Civil Engineering and Urban Planning IV

Editors: **Yuan-Ming Liu, Dong Fu, Zhen-Xin Tong, Zhi-Qing Bao, Bin Tang**

CRC Press
Taylor & Francis Group
A BALKEMA BOOK

CIVIL ENGINEERING AND URBAN PLANNING IV

This page intentionally left blank

PROCEEDINGS OF THE 4TH INTERNATIONAL CONFERENCE ON CIVIL ENGINEERING AND URBAN PLANNING, BEIJING, CHINA, 25–27 JULY 2015

Civil Engineering and Urban Planning IV

Editors

Yuan-Ming Liu
Shanghai Jianke Engineering Consulting Co. Ltd., Shanghai, China

Dong Fu
China First Metallurgical Group Co. Ltd., Wuhan, Hubei, China

Zhen-Xin Tong & Zhi-Qing Bao
Shanghai Jianke Engineering Consulting Co. Ltd., Shanghai, China

Bin Tang
College of Urban Construction, Wuhan University of Science and Technology, Wuhan, Hubei, China

CRC Press
Taylor & Francis Group
Boca Raton London New York Leiden

CRC Press is an imprint of the
Taylor & Francis Group, an **informa** business

A BALKEMA BOOK

CRC Press/Balkema is an imprint of the Taylor & Francis Group, an informa business

© 2016 Taylor & Francis Group, London, UK

Typeset by V Publishing Solutions Pvt Ltd., Chennai, India
Printed and bound in Great Britain by CPI Group (UK) Ltd, Croydon, CR0 4YY

All rights reserved. No part of this publication or the information contained herein may be reproduced, stored in a retrieval system, or transmitted in any form or by any means, electronic, mechanical, by photocopying, recording or otherwise, without written prior permission from the publisher.

Although all care is taken to ensure integrity and the quality of this publication and the information herein, no responsibility is assumed by the publishers nor the author for any damage to the property or persons as a result of operation or use of this publication and/or the information contained herein.

Published by: CRC Press/Balkema
P.O. Box 11320, 2301 EH Leiden, The Netherlands
e-mail: Pub.NL@taylorandfrancis.com
www.crcpress.com – www.taylorandfrancis.com

ISBN: 978-1-138-02903-3 (Hbk)
ISBN: 978-1-315-64515-5 (eBook PDF)

Civil Engineering and Urban Planning IV – Liu et al. (Eds)
© 2016 Taylor & Francis Group, London, ISBN 978-1-138-02903-3

Table of contents

Preface xv

Architecture and urban planning

The construction of livable city in the practice of historical town planning: A case of Luzhi town, Suzhou, China 3
Z.-L. Zhang & L.-D. Jiang

Application mode of the evaluation outcomes of mountainous land suitability for urban construction in compilation of general land-use planning in Yunnan Province—based on the strategy of "Constructing Mountainous Cities" and its effects 7
Z.-S. Yang, Q.-G. Zhao, S.-Q. Zhang, Y.-M. He, B.-S. Zhang & M.-J. Xu

Study on the decorative features of Huaxi Ba historical architecture 13
J.-N. Zhang, X. She & Y.-Z. Li

Inclusiveness and complexity in Nieuwmarkt neighborhood renewal project—lessons from Pentagon block and its surroundings 17
H. Jiang

Forecasting research on the functional evolution of the land area in the Dalian core port area 25
Q. Zhang, W.-Y. Wang, Z.-J. Guo & X.-Q. Song

The study on ecological risk assessment in the port of the coastal city based on the Landscape Pattern Analysis 31
W.-Y. Wang, G.-L. Tang, Y. Zhou & Q. Zhang

Evaluation of the parking permits scheme for residents in Thessaloniki, Greece 37
G. Mintsis, C. Taxiltaris, S. Basbas & Y. Stathis

A comprehensive research and design of the campus vehicle management system 45
Y. Li

Research on the relationship between ecological industry and sustainable development of industrial park 51
X. Niu

Research on the main risks and countermeasures of glass curtain wall 55
Q. Li & X. Zhu

Numerical study of leaked natural gas dispersion within an urban street canyon considering the distribution of ground surface flux 61
Y. Wang, H. Huang & L.-D. Huang

The quantitative risk assessment of the storage tank areas based on the domino effect 65
J.-L. Zhao, H. Huang, B.-N. Su & N. Zhang

Discussion on the contribution of the Bohai Strait Tunnel Project to freight transportation system and economic benefit 71
B. Wang, C.-N. Deng, F. Liu & J. Zhang

Study on the renovation of old industrial district combined with the creative industry in Guangdong, China 77
H. Ma & K. Zhu

Comprehensive evaluation research on the sustainable development of urban infrastructure 85
Y. Lin, M.-P. Zhang, H.-T. Wang & Y.-C. Li

Study on temperature-rising rules of self-heating airfield pavement with continuous carbon fiber heating wire 95
W. Xu, C.-M. Li, G. Xu & G.-Y. Li

Fuzzy optimization for pedestrian subjective route choice 101
A. Çekmiş

Fractal dimension—a new tool for quantitative analysis of urban skyline 107
J. Wang

Farming space in ancient Chinese cities: Harmonious urban development shaped by agricultural civilization and rural relations 111
Y. Tang & L.-X. Guo

Research on industrialized spatial features of Xi'an modern city 121
Y. Wei, Y. Wang & F.-F. Yang

Analysis of Urban Public Greenspace pattern based on landscape metrics in Kunming 127
M. Liu, Z.-M. Zhang, M.-Y. Yang, Y.-P. Geng, X.-K. Ou & D. Song

Research on the group layout of the space form in the intensive university campus 133
Q.-M. Deng & Y.-B. Liu

Residents' living experience and satisfaction in Chinese urban development: A case study of Ningbo 139
C.-H. Wen, Y.-L. Lin & J. Bie

Research on the strategies of urban spatial integration in the view of cultural heritage conservation 147
Y.-Q. Zhao, J. Xu & W. Tian

Public spaces of the social housing in Porto: Learning with design practice 153
N. Abrantes, F.B. Alves & V. Abrantes

From Nicholas Negroponte to Al Bahar Tower: The development in theory and technology of responsive architecture 161
H.-J. Liu

Regional Building Cooling Load Prediction Stochastic model based on Monte Carlo simulation 165
L.-Z. Wang, H.-W. Tan & Z. Zhuang

Seismic time history analysis of large-scale wind turbine 171
L. Fang, D. Zhang & J.-W. Wang

Study on population and land expansion and their coordinated relations—a case of Hebei Province 175
Y.-C. Wang, Y. Chen & Q.-N. Yan

Ecological rebuilding planning strategy of rural vacant land in South Jiangsu 181
Z.-X. Qin & Y.-Z. Huang

Introduction and forecast of creative industry parks of industrial heritage culture in China 185
Z. Qiao, H. Zhang & Y. Wei

Study on planning and construction standards of facilities for the aging population in Chinese urban residential areas in a deep aging society 189
X. Wang, Z.-G. Liu & Y.-L. Zhu

Application of a complex ecosystem theory in intensive planning of public facilities in residential areas 193
X. Wang, Y.-L. Zhu & S.-Y. Gao

Urban disaster prevention and mitigation planning optimization based on disaster prevention system construction 197
Z. Wang & Q.-F. Wang

Analysis of the differential parking charge policy in Nanjing based on the big data of Microblog 201
Y.-X. Sun, Y.-B. Yang, N.-N. Geng & Z.-W. Ji

An efficiency evaluation and a regional variance analysis of the provincial forest park tourism 207
C. Yu & M. Li

Deformation monitoring and control of the lateral karst cave tunnel 213
D.-D. Zhang, F. Xiong, L. Zhang & H. Shi

Research on the development of the non-motorized transportation system in the short time scale—taking Lianyungang as an example 219
H. Lu & Y.-Z. Ni

Advances in designing stainless steel second-skin façades 225
C.M. Houska

Quicker opening of bituminous asphalt pavements to traffic by use of mechanical impedance measurements 231
J. Huebelt , J. Lindemann, S. Wolf & F. Wellner

Research on an ecological blockhouse in the Zhaba area, Ganzi autonomous prefecture 235
X. She, J.-N. Zhang & Y.-Z. Li

Civil engineering

Structural protection after landslide phenomena: A case study in Northern Italy 241
M. Sassu, M. Andreini, A. De Falco, L. Giresini & M.L. Puppio

A new principle of virtual power for elastoplasticity mechanics 247
N.-Z. Lei, I.-L. Chung & Y.-H. Pao

Economic incentive policy design for fabricated construction based on externality analysis 253
G.-C. Liu, X. Li, C.-X. Wang & W.-J. Sun

Research on barriers analysis of formwork and BIM solution 257
X. Ji, H.-G. Zhu, X.-D. Zhang & L.-F. Dong

Study on the optimization design of the suspended dome structure 261
Q. Zhang, L.-Y. Ma & B.-X. Gu

Dynamic analysis on the stability of high reinforced soil slope under seismic effects 265
X.-S. Tang, J. Lai & Y.-R. Zheng

Seismic performance of the Self-Centering Confined Masonry Wall with external steel dampers 271
X.-B. Hu, W.-X. Li, K. Liu & L. Chen

Post-evaluation on wind power construction project 277
Y.-N. Wu, Z.-M. Lu & X.-Y. Zong

Numerical simulation of peak strength reduction in rock under uniaxial cyclical compression 281
H.-L. Zhang, Y. Tang, C.-C. Chen, W. Nie, K. Zhao & S.-M. Ma

The applied research of wind bolt and stable cable to the beam string structure 287
F.-T. Pan, Y. Lu & L. Zhang

The relation of kappa and distance in the case of Tohoku-oki earthquake 291
B.-H. Zhu, Z.-R. Tao & X.-X. Tao

A simplified method for calculating load transverse distribution coefficient of skew bridge 297
H.-L. Jin, X.-B. Tang & L. Jiang

An ontology-based context management system for diversion tunnel 303
X.-Y. Zheng & J. Shen

Dynamical reliability of internally resonant structural system under Gaussian white noise excitations 309
H.-Y. Wang, J. Lan & Y.-J. Wu

Historic and modern urban concrete bridges in Poland 313
J. Biliszczuk, J. Onysyk, W. Barcik & R. Toczkiewicz

Experimental investigation on the hysteresis behavior of beam-to-column connections of H-beams with corrugated webs 317
X. Fan & M. Li

Numerical analysis on mechanical behavior of masonry walls strengthened by BFRP 321
Z. Lei, Y. Xu, Y. Wang & J.-T. Qu

Research on the ecological stability technology of carbonaceous shale slope 327
X.-X. Liu & Y. Dai

Calculation of areas flooded in urban reservoirs of water supply 333
E.A. Silva, F. Leonardi, M.M. Pedrosa, F. Puga & V.S.S. Leonardi

Research on influencing factors of eutrophication of Tanghe reservoir 337
C.-X. Mi, J.-C. Chen & Y.-N. Mi

Engineering properties of Self-Compacting Concrete with stainless steel slags 341
Y.-N. Sheen, H.-Y. Wang, L.-J. Huang & T.-H. Sun

Reconstruction of three-dimensional road roughness 347
G. Yao, Y. Yang, W. Du & M. She

Improved punching shear capacity calculation method of reinforced concrete slab-column connections 351
H.-Y. Guo & J.-J. Cheng

Experimental research on elastic modulus of high-performance concrete in bridges 355
H.-X. Du, Q. Zhang, R.-Z. Yan, J. Yang & L.-L. Yao

Using Analytic Hierarchy Process to evaluate the improvement schemes of the Maoliling Tunnel based on the VISSIM simulation 361
P.-Q. Wang, Z.-G. Lu, H.-Q. Zhang & F.-J. Wang

Application of ambient vibration tests on an existing school building to evaluate the effectiveness of retrofitting 367
L. Li, T. Ohkubo, A. Teramoto & S. Matsumoto

Desertification risk assessment based on GIS in the Loess Plateau, China 373
J.-X. Zhang, W.-F. Liu, D.-Y. Zhang, J.-X. Pang, D. Wang, Y. Wang & X.-S. Li

Remediation of soil contamination on urban industrial sites—a case study on the old industrial base in Northeast China 381
Y.-C. Zhang

Performance of a level isolation device for cultural relics by shaking table tests 387
Q. Zhou, W.-M. Yan & J.-B. Ji

Experimental study on Tou-kungs of Tai-he Palace in the Forbidden City under vertical loads 393
Q. Zhou, W.-M. Yan & J.-B. Ji

Displacement calculation of helical curved beams based on ULM 399
J.-M. Liu, Z.-Y. Zhang & Q.-Y. Wei

Reinforcement optimization of Continuously Reinforced Concrete Pavement 403
L. Qing, Z.-M. Hu & R.-H. Liu

A gray-fuzzy evaluation method for soft foundation treatment based on genetic algorithm 407
Y.-P. Sun

One-way expansion of compacted lateritic soil and prediction of crack closure time 413
W. Bai, L.-W. Kong & R.-B. Lin

The time-dependent effect of interfacial stresses on strengthening RC beams with CFRP 417
B.-S. Xu, M. Ma, M. Zhang & G.-F. Li

Influence of anode follow-up on electro-osmosis 423
R.-B. Lin, L.-W. Kong, W. Bai, D.-L. Zhu, A.-W. Yang & P. Yang

Study on the construction mechanics of the road tunnel crossing underneath the overlying mining area 429
J.-W. Gong, X. Wang & P.-L. Qi

Construction deformation monitoring and application analysis for the neighborhood tunnel 433
H. Sheng, J.-W. Gong & X. Wang

Experimental study on the boundary slippage phenomenon of soft soil micropore seepage 437
H. Zhou & W.-F. Yan

Development of an urban rainstorm flood simulation model based on a plain flood model 443
B.-N. Su, H. Huang, N. Zhang & J.-L. Zhao

A study of engineering and electricity properties of cement mortar added with fly ashes and piezoelectric materials 449
S.-C. Chang, J.-C. Lin, S.-H. Chen & H.-Y. Wang

No-sand cushion vacuum preloading method to improve bearing capacity of fresh hydraulic fill mud 455
W. Bai, R.-B. Lin, D.-L. Zhu, Z.-X. Liu & G.-F. Yuan

Theoretical and experimental study on a new combined mild steel damper 461
J.-C. Wang, L.-Z. Yang, F.-F. Wang & M. Wei

Application study of mesh-based block identification method in an underground cavern complex 465
Y.-T. Zhang, X.-L. Ding & Z.-G. Zhang

Estimation of areas of experimental rainfall-eroded soil slope based on moving average time series models 471
X.-Y. Fan, F.-L. Xu, Y.-C. Liang, L. Chen, Y. You & W. Nie

Network arches for road and rail 477
P. Tveit

Analysis of anchorage zone and strut-and-tie design of single-eccentric concrete straight anchor 483
W.-X. Zhang, Q.-Y. Xie & L. Liu

Simplified analysis of cohesion layer of steel bridge deck pavement under different vehicle load cases 491
Z.-F. Wang, Z.-B. Cheng, M.-J. Zhang, B. Gao & K. Liu

Comparative study of intra-urban target performance on simulated WorldView-2 and WorldView-3 responses from hyperspectral data 497
S.C. Azevedo, G.P. Cardim, M.M. Pedrosa, E.H. Alcântara & E.A. Silva

Priming effects on people's safety decision in a virtual reality construction simulator 501
X.-Q. Lu & S.R. Davis

Seismic fragility analysis of complex landscape covered bridge 507
S. Song & Y.-J. Qian

Study on the unconfined compressive strength prediction of cement soil according to curing time 515
S.-Y. Zhang, Y.-G. Chen & Z.-W. Zhao

Research on critical slope for channel excavation based on finite arc and strength reduction methods 519
X.-P. Wu, P.-J. Jin & Y. Zhang

Liners and covers for landfills from cemented sands in arid areas 523
N.F. Ismael, A.A. Al-Rashidi & D.N. Ismael

Simulation study of bed shear stress distribution of wide and narrow alternated channels 529
S.-T. Miao, H. Lin & Y. Zeng

Study of the bearing capacity of lightweight wallboards under a uniform load 533
J.-Y. Li, L. Zhang & L.-H. Liu

Effect of scale and geometry features of fault on crustal stress 537
Q.-T. Pei, X.-L. Ding, Y.-T. Zhang, Z.-H. Dong & S.-L. Huang

Analysis and comparison of the most reasonable height based on the stiffness characteristic for different types of flat vierendeel structures 543
C.-X. Wei, J.-M. Tian & L.-Z. Jiang

Numerical damage analysis of masonry structure strengthened with FRP composite material 547
Z. Lei, Y. Xu, Y. Wang & J.-T. Qu

Improved Duncan-Chang model's application in pit lateral unloading simulation 551
L.-H. Cheng, G.-L. Liu & A.-F. Li

Earthquake response of cable-stayed bridge with local cable vibration under long-period ground motion 555
B.-B. Chen, Z.-R. Feng, B.-B. He & X.-F. Wang

Physico-mechanical characteristics of dune sand concrete as an emerging building material for light constructions 561
M. Chemrouk, M. Boukerrou & A.A. Rahmani

The elastic-plastic analysis of single buildings of prefabricated shear wall 569
H. Qi, M. Li & K. Liu

A new method for measuring hydraulic parameters of unsaturated soils 573
P.-P. Yi & S.-K. Niu

Cost risk analysis for the power transmission project-based network 579
H.-Y. Shen, P. Wang & Y. Liu

Numerical modeling: The evolution of tectonic stress field in the Longmenshan region 583
S.-R. Su, Y. Zhang & P. Li

Field settlement observations made on four Concrete Face Rockfill Dams 589
Z.-Z. Fu, T.-B. Wang & S.-S. Chen

Analysis of the lifting law of the lakeshore deepwater berth 597
H.-W. Sun

Key technique in the movement of the Yellow River Museum 603
Z.-M. Zhang & L. Cai

Research on the hard brittle clay shale water content and the mechanical strength distribution rule 607
G.-R. Lu, M. Liu, L.-W. Zhang & H. Zhou

Research development on seismic behavior of the short-pier shear wall 611
L.-M. Jiang & J.-F. He

Influence factor of surrounding roads on compacting displacements of jacked piles 615
Z.-Y. Luo, B.-P. Zhou & Y.-L. Tao

Application and exploration of ground penetrating radar to pipe jacking construction 619
K. Guo, P. Chen, L. Liu, Y. Ma & R.-J. Sun

Study on the drying shrinkage of the manufactured sand high-strength concrete 625
D.-H. Wu

Finite element analysis of hollow cylinder test taking torque rate into consideration 629
B.-B. Xu & T. Noda

The research of the impact load of a vehicle applied to the bridge based on a model experiment 633
X.-F. Lin, Y. Ding, X.-D. Zhang & G.-W. Tang

The state space method of free vibration analysis for frame-shear wall-thin-walled core skew structure 637
H. Zhang & L. Huang

Finite element method analysis—the mechanism of anti-slide piles to reinforce the slope title 643
D.-B. Ren, S.-H. Yu & J.-Y. Tu

Damage simulation of a concrete column in fire 649
S.-H. Tang, Y.-P. Cui, Y.-S. Luo & S.-P. Yin

Numerical analysis of foundation properties in a large artificial mountain 655
W.-D. Wang, Z.-R. Ye, K. Zeng, C. Zhao, H.-F. Chen & H.-W. Lu

Connection performance assessment of 2D steel frames under column-removal scenario 661
C. Chen, H.-R. Yu, Y. Xu & W.-B. Li

Analysis of beam-column joint in steel frame structure based on connection failure probability 665
H.-R. Yu, C. Chen, Y. Xu & W.-B. Li

Linear optimal semi-active control of earthquake response of vibration-absorption megaframe structure 671
M. Zhang & S.-L. Hu

Evaluation of Russia's innovation activity levels in construction 677
V.I. Telichenko & A.A. Benuzh

The influence of a bridge deck's relative height on the damping effect of a tower-girder elastic connecting device in cable-stayed bridges 681
J. Huang, W.-X. Zhang, L.-L. Zhao & J.-J. Wang

Causes of explosion in section c of the diversion tunnel under construction at Zengwen reservoir 685
P.C. Lee, H.H. Pan & S.P. Ho

The effects of hole ratio on the failure probability of masonry structures 691
T. Lv & R.-Y. Zheng

Dynamic behavior of a concrete building under mainshock-aftershock seismic sequence with a progressive damage and failure material model 695
J.M. Dulinska & I.J. Murzyn

Computational study on delamination detection in FRP beam with an ultrasonic-optic technique 701
Y. Xu, Y. Yu & L. Niu

Influence of Superabsorbent Polymer with different particle size and dosage on properties of cement mortar 707
Z.-L. Yi, H.-J. Li, Y.-B. Tan & Y.-J. Xie

Experiment study of retard-bonded pre-stressed concrete structure 713
T.-B. Liu & J.-C. Zhao

Analysis of deformation characteristics of pre-stressed steel girder in high temperature (fire) environment 721
Q. Sun, Y. Guan & W. Tian

Experimental analysis on mechanical properties of different types of steel fiber-reinforced concrete 727
J.-G. Shao

Research on the stability of stiffened plates with trapezoidal closed ribs in orthotropic steel box girder 733
X. Peng, J. Di & Y. Zou

Experimental study on road performance parameters of micro bonded graded broken stone 737
B.-Y. Yu, Y. Zhang & Z.-J. Wang

Performance observation and evaluation analysis of the graded broken stone base test road 741
B.-Y. Yu, Y. Zhang & Z.-J. Wang

Experiment study on the effect of freeze-thaw damage to chloride ion penetration performance of concrete 745
X.-H. Hao, Y.-N. Zhang, Y. Liu & Y.-D. Hu

Numerical simulation study on the freeze-thaw process of concrete 749
X.-H. Hao, W. Lan, Y. Liu & Y.-D. Hu

Experimental study on the flexural behavior of concrete beams strengthened with near-surface mounted CFRP laminates 753
L. Huang, X. Li & H. Zhang

Simulation analysis of the excavation with the support pile of the Shandong bookstore project 757
Y. Wang, F.-T. Lu, W.-K. Hu, G.-L. Hu & Y.-J. Zheng

Mechanical analysis of a new type of self-centering frame 763
Y. Liu, M.-X. Pan, Z. Zhou, Y.-K. Dong & T.-S. Zhou

Analysis of the displacement of soil around the shaft and cross channel based on MIDAS/GTS 769
J.-W. Zhong, Z.-Y. Duan & Y.-J. Xu

Numerical simulation of bearing characteristics of single pile in the Zhanjiang area 775
Y.-M. Liu, D. Fu, Z.-X. Tong, Z.-Q. Bao & B. Tang

The elastic mechanics equations of bi-curvature beam based on tensor theory 779
J.-M. Liu, Z.-Y. Zhang, Q.-Y. Wei & A.-G. Leng

Analysis on the influence of buckling performance of the U-stiffened plate on deck surfacing and wheel load 785
R.-P. Zhao

Transportation engineering

A new method for positioning Variable Message Signs 791
Y.-R. Guo, X.-M. Wang, M. Wang & H. Zhang

Traffic freight volume forecasting based on optimized GM (1,1) power model 797
S.-J. Zhang & S.-Y. Chen

Modeling of tree-roots effects on pavement stresses and strains 803
M. Mostafa Hassan & J.A. Adedeji

Navigation risk evaluation for channels based on the Belief Rule Base 811
W.-D. Gan, Z.-Y. Zhang & Y.-W. Li

Studying the effect of the difference in vehicles' mass on fatal accidents 817
S.M. Sadat Hoseini, F. Zera'at Peyma & S.S. Kashfi

Analysis and evaluation on depth perception of commercial vehicle drivers 821
L.-C. Zhang, L. Wei, J.-C. Zhou, S. Tian & S.-C. Wang

Research on the competitive character of urban rail transit and conventional bus—taking the Suzhou rail transit passenger corridor as an example 825
L.-J. Wang, W.-Z. Xiao, W.-W. Shen & J. Liu

Modeling of fly ash stabilized base layers 831
J.A. Adedeji & M. Mostafa Hassan

Automatic extraction of vector road based on bus GPS data 837
S.-H. Xu, F.-Z. Li, L.-G. Meng & Q.-T. Zhao

Research on the crack resistance of the high-viscosity emulsified asphalt sand seal 843
Y.-Z. Sun, J.-W. Pan, X.-Y. Tang & J.-C. Wang

Reliability assessment of port area road based on Bayesian analysis 847
X.-Q. Song, Y. Zhou, W.-Y. Wang & Q. Zhang

Study on the anti-cracking performance of fibrous high-viscoelastic asphalt sand 851
Y.-Z. Sun, X.-Y. Tang, Z. Guo & J.-C. Wang

Experimental study on the direct tensile experiment of high-viscoelastic asphalt sand 855
Y.-Z. Sun, Z.-Y. Gu, C. Liu & Z. Guo

An RFID based carbon footprint tracing method for product logistics 859
S.-L. Chen, J.-J. Yi, X.-M. Zhu & H. Jiang

Left-turn track function of bicycle flow in intersection 865
S.-C. Zhang, K.-K. He & R.-F. Yang

Study on the test of the CRTSII slab reinforced with Basalt Fiber Steel Tendon 871
Z.-P. Feng, H. Wang, Y. Wang, S.-X. Zhang, P. Wang & X.-A. Yan

Optimal bus station locations using a Voronoi diagram model 877
G.-Y. Zhu, W.-X. Zhang, J. Wei & P. Zhang

Optimization of sustainable biofuel network based on hybrid genetic algorithm 883
N.-N. Geng, Y. Zhang, Y.-X. Sun & Y.-J. Jiang

Mode choice behavior for access to the airport under a new mode: A case study of Nanjing Lukou Airport 889
D.-W. Bao, S.-Y. Hua & J.-H. Jia

Effect of rail transit box-girder with web opening on the structure noise radiation 895
L.-Y. Liu & D.-Y. Xu

A comprehensive model for facility location in disaster relief 899
Q.-S. Lei, Z.-D. Mo & X.-G. Zhou

A trans-shipment model for emergency relief distribution in unexpected disasters 903
Q.-S. Lei, Y.-Y. Wang & X.-G. Zhou

A cellular automata model for indoor evacuation based on artificial potential field and ant colony algorithm 909
Z.-W. Ye, Y.-J. Yin, X.-L. Zong, M.-W. Wang & Y.-L. Jiang

Intercity rail transit pricing based on the Ramsey model 915
Q.-Y. Luo, L. Mang, H.-F. Jia & S.-T. Gao

A model of avoiding traffic accidents between drivers and pedestrians in signalized intersections in VANETs 921
J. Sun

Hybrid life cycle and interval linear programming for the copying paper supply-chain management considering the Greenhouse Gas mitigation 927
W.-C. Yue, Y.-P. Cai, L.-Y. Xu, C.-H. Li, X. Wang & Q.-Q. Rong

Comparisons of resident trip characteristics in large and medium cities between the central and western regions in China 933
T. Liu & B.-F. Li

A multistage method on regional multimodal logistic network design from a logistic enterprise perspective: A case in China 939
H.-Q. Li

Research on mechanical properties of steel slag asphalt mixture 947
W. Li, H.-D. Wang, H.-B. Wang & C.-Y. Wang

Multi-objective evaluation of different traffic organizations for twelve-lane freeways 953
J. Han, C.-C. Xu, W. Wang, X.-Y. Tian & X.-D. Li

Urban public transportation system in China 961
H. Huang & L. Cheng

Crowd management in emergency situations: What can be learned from the existing video data? 967
B.-B. Liu & X.-C. Guo

Fuzzy-theory-based determination model for researching airport passenger flow radiative zone 973
W.-H. Zhang, L. Zhou, H.-J. Bai & Q.-Q. Li

Performance evaluation of recycled cement stabilized crushed stone 981
J. Wang, S.-F. Xu, J. Qiao, L.-T. Xu & Y.-J. Guo

Performance evaluation of the recycling asphalt binder regenerated with vegetable oil 985
Q. Man, J. Wang, S.-F. Xu & Z. Suo

Review on three road surface roughness simulation methods 989
F. Yang & J.-T. Zhao

Civil Engineering and Urban Planning IV – Liu et al. (Eds)
© 2016 Taylor & Francis Group, London, ISBN 978-1-138-02903-3

Preface

On behalf of the conference organizing committee, I feel so honored, truly honored to announce that the 4th International Conference on Civil Engineering and Urban Planning (CEUP2015) was successfully held in Beijing. As an initiative conference, CEUP has been dedicating to contemporary contributions from the most state-of-the-art fields such as Civil Engineering, Transportation Engineering, Architecture and Urban Planning. The past successful CEUP conferences will lay a solid foundation for the CEUP2016 in Zhangjiajie of Hunan province.

CEUP 2015 is hosted by Bosen Academic Conference Solutions Co. Ltd., China, with the main objective of providing a comprehensive global forum for experts and participants from academia to exchange ideas and presenting results of ongoing research in fields relative to the main theme of the conference.

During the conference, 5 famous scholars and engineers are invited to deliver their keynote speeches on their latest researches, including Professor Ramesh P. Singh (the Professor of School of Earth and Environmental Sciences Chapman University), Prof. Konstadinos Goulias Geography Department, University of California Santa Barbara), Prof. Kouros Mohammadian (the Professor of Department of Civil and Materials Engineering University of Illinois at Chicago), Prof. Giovanni Barla (Former Professor of Rock Mechanics at Politecnico di Torino), Prof. Ahmed Mebarki (the Professor in Civil Engineering at University Paris-Est (Marne-la-Vallée)). Taking this opportunity, we extend our heart-felt gratitude to all the attendees. Without all of you, the conference had not been so successful and glorious!

Certainly we should also express our acknowledgements to the tpc members, session organizers, the reviewers and all the authors, who together made the conference more successful. There is a long way to go and the responsibilities on our shoulders are huge, however, we believe ourselves that we can do better and more!

Last but not the least, thanks, gratitude and acknowledgements should also go to the CRC Press/Balkema (Taylor & Francis Group) who have been ever-lasting supporting us to publish the manuscripts. Let us hand by hand to create a win-win situation in the future!

Linda Lee
Editor

This page intentionally left blank

Architecture and urban planning

This page intentionally left blank

Civil Engineering and Urban Planning IV – Liu et al. (Eds)
© 2016 Taylor & Francis Group, London, ISBN 978-1-138-02903-3

The construction of livable city in the practice of historical town planning: A case of Luzhi town, Suzhou, China

Zhen-Long Zhang & Ling-De Jiang
School of Architecture and Urban Planning, Suzhou University of Science and Technology, Suzhou, Jiangsu, China

ABSTRACT: This research aims to explore the suitable approaches and strategies to reach a livable city in the planning of a historical town. This study first explores the relationship between the connotation of a livable city and historical town planning. Second, the idea of historical town planning which is based on the livable city principle has been put forward. Third, the research implemented the idea of livable urban development, combined urban characteristics, and explores the possible approaches and strategies of achieving the livable city in Luzhi town. In the end, the study concludes the contradictions and conflicts of achieving a livable city in Luzhi town.

1 INTRODUCTION

"Livable city" is a suitable human habitation, which requires a combination of residence, daily life, recreation, transportation, management, public services, cultural, and other complex elements in time and space. The aim of "Livable city" is to achieve a balance between the current development and future development in all social functions, and ultimately reach the "people—cities—nature" harmonious coexistence (Wu 2007). To build a livable city building goals and technical measures in urban planning and a long-term and a dynamic process are required. In order to identify urban master planning strategies and measures that are used to achieve the main objective of the livable city construction, the general ideas and methods of the urban development need to be rationally discussed.

The premise of "historical town planning" is to be focused on the protection of the elements of a historical town. The elements include three aspects. First, it improves basic living conditions, community environment, and public environment of the historical town; enhances the economic strength of the old town; and improves ecological environment in the new and old town. Second, the planning should pay attention to the development and protection of the built environment and respect the historical imprint of the town. Third, the planning should emphasize people-oriented ideas since people are the main body of the historical town (Xu et al. 2010). With rapid social and economic development, people in different living, cultural, and geographic backgrounds have different standards and requirements toward urban life. Therefore, the planning objectives are a diverse and dynamic development mechanism that meets people's understanding and pursuit of employment opportunities, physical life, social, and culture environment in different periods.

The study explored suitable approaches and strategies of reaching a livable city in the planning of a historical town from the aspects of urban spatial distribution, transport, environment, socio-economic development, social civilization and so on, and proposed the strategy of achieving a livable city in Luzhi town.

2 THE FRAMEWORK OF HISTORICAL TOWN PLANNING BASED ON LIVABLE CITY

In the construction of historical and cultural town, it is usually common to simply pursue the increase of economic indicators and urbanization rate of land space at the expense of a large amount of land resource and people's quality of life, which destroyed the historic elements of the old town to some extent. It focuses on the problem of how to balance development with protection, how to strengthen the protection of historical and cultural heritage, how to maintain scenic spots and green spaces in the domain of the historic town, and how to develop the new townships into a livable city.

2.1 *Protect the urban historical elements*

Historical town planning should combine nature and humanity to highlight the characteristic element of historic styles, natural resources, and geographical culture. That is to say, the planning

should help to keep the human landscape in harmony with the natural landscape, maintain the town's original historical type, highlight the dominant position of traditional local culture and form unique urban characteristics of urban humanity and natural landscape.

2.2 *The approach to protect the urban historic culture*

The construction of livable cities needs to arouse the internal driving force of urban development. The lack of urban personality and characteristics will inevitably lead to the loss of history and culture and the emptiness of spiritual life. Therefore, it is necessary to protect the personality of the prominent town and strive to create a unique charm of the town. The historical cultural heritage includes material culture and intangible cultural heritage, which enriches the cultural life of the people. And the planning focuses on the town's history, culture, customs, context memory, and its unique landscape. In addition, the planning pays more attention to self-culture in the spiritual pursuit and personality shaping in order to achieve change in material life. Moreover, what is important is to avoid negative phenomena, such as the construction of macro cyclic road, interchange, and too many high-rise residential buildings. Small towns ought to possess its characteristic and avoid homogenization (Wang 2009). Thereby it can lead a livable life, enhance the appeal of the local cultural, and create a unique sense of pride and intimacy.

2.3 *Search effective ways to create a beautiful ecological space*

In the process of ecological construction, an agreeable living environment and pleasant production space are created. Historical town planning should use the most of natural ecological resources and effectively organize the natural landscape and green space. And the historical town located in waterside should establish an idea to create eco-town from a perspective of ecology (Jiang et al. 2009).

2.4 *Construct a feasible and efficient integrated transport system*

The historical town planning focuses on a reasonable construction of transport infrastructure, improves the traffic management system, and vigorously develops alternative public transport. At the same time, it also builds a pleasant walking system, facilitates leisure travel, and reduces unnecessary vehicle traffic through the rational organization of passenger, cargo flow, and urban land function.

2.5 *Explore the models to promote industrial restructure*

In the process of historic town planning, we should pay special attention to the local resources and promote urban industrial transformation and upgrading. Then speed up and adjust the industrial structure and strengthen the technology research and development, change the backwardness of the enterprise, and provide the impetus for long-term sustainable development of a livable city. The current prevalence model of "land for capital" should also be reversed. To some extent, this pattern of development is an unusual sustainable development model at the expense of social equity and ecological environment.

3 THE LIVABLE CITY IN THE PRACTICE OF HISTORICAL PLANNING IN LUZHI TOWN

3.1 *The overview of Luzhi town*

Luzhi is a typical waterside town in the south of Yangtze River (Jiangnan), and has a long historical and cultural value (Fig. 1). Luzhi was granted the Chinese Historical and Cultural Town in 2003 and the Outstanding Achievement Award of UNESCO in protecting the ancient town in 2006. Luzhi town has an area of approximately 17 km², which keeps in a naturally close link with Taihu Lake. And the township has a simple spatial structure. Although it has a floating population, most of them are tourists. As a national historical town, Luzhi has rich cultural heritage of local, ethnic, and pluralistic character. In addition, there are pleasant natural and ecological environments and convenient traffic conditions between urban and rural areas, which are easy to build a harmonious, safe, and healthy living environment.

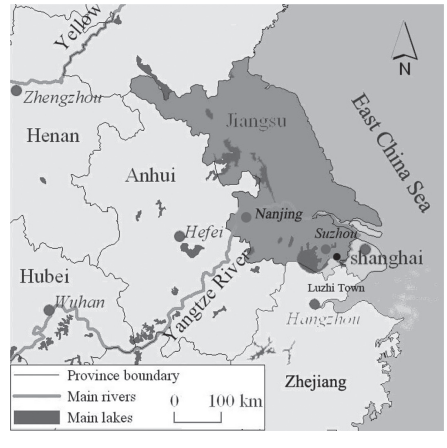

Figure 1. The site of Luzhi town.

3.2 *The construction of livable city in the historical planning of Luzhi*

3.2.1 *Transform the industry from industry-oriented to service-oriented*

The industry of Luzhi needs to be transferred from the industrial economy to service economy from the industrial perspective. The planning strengthens the adjustment and optimization of the industrial structure to achieve a win-win situation of economic development. During the development of manufacturing industries, it emphasizes that the resource-saving industries and environment-friendly industries, green economy, and low carbon economy replace the traditional extensive economic growth mode. At the same time, it also emphasizes that the ultimate objective of development is the all-round development of human beings.

The historical town planning resets and upgrades land use in the original old town. During the transition process of "industrial economy" to "service economy", the spatial reconstruction meets the demand of the "service economy".

3.2.2 *Construct beautiful "Green Waterside" based on "River City"*

The Luzhi town is historically near the water, and the planning should propose to establish the structure of an urban green space system which put forward building the corridor around the lake and river as well as increase green spaces along the road throughout the town (Fig. 2).

Building the corridor around the lake and river refers to the construction of two green belts around the Chenghu Lake on the southern part of the town and along the Wusongjiang River. The protective green corridor around the town clearly defined the boundary between the new town and old town. It is also an effective control of urban sprawl. "Increase green space along the road throughout the town" refers to the green network mainly organized by road green areas and ecologic green belt, and the green patch of green land and production of green organic links, which forms the town's green space system. The green structure system fully reflects the structural features of the natural landscape Luzhi, which highlights Luzhi as the "Green waterside" town.

3.2.3 *Highlight the geographical features through urban space reconstruction*

On the one hand, the built land in Luzhi is limited. On the other hand, the proportion of residential land and public service land in Luzhi is very low, which restricts the construction of a livable city. With the rapid development of industrialization, industrial enterprises have covered too much land last year. The small-scale residential areas with the imperfections of the surrounding facilities is one of the most important restricting factors to upgrade residence quality. The high population density also leads to a shortage of housing, environmental decline, and a series of other problems, which results in the decline of the old township. In addition, due to the land conditions and large population, the urban development has not yet got rid of the idea of "economy priority".

The planning controls the scale of the township land, stops further increase in the total amount of land for construction, and gives overall consideration to both needs and interests of the public. On one side, the quality of infrastructure in the old township is improved and public open space increases. On the other side, the plan focuses on improving the attractiveness of the new town by means of optimization, adjustment, and replacement of land features; find the internal potential; and transferring the simple outward expansion to the fully internal optimization and improvement (Fig. 3).

The plan establishes the idea of coordinating the relationship between economic development and environmental protection from the view of features creation, in order to build the "waterside towns in the south of Jiangsu Province". Furthermore, by

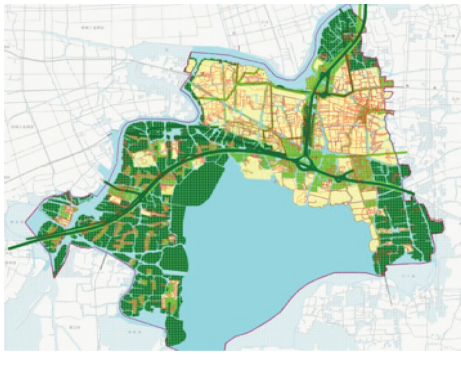

Figure 2. Green system planning of Luzhi town.

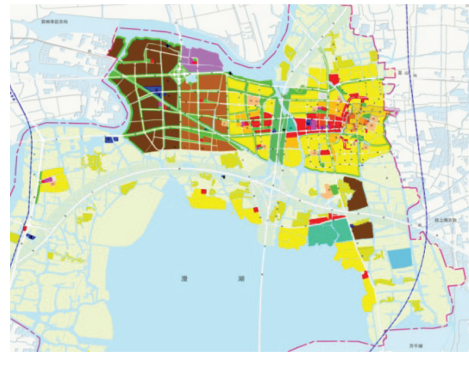

Figure 3. The land use planning of Luzhi town.

means of analysis and positioning of ecologically sensitive area, it forms the pattern of greenbelts by a barrier consisting of an urban periphery ecosystem, a combination of the road green belt and urban perimeter defense (Green Belt series) lines, and the various parks which effectively protect ecological sensitive area. It also creates a good urban living environment and a features available living space, which makes Luzhi a beautiful livable town.

3.2.4 *Integrate with a new modern urban transportation system*

In order to achieve the goal of livable city, Luzhi does not need to only allocate more public service facilities and open spaces according to the construction standards of the modern city, but also improve public transportation system and integrate in the bus network in the Suzhou City, make full use of the parking, pedestrian overpass, and the underground space to meet people's daily needs (Fig. 4).

The planning optimizes urban road nodes; reduces cross-border traffic interference; and creates complete internal blocks. Furthermore, it stresses the link between Luzhi, Suzhou Industrial Park (SIP), and Shanghai. Besides, it creates a close contact with the tourism in the old town area. The planning constructed new roads along the Chenghu Lake to connect the north of Chenghu Lake and the western settlements and eco-tourism zone, and built a livable network of a slow traffic system.

3.2.5 *Town feature reconstruction from the "industrial town" to the "water town"*

Following the idea of natural and cultural combination, the plan promotes the urban landscape with natural landscape in harmony, maintains the town's original historic scene, highlights the dominant position of the town's traditional culture, and forms a unique urban culture and natural landscape. In addition, using the design idea of "South of Yangtze River (Jiangnan)" and "Wu-Yue culture", the planning highlights the unique characteristics of Luzhi town.

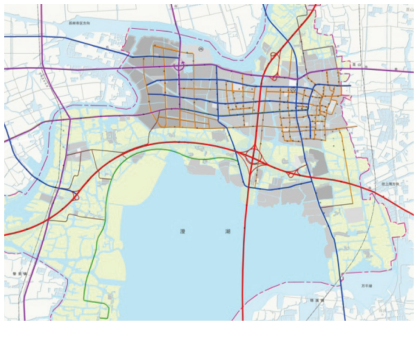

Figure 4. Transportation system of Luzhi town.

The planning simultaneously took advantage of industrial innovative landscape in the early-formed industrial area and expanded personalized space in industrial areas, which became a new platform for building regional characteristics. The ecological benefits of green spaces have reduced air pollution and improved environmental quality, which makes "Industrial style of Waterside town" as the new characteristic of Luzhi so as to show the new face of current industrial development. It also integrates a beautiful environment into the historical and cultural characteristics of Luzhi.

4 CONCLUSION

The strengthening of historical and cultural protection is a precondition of historical town planning. The appropriate economic development and the living environment improvement together with the town' comprehensive vitality enhancement can help achieve the ultimate goal of livable city. In the future, urban development will seek harmony in characteristics of Luzhi. It is the key to realizing the symbiosis of historical cultural characteristics and modern town that develops a green, ecological, livable, and harmonious town.

However, during the process of urban development, Luzhi Town faced contradictions between rapid development and historic preservation, and also other contradictions such as the pressure of industrial transformation and upgrading. The realization of livable cities still needs far more exploration and research.

ACKNOWLEDGMENT

This manuscript was funded by the "National Science Foundation of China (51208330)" and "A Project Funded by the Priority Academic Program Development of Jiangsu Higher Education Institutions (PAPD)".

REFERENCES

Jiang, Y.H., Zhen, F. & Wei, Z.C. 2009. The construction practice and its enlightenment of livable city abroad. *Urban Planning International* 24(4): 99–104.

Wang, Y. 2009. The related problems of building the livable city in Qinhuangdao. *Urban Studies* 16(2): 8–11.

Wu, T.Y. 2007. A dream of living poetically for modem people-Humility and aesthetic connotation of best city for living. *Urban Studies* 14(3): 1–6.

Xu, Y.H., Jia, X. & Xi, L. 2010. Urban master planning implementation evaluation system of medium and small cities by the perspective of livable city: case study of Wanzhou District in Chongqing. *Urban Studies* 17(2): 8–12.

Civil Engineering and Urban Planning IV – Liu et al. (Eds)
© 2016 Taylor & Francis Group, London, ISBN 978-1-138-02903-3

Application mode of the evaluation outcomes of mountainous land suitability for urban construction in compilation of general land-use planning in Yunnan Province—based on the strategy of "Constructing Mountainous Cities" and its effects

Zi-Sheng Yang
Institute of Land and Resources and Sustainable Development, Yunnan University of Finance and Economics, Kunming, Yunnan, China

Qiao-Gui Zhao
Institute of Land and Resources and Sustainable Development, Yunnan University of Finance and Economics, Kunming, Yunnan, China
Department of Land and Resources of Yunnan Province, Kunming, Yunnan, China

Shu-Qing Zhang
Institute of Land and Resources and Sustainable Development, Yunnan University of Finance and Economics, Kunming, Yunnan, China
Planning and Design Institute of Land and Resources of Yunnan Province, Kunming, Yunnan, China

Yi-Mei He, Bo-Sheng Zhang & Ming-Jun Xu
Institute of Land and Resources and Sustainable Development, Yunnan University of Finance and Economics, Kunming, Yunnan, China

ABSTRACT: Building cities and towns on mountains is an important mode of urban development in the 21st century, and carrying out and having a mountainous land suitability evaluation for urban development is the strategic base and the firm support for the implementation of the strategy of "Constructing Mountainous Cities". Since the second half of 2011, counties, districts or cities have carried out, one after another, evaluation of mountainous land suitability for urban development within their respective territory, and the evaluation results have been applied in the revision and compilation of "General Land Use Planning (2010–2020)" at the county- and town-level in Yunnan Province based on the strategy of "Constructing Mountainous Cities", especially with regard to how to ensure a reasonable landscape of urban and industrial development in mountainous areas, which achieved obvious effects. With evaluation results reported from these counties and towns, Yunnan eventually successfully implemented its strategy of "Protecting Farmland in Flatland Areas and Constructing Mountainous Cities", by which more than 80% of quality farmlands in flat areas throughout the province were brought under permanent effective protection and the occupation of farmlands for development purpose reduced substantially. Turning to mountains for suitable land for urban and industrial development provides a new and huge space for urbanization and industrialization, and offers a very effective solution to the outstanding conflict between farmland protection and ever-growing construction land demand.

1 INTRODUCTION

Building cities and towns on mountains is an important mode of urban development in the 21st century. This way of urban development can save a lot of precious flat lands otherwise occupied by buildings and structures, especially plains and high-quality flat arable lands, which are a nation's very base for food security and sustainable development, and thus is becoming a prevailing trend in many mountainous areas. Yunnan, as a typical mountainous border province in west China, has witnessed the constant conflict between the availability of flat lands and the fast-growing demand for occupation of land for development purpose, with nearly 93.60% of its territory being mountainous areas and only as low as 6.40% being flat areas (Yang et al. 2014). To protect its quality flat farmlands that are declining rapidly in the province, the Government of Yunnan Province devised and

implemented, in the first half of 2011, the strategy of "Protecting Farmland in Flatland Areas and Constructing Mountainous Cities", which is henceforth referred to as "Strategy of Constructing Mountainous Cities" or "Cities-on-Mountains Strategy" (He et al. 2015). Meanwhile, Yunnan was selected and included by the Ministry of Land and Resources of PRC on China's first list of pilot provinces and cities for comprehensive development and utilization in gentle-slope hilly areas.

The strategy of "Constructing Mountainous Cities" can go nowhere without a firm planning at hand. So, the province-wide compilation of General Land Use Planning at both county and town levels was initiated in the second half of 2011 throughout the province for the purpose of effective protection of flat farmlands and successful implementation of the above-mentioned strategy.

The first question to be answered regarding building a city or town on a mountain is what kind of mountain can be said qualified for urban development and what not? To answer this question, we must have a full and accurate evaluation of the suitability of mountains and hills for urban development, which is a precondition, and a crucial base and support too for the successful implementation of the strategy of "Constructing Mountainous Cities". From the aspect of urban disaster prevention, a key issue to be addressed or done first when making an urban land-use planning and designing the landscape of development is to have a risk evaluation on land's suitability for urban development (Zhu et al. 2010). For years, both home and foreign scholars have made evaluation of land's suitability for urban development as a very fundamental work to be done before making an urban planning or a urban land-use planning for a city. For this reason, counties, districts or cities throughout Yunnan Province have in turn carried out evaluation of mountainous land suitability for urban development within their respective territory in order to lay a firm base for the compilation of General Land Use Planning at the county and town levels so that Yunnan's strategy of "Constructing Mountainous Cities" can be implemented successfully.

2 THE APPLICATION MODE

During the period from June to September 2011, Department of Land & Resources of Yunnan Province in turn formulated "The Pilot Plan of Yunnan Province for Adjusting and Improving General Land Use Planning (2006–2020) at County- and Town-Level Based on Adjusting Urban and Rural Development Ideas and Strengthening Farmland Protection in Flatland Areas", "The Implementation Plan of Yunnan Province for Adjusting and Improving General Land Use Planning (2006–2020) Based on Strengthening Farmland Protection and Promoting the Scientific Development of Urbanization", and "The Technical Guidelines of Yunnan Province for Improving General Land Use Planning at County- and Town-Level (Trial)", in which 10 counties and cities were identified as the pilot counties or pilot cities for revision and compilation of general land-use planning. Based on the feedback and findings from these pilot counties and cities, the province-wide revision and compilation of general land-use planning at both county and town levels was initiated throughout Yunnan. In revision and compilation of general land-use planning, counties, districts and cities first carried out an evaluation of the suitability of all gently sloped mountains and hills in the peripheral areas of their respective towns, counties or cities for urban development, as required by "The Technical Guidelines of Yunnan Province for Improving General Land Use Planning at County- and Town-Level (Trial)", based on which a new landscape of urban and industrial development on gently sloped mountain was conceived and proposed.

2.1 *Overview of evaluation outcomes of mountainous land suitability for urban construction*

Counties, cities or districts carried out their respective evaluation of mountainous land suitability for urban development in accordance with "The Technical Guidelines of Yunnan Province for Improving General Land Use Planning at County- and Town-Level (Trial)", following the boundaries of flatlands in their respective territory as delineated on Yunnan Database of Flatlands Surveys as well as the database and maps of the Second National Land Survey. Considering the range of urban development as delineated in their respective Urban Master Plan, the areas to be assessed were those retrieved with ArcGIS9.3 from the Second National Land Survey Database by applying the criterion of "slope below 25°", i.e. all gently sloped mountains, tablelands and low hilly lands in the peripheral areas of a flat region. The evaluation unit is basic pattern spots of 1:10 000 land-use map in the Second National Land Survey Database, and is evaluated by applying the index system and technical method of land suitability for urban construction (Yang et al. 2010; He et al. 2014).

The main outcomes of the suitability evaluation comprise: (1) each county's, city's or district's area and percentage of land suitability grades for urban development in gently sloped mountainous areas; (2) each county's, city's or district's map of mountainous land suitability evaluation for urban

development (on the 1:10000 scale); (3) each county's, city's or district's database of mountainous land suitability evaluation for urban development.

2.2 *The application mode*

2.2.1 *Core tasks and objectives of general land-use planning for implementing the strategy of "Constructing Mountainous Cities"*

In Yunnan's case, there are two core tasks. One is the adjustment and optimization of the construction land layout. The layout of construction land as depicted in the former "General Land Use Planning (2006–2020)" was adjusted and optimized, following the fundamental principle of "intensive and economical use of land, effective protection of flat farmlands, building cities & towns and industry on mountains, and the coordinated development in both urban and rural areas". The revised one requires that counties, cities or districts should control the percentage of their flat lands to be allocated for constructions below 50% of their total lands to be allocated for this purpose, their farmlands on mountains to be occupied for constructions below 30% of their total lands to be allocated for this purpose, their constructive expansion conditionally permitted zone in flatland areas accounted for the proportion of generating new construction land in this areas should not be greater than 20%, and their constructive expansion conditionally permitted zone in mountainous areas accounted for the proportion of the total scale of the construction land in this areas should not be greater than 50%.

The second is for the adjustment of the layout of prime farmlands. The layout of prime farmlands depicted in the former General Land Use Planning (2006–2020) was adjusted, following the principle of "further increase the area of prime farmlands in flat areas, reduce the one in mountainous areas, and quality prevails". The revised one requires counties, cities and districts to increase or maintain their percentage of flat farmlands counted as prime farmlands at or over 80% of their total farmlands available in the flatland area by turning land in flat areas, rather than on mountains as previously proposed in the former land-use planning, into prime farmlands.

2.2.2 *The application mode*

In view of the core tasks detailed above, the main application of carrying out an evaluation of mountains' suitability for urban development in the compilation of general land-use planning for implementing the strategy of "Constructing Mountainous Cities" is to ensure the existence of a reasonable layout of both urban development and industrial development in a mountainous area.

By "reasonable layout" we chiefly mean that lands to be allocated for urban or industrial development purpose should always be within the delineated gently sloped areas with suitable conditions for the intended constructions. In other words, lands to be allocated for both urban and industrial development should spatially coincide with the suitable lands or areas as delineated on the "Map of Mountainous Land Suitability for Urban Construction", and in any way, should not be within "unsuitable area" with hard, even harsh, conditions. For the costs and safety considerations, lands to be allocated for such purposes should be better in a first-class and second-class developable area whenever possible.

Specifically, the application process and mode can be divided into the following three steps:

– Superpose the "New Urban Development Map (1:10000)" drawn by the government or by a urban construction authority and the "Map of Mountainous Land Suitability for Urban Construction (1:10000)" to see their spatial coincidence and interrelationship, as follows:
  If they completely coincide, then all mountainous lands as planned for urban development are said to be suitable for constructions; in this case, the use and allocation of land may be made in accordance with the "New Urban Development Map".
  If they coincide in most parts, with some not, that is, some parts in the new urban development planning are "unsuitable lands for construction", in this case, one may either ask the government or the urban construction authority to revise the "New Urban Development Map" to make it coincide with the "Map of Mountainous Land Suitability for Urban Construction (1:10000)"; or change the intended use of these "unsuitable lands" to "green space" rather than for construction when making land-use planning.
  If they do not coincide in most parts, that is, most parts in the area planned for urban development are "lands unsuitable for construction", in this case, the government or the urban construction authority must redraw the "New Urban Development Map (1:10000)" until it coincides with the "Map of Mountainous Land Suitability for Urban Construction (1:10000) in order to ensure a reasonable layout of urban construction land in the involved mountainous areas.
– Superpose the Boundary Map for New Industrial Development Projects (or for other independent development projects) (1:10000) drawn by the government or a competent authority and the "Map of Mountainous Land Suitability

for Urban Construction (1:10000)" to see their spatial coincidence and interrelationship, the same way as described in the preceding two paragraphs.
– Reshape the layout of prime farmlands in flat areas. All lands in a flat area that are previously planned for urban development or for industrial development will be cancelled and replanned as prime farmlands and allocate mountainous lands instead for such purposes to maintain the percentage of flat farmlands counted as prime farmlands at or over 80% of the total farmlands available in a flat area and to achieve the goal of "Protecting Quality Flat Farmlands and Building Cities & Towns on Mountains".

3 THE APPLICATION EFFECTS

By carrying out the evaluation of mountainous land suitability for urban development, Yunnan finally successfully completed the compilation and review of the county- and town-level General Land Use Planning (2010–2020), which is the firm base for the implementation of the province's strategy of "Constructing Mountainous Cities" and for the effective protection of farmlands in flat areas, which sets the goals for farmland protection and rules for land-use regulation in flat areas, which is a yardstick governing and regulating the use and protection of flat lands by authorities and developers, and is a remarkable blueprint for province-wide protection of quality farmlands in flat areas. Overall, by developing and preparing General Land Use Planning (2010–2020), counties and towns are enabled to protect their flat farmlands and implement the strategy of "Constructing Mountainous Cities" in a much more effective way. Specifically, by doing so, Yunnan' farmland protection and the strategy of "Constructing Mountainous Cities" achieve great success. This mainly reflects in the features detailed below.

3.1 *Effectively protecting prime farmlands in flat areas throughout the province*

– Prime farmlands in flat areas are effectively protected. The protected area of prime farmlands in the former General Land Use Planning of Yunnan Province (2006–2020), hereinafter referred to as the Former Planning, is 5.0236 million hectares, and that in the revised General Land Use Planning of Yunnan Province (2010–2020), hereinafter referred to as the Improved Planning, is 5.2627 million hectares, indicating an increase of 239,100 hectares; and the planned area of prime farmlands in flat areas is increased from the former 903,200 hectares up to 1.1158 million hectares, 23.54% higher, equivalent to a net increase of 212,600 hectares.
– The percentage of prime farmlands in flat areas is substantially increased. The province's total area of flat farmlands as of 2009 was 1.3549 million hectares and the area of flat farmlands counted as prime farmlands before the land-use planning improved was 903,200 hectares, indicating a protected percentage of flat farmlands of 66.66%. After the planning was improved, the area of farmlands counted as prime farmlands in flat areas was increased to 1.1097 million hectares, indicating a net increase of 206,500 hectares; and the protected percentage of flat farmlands rose to 81.90%, indicating a net increase by 15.24%, as given in Table 1.
– The ratio of prime farmlands to total farmlands in flat areas as well as the ratio of flat farmlands to total farmlands available province-wide both increased after the land-use planning was improved. Before the planning was improved, the total area of flat farmlands province-wide as of 2020 was determined to be 1.2842 million hectares, accounting for 19.89% of the province's total area of farmlands, and the total area of prime farmlands in flat areas to be 903,200 hectares, accounting for 17.98% of the province's total area of prime farmlands, which were then determined to be 5.0236 million hectares. However, after the planning was improved, the total area of flat farmlands province-wide as of 2020 was determined to be 1.3084 million hectares, accounting for 20.01% of the province's total area of farmlands, and the total area of prime farmlands in flat areas was determined to be 1.1158 million hectares, accounting for 21.20% of the province's total area of prime farmlands, which were then determined to be 5.2627 million hectares.

3.2 *Greatly promoting the layout of construction land on mountains throughout the province*

Before the planning was improved, the total area of lands planned for new construction was 190,500 hectares, out of which 90,600 hectares were in flat

Table 1. Protected percentage of flat farmlands before and after the improvement of Yunnan's general land-use planning.

Indicator	Before	After	Change by
Protected area of flat farmlands counted as prime farmlands (10,000 hectares)	90.32	110.97	+20.65
Protected percentage of farmlands in flat areas (%)	66.66	81.90	+15.24

Table 2. Proportion of construction land layout in mountainous areas before and after the improvement of Yunnan's general land-use planning.

Indicator	Before	After	Change by
Percentage of mountainous lands planned for new construction (%)	52.43	66.89	+14.46
Percentage of mountainous lands planned for new urban and rural construction (%)	38.04	55.02	+16.99

areas and 99,900 hectares were on mountains, which made up 52.43% of the total planned area of the province. After the planning was improved, however, the total area of lands planned for new construction was 220,600 hectares, out of which only 73,000 hectares were in flat areas and as high as 147,600 hectares were on mountains, which made up 66.89% of the total planned area of the province, indicating a remarkable increase by 14.46%.

Before the planning was improved, the total area of lands planned for new urban and rural construction was 90,800 hectares, out of which 56,300 hectares were in flat areas and 34,500 hectares were on mountains, which made up only 38.04% of the total planned area of the province for such purposes. After the planning was improved, however, the total area of lands planned for new urban and rural construction was 102,200 hectares, out of which only 45,900 hectares were in flat areas and as high as 56,200 hectares were on mountains, which made up 55.02% of the total planned area of the province for such purposes, indicating a remarkable increase by 16.99% (Table 2).

After the land-use planning was improved, the total area of mountainous lands for both industrial, and urban and rural development rose substantially, and the land development province-wide became more mountain-based. The new land-use planning will definitely promote the implementation of Yunnan's strategy of "Constructing Mountainous Cities".

4 CONCLUSION

A total of 129 counties, cities and districts throughout the province carried out the evaluation of mountainous land suitability for urban construction, developed and prepared their respective greatly improved general land-use planning, which proved to be an extremely effective way to protect high-quality farmlands in flat areas as well as an important base and support for the province-wide implementation of the strategy of "Constructing Mountainous Cities". By carrying out the suitability evaluation, county- and town-level general land-use planning (2010–2020) was revised, especially with regard to having a reasonable layout of urban and industrial development, on which the Government of Yunnan successfully implemented its "Protecting Flat Lands and Building Cities on Mountains" Strategy, brought more than 80% of its quality farmlands in flat areas under permanent effective protection and reduced the occupation of farmlands for development purpose down to a substantial extent. Turning to mountains for suitable lands for urban and industrial development provides a new and huge space for urbanization and industrialization, and offers a very effective solution to the outstanding conflict between farmland protection and ever-growing demand for development.

ACKNOWLEDGMENTS

This article is the result of project (No. 41261018) supported by the National Natural Sciences Foundation of China. We thank the Department of Land & Resources of Yunnan Province and Planning and Design Institute of Land & Resources of Yunnan Province for their help.

REFERENCES

He, Y.M., Yang, Z.S., Zhang, B.S., et al. 2014. Study on urban construction land suitability evaluation in southwestern mountainous areas of Yunnan Province based on the strategy of "protecting farmland in flatland areas and constructing mountainous cities": A case in Lianghe County. *Agricultural Science & Technology* 15(10): 1774–1777.

He, Y.M., Yang Z.S. & Zou J.L. 2015. Analysis on the necessity and feasibility of implementing the strategy of "protecting farmland in flatland areas and constructing mountainous cities" in Yunnan Province. *Agricultural Science & Technology* 16(4): 769–773.

Yang, Z.S., Wang, H. & Zhang, B.S. 2013. Study on constructive land suitability evaluation in China's southwestern mountainous areas: A case in Mangshi, Yunnan Province. In: Yang, Z.S. ed. *Research on Land Development & Rearrangement and Building Urban and Industrial Projects on Mountainland in China (in Chinese)*. Beijing: Social Sciences Academic Press.

Yang, Z.S., Zhao Q.G. & Xin, L. 2014. *Land Resources of Yunnan*. Beijing: Science and Technology Press of China.

Zhu, Q.J., Su Y.P. & Wu, D.S. 2010. Risk assessment of land-use suitability and application to Tangshan City. *International Journal of Environment and Pollution* 42(4): 330–343.

This page intentionally left blank

Civil Engineering and Urban Planning IV – Liu et al. (Eds)
© 2016 Taylor & Francis Group, London, ISBN 978-1-138-02903-3

Study on the decorative features of Huaxi Ba historical architecture

Jing-Ni Zhang, Xiao She & Yun-Zhang Li
College of Architecture and Environment, Sichuan University, Chengdu, Sichuan, China

ABSTRACT: The architectural decorations of Union University in Huaxi Ba area are extensive, interesting, and have high artistic accomplishments. In the age of great culture amalgamation, this research will help us to understand the concepts and practice of architects from home and abroad in that specific historical period. Their successful experience also has great significance on modern architectural creation.

1 INTRODUCTION

Huaxi Ba is located by the bank of Chengdu Jinjiang River, near the 3rd section of Renmin South Road, and the Tianfu Square in central Chengdu is to the north. In 1910, missionary O.L. Kilborn, Joseph Beech, and Zuoxin Tao, from Canada and America established Huaxi Union University here. The campus was mostly planed by a British architect named Fred Rowntree. The campus buildings massively started to be built in 1915, and more than 40 buildings had been finished by 1928. Expansion of the construction continued year by year. By 1949, the campus area was over a thousand mu and there were more than 70 buildings. The architecture adopted traditional Chinese style, but its decorations were obviously different from traditional Chinese way. This group of campus buildings in southwest China was a valuable combination of the East and West styles. Huaxi Union University, which was one of Chinese thirteen church universities as Shanghai St John's, Soochow Dongwu University, and Beijing Yenching University, is one of the earliest Christian Colleges in China (Zhang 2004). The architectural decoration was drawn from broad contents, uniquely and diversely shaped, and well preserved, which makes it outstanding in church universities. There are more than ten historical buildings remained in Huaxi Ba, among which the Huaide Hall built in 1919 and the Maode Hall built in 1926 were the most typical ones in decoration, so we take these two for deep study.

2 THE HUAIDE HALL

The Huaide Hall, which was started to be built in 1915 and was completed in 1919, has been used as the office building of Wangjiang campus of Sichuan University. It consists of administrative office department, arts classroom, photography department, auditorium, and so on. The front elevation of Huaide Hall is axisymmetric and the external wall is made of cyan bricks with a porch at the entrance. Although it looks like a single storey building from the outside, it actually has two storeys inside (Fig. 1).

The whole building is richly shaped in proper proportion and unique style. It's in accordance with traditional Chinese architectural composition, but if observing carefully, you will find there is a great difference. Compared to traditional Chinese architecture, the roof is much steeper in Huaide Hall, more like the sloping roof in western architecture. Upper windows and tiger windows are set to supply the indoor lighting. It is obvious to find typical western architectural features despite the use of hip roof and pyramidal roof, which is common in China. The entrance porch is slightly curved in the middle of the roof, which is similar to the Japanese construction in Tang wind breaking practice. The side windows of the hip roof with geometric pattern decoration is large, making it more similar to the western roof and the chimneys protruding from roof, which can also be seen in Shangqiu St Paul

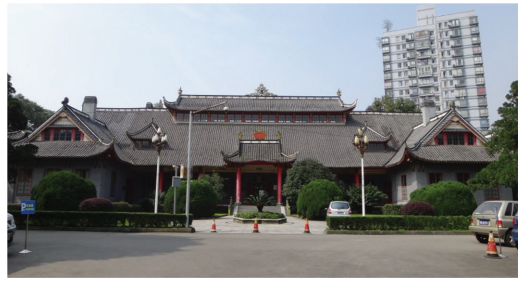

Figure 1. Façade of the Huaide Hall.

hospital, Henan (Shangqiu First People's Hospital now) are the very products of the combination of Chinese and western elements.

Partial decoration has the following characteristics: At the top of the entrance step railing is a flower-shaped column with four petals, which looks like tulips in western form. The front porch is supported by four big red columns, of which the bases have eight prismatic edges decorating with bat patterns. The main ridge of the porch has a red fan pattern on it with chrysanthemum-like ornaments above and below. The porch is decorated with animals on both ends of the ridge, whose curved shape is similar to the Chiwen in traditional Chinese architecture, but the overall shape is more like the dolphin image in European mythology (Fig. 2). The ends of vertical ridges are painted pearl with simple decoration. The ends of the diagonal ridges are decorated in pastem. Diagonal beam and the lower part of the eaves are decorated with the phoenix head. The decorated brackets on the columns are painted in eagles and the front gate door covering is painted with crane (Jin et al. 2007).

The main ridge over the top windows on the second floor is decorated with two dragons and a flower basket. The dragons turn their back against the flower basket and their bodies twist with the pastem in the basket. The ends of the main ridge are Chiwen, similar to the ones in the QingYang Temple. What makes it different is the position—it is at the top of the main ridge, not swallowing the ridge. There's also a phoenix head below the eaves. The supporting arches are less obvious. There is a large area of windows on the external walls of the second floor. The pane is also decorated with angle fillet, and the head of the beams is painted with flowers and grass.

Both sides of the main ridges on the roof covering are decorated with lizards, whose shapes are unique. They have strip-shaped ears, strong forelimbs, highly curly tails, trying to swallow the main ridge. In the front, the tiger window is decorated with pyramidal roof, resembling the tulip pattern at the railing. Below the eaves are decorated with phoenix heads.

Figure 2. Decorations of the main ridges.

Figure 3. Decorations of main ridge, under eave and on the column.

The main ridges on the roof at the side faces of Huaide Hall are also decorated with lizards that are slightly different from the ones at the front side. Their ears are larger, mouths are full of tusks, heads are heading towards outside of the ridge, and they are lying on the top of the ridge. Below the ridge are slant phoenix heads. The column on the walls are carved in western style lions with wings on the top, clearly different from the traditional ones (Fig. 3). Supporting arches on the side walls are carved in sea horses, two in a row. Xuan Yu at the side face is in the shape of five-petal peach with a pointed end, and is carved in auspicious clouds.

The lattice hanging above the indoor staircase is decorated with pigeons, columns in the staircase have double layers of four petal-lotus on their top. The central atrium of two storeys high has arches in bird shape.

3 THE MAODE HALL

The Maode Hall, now serving as a history exhibition hall at Huaxi campus of Sichuan University, was built in 1926. It used to be the university library of the Huaxi Union University. After completion, it became a library as well as history museum. The layout, shape, and style are all similar to the Huaide Hall, and with the church tower as the origin, Maode Hall and Huaide Hall are of the axis symmetrical layout (Fig. 4).

Compared to Huaide Hall, the porch of the Maode Hall is relatively narrow. The main ridge at the porch is decorated with two lizards and a vase, and the two lizards turn their tails against each other, they have fins at the back of the heads, thin tongues out of the mouth, and the shape of their

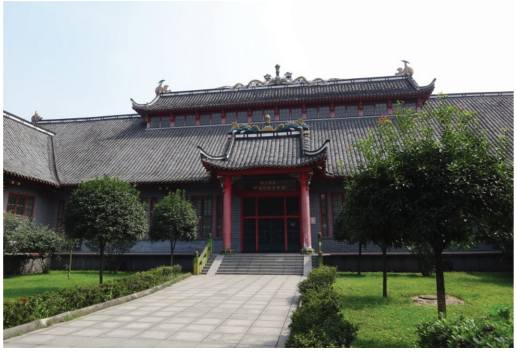

Figure 4. Façade of the Maode Hall.

heads are similar to the Chiwen at Huaxi Ba. They have strong legs and long fins at the back connected to the tail. The vase is like a three-layer lotus, with a pearl on the top and a base at the bottom. The ends of the diagonal ridges and the hip ridges have leaf-shape decorations. Below the roof is the slant pig head decoration and arches painted with eagles (Fig. 5). The column bases look like the ones in Huaide Hall, except they have eight piped edges rather than bats decorative patterns.

The main ridge above the top window on the second floor has an image of two dragons playing with a vase in the midst. The bodies of the dragons are surrounded by auspicious cloud, and there are not any antennas on their heads. The vase has a three-layer-lotus pedestal and a pearl on the top. At the ends of the main ridge are two lizards whose pose is slightly different from the ones on the top windows and in Huaide Hall, since they have fins on the back and tails pointing to the sky. The ends of the diagonal ridges are decorated with curve. Below the roof is a slant decoration. Supporting arches are simplified as petal, and the pane is also decorated with fillet.

The main ridges on the side roof have dragon heads decorations with big noses, curly tails, flakes, and heads beyond the roof pointing toward outside. The diagonal ridges are decorated with curves below which are symmetric roll shaped patterns. Under the roof are slant decorations.

The side of the gable wall has a fake door, on which flower-shape hanging fences are painted. The ends of roof ridges are decorated with lizards, similar to the ones at the front porch. The Tiger window has a pointed peak on it, which is a four-layer lotus with green leaves. The ends of hip ridge are curly.

The column cap of the railing of indoor staircase is in a shape of two-layer square lotus with four petals. At the center is a two-storey atrium surrounded by corridors. The structure part is decorated by curves (Fig. 6).

Figure 5. Slant pig head and arches.

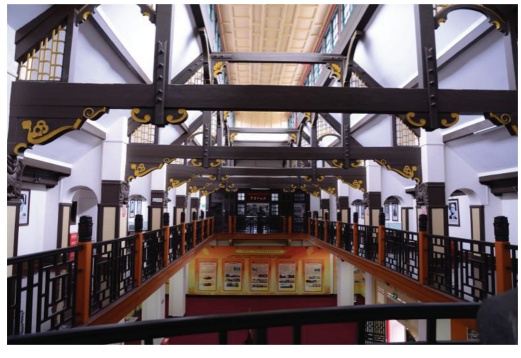

Figure 6. The two-storey atrium.

4 ANALYSIS OF DECORATIVE FEATURES OF HUAIDE HALL AND MAODE HALL

4.1 *The emergence of westernization*

Throughout the architectural decoration images of Huaide Hall and Maode Hall, a large number of western images turn up like lizard, hippocampus, eagle, pig head, stone line, dolphin, and tulip, which are totally different from what they are in traditional buildings despite the imitation of traditional Chinese compositions.

Take the lizards for example. They are usually used for decoration on the two sides of main ridge, which look like Chinese Wenshou and Wangshou in a far distance (Li et al. 2014). The seahorse image on the supporting arch at Huaide Hall, the eagle image on the arch at the porch of Huaide Hall and Maode Hall, the pig head image under the roof at the Maode Hall, the stone carved flying lion image at sides of Huaide Hall, the tulips image at the top of columns, the tiger window at Huaide Hall, the geometrical patterns painted on the roofs, and the

walls at both buildings are all western images. Under the control of traditional Chinese architectural decoration composition, the architects use their imagination to bring in large amounts of western architectural decoration themes (Chen et al. 2014).

4.2 *Westernization and misuse of traditional images*

Despite the Chinese traditional decorative themes, the practice and form in Huaide Hall and Maode Hall are all different from the local traditional Chinese architectural decoration, these traditional images are interpreted by the western designers in their own way. For example, most of the dragon head images are simplified in Huaide Hall and Maode Hall. The two dragons and vase decoration at the front high window show that dragon heads do not have horns. The dragons open their mouth and expose their teeth, which is similar to the head of a lizard. The fans at the ridge of porch in Huaide Hall are Chinese images, which are misused. Walls at the Maode Hall use traditional weight bearing component DouGong as decoration, which is far from the native.

4.3 *Differences in decorative features between Huaide Hall and Maode Hall*

The Huaide Hall was built 7 years before Maode Hall, so the management of decoration is different in some ways. Built in 1919, the Huaide Hall is the oldest campus building in Huaxi University, its decoration seems to be abrupt and strong. Taking the lizards on the roof for example, the form is strange and scary, and the dragon on the top of the ridge has a jerky face. But the lizards decoration in the Maode Hall built in 1926 seems to have a better interaction with dragon decoration at the roof ridge. At the same time, the designers started to pay more attention to the representative components in traditional Chinese architecture and imitate Chinese wood structure intentionally.

These changes indicate that in the sustaining process of campus construction, western designers have gradually gained experience in the intention of blending eastern and western decorative themes better while reserve the native designing intention.

5 CONCLUSION

The overall planning and campus designing of Huaxi Union University is conducted by the British architect Fred Rowntree, who arrived at China in 1912 and investigated many traditional Chinese buildings in Beijing and Chengdu. Before he started designing the campus, he had made a careful measurement and investigation in purpose of blending elements from traditional Chinese architecture and western architecture together.

It is obvious from what we have discussed that while building the Western Church University in Chengdu, the architect did not use his experienced western architectural composition, instead, he had a fully investigation of traditional local composition. Under the control of traditional Chinese architectural composition, the architect used western decorative themes and dissimilated traditional Chinese architectural themes. On the one hand, the designer himself was not familiar with the traditional Chinese culture, on the other hand, it may be the needs of the propaganda of western church culture.

The decoration of the ancient architecture in Huaxi Ba is bold and interesting. Though choppy and naïve, it is full of unique understanding of Chinese and western culture and exuberant creativity, which turned out to be a high artistic achievement. In the era of culture integration, a thorough study of architectural decoration is helpful to have a better understanding of foreign architects' view on Chinese architectural culture in specific history period and unique attempts in architectural design practice. Their successful experience also has a very strong influence for modern architectural creation.

ACKNOWLEDGEMENT

The introduction of talent research projects in Sichuan University, China Fundamental research funds for the Central Universities Research Projects China.

REFERENCES

Jin, J. 2007. Application of 3D laser scanner in the field of Architecture. *Architecture and Culture* 121(4): 168–171.

Kezhen, C. 2014. The study of the characteristics of the typical vernacular dwellings in Mount. Emei. *The 3rd International Conference on Civil Engineering and Urban Planning, Wuhan, Hubei, Jun. 20–22, 2014*.

Liping, Z. 2004. *Lovesickness for Huaxi Ba.* Chengdu: Hebei Education Press.

Qiang, L. 2014. The Characteristics Study on Typical Traditional Building in Mount Emei Regions. *Outline of 2014 Annual Meeting Academic Lecture, Kobe University, Sept. 12–14, 2014*.

Civil Engineering and Urban Planning IV – Liu et al. (Eds)
© 2016 Taylor & Francis Group, London, ISBN 978-1-138-02903-3

Inclusiveness and complexity in Nieuwmarkt neighborhood renewal project—lessons from Pentagon block and its surroundings

Hong Jiang
Shanghai Institute of Architectural Design and Research Co. Ltd., Shanghai, China

ABSTRACT: Urban renewal in housing supply is a multi-level urban renewal issue from political strategy to physical space solution. To study the links between the two large span levels, this paper evaluates the performance of physical renewal from six aspects of different scope based on the case study of a successful neighborhood block in Amsterdam. Under the premise of policy study and qualitative analysis based on field survey, physical attributes of the block in certain social political background are discussed. Through speculative thinking, it elaborates how collective demands are addressed within a traditional block form while still keeping surrounding tissue and space character and how different methods respond to the top–down requirement. In order to serve a highly political goal, it reflects that different scales of physical approaches are mutually enhanced and macroscopic proposals would compromise to the common premise which is necessary to be persisted.

1 INTRODUCTION

In Amsterdam, urban renewal has undergone far more complicated situations than other areas and has generated profound influence on both housing market and social context regarding housing renewal in the city center (Pistor 1994). Pistor's work gives a macro view on the characteristics and problems on the development of Amsterdam in different stages. It implies a kind of extensive correspondence between plan and policy by elaborating how the policy and strategy is slightly shifted as expanding urbanization has break through the existing pattern. In Jolles's research, the driving force behind the macroscopic process is explored including how sectorial plan transit to integral plan in a documentary way. Its discussion shows an excellent model of speculative research method which is embodied in reading different structure plan according to the policy emphasis of the period.

In terms of policy, the 'integrated' aspect of area-based policies in the Netherlands is discussed in 'Manuel B' research which reveals the unbalanced relationship between policies that focus on physical interventions and that focus on social interventions. Similarly, policy investigation is also conducted by Sako Musterd but he concentrated more on the problem oriented policy responses. Referring to the evaluation and effect of the evolution process of Amsterdam, a collection of distant and objective views from professional planners and architects is combined by Maarten Kloos to probe into the valuable aspects of relevant precedents that contribute to physical urban qualities in professional category e.g., human experience, building art and features of the heritage.

In order to fill the gap to make closer links between urban plan policy and practical project systematically, the research gives further insight into the subject that how small scale practical project can respond to different levels of policy demand in form, degree, and effect as shown in Figure 1.

Under the instruction of the urban renewal framework, Nieuwmarkt neighborhood renewal project was constructed in 1981 and it achieved a remarkable balance between demolishment and protection. It indicates a sophisticated process of urban evolvement and brought huge social benefits. It has managed to knit urban tissue and made it adaptable for increasing modern functions. Co-operation between community and planning authority shaped the planning process in a bottom–up way and made the project finally accepted by the mass residents. This essay, taking Pentagon block as a major example, focuses on exploring how such complexity is reflected in the project in different levels of policy, housing typology, transport need, and consideration of historical heritage protection.

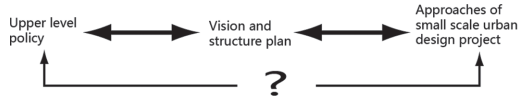

Figure 1. Research subject scope.

2 RESPONDING TO HOUSING POLICY IN 1978

In 1960s Amsterdam city prosperity has increased quite fast and has led to an expansion of business to suburbs and loss of function in the old city center. Under the pressure of protest of local residents following drastic slum clearance around 1964, preferences are shifted to smaller scale projects, but urban fabric are still maintained. "On the scale of city, urban planning, which traditionally focused on realization was superseded by the 'planological' approach, concentrating more on taking a 'plan as process' approach to a desired development" (Jolles et al. 2004) (Fig. 2). Besides, giving a clear boundary of the old city center, an important theme of the 1974, structure plan in preservation of the residential function in neighborhood of city center and development on the edge of city is shown in Figure 3.

Preference of the ground level housing is more accepted than impersonal high rise flats. With the introduction of "compact city" planning concept emerging in 1978, the third report of urban renewal "building for the neighborhood" came into action, which gives priority to keeping the vitality of city center and improving the social housing stock in the city center region. Instead of "opening up for corridors" with demolish, what is emphasized is "inward growth" (Klaas 2003). It is expanded in three aspects—rehabilitation, reconstruction, and preservation. Comprehensive consideration on the rich site context is deeply rooted in the design concept, which could be explored into different design thinking levels. The reconstructive plan of Nieuwmarkt neighborhood stresses on enhancing the centrality of the existing historical core through adding directive radiation shape streets rather than creating a new center public space.

The key point of housing policy highlights the renovation rather than demolishing which is shown in Figure 4. Attention is turned to the quantitative and qualitative reinforcement of the urban residential function of the city center and its surrounding urban residential neighborhoods which is shown in Figure 5. Besides, reinforcement of the local economy was the target of the

Figure 2. The twelve urban renewal areas.

Figure 3. 1974 structure plan.

Figure 4. Existing urban fabric after demolishment.

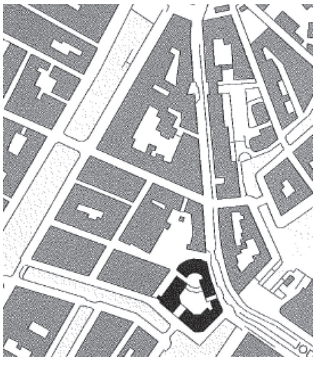

Figure 5. Site of the Nieuwmarkt neighborhood.

Figure 6. Contents in dominant upper level policy during the time period before and after the completion of the project.

same significance. As a result, smaller business sectors in the city center are promoted to stop the depopulation and diminishing prosperity of the city center. Located in an important historical site, the project confronted a radical resident movement and a national policy that was designed to solve the housing shortage through massive investment in social housing (Fainstein 2000).

Urban working class has become the main target for the customers of housing provision at that time, and social problems like gentrification was also on the list to be tackled. Under the pressure of local community and criticism on failure modern construction, the plan was going to meet the various needs of local residents and try to achieve social mixture.

Figure 6 displays a comprehensive list of contents in the policy review during the period. The design strategy and the corresponding relationship will be discussed in the following studies.

3 DESIGN PARAMETER

3.1 *Elaborative layout*

In order to rightly maintain the urban product of scientific rationality especially the heart of city intact, strict regulations such as the height of new construction and block size were introduced in the practice as planning the guidelines. Accordingly, many design principles were involved including restoration of the building skyline accompany with the narrow street profile, mixed function along the street and enhancing the separate identities of different lots by establishing a clear serious of space sequence which is shown in Figure 7.

Reconstructed blocks are basically controlled within the original building lines carved by permeable routes, so that traditional street patterns and

Figure 7. Pentagon block.

geometric division of the lots are preserved and continued.

All types of units are combined in unified form of patterns. In a larger site scale, it has double meanings regarding constituting wider urban tissue. According to the figure ground analysis, on one hand, it processed its own integrity in form. On the other hand, it has been successfully integrated into a larger scale cluster as a sub-element and contributed to maintaining connection to the existing urban fabric. Side square of the church list is kept with good access from street and riverbank, which is shown in Figure 8.

In order to be closely embedded to the complicated site context, each facade conveys a different meaning, what is especially worth has mentioned that the accurate corner smartly converts from the street facade to the small public square to invite public flowing inside which is shown in Figure 9. It provides a continuous gateway view to the church to enhance its symbolic position which is shown in Figure 10. There is much criticism on dwellers' privacy ruined by the intentionally designed public space inside, because local activities gave away to overwhelming public passing finally.

Along the river side, subtle transition from public to private is successfully achieved by ground level changes and front gardens design. It is such a brilliant inter between space design that makes communal life and individual life coexist which is shown in Figure 11.

Gateway view from the south begins with vibrant retail frontages on the ground floor and open café next to the canal. The vivid civic life images give a strong sense of belonging and unique character to the neighborhood.

3.2 *Coexistence of both old and new life styles*

Pentagon block is regarded as the turning points from private block to open block in terms of space define which is shown in Figure 12. From this aspect, it tries to open the closed block and conveys

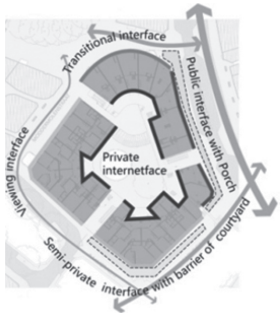

Figure 8. Hierarchy in block cluster.

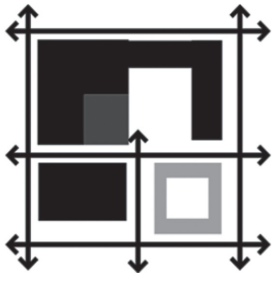

Figure 9. Interface analysis.

Figure 10. Gate view to the old church.

a willing to get residents' privately life involved in urban life, and then more open space are being given to public use for taking advantage of the existing landscape and building heritage. Elevated semi-open public corridor invites canal view into the street and creates a new kind of pedestrian space along the street. Accesses to the public inner courtyards are given by the three separated entrances of the block. In the ground floor, private rooms, and semi-private rooms are separated by shared stairs while half underground studio and retail have differently oriented accesses. Joined working and living space initiate a new city living style.

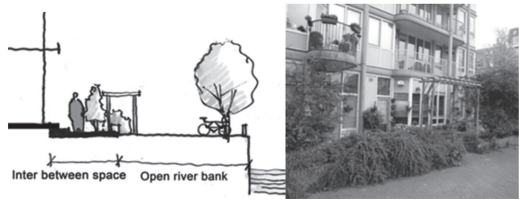

Figure 11. Interface along the riverbank.

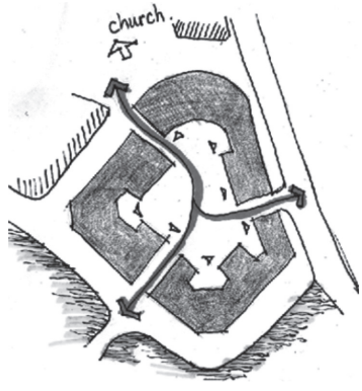

Figure 12. Public route and private entrance.

Flourish of both public and private life leads to the different five façade. For instance, along the major street, it becomes a part of the shopping street via extending the canopy of commercial corridor from adjacent building. While at the round corner, a continuous curved short gallery delivers the transform from public to semi-public realm.

Unfortunately, due to the insufficient landscape design of the collective courtyard and the probability of the incompatibility of private need for local collective space and public use, no local residents' activities that happen actually and are almost overwhelmed by uncontrolled random public crossing.

Thanks to the preservation of flexible ground nearby, an open street market and a music opera were latterly added on the opposite bank side with good access, therefore, diverse activities help to improve efficiency of space utilization in urban central area.

3.3 *Integrated approach to modern development demands*

As an inevitably common challenge in urban renewal project, the growing modern traffic needs to be addressed over the city center for future development. So what kind of development pattern should be selected is to be studied. As the old town displays a strong connection of urban morphology and building typology, any highway proposal should reconcile

to the wide city context. After a long time of suspension, the proposed constructions of an artery of our lane motorway, a subway underground and a parking garage were finally reduced to two separate roads for one way and a narrower subway route.

As a result, the construction of metro line goes in accordance with the old street layout rather than widening the street. Its boundary was confined within the old building lines to avoid any impact on the historical cityscape which is shown in Figure 13. This quite strict vehicle transport strategy contributes to a strong narrow visual direction to the Nieuwmarkt—a spirit square. Street design also aims at promoting the public transport and cycling tradition. Unlike most roads leading to the city center giving more space for vehicle transport, it actually allows only one lane for motor use and much more space for cyclist and pedestrian which is shown in Figure 14.

In parallel, height of new buildings is set no higher than the old buildings' eaves and help to shape a continuous street interface controlled by higher historical buildings.

As a result of restriction on transport, a clear visual distinction between sold city center and environs can be defined on the city scale. Meanwhile, good access from and to city center is well achieved without any impact.

3.4 *Complexity of urban space hierarchy in surrounding*

As the new emerging design theories are gradually applied to the following adjacent areas, the hierarchical urban space are interrelated and joint to others. "Open block" is one of the concepts that is relevant with defining communal urban space. Traditional private block became an element coordinating with the newly added single buildings to shape the open public space.

In J.W. Siebbeleshof, with a latter constructed residence on the east side of Sint Antoniesbreestraat, the existing building at the angle is combined into a newly constructed block with a private courtyard inside, which is shown in Figure 15. Furthermore, being linked with another two adjacent linear buildings, the continuity on of street is able to be completed. Elevated entrance into the block indicates the existence of a less open public space behind which is shown in Figure 16. To some

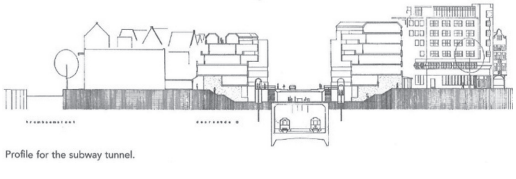

Figure 13. Sint Antoniesbreestraat section.

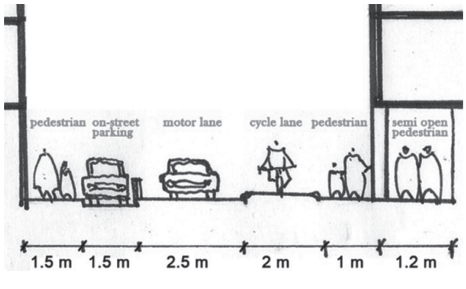

Figure 14. Sint Antoniesbreestraat street design.

Figure 15. Public route through J.W. Siebbeleshof block.

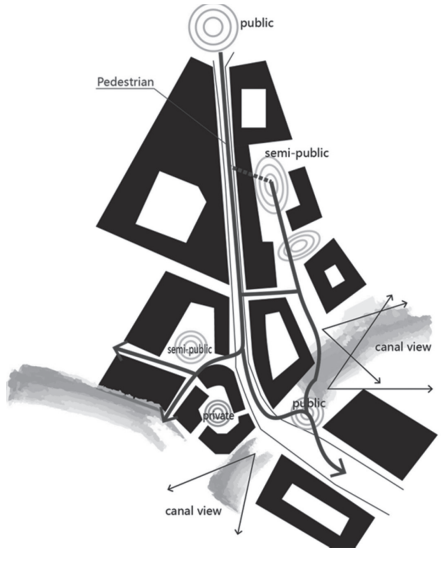

Figure 16. Continuous growing of space sequence.

extent, new sequence of space descripts a welcoming character of the city overlapping on previous urban tissue which is shown in Figure 17.

Thin building forms, on one hand, are developed at the time to allow sufficient sunlight to come into the narrow block to improve the quality of living environment compared to the traditional block. On the other hand, they have double frontages, which make it possible to accommodate spacious inner courtyard in smaller lots.

Since a view corridor to the canal is invited into the block, public use tends to be involved into the inner space. Carefully designed level changes are continued toward the bank, building projection and plants arrangement between the communal space and buildings help to create space hierarchy for the sake of residents' psychological need. All these results in the increased complexity of used pattern. Playground is able to be allocated and shared by other neighborhood nearby. Thanks to block structure gradually opened up, urbanscape is involved which is shown in Figure 18.

Besides, despite housing tenure proportion has changed a lot; traditional public life style was respected and got evolved to a new stage. Open space became more sophisticated and was subdivided into various uses with different hierarchies-view corridor, city meeting area and extended collective square which is shown in Figure 19.

3.5 *Coherence in architectural level*

As a leader of Structuralism at that time, Van Eyck (designer of Pentagon Block) had made great efforts in expressing housing language in technical way as well as keeping connection to the existing built environment. The inner facade of the block appears to be neutral and flat lacking identity of

Figure 17. Entrance to the block open space.

Figure 18. Sequence of space of J.W. Siebbeleshof block.

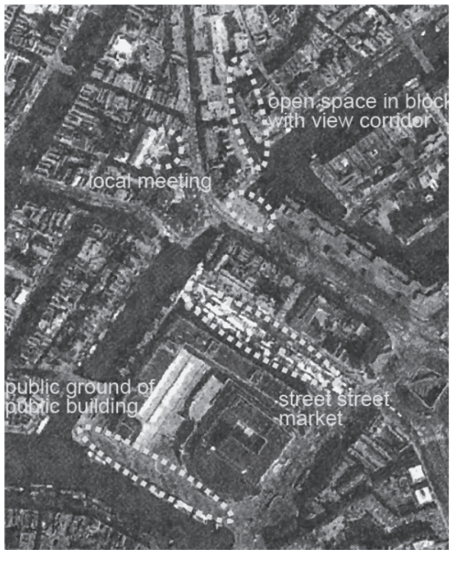

Figure 19. Newly added open spaces (before and after renewal).

individual dwellings. Continuous repetition of colonnades and uniform windows represented a typical appearance of social houses, the cantilevered balconies of which on the street side convey active participation in urban life. From that, subtle differences of single buildings are well fit into a general framework given by the rigorous grid of concrete skeleton, which offers freedom in variations in use. Meanwhile, fast construction can be also achieved through modern structure.

Pentagon block accommodates 87 dwellings with the house type of apartment, marionettes, senior citizen dwellings, and studio dwellings. Four shops and one pup are arranged on the ground floor.

Diverse dwelling types are carefully arranged in the single six storey block with personalized appearance, and their identities being well articulated through architectural language. In this way, legibility and sense of place are implemented in individual family level.

It is obvious that modern architectural manipulations are applied in urban design to enhance the context rather than branding itself. Certain privacy and variety in housing typology expression are merged together.

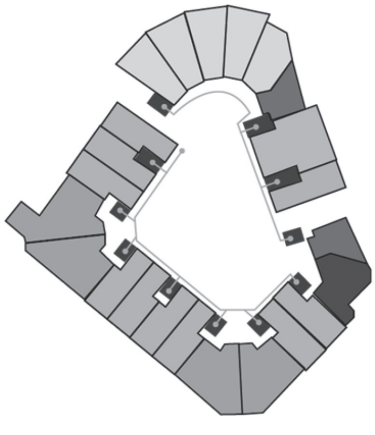

Figure 20. Unit diversity and circulation.

Plan design reflects the compact and efficient life mode as response. Sufficient shared stairs embedded in the units give way to the circular corridor as well as shaping the entrance space which is shown in Figure 20. The same type of unit is duplicated along straight segment while larger ones are set on the three corners. From the rational designed layout, it indicates the thoughtful efforts to achieve the balance between density and comfort.

4 CONCLUSION

From the analysis above, it can be concluded that the response to the upper level policy lies in the multi-level design strategy. Long-term policies need a variety of strategies to be implemented while single approach may also serve multiple goals in different degrees. (Fig. 21)

It is showed that under the background of urban renewal planning policy, a shift from large reconstruction to small scale renovation project in either sensitive city center or former industry area, organic renovation shows strong flexibility in not only reshaping intimate city scape but also keeping diversity. Following traditional block forms-regular cubic shape, human scale and low rise, the possibility of achieving high density within low rise residences has been somehow validated. Furthermore, they create a visual density as a residential area; entirely contrast to some earlier inhumane cases (Bijlmermeer) during 1960s and 1970s. Parking areas are restricted considering the comparatively lower income background and supporting for public transport. Mixed use rather than transport modes separation in street design proves to be an efficient way in increasing the road capacity. In a word, all the efforts contribute to a good balance between accessibility and livability.

DESIGN PARAMETER / POLICY & PRINCIPLES	Layout and fabric	Coexist of old and new life style	Modern traffic development	Extending urban space sequence	House typology & mixed use
Process planning	●			●	
Inward growth	●				●
Historical site renavation	●		●	●	
Social house					●
Keeping vitality of city center		●	●		
Neibourhood development		●		●	

Figure 21. Design parameters responding to different levels of policy demand.

In the perspective of development it is a gradual coordinated process to have later requirement and technology integrated in the previous framework. On a practical level, essential principles need to be persisted and sort according to the importance of grades so that the following measures can be taken in a consistent framework. Especially, in nowadays when land-scarce goes against with large demolition in city center, although achievement in every aspect is almost impossible, the implementation of systematic approach proves to be of crucial significance in leading efforts to an overall objective.

REFERENCES

Aalbers, M.B. & Beckhoven, E.V. 2010. The integral approach in neighbourhood renewal-more than just a philosophy. *Royal Dutch Geographical Society KNAG* 101(9): 1–13.

Beeldbank Stadsarchief Amsterdam. 2014. Beeldbank Stadsarchief Amsterdam. 2014. *http://beeldbank.amsterdam.nl/index.php?option=com_result&Itemid=9&qasked=1&qtype=nieuw&gn=1423291&view=1*.

Jolles, A., Klusman, E. & Teunissen, B. 2004. *Planning Amsterdam-Scenarios for Urban Development 1928–2003*. Rotterdam: NAi Publishers.

Jolles, A., Klusman, E. & Teunissen, B. 2004. *Planning Amsterdam-Scenarios for Urban Development 1928–2003*. Rotterdam: NAi Publishers.

Kloos, M. 1988. *Amsterdam-An Architectural Lesson*. Kloos, M. 1988. *Amsterdam-An Architectural Lesson*. Amsterdam: Toth Pub. House in co-ordination with ARCAM Foundation.

Nieuwmarkt Neighbourhood: Socio hohttp://www.rohmer.nl/?view = detail&pageAlias = projecten&projId = 68"*http://www.rohmer.nl/?view=detail&pageAlias=projecten&projId=68.*

Pistor, R. 1994. *City in Progress-Physical Planning in Amsterdam*. Amsterdam: Dienst Ruimtelijke Ordening.

Sako, M. & Wim, O. 2008. Integrated urban renewal in The Netherlands: a critical appraisal. *Urban Research & Practice* 1(3): 78–92.

Civil Engineering and Urban Planning IV – Liu et al. (Eds)
© 2016 Taylor & Francis Group, London, ISBN 978-1-138-02903-3

Forecasting research on the functional evolution of the land area in the Dalian core port area

Qi Zhang, Wen-Yuan Wang, Zi-Jian Guo & Xiang-Qun Song
Faculty of Infrastructure Engineering, Dalian University of Technology, Dalian, Liaoning, China

ABSTRACT: Dalian core port area is an important external transport hub and a development engine in the locality; the functional evolution of its land area is affected by natural conditions, relationship between the port and the city, and social economic development level. Based on remote-sensing images of Dalian, this paper classifies the types of land use and simulates the development pattern of this land area by the CA-Markov-MCE (multi-criteria evaluation) model. This paper considers the impact on the suitability of port construction caused by factors such as nature, society, economy and policy in the model, and determines the weight of each factor by the analytic hierarchy process. Based on the accurate simulation of the actual land area of the Dalian core port area in 2013, this paper forecasts the distribution situation of land area in 2020. The result indicate that the CA-Markov-MCE model can effectively quantify and predict the evolution of the land area, and the Dayaowan port area of Dalian will be the focus point of development in the future.

1 INTRODUCTION

Urbanization process is accelerating in the world in the new century. Meanwhile, the development trend of large-scale specialization of ships promotes the transformation and upgrading of the port, and the port has increasing conflicts with the city on the space expansion, which are reflected as the evolution of the land area in the port area influenced by the development of the port and the city.

Land area in the port area is a localized functional land in the city. Its evolution is affected by the combined action of factors such as nature, society, economy and policy. The existing related research has mostly concentrated on the discussion about the relationship between the port and the city (Bird 1963; Hoyle 1989; Ducruet & Jeong 2005; Notteboom & Rodrigue 2005; Li et al. 2008; Xu 1997; Guo & Han 2013), and failed to deeply study the evolution process of the port from the view of land use of land area in the port area.

In recent years, the research on Land-use Model supported by Remote sensing and geographical information technology has become mature; as a result, a variety of models for predicting land-use temporal and spatial evolution have been established (Pijanowski et al. 2002; Li et al. 2005; Nemmour & Chibani 2006; Niu & Ou 2007; Zhang et al. 2009; Zhang 2000; Luo et al. 2010; Pontius 2000). The CA-Markov-MCE model has a powerful spatial analysis ability in the CA model, predictive power for a long time in the Markov model, and ability of accurately and effectively simulating the changed trend of land use in the MCE model at the same time. Therefore, based on the impact on port construction suitability caused by various factors, this paper applies the CA-Markov-MCE model in forecasting research on the functional evolution of land area in the Dalian core port area, in order to provide a scientific basis for the development program of the port.

2 REGIONAL SITUATION AND DATA SOURCES

2.1 *Regional situation*

Dalian core port area is located in the Dalian bay and the Dayao bay close to the Huanghai Sea. It has the main port facilities in Dalian, such as container terminals, liquid bulk terminals, bulk grain terminals and ro-ro passenger ship docks. In recent years, with the rapid development of the port, the throughput of the container is over 10 million TEU. Regional development speeds up and the functional area of the port and the city has increased dramatically.

2.2 *Data sources and processing*

This paper selects the Dalian core port area and peripheral urban areas as the main study area. The selected data mainly come from Landsat remote sensing data, which were, respectively, acquired in 2000, 2006 and 2013. This paper selects both elevation and slope data, of which the accuracy is 30 m × 30 m.

3 RESEARCH METHOD

This paper divides land use into several types, namely ecological land, construction land, land area of the port and sea area, in accordance with the major characteristics of regional land. CA-Markov model features the spatial prediction characteristic of the CA model and the temporal and spatial characteristic of the Markov model. Combined with the geographic information system technology, it could research the evolution of the land area of the port by confirming the Markov transformation matrix, analyzing the suitability of the land area of the port on the basis of the MCE model, and constructing the cellular filter.

3.1 *Markov model*

Markov model is a stochastic model that determines the state change trend and predicts their future by the research on the initial probability and transition probability of different states. The matrix that consists of the collection of all primary transfer probability of the system is called the transfer matrix. If the data of land-use types of two phases are known, we can get the land-use transfer matrix between them, which is used for forecasting land conversion rules of the land area of the port:

$$P = \begin{bmatrix} p_{11} & p_{12} & \cdots & p_{1n} \\ p_{21} & p_{22} & \cdots & p_{2n} \\ \cdots & \cdots & \cdots & \cdots \\ p_{n1} & p_{n2} & \cdots & p_{nn} \end{bmatrix} \quad (1)$$

$$0 \le p_{ij} \le 1, \ \sum_{j=1}^{n} p_{ij} = 1 \ (i, j = 1, 2, 3 \cdots n) \quad (2)$$

where n is the number of land-use types, and p_{ij} is the probability of type i to type j. Land-use status at time t and t+1 is described by S_t and S_{t+1}, respectively. The relationship between them can be described as

$$S_{t+1} = S_t \times P \quad (3)$$

3.2 *MCE model*

Because the development of the land area of the port is sensitive to the influence of natural factors, economic factors and social factors, we need to analyze the suitability of the land in order to correct the probability of turning into the function area in the port. Based on a certain suitable area of port construction and specific factors of port construction, this paper applies the MCE model for calculating the suitability of port construction.

This paper selects some factors of port construction, including natural factors (elevation, slope), social factors (the distance between the new port and the built port area, the distance between the new port and the consolidation and distribution system) and policy factors (core port area) according to the scientific nature and the principle of accessibility of data. Policy factors are qualitative factors, so this paper quantifies the degree of the core levels of the port area as the integer value, which is used for quantifying policy factors. This paper standardizes factors by selecting different linear fuzzy membership functions according to the characteristic of each factor so as to make the influence degree of various factors on the evolution of land area comparable (Fig. 1). Then, the suitability of port construction within the study area can be described as 0~1, where 0 is the most inappropriate and 1 is the most appropriate. Finally, we get the weight of each factor through the AHP and get the suitability coefficient of the land area in the port by using the weighted average method.

3.3 *Cellular filter*

Cellular automaton follows the partial transformation rules; in other words, the state of cellular automata at a certain time is only related to that at the last moment. The cellular automaton used for forecasting land transformation is 30 m × 30 m. We select the space of 5 × 5 around the core cell as the neighboring effect area. Cellular filter is the effect weight of the cellular neighborhood on its state changes, and the 5 × 5 filter

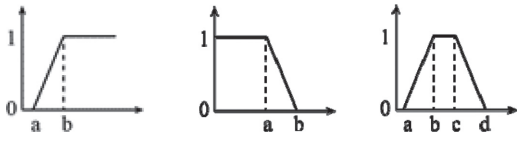

Figure 1. Standardized fuzzy membership function.

constructed according to Gaussian distribution can be described as

$$\begin{bmatrix} 1 & 2 & 3 & 2 & 1 \\ 2 & 7 & 11 & 7 & 2 \\ 3 & 11 & 17 & 11 & 3 \\ 2 & 7 & 11 & 7 & 2 \\ 1 & 2 & 3 & 2 & 1 \end{bmatrix} \quad (4)$$

When forecasting the land use, we carry out an iterative calculation through the CA-Markov-MCE model combined with built cellular filter on the basis of land conversion rules, land-use map in benchmark year and land-use suitability images in the year to be predicted. Iterative times are related to the span of time to be predicted.

4 SIMULATION AND ANALYSIS OF THE FUNCTIONAL EVOLUTION OF THE LAND AREA IN THE DALIAN CORE PORT AREA

4.1 *Basic data processing*

This paper classifies the study area by a supervised classification combined with the man-machine interaction. Because the key point of this paper is the evolution of the land area in the port area, we classified forest land, cultivated land and grassland as ecological land, and classified construction land in the port area as the single type of land use. Therefore, we obtain graphs of land-use data at different times, including ecological land, construction land and the land area in the port and sea area. We obtain the data of traffic, distance and industrial district from spatial data, and execute a process of grid transformation for them.

4.2 *Pattern evolution of the land area in the port*

During 2000 to 2013, construction land in Dalian continuously increased from the view of spatial distribution of land use (Fig. 2). The extent of old city expansion was limited because of the restriction of geomorphic feature, while new city expansion dominated the expansion of construction in recent years. Meanwhile, the focus of Dalian port construction is gradually transferred to the Dagushan peninsula and the Dayao bay area, which is in accordance with the expansion of the center of the city. By using GIS software. The land area in the port in 2000 and 2013 were calculated to be 0.93 km^2 and 2.79 km^2, respectively. The range of the land area in 13 years increased over 200%.

4.3 *The analysis of land-use transfer matrix*

The land-use transfer matrices in 2000~2006 and 2006~2013 were calculated by using the Markov model, as given in Table 1.

Land-use transfer matrix reflects transforming relationships among different land types. From Table 1, it can be found that the probability of sea land, ecological land and port land transferred to construction land exceeds the probability of them to other types. As shown in Figure 2, land area in the port turned into construction land is mainly caused by the relocation of the old port area in the Dalian bay. In recent years, the land area in the port transformed from construction that came from sea reclamation in the early period has contributed to the majority of the new land area. In addition, port land occupies a small amount of ecological land, reflecting that the development of the Dalian port has few effects on the ecological resources.

4.4 *Prediction of the evolution of the land area in the port*

Combined with the suitability of port construction in 2013, this paper simulates the land-use map used in 2013 by 7 times of iterative computation with the CA-Markov-MCE model on the basis of land-use data used in 2006 (Fig. 3). The forecasting land area in the port in 2013 was 2.74 km^2, and the relative error between it and the actual area was 1.8%. We test the result by the Kappa test. In the test, K_S is 0.75, which indicate that the comprehensive

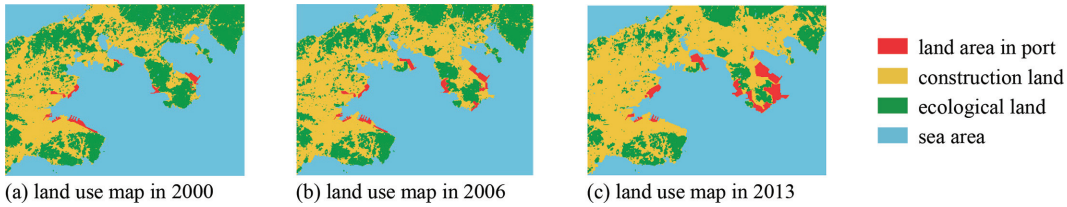

(a) land use map in 2000 (b) land use map in 2006 (c) land use map in 2013

Figure 2. Land-use map within the study area.

Table 1. Land-use type transition probability matrix within the study area.

		Transition probability			
	Land type	Sea area	Construction land	Ecological land	Land area in port
2000~2006	Sea area	0.8137	0.1542	0.0124	0.0196
	Construction land	0.0224	0.8179	0.1123	0.0474
	Ecological land	0.0031	0.3640	0.6220	0.0109
	Land area in port	0.0209	0.1979	0.0000	0.7812
2006~2013	Sea area	0.8145	0.1574	0.0005	0.0276
	Construction land	0.0155	0.7988	0.0746	0.1112
	Ecological land	0.0039	0.4184	0.5657	0.0121
	Land area in port	0.0014	0.2711	0.0005	0.7270

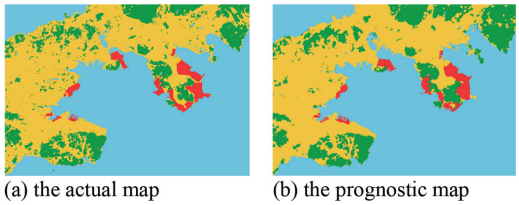

(a) the actual map (b) the prognostic map

Figure 3. The actual land-use map (a) and the prognostic land-use map (b) within the study area in 2013.

Figure 4. The prognostic land-use map within the study area in 2020.

information of the predicted results is good. In addition, because the location change of the land area in the port has more research significance, we test it with the location Kappa coefficient and $K_L = 0.76$. The predicted result has a high spatial accuracy. In short, the simulation result of the CA-Markov-MCE model conforms to the actual conditions and has high reliability.

Thus, on this basis, we forecast the pattern of the land area in the port in 2020 (Fig. 4). Compared with that in 2013, the forecasting land area in the port in 2020 increases by 118%, to 6.07 km^2. The new land area mainly comes from construction land and reclamation, and expands along the north shore of the Dayao bay. A continuous core port area will be built in the Dayao bay coastline and the Dagushan peninsula coastline.

5 CONCLUSION

This paper proposes the CA-Markov-MCE model to study the evolution of the land area in the Dalian core port area. This model considers the impact on the suitability of port construction caused by natural factors, such as social factors, economic factors and policy factors, so that we can enhance the rationality and simulation precision. The prediction result of the evolution of the land area in the Dalian port indicates that the land area in the Dalian core port area would increase continuously in the future. Besides, port constructions mainly concentrate in the Dagushan peninsula and constructions on both north and south shores of the Dayao bay port area are the construction emphasis.

ACKNOWLEDGMENT

This research received the financial support from the National Natural Science Foundation of China (Grant no. 51279026).

REFERENCES

Bird, J. 1963. *The Major Seaports of the United Kingdom*. London: Hutchinson.

Ducruet, C. & Jeong, O. 2005. *European Port-City Interface and Its Asian Application*. Gyeonggi-do: Korea Research Institute for Human Settlements.

Guo, J. & Han, Z. 2013. The port-city spatial system evolution theory and empirical study of Chinese seaport city. *Scientia Geographica Sinica* 33(11): 1285–1292.

Hoyle, B.S. 1989. The port-City interface: Trends, problems and examples. *Geoforum* 20(4): 429–435.

Li, J., Zhu, X. & Zhang, D. 2008. Spatio-temporal characteristics of urbanized area growth and outer spatial form evolution of group port city: Taking Ningbo city as a case. *Geographical Research* 27(2): 275–285.

Li, Z., Wang, Y., Wu, J., Zhang, X. & Li, L. 2005. Application of urban growth model in spatial decision-making of land supply the case of Longgang District of Shenzhen city. *Resources Science* 27(2): 51–58.

Luo, P., Jiang, R., Li, H., Zhang, X., Huang, B. & Xiang, Q. 2010. Research on the method of regional land use evolution based on the combination of spatial logistic model and markov model. *China Land Science* 24(1): 31–36.

Nemmour, H. & Chibani, Y. 2006. Multiple support vector machines for land cover change detection: An application for mapping urban extensions. *ISPRS Journal of Photogrammetry and Remote Sensing* 61(2): 125–133.

Niu, X. & Ou, M. 2007. Study on the forecast of land structure in Yangzhou city based on Markov theory. *Economic Geography* 27(1): 153–156.

Notteboom, T.E. & Rodrigue, J. 2005. Port regionalization: Towards a new phase in port development. *Maritime Policy & Management* 32(3): 297–313.

Pijanowski, B.C., Brown, D.C., Shellito, B.A. et al. 2002. Using neural networks and GIS to forecast land use change: a land transformation model. *Computers, Environment and Urban Systems* 26(6): 553–575.

Pontius, R.G. 2000. Quantification error versus location error in comparison of categorical maps. *Photogrammetric Engineering & Remote Sensing* 66(8): 1011–1016.

Xu, J. 1997. On the function of port to the development of port city. *Areal Research and Development* 16(4): 11–14.

Zhang, X. 2000. Cellular automaton based urban growth dynamics modelling and prediction. *Journal of Graduate School, Academia Sinica* 17(1): 31–36.

Zhang, X., Wang, W., Verburg, P.H. & Xu, Z. 2009. Scenarios simulation of land use pattern in Tangshan coastal zone. *Resources Science* 31(8): 1392–1399.

This page intentionally left blank

Civil Engineering and Urban Planning IV – Liu et al. (Eds)
© 2016 Taylor & Francis Group, London, ISBN 978-1-138-02903-3

The study on ecological risk assessment in the port of the coastal city based on the Landscape Pattern Analysis

Wen-Yuan Wang, Guo-Lei Tang, Yong Zhou & Qi Zhang
Faculty of Infrastructure Engineering, Dalian University of Technology, Dalian, Liaoning, China

ABSTRACT: With the rapid development of international trade, the scale of the coastal port expands unceasingly. Port and its adjacent area, where the incidence of ecological crisis and environmental pollution is high, have a great influence on the ecosystem of the coastal city. This paper proposes a method to assess the ecological risk assessment in the port of the coastal city comprehensively by using the landscape pattern analysis. And it takes a coastal city in Northern China as an example and uses this method to determine the port ecological risk level of all areas of the city. From the perspective of the ecological impact, this paper provides a reference for the port layout.

1 INTRODUCTION

Port is a key node of modern transportation system, generally located in the transition zone of water and land, on the brink of a variety of ecosystems, with a lot of characteristics of ecosystem of land, wetland, sea and city. According to the relationship among economic (production), environment (natural) and society (human) of production and management activities of the port, the ecosystem of the port can be divided into 3 subsystems: harbor living subsystem, natural environment subsystem and social environment subsystem. Material circulation, energy flow, species exchange, information transmission and value flow frequently and tempestuously among each subsystem. The complex economic behavior and production activities of the port can bring a great risk to the city's ecosystem of the port, so the ecological risk identification, measurement and evaluation of the city's ecosystem of the port are necessary. It can help to provide the basis for effective risk management plan and management measures.

In the aspect of regional ecological risk assessment, the research methods include landscape ecological method and relative risk evaluation method. Rand et al. adopted the method of landscape ecological analysis in the research on using habitat to assess the ecological risk (Rand & Newman 1998). Chen et al. adopted the method of landscape ecological analysis in the research on the ecological risk of inland of arid region, and assessed the Sangong River Basin in Fukang (Chen & An 2003). In the research on risk of the island ecosystem, Wang X assessed the probabilistic risk and common risk of the island ecosystem by using nonlinear assessment model for multiple probabilistic risks and the relative risk model, respectively (Wang 2006). Yu (2012) used the relative risk model as the instrument of ecological risk assessment for late decision-making in the research on strategic decision-making in the coastal zone. The research on the characteristics of the port ecosystem and ecological risk is very limited. The existing research from the perspective of ecological toxicology mainly considers the impact of pollution on the water area (Manzo et al. 2014; Manzo et al. 2014); or from the perspective of ecological evaluation endpoint, considers how to select the measuring end to reflect the risk tolerance (Huo 2011; Li & Xu 2014). In 1997, Landis and Wiegers put forward the Relative Risk Model (RRM), introduced the concept of exposure and responded coefficient between risk source, habitat and assessment endpoint, solved the problems of large scale with multiple levels of risk source, habitat and receptor evaluation, and used this model to make ecological assessment of Port Valdez (Wiegers 1998). Peng et al. (2004) used the Relative Risk Model (RRM) to make the ecological assessment of Bohai Bay harbor. This paper through in-depth research and analysis of the composition of the port ecosystem uses Landscape Pattern Analysis (LPA) to determine the risk identification, measurement and evaluation of different regional ports (port district) of the scope of the port city, and provides the basis for effective risk management plan and management measures.

2 THE SCOPE AND COMPOSITION OF THE PORT ECOSYSTEM

Port ecosystem is a compound ecosystem of nature, economy and society. It includes three

subsystems: environment subsystem of the port, economy subsystem of the port and society subsystem of the port.

2.1 *Environment subsystem of the port*

Environment subsystem of the port includes the biological factors of human and biology, and the non-biological factors includes natural environment and artificial environment. Environment subsystem of the port is the basis of the economy subsystem of the port and the society subsystem of the port. The components of the environment subsystem of the port are shown in Figure 1.

2.2 *Economy subsystem of the port*

Economy system takes economic activities of people as the main body. It is composed of production, exchange, distribution and consumption, including important elements such as population, environment, resources, goods, capital and information. Its core function is to exploit and use port resource, with the support of port city and hinterland, and achieve the economic growth of the port through the port transportation system. The economic activities of the economy subsystem of the port include loading and unloading services, passengers boarding service, port financial service, port business service and port-neighboring industry. There are six dynamical subsystems related to the port economy: city subsystem of the port, regional economy subsystem, resources and environment subsystem, port-neighboring industry subsystem and integrated transportation subsystem (Liu et al. 2012). The port has an important status in the transportation system, and the modern port has become an important part in the operation of national economy. The components of the economy subsystem of the port are shown in Figure 2.

2.3 *Society subsystem of the port*

The society subsystem of the port is composed of human, organization, culture and policy.

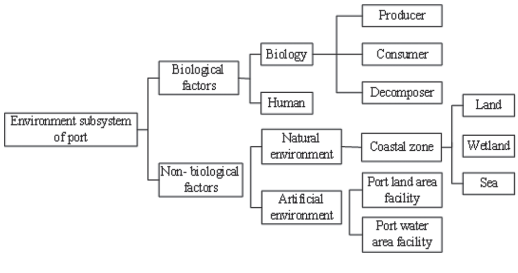

Figure 1. Components of the environment subsystem of the port.

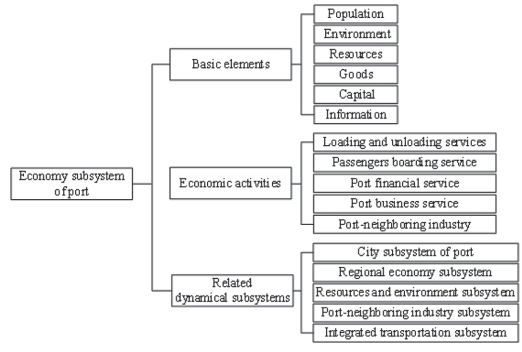

Figure 2. Components of the economy subsystem of the port.

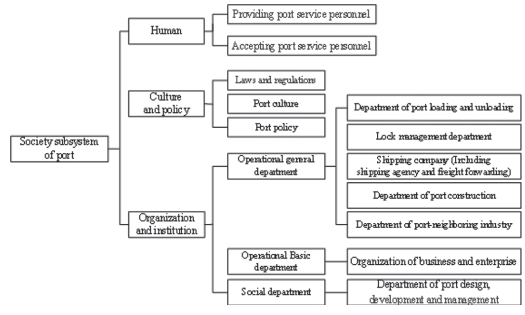

Figure 3. Components of the society subsystem of the port.

The components of the society subsystem of the port are shown in Figure 3.

3 THE LANDSCAPE PATTERN ANALYSIS OF THE ECOLOGICAL RISK OF THE PORT

This paper uses the landscape pattern index to build the ecological risk index, analyzes the distribution features of the global risk through the spatial statistical methods and mainly includes the following four steps:

– Through investigation and statistical analysis of data and information: Dividing into small-risk areas, using GIS and remote-sensing software (e.g. envi) to identify, explain and process the landscape of the study area, using landscape pattern analysis software (e.g. Fragstats) to calculate the landscape pattern index;
– Determining the vulnerability of different landscapes by the expert evaluation method and the analytic hierarchy process;

– Calculating the ecological risk index of each risk area, using statistical software to make spatial analysis and interpolation of global ecological risk;
– Dividing risk level, evaluating the regional ecological risk.

4 INSTANCE ANALYSIS

This paper takes a coastal area of Northeast China as an example, and evaluates the port ecological risk of all coastal areas of the city by using the landscape pattern analysis. Shoreline resources of the city are rich, the distribution of the port is intensive, and distribution is divided into five main parts.

4.1 *The division of risk districts*

By using the remote-sensing method to explain the landscape of the region in 2013, the landscape classification map can be obtained, as shown in Figure 4. The research area is divided into 1530 sampling plots by using the square grid of 5 km × 5 km. The division of risk areas is shown in Figure 5.

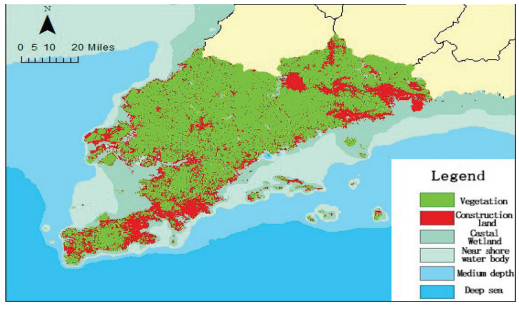

Figure 4. RS interpretation and classification results of landscape in Dalian in 2013.

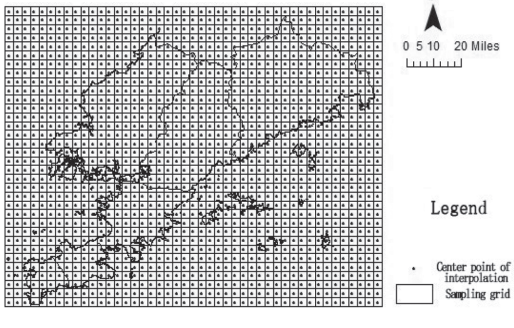

Figure 5. Risk districts dividing the map of Landscape Pattern Analysis (LPA).

4.2 *Landscape ecological risk calculation*

With the help of the GIS platform and Fragstats software to analyze the landscape pattern of each risk district, we get the landscape vulnerability index F_i, the landscape disturbance index S_i and the landscape risk index *ERI*. Assigning the landscape disturbance index S_i and the landscape risk index *ERI* of each risk district to the district center.

– The landscape vulnerability index F_i
Different landscape types represent different ecosystems of characteristics. There are four types of landscape in the study area: vegetation, construction land, coastal wetland and water body (putting near-shore water body, medium-deep water body and deep sea in the same class). In the above four kinds of landscape, the most vulnerable place is coastal wetland, followed by water and vegetation, and the construction land is the most stable place. There are 4 kinds of landscape vulnerability: coastal wetland = 6, water body = 4, vegetation = 3 and construction land = 1. Then, after normalizing the treatment, we get the landscape vulnerability index F_i of the four kinds of landscape.
– The landscape disturbance index S_i
With the help of the GIS platform and Fragstats software, we calculate the landscape index. According to the method provided in Section 3, we can get the landscape fragmentation index Ci, the landscape isolation index Ni and the landscape dominance index Di of each risk district. The landscape disturbance index needs to be determined for assigning to a, b and c. Through the analysis of the results of previous studies and comprehensive evaluation, we assign 0.6, 0.3 and 0.1 to a, b and c, respectively. That is to say, the most important index is the fragmentation index, followed by the isolation index and the dominance index.
– The landscape risk index ERI
With the help of the GIS platform, we calculate the landscape risk index ERI of 1530 risk districts.

4.3 *Spatial analysis and interpolation*

With the help of the geostatistical analysis function of ArcGIS, the spatial analysis and interpolation of the ecological risk of the 1530 risk districts in the study area can be realized. In this instance, we adopt the ordinary Kriging method to realize the analysis and interpolation of the landscape risk index *ERI* data.

– Distribution test of data points
Using the exploratory data statistical analysis function of the geostatistical analysis tool of ArcGIS, we can check the 1530 ecological

risk data. From Figure 6, we can see that the data of the landscape risk index *ERI* data are approximate to the normal distribution; in the trend test, there is no anisotropy of the landscape risk index *ERI* data.

– Surface analysis and interpolation
Using the geostatistical analysis tool of ArcGIS, we can carry out the analysis and optimal fitting of the variation function of the landscape risk index *ERI* data. Through the analysis and comparison, we find that the exponential model fitting effect is the most ideal, and the variation curve of fitting is shown in Figure 7.

The related parameters of the variation function model are listed in Table 1. We can see that the nugget/still of the *ERI* is 30.4%. It shows that, with the sampling interval of 5 km, there are some non-structural factors of a small scale influence the quality of the corresponding index of this area; however, the structural factor is still the leading factor; the range of the ERI is 78008 m. In this instance, the main port area is within the geographic range of 10 km and the maximum global geographical distance is 200 km, adopting that the interpolation prediction model can meet the actual demand basically.

Based on the variation function model, we use exponential model to fit and the grid size of the interpolation 50 m × 50 m can be determined. Kriging interpolation results processing the *ERI* of the study area are shown in Figure 8.

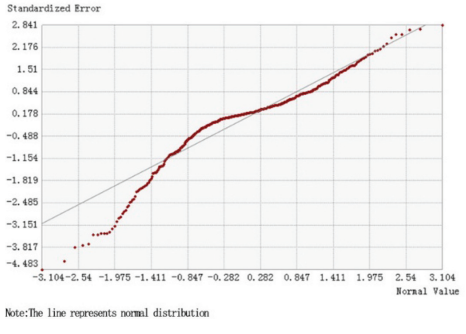

Figure 6. QQ plot of the risk index ERI.

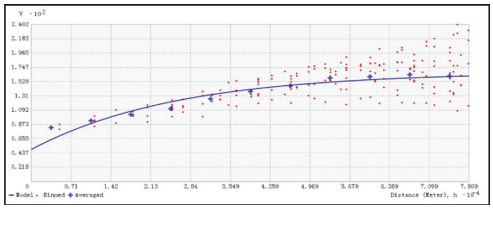

Figure 7. Experimental and model-fitted Semivario grams of the risk index ERI.

4.4 *Classification of risk ranking*

With the help of the ArcGIS platform, we classify the landscape ecological risk of the study area. The landscape ecological risk index is in accord with the normal distribution, so it can be classified according to the standard deviation. The ecological risk in the study area is classified into five rankings, the results of which are summarized in Table 2. The distribution of ecological risk after classification is shown in Figure 9.

By the analysis of the landscape pattern of the study area, we can get the distribution of ecological risk in the region. From Figure 9, we can see that district 2 is in the high-risk area; district 1 (including Dagang port, Dayaowan port and Shangdao port) and district 3 are in the higher-risk area; district 4 is in the medium-risk area and the adjacent area of the port is in the higher-risk area; district 5 is in the medium-risk area.

4.5 *Analysis of results*

District 2 is in the high-risk area. It belongs to the island ecosystem, the landscape type is rich and the degree of landscape fragmentation is higher. It may cause a great threat to the local ecosystem with the port area conduction here; special attention should be paid to the process of construction and operation of district 2. The port construction and urban construction of district 3 have been made for many years; the landscape pattern is basically in a stable state, the utilization of green space, beach and water body is large and the ecological risk is higher. The urban construction intensity of Pikou port and Zhuanghe port area is relatively (Dalian city) weak, and the scale of port construction is relatively small. And the utilization of green space, beach and water body is relatively weak. Most parts of it are in the medium-risk area and small parts of it are in the high-risk area. For district 3 and

Table 1. Corresponding parameters in diversity theoretical models.

Data	Year	Model	Nugget	Still	Nugget/still	Range/m
ERI	2013	Exponential model	0.0045	0.0148	30.4%	780088

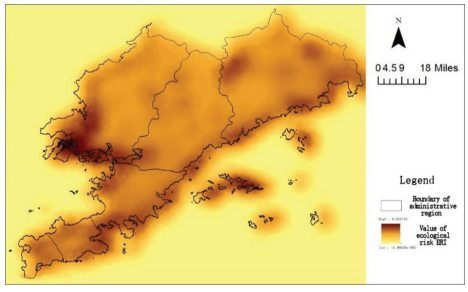

Figure 8. Kriging interpolation results of the risk index ERI in Dalian in 2013.

Table 2. Risk ranking basis.

Risk ranking	Basis of classification
High	$ERI \leq 0.085$
Higher	$0.085 \leq ERI \leq 0.253$
Medium	$0.253 \leq ERI \leq 0.420$
Lower	$0.420 \leq ERI \leq 0.587$
Low	$ERI \geq 0.587$

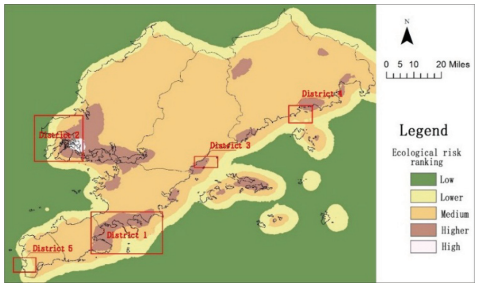

Figure 9. Spatial distribution and classification of ecological risk in Dalian in 2013.

district 4, attention should be paid to the protection of the ecosystem in the process of construction and operation. District 5 is in the medium-risk area and the urban construction intensity is relatively (Dalian city) weak. This area belongs to the new port, the scale of the port is relatively small, the utilization of green space, beach and water body is relatively weak, and the space of ecological use is large.

5 CONCLUSION

With the rapid development of international trade, the accident frequency of ecological pollution and environmental pollution in the coastal port and its adjacent area is high. Ecological risks are hazardous and uncertain; it has a great influence on the ecosystem of the coastal city. Based on the in-depth analysis of the port ecosystem, this article proposes an effective method to assess the ecological risk of the port. And it takes a coastal city in Northern China as an example, uses the landscape pattern analysis, researches the port ecological risk of all coastal areas of the city, and makes a comprehensive evaluation. This paper puts forward the port ecological risk level of all areas of the city and can provide a reference for the scale and timing of the port construction in different regions of the city.

ACKNOWLEDGMENT

This research was financially supported by the National Natural Science Foundation of China (Grant no. 51279026).

REFERENCES

Chen, P. & An, X. 2003. Ecological risk analysis of regional landscape in inland river watershed of arid area—A case study of Sangong River Basin in Fukang. *Chinese Journal of Ecology* 22(4): 116–120.

Huo, S. 2011. *Research on Distribution Characteristics and Ecological Risk of Heavy Metal in Surface Sediment of Bohai Sea*. Qingdao, China: Ocean University of China.

Li, F. & Xu, M. 2014. Heavy metals contamination levels at the ports zones of Jiangsu. *Resources and Environment in the Yangtze Basin* 2014(09): 1275–1282.

Liu, A., Wang, P. & Ding, Y. 2012. *The Introduction of Geostatistics*. Beijing: Science Press.

Manzo, S., Ansanelli, G. & Pappella, L. 2014. First evaluation of the threat posed by antifouling biocides in the Southern Adriatic Sea. *Environmental Science-Processes & Impacts* 16(08): 1981–1993.

Manzo, S., Schiavo, S. & Aleksi, P. 2014. Application of a toxicity test battery integrated index for a first screening of the ecotoxicological threat posed by ports and harbors in the southern Adriatic Sea (Italy). *Environmental Monitoring and Assessment* 186(11): 7127–7139.

Peng, S., Qin, X., Zhou, R., Wang, X. & Shi, H. 2014. Ecological risk evaluation of port in Bohai Bay. *Acta Ecologica Sinica* 34(1): 224–230.

Rand, G.M. & Newman, J.R. 1998. The applicability of habitat evaluation methodologies in ecological risk assessment. *Human and Ecological Risk Assessment: An International Journal* 4(4): 905–929.

Wang, X. 2006. *The Method and Application Research of Island Ecosystem Risk Assessment of Island*. Qingdao, China: Graduate School of Chinese Academy of Sciences.

Wiegers, J., Feder, H. & Mortensen, L. 1998. A regional multiple-stressor rank-based ecological risk assessment for the fjord of Port Valdez, Alaska. *Human and Ecological Risk Assessment* 4(5): 1125–1173.

Yu, W. 2012. *Ecological Risk Assessment of Strategic Decision Making in Coastal Area*. Xiamen: Xiamen University.

This page intentionally left blank

Civil Engineering and Urban Planning IV – Liu et al. (Eds)
© 2016 Taylor & Francis Group, London, ISBN 978-1-138-02903-3

Evaluation of the parking permits scheme for residents in Thessaloniki, Greece

G. Mintsis, C. Taxiltaris, S. Basbas & Y. Stathis
Department of Transportation and Hydraulic Engineering, Faculty of Rural and Surveying Engineering, School of Engineering, Aristotle University of Thessaloniki, Thessaloniki, Greece

ABSTRACT: In the center of the city of Thessaloniki, Greece, parking strategy includes short-term and long-term on-street parking with fees (1.7 euros/h) and on-street free parking for residents holding a specific parking permit. The aim of this paper is to evaluate the parking permit scheme for residents from the user's point of view. For this purpose, a questionnaire-based survey was carried out and 194 questionnaires were collected. The survey took place during September–November 2013 in the center of Thessaloniki. All the respondents were parking permit holders. The questionnaire consisted of three parts: the first one refers to the socioeconomic characteristics of the respondents, the second part refers to their mobility characteristics and the third part refers to their parking characteristics. The findings of the research could help the local authorities to improve the efficiency of such measures by taking into account the needs of their citizens.

1 INTRODUCTION

Parking strategies play a very important role in traffic management in urban areas, both in enhancing accessibility and in confronting congestion and the associated environmental impacts. Within the framework of a parking strategy, special attention is usually given to the residents. Parking permit for residents is an option for many local authorities worldwide, and this measure is implemented mainly in central areas.

There is always the question whether to charge residents for curb parking. According to the results of a research in New York City (Guo & McDonnell 2013) where a hypothetical parking permit program for residents was examined, "52.5% are willing to pay an average of $408 per year". In another research which was carried out in the city of Thessaloniki, Greece, three scenarios were considered for the residents (Giannopoulos et al. 1996): a) free parking, b) parking permit at a low cost (a standard fee without taking into account whether the parking permit holder could actually find a parking space or not as supply is in excess of demand in the city center), c) parking permit at a low cost (standard fee depending on the number of times the parking permit holder could actually find a parking space). The above-mentioned three scenarios were considered in conjunction with other two scenarios: a) residents can park their cars in curb parking spaces where the rest of the citizens pay a fee and b) residents can park their cars in exclusive curb parking spaces.

In the historical parts of the cities, the problem of parking for the residents becomes more severe due to the usual poor geometrical characteristics of the road network and the luck of empty space for parking. One such case is Ano Poli, which is the old part of the city of Thessaloniki, Greece, where according to a study (Basbas 1996), 90% of parking demand comes from the residents. The luck of empty space led to the formation of proposals for the implementation of parking permits scheme for the residents and at the same time to the introduction of mini-buses for the facilitation of the transport needs of the visitors.

The provision of "almost free of charge" parking permits to residents and the associated welfare losses is examined by a research conducted in The Netherlands (Van Ommeren et al. 2014). According to a research carried out in Amsterdam (Van Ommeren et al. 2011), it was found out that the residents' marginal Willingness-to-Pay for a parking permit is about 10 euros per day, an amount of money which exceeds the tariff for the permit and which is below the tariff paid by the non-residents for on-street parking.

It is also important to examine the impact that parking policies for residents have on car ownership and travel behavior. One such research was carried out in New York City (Guo 2013a) where these implications were examined. It is also important to note that the availability of parking space affects car usage. According to the results of a survey conducted in the city of New York (Guo 2013b), households for which parking is

convenient, i.e. on-street parking and garage, tend to increase their car usage.

Ordinary least-squares models were developed for the city of Shenzhen (Wang & Liu 2014) in order to examine the relationship between parking supply and a number of factors concerning the urban environment such as land-use characteristics, location and transportation characteristics. Suggestions based on the findings of the specific research include the formation of policy based on neighborhood-size areas and also differentiation of districts based on their land development density.

The aim of the present paper is to evaluate the parking permit scheme for residents in the central area of the city of Thessaloniki from the user's point of view. For this purpose, a questionnaire-based survey was designed and carried out and the results of the descriptive statistics, inferential statistics and regression analysis are presented hereinafter.

2 EXISTING PARKING STRATEGY IN THE CITY CENTER OF THESSALONIKI

The city of Thessaloniki, located in Northern Greece, is the second biggest urban agglomeration in the country. The biggest municipality in the city is the Municipality of Thessaloniki with 325,182 residents (Hellenic Statistical Authority 2014).

Parking strategy in the city center includes the use of a special parking card that allows the driver to park his/her car at specific parking spaces next to the curb. The cost of the card is 1.70 euros for one hour and cards are available at many stores in the city center. It must be mentioned at this point that there are specific parking spaces where parking is only allowed for a maximum period of 2 hours at a cost of 1.70 euros/hour (short-term parking). In this case, the driver uses parking ticket machines that are located in the city center. The driver inserts the fee together with the plate number of his/her car. The arrival time is displayed on the ticket.

The objective of the short-term parking scheme is to increase the parking turnover, which means that more drivers can use the same parking lot during the day. The scheme is in operation from 08:00 to 20:00 on Monday to Friday and from 08:00 to 15:00 on Saturdays.

Part of the parking strategy is the provision of parking permits to residents of the city center (residents' parking scheme). This specific measure was first introduced in the city center by the Municipality of Thessaloniki in May 2007. The implementation area of the parking permits scheme consists of two zones that are divided by a main arterial road in the city center. Residents with parking permits can only park their cars in the zone in which the permit is assigned to.

A special badge is provided to the residents of the city center by the respective municipality authorities. It must be mentioned at this point that there is no charge for the badge.

Each household can only apply for one parking permit. Therefore, households with more than one car need to pay parking fees for their additional cars in order to park these cars next to the curb. Permit holders must clearly display a valid permit (badge) in front glass of their cars.

It is crucial to say that parking is free for the permit holders in the two special zones in the city center, but there is no guarantee that they can find an empty parking space. This means that the demand is higher than the supply, something which is expected in a central area.

People who are eligible to apply for the badge must submit a number of documents to the municipality authorities including taxation documents, an electricity bill and a proof for their residence location.

The total number of available parking spaces in the city center is presented in Table 1 (Division of Sustainable Mobility and Networks 2013).

3 DESIGN OF THE QUESTIONNAIRE-BASED SURVEY

In order to investigate the characteristics of the on-street parking permit strategy for residents, a questionnaire-based survey was designed and carried out in the city center from September 2013 to November 2013 (Stathis 2013). The questionnaire was addressed to the residents of the city center who are holders of a parking permit. A total number of 194 questionnaires were collected and analyzed in the framework of the survey. It must be mentioned at this point that the questionnaire was tested in a pilot survey.

Table 1. Parking spaces per type of parking in the city center.

Type of parking	Number of parking spaces next to the curb
Parking control (1.70 euros/hour) and free parking for the residents	5622
Parking control (1.70 euros/hour—max. 2 hours) and free parking for the residents	783
Free parking spaces	800
Loading and unloading parking spaces	290
Total number of parking spaces	7495

The research methodology concerning the evaluation of the parking permits scheme for residents in Thessaloniki is shown in Figure 1.

The questionnaire consisted of three parts. The first part included seven questions that concerned the socioeconomic characteristics of the respondents (gender, age, occupation, monthly income, education level), resident ownership status (rental, privately owned) and the number of available cars in the household.

The second part included three questions that concerned the mobility characteristics of the respondents (use of the private car for the trip towards their workplace, location of their workplace in relation to the area of the parking permits scheme for residents, frequency of use of the private car—per day/week/month).

Finally, the third part included eight questions that concerned the parking characteristics (time spent for searching parking space in the area of the parking permits scheme for residents, time usually spent to walk from residence to parking place, willingness-to-pay for the parking permit, parking duration (usually), frequency of not finding a parking space (per day/week/month), actions of the driver after not finding a parking space, drivers' opinion about the parking permits scheme for residents, drivers' proposals for the improvement of the parking permits scheme for residents).

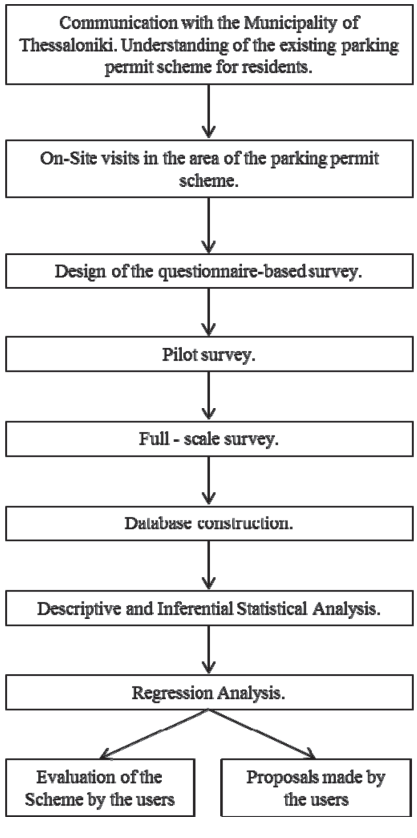

Figure 1. Research methodology.

4 DESCRIPTIVE STATISTICS

Tables 2–4 present the results of the descriptive statistical analysis concerning the first, second and third part of the questionnaire, respectively.

Table 2. Results from the first part of the questionnaire.

Socioeconomic characteristics	Results
Gender	Male: 67.53%
	Female: 32.47%
Age	18–24 years: 3.09%
	25–39 years: 30.41%
	40–54 years: 35.05%
	55–64 years: 20.62%
	≥65 years: 10.82%
Occupation	Employee in the public sector: 18.56%
	Employee in the private sector: 22.16%
	Self-employed worker: 34.54%
	Pensioner: 15.46%
	Student: 3.09%
	Unemployed: 6.19%
Monthly income	0–800 euros: 36.08%
	801–1600 euros: 47.94%
	1601–2400 euros: 9.28%
	≥2401 euros: 6.70%

Table 3. Results from the second part of the questionnaire.

Mobility characteristics	Results
Use of the private car for the trip towards their workplace	Yes: 42.67%
	No: 57.33%
Location of their workplace in relation to the area of the parking permits scheme for residents	In the area of the scheme: 45.33%
	Outside the area of the scheme: 54.67%
Frequency of use of the private car—per day/week/month	More than 2 times a day: 2.06%
	2 times a day: 6.19%
	Once a day: 33.51%
	1–3 times a week: 33.51%
	1–10 times a month: 22.68%
	Rarely: 2.06%

Table 4. Results from the third part of the questionnaire.

Parking characteristics	Results
Time usually spent in searching for parking space in the area of the parking permit scheme for residents	Find a parking space immediately: 6.70% Less than 10 min: 14.95% 11–20 min: 50.00% 21–60 min: 24.23% More than one hour: 4,12%
Time usually spent to walk from residence to parking place	Less than 2 min: 11.86% 2–5 min: 55.67% 5–10 min: 18.04% 10–15 min: 10.82% More than 15 min: 3.61%
Willingness-to-Pay for the parking permit	Nothing: 68.04% Less than 1 euro: 2.06% 1–2 euros: 3.61% 2–5 euros: 5.15% 5–10 euros: 12.89% More than 10 euros: 8.25 %
Parking duration (usually)	1–2 hours: 1.55% 2–8 hours: 7.73% More than 8 hours: 90.72%
Frequency of not finding a parking space (per day/week/month)	More than twice a day: 0.52% Twice a day: 1.03% Once a day: 23.20% 1–3 times a week: 31.44% 1–10 times a month: 17.53% Rarely: 26.29%
Actions of the driver after not finding a parking space	Keep searching: 47.16% Parking parallel to a car already parked and leaving a note on their cell phone number: 21.01% Parking at a faraway distance: 19.89% Parking with fee (on-street): 10.23% Illegal parking: 1.14% Parking station: 0.57%
Drivers' opinion about the parking permit scheme for residents	In favor of the scheme: 83.51% Opposed: 16.49%
Drivers' proposals for the improvement of the parking permit scheme for residents	Enforcement: 62.30% More parking spaces: 16.38% Reduced fees for residents: 4.92% Fewer documents to obtain the permit: 4.10% Employers to be eligible for permits: 2.46% Parking spaces only for residents: 1.64% Use of parking spaces with fees: 1.64% Fewer time intervals for loading and unloading lorries and vans: 1.64% More "free of charge" parking spaces: 0.82% Construction of parking stations: 0.82% Abolishment of the parking permit scheme: 0.82% Keeping the scheme as it is: 0.82% Expansion of the parking permits scheme for residents in order to cover the whole area of the city center: 0.82% Expansion of the parking permits scheme for residents to other areas (outside the city center): 0.82%

5 INFERENTIAL STATISTICS

In order to examine the possible factors that affect the positive or negative opinion of the respondents, the correlation coefficient rho, Spearman, for a significance level a = 0.05 was calculated. The main results of the analysis using IBM SPSS v.20 are presented hereinafter.

Concerning drivers' opinion about the parking permit scheme for residents, the analysis showed that their opinion is positively associated with their education level (N = 194, r_s = 0.157, p = 0.029), the frequency of the use of their private cars (N = 194, r_s = 0.184, p = 0.010), the time usually spent in searching for parking space in the area of the parking permit scheme for residents (N = 194, r_s = 0.204, p = 0.004), their Willingness-to-Pay for the parking permit (N = 194, r_s = 0.168, p = 0.019) and the frequency of not finding a parking space (N = 194, r_s = 0.190, p = 0.008). It is worthwhile to mention at this point that drivers who spent enough time in order to find a parking space had expressed a positive opinion for the parking permits scheme.

Those of the respondents who systematically spent enough time to find a parking space are positively associated with the walking time to their residence (N = 194, r_s = 0.536, p = 0.001) and their Willingness-to-Pay for the parking permits scheme (N = 194, r_s = 0.311, p = 0.001).

Respondents' Willingness-to-Pay for the parking permit is positively associated with their income (N = 194, r_s = 0.245, p = 0.001), their educational level (N = 194, r_s = 0.213, p = 0.003), the large amount of time spent in order to find a parking space (N = 194, r_s = 0.311, p = 0.001), the long-term parking duration (N = 194, r_s = 0.189, p = 0.008) and their positive opinion for the parking permits scheme (N = 194, r_s = 0.168, p = 0.019).

6 REGRESSION ANALYSIS

The multiple regression analysis is used in order to investigate the factors that affect the Willingness-to-Pay for the parking permits scheme. Two different models are examined. The dependent variable is the Willingness-to-Pay for the parking permits scheme. The first model includes the following two predictors and the constant.

a) The respondents' educational level and b) time usually spent in searching for parking space in the area of the parking permit scheme for residents.

The second model includes the following nine predictors and the constant plus the two predictors mentioned above.

a) Monthly income, b) number of available cars in the household, c) use of the private car for the trip towards the workplace, d) location of the workplace in relation to the area of the parking permits scheme for residents, e) frequency of use of the private car, f) parking duration (usually), g) frequency of not finding a parking space, h) opinion about the parking permits scheme for residents, i) zone (as previously mentioned, the implementation area of the parking permits scheme consists of two zones that are divided by a main arterial road in the city center). The regression model summary is presented in Table 5.

The contribution of the most important predictors is presented in Tables 6 and 7.

Therefore, time spent in searching for parking space and educational level seems to be the most

Table 5. Model summary having Willingness-to-Pay as the dependent variable.

	Model 1	Model 2
R	0.380	0.443
R^2	0.144	0.196
Adjusted R^2	0.133	0.134
Std. error of the estimate	1.647	1.646
R^2 change	0.144	0.052
F change	12.666	1.009
df1	2	9
df2	150	141
Sig. F change	0	0.436

Table 6. Contribution of the most important predictors for model 1.

	Constant	Educational level	Time usually spent for searching for parking space
Unstandardized coefficients			
B	–2.202	0.734	0.562
Std. error	0.897	0.198	0.144
Standardized coefficients			
Beta		0.283	0.298
t	–2.456	3.702	3.908
Sig.	0.015	0	0
95% confidence interval for B			
Lower bound	–3.973	0.342	0.278
Upper bound	–0.430	1.125	0.846
Collinearity statistics			
Tolerance		0.979	0.979
VIF		1.021	1.021

Table 7. Contribution of the most important predictors for model 2.

	Constant	Educational level	Time usually spent for searching for parking space
Unstandardized coefficients			
B	–4.874	0.616	0.492
Std. error	2.539	0.232	0.169
Standardized coefficients			
Beta		0.237	0.261
t	–1.920	2.657	2.916
Sig.	0.057	0.009	0.004
95% confidence interval for B			
Lower bound	–9.893	0.158	0.158
Upper bound	0.145	1.075	0.825
Collinearity statistics			
Tolerance		0.715	0.712
VIF		1.399	1.405

important factors that affect Willingness-to-Pay for the parking permit in the specific survey. The more the educational level is improved, the more the Willingness-to-Pay for the parking permits scheme is increased for the specific respondents. At the same time, monthly income is not an important factor, although some could expect the opposite. The increase in time usually spent for searching for parking space means the increase in the Willingness-to-Pay for the parking permits scheme. The examination of the additional nine predictors in the second model showed that these predictors do not affect the Willingness-to-Pay for the parking permits scheme. It is important to note that the location of the residences (in each one of the two zones) does not affect the Willingness-to-Pay for the parking permit scheme.

From the regression analysis, it is obvious that Model 1 is the most robust one.

7 CONCLUSIONS

The low percentage of young residents (18–24 years old) can be explained by the fact that they usually drive the family car. Thus, the age distribution refers to the parking permit holders and not to drivers in general. Residents with a university degree participated to a high extent in the questionnaire-based survey. More than half of the respondents (57.33%) did not use their private cars on their way to work. At the same time, 54.67% of the respondents stated that their workplace was located outside the area of the parking scheme. This could mean that residents who were commuters used public transport or other means of transport (e.g. environmental-friendly transport means such as bicycles). It is worthwhile to mention that more than half of the respondents did not use their car every day. Therefore, parking turnover for residents was not high. The usual parking duration was more than 8 hours for the vast majority of the respondents (90.72%). Although they were parking permit holders, they spent a considerable amount of time in order to find a parking space (more than half of them used to spend 11–20 min). For the residents who did not use their cars every day, 11–20 min could be an "acceptable" time, but for the rest of residents, this became a problem.

Almost two-thirds of the respondents stated that they were not prepared to pay anything in order to obtain the parking permit, something which can be explained by taking into account the difficult economic situation in the country. It is also interesting to note that 83.51% of the respondents were in favor of the parking permit scheme for residents. When they did not find a parking place at once, they continued to search (almost half of them), while double parking was an option for one out of five of them. When doing so, they also left a note on their cell phone number in order to inform the driver who had already parked legally to call in case of emergency. Among the proposals for the improvement of the parking permit scheme for residents, enforcement was of major importance (62.30%) followed by the creation of more parking spaces (16.38%).

Willingness-to-Pay for the parking permit scheme was positively associated with the parking permit holders' educational level and also with the time spent by the parking permit holders for searching parking space. Taking also into account the findings of the research in Amsterdam (Van Ommeren et al. 2011), a possible parking policy for the Thessaloniki case could include a small fee for the parking permit. The international experience (Guo 2013b) has also shown that parking convenience for residents tends to increase their car usage. Therefore, in a future redesign of the parking permit scheme for residents in Thessaloniki, the respective authorities should take into account that the more convenient the parking space for residents is, the fewer the alternative, environmental-friendly, transport modes will be. In this case, there is a need for further improvement of the public transport system in the city center, emphasizing on the old, historical part (Basbas 1996).

Citizens' involvement in the decision-making process is a new concept in Europe. Sustainable Mobility Plans (SUMPs), an initiative which have been supported by European Commission in

the last few years, are setting the framework for a better strategic planning in a metropolitan area by bringing all the relevant stakeholders, both policy makers and the end users in the same table (Politis et al. 2015). In this context, the outcomes of the present questionnaire-based survey could be considered as an argument tool by the residents of Thessaloniki's city center for any new parking policy scheme.

Differentiation of the districts in the design process of the parking strategy is also an important issue (Wang & Liu 2014). The findings in the Thessaloniki case showed that the location of the residence does not affect Willingness-to-Pay for the parking permit scheme for residents. However, differentiation of districts and of the associated parking policy could be proved essential in a future extension of the scheme to other parts of the city. The use of Geographic Information Systems (GIS) will be very helpful towards this direction.

The findings of the present research could help the local authorities to improve the efficiency of such measures by taking into account the needs of their citizens.

REFERENCES

Basbas, S. 1996. Organisation of the traffic and parking system in areas with special character–the case of Ano Poli, Thessaloniki. *Traffic in Thessaloniki. Proposals, Contradictions, Confrontations; Proc. Symp., Thessaloniki, 6–7 November 1996*. Thessaloniki: Technical Chamber of Greece, Institute of Thessaloniki's Architects, Municipality of Thessaloniki.

Division of Sustainable Mobility and Networks, Municipality of Thessaloniki. 2013. Personal communication.

Giannopoulos, G.A., Pitsiava-Latinopoulou, M., Aifandopoulou, G. & Basbas, S. 1996. Parking policy for the central area of the Municipality of Thessaloniki. *Traffic in Thessaloniki. Proposals, Contradictions, Confrontations; Proc. Symp., Thessaloniki, 6–7 November 1996*. Thessaloniki: Technical Chamber of Greece, Institute of Thessaloniki's Architects, Municipality of Thessaloniki.

Guo, Z. 2013a. Does residential parking supply affect household car ownership? The case of New York City. *Journal of Transport Geography* 26: 18–28.

Guo, Z. 2013b. Home parking convenience, household car usage, and implications to residential parking policies. *Transport Policy* 29: 97–106.

Guo, Z. & McDonnell, S. 2013. Curb parking pricing for local residents: An exploration in New York City based on willingness to pay. *Transport Policy* 30: 186–198.

Hellenic Statistical Authority. 2014. Demographic and social characteristics of the permanent population in the country according to revision of the census Population—Residence 2011. *Census Population–Residence 2011*. Piraeus, Greece.

Politis I., Papaioannou P. & Nikolaidou A. 2015. The Development of a National Cities Network in Order to Promote Sustainable Urban Mobility Plans: Barriers and Opportunities (Greek). *Accepted for Presentation at the 7th International Congress on Transportation Research, Athens 5–6 November, 2015.* Athens: Hellenic Institute of Transportation, Hellenic Institute of Transportation Engineers.

Stathis, Y. 2013. *Investigation of the Characteristics of the Parking Permits Scheme for Residents in the Center of the City of Thessaloniki*. Greece: Faculty of Rural & Surveying Engineering, Aristotle University of Thessaloniki.

Van Ommeren, J., Wentink, D. & Dekkers, J. 2011. The real price of parking policy. *Journal of Urban Economics* 70: 25–31.

Van Ommeren, J., De Groote J. & Mingardo, G. 2014. Residential parking permits and parking supply. *Regional Science and Urban Economics* 45: 33–44.

Wang, J.J. & Liu, Q. 2014. Understanding the parking supply mechanism in China: A case study of Shenzhen. *Journal of Transport Geography* 40: 77–88.

This page intentionally left blank

Civil Engineering and Urban Planning IV – Liu et al. (Eds)
© 2016 Taylor & Francis Group, London, ISBN 978-1-138-02903-3

A comprehensive research and design of the campus vehicle management system

Yu Li
Southwest Jiaotong University, Chengdu, Sichuan, China

ABSTRACT: This paper explains an intelligent campus vehicle management system for Chinese universities. Based on the principles of man-machine engineering and interactive design, utilizing systemic analysis, the system is built to target vehicle management deficiencies with regressive access control administration, such as traffic jams and long line-ups at campus entrances and exits. The object of this study on the access control administration was the Southwest Jiaotong University. This system will not only reduce the labor intensity of the public security workers on the campus by integrating automation and intelligence into the pay parking system, but will also decrease traffic jams by expediting the payment process. Additionally, it will increase the elements of "humanization" and add a "sense of warmth" to the management system, thus better supporting the humane atmosphere of the campus. The system provides a good reference for the design of university campuses.

1 INTRODUCTION

There are many differences in campus layout between Chinese and western universities. Influenced by traditional culture, the Chinese campus layout is "locked". The term "locked" can be interpreted in three ways: 1) the spatial form of the campus is segregated from the neighboring environment; 2) the activities of campus users are not available to outsiders; and 3) the psychological state of the people on campus is closed. In contrast, western universities mostly adopt an open campus layout. Neither model is good or bad, but merely influenced by cultural differences. However, different layouts will certainly have an influence on the overall design of campus vehicle management systems.

The opening of universities to society allows more vehicles to constantly flood into the campus, which further intensifies the traffic congestion on campus and increases the load of the vehicle management system.

Today, most campus vehicle management systems use ETC and IC card technology. Field investigation shows that these two technologies both have defects. For example, when a car passes ETC verification, the driver of a following vehicle may mistakenly think that the access control has an automatic release, and may try to pass the access control without verification. As a result, this is not only a potential safety hazard, but may also cause capital losses through not charging vehicles for parking. IC card technology also has certain problems. For example, 1) the distance between the case card swiping position and the vehicle is difficult to handle, and sometimes, drivers have to leave their vehicles to do it; 2) manual payment is time-consuming, which may lower the efficiency of vehicle access and increase the working intensity of security personnel; and 3) while waiting in line, vehicles produce a great deal of exhaust, thus degrading the surrounding air quality. A principal factor of slack campus roads is the tendency of drivers to park randomly in the limited space of a campus. As a consequence, complications between people and vehicles have emerged. The random choice of parking spots leads to unnecessary vehicle scratches, which will not only result in property damage, but will also make people suspicious of the safety of the campus environment and lead to a lack of confidence in the campus environment.

The weak ergonomics of the police box causes some application deficiencies, as is shown in Photograph 1. The vehicle passing issues can be summarized as follows:

- As the ergonomics design of the police box is unreasonable, the worker has to keep bending down when giving change.
- The unreasonable design of the window height makes it difficult for the worker to pass cards while sitting on the chair. At the same time, it is not easy to reach out and give change to the drivers.
- The height of the police box window is not properly designed, as the sightline of the worker may

Photograph 1. Survey photos.

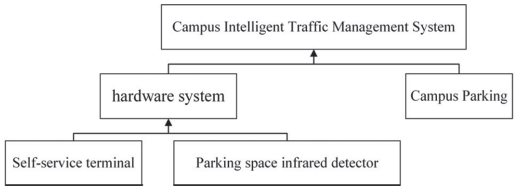

Figure 1. The elements of the intelligent traffic management system.

be blocked by the window frame when receiving the card from the driver.

– The low efficiency of the access control administration regularly causes a traffic jam.

Iana Zankina (2013) in *Campus driver assistant on an Android platform* mainly explores a navigational APP for freshmen on the campus based on an Android platform. The result of this research is, however, unsuitable for the study of locked management system of Chinese universities, nor does it have any coverage of campus transportation management.

The basic idea of the current study is to design a set of intelligent systems in the context of a university campus, combining the use of relevant hardware and software to regulate the management of motor vehicles on campus, as is shown in Figure 1.

The system offers different entrance payment methods for users. Specifically, the temporary vehicle drivers are divided into two groups: one with e-payment experience and one without. The former group pays by means of the new carrier, Campus Parking, while the latter pays by means of a self-service IC card. Campus Parking users can scan a two-dimensional code on the screen of the self-service terminal to input their entrance time and check the campus area distribution for available parking spaces as well as the service conditions of the nearest parking space; when leaving, the users can scan the two-dimensional code on the terminal again, enter the password, and complete the payment. In this way, the system will ease the congestion caused by lengthy payment systems in campus access control and reduce the working intensity of the security personnel. This is not only a beneficial supplement to the existing method on the campus, but will also increase efficiency according to the needs of different groups of users.

2 DESIGN ANALYSIS

The campus vehicle management system is a relatively complex integrated system consisting of diverse elements with multiple links and facilities. The problems to be solved are seen as an integrated system, and all conditions and elements are analyzed comprehensively so as to better find solutions. For example, 1) temporary vehicles are offered a brand new charging method and external vehicles are provided with the most reasonable parking and leaving service, thus solving the current major problems of static traffic; 2) the intelligent and self-service charging method reduces the working intensity of security personnel; and 3) integrating all subsystems into the vehicle management system will not only optimize the fragmentary access control in appearance, but will also create a unified design of all internal functions in the vehicle management system.

2.1 *Applying flow analysis*

The flow chart (Fig. 2) is drawn based on Visio to clarify the applying process.

After entering campus, drivers use the "visit" interface of a Campus Parking self-service terminal to select the area they wish to visit, such as the dormitories, teaching buildings, or family areas. According to infrared sensors of the parking spaces, the system can frequently update the availability of parking spaces. Then users can select a parking space near their destination according to the parking conditions of the area of their visit.

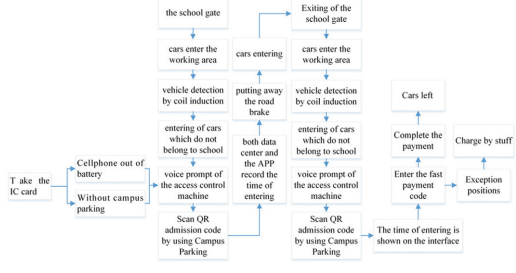

Figure 2. Flow analysis of the intelligent pilot system.

After parking, the Campus Parking map will automatically "put a positioning pin" so that the user can easily find the vehicle again later. Diagram 1 drawn by the author shows this system in use.

According to the design idea of "making the machine easy to understand" (Li 2007) in product semantics combined with the concept of "structure, shape, color, and materials to symbolize itself", the machine should accord with human behavioral characteristics and reduce the possibilities of human mistakes.

2.2 *Hardware system design*

To achieve the optimal functional dimension of the product in design, we must consider the average wingspan, sitting height, body correction, range of visibility, and best vision of adults (Ruan 2005), as is shown in Table 1.

By calculation, the average value of wingspan: L = (male + female)/2 = 1625 mm, so the developed width of one arm = the average value of wingspan/2 = 812.5 mm.

Under the natural and normal driving state of drivers, the seat height will fall by 44 mm, the dressing correction increases by 6 mm, and the shoulder width increases by 13 mm. Since users reach their arms out of their vehicles to operate access control equipment under the normal mental state, the mental correction is not considered in the calculation either. The condition of the user is shown in Diagram 2.

Finally, according to the formula, the product's optimal functional dimension = human body dimension of relevant percentiles + functional correction + mental correction, the one-arm optimal functional size (L) can be acquired: size (L) = 812.5 mm + 13 mm = 825.5 mm.

The view scope of eyes under the static state: 55° upward the horizontal line of the vertical direction. In system designs, the static field of view is usually taken as the basis. The range of visibility refers to the distance between the eyes and the object of observation. Usually, the optimum viewing distance is selected between 380 and 760 mm, according to the size and shape of the object of observation.

α is the optimum field of view, $\alpha = \alpha 1$ (25°) + $\alpha 2$ (30°) = 55°. According to the formula, H3 = L × tan$\alpha 1$ = 378.625 mm, the following is acquired: the maximum height of the whole access controller H = H1 + H2 + H3 = 1590 mm. In the formula D = (α/3438) L = 792.5 mm, D refers to the distance between the two endpoints of the display interface, while α is the optimum viewing angle and L is the range of visibility. Therefore, the optimum height of the self-service terminal and the optimum size of the viewing screen are confirmed.

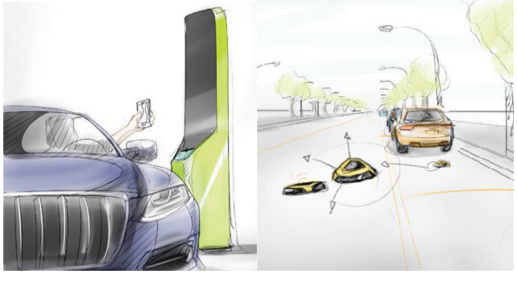

Diagram 1. Scenarios of the system in use.

Table 1. Man-machine size.

Item	Age group percentiles	
	Male (18–60)	Female (18–55)
Eye to seated surface	798	739
Wingspan	1691	1559
Recommended value of the sitting height of the car seat	440–480	440–480

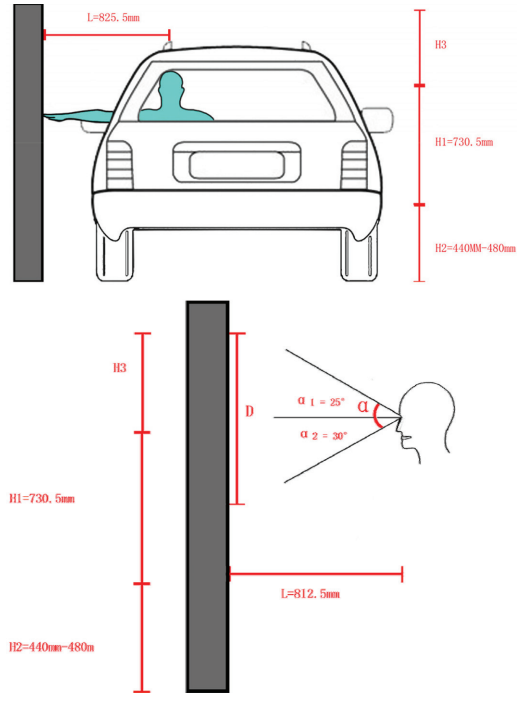

Diagram 2. The man-machine analysis.

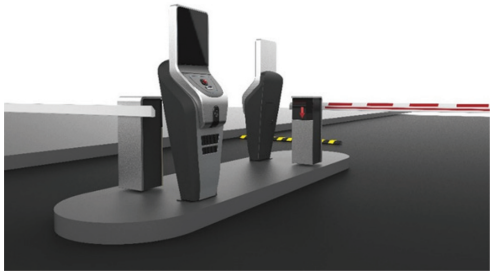

Diagram 3. Design sketch.

According to the users' man-machine size, redesign is carried out over the vehicle management system products so as to satisfy the users' needs with regard to aspects like vision and touch, as well as to optimize the users' experience.

Just as J.J. Gibson said, a man-machine interface should be designed to be a form that makes users perceive that it is designed to provide them with operation conditions. In this way, users become the initiators and machines follow them. (Li 2007)

The scenario sketch is given in Diagram 3.

3 MOBILE APPLICATION DESIGN

The information architecture of Campus Parking is shown in Figure 3.

Enter the main interface, click on "control point", and then the four basic functions are shown: pay, visit, information, and options. The circular white icon will turn yellow as a visual confirmation for users. The presentation of this process is given in Diagram 4A.

Pay: scan the QR code on the terminal screen. Then the fees will appear in an animated form. The striking color contrasts with the background, quickly and clearly showing the most important information. At last, enter the six fast payment codes to finish the payment. The visualization of this process is given in Diagram 4B.

Visit: after entering the campus and choosing a destination according to the classification the campus areas, the map will display empty parking spaces. When confirmed, users can drive their car toward the space by following the navigation. The visualization of this process is given in Diagram 4C.

For Campus Parking users, the interface should be easy to learn, highly efficient, easy to remember, and allow for few to no mistakes. In short, it must reflect the usability of the product. It specifically includes the following aspects:

– The icon designs are easy to understand and users can foresee the relevant functions of each icon;

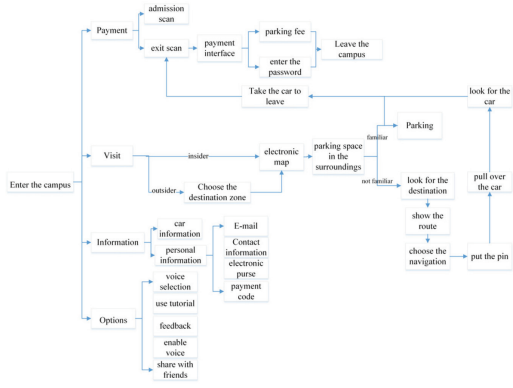

Figure 3. Information architecture.

Diagram 4A. Campus parking interface design.

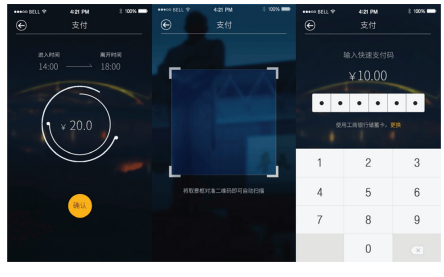

Diagram 4B. Campus parking interface design.

Diagram 4C. Campus parking interface design.

– The design reduces unnecessary hierarchy so that users can achieve their purpose with high efficiency;
– The interface's appearance is the main source of preset usage (Saffer 2006).

By refining the appearance of the interface, the interactive design can provide preset usage options to make it convenient for users to find out the functions, characteristics, and usage modes of the product, and thus improve the system's efficiency.

The interface icon design is mainly used to convey the meaning of the graph itself. A reasonable design can help users foresee the functions of buttons. By using reasonable icons, users instinctively connect the icons with their functions, making the abstract functions more familiar.

4 USABILITY TEST

The development of Campus Parking is based on the IOS system, and Axure7.0 was used to make the high fidelity model.

Test purpose: To establish the task models of cash payment and Campus Parking e-payment, and to make a comparison of the amount of time of these two different payments take.

4.1 *Time consumption under traditional parking payments scheme*

The task of paying for parking with cash can be deconstructed into the following five steps: the driver finds cash; the driver passes the IC card to the staff; the staff offers change; the balance is passed to the driver; the staff manually opens the gate. These five steps waste time, as is shown in Table 2.

The test takes the south vehicle management system of the Xipu Campus of Southwest Jiaotong University as the investigation site. Through the sampling survey of the external temporary vehicles' leaving time, it is found that the average time of vehicles in leaving payment is 11 seconds.

Table 2. Statistics of cash payment time.

	Actions of time consuming				
Subjects	The drivers get cash	Pass the cash	Offer the change	Open the gate	Total time
NO. 1	7s	1s	5s	1s	14s
NO. 2	2s	2s	7s	1s	12s
NO. 3	4s	1s	12s	1s	18s
NO. 4	1s	1s	4s	1s	7s
NO. 5	4s	2s	5s	1s	12s
NO. 6	5s	2s	4s	1s	12s
NO. 7	6s	1s	5s	1s	13s
NO. 8	4s	1s	4s	1s	10s

Table 3. Test results.

Payment	
Mean consumption time	Mean clicks
7s	8.5

According to field observation, 4 drivers took out their wallet to find money after parking, 13 drivers found cash in their vehicle and paid after parking, and only 3 drivers prepared cash in advance and directly handed it to the staff.

The action of finding cash and offering change is the most uncertain and time-consuming element, because it is mostly determined by the drivers' habits and the staff's working conditions, which are greatly influenced by human factors. In addition, the time it takes for the staff to offer change is determined by the amount of cash the driver offers, and a large amount of cash will consume more time.

4.2 *Time consumption under campus parking scheme*

With Campus Parking, the task of paying for parking can be divided into four steps: enter the main interface; scan the two-dimensional code; confirm the time and fees; input rapid payment code.

Test objects: 8 drivers (four male and four female)

Test sample: Hi-Fi test prototype of Campus Parking, which can be tested using mobile phones.

Test method: Click on the mobile device, make records, and fill in the test report.

The results of the test are shown in Table 3.

The test compares the time consumed by the two methods of paying. E-payment is faster and cash payment is also greatly influenced by human factors, such as the amount of cash paid and the staff's working state. Even worse, it is inevitable that staff will sometimes give faulty change given their intensive working conditions. E-payment is more reliable. There are no interactions between drivers and staff, which reduces the staff's working intensity. Additionally, the time consumed by e-payments will decrease as the users' proficiency with Campus Parking increases.

5 CONCLUSION

This paper demonstrates deep research and an intensive study of vehicle management on campus, combining the traditional vehicle management approach with new methods based on time features

and new technologies, so as to meet the current demand for vehicle management and to create new design ideas by applying the new technologies to the entire system, thus better coordinating the system with the campus environment as a whole.

As a set of brand-new, smart, and self-supporting payment management systems, this design considers people, machines, and the environment as a whole, and possesses the following characteristics:

– In terms of function, this design is usability-oriented. It aims to realize automation and intelligence through friendly human-computer interaction designs in order to improve traffic efficiency.
– In terms of management, the design reduces the error rate of cash payments and capital losses by applying a new form of e-payment. It also lowers the labor intensity of managers. By combining APP and the hardware system, this design aims to guide different groups of people in finding their own efficient and convenient approaches according to their individual characteristics.
– With the campus vehicle management system, all departments shall optimize the design by planning and integrating the scattered layout of the current vehicle management system, increasing the management systematization, and manifesting the organic connection between people, machines, and the environment, so as to make the flow of vehicles in the campus vehicle management system more humanized and humanistic, more helpful, and better fitted to the cultural atmosphere of the college.

REFERENCES

Colborne, G. 2011. *Simple and Usable Web Mobile and Interaction Design*. Beijing: Post & Telecom Press.

Li, L.S. 2007. *Approaches to Industrial Design.* Beijing: China Architecture & Building Press.

Norman, D.A. 2005. *Emotional Design.* Beijing: Publishing House of Electronics Industry.

Ruan, B.X. (Trans). 2005. *Industrial Ergonomic.* Beijing: China Machine Press.

Saffer, D. 2006. *Designing for Interaction Creating Innovative Applications and Devices*. CA: New Riders.

Simon, R. 1997. *Symbolic Images in Art as Therapy*. London: Routledge.

Zankina, I. 2013. Campus driver assistant on an Android platform. *http://proquest.calis.edu.cn/Detail.aspx?pid=GxSOsmfLBB4%3d.*

Civil Engineering and Urban Planning IV – Liu et al. (Eds)
© 2016 Taylor & Francis Group, London, ISBN 978-1-138-02903-3

Research on the relationship between ecological industry and sustainable development of industrial park

Xi Niu
Nanchang Institute of Technology, Nanchang, Jiangxi, China

ABSTRACT: Industrial park has played a major role in economic development these years. But there are also some issues restricting the further development of industrial park. The purpose of this research is to identify whether ecological industry significantly impacts the sustainable development of industrial park. Based on the relevant literature and theories, the paper confirmed the evaluation index system and built comprehensive evaluation model of industrial park and ecological industry. Data sources were got from Jiangxi Statistical Yearbook and China Industry Economy Statistical Yearbook. The paper used SPSS 20.0 to do correlation and regression analysis. The results confirm that ecological industry has a positive and significant impact on the sustainable development of industrial park. According to the results, industrial park should focus on the ecological industry in the future development.

1 INTRODUCTION

For a long time, industry has been the leading industry for economic development in China, and industrial park has played a major role in promoting industry development. Chinese traditional industrial park has many problems in the process of transition to modernization, such as excessive resource consumption and serious environmental pollution. That deepens contradictions between industrial park and its surrounding ecological environment. These contradictions are also restricting the further development of industrial park. It is necessary to explore an eco-development mode for sustainable development of industrial park. Until now, scholars have carried out studies on industrial park development from the perspective of ecology. Shi & Wang (2010) reviewed the background and development process of eco-industrial park in China, and summarized the development models of eco-industrial park. Sun et al. (2010) defined the connotation of operating efficiency of eco-industrial park, and established the operation efficiency evaluation index system of eco-industrial park. Zhang et al. (2011) constructed typical industry type of eco-industrial parks index system based on the basic concept. Liu et al. (2012) conducted empirical research on comprehensive eco-industrial parks environmental performance, and proposed quantitative adjustment for the future environmental control. Wang et al. (2013) evaluated the eco-industrial park symbiotic efficiency from the perspective of industrial symbiosis, and provided a reference for eco-industrial park symbiotic development in the future.

Existing research results mostly focused on index system building and environmental performance evaluation of eco-industrial park. Studies on the sustainable development of industrial park from the perspective of ecological industry remain scarce. And there is a gap in empirical studies on the relationship between ecological industry and industrial park. Therefore, the purpose of this paper is to explore whether ecological industry significantly impacts industrial park. First, the paper analyzed the basic concept of ecological industry and proposed the hypothesis of the relationship between ecological industry and industrial park. Then, the paper introduced the methodology used in empirical research. Finally, the paper put forward results and suggestion.

2 THEORETICAL FOUNDATION AND HYPOTHESIS

2.1 *Theory of ecological industry*

Due to problems of high energy consumption, high pollution and low efficiency in the development of traditional industries, people have to rethink the traditional patterns of industrial development. Under such background, people put forward the concept of ecological industry. It originated from repositioning the relationship between resource protection and social economic development. Ecological industry is the modern industrial development mode based on theories of ecological economics and industrial ecology. Ecological economics theory explores and describes

the ecosystem based on fully affirming the role of resources and environment. The theory considers that social economic system should also follow the ecosystem development principle in the process of economic development, and should keep the balance between energy flow and material flow to form whole society ecosystem (Xu & Zhang 2008). Based on the theory of ecological economics, Robert Frosch and Nicolas Gapllopoulos carried out the "industrial metabolism" research, which signified the emergence of industrial ecology. Industrial ecology theory considers that the modern industrial production process can be seen as the metabolic process of transforming raw material, energy and labor into products and waste. This metabolic process can make industry system more efficient and sustainable.

According to theories mentioned above, this paper defines ecological industry as the modern industrial development mode with the characteristic of resource-conservation and environment protection. Essentially, ecological industry is the mode performing industrial activities based on ecological and industrial principle and putting emphasis on the industry sustainable development.

2.2 *Industrial park sustainable development and its relationship with ecological industry*

In China, industrial park is a special designated area led by the government to achieve economic development goals. Industrial park construction and development can create conditions and infrastructure for local economic development. In recent years, the industrial park has achieved good results. But there are also some issues restricting the further development of the industrial park, such as less optimized industrial structure, increasing resources cost and environmental constraints. How to promote the sustainable development of the industrial park has become a focus in academia. Sustainable development is a new development concept. Sustainable development theory considers resource, environment and development as an interconnected organic whole, and emphasizes that people should follow basic principles of harmony between human and nature, economy and ecology, development and resource environment. The application of sustainable development principles in industry is to keep the rational allocation of resources when increasing output and income in industrial activities, and coordinate the relationship between industrial ecology and industrial economy through modern technology, and establish a coordinated industrial economy development pattern (Zheng & Guo 2010).

According to the above analysis, the paper proposed the hypothesis that there is a positive and significant relationship between ecological industry and industrial park sustainable development.

3 RESEARCH METHOD

3.1 *Evaluation index system*

Based on the existing literature research results, the paper considered representativeness, availability and quantifiability of the index (Chen & Zhang 2012), and then identified the evaluation index system of industrial park and ecological industry. The evaluation index system of industrial park includes Industrial Added Value (IAV), the proportion of IAV in the whole province industrial Gross Domestic Product (GDP), the number of employees, the proportion of the number of employees in the whole number of province industrial employees. The evaluation index system of ecological industry established from four aspects including the level of industrialization, the level of technology development, the capability of sustainable development and the level of human resource utilization. The level of industrialization consists of two second grade indexes including GDP per capita and the proportion of IAV in the whole province GDP; The level of technology development consists of three second grade indexes including the proportion of expenditure for Research and Development (R & D) in the whole province GDP, the proportion of high-tech IAV in the whole IAV and the number of fixed-line and mobile phone users per hundred population; The capability of sustainable development consists of two second grade indexes including energy consumption per ten thousand Yuan GDP and the proportion of output value of industrial "three wastes" comprehensive utilization in the whole province GDP; The level of human resource utilization consists of two second grade indexes including the employment growth rate and labor productivity in industrial enterprises above designated size.

3.2 *Data sources and processing*

The paper took Jiangxi 95 provincial industrial parks as the empirical study object. Data on the ecological industry have been taken from China Industry Economy Statistical Yearbook from 2005 to 2013. Data on the industrial park have been taken from Jiangxi Statistical Yearbook from 2005 to 2013. The paper used interpolation method and regression analysis to obtain missing data in some year. Because the data were in the different dimension and role direction, to enable them to be comparable, the paper used min-max standard method to standardize the data, and distinguished positive

and negative indexes. The equations are shown as follows:

$$X_i = \frac{K_i - K_{i\min}}{K_{i\max} - K_{i\min}} \quad (1)$$

$$X_i = \frac{K_{i\max} - K_i}{K_{i\max} - K_{i\min}} \quad (2)$$

Equation (1) is for calculation of positive indexes. Equation (2) is for calculation of negative indexes. In above equations, X_i = standardized value of the index; K_i = original value of the index; K_{imin} = minimum value of the index; K_{imax} = maximum value of the index.

Based on the relevant literature (Zhang et al. 2010; Yang 2012; Guo 2013), the paper used Delphi method and Analytic Hierarchy Process (AHP) method to determine the weight of each index. Due to the limited space, the weight processing is omitted.

3.3 *Comprehensive evaluation model construction*

Due to strong comprehensive explanation (Zhang & Chen 2012), the paper chose additive synthesis method to build the comprehensive evaluation model for industrial park and ecological industry as below:

$$K = \sum_{j=1}^{n} \lambda_j \omega_j \Big/ \sum_{j=1}^{n} \omega_j \quad (3)$$

In the equation, K stands for the comprehensive evaluation value of industrial park and ecological industry; n = the number of index; λ_j = evaluation value of each index; ω_j = weight of each index.

4 ANALYSES AND RESULTS

4.1 *Comprehensive evaluation values*

Based on the data source and the comprehensive evaluation model mentioned above, the paper calculated each comprehensive evaluation value from 2004 to 2012, as shown in Table 1.

4.2 *Correlation analysis*

Based on the result in Table 1, the paper used SPSS20.0 to do correlation analysis on the industrial park and ecological industry. The results are shown in Table 2.

The Table 2 shows that at the 0.01 significance level, the correlation coefficient between the industrial park and the ecological industry is 0.961.

Table 1. Comprehensive evaluation values of the industrial park and the ecological industry from 2004 to 2012.

Year	Industrial park	Ecological industry
2004	0.000000	0.106110
2005	0.107696	0.264114
2006	0.256302	0.460322
2007	0.393793	0.568744
2008	0.546842	0.542084
2009	0.662873	0.630839
2010	0.749150	0.693973
2011	0.879195	0.711506
2012	0.992608	0.887999

Table 2. Correlation analysis on industrial park and ecological industry.

	Industrial park	Ecological industry
Industrial park	1	0.961***
Ecological industry	0.961***	1

*** means correlation is significant at the 0.01 level (2-tailed).

The finding demonstrates that the industrial park and the ecological industry have a positive and significant relationship.

4.3 *Regression analysis*

To further illustrate the influence degree of ecological industry on industrial park, the paper did regression analysis. The ecological industry is taken as a predictor to explain its impact on the industrial park. The results are shown in Tables 3–5.

In the Table 3, R is 0.961 which means that industrial park and ecological industry have a significant correlation. R square is 0.923 which means ecological industry can explain 92.3 percent of the industrial park development. The finding shows that the impact of ecological industry on the sustainable development of industrial park reaches 92.3 percent.

In the Table 4, Sig. is 0.000[a]. It is less than 0.05, which indicates that the ecological industry and the industrial park have a significant linear relationship, so the regression model is tenable.

In the Table 5, the regression model constant is minus 0.242, and regression coefficient is 1.390. Therefore, the model of the sustainable development of industrial park is that $y = -0.242 + 1.390x$, where y = comprehensive evaluation value of industrial park; x = comprehensive evaluation value of ecological industry. Based on this model, we can

Table 3. Model summary.

Model	R	R square	Adjusted R square	Standardized error of the estimate
1	0.961[a]*	0.923	0.912	0.102424119

*a. Predictors: (Constant), ecological industry.

Table 4. Analysis of variance.

Model	Sum of squares	Degree freedom	Mean squares	F	Sig.
Regression	0.878	1	0.878	83.647	0.000[a]
Residual	0.073	7	0.010		
Total	0.951	8			

Table 5. Regression coefficients.

	Unstandardized coefficients		Standardized coefficients	T	
Model	B		Standardized error	Beta	Sig.
(Constant)	–0.242		0.089	–2.717	0.030
Ecological industry	1.390		0.152	0.961	0.000

predict the sustainable development of industrial park from the development of ecological industry in the future.

5 CONCLUSIONS

The research results in Table 3 show that the correlation coefficient between industrial park and ecological industry is 0.961 (at the 0.01 significance level). The results in Table 4 further show that ecological industry can explain 92.3 percent of the sustainable development of industrial park. And we can predict the future development from the results of Table 5. All results strongly confirm the hypothesis that there is a positive and significant relationship between ecological industry and industrial park sustainable development. Due to the important role of ecological industry, industrial park should pay more attention to the ecological industry to solve issues of development in the future.

ACKNOWLEDGMENTS

This paper is supported by youth foundation of Human Society Scientific Research of Ministry of Education of China (Grant No. 13YJC790208), and Jiangxi Province Social Sciences "Twelve-Five" Program (Grant No. 11YJ18) and Jiangxi Province Soft Science Program (Grant No. 20141BBA10024).

REFERENCES

Chen, F. & Zhang, X.Z. 2012. Study on the competitiveness of regional industry transfer in Midwest China. *Statistics & Decision* 28(2): 124–128.

Guo, L.J. 2013. Evaluation of coordinated development of new industrialization and new urbanization. *Statistics & Decision* 29(11): 64–67.

Liu, W. et al. 2012. Studies on environmental performance of sector-integrate eco-industrial parks with data envelopment analysis. *Ecological Economy* 28(7): 125–128.

Shi, L. & Wang, Z. 2010. Eco-industrial parks in China. *Journal of China University of Geosciences (Social Sciences Edition)* 10(4): 60–66.

Sun, X.M. et al. 2010. Establishment of indicator set for evaluating operating efficiency of eco-industrial parks. *China Population, Resources and Environment* 20(1): 124–128.

Wang, S.G. et al. 2013. Quantitative evaluation of symbiosis efficiency in eco-industrial parks. *Journal of Industrial Technological Economics* 33(6): 33–38.

Xu, C.H. & Zhang, J.B. 2008. A study of development of ecological industry economy in Sichuan province. *Ecological Economy* 24(3): 107–111.

Yang, Y.J. et al. 2012. Empirical study on the relationship between new industrialization and new urbanization in Central China. *Statistics & Decision* 28(2): 129–132.

Zhang, L.J. et al. 2011. A study on the evaluation index system and methods of ecological transformation of sector-based industrial parks-based on the theory of sustainable development. *Journal of Industrial Technological Economics* 31(5): 86–91.

Zhang, X.Z. et al. 2010. Empirical research on relation between industrial parks and process of industrialization and urbanization–taking Jiangxi province as an example. *Productivity Research* 25(8): 117–144.

Zhang, X.Z. & Chen, F. 2012. The occurred mechanism of regional industrial transfer–based on the synthetic evaluation and analysis of occurred potential difference. *Forum on Science and Technology in China* 28(4): 100–105.

Zheng, S.H. & Guo, L. 2010. Review on theories and issues of eco-industry. *Enterprise Economy* 31(2): 29–31.

Civil Engineering and Urban Planning IV – Liu et al. (Eds)
© 2016 Taylor & Francis Group, London, ISBN 978-1-138-02903-3

Research on the main risks and countermeasures of glass curtain wall

Qian Li & Xuan Zhu
Department of Engineering Management, Xi'an University of Architecture and Technology, Xi'an, Shaanxi, China

ABSTRACT: Glass curtain wall has numerous advantages that other building materials cannot compare with. However, with the increase of its service time, many shortcomings are becoming more and more prominent, causing a lot of inconvenience to the public. There were 23 risk factors which were evaluated from the aspects of the probability and potential loss of the risks by questionnaire survey. Via applying SPSS software for statistic analysis, nine main risks were identified. Then analyzed the causes of the main risks and proposed prevention countermeasures accordingly. This study has positive significance for preventing the main risks of glass curtain wall and promoting its better application.

1 INTRODUCTION

From the 1980's to now, glass curtain wall has over 30 years of application history in China. Its application scale and speed of development are quite rapid. With the advantages of light weight, short construction duration and fashionable appearance, the skyscrapers decorated with glass curtain wall become the symbol of urban modernization. According to statistics, China is the largest producer and user of glass curtain wall in the world (Huang 2013). However, with the increase of its service time, many shortcomings of the glass curtain wall are becoming more and more prominent, causing a lot of inconvenience to the public, even becoming a threat to people's lives and property, which result in widespread concern in the society.

At present, most researches on the risks of glass curtain wall only discuss some individual risks. There are also some articles discussing the risk management of glass curtain wall from the general view of project management, but researches on the major risks identification and prevention of glass curtain wall are very few. Due to the lack of authoritative and systematic historical data, a questionnaire survey was used in this research. Take the service time of glass curtain wall as main research interval and the existing glass curtain wall as basic research object. Identify main risks from various factors in its different application stage and then propose appropriate countermeasures from the aspects of design, manufacture, construction and maintenance, which can be taken as a reference for preventing main risks of new-built and existing glass curtain wall happening.

2 QUESTIONNAIRE SURVEY

2.1 *Design questionnaire*

On the basis of reference to related researches at home and abroad and expert interview, the questionnaire was designed. It incorporates three parts:

- Basic Information. It is used to understand respondents' areas of work, professional experience and knowledge level in order to analyze the questionnaire in the later stage.
- Risk Scale. Glass curtain wall is composed of four systems: a panel system, fastening device, supporting system, and structural adhesive. Use the Likert scale to evaluate specific risks in these four systems and other risks from both a risk possibility and potential risk loss perspective. Make P stand for the probability of risk, available options are: 1-almost impossible, 2-small, 3-occasionally, 4-very likely, 5-often. Make Q represent the potential loss of risk, options are: 1-very low, 2-low, 3-moderate, 4-high, 5-very high. The risk assessment theory normally uses the following equation to calculate the amount of risk-R (Liu 2013):

$$R = \overline{P} \times \overline{Q}$$

In this equation, $\overline{P}$ is mean value of risk probability and $\overline{Q}$ is mean value of risk potential loss.

The mean value can better summarize the views from the various respondents with good representativeness. The product of the mean value of risk probability and risk potential loss is the expected loss, which is defined as R.

– Note. It was used as explanation to non-commonsense risk so that to make respondents answer reasonably.

2.2 *Distribution and withdrawal of the questionnaires*

Questionnaires were distributed by e-mails and on-site distribution. A total of 100 questionnaires were distributed and 79 copies were returned. There were 68 valid questionnaires, valid ratio was 68%. Professions of the 68 valid respondents were related to real estate developer, design unit of curtain wall, curtain wall construction and maintenance, the owner and research and education institution. The proportions were 15%, 23%, 10%, 18%, 34% each. 74% of the 68 valid respondents have bachelor degree or above. The profession, knowledge level and life experience of the respondents can ensure that they have a better understanding of glass curtain wall and are able to make reliable answers to the questionnaire.

3 ANALYSIS OF DATA

3.1 *Reliability test*

In order to ensure the survey is scientific and reliable, a reliability test needs to be conducted before questionnaire data analysis. Cronbach's alpha is the most commonly used method for reliability analysis. The α coefficient ranges from 0 to 1, when the α coefficient is between 0.7 and 0.98, it indicates that the result is reliable. Use the SPSS software to calculate the α coefficient of the probability and the potential loss of the risks and the results are 0.873 and 0.814, which is with good reliability. Therefore further analysis can be carried out.

3.2 *Statistics of risk factors*

The data of 68 valid questionnaires was input into the SPSS software, and the mean values of the probability and the potential loss of 23 risks were calculated respectively. According to the equation $R = \overline{P} \times \overline{Q}$, calculated the R and sorted it from big to small, which is as shown in Table 1.

3.3 *Analysis and identification of main risks*

In the risk scale, P = 3 represents the occasional occurrence of risk events, which is in the middle position in the overall levels. Q = 3 represents the loss of the risk is average, also a middle position. Then when the probability and the potential loss of the risks are medium, that is P = 3 and Q = 3, the amount of risk-R is 9, this is an average level. Table 1 shows that there are 9 risk factors of which $R \geqq 9$ and 14 risk factors of which $R < 9$ in the 23 risk factors, which means the amount of risk of the top 9 is larger in R than its average level. So the top 9 risks were identified as the main risks.

As it is shown in Table 1 that in other risks category, the R of fire resistance of glass curtain wall is 16.942, which ranks first in the list and of great importance. In panel system, the R of self-explosion of tempered glass is 15.675 which ranks second. In the fasteners and fixtures category, four risk factors are listed. Three remaining risks' R are all higher than 9 except the risk of outer decorative thread loosen/fell off. Thus it can be seen that fasteners and fixtures is a part may cause lots of risk and potential loss. So it can be analyzed as a whole. Similarly, in the structural adhesive category, the R of the listed four risks are all more than 9 which needs to be analyzed as a whole as well.

4 CAUSES AND COUNTERMEASURES OF MAIN RISKS

4.1 *Causes of main risks*

The causes of main risks come from many aspects, including design, material selection, construction, supervision and management, etc. Causes of main risks are shown in Table 2 which was made on the basis of the reference to expert interviews and related research.

4.2 *Countermeasures of main risks*

4.2.1 *Countermeasures of self-explosion of tempered glass*

Self-explosion of tempered glass refers to glass automatic bursts without external force (Sun 2013). Decrease of the probability and the potential loss of the self-explosion of tempered glass should be taken as countermeasures.

From the point of view to reduce the probability of self-explosion. In design stage, we should specify the type of the glass via scientific and rigorous calculation. In the construction, attention should be paid to prevent damage to the edge of the glass. In order to ensure the safety of applying the glass, the geometric parameters, the surface defects and the surface stress of the glass should be examined in detail (Tan 2013). In addition, the application of ultra-white glass can avoid the risk inherently because its production process can greatly reduce the content of nickel which is the main reason for the self-explosion.

In terms of reduction of the potential loss of the risk. In order to prevent falling glass from injuring pedestrians and smashing objects, actions should be taken such as building canopy/cornice at the entrance and planting a certain width of the green

Table 1. Statistical analysis of risk factors of glass curtain wall.

Category	Risk factors	P-probability of risk		Q-potential loss of risk		R	Ranked list of R
		Mean value	Std deviation	Mean value	Std deviation		
Panel system	1. Glass break under outside force	2.22	0.875	3.74	0.648	8.306	12
	2. Self-explosion of tempered glass	3.44	0.398	4.56	0.436	15.675	2
	3. Uneven glass color, image deformity	2.65	0.857	2.06	0.698	5.460	23
	4. Hollow glass gets foggy/mildewy	2.87	1.056	2.49	0.759	7.140	21
	5. Poor privacy	3.64	0.963	2.25	0.774	8.270	13
	6. Transmittance reduces because of dust	4.35	0.988	1.90	0.788	8.196	15
Fasteners and fixtures	7. Hydrogen embrittlement cause ductility decrease	3.49	0.941	2.79	0.537	9.750	9
	8. Bolts, embedded parts, connections get loose	3.16	0.607	3.60	0.879	11.374	7
	9. External decorative thread loose/fall off	3.10	0.947	2.75	0.703	8.531	11
	10. Aging/corrosion of bolts, connectors, embedded parts, solder joint	3.53	0.752	3.75	0.793	13.227	3
Structural adhesive	11. Creep failure under lasting stress	3.43	0.838	3.54	0.768	12.149	4
	12. Substandard quality lead to failure	3.06	0.819	3.79	0.794	11.583	5
	13. Fatigue failure of structural adhesive because of dynamic load	2.87	0.729	3.61	0.764	10.347	8
	14. Aging of structural adhesive lead to bond failure	3.12	0.983	3.65	0.895	11.402	6
Supporting system	15. Proximate matter is damaged	2.51	1.086	2.92	0.803	7.342	20
	16. Aging of insulating strip	2.42	0.675	3.30	0.901	8.000	18
	17. Proximate matter gets loose/deformed	2.60	0.894	2.92	0.853	7.583	19
Other risks	18. The hardware of the window sash was damaged during use	2.97	0.794	2.28	0.605	6.773	22
	19. Rainwater leakage	3.34	0.983	2.43	0.621	8.255	14
	20. Light pollution	3.44	1.196	2.35	0.517	8.077	16
	21. Poor fire resistance of glass curtain wall	3.85	0.871	4.40	0.519	16.942	1
	22. Poor thermal insulation	2.87	0.797	3.01	0.830	8.643	10
	23. Poor ventilation	3.51	1.192	2.29	0.470	8.048	17

Table 2. Causes of main risks.

Category	Risk factors	Ranked list of R	Causes of main risks
Panel system	2. self-explosion of tempered glass	2	① Design and construction is not in accordance with the standard specification; ② NiS in glass; ③ Glass is mixed with grains of sand, stone, bubbles and other impurities; ④ Glass material uneven or surface defects; ⑤ Surrounded tightness of installed glass is different; ⑥ The wind load causes the variation of the main structure in different floor
Fasteners and fixtures	7. hydrogen embrittlement cause ductility decrease	9	① Production process of fastener
	8. bolts, embedded parts, connections get loose	7	① Construction is not standardized; ② The long-term effect of wind load, dynamic load and the weight of glass curtain wall
	10. aging/corrosion of bolts, connectors, embedded parts, solder joint	3	① Influence of natural environment; ② Corrosion of washing liquid; ③ Without protection; ④ Construction is not standardized
Structural adhesive	11. creep failure under lasting stress	4	① The long-term effect of glass weight; ② Stress relaxation of structural adhesive in service environment
	12. substandard quality lead to failure	5	① Production factory lack of industry self-regulation; ② Adverse supervision of the relevant departments; ③ Lack of corresponding test before using; ④ The service life of the structural adhesive is not in conformity with the service life of architectural
	13. aging of structural adhesive lead to bond failure	6	① The effect of the rain, sever cold, high temperature, ultraviolet radiation, salt fog, mist, microorganisms in the nature; ② Corrosion of washing liquid
	14. fatigue failure because of dynamic load	8	① Pressure effect of wind load; ② The vibration of the opening and closing of the window
Other risks	21. poor fire resistance of glass curtain wall	1	① The poor fire resistance of glass; ② The poor fire resistance of adhesive; ③ Steel, aluminum alloy under high temperature strength loss quickly; ④ Design, construction is not standardized

belt adjacent to the building. Besides, laminated glass is also a good choice, the plastic organic layer in laminated glass can fix the broken glass as a whole and keep the broken glass from falling down. Crowded street buildings should use laminated glass particularly.

4.2.2 *Countermeasures of fasteners and fixtures*

A reliable check on the fasteners and fixtures should be implemented before installation and only ones passing through the inspection can be installed. The regulations needs to be followed during installation to ensure the fasteners and fixtures are well installed. Rust prevention and anticorrosion protection needs to be implemented. To shorten the pickling time in the production process or add corrosion inhibitor can control hydrogen embrittlement of parts. During the operation, the maintenance work should be carried out and the aging, deformed and defect parts should be replaced or reinforced in time.

4.2.3 *Countermeasures of the failure of structural adhesive*

The related departments should enhance the supervision and management to ensure the product quality of the structural adhesive. The supporting sheet which can share the load of structural adhesive should be installed. It is better to implement appropriate reinforcement for the glass curtain wall which bears long-time or dynamic load. The structure adhesive should be made in a clean environment and its compatibility and bond strength should be tested before application (Tan 2013). In addition to the visual inspection, professional testing is also necessary during maintenance. The aged structural adhesive that can't meet the requirements should be added or cleared and re-glued. The glass curtain wall of which structure adhesive has met or exceeded the service life needs an overhaul.

4.2.4 *Countermeasures of the poor fire resistance of glass curtain wall*

First, design work should be strictly carried out in accordance with related codes and technical specification. The whole glass curtain wall system should be consistent with the basic requirements of smoke control, fire integrity and fire insulation. Different materials should be chosen according to different requirements of building fire protection and necessary calculation should be made in order to determine the appropriate size of glass. Flame-retardant measures should be taken to structural adhesive to avoid its failure in fire. Fireproof coating and fireproof heat insulation material can improve the fire resistance of steel and aluminum profile. The gap between the glass curtain and the floor slab should be plugged with nonflammable material to form a fire and smoke prevention band (Wang 2010).

5 SUMMARY

Through the questionnaire survey, nine main risks of glass curtain wall in service period were identified and countermeasures were proposed from the design, production, construction, maintenance and other different aspects. Glass curtain wall has advantages that other decorative building materials cannot compare with. Although there are some problems in the application, it is believed that it will better serve us and become the highlight of the city through the strict precaution, effective control and research and application on new material.

REFERENCES

Huang, X.K. 2013. 30 years of technology development of glass curtain wall. *Journal of Building Science* 29(11): 80–88.

Liu, X.J.M. 2013. *Technological Economics.* Beijing: Science Press.

Sun, W.Q. et al. 2013. Effect of stress on self-explosion of tempered glass. *Journal of Building Structure* 32(10): 88–89.

Tan, Z.C. et al. 2013. The method of detection and identification of existing glass curtain wall. *Journal of Industrial Buildings* 43(1): 651–654.

Tan, Z.C. & Wang, Y.H. 2013. Methods of glue's inspection for existing building curtain wall. *Journal of Industrial Construction* 43(6): 655–658.

Wang, Q.H. 2010. Analysis and solution to safety of fire plugging in curtain wall. *Journal of Fire Science and Technology* 29(1): 48–50.

This page intentionally left blank

Civil Engineering and Urban Planning IV – Liu et al. (Eds)
© 2016 Taylor & Francis Group, London, ISBN 978-1-138-02903-3

Numerical study of leaked natural gas dispersion within an urban street canyon considering the distribution of ground surface flux

Yan Wang, Hong Huang & Li-Da Huang
Department of Engineering Physics, Institute of Public Safety Research, Tsinghua University, Beijing, China

ABSTRACT: In this study, the dispersion of natural gas leaking from buried pipelines in an urban street canyon is investigated through computer simulation. The numerical simulations were performed using OpenFOAM, a free and open source software for Computational Fluid Dynamics (CFD). The standard solver simpleFoam was modified to include passive scalar turbulent transport, and was validated against a wind-tunnel experiment data. Then, six leaking cases representing different distribution of ground surface natural gas flux were numerically studied. The results show that the concentration distribution was much more sensitive to surface flux when the leaking point was at the leeward side of the street canyon than that at the windward side. And the concentration out of the canyon containing the leaking point was almost irrelevant to the distribution of surface flux. This knowledge will contribute to the better design of the monitoring and early warning system for urban natural gas system.

1 INTRODUCTION

Urban natural gas system is one of the critical infrastructures, on which the stable operation of modern cities strongly depend. However, the accidents caused by natural gas leakage are great threats to public safety, leading to casualties and economic losses (Han & Weng 2010; Han & Weng 2011). Large leakage rate caused by heavy equipment such as civil engineering machinery can be immediately discovered and repaired (Okamoto & Gomi 2011). But smaller leakage can go on for months, or even years. In addition to wasting energy, threatening safety and health, leaked natural gas can also add to global warming. So, monitoring and early warning of natural gas leakage are of great importance. For urban natural gas networks, leaked gas usually first migrates through the shallow subsurface before enters into the atmosphere. The distribution of natural gas flux through the ground surface is influenced by the position of the pipeline, soil properties as well as surrounding objects (Okamoto et al. 2014). These complex surroundings contribute to the uncertainty of the monitoring and early warning of natural gas leakage. This study aims to numerically analyze the impact of ground surface flux distribution on natural gas dispersion in an urban street canyon by computer simulation.

2 MODEL DESCRIPTION AND VALIDATION

2.1 *Model description*

The numerical simulations were performed using OpenFOAM, a free and open source software for Computational Fluid Dynamics (CFD). Details about OpenFOAM can be found at the website http://openfoam.org/.

The standard solver simpleFoam was modified to include passive scalar turbulent transport. Then the new solver was used to solve the incompressible Reynolds-Averaged Navier-Stokes (RANS) equations with the Standard k-ε model (Launder & Spalding 1974) using the SIMPLE algorithm (Ferziger & Perić 2002). The RANS equations include the continuity equation, the momentum equation, the passive scalar transport equation and turbulent closure equations, which can be expressed as the following:

$$\frac{\partial \overline{u_i}}{\partial x_i} = 0 \tag{1}$$

$$\frac{D\overline{u_i}}{Dt} = -\frac{1}{\rho}\frac{\partial \overline{p}}{\partial x_i} + \frac{\partial}{\partial x_j}\left(\nu \frac{\partial \overline{u_i}}{\partial x_j} - \overline{u_i' u_j'}\right) \tag{2}$$

$$\frac{Dk}{Dt} = P_k + \frac{\partial}{\partial x_j}\left(\frac{\nu_t}{\sigma_k}\frac{\partial k}{\partial x_j}\right) - \varepsilon \tag{3}$$

$$\frac{D\varepsilon}{Dt} = \frac{\varepsilon}{k}\left(C_{\varepsilon 1}P_k - C_{\varepsilon 2}\varepsilon\right) + \frac{\partial}{\partial x_j}\left(\frac{\nu_t}{\sigma_\varepsilon}\frac{\partial \varepsilon}{\partial x_j}\right) \tag{4}$$

$$-\overline{u_i'u_j'} = \nu_t\left(\frac{\partial \overline{u_i}}{\partial x_j} + \frac{\partial \overline{u_j}}{\partial x_i}\right) - \frac{2}{3}\delta_{ij}k \tag{5}$$

$$\nu_t = C_\mu \frac{k^2}{\varepsilon} \tag{6}$$

$$P_k = -\overline{u_i'u_j'}\frac{\partial \overline{u_i}}{\partial x_j} \tag{7}$$

$$\frac{DC}{Dt} = -\overline{u_i}\frac{\partial C}{\partial x_i} + \frac{\partial}{\partial x_i}\left[\left(D + \frac{\nu_t}{Sc_t}\right)\frac{\partial C}{\partial x_i}\right] + S_C \tag{8}$$

where x_i is the ith Cartesian coordinate, $\overline{u_i}$ is the mean velocity, u_i' is the fluctuating velocity, ρ is the air density, $\overline{p}$ is the mean pressure, ν is the kinematic viscosity, k is the turbulent kinetic energy, ν_t is the kinematic eddy viscosity, ε is the turbulent dissipation rate, δ_{ij} is the Kronecker delta, $C_\mu = 0.09$, $C_{\varepsilon 1} = 1.44$, $C_{\varepsilon 2} = 1.92$, $\sigma_k = 1.0$ and $\sigma_\varepsilon = 1.3$ are model constants, C is the mean scalar concentration, D is the diffusivity coefficient and $Sc_t = 0.7$ is the turbulent Schmidt number.

2.2 *Model validation*

A wind-tunnel experiment dataset for two-dimensional multiple street canyons is available at http://www2.dmu.dk/atmosphericenvironment/trapos/cfd-wg.htm, which is from the work of Meroney et al. 1996 and Rafailidis. 1997. From the available experimental case at a scale of 1: 500, the computational domain consists of five square canyons and six square buildings with flat roofs, which is shown in Figure 1. The measured concentration K of the experiment was normalized according to:

$$C = \frac{KUHL}{Q} \tag{9}$$

were C is the non-dimensional concentration, K is the measured tracer concentration, U is the free stream velocity measured at 0.5 m above the floor, H is the building height, L is the length of the line source across the flow and Q is the source strength.

At the inflow boundary, the velocity profiles, the turbulent kinetic energy k and the turbulent dissipation rate ε were specified according to the experiment. At the outflow boundary, the zero gradient condition was used. At the upper boundary, the symmetry condition was used. At solid walls, the no-slip condition was applied. The tracer source was placed on the ground in the central street canyon marked by 'S'.

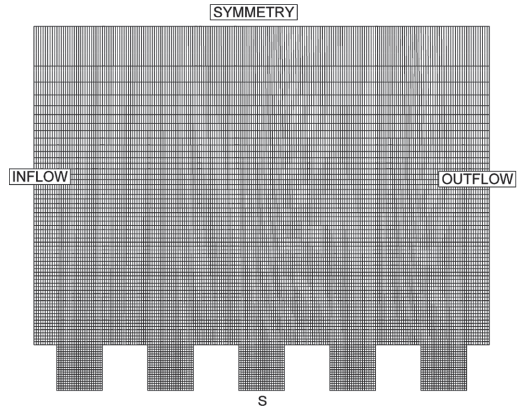

Figure 1. The computational domain and the grid mesh.

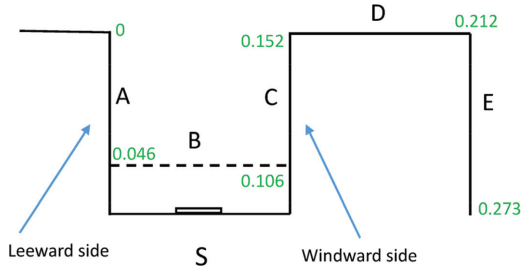

Figure 2. The measurement points of the wind-tunnel experiment. Sampling path: A-B-C-D-E. The numbers indicate the distance along the path.

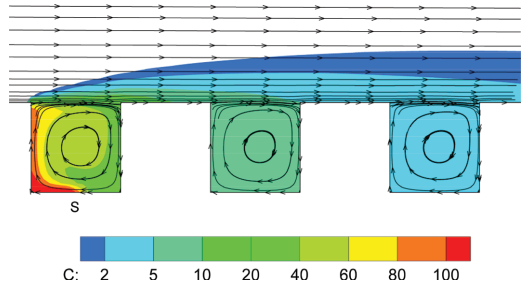

Figure 3. The streamlines and the contour of the normalized concentration simulated by OpenFOAM.

The measurement points were distributed along the path A-B-C-D-E shown in Figure 2.

A convergence criterion of 10^{-6} was used for all the variables. The simulated air flow and tracer gas dispersion are shown in Figure 3, and the comparison of normalized concentration between simulation and experiment is shown in Figure 4, where the shadow denotes path B and path D in Figure 2.

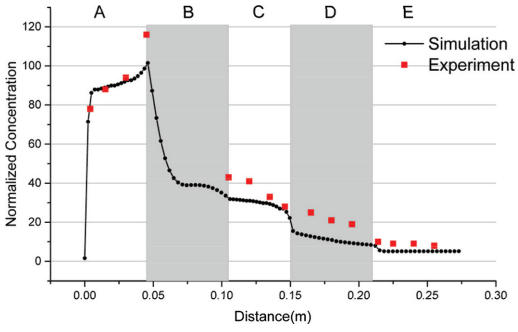

Figure 4. Comparison of the normalized concentration simulated along the sampling path 'A-B-C-D-E' by OpenFOAM (which will be referred to as experiment case in the following) and measured in the wind tunnel experiment.

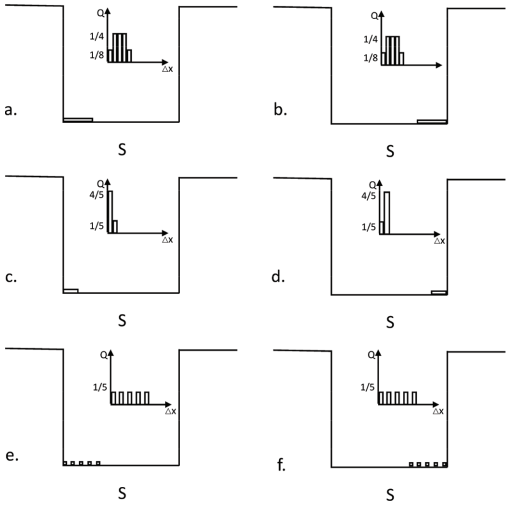

Figure 5. Setup of the six leaking cases. The total surface flux was all set to 1 g/s.

It can be seen that the simulation result of OpenFOAM agrees well with the wind tunnel experiment, proving that the new solver is capable of simulating atmospheric dispersion of passive gas in the two-dimensional urban street canyon.

3 NUMERICAL EXPERIMENTS

The validated OpenFOAM solver was applied to six leaking cases representing different distribution of ground surface natural gas flux, which is shown in Figure 5.

Case a, case c and case e occur at the leeward side of the central canyon marked by 'S' while case b, case d and case f occur at the windward side. The surface flux distribution for these cases is set according to typical scenes in real world.

4 RESULTS AND DISCUSSION

As is shown in Figure 6, the simulation results of case a, case c and case e are added to Figure 4. The concentration of case a is between that of case c and case e. For path A (see Fig. 2), the concentration order is c > a > e > experiment case. For path B, the concentration order is reversed. However, for path C, there is little difference; for path D and E, there is no visible difference.

The simulation results of case b, case d and case f are shown in Figure 7. Compared to Figure 6, the concentration difference is much smaller. It can be seen that the concentration distribution was much more sensitive to surface flux when the leaking point was at the leeward side of the street canyon,

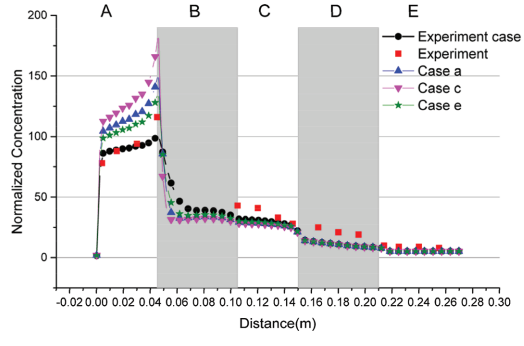

Figure 6. Normalized concentration of case a, case c, case e and the original wind-tunnel experiment simulated along the sampling path 'A-B-C-D-E'.

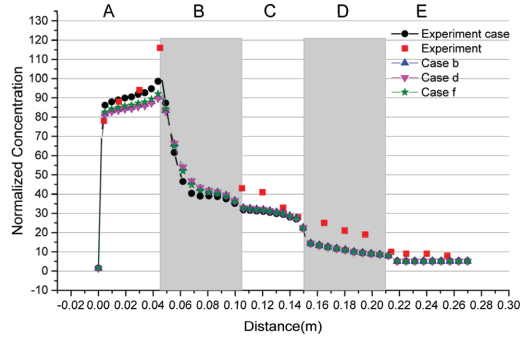

Figure 7. Normalized concentration of case b, case d, case f and the original wind-tunnel experiment simulated along the sampling path 'A-B-C-D-E'.

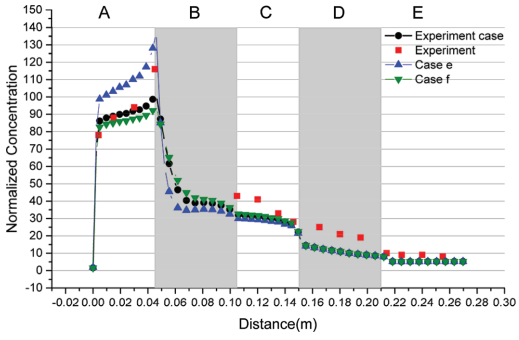

Figure 8. Normalized concentration of case e, case f and the original wind-tunnel experiment simulated along the sampling path 'A-B-C-D-E'.

and the concentration out of the canyon containing the leaking point was almost irrelevant.

In Figure 8, leeward leakage case e, windward leakage case f and middle leakage experiment case are put together. For path A, the concentration order is e > experiment case > f. For path B, the concentration order is reversed. So, leeward leakage causes more concentration at the leeward side while windward leakage causes more concentration at the windward side. And the concentration difference at the leeward side is bigger than that at the windward side. But when the downstream building roof and canyon walls was considered (path C, path D and path E), the concentration difference is very small.

5 CONCLUSION

The OpenFOAM software is reliable in simulating flows and dispersions in two dimensional street canyons. The concentration distribution was much more sensitive to surface flux when the leaking point was at the leeward side of the street canyon, and the concentration distribution out of the canyon containing the leaking point was almost unaffected. These findings can be helpful to the design of monitoring and early warning system for urban natural gas system. Future work can be devoted to investigating different urban configurations and wind profiles.

ACKNOWLEDGMENTS

This work was supported by the Ministry of Science and Technology of the People's Republic of China under Grant No. 2015BAK12B01 and the National Natural Science Foundation of China (Grant No. 71173128).

REFERENCES

Ferziger, J.H. & Perić, M. 2002. *Computational Methods for Fluid Dynamics.* Berlin Germany: Springer.

Han, Z.Y. & Weng, W.G. 2010. An integrated quantitative risk analysis method for natural gas pipeline network. *Journal of Loss Prevention in the Process Industries* 23(3): 428–436.

Han, Z.Y. & Weng, W.G. 2011. Comparison study on qualitative and quantitative risk assessment methods for urban natural gas pipeline network. *Journal of Hazardous Materials* 189(1–2): 509–518.

Launder, B.E. & Spalding, D.B. 1974. The numerical computation of turbulent flows. *Computer Methods in Applied Mechanics and Engineering* 3(2): 269–289.

Meroney, R.N., Pavageau, M., Rafailidis, S. & Schatzmann, M. 1996. Study of line source characteristics for 2-D physical modelling of pollutant dispersion in street canyons. *Journal of Wind Engineering and Industrial Aerodynamics* 62(1): 37–56.

Okamoto, H. & Gomi, Y. 2011. Empirical research on diffusion behavior of leaked gas in the ground. *Journal of Loss Prevention in the Process Industries* 24(5): 531–540.

Okamoto, H., Gomi, Y. & Akagi, H. 2014. Movement characteristics of hydrogen gas within the ground and its detection at ground surface. *Journal of Civil Engineering and Science* 3(1): 49–66.

Rafailidis, S. 1997. Influence of building areal density and roof shape on the wind characteristics above a town. *Boundary-Layer Meteorology* 85(2): 255–271.

Civil Engineering and Urban Planning IV – Liu et al. (Eds)
© 2016 Taylor & Francis Group, London, ISBN 978-1-138-02903-3

The quantitative risk assessment of the storage tank areas based on the domino effect

Jin-Long Zhao, Hong Huang, Bo-Ni Su & Nan Zhang
Department of Engineering Physics, Institute of Public Safety Research, Tsinghua University, Beijing, China

ABSTRACT: The domino effect brings a great threat to the tank areas and is responsible for many severe accidents. In this paper, a new method has been developed to quantitatively calculate the risk of the storage tank areas. This new method has been based on practical possible scenarios and closes to the actual situations. The individual acceptance criterion of the Netherland has been introduced to cut out the small probability accidents, which simplifies the scenarios and enlarges the range of applications. The results show that the risk distribution can be obtained by using this method and the domino effect is obvious for storage tank areas. While considering the domino effect, the region where the risk value is higher than 10^{-5} becomes 1.5 times than that without considering. Meanwhile, the planning region (risk value more than 10^{-8}) also enlarges greatly, which needs to pay more attention. Thus, this method can offer some meaningful suggestions on the layout design of the storage tank areas and avoid the accident escalation.

1 INTRODUCTION

Oil storage tank areas possessing large amounts of harmful substances and energy with great probability of accidental release, can pose risks to their personnel, equipment facilities and environment (Kang et al. 2014). The numbers of the severe tank accidents in the developed countries have been controlled by publishing strict engineering guidelines and standards for the construction, material selection, design and safe management of the storage tanks and their accessories (Chang & Lin 2006). However, along with the rapid growth of industrialization and population, the risk posed by probable tank accidents also continues to rise in the developing countries (Chen et al. 2012). The scale of tank areas and the volume of the single tank are continuous to expand especially developing countries. Meanwhile, due to the land utilization and economic reasons, distances between the installations are getting smaller and smaller (Chen et al. 2012). The domino effect is responsible for severe tank accidents because surrounding tanks are involved into primary accidents (Khan & Abbasi 1999). For instance, three tanks were damaged successively and resulted in a full surface fire in the Zhangzhou Gulei Petrochemical "4.6" fire explosion accident because of domino effect (Zhu 2015). Thus, evaluating the risk of storage tank areas based on the domino effects is vital for urban planning.

As an important part of the urban planning, the quantitative risk assessment of the chemical plants has been discussed and analyzed by Jonkman et al. (2003). The domino effect should be considered in the tank areas especially the high densities of tanks. The influence between the adjacent tanks was studied since the 1990s and the threshold model was developed by analysis of historical data (Bagster & Pitblado 1991). Based on the failure criterion of vessels, the failure probability model was built by Khan and Abbasi (1998). The tank has been classified into four types and the failure models were separately developed by Cozzani et al. (2005). Using the probability model, the failure probability of the tanks caused by the hazardous factors (radiation, overpressure, fragments) can be evaluated. These results have paid a solid foundation to the quantitative risk assessment of the storage tank areas.

2 METHOD

In the practical conditions, the development of accidents is constantly changing and the firefighters may be confronted to different scenarios. Thus, it is reasonable to calculate tank areas risk according to accident scenarios. Figure 1 summarizes the main steps of the methodology.

2.1 *Identification of primary scenarios and harmful factors*

The primary scenario usually involves just one tank failure at the first stage from the historical tank

accident cases (Abdolhamidzadeh et al. 2011). In the risk assessment process, the tank is considered as a basic assessment unit and the possible scenarios are built according to a primary accident tank. For an industrial park, the primary event and the harmful factors are shown in Table 1.

From the Table 1, the pool fire as the basic events accounts for 44%. In the study, atmospheric tanks are the main objects and the pool fire is set as a primary scenario. The frequency of the pool fire in the tank areas has been provided by some risk assessment institutions including LASTFIRE project and Health Safety and Environment Management (HSE). For atmospheric tanks, 1×10^{-4}/year is considered as the primary accident frequency and this value can be modified according to specific situations (Van Sciver 1990). Moreover, the event tree technique has usually been applied to determine the primary accidents frequently.

The solid model is often used to estimate the thermal radiation from the pool fire. Further details about the pool fires models have been discussed in SFPE (DiNenno 2008).

$$q = EF_{12}\tau \tag{1}$$

where E is the average emissive power at the flame surface, KW/m^2; F_{12} is the view factor (the value under the wind and windless is offered in SFPE); τ is the atmospheric transmissivity. The heat flux of the tank areas can be obtained according to the solid model as the primary accidents happen.

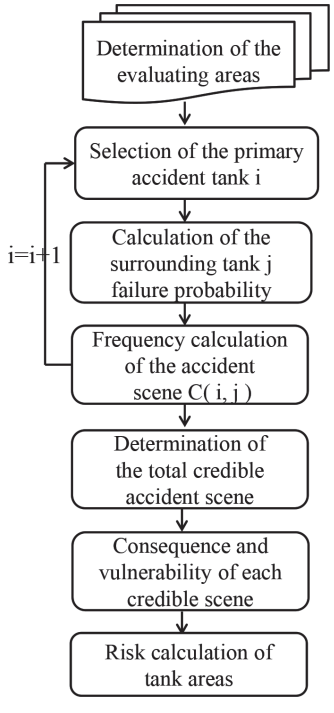

Figure 1. Flow diagram of the procedure used for the tank areas quantitative assessment of risk considering the domino effect.

2.2 *Failure probability and selection of credible scene*

The failure probability of the surrounding tanks is higher than the ordinary situations and this change should be considered. Based on the analysis of the historical data, the tank failure probability model is offered by Cozzani under the certain heat flux intensity (Cozzani et al. 2015).

$$Y = 12.54 - 1.847\ln(ttf) \tag{2}$$

$$\ln(ttf) = -1.128ln(q) - 2.667 * 10^{-5} * V + 9.877 \tag{3}$$

where Y is probit value for the failure given the primary accident; ttf is the time to failure, s; q is radiation intensity on the target equipment, kW/m^2; V is the tank volume, m^3.

The probability of the tank failure is expressed as:

$$P_{ij} = \frac{1}{\sqrt[2]{2\times\pi}}\int_{-\infty}^{Y-5} e^{-\frac{x^2}{2}}dx \tag{4}$$

Table 1. The primary event and the harmful factors of the 100 domino accidents.

		Harmful factors		
Primary event	Number	Radiation	Overpressure	Fragments
VCE	17	0	16	1
Mechanical explosion	17	0	10	7
BLEVE	13	0	0	13
Fireball	1	1	0	0
Jet fire	8	8	0	0
Pool fire	44	44	0	0

where P_{ij} is the failure probability of the tank j under the pool fire effect of the tank i. The target tanks failure probability can be calculated using this model.

The number of the possible scenarios are usually large for large storage tank areas and can achieve to 2^n (n is the tank number). However, the domino effect is extensively related with the distance and emergency response. Thus, some possible scenes' frequency is so small that we need not consider them. In order to limit the complexity of the analysis, it is important to perform a preliminary screening of the possible scenarios and determine credible them. In the quantitative risk analysis, the individual risk and the societal risk have been defined to describe the tank areas risk level. The risk acceptance criteria is given by some countries and shown in Table 2 (Sinopec Safety Engineering Institute 2007).

In the paper, the tolerance risk value of the Netherland is used to cut down the invalid scenes. The correlation can be expressed as:

$$P_s = \begin{cases} P_s;\ P_s > 10^{-6} \\ 0;\ P_s < 10^{-6} \end{cases} \tag{6}$$

where P_s is the probability of the possible scenarios.

According to the individual risk acceptance criteria, credible scenarios can be selected. This calculation process has been simplified greatly especially for large tank areas.

2.3 *Individual risk analysis*

The "probit analysis" is a well-known method to evaluate the dose-effect relation for human responses to thermal radiation that is derived from the cumulative expression for a normal Gaussian probability distribution function (Cozzani et al. 2005):

$$Y = -14.9 + 2.56 \ln\left(6 \times 10^{-3} \times q^{1.33} \times t_e\right) \tag{7}$$

Table 2. The individual risk acceptance criteria for different countries or regions.

Different countries or regions	Tolerance risk (per year)	Negligible risk (per year)
Netherlands existing installations	10^{-5}	10^{-8}
Netherlands new installations	10^{-6}	10^{-8}
United Kingdom existing installations	10^{-4}	10^{-6}
Hong Kong	10^{-5}	\
Santa Barbare	10^{-5}	10^{-7}

where Y is the probit unit, t_e is the exposure time, min; q is the thermal radiation under a credible scene, W/m^2.

The personal death equation is expressed as:

$$R = \frac{1}{\sigma\sqrt{2\pi}} \int_{-\infty}^{Y-5} e^{-u^2/2} du \tag{8}$$

where R is the probability of death ($0 \le R \le 1$), u is the variable of integration.

For the tank areas, the individual risk is related with all the credible scenes and can be expressed as:

$$P_{total} = \sum_{n=1}^{N} P_n \times R_n \tag{9}$$

where P_n is the happened probability of the nth scene; R_n is the people death probability under the nth scene.

3 CASE STUDY

The map in Figure 2 is a part of the Zhenhai industrial park. The volume of the tanks is 5 000 m^3 and the type of the contained fuel is gasoline. The tank diameter is 21 m. The case study is separated into two parts. The first part shows the failure probability of the surrounded tanks as the Tank 1 happens to pool fire, which is set as a primary accident. The second part compares the risk variation when the domino effect is considered.

3.1 *The Tank 1 happens to pool fire*

In order to quantitatively show the domino effect, the primary accident is set as the Tank 1 involved

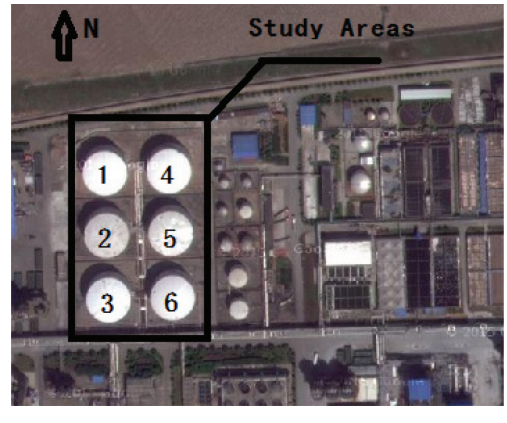

Figure 2. The layout of the tanks have been located at Zhenhai industrial park.

into the pool fire. In the tank areas, the volume of target tanks is 5 000 m^3 and the failure probabilities are shown in Figure 3. It obviously shows that the effect of Tank 2 and Tank 4 cannot be ignored as the Tank 1 has happened to pool fire.

According to the tanks failure probability, the credible scenarios can be obtained when the Tank 1 has been first involved into the pool fire. The credible scenarios are shown in Table 3.

From the Table 3, it can be concluded that the number of credible scenarios is not as large as compared with that before screening. The calculation time will be shortened a lot because of the primary screening especially for the large tank areas.

3.2 *Risk distribution*

In order to reflect the importance of considering domino effect, the comparison of the risk distribution change to the traditional method has been given in Figure 4.

From the Figure 4, the risk aversion region where the risk value is more than 10^{-5} enlarges nearly 1.5 times when the domino effect is to be considered. In this region, the important devices for example subsurface pumps are not emplaced strictly. The planning region where the risk value

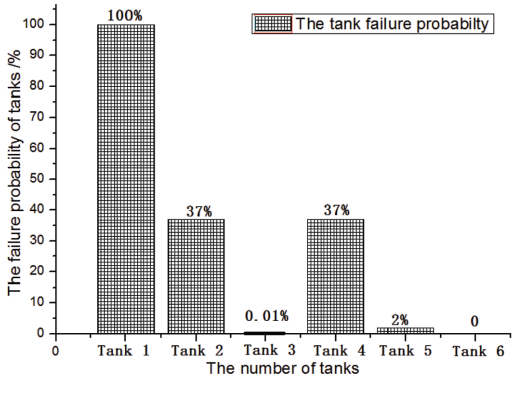

Figure 3. The tanks failure probability as the tank 1 happens to pool fire.

Table 3. The credible scenarios as the tank 1 happens to pool fire.

Number	Credible scenarios	Frequency/per year
1	Tank 1	1.0×10^{-4}
2	Tank 1, Tank 2	3.7×10^{-5}
3	Tank 1, Tank 4	3.7×10^{-5}
4	Tank 1, Tank 2, Tank 4	1.4×10^{-5}

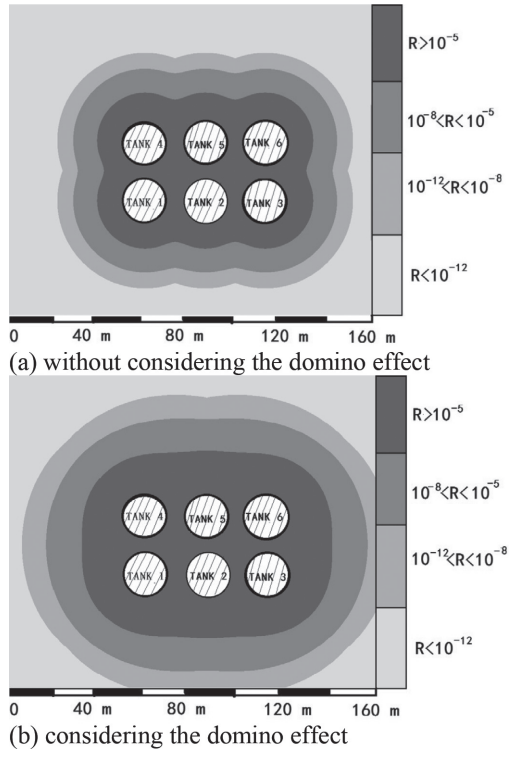

Figure 4. The comparison of the risk distribution variation for the tank areas.

is over 10^{-8} obviously enlarges when we considered the domino effect. In this region, new buildings or devices should not be built and the activity of human should be avoided as far as possible according to the risk acceptance rule. From the risk comparison, the concerned region has changed significantly and the domino effect is obvious. Therefore, the domino effect should be considered in the tank areas planning.

4 CONCLUSION

- The quantitative risk assessment method considering the domino effect and based on different credible scenarios is more close to the actual situations and has a direct significance for the tank areas planning.
- In the assessment process, it can be concluded that the surrounding tanks have been easily involved into the primary accident and the domino effect has been very obvious. Therefore, the layout of the important devices and the emergency material reserves should consider the complex situations.

– The individual acceptance criterion of the Netherland has been introduced in the screening, which can cut out many small probability (less than 10^{-6}) scenarios. This simplification enlarges the range of the risk calculation and can be extensively used into the large tank areas especially many tanks.

ACKNOWLEDGMENTS

This work was supported by the Ministry of Science and Technology of the People's Republic of China under Grant No. 2015BAK12B01 and the National Natural Science Foundation of China (Grant No. 71173128).

REFERENCES

Abdolhamidzadeh, B., Abbasi, T., Rashtchian, D., et al. 2011. Domino effect in process-industry accidents–An inventory of past events and identification of some patterns. *Journal of Loss Prevention in the Process Industries* 24(5): 575–593.

Bagster, D.F. & Pitblado, R.M. 1991. Estimation of domino incident frequencies-An approach. *Process Safety and Environmental Protection* 69(4): 195–199.

Chang, J.I. & Lin, C.C. 2006. A study of storage tank accidents. *Journal of Loss Prevention in the Process Industries* 19(1): 51–59.

Chen, Y., Zhang, M., Guo, P., et al. 2012. Investigation and analysis of historical Domino effects statistic. *Procedia Engineering* 45: 152–158.

Cozzani, V., Gubinelli, G., Antonioni, G., et al. 2005. The assessment of risk caused by domino effect in quantitative area risk analysis. *Journal of hazardous Materials* 127(1): 14–30.

DiNenno, P.J. 2008. *SFPE Handbook of Fire Protection Engineering.* United States of America: SFPE.

Jonkman, S.N., Van Gelder, P. & Vrijling, J.K. 2003. An overview of quantitative risk measures for loss of life and economic damage. *Journal of Hazardous Materials* 99(1): 1–30.

Kang, J., Liang, W., Zhang, L., et al. 2014. A new risk evaluation method for oil storage tank zones based on the theory of two types of hazards. *Journal of Loss Prevention in the Process Industries* 29: 267–276.

Khan, F.I. & Abbasi, S.A. 1998. Models for domino effect analysis in chemical process industries. *Process Safety Progress* 17(2): 107–123.

Khan, F.I. & Abbasi, S.A., 1999. The world worst industrial accident of the 1990s-What happened and what might have been: A quantitative study. *Process Safety Progress* 18(3): 135–145.

Van Sciver, G.R. 1990. Quantitative risk analysis in the chemical process industry. *Reliability Engineering & System Safety* 29(1): 55–68.

Sinopec Safety Engineering Institute. 2007. *A Guidance for Quantitative Risk Assessment in the Petrochemical Plant.* Beijing: China Petrochemical Press Co. Ltd.

Zhu, Y.J. 2015. Notes for large petrochemical fire fighting and rescue based on Zhangzhou Gulei petrochemical "4.6" fire explosion accident. *Journal of Value Engineering* 23(3): 059.

This page intentionally left blank

Civil Engineering and Urban Planning IV – Liu et al. (Eds)
© 2016 Taylor & Francis Group, London, ISBN 978-1-138-02903-3

Discussion on the contribution of the Bohai Strait Tunnel Project to freight transportation system and economic benefit

Bing Wang
The Communications Research Institute of Liaoning Province, Shenyang, Liaoning, China
College of Civil Engineering and Architecture, Zhejiang University, Hangzhou, Zhejiang, China

Chang-Ning Deng
The Communications Research Institute of Liaoning Province, Shenyang, Liaoning, China

Fei Liu
Shenyang Highway Plan and Design Institute, Shenyang, Liaoning, China

Jian Zhang
Liaoning Jianzhu Vocational University, Liaoyang, Liaoning, China

ABSTRACT: Bohai Strait Tunnel Project is a new planning major project of China. A key issue for this project is the transportation and economic benefit after implementation. The paper discusses the contribution of Bohai Strait Tunnel Project to freight transportation system and economic benefit. Modified Negative Exponent Network Flow Assignment model (MNENFA model) and economic benefit analysis were used in this manuscript. Three logistic routes were selected in this paper, including, Tongliao-Yantai, Dandong-Yantai, and Shenyang-Yantai. Two cases: "without Bohai Strait Tunnel" and "with Bohai Strait Tunnel" were used to make a comparison. Multiple transportation modes were considered, such as highway transportation, railway transportation, air transportation, water transportation, and their combined transportation. It was found that after implementation of Bohai Strait Tunnel project, tunnel transportation became the new main transportation mode and took up very large market share and freight volume. Besides, it was also found that Bohai Strait Tunnel project could bring great economic benefits; the benefit of time saving was larger than the benefit of distance reduction.

1 INTRODUCTION

Bohai Strait Tunnel Project is a new planning major project of China. The purpose of the project is to construct an undersea tunnel to link Dalian on the Liaodong Peninsula to Yantai on the Shandong Peninsula. At present, the transportation from Dalian to Yantai requires a detour around the Bohai Sea, and the heavy transportation pressure in Bohai Rim Region has brought much inconvenience to people and exerted negative impacts on the environment. If built, the trip between the two cities would be shorted by one hour. The project was purposed by Yantai City Government in 1992, and then it got a lot of attention. In 2008, the General Office of Yantai Municipal People's Government, State Scientific and Technological Commission et al. completed the study of the influence of Bohai Strait Tunnel on Bohai economic rim and northeast old industrial base (Liu & Liu 2009). In 2009, Transport Planning and Research Institute, Institute of Comprehensive Transportation of National Development and Reform Commission et al. conducted a strategic planning of Bohai Strait Tunnel (Project team of strategic planning of Bohai Strait Tunnel 2012). From 2009–2010, Ludong University performed analysis on construction investment and investment decision of Bohai Strait tunnel (Wu & Li 2009; Wu & Liu 2010). In 2012, the Communications Research Institute of Liaoning Province et al. studied some key problems of Bohai Strait Tunnel (The Communications Research Institute of Liaoning Province 2012). In 2012, Qingdao Institute of Marine Geology evaluated the crustal stability of Bohai Strait Tunnel (Zhao et al. 2014).

A key issue for this project is the transportation and economic benefit after implementation. Traffic volume and transportation network assignment are the basis of national planning and transportation construction. Project planning and design, investment budget will be decided according to the

future traffic volume. Investment return, operation, administration and maintenance after implementation of project will also be evaluated by future traffic condition. So, there is a need for a scientific and rational prediction of future traffic volume and transportation network assignment, and fixing on a developing target. Besides, economic benefit analysis is a key part of project feasibility study, which can assess the construction scale, construction period, economic benefit, and rationality of a project. It is very importance to evaluate economic benefit of planning project. The paper discussed the contribution of Bohai Strait Tunnel Project to freight transportation system and economic benefit, and is aim to provide policy recommendation on implementing national development plan.

2 MODELS

2.1 *MNENFA model*

Trip-makers or shippers always prefer to choose the most appropriate path: shortest, fastest, and cheapest. But due to complex traffic road and random traffic situation, trip-makers or shippers not always choose the shortest or cheapest route, and may choose the suboptimal route. So there are two factors which can influence trip-makers or shippers decision: most appropriate route factor and random factor. Modified Negative Exponent Network Flow Assignment model (MNENFA model) is a network flow model which is based on cheapest transportation cost and random factor. An additional inclination factor B_i was introduced in the model (Wang 2003), which represents some factors that can affect the trip-makers or shippers choices (Friesz & Bernstein 1996). The MNENFA model can be evaluated using the following equation:

$$K_i = A \cdot B_i \cdot \exp\left[-C_0 \cdot \left(D_i - D_j\right)/D_j\right] \quad (1)$$

where, K_i is the ratio of transport volume in route i to total transport volume, the sum of K_i is 1.

C_0 is the cost-sensitive parameter. In this paper, the freight transportation is low price goods, and low demand to transport quality and time, $C = 3.5$.

D_i is transportation cost in route i. In this paper, D_i in the year of 2050 was predicted by analyzing the past 20 years transportation cost.

D_j is the minimum transportation cost in all routes.

A is normalized parameter, and is given as follows:

$$A = 1/\sum B_i \cdot \exp\left[-C \cdot \left(D_i - D_j\right)/D_j\right] \quad (2)$$

B_i is inclination factor in route i, which represents some factors that can affect the trip-makers' or shippers' choices and can be obtained using the following expression:

$$B_i = B_{pi} \cdot B_{wi} \quad (3)$$

where, B_{pi} is the score of ports in route i.

B_{wi} is the score of route i.

B_{pi} and B_{wi} can be obtained by comprehensive assessment method.

And then, the freight volume in route i can be evaluated according to the following expressions:

$$Q_i = K_i \cdot Q \quad (4)$$

Q_i is the freight volume in route i.

Q is the total freight volume.

2.2 *Economic benefit analysis*

Economic benefit analysis (Wu 2009) is of vital importance to evaluate an engineering project, which can assess the construction scale, construction period, economic benefit, and rationality of a project. National economic benefit can be used generally in the study of economic benefit analysis. National economic benefit is the contribution of an engineering project to the national economy in a certain amount of capital investment, and can be analyzed by the "with" and "without" comparison method, i.e. evaluating the amount of traffic or freight volume under the two cases: with the project and without the project. The benefit can be estimated by two parameters: benefit of distance reduction B_{hd} and benefit of time saving B_{hs}.

$$B_{hd} = C_{h0} Q_h \left(L_0 - L_n\right) \quad (5)$$

where, B_{hd} is benefit of distance reduction of cargo transportation after implementation of project, million Yuan.

C_{h0} is the unit transportation cost of cargo transportation before implementation of project, Yuan/ton* kilometer.

Q_h is the predicted freight volume in the route that is shortened after implementation of project, million ton.

L_0 is the transportation distance before implementation of project, kilometer.

L_n is the transportation distance after implementation of project, kilometer.

$$B_{hs} = \bar{C} Q_h I_h T_{hs} \quad (6)$$

where, B_{hs} is benefit of time saving of cargo transportation after implementation of project, million Yuan.

$\bar{C}$ is average price of goods in transit, Yuan/ton.

I_h is interest rate or discount rate of fluid capital, %.

T_{hs} is shortened transportation time after implementation of project, hour.

3 PROGRAMS

As shown in Tables 1 and 2, three logistic routes were selected in this paper, including, Tongliao-Yantai, Dandong-Yantai, and Shenyang-Yantai. Each logistic route had two transportation routes. The length of the transportation route was listed in the tables. Two cases: "without Bohai Strait Tunnel" and "with Bohai Strait Tunnel" were used to make a comparison. Multiple transportation modes were considered, such as highway transportation, railway transportation, air transportation, water transportation, and their combined transportation. The freight volume in 2050 was predicted based on growth rate method and the OD survey data of freight transportation in 2010. The predicted freight volume is presented in Table 3.

4 RESULTS AND DISCUSSION

Market share and freight volume of three transport routes in 2050 could be evaluated by the MNENFA model, and benefit of distance reduction and benefit of time saving would be calculated by equations (5) and (6).

Table 1. Length of the transportation route and transportation mode without Bohai Strait Tunnel.

Code	Transportation route	Length of the transportation route (km)					
1	Tongliao-Shenyang-Dalian-Yantai	Mode	HW	RW	HA	RA	
		Length	824	938	899	1013	
	Tongliao-Chifeng-Beijing-Yantai	Mode	H	R	AT		
		Length	1629	1816	1221		
2	Dandong-Dalian-Yantai	Mode	HW	RW	HA	RA	
		Length	485	766	560	841	
	Dandong-Shenyang-Beijing-Yantai	Mode	H	R	AT		
		Length	1670	2153	1424		
3	Shenyang-Dalian-Yantai	Mode	HW	RW	HA	RA	DA
		Length	561	562	636	637	593
	Shenyang-Beijing-Yantai	Mode	H	R			
		Length	1430	1722			

* H = highway transportation; R = railway transportation; W = water transportation; DA = direct air; AT = air transit; HW = highway-water combined transportation; RW = railway-water combined transportation; HA = highway-air combined transportation; RA = railway-air combined transportation.

Table 2. Length of the transportation route and transportation mode with Bohai Strait Tunnel.

Code	Transportation route	Length of the transportation route (km)							
1	Tongliao-Shenyang-Dalian-Yantai	Mode	HT	RT	HW	RW	HA	RA	
		Length	820	934	824	938	899	1013	
	Tongliao-Chifeng-Beijing-Yantai	Mode	H	R	AT				
		Length	1629	1816	1221				
2	Dandong-Dalian-Yantai	Mode	HT	RT	HW	RW	HA	RA	
		Length	481	762	485	766	560	841	
	Dandong-Shenyang-Beijing-Yantai	Mode	H	R	AT				
		Length	1670	2153	1424				
3	Shenyang-Dalian-Yantai	Mode	HT	RT	HW	RW	HA	RA	DA
		Length	557	558	561	562	636	637	593
	Shenyang-Beijing-Yantai	Mode	H	R					
		Length	1430	1722					

* HT = highway transportation through Bohai Strait Tunnel; RT = railway transportation through Bohai Strait Tunnel.

4.1 *Result of MNENFA model*

The results of market share and freight volume in 2050 were presented in Tables 4 and 5.

For the transportation network without Bohai Strait Tunnel, it was found that highway-water combined transportation and railway-water combined transportation were main transportation ways, and the sum of HW and RW was up to 96.4% of total transportation volume (Dandong-Dalian-Yantai route), which played decisive roles in Bohai economic rim. And then, railway transportation also had large freight transport capacity and a certain market share, in which the market share of Tongliao-Chifeng-Beijing-Yantai route accounted for 14.6%; but due to a detour around the Bohai Sea, transport capacity and transport efficiency were restricted. Air transportation, including direct air, air transit, highway-air combined transportation and railway-air combined transportation, was mainly express transportation and had a small market share owing to higher prices and tiresome transfer.

For the transportation network with Bohai Strait Tunnel, it was apparently seen that highway transportation through Bohai Strait Tunnel and railway transportation through Bohai Strait Tunnel became the new main transportation modes. The reason is that Bohai Strait Tunnel can connect Dalian to Yantai and the distance between the two cities is shorten by 165 km from a total of 1596 km (by highway transportation), which reduce the transport time and transport cost, and freight transportation are captive to Bohai Strait Tunnel. Besides, it was also found that the water transportation such as HW and RW was replaced by tunnel transportation, but very low transportation cost made water transportation still occupy a certain market share. The market share of HW in Dandong-Dalian-Yantai route was 17.1%. Yet the water transportation is prone to suffering appalling weather, high wind and freezing winter, the market share and freight volume are far smaller than those of tunnel transportation. Finally, it was noted that air transportation was affected little by Bohai Strait Tunnel, and the market share and freight volume after the implementation of

Table 3. The predicted freight volume in 2050.

Transportation route	The predicted freight volume in 2050 (thousand ton)
Tongliao-Yantai	6201.4
Dandong-Yantai	640.7
Shenyang-Yantai	10284.8

Table 4. The result of MNENFA model in 2050 without Bohai Strait Tunnel.

Market share and freight volume in 2050 without Bohai Strait Tunnel								
Routes	Tongliao-Shenyang-Dalian-Yantai					Tongliao-Chifeng-Beijing-Yantai		
Transportation modes	HW	RW	HA	RA		H	R	AT
Market share (%)	48.2%	34.2%	1.5%	1.3%		0.3%	14.6%	0.0%
Freight volume (Thousand ton)	2991.9	2119.0	92.3	78.6		16.4	903.1	0.0
Routes	Dandong-Dalian-Yantai					Dandong-Shenyang-Beijing-Yantai		
Transportation modes	HW	RW	HA	RA		H	R	AT
Market share (%)	87.4%	9.0%	1.2%	0.8%		0.0%	1.5%	0.0%
Freight volume (Thousand ton)	560.0	57.9	7.7	5.3		0.1	9.6	0.0
Routes	Shenyang-Dalian-Yantai					Shenyang-Beijing-Yantai		
Transportation modes	HW	RW	HA	RA	DA	H	R	
Market share (%)	70.8%	20.6%	1.7%	1.3%	0.9%	0.1%	4.7%	
Freight volume (Thousand ton)	7279.1	2118.1	174.1	131.4	94.6	8.3	479.1	

Table 5. The result of MNENFA model in 2050 with Bohai Strait Tunnel.

Market share and freight volume in 2050 with Bohai Strait Tunnel									
Routes	Tongliao-Shenyang-Dalian-Yantai						Tongliao-Chifeng-Beijing-Yantai		
Transportation modes	HW	RW	HA	RA	HT	RT	H	R	AT
Market share (%)	4.9%	8.9%	1.3%	1.1%	16.6%	63.9%	0.0%	3.1%	0.0%
Freight volume (Thousand ton)	305.4	552.1	82.9	70.6	1029.5	3966.5	0.2	195.2	0.0
Routes	Dandong-Dalian-Yantai						Dandong-Shenyang-Beijing-Yantai		
Transportation modes	HW	RW	HA	RA	HT	RT	H	R	AT
Market share (%)	17.1%	2.1%	1.1%	0.8%	60.4%	18.4%	0.0%	0.2%	0.0%
Freight volume (Thousand ton)	109.5	13.2	7.1	4.9	387.0	117.8	0.0	1.1	0.0
Routes	Shenyang-Dalian-Yantai						Shenyang-Beijing-Yantai		
Transportation modes	HW	RW	HA	RA	DT	HT	RT	H	R
Market share (%)	7.2%	4.5%	1.6%	1.2%	0.9%	27.2%	56.9%	0.0%	0.6%
Freight volume (Thousand ton)	735.7	467.5	163.8	123.7	89.0	2798.1	5850.4	0.0	56.7

Table 6. Benefit of distance reduction of cargo transportation in 2050 B_{hd}.

Route	Transportation mode	Q_h (Thousand ton)	L_0 (Kilometer)	L_n (Kilometer)	B_{hd} (Million Yuan)	Sum (Million Yuan)
Tongliao-Yantai	HT	1029.5	1629	820	611.59	1452.46
	RT	3965.5	1816	934	840.87	
Dandong-Yantai	HT	387.0	1670	481	337.78	375.66
	RT	117.8	2153	762	37.89	
Shenyang-Yantai	HT	2798.1	1430	557	1796.27	3453.67
	RT	5850.4	1722	558	1657.40	
Total/Million Yuan						5281.79

tunnel were slightly lower than those without Bohai Strait Tunnel. The possible reason is that air transportation is mainly to provide express transportation and requires high transport quality and very short time, which differ from mass freight transportation of other transportation modes.

4.2 *Result of economic benefit analysis*

As shown in Table 6, the benefits of distance reduction in 2050 of three routes, including Tongliao-Yantai, Dandong-Yantai, and Shenyang-Yantai, were 1452.46 million Yuan, 375.66 million Yuan, and 3453.67 million Yuan, respectively. As presented in Table 7, the benefits of time saving in 2050 of three routes were 12158.50 million Yuan, 1411.93 million Yuan and 25314.99 million Yuan, respectively. The economic evaluation result indicated that Bohai Strait Tunnel project could bring great economic benefits, and the benefit of time saving is larger than the benefit of distance reduction. It was also noted that the benefits of route Shenyang-Yantai was largest. The reason is that Shenyang city is an important provincial capital city and serves as an important transport hub of northeast China. So Shenyang could benefit more from Bohai Strait Tunnel.

Table 7. Benefit of time saving of cargo transportation in 2050 B_{hs}.

Route	Transportation mode	Q_h (Thousand ton)	T_{hs} (Hour)	B_{hs} (Million Yuan)	Sum (Million Yuan)
Tongliao-Yantai	HT	1029.5	6.74	1665.72	12158.50
	RT	3965.5	11.03	10492.78	
Dandong-Yantai	HT	387.0	9.91	920.19	1411.93
	RT	117.8	17.39	491.74	
Shenyang-Yantai	HT	2798.1	7.28	4885.43	25314.99
	RT	5850.4	14.55	20429.56	
Total/Million Yuan					38885.42

5 CONCLUSIONS

– Bohai Strait Tunnel could reduce transportation distance, short transportation time and save transportation cost. After implementation of Bohai Strait Tunnel project, tunnel transportation took up large market share and freight volume, and became the new main transportation mode.
– Bohai Strait Tunnel project could bring great economic benefits, the benefit of time saving was larger than the benefit of distance reduction, and the two benefits in 2050 were 38885.42 Million Yuan and 5281.79 Million Yuan, respectively.

ACKNOWLEDGEMENT

This work was financially supported by the Key Research Items of Liaoning Province Communications Department (201523), Natural Science Foundation of Liaoning Province of China (2015020610), China Postdoctoral Foundation (2013M531459) and Zhejiang Postdoctoral Sustentation Fund (Bsh1201023).

REFERENCES

Friesz, T.L., Bernstein, D. & Stough, R. 1996. Dynamic systems, variational inequalities and control theoretic models for predicting time-varying urban network flows. *Transportation Science* 30(1): 14–31.

Liu, X.H. & Liu, L.Z. 2009. *The Influence of Bohai Strait Tunnel on Bohai Economic Rim and Northeast Old Industrial Base (in Chinese)*. Beijing: Economic Science Press.

Project team of strategic planning of Bohai Strait Tunnel. 2012. *Research on Strategic Planning of Bohai Strait Tunnel (in Chinese)*. Beijing.

The Communications Research Institute of Liaoning Province. 2012. *Key problems of Bohai Strait Tunnel (in Chinese)*. Shenyang.

Wang, X.F. 2003. *Network Flow Assignment Applied in National Economic Evaluation of Planned Port Construction Project (in Chinese)*. Dalian: Dalian Maritime University.

Wu, A.H., Li, F.X. & Liu, X.H. 2009. An Analysis of Bohai Cross Sea Channel Construction Investment to Economic Contribution. *ICNDS, '09 Proceedings of the 2009 International Conference on Networking and Digital Society. Guiyang, Guizhou, China, 30 May–1 June, 2009*.

Wu, A.H. & Liu X.H. 2010. Investment Decision for Bohai Strait Cross-sea Channel Investment Based on Fuzzy Risk Analysis. *3rd International Conference on Information Management, Innovation Management and Industrial Engineering. Kunming, China, 26–28 November, 2010*.

Wu, Z.L. 2009. *Comprehensive Transportation Planning (in Chinese)*. Beijing: Tsinghua University Press.

Zhao, T.H., Gao, X.H. & Qi, Q. 2014. Shallow structure characteristics in trans-sea channel of Bohai strait (in Chinese). *Hydrographic Surveying and Charting* 34(2): 38–42.

Civil Engineering and Urban Planning IV – Liu et al. (Eds)
© 2016 Taylor & Francis Group, London, ISBN 978-1-138-02903-3

Study on the renovation of old industrial district combined with the creative industry in Guangdong, China

Hang Ma
School of Urban Planning and Management, Harbin Institute of Technology, Shenzhen Graduate School, Shenzhen, Guangdong, China

Kan Zhu
China Nerin Engineering Co. Ltd., Shenzhen Branch, Shenzhen, Guangdong, China

ABSTRACT: The paper analyzes the renovation of old industrial districts combined with the creative industry in Guangdong, China, under the industrial structure transformation and urban renovation period, and puts forward the planning frame, which includes five basic principles, such as urban sustainability, protection and reconstruction, green ecology, combining with urban development, and interest balance. Then the evaluation system, control system, and target system are set up along with modes of renovation in order to attain unified planning and reasonable modes of renovation. Then it studies the specific requirements and methods of the different types of industrial renovation affected by the creative industry from planning layout and building reconstruction aspects, by the case studies in Guangdong. Finally the paper affords the specific suggestions after the relative existing problems on the renovation are put forward, which could be used as a reference in other such cases.

1 INTRODUCTION

Recently, a host of the obsolete industrial buildings and old industrial parks in China are confronted with the situation of demolishment, renewal, and functional transformation. Meanwhile, the rising and booming creative industry hungers for a lot of building space to meet its special needs. So the renewal of the buildings of the obsolete industrial area relieves this impact and brings in great economic and social benefits as well. Places like Beijing and Shanghai have already built creative industry parks such as 798 and M50. As a region of rapid economic growth, Guangdong starves for plentiful low-cost building space to meet the boost of its creative industry and at the same time, owing to the location conditions, market conditions, and its incompatibility with the environment, the original properties of the old industrial area requires an immediate update or functional transformation. Under this circumstance, it is quite practical to reshape those factories with historic significance into creative industry parks (Catier 2002; Altrock & Schoon 2013).

The problems with restructuring projects are:

– Creative industry parks usually take up a large area with hard landscapes outnumbering green landscapes;
– Experience from the successful creative industry parks, lessons from the failed cases, and an evaluation system for the restructuring are needed.

2 THE EVALUATION SYSTEM FOR RECONSTRUCTION

2.1 *An investigation on the current situation*

Before reshaping the obsolete industrial area, it is necessary to do a research on its current situation. The history and culture, the potential value, the basic information of the factory buildings, the surroundings of the factories, the facilities of the factories, and things alike should be taken into consideration before designing the blueprint for reconstructing. And a reconstructing plan should be made so as to avoid any destruction to the potential historic or cultural value for lack of preparation.

2.2 *The evaluation of values*

The values of old industrial buildings include historic value, scientific value, cultural value, sentimental value, and utility value. From the aspect of reusing the obsolete industrial area, the focus of reconstructing will be on its utility value. The factors that affect the reusing values of the old industrial buildings are: the locations, the surrounding

advantages, the conditions of the buildings, the available space area, the quality of the equipment, and the difficulty of reconstructing. The overall evaluation of these factors will determine the fate of these old industrial buildings: to be repaired, reshaped, or removed (Wang 2008).

2.3 *Economic assessment*

Since interests are the essential and lasting drive force, any practice of protection or recycling, reconstructing the old industrial building included, is essentially interest-driven, be it purely economic interests or complicated social interests. Therefore, under the market-oriented economy, the estimation of expected economic benefits will always be one of the highlighted goals of the developers and designers. The economic assessment should include the following aspects:

– Land cost
  Because the industrial buildings are always located within the factories or industrial parks, the value of land reacts slowly to the market demands for land, which makes the reconstructing and reusing costs of these buildings lower than that of the general old building and makes the costs lie between developing new sites and reconstructing general old buildings.
  As the old industrial buildings (groups) undergo the reconstruction for creative industry park purposes, the nature of the land does not change fundamentally (being industrial building parks), which makes the land cost relatively low and thus is of great advantage.
– Construction cost
  Usually, old industrial buildings are located in the central area of the city with mature public facilities; therefore, compared with the costs on building new industrial parks, the government and the developers can save money on public facilities like transportation, energy resources, water supply, culture and education, health, safety, disaster prevention, etc.
– Social cost
  Social cost which includes the cost related to ecological, historical, and cultural environment is a kind of intangible cost that is hard to be illustrated by money. But it will be reflected in our life in other ways. The reconstruction and reuse of old industrial buildings need to be analyzed and evaluated for any related social cost.

3 DEVELOPMENT MODE

3.1 *Classified by the development objective*

– A Top-down Mode Guided and Driven by Government
  It means that the local governments at all levels, following the overall development strategy and planning of the regional industry, draw up a development planning mode for regional creative industry by analyzing the environment needed, the location requirements, and space requirements and integrating with the evaluations on environment conditions and the development of regional economic, social, and cultural conditions.
– A mutual promotion mode of top-down and down-top
  It means the mutual promotion between spontaneous development and government-driven development. The rich cultural background, flexible creative space, and low-cost reconstruction expenses and rents attract a lot of artists and small and medium enterprises to gather here spontaneously. The governments learn about these gatherings and support them through unified planning, policy and infrastructure supporting, and subsidiary services perfecting so as to make the best out of these spontaneous gatherings on talents, funds, culture, creative ideas, views, etc.

3.2 *Classified the integrated way*

Based on the number of companies that are moving in and the number of buildings, there are three types of combinations of companies and buildings:

– "One-to-one"
  With one creative enterprise coming in, one old building will be reconstructed accordingly. For example, Sihang Warehouse was transformed into "Creativity Warehouse".
– "Many-to-one"
  With many creative enterprises coming in, one old building will be reconstructed accordingly. For example, Sihang Warehouse was transformed into "Creativity Warehouse".
– "Many-to-many"
  With many creative firms coming in, the whole industrial park is under reconstruction thus updated as creative industry park.

Most of the creative industry parks in Shenzhen are transformed from old industrial zones. The initial project of Shenzhen's OCAT attracts around 30 top creative institutes, covering fields as arts, designing, media, advertisement, photography, and culture, while the initial project of Tianmian's City of Design draws 70 creative institutes in, with 20 from abroad and 50 local; other creative industry parks, such as F518 Idea Land, Nanhai E-Cool, are all based on reconstructing old industrial buildings and attract many design-related creative institutes. That's

why they all fall into "Many-to-Many" classification (Cao 2008).

3.3 *Classified by functions*

Based on different types of functions, the creative industry parks in Guangdong can be classified into "Creative Pattern", "Experiential Pattern", "Consumption Pattern", and "Compound Pattern".

– Creative pattern
  This type of parks focuses on creating an environment for creation by offering hardware support like necessary technical equipment as well as soft services support like cultural facilities and counselling services. The enterprises that move in this type of parks are mostly engaged in business like architecture design, graphic design, advertisements, arts, etc. For all kinds of artists from these enterprises, this type of parks will provide work environment and communication platforms. Take Nanhai E-Cool as an example. This industry park mainly includes local and overseas enterprises of architecture design and landscape design with some service institutes of interior design, industrial design, costume design, advertisements design, furniture design, presentation design, artistic creation, space design, film & TV and comic & animated products making, visual arts, ceramic arts, photographic industry, art bookstores, and art galleries as its complements. Because designing is the dominant function of this category, these types of parks are labeled as "Creative Pattern" parks.
– Experiential pattern
  This kind of park emphasizes the participants' physical and emotional experience and the communications between the artists as well as the products from the park and the visitors to the park. This type of park always hosts exhibition activities which encourage the designers and the visitors to communicate with each other. Some examples of this sort of parks are OCT-LOFT in Shenzhen Overseas City, Guangzhou Xinyi Exhibition Hall, Dongguan Art Exhibition Centre.
– Consumption pattern
  This classification is similar to Experiential Pattern except that it highlights its consumption feature more. It mainly serves general audiences and cultural consumers by creating consumption areas which enable the consumers to experience and consume culture. The services provided by this kind of park often include comic and animation products, clothing exhibitions, bookstores, and fashion products. One example of this category is Guangzhou Rectory.
– Compound pattern
  This category contains at least two functions of the three classifications mentioned above. It emphasizes the comprehensive development of creativity, education, and business. Most of the creative industry parks fall into this category. Generally speaking, the size of this type of park is large so that it can provide enough creation space and communication space for the artists as well as enough room for large scale exhibitions, advisory services, communication, and consumption for the visitors.

  One typical example of this classification is Shenzhen F518 Idea Land. This park can be divided into several sections: "Creative Forefront" represents the high-end technology invention; "Modern Art Gallery" is for art creation; "Exhibition Centre" serves as the exhibition platform; "Status Arcade" offers entertainment services; and some of the other functional sections provide accommodation units as well. This multifunction park contains not only the functions of "Creative Pattern", "Experiential Pattern", and "Consumption Pattern", but also supporting services such as entertainment centers and accommodation units.

  The example from Guangzhou is Fangcun Cultural Creativity Industry Park. This park combines the functions of commerce, business, exhibitions, restaurants and hotels, detailing as headquarter of business groups, international conventions, cultural exhibitions, and supporting services as hotel and restaurant.

3.4 *Classified by industry categories*

There is no settled standard for nationwide creative industry park classification yet. But Program for Strategy Implemented to Establish Shenzhen as a Cultural City focuses on developing creativity and design-related industries and relating these industries with the industry parks reconstructed and recast from old industry buildings. Based on that, the creative industry park transformed from the old industry buildings in Guangdong can be classified as comic and animation industry, architecture design, decoration design, printing, costume design, etc. Some of the creative industry parks under these classifications are of unitary development while some others are developing with other creative industries; under this circumstance, the industry layouts of these parks lead to two different ways.

– Unitary industry—separated development
  Because of the diversity of creative industries, customized methods are always applied to the reconstruction of old industry buildings. The industries in this kind of industry parks are

always unitary with supporting services only. For example,

* Comic and animation industry
  One example of this category is the Shenzhen Comic and Animation City (currently under construction). Transformed from the old industry building and funded by Shangkai (Group) Co., Ltd., this park takes up an area of 24,000 square meters with a building area of 62,000 square meters.
* Design industries on architecture, graphics, and advertisement
  The example of this category is Tianmian "City of Design" Creative Industry Park. Funded and developed by Shenzhen Sphinx Culture and Communication Co., Ltd., this park holds an area of 15,000 square meters with a building area of 50,000 square meters. By now, over 70 companies, most of which are designing institutes, have moved in.
* Clothing industry
  An example of this category is Guangzhou TIT Textile Costume Creative Industry Park. Themed on costume ideas, it integrates information distribution, product exhibition, business communication, fashion, and recreation into one platform. This park is divided into six functional units which are creative studios, home of designers, exhibition and distribution centre, brand headquarter, fashion and recreation area, and supporting services. With a number of costume brands, costume designers, and artists gathering here, it will soon become the window of Guangzhou to show its creativity to the world. Another example of creative industry park for costume industry is Taigucang South China Costume Creative Base.
* Auto industry
  922 Creative Industry Park is a creative industry park with automobile culture as its theme and with high-level architecture style as its characteristic. It is aimed at high-end consumption combined with culture, business, art, humanity history, and tourism.
* Music industry
  The example of this category is B8 Music Studio which is a creative industry park developed specially for music industry. Equipped with stage, stereo system, musical instruments, lighting, and projecting equipment, it always hosts entertainment activities of music, exhibitions, operas, parties, etc.
* Ceramics industry
  The example taken here is Foshan Southerly Ancient Stove Creative Industry Park. It gathers not only the best traditional handicrafts such as old banyan, ancient architectures, ancient civilian dwellings, and straw sandals, but also the best folk arts like lion dance, martial arts, Cantonese operas. and paper-cuts.

– Compound industry—All-round development
  This type of park holds diverse industries. For example, OCT-LOFT is the result of the function renovation of the east part of Shenzhen Overseas City. It opens to industries like art design, architecture design, advertisement design, fashion design, planar design, and handicrafts design of the whole city or even the whole South China region and provides them with a place for creativities, exhibitions, productions, and communications. Invested by China Merchants Technology Holdings Co., Ltd., Nanhai E-Cool, the second project of Shekou Creative Industry Park, lies near Shekou Sea World with an area of 100,000 square meters. The main industries here are game animations and creative designs.

4 THE PLANNING LAYOUT AND THE RECONSTRUCTION MODE

4.1 *The planning layout of the obsolete industrial zone for creative industry*

– Perfection of transportation
  The surrounding environment of the old industrial parks such as the road condition and facility sites which were designed to serve the production of the former companies. With a strong function and an enormous space, it is good for product transportation but is not good for human activities. With a sense of monotony and dullness on the outer space of the old industrial parks, we could hardly feel any liveliness and human touch. Besides, in the long run, the layouts of some old industrial buildings become a mess after many unplanned extensions with narrow road space, messy and dirty environment, low using rate, and the cargo transport access, and fire-fighting access in disorder, which stops us from full taking the best out of its usage, safety, and social advantages. This messy environment also damages the historic and cultural atmosphere of the buildings greatly. So we need to reorganize the transportation to make it easily accessible and provide an unobstructed route for human traffic as well as cargos so as to eliminate the hidden danger in fire fighting and increase the space for auto parking.

  When planning the transportation for the reconstruction of the old industrial buildings, there are several factors that should be taken into consideration:

  * Design for accessibility and easy access
    Whether the traffic around this area is convenient, and the position and design of the access are easy to identify and approach.

* An appropriate allocation of human traffic and cargo transport to make traffic smooth
  Whether the traffic of humans will conflict with the traffic of cargos, and the instructions for and evacuation of human flow are reasonable.
* Enough parking spaces
  Whether the parking place is enough or do we need to broaden our underground parking lot.

– An improvement in landscape
  The outer space of the buildings which is a continuation of the inner space of the buildings is interpenetrating with public space of the city. Hence, an excellent outer environment which usually includes roads, site facilities, and environmental greening plays a main role in the old industrial parks' keeping up with the city renewal. Because the surrounding environment of the old industrial buildings is designed for production, transportation, and preservation of the industrial age, it is usually monotonous, mechanical, dull, and lack humanized designs. Plus, these old industrial buildings have long been abandoned, which lead to a severe state with crowded and cluttered surroundings, clogged road, the cargo transport access and fire-fighting access in disorder, and lack of green plants and recreation space. As a result, in order to create a comfortable and a convenient and humanized new community environment, a great effort has to be made to reconstruct the outer environment. One good example here is the landscaping square design of Nanhai E-Cool (Wu 2010).
– Reusing and reshaping of park features
  * Rebirth of the landscape and visual system
    We can reinforce the uniqueness of the original environment by providing scientific outdoor facilities and landscapes that match people's needs. The facilities of old industrial parks, such as a forest of chimneys, a group of buildings, the towering cranes, and the spanned pipelines, are the products of industrial age and also an important part of the landscape of the old industrial park. After we do some adjustment to these facilities, be it adding some design or removing some parts, we can highlight the representative features of the industrial park.
  • The artistic processing of industrial labels must create a striking effect with bright colours.
  • The reshaping and even the abrupt change of industrial units have a dramatic effect on the park.
  * Recycling of waste materials
    The waste materials can be a source of landscape under the secondary design and principles of sustainable development of ecosystem. In this way, the history record can be preserved as well.

5 THE RECONSTRUCTING MODE OF THE OBSOLETE INDUSTRIAL ZONE FOR CREATIVE INDUSTRY

5.1 *Updating and adjusting of the functions*

Based on the current situations of the old industrial zones and the development of creative industry in Guangdong, the functions to be replaced include creativity activities function, exhibition and communication function, and recreation and consumption space.

– Replaced as a creativity activity space—A place for creative movements
  The old industrial building space can be designed as a creativity activity space so that after reconstructing the original structure of the enormous space becomes flexible and meets different needs of creativity activities.
  An example of this kind of function replacement is Nanhai E-Cool which became a creative studio after replacing the functions of the huge space of the old industrial buildings.
– Replaced as exhibition and communication space—A showcase for creative achievements
  The layout of old industrial buildings space is so similar with the layout of large-scale exhibitions that we can simply do some space division or integration for exhibition purpose. What's more, the original structure of the buildings or the abandoned equipment can serve as a main role or supporting part for the exhibition. And the space between the buildings or the outdoor space within the park can be used as exhibition as well. An example of this kind of function replacement is Creative Culture Park of Overseas City which makes good use of the space of the old industrial park and is made into small and large exhibition halls for exhibitions.
– Replaced as recreation and consumption space—A place for creative product consumption
  The creative industry parks need the assistant function of consumption space to support the designing platform. Meanwhile, with a lot of people who follow the fashion trends coming in, the consumption area of the industrial park will become a new consumption place for the whole city as well. An example of this kind of function replacement is Overseas City LOFT Creative District which turns the space between factory buildings and the park into an exhibit market. It is a creative product consumption place with cultural and artistic atmosphere.

5.2 *Space transformation*

When the space provided by old industrial park doesn't meet the requirements of new functions, we can transform the space by dividing the whole space into small parts or combine small parts into a whole so as to meet the space requirements of the new functions.

- Overall space transformation
  The transformation of overall space includes separation, combination, and extension.
- Separation of space
  To meet the requirements of the new functions, the overall space inside the old industrial park can be separated vertically or horizontally into small parts for better use.
- Combination of space
  The space between individual buildings can be combined into a larger and connected continuation of space by knocking the obstacles between two buildings through or bridging two buildings with a corridor or linking two buildings with a roof.
- Extension of space
  The extension of space is based on the original building structure but builds new parts vertically or horizontally to complement the functions of the buildings. However, before adding new parts on the old buildings, we have to understand what the new parts are for and how the new parts function and how to handle the consistency between the newly-built space and the remaining space from the old building and make it a whole consistent space. Because the extension parts involve the bearing capability of the old buildings, an analysis of the bearing capability of the building structure is needed before starting the extension project.
- Partial space transformation
  - Partial space removal
    Three ways to remove partial space are adding new layers vertically, extending space horizontally, and using underground space. The first two methods are most commonly used in old industrial building reconstruction in China. Here are the details: removing part of the wall, or part of the floor slab, or part of the beams, or part of the pillars, or even part of the building.
  - Partial space addition
    Based on the space requirements of new functions, new space can be created by building additions inside or outside the building. The most common space additions are stairs, elevators, corridors, vestibules, and roofed patios. The style of the added space can either unite or contrast with the original building.
  - Partial space rebuilding
    Part of the building has to be removed and rebuilt so as to repair the damage of the original building caused by long term usage or to meet the requirements of the reconstructing design. The jumping-off points of these two conditions are different, so are the approaches taken in rebuilding. The former focuses on reinforcement and adjustment with the whole building style unchanged for repairing reasons; the latter always hopes to be different from the original building and have an ingenious façade by rebuilding.

5.3 *Building's façade design*

A building's façade design is a very important part in old industrial building reconstruction. Building style, building shape, decorating materials, building dimensions, and colours are the outer features of a building and are one of the significant factors that reflect the characteristics of the building itself. The reconstruction of building's façade has to meet the requirements of the new functions and take the consistency with the surrounding environment into consideration. Generally speaking, the ways to design a building's facade are:

- Repairing and preserving the façade of the old building
  This reconstructing approach is usually applied to architectural heritages which contain distinct regional characteristics and historical value. For this kind of industrial building, when handling its façade, a conservative attitude has been taken by preserving major parts of the outer features of the original building and doing some maintenance or repairing or replacing part of the units. Sometimes, the changes in building functions are so great that an overall removal has been taken inside the building—using steel structures to replace the original concrete structures or brick-timber structures just to save the whole building's façade. In this way, not only the historical features have been preserved, but new functions and new space are also achieved.
- Removing the façade of the old building
  This approach is aimed at many ordinary old industrial buildings whose value is mainly embodied in its excellent structure conditions, locations, and well-equipped facilities. These buildings do not have distinct historical or aesthetic value or features, so the updating of the façade of these buildings can enjoy a larger freedom. Only limited by the original structure potential, designers can give free rein to their imagination and creativities to redesign the façade of the building, to create new façades and make the old façade disappear.

– Updating the equipment technology
  Since the equipment inside the old industrial building serves the former production process, most of them do not meet the requirements of the new functions and thus will be dismantled and updated while some with historic value or features can be saved as an organic part of the old body.
  * Updating of the equipment
    During the reconstruction of the old industrial buildings, the updating of the buildings' facilities, which is aimed to improve the intrinsic physical environment of the buildings, is an indispensable step for enhancing the reconstructing quality. The main updating will involve equipment on electric power, telecommunication, elevators, water supply, sound and video systems, heating and air conditioning, and fire-fighting.
  * Application of low-energy consumption
    Two aspects of the application of low-energy consumption are the restructuring of the building's envelope structure and the application of intelligent control technology.

    Restructuring the Building Structure: This involves the restructuring of the building's envelope structure and the installation of ventilation systems. The envelope structure includes exterior walls, windows and doors, and the roofs. Take Shenzhen's Nanhai E-Cool as an example, the reconstructing of the wall body and the application of the "ventilating chimneys" technology are aimed at saving energy.

    Reconstruction of Wall Body: Corresponding with the new functions, designers kept as much original wall body as possible and added a layer of 100-millimeter thermal insulation masonry on the interior wall just to meet the energy-saving requirements of local public buildings. Besides, the measures of employing LOW-E insulating glass, external sun shading, and heat-insulating roofing with extruding polystyrene board also contributed to meet the energy saving requirements.
  * Application of intelligent control technology
    In order to operate and manage the low-energy consumption technology properly, the building can be equipped with a series of intelligent control technology such as heat accumulation measurement on the wall body and infrared ray thermal radiation. A comprehensive usage of the intelligent control technology can lower the heat energy demands of the building efficiently.

6 CONCLUSION

For the past several years, owing to the rapid economic growth of Guangdong, many cities are confronted with city function and industrial structure adjustments which lead to a function modification of partial land thus creating plenty of spare and abandoned industrial buildings. These buildings feature as firm main structure, highly flexible space, large building groups and have a great impact on environment if under removal or reconstructing, and possess unique design ideas, aesthetic values, and historic and cultural characteristics at the same time. Old industrial buildings can fulfil the basic building space demands of creative industry, but as practice, there are still some reconstructing blindfold actions which waste social resources. Hence, this article is intended to provide a reconstructing guide for the combination between creative industry and old industrial zones in China by setting up an appropriate reconstructing planning through carrying out the analysis on influence factors, the choice on function types and the reconstruction on physical space, and the examples of Guangdong as cases.

ACKNOWLEDGMENT

It is supported by the National Natural Science Foundation of China (51208138) and Shenzhen Key Laboratory of Urban Planning and Decision Making, Harbin Institute of Technology Shenzhen Graduate School.

REFERENCES

Altrock, U. & Schoon, S. 2013. Urban villages as local economic clusters: The case of the Zhongda cloth market in Guangzhou. *Rural Migrants in Urban China*. Wu, F.L. Zhang, F.Z. & Webster, C., eds. London: Routledge.

Cao, Z.L. 2008. *A Design Research on the Reuse of the Old Industrial Buildings in Combination with Creative Industry in Shenzhen*. Harbin: Harbin Institute Technology.

Catier, C. 2002. Transnational urbanism in the reform-era Chinese city: Landscapes from Shenzhen. *Urban Studies* 39(9):1513–1532.

Wang, J.G. 2008. *Protection and Renovation of Industrial Buildings of Post-industry*. Peiking: China Architecture & Building Press.

Wu, X.Y. 2010. To probe into the conversion of existing industrial buildings to creative industry park in Shenzhen. *Architectural Journal* (S1): 47–50.

This page intentionally left blank

Civil Engineering and Urban Planning IV – Liu et al. (Eds)
© 2016 Taylor & Francis Group, London, ISBN 978-1-138-02903-3

Comprehensive evaluation research on the sustainable development of urban infrastructure

Yang Lin, Meng-Ping Zhang, Hong-Tao Wang & Yi-Chen Li
School of Civil Engineering, Wuhan University, Wuhan, Hubei, China

ABSTRACT: Urban infrastructure is the important foundation for urban survival and development. How to alleviate and avoid "city disease" are realistic issues that everybody has to face. Making a comprehensive evaluation for the sustainable development of the city infrastructure is not only the need of urban sustainable development, but also the need of scientific and reasonable planning and construction, as well as meeting the urban sustainable development. This paper puts forward the index system of quantitative analysis, and builds the evaluation system of the urban infrastructure sustainable development. According to the quantitative indicators of the index system, this paper gathers the basic data of urban infrastructure during 2007~2014 in Wuhan, China and analyzes four secondary indices. Moreover, the paper uses the principal component analysis (pca) to measure the sustainable development of Wuhan infrastructure. Finally, it combines with the situation of Wuhan urban infrastructure sustainable development to put forward the corresponding countermeasures.

1 INTRODUCTION

As an open and complex ecosystem, the urban absorbs various resources from the outside and makes much negative effect through their internal operation mechanism (Corvellec et al. 2013). The early urban infrastructure has been built and put into use gradually in the process of the high-speed construction and development (Ma et al. 2012 & Shankar et al. 2009). Their function has been exerted, but it does not solve the existing problems. Instead, the urban problems tend to be more serious to some extent (Gilmour 2011), such as traffic jams, air pollution, heat island effect, strained resources, city garbage, sewage treatment, and municipal drainage facility falling. In 2013, the Government Work Report used "city diseases" to describe this phenomenon. This Report states that: "the urban infrastructure is not perfect." The financing difficulties, the 'city diseases' and the comprehensive governance mechanism of the environment need innovation urgently (Pandit et al. 2014). Urban sustainable development can embody the potential power of the current development and meet the need of the present development without compromising the ability of future development (Mell et al. 2009). The support and the guarantee capabilities are related to the urban development among all elements of the society, the economy and the environment.

Based on the fundamental role of the urban infrastructure, the urban sustainable development does not separate the urban infrastructure sustainable development. In the real world, many urban infrastructures have been built and put into use gradually (Asgarzadeh et al. 2009). Therefore, it is vital to assess the perfect degree of the existing urban infrastructure system, the sustainable development level and the potential of the urban infrastructure.

2 LITERATURE REVIEW

The international research and practice of the infrastructure sustainable development are advanced. The idea of the sustainable development runs into the life cycle, including the design, the construction, the operation and the maintenance of the infrastructure. In the theory research, the maneuverability of the sustainable development is related to the operation management of the urban road infrastructure (Wang 2010). It illustrates that the current management does not adapt to the urban sustainable development. So, it establishes the conceptual frame. The frame expands that the basic task of the operation management of the urban infrastructure is to obtain and keep the maximum of the mobility of people and goods, under the bearing capacity of the regional resources and the environment (Andrade et al. 2011). AlQahtany et al. (2013) studied the status of the urban infrastructure sustainable development using the knowledge management theory

and the life-cycle cost theory. Under the centralized background, Reiner et al. (2014) researched the problems of the sustainable development and the institutional incentive of the infrastructure, by presenting the evaluation of behavior criterion of the individual's and institute's performance on the environment. In terms of the development feature of the living environment of humans, Ma Tao summarized the ten steps of achieving the infrastructure sustainable development environment (Maotao et al. 2012). In the real world, towards the urban planning and design, on the one hand, the UK strengthened the strategy implementation of the sustainable development through adjusting the urban design policy. On the other hand, the UK began to propose and implement the sustainable development standards of the urban design. For example, in 2010, the greater London authority put forward the Strategy of Sustainable Design and Build for London in Supplementary Planning Guidance, stating that: "The authority proposed the concrete and sustainable design standards and guidelines, according to the actual development of London, aiming at several key areas of the sustainable development relating to the urban design, such as reusing the land and buildings, responding the climate change, saving the energy and water, reducing the noise and air pollution, enhancing the micro climate, improving the traffic accessibility and the environmental comfort, promoting the environmental tolerance and protecting the natural environment and biodiversity." These can be considered as the first implementation of the urban sustainable design standards environment (Zheng et al. 2009). In terms of the urban drainage infrastructure, the UK Environment Protection Department analyzed the defect of the traditional drainage system, through presenting the concept of "the sustainable drainage system". The new system included a series of sustainable management technologies relating to the surface water and groundwater. The technology could reduce the likelihood of the urban water logging, improve the utilization rate of the surface water and rainwater, minimize the pollution diffusion, maintain or restore the natural water and beautify the environment. Except those functions, the amount of the comprehensive cost was less than the traditional drainage system environment (Spth & Rohracher 2014). Marseille, the second biggest city in France, was affected by the Barcelona anellaverda and formulated the development plan of the green infrastructure. Consecrating the city's residual non-constructive space fully, the plan solved the problem of the sustainable development of the urban environment by the planning and construction of the urban green infrastructure environment (Sun & Hu 2012). It is also a part of the sustainable development spreading the green building concept and certification. In the USA, both official and non-governmental organizations advocated vigorously the green building authentication. By 2013, over the hemisphere, 10.5 billion square feet of the commercial and public buildings' design, the construction and the operation were authenticated by LEER. Since November 2013, in the USA, the green building council has begun to adopt the latest LEEDv4 authentication system. On the one hand, the new system enhanced the design and construction standards of the green building. On the other hand, the new system enlarged the application areas, such as data center, warehouse, logistics center, hospital, school and store (Zhong & Juan 2013; Morrissey et al. 2012; Ardekani et al. 2013). Thus, LEEDv4 in the USA adapted the demands of the sustainable development. Singapore paid great attention to the urban sustainable development. In order to promote the development of the domestic green building, the Singapore Construction Bureau established the awards of Green Mark, aiming at the construction industry. The index system of selecting Green Mark included five aspects: building the energy efficiency, building the water use efficiency, the construction of environmental protection, and building the indoor environment quality and other innovation designs of environmental protection related to building. And the government pushed the development of the green building construction to meet the long-term needs of the sustainable development, through making the incentive policy.

3 RESEARCH METHODOLOGY

The urban infrastructure is a complex system. Two main aspects can be divided: large-scale systems, such as energy power, transportation, water supply and drainage, posts and telecommunications, ecological environment and safety and calamity reduction; small-scale systems, containing a lot of specific evaluation index to measure the practical status environment (Yigitcanlar & Dur 2010). It is unreasonable to use a single index to evaluate comprehensively. This is because the evaluation index system has a lot of hierarchies and evaluates the environment (Aghasian & Charehjoo 2011). It is absolutely necessary to collect and fuse the information of the indicators to obtain the comprehensive index and reflect the whole situation of things evaluated. Therefore, it is more reasonable to adopt the method of the multi-index comprehensive evaluation.

At present, the comprehensive evaluation method includes two categories: subjective determining weights evaluation method and objective determining weights evaluation method environment

(Dou et al. 2011; Chenevey & Buchberger 2013). The former usually adopts the qualitative method, getting the weight from the subjective judgment of experts according to the practical experience, such as analytic hierarchy process and fuzzy comprehensive evaluation; the latter gets the weight according to the correlation between indicators and the variation coefficient of each index, such as gray correlation method, TOPS worker method and principal component analysis. For improving the reliability of the analytical results, it is a more scientific and objective way to get the weight according to the correlation between indicators and the variation coefficient of each index.

3.1 *Analysis principle*

The principal component analysis is one of statistical methods that is used to get a new set of independent comprehensive variables to substitute the original variables. Meanwhile, it chooses a few comprehensive variables from these according to the actual need. Those comprehensive variables are called principal components, which contain the most important information in the data and show the characteristics of the research object.

3.2 *Mathematical model*

We consider an original $n \times p$ matrix X with n variables and p sample data ($X_1, X_2, \ldots, X_p$), which is configured as follows:

$$x = \begin{bmatrix} \begin{bmatrix} x_{11} & x_{12} & \cdots & x_{1p} \\ x_{21} & x_{22} & \cdots & x_{2p} \\ \cdots & \cdots & \cdots & \cdots \\ x_{n1} & x_{n2} & \cdots & x_{np} \end{bmatrix} \end{bmatrix} \quad (1)$$

We define $X_1, X_2, \ldots, X_p$ for the original variable indicators. $Z_1, Z_2, \ldots, Z_m$ is the new comprehensive variable indicators ($m \leq p$). The purpose of the principal component analysis is to reduce dimensions to transform p original indicators ($X_1, X_2, \ldots, X_p$) to m comprehensive indices ($Z_1, Z_2, \ldots, Z_m$) on the premise of little information loss. Each new comprehensive variable is a linear combination of the original variables, which is configured as follows:

$$\begin{cases} Z_1 = I_{11}x_1 + I_{12}x_2 + \cdots + I_{1p}x_p \\ Z_2 = I_{21}x_1 + I_{22}x_2 + \cdots + I_{2p}x_p \\ \vdots \\ Z_m = I_{m1}x_1 + I_{m2}x_2 + \cdots + I_{mp}x_p \end{cases} \quad (2)$$

At the same time, new variables meet the following conditions:

1. Z_i is independent on Z_j ($i = j$, $j = 1, 2, \ldots, m$).
2. Z_1 is the maximum of the variance in the linear combination of $X_1, X_2, \ldots, X_p$; Z_2 is the maximum of the variance in the linear combination of $X_1, X_2, \ldots, X_p$, unrelated Z_1; Z_m is the maximum of the variance in the linear combination of $X_1, X_2, \ldots, X_p$, unrelated $Z_1, Z_2, \ldots, Z_m$ with each other. The new variable $Z_1, Z_2, \ldots, Z_m$ was regarded as the first, second, …, mth principal component of the original variable $X_1, X_2, \ldots, X_p$.

The essence of the principal component analysis is to determine the coefficient l_{ij} ($i = 1, 2, \ldots, m$; $j = 1, 2, \ldots, p$) of the original variable X_j ($j = 1, 2, \ldots, p$) in the principal component Z_i ($i = 1, 2, \ldots, m$). It can be proved that the coefficients lij are corresponding eigenvectors of larger eigenvalues of the related matrix, respectively, in all original variables ($X_1, X_2, \ldots, X_p$). The variance of the comprehensive variable Z_i is the corresponding characteristic root λ_i. The correlation coefficient matrix is a positive definite matrix, so the characteristic root λ_i is positive. Ranking them by size, we get $\lambda_1 \geq \lambda_2 \geq \ldots \geq \lambda_i \geq 0$.

In addition, n represents the number of evaluation objects; $X_1, X_2, \ldots, X_p$ represent the original variables and are used to measure the evaluation objects; l_{ij} represents the eigenvector of the correlation coefficient matrix of the original variable; λ_i represents the eigenvalues of the correlation coefficient matrix of the original variable; the principal component of $Z_1, Z_2, \ldots, Z_m$ has more superior performance than the original variables.

3.3 *Analysis steps*

1. Select the analysis variables: Determine the analysis variables, and collect the research data to construct the original data matrix, which is configured as follows:

$$x = \begin{bmatrix} \begin{bmatrix} x_{11} & x_{12} & \cdots & x_{1p} \\ x_{21} & x_{22} & \cdots & x_{2p} \\ \cdots & \cdots & \cdots & \cdots \\ x_{n1} & x_{n2} & \cdots & x_{np} \end{bmatrix} \end{bmatrix} \quad (3)$$

2. Normalize the raw data: Because the measurement unit of the analysis variable is different, they cannot be directly compared and analyzed. Therefore, the original data need to be converted to the dimensionless standard data by a specific mathematical formula. The standardized function is as follows:

$$Z_i = \frac{x_i - \overline{x}}{s_i} \quad (4)$$

It should be noted that

$$\bar{X} = \frac{1}{n}\sum_{i=1}^{n} x_{ij} \tag{5}$$

$$s_i = \sqrt{\frac{1}{n-1}\sum_{i=1}^{n}(x_{ij} - \bar{x})^2} \tag{6}$$

We obtain the standardized matrix by calculation, which can be configured as follows:

$$Y = \begin{bmatrix} \begin{bmatrix} y_{11} & y_{12} & \cdots & y_{1p} \\ y_{21} & y_{22} & \cdots & y_{2p} \\ \cdots & \cdots & \cdots & \cdots \\ y_{n1} & y_{n2} & \cdots & y_{np} \end{bmatrix} \end{bmatrix} \tag{7}$$

3. According to the standardized data, calculate the covariance matrix and obtain the correlation coefficient matrix as follows:

$$R = \frac{1}{n} Y'Y \tag{8}$$

It should be noted that R represents a $p \times p$ matrix.

4. Calculate the eigenvalue and the corresponding unit eigenvector of the correlation coefficient matrix.
5. According to the following formula, calculate the contribution rate of the principal component and the cumulative contribution rate.

The contribution calculation rate is defined as follows:

$$a_i = \lambda_i \Big/ \sum_{k=1}^{p} \lambda_k (i = 1, 2, \ldots, q; k = 1, 2, \ldots, q) \tag{9}$$

where λ represents the eigenvalue; a represents the eigenvector; q represents the count of the eigenvalue of the correlation matrix.

$$\sum_{k=1}^{i} a_k = \sum_{k=1}^{i} \lambda_k \Big/ \sum_{k=1}^{q} \lambda_k (i = 1, 2, \ldots, q;\ k = 1, 2, \ldots, q) \tag{10}$$

6. Obtain the principal components and determine the score of principal components. Follow the steps below:

1) Select the cumulative contribution rate from 85% to 95%;
2) Select the principal component whose $\lambda_i \geq 1$;
3) Accumulate the principal components, of which the eigenvalue product is more than 1;
4) Calculate the score of the principal components, which is defined as follows:

$$F = \sum_{k=1}^{i} a_k F_k \tag{11}$$

4 DATA COLLECTION

4.1 *Raw data of UISDL (Urban Infrastructure Sustainable Development Level) in Wuhan, China*

The comprehensive evaluation of the sustainable development status of the urban infrastructure involves not only the need of the sustainable development of the urban infrastructure, but also the need of scientific and reasonable planning, city construction and meeting the urban sustainable development. This paper takes Wuhan city infrastructure as the research object. According to the quantitative index evaluation system that Section 3 builds, the principal component analysis (p c a) is used to analyze and evaluate four secondary indices, respectively, including the level, the potential, the coordination and the regulation of the urban infrastructure sustainable development in Wuhan. Then, based on the results of the evaluation and analysis of the above four indices, it further analyzes and evaluates the comprehensive level of the sustainable development of the urban infrastructure in Wuhan. Through the descriptive statistics, the original variables are analyzed using the maximum variance method. Then, it works out the total variance explanation. Through the total variance explanation, the initial eigenvalue, the contribution rate and the cumulative contribution rate of the original variable can be obtained. Based on the condition of selecting the principal component, the principal component can be determined, which is presented in Table 1. Taking the contribution rate as the weight of each principal component, we calculate the score of each principal component.

4.2 *Standardized data on the UISDL outputs*

The standardized data of Wuhan city infrastructure sustainable development level are summarized in Table 2.

5 ANALYSIS AND EVALUATION

By using the Principal Component Analysis (PCA), the quantitative analysis and evaluation were carried out, respectively, on four secondary indices of the sustainable development of the urban infrastructure in Wuhan. Next, this paper takes the level, potential, coordination and regulation of the sustainable

Table 1. Raw data of Wuhan urban infrastructure sustainable development level.

	2007	2008	2009	2010	2011	2012	2013	2014
TEC	3102.33	3186.26	3828.17	3884.03	3914.27	3741.91	4071.71	5545
TEWC	185.5802	210.8743	230.8126	258.6728	286.4338	310.2749	353.6311	383.6469
TCGS	1.084	1.4092	1.802	2.8469	4.0859	5.6489	7.8444	10.5
GSPTL	2344	2649	3073	3475	3880	4688	5187	5532
TWS	7.6466	9.6096	9.2921	9.4203	9.6595	9.7612	10.0072	10.9602
TW	6.88	6.6676	6.232	7.1632	7.3235	7.4011	7.6856	8.4779
WSPL	5730	6130	6380	6644	6679	6708.4	6949.6	7156.8
UDPL	1684	1730	1810	6126	6321	6592	7543	7909
TLR	2132.19	2300.45	2369	2515	3034.7	2542	2682.2	2840.1
TAR	3583.13	4100	4328	4771	5809	6802	7273	7726.2
PTWS	1.28857	1.541344	1.61937	1.733836	1.888206	2.170397	2.289671	2.574322
RTOLL	10.6	10.6	10.6	10.6	10.6	10.6	29.3	29.3
BOLL	5213	5463	5986	6600	6976	7241	7001	5862
TNOPSC	5367	5213	5463	5986	6600	6976	7241	7465
BTOPATU	74.97	114.96	145.13	180.62	211.11	293.8215	109.47	128.94
LSTC	232.7	231.55	234.7	293.2	316	279	273	255
TMPS	454	556.15	691.99	624.08	815	1037	1145	1271
UTS	343.7	381.44	403.45	436.51	380	339	316	316
UGGA	6775.9	7066.2	7168	16837.74	17242	17479	17990	16347.32
PLG	202	207	211	215.35	219.03	217.42	219.14	224.4
EPI	6.7276	6.8199	8.43202	7.238184	3.74663	12.9085	19.28346	8.6697
ISWP	749.68	847.29	954.31	922.48	1094.49	1215.05	1324.84	1379.65
TEE	2489.42	2567.36	3060.35	3049.92	4014.7	4299.87	4720.8	6360
TWWE	7.21447	6.566527	6.574634	6.62832	7.88588	7.843506	7.837666	7.65819
FL	602.3	525.9	918.59	987.07	1101.5	1653.72	1188.37	2724
TAL	1820.39	469.8	475.26	670.16	469.89	440.42	387.67	486.3
D	1.9634	2.004	2.1145	2.1541	2.2728	2.3997	2.5069	2.5376
NOHD	3.58	3.74	3.81	4.07	4.34	4.81	5.12	5.65

Notes: TEC = Total energy consumption (ten thousand tons of standard coal); TEWC = Total electricity of whole society (million kilowatt hour); TCGS = Total city gas supply (a hundred million cubic meters); GSPTL = Gas supply pipeline total length; TWS = Total water supply (a hundred million cubic meters); TW = Total water (a hundred million cubic meters); WSPL = Water supply pipe length (kilometer); UDPL = Urban drainage pipe length (kilometer); TLR = Total length of road (kilometer); TAR = Total area of the road (ten thousand square meter); PTWS = Passenger traffic of the whole society (a hundred million person-time); RTOLL = Rail transit operation lines length (km); BOLL = Bus operating line length (km); TNOPSC = Total number of Public steam (electric) cars; BTOPATU = Business total of posts and telecommunications (one hundred million yuan); LSTC = Local subscribers total capacity (thousands of families); TMPS = Total mobile phone subscribers (thousands of families); UTS = Urban telephone subscribers (thousands of families); UGGA = Urban garden greenbelt area (ha); PLG = Pick-up living garbage (ten thousand tons); EPI = Environmental protection investment (one hundred million yuan); ISWP = Industrial solid waste production (ten thousand tons); TEE = Total exhaust emissions (one hundred million standard cubic meters); TWWE = Total waste water emissions (one hundred million tons); FL = Fire losses (ten thousand yuan); TAL = Traffic accident losses (ten thousand yuan); D = Doctor (ten thousand); NOHB = Number of health bed (ten thousand).

development of the city infrastructure in Wuhan as variable indicators. By using the Principal Component Analysis (PCA) again, the comprehensive evaluation of the sustainable development of the city infrastructure in Wuhan is carried out.

5.1 *Analysis of the comprehensive score of original data*

The respective composite scores of the level, the potential, the coordination and the regulation of the sustainable development of the urban infrastructure in Wuhan every year from 2007 to 2014 are taken as the original data of the comprehensive analysis and evaluation, as presented in Table 3.

5.2 *Processing the raw data*

The original data come from the different comprehensive scores each year from 2007 to 2014. So, they are dimensionless data and need not to be standardized. The index characteristic values, the contribution rate and the cumulative contribution rate are obtained by calculation, as given in Table 4.

Table 2. Standardized data of Wuhan city infrastructure sustainable development level.

	2007	2008	2009	2010	2011	2012	2013	2014
TEC	–1.07946	–0.96718	–0.10842	–0.03369	0.00677	–0.22382	0.2174	2.18839
TEOWS	–0.31733	–1.03	–2.0566	0.08127	0.31277	0.51158	0.87314	1.12344
TCGS	–0.98269	–0.88639	–0.77008	–0.46068	–0.0938	0.36902	1.01913	1.80548
GPTL	–1.27742	–1.01931	–0.6605	–0.32031	0.02243	0.7062	1.12848	1.42044
TWS	–2.05626	0.07043	–0.27354	–0.13465	0.1245	0.23468	0.50119	1.53366
TW	–0.35378	–0.35387	2.47487	–0.35365	–0.35358	–0.35354	–0.35341	–0.35305
WSPL	–1.79183	–0.9148	–0.36665	0.21219	0.28893	0.35339	0.88224	1.33654
UDPL	–1.19975	–1.18293	–1.15367	0.42485	0.49617	0.59528	0.9431	1.07696
TLOR	–0.45817	–0.41123	–0.3921	–0.35137	–0.20638	–0.34384	–0.30472	2.46781
TAOTR	–1.24655	–0.91881	–0.77424	–0.49334	0.16484	0.79448	1.09313	1.3805
PTOTWS	–1.39818	–0.80879	–0.62686	–0.35996	–0.00002	0.65796	0.93607	1.59978
RTOLL	–0.54006	–0.54006	–0.54006	–0.54006	–0.54006	–0.54006	1.62019	1.62019
BOLL	–1.41153	–1.08471	–0.40101	0.40166	0.8932	1.23963	0.92588	–0.56311
TNOPS	–1.02703	–1.1986	–0.92008	–0.33742	0.34662	0.76551	1.06073	1.31029
BTOPAT	–1.18438	–0.60964	–0.17603	0.33404	0.77225	1.961	–0.68854	–0.40871
LSTC	–1.01437	–1.05118	–0.95036	0.92196	1.65168	0.46748	0.27545	–0.30065
TMPS	–1.24989	–0.90508	–0.44654	–0.67578	–0.03132	0.71806	1.08262	1.50794
UTS	–0.48263	0.39254	0.90294	1.66959	0.35915	–0.59162	–1.12498	–1.12498
UGGA	–1.24555	–1.19066	–1.17141	0.65696	0.7334	0.77821	0.87483	0.56423
PLG	–1.69881	–1.01477	–0.46754	0.12757	0.63103	0.41076	0.64607	1.36568
EPI	–0.52036	–0.50115	–0.16569	–0.41411	–1.14066	0.76582	2.09238	–0.11623
ISWP	–1.35553	–0.93049	–0.46447	–0.60307	0.14595	0.67093	1.14901	1.38768
TEE	–1.01476	–0.95533	–0.57944	–58739	0.14823	0.36566	0.68661	1.93642
TWWE	–0.10171	–1.17021	–1.15684	–1.06831	1.00548	0.93561	0.92598	0.63001
FL	–0.86646	–0.9749	–0.78761	–0.32031	–0.15788	0.62595	–0.03458	2014569
TAL	2.43892	–0.3815	–0.3701	0.03691	–0.38131	–0.44286	–0.55301	–0.34704
D	–1.27082	–1.08703	–0.5868	–0.40754	0.12981	0.70428	1.18957	1.32854
NOHB	–1.09694	–0.88026	–0.78547	–0.43336	–0.06771	0.56879	0.9886	1.70636

Notes: TEC = Total energy consumption (ten thousand tons of standard coal); TEOWS = Total electricity of whole society (million kilowatt hour); TCGS = Total city gas supply (a hundred million cubic meters); GPTL = Gas supply pipeline total length (kilometer); TWS = Total water supply (a hundred million cubic meters); TW = Total water (a hundred million cubic meters); WSPL = Water supply pipe length (kilometer); UDPL = Urban drainage pipe length (kilometer); TLOR = Total length of road (kilometer); TAOTR = Total area of the road (ten thousand square meter); PTOTWS = Passenger traffic of the whole society (a hundred million person-time); RTOLL = Rail transit operation lines length (km); BOLL = Bus operating line length (km); TNOPS = Total number of Public steam (electric) cars; BTOPAT = Business total of posts and telecommunications (one hundred million yuan); LSTC = Local subscribers total capacity (thousands of families); TMPS = Total mobile phone subscribers (thousands of families); UTS = Urban telephone subscribers (thousands of families); UGGA = Urban garden greenbelt area (ha); PLG = Pick-up living garbage (ten thousand tons); EPI = Environmental protection investment (one hundred million yuan); ISWP = Industrial solid waste production (ten thousand tons); ISWP = Industrial solid waste production (ten thousand tons); TEE = Total exhaust emissions (one hundred million standard cubic meters); TWWE = Total waste water emissions (one hundred million tons); FL = Fire losses (ten thousand yuan); TAL = Traffic accident losses (ten thousand yuan); TAL = Traffic accident losses (ten thousand yuan); D = Doctor (ten thousand); NOHB = Number of health bed (ten thousand).

According to the score and the contribution rate of the principal component each year from 2007 to 2014, the annual comprehensive score is calculated, as presented in Table 5.

5.3 *Evaluation of the urban infrastructure comprehensive level*

From the figure, it can be seen that the comprehensive level of the sustainable development of the urban infrastructure in Wuhan is gradually increased from 2007 to 2014. Based on the table, we can divide the development process into two stages.

From 2007 to 2011, the structure and the function of the urban infrastructure were perfected year by year through the construction of four years from 2007 to 2011. Therefore, the comprehensive level of the sustainable development of the urban infrastructure in Wuhan was in a rapid ascension

Table 3. The comprehensive score of original data in Wuhan city infrastructure sustainable development.

	The composite scores of the level	The potential scores of the level	The coordination scores of the level	The macro-control scores of the level
2007	–0.94818	–0.72439	–0.37051	–0.573
2008	–0.52015	–0.74889	–0.40447	–0.71604
2009	–0.26164	–0.56877	–0.15932	–0.69246
2010	–0.16303	–0.22727	–0.37125	–0.2376
2011	0.047959	–0.07381	–0.81903	0.293831
2012	0.113302	0.30095	0.530462	0.468984
2013	0.313189	0.681266	1.433891	0.717649
2014	1.418566	1.360911	0.160227	1.254523

Table 4. The initial eigenvalue and extract sum of square by calculation.

	Initial eigenvalue			Extract sum of squares		
Principal component number	Eigenvalue	Contribution rate %	Cumulative contribution rate %	Eigenvalue	Contribution rate %	Cumulative contribution rate %
1	3.231	80.763	80.763	3.231	80.763	80.763
2	0.679	16.981	97.744			
3	0.085	2.119	99.864			
4	0.005	0.136	100			

Table 5. The annual comprehensive score in Wuhan city infrastructure sustainable development.

	First principal component scores	Composite scores
2007	–1.06121	–0.85707
2008	–0.96262	–0.77744
2009	–0.70054	–0.56578
2010	–0.39285	–0.31728
2011	–0.15308	–0.12363
2012	0.49078	0.396369
2013	1.094	0.883547
2014	1.68552	1.361277

period. Before 2007, the two factors, namely the current situation of the behindhand city infrastructure in Wuhan and the investment scale of the urban construction in this stage, directly affected the ascension speed of the comprehensive level of the city sustainable development in Wuhan. But the construction of this period laid a certain foundation for the promotion of the next period.

From 2011 to 2014, as the infrastructure was completed and put into use, the structure of the infrastructure system tended to be more perfect and the comprehensive ability of serving the society increased year by year. So, during this period, the comprehensive level of the sustainable development of the city infrastructure in Wuhan increased rapidly.

Combining the graph of the level, the potential, the coordination and the regulation of the sustainable development of the city infrastructure in Wuhan, it can be seen that the development tendency of the four-curve track is consistent, and all of them are a rising trend year by year. Only the coordination of the sustainable development showed substantial fluctuations and was in an unstable state. This suggested that through the urban infrastructure construction from 2007 to 2014, the current situation of the city infrastructure in Wuhan exhibited a lot of change: the constitution of the system tended to be perfect; the function and the level of serving the society were increasing; the infrastructure had a certain ability of the sustainable development. But in the process of the urban construction, the relations among the economic, social and natural environments should be well coordinated.

6 CONCLUSION

On the basis of the quantitative analysis conclusion of the previous chapter, the comprehensive level of

the sustainable development of the infrastructure in Wuhan was rapidly increasing year by year and the development level, the development potential and the development regulation all were in a state of increase year by year (Zito & Salvo 2011; Reiner M.B. 2014; Hadjri & Onyango 2013). It suggested that the infrastructure in Wuhan in the early stage improved the bearing capacity of the city and the urban ecological environment after being completed and put into use. It had a certain effect on promoting the sustainable and healthy development of the economic society in Wuhan. But only the index and the sustainable development coordination of the city infrastructure in Wuhan presented a fluctuation with large amplitude. The state of the coordination was not stable. It suggested that during the period from 2007 to 2014, the construction and the use of the infrastructure in Wuhan were not very good within the environment and the society. Recently, the current situation of the infrastructure construction in Wuhan reflected the blunt fact. During the stage of planning, investment, design, construction and operation of the infrastructure in Wuhan, the people-oriented, environmental-friendly and resource-saving concepts were not implemented and reflected in the whole life cycle of the project. Based on this, the article puts forward the corresponding countermeasures for the sustainable development of the urban infrastructure in Wuhan, respectively, from the phase of the planning and design and the phase of the construction of the project, and from the project implementation of the infrastructure. There are specific aspects that are detailed below.

The construction of various infrastructures should be strictly in accordance with the general planning of the city and the general planning of the urban land use in Wuhan. In the planning stage, the project should fully prepare the argument analysis for the bearing capacity of the resources and the environment, not only pay attention to the short-term economic benefit or just solve the current environmental problems (Xu et al. 2012). The planning should keep a long-term foothold, pay attention to the resource-saving and the environment protection, and avoid the disorderly and redundant construction. Also, it should pay attention to the protection of cultural relics in the planning process.

When making the planning, certain situations for the future development of the city should be fully considered. A lot of infrastructures are demolished and rebuilt, although they are not built for a long time or not used for the design working life. On the one hand, it makes a waste of resources; on the other hand, it impacts the traffic and the environment of the urban. The planning of the urban infrastructure should maintain properly in advance, in response to the unforeseen social needs in the future.

Once the urban planning is determined, it maintains relative stability and cannot change at will. If it is really necessary to modify, it should change strictly in accordance with the established procedure. But in fact, in the process of the implementation of much large-scale infrastructure, the established planning often gives way to the development and the construction of the infrastructure and even the commercial housing. In the process of our actual work, the so-called "rules" are very common, for example, presumptuously raising the volume rate, improving the commercial and residential housing area ratio, ignoring the sunshine and spacing requirements, and removing or reducing the area of land for public service facilities (e.g. refuse transfer station and welfare facilities). In addition, it is also used to ensure the continuity of the planning implementation and the coordination and order development of the city that the urban planning cannot modify at will.

At present, most funds of the urban construction in Wuhan are used for the construction of the road network and the rail transit of the urban. The investment proportion of the environmental infrastructure is very small. The environment problems in Wuhan city, such as water pollution, soil pollution and atmospheric pollution, still have not been fully improved. During the later period, the planning and the construction of the environmental protection infrastructure should be made perfect, such as the urban sewage treatment and the garbage disposal. On the one hand, its proportion in the fund investment of the whole city construction should be increased; on the other hand, the scientific establishment and the enforcement of the specialized planning should strengthen the environment (Hu et al. 2013).

In the process of designing the urban infrastructure, the infrastructure should have its own function. At the same time, it should follow the principle of the sustainable development. Under the condition that the investment control allows, the design concept of the green building should be fully embodied. For example, in terms of energy-saving, full use should be made of natural renewable energy sources, including the comprehensive utilization of the solar energy, the geothermal energy and the wind energy (Dou et al. 2011); with respect to the spatial structure and layout the natural lighting and the ventilation should be highlighted, including water resource recycling (Otegbulu 2010). In terms of the green building design, the USA, Singapore, Germany and Australia have been in the lead in the world. We should learn more about the experience and technology of the green building design from these countries. For example, in the architectural design, Singapore obeys the

design concept, "four saves and two environmental protections", including energy-saving, land-saving, water-saving and material-saving, and pays attention to the external ecological environment protection and the indoor environment protection. In terms of electricity-saving and energy-saving, there is a wide use of the energy-saving lamp, the induction illumination and the energy-saving escalator and the use of the solar energy as much as possible. For example, the Tree lodge, the first green group houses, gets Green Mark Platinum, installs solar panels in the roof, which occupies 20% to 30% of the roof area, and the electricity of which is used for lighting public places such as the parking lots and the corridor at night, saving as much as 80% electricity. In terms of water-saving, we use the latest technology in the architecture design phase, establish the urban rainwater collection system, adopt the water-saving automatic irrigation system, and set the rainwater collection system on the roof, to fully realize the water-saving and the water-recycling environment (Yang et al. 2014).

REFERENCES

Aghasian, E. & Charehjoo, F. 2011. A key to achieving sustainable development. *Proceedings—4th International Conference on Information and Computing,* 22(7): 451–456.

AlQahtany, A., Rezgui Y. & Li, H.J. 2013. A proposed model for sustainable urban planning development for environmentally friendly communities. *Architectural Engineering and Design Management* 9(3): 176–194.

Andrade, M.A., Romero-Gomez, P. & Choi, C.Y. 2011. Impact of sustainable urban water infrastructure on water quality. *World Environmental and Water Resources Congress 2011: Bearing Knowledge for Sustainability—Proceedings of the 2011 World Environmental and Water Resources Congress, California, 2011*. 22(05): 253–262. Reston, Virginia: American Society of Civil Engineers.

Ardekani Siamak A. & Bakhtiari Bahareh. 2013. A transportation sustainability index for urban communities. *Developing the Frontier of Sustainable Design, Engineering, and Construction—Proceedings of the 2012 International Conference on Sustainable Design and Construction* 11(2): 311–318.

Asgarzadeh, M., Koga, N., Takaaki, Yoshizawa, Munakata J. & Hirate, K. 2009. A transdisciplinary approach to oppressive cityscapes and the role of greenery as key factors in sustainable urbandevelopment. *2009 IEEE Toronto International Conference—Science and Technology for Humanity, Toronto, 2009.* 26(09): 1042–1047. New York: IEEE.

Chenevey, B. & Buchberger, S. 2013. Impact of urban development on local water balance. *World Environmental and Water Resources Congress 2013: Showcasing the Future—Proceedings of the 2013 Congress*, *Florida, 2013* 05(19): 2625–2636. Reston, Virginia: American Society of Civil Engineers.

Corvellec, H., Campos, M.J.Z. & Zapata, P. 2013. Infrastructures, lock-in, and sustainable urban development: The case of waste incineration in the Göteborg Metropolitan Area. *Journal of Cleaner Production* 50(1): 32–39.

Dou, X.H., Liu, R.Z. & Chen, X.Z. 2011. Reflections on water resource sustainable development in Wuhan metropolitan area. *Communications in Computer and Information Science* 211 CCIS(4): 363–369.

Gilmour, D., Blackwood, D., Banks, L. & Wilson, F. 2011. Sustainable development indicators for major infrastructure projects. *Proceedings of the Institution of Civil Engineers: Municipal Engineer* 164(1): 15–24.

Hadjri, K. & Onyango, J. 2013. The sustainability of new urban developments in Dubai. *Proceedings of the Institution of Civil Engineers: Urban Design and Planning* 166(2): 119–125.

Hu, S., Li, J. & Clément-Noël, D. 2013. Residence block design methods based on the concept of sustainable development-a case study of residence block design of Wuhan. *Applied Mechanics and Materials.* 2013.255(1): 199–202.

Ma Tao, Gao Tianjuan & Gao Zhijuan. 2012. Study on the sustainable development of municipal infrastructures. *Advanced Materials Research* 527(2): 2871–2874.

Ma, C.J., Cao, G.L. & Ma, Y.T. 2012. Discussion on the sustainable development of urban water conservancy infrastructure construction. *Advanced Materials Research* 430(1): 733–736.

Mell, I.C. 2009. Can green infrastructure promote urban sustainability? *Proceedings of the Institution of Civil Engineers: Engineering Sustainability* 162(1): 23–34.

Morrissey, J., Iyer-Raniga, U., McLaughlin, P. & Mills A. 2012. A Strategic Project Appraisal framework for ecologically sustainable urban infrastructure. *Environmental Impact Assessment Review* 33(1): 55–65.

Otegbulu, A.C. 2010. Assessment of user-demand preferences of urban infrastructure in lagos metropolis using the contingent valuation model. *Proceedings of the 2nd International Postgraduate Conference on Infrastructure and Environment* 1: 369–378.

Pandit, A., DesRoches, J., Reginald, R.G. & Crittenden, J.C. 2014. A framework to identify the sustainable and resilient zone of urban infrastructure system planning and design. *Creating Infrastructure for a Sustainable World Proceedings of the 2014 International Conference on Sustainable Infrastructure, Long Beach, California* 11(6): 434–441.

Reiner, M.B., Fisher, S. & Sperling, J. 2014. Evaluation of sustainable infrastructure: Development context matters. Creating Infrastructure for a Sustainable World-Proceedings of the 2014 International Conference on Sustainable Infrastructure. *Long Beach, California. 2014.* 11(6): 420–433. Reston, Virginia: American Society of Civil Engineers.

Shankar, R., Chadchan, J. & Sangeetha, P. 2009. Integrating urban land use and infrastructure for sustainable development. *2009 2nd International Conference on Infrastructure Systems and Services: Developing 21st Century Infrastructure Networks, Chennai, India 2009*. 12(9): 1–6. New York: IEEE.

Spth, P. & Rohracher, H. Conflicting strategies towards sustainable heating at an urban junction of heat infrastructure and building standards. Energy Policy. 2014.

Sun, H.L. & Hu, Y.P. 2012. Research on sustainable development evaluation system of large-scale infrastructure projects based on AHP. *Applied Mechanics and Materials* 174(7): 2931–2935.

Wang, P. 2010. RETRACTED ARTICLE: Idea and strategy of urban public transport sustainable development in Chongqing. *CCTAE 2010–2010 International Conference on Computer and Communication Technologies in Agriculture Engineering, Chongqing, 2010*. 24(1): 207–210. New York: IEEE.

Xu, M., Weissburg, M., Newell, J.P. & Crittenden J.C. 2012. Developing a science of infrastructure ecology for sustainable urban systems. *Environmental Science and Technology* 46(15): 7928–7929.

Yang, T.H., Zheng, Q.H. & Wang, Y. 2014. Fuzzy comprehensive assessment of urban underground power cable infrastructure safety risk. *Advanced Materials Research* 860(3): 2544–254.

Yigitcanlar, T. & Dur, F. 2010. Developing a sustainability assessment model: The sustainable infrastructure, Land-use, environment and transport model. *Sustainability* 2(1): 321–340.

Zheng, Z.H., Fu, L., Di, H.F. & Wu, Z. 2009. *Urban energy carrying capacity—A evaluation method on sustainable urban energy system.* Wuhan: Management and Service Science. 9(20): 1–5.

Zhong, W. & Juan, Z.C. 2013. Evaluation index system construction of coordination of road passenger terminal layout and urban development. *ICTE 2013—Proceedings of the 4th International Conference on Transportation Engineering* 10(5): 2561–2566.

Zito, P. & Salvo, G. 2011. Toward an urban transport sustainability index: An European comparison. *European Transport Research Review.* 3(4): 179–195.

Civil Engineering and Urban Planning IV – Liu et al. (Eds)
© 2016 Taylor & Francis Group, London, ISBN 978-1-138-02903-3

Study on temperature-rising rules of self-heating airfield pavement with continuous carbon fiber heating wire

Wei Xu, Chun-Ming Li, Gui Xu & Guang-Yuan Li
Department of Airfield Construction Engineering, Air Force Engineering University, Xi'an, Shaanxi, China

ABSTRACT: Three cement concrete pavement slabs were made, which, respectively, had inbuilt 6 k, 12 k and 24 k carbon fiber heating wire, and the temperature-rising law of plates was studied through field experiments in different natural environments and input powers. The results indicate that (1) the closer the heating wire, the faster the temperature would rise and the higher the temperature would reach. (2) Temperature of different points on the same plane of each concrete slab surface was less than 3°C when the spacing of heating wire was 10 cm, and the temperature uniformity was good. (3) The results of temperature rise were mainly decided by the input power. The temperature of the slab surface could rise to 0°C after 3.5 hours with the −10°C natural temperature and 382 W/m^2 input power. (4) The variation tendency of the temperature on the slab surface was always in correspondence with the environmental temperature. The temperature on the slab surface would reduce by more than 20% when the environment temperature reduced by 3°C.

1 INTRODUCTION

The accumulation of snow and ice on the surface will not only affect the service life of the airfield pavement in winter, but also frequently cause flight accidents induced by sideslip on a frozen pavement (Mo 2009). Snow-melting and deicing are important maintenance work in Chinese airfields that are located in cold and snowy areas (Lee et al. 1984). At present, a vehicle refitted with a jet engine is often used to remove snow and ice from the pavement by sending out hot or cold air. But this method costs high and needs lots of machines and manpower. In addition, clearing snow by manual labor has low work efficiency and chemicals used in this way can damage the pavement.

Now researchers put an emphasis on the initiative snow-melting method, including the method of heating pipe underground (Gao et al. 2007), solar heating storage method (Tang et al. 2001), conductive concrete heating method (Zhuang & Liu 2002), and heating cable method (Li 2008). The research puts a kind of calefaction medium that is supplied by electricity or other energy in the concrete pavement to remove snow and ice by self-heating. For example, Gu (2010) put forward a plan to lay the aluminum wire mesh in the pavement and control the pavement temperature by computers. Zhao & Che (2010) conducted an experiment on carbon fiber heating wire to remove the snow and ice on the surface of roads and bridges. Chen has long studied the application of carbon fiber grid to melt snow and deicing on the concrete road. Based on these positive results, the carbon fiber heating wire has many advantages, such rapid heating up, high efficiency of thermal conversion, light mass, small size, and lower price. Therefore, it is worthwhile to study the continuous installation of carbon fiber heating wire in the concrete pavement. This article studied the temperature change in the feature points during the heating process with different input powers and environment temperatures in order to find out the temperature-rising rules of the self-heating airfield pavement that is equipped with the continuous installation of carbon fiber heating wire.

2 GENERAL SITUATION OF EXPERIMENTS

The field experiment is located in Anshan, Liaoning province. The concrete slab for airport pavement is integral forming, which is 4 m in length and width and 30 cm in height. The top face of the slab is at the ground level, and the four sides and a bottom are insulated with EPS foam plates. The concrete and its mix proportion are the same with the apron pavement construction in one local airport. Three different kinds of carbon fiber heating wires covered with Tefzel are used in the experiment, which are respectively named 6 K, 12 K, and 24 K with the resistance of 70 Ω/m, 35 Ω/m, and 17 Ω/m. The concrete slabs with different wires are numbered by

S1, S2, and S3. The space among wires in one slab is 10 cm, and the depth is 5 cm from the surface. The DS18B20 temperature transducers are fixed up at different levels and heights by steel wires or high temperature glue in the plate. The temperature data are recorded by the DAM3061 chip.

3 ANALYSIS OF EXPERIMENTAL RESULTS

The influence on the temperature of the concrete slab is studied after being electrified at different input powers and environment temperatures (Table 1). The transfer rules of heat in the concrete medium are analyzed.

3.1 *Changing rules of temperature*

Figure 1 shows the temperature changing curves of slab S3 on depth direction under different input powers when power-on and power-off. At the beginning of heating, the bottom of the concrete slabs contacts with the ground, so the bottom temperature of concrete slab reaches the highest because there is an heat preservation effect on the bottom of the slab to a certain extent and the temperature of the foundation changes to a small extent. On the contrary, the temperature of the slab surface is lowest because of its more obvious heat convection and heat radiation effect with the air.

In the heating process, the temperature of the concrete slab decreases with the increase in the depth, the temperature increases with electrified time increasing in the same position, the velocity of temperature rise is faster first and then becomes gradually slow. According to Figure 1, the temperature of the points 5 cm below the surface is highest, which is 4.12°C, 6°C, and 12.56°C, respectively, after heating for 12 hours when the electric current is 0.8 A, 1 A, and 1.5 A. According to Figure 1b, the temperature of the points 5 cm below the surface increases by 10°C after heating for 12 hours and increases by 10.37°C after heating for 24 hours. The temperature increases in the first 12 hours and reaches 96.4% of the overall, so the heating time is prescribed for 12 hours. During the heating process, the temperature changes slowly with the increasing depth mainly because of the internal heat storage and heat exchange of the structure layer with the air. The deeper the depth, the more obvious the internal heat storage and the less the heat exchange with the air.

Form Figure 1c, it also can be seen that the heat of the concrete slab loses slowly. When the electric current on heating wire is 1.5 A, it needs 12 hours cooling to reach the original temperature after heating for 12 hours. So, it is considered to adopt the method of preheating or discontinuous heating to melt snow and ice by the residual heat of concrete with minimum electric consumption. Thus, the cost can be saved.

Table 1. Different input powers.

Input power (W/m^2)	Electric current (A)			
	0.5	0.8	1	1.5
Number of plates				
S1 (6 k)	170	448	700	/
S2 (12 k)	88	224	350	/
S3 (24 k)	43	109	170	382

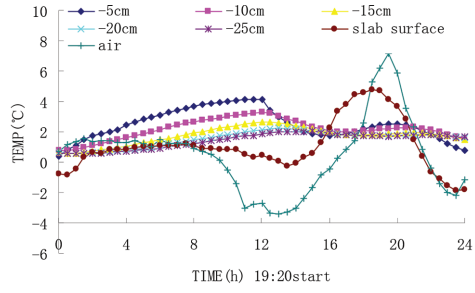

(a) S3 0.8A 109W/m^2

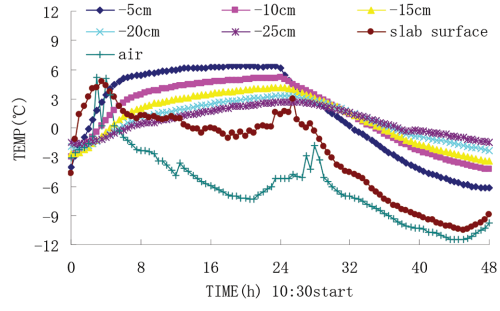

(b) S3 1A 170W/m^2

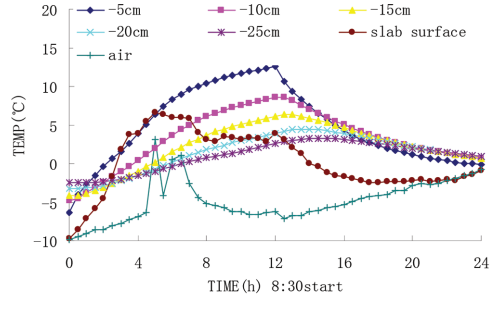

(c) S3 1.5A 382 W/m^2

Figure 1. Temperature changing curves on depth direction under different input powers.

3.2 *Analysis of the distribution uniformity of temperature*

3.2.1 *Distribution uniformity of slab surface*

As can be seen from the Figure 2, during the heating process, the temperature in the middle of the slabs is always highest, followed by the edges and finally by the corners, which is lowest. The reason is that the middle of the slabs is in the center of the temperature field and heat exchange is continuously balanced and less affected by the ambient temperature. The edge and corner are located at the edge of the temperature field. Heat exchange occurs between the corner and the surroundings so that heat loss is much more, and the temperatures of the edges and corners are lower. The temperature of the slab surface is maximum after heating for 6 h. The temperature of the (S1, S2, S3) center is 10.75°C, 2.93°C, and 1.25°C, respectively, which exceeds 17.2%, 65.5%, and 138.9% of the average temperature of the slab surface, respectively. The temperatures of the corners are, respectively, 7.75°C, 0.45°C, and –0.43°C, which are below 15.2%, 74.6%, and 182.2% of the average temperature of the slab surface. Thus, the higher the heating power is, the better the temperature uniformity of the slab surface, the stronger its ability to resist ambient temperature variation. In the initial stage (before the temperature reaching maximum), there is a narrow temperature difference between the corner and the center. The maximum temperature differences are respectively, 2.37°C, 2.49°C, and 1.62°C. With the decreasing environment temperature, the temperature of the slab surface decreases as well. Maximum temperature differences are, respectively, 6.5°C, 2.67°C, and 2.68°C. Except for S1 slab, the temperature difference of the slab surface is controlled within 3°C and temperature uniformity is better.

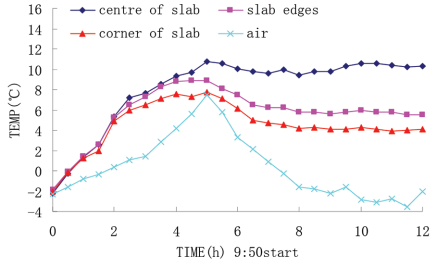

(a) S1 0.8A

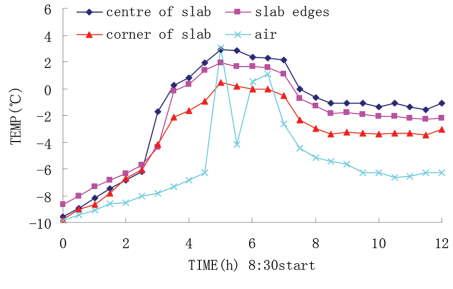

(b) S2 0.8A

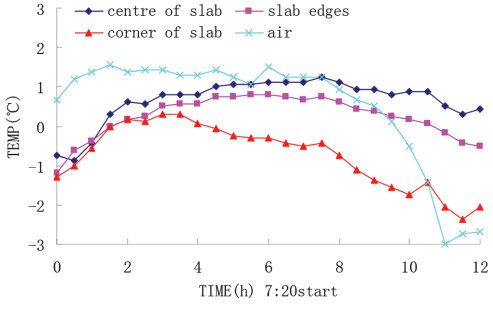

(c) S3 0.8A

Figure 2. Temperature variation curve of different positions at the slab surface and the air.

3.2.2 *Temperature distribution of feature points 10 cm downward from the surface*

According to the experiments, temperatures of each point on 10 cm downward from the surface are balanced during the heating process, the temperature of the slab center is highest and the quarter of the slab is lower. The temperature of the slab edge that is perpendicular to the heating wire is higher than that of another edge. Differences in the temperature at the center and corner of the slab increase equally with time changing and input power increasing. The temperature difference is maximum after heating, which are 8.25°C (S1), 4.37°C (S2), and 2.44°C (S3).

3.3 *Influence on temperature changing by input power*

3.3.1 *The same heating wire at different input powers*

Figure 3 shows that the temperature of the slab surface and inner points increases after heating for 12 h with different input powers. When the input power is 109 W/m^2, the temperatures of the slab surface and feature points (5 cm, 10 cm, 15 cm, 20 cm, and 25 cm downward from the surface) increase to 1.18°C, 3.75°C 2.56°C, 2°C, 1.5°C and 1.31°C, respectively. Based on these experiment data, the closer the heating wire is, the less the external environment influences. In addition, temperatures at different depths increase with the increasing input power. When the input power is 109 W/m^2, 170 W/m^2, and 382 W/m^2 respectively, the temperature of the feature point (5 cm downward from the surface) is increased by 3.75°C, 10°C, and 18.87°C.

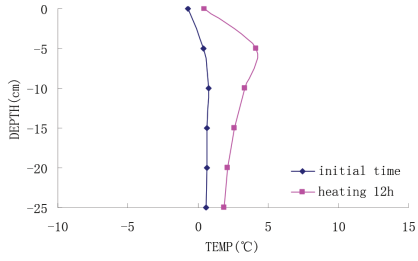

(a) S3 0.8A 109W/m^2

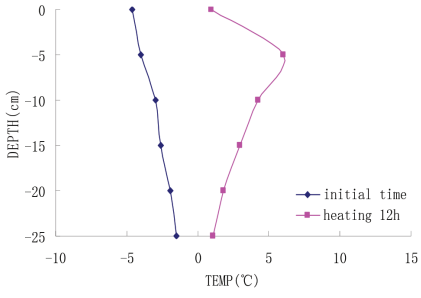

(b) S3 1A 170W/m^2

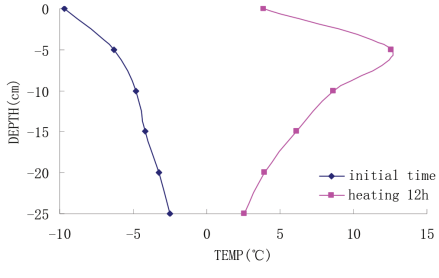

(c) S3 1.5A 382 W/m^2

Figure 3. Comparison of the temperature of the S3 slab at different depths of the initial time and 12 hours later.

3.3.2 *Different heating wires at the same input power*

When the input power of S1 and S3 slabs is 170 W/m^2, the temperature of the concrete slab surface and each feature point (5 cm, 10 cm, 15 cm, 20 cm, and 25 cm downward) is, respectively, increased by 9.37°C and 5.55°C; 10.3°C and 10°C; 8.49°C and 7.25 °C; 5.93°C and 5.55°C; 4.43°C and 3.74°C; and 2.18°C and 2.56°C. According to these data, temperature difference of the slab surface is great, while the temperature of other feature points change to a small extent. This shows that the temperature-rising rule of the concrete slab is mainly determined by the input power, and irrelevant to the specifications of heating wire and the input electric current.

For different heating wires with different maximum currents, the concrete slabs numbered S1 (6 K), S2 (12 K), and S3 (24 K) are able to bear the different maximum powers, which are 700 W/m^2, 590 W/m^2, and 750 W/m^2, respectively.

3.3.3 *Effective power of ice melting and deicing*

In Figure 4, the initial temperature of each slab is slightly different with the influence of the environment temperature, but the overall changing trend is consistent. Temperature rise is faster initially and slowly after a period of time, tending to be stable in the end. With the increase in input power, the maximum temperature and the stable temperature of the slab surface after heating increase gradually. Field test shows that when the environment temperature is about 0°C, and the heating power is 88 W/m^2 and 109 W/m^2, the temperature of the slab surface is always about 0°C after heating for 12 h. When the environmental temperature is about –10°C, and the heating power is 224 W/m^2 and 382 W/m^2, the temperature of the slab surface rises to a maximum value after heating for 5 h. But the temperature of the slab surface decreases slightly because of the impact of the external environment. The temperatures are, respectively, increased to 9.06°C and 13.37°C, and finally stabilized at 1°C and 3°C. Thus, 382 W/m^2 is the effective power of deicing and snow-melting under the environment temperature of –10°C. When the input power increases to 448 W/m^2 and 700 W/m^2, the temperature of the slab would increase to 10.31°C and 18.95°C after heating for 12 h.

The temperature changing curve versus input power of the slab surface after heating for 12 h is concluded in Figure 5. It is generally acknowledged that deicing and snow-melting can be achieved when the temperature reaches 2~3°C. The computing result indicates that the temperature of the slab surface can reach 3°C after heating for 12 h when the input power is 240 W/m^2. So, the input power of 240 W/m^2 is the minimum effective power of deicing and snow-melting when the environment temperature is between –10°C and 0°C.

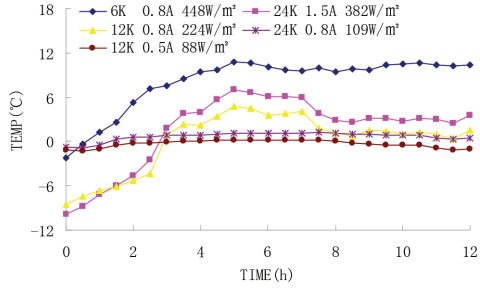

Figure 4. Temperature-rising curve of the slab surface.

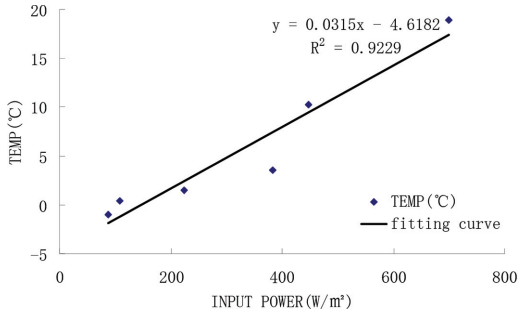

Figure 5. The curve of temperature versus input power under different input powers after heating for 12 h.

3.4 *Influence of the natural environment on the temperature-rising of the slab surface*

From Figure 2, it can be seen that temperature changing trend of the slab surface is always the same as the environment temperature during the whole heating process. When the environment temperature reaches the maximum value of each day, the temperature of the slab surface reaches the maximum value at the same time. When the environmental temperature suddenly decreases, the slab surface temperature would also decrease at different scopes. As can be seen from Figure 2a, when the environment temperature decreases by 3.93°C in the 8 h–11 h period, the temperature of the slab surface declines by 0.62°C, which decreases by 31.0% of the total rising temperature before cooling. As shown in Figure 2b, when the environment temperature decreases by 6.93°C in the 4 h–7 h period, the temperature of the slab surface declines by 3°C, which is a drop of 31.8%; As shown in Figure 2c, when the environment temperature decreases by 8.24°C in the 5 h-8 h period, the temperature of the slab surface declines by 3.62°C, which is a drop of 24.0%. Even if the environment temperature decreases greatly, the increasing input power can prevent the temperature from dropping to a certain extent.

4 CONCLUSION

- With the increasing heating time, the temperature of the slab rises evenly. The closer the heating wire is, the faster the temperature rises, even reaching to a higher temperature. The concrete slab cools slowly, so the residual heat of concrete could be made full use for melting snow and ice.
- Temperature of different points on the same plane of the surface and 10 cm downward of the concrete slab is less than 3°C when the spacing is 10 cm, and temperature uniformity is good. Temperature uniformity is influenced by the environment temperature change and input power. The more the environment temperature changes, the worse the surface temperature uniformity is. The bigger the heating power is, the better the temperature uniformity is.
- Effect of the slab surface's temperature rise is mainly determined by the input power and without direct relation with the category of heating wire and input electric current. The amplitude of the slab surface's temperature rise has plus relativity with input power. The results of the experiments indicate that the temperature of the slab surface exceeds to 3°C after heating for 3.5 hours with 382 W/m^2 input power when the natural temperature is –10°C. In conclusion, the minimum effective input power of snow melting and deicing is 240 W/m^2 when the range of the environment temperature is –10°C~0°C.
- Temperature of the slab surface is obviously influenced by the natural environment. The temperature change of slab surface is always consistent with the natural environment. The slab surface temperature will decease by more than 20% when the environment temperature reduces by 3°C.
- Heat insulation layer is not considered in the experiments, which causes loss of heat because of parts of heat exchange occurring downward. If an appropriate heat insulation layer made up of tin foil and other materials is laid under the plane of carbon fiber heating wire, the temperature of the pavement surface rises faster and higher.

REFERENCES

Chen, L., Sun, M.Q. & Li, B. 2010. Experiment research on Electric concrete pavement with heating carbon fiber grating deicing. *High Way* (4): 175–179.

Gao, Q., Yu, M. & Liu, X. 2007. Deicing and Snow melting Technology and Analysis Based on Energy Storage. *High Way* (5): 170–174.

Lee, R.C., Sacks, J.T., Nydahl, J.E., et al. 1984. Bridge heating using ground source heat pipes transportation research. *Transportation Research Record* (962): 51–57.

Li, H. 2008. *Research on Application of Spontaneous Heating Technology in Airport Pavement Deicing*. Xi'an: Air Force Engineering University.

Mo, L.T. 2009. *Preparation and Research of Electrically Conductive Asphalt Concrete*. Wuhan: Wuhan University of Technology.

Tang, Z.Q., Li, Z.Q. & Hou, Z.F. 2001 Conductive concrete snowmelt deicing mechanism analysis. Concrete 141(7): 8–12.

Zhao, H.M. 2010. *Experimental Investigation on Concrete pavement and bridge deck deicing with Carbon Fiber Heating Wire*. Dalian: Dalian University of Technology.

Zhuang, M. & Liu, G. 2002 Category and application of heating cables. *Electric Wire & Cable* (5): 14–16.

This page intentionally left blank

Civil Engineering and Urban Planning IV – Liu et al. (Eds)
© 2016 Taylor & Francis Group, London, ISBN 978-1-138-02903-3

Fuzzy optimization for pedestrian subjective route choice

A. Çekmiş
Istanbul Technical University, Istanbul, Turkey

ABSTRACT: In this paper, we introduce a pedestrian route optimization model depending on the users preference. The model uses fuzzy sets theory for its capacity to answer subjective and imprecise route choices. The structure of the model is explained and discussed on a pilot study. The proposed Fuzzy Inference System (FIS) model needs to be developed and proved on a detailed case study supported by a database. Yet, it is promising in terms of the effectiveness of fuzzy approach and the simplicity of the application process.

1 INTRODUCTION

There is a large amount of research on pedestrian movement from flow dynamics to individual's behavior. Route choice, way finding, activity scheduling, crossing, and crowd evacuation are modeled by using techniques range from macroscopic and microscopic simulations, of continuous or discrete time, of time- or event-based transition (Papadimitriou et al. 2009).

The pedestrian walk whether a goal directed or a more random motion, demands different methods for modeling (Khider et al. 2009). Pedestrian movement is more or less predictable, especially during the self-organization of collective moving (Helbing et al. 2001). However, human behavior becomes more chaotic and irregular during a singular and exploratory movement, which is intrinsically uncertain. To figure out such behavior patterns, many other research are undertaken, varying from static analyzes depending on the space syntax and visual integration (Turner 2001) to agent-based simulations that are interesting in attractive interactions (Wang 2014). Fuzzy sets theory is also appreciated to deal with the ambiguity in both motive for the movement and reaction to the environmental stimuli. In normal and non-panic situations, Nasir et al. (2014) shows the effectiveness of a fuzzy logic approach that is based on the modeling of a pedestrian steering behavior, and considering the level of attractive and repulsive effects of the surrounding environment.

The subjective and imprecise nature of pedestrian behavior gains importance in route choice. Hoogendoorn & Bovy (2004) argue that pedestrian route choice is based on utility optimization by addressing some criteria as follows (Chiolek 1978, Gipps 1986):

1. Distance or travel time between origin and destination.
2. Proximity of obstacles or other physical obstructions; closeness to walls.
3. Number of sharp turns and rapid directional changes (route directness).
4. Expected number of interactions with other pedestrians (level-of-service).
5. Stimulation of environment, and attractiveness (e.g., ambience conditions, shopping windows, and shelter in case of poor weather conditions).

They highlight that several empirical studies (Bovy & Stern 1990, Guy 1987, Senevarante & Morall 1986) have proved that these utility criteria are not mutually consistent, while their priority in route choice will vary among different pedestrians. For instance, Hill (1982) concludes that route directness is the most common criteria in pedestrian route selection strategies, which are widely subconscious. The term directness here not only deals with the length of the route, but also its level of complexity. Besides directness, pleasantness of the route is another important qualification for defining route preferences. Also, some other factors such as habit, number of crossings, pollution and noise levels, safety and shelter from poor weather conditions, and stimulation of the environment also have a role in route choice behavior studies (Bovy & Stern 1990). Additionally, trip purpose plays a substantial role in route choice behavior. For instance, scenery or attractiveness is quite significant for recreational trips, while it plays no role for work-related walking trips. So, it is obvious that different factors such as pedestrian's trip purpose, age, gender, and physical abilities affect utility values, which leads pedestrians to make a subjective rational choice. Therefore, it can be theoretically assumed that pedestrians can make different decisions about the routes they will take.

This paper presents an initial stage of a research on building a computational route choice model. The objective is to select the best route among the set of all available alternatives, with regards to the personal preferences for different characteristics of the routes. Fuzzy mathematics is applied as the suitable method to carry the subjective, linguistic, and unsharp decisions of an individual into the computation process.

The pioneering papers by Akasaka & Onisawa (2008) and Chakraborty & Hashimoto (2011) propose fuzzy logic in subjective preference based route selection in pedestrian navigation system. In a similar sense, the goal of this study is to develop a simple user-friendly plug-in upon existing desktop and mobile web mapping services like Google Maps, which currently give travel time and distance based on the routes for drivers, walkers, and cyclists. In spite, of providing objective choices, the subjective value as a route choice criterion is currently not provided by the existing map services. Apart from the early works, the purpose here is to propose a user interface where they can choose their satisfactory level of given subjective–objective linguistic parameter, which are directly connected with a fuzzy engine. So a robust, faster and less complicated application is attempted for the further results of this study.

The following part explains the methodology of the model; fuzzy optimization, the concept of fuzzy logic and sets theory, and Fuzzy Inference System (FIS).

Later, the preliminary model is introduced and applied to a pilot study of a limited route sample. The aim is to reveal the importance of the subjective decision-making on route choice and manage the optimization accordingly. The further study is addressed in the conclusion.

2 FUZZY OPTIMIZATION

The formulation of an optimization problem contains two essential elements: a set of feasible alternatives and an objective function as the purpose of comparing the alternative with each other. The goal is to determine the most suitable solution according to the given criteria. In a decision-making situation, either knowledge about alternatives or description of function (or both) may be imprecise, and it is important to adequately incorporate this type of information in an analytical framework (Kacprzyk & Orlovski 1987). Fuzzy logic and sets theory is seen as an ideal method and extensively studied since seventies (Jiménez et al. 2006) for its capacity to deal with the underlying uncertainty of the optimization problem. In a fuzzy optimization, it has aimed to find out the most satisfying values in a membership function. Fuzzy optimization can be considered as a viable approach to many cases in transportation, which are not completely mechanical or physical phenomena, and involve human interpretation (Kikuchi 2007). Yanyang et al. (2012) shows that fuzzy multi-objective optimization for flight planning can better represent the subjective inclination of decision maker directly. Murat et al. (2014) uses fuzzy optimization for the case of an urban bus lines organization, which accommodates the analyst ambivalence in selection of the exact value.

Fuzzy logic has emerged as an alternative to binary logical system. Zadeh (1975), who coined the term, says that fuzzy logic is not fuzzy; it is a precise logic of imprecision and approximate reasoning. It is based on the notion of partial or relative truth which fluctuates between completely true and completely false—different from the conventional dual logical statement which is either true or false, but not in between (Zimmermann 2001). It is a form of multivalued logic and everything is a matter of degree. Thus, it provides a great elasticity and accuracy in categorizing and analyzing of real situations. Only true and false is sometimes inadequate when we describe a vague phenomenon and make judgments. Fuzzy logic better imitates human reasoning in its use of imprecise information to generate decisions (Carlsson & Fullér 2002).

Fuzzy sets represent and manipulate data, which is not precise. It captures the subjective and lexical imprecision such as 'partly true,' 'very big,' and 'a long time' by using numeric intervals. The idea of gradual membership is mathematically expressed by overlapping fuzzy subsets. In classical (crisp) set theory—in a strong relation with Boolean logic—all the elements in a set are completely equal; having the membership degree: 1. However, in a fuzzy set, there exist members with varying degrees of membership between 0 and 1, thereby an element could belong to more than one set. Figure 1 shows a crisp and fuzzy set of age, which has subsets: young, middle-aged, and old. The crisp subsets on the left are strictly separated, where the limit values do not reflect a rational division—like '50' will be in the middle-aged set while '51' in the old set.

FIS is a computational process, operated in MATLAB, which uses fuzzy sets theory to map given inputs to an output. A FIS follows these steps: fuzzification, rules application, rules evaluation, and aggregation (and defuzzification if Mamdani type FIS is used). Fuzzification is the

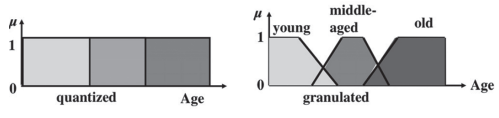

Figure 1. Granulation of age (Zadeh 2008).

process of transforming crisp input values into fuzzy truth values by using input Membership Functions (MFs). MFs are fuzzy subsets that represent granular information related to a set, such as young, middle-aged, and old. By assigning a membership degree in the fuzzy input subset the crisp input value is fuzzified. Later, the user decides if then the fuzzy controls rules, which shows the logical relation between the input (as antecedent) and output (as consequent). Fuzzy operators; –and, or, not—can be used to combine inputs. The rules are evaluated according to firing strength; the degree to which the antecedent part of a fuzzy rule is satisfied (MathWorks 2013). The output value is computed for each rule. In the aggregation process, the outputs of each rule are combined into a final output. Different from Sugeno type FIS, Mamdani method use fuzzy sets as rule consequent, thus requires defuzzification to result a single value.

3 MODEL PROPOSAL

The model is devised as a FIS structure. It interprets the values in the input vector; evaluates pre-defined rules; and assigns the values to the output vector.

The inputs are the parameters, which can be attributes of a route. That means a variety of criteria, including: (Nadi & Delavar 2011) travel distance, travel time, type of road, travel reliability, directness and quality of road, width, slope, number of stop signs, and number of scenic landscapes. Some criteria's are not expected to be a choice function, such as safety that is a requirement; not subject to choose. But steepness as a difficulty level can be a parameter for the young, or complexity for a flâneur.

Instead of using all the criterias, the most suitable parameters in a specific case are chosen for fuzzy optimization. The parameters have levels for pedestrians to select; 'minimum,' 'average,' and 'maximum,' which match up with the membership functions of FIS inputs. The user expresses his/her itinerary request between start (A) and destination (B) locations by deciding the most suitable level. This subjective information is directly carried into the calculation process through the granulation of inputs. The output is the "satisfaction level" of a route and also defined as MFs from 0 to 1.

The rules are created according to the users preferences. The rule with the highest MFs consequent has the antecedent that is exactly the same with the parameter combination stated by the user. FIS operates for all route alternatives between A and B, which are attainable on the map. The optimum route will be the one that has the highest output value. If another user prefers a different parameter combination, then the rules change accordingly, and FIS evaluates the routes anew.

4 PILOT STUDY

4.1 *Project area*

The case is selected in Istanbul, the most populated city in Turkey. Kadıköy, is an old and cosmopolitan neighborhood in Istanbul, on the northern shore of the Marmara Sea, facing the historic city center on the European side of the Bosporus. Both, residential and commercial areas characterize the urban fabric. There are well-established housing settlements, occupied by middle and high-income groups. Kadıköy center is a lively market area with shops, cafes, and bars. Many social and cultural facilities are provided as well, which makes Kadıköy the heart of the Anatolian part of Istanbul.

The start and destination locations of the proposed travel in Kadıköy are showed in Figure 2. It starts from the main transportation node on Kadıköy shore, where busses, ferries, and subway gather, and reaches to the Moda neighborhood. Besides, being an old housing settlement, Moda is known as the recreational zone of Kadıköy with cafes and parks, where people enjoy the beautiful sea view. Thus, a huge amount of local people and tourists visit Moda. Many of them come from the European side; get off in the center of Kadıköy, where it is marked as the starting point (A). Those people mostly prefer to walk to Moda (B) by choosing one of the numerous different route possibilities.

4.2 *Application*

The objective is to present the most suitable route to the users among the set of all routes between A and B with respect to their individual preferences.

Figure 2. Kadıköy map showing start and destination locations and three routes chosen for the application (on Google Maps).

In any application, the first step is the determination of parameters, which are the attributes of a route. For this case, three parameters are chosen:

1. *Distance*.
2. *Difficulty*, which is linked to the average slope.
3. *Social attractiveness*, which is linked to the relative majority of activities along each route. This criterion is important when we think of the heterogeneous structure of the neighborhood with its silent residential and lively market areas.

The next step is sorting all the possible routes together with their parametric variables. Although, there could have been many infinitely route alternatives, which will vary at each node, three of them are chosen as evaluation samples (Fig. 2). First, route stretches along the shore, which is the only route with scenery and no social facility. Second, route goes through the market area and follows the bars street. Last, route starts on the main avenue of Kadıköy (overlapping with the tram line) then enters into a residential area. Kadıköy cape is formed as a hill so slope affects all routes to a certain extent. The first route is flat for the great part of the route, but has slope at the end. The parametric variables of distance and average slope for routes are obtained from Google Earth. Social attractiveness is an uncountable value assigned from a 0–10 scale by researcher according to the site survey. All the information about the routes is listed in Table 1.

In the following phase, a hypothetic user preference is written as: "I prefer the route with the minimum distance and the minimum slope, and the maximum attractiveness." It is the formulation of the optimum route for this individual user.

Later, FIS is created in MATLAB software for this specific request as a 3 inputs–27 rules problem (Fig. 3). The input fuzzy sets are distance, slope, and attractiveness, with three subsets (MFs) for each:

Table 1. The input data of routes 1, 2, and 3.

Inputs	Route 1	Route 2	Route 3
Distance (m)	2360	1420	1860
Difficulty (Average slope) (%)	2.8	4.4	2.9
Social attractiveness	0	10	5

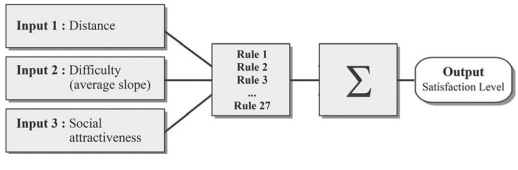

Figure 3. The FIS structure.

Table 2. The result of the FIS model.

Output	Route 1	Route 2	Route 3
Satisfaction level	0.116	0.603	0.425

maximum, average, and minimum. The domain of discourse (universe) is expected to include all the variables between the minimum and maximum in the data set for measurable parameters, or to be a subjective interval for non-countable parameters. So, if all the alternative routes have been sorted, the universe would be delimited by the minimum and maximum routes variable for distance and average slope. But in this limited study, the universe of the input sets is designed according to the three routes.

The output value is the "satisfaction level," as mentioned previously, and has MFs between 0 and 1, which will be the consequents of the rules. Combining all membership functions in the antecedents creates 27 rules. The rule that will promote the optimum route is "If the distance is minimum and slope is minimum and attractiveness is maximum, then the satisfaction is MF = 1." Of course the opposite premise will contradict with the users preferences and result in the least satisfaction as "If the distance is maximum and slope is maximum and attractiveness is minimum, then the satisfaction level is MF = 0." After the rule evaluation for each route in the FIS process, the outputs are listed in Table 2.

The results show that route 2 is the optimum route for this user. It is the shortest and most attractive option within those three, but at the same time has the highest average slope percentage. The fuzzy optimization under pre-defined goals and constraints says that it is the best route and the most feasible solution. The results might be predictable without a calculation for now. But, when the number of routes increases and only a slight difference emerges between the routes, it will be difficult to choose the best option. Then, the proposed model will be helpful to decide the optimum itinerary, especially when the users have a little knowledge about the area they travel through.

5 CONCLUSION

This paper proposes a fuzzy logic model based on pedestrian route selection according to a certain user preferences. The user describes a route with the attributes he/she preferred, and FIS evaluates all possible routes to select the most suitable one for the user.

Besides the requirement of new applications and validation of results, the computational model needs to be improved by:

Adding more inputs to provide more choice alternatives for users.
Detecting all possible routes in a GIS environment and storing their input variable data.
Creating FIS for each possible choice pattern in terms of rule application.
Designing an automatic process linking user interface with FIS and GIS.

The FIS model presents a considerable flexibility in terms of working with variable parameters (criteria). In future studies, the model can be designed on a more subjective-base by using only personal preferences, or specialized for different types of users with relevant criteria. Additionally, other factors such as time (day or night) and weather conditions (rainy or sunny) can be interpreted in the model.

REFERENCES

Akasaka, Y. & Onisawa, T. 2008. Personalized Pedestrian Navigation System with Subjective Preference Based Route Selection. In Da Ruan, Frank Hardeman and Klaas van der Meer (eds.) *Intelligent Decision and Policy Making Support Systems, Studies in Computational Intelligence*. 117: 73–91. Berlin: Springer-Verlag.

Bovy, P.H.L. & Stern, E. 1990. *Route choice: Wayfinding in transportation networks*. Dordrecht: Kluwer Academic Publishers.

Carlsson, C. & Fullér, R. 2003. A fuzzy approach to real option valuation. *Fuzzy sets and systems* 139(2): 297–312.

Chakraborty, B. & Hashimoto, T. 2011. Computational framework for subjective preference based route selection in pedestrian navigation system. In *Proceedings of TENCON 2011–2011 IEEE Region 10 Conference, Bali, Indonesia, 21–24 November 2011*: 1144–1148. Indonesia: IEEE Press.

Chiolek, M.T. 1978. Spatial behaviour in pedestrian areas. *Ekistics* 45(268): 120–122.

Gipps, P.G. 1986. *Simulation of Pedestrian Traffic in Buildings*. Karlsruhe: Institut für Verkehrswesen, Universität Karlsruhe.

Guy, Y. 1987. *Pedestrian Route Choice in Central Jerusalem*. Beer Sheva (in Hebrew): Department of Geography, Ben-Gurion University of the Negev.

Helbing, D., Molnar, P., Farkas, I.J. & Bolay, K. 2001. Self-organizing pedestrian movement. *Environment and planning B*, 28(3): 361–384.

Hill, M.R. 1982. *Spatial Structure and Decision-Making of Pedestrian Route Selection Through An Urban Environment*. Lincoln: ETD collection for University of Nebraska. Paper AAI8306484.

Hoogendoorn, S.P. & Bovy, P.H. 2004. Pedestrian route-choice and activity scheduling theory and models. *Transportation Research Part B: Methodological* 38(2): 169–190.

Jiménez, F., Cadenas, J.M., Sánchez, G., Gómez-Skarmeta, A.F. & Verdegay, J.L. 2006. Multi-objective evolutionary computation and fuzzy optimization. *International Journal of Approximate Reasoning* 43(1): 59–75.

Kacprzyk, J. & Orlovski, S.A. (eds.) 1987. *Optimization Models using Fuzzy Sets and Possibility Theory*, Dordrecht: Springer Science+Business Media: 396–414.

Khider, M., Kaiser, S., Robertson, P. & Angermann, M. 2009. Maps and Floor Plans Enhanced 3D Movement Model for Pedestrian Navigation. *Proceedings of the 22nd International Technical Meeting of The Satellite Division of the Institute of Navigation (ION GNSS 2009), Savannah, Georgia, 22–25 September 2009*: 790–802. USA: The Institute of Navigation (ION) Publications.

Kikuchi, S. 2007. Fuzzy Sets Theory Approach to Transportation Problems. In *Artificial Intelligence in Transportation, Transportation Research Circular E-C113*: 33–48. Washington: Transportation Research Board.

MathWorks. 2013. MATLAB. Fuzzy Logic Toolbox. http://www.mathworks.com/help/pdf_doc/fuzzy/fuzzy.pdf.

Murat, Y.S., Kutluhan, S. & Uludag, N. 2014. Use of Fuzzy Optimization and Linear Goal Programming Approaches in Urban Bus Lines Organization. *Proceedings of the 17th Online World Conference on Soft Computing in Industrial Applications; 10–12 December 2012*: (223) 377–387. Springer International Publishing.

Nadi, S. & Delavar, M.R. 2011. Multi-criteria, personalized route planning using quantifier-guided ordered weighted averaging operators. *International Journal of Applied Earth Observation and Geoinformation* 13(3): 322–335.

Nasir, M., Lim, C.P., Nahavandi, S. & Creighton, D. 2014. A genetic fuzzy system to model pedestrian walking path in a built environment. *Simulation Modelling Practice and Theory* 45: 18–34.

Papadimitriou, E., Yannis, G. & Golias, J. 2009. A critical assessment of pedestrian behaviour models. *Transportation Research Part F: Traffic Psychology and Behaviour* 12(3): 242–255.

Senevarante, P.N. & Morall, J.F. 1986. Analysis of factors affecting the choice of route of pedestrians. *Transportation Planning and Technology* 10(2): 147–159.

Turner, A. 2001. Depthmap: A program to perform visibility graph analysis. In John Peponis, Jean Wineman and Sonit Bafna (eds.) *Proceedings of the 3rd Space Syntax Symposium; Atlanta, Georgia, 7–11 May 2001*: 31.1–31.9. Michigan: A. Alfred Taubman College of Architecture and Urban Planning.

Wang, W.L., Lo, S.M., Liu, S.B. & Kuang, H. 2014. Microscopic modeling of pedestrian movement behavior: Interacting with visual attractors in the environment. *Transportation Research Part C Emerging Technologies* 44: 21–33.

Yanyang, W.A.N.G., Tietao, W.E.I. & Xiangju, Q.U. 2012. Study of multi-objective fuzzy optimization for path planning. *Chinese Journal of Aeronautics* 25(1): 51–56.

Zadeh, L.A. 2008. Is there a need for fuzzy logic? *Information Sciences* 178(13): 2751–2779.

Zadeh, L.A. 1975. Fuzzy logic and approximate reasoning. *Synthese* 30(3–4): 407–428.

Zimmermann, H.J. 2001. *Fuzzy set theory- and its applications*. USA: Kluwer.

This page intentionally left blank

Civil Engineering and Urban Planning IV – Liu et al. (Eds)
© 2016 Taylor & Francis Group, London, ISBN 978-1-138-02903-3

Fractal dimension—a new tool for quantitative analysis of urban skyline

Jun Wang
Department of Urban Planning and Architecture, Institute of Faculty of Architectural and Surveying and Mapping Engineering, Jiangxi University of Science and Technology, Ganzhou City, Jiangxi, China

ABSTRACT: This article discusses the relationship between urban skyline and fractal dimension. At first, it briefly reviewed the recent researches of urban skyline and introduced the basic knowledge of fractal geometry. Then, it selected a typical waterfront urban skyline photo each of Boston, Sydney, and Chicago and extracted their urban skylines. The fractal dimension (box-counting dimension) of each urban skyline was calculated by the software Fractal fox based on the fractal geometry theory. The calculated results were compared and analyzed at the end and they show that the value of the skyline's box-counting dimension is positively related to the understanding of the complexity of skyline in vision. It further concludes that fractal dimension could be an effective tool for quantitative analysis of urban skyline.

1 INTRODUCTION

Generally, urban architecture skyline refers to the rolling connection of buildings, which take the sky as the background in an urban environment.

Lots of literatures have constantly explored the urban skyline. But most of them are qualitative analysis. Such as, *Reading the Skyline of Chicago* (Huang 2006), *Skyline Interpretation* (Wang 2004) etc. So far, American scholar Wayne Attoe made the most profound analysis of the skyline. The book *Skylines: Understanding and Molding Urban Silhouettes* (Wayne 1981), which was published in 1981 by him introduced the evolutionary, aesthetical, and social significance systematically. However, his research also uses qualitative analysis and he did not carry out the rigorous quantification. The so-called quantitative analysis refers to the accuracy and strict comparison of the skyline through some mathematical formulas, values, and methods. The existing quantitative analysis method is based on the height of the building or the statistically significant histogram of the volume of the building, such as the *Research of Quantitative Analysis of Urban Skyline* from Qiu Maolin and Li Junli (1997).

2 OVERVIEW OF FRACTAL GEOMETRY

In 1975, French American Mathematician B.B., Mandelbrot (1924~) published his monograph *Fractals: Form, Chance and Dimension*. It declares the official birth of the fractal geometry theory which is one of the three major theoretical frontiers (Chaos, Solitons and Fractal) of nonlinear science. The basic idea of studying rough and self-similar fractal geometry is that the objective things have self-similar hierarchy structure; the local and the whole have the similarity in statistical sense in form, function, information, time, and space and then, becomes self-similarity. For example, each part of a magnet has a north pole and a south pole as a whole. When you continue to split down, each part has the same magnetic field as the whole magnet. For this kind of self-similar hierarchy, the whole structure is unchanged when it is appropriately zooming in geometry. The birth of fractal geometry created a new area for the description of complex irregular objects (especially natural substances). We might as well compare the differences between the Euclidean geometry and the fractal geometry:

Table 1. Differences of Euclidean geometry and fractal geometry (Jin & Lu 1998).

Comparison of Euclidean geometry and fractal geometry	
Euclidean geometry	Fractal geometry
Classical (>2000 years)	Modern monster (>30 years)
Based on characteristic length or proportion	No characteristic length or proportion
Suitable for artificial products	Suitable for the nature of the shape of various objects
Describe by formula	Describe by (recursion) algorithm

The word "fractal" mainly applies to pure mathematics fractal and part of natural fractal. The so-called natural fractal refers to the natural model that can be depicted by fractal set. Or you can understand like this: Pure mathematics fractal accords with strict self-similarity (such as Koch curve, as shown in Fig. 1). It is also called regular fractal. However, the natural fractal is an approximate self-similarity (statistic self-similarity) (Such as snow covered Himalaya Range Mountains, as shown in Fig. 2), and it is also called as irregular fractal.

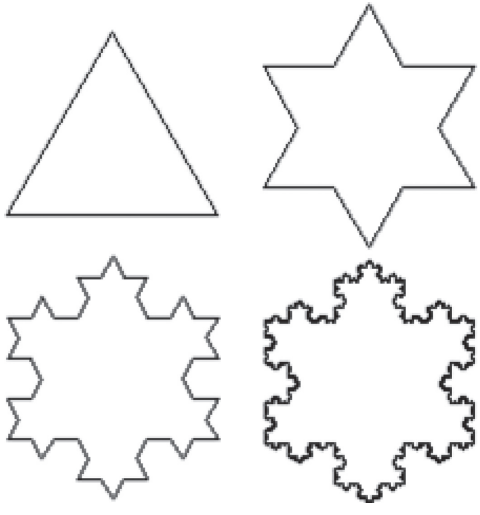

Figure 1. Koch curve (Source: Network).

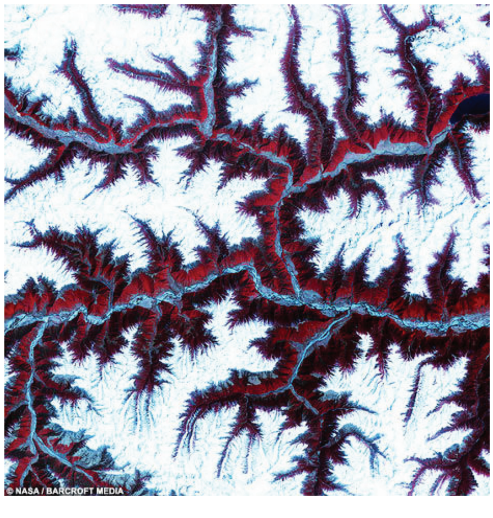

Figure 2. Snow covered Himalaya Range Mountains (Source: Network).

In mathematics, the most basic invariants to describe topological properties of geometric graphs are dimensions. The dimension of integers in Euclidean geometry is also called Topological dimension. But fractal dimension is the most important concept in fractal geometry theory. It includes the integer dimension in itself in order to be a measure of fractal complexity (or expressing the degree of fractal objects fills the space). However, fractal dimension is only a collective thing (such as Hausdorff dimension, self-similar dimension and box-counting dimension) in fractal applications. The calculation and the experience estimates of the box-counting dimension are relatively easy among them. It is one of the most widely used dimensions. It is suitable for general natural shapes. It has a series of equivalence definitions, like the method of mesh cover, in order to calculate the box dimension of a planar set F, we can construct some square of length δ or we could call it, "box". Then, calculate the number $N\delta(F)$ of intersection between the box with different length and F (box-counting dimension got its name from here). The dimension is when $\delta \to 0$, the logarithm rate that $N\delta(F)$ increased. Or it can be estimated by the slope that the function $\log N\delta(F)$ related to $-\log \delta$ (Kenneth 1991).

3 FRACTAL ANALYSIS OF URBAN SKYLINE

According to the theory of fractal geometry, self-similarity is the most important feature of fractal. The shape of the object is invariant when the scale changes. The skyline of mountains and forests belong to natural fractal as, it can always be found in a certain range of mountains and woods. Skyline contains a smaller structure of that having similar shapes, when we keep narrowing the scale of observation.

It is not hard to find, it also has fractal features through observation of the form of the urban architecture skyline. There are two main types of roof in modern city, which are flat roof and sloping roof. The volume of the building is mainly a single cuboid or a combination of cuboid. They eventually cause repeating registration and connection between urban architecture skylines from different angles and form self-similar fractal phenomenon such as the urban architecture skyline extracted from three famous waterfront cities as shown in Figures 3–5.

To verify the feasibility of fractal geometry applied to urban skyline quantitative analysis, this article selects three photos of typical waterfront city skyline from Boston, Sydney, and Chicago. (Sizes are all 1024×683, resolutions are all 72 PPI).

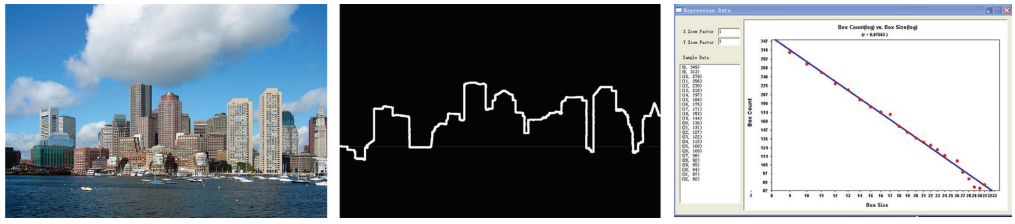

Figure 3. Calculation process of typical waterfront city in Boston, box-counting dimension Db = 1.056 (The left is from the internet, the middle and the right is screenshots from Fractal fox).

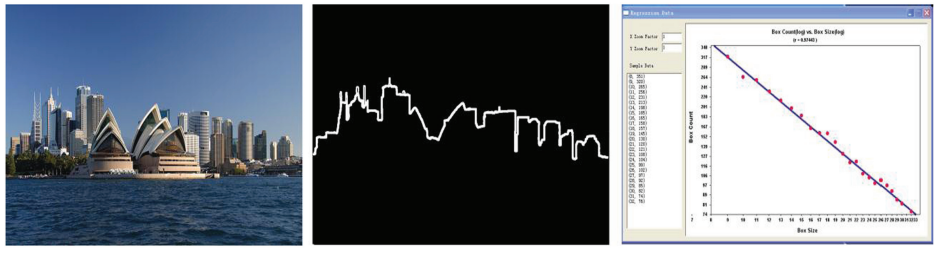

Figure 4. Calculation process of typical waterfront city in Sydney, box-counting dimension Db = 1.115 (The left is from the internet, the middle and the right is screenshots from Fractal fox).

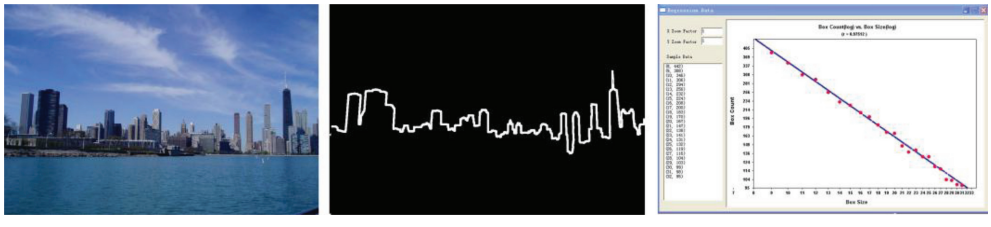

Figure 5. Calculation process of typical waterfront city in Chicago, box-counting dimension Db = 1.121 (The left is from the internet, the middle and the right is screenshots from Fractalfox).

The author has calculated the box-counting dimension of the skyline in the photograph. The operation is carried out in the software Fractal fox. Fractal fox is a fractal dimension calculating software. It provides twelve methods for calculating fractal dimension. This article chooses the box-counting dimension. Based on the aforementioned mesh cover method, the algorithm of box-counting dimension in the software is: the two-dimensional digital image is a two dimensional matrix composed of a series of pixel points. So when the software is calculating the box-counting dimension of the digital image, it counts the number of nonzero sub matrix under different sub matrix. Then carry out regression, analyzes of the number of sub matrix order and corresponds the nonzero sub matrix in the double logarithmic coordinates. If it is a linear correlation, the slope of fitting line is the image's box-counting dimension (Peng et al. 2004).

Three skylines are all extracted from the photos through the software Fractal fox. And then, the fitting linear of box-counting dimension is obtained. It comes to a conclusion that the skyline of the chosen photos have fractal feature. They belong to natural fractal. Finally, the dimension of the box is calculated. The process is shown in Figures 3–5.

The results show that the box-counting dimension Db of the three cities is Boston 1.056, Sydney 1.115, and Chicago 1.121. According to the Fractal geometry theory, the bigger the fractal dimension is, the more complex and rough the fractal objects will be. The smaller the fractal dimension is, the smoother the fractal objects will be. According to this, the Boston Waterfront skyline should be the most soothing and the Chicago waterfront skyline should be the most abundant. And, the actual situation of the visual is also true. From this we can know, the value of the urban skyline box-counting

dimension was positively related to the understanding of the complexity of skyline in vision.

4 CONCLUSION

The above results show that, the fractal dimension can indeed be applied to quantitative analysis of urban skyline. Which needs to be pointed out is that, urban architecture skyline belongs to irregular fractal (natural fractal). Its self-similarity is approximately self-similarity, but not strict self-similarity. That is, its fractal features exist only in a certain range. The broken line tends to become a one-dimensional straight line when we narrowed the observation scale to a single building. Then the skyline does not have fractal features. (This is also consistent with the fractal theory). In addition the validity of the method is verified only by the author. In order to make use of the fractal geometry in architecture and urban research area more deeply, the concrete evaluation criteria of fractal dimension of urban skyline still further needs to be studied.

ACKNOWLEDGMENT

This research has been supported by Science and Technology Development Foundation of Educational Commission of Jiangxi Province of China (No. GJJ13372).

REFERENCES

Huang, H. 2006. Interpretation of urban skyline in Chicago. *Foreign Urban Planning* 2006(21): 61–66.

Jin, Y.W. & Lu, S.J. 1998. *Principle and Application of Fractal Geometry*. Hangzhou: Zhejiang University Press.

Kenneth, F. 1991. *Fractal Geometry-Mathematical Foundations and Applications (translated by Zeng, W.Q. etc.)*. Shenyang: Northeastern University Press.

Peng, R.D., Xie, H.P. & Ju, Y. 2004. Calculation method of fractal dimension of two-dimensional digital image. *Journal of China University of Mining & Technology* 2004(1): 24.

Qiu, M.L. & Li, J.L. 1997. Research of quantitative analysis of urban skyline. *Architectural Journal* 97(22): 63–79.

Wang, X.K. 2004. *Interpretation of Skyline*. Wuhan: Huazhong University of Science and Technology.

Wayne, A. 1981. *Skylines: Understanding and Molding Urban Silhouettes*. New York: John Wiley and Sons.

Civil Engineering and Urban Planning IV – Liu et al. (Eds)
© 2016 Taylor & Francis Group, London, ISBN 978-1-138-02903-3

Farming space in ancient Chinese cities: Harmonious urban development shaped by agricultural civilization and rural relations

Yan Tang & Lei-Xian Guo
Beijing Key Laboratory of Spatial Planning Study for the Capital Region, School of Architecture, Tsinghua University, Beijing, China

ABSTRACT: Founded on agricultural civilization, the traditional China was indisputably a "rural society" in the farming era. On this basis, the article takes ancient Chinese cities of feudal times as research objects, and explores the influence of farming activities and rural relations on these cities. Mainly through literature review and deductive reasoning, and partly using typological analysis and ideological analysis methods, it finds out that whether in watercourses, vestibules, backyards or gardens, the urban space in ancient China was saturated with various kinds of "farming elements", such as livestock, grains, fruits, vegetables, flowers, etc. Through analyzing their existence, spatial distribution and values, the article tries to interpret the characteristics and significance of these urban farming elements and spaces that were deeply shaped by the Chinese philosophy of "Unity of Man and Nature" and profoundly influenced by agricultural civilization. Such an urban farming tradition enlightens that it can be a useful method to mix farming elements into modern Chinese cities so as to integrate the separated urban-rural relationship.

1 INTRODUCTION

1.1 *Research background: Urban-rural separation in modern China vs. harmonious urban-rural development in the farming era*

Under its rapid socio-economic development since the opening-up, China's urbanization has reached a significantly new level. However, despite its entry into the list of medium-income countries as estimated by the World Bank, China still faces obvious structural problems, the most prominent of which is the urban-rural dual structure, or the increasing urban-rural separation. Scholars (Mallee 2000; Fan 2002; Chan 2012) widely attribute the urban-rural dual structure to the administration measures concerning population flow that centers around the household registration system, which caused social problems on such aspects as labor supply and consequently hindered social prosperity. Wu et al. (2013) further argue that China's space management measures, which are based on differentiated urban and rural land ownership, have resulted in a number of conflicts (such as low-quality and informal urban construction projects, urban villages and forced demolition) that challenge the transition of China's cities. Christiansen (2009) contends that the loss of arable land under the collective ownership of rural land, in complicit with environment deterioration, has brought negative influences on food security and social stability. Well aware of the urban-rural separation and conflicts, the Chinese government has taken a number of measures to realize coordinating development between urban and rural areas especially since 2000.[1]

However, such urban-rural "confrontation" did not run throughout China's history. Instead, Chinese philosophy has an ancient tradition of pursuing urban-rural harmony: the human settlement construction in urban areas and their hinterlands practiced ideas like "mutual assistance between villages and cities" and "cities containing rural elements", which have been embodied in the 2000 years' history of China's urban construction. This renders special importance to a study on the harmonious urban-rural relation in federal China, to be specific, how rural elements found expression in the urban space of ancient Chinese cities, as well as how they provided support for urban development in turn. In this regard, Zeng (2005) conducted a preliminary exploration, but it remains largely understudied. A glance at the global reveals inspiring insights on ancient cities' employment of rural space: grains and vegetables were planted in the cities of ancient Mesopotamia as a way to prevent hunger during war periods (Mumford 1938; Mumford 1961); the courtyard of platoon residences was used as vegetable gardens in Renaissance Bologna, Florence and other Italian cities (Benevolo 1980); around the city wall of Theodosius there was an area of 15 km^2 used as fruit garden, grape garden and pasture in Constantinople of Byzantine era (Ljungkvist et al. 2010); and archaeology shows that agricultural production activities also existed in cities of ancient India, Burma, Java, Maya and

Inca (Smit et al. 2001). All this demonstrates that rural space in cities is determined by the productive level of ancient human society, but what renders special scholarly significance to the ancient Chinese context is the influence of philosophical thoughts like "unity of man and nature" and "physiocracy" on urban agricultural elements besides factors like China's productivity level at that time.

1.2 *Contents and analytical methods*

Acknowledging the realistic urban-rural separation but the harmoniousness in history, the article adopts a time span from the Warring States period to the Opium War, and explores agricultural farming in ancient Chinese cities under profound influences of agricultural society and feudal system.[2] Mainly through literature review and deductive reasoning, and partly using ideological analysis and class analysis methods, it finds that whether in watercourses, vestibules, backyards or gardens, the urban space in ancient China was saturated with various kinds of "farming elements". Through analyzing their existence, spatial layout, significance, and so forth, the article re-reads the farming characteristics of ancient Chinese urban spaces that were based on the Chinese philosophy and dominated by "farming civilization" and "rural relations".

The following part of the paper is organized into four sections. It begins with an ideological analysis about the influence of Chinese philosophy on its urban-rural relations and urban space. This is followed by an exploration into the physiocracy of feudal China using class analysis method from the perspective of both the ruling class and the ruled class. Focus is then turned to the evidence of farming space in ancient Chinese cities from ancient literature and paintings and the paper concludes with the deduction of the spatial significance of such space. The clues and contents that run throughout this article include: first, the relation between ancient city development and farming civilization; second, the influence of "infiltration of rural relations into the urban" as regards ancient urban space; third, the emergence of farming elements in ancient Chinese cities and their spatial layout; fourth, the role of farming elements in ancient Chinese cities and their significance.

2 THE INFLUENCES OF AGRICULTURAL CIVILIZATION AND RURAL RELATION ON ANCIENT URBAN SPACE

2.1 *Development of ancient Chinese cities under agricultural civilization*

Founded upon agricultural civilization of thousands of years, traditional China is indisputably a rural society. In the long-lasting agrarian age, China had never been a real "urban society" (Zhou 1999; Ma 1997). At that time, nostalgia[3] for most of the Chinese people means a return to homeland, and particularly, to a pastoral and rustic countryside life. In the agricultural society of dynastic China, a vast majority of government officials, regardless of high-, medium-, or low-rank, would return to their homeland after retirement. Indeed, the two Chinese idioms, "*rong gui gu li* (i.e., return one's native space with honor)" and "*gao lao huan xiang* (i.e., resign from office and return one's native space when old)" have captured Chinese people's nostalgic sentiments that are rooted somewhere in traditional Chinese culture.

As Engels (1884) pointed out, "Agriculture is the decisive production division for the entire ancient world". Indeed, monarchy in ancient China is called "*sheji*": "*she*", the owner of the land; "*ji*", the prime grain,[4] demonstrating agriculture as the lifeblood of the Chinese nation. Each dynasty unanimously laid special importance on agricultural production and management. The traditional Chinese thought prioritizes agriculture over industry and commerce, as reflected by the Chinese idioms "*zhong ben yi mo*" (which implies agriculture as the *ben*, foundation) and "*zhong nong yi shang*" (literally, to prioritize agriculture to commerce). It was these thoughts that regulated the social development in ancient China, which in turn highlights the irreplaceable role of farmers, agricultural production, and rural economy in both the family and the nation.

"In this era, cities, founded upon land property and farmers, were not only administration centers of a given region, but centers for services and trades". As cities were then in small quantities and scales, "they had not yet become a substantial force that could subvert the conventional productivity and its corresponding production relations", under which circumstance the whole society was under the domination of "rural relations" (Wu et al. 2014). Mote (2000) remarked on the urban and rural in ancient China that, Chinese people's lifestyle was not determined by urban but rural elements. It was like cities and towns scattered on a network of rural elements that was woven with "Chinese civilization". Mote's words delineated the basic historical conditions of ancient China: agriculture was the foundation of the national economy; farmers accounted for the vast majority of population; rural area was the most important form of existence in terms of land; and cities were like gems scattered among the vast rural area.

However, as cities evolved from village clusters, their significance of existence is at least three-fold: first, to guard the homeland. Since the Shang Dynasty, rulers would establish a city to control

the new land they explored (Wu et al. 2014; Liang 2005), which reflects a basic attribute of city as a tool for guard and defense. Second, to serve as the stronghold for political management, or in other words, a residence for the ruling classes. Compared with rural areas, cities had relatively mobile upper classes, accommodating landlords, intellectuals, merchants, and officials (Fairbank 2001). Third, as major places for industrial and commercial trade, cities promoted material exchanges and flows either within or among cities, as well as between the urban and the rural, which reflects the attribute of city as marketplace.

2.2 *Farming elements in ancient urban space: Infiltration of rural relations into the urban*

According to Marx (1859), the urban-rural tie in ancient China is primarily expressed through the infiltration of rural relations into the urban, which contradicts the modern mode characterized by the infiltration of urban relationships into the rural and the domination of the urban. "Rural relation" has a multi-facet meaning in ancient China. It could refer to farmers' dependence on agricultural land, the tenancy relationship between landlords and peasants, the kinship-structured social and cultural relation, etc. As a result of the constant projection of farming thoughts and rural relation onto ancient Chinese cities during the spatial construction, "farming elements" constituted a common spatial component of ancient cities. "Cities evolved from villages while villages emerged from fields. *Book of Songs* depicted this phenomenon as 'cottage in field'. When cottages developed into villages, and later into towns, farmland did not completely diminish from towns, presenting a scene known as 'farmland in the city'" (Zeng 2007). It can thus be seen that as though cities, after evolving from village clusters, had broken away from the rural pattern, their production and living modes remained similar to a rural society before it was further developed. The concept of "farming elements in ancient cities" in this article is premised on agriculture in the broad sense, designating the reflection of various agricultural production elements (e.g. land, plant, animal) on urban spaces.

3 THE ADVOCACY OF FARMING ELEMENTS BY VARIOUS SOCIAL CLASSES IN ANCIENT CHINESE CITIES

Even before the Physiocratic School, represented by Adam Smith and Anne-Robert-Jacques Turgot, proposed that all countries should take land products as the sole or major source of revenue and wealth (Smith 1776), China had already practiced agricultural production for thousands of years, with their importance constantly reiterated by all levels of social classes ranging from the Emperor to the general public in ancient China. In ancient Chinese cities, agriculture was advocated and emphasized, though at varying degrees, by all social classes on such aspects as agricultural production, cultivation, and etiquette, through which farming elements gained long-term development in cities.[5]

3.1 *Urban farming promoted by the ruling classes*

As the head of the ruling classes in federal China, the Emperor used to prioritize agricultural issues in state politics, national economics, as well as people's livelihood. Throughout all the stages of seeding, growth, and maturing, the Emperors would participate in agricultural rituals, at one time to pray for good climate and bumper harvest, and at another to celebrate the harvest afterwards. In the seeding season of early spring, the Emperor would do the first plow before farmers, so as to "set up a model and motivate farmers".[6] In case of drought or flood, the Emperor would offer sacrifices to the gods of mountains, the sun, the moon, and the stars. In the harvest season, the Emperor would hold large-scale rituals to pay tribute to the heaven and earth (Fu 2006). These agricultural rituals, more often than not, occurred in cities or their outskirts. For instance, in early spring, the Emperor would hold a ritual to pay tribute to the royal field in the Altar of the God of Agriculture, with his court officials. "Plow in the royal field in spring and quote poems to sing the praise of the God of Agriculture".[7] It was believed that this ritual could bestow farmers a special power in their farming activities afterwards. Clearly, the Emperor's participation in plow bridged the link between cities and rural areas (Fig. 1). Other nobles and

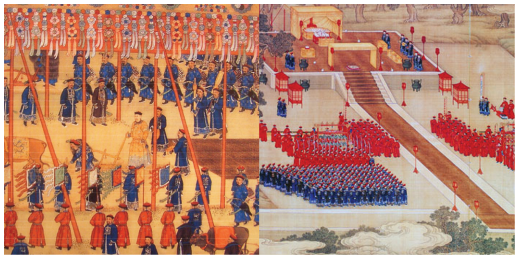

Figure 1. Part of the drawing of "Sacrifice in the Altar of the God of Agriculture" in Yongzheng period of the Qing dynasty (left: the ritual of plowing royal field, right: offering sacrifice to the God of Agriculture).
Source: painted by Giuseppe Castiglione (to be verified), http://www.ourjg.com, http://www.culture.gouv.fr/Wave/image/joconde/0037/m500604_0001240_p.jpg.

officials would then participate in urban agricultural activities more actively. For instance in the Wei country of the Three-Kingdoms era, General Yan Fei, when he served as the prefecture head of Jingzhao, put forward "to prosper agriculture and to enrich farmers" and "opened vegetable gardens at his residence and asked his men to do farming in spare time".[8]

3.2 *The publics' active participation in urban farming*

Ordinary people are representatives of the dominated classes in China's ancient hierarchical system. In cities, they constitute the major force of urban farming, who widely participated in farming activities such as cropping, planting, and breeding. China's traditional production mode of "men tilling and women weaving" is a "family economy" integrating agricultural and handicraft production, which is, in other words, a "small peasant economy" combining self-sufficiency with commodity economy (Lin 2007). Therefore, it was not a surprise that farming activities emerged in ancient Chinese cities where commercial and handicraft production mode dominated. For instance, in the wealthy Liangzhe region of the Song Dynasty, both landlords and peasants were urban residents, which were typically true in *fuzhou* (prefectural level cities) (Chen 2002). For ordinary people, their farming activities usually comprised, on the one hand, planting and cultivation in their own garden yard, and on the other hand, tilling, breeding, and maintenance on those special urban agricultural land (such as farmland, arable land, and animal farm). For example, in the North Wei Dynasty, residents of Zuomo City grew wheat;[9] in the Tang Dynasty, urban residents of Shuiwen County had paddy fields;[10] likewise in the Song Dynasty, citizens of Huangzhou City "planted rice along the urban avenues".[11] For the relatively low productivity, "in most of the Chinese cities, buildings were quite scattered in the urban area. Enclosed by the city walls are large areas of wasteland, orchard, garden, and arable land. This is typically so in Chang'an, capital of the Tang Dynasty" (Xie 1998) (Fig. 2).

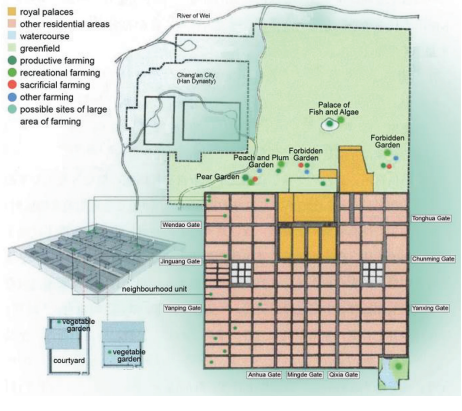

Figure 2. Farming elements of Chang'an city in the Sui and Tang Dynasties.
Source: (Shi, 2012: 13).

4 SPATIAL LAYOUT OF FARMING ELEMENTS IN ANCIENT CHINESE CITIES

In a study on the contribution of ancient Chinese cities to agriculture, Zeng (2007) defined farming elements as the agriculture in the inner city, as well as the agriculture of its surrounding areas managed by and served for urban residents. Under this conceptual framework constructed by Zeng (2007), Shi (2012) and Guo (2012), the article specifically discusses the spatial layout of farming elements in ancient Chinese cities in terms of inner and outer cities. It argues that farming elements was in all the important spatial components of ancient Chinese cities, both in inner and outer cities (Fig. 3).

4.1 *Farming elements in the inner city*

– Square-shaped city

Ancient Chinese cities constructed under the guidelines of feudal etiquette (*lizhi*) usually marked the core position of temples and palaces (Jiao 2012), presenting a chessboard "square-shaped city" pattern. A Chinese architecture classic, *Book of Diverse Crafts* (*Kao Gong Ji*), recorded that "architects design a capital city measuring 9 *li* by 9 *li* (1 *li* equals to 415.8 metres) with 3 gates on each side and the city has 9 north-south-oriented and east-west-oriented streets each with a width of 9 vehicles", which delineated

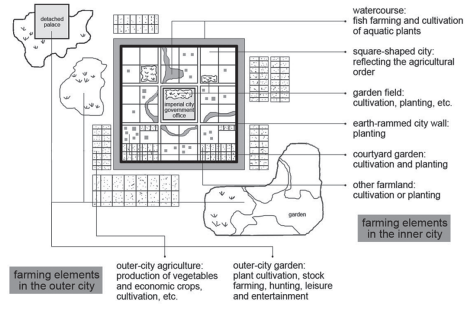

Figure 3. Distribution diagram of farming elements in ancient Chinese city (drawn by authors).

a clear urban spatial form which shaped the chessboard road system. Wu (2009) remarked that the square urban system was formed under the influence of the square-field system in pre-Qin period (Xie 1934; Cao 2005),[12] and was an extension of the agricultural land allotment system;[13] the urban shape, city gate setting, path-making methods and land-use relationship all reflect the agricultural order of that era. If this is true, ancient Chinese cities have been engraved with the "farmland pattern" from its very start, and the urban space is a signified projection of the rural spatial pattern.

– Courtyard garden

  As residents made use of every bit of space in their vestibules and backyards to plant and breed, "courtyard economy" was an important part of the ancient urban farming. Mencius once offered advice to His Majesty that "if a five-mu land are utilized for mulberry tree planting, a fifty-year-old man can wear silk".[14] It can thus be seen that "courtyard economy" was an important driving force in both urban and rural areas. Likewise in the Western Han Dynasty, Wang Mang's reform prescribed that "courtyards without trees would be viewed as deserted, and consequently, owners shall be fined three portions of taxation".[15] Nevertheless, this does not mean that courtyard planting could occupy public spaces like urban streets. According to the *Law of Ming Dynasty*, anyone whose residence and garden were built on lanes or alleys would be punished 60 whips.

– Earth-rammed city walls

  As an important defensive facility, city wall was the physical border that circled cities out of the vast rural area. Earth-rammed city wall is a vivid example of how ancient agriculture extended its realm. There was "compartment field" during the rule of the Han Emperor Chengdi, as recorded in *Book of Fan Shengzhi* (Zeng 2007). As compartment field drew on intensive human and material resources to small lands, it was undeniably a viable and effective planting method to prevent drought and guarantee harvest. This planting method was widely applicable in narrow fields, slopes and hills around the city wall, and more importantly, this type of agricultural cultivation was more effective than other cultivating methods for its "less input but more output" (*shao zhong duo shou*).

– Garden field

  In ancient Chinese cities there were flower and vegetable gardens of different sizes, as well as royal gardens, which were not only for sightseeing but for agricultural production. They were hence important components of the overall urban natural and ecological environment. In the early Spring and Autumn Period, gardens were mainly for production and those for sightseeing emerged only afterwards (Liu 2000). When Huang Xiang was promoted to the Chief of Wei Prefecture, "there were gardens in urban and suburban areas, either cultivated independently or jointly".[16] The present Guanyuan, or Official Garden, in Xicheng District of Beijing, was originally a vegetable production base named Guan Caiyuan (Official Vegetable Garden) in the Ming Dynasty. Similarly, Zhuang Zhuo recorded that "there were many vegetable gardens within the northeast gate of Yingchang City".[17] All this reflects the popularity of vegetable gardens in the city.

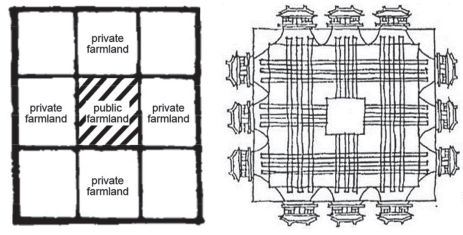

Figure 4. Homogeneous spatial structure between the "square-fields system" (left) and "square-shaped city system" (right).

– Watercourses

  In ancient Chinese cities, both natural and excavated watercourses, including rivers, lakes and moats, provided space for fish farming as well as the cultivation of aquatic plants. As an old Chinese rhetoric goes, "a fire on the city gate brings disaster to the fish in the moat". Fan Li, a millionaire of the Yue state in Spring and Autumn Period, recalled in his book *Tao Zhu's Methods for Fish Farming* that he had five ways to earn livelihood, the most efficient of which was fish farming. Fish in ancient Chinese cities was both for food and for appreciation. Until the Tang and Song Dynasties, four major freshwater fishes had been chosen for human consumption and several goldfish species for appreciation. Ji Cheng recorded in *Garden Management: Goldfish Bowl* that "put fish into one or two crude bowls [...] scientific feeding is more important than ornaments in the bowl". Until then, it was common to see goldfish breeding as an entertainment in ordinary households.

– Other farmland

  Due to small population and underdeveloped commodity economy, there were many vacant lands in ancient Chinese cities, providing huge possibilities for urban farming. Indeed, urban farming ran almost throughout China's entire dynastic period (Zeng 2005; Zeng 2007). For instance, in the Han dynasty, there was arable land within city walls besides residences (Zhang 2006); in the late stage of Emperor Xuanzong's

rule of the Tang dynasty when the originally liberal politics became corrupted, there was a large number of farmlands and gardens in the Capital region; as recorded by *New Tang Book: The Tale of Eunuchs*, "the fertile land that eunuchs occupied was almost equal to the size of half the Capital Region";[18] in Luoyang City in the period of Song Dynasty, paddy fields were scattered here and there. *Yijian's Collection* also documented that, Wang Ming, a citizen of Linchuan, Jiangxi Province, "bought the vacant land in western city to plant vegetables";[19] in the Ming Dynasty, "there were a huge number of farmlands accompanied with standby huts" in Shanghai,[20] and in Beijing, "vegetables and melons were planted in all vacant fields […] from Donghua Gate to Lichun Gate"; in the Qing Dynasty, "(Deyang) city and its nearby villages were covered by winter wheat".[21]

4.2 *Farming elements in the outer city*

– Outer-city garden

As all the detached palaces, royal gardens, and plant gardens, etc. in the urban periphery are special for plant cultivation, stock farming, hunting, leisure, and entertainment, they usually integrate multiple attributes, such as production and sightseeing. Compared with the royal gardens in the city center, these are usually larger in scale, providing the richest and most intensive urban agricultural production. For instance, Shanglin Garden, expanded by Emperor Wu of Han dynasty, crossed the border of five counties, with a dimension of 300 *li* by 300 *li*. According to *Han Book: Old Rituals*, there were a number of stocks in the garden; the Emperor went hunting in Spring and Autumn, and returned with numerous preys. *A Record on Guanzhong* further asserts that, apart from four-footed animals, fishes, birds, and silkworms, there were also fruit trees, grains, and even grapes imported from the western territories, as well as exotic flowers and trees from the south. Likewise, the Farming and Weaving Pictures (genzhi tu) captured the layout of the Summer Palace in Qianlong era of Qing dynasty, which was made up of Sightseeing Complex, Weaving and Dyeing Workshop, Silkworm Farming Building, Water Village Residence, and Pastoral Garden, reinforcing the importance of waters, paddy fields, and sericulture for ancient people. Agriculture also prospered in the South Garden of Beijing, which was a hunting place exclusively for the Emperors of Ming, Yuan, and Qing dynasties. "A variety of animals and plants were cultivated and ordinary people were forbidden to hunt deers, bucks, birds or rabbits".[22]

Figure 5. Farming scenario of Beijing "Southern Garden".
Source: http://beijingww.qianlong.com/221/2007/08/27/22@35522.htm.

– Outer-city agriculture

Besides grains, the outer-city agriculture in ancient China was dedicated to producing vegetables and economic crops, in order to gain profits by serving directly for cities. Scholars (Chen 2003; Xie 2007) found that: in Lin'an City of the Southern Song Dynasty, "there were no residents at all by the East Gate but a vast area of vegetable gardens";[23] in the western outskirts of Shaoxing City, "most of the households were chicken breeders, with one chicken farm occupying 18 li long";[24] flower farming prevailed in the outskirts of Suzhou City, "to the extent that one could not see the edge of the farms either in the eastern or western suburbs";[25] in the Northern Song Dynasty, "on the left side of the Capital City, gardens reached a length of around 100 li";[26] in Beijing of the Ming Dynasty, "east of Desheng Gate lied hundreds of acres of paddy fields";[27] in the outskirts of Chenzhou City of the Northern Song Dynasty, there were even flower farmer households. "Planting flowers was just like planting corn, which could easily take up hectares of land.[28]

5 THE VALUE AND FUNCTION OF FARMING ELEMENTS IN ANCIENT CHINESE CITIES

As the emergence of farming elements in ancient Chinese cities was not cultivated on purpose, the phenomenon reflects the farming civilization and

rural relationship, indicating that farming elements played an important role in promoting the healthy development of cities. Specifically, they contributed to composite dimensions such as food supply, human recreation, ecological protection, economic development, agricultural research, and farming education (Fig. 6).

– Agriculture, above all, provides food supply, thereby reducing cities' dependency on food import. For instance, in Beijing of the Qing Dynasty when the capital heavily relied on grain import from south China through watercourse shipping, Fengze Garden produced most of the rice for the royal family of Emperor Kangxi. As recorded, Fengze Garden fed the royal family "with an annual harvest of hundreds of kilograms for over 40 years".[29] In extreme circumstances such as war times and famines, urban farming became strategically important for their grain reserves.
– Agriculture in ancient Chinese cities provided pastoral scenery, such animals and plants, which not only entertained citizens, but also beatified the overall environment and cultivated people's soul. Indeed, there were numerous poems reflecting how the urban pastoral environment could cultivate poets' temperament. In Liu Zongyuan's "planting 200 orange trees and enjoying new leaves spreading all over the city next spring"[30] and Du Fu's "desiring to plant flowers around the cottage regardless of green or yellow plum",[31] both poets unanimously depicted their love for plants and expectation for their blossom. In the Tang and Song Dynasties, there were flower festivals in China's major cities, such as Chang'an, Luoyang, Yangzhou, and Hangzhou. The well-known saying, "the Capital flooded by flowers in the blossom season",[32] recorded the grand scene where people gathered to appreciate peonies. Besides, farming elements in ancient Chinese cities were also important means for the city to return to nature, and for the authorities to protect the ecological environment. They help to conserve water, protect nature, purify the air, adjust the micro climate, improve human settlements, and so forth.
– From the perspective of economics, as agricultural products, whether it was grain, fruits vegetables, or stocks, heavily relied on urban land for production, they promoted the development of commercialized exchange-based agricultural economy. This could be exemplified by the "garden household" (yuanhu) specialized in vegetable planting in the Capital City of Tang and Song Dynasties. According to Book of the Later Han, there were government positions exclusively serving for the management of agricultural plantation.
– Agriculture in ancient Chinese cities bore the mission of scientific research, thereby not only advancing agricultural technologies, but promoting the cultivation and marketing of agricultural products. Most of these products in ancient China had to undergo a so-called "urbanization" process. That is, they could only be spread to the vast rural areas after successful pilot planting in cities. A typical example is the Champa rice introduced during the reign of Emperor Zhenzong in the Song Dynasty (Zeng 2007). Due to their political, economical, and cultural advantages, cities were not only important bases for farming experimentation, but attracted and trained a number of outstanding agricultural technicians, including melon farmer Zhao Ping in the Han Dynasty, tree planter Guo Tuotuo in the Tang Dynasty, and peony-grafting expert Menyuanzi in the Capital City Luoyang of Song Dynasty.
– Agriculture in ancient Chinese cities also played a prominent educational role. It provided an opportunity for the rulers and the general public alike to understand nature, observe crops, learn about farming, as well as experience breeding and hunting. They would be naturally acquainted with farming skills on the way to learn the difficulties of livelihood. Indeed, the very existence of farming elements in cities was per se a promotion of traditional Chinese values that laid special emphasis to agriculture. Through these elements, traditional farming thoughts were effectively inherited by both the urban and the rural, including seasonal points (to guide the farm work), soil-crop suitability, crop classification, and human cultivation.

As urban development was molded by farming civilization and rural relationship in ancient China, urban space was thus permeated with various farming elements. The urban-rural relation was characterized by spatial integration and mutual mergence. Cities, therefore, share the natural law of farming with the rural such as "spring ploughing no later than lunar Feburary"[33] and "harvesting upland rice in lunar May".[34] In the meantime, urban merchants promoted the resource and economical exchanges between the urban and the rural, which to a certain extent facilitated the industrialization and commercialization of rural economy. Besides, Ancient Chinese cities were not only industrial and commercial centers, but also agglomeration places of landlords.[35] Urban landlords assumed two tasks of agricultural management and commodity manufacturing, which is expressed as an integration of urban (commercial) and rural (landlord) economy (Xie 2007). Under farming elements, the urban spaces in ancient China were more

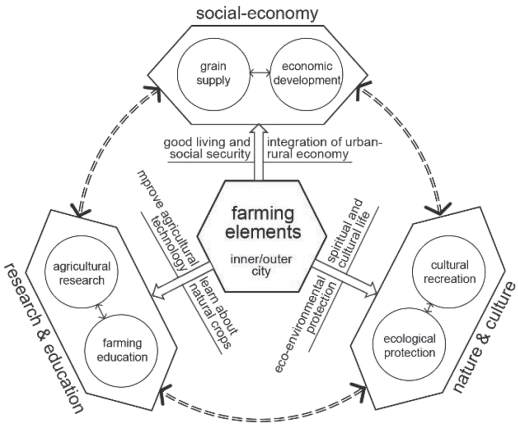

Figure 6. The value and function of farming elements in ancient Chinese cities (drawn by authors).

straightforwardly characterized by urban-rural integration and co-reliance. Sentiments of "nostalgia" were therefore always embedded within the urban farming lifestyle as captured by the well-known saying "go farming at sunrise and get back at sunset", which is a reflection of the ancient Chinese philosophy of "unity of man and nature", "zhong (moderation)" and "he (harmony)".

Despite that most of the ancient Chinese cities were partly or entirely demolished in recent decades, living history of urban farming can still be experienced in several sites today. One of the examples is Xuanhua Old City in Hebei Province, where grape gardens with a history of over 1,300 years are still well kept and operated within the city wall. The unique funnel-shaped trellis provides a place at its center for ancient religion believers to practice Buddhism or Taoism, integrating agricultural production and people's spiritual life. In 2013, Xuanhua Grape Garden was recognized as a Globally Important Agricultural Heritage Systems (GIAHS) site and its first and so far the only urban agriculture heritage by UN Food and Agriculture Organization.[36] With more and more sites to be discovered and investigated, such knowledge as how ancient Chinese people conducted farming activities in urban spaces may even continue to be expanded.

6 CONCLUSION

This article demonstrates that farming elements were virtually everywhere in the urban space of ancient Chinese cities, reflected by and embodied in the shape of the city, living unit courtyards, city walls, watercourses and gardens, both inside and outside the inner city. Evidences show that such a mixture of agricultural activities and urban life was quite an outcome of Chinese philosophy of "Unity of Man and Nature" and the corresponding harmonious urban-rural relationship. It adds to the existing scholarship by demonstrating that "urban/metropolitan agriculture" is by no means "novel" or "import" for China, but a pursuit of nature, a collective nostalgic look-back of its historical memories and a re-recognition of Chinese culture. China's urban farming tradition suggests that it could be an applicable method to incorporate farming elements, whether an allotment, a balcony garden, a roof field or an agricultural workshop, into modern China cities to alleviate the urban-rural problems and revitalize the native culture of human settlements.

ACKNOWLEDGEMENT

This research is sponsored by the National Natural Science Fund of the P.R. China (51408332), the Humanities and Social Sciences Research Youth Fund of the Ministry of Education of the P.R. China (YETP0074), and the Youth Talent Program of Beijing (YETP0074).

REFERENCES

Benevolo, L. 1980. *The History of the City*. Cambridge, MA: MIT Press.

Cao, Y. 2005. *A Study on Square-Field*. Wuhan: Central China Normal University Press.

Chan, K.W. 2012. Crossing the 50 percent population Rubicon: Can China urbanize to prosperity? *Eurasian Geography and Economics* 53(1): 63–86.

Chen, G. 2002. An analysis of the urban resident structure in Liangzhe of the Southern Song Dynasty. *Zhejiang Social Sciences* 2002(11): 177–180.

Chen, G. 2003. Material supply and consumption of river south cities in Song Dynasty. *The Journal of Chinese Social and Economic History* 2003(1): 36–38.

Christiansen, F. 2009. Food security, urbanization and social stability in China. *Journal of Agrarian Change* 9(4): 548–575.

Engels, F. 2003. *The Origin of the Family, Private Property and the State*. Central Compilation & Translation Bureau (trans). Beijing: People's Publishing House.

Fairbank, J. 2001. *The United States and China*. Zhang Lijing (trans). Beijing: World Affairs Press.

Fan, C.C. 2002. The elite, the natives, and the outsiders: Migration and labor market segmentation in urban China. *Annals of the Association of American Geographers* 92(1): 103–124.

Fu, J. 2006. *The Research of Chinese Traditioal Agriculture Ecological Thought*. Yangling: Northwest A & F University.

Guo, S. 2012. *Study of Urban Farming Space*. Beijing: Tsinghua University.

Gernet, J. 1998. *La Vie quotidienne en Chine: a la de l'invasion mongole, 1250–1276*. Liu Dong (trans). Nanjing: Jiangsu People's Publishing House.
Jiao, Z. 2012. The influence of the ritual ethnics of the Zhou Dynasty and "the national engineering standards for capital construction" on the capital urban form in ancient China. *Urban Planning Forum* 2012(1): 114–118.
Liang, G. & Liu, S. (eds). 2005. *The Urban and the Rural*. Beijing: Encyclopedia of China Press.
Lin, G. 2007. Benign interaction and vicious circle: Thoughts on the historical changes in China's urban-rural relation. *Rural China: An International Journal of History and Social Science, Volume V*. Huang, Z.Z., ed. Fuzhou: Fujian Education Press.
Lin, J.Y. 1992. Rural reforms and agricultural growth in China. *The American Economic Review* 82(1): 34–51.
Liu, Z. & Wang, Q. 2000. *A History of Residential Construction in China: City, Residence and Garden*. Beijing: China Architecture and Building Press.
Ljungkvist, J., Barthel, S., Finnveden, G. & Sörlin, S. 2010. The urban Anthropocene: Lessons for sustainability from the environmental history of Constantinople. *The Urban Mind: Cultural and Environmental Dynamics, Studies in Global Archaeology, 15*. Sinclair, P.J.J., Nordquist G, Herschend F, & Isendahl C., eds. Uppsala: Uppsala University Press.
Mallee, H. 2000. Migration, Hukou and resistance in reform China. In Elizabeth J.Perry and Mark Selden (eds.), *Chinese Society. Change, Conflict and Resistance*. London and New York: Routledge.
Marx, K. 1859. Pre-capitalist economic formations. In Karl Marx, *A Contribution to the Critique of Political Economy*. Moscow: Progress Publishers.
Ma, X. 1997. *A History of Rural Society in Western and Eastern Han Dynasties*. Jinan: QiLu Press.
Mote, F.W. 2000. The transformation of Nanking, 1350–1400. *The City in Late Imperial China*. William Skinner, G. ed. Ye, G.T. (trans.) Beijing: Zhonghua Book Company.
Mumford, L. 1938. *The Culture of Cities*. New York: Harcourt, Brace and Company.
Mumford, L. 1961. *The City in History, Its Origins, Its Transformation, and Its Prospects*. New York: Harcourt, Brace & World, Inc.
Shi, K. 2012. *Contemporary Revelation of the Historical Development of Urban Architecture Spatial Form*. Jinan: Shandong Jianzhu University.
Smith, A. 1776. *The Wealth of Nations*. Guo Dali et al. (trans). Shanghai: Shanghai Joint Publishing Campany.
Smit, J., Nasr, J. & Ratta, A. 2001. Urban agriculture yesterday and today. In United Nations Development Programme, Jac Smit (ed.), *Urban Agriculture Food, Jobs and Sustainable Cities*. New York: United Nations Pubns.
Wu, F., Zhang, F. & Webster, C. 2013. Informality and the development and demolition of urban villages in the Chinese peri-urban area. *Urban Studies* 50(10): 1919–1934.
Wu, J. 2009. Square-Field System and the Square Layout of Ancient Chinese Cities. *Architectural History & Theory, Volume X*. Yang, H.X. ed. Beijing: Science Press.
Wu, T., Xu, B. & Zhang, N. 2014. *Space Sharing: Neo-Marxism and China's Urbanization*. Beijing: The Commercial Press.
Xie, F. 2007. Comparing the staple food supply between the ancient China's cities and the meieval western European cities. *China Agriculture* 2007(4): 57–67.
Xie, W. 1934. *An Investigation of the Square-Field in ancient China*. Beijing: The Commercial Press.
Yu, L. 2008. Theory and practice of urban agriculture. *China Development* 2008(6): 95–105.
Zeng, X. 2005. Cities and agriculture in song China. *Selected Essays on the History of Song China*: 327–361, *Volume VI*. Jiang, X.D. ed. Baoding: Hebei University Press.
Zeng, X. 2007. On the role of city in agriculture of ancient China. *The Journal of Chinese Studies* 2007(2): 219–252.
Zhang, J. 2006. *A Study on the Urban Society in Han China*. Beijing: Social Sciences Academic Press (China).
Zhou, Y. 1995. China's reform of agricultural economy and the promotion of structural transformation in rural society. *Social Science Research* 1999(5): 85–91.

NOTES

1. For example, during the reforms starting from rural areas in the late 1970s and 1980s, agricultural productivity was greatly promoted through decollectivized agricultural production modes (Lin 1992); since 2004, the No. 1 Documents of the Central Committee of the Communist Party of China unanimously paid special attention to the three rural issues; represented by the slogans of "urban-rural coordination", "urban-rural integration", and "industry nurturing agriculture, cities nurturing villages", new policies are dedicated to promoting the equal exchange of elements and products between the urban and the rural, as well as to the balanced allocation of public resources, in the hope of minimizing urban-rural separation; in 2005, new countryside construction was launched nationwide; in 2006, the Chinese government canceled agricultural tax; in 2015, rural land system reform started to be implemented in the country's 33 county-level administrative regions, which allows the collective-managed construction land to enter the land market. Considering the scale and complexity of existing problems, to reduce urban-rural conflicts and separation still requires long-term efforts.
2. It refers to a city constructed under a certain planning guidance.
3. While embracing modern civilization, it is believed that contemporary cities with high-rise buildings cast by concrete and steel are nowadays encroaching on citizens'

"nostalgic memories". At the Central Government's Work Meeting on Urbanization held at the end of 2013, President Xi Jinping advocated to "merge cities into nature, let residents see mountains and waters, and evoke a sense of nostalgia".

4. Xu Shen, *Shuo Wen Jie Zi* (Word and Expression).
5. Chinese feudal hierarchy was classified according to the official rank and the social status of a family. The main social relation among different classes was characterized by the exploitation of the peasantry by the landlord class.
6. *Guoyu: Zhouyu.*
7. *Han Yi* (Han Ritual).
8. *San Guo Zhi* (Records of Three Kingdoms: Wei Book: A Tale of Yan Fen).
9. See *Song Yun Xing Ji*, that "there were more than 100 households in Zuomo City, […] (people) abstracted water and planted wheat."
10. See *A Record of Yuanhejuan County, Volume Sixteen*, that "ordinary people grew paddy in the city."
11. See Zhang Lei, *A Collection About Heshan*, that "(people) abstracted water and plant rice beside the official street."
12. Whether the square field system ever existed in history remains controversial in the academic circle. It is also speculated that this system may have been invented during Xia, Shang or Zhou Dynasty.
13. The square field system recorded in *Mencius: Emperor Wen of Teng Dynasty, Vol. 1* is as follows. "The land area measuring 1 *li* by 1 *li* amounted to 1 *jin*. 1 *jin* equaled to 900 *mu*. The portion of land in the centre of *jin* was public land. 8 households had their private lands and they cultivated public land together, each of which amounted to 100 *mu*."
14. *Mencius: Emperor Hui of Liang Dynasty, Vol. 1.*
15. *Han Book: A Record of Shihuo, Vol. 2.*
16. *Post-Han Book, Vol. 80: A Tale of Huangxiang.*
17. Zhuang Jiyu, *Jilie Bian*.
18. *New Tang Book: A Tale of Eunuchs.*
19. *Yijianzhi: Zhizhi*.
20. *A Record of Songjiang Government Building of Chongzhen Era*.
21. Year 19. Jiaqing, *Zhili Mianzhou Zhi*.
22. *Dijing Jingwu Lüe*.
23. Du Wenlan, *Guyaoyan*.
24. Zhou Bida, *Erlaotang Zaji*.
25. *A Record of Wujun*.
26. Meng Yuanlao, *Dongjing Menghua Lu*.
27. Dijing Jingwu Lüe.
28. Zhang Bangji, *Chenzhou Mudan Ji*.
29. *Kangxi Jixia Gewu Pian*.
30. Liu Zongyuan, Liuzhou Xibeiou Zhong Ganshu.
31. Du Fu, *Zhi Xuqin Mi Guozhai*.
32. Liu Yuxi, *Shang Mudan*.
33. Lu You, *Niao Ming*.
34. Li Deyu, *Zhe Linnandao Zhong Zuo*.
35. In broad sense, the Emperor, aristocracies, and nobles are all owners of rural land, or landlords.
36. See http://www.fao.org/giahs/giahs-sites/en/.

Civil Engineering and Urban Planning IV – Liu et al. (Eds)
© 2016 Taylor & Francis Group, London, ISBN 978-1-138-02903-3

Research on industrialized spatial features of Xi'an modern city

Yan Wei
Xi'an University of Technology, Xi'an, Shaanxi, China
Xi'an University of Architecture and Technology, Xi'an, Shaanxi, China

Yue Wang & Feng-Fan Yang
Xi'an City Construction Archives, Xi'an, Shaanxi, China

ABSTRACT: The Industrial Revolution is usually the beginning of a historical phenomenon. Under the impact and impetus of the industrialized historical development trend, Xi'an's modern history has undergone a transformation from the traditional handicraft industry city to the modern machine industrialized city. This thesis is to analyze the features of a planning pattern evolution of modern industry, industrial plant, industrial structures, and decorative styles of modern Xi'an. It has hoped that this thesis will have certain impetus role in the study of modern industrial construction in Xi'an city.

1 INTRODUCTION

These modern times are an important transition period in the Chinese history. Such kind of the transformation is reflected in the profound changes in all aspects of society, ideology, culture, and life, especially after the founding of People's Republic of China. China has then entered into constructing the road to socialism, and it has begun to enter the period of fast urbanization and industrialization. Industrialization has become an important part of urban development. Xi'an began to develop its modern industry from the end of the nineteenth century, and it formed a group of influential industries from the 1960s to 1970s. As the typical representative of industry in the twentieth century of Xi'an, these industrial plants affected the whole appearance of the urban construction. Historical value, social value, and artistic value were the witnesses of urban industrial development in Xi'an.

2 INDUSTRIAL PLANNING AND SPATIAL EVOLUTION OF XI'AN MODERN CITY

2.1 *The embryonic form period of modern industrial planning concept*

In the 1860s, under the impetus of the Self-Strengthening Movement, China began to introduce and study Western science and technology, establishing the modern military industry and civilian industry. In 1869, as the imperial envoy to supervise the military affairs in Shaanxi and Gansu, Zuo Zongtang founded the Xi'an Machinery Bureau in Xi'an, which became the beginning of the machinery industry in Xi'an. Although in Xi'an, modern machinery industry existed in the late nineteenth century, the planning concept of the industrial area had not started until the early 1930s. In 1932, the Chinese Nationalist Party determined to call Xi'an as Xijing by taking Chang'an as its provisional capital at the second plenary meeting, proceeding with organizing the preparation of Xijing urban planning (Zhu & Wu 2003).

In 1934, the *Partition Issue of Xijing Urban City* proposed by Ji Ping, based on the urban city planning in Britain and other countries, it was the earliest planning design program of modern scientific significance that could be found in the literature. According to the program, Xijing was divided into: commercial region, industrial district, cultural district, scenic district, and administrative district; there was a scenic area designed between the shores of Chanba and Duqu. There were higher education institutions designed along Qujiang and Fanchuan. The railways to the west of Hancheng and in the middle section of Weihe were considered as the industrial area, and the old Hancheng area was taken as the commercial district. In 1937, "First Meeting of Xijing Urban Plan" was held by Xijing Municipal Construction Committee, at the meeting "Xijing urban was proposed to be six districts, namely administrative district, cultural heritage district, industrial district, commercial district, agricultural experimental district, scenic district and others," and the meeting clearly pointed out the planning design of Xijing urban city of provisional capital. After that, the Xijing Municipal Construction Commission and

its relevant experts co-wrote the *Xijing planning*, in 1941, the *Xijing City Zoning Plan Instruction* that was proposed on the basis of *Xijing Planning*, which took the north city of Hancheng, east city of Great Wild Goose Pagoda, and the Qujiang Pool as the cultural heritage district; south city of Feng-qi-yuan was designed as the administrative district; the prefectural city of Ming & Qing dynasty was designed as the commercial district; and northern suburbs of railway station was taken as the industrial district, southwest city of Shenheyuan and Ziwu town were designed as the agriculture district, Zhong-nan mountain of Qinling was taken as scenic district (see Fig. 1) (Zhu & Wu 2003). The planning thoughts at that period were suitable for a gradual start of the industrial civilization, which was an important period of Xi'an city planning and industrial development. Although, it was still the outline nature for private scholar Ji Ping, Xijing Preparatory Committee, and Xijing Municipal Construction Committee Xijing to develop the urban planning, it reflected the impact of the urban construction thought starting from the functional approach and Western urban planning ideology on Xi'an's modern urban development.

2.2 *Gestation period of socialist industrial planning*

During 1950–1952, in order to meet the upcoming boom of the socialist economic construction, Xi'an prepared three consecutive times of urban planning. The Xi'an urban planning conducted in 1950 was one of the earliest overall urban city planning in the country, according to the planning, old urban area was separated from the new urban area, and the new urban area was built on the west side of the old urban area. The focus of the urban industrial layout was to expand toward the western suburbs, the industrial areas and residential areas were designed in the crossing layout, which were configured with commercial district, the central economic area, higher education zones, and others to serve for the industrial construction. In 1951, the industrial district was expanded to three directions of east, west and south, namely the three directions had the industrial districts. In 1952, the comprehensive introduction of Soviet urban planning principles, economic and technical indicators, procedures and methods of the preparation of overall urban planning were used for Xijing urban planning, which suspended the spatial strategy for focus westward urban development, thereby forming the structure of concentric circles by taking the old urban area as a center of development. According to the planning layout, the industrial district was a relatively concentrated arrangement in the western suburbs, and the mixed mode of industrial districts and residential districts was abolished (Local Chronicles Codification Committee of Shanxi Province 1999). In terms of the industrial district of planning, although the three times of planning had slightly different forms, they all were being avoided from the old urban area, selecting the construction of the undeveloped new area along the railway line, which to a certain extent protected the history of the old urban area. Meanwhile, the new industrial area planning was combined with urban development, and the use of the relatively concentrated layout guidelines created favorable conditions for developing the comprehensive industrial layout planning in the future (see Fig. 2).

2.3 *Formation period of urban industrial planning pattern affected by the Soviet Union*

The so-called large scale economic construction was launched in 1953, and Xi'an was listed as the first batch of cities for key construction, the construction of 17 items of 156 projects aided by the

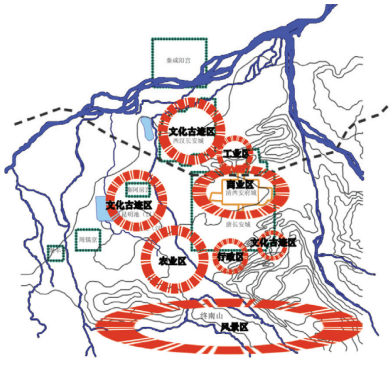

Figure 1. Functional instruction of Xijing partition plan.

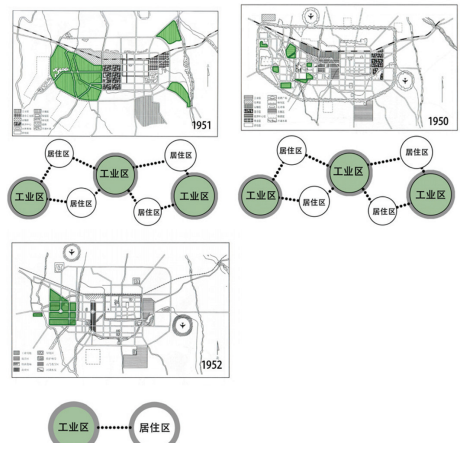

Figure 2. Xi'an urban planning in 1950, 1951, and 1952.

Soviet Union was fixed in Xi'an, Xi'an started to prepare for the new overall urban development plan with the combination of the site construction of industrial projects. In the *1953~1972 Urban Overall Planning of Xi'an City*, the designated function of the city was determined to be the light type of the precision machinery manufacturing city and textile industry city, urban industrial area was arranged in the eastern and western suburbs outside the old urban area, which was 4~4.5 km far from the old urban city, in west Chanhe, and east Weihe, southern district of Longhai railway (Local Chronicles Codification Committee of Xi'an City 2000). The planning was based on the positioning of the industrialized designated function of city, and therefore, the industrial space played a decisive role in the city. Meanwhile, under the influence of the urban planning concepts in the Soviet Union that the urban planning was to make the urban structure be adapted to social needs of mass machine production, the layout of the urban industrial planning along the Longhai railway was adopted, which was relatively in symmetrical distribution on both sides of the old urban area in eastern and western suburbs. The industrial development was focused on the relationship with the railway, and the railway branch lines were respectively introduced into the industrial area of eastern and western suburbs, which were easy for transporting the production materials, focusing on the relationship between the production and daily life (see Fig. 3).

During 1953–1957, the urban construction of Xi'an was implemented basically in accordance with *1953~1972 Urban Overall Planning of Xi'an City*. The new built urban area was based on the old urban area as the center, expanding toward three directions of east, west, and south; the vast majority of the key industrial enterprises were concentrated on eastern and western suburbs, forming the urban spatial frame structure based on old urban areas as the core, expanding toward eastern and western sides along Longhai lines. Therefore, Xi'an formed three major industrial districts at that time: the western suburbs was built as the concentrated "electricity industry city" for the power transmission equipment and instrumentation manufacturing; the Hansen Village and Hujiamiao in the eastern suburbs was built as "military industry city" for manufacturing a number of military machinery used in Kunlun, Yellow River, Hua Mountain, Qin Chuan, and East; and "textile city" composed of third, fourth, fifth, and sixth State Cotton factories manufacturing textile products in Baqiao of the eastern outskirts.

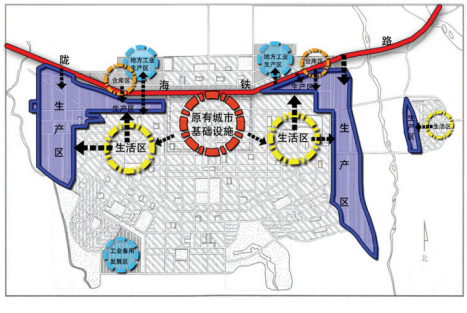

Figure 3. Industrial pattern of 1953~1972 Urban Overall Planning of Xi'an City.

In 1964, the implementation of "three-line construction" policy was started. China continuously introduced a lot of the medium-sized enterprises from Dalian, Shenyang, Shanghai, and other coastal cities into Xi'an, and most of the factories moved to Xi'an merged associated factories in Xi'an, using the original buildings for expansions and restructurings, maintaining the urban pattern of developing the eastern and western suburbs as industrial areas, building the industrial district in the western suburbs, the Sanqiao industrial district in the northwest outskirts, Hansen Village industrial district in the eastern outskirts, Hujiamiao industrial district in the eastern outskirts, Hongqing industrial point in the eastern suburbs, "textile city" in the eastern suburbs, industrial district in the Northeast suburbs, as well as Weibin industrial area in northern suburbs, and industrial point in southern suburbs. Thus, Xi'an gradually became the industrial base including aviation, electronics, textiles, machinery, and a variety of industries.

3 ANALYSIS OF MODERN INDUSTRIAL PLANTS AND INDUSTRIAL ARCHITECTURE FEATURES IN XI'AN

3.1 *Xi'an modern industrial plant planning*

The evolution course of Xi'an industrial plant planning was from exploration to the maturity, the industrial plant construction at the early stage of late Qing Dynasty was not sufficient in the design experiences. The industrial factory planning was arranged in accordance with the internal production and division of labor, there's basically no systematic planning theory served as guidance. The Western industrial construction concepts was introduced during the Republic of China, the industrial enterprises with relatively large-scale employed hepa designers that were more early affected by the Western design thoughts to conduct the designs. Not only the functional layout was considered in factory planning, but also the attention was paid to the AC streamline production organization, furthermore, the design contents of the auxiliary buildings for production, and living areas and

others should be taken into consideration (Wang et al. 2011). For example, the factory planning of Dahua cotton mill was built by Shanghai Xiangxin Construction Company, and the factory was with rational layout according to the textile process flow, while taking the layout of residential areas into account.

After the founding of People's Republic of China, the industrial construction theories and technologies aided by the Soviet Union were alien to the industrial construction field in domestic, most of the new built industrial districts in Xi'an were drawn on the construction experiences of the former Soviet Union, under the participation and guidance of the Soviet experts, the Architectural design theory of Western modern functionalism, building creation principle, construction procedures, construction methods and economic and technical indicators created by the Soviet Union in the period of command economy began to guide the design of the industrial districts. The modern factory planning concept was adopted in construction of Xi'an plant aided by the Soviet Union, where the planning layout was conducted rationally and orderly, the factory was clearly divided into front portion of factory area, production area, and warehouse area. The factory road was designed in accordance with the production transportation requirements, factory greening was increased, the cooperative design and coordination was conducted in the workshop according to the techniques and various types of work, combined with the characteristics of industrial workers, the nursing rooms and nurseries and others were incorporated into the plant planning, together with the complete construction workers' welfare facilities, and the design at each design stage had the preparation of the related technical documents. Such kind of Soviet industrial plant planning mode had affected Xi'an's industrial plant construction for nearly half of the twentieth century. Most of the newly built plants were drawn on planning concept of the Soviet factories, the plant layout was well structured by focusing on plant greening, and the auxiliary facilities were complete, the planning was somewhat forward-looking; therefore, those factories can still meet production needs till now (see Fig. 4).

3.2 *Structure features of Xi'an modern industrial building*

The differences that lies between the industrial buildings and civil buildings is that the two have special requirements of the architectural span, height, and loads; besides, the structural form of Chinese traditional timber-framed structure is not suitable for the mechanical-based industrial production mode. With the introduction of the Western architecture technology, as well as the use of the steel, iron, cement, and other new materials, the industrial buildings have been had a greater development in structure, material, size, and construction process. There are two kinds of the main structural form, namely the steel structure and bent structure of the reinforced concrete (Fu 2010).

The steel structure appeared earlier, the textile workshop of Dahua cotton mill was built with the steel structure, which was also the earliest steel industrial building in the northwest, the factory was supported by steel triangular roof trusses and steel columns, and the structure node was anchored by screws. The steel structure is with certain firmness, but it is easy to rust, so the steel structure was soon eliminated after the emergence of reinforced concrete structures. The pre-fabricated reinforced concrete bent structures were widely used after the implementation of the projects aided by the Soviet Union. According to the different production requirements, there were different types of the support columns, such as H-shape, rectangular-shape, cow-leg column, and so on. There were the pre-stressed concrete roof trusses, the pre-stressed concrete double-slope roof beams, reinforced concrete single-slope roof beams, pre-stressed concrete arched roof trusses, reinforced concrete combined roof trusses, and other forms (see Fig. 5).

3.3 *Decor style of Xi'an modern industrial building*

The decor style of Xi'an modern industrial building can be divided into three types: traditional Chinese style, modern Western style, and Soviet-style, imitated Soviet style (Wang et al. 2011).

Chinese traditional industrial building retains many features of traditional Chinese architecture,

Figure 4. Factory district planning in Xi'an electrical city.

Figure 5. Reinforced concrete single-slope roof beams Dahua Spinners.

and the building materials are mainly for the red brick, greay tiles, and timber. The ancient Chinese timber-framed structure style is used for roofs, roof-ridge, gables and other parts of the architecture, and this has been used in many office buildings of the factories. According to three-phase pattern of the traditional roof, architecture body and the base, the roof is saddle roof, the two wings have fire-sealing gables, and the rafters are used on eaves as simple decoration.

The Western style is mainly affected by European and American architectural styles, the column, arch, and other elements of Western classical architecture are integrated into industrial buildings. Compared with the coastal cities, Xi'an has fewer modern Western-style industrial buildings, those so-called western-style industrial buildings are with compromise features of Chinese and Western styles, and no large trend has been formed yet in Xi'an.

The so-called Soviet-style, imitated Soviet style refers to industrial buildings built with the aid of the Soviet Union, and the industrial buildings built by imitating the Soviet style of industrial buildings. During "The First Five Year Plan" and "The Second Five Year Plan" of Xi'an construction aided by the Soviet Union, the industrial buildings were finished under the impact of the "Soviet Socialism" national style, those buildings were integrated with the Soviet national architectural form, and the buildings were in central symmetry, the facades were decorated with the columns, arched window trims and embossing moldings. The most representative would be the main office building of Xi'an High Voltage Switch Factory (now Xi'an High Voltage Apparatus Co., Ltd) (see Fig. 6), clock tower on the central portion of the building roof and the steeple are the typical Soviet architectural style. Due to the lack of experience in the industrial construction after the founding of People's Republic of China, the industrial factory planning and industrial buildings during that period were subject to the influence of the Soviet-style industrial buildings, and the buildings were built by drawing on the Soviet industrial building modes.

Figure 6. First State-owned Northwestern printing and dyeing mill.

4 VALUES OF XI'AN MODERN INDUSTRIAL PLANNING AND INDUSTRIAL BUILDINGS

4.1 *Historical value*

The industrial construction was an important period for Xi'an to change from the traditional city to industrial city, and it also witnessed the process from the rise of Xi'an national industry to modern urban development, and an integral part of modern urban construction development process in Xi'an, which reflected the change course of Xi'an from traditional society to modern society, recording the urban landscape of a historical period.

4.2 *Social value*

The building environment, production machinery, processing technology, production processes, and others of industrial production are different from the production mode during the handicraft period, and the machinery industry has brought a tremendous impact to the traditional society of Xi'an. In particular, after the founding of People's Republic of China, with the socialist industrialized construction and the construction aided by the Soviet Union, Xi'an modern industrial buildings have an important social role in people's lifestyles, ways of thinking, change and transformation of values.

4.3 *Artistic value*

The planning, buildings, structures, and production equipment in industrial factories are with industrial features, these special elements are different from other landscape environment form the distinctive landscape arts (Lu 2006). Xi'an has rich forms of industrial buildings, especially the industrial buildings aided by the Soviet Union, the decorative moldings, columns, clock tower, and other Soviet classical architecture decorations and architecture details, these exotic architecture decorations and architecture details, reflecting the decorative features of the unique industrial building arts.

4.4 *Cultural value*

Cultural change is the eternal law of social and cultural systems, the most important event of modern social culture is the development of machinery

industry, and the industrialization promotes the development and progress of human civilization. Xi'an modern industrial building reflects the transition of Xi'an from traditional culture to modern culture, and it is with the typical cultural characteristics of the times, Xi'an is an important chain in the development of modern culture.

ACKNOWLEDGMENT

This paper has been supported by the Humanity and Social Science Youth foundation of Ministry of Education of China (13YJC760088) and Science Foundation of Xi'an University of Technology (117-211409).

REFERENCES

CPC Shaanxi Provincial Committee Party History Research Center. 2002. *The First Five Year Plan and Key Projects in Shanxi.* Xi'an: Shaanxi People's Publishing House.

Fu, Y. 2010. *Research on Xi'an Modern Buildings (1840–1949)*. Xi'an: Xi'an University of Architecture and Technology.

Local Chronicles Codification Committee of Shanxi Province. 1999. *Shanxi Province Construction.* Xi'an: Sanqin Press.

Local Chronicles Codification Committee of Xi'an City. 2000. *Xi'an City Volume II Urban Infrastructure.* Xi'an: Xi'an Press.

Lu, S.M. 2006. *Protection and Utilization of Urban Industrial Heritage*. Nanning: Planner.

Wang, X.J., Chen, Y. & Jin, X. 2011. *Research on Xi'an Industrial Heritage Protection and Reuse.* Beijing: China Building Industry Press.

Civil Engineering and Urban Planning IV – Liu et al. (Eds)
© 2016 Taylor & Francis Group, London, ISBN 978-1-138-02903-3

Analysis of Urban Public Greenspace pattern based on landscape metrics in Kunming

Min Liu
Institute of Ecology and Geobotany, Yunnan University, Kunming, Yunnan, China
Yunnan Key Laboratory of International Rivers and Transboundary Eco-Security, Yunnan University, Kunming, Yunnan, China

Zhi-Ming Zhang, Ming-Yu Yang, Yu-Peng Geng & Xiao-Kun Ou
Institute of Ecology and Geobotany, Yunnan University, Kunming, Yunnan, China

Ding Song
Kunming University of Science and Technology, Kunming, Yunnan, China

ABSTRACT: Urban Public Greenspace (UPGS) plays important functions in the metropolitan area. The objective of this study is to analyze Urban Public Greenspace (UPGS) status of Kunming tricyclic district. A GIS-based method, landscape metrics-based method was employed to insights into how the pattern of UPGS in the study area was and what spatial variance in different concentric ringways was. Results revealed that the UPGS pattern has some serious shortage provision, poor connectivity, and inequalities distribution in the study area. This study demonstrated a combination of remote sensing image classification and landscape metrics analysis can be regarding as a tool for UPGS and other urban landscape research. It has also revealed that the UPGS status analysis plays an important role in directing the future urban planning with rational principle for urban planners and stakeholders.

1 INTRODUCTION

Urban Public Greenspace (UPGS) is an important part in urban greenspaces system, and plays a major role in cities for aesthetic enjoyments, recreational opportunities and physical, and psychological well-being (Chen & Jim 2008). The increasing emphasis on UPGS is a current trend in the development of cities. But a large number of UPGS exist in single, uneven allocations and many other issues (Zhou & Wang 2009; Zhou & Li 2011).

Landscape metrics are useful tools in mapping and quantifying spatial land cover characteristics (Kong et al. 2012). It has widely been used in the urban green spaces pattern (Ghaffari & Monavari 2013; Mas et al. 2010; M'Ikiugu et al. 2012; Kong & Nakagoshi 2006; Zhou & Wang 2011). Studies have been taken out on green space using GIS in many countries (Kong et al. 2007; Oh and Jeong 2007; Senanayake et al. 2013). Thus, it is a suitable measure to analyze the rationality of UPGS using landscape index combined with GIS.

Kunming is selected for analysis in this study because it is the capital and the only one mega-city of Yunnan province in southwest of China with rapid urban expansion recently. This city has a higher rate of population growth (About 6 million permanent residents are living in a small mountain city environment). Besides, the city becomes a more attractive city for tourist around the world and its UPGS is a symbol of the impression to promote the value of tourism. The object of this study is to quantify the spatial patterns of UPGS in Kunming city. The following two research questions are put forward: (a) What was pattern of UPGS in tricyclic metropolitan area; (b) To investigate the spatial variance in landscape patterns along different concentric bypass roads.

2 STUDY AREA

Kunming city (102°10′–103°40′E, 24°23′–26°33′N; 1890 a.s.l.) located in central Yunnan province, with a total area of about 21 thousand km^2. The city began to receive more attention after 1999 when it held the International Horticulture Exposition and was recognized as an international radiation center for South and Southeast Asia (Zhou & Wang 2011).

The urbanization process of Kunming city conforms to the concentric model, with various intensities of development in different concentric belts and a relative shortage of green space in the urban

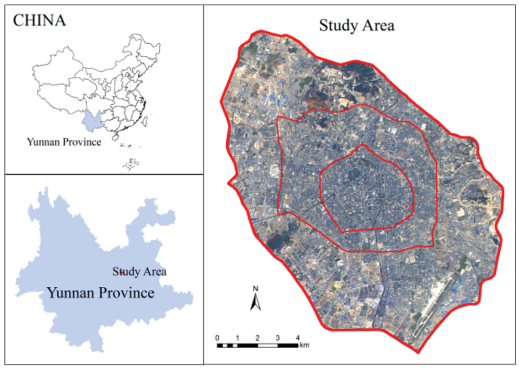

Figure 1. Location of Kunming tricyclic district.

core (Zhou & Wang 2011), and the main urban areas concentrated within tricyclic road. Thus, the study focused on the park land pattern in the Kunming tricyclic metropolitan area (Fig. 1). The study area covers 143.61 km^2. To rejuvenate the city with natural elements, the Kunming Landscape Bureau carried out several greening projects. A series of campaigns and activities were, therefore, implemented from 2006 to 2010 to allocate more green areas and corridors in the urban areas.

3 MATERIALS AND METHODS

3.1 *Data source*

Data used in this study were derived from remotely sensed images and field surveys. The following cloud-free remotely sensed images were used: ALOS Image (sensor AVNIR-2) acquired on March 22, 2010; ALOS Image (sensor PRISM) acquired on March 22, 2010. AVNIR-2 (AV) image has a resolution of 10 m in multispectral bands. PRISM (PS) image is panchromatic band with a resolution of 2.5 m. Field survey data included the ground control points collected using Global Positioning Systems for geo-referencing satellite images and photographs for assisting in image interpretation.

3.2 *Data processing*

For satellite images, they were firstly geo-referenced to the Universal Transverse Mercator (UTM) coordinate system by ERDAS IMAGINE 9.2 software package. Six spatial evenly distributed ground control points were selected for geometric correction using a second-order-polynomial transformation and the nearest neighborhood resampling method. Then IHS fusion was used to integrate the geometric detail of the PS image and the color information of AV image to produce a high-resolution Multispectral (MS) image (Daneshvar & Ghassemian 2010). Finally, the MS image was resampled to 2.5 m in order to match with the spatial resolution.

3.3 *Classification and extracting park green space*

Supervised classification is a new and effective approach to green space information extraction (Ghaffari & Monavari 2013; Zhou & Wang 2011). The object-oriented remote sensing image classification has been shown to improve land classification accuracy (Weng 2012). In this study, so the hierarchical classification and the neighboring classification rules in eCognition 8.7 were used in the image classification. Land use of the study area was classified into roads, agricultural land, building land, green space, water, and unutilized land (Kong et al. 2012), meanwhile the various types is composed of next level of different categories according to the different surface textures and color information. There are five main types of green spaces in the cities, namely forests, farmlands, parks, accessory greenbelt, and protective greenbelt (Ministry of Construction, PR China 2002).

Statistics of training samples for MS image was plotted to ensure that different land use classes could be separated. After classification, fifty sampling points in current Google earth image for each land use class were randomly selected to assess the classification accuracy. The current Google earth image has 1 m resolution or less in Kunming region, enough to replace the field sampling to examine the accuracy. At the same time, ALOS images in 2010, green space map in 2010, field survey, interview, and local knowledge, and experience of the study area were used as reference data for the assessment. Minor adjustments were done to correct the misclassified classes through field work verification. Finally, the overall accuracy of classification results is 0.92, overall kappa is 0.90.

For the classification result, we extracted park green space within the scope of the study area by visual interpretation. And then, the study area was classified into UPGS and non-UPGS. 110 polygon samples for each category in current Google earth image were randomly selected for the accuracy detection of visual interpretation. The error matrix analysis of samples was made for the urban public greenspace after extraction, with 0.98 of overall accuracy and 0.89 of overall kappa.

3.4 *Analysis of urban public greenspace pattern using landscape metrics*

To analyze the pattern of urban public greenspace, we tried to choose proper landscape metrics that are sensitive enough to detect the landscape pattern. In the present study, a total of seven

Table 1. Definition of landscape metrics used in this study.

Metrics	Description	Unit	Range	Justification
Number of Patches (NP)	The number of patches of the corresponding patch type (class).	None	NP ≥ 1	Aggregation index
Percentage of Landscape (PLAND)	The proportion of the area of certain land use class to the entire landscape area.	Percent	0 < PLAND ≤ 100	General index
Patch Density (PD)	The number of patches in certain class divided by the entire landscape area.	Number per 100 hectares	PD > 0	Index of fragmentation
Largest Patch Index (LPI)	The largest patch of certain class divided by the entire landscape area.	Percent	0 < LPI ≤ 100	Index of fragmentation and dominance
Landscape Shape Index (LSI)	Patch perimeter divided by the minimum perimeter possible for a maximally compact patch of the corresponding patch area.	None	LSI ≥ 1	Index of shape
Shannon's Diversity Index (SHDI)	Minus the sum, across all patch types, of the proportional abundance of each patch type multiplied by that proportion.	None	SHDI ≥ 0	Index of diversity
CONNECT	The number of functional joining's between all patches of the corresponding patches type.	Percent	0 < CONNECT ≤ 100	Index of connectance

landscape metrics (see in Table 1) were chosen including Number of Patches (NP), Percentage of Landscape (PLAND), Patch Density (PD), Largest Patch Index (LPI), Shannon's Diversity Index (SHDI), CONNECT. FRAGSTATS 3.4 software was used for the metric analysis.

Patch is the basic spatial unit to computing landscape index in this work; NP represents the number of the park patch, which quantitatively expresses the intensity of park patch. PLAND describes the relative abundance for UPGS in general. PD is associated with the degree of patch fragmentation in the traditional sense, not only that, it also sensitive to service ability of UPGS here. LPI can express the dominance of UPGS. LSI is closely related with the complexity of landscape pattern. SHDI was used to express the landscape diversity. CONNECT exhibits the patches's connectivity (Ghaffari Monavari 2013; Kong & Nakagoshi 2006).

We use these landscape metrics to analyze the UPGS in two aspects: synoptic landscape (UPGS) pattern, concentric landscape (UPGS) pattern, (Feng 2009; Li 2012; Ramachandra et al. 2012; Zhou & Wang 2011). First of all, a comparative analysis on whole study area was taken to the UPGS. Second, concentric analysis was executed to quantify spatial patterns of urban parks in each belt that radiated from the urban center to the fringe of the study area, which was divided into three concentric belts in full compliance with ring roads of Kunming, because the city currently has formed a three-ring concentric development pattern.

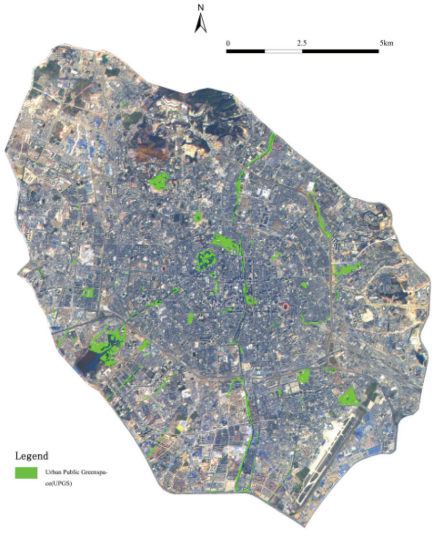

Figure 2. UPGS of the study area.

4 RESULTS

4.1 *Synoptic landscape (UPGS) pattern*

The landscape metrics were analyzed to present the characteristics of UPGS patterns. The synoptic analysis provided an overall summary of UPGS composition and configuration to examine the UPGS pattern (Fig. 2). Table 2 shows that the overall results of metrics. The results show that the park patch number of tricyclic district was relatively substantial,

Table 2. Landscape pattern comparison of landscape metrics.

	NP	PLAND	PD	LPI	LSI	SHDI	CONNECT
Overall area	299	1.85	2.08	0.15	36.44	0.09	0.81
I belt	72	4.07	4.92	1.44	17.95	0.17	27.86
II belt	66	1.43	2.01	0.56	15.38	0.07	11.28
III belt	181	1.66	1.88	0.20	28.26	0.08	8.00

at the same time, Landscape Shape Index (LSI) is also bigger, but the rest of the index value are low. It is revealed that there exists low abundance of UPGS types, poor connectivity and low park area ratios by three lower indexes of the Shannon's Diversity Index (SHDI), CONNECT and PLAND.

4.2 *Concentric landscape pattern*

To provide insights into the spatial variation of park landscape patterns in different concentric belts, analysis was performed in three concentric belts radiating from the city center to the fringe of study area. Apparently, the results showed that all index of I belt are greater than II belt and III belt, in addition to the NP. The old city of Kunming mainly located in belt 1 area, the index of NP in I belt is lower than II belt and III belt, instead, the PLAND of I belt exceeds the II belt and III belt. This means that a small number of park in the central district, but the overall area still accounts for a large advantage in current situation, mainly because of the large parks have left over in the region, such as Green lake park and the Yuantongshan park result in the higher proportion of park green space in I belt. Meanwhile, it shows they have good green infrastructure in central area, and the district of II belt and III belt behind pay more attention to commercial land development ignoring construction of the green space to relatively low proportion in PLAND. The greater other metrics value shows that the park green space of the central area can provide better service function than the peripheral space.

In II belt, the metrics of PD, LPI, and CONNECT were higher than III belt, except NP, PLAND, LSI, and SHDI. It suggests that II belt belongs to the city center in Kunming. The government strives to UPGS construction but was limited to the high value of land space, which is difficult to achieve. In contrast, in III belt, idle land can be used for the park construction and thus lead to the UPGS patch number and area ratio relatively high.

5 DISCUSSION

Landscape metrics are used to analyze the results of the UPGS in overall, concentric two aspects respectively. From the perspective of current UPGS status of Kunming city, the UPGS provision had a serious shortage with 1.85 of PLAND. UPGS type is very simple with more traditional types of integrative parks, while having less new types of UPGS such as wetland parks and theme parks, and with poor connectivity which could not form an organic network by lack of linear/corridor UPGS combined with roads and rivers. The concentric results seriously reflected the uneven distribution of UPGS from city center to the peripheral. I belt is the downtown area which was valued the development of public green, and III belt possess vacant spaces that can be used with the development of the park, which is not fair for residents to enjoy UPGS.

From the analysis of UPGS of Kunming tricyclic district, it shows that the most serious problem of UPGS is supply shortage and unreasonable distribution. In this context, it is an urgent need to increase the amount and area of UPGS in Kunming by setting various types of Shapes Park and thus increasing the Neighborhood Park. Simultaneously, we should increase linear/corridor neighborhood parks in the street and rivers to strengthen park accessibility and connectivity and form a UPGS network system.

Object-based image classification was used to extract existing green space, significantly costing savings compared to traditional field survey, which together with the previous fusion processing provides a credible precision. Similarly, the sampling for accuracy check is a new method based on current Google earth image to avoid labor waste for field sampling. Challenges remain for data resolution (preferably within 1 m accuracy for urban green extraction), classification techniques improvement and evaluation criteria.

6 CONCLUSION

This study employed GIS integrated with landscape pattern metrics to analyze the UPGS pattern in Kunming tricyclic district from the perspective of landscape ecology. The landscape pattern in concentric belts was also compared to examine the variation of UPGS. The results show that the

UPGS pattern has serious shortage provision, poor connectivity and inequalities significantly exist in cyclic structure.

Combination of landscape ecology and GIS is a worth new trying evaluation method to analyze UPGS pattern. This study can be applied to select priority greenspace planning scheme for planner and policymakers, and guide the urban planning in the future. Demographic factors and dynamic monitoring of UPGS implementation will be continue to study in our future works.

REFERENCES

Chen, W.Y. & Jim, C.Y. 2008. Assess and valuation of the ecosystem services provided by urban forests. In: *Ecology, Planning and Management of Urban Forests International Perspectives.* Carreiro, M.M., Song, Y.C. and Wu, J. Eds. New York: Springer.

Cohen, D.A., Mckenzie, T.L., Sehgal, A., Williamson, S., Golinelli, D. & Lurie, N. 2007. Contribution of public parks to physical activity. *American Journal of Public Health* 97(3): 509–514.

Dallimer, M., Tang, Z., Bibby, P.R. 2011. et al. Temporal changes in greenspace in a highly urbanized region. *Biology Letters* 7(5): 763–766.

Daneshvar, S. & Ghassemian, H. 2010. MRI and PET image fusion by combining IHS and retina-inspired models. *Information Fusion* 11(2): 114–123.

Feng, S. 2009. *Studies on 32 Year Land Use Cover Change and Its Drivering Forces in Kunming Suburbs (in Chinese)*. Mengla County: Xishuangbanna TroPical Botanical Garden Chinese Aeademy of Seienee.

Gao, J., Yang, M.J. & Tao, K.H. 2000. Analysis the pattern of urban greenary features in Shanghai. *Chinese Landscape Architecture (in Chinese)* 16(1): 53–56.

Ghaffari, P.O. & Monavari, S.M. 2013. Physical development trend and green space destruction in developing cities: A GIS approach. *Environment, Development and Sustainability* 15(1): 167–175.

Hobden, D.W., Laughton, G.E. & Morgan, K.E. 2004. Green space borders: A tangible benefit? Evidence from four neighbourhoods in Surrey, British Columbia, 1980–2001. *Land Use Policy* 21(2): 129–138.

Kaczynski, A. & Henderson, K. 2007. Environmental correlates of physical activity: a review of evidence about parks and recreation. *Leisure Sciences* 29(4): 315–354.

Kong, F. & Nakagoshi, N. 2006. Spatial-temporal gradient analysis of urban green spaces in Jinan, China. *Landscape and Urban Planning* 78(3): 147–164.

Kong, F., Yin, H. & Nakagoshi, N. 2007. Using GIS and landscape metrics in the hedonicprice modelling of the amenity value of urban green space: A case study in JinanCity, China. *Landscape and Urban Planning* 79(3–4): 240–252.

Kong, F., Yin, H., Nakagoshi, N. et al. 2012. Simulating urban growth processes incorporating a potential model with spatial metrics. *Ecological Indicators* 20(1): 82–91.

Li, Y.Y. 2012. *The Change of Urban Green Space and its impact on Eco-environmental effects: A case study in Shanghai (in Chinese)*. Shanghai: Fudan University.

Maller, C., Townsend, M., Pryor, A., Brown, P. & St Leger, L. 2006. Healthy nature healthy people: "Contact with nature" as an upstream health promotion intervention for populations. *Health Promotion International* 21(1): 45–54.

Mas, J.F., Gao, Y. & Pacheco, J.A.N. 2010. Sensitivity of landscape pattern metrics to classification approaches. *Forest Ecology and Management* 259(7): 1215–1224.

McGarigal, K., Cushman, S.A., Neel, M.C. et al. 2002. FRAGSTATS: Spatial Pattern Analysis Program for Categorical Maps. *http://www.umass.edu/landeco/research/fragstats/fragstats.html.*

M'Ikiugu, M.M., Kinoshita, I. & Tashiro, Y. 2012. Urban green space analysis and identification of its potential expansion areas. *Procedia-Social and Behavioral Sciences* 35(1): 449–458.

Ministry of Construction, PR China. 2002. *Standard for Classification of Urban Green Space, CJJ/T 85-2002, J185-2002 (in Chinese)*. Beijing: Ministry of Construction Press.

Oh, K. & Jeong, S. 2007. Assessing the spatial distribution of urban parks using GIS. *Landscape and Urban Planning* 82(1–2): 25–32.

Ramachandra, T.V., Aithal, B.H. & Sanna, D.D. 2012. Insights to urban dynamics through landscape spatial pattern analysis. *International Journal of Applied Earth Observation and Geoinformation* 18(1): 329–343.

Senanayake, I.P., Welivitiya, W. & Nadeeka, P.M. 2013. Urban green spaces analysis for development planning in Colombo, Sri Lanka, utilizing THEOS satellite imagery–A remote sensing and GIS approach. *Urban Forestry & Urban Greening* 12(3): 307–314.

Weng, Q. 2012. Remote sensing of impervious surfaces in the urban areas: Requirements, methods, and trends. *Remote Sensing of Environment* 117(1): 34–49.

Zhou, X. & Wang, Y.C. 2011. Spatial–temporal dynamics of urban green space in response to rapid urbanization and greening policies. *Landscape and Urban Planning* 100(3): 268–277.

Zhou, Y. & Li, J. 2011. Analysis and Evaluation to Park Green Spaces Status of Wuhan Main City in China. *2011 Second International Conference on Mechanic Automation and Control Engineering, Inner Mongolia, 2011.*

Zhou, Z. & Jiang-Ping, W. 2009. Evaluation of the Current Situation and Planning of the Greenspace System in Huaibei City Using GIS Based Network Analysis. *International Conference on Management and Service Science, MASS'09, Wuhan, 2009.*

This page intentionally left blank

Civil Engineering and Urban Planning IV – Liu et al. (Eds)
© 2016 Taylor & Francis Group, London, ISBN 978-1-138-02903-3

Research on the group layout of the space form in the intensive university campus

Qiao-Ming Deng & Yu-Bo Liu
State Key Laboratory of Subtropical Building Science, School of Architecture, South China University of Technology, Guangzhou, Guangdong, China

ABSTRACT: Intensive campus will be an inevitable choice of university construction in our country in the future. This paper researched on the effect of several different group layouts that improved the intensive extent in the campus by math models, through which it analyzed the space forms of university campus as well as the relationship between the intensive extent and the space quality. As a result, this paper tended to raise a proper type of group layout that will improve the intensive extent in the university campus and also provide some design suggestion.

1 INTRODUCTION

There is a large population with relatively little land in our country. However, even with such shortage of land resource, those limited land resources are not utilized to the fullest extent. Considering the conflict between the constant need from the development of higher educational construction and the preservation of limited land resource, and the actual need of higher education management, especially in those economic developed districts, an intensive construction mode of university campus will become an inevitable choice in a growing number of schools.

However, the intensive issue does not mean that the more the better, but it must take the space quality into consideration. Intensive campus construction is beneficial in improving the land-use efficiency, which will provide space for the future development of the school. Besides, intensive layout and function recombination can improve the efficiency of teaching and management. Sometimes they can also lead to the reduction in energy consumption. On the other hand, over-intensive campus may cause some problems such as ventilation, lighting, landscape view and noise, which will lead to the decline in the campus greening ratio, public activity space and environmental quality. Some may even have a detrimental influence on students' psychological health. Therefore, those intensive campus planning and design that lack of deep research will bring a negative effect and thus cause the deterioration of the whole environment in the campus.

As far as we are concerned, the key problem of intensive campus design is how to acquire comfortable space when the density of the campus is improved. Therefore, in order to achieve the balance between the density and quality, we need to further research on the complex relationship between the space form, the intensive extent and the space quality.

2 INTENSIVE EXTENT AND THE SPACE FORM OF THE CAMPUS

The intensive extent is mainly determined by the building floors, depth, height, distance between different buildings and their whole layout. Different space forms of the campus bring different intensive extents and results in various space qualities. "Space form of the campus" is similar to the concept of "urban space form", which not only focuses on the building floors, volume and compound mode, but also focuses on all kinds of campus space. Group layout is an important aspect that contributes to the space form of the campus. Different types of group layouts have different influences on improving the intensive extent, landscape view, natural ventilation and lighting, all of which are the key factors that are related to the satisfactory intensive space.

3 INTENSIVE EXTENT AND MODEL RESEARCH ON SPACE FORM OF THE CAMPUS

After research on the cases of better intensive campus, we discovered that there are four types of space forms that can be used to model and analyze the feature of group layouts in the intensive campus, including point layout, strip layout, enclosing layout and patio layout (Koen 2004). The research mainly

adopts three variables, including the floor area ration "F", building storey "n" and the building depth "d" (Fig. 1). According to every type of space form, we set up different math models to calculate the floor area ratio. Then, we compare the variation in the floor area ratio of different types of group layouts due to the variation in the number of floors and depth, in terms of the same space quality.

The basic hypothesis of the research is as follows:

The storey height "h" is the same and the angle of the external shade is set as 45°; in other words, the distance between the buildings "L" is the same with the height of the whole building "nh" (Rudy 2008).

Since there are too many factors related to the space quality, in order to simplify the research, we keep the angle of the external shade the same, which can make sure that there are same space qualities, including the same lighting, ventilation, sunshade and landscape view conditions in terms of different intensive extents.

3.1 *Point layout*

The calculation function for the FSI (Floor Space Index) of the point layout is as follows:

$$F = \frac{nd^2}{(d+nh)^2} \tag{1}$$

Calculated by the computer software, with the same building storey number, the influence on the variation in FSI by the variation in depth can be obtained, as shown in Figure 2. The influence by the variation in storey with the same depth is shown in Figure 3. As the figures show, for the point layout, with the increase in building depth, the FSI will increase and peak at a maximum; with the same building depth and the increase in storey, the FSI rises to a peak value and then begins to fall off.

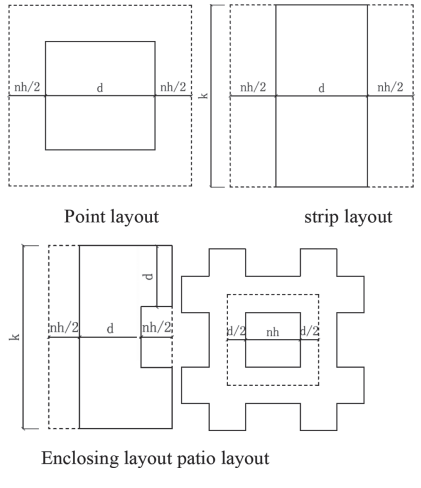

Figure 1. Model parameters.
Resource: analysis by the author.

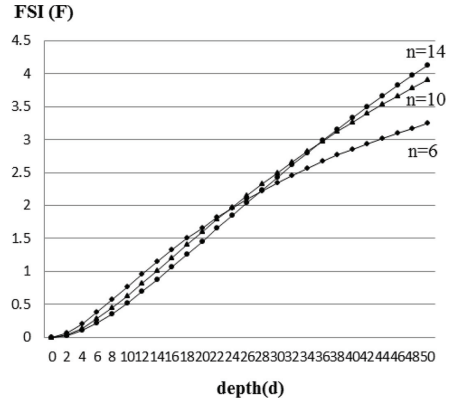

Figure 2. With the same storey, influence on the FSI by depth.
Resource: analysis by the author.

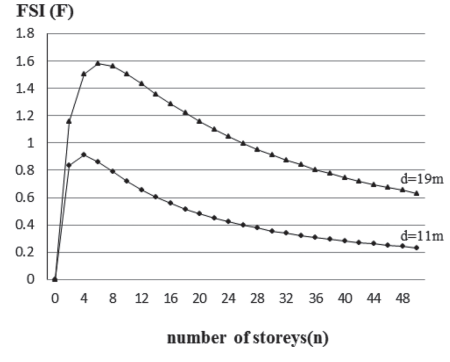

Figure 3. With the same depth, influence on the FSI by storey.
Resource: analysis by the author.

3.2 *Strip layout and enclosing layout*

Strip layout and enclosing layout have the same calculation function for the FSI:

$$F = \frac{nkd}{(d+nh)k} = \frac{nd}{d+nh} \tag{2}$$

Calculated by the computer software, with the same building storey number, the influence on the variation in FSI by the variation in depth can be obtained, as shown in Figure 4. The influence by the variation in storey with the same depth is shown in Figure 5. As the figures show, for the

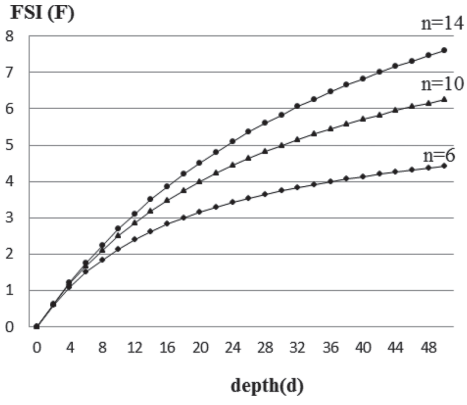

Figure 4. With the same storey, influence on the FSI by depth.
Resource: analysis by the author.

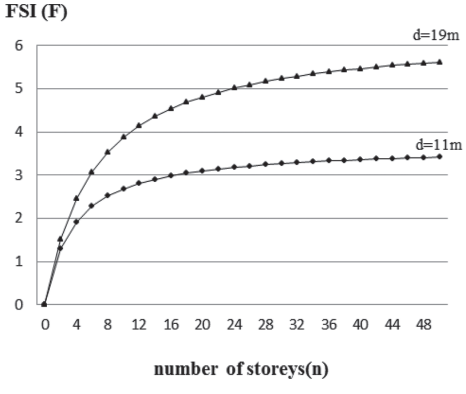

Figure 5. With the same depth, influence on the FSI by storey.
Resource: analysis by the author.

strip layout and enclosing layout, with the increase in building depth and storey, the increasing rate of FSI will slow down. It is because when the depth and storey increase to a certain extent, in order to keep the same angle of the external shade, the distance between buildings increases and thus leads to the decline in enhancive building areas and the improvement of the extent of FSI.

3.3 *Patio layout*

The calculation function for the FSI of the patio layout is as follows:

$$F = \frac{nd(d+2nd)}{(d+nh)^2} \quad (3)$$

Calculated by the computer software, with the same building storey number, the influence on the variation in FSI by the variation in depth can be obtained, as shown in Figure 6. The influence by the variation in storey with the same depth is shown in Figure 7. As the figures show, for the patio layout, the FSI will increase with the growth of both the depth and the storey. However, the increasing rate of FSI will slow down with the growth of the depth and the storey. Comparing these two factors on the effect of improving the FSI, the effect of the increase in building storey becomes much obvious.

3.4 *Comparative analysis of different types of group layouts*

After the comparative analysis of the calculation results for different types of group layouts, we discovered that except the FSI of point layout, almost all the FSI values of strip layout, enclosing layout

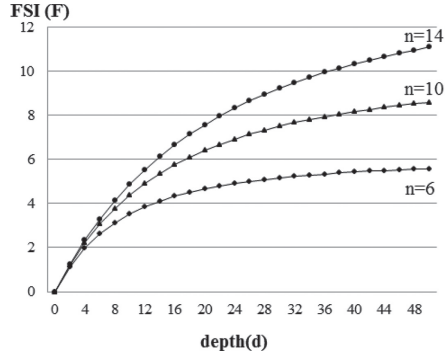

Figure 6. With the same storey, influence on the FSI by depth.
Resource: analysis by the author.

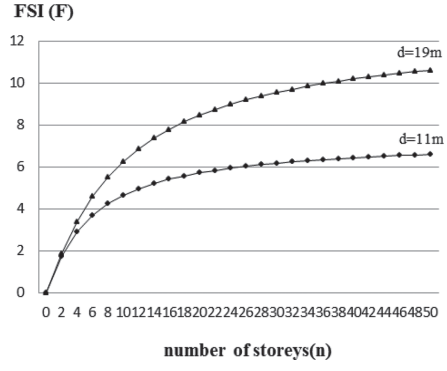

Figure 7. With the same depth, influence on the FSI by storey.
Resource: analysis by the author.

and patio layout, increase with the growth of building storey as well as the building depth.

1. When increasing the building depth, as shown in Figure 8, the FSI of all the four types of layout will rise, even though the increasing rate is declining and there is an extreme value in every type. Among all the types, the patio layout is the one that can achieve the highest FSI, which is nearly twice the strip layout and enclosing layout and even four times the point layout. However, with the increase in the building depth, the efficiency of inner ventilation and lighting declines dramatically and becomes difficult to meet the need of the normal teaching function. What is worse, the visions in front of the building also decline and thus bring the teachers and students a sense of stress. In order to improve the inner space quality, there need to be more courtyards to bring natural ventilation and lighting, which will decline the building areas and FSI and lead to a worse synthetical effect.
2. When increasing the building storey, as shown in Figure 9, the FSI of strip layout, enclosing layout and patio layout will increase, even though the increasing rate is declining. Among these three types, the patio layout can achieve the highest FSI, which is better than that under the condition of increasing building depth. By contrast, the FSI of point layout is the lowest, and it has the extreme value when the building height is the same with the depth, after which the FSI will decline as the building storey is increased. The FSI can be improved when the point building is located in a staggered way.

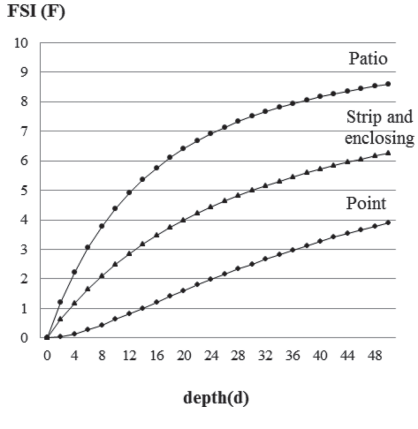

Figure 8. Comparative analysis of the influence on FSI of different types of layouts by the variation in depth with the same storey.
Resource: analysis by the author.

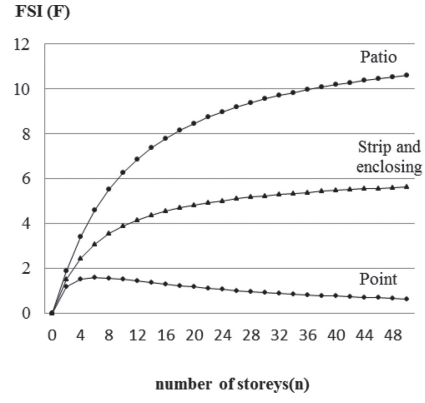

Figure 9. Comparative analysis of the influence on FSI of different types of layouts by the variation in storey with the same depth.
Resource: analysis by the author.

4 CONCLUSION

4.1 *Comparative analysis of different methods in improving the intensive extent*

In terms of a certain space quality, choosing a reasonable type of group layout is the most effective way among all sorts of methods in improving the intensive extent, as presented in Table 1.

Comparing these four types of layout modes, the patio layout is the most effective mode in terms of both the increase in storey and depth. Meanwhile, no matter which layout mode it was, increasing the building storey is the most effective way when the building is relatively low. Increasing the depth makes sense only when the building is relatively high.

4.2 *Suggestion on the application of the research results for the intensive campus planning and design*

4.2.1 *Choose a reasonable space layout*

The issue of intensive design is complex. It does not mean that the higher the FSI is, the better it is. We need to take the space quality into consideration. The space form of the campus is an important aspect that determines the intensive extent. Different types of group layout will lead to various campus space forms and thus result in different environmental quality. As shown by the above research, in terms of the same building storey, depth and space quality, there are differences between different types of group layout, among which the patio layout has the highest FSI, which is nearly twice the strip layout and enclosing layout and even four times the point layout. Therefore, patio layout is the most effective way to improve the FSI in the campus with increasing finance. In the complete cases of the intense

Table 1. Evaluation and application areas of the above-mentioned methods.

Methods of improving the FSI	Floor area ratio "F" calculation model	The proposal of improving the FSI	Advantages	Disadvantages	Suggestion on application
Different types of group layout					
Point layout 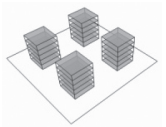	$\frac{nd^2}{(d+nh)^2}$	When the building height is the same with the depth, the FSI reaches its maximum. With the increasing building storey, the FSI declines. Under the same conditions, this type shows the lowest FSI	With a reasonable building depth, there are better natural ventilation and lighting conditions in every building	The FSI is relatively low; Inconvenience transport connection between every building; Low efficiency of inner space	Improve the FSI by locating the buildings in a staggered way. Reduce rooms that face to the east and west by combining some assistant space, such as staircase and toilets
Strip layout 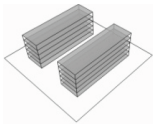	$\frac{nd}{d+nh}$	The FSI will increase with the growth of building storey and depth, even though the increasing rate is declining. The effect is nearly the same with that of the enclosing layout, which is in the middle stage of all the modes	All the buildings have better lighting conditions	There are bad influences on ventilation because of buildings in front or behind	Take the local wind direction into consideration to improve the ventilation conditions, such as bottom overhead construction or sky yard design
Enclosing layout 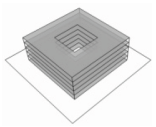	$\frac{nd}{d+nh}$	The FSI will increase with the growth of building storey and depth, even though the increasing rate is declining. The effect is nearly the same with that of the strip layout, which is in the middle stage of all the modes	Provide enclosing outer space, which has a better atmosphere that is beneficial for the communication between teachers and students	There are some rooms that face to the east and west as well as some problems in the ventilation of the courtyard	Take the local climate conditions into consideration. The northern area prefers the closed courtyard while the southern area tends to bottom overhead construction or open holes in the storey to improve the ventilation
Patio layout 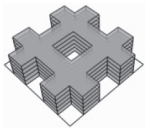	$\frac{nd(d+2nh)}{(d+nh)^2}$	The FSI will increase with the growth of building storey and depth even though the increasing rate is slowing down. In terms of the same conditions, this type shows the highest FSI.	Provide enclosing outer space, which has a better atmosphere. This type can greatly improve the FSI.	There are some rooms that face to the east and west, some problems in ventilation of the court yard as well as in the transport connection.	Take the local climate conditions and need of ventilation into consideration. The southern area can improve the transport connection and ventilation by bottom overhead construction.

(*Continued*)

Table 1. (*Continued*).

Methods of improving the FSI	Floor area ratio "F" calculation model	The proposal of improving the FSI	Advantages	Disadvantages	Suggestion on application
Increase in the building storey		It is an effective way to improve the FSI when the building has relatively few storey	Higher FSI and more open space	With the increase in building storey, the cost increases and the use efficiency declines. There is a problem of flow distribution in high rise	It is necessary to design divisional vertical transportation to solve the problem of flow distribution when the building is relatively high. It is beneficial to improve the inner space quality when the design combines the sky yard
Increase in the building depth		It is an effective way to improve the FAR when the building has relatively many stories	Low cost	With the increase in building depth, the lighting and ventilation of inner space turn worse	It is necessary to design landscape courtyard to improve the lighting, ventilation and view of landscape when the building depth is relatively deep

campus, both the Hong Kong Polytechnic University and City University of Hong Kong adopt similar types of layout and achieve a higher intensive extent. Therefore, choosing different types of group layout will directly determine the potential of the intensive extent in the campus. In the early stage of the campus planning and design, it is necessary to combine the land conditions, function requirements and the needs of intensive extent to choose a reasonable type of layout, through which the intensive extent of the campus can be significantly improved finally.

4.2.2 *Adapting to the local climate condition*

Due to a vast territory in our country, there are great differences of climate in different places. Choosing which type of group layout to improve the intensive extent needs to take the specific regional climate conditions into consideration. For example, given that the main climate features of South China district include high temperature and high humidity, the coping strategies in the architecture are ventilation, sunshade and heat insulation. Although patio layout can improve the highest FSI, the over closed yard is not beneficial for natural ventilation. In the design of the Hong Kong Polytechnic University, the designer adopted the bottom overhead strategy to connect every patio, which not only provides better ventilation conditions but also enhances the transport connection between different patios. Therefore, it achieves better space quality (Deng & Liu 2015). As to the northern area in our country, both the patio layout and enclosing layout are most beneficial in adapting to the local climate conditions, as they can not only provide better lighting conditions but also keep off the cold wind, and thus lead to a comfortable outer space in the campus. All in all, it is necessary to improve the layout according to the regional climate feature even after choosing an appropriate type of group layout that will improve the intensive extent.

ACKNOWLEDGMENT

This project was supported by the National Natural Science Foundation of China (No. 51508193) and the Fundamental Research Funds for the Central Universities (No. 2014ZM0029).

REFERENCES

Deng, Q.M. & Liu, Y.B. 2015. Research for the satisfaction of students in high density campus environment—take a university in Hong Kong as an example. *South Architecture* 165: 119–123.

Koen, S. 2004. Sustainable Urban Design: Issues, Research and Projects. *World Architecture* 170: 34–39.

Rudy, U. 2008. *Cities Full of Space, Qualities of Density*: 30. Rotterdam: 010 Publishers.

Civil Engineering and Urban Planning IV – Liu et al. (Eds)
© 2016 Taylor & Francis Group, London, ISBN 978-1-138-02903-3

Residents' living experience and satisfaction in Chinese urban development: A case study of Ningbo

Cong-Hua Wen & Yueh-Lung Lin
School of Mathematical Sciences, Faculty of Science and Engineering, The University of Nottingham, Ningbo, Zhejiang, China

Jing Bie
Department of Civil Engineering, Faculty of Science and Engineering, The University of Nottingham, Ningbo, Zhejiang, China

ABSTRACT: China has been experiencing very rapid urbanization and urban development in the past decades. This has led to worsening problems such as traffic congestion and poor air quality which reduced the urban residents' quality of life. The purpose of this study is to help achieve sustainable urban development, by investigating the crucial requirements of urban development on environmental protection, social and economic development and sustainability. Through a questionnaire survey on residents' living experiences and assessment of the built environment at five residential communities in the city of Ningbo, this study investigates the relationship between living standard and the living environment. The results show that there is a general desire to have more floor area at home; satisfaction with public transport is generally high but traffic noise causes a lot of disturbance and reduces residents' quality of life. Based on these results, recommendations are made on building sustainable communities in the future.

1 INTRODUCTION

China has a huge population. As a developing country, China has seen a rapid urbanisation in recent years. More living areas are needed to accommodate the growing urban population. Establishing a sustainable solution to urban development in China with rapid urban population growth is critical in global efforts towards achieving sustainability. In this paper a case study is carried out for the city of Ningbo. Here we focus on five residential areas (communities) and conduct a questionnaire survey with their residents. With the data collected, we can analyse the basic attitude people have towards their residence. We also analyse people's satisfaction level on a set of aspects related to their residence. With the results achieved we make recommendations for sustainable urban development in Ningbo (in particular) and China (in general).

2 BACKGROUND

The negative relationship between human activities and climate change is well established (IPCC 2001). More than 50% of the world's population currently live in urban areas (UN Habitat 2008), occupying only about 2% of the landmass, but consuming over 75% of the resources. This distinct difference in numbers indicates how improper and unreliable some urban forms can be. To avoid the potential problem of limited land availability under population growth, it is necessary to establish sustainable solutions of urban development in China. Urban development in Ningbo, experiencing rapid growth as a coastal city, has been suffering from the old-fashioned planning form which gradually cannot satisfy the social demands with high population density and rapid economic development. More integrated and innovative urban planning strategies are therefore needed as the new development form.

Researchers have been studying the requirements for sustainable cities (Jenks & Dempsey 2005). Sustainability has many facets; its assessment is not always straightforward: various assessment methodologies (Singh et al. 2009) and indicators (Winograd 2007) comes into play, covering economic, environmental as well as social aspects in urban development. The sustainability of urban development highly depends on the quality of the communities in the urban environment. The concept of community quality here concerns the standard of the designed environment in meeting the complex levels of human needs.

Smith et al. (1997) studied the relationship between the physical form of a urban community and its quality. The researchers investigated the physical elements that contribute to the quality of

a community. Six main categories of the quality principles have been adopted: liveability, character, connection, mobility, personal freedom, and diversity. A set of physical form criteria has been developed under the categories of community, urban block, buildings, streets, pedestrian ways, open space, vegetation, and feature areas. Case study applied to three communities in Toronto shows that the most important physical form criteria are: a walkable community, outdoor amenities, lots of seating, barrier free, and open space areas in residential areas.

Bender et al. (1997) conducted a questionnaire survey of 850 house owners in the greater Geneva area. They studied the preferred characteristics related to the environment of single-family houses and found out that distance to a green area and quietness of the area are the two most important factors. On the other hand, the proximity of shopping centres and schools is not as important as in other countries.

Zakaria El Adli Imam (2006) investigated the role of green areas (greenway, greenery) in the development of urban and sub-urban areas. It is argued that they help mitigate the loss of "natural" space by having scenic qualities and provide for recreation, education, a sense of well-being, and preservation of the natural habitat.

3 METHODOLOGY

In this study data are collected through a living experience questionnaire and a built environment survey. Five residential communities (neighbourhoods) are chosen for this survey.

3.1 *Living experience questionnaire*

The residents' living experience and satisfaction are investigated through a questionnaire survey. The questionnaire contains three parts: questions about the housing, questions about the living environment, and questions about the household. The questionnaire is purposely designed to avoid intruding respondent's privacy directly. Less privacy-sensitive questions are asked instead; for example, instead of household income, respondents are asked the amount of the cars they own, which can be an indicator on their income level.

Effort has been made to cover both genders and all age groups. With the cooperation of these communities, questionnaires are given out to local residents for filling in. In some cases survey is undertaken along the main street of the community, where pedestrians passing by are approached for the survey; in other cases, a gathering is preannounced where residents willing to participate come to a central location for filling the questionnaire. This is further complemented by door-to-door surveys where residents are approached at their front door.

The following questions are included in the questionnaire survey:

- Questions about the housing: type, ownership, facilities/furniture, satisfaction of home size, satisfaction of home location.
- Questions about the living environment: satisfaction of the neighbours, satisfaction/perception of neighbourhood safety (at night), satisfaction of neighbourhood sanitary conditions, satisfaction of neighbourhood noise levels, satisfaction of shopping convenience, satisfaction of neighbourhood landscaping.
- Questions about the resident and their household: gender, age, family members, occupation, commuting method, car ownership, years of residence in neighbourhood.

Five communities are chosen and results from a total of 116 respondents are collected:

- Qinglinwan: 19 respondents
- Lianfeng Shiji: 20 respondents
- Jinghuayuan: 26 respondents
- Haiguang Xingdu: 38 respondents
- Yonghe Yiju: 13 respondents.

In terms of gender distribution of the respondents, 58 are female and 57 male, with 1 unknown. Age distribution of the respondents is shown in Figure 1. Respondents at each community cover a wide range of occupations, including full-/part-time employment, student, housewife, unemployed, etc.

3.2 *Built environment survey*

The built environment survey attempts to characterise the neighbourhood and contains three parts: the street, the typical buildings and the

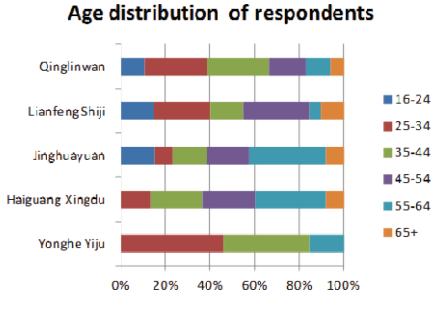

Figure 1. All age groups have been accounted for in the questionnaire survey.

land-use form. Surveys are taken by researchers walking through the communities, recording and assessing the conditions and characteristics of the neighbourhood features, based on a predefined set of criteria.

Firstly the appearance and the quality of the neighbourhood streets are evaluated. The quality of each street is assessed against the following criteria:

- Amount of litter on street
- Maintenance of street
- Presence of vandalism
- Perceived safety.

Secondly, buildings in the community are divided into several height/storey groups and each group is categorised/assessed separately against the following aspects/criteria:

- Type of building
- Age of building
- No of stories
- Maintenance of building
- Access to building
- Facilities in building (Lift, Basement parking, Concierge, Close circuit camera).

Lastly, the land-use form survey generally focuses on the availability of certain facilities in and around the community. These include the following aspects:

- Transport facilities (bus stops, parking facilities)
- Retail stores
- Educational institutions
- Communal services (community centre, public library, police station, etc.)
- Medical facilities
- Entertainment and recreation (clubs, sports facilities, public square, green land).

4 DATA ANALYSIS

Data from the living experience questionnaire and built environment survey are analysed for answering the research questions.

4.1 *General statistics and the household*

The general results suggest that the majority of homes are private properties (Fig. 2), meaning a lack of public housing in the surveyed communities. Most households are well equipped, with facilities such as television, washing machine, refrigerator at home. Automobiles are also readily available, with most households owning one or two cars (Fig. 3).

The majority of household are three-member satellite families (Fig. 4). Large households (≥5)

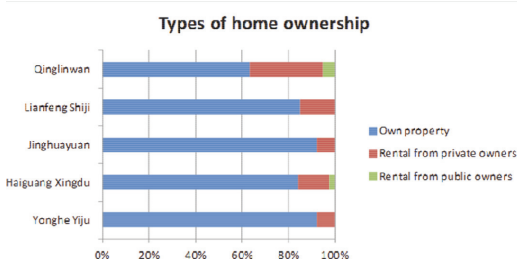

Figure 2. The vast majority of homes are owned privately.

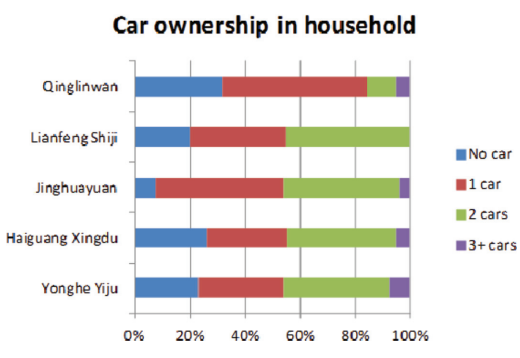

Figure 3. Car ownership has become common place in Ningbo, with the most households owning one or two cars.

do exist but they represent less than 20% of the respondents. It would be natural to assume that large households have large accommodations but this is not necessarily true (Fig. 5): many large households live in homes with two or less bedrooms.

4.2 *Current living standard*

Respondents are generally satisfied with their home size (Fig. 6), with 56% reporting satisfied or very satisfied. Still, 11% of the respondents are dissatisfied with their current home size. The satisfaction level seems to correlate with the home size (indicated by the number of bedrooms at home), as seen in Figure 7. This represents a general desire to have bigger (than current) homes.

Regarding their home location, the majority of respondents are satisfied, with less than 5% dissatisfied. However, this can vary significantly across different communities, as seen in Figure 8. This is natural as different communities are located in different areas of the city and may have different levels of service in terms of public transport (Fig. 9) and other facilities such as shopping (Fig. 10), employment, sports etc.

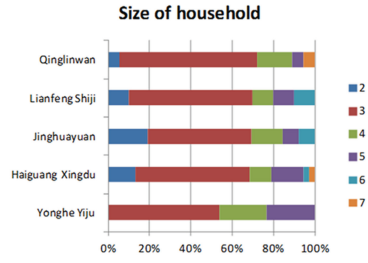

Figure 4. A typical household has three members: father, mother, and child.

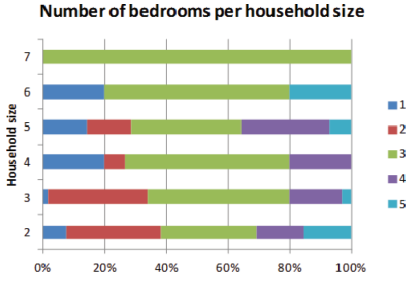

Figure 5. Large households do not necessarily own large homes.

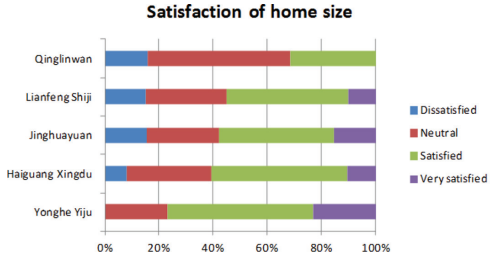

Figure 6. Most respondents are satisfied with their home size.

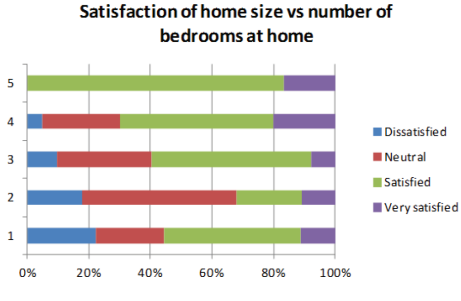

Figure 7. Satisfaction level of home sizes is strongly correlated to the number of bedrooms at home.

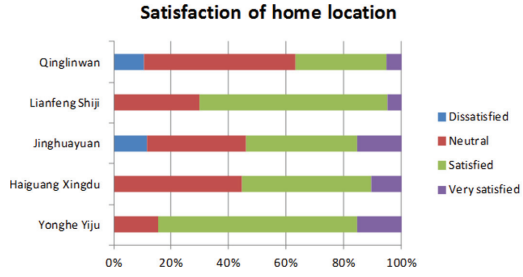

Figure 8. Satisfaction level of home location varies significantly across the communities.

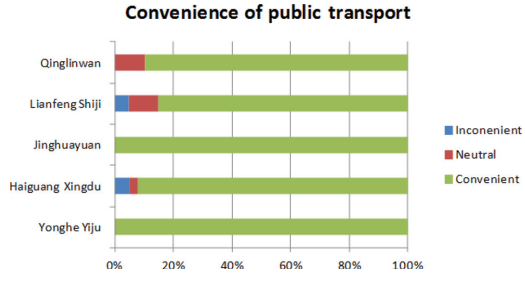

Figure 9. The great majority of the respondents have convenient access to public transport.

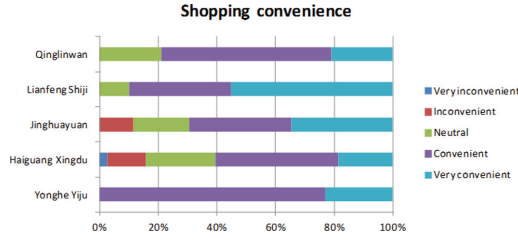

Figure 10. Perceived shopping convenience varies across the communities and seems to correlate to residents satisfaction of home location (Fig. 8) and their perceived convenience of public transport (Fig. 9).

On the other hand, it is found that satisfaction of home location may be correlated to residence length (Fig. 11): dissatisfied residents usually have a shorter period of residence at the current community, while long term residents are generally more satisfied of their home location. There can be several explanations for this: dissatisfied residents have a higher likelihood of changing residence after a few years, moving to a location perceived as better; "newer" residents need time to settle down and their appreciation of the community may be limited in the beginning; it also takes time to get oneself familiarised with all the facilities as well

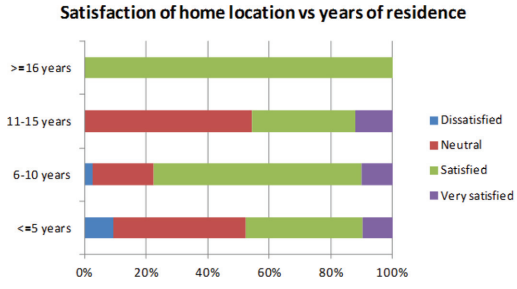

Figure 11. Satisfaction level of home location is positively correlated to the length of residence in the community.

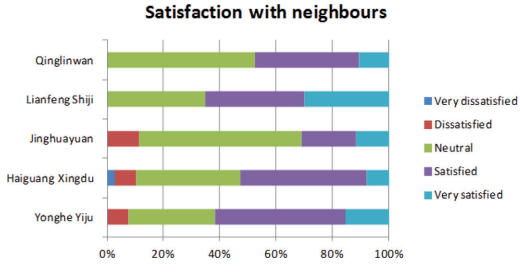

Figure 12. Respondents are generally satisfied with their neighbours in the community.

as opportunities of activities in the vicinity of the neighbourhood.

4.3 *The living environment*

When asked about their opinion on neighbours, the majority of the respondents are satisfied with the neighbours they have (Fig. 12). Only 6% are (very) dissatisfied with their neighbours. Dissatisfaction may stem from noisy neighbours (Fig. 13), although the biggest source of neighbourhood noise is actually from road traffic (Fig. 14). The seriousness of traffic noise has been overlooked in the past and its damage underestimated. This study shows that traffic noise is a serious concern for many if not all communities. This echoes the results from Bender et al. (1997), which shows that quietness of the residential area is highly desired by the residents in Geneva.

The respondents are also asked whether they feel safe when walking alone at night in their neighbourhood. The results show that the vast majority feel safe (Fig. 15), with two of the communities having more than 20% respondents feeling unsafe. We expect gender to make a huge difference in perceived safety, but the results (Fig. 16) show that this is not case. This may indicate that the type of danger is not necessarily person-related

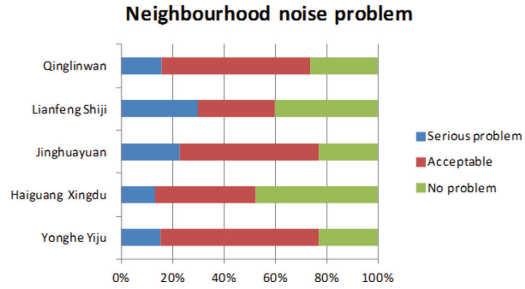

Figure 13. In all communities there are some residents who see noise as a serious problem.

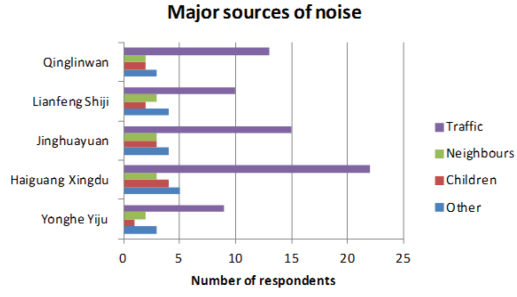

Figure 14. Road traffic is the biggest source of noise in all communities.

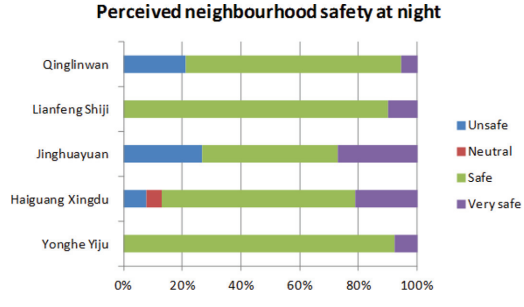

Figure 15. Most respondents feel safe in their neighbourhoods.

(such as assault) but often property-related (such as robbery) which both genders are likely to become victim of. Regarding neighbourhood sanitary conditions, there appears to be a huge difference between the communities (Fig. 17). Different communities are managed by different property management companies. This may partially explain the differences.

The results are similar for satisfaction level of neighbourhood landscaping (Fig. 18). Neighbourhood landscaping is to a large extent managed by

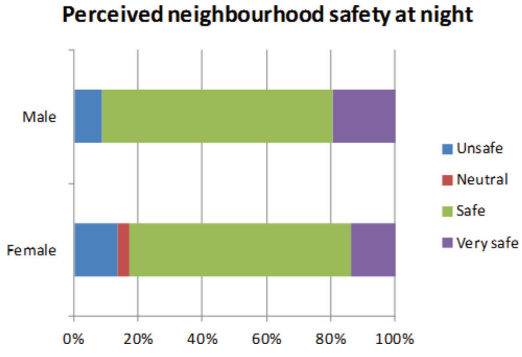

Figure 16. The difference between males and females is not very big when it comes to perceived neighbourhood safety.

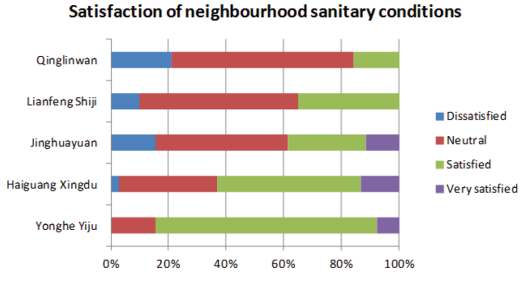

Figure 17. Satisfaction level of neighbourhood sanitary conditions varies significantly across the communities.

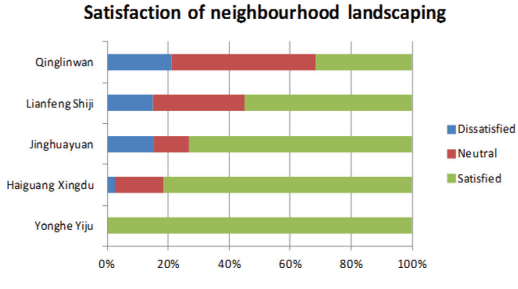

Figure 18. Satisfaction level of neighbourhood landscaping varies significantly across the communities.

the property management company. In some communities the neighbourhood greenery is better organised than in other communities. Frequency of visiting the greenery (Fig. 19) is positively correlated to satisfaction of landscaping. This means that when good greenery is present, residents are eager to spend time and enjoy it.

The major purposes of visiting the neighbourhood greenery (Fig. 20) are exercise and playing with children, followed by sightseeing and walking the dog.

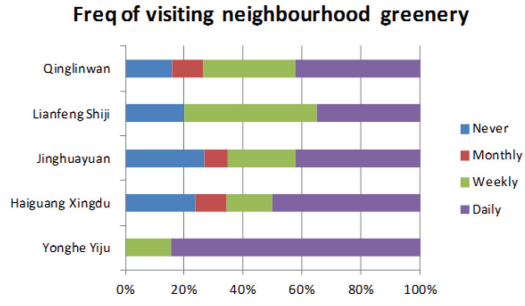

Figure 19. Frequency of visiting neighbourhood greenery is positively correlated to satisfaction of neighbourhood landscaping.

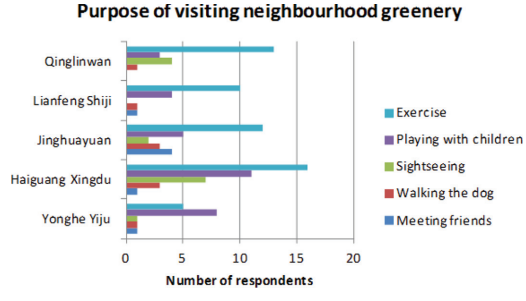

Figure 20. The major purposes of visiting the greenery are related to individual activities, while meeting friends as a group, community-binding activity is not frequently performed.

These activities can be considered as personal as they are performed alone (or with young children and dogs). The greenery is seldom used for gathering and meeting neighbourhood friends, which can be considered as a group, community-binding activity. This suggests that the functions of public spaces inside the neighbourhood have to be further explored, for building a harmonious community.

4.4 *Relationship with the built environment*

Results from the built environment survey shows that the five residential communities have diverse characteristics. The most important results are summarised in Table 1. Overall, Yonghe Yiju and Qinglinwan score better than the other three communities: they have newer buildings and better facilities. The types of residence vary from townhouses to high-rise residence blocks, with the majority being condominium (apartment, flat) buildings. Numbers of floors are generally 10~18, except townhouses which usually have 3~4 floors. Buildings with more than 8 floors are generally equipped with lifts (elevators). Conditions of

Table 1. Characteristics of the built environment at the residential communities.

Community	Yonghe Yiju	Haiguang Xingdu	Jinghuayuan	Lianfeng Shiji	Qinglinwan
Residential type	Block	Condominium	Townhouse	Condominium	Condominium
Age of buildings	0~5	15~20	10~15	10~15	5~10
No. of floors	11~17	7~10	3~4	8	6~12
Lift	Yes	No	No	No	Yes
Conditions of building	Good	Poor	Fairly poor	Fairly poor	Fairly good
No. of through roads	5	3	2	5	3
No. of dead-end roads	1	0	0	0	0
Street maintenance	Good	Fairly good	Fairly good	Fairly good	Good
Presence of litter	Little	Little	Little	Widespread	Little
Evidence of vandalism	None	Smashed windows & Graffiti	Smashed windows	Damage to street furniture & Graffiti	None
CCTV surveillance	Yes	No	Partially	No	Yes
Parking facilities	Underground	Surface	Surface	Surface	Surface & Underground
Bus stop nearby	Yes	Yes	Yes	Yes	Yes
No. of supermarkets	3	1	3	0	2
No. of retail stores	5	4	4	13	5
Educational institutions	Primary school	Primary school	Primary & secondary	Primary & secondary	Primary & secondary
Public library	Yes	No	No	No	Yes
Hospitals	No	No	No	No	No
Clinics	Yes	Yes	Yes	Yes	Yes
Sports facilities	Yes	Yes	Yes	Yes	Yes
Park	Yes	No	Yes	No	Yes
Public square	Yes	No	Yes	Yes	Yes
Greenery	Yes	Yes	Yes	Yes	Yes

buildings vary from good to poor and generally depend on how new the buildings are.

Roads inside the neighbourhood are mostly through roads (no dead end), well maintained and have little litter (except Lianfeng Shiji). Vandalism is present in some communities and varies from smashed windows to graffiti and damage to street furniture. CCTV surveillance is available in about half of the communities.

For home location, respondents from Jinghuayuan and Qinglinwan have the lowest satisfaction level (Fig. 8). It is however difficult to attribute this to the absence of various facilities in the neighbourhood: Jinghuayuan and Qinglinwan are fairly equipped with communal facilities such as transport access, retail, education and sports facilities, compared the other three communities. This implies that residents' satisfaction of home locations depends more on the geographical location (e.g. location within a city, distance to work) than on the facilities nearby.

For shopping convenience, it seems to depend more on the presence of (small) retail stores than on the presence of (big) supermarkets. Convenience level is the highest for respondents from Lianfeng Shiji (Fig. 10), where there is no supermarket nearby but an abundance of retail stores (Table 1). On the other hand, convenience level is the lowest for Haiguang Xingdu and Jinghuayuan, both of which have supermarkets nearby but only a limited number of retail stores, compared to other communities. This trend is, however, not so clear-cut, if we compare Yonghe Yiju and Jinghuayuan: the numbers of supermarkets and stores are almost the same yet there is a significant difference in perceived shopping convenience. This indicates that shopping convenience cannot be solely judged by the number of shops nearby but also other factors (e.g. types of shop and what they sell).

In terms of noise problem, it is difficult to attribute the differences between the five communities (Fig. 13) to the characteristics of their built environment. External traffic may be a bigger contributor than internal traffic. The same applies to safety at night: Jinghuayuan and Qinglinwan score the lowest in terms of perceived safety level (Fig. 15), yet both are (partially) equipped with CCTV surveillance. There does not seem to be a correlation between perceived safety and the presence of litter and/or vandalism, either.

It is also difficult to attribute the satisfaction levels of neighbourhood sanitary conditions (Fig. 17) and landscaping (Fig. 18) to the summary characteristics in Table 1. It was expected that the perceived neighbourhood sanitary conditions were highly influenced by the presence of litter and vandalism on street. The results show, however, such correlation does not seem to exist. A potential reason is that residents are more concerned of sanitary conditions within buildings than on streets, i.e. public spaces inside buildings such as staircases and lifts. For landscaping, it seems that the quality of the provided greenery can make a big difference on residents' satisfaction.

5 RECOMMENDATIONS FOR SUSTAINABLE URBAN DEVELOPMENT IN CHINA

Based on the study results, the following recommendations are made for achieving sustainable urban development in Ningbo and in China. It should be noted that the results above are more indicative than conclusive. The recommendations are therefore of a suggestive nature and further explorations are necessary before implementation is planned.

- Public housing should be better available (at reasonable prices), to ensure a fair and socially sustainable society. The dominance of private ownership of housing is disadvantageous to families with many members and/or lower income.
- More floor areas are desired by certain group of people, especially those with small-sized homes. Affordable public housing can help solve this, while on the other hand, a minimum floor area per head may need to be established as social requirement.
- Availability of public transport and other activities (incl. shopping) are important for a residential community. This means that urban planners should do their best in bringing their activities close to the residence, either by offering facilities nearby or with efficient public transport, so residents can easily access facilities/activities far away.
- Traffic noise is a serious problem that has been overlooked. More should be done in countering this, both in traffic planning (e.g. avoid houses next to high speed road) and through traffic management (e.g. speed limit, car free zones, traffic curfew at night hours).
- Neighbourhood greenery is a vital component to the community. More should be done to ensure its quality and to enhance its popularity, also for community-binding activities. Besides providing a location for activities, neighbourhood greenery may also help improve the neighbourhood air quality and have noise barrier effects, contributing to a better living environment. A well-planned and maintained greenery is crucial for the sustainability of the community.

ACKNOWLEDGEMENT

This paper was funded by The Qianjiang Talent Scheme (QJD1202001).

REFERENCES

Bender, A.R., Din, A., Favarger, P., Hoesli, M. & Laakso, J. 1997. An analysis of perceptions concerning the environmental quality of housing in Geneva. *Urban Studies* 34(3): 503–513.

IPCC. 2001. *Climate Change. Synthesis Report*.

Jenks, M. & Dempsey, N. (eds) 2005. *Futures Forms and Design for Sustainable Cities*. Oxford: Architectural Press.

Singh, R.K., Murty, H.R., Gupta, S.K. & Dikshit, A.K. 2009. An overview of sustainability assessment methodologies. *Ecological Indicators* 9(2): 189–212.

Smith, T., Nelischer, M. & Perkins, N. 1997. Quality of an urban community: A framework for understanding the relationship between quality and physical form. *Landscape and Urban Planning* 39: 229–241.

UN Habitat. 2008. *2008 Annual Report*. UN-Habitat, ISBN: 978-92-1-132046-6.

Winograd, M. 2007. Sustainability and vulnerability indicators for decision making: lessons learned from Honduras. *International Journal of Sustainable Development* 10(): 93–105.

Zakaria El Adli Imam, K. 2006. Role of urban greenway systems in planning residential communities: A case study from Egypt. *Landscape and Urban Planning* 76: 192–209.

Civil Engineering and Urban Planning IV – Liu et al. (Eds)
© 2016 Taylor & Francis Group, London, ISBN 978-1-138-02903-3

Research on the strategies of urban spatial integration in the view of cultural heritage conservation

Yi-Qing Zhao, Jian Xu & Wen Tian
Institute of Heritage Sites and Historical Architecture Conservation, Xi'an Jiaotong University, Xi'an, Shaanxi, P.R. China

ABSTRACT: This study aims at exploring the space integration strategy between rapid urbanization and the urban cultural heritage resources known as the—"isolated island." Urban spatial integration is a study, which relates to factors that are affecting and restricting the urban space. Cultural heritage resources are concentrated in Xi'an. In this process of developing space, how to protect cultural heritage resources and how to integrate and accrete with living space of residents in old blocks are important study issues to transmit cultural characteristics. By introducing cultural heritage protection concept into urban spatial development of old blocks in Xi'an, this paper analyzes historical evolution and studies status of Dongguan district, and also puts forward the current urban space problems existing in district. Through in-depth analysis of space integration method oriented by cultural heritage resources, this paper puts forward chronic walking system in road traffic space, combination between heritage space, and public space as well as integration strategy to assisting space integration to inherit regional culture and improve living environment thus inherit old blocks features and context.

1 INTRODUCTION

Since 30 years and above, China has carried out reform and opening-up policy. With urbanization process accelerating, amounts of development and construction lead to low efficiency in urban spatial utilization and memory fault (Figueiredo 2014, Janssen et al. 2014). Chinese cities are facing an unprecedented "urban characteristic" crisis. Urban space bears material level and social level in development and reflects urban cultural details. As to a historical city, the impact of modern rapid development led to reduction of regional features and lack of urban development context, so urban cultural heritage is gradually becoming the "isolated island" in old blocks. As the Zhongyuan cultural heritage city-one of China's four big historical culture areas, it can be seen from Figure 1 that Xi'an is one of the most unique historical and cultural city in our country and its urban construction land is completely covered by Tang Chang'an site. In recent years, rapid construction led to improper way of use, which further intensified the contradiction between cultural heritage conservation and urban construction. By means of space integration, this paper studies two aspects-protection and utilization of cultural heritage as well as urban planning and design, from which this paper seeks balance in urban construction, which has great significance to realize sustainable development in cultural heritage of historical city (Veldpaus 2013).

In recent years, the research works on theory and practice of cultural heritage protection as well as urban space integration have been improved. Cultural heritage protection mainly targets specific cultural heritage resources, such as large site, architectural heritage, historical blocks, which mainly studies cultural details and protection technique.

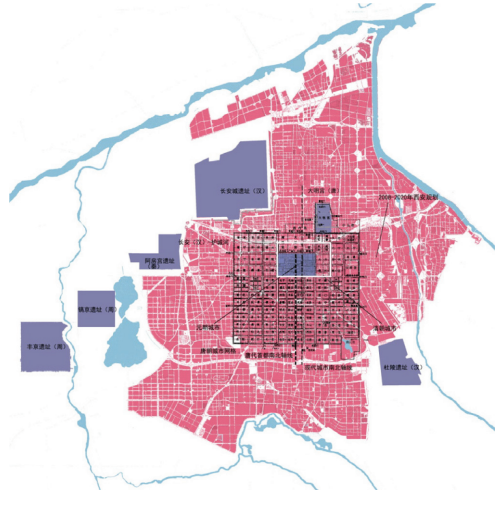

Figure 1. Overlapping diagram of Tang Chang'an site and construction land in Xi'an main city zone. (Source: Dongguan urban design project team of XJTU).

While urban spatial integration objects are wider, this includes special urban space, urban elements, and urban agglomeration so on (Lu 2004). Historical urban spatial integration oriented by cultural heritage resources is still at an initial stage. Research on urban space integration in our country is gradually turning from macro to micro level. In views of domestic research, professor Dong Wei of Southeast University and his team have made pioneering research on historical space integration which introduces ideas of history network integration based on analysis of cultural heritage resources (Tang & Dong 2009). Professor Li Heping of Chongqing University studied about the whole integrated mechanism of historical area and urban development and explored coupling path between historical area and multiple factors such as, society, economy, culture, space, and so on (Li et al. 2014). Space integration, as the new path to protect cultural heritage, tries to break antagonism state that takes heritage as "the static historical display," "history and modern paradox," changes traditional isolation protection thought and puts forward design ideas of urban overall symbiosis (Kong et al. 2006). "Space planning is the most important aspect in city, although space has no physical form, it is the core of basic skeleton forming one region in city" cultural heritage is the soul to active space (Zhang & Wang 2008). Based on this concept, cultural heritage space can be understood as the subsystem of the urban space, which embodies urban culture characteristic and avoids appearing as the phenomenon of "one side thousand cities." Foreign urban planning master Kevin lynch in his classic book "the city image" refers that "generation of city markers correlated with history plays a strong role in reinforcing city"(Shi 2003). Through integration of urban space resources, elements, and forms, urban historical context can be better inherited. So taking "Xi'an Dongguan area" as a research object, this paper starts from historical evolution to existing problems and designs city under the concept of restoring cultural heritage resources space system to provide basis for historical urban cultural heritage and protection.

As Figure 2 shows, the location of the case is in the west part of Xi'an.

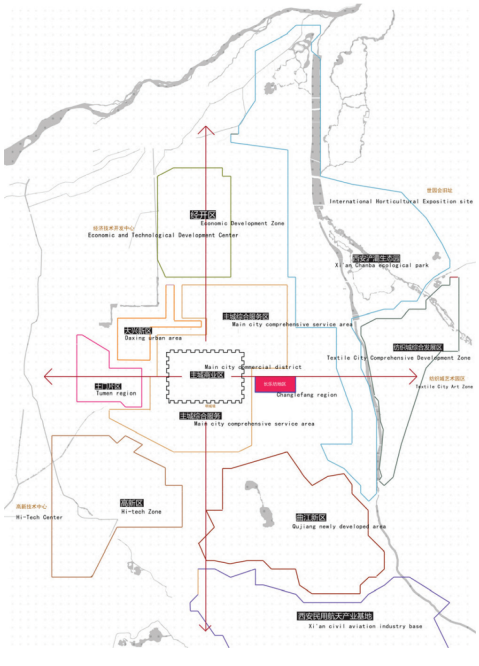

Figure 2. Research object location map. (Source: Dongguan urban design project team of XJTU).

2 ANALYSIS OF XI 'AN DONGGUAN DISTRICT HISTORICAL EVOLUTION AND CURRENT PROBLEMS

2.1 *Xi'an Dongguan district historical evolution*

2.1.1 *Political, economic, and cultural center in Tang dynasty*

The reign of Emperor Xuanzong of the Tang Dynasty experienced thriving period when Xingqing palace was built. Tang Chang'an City is the political, economic, and cultural center in Chang'an. Wangji temple and East Datang city were both built during this period. Tang Chang'an city is located in north of Anxingfang and Shengyefang distributing many tang king houses that located in Dongguan area now.

2.1.2 *Formation of function pattern during Ming and Qing dynasties*

At the earlier period of Ming dynasty, Xi'an expanded towards the east and four city walls that are formed in this period, of which east city wall was first built with a larger scale. The aim of building the four city walls is to defend the city gate which had certain military defense function. At that time city gate was the main channel for going in or out of the city, east city wall also had religion and business functions. In Qing dynasty, there existed confronted pattern between business district around north–south gate in west city area and Dongguan business district in east city area (Shi 2003). During this period, south city and Mang city were constructed in Xi'an, which hindered the urban traffic and formed two-district pattern. Changle gate directly connected with the living areas of Mang city and Dongguan area whose business had entered into prime time. In late Qing dynasty, Dongguan region was the largest distribution center for medicinal materials and forest products, accompanied by the emergence of other formats. The larger business hall "Shanxi hall" is located in this region.

2.1.3 *During the anti-Japanese war, the influx of refugees and gradual decline in business*

During the anti-Japanese war, a large number of refugees entered into Xi'an. Dongguan region, close to the railway station, was a residential area for the refugees who had techniques such as, weaving, bleaching, and so on. So, industry was concentrated in Dongguan region. The linking and running of Longhai railway was made a commercial prosperity along railway, so business in Dongguan region was affected. Combined with ten years of war, Dongguan region gradually lost prosperity.

2.1.4 *Since 1949, resident living region formation in old district*

After 1949, Dongguan business has revived. During this period, Dongguan has experienced common development since 1949, which included peer support, cooperatives, and public-private partnerships. Nowadays, under the collision between history and modern, Dongguan has developed to be the historical region of the old city with many functions such as, historical heritage, newly built residential region, old city resident, commerce, education, and religion.

2.2 *Existing problems of Dongguan Changle square in Xi'an*

2.2.1 *Urban land fragmentation*

Dongguan Changle square is located in Eastern Ring road of east gate of Xi'an city wall where it is positioned for education, culture, and business center in the fourth overall planning of Xi'an. Now the segmentation of the land is more fragmentary: small part of the land scattered in this region is used for cultural relics, education as well as less commercial land along the street, and most of the lands are residential land (Fig. 3). Distribution of residential land with fragmentarily embedded land function limits fusion and expansion in this region.

2.2.2 *Road system congestion*

Figure 4 shows that this region is located in east gate of the old city wall. Main Dongguan street

Figure 3. Current land function diagram. (Source: Dongguan urban design project team of XJTU).

Figure 4. Diagram of road traffic. (source: Dongguan urban design project team of XJTU).

connecting with East gate is the important hub to link Xi'an east–west traffic, whose primary road intersection is the main jam node at the peak time. At the same time, Xingqing road, is next the important south-north traffic trunk road within Xi'an second ring, links important regions (Changle square, Xingqing palace, and Xi'an Jiao Tong University district) within three areas of the city, traffic is also beyond the load. Road condition of this region is complicated. Road connecting the main trunk road links Paofang Street and Changlefang Street in the east–west direction. With poor road condition, there also exists dead end highway in the branch. With vehicle–pedestrian mixing, traffic condition is the worse in this region, which brings pressure to road system of this region (Fig. 5).

2.2.3 *Isolation between cultural heritage resources and surrounding living environment*

An amount of cultural heritage resources is being distributed in Dongguan Changle square region, with the old streets bearing Xi'an history and culture (as shown in Fig. 6). Those cultural resources are gradually separated with surrounding living environment in city development, which like mosaic are embedded in urban skin texture showing "fragmentation, island" crisis (Fig. 7). And their value has not been reflected, which reduces its original historical and cultural atmosphere. In addition, residents' cognition to urban culture plays an important role in protecting cultural inheritance of historical city. The lacking of it will separate heritage space and living space and cannot inherit culture.

2.2.4 *Fracture and lack in public space*

Public space is closely related to residents' daily life. As a bond connecting to residents activities in certain regions, public space should also carry and reflect the urban culture function. In process of continuous self-renewal, quantity, and quality of public

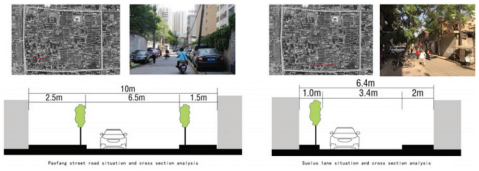

Figure 5. Section road situation.

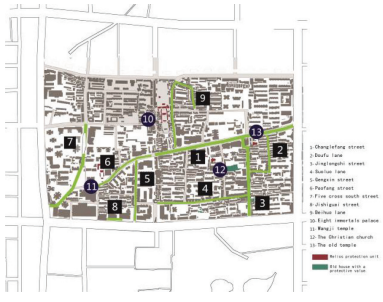

Figure 6. Cultural heritage resources distribution. (Source: Dongguan urban design project team of XJTU).

Figure 7. Photos of part of current cultural heritage within the region (left: Wangji temple desolately exists in the district, right: eight immortals palace in end of antique market).

space in Dongguan Changle square appear insufficient, due to newly building houses and population aggregation. Lack of communication between public spaces, residents' activities are mainly aggregated at the side of the road (Fig. 8). "Fragmented" public space is "devouring" public space by road transportation and parking lot existing in district.

2.2.5 *Imperfect infrastructure*

Due to uneven construction quality, the construction situation of Dongguan Changle square is complicated with weak infrastructure. Its current problems such as lack of open space, mixing parking and pedestrian, and deteriorating living environment, are the limiting factors affecting the development in this district. However, large-scale development and construction has not been carried out in Dongguan district, thick life breath of old Xi'an resident is persisting. So, the requirement to perfect infrastructure is the key factor for sustainable life space.

Figure 8. Public space and present residents' activities.

3 SPACE INTEGRATION STRATEGY ORIENTED BY CULTURAL HERITAGE RESOURCES

Dongguan Changle square is characterized by habitancy and religious culture. As a center district in historical city, the new urban design concept is needed to inherit living environment and cultural characteristics. The core problem of spatial integration is penetration and communication between heritage space and residents' behavior space. Spatial integration guide by cultural heritage resources are based on entity elements (Jing 2011). Through residents' activities, these entity elements that connect by the road system are integrated to space elements, which are integrated to regional space elements through ground and underground spatial integration. Finally, a continuous and unified network system is formed (as shown in Fig. 9). So space strategy research can be carried out from three aspects: integration of road space, public space and heritage space infiltration, and rational utilization of underground.

3.1 *Integration of road traffic space*

As the central region in the city, the region function of Dongguan Changle square will affect the whole city. It is necessary to consider the whole development of urban space to solve the traffic problem. With regional inside tunnel being auxiliary, urban road is the main skeleton to open road network that are based on the continuous original urban space texture and scale. East Ring road—crossing traffic in north–south direction is introduced into underground to increase completion and connection of ground walk channel. Characteristic old house and architectural heritage such as Wangji temple, eight immortals palace, and so on are nodes which through connection of distributed old streets radiate outward and become the cultural heritage spatial district. Residents' activity space-walking path-in district is used to connect chronic traffic system (as shown in Fig. 10) within building area and disperse various traffic ways of original road.

3.2 *Mutual penetration of public space and heritage space system*

Public space, behavior space for residents' activity, in Dongguan Changle square district is combined

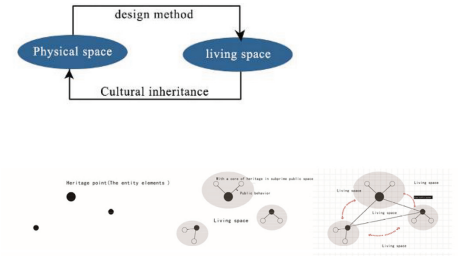

Figure 9. Idea of space integration oriented by cultural heritage resources.

Figure 10. Slow traffic system and dredging road.

with heritage space that is composed of cultural heritage to become the public activity space. Their intersection and penetration make urban space with continuous liquidity and integrity, which promote the heritage public space to build residents' activity space (Peng 2007).

Heritage space within district has shaped formation requirement of public space node, flake, and planar space. Also heritage space, the living place that has changed continuously, has the potential to inherit cultural atmosphere and active space. So public space transformation use heritage space originally to stitch broken space, construct new space connection and resolve fragmentary distribution of cultural heritage and fracture problems in the surrounding environment. This paper, integrates the functions of public space within the district to form a new one that cultural inheritance and residents' life merge into each other and are independent of each other, and finally catalyzing and accreting the lost heritage space and dynamic residents' living space. In addition, because Tang Chang'an city is completely under Xi'an old town, underground legacy, such as Lifang, its story, infiltrate and combine with public space by forms of identification of ground public space as well as city furniture to activate urban space (Fig. 11).

3.3 *Integration and utilization of auxiliary space*

Because of the special geographical location in old town-near main city, Dongguan Changle square

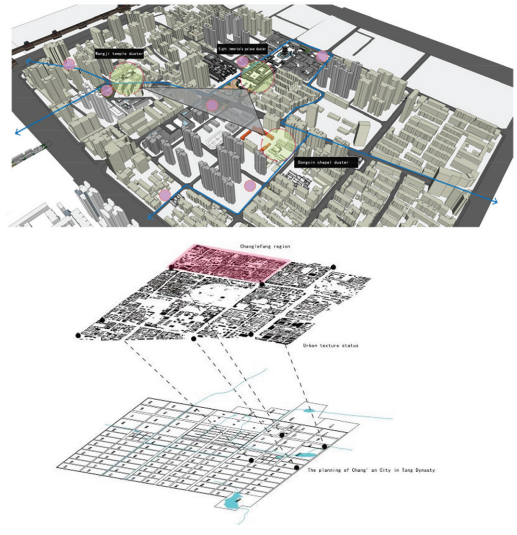

Figure 11. Penetration between public space and heritage space.

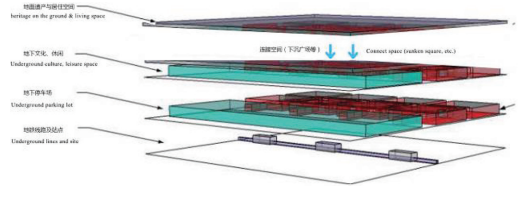

Figure 12. Stratified underground space diagram.

has such questions as larger population density, land tension, and poor environmental quality. Concept of planning and design needs to change from two-dimensional space thinking to three-dimensional space thinking, which can be realized through rational use of auxiliary space. The underground space is stratified vertically. Business culture, underground parking, and municipal disaster prevention are set for stratification and integration in each underground. It can rationally resolve "devouring phenomenon" that is because of ground parking, public space is devoured by road to increase the ground greening, perfect function of urban space. Besides, city function should be implanted in heritage space. When protecting its original true, it is easy to construct recognizing and remembering auxiliary space combined with residents' traditional life (Fig. 12).

3.4 *Integration of economic, social level, and utilization*

The city is a complex system, Dongguan Changle region of space is the outcome of physical space and life trajectory. Therefore, in addition to the

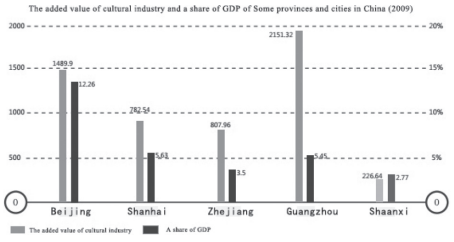

Figure 13. The added value of cultural industry and a share of GDP of some provinces and cities in China (2009).

means from the physical plane, darning their social networks is also an important aspect of building a vibrant space. In this case, social network reflects in the neighborhood, which is essential to retain the local culture. So, to retain the original texture, original neighborhood, and restore the original residential streets is a continuation of historical context effective method. At the same time, compared with other cities in China, the development of cultural industry in Xi'an is still in the initial stage, the excavation, and the revitalization of the cultural industry in this area, can also promote the development of Xi'an, as well as the rise of cultural industry in the region of the economic and social aspects of promotion.

4 CONCLUSION

Old city region with cultural heritages is the essence of cultural inheritance for a city. Rapid development of city in our country needs to explore heritage space development existing among urban spaces. It is easy for people to ignore heritage space that has not been included in protection area as well as residential culture characteristics. As continuation of old Xi'an traditional culture, Dongguan Changle square witnesses rise and fall of the city in process of urban development, which is also an important component of Xi'an city culture. Nowadays, because of cluttered space and backward infrastructure, cultural heritage is in jeopardy within this region; because this district has strong life breath, dismantling old building in traditional way cannot inherit the cultural and living atmosphere. Through research on urban design of Dongguan Changle square, this paper puts forward coordinated development between heritage space and urban living space to provide a new view for inheriting special culture of historical region with much more cultural relic and thick living atmosphere (Ahern 2013, Kong 2006, Nasser 2003, Puren & Jordaan 2014, Taylor 2014).

ACKNOWLEDGMENT

We would like to acknowledge support provided to us for the State National Science Fund of China (No. 51278416).

REFERENCES

Ahern, J. 2013. Urban landscape sustainability and resilience: the promise and challenges of integrating ecology with urban planning and design. *Landscape Ecology* 28(6): 1203–1212.

Figueiredo, V.G.B. 2014. Cultural heritage, city, sustainability: what is the role of urban legislation in preservation and development? *Ambiente & Sociedade* 17(2): 91–110.

Janssen, J. et al. 2014. Heritage planning and spatial development in the Netherlands: changing policies and perspectives. *International Journal of Heritage Studies* 20(1): 1–21.

Jing W.Z. 2011. Research on urban three-dimensional space integration. *Journal of Underground Space and Engineering* 12(6): 1047–1052.

Kong X.Y. et al. 2006. Research on space integration and evolution process of center region in historical city-taking conceptual urban design in Hangzhou Wulin square and surrounding area for an example. *Journal of Urban Architecture* 12(12): 42–45.

Kourtit, K. et al. 2014. Planning for Urban Historical-Cultural Heritage: A Geo-Imaging Multicriteria Approach. *Built Environment* 40(4): 521–533.

Li, H.P., Xiao, J. & Hu, Y.Y. 2014. Study of Fragmentary historical location coupled with overall city development mechanism. *Urban Development Research* 6(9): 62–68.

Lu, J.W. 2004. Theory of urban design integrated mechanism. *Journal of construction* 12(1): 24–27.

Nasser, N. 2003. Planning for urban heritage places: reconciling conservation, tourism, and sustainable development. *Journal of Planning Literature* 17(4): 467–479.

Peng, X.L. 2007. *Research on integration of urban public space design*. Hunan: Hunan University.

Puren, K. & Jordaan, T. 2014. Towards integrating built heritage resources in urban development through spatial planning. *The Sustainable City IX: Urban Regeneration and Sustainability* 2(191): 1209.

Shi, G.Z. 2003. *Ancient capital Xi 'an-Xi'an historical change and development*. Xi'an: Xi'an publishing house.

Tang, X.X. & Dong, W. 2009. The construction of urban historical and cultural spatial network-taking Ningbo city for an example. *Journal of Planning a Wide-angle* 12(1): 85–91.

Taylor, K. 2014. The Historic Urban Landscape. Managing Heritage in an Urban Century. *Landscape Research* 39(3): 326–329.

Veldpaus, L. et al. 2013. Urban Heritage: putting the past into the future. *The Historic Environment* 4(1): 3–18.

Zhang, S. & Wang, J. 2008. *Our heritage, our future—exploration and thinking about urban heritage protection*. Shanghai: Tongji University Press.

Civil Engineering and Urban Planning IV – Liu et al. (Eds)
© 2016 Taylor & Francis Group, London, ISBN 978-1-138-02903-3

Public spaces of the social housing in Porto: Learning with design practice

Nuno Abrantes, Fernando Brandão Alves & Vitor Abrantes
CITTA—Research Centre for Territory, Transports and Environment, Faculty of Engineering, University of Porto, Portugal

ABSTRACT: In the late twentieth century, the housing stock of Porto showed signs of social and urban imbalance. This characteristic is mostly due to the successive construction of the large suburbs since the second half of the twentieth century, related to the "Plano de Melhoramentos" (Plan of Improvements). These barrios concentrated thousands of families, who were economically disadvantaged, through a high concern for the amount of dwellings and a tiny concern for the environmental quality of these residential areas.

Nevertheless, most of these large housing estates barrios were absorbed by the expansion of the city and, as a result, there was a significant improvement of the access net, transports, and service network, thus, minimizing the isolation of these neighborhoods. In the nineties, social and economic problems of these populations have sharpened. Such problems are also related to the stigmatization phenomenon, compounded by a generalized process of degradation of the public space and built space, which results from the lack of conservation and rehabilitation programs.

The Municipality of Porto starts in 2004, together with the "Instituto Nacional da Habitação" (INH—National Institute for Residence) a program for the rehabilitation of 5000 dwellings in the municipal social housing and for the construction of 300 new dwellings under controlled costs.

The article presents the study that we have been developing concerning the best procedures that professionals and politicians should have while facing the renewal of social housing barrios. These operations are very important for the social and urban balance, since about 20% of the local people live in municipal dwellings. This financial effort aimed at the rehabilitation of the residential park underlines the policies of strengthening the social cohesion. Social actions at an educational, training, employment and social assistance levels should complement this effort. To illustrate this study we will present the ex-ante and post analytic scenarios of the "Bairro de Contumil" (Contumil Barrio), in Porto.

1 INTRODUCTION

1.1 *The city of Porto and the social housing*

The city of Porto has assumed a very important role in the history of Portuguese social housing, and continues its promotion until today. This activity began in the late nineteenth century, due to humanitarian, hygienists and public health concerns, in an attempt to curb the massive construction of "the islands" (Fig. 1)—original Portuguese designation: *as ilhas*[1].

At the beginning of the twentieth century, the "islands" contributed to the balance of the housing shortage that had resulted from the massive migration of the rural population to the city. In the late nineteenth century, the islands have harbored about 30% of the city population. While this type of housing grew significantly in the early twentieth century, thousands of buildings in the city of Porto were overbooked by the families with poor financial resources.

The first municipal neighborhoods (barrios) were built between 1899 and 1905—ex. *Monte Pedral*, *Ramalde,* and *Bonfim* neighborhoods, thanks to the initiative of a Portuguese Company: *O Comércio do Porto*, in partnership with the Municipality of Porto.

Therefore, in the 30s and 40s, the New State departs from the building multifamily housing solutions, mainly built in Lisbon, and privileges "Portuguese house" (perhaps referring to the Portuguese "Raul Lino's house models" in 1929

[1]The "islands" are small houses, usually one floor house, distributed in rows along the backside of the plots of middle-class homeowners. The access was assured through a narrow central (or aside) corridor that made the direct connection to the street. These housing units were highly precarious. Sanitary infrastructures were missing in its interior—the inhabitants had to use public baths to their hygiene and daily care.

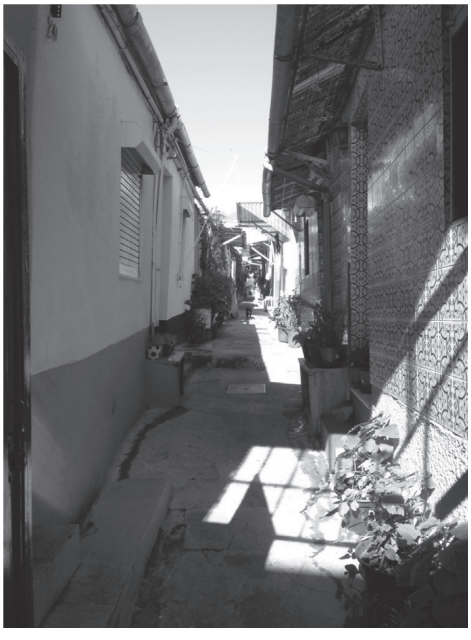

Figure 1. Typical image of Porto "islands".

and the Portuguese Houses 1933), on behalf of social and moral order. The neighborhoods of the Economics Houses developed into townhouses or band, with a markedly "traditionalist" and rural architectural characterization, designed according to the studies by minimum sizing.

1.2 *The economic houses of Porto*

The neighborhoods of the Economic Houses in Porto, constructed between 1935 and 1965 in distant areas of the city, represented about 2000 dwellings. In the 50s, more examples of the construction of multi-family housing appeared, primarily through direct state intervention in social housing: "What we see is a spatially monetization of land available and the need for more comprehensive solutions to problems of ordering of metropolitan life" (Baptista 1999).

The neighborhood of Ramalde, built in the western part of the city on the initiative of the Federation of Provident Funds (Fundo da Caixa de Previdência), designed by the architect Fernando Távora constitutes an experience of the adoption of affordable housing in the modernist principles enunciated in the Charter of Athens (1931) excellent multifamily blocks the object of an extremely well-detailed design, "(...) in intimate relationship with the urban green, (...) with a very strong human scale (Baptista Coelho 2006).

In 1956, he enters into force the Plan for Salubrity of Porto Islands (*Plano de Salubridade das Ilhas do Porto*), which gave rise to the Plan of Improvements for the City of Porto (1956–1966) in response to the worsening of the housing needs of the city. In the first phase (1956–1966) thirteen municipal districts are built for a total of 6072 dwellings for the relocation of families living on the islands. It is under this Plan that is built in 1977 in the Municipal District study: *Contumil* Quarter.

1.3 *The Porto plan of improvements*

The Plan of Improvements (*Plano de Melhoramentos*) (CMPorto 2006) is responsible for the emergence of a new urban typology in Porto through new housing estates. This typology has developed in other European countries, "dissolves the street as an essential urban element, turning it into a mere passageway and freeing a building direct relationship with it" (Cardoso 1996).

With the Revolution of April 1974 other initiatives are promoted with the same goal of fighting the shortage of housing for people of lower social classes. Noteworthy is the SAAL—Outpatient Services Local Support (1974–1976) created as the Housing Development Fund (FFH) Specialized Technical Corps.

This service has advocated "a radical model of the city and planning: a city where the poor are also entitled to the historic centre" (Costa 1998).

With this goal, operations of rehousing families, that inhabited the islands, are conducted, locating them in the same area of residence. The inhabitants themselves participated in the resettlement process, first in the design phase of the neighborhoods and in the later stages of construction. Good examples of this period are the neighborhood of Antas, designed by Pedro Ramalho, the neighborhood of St. Victor (Fig. 2), and the neighborhood of Bouça, both designed by Álvaro Siza Vieira.

Figure 2. Neighborhood of St. Victor, SAAL.

In the late twentieth century, the housing stock of Porto showed signs of social and urban imbalance. This characteristic is due in a large measure to the successive construction of large townships since the second half of the twentieth century, related to the Plan of Improvements. These projects concentrated thousands of economically disadvantaged families, through a high concern for the amount of dwellings and a tiny concern on the environmental quality of these residential areas (CMPorto 1999).

1.4 *The rehabilitation housing process*

In partnership with the National Housing Institute (INH), the Municipality of Porto started in 2004; a program for the rehabilitation of 5,000 dwellings in the social neighborhoods and even the construction cost of 300 new housing has been controlled. This operation began rehabilitation in more degraded neighborhoods built before the decade of 1980. The interventions were aimed, on the one hand, improving significantly the conditions of comfort and liveability of residential buildings, on the other hand, the qualification of the urban image of the neighborhoods. Accordingly, rehabilitation operations focus mainly on the building surroundings, roofing and facades (frames), infrastructure for water and electricity and even the common areas (stairwells) of the buildings.

Currently underway is the second phase of a new agreement between Porto's City Hall and IHRU for the rehabilitation of more than 5,000 social housing dwellings-about 20% of Porto citizens reside in council housing.

This rehabilitation policy is framed in Urban II (2000–2006) Community Initiative Programme, globally funded by the European Union, whose goal is the revitalization and redevelopment of urban areas in the social, economic and urban bankruptcy, under which the redevelopment projects in the public space of *Contumil* and Pius XII neighborhoods have been developed.

2 THE CASE STUDY ANALYSIS

2.1 *Morphological characterization of public space before the renewal*

2.1.1 *Circulation spaces*

Like other neighborhoods, there is a great dependence between road and pedestrian networks. The pedestrian network is developed parallel to the road network-adjacent to traffic one can see walks, pathways or even other areas that do not focus on motorization (Fig. 3).

There is a preponderance of the pedestrian network in the road network, latter materialized almost exclusively on two axes, and the Professor

Figure 3. View of *Contumil* Barrio before renewal.

Bonfim Barreiros street and Engenheiro Pedro Inácio Lopes street. These two main thoroughfares crossing the west end—the central and northern area of the neighborhood, respectively—most of the accesses to spaces of residence and entry area for the residential buildings made through the pedestrian network. The road network supports a direct contact with the four main axes regarding the local distribution of its urban grid network: *Contumil* street at south; *Ajuda* street at west; *Joaquim Alves Teixeira* street and *Santo António* street at *Contumil* north. These are the links that establish the degree of formal and functional integration of the housing development in the wider urban area. There is an imbalance at the level of penetration by the surrounding highways along the perimeter of the neighborhood.

This impermeability of the urban fabric to road accessibility, particularly the most inland areas will be a key factor in the morphology of the spaces of permanence and reading of the urban image of the entire residential complex. Already in functional terms, the low permeability of the road network is a conditioning accessibility to blocks of housing, not only for its residents but also for the use of urban services or even emergency. There are 213 parking spaces, less than half the number of dwellings in the neighborhood. Nowadays, the lack of parking meant one of the defects with greater visibility in the urban areas of the district. We may conclude by the photo archives that there was a riotous use of parking in the neighborhood. For example, the rules induced by the morphology of parking is often disregarded, particularly in areas where parking is longitudinal to the carriageway are used in perpendicular thereto. On the other hand, there is an indiscriminate occupancy of vehicles in the pedestrian areas and spaces remaining, not only contributing to inhibiting its use by

people but also for the degradation of existing vegetation and floors.

Moreover, the pedestrian network is structured by a network of pathways that develops in accordance with the accessibility to the various buildings and spaces of permanence. The mesh pedestrian circulation often separates the road infrastructure to ensure access to the areas where motor traffic is not enough. The pedestrian network opens seven innings in the neighborhood, four of which adjacent to the access road. The remaining three are transverse to *Contumil* Street and help break the physical barrier that limits the district conforming to the local urban fabric. Therefore, the network of pedestrian circuits is physically articulated with the engaging in a more balanced way than the road network. Most walkways are flat. Although, we may see some stairs in some of the residential building's entries. Therefore, there is no concern for the disabled residents.

Conversely, ownership of the rear ground floor spaces adjacent to buildings by the majority of the homes in the Ground floor significantly reduces the useful areas of pedestrian space adjacent to the public roads.

Finally, it has been emphasized that the one factor that potentiates the misuse of public space is that there is a slight difference in the coatings used for the parking and pedestrian circulation and road surfaces. Traffic lanes, parking spaces and sidewalks have the same bituminous pavement, and the separation of space for vehicles and pedestrian can be seen only by the snapping of the curbs. These three distinct spaces, therefore, present the same visual reading.

2.1.2 *Spaces of permanence*

The exterior spaces of permanence of *Contumil* neighborhood correspond, in general, the project approached in neighborhoods built by the Plan of Improvements. The urban fabric that is mostly defined by the built mass and the road circulation spaces, with public space to the rest, the negative, the areas left available by the conformation of this mass built and road infrastructure. Public spaces with significant levels of physical contention are more adequate for the success of spaces of permanence (Alves 2003).

Thus, the outside space for staying is delimited by a set of blocks scattered throughout the territory and a little road network by branched urban spaces in the neighborhood and in many places it is a little conversational with the built fronts. There is generally a strong irrigation of the urban fabric along the pedestrian network. However, the formal expression of this structure is somewhat pronounced given the magnitude of the spaces that it travels, and it is not considered as a relevant element in the morphology of the spaces of permanence. This must be, by far, the excessive size of the areas not crossed by roads, major axes in the direction of reading the urban fabric, and the lack of references in the geometric relationship between roads, buildings and spaces of permanence. The mesh spaces of permanence of *Contumil* neighborhood present three main centers, a playground, a square and a landscaped enclosure, which correspond to areas of residence with greater potential to attract users to the scale of the residential complex. This reality exposes a small hierarchy between the different areas of residence in the neighborhood, in terms of functionality, usage and type of most frequent users. Analyzing the different types of spaces of permanence that are existing and their location and distribution in the urban fabric of the neighborhood, we concluded that these spaces of permanence give no indication on the use or ownership that you must comply with the obvious exception of the playground. So, prevalent spaces of permanence without prepositional capacity, in other words, without formal characteristics or without street furniture that motivates your spontaneous enjoyment. These allocations reflect an inability of urban space in highlighting the zones of territorial influence, increasing the ambiguity in perception between public and private domains (Fig. 4).

In all blocks of housing in the neighborhood it manifests a phenomenon of privatization of the residual spaces adjacent to ground floors parks.

As a means to compensate for the small interior spaces of the housing with minimum dimensions, the most common grounds are suitable for storey dwellings. Despite the appropriation of these spaces brings benefits to most residents of the single-storey dwellings, their relatively random formalization in terms of materials used, promotes unqualified image of urban space. The spaces of

Figure 4. View of the public space in Contumil Barrio before renewal.

permanence in *Contumil* neighborhood, do not integrate, in general, urban furniture that invites its use by the residents of the neighborhood. Moreover, most garden areas do not receive the necessary care for the proper maintenance and operation (Pedrosa 2010).

2.2 *Morphological characterization of public space after the renewal*

2.2.1 *Circulation spaces*

The requalification of the spaces for access and circulation in *Contumil* neighborhood introduced the opening of new road sections, starting from the *Pedro Inácio Lopes* street and will intersect with the *Bonfim Barreiros* street at North, and with the *Contumil* street at south. Thus, there is a significant increase in the penetration assigned to motor traffic in the urban fabric of the neighborhood, along with the pedestrian pathways axes. Axes which are thus secure both types of accessibility.

This requalification provides benefits in terms of greater road accessibility to spaces of permanence and entry zones for residential buildings. Additionally it allows greater proximity of pedestrians to parking spaces. This new permeability of the urban fabric to the road network allows the inclusion of parking in the direct surrounding of all blocks, always adjacent to a roadway spaces. Increased accessibility to the road blocks housing and the redesign of the traces of roads resolved part of a major problem in urban areas of the neighborhood: Insufficient parking capacity. With the intervention, 455 new parking spaces were obtained—more than the double of the previous existing places, reaching almost the number of dwellings (502).

The proposed pedestrian network ensures that the links above, both the urban environment as the totality of apartment buildings and spaces of permanence. The new routes are located in the boundary areas of the neighborhood, intending to reverse the character of the residual space befitting it. Similar to what happens with the roads, the footpaths are reformulated by the orthogonal plotted in formal consistency with the other new elements of the urban space: buildings, spaces of movement, permanence and parking. This new condition favoring, firstly, an immediate interpretation of the structure of accessibility in housing development and secondly, the pedestrian network assigning an important role in the formal delimitation of the urban fabric.

A characteristic element of this intervention on the public space arises: the creation of urban furniture for staying. In this case, the new furniture marks the transition between the space frame of Building 12 and the adjoining footpath. This piece of precast concrete in the shape of an "L," which in this case comes in the form of a bench, part of the systematization provided by the formal vocabulary of the proposed solutions, representing that module adopted by architects (Fig. 5).

The choice of flooring material meets the requirements of the robustness, low cost and ease of the maintenance aspects considered very important in the competition program. This solution provides an easy implementation and adaptation to the complex situations of slope and different levels of threshold. Despite these constraints makes this option acceptable, bituminous floor is not the most suitable for paving outdoor spaces in the residential areas, especially in this way so extensive and widespread. The visual mischaracterization that this finishing induces in the urban landscape is high.

2.2.2 *Spaces of permanence*

The network of spaces of staying, resulting from the proposed redevelopment has been formally directly linked with the implementation of the housing blocks, made possible by the consistency of the new road layouts with the built mass. Since the deployment of the buildings has not changed, there is a subordination of the layout of the outdoor spaces to guiding axes of built masses. The new lattice stroke that takes to the road network allows the structuring of the urban fabric in a complementary fashion to buildings and in this way the conformation of space of permanence the regular and clearly

Figure 5. General view of Contumil Barrio after requalification.

discernible contours. The opening of the new routes in the road network was relevant for the characterization of mesh spaces of permanence in sets with more functional and controlled areas in its form.

The greater penetration of the road network and the geometric regularization of its layout consolidates and organizes the limits with the different neighborhoods constituting an essential element in the overall structuring of the urban fabric, which is important given the considerable size of this neighborhood. The pedestrian network also gains a new clearer readability in the redesigning of the urban fabric with its laid parallel to the road network layout and buildings, also contributing to the formal delimitation of areas of residence in the neighborhood. Spaces of permanence have been submitted to a geometric redefinition, which has also included the integration of urban furniture. The landscaped grounds next to the playground won a space character of permanence that it hadn't. For this reason, the significant size and its central position in the neighborhood, acquired an attractive potential for enjoyment by the majority of the neighborhood's population.

The design of the complementary poles in many areas in the proximate of neighborhood was one of the most important transformations in the neighborhood. The creation of these spaces of permanence comes to assign specific spaces before requalification represented neither established any relationship with potential users. The intervention has the ability to superimpose different capacities of use, providing a more widespread use of outdoor spaces (Fig. 6).

There was also an intention to assign each housing block, own areas of residence and socializing, helping to qualify the footpaths in the residence.

There is a redefinition of the meaning of collective space in their public and semi-public dimensions, which returns this zone district to the public domain. The trees that were planted at the intervention will be crucial, with a larger size, its shadow will be an asset to the appropriate areas of the residence and also the surrounding footpaths. This project clearly demonstrates that one of the major objectives in this intervention is achieving environmental comfort to outdoor spaces. In these spaces, the trees were respected and new trees were planted to ensure their shade. The redesign of the road network has resulted in the global restructuring of the urban fabric of the neighborhood. The unifying elements of the intervention contribute decisively to a continuous reading of identity and public space in the neighborhood. The reticulated mesh itself is fragmented into smaller pieces, allowing for a more immediate perception of the relative position in space of each set.

Figure 6. General views of the public space in *Contumil* Barrio after requalification.

The systematization of the formal vocabulary of the proposed concrete element in the shape of an "L" gives coherence to the intervention which involves the urban image of the set. These prefabricated elements adopted by the designers in different situations gives a decent look to the housing complex and warrant characteristics of functionality, durability, and resistance to the different elements: benches, stairs, handrails, ramps, retaining walls, etc.

The entry zones in the blocks of housing were designed to convey a hint of stay of residents by promoting good neighborliness, complemented by the provision of benches near the accesses to buildings. This implementation of the urban furniture stay has been complemented by the patches of vegetation or landscaped slopes well-defined boundary, making those areas more attractive. The versatility of the precasted element "L" is suitable for more than one function simultaneously, and also works as a bank or a containment wall delimiting distinct zones, clarifying the organization of spaces.

There is also an attempt to humanize the spaces of principal residence, either by the presence of street furniture as the careful differentiation of the floors in the green areas. The materials used in the intervention of public space were the bituminous pavement and pedestrian areas of the road traffic and in spaces of permanence of blocks of housing together. This lack of differentiation does not contribute to the characterization of the residential neighborhood. The urban landscape of the enterprise appears with a certain "hard look" for its extensive smooth surfaces and uniform dark color. There are, thus, imposing visual effects that acquire circulation spaces in some areas and, on the other hand, the positive visual impact caused by simply changing color and texture of the parking spaces. The use of concrete in all elements of the street furniture and in the delineation of areas emphasized in many situations such hardness of the assembly.

Finally, the external appearance of the buildings significantly affects the attractiveness of the urban image of the residential complex.

Entries in buildings were closed by installing frames, making the building much more secure for its residents. The architectural treatment of the input zones in the blocks was the subject of great care in the design of roofs guard and protection of the entrance door and access to mailboxes that are now accessible from the outside.

The intervention in the housing blocks contributed significantly to the enhancement of the urban image of the whole neighborhood.

3 GENERAL CONCLUSIONS FROM THE ANALYSIS OF THE CASE STUDY—CONTUMIL NEIGHBOURHOOD

The analysis of the morphological characteristics of the public spaces in the *Contumil* neighborhood before and after the intervention of physical rehabilitation has been allowed to study the factors that compromised the urban integration and architectural quality of the neighborhood. On the other hand, it has also us allowed to examine the degree of satisfaction of the neighborhood's residential population and the extent to which this intervention redevelopment responded to these conditions.

The reformulation of the accessibility plays an important role in this regard. The restructuring of the road network has been redesigned with orthogonal layout and new links that regulate the mesh spaces of permanence while solving gaps in accessibility and parking proximity.

The elimination of many of the physical barriers that conditioned the pedestrian accessibility for people with reduced mobility has facilitated the use of outdoor spaces by most residents. Intervention on the spaces of movement and residence, clarifies the areas of territorial influence in the urban space of the neighborhood, contradicting the ambiguity in the perception of the public and private domains, and function of each type of space. Illegal buildings in the public parks are removed and give rise to areas of residence that frame residential buildings that support the habits of conviviality that were occurring there, manning the long walking routes in the neighborhood stay with furniture and change the visual effect that all chaotic these appropriations gave the urban image of the neighborhood. Thereby, promoting the effective use of the external primary spaces in the consolidation of the habits of sociability among residents and feelings of the self-esteem, identifying themselves with the place of residence. This fact, along with the consolidation of the integration of the neighborhood in the city through urban continuity ensured from the surrounding areas to the limit of the collective/individual space. All these factors act as a functional contribution to the residential satisfaction of the inhabitants. Physical rehabilitation is also an asset to the city in the sense that values its residential heritage and promotes urban balance of this part of town. Moreover, all these factors minimize the neighborhood phenomena of stigma as perceived by its residents, one of the objectives of urban renewal.

The project-oriented strategy and how it was reflected in the proposal should be interpreted in the context of the intervention of *Contumil* neighborhood in its urban insertion and urban conditions of pre-existing situation but also from the impositions of the tender program and financial constraints the intervention.

We consider that this redevelopment in the *Contumil* neighborhood gathers important information for further studies within the field of architecture, and it constitutes an important reference for future interventions in public spaces, regarding the redevelopment strategies for the Economic Housing Neighborhoods.

It would be desirable to allow a greater effort to associate the asset management to a constant monitoring of issues involving social tensions and eventually creating initiatives in the areas of social work and education. The reverse of the negative social effects that sometimes occur in *Contumil* neighborhood, will be possible only if one applies for a medium/long term new performance. If no measures will be taken, the scenario of insecurity in the neighborhood may worsen, isolating a significant part of the population in their homes.

REFERENCES

Alves, F.B., 2003. *Avaliação da Qualidade do Espaço Público Urbano—Proposta Metodológica*. Lisbon, Portugal.

Baptista, L.A.V., 1999. *Cidade e Habitação Social*. Oeiras, Portugal, page 96.

Baptista Coelho, A., 2006. *1984-2004-20 anos a promover a construção de habitação social*. Lisbon, Portugal, page 52.

Cardoso, A., 1996. Do desenvolvimento do planeamento ao planeamento do desenvolvimento. Porto, Portugal, page 24.

CMPorto, Câmara Municipal do Porto, 1996. *Plano de Melhoramentos 1956–66*. Porto, Portugal.

CMPorto, Câmara Municipal do Porto - Pelouro de Habitação, Acção Social e Proteção Civil, *1999. Habitação Social no Porto*. Porto, Portugal.

Costa, A.A., 1998. *1974–1975, o SAAL e os anos da Revolução. Arquitectura do Século XX—Portugal*, page 68.

Pedrosa, C., 2010. *Da Cidade ao Indivíduo: O Papel da Requalificação Urbana de Conjuntos de Habitação de Interesse Social. Estudo da Requalificação Física do Espaço Público do Bairro de Contumil, na cidade do Porto*. Lisbon, Portugal.

This page intentionally left blank

Civil Engineering and Urban Planning IV – Liu et al. (Eds)
© 2016 Taylor & Francis Group, London, ISBN 978-1-138-02903-3

From Nicholas Negroponte to Al Bahar Tower: The development in theory and technology of responsive architecture

Hai-Jing Liu
Alfred Taubman College of Architecture and Urban Planning, University of Michigan, MI, USA

ABSTRACT: This paper reviews the development of responsive architecture and categorizes its practice into several directions based on Negroponte's definition. Some unpromising factors such as high energy cost and the question about building's overall efficiency are preventing the practical field of responsive architecture from making a significant step forward. These factors are carefully analyzed in this article, and several emerging technologies are introduced and discussed with its potential application in the practice area of responsive architecture. Among these, the hybridized model proposed by Sterk, together with interdisciplinary efforts will significantly accelerate the development of responsive architecture.

1 INTRODUCTION

The term responsive architecture, which is also called interactive, reactive or adaptive architecture, is defined as a class of architecture or building with the objective of physically reconfiguring themselves to meet changing needs with variable mobility, location or geometry (Pesenti, Masera, Fiorito, & Sauchelli, 2014). The term was first defined by Nicholas Negroponte who took the effort bringing digital technologies into the field of architecture. From its setup of definition in 1975, it has been 40 years of development of both theory and practice.

Comparing the digital devices' revolutionary progress over these years, however, the architectural technology does not see a significant breakthrough, especially in the field of responsive architecture. A large number of responsive architecture projects completed in recent years are still employing similar technologies 20 years ago. Why is that? The paper will go through researches and practices of responsive architecture based on Nicholas Negroponte's theory and explore new possibilities in responsive architecture with newly emerging digital technologies.

2 THE FORMATION OF THE THEORY OF RESPONSIVE ARCHITECTURE

2.1 *Simple kinetic models*

Dating back to history, early examples of flexible architectures exist, such as the North American tepees and Mongolian yurts. These tepees and yurts are nomadic architecture that will move with the migration of people. These structures are adaptable with the changing needs of its users. However, none of these structures are meant to last forever, so they are quite different from the architectural types of our common sense. It is not until William Zuk published his book *Kinetic Architecture* that brought this kind of building in the study field of architecture. The book addresses the importance of being able to accommodate the problem of change. Architecture should be adaptive, much as natural form is, thereby encouraging the original set of pressures to grow, to transform, to change (Zuk & Clark, 1970).

2.2 *The introduction of computer technology*

With the development of cybernetic theories and practices, some architects tried to bring the cybernetic ideas into the architectural field. The Control Theory was brought up by Wiener.N in 1948 (Packe & Jordan, 2001). The theory was mainly used to define and understand the process and function of the interaction of information between human and mechanical systems. Gordon Pask introduced the Control Theory into the field of architecture and formed the conception of Anticipatory Architecture (Pask, 1969). He insisted that the spatial environment should not strictly match our primary anticipations. It should allow the users to modify the space conditions based on their changing needs and objectives. His theory and models give a technical background to responsive architecture. (Wang, 2011).

From 1970 to 1975, Nicholas Negroponte published some books and articles, which are *The Architecture Machine* (Negroponte, 1970), *The Soft Architecture Machine* (Negroponte, 1975), and *The Semantics of Architecture Machines*

(Negroponte, 1970), that marks the first attempt to define and produce responsive architectures. In his book, Negroponte proposes that responsive architecture is the natural product of the integration of computing power into built spaces and structures. He also extends this belief to include the concepts of recognition, intention, contextual variation, and meaning into computed responses and their successful and ubiquitous integration into architecture (Sterk, 2005).

3 PRACTICE DEVELOPMENT IN RESPONSIVE ARCHITECTURE

There are four kinds of responsive actions defined by Negroponte in the soft architectural machine: reflexive, simulated, operational and informational (Negroponte, 1975). Quite a lot of built-up examples of architectural projects are based on his theory.

Responsive architecture could be categorized into three types based on its objectives (Wang, 2011):

Objective 1—Meeting the demand of sustainability
Objective 2—Meeting the demand of space organization
Objective 3—Meeting the demand of interaction between people and space.

This article will match one kind of responsive action with one particular objective to form 12 directions in responsive architecture. From which, four of them are closely related to architectural practice. They have been researched and developed intensely over these years. The followings are some examples in each direction.

3.1 *Reflexive and sustainability*

Most of the built responsive architectural examples fall in this direction. One of the emerging technologies in responsive architecture is in kinetic facades relating to the regulation of solar gains, ventilation and other energy saving method regarding the massive use of HVAC systems. The façade systems are responsive to changing environment.

The first realized responsive architectural project—Arab World Institute done by Jean Nouvel was completed in 1987. The building's façade system is composed of several hundreds of light sensitive diaphragms that regulate the amount of light allowed to enter the building. This façade system will control the interior temperature. The project was of great technical and idea advance at that time.

Since the completion of Arab World Institute, there are a lot of architectural projects using solar control systems. The latest example of this kind is the Al Bahar Tower in Abu Dhabi. The tower has a Mashrabiya shading system. The actuated façade panels are programmed to respond to the movement of the sun as a way to reduce solar gain and glare (Aedas, 2012).

3.2 *Operability and sustainability*

The dynamic tower proposed by Italian Architect David Fisher is said to gain its building energy entirely from wind and solar power (Fisher). The building has a central core which is the key structure and transportation support. There are 80 floors rotating around the core, the solar panels are implemented on the roof of every floor and turbine machines are located between the floors. As Fisher claimed, the building would produce not only enough energy for its own, but also will meet the energy demand of the buildings nearby. The project was proposed on 2008 but has never been built until now due to its unrealistically high initial cost.

3.3 *Reflexive and space organization*

The open columns project designed by University at Buffalo is designed to be responsive to carbon dioxide emissions. The columns do not have a conventional shape or carries their conventional structural ability. They are composed by urethane elastomers which reside collapsed in the ceiling in the installation. With more people coming to the space and the CO_2 level going up, the column will drop down, dividing the space and dispersing the people into smaller groups. When there is less people in the place, the column will go up and inviting people to the space. Therefore, the columns are used to reconfigure the space of inhabitation. (Khan, 2010).

3.4 *Operability and space organization*

The Sliding House in Suffolk, UK, designed by dRMM Architects was completed in 2009 (dRMM, 2009). The wall and roof structure can slide away entirely to reform its interior space. The interior space including bedrooms, guestrooms, garage and greenhouse would have combinations of enclosure, open-air living and framing of views according to position. It also helps control lighting conditions, provides additional insulation and creates a sense of openness and enclosure inside the house. (Stevenson, 2011).

4 OBSTACLES AND SOLUTIONS IN THE DEVELOPMENT OF RESPONSIVE ARCHITECTURE

As mentioned in the introduction, the field of responsive architecture is making progresses slowly compared to the fast development of computer science. There are two major obstacles in the development of responsive architecture.

One of the obstacles is that the kinetic structures often cost more energy, initial building cost as well as maintenance fee than normal buildings. Although many have claimed that the responsive building elements would reduce the energy cost, but few of them are approved statistically being energy efficient through the whole building life-cycle. To reduce the energy input for the kinetic structures, soft materials, like inflatable plastics are the first material that came into people's mind. It is easy to control and consume little energy but not that feasible, since not so many people would accommodate themselves in plastic bags (Negroponte, 1975). However, smart materials will be a research area which has great potential in responsive architecture.

The other obstacle is that in the built examples, responsive elements are only designed as one part, such as only the skin or façade; or designed toward only one reflexive aspect. For example, the Al Bahar tower has a responsive façade only react with sun exposure. The environmental problems are complex, the demand of space organization is not stable, and the person should also be collaborative in the design of spaces. With the development of digital technologies, this direction will have a strong potential in architectural field.

4.1 *Reducing energy cost and smart materials*

The Abu Dhabi tower is by far the largest scale responsive architecture that came in realization. Unlike Jean Nouvel's Arab World Institute, which is energy-consuming with a complicated system, the responsive façade of Abu Dhabi tower is simple and requires very little energy with the use of shape memory alloy wires to activate the origami patterns. The shape memory alloy is an alloy that remembers its original shape and that when deformed returns to its pre-deformed shape via heating. Origami can be used to construct various geometrical designs not possible with compass and straightedge constructions. The combination of the two offers a great solution for the kinetic aspect of responsive architecture (Pesenti, Masera, Fiorito, & Sauchelli, 2014).

The other material that requires even no external energy input to be kinetic is wood. It was discovered by Achim Menges and Steffen Reichert. In their studies, they found that wood can be carefully controlled to change its dimension directly in response to the moisture content (Menges & Reichert, 2012).

4.2 *Overall balance and the hybridized model of control*

Sterk built a hybridized model of control suitable for contemporary responsive architecture based on the work of Negroponte (Sterk 2005). The model was divided into two parts: the interior and the façade. It analyzed how these two parts got controlled. The model will build a system frame, introducing the operation mechanism of responsive architecture. Conceptually, responsive architectures treat the needs and of users as a set of ever changing conditions. Every element will be controlled by its relating factors. Low-level processes, high-level responses should be introduced. Responsive architecture should be able to recognize and guess the need of its users.

The model (Fig. 1) proposed by Sterk is to produce a form of responsive architecture that relates user needs to actual building components and their responsive actions, be they generated by low-or high- level processes. This model combined user's spatial needs, structure's environmental load and spatial response to control the internal spaces together. An example was built describing this model (Fig. 2). In this framework, activities of

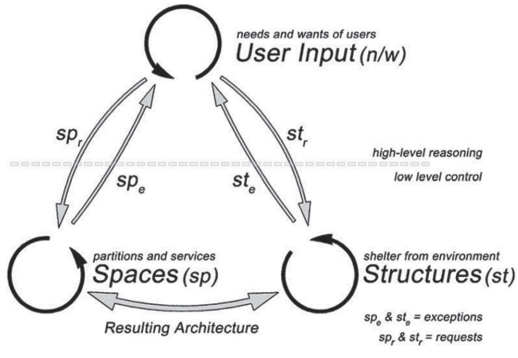

Figure 1. The proposed hybridized control model for use within a functional responsive architecture (Sterk, 2005).

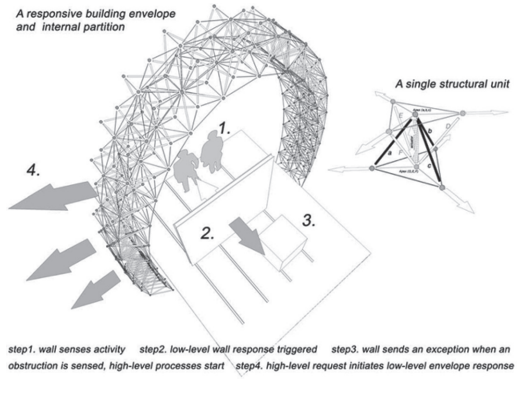

Figure 2. A structure and internal partition working cooperatively in response to changing patterns of use (Sterk, 2005).

each building elements are coordinated to reflect user needs. In step 1, the sensor will be monitoring the amount of people in the space. Step 2, when the amount of people reaching certain point, the low-level wall response will be triggered and sliding in the other way to give more space. Step 3, if the wall is sliding to its very extent, it will send an exception signal to the high-level processes. Step 4, now the envelope will adjust to increase the amount of space. By linking lower-level process with higher-level process and feed back to the central computer, future actions can be predicted through gathering these data. The hybridized model helps to simplify the tasks by delegating smaller, simpler, tasks to low-level processes before engaging higher levels of computing power to solve harder tasks that will involve many components. It will also be safer and easier for users to use.

Besides this model, the author also proposed the networks of hybridized control. So it is not only one building be responsive to its environment and its users, it is a community of buildings' interaction and action. The extended model is basically the same type of processes that occurs in the single building. But it will give better and comprehensive solution of the collaborate benefit of the community. Since it is also has feedbacks to the central computer, it will form a large data base that will also be instructional to new developments (Meyboom, 2009).

5 CONCLUSION

With the macroscopic system view discussed above, the possibilities of architecture have been proliferated. Moreover, if connecting the network of responsive architectures to a larger database, it will respond to larger sets of environmental and social conditions in a more cooperative and beneficial ways. The responsive buildings will be one loop in the larger database, constantly receiving inputs, giving out feedbacks and transforming themselves. The realization of this network will involve detailed technical progresses in areas other than architecture, such as smart materials, innovative mechanism of action etc.

In the future, people could customize their homes, workplaces. Through a mobile phone app, after answering some questions about your demand and aesthetic preferences, a 3d print home will be ready for you just after a few hours. These costume-made buildings' information will be gathered in a database. The database will include all the information about the urban environment and its infrastructures. And all responsive buildings or urban elements from one region are linked within the network. It is also of great benefit for dealing with extreme conditions. In normal days, the buildings will be in a stable state or run the low-processes to keep it work. When extreme situation happens, say a sudden flood exceeding the normal capacity of the city, or some big event that exceed the transportation and accommodation capacity, the buildings should be responsive to these sudden changes and be stimulated to take actions from low-processes to high-processes.

This kind of network system will blur the boundary of architecture. A building will be more like a product than a piece of architecture. The cultural and social meaning that should be carried in the long history of architecture would fade away. This significant building technology progress would also invoke the biggest argument in the meaning of architecture.

REFERENCES

Aedas. 2012. Retrieved from Archdaily: http://www.archdaily.com/270592/al-bahar-towers-responsive-facade-aedas.

dRMM. 2009. Retrieved from dRMM: http://drmm.co.uk/projects/view.php?p=sliding-house.

Fisher, D. (n.d.). 2009. dynamicarchitecture. Retrieved from http://www.dynamicarchitecture.net/home.html.

Khan, O. 2010. *Open Columns: A Carbon Dioxide(CO2) Responsive Architecture*. Newyork: Buffalo.

Menges, A., & Reichert, S. 2012. *Material Capacity-Embedded Responsiveness.* Newyork: John Wiley & Sons Ltd.

Negroponte, N. 1970. *The Architecture Machine.* Cambridge: Mass., M.I.T. Press.

Negroponte, N. 1975. *The Soft Architecture Machine.* Cambridge: Mass., M.I.T. Press.

Packe, R., & Jordan, K. 2001. *Multimedia: From Wagner to Virtual Reality*. New York: W.W. Norton.

Pask, G. 1969, September. *Architectural relevance of cybernetics*. Architectural Design 4(77): 54.

Pesenti, M., Masera, G., Fiorito, F., & Sauchelli, M. 2014. Kinetic solar skin: a responsive folding technique. *International Conference on Solar Heating and Cooling for Buildings and Industry*. Amsterdam: Elsevier Ltd.

Sterk, T.D. 2005. Building upon Negroponte: a hybridized model of control suitable for responsive architecture. *Automation in Construction* 2(14): 225–232.

Sterk, T.D. 2010. Responsive Architecture: User-centered Interactions within the Hybridized Model of Control. In: Proceedings of the Game Set and Match II, On Computer Games, Advanced Geometries, and Digital Technologies, Rotterdam: Episode Publishers: 494–501 (2006a).

Wang, J. 2011. *Biomimicry. Kinetics. Sustainability—Study on Kinetic Building Envelopes Based on Biological Acclimatization*. Tianjin: Tianjin University.

Zuk, W. & Clark, R.H. 1970. *Kinetic Architecture.* New York: Van Nostrand Reinhold; 1st edition (1970).

Civil Engineering and Urban Planning IV – Liu et al. (Eds)
© 2016 Taylor & Francis Group, London, ISBN 978-1-138-02903-3

Regional Building Cooling Load Prediction Stochastic model based on Monte Carlo simulation

Li-Zhen Wang
College of Mechanical Engineering, Tongji University, Shanghai, China

Hong-Wei Tan
College of Mechanical Engineering, Tongji University, Shanghai, China
Research Center of Green Building and New Energy, Tongji University, Shanghai, China

Zhi Zhuang
Research Center of Green Building and New Energy, Tongji University, Shanghai, China

ABSTRACT: Regional energy system planning and load forecasting make the great contributions to reduce the energy consumption. In light of the fact that we may not be able to obtain the complete building parameters during the period of regional energy planning, the conventional software for load calculation cannot accurately simulate the building's cooling load. In this paper, a new method based on Monte Carlo methodology is proposed for forecasting the regional building cooling load. We first establish the Regional Building Cooling Load Prediction Stochastic model (RBCLPS model), followed by the risk characteristics of the variable distribution in this model being determined. Besides, the distribution of peak cooling load probability for various buildings (including the whole regional building) as well as the annual average hourly cooling load can also be obtained by using Monte Carlo method. Furthermore, we also perform the simulation according to the case study by considering the cooling load characteristics of the regional building. Numerical results show that RBCLPS model can lead to the available area of the distribution as well as the cumulative probability of the peak cooling load frequency. It has been shown that the average and the standard deviation of regional building peak cooling load are 60.9 MW and 5.5, respectively. This study would be beneficial to achieving decision-making risk control and cost control for regional energy planning and providing a feasible solution for them.

1 INTRODUCTION

In recent years, urbanization construction has been quickly developed in China, and the construction project of low-carbon-ecological city becomes more and more complicated. Regional energy planning becomes increasingly important (Wang & Xu 2011).

In the construction planning phase, the selection of regional cooling system is based on the building cooling load calculation. Uncertainties of predicting building cooling load arise from a variety of sources like the lack of building basically information (Kavgic et al. 2013). In China, conventional regional building cooling load prediction is determined by the cooling load indicators method of superposition or estimated by building energy simulation program to simulate the regional building cooling load and the energy consumption.

In the building cooling load research field, several studies have been dedicated to the method. These researches include the neural network method (Abdullatif et al. 2004; Papalexopoulos et al. 1994), and the statistics regression method (Pagliarini & Rainieri 2012), and support the vector machine method (Li et al. 2009) and the grey theory combines improved of genetic algorithm (Lee & Tong 2011). Multi-forecast method (Yao et al. 2004) is used to integrate several common air conditioning load forecasting model, and introduced AHP method to air conditioning load combination forecasting model. These methods are better in the design stage for building cooling load forecast. Many factors affect the building load calculations in the architectural design phase. Fernando et al. (2010) studied on the uncertainty in peak cooling load of the individual buildings. Scenarioy analysis by setting several scenarios (Long et al. 2011) can predict the cooling load, but it also remains uncertain.

Monte Carlo simulation in real terms is through a large number of random tests, using a numerical method to solve the problem of probability

theory (Liu 2009). In recent years, scholars at the Monte Carlo simulation methods engaged in a large number of researches, which is mainly used in economics and finance, building thermal simulation, wind turbines, medical statistics and the reliability, and so on (Liu 2009; Soratana & Marriott 2010; Haarhoff & Mathews 2006; Marmidis et al. 2008).

However, regional building cooling load has not yet been incorporated into the statutory planning system in China, because there are no clear standards and specifications for these plans. In this paper, we propose a regional building cooling load prediction model based on the determined distribution function of random variables, using Monte Carlo simulation method to solve the uncertainty problem of regional building cooling load during the planning phase. Regional cooling load prediction is very significant on urban energy planning. Moreover, a case study of regional cooling load prediction energy planning for a new district of Fujian province is carried out.

2 MONTE CARLO SIMULATION METHODOLOGY

Monte Carlo simulation is a widely used whenever the uncertainty is expressed in the form of probability distributions. In a Monte Carlo analysis, Monte Carlo simulation method is through statistical sampling principle to establish a mathematical model to solve the problems. It contains the following main steps:

The first step is to set up the mathematical model for regional building cooling load. The second step in the uncertainty analysis is to determine main risk variables of Monte Carlo analysis model through research statistics and analysis to determine the probability distribution of risk variables. The third step preparation of procedures according to the given probability distribution generates large amounts of random numbers; random number can simulate the practical problems. The fourth and the last step of the analysis is that these random numbers as variables or parameters input the stochastic model, after many times simulations regional building cooling loads can be obtained, which predicted in numerous factors affecting the study area under the peak cooling load and its distribution.

Author wrote a MATLAB (Cao 2009) program to realize the Monte Carlo stochastic simulation, and the process is shown in Figure 1.

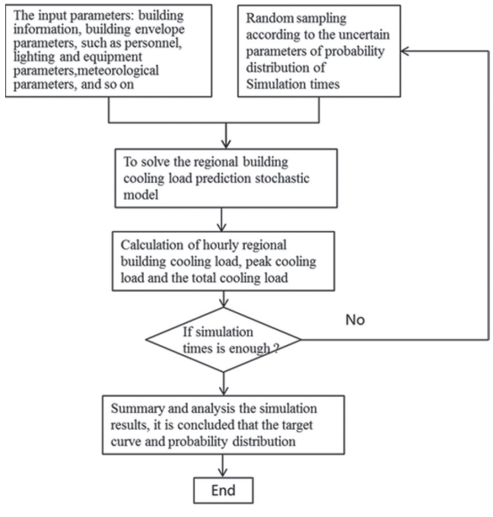

Figure 1. Flowchart of Monte Carlo simulation method.

3 REGIONAL BUILDING COOLING LOAD PREDICTION STOCHASTIC MODEL (RBCLPS MODEL)

3.1 *Regional building cooling load prediction model*

Judging from the architectural form of the new strict, building most of cuboids or multiple combinations of rectangular form, we choose rectangle of bottom shape of the building for research. Regional building cooling load of the problem can be expressed for: in a regional which has n class buildings, planning figure in the various building of function positioning, and area, and limited high has determines, simplified building internal layout separated will similar building as a overall, in the summary method (Lin et al. 2013) used the cooling load coefficient method (Shan 1989) combines regional building load uncertainty factors, established regional building cooling load forecast random model:

$$CL_j = \sum_{n=1}^{6} A^n \sum_{i=1}^{5} \alpha_{i,j}^n q_i^n \qquad j = 1,2\ldots\ldots 8760 \tag{1}$$

where CL_j denotes the total hourly building cooling load (W), n stands for building types, such as office buildings, hotels, hospital, school buildings, shopping malls, and residential buildings; A^n denotes the floor area of the nth type building (m^2), $\alpha_{i,j}^n$ is the ith kind hourly cooling load factor for the n type building; q_i is the ith type cooling load indicator the n kind building (W/m^2), $I = 1, 2 \ldots 5$ of the palisade structure, respectively, fresh air, people, lighting, and electrical equipment of the cooling load.

$$\alpha_{1,j}^{n} q_1^n = \frac{T_j - T_I^n}{T_W - T_I^n} \left\{ 2\left[K_1 \Delta t_1 \left(1 - \bar{\varepsilon}\right) + K_3 \Delta t_3 \bar{\varepsilon} + C_Z D_{j\max} C_{LQ} \bar{\varepsilon} \right] \frac{(m+1)h_0}{ma} + K_2 \Delta t_2 \frac{h_0}{h} \right\} \tag{2}$$

where T_j, T_I^n, T_w, respectively, stand for the outdoor dry bulb temperature, the indoor design temperature, and the summer air-conditioning outdoor dry bulb temperature (ºC); K_1, K_2, and K_3 are the heat transfer coefficients of the outside wall, roof, and the window; Δt_1, Δt_2, and Δt_3 are the cooling load temperature difference of the exterior wall, roof, and outside the window, ε denotes the window–wall ratio on average; a is the building base side length and ma is the another side length, h is the building height, and h_0 is the standard layer height; C_{LQ} is the cooling load factor; $D_{j,max}$ is the maximum value of solar radiation heat gain factor (W/m^2); C_z is the integrated block coefficient of window glass;

$$\alpha_{2,j}^{n} q_2^n = \left(\frac{h_j - h_I^n}{h_W - h_I^n} \right) \left[d_p^n \lambda_j^n G^n \rho \left(h_w - h_I \right) \right] \tag{3}$$

where h_j, h_I^n, and h_w are hourly outdoor air enthalpy, indoor design air enthalpy, and the outdoor design air enthalpy (kJ/kg), respectively; d_p^n is the indoor occupancy density (p/m^2), G^n is the fresh air (m^3/p·h), and ρ denotes the air density (kg/m^3);

$$\alpha_{3,j}^{n} q_3^n = \left(d_p^n \phi^n \lambda_j^n C_{3,LQ} \right) q_3^n \tag{4}$$

where ϕ^n is the aggregation coefficient, λ_j^n is the number of persons in the room by the hour, and $C_{3,LQ}$ is the occupant cooling load factor.

$$\alpha_{4,j}^{n} q_4^n = \mu_j^n C_{4,LQ} q_4^n \tag{5}$$

where μ_j^n is the hourly utilization rate of lighting; and $C_{4,LQ}$ is the lighting cooling load factor;

$$\alpha_{5,j}^{n} q_5^n = \left(\delta_j^n C_{5,LQ} \right) q_5^n \tag{6}$$

where δ_j^n is the hourly utilization rate of equipment; and $C_{5,LQ}$ is the equipment cooling load factor.

3.2 *Prediction of key parameters of the model and its probability distribution*

Meteorological conditions of the study area are assumed for the deterministic parameters. In the planning phase, architectural design is uncertain when there are a lot of uncertainty and unpredictability, such as heat transfer coefficient of the building envelope; indoor design temperature and the ratio of window to wall, indoor occupancy density lighting, and electrical equipment density are all the random variables.

Existing buildings of the city planning questionnaire survey, combined with the local statistical yearbook, and forecast the future development trend and requirements, such as parameter setting in the distribution, the membership function of the random variables can be obtained, such as the determination of the exterior wall heat transfer coefficient distribution coefficient and using the statistical methods heat transfer coefficient of the exterior wall can be obtained to obey normal distribution, and Table 1 is as follows.

3.3 *Sampling method of random variable*

This paper adopted the inverse function method for direct sampling of continuous and discrete random variables.

3.3.1 *Continuous random variables*

For the random variable x, the distribution function F (x) can solve its inverse function G (x). If R is in [0, 1] interval random variable of uniform distribution, by x = G (R) transform, a random variable X can be obtained according to the distribution of the F (x). By the above method, the triangle distribution and the uniform distribution of the transformation type x = G (R) can be retained.

3.3.2 *Discrete random variables*

For arbitrary discrete distribution $F(X) = \sum_{X_i < X} P_i$ $x_1, x_2, \ldots, x_n$ stands for discrete distribution function of hops, P_1, P_2 … denotes for the corresponding probability. Discrete distribution of the sampling method is as follows:

$$X_F = x_I, \quad \sum_{i=1}^{I-1} P_i < \xi \le \sum_{i=1}^{I} P_i \tag{7}$$

Table 1. Distribution of the stochastic parameters.

A random variable	Distribution
T_i^n	Uniform distribution
K_1, K_2, K_3	Normal distribution
d_p^n	Uniform distribution
q_4^n, q_5^n	Triangular distribution
G^n, $\bar{\varepsilon}$	Discrete distribution

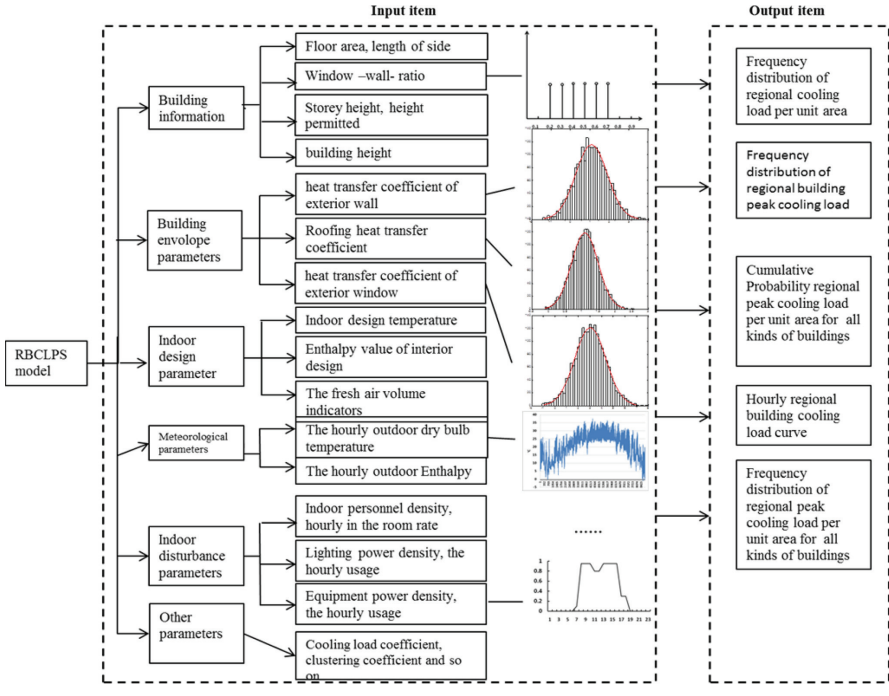

Figure 2. Composition of input and output parameters on the stochastic model.

3.4 *Stochastic model of input and output parameters*

The input and the output items of the stochastic model are as shown in Figure 2.

4 RESULT

4.1 *Case study*

A master planning in hot summer and warm winter area as the study area, as shown in Figure 3, is proposed to build for office, hotel, business, health care, education, and housing for the integration of comprehensive administrative region, in river west of development over the same area as the research object, using the Monte Carlo numerical simulation method to predict the area building cooling load.

4.2 *The parameters of RBCLPS model*

The input parameters including the deterministic parameters and the random variable of RBCLPS model, the deterministic parameter method is listed in Table 2.

The determination of the random variables for the urban buildings is to carry out the investigations, and the research includes the economic level, the industrial structure, the population status of local, and needs to select the part of the building in all kinds of buildings.

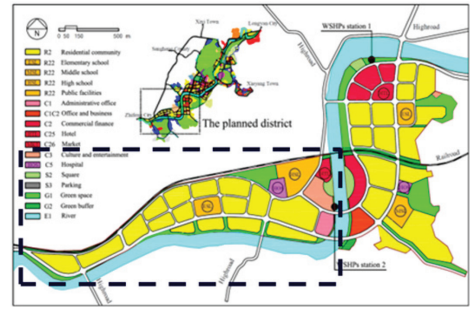

Figure 3. Master plan of the study area.

The investigation of building owner contains building information, envelope structure, user information, local conventional energy, energy model, energy prices, and incentive policies for renewable energy. On the basis of the local information, the building energy consumption information database is established. Random numbers generated by the MATLAB program.

Table 2. Deterministic parameters election method of RBCLPS model.

Parameter	Note
A^n (A^1 = 37 090, A^2 = 56 400, A^3 = 25 640, A^4 = 61 427, A^5 = 1296, A^6 = 679 025, m^2), H, h_0, a, m	The master plan
T_j, h_j	China building thermal environment analysis special meteorological data set
T_w, h_w, $D_{j,max}$, Δt_1, Δt_2, Δt_3, ϕ^n, λ_j^n, $C_{3,LQ}$ δ_j^n, μ_j^n, $C_{4,LQ}$ δ_j, $C_{5,LQ}$	"Concise handbook of air conditioning system design" and "Residential building energy saving standards in hot summer and warm winter area" "Design standard for energy efficiency of public buildings"

4.3 *The results of Monte Carlo simulation*

With the MATLAB simulation program that we develop, some input factors can be to programming. In this paper, we set up simulation number for 2000 times, so as to ensure sufficient statistical information can be obtained. The simulation results are shown in Figure 4.

From Figure 4(a) and (d), regional peak cooling load and cooling load of the unit building area is through the Anderson—darling normality test, normally distributed. Figure 4(a) in the regional peak cooling load average μ is 6×10^7 W, and Figure 4 classification architecture maximum probability of the peak cooling load superposition compared result was reduced by 10%. Figure 4(c) shows the hourly cooling load for the whole region at the scenarios of 50% cumulative probability.

Regional probability density distribution of the peak cooling load is Equation (8).

$$f(x) = 0.0725e^{-\frac{(x-60.9)^2}{60.5}}, (40 < x < 80, MW) \quad (8)$$

Regional unit building area of probability density distribution of the cooling load is Equation (9).

$$f(x) = 0.064e^{-\frac{(x-70.8)^2}{76.9}}, (45 < x < 90, w/m^2) \quad (9)$$

Figure 4(b) demonstrates the predicted peak cooling load in the 68.3% confidence interval for [55.4, 66.4] MW. In Figure 4, average μ point is in line with the recommended values in the current

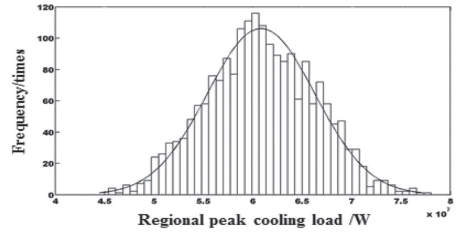

(a) Peak cooling load frequency distribution for the region.

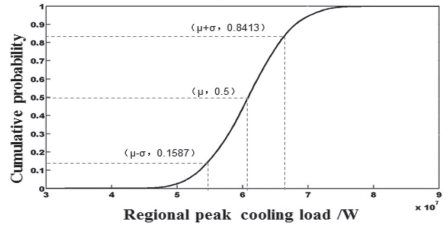

(b) Cumulative probability distribution of the peak cooling load for the region.

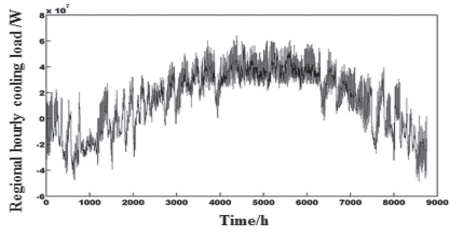

(c) Hourly cooling load for the region.

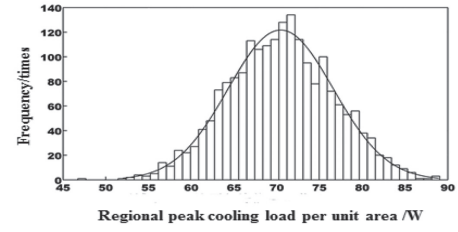

(d) Frequency distribution of peak cooling load per unit area.

Figure 4. The cooling load diagram for the region.

energy efficiency design standards, (μ, μ+σ] = (60.9, 66.4) is a regular interval value, [μ−σ, μ) = (55.4, 60.9) is the use of advanced technology of the low carbon scenario interval value.

5 CONCLUSION

We establish the Regional Building Cooling Load Prediction Stochastic model (RBCLPS model) based on Monte Carlo methodology and MATLAB program. RBCLPS model can predict

the cooling load for the whole studied area or each kind of buildings. At the same time, the paper takes a planning area as an example, simulate and predict the regional building cooling load. The main results are as follows: 1) RBCLPS model can solve the stochastic problem of regional building cooling load on regulatory detailed planning; 2) To determine the distribution of random variables and random number generation method; 3) Probability distribution and cumulative probability distribution of regional peak cooling load are obtained by the RBCLPS model of probability distribution and cumulative probability distribution; provide technical support for designers and decision makers; and 4) Prediction model is put forward the recommended value, regular scenario interval value and interval prediction method of low carbon scenario.

ACKNOWLEDGMENT

The authors would like to thank the Ministry of Science and Technology of the People's Republic of China for the financial support of science and technology research in the 12th Five-year Plan with Grant No. 2012BAJ15B03. The authors also appreciate the two anonymous reviewers for their detailed and constructive comments.

REFERENCES

Abdullatif, E., Nakhi, B. & Mahmoud, M.A. 2004. Cooling load prediction for buildings using general regression neural networks. *Energy Conversion and Management* 45(13–14): 2127–2141.

Cao, Y. 2009. *Training and Tutorials of MATLAB.* Beijing: China Machine Press, 150–168.

Fernando, D.M., Cejudo-Lopez, J.M. & Carrillo-Andres, A., et al. 2010. Uncertainty in peak cooling load calculations. *Energy and Buildings* 42 (7): 1010–1018.

Haarhoff, J. & Mathews, E.H. 2006. A Monte Carlo method for thermal building simulation. *Energy and Buildings* 38(12): 1395–1399.

Kavgic, M., Mumovic, D. & Summerfield, A. et al. 2013. Uncertainty and modeling energy consumption: Sensitivity analysis for a city-scale domestic energy model. *Energy and Buildings* 60(3): 1–11.

Lee, Y.S. & Tong, L.I. 2011. Forecasting energy consumption using a grey model improved by incorporating genetic programming. *Energy Conversion and Management* 52(1): 147–152.

Li, Q. Meng, Q.L., & Cai, J., et al. 2009. Applying support vector machine to predict hourly cooling load in the building. *Applied Energy* 86(10): 2249–2256.

Lin, D.M., Wang, Z.J., Zhai, Z.J., et al. 2013. A simplified method to predict hourly building cooling load for urban energy planning. *Energy and Buildings* 58(3): 281–291.

Liu, J. 2009. *Monte Carlo strategies in scientific computing.* Beijing: Higher Education Press, 2–15.

Long, W.D., Bai, W. & Fan, R., et al. 2011. *Community energy planning for built environment in low carbon cities.* Beijing: China Architecture and Building Press, 182–194.

Marmidis, G., Lazarou, S. & Pyrgioti, E. 2008. Optimal placement of wind turbines in a wind park using Monte Carlo simulation. *Renewable Energy* 33(7):1455–1460.

Ministry of Construction of the People's Republic of China. GB50189–2005. Design standard for energy efficiency of public buildings.

Ministry of Construction of the People's Republic of China. JGJ 75–2012. Residential building energy saving standards in hot summer and warm winter area.

Pagliarini, G. & Rainieri, S. 2012. Restoration of the building hourly space heating and cooling loads from the monthly energy consumption. *Energy and Buildings* 49(2): 348–355.

Papalexopoulos, A.D., Hao, S.Y. & Peng, T.M. 1994. An implementation of a neural network based load forecasting model for the EMS. *IEEE Transactions on Power Systems* 9(4):1956–1962.

Shan, J.P. 1989. *Cooling load calculation method.* Beijing: China Architecture and Building Press, 30–71.

Soratana, K. & Marriott, J. 2010. Increasing innovation in home energy efficiency: Monte Carlo simulation of potential improvements. *Energy and Buildings* 42(6): 828–833.

Wang, D.Y. & Xu, W.F. 2011. Low-carbon city and building energy planning. *Heating Ventilation Air conditioning* 4(4): 17–18.

Yao, Y., Lian, Z.W., & Liu, S., et al. 2004. Hourly cooling load prediction by a combined forecasting model based on Analytic Hierarchy Process. *International Journal of Thermal Sciences* 43(11): 1107–1118.

Zhao, R.Y. 1998. *Concise Handbook of air conditioning system design.* Beijing: China Architecture and Building Press, 26–61.

Civil Engineering and Urban Planning IV – Liu et al. (Eds)
© 2016 Taylor & Francis Group, London, ISBN 978-1-138-02903-3

Seismic time history analysis of large-scale wind turbine

Lin Fang, Di Zhang & Jian-Wei Wang
Yellow River Conservancy Technical Institute, Kaifeng, Henan, China

ABSTRACT: Integrated digital 3D blade-tower-foundation-subgrade FEM model and foundation-subgrade model of the wind turbine structure are established. Dynamic characteristics and response results of the wind turbine coupled structure influenced by ground motion are researched, response patterns of stress and displacement of the foundation are obtained, and some reference basis is provided for design and construction of the wind turbine foundation.

1 INTRODUCTION

Wind turbine structure is slender and its mass distributes unevenly (Cao & Zhang 2011). For the sake of power generation, it violates the structural requirements of high building: appropriate height-to-width ratio and even distribution of mass (Ding et al. 2013). Destructive power of seismic loads is strong so the study on the seismic behavior of the wind turbine structure is an important part of structure design. (Zhu et al. 2012).

2 BASIC STRUCTURAL CHARACTERS

Taking Huitengxile wind farm as a calculation example, the wind turbine structure mainly consists of three rotor blades, hub, engine room, tower and foundation (Zhang et al. 2008). The type of unit is GE1.5sle 50 HZ. The height of the conical tower is 77.3 m. The bottom diameter of the tower is 4.3 m and the top diameter of the tower is 2.4 m. The total weight of the engine room, hub and blades is 88 t. The distance between the center of mass of the hub, the engine room and the tower central line is 0.687 m. The radius of the impeller is 38.5 m, and the foundation is of spreading type.

3 CALCULATION MODEL

Global coordinate system origin of the model is the center of the bottom of the plain concrete cushion. Z axis is the vertical central axis of the foundation and the tower. The positive direction of the X axis is the direction of the horizontal wind load. The X axis, Y axis and Z axis follow the rules of right-hand coordinate system. In order to reduce the influence of the boundary constraint on the stress of the foundation, the depth of the subgrade is set 9 times the diameter of the foundation, which is equal to 144 m, and the diameter of the horizontal calculation region is set 18 times the diameter of the foundation. The boundary conditions of the bottom of the subgrade model are fixed and the boundary conditions in the horizontal direction of the subgrade are fixed (He et al. 2009). The integrated FEM model of the wind turbine is shown in Figure 1, and the FEM model of the foundation and the upper structure is shown in Figure 2.

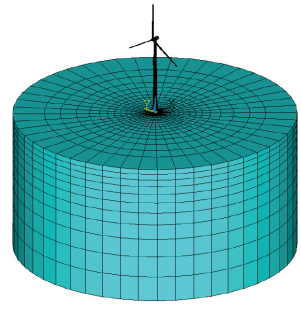

Figure 1. Whole FEM model.

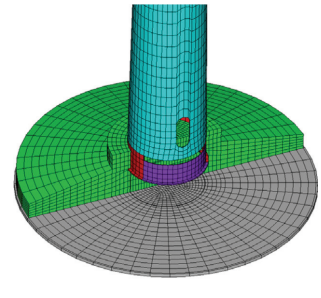

Figure 2. FEM model of the foundation and the upper structure.

4 LOADS AND SCHEMES

The maximum seismic fortification intensity of Huitengxile wind farm is 7. In the seismic analysis, the influence of the horizontal ground motion is only considered in the calculation. Through comparison and analysis, Ninghe Tianjin seismic wave is adopted in the dynamic time history analysis of the wind turbine structure and the recorded duration is 19.11 s, the time interval is 0.01 s, and the peak acceleration is 141.3 cm/s^2. In every 0.1 s of the record, a value is selected and the number of values reaches to 190. For the rare earthquake whose fortification intensity is 7, the maximum acceleration is 220 cm/s^2, and the acceleration values chosen for Ninghe Tianjin seismic wave are multiplied by 1.56 to meet the requirements of rare earthquake. This seismic wave is taken as input data in the time-history analysis (Clough & Penzien 2003).

In order to analyze and compare the calculation results of the foundation-subgrade FEM model, two different schemes are chosen, as presented in Table 1. In order to study the stress and deformation of the foundation under the influence of ground motion, typical section A-A is selected, as shown in Figure 3, and in this section, seven characteristic points A, B, C, D, E, F, G are selected for analysis, as shown in Figure 4.

Table 1. Ground motion time-history analysis scheme.

Calculation scheme	FEM model
Scheme 1	Integrated "blade-tower-foundation-subgrade" model
Scheme 2	"Foundation-subgrade" comparison model

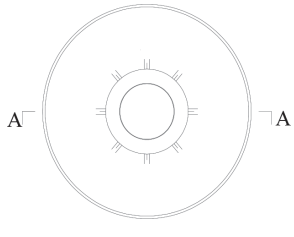

Figure 3. Section A-A.

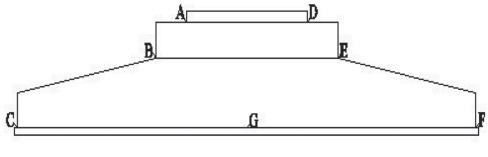

Figure 4. Characteristic points of section A-A.

5 CALCULATION RESULT ANALYSIS

5.1 *Foundation stress analysis for ground motion*

In order to analyze the response patterns of stress of the foundation under the influence of ground motion, principal tensile stress time-history curves of A, B, D and E are obtained, as shown in Figure 5 and Figure 6. The direction of the acceleration is the X direction. The principal tensile stress of A, B, D, E changes as the acceleration of seismic wave varies. The left tension, right compression and left compression, right compression of the foundation change based on the process of propagation of acceleration wave. But in scheme 1, because of the upper structure, namely the blades and tower, the change in the range of principal tensile stress of A, B, C, D is significantly larger than that observed in scheme 2.

5.2 *Foundation displacement analysis for ground motion*

X, Y, Z displacement time-history curves of the characteristic points C, G, F are shown in Figures 7–12. From Figure 7 and Figure 8, it can be seen that the X displacement time-history curves of the characteristic points C, G, F are basically consistent. Y displacement time-history curves of the characteristic points C, G, F are shown in Figure 9 and Figure 10 and it can be seen that the variation in Y displacement is small.

Z displacement time-history curves of the characteristic points C, G, F are shown in Figure 11 and Figure 12, and the variation is similar to that of principal tensile stress time-history curves. Because of the influence of horizontal seismic wave and gravity, when the X axis negative direction side of the foundation is tensile and the downward displacement of the foundation is produced, the X axis negative direction side of the foundation is

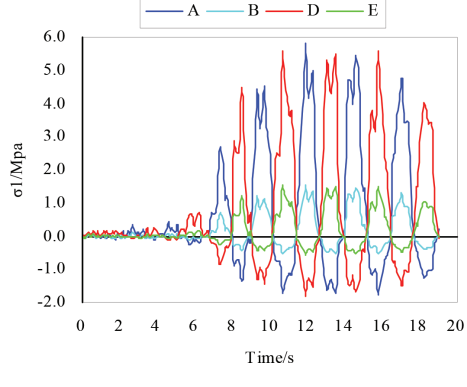

Figure 5. σ1 time-history curve of A, B, D, E in scheme 1.

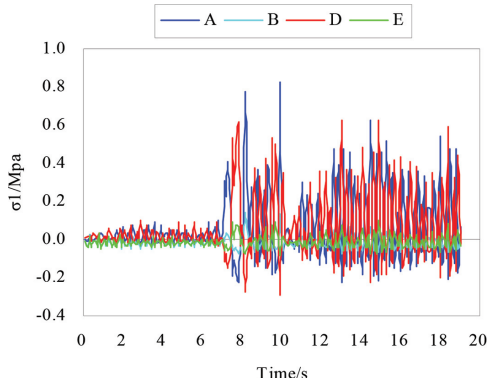

Figure 6. σ1 time-history curve of A, B, D, E in scheme 2.

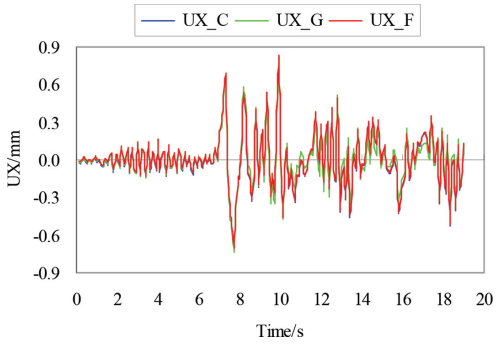

Figure 7. X displacement curve of C, F, G in scheme 1.

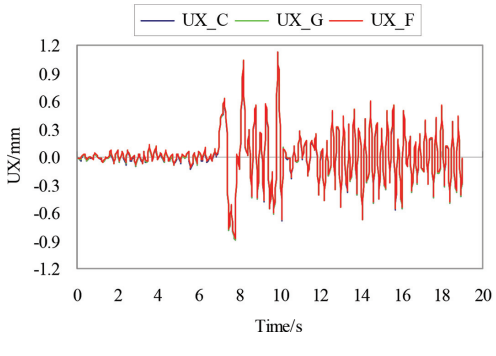

Figure 8. X displacement curve of C, F, G in scheme 2.

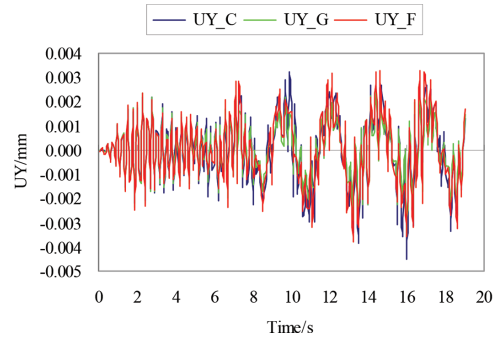

Figure 9. Y displacement curve of C, F, G in scheme 1.

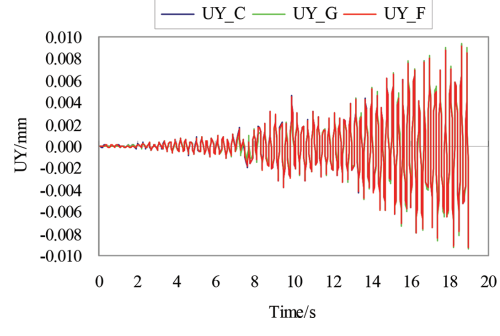

Figure 10. Y displacement curve of C, F, G in scheme 2.

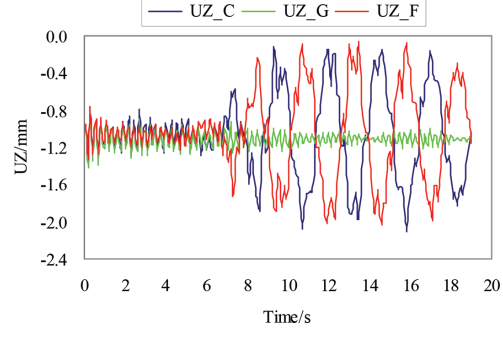

Figure 11. Z displacement curve of C, F, G in scheme 1.

relatively upward, but the X axis positive direction side of the foundation is relatively downward. When the X axis positive direction side of the foundation is tensile, the trend is just opposite. Z displacement alternative variation of the characteristic points C and F can be seen clearly and the Z displacement of the middle characteristic point G is small.

Above all, among the time-history variation of the displacement of three characteristic points, Z displacement of each point is the largest, and when the foundation is under the influence of horizontal ground motion and gravity, Z displacement is the main feature, but the biggest displacement meets the specification requirements.

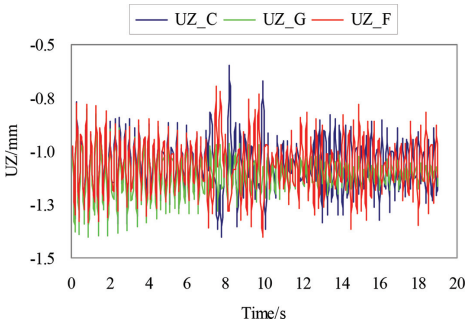

Figure 12. Z displacement curve of C, F, G in scheme 2.

6 CONCLUSIONS

From the calculation results of the two schemes, under the influence of horizontal ground motion, the stress status of the entire structure is low, Z displacement is the main feature of displacements, but it meets the specification requirements. Response patterns of stress and displacement provide some reference basis for design and construction of the wind turbine foundation.

REFERENCES

Cao, Q. & Zhang, L.J. 2011. Study of Effects of Foundation on Seismic Response for Wind Turbine Tower System *China Academic Journal Electronic Publishing House* (in Chinese).

Clough S. & Penzien J. 2003. Dynamics of Structures. *Computer & Structures Inc.* 2(30): 3–5.

Ding, L., Zheng, Y., & Zhang, F.X. 2013. Stress Analysis of Vertical Axis Wind Turbine Based on Fluid-Structure Coupling. *South to North Water Transfer and Water Science & Technology* 11(4): 84–88. (in Chinese).

He, G.L., Zhou, Y., Li, J. 2009. Seismic Analysis of Wind Turbine System. *Engineering Mechanics* 26(7): 72–77. (in Chinese).

Zhang, Y.M., Song, Y.P. & Zhang, X.D. 2008. Investigating the Soil-Structure Dynamic Interaction for Tall Buildings under Coupled Action of Multi-Directional Earthquake *Engineering Mechanics* 25(2): 154–159 (in Chinese).

Zhu, L., Yao, X.Q., & Wang, Y.Q. 2012. Earthquake Response Spectrum Analysis of 600 MW Wind Turbine Generator System. *Solar Energy Journal* 33(10): 1672–1675. (in Chinese).

Civil Engineering and Urban Planning IV – Liu et al. (Eds)
© 2016 Taylor & Francis Group, London, ISBN 978-1-138-02903-3

Study on population and land expansion and their coordinated relations—a case of Hebei Province

Yin-Chuan Wang, Ying Chen & Qiao-Na Yan
College of Land and Resources, Agricultural University of Hebei, Baoding, Hebei, China

ABSTRACT: Urbanization is one of main reasons for world progress and development. In order to understand the urban population size of Hebei as well as land scale development law and status, this paper analyzed the coordinated relationship between urban population and land to guide the future urban development. The time span considered in this paper was 13 years, from 2000 to 2012, and the rank-size rule was used to analyze the development laws of urban population and urban built-up area of 33 cities in Hebei Province, and then the allometric growth and urban land expansion parameters were adopted to analyze their relationship from the levels of time and space. The results showed that the Hebei urban system was not perfect and the urban size was small. The primacy ratios of population size knots and built-up area were low. From the vertical perspective, the allometric relationship of the whole province was gradually significant from 2006, and the growth rate of the built-up area was significantly higher than that of urban population. From the horizontal perspective, the land expansion coefficients of most cities were higher than the reasonable value, the urban population density was low, and land-use efficiency was yet to be improved.

1 OVERVIEW OF RESEARCH AREA AND DATA SOURCE

1.1 *Overview of research area*

The geographic location of Hebei Province is east longitude 113°04′ to 119°53′ and north latitude 36°01′ to 42°37′. It is located in the North China Plain and encompasses two major cities: Beijing and Tianjin. It covers an area of 187,693 km^2 and was estimated to have a population of 72.8751 million (in 2012). In the administrative region, it has 11 prefecture-level cities, 22 county-level cities, 108 counties and 6 autonomous counties.

1.2 *Data source*

The basic data in this paper were derived from the "Annual Statistical Report on Construction of Cities and Counties in Hebei (2001–2013)". Compared with the data of each year, it was found that on February 1, 2002, County-level Fengnan City was removed upon the approval of the State Council (Guohan [2002] No. 7), and the Fengnan District, Tangshan City was established. From 2002, there were no statistical data about Fengnan City; therefore, it was removed from data. The population data used in this paper included the urban population but not the non-agricultural population. The is sue to the limitation of the existing household registration system. The gap between the non-agricultural population and the actual population living in cities has gradually widened. If the non-agricultural population data were used as the basic data for research, it would have a little practical significance.

2 RESEARCH ON THE DEVELOPMENT STATUS OF POPULATION AND LAND SCALE

Urban scale is the major issue of urban research as well as the basis for the formulation of overall urban planning. In general, urban scale has the fractal nature and satisfies the Zipf rank-size rule. Population scale and land scale are the two best indicators that reflect the urban scale. This paper carries out a rank-size analysis of two groups of data on the urban population and urban built-up area. The rank-size expression is as follows:

$$P_i = P_1 R_i^{-q} \tag{1}$$

where R_i is the rank of the city i; P_i is the urban population (land) scale with the rank of R_i; P_1 is the first theoretical urban population (land); and q is the Zipf dimension (Chen & Liu 2001).

During data processing, the logarithmic form of the above equation is generally used, i.e.

$$\log P_i = \log P_1 - q \log R_i \tag{2}$$

It is generally considered that the reasonable value of q is 1. At this point, the urban system development is relatively balanced, and it has the rank-size distribution pattern. When the value of q is greater than 1, the population (land) is more concentrated in large cities. Thus, the population (land) scale in large cities is too large, while the population (land) scale in small and middle cities is relatively small. At this point, the primacy ratio of cities in the region is relatively high. When the value of q is smaller than 1, the case is opposite. In other words, population (land) is more concentrated in small and middle cities and the scale of larger cities is not large enough (Tang & Zhang 2011).

2.1 *Research on the features of urban population scale*

Hebei is a province with a large population. The urban population increased from 1,170,460 in 2000 to 14,987,700 in 2012, ranking the sixth place in the country, with the annual growth rate of 2.08%. Table 1 presents the urban population data from 2000 to 2012.

(1) From the angle of the correlation coefficient R^2, the model fitting ji degree is better. (2) Zipf index q changes about 0.83 and its value becomes smaller, indicating that the primacy ratio of cities in Hebei is low, the population size in large cities is small, while the population size in small and middle cities is large. Meanwhile, q is constantly becoming smaller, indicating that decentralized power is greater than centralized power. In general, when the primacy ratio is too low, the core and support roles of central cities in city groups are not obvious, their leadership and economic driving force for the economy of the surrounding areas are not significant enough, and they cannot form the core source of radiation that affects the overall economic development of the whole region. Only if the urban system is in a rank-size distribution pattern will it facilitate the reasonable and effective utilization of resources in the whole province, and promote the benign development of economy, society and other aspects, thus making the system in the region evolve into an orderly ideal form. According to the actual situation of Hebei Province, the urban scale is often small. Though q is smaller than 1, small cities are not prominent relative to cities in other provinces. (3) Structural capacity LnA reflects the complexity of the urban system. The complexity is in direct proportion to the value of LnA. According to Table 1, though LnA fluctuates, in general, it gradually becomes larger, and the change amplitude is not large, indicating that the urban population gross of Hebei Province is constantly increasing, and the complexity of the urban system increases by a small amplitude. (4) The theoretical value of the urban population increased from 2,182,400 to 2,693,000. The ratio of the theoretical value of primate city to actual value reduced from 1.2964 to 1.1550. The small amplitude of the reduction in the ratio indicates that the urban system gradually becomes complex and the overall scale is constantly increasing. In addition, Hebei is a province with a large population, ranking the sixth in China, but the populations of its cities rank lower in the world. The population of its primate city, Shijiazhuang, is only ranked 20th in China, indicating that Hebei Province needs to think of the future development direction of its cities seriously, develop

Table 1. The rank-size analysis table of the city population of Hebei Province.

Year	Rank-size expression	q	R^2	LnA	Population of primate city (ten thousand)	Theoretical population (ten thousand)	Theoretical/ actual
2000	$Y = 218.24X^{-0.8673}$	0.8673	0.946	5.3856	168.34	218.24	1.2964
2001	$Y = 210.29X^{-0.8462}$	0.8462	0.9511	5.3485	185.2	210.29	1.1355
2002	$Y = 214.78X^{-0.8426}$	0.8426	0.9497	5.3696	197.96	214.78	1.0850
2003	$Y = 214.18X^{-0.8364}$	0.8364	0.95	5.3668	201.4	214.18	1.0635
2004	$Y = 220.50X^{-0.8284}$	0.8284	0.9592	5.3959	207.56	220.5	1.0623
2005	$Y = 224.98X^{-0.8279}$	0.8279	0.9604	5.416	214.4	224.98	1.0493
2006	$Y = 231.09X^{-0.8188}$	0.8188	0.9652	5.4428	195.05	231.09	1.1848
2007	$Y = 224.05X^{-0.8265}$	0.8265	0.9697	5.4974	204.08	224.05	1.0979
2008	$Y = 245.14X^{-0.8197}$	0.8197	0.9695	5.5018	206.75	245.14	1.1857
2009	$Y = 247.59X^{-0.8128}$	0.8128	0.971	5.5118	224.5	247.59	1.1029
2010	$Y = 259.82X^{-0.8184}$	0.8184	0.9728	5.56	227.6	259.82	1.1416
2011	$Y = 268.23X^{-0.8158}$	0.8158	0.9736	5.5919	230.84	268.23	1.1620
2012	$Y = 269.30X^{-0.8143}$	0.8143	0.9699	5.5958	233.16	269.3	1.1550

scientific policies, and improve the healthy and orderly development of the urban system.

2.2 *Research on the features of urban built-up area scale*

The rank-size rule in the fractal theory applies not only to research on the urban population size, but also to research on the urban land scale. In 2000, the built-up area in Hebei was 962.87 square kilometers; in 2012, it increased to 1,738.89 square kilometers, with the average annual growth rate of 5.05%. The same method is used for processing and analysis of urban built-up area data from 2000 to 2012, as given in Table 2. (1) Zipf index q is less than 1, indicating that the urban built-up area has a relatively uniform size, the scale of high-ranking cities is not prominent enough, while small and middle cities are relatively developed. After the analysis of the change in q, it can be seen that, though q changes, it gradually becomes large in general, from 0.75 in 2000 to 0.790 to 2012. This development trend clearly indicates that the development of the built-up area scale of cities at all levels in Hebei Province tends to equilibrium, but the change is very slow. The scale of large cities is far from a reasonable level, and the situation of the relative prominence of small and middle cities changes little. (2) Structural capacity LnA becomes larger, indicating that the urban system gradually becomes perfect, and the overall size becomes larger, and the magnitude of this change is greater than that of the change in the above population structural capacity. (3) The ratio of the theoretic value of primate city to actual value slightly increases from 1.327 to 1.389, indicating that the expansion speed of the built-up area of primate city is lower than the average expansion speed of the whole province.

3 RESEARCH ON THE RELATIONSHIP OF SCALE EXPANSION BETWEEN URBAN POPULATION AND LAND

3.1 *Research on the features of allometry*

Allometry was a geometric measurement method first applied in the field of biology. Now it is applied in the research on urban development as well as on scale features of population and land in the process of urban development, reflecting the longitudinal growth law of the urban system in the process of historical development (Lee 1989). P represents the urban population and L represents the urban built-up area. P and L generally have the following power exponential relationship:

$$L = \alpha P^{\beta}$$

where α is the proportionality factor and β is the scaling exponent (Liu & Chen 2005).

A regression analysis of power function and linear function of urban population and built-up area from 2000 to 2012 (Fig. 1) is made, and the results are summarized in Table 3.

The key of the allometric model is to inspect the value of the parameter β. Based on the assumption of equal dimension between P and L, it is generally considered that:

The value of β greater than 1, i.e. positive allometry, indicates that the growth of urban land is faster than that of the urban population, and the urban population density decreases;

The value of β smaller than 1, i.e. negative allometry, indicates that the growth of urban land is

Table 2. The rank-size analysis table of the city area of Hebei Province.

Year	Rank-size expression	q	R^2	LnA	Area of primate city (km^2)	Theoretical area (km^2)	Theoretical/ actual
2000	$Y = 162.19X^{-0.7541}$	0.754	0.942	5.089	122.21	162.19	1.327
2001	$Y = 166.56X^{-0.7484}$	0.748	0.950	5.115	122.21	166.56	1.363
2002	$Y = 178.32X^{-0.7532}$	0.753	0.950	5.184	152.30	178.32	1.171
2003	$Y = 193.69X^{-0.7544}$	0.763	0.948	5.266	187.38	193.69	1.034
2004	$Y = 218.64X^{-0.7759}$	0.776	0.960	5.387	187.38	218.64	1.167
2005	$Y = 225.08X^{-0.7717}$	0.772	0.958	5.416	196.03	225.08	1.148
2006	$Y = 246.01X^{-0.7739}$	0.774	0.965	5.505	209.11	246.01	1.176
2007	$Y = 260.63X^{-0.7785}$	0.779	0.967	5.563	209.11	260.63	1.246
2008	$Y = 270.96X^{-0.7804}$	0.780	0.969	5.602	213.00	270.96	1.272
2009	$Y = 278.85X^{-0.7749}$	0.775	0.964	5.631	224.00	278.85	1.245
2010	$Y = 286.59X^{-0.7728}$	0.773	0.970	5.658	234.00	286.59	1.225
2011	$Y = 296.65X^{-0.7622}$	0.762	0.966	5.693	234.00	296.65	1.268
2012	$Y = 343.02X^{-0.7901}$	0.790	0.970	5.838	247.00	343.02	1.389

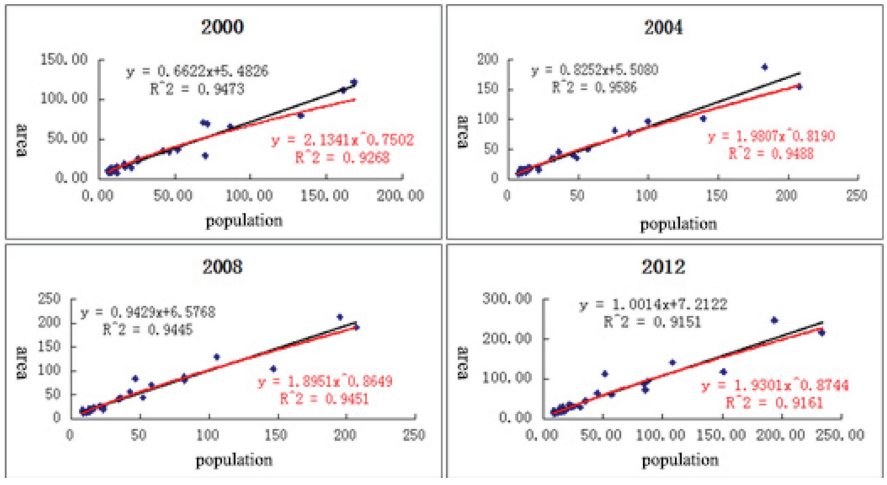

Figure 1. Models of urban land-population allometric growth in Hebei (2000–2012).

Table 3. The table of goodness-of-fit test of allometric growth in prefecture-level cities in Hebei.

Year	Goodness-of-fit	
	Power function	Linear function
2000	0.9268	0.9473
2001	0.9678	0.9634
2002	0.9498	0.9463
2003	0.9281	0.9445
2004	0.9488	0.9586
2005	0.951	0.9563
2006	0.9378	0.9428
2007	0.9474	0.9498
2008	0.9451	0.9445
2009	0.9397	0.939
2010	0.926	0.9266
2011	0.9329	0.9308
2012	0.9161	0.9151

lower than that of the urban population, and the urban population density increases;

If the value of β is 0, it indicates no change in urban population density;

If the value of β is 1, i.e. the same growth rate of the urban population and land, it indicates a linear relationship between their growths.

In the research on allometry, only if the standard value of the scaling exponent is reasonable, and the population and land dimensions reach the maximum balance, will the analysis of relative growth relationship between built-up area and population in the urban system be more reasonable. The scaling exponent used in this paper was first proposed by scholars such as Liu Yan'guang. Its standard value that is applicable to China's situation is 0.85 (Chen & Xu 1999).

Table 3 presents the sign of degradation of allometric relationship from 2000 to 2007. On the one hand, it may be caused by the difference between the statistical range of the urban population and the statistical range of the built-up area. Therefore, from the accurate angle of research on cities, it is necessary to form the basic data on the urban population and land equipotent in the territory. On the other hand, it indicates that an ordered and reasonable urban system has not yet been formed in Hebei Province. Affected by various factors such as resource and location, there is an obvious regional difference in the urban development of the whole province, which is specifically reflected in northern regions such as Zhangjiakou and Chengde and eastern regions such as Cangzhou and Hengshui. Due to factors such as location and landform, the urban development is lower. Since 2008, the allometric feature of the urban system has gradually been significant, and the urban system has gradually become complex and perfect. The reason is that in recent years, Hebei Province has begun to enhance the economic development and urban construction in regions at a lower development speed.

The research on the allometric scaling exponent shows that the development of the urban system from 2000 to 2006 (linear function till 2005) is in a negative allometric phase, i.e. the population growth rate is larger than the land growth rate. At this point, cities longitudinally develop towards a high level and population density shows a rising trend.

Since 2007 (linear function from 2006), the scaling exponent has exceeded the standard value of 0.85. The development of the urban system enters in a positive allometric phase, i.e. the land growth rate is larger than the population growth rate. At this point, cities horizontally develop towards "flattening" and the population density shows a decreasing trend. The reasonable urban development mode is that with the expansion of urban scale, cities should longitudinally develop towards a high level when the area of the urban infrastructure is smaller. However, at present, the development trend of urbanization of the whole province is in the opposite way, so the urban development of Hebei Province does not make intensive use of land (Tang & Zhang 2011).

3.2 *Research on urban land expansion coefficient*

After an allometric analysis of previous data of cities, it is found that the fitting results are not satisfactory. Therefore, the indicator-urban land expansion coefficient is used to analyze the relationship between the population and land at the spatial level. Land expansion coefficient refers to the ratio of urban land growth rate to urban population growth rate in a certain period. Its expression is as follows:

$$K = GR/PR \times 100\%$$

where K is the urban land expansion coefficient; GR is the annual average growth rate of the urban built-up area; and PR is the annual growth rate of the urban population (Lee 1989). Table 4 presents the urban land expansion coefficients from 2000 to 2012.

According to the research on the China Institute of Urban Planning and Design (1989): the reasonable value of China's urban land expansion coefficient is 1.12, i.e. when the urban population increases by 1%, the built-up area increases by about 1.12%. When the value is less than 1.12, it indicates that the urban construction land is small; when the value is greater than 1.12, it indicates that urban construction area is too large. According to the actual situation of Hebei Province, the expansion coefficients are divided into three levels: expansion coefficients greater than 2 belong to Level I, representing that the built-up area expansion is faster than urban population expansion and the land utilization is lower; expansion coefficients between 1 and 2 belong to Level II, which is a relatively coordinated range; expansion coefficients smaller than 1 belong to Level III, representing that the built-up area scale is obviously smaller than the urban population scale and the urban land is small.

Hebei Province has 33 cities (11 prefecture-level cities, 22 county-level cities). Of these, 9 cities are at Level I, with the land expansion coefficient higher than 2, exceeding the relatively coordinated range, indicating that their construction land expansion is fast. And 14 cities are at Level II, indicating that the development of their urban land and population is relatively reasonable. The remaining 9 cities are at Level III, with the land expansion coefficient obviously lower than the reasonable value, indicating

Table 4. The coefficient table of urban land expansion.

City	Expansion coefficient	Population density 2012 (/km^2)	City	Expansion coefficient	Population density 2012 (/km^2)
Chengde	6.159	702	Gaocheng	1.232	1455
Tangshan	5.179	1605	Nangong	1.211	730
Jizhou	4.065	1228	Qinhuangdao	1.203	2626
Baoding	3.468	3879	Huanghua	1.143	953
Handan	3.123	3745	Wuan	1.120	2587
Cangzhou	2.845	3352	Gaobeidian	1.065	4450
Luquan	2.188	1388	Bazhou	0.807	1971
Anguo	2.185	1136	Zunhua	0.798	2538
Renqiu	2.073	5151	Jinzhou	0.702	1153
Hengshui	1.968	1322	Shenzhou	0.657	2044
Dingzhou	1.892	8325	Sanhe	0.620	1196
Zhuozhou	1.845	5002	Hejian	0.589	2507
Shijiazhuang	1.796	8210	Xinle	0.181	1803
Xinji	1.454	1303	Langfang	–1.861	1788
Xingtai	1.360	7818	Shahe	–2.226	2559
Qianan	1.351	1824	Botou		7659
Zhangjiakou	1.323	2307	Province	2.404	2411

that the land growth range is smaller than the population growth range. Data on Langfang, Shahe and Botou are abnormal: data on Langfang and Shahe are negative, and the population growth rate of Botou is 0. A problem is found after the data of the three cities are analyzed, i.e. the urban population data are too high in 2000, which have a big gap with the following data. This is caused by different statistical calibers in different years. According to the spatial analysis chart, 5 of the 11 prefecture-level cities are at Level I, and there is a phenomenon of land waste; 5 cities are at Level II, which are in a relatively coordinated phase. And 22 county-level cities are located in central regions such as Shijiazhuang, Hengshui, Cangzhou and Baoding, 4 of which are at Level I, 9 of which are at Level II, and the other 9 are at Level III. A comparison between the prefecture-level cities and the county-level cities shows that the ratio of prefecture-level cities at Level II to these at Level III is 55%, while the ratio of county-level cities is 81%. Thus, the larger the city is, the faster the built-up area expansion is than urban population expansion, and the more serious the phenomenon of land waste is.

Expansion coefficient cannot express the concept of urban land per capita. To more comprehensively analyze the relationship between the urban population and land, the urban population density indicator data are added for comparison. From Table 4, it can be found that the urban land expansion coefficient of the whole province is 2.404; the population density is 2411 persons/km^2, nearly similar to the national average value of 2378 persons/km^2. Especially, (1) among the 11 cities with expansion coefficients not higher than 1.12, the population density of Gaobeidian City is significantly higher than the provincial average value of 2411 persons/km^2, reaching 4450 persons/km^2; the population density of Huanghua City is significantly lower than the provincial average value, only 953 persons/km^2; (2) Among the 21 cities with an expansion coefficient larger than 1.12, the expansion coefficients of Chengde, Tangshan and Jizhou far exceed 1.12, and the expansion coefficient of Chengde is the largest, reaching 6.159. Moreover, the population densities of the above three cities are significantly low, and the population density of Chengde with the largest expansion coefficient is the lowest in the whole province, only 702 persons/km^2, indicating the irrational use of land to a certain extent. In addition, the population density of Nan'gong City with the urban expansion coefficient being close to a reasonable value is significantly lower, only 730 persons/km^2. However, it can be seen that in most region of Hebei Province, there is a phenomenon of large construction land area and low land utilization. It is related to land economy implemented by local governments in recent years. Driving GDP increase by selling land promotes the excessively rapid growth of construction land.

4 CONCLUSION

This paper uses the rank-size rule to analyze the population and land scale as well as allometry and urban land expansion coefficient to analyze their relationship. Rank-size rule is used to better analyze the scale of population and construction land, but the two parts are separate, so that they cannot intuitively reflect the relationship between population and land. Allometry and urban land expansion coefficient can be used to analyze their growth ratio relationship, and reflect the coordination between built-up area expansion and population growth. The fitting result of allometry through horizontal analysis is not satisfactory, so urban land expansion coefficient is introduced, but they cannot reflect the factor-status of urban population density. Therefore, the indicator-urban population density is used for comparison, so that the status of urban scale development can be analyzed in a more dimensional and comprehensive manner.

REFERENCES

Chen, Y.G. & Liu, J.S. 2001. Allometry Relations of Urban System and Rank-Size Rule—Revision and Development of Steindl Model. *Scientia Geographica Sinica* 21(5): 412–416.

Chen, Y.G. & Xu, Q.H. 1999. Fractal Geometric Model of Population-Area Allometry of Regional Cities—Revision and Development of Nordbeck-Dutton Theory of Allometry of Urban System. *Journal of Xinyang Normal University (Natural Science)* 12(2): 198–203.

Lee, Y. 1989. An allometric analysis of the US urban system;1960–1980. *Environment and Planning A* 21(4): 463–476.

Liu, J.S. & Chen Y.G. 2005. Discussion on Population-Area Allometric Features of Regional Cities. *Scientia Geographica Sinica* 25(2): 135–141.

Tang, Y. & Zhang, R.H, 2011. Primary Exploration of Taiwan Urban Scale Distribution-Analysis Based on Rank-Size Rule. *Journal of Jimei University* 14(2): 59–64.

Civil Engineering and Urban Planning IV – Liu et al. (Eds)
© 2016 Taylor & Francis Group, London, ISBN 978-1-138-02903-3

Ecological rebuilding planning strategy of rural vacant land in South Jiangsu

Zhen-Xing Qin & Yao-Zhi Huang
Suzhou University of Science and Technology, Suzhou, Jiangsu, China

ABSTRACT: As an important economic development hinterland in Yangtze River Delta, South Jiangsu's land utilization is obviously very important. But during the process of new type of urbanizations, hollow villages, demolitions, and merging of villages have led to large amounts of rural vacant lands. It has been very urgent for us to ecologically rebuild these vacant lands and realize intensive sustainable development in rural planning. Using the research methods of investigation and observation, the paper analyzes and studies the issue of rural vacant land existing in rural planning of South Jiangsu and proposes corresponding planning strategies of ecological rebuilding.

1 INTRODUCTION

China's economy developed rapidly since the beginning of reforms that opened up the market, which unavoidably leads to urban and rural segregation and highlighted dual structures. With the economic development influenced by the urban-rural integration policy, China's rural construction has developed continuously but has many problems. Taking Suzhou as an example in the three concentrate and three replacement strategies proposed in urban-rural integration, the space structure is further adjusted and 5515 villages are planned to be merged, which will save a lot of unincorporated villages from the danger of disappearing. Meanwhile, because of economic transformation and lack of planning, large amounts of internal rural housing land, construction land for industrial and mining enterprises, and disengaged and deserted lands are left unused during the process of village movement and merging. Lands are being seriously wasted.

In the background of constructing an ecological conservation-minded society and great reduction of arable lands at present, saving and appropriately using lands is extremely urgent. Rebuilding and utilizing rural vacant lands has attracted great attention. But current researches mainly focus on conversions of rural vacant lands into industrial lands, mainly by recovering landscape to transform these lands into parks and such. But at present there is lack of deep study about how to ecologically rebuild these vacant lands in rural planning. Based on the reconfiguration plan of rural-urban systems in rural areas, the article regards rural vacant lands as points and renovates these lands by adjusting measures to different types of vacant lands, to achieve the greatest benefit in reusing the vacant lands at the lowest cost.

2 SIGNIFICANCE OF REUSING RURAL VACANT LANDS

2.1 *Requirement by national policy on rural development*

The National New-Type Urbanization Planning (2014~2020) suggests strengthening the balance of urban and rural development, enhancing the vitality of rural development, shortening the gap between urban and rural places, and promoting the coordinated growth of urbanization and new rural construction. Scientific planning is needed to create townships and villages, build a beautiful countryside with different characteristics, and, while respecting villagers' sentiments, scientifically guide the construction of rural housing and settlements to make the villagers' lives more productive and convenient, enhance the function of natural villages and maintain a scenic countryside, promote regional culture and ecologicalization according to the requirements of developing central village, and preserve special village and renovate vacant villages (Central Government Portal 2014). So reusing rural vacant lands is not only the development requirement to economically and intensively utilize resources like land, water, and energy; promote overall utilization of resources; control total consumption; and improve the efficiency not only during national new-type urbanization construction, but also the foundation for developing ecological construction of green cities.

2.2 *Demands for economic and social development in rural areas*

Planning and constructing rural areas, rapidly developing agricultural economy and improving the orderly life of peasants at present are the current urgent demands of each rural area and are the basic solutions for various problems of rural areas (Du 2013). It is indicated by transforming the South Jiangsu mode to a new one that satisfies the higher demands made for economic and social development of rural areas. The existing vacant lands are obviously an extremely waste. So ecologically rebuilding the vacant lands can not only effectively improve the rural image, but benefit the development of the overall economy and society.

2.3 *Purchases for ecological construction in rural planning*

With the continuous strengthening of rural areas required by national policy, more and more attention is being paid to rural planning and construction. The national standard *Beautiful Village Construction Guidelines* took effect on June 1, 2015. The standard puts forward ideas to construct the ecological environment of rural areas; regulate the environmental quality requirements of water, land, air, etc.; prevent and cure agricultural, industrial, and domestic pollution; protect the ecosystem of forests, vegetation, watercourses, etc.; and guide the environmental renovation like maintenance of village appearance, environmental greening, lavatory reconstruction, and develop 11 items of quantitative indexes for ecological environment. South Jiang is the leader in constructing beautiful villages. Its requirements on reusing rural vacant lands and on ecological reconstruction are higher to enhance the rural image and landscape environment.

3 CURRENT ISSUE OF RURAL VACANT LANDS

With the rapid development of China's urbanization, a large rural population flocks to cities; this leads to rural hollowness, abandonment of villagers' real estates, factories, farms, etc. The proportion of vacant rural lands increases continuously, the layout of rural lands is seriously messy, and these lands are used extensively, which greatly influences village appearance, causes environmental pollution, and waste of land resources. The article combines the rural construction characteristics of South Jiangsu, concludes with four types of causes of vacant rural lands, and starts with the types of vacant rural lands to point out what does matter really from each type.

3.1 *Problem of vacant rural housing lands*

During the process of constructing beautiful villages in South Jiangsu, vacant housing lands are generated as a result of movement and merger of villages and plan adjustment, rural population emigration, land use rights, and the incoordination between assets and rural resident relocation (Zhang et al. 2010). These lands generally occupy small areas, their layouts are relatively scattered, and they are differently damaged and generate building wastes. And the soil geology also greatly changes due to construction. In general, these housing lands aren't used or fully used, which generates large amounts of short-term or medium-term vacant lands and causes a huge waste of land resource; on the other hand, the environment surrounding deserted housing land is generally bad, which causes a rather bad effect on the improvement of human settlement and rural civilization construction and leads to disordered land management (Luo 2009).

3.2 *Problem of industrial vacant lands*

The so-called industrial vacant land means the lands which seem useless are ignored by human beings because they are damaged due to industrial production or other reasons but can be redeveloped by certain treatments (Zhang 2006). During the mode transformation of South Jiangsu, the industrial structure adjustment of village construction or the promotion of ecological construction ideas may close or move some factories and township enterprises, which form industrial vacant lands. These lands occupy different areas; some are large, some scattered, and most leave far away from villages. Some factories and township enterprises generate pollutants. All these not only cause serious waste of land resource, but sharpen the environmental pollution issue, lead to degeneration of ecological system, and, to some degree, affect the landscape image shaping of ecological village.

3.3 *Problem of disengaged and deserted lands*

For the current situation of villages, unavoidably there will be small amounts of vacant land in internal construction lands of villages. These vacant lands include space along street, construction dead space, and unused village land. They are generally deserted or overgrown with weeds, or used for stocking sundries and rubbish, which will breed mosquitoes, give out bad odors, worsen hygienic conditions, and cause land pollution and waste which have a seriously bad effect on the village environment and the whole landscape style.

4 ECOLOGICAL RECONSTRUCTION STRAREGY FOR VACANT LANDS IN SOUTH JIANGSU

We need to take full advantage of the goods ecological environment of South Jiangsu and comprehensively plan the coordinated sustainable development of rural economy, society, and nature as a whole to form a complete development mode for overall efficiency of the economic-social-natural compound ecosystem and construct a healthy and harmonious rural ecological system (Ma 2011) with ecological construction as the basis when transforming and reusing the rural vacant lands in South Jiangsu area.

4.1 *Reconditioning of vacant housing lands*

Deserted housing land occupies a relatively great proportion in rural vacant land, so sufficient attention should be paid to it in ecological construction. Generally new village construction and waste land reclamation are adopted to transform and reuse the deserted housing land as residential and agricultural land. In rural construction, generally there are three types of deserted housing lands as follows:

- Reusing vacant housing lands far away from planned residential districts and lands with small scope and scattered distribution for agriculture. Develop ecological agriculture based on ecologically agricultural mode of modern villages to enhance land utilization efficiency and increase the agricultural area. But lands with pollution or relatively bad geology or vacant housing with good construction position or stable structure can be replaced as public supporting houses, like chess room for villagers, recreation room for children, etc., by external wall rebuilding and internal space transformation.
- Reusing vacant housing land of a certain scale with convenient transportation and relatively good environment as an urban-rural integrated community to develop rural leisure industry depending on good ecological environment in South Jiangsu. Reuse the vacant housing land to develop rural tourism like Agricola, rural eco-sightseeing agriculture, agricultural experience, etc., which brings good economic benefit while implementing ecological construction on deserted housing land (Xie 2011).
- Reusing the scattered small-area vacant housing land which is surrounding or inside the planned residential district by rebuilding it as a public cultural service place of ecological village or small green parks or landscape nodes along streets because of its close connection to the residential area or develop a waterfront landscape by combination with a water network for villages to carry out cultural activities and recreation so as to enrich their living standard and improve environment quality.

4.2 *Reconstruction of vacant industrial lands*

Factors affecting the ecological reconstruction and reuse of urban vacant industrial lands mainly include: pollution level, geographic position, and adjustment of production and industrial structures (Guo 2007). Industrial vacant lands should be far away from villages and are of various types. Vacant lands with different characteristics should be reconstructed and reused with different methods to maximize the value of their ecological construction.

- Reusing industrial vacant land without pollution. Such vacant lands have no or little pollution, which can be ecologically repaired and transformed. For those near the residential area, they can be used as industrial land without pollution continuously according to the development demand of rural production and industrial structures. This can not only make full use of original sources for reuse, but also is convenient for residents' work and life, drives economic development, and realizes the high unity between ecology and benefit; those lands far away from ecological villages or not appropriate as industrial land according to industrial structure planning can be rebuilt as agricultural land by combing local agricultural characteristics of South Jiangsu after ecological restoration.
- Reusing pollutant industrial vacant land. Such industry produces a certain amount of pollution, which may pollute the soil texture, vegetation to a certain degree. More attention should be paid to ecological restoration on it during reusing. It can be transformed into parks or land for tourism services during ecological restoration according to the original facilities and resources of the vacant land. For example, the former address of Zhongshan Qijiang Park is Yuezhong Shipyard. The landscape planning and design of the park was completed by Professor Yu Kongjian of Pecking University, which opens the door to reusing industrial vacant land in China. It organizes and constructs the park landscape system from multi-dimensional perspectives like protecting and continuing industrial culture, reusing industrial facilities, re-creating embellishment, ecological protection and reconstruction, etc., which realizes the goal of maximizing ecology (Zu 2014).

4.3 *Reshaping of vacant and deserted lands*

Generally, such lands lay out scattered and occupy less land. For the vacant lands along street, we have

make full use of the vacant deserted land based on the street space to constitute network street space during ecological restoring, which can meet the demand for driving and developing fire-fighting access or establish waterfront landscapes along water networks; for construction of dead space or vacant land inside the village, we have to adjust measures to local conditions to establish green spaces for "fruit tree and vegetable garden"; for water pools which can't be connected with water networks, we can dig them into lily ponds as rain purifying pools and space for viewing lotuses; in addition, the vacant land can also be flattened. We need to add leisure facilities, encourage villages to communicate with each other to get along well with each and create a happy and peaceful village environment.

5 CONCLUSION

Rural ecological construction in China's South Jiangsu is still continuously developing and perfecting itself at present and faces many problems that need to be solved urgently. We have to take ecological construction as the basis to adjusting measures to local conditions of internal rural housing land, industrial vacant land, and vacant and deserted land to realize scientific and ecological reconstruction of vacant land and constitute a healthy and harmonious rural ecological system when transforming and reusing rural vacant lands. With more attention paid to healthy and ecological lifestyles by human beings, the ecological construction has gradually developed in countries and cities. And the ecological reconstruction of rural vacant lands will be a significant issue to be considered particularly during the ecological village construction in future.

ACKNOWLEDGMENT

This work was financially supported by scientific research innovation projects for post graduates of regular institutions of higher learning in Jiangsu province, 2015 with project number: KYLX15-1304.

REFERENCES

Central Government Portal. 2014. National New Urbanization Plan (2014~2020). *www.gov.cn*.

Du, P. 2013. *Social Policy Based in New Rural Construction Planning and Economic Development Research*. Wuhan: Central China Normal University.

Guo, S.F. 2007. *A Preliminary Study on Method of City Industrial Wasteland's Ecological Planning Renovation and Renewal*. Tianjin. Tianjin University.

Luo, L.T. 2009. Thinking on the reclamation of abandoned house land in old village. *Shaanxi Journal of Agricultural Sciences* (5): 173–175.

Ma, P. 2011. The type and planning regulation of Idle land in the village. *Jilin Agriculture* (11): 51–55.

Xie, N. 2011. *Study on Rural Idle Residential Land Utilizing on Building a Resource-saving and Enviromnent–friendly Society*. Changsha: Hunan Agricultural University.

Zhang, J.H. 2006. *An Explore on the Reuse of Beijing Urban Industry Abundant Lands.* Beijing: Beijing University of Civil Engineering and Architecture.

Zhang, L.F., Pu L.J. & Tu X.S. 2010. Analysison the connotation, classification and formation cause of the wastel and. *Resources and Environment in the Yangtze Basin* (19): 180–185.

Zu, Y.J. 2014. *Research on Transformation and Utilization Methods of Industrial Wasteland*. Beijing: Chinese Academy of Forestry.

Civil Engineering and Urban Planning IV – Liu et al. (Eds)
© 2016 Taylor & Francis Group, London, ISBN 978-1-138-02903-3

Introduction and forecast of creative industry parks of industrial heritage culture in China

Zhi Qiao, Hao Zhang & Yan Wei
Xi'an University of Technology, Xi'an, Shaanxi, China

ABSTRACT: Post industrial revolution, which was under the background of economic globalization and establishment of new China, the industry of China gained rapid development, which gave significant opportunities for the growth of creative industry parks of industrial heritage culture (such as "798" in Beijing). In the recent years, with the urgency of economical restructure, the re-utility of industrial heritage has become a hot issue, thus making the development of creative industry parks a must in China. However, the feasibility research of the creative industry parks draws little attention. This paper, with the purpose of providing reference to the themes selection, space plan, and market operation of the parks, makes researches on the development history, value trend, construction strategy, existing problems, and development direction of the parks.

1 CURRENT SITUATION OF CREATIVE INDUSTRY PARK OF INDUSTRIAL HERITAGE CULTURE

Since mid-1990s, the creative industry park of the industrial heritage culture has been developing gradually in the context of corporate reengineering, such as 798 art area in Beijing. The essence of cultural industries is a combination of culture and economy to meet the cultural consumption of society. Cultural industries can be analyzed as three concentric circles: the inner circle as the "culture," the middle layer for the "creativity," the outer layer for the "market." "Creativity" is a medium between "culture" and "market," aiming at producing material culture for consumption. It requires the following production conditions: funds, environment (park), team (talents), technology, and so on. According to the standards of Classification of Culture and Related Industries (2012), it is a category of cultural creativity and design services that deepens the understanding of cultural industries. As the unique historical remains, industrial heritage records great exploration which the Communist Party of China leads the people to practice socialist industrialization and embodies the Chinese people's entrepreneurial spirits of self-reliance, hard work, deserving, protecting, and goes on. Therefore, industrial heritage has important historical values.

On the premise of sustainable development, this paper explores the influence of creative industry park of industrial heritage culture from multiple perspectives and dimensions through its in-depth research value so that, we position the theme of parks and give them new meanings. This paper also has advance explorations on plans and development of parks from national purposes of socialist core values, social purposes, and personal purposes and aims at achieving effective combination of protection and utilization of industrial heritage and urban vitality and revival.

The value of creative industry park of industrial heritage culture lies in providing beneficial and necessary conditions for selecting geo-cultural environment for cultural production, attracting talents, raising funds, updating technology, materials, and tools. The use of the city remains for the production of selected geo-cultural environment, talent attraction, to raise funds to update technology, materials and tools and constructive strategy of China's "Five in One." That requires researching and studying of the urban origins and histories, current situation and development trend, environmental ecology, heritage protection, and so on. Then, we can analyze deeply the relationship between urban industrial heritage and cultural and creative industries so that we can provide theoretical support and near plan for construction of creative industry park of industrial heritage culture necessarily and feasibly.

Foreign researches on cultural and creative industry park mainly concentrate on three respects: influencing elements, choice of location, and regional functions. In side of theories, Landry put forward the theory of urban creativity in 2001. Hutton thought that most creative industry parks were grouped in inner place of big cities and the edges of CBD and preferred architectures which had a rich culture. Terry Flew demonstrated

mutual promotion mechanism between that urban renewal and cultural and creative industries in 2010. David C. Harvey elaborates a planning method of cultural and creative industrial park of regional culture. Results of domestic researches mainly involve factors affecting formation and development of cultural and creative industries parks, location selection and its functions on industrial restructuring, and economic development. Combined with the cultural and creative industry cluster theory and the physical properties of the stacking space, cultural and creative industry park is divided into urban industrial heritage transformation, traditional, historical, and cultural street change, development of tourist attractions, construction of the new buildings, and reliance on universities. Professor Niu (2010) proposed evaluation index system in accumulation areas. Feng (2009) classified the areas according to the economic spatial patterns. Overall, a theoretical system with Chinese characteristics in line with national conditions is forming. Researches on cultural and creative industrial park pay attention to both theory and practice and become gradually mature.

From the theoretical aspect, there are many articles that showed up respectively, such as the earliest article named "the Reconstruction of the Brooklyn Bridge," written by American scholar Steinman; the Nizhny Tagil Charter, approved by the International Protection of Industrial Heritage Committee in 2003; the Venice Charter, sited through by the International Council of Monuments and Site in 1964; the Bala Charter, an Australian charter on architectural heritage protection in 1979. Domestically, there are files like "Wuxi Proposal" on industrial heritage protection in 2006, and on strengthening the Protection of Industrial Heritage issued by the State Administration of Cultural Heritage in May, 2006.

As for the scholars, Mr. Ruan Yisan came up with the ecology theory about the protection of urban history and environment; Yu Kongjian, Shan Jixiang, Tian Yan, and others made a study on the general-investigation mechanism of industry heritages; Ye Yanbing and Liu Xi made a classification of old industrial buildings from their spatial characters; Han Fuwen, Li Li, and Liu Wei, along with other scholars, did a research on the evaluation mechanism of industry heritages; Weng Linmin and Li Jianhua promoted to classify the level of protection; Xie Xuefang and Huang Changyong introduced five protection models of International industry heritages (Shan 2006, Yu et al. 2006).

In practice, according to the definition of the Nizhny Tagil Charter, industrial heritage refers to the remains of the industrial civilization. They possess historical, scientific, and technological, social, architectural, or scientific value. The redevelopment of urban industrial heritage is to basically transform the building and environment in old urban industrial heritage area, thus realizing the aim of functional space transformation. In this way, the transformed space not only conforms to the demands of the development of creative industry gathering area, but also protects the industrial historical building which possessed cultural value. At present, both domestic and foreign research of cultural and creative industry park in industrial heritage type are mainly focus on the classification management, utilization, and protection, the museum exhibition, tourism development, office, public leisure space, etc. Such examples like the protection and renovation of the Ruhr industrial area in Germany, SOHO art district in the United States, "798" in Beijing (see Fig. 1), Shanghai "M50" in Shanghai, "Redtory" in Guangzhou, "Textile City Art District" in Xi'an (see Fig. 2), and "Dahua 1935" etc. are all can be roughly divided into spontaneous development mode or centralized development mode.

Based on the present situation of insufficient prospective planning in domesticate park and the trend that designs walk almost the same way as the plan, viewed under the strategic background of construction with "Five-in-One Principle," the insufficiency

Figure 1. Beijing DAD—Dashanzi art district.

Figure 2. Xi'an Banpo international art district.

of existing research was showed in: the lack of identifying the value connotation of industrial heritage traits of the old industrial; the lack of multi-tiered inductive research on industrial heritage protection; the lack of concerns on campus environment and vitality, while only the protection of "building shell" was highlighted; the lack of exploration on sustainable development between industrial heritage and cultural creative industry; the lack of quantitative research and thematic study on its current environment; the lack of oriented study in guiding space function partition and designing strategy of industrial heritage cultural creative industry park.

Literature shows that research in China is mainly limited to the case study, thus the influence factors, dynamic mechanism, and growth pattern of the formation and development in cultural creative industrial area has formed a preliminary study. The research mainly focuses on the theory of cluster, self-organization, and symbiosis and observes the formed mechanism of cultural creative industry area in both the external macro factors and internal microscopic dynamics and elements (Qiao 2010). However, domestic research on studying and analyzing the related value, influence, theme, and non-material elements of the cultural and creative industry park in industrial heritage type is little, let alone the literature studied based on the strategic targets and the socialist core values of "Five Developments" proposed on the 18th CPC National Congress. Under the strategic guidelines of "Five Developments" proposed on the 18th CPC National Congress and based on the Athens Charter, Venice Charter, Nairobi, Washington Charter, Machu Picchu Charter, and other research results, the cultural and creative industry park was fully developed. Therefore, it possessed huge realistic significance and practical value on studying the positive effect of industrial heritage protection and renovation, searching its right direction, and balancing with the demand of urban renewal and expansion.

2 DESIGNING DIMENSIONS OF CREATIVE INDUSTRY PARK OF INDUSTRIAL HERITAGE CULTURE

Adhering to the instruction of socialist core values and the trend of eco-friendly construction, the status analysis of creative industry park of industrial heritage culture discusses the sustainable development of aforementioned parks and seeks theoretical support and practical purposes to further its value impact analysis. The analysis also points out the constructional significance and theme tuning of cultural and creative industrial parks utilizing heritage and deplores their values to a country, society, and individual.

First it comes to the re-utilization value of industrial heritage. Starting from the angle of urban development that includes history and culture, industrial development, and physical transformation, the analysis is founded on the relative methods of gradient theory and mainly makes stratification and induction of heritage value based on historical information and physical formation (see Fig. 3). Among the three stratification layers that involve protection layer (elements requiring protection), renewable layer (elements that can be transformed), and deletion layer (elements that should be deleted), renewable layer is the priority that features such factors as district renewal, image updating, physical and structural renewal, function updating, and regulations refreshment. Site marks are screened and induced to reveal their prime motive value and to achieve inheritance and promotion of cultural heritage and its forms.

Next is cultural creativity value. Materials are finite but creativity is not, which makes it the fundamental drive of cultural industry and guarantee of sustainable development. To achieve sustainable development of creative industry park of industrial heritage culture, investigation and induction must be conducted on presentation of creative design, creativity serialization, extensibility and added-value for the purpose of putting forward R&D model for fine cultural creativity project, and analyzing the sustainability of its creativity vitality.

In the end, as urban development is a dynamic historical process of constant changes, the transformation from appearance-empathized to space-empathized should be achieved by a space combination of a display zone of heritage protection, construction control area and cultural creativity industrial garden. Through deploring a new model that combines fashion and consumption, creative designing and art zone, a way of thinking and procedures of how industrial parks

Figure 3. Xi'an Dahua—1935.

Figure 4. Xi'an Banpo international art district.

can dive industrial heritage to positive sustainable development can be extracted from sustainability of designing technique and marketing and creativity. Hence, the space reorganization of the park can be fully realized (see Fig. 4).

The 18th National Congress of Communist Party of China juxtaposes ecological development with ecological, political, cultural, and social development to build socialist of Chinese characteristics in the aforementioned manner, or Five-in-One. Regarding the current situation in China where relevant parks have a convergence tendency, this paper sets Five-in-One as construction objection, conducts investigation with professional disciplinary research methods from perspective of heritage protection, ecological design, cultural carrier, creativity value, and marketing environment while taking sustainability and value impact as reference. The research on creative industry park of industrial heritage culture requires to pinpoint inherent features of industrial heritage, establish the meaning of park construction and development, discuss construction value, theme tuning and planning, and layout of the park, and provides an insightful investigation to the future development of the park by harnessing micro-advantages into macro-positioning.

3 ANALYSIS DIMENSIONS OF CREATIVE INDUSTRY PARK OF INDUSTRIAL HERITAGE CULTURE

3.1 *A clear objective—to deplore the sustainable development focus of creative industry park of industrial heritage culture*

Pay emphasis on the stratification of industrial heritage and the spread of urban culture. To balance sustainable development of the parks from designing technique sustainability, operation sustainability, and creativity sustainability is on the basis of gradient theory with stratification and induction as standpoints.

3.2 *Method updating—to improve the research method of creative industry park of industrial heritage culture*

Intensify research and investigation through comparisons, stratification analysis, quantitative analysis, value impact synthetic analysis of the parks, and designing strategies of spatial function distribution in order to find the planned theme of parks' development.

3.3 *Theoretical exploration—to resolve the value cognition issue of the value of creative industry park of industrial heritage culture in the modern society*

Globalization and a major country position require China's economy and society to fit the international economic, political, and technological development. China has to constantly adjust its development strategies and economic structure, and industrial transformation has become normal. In the transformation, creative industry park of industrial heritage culture cost little and is effective. Its transformation is smooth and resource-conservative as well as environmentally-friendly, which supplies it a special value under the construction strategies and core socialist value.

ACKNOWLEDGMENT

This paper is supported by special scientific research project under Shaanxi Provincial Education Department (Humanities and Social Sciences Project): The Study of the Homogeneous Construction of Culture and Creativity Industrial Park Featured by Industrial Heritage; Humanity and Social Science Youth Foundation of Ministry of Education of China (13YJC760088). We would like to thank them all for their support.

REFERENCES

Feng, G.Y. 2009. On the internationalization strategy transformation of the cultural and creative industry in China. *Contemporary Economics* 9: 78–79.

Niu, W.L. 2010. Industrial agglomeration and cultural industry park construction. *China Higher Education* 21: 29–31.

Qiao, Z. 2010. The art design of the park of the park in Qujiang. *Journal of Northwest University Philosophy and Social Sciences Edition* 6.

Shan, J.X. 2006. Attention to new cultural heritage—The protection of industrial heritage. *China Cultural Heritage* 4: 10–45.

Yu, K.J., et al. 2006. Preliminary exploration of Chinese industrial heritage. *Architectural Journal* 8: 12–15.

Civil Engineering and Urban Planning IV – Liu et al. (Eds)
© 2016 Taylor & Francis Group, London, ISBN 978-1-138-02903-3

Study on planning and construction standards of facilities for the aging population in Chinese urban residential areas in a deep aging society

Xiao Wang, Zhi-Guo Liu & Yan-Lin Zhu
School of Civil Engineering, Nanjing Tech University, Nanjing, Jiangsu, China

ABSTRACT: There is a huge increase in the number of aging population that requires a new standard for the social service and public facilities for the aged in Chinese urban residential areas. Based on the analysis of the problems and the summary of experience in the exploration on the existing planning and construction standards for aging population, this research pays attention to indicators like category, classification, layout of the facilities for aging population in Chinese urban residential areas, and put forward a new idea of the standard, which conforms to the requirement of the development for the aging population.

1 INTRODUCTION

The planning of public facilities is one of the most important content in planning and construction standards for urban residential areas (Yang 2013). As the level of aging population is aggravating (Mu 2011), it is becoming an important issue in the urban planning. In addition, that the traditional family structure is getting smaller and the aged people prefer different and specific service, the imbalance of social and economic development and the difference in population age structure are also the causes of higher level requirement of service facilities for the aging population in urban residential areas.

2 RESEARCH ON RECENT PLANNING AND CONSTRUCTION STANDARDS OF FACILITIES FOR AGING POPULATION IN CHINA

In order to reduce the stress of the increasing aging population, Chinese government has put forward a series of planning and construction standards of facilities since China has stepped into the aging society in October 1999, which was beyond the expectation. For specific national regulations and standards, please see Table 1.

The existing national standards play a guiding role in the construction of facilities for aging population, but the guiding function in the pattern for the aged is not that strong. The problems concentrate on the lack of overall planning between the old and new city areas, and the correspondence between the planning and the pattern is not that clear either. Some indicators are too vague to achieve. Contradiction between supply and demand of facilities for the aged in urban residential areas still exists. The configuration of facilities is too simple and crude to meet the requirement of the aging people.

3 THE CLASSIFICATION SYSTEM OF FACILITIES FOR AGING POPULATION IN URBAN RESIDENTIAL AREAS

3.1 *The existing classification system of regulation and standards*

Most of the existing standards were put forward 10 years ago; out of which some of them were set up in the last century, which cannot meet up with the endowment mode nowadays. The classification of the endowment facilities differs in different standards, which is very incomplete and inconsistent to guide the construction planning facilities for the aging population in urban residential areas. We need a new series of standards as guidance.

3.2 *The classification of facilities for the aging population in residential areas*

According to the requirements of the city and the experience in other countries, we offer a suggestion to divide the facilities into 4 types including Daytime Care and Service Centre, Full-time Care and Service Centre, Rehabilitation Service Centre, and Activity and Learning Centre.

Table 1. National regulation and standards of facilities construction for aging population.

Name of the standards	Number of the standards	Characteristics of the standards	Shortage of the standards
Planning and design standards for urban residential areas	GB50180-93 (2002)	Dividing residential areas into residential zone, residential quarter and housing cluster	Did not pay enough attention to the new type of construction planning for aging population in residential areas
Planning regulations for urban public facilities	GB50442-2008	Classifying facilities for the elderly into social welfare facilities, putting forward a standard for the land per person	Did not set a specific category for facility of aging population, low applicability
Planning regulations for urban elderly facilities	GB50437-2007	Dividing facilities for the aging population into 7 categories, according to city level, district level, residential zone level, residential quarter level and housing cluster level	Rarely used by the government
Design specification for endowment facilities construction	GB50867-2013	Stipulating the object of the service, content of the construction, scale of the classification and design of the construction	Laying particular emphasis on construction design
Design specification of architectural for the elderly	JGJ122-99	Appropriate for new constructions, expansion constructions and rebuilding constructions for the elderly (including residential buildings and public facilities)	Put forward in last century and not suitable for the facilities for the elderly nowadays

4 THE STAGING HIERARCHY OF FACILITIES FOR THE AGING POPULATION IN RESIDENTIAL AREAS

4.1 *The existing staging hierarchy system of regulation and standards*

Chinese existing staging hierarchy system of regulation and standards for facilities for the aged in urban residential areas is usually based on two elements, the influenced number of people and the scope of administrative jurisdiction. In Planning and Design Standards for Urban Residential Areas, the planning of the endowment facilities in residential areas is divided into residential zone, residential quarter, and housing cluster. In Planning Regulations for Urban Elderly Facilities, it's divided into residential district, residential quarter.

4.2 *Practice of classification of facilities for the aging population in urban residential areas*

Most standards of public facilities in the residential areas of China are based on the local population structure, terrain, and traditional customs for the elderly. The development degree of economy is also an affecting factor in setting up a grading standard of facilities for the aging population with geographical characteristics (Jiang 2005). For instance, Shanghai government divides residential areas into residential zones, residential quarters and streets. Nanjing divides it into residential communities and grassroots communities. In Guangzhou, it is divided into district planning, residential zones, residential quarters, and clusters.

4.3 *The service system classification of facilities for the aging population in urban residential areas*

The planning and construction standards system of facilities for the aging population in urban residential areas must reveal all the details when formulating. Advancement and foresight must be involved in the standards. Based on the existing standards and the analysis on the planning layout of specific cities, we would like to suggest dividing urban residential areas into streets, community residential committees and construction projects; so that the city can supply service for the aged in organize.

5 IMPORTANT ELEMENTS OF FACILITIES FOR THE AGING POPULATION IN URBAN RESIDENTIAL AREAS

5.1 *Considering the absolute number of aging population and its distribution characteristic*

The type, quantity, and scale of facilities for the aged are determined by the number, increasing

Table 2. Settings of classification of facilities for the aging population in urban residential areas.

Types of the facilities	Staging hierarchy of facilities			How to set
	Street (village, town and residential areas)	Community residential committees (also called residential quarters)	Construction projects (also called dwelling house projects)	
Daytime Care and Centre	Required	Suitable	–	Independent or combine with others
Daytime Service Centre	Required	Required	Suitable	Combine with Daytime Care Centre
Rehabilitation Service Centre	Suitable	Suitable	–	Combine with hospitals in committees, villages and towns
Activity and Learning Centre	Required	Suitable	Suitable	Combine with Daytime Care and Service Centre
Full-time Care and Service Centre	Required	–	–	Set nursing home if required

trend, and the level of the aging population. The layout and location of the facilities should be suitable with the distribution of the aging population, economic social characteristic, and the spatial development trend in the first time. It suggests setting the facilities in relative concentration areas of the aged.

5.2 *Considering suitable location condition and dwelling environment*

Facilities for the aging population have worked for the aged. Since their physiological function is getting weaker and weaker, we need to set the facilities depending on their perspective of psychology and physiology. A flat land with beautiful sunshine, medical treatment, public greenbelt and without pollution and construction site will be a suitable location.

5.3 *Considering convenience of transportation and condition of infrastructure*

Since the physiological function of the elderly are getting weaker and their reaction and stain capacity are degenerating, when we plan the facilities, the convenience of transportation must be considered. It should be to set nearby the bus station but not on the city expressway and main streets.

5.4 *Considering combination of public facilities in residential areas*

Facilities for the aged belong to quasi-public goods, so the service for the aged supplied by the government and the society is part of public service. Lots of facilities are required to offer impeccable and professional service for the aged. It has encouraged combining the facilities with the infrastructure in residential areas so that, we can take full advantage of public resources to reduce repeated construction and waste.

5.5 *Considering different arrangement between the new urban areas and the old*

Density of distribution and trend of variation of the aging population in new and old city areas should be considered by planning and construction department, so that pointed requirement can be met. Planning and construction department and managers of old city areas should survey and clear up the resources and facilities in ordinary to recombine them into facilities for the aged. As the land in new city areas is out of requirement and the proportion of the aging population is small, it is compulsory required that the new project should involve facilities for the aged, and it must be planned, designed, build, and put into service in the same time (Fei 2013).

6 SUMMARY

A new concept of standard for the social service and public facilities for the aging population in Chinese urban residential areas is raised in this article. We have made some promotion in the existing standards. Before, we step into deep aging society; we wish this research can contribute a little to help the Chinese government in reducing the stress of aging population.

REFERENCES

Fei, Y. 2013. Study on supply for public facilities of residential areas in Guangzhou. *College Journal of South China University of Technology* 5: 45–47.

Jiang, L.X. 2005. New development mode of Chinese urban residential areas. *College Journal of Nanjing Tech University* 1: 47–50.

Mu, G.Z. & Zhang, T. 2011. Development trend and strategy reply of theaging population in China. *College Journal of Central China Normal University* 5: 29–36.

Yang, G.X. & Miao, T.Q. 2013. Study on the adjustment of the planning of public facilities in urban residential areas. *Urban Planning* 10: 71–76.

Civil Engineering and Urban Planning IV – Liu et al. (Eds)
© 2016 Taylor & Francis Group, London, ISBN 978-1-138-02903-3

Application of a complex ecosystem theory in intensive planning of public facilities in residential areas

Xiao Wang, Yan-Lin Zhu & Shen-Yuan Gao
School of Civil Engineering, Nanjing Tech University, Nanjing, Jiangsu, China

ABSTRACT: Based on the complex ecosystem theory, this article points out a concept about the intensive planning of public facilities in residential areas. We should obey the three rules of society, nature, and economy that will attach great importance to people, hold the flow of the resources, and balance the social management. This way we will be able to achieve the situation of stable residential system of public facility, which can make the city complex ecosystem self-organized.

1 INTRODUCTION

As the basic component of urban structure, residential areas play an important role in achieving the city function (Giannakodakis 1994). That is why its construction and development play an important role in urban development. The traditional mode of urbanization has brought a series of problems like draining resources, ecological environmental deterioration, and increase of social contradictions. So in order to deal with these problems and to build an appropriate ecological resident area this has become a new focus in this study during the period of new-type urbanization. In March 2014, Chinese government put forward a provision which underlined high density and function mixed and transit oriented mode. We have boldly proposed the self-organization and complex ecosystem theory in this article to realize the goal.

2 PROBLEMS IN TRADITIONAL PLANNING OF PUBLIC FACILITIES IN RESIDENTIAL AREAS

Complex ecosystem theory points out that human society is a special artificial ecosystem on the basis of human transform and natural environment, which is consisted of natural subsystem, economic subsystem, and social subsystem (Chin-Hsien & Hsueh-Sheng 2009). Among these three subsystems, intensive material flow, energy flow, and information flow interact with each other, in which human decision and management plays a decisive function. And the contradiction produced in the process of development can be roughly summed up as the contradictions between the three subsystems.

2.1 *The contradiction between the social subsystem and natural subsystem*

The development of human society is a process of constantly using various resources, creating material, and spiritual wealth (Haq 1997). But artificial urban system cannot achieve self-sufficiency and it must rely on the supply of natural systems. With the continuous development of the social system, social system relies more on natural resources, but most of the natural resources are non-renewable resources. With the blindly exploitation of human, the natural resources of our country present the phenomenon of shortage and uneven distribution, irreconcilable contradiction is caused between social demand and resource crisis, inequality has led to more social conflicts and safety hidden trouble.

2.2 *The contradiction between natural subsystem and economic subsystem*

According to the statistics from 2003 to 2011, our country's economy has grown stably but two-thirds of them are on the basis of the environmental pollution and ecological destruction. Can you believe that among the 20 most polluted cities of the world, 16 of them are Chinese cities! In 2013 the national average fog days of record in 52 years, and land desertification, soil erosion, typhoons, floods, dust storms and other natural disasters are becoming more frequent.

2.3 *The contradiction between economic subsystem and social subsystem*

City governments in our country seek for the rapid growth of regional economy continuously at the price of the ignorance of city history and

cultural personality. The quick buck has impacted on thousands of cities. The government emphasizes immediate interests and ignores the long-term development of cities, urban social development, and ecological system was destroyed.

3 ADVANTAGES OF COMPLEX ECOSYSTEM THEORY USED IN INTENSIVE PLANNING OF PUBLIC FACILITIES IN RESIDENTIAL AREAS

As a component unit of the city, living area is one of the important parts of the complex ecological system of the human society (Olsson 2000). It has the characteristics of openness and contact with other function system through material flow, energy flow and information flow. The core of living area provides matter, energy, and living guarantee for the normal living life in the residential areas (Jin 2004). Public facility system consists of energy, greening, traffic, water supply, and drainage and the network communication facilities. These facilities undertake different requirements from people, but they interact and restrict with each other, realizing their function.

Public facility system has much external boundary conditions. It needs exchange with other functional system in residential areas (Li 2009). At the time, it has more closely communication with the urban complex ecosystem. Residential area of public facility system is based on the development of urban infrastructure system (Nip 2009). Public infrastructure needs a huge investment and some can bring profit for the economy system. Public facility accept the gifting from natural system, meanwhile, it brings catastrophic pollution problem to the natural system.

Therefore, the ultimate goal of the intensive planning ideas of public facilities in residential areas is to realize the self-organization balance of public facility system and the virtuous circle of social, economic and natural system.

4 INTENSIVE PLANNING IDEAS OF PUBLIC FACILITIES IN RESIDENTIAL AREAS BASED ON COMPLEX ECOSYSTEM

Considering the close connection of residential areas and the city system, the intensive planning of public facilities should be based on both of them, especially on the channels of materials, energy, and information between the residential areas and the city system. It's the public facilities that ensure the smoothness of the channels.

And here are the ideas.

4.1 *Economic subsystem: Stable economy concept*

As part of public financial expenditures, the investment of public facilities represents public advantages. It needs to meet people's living demands. Since, we are trying to change the current situation that people only focus on the growing of the Per Capita GDP, Stable Economy Concept made it a possibility that public facility system being brought into the whole natural system and social system, which makes the goal of the intensive planning from economic to only economic, natural, and social.

4.2 *Social subsystem: Moderate and advance development concept*

Great importance should be attached to moderate the planning of public facility. Considering the bearing capacity of the social system and natural system, the scale and quantity of the public facility development need a limit and control, which can bring the system to a stable self-organized situation. Under the maximum bearing capacity of the society, we need to plan the public facilities of residential areas in advance so that we can reserve enough space for the rapid rise of the population.

4.3 *Natural subsystem: Nature symbiosis concept*

Increasing proportion of public lawn should be included in the intensive planning of public facilities, which can not only diversify the city landscape, but also improve the metabolism ability of the residential areas system. In traditional planning way, a huge amount of waste of the public facility system will be discharged into the natural system directly (Wang 2009). It will increase the burden of the degradation and cause irreversible damage to the natural system in the long time. So, we should pay attention to the construction of natural facilities like the river system, and also when designing an intensive plan for public facility in the natural subsystem. Only in this way can improve the self-repairing capability of the system and reduce the burden of the system.

The complex ecosystem consists with the factors of nature, society, and economy. The three factors are depending with each other but also independent by themselves. They insist each other but also restrict each other. They interact with each other but also develop together. The fundamental motivation of the self-organization of the complex ecosystem is the inter cooperation of the different rules inside the system. It is the cooperation between the social rules, economic rules, and natural rules that can determine the harmony of the system.

The essence of sustainable development is to establish a balance between the human beings and nature in order to make both of them develop in a healthy manner. It must include the three systems. The development of only one or two of them is not a sustainable development.

We need to achieve the goal to the three plans into one, which means when we do the intensive planning of the public facilities of the residential areas, we must pay attention to the cooperation between the natural subsystem, economic subsystem and social subsystem.

5 SUMMARY

This article is focused on the intensive planning ideas of public facilities in residential areas, which are based on the complex ecosystem. By analyzing the flow and scale of the factors in the subsystem, this concept guarantees the smoothness of the channels between the materials, energy, and information. To achieve the intensive plan of public facility in the residential areas, we need to attach great importance to people, depend on the natural environment, hold the flow of the resources, and require the social management. All in all, intensive planning is divided into three levels: guarantee the stability of residential areas system on the first level, then, find the balance between the residential areas and the city system, and achieve the self-organization of the city complex ecosystem in the end.

REFERENCES

Chin-Hsien L. & Hsueh-Sheng C. 2009. *Exploration assessment of the service distance based on Geographical Information. Systems and Space Syntax analysis on the urban public facility [A]*. Second International Conference on Environmental and Computer Science. *Dubai*. 28–30.

Giannakodakis G. 1994. *Transport Planning: A Holistic Systems Approach [A]*. Proceedings-Conference of the Australian Road Research Board. Sydney. 53–71.

Haq G. 1997. *Towards Sustainable Transport Planning: A Comparison between Britain and the Netherlands [M]*. London. Arebury Press. 79–83.

Jin Z.M. 2004. *Way to Intensive Urbanization: Study on Urbanization in Aojiang Drainage Basin [D]*. Zhejiang University. 17–22.

Li J.B. 2009. First Exploration of Intensive Design in Urban Commercial Complex in Modern Cities [D]. Chongqing University. 39–42.

Nip D. 2009. *Planning in the Process for Multiplex Sports Facilities: Integrating and Empowering the 'Public' in Public-Private Partnerships [D]*. University of Manitoba. 1–3.

Olsson L. 2000. *Actors and Actions for Environmental Adaptation of Transport [C]*. Sixth International Conference on Urban Transport and the Environment for the 21st Century. Townsville. 433–438.

Wang H.Y. 2009. *A Development Strategy Research of Group Urban Development in a Compact Type [D]*. Zhongnan University. 117–121.

This page intentionally left blank

Civil Engineering and Urban Planning IV – Liu et al. (Eds)
© 2016 Taylor & Francis Group, London, ISBN 978-1-138-02903-3

Urban disaster prevention and mitigation planning optimization based on disaster prevention system construction

Zheng Wang & Qi-Fan Wang
Logistics Engineering University, Chongqing, China

ABSTRACT: In recent years, the various disasters like flood, earthquake, and landslide, had brought a large number of casualties and property loss to the urban. It also revealed that the security and recovery ability of a city lifeline system is insufficient. According, to the problem of disaster prevention and mitigation planning in Chinese cities, the content system of disaster prevention and mitigation planning should be further optimized and make full use of planning in disaster prevention and mitigation.

1 INTRODUCTION

In recent years, the natural and man-made disasters had taken place. It has a great influence on the cities, such as the Beijing floods in 2012 and the Southern China typhoon disaster in 2014. For a long time, we are involved in the content of urban disaster prevention and reduction in the compilation of the plan for each city. But part of the disaster prevention and mitigation planning cannot play its due role, in the face of adversity. It has become an important problem to be solved in the planning of urban disaster prevention and mitigation, Such as lack of self-protection ability of urban infrastructure and the urban lifeline system is not perfect.

2 CURRENT SITUATION OF DISASTER PREVENTION AND MITIGATION PLANNING IN CHINA

Chinese urban planning usually includes two phases of compilation and management. According, to the provisions of relevant laws and regulations of urban planning, these two phases are covered with the content of disaster prevention and mitigation. But the contents, requirements, and implementation model of the disaster prevention and mitigation in different phases are not all the same. In actual operation of the process in urban planning, disaster prevention, and mitigation plan shows different status of compilation and management, for a difference of the condition and the policy.

For a long time, disaster prevention and mitigation has been paid more attention in urban planning. The compilation requirements and content of city disaster prevention and mitigation planning are defined in urban planning legal norms of each period. Among which, disaster prevention and mitigation will be the content as a mandatory content of the urban and town master planning in the second chapter seventeenth of the current "urban and rural planning law." In the urban and town master planning in the actual preparation, usually they are composed exclusively of disaster prevention and mitigation planning. It included text and drawings, which can provide the basis for the compilation the regulatory detailed planning and implementation of disaster prevention and mitigation planning. For the regulatory detailed planning, there are no clear requirements for disaster prevention and mitigation in the legal norms. But in order to implement the requirements of the master planning, a lot of city disaster prevention and mitigation will form a special expression in the chapter text and specification of the regulatory detailed planning, or in drawings.

3 THE PROBLEMS OF URBAN DISASTER PREVENTION AND MITIGATION PLANNING IN CHINA

3.1 *Disaster prevention and mitigation planning is not specific*

The content of disaster prevention and mitigation planning was generally based on the text description in urban master planning of Chinese cities. The one put forward was the overall goal, protection requirement, and construction principle of disaster prevention system. The two put forward was the principles and standards of disaster prevention, based on the disaster that the city was facing, and in accordance with the Flood control, earthquake proof, fire protection, and civil

air defense. These principles and standards are the requirements of the overall urban planning of disaster prevention and mitigation but also in line with the provisions of laws and regulations. But under these principles and standards should be how to compile the detailed content of disaster prevention and mitigation planning? It did not reflect in the urban planning legal norms and the various phases of urban planning. There is a lack of planning content that can really guide the city disaster prevention and mitigation.

3.2 *Disconnection among the relevant planning*

Urban planning is the overall layout of covering the whole city and covering the construction content. It contains the city land layout, coordination function, traffic organization, infrastructure layout, and other aspects of the planning content. And these contents are often related to each other. However, in most of the urban master planning, special planning of road traffic, municipal public facilities are out of touch with disaster prevention and mitigation planning. These special planning is formulated based on the needs of daily use. Such as road traffic planning is often based on the need to develop the daily traffic flow and traffic connection, the municipal pipe network capacity and layout are also according to the city population and industry needs. These did not combine with disaster prevention and mitigation planning and there were no specific controlled requirements to improve the capacity of disaster prevention and mitigation of lifeline system and guide the construction.

3.3 *Pay attention to the prevention of pre-disaster and contempt for post-disaster disposal*

The majority of urban disaster prevention and mitigation planning focuses on the prevention of pre-disaster, such as setting the flood control standard dredge the river and disaster monitoring. These contents are no ground for blame as the important content is disaster prevention and mitigation planning. But these are missing in many of the cites' disaster prevention and mitigation planning, about how to repair the lifeline system, and what should the layout of facilities and land for post-disaster rescue and resettlement conditions in urban planning.

4 THE RECONSTRUCTION OF URBAN DISASTER PREVENTION AND MITIGATION PLANNING CONTENT SYSTEM

In order to strengthen the guidance of urban disaster prevention and mitigation planning, its content system should be further refined, and disaster prevention and mitigation measures in more detail will be formulated. According to the situation of city disaster response, city disaster prevention is usually divided into four stages, i.e., disaster analysis, disaster prevention, emergency rescue, and post-disaster resettlement. The content system of urban disaster prevention and mitigation planning can be divided into four parts correspondingly.

4.1 *Hazard analysis and monitoring*

Disaster prevention and mitigation planning should be combined with the historical data of local climate, geology, hydrology, and disaster, which should be a comprehensive analysis of city disaster types and occurrence probability, and should establish a basic database of spatial distribution of city disaster. At the same time, the planning can arrange all kinds of disaster monitoring points, work with city planning, construction, land, environment, municipal, fire, weather, health departments, and construct the city disaster monitoring network, to provide the basis for the strategy, countermeasures, and data correction of disaster prevention and mitigation.

4.2 *Disaster prevention countermeasures*

The existing city disaster prevention and mitigation planning would make a standard for flood prevention, earthquake, and also have clear requirements on fire, the civil air defense facilities planning layout. These measures had played a crucial role on the current city disaster prevention and mitigation. But even so, the cities had still often faced water logging, mudslides, pollution and other hazards and accidents. One reason is the city management is not strict, on the other hand, is also due to the content of planning is not detailed. Therefore, the city disaster prevention and mitigation planning should also be designed to tease out the disaster prevention and mitigation measures of city space layout and compile the district planning.

The disaster prevention and mitigation measures of city space layout refers to the influence for disaster response, optimization of the layout of the measures of city function, land, space, as far as possible to reduce the disaster damage to the city and people. Such as, the mandatory requirements of pollution industry layout, the control request of disaster area land use, and the effective organization of city building layout and open space, forming the environment of anti wind and inductive ventilation of city space. According, to the characteristics of the future development of the city, the disaster prevention and mitigation measures of city space layout in detail will be compiled.

Reasonable partition of city disaster prevention can also be considered about city disaster prevention and mitigation planning, for the large land and dense buildings cities (Zhang 2012). The cities have large population and dense buildings. The city disaster causes serious damage and casualties, and it is not conducive to rescue in the internal of the city. Especially, the external rescue is difficult to enter city center, and the internal personnel of city is not conducive to evacuate. Division of disaster prevention subarea of the city range is divided into small areas, be combined with the administrative jurisdiction, disaster sites, disaster relief channel, natural geographical environment, land planning, and comprehensive consideration. It should also put forward the requirements for the construction of disaster prevention and mitigation inside and outside the subarea. The first is the location, range, standard of emergency shelters, and rescue supply temporary storage point internal disaster prevention subarea. The second is the relief channel layout and the channel and the surrounding construction requirements, between the internal disaster prevention subarea, disaster prevention subarea and others, disaster prevention subarea and outside. The third is disaster prevention separation strip layout which is constructed by the wide and open belt such as city green space, main roads between disaster prevention subarea and others, and the requirements of scale control of separation strip, the construction of supporting facilities, and land use development intensity on both side. It makes the layout of the city convenient for disaster relief, post-disaster resettlement, also conducive to the prevention of disaster spreading.

4.3 *Disaster emergency rescue*

City lifeline system is an important basis for disaster emergency rescue. Disaster prevention and mitigation planning should clear the relief of the standards of own disaster prevention and construction of lifeline engineering at first, such as channel, electricity, communications, fire protection, water supply, and drainage, command center, the hospital. The construction control requirements should also be put forward with the surrounding construction effect on the lifeline engineering, in order to enhance the ability to resist disasters of lifeline engineering. Second, the layout of the post-disaster rescue command center should be done, and the standby system planning should be done for disaster relief key facilities such as relief channel, emergency power, emergency communications, emergency water, command center and so on, to enhance the reliability of these relief key facilities in disaster rescue. The third, making use of co-ordination of planning, the coordination measures of rush-repair should be formulated for power, communication, water supply and drainage, heating, in order to restore the lifeline system as soon as possible after the disaster. The fourth, there should be a corresponding emergency plan, from the point of view of the whole city and even greater range. Including emergency evacuation plan, emergency rescue plan, and rescue channel repair plan. To clear how the rescue should be efficiently carried out after the disaster from various aspects. The emergency evacuation plan should be of clear evacuation routes and hiding places when the disaster or after the disaster, to guide the orderly evacuation of personnel. Emergency rescue plans need to be clear, after the disaster the moving route of relief supplies and rescue equipment from all levels of relief supplies reserves to disaster, rescue shelters, and the coordination of relief is supplied to the city and the greater region, making full use of the whole city and regional city group resources for rescue. The rescue channel repair plan needs to be clear on all kinds of emergency line after the destruction or blocked of the rescue channel and the organization plan of rescue channel repairing, in order to quickly open up the rescue channel.

4.4 *The resettlement and support after the disaster*

For post-disaster resettlement, disaster prevention and mitigation planning needs unified planning of emergency shelters in the city. According to the requirements of the disaster prevention subarea and the layout of school, green, and square, it should plan scale, service radius, facilities, evacuation routes, surrounding the construction of emergency shelters, and put forward the control requirements. For the support to public after the resettlement, it should focus on electric power, communication, water supply and drainage, heating, rescue supplies and other issues. First of all, according to the layout of emergency shelter, the planning needs the overall layout of electric power, communication, water supply and drainage, heating supply facilities and network of the emergency shelter, and puts forward the construction requirements of the standby system, on the basis of the municipal facilities planning.

Second, the planning should plan the various rescue materials reserve system. It can set up a rescue reserve system composed of "Regional rescue materials storage—city rescue material support storage—rescue material temporary storage point." Regional rescue materials storage is the supporting material reserve site across the city and area. It can provide material support for post-disaster resettlement of more than one city. It's planning should be compiled collaboratively by multi-city, or be

led to compile by the provincial or national level institutions. City rescue material support storage is a reserve point that is distributed inside the city or suburban. Rescue material temporary storage point is distributed inside the city; it can provide the support of material for the resettlement immediately. It can be planned by combining with the disaster prevention subarea and emergency shelters. The planning of city rescue material support storage and rescue material temporary storage point should be compiled in disaster prevention and mitigation planning of urban master planning level. On one side, the planning needs to combine its position, size, construction standard of facilities and the construction control requirement of surrounding area. On the other hand, it should also plan the emergency channel connecting the three materials reserve system, and between the rescue material temporary storage point and emergency shelters, in order to build post-disaster resettlement materials support system covering the whole city.

5 CONCLUSION

Through the content system of urban disaster prevention and mitigation planning are optimized to four parts of disaster analysis, disaster prevention, emergency rescue, post disaster resettlement, the planning can guide the works of before and after the city disaster correspondingly. It plays an important role to respond to the disaster timely and improve efficiency.

REFERENCES

Guo, J.Z. 2009. Study on the construction of urban disaster prevention and reduction system. *City* 174(1): 71–76.

Shen, L.F. & Chen, N.Z. 2006. Study on the urban public safety planning. *Planners* 22(11): 27–30.

Wang, J.B., Dai, S.Z. & Gou, A.P. 2013. Urban disaster prevention planning compilation. *Planners* 29(1): 45–49.

Yu, H.W., Wu, G.Z. & Liu, H.U. 2008. Exploration on safeguarding strategies of urban lifeline systems. *China Safety Science Journal* 18(5): 18–22.

Zhang, F. 2012. Exerting the advantages of city planning, constructing a safe city. *City Planning Review* 36(11): 45–66.

Zhang, M. & Chen, J.F. 2007. Urban public safety from the perspective of urban planning. *Urnan and Rural Development* 388(1): 8–9.

Civil Engineering and Urban Planning IV – Liu et al. (Eds)
© 2016 Taylor & Francis Group, London, ISBN 978-1-138-02903-3

Analysis of the differential parking charge policy in Nanjing based on the big data of Microblog

Yi-Xiang Sun
School of Civil Aviation, Nanjing University of Aeronautics and Astronautics, Nanjing, Jiangsu, China
School of Business, Yancheng Teachers University, Yancheng, Jiangsu, China

Ying-Bao Yang
School of Civil Aviation, Nanjing University of Aeronautics and Astronautics, Nanjing, Jiangsu, China

Na-Na Geng
School of Transportation, Southeast University, Nanjing, Jiangsu, China

Zhi-Wei Ji
School of Civil Aviation, Nanjing University of Aeronautics and Astronautics, Nanjing, Jiangsu, China

ABSTRACT: The social media is becoming more and more popular nowadays. In addition to a relatively centralized occupation of the media, it also has the features of a big population base, frequent status updates and rapid information transmissions. The research on the data of social media has been a field of great concern. Meanwhile, the differential parking charge policy is well-known as one of the measures to ease the traffic congestion that was implemented on June 15, 2014 in Nanjing, but the effect of the policy implementation is unknown. For the two points, the main purpose of this thesis is to study the impact on the differential parking charge policy in the prospect of big data collected from the Microblog. This thesis discusses the effect of policy implementation from the perspective of public attitude before and after the policy. It chooses some hot words about the policy for data mining from the Microblog and then makes some effective statistical analyses to get the result. At last, the thesis gives some specific suggestions in order to get better practical results and alleviate urban traffic congestion.

1 INTRODUCTION

1.1 *Background*

Social media, in general, has become an important source for unprecedented reach, speed, and democratization of communication. The social media plays a crucial role in the modern life, including potentially for transport (Ayelet et al. 2014). Studies have focused on big data analysis in transport (Wang et al. 2013). Recent studies have demonstrated the utility of the social media data sources for a wide range of transportation. Collins et al. (2012) demonstrated the use of an innovative social media-based data source, Twitter, to evaluate transit rider satisfaction. Only recently has attention been given to studying the Transportation Network Policy based on the Big Data Analysis (Wang et al. 2014). The advent of the era of big data causes the wide attention to scholars from all walks of life. Whether in academic circle or government, all fields are to begin this kind of process. Corporations generalize the big data into three V, namely, Volume, Variety, and Velocity (Zikopoulos & Eaton 2011).

Sina Weibo whose users state restricted to 280 characters in length, which is not only more adoptable to the need of rapid life pace in modern society, but also more convenient for users to update and share their interests in Microblog information via mobile communication terminal. In the United States, from its establishment in 2006, the number of Weibo Website users has extremely increased and has exceeded one billion by the end of December in 2013. So users generating data size is obvious (Pieter & Michiel 2010). Microblog is regarded as the typical example of the era of big data for that it is a simple and a convenient operation, abundant information, fast transmission, and rapid update accord with the general characteristics of the big data. At the same time, the mass data generated by the Microblog users also becomes an important resource of social research in the big data environment (Liu et al. 2013).

Traffic congestion has become a co-existing headache for the large cities. The history of the

domestic and foreign urban traffic shows that parking problem is one of the cruxes. The only way to solve the problem of parking management is that we can make full use of road (Duan & Mao 2012).Nanjing municipal committee and government highly values the urban traffic management. In the face of severe urban traffic situation that we have lots of vehicles, population density, and the shortage of land resources. Parking charge policy has been formally implemented on June 15, 2014 in Nanjing. The policy actively advocates bus priority and green travel, enabling traffic to flow freely. As one core means of traffic demand management, parking demand management curb the usage of automobiles by raising the parking fee standards and increasing the cost–use of automobiles.

On the basis of mass data of people's responses on Weibo (the Microblog) before and after the implementing of differential parking policy in Nanjing, this paper will study and discuss the effect of the implementation of the Nanjing differential parking charges policy, which aims to provide suggestions for perfecting the development of urban transportation.

1.2 *Nanjing traffic and parking situation*

Currently, the ownership of vehicles has been up to 180, 68 million, including the ownership of cars and private cars that are amounting to 140.41 and 117.73, respectively (Nanjing Daily 2014). In recent years, a rapid growth of private cars has been seen in Nanjing, which the ownership has reached to 50.19 million. This figure has doubled during 5 years, aggravating the traffic congestion and jams. The average congestion delay index of the congested road in Nanjing is about 3.17, and the travel time people spend due to traffic congestion is above three times of the travel time under state of the free flow (AutoNavi 2014). The expansion of parking facilities in the main urban area of Nanjing cannot catch up with the rapid increase of car ownership in those years, which makes parking a more and more difficult problem when people go out.

1.3 *Differential parking charge policy in Nanjing*

Considering the traffic congestion and difficult parking in Nanjing City, Nanjing Municipal Government officially implemented a new policy about the differentiated parking charge on June 15, 2014. The following content is the analysis on such a new policy.

The parking areas in six districts in the regions south of Yangtze River can be divided into core area, first-level area, second-level area, and three-level area, with tiered pricing standard implemented. The core area approximately accounts for 0.4% of total area of six districts, the first-level area approximately accounts for 4%, the second-level area approximately accounts for 12.6%, and the third-level area approximately accounts for 83%. The parking lot is divided into main line, branch, public parking lot, and residential property parking, etc., and the descending tiered price is implemented. Figure 1 shows the division of parking areas in the new policy.

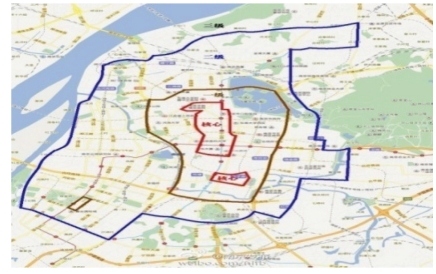

Figure 1. Nanjing parking area dividing map.

2 DATA ANALYSIS

2.1 *Data sources—Weibo*

Weibo (SinaWeibo) is one of the most popular sites in China. It was launched by SINA Corporation on 14 August 2009, and has more than 300 million registered users as of February 2012. About 100 million messages are posted each day on SinaWeibo (Wikipedia 2012). A user on Weibo can post an original short message no longer than 140 characters, called Weibo, or rebroadcast someone else's messages to his or her followers, which is called "repost." A reposted Weibo usually starts with "@," where the sign represents a reference to the one whom you originally posted the messages to. A message, or Weibo, may consist of a text, images, emotions, topics, or videos. Topic is a short text within two hash tags, which usually represents popular events that many people repost.

2.2 *Data analysis methods*

The main task in the data analysis stage is to carry out feature extraction and analysis on the basis of collecting the relevant Microblogging data. This research adopts the following methods of the data mining. The data mining method is to adopt automatic or semi-automatic intelligent way, make use of technologies, such as correlation analysis, and clustering analysis and classification to predict the time–sequence mode and variance analysis, to make analysis on the large quantity of data and obtain conclusive reasoning, obtain the trend and correlation of data information, and then mine out implicit information, which is previously unknown and has potential value (Yu et al. 2011). The overall

goal of the data mining process is to extract information from a data set and transform it into an understandable structure for further use (Liu & Jia 2012). In this research, the clustering analysis method is utilized to cluster short texts on the Microblog, make division on Microblog content or users based on topic, territory or other common points, and then carry out the calculation analysis according to the research purpose on this basis. Besides, it is also able to make use of the decision tree to analyze user features, potential relations, or other contents according to the large quantity of users' identification and other user information.

2.3 *Data analysis*

The new parking policy was officially implemented on June 15, but the government firstly released that "Nanjing will implement a leverage adjustment on parking charge" through the Weibo platform on May 30; on May 31, CCTV news also released the news about the new parking policy through Weibo platform. The new Nanjing parking policy became concerned and discussed focus.

All data in this research comes from Weibo. Through advanced search function of Weibo, all Weibo contents about Nanjing parking from May 30 to July 15 are searched out. There are totally 107,152 relevant microblog contents. This paper carries out analysis on the influence of new Nanjing parking policy through more than 100,000 relevant microblog contents.

It can be seen through the data searching that there are 107,152 microblog contents about "Nanjing parking" released; the quantity of microblog contents about complaints due to "worry about illegal parking" and "worry about punishment" is ranked at the first place, and the quantity is 59,334; the quantity of microblog contents about complaint of "high charge" due to "worry about rise of parking fee" follows, and the quantity is 28,022. Except for the above main keywords, the big data shows that the topics such as "whether the parking space is sufficient," "whether the implementation of new policy is effective," "whether the quantity of infringement notice will increase," "whether the parking lot can catch up with such new policy" are the concerned focus.

Among all Weibo contents, the news about new Nanjing parking policy released by CCTV News on May 31 has been forwarded for 380 times and commented for 814 times, and this is a most noteworthy Weibo content. We consider that this Weibo is the key Weibo before the implementation of the policy.

We carry out detailed analysis on this Weibo content. In the analysis process, the basic information about Weibo users we seize include user id, nickname, detailed information, number of Weibo contents released, number of concerned Weibo, number of fans, and whether such user is a verified user of Weibo, as well as users' reply and forwarding relation, and specific number of statistic reply and forwarding upon catching those contents.

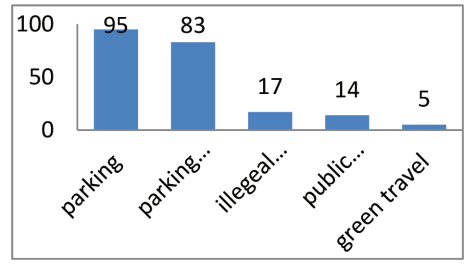

Figure 2. Forwarding mentioned keywords of key Weibo before the implementation of the policy.

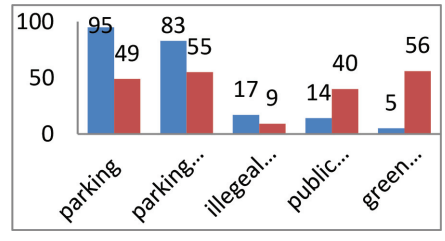

Figure 3. Forwarding mentioned keywords of key Weibo after the implementation of the policy.

Through the Weibo analysis tool, we carry out a detailed analysis on this Weibo content. The quantity of exposure of this news is 21,845,597, which is more than that of 91% of Weibo content. It is obvious that men are more interested in this Weibo than women; except that people in Jiangsu are concerned about this Weibo, the users in Beijing, Shanghai, and Zhejiang, etc., have a high degree of participation; furthermore, there are no invalid Weibo users found.

Through Weibo analysis of keywords that have been forwarded, we can find that the focus of public the first three keywords, followed by: parking, charge and parking charge, and illegal parking. The specific content is shown in Figure 2.

Next, @Nanjing Fabu released an important Weibo content on June 15 to further explain the new policy.

The Weibo had been reposted a total of nearly 686 times and has attracted more than 516 comments by the people. Through the analysis on this Weibo's forwarding and comments, we can find the influence before and after the implementation of the new policy.

We can see the forwarding mentioned keywords of the key Weibo after the implementation of the policy in Figure 3.

3 RESULTS

3.1 *Before implementation of the new policy, citizens are doubtful about the expected effect of the new Nanjing parking policy, and people are on the same wavelength*

Through the analysis on Weibo net friends' comment contents, 90% of net friends are doubtful about the expected effect of the new Nanjing parking policy, and they mainly focus on the problem that "more problems may appear if the government merely depends on 'economic sanction,'" but does not improve parking guidance and other services. Besides, some net friends worry that "the disordered parking phenomenon will get worse if only parking fee rises and no parking guidance is given."

3.2 *Green travel attracts people's attention after the implementation of new policy; the effects of the policy begin to emerge*

With the official implementation of the new policy, it can be seen through comparison on Weibo data before and after the implementation of the new policy that the "green travel" attracts people's attention after the implementation of the new policy. After the parking fee rises, among the key words mentioned by net friends, "travel" becomes the hottest word, followed by "new street" and "green travel," while the mentioning frequency of words "parking" and "parking lot" greatly decreases. This situation is shown in Figure 4.

The attention paid to "parking" decreases, while the attention paid to "green travel" increases. Many net friends say that it is unexpected that the road becomes more unobstructed, although, they are forced to select a transit trip after the implementation of a new policy, "in the past, Xinjiekou was much obstructed; however, it is more unobstructed than ever."

It can be seen that the implementation of a new policy causes a great positive influence on people's selecting green travel, which also improves traffic congestion. The following data also prove this point.

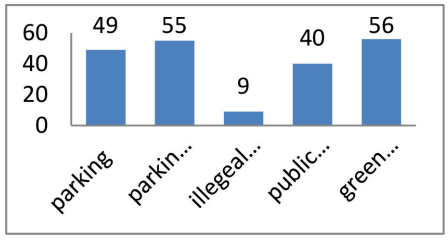

Figure 4. Forwarding mentioned keywords comparison.

Nanjing traffic police released the Microblog content on June 23: from June 15 to June 20, since the new parking charge policy is implemented in Nanjing, the green travel increases, the metro newly increases by 236,500 person–time within 5 days; the parking in core area decreases, the road becomes unobstructed, and the vacancy rate of the parking space is more than 20%; the traffic flow decreases by 15%; 15,306 yellow notices have been given within 5 days in six districts in the regions south of Yangtze River, and the quantity of illegal parking decreases by almost 50%.

"The new parking charge policy causes obvious influence on urban traffic." The data of Nanjing Traffic Administration shows that the traffic flow within urban area decreases by 3% and the traffic flow in core area decreases by 9% after the implementation of the new policy; the congestion situation in the core roads such as East Zhongshan Road, Hanzhong Road, South Zhongshan Road, and Hongwu Road is greatly improved compared with that before implementation of new policy.

Some problems exist in the implementation of the New Policy. The Microblog data show that the implementation of the new differentiated parking policy actually brings obvious effect based on data; however, some problems also exist in the implementation of new differentiated parking policy.

3.3 *Suggestions for implementation of new policy*

It seems feasible to enhance the quickness and comfort of public traffic system, and realize the public's willing alienation of private car trip. The citizens will prefer public transportation to private car only after the public transportation becomes more convenient. If the construction of public transportation is lagged, the public living in the urban areas cannot afford the cost of a private car, and there is no traffic congestion but people congestion on road, we shall introspect on the policy about eliminating traffic congestion. All good polices shall start from the public's convenient trip. The urban administrators shall start from a more convenient trip and the perspective of serving for taxpayers to think about problems.

3.3.1 *To build more multi-storey parking garages*

The parking in the central urban area is really difficult. Therefore, it is able to build more multi-storey parking garages, reduce rather than increase the charging standard of underground parking, and guide more vehicles to realize multi-storey parking. As for internal parking space in some units, it is able to allow the surrounding residents to park at night or weekend. As for some non-commercial central belt, the parking fee can be free. Through differentiated management, the difficult parking can be effectively mitigated.

3.3.2 *To quicken the construction of the parking system and perfect parking management*

The parking lot management company can be established in each district to operate all parking spaces in each district in a uniform and standard way; it is suggested that all parking lots are installed with an IC card device so that the card-swiping charge is implemented for parking; it is also suggested that the fees collected by all parking lots are used for a fixed purpose, and all of them are used in the construction of the parking lot so that more parking lots are available for citizens.

4 CONCLUSION

In this paper, we have two purposes: one is to analyze the attitude of the people toward the new parking policy, and the other is to analyze the influence of the implementation of the new policy on people. We find that about 90% of microblog users are doubtful about whether the actual effect can be obtained via this new parking policy, and they mainly worry that the parking fee rises but the parking service is still bad, the rise of parking fee and difficult parking further increase car owners' parking burden, and the government does not make an effective supervision on the use of parking management fee. Actually, we find through data that people pay more and more attention to the green travel after the implementation of the new policy, and more and more people select public transport due to implementation of new policy, which also mitigates the traffic congestion in Nanjing to a certain degree. In general, we think that it is necessary to further perfect the urban public transportation, encourage citizens to take a transit trip, build more multi-storey parking garages, quicken the construction of intelligent parking system, and perfect parking management in order to make people accept the new policy and improve the implementation effect of the new policy.

ACKNOWLEDGMENTS

This work was supported by the Fundamental Research Funds for the Central Universities and Funding of the Jiangsu Innovation Program for the Graduate Education (KYLX15_0312).

REFERENCES

AutoNavi. 2014. China's traffic data in the 1st quarter of 2014. *http://bbs.amap.com/TV/2014_Q1_traffic.pdf.*

Ayelet, G., Susan, M., Einat, M. & Silvio, N. 2014. The Impact of Social Media Usage on Transport Policy: Issues, Challenges and Recommendations. *Procedia-Social and Behavioral Sciences* 111: 937–946.

Collins, C., Hasan, S. & Ukkusuri, S.V. 2012. A novel transit rider satisfaction metric: Rider sentiments measured from online social media data. *Journal of Public Transportation* 16(2): 21–45.

Duan, L.R. & Mao, L.Z. 2012. Basic concepts and international experience of Parking Management. *Comprehensive Transportation* 2: 69–73.

Liu, L. & Jia, K. 2012. Detecting Spam in Chinese Microblogs-Astudyon SinaWeibo. *2013 Ninth International Conference on Computational Intelligence and Security, Guangzhou, China, 17–18 Nov. 2012.* Washington, DC: IEEE Computer Society.

Liu, X.J., You, B. & Zhang, A.Y. 2013. Review on the Data Used in Researches of Microblog. *Journal of Intelligence* 32: 39–45.

Nanjing Daily. 2014. The number of private cars in Nanjing. *http://www.njdaily.cn/2014/0313/774615.shtml.*

Pieter, N. & Michiel, H. 2010. Mining Twitter in the cloud: A case study. *2010 IEEE 3rd International Conference on Cloud Computing, Miami, FL, USA, 5–10 July 2010.* Washington, DC: IEEE Computer Society.

Wang, M.Q., Wang, J. &Tian, F. 2014. City Intelligent Energy and Transportation Network Policy—Based on the Big Data Analysis. *Procedia Computer Science* 32: 85–92.

Wang, P., Huang, Z.R. & Gong, H. 2013.Transportation Engineering in the Big Data Era. *Journal of University of Electronic Science and Technology of China* 42: 806–816.

Wikipedia. 2012. Wikipedia: Sinaweibo. *http://en.wikipedia.org/wiki/SinaWeibo.*

Yu, L., Asur, S. & Huberman, B.A. 2011. What trends in Chinese social media. *The 5th SNA-20 KDD Workshop'11 (SNA-KDD'11), San Diego CA, USA, August 21, 2011.* Rochester, NY, USA: Social Science Electronic Publishing.

Zikopoulos, P. & Eaton, C. 2011. Understanding Big Data: Analytics for Enterprise Class Hadoop and Streaming Data. New York: McGraw-Hill.

This page intentionally left blank

Civil Engineering and Urban Planning IV – Liu et al. (Eds)
© 2016 Taylor & Francis Group, London, ISBN 978-1-138-02903-3

An efficiency evaluation and a regional variance analysis of the provincial forest park tourism

Chao Yu & Mei Li
Forestry College of Sichuan Agriculture University, Wenjiang, Sichuan, China

ABSTRACT: The data envelopment analysis model was applied hereby to make an analysis of the Chinese provincial forest park tourism and the results have been obtained as follows: (1) the average comprehensive efficiency of the Chinese provincial forest park tourism is 0.507, right on the medium level; (2) the comprehensive efficiency of the Chinese provincial forest park tourism varies with the region, i.e., "higher in the east than in the west, higher in the west than in the northeast, and higher in the northeast than in the central regions"; (3) tourism investment cannot be fully utilized and well repaid, with only 29.03% of it can be fully converted. According to the investigation in the development and the management of the Chinese provincial forest park tourism, adjustment is supposed to be made in the structure of the input factors and more emphasis should be put on the forest park tourism market surveys, re-evaluation, and planning of the provincial forest parks.

1 INTRODUCTION

Forest park is a specific forest location with a certain scale and a high quality of forest landscape resources and the environment conditions, which can develop the forest tourism (Chen et al. 2007). A forest park tends to have the most abundant forest resources and the best eco-environment so that it is endowed with various irreplaceable functions, such as resource conservation, environment education, and tourism economy. In other words, a forest serves as a multifunctional carrier which can be utilized in terms of resource conservation, environment protection, ecological knowledge popularization, ecological civilization promotion, and ecological tourism development. Forest park tourism has become a main force in the Chinese ecological tourism and a hot spot in the academic circles.

With intensifying resource exhaustion and environment disruption in recent years, such concepts as low-carbon economy, efficiency and fairness, and sustainable development have been deeply rooted in people's heart, and a reasonable tourism evaluation has been an essential part in the forest park development. According to the existing literature, foreign scholars in tourism efficiency study are inclined to focus on such micro aspects as measurement and assessment of management efficiency, and to adopt such study methods as Data Envelopment Analysis (DEA) and Malmquist index model (Barros & Dieke 2008, Hsieh & Lin 2010); meanwhile, domestic scholars focus more on such aspects as the utilization efficiency of tourism industry and their comparatively few studies are basically focused on the eco-efficiency rating of forest resources (Ma & Bao 2010, Liang & Yang 2012) and the development of tourism efficiency (Huang 2011). By reviewing foreign and domestic literature, the author finds that the objects of tourism efficiency study are more concentrated on urban tourism or hotel industry, and less in mesoscale forest parks and scenic spots. Based on these findings, DEA is adopted hereby to make a quantitative measurement of the Chinese provincial forest park tourism efficiency, to reveal the efficiency feature of the Chinese forest parks' investment and output, and finally to provide the theoretical basis and reference to the effective investment and the sustainable development of the Chinese forest parks.

2 RESEARCH DESIGN

2.1 *Research methods*

DEA proposed by Charnes and Cooper, two distinguished operational research experts, is an important offshoot of the operational research. By introduction of the change of relative efficiency, this research method can be widely applied into various fields only if the input and the output indexes conform with the mathematics model and the axiom system. The working mechanism is as follows: supposing there are n decision

making units in an model, the input and the output vector of the number j decision making unit is respectively: input vector $x_j = (x_1^j, x_2^j, x_3^j, x_4^j, \ldots, x_m^j)$, output vector $y^j = (y_1^j, y_2^j, y_3^j, \ldots, y_n^j)$, $j = 1, 2, \ldots, n$; herein, $(x^j, y^j) \in T$, T is production possibility set (Wei 2004).

$$\begin{cases} \min\left[\theta - \varepsilon\left(\hat{e}^T s^- + e^T s^+\right)\right] \\ st. \sum_{j=1}^{n} x_j \lambda_j + s^- = \theta x_0 \\ \sum_{j=1}^{n} y_j \lambda_j - s^+ = y_0 \\ \lambda_j \geq 0, j = 1, 2, \ldots, n \\ s^- \geq 0, s^+ \geq 0 \\ \sum_{j=1}^{n} \lambda_j = 1 \end{cases} \quad (1)$$

In this formula, θ ($0 < \theta \leq 1$) stands for comprehensive efficiency, λ_j ($\lambda_j \geq 0$) for weighted variable, s^- ($s^- \geq 0$) for slack variable, s^+ ($s^+ \geq 0$) for remaining variable, ε for non-archimedean infinitesimal, $e_1^T = (1,1, \ldots, 1) \in E_m$ for m-dimension unit vector space, $e_2^T = (1,1, \ldots, 1) \in E_k$ for k-dimension unit vector space. Herein, $e^T = (1,1, \ldots 1) \in E_m$, $e^T = (1,1, \ldots 1) \in R_k$.

Optimal value can be achieved upon the results calculated as $\theta = 1$ or $SE = 1$ and then (x_0, y_0) is the optimum solution which means the pure technical efficiency and the optimal scale efficiency reach the optimum value and that the input has gained the most output.

2.2 *Research object and source of data*

Thirty one provincial forest parks in mainland China are chosen as research objects in this paper, with all forest parks involved in the same provincial area as a DMU. According to the China's regional division methods, china is divided into four regions, namely the eastern area (including Beijing, Tianjin, Shanghai, the provinces of Hebei, Shandong, Jiangsu, Zhejiang, Fujian, Guangdong, and Hainan), the central China (Inner Mongolia Autonomous Region and the provinces of Shanxi, Henan, Hubei, Hunan, Anhui, and Jiangxi), the western area (Chongqing, Ningxia Hui Autonomous Region, Xinjiang Uygur Autonomous Region, Guangxi Zhuang Autonomous Region, Tibet Autonomous Region, and the provinces of Shaanxi, Gansu, Qinghai, Yunnan, Guizhou, Sichuan), and the northeastern area (the provinces of Heilongjiang, Jilin and Liaoning). Forest parks can be found in every province and can serve as a mirror of the current investment and development situation of the Chinese forest parks. The data used in this research are obtained mainly from the China Forestry Statistical Yearbook (2013) and The Yearbook of China Tourism Statistics (2013).

2.3 *Index selection*

Based on the domestic and foreign research literature and data information in point, this paper intends to reflect the forest park production units' input and output data to a greater degree, in the hope that a real representation of tourism producing process and an effective evaluation of the total factor productivity can be made. Taking into consideration the real situation of the forest park production units, input indexes adopted in this research include number and size of the forest park, capital input amount, and the number of employees while the output indexes involved are operation revenue and overall productivity. In essence, the direct output of the forest park should cover the whole industrial chain in the tour process, however, only tourism revenue and tourism receipt are chosen as tourism output indexes in most tourism efficiency researches (Barros & Matias 2006). Therefore, operation revenue and mean productivity of all employees are hereby adopted as the forest park tourism output indexes in this research.

3 RESULTS AND DISCUSSION

3.1 *Overall characteristics of the Chinese provincial forest park tourism efficiency*

By the DEA model, which was explained before in this paper, the 2012 comprehensive efficiency, technical efficiency, and scale efficiency of all the provincial forest parks involved are figured out in Figure 1. Among the 31 provinces, the mean value of forest park tourism comprehensive efficiency is 0.507 and the optimum efficiency is attained only in seven provinces with the optimal efficiency

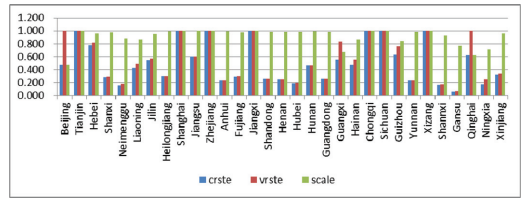

Figure 1. Chinese forest park tourism efficiency analysis.

value as 22.58%. This means that in 2012, only few provinces achieved optimal output in terms of forest park tourism development while in most cases the input–output relation was far from optimized. In terms of decomposition efficiency, in 2012, the pure technical efficiency attained optimization in nine provinces which accounts for 29.03% of the total number of provinces. At the meantime, optimal scale efficiency was achieved in eight provinces, which accounts for 25.8% of the total number of provinces. It is worth mentioning that the number of provinces with optimal technical efficiency is bigger than that of provinces with optimal comprehensive efficiency and scale efficiency. Through analysis, the Chinese provincial forest park tourism development features a lower level of resources exploitation and a yet-to-be-improved input–output efficiency.

3.2 *Regional characteristics of the Chinese forest park tourism efficiency*

According to the regional division of the east, the central, the west, and the northeast, the Chinese forest park tourism efficiency in 2012 presents generally the characteristics, "high in the east and west and lower in the central," and in detail, the provincial forest park tourism comprehensive efficiency in each area is respectively 0.613 in the east, 0.522 in the west, 0.423 in the northeast, and 0.367 in the central China. The province with the lowest tourism comprehensive efficiency value of 0.055 is the Gansu province, located in the west area where the mean value of the provincial forest park tourism efficiency is 0.522 and the standard deviation is 0.361. These numbers indicate that the forest park tourism efficiency varies a lot with the western provinces. Regarding the forest park tourism in the four major regions, the pure technical efficiency is higher in the east and west, lower in the central area, while the scale efficiency is higher in the east, central, and northeastern areas, lower in the west. In general, the average tourism technical efficiency of the provincial forest parks in China is 0.562, less than the average tourism scale efficiency (0.913), which implies that the technical return level of the Chinese provincial forest park tourism is yet to be improved to a larger extent. Thus this can be seen that provincial forest parks in the eastern area stand in the front row in China in terms of comprehensive efficiency, pure technical efficiency, and scale efficiency, and boast of higher input–output efficiency; mainly owning to the agglomerative advantages of the forest resources, the provincial forest park tourism scale in the central China is higher than in other areas; the provincial forest park tourism in the western areas is higher in pure technical efficiency than in central and northeastern areas; by comparison with those in other three areas, forest parks in the northeast develop in a more balanced way with the comprehensive efficiency, pure technical efficiency, and scale efficiency on the national average level. More details are provided in Table 1.

3.3 *Classification features of the Chinese forest park tourism efficiency*

In accordance with the average tourism efficiency value of the 31 Chinese provincial forest parks and compared with the average national tourism efficiency value (0.507), the Chinese provinces fall into four levels: first, seven highest-efficiency provinces which account for 25.8% of the total number of the Chinese provinces, and have achieved the optimal input–output efficiency with the forest park tourism comprehensive efficiency between 0.750 and 1.000; secondly, higher-efficiency provinces including the Jilin Province, the Jiangsu Province, the Guangxi Province, the Guizhou Province, and the Qinghai Province, which account for 16.13% of the total number of the Chinese provinces and have a forest park tourism comprehensive efficiency between 0.500 and 0.750; thirdly, the 11 lower-efficiency provinces (all located in the middle and the eastern area except for the Xinjiang Province) which account for 35.48% of the total number of the Chinese provinces and have a forest park tourism comprehensive efficiency between 0.250 and 0.500, which is below the national average level; last, the lowest-efficiency provinces including Inner Mongolia, Anhui, Hubei, Guangxi, Yunnan, Shaanxi, Gansu, and Ningxia, which account for 25.8% of the total number of the Chinese provinces, and desperately need to improve the provincial forest park tourism's input–output efficiency, which is the lowest level in the nation.

High tourism efficiency means that the tourism input is fully utilized whereas the asymmetry of the input and the output leads to a low tourism efficiency. Nationally speaking, forest parks' quantity and the size redundancy rates are less than the capital input and the employment redundancy rates, and meanwhile, forest

Table 1. Average forest park tourism efficiency of the four areas in China (2012).

Area	Crste	Vrste	Scale
The east	0.613	0.679	0.924
Central China	0.367	0.374	0.973
The west	0.522	0.604	0.860
The northeast	0.423	0.455	0.937

Table 2. Average redundancy rate of the Chinese provincial forest park tourism input in 2012 (%).

Province (municipality)	Forest park quantity (%)	Forest park size (%)	Capital input (%)	Employees' number (%)
Beijing	0.00	0.00	0.00	0.00
Tianjin	0.00	0.00	0.00	0.00
Hebei	83.68	90.79	18.88	85.43
Shanxi	84.29	88.30	70.93	70.93
Inner Mongolia	85.23	97.94	82.20	82.20
Liaoning	53.48	50.71	50.71	50.71
Jilin	42.67	40.05	42.67	48.67
Heilongjiang	70.16	94.62	70.16	70.16
Shanghai	0.00	0.00	0.00	0.00
Jiangsu	54.48	39.63	72.53	74.92
Zhejiang	0.00	0.00	0.00	0.00
Anhui	80.22	76.62	76.62	76.62
Fujian	87.11	69.60	69.60	85.23
Jiangxi	0.00	0.00	0.00	0.00
Shandong	85.06	74.37	74.37	84.28
Henan	80.80	74.81	74.81	82.13
Hubei	80.65	88.85	80.65	85.47
Hunan	53.32	64.40	53.32	73.77
Guangdong	85.75	79.44	73.99	73.99
Guangxi	44.74	17.31	17.31	53.69
Hainan	44.85	44.84	50.02	75.10
Chongqing	0.00	0.00	0.00	0.00
Sichuan	0.00	0.00	0.00	0.00
Guizhou	40.66	24.13	61.95	24.13
Yunnan	84.94	77.39	76.84	76.84
Xizang	0.00	0.00	0.00	0.00
Shaanxi	86.52	82.91	82.81	82.81
Gansu	96.21	98.95	92.90	93.31
Qinghai	0.00	0.00	0.00	0.00
Ningxia	85.64	90.81	91.36	75.38
Xinjiang	87.81	79.79	70.83	66.23

parks' quantity redundancy rate is higher than the size redundancy rate. Among all the Chinese provinces, typical examples of the high forest park tourism input–output efficiency are Beijing, Tianjin, Shanghai, Zhejiang, Jiangxi, Chongqing, Sichuan, and Qinghai which have no redundancy in the forest park tourism input, tourism facilities, and employment.

4 CONCLUSION AND SUGGESTIONS

Taking the China's provincial forest park tourism development in 2012 as a research object and applying the DEA method to measure the provincial forest park tourism efficiency, we obtained the conclusions as follows:

1. In general, the Chinese provincial forest park tourism efficiency lies in the mediate level, with the 2012 average comprehensive efficiency as 0.507 and only few provinces attaining the DEA optimal value in the comprehensive efficiency, pure technical efficiency, and scale efficiency. More specifically, the average scale efficiency of the Chinese provincial forest park tourism is higher than the average pure technical efficiency and the average comprehensive efficiency while the number of provinces (municipalities or regions) with the optimal pure technical efficiency is bigger than that of the provinces with the optimal comprehensive efficiency and the optimal scale efficiency.
2. In spatial patterns, Chinese provincial forest park tourism efficiency is higher in the east than in the west, higher in the west than in the northeast, and higher in the northeast than in the central China. Pure technical efficiency shares the similar spatial distribution pattern with the

comprehensive efficiency. Scale efficiency varies little with the region divisions. Therefore, in general, the Chinese provincial forest park tourism efficiency possesses a spatial development feature of "central sag."

3. Disproportion of input and output is almost present in the whole Chinese provincial forest park tourism, which means that the tourism input is not effectively utilized and fully returned. Only 29.03% of the provincial forest park tourism input is returned without redundancy, which is a sign of serious uneconomical scale in the Chinese provincial forest park tourism input. Based on the research conclusions, the following suggestions can be given for the sake of the Chinese provincial forest park tourism development: first, an adjustment of the provincial forest parks' input factor structure should be made in order to increase the factor conversion rate. The factor input redundancy was very popular in the Chinese provincial forest park tourism industry. It is advisable to increase efficiency of the resource utilization by means of the rational distribution of the input resource factors, industrial structure optimization, and highlight of the tourism features and upgrading of the industrial technologies. Secondly, more emphasis should be put on forest tourism market investigation so as to determine the reasonable input scale. Local authorities involved should carry out more market researches to figure out their needs in developing the provincial forest park tourism, and further to determine the reasonable factor input scale which can bring about more tourism output. And lastly, more importance should be attached to the evaluation and planning of the provincial forest park tourism. Evaluation of the provincial forest parks' input and output should be made according to the specific conditions of each province. Only by the control and optimization of the provincial level can attain the optimal efficiency in the Chinese provincial forest park tourism.

REFERENCES

Barros, C.P., Dieke, P. 2008. Technical efficiency of African hotels. *International Journal of Hospitality Management* 27(3): 438–447.

Barros, C.P. & Matias, A. 2006. Assessing the efficiency of travel agencies with a stochastic cost frontier: A Portuguese case study. *International Journal of Tourism Research* 8(5): 367–379.

Chen, G., Xia, Z.K. & Yu, H. 2001. Types and Functions of Forestpark. *Forest Resources Management* 03: 41–45.

Hsieh, L.F. & Lin, L. H. 2010. A performance evaluation model for international tourist hotels in Taiwan—An application of the relational network DEA. *International Journal of Hospitality Management* 29(1): 14–24.

Huang, X.J. 2011. Comparison and analysis on the tourism efficiency of forest parks in China. *Scientia Silvae Sinicae* 47(12): 22–27.

Liang, L.T & Yang J.T. 2012. Analysis of the tourism efficiency and its decomposition based on DEA. *Geographical Research* 31(8): 1422–1430.

Ma, X.L. & Bao, J.G. 2010. Regional difference and spatial patterns of the tourism efficiency in Chinese primary tourist cities. *Human Geography* 25(1): 105–110.

Wei, Q.L. 2004. *Effective Methods on Evaluating Relative Efficiency*. Beijing: Science Press, 28–30.

This page intentionally left blank

Civil Engineering and Urban Planning IV – Liu et al. (Eds)
© 2016 Taylor & Francis Group, London, ISBN 978-1-138-02903-3

Deformation monitoring and control of the lateral karst cave tunnel

Dan-Dan Zhang
Civil Engineering Department, Chongqing Energy College, Chongqing, China

Fu Xiong
China Railway Engineering Group Co. Ltd., Chongqing, China

Lan Zhang
China Coal Technology Engineering Group, Chongqing Research Institute, Chongqing, China

Hong Shi
Shenzhen Municipal Engineering Company, Shenzhen, Guangdong, China

ABSTRACT: Based on the Huangshanpe tunnel which has the lateral karst caves, the contents, the technique, and the method of deformation monitoring are described. The results show that: (1) The surrounding rock is graded III, so that it becomes stable in a short time after being excavated and the total deformation is small; (2) The influence distance is about two times as long as the tunnel diameter, so the distance from the excavation section to the karst caves is beyond that; and (3) The construction method and the composite lining are reasonable, which can provide some references for the similar engineering.

1 INTRODUCTION

Our country is a country with a very wide distribution of karst. Along with the rapid development of the road constructions, the highway and the railway tunnels in the karst area are more and more. Especially in the western mountainous area, large section tunnel constructions in the limestone karst area are universal. According to the statistics, tunnels are limestone karst areas, which are above 50%. The existence of the karst is a serious threat to the excavation and the operation of the tunnels.

Karst often leads to deformation and instability of the surrounding rock in the tunnels, e.g., a partial collapse in the tunnel excavation, off fall-block, and rock-fall (Li et al. 2008; Li et al. 2007; Shang 2007; Zeng & Zhang 2006; Zhang et al. 2007). In addition, water gushing from the karst caves is another influence of the karst, which not only makes the construction slow but also threats the safety of the workers and the machines.

2 ENGINEERING SITUATION

2.1 *Geological condition*

According to the geological investigation in Figure 1, the soil present upper the tunnel is the residual soil which includes silt clay, red clay, and the silt clay formed by flood alluvial, and also it contains a mixed backfill soil partially, mudstone with limestone, limestone, and shale with the limestone underground.

The tunnel crosses the sections with full of karst, and the karst morphology is mainly the surface melting groove, solution groove, karst, karst caves, sinkholes, and so on. The height of the highest cave roof is about 861.20 m, which is 6.5 m below. The detailed information of these lateral karstes is given in Table 1.

In usual period, the tunnel water inflow rate can reach 10 000 m^3/d, in wet periods; the maximum

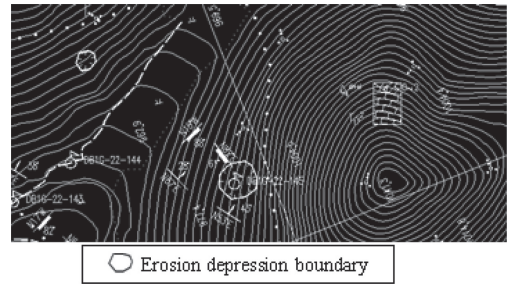

Figure 1. Geological map in the karst area.

Table 1. Survey results of the karst caves.

Location	Investigation results
One hundred meters from the left side of section DK219+785	The elevation of the structural opening is 976 m, the width of the hole is about 10–15 m, and there is no water inside.
One hundred and seventy meters from the right side of section DK219+870	The elevation of the structural opening is 984 m, and the elevation of the bottom of the cave is 934 m. The maximum diameter of the karst cave is about 5 m. Dripping water exists from the cave. The karst cave is along the development of the tendency, the slope is about 30 degrees.
Two hundred and twenty-five meters from the right side of section DK219+870	The elevation of the structural opening is 980 m, and the length of the karst cave is about 30 m The karst cave is along the slope, the slope is about 5 degrees, and there is no water in it.

Table 2. Tunnel excavation method.

Rock grades	Construction scheme
II	Bench method or entire section method
III	Bench method
IV	Bench method or bench method with big arch springing
V	Bench method with big arch springing CRD

inflow can reach 20 000 m^3/d. The tunnel is located in the level cycle of the karst water.

Water inrush and burst mud can occur during the construction. A larger gushing can occur between the lava and the lava contact zone.

2.2 *Construction scheme*

It contains the rock grades from II to V in the tunnel. Construction scheme is determined as mentioned in Table 2.

The tunnel is mainly excavated by the three-step method, and the initial support is carried out timely after excavation.

In the areas with a very wide distribution of the karst, composite lining called IV_{aw} or IV_{ay} is carried out on excavation sections. Grid steel frame is used, and their space is 1.0 m. Advance ductile grouting is also used to strengthen the surrounding rock of the excavation sections.

3 MONITORING PROGRAM

According to the basic requirements of the highway tunnel construction technical specification, monitoring contents and monitoring methods which meet the need of structural characteristics of the tunnel are listed in Table 3, and the construction process and the geological conditions are determined. Space between the monitoring sections is

Table 3. Main monitoring contents and instruments.

Monitoring contents	Monitoring instrument	Remarks
Geological observation	Geological compass	
Convergence of surrounding rock	Sophisticated level gauge, digital convergence gauge	
Crown settlement	Sophisticated level gauge	
Ground settlement	Sophisticated level gauge, grade rod	This monitoring is executed in structural opening, shallow-embedded sections and bias voltage sections.
Surrounding rock pressure	Earth pressure cell, stress gauge, frequency receiver	This monitoring is executed in fault fracture zone and its influence zone.

Table 4. Section spacing.

Rock grades	Section spacing (m)
V	5
IV	10
II–III	30–50

Table 5. Monitoring frequency.

Displacement velocity (mm/d)	Monitoring frequency
>5	Two times a day
1–5	One times a day
0.5–1	Once every two or three days
0.2–0.5	Once every three days
<0.2	Once every seven days

provided in Table 4. Monitoring frequency is also provided in Table 5.

4 ANALYSIS OF THE MONITORING RESULTS

4.1 *Analysis of the surrounding rock convergence*

A karst cave exists 100 m from the left side of the Section DK219+785. According to the requirements of the construction organization, Section DK219+790 is set up, of which surrounding rock convergence is shown in Figure 2 and Table 6.

Two karst caves exist on the right side of the Section DK219+870, one is 100 m away and the another one is 225 m away. Section DK219+790 is set up, and its surrounding rock convergence is shown in Figure 3 and Table 3.

According to Figures 3 and 4, it can be seen that the deformation of the surrounding rock is stable, and the convergence of the surrounding rock is obvious: After excavation, a sharp increase in the horizontal convergence speed of the surrounding rock occurs, convergence speed reaches a maximum value on the first day, and the horizontal convergence speed reaches 1.2 mm/d. From the second day, the convergence rate begins to decrease; Convergence speed comes to zero on the fourth day, surrounding rock comes stable. From the beginning to the end, the convergence lasts only 4 days and the maximum convergence speed is just only 1.2 mm/d, which indicates that these Lateral karst caves have a little influence on the excavation sections in the Huangshanpe tunnel.

Although the diameter of the karst cave on the left side of Section DK219+790 reaches 15 m, the distance between the cave and the excavation sections is as far as 100 m, beyond the influence range of the cave to the surrounding rock according to a theory that impacts the range of the lateral cave on the surrounding rock is about two times the diameter of the tunnel hole.

There are two caves in the right side of Section DK219+873, and their distances are respectively 170 m and 225 m from the monitoring sections which are far from the impact range. Seen from the monitoring results, the two karst caves have little influence on the convergence of the monitoring sections.

Contrast diagram between the influence of the cave on the right side of Section DK219+790 and the influence of the cave on the right side of Section DK219+873 is shown in Figure 4. It can be seen that the horizontal convergence of Section DK219+790 is less than that of DK219+873 for the middle step, but the horizontal convergence of Section DK219+790 is more than that of DK219+873 for the bottom step. There is no obvious regularity in the monitoring results. This also shows that the lateral caves have no obvious effect on the surrounding rock.

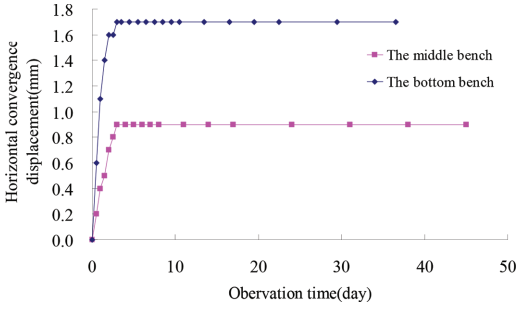

Figure 2. Curves of horizontal convergence at section DK219+790.

4.2 *Analysis of crown settlements*

Monitoring results are shown in Table 7 and Figure 5. For Section DK219+790 and Section DK219+873, deformations have become stable on the fifth day. The maximum crown settlement speed is just 1.0 mm/d. In addition, the total settlements of the two monitoring sections are small. The results show that surrounding rock of these two monitoring sections is relatively stable, which is because of the good quality of the rock and the long distance between the karst caves and the monitoring sections.

Table 6. Results of the surrounding rock convergence.

Location of measured section	Observation days (d)	Convergence time (d)	Maximum deformation rate (mm/d)	Maximum convergence value (mm)
DK219+790	45	4	0.4	0.9
	36.5	3.5	1.2	1.7
DK219+873	47	4	1.2	1.5
	52.5	3.5	0.6	0.5

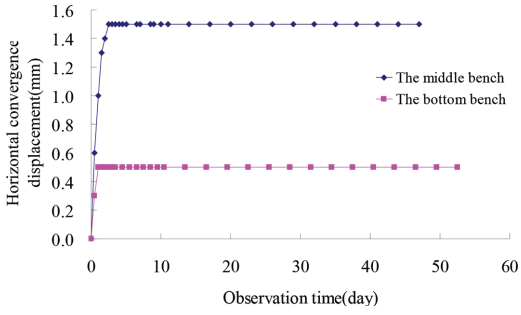

Figure 3. Curves of horizontal convergence at section DK219+873.

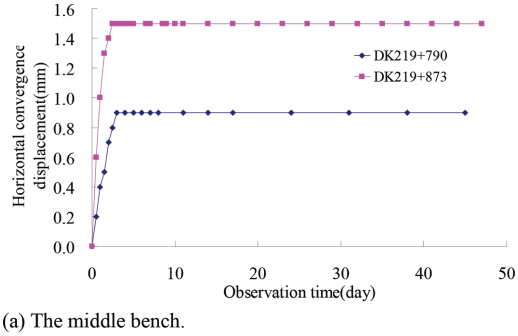

(a) The middle bench.

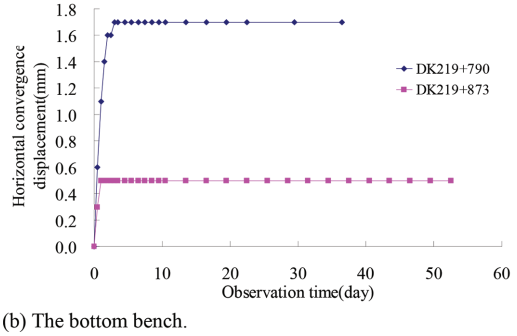

(b) The bottom bench.

Figure 4. Contrast diagram of the horizontal convergence between the sections DK219+790 and DK219+870.

4.3 *Analysis of the rationality of construction method*

The rationality of the tunnel construction method is verified by the allowable range of the tunnel deformation.

Platts formula and the French standards for the tunnel roof subsidence provide an allowable displacement value of the crown settlement and an allowable ratio between the displacement and the span. According to Platts formula, vault allowable values can be expressed as:

$$\delta_1 = 12 \cdot \frac{b_0}{f^{1.5}} \tag{1}$$

where δ_1 is the allowable displacement value of the crown settlement, f is the consistent coefficient, and b_0 is the cavern span.

Allowable displacement values calculated according to Platts formula are listed in Table 8. It can be seen that the crown settlements of both Section DK219+790 and Section DK219+873 are less than the allowable displacement value calculated according to the Platts formula. In addition, ratios between the displacement and the span of the two monitoring sections are both less than those in French standards for the tunnel roof subsidence.

According to the statistical analysis of the results of tunnel convergence, the relative convergences of Section DK219+790 and Section DK219+873 are

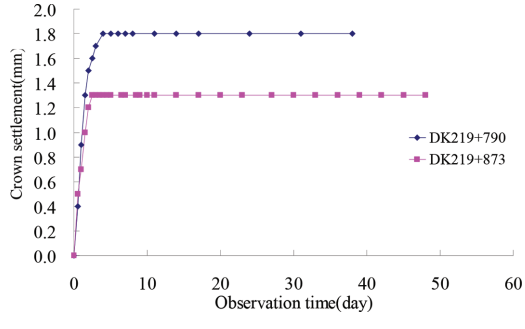

Figure 5. Curves of the crown settlements.

Table 7. Results of the crown settlement.

Location of measured section	Observation days (d)	Required time for stability (d)	Maximum deformation rate (mm/d)	Cumulative settlement (mm)
DK219+790	45	5	1.0	1.8
DK219+873	48	5	1.0	1.3

Table 8. Analysis of the extremum and admissible value of settlement.

Location of measured section	Consistent coefficient	Ratio between displacement and span (%)	Maximum displacement (mm)	Allowable displacement value (mm)
DK219+790	4.5	0.007	1.0	16.8
DK219+873	4.5	0.007	1.0	17.2

0.013% and 0.011%, respectively which are in the range of relative convergences value of surrounding rock regulated in specification about composite lining.

From the results of the rock convergence and the crown settlement, the construction method used in the tunnel is reasonable.

5 CONCLUSION

The valuable conclusions include:

1. The surrounding rock is graded III, so that it becomes stable in a short time after being excavated and the total deformation is small;
2. The influence distance is about two times as long as the tunnel diameter, so the distance from the excavation section to the karst caves is beyond that; and
3. The construction method and the composite lining are reasonable, which can provide some reference for the similar engineering.

ACKNOWLEDGMENTS

This study was supported by 2014 annual scientific and technological research project of the Chongqing Municipal Education Commission (KJ1405301). The author is grateful to the engineers of China Railway Engineering Group Co., Ltd during the different stage of this study, and to the reviewers for their constructive comments on the manuscript.

REFERENCES

Li, S.C., Zhang, Q.S. & Li, S.C. et al. 2007. Forecast of karst-fractured groundwater and defective geological conditions. *Chinese Journal of Rock Mechanics and Engineering* 26(2): 217–227. (in China).

Li, S.C., Xue, Y.G. & Zhang, Q.S. et al. 2008. Key technology study on comprehensive prediction and early-waming of geological hazards during tunnel construction in high-risk karst areas. *Chinese Journal of Rock Mechanics and Engineering* 27(7): 1297–1306. (in China).

Shang, H.C. 2007. Analyses of karst at eastern portal of Huafu Mountaion tunnel and treatment of karst cave. *Journal of Railway Engineering Society* 58(8): 58–60. (in China).

Zeng, W. & Zhang, M.Q. 2006. Study on parallel drift construction technique of karst cave No.2 in Yuanlngshan tunnel. *Chinese Journal of Rock Mechanics and Engineering* 25(1): 191–198. (in China).

Zhang, M.Q., Huang, H.J & Tian, S.M. et al. 2007. Safe design, construction and management of karst Tunnel. *Journal of Railway Engineering Society* (5): 75–85. (in China).

This page intentionally left blank

Civil Engineering and Urban Planning IV – Liu et al. (Eds)
© 2016 Taylor & Francis Group, London, ISBN 978-1-138-02903-3

Research on the development of the non-motorized transportation system in the short time scale—taking Lianyungang as an example

Hua Lu
Lianyungang Planning Bureau, Lianyungang, Jiangsu, China

Ya-Zhou Ni
Chief Engineer's Office, Lianyungang Planning Bureau, Lianyungang, Jiangsu, China

ABSTRACT: Taking short time scale as a research module, the theory and the practical experience of the city non-motorized transportation system are analyzed and summarized, and the rationality and the necessity of the research on the non-motorized transportation system in a short time scale are analyzed. Combined with the actual situation of Lianyungang, the planning strategy is constructed to provide an effective support for the sustainable development of the urban ecological health.

1 INTRODUCTION

1.1 *Research significance*

The non-motorized transportation system, which is used as the main travel characteristics, such as walking, bicycle, and the electric vehicle, is not only an important part of the urban comprehensive transportation, but also an important component of the urban life system. At the same time, the resource environment is gradually strengthening the traffic constraints, as a popular way to relieve traffic congestion, reduce traffic pollution, and promote social justice, order, safe and comfortable, low energy consumption and low pollution.

1.2 *Research type*

As the main form of the non-motorized transportation system is walking, bicycle, and electric vehicle, it has some limitations. The research on the short time scale of the city's non-motorized transportation is highly complementary and fit.

2 NON-MOTORIZED TRANSPORTATION SYSTEM OF THE CITY

2.1 *Origin non-motorized transportation system*

Non-motorized transportation system, also known as the slow traffic system of the city, mainly to meet the residents travel, shopping, sports, exchanges, leisure, tourism, and the other needs, throughout the city in every corner of the life (Bao 2011). Slow traffic of the system in foreign countries more rapidly, originated in the United Kingdom, developed in Denmark (Denmark's capital, Copenhagen is known as the car era of the bicycle) Germany, Sweden and other countries, and mature in Holland. The Holland government encourages people to walk and ride bicycles, and to develop the policies to build the pedestrian corridors and the bicycle lanes. It has one of the world's most dense bicycle transportation networks, a total length of 22,000 km, is ten times the length of its highway. Throughout the city's bicycle lanes, the traffic control, which has to ensure the bikes on the roads in the morning and evening during the rush hours, rarely encountered a red light, and made sure the bike compared with the motor vehicles have the absolute path priority with the maximum speed up to 20 km/h. The construction of the bicycle special tunnels, bridges, parking spaces (even double the double parking spaces), and the bike are all free. To achieve a virtuous connection between the bicycle and the public transport, the subway and the light rail cars are set to have a special bike–bicycle parking space. After decades of development of the people of Holland who had long been got rid of the idea of riding a bicycle unless they were poor or had no car payment ability, there are more than 90% of the people keen to travel by bike, which was considered as slow travel only for fitness, environmental protection and fast, has become a fashion. The development of the non-motorized transportation system further expands the accessibility of traffic and can expand the accessibility of the city center to form and improve the urban public transport (Tian 2011). The development of the urban non-motorized transportation system in our country can be divided into four stages (Table 1).

Table 1. Four stages of the development of the urban non-motorized transportation system in our country.

Development stage	Representative of the time	Main way	Influence factors
First stage	Before 1940s	The more primitive way of walking.	Productivity development level is low, bicycle travel mode is less.
Second stage	From 1940s to 1980s	Bicycle gradually rises, walking and bicycle as the main way to travel by the residents.	Economic level limit, walking, bicycle travel cost is relatively low.
Third stage	From 1980s to the 21st century	Motor vehicle traffic has gradually become the main mode of the transportation in the city.	The promotion of the industrial civilization, the level of the automobile productivity increased significantly.
Fourth stage	Since the beginning of the 21st century	Begin to realize the importance of walking and bicycle traffic.	Urban traffic has gradually deteriorated.

In view of the large number of domestic and foreign scholars on the non-motorized transportation system planning, many optimization strategies and measures are put forward from the aspects of strategic planning, non-motorized transportation system system planning, non-motorized transportation system system planning, non-motorized transportation system management, and so on. However, because of the research background, the basic model and the different research perspective, the research on the strategy of the urban chronic system planning in our country is based on the short time scale (Liu 2011).

2.2 *Concept definition of the short time scale*

Research on the planning strategy of the urban non-motorized transportation system in short time scale, we should define the concept of short time scale. Statistical data show the slow travel speed is generally refers to the speed that is not more than 20 km/h, usually human walking speed is about 0.5 m/s to 2.16 m/s, comfortable travel time in about 20 minutes (Shi 2011); bicycle speed in general is about 10 km/h, comfortable travel distance is about 3 km is the best, i.e., travel time in 20 minutes or so; electric vehicles in general is about 20 km/h, comfortable travel distance is generally not more than 10 km, travel time in about 30 minutes. Therefore, the short time scale concept is defined as a time of travel for less than 30 minutes.

3 THE PRESENT SITUATION AND SUPPORT IN LIANYUNGANG CITY

3.1 *Development status*

The proportion of the non-motorized travel in Lianyungang is significantly higher than that in other cities, and the residents receiving the non-motorized travel will have higher willingness to accept and have higher practical feasibility. The status of the city is not big, the city's household population changes a little, the two major groups contact is weak, each group relative to the system, a group of people to meet the internal and the non-motorized vehicles to meet the daily travel needs. Bus travel ratio is low, the level of public transport service is low, and the attraction is not strong. One day travel there are four peaks, respectively, the morning and evening of the two peaks and two peaks at noon. High proportion of basic travel, relatively small elastic travel (Table 2).

Table 2. The percentage of the urban traffic structure in Lianyungang in the last 5 years.

Travel mode	Walking (%)	Bicycle/ electric vehicle (%)	Bus/rail (%)	Taxi (%)	Car (%)	Other (%)
2009	27	45	7	2	17	2
2010	27.5	43	6.5	2.5	18	2.5
2011	25.8	43	7.2	3	19	2
2012	22.7	42	9	2.8	21	2.5
2013	19	43.5	9.5	3	22	3.0

Lianyungang urban residents travel has five major characteristics (Chen 2012). First, the travel times on the high side. 2013 Lianyungang residents per capita travel for 3.2 times/day, not including the children under the age of 3.3 to 6 times/day. The average number of people who have a trip is 3.8 times per day, and the travel rate is 87%, compared with other cities, travel times are high. Second, not high. Lianyungang urban residents travel to work, school and return, and the other rigid travel, accounting for 78% of the total travel. Entertainment sports, life shopping, such as the low elasticity of travel. Third, the proportion of the motorized travel is relatively low. Lianyungang city residents travel

by foot, bicycle, and the electric vehicles, the total ratio of 50% or more. Fourth, Lianyungang urban residents travel performance is typical of the four peak, respectively, is a morning and evening peak of two and two peak in the noon, in which the peak (7:00–8:00) and late peak (17:00–18:00) travel accounted for 24% of the total day trips, two peak (11:00–12:00 and 14:00–15:00) accounted for 17% of the total travel volume. Fifth, a short time scale of travel, travel distance is relatively short, i.e., the average travel distance of about 3 km.

3.2 *Development support*

Non-motorized transportation system for a short distance travel has obvious advantages, it can be used as the main way to travel in a short distance, as a medium, long distance travel and public transportation is an indispensable way of the transportation. Lianyungang belongs to the plain city, the road gradient is relatively low, and the natural conditions are very suitable for the development of the non-motorized transportation system. In addition, the development of Lianyungang city, the development of a group development model is shown (Fig. 3). 08 version of the master plan proposed the "pole" urban spatial structure although the layout of the urban space form towards the port city of the integration development trend, after 5 years of urban development, cities can still broadly be divided into the group of Xinhai district and Lianyun tours, Xu Wei District as industrial zone, not within the scope of this study, group within the main city were within a distance of 10 km range, which group internal non-motorized transportation system was constructed to provide a natural soil (Fig. 1).

Within the travel time of each group, people's travel time is within 30 minutes, which is typical of the short time scale. Cross group head of travel

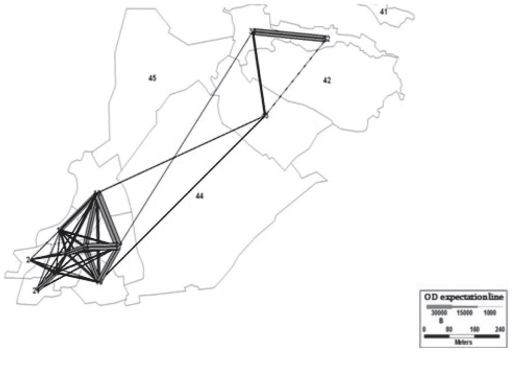

Figure 1. The distribution of travel destination and the distribution of consumption of different travel destination in Lianyungang city of Lianyungang.

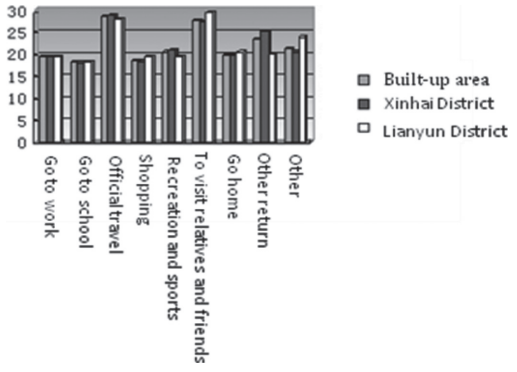

Figure 2. Lianyungang urban residents travel 24 hours distribution map and the status of the residents travel in the OD distribution area.

distance ratio is relatively low, between the groups mainly the BRT bus rapid transit line of the effective connectivity service ranks relatively tight binding, elastic travel group in the internal travel, Xinhai district group internal travel and Lianyun tours in travel, population and post-basic balance on the spot, with certain post-residency without the separation characteristics (Fig. 2).

4 PLANNING STRATEGY

4.1 *Policy support*

Non-motorized transportation system planning should be formulated at the national, provincial, and municipal levels, and the important role and status of the non-motorized transportation system in urban traffic and urban development should be clearly defined in the government documents (Gao & Wang 2008).

In 2013, the Ministry of housing and urban development proposed to implement the State Council on strengthening the urban infrastructure construction ([2013]36), the State Council on the issuance of air pollution prevention action plan ([2013]37) file spirit, accelerate the transformation of urban transport development model, and promote the urban transport sector energy conservation, to further strengthen the urban pedestrian and bicycle transportation system, and expand the social impact of the demonstration project, we will carry out the urban pedestrian and bicycle transportation system demonstration projects. To optimize the urban traffic structure as the main line, to improve the proportion of walking and bicycle travel, to improve the environment for the purpose of walking and bicycle travel, to strengthen the urban road transport infrastructure, to promote

Table 3. Planning strategy for the non-motorized transportation system.

Mode	Features	Operation mode	The appropriate level of planning
Macro-scale integration	The planning process of the slow running system through the overall level of the urban planning process, and closely integrated with it.	Non-motorized transportation system planning is a necessary structure of the overall planning of the city, the following guidance of the following levels of the urban planning.	Urban master plan Overall urban design
Micro-scale integration	The non-motorized transportation system planning is a special kind of a special planning.	Non-motorized transportation system planning to refer to the operation mode of the special planning and examination and approval procedures carried out separately.	Detailed planning of the city Special planning of the city

low-cost, efficient, low environmental impact of the transportation system, encourage and support green travel, forming a number of systems, environmental friendly walking and bicycle traffic system, promote urban green transportation development. The first batch (2010) included six demonstration projects. The second batch (2012) included six demonstration projects. The third batch (2014) included 94 demonstration projects. Total is 106.

We should actively appeal to and encourage the local planning and construction departments to lead the local planning and construction departments, research and formulate the standard of the local non-motorized transportation system. The implementation scope of the non-motorized transportation system system, the implementation strategy, the connection between the public and the public facilities, and the supporting construction standards, etc.

4.2 *The strategy of planning establishment*

Non-motorized transportation system planning can be integrated with the overall planning, control detailed planning, urban design, and planning and design (Duan 2013). It is proposed that the design is divided into two levels: macro- and micro-scale. At the macro level, the planning process of slow running system can be carried out through the overall level of urban planning, and it is necessary to guide the planning of urban planning, and can refer to the operating mode and the examination and approval of special planning (Shen et al. 2010). Through the macro level of the statutory, to guide the micro level of the non-motorized transportation system special planning, hierarchical control (Table 3).

The preparation of the special planning of the non-motorized transportation system should be based on the urban master plan and the urban comprehensive transportation system, which is connected with the urban rail transit, public transportation, parking facilities, and other special planning (Fig. 3).

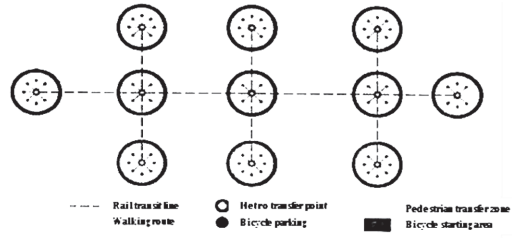

Figure 3. The schematic diagram of the city's slow transit system and the bus feeder.

4.3 *The spatial organization strategy and space division*

The spatial organization of the slow traffic system can be divided into a high frequency generating area and a recreational area (Liu 2014). High frequency generation division including the area of contact part, adjacent contact part, and cross connection part. Area in the contact part with high density and small block type bicycle road network, mainly to low grade road bike, they should be as far as possible into the net, need to increase the connectivity, the need to separate the space between motor vehicles and bicycles, encourage bicycles, bicycle priority can divided into three regions of Haizhou district, Xinpu district, and Lianyun district. Adjacent areas should provide a relatively perfect adjacent area link channel, the bicycle road as the auxiliary road, connecting adjacent partition (Wu et al. 2014). They and transfer hub, etc., need to have good convergence, encourage public bicycle and "B+R" mode of implementation, such as the Haizhou district and Sinpo district. Cross links should be limited by high standard channel, combined with the public transport of effective connection to meet the connectivity such as Haizhou district and Lianyun district, Xinpu district, and Lianyun district (Table 4).

Table 4. The regional traffic organization strategy of bicycle.

Partition type	Relation grade	Transportation facilities	Traffic organization strategy	Remarks
High frequency area Leisure sports area	Area connection	High density small block type bicycle road network, based on the main road of low grade bicycle	As far as possible into the net, increased connectivity, non-spatial separation, bicycle priority, encourage bicycle travel	Haizhou district, Sinpo district, Lianyun district
	Adjacent area connection	High density and small block type bicycle road network, the main road to the low level of the road, to provide a more perfect adjacent to the channel, with a bike path as a supplement	Connect adjacent partitions, and transfer hub, etc., have good convergence, encourage public bicycles and the implementation of the "B+R" mode	Haizhou district and Sinpo district
	Cross area connection	Provide limited access to high standards to meet the purpose of connectivity	Limited by the long distance cross channel weakening travel, reduce the amount of bicycle travel long distances	Haizhou district and Lianyun district
		Along the scenic areas, parks and green belts set up dedicated bike landscape leisure road	Provide a good condition, encourage the purpose of leisure sports bicycle traffic	The Dongyanhe road and the Huanshan road, etc.

Source: According to Kong Linglong, Shi Xudong from the car of the city to return to the human nature of the city—based on the situation of the city's the non-motorized transportation system construction plan.

Leisure sports area mainly refers to the special bicycle road along the scenic landscape and leisure area, the park green space, and the green belt. According to the specific location of the terrain system planning, provide a good convergence of the traffic conditions, to encourage bicycle traffic, such as the east salt river belt, the ring road, etc.

5 CONCLUSION

Yang Gail of Danish planning expert in the "communication and space," a book, once said that non-motorized transportation system means a vivid city. It can not only increase the accessibility of the city, so that the city is vivid, but also to bring a slow paced life culture. Under the dome, so that the general public is willing to accept and participate in the way of the green ecology, which is not only healthy, but also will become a trend of the urban development.

REFERENCES

Bao, X.Z. 2011. *The implementation method and application of the bicycle based road*. Xi'an: Chang'an University.

Chen, Y.W. 2012. *The spatial characteristics and construction strategy of urban non-motorized transportation system under public transportation and urban background*. Harbin: Harbin Institute of Technology.

Duan, X.Y. 2013. *Research on the land use planning of Yuelu District in Changsha based on the concept of green city*. Changsha: Hunan University.

Gao, S.M. & Wang, L. 2008. The construction of non-motorized transportation system in Urban New Area—Taking Tieling city as an example; *City Planning Review* (10): 27–29.

Liu, Y.X. 2011. *New urban bicycle transportation system planning research*. Harbin: Harbin Institute of Technology.

Liu, C. 2014. *Research on the construction method of urban non-motorized transportation system transportation network*. Chengdu: Southwest Jiao Tong University.

Shen, Q.J., An, C. & Liu, C.S. 2010. The connotation of low carbon eco city, characteristics and the planning and construction of basic principle. *Journal of urban planning* (05): 12–16.

Shi, X.F. 2011. *The development of public bicycle system planning and development in Hangzhou based on the experience*. Hangzhou: Zhejiang University.

Tian, X.M. 2011. *The characteristics of bicycle traffic in the big cities and the development strategy research of the city*. Beijing: Beijing Jiaotong University.

Wu, H.L., Yuan, Z.Z., Tian, J.F. & Li, H.X. 2014. Ecological district traffic planning and practice which is based on green traffic idea. *Urban development research* (02): 23–26.

This page intentionally left blank

Civil Engineering and Urban Planning IV – Liu et al. (Eds)
© 2016 Taylor & Francis Group, London, ISBN 978-1-138-02903-3

Advances in designing stainless steel second-skin façades

C.M. Houska
TMR Consulting, Pittsburgh, Pennsylvania, USA

ABSTRACT: Long before central heat or air-conditioning, mankind modified building designs to suit the climate and naturally make them cooler or retain heat better. Bioclimatic design builds on this ancient concept to better harmonize buildings with their environment to achieve energy-reduction goals, and it is growing in popularity globally as new tools are introduced to improve building analysis and products become more available. Screening exterior façades from the sun or winter storms is an old idea that has regained popularity with the growth of the bioclimatic design movement. Exterior walls can be transformed from relatively simple "climate-defensive" mechanisms into more active membranes using second façades to shelter the building envelope. This concept is suited to buildings of all sizes, outdoor public spaces, and transit facilities. Both the advancements in building design and energy modeling technology will be discussed along with the unique corrosion considerations for specifying the system materials.

1 INTRODUCTION

Bioclimatic architecture refers to the design of buildings and spaces using local climatic conditions to improve thermal and visual comfort. These designs reduce the energy required for heating, cooling, and lighting buildings; increase fresh air circulation; and improve occupant comfort. Designing for the local climate is economical, ecologically sound, and suitable for countries at all stages of development.

Bioclimatic façade systems can use traditional overhangs and setbacks, but increasingly a layer of screens is placed outside of the primary environmental barrier. These screens serve as a double envelope or second skin to achieve the building's energy reduction goals. European and US research has improved the ability to model their potential benefits (European Commission 2005, European Commission 2007, Klems 2000, LBNL 2009, Schuman et al. 1992).

The increased use of whole building Life Cycle Assessments (LCAs) is making designers more aware of the high environmental impact associated with repeated material replacement and encourages specification of durable products that are not replaced over the project's service life. Stainless steel is a logical material for corrosive environments with pollution or salt exposure, particularly when there will be minimal to no maintenance and at least 50 years of service life. Screening elements are highly visible design elements but maintenance is often difficult making material choice critical.

2 UTILIZING PREDICTIVE SOFTWARE

There are several software tools for assessing the energy efficiency of façades and fenestration systems, including the North American developed COMFEN, EFEN (DesignBuilder), Daylight1-2-3 (NRC Canada), SPOT (AEC), Ecotect (Autodesk), and the MIT Design Advisor (MIT).

COMFEN 5.0 (Beta release January 2013) is the most recent iteration of free software developed by the U.S. Government's Lawrence Berkeley National Laboratory and primarily funded by the U.S. Department of Energy (DOE). It draws on existing research, previous modeling developments, and evaluations of a large number of existing European and North American buildings. It is an important tool for assessing potential energy savings.

While the software contains a default set of common interior and exterior shading systems, users can create new shading system options and assess their energy saving potential. COMFEN 5.0's sophisticated Energy Plus analysis software looks at each room's unique design and exposure rather than using larger zones. Different fenestrations and shading system types can be assessed for each room type and orientation. Weather, sun angle change, and other data is automatically pulled in from the US DOE database making annual and monthly projections for energy consumption, thermal comfort, hourly daylight luminance, and possible glare index.

3 GERMANY–UAE COMPARISON

The German firm Heliograph created a detailed whole building 3-D computer model based on the Light Cube, a 1998 Kramm & Strigl designed, 7-storey, 1880-m^2 office building in Saarbrûcken, Germany. All aspects of the existing building, including insulation, thermally insulated glass type, and window treatments, remained the same. The software used the same predictive formulas as COMFEN for analysis. The Light Cube model divides the building into zones based on the floor, orientation, and location. Using multi-year US DOE hourly weather data for Dubai, expected building performance was modeled using four options: no shading, interior shading, and exterior shading with either tinted glass or full height woven sunscreens.

In Dubai (UAE), the model predicted annual cooling energy requirements as follows: no shading (416 MWh/a), internal shading (257 MWh/a), internal window shading (279 MWh/a), and exterior woven mesh shading (248 MWh/a). Relative to externally tinted glass, woven mesh second skins provided an annual cooling energy reduction of 12 MWh/a in Germany and 31 MWh/a in Dubai, UAE (Heliograph 2006).

4 BIOCLIMATIC SECOND-SKIN FAÇADES

Bioclimatic second-skin façades are typically 0.2–4.5 m away from the environmental barrier. The intermediate space can be used to moderate heat, light, wind, noise, pollution, and other environmental stresses. The second-skin façade can provide shading, light and air redirection; thermal load balancing; and resistance to heat loss and gain.

The inner environmental barrier wall frequently has operable windows or provides other provisions for ventilation. At least partial shading of the inner wall reduces summer cooling requirements while still allowing daylight to enter the building. During the winter, some second skins shelter the inner wall from winter storm buffeting, while allowing the sunlight to enter and warm up the building, lowering heating loads. Seasonal daylight modeling is necessary for energy design optimization.

Bioclimatic second skin weather screens can be either active, computer-controlled systems that constantly adjust to the environment or low-tech, fixed passive systems. This paper focuses on four screen types with active and passive screen examples: fixed and operable louvers, woven mesh, perforated panels, and green (*i.e.*, vegetated) façade screens.

Tension-supported systems, such as green (vegetated) screens and louvers, parallel the inner wall. Alternatively, lightweight framing can be used to vary the distance between the inner insulated skin and second skin, making seamless curving, geometric, and other shapes possible.

On existing buildings, second weather-screening skins can reduce energy while modernizing the appearance. For new constructions, they can provide a unique appearance at a much lower cost than is possible through modifying load-bearing walls. These façades can also enhance building security and safety by providing barriers.

5 ACTIVE SECOND-SKIN FAÇADES

The most common active second-skin façades are operable metal louvers, wooden slats, or perforated panels. Integrated computer-controlled systems work with the building's heating and cooling to respond dynamically to varying conditions (European Commission 2005, European Commission 2007, Klems 2000, LBNL 2009, Schuman et al. 1992).

Sections of the shading system adjust (*e.g.,* open or close) with changes in the sun's trajectory or weather. This maximizes the benefits of solar radiation or lighting, minimizes heat gain, and, in some cases, shields the inner wall during winter storms to reduce heat loss. Natural ventilation is maximized to improve occupant health and control building temperature levels.

Energy is necessary to operate these systems, and maintenance of the mechanical and sensing systems is required. Active second-skin façades have been particularly popular in Europe, Asia, and Australia, although some of the earliest examples are in North America (*e.g.*, Occidental Chemical Center, Niagara Falls, New York, completed in 1980).

5.1 *German corporate campus*

The TKQ architect consortium designed a seven-building corporate campus in Essen, Germany for ThyssenKrupp, which was awarded a Gold certificate based on the new German Certification

Figure 1. ThyssenKrupp Quarter. Credit Thyssen Krupp AG.

for Sustainable Buildings. Energy requirements are expected to be 20–30% below statutory requirements. The integrated computer-controlled environmental systems adjust the natural ventilation and sun-shading levels to respond to changing weather conditions. In combination with geothermal heating and cooling, air-conditioning was eliminated and winter heating requirements were greatly reduced.

All the buildings are simple, glazed shapes with Type 316 sunshade systems. Building Q2, the corporate conference and training center, has custom, perforated, and passive sunscreens. Active motorized horizontal slat sunshades were used on Building Q1. Motorized triangular, square, and trapezoidal fins were employed on Buildings Q5 and Q7. Adjustment of the slats' angles determines interior light and temperature levels (ThyssenKrupp 2010).

5.2 *San Francisco Federal Building*

The USGBC LEED Silver San Francisco Federal Building is a narrow, 56,205-m^2, 18-storey tower connected to a four-storey annex and adjoining a public plaza. Built in 2007 using COMFEN to assist with design, it was the first office tower in the United States to give preference to natural ventilation. The computer-controlled ventilating inner skin adjusts to daily and seasonal climate fluctuations, providing natural temperature control. About 70% of the work area is naturally ventilated rather than air-conditioned. Approximately 90% of the workstations have natural lighting.

The southeast façade has computer-controlled, perforated Type 316 stainless steel sunscreens covering the full height of glass window walls. The building surpasses the U.S. General Services Administration's (GSA's) energy performance criteria by 50% (Gonchar 2007, Klems 2000, LBNL 2009, Schuman et al. 1992).

5.3 *41 Cooper Square*

Built in 2009, 41 Cooper Square is an engineering building at the Cooper Union. It was the first USGBC LEED certified educational building in New York City. This 16,258 m^2 multi-award-winning project received a Platinum rating.

Stainless steel perforated panels have varying opening sizes and are at different distances from the window wall. The building's computer-controlled environmental system adjusts the panel angle to reduce energy use and allow natural light to enter. While the underlying building is traditional in shape, the screen gives it a dramatic sculptural presence.

The sunscreen, natural ventilation, a vegetated roof, and radiant heating and cooling ceiling panels reduced the building's energy requirements by 40% relative to a standard building of its type. About 75% of the building's interior spaces are lit with natural light (Morphopedia 2009).

6 PASSIVE SECOND-SKIN FAÇADES

Passive systems are simple second-skin façades with fixed semi-permeable membranes. They are typically woven mesh, perforated sheets, fixed louvers, or vegetated screens. These assemblies are ideal when minimal maintenance is expected or electricity is less reliable. They are not mechanically tied to the internal climate management systems.

Like active screens, passive systems provide shelter from the harsh weather by reducing the impact of rain, direct sunshine, and winter storms. Abu Dhabi's Capital Gate Building is a striking example of partial shading with stainless-steel woven mesh sweeping down its south side to eliminate more than 30% of the sun's heat.

6.1 *Eastern Michigan University*

When Eastern Michigan University in Ypsilanti, Michigan wanted to expand the Mark Jefferson Science Complex, the architects designed the 7432-m^2 five-storey addition and renovated the original 1969 16,723-m^2 building. The project was awarded US Green Building Council (USGBC) LEED Gold in 2013, and, in the energy and atmosphere category, it achieved a 31.5% improvement relative to the baseline building performance rating.

Woven Type 316 stainless steel fabric (929 m^2) sun screen panels span the building's height on the large western and smaller eastern façades. The custom sunshade system angles outward from the building on Type 316 structural supports to avoid galvanic corrosion.

On a sunny 23.9 °C August day, temperature readings performed on adjoining exterior locations

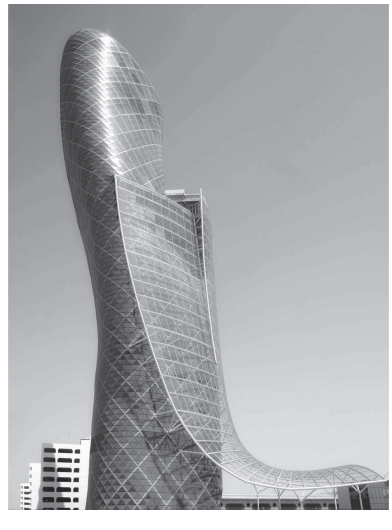

Figure 2. Abu Dhabi's Capital Gate Tower. Photo GKD USA.

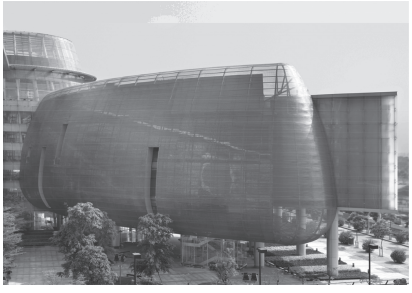

Figure 3. Guangzhou, China's Second Children's Activity Centre. Photo Steffian Bradley Architects.

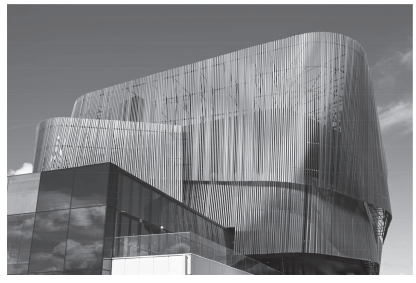

Figure 4. Stockholm Congress Centre. Photo Outokumpu.

showed that the area shaded with metal fabric was 9.3% above ambient (27.8 °C) and the adjoining unshaded area was 25.3% above ambient (34.4 °C). Even in temperate climates, shading exterior building surfaces can significantly reduce air conditioning requirements.

6.2 *Guangzhou Second Children's Activity Center*

Completed in 2006, Guangzhou Second Children's Activity Center provides arts education courses for primary and secondary school students.

This 42,735-m^2 concrete and glass building uses a Type 316 stainless-steel mesh sunscreen system and natural ventilation to eliminate air-conditioning in common spaces. It is elevated to retain open circulation at street level.

The sunscreen curves outward sheltering the linear inner wall while maximizing natural light exposure, creating a distinctive identity, and minimizing energy requirements in a hot climate.

6.3 *Stockholm Congress Centre*

Completed in 2011, the Stockholm Waterfront Congress Centre is located on the city's harbor. It was designed for significant energy reduction and received the Swedish green-building certification. The second façade stainless sunscreen is composed of Z-shaped duplex 2205 stainless steel structural sections.

Stockholm is a coastal environment. The building side of the sun screen is sheltered from rain, and maintenance cleaning is not expected. Corrosion-resistant, high-strength duplex stainless steel 2205 was specified to meet durability requirements and prevent corrosion staining.

7 VEGETATED PASSIVE FAÇADES

Vegetated screens are a low-technology option that passively adjusts to the seasons, shielding windows from the summer sun and, after the leaves fall, allowing the winter light to warm buildings. European and Australian researches have shown they have significant potential for energy reduction. When fully vegetated, these assemblies also reduce noise and electromagnetic pollution; increase green spaces; improve air quality and occupant health; offset carbon taxes (for countries that have them); and can be used for food production.

Success depends on appropriate vine and structural material selection. Protective coatings cannot be reapplied to the support structure and some release metals that kill plants (*e.g.*, biocides like zinc). High strength is necessary to withstand wind loads when fully vegetated and it cannot deteriorate over time with Ultraviolet (UV) exposure, as will occur with plastics. Exposure to corrosive salts, pollutants, and even fertilizers must be considered. For these reasons, stainless steel is the most suitable choice for long-term installations (Helzel & Taylor 2012, Murphy 2009, 2011).

7.1 *Council House 2*

Completed in 2006, Melbourne, Australia's 10-storey government building Council House No. 2 (CH2) has won many awards including the Green Building Council of Australia's (GBCA's) Green Star '6' rating. Relative to the city's Council House No. 1, it uses 85% less electricity, 87% less gas, and 72% less potable water. The carbon dioxide (CO_2) emissions associated with building operation were reduced by about 60%.

Air-conditioning is responsible for half the energy consumption of a typical Melbourne building. Passive stainless steel sunscreens, natural ventilation, and conductive ceiling cooling reduced energy requirements. The building's north side (which receives the most sun) has balcony projections with vegetated screens along their sides to minimize sun heating, filter glare, and connect occupants with their environment (Hopkins et al. 2012, Tan 2007).

The plants are supported by a Type 316 mesh and tension cable system with planters on each floor. The screen extends over the roof terrace, providing

an arbor-like sunshade and energy-consumption reduction levels equivalent to a vegetated roof.

7.2 *University housing*

The residence hall at the Munich University of Technology (Garching, Germany) has encircling walkways instead of traditional balconies to encourage resident interaction. A second skin of Type 316 woven mesh provides greater security and safety than traditional balcony railings and supports a green screen.

The vines keep the simple concrete and glass building and terraces cooler in the summer, transform its appearance, and provide an important link with nature as leaves change color with the seasons. In the winter, the sun warms and lights the building. This concept was also used by Kissler + Effgen Architects for a seminary lecture building at Sankt Georgen Graduate School for Philosophy and Theology in Frankfurt.

8 LANDSCAPING SCREENS

Arbors, plant and perforated screens, and other shading concepts can make outdoor spaces more comfortable, private, and inviting.

The South Bank Parklands in Brisbane, Australia has a long, meandering arbor. Large sculptural pieces of Type 316 stainless steel plate form the primary framework and the tension cable system in-between supports the vines spreading up from the surrounding beds.

Insurance company Swiss Re installed a 'floating hedge' around the three buildings in their Munich corporate headquarters. Open at the first floor level to allow easy access, it is densely vegetated from 6.5 to 17 m above the ground. In the summer, this green wall shields the buildings from sun, reducing energy requirements. During winter, after the deciduous leaves fall, interior light levels and solar warming increase. Arbors create sheltered pathways between the buildings.

9 TALL BUILDING POTENTIAL

Weather-screening design concepts are not new concepts and they are increasingly being applied to taller buildings (Olyay 1963, Yeang 1994 1995, 1996). The curving woven stainless steel mesh screen up to the 19th floor of Capital Gate Tower (160 m) illustrates the potential of shading on tall buildings (Schofield 2012).

On traditional tall building shapes, high and shifting winds, particularly at corners, make wind modeling critical to determine the impact of building structural loading of any design element projecting from the surface. It may be necessary to move sunscreens away from corners, limit their outward projection, and make similar adjustments.

However, a significant evolution in tall building design concepts is occurring. The innovative design of Kingdom Tower (Jeddah, Saudi Arabia, Adrian Smith + Gordon Gill) creates areas that are so sheltered from wind that open-air balconies are feasible on very high floors. Rethinking tall buildings by creating aerodynamic shapes will make it possible to use screening systems at much greater heights, including gardens supported by plant screens climbing toward the sky.

10 STAINLESS STEEL SELECTION

The term "stainless steel" refers to a family of alloys that provide varying levels of corrosion resistance, strength, and formability. While the most commonly specified stainless steels are Types 304/304 L, 316/316 L, and, to a lesser extent, 2205, 904 L, and 317 LMN, many other alloys have been used. Stainless steels provide much higher corrosion resistance than other common architectural metals, particularly when there is pollution and chloride salt exposure (*i.e.*, deicing or coastal salt). There are numerous articles and industry association brochures to assist with stainless steel selection (Houska 2000, 2001, 2007, 2014, 2011, Houska & Wilson 2007).

Second skins are at least partly sheltered from rain-washing, particularly on the inner side facing the environmental barrier. This area is visible to building occupants. Corrosion research shows that sheltered surfaces typically accumulate much higher levels of corrosive pollutants, salts, and particulate. Most climates have high enough temperatures and enough moisture present (*e.g.,* condensation, humidity, fog) to initiate corrosion and, in combination with higher corrosive deposit levels, more corrosive conditions are created. Surfaces that are fully exposed to heavy rain are naturally cleaned, reducing deposit accumulations and the severity of the environment.

Climates with minimal rain and very high levels of particulate and chloride salt deposition rates, as occurs in arid coastal areas like the Middle East, are a documented exception. These areas have higher deposit accumulation and corrosion rates on fully exposed surfaces.

Care should be taken in specifying tightly woven and cable products since chloride crevice corrosion can occur if the wrong alloy is selected, and, under some conditions, chloride stress corrosion cracking must also be considered. Additionally, stainless steel structural components should be used to support stainless steel screens—galvanic corrosion of structural supports should be expected if carbon steel or aluminum is used.

Type 304/304 L is generally appropriate for mild outdoor applications with low levels of

urban pollution. Type 316/316 L is suggested for exposure to low to moderately corrosive coastal and deicing salts, moderate industrial, and higher urban pollution levels.

Unless there will be regular cleaning, type 316/316 L does not provide sufficient corrosion resistance for applications with higher surface chloride salt or pollution accumulations, as might occur in some sheltered or more severe environments. In more corrosive or sheltered applications, duplex 2205 is generally the most cost-effective non-proprietary option. Cable and woven products that might be susceptible to chloride salt crevice corrosion can be obtained in 904 L and 317 LMN, which have equivalent corrosion resistance to 2205. When an environment appears severe, the advice of a stainless steel corrosion specialist should be obtained.

11 SUSTAINABLE DESIGN BENEFITS

On average, international stainless steel production contains about 60% recycled scrap content and, in some regions, recycled content can reach 90%. More than 92% of the stainless steel used in architecture, building, and construction is recycled at the end of service into new metal.

Numerous studies around the world have examined runoff from various materials to determine whether it is potentially toxic to humans, plants, or wildlife. Stainless steel has extremely low runoff levels (often below detectable limits), and it is not a biocide or otherwise toxic to the environment. When properly specified, stainless steel can last the life of a project even if it will span hundreds of years. There has been extensive structural research and it is included in structural codes and design guides.

12 CONCLUSION

Successful sustainable bioclimatic design requires material selections that can last the project's life. Stainless steel is the most corrosion-resistant of the readily available architectural metal options and is capable of providing the structural strength required for weather screens. When an appropriate stainless steel alloy and finish are specified, they provide attractive performance over the building's life.

REFERENCES

European Commission. 2005. *BESTFAÇADE: Best Practice for Double Skin Façades.* European Commission, Intelligent Energy Europe, EIE/04/135/S07.38652, WP 1 Report "State of the Art".

European Commission. 2007. *Simple Calculation Method.* EIE/04/135/S07.38652, WP 4 Report.

Gonchar, J. 2007. Morphosis and arup engineers create dynamic form that follows function for the U.S. Federal Building in San Francisco. *Architectural Record.*

Heliograph. 2006. Thermical Research Study of the Expomedia Light Cube in Saarbrüken and Dubai.

Helzel, M. & Taylor, I. 2012. Green Walls in Stainless Steel. *EuroInox.*

Hopkins, G., Goodwin, C., Milutinovic, M. & Andrew, M. 2012. *Post Construction Monitoring report: Living Wall System for Multi-storey Buildings in the Adelaide Climate*. Government of Australia.

Houska, C. 2000. *Guidelines for Corrosion Prevention*. Nickel Institute.

Houska, C. 2001. *Timeless Stainless Architecture.* Nickel Institute.

Houska, C. 2004. Which Stainless Steel Should be Specified for Exterior Applications. *IMOA.*

Houska, C. 2007. Designing on the waterfront. *The Construction Specifier*.

Houska, C. & Wilson K. 2007. Pushing the design envelope with structural stainless steel. *The Construction Specifier*.

Houska, C. 2011. Stainless steel for severe coastal environments. *The Construction Specifier*.

Klems, J.H. 2000. *Solar Gain through Fenestration Systems Containing Shading: Procedures for Estimating Performance from Minimal Data*. Building Technologies Dept., Lawrence Berkeley National Laboratory.

LBNL. 2009. *High Performance Building Façade Solutions, Final Project Report*. Lawrence Berkeley National Laboratory, Project CEC-500-06-041.

Morphopedia. 2009. 41 Cooper Square. *Morphopedia*, and press releases on website.

Murphy, R. 2011. Lightweight facades. *Architecture Australia*.

Murphy, R. 2009. Tensile facades. *Architecture Australia* 98(6): 121.

Olyay, V. 1963. *Design with Climate.* Princeton University Press.

Schofield, J. 2012. Case study: Capital gate, Abu Dhabi. *CTBUH Journal* (2): 12–17.

Schuman, J., Rubinstein, F., Papamichael, K., Lee, E.S. & Selkowitz, S. 1992. *Technology Reviews Shading Systems.* Berkeley, CA: Windows and Daylighting Group Energy and Environment Division, Lawrence Berkeley Laboratory, University of California.

Tan, S. 2007. CH2 6 Stars, but How Does it Work? and CH2 6 Stars, but is it Architecture? *Australian Architecture*.

ThyssenKrupp. 2010. *Elegance and Functionality: ThyssenKrupp Nirosta Supplies Stainless Steel for Innovative Unshade Elements on Façade of New ThyssenKrupp Headquarters in Essen*. ThyssenKrupp Quarte.

Yeang, K. 1994. *Bioclimatic Skyscrapers.* Artemis London Ltd.

Yeang, K. 1995. *Designing with Nature.* McGraw-Hill.

Yeang, K. 1996. *The Syscraper Bioclimatically Considered*. Academy Press.

Civil Engineering and Urban Planning IV – Liu et al. (Eds)
© 2016 Taylor & Francis Group, London, ISBN 978-1-138-02903-3

Quicker opening of bituminous asphalt pavements to traffic by use of mechanical impedance measurements

J. Huebelt & J. Lindemann
Hochschule Mittweida, Mittweida, Germany

S. Wolf
Wolf Straßen- und Tiefbau GmbH, Reinsdorf, Germany

F. Wellner
Fakultät Bauingenieurwesen, Technische Universität Dresden, Dresden, Germany

ABSTRACT: Among others, the long term durability of road pavements is influenced by the time gap between the laying process and the opening to traffic. Here, in this project a rather simple method for the estimation of the time for opening the pavement to traffic after the laying process is discussed.

Therefore in the first part of the paper a technique for the measurement of the mechanical input impedance is introduced. On the basis of this measurement the Young's modulus is estimated at 5 Hz and 20 °C by use of the temperature/frequency equivalence. In the second part of the project the method has been applied to five new built German pavements. Moreover, by applying a first rough assumption for the setting of asphalts the time for opening the pavements to traffic has been estimated.

1 INTRODUCTION

In Germany the time of opening the pavement to traffic after the laying process is specified in ZTV-Asphalt-StB (2007). According to that directivity the opening time for a single layer is given by 24 hours. In this time the traffic has to be detoured. Hence, huge traffic jams, can occur anywhere and not only in urban areas. To shorten this time gap accurate information about the mechanical properties of the asphalt during and after the laying process were required.

Among others, the mechanical behavior of a bituminous structure can be described by Young's modulus. Thus, a procedure for measuring the Young's modulus in situ could give more information about the mechanical condition of the new built road pavement. An indicator for the Young's modulus of a pavement could be the mechanical input impedance. Therefore, in this paper, the convenient use of the measurement of the mechanical input impedance for predicting the time of opening the pavement to traffic will be discussed.

2 THEORY

2.1 *Estimation procedure*

The basic idea of the procedure discussed here is the fit of predicted values of the mechanical impedance $\underline{Z}_{theory}$ to the results of impedance measurements $\underline{Z}_{data}$ by use of Equation (1). For that, the applied model has to be a function of Young's modulus E. Exactly that value of E which fulfills Equation (1) ($\Delta(E) \rightarrow \min$) for all frequencies ω_i give the best estimation of E. Such estimation procedures, e.g. Newton approximation, are usually iterative methods. After starting with initial values, the procedure tries to converge to a local minimum of an objective function $\Delta(E)$ which quantifies the deviation of the fitted values from the measured data. A strategy for finding a global minimum is discussed in (Huebelt et al. 2010)

$$\Delta(E) := \sqrt{\sum_{i=1}^{n} \left| \underline{Z}_s^{data}(\omega_i) - \underline{Z}_s^{theory}(\omega_i) \right|^2} \longrightarrow \min \quad (1)$$

2.2 *A simple model of the structure of the pavement*

As a first simple assumption, the Rayleigh-Wave-Model has been applied for the calculation of the mechanical input (point) impedance $\underline{Z}_{data}$ of a pavement (see Equation (3) and Heckl et al. 1994). Moreover, Equation (2) defines the mechanical point impedance $\underline{Z}$. Here $\underline{F}$ is the dynamic (frequency dependent) force and $\underline{v}$ the dynamic velocity on a small contact area of the observed surface. All the values are complex numbers.

$$\underline{Z} \equiv \frac{\underline{F}}{\underline{v}} \tag{2}$$

$$\underline{Z} = \frac{1}{\frac{\omega k_T}{G}(1-\mu)\left[0{,}19 + \frac{0{,}3\,j}{k_T\,a}\right]} \tag{3}$$

In Equation (3), ω is the angular frequency and G indicates the shear modulus. The value μ stands for the Poisson's ratio that can be estimated as a function of temperature θ by using Equation (4) according to Witczak (2004). The variable k_T is the wave number of the transversal wave and a is the diameter of the contact area.

$$\mu(\vartheta) = 0.15 + \frac{0.35}{1 + e^{3.1849 - 0.04233\left(\frac{9}{5}\vartheta + 32\right)}} \tag{4}$$

The shear modulus G in Equation (3) is calculated by:

$$G = \frac{E}{2(1+\mu)}. \tag{5}$$

Here, the strong frequency and temperature dependency (Master Curve) of the Young's modulus E and the Poisson's ratio μ has to be mentioned. This behavior can be considered according to Francken & Verstraeten (1974) by applying the variable R (reduction function) in Equation (6) or by determining the master curve by conventional laboratory measurements before the laying process:

$$|E| = R \cdot E_{\infty}. \tag{6}$$

3 MEASUREMENT SETUP

According to the block diagram in Figure 1, the measurements have been carried out for the determination of the mechanical impedance $\underline{Z}$. Here an impedance sensor as well as the combination of a force sensor and an accelerometer has been used. For the excitation of the pavement, the use of a shaker was necessary. For that purpose the shaker had to be supported by a rack shown in Figure 3.

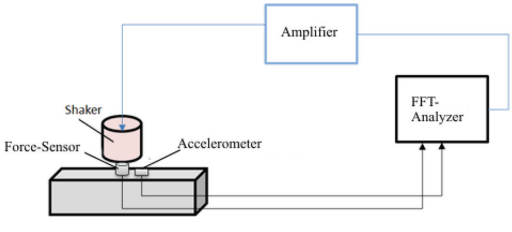

Figure 1. Block diagram of the measurement setup.

Figure 2 shows the measured (oscillating curve) mechanical point impedance of a pavement under test as a function of frequency. The prediction (smooth curve) is carried out by assuming the Young's modulus to be frequency dependent by use of Equation (6). By applying of Equation (1), the minimum of deviation between measured and predicted values has been found. The result of that

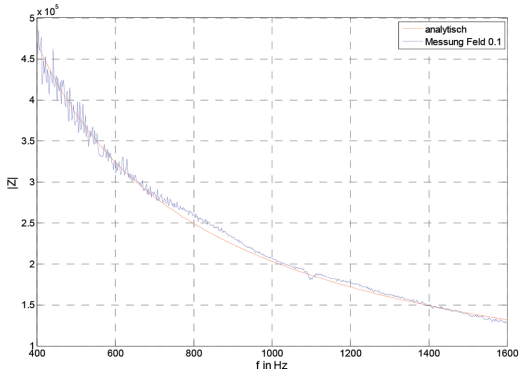

Figure 2. Magnitude of the mechanical point impedance $\underline{Z}$ of a pavement under test versus frequency f. Here, the Young's modulus is considered by the temperature/frequency equivalence; *Oscillating curve*: measured mechanical point impedance. *Smooth curve*: predicted mechanical point impedance; the computation has been carried out by assuming the Young's modulus to be a function of frequency and temperature (see Equation (6)) and by the minimization procedure denoted by Equation (1).

Figure 3. Measurement setup applied on a new built German motorway.

procedure is the function Young's modulus versus frequency.

For comparison of the results achieved by the measurements discussed here with the results of conventional laboratory measurements the value of the Young's modulus $E_{5\ Hz}$ at a frequency of 5 Hz and a temperature of 20 °C is calculated. This value is used in the following discussion.

4 DETERMINATION OF THE TIME FOR OPENING THE ROAD TO TRAFFIC

After the laying process the mechanical point impedance has been measured on five different bituminous pavements. In Figure 4 the Young's modulus $E_{5\ Hz}$ as described in Section 3 is given as a function of time. The time axis starts here exactly with finishing the laying process.

In Germany the time of opening to traffic after the laying process is specified in ZTV-Asphalt-StB (2007). According to that directivity the opening time for a single layer is given by 24 hours. Thus, in the following discussion the Young's modulus $E_{5\ Hz}$ measured 24 hours after the laying process is denoted as $E_{5\ Hz,traffic}$. The final strength of the asphalt should occur at least 24 hours after finishing the laying process. Therefore the Young's modulus measured after 72 hours seems to be a good guess for the final strength. So the aforementioned value is denoted as $E_{5\ Hz,final}$. Please note that all the values of $E_{5\ Hz}$ have been determined by measurements and normalized to the temperature of 20 °C and a frequency of 5 Hz (by use of the temperature/frequency-equivalence).

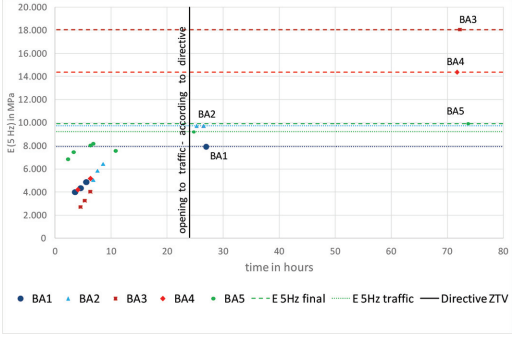

Figure 4. Young's modulus $E_{5\ Hz}$ at 5 Hz and 20 °C vs. time (time after the laying process of the bituminous pavements) determined on new built German bituminous pavements. The value of $E_{5\ Hz,traffic}$ can be found after the time of 24 h (horizontal pointed lines) after the laying process. The Young's modulus measured after 72 hours seems to be a good guess for the final strength ($E_{5\ Hz,final}$ indicated by dashed lines).

In Figure 4 the value $E_{5\ Hz,final}$ is indicated by horizontal dashed lines. As aforementioned the value of $E_{5\ Hz,traffic}$ can be found after the time of 24 hours (pointed lines). So, as an example for a good agreement between the both values the project "BA5" (indicated by circles in Fig. 4) has to be mentioned. Here the $E_{5\ Hz,final}$ is approximately 10.000 MPa and the value for $E_{5\ Hz,traffic}$ is 9.300 MPa. That means, the deviation between the discussed values is less than 10%. The time for opening is in accordance with the directive (24 hours).

Moreover, by applying a rough assumption for the setting of asphalts the time for opening to traffic has been estimated. That means, a linear behavior of $E_{5\ Hz}$ vs. time is assumed during the setting of the asphalt. By caring out that rough estimation for project "BA2" the time for opening the pavement to traffic can be indicated approximately at 15 hours. The guess for the opening time of the projects "BA3" and "BA4" is 24 hours and 72 hours, respectively.

Future work: In the next part of the project the setting process of asphalt pavements will be considered more precisely and additional measurements on new built pavements will be carried out.

5 CONCLUSION

In the project discussed here a rather simple method for the estimation of the time for opening the pavement to traffic after the laying process is discussed.

Therefore, in the first part of the paper a technique for the measurement of the mechanical input impedance is introduced. Here, the Young's modulus is estimated by use of the temperature/frequency equivalence. On the end of that procedure the value of the Young's modulus at 5 Hz and 20 °C is indicated.

In a second part of the project the presented method has been applied to new built German pavements directly after the laying process. For the discussion of the results the Young's modulus $E_{5\ Hz}$ measured 24 hours after the laying process is introduced as $E_{5\ Hz,traffic}$. The value $E_{5\ Hz,final}$ measured 72 hours after the laying process stands for the final strength of the pavements. Thereby, by executing a first rough assumption the time for opening the pavement to traffic has been estimated by the comparison of the values $E_{5\ Hz,final}$ and $E_{5\ Hz,traffic}$.

ACKNOWLEDGMENTS

Europäische Union

Europa fördert Sachsen.
EFRE
Europäischer Fonds für regionale Entwicklung

We like to acknowledge the European Union for granting this research project by the EFRE funds.

REFERENCES

Francken & Verstraeten. 1974. Methods for predicting moduli and fatigue laws of bituminous road mixes under repeated bending. *Transportation Research Record* 515: 114–123, Washington D.C.

Heckl, M., Müller, A. & Helmut, A. 1994. *Taschenbuch der Technischen Akustik.—2*. Auflage, Berlin: Springer.

Huebelt, J., Kuehnert, Ch., Figula, U., Wellner, F. & Blasl, A. 2010. Estimation of the porosity of asphalts by surface impedance measurement. *17th International Congress on Sound and Vibration (ICSV17), Cairo, 2010*. Cairo: ICSV.

Witczak, M.W. 2004, Material Properties for Implementation of Mechanistic-Empirical Pavement Design Procedures Material Properties for Implementation of Mechanistic-*Empirical (M-E) Pavement, Design Procedures Final Report*. Athens: Stocker Center Ohio University.

ZTV-Asphalt-StB. 2007. *Zusätzliche technische Vertragsbedingungen und Richtlinien für den Bau von Verkehrsflächenbefestigungen aus Asphalt.*—Köln: FGSV.

Civil Engineering and Urban Planning IV – Liu et al. (Eds)
© 2016 Taylor & Francis Group, London, ISBN 978-1-138-02903-3

Research on an ecological blockhouse in the Zhaba area, Ganzi autonomous prefecture

Xiao She, Jing-Ni Zhang & Yun-Zhang Li
Sichuan University, Chengdu, Sichuan, China

ABSTRACT: Blockhouse in the Zhaba area, which is in the Ganzi autonomous prefecture, Sichuan province, is quite mysterious as it is located at the great canyon where traffic is rather inconvenient. In recent years, a growing number of humanity scholars started to study the unique human history and walking marriage custom, attentions are gradually drawn to this area. This paper is aimed at studying the master plan form, space characteristics, construction methods and details of rural blockhouses in Zhaba area based on the first-hand on-site survey and drawings. After the comprehensive introduction, we compare the blockhouse in this area with the similar ones in other Tibetan regions. In this way, we can clarify its geographical features as the foundation materials for further study on Zhaba.

1 INTRODUCTION

"Zhaba" is a geographic concept, which means the joint of Daofu and Yajiang, in Ganzi State, Sichuan Province, through which the Xianshui River flows. It is surrounded by 1150 m^2 of continuous succession of standing peaks. The Zhaba area is an administrative division of Daofu. It borders Bamei area to the east, Waerri area to the north, Yajiang county to the south and Xinlong county to the west. About 900 families, 6000 natives live there now (Tu 2011).

As Zhaba area locates in a great canyon of Hengduan Mountains, too dangerous to come in and go out, it still remains a system of matriarchy under which people morally do not marry each other, nor do the couples live together (Lin 2006). The whole race seems mysterious and original. It is believed that the natives might be survivors from ancient DongNv country where there was a tribe quite good at making pottery, called "Zha" after it was annexed by Tubo Empire. "Zha" means "pottery", meanwhile "Zhaba" means "potter" (Lin 2005). We can't tell if the inference is true unless further progress is made about Zhaba. Due to the remote location, Zhaba blockhouses reserve authenticity of original tibetan dwellings and also formed its own characteristics in the long term of development. Thus they become an important source for researches on the history of Khampa Tibetan area.

Existing studies mainly focus on the unique marriage custom and mysterious origin. There hasn't been any deep study on Zhaba Blockhouses based on the first-hand on-site survey and drawings. Researches on Zhaba Blockhouses are demanded urgently to conserve the ancient and precious vernacular architecture which was built by local craftsmen who learned the technique only from their master orally. Besides, a great number of the vernacular architecture will be inundated by the reservoir being built in the upper reaches of Xianshui River. New techniques of construction and materials brought from outside will also change the origin ones. Tradional Zhaba blockhouses, whose history is ancient and mysterious even throughout the whole Khampa Tibetan area, have great significance on completing the historical culture venation. We performed detailed surveying and mapping on these blockhouses on its layout, structure, construction technology, decoration and so on, aiming at saving the ethnically cultural diversity and understanding Zhaba's historical changes.

We measured the oldest two dwellings there. Although they look shabby now, they were constructed as the original Zhaba blockhouses. This paper is part of the research series on Khampa Tibetan traditional dwellings.

2 OVERALL LAYOUT

The Zhaba area locates in a great canyon of Hengduan Mountains, along Xianshui River. Due to the extreme weather on the plateau, buildings mostly face the river to gain more sunlight and take hills on the bank as a shelter from wind. Vernacular architectures here are mainly blockhouse-like dwellings, star-shaped watchtowers and Buddhist temples. In the past, rich families built star-shaped watchtowers nearby for defense in wars. Buddhist temples are surrounded by dwellings for the convenience of sacrifice rites. Since mountainside is

Figure 1. Overall arrangement.

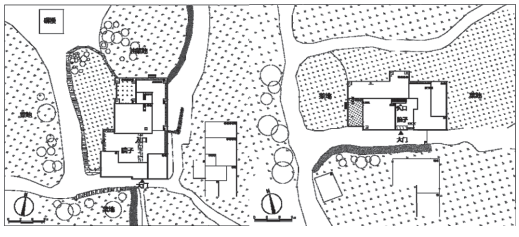

Figure 2. Masterplan of Basang' house/Renching's house.

the best location on which buildings are protected from flood at the foot and strong wind blowing over the peak, dwellings here were firstly built on the mountainside and then spread to the foot over time. Natives there are mainly living a life depended on farming and animal husbandry (Fig. 1).

A Zhaba dwelling consists of a four-storey blockhouse, a wing-room or two and the yard in-between. The main building-the blockhouse normally occupies a square area of 100 to 200 m^2. The semi-open wing-room of one or two storeys is used for crop airing and storing. In mountainous terrain, this kind of plan arrangement contributes to better land use, cohesion and defense (Fig. 2).

3 ARCHITECTURE ANALYSIS

3.1 *The plane*

We mainly measured blockhouses of the Basangs' and the Renchings'. The latter has been existed over 200 years. The plane of the main building is rectangular. The Basangs' overall floorage is 560 m^2, covering an area of 170 m^2. The Renchings' overall floorage is 500 m^2, covering an area of 154 m^2. Main rooms of the two houses all face the south and have mountains behind to gather heat and light, also avoid cold wind from northwest (Fig. 3).

The first floor is used for keeping livestock, wood and fodder. The tradition helps to make it convenient for people to take care of animals without going outside in winter. There are barely no windows and

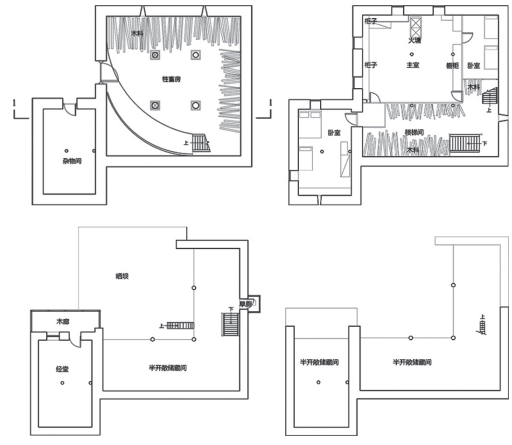

Figure 3. First/second/third/forth floor plan (Renching's house).

just several small holes allowing poor lighting and ventilation in for defense and warmth. There are four indoor wooden pillars, under which are column bases piled up by gallets. The distance between the columns is about three meters. Since the Zhaba blockhouse uses stone wall and the indoor wooden construction to bear weight jointly, the number of columns can reflect the scale of a building. The stairs are made of wood. It is very steep with a slope of about 45–60 to prevent livestock climbing.

The second floor is the main residential area of a family, with the best lighting and ventilation. Bedrooms are on the south. The main room performing as kitchen and living room is the most representative part in the house, and its furniture and decoration have combined into a relatively fixed form. The fireplace is set next to the southern wall. Besides the function of cooking and heating, it is also the sacred symbol. Compared to the Renching's, the Basang's house has a more compact layout with a smaller stair hall and an added storeroom.

On the third floor, there is a unique wooden aqua privy, adhering to stone wall in the west. It occupies an area of about 1 m^2, allowing feces fall directly to the corner of the external wall, thus people can collect them as fertilizer when they are dried. Tibetan people take cleanness as an important part in their religion, so the hanging aqua is gradually formed. The scripture room is at the top of all the function rooms, and the space is enclosed by stone walls from the first floor, which indicates the state of the scripture room. What's worth mentioning is that outcomers are not allowed to go up to the roof, which will bring disasters in the natives' belief.

The fourth floor is semi open, mainly used for storing hay.

Figure 4. Elevation of Basang's house/Renching's house.

3.2 *The façade and section*

Zhaba blockhouses are normally 10 to 15 meters high, and have 4 or 5 storeys, each is about 3 meters high. The walls are constructed by flaky mixture and clay loam which relates to the location of Zhaba-canyon lands with few forests. It makes stones become a substitute, which also contributes to defense. The walls are rough. It's believed that rough metopes help men to clime the wall to get into woman's room. This weird use is related to the unique local walking marriage custom. Now new walls are built more smoothly due to the external cultural influence. Blockhouse in Zhaba has a lot in common with other Tibetan blockhouses, even with stockade in Qiang ethnic minority villages, such as the thick stone external walls and the way to make the wall thinner on the top by which the upper weight decreases, and the center of gravity lowers, strengthening walls in seismicity. Trapezoid external elevations make people feel stable while interior walls can still keep vertical. What's more, lower buildings have thinner walls, so as windward sides.

The windows of Zhaba dwellings are high and small. There are just few on west elevation, and the section of window is trapezoid-the outer aperture is bigger. All of these help to prevent chill wind. The blockhouse looks grey as the flaky mixture is on the whole, but some parts are brushed alternately into blue and white stripes of 500 mm wide which are regarded as a talisman according to Zhaba people's religion-The shamanism, or maybe the earliest Bonism (Fig. 4).

4 FRAMEWORK AND CONSTRUCTION

The construction methods of Zhaba blockhouses and the traditional Tibetan dwellings are similar, they all use stone walls for basic weight bearing and the wooden structure for further weight bearing. When making walls, the natives use the combination of big and small gallets: the big ones to form the structure, the small ones to fill the gaps aiming at avoiding vertical crevice (Wang & Wang 2014). The process of construction would be setting up columns at first, building the wooden construction,

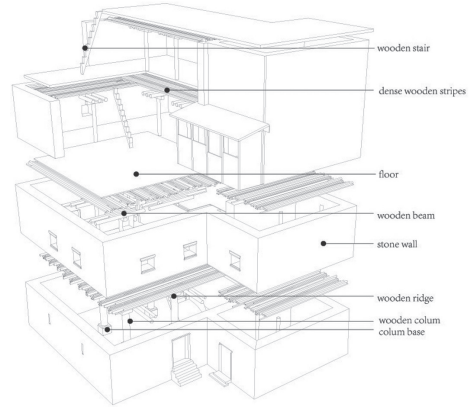

Figure 5. Structure detail analysis.

then forming the stone walls. After the reinforcement, people begin to put on beams, rafters and other structure parts. So on and so forth, the whole building would be finished (Fig. 5).

5 THE DETAILS

Tibetan people are crazy about decoration, their decoration is rough and bold with high color purity, which always contains religion and auspicious implication. Because roof is the closest part to sky, the natives usually show their respect to the sky there. We can see facilities used to simmer mulberry, piles of Mani stone slabs and many Mani flags on the roof. The flags and slabs have scripture on them.

At the top of the building, there is a small golden pagoda. All of these reveal the natives' religion and belief for their gods and nature.

At corners on the roof, there are horn-shaped decorations, about 1 meter high. They represent the natives admiration for the mountains. We can infer that it relates to the tradition of piling up white stones at the roof corners in Qiang ethnic minority. Every horn-shaped decoration has several thin stone flakes on it, which makes it an important feature of Zhaba blockhouse.

The special outdoor ladder is a log carved into a jagged one, leaning against the roof directly. This wooden ladder is easy to make, convenient to move, but not easy to use if with no experience (Fig. 6).

6 COMPARISON BETWEEN DWELLINGS IN ZHABA, DAO FU, DANBA AND LUOHUO AREA

Dwellings in these areas have complex relationships. Due to the alpine terrain, small horizontal

Figure 6. Facilities at the top/small golden tower horn-shaped decoration/Tibetan wooden stair.

distance can lead to huge difference in atmosphere, geography, geological conditions and so on. Thus dwellings in these adjacent areas vary in function, plan, form and so on (Fig. 7).

6.1 *The similarities*

In general, dwellings in Zhaba and Danba use stone walls and wood structure for load-bearing while dwellings in Daofu and Luhuo are in log cabin construction. These two structures have something in common, taking the layout for example. Firstly, the main functional parts of the two kinds of dwellings are the same-livestock at the bottom and the scripture on the top, following the order of animal-people-god, which relates to the tibetan Buddhism. Secondly, they all have back stages for drying. Thirdly they all try their best to keep the safety and state of scripture room.

6.2 *The differences*

The blockhouse in Zhaba and Danba area are different from the wooden structure house in Daofu and Luhuo area in the following aspects. Blockhouse in Zhaba area use the combination of stone walls and wood structure for weight bearing, similar to this structure, blockhouse in Danba area use wood supportive structure from second floor. Nevertheless, dwellings in Daofu and Danba mainly use the log cabin structure, in which walls are used to supporting and enveloping. These two typical structures can be ascribed to natural reason, social reasons and so on. Speaking of natural reason, Zhaba and Danba area are located in great canyons, where the forest is relatively insufficient. At the meantime, Dao fu and Luhuo are located in seismic zone, the wooden log cabin construction is better for further reservation. For social respect, Zhaba and Danba had experienced a great amount of wars in history, so they pay more attention on defense, and the stone structure meets this criterion

Figure 7. Map of Ganzi autonomous prefecture.

Figure 8. Blockhouses in Luhuo area/Zha Ba area.

better (Xie 2010). On the contrary, wooden structure in Daofu and Luhuo is pretty poor at defense as wood is weak at strength and hardness, not to mention it is easy to burn. So they are mainly used for people living and storage, which reflects the relatively stable social condition (Fig. 8).

7 CONCLUSION

The Zhaba blockhouses are very important part of Khampa Tibetan dwellings. Due to the remote location, Zhaba blockhouses reserve authenticity of original tibetan dwellings but also formed its own characteristics in the long term of development. Nowadays, it is hard for Zhaba to avoid being eroded by the outside world. We performed detailed surveying and mapping on these blockhouses urgently, aiming at saving the ethnically cultural diversity for future.

REFERENCES

Lin, J.H. 2005. Research on the origion of Zhaba. *Second Series of Tibetology Journal*: 100–105.

Lin, J.H. 2006. Zhaba-The history and culture of a walking marriage tribes. *Journal of Kangding Nationality Teachers College* 15(4): 6–9.

Wang, J.H. & Shi, S. 2014. King of Tibetan blockhouse. *National Architecture* (6): 141–144.

Xie, J. 2010. *Study on the Traditional Tibetan Residential of Ganzi Areas in Southeastern Sichuan-Take Jiaju Mountain Village as an Example.* Xi'an, Shanxi: Xi'an University of Architecture and Technology.

Yuan, X.C. 2011. Walking marriage system research in Zhaba area. *Journal of Southwest China (Social Sciences Edition)* 37(4): 196–200.

Civil engineering

This page intentionally left blank

Civil Engineering and Urban Planning IV – Liu et al. (Eds)
© 2016 Taylor & Francis Group, London, ISBN 978-1-138-02903-3

Structural protection after landslide phenomena: A case study in Northern Italy

M. Sassu, M. Andreini & A. De Falco
DESTEC, University of Pisa, Italy

L. Giresini
DADU, University of Sassari, Italy

M.L. Puppio
DESTEC, University of Pisa, Italy

ABSTRACT: The protection of a vehicular road after a landslide due to heavy rainfall is described in this paper. With a vision to design steel barriers and wires, collapse scenarios with simple failure models of single falling blocks are presented. The content refers to an application in a vulnerable area of Northern Italy, where a landslide occurred next to an important road. Specific reinforcements and safety features against rolling blocks are illustrated.

1 INTRODUCTION

In recent years a significant increase in hydro-geologic instability cases is observed. It is mainly due to climate changes causing disasters and also in cultural heritage, urban land, and infrastructures. Within La Spezia District, one of the most vulnerable in Italy, during the last two years an exponential growth of large and small landslides occurred. Therefore, the government was forced to conduct top urgency interventions in the context of around an impressive number of ten collapse events (about 150 in 2011).

The outcomes of such natural events has an impressive cost on the society in terms of flood and landslide damage (i.e., the events in the Calabria, Sicily, Tuscany, Campania, and Liguria region), with its fatality occurring most in populated areas. Unfortunately, the resurgence of high intensity rainfall is often accompanied by the decrease of investment in prevention planning.

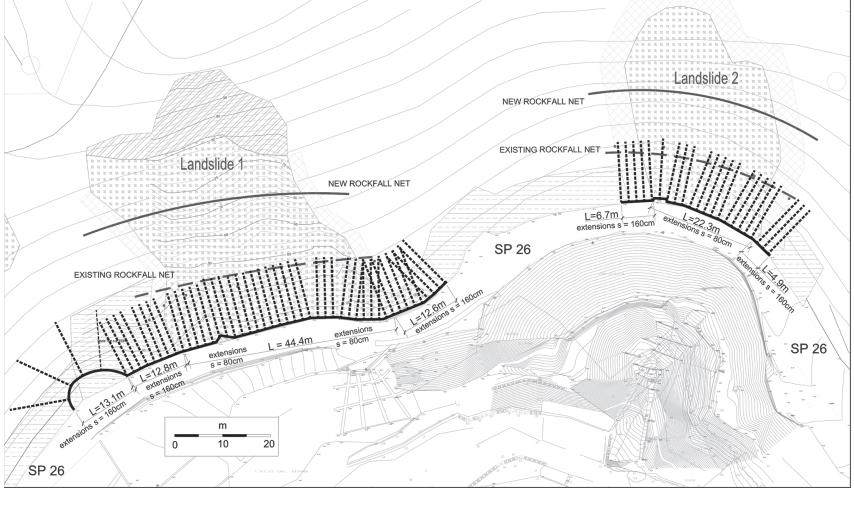

Figure 1. Map of Tellaro landslide with indications of the involved areas and the safety features.

Figure 2. Images of the landslide over the SP26 road (top left, before collapse—top right, after collapse).

This research field involves the entire civil society, as well as technicians, the actual political class, and the government. In this paper, a recent landslide that hit the village of Tellaro (Fig. 1) in the town of Lerici (SP) in December 2010 is examined as a typical event of territorial soil collapse due to rainfall.

Between 21st and 23rd December, many and reiterated heavy rainfall events have affected the entire area (Fig. 2) and activated two wide landslide fronts for a total of about one hundred meters and an height of about eighty meters.

A mudslide of over a thousand cubic meters has flooded the provincial road SP26, isolating the village of Tellaro for many days. Due to a lucky circumstance, there were no fatalities and thanks to additional provisional works downstream the road, the great mass mud falling from the mountain did not result in further serious collapses, limiting the damage to the road surface.

2 A MEANINGFUL CASE: THE LANDSLIDE OF TELLARO ON DECEMBER 2010

The causes of the examined landslide can be summarized in four points:

- *Lack of upstream control of meteoric waters*—the old ditches and runoff lines had been clogged over the years with organic and soil debris; in addition, PVC pipes for sewage disposal had been inserted under the surface and not adequately managed in the context of the existing culverts.
- *Lack of maintenance of the forest*—the undergrowth of the entire privately owned area was in a state of disuse because its steep incline makes it unusable for recreational or tourist activity. Furthermore, due to premature aging and weakening of trees, they are not even able to stabilize the strong steep slope of the hill.
- *Unfavorable geological conditions*—due to the presence of a debris blanket on fractured shale formation, the shape and stratigraphy of the slope surface showed an unstable condition: in presence of rainwater infiltration, such shales significantly reduce the internal cohesion and ease the downstream sliding.
- *Progressive sluices closure*—in order to enable a better use of land in the valley near the sea, the closing of culverts had been carried out downstream the road. This operation reduced the uptake capacity of the culvert system and caused a reverse flow of the water, which may have increased the instability of the slope.

The "post-landslide" configurations of the territory are even more vulnerable: the blanket slips with the shallow organic debris, leaving the inclined surface of the slope unguarded against

future rainfalls. Human intervention therefore involves the application of rockfall protection kits and protection devices for the roadway, waiting for a reforestation aimed at restoring the natural landscape aspect of the surrounding Ligurian coast.

3 ASSESSMENT OF THE POST-LANDSLIDE: FALLING BOULDERS

One of the most dangerous situations after landslides is the detachment and rolling of ruinous boulders. In fact, while the landslide motion is sometimes slow and in so many cases it is possible to defend the people on time, falling boulders is a sudden and unannounced phenomenon (Mazziotti 2010). The phenomena are essentially the following:

- Fall for sliding,
- Free fall in the air,
- Fall for rolling,
- Fall to rebound.

The first is the fall along the sliding slope. Using a model of rigid block, the boulder acceleration a is given by the two expressions (Fig. 3).

$$a = g(\sin\beta - \cos\beta\tan\delta), \tag{1}$$

$$a = \frac{g\sin(\beta-\delta)}{\cos\delta}, \tag{2}$$

where g is the gravity acceleration, δ is the friction angle between the sliding block and the floor, β is the inclination of the slope.

The tangential velocity of the block as function of time t is therefore:

$$v = v_0 + gt(\sin\beta - \cos\beta\tan\delta), \tag{3}$$

where v is the linear velocity at time t and v_0 is its eventual initial velocity. The motion is uniformly accelerated if $\delta < \beta$, whereas the condition $\beta = \delta$ represents the extreme situation of rock stability.

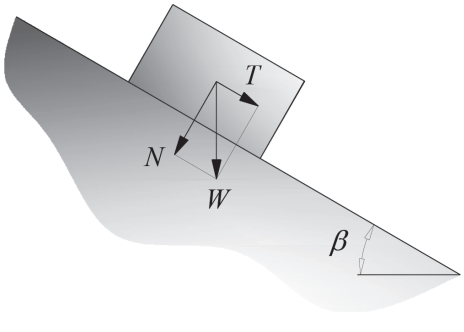

Figure 3. Scheme of sliding boulder.

The phenomenon of free fall from height h, whose only obstacle is the resistance offered by the air, is an extreme case. The well-known kinematic relationship of a particle with initial velocity v_0 gives

$$v_f = \sqrt{v_0^2 + 2gh}. \tag{4}$$

In the presence of air resistance, the acceleration is reduced from g to the value a given by

$$a = g\cdot\left(1 - \frac{v^2}{V^2}\right), \tag{5}$$

being:

$$V^2 = \frac{mg}{KAf}, \tag{6}$$

where V (m/s) is the speed limit, or critique speed, of the falling body. In particular, placing the shape factor f equal to 1 (square section bodies that move normally to the plane of the section) and the coefficient of air resistance $K = 0.08$ kg/m^2, being the footprint area A of the body expressed in m^2 and its weight mg in kg, figured out that:

$$V = \sqrt{\frac{mg}{0.08A}} = 3.5\sqrt{\frac{mg}{A}}. \tag{7}$$

The most common values of the expression (7) are tabulated in the literature and are reported herein in Table 1.

More frequently, the fall of boulders occurs by rolling and can trigger the further fall of other boulders, starting the so-called "avalanche effect".

In a first approximation, the phase of rolling can be interpreted by the known relations that describe the tangential velocity of a solid sphere or a cylinder in references. The physical model, derived from the rotational kinematics of the rigid body, takes the linear velocities from the two following relations, respectively, valid in the case of a solid sphere and of a full cylinder:

$$\begin{aligned} v &= \sqrt{v_0^2 + \frac{10}{7}gs(\tan\beta - \tan\lambda)\cos\beta} \quad \text{(Sphere)} \\ v &= \sqrt{v_0^2 + \frac{4}{3}gs(\tan\beta - \tan\lambda)\cos\beta} \quad \text{(Cylinder)} \end{aligned} \tag{8}$$

in which λ is the angle of rolling friction, while s is the length of the slope.

Table 1. Falling boulders speed (h = height of falling block; $v(h)$ = final speed with air resistance; *v.v.* = final speed without air resistance).

Volumes (m^3)	h = 10 m	h = 20 m	h = 30 m	h = 40 m	h = 50 m	h = 100 m	h = 200 m
	$v(10)$	$v(20)$	$v(30)$	$v(40)$	$v(50)$	$v(100)$	$v(200)$
0.001	13.82	19.28	23.29	26.29	29.22	38.18	43.49
0.008	13.89	19.48	23.67	27.11	30.05	40.65	51.86
0.027	13.93	19.59	23.86	27.41	30.48	41.89	55.68
0.125	13.95	19.67	24.02	27.65	30.81	42.86	57.27
1	13.98	19.74	24.13	27.82	31.06	43.57	60.61
2	13.99	19.77	24.19	27.91	31.18	43.92	61.62
20	13.99	19.79	24.22	27.96	31.26	44.13	62.22
v.v.	14.00	19.80	24.25	28.00	31.30	44.27	62.61

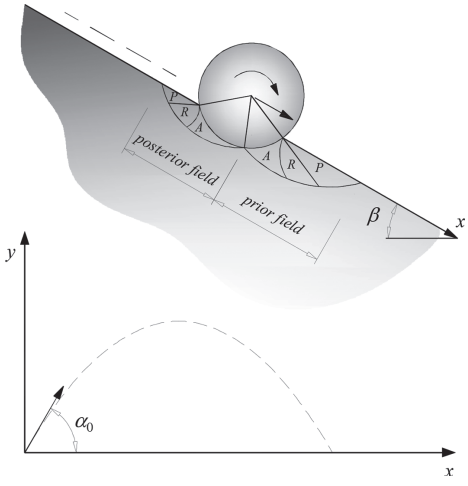

Figure 4. Rolling block on collapsing soil (above) and trajectory of the rebounds (below).

In order to characterize the parameter λ, it must be observed that during the fall, the body performs rolling movements mixed with sliding and rebounds, which occur during the possible phases of rupture of the underlying soil as in Figure 4 (Karafiath & Nowatzki 1978).

Assuming for soil the well known Mohr-Coulomb law, the shear strength along the surface of the rolling interface is

$$\tau = (\phi + \sigma_n)\tan\lambda, \tag{9}$$

where $\phi = c \cot \varphi$ (c cohesion; φ friction angle of the soil). An analytical procedure for determining the average values of these two parameters by observing the shape of the landslide mechanism is presented by Sassu et al. (2013) for masonry walls filled by cohesive earth.

In this way, the friction angle at the interface is defined as a function of the geotechnical parameters c and φ. From the previous expression it can be deduced that:

$$\tan\lambda = \frac{\tau}{(\varphi + \sigma_n)}. \tag{10}$$

Laboratory tests (Mazziotti 2010) have allowed the comparison of shear strength along the solid-soil interface and of that of the soil itself, founding the empirical relation

$$\lambda = 0.7 - 1.0\varphi, \tag{11}$$

for which the rolling friction is, however, lower than the internal friction of the ground on which it occurs. Tests of rolling in references have shown the importance of size factors and the shape of the rolling block: displacements increase with the volume of the body which is moving with a speed that is directly proportional to the size and shape factor, as represented in the graph of Figure 5.

Finally, the mode of formation of rebounds, often combined with slips and tumbles, may be briefly summarized as follows.

The kinematics of a particle provides the parabolic trajectory $y(x)$ of a point bouncing with initial velocity v_0 and an angle of incidence α_0 (Fig. 4):

$$y = x \cdot \tan\alpha_0 - \frac{g \cdot x^2}{2 \cdot v_0^2 \cdot (\cos\alpha_0)^2}. \tag{12}$$

The relation between the speed before (v_i) and after the impact (v_0) is given by

$$v_0 = e\, v_i, \tag{13}$$

where e is the coefficient of restitution (for inelastic collision, it is between 0 and 1; for elastic collision it is

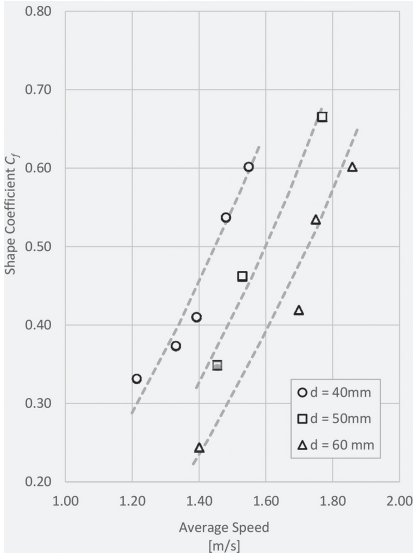

Figure 5. Shape coefficient vs speed.

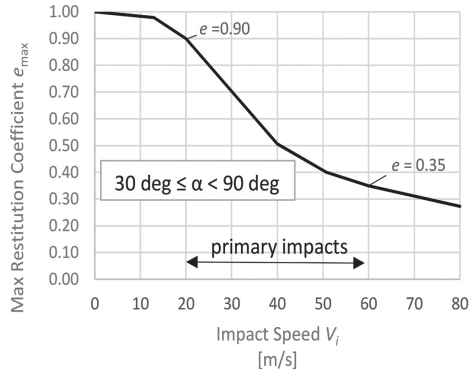

Figure 6. Maximum values of the restitution coefficient as a function of the impact speed.

Figure 7. The road protection device against falling boulders.

equal to 1). Hallbauer (Wyllie & Mah 2005) proposed a method for prediction of the maximum rebound in the case of $e = 0.5$ and $\alpha_0 = 45$deg, but it is desirable carrying out some experimental tests to evaluate the safety conditions in situations post-landslide. In this sense, the available results of the experimental tests have shown that the restitution coefficient decreases with increasing impact speed. This is due to the greater damage produced by the impact of the block on the collided surface, thus transforming an elastic collision, in the case of reduced speed, to an inelastic collision for high impact speed. The trend of Figure 6 may constitute a reference, assuming that the boulder has an impact resistance greater than that of the ground surface bumped.

The technical solution to avoid any rolling of blocks on the road is reported in Figures 7 and 8, where vertical tubes are supporting a series of steel rows and high strength wires. The base of each tube is anchored on an r.c. beam connected to micro-poles. Further wires are suspended to avoid the excessive speed of falling rocks.

In case of the absence of wire and tube protections, the falling boulders will interest the road. The structure is calculated using a conventional method; considering both risks, the falling boulders and the landslide: for this last situation, a static transverse force is applied by unstable soil, considering a conservative scenario of the presence of hydrostatic mud (self-weight 20 KN/m^3) due to a possible further passive depot on the slope. In fact, the lack of maintenance of the overlying private areas causes us to assume a drastic hypothesis (Sassu et al. 2013) of protecting the public road with a landslide return period of 100 years (Corominas et al. 2014).

The case of falling boulders is conservatively designed by the application of a direct elastic impact on a single steel tube. The kinetic energy of a mass m and speed v is equal to the elastic work of a tube of stiffness EJ and height h, obtaining the displacement

$$w = v\,(h^3\ m/3EJ)^{1/2} \tag{14}$$

and, from classic Clapeyron theorem, the design transverse force P is

$$P = mv^2/w \tag{15}$$

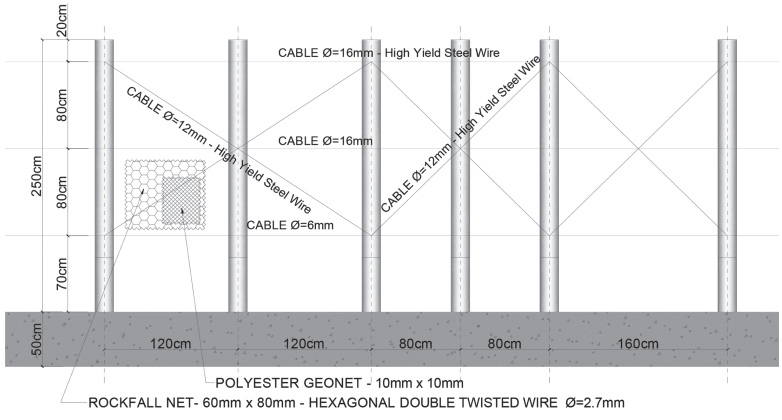

Figure 8. Details of steel barrier and protection wires.

4 CONCLUSIONS

Soil protection from landslides caused by rainfalls is a relevant theme in the management of territorial prevention. Periodical maintenance activities, such as cleaning and conservation of forest equilibrium, are crucial to preserve the land from the damage caused by climate change.

The illustrated example shows that periodical low-cost maintenance activities of the mountainside on a roadway could avoid relevant inconveniences for safety after a landslide has occurred, where the risk of detachment and rolling of blocks in absence of vegetation is increased. Simple models of several collapse scenarios of single blocks and of the entire slope are presented in order to provide tools for designing barriers and specific wires as in the described case study.

REFERENCES

Anderson, S. & Sitar, N. 1995. Analysis of rainfall-induced debris flow, *J. Geotech. Engineering* 121(7): 544–552.

Andreini, M., De Falco, A., Giresini L. & Sassu, M. 2013. Collapse of the historic city walls of Pistoia (Italy): Causes and possible interventions. *Advances in Civil Structures, Applied Mechanics Materials* 352: 1389–1392.

Andreini, M., De Falco, A., Giresini, L. & Sassu, M. 2013. Structural analysis and consolidation strategy of the historic Mediceo aqueduct in Pisa (Italy). *Advances in Civil Structures Applied Mechanics Materials* 351–352: 1354–1357.

Carrara, A., Crosta, G. & Frattini, P. 2008. Comparing models of debris-flow susceptibility in the alpine environment. Geomorphology 94(3–4): 353–378.

Corominas, J. & Moya, J. 2008. A review of assessing landslide frequency for hazard zoning purposes. *Engineering Geology* 102(3–4): 193–213.

Corominas, J., Westen, C., Frattini, P. et al. 2014. Recommendations for the quantitative analysis of landslide risk. *Bulletin of Engineering Geology and Environ.* 73(2): 209–263.

Crosta, G.B. & Frattini, P. 2008. Rainfall-induced landslides and debris flows. *Hydrological Processes* 22(4): 473–477.

Fell, R. 1994, Landslide risk assessment and acceptable risk. *Canadian Geotechnical Journal* 31(2): 261–272.

Gabet, E.J. & Mudd, S.M. 2006. The mobilization of debris flows from shallow landslides. *Geomorphology* 74(1–4): 207–218.

Gariano, S.L., Brunetti, M.T., Iovine, G., Melillo, M., Peruccacci, S., Terranova, O., Vennari, C. & Guzzetti, F. 2015. Calibration and validation of rainfall thresholds for shallow landslide forecasting in Sicily, southern Italy. *Geomorphology* 228(1): 653–665.

Guzzetti, F., Carrara, A., Cardinali, M. & Reichenbach, P. 1998. Landslide hazard evaluation: A review of current techniques and their application in a multi-scale study. *Central Italy Geomorphology* 31(1–4): 181–216.

Jaeger, C. 1979. *Rock Mechanics and Engineering.* 2nd edn. Cambridge: Cambridge University Press.

Karafiath, L.L. & Nowatzki, E.A. 1978. *Soil Mechanics for Off-road Vehicle Engineering.* Clausthal, Germany: Trans. Tech. Publications.

Mazziotti, L. 2010. *The Defence of Soil and Landslides in Italy.* Department of National Italian Fire Corps, Ministry of the Interior (in Italian).

Sassu, M., Andreini, M., Casapulla, C. & De Falco, A. 2013. Archaeological consolidation of UNESCO masonry structures in Oman: The sumhuram citadel of khor rori and the Al balid fortress. *Int. Journal of Architectural Heritage* 7(4): 339–374.

Stoffel, M., Butler, D.R. & Corona, C. 2013. Mass movements and tree rings: A guide to dendrogeomorphic field sampling and dating. *Geomorphology* 200(10): 106–120.

Van Westen, C.J., Castellanos, E. & Kuriakose, S.L. 2008. Spatial data for landslide susceptibility, hazard, and vulnerability assessment: An overview. *Engineering Geology* 102(3–4): 112–131.

Wyllie, D.C. & Mah, C.W. 2005. *Rock Slope Engineering-civil and Mining*. 4th edn. London: Spon (Taylor and Francis).

Civil Engineering and Urban Planning IV – Liu et al. (Eds)
© 2016 Taylor & Francis Group, London, ISBN 978-1-138-02903-3

A new principle of virtual power for elastoplasticity mechanics

Neng-Zhong Lei & Ie-Lung Chung
Department of Civil Engineering and Architecture, Wuyi University, Fujian, China

Yih-Hsing Pao
Theoretical and Applied Mechanics, Cornell University, Ithaca, New York, USA
Institute of Applied Mechanics, National Taiwan University, Taipei, Taiwan

ABSTRACT: In this paper, a new variational principle of virtual power is proposed based on the concept of rate variation. According to the principle of energy conservation, the power equation is derived by expressing the deformation power in terms of the variation rate of strain energy and dissipation power. By virtue of Poisson's transform, the complementary dissipation power is expanded as Taylor's series of stress rate, in which only a one-order quantity of the stress rate is considered. The variation of the power equation with respect to the quantity of the one-order derivative gives the general form of an elastoplastic constitutive equation. Different coefficients of one-order quantity may lead to different elastoplastic constitutive relations. The Prandtl-Reuss constitutive equation and Huang's constitutive equation are the two special examples of the result obtained in the present work.

1 INTRODUCTION

In early times, the yield surface elastoplastic model (yield surface) principle was used to construct the elastic and inelastic constitutive equations (Hill 1950; Ducker et al. 1957). Based on traditional plastic mechanics, the process could be divided into the yield function, the flow rule, and hardening law of three parts, but the relation of the three parts did not have a close contact with each other. Ziegler (1983) introduced the traditional theory of thermodynamics in solid mechanics. In Ziegler & Wehrli (1987), traditional thermodynamics were introduced into generalized strain and disperse stress, and assumes the dissipation function of energy function, so that the "dissipative generalized stress" is orthogonal to the level surfaces of the dissipation. The Second Law requires that energy be dissipated; the orthogonal principle requires the dissipation to be maximal. Under the orthogonal principle, the plastic constitution equation can be derived by using virtual work through the free energy function, and dissipation function can be derived into three parts of yield function, the flow rule, and hardening law. At first, the orthogonal principle, (Houlsby 1981; Houlsby 1982) was applied to the plastic mechanics and soil mechanics by using Ziegler theory. Houlsby & Puzrin (2000) used the thermodynamic model in rates independent of the material to construct the constitutive relation of elasticplastic mechanics; the elastoplastic theory was based on the laws of thermodynamics by using a free energy function and dissipation function. Meanwhile, the elastoplastic theory was combined with Ziegler orthogonal assumption to establish the constitutive model, and the yield function. The flow rule and hardening law are obtained from the free energy function and dissipation function.

By these research results, we first applied the laws of thermodynamics through the virtual power principle derived constitutive behavior of solid mechanics and fluid mechanics (Pao et al. 2011). In the previous study of the wider variational principles, the constitutive equations have to be known, which are the constraint conditions during the variational calculation. It is known that the distribution of the total energy in a material determines the constitutive equation. A power unit of volume in an elastoplastic body can be divided into two parts. One is the reversible part of the elastic potential energy, and the other is the irreversible part of energy dissipation. According to the law of conservation of energy, a power unit of volume can be derived from this law, and then, a concept of the linear term of variational principle is defined. A virtual power equation can be obtained by the combination of the linear term of variational principle and the Poisson transformation (Lanczos 1949). The energy dissipation function can be expanded into a Taylor series. By retaining only the linear term, the linear term of the elastoplastic

constitutive equation can be derived. The form of elastoplastic constitutive equation derived from Lubliner (1990) and Huang (1994) can be easily demonstrated by using this method.

1.1 *Derivation of elastoplasticity constitutive equations by using virtual power*

For the classical plasticity theory of the first and fundamental assumption, the strains ε can be decomposed into additive elastic and plastic components (Houlsby 1981):

$$\varepsilon = \varepsilon^e + \varepsilon^d \tag{1}$$

where ε^e is elastic part and the ε^d is plastic part. The principle of balance of energy states that the rate of change of energy equals the rate of work done by the external forces acting in the elastoplastic body. The mechanical rate of work can be shown that (Einav 2012):

$$\dot{w} = \sigma : \dot{\varepsilon} \tag{2}$$

where w is the internal energy per unit of volume of a strained body. To describe the elastoplastic behavior of the material, a power unit of volume can be decomposed into two parts. One is the reversible part of the elastic potential energy, and the other is the irreversible part of energy dissipation, which are defined as follows:

$$\sigma : \dot{\varepsilon} = \rho\dot{\hat{U}}(\varepsilon^e) + \hat{R}^w(\dot{\varepsilon}^d; \varepsilon^d) \tag{3}$$

where σ is the stress tensor, ε is the strain rate tensor, ρ is the density if the material, $\hat{U}(\varepsilon^e)$ is the elastic energy per mass of the material, and $\hat{R}^w(\dot{\varepsilon}^d; \varepsilon^d)$ is the complementary dissipating function. The rate of the elastic energy can be expressed as follows:

$$\rho\dot{\hat{U}}(\varepsilon^e) = \rho\frac{\partial\hat{U}(\varepsilon^e)}{\partial\varepsilon^e} : \dot{\varepsilon}^e \tag{4}$$

By using the variational operation, equation (3) can be expressed in terms of the form of increments as follows:

$$\sigma : \delta_1\dot{\varepsilon} = \rho\delta_1\dot{\hat{U}}(\varepsilon^e) + \delta_1\hat{R}^w(\dot{\varepsilon}^d; \varepsilon^d) \tag{5}$$

Using the Poisson transformation (Lanczos 1949), $\rho\hat{U}(\varepsilon^e)$ can be expressed as follows,

$$\rho\hat{U}(\varepsilon^e) \equiv -\rho\hat{G}(\sigma) + \sigma : \varepsilon^e \tag{6}$$

where $\rho\hat{G}(\sigma)$ is the elastic potential energy.

Differentiation of equation (6) with respect to time yields,

$$\rho\dot{\hat{U}}(\varepsilon^e) = -\rho\dot{\hat{G}}(\sigma) + \dot{\sigma} : \varepsilon^e + \sigma : \dot{\varepsilon}^e \tag{7}$$

In which

$$\rho\dot{\hat{G}}(\sigma) = \rho\frac{\partial\hat{G}}{\partial\sigma} : \dot{\sigma} \tag{8}$$

The variational of equation (7) yields

$$\rho\delta_1\dot{\hat{U}} = \rho\delta_1\dot{\hat{G}} + (\delta_1\dot{\sigma}) : \varepsilon^e + \sigma : (\delta_1\dot{\varepsilon}^e) \tag{9}$$

in which,

$$\delta_1\dot{\hat{G}} = \frac{\partial\hat{G}}{\partial\sigma} : \delta_1\dot{\sigma} \tag{10}$$

Similarly, we assume the dissipating function as follows,

$$\hat{R}^W(\dot{\varepsilon}^d; \varepsilon^d) = -\hat{R}^G(\dot{\sigma}; \sigma) + \sigma : \dot{\varepsilon}^d + \varepsilon^d : \dot{\sigma} \tag{11}$$

where $\hat{R}^G(\dot{\sigma}; \sigma)$ is the complementary dissipating function. The variational of equation (11) yields

$$\frac{\partial R^W(\dot{\varepsilon}^d; \varepsilon^d)}{\partial\dot{\varepsilon}^d} : \delta_1\dot{\varepsilon}^d = \frac{\partial\hat{R}^G(\dot{\sigma}, \sigma)}{\partial\dot{\sigma}} : \delta_1\dot{\sigma} + \sigma : (\delta_1\dot{\varepsilon}^d) + \varepsilon^d : (\delta_1\dot{\sigma}) \tag{12}$$

Substituting equations (1) and (7)~(12) into (3), it yields

$$\begin{aligned}\sigma : \delta_1(\dot{\varepsilon}^e + \dot{\varepsilon}^d) &= \left[\rho\frac{\partial\hat{G}(\sigma)}{\partial\sigma} : \delta_1\dot{\sigma} + (\delta_1\dot{\sigma}) : \varepsilon^e + \sigma : \delta_1\dot{\varepsilon}^e\right] \\ &+ \left[\frac{\partial\hat{R}^G(\dot{\sigma};\sigma)}{\partial\dot{\sigma}} : \delta_1\dot{\sigma} + \sigma : \delta_1\dot{\varepsilon}^d + \varepsilon^d : (\delta_1\dot{\sigma})\right]\end{aligned} \tag{13}$$

Eliminating $\sigma : \delta_1(\dot{\varepsilon}^e + \dot{\varepsilon}^d)$ from both sides of equation (13), it yields

$$(\varepsilon^e + \varepsilon^d) : \delta_1\dot{\sigma} = \rho\frac{\partial\hat{G}(\sigma)}{\partial\sigma} : \delta_1\dot{\sigma} + \frac{\partial\hat{R}^G(\dot{\sigma};\sigma)}{\partial\dot{\sigma}} : \delta_1\dot{\sigma} \tag{14}$$

Equation (14) represents a new variational constitutive equation for dissipative materials.

2 THE CONSTITUTIVE EQUATIONS

2.1 *Elastoplasticity*

Form equation (14), we eliminate the term $\delta_1\dot{\sigma}$ from both sides. The following equation is obtained:

$$\varepsilon^e + \varepsilon^d = \rho\frac{\partial \hat{G}}{\partial \sigma} + \frac{\partial \hat{R}^G(\dot{\sigma},\sigma)}{\partial \dot{\sigma}} \tag{15}$$

We split the both sides of equation (15) into the elastic and dissipative parts, i.e.,

$$\varepsilon^e = \rho\frac{\partial \hat{G}}{\partial \sigma} \tag{16}$$

$$\varepsilon^d = \rho\frac{\partial \hat{R}^G}{\partial \dot{\sigma}} \tag{17}$$

where $\hat{G}$ is the Gibb's function, and $\hat{R}^G$ is the complementary dissipating function. To determine the conservative part of the strain from the complementary energy function $\hat{G}(\sigma)$, we approximate Gibb's function in equation (16) by expanding $\hat{G}(\sigma)$ into a power series of σ, that is,

$$\hat{G}(\sigma) = S_{(0)} + S_{(2)} : \sigma + \frac{1}{2} S_{(4)} : \sigma : \sigma + \ldots \tag{18}$$

where $S_{(0)}, S_{(2)}, S_{(4)}$ are the zero-, second-, and fourth-order tensors independent of the stress tensor σ, respectively. Substituting equation (18) into (15), keeping the complementary energy function $\hat{G}(\sigma)$ to be the second-order of the stress tensor and applying the boundary conditions of $\sigma = 0$ and $\varepsilon^e = 0$, it yields

$$\varepsilon^e = \rho\frac{\partial \hat{G}}{\partial \sigma} = S_{(4)} : \sigma \tag{19}$$

Physically, $S_{(4)}$ represents the flexibility tensor of fourth-order. If the force rank tensor C is known, $S_{(4)}$ can be expressed in terms of C as follows:

$$C = S_{(4)}^{-1} \tag{20}$$

Substituting equation (20) into (19) yields,

$$\varepsilon^e = \rho\frac{\partial \hat{G}}{\partial \sigma} = C^{-1} : \sigma \tag{21}$$

It is obvious from equation (21) that when the elastic potential energy chooses a second-order tensor, the relation of the stress and strain is linear. The form of the plastic constitutive equation can be derived from the part of the complementary dissipating function. Similarly, we approximate the complementary dissipating function defined by equation (17) by expanding $\hat{R}^G(\dot{\sigma};\sigma)$ into a power series of $\dot{\sigma}$, that is,

$$\hat{R}^G(\dot{\sigma};\sigma) = \alpha_{(0)}(\sigma) + \alpha_{(2)}(\sigma) : \dot{\sigma} + \frac{1}{2}\alpha_{(4)}(\sigma)\dot{\sigma} : \dot{\sigma} + \cdots \tag{22}$$

where the $\alpha_{(0)}, \alpha_{(2)}, \alpha_{(4)}$ are the stress-dependent zero-, second-, and fourth-order tensors, respectively. If only the linear term of $\dot{\sigma}$ is retained in equation (22), we have

$$\frac{\partial \hat{R}^G(\dot{\sigma};\sigma)}{\partial \dot{\sigma}} = \alpha_{(2)}(\sigma) \tag{23}$$

For an elastoplastic material, when the stress exceeds its elastic limit stress, irreversible plastic deformation will develop.

Since $\dot{\sigma}$ changes its sign from positive to negative as the applied force changes from the case of loading to unloading, the value of $\hat{R}^G$ and thus ε^d fluctuate between positive and negative accordingly. The constitutive relation determined from the linear term as shown in equation (23) is then inherently unstable, and is usually discarded on physical ground. Let $\beta = 0$ for unloading after yielding and/or neutral loading and $\beta = 1$ for loading after yielding. Therefore, the plastic strain can be expressed as follows:

$$\varepsilon^d = \beta\frac{\partial \hat{R}^G}{\partial \dot{\sigma}} = \beta\,\alpha_{(2)}(\sigma) \tag{24}$$

The total strain of the elastoplastic body thus can be expressed as follows:

$$\varepsilon = \varepsilon^e + \varepsilon^d = C^{-1} : \sigma + \beta\,\alpha_{(2)}(\sigma) \tag{25}$$

Equation (24) is the elastoplastic constitutive equation. Differentiation on the both sides of equation (25) yields

$$d\varepsilon = d\varepsilon^e + d\varepsilon^d = C^{-1} : d\sigma + \beta\, d\alpha_{(2)}(\sigma) \tag{26}$$

The stiffness coefficient C in equation (25) is a material constant at a natural state, which is either known or experimentally measurable. The dissipative coefficient $\alpha_{(2)}$ is an unspecified function of stress at the current time t. For metal materials, the material can be assumed to be isotropic, and thus $\mathrm{d}\,\alpha_{(2)}$ is derivable from a scalar function $f(\sigma_f)$, where the argument σ_f is a scalar function of stress invariant. Thus, we obtain:

$$\mathrm{d}\,\alpha_{(2)} = \mathrm{d}\gamma \cdot \frac{\partial f(\sigma_f)}{\partial \sigma} \tag{27}$$

Substituting equation (27) into equation (26), it yields

$$\mathrm{d}\varepsilon = \mathrm{d}\varepsilon^e + \mathrm{d}\varepsilon^d = C^{-1} : \mathrm{d}\sigma + \beta \mathrm{d}\gamma \cdot \frac{\partial f(\sigma_f)}{\partial \sigma} \tag{28}$$

By assuming $\mathrm{d}\lambda = \beta \mathrm{d}\gamma$, equation (28) can be simplified as follows:

$$\mathrm{d}\varepsilon = \mathrm{d}\varepsilon^{e} + \mathrm{d}\varepsilon^{d} = C^{-1} : \mathrm{d}\sigma + d\lambda \cdot \frac{\partial f(\sigma_f)}{\partial \sigma} \tag{29}$$

where $\mathrm{d}\lambda = 0$ is for unloading after yielding and/or neutral loading, and $\mathrm{d}\lambda = 1$ is for loading after yielding. If the scalar function f is chosen as $f = 3J_2'$, where J_2' is the differentiation of the second-order of stress invariant, which can also be expressed as $J_2' = \frac{1}{2} S_{ij} S_{ij}$, where the S_{ij} is deviatoric stress. Note that

$$\frac{\partial f(\sigma_f)}{\partial \sigma} = S_{(2)} \tag{30}$$

$$\mathrm{d}\varepsilon = \mathrm{d}\varepsilon^{e} + \mathrm{d}\varepsilon^{d} = C^{-1} : \mathrm{d}\sigma + \mathrm{d}\lambda \cdot S_{(2)} \ (t_0 < t_Y < t) \tag{31}$$

Equation (31) is the constitutive equation, which, in the form, is the same as Prandtl-Reuss equation (Lubliner 1990). Similarly, if equation (22) is chosen as a second-order, and both of $\alpha_{(0)}$ and $\alpha_{(2)}$ are assumed to zero, then we have

$$\hat{R}^{G}(\dot{\sigma};\sigma) = \frac{1}{2}\alpha_{(4)}(\sigma)\dot{\sigma} : \dot{\sigma} \tag{32}$$

Substituting equation (32) into (17), it yields

$$\varepsilon^{d} = \frac{\partial \hat{R}^{G}}{\partial \dot{\sigma}} = \alpha_{(4)} : \dot{\sigma} \tag{33}$$

Again, differentiation of equation (33) on both sides, we obtain,

$$\mathrm{d}\varepsilon^{d} = \mathrm{d}\alpha_{(4)} : \dot{\sigma} \tag{34}$$

Let

$$\mathrm{d}\alpha_{(4)} = \mathrm{d}\lambda \cdot \frac{\partial f}{\partial \sigma}\frac{\partial f}{\partial \sigma} \tag{35}$$

Substituting equation (35) into (34), it yields

$$\mathrm{d}\varepsilon^{d} = \mathrm{d}\lambda \cdot \frac{\partial f}{\partial \sigma}\frac{\partial f}{\partial \sigma}\dot{\sigma} \tag{36}$$

After the plastic strain in the constitutive equation is solved, we can substitute equation (36) into (31). In this case the total strain can be expressed as follows:

$$\mathrm{d}\varepsilon = \mathrm{d}\varepsilon^{e} + \mathrm{d}\varepsilon^{d} = C^{-1} : \mathrm{d}\sigma + \mathrm{d}\lambda \cdot \frac{\partial f}{\partial \sigma}\frac{\partial f}{\partial \sigma}\dot{\sigma} \tag{37}$$

By assuming $\frac{\mathrm{d}\lambda}{\mathrm{d}t} = \frac{a}{h}, (h \neq 0)$ equation (37) can be expressed as follows:

$$\mathrm{d}\varepsilon = C^{-1}\mathrm{d}\sigma + \left(\frac{a}{h}\right)\frac{\partial f}{\partial \sigma}\frac{\partial f}{\partial \sigma}d\sigma \tag{38}$$

$$\Delta\varepsilon = C^{-1}\Delta\sigma + \left(\frac{a}{h}\right)\frac{\partial f}{\partial \sigma}\frac{\partial f}{\partial \sigma}\Delta\sigma \tag{39}$$

Equation (39) represents the differential form of the elastoplastic constitutive equation by (Huang 1994).

3 CONCLUSION

In this paper, we proposed the concept of the linear term of variational principle. According to this principle, we established a new principle of virtual power. According to the law of conservation of energy, the total energy of an elastoplastic body can be split into two parts. One is the reversible part of the internal energy, and the other is the irreversible part of energy dissipation. After variational and the use of Poisson transformation, the total energy of the elastic potential energy and the energy dissipation function can be expanded into a Taylor series in terms of the rate of stress. In this process, the differential form of Prandtl-Reuss constitutive equation can be derived by using the proposed new variational principle of virtual power.

ACKNOWLEDGMENT

This work is sponsored by Finance Department in Fujian of China under Contract No. 2014Y0040. The support is greatly appreciated.

REFERENCES

Ducker, D.C., Gibson, R.E. & Hankle, D.J. 1957. Soil mechanics and work hardening. *Theories of Plasticity Trans. ASCE*. 122(3): 338–346.

Einav, I. 2012. The unification of hypo-plastic and elasto-plastic theories. *International Journal of Solids and Structures* 49(11–12): 1305–1315.

Hill, R. 1950. *The Mathematical Theory of Plasticity*. Oxford: Oxford University Press.

Houlsby, G.T. & Puzrin, A.M. 2000. A thermomechanical Framework for Constitutive Models for Rate-independent Dissipative Materials. *International Journal of Plasticity* 16(9): 1017–1047.

Houlsby, G.T. 1981. *A Study of Plasticity Theories and Their Applicability to Soils*. Cambridge: University of Cambridge.

Houlsby, G.T. 1982. A Derivation of the Small-Strain Incremental Theory of Plasticity from Thermomechanics. Amsterdam: Proceedings of the International Union of Theoretical and Applied Mechanics (IUTAM), *Conference on Deformation and Flow of Granular Materials, Holland, Delft, 28–30 August, 1928*.

Huang, Z.P. 1994. A rate-independent thermoplastic theory at finite deformation. *Arch. Mech*. 46(6): 855–879.

Lanczos, C. 1949. *The Variational Principles of Mechanics*. 4th ed. New York: University of Toronto Press.

Lubliner, J. 1990. *Plasticity Theory*. New York: Macmillan Publishing Company.

Pao, Y.H., Wang, L.S. & Chen, K.C. 2011. Principle of virtual power for thermomechanics of fluids and solids with dissipation. *International Journal of Engineering Science* 49(1): 1502–1516.

Ziegler, H. & Wehrli, C. 1987. The derivation of constitutive relations from the free energy and the dissipation function. *Advances in Applied Mechanics* 25(1): 183–238.

Ziegler, H. 1983. *An Introduction to Thermomechanics*. Amsterdam: North-Holland.

This page intentionally left blank

Civil Engineering and Urban Planning IV – Liu et al. (Eds)
© 2016 Taylor & Francis Group, London, ISBN 978-1-138-02903-3

Economic incentive policy design for fabricated construction based on externality analysis

Guang-Chen Liu, Xin Li & Chun-Xia Wang
School of Management, Shenyang Jianzhu University, Shenyang, Liaoning, China

Wen-Jing Sun
School of Business, Liaoning University, Shenyang, Liaoning, China

ABSTRACT: Strong externality will lead to the failure of fabricated construction market. The Chinese government should urgently formulate corresponding economic incentive policies to promote the development of fabricated construction. In this paper, we use economic principles to analyze external hazards of fabricated construction. And the qualitative analysis on the main incentive bodies, incentive objects and targets are presented. Then, the evolutionary game model between the government and the developer group is established. From the model, we can obtain an effective range of government incentive strength and propose effective incentive proposals according to the different objects.

1 INTRODUCTION

Fabricated construction is a building technology system, which is a kind of generic Prefabricated Components (PC) that via proprietary connection technologies upgrade for factory production and field-based special mechanized assembly. Its mold production of components and parts can reduce material consumption and speed up the construction pace (Li 2012). The mechanization of site construction reduces the noise pollution and wastewater to ensure green construction. Fabricated construction reflects the good social, economic and environmental benefits, becoming a new construction mode to take the way of sustainable development. Papers about fabricated construction based on externality analysis are very few. Yang (2013) described the impacts of externalities on producers but not on consumers. Jin (2010) called for government subsidies, but did not give a reasonable explanation about the strength of subsidies. In this paper, the external influence on consumers is analyzed, and the quantitative analyses of subsidies are presented to provide new ideas for the government.

2 THE ORIGIN AND IMPACTS OF FABRICATED CONSTRUCTION'S EXTERNALITIES

2.1 *The origin of fabricated construction externalities*

Externalities refer to the behavior of economic agent damage or to other economic benefits, but there are no corresponding obligations or return. It can be divided into positive externalities and negative externalities. Positive externalities refer to an economic subject activity that benefits other people or society but cannot be compensated from other beneficiaries. The fabricated construction development of related subjects can save resources, reduce dust and noise pollution, reduce worker safety problems, alleviate labor shortages, greatly contribute to the progress of related industries, and effectively promote national economic development. Other subjects can gain benefits but do not pay the appropriate corresponding compensations to the related subjects. Therefore, fabricated construction has positive external effects.

2.2 *Positive external effects of fabricated construction's consumption*

Fabricated construction's consumption will produce external effects. External effects make a Marginal Private Benefit (MPB) less than the Marginal Society Benefits (MSB). So, the marginal private revenue curve below the marginal society benefits the curve. From the consumer's perspective, purchase quantity should be set at Y_1 to maximize profits, but consumption should be set at Y_2 to ensure the maximization of social benefits. Obviously, positive externalities lead to fabricated construction's consumption Y_1 and cannot achieve Pareto optimal social consumption Y_2. In Figure 1, Y represents fabricated construction's consumption, S is the fabricated construction's supply curve and MC is the marginal cost curve.

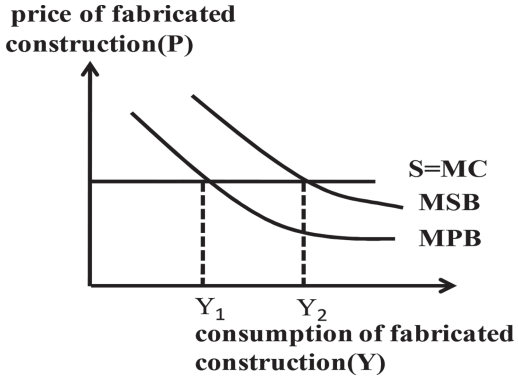

Figure 1. Positive external effects analysis of fabricated construction's consumption.

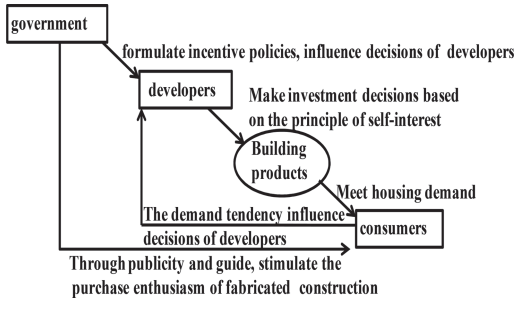

Figure 2. The relation diagram of incentive targets.

2.3 *Impact analysis of fabricated construction's externalities*

Based on the analysis of Figure 2, because of the positive externality, only through the market, it is difficult to guarantee that the supply and consumption of fabricated construction could meet the Pareto optimal market demand. So, the government must formulate reasonable economic incentive policies to ensure the fabricated construction products economically feasible and improve the enthusiasm of relevant subjects to promote fabricated construction development.

3 ECONOMIC INCENTIVE MECHANISM CONSTRUCTION OF FABRICATED CONSTRUCTION

Incentive mechanism design theory was presented by the famous American economist Holloway Hereby. Design theory studies about what kind of incentive mechanism makes people take actions to achieve social goals in the self-interest behavior driven by a certain economic, environmental and social goal. This paper is based on this theory and design for the fabricated construction incentive system, specifically including the main incentive bodies, incentive targets and incentive goals (Wang 2009).

3.1 *The main incentive bodies*

The development of fabricated construction will involve many stakeholders. As measured by the level of participation, high participation incentive key subjects include government, developers and consumers. At the same time, they also include incentive minor subjects such as the planning and design units, construction enterprises, supervision units, equipment suppliers and material property enterprises.

3.2 *Incentive objects*

Government should choose developers and consumers as the main incentive objects, and other related subjects as secondary incentive targets in accordance with the participation of different targets. According to the current situation, the leading real estate developers will be more likely to be engaged in the development of fabricated construction and have higher enthusiasm due to the in-depth understanding of the concept and advantages of fabricated construction. Therefore, the government should develop appropriate incentives for that type of real estate developers in order to better improve the supply of fabricated construction products.

3.3 *Incentive goals*

The first overall incentive goal is that, through the concept propaganda and the corresponding economic incentives, more consumers will accept fabricated construction and form the consumption demands gradually. The second one is to gradually cultivate and improve fabricated construction market mechanism so that market demands can be transmitted to the developers in a better way. With the government's administrative command policies and economic support, developers will choose fabricated construction as their best choice.

4 ANALYSIS OF THE INCENTIVE MECHANISM IMPLEMENTATION

4.1 *Condition constraints of incentive mechanism implementation*

The incentive mechanism enforcement of fabricated construction should be based on the principles of

"the internalization of external effects" and meet two condition constraints (Ji 2014) as follows:

- The government incentives should be moderate to achieve the desired effects and avoid excessive fiscal profligacy.
- Developers have the highest opportunity cost when they develop the fabricated construction with the economic incentives. It will be the optimal choice of all the investment programs consistent with the government's desired targets.

4.2 *Game analysis of incentive mechanism implementation*

Evolutionary game theory is based on the game analysis of the bounded rationality of game party to research the strategy adjustment process, trend and stability of group members.

Evolutionarily Stable Strategy (ESS) refers to the strategy adopted by the majority of the members of the population. Replicator dynamics equation is a dynamic differential equation, which describes that a specific strategy has been adopted in a group ratio equation (Zhu 2007).

Assuming that the government is a fully rational agent, the developer group is bounded rational agents, and they start actions after observing incentive policies proposed by the government. Developers adjust their strategies by following constantly and ongoing learning about other developers. Finally, the developer group finds the optimal strategy and reaches the game equilibrium state. Due to the different roles between developers and the government, there are also differences of their benefits. Their games are analyzed as follows.

P stands for the government incentive strength ($P \geq 0$, a larger P value indicates that the government incentive strength is greater). Q stands for the decision of the developer group. $Q = (Q_1, Q_2) =$ (the development of traditional architecture, the development of fabricated construction). And x stands for the proportion of Q_1 in the group and $1 - x$ represents the proportion of Q_2 in the group.

When the developers develop the traditional architecture, the developers and the government payment function U_d and U_g are expressed as follows:

- $U_d(Q_1) = m_1$. m_1 refers to the revenue of developers when they develop the traditional architecture.
- $U_g(Q_1) = n_1$. n_1 refers to the revenue of the government when the developer group develops the traditional architecture.

When the developer group develops fabricated construction, the developer group and the government payment function U_d and U_g are expressed as follows:

- $U_d(Q_2) = m_2 - k + m_3 + p$. m_2 refers to the income of the developers when they develop fabricated construction. k refers to the cost of the developers when they develop fabricated construction. m_3 refers to the additional income (e.g. brand benefits improvement) when the developer group develops fabricated construction. p refers to government incentive subsidies.
- $U_g(Q_2) = n_2 + n_3 - p$. n_2 refers to the revenue of the government when the developer group develops fabricated construction. n_3 refers to the government extra benefits such as resource-saving and environment improvement.

The average expected return for the developer group is $\bar{U}_d = U_d(Q_1) + (1 - x) \times U_d(Q_2) = x \times m_1 + (1 - x) \times (m_2 - k + m_3 + p)$.

The replicator dynamics equation $F(x) = dx/dt$ indicates the change rate when the developer group chooses the Q_1 strategy and the ratio is x. Then, $F(x) = dx/dt = x \times [U_d(Q_1) - \bar{U}_d] = x \times (1-x) \times [m_1 - (m_2 - k) - m_3 - p]$.

By solving $F(x) = 0$, we can get the steady-state point of the dynamic replication equation. Then, $x = 0$, $x = 1$, $P^* = m_1 - (m_2 - k) - m_3$. According to the stability theorem of differential equations, an evolutionary stable strategy requirement is $F'(x) < 0$. We can get $F'(x) = (1 - 2x) \times [m_1 - (m_2 - k) - m_3 - p]$.

When $P = P^* = m_1 - (m_2 - k) - m_3$. F (x) is always 0, and the proportion of the traditional architecture developer and the fabricated construction developer is in a relatively stable state.

When $p > p^*$, consider the two stable states $x = 0$ and $x = 1$, due to $F'(x = 0) > 0$, $F'(x = 1) < 0$, $x = 0$ is the only evolutionarily stable strategy. The developers will be able to benefit with this kind of incentive policy. Individuals will learn and imitate from each other. Finally, they will choose to develop fabricated construction and tend to be stable.

When $p < p^*$, due to $F'(x = 0) > 0$, $F'(x = 1) < 0$, $x = 1$ is the only evolutionarily stable strategy. The government incentive strength is lower than the expectation of incentive objects and the development of prefabricated construction will cause damage to the benefits of the developers. So, the developers choose the development of traditional architecture as an equilibrium strategy.

The government's expected revenue would be greater than or equal to the actual revenue when all developers choose to develop the traditional construction, and thus $\bar{U}_g = x \times U_g(Q_1) + (1 - x) \times U_g(Q_2) = x \times n_1 + (1 - x)(n_2 + n_3 - p) \geq n_1$. We can get $p \leq n_2 + n_3 - n_1$. A rational government should formulate the visionary incentive policy. In other words, $m_1 - (m_2 - k) - m_3 \leq p \leq n_2 + n_3 - n_1$. This incentive policy can make "the internalization of external economy" ensure resources, environment and long-term interests of the whole society.

5 SUGGESTIONS OF FABRICATED CONSTRUCTION PROMOTION

The government should take the form of "grass and sticks" to determine the guide mechanism mainly on the supply side and provide preferential subsidies in order to improve the enthusiasm of relevant subjects. At the same time, the government should take compulsory measures to make the related subject activities conform to the requirements of the policy and clear their responsibilities and obligations in order to better promote the development of fabricated construction. Concrete ways are given below.

5.1 *Financial support*

The government can set up "fabricated construction special research fund" to encourage enterprises and universities to do research work in the following areas in order to ensure fabricated construction technological innovation, products and management innovation:

- Sound module system, promote standardization of components and connection technology, develop evaluation system and technical regulations, form localization fabricated construction universal system.
- Promote the development of fabricated construction technology patents.

Moreover, the government should supply financial subsidies to fabricated construction developers according to the above analysis of the economic incentive intensity interval.

5.2 *Tax preferential*

- Technical advisory services fee and design fee in project decision-making and design stage should be plus 50% before the development enterprise income tax deduction (Li 2012).
- Social security fee of development projects that use the recommended directory components would be deducted from total project costs of fabricated component costs as the base to take into account.
- Corporate income tax, land tax, business tax and surcharges in the sales process of fabricated construction, which in line with the national standard of fabricated construction should be given a certain deferment and be exempted.
- For consumers, the government should reduce the house deed and fund loans payment proportion. Moreover, the government can give appropriate preferential lending rates to stimulate consumption demands.

5.3 *Other subsidies*

- The government should formulate volume rate rewards such as part of eligible construction area should be exempted and a certain percentage of roof greening can be included in the total green area.
- The government should open up the green channel to the examination and approval of the required documents related to fabricated construction.
- The depreciation and amortization period of the fabricated project land, factory buildings, equipments should be rationally determined according to their particularity.
- Fabricated construction projects should give priority to participate in all kinds of engineering construction awards.

6 CONCLUSION

At present, the construction industry is still in the extensive operational phase with the high consumption, high pollution and low efficiency. In order to better promote the transformation of the construction industry structure, we must promote the development of fabricated construction actively. Fabricated construction products have strong externality. Moreover, ordinary consumers lack enough understanding of fabricated construction and have no real feelings about house quality improvement. So, it is difficulty to improve the enthusiasm of producers and consumers at this stage. Only by establishing the scientific incentive mechanism and using a reasonable incentive means can we improve the fabricated construction market and promote the development of modern construction industry effectively.

REFERENCES

Ji, B.Y. et al. 2014. Obstacles and countermeasures for BIM application in building industry based on the externalities analysis. *Construction Technology* 43(03): 84–87.

Jin, Z.Y. et al. 2010. Economic Incentive Policy Design for Green Buildings Based on Externality Analysis. *Building Science* 26(06): 57–62.

Li, J.H. et al. 2012. *Study on the Restricting Factors of Development of Housing Industrialization and Countermeasures of China*. Chongqing: Chongqing University.

Li, T.H. et al. 2012. BIM and RFID assisted life cycle management of prefabricated buildings. *Journal of Engineering Management* 26(03): 28–32.

Wang, H.B. & Liu, C.B. 2009. Incentive mechanism design based on game analysis for new building energy efficiency. *Building Science* 25(02): 24–28.

Yang, J. 2013. Research on government economic incentive mechanism for green building promotion. *Journal of Shandong Jianzhu University* 28(04): 298–302.

Zhu, Q.H. et al. 2007. An evolutionary model between governments and core-enterprises in green supply chains. *Systems Engineering-Theory & Practice* 12(12): 85–89.

Civil Engineering and Urban Planning IV – Liu et al. (Eds)
© 2016 Taylor & Francis Group, London, ISBN 978-1-138-02903-3

Research on barriers analysis of formwork and BIM solution

Xuan Ji, Hong-Guang Zhu, Xiao-Di Zhang & Long-Feng Dong
School of Mechanics and Civil Engineering, China University of Mining and Technology, Beijing, China

ABSTRACT: As a concealed work phase in the building industry, formwork engineering has always been given less attention. Nowadays, in practice, formwork engineering continues to be in a state of disorder in terms of dispersed installation and detaching, careless slicing and cutting, and scattered remnants in the construction site. The current extremely far behind technological level, quality, lapping technique, formwork matching, cutting and turnover have a direct inverse influence on project quality, construction cost and duration. Building Information Modeling (BIM) technology has been increasingly and widely applied in the engineering project. Because it has quite obvious effects in the aspects of improving project quality, saving costs and shortening the construction period. Thus, the effective way to solve the problem of backward status of formwork engineering is by improving the involved people's attention to formwork engineering and by promoting the application of BIM technology in the field of construction formwork. The present paper attempts to shed some light on the current status of formwork engineering in China and the obstacles faced in the use of BIM solution in the construction industry.

1 INTRODUCTION

Formwork engineering refers to the fresh concrete modeling formwork and the whole set of structural system supporting it. In formwork engineering, the construction part in contact with the concrete and controlling its predetermined size, shape and location is known as the formwork. Members, trusses, connecting pieces, metal accessories and temporary bridges for construction support and fixing the formwork constitute the supporting system. Although formwork is a type of temporary structures in the construction of architectural engineering, it actually represents an important link between the engineering of reinforced concrete construction and the degree to which the technology is advanced. The latter fact has a direct influence on the quality, construction period and cost of the entire project [1]. These three aspects are further discussed as follows:

– Influence of Formwork Engineering on Project Quality: Formwork construction quality has played a decisive role in geometric dimensioning and appearance quality of concrete. Formworks with less joints, high-quality and smooth surface can reduce the face-work after the form is removed, which not only cut down materials expenses or labor cost required by face-work technique, but also increase the overall level of the project quality.
– Influence of Formwork Engineering on Construction Duration: Although the formwork engineering is considered a temporary, but instrumental, job, it occupies almost 30%–40% of the overall construction duration. Primary technical difficulties face many concrete structural engineering practices, such as stem from formwork engineering, thus the construction duration of the entire project is directly influenced by the formwork's technological level.
– Influence of Formwork Engineering on Construction Cost: In a typical construction project, the general cost of formwork represents 25%–30% of the total cost of reinforced concrete, while 30%–40% of the amount of labor required for the entire project is expended by the formwork works. Therefore, promoting the progress of formwork technology is an effective way to reduce the amount of formwork work and save labor expenses.

2 ANALYSIS OF BARRIERS TO FORMWORK IN CHINESE CONSTRUCTION INDUSTRY

The current state of technology of formwork engineering and scaffolding in China has not made much progress. Compared with developed countries, there still exist a comparatively large gap and numerous challenges with regard to the development of formwork industry. Among those challenges, the following features can be defined, as shown in Figure 1.

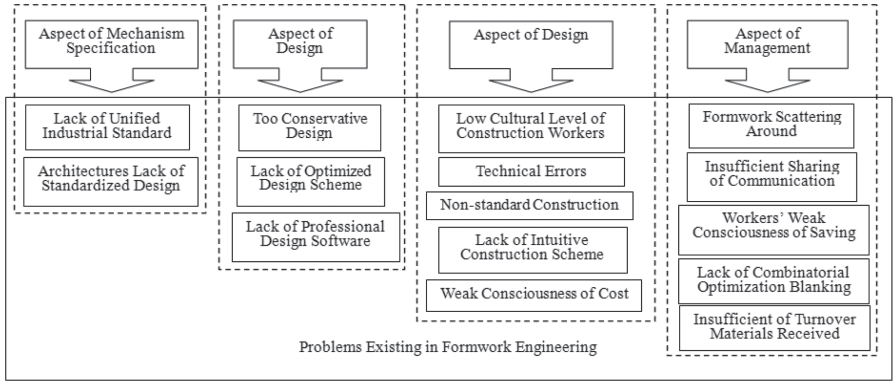

Figure 1. Obstructive factors affecting the development of formwork engineering.

– The aspect of mechanism specification
– The aspect of design
– The aspect of construction
– The aspect of management.

3 A NEW TECHNOLOGY PROMOTING THE DEVELOPMENT OF FORMWORK—BIM TECHNOLOGY

3.1 *BIM technology*

Using BIM, which stands for Building Information Modeling, a three-dimensional computer model is established for the building under consideration by means of digital technology. BIM also provides a database about the full life cycle of this building model. This information can be accessed, inserted, extracted, modified and updated by any party related to the project, with the continuous promotion of construction project. Therefore, BIM enables engineers, designers, supervisors and owners to comprehensively understand the project and improve the coordination skills among each party involved in the project. Compared with traditional project management, the advantages of BIM lie in the following aspects: helping to shorten project duration, providing a more reliable and accurate project budget, strengthening collaboration and information exchange among different project parties, providing a more efficient construction management, improving innovation and advancement of the project and offering a more convenient management and maintenance of equipment.

3.2 *The effect and application of BIM technology in domestic projects*

BIM has been applied relatively early in many countries around the world and has been effectively

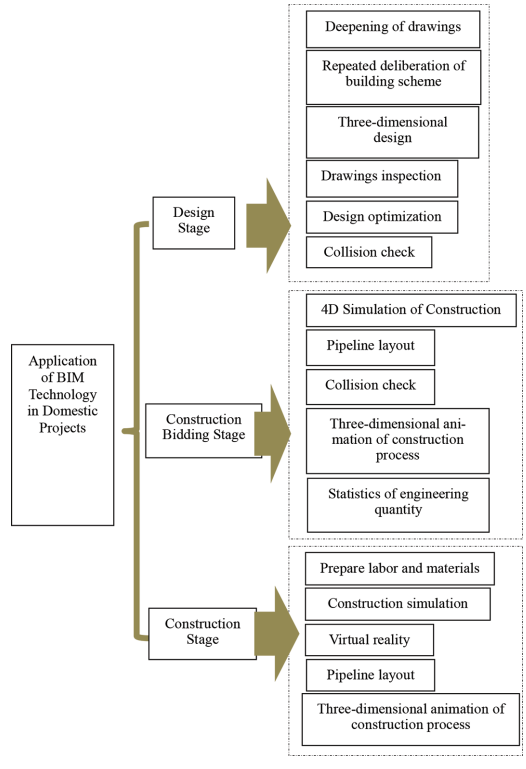

Figure 2. The application of BIM technology in domestic projects.

and successfully implemented in various projects. In China, on the other hand, research and application of BIM have been relatively late, and it has only been applied in some large-scale and complicated projects. At the present stage, the application of BIM in China has been concentrating on project display, communication and coordination

in the design stage, 4D simulation demonstration in the bidding phase and also engineering quantity statistics and construction simulation in the construction stage. Figure 2 shows a flow chart for the current application of BIM in China.

4 PROMOTING THE APPLICATION OF BIM IN THE FIELD OF FORMWORK ENGINEERING IN CHINA

According to the BIM system structure and data structure based on the IFC, the formwork engineering BIM system has been developed by using Autodesk Revit Architecture as the platform.

4.1 *Formwork engineering modeling based on BIM*

4.1.1 *3D geometric modeling based on Revit*

According to the definition of formwork engineering component in China's Construction Industry and special structural organization, it provides formwork components of different specifications and types and 4D modeling of construction facilities as the formwork supporting system, and also takes advantage of Internet explorer to realize the organization, classification, association and browsing of component modeling.

4.1.2 *Introduction of the optimization model of formwork engineering*

Establishing data exchange between 4D modeling and the formwork optimization model, it realizes the optimization process of formwork resources based on the information model of formwork construction optimization.

- Establishing, editing and querying of formwork engineering information: In this stage, establishing, editing and querying of formwork construction information are realized. This includes material properties, formwork collocation, formwork turnover, construction workers, machine and construction schedule. It can also provide the application of construction management system and operation maintenance system based on BIM.
- Input and output module of BIM model: In this stage, a BIM construction model is quickly created through introducing other BIM design software and the simulation process of formwork engineering construction is completed.

4.2 *Dynamic management system of formwork engineering based on BIM*

Dynamic Management System of Formwork Engineering mainly consists of three parts: optimization system of formwork engineering, construction simulation system of formwork engineering and project management system of formwork engineering. These three parts are shown in Figure 3 and discussed in further detail below.

- Optimization system of formwork engineering: In the part of the formwork optimization model, the formwork collocation is optimized, specifically the least break size, with the purpose of avoiding the waste produced due to cutting without plans. According to the divided

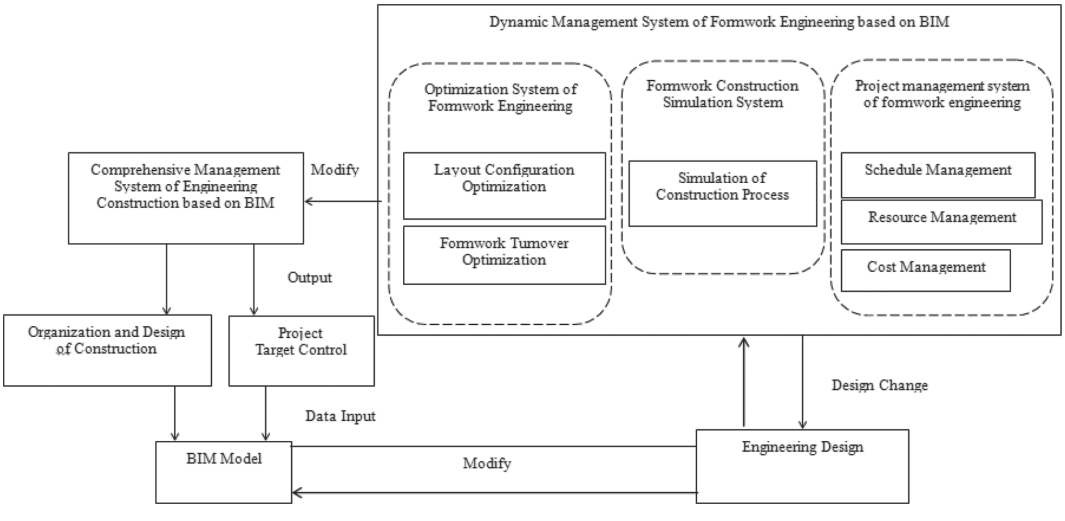

Figure 3. Overall structure of the BIM application system of formwork engineering.

construction segments, quantity of construction is segmented.

- Construction simulation system of formwork engineering: Depending on the divided construction segments and arranged construction schedule, in this part, the construction simulation of the formwork engineering is made. In the simulation process, formworks of different sizes are designated different colors. Being intuitive, clear and easier to understand, coloring the different formworks is convenient for workers to operate and reduce the error rate of formwork installation and improve the formwork turnover rate and work efficiency.
- Project management system of formwork engineering: During the construction process, various items can be automatically calculated. The items include engineering quantity and relative construction schedule's consumption of labor, materials and machine budget. According to the established Dynamic Management System of Formwork Engineering, an all-round management of formwork from optimized design can be made.

5 CONCLUSION

This paper focuses on the current status of formwork engineering in China. In recent years, BIM technology has been increasingly widely applied in the engineering of construction projects. Because BIM has many obvious positive effects in terms of improving project quality, saving costs and shortening the construction period, it has been appreciated by the public. Nowadays, formwork engineering practice in China is still in a chaotic state of dispersed installation and detaching, careless slicing and cutting, scattered remnants. The undeveloped current technological level, quality, lapping technique, formwork matching, cutting and turnover have directly affected the overall project quality, construction cost and duration. Therefore, the effective way to solve the problem of backward and stalemated status of formwork engineering is by improving the involved people's attention to formwork engineering and by encouraging the promotion of the application of BIM technology in the field of construction formwork.

REFERENCES

Bynum, P., Issa, R.R.A. & Olbina, S. 2013. Building information modeling in support of sustainable design and construction. *J. Constr. Eng. Manage.* 78(6): 24–34.

Bosché, F., Turkan, Y., Haas, C., & Haas, R. 2010. Fusing 4D modeling and laser scanning for automated construction progress control. *Proc., 26th ARCOM Annual Conf. and Annual General Meeting, Association of Researchers in Construction Management* 8(23): 28–33.

Choi, B., Lee, H.S. & Park, M., et al. 2014. Framework for work-space planning using four-dimensional BIM in construction projects. *J. Constr. Eng. Manage.* 5(34): 24–44.

Doloi, H. 2014. Rationalizing the implementation of web-based project management systems in construction projects using PLS-SEM. *J. Constr. Eng. Manage.* 10(106): 10–18.

El-Omari, S. & Moselhi, O. 2011. Integrating automated data acquisition technologies for progress reporting of construction projects. *Autom. Constr.* 20(6): 699–705.

Geem, Z.W. 2010. Multiobjective optimization of time-cost trade-off using harmony search. *J. Constr. Eng. Manage.* 34(5): 711–716.

Goedert, J.D., Sacks, R. & Hazzan, O. 2013. Integrating construction process documentation into building information modeling. *J. Constr. Eng. Manage.* 3(12): 78–86.

Hartmann, T. 2011. Goal and process alignment during the implementation of decision support systems by project teams. *J. Constr. Eng. Manage.* 36(2): 1134–1141.

Hasselhoff, J., Cheng, L.J. & Waimer, F. 2015. Design, manufacturing and testing of shear-cone connectors between CFRP stay-in-place formwork and concrete. *Composite Structures* 7(29): 47–54.

Lu, W.S., Peng, Y., Shen, Q.P., et al. 2013. Generic model for measuring benefits of BIM as a learning tool in construction tasks. *J. Constr. Eng. Manage.* 6(23): 195–203.

Mohammed, T.A., Rozana, Z., Rosli, M.Z., et al. 2014. Sustainability indicators for concrete formwork system. *Cement and Concrete Composites* 4(50): 60–72.

Ramesh, K. & Baskar, N. 2015. The simple genetic algorithm approach for optimization of nesting of sheet metal parts in blanking operation. *J. Constr. Eng. Manage.* 8(18): 41–53.

Salem, O. 2008. Project management practices and information technology research. *J. Constr. Eng. Manage.* 10(2): 501–508.

Sacks, R., Treckmann, M. & Rozenfeld, O. 2009. Visualization of work flow to support lean construction. *J. Constr. Eng. Manage.* 12(39): 1307–1315.

Turkan, Y., Bosché, F., Haas, C.T., Haas, R., et al. 2013. Toward automated earned value tracking using 3D imaging tools. *J. Constr. Eng. Manage.* 34(1): 423–433.

Civil Engineering and Urban Planning IV – Liu et al. (Eds)
© 2016 Taylor & Francis Group, London, ISBN 978-1-138-02903-3

Study on the optimization design of the suspended dome structure

Qiong Zhang, Ling-Yong Ma & Bing-Xin Gu
Architecture Engineering Department, Northeast Petroleum University, Daqing, Heilongjiang, China

ABSTRACT: In this paper, ANSYS software is applied to the optimal prestress and the vibration characteristic analysis of the suspended dome structure. According to the comparison with single-layer lattice shells, the structural characteristics of the suspended dome structure are superior to those of the single-layer lattice shells structure after the comprehensive action by the cable and the hoop cable. Through the modal analysis of the suspended dome structure, the structural natural vibration characteristics are determined, further understanding of the structural resonance region is acquired, weak links of the structure vibration are found, and guidance for the further engineering application is provided.

1 INTRODUCTION

With the rapid economic development, the demand on the construction has significantly increased. The new calculation theory, new structural materials and the new industrial technology promote a wide application of the spatial structure.

In the recent years, the string structure system has been applied more extensively in the structure of a large span of the new types of prestressed lattice structure (Chen 2011). Suspended dome structure first appeared in Japan, in 1993. Kawaguchi, a professor at Japan Hosei University, who made the combination of the cable-strut tensile structure and the single reticulated shell, formed a new hybrid space structure. Suspended dome structure is a new type of roof structure based on the tensegrity concept.

The concept of "Tensegrity" was put forward by the famous American architect Fuller. Its ideas are to minimize the compression state in structure; thus, the structure is in a continuous state of tension. It belongs to the balance spatial structure system of prestressing, as it uses the wire rope instead of the pull rod, typical for the traditional space structure, both to reduce the structure weight and to the benefit from the advantages of the cable tensile strength.

Prestress has a great influence on the static performance, stable performance and dynamic performance of this structure (Zhang et al. 2004). The main issues when designing the suspended dome structure are how to reasonably layout the lower cable-strut system, how to determine the appropriate prestress and how it can be distributed reasonably. If the prestress numerical is too large, it will cause the cable damage due to overload. If the prestress numerical is too small, it will not be able to satisfy the stress effect of the structure, falling short of the required stiffness. This paper proposes an effective and practical optimal design method to solve the problem of distribution and value of the prestressed suspended dome structure.

2 SUSPENDED DOME PRESTRESS OPTIMIZATION THEORY

Suspended dome structure can be called a high efficacy spatial structure system, and the main cause is the introduction of high strength cable and prestress. By applying prestress to the cable, the structure obtains the reverse displacement and internal force under the normal working load, and it effectively improves the mechanical behavior of the upper single-layer reticulated shell structure. Suspended dome prestress cannot be set too large, otherwise the permanent load on the structure will not be offset with the action of the upward and centripetal horizon. It produces an adverse effect on the structure, so prestress of the suspended dome structure setting exists as a group of optimal solution.

2.1 *Prestress optimization principle*

The main function of the prestress in the suspended dome structure is to reduce the radial horizontal constraint counterforce to peripheral components and the internal force peak value of the upper net shell structure, controlling the structural deformation and improving the stability of the structure. Regardless of the change in the member section, only the prestress of the lower ring of d cable-strut is used as an optimization variable.

In this paper, the ideal prestressed state should meet the following requirements:

– To ensure that all cables of the tensegrity structure should not slack under the normal working condition;
– To ensure that the prestressed state that is imposed can guarantee the desired geometry;
– To use the lowest prestress level to satisfy the above two conditions.

2.2 *Optimization steps*

This paper uses the ANSYS optimization module for the prestress optimization of the suspended dome structure to realize the optimization steps as follows:

– To build an optimization analysis file, including parameterized modeling, loading and solving of the model, extracting the finite element analysis results, assigning the value to the state variables (constraints) and using the objective function. To minimize the prestress level, the objective function is the minimum sum of squares of the structural member internal force after the prestressing, which is as follows:

$$f(x_i) = \sum_{i=1}^{m} \frac{1}{2}\left(M_{iL}^2 + M_{iR}^2\right) + \sum_{i=1}^{m} N_i^2, \quad j = 1, 2, ..., n. \tag{1}$$

where n is the number of cables; m is the number of structural variables; x_j is the initial strain of the first j root lasso; M_{iL} is the ith bar of the structure left end bar moment; M_{iR} is the ith bar of the structure right end bar moment; N_i is the ith bar of the structure axial force. The variable is given priority with accordance to tension and compression, while the moment can be ignored. The objective function can be further simplified to

$$f(x_i) = \sum_{i=1}^{m} N_i^2, \quad j = 1, 2, ..., n. \tag{2}$$

The constraint is the initial strain of the upper and lower limits of lasso.

– To build an optimized control file, including specifying optimization analysis file, declaring optimization variables, selecting the optimization tool or optimization method, specifying the optimization loop control method and evaluating the optimization parameters.
– Fixing the design variables, backing into circulation according to the completed optimization loop and the current state of the optimized variables.
– Checking the results of the implementation sequence and the post-processing design.

3 THE SUSPENDED DOME PRESTRESS OPTIMIZATION

3.1 *Suspended dome structure model*

In the process of the establishment of the model based on the parametric design language, APDL, which is easy to modify and maintain at work, the use of its loop statement can greatly reduce the analysis time and improve the efficiency of optimization (Mu 2006). Modeling steps are as follows:

– Establishing the node coordinates
Classifying and summarizing coordinates in this picture, establishing node coordinates of the suspended dome model, according to the design of CAD drawings (Industry standard 2011).
– Defining the type of element bar, real constant and material properties.
According to the mechanical characteristics, reticulated shell of the suspended dome is simulated by the beam-4 element. The connection between the upper brace strut and single-layer lattice shells is simplified to articulate; therefore, the brace strut is simulated by the Link-8 element; according to the characteristics of the ring cable, it can be pulled but cannot be pressured, so it is simulated by Link-10 unit element.
– Connection of unit bar
The variables of the suspended dome structure include the upper grid connection with brace strut, connection of the middle grid as well as ring cable.

Then, the finite element modal of the suspended dome structure is established by using the APDL language, as shown in Figure 1.

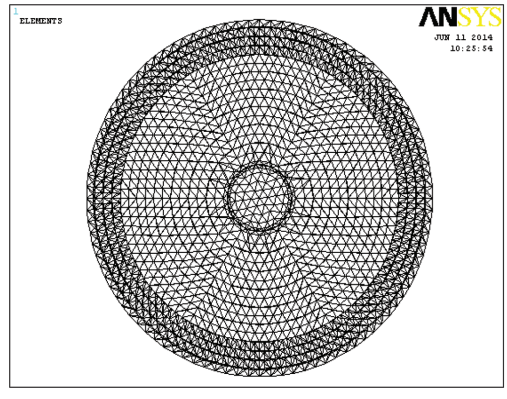

Figure 1. Suspended dome structure model of ANSYS.

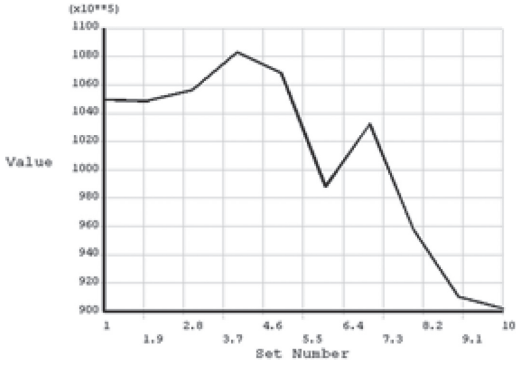

Figure 2. Relation curve of the set number and target variable.

3.2 *Specific optimization process*

– Applied load and constraints
  Applied load in this paper is the uniform load. the concentrated load of the upper grid is placed in the vertical position facing downward. However, in this way, it is unable to exert the unit load; therefore, the transformation is necessary as the concentrated load is applied into each node by simplifying. The uniform load is applied to each node on average.
– Optimization to solve
  According to the effect of the prestressed suspended dome, a maximum stress of the upper structure is defined as the target variable. The initial strain is controlled by means of virtual prestress. The initial values of a given virtual prestress are as follows: P1 = 250 KN; P2 = 450 KN; P3 = 650 KN; P4 = 850 KN; P5 = 1000 KN; P6 = 1200 KN.

To solve the analysis, 10 substeps, the N—R method and double constant loading + 0.5 times equivalent node load of the live load are considered.

After running an analysis in ANSYS, all optimized analysis results are obtained through the post-processing and are shown in Figure 2.

For the 10th step of the ridge cable, the best prestress value is 90 MPa and the initial value is 105.5 MPa. After the ANSYS optimization, the original value of the optimal rate approximates to 15%.

4 FINITE ELEMENT MODAL ANALYSIS OF SUSPENDED DOME STRUCTURE

Modal analysis is a type of a linear analysis, which can be used to determine the natural vibration frequency and a natural vibration type of the structure. The influence of any other nonlinear factor can be ignored in the analysis. It is the foundation of the dynamic analysis.

The modal analysis of the suspended dome structure is performed in order to reach the following goals: to determine the natural structural frequency and vibration mode, to obtain further understanding of the structural resonant region and to provide guidance for structural strengthening design.

The first five orders of the vibration mode diagram of the suspended dome structure are obtained through the modal analysis and are shown in Figure 3. The biggest displacement situation of the first five orders of the suspended dome structure are presented in Table 1. According to the analysis:

– Each vibration mode of the suspended dome structure shows different characteristics due to the symmetry of the structure. The intensive vibration frequency spectrum also appears at a condition when the multiple modal frequency is equal;
– Suspended dome structural vibration mode is divided into horizontal and vertical vibration; the horizontal and vertical displacement of

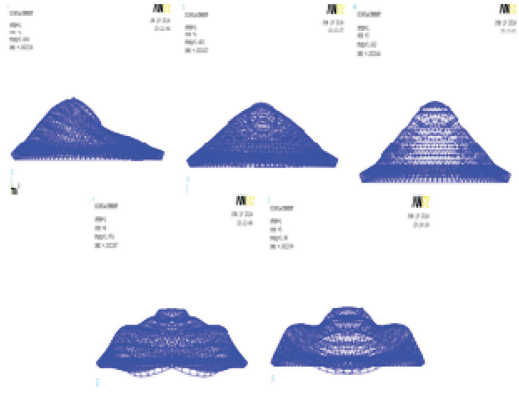

Figure 3. The first five orders of the vibration mode diagram of the suspended dome structure.

Table 1. The biggest displacement situation of the first five orders of the suspended dome structure.

Vibration mode	Period	UX (mm)	UY (mm)	UZ (mm)
1	0.313	0.894	0.958	1.584
2	0.313	0.957	0.890	1.870
3	0.282	0.579	0.610	2.563
4	0.252	0.564	1.245	3.062
5	0.252	1.234	0.556	3.088

each vibration mode is small and in the same magnitude;

– The first two orders of modal frequency are similar, the vibration mode is manifested as the horizontal vibration on the X-axis, the first order modal vibration along the reverse direction of the X-axis, the second order along the direction of the X-axis. The suspended dome structure produced an overall vertical vibration along the direction of the Z-axis in the third order of the vibration mode; the fourth and the fifth orders of vibration mode are the combination form of the horizontal vibration with the vertical vibration, the fourth order of the vibration mode is given the priority to the horizontal vibration and vertical vibration of the Y direction, while the fifth order of the vibration mode is given priority to the horizontal vibration and vertical vibration of the X direction, and the vibration mode is relatively stable.
– Due to the role of the lasso, in the bearing place of the suspended dome structure, the vertical and torsion deformation is produced, which goes against the stability of the structure.

5 CONCLUSION

Optimizing prestress of the upper part of the suspended dome structure by using the finite element analysis software ANSYS and the modal analysis is carried out on the structure at the same time. The conclusions are drawn as follows:

The prestress of this structure increases by 15% after the optimization, and the reduction in prestressing force is beneficial in decreasing construction difficulty.

The modal analysis of the results demonstrated that this structure produces a larger shift in the middle part, torsional deformation in the bearing part, and the resonance occurs over parts prone to damage; therefore, reinforcement treatment should be used across the parts of the structure in practical engineering.

REFERENCES

Chen, Z.H., 2011 Suspended-dome structural research and engineering practice. *Progress in Construction Steel Structure* 13(5): 11–20.

Industry Standard. 2011. *Technical Regulations of Space Grid Structure (JGJ7-2010)*. Beijing: China Building Industry Press.

Mu, Z.G., Hou, X.W., Ning, P.H. & Wu, J.R. 2006. Grid structural optimization design Based on discrete variables in ANSYS environment. *Journal of University of Science and Technology Beijing* 28(5): 417–421.

Zhang, M.S., Bao, H.Z., Zhang, Z.H. & Dong, S.L. 2004. Optimum design of Suspended-dome. *Journal of Spatial Structures* 10(3): 26–30.

Civil Engineering and Urban Planning IV – Liu et al. (Eds)
© 2016 Taylor & Francis Group, London, ISBN 978-1-138-02903-3

Dynamic analysis on the stability of high reinforced soil slope under seismic effects

Xiao-Song Tang
School of Civil Engineering, Chongqing University, Chongqing, China
Logistical Engineering University Chongqing, Chongqing, China

Jie Lai
Logistical Engineering University Chongqing, Chongqing, China

Ying-Ren Zheng
Logistical Engineering University, Chongqing, China
Engineering and Technology Research Center of Geological Hazard Prevention and Treatment, Chongqing, China

ABSTRACT: At present, there is a lack of reasonable design and calculation method for the high slope of reinforced soil. Based on the strict mechanic theories, the paper adopts FEM strength reduction to carry out static analysis and dynamic analysis under seismic effects on the high reinforced soil slope in Hechi Airport, Guangxi Province. The calculation results indicate that both the dynamic and static safety factors and the length of reinforced belt can satisfy the design requirement. The monitored data in the field are in coincidence with the result of numerical calculation, and the engineering project is stable and reliable after the completion of construction.

1 INTRODUCTION

At present, traditional calculation method of reinforced earth-retaining wall and slope is commonly used in the design, which is empirical to some degree and the scope of application is limited strictly according to the design code; for example, the slope height should be less than 20 meters (British Standards Institution 2010; Chinese Standards Institution 2002). So, the method in the code cannot be used for the high slope. FEM strength reduction can conduct a strict mechanic analysis on the reinforced earth-retaining wall and slope, so it is becoming widely used and adopted by some general and professional software applications, but it has been only used in static analysis so far (Damians et al. 2013; Bathurst et al. 2011; Liu et al. 2012; Miyata & Bathurst 2012). This paper induces the dynamic analysis of FEM strength reduction into the seismic design for reinforced soil slope through FLAC3D numerical analysis (Zheng et al. 2010; Zheng et al. 2009; Ye et al. 2010). Wenchuan Earthquake in 2008 proved that the reinforced earth-retaining wall and slope had good seismic performance. This paper also conducts dynamic analysis on the high reinforced soil slope under seismic effects in Hechi Airport, Guangxi. The results indicate that the engineering project has good seismic behavior and satisfies the dynamic design requirement. The methods in this paper are feasible and reasonable to analyze the seismic performance of reinforced earth-retaining wall and slope.

2 MECHANISM OF REINFORCED MATERIAL

In order to simulate the sliding phenomena between geo-grid and soil, contact elements are set in the calculation model, which can resist tensile and shear loads but cannot bear bending loads. The mechanic condition of the contact elements, assuming that the model can satisfy Mohr-Coulomb yielding criteria (Itasca Consulting Group 2003), is shown in Figure 1.

$$\tau = \sigma_m \tan\varphi_{inter} + c_{inter} \quad (1)$$

where φ_{inter} is the inner friction angle and c_{inter} is the cohesion of the contact element.

φ_{inter} and c_{inter} can be measured by drawing or shear experiments of reinforced material.

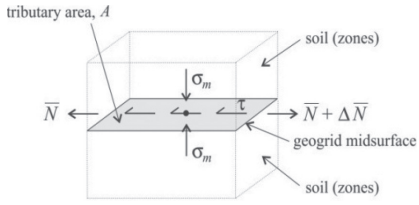

Figure 1. Mechanic condition of contact element between reinforced material and soil.

3 COMPLETE DYNAMIC ANALYSIS OF FEM STRENGTH REDUCTION

Different from the failure mechanism of the slope under the static condition, tensile failure would occur on the slope more easily due to the repetition of seismic load, so the tensile strength of rock and soil mass should be considered. The criteria of shear yield can be expressed as follows:

$$f^s = \sigma_1 - \sigma_3 N_\varphi + 2c\sqrt{N_\varphi} \quad (2)$$

The tensile yielding criterion is as follows:

$$f^t = \sigma_3 - \sigma^t \quad (3)$$

where c, φ and σ^t are, respectively, the cohesion, inner friction angle and tensile strength, where $N_\varphi = (1 + \sin\varphi)/(1 - \sin\varphi)$.

In the numerical analysis, the software of FLAC3D is combined with the complete dynamic analysis of FEM strength reduction to conduct the static and dynamic stability analysis on the high reinforced soil slope under static and seismic conditions. The strength is reduced according to Equations (4) and (5):

$$c' = c/\omega, \varphi' = \arctan(\tan\varphi/\omega) \quad (4)$$

$$\sigma' = \sigma^t/\omega \quad (5)$$

where ω is the reduction coefficient.

Through increasing ω continuously in the calculation to reduce the shear and tensile strength of rock and soil mass, the structure of reinforced soil can reach the limit equilibrium state so that failure will occur. Strength reduction is required to judge the failure, so the paper applies the following criteria to judge comprehensively: (1) the transfixion of failure surface (tensile-shear failure surface); (2) the mutation of displacement of the key points outside the failure surface. Under the seismic condition, loads on the slope would change with time so the displacement would change with time, which differs from the static condition. So, the mutation at a certain moment cannot be used to judge the slope failure. But the mutation of displacement after the seismic effects can be taken as a criterion. As a result, the mutation of the relationship curve between reduction coefficient and displacement can be usually used to judge the failure. (3) The convergence of the calculation. In the dynamic analysis of slope stability, all the above three criteria should be used at the same time to judge the slope failure.

4 PRACTICAL ENGINEERING IN HECHI AIRPORT

The calculation example is the DQ1 section, located in Hechi Airport, Guangxi Province, China. In order to reduce the engineering cost and space needed, the high reinforced soil slope is used to support, where the slope is 60 meters high, and is divided into 4 stages with 15 meters high per stage. Sidewalks with 3 meters wide are set between two stages.

4.1 *Selection of material parameters*

4.1.1 *Parameters of filling material*

In the DQ1 section, the size and composition of filling materials are complicated, mainly including coal gangue, medium-weathered mud, shale, limestone and the mixture of strong-weathered mudstone and coal gangue. The basic physical and mechanical parameters can be obtained through a large-sized triaxial compressive tester (as shown in Fig. 2), where the diameter of the sample is 300 mm and the height is 600 mm.

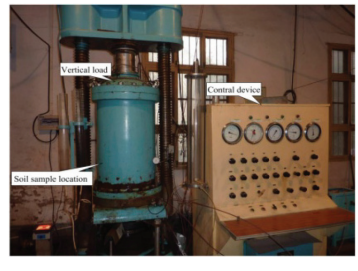

Figure 2. Large-sized triaxial compressive tester.

Table 1. Physical and mechanical parameters of soil.

Soil	Dry density (g/cm³)	c (kPa)	φ (°)
Coal gangue	2.15	260.57	38.8
Strong- and medium-weathered rock and soil	2.2	1700.65	31.4

Saturated and consolidated drained shear is used and the confining pressure is 0.1 MPa, 0.2 MPa, 0.4 MPa and 0.8 MPa, respectively. The physical and mechanical parameters of the two filling materials are listed in Table 1.

Due to the occlusion between rock particles, c is comparatively larger, as revealed by the test. Considering that the occlusion cannot be ensured in practical engineering, c is usually ignored or evaluated as a small value. For the sake of safety, the inner friction angle $\varphi = 30°$, $c = 5$ kPa and $\gamma = 20$ kN/m^3 are adopted in the calculation. The calculated parameters of filling materials and bedrocks in the numerical simulation are listed in Table 2.

4.1.2 *Parameters of reinforced materials*

The mechanical properties of the reinforced materials would influence the engineering safety directly, so the geosynthetic materials are tested in the the experiment. In practical engineering, steel and plastic cladding stripe (CAT stripe) is used. Its drawing force is 118 kN/m and the elongation is 2.5%, which is less than the requirement of 3%. The tensile stiffness of the reinforced belt can be worked out though the standard yielding elongation provided by the manufacturer, and the tensile stiffness EA is about 4700 kN/m to $EA = NL/\Delta l = 118/2.5\%$.

The φ_{inter} and c_{inter} of contact element are measured by the large-sized direct shear test, as shown in Figure 3. The diameter of the shear box in the test is 500 mm and the height is 500 mm; the maximum vertical pressure and the horizontal thrust is 700 kN; the maximum horizontal displacement is 150 mm. It was found that $\varphi_{inter} = 17°$ and $c_{inter} = 26$ kPa. The final mechanical parameters of the reinforced material and contact element are listed in Table 3. In the numerical simulation, the contact between the reinforced material and the surrounding soil is simulated through setting the coupling springs in FLAC3D. The transfer of stress between soil and grid should satisfies Mohr-Coulomb criteria, i.e. Equation (1).

4.2 *Layout of the high reinforced soil slope*

The height of the reinforced soil slope is 60 meters, being completed individually by four stages. Sidewalk with 3 meters wide is set every 15 meters along the height, as shown in Figure 4.

The comprehensive slope gradient of engineering is 1:2.5. The details of the engineering after construction are shown in Figure 5.

4.3 *Input seismic wave and boundary condition in dynamic analysis*

The input seismic wave in the calculation is Linghe Wave (Linghe 1995) and the peak value of acceleration is 0.17 g. The seismic wave is input bidirectionally in the numerical analysis, where the peak value of acceleration in the vertical direction is 2/3 of that in the horizontal direction. Free boundary field is adopted to prevent the reflection of seismic wave on the grid boundary, thus the boundary condition of unlimited field during earthquake can be simulated. Local damping of FLAC3D is used, which can satisfy the precision requirement in common engineering. The damping coefficient is 0.157. The major energy section is obtained artificially. The seismic wave after the correction of baseline is shown in Figure 6 when the seismic wave is input for 10 seconds.

4.4 *Results of numerical analysis*

First, the stability of engineering under gravity in static condition should be calculated to judge whether it can satisfy the static design requirement. Then, the dynamic safety factor of stress field under gravity and seismic effects is calculated to judge whether it can satisfy the dynamic design requirement.

4.4.1 *Calculation model*

The grid dividing and the location of monitoring points A-H during the numerical simulation are shown in Figure 7.

4.4.2 *Safety factor under gravity field*

The slope engineering is hierarchical construction. From Table 4, it can be seen that the safety factors of each stage are analyzed based on the theory of limit equilibrium and combined with the FEM strength reduction of FLAC3D to ensure the slope safety during the construction. Obviously, the safety factor of each stage can satisfy the specification requirements and the safety factor after supporting is 1.39 under gravity. The maximum force

Table 2. Physical and mechanical parameters of soil material in numerical simulation.

Materials	Density (kg/m^3)	Elastic modulus (MPa)	Passion ratio	c (kPa)	Φ (°)	Tensile strength (kPa)
Filling materials	2.0	90	0.3	5	30	–
Bedrocks	2.3	1600	0.14	1000	33	250

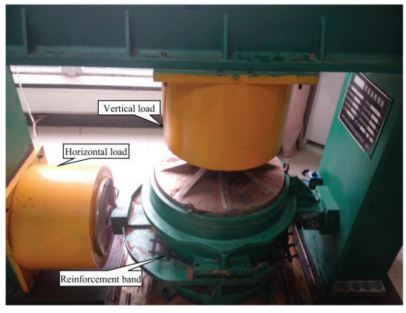

Figure 3. Large-sized direct shear test of the filling material.

Table 3. Parameters of reinforced material and contact element.

Types	Tensile stiffness EA (kN/m)	Cohesion (kPa)	Inner friction angle (°)
Reinforced material	4700	–	–
Contact element	–	26	17

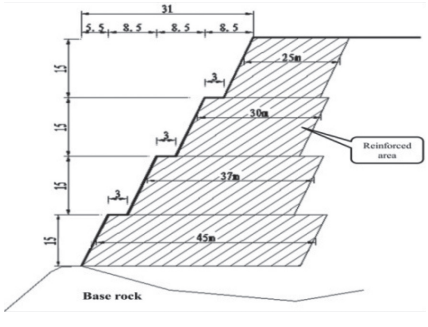

Figure 4. Layout of the reinforced earth-retaining wall in the DQ1 section.

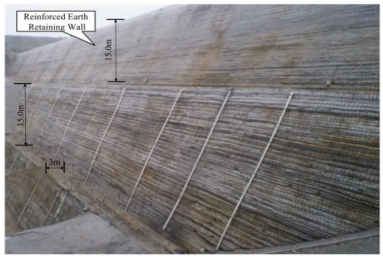

Figure 5. Reinforced earth-retaining wall after construction.

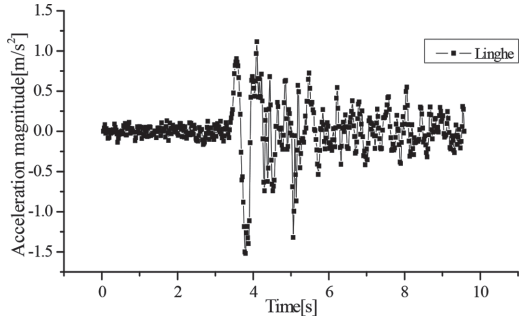

Figure 6. Time history of acceleration of the input seismic wave.

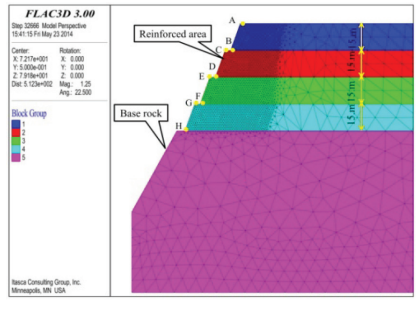

Figure 7. Numerical calculation of the slope.

Table 4. Safety factor of each stage.

Stages	The 4th stage	The 3rd stage	The 2nd stage	The 1st stage
Safety factor	1.75	1.58	1.45	1.39

on the reinforced belt is 92.54 kN/m and its strength reservation coefficient is 2.18, which can satisfy the design requirement under the static condition.

4.4.3 *Safety factor under gravity and seismic effects*

Dynamic analysis of FEM strength reduction is combined with FLAC3D analysis software to conduct the numerical simulation. To ensure safety, the peak value of the input Linghe seismic wave is set as 0.17 g, which is higher than the required fortification intensity in the area.

Figure 8 shows that mutation of the accumulated displacement of monitoring points occurs after the earthquake when the reduction coefficient is 1.17, and the slope failure can be judged initially.

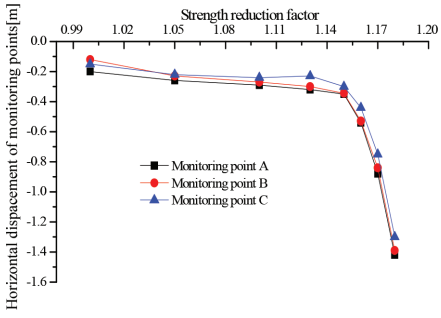

Figure 8. Relationship curve between displacement and reduction coefficient of monitoring points after earthquake.

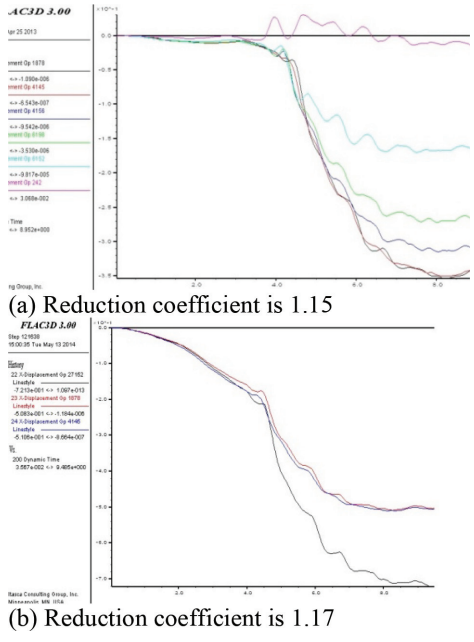

Figure 9. Time history of horizontal displacement of monitoring points under different reduction coefficients.

The dynamic safety factor of the slope should be between 1.16 and 1.18.

Figure 9a shows that the displacement convergence and the structure can still bear the loads after the earthquake when the reduction coefficient is 1.15. In Figure 9b, the displacement would be non-convergence and failure occurs when the reduction coefficient is 1.17. So, the dynamic safety factor under the seismic effects of the slope is 1.16.

When the failure occurs on the slope, the mutation of shear strain is especially obvious. Some phenomena in Wenchuan earthquake show that

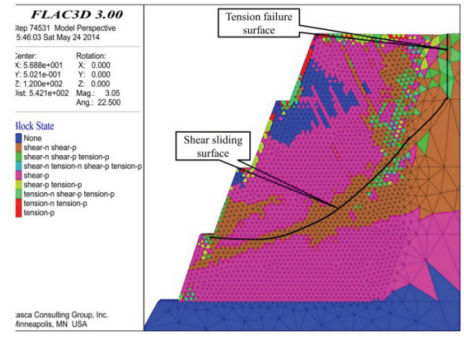

Figure 10. Failure state of elements.

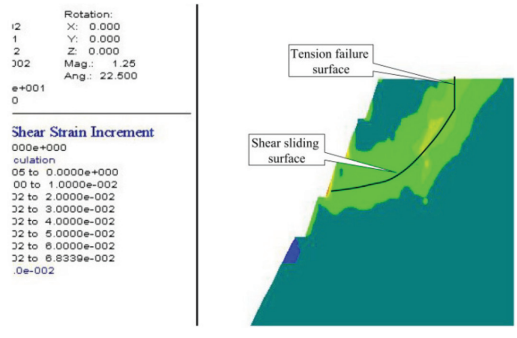

Figure 11. Nephogram of shear increment.

the failure surface of the slope is mainly composed of tensile failure in the upper part and shear failure in the lower part, so the tensile failure of the slope should be considered. As the failure state shown in Figure 10, tensile failure elements with a certain thickness exist on the top of the slope, so the location and state of failure surface can be judged comprehensively through the mutation points of shear strain and the failure state of elements. The location of failure surface under earthquake is indicated by the black line in Figures 10 and 11.

5 CONCLUSIONS

- The safety factor of the high reinforced soil slope in Hechi Airport is 1.39 under gravity, so the engineering is stable and reliable.
- Through inducing FEM strength reduction into the seismic design of high reinforced soil slope, the dynamic safety factor of the high slope is found to be 1.16 under Linghe wave whose peak value of acceleration is 0.17 g, which can satisfy the specification requirements.

– Dynamic analysis of FEM strength reduction is adaptable in the analysis on the high reinforced soil slope under seismic effects and can work out the combined tensile and shear failure surface of reinforced soil.

ACKNOWLEDGMENTS

This work was supported by the National Basic Research Program of China (973 Program, Grant No. 2011CB710603, 973 Program and Grant No. 2011CB013600) and the Chongqing natural science fund (Grant No. CSTC2013jcyjys0002).

REFERENCES

Bathurst, R.J., Huang, B. & Allen, T.M. 2011. Load and resistance factor design (LRFD) calibration for steel grid reinforced soil walls. *Georisk* 5(3–4): 218–228.

British Standards Institution. 2010. *Code of Practice for Strengthened/Reinforced Soil and Other fills.* BS 8006. U.K.: Milton Keynes.

Chinese Standards Institution. 2002. *Code for Seismic Design of Nuclear Power Plants.* GB50267–97. Beijing: China Planning Press.

Damians, I.P., Bathurst, R.J., Josa, A., Lloret, A. & Albuquerque, P.J.R. 2013. Vertical-facing loads in steel-reinforced soil walls. *J. Geotech. Geoenviron. Eng.* 139(9): 1419–1432.

Itasca Consulting Group, Inc. 2003. *FLAC. (Fast Lagrangian Analysis 2D) User's Manual, Version3.0. MI.Is.1.J.*

Liu, C.N., Yang, K.H., Ho, Y.H. & Chang, C.M. 2012. Lessons learned from three failures on a high steep geogrid-reinforced slope. *Geotextiles and Geomembranes* 34(5): 131–143.

Miyata, Y. & Bathurst, R.J. 2012a. Analysis and calibration of default steel strip pullout models used in Japan. *Soils Found.* 52(3): 481–497.

Ye, H.L., Zheng, Y.R., Huang, R.Q., Li, A.H., & Du, X.L. 2010. Application of dynamic analysis of strength reduction in the slope engineering under earthquake. *Eng. Sci.* 8(3): 41–48.

Zheng, Y.R., Ye, H.L. & Huang, R.Q. 2009. Analysis and Discussion of Failure Mechanism and Fracture Surface of Slope under Earthquake. *Chin. J. Roc. Mec. Eng.* 28(8): 1714–1723.

Zheng, Y.R., Ye, H.L. & Huang, R.Q. 2010. Study on the seismic stability analysis of a slope. *J. Earth. Eng. Eng. Vib.* 30(2): 173–180.

Civil Engineering and Urban Planning IV – Liu et al. (Eds)
© 2016 Taylor & Francis Group, London, ISBN 978-1-138-02903-3

Seismic performance of the Self-Centering Confined Masonry Wall with external steel dampers

Xiao-Bin Hu
College of Civil Engineering, Wuhan University, Wuhan, Hubei, China

Wen-Xia Li
Shandong Electric Power Engineering Consulting Institute Co. Ltd., Jinan, Shandong, China

Kun Liu & Lu Chen
College of Civil Engineering, Wuhan University, Wuhan, Hubei, China

ABSTRACT: The self-centering or rocking wall is characterized by a special base connection that isolates the wall from its foundation which ensures the controlled rocking behavior of the wall. This paper proposes a new type of Self-Centering Confined Masonry Wall (SCCMW) equipped with both unbonded tendons and external steel dampers. To investigate the seismic performance of the SCCMW developed in this paper, pseudo-static tests of the wall subjected to cyclic loading were performed. A special emphasis was given to evaluate the influence of parameters including the initial prestress in tendons as well as the yield force of dampers on the hysteresis behavior of the SCCMW. It is showed that the SCCMW remained intact during the loading process and no significant degradation in strength and stiffness was observed. It is also revealed that with the increase of the initial prestress in tendons, the self-centering ability of the wall is enhanced but its energy dissipation capacity is impaired. In addition, with the increase of the yield force of steel dampers, the energy dissipation capacity of the wall is improved but some residual displacement occurs.

1 INTRODUCTION

As one type of self-centering structural system, the self-centering wall or rocking wall consists of three parts including the wall, post-tensioned unbounded prestressed tendons and dampers. In contrast with the conventional wall structure, the self-centering wall is detailed to rock about the foundation by utilizing gap-opening behavior of horizon connections at the base or along the height of the wall.

To achieve a basic understanding of rocking behavior of the self-centering wall, a rigid wall model was proposed by Armouti (1993) and Kurama (1997), which describes the lateral hysteresis behavior of the wall as a rigid block on a rigid foundation. In the model, the gap opening at the base of the wall is resisted by spring elements at both ends and the concrete in compression is represented by compression link elements. Toranzo (2001, 2004) developed rocking confined masonry walls with hysteretic-energy-dissipators at their base and conducted shake-table tests on the reduced-scaled model. The experimental results show that the rocking confined masonry walls experienced no significant damage and can be successfully adapted to confined masonry structures. In addition, Toranzo (2001, 2004) proposed a numerical analytical model for the rocking wall, in which the wall is modeled by diagonal struts and the rocking at the base is simulated by a group of contact springs.

It can be seen that in the researches concerning the SCCMW, the wall is only equipped with the energy dissipators but not including the prestressed tendons, although they play a key role of improving the self-centering ability of the wall (Hu 2013). Therefore, a new type of SCCMW installed with both unbonded post-tensioned prestressed tendons and external steel dampers was developed in this paper. Its hysteresis behavior was then investigated by pseudo-static tests with attentions paid to evaluate the effect of parameters including the initial prestress in tendons as well as the yield force of dampers.

2 MECHANICS OF THE SCCMW PROPOSED IN THIS STUDY

2.1 *Configuration of the SCCMW*

The SCCMW proposed in this paper is schematically illustrated in Figure 1. The SCCMW is comprised of three main parts including the confined masonry wall, prestressed tendons and steel dampers. The masonry wall is confined by the peripheral concrete columns and beams. To avoid the likely occurrence

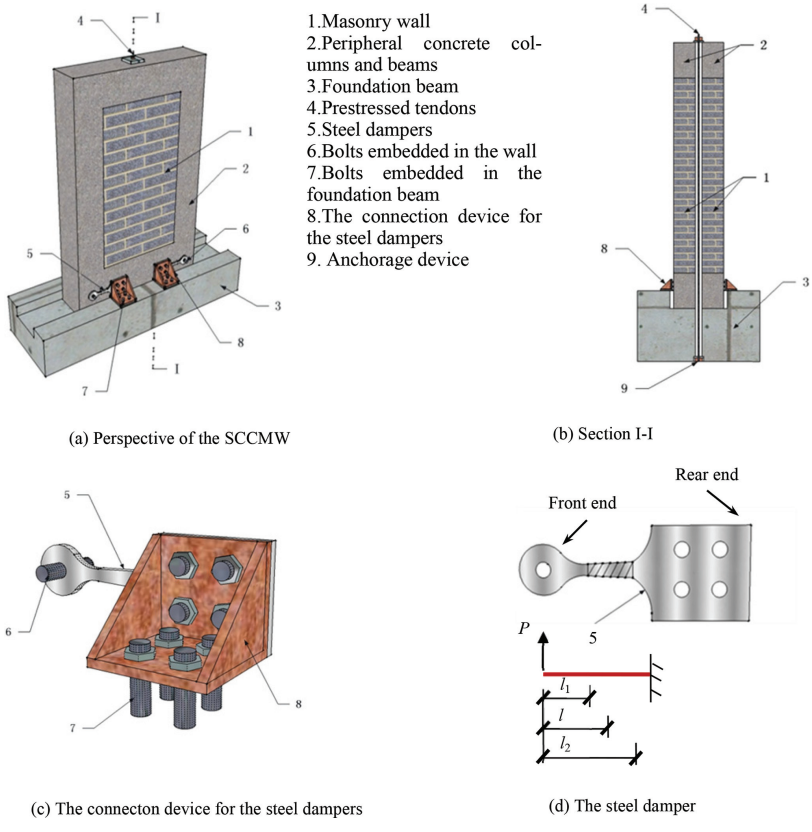

Figure 1. Schematics of the SCCMW proposed in this study.

of out-of-plane overturn, the masonry wall is placed on the foundation beam with grooved sections. The isolation interface between the wall and the foundation beam enables the controlled rocking mechanism of the wall dictated by the gap opening at the connection interface. A total of four steel dampers, two on each side of the wall, are placed near the two edges of the wall with the front end connected by bolts embedded across the wall. The rear end of dampers are bolted to a specially-designed device, as seen in Figure 1c, which is then connected to the foundation beam by embedded bolts. The prestressed tendon passes through the wall vertically by an embedded pipe along the centerline of the wall and has both ends fixed by anchorage devices.

2.2 *Detailing of the steel dampers*

The steel damper is made of mild steel with the nominal yield strength of 235 MPa. The damper rocks about its rear end as the rotation of the wall. It is desired that a large amount of energy dissipation happens in the middle hatched region of the damper when it yields in flexure, as seen in Figure 1d. In addition, the transition zones near the energy dissipation region are rounded to avoid stress concentration.

The steel dampers can be modeled approximately as a cantilever with variable sections, as seen in Figure 1d, where P denotes the force acting on the center of the front end of the damper. For an arbitrary section located in the energy dissipation region, the force upon its yielding can be calculated as

$$P_{\mathrm{y}} = \frac{f_{\mathrm{y}} W_{\mathrm{p}}}{l} = \frac{f_{\mathrm{y}} t h^2}{4l} \tag{1}$$

where f_{y} is the steel yield strength; W_{p} is the plastic section modulus; h and t is the height and width of the section respectively; l is the distance of P from the section. It is assumed that all the sections in the energy dissipation region yield simultaneously. Taking two end sections into account, from equation (1) it can be derived as follows,

$$\frac{h}{\sqrt{l}} = \frac{h_1}{\sqrt{l_1}} = \frac{h_2}{\sqrt{l_2}} \tag{2}$$

where, l_1 and l_2 are the distances of P from the end sections respectively; h_1 and h_2 are the corresponding section height, as seen in Figure 1d.

Equation (2) indicates that a parabolic shape of the energy dissipation region is required. However, the straight line shape is adopted alternatively, which can closely represent the parabolic curve and, what's more, ease the manufacturing process.

3 DESCRIPTION OF THE PSEUDO-STATIC TEST OF THE SCCMW

3.1 *Design of the test specimen*

The scaled prototype SCCMW is used in the test. The dimension of the test SCCMW is set to be 1.35 m × 1.0 mm × 0.24 m (height × width × thickness). The section dimensions of the peripheral concrete column and beam are both 0.2 m × 0.24 m (height × width). The foundation beam has the section dimension of 0.6 m × 0.4 m (height × width), and the groove depth is 0.1 m. In addition, to facilitate applying the initial prestress to the tendon, the concrete block with the dimension of 0.8 m × 0.6 m × 0.6 m (length × width × height) was placed between the foundation beam and the test floor.

The confined masonry wall was constructed by autoclaved sand-lime perforated bricks with the nominal compressive strength of 10 MPa. The reinforcements in the peripheral concrete column and beam as well as the foundation beam were detailed according to the constructional requirement, while the plain concrete was used for the concrete block. The concrete nominal compressive strength is 20 MPa and the steel nominal strength is 335 MPa. The prestressed steel strand with the nominal diameter of 15.2 mm and the nominal strength of 1860 MPa was selected to apply the initial stress.

To evaluate the effect of steel dampers on seismic performance of the test SCCMW, two steel dampers with different dimensions were fabricated, as showed in Figure 2. The two dampers are denoted as SD-1 and SD-2 respectively and have the same thickness of 10 mm. From equation (1), it can be obtained as follows

$$P_{y2} = 4P_{y1} \tag{3}$$

where, P_{y1} and P_{y2} represent the yield force of the SD-1 and SD-2 respectively.

3.2 *Loading device and instrumentation*

The loading device is displayed in Figure 3. The 60-ton capacity hydraulic actuator was attached to the reacting-force wall and exerted lateral load at the top of the test SCCMW by a connective holder. The foundation beam was fixed through the concrete block to the floor by four anchor bolts. A total of 3 displacement instruments were installed, among which the displacement instrument #1~#2 were mounted symmetrically at the top of the test SCCMW and used to measure the lateral displacement, and the displacement instrument #3 was arranged at the bottom aimed to monitor any horizontal slip of the wall relative to the foundation beam. Two load cells were used in the test but not shown in Figure 3, in which one was attached to the tendon to monitor the axial force and another one was connected to the load actuator to acquire the lateral force.

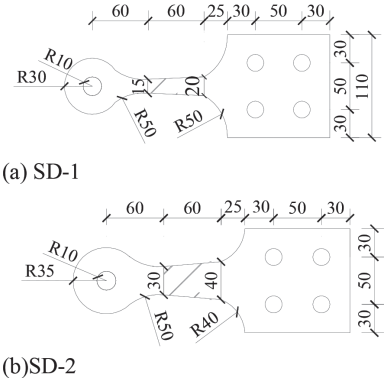

Figure 2. Dimensions of the steel dampers used in the test (unit: mm).

3.3 *Testing procedure*

The test SCCMW was loaded laterally using a displacement-control approach, for which the wall was subjected to various lateral drift cycles. The prescribed displacement loading history at the top of the test SCCMW is shown in Figure 4, where the positive value represents that the wall was pushed and the negative value represents that the wall was pulled. The magnitude of the first cycle is 4 mm, and it increases progressively by 4 mm until reaching 20 mm that corresponds to a roof drift ratio of 1.5 percent.

To investigate the effect of the tendon on seismic performance of the test SCCMW, three cases were taken into account: 1) the tendons were not installed; 2) the initial prestress in the tendon is zero; 3) the initial prestress in the tendon is 0.1 f_{ptk}, where f_{ptk} denotes the tendon nominal strength (1860 MPa). Similar to the prestressed tendon, three cases were also considered for the steel dampers: 1) the steel dampers were not installed; 2) SD-1

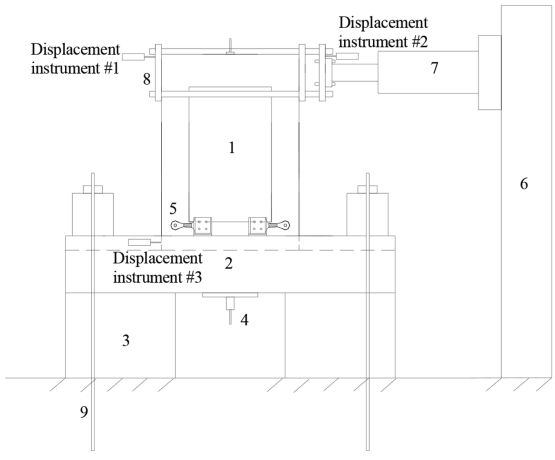

1.The test SCCMW
2.Foundation beam
3.Concrete block
4.Prestressed tendon
5.Steel damper
6.Reacting-force wall
7.Hydraulic actuator
8. Connective holder
9. Anchor bolts

Figure 3. Loading device and instrumentation.

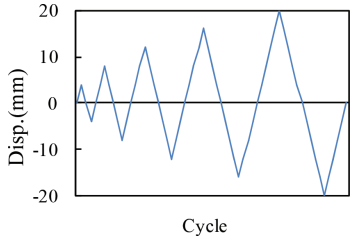

Figure 4. Displacement loading history.

Table 1. Loading cases scheduled in the test.

No	Type of the steel damper	Initial prestress in the tendon
1	*	*
2		0
3		0.1 f_{ptk}
4	SD-1	*
5		0
6		0.1 f_{ptk}
7	SD-2	*
8		0
9		0.1 f_{ptk}

* "*" in the Table means the steel damper or tendon is not included.

Figure 5. Photograph of the SCCMW test.

damper and 3) SD-2 damper were deployed respectively. Therefore, a total of 9 loading cases were scheduled as listed in Table 1. Figure 5 shows the photograph of the test.

4 EXPERIMENTAL RESULTS

4.1 *Observations in the test*

During the whole loading process, the peripheral column and beam of the test SCCMW remained intact and no obvious damage was observed in the masonry wall. The wall pivoted about its bottom edges and no obvious slip occurred between the wall and the foundation beam, which demonstrates the effectiveness of the detailing of the SCCMW. Obvious plastic deformation exhibited in the steel damper, indicating that it worked well as expected.

4.2 *Axial force in the tendon*

The loading case #6 is selected to investigate the variation of axial force in the tendon. Figure 6a shows the axial force in the tendon vs. the lateral displacement at the top of the wall curve. It can be seen that the axial force in the tendon varied incrementally with the rise of the lateral displacement of the wall. As the wall was unloaded completely, the axial force in the tendon basically returned to its initial value. The time history of the axial force in the tendon is presented in Figure 6b, showing that the maximum axial force in the tendon is 77.7 kN which corresponds to the maximum stress of 558.9 MPa. This value is much less than the nominal strength of the tendon (1860 MPa), indicating that the tendon kept elastic during the whole loading process.

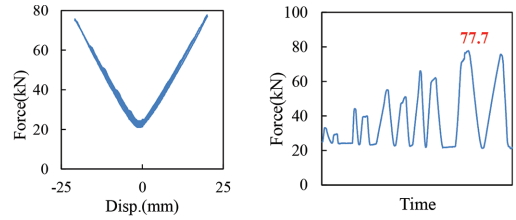

(a) *P-d* curve (b) *P- t* cuve

Figure 6. The axial force in the prestressed tendon.

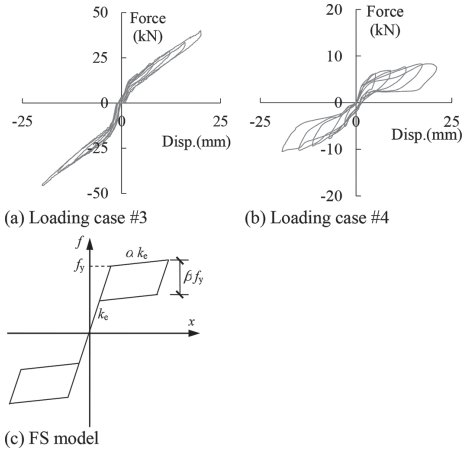

(a) Loading case #3 (b) Loading case #4

(c) FS model

Figure 7. Typical hysteresis curve.

4.3 *Hysteresis curves of the test SCCMW*

– Characteristics of the hysteresis curves

The lateral load vs. displacement hysteresis curves of the test SCCMW for some representative loading cases are plotted in Figure 7. It is found that no obvious stiffness degradation happened and negligible residual displacement occurred. It can be also seen that flag shape is typical of these hysteresis curves, thus the Flag-Shaped (FS) model (Christopoulos et al. 2002) can be well used to capture its hysteresis behavior. As shown in Figure 7c, the FS model can be determined fully by four independent parameters including the yield force f_y, the elastic stiffness k_e, the post-yield stiffness ratio α and energy-dissipation coefficient β.

It is interesting to find that the test SCCMW can still dissipate certain energy even though the steel dampers were not installed in the wall (e.g., Loading cases #1~3), as shown in Figure 7a. The reason may attribute to the certain friction force existing between some interfaces, e.g., the one between the wall and the foundation beam or that between the tendon and the pipe embedded in the wall. It is also worth noting that the test SCCMW has negligible residual displacement even though the prestressed tendon was not installed in the wall (e.g., Loading cases #1, #4, #7), indicating that the wall may achieve self-centering ability only by utilizing its self-weight.

– Effect of parameters on the hysteresis curves.

To investigate the effect of initial prestress in the tendon on hysteresis behavior of the test SCCMW, the hysteresis curves of the test SCCMW corresponding to various initial prestress in the tendon are plotted in Figure 8. It can be seen that the strength and stiffness of the test SCCMW are enhanced remarkably due to the addition of the prestressed tendon. The strengthening effect is more pronounced for the post-yield stiffness of the test SCCMW, which is positive after the installation of the prestressed tendon while tending to be zero or negative without the tendon.

It is also observed that with the increase of initial prestress in the tendon, the strength of the test SCCMW augments remarkably while the post-yield stiffness remains basically unchanged, indicating that the post-yield stiffness of the SCCMW is likely independent of the initial prestress in the tendon. In addition, the residual displacement of the test SCCMW upon the completion of unloading reduces with the increase of the initial prestress in the tendon, which means that it is effective to improve the self-centering ability of the SCCMW by increasing the initial prestress in the tendon.

Figure 9 displays the hysteresis curves of the test SCCMW corresponding to different steel dampers. It can be seen that after the addition of the steel damper, the hysteresis curves get plumper with larger enclosed areas, meaning that installation of the steel damper can enhance the energy dissipation capacity

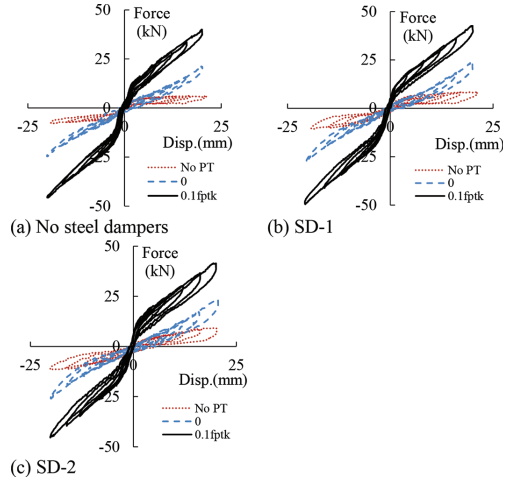

(a) No steel dampers (b) SD-1

(c) SD-2

Figure 8. Hysteresis curves corresponding to various initial prestress in the tendon.

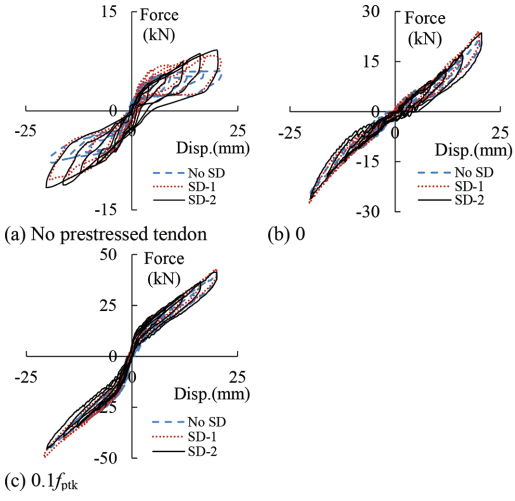

Figure 9. Hysteresis curves corresponding to different steel dampers.

of the SCCMW effectively. It is also found that the area enclosed by the hysteresis loop gets larger with the increase of the yield force of the steel damper, which indicates that the energy dissipation capacity of the SCCMW can be enhanced by raising the yield fore of the steel damper, whereas the residual displacement of the test SCCMW increases.

5 CONCLUSIONS

This paper developed a new type of SCCMW equipped with both unbounded prestressed tendons and external steel damper. The pseudo-static test of the wall subjected to cyclic loading was conducted to investigate its hysteresis behavior. The following conclusions can be drawn:

– During the loading process, the test SCCMW experienced no obvious damage and stiffness degradation. The hysteresis curve is characterized by flag shape, which can be described by the FS model.
– The strength and stiffness of the test SCCMW augment remarkably by the addition of prestressed tendon. With the increase of initial prestress in the tendon, the self-centering ability of the test SCCMW is enhanced but its energy dissipation capacity is impaired.
– The energy dissipation capacity of the test SCCMW gets improved with the installation of steel dampers. With the rise of yield force of steel dampers, the energy dissipation capacity of the SCCMW is enhanced but some residual displacement occurs.

ACKNOWLEDGEMENT

This work was supported by grants from The National Natural Science Foundation of China (51208386) and The Hubei Provincial Natural Science Foundation of China (2011CDB266) respectively. The authors are grateful to the sponsors. However, the opinions and conclusions expressed in this paper are solely those of the writers and do not necessarily reflect the views of the sponsor.

REFERENCES

Armouti, N. 1993. *Seismic Performance of Precast Concrete Structural Walls.* Bethlehem, PA: Department of Civil and Environmental Engineering, Lehigh University.

Christopoulos, C., Filiatrault, A.E. & Folz, B. 2002. Seismic response of self-centering hysteretic SDOF systems. *Earthquake Engineering and Structural Dynamics* 31(5): 1131–1150.

Hu, X. & He, H. 2013. Study on the mechanical behavior of self-centering wall under cyclic loading. *Engineering Mechanics (in Chinese)* 30(11): 202–206.

Hu, X., He, H., Peng, Z., et al. 2013. Study on the hysteretic performance of self-centering wall subjected to cyclic loading. *Journal of Building Structures (in Chinese)* 34(11): 23–28.

Kurama, Y.C. 1997. *Seismic Analysis, Behavior and Design of Unbonded Post-tensioned Precast Concrete Walls.* Bethlehem, PA: Lehigh University.

Mazzoni, S., McKenna, F., Scott, M.H., et al. 2006. Open system for earthquake engineering simulation user command-Language manual. OpenSees version 1.7.3, 2006.

Toranzo, L.A., Carr, A.J. & Restrepo, J.I. 2001. Improvement of Traditional Masonry Wall Construction for Use in low-rise/low-wall-density Buildings in Seismically Prone Regions. *New Zealand Society for Earthquake Engineering 2001 Conference, Wairakei, New Zealand, March 23–25, 2001.* New Zealand: New Zealand Society for Earthquake Engineering Inc.

Toranzo, L.A., Carr, A.J. & Restrepo, J.I. 2001. Displacement based design of rocking walls incorporating hysteretic energy dissipaters. *7th International Seminar on Seismic Isolation, Passive Energy Dissipation and Active Control of Vibrations of Structures, Assisi, Italy, October 2–5, 2001.* Italy: Foundation of the Anti-Seismic Systems International Society (ASSISi).

Toranzo, L.A. 2002. *The Use of Rocking Walls in Confined Masonry Structures: A Performance-based Approach.* Christchurch: University of Canterbury.

Toranzo, L.A., Carr, A.J., Restrepo, J.I., et al. 2004. Rocking Confined Masonry Walls with Hysteretic Energy Disspators and Shake-table Validation. *13th World Conference on Earthquake Engineering, Vancouver, Canada, August 1–6, 2004.* Canada: The Canadian Association for Earthquake Engineering under the auspices of the International Association for Earthquake Engineering (IAEE).

Civil Engineering and Urban Planning IV – Liu et al. (Eds)
© 2016 Taylor & Francis Group, London, ISBN 978-1-138-02903-3

Post-evaluation on wind power construction project

Yun-Na Wu, Zhi-Ming Lu & Xiang-Yu Zong
North China Electric Power University, Beijing, China

ABSTRACT: At present, with the increasing shortage of traditional energy and state support for the development of new energy industry, wind power industry seizes a great opportunity of development. In practice, the wind power project has many problems. Therefore, this paper conducted a post-evaluation research based on four aspects by applying the only reference comparison judgment method and fuzzy comprehensive evaluation, and put forward some valuable comments and suggestions.

1 INTRODUCTION

China is one of the largest contributors to the international carbon market (Zhou & Tong 2010). The government put forward "energy conservation and emissions reduction" to reduce the pollutant emissions and improve the utilization rate of unit energy in the 11th five-year plan for the first time (Wang & Peng 2012). At the same time, wind power causes less pollution. Development of wind power will help reduce air pollution. However, currently, post-evaluation on wind power construction project encounters the development bottleneck. Post-evaluation will provide a powerful guarantee for the successful implementation and operation of the future project if it is carried out very well. Researchers both at home and abroad have paid enough attention to the wind power project. Barroso made a project evaluation on the wind power projects in Germany (Barroso & Iniesta 2014). Wu studied the enterprises in China in order to determine how to make an evaluation on wind power project (Wu & Sun 2015). In order to lead the wind power construction projects to improve efficiency and achieve long-term sustainable development, this paper established the evaluation index system, and then an example was studied. Thus, this research will promote the development of wind power and contribute to the long-term development.

2 BUILDING THE EVALUATION INDEX SYSTEM

When selecting the evaluation indicators, we fully considered the differences between the wind power construction project and the general construction project. In addition, according to the actual characteristics of the wind power construction project and general principles, such as relevance, the evaluation system can be divided into four dimensions: early period of the construction process, middle period of the construction process, late period of the construction process and operational period. The final post-evaluation index system of the wind power construction project is presented in Table 1.

3 INTRODUCTION OF RELEVANT THEORIES

3.1 *The only reference comparison judgment method*

Suppose there is an index set $\{x_j\}$, first, the decision-maker finds the least important one from the index set and denotes it as x_{jm}, and then records them. The result is x_{ji}, x_{j2}, ... ,x_{jm} (Zhang et al. 2010):

$$x_{km} = x_{jk}/x_{jm} = a_k \in [d_{1k}, d_{2k}] = D_k \quad k = 1, \ldots m-1, d_{2k} > d_{1k}, d_{1m} = d_{2m} \tag{1}$$

$$d = d_{2k} - d_{1k} \tag{2}$$

$$c = (d_{1k} + d_{2k})/2 \tag{3}$$

$$e_k = c + \alpha d, \ -0.5 \le \alpha \le 0.5 \tag{4}$$

$$w_k = \frac{e_k}{\sum_{i=1}^{m} e_i}, \ k = 1,2,...,\mathrm{m} \tag{5}$$

3.2 *Fuzzy comprehensive evaluation*

Fuzzy comprehensive evaluation based on the fuzzy set theory is regarded as a new decision-making

Table 1. The post evaluation index system of the wind power construction project.

First class indicator	Second class indicators	Third class indicators
The post-evaluation index system of the wind power construction project	The early period of the construction process	International situation
		National policy
		Public support
	The middle period of the construction process	Construction schedule
		Construction cost
		Interest during construction
		Intermediate inspection program
	The late period of the construction process	Improvement of air quality
		Climate change
		Enhancement of regional impression
		Final delivery
	Operational period	Concept innovation
		Technical progress
		Routine maintenance
		Operating income

method that is particularly useful in a multi-variable circumstance (Guo et al. 2009). Results of project evaluation can be divided into five levels: very good, good, ordinary, bad and very bad.

4 BUILDING THE EVALUATION MODEL

- Determine the factor set $X = \{x_1, .., x_m\}$;
- Determine the evaluation set $Y = \{y_1,..., y_n\}$;
- Determine the weight;
- Determine the domain of comment;
- Assign the score to each evaluation project; and
- Make comprehensive evaluation and comparison.

5 EXAMPLE ANALYSIS

Based on the established index system in this paper, we carried out an analysis for wind power construction projects A, B and C. Three projects were located in three different places where the wind resource was abundant. In the process of building, relatively advanced technology was adopted, some equipment completed in batches was running for several years. During this period, regular maintenance and some routine overhaul activities were performed.

- x_1, x_2, x_3, x_4 represented the early period of the construction process, the middle period of the construction process, the late period of the construction process and operational period, respectively.
- y_1, y_2, y_3, y_4, y_5, represented very good, good, ordinary, bad and very bad levels, respectively.
- In terms of the secondary index, the late period of the construction process was regarded as the least important one through the expert's judgment. We obtained D1 = [2.2,2.8], D2 = [2.5,3], D3 = 1, D4 = [1.6,1.8], e = –0.3. The calculation result of the first class weight is given in Table 2.

So, the weight of the second class index was $w_2 = (0.31, 0.34, 0.13, 0.22)$.

Similarly, the weights of the third class index are given as follows:

$$w_{31} = (0.312, 0.375, 0.313),$$
$$w_{32} = (0.213, 0.234, 0.372, 0.181)$$

$$w_{33} = (0.101, 0.254, 0.237, 0.408),$$
$$w_{34} = (0.123, 0.241, 0.301, 0.335)$$

- The range of the very good level was (90,100], the range of the good level was (80,90], the range of the ordinary level was (70,80], the range of the bad level was (60,70], and the range of the very bad level was [0,60].
- Through the expert scoring, we obtained the following scores:

$$A: A_{31} = (70,85,80), A_{32} = (45,60,80,70),$$
$$A_{33} = (62,73,86,80), A_{34} = (80,70,85,90)$$

$$B: B_{31} = (62,80,82), B_{32} = (55,65,70,90),$$
$$B_{33} = (65,77,80,90), B_{34} = (70,75,83,82)$$

$$C: C_{31} = (65,88,86), C_{32} = (62,73,65,78),$$
$$C_{33} = (60,78,72,85), C_{34} = (73,72,78,88)$$

* The comparison of the early period of the construction process is given by

Table 2. The calculation result of the first class weight.

d	C	e_k	w_2
0.6	2.5	2.32	0.31
0.5	2.75	2.6	0.34
0	1	1	0.13
0.2	1.7	1.64	0.22
		7.56	1

$$\begin{bmatrix} 70 & 85 & 80 \\ 62 & 80 & 82 \\ 65 & 88 & 86 \end{bmatrix} * \begin{bmatrix} 0.312 \\ 0.375 \\ 0.313 \end{bmatrix} = \begin{bmatrix} 78.755 \\ 75.01 \\ 80.198 \end{bmatrix}$$

The result analysis indicated that in terms of the early period of the construction process, we could draw the conclusion C > A > B. In this period, B and A were ordinary, and C was good.

* The comparison of the middle period of the construction process is given by

$$\begin{bmatrix} 45 & 60 & 80 & 70 \\ 55 & 65 & 70 & 90 \\ 62 & 73 & 65 & 78 \end{bmatrix} * \begin{bmatrix} 0.213 \\ 0.234 \\ 0.372 \\ 0.181 \end{bmatrix} = \begin{bmatrix} 66.055 \\ 69.255 \\ 68.586 \end{bmatrix}$$

The result analysis indicated that with respect to the middle period of the construction process, we know that B > C > A, which were all bad.

* The comparison of the late period of the construction process is given by

$$\begin{bmatrix} 62 & 73 & 86 & 80 \\ 65 & 77 & 80 & 90 \\ 60 & 78 & 72 & 85 \end{bmatrix} * \begin{bmatrix} 0.101 \\ 0.254 \\ 0.237 \\ 0.408 \end{bmatrix} = \begin{bmatrix} 77.826 \\ 81.803 \\ 77.616 \end{bmatrix}$$

The result analysis indicated that with regard to the late period of the construction process, we know that B > A > C, B was good, and A and C were ordinary.

* The comparison of the operational period is given by

$$\begin{bmatrix} 80 & 70 & 85 & 90 \\ 70 & 75 & 83 & 82 \\ 73 & 72 & 78 & 88 \end{bmatrix} * \begin{bmatrix} 0.123 \\ 0.241 \\ 0.301 \\ 0.335 \end{bmatrix} = \begin{bmatrix} 82.445 \\ 79.138 \\ 79.289 \end{bmatrix}$$

The result analysis indicated that with respect to the operational period, we know that A > C > B, A was good, and B and C were ordinary.

* The comparison of the whole project is given by

$$\begin{bmatrix} 78.755 & 66.055 & 77.826 & 82.445 \\ 75.01 & 69.255 & 81.803 & 79.138 \\ 80.198 & 68.586 & 77.616 & 79.289 \end{bmatrix} * \begin{bmatrix} 0.31 \\ 0.34 \\ 0.13 \\ 0.22 \end{bmatrix} = \begin{bmatrix} 75.12803 \\ 74.84455 \\ 75.71428 \end{bmatrix}$$

The result analysis indicated that with respect to the whole project, we know that C was better than A and B, and B was the worst. They were all ordinary, so the wind projects needed some improvements.

6 CONCLUSION AND SUGGESTIONS

This article not only evaluated a project, but also made an evaluation of three projects, compared them, improved the accuracy of the results, and put forward some valuable advice for the development of Chinese wind power industry. Development of wind power that conforms to the sustainable development strategy will get a strong support from the state. Post-evaluation should be strengthened for the wind power construction project in the future. In addition, special attention should be paid to the middle period of the construction process.

ACKNOWLEDGMENTS

This work was financially supported by the National Nature Science Foundation of China (No. 71271085) and the Beijing Twelfth Five Year Plan Project of Philosophy and Social Sciences (No. 12JGB044).

REFERENCES

Barroso, M.M. & Iniesta, J.B. 2014. A valuation of wind power projects in Germany using real regulatory options. *Energy* 77: 422–433.

Guo, L., Gao, J., Yang, J. & Kang, J. 2009. Criticality evaluation of petrochemical equipment based on fuzzy comprehensive evaluation and a bp neural network. *Journal of Loss Prevention in the Process Industries* 22(4): 469–476.

Wang, W.M. & Peng, L.J. 2012. North China wind power layout evaluation under energy conservation and emissions reduction. *Renewable Energy* 4: 106–109.

Wu, Z.Q. & Sun, H. 2015. Behavior of Chinese enterprises in evaluating wind power projects: A review based on survey. *Renewable & Sustainable Energy Review*s 43: 133–142.

Zhang, P.F., Gu, J.A., Lv, X.F. & Zhang, Q.F. 2010. Research on manufacturing resources comprehensive valuation method based on user evaluation information. *The Mechanical design and Manufacturing* 7: 258–260.

Zhou, S. & Tong, Q. 2010. Study on the risk of uncertainty in the clean development mechanism project development. *Ecological Economy* 9: 26–29.

Civil Engineering and Urban Planning IV – Liu et al. (Eds)
© 2016 Taylor & Francis Group, London, ISBN 978-1-138-02903-3

Numerical simulation of peak strength reduction in rock under uniaxial cyclical compression

Hai-Long Zhang
Faculty of Architecture Engineering, Chongqing University of Arts and Sciences, Chongqing, China

Yang Tang, Can-Can Chen, Wen Nie, Kai Zhao & Shu-Min Ma
State Key Laboratory of Coal Mine Disaster Dynamics and Control, Chongqing University, Chongqing, China

ABSTRACT: Currently most rock fatigue damage models aim to calculate damage factor which cannot be directly used for estimation of peak strength changes. If reduction of peak strength links the cyclic loading directly, the evaluation of peak strength reduction under dynamic loading problem would be more effective. We numerically simulate rock damage under different cyclical stress amplitudes and average stress for the relation between peak strength reduction and number of cyclic loading. The primary damage model in terms of peak strength reduction under different cyclical stress amplitudes and average stress is constructed.

1 INTRODUCTION

Dynamic issues (fatigue damage) in rock mass as foundation, bridge, or slope, are very complex (Huang et al. 2008; He et al. 2009). Currently most rock fatigue damage models are developed from damage mechanics basic theory (Lemaitre 1984; Kachanov 1986; Lemaitre & Lippmann 1996). The linear fatigue damage models are developed from the Miner's rule which is probably the simplest cumulative damage model (Shimokawa & Tanaka1980) as

$$D = \sum_{i=1}^{k} \frac{n_i}{N_i} \tag{1}$$

If there are k different stress levels and the average number of cycles to failure at the ith stress, S_i, is N_i, then cumulative damage factor, D, where, n_i is the number of cycles accumulated at stress S_i. For nonlinear damage, considering micro-plastic strain (Fatemi and Yang 1998; Chaboche & Lesne 1988; Ge et al. 2003; Jian and Xu 2014), a model in the format of equation (2) is put forward as follows:

$$D = 1 - \left(1 - \frac{N}{N_f}\right)^{\frac{1}{\alpha+1}} \tag{2}$$

where, D is the cumulative damage factor. N is accumulated consuming life. N_f is the service life. α is material parameter.

It found that the key part is to determine the cumulative damage factor D for most fatigue damage model (Diederichs et al. 2004; Tang et al. 2002; Cai et al. 2004; Huang et al. 2002).

However, material peak strength is an important index in evaluation of construction reliability (VandenBerge et al. 2013; Cheng et al. 2007; Dawson et al. 1999) which few consider the effort from dynamic loading. If peak strength reduction and cyclic loading are linked directly, the evaluation of peak strength reduction under dynamic loading would be more effective.

In order to find how the cyclic loading affects the material peak strength and the relationship between strength and consuming and service fatigue life. This paper carried out the following work:

- Numerically simulate rock damage under different stress amplitudes and average stress of uniaxial cyclical compression;
- Test peak strength after different stress amplitudes, average stress, and number of cyclic loadings;
- Investigate the relation between residual peak strength and number of cyclic loadings given different stress amplitudes and average stress;
- Constructing the primary damage model in terms of peak strength reduction under uniaxial cyclical compression.

2 METHODS

2.1 *Brief descriptions of RFPA2D software*

A numerical tool, Rock Failure Process Analysis (RFPA2D) code (Tang & Kou 1998; Tang 1997),

has been used to simulate the failure process of specimens under uniaxial loading. The application of RFPA2D code shows some promises on genuinely modelling the failure behaviour of actual rock in a more realistic way (Tang et al. 1998; Tang et al. 2000a; Tang et al. 2000b; Tang et al. 2001; Wang et al. 2000; Wang et al. 2001). The idea of RFPA2D is fatigue damage of rock is caused by irreversible micro damage accumulation under load. Statistic damage model is based on Krajcinovic et al. (1982).

$$c(v) = \int_0^v TP(x)dx \tag{3}$$

$$D = c/T \tag{4}$$

$$D(v) = \int_0^v P(x)dx \tag{5}$$

where $c(v)$ is the damage elements in rock given loading v; T is the total elements in rock $p(x)$ is the PDF of damage elements in rock. In this software, the consideration of elements in rock is achieved by assigning the elements random strength and elastic modulus by assuming a Weibull's distribution, $\varphi(m,a_0)$, where the Parameter m is defined as homogeneity index, which controls the shape of the distribution function relating to the degree of material heterogeneity; a_0 is the parameter related to the mean value of the material parameters for the elements, such as strength and elastic modulus. The damage in the model is simulated as the reduction of material elastic properties. In order to quantitatively describe the damage accumulation, the code assumes that the Young's modulus of the damaged material E' can be estimated by reducing the Young's modulus of the initially undamaged solid E_0 as

$$E' = E_0(1 - D') \tag{6}$$

$$\sigma = E_0(1 - D')\varepsilon \tag{7}$$

D' is the damage parameter, depending on the loading history and determined by the failure criterion. The Poisson's ratio v for all the elements is assumed to be constant. The simulated elastic material, defined by E and v, is discretized using a finite element method to calculate the stress state in each element due to the loading.

Table 1. Parameters of numerical experiment.

Homogeneity index-m	5
Poisson's ratio-v	0.2
Young's modulus-E (average)	5900 MPa
Friction angle	30°
Density	2700 Kg/m^3
Compressive strength	23 MPa
Compressive-tensile ratio	10
Residual strength percentage	0.1
Residual Poisson's percentage	1.1

2.2 *Material property and experimental condition*

In our study, the model grid is 100 time 200. And the numerical specimen is 50 mm wide and 100 mm high whose parameters are shown in Table 1. The experimental steps are as follows:

- Stress-strain process: uniaxial loading is added gradually by increment of 0.5 MPa at every step until failure.
- Uniaxial loading is added in supposed value (stress amplitudes is 8, 9, 10, 11, and 12 MPa in our case) at step 2 and then unload to 1 MPa at step 3 (which means average stress is 4.5, 5, 5.5, 6, 6.5 MPa). Both the steps mean a cyclic loading.
- Residual peak strength: after different number of cyclic loading of fixed stress amplitude the uniaxial loading is added by an increment of 0.5 MPa until a failure.

3 RESULTS ANALYSIS

- Determining the stress amplitudes for fatigue failure. In Figure 1 the initial peak strength of rock specimen is 13 MPa. Generally, the fatigue strength of rock is in the range of 60–70% of peak strength. Thus, the minimum stress amplitude in our study is 8 MPa.
- "Structural" failure or "survival ratio" of rock specimens under different cyclic loading. The Figure 2 demonstrates the strains under different stress amplitudes of cyclical loading. It could be found that the high stress amplitude means short

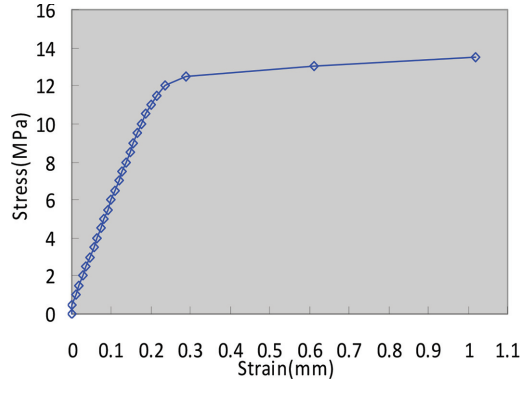

Figure 1. Strain-stress curve of numerical simulation.

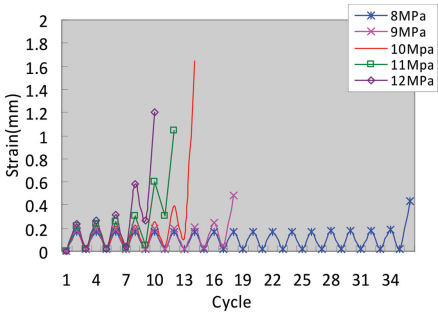

Figure 2. Strains-cyclical loading curve under different stress amplitudes.

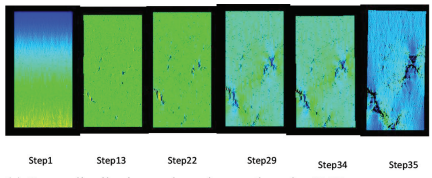

(a) Stress distribution and crack growth under 8MPa stress amplitudes

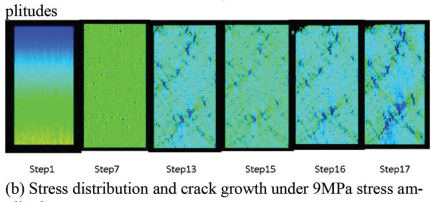

(b) Stress distribution and crack growth under 9MPa stress amplitudes

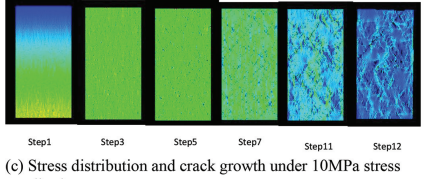

(c) Stress distribution and crack growth under 10MPa stress amplitudes

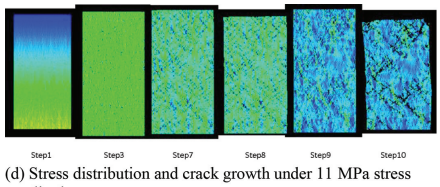

(d) Stress distribution and crack growth under 11 MPa stress amplitudes

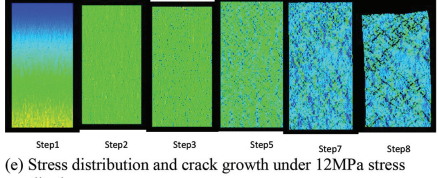

(e) Stress distribution and crack growth under 12MPa stress amplitudes

Figure 3. Stress distribution and crack growth under different stress amplitudes (Step1- no stress; the every following two steps mean a cyclical stress eg: step 2–3 is cycle 1).

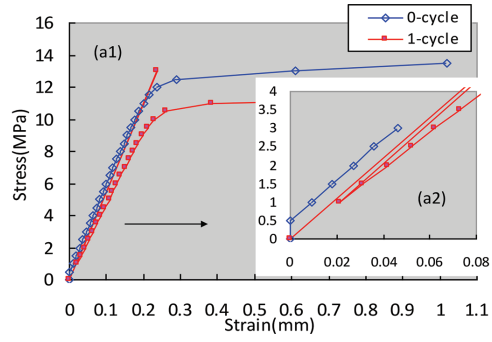

(a)Peak strength test after 1 cyclic loading

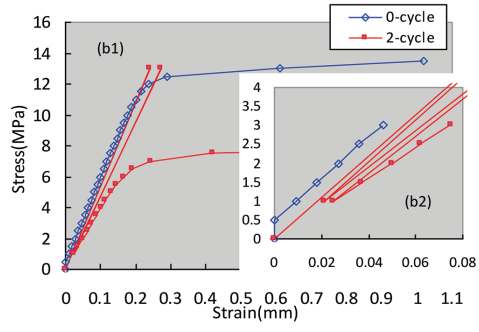

(b) Peak strength test after 2 cyclic loading

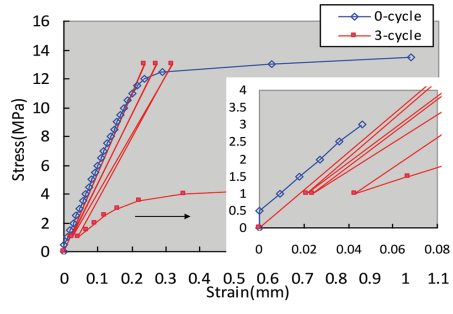

(c) Peak strength test after 3 cyclic loading

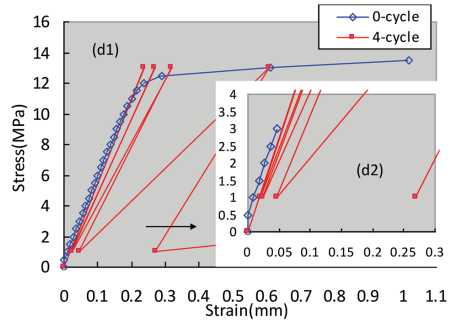

(d) Peak strength test after 4 cyclic loading

Figure 4. Peak strength test after cyclic loading (12 MPa).

survival life for example the 12 MPa stress refers to 5 cycles while the 8 Mpa stress needs 18 cycles for failure. Stress distribution and crack growth under different stress amplitudes could be seen in Figure 3.

– Peak strength test after different cyclic loadings (for example: 12 MPa) are shown in Figure 4. We could find that after every cycle the non-recovered displacement is increased. The peak strength also decreased with the increment of cycles.

4 DISCUSSION

In order to investigate the peak strength reduction under uniaxial cyclical compression, we separately obtain the peak strength under different loading cycles and stress amplitudes (average stress). And the strength is plotted to cyclic loading number in Figure 5. In addition, we introduced the peak strength factor S which could be considered as S_c/S_i vs. a cycle ration (life) as N/N_f.

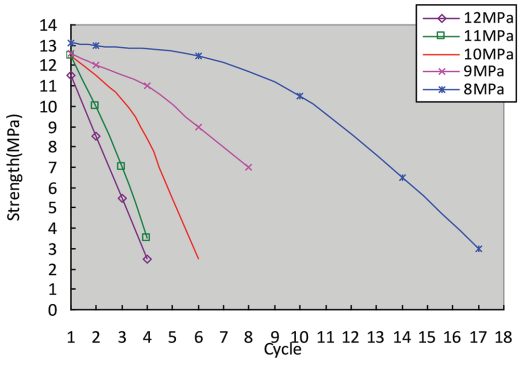

Figure 5. Peak strengths related to cyclic loading.

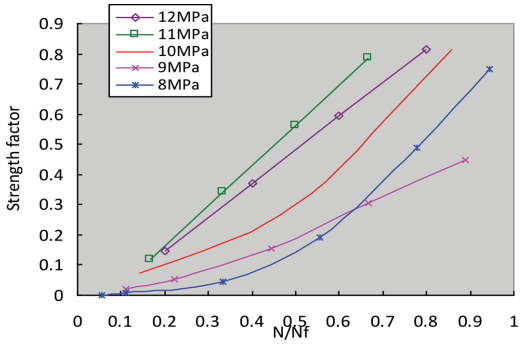

Figure 6. Curve between peak strength factor and cycle ratio.

Table 2. The parameters and error analysis.

Stress amplitude	8 MPa	9 MPa	10 MPa	11 MPa	12 MPa
β	0.396	0.297	0.657	1.0172	0.971
R-squares	0.964	0.986	0.951	0.961	0.987
SSE	0.025	0.0019	0.02	0.01	0.003
RMSE	0.071	0.021	0.063	0.06	0.032

where, S_c is the consuming peak strength; S_i is the initial peak strength. N is current number of cycles; N_f is the total number of cycles until failure. Thus, in Figure 6, we investigate the relation between peak strength factor and cycle ratio (both S and N/N_f are dimensionless units). The Table 2 shows the parameters and error analysis under stress amplitudes-8, 9, 10, 11, and 12 MPa.

It found that the relation between peak strength factor and cycle ration (consuming life) in equation (8) is very similar with equation (2)

$$S = 1 - \left(1 - \frac{N}{N_f}\right)^{\beta} \tag{8}$$

5 OUTLOOK

Crack growth under uniaxial compression could be estimated by equation (9) from Okubo (1984) for structural stability.

$$\frac{dl}{dt} = K^e (D_1 l^{-r} + D_2) \tag{9}$$

Here, l is the main crack length, K is the stress strength factor (proportional to peak stress), r, $D_1$and D_2 are constant, e is loading-rate dependent constant. While, crack growth under uniaxial cyclical compression will need more concerns in the future. In uniaxial cyclical compression environment, $1 - S$ is proportional to peak stress. Thus, $K = f(1-S)$ is assumed. Combining equations (8) with (9) the model of crack growth under loading-rate and cyclic loading could be as follows:

$$\frac{dl}{dt} = f(1-S)(D_1 l^{-r} + D_2) \tag{10}$$

The definition of this model will be our next jobs. We also have to point out in our study, different stress frequency, initial strength in rock, and homogeneity are not considered. In the future, these factors will affect the peak strength factor, which should be studied.

6 CONCLUSIONS

The test results revealed that the peak strength of the rock reduced while amplitude and dynamic loading average stress increased. The process can be described using peak strength factor not only cumulative damage factor. We consider rock mass stability under dynamic loading could be more conveniently estimated by peak strength factor.

ACKNOWLEDGMENTS

The research is supported by Study on the basic and frontier of Chongqing (ordinary, cstc2014jcyjA0994) and the Opening Fund of the State Key Laboratory of Coal Mine Disaster Dynamics and Control at the Chongqing University (2011DA105287-KF201312).

REFERENCES

Cai, M., Kaiser, P.K., Tasaka, Y., Maejima, T., Morika, H. & Minami, M. 2004. Generalized crack initiation and crack damage stress thresholds of brittle rock masses near underground excavation. International. *Journal of Rock Mechanics and Mining Sciences* 41(5): 833–847.

Chaboche, J.L. & Lesne, P.M. 1988. A continuous fatigue damage model. *Fatigue & Fracture of Engineering Materials & Structures* 11(1): 1–17.

Cheng, Y.M., Lansivaara, T. & Wei, W.B. 2007. Two-dimensional slope stability analysis by limit equilibrium and strength reduction methods. *Computers and Geotechnics* 34(3): 137–150.

Dawson, E.M., Roth, W.H. & Drescher, A. 1999. Slop stability analysis by strength reduction. *Geotechniue* 49(6): 835–840.

Diederichs, M.S., Kaiser, P.K. & Eberhardt, E. 2004. Damage initiation and propagation in hard rock during tunneling the influence of near face stress rotation. *International Journal of Rock Mechanics and Mining Sciences* 41(5): 785–812.

Fatemi, A. & Yang, L. 1998. Cumulative fatigue damage and life prediction theories: a survey of the state of the art for homogeneous materials. *International Journal of Fatigue* 20(1): 9–34.

Huang, C., Subhash, G. & Vitton, S.J. 2002. A dynamic damage growth model for unixal compressive response of rock aggregates. *Mechaincs of Material* 34(5): 267–277.

Kachanov, L. 1986. *Introduction to Continuum Damage Mechanics*. Berlin: Springer.

Krajcinovic, D. & Silva, M.A.G. 1982. Statistical aspects of the continuous damage theory. *International Journal of Solids and Structures* 18(7): 551–562.

Lemaitre, J. 1984. How to use damage mechanics? *Nuclear Engineering and Design* 80(2): 233–245.

Lemaitre, J. & Lippmann, H. 1996. *A Course on Damage Mechanics*. Berlin: Springer.

Okubo, S., Shin, K. & Nishimatsu, Y. 1984. Mathematical model of crack growth for sanjome andesite. *Journal of the Society of Materials Science* 33(370): 882–887.

Tang C.A., Lin, P., Wong, R.H.C. & Chau, K.T. 2001. Analysis of crack coalescence in rock-like materials containing three flaws-Part II: Numerical approach. *International Journal of Rock Mechanics Mining Sciences* 38(7): 925–939.

Tang, C.A. & Kou, S.Q. 1998. Fracture propation and coalescence in brittle materials under compression. *Engineering Fracture Mechanics* 61(3–4): 311–324.

Tang, C.A. 1997. Numerical simulation of progressive rock failure and associated seismicity. *International Journal Rock Mechanics and Mining Sciences* 34(2): 249–261.

Tang, C.A., Liu, H.Y. & Lee, P.K.K. 2000. Numerical tests on micro–macro relationship of rock failure under uniaxial compression, part I: Effect of heterogeneity. *International Journal of Rock Mechanics Mining Sciences* 37(4): 555–569.

Tang, C.A., Tham, L.G., Lee, P.K.K., Tsui, Y. & Liu, H. 2000. Numerical tests on micro–macro relationship of rock failure under uniaxial compression, Part II: Constraint, slenderness and size effects. *Internal Journal Rock Mechanics Mining Sciences* 37(4): 570–577.

Tang, C.A., Tham, L.G., Lee, P.K.K., Yang, T.H. & Li, L.C. 2002. Coupled analysis of Flow, Stress and Damage (FSD) in rock failure. *International Journal of Rock Mechanics and Mining Sciences* 39(4): 477–489.

Tang, C.A., Yang, W.T., Fu, Y.F., & Xu, X.H. 1998. A new approach to numerical method of modelling geological processes and rock engineering problems—continuum to discontinuum and linearity to nonl-inearity. *Engineering Geology* 49(3–4): 207–214.

VandenBerge, D.R., Duncan, J.M. & Brandon, T.L. 2013. Rapid Drawdown Analysis Using Strength Reduction. Proceedings of the 18th International Conference on Soil Mechanics and Geotechnical Engineering, Paris, September, 2–6, 2013. IOS Press.

Wong, R.H.C., Chau, K.T., Lin, P. & Tang, C.A. 2001. Analysis of crack coalescence in rock-like materials containing three flaws-I: Experimental approach. *International Journal of Rock Mechanics Mining Sciences* 38(7): 909–924.

Wong, R.H.C., Lin, P., Chau, K.T. & Tang, C.A. 2000 The effects of confining compression on fracture coalescence in rock-like material. *Key Engineering Materials* 183–187(2000): 857–862.

Wong, T.F. & Biegel, R. 1985. Effects of pressure on the micromechanics of faulting in San Marcos gabbro. *Journal of Structural Geology* 7(6): 737–749.

This page intentionally left blank

Civil Engineering and Urban Planning IV – Liu et al. (Eds)
© 2016 Taylor & Francis Group, London, ISBN 978-1-138-02903-3

The applied research of wind bolt and stable cable to the beam string structure

Fu-Ting Pan & Yi Lu
College of Civil and Environmental Engineering, Anhui Xinhua University, Hefei, Anhui, China

Li Zhang
Audit Department, Anhui Audit Vocational College, Hefei, Anhui, China

ABSTRACT: Beam string structure is a new type of long-span pre-stressed steel structure. When the wind suction exceeds the vertical downward load, the lower chords which are always made of cables will be inactive because of its zero tension stress. In this paper, the wind bole and stable cable are applied to the beam string structure, the bearing capacity and the overall stability of the structure after cable failure are analyzed using the general finite element software SAP2000. All of the work is aiming to provide references for designing.

1 INTRODUCTION

Beam string structure has been widely used in China because of its reasonable bearing behavior, beautiful appearance and economy. The overall stiffness of the structure is ensured by the cable tension to form a self-balancing system (Zhang et al. 2005). If the wind suction exceeds the vertical downward load, the lower chords which are always made of cables will be inactive (Bai et al. 2001). The bearing capacity and the overall stiffness of the structure are significantly reduced, so the wind resistance design is particularly important (Zhuang 2014).

2 THE BEARING CAPACITY CALCULATION

2.1 *The engineering situation*

The project is a corridor between two tall buildings, and the span of the beam string structure is 25 meters. Purlins are set up along the longitudinal direction, and it can be used as a vertical support for the beam string structure. The material selection and mechanical properties of the components are shown in Table 1.

According to the wind tunnel test, the air pressure is three times as much as the basic wind pressure in the region. In this paper, the bearing capacity and the overall stability of the beam string structure are analyzed by the general finite element software SAP2000 (Yang et al. 2002), and the calculation model is shown in Figure 1. The main chord is fixed on both ends hinged, and the torque is limited at the same time. Adopts the hinged connection between the purlin and the main chord (Spence & Gioffre 2011).

2.2 *The first design condition*

The bearing capacity of the beam string structure is calculated considering the combination of the dead load, the snow load, the wind pressure and the prestress. The program calculated the internal force of the structure under each load separately,

Table 1. Mechanical properties of components.

Component	Section shape	Steel material	Modulus of elasticity (MPa)
Main chords	$\Phi 324 \times 15$	Q345B	2.06×10^5
Truss braces	$\Phi 120 \times 10$	Q345B	2.06×10^5
Purlins	$300 \times 10 \times 12$	Q345B	2.06×10^5

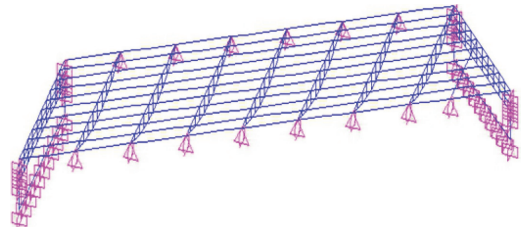

Figure 1. The calculation model of the beam string structure.

and then completed the internal force combination according to the requirement. The stress ratio of each bar are checked, which is shown in Figure 2. It can be seen that the stress ratio of each member is less than one, which means that all of the member are satisfied for the bearing capacity (Zhao & Liang 2015).

2.3 *The second design condition*

Since the wind suction exceeds the vertical downward load, the prestress cables will be inactive. The bearing capacity of the beam string structure is calculated considering the combination of the dead load, the wind suction and the prestress. After the procedure, the bearing capacity of some members is not satisfied (Zhang et al. 2004).

Stainless steel wind bolts are added between the vertical bearing structure and the main chord, and stable cables are set up between the main chords. Simultaneously, stability brace are set up between the main chord and lateral load bearing structure. The material selection and mechanical properties of the components are shown in Table 2, and the calculation model after the inactive of the prestressed cable is shown in Figure 3. Software analysis shows that all the members meet the load requirements through the procedure check. By increasing the wind bolt, the calculation length of the main chord is reduced, and the structure can meet the strength requirement (Zhang 2013).

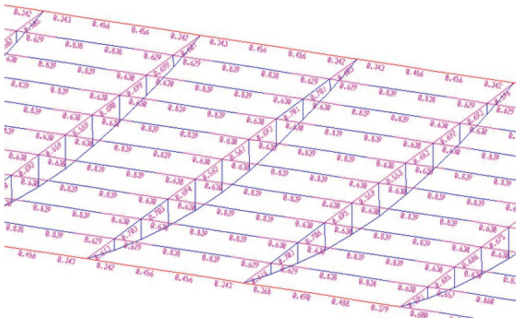

Figure 2. The stress ratio of each member.

Table 2. Mechanical properties of components.

Component	Section shape (mm)	Modulus of elasticity (MPa)
Wind bolts	Φ60	1.6×10^5
Stable cables	$\Phi 5 \times 61$	1.6×10^5
Stability brace	$\Phi 219 \times 6$	2.06×10^5

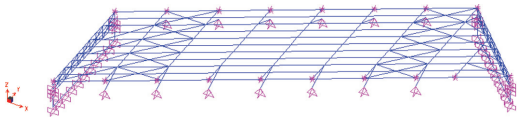

Figure 3. The calculation model after the inactive of the prestressed cable.

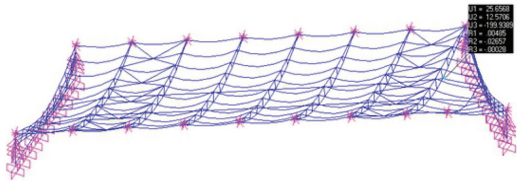

Figure 4. The deformation of the structure under the wind pressure.

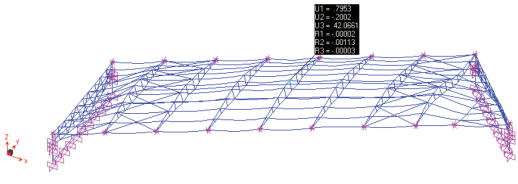

Figure 5. The deformation of the structure under the wind suction.

2.4 *Overall stability checking*

In order to enhance the overall stability of the structure, the cross stabilizer bar is added between the main chord of the roof plane, and two long prestressed cables are added between the prestressed cables. In order to analyze the overall stability of the structure, the nonlinear deformation of structure is analyzed (Zhang et al. 2005). Under three times of the design load, the program calculation can still converge. The deformation of the structure is shown in Figures 4 and 5. From the diagram, it can be seen that the deformation of the structure is mainly the vertical deformation, and the maximum lateral deformation is relatively small.

3 CONCLUSION

In this paper, the bearing capacity and the overall stability of the beam string structure under the wind pressure and wind suction are checked. The results show that: 1) After the failure of the cable, the load can be borne by the main chord, and the bearing capacity of each member can be satisfied after the addition of the wind bolt; 2) After the addition of stable cable, the lateral deformation

and the vertical deformation of the structure are not exceed the specification, and the overall stability is well.

REFERENCES

Bai, Z.X., Liu, X.L. & Li, Y.S. 2001. A new spatial structure-Beam string structure. *Spatial Structures* 7(2): 33–38.

Qiao, W.T. & Han, Q.H. 2006. Analysis of wind-induced vibration response of plane beam string structure. *Journal of Hebei University of Technology* 35(6): 92–98.

Spence, S. & Gioffre, M. 2011. Efficient algorithms for the reliability optimization of tall buildings. *Journal of Wind Engineering and Industrial Aerodynamics* 99 (6–7): 691–699.

Yang, R., Dong, S.L. & Ni, Y.G. 2002. Form finding ansysis of prestressed beam string structures-modified Inverse iteration method. *Spatial Structures* 8(4): 29–35.

Zhang, C.R. 2013. *Design and Application of Large-span Beam String Structure*. Tianjin: TianJin University.

Zhang, E.W., Yang, W.G. & Zhen, W. 2005. Software practicalization for analysis of wind-induced vibrations of large span roof structures. *Tsinghua Science and Technology* 10(3): 354–358.

Zhang, Y., Tian, X.Y. & Wang, Y.Q. 2005. Elasto-plastic large displacement analyses of beam string structure. *Journal of Beijing Jiaotong University* 29(4): 19–24.

Zhang, Z.H., Zhang, M.S. & Dong, S.L. 2004. Some aspects of beam-string structures. *Engineering Mechanics* 21(6): 26–30.

Zhao, J.D. & Liang, C.Z. 2015. Analysis and mechanical behavior research of beam string structures. *Building Science* 31(1): 1–6.

Zhuang, X.Z. 2014. Design and construction of the large-span roof with string structure in typhoon area. *Construction Technology* 43(2): 42–45.

This page intentionally left blank

Civil Engineering and Urban Planning IV – Liu et al. (Eds)
© 2016 Taylor & Francis Group, London, ISBN 978-1-138-02903-3

The relation of kappa and distance in the case of Tohoku-oki earthquake

Bai-Hui Zhu & Zheng-Ru Tao
Key Laboratory of Earthquake Engineering and Engineering Vibration, Institute of Engineering Mechanics, China Earthquake Administration, Harbin, Heilongjiang, China

Xia-Xin Tao
Harbin Institute of Technology, Harbin, Heilongjiang, China

ABSTRACT: In seismology, kappa (κ) values have been used as an important input parameter for 30 years. However, the mechanism is not clear till now. The relation with distance is discussed as the influence of propagation path on κ values, the influence of magnitude and focal mechanism is not our focus. Data is from the main shock of 2011 Tohoku-oki Earthquake, recorded by K-NET and KiK-net stations with distance less than 300 km. The linear dependence with distance is more visible from the KiK-net borehole records than that from the K-NET and KiK-net surface records.

1 INTRODUCTION

With the accumulation of the strong ground motion data, seismologists find that the acceleration Fourier amplitude spectra decrease quickly at high frequencies. Papageorgiou & Aki (1983), Anderson & Hough (1984) introduce high-frequency spectral attenuation quantitatively. They indicate that the decay of acceleration Fourier amplitude spectrum should be considered as linear for frequencies higher than a specific frequency f_E: $A(f) \sim \exp(-\pi\kappa f)$, in a log-linear space. Assuming the quality factor Q is independent with frequency, κ is directly proportional to the slope of acceleration Fourier amplitude spectrum when frequency is higher than a specific frequency f_E.

The mechanism of κ is under discussed and no consistent conclusion has been achieved. Anderson & Hough (1984), Anderson (1986) & Anderson (1991) find that κ is positively correlated with epicenter distance and is influenced by site condition, using the strong ground motion data in California. Atkinson (1996) considers that κ is associated with site and source. Tsai & Chen (2000) use the strong motion data of 16 earthquakes of 7 stations of SMATR1 and FA1–5 station in lotung, Taiwan to analyze the model comprised of distance, magnitude and site condition, propose the high-frequency decay is mainly related to source and site, and the propagation component is small. Petukhin & Irikura (2000) indicate it is mainly controlled by source. Purvance & Anderson (2003) propose that κ mainly influenced by source (include magnitude and focal mechanism). Boore (2003) considers κ_0 is related to source or site condition. Same as Papageorgiou & Aki (1983), Halldorsson & Papageorgiou (2005) also think κ is related to source. Cotton et al. (2006) consider that κ is mainly related to site factors. Houtte et al. (2011) adopt an inversion procedure following Purvance & Anderson (2003) to aim at the decomposition of κ into source, site and propagation components, taking advantage of KiK-net strong motion data between 1998 and 2006, and the results show that κ depends on shallow S-wave velocity. Kilb et al. (2012) consider that site condition contributes to κ, using 1137 small earthquakes recorded by the ANZA seismic network in southern California. Atik et al. (2014) consider source, site and propagation path can be the factors of κ.

So far, it is not consistent on the mechanism of κ. The influence of propagation path on κ value is discussed. Anderson & Hough (1984) is adopted to obtain κ of each record, with distance less than 300 km, from K-NET and KiK-net stations in the main shock of Tohoku-oki Earthquake, occurred on March 11, 2011.

2 DATASET AND ANALYSIS METHOD

The data used here are from 116 K-NET stations and 89 KiK-net stations during the main shock of Tohoku-oki Earthquake on March 11, 2011. For each record, the Fourier amplitude spectrum is calculated from the S wave arrival to the time

point with 80% of total energy accumulated, the window is chosen to involve only direct S-wave arrival. Tsai & Chen (2000) point out that spectral shape is fairly insensitive to the window length as long as the main energy of the S wave is involved. Each record is dealt with 30 Hz low-pass filtering by the butterworth filter, which is the same with Laurendeau et al. (2013).

Two horizontal acceleration time histories are transferred to acceleration Fourier amplitude spectra by FFT. In log-linear space, the decay of acceleration Fourier amplitude spectrum at high-frequency is fitted linearly, and the slope is divided by $-\pi$, and the result is the value of κ, followed the steps in Anderson & Hough (1984). In other words, Anderson & Hough (1984) hypothesize that to first order the shape of the acceleration spectrum at high frequencies can generally be described by the equation (1)

$$a(f) = \mathrm{A}_0 e^{-\pi\kappa f} \tag{1}$$

where A_0 depends on source properties, epicentral distance, and perhaps other factors, κ is described by the equation (2)

$$\kappa = -\lambda/\pi \tag{2}$$

where λ is the slope of high-frequency of Fourier amplitude spectrum, and it can be described by the equation (3)

$$\lambda = \Delta(\ln a)/\Delta f \tag{3}$$

where a is Fourier amplitude, f is frequency.

Figure 1 is an example from the borehole record No. GNMH08110311144 of KiK-net, in which the gray line is Fourier amplitude spectrum and the black line is the fitting line of high-frequency decline. In Figure 1, above 12 Hz, the acceleration Fourier amplitude spectrum is flat, which is considered as noise.

3 INFLUENCE OF EPICENTRAL DISTANCE

The relation with epicentral distance (≤300 km) can be verified by the data of above 116 K-NET stations with epicentral distance less than 300 km, shown in Figure 2.

The linear regression of κ with the epicentral distance, and the result is listed in Table 1.

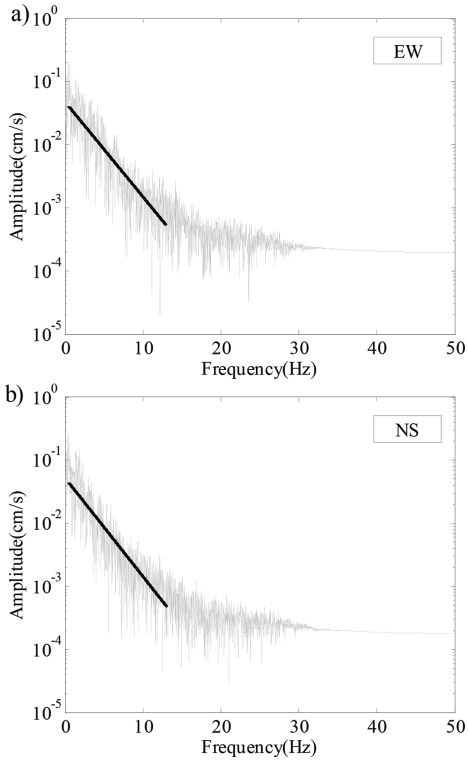

Figure 1. Two horizontal Fourier amplitude spectra and fitting lines (GNMH08110311144).

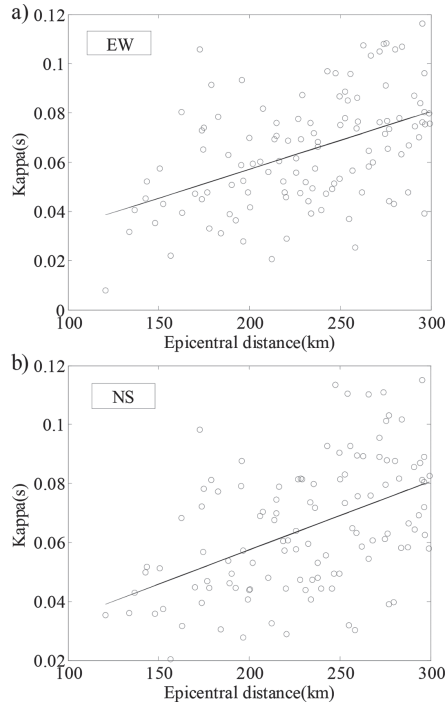

Figure 2. The relation between κ and epicentral distance by records from K-NET stations.

Table 1. The relation between κ that is calculated by two horizontal records at K-NET stations and epicentral distance.

Direction	Equation	R^2	F statistics
EW	$\kappa = 0.0002R + 0.0010$	0.2252	$33.13 > F_{0.05} = 3.928$
NS	$\kappa = 0.0002R + 0.0109$	0.2355	$35.12 > F_{0.05} = 3.928$

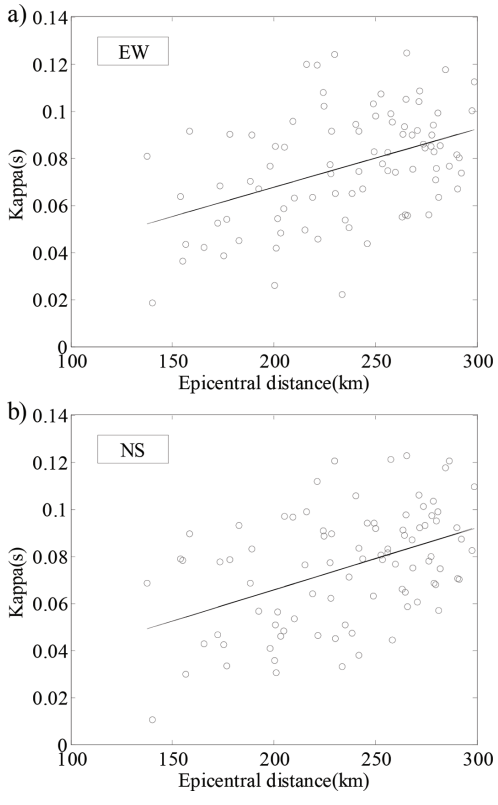

Figure 3. The relation between κ and epicentral distance by records from KiK-net surface stations.

From Table 1, the values of κ of two horizontal directions have little difference and increase with epicentral distance. Coefficients of determination R^2 are around 0.23, which indicates that the epicentral distance can interpret the value of κ, to some extent. F statistics are more than the critical values on the 0.05 significance level, which indicates the null hypothesis is rejected, the regression equations are significant.

Figure 3 shows the relation with epicentral distance (≤300 km) by the data of 89 KiK-net surface stations.

Results of the linear regression are listed in Table 2.

It is indicates that the linear regression equations are significant at the level of 0.05.

In Figures 2 and 3, the scattering is obvious. To avoid the influence of site condition, the data of 89 KiK-net borehole stations, with epicentral distance less than 300 km, is adopted to observe the relation between κ and epicentral distance, as shown in Figure 4.

The linear regression results of κ with the epicentral distance are listed in Table 3.

In Table 3, the κ values of two horizontal directions have little difference and increase with

Table 2. Results of the linear regression between κ and epicentral distance by records from KiK-net surface stations.

Direction	Equation	R^2	F statistics
EW	$\kappa = 0.0002R + 0.0181$	0.1878	$20.12 > F_{0.05} = 3.964$
NS	$\kappa = 0.0003R + 0.0126$	0.2062	$22.60 > F_{0.05} = 3.964$

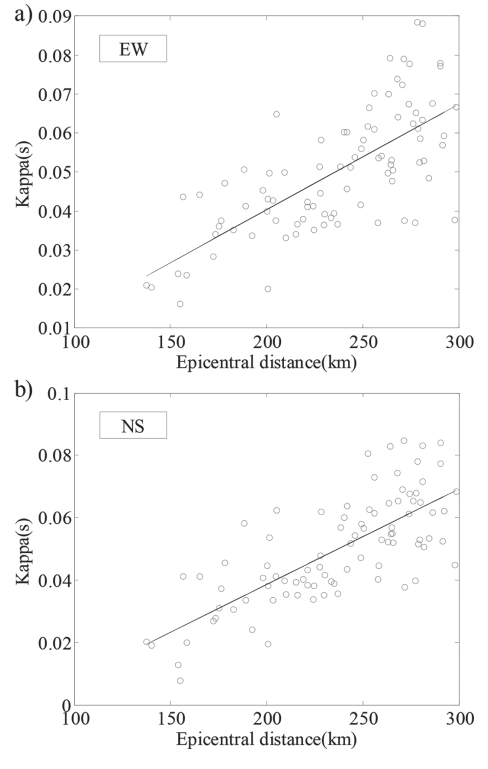

Figure 4. The relation between κ and epicentral distance by records from KiK-net borehole stations.

Table 3. Results of the linear regression between κ and epicentral distance by records from KiK-net borehole stations.

Direction	Equation	R^2	F statistics
EW	$\kappa = 0.0003R - 0.0138$	0.5050	$88.82 > F_{0.05} = 3.964$
NS	$\kappa = 0.0003R - 0.0226$	0.5566	$102.20 > F_{0.05} = 3.964$

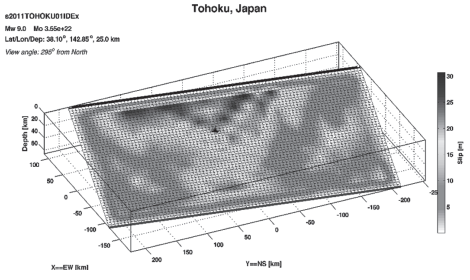

Figure 5. Finite fault model of Ide et al. (2011).

epicentral distance. Coefficients of determination are around 0.54, which indicates that the epicentral distance has a great interpretation to κ.

Comparing Figure 3 with Figure 4, site condition has an effect on κ so that it weakens the linear relation between κ and epicentral distance and increases the discreteness. κ values of borehole-station records are 0.01 s~0.09 s, meanwhile, those of surface-station records are 0.02 s~0.13 s, the amplification to κ might be caused by soil layers. It is proved that ground motion attenuation on soil site is faster than that on rock site as well.

4 INFLUENCE OF RUPTURE DISTANCE

One finite fault model is proposed by Ide et al. (2011), as shown in Figure 5.

The rupture distance is the closest distance from site to the rupture plane. The relation between two horizontal κ values and rupture distance is shown as Figure 6. These κ values are from 408 K-NET stations (rupture distance ≤300 km).

By least squares method, κ values are regressed with rupture distance linearly. The regression equation on east-west direction is: $\kappa = 0.0001R_d + 0.0574$, $R^2 = 0.1612$; the regression equation of south-north direction is: $\kappa = 0.0001R_d + 0.0556$, $R^2 = 0.1717$. The values of κ of two horizontal directions have little difference and increase with rupture distance.

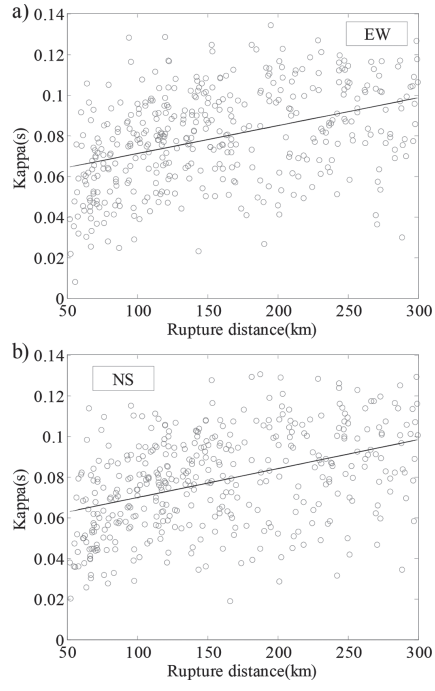

Figure 6. The relation between κ and rupture distance by records from K-NET stations.

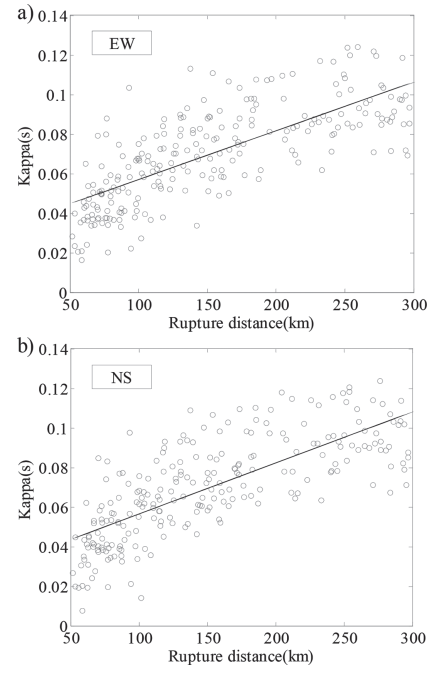

Figure 7. The relation between κ and rupture distance by records from KiK-net stations.

Comparing with the relation in section 3, this scattering is larger and the coefficient of determination is smaller.

The relation with rupture distance, from data of 238 KiK-net stations (borehole, rupture distance ≤300 km), is shown in Figure 7.

The regression equation on east-west direction is: $\kappa = 0.0002R_d + 0.0324$, $R^2 = 0.5490$; the regression equation on south-north direction is: $\kappa = 0.0003R_d + 0.0307$, $R^2 = 0.5593$. The κ values on two horizontal directions have little difference and increase with rupture distance. Comparing with the relation in section 3, the coefficient of determination is larger, which indicates the fitting degree is better.

5 CONCLUSIONS

The relation between κ and distance is discussed preliminarily, by the main shock data of 2011 Tohoku-oki Earthquake, recorded by K-NET and KiK-net stations. The results from K-NET and KiK-net surface records are similar, the linear relations are weaker and discreteness is larger. However, by the data of KiK-net borehole stations, the coefficient of determination of linear regression is larger, which reveals the relation is stronger. Meanwhile, site condition has an effect on κ since it weakens the linear relation between κ and increase the discreteness.

Two distance definitions are adopted here, epicentral distance and rupture distance, the linear relation between κ values and rupture distance is stronger, using the borehole data.

ACKNOWLEDGEMENTS

This work was financially supported by National Nature Science Foundation of China (51478443, 51178435 and 51178151).

REFERENCES

Anderson, J.G. & Hough, S.E. 1984. A model for the shape of the Fourier amplitude spectrum of acceleration at high frequencies. *Bull. Seismol. Soc. Am*. 74(5): 1969–1993.

Atik, L.A., Kottke, A., Abrahamson, N. & Hollenback, J. 2014. Kappa (κ) scaling of ground-motion prediction equations using an inverse random vibration theory approach. *Bull. Seismol. Soc. Am*. 104(1): 336–346.

Atkinson, G.M. 1996. The high-frequency shape of the source spectrum for earthquakes in eastern and western Canada. *Bull. Seismol. Soc. Am*. 86(1A): 106–112.

Boore, D.M. 2003. Simulation of ground motion using the stochastic method. *Pure Appl. Geophys*. 160(3–4): 635–676.

Cotton, F., Scherbaum, F., Bommer, J.J. & Bungum, H. 2006. Criteria for selecting and adjusting ground-motion models for specific target regions: Application to Central Europe and rock sites. *J. Seismol*. 10(2): 137–156.

Halldorsson, B. & Papageorgiou, A.S. 2005. Calibration of the specific barrier model to earthquakes of different tectonic regions. *Bull. Seismol. Soc. Am*. 95(4): 1276–1300.

Houtte, C.V., Drouet, S. & Cotton, F. 2011. Analysis of the origins of κ (Kappa) to compute hard rock to rock adjustment factors for GMPEs. *Bull. Seismol. Soc. Am*. 101(6): 2926–2941.

Ide, S., Baltay, A.G. & Beroza, C. 2011. Shallow dynamic overshoot and energetic deep rupture in the 2011 Mw 9.0 Tohoku-Oki earthquake. 332(10): 1426–1429.

Kilb, D., Biasi, G., Anderson, J., Brune, J., Peng, Z.G. & Vernon, F.L. 2012. A comparison of spectral parameter kappa from small and moderate earthquakes using southern California ANZA seismic network data. *Bull. Seismol. Soc. Am*. 102(1): 284–300.

Laurendeau, A., Cotton, F., Ktenidou, O.J., Bonilla, L.F. & Hollender, F. 2013. Rock and stiff-soil site amplification: dependency on VS30 and Kappa (κ0). *Bull. Seismol. Soc. Am*. 103(6): 3131–3148.

National Research Institute for Earth Science and Disaster Prevention. 2015. *http://www.kyoshin.bosai.go.jp/*.

Papageorgiou, A.S. & Aki, K. 1983. A specific barrier model for the quantitative description of inhomogeneous faulting and the prediction of strong ground motion, part I: Description of the model. *Bull. Seismol. Soc. Am*. 73(3): 693–722.

Petukhin, A. & Irikura, K. 2000. A method for the separation of source and site effects and the apparent Q structure from strong-motion data. *Geophys. Res. Lett*. 27(20): 3429–3432.

Purvance, M.D. & Anderson, J.G. 2003. A comprehensive study of the observed spectral decay in strong-motion accelerations recorded in Guerrero, Mexico. *Bull. Seismol. Soc. Am*. 93(2): 600–611.

Tsai, C.C.P. & Chen, K.C. 2000. A model for the high-cut process of strong motion accelerations in terms of distance, magnitude, and site condition: an example from the SMART 1 array, Lotung, Taiwan. *Bull. Seismol. Soc. Am*. 90(6): 1535–1542.

This page intentionally left blank

Civil Engineering and Urban Planning IV – Liu et al. (Eds)
© 2016 Taylor & Francis Group, London, ISBN 978-1-138-02903-3

A simplified method for calculating load transverse distribution coefficient of skew bridge

Hua-Lei Jin, Xiao-Bing Tang & Lei Jiang
School of Transportation, Wuhan University of Technology, Wuhan, Hubei, China

ABSTRACT: Owing to imperfections and complexities in calculating load transverse distribution coefficients of skew bridges, the modal parameters method was put forward through the researches on the orthogonal straight bridges, which is not limited to bridge types and can be used for skew bridges. To further explore the precision of this method, a Midas/civil space beam gird model was built and the load transverse distribution coefficients were contrasted with another method. The results showed that modal parameters method meets the needs of engineering calculation and can be applied to skew bridges. It is hoped that the modal parameters method can put more emphasis on bridge design and testing in the future.

1 INTRODUCTION

In recent years, demands for skew bridge construction got bigger with the rapid development of China's highways. Skew bridges obviously show the characteristics of spatial stress, and their mechanisms are more complicated than the orthogonal ones. The mechanical properties of skew bridges include the coupling effect of bend-twist, uneven reaction distribution and discount of the bending moments at mid-span, and so on (Wang et al. 2004). The load transverse distribution coefficient is the main basis to evaluate lateral force transmission performance, and it refers to the distribution percentage of a highway's vehicle load in each girder. It is a complex spatial structure and often simplified to plane problems in bridge designs. Calculating load transverse distribution coefficient in orthogonal bridges is simple, but for skew bridges is not so easy, because there are many factors that impact skew bridges, such as skew angle, wide cross ratio, flexural stiffness, torsional stiffness, and support conditions, and load types (Yu et al. 2013). Among them, the effect of inclination cannot be ignored; therefore, it seems that the accuracy and reliability of a simplified method are particularly important.

Domestic and international articles about solving the load transverse distribution coefficient of skew bridges are massive, and major computational methods can be classified into two parts, one is the common method and the other is the spatial numerical method. Common methods include the lever principle method, the rigid-diaphragm method, the hinge-jointed plate method, the rigid-jointed beam method, the G-M method, and so on, while spatial numerical methods include the space beam element method, the plate element method, the 3D finite element method, and the beam-grid method. Among them, elastic support continuous beam method and the generalized rigid-jointed beam method are suitable for orthogonal bridges, while skew ones always take spatial numerical method. Finding a simplified method for calculating load transverse distribution coefficient in skew bridges is particularly urgent and meaningful. The literature (Liu et al. 2009) proposed the modal parameters method to calculate the load transverse distribution coefficient, mainly by using modal flexibility, and this method is not limited by bridge types. On this basis, taking a skew bridge as an example, the load transverse distribution coefficient was calculated and compared with another method; this will further verify the feasibility and applicability of the modal parameters method.

2 THEORY EVIDENCE

Literature (Yang et al. 2014) compared the rigid-diaphragm method, the rigid-jointed beam method, and the G-M method for calculating the load transverse distribution coefficient of prefabricated bridges and concluded that when there are 3–5 pieces of beams, the rigid-diaphragm method is recommended; while when there are 5–9 pieces of beams, the G-M method is suggested. However, the above suggestions were just suitable for small box girders and whether it is suitable for any skew bridge is not mentioned. According to

literature (Dui 2013), it is recommended to use the rigid-diaphragm method for skew bridges at present, and (Zhang 1985) also discussed the rigid-diaphragm method for orthogonal bridges, skew bridges as well as plane curved bridges; moreover, it derived the calculation formulas of the load distribution influence line in various bridge types. But (Guo 2007) made it clear that the rigid-diaphragm method is not applicable to skew slab bridges and girder bridges; it usually uses numerical methods for calculation. Thus, this paper used modal parameters method and the rigid-diaphragm method for calculating the load transverse distribution coefficient and their results were compared.

2.1 *Influence line and load transverse distribution coefficient*

The influence line is that in a unit moving load $p = 1$ under the action, variation rule of a certain value Z is represented by a function image, which is called the influence line of value. The load transverse distribution coefficient (Han 2009) is used to solve the section internal force of point K on the beam; it can make use of the influence line of load transverse distribution coefficients. First, calculate the total loads which refer to the total wheel loads acting on the bridge; then, according to the internal force influence line of point K, calculate maximum internal force value under the action of the distributed loads. The formula for calculating the transverse distribution coefficient of the vehicle load is as follows:

$$m_q = \frac{\sum \eta_q}{2} \tag{1}$$

where η_q = vertical value corresponding to the car load of lateral distribution influence line.

2.2 *Introduction of calculation method*

The principle of calculating the load transverse distribution coefficient by using modal parameters method (Zeng et al. 2001) is that the load transverse distribution coefficient is determined by the deflection rule of the main girder. The task of this method is to determine the ratio of each girder under the loads. It needs to get the modal flexibility which refers to deflection of the beam under the unit load first; further, according to the calculated modal flexibility, extract the deformation value of the mid-span cross-section, and it can get the load lateral distribution influence line with the help of this value and the number of beams. Based on this, arrange the loads in the most unfavorable position, and the load position's influence on the line of vertical value is calculated. Finally, according to equation (1), we get the values of the load transverse distribution coefficient.

In the modal parameters method, displacement vector at t moment can be expressed as follows:

$$u(t) = q_1(t)\varphi_1 + q_2(t)\varphi_2 + \ldots + q_p(t)\varphi_p = \Phi Q(t) \tag{2}$$

where $q_i(t)$ = generalized coordinate of the structure; φ_i = the ith mode shape vector; Φ = the mode shape matrix; $Q(t)$ = the $n \times 1$ vector of generalized modal.

Use the application of the orthogonality conditions, then it can get a system's uncoupled single-degree-of-freedom equation:

$$\ddot{q}_i(t) + 2\zeta_i\omega_i\dot{q}_i(t) + \omega_i^2 q_i(t) = \frac{\varphi_i^T f(t)}{m_i} \tag{3}$$

where ω_i = un-damped natural frequency; ζ_i = modal damping ratio; m_i = modal mass of the ith mode.

The physical meaning of equation (3) refers to the approximation of modal static displacement when the unit load occurs on the jth DOF.

As the static response is independent of time, the first two terms in equation (3) vanish; it becomes:

$$q_i = \frac{\varphi_i^T f}{\omega_i^2 m_i} \tag{4}$$

where f = unit force vector, its value is unity for an applied load at jth DOF. It can be expressed as:

$$\varphi_i^T f = \varphi_{j,i} \tag{5}$$

Then equation (4) can be written as:

$$q_i = \frac{\varphi_{j,i}}{\lambda_i m_i} \tag{6}$$

Because low order modes are more than the high ones, take the front r orders of the modes. Then equation (2) can be expressed as:

$$u_j = \sum_{i=1}^{r} c_{j,i}\varphi_i = \sum_{i=1}^{r} \frac{\varphi_{j,i}}{\lambda_i m_i}\varphi_i \tag{7}$$

where $c_{j,i}$ = the ith modal coefficient, refers to the ith component of the generalized modal contribution vector; λ_i = eigenvalue of the ith mode.

Because the load on any piece of beam equals the vertical value of influence line under the unit load in an arbitrary beam, in addition, to the elastic beam, load and deflection are proportional to each other. Thus, the influence line of

any number of beams is derived with the *j*th beam as an example; the vertical value of influence line is marked as:

$$\eta_{j,i} = u_{i,j} \Big/ \sum_{i=1}^{n} u_{i,j} \tag{8}$$

Above all, the steps to solve the load transverse distribution coefficient by using modal parameters method are: first, calculate the natural frequencies and modal shapes, then, according to the equation (7), get the modal flexibility at the mid-span cross-section. At last, calculate the vertical values by equation (8).

3 ENGINEERING CASE

3.1 *Engineering background*

A skew bridge with skew angle of 20 degrees, beam height of 150 cm, width of 1500 cm, and thickness of 20 cm (top plate) and 25 cm (bottom one) is considered. In addition, the belly is 45 cm, the width at the middle support is 120 cm, and the end width is 200 cm.

The speed of the bridge is 100 km/h; the designed load rating is Automobile-over 20, Trailer-120, and the width of the bridge deck is 0.50 m (barrier) +6.92 m (lane) +0.66 m (central separation guardrail) +6.92 m (lane) +0.50 m (barrier) = 15.50 m.

The upper structure is C50 prestressed concrete beam, compressive modulus of elasticity is 3.45×10^4 MPa, the bulk density is 26 kN/m^3; also, the design value of axial compressive strength is 22.4 MPa, and design value of tensile strength of axial is 1.83 MPa. Besides, the density of crash barrier is 26 kN/m^3 and asphalt concrete is $24\,kN/m^3$. Elevation of intermediate span and plan of intermediate span as well as the cross section of the bridge are shown in Figures 1–3.

3.2 *Model establishment and result analysis*

The finite element program Midas civil 2012 was used for calculation and analysis, and space beam gird model was used to establish the upper structure. There were 532 units and 333 nodes, and the calculation model is shown in Figure 4.

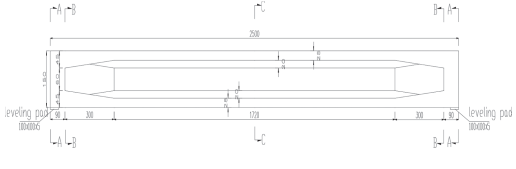

Figure 1. Elevation of intermediate span. (unit: cm).

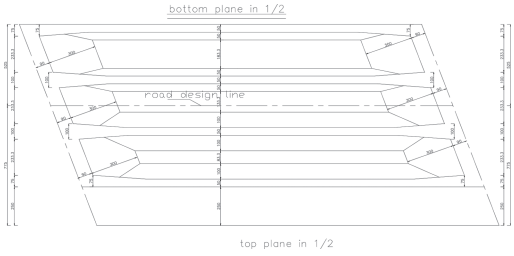

Figure 2. Plan of intermediate span. (unit: cm).

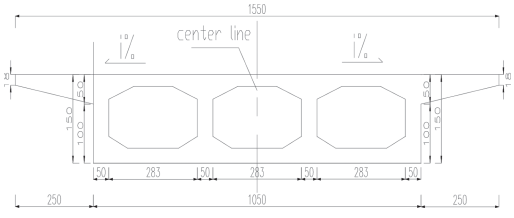

Figure 3. Cross section of box girder. (unit: cm).

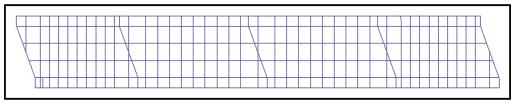

Figure 4. Calculation model.

The whole cross section was divided into four beams, as shown in Figure 5. At the same time, the asphalt concrete pavement and guardrail quality were as per meter in quality, and the overall structure of the bridge was calculated and the fundamental frequency of the structure is shown in Table 1. The first and two orders vibration shape diagrams are shown in Figures 6 and 7.

We acquired the data of the load transverse distribution coefficient by using the modal parameters method and the rigid-diaphragm method, as shown in Tables 2 and 3 and Figures 8 and 9.

It can be observed from Tables 2 and 3 that the load transverse distribution coefficients of the skew bridge were calculated with the modal parameters method and the rigid-diaphragm method under the action of the load Automobile-over 20 and Trailer-120, respectively, and the deviation values of the two methods were also listed. Figures 8 and 9 showed the comparison chart of the two methods, which are intuitive and clear. It had been found that the basic law of the two methods is the same and the results of the modal parameters method are larger. The concept of rigid-diaphragm method is clear, but it assuming that the diaphragm

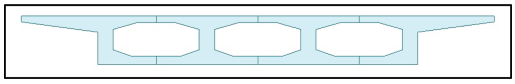

Figure 5. Model of cross section.

Table 1. Natural frequencies.

Fundamental frequency of positive bending moment f1/Hz	Fundamental frequency of negative bending moment f2/Hz
5.55	7.22

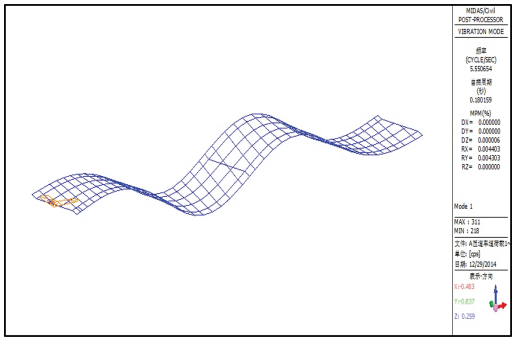

Figure 6. The first order vibration shape diagram. (vertical base frequency).

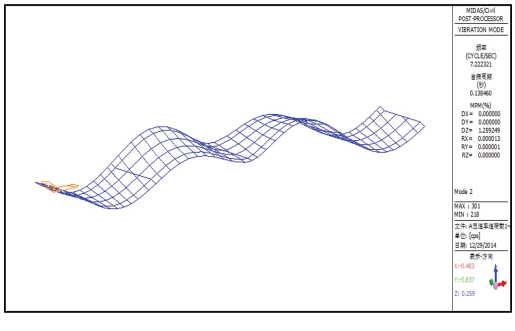

Figure 7. The second order vibration shape diagram (vertical base frequency).

is absolutely rigid and the torsional rigidity of the main girder is not considered. However, the simple method proposed by this paper is not restricted by bridge types and it is simple and fast in computation. Furthermore, the changing trends of the transverse distribution coefficient of the Automobile-over 20 load and the Trailer-120 are

Table 2. Load transverse distribution coefficient (1).

Load transverse distribution coefficient	Auto-over 20			
	Beam 1	Beam 2	Beam 3	Beam 4
Modal parameters method	0.517	0.540	0.516	0.538
Rigid-diaphragm method	0.506	0.531	0.506	0.531
The deviation/%	2.20	1.65	1.97	1.30

Table 3. Load transverse distribution coefficient (2).

Load transverse distribution coefficient	Trailer-120			
	Beam 1	Beam 2	Beam 3	Beam 4
Modal parameters method	0.298	0.269	0.297	0.268
Rigid-diaphragm method	0.292	0.264	0.292	0.264
The deviation/%	2.14	1.71	2.02	1.52

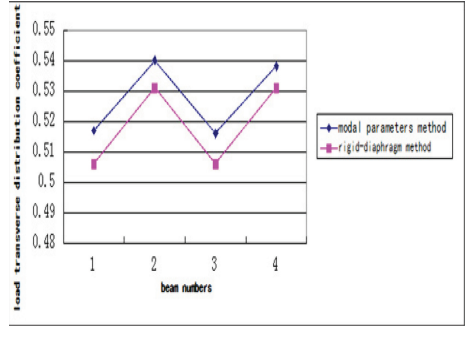

Figure 8. Contrast figure of the load transverse distribution coefficient under Automobile-over 20.

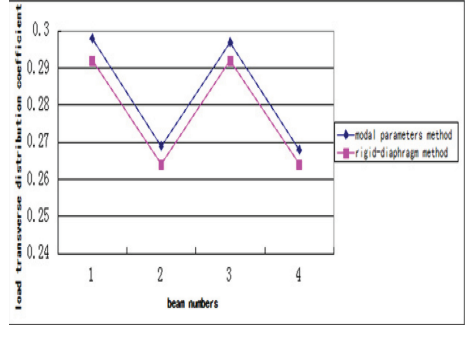

Figure 9. Contrast figure of the load transverse distribution coefficient under the load Trailer-120.

the same. The maximum error is no more than 5%, and it can meet the actual needs of the project.

4 CONCLUSION

- Based on the knowledge of structural dynamics, the modal parameters method was conducted to compute the load transverse distribution coefficient of the skew bridge, and the calculation formulas and steps were derived.
- Taking a skew girder bridge as an example, the data of modal parameters method and the rigid-diaphragm method were compared. The maximum error of the two is not more than 5%. Typically, it is also found that the modal parameters method is better than rigid-diaphragm method in rapid calculation.
- In the actual bridge design and testing, we should pay more attention to the modal parameters method, which can serve as a more efficient way to calculate the load distribution coefficient.

REFERENCES

Chen, C.L. 2014. Analysis and calculation of transverse load distribution of small box girder bridge. *Transportation Standardization* 42(7): 115–117.

Dui, H. 2013. Design Method of Transverse Load Distribution of Continuous T Girder Bridge and Its Experimental Study. Changan: Changan University.

Guo, S.J. 2007. Research on Transverse Force Distribution of Medium or Medium Small Span Box-girder Bridge with Flanges. Chengdu: Southwest Jiaotong University.

Han, H.Q. 2009. Research and Application of Lateral Load Distribution Factor Calculating Method for Small and Medium-span Bridges. Changchun: Jilin University.

Li, S.H. et al. 2009. Investigation and application of transverse load distribution coefficients measured in existing bridge. *Journal of Shandong University of Science and Technology* 28(5): 27–29.

Liu, H. et al. 2009. Calculation method of transversal distribution factor for bridge load. *Journal of Traffic and Transportation Engineering* 9(1): 62–66.

Nie, X. et al. 2009. Transverse load distribution on box section continuous composite steel-concrete bridges. *Journal of Tsinghua University* 49(12): 1930–1933.

Wang, L.B. 2004. Analysis on Mechanical Characteristics and Bearing Capacity of Assembly Skew Hollow Slab Bridge. Changsha: Changsha University of Science & Technology.

Yang, M.L. & Shi, C.E. 2014. Research of load transverse distribution coefficient in simply-supported-continuous bridge. *Journal of China & Foreign Highway* 34(5): 142–146.

Yu, Q.H. et al. 2013. Research of load transverse distribution coefficient in oblique wide continuous hollow slab bridge. *Journal of China & Foreign Highway* 33(3): 127–130.

Zeng, H. & Bert, C.W. 2001. Free vibration of discretely stiffened skew plants. *International Journal of Structure Stability and Dynamics* 1(1): 125–144.

Zhang, S.D. 1985. Calculate transverse load distribution influence line of rectangular bridge, skew bridge and plane bending bridge with rigid transverse beam method. *Journal of Chongqing Jiaotong University* 4(15): 32–40.

This page intentionally left blank

Civil Engineering and Urban Planning IV – Liu et al. (Eds)
© 2016 Taylor & Francis Group, London, ISBN 978-1-138-02903-3

An ontology-based context management system for diversion tunnel

Xiao-Yu Zheng
Chengdu Engineering Corporation Limited, Chengdu, Sichuan, China

Jie Shen
School of Computer Science and Engineering, University of Electronic Science and Technology, Chengdu, Sichuan, China

ABSTRACT: Diversion tunnel is often characterized by long tunnel line, extremely complicated geologic conditions and construction techniques, great embedded depth, inspection and maintenance difficulties. Consequently, the problems of construction management and engineering construction schedule control could occur, especially diversion tunnel groups. In this paper, a new ontology-based model for diversion tunnel is proposed, and design and development of the context management system for mobile computing, which is an intelligent context-aware system, is described. Moreover, knowledge sharing and knowledge reuse are also provided by using the ontology model. The context management system makes use of rule-based reasoning that provides derivation of a high-level context from a low-level context. The test results validate the feasibility of the context management system. The achievements of this paper could provide references for the management of diversion tunnel or similar rock engineering. Technical support and scientific basis are also provided for its process control, safety warning, later inspection and maintenance.

1 INTRODUCTION

Diversion tunnel is often characterized by long tunnel line, extremely complicated geologic conditions and construction techniques and great embedded depth (Hu et al. 2012), and so the problems of construction management, engineering construction schedule control, and later maintenance could occur, especially long-distance diversion tunnel group (Wang et al. 2011; Liu et al. 2007; Lee et al. 2006; Li et al. 2014). The simulation of the whole construction progress of diversion tunnel was researched by Hu et al. (2012), Zhong et al. (2007), Li et al. (2006) and Shi et al. (2012), which can provide the real-time control of the whole construction progress and scientific basis for feasibility studies and evaluation of the construction program. But the key issues are not addressed, including how to link between simulation of the construction process and the site construction process, and how to acquire real-time site data that determine the accuracy of simulation and control of the construction process. Obviously, it is important for the system to get the site data of the construction process quickly, easily and accurately. Furthermore, the information would provide data support for safety warning, later inspection and maintenance. The features of diversion tunnel make the information many and varied about its geology, construction process, inspection and maintenance. Accordingly, traditional diversion tunnel shows either a lack of complete data management for construction process, inspection and maintenance or a simple storage of process data in the database that is used for query function, managing and visualizing (Li et al. 2013; Klaus et al. 2013). Since there are no data modeling and universal description of data at the semantic level, it is difficult to implement an advanced data application. This paper aims to fulfill this research requirement based on mobile computing, ontology-based context management, NFC (Near Field Communication) and semantic computing, and a context-aware web middleware is presented. Using NFC technology, the middleware can acquire the contexts in ever-changing environments, and provide the end-to-end management service for diversion tunnel. The context engine mentioned is based on Jena, which implements a context engine and provides APIs to perform context-related operations.

2 CONTEXT-AWARE MIDDLEWARE

Based on the above idea, we design the architecture of the context-aware system (as shown in Fig. 1), which aims to provide an efficient infrastructure support for building context-aware services in pervasive computing environments.

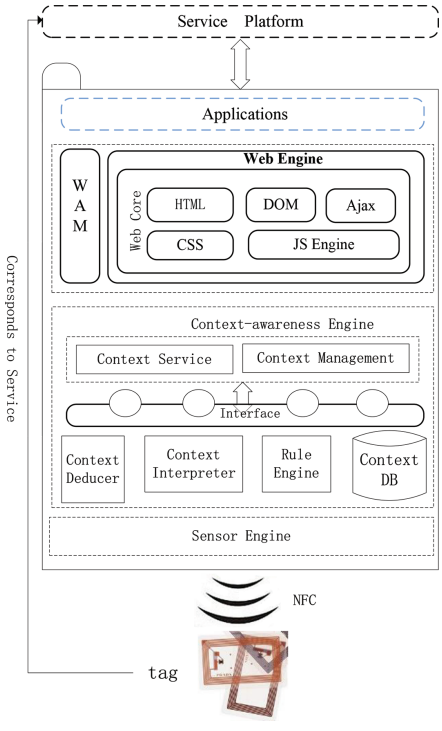

Figure 1. Architecture of the proposed context-aware system.

There are three separate domains that we combine in our approach: tags or NFC mobile phones within which there are applications or service contexts, and the service platform and the mobile phone that connects other two domains and acts as a mediator between them. To interact with both domains, the mobile phone uses web middleware with context awareness that detects applications or service contexts from pervasive environments and acquires them from the service platform. In pervasive environments, tags or mobile phones contain context information for applications or services.

Our mobile web middleware of NFC context-awareness is a distributed middleware that transfers and converts low-level contexts in physical spaces into semantic spaces where applications and services can be easily shared and accessed by mobile devices. It consists mainly of a context-awareness engine, a sensor engine which is responsible for acquiring contexts, a widget runtime, a WAM (Web Application Manager) and a web engine, as shown in Figure 1. This mobile web middleware has a more functional set of applications and an adequate infrastructure support for building context-aware applications, which significantly improves the user's quality of experience.

The web engine provides a lightweight web runtime on mobile devices, and an interoperable and platform-independent solution to applications. Our mobile web engine mainly consists of the following components.

The context engine is a lightweight modular architecture for the development and implementation of context-aware middleware. It consists of the following components: the context deducer is responsible for deducing a high-level context from a static and dynamic low-level context in the physical space, and storing them in the context database; in other words, the place where the physical space is turned into the semantic space. The context interpreter is composed of a context reasoner and a knowledge base. The context reasoner provides logic reasoning services in conjunction with a knowledge base and applies the rules contained in the knowledge base to process context information. The rule engine manages context-awareness rules and behaviors relevant to specific applications. These rules are explicitly updated and changed by users using the user interface and implicitly learnt by the rule engine itself. The context database can be used to store not only the context ontology instance and history, but also the domain knowledge. Especially when the network is offline, the local context database is very important. The context is modeled with the context ontology using OWL (Web Ontology Language) to provide knowledge sharing, knowledge reuse and logical reasoning. The context management component is responsible for acquiring the low-level context from WAM and managing the context components to translate the low-level context into a high-level one. Based on it, the context service generates the necessary knowledge for decision on adaptation actions to provide a context-aware support.

The sensor engine is responsible for acquiring various contexts from environments. It is made up of four main layers: abstract sensor hardware layer, software stack layer, interface layer and service layer. The mobile operating system generally implements the preceding three layers that are known as the sensor stack. The service layer of the sensor engine expands and enhances the existing sensor stack on mobile operating systems. Its core idea is to utilize the sensor for applications, which are capable of providing high-level services for users, thus we named it the service layer of sensor stack.

3 SERVICE PLATFORM

The service platform is responsible for managing domain knowledge, and storing and processing the context. On the one hand, the service platform must hide the complexity associated with services and applications crossing over different service domains. It allows mobile users to be connected anytime,

anyplace, with any service in different scenarios. If the application in the application context is not local, WAM on mobile phones will download it from the service platform. On the other hand, the service platform manages domain knowledge, and handles contexts, which provides knowledge sharing and knowledge reusing by using ontology-based models. Also, it makes use of the rule-based context interpreter to provide derivation of high-level implicit contexts from low-level explicit contexts. For example, a context-aware scheme recommendation system is implemented by the history data of other diversion tunnels, site contexts and context rules.

The implementation on servers is mainly composed of four modules: Network Communication Module, Command Processing Module, Query and Reasoning Module and Data Model Module. The function of Network Communication Module and Command Processing Module is similar to that of the intelligent terminals, which will not be detailed here. The Query and Reasoning Module performs reasoning and query operations on the data model so as to extract services and contents according to site contexts and knowledge database. The modeling of data, with the aim of meeting requirements of the Query and Reasoning Module, is completed in the Data Model Module.

When employing ontology-based modeling in reasoning procedures, we can utilize the rule-based reasoning method, where rules can be obtained and added dynamically, to extract knowledge that will be preferred by users. Besides, rule-based reasoning has a high quality for scalability and self-adaptation. It may to some extent improve the precision of reasoning as well. Assuming that the set A (A = {a_1, a_2, …, a_i, …}) represents the obtained knowledge, and the set P represents the weight set. For every knowledge a_i in set A, we first calculate its corresponding recommendation value w_i. Consecutively, a weight-based algorithm is applied to calculate the weight of each knowledge. The algorithm is defined as follows:

- First, obtain high-level contexts, which are represented by set Nr (Nr = {n_1, n_2, …, n_i}), and initial w_i as $w_i = 0$;
- Obtain the set Pr (Pr = {p_1, p_2, …, p_i}), the corresponding weight set of Nr;
- for (each knowledge a_i in set A)
- Initiate the information type set as Ni = Nr, where Ni is the corresponding content set of each a_i;
- for (each n_i in set Ni)
- if (a_i matches n_i) w_j += p_i;
- Finally, descending sort elements in set A according to the value of w_i.

The values in weight set P are not invariable, where their weights can be modified by a feedback mechanism (e.g. by the ratio of the knowledge's recommendation frequency and its acceptance frequency). Combined with the above method, the precision of knowledge push can be further improved.

4 ONTOLOGY MODEL

The term 'Ontology' has a long history in philosophy (Gruber, 1993), which is a formal explicit description of concepts in a domain of discourse. It defines a set of representational primitives with which a domain of knowledge can be modeled and specific situations can be described in a domain.

The actual context data model for diversion tunnel may be of many different kinds of format, which can be XML, JSON or even the customized, and these data in physical space will be turned into semantic space. In semantic space, the contexts are modeled using an ontology-based approach to help us describe contexts semantically, in a way which is independent of programming language, middleware or operating system. The context model is described by ontology written in OWL (Web Ontology Language), and it is a Semantic Web language proposed by W3C's Web Ontology Working Group. The generalized ontology for diversion tunnel defines the

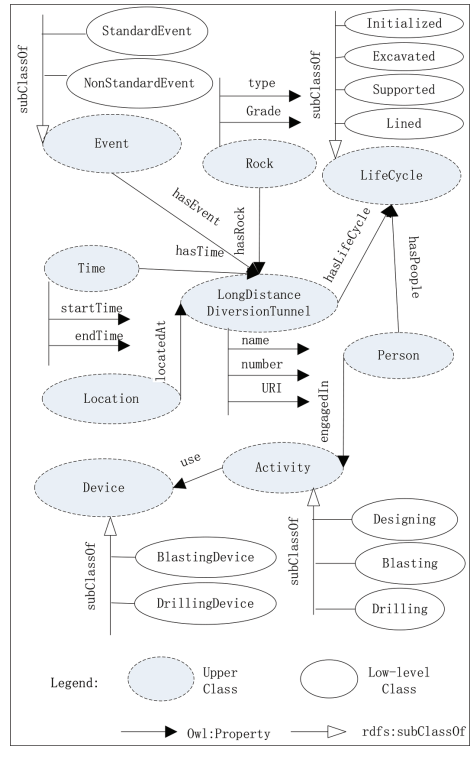

Figure 2. Partial definition of ontology for diversion tunnel.

basic concepts of person, location, device, event, time, inspection channel, activity, diversion tunnel, life cycle and rock, and consists of 10 classes and corresponding properties, as shown in Figure 2.

Moreover, the reasons for using ontology-based context modeling for diversion tunnel are to provide knowledge sharing, logical reasoning and knowledge reuse. All context knowledge recorded in a diversion tunnel project will provide the technical support and scientific basis for other diversion tunnel projects, and realize knowledge sharing and reuse. Based on the current diversion tunnel design and these knowledge bases, the platform can implement the logical reasoning for its construction process in the life cycle.

5 VERIFICATION IMPLEMENTATION

We designed an ontology-based context management system that is intended to verify the validity of the proposed model. To construct the system, the first step is to instantiate information on NFC tags in line with the proposed modeling method. To illustrate, a tag containing context information for diversion tunnel should be created. Once being instantiated by the model, it is presented in Table 1. For keeping it short, Table 1 only presents a partial view of context data model instance. The "BasicInfo" node will provide the serial number and common information data of each tunnel segment. The serial number has two parts. The first part is a byte that designates which hydraulic engineering the tunnel segment belongs to. For example, the Jinping II hydropower station may be encoded as "00000001". And the second part is three bytes that designates the tunnel segment number, such as "00000000 00000000 00000001" for the first tunnel segment. The coding method can ensure that each tunnel segment number is unique in all hydraulic engineering, which is convenient to query and retrieve in the knowledge database. The "URI (Uniform Resource Identifier)" element has a web address that links directly to the website of hydraulic engineering or diversion tunnel, and more information can be found. The "Excavation-Method" element indicates the excavation way of each tunnel segment. The "SupervisorInfo" element describes the information of supervisor who is responsible for the quality of tunnel segment, which is convenient to issue tracking. The "event" element is an independent object that can occur in any node, and records the information related to the event.

As for the implementation on intelligent terminals, we developed a client application on an NFC-enabled mobile phone with the Android system, and the application architecture is based on Figure 1.

Table 1. The instance of context information (partial).

```
…
<BasicInfo>
<Number>00000001000000000000000000000001</
  Number>
<URI> www.scyw.com.cn </ApplicationURI>
<ExcavationMethod > DrillBlastMethod </Excavation-
  Method >
<SupervisorInfo > LiChun,510107197902310028</
  SupervisorInfo >
…
</BasicInfo >
<Initialized>
<RockCharateristics>
<RockType>Granite</RockType>
<RockGrade>Grade-III</RockGrade>
</RockCharateristics>
…
</Initialized>
<Excavated>
<Event>The collapse occurs during excavation</Event>
…
</Excavated>
…
```

When we develop the server application, the ontology-based modeling is applied to the modeling of catering data. Its query and reasoning engine is derived from an open source project, Jena, where a data-oriented query language, SPARQL, and a rule-based mechanism are used separately to implement the query and reasoning process. The query process aims at obtaining services that the user requires. Accordingly, the reasoning process intends to work out contents that users want to know. When the mobile phone touches an NFC tag mentioned above, it establishes a connection to the server and transfers the entity information from the NFC tag to the server. As the server gets the entity information, it exacts the element whose type value is "Number". For the reason that this element is unique in the knowledge base, it can be used as an identifier of an entity. Two threads, one for query and the other for reasoning, are created upon getting the value of "Number" element (assuming that its value is stored in a variable called *Number*). The priority of the query thread is to acquire detailed information of the corresponding entity. In contrast, the reasoning thread, with the aim of getting a set of recommended knowledge, performs reasoning procedures on the basis of the corresponding rules of entity information. For example, some recommended methods based on the processing rules of collapse during excavation are provided for the corresponding event

in Table 1. The activity diagraph of the server is shown in Figure 3.

After obtaining the reasoning results, the server begins to sort the set with the algorithm mentioned in Section 3.

Ultimately, a recommendation set is worked out. Consecutively, after the whole preceding procedures, the server pushes all the results to the mobile terminals. The parsing and processing of results are completed on terminals and eventually presented to the user with a visual interface, as shown in Figure 4.

With the above example, the validity of the proposed model is verified, which can be recognized as a convincing proof of the feasibility of applying ontology-based context management technology in diversion tunnel.

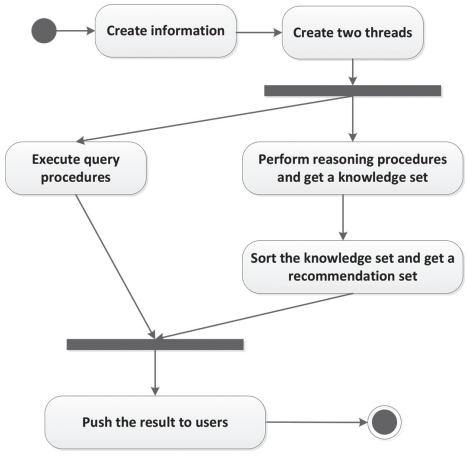

Figure 3. Activity diagraph in the server.

Figure 4. Results presenting the query and reasoning for collapse.

6 CONCLUSION

This paper is intended for analyzing mobile management technology in diversion tunnel. In addition, a brand-new context management model for diversion tunnel is proposed and verified with an example. We believe that the ontology-based context and NFC technology will revolutionize the user experience in diversion tunnel management.

REFERENCES

Gruber, T.R. 1993. A translation approach to portable ontologies. *Knowledge Acquisition* 5(2): 199–220.

Hu, L.X., Zhong, D.H. & Tong, D.W. 2012. Simulation and real-time control of whole construction progress of long-distance diversion tunnels under unfavorable geological conditions. *Chinese Journal of Geotechnical Engineering (in Chinese)* 34(3): 497–503.

Klaus, C., Klaus, R. & Gerd, K. 2013. A tunnel information system for the management and utilization of geo-engineering data in urban tunnel projects. *Geotechnical and Geological Engineering* 31(3): 845–859.

Lee, C.H., Wang, T.T. & Chang, C.S. 2006. Case study hydraulic tunnel rehabilitation. *Rock Engineering Symposium, Taiwan, 2006*. Tainan, Taiwan: Cheng Kung University Press.

Li, J.R., Zhong, D.H., Liu D.H., et al. 2006. Methodology and application of three-dimensional dynamic visual simulation of hydraulic and hydroelectric engineering. *Journal of System Simulation (in Chinese)* 18(1): 116–119.

Li, X.J. & Zhu, H.H. 2013. Development of a web-based information system for shield tunnel construction projects. *Tunnelling and Underground Space Technology* 37(1): 146–156.

Li, X.P. & Li, Y.A. 2014. Research on risk assessment system for water inrush in the karst tunnel construction based on GIS: Case study on the diversion tunnel groups of the Jinping II Hydropower Station. *Tunnelling and Underground Space Technology* 40(1): 182–191.

Liu, H.S., Chen, S.T., Chang, C.T., Ku, C. & Liao, Y.H. 2007. Design and construction of rehabilitation of the raw water transport main of Chin-Tan Weir. *Sino-Geotechnics* 114(12): 63–72.

Shi, Z.Q., Gao, L.L. & Zhang, L. 2012. Simulation model of deep buried diversion tunnel construction. *Yellow River (in Chinese)* 34(10): 141–143.

Wang, T.T., Lee, C.H., Weng, M.C. & Ho, T.Y. 2011. Life cycle design considerations of hydraulic tunnels based on inspection and maintenance cases. *WTC2011 Congress, Finland, Helsinki, 2011.* Helsinki, Finland: ITA.

Zhong, D.H. & Liu, K.J. 2007. Schedule forecasting and control based on real time simulation of underground structure group construction. *Journal of Tianjin University (in Chinese)* 40(6): 721–725.

This page intentionally left blank

Civil Engineering and Urban Planning IV – Liu et al. (Eds)
© 2016 Taylor & Francis Group, London, ISBN 978-1-138-02903-3

Dynamical reliability of internally resonant structural system under Gaussian white noise excitations

Hao-Yu Wang, Jun Lan & Yong-Jun Wu
Department of Engineering Mechanics, Shanghai Jiao Tong University, Shanghai, China

ABSTRACT: Theoretically, the dynamical reliability of internally resonant structural system with Many-Degrees-of-Freedom (MDOF) under Gaussian white noise excitations is studied. By using stochastic averaging method, the equations of motion of the original system are reduced to a set of averaged Itô stochastic differential equations. The backward Kolmogorov equation governing the conditional reliability function and the Pontryagin equation governing the mean first-passage time are established under appropriate boundary and (or) initial conditions. An example is given to show the accuracy of the theoretical method. All results are verified by Monte Carlo simulation.

1 INTRODUCTION

Structural and mechanical systems are often modeled as vibration system with Many-Degrees-of-Freedom (MDOF). Due to the coupling effect involved in the system, internal resonance can emerge, inducing many notable dynamical phenomena, such as energy transfer (Costa et al. 2009), energy harvest (Liu & Kremer 2014), vibration absorption (Ji 2014), etc. It is widely been recognized that the stochastic excitations are ubiquitous in engineering, such as turbulent wind, seismic ground motion, etc. So far, there are abundant literatures about the stochastic response, stochastic stability of stochastically excited Single-Degree-of-Freedom (SDOF) linear or nonlinear systems. For internally resonant MDOF stochastic nonlinear systems, less work has been done (Wu et al. 2013).

Reliability problem (first-passage) is a key issue in the analysis of stochastic dynamics (Ghazizadeh et al. 2012; Goller et al. 2013). In this work, the reliability problem based on the first-passage model of Many-Degrees-of-Freedom (MDOF) system under Gaussian white noise excitations is studied theoretically. In the case of internal resonance, the equations of motion of the original system are reduced to a set of averaged Itô stochastic differential equations after stochastic averaging. The Backward Kolmogorov (BK) equation governing the conditional reliability function and the Pontryagin equation governing the mean first-passage time are established under appropriate boundary and (or) initial conditions. An example is given to show the accuracy of the analytical method. Monte Carlo simulation is performed to verify the theoretical results.

2 AVERAGED ITÔ EQUATIONS

Consider the following n-DOF system

$$\ddot{X}_i + g_i(X_i) = \varepsilon d_i(\mathrm{X},\dot{\mathrm{X}}) + \varepsilon^{1/2} h_{ik}(\mathrm{X},\dot{\mathrm{X}}) W_k(t)$$
$$i, j = 1, 2, \ldots n; \quad k = 1, 2, \ldots m. \tag{1}$$

where X are generalized displacements; $g_i(X_i)$ is a nonlinear function of X_i. d_i denote weak damping and coupling terms; h_{ik} denote amplitudes of stochastic excitations; ε is a small positive parameter; $W_k(t)$ are stationary Gaussian white noises with correlation functions $R_{kl}(\tau) = E[W_k(t)W_l(t+\tau)] = 2D_{kl}\delta(\tau)$. The repeated subscript denotes summation.

The energy of each sub-system can be expressed as

$$E_i = \dot{X}_i^2/2 + \int_0^{X_i} g_i(X_i)\,dX_i. \tag{2}$$

Express the solution of equation (1) as the following form of generalized harmonic function (Cheung & Xu 1995)

$$X_i(t) = A_i \cos\Phi_i(t) + B_i,$$
$$\dot{X}_i(t) = -A_i \nu_i(A_i,\Phi_i)\sin\Phi_i(t), \tag{3}$$

where

$$\Phi_i(t) = \eta_i(t) + \Theta_i(t),$$
$$\nu_i(A_i,\Phi_i) = \frac{\mathrm{d}\eta_i}{\mathrm{d}t} = \sqrt{\frac{2[U_i(A_i+B_i) - U_i(A_i\cos\Phi_i + B_i)]}{A_i^2\sin^2\Phi_i}},$$
$$U_i(A_i+B_i) = U_i(-A_i+B_i) = E_i,$$
$$U_i = \int_0^{X_i} g_i(X_i)\,dX_i. \tag{4}$$

A_i, η_i, ν_i and Θ_i are all stochastic processes. A_i and ν_i are the amplitude and instantaneous frequency of the ith sub-system of the system (1), respectively.

If the system is resonant, there are α ($1 \le \alpha \le n-1$) relations of internal resonance, i.e.,

$$N_{uj}\omega_j = \varepsilon\sigma_u, \quad u = 1,2,\ldots,\alpha; \quad j = 1,2,\ldots,n, \tag{5}$$

where N_{sj} are integers, σ_s are small detuning parameters.

Introduce α new variable

$$\Gamma_u = N_{uj}\Phi_j, \quad u = 1,2,\ldots\alpha; \quad j = 1,2,\ldots n. \tag{6}$$

According to Stratonovich-Khasminskii limit theory (Khasminskii 1996; Stratonovitch 1963) and performing averaging with respect to the rapidly varying variables, one can obtain the following averaged Itô equations about A and Γ:

$$\begin{aligned} dA_i &= \varepsilon\bar{m}_i^{(1)}(A,\Gamma)dt + \varepsilon^{1/2}\bar{\sigma}_{ie}^{(1)}(A,\Gamma)dB_e(t),\\ d\Gamma_u &= \varepsilon\bar{m}_u^{(2)}(A,\Gamma)dt + \varepsilon^{1/2}\bar{\sigma}_{ue}^{(2)}(A,\Gamma)dB_e(t),\\ & i = 1,2,\ldots,n; \quad u = 1,2,\ldots,\alpha. \end{aligned} \tag{7}$$

3 CONDITIONAL RELIABILITY FUNCTION AND MEAN FIRST-PASSAGE TIME

It is reasonable to assume that first-passage occurs once $A_i(t)$ exceeds a certain critical value A_{ic} for the first time. The conditional reliability function, denoted by $R(t\,|A_0, \Gamma_0)$, is defined as the probability of $[A(t), \Gamma(t)]$ being in the safety domain Ω_s within interval $(0, t]$ given initial state being in Ω_s. $R(t\,|A_0, \Gamma_0)$ is determined by the following BK equation (Zhu 2006):

$$\begin{aligned} \frac{\partial R}{\partial t} &= \varepsilon\bar{m}_{i0}^{(1)}\frac{\partial R}{\partial A_{i0}} + \varepsilon\bar{m}_{u0}^{(2)}\frac{\partial R}{\partial \Gamma_{u0}} + \frac{1}{2}\varepsilon\bar{b}_{ij0}^{(11)}\frac{\partial^2 R}{\partial A_{i0}\partial A_{j0}}\\ &\quad + \frac{1}{2}\varepsilon\bar{b}_{u_1u_2 0}^{(22)}\frac{\partial^2 R}{\partial \Gamma_{u_1 0}\partial \Gamma_{u_2 0}} + \varepsilon\bar{b}_{iu0}^{(12)}\frac{\partial^2 R}{\partial A_{i0}\partial \Gamma_{u0}}, \end{aligned} \tag{8}$$

where

$$\begin{aligned} &\bar{m}_{i0}^{(1)} = \bar{m}_i^{(1)}\,|_{A=A_0,\Gamma=\Gamma_0}, \quad \bar{b}_{ij0}^{(11)} = \bar{\sigma}_{ie}^{(1)}\bar{\sigma}_{je}^{(1)}\,|_{A=A_0,\Gamma=\Gamma_0},\\ &\bar{b}_{u_1u_2 0}^{(22)} = \bar{\sigma}_{u_1e}^{(2)}\bar{\sigma}_{u_2e}^{(2)}\,|_{A=A_0,\Gamma=\Gamma_0},\\ &\bar{b}_{iu0}^{(12)} = \bar{\sigma}_{ie}^{(1)}\bar{\sigma}_{ue}^{(2)}\,|_{A=A_0,\Gamma=\Gamma_0}. \end{aligned} \tag{9}$$

The initial and boundary conditions of equation (8) are

$$\begin{aligned} &R(0\,|\,A_0,\Gamma_0) = 1,\ A_{i0} \in [0, A_{ic}),\ \Gamma_0 \in [0,2\pi],\\ &R(t\,|\,A_0,\Gamma_0) = 0,\ \ A_{i0} = A_{ic},\ \Gamma_0 \in [0,2\pi],\\ &R(t\,|\,0,\Gamma_0) = \textit{finite},\ \ \Gamma_0 \in [0,2\pi],\\ &R(t\,|\,A_0,0) = R(t\,|\,A_0,2\pi). \end{aligned} \tag{10}$$

The conditional Mean First-Passage Time (MFPT) $T(A_0, \Gamma_0)$ is also a function of the initial state $[\mathbf{A}_0, \Gamma_0]$. T is determined by the following Pontryagin equation:

$$\begin{aligned} -1 &= \varepsilon\bar{m}_{i0}^{(1)}\frac{\partial T}{\partial A_{i0}} + \varepsilon\bar{m}_{u0}^{(2)}\frac{\partial T}{\partial \Gamma_{u0}} + \frac{1}{2}\varepsilon\bar{b}_{ij0}^{(11)}\frac{\partial^2 T}{\partial A_{i0}\partial A_{j0}}\\ &\quad + \frac{1}{2}\varepsilon\bar{b}_{u_1u_2 0}^{(22)}\frac{\partial^2 T}{\partial \Gamma_{u_1 0}\partial \Gamma_{u_2 0}} + \varepsilon\bar{b}_{iu0}^{(12)}\frac{\partial^2 T}{\partial A_{i0}\partial \Gamma_{u0}}. \end{aligned} \tag{11}$$

The boundary conditions of equation (11) are

$$\begin{aligned} &T(A_0,\Gamma_0) = 0,\ A_{i0} = A_{ic},\ \Gamma_0 \in [0,2\pi],\\ &T(0,\Gamma_0) = \textit{finite},\ \ \Gamma_0 \in [0,2\pi],\\ &T(A_0,0) = T(A_0,2\pi). \end{aligned} \tag{12}$$

Solving the partial differential equations (8) and (11) by finite difference method, one can obtain the approximate reliability function and mean first-passage time of the original system (1).

4 NUMERICAL EXAMPLE

Consider the following 2-DOF coupled Duffing-van der Pol system.

$$\begin{aligned} &\ddot{X}_1 + (\beta_{10} + \beta_{11}X_1^2 + \beta_{12}X_2^2)\dot{X}_1 + \omega_{01}^2 X_1\\ &\quad + \gamma_1 X_1^3 + \eta_{12}\dot{X}_2 = W_{11}(t) + X_1 W_{12}(t),\\ &\ddot{X}_2 + (\beta_{20} + \beta_{21}X_1^2 + \beta_{22}X_2^2)\dot{X}_2 + \omega_{02}^2 X_2\\ &\quad + \gamma_2 X_2^3 + \eta_{21}\dot{X}_1 = W_{21}(t) + X_2 W_{22}(t), \end{aligned} \tag{13}$$

Herein, $W_{ik}(t)$ are independent Gaussian noises with intensity $2D_{ik}$.

Consider the 1:1 internal resonance in the system. In this case, the following relationship exists:

$$\omega_1(A_1)/\omega_2(A_2) = 1 + \varepsilon. \tag{14}$$

The parameters are chosen as: $A_{ic} = 0.5$, $\beta_{ij} = 0.01$, $\eta_{ik} = 0.05$, $\omega_{0i} = 2.0$, $D_{ik} = 0.03$ (i, k = 1, 2; j = 0, 1, 2). The averaged Itô stochastic differential equations are:

$$dA_1 = \bar{m}_1^{(1)}(A,\Gamma)dt + \bar{\sigma}_{11}^{(1)}dB_1(t) + \bar{\sigma}_{12}^{(1)}dB_2(t),$$
$$dA_2 = \bar{m}_2^{(1)}(A,\Gamma)dt + \bar{\sigma}_{21}^{(1)}dB_1(t) + \bar{\sigma}_{22}^{(1)}dB_2(t),$$
$$d\Gamma = \bar{m}_1^{(2)}(A,\Gamma)dt + \bar{\sigma}_{11}^{(2)}dB_1(t) + \bar{\sigma}_{12}^{(2)}dB_2(t). \quad (15)$$

The drift coefficients are

$$\begin{aligned}
\bar{m}_i^{(1)} &= \bar{m}_{i1}^{(1)} + \bar{m}_{i2}^{(1)},\\
\bar{m}_{i1}^{(1)} &= \Big\{-4A_i\Big[4\beta_{i0} + A_i^2\beta_{ii} + 2\beta_{ij}A_j^2\Big]\\
&\quad + \frac{2A_i^3\left(6D_{i1} + A_i^2D_{i2}\right)\gamma_i^2}{\left(A_i^2\gamma_i + \omega_{0i}^2\right)^3} - \frac{A_i\left(26D_{i1} + 7A_i^2D_{i2}\right)\gamma_i}{\left(A_i^2\gamma_i + \omega_{0i}^2\right)^2}\\
&\quad + \Big[16D_{i1} + 12A_i^2D_{i2} + A_i^6\gamma_i\beta_{ii} + 3A_i^4\gamma_i\\
&\quad \times\left(2\beta_{i0} + A_j^2\beta_{ij}\right)\Big]\Big/\Big[A_i\left(A_i^2\gamma_i + \omega_{0i}^2\right)\Big]\Big\}\Big/32,\\
\bar{m}_{i2}^{(1)} &= A_iA_j^2\beta_{ij}\left(\gamma_iA_i^2 + 2\omega_{0i}^2\right)\\
&\quad \times\cos(2\Gamma)\Big/\Big[16\left(\gamma_iA_i^2 + \omega_{0i}^2\right)\Big]\\
&\quad - A_j\left[2b_{10}(A_1) - b_{12}(A_1)\right]\left[2b_{20}(A_2) - b_{22}(A_2)\right]\\
&\quad \times\eta_{ij}\cos\Gamma\Big/\Big[8\left(\gamma_iA_i^2 + \omega_{0i}^2\right)\Big]\\
&\quad - A_j\left[b_{12}(A_1) - b_{14}(A_1)\right]\left[b_{22}(A_2) - b_{24}(A_2)\right]\\
&\quad \times\eta_{ij}\cos3\Gamma\Big/\Big[8\left(\gamma_iA_i^2 + \omega_{0i}^2\right)\Big]\\
&\quad - A_j\left[b_{14}(A_1) - b_{16}(A_1)\right]\left[b_{24}(A_2) - b_{26}(A_2)\right]\\
&\quad \times\eta_{ij}\cos5\Gamma\Big/\Big[8\left(\gamma_iA_i^2 + \omega_{0i}^2\right)\Big]\\
&\quad - A_jb_{16}(A_1)b_{26}(A_2)\eta_{ij}\cos7\Gamma\Big/\Big[8\left(\gamma_iA_i^2 + \omega_{0i}^2\right)\Big],\\
&\quad (i,j = 1,2,\ i \neq j,\ \textit{no summation about } i)\\
\bar{m}_1^{(2)} &= b_{10}(A_1) - b_{20}(A_2) - A_2^2\beta_{12}\left(3\gamma_1A_1^2 + 4\omega_{01}^2\right)\\
&\quad \times\sin(2\Gamma)\Big]\Big/\Big[32\left(\gamma_1A_1^2 + \omega_{01}^2\right)\Big]\\
&\quad - A_1^2\beta_{21}\left(3\gamma_2A_2^2 + 4\omega_{02}^2\right)\sin(2\Gamma)\Big/\Big[32\left(\gamma_2A_2^2 + \omega_{02}^2\right)\Big]\\
&\quad + A_2\left[2b_{10}(A_1) + b_{12}(A_1)\right]\left[2b_{20}(A_2) - b_{22}(A_2)\right]\\
&\quad \times\eta_{12}\sin\Gamma\Big/\Big[8A_1\left(\gamma_1A_1^2 + \omega_{01}^2\right)\Big]\\
&\quad + A_2\left[b_{12}(A_1) + b_{14}(A_1)\right]\left[b_{22}(A_2) - b_{24}(A_2)\right]\\
&\quad \times\eta_{12}\sin3\Gamma\Big/\Big[8A_1\left(\gamma_1A_1^2 + \omega_{01}^2\right)\Big]\\
&\quad + A_2\left[b_{14}(A_1) + b_{16}(A_1)\right]\left[b_{24}(A_2) - b_{26}(A_2)\right]\\
&\quad \times\eta_{12}\sin5\Gamma\Big/\Big[8A_1\left(\gamma_1A_1^2 + \omega_{01}^2\right)\Big]\\
&\quad + A_2b_{16}(A_1)b_{26}(A_2)\eta_{12}\sin7\Gamma\Big/\Big[8A_1\left(\gamma_1A_1^2 + \omega_{01}^2\right)\Big]\\
&\quad + A_1\left[2b_{10}(A_1) - b_{12}(A_1)\right]\left[2b_{20}(A_2) + b_{22}(A_2)\right]\\
&\quad \times\eta_{21}\sin\Gamma\Big/\Big[8A_2\left(\gamma_2A_2^2 + \omega_{02}^2\right)\Big]\\
&\quad + A_1\left[b_{12}(A_1) - b_{14}(A_1)\right]\left[b_{22}(A_2) + b_{24}(A_2)\right]\\
&\quad \times\eta_{21}\sin5\Gamma\Big/\Big[8A_2\left(\gamma_2A_2^2 + \omega_{02}^2\right)\Big]\\
&\quad + A_1b_{16}(A_1)b_{26}(A_2)\eta_{21}\sin7\Gamma\Big/\Big[8A_2\left(\gamma_2A_2^2 + \omega_{02}^2\right.\\
b_{i0}(A_i) &= \left(\omega_{0i}^2 + 3\gamma_iA_i^2/4\right)^{1/2}\left(1 - \lambda_i^2/16\right),\\
b_{i2}(A_i) &= \left(\omega_{0i}^2 + 3\gamma_iA_i^2/4\right)^{1/2}\left(\lambda_i/2 + \lambda_i^3/64\right),\\
b_{i4}(A_i) &= \left(\omega_{0i}^2 + 3\gamma_iA_i^2/4\right)^{1/2}\left(-\lambda_i^2/16\right),\\
b_{i6}(A_i) &= \left(\omega_{0i}^2 + 3\gamma_iA_i^2/4\right)^{1/2}\left(\lambda_i^3/64\right),\\
\lambda_i &= \gamma_iA_i^2\Big/\Big[4\left(\omega_{0i}^2 + 3\gamma_iA_i^2/4\right)\Big].
\end{aligned} \quad (16)$$

The diffusion coefficients are

$$\begin{aligned}
\bar{b}_{ii}^{(11)} &= \bar{\sigma}_{i1}^{(1)}\bar{\sigma}_{i1}^{(1)} + \bar{\sigma}_{i2}^{(1)}\bar{\sigma}_{i2}^{(1)}\\
&= \left(3A_i^4D_{i2}\gamma_i + 16D_{i1}\omega_{0i}^2\right)\Big/\Big[16\left(A_i^2\gamma_i + \omega_{0i}^2\right)^2\Big]\\
&\quad + 2A_i^2\left(5D_{i1}\gamma_i + 2D_{i2}\omega_{0i}^2\right)\Big/\Big[16\left(A_i^2\gamma_i + \omega_{0i}^2\right)^2\Big],\\
&\quad (i = 1,2,\ \textit{no summation about } i)\\
\bar{b}_{11}^{(22)} &= \bar{\sigma}_{11}^{(2)}\bar{\sigma}_{11}^{(2)} + \bar{\sigma}_{12}^{(2)}\bar{\sigma}_{12}^{(2)}\\
&= D_{11}\left(7A_1^2\gamma_1 + 8\omega_{01}^2\right)\Big/\Big[8\left(A_1^3\gamma_1 + \omega_{01}^2A_1\right)^2\Big]\\
&\quad + D_{12}\left(11A_1^2\gamma_1 + 12\omega_{01}^2\right)\Big/\Big[16\left(A_1^2\gamma_1 + \omega_{01}^2\right)^2\Big]\\
&\quad + D_{21}\left(7A_2^2\gamma_2 + 8\omega_{02}^2\right)\Big/\Big[8\left(A_2^3\gamma_2 + \omega_{02}^2A_2\right)^2\Big]\\
&\quad + D_{22}\left(11A_2^2\gamma_2 + 12\omega_{02}^2\right)\Big/\Big[16\left(A_2^2\gamma_2 + \omega_{02}^2\right)^2\Big],\\
\bar{b}_{i1}^{(12)} &= \bar{b}_{1i}^{(21)} = \bar{\sigma}_{i1}^{(1)}\bar{\sigma}_{11}^{(2)} + \bar{\sigma}_{i2}^{(1)}\bar{\sigma}_{12}^{(2)} = 0.
\end{aligned} \quad (17)$$

The BK equation associated with the averaged system (15) is

$$\begin{aligned}
\frac{\partial R}{\partial t} &= \bar{m}_{10}^{(1)}\frac{\partial R}{\partial A_{10}} + \bar{m}_{20}^{(1)}\frac{\partial R}{\partial A_{20}} + \bar{m}_{10}^{(2)}\frac{\partial R}{\partial\Gamma_0}\\
&\quad + \frac{1}{2}\bar{b}_{110}^{(11)}\frac{\partial^2R}{\partial A_{10}^2} + \frac{1}{2}\bar{b}_{220}^{(11)}\frac{\partial^2R}{\partial A_{20}^2} + \frac{1}{2}\bar{b}_{110}^{(22)}\frac{\partial^2R}{\partial\Gamma_0^2}.
\end{aligned} \quad (18)$$

The Pontryagin equation associated with the averaged system (15) is

$$\begin{aligned}
-1 &= \bar{m}_{10}^{(1)}\frac{\partial T}{\partial A_{10}} + \bar{m}_{20}^{(1)}\frac{\partial T}{\partial A_{20}} + \bar{m}_{10}^{(2)}\frac{\partial T}{\partial\Gamma_0}\\
&\quad + \frac{1}{2}\bar{b}_{110}^{(11)}\frac{\partial^2T}{\partial A_{10}^2} + \frac{1}{2}\bar{b}_{220}^{(11)}\frac{\partial^2T}{\partial A_{20}^2} + \frac{1}{2}\bar{b}_{110}^{(22)}\frac{\partial^2T}{\partial\Gamma_0^2}.
\end{aligned} \quad (19)$$

Solving the 3+1-dimensional BK equation (18) and 3-dimensional Pontryagin equation (19), we

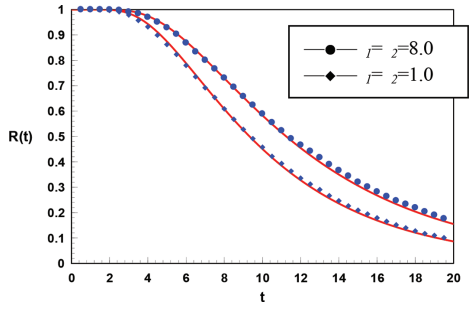

Figure 1. Conditional reliability functions of system (13).

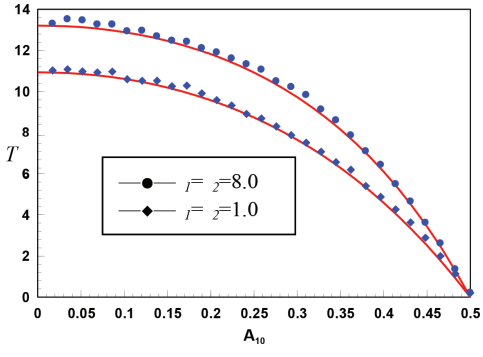

Figure 2. MFPT of system (13). A_{10} is a variable.

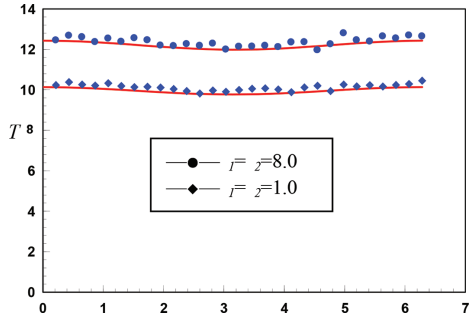

Figure 3. MFPT of system (13). Γ_0 is Γ_0 a variable.

obtain the conditional reliability function and mean first-passage time of system (13), respectively. Figure 1 shows results of conditional reliability function. The solid lines are analytical results while the discrete symbols are results from Monte Carlo Simulation (MCS). Obviously, the agreement is very good. Figure 2 shows that the mean firs-passage time is a decreasing function of the initial state A_0, while Figure 3 demonstrates that the mean firs-passage time is not sensitive to the initial state Γ_0. This is physically meaningful.

5 CONCLUSION

In the present paper, the reliability problem of MDOF internally resonant strongly nonlinear structural systems is studied. The stochastic excitations are modeled as Gaussian white noise. The averaged Itô stochastic differential equations are obtained in the case of internal resonance. The BK equation and the Pontryagin equation are established to determine the conditional reliability function and the conditional mean first-passage time, respectively. A 2-DOF coupled Duffing-van der Pol system is given as an example to illustrate the application of the analytical method. The 3+1-dimensional BK equation and 3-dimensional Pontryagin equation are solved under suitable initial and boundary conditions. It is seen that the agreement between the theoretical method and MCS is very good.

ACKNOWLEDGEMENT

This work was financially supported by the National Natural Science Foundation of China (Grant Nos. 11272201, 11132007 and 11372271).

REFERENCES

Cheung, Y.K. & Xu, Z. 1995. Internal resonance of strongly non-linear autonomous vibrating systems with many degrees of freedom. *Journal of Sound and Vibration* 180(2): 229–238.

Costa, S.N.J. et al. 2009. On energy transfer between vibrating systems under linear and nonlinear interactions. *Nonlinear Dynamics* 57(1): 57–67.

Ghazizadeh, S. et al. 2012. New analytical solution of the first-passage reliability problem for linear oscillators. *ASCE Journal of Engineering Mechanics* 138(6): 695–706.

Goller, B. et al. 2013. Reliability assessment in structural dynamics. *Journal of Sound and Vibration* 332(10): 2488–2499.

Ji, J.C. 2014. Design of a nonlinear vibration absorber using three-to-one internal resonances. *Mechanical Systems and Signal Processing* 42(1–2): 236–246.

Khasminskii, R.Z. 1966. A limit theorem for the solutions of differential equations with random right-hand sides. *Theory of Probability and Its Applications* 11(3): 390–406.

Kremer, D. & Liu, K.F. 2014. A nonlinear energy sink with an energy harvester: Transient responses. *Journal of Sound and Vibration* 333(20): 4859–4880.

Stratonovitch, R.L. 1963. *Topics in the Theory of Random Noise*. New York: Gordon and Breach.

Wu, Y.J. et al. 2013. First-passage problem of strongly nonlinear stochastic oscillators with external and internal resonances. *European Journal of Mechanics A/Solids* 39: 60–68.

Zhu, W.Q. 2006. Nonlinear stochastic dynamics and control in Hamiltonian formulation. *Applied Mechanics Reviews* 59(4): 230–248.

Civil Engineering and Urban Planning IV – Liu et al. (Eds)
© 2016 Taylor & Francis Group, London, ISBN 978-1-138-02903-3

Historic and modern urban concrete bridges in Poland

J. Biliszczuk & J. Onysyk
Research and Design Office Mosty-Wrocław, Wrocław University of Technology, Wrocław, Poland

W. Barcik & R. Toczkiewicz
Research and Design Office Mosty-Wrocław, Wrocław, Poland

ABSTRACT: This paper presents development of urban concrete bridges, built over the last century in Poland. Changes of structural and architectural configuration on examples of selected bridge structures are described. In particular, early Polish reinforced concrete and prestressed concrete structures as well as first bridges built with use of innovative construction technologies are presented. The paper is concluded with examples of modern structures.

1 INTRODUCTION

Cities were usually established along rivers, in places where communication routes were crossing. There the bridges, facilitating traffic of people and goods and flow of ideas, were built. Bridges constructed in cities, apart from their utility functions, were symbols showing the economic strength of agglomerations and set new trends in architecture and technology.

This paper presents briefly the development of urban concrete bridges in Poland since the beginning of the twentieth century to the present time.

2 INNOVATIVE HISTORIC BRIDGES

This section presents urban bridges, which at the time of construction were innovative in terms of used materials and erection technology. The first use of reinforced concrete by Polish engineer was in 1894. Professor Maximilian Thullie from Lviv University of Technology (now Ukraine) designed a reinforced concrete footbridge with a span of 11.05 m.

Examples given below are flagships of Polish engineering of the 20th century and in most cases are still in use.

2.1 *First reinforced concrete bridges*

The Poniatowskiego Bridge over the Vistula River in Warsaw was built in 1904–1914. Its main part, 506 m long, consists of eight steel trusses with spans of 32 to 80 m. Along with the bridge a 701 m long viaduct over the Powiśle district, an extension of Jerozolimskie Avenue, was built (Fig. 1).

Figure 1. Present view of the Poniatowskiego Bridge in Warsaw (upper photo) and the Warszawski Bridge in Wrocław.

Viaduct of the Poniatowskiego Bridge was the first structure designed by Polish engineers, in which a new material—reinforced concrete was implemented on a large scale. Reinforced concrete arches with spans of 12.5 m to 20.0 m support deck of the viaduct. The deck is a steel grid consisting of longitudinal floor beams, supporting steel plates and main crossbeams with overhangs placed on reinforced concrete columns. In the axes of arch supports, concrete piers braced by Vierendeel cellular cross-beams are localized. Architectural design of the viaduct was emphasized, hence the presence of Neo-Renaissance ornamental towers, leading to the deck and pavilions built in the structure of the viaduct.

The Old Warszawski Bridge (initially called Hindenburgbrücke) was built in Wrocław in 1916

and has been used till the present day. The bridge has five reinforced concrete arch barrels with spans of 27.8 to 33.5 m and a reinforced concrete tied arch with a span of 55.9 m (Melan & Gesteschi 1932). In 2007 selected structural elements of the arch span (reinforced concrete crossbeams and hangers) were strengthened with CFRP plates and fabrics and the whole structure was rehabilitated (Fig. 1).

Intensive development of reinforced concrete bridge structures, including urban bridges, took place in Poland in the interwar period. In particular, many reinforced concrete arch bridges of various types (barrel arches, upper deck arches, tied arch bridges and Langer type arches) were built. Many of them were unfortunately destroyed during the Second World War.

2.2 *Early prestressed concrete urban bridges*

Technology of concrete prestressing has enabled to design concrete bridges with spans and shapes that were unattainable in the case of reinforced concrete, while increasing their durability. Prestressed concrete has been used in Polish bridge engineering since 1953 (Biliszczuk 1997).

Built in 1954–1959 road-tram Pokoju Bridge over the Odra River in Wrocław (Fig. 2) is 125.3 m long. This light, elegant bridge of horizontal outline consists of two parallel structures with a total width of 25.7 m, separated by a narrow longitudinal gap. Separate post-tensioned concrete structures have multi-cell box cross-section and a static scheme of a three span Gerber's beam. Span lengths are 33.1 + 52.5 + 33.1 m, including the middle suspended span with a length of 14.5 m.

The same static scheme was adopted in the Cłowy Bridge built over the Regalica River in Szczecin, in 1959. It is a post-tensioned concrete structure with spans of 58.60 + 78.60 + 58.25 m. The superstructure consists of six beam girders, which in the hogging moment zones (over supports) were modified into three box girders with a height varying from 2.0 m to 4.7 m. Middle part of the main span (suspended span) with a length of 34 m consists of precast prestressed T-beams with a height of 2.0 m in the middle of the span and of 2.2 m over the hinge support. Assembly of prefabricated beams weighing 70 tons each was carried out with use of a floating crane.

2.3 *Implementation of new construction technologies*

The first Polish cantilevered, cast in-situ concrete bridge—the Bernardyński Bridge over the Brda River in Bydgoszcz (Fig. 3) was opened in 1963. The basic dimensions of the bridge are: span lengths 12 + 40 + 12 m, deck width 27.3 m. Height of the superstructure varies from 0.95 m in the span to 2.5 m over the piers. The bridge is a three span structure with a hinge in the middle of the main span. Two girders forming the superstructure have a box cross-section with wide spacing of webs equal to 6.65 m. The middle span over the river was cantilevered with use of two sets of steel movable scaffolding. Each segment with a length of 3 m and width of 14.5 m (concrete volume equal to 20 m^3) was erected in 4 days. The main girders were prestressed by 37Ø5 mm cables. Transverse prestressing was carried out using Freyssinet 18Ø5 mm cables (Wolff 2003).

The Pomorski Bridge (Fig. 3), built in 1969, was the first bridge implementing a cantilever assembly of precast concrete segments. It is a three-span structure with a hinge in the middle of the main span. The superstructure consists of

Figure 2. Early prestressed concrete bridges: the Pokoju Bridge in Wrocław (upper photo) and the Cłowy Bridge in Szczecin.

Figure 3. First cantilevered bridges: the Bernardyński Bridge (upper photo) and the Pomorski Bridge.

five box girders of variable height, with spans of 18 + 43 + 18 m. The central span over the Brda River was cantilevered. The number of segments was 70, and their length varied from 2.0 to 2.9 m, while a constant weight of 16 tons was maintained. The segments were joined using epoxy glue and prestressed by 48Ø5 mm cables anchored in the webs. The segments were precast in inverted position, transported to the assembly site and then rotated into the final position by a special platform (Wolff 2003). This method was an original concept.

3 MODERN STRUCTURES

A rapid development of urban road infrastructure during the last years resulted in construction of many new bridges in centers of cities as well as along new city ring roads. Their location in urbanized areas (over railway lines, streets and crossroads) often results in construction of multi-span structures. In this section selected examples of such structures, built recently in Poland are described.

3.1 *Multi-span flyovers*

Gądowska flyover in Wrocław, built in 2000–2002 along the inner city ring road, consists of two parallel, curved in plan 15-span box structures (Fig. 4), made of prestressed concrete class C50/60. Side junctions (beam-plate structures) are joined to both superstructures in their middle section. Span length varies from 33.0 to 52.0 m. The flyover is located in an urbanized area, crossing a busy street and two-level multi-track railway lines, therefore it was erected by means of longitudinal launching method. Only side parts were cast on scaffolding. An interesting feature of this structure was assembly of precast, curved elements, forming side parts of the three-cell box cross-section of the girders (Biliszczuk et al. 2011).

Figure 4. Modern multi-span flyovers: the Gądowska flyover (upper photo) and WA-17 flyover.

Multi-span flyovers denoted as WA-19 and WA-17 were built in 2011 along the A8 motorway ring road of Wrocław (Biliszczuk et al. 2012). WA-17 viaduct is a seven-span horizontally curved structure, crossing several streets and a railway line. Its total length is 300.0 m, the length of spans varies from 30.0 to 60.0 m. The superstructure is a single-cell box girder. Due to the significant length of deck plate overhangs, they are supported by steel tube struts forming a "V" shape in side view (Fig. 4). The struts carry loads in transverse and longitudinal direction, and dominate the architectural reception of the flyover. Superstructures for both carriageways were longitudinally launched.

WA-19 flyover has a similar structural configuration. It crosses a city road interchange and a railway line in the vicinity of EURO 2012 football stadium. It was constructed on traditional scaffolding in five multi-span sections (Biliszczuk et al. 2012). WA-19 flyover consists of two structures curved in plan, separate for each of the carriageways. 16-span continuous beam superstructures are made of prestressed concrete class C50/60. Span length varies from 35.0 to 58.0 m and the total length of the flyover is 750 m.

3.2 *Urban bridges*

The Zwierzyniecki Bridge over the Vistula River built in 2000 (Fig. 5) connects two districts of the city—Dębniki and Zwierzyniec. Its configuration was based on the result of an architectural competition (Flaga et al. 2002). The bridge is a single beam with a span of 132 m, fixed in both abutments. Assumed static scheme imposed design of large complex support zones, providing a proper fixing of the span. They consist of a system of massive frames, transoms and struts, pressed to the heavy abutments by vertical cables. Double-cell box main girder was cantilevered. Its height varies from 7.0 m at the abutments to 3.5 m in the middle of the span. Architectural design of the bridge was emphasized: the bottom edge of the box girder is curved and facade panels of the same curvature were mounted on the steel struts supporting the deck overhangs.

Rędziński Bridge in Wrocław, completed in 2011, consists of three substructures: two approach flyovers (610 m and 520 m long, multi-span continuous beams made of prestressed concrete, span lengths

Figure 5. Modern urban bridges: the Zwierzyniecki Bridge in Cracow (upper photo), the Rędziński Bridge in Wrocław (middle photo) and viaduct in Opole.

up to 60 m) and a cable-stayed main bridge (Fig. 5): 612 m long, span lengths $50 + 2 \times 256 + 50$ m. The superstructure of the main bridge consists of two separate prestressed concrete box girders of a constant height (one for each carriageway of the motorway), suspended to a single, 122 m high, H-shaped concrete pylon (Biliszczuk et al. 2014). As the bridge is situated in recreational area of Wrocław, a great attention during the design process was paid to the aesthetics and architectural issues. To achieve a light, elegant structure a small deck thickness equal to 2.58 m, which is about 1/100th of the main span was designed.

The viaduct in Opole (2010) is located in the strict city center over a railway station and a local street (Fig. 5). It is a single pylon cable-stayed structure with a main span of 72.0 m. The pylon is fixed in the asymmetric concrete deck of a complex geometry. The superstructure is a prestressed concrete plate with a thickness of 0.90 m in the area of the pylon and a beam-slab structure (three main prestressed concrete girders in the cross-section) in the main span and in the back span. The pylon is a hybrid structure: bottom and central parts are made of concrete prestressed by vertical cables; the upper part is a steel box, where passive anchorages of main stays and back stays are located. Cable stays are arranged in a single plane in the axis of the viaduct.

4 CONCLUSIONS

The paper describes development of Polish urban concrete bridges since the beginning of the last century. Presented examples illustrate changes in structural and architectural design. In particular, the early reinforced concrete and prestressed concrete structures and first bridges built with use of modern construction technologies are described.

This brief review clearly shows that the most innovative structures in terms of architectural and structural form, technology and new materials are built in cities.

REFERENCES

Biliszczuk, J. 1997. Historia rozwoju mostów z betonu sprężonego w Polsce (History of prestressed concrete bridges in Poland—in Polish). *Inżynieria i Budownictwo* 9: 427–431.

Biliszczuk, J., Barcik, W., Onysyk, J., Sadowski, K., Toczkiewicz, R. & Tukendorf, K. 2011. Use of Prefabricated Elements in Structural and Architectural Designing of Concrete Bridge Superstructures. *Proc. of the 7th Central European Congress on Concrete Engineering, Balatonfured, 22–23 September 2011.* B udapest: FIB Hungary.

Biliszczuk, J., Barcik, W., Onysyk, J., Toczkiewicz, R., Tukendorf, A. & Tukendorf, K. 2014. Rędziński Bridge in Wrocław—the largest concrete concrete cable-stayed bridge in Poland. *Structural Engineering International* 24(2): 285–292.

Biliszczuk, J., Onysyk, J., Barcik, W., Prabucki, M., Sułkowski, M., Sadowski, K. & Toczkiewicz, R. 2012. Construction of Multi-span Motorway Viaducts Using Various Technologies. *Proc. of fib Symposium "Concrete Structures for Sustainable Community", Stockholm, 11–14 June 2012.* Stockholm: Swedish Concrete Association.

Flaga, K., Matuszkiewicz, T. & Wanecki, P. 2002. The New Prestressed Concrete Bridge over the Vistula River in Kraków. *Proc. of the 1st fib Congress "Concrete Structures in the 21st Century", Osaka, 13–19 October 2002.* CD-ROM.

Melan, J. & Gesteschi, T.H. 1932. *Bogenbrucken Vierte Neubearbeitete Auflage* (in German). Berlin: Wilhelm Ernst & Sohn.

Wolff, M. 2003. Pierwsze w Polsce betonowe mosty zrealizowane metoda nawisową (in Polish). *Proc. of the Workshop "Budowa Mostów Betonowych Metodą Nawisową", Warsaw, 23 January 2003.* Warsaw: Warsaw University of Technology.

Civil Engineering and Urban Planning IV – Liu et al. (Eds)
© 2016 Taylor & Francis Group, London, ISBN 978-1-138-02903-3

Experimental investigation on the hysteresis behavior of beam-to-column connections of H-beams with corrugated webs

Xin Fan
China State Construction Technical Center, Beijing, China
Harbin Institute of Technology, Harbin, Heilongjiang, China

Ming Li
China State Construction Technical Center, Beijing, China

ABSTRACT: Steel H-beams with corrugated webs can provide high shear buckling resistance with very thin webs, which results in saving steels. Common beam-to-column rigid connections are not suitable for H-beams with corrugated webs, so two types of beam-to-column connections are proposed for H-beams with corrugated webs. One beam-to-column connection is to weld a short cut of the common H-beam at the end of the H-beam with corrugated webs, and the other one is bolted endplate connection. To investigate the hysteresis behavior of the beam-to-column connections of H-beam with corrugated webs, four specimens of the two types of connections were tested. Failure modes and hysteresis loops were obtained. The failure modes of the specimens were all shear buckling of the corrugated webs, and no failure was found at the connection parts. The specimens with initial imperfection showed early buckling in the tests. The test results revealed that the two types of the beam-to-column connections of H-beams with corrugated webs had good cyclic performance without brittle failure, and that the initial imperfection of the corrugated webs influenced the hysteresis behavior of the connections.

1 INTRODUCTION

H-beams with corrugated webs have been widely used in steel structures due to the advantages such as higher shear buckling resistance and thinner webs compared with beams with common flat webs (Zhang 2008). Behaviors of H-beams with corrugated webs have been investigated thoroughly (Elgaaly 1997; Guo 2012), but research on the behavior of connections of H-beams with corrugated webs is scarce. Since the performance of connections has an important effect on the safety and economy of steel structures, it is necessary to investigate the behaviors of connections of H-beams with corrugated webs.

2 DESIGN OF SPECIMENS

Common beam-to-column rigid connections are usually presented by welded flanges and bolted webs. But they are not suitable for beams with corrugated webs. So two types of beam-to-column connections are proposed for H-beams with corrugated webs. One beam-to-column connection is to weld a short cut of the common H-beam at the end of the H-beam with corrugated webs, and the other one is bolted endplate connection. For the hysteresis experimental research, four specimens were prepared. Two of them with the names A1 and A2 are connections with a short cut of H-beam with flat webs and the other two with the names B1 and B2 are bolted endplate connections. H-beams with corrugated webs CWA500-200 × 10 are used. CWA500-200 × 10 indicates that the flanges are 200 mm wide and 10 mm thick, and the webs are 500 mm high and 2 mm thick. The geometric parameters of the web corrugation are shown in Figure 1.

The dimensions of the connection are shown in Figures 2 and 3.

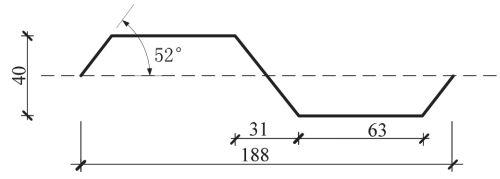

Figure 1. Geometric parameters of the web corrugation.

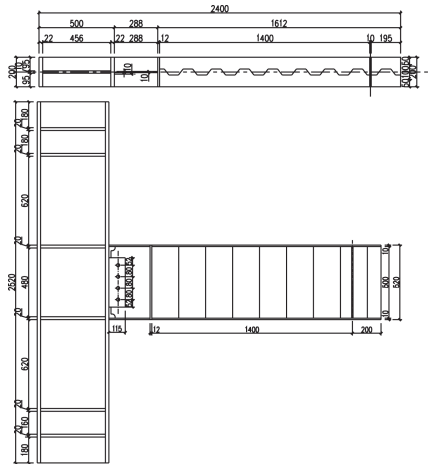

Figure 2. Dimension of specimens A1 and A2.

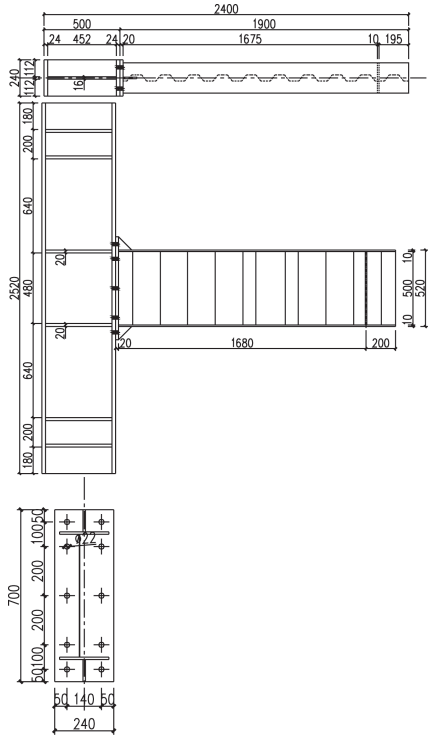

Figure 3. Dimension of specimens B1 and B2.

3 MATERIAL TEST RESULTS

Rectangular specimens for material property tests were prepared following the Chinese standard GB/T 2975-1998 and GB 6397-86. The specimens were loaded following the GB/T 228-2002. The test results are summarized in Table 1.

Table 1. Material test results.

Thickness (mm)	Yielding Strength σ_y (MPa)	Tensile Strength σ_u (MPa)	Elongation (%)
2	244	394	34.7
6	297	413	35.7
10	303	435	34.7
12	320	457	38.5
20	281	434	35.5

Figure 4. Photo of A1 and A2 at the test site.

Figure 5. Photo of B1 and B2 at the test site.

4 LOADING AND MEASURING SCHEME

The experiments were carried out in the laboratory of Tongji University. The test equipment included the horizontal reaction frame, hoisting jack, sensors and data collection systems.

The test setup is shown in Figures 4 and 5. The column is fixed horizontally at the test site by pressing beams, and the end of the column is fixed by hoisting jack in case of flipping. The out-of-plane deformation of specimens is restrained during tests. The beam is loaded cyclically by tension jack that is fixed at the horizontal reaction frame. The loading protocol specifies a series of load steps and the number of cycles for each. Each load step corresponds to the displacement of the loading point. The load steps were executed and data points recorded at regular intervals. The load steps are continued until the limits of the test frame are reached or until the specimen failed.

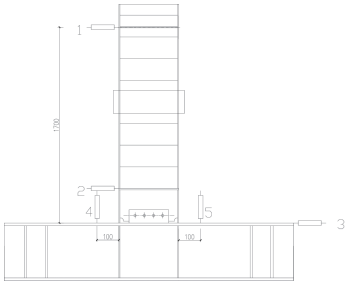

Figure 6. Displacement meters of A1 and A2.

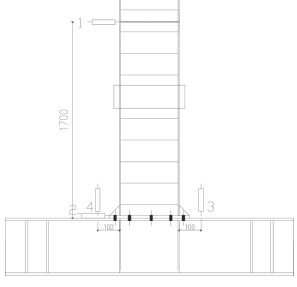

Figure 7. Displacement meters of B1 and B2.

The displacements of loading and supporting point were monitored by displacement meters. Arrangement of measuring points is shown in Figures 6 and 7.

5 FAILURE MODES OF SPECIMENS

5.1 *Failure mode of specimen A1*

When the specimen was loaded at the second circle of displacement 18 mm, some noise could be heard. The noise was even louder at the first circle of 24 mm, and the corrugated webs showed local buckling near the loading point. The corrugated webs buckled across the beam section and the specimen failed at the third circle of 24 mm. The initial and final failure modes of specimen A1 are shown in Figure 8.

5.2 *Failure mode of specimen A2*

When the specimen was loaded at the first circle of displacement 9 mm, some noise could be heard. The noise was even louder at the first circle of 12 mm, and the corrugated webs showed local buckling near the stiffener. A huge bang was heard at the first circle of 30 mm. The corrugated webs buckled across the beam section and the specimen failed at the third circle of 30 mm. The initial and final failure modes of specimen A1 are shown in Figure 9.

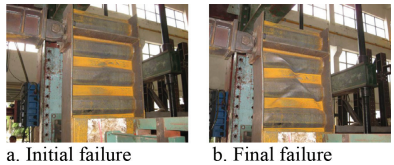

a. Initial failure b. Final failure

Figure 8. Failure mode of specimen A1.

a. Initial failure

b. Final failure

Figure 9. Failure mode of specimen A2.

Figure 10. Failure mode of specimen B1.

5.3 *Failure mode of specimen B1*

When the specimen was loaded at the third circle of displacement 24 mm, some noise could be heard. The noise was even louder at the second circle of 30 mm, and the corrugated webs showed local buckling in the middle of the beam, and then the specimen failed. The failure modes of specimen B1 are shown in Figure 10.

5.4 *Failure mode of specimen B2*

When the specimen was loaded at the first circle of displacement 12 mm, some noise could be heard. The noise was even louder at the third circle of 12 mm, and the corrugated webs showed local buckling in the lower part of the beam.

Even bigger noise was heard at the second circle of 30 mm and the local buckling was developed, which then caused the failure of the beam. The initial and final failure modes of specimen B2 are shown in Figure 11.

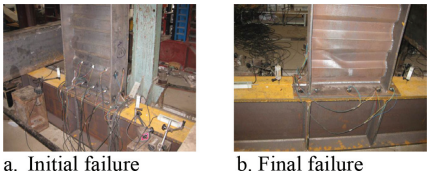

a. Initial failure b. Final failure

Figure 11. Failure mode of specimen A2.

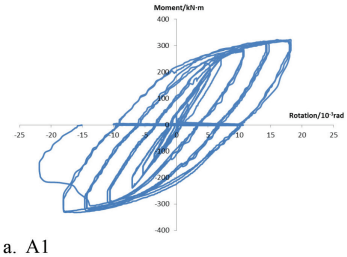

a. A1

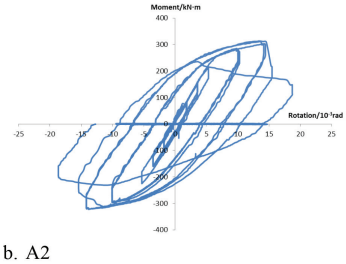

b. A2

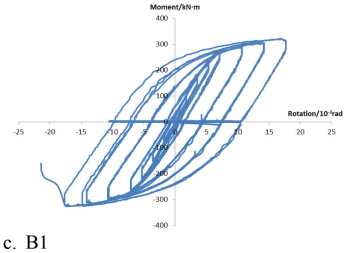

c. B1

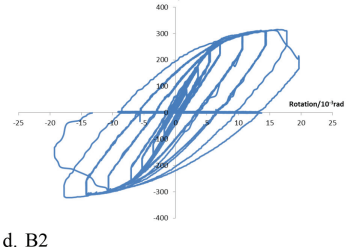

d. B2

Figure 12. Moment-rotation hysteresis loops at the beam end.

6 TEST RESULTS AND ANALYSIS

The hysteretic curve is the important evidence for the evaluation of the seismic performance of the structure. Figure 12 shows the moment-rotation hysteretic curves of the specimens. It could be concluded from the figure that

– All the hysteretic curves of the specimens are plump, and no obvious pinching could be observed. Before the specimens failed, the curves of the same loading step coincided with each other.
– The corrugated webs of specimen A2 was conducted with local initial imperfection, so the local buckling was earlier than specimen A1, and the decrease in the loading capacity was earlier and more obvious.
– The decrease in the stiffness of specimen B2 was earlier than specimen B1, and the shape was not as plump as B1 due to the initial imperfection.

7 CONCLUSION

The seismic performance of two types of beam-to-column rigid connections was investigated through four cyclic loading tests. The failure modes and hysteretic performance of the connections were studied. The main conclusions of the tests are as follows:

– There was no obvious cracking in all the connection zones of the specimens. The connections designed following the static capacity could meet the need of seismic codes
– All the hysteretic curves of the specimens were plump, and no obvious pinching could be observed. The seismic behavior of the connection could be described as very good.
– The seismic performance was sensitive to the initial imperfection of the corrugated webs.

REFERENCES

Elgaaly, M. & Seshadri, A. 1997. Girders with corrugated webs under partial compressive edge loading. *Journal of Structural Engineering ASCE* 123(6): 783–791.

GB/T228-2002. 2002. *Metallic Materials-Tensile Testing at Ambient Temperature (in Chinese)*. Beijing, China: China Architecture & Building Press.

GB/T2975-1998. 2004. *Steel and Steel Products-Location and Preparations of Test Pieces for Mechanical Testing (in Chinese)*. Beijing, China: China Architecture & Building Press.

GB6397-86. 1986. *Metallic Materials-Test pieces for Tensile Testing (in Chinese)*. Beijing, China: China Architecture & Building Press.

Guo, Y.L., Wang, X.A. & Zhang, B.H. 2012. The State of Art Design Theory of Sinusoidal Web Steel Structures. *Industrial Construction (in Chinese)* 42(7): 1–13.

Zhang, Z. *Theoretical and Experimental Research on the H-beams and the Composite Beams with Corrugated Webs (in Chinese)*. Shanghai: Tongji University.

Civil Engineering and Urban Planning IV – Liu et al. (Eds)
© 2016 Taylor & Francis Group, London, ISBN 978-1-138-02903-3

Numerical analysis on mechanical behavior of masonry walls strengthened by BFRP

Zhen Lei
School of Urban Construction and Management, Yunnan University, Kunming, Yunnan, China

Yan Xu
Institute of Technology, Baoshan College, Baoshan, Yunnan, China

Yong Wang
Chengdu JZFZ Architectural Design Co. Ltd., Chengdu, Sichuan, China

Jun-Tong Qu
School of Urban Construction and Management, Yunnan University, Kunming, Yunnan, China

ABSTRACT: Nonlinear FEA models of BFRP-strengthened masonry structure under in-plane loading tests are built by using ABAQUS software, in which large deformation, material nonlinear property and interface property are considered. Here, representative volume element method was used to simplify the simulation of masonry. The numerical simulation results are compared with the experimental results to validate the reliability and accuracy of nonlinear finite analysis. Besides, parameter analysis is conducted to further study the effect of masonry strength, vertical compression, aspect ratio and strengthening amount on the bearing capacity of FRP-strengthened masonry wall.

1 INTRODUCTION

FRP strengthened masonry structure is a kind of composite structure which is composed of masonry and FRP sheet, including the bonding material. Therefore, its mechanical behavior depends on the material characteristics and the coordinated working performance. Once the masonry wall cracked, the masonry material exhibits obvious nonlinear behavior and it is difficult to analysis the whole loading process using analytical method. Nonlinear finite element method can effectively consider the effect of material nonlinear property and interface property as well as geometric nonlinearity. Besides, the current experiment has certain limitation, which can only study a single or a few specific parameters. Finite element analysis can make up the insufficient of experimental study and avoid the limitation of test funds and periods. Based on the former experiments (Lei et al. 2013), this paper makes a finite element modeling and parameter analysis of FRP strengthened masonry structure under in-plane loading using ABAQUS.

2 NUMERICAL MODELING FOR (BFRP-STRENGTHENED) MASONRY WALLS

The detailed dimension of (BFRP-strengthened) masonry wall refers to the in-plane low cycle loading tests in (Lei et al. 2013). The bricks and mortars are taken as a whole (Ma et al. 2013), the modeling of masonry walls are solid element using C3D20R. Based on the existing research and trial analysis (Liu et al. 2005; Liu et al. 2009), the compression constitutive model for masonry shown in equation (1) is adopted.

$$\begin{cases} \dfrac{\sigma}{f_m} = 1.96\dfrac{\varepsilon}{\varepsilon_0} - 0.96\left(\dfrac{\varepsilon}{\varepsilon_0}\right)^2 & 0 \le \dfrac{\varepsilon}{\varepsilon_0} \le 1 \\ \dfrac{\sigma}{f_m} = 1.2 - 0.2\dfrac{\varepsilon}{\varepsilon_0} & 1 \le \dfrac{\varepsilon}{\varepsilon_0} \le 1.6 \end{cases} \quad (1)$$

where ε = masonry strain; σ = masonry stress; f_m = the average compression strength; ε_0 = masonry strain corresponding to f_m. Here, the value of ε_0 is 0.0038.

The concrete damage energy criterion provided in ABAQUS is adopted as the tension constitutive model for masonry. The damage tension strain-fracture energy relationship is shown in Figure 1.

Where G_f^{I} = fracture energy, which is defined as the energy needed for one continual crack per unit area; σ_{tu}^{I} = damage strain. G_f^{I} has a value between 40~120 *N/m*. the value of σ_{tu}^{I} is obtained by tests.

The elastic modulus E is calculated according to equation (2) (Liu 2013).

$$E = 370 f_m \sqrt{f_m} \tag{2}$$

The average compression strength of bricks is 12.8 MPa. When mortar type is M5.0, f_m is 3.73 MPa, and when mortar type is M2.5, f_m is 3.15 MPa.

The elastic modulus E is 2665 and 2069 MPa, respectively.

Masonry damage plastic material model adopts DAPL (Damaged Plasticity Concrete Model) model provide by ABAQUS. The fault value is set as the value of eccentricity, K and f_{b0}/f_{c0}. The dilation angle is 30 degree.

The modeling of BFRP strips are membrane element using M3D4R. Anisotropy single linear elastic composite material provided in ABAQUS is adopted for BFRP sheet. The elastic modulus along the length E_1 is 105 GPa, and the elastic modulus along the length E_2 equals $0.001E_1$. Shear modulus is $0.001E_2$.

The diagonal FRP strips did not exhibit bond-slip due to the confinement of the horizontal FRP strips, which had no influence on the tensile contribution. It is assumed that there is no relative slip between masonry wall and FRP strips, tie constraint is adopted between masonry wall and FRP strips. The position and direction of the loading force are applied to the model in the same way as in the test (Lei et al. 2013). The finite element analytical models are shown in Figure 2.

The material model in current numeral simulation software under low cyclic loading is still difficult to exhibit the pinch phenomenon of hysteresis curve and easily leads to non-convergence. Besides, researches have proven that the load-displacement (P-Δ) curve under monotonic loading is basically the same as envelope curves under low cyclic loading. Therefore, the paper only conducts the nonlinear numerical analysis of (BFRP-strengthened) masonry walls (W1, SW1) under monotonic loading.

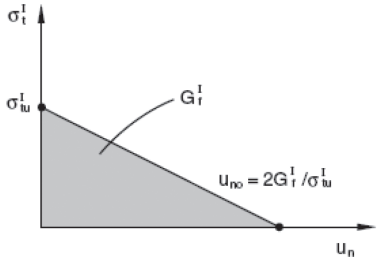

Figure 1. Damage tension strain-fracture energy curve.

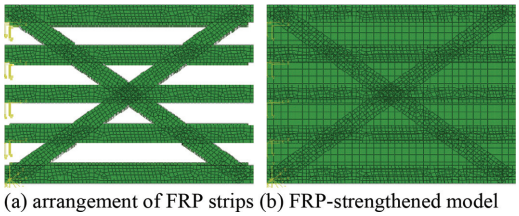

(a) arrangement of FRP strips (b) FRP-strengthened model

Figure 2. Finite element analytical model.

3 EXPERIMENTAL VERIFICATION

3.1 *Analysis of mechanic behavior*

The stress distributions (S11 and Mises stress contour) of specimen at the moment of failure are shown in Figures 3 and 4. The failure state has

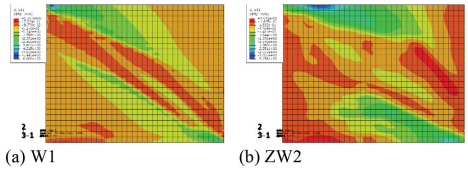

(a) W1 (b) ZW2

Figure 3. S11 stress contour.

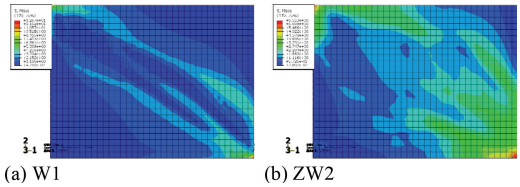

(a) W1 (b) ZW2

Figure 4. Mises stress contour.

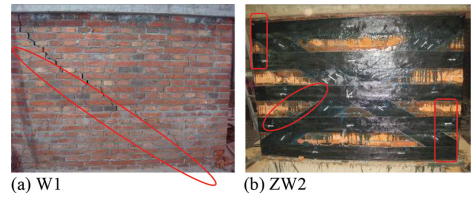

(a) W1 (b) ZW2

Figure 5. Experimental damage modes.

defined at (Lei et al. 2013). According to S11stress contour, the Finite element failure patterns (Fig. 5) are basically agreed with Experimental failure modes (Lei et al. 2013).

Numerical model of un-strengthened wall W1 exhibits diagonal crack under shear-compression loading when the principal tensile stress exceeds the crack stress. It is agreed with the experimental phenomenon of W1. While for the FRP-strengthened wall SW2, FRP strips have taken parts of the load. The stress distribution of masonry has been changed (Fig. 3b), which proves the availability of FRP strengthening technique.

3.2 *Load-displacement curves*

The numerical load-displacement curves obtained at the top of wall are compared with the experimental hysteresis loops shown in Figure 6.

The numerical curves of W1 and ZW2 are all exhibit inverse "S" shape, which are basically fit with the envelope curves from these hysteretic responses curves.

The numerical curve of W1 is slightly higher than that of experimental result due to the modeling incapability of construction errors and material defects.

At the later stage of loading, the numerical curve of FRP-strengthened wall W2 is lower than the experimental envelope curve, because the closed horizontal FRP strips, which offer an effect of confinement, play an important role in the improvement of lateral strength in the test, while this effect cannot be modeled in ABAQUS.

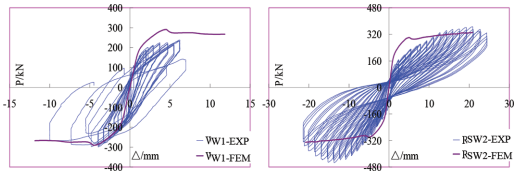

Figure 6. Load-displacement curves of experiment (EXP) and FEM.

The numerical characteristic strengths, including the cracking load, maximum strength are list in Table 1 and compared with the experimental results. The error rates in cracking load between the numerical simulations and experiments reach the range of –4%~+3%, while the average error rates in ultimate load is higher ranging from –20%~+9.5%, which is caused by the modeling incapability of FRP confinement.

4 PARAMETER ANALYSIS

In order to further study the mechanical behavior of FRP-strengthened masonry wall, Parameters, including mortar strength, strengthening amount, axis-compression ratio and aspect ratio are analyzed in term of the load-displacement (P-Δ) curve based on the former study. The experimental FRP strengthening patter is applied in the simulation.

4.1 *Masonry strength*

The strength of brick remains unchanged, two kinds of mortar strength are considered: M2.5 and M5.0. The basic parameters are listed as follows: W = 2100 mm; H = 1500; σ = 0.6 MPa; SP-N = 150 mm^{-1}; X-N = 150 mm^{-1}. The numerical results are shown in Figure 7.

Note: W = width of masonry wall; H = height of masonry wall; SP = width of horizontal FRP strip; X = width of diagonal FRP strip; N = layer number of FRP strip; σ = vertical compression; M = mortar strength.

The lateral shear strength increases with the improvement of mortar strength, and the curves exhibit similar rising trend. At the early stage of loading, the wall and FRP strips bear the load coordinately, there is basically a linear relationship between lateral load and displacement. Once the

Table 1. Characteristic strengths of experiment (EXP) and FEM.

Loading direction	Cracking load/kN			Ultimate load/kN		
	$P_{cr,FEM}$	$P_{cr,EXP}$	$\frac{P_{cr,FEM}}{P_{cr,EXP}}$	$P_{cr,FEM}$	$P_{cr,EXP}$	$\frac{P_{cr,FEM}}{P_{cr,EXP}}$
W1						
+	185	180	1.03	279.5	297.4	0.94
–				279.5	223.3	1.25
SW2						
+	195	204	0.96	321.3	452.5	0.71
–				321.3	360.1	0.89

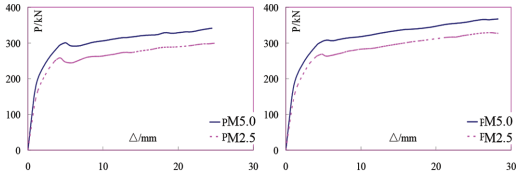

(a) X-N=150mm-2 (b) X-N=300mm-2

Figure 7. *P*-Δ curves corresponding to different mortar strength.

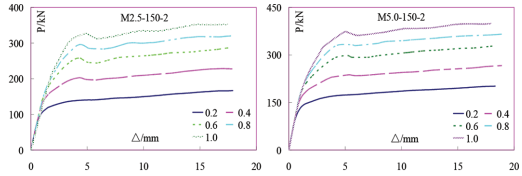

(a) M2.5 (b) M5.0

Figure 8. *P*-Δ curves corresponding to different vertical compression.

wall cracks, the curves present a significant turning point and the strengthening effect of FRP strips is more obvious.

4.2 *Vertical compression*

Some researchers have proven that the vertical compression have a positive effect on improving the shear strength. Here, the vertical compression ranges from 0.2 to 1.0 MPa. Other parameters are listed as follows: W = 2100 mm; H = 1500; SP-N = 150 mm^{-1}; X-N = 150 mm^{-2}. The numerical results are shown in Figure 8.

The lateral strength of FRP-strengthened masonry increases with the improvement of vertical compression within certain limits, but the extent of increase gradually decreases as the vertical compression goes up. The vertical compression has little influence on the initial lateral stiffness, but influences the crack load greatly.

4.3 *Aspect ratio*

Unreinforced Masonry (URM) Walls with low aspect ratio exhibit shear-dominant failure mode, while walls with higher aspect ratio exhibit flexural-dominant or shear-flexural failure mode. The former walls have larger lateral strength (Liu 2013). By far there is no research on the aspect ratio effect on the FRP-strengthened masonry wall. Here, the height of wall ranges from 1300 to 2300 mm. Other parameters are listed as follows: W = 2100 mm; M = M5.0; SP-N = 150 mm^{-1}; X-N = 150 mm^{-2}. The numerical results are shown in Figure 9.

The lateral strength of strengthened specimens decreases with the improvement of aspect ratio, which is similar to that of URM walls. The lower aspect ratio has a positive effect on the lateral stiffness and crack load.

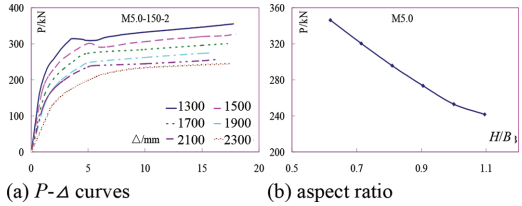

(a) *P*-*Δ* curves (b) aspect ratio

Figure 9. *P*-Δ curves corresponding to different aspect ratio.

4.4 *Strengthening amount*

After crack happened, FRP strips play an important role in bearing load. Here, the width of diagonal strips ranges from 150 to 300 mm, and the layer number ranges from 1 to 3. Two kinds of mortar

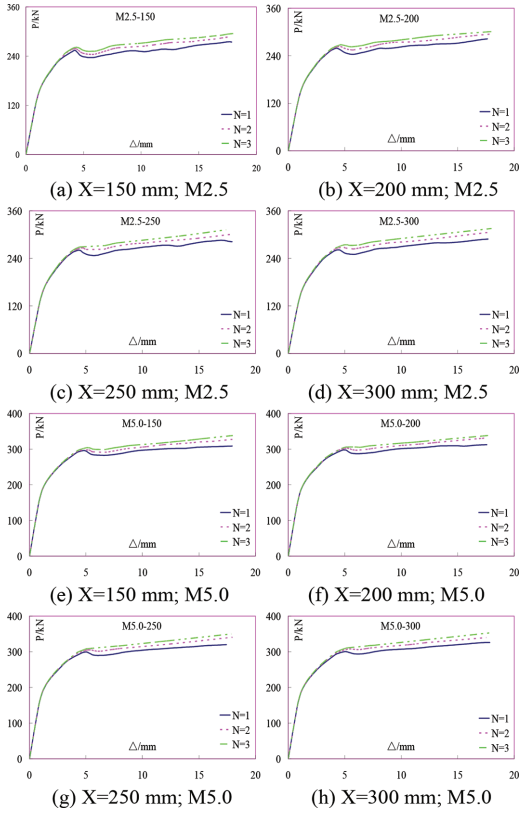

(a) X=150 mm; M2.5 (b) X=200 mm; M2.5
(c) X=250 mm; M2.5 (d) X=300 mm; M2.5
(e) X=150 mm; M5.0 (f) X=200 mm; M5.0
(g) X=250 mm; M5.0 (h) X=300 mm; M5.0

Figure 10. *P*-Δ curves corresponding to different FRP strengthening amount.

strength are considered: M2.5 and M5. Other parameters are listed as follows: W = 2100 mm; H = 1500 mm; SP-N = 150 mm^{-1}. The numerical results are shown in Figure 10.

The lateral strength of FRP-strengthened wall increases in proportion to the FRP layer number. Before cracking, the curves corresponding to different FRP strengthening amount are almost coincided, which is consistent with the experimental results.

The improvement of maximum lateral strength rises slowly once the FRP width exceeds a certain limit, then the improvement of strength can be achieved by increase the layer number. This is because the overlarge width of FRP impairs the strength effect.

The width of FRP has no obvious effect on the initial lateral stiffness and crack load.

Under the same condition of FRP strengthening amount, walls with low mortar strength can achieve a higher maximum strength by increasing the FRP width compared to the improvement of layer number, which is contributed to the effective confinement of FRP strips.

5 CONCLUSIONS

- Based on the FEM numerical results of FRP-strengthened masonry wall in terms of the deformation, stress distribution and failure mechanism, the effectiveness of FRP strengthening technique is further validated.
- The numerical results are basically coincided with experimental results, which verifies the reasonability of numerical modeling and material parameters.
- The lateral strength of FRP-strengthened masonry walls is greatly influenced by the masonry strength, vertical compression, aspect ratio strengthening amount, and the improvement caused by each parameter is different.
- FRP-strengthening technique is more applicable to the strengthening of old or existing masonry structures with low mortar strength.

ACKNOWLEDGEMENTS

The research was sponsored by Yunnan Provincial Education Office Scientific Research Foundation (2014Z008), Scientific Research Projects Foundation of Yunnan University (2014CG012) and Yunnan Applied Basic Research Projects Foundation (2015FD005).

REFERENCES

Lei, Z., Zhou, D.Y. & Wang, J.B. 2013. Seismic performance of masonry walls strengthened with fiber-reinforced polymer. *Journal of South China University of Technology* 41(3): 43–49.

Liu, G.Q. 2005. *The Research on the Basic Mechanical Behavior of Masonry Structures*. Changsha: Hunan University.

Liu, G.Q., Shi, C.X. & Lu, W.R. 2005. Shear behavior and calculation of load-bearing capacity of masonry shear wall. *Journal of Building Structures* 26(5): 81–117.

Liu, G.Q., Yan, Y.Q. & Shi, C.X. 2009. Research on the unified model of the compressive constitutive relations of masonry. *Journal of Hunan University* 36(11): 6–9.

Ma, G.W., Hao, H. & Lu, Y. 2001. Homogenization of masonry using numerical simulations. *Journal of Engineering Mechanics* 127(5): 421–431.

This page intentionally left blank

Civil Engineering and Urban Planning IV – Liu et al. (Eds)
© 2016 Taylor & Francis Group, London, ISBN 978-1-138-02903-3

Research on the ecological stability technology of carbonaceous shale slope

Xin-Xi Liu & Yi Dai
School of Civil Engineering and Architecture, Changsha University of Science and Technology, Changsha, Hunan, China

ABSTRACT: Based on the carbonaceous shale slope on the left of the Guangxi Liuzhai-Hechi highway K20 + 450~960 segment, research on the ecological stability technology of the carbonaceous shale slope is launched, and the curing mechanism, membrane-forming mechanism and curing performance of the polymer cement are analyzed. A new method is proposed that ecological soil is laid on the polymer membrane layer after curing the carbonaceous shale slope, and then the seeds are sown on the ecological soil layer. This ecological stability technology can effectively solve the contradiction between slope protection and ecological damage, slope stability is ensured, and also a rapid recovery of slope vegetation is achieved.

1 INTRODUCTION

With the rapid development of highway construction, carbonaceous shale slope protection issues have become increasingly prominent. Because carbonaceous shale can be easily softened and gradually disintegrated when it contacts with water (Che 2008), it makes many collapses and landslides in many carbonaceous shale slopes because there is not enough time to protect when doing excavation; dumping-tension type landslide often occurs especially in some carbonaceous shale slope with a top hard, bottom soft structure due to creep and differential weathering. This phenomenon is very prominent in the Guangxi Liuzhai-Hechi highway. Currently, hang net shotcrete and mortar rubble are commonly used for carbonaceous shale slope protection, although it can be used to effectively protect such soft rock slope, but a far cry from the eco-friendly concept in highway construction. Growth of vegetation and creation of landscape effects are mainly emphasized for the existing soft rock slope for ecological protection, but weathering and stability of the shallow layer for soft rock slope vegetation protection are ignored, and they have been the main bottleneck for carbonaceous shale slope ecological protection. For this reason, it has a very important application value for conducting carbonaceous shale slope ecological stability technology research (Zhou et al. 2010). This paper aims at solving the problem of softening and disintegration stability by using polymer cement to cure the carbonaceous shale slope, and then the seeds are sown for ecological protection after ecological soil is laid in order to achieve good ecological stability effects.

2 CURING MECHANISM OF POLYMER CEMENT

The process of the water-soft rock internal structure interaction is the main factor for soft rock slope softening and unstable collapse (Luo et al. 2012). Soft rock slope can be slowly softened by preventing or reducing the chance of the contact between water and the soft rock slope surface. Soft rock surface is coated and adhered by using a curing agent for soft rock curing (Chai et al. 2009), and thus the properties of the soft rock surface are changed. This prevents the dehydration-absorbent-soften process, and volatility of the soft rock's physical and mechanical properties can be further prevented, weakened or slowed down, so the long-term stability of the soft rock slope can be improved.

2.1 *Membrane-forming mechanism of polymer cement*

At present, a more consistent view about the membrane-forming mechanism (Chen et al. 2006) of polymer cement is that higher adhesion of the membrane layer can be formed on the surface of cement hydration products for polymer emulsion after the hydration of cement slurry. Pores of cement hydration products are filled with some high polymer, and the cement after hardening

becomes denser. Membrane-forming of polymer cement and hydration of cement occur at the same time. The interconnected network structure membrane layer is formed after the polymer membrane layer and cement hydration products are interwoven together.

2.2 *Curing performance of polymer cement*

Hydrophobe, firmness and waterproofness of the membrane layer are the main performance for the curing performance of polymer cement. Physical and chemical methods of scratch, test contact angle of static water and the bibulous rate of soft rock samples are used for analyzing the physical and chemical properties of the polymer cement curing agent, showing that the membrane layer has good performance of hydrophobic, film, and waterproof by characterizing and measuring the membrane layer. Specific curing performance of polymer cement is described below.

2.2.1 *Hydrophobic performance*

As shown in Figure 1, wetting angle of the surface of the rock samples increases significantly after curing the soft rock by using the curing agent. This increase is due to the fact that the interconnected network structure membrane layer is formed and fully covers the soft rock sample surface, and also the hydrophilic group on the surface of the soft rock samples is changed into the hydrophobic group, so it has a good hydrophobic performance. From Figure 1a and b, it can be observed that the wetting angle of the surface of the rock samples increases from 37.5° to 82.9° after curing.

(a) Before curing

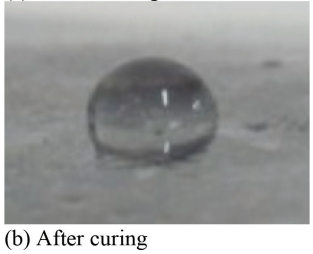

(b) After curing

Figure 1. Photos showing the droplets on the soft rock surface.

2.2.2 *Film performance*

The bond strength between the membrane layer and the rock surface is a key performance indicator to evaluate the quality of the curing agent. It largely determines the application of the possibility and reliability of the curing agent. It is generally measured by the method of scratch. Scratch tool is used to scratch some regular shape with a fixed pattern on the test sample surface membrane layer in the method of scratch (as shown in Fig. 2a). The bond strength between the membrane layer and the rock surface is determined according to the membrane layer shedding situation (as shown in Fig. 2b) between scratches.

Figure 2 and Table 1 shows that the bond strength between the membrane layer and the rock surface is good. This is because when the soft rock

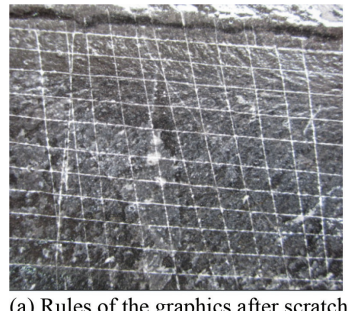

(a) Rules of the graphics after scratch

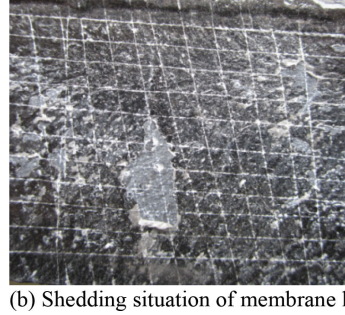

(b) Shedding situation of membrane layer

Figure 2. Photos showing the scratches on the membrane layer.

Table 1. Results of bonding strength between the curing agent and the rock surface.

Number	Number of shedding	Percentage loss
1	3	3%

sample is solidified by the polymer cement curing agent, a strong Si-O-Si bond is formed by the dehydration condensation reaction between Si-OH in the hardener and -OH on the surface of the soft rock samples. An integral and continuous airtight structure is formed on the rock surface, so it has an excellent film performance.

2.2.3 *Waterproof performance*

It can be seen from Figure 3 and Table 2 that large pores inside the soft rock samples are filled with water molecules due to infiltrating when carbonaceous shale samples (unmodified) immersed in water. After a period of time, large pores are full of water and the growth rate of water absorption slows down. The interconnected network structure membrane layer is formed due to the hydroxyl radical interaction between the high polymer and the soft rock surface in carbonaceous shale samples (modified). The rate of the water molecules that infiltrate into internal pores can be slowed down effectively and the rate of water absorption increases slowly. This shows that the waterproof performance of the carbonaceous shale samples is good.

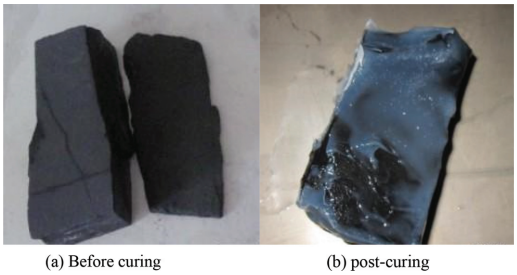

(a) Before curing (b) post-curing

Figure 3. The rock sample soaked failure modes.

Table 2. Measured values of soft rock sample quality changes at different soaking times.

Soaked time/day	0	1	2	3
Before curing	279.32	284.52	284.59	284.6
Post-curing	257.48	257.5	257.54	257.59
Soaked time/day	4	5	6	7
Before curing	284.62	284.63	284.65	284.67
Post-curing	257.73	257.96	258.23	258.57

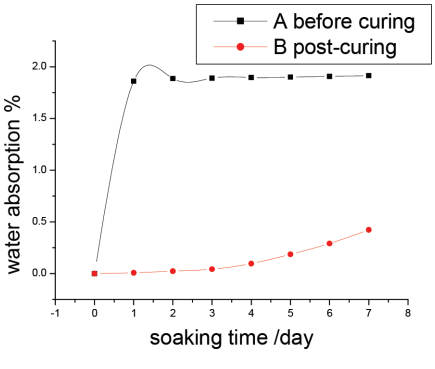

Figure 4. Soft rock absorption and immersion time curves.

3 ENGINEERING APPLICATION

3.1 *Engineering situation*

The main component is carbonaceous shale on the left of the Guangxi Liuzhai-Hechi highway K20 + 450~960 segment. Carbonaceous shale has poor diagenesis and weathering resistance degree; it can be easily softened and disintegrated when it contacts with water, and thus the slope surface is broken and very unstable. It makes the exudate of the carbonaceous shale acidic because large amounts of carbon and sulfur chemical composition are contained in carbonaceous shale and the contents of nitrogen, phosphorus and potassium element are low, and these elements are required for plant nutrient composition. Thus, plants are difficult to grow on the carbonaceous shale surface.

3.2 *Construction program*

Polymer cement curing agent is prepared for the curing of the free face of the carbonaceous shale slope, the polymer membrane layer is formed on the slope surface, and then the seeds are sown on the ecological soil layer after ecological soil is laid on the polymer membrane layer, as shown in Figure 5. After the seeds survive in ecological

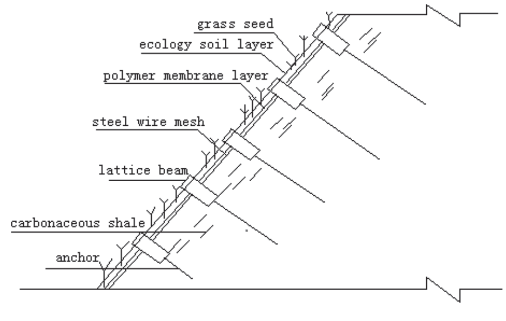

Figure 5. Ecological protection structure of the slope.

soil, it can break through the polymer membrane layer with the growth of the root. The goal of the fixed slope is achieved when the root is more stable in the rock layer of the depths of the slope (Ji & Yang 2013).

3.2.1 *Construction technology process*

The process of construction technology is as follows: clean up the slope → install anchor → hang and fix steel wire mesh → install frame beam → curing the soft slope → spray organic base material (ecological slope stabilizer is added according to the proportion) → spray and sow grass → maintenance and management.

3.2.2 *Construction matters need attention*

To make the curing agent better infiltrate on the carbonaceous shale surface to a certain depth and form a membrane layer of a certain thickness, the cataclastic structure in the slope and weathered carbonaceous shale should be cleaned to ensure quality. The curing agent and the first layer with caking property of soil should directly adhere to the surface of carbonaceous shale. The first layer is 2–3 cm and spraying is done three times. The ratio of the curing agent should be changed every time and the curing agent should be sprayed three times. Grass seeds and shrubs should be mixed and made suitable for the local climate conditions to ensure that the slope can resist washout due to rain. The main grass seeds include tall fescue, bermuda grass, butch clover, perennial ryegrass and main shrubs include privet, *Amorpha fruticosa*, burn mark, and *Lespedeza bicolor*.

3.3 *Test results*

There are some findings at the construction site: weathering and disintegration of carbonaceous shale were effectively suppressed and the rain washing was effectively prevented by adding the curing agent to the outside soil. There was good adhesion between planting soil and galvanized wire mesh because viscosity was obtained when the soil for planting is sprayed on the surface of carbonaceous shale so that it can form a flexible protective layer of the slope. Nutrient and moisture for the germination and growth of vegetation were obtained by planting soil, thus the needs of vegetation were satisfied. Grass seeds basically germinated at the site by observing and the rate of germination reached 90%. Vegetation on the slope grew well (as shown in Fig. 6) and slope was in the steady state after months of testing. Slope without curing and curing slope without the outside soil were compared for analysis. Plant growth situation is shown in Figures 7 and 8.

Figure 6. Vegetation grew well.

Figure 7. Slope without curing.

Figure 8. Cured slope (without the outside soil).

4 CONCLUSIONS

Weathering and disintegration of carbonaceous shale are effectively suppressed by using the polymer cement curing agent in carbonaceous shale slope. Soil stabilizer is used in the outside soil with spray technology to ensure that soil has water moisturizing performance and good strength. The plant growth environment is improved and good

structure of the soil is maintained, which creates favorable conditions for recovery and maintenance of vegetation. The purpose of building a solid, economical and environmental-friendly highway slope is achieved. Ecological soil is sprayed on the polymer membrane layer after curing the carbonaceous shale slope by using polymer cement curing agent; finally, the seeds are sown on the ecological soil layer. This new ecological stability technology has a certain guiding significance for dealing with the problem of carbonaceous shale slope stability in the future.

ACKNOWLEDGMENTS

This study was supported by the National Natural Science Foundation (No. 51378082).

REFERENCES

Chai, Z.Y., Kang, T.H., et al. 2009. Evaluation of silicon modified resin for coated soft rock with high montmorillonite content and its effects. *Chinese Journal of Rock Mechanics and Engineering* 28(1): 81–87.

Che, P. 2008. *Research on Solidifying Characteristics of Soft Rocks-water Interaction and Mud Compounds of Soft Rocks*. Shanghai: Tongji University.

Chen, L.J., Chen, L.Q., Zhang, X.Y., et al. 2006. The research and film forming mechanism of polymer-cement waterproof coating. *New Building Materials* 8: 33–36.

Ji, X.L. & Yang, P. 2013. Numerical analysis of the effects of roots on the slope reinforcement based on the roots forms. *Journal of Nanjing Forestry University (Natural Sciences Edition)* 37(2): 113–117.

Luo, G.C., Fu, H.Y. & He, W. 2012. Experimental study on the characteristics of carbonaceous shale disintegration. *Journal of China & Foreign Highway* 32(3): 309–311.

Zhou Y.X., Xie, F.Y., et al. 2010. The application of new ecological slope stability technology in Baoteng highway. *Highway* 8(8): 93–97.

This page intentionally left blank

Civil Engineering and Urban Planning IV – Liu et al. (Eds)
© 2016 Taylor & Francis Group, London, ISBN 978-1-138-02903-3

Calculation of areas flooded in urban reservoirs of water supply

E.A. Silva, F. Leonardi, M.M. Pedrosa, F. Puga & V.S.S. Leonardi
Faculty of Science and Technology, University Estadual Paulista—UNESP, Presidente Prudente, Brazil

ABSTRACT: In 2014, Brazil suffered a long drought period. The unusual lack of rainfall has resulted in a decrease in the water levels over the main reservoirs in the country. In this sense, images from remote sensing and techniques of digital image processing can be used as a tool to monitor the water level decrease. Two images from LandSat-8 were used in this work. The images were obtained in June 2015 and the actual situation of the Billings and Guarapiranga reservoirs was shown. The MATLAB software together with the mathematical morphology's toolbox was used to detect and determine the area of the reservoirs. For this purpose, a routine was developed to filter, highlight, and threshold the image.

1 INTRODUCTION

1.1 *General view*

The Brazilian hydrography can be described as the most extensive river system of the world (Butler 2006). Besides having a unique configuration that allows diversification of economic exploitation as a source of drinking water, agricultural irrigation, and production of hydroelectric power (Choudry 2013). However, in 2014, Brazil suffered a long drought period that significantly reduced total water available for human consumption.

São Paulo has the largest population concentration in the country. Among the biggest water reservoirs that provide water supply to the population are Guarapiranga and Billings. With the intention to determine the impact of the lack of rainfall on the reservoirs, we present a morphological routine to detect reservoirs in digital images.

The number of published works dealing with detection of reservoirs from urban areas is high (Silva et al. 2009, Statella & Silva 2009, Stroppa et al. 2010). Most of the studies concern the detection of these features, but depending on the application, we need to calculate some characteristics and the analysis of the changes that occurred needs to be performed. So our approach consists of two main objectives. The first one consists of detecting the reservoir, followed by the second one where we calculate the volume of the reservoirs to assess the level of reduction caused by the lack of the rainfall.

The images used in the paper were obtained by LandSat-8, which covered the two main water reservoirs of São Paulo city, Billings and Guarapiranga. The morphological processing used to detect both reservoirs allows highlighting, thresholding, and filtering the interested features. Initially, the sequence of operations adopted was to smooth the original image to obtain homogenous areas. Next, highlights were applied to contrast the interesting area from the background. The reservoirs are detected by binarization using the ideal threshold. Finally, some noise was removed by filtering.

The areas from the reservoirs were calculated and compared with the value indicated in the literature. The results obtained by the proposed methodology indicate that the routine was efficient to detect the whole area of the reservoirs, since the achieved values matched with the value found in the literature. It means that a routine composed of morphological operations can be used for mapping in conventional processes for updating cartographic products and also monitoring and planning environmental events.

1.2 *Objective*

The goal of this paper is to determine the area of Billings and Guarapiranga reservoirs by morphological image processing with the purpose of verifying the efficiency of the routine in different situations and analyze the impact of the lack of rainfall on the two reservoirs in São Paulo.

2 THEORETICAL RECITAL

2.1 *Mathematical morphology*

The basic principle of MM is to use a geometric form named structuring element to probe a digital

image, quantifying the mode in which this element fits within this image (Facon 1996).

The mathematical morphology is based on two operations: erosion and dilation, which are used for the development of other morphological operations. The operations used are described as follows.

2.2 *Morphological operators*

The operation regional extrema is a tool which filters the image extrema using a contrast criterion. It removes random noise in the input image (f) through the elimination of peaks with higher contrast than the defined threshold (h). This is achieved through reconstructing by dilation of f from $f–h$, as defined in Equation (1) (Soille 2003):

$$HMAX_h(f) = R_f^{\delta}(f-h) \tag{1}$$

where R_f^{δ} is the morphological reconstruction by dilation.

The histogram equalization consists of changing the original histogram to a uniform histogram. This is achieved by distributing the histogram of the original image so that each gray level can be shown with a similar frequency.

One way to highlight objects from the background of images is by choosing a threshold value T that separates these two groups. The values of the pixels below the threshold T are all associated with zero and above one, as show the Equation (2):

$$g(x,y)=\begin{cases}1 \ if \ \ f(x,y) > T \\ 0 \ if \ \ f(x,y) \le T\end{cases} \tag{2}$$

The area-opening transform removes any component connected to the image f whose area is less than a given threshold. The connectivity is given by the structuring element Bc. The Equation (3) presents the mathematical formulation (Soille 2003):

$$\gamma_{\lambda} = \bigvee_i \left\{ B_i \, is \, connected \, and \, card(B_i) = \lambda \right\} \tag{3}$$

3 TEST AREA OF RESEARCH

For the development of the routine, we used two sub-images obtained by LandSat-8, band 5 corresponding to near infrared, acquired on 06/15/2015. The Guarapiranga reservoir is showed in Figure 1a and Billings reservoir in Figure 1b. The reservoirs are located in São Paulo city, in the state of São Paulo.

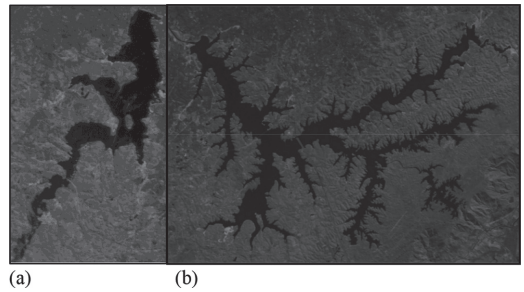

(a) (b)

Figure 1. Original images.

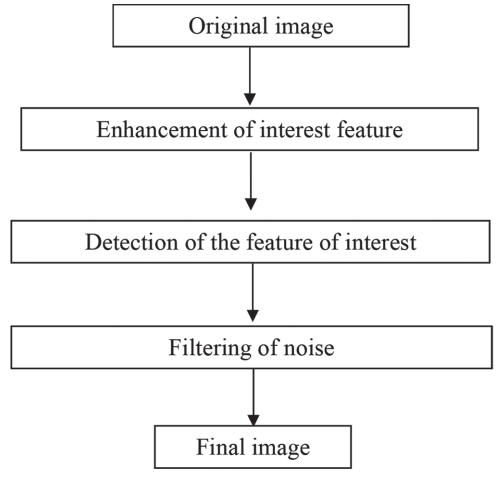

Figure 2. Flowchart of methodology proposed.

4 METHODOLOGY

The methodology proposed consists of morphological operations in order to extract the reservoirs contained in remotely sensed images, such as the calculation of the areas of the reservoir and flooded areas.

The flowchart presented in Figure 2 shows the sequence of the steps used for detecting the reservoir and the area's calculation.

The flowchart presented in Figure 2 shows the sequence of the steps used for the detection of the reservoir and the area's calculation.

5 RESULTS

We applied the developed methodology to detect the reservoirs in two images from the same satellite. The first step consisted of enhancing the values of brightness and contrast. For this propose, the regional extrema was applied to the original image.

The adopted intensity threshold values were 80 and 110 to Guarapiranga and Billing reservoirs, respectively. These values were chosen based on histograms of each image. The results are illustrated in Figure 3. Aiming to obtain highlighted reservoirs in relation to the other features presented in the scene, the histogram equalization was applied to the previous result, as showed in Figure 4.

In order to detect the reservoirs, the two images were binarized based on the analysis of the histogram of each image resultant from the application of the equalization. The intensity threshold value for each image was 88 and 40 for Guarapiranga and Billing reservoirs, respectively. These values allow separating the regions corresponding to the reservoirs from the background of our images. The result of binarization is showed in Figure 5.

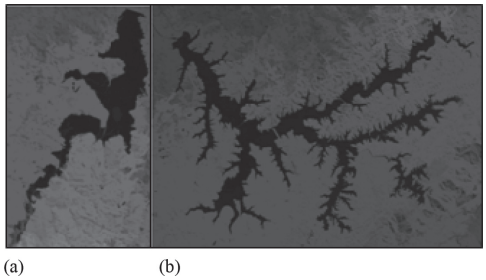

Figure 3. Result of the regional extrema application.

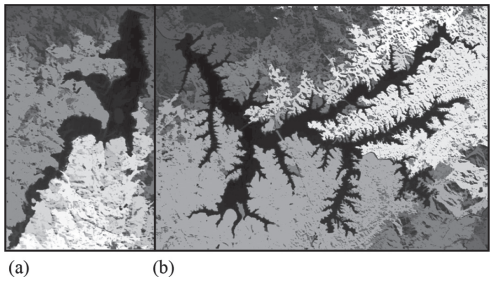

Figure 4. Results of the applying the *histeq* operator.

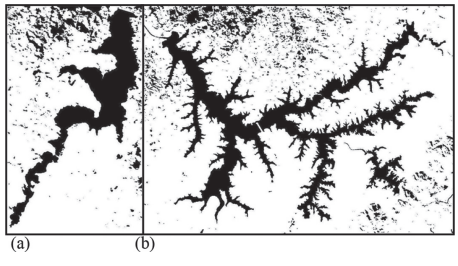

Figure 5. Results of applying the binary operator.

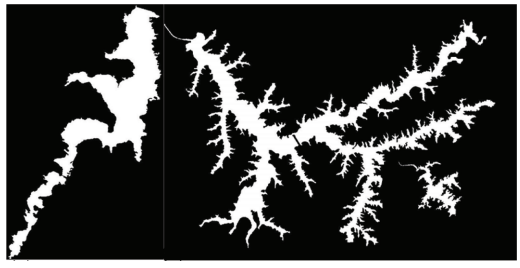

Figure 6. Results of applying the area opening operation.

The last step of the proposed methodology consists of eliminating some areas that are not of interest for this propose.

Thus, it was applied in the area opening operation, which removes connected components whose area, in number of pixels, is smaller than a given threshold value. In our case, the threshold values chosen were 6.450 and 10.010 pixels. These values were obtained empirically. Figure 6 shows the reservoirs completely detected with no noise.

Knowing that the spatial resolution of LandSat-8 images is 30 m, it was possible to determine the area occupied by the reservoirs. The image of the Billings reservoir was determined as 52,854 pixels, which when multiplied by the pixel area results in a total area of 47.568 km². The image of the Guarapiranga reservoir was calculated as 15,733 pixels, which corresponds to a total area of 14.159 km².

6 CONCLUSION

Analyzing the visual results achieved by the methodology proposed, we concluded that the work reached the main objective that was to detect Billings and Gurapiranga reservoirs from images and then determine its respective flooded area.

The areas calculated for the two reservoirs are not close to the values mentioned in the literature. The area of Billings reservoir calculated in the study was 47.568 km², while the value in real literature is 106.6 km². The area of Guarapiranga was calculated as 14.159 km² and the normal area is 26.6 km². The area differences can be justified due to fluctuations in water levels and mainly due to the lack of rain during a large time scale. As well known, 2014 was the driest year of the last decade in Brazil.

The quality of feature detection is directly linked with the choice of the threshold value. In this work, the value was defined by the histogram analysis; even when there are alternatives which can determine this value automatically.

Visually, the results obtained by mathematical morphology techniques seem to be corrected. However, it is necessary to use more images to test the routine in order to evaluate its performance statistically. The evaluation will allow the use of routine in different areas of knowledge, such as ambient monitoring and planning.

ACKNOWLEDGMENTS

We are thankful to the INPE for the supply of the images without which this work could not have been carried out and the CAPES and FAPESP for financial support.

REFERENCES

Butler, R.A. 2006. The Amazon: The World's Largest Rainforest. Mongabay.com/A Place Out of Time: Tropical Rainforests and the Perils They Face. *http://rainforests.mongabay.com/amazon.*

Choudry, U.A. 2013. Brazil as an emerging economic power: Dynamics & implications. *Global Journal of Human Social Science Political Science* 13(2): 1–8.

Facon, J. 1996. *Morfologia Matemática: Teorias e Exemplos.* Curitiba: Editora Universitária Champagnat da Pontifícia Universidade Católica do Paraná.

Serra, J. 1982. *Image Analysis and Mathematical Morphology*. London: Academic Press.

Silva, E.A., Leonardi, F. & Stroppa, R.G. 2009. Aplicação de Morfologia Matemática e técnicas de PDI na extração de imagens digitais com interesses em cálculos de reservatório e área inundada por hidrelétricas. *Revista SELPER* 29(2): 22–29.

Soille, P. 1999. *Morphological Image Analysis: Principles and Applications*. Berlin: Springer-Verlag.

Statella, T. & Silva, E.A. 2009. Extração de drenagens em imagens digitais através de técnicas de morfologia matemática. P*rofiscientia (Cuiabá)* 04(1): 359–376.

Stroppa, R., Leonardi, F. & Silva, E.A. 2010. Digital Image Processing using techniques of mathematical morphology. *Proceedings of 3rd International Mutil-Conference on Engeneering and Technological Innovation. International Institute of Informatics and Systemics, Orlando, 2010*. Orlando: International Institute of informatics and Systemics.

Civil Engineering and Urban Planning IV – Liu et al. (Eds)
© 2016 Taylor & Francis Group, London, ISBN 978-1-138-02903-3

Research on influencing factors of eutrophication of Tanghe reservoir

Chen-Xi Mi, Jing-Chao Chen & Yong-Ning Mi
College of Water Conservancy, Shenyang Agricultural University, Shenyang, Liaoning, China

ABSTRACT: At present, eutrophication exerts profound effect on the water quality of reservoirs and lakes. It is essential to ascertain the influencing factors of the phenomenon and identify effective solutions. In this paper, factor analysis method is used to evaluate eutrophication level of Tanghe reservoir and the conclusion conforms to the current situation. Additionally, it is found that nitrogen, phosphorus, and water temperature are the main factors which have influenced the reservoirs' eutrophication.

1 INTRODUCTION

Both of the reservoirs and lakes belong to the surroundings of still water. Flow velocity in such places is low so that different nutrient substances are accumulated gradually (Rast & Thornton 2012). As a result, such pollutants pose a severe threat to the water quality of the water bodies. The so-called eutrophication is indicated as the process in which the reservoirs and lakes with a low production rate of planktons become the places with high rate. During the process, first a little amount of diatom and chlorella are found and then plenty of blue-green algaes are grown when the water is smelly by which its quality declines drastically.

Considering the regular development of the lakes and reservoirs, it is a natural process to transfer oligotrophy to eutrophy. In a normal situation, this process is quite slow and needs to be measured in terms of geologic time scale. However, because of large scale human activities, the speed of the process has increased sharply. The factors affecting eutrophication includes light, temperature, geological conditions and nutrient substances such as TP and TN (He & Jin 2011). The paper analyzes common indexes which have an influence on the evaluation of eutrophication based on factor analysis method and major factors leading to the phenomenon are found so as to propose corresponding suggestions for addressing the problem.

2 THE SUMMARY OF FACTOR ANALYSIS METHOD

Factor analysis method is a kind of statistical approach which is used to study on correlativity among a group of variables. In the analyzing process, the known data is calculated, which is aimed at recognizing common factors exerting profound influence on the total process and then the scientific assessment is made based on the calculation. The mathematical model is shown as follows (Wang et al. 2004; Mi et al. 2011; Yei et al. 2011):

$$\begin{cases} X_1 = a_{11}F_1 + a_{12}F_2 + \cdots + a_{1m}F_m + a_1 \in_1 \\ X_2 = a_{21}F_1 + a_{22}F_2 + \cdots + a_{2m}F_m + a_2 \in_2 \\ \cdots \\ X_p = a_{p1}F_1 + a_{p2}F_2 + \cdots + a_{pm}F_m + a_p \in_p \end{cases} \quad (1)$$

In the model, x_1, x_2…..x_p represent several original variables. They are standard variables with the average value 0 and standard deviation 1. F_1, F_2, and F_m represent common factors and m is less than p. The matrix can be shown as follows (Zeng et al. 2006):

$$X = AF + a\in \quad (2)$$

In the matrix, F represents common factor, A is the symbol of factor loading matrix, a_{ij} represents loading factor, and $\in$ represents special factor, which is equal to the residual error in the multiple regression analysis.

3 THE STUDY ON EUTROPHICATION OF TANGHE RESERVOIR

3.1 *The natural condition of the reservoir*

The Tanghe reservoir is located in the upper river of Tanghe which is the main tributary of Taizi River. The drainage area of the reservoir is 1228 km^2 which accounts for 84% of the whole area of Tanghe. The reservoir is established in the mountain area of Liaoyang City and its average height is 300 m (Li & Li 2013). The place is characterized by temperate monsoon climate and it has four distinct seasons. The average rainfall and runoff among several years are 774 mm and 289 million m^3, respectively.

Table 1. Annual average value of pollutants in the Tanghe reservoir in 2014.

Name of section	COD_{MN} (mg/L)	BOD_5 (mg/L)	TN (mg/L)	TP (mg/L)	Chla (mg/m³)	Temp (°C)	SD (m)	DO (mg/L)
Front of the dam	2.917	1.200	0.695	0.005	1.959	19	3.487	7.850
Middle of reservoir	2.881	1.000	0.591	0.005	2.887	19	3.514	7.871
Middle of Dongcha	2.885	1.157	0.632	0.005	3.375	19	2.714	7.385
Front of Dongcha	2.940	1.171	0.581	0.005	3.992	19	2.042	7.357
Middle of Xicha	3.064	1.000	0.625	0.005	3.268	19	2.685	8.485
Front of Xicha	2.918	1.171	0.687	0.005	3.701	19	1.957	7.785

Table 2. The correlation matrix of different indexes.

	COD_{MN}	BOD_5	TN	TP	CHLA	TEMP	SD	DO
COD_{MN}	1.000	–0.420	–0.059	–0.124	0.143	0.124	–0.225	0.740
BOD_5	–0.420	1.000	0.510	0.446	0.009	–0.446	–0.338	–0.670
TN	–0.059	0.510	1.000	0.620	–0.467	–0.620	0.055	0.179
TP	–0.124	0.446	0.620	1.000	–0.849	–1.000	0.549	0.072
CHLA	0.143	0.009	–0.467	–0.849	1.000	0.849	–0.884	–0.319
TEMP	0.124	–0.446	–0.620	–1.000	0.849	1.000	–0.549	–0.072
SD	–0.225	–0.338	0.055	0.549	–0.884	–0.549	1.000	0.279
DO	0.740	–0.670	0.179	0.072	–0.319	–0.072	0.279	1.000

Table 3. The results of eigenvalue and accumulated variance contribution rate.

No	Eigenvalue	Percentage (%)	Accumulated percentage (%)
1	3.819	47.734	47.734
2	2.369	29.612	77.346
3	1.338	16.725	94.072
4	0.441	5.510	99.582
5	0.033	0.417	100
6	0	0	100
7	0	0	100
8	0	0	100

3.2 *Analysis of factors influencing the eutrophication of Tanghe reservoir*

Eutrophication is indicated as the water quality problem caused by an excessive input of nutrient substances such as N and P. The paper chooses the commonly-used indexes and uses factor analysis method based on the annual average value of pollutants in 2014 to find out key factors leading to eutrophication of the reservoir. The value is shown as follows in Table 1.

3.2.1 *The establishment of the correlation coefficient matrix*

To avoid considerable degree of dispersion caused by the difference of dimension, which has a negative influence on the final analysis, the original data Z_{ij} (i = 1, 2, …., n, j = 1, 2, …., p, i represents the number of variables and p represents sample point) is standardized into the variable which has an average value 0 and variance 1, the equations are shown as follows:

$$X_{ij} = \frac{z_{ij} - \overline{z_j}}{S_{jj}} \tag{3}$$

$$\overline{z_j} = \frac{1}{n}\sum_i^n z_{ij} \tag{4}$$

$$S_{jj}^2 = \frac{1}{n-1}\sum_i^n \left(z_{ij} - \overline{z_j}\right)^2 \tag{5}$$

In the equations, $\overline{z_j}$ and S_{ij} represent the average value and standard deviation of original data, respectively.

The correlation matrix R is shown in Table 2 which is based on the result of calculation of $R = \frac{1}{n}X' X$.

3.2.2 *The calculation of eigenvalue and eigenvector*

The eigenvalue λ and eigenvector u can be obtained based on the calculation of $|\lambda I - R| = 0$; the results are shown in Tables 3 and 4.

As the requirement of the accumulated variance contribution rate in which $\sum_{i=1}^{m}\lambda_i / \sum_{i=1}^{p}\lambda_i \geq 85$,

Table 4. The results of eigenvector.

	Factor 1	Factor 2	Factor 3	Factor 4	Factor 5	Factor 6	Factor 7	Factor 8
COD_{MN}	–0.113	0.442	0.530	–0.487	0.510	–0.001	–0.034	–0.115
BOD_5	0.178	–0.563	0.288	–0.183	0.218	0.101	0.183	0.666
TN	0.342	–0.108	0.485	0.687	0.252	0.116	–0.102	–0.275
TP	0.496	–0.038	0.093	–0.314	–0.302	0.228	0.592	–0.390
CHLA	–0.475	–0.193	0.188	–0.053	–0.223	0.777	–0.170	–0.130
TEMP	–0.496	0.038	–0.093	0.314	0.302	–0.003	0.745	–0.012
SD	0.343	0.278	–0.519	0.041	0.447	0.553	–0.045	0.161
DO	0.063	0.598	0.281	0.236	–0.444	0.124	0.136	0.0522

the first m factors in the table are chosen as factor variables. From Table 4, we can see that the accumulated contribution rate of the first three factors is 94.07%, so these factors are chosen to make the analysis of factor loading.

3.2.3 *The establishment of factor loading matrix*
In the analysis, the matrix is rotated in order to obtain a clear understanding of loading factors and making them be used to account for original variables efficiently. What's more, by doing so, each variable has larger load on only one public factor than the other ones. In the paper, the method of varimax is used to rotate the loading matrix and the final result is shown in Table 5.

As shown in the table above, TN, TP, and temperature have larger influence on factor 1 which is the principal factor than the other parameters. It means that these three parameters are the main influencing factors making contribution to eutrophication of Tanghe reservoir. To factor 2, COD_{MN} and DO make the greatest contribution and it reflects the extent of impacts of these two factors on eutrophication. Additionally, by analyzing the result of factor 3, it can be seen that Chla and SD are also important indexes to reflect the degree of eutrophication.

3.2.4 *The scores of sample factors*
Based on the calculation results of different correlation matrixes, the F_{ij}, which is the score of different factors in six samples, can be obtained in order to calculate the F_i, which represents the synthesis score of different samples. The equations are shown as follows and the final scores are shown in Table 6.

$$F_{ij} = \sum_{k=1}^{8} X_{ik} \cdot p_{jk} \tag{6}$$

$$F_i = \sum_{j=1}^{3} F_{ij} \cdot \frac{\lambda_j}{\sum_{j=1}^{3} \lambda_j} \tag{7}$$

Table 5. The maximum rotating results of variances to the factor loading matrix.

	Factor 1	Factor 2	Factor 3
COD_{MN}	0.015	0.908	0.248
BOD_5	0.733	–0.601	0.292
TN	0.879	0.098	–0.075
TP	0.771	–0.054	–0.597
CHLA	–0.423	–0.089	0.901
TEMP	–0.771	0.055	0.597
SD	–0.043	0.025	–0.995
DO	–0.002	0.949	–0.258

Table 6. The synthesis scores of different samples.

No	Y (i, 1)	Y (i, 2)	Y (i, 3)	Synthesis score
Front of the dam	–3.669	–0.028	4.232	–1.119
Middle of reservoir	0.198	0.365	–6.283	–0.902
Middle of Dongcha	–11.454	–3.711	25.735	–2.405
Front of Dongcha	5.608	0.225	–10.091	1.123
Middle of Xicha	–0.982	1.907	1.848	0.431
Front of Xicha	10.301	1.243	–15.441	2.872

In the equations, x_{ik} represents the value of the k-th variable in the i-th sample after standardization (i = 1, 2, … 6; j = 1, 2, 3), p_{jk} represents the loading of the k-th variable onto the j-th factor after rotation.

As seen from the values in Table 6, among 6 samples, the score of front of Xicha is higher than the others while the front of Dongcha is the second one, followed by the middle of Xicha and middle of the reservoir. Middle of Dongcha got the lowest

score in the table. These results reflect the rank of the nutrition level in such places. Comparing the results with the actual situation, such values conform to current level of eutrophication in Tanghe reservoir.

4 CONCLUSION

The advantage of the factor analysis method is to make use of few independent factors to replace the massive information of the original data. In the paper, this method is taken to do the research on factors which are commonly used to evaluate the degree of eutrophication for different water bodies. Among the factors, TP, TN, and temperature exert considerable influence on the principal factor, COD_{MN} and DO make great contribution to the factor 2 while the result of factor 3 reflect the impacts of Chla and SD on eutrophication of the reservoir. By analyzing the results, it can be seen that, to Tanghe reservoir, the main influencing factors of eutrophication are TN, TP, and temperature, which conform to the known conclusion. Additionally, the synthesis scores of different samples accord with current eutrophication level of the reservoir. Consequently, it is appropriate to utilize the factor analysis method to do the research on the eutrophication of Tanghe reservoir and the conclusion of this research can be used to provide effective suggestions to improve the water quality of the reservoir.

REFERENCES

He, B. & Jin, Y.M. 2011. Water quality eutrophication assessment of Liaoning Shenwo Reservoir. *Journal of Hydroelectric Engineering* 23(2): 27–32.

Li, G.B. & Li, X.S. 2013. Quality appraisal of water environment and measures for water resources protection of Tanghe reservoir. *Journal of Shenyang Agricultural University* 34(2): 135–137.

Mi, Y.N., Wang, X. & Liu, Q.S. 2011. Research on water environmental capacity of Chaihe reservoir. *Water Resources and Power* 29(11): 40–43.

Rast, W. & Thornton, J.A. 2012. Trends in eutrophication research and its control. *International Journal of Environment and Pollution* 33(4): 57–62.

Wang, L.J., Sun, S.Q. & Tian, F. 2004. Application of uncertainty mathematic analysis methods in river water quality assessment. *Journal of Hefei University of Technology* 27(11): 1425–1429.

Yei, C., Li, C.H. & Song, X.F. 2011. Study on ecological restoration in near-shore zone of a eutrophic lake, Wuli Bay, Taihu Lake. *Ecological Engineering* 37(9): 1434–1437.

Zeng, S.Y., Du, P.F. & Chen, J.N. 2006. Capability comparison among watershed pollution loading models. *Advances in Water Science* 17(1): 109–112.

Civil Engineering and Urban Planning IV – Liu et al. (Eds)
© 2016 Taylor & Francis Group, London, ISBN 978-1-138-02903-3

Engineering properties of Self-Compacting Concrete with stainless steel slags

Yeong-Nain Sheen, Her-Yung Wang, Li-Jeng Huang & Te-Ho Sun
Department of Civil Engineering, National Kaohsiung University of Applied Sciences, Kaohsiung, Taiwan, R.O.C.

ABSTRACT: The study is expected to effectively consume slag waste, reduce the amount of conventional material, and provide a low-cost concrete. In the SCC mixture, the Stainless Steel Oxidizing Slag (SSOS) replaces natural coarse and fine aggregates with various ratios (e.g., 0%, 50%, and 100%); and the Stainless Steel Reducing Slag (SSRS) partially substitutes for Portland cement (e.g. 0%, 10%, 20%, and 30%). A series of 12 mix proportions with a constant water-binder ratio was provided in this study. The hardened properties of the proposed SCC such as compressive strength, ultrasonic pulse velocity, and surface resistivity was experimentally investigated to examine the feasibility of SCC made with stainless steel slags. The testing results show that SSOS replacing natural aggregates in SCC could increase the compressive strength, electrical resistivity, and the ultrasonic pulse velocity to be a good quality concrete.

1 INTRODUCTION

1.1 *Stainless steel slag*

Stainless steel slag is a byproduct of manufacturing stainless steel from scrap iron. The characteristics of stainless steel slag differ from those of electric arc furnace carbon steel because of the additional elements of ferrochrome and nickel in stainless steel (Das et al. 2007; Zhang et al. 2011). Because the content of the stainless steel slag includes chromium, lead, nickel, and cadmium element, these elements create problems for both occupational and environmental health threats (Das et al. 2007; Durinck et al. 2008; Mar et al. 2009). Although, chromium has been reported as the most harmful element found in stainless steel waste (ICDA 2007), based on the results from the Toxicity Characteristic Leaching Procedure (TCLP) (US Environmental Protection Agency 2003) for stainless steel slag that were obtained from Italy, China, and Taiwan, the quantity of heavy metals recovered via leaching was found below detection limits (ICDA 2007; Zhang et al. 2011). Hence, the pollution risks posed by the heavy metals in stainless steel slag are minimal. Moreover, in most areas, stainless steel slag can be simply treated as a common, nonhazardous waste. In general, stainless steel slag can be used as a landfill material for the earth engineering (Zhang et al. 2011). However, the material also has both the cementation and pozzolanic reaction characteristics like Blast Furnace (B.F.) slag, thus, making it a viable concrete binder (Zhang et al. 2011; Sheen et al. 2013).

1.2 *Self-compacting concrete*

Self-Compacting Concrete (SCC) is characterized by its ability to be casted and filled into a framework entirely under its own weight and without the need for any type of compaction or external vibration. Additionally, SCC is highly resistant to segregation and flows easily around reinforcements and is hard-to-reach areas (Okamura 1999; Hwang 2010). Because the easy-to-pour SCC requires neither additional equipment nor skilled labor to consolidate, it has recently gained popularity (Kou et al. 2009; Hwang 2010; Mucteba et al. 2011). However, SCC does contain waste and industrial by-products, such as fly ash, limestone powder, which are generally used as mineral admixtures (Zhang et al. 2011; Kriskova 2012; Wang et al. 2013; Sheen et al. 2013; Chen et al. 2013).

According to the literature, when the fineness of Stainless Steel Reducing Slag (SSRS) is 4400 cm^2/g and cement content that replaces less than 30% by weight, the compressive strength of cement mortar is greater than that specified by ASTM C150 (Sheen et al. 2013). Moreover, replacing the natural aggregate with Stainless Steel Oxidizing Slag (SSOS) improves the compressive strength, with the value for 100% SSOS aggregate being nearly 1.13~1.14 times the natural aggregate after 28 days (Sheen et al. 2014). The test variables and mixture proportions of stainless steel slags is of a highest percentage, in order to use the stainless steel slags as much as possible,. The purpose of the study is aimed at increasing the economic value of stainless steel slag

and reducing the cement content in SCC, thereby, contributing to the resource recycling initiative.

2 EXPERIMENTAL PLAN

2.1 *Experimental materials*

The Portland cement used in this study was produced according to the ASTM C150 type I Portland cement with a specific gravity of 3.15 and a fineness of 3851 cm^2/g (manufactured by Taiwan Cement Corporation, Taiwan, and ROC). Class F fly ash was produced by Shin-Ta Thermal Power Plant of the Taiwan Power Company. SSRS was crushed by Fluidized bed opposed jet mill into powders. The fineness of SSRS is 5500 cm^2/g and the specific gravity is 2.85. The tap water was used to mix materials of concrete. The stainless steel slag was obtained from Lihwa Corp. SSOS was crushed and sieved after performing magnetic. The SSRS and SSOS are shown in Figure 1. The Figure 2 shows the Natural and SSOS aggregate particle size distribution curves. The sieve grading of the aggregates used matched the ASTM C33. The material properties are shown in Table 1.

2.2 *Experimental variables and mixture*

According to Hwang's Densified Mixture Design Algorithm (DMDA) (Hwang 2010), the SCC mixture was made with a constant water-to-binder ratio (W/B = 0.40) in which a portion of the aggregate was replaced by SSOS in weight ratios of 0%, 50%, and 100% and cement were replaced by SSRS in weight ratios of 0%, 10%, 20%, and 30%. The design compressive strength of 28 days

Figure 1. SSRS and SSOS.

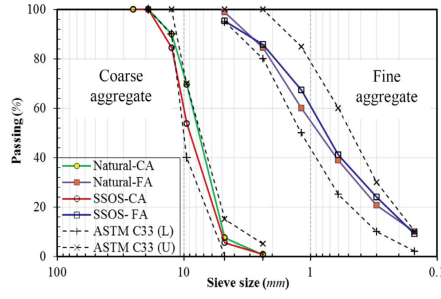

Figure 2. Particle-size distribution of N.A. and SSOS aggregates.

Table 1. Material properties.

Physical properties					
Items (Aggregate)		SG_{SSD}	Water absorption (%)		Fineness (cm^2/g)
Natural fine		2.65	2.2		–
Natural coarse		2.64	1.3		–
Fine SSOS		2.86	2.8		–
Coarse SSOS		2.88	1.9		–
SSRS		2.85	–		5500
Chemical composition (%)					
		SiO_2	CaO	Al_2O_3	MgO
SSOS		38.61	31.5	2.43	12.8
SSRS		23.5	50.6	4.1	8.2
TCLP (mg/L)					
Cr	Cu	Cd	Pb	Zn	Ni
N.D	N.D	N.D	N.D	N.D	N.D

*N.D = Not detected, less than the test detection value.

Table 2. Mixture proportion (kg/m^3).

Sample	SSOS Aggregate		Natural Aggregate		SSRS	Cement	Water
	Fine	Coarse	Fine	Coarse			
S-0-0	849	787	0	0	0	448	232
S-0-10	849	787	0	0	45	403	232
S-0-20	849	787	0	0	90	358	232
S-0-30	849	787	0	0	134	314	232
S-50-0	425	394	424	393	0	448	232
S-50-10	425	394	424	393	45	403	232
S-50-20	425	394	424	393	90	358	232
S-50-30	425	394	424	393	134	314	232
S-100-0	0	0	849	787	0	448	232
S-100-10	0	0	849	787	45	403	232
S-100-20	0	0	849	787	90	358	232
S-100-30	0	0	849	787	134	314	232

is 280 kgf/cm^2. Table 2 shows the replacement of a weight basis and the mixture proportion.

2.3 *Hardened properties test items and methods*

The compressive strength was tested according to ASTM C39. A cylinder specimen of 100 mm diameter and 200 mm height was made, and tested at 1 day, 7 days, 28 days, 56 days, and 91 days. Ultrasonic pulse velocity detection was performed according to ASTM C597. An ultrasonic instrument was used to transmit ultrasonic pulse waves to the cylinder specimen, and the signals were returned to the pulse wave receiver. As the concrete test block ages with time, the block becomes more compact, and the measured ultrasonic pulse velocity also increases (Leslie et al. 1949; Hwang et al. 2001; Hwang 2010). According to the ASTM C876 standard on surface resistance, the resistivity can be measured by the contact section of concrete. During the test, the specimen was dry on the outside and saturated on the inside. The concrete surface resistance was the degree of concrete density and the index of impermeability (Hwang et al. 2001; Hwang 2010; Sheen et al. 2013).

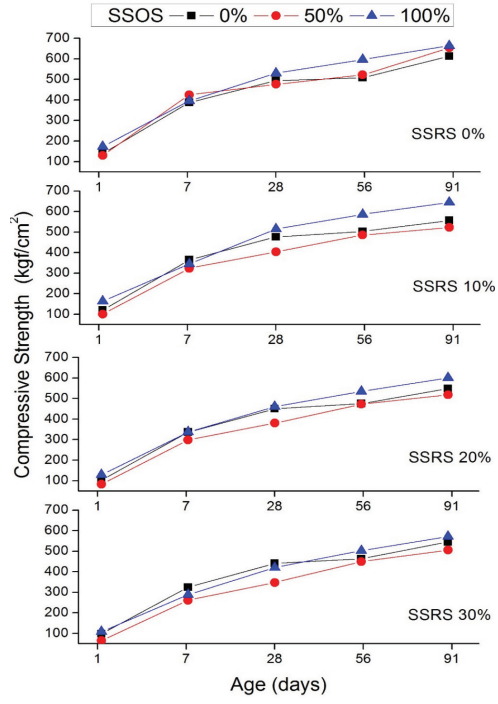

Figure 3. Compressive strength of SS-SCC.

3 RESULTS AND ANALYSIS

3.1 *Compressive strength*

As shown in Figure 3, the compressive strength of stainless steel slag SCC (SS-SCC) tends to increase when the SSRS replacement ratio of the cement decreases, and the compressive strength tends to decrease when the SSOS replacement ratio of the aggregate decreases. The compressive strength of 28 days is 348–580 kgf/cm^2 higher than the design compressive strength 280 kgf/cm^2. The compressive strength of S-100-10 (100% SSOS and 10% SSRS substitution) is higher than the control group S-0-0 after 28 days. However, after 56 days, the compressive strength of S-100-30 (100% SSOS and 30% SSRS substitution) is higher than the control group. The results indicate that SSOS and SSRS replace aggregate and cement material of

SCC is acceptable. The maximum substitution is 100% SSOS and 30% SSRS.

3.2 *Ultrasonic pulse velocity*

Figure 4 shows the ultrasonic pulse velocity for the SS-SCC after 1 day, 7 days, 28 days, 56 days, and 91 days. Ultrasonic pulse velocity tends to increase with the SSOS aggregate proportions and age. The ultrasonic pulse velocity is in range of 4028–4393 m/s after 28 days. The measured values are within 3660–4575 m/s; it means that the quality of SS-SCC is "good" in density (Whitehurst 1951). The results indicate that SS-SCC density is the same as the one of the control group. Meanwhile, the ultrasonic pulse velocity of S-30-100 (4230 m/s) is higher than S-0-0 (4212 m/s) after 28 days.

3.3 *Surface resistance*

when there is a corrosion risk in a reinforced concrete structure, the resistivity after 56 days should be above 20 kΩ-cm to prevent corrosion of the reinforcement. Figure 5 indicates the surface resistance of the SS-SCC, which had a resistance between 20 and 50 kΩ-cm after 56 days, could reach the required value of 20 kΩ-cm to prevent corrosion. The results indicate that SS-SCC can prevent the corrosion risk in a reinforced concrete structure as good as the specimen of the control group. The

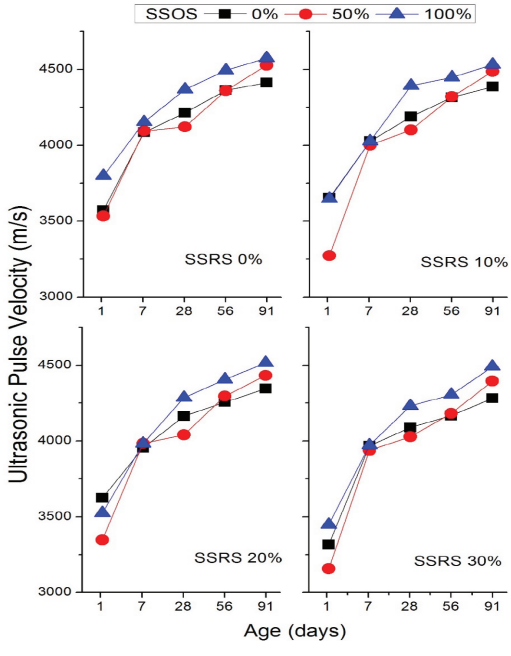

Figure 4. Ultrasonic pulse velocity of SS-SCC.

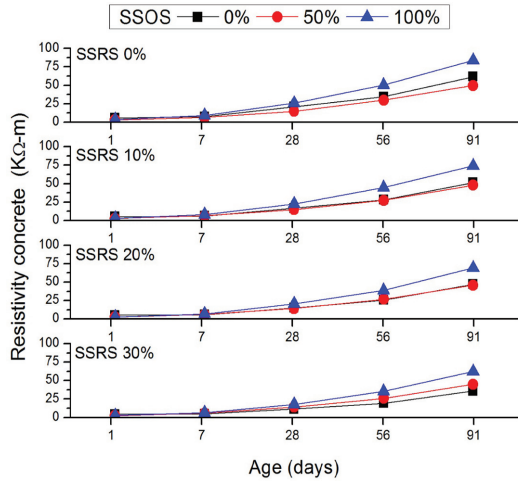

Figure 5. Surface resistance of SS-SCC.

surface resistance of S-30-100 (35.3 kΩ-cm) is greater than S-0-0 (34.4 kΩ-cm) after 56 days.

4 CONCLUSION

- The SS-SCC compressive strength tends to decrease when the SSRS replacement ratio of the cement increases, and the compressive strength tends to increase when the SSOS replacement ratio of the aggregate increases. Due to these characteristics, the compressive strength of SS-SCC is similar the control group.
- The ultrasonic pulse velocity measured values show that SS-SCC density is the same as the one of the control group.
- The SS-SCC surface resistance values were over 20 kΩ-cm. The results indicate that SS-SCC can prevent the corrosion risk in a reinforced concrete structure.

The SS-SCC hardened properties of S-30-100 are similar to the control group S-0-0. This study shows that it is viable to use only 314 kg/m^3 cement and an amount of stainless steel slags to produce SCC. The results will reduce stainless steel slag wastes and increase the economic value of stainless steel slag. Additionally, it will contribute to environmental protection and the resource recycling initiative.

ACKNOWLEDGMENTS

The authors would like to thank the Ministry of Science and Technology of the Republic of China, Taiwan, for the financial support they provided

to them, during this research under Contract No. MOST 103-2221-E-151-046.

REFERENCES

Chen, Y.Y., Tuan, B.L.A. & Hwang, C.L. 2013. Effect of paste amount on the properties of self-consolidating concrete containing fly ash and slag. *Construction and Building Materials* 47: 340–346.

Das, B. & Prakash, S. 2007. An overview of utilization of slag and sludge from steel industries. *Resources, Conservation and Recycling* 50(1): 40–57.

Durinck, D., Arnout, S., Mertens, G., Boydens, E., Jones, P.T. & Elsen, J. 2008. Borate distribution in stabilized stainless-steel slag. *Journal of the American Ceramic Society* 91(2): 548–554.

Hwang, C.L. 2010. *The Theory and Practice of High Performance Concrete*. Taipei: Chan's Arch-Publishing Co., Ltd.

Hwang, C.L. & Zhan, Y.Y. 2001. The resistance and the chloride ion permeability behavior of concrete. *Chinese Institute of Civil and Hydraulic Engineering Journal* 2(13): 293–302.

ICDA. 2007. *Health Safety and Environment Guidelines for Chromium*. Paris: ICDA.

Kou, S.C., & Poon, C.S. 2009. Properties of self-compacting concrete prepared with coarse and fine recycled concrete aggregates. *Cement and Concrete Composites* 31(9): 622–627.

Kriskova, L., Pontikes, Y. & Cizer, Ö. 2012. Effect of mechanical activation on the hydraulic properties of stainless steel slags. *Cement and Concrete Research* 42(6): 778–788.

Leslie, J. & Cheesman, W. 1949. Ultrasonic method of studying deterioration and cracking in concrete structures. *ACI Journal* 46(1): 17–24.

Ma, G. & Garbers-Craig, A.M. 2009. Stabilizations of Cr (VI) in stainless steel plant dust through sintering using silica-rich clay. *Journal of Hazardous Material* 169(3–1): 210–216.

Mucteba, U. & Kemalettin, Y. 2011. Effect of mineral admixtures on properties of self-compacting concrete. *Cement & Concrete Composites* 33(7): 771–776.

Okamura, H. & Ouchi, M. 1998, Self-compacting high performance concrete. *Progress in Structural Engineering and Materials* 1(4): 378–383.

Sheen, Y.N., Wang, H.Y. & Sun, T.H. 2013. A study of engineering properties of cement mortar with stainless steel oxidizing slag and reducing slag resource materials. *Construction and Building Materials* 40: 239–245.

Sheen, Y.N., Wang, H.Y. & Sun, T.H. 2014. Properties of green concrete containing stainless steel oxidizing slag resource materials. *Construction and Building Materials* 50: 22–27.

US Environmental Protection Agency. 2003. *RCRA Training Modules*, *Introduction to Hazardous Waste Identification*. Washington, DC: US Environmental Protection Agency.

Wang, H.Y. & Lin, C.C. 2013. A study of fresh and engineering properties of self-compacting high slag concrete (SCHSC). *Construction and Building Materials* 42: 132–136.

Whitehurst, E.A. 1951. Soniscope test concrete structures. *ACI Journal* 47(2): 433–444.

Zhang, H.W. & Hong, X. 2011. An overview for the utilization of wastes from stainless steel industries. *Resources*, *Conservation and Recycling* 55(8): 745–754.

This page intentionally left blank

Civil Engineering and Urban Planning IV – Liu et al. (Eds)
© 2016 Taylor & Francis Group, London, ISBN 978-1-138-02903-3

Reconstruction of three-dimensional road roughness

Gang Yao, Yang Yang, Wen Du & Min She
College of Civil Engineering, Chongqing University, Chongqing, China

ABSTRACT: In this research, road roughness is a key factor for human-vehicle-road, wind-vehicle-road, and wind-vehicle-bridge vibration systems. A new three-dimensional road roughness to be reconstructed with random harmonic function had been proposed by the author. Reconstructed random harmonic function has proved to have stability and zero-mean properties and follow Gaussian distribution in theory. The three-dimensional road roughness was simulated with random harmonic method by MATLAB. The distribution characteristic and range of road roughness had been developed. And the result has proved to be right by power spectral density and the coherence curve. Therefore, it is feasible to reconstruct a three-dimensional road roughness with random harmonic method.

1 INTRODUCTION

Road roughness, which is closely related to passengers' comfort, vibration of vehicle and friction loss, is an important factor in evaluating the pavement properties (Duan et al. 2009). Vibration of vehicle is mainly caused by road roughness in the process of moving. Road roughness is an excitation source in research of human-vehicle-road (Liu et al. 2014), wind-vehicle-road, and wind-vehicle-bridge vibration system (Zhang & Li 2011; Ma et al. 2012; Han & Chen 2008). With the development of numerical simulation technology, a series of theories to simulate road roughness have been put forward. Two-dimensional road roughness is simulated mainly on four theories: power spectrum analysis model, time series analysis model, wavelet analysis model, and fractal analysis model (Zhang & Li 2011).

In this paper, a three-dimensional road roughness with random harmonic function has been proposed. Reconstructed random harmonic function has proved to have stability and zero-mean properties and follow Gaussian distribution in theory (Grigoriu 2006). The three-dimensional road roughness was simulated with random harmonic method by MATLAB (Agostinacchio et al. 2014). The distribution characteristic and range of road roughness had been developed.

2 THE RECONSTRUCTED FUNCTION WITH RANDOM HARMONIC

Road surface displacement power spectral density can be expressed in Equation (1).

$$G_q(n) = G_q(n_0)\left(\frac{n}{n_0}\right)^{-w} \tag{1}$$

where $G_q(n)$ = road roughness power spectral density; n = space frequency, m^{-1}; n_0 = reference space frequency, $n_0 = 0.1$, m^{-1}; $G_q(n_0)$ = road roughness coefficient, m^{-2}/m^{-1}; w = frequency index, $w = 2$.

The vehicle tire's excited frequency is related to the space excitation frequency and the vehicle speed in this process (Liu & Qian 2008), and space power spectral density function is expressed in Equation (2).

$$\begin{aligned} G_q(f) &= \frac{1}{u}G_q(n) = \frac{1}{u}G_q(n_0)\left(\frac{f}{n_0}\right)^{-w}\left(\frac{1}{u}\right)^{-w} \\ &= G_q(n_0){n_0}^{w} f^{-w} u \end{aligned} \tag{2}$$

where f = vehicle tire's frequency in the process, $f = u \cdot n$, Hz; u = vehicle speed, m/s; (f_1, f_2) could be divided into N intervals, middle frequency of i interval is $f_{mid\text{-}i}$; $f_{mid\text{-}I}$ could take the place of power spectral density if there are enough intervals. Power spectral density in i interval can be developed in Equation (3).

$$G_i = G_q(f_{mid-i}) f_i (i = 1, 2, 3 \ldots N) \tag{3}$$

The relation between power spectral and value of amplitude is $A^2 = G$, so the value of amplitude in each interval can be developed in Equation (4).

$$A_i = \sqrt{G_i} = \sqrt{G_q(f_{mid\text{-}i}) g V f_i} \tag{4}$$

where A_i = value of amplitude in each interval. The cumulative sum of N individual cosine waves that has the A_i standard deviation is expressed in Equation (5).

$$Z_a = \sum_{i}^{N} \sqrt{2} A_i \cos(2\pi f_i t + \phi_i) \tag{5}$$

where Z_a = displacement that vertical to road surface, m. Substituting $t = y/u$ and $f_i = u \cdot n_i$ into Equation (6).

$$Z_a = \sum_{i}^{N} \sqrt{2} A_i \cos(2\pi n_i y + \phi_i) \tag{6}$$

where y = displacement along the road; ϕ_i = a random number in the range of [0, 2π], matching the standard normal distribution. It can be found that road roughness is only related to the displacement, and it has no relation to vehicle speed. Vehicle speed is an intermediate variable participating in the transformation. X direction is assumed as the direction cross the road, and Y direction is assumed as the direction along the road. Z direction is assumed as the direction, which is vertical to x, y plane. Road roughness along and cross the road can be expressed with random harmonic function in Equations (7) and (8).

$$\begin{aligned} X &= \sum_{i=1}^{N} X_i = \sum_{i=1}^{N} \sqrt{2} A_i \cos\left(2\pi n_i x + \phi_{1i}\right) \\ &= \sum_{i=1}^{N} \sqrt{2} A_i \cos\left(2\pi f_i t_x + \phi_{1i}\right) \end{aligned} \tag{7}$$

$$\begin{aligned} Y &= \sum_{i=1}^{N} Y_i = \sum_{i=1}^{N} \sqrt{2} A_i \cos\left(2\pi n_i y + \phi_{2i}\right) \\ &= \sum_{i=1}^{N} \sqrt{2} A_i \cos\left(2\pi f_i t_y + \phi_{2i}\right) \end{aligned} \tag{8}$$

Z_1, Z_2, …, Z_N are independent bi-variety random vectors, $Z_i = (X_i, Y_i)$, $i = 1, 2, 3, \ldots N$. Sum of the vector can be developed in Equation (9).

$$Z = \sum_{i=1}^{N} Z_i = \left(\sum_{i=1}^{N} X_i, \sum_{i=1}^{N} Y_i \right) = (X, Y) \tag{9}$$

Theorem of Laning–Battin has pointed out if N tending to infinity then $Z = (X, Y)$ matching Gaussian distribution:

$$\begin{cases} \lim\limits_{N\to\infty} \dfrac{1}{\sigma x^3} \sum\limits_{i=1}^{N} E\left\{ \left| X_i - E(X_i) \right|^3 \right\} = 0 \\ \lim\limits_{N\to\infty} \dfrac{1}{\sigma y^3} \sum\limits_{i=1}^{N} E\left\{ \left| Y_i - E(Y_i) \right|^3 \right\} = 0 \end{cases} \tag{10}$$

If f_i is independent in random harmonic function, then Equation (11) is the probability density function.

$$p_{f_{mid-i}}(f) = \frac{G_x(f)}{2\pi E_i} I\left[f \in \left(f_{i-1,}\ f_i \right) \right] \tag{11}$$

$I[f \in (f_{i-1}, f_i)]$ is a indicative function, if $f \in (f_{i-1}, f_i)$, then $I[\cdot] = 1$, otherwise $I[\cdot] = 0$. Equations (12)–(14) could be set up since the probability is compatible.

$$\int_{f_{mid-i-1}}^{f_{mid-i}} p_{f_{mid-i}}(f) d_f = 1 \tag{12}$$

$$\begin{aligned} &\sum_{i=1}^{N} E\left| X_i \right|^3 \\ &= \sum_{i=1}^{N} \int_{f_{i-1}}^{f_i} \int_{0}^{2\pi} \frac{1}{2\pi} p_{fi}(f) \left| \sqrt{2} A_i \cos\left(2\pi f_i t_x + \phi_i\right) \right| d_{\phi_i} d_f \\ &= \sum_{i=1}^{N} \frac{8\sqrt{2} A^3(f_i)}{3\pi} \end{aligned} \tag{13}$$

$$\begin{aligned} \lim_{N\to\infty} \sum_{i=1}^{N} E\left| X_i \right|^3 &= \lim_{N\to\infty} \frac{8\sqrt{2}}{3\pi} \sum_{i=1}^{N} E_j \sqrt{E_j} \\ &= \lim_{N\to\infty} \sum_{i=1}^{N} \frac{8\sqrt{2}}{3\pi} \int_{n_u}^{n_l} \left[\frac{G_x(f_i)}{\pi} (\Delta f_i) \right]^{3/2} \\ &\le \lim_{N\to\infty} \sum_{i=1}^{N} \frac{8\sqrt{2} G_{\max}{}^{3/2}}{3\pi (2\pi)^{3/2}} (\Delta f_i)^{3/2} \end{aligned} \tag{14}$$

$G_{max} = max|\ G_x\ (f)|$, $E(X_i) = 0$, $E(Y_i) = 0$, when $N \to \infty$, and $\Delta \to 0$, Equation (15) could be set up.

$$\lim_{N\to\infty} \frac{1}{\sigma x^3} \sum_{i=1}^{N} E\left\{ \left| X_i - E(X_i) \right|^3 \right\} = 0 \tag{15}$$

According to Laning–Battin theorem, Equation (9) can match up to the Gaussian distribution. So, Equation (16) can be built according to Equation (9).

$$\begin{aligned} Z = \frac{1}{2} \Bigg(&\sum_{i=1}^{N} \sqrt{2} A_i \cos\left(2\pi f_i t_x + \phi_{1i}\right) \\ &+ \sum_{i=1}^{N} \sqrt{2} A_i \cos\left(2\pi f_i t_y + \phi_{2i}\right) \Bigg) \end{aligned} \tag{16}$$

When vehicle runs on road, $t_x = x/u$, $t_y = y/u$ and $f_i = u \cdot n$ are brought into Equation (16), and Equation (17) could be developed.

$$\begin{aligned} Z = \frac{1}{2} \Bigg(&\sum_{i=1}^{N} \sqrt{2} A_i \cos\left(2\pi n_i x + \phi_{1i}\right) \\ &+ \sum_{i=1}^{N} \sqrt{2} A_i \cos\left(2\pi n_i y + \phi_{2i}\right) \Bigg) \end{aligned} \tag{17}$$

$E(X) = 0$ and $E(Y) = 0$, X and Y are independent variables, so $E(Z) = 0$. When N tends to infinity, Equation (17) expresses a stable zero-mean process

following Gaussian distribution because random harmonic has a stability character.

3 THREE-DIMENSIONAL ROAD ROUGHNESS SIMULATED BY RANDOM HARMONIC METHOD

Usually, road space frequency ranges from 0.011 to 2.83 m^{-1} and time frequency ranges from 0.44 to 28.3 Hz including the suspension quality natural frequency 1~2 Hz and the non-suspension quality natural frequency 10~15 Hz. Three-dimensional road roughness of B level was simulated at the condition of time frequency, which was divided into 200 portions and sampling frequency was taken as 0.01 s with MATLAB. Road roughness with 40 m both in width and length was shown in Figure 1.

In order to find out space distribution of road roughness clearly, contour lines of the road were specified in Figure 2. It can be seen directly that the distribution of road roughness was irregular, so the road roughness was a random distribution.

When the width of road was known, roughness along the road could be developed in Figure 3. When the length of road was known, roughness cross the road could be developed in Figure 4. Figures 3 and 4 showed variations of road roughness that in width and in length were chosen randomly. Variations of road roughness remained stable and fluctuated around zero. The range of variation mainly focused on –0.03 m.

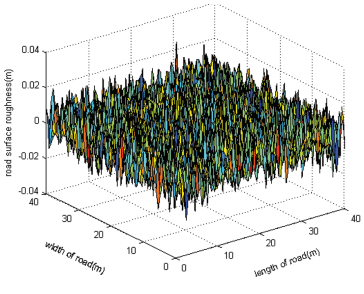

Figure 1. Three-dimensional road roughness of B level.

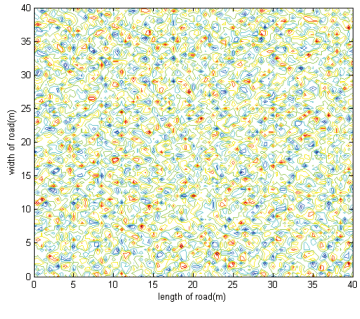

Figure 2. Contour lines generated.

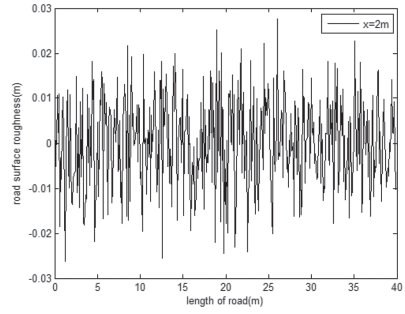

Figure 3. Roughness along the road generated by random harmonic method at 2 m width of road.

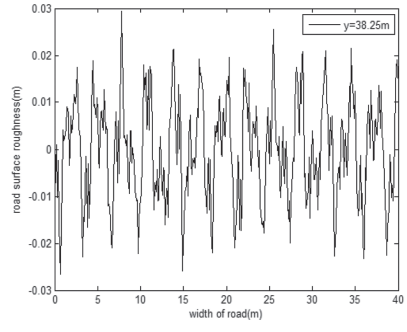

Figure 4. Roughness across the road generated by random harmonic method at 38.25 m length of road.

In order to confirm the correctness of road roughness reconstructed by random harmonic method, power spectral density was simulated. The simulated power spectral density curve was compared with the standard power spectral density in Figure 5. It can be seen that the simulated power spectral density agreed well with the standard power spectral density. Therefore, power spectral density simulated by random harmonic method was similar to the standard one. Deviation between simulated power spectral density and standard power spectral density was brought in because of the limited sampling points and the random phase data. In the coordinate system, displacement points were taken on average which led to regional focus in power spectral density curves.

When the vehicle model was built with more than five degrees of freedom, road roughness was needed to be imported in each vehicle wheel. Motivation on the left and right side of vehicle wheel had the same power spectral density, so it is necessary to consider the coherence. Road roughness in 3.0 m width and

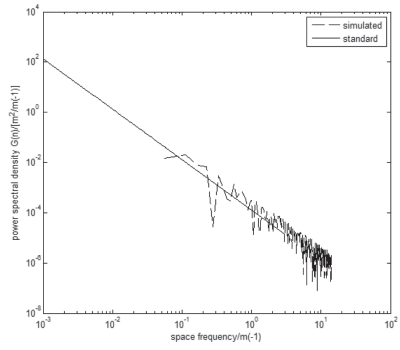

Figure 5. Simulated power spectral density by random harmonic method and the standard one.

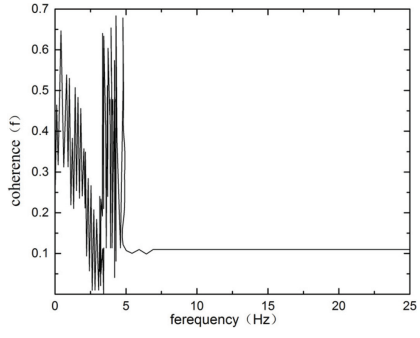

Figure 6. Coherence curve.

14.0 m width were used in simulating the coherence function curve, and it is shown in Figure 6.

As shown in Figure 6, the road roughness was almost the same when $f > 5$ Hz. The slope of coherence curve was almost identical when $0 < f < 2.5$ Hz. Deviation existed in $2.5 < f < 5.0$ Hz because of large vibration amplitude. Frequency domain which fitted in good condition included the natural frequency of vehicle body quality that is 1.0~2.0 Hz and the natural frequency of vehicle wheel quality that is 10.0~16.0 Hz. In conclusion, the three-dimensional road roughness with random harmonic method can reflect the real condition of road roughness.

4 CONCLUSION

- It has been proved that reconstruction of random harmonic function has stable and zero-mean characters and it follows the Gauss distribution well. Three-dimensional road roughness reconstructed with random harmonic function is correct and feasible.
- Simulated power spectral density curves were compared with standard power spectral density to confirm the correctness of results. Deviation of power spectral density simulated by random harmonic method was brought in because of the limited sampling points and the random phase data.
- Coherence curve was generated by choosing road roughness at different width, and it proved that the three-dimensional road roughness with random harmonic method can reflect the real condition of road roughness.

ACKNOWLEDGMENTS

This work has been financially supported by Science and Technology project of Chongqing Municipal Construction Commission (20130844) and it is gratefully acknowledged.

REFERENCES

Agostinacchio, M., Ciampa, D. & Olita, S. 2014. The vibrations induced by surface irregularities in road pavements–A Matlab approach. *Eur. Transp. Res. Rev* 11(6): 267–275.

Duan, H.M., Shi, F. & Xie, F. 2009. A survey of road roughness study. *Journal of Vibration and Shock (in Chinese)* 28(9): 95–102.

Grigoriu, M. 2006. Evaluation of Karhunen-Loeve, spectral and sampling representations for stochastic processes. *Journal of Engineering Mechanics* 132(2): 179–189.

Han, W.S. & Chen, A.R. 2008. Three-dimensional coupling vibration of wind-vehicle-bridge systems under random traffic flow. *China Civil Engineering Journal (in Chinese)* 41(9): 97–103.

Huang, S.P., Quek, S.T. & Phoon, K.K. 2001. Convergence study of the truncated Karhunen-Loeve expansion for simulation of stochastic processes. *International Journal for Numerical Methods in Engineering* 52(9): 1029–1043.

Kovantsov, A. & Krumbergs, R. 2012. Creation of graphs of functions with use of theorems of elementary geometry. *Computer Modelling and New Technologies* 16(2): 50–59.

Liu, B., Wang, Y.Z., An, J.J., et al. 2014. The spatial model of vehicle—pavement coupling vibration and its dynamic responses analysis. *Journal of Shandong University: Engineering Science (in Chinese)* 43(3): 83–90.

Liu, Y. & Qian, Z.D. 2008. Review of road roughness and vehicle vibration mode. *Journal of Highway and Transportation Research and Development (in Chinese)* 25(1): 51–57.

Ma, L., Han, W.S. & Ji, B.H. 2012. Study of vehicle-bridge coupling vibration under actual traffic flow. *China Journal of Highway and Transport (in Chinese)* 25(6): 80–87.

Zhang, B.Q. & Li, L. 2011. Dynamic model and comfortableness evaluation of a body-vehicle-road coupled system. *Journal of Vibration and Shock (in Chinese)* 30(1): 1–6.

Zhang, H.L. & Yang, W.Q. 2010. Evaluation method of pavement roughness based on 5-DOF human-vehicle—road vibration model, *Journal of Traffic and Transportation Engineering (in Chinese)* 10(4): 16–22.

Civil Engineering and Urban Planning IV – Liu et al. (Eds)
© 2016 Taylor & Francis Group, London, ISBN 978-1-138-02903-3

Improved punching shear capacity calculation method of reinforced concrete slab-column connections

Hui-Yong Guo & Jin-Jun Cheng
School of Civil Engineering, Chongqing University, Chongqing, China
Key Laboratory of New Technology for Construction of Cities in Mountain Area of the Ministry of Education, Chongqing, China

ABSTRACT: In order to solve strength analysis problem of reinforced concrete slab-column connections, a comparison study is done and an improved punching shear capacity method is presented. First, the punching shear capacity methods of the codes: GB50010-2010, ACI318-08 and EN1992-1-1-2004, are analyzed. Then, a comparison study of punching shear capacity calculation methods is done by using ANSYS finite element software. The effects of concrete strength, slab thickness and longitudinal reinforcement ratio are considered in the study. Finally, an improved punching shear capacity formula is proposed. The results indicate that because of the consideration of longitudinal reinforcement ratio, the improved punching shear capacity formula is more reasonable.

1 INTRODUCTION

In general, a flat plate is susceptible to punching shear failure at its slab–column connection. This punching shear failure significantly degrades the overall resistance of the structure against gravity load, and thus the structure may collapse. For this reason, many studies have been performed to evaluate the punching shear strength of slab-column connections. Theodorakopoulos and Swamy (2002) presented a simple analytical model to predict the ultimate punching shear strength of slab–column connections. The model is based on the physical behavior of the connections under load, therefore applicable to both lightweight and normal weight concrete. Choi et al (2007) performed a theoretical study to investigate the punching shear strength of interior slab-column connections made of steel fiber reinforced concrete. Park et al (2011) developed a strength model to predict the direct punching shear strength of interior slab-column connections without shear reinforcement. At slab-column connections damaged by flexural cracking, it was assumed that the punching shear force was resisted mainly by the compression zone of the critical section. Abdullah et al (2013) investigated the effectiveness of bonding non-prestressed and prestressed carbon fiber reinforced polymer plates to the tension surface of concrete column-slab connections in both the serviceability and ultimate limit state. However, the punching shear capacity calculation methods of several national building codes are different, the punching failure mechanism is still not clear yet. Especially the effect of longitudinal reinforcement ratio isn't considered in China codes GB50010-2010. Therefore, the punching shear calculation method of reinforced concrete slab-column connections is studied in this paper.

2 PUNCHING SHEAR CAPACITY

Punching shear performance of slab around the joint area of reinforced concrete slab-column structure is very important. Here, the punching shear capacity of reinforced concrete slab without stirrup or bent-up reinforcement is considered. Different punching shear capacity calculation methods are proposed by these codes: GB50010-2010 (2010, China), ACI318-08 (USA) and EN1992-1-1-2004 (Europe). For these codes, the punching shear capacity formula can be simply written as.

$$V_c = C_0 \eta \mu_m h_0 \tag{1}$$

in which, C_0 is punching shear coefficient; η is influence coefficient, $\eta = \min(\eta_1, \eta_2)$; $\mu_m$sss is critical section perimeter; h_0 is sectional effective height. For different codes, the punching shear coefficient C_0 and influence coefficient η are listed in Table 1.

In Table 1, f_t is concrete tensile strength, f'_c is concrete compressive strength, f_{ck} is standard value of concrete compressive strength, β_h is influence coefficient of sectional height, β_s is long side to short side ratio, α_s is influence coefficient of column type.

Table 1. Calculating parameters of punching shear capacity without abdominal reinforcement.

Codes	C_0	η_1	η_2
GB50010-2010	$0.7\,\beta_h f_t$	$0.4+\frac{1.2}{\beta_s}$	$0.5+\frac{\alpha_s h_0}{4\mu_m}$
ACI318-08	$0.333\lambda\phi\sqrt{f'_c}$	$0.5+\frac{1}{\beta_s}(\beta_s \geq 2)$	$0.5+\frac{\alpha_s d}{4b_0}$
EN1992-1-1-2004	$C_{Rd,c}k(100\rho_l f_{ck})^{1/3}$ $\geq v_{\min}+0.1\sigma_{cp}$	–	–

Table 2. Main factors in different national codes.

Influencing factors	GB50010-2010	ACI318-08	EN1992-1-1-2004
Concrete strength	f_t	f'_c	f_{ck}
Shape of loading area	Yes	Yes	No
perimeter-height ratio	Yes	Yes	No
Longitudinal reinforcement ratio	No	No	Yes
Punching shear cone angle and critical width	45° or $\frac{h_0}{2}$	45° or $\frac{d}{2}$	45° or $\frac{d}{2}$

In general, the punching shear capacity is related to many influencing factors such as concrete strength, shape of loading area, longitudinal reinforcement ratio, anti-punch reinforcement placing etc. For different codes, the main influencing factors are listed in Table 2.

From Table 2, it can be seen that the effect of longitudinal reinforcement ratio hasn't been considered in the code GB50010-2010 and code ACI318-08. The code EN1992-1-1-2004 considers the effect of longitudinal reinforcement ratio but doesn't consider the shape of loading area and perimeter-height ratio. Therefore, it is necessary to improve the punching shear capacity formula.

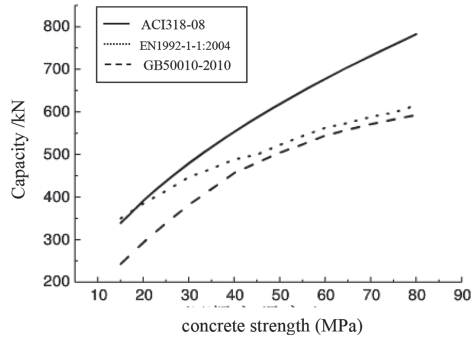

Figure 1. Influence curve of concrete strength.

3 COMPARISON CALCULATION ANALYSIS

A reinforced concrete slab-column connection structure is considered in this paper. In the connection structure, slab depth h = 200 mm, column size $a \times b$ = 350 mm × 350 mm, concrete strength is C30, two-way longitudinal reinforcement configuration is Φ12@100, reinforcement area per meter is A_s = 1131 mm^2, steel reinforcement strength standard value is 335 MPa. ANSYS finite element software is applied to calculate the punching shear capacity of reinforced concrete slab-column connection. Here, the punching shear capacity of reinforced concrete slab without stirrup or bent-up reinforcement is only considered.

The calculation results of concrete strength change are shown in Figure 1. From Figure 1, it can be seen that the change trends of the three codes are similar in concrete strength. The calculation results of slab thickness change are shown in Figure 2.

From Figure 2, it can be observed that the change trends of the three codes are still similar in slab thickness. The calculation results of column edge length change are shown in Figure 3. From Figure 3, it can be seen that the change trends of the three codes are approximately similar in

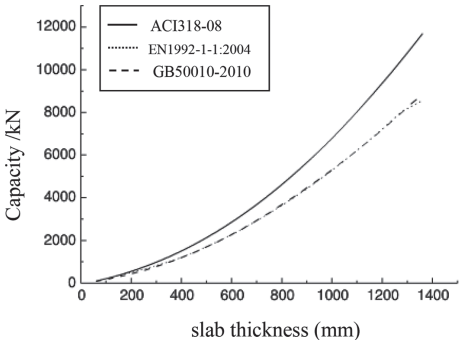

Figure 2. Influence curve of slab thickness.

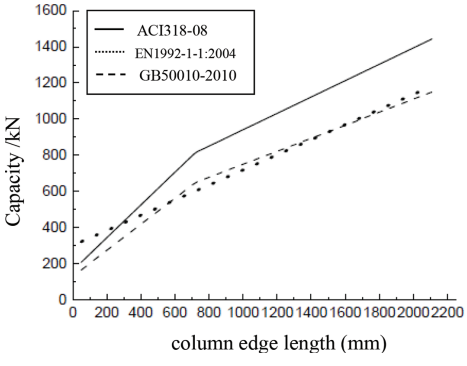

Figure 3. Influence curve of column edge length.

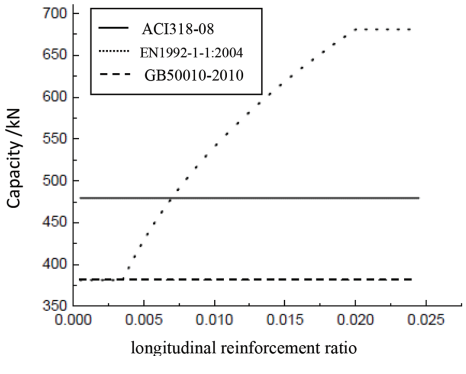

Figure 4. Influence curve of longitudinal reinforcement ratio.

column edge length. The calculation results of longitudinal reinforcement ratio change are shown in Figure 4. From Figure 4, it can be observed that the longitudinal reinforcement ratio doesn't have an effect on punching shear capacity for the codes GB50010-2010 and ACI318-08. In addition, it has a linear change for the code EN1992-1-1-2004. The punching shear capacity value of the code GB50010-2010 is lowest in the three codes. Therefore, the code GB50010-2010 is more conservative than the code ACI318-08 and code EN1992-1-1-2004. Thus, it is necessary to consider the effect of longitudinal reinforcement ratio for the code GB50010-2010.

4 IMPROVED PUNCHING SHEAR CAPACITY EQUATION

In China code GB50010-2010, the effect of longitudinal reinforcement ratio isn't considered. Thus, the calculation value is too conservative. Through the comparison of punching shear capacity formulas of the three codes: GB50010-2010, ACI318-08 and EN1992-1-1-2004, it can be seen that the punching shear capacity should include four main parts: correction coefficient, influence coefficient, concrete strength, and critical section area. Thus,

$$V_c = \gamma \eta f \mu_m h_0 \tag{2}$$

In order to solve the problem that the punching shear capacity and the longitudinal reinforcement ratio are uncorrelated in China code GB50010-2010, the punching shear capacity equation should be improved. In the code EN1992-1-1-2004, the punching shear capacity is proportional to $\rho^{1/3}$. Therefore, the fitting equation form $y = ax^b$ can be used, in which, x is reinforcement ratio, y is punching shear capacity. The fitting results are shown in Figures 5 and 6.

The fitting value of b is 0.445, the correlation coefficient is 0.659. It can be seen that the fitting correlation coefficient is close to that of the code EN1992-1-1:2004. Thus, the influence coefficient of longitudinal reinforcement ratio can be given by

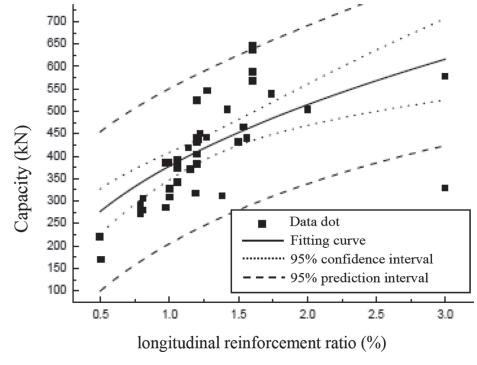

Figure 5. Fitting curve of the equation.

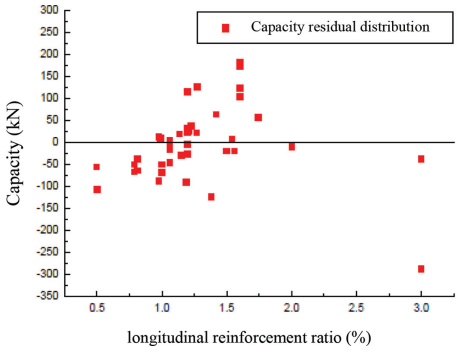

Figure 6. Residual distribution.

$$\xi = (100\rho_L)^{0.445} \tag{3}$$

In order to avoid the calculation result of ξ is less than that of the old codes, it is required that $\xi \geq 1$. Thus, the improved punching shear capacity can be written as

$$V_c = 0.7\beta_h \xi f_t \eta \mu_m h_0 \tag{4}$$

in which,

$$\eta = \min\{\eta_1, \eta_2\}, \eta_1 = 0.4 + \frac{1.2}{\beta_s}, \eta_2 = 0.5 + \frac{\alpha_s h_0}{4\mu_m} \tag{5}$$

$$\xi = \begin{cases} 1 & \rho_L \leq 0.01 \\ (100\rho_L)^{0.445} & \rho_L > 0.01 \end{cases} \tag{6}$$

5 CONCLUSIONS

In this paper, a comparison study of punching shear capacity based on GB50010-2010, ACI318-08 and EN1992-1-1-2004, is performed and an improved punching shear capacity formula is presented. By taking into account the analysis results of the reinforced concrete slab-column connections, the following conclusions can be drawn:

(1) The codes GB50010-2010 and ACI318-08 don't consider the effect of longitudinal reinforcement ratio for punching shear capacity. (2) The code EN1992-1-1-2004 considers the effect of longitudinal reinforcement ratio but doesn't consider the effect of loading area shape and perimeter-height ratio. (3) The improved punching shear capacity formula considers not only the effect of longitudinal reinforcement ratio but also the effect of loading area shape. Therefore, the improved punching shear capacity formula is closer to the fact of reinforced concrete slab-column connections.

ACKNOWLEDGMENTS

Project supported by Construction science and technology Foundation of Chongqing (Grant No. 2014-372). Project supported by the National Natural Science Foundation of China (Grant No. 51578094) and supported by the National Natural Science Foundation of China (Grant No. 51468058).

REFERENCES

Abdullah, A., Bailey, C.G. & Wu, Z.J. 2013. Tests investigating the punching shear of a column-slab connection strengthened with non-prestressed or prestressed FRP plates. *Construction and Building Materials* 48(11): 1134–1144.

Choi, K.K., Taha, M.M.R., Park, H.G. et al. 2007. Punching shear strength of interior concrete slab-column connections reinforced with steel fibers. *Cement & Concrete Composites* 29(5): 409–420.

Ministry of Housing and Urban-rural Development of the People's Republic of China. 2010. *Code for Design of Concrete Structures (GB50010–2010)*. Beijing: China Architecture & Building Press.

Park, H.G., Choi, K.K. & Chung, L. 2011. Strain-based strength model for direct punching shear of interior slab-column connections. *Engineering Structures* 33(3): 1062–1073.

Theodorakopoulos, D.D. & Swamy, R.N. 2002. Ultimate punching shear strength analysis of slab-column connections. *Cement & Concrete Composites* 24(6): 509–521.

Civil Engineering and Urban Planning IV – Liu et al. (Eds)
© 2016 Taylor & Francis Group, London, ISBN 978-1-138-02903-3

Experimental research on elastic modulus of high-performance concrete in bridges

Hong-Xiu Du, Qiao Zhang & Rui-Zhen Yan
College of Architecture and Civil Engineering, Taiyuan University of Technology, Taiyuan, Shanxi, China

Jun Yang & Li-Lang Yao
Shanxi Traffic Construction Supervision Company, Taiyuan, Shanxi, China

ABSTRACT: Based on Shanxi local raw materials, the highway project from Jixian to Hejin and the investigation for C50 HPC of the superstructure in bridges, we research the law of elastic modulus of HPC under different curing conditions with an increase in age. We establish hyperbolic function model, logarithmic function model, and exponential function model to fit the elastic modulus of HPC and the age. According to the comparative analysis, the elastic modulus of HPC at early age can reach more than 80% in 28 days; the responding value of HPC under the same curing condition is lower than the values under the standard curing condition at the same age. The hyperbolic function is recommended to characterize the elastic modulus of HPC under standard condition and the logarithmic function is recommended under the same curing condition. By using the X-ray CT image analysis technique, it is concluded that the internal porosity rate is more less, concrete structure is more compact, and elastic modulus is greater as the growth of the age.

1 INTRODUCTION

With the new building materials in excellent working performance and good durability, HPC has been widely used in the construction of traffic engineering (Gao 2015; Pan & Wu 1997). However, there are still some problems to be solved in the application of HPC in modern bridge construction, especially the superstructure. The compressive strength of HPC develops quickly at early age (Hazim et al. 2010), but the growth of the elastic modulus develops relatively slowly (Zhang et al. 2003; Feng 2007). When the elastic modulus of HPC is lower the prestressing tensioned bar will lead to the increase of the concrete creep, particularly continuous frame bridge, and large-span box girder will produce a large deformation and deflection after completing a number of years (Xiong et al. 2010), which will directly affect the use and durability of the bridge. For some projects, which have schedule restrictions and also require prestressing in 3d age or earlier age, not only the early strength of HPC needs to achieve tensile requirements, but also the early elastic modulus requires reaching the specification (Li et al. 2010).

According, to the raw materials with regional characteristics and the superstructure of the box girder bridge in Shanxi Province, we investigate the evolution law of elastic modulus at age changes under different curing conditions (Yang et al. 2010) in prestressed concrete. The expected research results can not only provide practical and reliable engineering bases for dual controlling engineering progress, ensuring construction quality, and other aspects during construction of the highway bridge superstructure, but also provide experimental data for preparing relevant specifications.

2 TEST METHOD

2.1 *Raw materials and concrete mixture ratio*

Portland P.O 42.5 cement; class I fly ash; S95 slag.

Medium sand, II area, the fineness modulus is 2.82 and the grain size is qualified.

Gravel: continuous gradation from 5 mm to 20 mm, 5–10 mm content is 30%; 10–20 mm content is 70%.

The HPC design strength is C50; the slump is from 140 to 160 mm, the mixture ratio is shown in Table 1.

Table 1. Mixture ratio of C50 (kg/m^3).

Cement	Fly ash	Slag	Sand	Gravel	Water	Water reducer
400	28	43	707	1107	165	4.71

2.2 *Specimen size and the number of specimen*

The standard prism specimen sizes are 150 mm × 150 mm × 300 mm. The elastic modulus of concrete are tested under the standard curing condition and the same curing condition is there at the age of 3d, 5d, 7d, 28d, and 56d. Three specimens are used to make static axial compression tests at each age and ten specimens are used to make elastic modulus tests.

2.3 *Index of inspection*

Test the elastic modulus at the age of 3d, 5d, 7d, 28d, and 56d of HPC.

Use X-ray CT technology to analyze the microstructure of concrete at the age of 7d and 28d.

3 TEST RESULTS AND ANALYSIS

3.1 *Data inspection and analysis*

3.1.1 *Data inspection*

The experiment measures the elastic modulus under two curing conditions at the different age. According to statistical methods, all the data are effective under the case of $T(1) \leq T(10,0.05)$ and $T(10) \leq T(10,0.05)$. All the data are also effective (Li 2010; Lin 2010) at the different ages under the case of $V(1) \leq W_C S$, $V(10) \leq W_C S$.

3.1.2 *Data analysis*

According, to the trend of the change of the elastic modulus, we selected hyperbolic function, exponential function, and logarithmic function to fit the data and obtain the regression model and the fitting curve of elastic modulus with age changes.

3.2 *The elastic modulus of HPC under different curing conditions*

The samples are maintained under standard curing condition to the stipulated age in construction site laboratory and the samples are maintained under the same curing condition with box girder structure to the stipulated age in the construction site. The elastic modulus for these samples are shown in Table 2. And the fitting results are shown in Table 3 and Figures 1 and 2.

3.3 *Comparison and analysis*

3.3.1 *The relationship between the concrete modulus and age under different curing conditions*

The test results show that the elastic modulus at the age of 3d, 5d, 7d, and 56d, respectively reach to 81.84%, 89.64%, 91.16%, and 97.35% of its 28d under the standard curing condition. Under the

Table 2. Test values of elastic modulus under different curing conditions.

	Age	Test values ($\times 10^4$ MPa)									
Standard curing condition	3d	3.77	3.98	3.73	3.77	3.81	4.02	4.11	4.16	3.89	4.16
	5d	4.26	4.3	4.1	3.99	4.3	4.14	4.22	4.14	4.03	4.3
	7d	4.47	4.51	4.47	4.65	4.61	4.38	4.3	4.3	4.61	4.38
	28d	4.7	4.88	5.07	4.62	4.83	5.22	4.54	5.17	4.83	4.79
	56d	4.75	4.74	4.81	4.84	4.64	4.71	4.81	4.64	4.71	4.71
Same curing condition	3d	3.67	4.01	3.88	3.79	3.48	3.71	3.83	3.75	3.63	3.56
	5d	3.75	4.01	4.06	3.9	3.98	4.28	4.19	4.19	4.1	4.38
	7d	4.02	4.22	4.14	3.76	3.91	4.1	4.27	3.94	4.4	4.45
	28d	4.8	4.42	4.21	4.28	4.28	4.56	4.31	4.56	4.64	4.52
	56d	4.49	4.92	5.00	4.84	4.59	4.96	4.88	4.66	4.59	4.46

Table 3. Fitting formula between concrete elastic modulus and age.

	Types	Fitting formula between elastic modulus and age	R^2	Note
Standard curing condition	Hyperbolic function	$y = 1/(0.2042 + 0.153/x)$	0.965	Recommend
	Exponential function	$y = 4.8808e^{-0.6681/x}$	0.96	
	Logarithmic function	$y = 3.7442 + 0.29\ln x$	0.8485	
Same curing condition	Hyperbolic function	$y = 1/(0.2142 + 0.1644/x)$	0.9543	
	Exponential function	$y = 4.6562e^{-0.6859/x}$	0.9422	
	Logarithmic function	$y = 3.4886 + 0.3072\ln x$	0.9603	Recommend

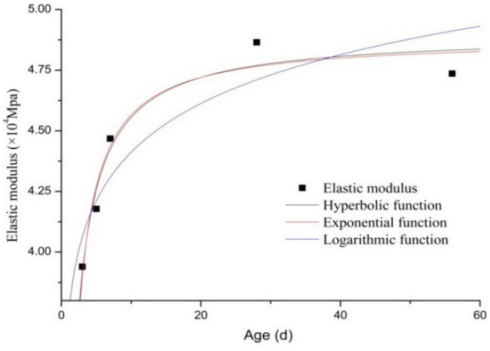

Figure 1. Fitting curve of the elastic modulus and age under the standard curing condition.

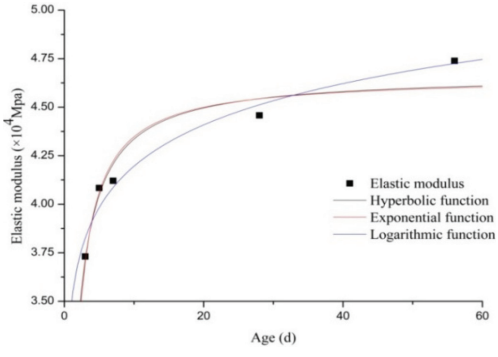

Figure 2. Fitting curve of the elastic modulus and age under the same curing condition.

same curing condition, the elastic modulus at the age of 3d, 5d, and 7d, respectively reach to 83.59%, 90.44%, and 92.08% of its 28d. No matter what the curing condition, the early age elastic modulus of HPC is higher and grows faster. The result is shown in Figure 3.

3.3.2 *The comparison analysis of concrete elastic modulus at the same age under different curing conditions*

The elastic modulus under the same curing condition is about 3% lower as compared to the values under the standard curing condition. The concrete elastic modulus are, respectively 2.25%, 3.23%, 3.13%, 4.09%, and 4.41% lower at the age of 3d, 5d, 7d, 28d, and 56d. In practical application, the elastic modulus values under the same curing condition should be 95%~97% of the values under the standard curing condition. The result is shown in Figure 4.

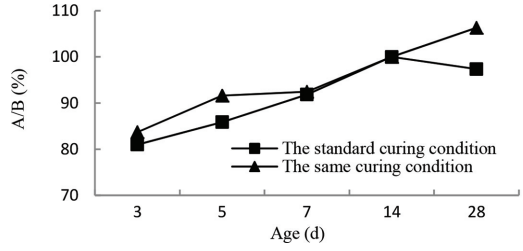

Figure 3. The relationship between elastic modulus and age under different curing conditions 28d.
* A: the test values of each age; B: the test values of 28d.

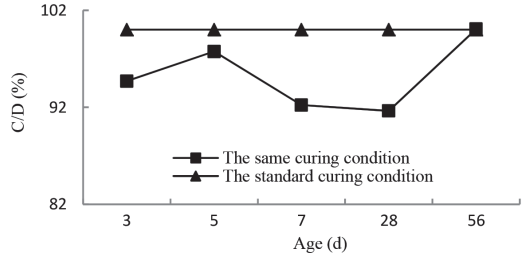

Figure 4. The relationship of elastic modulus under different curing conditions.
* C: the test values under the same curing condition; D: curing condition in the same age the test values under the standard curing condition.

3.4 *Analysis on the microstructure of concrete defects using X-ray CT*

3.4.1 *X-ray CT image analysis technique*

The core samples' size is 6 mm × 5.65 mm drilled from the specimen under the standard curing condition at the age of 7d and 28d. We use High-resolution Micro CT System to analyze its microstructure and then convert CT-scanning data into 1,500 cross-sectional 2D images. The typical layers are shown in Figure 5.

In order to describe and count defect rate accurately, we use MATLAB to process CT images by noise reduction and gray scale processing. By calculating the threshold, binary images of the different typical layers at different ages are shown in Figure 6, corresponding to the same layer in Figure 5.

3.4.2 *Analysis of concrete internal defect*

We select 3 typical layers and use IPP image analysis software. Through the theory of statistical analysis, the average concrete pore sizes of different layers are concluded at the age of 7d and 28d. The results are shown in Table 4. Binarization image can be analyzed by IPP image analysis software and the defect rate of each representative layer

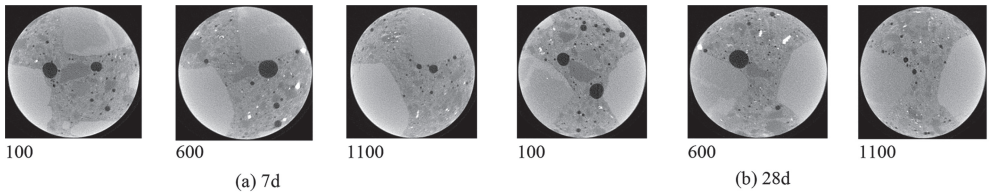

Figure 5. The 2D images of each typical layers in different ages.

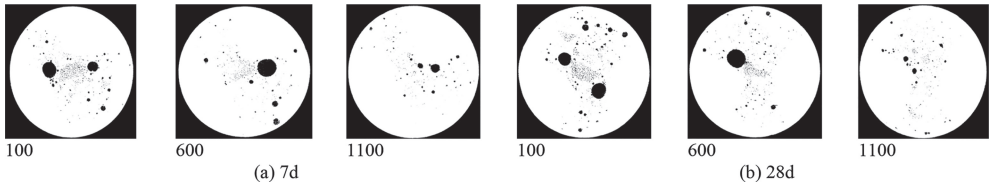

Figure 6. The binary images of different typical layers in different ages.

Table 4. Average pore size and defect rate of each representative layer.

	Pore size (μm)			Defect rate (%)		
Layer	100	600	1100	100	600	1100
7d	3.47	4.68	3.76	0.81	3.02	1.62
28d	3.67	4.20	4.03	0.58	2.92	1.60

can be obtained (Fukuda et al. 2012; Tian et al. 2012). Defect rate is expressed as $P_c = n_c/n$, where n_c indicates the set of pixels whose gray value is lower than the threshold value, n is the total number of pixels in the image. Analysis and calculation results are shown in Table 4.

From Table 4, we can see the defect rate of 28d is less than 7d, which show that the degree of cement hydration is higher with the growth of the age and the compactness of concrete is greater, the defect rate is smaller.

4 CONCLUSION

Combined with the highway engineering from Jixian to Hejin, we study the elastic modulus of C50 HPC in the bridge superstructure and conclude the conclusions as follows:

– Under the standard curing condition, logarithmic functions and exponential functions can also reflect the concrete elastic modulus variation with age, considering the practical application of convenience, hyperbolic function model is recommended.
– Under the same curing condition, logarithmic function model can reflect the concrete elastic modulus variation with age better.
– Under the standard curing condition and the same curing conditions, the HPC elastic modulus can reach more than 80% of 28d value at an early age; it even can reach more than 90% after 5d. Whatever the curing condition, the elastic modulus of HPC is higher and grows faster in an early age.
– The elastic modulus values under same curing condition are less than values under the standard curing condition.
– By contrast the microstructure and elastic modulus of concrete under the standard curing condition at the age of 7d and 28d, we can come to a conclusion as follows: as the growth of the age, internal porosity rate tend to be less, concrete structure will be more compact and elastic modulus will be greater.

ACKNOWLEDGMENT

We would like to thank and acknowledge the National Natural Science Foundation of China (51278325) and Shanxi Province Natural Science Foundation (2011011024-2) for all the financial support they provided, during this project.

REFERENCES

Feng, T.K. 2007. Experimental research on the growth of compressive elastic modulus and strength of concrete. *China High-Tech Enterprises* 11(4):158.

Fukuda, D., Nara, Y., Kobayashi, Y., et al. 2012. Investigation of self-sealing in high-strength and ultra-low-permeability concrete in water using micro-focus X-ray CT. *Cement and Concrete Research* 42(11): 1494–1500.

Gao, Y.Q. 2015. The analysis of application of high-performance concrete in road and bridge construction process. *Technology Innovation and Application* 15(4):221.

Hazim, M.D., Matthew, C.W., Mervyn, J.K. & Paul, Z. 2010. Behavior of instrumented prestressed high-performance concrete bridge girders. *Construction and Building Materials* 24(11):2294–2311.

Li, M. 2011. Application of nondestructive testing technique in pre-stressed concrete box girder of a super-large bridge based on the Grubbs criterion. *Supervision Test and Cost of Construction* 07–08(4):61–65.

Li, X.W., Zhu, Y.N. & Huang, K.C. 2010. Experimental research on elastic modulus of prestressed concrete. *Ready-Mixed Concrete* 12(3):67–70.

Lin, Y. 2010. Elimination of abnormal value in inspection lot concrete strength testing with drilled core method. *Fujian Construction Science & Technology* 28(2):25–28.

Pan, Y. & Wu, M. 1997. Application of high-properties concrete in road bridge. *Northeastern Highway* 12(3): 65–67.

Tian, W., Dang, F. & Chen, H.Q. 2012. Fractal analysis on meso-fracture of concrete based on the technique of CT image processing. *Journal of Basic Science and Engineering* 20(3):424–431.

Xiong, H.X., Sima, Y.Z. & Zhang, Y.T. 2010. Elastic modulus of prestressed concrete beam based on damage mechanics. *Engineering Mechanics* 12(27): 217–221.

Yang, C.X., Liu, H. & Huang, B.T. 2012. Influence of steam-curing on the elastic modulus of high performance concrete. *Journal of Sichuan University of Science & Engineering (Natural Science Edition)* 25(5):73–75.

Zhang, J.R., Wang, H.C. & Yang, W.J. 2003. Experimental research on compressive strength and elastic modulus of concrete in early age. *Journal of China & Foreign Highway* 23(2):89–92.

This page intentionally left blank

Civil Engineering and Urban Planning IV – Liu et al. (Eds)
© 2016 Taylor & Francis Group, London, ISBN 978-1-138-02903-3

Using Analytic Hierarchy Process to evaluate the improvement schemes of the Maoliling Tunnel based on the VISSIM simulation

Pei-Qing Wang
Taizhou Highway Administration of Zhejiang Province, Taizhou, Zhejiang, China

Zhi-Gang Lu
Department of Intelligent Transportation System, Zhejiang Scientific Research Institute of Transport, Hangzhou, Zhejiang, China

Hou-Quan Zhang
Taizhou Highway Administration of Zhejiang Province, Taizhou, Zhejiang, China

Fu-Jian Wang
College of Civil Engineering and Architecture, Zhejiang University, Hangzhou, Zhejiang, China

ABSTRACT: This paper aims to evaluate the improvement schemes of the Maoliling Tunnel in Shenhai Freeway based on VISSIM simulation results, using the Analytic Hierarchy Process (AHP) methodology. An evaluation index system, including average speed, average speed variance, emergency brake number and lane change number, is applied to analyze the merits and defects of the four improving schemes under review. The results reveal that Scheme 1, setting speed limits and deceleration zones along the tunnel, has the highest evaluation among the four schemes. The methodology introduced in this paper can enhance the feasibility of plans or measures that are difficult to rehearse in the real world, and obtain the best plan or measure among alternative choices.

1 INTRODUCTION

The Maoliling Tunnel in Shenhai Freeway (G15) is a twin 4-lane and 3,590 m-long highway tunnel section, situated in Taizhou, Zhejiang Province of China. From the Southbound Section, the forepart of the tunnel measuring 1,360 m is the continuous uphill section, followed by a continuous 2,230 m-long downhill section; the elevation of the tunnel increases from 120 m to 130 m, and then reduces to 99 m. In addition, the traffic flow of the tunnel increases annually. By the end of 2014, the Annual Average Daily Traffic (AADT) had already reached 70,425 pcu/d, where "pcu" stands for "passenger car unit". Traffic accidents occur frequently in this highway section due to the special geographical environment and traffic status, and sometimes serious or major traffic accidents also occur. A total of 543 traffic accidents have occurred from December 2004 to May 2005, which have resulted in 24 deaths. Thus, how to improve the traffic safety of this tunnel section has attracted great attention, which has been discussed to work out effective strategies by the relevant departments.

Many scholars have attempted to explore or study tunnel traffic accidents and have obtained some achievements. A study conducted by the Norwegian Public Roads Administration has indicated that the accidents rates were higher at the tunnel entrance zone than at other zones and the severity of accidents was higher in tunnels than on stretches of the road (Amundsen & Ranes 2000), the results of which are similar to those reported by Lemke (2000). Specifically in China, Ma et al. (2009) investigated the monthly and hourly distribution characteristics of four Chinese freeway tunnel traffic accidents, using data obtained from police records. Their results indicated that the zone next to 300 m inside the tunnel had highest accident and casualty rates. Jiang (2002) investigated a fire accident that occurred in the Maoliling Tunnel, and put forward some measures to prevent or reduce a similar accident.

However, the existing literature mainly focuses on the accident characteristics analysis, little on how to improve the traffic environment to reduce accident rates. Previous studies have proved that information and verbal instructions have positive effects on improving safety behavior according to the simulation results (Kinateder et al. 2013). For improving the driving environments of the Maoliling Tunnel, some measures have been put

forward, but must be verified as valid before their implementation. Thus, it is necessary and important to pre-evaluate the merits and defects of these improvement measures in the virtual environment based on the simulation reports.

In this study, we put forward four schemes to improve the traffic environment along the Maoliling Tunnel. Based on the VISSIM simulation report, we use the AHP to evaluate which scheme has the best effect, considering the following four aspects: Average Speed (AS), Average Speed Variance (ASV), Emergency Brake Number (EBN), and Lane Change Number (LCN). The traditional AHP always uses the scoring method to adjust the weighting of factors, e.g. expert scoring method. This study is the first to objectively evaluate the merits and defects of improvement measures in the virtual environment, which would enhance the feasibility of these measures and reduce costs in the real world.

2 METHODOLOGY

2.1 *Analytic Hierarchy Process (AHP)*

AHP, proposed by Saaty (1990), is a decision-making technique with multi-criteria. It is a systematic, concise and practical method with the advantages of combining the qualitative and quantitative analysis. The main idea of the AHP is to convert a complicated problem to a recursion order hierarchy structure, and then to sort the different choices by the evaluation and judgment using a certain criterion.

The modeling process of the AHP can be divided into the following six steps:

- Defining the problem and determining the goal.
- Modeling hierarchical structure: this step is to analyze the factors that are related to the decision problem, and it is vital to find the relationships among the factors; grouping the factors into different hierarchies from the top (the target) through the intermediate levels (criteria) to the lowest level (solution).
- Establishing judgment matrices of each hierarchy: identify the priorities among all elements by making pairwise comparisons of elements based on a certain criterion of the previous hierarchy; use the comparison scale to quantify the priorities; and then formulate the judgment matrix for different hierarchies. The comparison scale is presented in Table 1.
- Exploring the priorities of each criterion among all solutions: synthesize the above judgments about all solutions for each criterion to yield a set of overall priorities for each hierarchy.
- Checking the consistency of the judgments: in this step, it needs to test whether the deviation of judgment matrices is acceptable; the judgment matrix is valid when the consistency is acceptable, otherwise the judgment matrix should be revised (Awasthi & Chauhan 2011).

Table 1. Comparison scale for AHP preferences.

Numerical Rating	Verbal judgment of preferences
1	Equally important
3	The former factor is slightly more important than the latter
5	The former factor is more important than the latter obviously
7	The former factor is more important than the latter strongly
9	The former factor is more important than the latter extremely
2, 4, 6, 8	In the middle of the above two adjacent judgment scales
Reciprocals	The latter factor is more important than the former

The consistency is determined by using the eigenvalue $\lambda_{\max}$ to calculate the consistency index CI, which can be calculated as given in Equation (1), where n is the matrix size. Judgment consistency can be checked by checking the value of the consistency ratio CR, which can be calculated as in Equation (2), where RI is the average random consistency. Table 2 lists the appropriate matrix value of RI. When the CR is no more than 0.1, the result of the judgment matrix is acceptable. Otherwise, the judgment matrix is inconsistent, and it should be revised and improved:

$$CI = (\lambda_{max} - n)/(n-1) \quad (1)$$

$$CR = CI/RI \quad (2)$$

- In the end, a final decision is made based on the results of the above processes.

2.2 *AHP for improvement scheme evaluation*

The AHP is most useful where teams of people are working on a complex problem, especially it has unique advantages when important elements of the decision are difficult to quantify or compare, or when the communication among team members is impeded by their different specializations, terminologies or perspectives (Bhushan & Rai 2004). The AHP methodology can be applied to these decision situations (Forman & Gass 2001):

- Choice: the selection of one alternative from a given set of alternatives, usually when multiple decision criteria are involved.

Table 2. Average random consistency (*RI*).

Order of matrix	1	2	3	4	5	6
RI	0	0	0.52	0.89	1.11	1.25

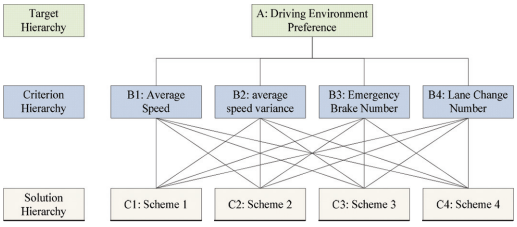

Figure 1. The AHP structure for improvement schemes.

– Ranking: putting a set of alternatives in order from most to least desirable.
– Prioritization: determining the relative merit of members of a set of alternatives, as opposed to selecting a single one or merely ranking them.

The target of this paper is to rank the four schemes and choose the best scheme; thus, the AHP is the appropriate and applied in this paper to reach this target. There are a total of three hierarchies in the AHP, namely target hierarchy, criterion hierarchy and solution hierarchy. As stated above, this paper focuses on the evaluation of improvement schemes that optimize the driving environments of the Maoliling Tunnel. Therefore, the three hierarchies of the structure in this paper can be described as follows: the driving environment preference is set as the target hierarchy; the four evaluation indices, including average speed, average speed variance, emergency brake number and lane change number, are set as the criterion hierarchy; the solution hierarchy includes the improvement schemes awaiting evaluation. With the three hierarchies, the AHP model of travel mode evaluation can be formulated, as shown in Figure 1.

2.3 *Improvement schemes and VISSIM simulation results of the four evaluation indices*

According to the official design material of the Maoliling Tunnel and the detected traffic data provided by the operation and management department, we simulated the actual traffic environment of the tunnel section using the simulation software VISSIM. VISSIM is a microscopic, time step- and behavior-based simulation model developed to analyze the full range of functionally classified roadways and public transportation operations. The related parameter settings, including road sections, Vehicle Composition and Proportion (VCP), Traffic Volume (TV) and Desired Speed (DS), are presented in Table 3, where "HGV" stands for "Heavy Goods Vehicle". The road sections include Northbound Section (NS) and Southbound Section (SS), and each section has three subsections.

Table 3. The actual situation simulation setting.

Parameters	
NS	
Length (m)	1: 200; 2: 1160; 3: 2210
Slope (%)	1: 2.5; 2: 5; 3: –1.5
Height (m)	1: from 121.34 to 124; 2: from 124 to 130; 3: from 130 to 98.87
SS	
Length (m)	1: 225; 2: 1160; 3: 2195
Slope (%)	1: –2.5; 2: –5; 3: 1.5
Height (m)	1: from 121.34 to 124; 2: from 124 to 130; 3: from 130 to 98.87
VCP (%)	
Car	60.3
Bus	10.3
HGV	28.8
TV (pcu/h)	
Northbound	3928
Southbound	3928
DS (km/h)	
Car	90–125
Bus	77–110
HGV	55–90

Table 4. The improvement schemes and measures.

Improvements	Measures
Scheme 1	Speed limit: car and bus less than 80 km/h; HGV less than 70 km/h; Deceleration zone 1: 100 m before the Tunnel, deceleration = –2 m/s^2; Deceleration zone 2: the first 50 m of the downhill section, deceleration = –2 m/s^2; Deceleration zone 3: the intermediate 50m of the downhill section, deceleration = –2 m/s^2.
Scheme 2	Speed limit: car and bus less than 80 km/h; HGV less than 70 km/h.
Scheme 3	Speed limit: car and bus less than 80 km/h; HGV less than 70 km/h; Lane restriction: HGV only outside lane permission
Scheme 4	Lane restriction: HGV only outside lane permission

Table 5. Simulation results.

Simulations	AS	ASV	EBN	LCN
Actual situation	69.33	236.202	165378	21222
Scheme 1	59.63	63.904	148752	10208
Scheme 2	58.34	88.166	311624	20605
Scheme 3	59.58	102.989	295517	15929
Scheme 4	72.49	416.802	297319	33861

In order to improve the traffic environments, we carried out four improvement schemes and the measures in detail, as summarized in Table 4. At the situation of each scheme, we collected 900-second simulation data of the four criterions. The simulation results of each scheme were saved in a "*.fzp" type file by setting the "Vehicle Record" of the "VISSIM-Evaluation-Files". We wrote a C# program for the statistical analysis of the data and obtained the final criterion results of each scheme. The final simulation results of the four schemes are summarized in Table 5. Here, AS, ASV, EBN and LCN represent the average speed, the average speed variance, the vehicles' emergency brake number and the vehicles' lane change number of the Maoliling Tunnel, respectively.

3 AHP DEVELOPMENT

3.1 *Evaluation from building of travel mode*

Previous researchers have proved that a speed limit decrease generally induces a decrease in the number of road injuries and fatality accidents (De Pauw et al. 2014). The accident reports of the Maoliling Tunnel provided by the police department also verify that the excessive speed or speed variance is the main factor causing an accident. Thus, to build the evaluation form, we score each criterion of each improvement scheme by using the actual situation simulation results dividing the improvement scheme simulation results. The evaluation form of each improvement scheme is given in Table 6.

3.2 *Judgment matrix and solutions of hierarchical single sorting*

By a pairwise comparison of the weight sets of evaluation criteria over each improvement scheme, the judgment matrix A-B, i.e. target hierarchy to criterion hierarchy, can be established. Similarly, by a pairwise comparison of the evaluation form of the improvement scheme over each evaluation criterion, we can obtain judgment matrices B1-C to B4-C by using the criterion of Scheme i (i = 1, 2, 3, 4) dividing criterion of Scheme j (j = 1, 2, 3, 4), i.e. criterion hierarchy to solution hierarchy. In this paper, a specialized AHP software YAAHP is applied to calculate the maximum eigenvalue and eigenvector of the judgment matrices.

After normalization, the eigenvectors (relative weight) of each judgment matrix are represented in Equation (3). Moreover, all the consistency ratio CR values are less than 0.1. Therefore, the results of judgment matrices are acceptable.

$$\begin{aligned}
&Judgment\ Matrix\ A \to B \\
&\quad = [0.0882, 0.2720, 0.4829, 0.1570]^T \\
&Judgment\ Matrix\ B1 \to C \\
&\quad = [0.2593, 0.2668, 0.2593, 0.2146]^T \\
&Judgment\ Matrix\ B2 \to C \\
&\quad = [0.4006, 0.2900, 0.2477, 0.0617]^T \\
&Judgment\ Matrix\ B3 \to C \\
&\quad = [0.4018, 0.1925, 0.2028, 0.2028]^T \\
&Judgment\ Matrix\ B4 \to C \\
&\quad = [0.4100, 0.2027, 0.2629, 0.1244]^T
\end{aligned} \tag{3}$$

From our point of view, compared with AV, reducing EBN is the most important target to improve the travel environments, followed by AVS and LCN. The pairwise comparison results are summarized in Table 7.

From Table 8, it can be found that Scheme 2 is the most competitive at the average speed, with an absolute advantage of 0.2668, compared with the

Table 6. Evaluation form of each improvement scheme.

Simulations	AS	ASV	EBN	LCN
Scheme 1	1.16	3.70	1.11	2.08
Scheme 2	1.19	2.68	0.53	1.03
Scheme 3	1.16	2.29	0.56	1.33
Scheme 4	0.96	0.57	0.56	0.63

Table 7. Judgment matrix A-B.

A	B1	B2	B3	B4	Value of single sort
B1	1	1/3	1/5	1/2	0.0905
B2	3	1	1/2	2	0.2890
B3	5	2	1	1	***0.3945***
B4	2	1/2	1	1	0.2260

Table 8. Judgment matrix B1-C.

B1	C1	C2	C3	C4	Value of single sort
C1	1.00	0.97	1.00	1.21	0.2593
C2	1.03	1.00	1.03	1.24	***0.2668***
C3	1.00	0.97	1.00	1.21	0.2593
C4	0.83	0.81	0.83	1.00	0.2146

Table 9. Judgment matrix B2-C.

B2	C1	C2	C3	C4	Value of single sort
C1	1.00	1.38	1.62	6.49	***0.4006***
C2	0.72	1.00	1.17	4.7	0.2900
C3	0.62	0.85	1.00	4.02	0.2477
C4	0.15	0.21	0.25	1.00	0.0617

Table 10. Judgment matrix B3-C.

B3	C1	C2	C3	C4	Value of single sort
C1	1.00	2.09	1.98	1.98	***0.4018***
C2	0.48	1.00	0.95	0.95	0.1925
C3	0.51	1.05	1.00	1.00	0.2028
C4	0.51	1.05	1.00	1.00	0.2028

Table 11. Judgment matrix B4-C.

B4	C1	C2	C3	C4	Value of single sort
C1	1.00	2.02	1.56	3.30	***0.4100***
C2	0.50	1.00	0.77	1.63	0.2027
C3	0.64	1.30	1.00	2.11	0.2629
C4	0.30	0.61	0.47	1.00	0.1244

other three schemes. Scheme 1 and Scheme 3 have the same value of single sort, which is the second competitive.

From Table 9, it can be found that Scheme 1 has the highest evaluation on average speed variance. In other words, Scheme 1 can reduce the vehicle speed variance to the utmost extent compared with the other three schemes.

According to Table 10, Scheme 1 has an obvious advantage on reducing the emergency break number. In other words, the improving measures provided by Scheme 1 have a great effect on optimizing the driving behaviors.

From Table 11, it can be found that Scheme 1 is the most competitive in reducing the lane change number, with the highest score of 0.4100.

4 AHP RESULTS

Based on the above calculations, the eigenvectors of judgment matrixes B1-C to B4-C could be made up into a new matrix of the whole four travel modes, to calculate the weight of criteria at different travel modes, and thus we could get the result of the comprehensive evaluation on the improvement schemes based on the simulation results, which is summarized in Table 12.

Table 12. Comprehensive evaluation result.

	B				
C	B1	B2	B3	B4	Order of 4 Schemes
	0.0905	0.2890	***0.3945***	0.2260	
C1	0.2593	***0.4006***	***0.4018***	***0.41***	***0.3904***
C2	***0.2668***	0.29	0.1925	0.2027	0.2272
C3	0.2593	0.2477	0.2028	0.2629	0.2345
C4	0.2146	0.0617	0.2028	0.1244	0.1454

From the results of Table 12, it could be found that Scheme 1 (0.3904) has the highest evaluation among the four improvement schemes, followed by Scheme 3 (0.2345), Scheme 2 (0.2272) and Scheme 4 (0.1454). It indicates that the measures included in Scheme 1 are the most effective among the four schemes.

5 CONCLUSIONS

The Maoliling Tunnel is an accident-prone highway section, and the increasing traffic flow makes the travel environments more serious along this section. In this study, we put forward four schemes to improve the traffic environments along the Maoliling Tunnel and use the VISSIM software to simulate the operating effects of the four schemes. The AHP methodology is used to analyze and evaluate the merits and defects of the four schemes comprehensively.

The findings reveals that in the evaluation of improving the driving environments, emergency brake number is obviously the most important factor, followed by the average speed variance. Moreover, measures of Scheme 1 have the highest evaluation on reducing the average speed of the vehicles, decreasing the emergency brake number of the vehicles and the lane change number of the vehicles. The measures of Scheme 2 have the biggest effect on reducing the average speed of the vehicles.

In summary, this paper applies the AHP to evaluate the merits and defects of improvement measures in the virtual environment, which aims to improve the driving environments of the Maoliling Tunnel. It certifies that the methodology introduced in this paper can enhance the feasibility of plans or measures that are difficult to rehearse in the real world, and obtain the best plan or measure among alternative choices.

ACKNOWLEDGMENTS

This work was financially supported by a grant from the Department of Transportation in Zhejiang

Province (Grant No. 2014H55) on the research of present situation and development direction of Taizhou highway network based on spatial and temporal characteristics of traffic volume.

REFERENCES

Amundsen, F.H. & Ranes, G. 2000. Studies on traffic accidents in Norwegian road tunnels. *Tunneling and Underground Space Technology* 15(1): 3–11.

Awasthi, A. & Chauhan, S.S. 2011. Using AHP and Dempster–Shafer theory for evaluating sustainable transport solutions. *Environmental Modelling & Software* 26(6): 787–796.

Bhushan, N. & Rai, K. 2004. *Strategic Decision Making: Applying the Analytic Hierarchy Process*. London: Springer-Verlag London Limited.

De Pauw, E., Daniels, S., Thierie, M. & Brijs, T. 2014. Safety effects of reducing the speed limit from 90 km/h to 70 km/h. *Accident Analysis and Prevention* 62: 426–431.

Forman, E.H. & Gass, S.I. 2001. The analytic hierarchy process—an exposition. *Operations Research* 49(4): 469–486.

Jiang, S.P. 2002. Investigation on and lesson from the fire in maoliling tunnel. *Underground Space (in Chinese)* 22(2): 172–172.

Kinateder, M., Pauli, P., Müller, M., et al. 2013. Human behaiour in severe tunnel accidents: Effects of information and behaioural training. *Transportation Research Part F: Traffic Psychology and Behaviour* 17: 20–32.

Lemke, K. 2000. Road safety in tunnels. *Transportation Research Record: Journal of the Transportation Research Board* (1740): 170–174.

Ma, Z.L., Shao, C.F. & Zhang, S.R. 2009. Characteristics of traffic accidents in Chinese freeway tunnels. *Tunneling and Underground Space Technology* 24(3): 350–355.

Saaty, T.L. 1990. How to make a decision: The analytic hierarchy process. *European Journal of Operational Research* 48(1): 9–26.

Civil Engineering and Urban Planning IV – Liu et al. (Eds)
© 2016 Taylor & Francis Group, London, ISBN 978-1-138-02903-3

Application of ambient vibration tests on an existing school building to evaluate the effectiveness of retrofitting

Liang Li, Takaaki Ohkubo & Atsushi Teramoto
Hiroshima University, Hiroshima, Japan

Shinya Matsumoto
Kinki University, Hiroshima, Japan

ABSTRACT: The vibration characteristics of structures have been considered to be one of the important evaluation indices to clarify the seismic performance. This paper presented the results that were obtained from the ambient vibration of an existing school building before and after measurements of seismic retrofitting using a wireless measurement system. Results and comparisons between the modal parameters, natural periods and displacements obtained by the before and after measurements of seismic retrofitting demonstrated that the measurement and data processing techniques used are valid for evaluating the seismic retrofitting works. Furthermore, to improve the reliability of this approach, a comparison of story rigidity between the measurement results and design documents was conducted. It is shown that this technique has high accuracy and usefulness.

1 INTRODUCTION

Improving the earthquake resistance of existing buildings is an international task because of the frequent occurrence of earthquakes. As an earthquake-prone country, Japan strived to establish regulations and promote researches for improving earthquake resistance because lots of buildings had been built since the high economic growth period. In Japan, seismic capacity is mainly calculated based on "Seismic Evaluation and Retrofit" established by The Japan Building Disaster Prevention Association (2001). However, in many countries, for example Sudan, buildings are designed and constructed without any seismic load consideration (Hassaballa et al. 2014). Therefore, it is necessary to establish an objective method and apparatus for diagnosing the safety of buildings.

Dynamic identification, a technique increasingly used in existing buildings and studies about the vibration characteristics, has been conducted energetically, for example, used in traditional timber buildings (Takahashi et al. 2009) and reinforced school buildings (Davide et al. 2014). Due to the development of sensing technical fields, the convenience of wireless measurement has been pointed out (Li et al. 2014).

To identify and evaluate the seismic properties, many ambient and forced vibration tests on before and after measurements of retrofitting works have been reported in the literature (Celebi et al. 1998; Taleb et al. 2012), but the safety precautions of the forced vibrations were also pointed out. Therefore, it is important to clarify the method to apply vibration tests and data processing techniques to evaluate buildings. The purpose of this study is to propose a simple and effective method for evaluating the effectiveness of seismic retrofitting based on vibration characteristics, and in this paper ambient vibration tests, namely before and after measurements of seismic retrofitting were conducted on an existing school building. It is shown that the dynamic behavior such as natural periods and mode shapes of the building can be effectively represented. By comparing the results from before and after measurements of the retrofitting works, the effectiveness of seismic retrofitting can be verified.

2 DESCRIPTION OF THE EXPERIMENT

2.1 *Test equipment and measurement methodology*

The wireless acceleration measurement system used in ambient vibration tests was developed by Hiroshima University and a private enterprise. Figure 1 shows the measurement system. It is composed of commercial servo-type acceleration sensors and wireless transmitting units which

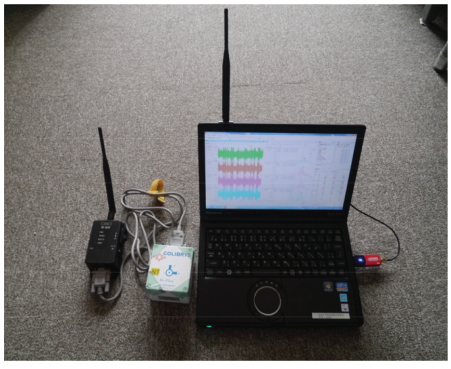

Figure 1. Image of the wireless measurement system.

were developed. The accelerometers have a wide frequency and acceleration range (DC to 1000 Hz and ±3 g, respectively) and the wireless signal units provide signal conditioning, 24-bit A/D conversion, and time synchronization of multiple sensors (maximum 7).

2.2 *Analysis method*

In the two ambient vibration tests on before and after measurements of the seismic retrofitting, 5 minutes of data with a 100 Hz sampling frequency were recorded and a direct current acceleration input was used. To perform Fourier spectrum analysis, the simple average of 20.48 seconds of data was taken from the measurement data. In addition, to obtain deformation of each story, data of acceleration was integrated twice. In addition, an explanation of this wireless measurement system and evaluation method to confirm the effectiveness of seismic retrofitting qualitatively and quantitatively has been proposed (Li et al. 2015).

2.3 *Description of the building and the seismic retrofitting*

The existing school building is sited in Hiroshima, which is located in the south, central area of the Chugoku region of Japan. The earthquake resistant performance of school buildings has been demand strictly as disaster prevention centers in Japan. Moreover, a national project was initiated in 2006 to reduce the seismic risk in existing school buildings (Oscar et al. 2014). Therefore, it is important to grasp the vibration characteristics data of school buildings. The building was constructed before 1980; according to Japanese law, it is an inadequate building. It is a three-story, nearly rectangular, reinforced concrete building, with one of its dimensions being considerably longer than the other one (54 m × 10 m). Under the ground floor, the building has an irregular shape consisting of a basement and oblique beams only in one section. The longitudinal direction consists of a pure rigid frame structure; the transversal direction is equipped with an earthquake-resisting wall structure. A schematic view and seismic retrofitting of the school building is shown in Figure 2.

The seismic retrofitting construction was carried out in 2013 in order to satisfy the target value of aseismic performance. In the longitudinal direction, additional framed steel braces were built in order to increase strength. Also, structural slits were constructed in the staircases in order to improve the ductility of their columns. In the transversal direction, additional earthquake resistant walls were constructed in the first floor. To improve the transmission efficiency of seismic force in the transversal direction when an earthquake occurs, additional slabs were built due to the large opening of slabs in the staircases, as shown in Figure 2. Figure 3 shows the details of the framed steel brace and removal of the existing wall.

In this experiment, ambient vibration tests, namely the before and after measurements of the seismic retrofitting at 2012 were applied to this

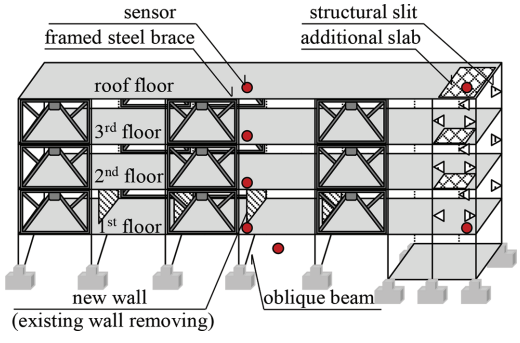

Figure 2. Image of the building and summary of the seismic retrofitting.

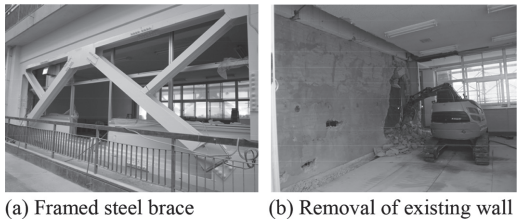

(a) Framed steel brace (b) Removal of existing wall

Figure 3. View of the details of the seismic retrofitting.

school building. In order to obtain the vibration characteristics and confirm the effectiveness of the seismic retrofitting works, acceleration sensors were placed in the central part and the staircase, as shown in Figure 2.

3 RESULTS OF THE VIBRATION TESTS

3.1 *Changes of vibration characteristics*

Chrysostomou et al. (2013) conducted in-situ measurements using a wireless monitoring system and compared the results of the mathematical models to discuss the feasibility for establishing the changes before and after data of retrofitting and the health monitoring of school buildings. It is considered that it is important to develop a measurement system and evaluation methodology for grasping the changes of the dynamic characteristics. Many studies have proposed to pay attention to the natural periods to evaluate the retrofitting effect (Muraoka et al. 2005). Moreover, the importance of soil-structure interaction and changes of each story should be considered.

In this study, to separate the vibration characteristics of each story, transfer functions of each story were analyzed by inputting a lower story and outputting upper stories. The natural periods obtained from the transfer functions were the removing of the lower story then the inputting of the story in the soil-structure interaction system, in other words, only the upper stories of the building were extracted. A comparative presentation of the natural periods is given in Table 1. The comparison between natural periods given by ambient vibration tests shows that they become shorter by about 90% in the longitudinal direction and the first story in transversal direction. Therefore, the increase of rigidity by the reinforcement can be confirmed.

Table 1. Natural periods of the building before and after the seismic retrofitting.

Direction	Story	Natural periods (sec)		Rate of change*
		Before	After	
Longitudinal	3rd	0.125	0.110	88.0%
	2nd	0.196	0.174	88.0%
	1st	0.293	0.269	91.8%
Transversal	3rd	0.070	0.070	100.0%
	2nd	0.097	0.095	97.9%
	1st	0.108	0.095	88.0%

*Rate of change = Natural period (After)/(Before).

The first vibration-mode shapes obtained from the ambient vibration tests on before and after measurements of the seismic retrofitting are shown in Figure 4. Natural periods of the whole building, as shown in Table 1, are regarded as 0.293 and 0.269 seconds in the longitudinal direction, 0.108 and 0.095 seconds in the transversal direction at before and after retrofitting, respectively. Figure 4 shows that the response magnifications in both directions after the seismic retrofitting are smaller than before. Particularly, the change in the longitudinal direction became larger. On the contrary, there were almost no changes in the transversal direction other than the roof floor. It shows that the effect of increasing the strength by using many framed steel braces in the longitudinal direction has been improved dramatically. The removing of existing walls and constructing new earthquake-resistant walls on the first floor in the transversal direction cannot reduce the vibration response; however, the effect in the upper stories can be expected.

3.2 *Evaluation of story rigidity*

It is considered that story rigidity as an index value has been recognized broadly and used frequently. Several methods for evaluating story rigidity have been proposed by using microtremor measurements. For example, assuming that the building is a shear deformation model so that the story rigidity can be calculated by inverse eigenvalue analysis based on natural periods and the mass of the building (Sakuma et al. 2011). In this study, to evaluate the seismic effect quantitatively, the story rigidity of the school building was calculated based on acceleration and deformation obtained from the vibration tests.

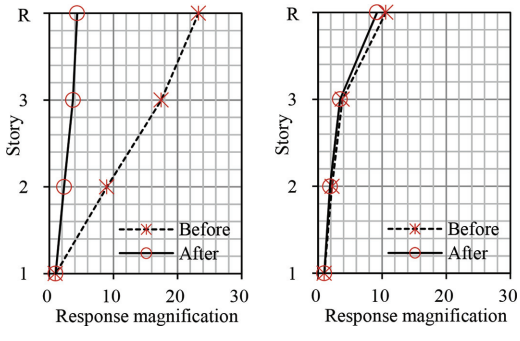

Figure 4. The first vibration-mode shape obtained from the vibration tests (Left: longitudinal direction; Right: transversal direction).

A stable waveform of 20 seconds was extracted, and then the absolute value of acceleration and displacement averaged to obtain the relationship between power and displacement. The interlayer deformation was calculated by the displacement of the upper and lower stories and the force was calculated using the acceleration obtained from the measurement and mass based on the design documents. Figure 5 shows the comparison of change rates in story rigidity at before and after measurements of the seismic retrofitting between the design documents and ambient vibration results. Due to the influence of secondary members and infinitesimal deformation of ambient vibration, the true values of the story rigidity obtained from the vibration tests have some variations with design documents. Therefore, the change rate of story rigidity in Figure 5 was proposed to evaluate the seismic effect. In the longitudinal direction, the deviation of change rate between measurement results and design documents is less than 10%. Similar results were obtained in the longitudinal direction that the retrofitting effect using framed steel braces can be confirmed even though the rigidity of steel brace is small (Abe et al. 2003). However, in the transversal direction, the results obtained from the vibration tests are 1.1 to 1.4 times larger than the design documents. Although a part of the school building is four stories, it is designed as a three-story building for seismic property diagnosis. Furthermore, the calculation method for the walls in the transversal direction of the one-sided corridor-type school building is difficult and the shearing rigidity lowering rate of the new wall should be considered. Mori et al. (2003) have proposed that the increased rate of rigidity of the new wall obtained from ambient vibration is about 50% of the calculated value. On the other hand, in both directions the trends of change rates of story rigidity between the ambient vibration tests and design documents look the same.

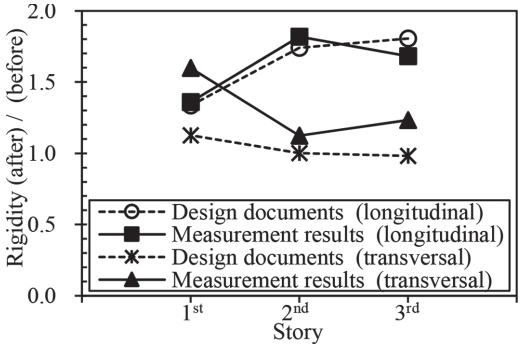

Figure 5. Story rigidity change rate before and after the seismic retrofitting.

4 CONCLUSIONS

This paper presents the results from the vibration tests performed on an existing school building at before and after measurements of seismic retrofitting using a wireless measurement system. Despite the fact that some discrepancies in story rigidity have generated between the estimates and designed values, the reliability of the method for grasping vibration characteristics and evaluating the retrofitting effect of buildings, qualitatively and quantitatively, has been better verified.

A clear decrease of the natural periods was observed only in the stories that had been reinforced. Natural periods of each story were obtained by separating the upper stories. The change rates of the natural periods of each story in the longitudinal direction were almost the same due to the same number of framed steel braces were constructed for each story. Similarly, the reduction of vibration response was observed, though the change in the transversal direction was extremely small.

Story rigidity was estimated based on the data of acceleration and displacement obtained from the vibration tests. The method that focuses on the change rate of story rigidity was considered valid for evaluating the effect of seismic retrofitting. However, the evaluation methods for the newly reinforced concrete walls in aseismic repair designs should be discussed. To improve the accuracy of this evaluation method, more buildings will be measured and more structure analysis methods should be implemented.

REFERENCES

Abe, Y., Mori, K. & Sato, S. 2003. Case Study on Verification of Earthquake Resistant Reinforcement by Microtremor Measurement: Part 3. Two Cases of Side Corridor Type School Building Reinforced by Steel Braces. *AIJ Tohoku Chapter Architectural Meeting, Tokai, Japan, 30 July 2003*. Tokyo, Japan: AIJ Press.

Celebi, M. & Liu, H.P. 1998. Before and after retrofit-response of a building during ambient and strong motions. *Journal of Wind Engineering and Industrial Aerodynamics* 77–78: 259–268.

Chrysostomou, C.Z. et al. 2013. Seismic retrofitting and health monitoring of school buildings of Cyprus. *The Open Construction and Building Technology Journal* 7(1): 208–220.

Davide, R., Fabrizio, G., Alessandro, B. & Luigino, D. 2014. Ambient Vibration Tests on a Reinforced Concrete School Building before and after Retrofitting Works with External Steel "Dissipative Towers". *Proceedings of the 9th International Conference on Structural Dynamics, EURODYN 2014, Porto, Portugal, Rome, 30 June–2 July 2014*. Germany: Department of Civil and Environmental Engineering.

Hassaballa, A.E., Ismaeil, M.A. & Adam, F.M. 2014. Seismic evaluation and retrofitting of existing hospital building in the Sudan. *Open Journal of Civil Engineering* 4(2): 159–172.

Li, L., Ohkubo, T., Matsumoto, S. & Miyamoto, A. 2014. The Application and Effectiveness of Vibration Measurement System Using a Wireless Acceleration Sensor to the Superannuated Bridge. *Proceeding of the Japan Concrete Institute, Takamatsu, Japan, 9–11 July 2014*. Tokyo, Japan: JCI Press.

Li, L., et al. 2015. An Empirical Study on the Effectiveness of Seismic Retrofitting Based on Wireless Microtremor Measurement. *International Conference on the Regeneration and Conservation of Concrete Structures, Nagasaki, Japan, 1–3 June 2015*. Tokyo, Japan: JCI Press.

Mori, K., Abe, Y. & Sato, S. 2003. Case Study on Verification of Earthquake Resistant Reinforcement by Microtremor Measurement: Part 5. Three Cases of School Building Reinforced by RC Walls. *AIJ Tohoku Chapter Architectural Meeting, Tokai, Japan, 30 July 2003*. Tokyo, Japan: AIJ Press.

Muraoka, N. et al. 2005. Evaluation of the Effects of Seismic Retrofit for Reinforced Concrete School Building Using Microtremor Observation. *The 1st International Conference on Urban Disaster Reduction, Kobe, Japan, 18–21 January 2005*. Tokyo, Japan: ISSS Press.

Oscar, A. & Yamazaki, F. 2014. Seismic Evaluation and Retrofitting of School Building in Venezuela. *The 14th World Conference on Earthquake Engineering, Beijing, China, 12–17 October 2014*. Kanpur: NICEE.

Sakuma, R. et al. 2011. Case Study on Estimation of Seismic Retrofit Performance by Microtremor Measurement. *AIJ Tohoku Chapter Architectural Meeting, Akita, Japan, 25–26 June 2011*. Tokyo, Japan: AIJ Press.

Takahashi, A., Fukumoto, M. & Kohara, K. 2009. A Study on Vibration Performances of Japanese Traditional Timber Buildings Based on Microtremor Measurements. *Protection of Historical Buildings, Prohitech 09, Rome, 21–24 June 2009*. Boca Raton, USA: CRC Press.

Taleb, R. et al. 2012. Use of Ambient and Forced Vibration Tests to Evaluate Seismic Properties of an Unreinforced Masonry Building Rehabilitated by Dampers. *15th World Conference on Earthquake Engineering, Lisboa, 24–28 September 2012*. Kanpur: NICEE.

The Japan Building Disaster Prevention Association. 2001. *Seismic Evaluation and Retrofit*. Japan: The Japan Building Disaster Prevention Association.

This page intentionally left blank

Civil Engineering and Urban Planning IV – Liu et al. (Eds)
© 2016 Taylor & Francis Group, London, ISBN 978-1-138-02903-3

Desertification risk assessment based on GIS in the Loess Plateau, China

Jian-Xiang Zhang & Wan-Feng Liu
College of Civil Engineering and Key Disciplines of Geotechnical Engineering, Longdong University, Qingyang, Gansu, China
Provincial Key Laboratory of Loess Engineering Properties and Applications in Gansu Province Universities, Qingyang, Gansu, China

Duo-Yong Zhang
Research Center of Desertification Control, Longdong University, Qingyang, Gansu, China

Jia-Xing Pang
School of Resources and Environmental Sciences, Lanzhou University, Lanzhou, Gansu, China

Dong Wang, Yun Wang & Xu-Sheng Li
College of Civil Engineering and Key Disciplines of Geotechnical Engineering, Longdong University, Qingyang, Gansu, China

ABSTRACT: Desertification is one of the most significant global environmental threat to human survival and development. We conducted a research in ecologically fragile areas of the Loess Plateau in China, and obtained the research data from historical research, remote sensing, field research and other ways. Soil, vegetation, land use and management, and other socio-economic data were used to set up the desertification risk assessment model. The results indicated that the ESAI model made a good description of the spatial distribution pattern of the desertification risk in the Loess Plateau, and the human activities broke the long-term stability conditions of the natural ecosystem to some degree. It has reference and guiding significance for the desertification control, and provides the necessary decision support for the local government.

1 INTRODUCTION

Desertification was formally adopted as an ecological problem and recognized by the world from the United Nations Conference on Desertification (UNCD) in 1977. The United Nations Environment Programme (UNEP) convened the 8th meeting advisor desertification control in Geneva in 1991. The meeting made a comprehensive study to combat desertification all over the world. In recent years, the main aim has been to study the evolution of desertification, desertification drive mechanism, detection and assessment of desertification and the establishment of the index system and other aspects. At the same time, the geographic information system technology is widely used in the study of desertification (Ladisa et al. 2012; Paolo D'Odorico et al. 2013) and by the majority of other Italian scholars. Desertification is one of the most serious environmental problems in China, and the Loess Plateau is the typical fragile ecological environment area. In order to set up the desertification risk assessment system (Environmental Sensitive Areas index, ESAI), we integrated bio-physical data with environmental quality factors (Coscarelli et al. 2005; Ladisa et al. 2012).

2 MATERIALS AND METHODS

2.1 *Study area*

The Loess Plateau is situated in the middle reaches of the Yellow River basin in northern China and covers a surface area of approximately 622,600 km^2 (Fig. 1).

The plateau lies between 33°43′–41°08′ E and 100°52′–114°34′ N, extending to the Taihang Mountains in the east, Riyue Mountains and Wushaoling in the west, the Great wall in the north, and the Qinling Mountains in the south, with an average elevation ranging between 1500 and 2000 m above sea level (The Integrated Survey Team of Chinese Academy of Sciences (CAS) of the Loess Plateau 1992; Zhao et al. 2014). The Loess Plateau has a typical continental monsoon climate: dry and cold in winter; hot and humid

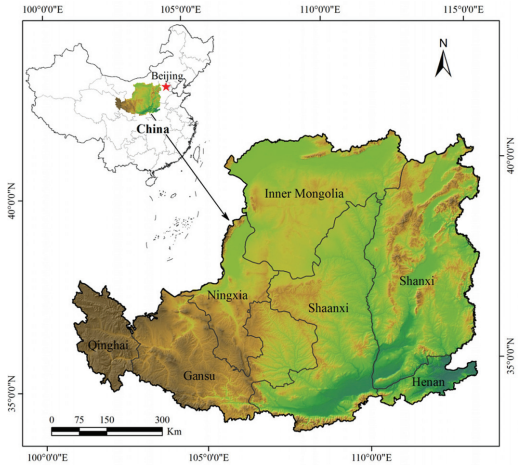

Figure 1. Loess plateau region and its seven provinces.

in summer. The average annual temperature ranges from 4.3°C in the northwest to 14.3°C in the southeast. The average precipitation is about 460 mm with large interannual variability (Li et al. 2009). Most of the region is covered by the loess of 100 m thick. Therefore, the Loess Plateau has become the most extensive, the most profound and the most typical loess landform in the world. At the same time, it is one of the most severely ecological degradation regions in the world because of its frequent heavy rainfalls during summer, steep topography, low vegetation cover and highly erodible loess soil (Zhang & Liu 2005; Sun et al. 2014).

2.2 *Reference framework and applied methodology*

The ESAI (Environmental Sensitive Areas index) model is based on five groups of indicators, including soil quality (parent material, soil texture, rocky fragments, soil depth, drainage, slope), climate quality (precipitation, aridity, aspect, rainfall erosivity), vegetation quality (vegetation cover, fire risk, soil erosion protection, vegetation resistance to drought), land-use management quality (cropland, pasture land, natural areas (forests and shrubland), mining areas (erosion control measures), recreational areas), and human pressure (population density, employment in agriculture, tourism pressure) (Ladisa et al. 2012; Ferrara et al. 2012). It includes some new indicators (land-use management quality, human pressure) compared with the Desertification Sensitivity Index-DSI methodology (Gad & Lofty 2008). The DSI method can be described as the Environmental Sensitive Areas index with Soil, Climate and Vegetation (ESAI_SCV):

$$\mathrm{ESAI_SCV} = (\mathrm{SQI} \times \mathrm{CQI} \times \mathrm{VQI})^{1/3}. \quad (1)$$

Then, the Environmental Sensitive Areas index (ESAI) can be determined as follows:

$$\mathrm{ESAI} = (\mathrm{SQI} \times \mathrm{CQI} \times \mathrm{VQI} \times \mathrm{LU_MQI} \times \mathrm{HPI})^{1/5}. \quad (2)$$

In order to reflect the degree of land degradation, we divided the ESAI into eight classes (C3-h, C2-critical, C1-critical, F3-fragile, F2-fragile, F1-fragile, Potential and Non-affected).

The SQI (Soil Quality Index) can be estimated according to the original ESI (Ferrara et al. 2005) model that considers the Parent Material (PM), Soil Texture (ST), Rocky Fragments (RF), Soil Depth (SD), drainage and slope. Then, the SQI can be calculated as follows:

$$\mathrm{SQI} = (\mathrm{PM} \times \mathrm{ST} \times \mathrm{RF} \times \mathrm{SD} \times \mathrm{Drainage} \times \mathrm{Slope})^{1/6}. \quad (3)$$

The CQI (Climate Quality Index) considers the average annual precipitation (mm), aridity, aspect and the fact R of the USLE (Universal Soil Loss Equation). So, the CQI can be described as follows:

$$\mathrm{CQI} = (\mathrm{P} \times \mathrm{Aspect} \times \mathrm{BGI} \times \mathrm{R})^{1/4}. \quad (4)$$

where P is the annual precipitation (mm); Aspect means the direction in which the land faces the cardinal points; and BGI is the Bagnouls-Gaussen Aridity Index (Bagnouls & Gaussen 1952), which can be calculated as:

$$\mathrm{BGI} = \sum_{i=1}^{12} (2t_i - p_i) k_i. \quad (5)$$

where t_i is the average air temperature of month i (i = 1–12); p_i is the average monthly rainfall; and k is the coefficient indicating the number of months, in which $2t > p$.

The VQI (Vegetation Quality Index) considers Vegetation Cover (VC), Fire Risk (FR), Soil Erosion Protection (SEP) and Vegetation Resistance to Drought (VRD). Then, the VQI can be defined as follows:

$$\mathrm{VQI} = (\mathrm{VC} \times \mathrm{FR} \times \mathrm{SEP} \times \mathrm{VRD})^{1/4}. \quad (6)$$

The LU_MQI (Land Use-Management Quality Index) includes both the land use (cropland, pastureland, forest) and management policies. It can be computed by two indices as follows:

$$\mathrm{LU_MQI} = (\mathrm{LUI} \times \mathrm{MQI})^{1/2}. \quad (7)$$

$$LUI = (CLUI \times PLUI \times FLUI)^{1/3}. \quad (8)$$

The LUI (Land Use Index) includes the CLUI (Crop Land Use Index), the PLUI (Pasture Land Use Index) and the FLUI (Forest Land Use Index), combined with management policies in order to obtain the integrated land-use management quality index.

The CLUI contains five groups of indicators. They include the intensity of land cultivation, the intensity of irrigation, the use of agricultural machinery, the use of agricultural fertilizers and insecticides, and the use of plant protection products. The PLUI includes both the areas of pastoral land and the number of animals present in the total area. The FLUI estimates the degree of forest cover.

The MQI is the Management Quality Index, representing the land protection. Afforestation, terracing and silt dam are considered as the soil conservation measures.

Taking into account the negative impact of humans on the environment, we set up the Human Pressure Index (HPI) (Ladisa et al. 2000). Because of the less tourists in the Loess Plateau area, we did not consider the impact of tourism for the land degradation on the study area. Then, the new HPI can be calculated as follows:

$$HPI = (PD \times RP \times EA)^{1/3}. \quad (9)$$

where PD is the population density; RP is the resident population at the end of the year; and EA is the employment in the agricultural sector.

2.3 *Data acquisition and pre-processing*

In this study, we obtained a series of climate, soil, vegetation and socio-economic data (Table 1).

All these data were used to set up the ESAI model for desertification risk assessment. The different themes (layers) were developed to five quality indices (SQI, CQI, VQI, LU_MQI and HPI). These quality indices of different layers of the Loess Plateau were elaborated in the GIS and characterized the impact of each factor by means of several quality classes, as given in Table 2.

3 RESULTS AND DISCUSSION

Desertification is a complicated process due to the variety of natural conditions and human activities involved (Wu and Ci, 2002). The overall results of ESAI for SQI, CQI, VQI, LU_MQI and HPI, respectively, are shown in Figures 2–6.

The Soil Quality Index (Fig.2) indicates that more than half of the Loess Plateau is of medium quality (52.5%), almost one-half (44.2%) is of high soil quality and only 3.3% is low quality. The areas of high quality are located mainly in the center of the Loess Plateau. So, much high soil quality is attributed to the deep soils (100 m deep). The Loess Plateau has been known to contain the thickest loess in the world. In addition to a small area of shallow soils, the poor soil drainage conditions also contribute to the low soil quality index.

The precipitation and air temperature data of 61 national meteorological stations were interpolated based on the GIS. After a series of calculations, we obtained the Vegetation Quality Index (VQI) (Fig. 3). The VQI shows that climate quality gradually decreases from southeast to northwest, while there also exists a clear Boundary: Ningxia—Lanzhou—Haiyuan—Dingbian—Suide—Hequ—Hohhot. The north of the boundary mainly distributes low-climate quality areas (23.7%), and the south of the line mainly distributes high-climate quality areas (29.8%), while the medium-quality climate areas are distributed on both of them (46.5%).

The Vegetation Quality Index shows that less than one-fifth of the Loess Plateau region is of

Table 1. Description of the ESAI themes and data source.

Theme	Layer name	Data source
Topography	Aspect, slope	30 m ATSTER Digital Elevation Model
Climate	Rainfall, aridity index, rainfall erosivity index	Monthly temperature and precipitation from 1980 to 2010
Soil	Parent material, rock fragments, soil depth and drainage	China Soil Map Based Harmonized World Soil Database (v1.1)
Vegetation	Vegetation cover, erosion protection, fire risk, and drought resistance	MOD12Q1 for land cover types of MODIS products
Land management	Land-use intensity, policy	Socio-economic dataset of the Loess Plateau (1980–2010)
Human pressure	Population density, agriculture population	Socio-economic dataset of the Loess Plateau (1980–2010)

Table 2. Description of classes and range of scores for five indicators of ESAI.

Class	Description	Range
SQI (Soil Quality Index)		
1	High quality	<1.1
2	Medium quality	1.1–1.3
3	Low quality	>1.3
CQI (Climate Quality Index)		
1	High quality	<1.3
2	Medium quality	1.3–1.5
3	Low quality	>1.5
VQI (Vegetation Quality Index)		
1	High quality	<1.3
2	Medium quality	1.3–1.5
3	Low quality	>1.5
LU_MQI (Land-Use Management Quality Index)		
1	Very high quality	<1.0
2	High quality	1.0–1.3
3	Medium quality	1.3–1.5
4	Low quality	>1.5
HPI (Human Pressure Index)		
1	High quality	<1.0
2	Medium quality	1.0–1.5
3	Low quality	>1.5

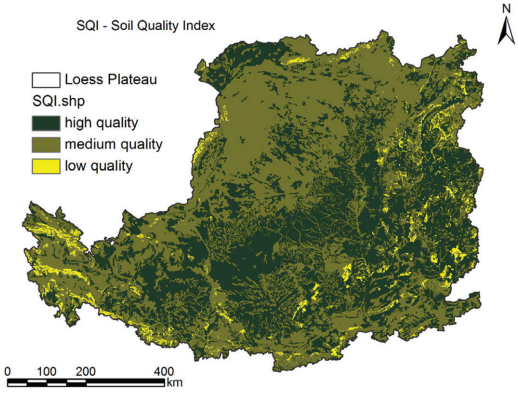

Figure 2. Spatial distribution of the soil quality index.

high quality (19.0%), nearly half the region is of medium quality (42.1%) and about 38.0% is of low quality (Fig. 4). The high vegetation quality areas are located in the southeast of the Loess Plateau, and mainly determined by the forests of high vegetation cover. They are mainly distributed in the north of Qingling, Ziwuling and Taihang Mountains. Because of the low vegetation cover, most of the plateau areas belong to the medium or low vegetation region, especially the grass-based Hetao

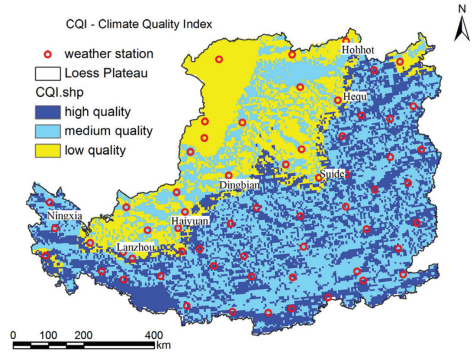

Figure 3. Spatial distribution of the climate quality index.

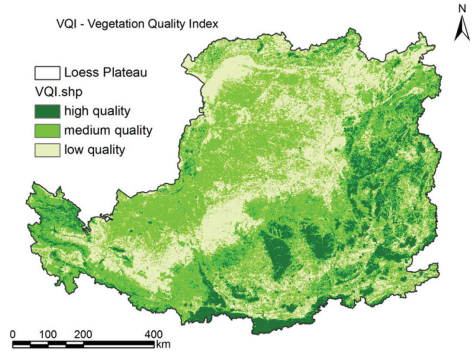

Figure 4. Spatial distribution of the vegetation quality index.

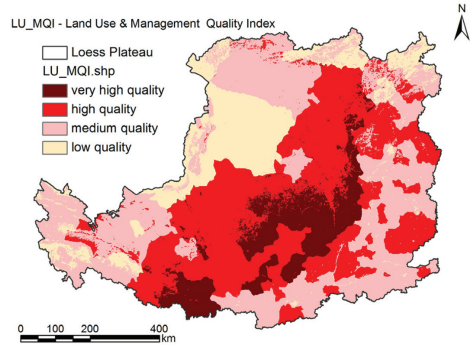

Figure 5. Spatial distribution of land use and management quality index.

Plain in Inner Mongolia. The transition areas from southeast to northwest are also mainly of low quality for the vegetation types of vulnerable crops.

Land use and management quality on desertification is mainly estimated from the different

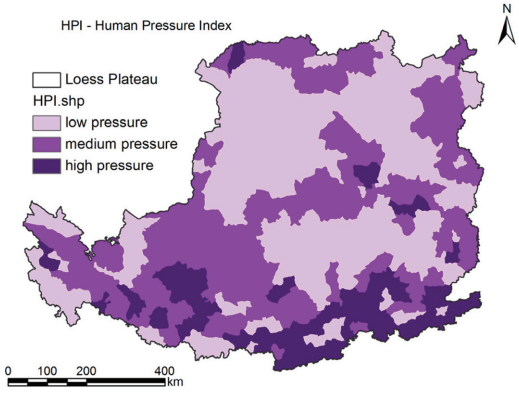

Figure 6. Spatial distribution of the human pressure index.

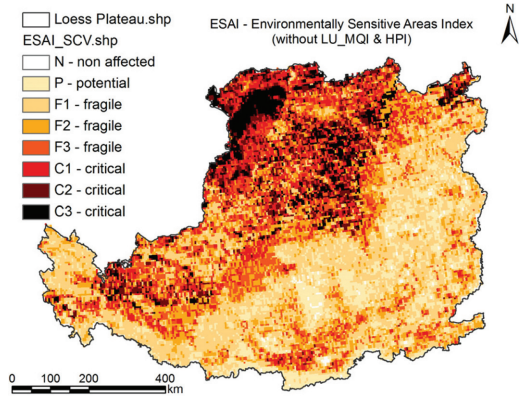

Figure 7. Spatial distribution of the ESAI (Environmentally Sensitive Areas Index) considering only the biophysical factors.

disturbances of cropland use, pasture land use and forest land use on the county scale. The Land Use and Management Quality Index (LU_MQI) shows that almost half of the plateau (48.3%) is of high or very high quality, which is distributed in the center of the Loess Plateau. This is because there is the key soil and water conservation division divided by the Chinese Academy of Sciences (CAS). The medium-quality area occupies 36.1%, which is similar to the high-quality one. There is only 12.2% of low-quality area located in Ertuokeqi, Ertuokeqianqi and Wushenqi of Inner Mongolia (Fig. 5). The low quality indicates the poor management policies and low degree of land use in the region.

The Human Pressure Index shows that almost half of the Loess Plateau is of low quality (46.2%), 39.8% is of medium quality and only about 14.0% is of high quality (Fig. 6). The Loess Plateau is almost covered by the entire Yellow River basin. The good soil and moisture conditions of the basin formed the farming culture of the Loess Plateau for thousands of years. Therefore, the high population density in the Loess Plateau region and also the agricultural population centers must be the important reasons for deciding the space distribution pattern of HPI in the Loess Plateau.

The three primary indices of soil, climate and vegetation quality index derive the ESAI_SCV (Environmental Sensitive Areas Index with Soil, Climate and Vegetation quality index) (Fig. 7). It includes only bio-physical aspects of the Loess Plateau region. In order to make effective measures to combat desertification, we also need to consider the human-induced factors. Thus, the sensitivity of the areas to desertification risk was determined by five indices of soil, climate, vegetation, land use and management quality and human pressure (Fig. 8).

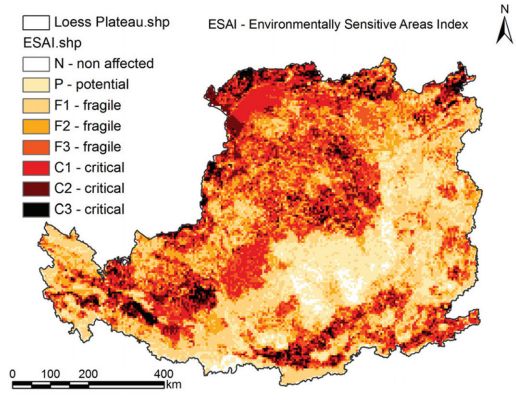

Figure 8. Spatial distribution of the ESAI (Environmentally Sensitive Areas Index).

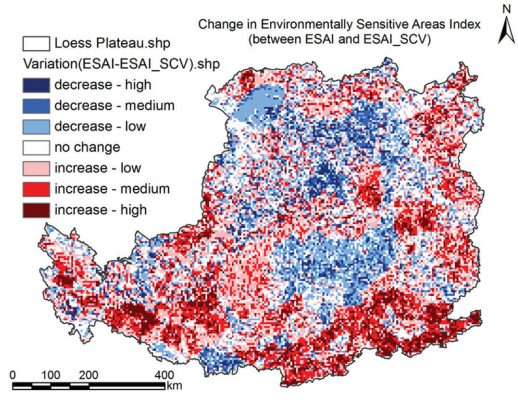

Figure 9. Spatial distribution of the ESAI (Environmentally Sensitive Areas Index) between the ESAI and ESAI_SCV.

Table 3. Description of the difference between the ESAI and ESAI_SCV.

Description	Range	ESAI_SCV (10^4 km^2)	%	ESAI (10^4 km^2)	%	Δ%
N-non affected	<1.25	0.32	0.5	0.99	1.6	1.1
P-potential	1.25–1.34	7.15	11.5	7.35	11.8	0.3
F1-fragile	1.35–1.45	18.99	30.5	15.50	24.9	−5.6
F2-fragile	1.45–1.50	11.57	18.6	10.87	17.5	−1.1
F3-fragile	1.50–1.55	8.50	13.7	11.23	18.0	4.4
C1-critical	1.55–1.60	7.18	11.5	9.97	16.0	4.5
C2-critical	1.60–1.65	4.45	7.1	4.58	7.4	0.2
C3-critical	>1.65	4.09	6.6	1.76	2.8	−3.8
Total		62.26	100.0	62.26	100.0	0.0

The estimation of desertification risk by means of the bio-physical factors (ESAI_SCV) shows that about one-fourth of the plateau (25.2%) could be classified as critical, almost two-thirds (62.8%) as fragile, 11.5% as potentially affected by desertification processes, and only 0.5% as non-affected land (Fig. 7). Overall, the extent of desertification of the northwestern region is significantly greater than that of the southeastern region in the Loess Plateau. Hangjinqi of Inner Mongolia is the most critical area for desertification, followed by Yulin City of Shaanxi Province. In contrast, many counties of Shaanxi and Shanxi are of lower-risk regions with weak or potential desertification risk.

The inclusion of human-induced factors changes the situation for desertification risk in the Loess Plateau. (Fig. 8) Desertification risk areas of F1-fragile, F2-fragile and C3-critical were reduced by 5.6%, 1.1% and 3.8%. At the same time, F3-fragile and C1-critical increased by 4.4% and 4.5%, respectively (Fig. 9 and Table 3). These results show that the human-induced factors have narrowed the gap between the classes of desertification risk. It is mainly due to the lower human pressure impact in the cities of Inner Mongolia than in the other cities (e.g. Lanzhou, Xi'an, Baoji, Xianyang, Luoyang) on the Loess Plateau. In addition, more effective management practices of soil and water conservation (e.g. afforestation, grazing prohibition, terracing and silt dam) form the new pattern of the ESAI. The practices reduced the risk of desertification in most areas except the high population in several municipalities of the Loess Plateau (Tianshui in Gansu province, Yan'an in Shaanxi province and most municipalities of Shanxi province).

4 CONCLUSIONS

In this paper, desertification risk of the Loess Plateau was assessed by considering a series of indices involving both the natural ecosystem (ESAI_SCV) and the human social system (ESAI).

The natural ecosystem of ESAI_SCV (Environmental Sensitive Areas index without LU_MQI and HPI) shows that climate determined the basic pattern of desertification risk, which decreased from the southeast to the northwest of the Loess Plateau. Vegetation is a significant indicator of desertification risk among others. This is because of the similar spatial distribution between the map of the Vegetation Quality Index (Fig. 4) and the Environmental Sensitive Areas index without LU_MQI and HPI (Fig. 7). The Soil Quality Index weakened the strength of Soil desertification risk in the center of the Loess Plateau to some degree (Fig. 2). It is mainly due to the large soil depth (almost 90% of the Loess Plateau with 100 m deep soil).

The human social system (ESAI) indicates the negative impact of large population south of the Loess Plateau; on the contrary, the effective policies of water and soil protection reduced the risk of desertification in most provinces and municipalities of the Loess Plateau. Therefore, we need to strengthen the prevention and control of desertification, while reducing the population pressure. However, the human social system is more variable than the natural ecosystem. We need to focus on the impact of human activities resulting in desertification on the Loess Plateau, and make positive and effective measures to combat desertification timely.

ACKNOWLEDGMENT

The authors are grateful for the funding from the National Natural Foundation of China (No. 31460090), the Science Planning Project of Gansu Province in 2015 (No. YB095), the Youth Science and Technology Innovation Project of Longdong University (No. XY2 K1409) and the Science

Planning Project of Gansu Province in 2014 (No. YB108).

REFERENCES

Bagnouls, F. & Gaussen, H. 1952. The xerothermic index. *Bulletin of the Association of French Geographers* 222–223: 10–17.

Dawelbait, M. & Morari, F. 2012. Monitoring desertification in a Savannah region in Sudan using Landsat images and spectral mixture analysis. *Journal of Arid Environments* 80(5): 45–55.

Ferrara, A. 2005. Expert system for evaluating the Environmental Sensitivity Index (ESI) of a local area. DIS4ME: Desertification Indicator System for Mediterranean Europe. *http://www.kcl.ac.uk/projects/desertlinks/indicator system/index.htm.*

Ferrara, A., Salvati, L., Sateriano, A., et al. 2012. Performance evaluation and cost assessment of a key indicator system to monitor desertification vulnerability. *Ecological Indicators* 23(12): 123–129.

Fischer, G., Nachtergaele, F., Prieler, S., van Velthuizen, H.T., Verelst, L. & Wiberg, D. 2008. *Global Agro-ecological Zones Assessment for Agriculture (GAEZ 2008)*. Rome, Italy: IIASA, Laxenburg, *Austria and FAO*.

Gad, A. & Lofty, I. 2008. Use of remote sensing and GIS in mapping the environmental sensitivity areas for desertification of Egyptian territory. *eEarth Discuss* 3(6): 41–45.

Integrated Survey Team of Chinese Academy of Sciences (CAS) of the Loess Plateau. 1992. *Dataset of Resources, Environment and Society for the Loess Plateau Region (in Chinese)*. Beijing: China Economic Publishing House.

Ladisa, G., Todorovic, M. & Trisorio Liuzzi, G., 2012. A GIS-based approach for desertification risk assessment in Apulia region, SE Italy. *Physics and Chemistry of the Earth* 49(5): 103–113.

Li, Z., Liu, W.Z., Zhang, X.C. & Zheng, F.L. 2009. Impacts of land use change and climate variability on hydrology in an agricultural catchment on the Loess Plateau of China. *Journal of Hydrology* 377(10): 35–42.

Paolo, D., Abinash, B., Kyle, F.D., et al. 2013. Global desertification drivers and feedbacks. *Advances in Water Resources* 51(1): 326–344.

Sun, W.Y., Shao, Q.Q., Liu, J.Y. et al., 2014. Assessing the effects of land use and topography on soil erosion on the Loess Plateau in China. *Catena* 121(10): 151–163.

Wu, B. & Ci, L.J., 2002. Landscape change and desertification development in the Mu Us Sandland, Northern China. *Journal of Arid Environments* 50(3): 429–444.

Xu, L.P., 2008. *Influence and Reciprocal Effects of Vegetation Rehabilitation on Regional Climate in Loess Plateau*. Yangling: Northwest A & F University.

Zhang, X.C. & Liu, W.Z. 2005. Simulating potential response of hydrology, soil erosion, and crop productivity to climate change in Changwu tableland region on the Loess Plateau of China. *Agricultural and Forest Meteorology* 131(3–4): 127–142.

Zhao, Y.F., Zou, X.Q., Zhang, J.X., et al. 2014. Spatiotemporal variation of reference evapotranspiration and aridity index in the Loess Plateau Region of China, during 1961–2012. *Quaternary International* 349(10): 196–206.

This page intentionally left blank

Civil Engineering and Urban Planning IV – Liu et al. (Eds)
© 2016 Taylor & Francis Group, London, ISBN 978-1-138-02903-3

Remediation of soil contamination on urban industrial sites—a case study on the old industrial base in Northeast China

Yao-Chi Zhang
Geography Institute of Paris-Sorbonne University, Paris, France

ABSTRACT: During the process of rapid development of China's urbanization and industrialization, early uncontrolled exploitation of resources and misuse of the land in the rough type of production process resulted in a series of urban environmental problems like soil contamination and the majority of the urban industrial sites being unused, which seriously restricted the sustainable development of cities. This paper, taking the research on the remediation of soil contamination on the city industrial sites in the Old Industrial Base in Northeast China for example, analyzes the current situation of contaminated land and the main problems in the remediation process, and by drawing on experience of developed countries to combat land pollution, provides new and constructive suggestions for soil pollution control measures of industrial sites in old industrial cities.

1 INTRODUCTION

The Old Industrial Base in Northeast China, enjoying rich natural resources and a large number of industrial enterprises, has been providing a lot of energy supplies and industrial products for the construction of the country. However, in the historical context of paying great attention to capacity and ignoring sustainable development, the majority of resource-based industrial cities have experienced uncontrolled resource exploitation and rough methods of production, resulting in rather serious soil contamination on most of the original industrial sites. Currently, under the guidance of the "retreat two into three" policy and with the rapid expansion of urban functions and urban layout adjustment, most high pollution, high energy-consuming enterprises located within the city have gradually moved out of the heartland, and part of the industrial enterprises in marginal areas of the city, because of factors like industrial adjustment and resource integration, have moved into the industrial park farther away from the city. The remaining contaminated land has seriously affected the health of local residents and damaged the local ecological environment, which directly threatens the healthy development of the city.

Treating and recycling of the contaminated land is of crucial importance to urbanization and urban revitalization. First of all, clean land is the basis of human being's healthy life; secondly it can ease the pressure of lacking land resources in the process of urbanization, stimulate economic growth, and attract foreign investment; finally, it can maintain and increase the value of land assets.

2 HISTORICAL CAUSES OF CONTAMINATED SOIL ON URBAN INDUSTRIAL SITES

The Old Industrial Base in Northeast China embraces a long history, and there are three stages in the formation of its contaminated soil on the urban industrial sites: in the first stage, that is, in the planned economy era (1949–1978), the state set up a lot of resource-based cities in the northeast area, in the economic development model then in which mine and the oil field developed simultaneously, a large number of polluting enterprises sprang up. During this period, industrial enterprises, in order to maximize the yield, exploited resources without restraint, severely damaging the original topography and geological structure, and meanwhile the rough way of storage of materials in large enterprises also generated a lot of toxic substances, further contaminating the land and groundwater sources. In addition, the discharge of a large number of untreated industrial waste gas has seriously polluted the local ecological environment; in the second stage, after the reform and opening up (1979–1993), the cities, in the meantime of economic development, put too much emphasis on the growth of GDP, while ignoring environmental protection, and issued some preferential policies to attract high pollution, high energy-consuming enterprises to enter without legal management of the sewage of enterprises, which caused further increased land pollution; in the third stage, the State Council proposed to revitalize the Old Industrial Base Northeast China (1993-present). Since then the city's industrial structure has been

adjusted (switching secondary industry to tertiary industry, and with the rise of post-industrial era, clean industry replacing high pollution industries), a lot of abandoned industrial sites were generated in the central city, and at the same time, urban development transformed from a scattering way to a gathering one, forming a land use style of specialized industrial areas. Furthermore, a great deal of arable land, forest land and other agricultural land as well as scattered rural settlements have been transformed into new urban industrial sites. All of the above factors brought about new requirements for the comprehensive management of industrial pollution.

3 CURRENT SITUATION OF CONTAMINATED SOIL ON URBAN INDUSTRIAL SITES

Soil contamination in the Old Industrial Base in Northeast China has displayed a tendency of increasing intensity. In the areas around mining perimeter, around the plant, around the town, on both sides of the highway, parks and other areas dense with economic and human activities, the soil is almost all subject to different degrees of pollution. Soil contamination displays very complex characteristics, showing a situation where industrial pollution, agricultural fertilizers, and plastic pollution organically mixed together. Among these, soil contaminated on industrial sites in the city is mainly from mining, smelting and other industrial pollution, specifically, the emissions of industrial "three wastes" (waste gas, waste, waste water), soil acidification caused by sedimentation of pollutants in the waste gas emitted in the atmosphere and other pollution caused by heavy metals and other contaminants, the piling of solid waste, the soil pollution caused by heavy metal contamination minerals and pathogens like due to waste water irrigation. Soil pollution brings grave risks, such as high occupational and surged mortality.

In terms of spatial distribution, the distribution of the major sources of industrial pollution in the Northeast region presents features that the major sources of industrial pollution continue to gather along the Harbin-Dalian railway and highways and into Liaoning Province, among which the largest number of sources exist in Liaoning Province accounting for more than 50% of the total sources of pollution in Northeast China; the main sources of pollution in Liaoning Province keep moving to and congregating in the Bohai Sea region, Shenyang—Dalian railway and the central cities of Liaoning; the ones in Jilin and Heilongjiang provinces continue to focus on the Harbin-Dalian railway (Li 2008). Specific cases are as follows: in the area of Hulu Island, Jinzhou, Liaoning Province, the land is mainly affected by pollution of zinc plants, pollution elements mainly including cadmium, lead, zinc, but the biggest impact is that there are comparatively large numbers of people getting cancer, dying young, living in single-parent families. Such elements attack human kidney organs and bones, causing osteoporosis; in the Zhangshi irrigation area in Shenyang province, due to the long time of irrigation with industrial waste water, the level of cadmium in soil and rice is highly above conventional measures, with human being and livestock unable to eat the rice. Consequently, the soil can no longer be used as arable land, only for other purposes; in Hetao region of Inner Mongolia, due to poor land quality and groundwater contamination, endemic diseases like arsenic poisoning and fluorosis are more serious, with nearly 30 million people threatened by arsenic poisoning, within which more than 2,000 people are suffering patients; the Yangjiageda village in Wuyuan County of Bayannao'er city is the key area of arsenic poisoning where there are lots of patients and deaths mainly of cancer and mostly in their prime time due to the torture of illness. These above tragedies caused by soil contamination have seriously warned people that we have reached a point where contaminated soil on industrial sites has to be remedied.

4 TECHNICAL REMEDIATION OF CONTAMINATED SOIL ON URBAN INDUSTRIAL SITES

Our technical remediation of soil pollution generally takes the following three ways: First, chemical method. Applying chemical amendments, like lime, phosphate, iron and other substances, adjusting soil pH, thus transforming heavy metals into insoluble forms can reduce the concentration in the soil solution, thereby we can reduce the toxic of heavy metals in the soil to crops. It also works to improve soil texture, apply organic fertilizer, and increase soil colloids' ability to absorb heavy metal ions and pesticides. However, this method can not solve the problem fundamentally. Second, biological control. Take biological improvement measures. Some plants such as sunflower have a strong absorption and enrichment capability of heavy metals. Therefore continuous cultivation a few years can significantly reduce the content of heavy metals in soil. Applying to soil organic substances, enhancing the activity of microorganisms, or inoculating to soil micro-organisms with special features can speed up the decomposition of harmful substances (Jiang 2004). Finally, physical control. As for seriously polluted soil, we can

employ different methods such as changing soil, improving soil by importing soil from other places, digging deep and other methods to dilute pollutants. Among them, the ex-situ remediation, a way of the physical control, has become a widely used restoration method across the country. For example, in the westward move project of the northern heavy industry Shenyang Heavy Machinery Group Co., it left an area of 800 square meters of land heavily polluted by coal tar after its relocation, so the original contaminated soil was cleared out and replaced with new earth and then implemented hard cover. After the treatment, the piece of land once contaminated has been built into a cultural square. This way of remediation has several features such as a short cycle, cheap, easy to operate and so on.

5 PROBLEMS IN THE REMEDIATION OF CONTAMINATED SOIL ON URBAN INDUSTRIAL SITES

In the background where the government strongly advocates to revitalize the Northeast, the northeast old industrial cities are actively carrying out urban renewal in order to achieve the sustainable development of urbanization and industrialization. In the urban renewal process, in order to make full and rational reuse of industrial land resource, several urgent problems needing to be resolved are as follows.

First, the lack of systematic statistics and summary of soil pollution data. Statistics of most urban contaminated industrial sites and information of environmental remediation are incomplete, hence it is rather difficult for government departments to grasp accurate information of every polluted industrial sites, which not only brings considerable difficulties to developing and implementing national laws and regulations, but also weakens to some extent the effectiveness of the national macro—control of the real estate industry. The public's supervision is short of sources of information, legal basis and institutional guarantee.

Second, the imperfect legal system of soil pollution control. Relevant legislation, policies and standards lag behind, and local regulations and environmental standards are in confusion, unable to meet the ever-changing needs of urbanization. Some provisions on land pollution prevention can be divided into three categories, the first category includes provisions relating to soil pollution control in land and agricultural law, specifically referring to "Agriculture Law", "Land Management Law", "Regulations on the Protection of Basic Farmland" and "Land Reclamation Provisions"; the second category includes comprehensive laws of environmental protection and single laws, such as the "Environmental Protection Law", "Environmental Impact Assessment Law" and "Cleaner Production Promotion law", etc.; the third category is single regulations on pollution prevention, such as those on water pollution, air pollution, solid waste pollution and radioactive pollution prevention and other laws and regulations. In recent years the country has unveiled a series of local regulations and policies (implementation and other opinions or approaches) related to industrial pollution remediation and control. For example, on May 25, 2007, Shenyang Environmental Protection Bureau and Shenyang Municipal Planning and Land Resources Bureau jointly promulgated the "Measures for Shenyang contaminated sites environmental remediation and restoration (trial)." However, due to the lack of feasible deterrent rules and powerful terms of accountability and no specific policies and regulations for contaminated land in the development, there is no law to follow in the management and restoration of contaminated land. In addition, the inadequate attention of current society to soil remediation also causes improper responsibilities and unclear duties. In some areas, the demolished plant sites omit even simple flat clearance work, directly access to auction procedures, and are sold to developers. At present only in Beijing and Chongqing, environmental protection departments have a contaminated site management division, while in other cities there is no mandatory requirement for developers to investigate those contaminated sites. Also in different cities, the standards of urban industrial pollution remediation and restoration are not unified, the implementation of those standards is difficult to coordinated, and information is not disclosed. The legal duties and obligations which the person and polluter liable for the historically remaining contaminated land should bear are not clearly defined.

Third, affected by "land finance" and administrative assessment system, forced by the pressure of short-term high growth performance, in the name of increasing the level of urbanization, and in order to respond to the lack of land resources, many local governments blindly use uncontrolled contaminated land, which exacerbates the difficulties in the remediation of polluted urban industrial sites.

Fourth, the lack of appropriate technical standards for soil pollution remediation and restoration. Technology and method of remediation and restoration of contaminated land in China is still in its infancy. The number of enterprises engaged in contaminated land remediation is in a serious shortage, most of the treatment technology and equipment rely on imports, and independent technologies

are inadequate. Hence an urgent needs to develop a variety of repair techniques. Faced with diverse types of soil contamination and the complex situation of pollution, we lack the experience of the comprehensive remediation of soil pollution.

Finally, the remediation and restoration of contaminated soil confronting with financial difficulties. At present the main source of funds mainly relies on the national government agencies and local governments, lacking the participation of non-profit organizations, individual volunteers, private organizations, civil society and specialized funding agencies abroad. Legislation and financial support from government and investment of private companies are not well combined. There exists a great need to establish multiple financing mechanisms and platforms (Xu 2008).

6 ENLIGHTENMENT FROM THE EXPERIENCE OF REMEDIATION OF CONTAMINATED LAND IN DEVELOPED COUNTRIES

Although the developed countries have fully proceeded into the industrialized or deindustrialization stage of development, up till now, they are still paying a heavy price for the ignored environmental damage in a period of rapid economic development in the past. Historically, most developed countries have taken massive re-investment and hundreds of years to gradually improve the ecological environment, whose remediation experience offers a variety of enlightenment to China's soil pollution remediation.

6.1 *Enlightenment from the experience of remediation of contaminated land in Germany*

In the post-industrial era, soil protection has become an important task in Germany's environmental protection. First, the German soil pollution investigation team is set up to carry out comprehensive and long-term soil testings. Nearly 800 monitoring stations distribute throughout the country, mostly carrying out soil environmental quality monitoring for land for different purposes, analyzing and recording their physical, chemical and biological indicators in order to determine changes in soil at different times. In addition, the environmental protection departments conduct a comprehensive investigation, screening, risk assessment all over the country for potential pollution sources, old factories, waste dumps and suspected contaminated land. In particular, they conduct a thorough investigation for focused contaminated land, including the types and concentration of pollutants, as well as their hazards to the surrounding environment and human health. And then according to the survey results, they establish a detailed database on the contaminated sites for the polluted land, which is a kind of effective dynamic management on national soil protection. Finally, through simulation of soil remediation, they implement a soil remediation plan. By soil risk assessment Germany divides soil into three levels as green, yellow and red, green for the prevention of land degradation, yellow for a warning, red for a must to be cleaned. Land of different functions, are treated differently. According to this theory, there is only about 10% out of Germany's 300,000 pieces of land requiring technological transformation. Now, Germany's land transformation and utilization takes the form of total control, expected to be used no more than 30 hm^2 by mid-2020 (Chen 2008).

6.2 *Enlightenment from the experience of remediation of contaminated land in France*

French Ministry of Environmental Protection released in 1933 the restoration of soil pollution policy. Through modifying and improving the existing industrial law, waste law and civil law and other laws, France stipulates related responsibilities of soil polluters so as to achieve the purpose of soil pollution prevention. Firstly, the basic soil pollution control strategy of France is based on the principle of prevention. The French environmental management departments control activities of pollutants emissions through the use of environmental laws including Industry Act, Waste Act and civil law, etc., controlling potential contamination from the source, establishing a regular monitoring system for soil pollution prevention and a soil risk assessment and restoration system. Secondly, in order to raise public awareness of environmental protection, recognition and preservation of information of contaminated land, the French Ministry of Environmental Protection establishes a public information management database of contaminated land, which includes information about the existing contaminated sites and contaminated sites that have been remedied. Finally, environmental management department can impose obligations of soil environmental remediation on related responsible person, after an accurate risk assessment of the contaminated land, based on the consideration of the future use of the land. For terra nullius, the state is responsible for environmental remediation.

6.3 *Enlightenment from the experience of remediation of contaminated land in the United States*

The remediation of American Brownfields began with the Musharraf River canal (LoveCanal)

event in the late 1970 s. Brownfields is for short for Brownfield land or Brownfield lots, as defined by the United States Environmental Protection Agency (EPA), referring to a piece of land contains or may contain toxic substances or pollutants. According to EPA statistics, there are roughly 450,000 pieces of brownfields across the country. The Congress passed in 1980 the "Environmental Response, Compensation, and Liability Act" (CERCLA) (He 2010), commonly known as the Superfund law. Superfund Act authorized EPA to manage contaminated sites across the country, and ordered those responsible for the pollution to restore seriously polluted grounds; the Superfund shall pay for site remediation costs for those with no polluters or polluters who cannot have repair capacity; and for those sites unable to find responsible polluters, the site remediation costs are paid by the Superfund and are recoverable by the EPA from those responsible. Funds are from the tax of domestic production of oil and imported petroleum products, chemical raw material taxes, environmental taxes, grants and conventional, restoration and administrative fees recoverable from those responsible, penalties, interest and other investment income. The US government in 1986 passed the "Superfund Amendments and Reauthorization Act", and spawned a series of related environmental management policies, such as "green credit policy", "environmental liability insurance policy", and so on, these policies had a profound influence on environmental protection, business production and development of US. According to EPA statistics, from the start of the brownfield project to 2013, more than twenty thousand projects nationwide completed the assessment, completed the management of 854 sites, and there were nearly 40,000 acres of land turned from waste into treasure, available for development. The completed project will not only provide for locals nearly 85,000 jobs, but also makes the average value of the real estate of the surrounding area increase by 2 to 3 percent, with considerable social benefits (http://site.douban.com/119254/widget/notes/3502751/note/273470253).

7 CONCLUSIONS

The Old Industrial Base in Northeast China has gone through the early industrialization period of predatory exploitation of resources, and the era of reform and opening up period of blind introduction of polluting enterprises, and has now entered into a new phase of urban renewal. Given the severity of hazards and extensiveness of the soil pollution, the remediation of contaminated soil on urban industrial sites has reached a critical point. Based on the characteristics of industrial sites in the old northeast industrial cities, some suggestions on soil pollution prevention and industrial sites recycling in the process of urbanization of the old industrial cities are put forward as follows.

Environmental supervision: a database of land contamination with multi-level management oversight from the central to the local government should be established as soon as possible, its data platform open to the public; environmental supervision and management should be strengthened, and environmental approvals to control new pollution sources should be stricken; real-time supervision should be conducted to the those who have the land use rights whose land is possible to generate pollution and the management and comprehensive utilization of industrial waste water, waste gas and waste is to be strengthened to prevent any discharge of waste containing various pollutants into the soil; regulate the collection, storage, transfer, transport and disposal activities of hazardous waste to prevent new soil pollution; for the contaminated land, it is necessary to find out and cut off pollution sources.

Legal support: the government should carry out special operations to rectify illegal sewage companies, to speed up the remediation of old pollution sources, and establish soil pollution liability lifelong accountability mechanisms; as for re-use of industrial pollution of land, it must be done according to the law. The government should improve specific the policy standards and laws regulations, and timely amend relevant laws and regulations, strengthen law enforcement to secure effective management and reasonable redevelopment of land contamination (Sang 2003).

Policy support: institutionalize the management and development of contaminated land as soon as possible, and the government takes the lead and the ministry, together with other relevant departments, shall draw up soil pollution prevention action plans. They shall make a list of remediation objectives or land use planning recommendations to reduce management costs on the premise of the land safety and security of the groundwater; in addition, they shall implement soil remediation projects, to carry out a pilot demonstration of soil pollution in typical areas, and gradually establish a soil pollution remediation technology system, finally to promote the restoration of soil pollution step by step. Meanwhile promote the recycling process of contaminated land and give preferential terms the appropriate use and auction of brownfields, and guide enterprises to transform and develop brownfield reasonably, jointly promoting renewal and development of brownfields. In regard to the acceptance of contaminated soil remediation project, form realistic acceptance evaluation program for soil pollution remediation.

Technical support: the relevant government departments can cooperate with research institutes to set up soil pollution research laboratories to carry out investigation and research on soil pollution control technology, to conduct verification, improvement combined with soil type and pollution status, and to summarize the most economical and reasonable treatment and re-use program for brownfields according to brownfields caused by different pollution sources. Accelerate the introduction of mature soil remediation technology from abroad and development and innovation. Strengthen the development of practical technology, in particular, to vigorously promote the development of low cost, simple and practical technology. Because soil contamination is generally more complex, it is difficult to use only one method to completely solve the problem. We must first harmonize multi-sectoral action, according to the actual situation, use a variety of methods, combined with comprehensive management and comprehensive planning, to make reasonable use of the contaminated soil.

Financial support: establish a special fund, and depending on the circumstances, give timely funding to the remediation of polluted land in different areas, the source of the funds being raised by more environment tax (Zhu 2009); at the same time, carry out tax relief policies for the companies which effectively control the generation of brownfield; as for the financing model for remediation fund, to promote partnership between government and private companies, namely the government obtain the rights to remedy and run the contaminated land by authorizing private companies to have the usufruct and income right of the contaminated land in a certain number of years; issue contaminated land securities, impawn the income right of the remedied land to issue securities, and again take the securities as (collateral) bonds to attract investors to buy, in order to gain the capital for the remediation of the contaminated land (Luo 2002).

Moreover, we should actively promote urban industrial wasteland pollution and human health, the importance of urban ecological and environmental protection, pollution control laws and regulations and other knowledge to improve people's awareness of environmental protection. In today's background of promoting sustainable development, we should try to avoid the tragedy of the developed countries which have experienced pollution first and then remediation. Today we are paying for what our predecessors have done, therefore our present thoughts and actions also determine the happiness of our future children and grandchildren!

REFERENCES

Chen, C. & Yang, L. 2008. Redevelopment strategies of brownfields in western countries and their enlightenment to China. *Land and Resources Information* 9(6): 16–20.

He, F., Chen, Y.Y. & Feng, Y. 2010. Enlightenment of the redevelopment of brownfields in the west. *Shanghai Real Estate* 29(4): 45–48.

Jiang, H.Y., Liu, M., Huang, S.F. et al. 2004. Current research and trends in urban contaminate soil remediation. *Journal of Safety and Environmental Safety* 4(5): 73–77.

Li, H.Y., Du, X.M., et al. 2008. Research on the sptiotemporal variation of industrial waste water pollution in the three provinces of northeast of China. *Research of Environmental Sciences* 21(2): 168–174.

Luo, S.D. 2002. Brownfields site in American cities and its administering. *Urban Problems* 21(6): 64–67.

Sang, D.L. 2003. Research on urbanization in China and reasons of legislation for sustainable use of land resource. *Urban Problems* 22(6): 61–64.

Xu, D.Y., Xu, Z.X. & Jin, W. 2008. Study on city land remediation in urbanization process: An America case. *Henan Science* 27(1): 95–99.

Zhu, Y.M., Su, H.T. & Guo, P. 2009. Comparison study on policies and regulations of brownfields cleanup and redevelopment at home and abroad. *Science of Environmental Protection* 35(3): 40–43.

Civil Engineering and Urban Planning IV – Liu et al. (Eds)
© 2016 Taylor & Francis Group, London, ISBN 978-1-138-02903-3

Performance of a level isolation device for cultural relics by shaking table tests

Qian Zhou
Palace Museum, Beijing, China

Wei-Ming Yan & Jin-Bao Ji
Beijing University of Technology, Beijing, China

ABSTRACT: To protect museum cultural relics against seismic damage, a level isolation device for cultural relics is developed. To study its isolation performances, shaking table tests are carried out. Model of showcase and replica of a ceramic cultural relics are made, the replica is set in the showcase by free-standing status. Two cases of the showcase are considered: the showcase is fixed on shaking table board; the showcase is fixed to top of the isolation device, and the free device is kept on shaking table board. *Chichi* earthquake waves of PGA (Peak Ground Acceleration) = 0.1 g, 0.3 g, and 0.5 g are made to act on the showcase in x and y directions. Parameters such as basic frequency, stiffness, displacement response, acceleration response, dynamic magnification coefficient, and so on, of the replica are obtained and the isolation performances of the device are verified. Results show that basic frequency of the isolation device is 0.775 Hz, with its level stiffness is 1.52 N/mm. For the replica, the isolation device makes oscillation motions which are similar to those in case of earthquakes, which overturns quickly due to overlarge amplitude. In comparison, the replica placed in the isolation device makes translation motion with much lower acceleration response, relative displacement, and magnification coefficient, which proves good performances of the isolation device.

1 INTRODUCTION

Cultural relics kept in museums are important components of movable cultural heritage and deserve protection for their historical and artistic importance. As these cultural relics usually are in free-standing status, they are prone of being damaged during earthquakes. Recent earthquakes such as the Wenchuan earthquake in May 2008 that measured 8.0 according to Richter Magnitude Scale (Ms) (Zhou et al. 2010a), Yushu earthquake in April 2010 that measured 7.1 Ms (Song and Li, 2010), and the Ya'an earthquake in April 2013 that measured 7.0 Ms (The Sichuan Provincial Cultural Relics and Archaeology Research Institute 2013) amongst others caused serious collateral damage of museum cultural relics. Under earthquakes, typical damage symptoms of museum cultural relics include slide, oscillation, and overturn; some relics even drop down from their bases and get damaged, as shown in Figure 1. Thus, it is important to reinforce these cultural relics on time. Traditional aseismic methods include binding or gluing the relic to its base, providing additional supports for the relic, decreasing height of barycenter of the relic and so on, which can mitigate seismic damage that might incur to the relic. However, problems such as damage to the relic, poor strengthening effects and so on also appear (Zhou et al. 2010). Application of vibration control technique in the field of cultural relic protection makes it possible to develop isolation devices for museum cultural relics (Zhou et al. 2013). The authors develop a

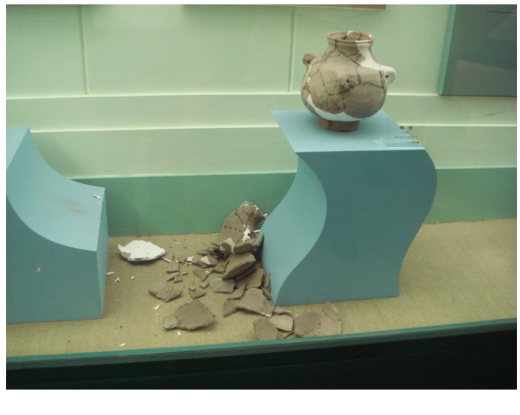

Figure 1. Seismic damage of museum cultural relics.

linear rail type of level isolation device for museum cultural relics. In the following, shaking table tests are carried out to verify its isolation performances, results will be helpful for aseismic protection of the cultural relics.

2 TEST SITUATION

2.1 *Constitution of isolation device*

The developed isolation device for relics is of linear rail-type, size of which is 760 × 760 × 120 mm (length × width × height), permission stroke of which is 180 mm in x or y direction. By constitution, the device is composed of components such as bottom plate, middle plate, top plate, sliders, springs, linear rails, damping blocks, and so on, as shown in Figure 2. The device is usually installed below showcase. When earthquakes are felt, the sliders move along linear rails and produce long period of the showcase, which avoids natural frequency scopes of earthquake waves and produces isolation effects.

2.2 *Test scheme*

Shaking table tests are used to study the performance of the isolation device for relics. The test models include replica of relic (ceramic material, bottom radius: 44 mm, barycenter height: 138 mm), showcase (steel frame, glass cover, size: 760 × 760 × 2200 mm) and isolation device, where the replica in the showcase is in free-standing condition. When isolation device is used, it is set under the showcase, with its top plate fixed to the bottom of the showcase. Measuring positions of models are shown in Figure 3, where 2 cases are considered: the showcase is installed with isolation device (left part of Fig. 1) the showcase directly stands on shaking table (right part of Fig. 1). Acceleration sensors are set on shaking table board (point 2), replica top (point 3), showcase top (point 4) to study acceleration responses of the models; displacement sensors are set under the isolation device (point 1) to study displacement responses of the device.

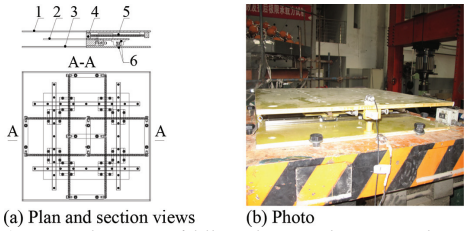

(a) Plan and section views (b) Photo

(1-top plate; 2-middle plate; 3-bottom plate; 4-damping block; 5-spring; 6-slider and rail)

Figure 2. The isolation device for relics.

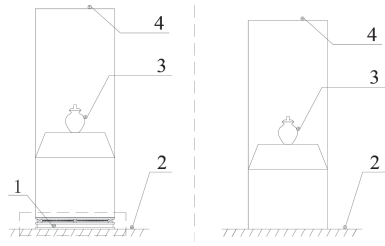

Figure 3. Test positions of models.

Table 1. Testing cases.

No	Use isolation device	Earthquake wave direction
C1	no	x
C2	yes	x
C3	no	x and y
C4	yes	x and y

The *Chichi* earthquake waves are applied to the model, which are in x direction or in both, x and y directions; strength of which are PGA (Peak Ground Acceleration) = 0.1 g, 0.3 g, 0.5 g, where g represents gravity acceleration. Responses of the replica under earthquakes are studied considering the model is/is not installed with isolation device. Different testing cases are listed in Table 1.

3 TEST PHENOMENA

For replica in showcase which stands directly on the shaking table board, it makes oscillation motions under earthquakes. When earthquake intensity increases, the replica overturns due to overlarge oscillation amplitude, as shown in Figure 4a. After the showcase is kept on the isolation device, the relic in the showcase makes translation motions under earthquakes. Although stroke of the replica relative to ground is large, it is nearly static relative to the isolation device during the whole process of earthquake action. It keeps stable vibration status even under high intensity of earthquakes, as shown in Figure 4b. Test phenomena of the replica under different cases are listed in Table 2.

4 TEST ANALYSIS

4.1 *Basic frequency*

For the showcase installed with isolation device, its basic frequency value is obtained by free

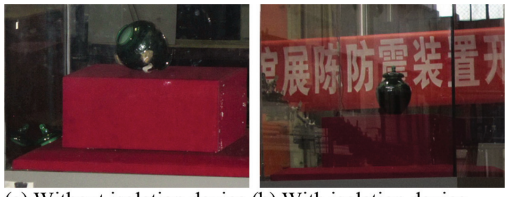

(a) Without isolation device (b) With isolation device

Figure 4. Test photos.

Table 2. Test phenomena of the replica.

	PGA = 0.1 g	PGA = 0.3 g	PGA = 0.5 g
C1	Oscillation	Oscillation	Overturn
C2	Translation, almost static relative to showcase		
C3	Oscillation	Overturn	Overturn
C4	Translation, almost static relative to showcase		

vibration method. The device is pushed to 100 mm location by level forces initially and then released to produce attenuation vibration. Acceleration response curve of top point of the showcase is shown in Figure 5a. By Fourier transform, frequency-spectrum curve of the point is obtained, as shown in Figure 5b. It is found that basic frequency of the showcase under this condition is $f_i = 0.775$ Hz.

To obtain level stiffness of the isolation device, level forces are applied to the device to make it produce displacement. Curves of the force (F) and displacement (u) are shown in Figure 6, where A and B represent measuring and fitting results respectively. Formula of the fitting curve is as follows:

$$y = 1.52x \quad (1)$$

By equation (1), it is found that level stiffness of the isolation device is $k = 1.52$ N/mm.

For the showcase without isolation device, white noise of PGA = 0.05 g is applied to it, and acceleration response of its top is obtained, as shown in Figure 7a. Fourier transform of the curve is carried out and the corresponding frequency-spectrum curve is obtained, as shown in Figure 7b. It is found the basic frequency value of the showcase under this condition is $f_n = 13.5$ Hz.

Besides, Fourier transform is applied to *Chichi* earthquake wave to get its basic frequency. Result shows that the value is $f_c = 1.47$ Hz. As $1/f_i > 1/f_c > 1/f_n$, it is easy to find that the isolation device extends the natural period of the showcase to reduce seismic damage of the replica kept in it.

4.2 *Displacement*

By tests, displacement response curves of the replica under different cases are obtained, as shown

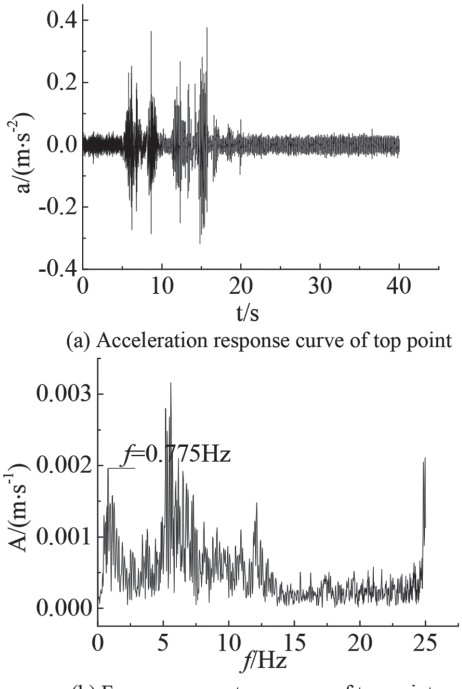

(a) Acceleration response curve of top point

(b) Frequency spectrum curve of top point

Figure 5. Determination of basic frequency of showcase with isolation device.

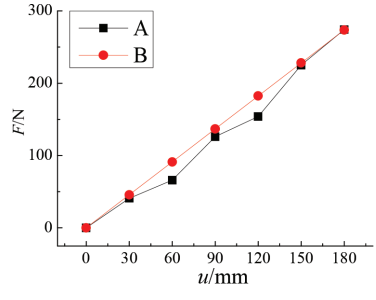

Figure 6. *F-u* curves of the isolation device.

in Figure 8. It's found that: (1) so far as shapes of the curves are concerned, the curves of C2 and C4 cases are stable, which behave nearly as even vibration based on balance location, reflecting stable vibration status of the replica under earthquakes. For cases of C1 and C3, the replica makes stable vibrations under earthquakes of PGA = 0.1 g. However, as the intensity of earthquake increases, the curves tend to break due to overturn of the replica. (2) As far as peak values of the curves are concerned, peak displacement values of replica (relative to ground) under C2 and C4 cases are larger than those under

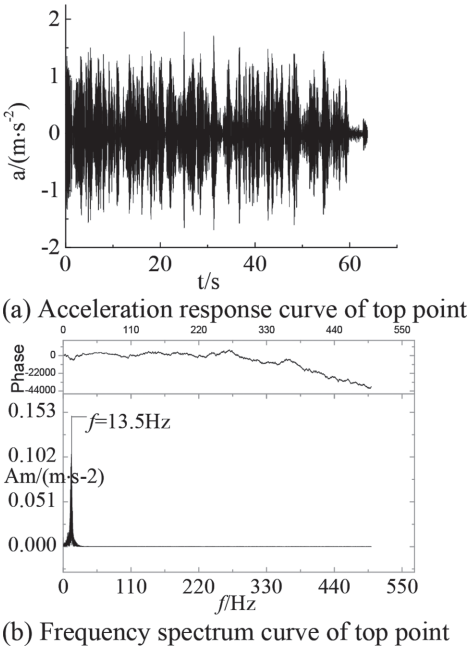

Figure 7. Determination of basic frequency of showcase without isolation device.

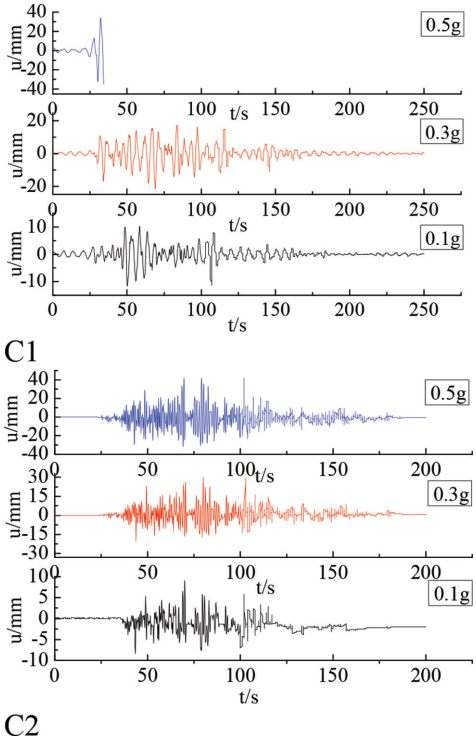

Figure 8. (*Continued*)

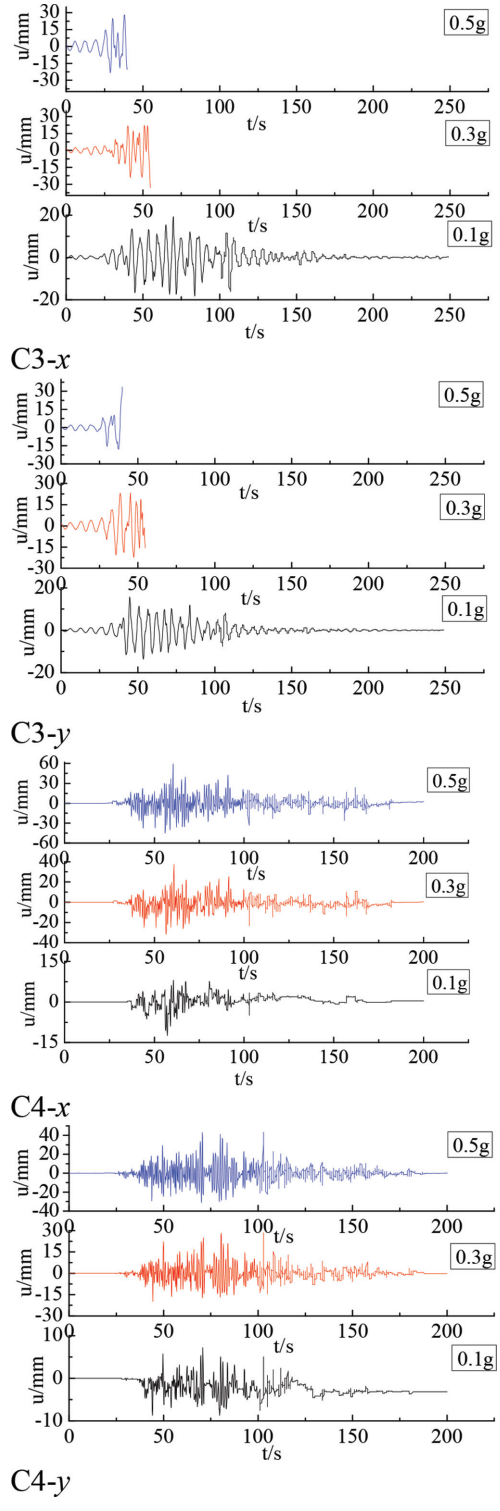

Figure 8. Displacement response curves of the replica.

C1 and C3 cases. For example, peak displacement value of the replica composites from x and y directions reaches 77.4 mm considering effects of isolation device (C4, PGA = 0.5 g), while only 44.2 mm under conditions without isolation device (C3, PGA = 0.5 g). This is mainly because of different movement modes of the replica under different cases. Under cases C1 and C3, the replica makes oscillation motion under earthquakes, which tends to overturn in case its oscillation amplitude is overlarge. However, under cases C2 and C4, the replica makes translation motion due to effects of isolation device. Peak displacement values of the replica relative to ground are larger than those under C1 and C3 cases, but much smaller relative to isolation device. The replica is still stable under strong earthquakes due to isolation effects.

To study the restoring performance of the isolation device after earthquakes, residue displacement values of the isolation device are obtained, as shown in Table 3. It is found that under different earthquake cases, the residue displacement values are relatively small (maximum values: 2.05 mm in x direction and 3.18 mm in y direction). Thus, it can be considered that the isolation device has good restoring performance, which can restore to origin location even under strong earthquakes.

4.3 *Acceleration*

Seismic forces on the replica can be reflected by its acceleration values. By tests, peak acceleration values of shaking table board (a_1) and the replica (a_3) under different cases are obtained, as shown in Tables 4 and 5. It is found that: (1) under the same intensity earthquake, a_3, value of the replica omitting effects of isolation device is greater than a_1, however lower than a_1 when isolation device is considered. (2) when earthquake intensity increases, a_3, values of cases C1 and C3 cases increase obviously, reflecting the replica is easy to be damaged. While for cases C2 and C4, a_3 values increase little when earthquake intensity increases, reflecting weak seismic forces on the replica even when input earthquake intensity is large. (3) The isolation device can effectively decrease acceleration response of the replica in both x and y directions.

Table 3. Residue displacement values of the isolation device (Units: mm).

	PGA = 0.1		PGA = 0.3		PGA = 0.5	
	x	y	x	y	x	y
C2	2.01	–	0.67	–	1.01	–
C4	0.43	3.18	0.22	0.16	2.05	0.34

Table 4. Peak acceleration values (Units: g).

	C1		C2		C3-x	
PGA/g	a_1	a_3	a_1	a_3	a_1	a_3
0.1	0.09	0.17	0.09	0.05	0.09	0.20
0.3	0.26	0.42	0.33	0.13	0.27	0.95
0.5	0.42	1.62	0.68	0.15	0.42	1.23

Table 5. Peak acceleration values (Units: g).

	C3-y		C4-x		C4-y	
PGA/g	a_1	a_3	a_1	a_3	a_1	a_3
0.1	0.09	0.20	0.10	0.05	0.09	0.07
0.3	0.37	1.03	0.27	0.12	0.27	0.11
0.5	0.50	1.18	0.49	0.19	0.66	0.19

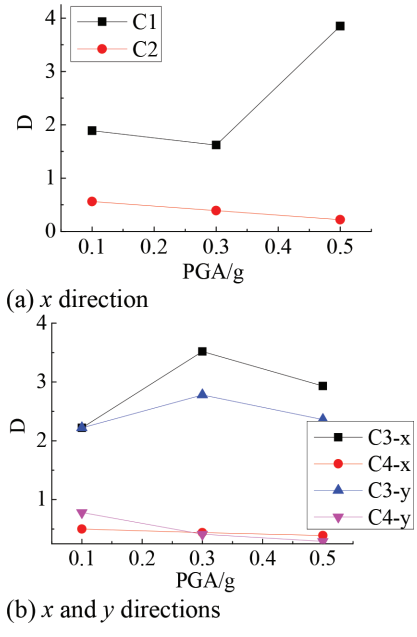

Figure 9. D curves of the replica.

4.4 *Dynamic magnification coefficient*

By definition, dynamic magnification coefficient D is introduced to estimate earthquake mitigation effects of the replica, $D = a_3/a_1$. Smaller value of D represents better mitigation effects. Based on Table 4, D curves of the replica are drawn as shown in Figure 9. It is found that: (1) under cases of C1

and C3, *D* values are always greater than 1 (maximum value reaches 3.85), reflecting that seismic wave is amplified after transferred from shaking table board to replica. Besides, the amplification effect tends to be obvious under strong earthquake, which makes the replica easy to be damaged. (2) under cases of C2 and C4, *D* values are always less than 1 (minimum value is only 0.22). This is because during process of earthquake, wave transferred from shaking table board to replica, the wave is attenuated due to isolation effects from the isolation device. As the device still performs good under high intensity of earthquakes, the replica is hardly damaged. (3) with the increase of earthquake intensity, *D* values of C1 and C3 cases tend to increase, while decrease under C2 and C4 cases. This also reflects good isolation performance of the isolation device.

5 CONCLUSION

Basic frequency of the isolation device is 0.775 Hz, its level stiffness is 1.52 N/mm.

For the replica omitting isolation device, it makes oscillation motions under earthquakes, which quickly overturns due to overlarge amplitude. *D* value of the replica exceeds 1, which tends to increase under strong earthquakes.

For the replica considering effects of isolation device, it makes stable translation motions under earthquakes. *D* value of the replica is always less than 1, which tends to decrease when earthquake intensity increases.

REFERENCES

Song, Y.C. & Li, Z.G. 2010. Damage survey and emergency protection methods of ancient buildings caused by Yushu earthquake on 14th Apr., 2010. *Qinghai Social Sciences* 11(04): 94–98.

The Sichuan Provincial Cultural Relics and Archaeology Research Institute. 2013. Damage survey of cultural relics sites in Sichuan caused by Lushan earthquake on 20th Apr., 2013. *Sichuan Cultural Relics* 13(03): 3–8.

Zhou, Q., Yan, W.M. & Yang, X.S. 2010a. Damage of ancient Chinese architecture caused by Wenchuan earthquake. *Sciences of Conservation and archaeology* 22(1): 37–45.

Zhou, Q., Yan, W.M. & Zhou, X.Y. 2010. Present status of aseismic techniques for domestic museum cultural relics. *Journal of Catastrophology* 25(S): 201–206.

Zhou, Q., Yan, W.M., & Ji, J.B. 2013. Development of isolation devices for free-standing museum cultural relics. *Journal of Disaster Prevention and Mitigation Engineering* 33(2): 147–154.

Civil Engineering and Urban Planning IV – Liu et al. (Eds)
© 2016 Taylor & Francis Group, London, ISBN 978-1-138-02903-3

Experimental study on Tou-kungs of Tai-he Palace in the Forbidden City under vertical loads

Qian Zhou
Palace Museum, Beijing, China

Wei-Ming Yan & Jin-Bao Ji
Beijing University of Technology, Beijing, China

ABSTRACT: To protect Chinese ancient timber buildings effectively, three types of Tou-kungs (bracket sets) in Tai-he Palace in the Forbidden City-intermediate set, column set, and corner set were taken as examples to study bearing performances of Chinese ancient Tou-kung of *Qing* Dynasty under vertical loads. Based on constituent characteristics of the Tou-kungs, the 1:2 scaled models were built, on which experiments of vertical loading were carried out. By experiments, damage modes, internal forces, and deformation of the Tou-kungs were discussed. Then, calculation model of vertical stiffness of the Tou-kungs were deduced. Results show that under vertical loads, the Tou-kungs are easy to be damaged on the top two-layer parts. Compared to the underparts, the upper parts of the Tou-kungs bear more forces. For different Tou-kungs, intermediate set, corner set, and column set on ultimate bearing capacity; corner set, column set, and intermediate set on ductility. Under vertical loads, calculation model of vertical stiffness of the Tou-kungs can be simplied as three-part line segments.

1 INTRODUCTION

Tou-kung (bracket sets) belongs to a special type of constitution of Chinese ancient buildings. It is composed of several layers of wooden components assembled vertically. The Tou-kung is usually located between column-top and roof-beam, whose main functions include transferring load from the roof to the column, mitigate aseismic damage of the whole building, architectural decoration, and so on. Types of Tou-kung can be defined by several means. Taking Tou-kung of Qing Dynasty as example, according to location, it can include intermediate set (each Tou-kung is located between columns), column set (the Tou-kung is located on top of the column, but not the corner column) and corner set (the Tou-kung is located on top of corner column); according to shape, it can include ping-zuo set (the Tou-kung has a symmetry) and Liu-jin set (the Tou-kung is asymmetrical, some components of its back part extend to neighbor beams); according to extending size, it can include 3-cai (extending the modulus size), 5-cai (extending 2 times of the modulus size), 7-cai (extending 3 times of the modulus size) and so on. Tai-he Palace in the Forbidden City is two-story ancient building of Qing Dynasty, which is the largest amongst Chinese ancient palace buildings. Height and extending sizes of Tou-kungs of Tai-he Palace are also large: 875×685 mm of 1st floor and 1050×900 mm of 2nd floor. Figure 1 shows photos of different types of Tou-kung in Tai-he Palace.

As Tou-kung has special structure and important mechanical functions, relative studies on it have been carried out. Wang (1992) studied influence of section

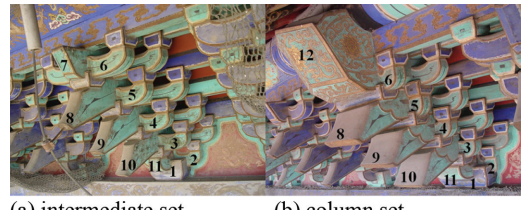

(a) intermediate set (b) column set

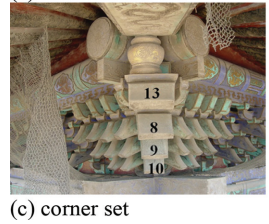

(c) corner set

Figure 1. Photos of tou-kungs in Tai-he Palace.
* 1: zuo-tou; 2: zheng-xin-gua-kung; 3: dan-cai-gua-kung; 4, 5: wai-zhuai-gua-kung; 6: wai-zhuai-xiang-kung; 7: shua-tou; 8: san-ang; 9: er-ang; 10: tou-ang; 11: tou-qiao; 12: tao-jian-liang-tou; 13: you-ang.

sizes of Tou-kung to its static performances. Zhao et al. (2008 & 2014) and Yuan et al. (2011) separately studied mechanical performances of Tou-kungs in Song and Liao dynasties. They both considered that in the Tou-kung had good bearing capacity in vertical direction, while in level directions the Tou-kung could consume part of earthquake energy by friction among components. Fujita et al. (1997) studied influence of extending sizes of Tou-kung to its aseismic performances by static and shaking table tests. Tsuwa et al. (2008) studied basic frequencies and damping ratios of Tou-kungs in Japan by free attenuation vibration methods. To further study mechanical performances of Tou-kung of Qing Dynasty under vertical loads, the Tou-kungs of Tai-he Palace are taken as example for static experiments. Results will be helpful for protection and maintenance of Chinese ancient wooden buildings.

2 EXPERIMENTAL OUTLINE

Korean pine is selected as material for experimental models of Tou-kung in *Tai-he* Palace. 1:2 scaled models of different types of Tou-kung are built, as shown in Figure 2. All models are upended for convenience of loading. To guarantee smooth bearing surface for each Tou-kung, a layer of sand is spread on ground, then a timber plate is put on sand, and the tou-kung is set on the plate. For Liu-jin type of Tou-kung, its central part is supported by concrete block and its extended end is fixed directly to the ground.

To obtain deformation of the Tou-kung under vertical loads, dial indicators (scope of ±50 mm) are set on tops of plate and zuo-tou. Besides, strain gauges are set on components such as zheng-xin-gua-kung, dan-cai-gua-kung, wai-zhuai-gua-kung and so on to study their internal forces. A hydraulic jack (scope of 100 kN) is used to load on the models. To avoid systematic error, the models are pre-loaded before formal experiments. During each experiment, the loading is continuously applied to the model, which starts from 4 kN, then increases by 3 kN/min, until the Tou-kung is destroyed. By experiments, damage modes, deformation and internal force characters of the Tou-kungs are studied.

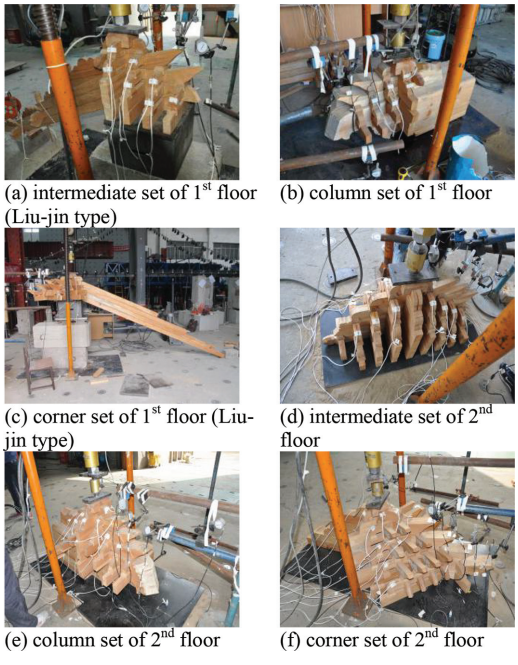

(a) intermediate set of 1st floor (Liu-jin type)
(b) column set of 1st floor
(c) corner set of 1st floor (Liu-jin type)
(d) intermediate set of 2nd floor
(e) column set of 2nd floor
(f) corner set of 2nd floor

Figure 2. Photos of tou-kung models.

3 EXPERIMENT PHENOMENA

3.1 *Intermediate set*

At initial loading stage, there appear slight sounds on top of the Tou-kung, reflecting compression behaviors among the components. With the increase in vertical load value, rotation of the dial indicators increases rapidly, reflecting obvious deformation of the Tou-kung. Under load, cracks appear successively on the components of zuo-dou, zheng-xin-gua-gong, and tou-qiao. Then, the tou-qiao is inclined, which leads to instability of the whole tou-kung. Other components keep intact during the loading process.

3.2 *Column set*

Under vertical load, the initial compression behaviors among components are not as obvious as those from the intermediate set. This is because the component number of column set is low (many small components are replaced by a beam with huge section sizes). When the load reaches about 20% of the ultimate value, there appears the first crack on zuo-tou. Then, components such as the shi-ba-tou, zheng-xin-gua-gong, tou-qiao successively crack due to insufficient strength of shearing or compression.

3.3 *Corner set*

There appear slight sounds among components during the first loading stage. Under the vertical load, the first crack appears on zuo-tou, which tends to extend downwards. With the increase of load, width of the crack increases simultaneously. Deformation also appears on zuo-tou. Then the tou-qiao cracks and inclines, leading to instability

Table 1. Main damage forms of the Tou-kungs.

Tou-kung	Damage forms
Intermediate set	Cracks of zuo-dou, tou-qiao and zheng-xin-gua-gong; incline of tou-qiao
Column set	Cracks of zuo-dou, shi-ba-tou, zheng-xin-gua-gong and tou-qiao
Corner set	Cracks of zuo-tou and tou-qiao, deformation of zuo-tou, incline of tou-qiao

of the whole T-kung. As only zuo-tou and tou-qiao are damaged during the whole loading process, it can be considered that the corner set of the Tou-kung has good bearing performance.

Main damage forms of different Tou-kungs under vertical loads are listed in Table 1.

4 EXPERIMENT ANALYSIS

4.1 *Load-deformation (F-u) curves*

By experiment, load-deformation (*F-u*) curves of the Tou-kungs are drawn in Figure 3, where positive and negative signs respectively represents compression of Tou-kung components. Meanings of different signs are: *p*-intermediate set, *z*-column set, and *j*-corner set. During loading stage, deformation of each Tou-kung increase with the increase of loading values. Slope of the curves tend to decrease, reflecting yielding process of the Tou-kungs. When the load is unmounted, the initial stiffness of column set is larger than those of other two sets of Tou-kung, but decreases quickly to the lowest value, reflecting its good restoring performance. For each Tou-kung, there exists residual deformation when the load is completely unmounted, which is composed of interspace between Tou-kung components and deformation of the component self. Order of ultimate bearing capacity of different set of Tou-kung is intermediate set (1st floor: 74.72 kN, 2nd floor: 72.43 kN) < corner set (1st floor: 90.07 kN, 2nd floor: 92.85 kN) < column set (1st floor: 95.64 kN, 2nd floor: 98.47 kN).

4.2 *Ductility coefficient*

Under loads, with the increase of deformation of the Tou-kung, it tends to be yielded, but can still bear loads, reflecting certain ductility performance. It is usually defined that ductility coefficient represents ductility of the Tou-kung, which can be expressed as ratio of ultimate deformation value against yielding value, as shown in Equation (1) (Gao et al. 2014).

$$\mu_\Delta = \Delta u/\Delta y \quad (1)$$

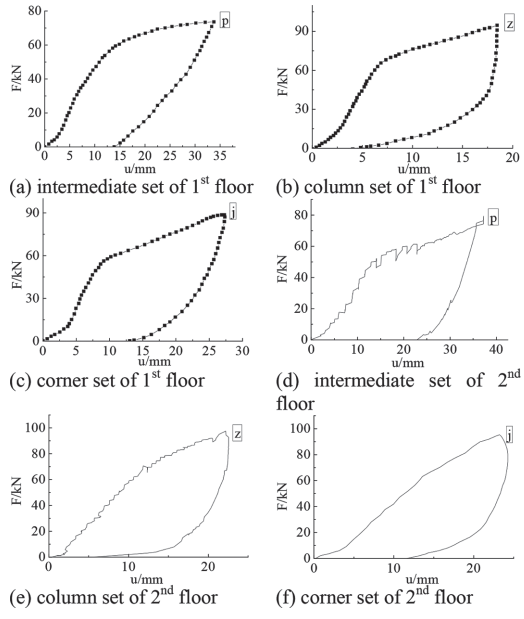

Figure 3. *F-u* curves of Tou-kungs.

In Equation (1), μ_Δ represents ductility coefficient, Δu represents ultimate deformation of Tou-kung, Δy represents yielding deformation of Tou-kung.

By *F-u* curves above as well as Equation (1), μ_Δ values of different sets of Tou-kung are calculated, as listed in Table 2. It is found that all sets have good deformation performance, and the intermediate set tends to be better than the other two sets. As most of the Tou-kungs in the Tai-he Palace belong to intermediate set, it can be considered that the whole Tou-kung layer of Tai-he Palace has good deformation performance in vertical direction, which can mitigate damage of the Tou-kung components under vertical loads.

4.3 *Load–strain (F-ε) curves*

To study bearing performances of different layers of Tou-kung under vertical loads, some components are selected for analysis. Strain gauges are set on the components to test their strain values under vertical loads. By data of the strain gauges, load-strain (*F*-ε) curves of Tou-kungs are drawn in Figure 4. Meanings of different signs are: *c*: zheng-xin-gua-kung; *d*: dan-cai-gua-kung; *e*: wai-zhuai-gua-kung; *f*: xiang-kung; *g*: end of balance pole of Liujin type of tou-kung. Means of *p*, *z*, and *j* are just as in Figure 3. As the strain value of the Tou-kung component is in direct proportion to internal force, thus its bearing performance can be reflected.

Table 2. μ_Δ values of Tou-kungs.

Set type	Floor No.	Δy/mm	Δu/mm	μ_Δ	μ_Δ/average
Intermediate	1	19.11	33.78	1.77	1.97
	2	17.18	37.25	2.17	
Column	1	12.06	18.75	1.55	1.76
	2	11.49	22.59	1.97	
Corner	1	19.34	27.65	1.43	1.59
	2	13.78	24.73	1.75	

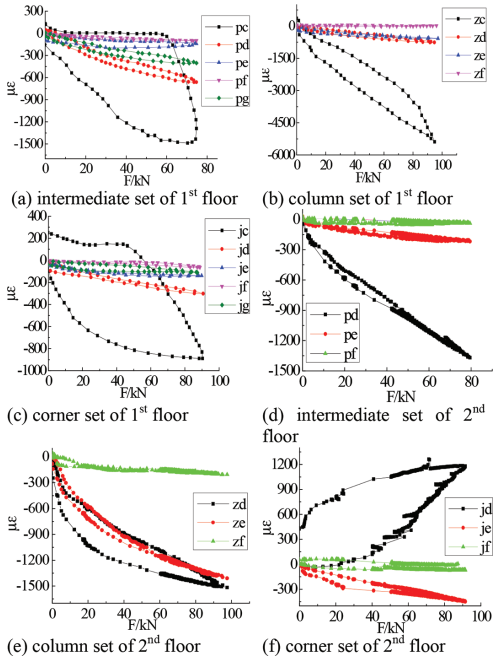

(a) intermediate set of 1st floor (b) column set of 1st floor

(c) corner set of 1st floor (d) intermediate set of 2nd floor

(e) column set of 2nd floor (f) corner set of 2nd floor

Figure 4. *F-ε* curves of Tou-kung components.

It is found that: (1) for each Tou-kung, internal forces of the upper layer components are larger than those of the underparts, reflecting upper components such as zuo-tou, zheng-xin-gua-gong, and tou-qiao are easy to be destroyed under vertical loads. This is also consistent with experiment phenomena. (2) the strain values are usually negative, reflecting compression process of the Tou-kung components under loads. However, some strain values of upper layers of Tou-kung are positive, reflecting warping of the components due to cracks. (3) strain values (internal forces) of column set of Tou-kung are larger than those of other two sets, reflecting components of the column set Tou-kung is more easily to be destroyed under vertical loads. This is because number of components of column set Tou-kung is low, which leads to relative large load each component bears. (3) strain values of intermediate set Tou-kung are larger than those of corner set. This is because section sizes of components of the former set Tou-kung are smaller, which leads to larger stress values. Calculation model of vertical stiffness.

4.4 *Calculation model of vertical stiffness*

Relation between point load on structural model and that on actual structure can be expressed as equation (2) (Yao & Chen 2001):

$$S_p = F_m/F_p = (A_m/A_p)^* (\sigma_m/\sigma_p) = S_\sigma * S_l^2 \quad (2)$$

In Equation (2), S_p, S_σ, and S_l separately represent similarity coefficients of load, stress, and size; F_m, A_m, σ_m separately represent point load, section area and section stress of structural model; F_p, A_p, σ_p separately represent point load, section area, and section stress of actual structure. By equation (2), it is calculated that ultimate force of each actual Tou-kung is about 350 kN. Besides, in normal status, vertical load on each actual Tou-kung is about 34 kN, which is about 1/10 of the ultimate value.

Vertical stiffness model of Tou-kung in Tai-he Palace can be determined by reference of curves in Figure 3, where each curve can be simplified by 3 part line segments, as shown in Figure 5. OA part represents initial compression stage of Tou-kung components, the Tou-kung is in elastic state, with its stiffness value small. AB part represents friction and compression stage of Tou-kung components, the Tou-kung is in yielding state, its stiffness value is large, point B can be considered as yielding point of the Tou-kung. BC part represents local damage stage of Tou-kung components, the Tou-kung is in ultimate bearing status, its stiffness value decreases, point C can be considered as ultimate damage point of the Tou-kung. The stiffness model is similar to results of Gao et al. (2008) and Yuan et al. (2011).

Based on experiment data, stiffness values of each Tou-kung in different stages are calculated, as listed in Tables 3–5, where "Cal" and "Ave" separately represent calculation and average results. It is found that stiffness of intermediate set Tou-kung

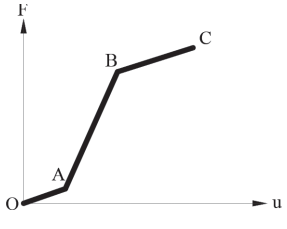

Figure 5. Calculation model of the vertical stiffness of Tou-kungs.

Table 3. Vertical compression stiffness values of Tou-kungs of Tai-he Palace (Units: kN/mm).

Set type	Floor No.	OA part	
		Cal	Ave
Intermediate	1	2.73	2.20
	2	1.67	
Column	1	4.04	3.04
	2	2.03	
Corner	1	2.86	2.44
	2	2.01	

Table 4. Vertical compression stiffness values of Tou-kungs of Tai-he Palace (Units: kN/mm).

Set type	Floor No.	AB part	
		Cal	Ave
Intermediate	1	3.55	4.03
	2	4.50	
Column	1	6.89	7.26
	2	7.63	
Corner	1	4.23	5.23
	2	6.22	

Table 5. Vertical compression stiffness values of Tou-kungs of Tai-he Palace (Units: kN/mm).

Set type	Floor No.	BC part	
		Cal	Ave
Intermediate	1	0.44	0.63
	2	0.81	
Column	1	2.19	2.65
	2	3.10	
Corner	1	1.69	2.30
	2	2.91	

is the lowest of all, the main reason lies in that its section sizes are smaller than the other two sets.

5 CONCLUSION

Under vertical loads, internal forces of the upper layer of Tou-kung components of Tai-he Palace are larger than those of its underparts, which means upper components such as zuo-tou, tou-qiao and so on are more prone to damage than the others.

For different types of Tou-kung, the order of ultimate bearing capacity is: column set > corner set > intermediate set, the order of ductility performance is: intermediate set > column set > corner set, the order of strain value is: column set > intermediate set > corner set.

Calculation model of vertical stiffness of Tou-kung in Tai-he Palace can be simplified as three part line segments, which separately represent compression, yielding and damage stages of the Tou-kung components.

REFERENCES

Fujita, K., Kimura, M. & Ohashi, Y. 1997. Shaking Table Tests on Tou-kung of Traditional Wooden Buildings (No. 3): Action of Earthquake Waves. *Research Proceedings of Kanto Branch of Architectural Institute of Japan, Kanto, 25 February 1998.* Kanto: Architectural Institute of Japan.

Gao, D.F., Zhao, H.T. & Xue, J.Y. 2008. Aseismic characteristics of bucket arch and mortise-tenon joint of ancient Chinese timber buildings-experimental research. *Journal of Natural Disasters* 17(2): 58–64.

Gao, D.F., Li, F. & Liu, J. 2014. Experimental study on the seismic performance of the structural layer with corbel bracket set of ancient Chinese timber structure. *Earthquake Engineering and Engineering Dynamics* 31(1): 131–139.

Kato, K., Tsuwa, I. & Koshihara, M. 2008. Shaking Table Tests of Traditional Timber Frames Including Tou-kung (Part 1): Experimental Outline and Results. *Proceedings of Lecture Abstracts of Architectural Institute of Japan, Chugoku, 20 July, 2008.* Chugoku: Architectural Institute of Japan.

Kimura, M., Fujita, K. & Sakamoto, I. 1997. Shaking Table Tests on Tou-kung of Traditional Wooden Buildings (No. 2): Vibration Characteristics of Tou-kung. *Research Proceedings of Kanto Branch of Architectural Institute of Japan, Kanto, 25 February 1998.* Kanto: Architectural Institute of Japan.

Sui, Y., Zhao, H.T., & Xue, J.Y. 2011. Experimental study of the seismicity of dougong and wooden frame in Chinese historic buildings. *China Civil Engineering Journal* 44(1): 50–57.

Sakamoto, I., Fujita, K. & Kimura, M. 1997. Shaking Table Tests on Tou-kung of Traditional Wooden Buildings (No. 1): Experiment Summarization and Static Experiment. *Research Proceedings of Kanto Branch of Architectural Institute of Japan, Kanto, 25 February 1998.* Kanto: Architectural Institute of Japan.

Tsuwa, I., Kato, K. & Koshihara, M. 2008. Shaking Table Tests of Traditional Timber Frames Including Tou-kung (Part 2): Modeling of Horizontal Resistance Force and the Analysis. *Proceedings of Lecture Abstracts of Architectural Institute of Japan, Chugoku, 20 July, 2008.* Chugoku: Architectural Institute of Japan.

Wang, T. 1992. *Probe of Statics of Chinese Timber Structures.* Beijing: Cultural Relics Publishing House.

Yao, Q.F. & Chen, P. 2001. *Structural Experiment of Civil Engineering.* Beijing: China Architecture & Building Press.

Yuan, J.L., Chen, W. & Wang, Y. 2011. Experimental research on bracket set models of Yingxian Timber Pagoda. *Journal of Building Structures* 32(7): 66–72.

This page intentionally left blank

Civil Engineering and Urban Planning IV – Liu et al. (Eds)
© 2016 Taylor & Francis Group, London, ISBN 978-1-138-02903-3

Displacement calculation of helical curved beams based on ULM

Jie-Min Liu
School of Science, Shenyang Jianzhu University, Shenyang, Liaoning, China

Zhi-Ying Zhang
School of Civil Engineering, Shenyang Jianzhu University, Shenyang, Liaoning, China

Qiu-Yu Wei
School of Science, Shenyang Jianzhu University, Shenyang, Liaoning, China

ABSTRACT: This paper aims to establish a method of calculating the displacement of helical curved beams. The orthogonal curvilinear coordinate system based on center principal axes is assumed to be agreement with natural coordinate system. The principal vector equation of internal force and principal moment of internal force on arbitrary cross section are obtained using the method of equivalent section and displacements of the helical curved beams are solved by means of Unit Load Method (ULM). A calculating example of vertical helical cantilever curved beams subjected to axial concentrated force is given. The derived equations and the results of this example are found to be more universal.

1 INTRODUCTION

The helical curved beams are often used in architecture design because of its iconic beautiful appearance and multiple functions. The theory of curved beams in applications of arch bridge and helical stair is especially more extensive (Chen 2005; Qi 1981; Tore 2004; Yuan & Chen 2013; Zhou, et al. 2012; Zeng 2010;). Some predecessors divided the curved beams approximately to many straight beam segments and then carried out analysis using the theory of straight beams (Yuan & Chen 2013; Zhou, et al. 2012).

Tore Dahlberg had the displacement prediction about one quarter elliptic curved beam based on Cassette theorem (Tore 2004). The elasticity equation of large displacement and small rotation has been given by Zeng (Zeng 2010). Chen C N studied deflection of the curved beams using the differential quadrature method (Chen 2005). To improve the calculative efficiency and reflect the character, the unit-load method of calculating the displacements of helical curved beams is suggested in this paper, and the vertical displacement equations of the beam are also given.

2 THE UNIT LOAD METHOD OF HELICAL CURVED BEAMS

When the unit load method based on principal of virtual work applies in the curved beam, the displacement of arbitrary point can be expressed as

$$\Delta = \int_L \bar{F} \cdot d\Delta \tag{1}$$

where Δ = the generalized displacement of arbitrary point P on given structure; $\bar{F}$ = internal force vector caused by virtual unit force, which is exerted at the point P and along the direction of generalized displacement, $\bar{F}$ can be expressed as

$$\bar{F} = (\bar{F}_\tau \;\; \bar{F}_n \;\; \bar{F}_b \;\; \bar{M}_\tau \;\; \bar{M}_n \;\; \bar{M}_b)^T \tag{2}$$

where $\bar{F}_\tau$ = axial force; $\bar{F}_n$ and $\bar{F}_b$ = shear force along n and b directions respectively; $\bar{M}_\tau$ = torque; $\bar{M}_n$ and $\bar{M}_b$ = bending moment along n and b axes respectively; and $d\Delta$ = deflection vector of the infinitesimal-segment under action of external loads, and can be expressed as

$$\mathrm{d}\Delta = (\mathrm{d}u_\tau \;\; \mathrm{d}u_n \;\; \mathrm{d}u_b \;\; \mathrm{d}\theta_\tau \;\; \mathrm{d}\theta_n \;\; \mathrm{d}\theta_b)^{\mathrm{T}} \tag{3}$$

In equation (3)

$$\begin{aligned} \mathrm{d}u_\tau &= \frac{F_\tau \mathrm{d}x^1}{EA} & \mathrm{d}\theta_\tau &= \frac{M_\tau \mathrm{d}x^1}{GI_p} \\ \mathrm{d}u_n &= \frac{k_n F_n \mathrm{d}x^1}{GA} & \mathrm{d}\theta_n &= \frac{M_n \mathrm{d}x^1}{EI_2} \\ \mathrm{d}u_b &= \frac{k_b F_b \mathrm{d}x^1}{GA} & \mathrm{d}\theta_b &= \frac{M_b \mathrm{d}x^1}{EI_3} \end{aligned} \tag{4}$$

where, k_n and k_b are the factors associated with shape of the section, for the circular section, $k_n = k_b = 10/9$.

Substituting Equations (2) and (3) into (1), the displacement of arbitrary point can be expressed as

$$\Delta = \int_L \frac{\bar{F}_\tau F_\tau}{EA} dx^1 + \int_L \frac{\bar{F}_n k_n F_n}{GA} dx^1 + \int_L \frac{\bar{F}_b k_b F_b}{GA} dx^1 + \int_L \frac{\bar{M}_\tau M_\tau}{GI_p} dx^1 + \int_L \frac{\bar{M}_n M_n}{EI_2} dx^1 + \int_L \frac{\bar{M}_b M_b}{EI_3} dx^1 \quad (5)$$

The Equation (5) is the general formula of Unit Load Method (ULM) calculating displacement of curved beams.

3 CALCULATING EXAMPLE

3.1 *The principal vector equation of internal force and principal moment equation of internal force*

A helical curved rod fixed at one end subjected to vertical concentrated force *F* along center axis with pitch of *H*, height of $l = nH$, radius of *R* is shown in Figure 1. Diameter of the rod is *d*, radius of the rod is *r*. tilt angle of center axis is φ. Elastic modulus is *E,* and shear modulus is *G*. The segment of *BC* is assumed as a rigid rod, thus, the displacement caused by deflection of *BC* is neglected. Try to calculate Δ_C at point *C*.

Cartesian coordinate system is marked as *O-ijk*, and natural coordinate system of the axis is marked as *D-*τ*nb*. *D* is arbitrary point of the helical curved beam. The parameter equation for point *D* on the helical curved beam can be expressed as

$$r_{OD} = R\cos ti + R\sin tj + Ktk \quad (6)$$

where, r_{OD} = the position vector of point *D*; *t* = the angle between axis *x* and *OD′*; *D′* = the projection of point *D* on the *O-xy* coordinate plane, *i j* and *k* = the unit vectors of Cartesian coordinate system.

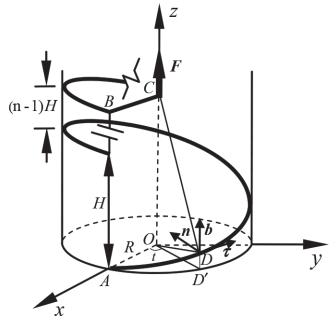

Figure 1. Model of the helical curved beam.

Based on the method of equivalent section (Liu 2011), we can obtain the principal vector of internal force F_R and principal moment of internal force *M* on cross section *D*, and can be expressed as

$$F_R = F = Fk \quad (7)$$

$$M = r_{DC} \times F = -FR\sin ti + FR\cos tj \quad (8)$$

The conversion relation for base vectors between Cartesian coordinate system and natural coordinate system is expressed as (Tuma & Walsh 2002)

$$\begin{Bmatrix} i \\ j \\ k \end{Bmatrix} = \begin{bmatrix} \alpha_\tau & \alpha_n & \alpha_b \\ \beta_\tau & \beta_n & \beta_b \\ \gamma_\tau & \gamma_n & \gamma_b \end{bmatrix} \begin{Bmatrix} \tau \\ n \\ b \end{Bmatrix} = \begin{bmatrix} \frac{-\sin t}{a} & -\cos t & \frac{\tan\varphi \sin t}{a} \\ \frac{\cos t}{a} & -\sin t & \frac{-\tan\varphi \cos t}{a} \\ \frac{\tan\varphi}{a} & 0 & \frac{1}{a} \end{bmatrix} \begin{Bmatrix} \tau \\ n \\ b \end{Bmatrix} \quad (9)$$

where,

$$a = \sqrt{1 + \tan^2\varphi} \quad (10)$$

$$K = H/2\pi = R\tan\varphi \quad (11)$$

Substituting Equations (9) into (7) and (8), we have

$$F_R = \begin{pmatrix} F_\tau & F_n & F_b \end{pmatrix}^T = \begin{pmatrix} \frac{F\tan\varphi}{a} & 0 & \frac{F}{a} \end{pmatrix}^T \quad (12)$$

$$M = \begin{pmatrix} M_\tau & M_n & M_b \end{pmatrix}^T = \begin{pmatrix} \frac{FR}{a} & 0 & \frac{-FR\tan\varphi}{a} \end{pmatrix}^T \quad (13)$$

Thus,

$$\bar{F} = \begin{pmatrix} \bar{F}_\tau & \bar{F}_n & \bar{F}_b \end{pmatrix}^T = \begin{pmatrix} \frac{\tan\varphi}{a} & 0 & \frac{1}{a} \end{pmatrix}^T \quad (14)$$

$$\bar{M} = \begin{pmatrix} \bar{M}_\tau & \bar{M}_n & \bar{M}_b \end{pmatrix}^T = \begin{pmatrix} \frac{R}{a} & 0 & \frac{-R\tan\varphi}{a} \end{pmatrix}^T \quad (15)$$

3.2 *The equations of vertical displacement at point C*

Substituting Equations (11), (14) and $dx^1 = (K^2 + R^2)^{1/2} dt$ into (5), we have

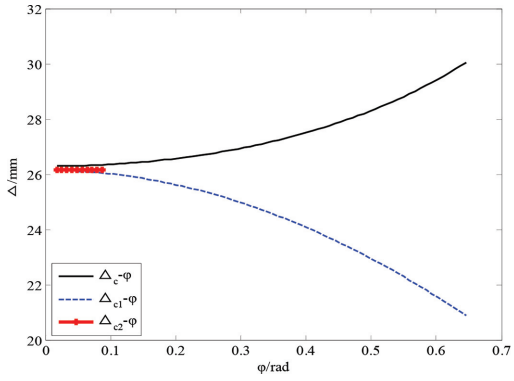

Figure 2. Curves of vertical displacements at point C with φ.

$$\Delta_C = F\sqrt{K^2+R^2}\,t_0\left[\frac{R^2}{GI_p a^2}+\frac{K^2}{EAa^2R^2}+\frac{K_b}{GAa^2}+\frac{K^2}{EI_3a^2}\right] \quad (16)$$

where, $A = \pi d^2/4$, polar moment of inertia $I_p = \pi d^4/32$, moment of inertia $I_3 = \pi d^4/64$.

When only the M_τ is considered, Equation (16) is reduced as

$$\Delta_{C1} = \frac{FR^2t_0}{GI_p a^2}\sqrt{K^2+R^2} \quad (17)$$

When φ is less than $\pi/36$ radian and r is far less than R, the vertical displacement can be approximately expressed as (Liu 1999)

$$\Delta_{C2} = \frac{64FR^3n}{Gd^4} \quad (18)$$

When $F = 2{,}510$ N, $t_0 = 2n\pi$, $n = 5$, $R = 240$ mm, $r = 24$ mm, $E = 210$ GPa, $G = 80$GPa, the variation of vertical displacements at point C with φ is shown as Figure 2.

In Figure 2, the solid line is obtained from equation (15), the dotted line is from Equation (16), and the asterisk line is from Equation (17). From Figure 2, we can see the effect of the torque to the vertical displacement is bigger with φ changing smaller. When φ is very small, the results obtained from Equations (15) to (17) are almost agreement. However, with the φ changing bigger, there is a bigger gap of data between the results obtained from Equations (15) to (17).

4 CONCLUSION

The equations for calculating displacements about helical curved beams which are derived by the authors are more general and extensive, that cannot be restricted to the φ. The equations can be used in the curved beam structures which need higher precision requirements. Essentially, the safety factor will be decreased in the case of only considering the effect of torque. Thus, the method established to calculate displacement of helical curved beams by authors is more meaningful.

REFERENCES

Chen, C.N. 2005. Differential quadrature element method analysis of in-plane deflection of vertically curved beam structures. *Computer-Aided Civil and Infrastructure Engineering* 20(2): 132–141.

Liu, H.W. 1999. *Mechanics of Materials.* Beijing: Higher Education Press.

Liu, J.M. 2011. *Mechanics of Materials.* Beijing: China Electric Power Press.

Qi, Z.C. 1981. The calculation of spiral stairways. *Building Structure* 01(05): 47–59.

Tore, D. 2004. Procedure to calculate deflections of curved beams. *Int. J. Eng Educ.* 20(3): 503–513.

Tuma, J.J. & Walsh, R.A. 2002. *Engineering Mathematics Handbook.* Beijing: Science Press.

Yuan, F.Y. & Chen, Q. 2013. Study on applicability of replacing the curve with a straight line to simplify the algorithm for curved girder bridge. *Engineering Construction* 45(2): 42–45.

Zeng, S., Chen, S.F., Qu, T. & Wang, H.D. 2010. Elasticity equations for spatial curved beams with large displacement and small rotation. *Engineering Mechanics* 27(12): 14–20.

Zhou, P.H., Zhang, Q.L. & Yang, X.L. 2012. Spatial curved beam model and mechanical analysis of elliptical spiral stairs. *Building Structure* 42(8): 137–141.

This page intentionally left blank

Civil Engineering and Urban Planning IV – Liu et al. (Eds)
© 2016 Taylor & Francis Group, London, ISBN 978-1-138-02903-3

Reinforcement optimization of Continuously Reinforced Concrete Pavement

Liu Qing, Zhi-Min Hu & Run-Hong Liu
University of South China, Hengyang, Hunan, China

ABSTRACT: Based on the simulation analysis of the orthogonal experiment which uses the panel thickness, concrete grade, longitudinal reinforcement ratio and longitudinal steel bar diameter as four horizontal factors by Abaqus, the most important sensitive parameter of Continuous Reinforced Concrete Pavement (CRCP) plate bottom stress is determined. Further, through the control of a single variable of the reinforcement rate, bar diameter, reinforcement position one by one to analysis the vehicle stress as well as temperature stress effect laws on continuous reinforcement concrete pavement, then puts forward a structural reasonable, economical concrete pavement reinforcement method.

1 INTRODUCTION

Continuous Reinforced Concrete Pavement (CRCP) is a kind of high performance concrete pavement structure, which is designed to reduce and eliminate the common diseases of ordinary concrete pavement. In 1921, the United States built the first CRCP trial section in Washington, D.C. (Garnham 1989). It has the advantages especially in the current heavy traffic volume and poor geological conditions such as comfortable driving, high bearing capacity, long service life, low maintenance cost, and the continuous reinforcement concrete road also has good effect in the road reconstruction process (Gregory 1983). However, the reinforcement is one of the important factors that affect the mechanical performance as well as economic cost of CRCP pavement. This paper uses the Abaqus to simulate the CRCP pavement and seek a reasonable and economical reinforcement scheme.

2 CRCP ORTHOGONAL EXPERIMENTAL DESIGN

The design of reinforcement for the reinforced concrete pavement mainly includes: the longitudinal reinforcement ratio, the bar diameter, and the position of the steel bar position. First, determine the horizontal factors of orthogonal test design. The CRCP with reinforcement design orthogonal test with four factors: A panel thickness, B concrete grade, C longitudinal reinforcement ratio, D longitudinal reinforcement diameter; adopt L^9 (3^4) orthogonal table to arrange the experiment as shown in Table 1 for the interaction among the factors and orthogonal test results as shown in Table 2.

2.1 *Visual analysis method*

The results were analyzed by the method of direct analysis, and the effect of the factors on the stress of CRCP was compared. As shown in Table 2, respectively mean the average numerical of the stress of the plate under the different level of the CRCP panel. The average value of the stress of the plate is reflected by the same factors as the different levels of the experimental results. At the same time, the optimum level of the factors is determined. And the influence of different factors on the experimental results is also influenced by the range of the difference.

Table 1. Orthogonal experimental design.

Serial number	1	2	3	4
Factor name	Panel thickness (cm)	Concrete grade	Longitudinal reinforcement ratio C (%)	Longitudinal reinforcement diameter (mm)
Level 1	27	C30	0.6	14
Level 2	30	C35	0.7	16
Level 3	33	C40	0.8	18

Table 2. Result of orthogonal experiment.

Factor	Panel thickness (cm)	Concrete grade	Longitudinal reinforcement ratio (%)	Longitudinal reinforcement diameter (mm)	Experimental stress results (MPa)
No. 1	27	C30	0.6	14	1.385
No. 2	27	C35	0.7	16	1.414
No. 3	27	C40	0.8	18	1.428
No. 4	30	C30	0.7	18	1.316
No. 5	30	C35	0.8	14	1.339
No. 6	30	C40	0.6	16	1.354
No. 7	33	C30	0.8	16	1.251
No. 8	33	C35	0.6	18	1.272
No. 9	33	C40	0.7	14	1.286
Average 1	1.409	1.317	1.337	1.337	
Average 2	1.336	1.342	1.339	1.340	
Average 3	1.270	1.356	1.342	1.339	
Range	0.139	0.039	0.012	0.013	

From Table 2 visual range analysis results can be seen in the range of the factors of the change, the effect of CRCP slab stress four sensitive parameters, the influence order from big to small: a > b > d > C. Under the load design of CRCP slab reinforcement scheme, panel thickness is the main factors affect the panel reinforcement and the best combination of factors in the orthogonal test of CRCP panel design. A3B3C2D2 is recommended.

3 CRCP REINFORCEMENT OPTIMIZATION DESIGN

ABAQUS modeling basic calculation parameters: concrete panel thick By the CRCP reinforcement design of orthogonal test the best panel corresponding to the reinforcement scheme combination, only for the various factors and conditions of best which need to be considered is not comprehensive enough. Therefore need to further optimize. In order to determine the reasonable reinforcement scheme, establish the finite element model, control the single variable, and analyze the change of the stress.

Ness h1 = 0.28 cm, modulus E = 30 GPa; Poisson's ratio μ = 0.15, density 2400 kg/m^3, thermal conductivity of 1.5 W/(m•K), specific heat capacity 0.980 KJ/Kg°C; base modulus thickness h2 = 22 cm, E = 1800 GPa, Poisson's ratio μ = 0.20; subbase thickness h3 = 20 cm, modulus E = 1400 GPa, Poisson's ratio μ = 0.20; subgrade modulus E = 100 MPa, Poisson's ratio μ = 0.28; reinforced parameters: longitudinal bar diameter d = 16 mm, modulus E = 210 GPa, Poisson's ratio μ = 0.10; transverse reinforcement diameter d = 14 mm; reinforcement spacing a = 0.5 cm, modulus E = 210 GPa, Poisson's ratio μ = 0.10; based on norms of cement concrete pavement design life of 30 years, the cumulative number of axle load values by especially heavy traffic, load type selection BZZ-100 wheel set of standard uniaxial load, load at worst load position crack spacing L = 1 m, crack width l = 1 mm; temperature stress calculation of the maximum temperature gradient value takes Tg = 88 (°C/m). Overall stress for CRCP is as shown in Figure 1.

3.1 *Effect of reinforcement ratio on the panel fatigue stresses*

As is shown in Figure 2, the panel fatigue stress decreases with the reinforcement ratio increasing. It decreases greatly between the range of 0.3%–0.6%. When the reinforcement ratio is lower than 0.3%, the fatigue stress exceeds the cement concrete flexural tensile strength standard value; when greater than 0.6%, the magnitude of this reduction is smooth. When the reinforcement ratio exceeds 0.7%, it will have little positive effect on the stress of the structure but result in the corresponding increasing amount of steel bars. According to the orthogonal experiment results, the panel reinforcement rate suggested between 0.7%–0.8% is reasonable and economic.

3.2 *Effect of steel bar diameter on the principal stress of the vehicle load on the panel*

The orthogonal experiment result shows that the longitudinal bar diameter is not significant for panel structure stress through controlling a single variable for further understanding of its role in the structure. So, taking the longitudinal reinforcement ratio 0.75% and keeping other parameters constant to build the finite element calculation model, only

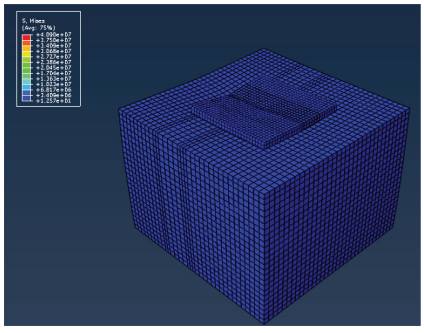

Figure 1. Overall stress for CRCP.

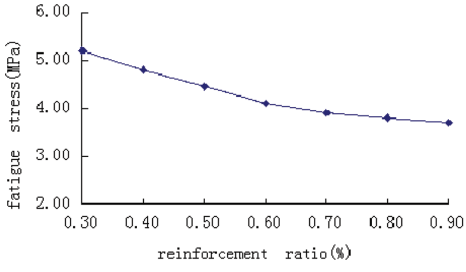

Figure 2. Reinforcement ratio and panel fatigue stress diagram.

change the diameter of the steel bar and the results are shown in Figure 3.

Table 3 shows when reinforcement rate remained constant, the reinforcement spacing increases with the increasing diameter of longitudinal reinforcement. Figure 3 calculation result shows that with the increasing of bar diameter, the panel vehicle load stress increases slightly, but it is not too obvious. The smaller of bar diameter, the smaller of bar spacing, then forming a tight steel mesh. So that the road structure under vehicle loads relatively uniform. Naturally, the reinforced steel bars are far from reaching its yield strength. Consider the structural characteristics and construction technology of the structure, it is suggested that the diameter of the steel bar for 14 mm–16 mm is reasonable and application.

3.3 *Effect of steel bars position on the principal stress of the vehicle load on the panel*

Section reinforced placement is reinforcement scheme design is one of the main contents and Figure 4 analysis the changing stresses of steel bars in section position of 1/3, 1/2, 2/3 of the CRCP slab under the vehicle and temperature load. Figure 5 analysis the changing stresses of transverse reinforcement in 30–80 cm under vehicle load.

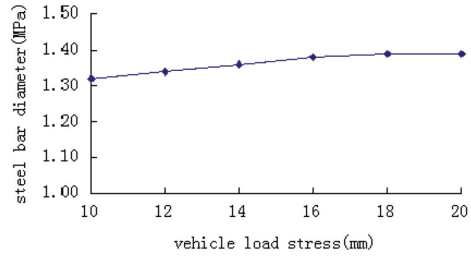

Figure 3. Effect of steel bar diameter on the principal stress of the vehicle load on the panel.

Table 3. Longitudinal reinforcement spacing corresponding to the diameter of the bar.

The diameter of the bar (mm)	10	12	14	16	18	20
Transverse distance	3.5	5.5	7	9.5	12	15

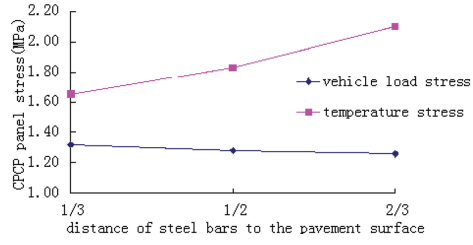

Figure 4. Effect of steel bars position on the principal stress of the vehicle load on the panel.

Figure 4 shows reinforced pitch road surface distance from the vehicle at the change of 1/3 to 2/3 tends to decrease, but stress slightly reduces. Steel bars position has little effect on the principal stress of the vehicle load on the panel. However, the temperature stress increases with the larger distance to the road surface and the growth rate was significantly greater than the magnitude of under vehicle loads. Steel bars position has a great influence on CRCP pavement temperature stress. In this paper, the results of the reinforced section and the design code of concrete pavement in China are consistent with the requirements of the steel bar design.

Figure 5 shows that the transverse reinforcement holds up and participates in the structure of the CRCP plate, and the main stress of the CRCP plate increases by 45.5% as the rises of the steel bars spacing from 30 to 80 cm. At present, the design of pavement design specification for in China is only considers the horizontal bar as the supporting structure (Industry standard of the People's Republic of China 2011). In this paper,

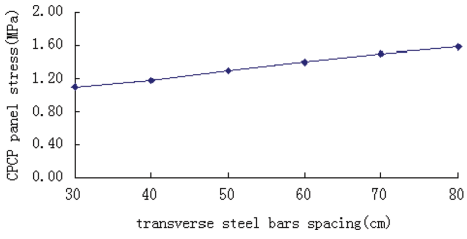

Figure 5. Effect of transverse distance on the principal stress of the vehicle load on the panel.

the calculation results show that transverse reinforcement effect stress of CRCP pavement. At the same time, transverse reinforcement design, integrated its structure characteristics and economic factors suggested transverse reinforcement spacing take between 30–45 mm is reasonable, economical and applicable.

4 CONCLUSIONS

- The panel reinforcement scheme design and orthogonal experiment under vehicle loads calculation results showed that the panel reinforcement scheme design factors order of magnitude is the panel thickness, grade of concrete, longitudinal steel bars diameter, longitudinal reinforcement rate;
- According to the analysis of the fatigue stress and the results of the orthogonal test of the reinforced concrete, it is suggested that the rate of the longitudinal reinforcement takes 0.7%–0.8% and the longitudinal steel bar diameter is recommended for 14 mm–16 mm by controlling a single variable.
- According to the analysis of the transverse CRCP pavement stress results, combine the stress characteristics of structure and economic factors. Horizontal bar spacing between 12 mm–16 mm is recommended which is reasonable, economical and applicable.

ACKNOWLEDGMENTS

This project was supported by the National Natural Science Foundation of China (grant no. 51304122), the university innovation platform open fund projects of Hunan province (grant no. 14K082) and the Young talents program of the University of South China (grant no. 2014-001).

REFERENCES

Garnham, M.A. 1989. The development of CRCP design curves. *Highways & Transportation* 36(12): 14–18.

Gregory, J.M. 1983. *Continuously Reinforced Concrete Overlays of Flexible Pavements on Trunk Road A2*. London: Transport and Road Research Laboratory.

Industry standard of the People's Republic of China. 2011. *Highway Cement Concrete Pavement Design Specifications.* Beijing: The Traffic People Press.

Civil Engineering and Urban Planning IV – Liu et al. (Eds)
© 2016 Taylor & Francis Group, London, ISBN 978-1-138-02903-3

A gray-fuzzy evaluation method for soft foundation treatment based on genetic algorithm

Yue-Ping Sun
Cangzhou City Administration of Highway Construction, Cangzhou, Hebei, China

ABSTRACT: Aimed at the subjectivity of the current soft foundation evaluation and clear grayness and ambiguity of the evaluation information, the gray-fuzzy comprehensive evaluation method for the soft foundation treatment based on the genetic algorithm was proposed. First, an evaluation index system hierarchy model was established using a Delphi method; then, the weight factor of each index to the soft foundation treatment was determined by AHP law, and the accelerating genetic algorithm was applied to determine the consistency of the judgment matrix; pros and cons of the various options were drawn based on the gray-fuzzy comprehensive evaluation method. Finally, the feasibility of the method was verified by instance analysis.

1 INTRODUCTION

Soft soil foundation generally refers to the compression layer including fill, silty soil, miscellaneous fill, or the foundation consisting of other highly compressible soils. Its instability often makes the road crack, sink, or even develop potholes. In order to eliminate the adverse effects of the soft soil foundation on the overall stability of the road, the stability of the soft soil foundation needs to be enhanced, the side sliding displacement needs to be eliminated, and the shallow or deep processing must be carried out on the soft soil foundation. Road soft foundation treatment schemes consist of single treatment methods, such as soil removal and replacement, drainage consolidation method, dynamic compaction, compaction and chemical strengthening method, and composite treatment schemes constitute two or more treatment methods (Feng et al. 2002; Pan et al. 2012).

There are a lot of decision-making problems in the comprehensive evaluation of the highway soft foundation treatment technology. Many factors have the effect on the choice of the soft foundation treatment schemes, including project investments, materials and equipments, environmental impacts, geological conditions, and personnel status. Due to the subjective judgments and difficulty of direct quantifications, most of the soft foundation treatment projects will depend on the experience of the engineering personnel, which increase the uncertainty of the effect of the foundation treatment. How to convert the experience of decision-making to the objective and smart decisions and choose reasonable soft foundation treatment schemes is a problem that needs to be solved for the engineering personnel, and also the main direction of the soft foundation treatment scheme evaluation.

In recent years, many researchers have proposed a variety of soft foundation treatment decision-making methods to optimize the soft foundation treatment scheme, such as principal component analysis, fuzzy comprehensive evaluation method, AHP, neural network, gray correlation method, and case-based reasoning method. Different decision models were established by combining various theoretical and actual situations. Among them, the gray correlation evaluation method and fuzzy comprehensive evaluation method have been widely applied in many fields, and have also achieved satisfactory results. However, shortcomings exist in policy-making models, which need to be optimized continually (Liu et al. 1999).

In the comprehensive evaluation of the soft foundation treatment scheme, the fuzzy evaluation method has been widely applied due to the fuzziness of evaluation criteria; on the other hand, a certain gray level of evaluation information due to the different abilities and preferences of the judge provides a basis for the application of gray theory in the comprehensive evaluation of the soft foundation treatment scheme. Therefore, there exist grayness and ambiguity in the comprehensive assessment of the soft foundation treatment scheme. It will result in the loss of information only using the fuzzy method; it cannot take full advantage of the characteristics of ambiguity only using the gray theory. Both of them will result in the deviation between evaluation results and actual situations, so the impact of both ambiguity and

grayness requires to be taken into account during the comprehensive evaluation (Xia 1997).

Based on existing research results, the evaluation system of the soft foundation treatment scheme was built scientifically. A gray-fuzzy comprehensive evaluation method for the soft foundation treatment based on a genetic algorithm was established by combining the gray theory and fuzzy evaluation method and applying acceleration genetic algorithm to test the consistency of judgment matrix, which has a theoretical and practical significance.

2 THE BASIC PRINCIPLE OF GRAY AND FUZZY ALGORITHM

Gray system theory, which deals with complex system theory from the completeness of information, rather than a special rule inside the system, knows the mechanisms of internal trends, mutual relations of systems in the higher level through the observation data and mathematical treatment. Its mathematical method is not a statistical method, and requires few data in system and conditions without meeting the requirements (Yu 2004).

Fuzzy mathematics is a tool used to process fuzzy information, and also a mathematical method to describe and process fuzzy information. It makes mathematics enter into the objective existence world with fuzzy phenomena. It is a bridge between the traditional classical mathematics and fuzzy real world. The essence and laws of the fuzzy phenomena are revealed through mathematics method.

2.1 *The basic theory of gray-fuzzy algorithm*

If $\tilde{A}$ is a fuzzy subset of space $X = \{x\}$, x is a gray number in [0,1] for the membership $\mu_A(x)$ of $\tilde{A}$, the point of gray level is $V_A(x)$ and A is the subset of $\tilde{A}$, $\tilde{A}$ is known as gray fuzzy or gray fuzzy sets in x, referred to as GF collection, $\underset{\otimes}{\tilde{A}}$, namely

$$\underset{\otimes}{\tilde{A}} \triangleq \left\{ \left(x, \mu_A(x), \nu_A(x) \right) \middle| x \in X \right\}$$

The equation can be expressed by "set pairs" as $\underset{\otimes}{\tilde{A}} = \left(\tilde{A}, \underset{\otimes}{A} \right)$. Among them, $\tilde{A} = \{(x, \mu_A(x)) | x \in X\}$ is known as the fuzzy areas of $\underset{\otimes}{\tilde{A}}$; $A = \{(x, \nu_A(x)) | \mu_A(x) > 0, x \in X\}$ is the gray section of $\underset{\otimes}{\tilde{A}}$. If the gray section $\underset{\otimes}{\tilde{A}}$ of GF set $\underset{\otimes}{\tilde{A}}$ is the classical set A, then $\underset{\otimes}{\tilde{A}} = (\tilde{A}, A) = \tilde{A}$. So the fuzzy set is a special case of gray fuzzy sets, and if the mold part $\tilde{A}$ of GF set $\underset{\otimes}{\tilde{A}}$ is the classical set A, then $\underset{\otimes}{\tilde{A}} = \left(A, \underset{\otimes}{A} \right) = \underset{\otimes}{A}$. So the gray set is a special case of gray fuzzy sets. Therefore, the gray fuzzy set is a promotion of both fuzzy and gray, and also a promotion of classical sets.

Given that space X = {x}and Y = {y}, if the gray of x and y to the membership μ_R(x,y) of fuzzy relation $\tilde{R}$ is $\nu_R(x,y)$, the direct product space X × Y is called gray fuzzy sets, referred to as GF relationship:

$\underset{\otimes}{\tilde{R}} = \left\{ \left((x,y), \mu_R(x,y), \nu_R(x,y) \right) \middle| x \in X, y \in Y \right\}$ is a gray fuzzy relation on X × Y, which can also be represented in the form of the gray fuzzy matrix:

$$\underset{\otimes}{\tilde{R}} = \left[\left(\mu_{ij}, \nu_{ij} \right) \right]_{m \times n} = \begin{bmatrix} (\mu_{11}, \nu_{11}) & (\mu_{12}, \nu_{12}) & \cdots & (\mu_{1n}, \nu_{1n}) \\ (\mu_{21}, \nu_{21}) & (\mu_{22}, \nu_{22}) & \cdots & (\mu_{2n}, \nu_{2n}) \\ \cdots & \cdots & \cdots & \cdots \\ (\mu_{m1}, \nu_{m1}) & (\mu_{m2}, \nu_{m2}) & \cdots & (\mu_{mn}, \nu_{mn}) \end{bmatrix}$$

GF relationship can also be expressed as: $\underset{\otimes}{\tilde{R}} = \left(\tilde{R}, \underset{\otimes}{R} \right)$, where $\tilde{R}$ is the fuzzy relation on X × Y, and $\underset{\otimes}{R}$ is the gray relationship on X × Y.

If $\underset{\otimes}{R}$ and $\underset{\otimes}{\tilde{R}}$ are the GF relations on X × Y and Y × Z, the synthesis relationship of $\underset{\otimes}{R}$ and $\underset{\otimes}{\tilde{S}}$ is given by

$$\underset{\otimes}{\tilde{R}} \circ \underset{\otimes}{\tilde{S}} = \left\{ \left((x,z), \bigvee_{y \in Y} \left(\mu_R(x,y) \wedge \mu_S(y,z) \right), \bigwedge_{y \in Y} \left(\nu_R(x,y) \wedge \nu_S(y,z) \right) \right) \middle| x \in X, y \in Y, z \in Z \right\}$$

2.2 *Gray-fuzzy comprehensive evaluation method*

The mathematical model and the method of gray-fuzzy comprehensive evaluation were provided according to the gray-fuzzy theory and common fuzzy evaluation methods.

2.2.1 *The establishment of the evaluation index system*

The factors of the soft foundation treatment scheme were attributively classified according to the system engineering and system hierarchy theory to build index system hierarchical structure model, which can be divided into the target layer, primary index layer, and secondary index layer. The evaluation index system was finally determined by the Delphi method and collecting statistical information.

2.2.2 *Determination of the weight set of evaluation index*

Guideline layers and schemes were used to determine the weight value through the AHP method.

This method requires less information and shorter time to make decisions. The process of the realization of the AHP method is as follows [6].

– The construction of the judgment matrix
If the index set of some floor is $A=\{A_1, A_2, \ldots, A_n\}$ and a scale of 1 to 9 ratio method is introduced, the judgment matrix is constructed by comparing the importance of layer of all the factors on pairwise as follows:

$$A=\begin{bmatrix} a_{11} & a_{12} & \cdots & a_{1n} \\ a_{21} & a_{22} & \cdots & a_{2n} \\ \cdots & \cdots & \cdots & \cdots \\ a_{n1} & a_{n2} & \cdots & a_{nn} \end{bmatrix}$$

where $a_{ij}(i, j=1, 2, \ldots, n)$ represents the relative importance of A_i and A_j, and has the following properties:

$$a_{ij}>0;\ a_{ii}=a_{jj}=1;\ a_{ji}=1/a_{ij}$$

– Single hierarchical arrangement and consistency check based on the genetic algorithm
Analyzing solution of the eigenvalue matrix $MW=\lambda_{\max}W$ in judgment matrix is W, which is the relative ranking of importance weights between the factors in the same layer and the factors in the previous level after normalization. If the weight ranking of each factor is $W_i(i=1, 2, \ldots, n)$ and meets $0<W_i<1$ and $\sum_{i=1}^{n} W_i=1$. There is $a_{ij}=\frac{W_i}{W_j}$ according to the definition of the judgment matrix theory. A single ranking weight of each factor and consistency test can boil down to the following nonlinear optimization problem:

$$\min CIF(n)=\frac{1}{n(n-1)}\sum_{i=1}^{n}\sum_{j=i+1}^{n}\left(a_{ij}\frac{W_j}{W_i}+a_{ji}\frac{W_i}{W_j}-2\right)$$

where $CIF(n)$ is the consistency index function. The formula is a nonlinear optimization problem. It is very simple and effective by Accelerating Genetic Algorithm (AGA) to solve this problem and the main steps of accelerating the genetic algorithm are: ① discrete and coding of initial change in the space; ② random generation of initial parent groups; ③ decoding and fitness of parent individuals list; ④ probability of selection and hybridization of parent individuals; ⑤ variation of offspring; ⑥ evolutionary iteration; ⑦ acceleration cycle. Variable space, generated by outstanding individuals in the first, second, and second iterations of the evolutionary, is a variable interval of the new initial change to enter step ① and rerun the standard genetic algorithm. The entire algorithm will end until the criterion function value of the optimization individual is smaller than a set value or algorithm acceleration reaches a predetermined number of cycles (Wang et al. 2002).

The consistency index coefficient CIF (n) value is different for the judgment matrix in different orders n. When CIF (n) < 0.1, the judgment matrix has satisfactory consistency, and the weight W_i of each index value calculated is acceptable; otherwise, the judgment matrix A needs to be adjusted until a satisfactory consistency is reached.

2.2.3 *The determination of the evaluation grade of the comprehensive evaluation and the sample matrix*

If evaluation grade is $V=\{V_1, V_2, \ldots, V_p\}$, serial number of evaluation specialists is $i(i=1, 2, \ldots, n)$, and the evaluated is $j(i=1, 2, \ldots, m)$, $D_{ij}^{(A)}$ as the evaluation index value sample matrix of evaluation specialists i on index factor A is the evaluated object j, i.e.:

$$D_{ij}^{(A)}=\begin{bmatrix} d_{11}^{(A)} & d_{12}^{(A)} & \cdots & d_{1j}^{(A)} \\ d_{21}^{(A)} & d_{22}^{(A)} & & d_{2i}^{(A)} \\ \vdots & & & \vdots \\ d_{i1}^{(A)} & d_{i2}^{(A)} & \cdots & d_{ij}^{(A)} \end{bmatrix}$$

2.2.4 *Determination of the assessment gray class*

The determination of the assessment gray is to determine the rank number, gray number and the number of gray whitenization weight functions. The evaluation gray class is divided into three levels, namely the upper class, middle class, and lower class and its gray type; whitening weight function is represented as follows:

If the gray number is $\otimes\in[d_1, \infty)$ in the upper class, the whitening power function is:

$$f_1(d_{ij})=\begin{cases} \dfrac{d_{ij}}{d_1}, & d_{ij}\in[0, d_1] \\ 1, & d_{ij}\in[d_1, \infty) \\ 0, & d_{ij}\in(-\infty, 0) \end{cases}\rightarrow$$

If the gray number is $\otimes\in[0, d_1, 2d_1]$ in the middle class, the whitening power function is:

$$f_2(d_{ij})=\begin{cases} \dfrac{d_{ij}}{d_1}, d_{ij}\in[0, d_1] \\ 2-\dfrac{d_{ij}}{d_1}, d_{ij}\in[d_1, 2d_1] \\ 0,\ d_{ij}\notin(0, 2d_1] \end{cases}$$

If the gray number is $\otimes \in (0, d_1, d_2)$ in the lower class, the whitening power function is:

$$f_3(d_{ij}) = \begin{cases} 1, d_{ij} \in [0, d_1] \\ \dfrac{d_2 - d_{ij}}{d_2 - d_1}, d_{ij} \in [d_1, d_2] \\ 0, d_{ij} \notin (0, d_2] \end{cases}$$

The gray evaluation coefficient $C_{ik}^{(A)}$ belongs to k classes determined by the evaluation objective j on evaluation index A through $D_{ij}^{(A)}$ and $f_k(d_{ij})$, and shown as $C_{ik}^{(A)} = \sum_{i=1}^{m} f_k\left(d_{ij}^{(A)}\right)$.

Total gray evaluation coefficient $C_j^{(A)}$ is

$$C_j^{(A)} = \sum_{i=1}^{n} C_{ij}^{(A)}.$$

The gray evaluation $r_{ik}^{(A)}$ belongs to the k classes determined by the evaluation matrix A on the estimator j through $C_{ik}^{(A)}$ and $C_j^{(A)}$, and shown as $r_{ik}^{(A)} = \dfrac{C_{ik}^{(A)}}{C_j^{(A)}}$.

So a gray evaluation weight matrix of all the evaluated objects for the evaluation indices A is:

$$R^{(A)} = \begin{pmatrix} r_{11}^{(A)} & r_{12}^{(A)} & \cdots & r_{1k}^{(A)} \\ r_{21}^{(A)} & r_{22}^{(A)} & & r_{2k}^{(A)} \\ \vdots & & & \vdots \\ r_{i1}^{(A)} & r_{i2}^{(A)} & \cdots & r_{ij}^{(A)} \end{pmatrix}$$

2.2.5 *Calculation of the gray-fuzzy comprehensive evaluation results*

Comprehensive evaluation matrix B is obtained by the fuzzy arithmetic with the index weight set and gray evaluation matrix:

$$B = W \circ R^{(A)}$$

which again is normalized to meet $\sum_{i=1}^{m} B_i = 1$.

The review set is $V = \{V_1, V_2, \ldots, V_p\}$ and comprehensive evaluation result Z of the evaluated is $Z = B \cdot V^T$.

3 INSTANCE ANALYSIS

3.1 *Project profile*

Taking a soft foundation treatment project as an example, silt and clay in the soft foundation section was fluid plastic and soft plastic state, so it must be treated in order to build the embankment. Construction units proposed a high demand to the duration and effect, which was an important factor of technical decisions.

We carried out a comprehensive evaluation on vibro gravel pile, plastic drainage board, two ash piles and powder mixing piles and other programs with a gray-fuzzy comprehensive evaluation method for the soft foundation treatment based on the genetic algorithm and selected the best solution.

3.2 *Calculation and analysis*

– The contrastive hierarchical structure model of the soft foundation treatment scheme
  The evaluation index system determined by the 10 experts is shown in Table 1, and the structure is the hierarchical structure.
– Weight value of the first-class index level and second-class index level
  Judgment matrix of the guideline layer is shown in Table 2 and judgment matrices of index layer are shown in Tables 3–5.
  W is the ranking value of relative importance of factors with the above layer.
– Determination of the sample matrix and gray weight matrix
  Evaluation order of the soft treatment scheme is divided into four levels: excellent, good, middle, bad. Its corresponding scores are 4, 3, 2, and 1.
  Taking the scenario 1 vibro gravel pile as an example, we employed 10 experts to score 9 indices in the C layer scoring, and the sample matrix of the expert evaluation is shown in Table 6.

Table 1. The evaluation index system of the soft foundation treatment scheme.

Target layer	Primary index layer	Secondary index layer	Project layer
General objective A best option	B1 economy	C1 investment, C2 amount of maintenance	D1 gravel pile method
	B2 technicality	C3 technical reliability, C4 treatment effect, C5 construction difficulty, C6 duration	D2 plastic drainage plate D3 two-ash pile
	B3 environment	C7 noise, C8 resource consumption, C9 influence on building	D4 powdered mixed-pile

Table 2. Judgment matrix of guideline layer.

A	B1	B2	B3
B1	1	2/3	1/5
B2	3/2	1	3
B3	5	1/3	1

Table 3. Judgment matrix 1 of index layer.

B1	C1	C2
C1	1	5
C2	1/5	1

Table 4. Judgment matrix 2 of index layer.

B2	C3	C4	C5	C6
C3	1	1	2/3	1/5
C4	1	1	5	1/3
C5	2/3	1/5	1	1/7
C6	5	3	7	1

Table 5. Judgment matrix 3 of index layer.

B1	C1	C2	C3
C1	1	3	5
C2	1/3	1	3/2
C3	1/5	2/3	1

Table 6. Sample matrix of expert evaluation.

3.5	4.0	2.5	3.0	4.0	4.0	3.0	2.5	2.0	3.5
3.0	3.5	4.0	1.5	2.0	3.5	1.5	2.0	2.5	4.0
2.5	1.5	2.0	2.5	3.5	4.0	3.5	3.5	2.0	3.0
4.0	1.5	2.0	3.0	3.5	3.0	4.0	2.0	1.0	4.0
3.5	2.5	3.0	2.5	3.0	3.5	3.0	1.5	1.5	3.0
3.0	3.0	3.5	3.5	3.0	3.5	3.0	1.5	1.5	4.0
2.5	3.5	2.5	3.0	2.5	2.5	4.0	2.5	2.0	3.0
4.0	2.5	4.0	3.5	4.0	2.5	4.0	1.5	3.5	3.5
4.0	1.0	2.5	2.5	2.0	3.0	3.5	1.0	2.5	3.5

Its corresponding gray number and whitening weight function are:

First gray type is "excellent," gray number is $\otimes \in [4,\infty)$, whitening weight function is the first stage;

Second gray type is "good," gray number is $\otimes \in [0,3,6]$, whitening weight function is the second stage;

Third class gray is "middle," gray number is $\otimes \in [0,2,4]$, whitening weight function is the second stage;

Fourth gray type is "bad," gray number is $\otimes \in [0,1,2]$, whitening weight function is the third stage;

Gray evaluate weight matrix $R^{(1)}$ of scenario 1 was obtained.

– Calculation of gray fuzzy comprehensive evaluation results:

$$B = W \circ R^{(1)} = (0.4071, 0.3222, 0.1426, 0.1280)$$

Other solutions adopted the same evaluation method, and the results are shown in Table 7.

Table 7. Comprehensive evaluation results of each scheme.

	Evaluation results			
Scheme	Excellent	Good	Middle	Bad
1	0.4071	0.3222	0.1426	0.1280
2	0.5270	0.2674	0.1081	0.0975
3	0.2880	0.3813	0.2844	0.0463
4	0.1947	0.3745	0.3446	0.0863

According to the results in Table 7, the comprehensive evaluation results Z of scheme 1 can be obtained $Z = B \cdot V^T = 3.01$.

Thus, four schemes can be ranked as superior to inferior as scheme 1 (3.01 points), scheme 4 (2.95 points), scheme 3 (2.38 points), and scheme 2 (2.23 points).

4 CONCLUSION

This paper established the evaluation method of the soft foundation treatment scheme by the combination of Delphi method, AHP method, genetic algorithms, and gray-fuzzy comprehensive evaluation method. This method avoided the uncertainty and inadequate information of the soft foundation treatment scheme, and the application of the acceleration genetic algorithm to test the consistency of the judgment matrix made the evaluation results more reasonable. Furthermore, the feasibility of the method was verified by instance analysis.

REFERENCES

Feng, Z.R., Zhu, R.G. & Yao, A. 2002. Multi-layer fuzzy decision for improvement of expressway foundation. *Chinese Journal of Rock Mechanics and Engineering* 21(6): 915–918.

Pan, R.C., Huang, R.Z. & Zhou, X.N. 2012. The research of the treatment scheme selection for the soft soil foundation of road engineering. *Highway and Transportation Research* 94(10): 23–27.

Liu, R.L., Tan, G.H. & Li, Q.G. 1999. The stability of rock slope and fuzzy comprehensive evaluation method. *Chinese Journal of Rock Mechanics and Engineering* 18(2): 170–175.

Xia, Y.Y. 1997. *Researches on an Integrated Intelligent Decision Support System for Slope Engineering*. Beijing: University of Science and Technology Beijing.

Yu, X.F. 2004. Evaluation methods of comprehensive multiple indicators. *Statistics and Decision* 11(1): 119–121.

Zhao, H.C., Xu, S.B. & He, J.S. 1996. *Analytic Hierarchy Process.* Beijing: Science Press.

Wang, S., Tang, X. & Zeng, Y. 2002. A research on combination forecasting approach based on accelerating genetic algorithm. *Science Research Management* 23(3): 118–121.

Civil Engineering and Urban Planning IV – Liu et al. (Eds)
© 2016 Taylor & Francis Group, London, ISBN 978-1-138-02903-3

One-way expansion of compacted lateritic soil and prediction of crack closure time

Wei Bai, Ling-Wei Kong & Rong-Bing Lin
State Key Laboratory of Geomechanics and Geotechnical Engineering, Institute of Rock and Soil Mechanics, Chinese Academy of Sciences, Wuhan, Hubei, China

ABSTRACT: Consolidation apparatuses are applied to explore one-way expansion of compacted lateritic soil with five different initial dry densities and four different initial water contents. Results indicate that the expansion process can be divided into three stages: an initial expansion stage, a rapid expansion stage, and a stable stage during the whole experiment time. The lower the initial water content, the larger the final amount of expansion soil under the same initial dry density; the greater the initial dry density, the larger the final amount of expansion soil under the same initial water content. According to the calculated expansion deformation of the soil, the crack closure time can be predicted.

1 INTRODUCTION

Because lateritic soil has the properties of high water sensitivity and high liquid limit, it will more easily fissure than ordinary clay during the drying process. The lateritic soil surface is always separated by a crack network, and the shapes of the clods closely resemble quadrangles or pentagons (Bai et al. 2012). Fissures in lateritic soil are the main channel of rainfall infiltration and the existence of the fissures increase the infiltration rate greatly. Previous studies have indicated that the hydraulic conductivity of cracked clay is several orders of magnitude greater than that of intact clay (Albrecht et al. 2001; Bouma et al. 1979; Boynton et al. 1985; Ketelaars et al. 1994), which suggests that the hydraulic properties of soil are controlled by desiccation crack networks (Chertkov 1998; Chertkov 1999; Chertkov 2000). In the process of rainwater infiltration into lateritic soil, its infiltration rate is not a fixed value. For unsaturated fissured lateritic soil, the soil will expand and gradually close the fissures with the increase of water content. That is the reason the permeability coefficient of soil gradually changed. This phenomenon is commonly referred to as soil self-healing. The process can be considered as the soil around the fissure is expanded with water immersed into it, which makes the crack close gradually. Due to the preferential flow phenomenon in the process of infiltration process, the fissure is filled with water earlier, and then the soil self-healing occurs. Although the expansion of soil mass is a three-dimensional process, the expansion process is closing to one-way expansion for a single crack. Therefore, it is an important way to explore expansion of compacted lateritic soil by studying the process of one-way immersion expansion deformation.

In this investigation, the consolidation apparatus is applied to explore one-way expansion of compacted lateritic soil and prediction of crack closure time.

2 MATERIALS AND TEST METHOD

2.1 *Materials*

Lateritic soil is widely distributed in several southwestern provinces of P.R. China. These provinces include Hunan, Guizhou, Yunnan, and Guangxi (Zhao et al. 2004). The effects of the alternating seasons in this region cause lateritic soil to undergo repeated cycles of wetting and drying, thus resulting in the formation of abundant shrinkage cracks or fissures. The disturbed lateritic soil samples (depth: 0.8–1.5 m) were taken from Chenzhou section, Hunan Province. The soil transported to the laboratory was air-dried, crushed, and sieved through a 2-mm sieve.

The basic Geotechnical properties are below: specific gravity is 2.75, liquid limit is 65.2%, plastic limit is 34.7%, plasticity index is 30.5%, according to the Unified Soil Classification System, the group symbol is MH, optimum water content is 23.2%, and the maximum dry density is 1.66 g·cm^{-3}, whose mineral include chlorite (20%), feldspar (5%), illite (15%), kaolinite (25%), quartz (30%), hematite (5%). The grain composition is shown in Table 1.

Table 1. The grain composition of the lateritic soil.

Grain size (μm)					
Grain composition	75~50	5~10	10~5	5~2	<2
Value (%)	17.8	39.3	10.6	8.1	24.2

2.2 *Test method*

Firstly, crush the air-dried soil artificially, and put through a 2-mm sieve, and measure its water content. Calculate the required water of soil samples with different initial water content, which are set as 30%, 25%, 20%, 16%, separately. Thereafter, spray the required water on soil with an atomizer and mix it for 30 minutes at the same time. And then, put it into a hermetic bag, and then store it in a wet-protection cylinder for 24 hours to make the distribution of humidity uniform.

Secondly, calculate required wet soil's quality according to the expected dry density of soil and put corresponding quality of wet soil into a well-prepared sample pressure, level the sample surface, and press the sample soil into the preparation mould (inner diameter is 61.8 mm and height is 20 mm) with static pressure. Five dry densities were considered, they are as follows: 1.30 g/cm^3, 1.38 g/cm^3, 1.46 g/cm^3, 1.54 g/cm^3, 1.58 g/cm^3; four types of initial water content are prepared as follows: 30.8%, 23.4%, 19.1%, 14.7%.

Because the surrounding lateritic soil of fissure has a one-way immersion condition, a one-way immersion was used in the experiment. The automatic acquisition instrument was applied to record the deformation of soil samples, the time intervals of record were 0.1 min, 0.25 min, 1 min, 2.25 min, 4 min, 6.25 min, 9 min, 12.25 min, 16 min, 20.25 min, 25 min, 30.25 min, 36 min, 49 min, 60 min, 2 h, 4 h, 23 h, 24 h. In the process of experiment, water quantity should be replenished in time to avoid the loss of water due to evaporation. The deformation of 6 h cannot have more than 0.01 mm as the termination condition of the test.

3 RESULTS

One-way expansion curves of compacted lateritic soil with different initial dry density and initial water contents are shown as Figures 1 and 2.

It can be seen from Figures 1–6, the lower the initial water content, the larger the final amount of expansion soil under the same initial dry density; the greater the initial dry density, the larger the final amount of expansion soil under the same initial water content.

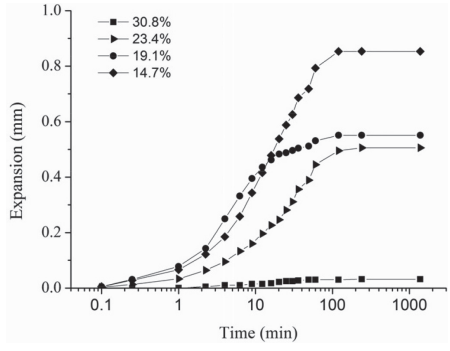

Figure 1. Relationship between one-way expansion and time of ρ_d = 1.58 g/cm^3.

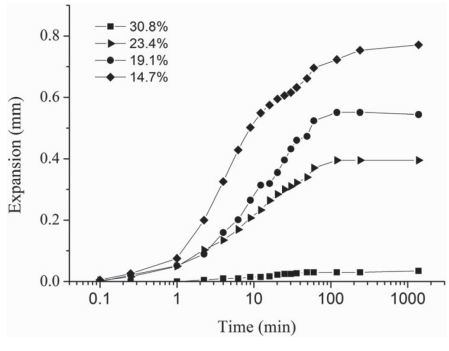

Figure 2. Relationship between one-way expansion and time of ρ_d = 1.54 g/cm^3.

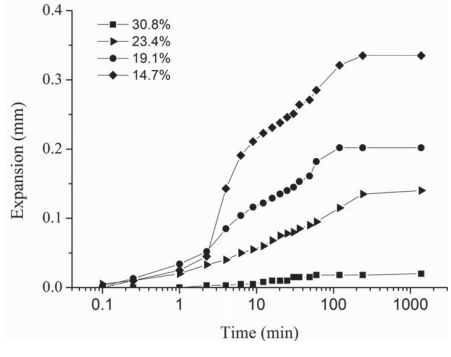

Figure 3. Relationship between one-way expansion and time of ρ_d = 1.46 g/cm^3.

The expansion process can be divided into three stages, initial expansion stage, rapid expansion stage, and stable stage, during the whole experiment time. The first stage of the expansion occurred in the flooded soil surface. Then, with water immersed

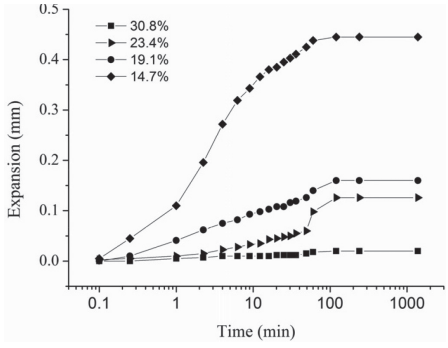

Figure 4. Relationship between one-way expansion and time of $\rho_d = 1.38$ g/cm^3.

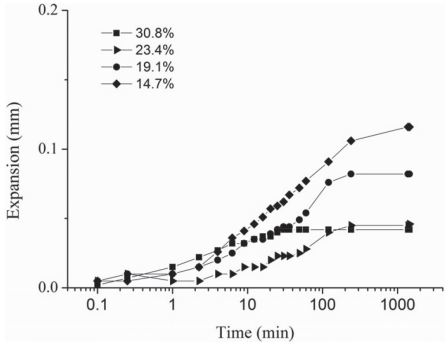

Figure 5. Relationship between one-way expansion and time of $\rho_d = 1.30$ g/cm^3.

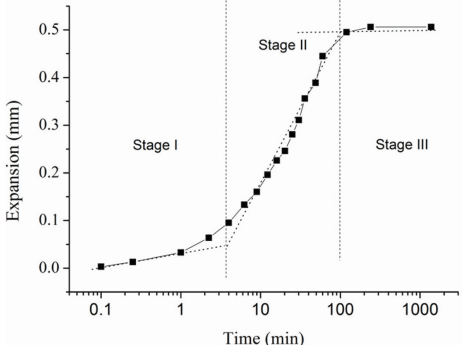

Figure 6. Schematic diagram of three stages during the expansion process of lateritic soil.

into soil specimens by capillary action, soil water interface area was expanded, the rapid expansion stage began. With the increased water content of soil specimen, suction decreases gradually, and the rate of water absorption decreases; the third stage (stable stage) is appears. Its schematic diagram is shown in Figure 6.

4 DISCUSSION

The three stages of the above-mentioned amount of expansion versus time can be simplified as a linear equation,

$$\delta = a_i \lg t + b_i \qquad (i = 1, 2, 3) \tag{1}$$

As motioned above, the permeability coefficient of fissures are larger than homogeneous soil itself; therefore, both sides of the lateritic soil around fissures is a one-way immersion condition in the soaking process. According to calculate the expansion deformation of the soil, the crack closure time can be predicted.

To make assumptions about cracks are paralleled and perpendicular to bedding the distance of three fissures adjacent marked as l_a and l_b, the initial width of fissure is w_0, the thickness of the soil is h, soil properties on both sides of fissure are the same. And then, the crack closure time can be predicted as follows:

$$\delta_{a(b)}(t) = \begin{cases} (a_1 \lg t + b_1)(l_a + l_b)/2h & t < t_1 \\ (a_1 \lg t + b_1 + a_2 \lg(t - t_1) \\ \quad + b_2)(l_a + l_b)/2h & t_1 \le t \le t_2 \\ (a_1 \lg t + b_1 + a_2 \lg(t_2 - t_1) \\ \quad + b_2 + a_3 \lg(t - t_3) + b_3)(l_a + l_b)/2h & t \ge t_2 \end{cases} \tag{2}$$

The fissure width is $w_t = w_0 - (\delta_a + \delta_b)/2$ at time t when $w_t = 0$, it can be considered that fissure has been closed.

5 CONCLUSIONS

Consolidation apparatus is applied to explore one-way expansion of compacted lateritic soil; the following conclusions can be drawn:

The expansion process can be divided into three stages, initial expansion stage, rapid expansion stage, and stable stage during the whole experiment time.

The lower the initial water content, the larger the final amount of expansion soil under the same initial dry density; the greater the initial dry density, the larger the final amount of expansion soil under the same initial water content.

According to the calculated expansion deformation of the soil, the crack closure time can be predicted from equation (2).

ACKNOWLEDGMENTS

The financial supports from the National Natural Science Foundation of China (Grant No. 51209196) and the project was funded by GuangXi Key Laboratory of Geomechanics and Geotechnical Engineering (14-KF-04) are gratefully acknowledged.

REFERENCES

Albrecht, B.A. & Benson, C.H. 2001. Effect of desiccation on compacted natural clays. *Journal of Geotechnical and Geoenviromental Engineering* 127(1): 67–75.

Bai, W., Kong, L.W. & Guo, A.G. 2012. Physical and Mechanical Properties of Fissured Lateritic Soil in Southwestern China. *Proceedings of the 4th International Conference on Problematic Soils, China, Wuhan, September 21–23, 2012.*

Bouma, J., Dekker, L.W. & Haans, J.C.F.M. 1979. Drainability of some Dutch clay soils: A case study of soil survey interpretation. *Geoderma* 22(3): 193–203.

Boynton, S.S. & Daniel, D.E. 1985. Hydraulic conductivity tests on compacted clay. *ASCE Journal of Geotechnical Engineering* 111(4): 465–478.

Chertkov, V.Y. 2000. Using surface cracks spacing to predict crack network geometry in swelling soils. *Soil Science Society of America Journal* 64(6): 1918–1921.

Chertkov, V.Y. & Ravina, I. 1998. Modeling the crack network of swelling clay soils. *Soil Science Society of America Journal* 62(5): 1162–1171.

Chertkov, V.Y. & Ravina, I. 1999. Tortuosity of crack networks in swelling clay soils. *Soil Science Society of America Journal* 63(6): 1523–1530.

Ketelaars, A., Kaasschieter, E.F., Coumans, W.J. & Kerkhof, P. 1994. The influence of shrinkage on drying behavior of clays. *Drying Technology* 12(7): 1561–1574.

Zhao, Y.W., Kong, L.W., Guo, A.G. & Tuo, Y.F. 2003. Mechanical behaviors and water-sensitive properties of intact Guangxi laterite. *Rock and Soil Mechanics* 24(4): 568–572.

Civil Engineering and Urban Planning IV – Liu et al. (Eds)
© 2016 Taylor & Francis Group, London, ISBN 978-1-138-02903-3

The time-dependent effect of interfacial stresses on strengthening RC beams with CFRP

Bai-Shun Xu, Ming Ma & Miao Zhang
School of Civil Engineering, Southwest Jiaotong University, Chengdu, Sichuan, China

Gui-Feng Li
Tianjin Municipal Engineering Design and Research Institute, Tianjin, China

ABSTRACT: The Reinforced Concrete (RC) beam can be strengthened by bonding Carbon Fiber-Reinforced Plastic (CFRP) to the bottom of the beam. In such reinforced beams, the bonding interface between CFRP and RC beam, when the forces must be transferred from CFRP to RC beam, will produce shear and peeling stresses. Although many research results have been provided, there are still many fields that need further research, such as the time-dependent effect of concrete. In this article, an analytical solution for interfacial stresses including creep and shrinkage effect of concrete is presented. The results show that the time-dependent effect of concrete will increase the shear and peeling stresses. The study can provide a reference to reinforce design engineering.

1 INTRODUCTION

Due to the rapid development of infrastructure construction, more and more existing structures are damaged. In the last few years, CFRP has been widely applied in maintenance and reinforcement of civil structures due to its excellent performances. Because of higher stresses in the end of CFRP, CFRP will debond from the reinforced beam as a significant failure mode. Therefore, a reasonable strengthening design needs accurate analysis of the shear and peeling stresses.

In the past 25 years, some exact analytical solutions have been established for interfacial stresses between CFRP and RC beam. In all these analytical solutions, two different analysis methods have been used. Roberts (1989) and Roberts and Haji-Kazemi (1989) used a staged analysis method; however, Vilnay (1988), Taljsten (1997), Malek et al (1998), Liu and Zhu (1994), Smith and Teng (2001) used allowable deformation conditions.

The short-term properties of interfacial stresses have been investigated by many achievements. However, there is only little research on the long-term characteristics. In this paper, the time-dependent effect of interfacial stresses is mainly researched, considering the creep and shrinkage of concrete in the original concrete beam. The results show that the time-dependent effect of concrete will increase the shear and peeling stresses, which need to pay more attention when the shear force equal to zero is not satisfied in the end region of CFRP. The influence can be neglected because it only can influence in a small region (Roberts 1989).

2 MATHEMATICAL FORMULATION

2.1 *Basic equation*

The RC beam strengthened with CFRP is shown in Figure 1. The micro-unit stress analysis for strengthening RC beams can be seen in Figure 2. The three layers from top to bottom of reinforced beam are concrete, glue layer, and CFRP. It is assumed that all compositing component of reinforced beam obey linear elastic.

In this paper, the subscript *c*, *p*, and *a* refer to concrete beams, CFRP plate, and adhesive layer; the symbol *E*, *I*, *G*, and *t* identify elastic modulus, inertia moment, shear modulus, and thickness; the symbol *N*, *V*, and *M* respectively represent axis, shear, and bending moment. Through the balance conditions of the differential element, there are

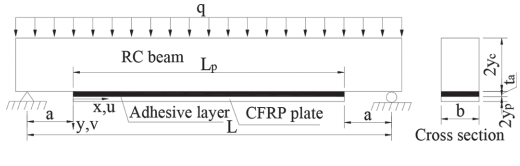

Figure 1. RC beam strengthened by CFRP.

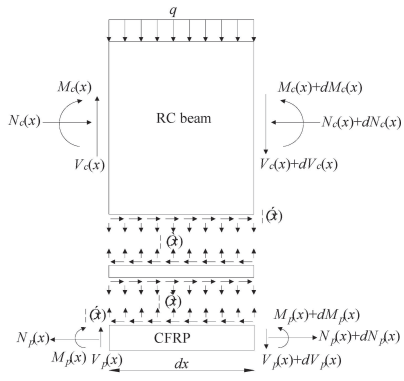

Figure 2. Differential element for strengthening RC beams.

$$\frac{dN_c(x)}{dx} = \tau(x)b \tag{1}$$

$$\frac{dV_c(x)}{dx} = -\sigma_y(x)b - q \tag{2}$$

$$\frac{dM_c(x)}{dx} = V_c(x) - \tau(x)by_c \tag{3}$$

$$\frac{dN_p(x)}{dx} = \tau(x)b \tag{4}$$

$$\frac{dV_p(x)}{dx} = \sigma_y(x)b \tag{5}$$

$$\frac{dM_p(x)}{dx} = V_p(x) - \tau(x)by_p \tag{6}$$

Differential equation of deflection in RC beams, is as follows:

$$\frac{d^2w_p(x)}{dx^2} = -\frac{M_p(x)}{E_pI_p} \tag{7}$$

$$\frac{d^2w_c(x)}{dx^2} = -\frac{M_c(x)}{E_cI_c} \tag{8}$$

where $w_p(x)$ and $w_c(x)$ are the deflections of CFRP plate and RC beams. Assuming that creep and shrinkage are independent. The strain which is at the bottom of the RC beams at time t ($t \geq t_0$) can be expressed as (Zhou & Chen 1994)

$$\varepsilon_c(x) = \frac{du_c(x)}{dx} = \frac{y_cM_c(x)}{E_c(t,t_0)I_c} - \frac{N_c(x)}{E_c(t,t_0)A_c} + \varepsilon_{cs}(t,t_s) \tag{9}$$

where $\varepsilon_{cs}(t,t_s)$ is the shrinkage strain, which is defined by JTG D62-2004 (JTG D62-2004 2004); $E_c(t,t_0)$ is the Young's modulus for concrete, changing with time

$$E_c(t,t_0) = \frac{E_c}{1+\chi(t,t_0)\cdot\varphi(t,t_0)} \tag{10}$$

where E_c is the Young's modulus for concrete at time t_0; $\varphi(t,t_0)$ is the creep coefficient related to the elastic deformation at time t_0, defined by JTG D62-2004 (JTG D62-2004 2004); $\chi(t,t_0)$ is an aging coefficient, which is defined as (Wang & Pan 1996)

$$\chi(t,t_0) = \frac{1}{1-e^{\left[-0.665\varphi(t,t_0)-0.107(1-e^{-3.131\varphi(t_0)})\right]}} - \frac{1}{\varphi(t,t_0)} \tag{11}$$

The strains at the top of CFRP, can be expressed as

$$\varepsilon_p(x) = \frac{du_p(x)}{dx} = -\frac{y_pM_p(x)}{E_pI_p} + \frac{N_p(x)}{E_pA_p} \tag{12}$$

2.2 *Interfacial shear stresses*

The shear stresses in the glue layer is given as

$$\tau(x) = \frac{G_a}{t_a}\left[u_p(x) - u_c(x)\right] \tag{13}$$

Differentiation twice the upper equation refers to x, with utilization of equations (1) to (6), (9), and (12). The solution of differential control equation of shear stresses can be given as

$$\frac{d^2\tau(x)}{dx^2} - \lambda^2\tau(x) + \lambda^2m_1V_T(x) = 0 \tag{14}$$

where

$$m_1 = \frac{G_a}{t_a\lambda^2}\left(\frac{y_c+y_p}{E_cI_c+E_pI_p}\right) \tag{15}$$

and

$$\lambda^2 = \frac{G_ab}{t_a}\left(\frac{(y_c+y_p)(y_c+y_p+t_a)}{E_cI_c+E_pI_p} + \frac{1}{E_cA_c} + \frac{1}{E_pA_p}\right) \tag{16}$$

The general solution to equation (14) can be expressed as

$$\tau(x) = B_1 \cosh(\lambda x) + B_2 \sinh(\lambda x) + m_1 V_T(x) \quad (17)$$

B_1 and B_2 are ordinary coefficients which are determined by boundary condition. The boundary condition of a simply-supported beam, which is acted by uniform load, is quoted to find the solution to the integration constant. The reasonable boundary conditions are: (a) $x = 0$, $N_c(0) = N_p(0) = M_p(0)$; (b) $x = L_p/2$, $\tau(x) = 0$. The formula of shear stresses in adhesive layer in arbitrary position is given as

$$\tau(x) = \left[\frac{m_2 a}{2}(L-a) - m_1\right]\frac{qe^{-\lambda x}}{\lambda} + m_1 q\left(\frac{L}{2} - a - x\right) \quad (18)$$

where

$$m_2 = \frac{G_a}{t_a}\left[\frac{y_c}{E_c I_c} + \frac{2\varepsilon_{cs}(t,t_s)}{qa(L-a)}\right] \quad (19)$$

2.3 *Interfacial peeling stresses*

The peeling stresses in the glue layer can be expressed as

$$\sigma_y(x) = \frac{E_a}{t_a}\left[w_p(x) - w_c(x)\right] \quad (20)$$

Differentiation four times the upper equation refer to x, and utilization of equations (1) to (8). The solution of differential control equation for peeling stresses can be given as

$$\frac{d^4\sigma_y(x)}{dx^4} + 4\beta^4\sigma_y(x) + n_1\frac{d\tau(x)}{dx} + \frac{E_a q}{t_a E_c I_c} = 0 \quad (21)$$

where

$$\beta = \sqrt[4]{\frac{E_a b}{4t_a}\left(\frac{1}{E_c I_c} + \frac{1}{E_p I_p}\right)} \quad (22)$$

and

$$n_1 = \frac{E_a b}{t_a}\left(\frac{y_c}{E_c I_c} - \frac{y_p}{E_p I_p}\right) \quad (23)$$

The general solution to equation (21) is as follow

$$\sigma_y(x) = e^{-\beta x}\left[C_1\cos(\beta x) + C_2\sin(\beta x)\right] + e^{\beta x}\left[C_3\cos(\beta x) + C_4\sin(\beta x)\right] - n_2\frac{d\tau(x)}{dx} - n_3 q \quad (24)$$

where

$$n_2 = \left(\frac{y_c E_p I_p - y_p E_c I_c}{E_c I_c + E_p I_p}\right) \quad (25)$$

and

$$n_3 = \frac{E_p I_p}{b\left(E_c I_c + E_p I_p\right)} \quad (26)$$

C_3 and C_4 will be zero when the peeling stress is zero induced by large scale of x. The general solution equation (21) therefore becomes

$$\sigma_y(x) = e^{-\beta x}\left[C_1\cos(\beta x) + C_2\sin(\beta x)\right] - n_2\frac{d\tau(x)}{dx} - n_3 q \quad (27)$$

Utilization of the boundary conditions: (a) $x = 0$, $N_c(0) = N_p(0) = M_p(0) = 0$; (b) $x = 0$, $V_p(0) = 0$. The ordinary coefficient C_1 and C_2 can be expressed as

$$C_1 = \frac{E_a}{2\beta^3 t_a E_c I_c}\left[V_T(0) + \beta M_T(0)\right] - \frac{n_3}{2\beta^3}\tau(0) + \frac{n_1}{2\beta^3}\left(\frac{d^4\tau(0)}{dx^4} + \beta\frac{d^3\tau(0)}{dx^3}\right) \quad (28)$$

$$C_2 = -\frac{E_a}{2\beta^2 t_a E_c I_c}M_T(0) - \frac{n_1}{2\beta^2}\frac{d^3\tau(x)}{dx^3} \quad (29)$$

3 RESEARCH AND ANALYSIS

3.1 *Comparative analysis*

In order to investigate the difference between the suggested method and the existing analytical solutions on the interfacial stresses, the effect of time dependent on concrete for calculating of shear and peeling stresses is not included. As shown in Figure 1, an RC beam strengthened by CFRP is acted on by uniform loads. The total length L is 3000 mm, the length of CFRP plate L_p is 2400 mm, the length of a is 300 mm and the uniform load q is 50 kN/m. The other relative size and material characteristics are showed in Table 1.

Figure 3 shows the calculating results of the interfacial shear and peeling stresses by different analysis methods for an RC beam reinforced by CFRP. The results of the interfacial shear and peeling stresses calculating by the suggested method agree well with the existing analytical solutions. There are very small differences among all these

Table 1. Relative size and material characteristics.

Name	Width (mm)	Height (mm)	Young's modulus (MPa)	Poisson's ratio
RC beam	200	300	30000	0.2
Adhesive layer	200	2.0	2000	0.35
CFRP plate	200	4.0	100000	0.28

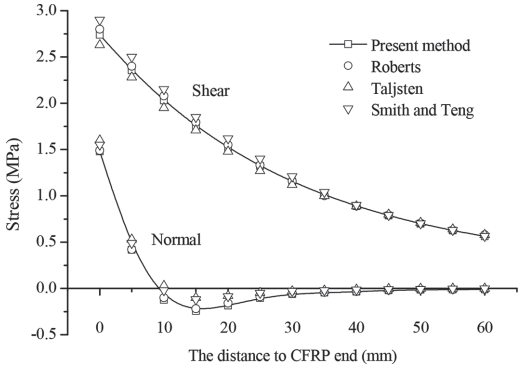

Figure 3. The results of interfacial shear and peeling stresses calculating by different analysis methods for an RC beam reinforced by CFRP (not including the time-dependent effect).

methods. It shows that the suggested method in this paper is feasible.

3.2 *The time-dependent analysis of interfacial stresses*

Since the suggested method for interfacial stresses in the article is feasible, the influence of creep and shrinkage of concrete is investigated by writing programs and numerical analysis. In order to investigate the effect of time-dependent, the concrete strength grade *C*30 and the environmental relative humidity 40% are adopted, the age of concrete while loading is 28 days, and the elastic modulus of concrete is 30 GPa. The total length L is 3000 mm, the length of CFRP plate L_p is 2400 mm, the length of a is 300 mm and the uniform load q is 50 kN/m. Other useful information can be obtained from Table 1.

Figure 4 shows the creep coefficient and the shrink-age strain change with time, which is defined by JTG D62-2004 (JTG D62-2004 2004). The relationship between the aging coefficient and time, which is defined by Wang and Pan (Wang & Pan 1996), is also included in Figure 4.

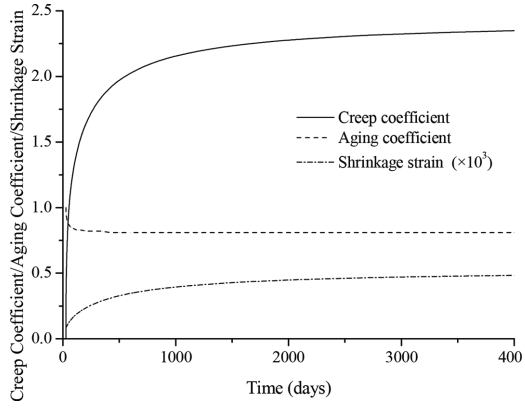

Figure 4. The relationship between creep coefficient, aging coefficient, shrinkage strain, and time.

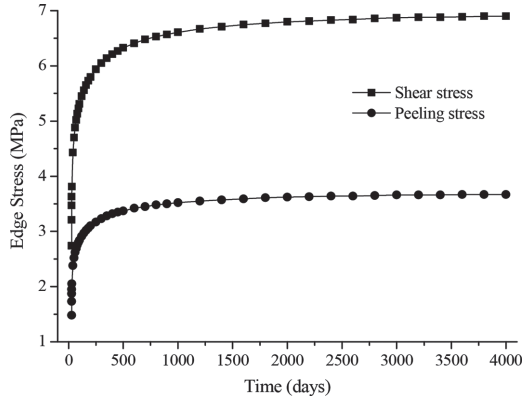

Figure 5. Time variation laws of interfacial shear and peeling stresses on the end of CFRP.

Figure 5 shows the time variation laws of the edge interfacial shear and peeling stresses by presented analysis method for an RC beam reinforced by CFRP. On the basis of the obtained results, we can conclude that the edge interfacial stresses exhibit a rapid increase during the first months and begin to increase slowly until they become almost constant after a very long time. The reason is that the creep coefficient and the shrinkage strain exhibit same change with time in Figure 4.

4 CONCLUSION

This paper investigates the time-dependent effect of interfacial shear and peeling stresses for an RC

beam reinforced with CFRP. A relative simple analytical method is proposed according to the creep and shrinkage effect of concrete. This research is helpful for comprehending the CFRP-to-concrete interfacial debonding in strengthened RC beams. The interfacial shear and peeling stresses change with the growth of time and exhibit the same variation with the effects of creep and shrinkage. The higher interfacial stresses on the edge of adhesive layer, which is harmful to the reinforced structure, may cause the interfacial debonding. Therefore, much attention should be attached to designing RC beams strengthened with CFRP. The research can provide a reference to the strengthening of design engineering.

REFERENCES

JTG D62-2004. 2004. *Code for Design of Highway Reinforced Concrete and Prestressed Concrete Bridge and Culverts*. Beijing: China Communications Press.

Liu, Z.H. & Zhu, B.L. 1994. Analytical solutions for R/C beams strengthened by externally bonded steel plates. *Journal of Tongji University* 22(1): 21–26.

Malek, A.M., Saadatmanesh, H. & Ehsani, M.R. 1998. Prediction of failure load of R/C beams strengthened with FRP plate due to stress concentration at the plate end. *ACI Structural Journal* 95(1): 142–152.

Roberts, T.M. 1989. Approximate analysis of shear and normal stress concentrations in the adhesive layer of plated RC beams. *The Structural Engineer* 67(12): 229–233.

Roberts, T.M. & Haji-Kazemi, H. 1989. Theoretical Study of the Behavior of Reinforced Concrete Beams Strengthened by Externally Bonded Steel Plates. *Proceedings of the Institution of Civil Engineers* 87(Part 2): 39–55.

Smith, S.T. & Teng, J.G. 2001. Interfacial stresses in plated RC beams. *Engineering Structures* 23(7): 857–871.

Taljsten, B. 1997. Strengthening of beams by plate bonding. *Journal of Materials in Civil Engineering* 9(4): 206–212.

Vilnay, O. 1988. The analysis of reinforced concrete beams strengthened by epoxy bonded steel plates. *The International Journal of Cement Composites and Lightweight Concrete* 10(2): 73–78.

Wang, X.W. & Pan, J.Y. 1996. Evaluating aging coefficient x in age-adjusted effective modulus method. *China Academy of Railway Sciences* 17(3): 12–23.

Zhou, L. & Chen, Y.C. 1994. *Shrinkage and Creep*. Beijing: China Railway Publishing House.

This page intentionally left blank

Civil Engineering and Urban Planning IV – Liu et al. (Eds)
© 2016 Taylor & Francis Group, London, ISBN 978-1-138-02903-3

Influence of anode follow-up on electro-osmosis

Rong-Bing Lin, Ling-Wei Kong & Wei Bai
State Key Laboratory of Geomechanics and Geotechnical Engineering, Institute of Rock and Soil Mechanics, Chinese Academy of Sciences, Wuhan, Hubei, China

Dong-Liang Zhu
Hubei Shuizong Water Resources and Hydropower Construction Co. Ltd., Wuhan, Hubei, China

Ai-Wu Yang
School of Civil Engineering, Tianjin Chengjian University, Tianjin, China

Ping Yang
Yiyang City Water Conservancy and Hydropower Construction Co. Ltd., Yiyang, Hunan, China

ABSTRACT: Electro-osmosis method is an effective way to quickly solve the problem of sludge drainage reinforcement. In this paper, the super soft soil of the Ezhou Liangzi area was taken as the test soil sample, and an improved method called anode follow-up was explored to improve the electro-osmotic effects. Three groups of different test schemes were carried out under the same voltage. The research provides a basis for on-site electro-osmosis test and proposes an optimization for multi-factor electro-osmosis test.

1 INTRODUCTION

Since 200 years, researchers have been focusing on electro-osmosis. In the early 19th century, Reuss, a Russian scientist, first discovered the clay electro-osmosis phenomenon: the pore water flows to the cathode while putting a DC voltage at both ends of the porous medium, and the phenomenon disappears soon once the electric field is removed. Similarly, the soil particles are negatively charged and the positive ions are adsorbed on the water molecules under natural conditions. When metal electrodes are installed at both ends of the soil, the cations drag the water molecules to the cathode, then the soil moisture decreases and the draining effect is achieved under the effect of external electric field. Once the cathode water is discharged, soil moisture will be reduced. In the 1930s, Leo Casagrande (Casagrande 1949) used electro-osmosis technology for soft soil reinforcement, so as to increase the shear strength of the fine-grained soil. Electro-osmosis method has been proven to be effective in strengthening low permeability coefficient silt subsoil (Jiao et al. 2011). The electric field generates negative pore water pressure, while the total stress remains unchanged; the effective stress is increased, promoting the consolidation of the soil. Its most prominent feature is that the soil under the pore water flows from the anode to the cathode driven by the electric field, and the pore water flow is hardly affected by the soil particle size. Other reinforcement measures such as preloading, and heaping have a good effect on free water, but they are ineffective on weakly bound water. The electro-osmosis method can overcome the limitation, which is very important. In the late 20th century, Shang and Lo (1997) pointed out that "although there are successful examples, the electro-osmosis technology is not widely used, mainly due to the smattering of electro-osmotic theory, and it results to high energy consumption, poor and unreasonable electro-osmosis system." In China, Wang (1999) deduced the laws of mechanics in electro-osmosis process in 1955. After the 1980s, national experts and engineers paid more and more attention to the electro-osmosis method, and the areas are gradually expanding. Shang and Lo (1997) summarized the information of the United States and Australia tailings processing and pointed out the main factors affecting the electro-osmotic effect in 1997: the internal factors refer to properties of the soil, including the following four types: soil particle size, mineral salt content, PH, and hydraulic conductivity; external factors include electro-osmosis system settings, including electrode materials and configurations, electrode layout, and power. Internal factors have been determined in engineering, and external factors should

be considered to improve the efficiency of electro-osmosis (Gao et al. 2005). For a one-dimensional electro-osmotic test, electrode arrangement is relatively simple, and usually only two parallel electrode plates are applied on both sides of the soil.

Electro-osmosis method faces many problems such as the development of surface resistance, different moistures between the soil near anode and cathode, and the soil electric permeability coefficient decreasing etc. (Liu & Zhang 2013). An improved method named follow-up action of the anode to improve the electro-osmotic effects was explored. In this experiment, super soft soil in the Liangzihu District of Ezhou city was processed. The author embedded the temperature and humidity sensors to monitor the moisture and temperature changes of the soil near the cathode and anode, and the multimeter was used to measure the current, voltage, and the displacement, which was collected with the sump during the electro-osmosis process.

2 RESEARCH CONTENT

2.1 *Basic physical and mechanical properties*

The average thickness of the soft soil in Ezhou Liangzihu ultra-soft silt dredger fill area is about 3–12 m. Recently, the dredger fill has been observed to have high moisture content, large compression, poor permeability, low strength, and other characteristics. The soil structure is destroyed, and the initial bearing strength of the ground is almost zero. The soil is still in a plastic state after standing for one month. The basic physical indicators are shown in Table 1.

2.2 *Test content*

The plexiglass box used in the experiments is shown in Figure 1. The size of the plexiglass box is 20 cm* 10 cm* 10 cm with three holes (diameter 6 mm) on one side of the bottom of the plexiglass box, which is used as a cathode. The water in the soil is collected and measured in the cathode side. The electrode plate is 11 cm*10 cm*5 mm with 16 holes in each electrode plate with a diameter of 5 mm is to ensure a good contact between the electrode and muddy soil, and the holes are channels of collection of drainage to the cathode water; there is a layer of non-woven fabric between the electrode plates and plexiglass box, to prevent soil particles from clogging the drainage holes.

Table 1. Physical parameters of the soft mud in Liangzihu dredger fill.

Moisture content (%)	Specific gravity	Wet density (g/cm^3)	Dry density (g/cm^3)	Liquid limit (%)	Plastic limit (%)
82.0	2.70	1.56	0.86	93.9	38.5

Figure 1. Plexiglass box.

Table 2. Experimental program.

	Original moisture	Termination condition
1	77.61	When anode moisture <40%, follow up 10 cm, Anode moisture <40%, cathode moisture <60%, I < 0.5 mA
2	78.30	When I < 0.5 mA, follow up 7 cm, Anode moisture <40%, Cathode moisture <60%, I < 0.5 mA
3	80.00	No anode follow-up, and under the continuous power for 72 h,
4	82.60	(Control group) no voltage at the ends of the soil

Test is divided into four groups, as shown in Table 2. The electrode plate is made of steel. When the current and soil conditions reach a certain level, the anode follows up. The anode plate will be pulled out from its original position and inserted in the new position. The first group follows up 10 cm, the second group follows up 7 cm, and the third group remains constant. There is no voltage in Group 4, and the voltages in the other three groups are 24 V.

3 RESULTS

3.1 *The effect of electro-osmosis*

During the process of electro-osmosis, the moisture of the soil changes a lot (as shown in Fig. 2). The moisture of the soil where there is no voltage,

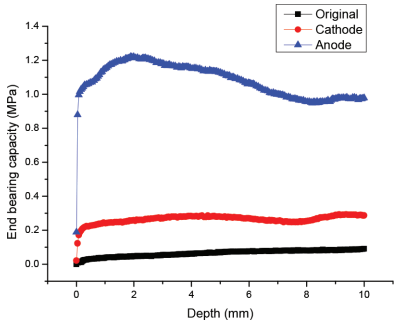

Figure 2. Changes of the soil moisture.

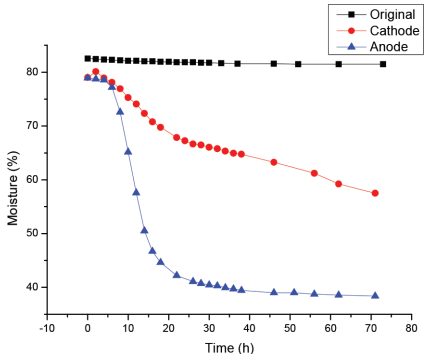

Figure 3. End-bearing capacity.

at both ends of it, changes little during the group 4. At 72 hours later, the soil moisture of the anode in group 3 is only about 48.7% of group 4, and the cathode is 72.9%. The end-bearing capacity increases a lot during the process (as shown in Fig. 3). Before the test, the end-bearing capacity is just 80 kPa and the anode is almost 950 kPa and the cathode is 280 kPa. It means that the electro-osmosis is an effective way to quickly solve the problem of sludge drainage reinforcement.

In the later period of group 3, cracks appear and develop in the soil. According to the interface resistance theory (Zhuang & Wang 2004), the resistance between the interface of the electrode plate and soil is very large, and there is a large potential loss at the interface between the soil and the electrode plate. But the loss is often subtracted from the total potential, and the final potential has effective potential effects on the soil. In order to detect the loss of the effective potential and the change in the interface resistance potential over the time, probes are inserted in the direction of the electrode plate midline in the middle of the soil. Cathode plate has a zero potential point, and the potential of the probes are measured and referred as ε_m, anode ε_p cathode ε_n. $V_n = \varepsilon_m - \varepsilon_n, V_p = \varepsilon_p \quad \varepsilon_m$, and they are the voltage of the soil on the anode (cathode) side.

As shown in Figure 4, initially, the moisture is approximately the same throughout the soil and the resistances of the soil are equal on both sides. According to the characteristics of the series circuit, the voltages are the same on both sides. With the electro-osmotic being, the soil moisture has decreased and cracks developed near the anode; therefore, resistance on the anode side of the soil has increased more greatly than that on the cathode side. The $V_p : V_n$ ratio is about 5:1 when it is stable. The anode is the main factor for low efficiency of electro-osmosis, but the anode soil reaches a certain strength. So the anode plate moves closer to the cathode, to avoid original cracks in the anode side and enhance the electro-osmotic effect.

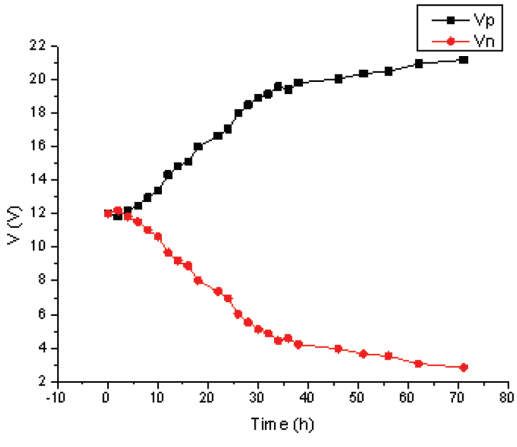

Figure 4. Voltage of the soil.

3.2 *Energy consumption*

Engineering economy is an important factor for restricting the development of the electro-osmosis method in engineering practice, power consumption is an important indicator of economic assessment, and energy consumption per unit displacement is proposed, which reflects the desired displacement of power consumption per milliliter. It can be calculated as follows:

$$E = \frac{UI\Delta t}{V_w}$$

where P is the power; U is the total voltage; I is the current; v_w is the drainage rate; V_w is the displacement; Δt is the drainage time; and E is the energy consumption per unit displacement.

As shown in Figure 5, with the decrease in anode moisture, E increases. The electro-osmosis method causes an enormous waste after reaching

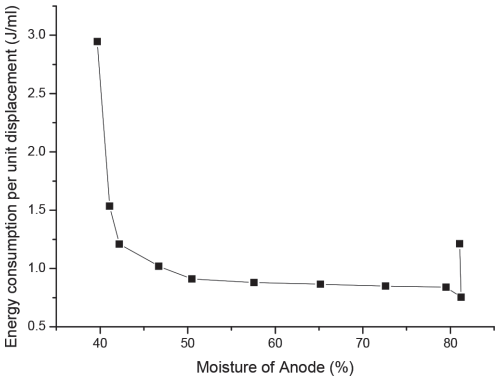

Figure 5. Energy consumption per milliliter.

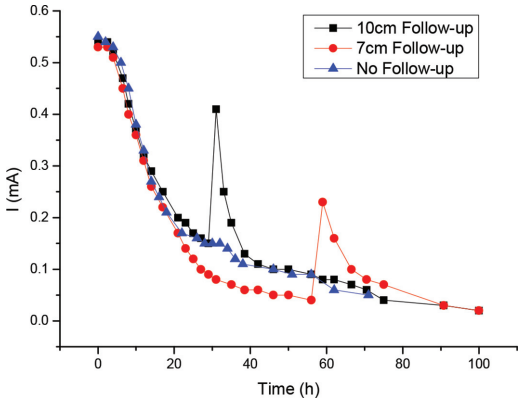

Figure 6. Current changes over the time.

a certain moisture. At 24 V, when the anode moisture is below 40, E increases sharply. Then, the anode should be pulled out and moved closer to the cathode.

3.3 *Anode follow-up*

The experimental program is shown in Table 2. The current curves are almost identical with those in the first 20 hours (as shown in Fig. 6). At 20 hours later, the current is only about one-third of the original, and the electro-osmotic efficiency is greatly reduced. According to the above-mentioned E, anode follows up in test 1. The anode plate is removed and inserted into the middle of the glass box, the current becomes three times as much as the original immediately, but it decreases rapidly in the next 10 hours. The anode follows up when the current is stable (probably around 0.05 mA) in group 2, the anode plate is removed and inserted into a one third division point closer to the anode side and the current increases nearly five times as much as the original instantly, but it also decreases rapidly in the next 10 hours. A hundred hours later, the current I is still at 0.05 mA in the three curves. The final current matters little with the potential gradient because of the cracks in the soil.

When the anode moisture is stable, the resistance near the anode is very large and it is the main factor for the low efficiency of electro-osmosis, but the anode soil has achieved certain strength, and has reached the effect of electro-osmosis process. Anode follow-up reduces cathode moisture quickly again (as shown in Fig. 7), and the new anode, which is closer to the cathode, is in fact in the intermediate position of the original soil. The final moisture of cathode in the experimental group in which the anode follows up is significantly reduced compared with the continuous conduction method. It is difficult to decrease the

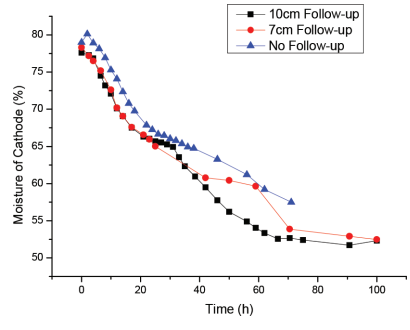

Figure 7. Cathode moisture over the time.

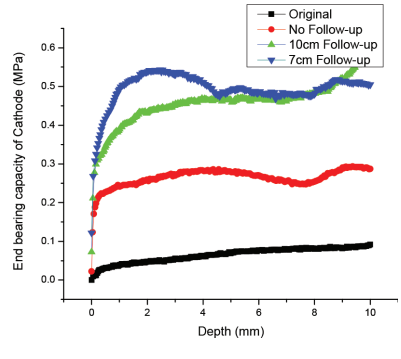

Figure 8. End-bearing capacity of cathode.

cathode moisture below 58 percent, but the cathode moisture can be as low as 50% in the follow-up group. The end-bearing capacity develops a lot in the process of the electro-osmotic (as shown in Fig. 8), it is only 80 kPa before the process; the end capacity around the cathode increases to 287 kPa

after 72 hours of reinforcement in test 3. The end-bearing capacity is as high as 560 kPa in test 1, and it is nearly 200% of it in test 3; it is 510 kPa in the test, about 177% of it in the test. In other words, the anode follow-up effectively improves the cathode treatment effect.

4 CONCLUSION

Through the one-dimensional electro-osmotic test carried out in the laboratory, the electro-osmosis method is considered to be an effective method of the fine-grained soil drainage consolidation process. The following conclusion can be drawn:

- When the soil moisture is reduced to a certain degree, the energy consumption per unit displacement significantly increases. It is not economically feasible;
- Anode follow-up can improve the current as high as five times after a period of time;
- Cathode moisture can be significantly reduced to 55% by anode follow-up;
- End-bearing capacity of cathode can be improved by 200% by anode follow-up.

ACKNOWLEDGMENTS

This work was supported by the Natural Science Foundation of Hubei Province, China (Grant No. 2014CFB370) and the Key Laboratory of Tianjin Soft Soil Character and Engineering Environment (Grant No. 2014SCEEKL01).

REFERENCES

Casagrande, L. 1949. Electro-osmosis in soils. *Geotechnique* 1(3): 159–177.

Gao, Z.Y., Zhang, M.Y. & Zhang, J. 2005. Laboratory model test of vacuum preloading in combination with electro-osmotic consolidation. *China Harbour Engineering* 05(01): 58–61.

Jiao, D., Gong, X.N. & Li, Y. 2011. Experimental study of consolidation of soft clay using electro-osmosis method. *Chinese Journal of Rock Mechanics and Engineering* 30(s1): 3208–3216.

Liu, F.Y. & Zhang, L. 2013. Experimental analysis of the electro-osmosis consolidation of soft clay under anode follow-up. *Journal of Civil, Architectural and Environmental Engineering* 01(1): 52–58.

Shang, J.K. & Lo, K.Y. 1997. Electrokinetic dewatering of a phosphate clay. *Journal of Hazardous Materials* 55(l–3): 117–133.

Wang, W.S. 1999. *Academician Geotechnical Selected Papers.* Beijing: China Architecture & Building Press.

Zhuang, Y.F. & Wang, Z. 2004. Study on interface electric resistance of electro-osmotic consolidation. *Rock and Soil Mechanics* 25(01): 117–120.

This page intentionally left blank

Civil Engineering and Urban Planning IV – Liu et al. (Eds)
© 2016 Taylor & Francis Group, London, ISBN 978-1-138-02903-3

Study on the construction mechanics of the road tunnel crossing underneath the overlying mining area

Jian-Wu Gong, Xin Wang & Pei-Lin Qi
School of Urban Construction, Wuhan University of Science and Technology, Wuhan, Hubei, China

ABSTRACT: With the development of highway in the mountain area, it is usually inevitable for the road tunnel to cross underneath the overlying mining area. Some numerical analysis models were built, and the influence between the mining area and the tunnel structure at different distances was analyzed. According to the analysis of the periphery displacement of the tunnel, the internal force of the supporting structure, and the distribution of the surrounding rock plastic zone, it is deduced that the overlying mining area has a remarkable influence on the stability of the tunnel structure and the surrounding rock. When the distance from the overlying mining area to the tunnel is less than 10 m, the adverse influence is fairly obvious, and strong pre-consolidation measures should be taken. The critical distance from the overlying mining area to the tunnel is about 30 m. When the distance is less than 30 m, the adverse effect must be taken into consideration during the design and construction of road tunnels.

1 INTRODUCTION

With the implementation of the West development strategy in China and vigorous promoting of the transportation infrastructure, the construction of highway tunnels is becoming more and more prominent. Since the 1980s, the order of mining activities in China has been chaotic, and illegal exploitation without planning left a lot of mining area (Chen et al. 2014, Zhang et al. 2010).

The interaction between the mining area and the tunnel brings about special difficulties for tunnel construction, so it is suggested that the tunnel should keep away from mining area as far as possible. Owing to the wide distribution of the mining area, it is usually inevitable for the tunnel to cross underneath the mining area, so there are lots of risks and potential hazards during tunnel construction (Huang et al. 2012a, 2012b).

Although research on highway tunnel construction in the mining area has been conducted for many years, and lots of valuable experience have been accumulated by investigation, stability evaluation and treatment of the mining area, the mature theory, and the engineering design system has not yet been performed (Tong et al. 2006). Many studies mainly aim at the mining area under tunnel, while there are few research results for the tunnel crossing underneath the overlying mining area (Cui et al. 2006, Wang et al. 2008).

Based on the distance between the tunnel and the overlying mining area, the influence degree and regulation of the overlaying mining area on the tunnel structure has been evaluated by the dynamic numerical simulation. The critical distance between the overlying mining area and the tunnel was put forward to ensure the safety of tunnel construction.

2 FINITE ELEMENT MODEL

2.1 *Model and working condition*

According to the influence scope of tunnel excavation, the distance of the model boundary to the tunnel boundary is more than five times the tunnel excavation span (Gong et al. 2009). In the model, the triangle solid element is adopted to simulate the surrounding rock, the link element for initial lining, and the beam element for secondary lining. The model was horizontally fixed at the left and right boundary, vertically fixed at bottom boundary. The mining area size is set at 3 m × 9 m, and takes the distance of 30 m from the overlying mining area to the tunnel for example. The full mesh map of the model is shown in Figure 1.

Based on the purpose of the research, six kinds of working conditions were selected at different distances between the overlying mining area and the tunnel: 5 m, 10 m, 20 m, 30 m, 40 m, and 60 m.

2.2 *Mechanical parameters*

In practical engineering, the rock mass in the mining area is usually weak, so the V-grade surrounding rock is selected in the simulation model.

The mechanical parameters of the surrounding rock are shown in Table 1, which is determined by the *Code for Design of Road Tunnel* (JTG D70-2004) and the exploration report of relative engineering (Gong et al. 2009, Song et al. 2007).

3 RESULTS

3.1 *Analysis on the periphery displacement of the tunnel*

Table 2 shows the periphery displacement value of the tunnel caused by the mining area construction at different distances. Figure 2 is the relation curve of the displacement value with the corresponding distances (In the tables and figures, the positive value represents the upward displacement for crown and bottom settlement, and relative reduction for convergence).

From Table 2, it can be seen that the tunnel structure is stretched in the vertical direction and compressed in the transverse direction due to the influence of overlying mining. At a certain distance, the periphery displacement of the tunnel increases gradually with the decrease in the distance between the overlying mining area and the tunnel. The change in the internal force in the lining structure is obvious, especially, at the crown of the tunnel, which is fairly adverse for the safety of the tunnel structure.

As shown in Figure 2, when the distance between the overlying mining area and the tunnel is less than 10 m, the influence of distance change on the periphery displacement of the tunnel is dramatic. The characteristic displacement, which is nearly linear, decreases with the distance from 10 m to 30 m. When the distance is more than 30 m, the influence degree is little. The result shows that the safe distance of the overlying mining area to the tunnel is about 30 m.

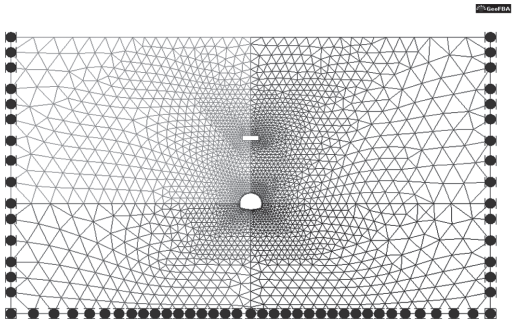

Figure 1. Mesh map of finite element model.

Table 1. Mechanical parameters of the surrounding rocks.

Item	E (GPa)	μ	γ (kN/m^3)	c (kPa)	φ (°)
V-grade rock	1.2	0.38	20	80	27

3.2 *Internal force analysis of the supporting structure*

Table 3 shows the axial force of the primary lining and the moment of the secondary lining caused by the mining area construction at different distances. Figure 3 shows the relation curve of the internal force value with the corresponding distance.

As can be seen from Table 3 and Figure 3, a regular change in the internal force of the tunnel supporting structure has occurred with the increase in the distance between the overlying mining area and the tunnel within a certain depth. When the distance is less than 10 m, the influence that the distance change has on the internal force of the tunnel supporting structure is dramatic. The change decreases gradually with the increase in the distance. When the distance is more than 30 m, the changing trend decreases rapidly. It also

Table 2. Deformation value of the surrounding rocks in the different distances of the overlying mining area to the tunnel.

Distance* (m)	Crown settlement (mm)	Bottom deformation (mm)	Vertical convergence (mm)	Horizontal convergence (mm)
5	22.9	3.2	–19.7	10.0
10	11.6	2.6	–9.0	6.2
20	5.7	1.8	–3.9	2.7
30	3.2	1.2	–2.0	1.4
40	1.7	0.7	–1.0	0.7
60	0.6	0.3	–0.3	0.2

* Distance from the overlying mining area to the tunnel.

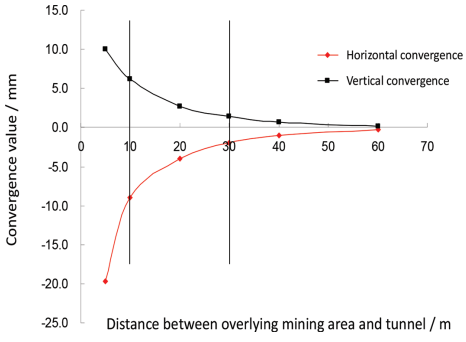

Figure 2. Curves of the deformation value of the surrounding rocks with the distance of the overlying mining area to the tunnel.

Table 3. Internal force of the lining at different distances of the overlying mining area to the tunnel.

Distance* (m)	Axial force of primary lining (kN)	Moment of secondary lining (kN·m)
60	2533	–80
40	2575	–66
30	2647	–42
20	2819	16
10	3371	187
5	4659	920

* Distance from the overlying mining area to the tunnel.

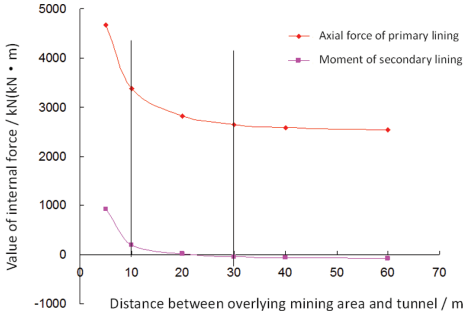

Figure 3. Curves of the lining internal force with the distance of the overlying mining area to the tunnel.

shows that the main influence scope in the overlying mining area to the tunnel is about 30 m.

3.3 *Analysis of the surrounding rock plastic zone*

At the different distances of the tunnel structure to the overlying mining area, the scope of the surrounding rock mass plastic zone can be obtained under different working conditions. The analysis results are shown in Figure 4.

From Figure 4, it can be seen that the distance of the overlying mining area to the tunnel has an obvious influence on the size and distribution of the plastic zone in the surrounding rock mass. When the distance is small, the plastic zone is connected

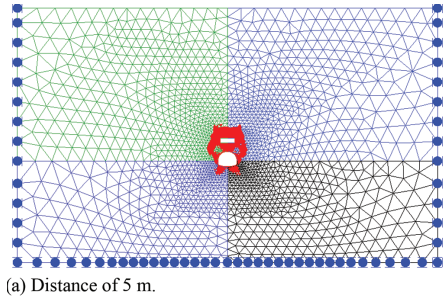

(a) Distance of 5 m.

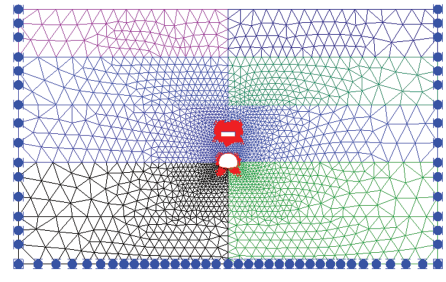

(b) Distance of 10 m.

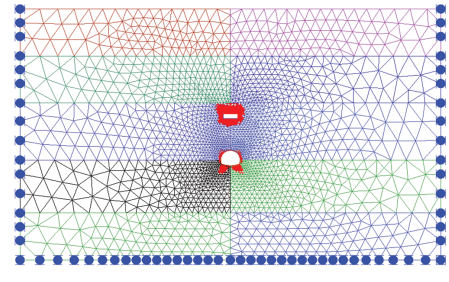

(c) Distance of 20 m.

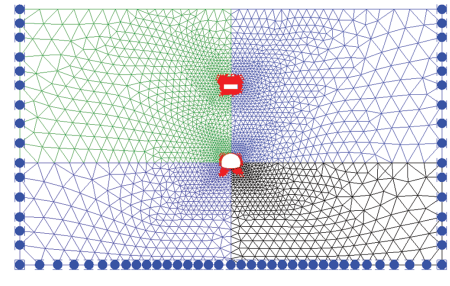

(d) Distance of 40 m.

Figure 4. Plastic zone range of the surrounding rocks with the distance of the overlying mining area to the tunnel.

between the tunnel and the mining area, and the scope of the plastic zone is relatively larger, which is fairly unfavorable for the stability of the tunnel and the surrounding rock. When the distance increases to 10 m, the plastic zone reduces, but the scope is still large. When the distance increases to 20 m, the plastic zone further reduces, and the interaction between the tunnel and the mining area becomes weaker gradually. While the distance is 40 m, the scope of the plastic zone almost keeps unchanged, which indicates that the mining area has a slight influence on tunnel stability.

According to the *Code for Design of Road Tunnel* (JTG D70-2004), the equivalent load height of the tunnel (h_q) is about 12.8 m in the V-grade rock mass, and the critical depth of the shallow and deep tunnels (H_p) is 32 m. Combining with the periphery displacement of the tunnel, the internal force of the supporting structure, and the distribution of the surrounding rock plastic zone, it can be deduced that the main influence scope of the overlying mining area on the tunnel structure is about 30 m at a certain size of the mining area.

4 CONCLUSION

Based on the numerical simulation, an analysis of the influence between the overlying mining area and the tunnel structure at different distances was carried out, and some conclusions are presented as follows.

The overlying mining area has a remarkable influence on the stability of the tunnel structure and the surrounding rock. When the distance from the overlying mining area to the tunnel is less than 10 m, the adverse influence is fairly obvious, and a strong pre-consolidation measure should be taken. At a certain depth, the influence decreases gradually with the increase in the distance between the overlying mining area and the tunnel. When the distance is less than 30 m, the adverse effect must be taken into consideration during the design and construction of the road tunnels. The critical distance between the overlying mining area and the tunnel can be set to 30 m.

While it must be pointed out that the effect mentioned above is closely related to the size and properties of the mining area, the condition of the surrounding rock and the construction method, the influence degree and scope are different under different conditions. In practical engineering, it is appropriate to combine the actual conditions for a comprehensive analysis.

ACKNOWLEDGMENTS

This work was financially supported by the National Natural Science Foundation of China (51208395) and the Research project of Education Department of Hubei Province of China (Q20111101).

REFERENCES

Chen, J.X., Gao, Y.T. & Jin, A.B. 2014. Influence of coal on tunnel stability and treatment technology. *Coal Technology* 33(10): 275–277.

Cui, Z.S., Zhao, K. & Gong, J.W. 2011. Numerical analysis on construction effect of underlying goaf on road tunnels. *Exploration Engineering* 38(7): 76–79.

Gong, J.W., Xia, C.C., Zhu, H.H., et al. 2009. Optimal analysis of construction schemes for Heshang small-space tunnels with large section. *Rock and Soil Mechanics* 30(1): 236–240.

Huang, L., Lu, Y.Y. & Su, D.F. 2012a. Treatment technology of highway tunnel through steep inclined goaf. *Journal of Highway and Transportation Research and Development* 29(11): 80–85.

Huang, M., Zhang, X.D. & Liu, H.R. 2012b. Stability analysis of surrounding rock of large-span arch tunnel in coal gob and its reinforcement. *Journal of Guangxi University* 37(1): 128–133.

Song, N.T., Chen, W.T. & Wang, M.N. 2007. Safety analysis of tunnelling in coal-minded area. *Railway Construction Technology* (3): 48–51.

The Professional Standards Compilation Group of People's Republic of China. 2004. *Code for Design of Road Tunnel* (JTG D70-2004). Beijing: China Communications Press.

Tong, L.Y., Liu, S.Y. & Qiu, J. 2006. *Harmfulness Evaluation and Treatment Technology of Highway Underlying the Goaf*. Nanjing: South East University Press.

Wang, S.R., Shen, N.Q. & Zhang, H.Q. 2008. Numerical analysis of deformation characteristics for highway tunnels through the mined-up regions. *China Mining Magazine* 17(3): 76–79, 81.

Zhang, Y.P., Cao, P., Yuan, H.P., et al. 2010. Numerical simulation on stability of complicated goaf. *Journal of Mining and Safety Engineering* 27(2): 233–238.

Civil Engineering and Urban Planning IV – Liu et al. (Eds)
© 2016 Taylor & Francis Group, London, ISBN 978-1-138-02903-3

Construction deformation monitoring and application analysis for the neighborhood tunnel

Hao Sheng, Jian-Wu Gong & Xin Wang
School of Urban Construction, Wuhan University of Science and Technology, Wuhan, Hubei, P.R. China

ABSTRACT: As a special type of tunnel structure, it is particularly necessary to monitor the deformation of the surrounding rock and tunnel for the neighborhood tunnel. Combined with practical neighborhood tunnel engineering, the deformation monitoring program for tunnel construction was introduced. The main monitoring items were discussed, including surface subsidence, crown settlement, convergence, and internal displacement of the surrounding rock. The excavation of the upper bench and inversion of the tunnel have a significant effect on surrounding rock deformation, and the influence scope of tunnel construction was about twice that of the tunnel diameter before and after the working face. The deformation stability time of the surrounding rock is about 40 days after the shotcrete bolt support in IV and III grade rock mass, and about 60 days in V grade rock mass. The experience and conclusions presented in this paper can provide a valuable reference for the determination of secondary lining supporting time and the optimization of lining parameters.

1 INTRODUCTION

Deformation monitoring plays an important role in tunnel engineering construction, which requires attention during not only the operation period, but also the construction stage. Due to the influence of the rock structure, geotechnical situation, and the blasting vibration in the excavation, the tunnel condition will change with the excavation process. Deformation monitoring of the tunnel must be carried out in order to ensure construction safety. It can provide accurate and timely information of the tunnel condition to adjust construction parameters and process (Yun & Tang 2015, Zhang et al. 2015).

Due to the limitations of the special geological and topographical condition, the spacing of the high-grade highway is generally difficult to meet the demand of the design code. So, as a special structure type, the neighborhood tunnel should be used. However, there are no more adequate designs and construction experiences about the neighborhood tunnel at present, and related deformation monitoring during the tunnel construction process is particularly necessary (Deng et al. 2014, Xia et al. 2007).

Tunnel deformation monitoring, which is an important link of the construction survey, not only provides important safety monitoring facility for tunnel construction, but also provides scientific information for adjusting the design parameters, determining the reasonable supporting time of the secondary lining and the comprehensive evaluation of the surrounding rock stability.

2 ENGINEERING PROFILE

A certain highway double line tunnel in the mountain area, with the length of 450 m, is a typical small spacing tunnel. The maximum excavation span of the single tunnel is about 16.69 m, and the net spacing between two tunnels is only 5.66 m, which is far less than the minimum limit in the *Code for Design of Road Tunnel* (JTG D70-2004). The whole tunnel passes through V, IV, and III grade rock mass. The maximum and minimum burial depth of the tunnel is about 62 m and 4 m, respectively.

The tunnel is constructed by NATM, and composite lining is designed for tunnel structure. Based on the system supporting, the advanced grouting using small duct for pre-reinforcement is adopted. During the construction of the tunnel, a series of deformation monitoring works have been done.

3 DEFORMATION MONITORING PROGRAM

For the mountain tunnel, the main purpose of deformation monitoring during the construction process is to ensure that the rock pressure acting on the temporary support system is within the control range. That is, it ensures that excessive vaults

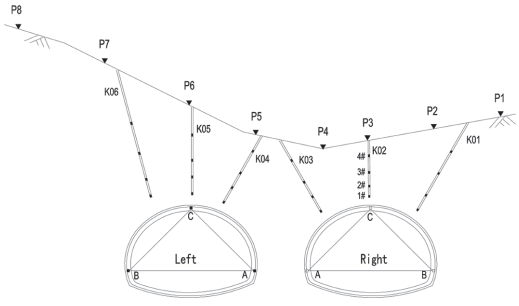

Figure 1. Schematic of deformation monitoring points of the monitoring section.

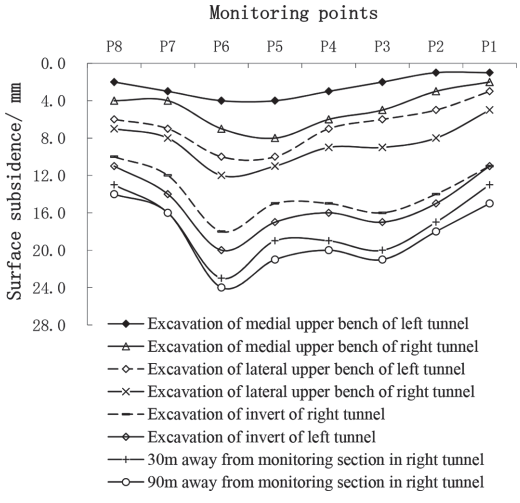

Figure 2. Curves of surface subsidence with construction process.

and floor uplift are not produced, and the instability of the excavation surface and the yield of the supporting system is prevented (Kavvadas 2005). Since the mechanics character of the surrounding rock is affected by many factors in the tunnel construction process, and the physical mechanical model to reflect the correct rock mass behavior is very difficult to obtain. The deformation and strength parameters of the surrounding rock are usually got based on the results of the deformation monitoring of the tunnel excavation by back analysis. So, in order to guide the construction and achieve a perfect design, it is necessary to monitor the deformation state of the surrounding rock in construction and to make a comprehensive analysis and judgment for the monitoring data (Xia & Li 1999, Zhang & Shi 2015).

According to the *Technical Specifications for the Construction of Highway Tunnel* (JTG F60-2009), construction technology and geological condition of the neighborhood tunnel, the tunnel deformation monitoring items should include tunnel surface subsidence, crown settlement, convergence, and internal displacement of surrounding rock and so on. The measuring point arrangement of the monitoring items is shown in Figure 1. In the figure, P1–P8 are surface subsidence observation points, K01–K06 are multi-point extensometer monitoring holes. Points A, B, and C are the measuring points of the crown settlement and convergence.

4 ANALYSIS OF THE MONITORING RESULTS

4.1 *Surface subsidence*

Taking a monitoring section at the exit part of tunnel for example, Figure 2 shows the surface subsidence displacement trend line corresponding to the different construction process and stage.

In the early time of tunnel construction, the surface settlement above the tunnel basically shows a funnel shape curve, and gradually spreads from the center to the outside of the tunnel. The settlement occurs mainly above the tunnel, which is basically identical to the Peck curve.

The surface subsidence of left tunnel is slightly larger than the right tunnel, which is related to surface geology and excavation condition. The surface soil of the left tunnel is loose, and the deformation is seriously affected by the construction and blasting vibration. At the same time, the excavation disturbance and vibration blasting of the followed right tunnel make the surface subsidence of the first left tunnel increase, the interaction between the construction of two tunnels is obvious.

The surface settlement at interlaid rock is larger than the lateral tunnel, which shows that it is influenced by the excavation of both tunnels, and the support method at this part should be strengthened in construction. From the different construction stages, the excavation of the upper bench and the inversion of the tunnel have a significant effect on the surface subsidence, while the lower bench is relatively smaller.

When the tunnel working face passes through the monitoring section about 30 m, the settlement of each measuring point reaches about 85% of the final settlement, and the subsidence rate becomes slower. When the tunnel working face passes through monitoring surface about 90 m, the settlement of each point is nearly stable, which shows that the influence scope of the working face was about twice the tunnel diameter.

4.2 *Crown settlement and convergence*

The crown settlement and convergence monitoring points are set at the same section, as shown in Figure 1. Taking the right tunnel as an example, the measurement results of the tunnel crown settlement and convergence deformation in each monitoring section and the time that the deformation tends to be stable are showed in Table 1.

Combined with the construction stages, the following can be obtained from monitoring results.

The average crown settlement of the right tunnel is slightly lesser than that of the left tunnel, and the average settlement of the right tunnel is 11 mm, which also shows the excavation of the following right tunnel that has a certain influence on the left tunnel. The rock at shallow-buried section of the tunnel entrance is poor, and the excavation is complex with large disturbance, crown settlement and convergence deformation are relatively large.

Corresponding to the different grades of the surrounding rock, the deformation value of III grade surrounding rock is significantly lesser than IV and V grade surrounding rock, which shows that the bench construction method for the III grade surrounding rock is feasible and it can ensure the stability of surrounding rock. However, the deformation at V grade surrounding is relatively larger, and the partial primary supports appear crack, which shows that the neighborhood tunnel has certain risks at V grade surrounding rock.

The deformation of the surrounding rock and stability time are closely related to the geological conditions. For IV and III grade surrounding rock mass, about 20 days after shotcrete bolt support, the rate of deformation was slowed down, and it was stable basically after 40 days; for V grade surrounding rock mass, about 30 days after the shotcrete bolt support, the rate of deformation was slowed down, and it was stable basically after 60 days.

Table 1. Deformation value of the monitoring sections of right tunnel and its stabilized time.

Monitoring section	Crown settlement (mm)	Convergence (mm)	Stabilized time (d)	Rock grade
1	17.21	2.40	26	V
2	17.01	4.79	15	V
3	17.11	2.76	13	IV
4	7.51	2.03	12	IV
5	4.55	1.01	17	III
6	2.60	1.75	14	III
7	4.30	3.25	26	III
8	7.05	4.46	17	III
9	10.95	5.38	28	IV
10	13.60	4.99	32	V
11	14.05	1.92	17	IV
12	13.25	5.11	24	IV
13	8.45	1.42	19	III
14	9.20	12.33	21	III

According to the deformation measurement results, combining with surrounding rock conditions, it is suggested that the secondary lining can be made 20 m to 30 m away from the working face in the portal section. For the middle part of the tunnel, it is 40 m away from the working face to construct the secondary lining.

4.3 *Internal displacement of surrounding rock*

The internal displacement of the different depth points in the rock can be measured using multi-point extensometers. According to displacement–time curve, the deformation law and the range of the loosening area of the surrounding rock are obtained, which provides a reference for judging the rationality of the anchor design. Taking the K02 measure hole as an example, the four measuring points' deformation curve with time are shown in Figure 3.

From Figure 3, it can be seen that the displacement of the surrounding rock has basically experienced a process of "rapid increase-slow change-basic stability." The displacement curve can be divided into five stages as following:

Stage I: The instrument was installed and the working face of the right tunnel was close to the monitoring section, the instrument was in a self-adjustment phase, and the displacement change of each point was little.

Stage II: When the working face of the medial upper bench of right tunnel was close to the measuring section, the displacement rate started to increase. When the working face of lateral upper bench of right tunnel reached measuring section, the displacement increase was rapid, and the displacement of each monitoring point produced about 50% of the total deformation.

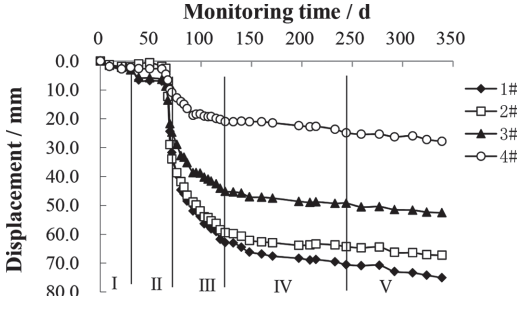

Figure 3. Curves of the internal deformation of the surrounding rock in K02 hole with monitoring time.

Stage III: When the working face of the bottom bench of the right tunnel reached monitoring section, the displacement of each point produced more than 65% of the total deformation, and when inverted working face passed the monitoring section, the displacement of each point produced more than 80% of the total deformation.

Stage IV: After the inverted excavation face of the right tunnel passed, the displacement change rate of each point decreased. When the inverted working face passed the monitoring section about 30 m, each monitoring point basically got stable.

Stage V: For some reason, the rate of the secondary lining construction was slow. When the secondary lining construction reached the monitoring section, the surrounding rock displacement curve was gentle, and each monitoring point nearly reached stability.

In addition to that, from the perspective of the data of displacement of each measuring point, when the construction of each working face passed monitoring section, surrounding rock displacement of 1#, 2#, and 3# points were relatively large, while the displacement of 4# measuring point was relatively small. It can be deduced that the surrounding rock near 3# point had a rupture, and the rock loose circle located between 3# and 4# point was about 3.0 m. Similarly, by analyzing the results of the other test holes, the surrounding rock loose circle was of about 3.0–3.5 m. As a whole, the crack range of surrounding rock was mainly within control limits, and the designed bolt length was reasonable.

5 CONCLUSION

Deformation monitoring is an important method to ensure the safety of tunnel construction. Through the monitoring of the construction process, the first-hand actual measurement data are obtained quickly and accurately. Based on the data analysis, the instability trend on part of the surrounding rock section can be forecasted.

The excavation of the upper bench and the inverted part of the tunnel have a significant effect on the surrounding rock deformation, and the influence scope of tunnel construction was about twice the tunnel diameter before and after the working face. The deformation stability time of the surrounding rock is about 40 days after shotcrete bolt support in IV and III grade rock mass, and about 60 days in V grade rock mass.

The experience and conclusions presented in this paper provide a valuable reference for the determination of the reasonable time of tunnel secondary lining and optimization of supporting parameters.

ACKNOWLEDGMENTS

The authors acknowledge the financial support provided by the National Natural Science Foundation of China (No. 51208395) and the Research project of Education Department of Hubei Province of China (No. Q20111101).

REFERENCES

Deng, W.B., Huang, S.X. & Alifu, N. 2014. Super close tunnel vault subsidence monitoring and forecast method research. *Journal of Geomatics* 39(3): 24–26.

Kavvadas, M.J. 2005. Monitoring ground deformation in tunneling: Current practice in transportation tunnels. *Engineering Geology* 79: 93–113.

The Professional Standards Compilation Group of People's Republic of China. 2004. *Code for Design of Road Tunnel (JTG D70-2004)*. Beijing: China Communications Press.

The Professional Standards Compilation Group of People's Republic of China. 2009. *Technical Specifications for Construction of Highway Tunnel (JTG F60-2009)*. Beijing: China Communications Press.

Xia, C.C. & Li, Y.S. 1999. *Testing Theory and Monitoring Technology of Underground Engineering*. Shanghai: Tongji University Press.

Xia, C.C., Gong, J.W., Tang, Y., et al. 2007. Study on site monitoring of large-section highway tunnels with small spacing. *Chinese Journal of Rock Mechanics and Engineering* 26(1): 44–50.

Yun, Y.F. & Tang, G. 2015. Deformation monitoring of tunnel surrounding rock convergence and stability study. *Journal of China and Foreign Highway* 35(3): 210–213.

Zhang, H.S., Chen, S.G. & Meng, J.H. 2015. Deformation monitoring and regression analysis of surrounding rock during the construction of Zhegu mountain tunnel. *Sichuan Building Science* 41(1): 141–145.

Zhang, T.Q. & Shi, Z.B. 2015. Deformation monitoring and analysis of soft rock tunnel. *Journal of Lanzhou Institute of Technology* 22(2): 36–39.

Civil Engineering and Urban Planning IV – Liu et al. (Eds)
© 2016 Taylor & Francis Group, London, ISBN 978-1-138-02903-3

Experimental study on the boundary slippage phenomenon of soft soil micropore seepage

Hui Zhou
School of Civil Engineering and Transportation, South China University of Technology, Guangzhou, Guangdong, P.R. China

Wei-Feng Yan
Guangzhou City Construction College, Guangzhou, Guangdong, P.R. China

ABSTRACT: By the mercury injection test and the constant head seepage test, seepage properties of the fine particles artificial soil and natural soil are tested. The research shows that the two samples tested meet the conditions necessary for the occurrence of the boundary slippage of micropore seepage. Under the same hydraulic gradient, as the permeability coefficient of the artificial soil sample with the pore fluid concentration increases, the largest scale can reach 300 times; "differentiation" appears when the permeability coefficient of the samples with different pore fluid concentrations changes with hydraulic gradient. Samples with a low pore fluid concentration will cause the microporous filtration "boundary slippage" phenomenon. When the hydraulic gradient is small, the k_i–I curve decreases with the increasing hydraulic gradient; when the hydraulic gradient is large, the k_i–I curve changes weakened; in contrast, soil samples with a higher pore fluid concentration do not cause the "boundary slippage" phenomenon, and the permeability coefficient increases along with the hydraulic gradient.

1 INTRODUCTION

Classic fluid flow in the solid surface assumed the fluid mechanics of the fluid molecules and the solid surface relative speed is zero, i.e., "no slip boundary." The assumption of the macroscopic experiment has been valid and has been widely used (Cai et al. 2007, Gu et al. 2004, Wu et al. 2008). However, as the thorough study of micro- and nanopore seepage, scholars have found that when the porosity decreases to a certain scale, the "boundary slippage phenomenon of seepage" appears (Granick et al. 2003, Neto et al. 2005, Stemme et al. 1990, Zhong et al. 2001), which is a law different from the macro flow. Soft soil is mainly composed of a very fine particle size of clay gel composition, with the particle size of micron grade. The intergranular per part can form the pore of less than 10 microns (Liang et al. 2010), and its permeability is influenced by the mineral composition, pore size distribution, pore water ionic composition, and concentration, and many other factors. By the mercury injection test and constant head seepage test, this article conducts a test of the seepage features with different pore fluid concentrations of the artificial soil and natural soil under different hydraulic gradient levels, and explores "the boundary slippage effect" of the soil micropore seepage from the microscopic view, which will provide a reference for soft soil engineering.

2 SAMPLE PREPARATION

The artificial soil for the experiment is made by kaolin and bentonite according to the dry mixing mass ratio of 1:2, dry density 0.82 g/cm^3, void ratio 2.20, and the pore fluid solute level for the analysis of pure sodium chloride (NaCl) particles is level 4 concentration with a specimen for every concentration (mol/L); natural soil samples include silt soil in Panyu, Guangzhou city, with the sampling depth of 7.8 m–8.0 m. The soil samples are in grayish black color with a slight odor and a high organic matter content, water content of 74.1%, void ratio of 2.06, pore fluid that of pure distilled water, a sample for the experiment. Physical parameters of the soil are as shown in Table 1.

3 THE BOUNDARY SLIPPAGE EFFECT TEST

3.1 *Mercury injection test and analysis*

Mercury injection test method is a commonly used method for the determination of pore size and

Table 1. Physical properties of test soft soil.

Sample number	Category	Sample composition	Pore fluid concentration n (mol/L)	Void ratio e	Dry density ρ_d (g/cm^3)	Plastic index I_P (%)	Moisture content w (%)
Y1	Artificial soil	Bentonite 33.3% Kaolin 66.7%	0	2.20	0.82	46.6	82.3
Y2			8.3×10^{-3}				82.4
Y3			8.3×10^{-2}				82.9
Y4			8.3×10^{-1}				83.2
Y5	Natural soil (silt soil in Panyu)	Quartz 32.9%, montmorillonite 26.5%, kaolinite 19.5%, feldspar 10.1%, white mica 8.3%, rock salt 2.7%	0	2.06	0.87	32.1	74.1

The test results of natural soil mineral composition were obtained from Guangzhou Institute of Geochemistry, Chinese Academy of Sciences.

distribution of the soil (Liang 2010, Liu 2006, Zhou et al. 2011). The experimental sample was pierced by the cyclization knife (61.8 mm in diameter, 40 mm in height), and was pushed gently by the porous stone from the ring knife, and then made a deep groove in the blade in order to reveal the fresh experimental section. This method was repeated and the cube of approximate length of 1 cm was got as the sample. After that the freezing drying treatment, the samples of low and high pressure are analyzed by AutoPore9510 mercury injection apparatus. When the mercury is injected, the in-mercury pressure, aperture and relational data were automatically acquired by using the inverse relationship of the in-mercury pressure and the aperture, and then converted to the percentage less than the certain aperture. The specific test principle and the conversion method can be found in the reference (Zhou 2013), so the explanation is omitted here. Figures 1 and 2 are shown in the pore distribution curves of artificial soil and natural soil sample.

Based on the research on the existing standard of soil pore (Kodikara et al. 1999, Shear et al. 1993, Zhou et al. 2010) and the measured results of pore distribution of the silt soils in the Pearl River Delta, the silt soil pore is divided into five categories: macroporous (D > 10 microns), middle hole (2.5 mu m < D < 10 microns), small hole (0.4 mu m < D < 2.5 microns), microporous (0.03 mu m < D < 0.4 microns), and ultramicro hole (D < 0.03 microns), particularly pores between the aggregates, in aggregates pores, between particles and part pores, inside particles pore and pore in the granules. The results of the pore size distribution of the soil samples are summarized in Table 2.

As shown in Table 2, the artificial soil specimen is dominated by the majority of pores in the middle hole, which account for 32.1%. The natural

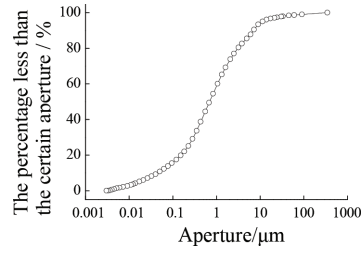

Figure 1. Pore distribution curves of the artificial soil sample.

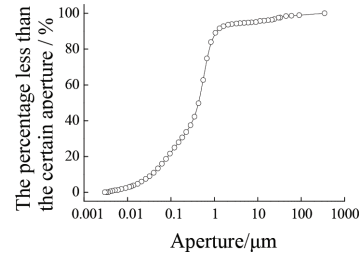

Figure 2. Pore distribution curves of the natural soil sample.

soil specimen is dominated by the majority pores between particles and inside the aggregates pore, which account for 48.7%. The percentage of both the macropore and ultramicro-hole is small. The results of both gentle curve ends obtained by steep morphological analysis is consistent with Figure 1, in contrast, the void ratio of the natural soil is smaller than that of the artificial soil. Mercury injection test results show that both contain a large number of micron grade pores (namely, the pore

Table 2. Pore size distribution of the soil samples.

Sample category	Macroporous (%)	Middle hole (%)	Small hole (%)	Microporous	Ultramicro hole
	>10 μm	2.5–10 μm	0.4–2.5 μm	0.03~0.4 μm	<0.03 μm
Artificial soil	10.9	32.1	26.8	24.1%	6.1%
Natural soil	5.5	13.9	48.7	27.4%	4.5%

Table 3. Permeability coefficient of the soil samples under different hydraulic gradient levels.

	Sample				Permeability quotient k_i /(10^{-8} cm/s)						
Number	$I = 6.25$	$I = 12.5$	$I = 25$	$I = 50$	$I = 75$	$I = 112.5$	$I = 150$	$I = 200$	$I = 250$	$I = 325$	$I = 375$
Y1	5.6	5.3	5.1	4.8	4.5	4.2	4.1	4.0	3.9	3.8	3.7
Y2	9.1	7.5	6.5	6.1	5.8	5.7	5.5	5.1	4.9	4.7	4.6
Y3	42.3	40.1	40.1	44.6	51.4	55.2	57.8	61.2	64.7	82.2	105.3
Y4	1009.6	1010.9	1015.7	1022.6	1032.5	1033.1	1053.1	1051.6	1079.1	1132.0	1169.9
Y5	279.0	235.0	210.0	193.0	187.0	183.1	179.0	164.0	153.0	129.0	121.0

*$I = H_0/L$, I for hydraulic gradient, H_0 for test head, L for sample height, and $L = 40$ mm = 4 cm in this experiment.

diameter is less than 10 microns), the percentage of 89.1% and 94.5%, respectively, which is the necessary condition to cause the micropore seepage boundary slippage effect.

3.2 *The seepage test and analysis*

In order to study the boundary slippage effect of the micropore seepage in soils, this paper uses the constant head test method and different concentrations of the pore fluid and distilled water to test the seepage characteristics of the artificial soil and the natural soil under different hydraulic gradient levels. Samples are prepared by blow samples, sample size 61.8 mm in diameter, 40 mm high, and the preparation method refers to the "standard of soil test method" (GB/T 50123-1999), and the samples are extracted in the saturated state. The experiment was carried out by using south 55 permeameter according to the low to high order of the head. The test head H_0 is, respectively, 25, 50, 100, 200, 300, 450, 600, 800, 1000, 1300, and 1500 cm, records the seepage flow of each sample within the given time, thus the permeability coefficient of the corresponding can be calculated. The average level of the three tests is the permeability coefficient k_i under the head, as shown in Table 3. The permeability coefficient, hydraulic gradient curves of artificial soil, and natural soil (i.e., k_i–I curve) are shown in Figures 3 and 4.

From Table 3 and Figures 3 and 4, constant head test results show that the permeability coefficient of the soil samples with the different concentrations of pore fluid can show the "abnormal" phenomenon of increase or decrease at all levels of hydraulic gradient, which is summarized as follows:

- Under the same hydraulic gradient level, the permeability coefficient of the artificial soil samples increases along with the increase in the pore fluid concentration, and its maximum magnitude can be 300 times. In addition, with the increase in hydraulic gradient, such as hydraulic gradient $I = 6.25$, the permeability coefficient of Y4 sample is 180 times of Y1, and for $I = 375$, it is 316 times.
- With the increase in the hydraulic gradient, the change trend of the permeability of the artificial soil sample under different concentrations of the pore fluid is "abnormal." When the pore fluid concentration is low (as shown in Fig. 3a and b), the permeability coefficient of the soil samples with an increased hydraulic gradient declines, with the largest decline of 51.4% (n = 0 mol/L) and 97.8% (n = 8.3×10^{-3} mol/L); on the other hand, when the pore fluid concentration is higher (as shown in Fig. 3c and d), the permeability coefficient of the soil samples with the increase in the hydraulic gradient increases gradually, $I = 375$ compared with $I = 6.25$, permeability coefficient of the former is 2.49 times higher than that of the latter (n = 8.3×10^{-2} mol/L) and 1.16 ($n = 8.3 \times 10^{-1}$ mol/L).
- The permeability coefficient of the soft soil specimen in Panyu is similar to that of a low concentration of the pore fluid trend along with the change in the hydraulic gradient of the artificial soil sample, and the soil permeability coefficient decreases with increasing hydraulic gradient.

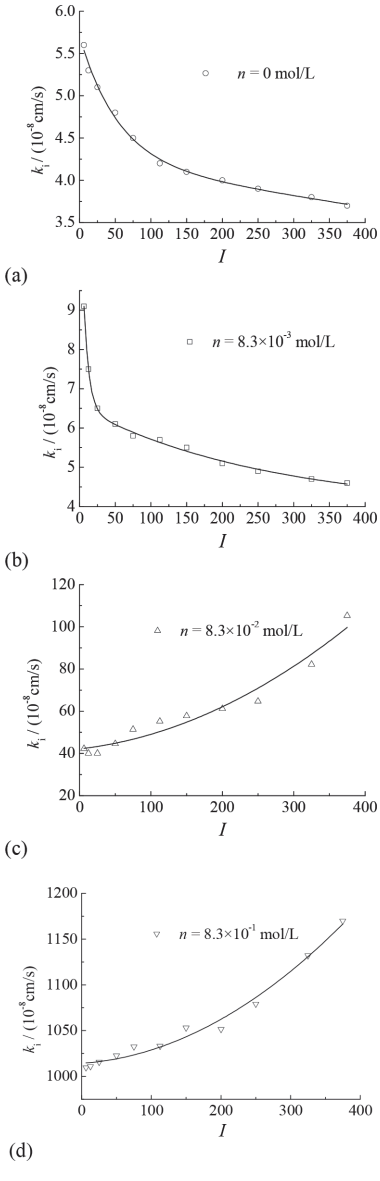

Figure 3. Curves with k_i and I of artificial soils.

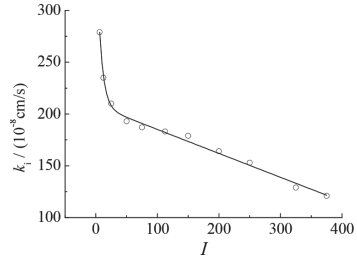

Figure 4. Curve with k_i and I of natural soil.

4 THE MICROSCOPIC MECHANISM ANALYSIS OF "THE BOUNDARY SLIPPAGE PHENOMENON"

The above-mentioned "abnormal" phenomenon of the artificial soil and natural soil permeability coefficient decreases with the increasing hydraulic gradient. This paper tries to discuss the very fine particles of clay micropore seepage in terms of the micro mechanism of "boundary slippage" formation. There are two specific situations:

– For the soil of the larger pore or the very fine particles of the soils with higher pore fluid concentrations, the permeability coefficient increases along with the hydraulic gradient. Particle surface can have a combination of thicker adsorption layer (i.e., the electric double layer) because of its large surface area, and the equivalent seepage aperture changes over electric double layer thickness. When the pore fluid concentration is higher, according to Gouy–Chapman diffusion theory, the combination of the adsorption layer thickness is small (i.e., the thickness of electric double layer is small), the equivalent aperture of microporous filtration is bigger, and no "boundary slippage" arise, as shown in Figure 5a. At this point, when the hydraulic gradient is small, free water can only be driven to flow in the pore, but bound water cannot be driven to flow, making the equivalent permeability pore relatively small, seepage resistance bigger, and the macro performance for the permeability coefficient small; along with the increase of the hydraulic gradient in the free water flow, at the same time, a viscosity of weakly bound water flow occurs gradually, the equivalent permeability hole enlargement and seepage resistance decreases, and macro shows the permeability coefficient increases along with the hydraulic gradient.
– As for the very fine particles of soil with low pore fluid concentration, the permeability coefficient decreases with the increasing hydraulic gradient, the boundary slippage effect can be used as an explanation. When the concentration of the pore fluid is reduced, the electric double layer thickness increases, the thickening of the adsorption layer enables the equivalent aperture of micropore seepage decrease greatly, leading to the "boundary slippage" phenomenon as shown in Figure 5b. At this point, when the hydraulic gradient is small, water seepage flow is reduced

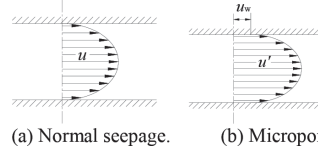

(a) Normal seepage. (b) Microporous filtration.

Figure 5. Boundary conditions of fluid flows.

because of the large account of "boundary slippage" that increases, the permeability coefficient curve falls sharply with the increasing hydraulic gradient; when the hydraulic gradient is larger, the hydraulic seepage flow is dominant, the permeability coefficient curve abates to change with hydraulic gradient, indicating a weak decrease.

The "boundary slippage" of the microporous filtration phenomenon can be interpreted as when the seepage characteristic of the pore size is very small, the intermittent solid–liquid interface appears and leads to the "boundary slip," the hole wall adsorption of the water molecules is reduced, and the water resistance decreases. This paper tries to explain the "abnormal" phenomenon in the constant head permeability test by the boundary slippage effect, but for other reasons, further research remains to be done from a microscopic view.

5 CONCLUSIONS

The following main conclusions can be obtained by analyzing the very fine particles of the artificial soil and natural soil seepage situation:

- The pore of the artificial soil of bentonite mixed with kaolin and natural soft soil samples in Panyu are mainly of micron grade, which fall into the category of very fine particles of clay and meet the necessary conditions arising from the micropore seepage "boundary slip" phenomenon.
- At the same hydraulic gradient level, the permeability of the artificial mixture of soil samples increases with the pore fluid concentration; its largest scale can reach 300 times, and with the increase in the hydraulic gradient, there is a sharp growth.
- For the soil of larger pores or the very fine particle soils with higher pore fluid concentrations, no microporous filtration "boundary slippage" phenomenon occurs, and its permeability coefficient increases with the hydraulic gradient; for very fine particles of soil with a low pore fluid concentration, its permeability coefficient decreases with increasing hydraulic gradient, which can be explained by the boundary slippage effect.

ACKNOWLEDGMENTS

This study was financially supported by the National Natural Science Foundation of China (Grant No. 51508200) and the Natural Science Foundation of Guangdong Province (Grant No. 2015A030310397).

REFERENCES

Cai, G.J., Liu, S.Y., Tong, L.Y. et al. 2007. Study on consolidation and permeability properties of Lianyungang marine clay based on piezocone penetration test. *Journal of Rock Mechanics and Engineering* 26(4): 846–852.

Granick, S., Zhu, Y.X. & Lee, H.J. 2003. Slippery questions about complex fluids flowing past solids. *Nature Materials* 2(4): 221–227.

Gu, Z.H., Gao, G.Y. & Wang, J.H. 2004. Experimental study on effects of structural properties to permeability of soft soil clay in shanghai. *Exploration Engineering: Rock & Soil Drilling and Tunneling* 31(5): 1–3.

Kodikara, J., Barbour, S.L. & Fredlund, D.G. 1999. Changes in Clay Structure and Behavior due to Wetting and Drying. *Proceedings of the 8th Australian-New Zealand conference on Geomechanics*. Hobart, Australia: Australian Geomechanics.

Liang, J.W., Fang, Y.G. & Gu, R.G. 2010. Analysis of microelectric field effect of seepage in tiny-particle clay. *Rock and Soil Mechanics* 31(10): 3043–3050.

Liang, J.W. 2010. *Experimental Study on Soft Soil Deformation and Seepage Characteristics with Microscopic Parameter Analysis*. Guangzhou: South China University of Technology.

Liu, P.S., & Ma, X.M. 2006. *Porous Materials Detection Method*. Beijing: Metallurgical Industry Press.

Neto, C., Evans, D.R., Butt, H.J. et al. 2005. Boundary slip in Newtonian liquids: A review of experimental studies. *Reports on Progress in Physics* 68(12): 2859–2897.

Shear, D.L., Olsen, H.W. & Nelson, K.R. 1993. Effects of desiccation on the hydraulic conductivity versus void ratio relationship for a natural clay. *Transportation Research Record.* Washington DC: National Academy Press.

Stemme, G., Kitttilsland, G. & Norden, B. 1990. A sub micron particle filter in silicon channels. *Sensors and Actuators* 431(4): 21–23.

Wu, C.W., Ma, G.J. & Zhou, P. 2008. A review of the study on the boundary slip problems of fluid flow. *Advances in Mechanics* 38(3): 265–282.

Zhong, Y.C., Tan, X.Q. & Yang, Y.M. 2001. Discussion on several issues in microfluid mechanism. *Journal of Guangdong University of Technology* 18(3): 46–48.

Zhou, H. 2013. *Study on Soft Soil Microstructure and Mechanism of Seepage and Consolidation in Pearl River Delta*. Guangzhou: South China University of Technology.

Zhou, H., Fang, Y.G., Gu, R.G. et al. 2011. Microscopic analysis of saturated soft clay in Pearl River Delta. *Journal of Central South University of Technology* 18(2): 504–510.

Zhou, H., Fang, Y.G. & Zeng, C. 2010. The experimental analysis on micropore change of Guangzhou saturated soft soil in the consolidation process. *Rock and Soil Mechanics* 31(S1): 138–144.

This page intentionally left blank

Civil Engineering and Urban Planning IV – Liu et al. (Eds)
© 2016 Taylor & Francis Group, London, ISBN 978-1-138-02903-3

Development of an urban rainstorm flood simulation model based on a plain flood model

Bo-Ni Su, Hong Huang, Nan Zhang & Jin-Long Zhao
Department of Engineering Physics, Institute of Public Safety Research, Tsinghua University, Beijing, China

ABSTRACT: Recently, urban floods caused by the rainstorms occur frequently. Studying the numerical simulation method of the urban rainstorm floods is helpful for disaster prevention and mitigation. In this paper, an urban flood simulation model is established based on a plain flood simulation model. Many improvements have been made, including modeling methods of the buildings, rainfall and drainage system. An area in Beijing was selected as the study area. The method is compared with a non-hydrodynamics flood simulation method. Different rainstorm scenarios are simulated and compared. The effects of the drainage wells are also tested for urban planning.

1 INTRODUCTION

Recently, urban floods have been caused by the rainstorms occuring frequently. Risk analysis is needed to reduce the losses for the urban rainstorm floods. Numerical simulation is an effective approach for the quantitative risk assessment. Studying the numerical simulation method of the urban rainstorm floods is helpful for the disaster prevention, urban planning and sponge city building.

Many kinds of flood simulation methods have been developed based on hydrodynamics (Caleffi et al. 2003; Kärnä et al. 2011). However, most of them have been focused on the river floods and the plain floods, and did not take urban rainstorm floods into consideration. Many important details, such as the modeling methods of the buildings and rainfall, were not given enough attention. At the same time simulation methods that are not based on hydrodynamics, such as "non-source flood" method (Renyi & Nan 2002) are still widely used in urban rainstorm floods simulations (Yin et al. 2011). Although, these methods are simple and fast, they cannot obtain the spatio-temporal distribution of the water accurately because the details of the water flow are ignored. Therefore, an urban flood simulation model based on the hydrodynamics is needed to make simulations more accurate.

In this paper, an urban flood simulation model is established based on a plain flood simulation model. Many improvements have been made, including modeling methods of buildings, rainfall and drainage system. An area in Beijing was selected as the study area. The method is compared with "non-source flood" method. Different rainstorm scenarios are simulated and compared. The effects of the drainage wells are also tested for urban planning.

2 METHODS

The urban flood simulation model established in this paper is based on a plain flood simulation model, LISFLOOD-FP. Many improvements have been made so that the new model is suitable for urban flood simulation.

2.1 *Introduction to LISFLOOD-FP model*

LISFLOOD-FP (Bates & De Roo 2000) is a flood simulation model based on the diffusion wave approximation of the two-dimensional SWEs (Shallow Water Equations). In this model, simulation area is divided into cells (usually squares with the same size) according to DEM (Digital Elevation Model) raster. Each cell is connected with its four neighbor cells. In the simulation, the (depth averaged) flow velocity between the adjacent cells i and j is calculated using Manning Formula:

$$v_{ij} = \frac{k \cdot d_{ij}^{2/3} \cdot S_{ij}^{1/2}}{n} \tag{1}$$

where v_{ij} = flow velocity (m/s); k = conversion factor (= 1 $m^{1/3}$ s^{-1}); d_{ij} = water depth at the interface between two cells (m); S_{ij} = water surface slope between two cells (dimensionless); n = Manning

coefficient (dimensionless). Flowrate can be obtained using:

$$Q_{ij} = v_{ij} \cdot d_{ij} \cdot w \tag{2}$$

where Q_{ij} = flowrate at the interface between two cells (m^3/s); w = the width of cells (m). The original literature of the LISFLOOD-FP (Bates & De Roo 2000) did not explicitly provide the calculation method of d_{ij}. In this paper, the following formula, which is used in JFLOW model (Bradbrook 2006), is applied.

$$d_{ij} = \max\left(h_i, h_j\right) - \max\left(z_i, z_j\right) \tag{3}$$

where h_i, h_j = water surface elevation in cells i and j (m), which equal to ground elevation plus water depth; z_i, z_j = ground elevation in cells i and j (m). After all flowrates between cells are calculated, the change rates of the water volume in the cells can be calculated using the following formula:

$$\frac{\mathrm{d}\left(V_i\right)}{\mathrm{d}t} = Q_{North} + Q_{South} + Q_{East} + Q_{West} \tag{4}$$

where V_i = water volume in cell i (m^3); t is time (s); $Q_{North}, Q_{South}, Q_{East}, Q_{West}$ = flowrates in the four directions, positive for inflow, negative for outflow. The change rates of water depth are:

$$\frac{\mathrm{d}\left(d_i\right)}{\mathrm{d}t} = \frac{\mathrm{d}\left(V_i\right)}{\mathrm{d}t} / w^2 \tag{5}$$

where d_i = water depth in cell i (m). The water depth in the next step can be determined if a time step Δt is given. Calculate the flow rate and update the water depth alternately until the simulation ends, and the spatio-temporal distribution of the water depth can be obtained. Time step can be determined using the following formula:

$$\Delta t = C \frac{w}{\max\left(v\right) + \sqrt{g \cdot \max\left(d\right)}} \tag{6}$$

where C = Courant number (dimensionless); g = gravitational acceleration (= 9.8 m/s^2); max (v) and max (d) are the maximum flow velocity (m/s) and maximum water depth (m) in the whole simulation area. In order to ensure accuracy, a maximum time step $\Delta t_{\max}$ is set. If time step obtained by the equation (6) is greater than $\Delta t_{\max}$, time step is set to $\Delta t_{\max}$.

2.2 *Model improvements*

There are some differences between the urban rainstorm floods and plain floods. Therefore, some improvements are needed to make the model suitable for the urban rainstorm flood simulation.

– Modeling method of the buildings
In this paper, buildings are treated as solid blocks. Cells that are occupied by buildings are excluded from simulation area. Also, flowrates between building cells and normal cells are always zero, as water cannot flow inside or outside building cells.
– Modeling method of source terms
Source terms mainly include effects of rainfall, infiltration, and drainage. It can be expressed by:

$$s = s_{rain} + s_{inf} + s_{drain} \tag{7}$$

In common cells, rainfall source term s_{rain} equals to rainfall intensity (in m/s, converted form common mm/h). However, in cells adjacent to building cells, rainfall source term is slightly greater than rainfall intensity. The difference equals to the total number of cells covered by the building divided by the total number of cells surrounding the building. In this way, the total rainfall in the simulation area will not decrease due to the buildings. It is also consistent with the actual situation that most buildings directly discharge rain water on roofs to the ground.

Although, infiltration parameters of the different kinds of soil are available, data of the common urban ground surface, such as concrete and asphalt, still lack. In this paper, urban ground surface is treated as impervious, and infiltration is neglected.

The drainage source term s_{drain} can be calculated using orifice discharge formula, as long as drainage pipe system works properly.

$$s_{drain} = -CA\sqrt{2gd} \tag{8}$$

where C = discharge coefficient (between 0 and 1); A = cross-sectional area of drainage wells (m^2), which is the total area of holes on drainage well covers in a cell.

The source term is considered by replacing the equation (5) with the following equation:

$$\frac{\mathrm{d}\left(d_i\right)}{\mathrm{d}t} = \frac{\mathrm{d}\left(V_i\right)}{\mathrm{d}t} / w^2 + s \tag{9}$$

– Prevention of the "checkerboard oscillation" phenomenon
The inertial terms are neglected in the diffusion wave approximation. This leads to "checkerboard oscillation" phenomenon when cells are

small and time step is large (Hunter 2005). In one time step, the volume of the water flow between two adjacent cells is so great that the water surface elevations of these two cells reverse in the next time step and oscillation occurs. This phenomenon is harmful for the simulation accuracy. In river flood simulations, this phenomenon seldom occurs because the cells are large. However, in the urban rainstorm flood simulations, cells are often very small to represent the complex landforms caused by the buildings and infrastructures. "Checkerboard oscillation" phenomenon becomes common and must be prevented. Hunter (2005) pointed out that there are two simple solutions for the "checkerboard oscillation" phenomenon. The first is to add a flow limiter, the second is to use an adaptive time step. Both of them can eliminate the "checkerboard oscillation", but they have drawbacks. Using a flow limiter will probably underestimate the flowrates and introduce errors. Using an adaptive time step will cause very small time step when water surface is flat, making simulation speed drop sharply. A workaround is to use a modified formula for a flow velocity when the difference in the water surface elevation between the two cells is less than a given threshold. However, artificial parameters and formulas are introduced, which is not good for the simulation to reflect the nature of water flow.

In this paper, a new method is used to solve this problem. In the simulation, change rates of the water depth in cells can be calculated using equation (5). These change rates are also change rates of the water surface elevation, as the ground elevation is constant. For adjacent cells i and j, introduce "chasing time" t'_{ij}:

$$t'_{ij} = -\frac{h_i - h_j}{d(d_i)/dt - d(d_j)/dt} \tag{10}$$

If $t'_{ij} > 0, t'_{ij}$ will represent the time needed for the water depth in two cells to be equal. If $0 < t'_{ij} < \Delta t$, the water depth in two cells will inverse in one step, thus, "checkerboard oscillation" phenomenon will occur. At that time, the flowrate between the two cells should be adjusted to avoid the oscillation. In this paper, the adjusted flowrate is:

$$Q'_{ij} = Q_{ij} \frac{t'_{ij}}{\Delta t} \tag{11}$$

This is equivalent to stop water flow after time t'_{ij}, when the water depth in the two cells is equal. In this way, "checkerboard oscillation" can be eliminated. This method can be seen as a generalized flow limiter. It uses not only water surface elevation but also change rates of the water surface elevation. Artificial influence introduced by this method is much lower than the traditional flow limiters.

3 RESULTS AND DISCUSSION

3.1 *Study area*

A region in Beijing is selected as the study area. It stretches to 1.1 kilometers from north to south and 1.5 kilometers from east to west, and covers an area of 1.65 square kilometers. In order to prevent the influence caused by edges, the simulation area was extended by 50 meters in all four directions. Figure 1 shows the region of the study area and the extended simulation area.

Landform is a very important factor in floods. In this paper, DEM data are provided by the Beijing Institute of Surveying and Mapping. Figure 2 shows the elevation map of simulation area.

The distribution of drains was carefully investigated one by one, on site. The investigation results show that there are about 360 drains in this region and most of them have a cross sectional area of about 0.17 square meters.

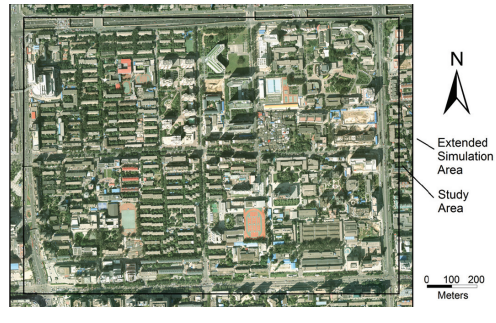

Figure 1. Study area and extended simulation area.

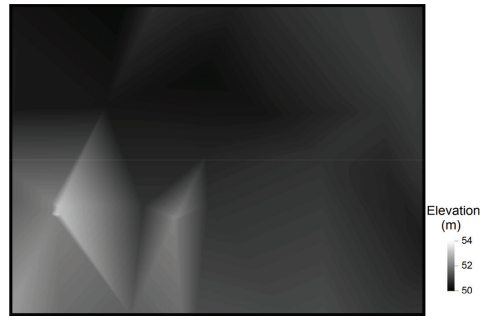

Figure 2. Elevation map of simulation area.

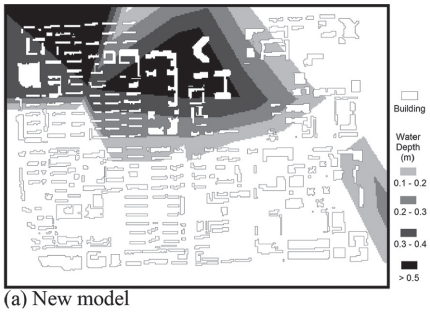

(a) New model

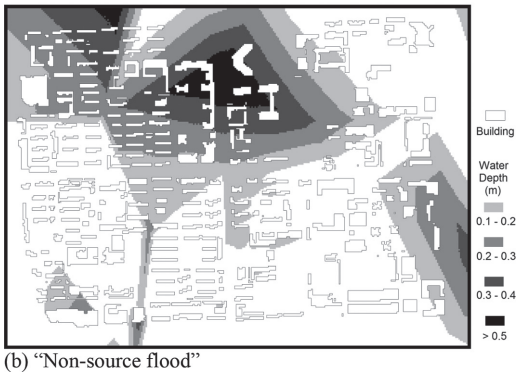

(b) "Non-source flood"

Figure 3. Distribution of the water depth obtained by the two methods.

3.2 *Comparison of the new model and "non-source flood" method*

The new model and "non-source flood" methods are compared by simulating a same rainstorm with a duration of 1 hour and rainfall intensity of 100 millimeter per hour. The effect of the drainage system has neglected to reduce influence factors and make the comparison easier. Figure 3 shows the distribution maps of the water depth at 1 hour obtained by the two methods.

The results obtained by the two methods are different, especially in local low-lying sections. The results obtained by a new model are more reasonable than those obtained by the non-hydrodynamics methods. The comparison indicates using non-hydrodynamics simulation methods in the urban rainstorm flood simulation that may introduce significant errors.

3.3 *Simulations under different rainfall scenarios*

Simulations under different rainfall scenarios were carried out with drainage wells ignored. Table 1 shows the maximum water depth during the whole rainstorm under different scenarios.

It can be seen that the rainstorms with a longer duration and greater rainfall intensity cause more serious floods. Flood situation caused by the rainstorms with the same total rainfall (for example, 60 min 25 mm/h rainstorm, 30 min 50 mm/h rainstorm, and 15 min 100 mm/h rainstorm) is similar.

Table 1. Maximum water depth without drainage wells (m).

Rainfall duration	Rainfall intensity			
	25 mm/h	50 mm/h	75 mm/h	100 mm/h
15 min	0.218	0.250	0.281	0.317
30 min	0.248	0.323	0.378	0.423
45 min	0.292	0.386	0.439	0.494
60 min	0.332	0.422	0.494	0.557

Table 2. Maximum water depth with drainage wells (m).

Rainfall duration	Rainfall intensity			
	25 mm/h	50 mm/h	75 mm/h	100 mm/h
15 min	0.194	0.230	0.254	0.269
30 min	0.227	0.264	0.285	0.301
45 min	0.243	0.276	0.291	0.305
60 min	0.247	0.276	0.291	0.308

Another group of simulations, which took the drainage wells into consideration were also carried out. Table 2 shows the simulation results.

It is obvious that water depth is lower with the help of drainage system. Still, rainstorms with longer duration and greater rainfall intensity cause more serious floods. However, for rainstorms with the same total rainfall, short-time strong rainstorms will cause more floods than the rainstorms with a longer duration. In other words, the effect of drainage system is limited to short-time strong rainstorms. Other measures, such as land leveling, maybe more useful to prevent and mitigate urban floods caused by short-time strong rainstorms.

4 CONCLUSION

In this paper, an urban flood simulation model is established based on a plain flood simulation model. Many improvements have been made, including modeling methods of buildings, rainfall and drainage system. An area in Beijing was selected as the study area. The method is compared with the "non-source flood" method. The results obtained by the two methods are quite different.

It indicates that using non-hydrodynamics simulation methods in the urban rainstorm flood simulation may introduce significant errors. Different rainstorm scenarios are simulated and compared. The results show rainstorms with longer duration and greater rainfall intensity cause more serious floods. Flood situations caused by rainstorms with the same total rainfall are similar. The effects of drainage wells are also tested. Water depth is significantly lower with the help of a drainage system. However, the effect of the drainage system is limited in short-time strong rainstorms. The simulation model is helpful for the prevention and mitigation of the urban rainstorm floods. It is useful for the urban planning and sponge city building.

ACKNOWLEDGMENTS

This work was supported by China Clean Development Mechanism Fund under Grant No. 2013049 and National Natural Science Foundation of China under Grant No. 71173128.

REFERENCES

Bates, P.D. & De Roo, A.P.J. 2000. A simple raster-based model for flood inundation simulation. *Journal of Hydrology* 236(2000): 54–77.

Bradbrook, K. 2006. JFLOW: A multiscale two-dimensional dynamic flood model. *Water and Environment Journal* 20(2006): 79–86.

Caleffi, V. et al. 2003. Finite volume method for simulating extreme flood events in natural channels. *Journal of Hydraulic Research* 41(2): 167–177.

Hunter, N.M. et al. 2005. An adaptive time step solution for raster-based storage cell modelling of floodplain inundation. *Advances in Water Resources* 28(9): 975–991.

Kärnä, T. et al. 2011. A fully implicit wetting–drying method for DG-FEM shallow water models, with an application to the Scheldt Estuary. *Computer Methods in Applied Mechanics and Engineering* 200(5–8): 509–524.

Renyi, L. & Nan, L. 2002. Flood area and damage estimation in Zhejiang, China. *Journal of Environmental Management* 66(1): 1–8.

Yin, J. et al. 2011. Community-based scenario modelling and disaster risk assessment of urban rainstorm waterlogging. *Journal of Geographical Sciences* 21(2): 274–284.

This page intentionally left blank

Civil Engineering and Urban Planning IV – Liu et al. (Eds)
© 2016 Taylor & Francis Group, London, ISBN 978-1-138-02903-3

A study of engineering and electricity properties of cement mortar added with fly ashes and piezoelectric materials

Shu-Chuan Chang, Jhan-Cyue Lin, Shyh-Haur Chen & Her-Yung Wang
Department of Civil Engineering, Institute of Civil Engineering Technology, K.U.A.S. Kaohsiung, Taiwan, R.O.C.

ABSTRACT: Taiwan, which is located on a plate junction, experiences frequent earthquakes, abundant rainfall during the typhoon season, and frequent natural disasters. Improvements in the intelligent disaster prevention functions of the buildings are imperative. The cement mortar materials prepared by replacing the cement component with varying amounts of fly ash 0%, 10%, 20%, and 30%, respectively (comparison group). The piezoelectric materials were prepared by replacing the 5% fine aggregate with piezoelectric powder (PZT group). The engineering and electricity properties were tested to assess the correlations among flow, compressive strength, water absorption, and electricity at 50 V and 100 V. The correlations between these properties were also investigated. At the curing age of 28 days, the compressive strength of the comparison group was in the range of 31.0–20.4 MPa, whereas, the compressive strength of PZT group was in the range of 29.0–19.0 MPa. The comparison group exhibited higher results (1870–1588 Ω) in the electricity property test under 50 V, whereas PZT group exhibited lower results (1419–1286 Ω). The compressive strength and results of the electricity property tests demonstrated that the compressive strength and electrical resistance decreased as the replacement of the fly ash increased. The strength of the comparison group was higher than the strength of PZT group because 5% of the fine aggregates were replaced by the piezoelectric material and the piezoelectric material was water-resistant. However, this study was just 5% of the fine aggregates replaced by the piezoelectric materials that, to the compressive strength, these effects are small.

1 INTRODUCTION

Taiwan is located on the border of the tectonic plates with frequent earthquakes, and extreme heavy rains brought by typhoons often causing severe disasters. Thus, buildings in Taiwan need smart solutions to strengthen their endurance. Along with the progression of science and technology, the development of piezoelectric composite materials has gradually become a trend. Piezoelectric composite materials are used in civil engineering to make up for the functional deficiencies of the original base materials. The piezoelectric effects of the piezoelectric materials also can be used while making controllers or sensors that has greatly increased the capacity of the civil engineering. Concrete, the most commonly applied material in civil engineering no longer functions to resist pressures, with the intelligence of the piezoelectric materials, it will be able to conduct self-monitoring, self-repair, mechanical sensing, among other things.

Previous studies have proved that making good use of piezoelectric materials in buildings can reduce damages caused by natural disasters and create more business opportunities (Clipsham et al. 2010; Jaitanong et al. 2008; Li & Gong et al. 2009; Li et al. 2008; Li et al. 2009; Xing et al. 2009; Yan et al. 2009).

Each year the thermal power plants in Taiwan produce about 100 million tons of fly ash, which can be a hundred percent recycled. This not only saves money, but also solves the shortage of the sandstone. There are studies showing that fly ash replacing cement actually carry out better construction quality and create economic benefits (Ahmaruzzaman 2010; Hwang et al. 2010; Maciej et al. 2014).

Piezoelectric materials are divided into: piezoelectric ceramic, piezoelectric polymer, and piezoelectric composites. Commonly used Piezoelectric Materials Are Lead Zirconate Titanate (PZT), quartz, Barium Titanate ($BaTiO_3$), Lead Zirconate Titanate (PLZT) that might create electro-optical effect, Poly Vinylidene Fluoride (PVF_2), etc. Piezoelectric ceramic (PZT) can have a good pyroelectric effect and piezoelectric effect, which is increasingly applied in civil engineering (Kolania et al. 2012; Ye & Breugel 2009).

This study investigated the cement mortars prepared using fly ash and piezoelectric materials

(PZT) to induce electromechanical properties. By examining the mechanical properties and electrical properties of these mixtures (Kuo et al. 2013), these materials can be used to facilitate and promote disaster prevention projects.

2 EXPERIMENTAL PLAN

2.1 *Experimental materials*

The cement used in this study was ASTM C150 type I Ordinary Portland cement. The mixing water met the ASTM C94 requirements for mixing concrete. Similarly, the fine aggregates produced in the Taiwan Ligang region met the requirements of the ASTM C33. Class F ASTM C618 fly ash was supplied by the Taiwan Xing-Da Thermal Power Plant. The PZT material used in this study was S-44 PZT powder with a density of 7.7 cm^3/g, which was purchased from Taiwan Kaohsiung Sunnytec Electronics Co. Table 1 describes the physical properties of the materials, and Table 2 summarizes their chemical properties.

2.2 *Experimental variables*

Table 3 shows that the mixtures of the cement mortars were prepared according to the ASTM C109 standards, and the ratio of the cement, water, and sand was set to 1:0.64:2.75. In the comparison group, cement was replaced with fly ash at concentrations of 0%, 10%, 20%, and 30%. Similarly, in the PZT group (the experimental group), the 5% fine aggregate was replaced with piezoelectric powder.

Table 1. The physical properties of material.

Items	Specific gravity	Water absorption (%)	F.M	Fineness (cm^2/g)
Fine aggregate	2.65	2.3	3.1	–
Cement	3.15	–	–	3500
Fly ash	2.8	–	–	3140
PZT	7.7	–	–	–

Table 2. The chemical properties of material (unit: %).

Properties	Cement	Fly ash	PZT
SiO_2	20.22	50.79	–
Al_2O_3	4.96	24.97	
Fe_2O_3	2.83	7.87	–
CaO	64.51	5.68	–
MgO	2.33	1.72	–
LOI	2.4	3.1	–
SO_3	2.46	0.3	–
Alkalis	0.48	–	–
$PbZrO_3$	–	–	55
$PbTiO_3$	–	–	45

Table 3. Compositions of the mixtures (unit: kg/m^3).

No.	Cement	Fly ash	PZT	Sand	Water
F0	543	–	–	1494	348
F10	462	38			
F20	408	75			
F30	353	113			
PZT- F0	543	–	217	1420	348
PZT-F10	462	38			
PZT-F20	408	75			
PZT-F30	353	113			

2.3 *Experimental methods and specimen processing*

The flow tests were performed on cement mortar specimens with dimensions of 5 cm × 5 cm × 5 cm in accordance with ASTM C109 standards. The molds were removed after 24 hours, and the specimens were allowed to cure in the saturated lime-water for 1, 7, 28, and 56 days. Subsequently, the compressive strength and water absorption properties were examined in accordance with ASTM C109 and ASTM C642-90 standards, respectively. The electrical properties were tested under the SSD and OD conditions, and the resistance was measured at 50 V and 100 V with a current of 0.01 A.

The samples were cured until the saturated surface was dry, and the square specimens were polished using sandpaper of three different grits. Next, the two sides of each square were painted with conductive silver paint. A conductive copper foil was then attached to the painted sides of the specimens leaving approximately 0.5 cm–1.0 cm of uncovered space in which to place the electrode clips for testing. Insulating tape was wrapped around the squares to avoid electrical leakage. All of this was completed before performing the resistance test.

3 RESULTS AND ANALYSIS

3.1 *Flow value*

The standard water cement ratio of the fly ash cement mortar was 0.64, which reached flow value 20.0 cm, meeting the standards required. As shown in Figure 1 the specimen in the comparison group which fly ash substituted cement from 0% to 30%, the standardized flow values ranged

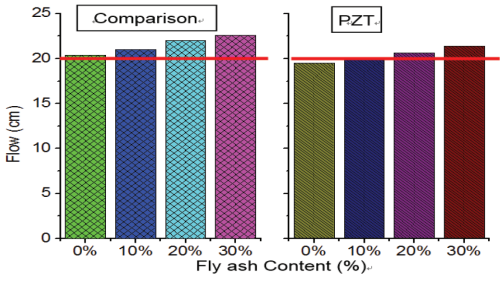

Figure 1. Flow values of piezoelectric fly ash cement mortar materials.

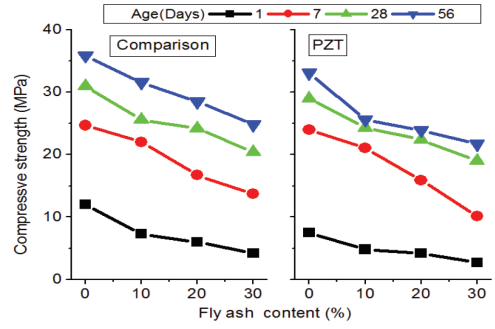

Figure 2. Compressive strengths of piezoelectric fly ash cement mortar.

from 20.4–22.6 cm. Specimens of the PZT group (experimental group) with the fly ash substituting cement from 0% to 30% had flow values of 19.5 cm–21.4 cm. As the ratio of fly ash increased, the flow values increased. Specimens with 30% of the fly ash substitution had the flow value of 2.2 cm higher than that of 0%. Specimens with piezoelectric materials had lower flow value (1.2 cm) compared to the comparison group. It might be as the piezoelectric materials did not mix with cement and fine aggregate well enough.

3.2 *Compressive strength*

Figure 2 shows that the specimens in the comparison group, with fly ash substitution from 0% to 30%, showed different compressive strengths and the different lengths of curing. Compressive strength values of 12.0–4.2 MPa, 24.7–13.7 MPa, 31.0–20.4 MPa, and 35.9–24.8 MPa were observed for the 1-day, 7-day, 28-day, and 56-day cured specimens, respectively. Similarly, the PZT group with the fly ash substitution exhibited compressive strength values of 7.5–2.7 MPa, 24.0–10.1 MPa, 29.0–19.0 MPa and 33.1–21.7 MPa for the 1-day, 7-day, 28-day, and 56-day cured specimens, respectively. The compressive strength decreased as the amount of fly ash increased. Mainly as the use of Class F fly ash genus low calcium fly ash its CaO content is low, caused by a reduced intensity and, thus, could not densify. The strength of the comparison group was higher than the strength of the PZT group because 5% of the fine aggregates were replaced by the piezoelectric material and the piezoelectric material was water-resistant. However, this study was just 5% of the fine aggregates replaced by the piezoelectric materials that regarding the compressive strength these effects are small.

3.3 *Water absorption*

Figure 3 shows that the rate of water absorption of the comparison group was 14.2%–15.0% for

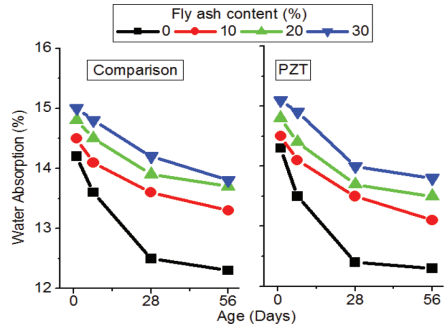

Figure 3. Water absorption of piezoelectric fly ash cement mortar materials.

the 1-day cured specimen and 12.5–14.2% for the 28-day cured specimen. The rate of water absorption of the PZT group was 14.3%–15.1% for the 1-day cured specimen and 12.4%–14.0% for the 28-day curing specimen. Specimens with higher fly ash substitution exhibited higher rate of water absorption. As the use of Class F fly ash genus low calcium fly ash has low CaO content caused by reduced intensity, the cement mortar becomes less hard due to the increased number of internal pores, which can absorb water. In the PZT group, because the piezoelectric materials were finer than the fine aggregates, these materials were able to fill the pores, resulting in a more significant decrease in the water absorption with an increasing fly ash substitution relative to the comparison group.

3.4 *The SSD-50 V resistance value*

As shown in Figure 4, the fly ash cement mortar specimens under the SSD state at 50 V and 0.01 A exhibited increasing resistance values with an increased curing time, which was indirectly related to the rate of water absorption. The resistance

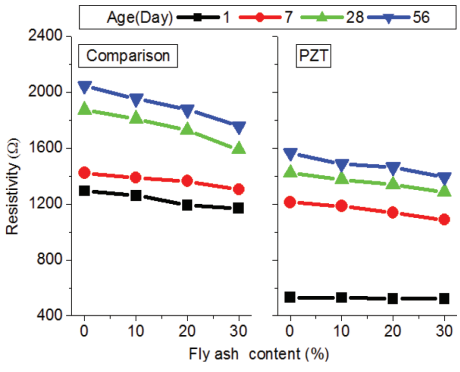

Figure 4. The SSD-50 V resistance value of piezoelectric fly ash cement mortar materials.

values of the comparison group specimen obtained after 1-day of curing were 1293–1168 Ω, whereas, those of the PZT group were 532–521 Ω. The resistance values of the control specimen obtained after 28-days of curing were 1870–1588 Ω, whereas those of the PZT group were 1419–1286 Ω. The specimens obtained after 1-day of curing were not completely hydrated, the resulting piezoelectric materials exhibited excellent conductivity, and the resistance values of the PZT group were lower than those of the comparison group. After hydration was complete during the curing process, the conductivity of the piezoelectric materials was restricted, resulting in higher values than those of the comparison group.

3.5 *The OD-50 V resistance value*

Figure 5 shows the resistance values of the fly ash cement mortar specimens prepared after 28 days of curing. The samples were examined under OD conditions at 50 V and 0.01 A. The resistance values of the comparison group were 3485–3908 Ω, whereas, those of the PZT group were 4092–4659 Ω. The higher resistance of the PZT group is caused by the lack of water permeation throughout the piezoelectric materials, which causes the electrical energy to become capacitive and leads to higher resistance. According to the comparison of the SSD state with the OD state when the voltage is 50 V, the electricity of the PZT in a SSD state ranges from 1419–1286 Ω, and the electricity of PZT in an OD state ranges from 4092–4659 Ω. Thus, the piezoelectric material generates capacitance in the specimen without moisture transfer, and the electricity in an OD state is greater than the electricity in a SSD state.

3.6 *The SSD-100 V resistance value*

As shown in Figure 6 the decrease in the resistance values of the cement mortar specimen was

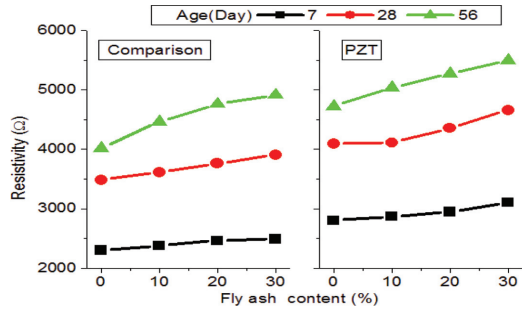

Figure 5. The OD-50 V resistance values of piezoelectric fly ash cement mortar materials.

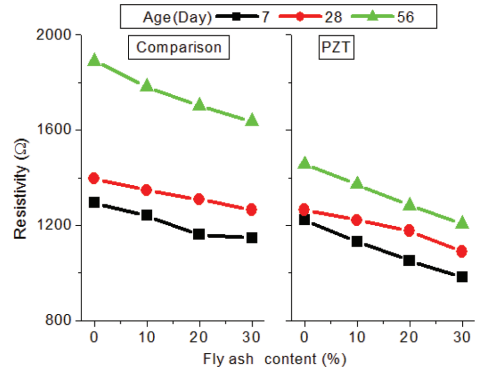

Figure 6. The SSD-100 V resistance values of the piezoelectric fly ash cement mortar materials.

observed under the SSD state at 100 V and 0.01 A with increasing fly ash concentration due to an decrease in the degree of hydration. Under the SSD state at 50 V, the comparison group specimens that were cured for 28 days exhibited resistance values of 1870–1588 Ω. When the voltage was increased from 50 to 100 V, the resulting resistance values were 1397–1264 Ω. These results indicate that the lower resistance was observed due to power transmission at a higher voltage. As the enhanced voltage caused an improvement in the conductivity of the specimens, the relative resistance value decreased.

3.7 *The OD-100 V resistance value*

As shown in Figure 7 the resistance values of the comparison group specimens that were cured for 28-days were 2644–3013 Ω under the OD state at 100 V with 0.01 A. Under the same conditions, the values of the PZT group were 3153–3415 Ω. The higher resistance of the PZT specimen was due to the formation of a capacitive state in the absence of water, as discussed earlier. Under the OD

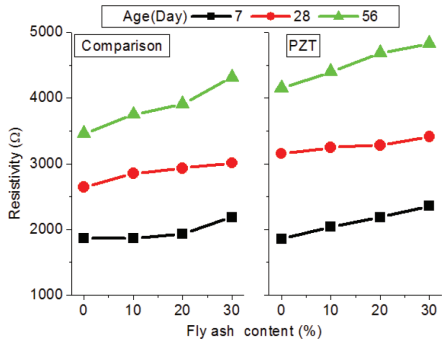

Figure 7. The OD-100 V resistance values of piezoelectric fly ash cement mortar materials.

state and 50 V, the comparison group specimens obtained after 28 days of curing exhibited resistance values of 3485–3908 Ω. When the voltage was increased to 100 V, the resulting resistance values were 2644–3013 Ω. These results indicate that the lower resistance was observed during the power transmission at a higher voltage. As the enhanced voltage caused an improvement in the conductivity of the specimens, the relative resistance value decreased.

4 CONCLUSION

- Flow value of the standard cement mortar, namely the 0% fly ash in the comparison group, was 20.0 cm. The PZT group has a slightly lower flow because the piezoelectric materials could not mix with the cement and fine aggregates well.
- The comparison group specimens that were cured for the 28-day exhibited compressive strength values of 31.0–20.4 MPa, whereas, those of the PZT group exhibited values of 29.0–19.0 MPa. The compressive strength decreased as the amount of fly ash increased because the use of Class F fly ash genus low calcium fly ash has a low CaO content caused by the intensity reduction and thus cannot densify. The strength of the comparison group was higher than the strength of the PZT group because 5% of the fine aggregates were replaced by the piezoelectric materials and the piezoelectric materials was water-resistant. However, this study was just 5% of the fine aggregates being replaced by the piezoelectric materials that for the compressive strength these effects are small.
- As the amounts of substituting fly ash increased, the rates of water absorption also increased. Specimen from the comparison group that had cured for 28-day had water absorption rates of 12.5–14.2%, compared to the 12.4%–14.0% of the specimen from the PZT group cured for the same period of time. It was because the fly ash increased the internal pores of the cement mortar, resulted in higher rates of water absorption. Piezoelectric materials filled in the pores in the specimen of the PZT group, thus, the rates of water absorption dropped more obviously when more fine aggregates were replaced.
- Specimens that were cured for longer amounts of time exhibited higher resistance values. Under the SSD state, the resistance values of the comparison group were 1264–1870 Ω, which were higher than the values of 1089–1419 Ω of the PZT group because the piezoelectric materials improved the conductivity. In contrast, under the OD state, the resistance values of the comparison group were 2644–3908 Ω, which was lower than the values of 3153–4659 Ω that were observed for the PZT group. The higher resistance of the PZT specimens was due to the absence of water, which caused the electrical energy to become capacitive. The resistance values at 50 V of 1286–4659 Ω were higher than the values of 1089–3415 Ω observed at 100 V, indicating that the samples exhibited less resistance at higher voltages. As the enhanced voltage improved the conductivity of the specimens, the relative resistance decreased.

ACKNOWLEDGMENT

The authors would like to thank the National Science Council of the Republic of China, Taiwan, for financially supporting this research under the Contract No. NSC 101-2221-E-151-063.

REFERENCES

Ahmaruzzaman, M. 2010. A review on the utilization of fly ash. *Progress in Energy and Combustion Science* 36(3): 327–363.

Clipsham, T.J. & Button, T.W. 2010. 1–3 Piezocomposites realised from small feature size, high aspect ratio, hot embossed moulds. Part II: Piezocomposite fabrication. *Microsyst Technol* 16(11): 1983–1988.

Hwang, C.L., Lai, C.I. & Hsieh, S.L. 2010. The fabrication and properties of high volume fly ash concrete. *Monthly Journal of Taipower's Engineering* 737: 84–93.

Jaitanong, N., Chaipanich, A. & Tunkasiri, T. 2008. Properties 0–3 PZT-Portland cement composites. *Ceramics International* 34(4): 793–795.

Kolani, B., Buffo-Lacarrière, L., Sellier, A., Escadeillas, G., Boutillon, L. & Linger, L. 2012. Hydration of slag-blended cements. *Cement & Concrete Composites* 34(9): 1009–1018.

Kuo, W.T., Chen, S.H., Wang, H.Y. & Lin, J.C. 2013. A study on the mechanical and electricity properties of cement mortar added with GGBFS and piezoelectric powder. *Construction and Building Materials* 49: 251–256.

Li, G.j., Quan, J., Gong, H.Y. & Sun, L.C. 2009. Research progress in cement based piezoelectric composites. *Materials Review* 23(12): 52–55.

Li, X., Huang, S.F., Liu, F.T. & Xu, D.Y. 2008. Properties of 0–3 cement-based piezoelectric composites modified by carbon black. *Journal of Building Materials* 11(3): 271–275.

Li, Z., Gong, H. & Zhang, Y. 2009. Fabrication and piezoelectricity of 0–3 cement based composite with nano-PZT powder. *Current Applied Physics* 9(3): 588–591.

Maciej, Z. & Mohsen, B.H. 2014. Experimental investigation and modeling of hydration and performance evolution of fly ash cement. *Materials and Structures* 47(7): 1259–1269.

Xing, F., Dong, B. & Li, Z. 2009. The study of pore structure and its influence on material properties of cement-based piezoelectric ceramic composites. *Construction and Building Materials* 23(3): 1374–1377.

Yan, S., Sun, W., Song, G., Gu, H., Huo, L.S., Liu, B. & Zhang, Y.G. 2009. Health monitoring of reinforced concrete shear walls using smart aggregates. *Smart Materials and Structures* 18(4): 1–7.

Ye, G. & Breugel van, K. 2009. Simulation of connectivity of capillary porosity inhardening cement-based systems made of blended materials. *Concr Technol* 54(2/3): 163–184.

Civil Engineering and Urban Planning IV – Liu et al. (Eds)
© 2016 Taylor & Francis Group, London, ISBN 978-1-138-02903-3

No-sand cushion vacuum preloading method to improve bearing capacity of fresh hydraulic fill mud

Wei Bai & Rong-Bing Lin
State Key Laboratory of Geomechanics and Geotechnical Engineering, Institute of Rock and Soil Mechanics, Chinese Academy of Sciences, Wuhan, Hubei, China

Dong-Liang Zhu
Hubei Shuizong Water Resources and Hydropower Construction Co. Ltd., Wuhan, Hubei, China

Zhu-Xiong Liu
Hubei Provincial Road and Bridge Co. Ltd., Wuhan, Hubei, China

Guan-Fu Yuan
United Investment Real Estate Co. Ltd., Wuhan, Hubei, China

ABSTRACT: No-sand cushion vacuum preloading method to improve bearing capacity of fresh hydraulic fill mud was proposed and carried out in a 10000 m^2 testing region. The results indicated that the ground surface settlement augmented linearly and sharply within 60 d. After 60 d, the sedimentation rate of all the monitoring sites decreased. The sedimentation rate tended to stabilize after 120 d. In addition, the fresh hydraulic fill mud with an initial bearing capacity of close to 0 kPa became a hard shell layer with a strength value around 50 kPa. The hard shell layer thickness was 0.2 m to 0.3 m. No-sand cushion vacuum preloading method has characteristics of low cost, short construction period and simple process, and provides a hard shell layer with a certain bearing capacity which fully meets the pile driver, self-discharging car and other machines work on it.

1 INTRODUCTION

In the past decade, hydraulic reclamation has been increasingly used in coastal regions, such as Binhai new area, which is located in Tianjin City, China. Binhai has an area of about 477 km^2. Furthermore, an increasing number of provinces are using hydraulic reclamation to obtain more ground for construction. The fresh hydraulic fill mud is deposited by a flowing stream of water, with the initial water content being more than 150%. The connection among the particles is extremely weak, and the initial foundation bearing capacity is close to 0 kPa. Fine particles (with a particle diameter of ≤0.005 mm) are located in the upper layer, and these particles exhibit high compressibility, low intensity, and poor penetrability, as shown in Table 1. Given the aforementioned special characteristics of hydraulic fill mud, improving hydraulic fill mud ground rapidly, effectively, and economically is a difficult technical problem that must be solved.

One of the widely used soft ground improvement methods is drainage through Prefabricated Vertical Drains (PVDs) to reduce consolidation time (Shen et al. 2005; Chai et al. 2006; Abuel-Naga et al. 2006; Rowe & Taechakumthorn 2008). PVDs are artificial drainage paths made of geosynthetics inserted into the soft ground to shorten the drainage path and the consolidation time.

Table 1. Geotechnical properties of the fresh hydraulic fill mud.

Properties	Values
Grain composition	
0.075~0.005 (mm)	44.1%
0.005~0.002 (mm)	20.5%
<0.002 (mm)	35.4
Water content	162.4%
Specific gravity	2.70
Density	1.42 g/cm^3
Dry density	0.54 g/cm^3
void ratio	3.98
Liquid limit W_L	93.9%
Plastic limit W_P	38.5%
Plasticity index I_p	55.4%

Vacuum consolidation is initially proposed by Kjellman (Chu et al. 2000). Studies on vacuum-induced consolidation continue to date (Chai et al. 2006; Bergado et al. 1998). In vacuum preloading, negative pressure is produced and propagated along PVDs, and then a nearly isotropic compression zone is created within the subsoil zone. Instead of increasing total stress, the advantages of applying vacuum preloading include reducing pore pressure and maintaining a constant total stress, which increase effective stress because of the reduction in pore pressure (less atmospheric) in the soil mass. Thus, stability problem of load preloading is avoidable. The sand cushion plays an important role for the aforementioned methods in consolidation the supply to horizontal drains and propagation of negative pressure because of its good permeability.

However, given that the initial ground bearing capacity of fresh hydraulic fill mud is close to 0 kPa, sand cushion cannot be implemented on fill mud, let alone spile machine land to work on the cushion. Moreover, as the reclamation project increases and the scale continuously expands, sand materials become insufficient in this region.

In this research, a no-sand cushion vacuum preloading method is investigated in-situ to improve the bearing capacity of fresh hydraulic fill mud. Based on the test results, the feasibility of no-sand cushion vacuum preloading treatment for fill mud is discussed.

2 MATERIALS AND METHODOLOGY

The no-sand cushion vacuum preloading testing position is located in Ezhou city, Hubei province, China. The fresh hydraulic fill mud area is 270,000 m^2 (see Fig. 1). The depth of the fresh hydraulic fill mud is about 4 m to 6 m. A 10000 m^2 region is chosen to be the testing area used with the no-sand cushion vacuum preloading technology (see Fig. 2).

Figure 1. The fresh hydraulic fill mud area (dredger filling).

Figure 2. The fresh hydraulic fill mud testing area (after).

Figure 3. Artificial pre-installing a layer of bottom woven cloth.

2.1 *Engineering characteristics of fresh hydraulic fill mud*

The initial foundation bearing capacity is close to 0 kPa. The geotechnical properties of fresh hydraulic fill mud are shown in Table 1.

2.2 *Test setup*

The main test procedures were as follows:

- The first critical process was the artificial pre-installation of a bottom layer of woven cloth. This cloth mainly provided the necessary platform for the subsequent process and separated the lateral drainage system from the fresh hydraulic fill mud, as shown in Figure 3.
- The laying lateral drainage branch pipe. This pipe is an important component of the horizontal drainage system, as shown in Figure 4.
- The installation of PVDs using manpower. Given the weakness of fresh hydraulic fill mud, mechanical equipment cannot settle and work on this mud. Therefore, manpower is used to install PVDs instead of the traditional spile machine, as shown in Figure 5.

Figure 4. Laying lateral drainage branch pipe.

Figure 5. Installing PVDs by manpower.

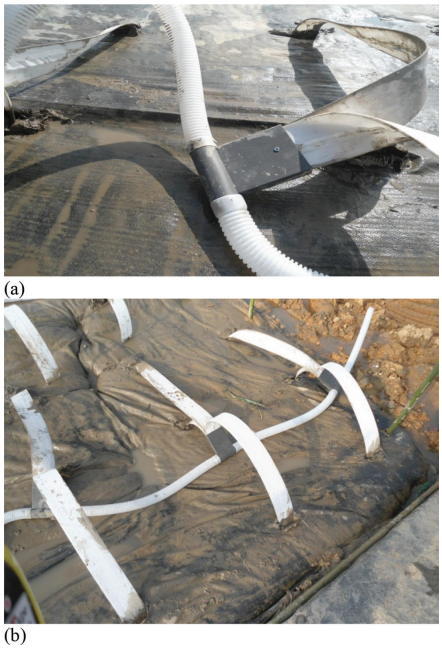

(a)

(b)

Figure 6. (a) Connection between PVD and plastic corrugated hose using connector (signal); (b) Connection between PVDs and plastic corrugated hoses using connector (multiple).

– The connection between PVD and a plastic corrugated hose as the connector, as shown in Figure 6a and b.
– The laying of non-woven geotextile (300 g/m^2). Drainage sand cushion cannot be used on fresh hydraulic fill mud area. Therefore, non-woven geotextile was used to replace the sand cushion as the drainage blanket to improve the efficiency of the horizontal drainage system, as shown in Figure 7.

Figure 7. Laying of non-woven geotextile.

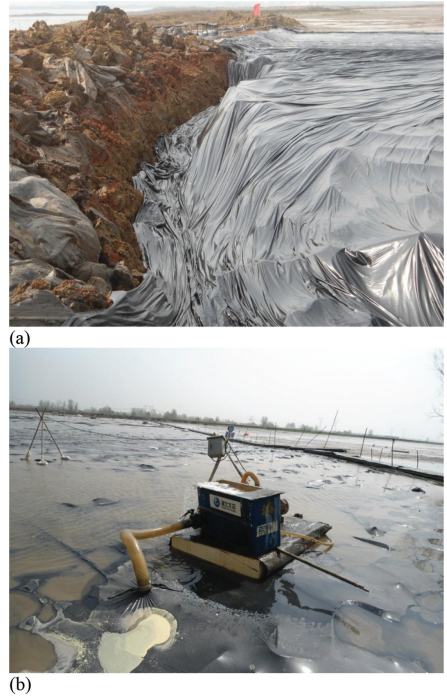

(a)

(b)

Figure 8. (a) Laying of membrane and sealing the membrane to soil; (b) Laying of vacuum jet pump (7.5 KW).

– The laying and sealing of the membrane to the soil and the laying of the vacuum jet pump (7.5 KW), as shown in Figure 8a and b.

2.3 *Monitoring and in situ testing program*

To evaluate the improvement effect of no-sand cushion vacuum preloading on the fresh hydraulic fill mud, vacuum degree and ground surface settlement were monitored. And after the vacuum was unloaded, cone penetration tests, vane shear tests, and shallow plate load tests were carried out, respectively.

3 RESULTS

The vacuum degree in the pipes was –62 kPa after 1 d since the vacuum jet pump started. The degree increased from –80 kPa to –87 kPa after 3 d and subsequently remained stable until the end of the experimental procedure.

The relationship between ground surface settlement and time is shown in Figure 9.

As shown in Figure 9, the ground surface settlement of the no-sand cushion vacuum preloading on the fresh hydraulic fill mud augmented linearly and sharply within 60 d. The gradients were 12.18, 8.83, 8.40, 13.03, 13.10, and 10.25 mm/d for monitoring sites #1–#6, respectively. Evidently, the ground surface settlement of monitoring site #5 was the largest and fastest among all the 6 monitoring sites. The reason was that the thickness of the fresh hydraulic fill mud at monitoring site #5 was the biggest at about 5.6 m, which indicated that thickness influenced the sedimentation rate. After 60 d, the sedimentation rate of all the monitoring sites decreased. In addition, the sedimentation rate tended to stabilize after 120 d.

Cone penetration or cone penetrometer test was the method used to determine the geotechnical engineering properties of the soil. Figure 10 shows the cone resistance curves versus depth. The fresh

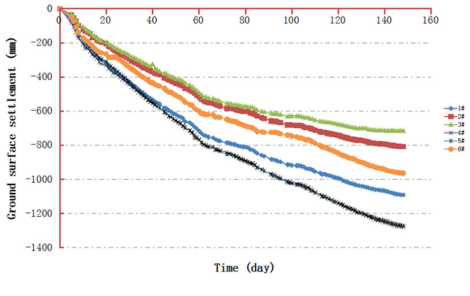

Figure 9. The relationship between ground surface settlement and time.

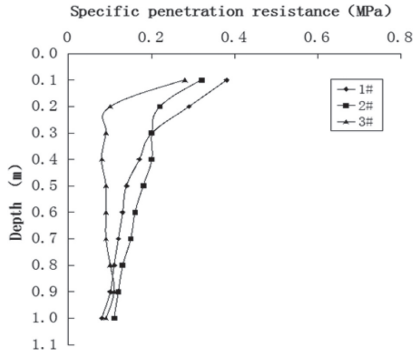

Figure 10. Curves of cone resistance versus depth.

hydraulic fill mud with an initial bearing capacity close to 0 kPa became a hard shell layer with a certain strength. The thickness of the hard shell layer was 0.2 m to 0.3 m. It directly proved the improvement of the no-sand cushion vacuum preloading technology on the fresh hydraulic fill mud. However, when the depth was larger than 0.3 m, the soil specific penetration resistance dampened quickly, which indicated that the no-sand cushion vacuum preloading technology could not improve the deeper hydraulic fill mud effectively.

Vane shear test was another useful in-situ testing method to investigate the geotechnical engineering soil properties. Figure 11 showed the vane strength curves versus the revolution angle of the undisturbed and disturbed soils, respectively. According to Figure 11, the vane strength of the undisturbed soil (marked as C_u) in the depth of 0.5 m was 8.5 kPa, whereas the vane strength of the disturbed soil (marked as C'_u) was 2.2 kPa, which indicated that the fresh hydraulic fill mud was formed with a certain structural strength. S_t was defined as the sensitivity in describing the structural soil. S_t was expressed as $S_t = C_u / C'_u$, and the S_t value was 3.9.

The *P-S* curve was obtained from the shallow plate load test, as shown in Figure 12. The area of the plate was 0.56 m^2. The *P-S* curve reduced gently and smoothly, therefore, the strength-controlled method was used to decide the ground bearing capacity, which was close to 50 kPa.

The system in the projects showed that the no-sand cushion vacuum preloading method was used to improve the fresh hydraulic fill mud and became workable. However, some problems required deeper investigation. For example, the effects of soil disturbance, which is commonly called smear, around vertical drains installed would reduce the permeability coefficient of soil. The strength and thickness of the hard shell layer was limited after improvement, therefore, further research could

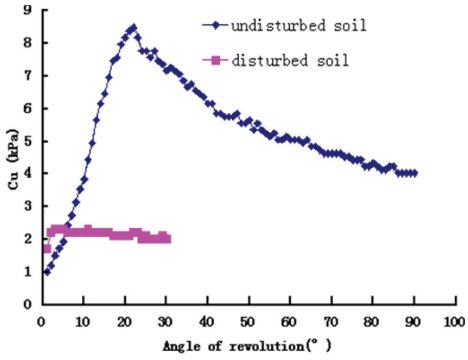

Figure 11. Curves of vane strength versus angle of revolution.

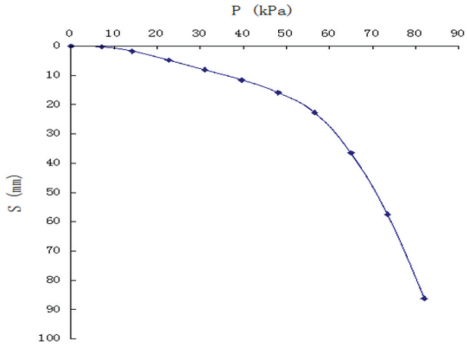

Figure 12. P-S curve on the improved ground of hydraulic fill mud.

benefit the optimization of the drainage system and enhance the effect of the no-sand cushion vacuum preloading on the fresh hydraulic fill mud.

4 CONCLUSIONS

The following conclusions were drawn from the work presented in this paper:

– The ground surface settlement of the no-sand cushion vacuum preloading on the fresh hydraulic fill mud augmented linearly and sharply within 60 d. After 60 d, the sedimentation rate of all the monitoring sites decreased. In addition, the sedimentation rate tended to stabilize after 120 d.
– The thickness of the fresh hydraulic fill mud influenced the sedimentation rate. Greater thickness meant a greater sedimentation rate.
– According to the results of the in-situ tests, the fresh hydraulic fill mud with an initial bearing capacity of close to 0 kPa became a hard shell layer with a certain strength value around 50 kPa, and the hard shell layer thickness was 0.2 m to 0.3 m, which fully meets the pile driver, self-discharging car and other machines work on the hard shell layer. The method has characteristics of low cost, short construction period and simple process and it is worth popularizing.

ACKNOWLEDGMENTS

This paper was supported by Natural Science Foundation of Hubei Province, China (Grant No. 2014CFB370) and Key Laboratory of Tianjin Soft Soil Character and Engineering Environment (Grant No. 2014SCEEKL01).

REFERENCES

Abuel-Naga, H.M., Bergado, D.T. & Chaiprakaikeow, S. 2006. Innovative thermal technique for enhancing the performance of prefabricated vertical drain during the preloading process. *Geotextiles and Geomembranes* 24(6): 359–370.

Bergado, D.T., Chai, J.C., Miura, N. & Balasudramaniam, A.S. 1998. PVD improvement of soft Bangkok clay with combine vacuum and reduced sand embankment preloading. *Geotechnical Engineering Journal* 29(1): 95–121.

Chai, J.C., Carter, J.P. & Hayashi, S. 2006. Vacuum consolidation and its combination with embankment loading. *Canadian Geotechnical Journal* 43(10): 985–996.

Chu, J., Yan, S.W. & Yang, H. 2000. Soil improvement by the vacuum preloading method for an oil storage station. *Geotechnique* 50(6): 625–632.

Rowe, R.K. & Taechakumthorn, C. 2008. Combined effect of PVDs and reinforcement on embankments over rate-sensitive soils. *Geotextiles and Geomembranes* 26(3): 239–249.

Shen, S.L., Chai, J.C., Hong, Z.C. & Cai, F.X. 2005. Analysis of field performance of embankments on soft clay deposit with and without PVD-improvement. *Geotextiles and Geomembranes* 23(6): 463–485.

This page intentionally left blank

Civil Engineering and Urban Planning IV – Liu et al. (Eds)
© 2016 Taylor & Francis Group, London, ISBN 978-1-138-02903-3

Theoretical and experimental study on a new combined mild steel damper

Jia-Chang Wang, Lin-Zhi Yang, Feng-Fan Wang & Ming Wei
College of Civil Engineering, Southeast University, Nanjing, Jiangsu, China

ABSTRACT: At present, the structure and form of energy dissipation of the mildest steel damper is very simple, which is unable to meet the requirements of slight and strong earthquakes at the same time. In order to solve this problem, this paper presents a new combined energy dissipation device composed of shearing and bending energy dissipation steel slabs. Then we carried out the material experiment on low yield point steel and low-frequency cyclic load experiment on the new damper. The results show that shearing energy dissipation steel slab works under the action of small and large displacement, while the bending energy dissipation steel slab only worked under large displacement. So we can reach the conclusion that the new combined energy dissipation device can work both in slight and strong earthquakes.

1 INTRODUCTION

Earthquakes are one of the greatest natural disasters on earth, with characteristics of high frequency, wide distribution, and difficulty to predict. In cities, secondary disasters resulting from it often cause damage or collapse of buildings. So the stability issues of buildings during earthquakes deserve increasing attention. Therefore, carrying out research on the seismic performance of structures has far-reaching meanings.

At present, energy dissipation technology has obvious advantages in the seismic strengthening of structures. Its main method is adding energy dissipation devices to structures without changing their basic form or reducing design requirements. So the energy dissipation device takes the lead in energy consumption when earthquakes hit, which can protect the main structure and reduce the damage. Metal energy dissipation devices are very commonly used for energy consumption when it comes to energy dissipation devices, especially low yield point steel with low yield strength and good malleability.

However, the most commonly used mild steel dampers at present almost have the same shape and way of consumption, unable to meet the different requirements in earthquakes which can be small or strong. Therefore, in view of this shortcoming, the concepts of mild steel dampers which can dissipate energy in several periods are put forward and bring out a lot of research. This paper also gives out a new type of mild steel damper device under similar principle.

2 THE CONSTRUCTION OF THE NEW COMBINED MILD STEEL DAMPER

The new combined mild steel damper includes the core energy-dissipating components and the fixed part of devices. Core energy-dissipating components consist of shearing and bending energy-dissipating components all processed by mild steel of low yield point. The fixed portion of the device is processed by ordinary steel (Fig. 1).

The new combined mild steel dampers involve many advantages. In practical engineering applications, the bending energy dissipation steel slabs can increase or decrease upon needs and reach reasonable earthquake resistance effects of established structures. In addition, dampers are easy to remove and replace when damaged as it is bolted.

3 TWO-STAGE MECHANISM OF ENERGY DAMPERS' ENERGY CONSUMPTION

According to the idea that the bending displacement comes bigger than the shearing displacement,

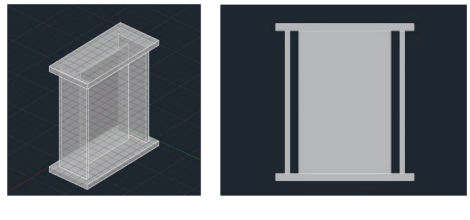

Figure 1. The shape of the damper.

energy-dissipating steel slabs are assembled together in different ways for different ways of working together.

When the small earthquake occurs, the shearing energy dissipation steel slab with a smaller yield displacement reaches the yield strength of steel at first. At this time, the bending energy dissipation steel slabs with a larger yield displacement are still in elastic state which is the first stage. Under the strong earthquake, the bending energy dissipation steel slabs with a larger yield displacement reach their yield strength as well and begin to enter the plastic state. Then the two types of energy dissipation steel slabs dissipate the earthquake energy together which is the second stage. So, it effectively reached the purpose of a phased energy dissipation.

4 EXPERIMENTAL STUDY ON MATERIAL OF LOW YIELD POINT STEEL

In order to dissipate seismic energy with high efficiency, the choice of rational energy dissipation metal material becomes essential. During the long-term study we find that mild steel is a kind of low yield point and good energy dissipation materials which are widely used among metal energy dissipation devices.

Prior to the mechanical test, we first conducted a material test on the low yield point steel. The experiment measuring the yield strength of the low yield point steel, tensile strength, elongation, yield ratio, and other parameters will give the strain-stress curve of the mild steel to provide an important basis for the analysis of subsequent mechanical test results.

Samples are prepared according to the requirement of "metal tensile test specimens" (GB6397-86), "metallic materials at room temperature tensile test method" (GB/T228-2002), and "steel products-location and preparation of test samples" (GB/T2975-1998) while the specific sample is shown in Figure 2. The test material is divided into three groups whose loading rates are 0.005 mm/s, 0.03 mm/s, and 0.1 mm/s, respectively.

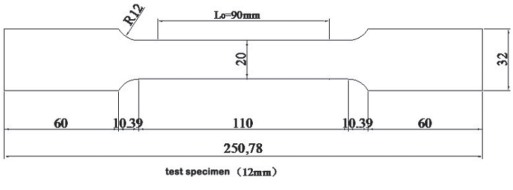

Figure 2. The shape of the sample.

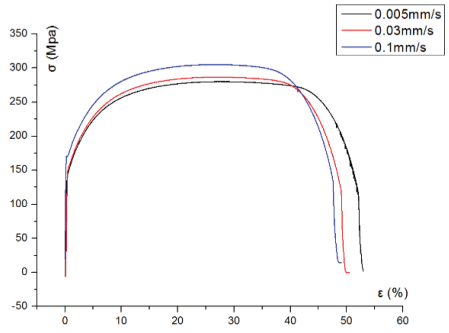

Figure 3. The stress-strain curve of different loading speeds.

The results show that the elongation of the low yield point steel is about 1.5 times of ordinary steel and it takes on good plastic deformation. Loading rate has a certain influence on both the yield strength and ultimate strength of mild steel and the intensity of the specimen varies proportionally as the loading rate while ductility is opposite. At the same time, the loading rate shows a stronger influence on yield strength while the impact on ultimate strength is not obvious. In short, the low yield point steel is similar to the ordinary steel, which respectively comes through the linear elastic stage, yield stage, stress strengthening stage, and necking stage. But the yield strength and ultimate strength of the low yield point steel is very low, and there is no obvious yield platform (Fig. 3).

5 EXPERIMENTAL STUDY ON A NEW COMBINED MILD STEEL DAMPER

5.1 *Experiment objectives*

The experiments adapt the method of low-frequency cyclic loads. We focus on the displacement change of shearing and bending energy dissipation steel discs and their own yield loads when they reach their yield displacements under the quasi static loading. The data of displacement, strain, yield load, and other indicators will be collected. The results will be showed in the strain-time curve and force-displacement curve.

5.2 *Experiment contents*

The experiment loading device can be seen in Figure 4, which includes the loading base, the steel loading beam, the four connecting rod devices, the lateral support device, and other accessories. The data of displacement and strain is mainly collected during the experiment. So, several external

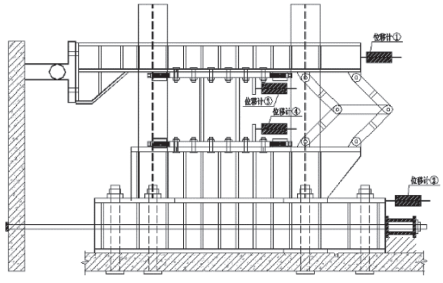

Figure 4. The loading device.

displacement sensors are placed on the damper to monitor and collect the displacement. The specific layout is showed in Figure 4. The No. 1 displacement gauge is set on the end of the steel loading beam, which measures the displacement of the beam under the action of horizontal load. The No. 2 displacement gauge is set on the end of the loading base, which measures the displacement of slip during the load. The No. 3 displacement gauge is set on the end of the top slab, which measures the relative slippage between the damper and the steel loading beam during the load. The No. 4 displacement gauge is set on the end of the bottom slab, which measures the relative slippage between the damper and loading base.

In addition, several strain gauges are placed on the shearing and bending energy dissipation steel slabs to collect the data of strain. Each slab has five strain monitoring points. On the shearing energy dissipation steel slabs, there are two strain monitoring points in the diagonal corner and the other three are set in the central axis symmetrically from top to bottom. There are also five strain monitoring points on the bending energy dissipation steel slabs, which lie in the central axis symmetrically from top to bottom. In order to ensure the completely same deformation between the strain gauge and the steel slab, all the strain gauges have been polished bright and then are pasted on the steel slabs with the 502 glue. Each strain gauge is also covered with the silicone in case of crash.

5.3 *The experimental phenomena and analysis*

With the increase in the loading displacement, the shearing energy dissipation steel slab starts to deform gradually. The bulging deformation out of the plane occurs in the middle of the steel slab while the bending deformation occurs on the edge. The deformation out of the plane is up to 19.1 mm when the loading displacement comes to 15 mm. The plastic deformation of the shearing energy dissipation steel slab cannot be restored when the loading displacement returns to zero, but the bending energy dissipation of steel slabs on the edge does not exist in the obvious residual plastic deformation.

The data of the strain in the experiment at any time of each monitoring point is true. We can observe the yield time of two kinds of energy dissipation steel slabs according to the development speed of the strain. We have digested all the data and drawn the two strain-time curves based on the certain monitoring points, which can be seen in Figures 5 and 6. It is noteworthy that the axis of abscissas is the time axis which is not the real time but the measurements to measure the sequences of the strain. The axis of ordinates is the strain axis.

As can be seen from Figures 5 and 6, the strain development speed of the shearing energy dissipation steel slab is faster than the bending energy dissipation steel slab and the peak is higher as well. We can conclude that the shearing energy dissipation steel slab is able to reach the yield point earlier than the bending energy dissipation steel slab. Therefore, the new combined mild steel damper has the ability to yield in the two stages.

In addition, in order to ensure that energy dissipation devices have good mechanical stability and energy dissipation properties, we also draw the

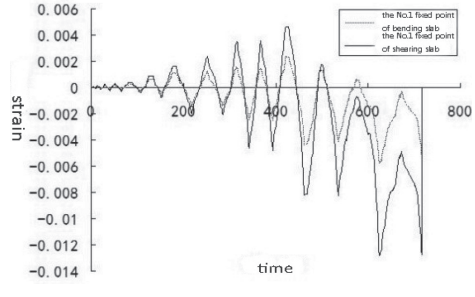

Figure 5. The strain-time curve of the no. 1 monitoring point.

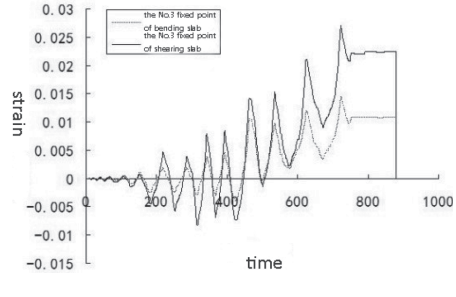

Figure 6. The strain-time curve of the no. 3 monitoring point.

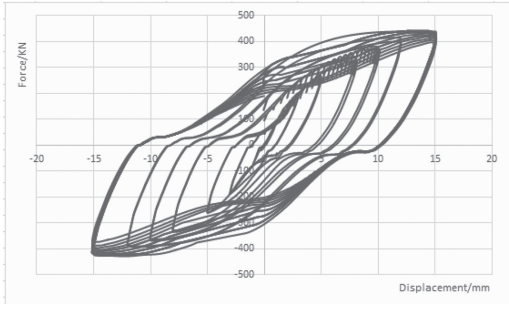

Figure 7. The force–displacement curve.

force-displacement curve of the specimens to verify. According to fullness of the curve, we can evaluate the effect of energy dissipation specimens as shown in Figure 7, after loading between ±15 mm (amplitude of design displacement) to and fro by 30 laps, no obvious deformation of the force-displacement curve takes place, as well as no obvious phenomenon of low-cycle fatigue, which satisfy the requirement of related standard.

6 CONCLUSION

After the experiment mentioned above, we draw the conclusion that the new combined mild steel energy dissipation device has two stages to yield and carry out energy dissipation, which can effectively protect the main structure when applied. By the way, only shearing steel slabs yield under small earthquakes and the bending ones will help when it is strong. All of these characteristics meet the demand of the different types of earthquakes, which makes it worthy of promotion and application.

REFERENCES

Bhart, S.D., Dumne, S.M. & Shrimali, M.K. 2014. Earthquake response of asymmetric building with MR damper. *Earthquake Engineering and Engineering Vibration* 13(2): 305–316.

Li, Y.S., Shen, S.Z., Liu, R. 2007. Study on optimum arrangement of hysteretic dampers in frame structure. *Journal of Harbin Institute of Technology* 4(025): 566–570.

Liu, Z. 2013. *The Hysteresis Behavior of the Mild Steel Damper Performance Study*. Beijing: Beijing Jiaotong University.

Liu, F., Wang, S.G., Du, D.S. & Liu, W.Q. 2012. Hysteretic performance test and simuiation analysis of a new type of mild steel damper. *Earthquake Resistant Engineering and Retrofitting* 6(014): 80–86.

Mito, M., Tamura, R., Isogai, Shimizu, K. & Fuchi, K. 1997. Study on seismic design method for building with steel damper (Part1). *Proc. A IJ Annual Meeting B, Japan, 1997.*

Song, F.M., Wen, D.H., Li, Z.G. & Bai, M.Z. 2008. Application and development of low yield point steel. *Hot Working Technology* 37(6): 85–88.

Wan, Z.P. & Liu, P. 2010. Application of low yield point steel in structural energy dissipation. *Steel Construction* 25(2): 35–38.

Wang, W., Lu X.L. & Xu, C.E. 2007. Engineering applications of low yield point steel in structural vibration control. *Structural Engineers* 23(6): 83–93.

Xing, S.T. & Guo, X. 2003. Study on mechanical behavior and effectiveness of a new type of mild steel damper. *Earthquake Engineering and Engineering Vibration* 23(6): 179–186.

Zhou, X. & Peng, L. 2009. A new type of damper with friction-variable characteristics. *Earthquake Engineering and Engineering Vibration* 8(4): 507–520.

Civil Engineering and Urban Planning IV – Liu et al. (Eds)
© 2016 Taylor & Francis Group, London, ISBN 978-1-138-02903-3

Application study of mesh-based block identification method in an underground cavern complex

Yu-Ting Zhang & Xiu-Li Ding
Yangtze River Scientific Research Institute, Wuhan, Hubei, China

Zhi-Guo Zhang
Changjiang Survey, Planning, Design and Research Co. Ltd., Wuhan, Hubei, China

ABSTRACT: For rock excavation projects in blocky and fractured rock masses such as caverns, slopes and foundations, block instability and related rock failure accounts for one of the most primary engineering concerns. Mesh-based block identification method is a newly proposed method for block identification. This paper firstly gives a general introduction of mesh-based block identification method, and then illustrates the removability determination method and block stability evaluation method that will be used in the subsequent application study. Afterwards, application study is conducted focusing on an ongoing underground cavern complex using the introduced methods. It is indicated that the mesh-based block identification achieves a satisfactory result and is able to associate with current block removability and stability evaluation method to obtain a reliable solution. Further issues regarding the mesh-based block identification method are discussed.

1 INTRODUCTION

Rock mass is a unique material characterized by its anisotropy and heterogeneity. Geological discontinuities, from geological faults and fractured zones in macroscopic view to fractures and fissures in mesoscopic view, largely determine the stability condition of rock mass. It is also due to their existence that makes rock materials behave different from rock masses. The efforts to gain insights into characteristics of geological discontinuities constantly progress along with the development of rock mechanics (Barton 1976). The physical and hydraulic properties of geological discontinuities have been extensively studied by many scholars (Grasselli 2003; Huang 2002). Moreover, not only their presences considerably affect the overall performance of rock masses, but also their combination, which leads to block instability failure, counts. Rock blocks are generated by intersection of geological discontinuities and excavation surfaces. Due to the arbitrary distribution of geological discontinuities, blocks around excavation surfaces, such as surrounding rock of underground openings and slope surfaces, should be attached with sufficient attention. In an attempt to cope with this issue, Goodman and Shi (Goodman 1985) proposed the well-known Block Theory. Its substantial parts include identification, removability determination and safety evaluation of blocks. Focusing on different aspects of the above topics, many scholars (Ikegawa 1992; Peng 2002; Warburton 1983; Yu 2009; Zhang 2006) proposed many useful tools, thus enhancing the effectiveness and power of Block Theory.

Despite of the achievements, the current methodologies still lack flexibility when complex excavation profile is encountered. To address this issue, the mesh-based block identification method is proposed. This paper is an application study of the newly proposed method (Zhang 2010). The traditional block removability and safety evaluation methods are also used, indicating the new block identification method is able to associate with current methodological frame.

2 MESH-BASED BLOCK IDENTIFICATION METHOD

2.1 *Review of traditional identification method*

Traditional block identification method is mainly topological approaches, which are constituted by the following procedures:

Step 1: generation of the network of fracture planes based on geological data.
Step 2: definition of rock excavation profile, such as the dimension and shape of caverns.
Step 3: cutting operation of fracture planes and excavation surfaces to obtain information of intersection points, intersection lines.

Step 4: search of closed loops based on the obtained points and lines to identify blocks.

In two dimensional cases, a block can be identified by selecting a set of surrounding lines with closed loop. In three dimensional cases, each selected line set with closed loop is viewed as a finite plane. These planes are combined together and further processed to determine the existence of blocks. If a spatial entity is found to be completely surrounded by finite planes, then it is identified as one block. The finite planes can be either excavation surfaces or geological planes of various types of discontinuities. The excavation surfaces defined in step 2 are always simplified as conventional shape, such as circular, horse-shoe and quadrilateral shape. This simplification is suitable for rock excavation projects with common shape, but lacks flexibility in describing projects with complex excavation profile. Therefore the mesh-based block identification method is introduced.

2.2 *Basic idea of mesh-based block identification method*

This method (Zhang 2010) essentially employs mesh grids to identify rock blocks, so it is both theoretically and practically different from traditionally topology-based methods. The mesh grids are normally established using mesh discretization method, which is more commonly named as preprocessing in finite element method or finite difference method. As mesh discretization of studied objects is so far very sophisticated technique, rock excavation projects with complex profile can be conveniently defined by mesh grids. Therefore, the problem that traditional identification method is always encountered can be solved.

Subsequently, based on the mesh grids, the method takes following four steps to identify blocks:

Step 1: generation of the network of fracture planes based on geological data. This step is identical to traditional method.

Step 2: mesh being further discretized to include fracture planes into mesh grid using mesh reconstruction technique. This step is to insert fracture planes into mesh grid that originally does not contain them. The mesh reconstruction technique is to re-mesh the elements that are crossed by fracture planes to reflect their existence. The reconstruction algorithm can be divided into two dimensional cases and three dimensional cases. The procedure is concise and can be implemented repeatedly. Fracture planes are thus automatically inserted into the existing mesh grids.

Step 3: spatial position relationship judgment among mesh elements and fracture planes. Each element of the mesh grid is located on either the upper part or the lower part of a fracture plane. Label all mesh elements with their spatial relationships with all considered fracture planes.

Step 4: combining such elements that share identical spatial position relationships with all fracture planes together to form a block. For instance, if a certain group of elements are all labeled as being on the upper, lower… upper part of fracture plane P_1, P_2 … P_n, then these elements can form a block.

As the above step 2 to step 4 can be compiled into computer codes, the identification procedures can be implemented automatically. So the overall efficiency of the proposed method is favorable.

3 REMOVABILITY AND SAFETY EVALUATION OF BLOCKS

3.1 *Removability analysis*

For identified blocks, only removable blocks are of engineering concerns. So it is required that all blocks should be examined to find removable ones. Generally, there are three types of motion pattern for removable blocks. They are separation motion from rock mass, sliding motion along single surface, and sliding motion along double surfaces (Goodman 1985).

For separation motion pattern (Fig. 1), blocks surfaces will be directly separated from rock mass under joint forces (denoted as r) imposed on the block. As all fracture planes have opened, the friction and cohesion forces along all surfaces are zero. In this case, there is no resistance against block movements and the anti-sliding force is zero. The sliding force (denoted as F_s) directly determines the direction of block motion (denoted as s). Therefore we have $F_s = |r|$. The judgment expression for this motion is $r \cdot v_l > 0$, where v_l is the normal vector of fracture planes.

For sliding motion along single surface (Fig. 2), blocks will slide along one plane v_i and separate from the other planes v_l ($l \neq i$). The judgment expression for this motion are $r \cdot v_i \leq 0$ and $s \cdot v_l > 0$. The resistance against sliding is provided by the friction

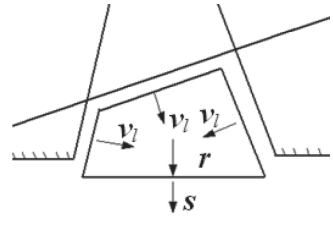

Figure 1. Separation motion.

and cohesion from plane v_i, while the sliding force is still provided by the projection force along sliding direction of joint force imposed on the block.

For sliding motion along double surfaces (Fig. 3), blocks will slide along two planes, whose normal vectors are v_i and v_j, respectively, and separate from the other planes v_l ($l \neq i \neq j$). The judgment expression for this motion are $s_i \cdot v_j \leq 0$, $s_j \cdot v_i \leq 0$, and $s \cdot v_l > 0$, where s_i and s_j are projections of joint force r on sliding surfaces. The resistance against sliding is provided by the friction and cohesion from planes v_i and v_j. while the sliding force is still provided by the projection force along sliding direction joint force imposed on the block.

3.2 *Safety evaluation*

A safety factor is introduced to quantify the safety extent of identified removable blocks. According to block removability analysis, the sliding force is provided by the projection force of joint force on sliding direction of block, and the anti-sliding forces are primarily provided by the friction and cohesion of sliding surfaces. Table 1 summarizes these forces that contribute to block stability. Normally, only block gravity is considered as joint force r in static analysis. If other loads, such as seismic load and seepage load, are considered, then r can be calculated accordingly.

Finally, the safety factor f for an identified removable block can be calculated by:

$$f = (F_c + F_f)/F_s \tag{1}$$

From mechanical point of view, a block with its safety factor larger than 1.0 will be stable. However, given the inaccuracies of input geometrical and physical parameters and the significance of projects, a safety margin should be considered. Normally, the condition of $f > 1.5$ is required to guarantee block stability. Therefore, for blocks with safety factor lower than 1.5, reinforcement measures are necessary to provide additional forces (denoted as F_a) against sliding. The safety factor for reinforce blocks is obtained by:

$$f = (F_c + F_f + F_a)/F_s \tag{2}$$

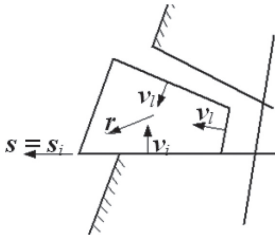

Figure 2. Sliding motion along single surface.

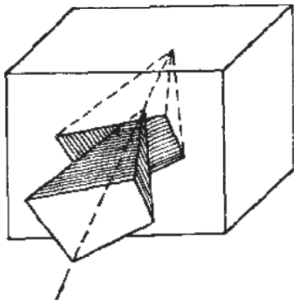

Figure 3. Sliding motion along double surfaces.

4 APPLICATION STUDY

4.1 *Project outline*

The studied project is a major hydropower station located in southwestern China. Its electricity generators are placed underground in a large scale cavern complex that consists of a series of caverns such as powerhouse, transformer hall, surge chamber, tailrace tunnel, and traffic tunnel, etc. During the excavation process, the surrounding rock is revealed blocky and fractured. Large amounts of geological discontinuities are found distributing widely within construction area. By comprehensive field investigation, it is preliminarily concluded that block instability and related rock failure will be a probable threat to the safety

Table 1. Forces considered for safety evaluation.

Motion pattern	Sliding force F_s	Friction force F_f	Cohesion force F_c
Separation motion	$\lvert r \rvert$	0	0
Slide along single plane i	$\lvert n_i \times r \rvert$	$\lvert n_i \cdot r \rvert \tan\Phi_i$	$c_i A_i$
Slide along double plaenes i and j	$\lvert r \cdot (n_i \times n_j) \rvert / \lvert n_i \times n_j \rvert$	$\{\lvert (r \times n_j) \cdot (n_i \times n_j) \rvert \tan\Phi_i + \lvert (r \times n_i) \cdot (n_i \times n_j) \rvert \tan\Phi_j\} / \lvert n_i \times n_j \rvert^2$	$c_i A_i + c_j A_j$

of both project and personnel. Therefore locating potentially instable blocks and reinforcing them with proper support measures are crucial.

4.2 *Establishing mesh grid*

According to the newly proposed block identification method, mesh grid is firstly obtained. The mesh is always borrowed from other numerical procedures which mainly deal with stress and strain analysis of rock masses using finite element method or finite difference method. Figure 4 plots the established mesh grid both on project area scale and on cavern complex scale. Totally over 130 000 nodes and almost 600 000 elements are discretized within the given range. The complex layout and spatial distribution of cavern complex can be precisely reflected by mesh elements. It is obviously very difficult to define such a complex profile using traditional method. It is noted that current mesh does not contain any fractures that are intended for block identification purpose.

4.3 *Identification of blocks*

Based on the obtained fracture plane information, the mesh grid is reconstructed to reflect their existence. Afterwards, block identification algorithm is implemented to combine elements with identical spatial relationship with all fracture planes together to form one block. Due to the wide distribution and large amounts of fracture planes, dozens of blocks are found around excavation surfaces. Therefore, only major blocks with large volume are listed here.

Figures 5–11 plot the location of 7 blocks, denoted as B1 to B7, around the top arch region of powerhouse and surge chamber. The illustrations are given both by mesh lines and by rendering effect.

It is compared based on field observation that the exposed location of identified blocks well agrees with field investigation results. This indicates the proposed method is effective and reliable. The information of blocks can be all obtained from mesh grid, thus providing subsequent block safety evaluation with necessary data.

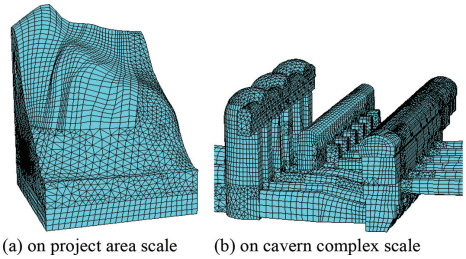

(a) on project area scale (b) on cavern complex scale

Figure 4. Mesh grid.

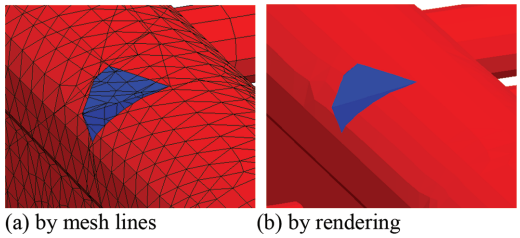

(a) by mesh lines (b) by rendering

Figure 5. Identified block: B1.

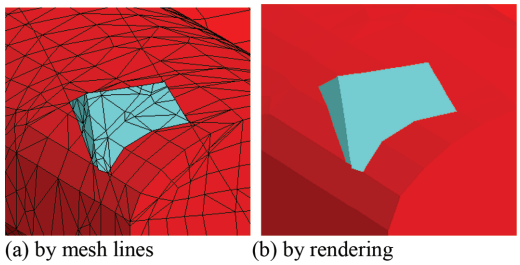

(a) by mesh lines (b) by rendering

Figure 6. Identified block: B2.

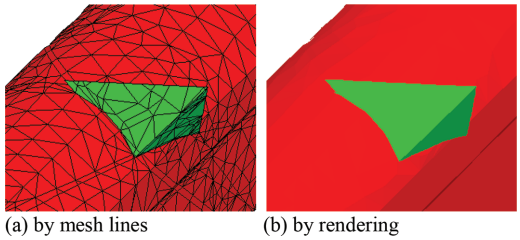

(a) by mesh lines (b) by rendering

Figure 7. Identified block: B3.

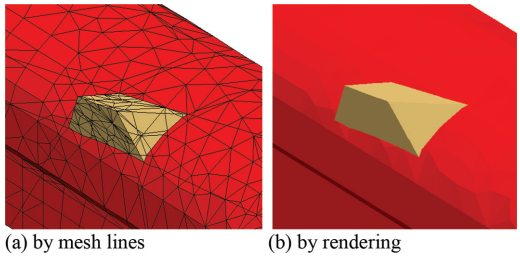

(a) by mesh lines (b) by rendering

Figure 8. Identified block: B4.

4.4 *Safety evaluation*

Based on the information drawn from mesh grid, block removability analysis and safety evaluation are done using the methods described in 3.1 and 3.2. Table 2 summarized the results of safety evaluation for identified blocks.

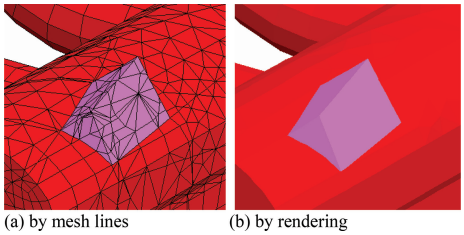

(a) by mesh lines (b) by rendering

Figure 9. Identified block: B5.

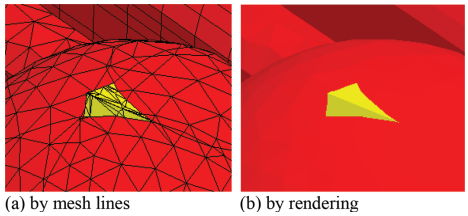

(a) by mesh lines (b) by rendering

Figure 10. Identified block: B6.

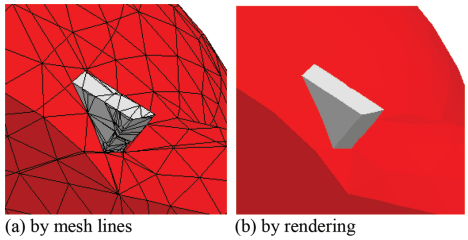

(a) by mesh lines (b) by rendering

Figure 11. Identified block: B7.

Table 2. Safety evaluation results of identified blocks.

Block no.	Number of cutting facture planes	Volume m^3	Motion pattern	Safety factor
B1	4	260	Double slide	1.40
B2	5	485	Collapse	0
B3	3	440	Single slide	1.05
B4	4	245	Double slide	1.05
B5	4	600	Collapse	0
B6	3	60	Collapse	0
B7	4	100	Double slide	1.55

It is found that each block is assigned with its volume, motion pattern and safety factor. This information is of great engineering value to reinforce instable blocks and then guarantee the stability of surrounding rock.

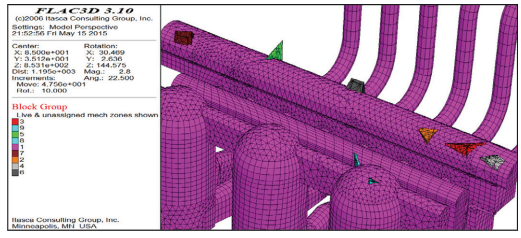

Figure 12. Identified blocks around excavation surface displayed on FLAC^{3D} platform.

5 DISCUSSIONS

Essentially, the identified blocks based on the proposed method are defined using mesh grids that are commonly adopted for finite element method or finite difference method. Figure 12 plots the identified blocks around excavation surface displayed on FLAC^{3D} platform. It is intuitively considered that whether the identified blocks can be involved in strain and stress calculation process, or say, whether the obtained stress and deformation results can be reflected in block safety evaluation process. If the safety evaluation of blocks is coupled into the stability analysis of surrounding rock, then the block safety evaluation results would be more reliable.

6 CONCLUSIONS

This paper introduces a newly proposed block identification method and its application study in an underground cavern complex. The results of application study well illustrates the advantages of the proposed method, indicating that the method is both effective and reliable in block identification and safety evaluation analysis, especially for rock excavation projects with complex profile. A potential research topic for future enhancement of the proposed method is also discussed.

ACKNOWLEDGMENT

Financial supports from National Natural Science Foundation of China (Nos. 51209021 and 51539002) and China Postdoctoral Science Foundation Funded Project (No. 2014M552021) are greatly acknowledged.

REFERENCES

Barton, N. 1976. Rock mechanics review: The shear strength of rock and rock joints. *International Journal of Rock Mechanics and Mining Sciences & Geomechanics Abstracts* 13(9): 255–279.

Goodman, R.E. & Shi, G.H. 1985. *Block Theory and Its Application to Rock Engineering*. New Jersey: Prentice Hall.

Grasselli, G. & Egger, P. 2003. Constitutive law for the shear strength of rock joints based on three-dimensional surface parameters. *International Journal of Rock Mechanics and Mining Sciences* 40(1): 25–40.

Huang, T.H., Chang, C.S. & Chao, C.Y. 2002. Experimental and mathematical modeling for fracture of rock joint with regular asperities. *Engineering Fracture Mechanics* 69(17): 1977–1996.

Ikegawa, Y. & Hudson, J.A. 1992. A novel automatic identification system for three-dimensional multi-block systems. *Engineering Computations* 9(2): 169–179.

Peng, X.C. & Tang, H.B. 2002. Three-dimensional Discontinuity Network Analysis (TDNA) on Rock Mass. *Proceedings of the Fifth International Conference on Analysis of Discontinuous Deformation, Stability of Rock Structures, Wuhan, 6–10, October, 2002*. Lisse: Balkema.

Warburton, P.M. 1983. Application of a New Computer Model for Reconstructing Blocky Block Geometry Analysis Single Block Stability and Identifying Keystones. *Proceedings of International Congress on Rock Mechanics, Melbourne, 10–15, April, 1983.* Rotterdam: A.A. Balkema.

Yu, Q., Ohnishi, Y. & Chen, D. 2009. A generalized procedure to identify three-dimensional rock blocks around complex excavations. *International Journal for Numerical and Analytical Methods in Geomechanics* 33(3): 355–375.

Zhang, Y.T., Xiao, M. & Chen, J.T. 2010. A new methodology for block identification and its application in a large scale underground cavern complex. *Tunnelling and Underground Space Technology* 25(2): 168–180.

Zhang, Z.X. & Kulatilake, P. 2006. A new stereo-analytical method for determination of removal blocks in discontinuous rock masses. *International Journal for Numerical & Analytical Methods in Geomechanics* 27(10): 791–811.

Civil Engineering and Urban Planning IV – Liu et al. (Eds)
© 2016 Taylor & Francis Group, London, ISBN 978-1-138-02903-3

Estimation of areas of experimental rainfall-eroded soil slope based on moving average time series models

Xiang-Yu Fan, Feng-Lin Xu & Yong-Chang Liang
School of Petroleum and Natural Gas Engineering, Southwest Petroleum University, Chengdu, Sichuan, China

Lin Chen
School of Sciences, Southwest Petroleum University, Chengdu, Sichuan, China

Yu You
School of Civil and Architectural Engineering, Chongqing Jiaotong University, Chongqing, China

Wen Nie
State Key Laboratory of Coal Mine Disaster Dynamics and Control, Chongqing University, Chongqing, China

ABSTRACT: Rainfall-induced soil erosion in mountain areas plays a significant role in supplying the sediment and shaping the landscape. Traditionally, related prediction models of soil erosion usually require many parameters. Besides, the model output considers the soil loss weight more. For evaluation of the changed landscape, involved area of soil erosion should be emphasized. Considering the two challenges, in our study we apply a simple and effective moving average time series model to simulate development of soil erosion area in a laboratory. The results show that the moving average model can swiftly estimate the growth of the soil erosion area within average relative error –8.9%.

1 INTRODUCTION

Soil erosion caused by overland flow is one of the most common geological phenomena in nature. Soil erosion models like USLE (Wischmeier & Smith, 1978), RUSLE (Renard et al. 1997), WEPP (Flanagan & Nearing 1995), EUROSEM (Morgan et al. 1993), KINEROS2 (Smith et al. 1995), and GUEST (Fentie 2001) usually depend on many parameters to predict soil erosion weight rate which is not easy for estimating hazard scope. Since the erosion area or scope is a significant target of topographic changes, we aim to develop a relatively simple model to estimate the erosion area. In this study, the physical experiments of rainfall-induced soil erosion were conducted under different rainfall intensities in the laboratory (three materials). The extent of erosion was reflected by the observation of the eroded area. In addition, the prediction model for soil erosion area was built based on the moving averages time series method.

2 METHODS

2.1 *Physical model and related issues*

In our case, a slope model is constructed in a flume device made of Plexiglas (Fig. 1). The slope inclination is 34° and the material from Fengdu Mountain, near to Yangtze River Bank, Chongqing, China whose surface soil can be easily eroded under heavy rainfall. The soil was air-dried and crushed to different test samples owning three particle size distributions as shown in Figure 2. The soil sample was squeezed by a plate with 120 N force for formation of the slope. In Figure 1, the *m* is moisture transducer whose contact area with soil is less than 20 mm^2 (measuring range 0–100%, resolution 0.1%, deviation ±2%); the *d* is a channel for drainage; one high-definition digital camera is used to record the changes of eroded soil area (front scene). Every test is conducted under

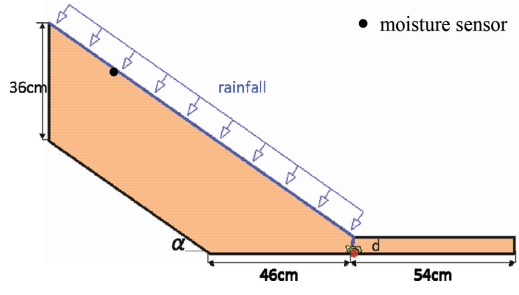

Figure 1. Geometry of the physical model.

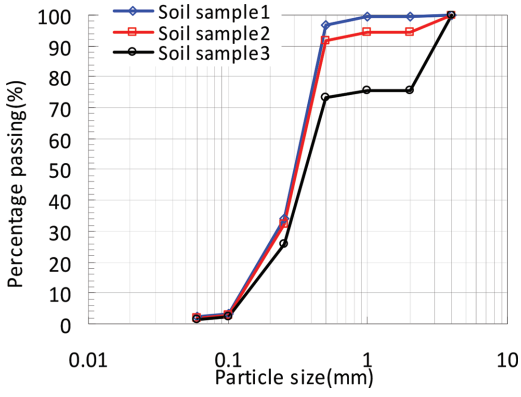

Figure 2. Particle-size distribution curves.

Table 1. Experimental scheme.

Soil types	Rainfall intensity (mm/hr)
12% of clay, 88% of fine sand with 5% of coarse sand	45
12% of clay, 88% of fine sand with 20% of coarse sand	
12% of clay, 88% of fine	25, 45, 65

similar initial geometry, and pre-added water content (deviation ±3%). Rainfall is simulated by three nozzles in five rainfall events. For the same material (soil sample 1), rainfall intensity levels in three experiments are approximately 25, 45, and 65 mm/hr, respectively. For the different materials (sample 1-sample 3), all the rainfall intensity in experiments is 45 mm/hr (Table 1).

2.2 *Erosion area calculation*

A fast way to calculate a two-dimensional area of the object is to use the BOUNDARY command in the software-Auto CAD. Using BOUNDARY, a point can be picked within the area to create a closed poly line or polygon domain. 'Features' palette can be used to find the area and perimeter of the poly line or polygon domain. By using MEASUREGEOM and AREA commands, a series of points or selected an object is specified to calculate area. In Figure 3(a), a coordinate is firstly established. And then contour of soil eroded area is extracted in Figure 3(b). Finally, in Figure 3(c) selected area calculation is executed by AutoCAD. In every experiment, the video data per minute is intercepted for area calculation and the error from the lens is about ~4.2%.

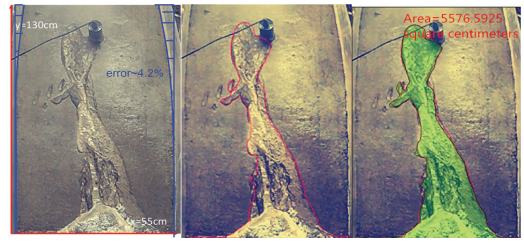

Figure 3. Area calculations by AutoCAD (soil sample 1–65 mm/hr) (a) Establishment of Coordinate (b) Extraction of contour (c) Calculation of areas.

3 RESULTS AND DISCUSSIONS

3.1 *Erosion area characters*

Figure 4 illustrates that the toe of the slope is more eroded than other positions because of more ground water supply from the upper parts. The erosion of top part of the slope without ground water supply from other parts has a slow increase. Thus, it could be progressive soil erosion. Figure 5 indicates the erosions of different materials under the same time domain and rainfall intensity. It is found that the coarse particles in soil sample 3 own lower erosion than fine particles because of higher permeability and stronger framework.

In the Figure 6, Soil sample 1–25 mm/hr has a most obvious initial phase (threshold of soil erosion action) because of small rainfall intensity. While compared to Soil sample 1–25 mm/hr the soil sample 1–45 mm/hr and soil sample 1–65 mm/hr have fewer time lags. In second acceleration stage, the erosion under higher rainfall intensity is obviously improved faster because of more surface runoff production. In the last phase, for one thing coarse particles remained and loss of fine particles makes the soil structure stronger; for another the water erosion develops towards deep direction. Therefore, the soil eroded area has a maximum value but the volume could still increase. By contrast, for different materials, coarse particle like the soil sample 3 has stronger structure (friction angle) and higher infiltration rate (producing less surface runoff) than fine particle as the soil sample 1. Two aspects of soil sample 3 make the resistance against the rainfall erosion more obvious. Summarily, the soil erosion is decided by both rainfall and materials strength.

3.2 *Moisture content analysis*

Monitoring data from moisture sensor describes the moisture content changes of slope surface (Fig. 7). When moisture is close to the saturated state, soil erosion increased suddenly. It could be the signal of the second stage coming.

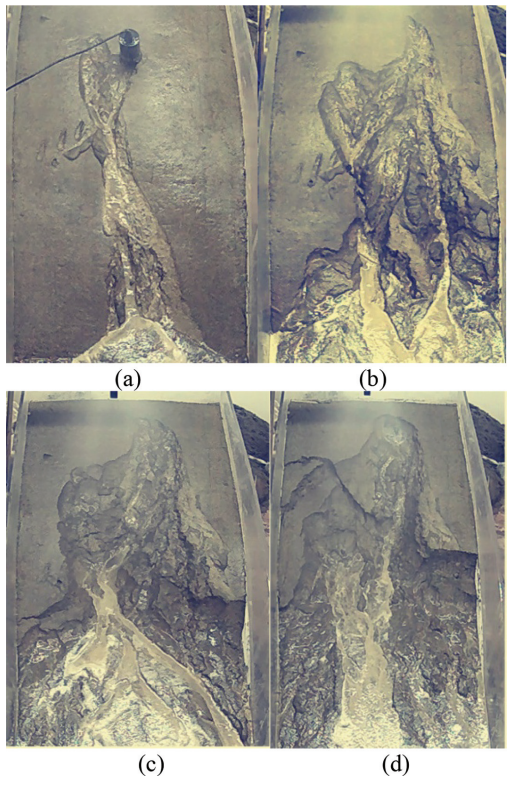

Figure 4. Different time domains in sample 1–65 mm/hr test (a) t = 6 min (b) t = 19 min (c) t = 45 min (d) = 70 min.

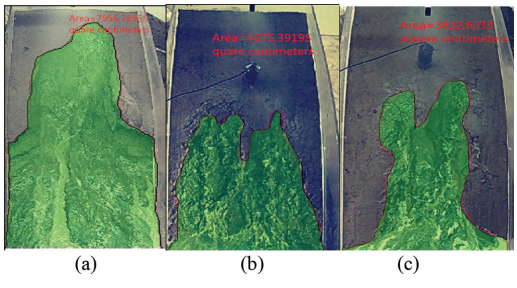

Figure 5. Different materials under the same time domain (a) sample 1 (b) sample 2 (c) sample 3.

3.3 *Prediction models based on moving averages*

Four moving averages models are employed to predict the soil erosion area development (the results of model prediction are shown in Fig. 8).

– Moving averages

$$y'_n = \frac{y_{n-1} + y_{n-2} + y_{n-3}}{3} \ (n \geq 4) \qquad (1)$$

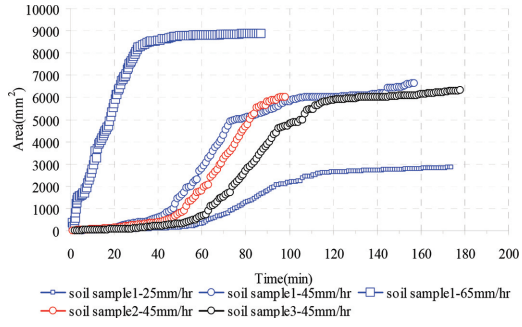

Figure 6. Results of soil eroded experiments.

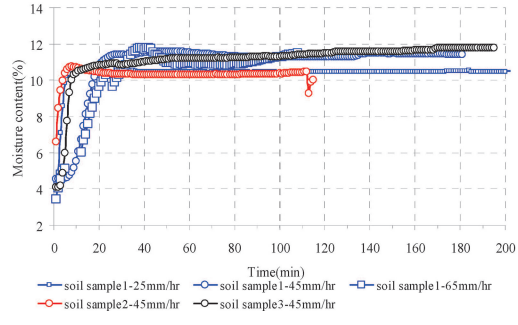

Figure 7. Moisture content in five experiments.

where y'_n is the output object of the prediction model; y_n is observation value. After every prediction, the responded observation is used to refresh the prediction value.

– Weight moving averaging method

$$y'_n = w_1 y_{n-3} + w_2 y_{n-2} + w_3 y_{n-1} \ (n \geq 4) \qquad (2)$$

where y'_n is the output object of the prediction model, w_1, w_2, w_3 are mathematic weights ($w_1 = 20\%$, $w_2 = 30\%$, $w_3 = 50\%$). y_n is observation value. After every prediction, the responded observation is used to refresh the prediction value.

– Slope moving averaging method

$$y'_n = \frac{\left(\frac{y_{n-2} - y_{n-3}}{t_{n-2} - t_{n-3}}\right) + \left(\frac{y_{n-1} - y_{n-2}}{t_{n-1} - t_{n-2}}\right)}{2} \ (n \geq 4) \qquad (3)$$

where y'_n is the output object of the prediction model. t_n is the time step. y_n is observation value. After every prediction, the responded observation is used to refresh the prediction value.

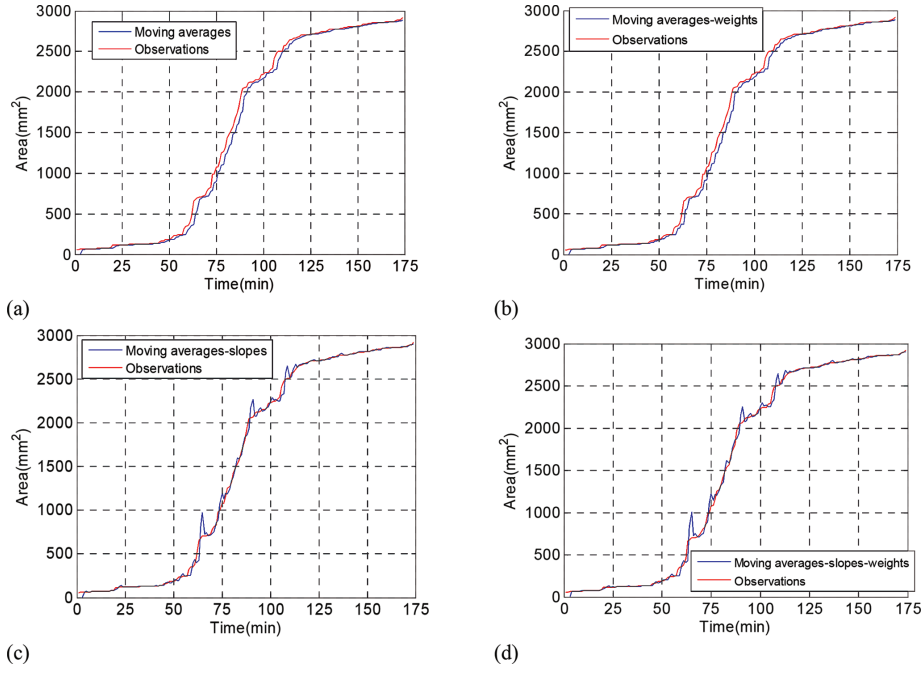

Figure 8. Forecast performances of four models (a) Moving averages (b) Moving averages-weight (c) Moving averages-slopes (d) Moving averages-slopes-weight.

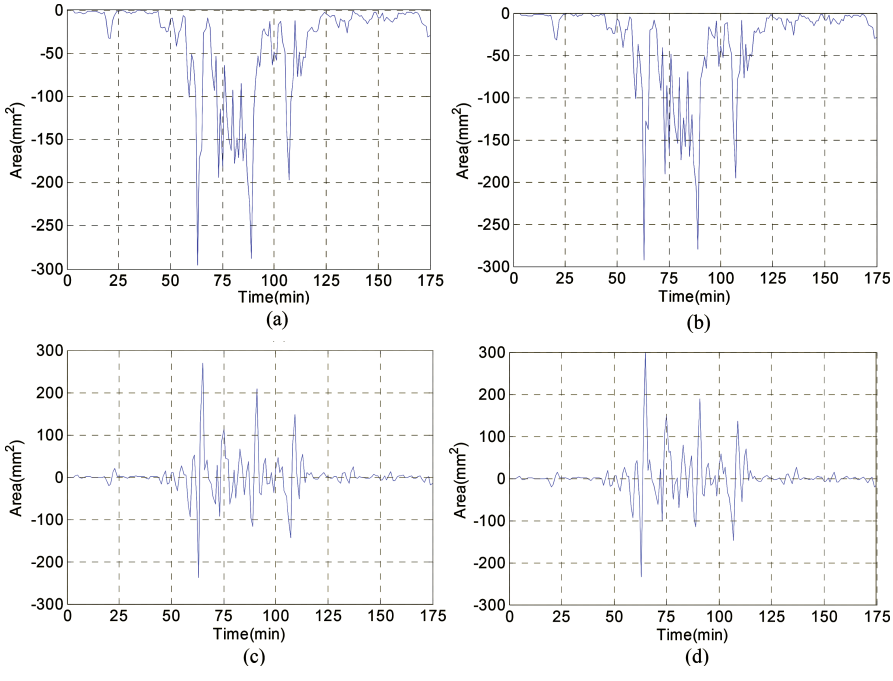

Figure 9. Error comparisons of four models (a) Moving averages (b) Moving averages-weight (c) Moving averages-slopes (d) Moving averages-slopes-weight.

– Weight slope moving averaging method

$$y'_n = w_1\left(\frac{y_{n-2}-y_{n-3}}{t_{n-2}-t_{n-3}}\right)+w_2\left(\frac{y_{n-1}-y_{n-2}}{t_{n-1}-t_{n-2}}\right)(n\geq 4) \quad (4)$$

where y'_n is the output object of the prediction model. t_n is the time step, w_1 and w_2 are mathematic weights ($w_1 = 20\%$, $w_2 = 80\%$). y_n is observation value. After every prediction, the responded observation is used to refresh the prediction value.

3.4 *Error analysis*

Figure 9 indicates error comparison of four models. Moving averages and Moving averages-weight models underestimate the soil erosion area with less 15% error in the second acceleration stage. While Moving averages-slopes and Moving averages-slopes-weight models overestimate the soil erosion area with less 15% error in the second phase.

4 CONCLUSIONS

Rainfall induced soil erosion experiments were carried out in a laboratory. And the soil erosion area developments are revealed under different rainfall intensities and materials. In addition, we applied the moving averages models to predict the growth of rainfall induced soil erosion area. The valuable conclusions include:

– The area of soil erosion obeys a trend of S-growth curve under continuous rainfall;
– The higher rainfall intensity can produce more area of soil erosion than lower rainfall intensity for same material;
– Under same rainfall intensity coarse material (stronger material) has a time lag against the soil erosion but finally a similar area of soil erosion compared to fine material;
– Moving averages models can effectively predict the soil erosion just by inputting the rainfall information.

ACKNOWLEDGMENTS

The research is supported by The National Natural Science Foundation of China (Grant No: 51474185), National Key Basic Research Program of China (973 Program) "Shale gas horizontal well drilling and completion key basic research" (Grant No: 2013CB228003), and Opening Fund of State Key Laboratory of Geo-hazard Prevention and Geo-environment Protection (Chengdu University of Technology)-SKLGP2013K007.

REFERENCES

Fentie, B. 2001. *Catchment-Scale Water Erosion and Deposition Modelling: A Physically-Based Approach. Queensland*: The University of Queensland.

Flanagan, D.C. & Nearing, M.A. 1995. *USDA Water Erosion Prediction Project: Hillslope Profile and Watershed Model Documentation.* NSERL Report No. 10. Indiana: USDA-ARS National Soil Erosion Research Laboratory, West Lafayette.

Morgan, R.P.C., Quinton, J.N., Smith, R.E., Govers, G., Poesen, J.W.A., Auerswald, K., Chisci, G., Torri, D. & Styczen, M.E., 1993. The European soil erosion model EUROSEM: A dynamic approach for predicting sediment transport from fields and small catchments. *Earth Surf. Processes Landforms* 23(6): 527–544.

Renard, K.G., Foster, G.R., Weesies, G.A., McCool, D.K. & Yoder, D.C. 1997. *Predicting Soil Erosion by Water: A Guide to Conservation Planning with the Revised Universal Soil Loss Equation Rusle.* U.S. Dept. of Agriculture, Agriculture Handbook No. 703. Washington, DC: United States Department of Agriculture.

Smith, R.E., Goodrich, D.C. & Quinton, J.N. 1995. Dynamic, distributed simulation of watershed erosion: The KINEROS2 and EUROSEM models. *Journal of Soil and Water Conservation* 50(5): 517–520.

Wischmeier, W.H. & Smith, D.D. 1978. *Predicting Rainfall Erosion Losses.* USDA Agricultural Handbook No. 537. Washington, DC: United States Department of Agriculture.

This page intentionally left blank

Civil Engineering and Urban Planning IV – Liu et al. (Eds)
© 2016 Taylor & Francis Group, London, ISBN 978-1-138-02903-3

Network arches for road and rail

Per Tveit
Agder University, Grimstad, Norway

ABSTRACT: Network arches normally save 2/3 of the structural steel needed in arch bridges with vertical hangers. That is because the bridge type has much tension and little bending. The arch has compression, but it has good sideways support. Network arches are best suited for spans between 80 and 180 m with a concrete deck that spans around 10 m between the rows of hangers. Network arches are very economic when a light steel skeleton can be put on the pillars. The steel tube arch can be filled with concrete. Then the concrete end beam can be cast, and then the tie. Maybe 200 network arches have been built in 25 countries. The spans are between 41 m and 380 m.

1 INTRODUCTION

I will start by pointing out some fundamental facts about the network arch (see Fig. 1). It has similarities to a simply supported beam. Arch and tie correspond to the tension- and compression zones of the beam. The hangers are a light replacement of the web.

In the author's opinion the maximum distance between the tension and the compression zone should normally not be over 20% of the span. Near 15% of the span normally looks best.

Steel efficiently carries tension which dominates hangers and tie. The distances between supports of the arch are small. This gives good utilization of steel in compression. Bending is unfavourable. There is very little bending in network arches. All this leads to an arch bridge that normally saves around 2/3 of the structural steel needed in arch bridges with vertical hangers.

2 THE TIE

Many smaller network arches should have simple concrete ties with edge beams (Fig. 2). Under daily loads this gives a beneficial compression in the concrete in the tie. The biggest bending in the tie is usually in the middle of the deck. Thus the edge beam with prestressing cables can be very slim.

In many network arches the tie has a lot of steel beams. That is a necessity in very wide spans.

When the span of the concrete plate is 12 to 18 m, it might be difficult to control deflection, especially if the plate deflects upward due to prestressing.

If the plate in the concrete has an upwards chamber, but gets too big deflection over time, the deflection could maybe be counteracted by fibre-reinforced polymer treads in tension under the plate. The treads can be fastened in holes from a temporary chord used in the erection. Little stools could be put in between the treads and the plate. We can always hope that these contraptions will not be necessary.

Figure 1. Network arch spanning 200 m.

Figure 2. Tie of a network arch.

3 THE ARCH

Wide flange beams are economic and give simple details. For longer spans bigger cross-sections are needed. Tubular arches attract 1/3 of the wind force on rectangular arches and can be filled with concrete (see Fig. 3).

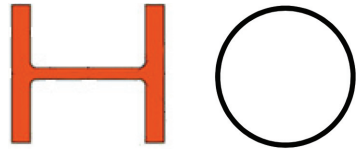

Figure 3. Two cross sections of arches.

4 HANGERS

The hangers can be steel rods or wires. Where hangers cross they should be covered by plastic tubes. That would prevent damage where they cross. Rubber bands could keep the crossing hangers near to each other in storms. See also page d-1 to d-4 in (Tveit 2014).

The author prefers hangers that are adjustable and replaceable. In the very unlikely event of a hanger breaking, hangers from a standard tension rod system are easy to replace.

5 AESTHETICS

Network arches are usually slender. Let us define slenderness as the span divided by the combined height of the tie and the arch. The bridge in Figure 4 spans 220 m. It has a slenderness of 198. It is the world's most slender arch bridge (Larsen 2011). The picture was taken before the railings were erected.

Looking at Figure 5, we can see a vase or two profiles facing each other. However, we hardly see both at the same time. Similarly looking at a bridge, we can see the bridge or the surrounding countryside, but we hardly see both at the same time. This speaks for slim bridges.

Figure 4. The Brandanger Bridge in western Norway.

Figure 5. Shows either a vase or two profiles.

Architects give valuable help in the design of bridges, but they should not take the driver's seat in the design process. That could lead to unnecessary costs and awkward bridges.

6 SHAPE OF ARCH

In his Ph.D thesis, Stephan Teich (2012) found that the optimal shape of an arch is a part of an ellipse. It is probably almost equally good if the arch has a continuous curvature that is slightly reduced in the wind portal near the ends of the arches. This gives a constant maximum force in a longer part of the arch, and a more even force in the hangers near the end of the arches.

7 ROBUSTNESS

Network arches are robust structures, more so than trusses (Zoli 2005; Zoli 2007).

If a few hangers are broken because a vehicle runs into them, the network arch is unlikely to break down because hangers that are near each other at the tie are far apart at the arch. Thus the support of the arch is reduced, but does not disappear. This speaks for a slight increase in the number of hangers. At the tie the big forces in the prestressing cables will prevent a breakdown before many hangers have been broken.

8 FOUR INTERESTING NETWORK ARCHES

8.1 *Providence Bridge in Rhode Island*

This bridge was the first network arch built in USA. It has five lanes in each direction. The bridge with some general information can be seen in Figure 6.

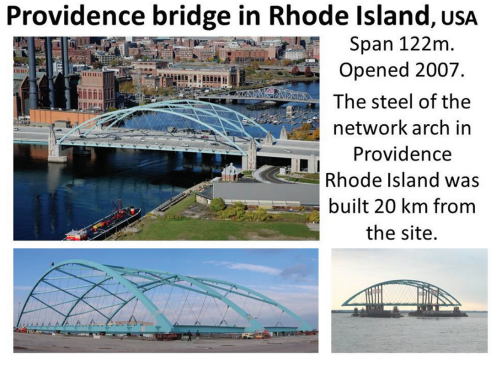

Figure 6. The first network arch built in the USA.

The tide helped putting the steel skeleton in place (Steere 2008).

The river was to be kept open when the bridge was built. This gave extra difficulties (Wollmann 2008).

8.2 *Blennerhassett Bridge over Ohio, USA*

From 2008 to 2014 the Blennerhasset Bridge was the world's longest network arch. Span 268 m (see Fig. 7). The use of sloping instead of vertical hangers reduced the deflection due to movable loads with a factor 11 (Wollmann 2007). In railway bridges for high speed trains this is important. Bending moment in arch and tie were reduced by a factor 4 and 5, respectively.

8.3 *The Mangamahu network arch*

The Mangamahu network arch replaced a bridge that fell down because a pillar failed (Chan 2008). It was lifted up by two red cranes and joined at the top by two men lifted by the yellow crane (see Fig. 8). It has a span of 85 m. It was the world's most slender arch bridge from 2008 to 2011. The Maoris like the bridge because it does not disturb the spirits in the river.

Figure 7. Blennerhasset Bridge.

Figure 8. Erection of the Mangamahu Bridge in New Zealand.

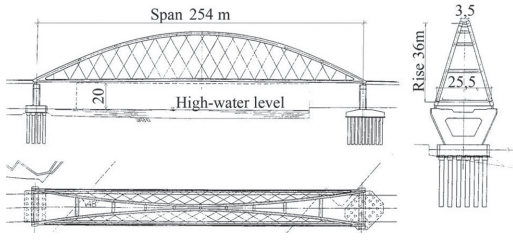

Figure 9. Network arch built in Japan in 1991.

8.4 *The Shinhamadera Bridge*

In the Shinhamadera network arch the arches slope towards each other. That looks good (see Fig. 9). In shorter bridges the sloping arches make the tie wider in order to avoid collision with the sloping arch and hangers. This makes the transverse beams longer.

The main span of the Shinhamadera Bridge was built on a quay and moved to the pillar by two big floating cranes. (Yoshikava, 1993) They have many earthquakes in Japan. Network arches have little weight compared to their strength. Thus they can withstand big earthquakes. The strong edge beams helps against the horizontal vibrations.

9 RAILWAY BRIDGES

As mentioned in 8.2 the network arches have small deflections. This is a great advantage for bridges for high speed trains. Because the live load might be big compared to the dead load of the tie, it might be sensible to let some hangers relax.

When some hangers relax, there is not full load on the whole span. Thus there is extra capacity to take the extra bending that occurs when hangers relax. Stresses due to relaxing of hangers is shown in pages 38 to 46 (Tveit 2015) and in page C4 to C6 in (Tveit 2014).

It would make the calculations much simpler if there was no relaxation of hangers in the serviceable limit state, and influence lines could be even more useful for a preliminary calculation. See p. 39 (Tveit 2015). Then there would probably be no problems in the collapse limit state.

10 STUDENTS WORK ON NETWORK ARCHES

Students have done a lot to develop network arches. Teich & Wendelin (2001) designed the Åkviksundet Bridge in Figure 10 according to EU norms. Calculations in German can be found at: http://fag.grm.hia.no/fagstoff/ptveit/.

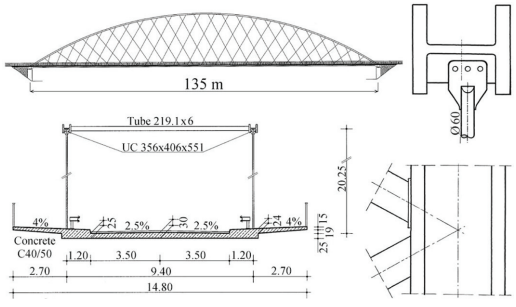

Figure 10. The Åkvik Sound Bridge.

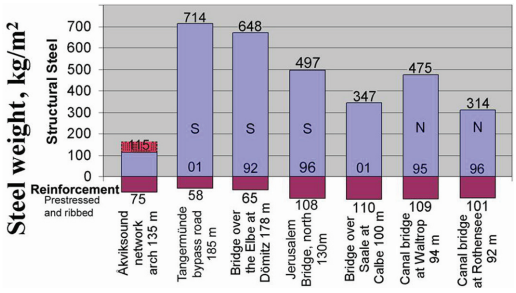

Figure 11. Steel needed for various road bridges.

The main span was to be made on shore to be moved out by pontoons or big floating cranes. Figure 11 compares the steel weight per m² of bridge area of the Åkvik Sound Bridge (Fig. 10), to the same for German arch bridges with vertical hangers.

The gray background indicates two bridges with nearly the same span. The German bridge uses four times as much structural steel. The dotted red area on Åkvik Sound Bridge shows steel weight for a temporary lower chord.

S shows that the arches slope towards each other. N means that there is no Windbracing. The year when the bridges were built is also shown in Figure 11.

Usually a network arch saves around 2/3 of the structural steel compared to arch bridges with vertical hangers.

Brunn and Schanack's bridge (Fig. 12) used 1/3 of the steel needed according to Herzog's diagram (Fig. 13). Max Herzogs diagram was compiled in 1975 and shows the steel weight per meter of railway track in several bridges.

Brunn and Schanack's bridge was made of stronger materials, but maybe it carried bigger loads.

Schanack did his Ph.D on network arches in Spain (Schanack 2008). He is now a professor

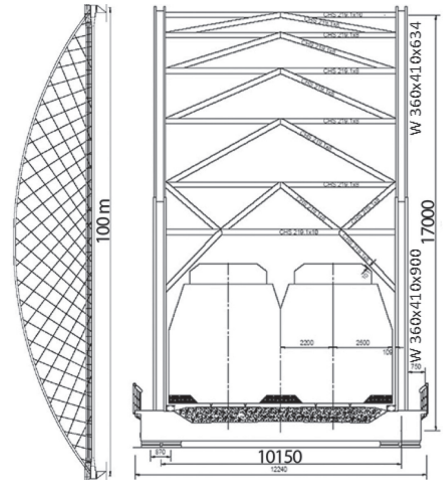

Figure 12. Graduation thesis of (Brunn & Schanack 2003).

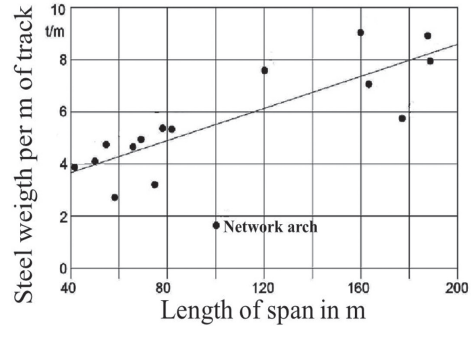

Figure 13. Comparison of steel weights in railway bridges.

in Chile. Teich did his Ph.D on network arches in TU-Dresden. (Teich 2012).

11 WORK OF MATIAS VALENZUELA

Matias Valenzuela analyzed the feasibility of designing a network arch in Chile, then in (Valenzuela 2010) he wrote: From continuous beam to network arch. A 60 m long multispan beam bridge from 1930 had been closed because sand and gravel had been washed away from under the pillars.

In 2012 Valenzuela, in his Ph.D thesis suggested that the bridge could be strengthened installing arch and hangers of a network above the lane. Then the pillars under the continuous beam could be removed. He proposed a criterion for the design of this strengthening (Fig. 14).

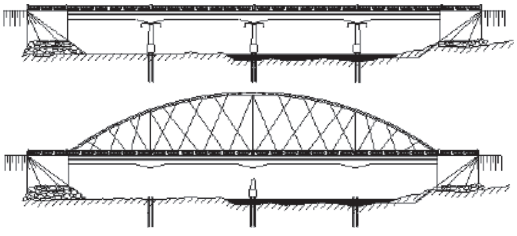

Figure 14. Repairs of a Chilean multispan bridge from 1930.

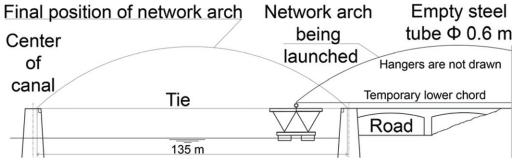

Figure 15. Economical erection of a network arch over a canal.

It is an advantage that the strengthening takes place mainly above the lane and at the end pillars. The dismantling takes place below the tie. The new bridge is less likely to be damaged by earthquake and scour.

12 BRIDGE OVER A CANAL IN CHINA

In Figure 15, a way of building an economical network arch over a canal in China is shown.

First the steel skeleton is built on one side of the canal. Then a pontoon is fastened to the pillar nearest to the steel skeleton. The steel skeleton is then rolled on to the pontoon. Then the steel skeleton is pulled over the canal and the steel skeleton is pulled till it is over the pillars. Then the water is pumped into the pontoons or the level in the canal is decreased.

The steel tube in the arch can be filled with concrete. Afterwards, the lower chord is cast. The beam between the ends of the arches is cast first. Then the edge beam is cast. Finally the concrete plate is cast. Then the temporary lower chord is removed. It can be reused in many similar spans of various lengths.

The concrete filled arch would be stronger if the concrete expanded a little to ensure good contact between the steel tube and the concrete. It is probably easier to increase the concrete strength.

It is important that there is little air in the steel tube. Banging on the steel tube while it is filled with concrete can help to achieve this. The result can be controlled with ultrasound.

Figure 16. Network arch over Ob in Siberia. Span 380 m.

By injecting strong mortar or epoxy under high pressure in between the concrete and the steel, we could make sure that there were no big air bubbles. Furthermore it would give three-dimensional compressive stresses like in a concrete column with helical reinforcement.

13 NETWORK ARCHES AROUND THE WORLD

The author's master thesis (Tveit 1955) was on Nielsen Bridges (Nielsen 1929). He suggested that some hangers of the Nielsen Bridges should cross each other at least twice. He later suggested that the new bridge type should be called network arches.

The author's first network arch was built in Norway in 1963 (Tveit 1964). It is likely to last at least 50 more years (Tveit 2007). Between 100 and 200 network arches have been built in around 25 countries. Many have been built in Germany, USA and Japan.

The road bridge in Figure 16 was opened by president Putin in 2014. It is the longest network arch in the world. Those who designed the bridge got the idea from a lecture given by the author in Moscow 2007.

Under the bridge there is a volcanic crack in the earth. Therefor the distance between the main pillars will change over time.

14 CONCLUSIONS

Network arches are economic, slender, good-looking, and have durable spans that use very little materials. They are equally well suited for road and rail bridges. The high strength to weight ratio of network arches gives good resistance to earthquakes.

Thin walled steel tubes in arches can be filled with concrete. By pumping strong mortar or epoxy under big pressure in between the steel and the concrete, a three-dimensional stress like in concrete columns with helical reinforcement, can be obtained.

Over 300 m long steel skeletons with temporary lower chords and thin walled steel tubes can be erected on land and floated to the pillars using pontoons or big floating cranes.

These facts speak for using network arches more often.

REFERENCES

Brunn, B. & Schanack, F. 2003. *Calculation of a Double Track Railway Network Arch Bridge Applying the European Standards*. Germany: TU-Dresden.

Chan, M. & Romanes, M. 2008. New Zealand's First Network Arch Bridge. *Conference paper for the 4th New Zealand Metal Industry Conference, HERA, New Zealand, October 2008*.

Herzog, M. 1975. *Stahlgewichte Moderner Eisenbahn-und Strassenbrücken. (Steel Weights of Modern Rail and Road Bridges)*. Der *Stahlbau 9/1975*. Berlin.

Keller, T. 2003. *Use of Fibre Reinforced Polymers in Bridge Construction Structural Engineering Documents*. Zurich, Switzerland: IABSE.

Larsen, R.M. & Jakobsen, S.E. 2011. *Brandangersundet Bridge–A Slender and Light Network Arch. Taller, Longer, Ligher*. London, UK: IABSE.

Nielsen, O.F. 1929. *Foranderlige Systemer Med Anvendelse På buer Med Skraatstillede Hængestenger. (Discontinuous systems used on arches with inclined hangers)*. Gad, Copenhagen, Denmark.

Schanack, F. 2008. *Puentes en Arco Tipo Network (Network Arch Bridges)*. Espãnia: Departemento de Ingeniera Estrutural y Mecánica, Escuela Técnica de Caminos, Canales y Puertos, Universitad de Cantabria Santander.

Steere, P. & Wu, Y.H. 2008. Design and Construction of the Providence River Bridge. *Official Proceedings of the 25th Annual International Bridge Conference, June 2–4, 2008.* Pittsburgh, Pennsylvania, USA: Engineers Society of Western Pennsylvania.

Teich, S. & Wendelin, S. 2001. *Vergleichsrechnung einer Netzwerkbogenbrücke unter Einsats des Europäishen Normenkonsepts*. Germany: TU-Dresden.

Teich, S. 2012. *Beitrag zur Optimierung von Netzwerkbogenbrüken (Contrbution to Optimizing Network Arch-Bridges)*. Germany: TU-Dresden.

Tveit, P. 1955. *Graduation Thesis on Arch Bridges with Inclined Hangers.* Norwegian: Technical University of Norway.

Tveit, P. 1964. Nettverkbogar, ein ny brutype. (Network Arches, a New Type of Bridge) *Bygg* 12(5): pp. 105–113.

Tveit, P. 2007. Visit to the Steinkjer Network Arch 44 Years Later. *5th International Conference on Arch Bridges, Madeira, 12–14 September 2007.* Portugal: University of Minho.

Tveit, P. 2014. A Systematic Thesis on Network Arches. *http://home.uia.no/pert/.*

Tveit, P. 2015. The Network Arch. Bits of Manuscript in March 2014 after Lectures in 50 Countries. *http://home.uia.no/pert/.*

Valenzuela, M & J.R. Casas. 2010. Bridge Strengthening by Structural Change: from Continuous Beam to Network Arch. *IABMAS 2012-Fifth International Conference on Bridge Maintenance, Safety and Management, Philadelphia, USA, July 11–15, 2010*.

Valenzuela. 2012. *Refuerzo de Puentes de Luces Medias Por Conversión en Arco Atirantado Tipo Network (Strengthening Method of Médium Span Bridges by Change Using Network Arch System)*. Spain: UPC-BarcelonaTECH (Universitat Politecnica de Catalunya).

Wollman, G., et al. 2007. Construction of Tied Arch Bridge Across Ohio River and Blennerhassett Island. *Proceedings of 24th Annual International Bridge Conference, Pittsburgh, Pennsylvania, June 4–6, 2007.* Pittsburg, Pennsylvania, USA: Engineers Society of Western Pennsylvania.

Wollmann, G. & Zoli, T. 2008. Bridge across Ohio River and Blennerhassett Island. *Structural Engineering International* 18(1): 28–30.

Yoshikava, O. et al. 1994. Construction of the Shinamadera Bridge. *Stahlbau* 63(1): 125–136.

Zoli, T. & Woodward, R. 2005. Design of Long Span Bridges for Cable Loss. *IABSE Symposium, Structures and Extreme Events, Lisbon, Portugal, September 14–17.* Zurich: IABSE.

Zoli, T. & Steinhouse, J. Some Considerations in the Design of Long Span Bridges against Progressive Collapse. *http://www.pw i.go.jp/eng/ujnr/tc/g/pdf/23/23-2zoli.pdf.*

Civil Engineering and Urban Planning IV – Liu et al. (Eds)
© 2016 Taylor & Francis Group, London, ISBN 978-1-138-02903-3

Analysis of anchorage zone and strut-and-tie design of single-eccentric concrete straight anchor

Wen-Xue Zhang, Quan-Yi Xie & Long Liu
Beijing University of Technology, Beijing, China

ABSTRACT: T Substantial studies have been conducted on the force analysis and design issues of the anchorage zone of prestressed concrete structure and significant discrepancies exist within different methodologies and the respective results in different countries. In the proposed research, local stress of the anchorage zone of single-eccentric straight anchor with rectangular section was analysed and the effect of pressure-bearing ratio λ and eccentricity γ on the stress distribution in the anchorage zone was studied. Based on the stress analysis, the single-eccentric straight anchor was categorised into small eccentricity, large eccentricity and critical eccentricity. The respective strut-and-tie design model was proposed. Finally, equations to predict the cracking load of single-eccentric straight anchor were proposed and verified by comparing the results based on the experiments.

1 INTRODUCTION

The European Federation for Precast Concrete (BIBM) conducted an investigation on the design of prestressed anchorage zone in 5 different countries. The investigation was based on a prestressed simply supported concrete beam with 6 prestressing tendons. The standards in the 5 countries are applied to design the prestressing anchorage zone. The main design parameters include bursting force, range of bursting tensile force and reinforcement ratio required for the section of anchorage zone (CEB 1987). Design results based on different standards show that the design parameters scattered in a great range and significant difference exists regarding the design of prestressing anchorage zone. This can possibly cause safety hazard. Therefore, further studies of prestressing anchorage zone are necessary.

Prestressing anchor can be categorised into end anchor and centre anchor in terms of Longitudinal location of anchoring point along concrete beam. According to the vertical location of anchoring point along the section, end anchor can be further divided into six categories: 1) single-concentric straight anchor; 2) single-eccentric straight anchor; 3) single inclined anchor (including eccentric inclined anchor and inclined and bended anchor); 4) multi-concentric straight anchor; 5) multi-eccentric straight anchor; 6) multi inclined anchor (Breen et al. 1991; Schlaich & Schafer 1991; Zhang 2007). In this study, prestressed concrete single-eccentric straight anchor was used as the research object; the stress distribution under anchor was systematically analysed and relevant strut-and-tie design model was proposed to predict the bursting load and spalling load under anchor. The prediction was compared with results obtained in the experiments and meaningful conclusions were drawn to provide further reference for relevant structural design.

2 LOCAL STRESS ANALYSIS SINGLE-ECCENTRIC STRAIGHT ANCHOR

Set the ratio of bottom plate dimension a to the height of the section of specimen h, i.e. the pressure-bearing ratio $\lambda = a/h = 0.1$ and the modified eccentricity $\gamma = 2e/h$, as shown in Figure 1. The conversion of single-eccentric straight anchor to single-concentric is shown in Figure 2.

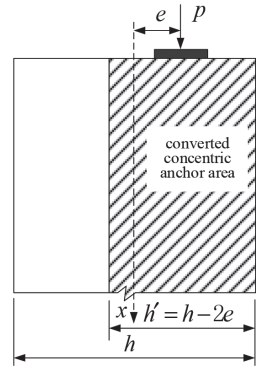

Figure 1. The converted single-concentric straight anchor.

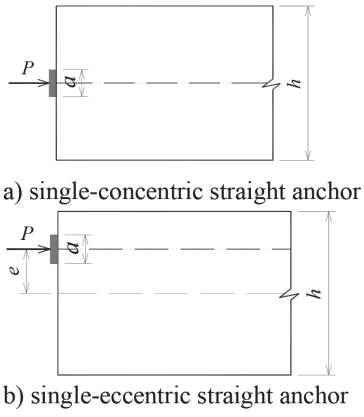

Figure 2. Prestressed anchoring type diagram and main parameters.

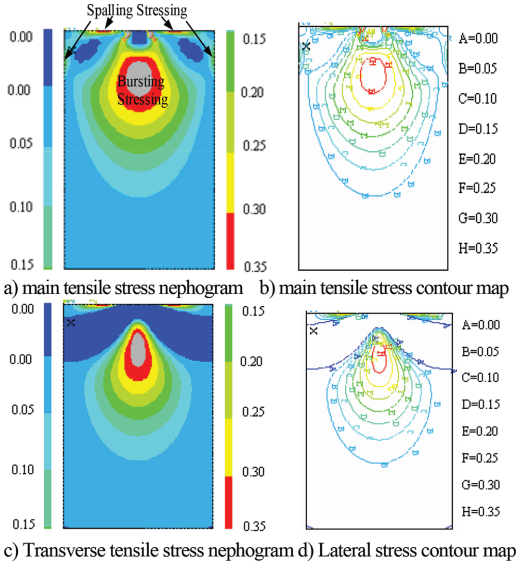

Figure 3. Anchorage stress distribution ($\lambda = 0.1$).

Setting the rectangular cross-section of single-concentric straight anchor as the plane structure, established the finite element model of an elastic plane and anchorage stress distribution was shown in Figure 3.

The distribution of bursting stress in different eccentricity was analysed and shown in Figure 4. Figure 5 shows the variation of bursting force under anchor with eccentricity in different pressure—bearing ratio. It is obvious that:

– For the same pressure-bearing ratio, the maximum bursting stress increased steadily with the increase of eccentricity. When the eccentricity was large, the maximum bursting stress increased significantly with the increase of eccentricity.
– The variation of bursting force under anchor was opposite to that of bursting stress: when the eccentricity was small, the bursting stress reduced with the increase of eccentricity; when the eccentricity was large, the bursting stress reduced significantly with the increase of eccentricity.

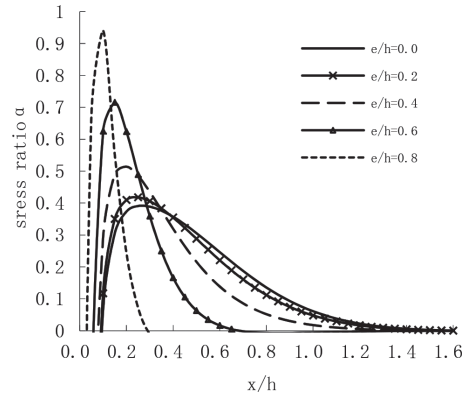

Figure 4. Effect of eccentricity on the bursting stress under anchor.

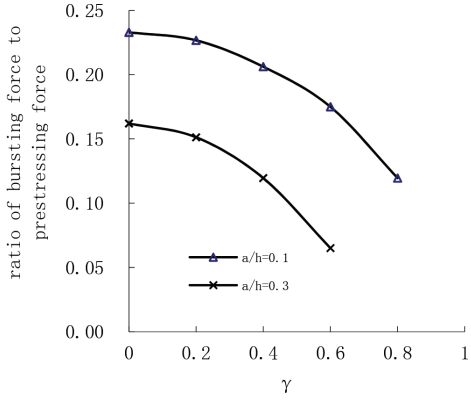

Figure 5. Effect of eccentricity on the bursting force under anchor.

On the basis that the dimension of the bottom plate of anchor remained the same, the pressure-bearing ratio was taken respectively as 0.1 and 0.3. In order to evaluate the relationship of the bursting force of single-eccentric straight anchor and the converted single-concentric straight anchor and the location of bursting force centre, the single-eccentric straight anchor was converted to single-concentric straight anchor to analysis. As shown

in Figure 1, the sectional dimension of the specimen after conversion was $h' = h - 2e$, and thus the pressure-bearing ratio under different eccentricities can be calculated as:

$$\lambda' = \frac{a}{h'} = \frac{a}{h - 2e} \quad (1)$$

where a = anchor plate size; e = eccentric distance.

The bursting force under anchor and the location of centre in the two models are shown in Figure 6. It is clear that:

– The magnitude and variation of bursting force under anchor for single-eccentric straight anchor and the converted single-concentric straight anchor were similar. Thus it is reasonable to calculate the bursting force under anchor for single-eccentric straight anchor using the calculating equation of bursting force under anchor for single-concentric straight anchor by replacing pressure-bearing ratio λ with λ'.

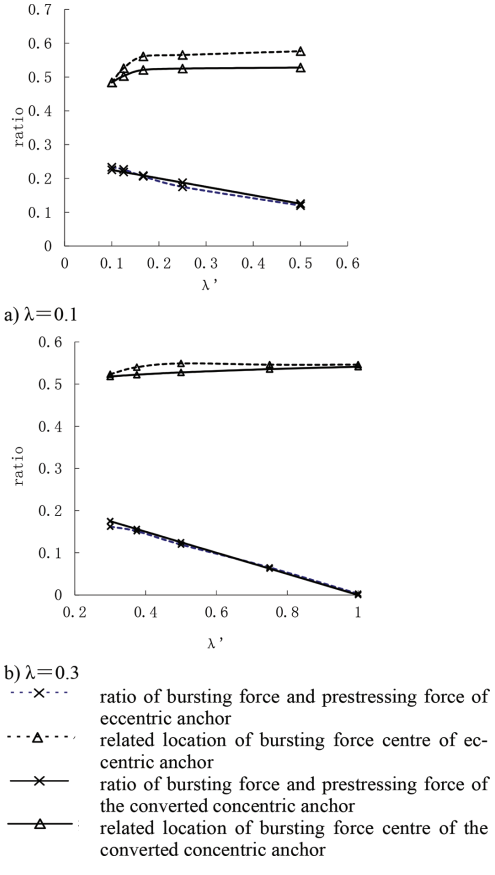

Figure 6. Comparison of bursting force.

– The related location of bursting force centre to the bottom plate of anchor for single-eccentric straight anchor was farther than that for the converted single-concentric straight anchor, but similar variation trend was found.

It is clear from the analysis of single-concentric straight anchor that although spalling stress exists in the section of the fixed end of anchor, the spalling tensile force was small. Guyon proposed that for single-concentric straight anchor, the spalling tensile force can be taken as 4% of the prestressing force P (He & Liu 2011). However, with the increase of eccentricity, especially when the eccentricity is large, spalling tensile force increases dramatically (Schlaich 1987; Thompson 2002). Therefore, it is necessary to analyse the relationship of spalling tensile force under eccentric straight anchor and eccentricity. Figures 7 and 8 show the variation of maximum spalling stress and total spalling force with eccentricity where the pressure-bearing ratio was taken as 0.1, 0.2 and 0.3. It is evident that:

– Both the maximum spalling stress and total spalling force increased with the increase of eccentricity. When the eccentricity was smaller than the critical eccentricity, i.e. in the state of small eccentricity, the rate of increase of the maximum spalling stress and total spalling force was small; when the eccentricity exceeded the critical eccentricity, the maximum spalling stress and total spalling force increased dramatically with the increase of eccentricity. When the pressure-bearing ratio was 0.1 and 0.2, and eccentricity was 0.8, the maximum spalling stress was approximately 1.6 times of the average sectional compressive stress σ_0 and the total spalling force was 0.164 time of the prestressing force P.

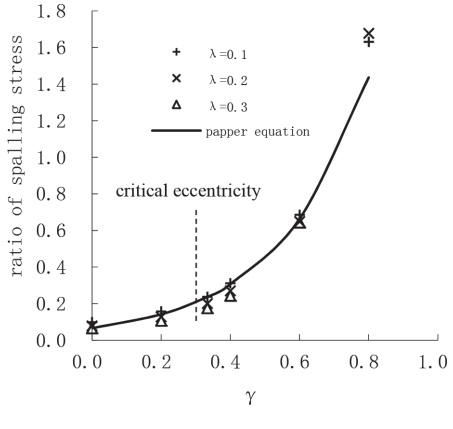

Figure 7. Relationship of the maximum spalling stress and eccentricity.

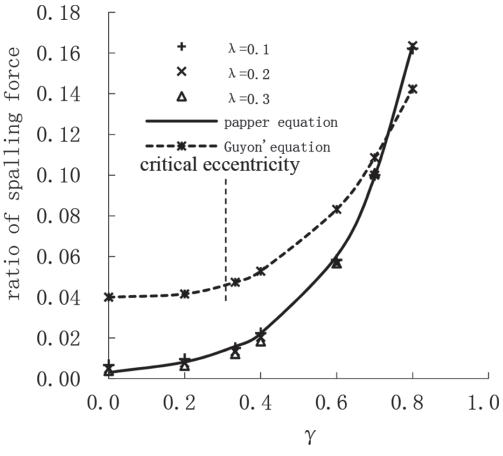

Figure 8. Relationship of total spalling tensile force and eccentricity.

– In the condition of small eccentricity, the related value of maximum spalling stress and total spalling force were significantly affected by different values of pressure-bearing ratio λ, but the absolute value of maximum spalling stress and total spalling force were small; with the increase of eccentricity, the contribution of eccentricity increased and the effect of pressure-bearing ratio reduced. Little difference was found for maximum spalling stress and total spalling force under different pressure-bearing ratios. Therefore, the effect of pressure-bearing ratio λ can be ignored during practical design.
– The relationship of maximum spalling stress and eccentricity, which 3 cm under the surface of concrete under different pressure-bearing ratios for the single-eccentric concrete straight anchor, can be fitted using the following equation:

$$\sigma_{msp} = 0.065 \times e^{3.86\gamma}\sigma_0 \tag{2}$$

where σ_{msp} = maximum expansion crack stress of concrete surface; σ_0 = section average compressive stress; γ= eccentricity rate; e = eccentric distance.

– The relationship of total spalling force and eccentricity can be fitted by

$$\begin{aligned} F_{sp} &= \left(0.003 \times e^{5\gamma}\right) P \\ F_{sp} &\geq 0.02P \end{aligned} \tag{3}$$

where F_{sp} = total spalling force; P-tensile; γ = eccentricity rate; e = eccentric distance.

In order to analyse the relationship of bursting force and bending tensile force in the condition of large eccentricity, the eccentricity was set from 0.4 to 0.8 in the cases where the pressure-bearing ratios were set as 0.1, 0.2 and 0.3. Results are given in Figure 9a, in which the vertical coordinate is the arctangent value of the ratio of bursting force and bending tensile force. Figure 9b shows the comparison of calculated ratio of bursting force and prestressing force P and FEA result when T_{sp}/T_m = 1.19 and act (T_{sp}/T_m) = 50°. It can be seen from Figure 9 that for different pressure-bearing ratio, the variation of the ratio of bursting force and bending tensile force with eccentricity was similar and when the eccentricity was larger than 0.5 and act (T_{sp}/T_m) was smaller than 50°, it is safe that:

$$T_{sp} = \tan 50^\circ \cdot T_m = \frac{\tan 50^\circ (3\gamma - 1)^2 P \cdot}{18\gamma}, T_{sp} \geq 0.02P \tag{4}$$

where T_{sp} = bursting force; T_m = bending tensile force; P = tensile; γ= eccentricity rate; e = eccentric distance.

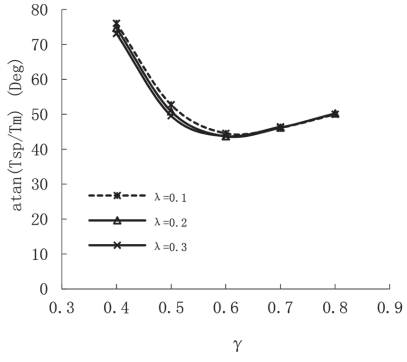

a) Act (T_{sp}/T_m) in different conditions

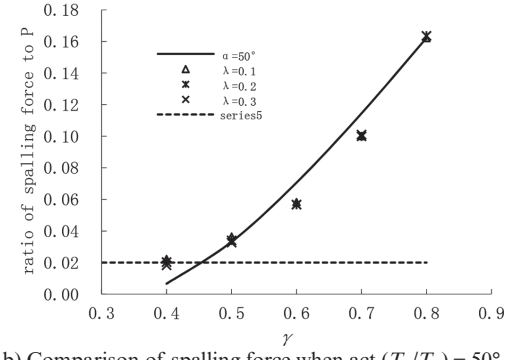

b) Comparison of spalling force when act (T_{sp}/T_m) = 50°

Figure 9. Strut-and-tie design model of anchorage zone in different conditions of eccentricity.

3 STRUT-AND-TIE DESIGN MODEL OF SINGLE-ECCENTRIC STRAIGHT ANCHOR

It is clear from the local stress analysis of single-eccentric straight anchor that the design of anchorage zone for eccentric straight anchor can be categorised into three conditions: 1) small eccentricity. In the condition of small eccentricity, the single-eccentric straight anchor can be designed as the converted single-concentric straight anchor (Wang 2005; You 2009) as shown in the strut-and-tie model in Figure 10a; 2) large eccentricity. In the condition of large eccentricity, bending tensile stress exists at the side away from the anchoring point and it must be accounted for.

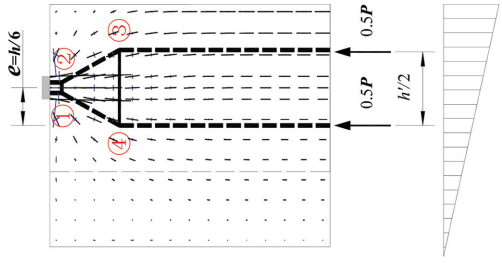

a) Condition of small eccentricity

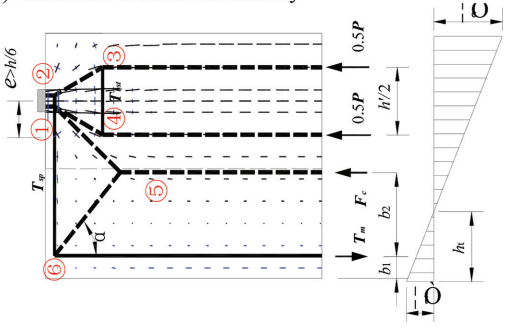

b) Condition of large eccentricity

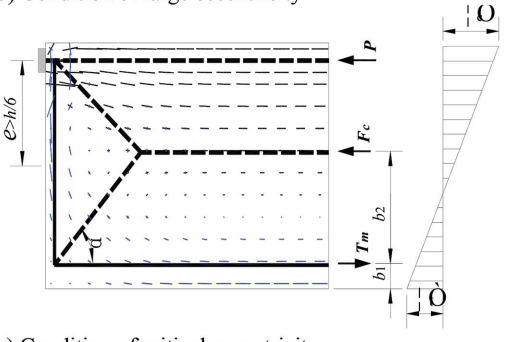

c) Condition of critical eccentricity

Figure 10. Strut-and-tie design model of anchorage zone in different conditions of eccentricity.

The strut-and-tie model as shown in Figure 10b can be used and the parameters can be taken as the following values. 3) Critical eccentricity. In this condition, the corresponding converted concentric anchor has a pressure-bearing ratio $\lambda \approx 1$, the bursting tensile force under the converted anchor was small and it can be simplified as a single strut (Wen & Zhou 1998; Luo et al. 2003). Other parameters can be calculated as in the condition of large eccentricity as shown in Figure 10c:

- Sectional dimension of the converted single-concentric straight anchor $h' = h - 2e$;
- Distance of nodes under anchor to the bottom plate of anchor $y_c = 0.04\, h'$;
- Distance to the bursting force centre $d_1 = 0.05\, h$;
- In the condition of large eccentricity, the maximum tensile stress $\sigma_t = (3\gamma - 1)p/(bh)$;
- In the condition of large eccentricity, the maximum compressive stress $\sigma_c = (3\gamma + 1)p/(bh)$;
- Tensile stress range $h_t = (3\gamma - 1)h/(6\gamma)$;
- Distance between tie 6–6 to the tension side $b_1 = h_t/3$;
- Distance between tie 5–5 to the tension side $b_2 = 5h_t/3$;
- Angle α was determined by T_{sp} and T_m taken as $\alpha = 50^\circ$.

4 PREDICTION OF CRACKING LOAD OF SINGLE-ECCENTRIC STRAIGHT ANCHOR

Compared with single-concentric straight anchor, it is more complex to predict the cracking load of single-eccentric straight anchor. The effect of eccentricity should be considered besides other factors with single-concentric straight anchor.[7] Possible mode of cracking for single-eccentric straight anchor includes: 1 cracking caused by bursting stress under anchor; 2 cracking due to spalling stress on the fixed ends of anchor; 3 bending cracking at tensile face due to large eccentricity. For the 3rd case, the cracking can be calculated according to beam theory to predict the cracking load, and is not discussed in this study. The first and second types of cracking load were discussed as follows:

- Prediction of bursting force of single-eccentric straight anchor
  It is clear from the local stress analysis of single-eccentric straight anchor that although the location of bursting force and spalling force centres of single-eccentric straight anchor can be approximated by the converted single-concentric straight anchor, significant discrepancies were found between the maximum bursting stress of single-eccentric straight anchor and the converted single-concentric straight anchor.

Therefore, specific pressure-bearing ratio and eccentricity should be incorporated in the calculation to predict the bursting load. The burst—cracking load of revised single-concentric straight anchor can be calculated as:

$$P_{bcp} = P_{cc} + P_{sc} = \frac{0.19K_{ec} \cdot t \cdot h \cdot f_{cu}^{0.75}}{K_b} + 48.8 \times 10^{-6} f_{cu}^{0.41} E_s A_{bst} \quad (5)$$

where P_{bcp} = burst-cracking load of revised single-concentric straight anchor; P_{cc} = Concrete alone bear the biggest load; P_{sc} = Splitting reinforced bear load; f_{cu} = Standard concrete cube compressive strength; E_s = Modulus of elasticity of splitting and steel; A_{bst} = The area of the splitting of reinforcement; t = Concrete section thickness; K_{ec} = general reduction factor taken as $K_{ec} = 0.75$; K_b = ratio of maximum bursting stress to the average prestress, $K_b = \sigma_{bst} \cdot h \cdot t / P$ as calculated by elastic finite element analysis.

To validate the reliability of the method in predicting the bursting load of single-eccentric straight anchor, an experiment was conducted by David Howard (Sanders 1990) was used for comparison as shown in Table 1. It is evident that the predicted value matched favourably with the measured results. The average value of the measured initial bursting force P_{bc} and the predicted value P_{bcp} was $\overline{K}$, the standard deviation $\sigma = 0.09$ and the coefficient of variation $c_v = 0.07$.

– Prediction of spalling force of single-eccentric straight anchor

Based on the same method and with consideration of the gradient of spalling stress decreasing inwards at the loading surface of the structure was large, the maximum spalling stress at 3 cm beneath the concrete surface was used to predict the spalling force. The equation to calculate the initial spalling force is given as:

$$P_{scp} = P_{cc} + P_{sc} = \frac{0.19K_{ec} \cdot t \cdot h \cdot f_{cu}^{0.75}}{0.065 \times e^{3.86\gamma}} + 48.8 \times 10^{-6} f_{cu}^{0.41} E_s A_{sp} \quad (6)$$

where P_{scp} = initial spalling force; P_{cc} = Concrete alone bear the biggest load; P_{sc} = Burst of reinforced bear the load; f_{cu} = Standard concrete cube compressive strength; E_s = Burst of reinforcement modulus of elasticity; A_{sp} = The area of the burst of reinforcement; t = Concrete section thickness.

To validate the reliability of the above method in predicting the spalling load of single-eccentric straight anchor, the experiment was conducted by David Howard was used for comparison as shown in Table 2. To product the results of the experiments by David Howard, Specimens E_1 and E_5 were in the case of critical eccentricity, no spalling crack was found before the ultimate load was achieved. For Specimen E_3, no spalling

Table 1. Comparison of predicted bursting load and measured initial bursting load.

Specimen	f_{cu} (Mpa)	K_b	h (mm)	t (mm)	E (GPa)	A_{bst} (mm)	Measured P_{bc} (kN)	Predicted P_{bcp} (kN)	P_c/P_{cp}
E1	37.6	0.371	914	279	198	1562	1535	1167	1.32
E2	41.0	0.469	914	279	198	1704	1179	1005	1.17
E3	42.3	0.469	914	279	198	1562	1113	1020	1.09
E4	39.2	0.469	914	279	198	1562	1113	967	1.15
E5	39.4	0.399	914	216	198	568	957	791	1.21
E6	39.0	0.428	914	254	198	316	1001	903	1.11
M5	32.2	0.428	813	432	198	306	1780	1348	1.32

* The average value of P_c/P_{cp} $\overline{k} = 120$, standard deviation $\sigma = 0.09$, coefficient of variation $c_v = 0.07$.

Table 2. Comparison of predicted spalling load and measured initial spalling load.

Specimen	f_{cu} (Mpa)	λ	h (mm)	t (mm)	E (GPa)	A_{bst} (mm)	Measured P_{bc} (kN)	Predicted P_{bcp} (kN)	P_c/P_{cp}
E2	41.0	0.67	914	206	279	787	1469	759	1.93
E4	39.2	0.67	914	206	279	142	1001	695	1.44
E6	39.0	0.5	914	187	254	126	1335	1175	1.14

* The average value P_c/P_{cp} $\overline{k} = 1.50$, standard deviation $\sigma = 0.33$, coefficient of variation $c_v = 0.22$.

crack was found as the concrete was blocked by plastic plates in order to test the strain in the spalling reinforcement. The comparison of predicted value of spalling force and measured initial spalling force for specimens with spalling cracks demonstrated large discrepancies between the predicted and measured values.

5 CONCLUSIONS

– On the basis that the pressure-bearing ratio remained the same, the maximum bursting stress under anchor increased with the increase of eccentricity. The variation of bursting force under anchor was opposite to the variation of bursting stress.
– Both maximum spalling stress and total spalling tensile force increased with the increase of eccentricity. When the eccentricity was smaller than the critical eccentricity, i.e. in the state of small eccentricity, the rate of increase for the maximum spalling stress and total bursting tensile force with the increase of eccentricity was small. When the eccentricity was larger than the critical value, the maximum spalling stress and total bursting tensile force increased significantly with the increase of eccentricity.
– In the condition of small eccentricity, the related value of the maximum spalling stress and total bursting tensile force was significantly affected by the variation of pressure-bearing ratio but the absolute values of the maximum spalling stress and total bursting tensile force were small; with the increase of eccentricity, the contribution of eccentricity increased while the effect of pressure-bearing ratio reduced and the difference of the maximum spalling stress and total bursting tensile force under different pressure-bearing ratios was small. Therefore, the effect of pressure-bearing ratio can be ignored during practical design.
– For single-eccentric straight anchor, the anchorage zone of single-eccentric straight anchor can be designed as the converted single-concentric straight anchor and the effect of spalling force at the fixed end section of the anchor can be ignored.
– It was shown that the prediction of the bursting load of single-eccentric straight anchor matched well with the measured results and the model can be applied in engineering practice. However, there were large discrepancies between the predicted and measured values of bursting load of single-eccentric straight anchor and further studies are required.

ACKNOWLEDGEMENTS

This paper was funded by Department of technological education, Ministry of Transport (201231882225).

REFERENCES

Breen, J.E., Burdet, O. & Roberts, C. 1991. *Anchorage Zone Reinforcement for Post-tensioned Concrete Girders*.

CEB. 1987. *Anchorage Zones of Prestressed Concrete Members*. CEB-FIP model code: No. 181.

Chen, J.Y. 2006. *Large Span Prestressed Concrete Box Girder Anchorage Zone of the Local Stress of Theoretical Analysis and Experimental Research*. Zhejiang: Zhejiang University.

He, Z.Q. & Liu, Z. 2011. Investigation of bursting forces in anchorage zones: Compression-dispersion models and unified design equation. *Journal of Bridge Engineering* 16(6): 820–827.

Luo, J.Q., Xiao, L.J., Wang, W.F., Yan, Q.S. & Tan, Y.P. 2003. Anchor under local stress analysis of prestressed concrete continuous girder Bridges. *The Chinese and Foreign Road* 23(6): 48–50.

Sanders, D.H. 1990. *Design and Behavior of Anchorage Zones in Posttensioned Concrete Members*. The University of Texas at Austin.

Schlaich, J. & Schafer, K. 1991. Design and detailing of structure concrete using strut-and-tie models. *Struct. Eng.* 69(6): 113–125.

Schlaich, J., Schafer, K. & Jenneweun, M. 1987. Toward a consistent design of structural concrete. *PCI Journal* 32(3): 74–150.

Thompson, M.K. 2002. *The Anchorage Behavior of Headed Reinforcement in CCT Nodes and Lap Splices*. The University of Texas at Austin.

Wang, Y. 2005. Local stress analysis under anchor of prestressed concrete box girder. *Urban Road and Bridge and Flood Control* (3): 50–52+4.

Wen, W.S. & Zhou, L.V. 1998. Single beam center straight anchor post tensioned anchorage areas. *Foreign Bridges* (3): 35–44.

You, W.G. 2009. The anchorage zone of stress analysis and the pull rod model. *North Traffic* (11): 43–46.

Zhang, W.X. 2007. *The Local Stress Analysis of Continuous PC Box Girder and Strut-and-Tie Design Method*. Shanghai: Bridge Engineering of Tongji University.

This page intentionally left blank

Civil Engineering and Urban Planning IV – Liu et al. (Eds)
© 2016 Taylor & Francis Group, London, ISBN 978-1-138-02903-3

Simplified analysis of cohesion layer of steel bridge deck pavement under different vehicle load cases

Zhan-Fei Wang, Zhi-Bin Cheng, Min-Jiang Zhang & Bin Gao
School of Traffic Engineering, Shenyang Jianzhu University, Shenyang, Liaoning, China

Ke Liu
School of Civil Engineering, Shenyang Jianzhu University, Shenyang, Liaoning, China

ABSTRACT: In order to study the relationship between the compressive stress and cohesion under the coupling action between zero load, standard load and over load and cohesion of cohesion layer, the three-dimensional model of steel bridge deck pavement system is established by finite element analysis software. In this study, we use friction coefficient instead of cohesion between layers to establish a simplified model on the basic of analysis of the shearing performance of steel bridge deck pavement. In order to provide simplified analysis of cohesion layer of steel bridge deck pavement, though the relationship equations of stresses and friction coefficients are put forward.

1 INTRODUCTION

The common harms that occur on the orthotropic steel bridge deck pavement can be divided into 4 kinds (Li 2008) (1. longitudinal and transverse cracks; 2. Rutting damage; 3. The pavement layer loss and removal; 4. Pits occurring). The main reasons for these damages are the over-load vehicles that result in large deformation of the deck surface and the braking and starting that result in the removal of the pavement layers. Because of the difference between the rigidity of the pavement layer and the steel bridge deck, it's essential for the coherent layers to limit the integrated deformation and shearing removal between the pavement layer and the bridge deck. Currently, some scholars have carried out FEM analysis on the stress, deformation and fatigue of the steel bridge, however, considering little investigation on the aspect of the shearing and integrated deformation between the steel bridge deck and the pavement layer. Besides, while executing the entire analysis on the bridge by FEM, the more complex the calculated process becomes, the more the material and structure layers are, the problems that internal memory lacks and the calculation process doesn't converge may occur. Aiming at solving the problems mentioned above, the 3-D FEM (Finite elements model) is planned to be established to simulate the steel bridge deck pavement system and investigate the relationship between the compressive stress and the coherent performance of the coherent layers in the condition of the coupling interaction between the coherent layers and the non-load, the standard load and the overload (Li 2003). Based on the analysis and summary of the shearing between the structure layers, the simplified model that the coherent layers contact could be replaced by the frictional contact is put forward. Eventually, the related formula which represents the relationship between friction ratios and different compressive stresses is fitted and it provides the theoretical foundation for the further FEA in the aspect of asphalt concrete steel bridge deck pavement.

2 CONSTRUCTIONS OF STEEL BRIDGE DECK ASPHALT CONCRETE AND VEHICLE LOADS

2.1 *Bridge construction and mechanical models*

The model of the steel bridge deck system is shown in Figure 1. The size of the deck is $150 \times 150 \times 20$ mm^3, E = 2.06×10^5 MPa, the

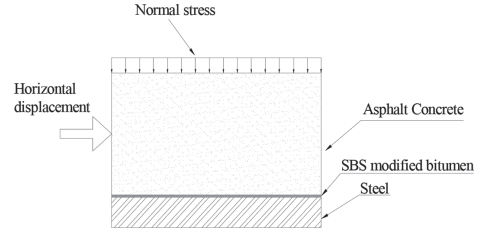

Figure 1. Steel bridge deck construction.

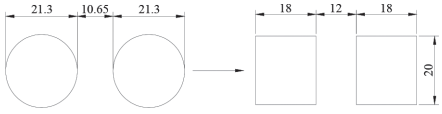

Figure 2. Loading model (Unit/cm).

Poisson ratio is 0.3. The thickness of the asphalt concrete layer is 80 mm. The elastic modulus of the asphalt concrete layer E_1 = 1200 MPa. The Poisson ratio of asphalt concrete layer is 0.25 (Ye 2007). The thickness of SBS is 1.5 mm. E_2 (the elastic modulus of SBS) = 15 MPa. The Poisson ratio of SBS is 0.35 (Liu 2009).

2.2 *Loading*

According to the Specifications for Design of Highway Asphalt (JTG D50-2006), the wheel group and single axial load (100 kN) is adopted for the standard axial load of the designed pavement. It has been simplified for BZZ-100. The conclusion that it's reasonable that loading region is simplified for rectangle has been raised by Wei Huang (Huang 2003) through the finite element simulation for the tire contact pressure. It can simplify the calculation and accurately reflect the law of the deck pavement under the axial load. Therefore, the rectangle vehicle loading graph which is recommended by AASHTO has been adopted for the calculation. The lateral dimension of the two rectangles is 18 cm, the longitudinal dimension is 20 cm, the tire contact pressure is 0.7 MPa, and the distance between margins of two rectangles is 12 cm. The accurate form is shown in Figure 2. Due to the limitation of the models, the area load takes 0.7 Mpa as the standard load. In addition, it takes 0.2 Mpa as the non-load pressure and takes 0.5 Mpa as the light-load pressure. 1.0 Mpa and 1.25 Mpa are respectively heavy load and over load.

When the bridge deck is under the vehicle load, as the vehicles may brake, start and decelerate, in response, the vehicle load may also result in the lateral force and eventually create the lateral displacement of the deck. Thus the lateral displacement is taken into consideration in the shearing analysis between the bridge deck pavement layers. The maximum is 0.2 mm.

3 FEM ESTABLISHING OF ASPHALT CONCRETE STEEL BRIDGE DECK

Model of asphalt concrete steel bridge deck pavement is established by ABAQUS package. The simulations of the steel bridge deck, the solid element SOLID45 was adopted in the simulation of the asphalt concrete and the SBS coherent layer. Tie was adopted in the contact between the asphalt concrete and SBS coherent layer, and the contact form between the deck and the SBS is Tie, either. The element type of the asphalt concrete and the steel bridge deck after the simplification that the coherent layer switched to frictional model is similar to the type which was before the simplification, however, the contact form between the asphalt concrete and the steel bridge deck was friction contact. Because of the visco-elastic plasticity of the asphalt concrete, the material may wriggle or loosen as the temperature and stress change. Therefore, the Drucker-Prager model was adopted in the constitutive relation of the asphalt concrete. The constitutive relation of the steel plate is shown in Figure 3. The mesh generation of the conventional shearing model between layers is basically identical with the simplified model, and the coherent layers of the conventional model consist two layers for the precision of the calculation. The accurate model is shown in Figure 4.

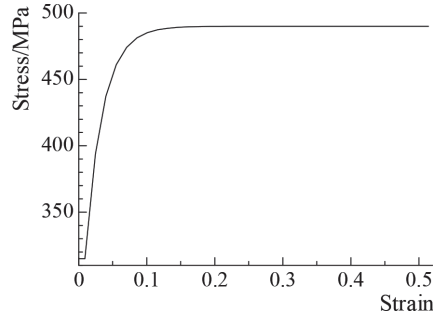

Figure 3. Stress-stain relation of steel.

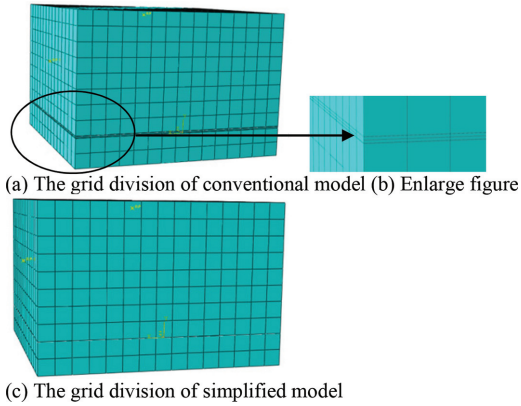

(a) The grid division of conventional model (b) Enlarge figure

(c) The grid division of simplified model

Figure 4. Contrast mesh partition conventional model and the simplified model.

4 THE FEM ANALYSIS FOR THE SIMPLIFIED MODEL AND SOLID MODEL OF THE ADHESIVE LAYERS

To discuss the relationship between the positive stress and the binder under the condition of the coupling effect and the simplified form that the coherent layers is replaced with friction ratio, the models of the non-load, the standard load and the overload conditions was investigated. And the results from the stress distribution and the load-displacement curves were analyzed.

4.1 *The stress distribution and deformation*

Two sorts of contact types (the coherent layers contact and the friction contact) were adopted in the contact between layers. The maximum stress distribution and deformation between layers under different vehicle loads is shown in Figure 5. Figure 5a to c respectively represent the analyzed results of the simplified models under the non-load, the standard load and the overload. Figure 5d to f respectively represent the results of the models which consist the coherent layers that are solid elements under the non-load, the standard load and the overload.

It could be concluded through observing the stress distribution and the shearing deformation between layers that the maximum shearing stress of the conventional models is 34.28 MPa, the maximum shearing stress of the simplified one is 36.83 MPa, the stress concentrates on the left end of shearing surface, and the deformations between layers of either the conventional models or the simplified ones are similar. The deformations are also basically identical either under the non-load condition or under the overload condition; the maximum stress concentrated conditions are almost same though the values differ a bit.

4.2 *The compared analysis between load-displacement curves*

To thoroughly study the relationship between the positive pressure and the binder under the condition of the coupling effect and the simplified form that the coherent layers is replaced with friction ratio, the load-displacement curves of the non-load condition, the standard load condition and the overload condition were compared. The results are shown in Figure 6. Figure 6a to c shows the results of the frictional contact and coherent layers contact between the bridge deck layers under the non-load condition. Figure 6d shows the results under the standard load condition. Figure 6e and f show the results that were under the overload condition. The horizontal coordinate represents the

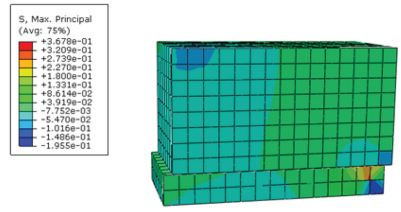

(a) Under the pressure of 0.2

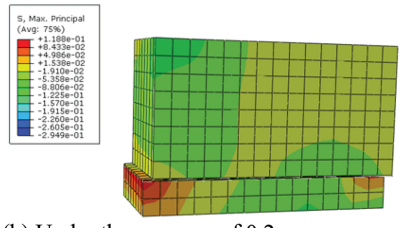

(b) Under the pressure of 0.2

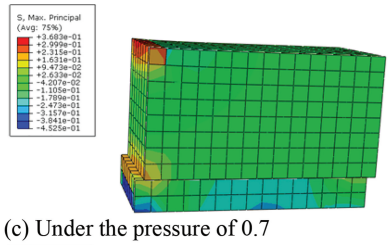

(c) Under the pressure of 0.7

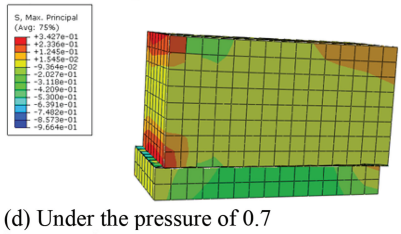

(d) Under the pressure of 0.7

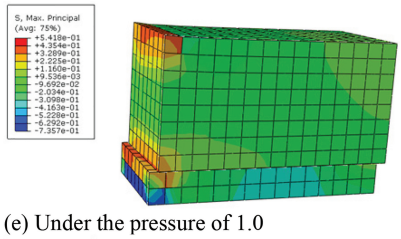

(e) Under the pressure of 1.0

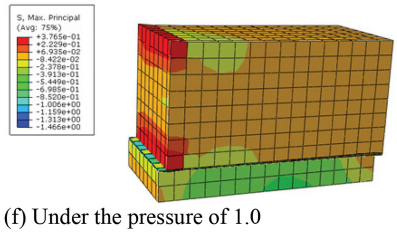

(f) Under the pressure of 1.0

Figure 5. The maximum stress distribution and deformation of connection between different layers under different load cases.

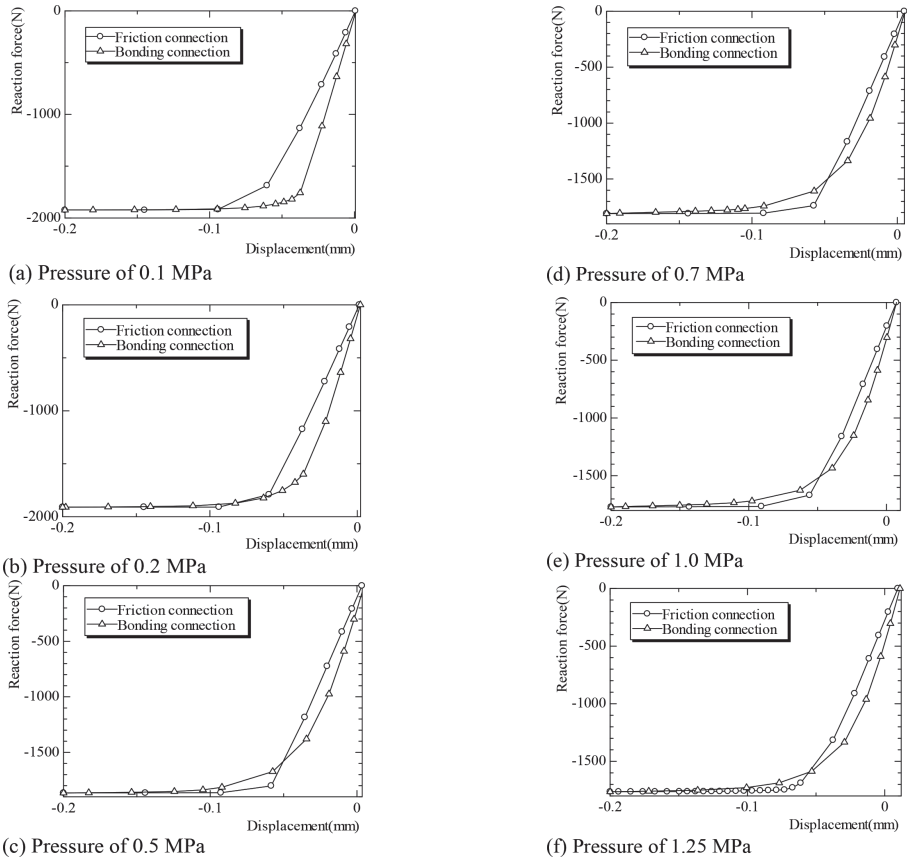

Figure 6. The comparison of the load-displacement curves between different layers under different loading cases.

horizontal displacement that was exerted on the asphalt pavement layer, the longitudinal coordinate represents the reaction force that occurs after the horizontal displacement exerts.

It can be concluded from the figures that the trend of the load-displacement curves of the frictional contact models and the coherent layers ones tends to be the same, and when the exerted displacement approaches 0.2 mm, the reaction forces of the models which adopted different contact types (the frictional contact and the coherent layers contact) tend to be identical and stable. Thus, the proposal that the coherent layers contact is replaced with friction ratio is feasible.

4.3 *The relationship between the pressure and the setting friction ratio when the simplified model is adopted*

Through the FEM analysis, the 12 finite elements models were investigated under 6 kinds of loads (including zero load, standard load, overload).

Table 1. Pressure and friction coefficient.

Pressure (MPa)	Friction coefficient
0.1	0.8615
0.2	0.4269
0.5	0.1668
0.7	0.1155
1.0	0.07905
1.25	0.0626

On the condition of the same load, when the analyzed horizontal load of the solid models equal the ones of the simplified ones, the setting friction ratios which were adopted in the process that the coherent layers is simplified for friction contact are shown in Table 1.

The results from Table 1 can be used to fit the curve which presents the relationship between different wheel loads and friction ratios, and the curve is shown in Figure 7. The related formula

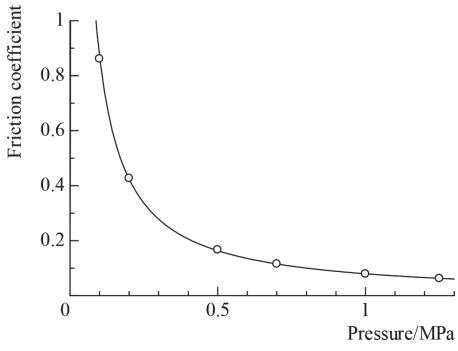

Figure 7. Relationship between pressure and friction coefficient.

is shown below. The accuracy of the formula is 99.994% after the comparison with the data from the results of the analysis.

$$y = \frac{0.08}{x^{1.04}} \quad (1)$$

5 CONCLUSIONS

Through the comparison among the load-displacement curves of the coherent layers contact and the frictional contact under different loads, the trends of the curves are the same, and the values are equal. When the exerted displacement approaches 0.2 mm, the reaction forces of the models which adopted different contact types tend to be identical and stable. Thus, the proposal that the coherent layers contact is replaced with friction ratio is feasible.

Through the analysis of the relationship between different wheel loads and friction ratios, the related formula of normal stress and friction ratio can be fitted, it presents highly precise, and it provides theoretical base for the further FEM model simplification.

ACKNOWLEDGMENT

This study is supported by Ministry of Housing and Urban-Rural Development of China (serial number: 2014-K2-047), the support is gratefully acknowledged.

REFERENCES

Huang, W. 2006. *Theory and Method of Deck Paving Design for Long-span Bridges*. Beijing: China Architecture & Building Press.

Li, X.L. 2008. *Research of Composite Pavement Structure on Orthotropic Steel Deck.* Hunan: Changsha University of Science & Technology.

Li, Y.C. & Zhang, J. 2013. Effect of compressive stress and temperature coupling action on the mechanical properties of the steel bridge deck. *Journal of Wuhan University of Technology* 35(11): 98–102.

Liu, N. 2009. *Experimental and Finite Element Analysis of Concrete Asphalt Deck Overlay*. Dalian: Dalian University of Technology.

Ye, Y. 2007. *Nonlinear Analysis of Asphalt Pavement by Using ABAQUS*. Hengyang: University of South China.

Zhu, X.H. 2013. A laboratory study of interlaminar shear properties on steel bridge deck pavements. *Science Technology and Engineering* 13(27): 8217–8221.

This page intentionally left blank

Civil Engineering and Urban Planning IV – Liu et al. (Eds)
© 2016 Taylor & Francis Group, London, ISBN 978-1-138-02903-3

Comparative study of intra-urban target performance on simulated WorldView-2 and WorldView-3 responses from hyperspectral data

S.C. Azevedo, G.P. Cardim, M.M. Pedrosa, E.H. Alcântara & E.A. Silva
Faculty of Science and Technology, University Estadual Paulista—UNESP, Presidente Prudente, Brazil

ABSTRACT: Urban areas are characterized by high heterogeneity of natural and artificial targets. The hyperspectral data has shown the potential use in urban applications due to discrimination capability of a variety of features. At the same time, the evolution of multispectral sensors is supporting these innovations through improvement of spatial and spectral resolution. This study aims to compare and evaluate the responses simulated for two multispectral satellite WorldView series. Experimental results show that responses simulated for WorldView-3 were consistent with the hyperspectral data. This indicates that the WV-3 simulation results are promising and that improvements incorporated in this sensor, launched last year, will be able to discriminate urban features.

1 INTRODUCTION

The comprehension of population dynamics has been a challenge for urban planning. High heterogeneity of urban environment hampers land cover identification and, consequently, the maintenance of updated urban cartographic databases. Although development in remote sensing technology has provided suitable information about urban areas, there are still many challenges in the discrimination of urban materials.

High spatial resolution was one of the requirements overcome by a recent commercial system. This improvement of spatial detail depicted in an image has introduced significant benefits in identifying land cover objects such as residential structures or urban vegetation (Herold et al. 2003). However, due to heterogeneity of urban materials, high spatial resolution alone is not enough to separate targets.

In general, most multispectral sensors are designed primarily for mapping land surfaces with a few limited bands and bandwidth compared with hyperspectral sensor system capability (Herold & Roberts 2006). However, imaging satellites from DigitalGlobe, such as WorldView-2 (WV-2), have received a lot of attention, since they were the first systems to collect eight multispectral bands, enabling applications in vegetation, coastal, and land-use (Digital Globe 2013).

Innovative perspectives were expected with the launch of WorldView-3 (WV-3) that happened in August 2014, mainly due to 12 multispectral bands additionally included. Furthermore, WV-3 will be the first commercial system to provide images with 31 cm of spatial resolution. It is expected that this advanced combined resolution will be able to reduce spectral mixtures and identify urban land cover types, contributing effectively in urban mapping (Digital Globe 2014).

While the availability of WV-3 images is recent and studies dealing with its applications are still rare in the literature, a way of checking the multispectral capability of these products is through response simulation of bands of interest.

In this respect, this paper aims to compare simulated responses for WV-2 and WV-3 from field hyperspectral data of common urban targets such as concrete, vegetation and cast shadow. Our objective was therefore to verify which multispectral sensor provided spectral responses similar to hyperspectral results, since this data can clearly discriminate urban features. Thus, the simulated responses in multispectral sensors will help to identify the real possibilities provided by the new sensors on board satellites.

This paper is organized as follows: in section 2 we describe and compare the sensors' characteristics; in section 3 the proposed methodology is discussed and experimental results are shown in section 4. Finally, general conclusions are presented in section 5.

2 SENSORS CHARACTERISTICS

WorldView imaging satellites developed by DigitalGlobe have assumed a prominent role among current commercial systems providing high-resolution data. The latest satellite in the WV series was launched in the end of last year and was called WV-The characteristics available had to improve on their closest "brother", WV-2, and promised to live up to expectations of providing better spectral

and spatial discrimination. More information about characteristics of both sensors can be seen in Digital Globe (2013) and Digital Globe (2014).

In relation to multispectral bands, WV-2 presented four new bands (Coastal, Yellow, Red Edge, and Near Infrared 2) in addition to the four traditional bands available until that time. WV-3 has maintained these 8 multispectral bands, as well as the panchromatic band. In addition, 12 new bands called CAVIS were also incorporated. These claim to improve measurement of atmospheric effect compensation (Digital Globe 2014).

Also, Eight Short-Wave Infrared (SWIR) bands were incorporated which may also offer additional capabilities in geological mapping, disaster monitoring, and exploration for mineral and petroleum resources (Kruse & Perry 2013), which fall outside the scope of this investigation.

3 RESEARCH METHODOLOGY

To evaluate the capacity of multispectral bands from WV-2 and WV-3 in discriminating urban targets, the first step was a field survey of the selected targets. Field spectra were acquired from four urban targets commonly found in multispectral images. The targets of interest were concrete, shrubby vegetation, grass vegetation and shadow cast in concrete and its characteristics is shown in Figure 1. The activities and procedures adopted to obtain the spectral responses are described below.

3.1 *Acquisition and data processing*

The field survey was carried out inside the campus of São Paulo State University, located in Presidente Prudente, to the west of São Paulo state, on 12 November 2014. The data was collected between 10 h 30 min and 11 h 30 min (Brasilia time) with clear and cloudless skies.

An ASD FieldSpec® portable spectroradiometer, model HandHeld, which records a continuous spectrum, ranging from 325–1,075 nm, was used. At each sampling target, measurements were first made from a reference panel (white Spectralon panel), in order to calculate the reflectance factors. The calibration of the Spectralon panel was discarded after verification in the laboratory and measurements were carried out sequentially, with no time for different light conditions to occur, preventing target radiance acquisition with the occurrence of larger errors.

The reflectance factor estimated from field spectral measurements can be described as Hemispherical–Conical Reflectance Factor (HCRF). However, we note that, in this case, Hemispherical–Directional Reflectance Factor (HDRF) was obtained due to data collection geometry (Fig. 2) with a very narrow Field-of-View (FOV) of 3° (Schaepman-strub et al. 2006).

Thus, HDRF was estimated by the ratio of the radiance of the target (L_r^{target}) and the Spectralon panel radiance (L_r^{refer}) for each recorded measurement multiplied by a calibration factor of the white reference panel, as shown in equation (1).

$$FRHD = \frac{L_r^{target}(\theta_i, \phi_i, 2\pi, \theta_r, \phi_r, \lambda)}{L_r^{refer}(\theta_i, \phi_i, \lambda)} * k \quad (1)$$

whereas 2π represents the contribution of diffuse illumination, θ and ϕ are the zenith and azimuth angles of incoming (i) and reflected (r) radiance, respectively, and k the calibration factor of the white reference panel (Milton 1987).

At each sampling target, 10 measurements were collected and the mean was used. A moving average filter with three points was applied to remove noises, which ensured that spectral details were not suppressed. Also, the spectrum interval between 400–900 nm was delimited to remove noises in the initial and final regions of the electromagnetic spectrum collected and to ensure reach from multispectral sensors from WorldView-2 and 3.

3.2 *Simulation of bands response*

The simulation of spectral responses from targets was performed using WorldView-2 and 3 bands. The principle used was based on the response function of most instruments, as shown in equation (2) (Schowengerdt, 2007).

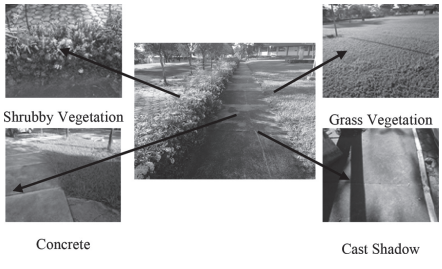

Figure 1. Characteristics from urban targets of study.

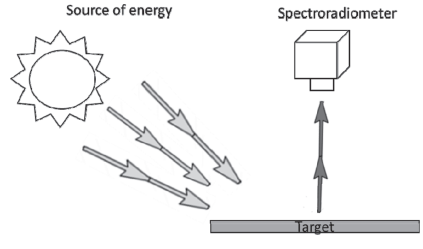

Figure 2. Field data collection geometry.

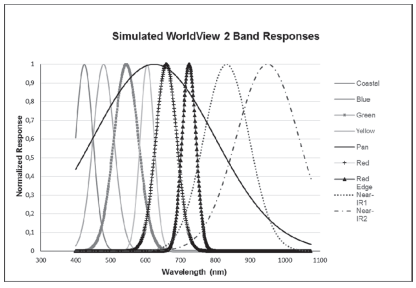

Figure 3. Response function for WV-2 spectral bands.

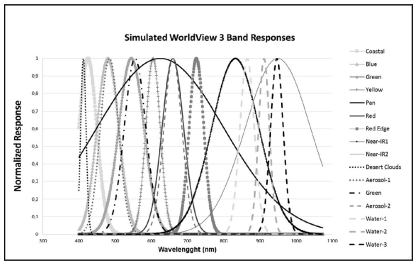

Figure 4. Response function for WV-3 spectral bands.

$$O(z_0) = \int_W i(\alpha)\, r(z_0 - \alpha)\, d\alpha \qquad (2)$$

The approach consisted of determining an output response $O(z_0)$ from the input signal convolved with a response function in the vicinity (W) of z_0 and integrating the result where instrument response is significant. The average value from each bandwidth and its spectral resolution was used for this. Finally, the radiance obtained for each target in each spectral sensor channel was the weighted sum of the radiance spectrum in the delimited interval for spectral bandwidth. Figures 3 and 4 shows the spectral curves obtained for the normalized responses of the sensors on board WV-2 and WV-3, respectively.

4 RESULTS AND DISCUSSION

Field data collected from selected urban targets were processed and its HDRF spectra calculated in accordance to equation (1). The original normalized HDRF curves for the four targets within the spectral resolution of the spectroradiometer are shown in Figure 5.

Although the characteristics of primary absorption by chlorophyll (Jensen 2007) were more severe for grass vegetation, it was observed that shrubby

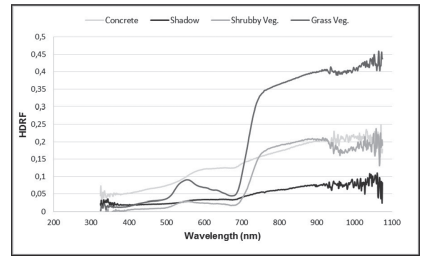

Figure 5. Original HDRF spectra obtained by field hyperspectral data.

vegetation had a lower response than grass vegetation across the whole spectrum.

The depth of absorption by chlorophyll in the grass vegetation resulted in a lower response than the shadow, which theoretically should not have occurred since it does not receive direct illumination. However, due to factors such as the influence of the atmosphere and diffuse radiation of other targets, the shadow response ends up not being null.

A simple moving average filter with three points was used in order to remove remaining noises in the spectrum, especially at the beginning and end of the spectrum. Despite there being no significant improvement in the data, it was observed, that the HDRF curves presented a homogeneous shape without feature loss. This was verified even after spectral delimitation, as shown in Figure 6.

Field spectra were used after smoothing by moving the average filter to simulate nine WV-2 bands and sixteen WV-3 bands, where the multispectral and panchromatic bands were considered. In the case of WV-3, panchromatic and eight multispectral bands has similarity with the WV-2 band set. In addition, WV-3 responses were simulated for a further seven bands among the twelve-band set from the CAVIS system. The results of the simulated responses for WV-2 and WV-3 are presented in Figures 7 and 8, respectively.

Results showed a similar shape of HDFR spectra to the WV-2 and WV-3 simulated responses. However, detailed features on the spectrum provided by the hyperspectral sensor (as shown in Fig. 6) were not retained for multispectral curves. Among the features that must be highlighted, the information content for grass vegetation spectra, such as the inflection point due to combined effects of absorption in red and high reflectance in the infrared region (between 680–800 nm), remained for multispectral response. Discrimination of this vegetation feature could be associated with a particular band to red edge position, provided by both multispectral sensors.

Confusions in data interpretation can occur, since multispectral data is not suitable for distinguishing characteristic reflectance signatures with

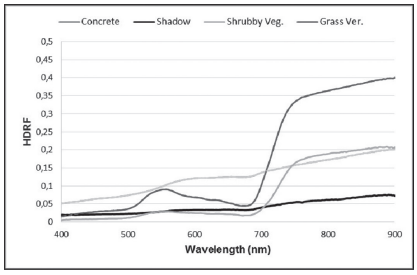

Figure 6. Result of moving average filter and spectral delimitation.

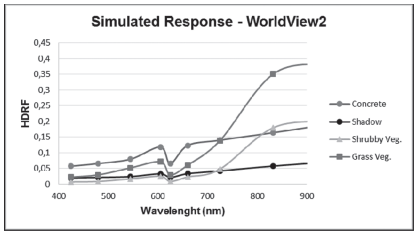

Figure 7. HDRF spectral curves of simulated WV-2 responses.

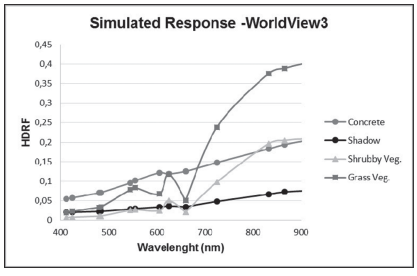

Figure 8. HDRF spectral curves of simulated WV-3 responses.

the same detail as using hyperspectral systems. An example was the pseudo absorption feature created at 625 nm in the concrete spectral curve from the WV-2 simulated response (Fig. 7). The absorption feature, which was not observed in the simulated WV-3 response, was due to the high bandwidth of the panchromatic band from WV-2 and resulted in a coarse separation of characteristic spectral features.

In addition, the experimental results simulated WV-3 spectral curves (Fig. 8) were similar to hyperspectral data, showing significant capabilities of additional new multispectral bands, which should enable identification of urban targets features. Therefore, further analysis with others urban targets and different scene composition should be carried out.

5 CONCLUSION

The comparison of response simulation for WV-2 and WV-3 multispectral sensors was performed using hyperspectral data from urban targets. Based on spectral curve observations, WV-3 bands provided responses close to the hyperspectral curves, showing increased spectral capabilities for discriminating urban targets provided by better spectral resolution than WV-2. It therefore offers the possibility of an advantage on response simulation, to assess whether the sensor will provide data that generates images that can be used in specific applications.

Since the WV-3 results indicate that this sensor will be a significant tool for discriminating urban targets, other studies must now show the possibilities for applications that can be explored. One drawback is that it is a commercial sensor, so image acquisition involves costs. Consequently, the advantage in the simulation of responses lies in identifying discrimination capability for the target of interest before acquiring the image, bringing facilities in the definition of spectral bands of interest.

ACKNOWLEDGEMENT

The authors are thankful to FAPESP for the financial support to perform this work.

REFERENCES

Digital Globe. 2013. WorldView-2 Spacecraft Information and Specifications. *https://www.digitalglobe.com/sites/default/files/DG_WorldWorl2_DS_PROD.pdf*.

Digital Globe. 2014. WorldView-3 Spacecraft Information and Specifications. *https://www.digitalglobe.com/sites/default/files/DG_WorldView3_DS_forWeb_0.pdf*.

Herold, M., Gardner, M. & Roberts, D. 2003. Spectral resolution requirements for mapping urban areas. *IEEE Transactions on Geoscience and Remote Sensing* 41(9): 1907–1919.

Herold, M. & Roberts, D.A. 2006. Multispectral satellites–imaging spectrometry–LIDAR: spatial–spectral tradeoffs in urban mapping. *International Journal of Geoinformatics* 2(1): 1–14.

Jensen, J.R. 2007. *Remote Sensing of the Environment-An Earth Resource Perspective*. 2nd ed. Upper Saddle River, N.J: Prentice Hall.

Kruse, F.A. & Perry, S.L. 2013. Mineral mapping using simulated worldview-3 short-wave-infrared imagery. *Remote Sensing* 5(6): 2688–2703.

Milton, E.J. 1987. Principles of field spectroscopy. *International Journal of Remote Sensing* 8(12): 1807–1827.

Schaepman-Strub, G., Schaepman, M.E., Painter, T.H., Dangel, S. & Martonchik, J.V. 2006. Reflectance quantities in optical remote sensing–definitions and case studies. *Remote Sensing of Environmen*t 103(1): 27–42.

Schowengerdt, R.A. 2007. *Remote Sensing: Models and Methods for Image Processing*. 3rd ed. Amsterdam: Elsevier Academic Press.

Civil Engineering and Urban Planning IV – Liu et al. (Eds)
© 2016 Taylor & Francis Group, London, ISBN 978-1-138-02903-3

Priming effects on people's safety decision in a virtual reality construction simulator

Xue-Qing Lu & S.R. Davis
University of New South Wales, Sydney, Australia

ABSTRACT: A Virtual Reality (VR) simulation is the imitation of a real-world process or system in a virtual environment. It has been considered to assist training in many fields. This study investigated the priming effects on people's safety decision in a virtual construction simulator, in order to improve the design of a virtual reality simulator to be used in training. Preliminary study results show that the addition of priming factors to a VR simulator contributes to people's sense of presence in a virtual environment. When people are primed by the concept of safety, they are more likely to perceive more risks and observe the environment carefully. Limitations of the research are that it applies to a specific problem and results need to be generalized over a larger set of problems. Future research is required to collect data over a large sample size.

1 INTRODUCTION

1.1 *Training with VR simulators*

The construction industry is well known to have high fatality and injury rates (Abudayyeh et al. 2006; Cameron & Duff 2007; Cheng et al. 2012; Choudhry et al. 2009). Thus safety management plays a vital role in construction management. Research has suggested that construction workers' safety performance is highly related to how they are trained (Sawacha et al. 1999). Carrying out safety training is helpful in changing the safety culture among workers, and positively changes workers' safety attitudes (Harvey et al. 2001). Therefore, adequate health and safety training can effectively reduce the injury rate in a construction project.

Methods that have been used in construction safety training involve lecture/discussion, demonstration, conference, simulation, videotapes, programmed instruction, and interactive video (Xie et al. 2006). With the advancement of the computer technology, e-learning (computer-aided learning) has become a widely used method to assist construction training.

1.1.1 *Appling VR simulator to construction safety training*

In the past few decades, a new technology, VR simulation, has been raised as a training tool. A VR environment is a simulated environment generated by a computer (Park et al. 2011). Books are the oldest form of VR. Other forms such as images and videos arose with the improvement of technology.

Simulation is the imitation of a real-world process or system over time (Banks et al. 2000). Thus a VR simulation can be defined as the imitation of a real-world process or system in a virtual environment.

Although there are many existing training methods, more realistic and interesting ways are demanded by trainees (Filigenze et al. 2000). Past studies have evaluated the effectiveness of applying VR in construction education. Sacks et al. (2013) examined the training value of VR in conventional safety training, and they found that training with VR is more effective, and the duration of participants' concentration is longer than traditional safety training.

1.1.2 *Problem justification*

One benefit of VR simulators is that when the trainees make incorrect decisions, they can experience the consequences without being exposed to any real dangerous situation (Filigenzi et al. 2000). However, there is also a problem that trainees may not take the safety consequences as seriously in a virtual world as in the real world. To deal with this problem, enhancement of trainees' sense of presence in the virtual environment is one of the major solutions (Schuemie et al. 2001). Hecht et al. (2006) found that the sense of presence is enhanced in a multimodal virtual environment (including visual, sound, and haptic feedback) than in a purely visual environment. However, as using 3D games for construction safety education is a new technology, the features still need to be enriched (Lin et al. 2011).

1.2 *Priming effect in VR simulators*

1.2.1 *Cognition and attention*

Attention is a process of selection and selective processing (Wood et al. 2006). Research has found that people can observe more objects in a virtual

environment when they have been primed by related information, and their memory about the objects in the virtual environment lasts longer after priming (Dinh et al. 1999). This finding supports the conclusion by Wood et al. (2006) that attention is a top-down, cognitively driven process. Research also shows that strong stimuli can capture people's visual attention, and people can observe more objects in a high fidelity virtual environment (Nunez & Blake 2003). Nunez (2004) proposed a constructionist cognitive model that describes the construction and reconstruction of cognitive processes considering the information flow between working memory and long term memory. Thus the addition of different stimuli (related or unrelated to people's expectation of the virtual environment) result in paying attention to different things.

1.2.2 *Priming effect on cognition*

Priming is the implicit memory effect that previous stimuli have on the response to a subsequent stimulus (Gulan & Valerjev 2010). It can occur in many circumstances. The priming effects being studied in this research are conceptual priming and repetition priming.

Conceptual priming occurs when an item with a similar form or meaning is primed (Nunez & Blake 2003). People tend to determine their behaviour by looking what others do when they are placed in a situation. It happens either when people feel another person has more expertise in this situation, or when they are seeking social acceptance (Pendry & Carrick 2001).

Repetition priming occurs when a stimulus or a task is similar to what people have experienced previously (Schacter & Addis 2007). When a similar situation is experienced, people can respond faster and make more accurate responses (Allenmark et al. 2015). When a subject repeats a task in a second virtual construction simulator, the previous experience in the first virtual construction simulator is the repetition priming factor.

Previous research also suggests that priming is a mediator variable for presence (Nunez & Blake 2003). This means that priming will increase the effects of other variables on presence, compared to their effect without the priming present. Thus if the designers make good use of stimuli in a virtual environment, priming can reinforce the effects of these stimuli on people's sense of presence.

1.3 *Hypothesis*

Based on the literature, the hypotheses of this study are:

- People can observe more risk situations in a virtual environment with obvious stimuli.
- Priming of safe choices helps people make safe decisions in a VR simulator.
- The priming effect is persistent to a different environment.

2 METHODS

2.1 *Test environment*

In this study two 3D VR simulations of construction sites (VE1 and VE2) were created. Participants were given the task of moving 60 virtual bricks around the construction site using a virtual wheelbarrow in each simulator. Each virtual environment contained two routes. A safe route that was further and longer and an unsafe route that was closer and shorter were given for participants to choose. (Fig. 1).

The interfaces for the participants to manipulate the VR simulators were mouse and keyboard. Participants can use function keys on the keyboard to move the virtual, and use the mouse to control where they look in the virtual environment.

Four priming factors were added to the virtual environments, which include three visual factors and one audio factor:

- Virtual workers pushed wheelbarrows via the safe route as a hint that people should use that route.
- Broken virtual temporary barriers were placed so that they looked as if they were intended to block the unsafe route, but had been damaged. This provides a hint that people should not use the unsafe route.
- Warning signs were placed in the environment to warn people of the relevant danger.
- A warning sound when the wheelbarrow was pushed along the unsafe route. The warning sound was 'Stop! Stop!' shouted by virtual people.

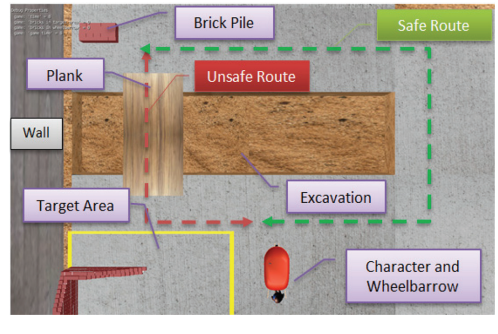

Figure 1. A plan view of VE1.

Table 1. Subject grouping.

Priming No priming	VE1 (P) VE2	VE1 VE2	VE2 (P) VE1	VE2 VE1
Sound	A1	A2	A3	A4
No sound	B1	B2	B3	B4

2.2 *Subjects*

University students studying civil engineering were invited to participate in the research. Each student will manipulate two virtual construction simulators. Table 1 shows the grouping of participants.

Participants were divided into eight groups: participants in Groups A1, A2, A3 and A4 manipulated the virtual environments with sound, and participants in Groups B1, B2, B3 and B4 manipulated the virtual environments without sound; participants in Group A1, B1, A2, and B2 manipulated VE1 first, and participants in Group A3, B3, A4 and B4 manipulated VE2 first. For the participants in Group A1, B1, A3, and B3, their first virtual environment contained all four priming factors.

2.3 *Test procedure*

Participants watched a 3 minute induction of the interface of the 3D virtual environment before they started using them. They were also given a 1 minute trial to familiarize themselves with the VR simulator before their real tasks began. After using the environments, the participants were asked to fill in a questionnaire about their safety decisions.

During the tests, participants were briefed that the aim of the experiments was testing the VR wheelbarrow simulator. The reason to test the VR wheelbarrow simulator was that wheelbarrow was considered difficult to maneuver. After they filled the questionnaire, they were debriefed that the real aim was testing their safety decisions in virtual construction environments. The reason of briefing them was to make sure that the participants would not guess the purpose of the research so that the data would not be compromised. The reason of debriefing them was to make sure that the participants were fully informed about the experiments.

Data were collected through participants' feedback of the questionnaire, and their rate of success or 'injuries' in the virtual tests. Participant behaviors were recorded by screen capture software.

3 PRELIMINARY RESULTS

43 civil engineering students participated in a preliminary study on conceptual priming. The conceptual priming factor was virtual workers walking on the safe route in the virtual construction environment (Fig. 2). The result showed a big difference between the students who were primed and those who were not.

3.1 *Environment observation*

Table 2 is the statistical results of the preliminary study. The proportion of the students who did not notice the further route was analyzed.

There was a significant difference between the two conditions, that when the participants were not primed of choosing the safety route, they were more likely to ignore the further route but focus on the closer route.

As the virtual workers were bright colored characters, it also proved that obvious stimuli can attract people's attention.

However, a previous study found that people with more action game experience can obtain more objects in a virtual environment (Vallett et al. 2013). Thus the influences of action game experience and construction work experience on people's attention in the virtual environment were also analyzed.

Table 3 shows the difference between the participants who have action game experience and those who don't have action game experience.

Table 4 shows the difference between the participants who have more than 3 months' construction work experience and those who have less than 3 months' construction work experience.

From the results given by Tables 3 and 4, in the following study, participants' action game

Figure 2. Priming factor–virtual worker.

Table 2. Preliminary results–priming and cognition.

Priming No priming	Sample Size	Proportion (%)	P-value
Primed	9	0	0.049
Not primed	24	25	

Table 3. Preliminary results–action game experience and cognition.

Game experience/ No game experience	Sample size	Proportion (%)	P-value
Game experience	8	0	0.031
No game experience	18	33.3	

Table 4. Preliminary results–construction work experience and cognition.

Work experience/ No work experience	Sample size	Proportion (%)	P-value
Work experience	13	15.4	0.066
No work experience	9	44.4	

experience and construction work experience should be asked before they do the experiments. Each group will be assigned evenly with the number of participants who have similar action game experience and construction work experience.

3.2 *Risk perception*

In the preliminary study, 19 out of the 43 participants also did a physical test with the same task in the laboratory either before (9 participants) or after (10 participants) their virtual tests (Fig. 3).

Participants were asked to choose the risks they recognized in the virtual construction site from 7 risks given in the questionnaire. Tables 5 and 6 show the results of 8 participants who did the physical tests first, 5 participants who had priming factors in their VR simulators, and 8 participants who did not have priming factors in their VR simulators but saw both routes. All these participants had background sound in their test environments.

In terms of the number of risks participants perceived in the VR simulator, the participants who were primed in the virtual environments perceived more risks than those who were not primed.

According to Table 6, there is also a difference between the feedbacks from the participants who did physical tests and those who did virtual tests. This difference suggests that the VR simulator still needs to be improved. However, the results are not significant, so the sample size needs to be enlarged in order to get more accurate results.

3.3 *Sense of presence*

Sense of presence is the sense of realism when people are manipulating a VR simulator (Slater & Wilbur 1997). In the questionnaire, participants were asked to answer two questions related to their sense of presence in the tests: a) How similar did the virtual world feel to the real world? b) How much do you think the control of wheelbarrow in the virtual world is similar to that of real world? They were asked to answer this question by rating their feelings on a 5-point scale. Table 7 shows the feedback of these two questions.

It could be seen from Table 7 that the addition of priming factors to the VR simulator increases the participants' sense of presence.

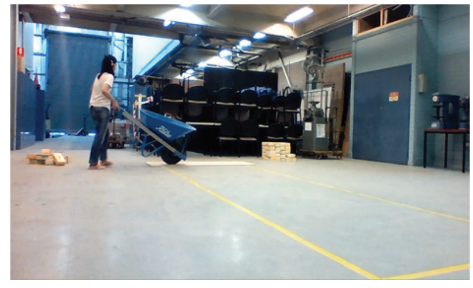

Figure 3. Physical test.

Table 5. Preliminary results–priming and risk perception.

Test environment	Sample size	Mean	P-value
Virtual without priming	8	3.0	0.286
Virtual with priming	5	3.6	

Table 6. Preliminary results–validity of the virtual reality simulator.

Test environment	Sample size	Mean	P-value
Physical	8	4.4	0.299
Virtual with priming	5	3.6	

Table 7. Preliminary results–priming and sense of presence.

Question	Priming/ no priming	Sample size	Mean	P-value
a	Priming	9	3.78	0.056
	No priming	12	3.17	
b	Priming	9	3.44	0.200
	No priming	12	3.08	

4 CONCLUSIONS

The results of this study highlight the priming effect on people's safety decision in a VR simulator. The addition of priming factors to a virtual reality simulator contributes to people's sense of presence in a virtual environment. When people are primed by the concept of safety, there is an increase chance that they will observe the environment more carefully.

As this study was designed as a pilot investigation of the effects of priming on people's safety decision, future study will refine the study methods and enlarge the sample size in order to collect more adequate and accurate data.

REFERENCES

Abudayyeh, O., Fredericks, T.K., Butt, S.E. & Shaar, A. 2006. An investigation of management's commitment to construction safety. *International Journal of Project Management* 24(2): 167–174.

Allenmark, F., Hsu, Y.F., Roussel, C. & Waszak, F. 2015. Repetition priming results in sensitivity attenuation. *Brain Research* (2015).

Banks, J., Carson, J. & Nelson, B. 2000. *DM Nicol, Discrete-Event System Simulation.* NJ, USA: Prentice hall Englewood Cliffs.

Cameron, I. & Duff, R. 2007. A critical review of safety initiatives using goal setting and feedback. *Construction Management and Economics* 25(5): 495–508.

Cheng, E.W., Ryan, N. & Kelly, S. 2012. Exploring the perceived influence of safety management practices on project performance in the construction industry. *Safety Science* 50(2): 363–369.

Choudhry, R.M., Fang, D. & Lingard, H. 2009. Measuring safety climate of a construction company. *Journal of Construction Engineering and Management* 135(9): 890–899.

Dinh, H.Q., Walker, N., Hodges, L.F., Song, C. & Kobayashi, A. 1999. Evaluating the Importance of Multisensory Input on Memory and the Sense of Presence in Virtual Environments. *Proceedings of IEEE Virtual Reality, March 13–17, 1999.* Houston, Texas: The Institute of Electrical and Electronics Engineers.

Filigenzi, M.T., Orr, T.J. & Ruff, T.M. 2000. Virtual reality for mine safety training. *Applied Occupational and Environmental Hygiene* 15(6): 465–469.

Gulan, T. & Valerjev, P. 2010. Semantic and related types of priming as a context in word recognition. *Review of Psychology* 17(1): 53–58.

Harvey, J., Bolam, H., Gregory, D. & Erdos, G. 2001. The effectiveness of training to change safety culture and attitudes within a highly regulated environment. *Personnel Review* 30(6): 615–636.

Hecht, D., Reiner, M. & Halevy, G. 2006. Multimodal virtual environments: response times, attention, and presence. *Presence: Teleoperators and Virtual Environments* 15(5): 515–523.

Lin, K.Y., Son, J.W. & Rojas, E.M. 2011. A pilot study of a 3D game environment for construction safety education. *Journal of Information Technology in Construction* 16: 69–83.

Nunez, D. 2004. A Constructionist Cognitive Model of Virtual Presence. *7th International Workshop on Presence (PRESENCE 2004), Valencia, Spain, October 13–15, 2004*.

Nunez, D. & Blake, E. 2003. Conceptual Priming as a Determinant of Presence in Virtual Environments. *Proceedings of the 2nd International Conference on Computer Graphics, Virtual Reality, Visualisation and Interaction in Africa: ACM, ACM New York, NY, USA, February 3–5, 2003*. Cape Town, South Africa: Afrigraph.

Park, A.J., Hwang, E., Spicer, V., Cheng, C., Brantingham, P.L. & Sixsmith, A. 2011. Testing Elderly People's Fear of Crime Using a Virtual Environment. *Intelligence and Security Informatics Conference (EISIC), Athens, Greece, 2011.* European: IEEE.

Pendry, L. & Carrick, R. 2001. Doing what the mob do: Priming effects on conformity. *European Journal of Social Psychology* 31(1): 83–92.

Sacks, R., Perlman, A. & Barak, R. 2013. Construction safety training using immersive virtual reality. *Construction Management and Economics* 31(9): 1005–1017.

Sawacha, E., Naoum, S. & Fong, D. 1999. Factors affecting safety performance on construction sites. *International Journal of Project Management* 17(5): 309–315.

Schacter, D.L. & Addis, D.R. 2007. The cognitive neuroscience of constructive memory: remembering the past and imagining the future. *Philosophical Transactions of the Royal Society B: Biological Sciences* 362(1481): 773–786.

Schuemie, M.J., Van Der Straaten, P., Krijn, M. & Van Der Mast, C.A. 2001. Research on presence in virtual reality: A survey. *CyberPsychology & Behavior* 4(2): 183–201.

Slater, M. & Wilbur, S. 1997. A Framework for Immersive Virtual Environments (FIVE): Speculations on the role of presence in virtual environments. *Presence: Teleoperators and Virtual Environments* 6(6): 603–616.

Vallett, D.B., Lamb, R.L. & Annetta, L.A. 2013. The gorilla in the room: the impacts of video-game play on visual attention. *Computers in Human Behavior* 29(6): 2183–2187.

Wood, S., Cox, R. & Cheng, P. 2006. Attention design: Eight issues to consider. *Computers in Human Behavior* 22(4): 588–602.

Xie, H., Tudoreanu, E. & Shi, W. 2006. Development of a Virtual Reality Safety-training System for Construction Workers. *Digital Library of Construction Informatics and Information Technology in Civil Engineering and Construction.* http://itc.scix.net/data/works/att/ff9b.content.00092.pdf.

This page intentionally left blank

Civil Engineering and Urban Planning IV – Liu et al. (Eds)
© 2016 Taylor & Francis Group, London, ISBN 978-1-138-02903-3

Seismic fragility analysis of complex landscape covered bridge

Shuai Song & Yong-Jiu Qian
School of Civil Engineering, Southwest Jiao Tong University, Chengdu, Sichuan, China

ABSTRACT: The finite element models of landscape covered bridges with and without upper building structures and models with node qualities simulating upper building structures were established accounting for uncertainties of ground motions and structures. Seismic fragility curves of the three models were developed using nonlinear time history analysis method and the impacts of upper building structures on bridge seismic performance were assessed. The results show that: in the earthquake, the upper building structures increased the seismic demands of pier and bearing as well as the seismic vulnerability of landscape covered bridges, especially under severe and completely damaged states. Therefore, the effects of upper building structures must be accurately assessed in the seismic design or vulnerability assessment of landscape covered bridge structures.

1 INTRODUCTION

Landscape covered bridges are structures with some upper buildings built on a common bridge for beautification and decoration. With the increasing demands of people's aesthetic requirements, landscape bridges with new and unique structures are emerging continually. However, the mechanical properties of landscape-covered bridge structures are more complex than common bridges, especially during earthquakes. So further studies are required to assess the seismic performances of landscape bridges. Due to the uncertainties of earthquake ground motions and structural parameters, seismic fragility analysis is increasingly being used in probabilistic seismic risk assessment of structures (Billah & Alam 2015, Modica & Stafford 2014). The current fragility curves of bridge can be developed using expert opinions, empirical data from past earthquakes, and analytical methods (Shinozuka et al. 2003, Yang et al. 2009). Due to the lack of sufficient structural seismic damage data and subjectivity of expert judgments, the first two methods have certain limitations in the practical application. Analytical seismic fragility curves are established based on the probabilistic seismic demand and capacity of the bridge using static or dynamic nonlinear analysis (Hwang et al. 2001, Nielson 2005). Therefore, analytical seismic fragility curves have few constraints and are widely used to study the seismic vulnerability of the bridge. However, previous research on the seismic vulnerability of bridges mainly focused on simply supported or cable-stayed bridges (Feng & Yuan 2010, Hwang & Liu 2004, Li et al. 2012), and very few studies on the landscape covered bridges had been performed. Therefore, the seismic vulnerability of three-span continuous rigid frame landscape covered bridges with four-story reinforced concrete frame structures was studied in this paper. The uncertainties of ground motions and structures were treated in a probabilistic way using the Latin hypercube sampling method. Seismic fragility curves of components were developed under various damage states taking spectral acceleration of ground motion and cumulative failure probability as parameters. Then, the bridge system's seismic fragility curve was obtained using the first-order boundary method, which provided a theoretical basis for seismic design and assessment of such structures.

2 BRIDGE CHARACTERISTICS AND MODELING

2.1 *Bridge description*

The four-layer structures are arranged on the bridge with each layer height of 4.5 m. Building structures adopt reinforced concrete frame structure form with column section size of 0.6 m × 0.6 m and beam section size of 0.5 m × 0.3 m. The lower part is a continuous prestressed concrete rigid frame bridge divided into three spans of 31.5 m, 36 m, and 31.5 m. Piers of height 11 m are constructed from three rectangular cross sections, whose dimensions are 4 m × 1.4 m, with spacing of 10 m. There are 14 expansion basin rubber bearings placed on each abutment. The structure was shown in Figure 1.

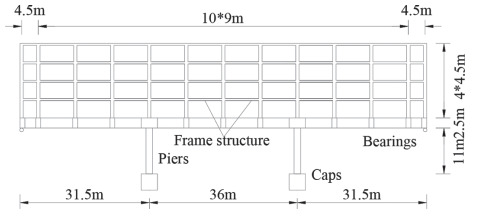

Figure 1. Caption layout of the landscape covered bridge.

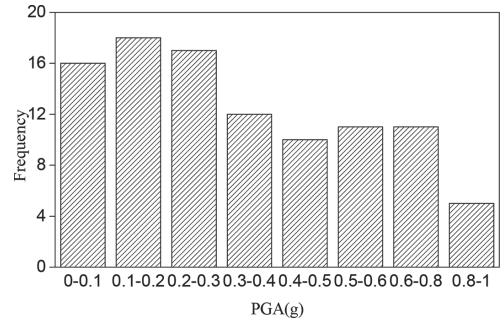

Figure 2. PGA distribution of the ground motion records.

2.2 *Modeling details*

Three models were developed using the finite element analysis package OpenSees to evaluate the impacts of upper building structures on the bridge seismic vulnerability. Model I: common continuous rigid frame bridge model without upper structures; Model II: the upper structures were equivalent to the node qualities and applied to the bridge structure; Model III: the whole model, including the upper structures was developed.

For the upper building structures, the columns at the ground floor of frame structures and beams were modeled using nonlinear beam-column elements with fiber-based cross sections; the remaining columns were modeled using elastic beam-column elements. For the bridge, the beams were modeled as a lumped centerline using elastic beam-column elements. The piers were modeled using nonlinear beam-column elements with fiber-based cross sections. The expansion basin rubber bearings were modeled using zero-length elements with a bilinear material model behavior in both horizontal directions. Nonlinear springs were used to model the behavior of the abutments in both longitudinal and transverse directions. The foundations were modeled using lumped translational and rotational springs at the base of the column.

3 GROUND MOTION RECORDS

Due to the characteristics of ground motion amplitude, spectrum and duration have significant impacts on the seismic response of structure, it is essential to choose the appropriate ground motion records for the nonlinear time history analysis. A set of 100 ground motion records were selected from the Pacific Earthquake Engineering Center strong database using the interval grouping method (Shome 1999) due to few realistic records were available in this area. The selected seismic records satisfies the following conditions: (1) the magnitude were larger than 6.0; (2) the epicentral distances were less than 100 km; (3) the high-pass filter corner frequency of ground motion horizontal components were less than 0.2 Hz, while the low-pass filter corner frequency were greater than 18 Hz. Furthermore, the selected ground motion records should meet the requirements of statistical analysis, which taking into account the universality of ground motion under regression analysis. The peak ground accelerations of the selected profile were shown in Figure 2.

4 SEISMIC FRAGILITY ANALYSIS

The seismic vulnerability of structures can be defined by the probability of structural seismic demand S_d exceeds the structural ductility capacity S_c:

$$P_f = P_r\left(S_c \Big/ S_d \le 1\right) \tag{1}$$

Due to both the seismic demand and ductility capacity can be represented by lognormal probability distribution (Shinozuka et al. 2000), the structure failure probability P_f can be expressed as the following normal distribution function:

$$P_f = \Phi\left[\frac{-Ln\left(\tilde{S}_c / \tilde{S}_d\right)}{\sqrt{\beta_c^2 + \beta_d^2}}\right] \tag{2}$$

where Φ [•] is a standard normal distribution function; $\tilde{S}_c$ and $\tilde{S}_d$ are the mean value of ductility capacity and seismic demand respectively; β_c and β_d are the logarithmic standard deviation of ductility capacity and seismic demand respectively.

To facilitate the application, Nielson used coefficient of variation COV to describe the uncertainty in ductility capacity (Nielson 2005). For minor and moderate damage states COV = 0.25,

while COV = 0.5 in severe and completely damage states. The logarithmic standard deviation could be derived by the coefficient of variation using the following equation:

$$\beta_c = \sqrt{\ln(1+\mathrm{COV}^2)} \tag{3}$$

Studies have shown that there is an exponential relationship between the ground motion intensity index IM and the mean value of seismic demand (Cornell et al. 2002):

$$\tilde{S}_d = a\mathrm{IM}^b \tag{4}$$

The logarithmic standard deviation of seismic demand β_d can be obtained by statistical analysis of structural seismic demand samples:

$$\beta_d \cong \sqrt{\frac{\sum_i^N (\ln S_d - \ln(a\mathrm{IM}^b))^2}{N-2}} \tag{5}$$

4.1 *Seismic demand parameters*

For the pier, plastic hinge may appear at the top or bottom of the pier during earthquakes. Therefore, the displacement ratio at the top of pier can represent structural seismic demand efficiently. Relative displacement ductility ratio at the top of pier can be expressed by the following equation:

$$\mu_d = \frac{\Delta}{\Delta_{\mathrm{cy1}}} \tag{6}$$

where Δ represents maximum relative displacement at the top of the pier; Δ_{cy1} represents relative displacement at the top of the pier when the steel first yield.

The horizontal movement of expansion basin rubber bearings is achieved through the relative slide between the top plate and sliding plate. In severe earthquake, steel liner plate shows sign of wear and tear and rubber seal rings are also in danger of being extruded. If the displacements of expansion basin rubber bearings are too large, the bearings will be tilted or even fall off or even worse unseating of superstructures may occur. Therefore, the seat relative sliding displacement can define the seismic demand and damage states of bearings accurately.

4.2 *Seismic damage states*

To evaluate the damage states quantitatively, the bridge failure process was divided into slight damage, moderate damage, extensive damage, and complete damage states during earthquakes (HAZUS-MH 2.1 2012). For the pier, the four damage states correspond to the minor spalling of concrete cover, cracking of concrete core, great residual displacement at the top of pier, and collapsing of pier respectively. In order to describe the four damage states of pier, the moment–curvature analysis of pier cross-section was performed using XTRACT section analysis software. Then, the relative displacements at the top of pier could be obtained using pushover analysis method under each damage state. The mean values of ductility capacity were derived using Equation (6) and the results were shown in Table 1.

When the actual displacement of bearing was less than the design allowable displacement, the bearing was in good working condition. So the relative sliding displacements of 100 mm and 50 mm were defined as the slight damage limit values for the longitudinal and transverse direction respectively. However, if the sliding displacement of basin rubber bearings was greater than 1/2 diameter of the polysaccharides slide, the bearings had the risk of falling. Therefore, the 1/2 diameter of polysaccharides slide was defined as completely damage limit value. Furthermore, when the displacement of bearing exceeded a certain value, the steel liner plate was worn out and rubber seal rings were extruded. So, the values of 150 mm and 200 mm were defined as moderate damage and serious damage limit values in longitudinal direction respectively, while the values of 100 mm and 150 mm were defined as moderate damage and

Table 1. Median values of component ductility capacity at different damage states.

Median values	Slight	Moderate	Extensive	Complete
Pier of Model I longitudinal	1	1.0452	3.1234	6.1234
Pier of Model I transverse	1	1.0944	2.8035	5.8035
Pier of Model II & III longitudinal	1	1.0315	1.6983	4.6983
Pier of Model II & III transverse	1	1.0697	1.7173	4.7173
Bearing—longitudinal (mm)	100	150	200	300
Bearing—transverse (mm)	50	100	150	300

serious damage limit values in transverse direction. The results were also shown in Table 1.

4.3 *Probabilistic seismic demand analysis*

The uncertainties may arise from the earthquake ground motions and bridge structures in the calculation of structural seismic demand. The seismic uncertainty can be considered in the selection of ground motion records. The uncertainties of bridge structure mainly arise from concrete and steel material properties, size of component in the structure, and the bearing characteristics. Specifically, yield strength of steel, weight of the upper structure, and the compressive strength of concrete are the most significant factors (Pan et al. 2010). Following the previous works (Padgett & DesRoches 2007, Zheng et al. 2013), the compressive strength of C40 concrete is normally distributed with a mean of 33.4 MPa and a COV of 0.12; the yield strength of HRB335 steel follows logarithmic normal distribution with a mean of 380.1 MPa and a COV of 0.06; the concrete density is considered as a normal random variable with a mean of 26.0 kN/m^3 and a COV of 0.1. According to the probability distribution, the 5%–95% intervals of the cumulative probability distribution were divided into ten parts equiprobably. Taking the average of each section as a representative value, ten bridge samples were established using Latin-hypercube sampling method (Olsson et al. 2003). The results were shown in Table 2.

The 100 Bridges–Earthquake samples were obtained when the ten bridge models were paired with the 100 ground motion records randomly. Based on the results of nonlinear dynamic time history analysis performed for the three models respectively, the functional relationships between structural seismic demand and ground motion intensity indices were achieved by using least squares regression analysis. The results were shown in Table 3.

Table 2. Parameters of the bridge samples.

	C40		Weight	HRB335
Samples	f_c (MPa)	*Ec* (MPa)	W (kN/m^3)	f_y (MPa)
1	29.8	25,840.2	28.4	350.6
2	34.8	27,923.1	25.1	360.5
3	38.9	29,526.3	24.4	367.1
4	35.8	28,325.6	25.7	372.7
5	27.9	25,007.4	26.9	377.7
6	32	26,774.8	23.6	382.7
7	37	26,355.5	29.5	387.7
8	31	30,362.9	22.5	393.3
9	32.9	27,151.7	26.3	399.9
10	33.9	27,566.8	27.6	409.8

Table 3. Probabilistic seismic demands of the components.

Models	Demand	Regression equation	R^2	β_d
Model I	ln (μ_z)	1.482 + 0.915 ln (Sa)	0.833	0.381
	ln (μ_h)	1.054 + 0.888 ln (Sa)	0.840	0.349
	ln (Δ_z)	4.660 + 0.917 ln (Sa)	0.838	0.375
	ln (Δ_h)	3.626 + 0.820 ln (Sa)	0.871	0.284
Model II	ln (μ_z)	2.258 + 0.950 ln (Sa)	0.825	0.428
	ln (μ_h)	1.869 + 0.931 ln (Sa)	0.819	0.398
	ln (Δ_z)	5.610 + 0.948 ln (Sa)	0.826	0.426
	ln (Δ_h)	4.522 + 0.789 ln (Sa)	0.864	0.284
Model III	ln (μ_z)	2.044 + 0.870 ln (Sa)	0.817	0.430
	ln (μ_h)	1.768 + 0.782 ln (Sa)	0.747	0.465
	ln (Δ_z)	5.399 + 0.870 ln (Sa)	0.813	0.435
	ln (Δ_h)	4.362 + 0.718 ln (Sa)	0.729	0.447

4.4 *Fragility curves of components*

Fragility curves for the pier and bearing were easily calculated using the seismic demand model and ductility capacity at different limit states in the framework of Equation (2). For clarity, only the fragility curves at minor damage state was given in Figure 3.

Figure 3a shows that in longitudinal direction, slight damage probabilities of pier and bearing in model II are larger than those of Model III and Model I. Figure 3b shows that in transverse direction, the pier in model II and model III have a similar slight damage probability; but the slight damage probability of bearing in model I is the largest. Therefore, the upper building structures increased the slight damage vulnerability of pier and bearing, but the impacts of the upper building structures on pier and bearing would be overestimate under slight damage state if the upper building structures were modeled using equivalent node qualities. In order to compare the components vulnerability of three models under various damage states in detail, the spectral acceleration median values of the bridge components under each damage states were listed in Table 4.

Comparisons among the three models show that upper building structures have a great impact on the vulnerability of pier and bearing during earthquakes. The spectral acceleration median values of pier and bearing under each damage states decrease significantly due to the upper building structures. If the impacts of upper building structure are ignored, the seismic capacity of the structure will be overestimate seriously. Comparisons between model II and model III show that the seismic vulnerability of the bridge components are larger if the upper building structures are modeled using equivalent node qualities. The reason for this observed phenomenon is that the upper building

structures can absorb energy by undergoing plastic deformation during earthquakes.

4.5 *Fragility curves of bridge system*

Bridge system is mainly composed of piers, beams, and bearings. Establishing the seismic vulnerability of bridge system based on multiple components need to identify the joint probability distribution of multi components. Due to the interaction between the seismic demands of bridge components, the joint distribution function of multiple components is very difficult to determine. In this study, the upper and lower bounds of bridge system vulnerability were computed using the first-order boundary method to approximate the bridge system vulnerability.

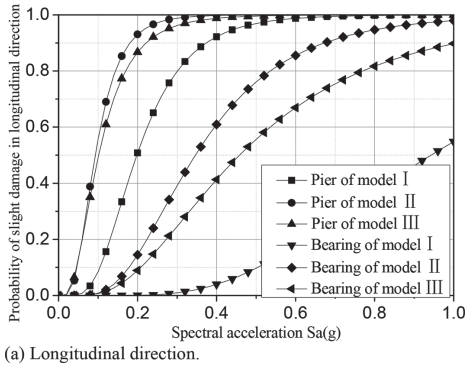

(a) Longitudinal direction.

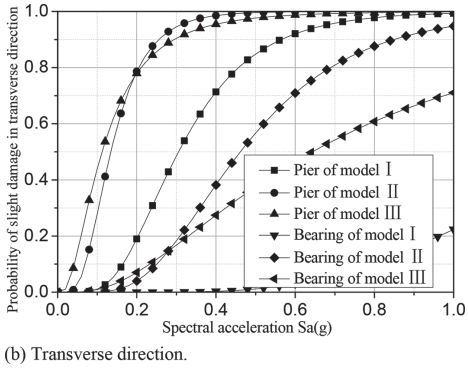

(b) Transverse direction.

Figure 3. Seismic fragility curves of components for slight damage state.

According to the first-order boundary method, bridge system failure probability can be expressed as (Choi et al. 2004):

$$\max_{i=1}^{m}\left[P_i\right] \le P_{sys} \le 1-\prod_{i=1}^{m}\left[1-P_i\right] \tag{7}$$

where P_{sys} is the bridge system failure probability; P_i is the failure probability of component i and m is the number of components.

Based on the vulnerability of each component, the lower and upper bounds of bridge system vulnerability can be determined by Equation (7). Due to space limitations, only the lower and upper bound of bridge system vulnerability under slight damage state were shown in Figure 4.

Figure 4 shows that without the upper building structures, the probabilistic upper and lower bounds of bridge system failure in transverse direction are 33% and 19% respectively under slight damage state when Sa = 0.2 g; after the upper building structures are added to the structures, the upper and lower bounds increased to 96% and 78%. Comparisons between Figures 4a and b show that the vulnerability of bridge system in transverse direction is more susceptible to the upper building structures than that in longitudinal direction.

Table 4. Medians of spectral acceleration for different damage states.

		Slight	Moderate	Extensive	Complete
	Components	Median (g)	Median (g)	Median (g)	Median (g)
Model I	Pier-long	0.2	0.21	0.69	1.44
	Pier-trans	0.31	0.34	0.97	>2
	Bearing-long	0.94	1.43	2	>2
	Bearing-trans	1.42	>2	>2	>2
Model II	Pier-long	0.09	0.1	0.16	0.47
	Pier-trans	0.13	0.15	0.24	0.71
	Bearing-long	0.35	0.53	0.72	1.1
	Bearing-trans	0.46	1.11	1.86	>2
Model III	Pier-long	0.1	0.11	0.18	0.57
	Pier-trans	0.11	0.12	0.21	0.76
	Bearing-long	0.4	0.64	0.89	1.42
	Bearing-trans	0.53	1.4	>2	>2

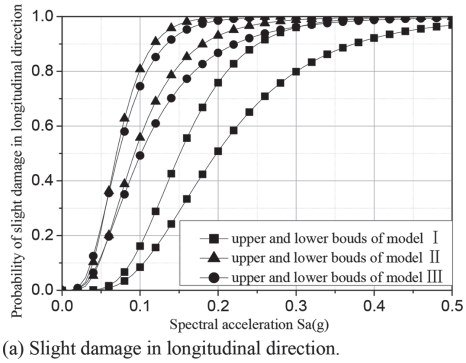

(a) Slight damage in longitudinal direction.

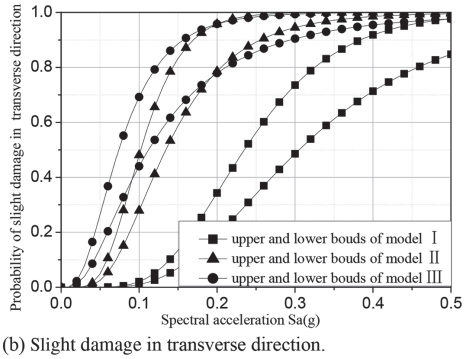

(b) Slight damage in transverse direction.

Figure 4. Bounds of system fragility curves for slight damage state.

Nelson et al. (2007) developed the bridge system vulnerability using Monte–Carlo method and found it was close to the upper bound of the first order method. So, using the upper bound of the first order method to assess the vulnerability of the system is safer. Therefore, the bridge system vulnerabilities of the three models were compared using the upper bound of the first order method in this study. For simplicity, the median values of the three models under various damage states were shown in Figure 5.

Figure 5 shows that spectral acceleration median values of model I are all larger than those of model II and model III in the four damage states. As the degree of damage increasing, the gaps between spectral acceleration median values of the three models become larger. In longitudinal direction, the spectral acceleration median values of the three models under completely damage state are 0.95 g, 0.31 g, and 0.41 g respectively. For transverse direction, the spectral acceleration median values of the three models under completely damage state are 1.54 g, 0.49 g, and 0.56 g respectively. So the upper building structures increase the system vulnerability in longitudinal and transverse directions

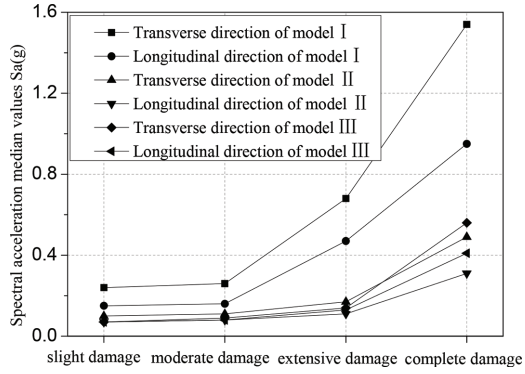

Figure 5. Median values for the fragility curves of the bridge system.

significantly, and the system vulnerability is larger if the upper buildings are modeled using equivalent node qualities.

5 CONCLUSION

The fragility curves of three models are developed using analytical method to evaluate the impact of the upper buildings. Comparisons between the damage probabilities and spectral acceleration median values of pier, bearing and bridge system under four damage states in the three models show that:

The upper building structures increase the vulnerability of pier and bearing under the four damage states, especially in severe and completely damage states. Subsequently, the upper building structures increase the vulnerability of bridge system both in longitudinal and transverse direction. The seismic vulnerability of such bridges will be overestimate if the upper building structures are modeled using equivalent nodal qualities. So the overall finite element models including upper building structures should be established in assessing the seismic vulnerability of such bridge structures, otherwise it will have a noticeable deviation. Since the types of upper building structures are complex, the effects of different types of structures on the vulnerability of landscape covered bridge need to be further studied.

REFERENCES

Billah, A.H.M.M. & Alam, M.S. 2015. Seismic fragility assessment of highway bridges: A state-of-the-art review. *Structure and Infrastructure Engineering* 11(6): 804–832.

Choi, E., DesRoches, R. & Nielson, B.G. 2004. Seismic fragility of typical bridges in moderate seismic zones. *Engineering Structures* 26(2): 187–199.

Cornell, A.C., Jalayer, F., Hamburger, R.O. & Foutch, D.A. 2002. Probabilistic basis for 2000 SAC federal emergency management agency steel moment frame guidelines. *Structure of Engineering* 128(4): 526–533.

Feng, Q.H. & Yuan, W.C. 2010. Method and application of seismic risk probability analysis for large- long span bridge based on IDA-MC. *Journal of Chang'an University* 30(3): 60–65.

HAZUS-MH 2.1. 2012. *Multi-Hazard Loss Estimation Methodology: Earthquake Model HAZUS-MH 2.1 Technical Manual*. Washington, DC.: Federal Emergency Management Agency.

Hwang, H. & Liu, J.B. 2004. Seismic fragility analysis of reinforced concrete bridges. *China Civil Engineering Journal* 37(6): 47–51.

Hwang, H., Liu, J.B. & Chiu, Y.H. 2001. *Seismic Fragility Analysis of Highway Bridges*. Memphis: Mid-America Earthquake Center.

Li, L.F., Wu, W.P., Huang, J.M. & Wang, L.H. 2012. Study on system vulnerability of medium span reinforced concrete continuous girder bridge under earthquake excitation. *China Civil Engineering Journal* 45(10): 152–160.

Modica, A. & Stafford, P.J. 2014. Vector fragility surfaces for reinforced concrete frames in Europe. *Bulletin of Earthquake Engineering* 12(4): 1725–1753.

Nielson, B.G. 2005. *Analytical Fragility Curves for Highway Bridges in Moderate Seismic Zones*. Atlanta: Georgia Institute of Technology.

Nielson, B.G. & Desroches, R. 2007. Seismic fragility methodology for highway bridges using a component level approach. *Earthquake Engineering and Structural Dynamics* 36(6): 823–839.

Olsson, A., Sandberg, G. & Dahlblom, O. 2003. On Latin hypercube sampling for structural reliability analysis. *Structural Safety* 25(1): 47–68.

Padgett, J.E. & DesRoches, R. 2007. Sensitivity of seismic response and fragility to parameter uncertainty. *Journal of Structural Engineering-ASCE* 133(12): 1710–1718.

Pan, Y., Agrawal, A.K., Ghosn, M. & Alampalli, S. 2010. Seismic fragility of multi-span simply supported steel highway bridges in New York State. I: bridge modeling, parametric analysis, and retrofit design. *Journal of Bridge Engineering-ASCE* 15(5): 448–461.

Shinozuka, M., Feng, M.Q., Kim, H., Uzawa, T. & Ueda, T. 2003. *Statistical Analysis of Fragility Curves*. Buffalo, NY: Multidisciplinary Center for Earthquake Engineering Research.

Shinozuka, M., Feng, M.Q., Lee, J. & Naganuma, T. 2000. Statistical analysis of fragility curves. *Journal of Engineering Mechanics-ASCE* 126(2): 1224–1231.

Shome, N. 1999. *Probabilistic Seismic Demand Analysis of Nonlinear Structures*. California: Stanford University.

Yang, C.S., DesRoches, R. & Padgett, J.E. 2009. Fragility curves for a typical California box girder bridge. *Lifeline Earthquake Engineering in a Multihazard Environment*. California: Oakland.

Zheng, K.F., Chen, L.B., Zhuang, W.L., Ma, H.S. & Zhang, J.J. 2013. Bridge vulnerability analysis based on probabilistic seismic demand models. *Engineering Mechanics* 30(5): 165–171.

This page intentionally left blank

Civil Engineering and Urban Planning IV – Liu et al. (Eds)
© 2016 Taylor & Francis Group, London, ISBN 978-1-138-02903-3

Study on the unconfined compressive strength prediction of cement soil according to curing time

Shi-You Zhang
Henan Electric Power Survey and Design Institute, Zhengzhou, Henan, China

Yan-Guo Chen
Yellow River Engineering Consulting Company, Zhengzhou, Henan, China

Zi-Wen Zhao
Henan Zhonghui Electric Power Engineering Consulting Co. Ltd., Zhengzhou, Henan, China

ABSTRACT: The strength characteristics of cement-stabilized soil were analyzed at different curing time or with different cement content. The strength data used for analysis were from unconfined compressive tests conducted in the laboratory. The experience equation was concluded which can predict the strength with different curing time. It has guiding significance for the design and construction of cement mixing pile.

1 INTRODUCTION

Cement mixing method is suitable for reinforcement treatment of soils such as normally consolidated peat, silt, saturated loess, fill, clay, and saturated loose sand. It has widely been used in foundation reinforcement, embankments seepage control, and deep excavation seepage control (Committee of "Foundation treatment manual" 2000, Hao 1991, Miao & Liu 2005, Xiao & Leng 2004). In this paper, laboratory tests are conducted to study the unconfined compressive strength of cement–soil. A cement–soil strength prediction method based on the cement content is proposed to meet the practical engineering design, construction, and quality control requirements.

2 TEST MATERIALS AND TEST METHODS

Original soil for cement stabilization is taken from a site in Zhengzhou city. It is classified into silty clay. Its basic physical properties and mineral composition are shown in Table 1. The cement used for the tests is an ordinary Portland cement which is produced by Henan Duoyangda Company. Its strength level is 325. Its stability, strength, and mortar additive species are in line with national standard "Common Portland cement" (General Administration of Quality Supervision, Inspection and Quarantine of the People's Republic of China 2007). Cement content of, 10%, 14%, and 17% are used in testing the mass of soil separately. Water–cement ratio is 1.6. Three test specimens for each group are made to perform the unconfined compressive tests for 7 days, 14 days, 28 days, 60 days, and 90 days of age.

When the samples are prepared, the amount of cement and water can be calculated from cement content and water–cement ratio. The amount of cement and water weighted by weighting scale are poured into light mixer, after they are mixed with the soils. The cement–soil is stratified into the cylindrical molds with the inner diameter of 3.91 cm and 8 cm height. Then, exposed in air indoor for conservation, they are released from the

Table 1. Properties and mineral components of soil.

				Mineral content (%)			
Water content w (%)	Volume gravity γ (kN·m^{-3})	Liquid limit w_L (%)	Plastic limit w_P (%)	Quartz	Illite	Calcium feldspar	Vermiculite
28.6	19.0	37.9	21.1	49.74	19.88	27.95	2.43

mound after 24 hours. The samples are sealed with plastic bags and continue conservation in a standard room until the scheduled time has arrived.

The unconfined compressive strength tests of cement–soil are conducted in accordance with "soil test method standards" (The Ministry of Water Resources of the People's Republic of China 1999) and the traditional instrument is used. Before the test, measure and calculate the average height of the initial sample, the initial average cross-sectional area of the specimen, and wipe a layer of Vaseline on both ends of the specimen. During the test, the sample is placed on the lower plate, the axial pressure and displacement gauge are adjusted to zero, so that the pressure plate just touch the sample. Start the machine to begin the tests. Record the pressure readings at each certain strain. Draw the stress–strain curves. If the curve is of a soft type, then the test can stop when the axial strain has reached 3%–5% after the peak value. The peak value of the curve is the unconfined compressive strength. If there is no stable value on the curve, the test should be carried out to 20% of the axial strain and take the value at 15% of axial strain as the unconfined compressive strength.

3 TEST RESULTS AND DISCUSSION

3.1 *Test results*

The unconfined compressive strength test results of cement–soil for different cement content and different ages are shown in Table 2. From the table, the maximum unconfined compressive strength of 90 days soil–cement is 1.38 MPa, corresponding to 20% of cement content.

3.2 *The influence of age on strength*

The relationship between the unconfined compressive strength and curing time at different cement content is shown in Figure 1. It can be concluded from Figure 1 that the unconfined compressive strength increases with the curing time at the same other conditions. But the increasing rate decreases with the curing time. The unconfined compressive strength of cement–soil for 7 days curing time is 0.33 to 0.47 times for 28 days curing time. The unconfined compressive strength of cement–soil for 90 days curing time is 1.71–1.86 times of 28 days curing time. It is different from the concrete that the strength of cement–soil has an obvious increase after 28 days. But the increasing rate becomes slower from 28 days to 90 days than from 7 days to 28 days.

Studies have shown that under the same conditions, the unconfined compressive strength ratio of

Table 2. The unconfined compressive strength value (MPa).

Cement content (%)	Age (day)				
	7	14	28	60	90
10	0.31	0.41	0.67	1.04	1.14
14	0.18	0.36	0.55	0.89	0.94
17	0.25	0.45	0.67	1.15	1.21
20	0.25	0.50	0.74	1.30	1.38

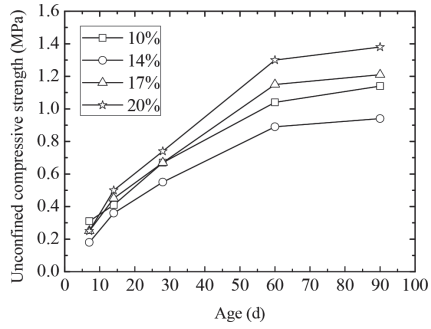

Figure 1. Relationship between the unconfined compressive strength and curing time.

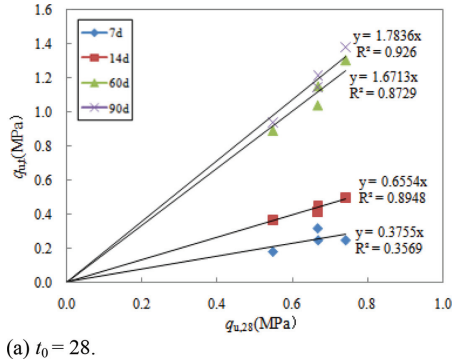

(a) $t_0 = 28$.

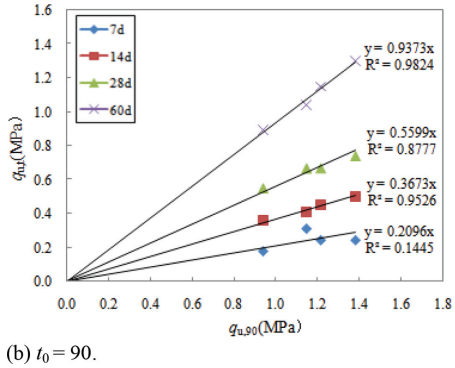

(b) $t_0 = 90$.

Figure 2. Relationship between $q_{u,t}$ and q_{u,t_0} of cement–soil.

Table 3. The prediction coefficient A_t from fitting.

Curing time (day)	$t_0 = 14$		$t_0 = 28$		$t_0 = 60$		$t_0 = 90$	
	A_{14}	R_{14}	A_{28}	R_{28}	A_{60}	R_{60}	A_{90}	R_{90}
$t = 14$	1	1	0.655	0.946	0.392	0.987	0.367	0.976
$t = 28$	1.524	0.932	1	1	0.597	0.886	0.560	0.937
$t = 60$	2.551	0.990	1.671	0.934	1	1	0.937	0.991
$t = 90$	2.721	0.982	1.784	0.962	1.067	0.991	1	1

cement–soil with different curing time has a linear relationship. The unconfined compressive strength predicting equations for different cement content is proposed as shown in Equation (1).

$$q_{u,t} = A_t \cdot q_{u,t_0} \tag{1}$$

where q_{u,t_0} is the unconfined compressive strength for curing time t_0, $q_{u,t}$ is the unconfined compressive strength for curing time t, and A_t is the coefficient.

According to the test results, if the strength values of different curing time are known the strength for other curing times can also be analyzed. The relationships of the strength for 28 days, 90 days with other curing time is shown in Figure 2. It can be seen from Figure 2 that the linear relationship of the strength for 28 days, 90 days, and 7 days is not obvious. However, it has an approximate linear relationship with other curing times. The corresponding slope is the coefficient A_t. The data of 7 days are excluded and the similar analysis is conducted for 14 days and 60 days. The result is shown in Table 3, and the R_t is the fitting coefficient.

It can be seen from Table 3 that the prediction coefficient A_t between q_{u,t_0} and $q_{u,t}$ has a relationship with t. The corresponding A_t for different curing time t is shown in Figure 3.

It can be seen from Figure 3 that A_t increases with curing time t and decreases with t_0. The fitting can be conducted by using Equation (2) for A_t and t for different t_0.

$$A_t = at^b \tag{2}$$

where a and b are fitting parameters shown in Table 4. R is relative coefficient.

It can be seen from Table 4 that for different t_0 Equation (3) can be obtained.

$$b = 0.565 \tag{3}$$

The parameter a has a relationship with t_0 which is shown in Figure 4.

Equation (4) can be used to fit the relationship between parameter a and t_0.

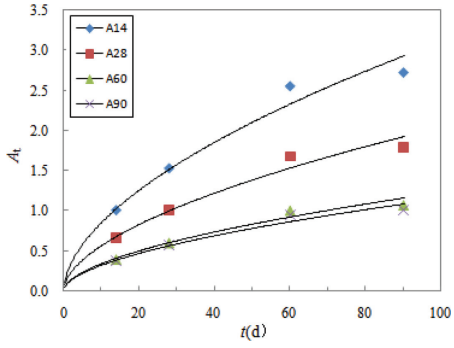

Figure 3. Relationship between A_t and t.

Table 4. The fitting parameters a and b for different t_0.

Curing time t_0 (d)	a	b	R^2
$t_0 = 14$	0.231	0.565	0.98
$t_0 = 28$	0.151	0.565	0.98
$t_0 = 60$	0.09	0.565	0.98
$t_0 = 90$	0.085	0.565	0.98

$$a = t_0^{-0.565} \qquad R^2 = 0.977 \tag{4}$$

The parameter A_t can be obtained from Equations (3), (4), and (2).

$$A_t = t_0^{-0.565} \cdot t^{0.565} \tag{5}$$

The experimental equation of predicting the strength of $q_{u,t}$ for any curing time t can be obtained by integrating Equations (5) into (1).

$$q_{u,t} = t_0^{-0.565} \cdot t^{0.565} \cdot q_{u,t_0} \tag{6}$$

The predicting strength values for other curing time are shown in Figure 5 from the known strength of 14, 28, 60, and 90 days.

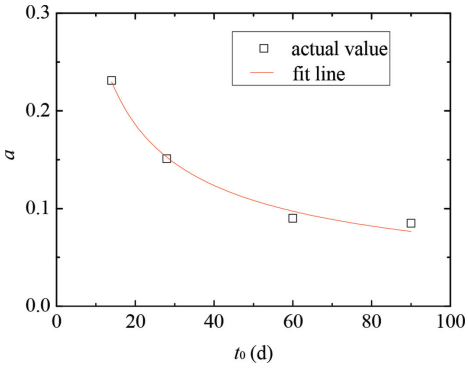

Figure 4. Relationship between a and t_0.

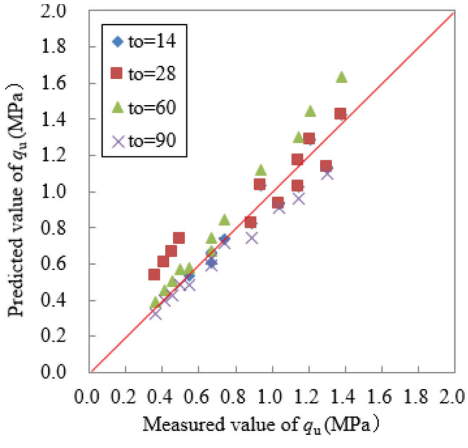

Figure 5. Comparison between measured values with predicting values by Equation (6).

In practical engineering, the predicting strength of other curing time is obtained according to 28 days.

$$q_{u,t} = 0.152 q_{u,28} \cdot t^{0.565} \tag{7}$$

4 CONCLUSION

In this paper, the unconfined compressive strength tests are conducted. Predicting equations of strength based on curing time is proposed. Conclusions can be made that:

- The unconfined compressive strength of cement–soil for the same cement content increases with curing time. The increasing rate becomes smaller with the curing time.
- The predicting equation is proposed to predict the unconfined compressive strength for any curing time from the strength of certain curing time. The equation is suitable for any cement contents. Because of the unstable data for 7 days, the equation is only used for 14 days to 90 days.

REFERENCES

Committee of "Foundation treatment manual". 2000. *Foundation Treatment Manual (Second Edition)*. Beijing: China Building Industry Press.

General Administration of Quality Supervision, Inspection and Quarantine of the People's Republic of China. 2007. *Common Portland Cement (GB175-2007)*. Beijing: Chinese Standard Press.

Hao, J.T. 1991. Discuss on the mechanical properties of cemented soil. *Chinese Jounal of Geotechnical Engineering* 13(3): 53–59.

Luan, M.L., Wei, H. & Lin, W.S. 2012. Transient Rayleigh wave technique in the engineering exploration. *Geophysical and Geochemical Exploration* 36(5): 878–883.

Miao, Z.P. & Liu, H.L. 2005. Laboratory study on unconfined strength of cement-stabilized soil in embankment. *Journal of East China Shipbuilding Institute (Natural Science Edition)* 19(5): 20–24.

The Ministry of Water Resources of the People's Republic of China. 1999. *Standard for Soil Test Method (GB/T 50123-1999)*. Beijing: China Planning Press.

Xiao, W.Q. & Leng, W.M. 2004. Laboratory test for treatment of the poor soil using deep mixing method. *Journal of Central South University of Technology (Natural Science)* 35(3): 490–494.

Civil Engineering and Urban Planning IV – Liu et al. (Eds)
© 2016 Taylor & Francis Group, London, ISBN 978-1-138-02903-3

Research on critical slope for channel excavation based on finite arc and strength reduction methods

Xiu-Ping Wu
Xi'an Research Institute, China Coal Technology and Engineering Group, Xi'an City, Shaanxi, China

Pei-Jie Jin & Yu Zhang
College of Pipeline and Civil Engineering, China University of Petroleum, Shandong, Qingdao, China

ABSTRACT: According to the element stresses, strains, and displacements calculated by the Finite Difference Method (FDM), the Finite Arc Method that is based on the limit equilibrium theory and the Strength Reduction Method with deformation trend as the failure standard are established in this paper. The two methods coupled with the Limit Equilibrium Method are mutually applied to study the critical slope degree of large channel excavation in South-to-North Water Diversion project in China. Three typical channel slope modes, which high slope, reclaimed slope and deeply excavated slope mode, are selected to acquire the variation curve of safety factor with the changes of excavation slope. Through comparison and analysis of the results, the critical excavated slope of the channel can be determined.

1 INTRODUCTION

In recent years, the Limit Equilibrium Method (LEM) and the Finite Difference Method (FDM) have been used extensively to determine the stability of the slope. The advantages of the LEM are explicit in concept and straightforward in process (Alejano et al. 2001; Chen 2003; Chen et al. 2007; Cheng et al. 2007). However, it has many limitations such as, too much simplified assumptions, incapable of reflecting the stress-strain relationship within the rock mass, and failing to consider the complicated load flaw. The defects result in low accuracy and difficulty to analyze failure process of slope. Considering the constitutive relation of the rock and soil, the initial stress state, the simulation for excavation or filling in the calculation process, the FDM can accurately reflect slope deformation characteristics, stress state and failure mechanism, but it cannot directly obtain the safety factor and the critical slip surface that are commonly used in engineering practice (Huang & Jia 2009; Chen et al. 2004). With the rapid development of computer technology, it has been an increasingly important research topic in the rock and soil slope engineering to combine the calculation results of FDM with traditional search for critical slip surface as well as the calculation of sliding stability safety factor.

This study aims at developing two practical procedures for searching critical slope and corresponding safety factor of channel excavation in the water diversion project. According to the results of the element stress, strain and displacement, the new approaches for the Finite Arc Method (FAM) and the Strength Reduction Method (SRM) have been applied in slope engineering availability.

2 FAM AND SRM

2.1 *Finite Arc Method*

In order to evaluate the slope stability, the results of the element stress, strain and displacement obtained from the calculation of FDM have been introduced into the search for critical slip surface and slope safety Factor (Fs). It has reduced some unnecessary assumptions, taking into account the complex constitutive relation of the rock and soil and acquired the slope stability under the complicated geology and environmental disturbance. Considering the soil slope, for example, here is a brief introduction to the calculation principle and steps.

The failure shape of soil slope is usually single and shears failure as the dominant failure pattern. The sliding surface would be of a circular arc or the combination of a circular arc with a slurry mingled layer. For a given circular sliding surface (Fig. 1), the safety factor is defined as the ratio of the sum of sliding force (τ_{ni}) and resistance force (τ_{fi}) along the sliding surface:

$$F_s = \frac{\sum \tau_{fi} L_i}{\sum \tau_{ni} L_i} \tag{1}$$

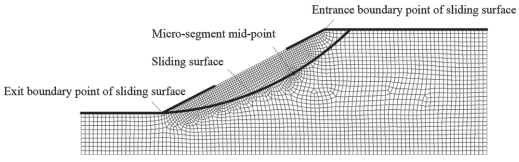

Figure 1. Calculation of slope safety factor with FAM.

L_i is the length of micro-segment. The steps for stability analysis are as follows:

- Calculate the stress components (σ_{xj}, σ_{yj}, τ_{xyj}) of every node of the slope element (planar linear quadrilateral element $j = 1, 2, 3, 4$; triangular element $j = 1, 2, 3$).
- Distinguish the element of each midpoint in micro-segment of the sliding surface.
- Use stress interpolation method to get the stress of each micro-segment midpoint.
- Determine resistance force and sliding force of micro-segment midpoint on sliding surface.
- Search for the critical slip surface and the minimum safety factor.

For any sliding surfaces, substitute the above results into Equation (1), the corresponding safety factor can be obtained. According to the zone of the slide point on the sliding surface, the scope of all the potential and the corresponding circle center in the sliding surface are determined, the calculation for the entire potential sliding surface is optimized, and the minimum safety factor is found. Then, the corresponding critical slip surface is defined.

2.2 *Strength Reduction Method*

The previously works have defined the reduction factor as the slope safety factor (F_s) and the shear strength reduction factor (F_{sr}) as the ratio of maximum shear strength and real shear stress produced by external loads. The process of the calculation gradually reduces the shear strength of each unit in the slope through the procedure. The cohesion (c) and internal friction angle (φ) are divided by the same reduction factor, thus a new cohesion and internal friction angle are obtained. Carry out the finite difference analysis and repeat the calculation until the slope reaches the critical failure state, which is defined by some failure criterion. At this point, the ratio of this strength index and the original strength index is the slope safety factor.

$$c' = c/F_{sr} \tag{2}$$

$$\varphi' = \arctan(\tan\varphi/F_{sr}) \tag{3}$$

In order to ensure the accuracy and reasonableness of the results, it is necessary to study the slope failure criterion by, which it judges whether the slope has stability or not. The present failure criterion is as follows: non-convergence of iterative solution; transfixion of shear strain; scope and connectivity status of plastic zone; the relation curve between the displacement of a point in a slope and the reduction factor. This paper takes the deformation trend of test points on the sliding surface as the failure criterion. Referring to result of LEM, the test points shall be located on a potentially sliding surface as much as possible. When the physical parameters of soil are continuously reduced, the safety factor is determined according to the relation curve between the reduction factor (F_{sr}) and the ratio of the displacement increment ($\Delta\delta$) of the test points and the reduction factor increment (ΔF_{sr}). When the ratio of $\Delta\delta/\Delta F_{sr}$ increases rapidly, the slope will reach the critical state and the reduction factor shall be the safety factor. Meanwhile, the position and shape of the critical slip surface are identified by the shear strain increment or the plastic zone.

3 RESEARCH ON CRITICAL EXCAVATED SLOPE FOR LARGE-SCALE CHANNEL SOIL SLOPE

For large-scale channel slope, the resistance of both ends of the sliding soil is not taken into consideration due to four factors: flat terrain, little changes of stratum structure along the channel

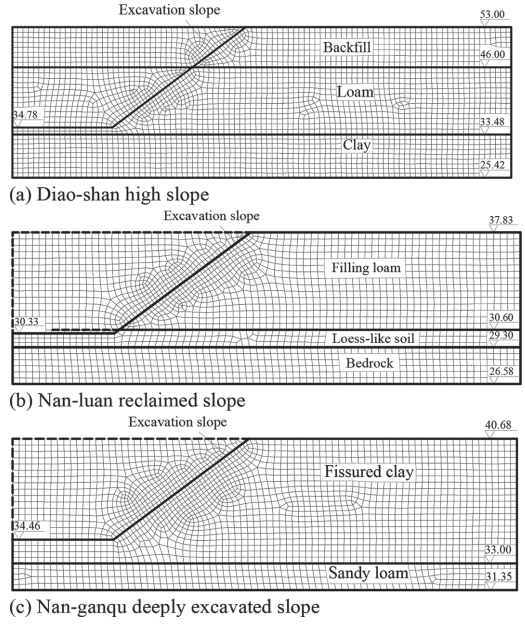

Figure 2. Typical cross-section and its mesh generation (unit: m).

Table 1. Values of mechanical parameters of channel slope.

Cross-section	Formation	Natural density/ ($kN \cdot m^{-3}$)	Elastic modulus/ MPa	Poisson ratio	Shear strength	
					c/kPa	φ/(°)
Diao-shan high slope	Backfill	19.10	5.86	0.31	17.40	19.00
	Loam	19.70	4.90	0.33	25.40	20.50
	Clay	19.80	9.40	0.30	32.30	19.00
Nan-luan reclaimed slope	Filling loam	20.10	5.86	0.31	15.67	16.00
	Loess-like soil	19.80	4.90	0.33	15.00	15.00
	Bedrock	24.00	3500	0.17	200.00	48.00
Nan-ganqu deeply excavated slope	Fissured clay	18.50	1.9	0.34	16.00	13.00
	Sandy loam	19.80	4.8	0.33	8.25	19.00

route, slopes in pairs and the same characters of left side and right side. It is enough to study one side for the selected typical cross-sections (Fig. 2). According to relevant information provided by design institute, the influence of groundwater can be ignored. The mechanics parameters of rock and soil are adopted and the critical state of the slope is obtained (Table 1).

According to the information provided by the design institute (The Professional Standards Compilation Group of People's Republic of China 2007), $F_s \geq 1.3$ can meet the excavation design requirements under the construction completed condition of the soil slope for large-scale channels. Stability evaluation on the selected channel cross-section is made under different excavation slopes, which uses the LEM, FAM, and SRM. The curves between the safety factor and the changes of excavation slope are as shown in Figure 3.

The three methods have evaluated the stability of the selected cross-section under different slope excavations. And the results have certain differences. Moreover, the safety factors obtained from FAM and SRM are all lower than that from LEM which take consideration the impact of excavation unloading or filling loading on the soil. The slope of *Diao-shan* has minor differences with that of *Nan-ganqu*. It does not only show that the excavation unloading has less effect on the slope compared with filling loading for channel slope with low slope height, but also indirectly proves the accuracy of the method mentioned. For *Nan-luan* reclaimed slope, the results exhibit relatively large differences. It indicates that filling loading has a great impact on stability of the channel slope and proves the reasonableness of the method mentioned as well. Therefore, for *Nan-ganqu* deeply excavated slope, it requires relatively low level of excavation slope. When the slope is 1:0.95, it meets the requirement perfectly. And the slope at this period is considered to be at its critical state. The high slope and reclaimed slope have relatively high requirements for the excavation slope due to its properties. Therefore, the slope shall be slowed down during the construction process. The results are then compared and analyzed to find out that the critical

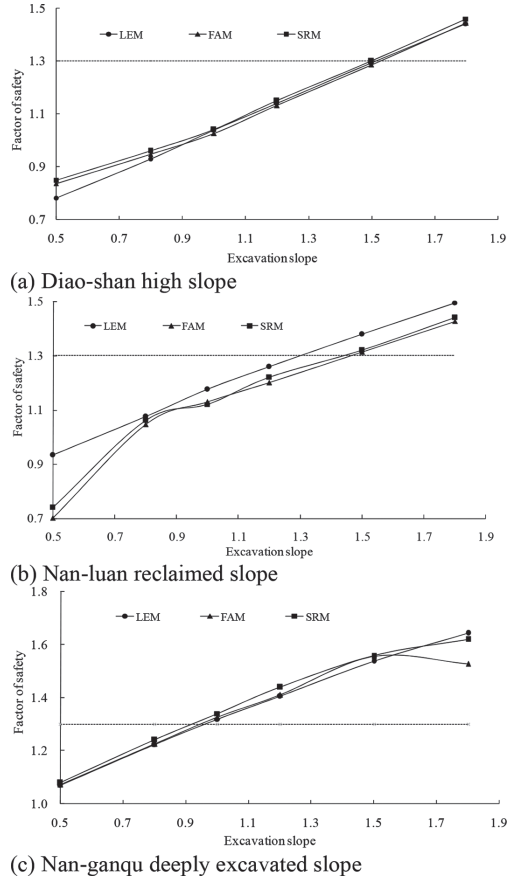

Figure 3. Safety factors change with excavation slope.

excavation slope of the *Diao-shan* high slope and *Nan-luan* reclaimed slope are 1:1.50 and 1:1.46, respectively.

4 DISCUSSION AND CONCLUSION

Based on the results of stress, strain and displacement, the FAM and SRM are established and corresponding computation procedure is developed. And the deficiencies of LEM and FDM are compensated. The results are compared and analyzed to show that the critical excavation slope of the *Diao-shan* high slope, *Nan-luan* reclaimed slope and *Nan-ganqu* deeply excavated slope are 1:1.50, 1:1.46, and 1:0.95, respectively. The results from the present investigation suggest that high slope and the reclaimed slope have high requirements to excavation slope degree. The construction process shall be slowed down. It has provided an important reference for optimization of excavation slope. Compared with the excavation slope of 1:2.50 proposed in South-to-North Water Diversion project in China, the critical degree obtained in this paper assures the project's quality, shortens construction time and reduces the project's costs.

REFERENCES

Alejano, L.R., Ferrero, A.M., Ramírez-Oyanguren, P. & Álvarez Fernández, M.I. 2011. Comparison of limit-equilibrium, numerical and physical models of wall slope stability. *International Journal of Rock Mechanics and Mining Sciences* 48(1): 16–26.

Chen, S.H., Qing, W.X. & Shahrour, I. 2007. Comparative study of rock slope stability analysis methods for hydropower projects. *Mechanics Research Communications* 34(1): 63–68.

Chen, Y.M., Li, Y.C. & Ling, D.S. 2004. Locating critical slip surfaces by a method combining monte Carlo technique and FEM. *Chinese of Rock and Soil Mechanics* 25(2): 75–80.

Chen, Z.Y. 2003. *Soil Slope Stability Analysis-theory Methods and Programs*. Beijing: China Water Power Press.

Cheng, Y.M. Lansivaara, T. & Wei, W.B. 2007. Two-dimensional slope stability analysis by limit equilibrium and strength reduction methods. *Computers and Geotechnics* 34(3): 137–150.

Huang, M.S. & Jia, C.Q. 2009. Strength reduction FEM in stability analysis of soil slopes subjected to transient unsaturated seepage. *Computers and Geotechnics* 36(1–2): 93–101.

The Professional Standards Compilation Group of People's Republic of China. 2007. *Design Code for Engineered Slopes in Water Resources and Hydropower Projects, SL386-2007.* Beijing: China Water Power Press.

Civil Engineering and Urban Planning IV – Liu et al. (Eds)
© 2016 Taylor & Francis Group, London, ISBN 978-1-138-02903-3

Liners and covers for landfills from cemented sands in arid areas

Nabil F. Ismael
Civil Engineering Department, Kuwait University, Kuwait City, Kuwait

Abdullah A. Al-Rashidi
Public Authority for Applied Education and Training, Kuwait City, Kuwait

Dalya N. Ismael
Civil Engineering Department, Australian College of Kuwait, Kuwait City, Kuwait

ABSTRACT: The potential use of crushed cemented sands, locally called 'gatch', as liners and covers for landfills in Kuwait was examined by laboratory tests. When excavated, the material is transformed into silty sands with fines ranging from 20% to 50%. Samples were obtained from one site in Keifan, Kuwait for testing. Modified Proctor Compaction Tests; and falling head permeability tests were carried out at different molding moisture contents. The results revealed a coefficient of permeability less than 1×10^{-7} cm/sec for samples compacted at or larger than the optimum moisture content which meets international standards for landfill conductivity. The use of ordinary Portland cement, in the amount of 2% by weight as an additive, was examined.

1 INTRODUCTION

With the rapid development of Kuwait and the Gulf states in the past 25 years, and the increased per capita consumption, the need for landfill sites for waste disposal has intensified. Every new landfill must have a base liner to prevent contaminants from leaching into the soil and entering groundwater or surface waters (Richardson and Sprague 2000). The liner must be a composite of a geomembrane installed on top of a compacted clay liner. The compacted clay liner must be at least 0.6 to 0.9 m thick and meet permeability standards of 10^{-7} cm/sec or less. The cap system must be at least 0.5 m thick and must also meet the same permeability standards. In the absence of clay deposits in the desert except along the shorelines, interest in using the local deposits of cemented sands has grown. The degree of cementation of these competent deposits varies with depth from very weak or uncemented to very strongly cemented material at the same location. The properties of the cemented deposits were investigated in detail by Ismael (1999). In brief the material locally called 'gatch' has a cohesion intercept due to the increased interlocking and bonding by cementing agents. Among the principal cementing agents are carbonates, hydrous silicates, iron oxides, and gypsum. When excavated, the cementation bonds are crushed and the material transforms to silty sands with fines content (<0.075 mm) of 20% to 50% depending on the location and the depth of excavation.

This paper examines the potential use of crushed cemented sands as liners in landfill construction. For this purpose a soil investigation and sampling from a site in Kiefan, Kuwait was carried out. This was followed by a laboratory testing program comprised of Modified Proctor Compaction tests and falling head permeability tests. The purpose being to determine whether the compacted specimens meet the U.S. Environmental Protection Agency minimum requirement for the coefficient of permeability ($K = 1 \times 10^{-7}$ cm/sec).

The use of ordinary Portland cement in the amount of 2% by weight was examined. Adding cement reduced the permeability of samples compacted on the wet ride of the optimum moisture content.

2 SITE INVESTIGATION

Two 150 mm diameter hollow stem auger borings were drilled at the site. Sampling and standard penetration tests were carried out at 0.5 m intervals to a depth of 2 m, and at 1 m intervals below this depth. Figure 1 shows a summary of the soil conditions at the test site. Indicated from left to right are the coring data including the length of each core run, the coring time, the rate of penetration in mm/min, and the recovery percentage. This is followed by the

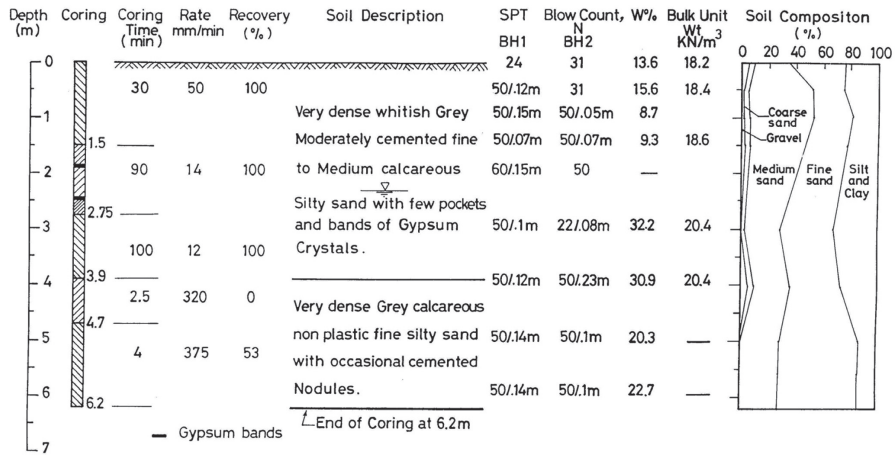

Figure 1. Soil conditions at the test site in Keifan (after Ismael 1999).

soil description, standard penetration test results, moisture content, bulk unit weight, and the soil composition. The soil profile consists of very dense whitish gray moderately cemented, fine to medium calcareous silty sand, with a few pockets and bands of gypsum crystal concretions to a depth of 3.9 m. this is underlain by very dense gray, calcareous, non-plastic, fine silty sand with occasional cemented nodules to the bottom of the boreholes. The lower layer being uncemented is typical of the soil profile in Kuwait where very dense cemented and uncemented layers appear in succession in the boreholes. Groundwater was encountered at a depth of 2.35 m below the existing grade.

Several bands of gypsum crystals were encountered between 1.85–1.9 m and 2.45–2.5 m. A few pockets of gypsum crystals were also found between 0–0.7 and 1.9–2.15 m. The standard penetration resistance generally exceeded 50 and most often it was not possible to drive the spoon required 0.45 m depth of penetration. The amount of fines comprising silt and clay is generally limited to about 20%, with the main component being fine to medium sand.

2.1 *Sampling*

Pits of 1.5 × 1.5 m were first excavated manually to a depth of 0.3 m. Undisturbed samples were taken first in brass liners using the drive cylinder method (Al-Rashidi 2004). Disturbed samples were excavated, placed in plastic bags and transported to the laboratory for testing.

3 MINERAL COMPOSITION

A summary of the chemical analysis on four soil samples at different depths is given in Table 1.

Table 1. Chemical analysis of the soil samples (after Ismael 1999).

	Weight %			
Element	0.3 m	0.6 m	1.2–1.5 m	3.2–3.9 m
SiO_2	64.1	57.8	78.5	65.2
Al_2O_3	2.19	1.89	2.27	9.94
Fe_2O_3	0.63	0.57	0.95	5.88
CaO	9.81	17.99	5.27	1.75
MgO	1.55	4.15	3.70	3.00
Cl	0.011	0.019	0.011	0.008
CO_2	0.53	10.8	9.30	3.40
SO_3	13.06	6.0	0.65	0.11
Na_2O	0.13	0.12	0.06	0.6
K_2O	0.57	0.45	0.63	1.92
MnO	0.01	0.026	0.03	0.05
P_2O_5	0.01	0.025	0.05	<0.05
SrO	0.11	0.06	0.03	0.007
TiO_2	0.12	0.10	0.2	0.77
LOI*	20.7	16.8	8.22	10.88
PH**	8.5	8.6	–	–
Compounds %				
Carbonates	1.2	25.2	17	5
Sulphates	28	12.5	1	0.2

*Loss on ignition at 1300°C

**1:2 water extract

–Not measured.

As shown the principal component is quartz which constitutes ~60% or more. There is a concentration of gypsum (28%) near ground level which decreases substantially with depth to 1% at a depth of 1.2–1.5 m. The amount of carbonates generally

decreased with depth. A comparatively large amount of ferrous oxides (~6%) was detected in the samples at 3.2–3.9 m which was not uniformly distributed. This was evident from the red colored bands seen in these samples.

4 THE TESTING PROGRAM

The following tests were carried out:

- Modified Proctor Compaction tests were performed on samples derived from excavated cemented sands.
- Falling head permeability tests on compacted samples at maximum density and optimum moisture content, and at 98% and 95% relative compaction on the dry and the wet ride of optimum.
- Falling head permeability tests on undisturbed samples.
- Repeat tests in 1 and 2 above but with 2% by weight ordinary Portland cement additive.

Two permeability tests were conducted at each moisture content to ensure the repeatability of the results. Curing was performed for 7 days for the samples which was mixed with cement. All samples were saturated prior to testing, and it took 7 to 10 days to achieve full saturation.

The above program was designed to examine the natural cemented sand, the excavated compacted material as base liner and caps for landfills, and the influence of cement additive on the hydraulic conductivity of the soil.

5 TEST RESULTS

The grain size distribution curve of the crushed cemented sand is shown in Figure 2. Table 2 shows the results of sieve analysis on these remolded samples (Al-Rashidi 2004). All cementation bonds were destroyed by tamping and light hammering prior to the tests. The results indicate that there is no gravel and the fines content is 34.4% and that the predominant component is fine to medium sand. This is in agreement with the requirements of the Environmental Protection Agency (1989) to achieve low hydraulic conductivity of 10^{-7} cm/sec or less.

Table 3 summarizes the test results for the remolded and the undisturbed samples. Indicated from left are the relative compaction, dry density, moisture content, and the average coefficient of permeability. Figure 3 shows the variation of the dry density and the permeability with the moisture content. From Table 3 and Figure 3, it is clear that the samples that were compacted on the dry side of the optimum moisture content and the undisturbed samples did not meet the minimum requirements of 10^{-7} cm/sec or less for the coefficient of permeability. Samples compacted at optimum moisture content and maximum modified proctor density, or on the wet side of optimum had a coefficient of permeability less than 10^{-7} cm/sec.

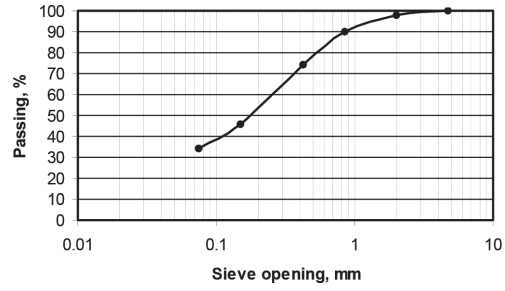

Figure 2. Grain size distribution curve.

Table 2. Sieve analysis on remolded samples, depth = 0.30 m.

US Sieve number	Percent passing
4	100.00
10	97.78
20	89.84
40	73.99
100	46.05
200	34.40
Pan	0.00

Table 3. Summary of compaction and permeability test results for remolded and undisturbed samples.

Relative compaction R_c (%)	Dry density (gm/cm^3)	Water content (%)	Coefficient of perm (K_{avr})
95 Dry	1.77	9.70	9.56 E-07
98 Dry	1.83	11.65	2.83 E-07
100 Opt	1.87	14.40	1.39 E-08
98 Wet	1.83	17.40	1.0 E-08
95 Wet	1.77	19.00	5.66 E-9
Undisturbed	1.73	7.4	6.04 E-6

5.1 *Use of cement additive*

The variation of the dry density and the coefficient of permeability with the moisture content for the compacted samples with 2% cement additive are shown in Figure 4 along with the compacted

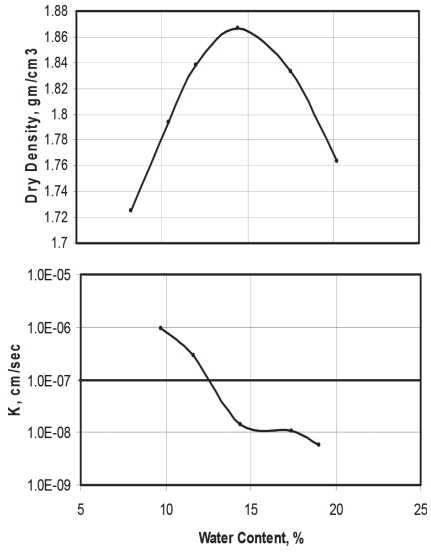

Figure 3. Variation of the dry density and permeability with moisture content for compacted gatch samples.

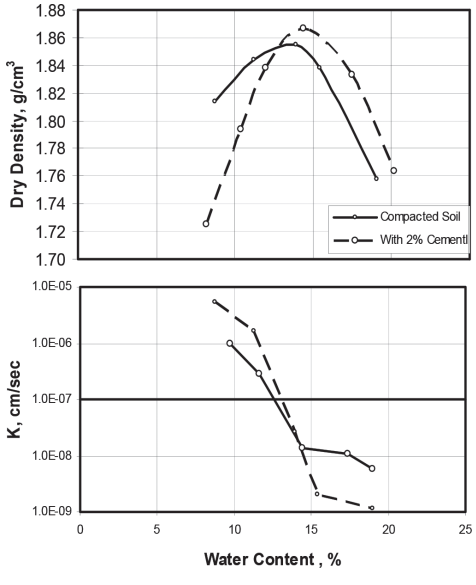

Figure 4. Comparison of the dry density & permeability with moisture content for the compacted gatch samples with and without cement additive.

samples with no cement additive. As shown by dotted curves the addition of cement decreased the permeability for the samples compacted wet of optimum to about 20% of their original value. Conversely, however, the permeability values increased with the cement additive for the samples compacted dry of optimum, and little change occurred for the samples compacted at maximum dry density and optimum moisture content.

6 DISCUSSION

It is pleasing to note the suitability of the crushed gatch soil as liners and caps for landfill construction. Due to its low plasticity this material will not desiccate and will not show the shrinkage cracks reported in highly plastic clays used as liners in arid areas (Daniel & Wu 1993; Kleppe 1981; Kleppe and Olson 1985). However, these soils are anisotropic and could vary from site to site in composition and degree of cementation depending upon the environmental factors and the stress history.

Test results associated with the cement additive is interesting and can readily be explained. At low molding moisture content, the presence of cement has dried the mix further leading to fluccuent matrix with large void ratio, and permeability, and proper hardening could not be realized. Conversely, samples compacted wet of optimum had sufficient moisture for proper lubrication and interaction and hardening due to the presence of cement.

The preceding results do not show any advantage in using cement additive to the test soils since the permeability values were below the minimum required by standards without cement additive. However, it may be necessary for other cemented deposits not meeting the minimum permeability criteria provided that the material is compacted wet of optimum and allowed sufficient time for curing and hardening. In general the use of additives is not encouraged due to the required strict supervision and quality control measures during mixing and placement.

7 CONCLUSIONS AND RECOMMENDATIONS

A program of site investigation, sampling and laboratory testing was carried at one site in Keifan, Kuwait to assess the suitability of using crushed cemented sands 'gatch' in landfill construction as liner and caps. Based on test results, the following conclusions are reached:

– Crushed cemented sands can be used as liners and caps in landfill construction. This is provided that they are compacted to the maximum

modified Proctor density and optimum moisture content, or compacted on the wet side of optimum. The corresponding coefficient of permeability of the compacted samples was less than 1×10^{-7} cm/sec.

– The use of ordinary Portland cement as additive in the amount of 2% by weight has reduced the permeability for the samples compacted at optimum moisture content or wet of optimum and increased the permeability for samples compacted dry of optimum. As such it is not recommended herein. However, it may be advantageous for materials that do not meet the permeability standard, if compacted on the wet side of optimum.
– Since cemented sand deposits vary in composition and degree of cementation from site to site, and with depth for the same site. It recommended to extend this site specific study to other sites with different soil composition, and percent of fines.

REFERENCES

Al-Rashidi, A.A. 2004. *Compaction and Permeability Study on Cemented Sands in Kuwait.* Kuwait: M.S. Project, Civil Eng. Dept., Kuwait University.

Daniel, D.E. & Wu, Y.K. 1993. Compacted clay liners and covers for arid sites. *Journal of Geotechnical Engineering* 119(2): 223–237.

Environmental Protection Agency. 1989. *Requirements for Hazardous Waste Landfill Design, Construction, and Closure.* Publication No. EPA-625/4-89-022, Cincinnati, Ohio.

Ismael, N.F. 1999. Properties and behavior of cemented sand deposits in Kuwait. *Soil and Foundations* 39(4): 47–57.

Kleppe, J.H. 1981. *Desiccation Cracking of Cohesive Soils.* Austin, Tex: University of Texas.

Kleppe, J.H. & Oson, R.E. 1985. Desiccation cracking of soil barriers. *Hydraulic Barrier in Soil and Rock (ASTM STP 874).* A.J. Johnson, R.K. Frobel, N.J. Cavalli, and C.B. Pettersson, eds.. Philadelphia: ASTM.

Richardson, G.N. & Sprague, R.T. 2000. Coordinating regulations in design and construction of modern landfill liners and closure caps. *MSW Management Magazine.* USA: Forester Communications, Inc.

This page intentionally left blank

Civil Engineering and Urban Planning IV – Liu et al. (Eds)
© 2016 Taylor & Francis Group, London, ISBN 978-1-138-02903-3

Simulation study of bed shear stress distribution of wide and narrow alternated channels

Shu-Ting Miao, Hu Lin & Yun Zeng
College of Water Conservancy and Hydropower Engineering, Sichuan Agriculture University, Ya'an, Sichuan, China

ABSTRACT: This paper chooses the wide and narrow alternated channels as the research object and establishes a three-dimensional flow calculation model to study the flow characteristics and the distribution of bed shear stress of the wide and narrow section with different flow rates. The results show that due to the large flow capacity in the wide section, but an insufficient flow in the narrow section, the water level upstream of the gap rises violently. From the narrow section to the wide section and then the narrow section, the average sectional velocity presents the distribution of "increase—decrease—stability—increase", which is contrary to the distribution rule of the water depth changes of the midstream. Under different flow conditions, the drastic changes of the bed shear stress of wide section swill results in the discontinuous movement of pebbles, causing the bed reversion deformation of cyclical reciprocating development. But in the narrow section, the bed shear stress increases with the flow rate, showing the linear relationship.

1 CHANNEL PROFILES

The mountain river systems pattern and flow direction are affected significantly by tectonic movements. Due to the changes in the structure and lithology, it often shapes into wide and narrow alternated channels like the lotus root. The gap section is narrow with a steep valley slope, exposed to bedrock, and towering peaks on both the sides. While the wide section is open with a gentle slope and developing terrace.

The wide section is up to 60 m in width, while the narrowest is only about 10 m. Moreover, gradient of the bed changes severely in the wide and narrow section, with 36% gradient in the narrow section, about twice as much as the wide section. A lot of pebbles piling up in the channel and the flow have great effect on sorting pebbles with the change of the channel's width. The median diameter of the pebbles is about 30–50 mm in the wide section, while at least 200 mm in the gap section. The channel of the river often forms a U-shape in the long evolution. In the dry season, the flow is small and is limited to the deep groove. While in the flood season, riverbed suffered severe erosion (Wang et al. 2008). By generalizing the actual river, we use numerical simulation to study the flow characteristics and bed shear stress distribution of wide and narrow alternated channels under different flow conditions. Figure 1 is the contrastive channel between wide section and narrow section (Aamarre & Roy 2008).

(a) Wide section

(b) Narrow section

Figure 1. Contrastive channel between wide section and narrow section.

2 ESTABLISHMENT OF THE MODEL

2.1 *Governing equation*

Use $k-\varepsilon$ turbulence model, continuity equation, momentum equation and k, ε equation, shown as follows:

Continuity equation:

$$\frac{\partial \rho}{\partial t}+\frac{\partial \rho u_i}{\partial x_{\mathrm{i}}}=0 \tag{1}$$

Momentum equation:

$$\frac{\partial \rho u_i}{\partial t}+\frac{\partial}{\partial x_j}(\rho u_i u_j) =-\frac{\partial P}{\partial x_i}+\frac{\partial}{\partial x_j}\left[(\mu+\mu_t)\left[\frac{\partial u_i}{\partial x_j}+\frac{\partial u_j}{\partial x_i}\right]\right] \tag{2}$$

k equation:

$$\frac{\partial \rho k}{\partial t}+\frac{\partial(\rho u_{ik})}{\partial x_i}=\frac{\partial}{\partial x_i}\left[\left[\mu+\frac{\mu_t}{\sigma_k}\right]\frac{\partial k}{\partial x_i}\right]+G+\rho\varepsilon \tag{3}$$

ε equation:

$$\frac{\partial(\rho\varepsilon)}{\partial t}+\frac{\partial(\rho u_i\varepsilon)}{\partial x_i} =\frac{\partial}{\partial x_i}\left[\left[\mu+\frac{\mu_t}{\sigma_\varepsilon}\right]\frac{\partial \varepsilon}{\partial x_i}\right]+C_{1\varepsilon}\frac{\varepsilon}{k}G-C_{2\varepsilon}\rho\frac{\varepsilon^2}{k} \tag{4}$$

$$\mu_t=\rho C_\mu\frac{k^2}{\varepsilon} \tag{5}$$

$$G=\mu_t\left[\frac{\partial u_i}{\partial x_j}+\frac{\partial u_j}{\partial x_i}\right]\frac{\partial u_i}{\partial x_j} \tag{6}$$

In the above formulas, ρ and μ are respectively density and molecular viscosity coefficients; p is the pressure term considering the gravity; μ_t the turbulent viscosity coefficient that can be calculated by the turbulent energy k and turbulence dissipation rate ε by Equation (5), in which C_μ is empirical constant, $C_\mu = 0.09$; $C_{1\varepsilon}$ and $C_{2\varepsilon}$ are constant of the equations, $C_{1\varepsilon} = 1.44$, $C_{2\varepsilon} = 1.92$; σ_k and σ_z are respectively turbulent Prandtl number of k and ε, $\sigma_k = 1.0$, $\sigma_z = 1.3$; G is a term from the turbulent kinetic energy generated by the average velocity gradient, which can be defined by Equation (6).

2.2 *The numerical method*

Finite volume method is used for discreteness, the governing equation is:

$$\frac{\partial(\rho\phi)}{\partial t}+\frac{\partial(\rho u\phi)}{\partial x}+\frac{\partial(\rho v\phi)}{\partial y} =\frac{\partial}{\partial x}\left(\Gamma\frac{\partial\phi}{\partial x}\right)+\frac{\partial}{\partial y}\left(\Gamma\frac{\partial\phi}{\partial y}\right)+s \tag{7}$$

In the above formulas, ϕ is generalized variable; Γ is the generalized diffusion coefficient corresponding to ϕ; s is a generalized source corresponding to ϕ; we use SIMPLE algorithm for the velocity pressure coupling, choose standard format for pressure interpolation, adopt the first-order windward format to discrete turbulent energy and turbulent dissipation rate equation and choose *QUICK* for momentum equation (Abrahams et al. 1995).

2.3 *Calculation model*

We get the model by generalizing the actual river, simulating a total of 206.5 m channel in length, with the gradient 17% in wide section, and 36% in a narrow section. The generalized diagram is shown in Figure 2. The model was divided into three typical sections such as inlet section (52 m), wide section (101 m), and narrow section (38 m). It is 40 min width at the inlet, and up to 60 min the wide section, but only 10 min for the narrow section. Eight flow conditions are set up in the simulation in total. They are respectively 25 m³/s, 35 m³/s, 45 m³/s, 55 m³/s, 65 m³/s, 75 m³/s, 95 m³/s, and 105 m³/s.

Hexahedral unstructured grid is used for discrete calculation area as shown in Figure 3. Water inlet is defined as velocity inlet. Non-slip boundary is used for the solid side wall, free outflow for outlet

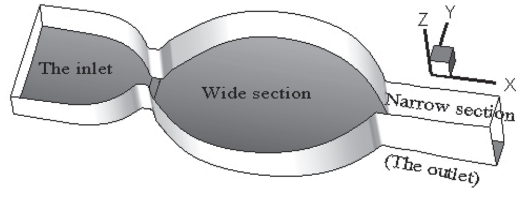

Figure 2. Generalized mathematical model.

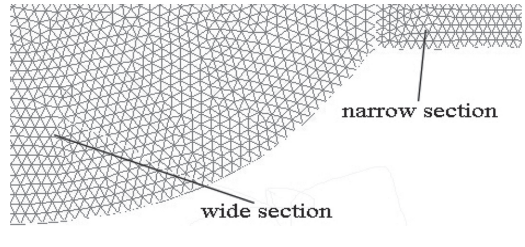

Figure 3. Meshing of the bottom of the model.

boundary, and pressure inlet for the upper boundary (PAIEMENT-PARADISG et al. 2011).

3 CALCULATION RESULTS AND ANALYSIS

3.1 *The water surface profile and the velocity distribution*

Water surface profile and velocity distribution in all conditions have similar rules. We only take condition 5 as an example here. Figure 4 is the water surface profile of condition 5 (Q = 65 m³/s) at Y = 0, and Figure 5 is the velocity distribution of condition 5. Water flows into the wide section at X = 57 m, where the water spreads and become shallow while the velocity increases. Due to the large flow capacity in the wide section, but insufficient in the narrow section, the water level upstream of the gap rises violently at the scope of X = 102–157 m. In the backwater area, the velocity presents the distribution rule of "reduction—stability—increase". The velocity goes down to 0.3 m/s from 1.1 m/s in the range of X = 102–110 m, it reaches a decline of 73%. In the range of X = 110–150 m, the flow velocity is relatively stable, about 0.3 m/s. In the vicinity of X = 150 m, the flow close to the narrow section begins to fall and becomes shallow along with a rise in flow velocity. When the water flows into the narrow section at X = 157 m, the velocity increases stably under the action of gradient.

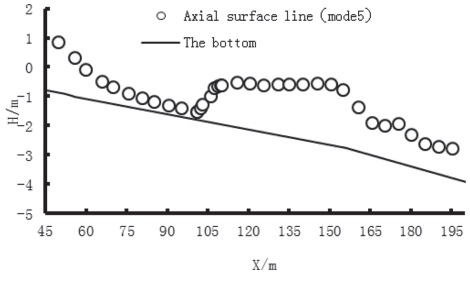

Figure 4. Water surface profile distribution of axis (condition 5).

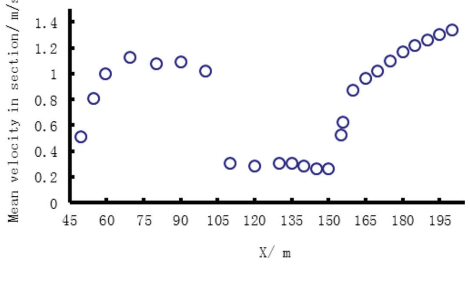

Figure 5. Cross-sectional average velocity distribution (condition 5).

3.2 *Cross-sectional bed shear stress*

Since the reflux have different effects on the mainstream, the distribution rule of the bed shear stress in wide section is different under different flow and the distribution rule in the narrow and wide section under the same condition also has significant differences. Figure 6 is the distribution comparison chart of cross-sectional bed shear stress in the wide section (X = 120) and the narrow section (X = 180) under four conditions (2, 4, 6, and 8). The peaks of cross-sectional bed shear stress at X = 120 m occurs in the middle of cross section, while the smaller the bed shear stress value is, the closer it is to the river bank. However, affected by reflux, the peak distribution rule of cross-sectional bed shear stress in condition 6 and condition 8 at X = 120 m are different from condition 2 and condition 4. The former peak occurs at the junction of mainstream and recirculation zone. For example, condition 6 reached the peak 22 pa at around Y = 3 m (or Y = –3 m), while condition 8 reached the peak 11pa at around Y = 13 m (or Y = –13 m). In narrow sections, the bed shear stress of the overall cross section in each condition has a uniform distribution. It reduces only when it is close to the 1/5 of the river bank, and the maximum bed shear stress

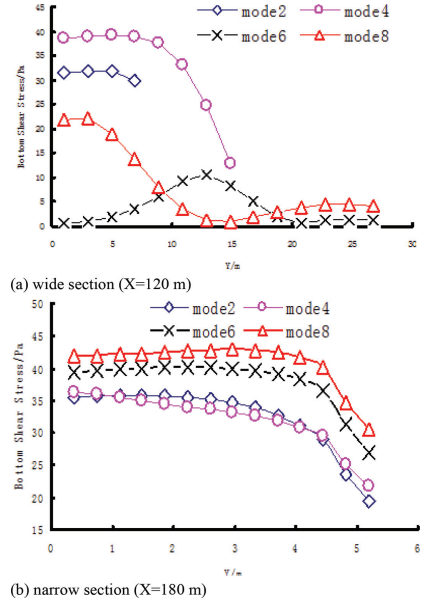

Figure 6. The cross-sectional bed shear stress distribution.

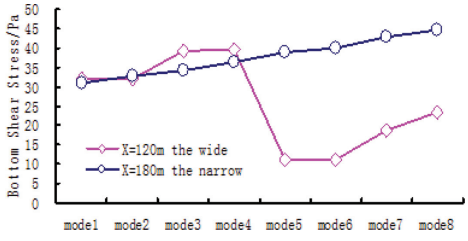

Figure 7. The comparison chart of bed shear stress in wide and narrow sections under different flow.

distributed in the middle area, increases with the flow rate.

3.3 *Bed shear stress comparison chart*

Figure 7 is the comparison chart of the wide and narrow section of bed shear stress. It shows the linear change in narrow sections and no simple function-correspondence in wide sections between the bed shear stress and the flow. We divide the eight conditions into three states according to the backwater, among which state I: no obvious backwater in wide section (condition 1, 2); state II: backwater not in the entire section (condition 3–6); state III: full backwater in wide section (condition 7, 8). The bed shear stress of state I in wide and narrow section seems similar, indicating that under a small flow, the flow characteristics of the wide and narrow alternated channels are similar to the straight channels. The bed shear stress of state II in wide sections is greater than in narrow sections (condition 3 and 4). With the increase of flow rate, the cross section is affected by the backwater in condition 5 and condition 6 at X = 120 m, the water becomes deeper and the bed shear stress declines sharply, which is only 29% of the bed shear stress in narrow sections of the corresponding conditions. Therefore, when the flood comes, the bed shear stress of the backwater area will greatly reduce and the gravel storage area will form in upstream of gap; when the backwater disappears at the end of the flood, the bed shear stress will greatly increase and the gravel will transport to the downstream once again, thus, making the bed reversion deformation of cyclical reciprocating development. For state III, the bed shear stress in wide sections increases with the flow. The increase rate is greater than in the corresponding narrow section. This shows that in catastrophic floods, the bed shear stress value in wide sections will also be great.

4 CONCLUSION

– The water level tends to rise violently in upstream of gap, because of the large flow capacity in the wide sections and insufficient flow capacity in the narrow sections. The average velocity distribution presents the rule of "increase-reduction—stability-increase" contrary to the distribution rule of the water depth of midstream.
– Affected by backwater and reflux and different from the narrow sections with uniform bed shear stress, the distribution of bed shear stress in wide sections changes from non-uniform to uniform in the cross section. Simultaneously, the peaks of bed shear stress are first off and then back to the middle region with the increase in flow.
– The bed shear stress in wide section changes violently as the flow varies, resulting in the discontinuous movement of pebbles and making the bed reversion deformation of cyclical reciprocating development. While the bed shear stress in the narrow sections increases with the flow, showing the linear relationship between them.

ACKNOWLEDGMENT

This work has been supported by both Innovative Training Program and Interest Cultivation Program for Scientific Research in Sichuan Agricultural University.

REFERENCES

Aamarre, H. & Roy, A.G. 2008. The role of morphology on the displacement of particles in a step-pool river system. *Geomorphology* 99(1–4): 270–279.
Abrahams, A.D., Li, G. & Atkinson, J.F. 1995. Step-pool stream: Adjustment to maximum flow resistance. *Water Resources Res* 31(10): 2593–2602.
Afzalimhr, H., Dey, S. & Rasoulianfar, P. 2007. Influence of decelerating flow on incipient motion of a gravel-bed stream. *sadhana* 32(5): 545–559.
Chartrand, S.M. & Whiting, P.J. 2000. Alluvial architecture in headwater streams with special emphasis on step-pool topography. *Earth Surface Processes and Landforms* 25(6): 583–600.
Geneviève, P., Geneviève, M. & André, R.2011. Effects of turbulence onthe transport of individual particles as bedload in a gravel-bed river. *Earth Surface Processes and Landforms* 36(1): 107–116.
Grant, G., Swanson, F.J. & Wonlman, M.G. 1990. Pattern and origin of stepped-bed morphology in high-gradient streams, western Cascades, Oregon. *Geological Society American Bulletin* 102(3): 340–352.
Montgomery, D.R., Buffington, J.M., Smith, R.D. et al. 1995. Pool spacing in forest channels. *Water Resources Res* 31(4): 1097–1105.
Wang, Z.Y., Melching, C.S., Duan, X.H. et al. 2008. Ecological and hydraulic studies of step-pool system. *Journal of Hydraulic Engineering* 130(7): 792–800.
Wang, Z.Y., Xu, J. & Li, C.Z. 2004. Development of step-pool sequence and its effects in resistance and stream bed stability. *Int J Sediment Res* 19(5): 161–171.

Civil Engineering and Urban Planning IV – Liu et al. (Eds)
© 2016 Taylor & Francis Group, London, ISBN 978-1-138-02903-3

Study of the bearing capacity of lightweight wallboards under a uniform load

Jiu-Yang Li, Li Zhang & Li-Hua Liu
School of Civil Engineering, Changchun Institute of Technology, Changchun, Jilin, China

ABSTRACT: This paper first conducted a theoretical analysis of the bearing capacity of lightweight wallboards by a program to determine the factors impacting the bearing capacity of the wallboard, and then performed tests and research under a uniform load on the basis of the analysis. The test data obtained can be used as a reference for the wallboard research.

1 INTRODUCTION

At present, the frame structure's exterior enclosure system is mainly equipped with lightweight small- and medium-sized building blocks as a substrate, and pasted with thermal insulation materials. This enclosure structure has the advantages of a simple construction technology and low cost, but its integrity is poor because it is built with the blocks compared with the frame structure having excellent ductility; it has a major disadvantage in the application, that is, loss arising from the damage of the filled wall. As a result, under the guidance of the national policy for housing industrialization, the research and development of a large-scale integral wallboard has become the research direction of the frame structure's enclosure system. This project group has researched, developed, and integrated a new-type of lightweight energy-saving wallboards that use the steel wire (reinforced bar) mesh as a framework, cement as cementing material, and industrial waste such as waste polystyrene foam plastic particles, expanded perlite and coal ash as aggregates for constituting lightweight concrete and pouring into structural layer and insulating layer. This lightweight wallboard can integrate the base material and the thermal insulating material, so that it has good integrity (Zhang 2012). It is equipped with wire-mesh as a framework, so it has big deformation and energy consumption capacity under load. In order to test the bearing capacity under a uniform load, this paper conducted the corresponding theoretical and experimental research.

2 THEORETICAL ANALYSIS OF FACTORS IMPACTING THE BEARING CAPACITY OF THE LIGHTWEIGHT WALLBOARD

2.1 *Finite element analysis for operating conditions*

Considering the influence of the lightweight wallboard thickness, cross-section steel wire (reinforced bar) diameter, vertical wire-mesh spacing and horizontal rebar mesh spacing on the deformation under a uniform load, parameter operating conditions for finite element analysis has been designed. A two-way wire-mesh frame is made of φ4, 5, and 6 cold-drawing galvanized steel wires. The wallboard thickness is between 250 mm and 300 mm, vertical wire-mesh spacing is between 150 mm and 250 mm, and horizontal wire-mesh spacing is between 300 mm and 500 mm. Twelve finite element samples of four groups have been designed (Li 2011a). The calculation parameter operating conditions are as shown in Table 1 (Li 2010).

During finite element analysis, the boards adopt an eight-node 3D stress unit with thickness equal to that of the material layer. Length and width will be determined according to operating conditions. Steel wire adopts 3D finit stn 180 wire unit. Therefore, there are two unit types: concrete and steel wire. Elasticity modulus of lightweight concrete is E = 1e3 N/mm^2, Poisson's ratio μ = 0.2, density ρ = 1.0 × 10^{-6} N/mm^3; rebar elasticity modulus E = 2e5 N/mm^2, Poisson's ratio μ = 0.3, and density ρ = 7.8 × 10^{-6} N/mm^3. The lightweight wallboard adopts four-point connection support with fixed pins. The support position is as shown in Figure 1.

Table 1. Combination table of wallboard finite element analysis operating conditions.

Operating conditions	Sample no	Steel wire diameter	Wallboard thickness (mm)	Vertical grid spacing (mm)	Horizontal grid spacing/mm
Group 1	1	4	250	200	400
	2	5	250	200	400
	3	6	250	200	400
Group 2	4	4	300	200	400
	5	5	300	200	400
	6	6	300	200	400
Group 3	7	4	250	200	200
	8	5	250	200	200
	9	6	250	200	200
Group 4	10	4	250	400	200
	11	5	250	400	200
	12	6	250	400	200

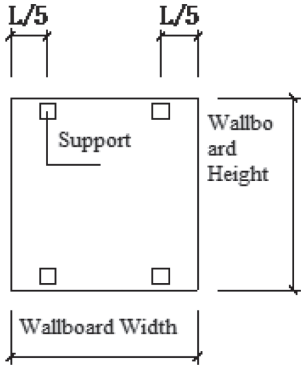

Figure 1. Wallboard calculation diagram.

The load form is uniform pressure, acting on all nodes on the surface course.

2.2 *Finite element calculation conclusion*

The finite element program is used to analyze the above operating condition samples and get the corresponding deformation and stress. The factors influencing deformation are analyzed to determine the factors influencing the wallboard's bearing capacity and rigidity.

2.2.1 *Contribution of the steel wire diameter change for the wallboard deformation*

In Table 1, according to the deformation analysis of the lightweight wallboard when the steel wire diameter is 4 mm, 5 mm, and 6 mm, the following conclusion is obtained: when the steel wire diameter increases from 4 mm to 5 mm and 6 mm, lightweight wallboard deformation will be reduced by 0.091% and 0.0 16%, respectively; however, the steel wire diameter change causes little influence on wallboard deformation. The main reason is that the wire-mesh frame appears to have a two-way distribution under a uniform load; when the deformation in the horizontal effect is smaller in the elastic stage, wire-mesh frame will act as a framework, having little deformation, and still standing in the serviceability limit state, so the steel wire diameter change causes little influence on the bearing capacity and rigidity of the lightweight wallboard in the elastic stage.

2.2.2 *Contribution of the wallboard thickness change for wallboard deformation*

In Table 1, the sample in Group 2 changes in the wallboard thickness on the basis of the corresponding steel wire diameter of the sample in Group 1. When the thickness changes from 250 mm to 300 mm, the conclusion we get from the analysis of the wallboard deformation is that when the wallboard thickness increases to 50 mm, steel wire diameter is 4 mm, 5 mm, and 6 mm, and deformation reduces by 49.84%, 46.06%, and 46.63% respectively. Therefore, in the elastic stage, the wallboard thickness changes plays an important role in the stress and deformation capacity, that is, the wallboard thickness can greatly influence the wallboard deformation rigidity and bearing capacity.

2.2.3 *Contribution of the horizontal wire-mesh spacing change for the wallboard deformation*

On the basis of the sample in Group 1, the sample in Group 3 changes the horizontal wire-mesh spacing correspondingly. By comparing samples 1 and 7, 2 and 8, 3 and 9 we find that wallboard thickness has not changed. The steel wire diameter is, respectively, 4 mm, 5 mm, and 6 mm; the horizontal wire-mesh spacing changes from 400 mm to 200 mm, respectively; and the wallboard deformation changes by

0.79%, 0.12%, and 0.13%. Therefore, if the horizontal wire-mesh spacing reduces, deformation will reduce correspondingly, but in a small proportion.

2.2.4 *Contribution of vertical steel wire grid spacing change to wallboard deformation*

The sample in Group 4 changes the vertical steel wire grid spacing according to the sample in Group 3. While other conditions have not changed, vertical wire-mesh spacing, respectively, changes from 200 mm to 400 mm. By conducting a comparative analysis for samples 7 and 10, 8 and 11, 9 and 12, wallboard deformation value increases by 1.38%, 2.05%, and 2.8% respectively, so the following conclusion is obtained: if the vertical steel wire grid spacing increases, wallboard deformation will increase, and the bearing capacity will reduce correspondingly.

2.2.5 *Summary*

In the range of the horizontal load and small elastic deformation, the contribution of wallboard thickness, cross-section steel wire diameter, horizontal wire-mesh spacing, and vertical steel wire grid spacing for lightweight wallboard deformation is successively: wallboard thickness, steel wire diameter, vertical steel wire grid spacing, and horizontal wire-mesh spacing. Although vertical steel wire grid spacing causes little influence, in the actual engineering, wallboard deformation under the horizontal and vertical loads should be considered. Therefore, horizontal and vertical wire-mesh spacing should not be too big. In addition, horizontal wire-mesh spacing should not be very small, because horizontal steel wire has a big influence on the wallboard's thermal insulation and energy conservation. If the steel wire spacing is too small, the heat conduction will increase, and the insulation performance of the lightweight wallboard will be greatly impacted. Therefore, the cross-section design of the lightweight wallboard should consider the bearing capacity under a uniform load and meet the other stress and energy-saving requirements.

3 EXPERIMENTAL RESEARCH

3.1 *Preparation for test*

Concrete was mixed according to the lightweight concrete mixing proportion developed by the project group, an optimal plan was selected based on the result of the theoretical analysis of the above cross-section composition, process and product 1:1 lightweight wallboard sample. Figure 2 shows the sample's external dimension: steel wire grid is φ4@300 galvanized steel wire, horizontal

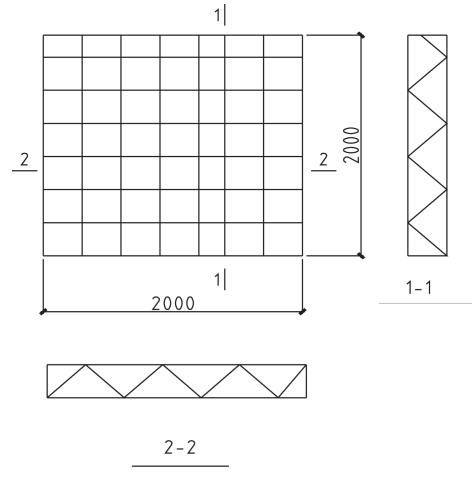

Figure 2. Schematic diagram of sample dimension and rebar mesh wallboard.

wire-mesh has a slant angle of 45° and an internal spacing of 500 mm; the end is equipped with four lanes of vertical wire-mesh (Liu 2011).

Before producing a sample, the rebar strain plate was pasted and maintained for more than 28 days; the strain box was connected and strain was tested; and the dial gauge was placed according to the design position and test deflection. The lightweight wallboard was placed horizontally, and fixed pins were used at two opposite angles and rolling pins at two opposite angles for four-point supports. In the loading plan, first, the uniform wind load borne by the lightweight wallboard was calculated. A larger value of 3.3 kN/m^2 was taken between the small earthquake and the big earthquake. The load was divided into three stages: load 1.1 kN/m^2 in the first stage, load 1.1 kN/m^2 in the second stage after 30 min, and then load 1.1 kN/m^2 in the third stage after another 30 min, totaling 3.3 kN/m (Li 2011b). If the wallboard did not develop an obvious crack when the load increased to the limit load, then load 1.1 kN/m^2 in the fourth stage was considered. If the wallboard did not have an obvious deflection, then the fifth stage load after 30 min was considered (the load of 3.3 kN/m^2 in this stage was determined according to the laboratory conditions) until the wallboard was damaged. Figure 3 shows the deflection test point position.

3.2 *Test process and conclusion*

The deflection value was recorded at each point under the load of the first three stages. After the load of the three stages, the concrete wallboard would slightly crack. For the sake of safety, the dial gauge was removed. Table 2 lists the deflection

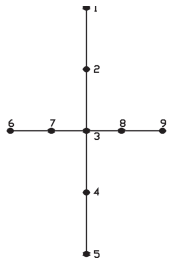

Figure 3. Diagram of dial gauge placing position under the load of first three stages.

Table 2. Corresponding deflection value at each test point (mm).

Load test point	1st stage load (1.1 kN/m^2)	2nd stage load (2.2 kN/m^2)	3rd stage load (3.3 kN/m^2)
1	0.04	0.19	0.24
2	0.02	0.16	0.24
3	0.01	0.17	0.26
4	0.01	0.10	0.17
5	0.01	0.06	0.10
6	0.01	0.20	0.30
7	0.01	0.19	0.28
8	0.01	0.14	0.24
9	–0.03	0.07	0.17

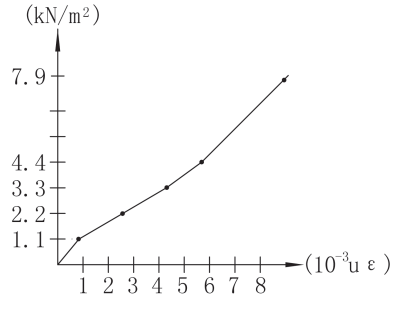

Figure 4. Load–strain at test point.

values at each point under the load of the first three stages.

The rebar strain was recorded by the computer and the load–strain diagram of several test points was generated. Figure 4 shows the load–strain of rebar at a test point. Other test points were similar to this, but the strain was different.

Deflection of the lightweight wallboard and rebar strain were tested. The following conclusion was drawn from the data analysis: the wire-mesh and concrete materials in the lightweight wallboard could fully exert their material performance under a uniform load, the crack load of the wallboard was 3.3 kN/m^2, the limit load was 7.9 kN/m^2, the maximum strain value corresponding to the limit load was 8905e^{-6}, and the limit deflection corresponding to the load was 0.78 mm.

4 CONCLUSION

Based on the theoretical research as well as finite element program analysis and test verification, this paper conducted a systematic and complete analysis and research on the bearing capacity of the lightweight concrete wallboard under a uniform load, and obtained the proportion ratio, bearing capacity, deflection, and material strain of the cross-sectional lightweight wallboard. The bearing capacity can ensure that the wallboard does not develop crack during a small earthquake and is not susceptible to damage during a big earthquake. Concerning the deflection of the lightweight wallboard obtained from the test, the deflection span ratio can reach the specified value of l/200. The tested maximum tensile strain of the rebar is close to the rebar's ultimate strain value of 0.01, thus guaranteeing the full utilization of material strength. The test data can provide a reference for further research and development of the lightweight wallboard.

ACKNOWLEDGMENTS

This work was financially supported by the Jilin Science and Technology Development Planned Topics [20140203014SF], Jilin Education Development Planned Topics [2015296], and the Changchun Institute of Technology Key Discipline.

REFERENCES

Li, J.Y. 2010. Deformation analysis of composite wallboard in finite element under the action of horizontal loading. *Industrial Building* 40(12): 87–89.

Li, J.Y. 2011a. Finite element analysis of displacement of composite wall cladding under wind load. *2011 International Conference on Electrical Technology and Civil Engineering, Lushan, China, April 22–24, 2011*. NY: Curran Associates, Inc.

Li, J.Y. 2011b. Analysis of deformation of composite wall cladding panel. *2011 International Conference on Electrical and Control Engineering, Yichang, China, Sept. 16–18, 2011*. NY: *Curran Associates,* Inc.

Liu, L.H. 2011. Design of Energy-saving Wire-mesh Frame Wallboard in Extreme Cold Area under Horizontal Load. *Journal of Changchun Institute of Technology* 12(1): 1–3.

Zhang, L. 2012. Finite Element Analysis on the Deformation of Energy-saving Wire-mesh Frame Wallboard. *Journal of Changchun Institute of Technology* 13(4): 1.

Civil Engineering and Urban Planning IV – Liu et al. (Eds)
© 2016 Taylor & Francis Group, London, ISBN 978-1-138-02903-3

Effect of scale and geometry features of fault on crustal stress

Qi-Tao Pei, Xiu-Li Ding, Yu-Ting Zhang, Zhi-Hong Dong & Shu-Ling Huang
Key Laboratory of Geotechnical Mechanics and Engineering of Ministry of Water Resources, Yangtze River Scientific Research Institute, Wuhan, Hubei, China

ABSTRACT: Up till now, it has been shown that if faults exist in rock mass, regardless of their strike, dip, shape, size, and other difference, they will have some effect on distribution characteristics of crustal stress. Discontinuous contact model based on the finite difference method is a newly proposed method for studying the effect of the fault on crustal stress. This paper, firstly, gives a general introduction on the effect of fault on crustal stress, and then illustrates the discontinuous contact theory and a finite difference method that will be used in the subsequent study. Afterwards, numerical simulation is conducted focusing on the effect of scale and geometry features of fault on crustal stress by using the introduced method. It is found that the indicator of the fault area can be used to describe the impact of the fault scale on crustal stress. When other conditions are the same, the maximum principal stress and shear stress at the end of fault are positively correlated with the fault scale. In addition, the principal stress values in the vicinity of the arc fault depend primarily on the central angle, which reach a maximum at a central angle of 90°. However, the magnitude of the principal stress near piecewise linear faults depend crucially on the angle, which is between the fault strike and regional maximum principal stress.

1 INTRODUCTION

Faulting is a prevalent structural geological phenomenon in the earth's crust. According to the statistical data (Wang et al. 2006, Zoback & Roller 1979), it is shown that the Tanlu fault is about three times the length of San Andreas fault. When the shear stress tends to be stable, the distance from Tanlu fault is about 100 km but from the San Andreas fault is 15–20 km. It can clearly be seen that the disturbed scope of the crustal stress increases with the increment of fault scale. As mentioned above, we believe that the fault scale has a great effect on the distribution rule of the crustal stress. In addition, the geometry features of the fault in the earth's crust often appears to be piecewise linear or irregular (Chen et al. 2014). So, it is of an important significance to study the effect of scale and geometry features of the fault on the distribution rule of the crustal stress.

In the past, the continuous model was often used to study the effect of fault on crustal stress. However, it could not reflect some characteristics of fault slip. Apart from this, the effect of the scale and geometry features of the fault on crustal stress was rarely studied due to the limited measurement data. On this basis, a discontinuous contact model was established in the paper by FLAC^{3D} to study the effect of scale and geometry features of fault on distribution characteristics of crustal stress. The results in the paper can provide important reference for obtaining reliable distribution rule of crustal stress when encounters different scales and geometry features of fault.

2 DISCONTINUOUS CONTACT THEORY BASED ON THE FINITE DIFFERENCE METHOD

Interface in FLAC^{3D} is taken as a single-sided, which can be stretched in the designated surface. It can also simulate slippage among the contact parts. Figure 1 plots the difference between continuous and discontinuous model. Comparing with continuous model, a discontinuous model

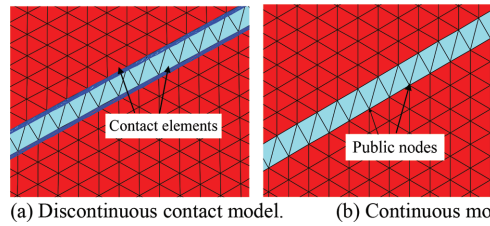

(a) Discontinuous contact model. (b) Continuous model.

Figure 1. Diagrams of continuous and discontinuous model.

takes in-continuous contact relationship between the surrounding rock and faults into account by setting contact elements. It may lead to slippage that occurs at the contact position, which is consistent with the actual situation. Moreover, the discontinuous model highlights the effect of faults on crustal stress and improves stress-weakening.

As the interface is elastic, the normal stress $f_n^{(t+\Delta t)}$ and shear stress $f_{si}^{(t+\Delta t)}$ on the interface at the time $t + \Delta t$ can be expressed as follows (Itasca Consulting Group 2015):

$$f_n^{(t+\Delta t)} = k_n u_n A + \sigma_n A \tag{1}$$

$$f_{si}^{(t+\Delta t)} = f_{si}^{\ t} + k_s \Delta u_{si}^{(t+0.5\Delta t)} A + \sigma_{si} A \tag{2}$$

Here, u_n is the absolute normal displacement of the interface node penetration into the target surface, Δu_{si} is the relative shear displacement increment vector, σ_n is the additional normal stress caused by the interface initialization, k_n and k_s are normal stiffness and shear stiffness, A is representative area of interface node.

When relative sliding occurs, the maximum tangential stress $f_{s\max}$ can be calculated by Mohr–Coulomb slip criterion. That is:

$$f_{s\max} = c_{if} A + \tan\varphi_{if} (f_n - uA) \tag{3}$$

Here, c_{if} is the interface cohesion, φ_{if} is the internal friction angle of interface, and u is pore pressure.

Based on the Mohr–Coulomb slip criterion, when the shear stress on the interface meets the condition $|f_s| < |f_{s\max}|$, the interface will be elastic. When the shear stress on the interface meets the condition $|f_s| = |f_{s\max}|$, the interface will be plastic. When relative sliding occurs, shear stress on the interface will keep unchanged $|f_s| = |f_{s\max}|$, and effective normal stress caused by shear displacement will increase. Then, we can get:

$$\sigma_n' = \sigma_n + \frac{\left(|f_s|_O - f_{s\max}\right) k_n}{k_s A} \tan\psi \tag{4}$$

Here, ψ is expansion angle of interface, $|f_s|_o$ is shear stress before correction.

On a separate note, if tensile stress exceeds the tensile strength of interface, interface damage will happen. Then, the normal stress and shear stress on the interface become zero.

3 EFFECT OF THE FAULT SCALE ON THE CRUSTAL STRESS

3.1 *Basic assumptions and boundary conditions*

For the quasi-three-dimensional model, some assumptions are listed as follows based on the natural state of rock mass and fault: (1) Rock is a homogeneous and isotropic; (2) The fault is treated as perfectly elastic material; (3) The fault is connected with the surrounding rock by discontinuous interface; (4) Boundary stress is regional, and the applied direction is perpendicular to the border; and (5) the fault is only affected by current tectonic stress field, and the residual stress by ancient tectonic stress field is negligible.

A separate "non-penetrating fault" is adopted in the model, which can be described by the multimedia method (Chen & Tian 1998). The direction of the regional maximum principal stress is from east to west, and $\sigma_1 = 16$ MPa, $\sigma_2 = 10$ MPa. Here, σ_1 refers to maximum principal stress, and σ_2 refers to minimum principal stress (same as below). Mechanical properties of rock, fault, and interface are shown in Tables 1 and 2. Right and bottom borders of the model are fixed. The established model by FLAC^{3D} and applied boundary conditions are shown in Figure 2.

3.2 *Calculation results*

During the calculation, fault width ranges from 50 m to 400 m, corresponding to the fault length which is 500 m, 1000 m, 1500 m, 2000 m, 2500 m, 3000 m, and 4000 m, respectively.

Contour diagrams of the maximum principal stress at the different fault length are shown in Figure 3. Here, l refers to the fault length (same as below). We can know that the crustal stress at the end of the fault concentrates significantly.

Table 1. Mechanical properties of rock and fault.

	Density (kg/m^3)	Deformation modulus (GPa)	Poisson's ratio	Cohesion (MPa)	Internal friction angle (degree)
Rock mass	2650	20.0	0.26	1.7	54.5
Fault	2350	3.0	0.35	0.1	20.0

Table 2. Mechanical properties of interface.

Cohesion (MPa)	Internal friction angle (Degree)	Normal stiffness (GPa)	Shear stiffness (GPa)
0.05	15.0	3.0	1.5

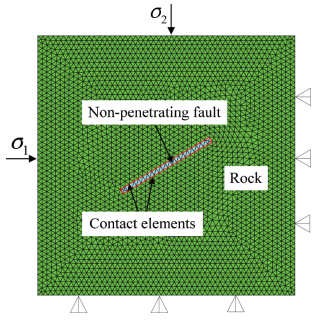

Figure 2. Finite difference model with boundary conditions.

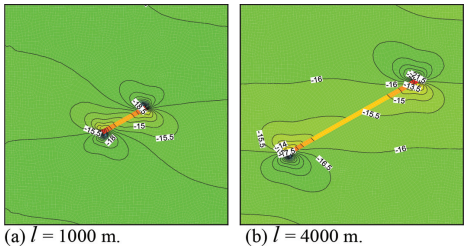

(a) l = 1000 m. (b) l = 4000 m.

Figure 3. Contour diagram of the maximum principal stress at different fault length (l) (unit: MPa).

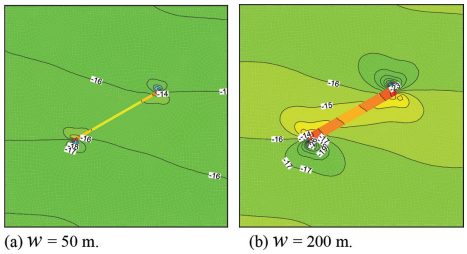

(a) w = 50 m. (b) w = 200 m.

Figure 4. Contour diagram of the maximum principal stress at different fault widths (w) (unit: MPa).

Furthermore, when the fault width is constant, as fault length increases, the magnitude of the maximum principal stress tends to be larger and the degree of stress concentration at the end of fault enhances gradually. In addition, the disturbed

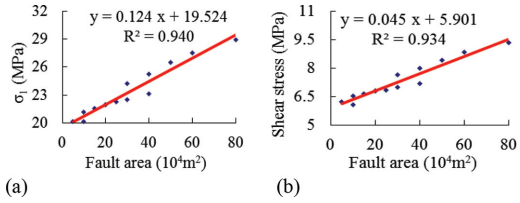

(a) (b)

Figure 5. Variation of the maximum principal stress and shear stress at the end of the fault with fault area.

scope of the maximum principal stress extends with the increment of the fault length. So, we can conclude that the fault length has a great impact on distribution characteristics of crustal stress.

Contour diagrams of the maximum principal stress at the different fault widths are shown in Figure 4. Here, w refers to fault width (same as below). It can be seen from the figure that the crustal stress at the end of the fault concentrates significantly, and the principal stress values on both sides of the fault are asymmetrical. Moreover, when the fault length is constant, with the increment of the fault width, the maximum principal stress values increase and the degree of the stress concentration at the end of fault enhances significantly. Besides, the disturbed scope of the maximum principal stress extends obviously. So, we can obtain the fault width has a great effect on the distribution rule of the crustal stress.

Variation of the maximum principal stress and shear stress at the end of fault with the fault area is shown in Figure 5. With reference to Figure 5, we can see that the magnitude of the maximum principal stress and shear stress at the end of the fault increases linearly with the fault area, and the linear correlation coefficient is close to 1. Further analysis indicates that the principal stress values increase and the degree of stress concentration at the end of the fault enhances more significantly with the increment of fault area. So, it is of reliable significance to quantitatively determine the impact of fault scale on the crustal stress by the indicator of the fault area.

4 EFFECT OF GEOMETRY FEATURES OF FAULT ON CRUSTAL STRESS

This section is mainly used to study the distribution characteristics of the crustal stress, which is affected by the geometry features of the fault. Assuming that the regional principal stress satisfies the conditions σ_1 = 16 MPa and σ_2 = 10 MPa, mechanical properties of the rock, fault, and

interface are selected in Table 1. Sketch of geometry features of the arc fault and Piecewise linear faults is shown in Figure 6.

4.1 *Arc fault*

During the calculation, chord length remains unchanged, and the central angle ranges from 60° to 180°. Variation of the maximum principal stress and shear stress at the end of arc fault with different central angles are shown in Figure 7. With reference to Figure 7, it can be seen from the figure that the crustal stress values at the end of the fault increase firstly and then decrease with the increment of the central angle, and the critical value is 90°. When the central angle is less than the critical value, the principal stress values increase and the degree of stress concentration at the end of the fault enhances with the increment of the central angle, but the relative rate of change is smaller. However, as the central angle is more than 90°, the principal stress values and the degrees of stress concentration at the end of fault decrease more significantly with the increment of the central angle and the relative rate of change are larger.

In addition, the direction of the maximum principal stress in the vicinity of the fault deviates from the original one to varying degrees. While exceeding a certain distance, the direction tends gradually to be in line with the regional tectonic stress field.

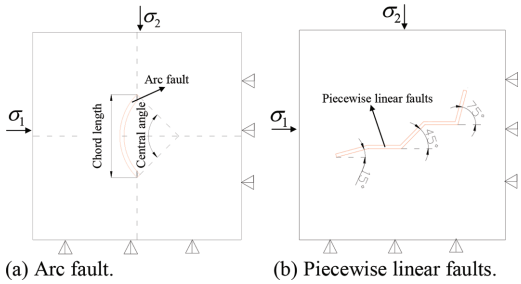

(a) Arc fault. (b) Piecewise linear faults.

Figure 6. Sketch of the different geometry features of the faults.

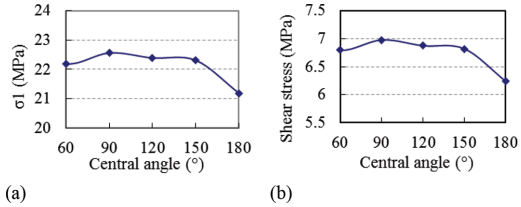

(a) (b)

Figure 7. Variation of the maximum principal stress and shear stress at the end of arc fault with central angle.

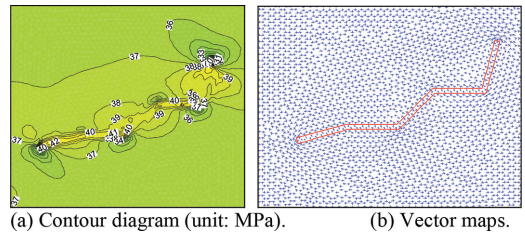

(a) Contour diagram (unit: MPa). (b) Vector maps.

Figure 8. Distribution characteristics of the principal stress in the vicinity of piecewise linear faults.

4.2 *Piecewise linear faults*

During the calculation, other conditions stay unchanged, and the angle between the fault strike and regional maximum principal stress ranges from 15° to 60°. Distribution characteristics of the principal stress in the vicinity of the piecewise linear faults are shown in Figure 8. We can obtain the crustal stress at the end or intersection of the faults concentrates significantly. Moreover, the principal stress values increase and the degree of stress concentration at the end of the intersection of faults enhances with the increment of angle.

Additionally, the direction of the maximum principal stress near the piecewise linear faults is quite complex, which deviates from the original one to varying degrees. The direction can be oblique, parallel, or perpendicular to fault. However, while exceeding a certain distance, the direction tends to be in line with the regional tectonic stress field.

5 CONCLUSION

This paper introduces a newly proposed method for studying the effect of fault on crustal stress. The results of the numerical simulation well illustrate the advantages of the proposed method, indicating that the method is both effective and reliable. The following conclusions can be drawn.

1. It is of a reliable significance to quantitatively describe the impact of the fault scale on the crustal stress by the indicator of the fault area. The principal stress values at the end of the fault are linearly correlated with the fault scale. Besides, with the increment of fault area, both of the principal stress values and the degree of stress concentration at the end of fault increase.

2. For an arc fault, crustal stress values at the end of fault increase firstly and then decrease with the increment of central angle, and the critical value is 90°. When the central angle is less than the critical value, the relative rate of change is smaller. However, as a central angle is more than 90°, the relative rate of change is larger.
3. For a piecewise linear faults, crustal stress near fault depends primarily on the angle, which is between fault strike and regional maximum principal stress. The principal stress values increase and the degree of stress concentration at the end or intersection of faults enhances with the increment of angle.
4. The direction of maximum principal stress near fault is quite complex, which can be oblique, parallel, or perpendicular to fault. While exceeding a certain distance, the direction tends gradually to be in line with the regional tectonic stress field.

ACKNOWLEDGMENT

Financial supports from National Natural Science Foundation of China (Nos. 51209021, 51379022, and 51179013) and Basic Research Fund for Central Research Institutes of Public Causes (Nos. CKSF2014065) are greatly acknowledged.

REFERENCES

Chen, B. & Tian, C.L. 1998. Numerical simulation technique for structures fractures in a reservoir case studies. *Acta Petrolei Sinica* 19 (04): 50–54.

Chen, N., Tang, Y.X. & Zhang, Q. 2014. Experimental Research about the Current Characteristic of the Fault Arc in Series based on Wavelet Analysis. *Procedia Engineering* 84: 736–741.

Itasca Consulting Group. 2015. Inc. Fast Lagrangian Analysis of Continua in 3 dimensions, *Users manuals*. version 5.0. USA: Itasca Consulting Group Inc.

Wang, Z., Deng, Q. & Du X. et al. 2006. Active fault survey on the Tanlu fault zone in Laizhou Bay. *Acta Seismologica Sinica* 19(05): 530–541.

Zoback, M.D. & Roller J.C. 1979. Magnitude of shear stress on the San Andreas fault: Implications of a stress measurement profile at shallow depth. *Science* 206(4417): 445–447.

This page intentionally left blank

Civil Engineering and Urban Planning IV – Liu et al. (Eds)
© 2016 Taylor & Francis Group, London, ISBN 978-1-138-02903-3

Analysis and comparison of the most reasonable height based on the stiffness characteristic for different types of flat vierendeel structures

Cui-Xia Wei, Ji-Ming Tian & Lu-Zhen Jiang
School of Civil Engineering, Hebei University of Science and Technology, Shijiazhuang BRA, Shijiazhuang, Hebei, China
Beijing Western Architectural Design Co. Ltd., Shijiazhuang BRA, Shijiazhuang, Hebei, China

ABSTRACT: For a long-span concrete floor and roof, the deformation is the main control index, therefore, analyzing the stiffness characteristics for the concrete floor and roof is very important. Based on this the stiffness characteristics for the vierendeel sandwich plate structure, including the flat vierendeel structure with upper ribbed slab, the flat vierendeel structure with the upper and down ribbed slab, were analyzed by FEM. The effects of the slab thickness, upper and down chord, vertical web member were studied. The analysis results show that: there is a most reasonable height for three types flat vierendeel structures, which could make the stiffness best and the deformation least. Furthermore, the most reasonable height decreases gradually for the different types flat vierendeel structures. Meanwhile the most reasonable height decreases gradually along with the slab thickness increasing, upper and down chord dimension increasing or vertical web member dimension decreasing. The conclusions could provide a theoretical basis for the design of the relevant projects to increase the stiffness and reduce the deformation.

1 INTRODUCTION

The flat vierendeel structure includes the vierendeel truss structure, the vierendeel gird structure, the vierendeel sandwich plate structure with the upper and down ribbed slab, the vierendeel sandwich plate structure with the upper ribbed slab, and so on. The flat vierendeel structure due to high stiffness, good economic index, and so on, is widely applied in all kinds of the long-span and large column-gird structure as the floor or roof in the building, such as Industrial Design Comprehensive Story in Guizhou University of Technology, Canteen in Hefei University of Technology, and so on. The flat vierendeel structure has been the main type in the concrete spatial structure.

For long-span concrete floor and roof, the deformation is the main control index, therefore, analyzing the stiffness characteristics for the concrete floor and roof is very important. But as the main structure type the theoretical system of the flat vierendeel structure is not perfect. The current studies about the flat vierendeel structure focus on the calculation method (Ma et al. 2006), the mechanical behavior (Dong 2009), and so on, but little on the stiffness characteristics. The literature (Wei 2007, Wei et al. 2012) only analyzed the stiffness characteristics for the vierendeel truss structure and the vierendeel gird structure, but did not analyze the stiffness characteristic for the vierendeel sandwich plate structure.

In view of this, firstly, the stiffness analysis of the vierendeel sandwich plate structure, which had the flat vierendeel structure with the upper ribbed slab, the flat vierendeel structure with upper and down ribbed slab, was taken into account. Furthermore, the comparison and analysis for three types' stiffness characteristic and the most reasonable height were done which could provide theoretical basis for the design of relevant projects using the reasonable height to increase the stiffness and reduce the deformation.

2 FINITE ELEMENT MODELING

In order to analyze the stiffness characteristic for the vierendeel sandwich plate structure, the orthogonal spatial finite element model simply supported on four sides was established, based on the finite element software ANSYS, the geometric parameters were as follows: the area of the plate was 13.5 m × 13.5 m, the dimension of the grid was 1.5 m, the number of the gird was 9 × 9. Applied unit vertical load on the model, concrete strength grade C30, using solid65 element, assumed that the material was uniform and linear, the effect of steel was ignored. The finite element models were established for the flat vierendeel structure with the upper and down ribbed slab, the flat vierendeel structure with upper ribbed slab in Figure 1.

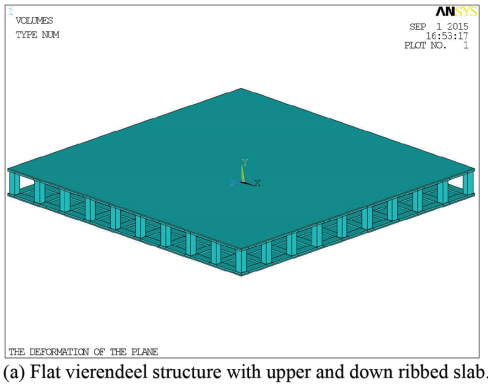

(a) Flat vierendeel structure with upper and down ribbed slab.

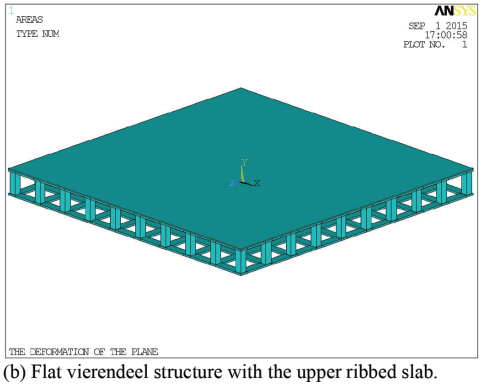

(b) Flat vierendeel structure with the upper ribbed slab.

Figure 1. Finite element models of the vierendeel sandwich plate structure.

Table 1. Model conditions.

Slab thickness (mm)	Upper and down chord dimension (mm × mm)	Vertical web member dimension (mm × mm)	Structure height (m)
45	400 × 75	300 × 300	[0.3:0.1:2.0]
55	400 × 95	250 × 250	
65	400 × 115	200 × 200	

In order to analyze the effects of the slab thickness, upper and down chord, vertical web member on the most reasonable height, the finite element model conditions were shown in Table 1, for every circumstance, the structure's height changed from 0.3 to 2.0 m, a total of 18 structure height, the deformation of the structure for every height was calculated.

For every circumstance, the bold data was the basic data in Table 1. Based on the bold data, other parameters are changed to calculate the corresponding deformation.

3 ANALYSIS OF THE STIFFNESS CHARACTERISTICS FOR THE VIERENDEEL SANDWICH PLATE STRUCTURE

3.1 *Effect of the slab thickness on the stiffness*

For the models shown in Figure 1, the dimension of the upper and down chord, and the vertical web member were same as in the bold data in Table 1, only changed was the slab thickness as shown in Table 1. For every circumstance, the deformation of the structure for every height could be obtained, and the results were shown in Figure 2.

As shown in Figure 2, there was a most reasonable height, which could make the stiffness best and the deformation least for the two types of flat vierendeel structure. The most reasonable height decreased gradually along with slab thickness increasing. Meanwhile, due to the down slab's effect, the deformation and the most reasonable height for the flat vierendeel structure with the upper ribbed slab were bigger than them for the flat vierendeel structure with the upper and down ribbed slab.

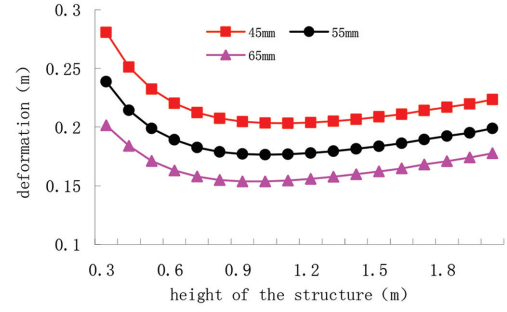

(a) Flat vierendeel structure with the upper and down ribbed slab.

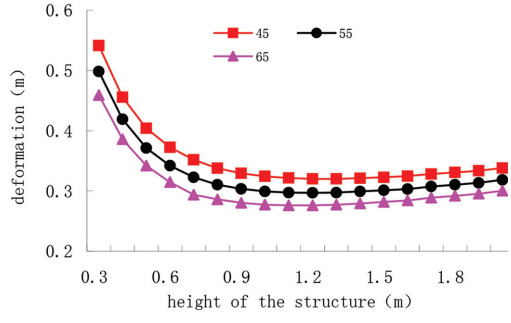

(b) Flat vierendeel structure with upper ribbed slab.

Figure 2. Diagram of deformation vs structural height for various slab thickness.

3.2 *Effect of the upper and down chord dimension on the stiffness*

For the models shown in Figure 1, the slab thickness and the dimension of the vertical web member were same as in the bold data in Table 1, only changed was the dimension of the upper and down chord as shown in Table 1. For every circumstance, the deformation of the structure for every height could be obtained and the results were shown in Figure 3.

As shown in Figure 3, there was a most reasonable height, which could make the stiffness best and the deformation least for the two types of flat vierendeel structure. The most reasonable height decreased gradually along with the upper and down chord dimension increasing. Meanwhile, due to the down slab's effect, the deformation and the most reasonable height for the flat vierendeel structure with upper ribbed slab was bigger than them for the flat vierendeel structure with the upper and down ribbed slab.

3.3 *Effect of the vertical web member dimension on the stiffness*

For the models shown in Figure 1, the slab thickness, the dimension of the upper and down chord,

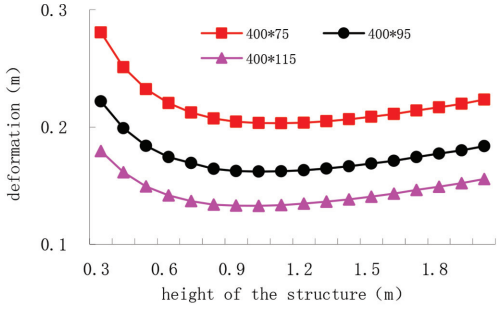

(a) Flat vierendeel structure with upper and down ribbed slab.

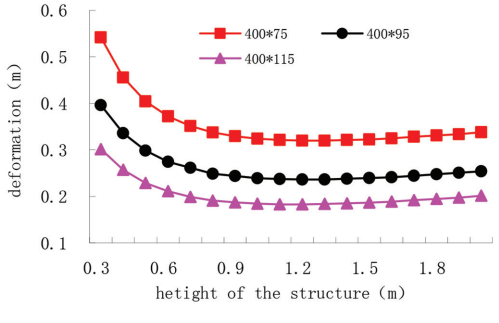

(b) Flat vierendeel structure with upper ribbed slab.

Figure 3. Diagram of deformation vs structural height for various upper and down chord dimensions.

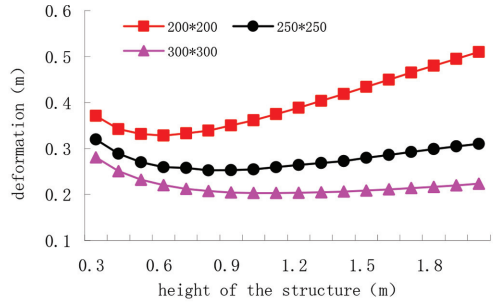

(a) Flat vierendeel structure with upper and down ribbed slab.

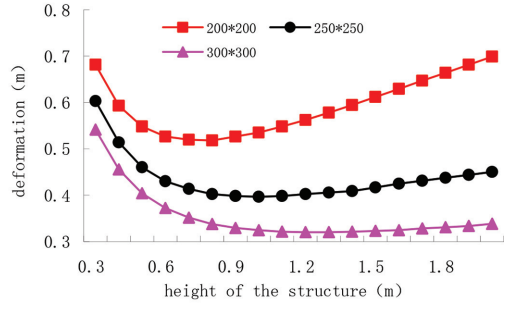

(b) Flat vierendeel structure with upper ribbed slab

Figure 4. Diagram of deformation vs structural height for various vertical web member dimensions.

were same to the bold data in Table 1, only changed the dimension of the vertical web member as shown in Table 1. For every circumstance, the deformation of the structure for every height could be obtained and the results were shown in Figure 4.

As shown in Figure 3, there was a most reasonable height, which could make the stiffness best and the deformation least for the two types of flat vierendeel structure. The most reasonable height increased gradually along with the vertical web member dimension increasing. Meanwhile, due to the down slab's effect, the deformation and the most reasonable height for the flat vierendeel structure with upper ribbed slab were bigger than them for the flat vierendeel structure with the upper and down ribbed slab.

4 COMPARISON AND ANALYSIS FOR THREE TYPES FLAT VIERENDEEL STRUCTURES

In order to analyze the stiffness characteristics for the three types flat vierendeel structures, three finite element models were established, the models for the flat vierendeel structures with upper and

down ribbed slab, the flat vierendeel structure with upper ribbed slab were still shown in Figure 1, the model for the vierendeel gird structure was shown in Figure 5. The three models had the same dimension to the bold data in Table 1. For the complete equivalent load, applied unit vertical surface load on the models shown in Figure 1, applied the complete equivalent vertical load on the upper ribbed beam in the Figure 5, the results for the three models were shown in Figure 6.

As shown in Figure 6, there was a most reasonable height for the three models, which can make the stiffness best and the deformation least. Meanwhile, due to the slab's effect, the deformation and the most reasonable height for the three types of flat vierendeel structures decreased significantly.

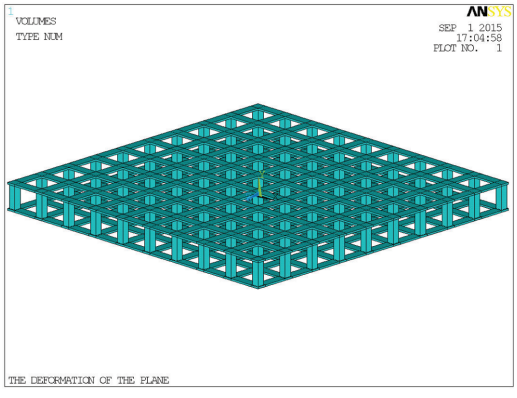

Figure 5. Finite element model of the vierendeel gird structure.

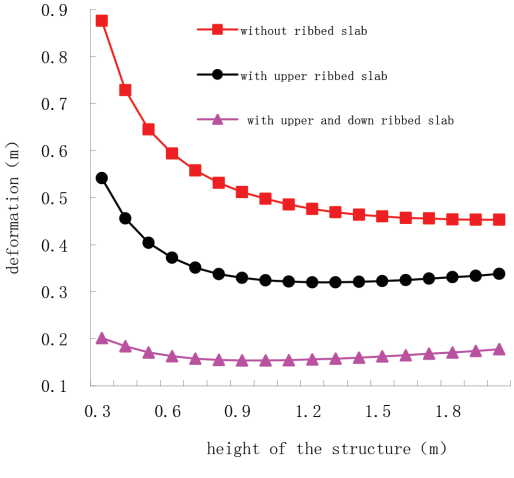

Figure 6. Diagram of deformation vs structural height for three types flat vierendeel structures.

5 CONCLUSION

Through comparison and analysis of the three types flat vierendeel structures, the flat vierendeel structure with upper and down ribbed slab, the flat vierendeel structure with upper ribbed slab and the vierendeel gird structure, the conclusions could be obtained as follows:

1. Three types of flat vierendeel structures all have a most reasonable height, which could make the stiffness best and the deformation least;
2. The influence law of the most reasonable height for the two types of vierendeel sandwich plate structures by the geometric parameters were analyzed. For instance, the most reasonable height decreases gradually along with the slab thickness increasing, upper and down chord increasing or vertical web member decreasing. The change flaw of the reasonable height could provide a theoretical basis for the design of relevant projects using the reasonable height to increase the stiffness and reduce the deformation.
3. For three types of flat vierendeel structures, the vierendeel gird structure, the flat vierendeel structure with upper ribbed slab, the flat vierendeel structure with upper and down ribbed slab, due to the slab's effect, the most reasonable height and the deformation decrease significantly.

ACKNOWLEDGMENT

This work was supported by the National Natural Science Foundation of China (51308182.), Natural fund of Hebei Province (E2014208143), and Shijiazhuang Science and Technology Support Program (11123511).

REFERENCES

Dong, S.L. 2009. The development history, innovation, classification and practical application of spatial structures. *Spatial Structures* 15(3): 22–43.

Ma, K.J., Zhang, H.G. & Zheng, T. 2006. *Theory and practice of new type architectural space griding structur.* Beijing: People's Communications Press.

Wei, C.X. 2007. *Study the Mechanics Inbeings of Open-web Grids and Open-web Sandwich Plates from the Stiffness Variety*. Hangzhou: Zhejiang University.

Wei, C.X., Liu, W.P. & Haung, L. 2012. Determination of the most reasonable height based on the stiffness characteristic for flat vierendeel structures. *Journal of Hebei University of Science and Technology* 8(1): 355–359.

Civil Engineering and Urban Planning IV – Liu et al. (Eds)
© 2016 Taylor & Francis Group, London, ISBN 978-1-138-02903-3

Numerical damage analysis of masonry structure strengthened with FRP composite material

Zhen Lei
School of Urban Construction and Management, Yunnan University, Kunming, Yunnan, China

Yan Xu
Institute of Technology, Baoshan College, Baoshan, Yunnan, China

Yong Wang
Chengdu JZFZ Architectural Design Co. Ltd., Chengdu, Sichuan, China

Jun-Tong Qu
School of Urban Construction and Management, Yunnan University, Kunming, Yunnan, China

ABSTRACT: In this paper, representative volume element is used to present the material composed of brick and mortar to simplify the modeling of masonry structure. A kind of concrete damage plasticity model is chosen for masonry, which can be used for a good simulation of structural damage and failure process. Based on the former experimental test, a finite element model of (FRP-strengthened) masonry structure is built to make a research on the damage analysis in terms of damage contour and damage parameter under the earthquake wave input. The numerical results are compared to the experimental damage phenomenon to verify the effectiveness of numerical analysis.

1 INTRODUCTION

Based on the experimental researches (Cao et al. 2014; Fan et al. 2012; Lei et al. 2013; Zhou et al. 2013; Lei et al. 2014), the results show that FRP-strengthening technique has no significant effect on the improvement of structure stiffness, but it can greatly improve the ultimate deformation capacity. Due to the confinement effect offered by FRP, the failure mode gets changed which postpones and even prevents the development of a major crack and yields more smeared crack distribution. The FRP-strengthened masonry wall or structure has better energy dissipation capacity and safety reservation.

Once the main tensile stress or main compressive stress exceeds the ultimate tensile or compressive strength of masonry material, the cracks develop in a horizontal or diagonal direction. In the former test, the experimental specimens exhibited no obvious compression failure, which only can be found at the bottom corner. Therefore, the paper focuses on the numerical tension damage analysis.

2 NUMERICAL MODELING FOR (FRP-STRENGTHENED) MASONRY STRUCTURE

The modeling of (FRP-strengthened) masonry structure has been illustrated in (Lei et al. 2014) detailed. Here, masonry walls, structural columns and floor slabs are modeled using solid element C3D8R, and FRP strips are modeled using membrane element M3D4R. The constitutive curves of masonry compression and tensile relationship are shown in (Yang 2008). According to the principle of energy equivalence, the compression and tension damage equation of masonry material can be obtained as follows:

$$\begin{cases} D = 0 & 0 \le \dfrac{\varepsilon}{\varepsilon_t} \le 1 \\ D = 1 - \sqrt{\dfrac{1}{\alpha_t (x-1)^{1.7} + x}} & \dfrac{\varepsilon}{\varepsilon_t} \ge 1 \end{cases} \tag{1}$$

The final meshed models (Lei et al. 2014) are shown in Figure 1.

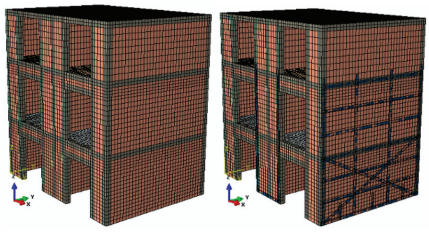

(a) Unstrenthened model A_{FEM} (b) FRP-strengthened model B_{FEM}

Figure 1. Finite element analytical model.

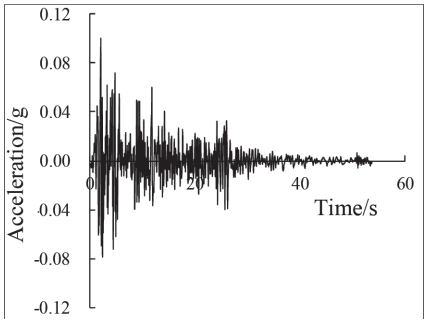

Figure 2. El-Centro wave diagram.

During the modeling process, no parameters related to crack are introduced; no crack can be shown in the numerical result, but the shape and position of the crack can be confirmed according to the tension damage contour (DAMAGET), which reflects the value of plastic strain and the extent of damage. The models are still in the elastic state under basic 7 seismic waves, and the value of damage parameter is relatively small. As the seismic intensity increases, the structure damage gets more serious. Therefore, this paper studies the damage state of (FRP-strengthened) masonry structure under rare 8 seismic El-Centro waves. The seismic wave diagram is shown in Figure 2, which is input to the loading system with a designed acceleration peak value of 0.4 g.

3 RESULTS AND DISCUSSION

3.1 *Tension damage contour*

Tension damage contours (DAMAGET) of model A_{FEM} and B_{FEM} at different loading moment are shown in Figures 3 and 4, and the final damage contours are compared with the experimental phenomenon (Lei et al. 2013). The damage extent gets more serious from blue to red in the contour.

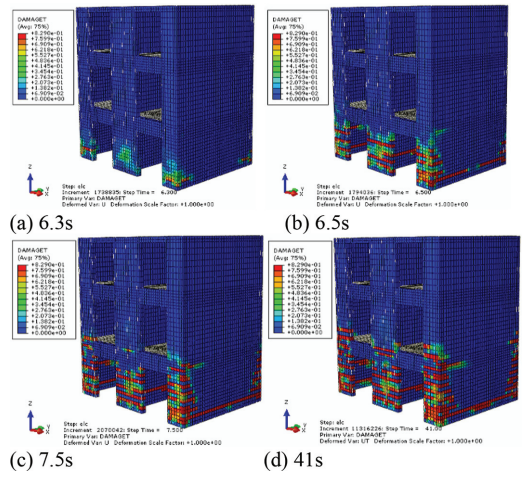

Figure 3. Tension damage contour of model A_{FEM}.

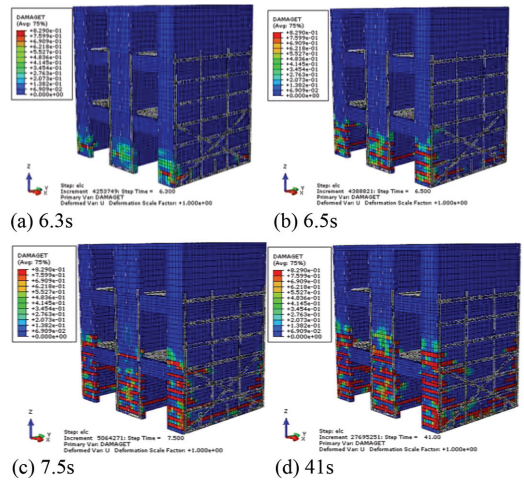

Figure 4. Tension damage contour of model B_{FEM}.

The location and developing trend of crack exhibited in numerical analysis is basically agreed with the experimental phenomenon. Horizontal cracks can be observed at the bottom transverse walls (axis ① and ③) and longitudinal walls (axis Ⓐ) as well as structural columns. Diagonal crack cannot be obviously reflected in the contour, because the effect of cumulative damage cannot be considered in the modeling process. Both models (A_{FEM} and B_{FEM}) have the same trend of cracking development. At the same loading moment, model B_{FEM} shows more severely damage and yields a more smeared crack distribution.

3.2 *Tension damage parameter*

At the later stage of loading process (≥20s), the damage phenomenon of the models stays unchanged which means that the tension damage value of each masonry element remains stable. In Figures 5 and 6 it shows the average value of tension damage parameter-time curve of transverse walls in each floor between 0 and 20 seconds. Table 1 shows the average value of tension damage parameter of transverse walls in 1 st and 2nd floor (axis ① and ③) after 20 seconds.

As the loading continues, the structural damage tends to be more serious. Due to the brittle characteristics of masonry structure, the model reaches the maximum damage extent at the maximum acceleration peak value and then keeps it unrecoverable till the end of seismic wave input. The structural damage mainly focuses on the first floor and gradually reduces from bottom to top. The damage extent of transverse walls in axis ① and ③ is closer because of asymmetrical model.

Both models almost turn to plastic state at the same loading moment (6s) corresponding to the ground motion amplitude (0.166 g), and reach the maximum state at 12 seconds corresponding to the ground motion amplitude 0.023 g. Compared to model A_{FEM}, the damage extent of transverse walls of strengthened model B_{FEM} is 30.4% and 21.6% higher in axis ① and ③, respectively. It proves that the FRP-strengthening technique can make the masonry wall crack more fully and increase the energy dissipation capacity. At the same time, FRP laminates can restrain the crack width and maintain the integrity of the structure.

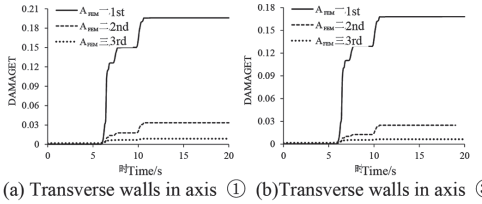

(a) Transverse walls in axis ① (b)Transverse walls in axis ③

Figure 5. Tension damage contour of model A_{FEM}.

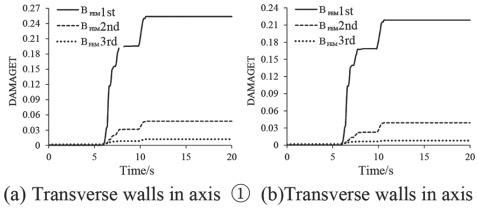

(a) Transverse walls in axis ① (b)Transverse walls in axis ③

Figure 6. Tension damage contour of model B_{FEM}.

Table 1. Average value of tension damage parameter.

	Transverse walls of model A_{FEM}			
Floor	1 st floor	2nd floor	1 st floor	2nd floor
axis	axis ①	axis ①	axis ③	axis ③
A_{FEM}	0.1959	0.0334	0.1681	0.0248
B_{FEM}	0.2539	0.0476	0.2187	0.0392

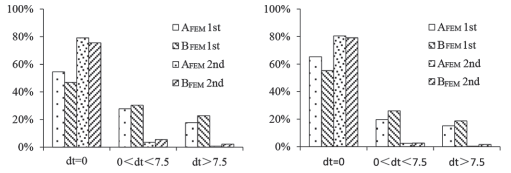

(a) Transverse walls in axis ① (b)Transverse walls in axis ③

Figure 7. Distribution of tension damage.

Table 2. Distribution ratio corresponding to dt > 0.75.

	Transverse walls of model A_{FEM}			
Floor	1 st floor	2nd floor	1 st floor	2nd floor
axis	axis ①	axis ①	axis ③	axis ③
A_{FEM}	17.71%	0.83%	15.10%	0.42%
B_{FEM}	22.74%	2.71%	18.75%	1.88%

3.3 *Distribution of tension damage*

According to the constitutive relationship model and defined criteria of plastic parameters for masonry material, the strain reaches 4 times the strain corresponding to the maximum stress when the value of tension damage parameter (dt) equals 0.75. Therefore, crack develops when dt > 0.75. Figure 7 shows the distribution of tension damage at different extent (dt = 0, 0 < dt ≤ 0.75, dt > 0.75) for transversal walls located in the 1 st and 2nd floor. Table 2 lists the detailed value of distribution ratio corresponding to dt > 0.75.

A large proportion of the walls both in the 1 st and 2nd floor are still in the elastic state (dt = 0). At the region of dt > 0.75, Distribution ratio in 1 st and 2nd floor for model B_{FEM} is 15.8% and 44.5% higher than that for model A_{FEM}.

4 CONCLUSION

The numerical results prove that the tension damage contour and parameter can effectively simulate

the crack development in the experimental test. Due to the more smeared crack distribution, the FRP-strengthened masonry structure has better energy dissipation capacity and seismic performance as well as higher safety reservation, which can make the structure withstand more severe earthquake. Representative volume element can significantly simplify the numerical analysis of masonry structure and accurately reflect the seismic response of FRP-strengthened masonry structure.

ACKNOWLEDGMENTS

The research had been sponsored by Yunnan Provincial Education Office Scientific Research Foundation (2014Z008), Scientific Research Projects Foundation of Yunnan University (2014CG012) and Yunnan Applied Basic Research Projects Foundation (2015FD005).

REFERENCES

Cao, L.Y., Wang, L.H., Li, Z.W. et al. 2014. Experimental study on the reinforcement masonry structure of carbon fiber nail and carbon fiber cloth. *Journal of Wuhan University of Technology* 36(6): 109–114.

Fan, Y., Zuo, H.L. & Guo, L. 2012. Experimental study on the test of masonry walls strengthened with CFRP under low-cyclic loads. *Journal of Shenyang Jianzhu University* 28(22): 208–214.

Lei, Z., Zhou, D.Y. & Li, Y.M. 2013. Shaking Table Test of Earthquake-damaged Masonry Structure Strengthened with External FRP. *IABSE Symposium Report, Rotterdam, 2013*.

Lei, Z., Wang, Y. & Qu, J.T. 2014. Nonlinear dynamic finite analysis of FRP-strengthened masonry structure based on ABAQUS. *Advanced Materials Research* 936: 1331–1335.

Yang, W.Z. 2008. Constitutive relationship model for masonry materials in compression. *Building structures* 38(10): 80–82.

Zhou, D.Y., Lei, Z. & Wang, J.B. 2013. In-plane behavior of seismically damaged masonry walls repaired with external FRP. *Composite Structure* 102: 9–19.

Civil Engineering and Urban Planning IV – Liu et al. (Eds)
© 2016 Taylor & Francis Group, London, ISBN 978-1-138-02903-3

Improved Duncan-Chang model's application in pit lateral unloading simulation

Li-Hong Cheng
State Key Laboratory Breeding Base of Nuclear Resources and Environment, Fundamental Science on Radioactive Geology and Exploration Technology Laboratory, Nanchang, Jiangxi, China
College of Architecture Engineering, East China Institute of Technology, Nanchang, Jiangxi, China

Guo-Lin Liu
No 2 Hydropower Force of Armed Police, Nanchang, Jiangxi, China

Ai-Fei Li
College of Architecture Engineering, East China Institute of Technology, Nanchang, Jiangxi, China

ABSTRACT: This Paper improved the nonlinear elastic Duncan-Chang model by using the rock and soil elastic plastic theory. This paper introduces finite element program to simulate pit excavation lateral unloading process, according to Duncan-Chang model and Goodman surface unit. The theoretical calculation results fairly approach measured values, which verifies the rationality of the improved Duncan-Chang model.

1 INTRODUCTION

Because of the complexity of soil deformation characteristics, the calculation of soil deformation should use different models or parameters according to different load conditions.

Because the Duncan-Chang model (Li 2004) parameters could be obtained by the conventional triaxial test, Duncan-Chang model is widely used as one of the constitutive models. For example, Donald, Abdulaziz, Xiao-yan Li, Jian-lin Yu, Yi-hong Lou, etc., they all used the Duncan-Chang model to simulate pit excavation process (Abdulaziz & Clough 1981; Donald et al. 1975; Li 2004; Lou et al. 2003; Yu & Gong 2002). However, the Duncan-Chang model was obtained in the case of the lateral stress invariant and the axial stress increased. But in the pit excavation project, the soil is in the unloaded condition which is different from the characteristics of loading. Therefore, the results would be a large deviation if we use the loading test parameters to calculate the lateral displacement of pit project. It caused the Duncan-Chang model to not be used well to simulate pit project. So, this paper firstly according to the Duncan-Chang model to derive a modulus equation of the lateral unloading stress path; then, the finite element program is compiled to simulate the elastic-plastic characteristics of soil deformation. Comparing the finite element calculation results with the measured values, we find that the calculation results from the improved Duncan-Chang model are more reasonable, which is suitable for the pit excavation simulation analysis.

2 FINITE ELEMENT MODEL OF LATERAL UNLOADING STRESS PATH

2.1 *The improved Duncan-Chang model (Yin et al. 2007)*

Homogeneous isotropic soil is assumed, according to the increment of the generalized Hooke's law:

$$E = \frac{\Delta\sigma_a\left(\Delta\sigma_a + \Delta\sigma_r\right) - 2\Delta\sigma_r^{\,2}}{\Delta\varepsilon_a\left(\Delta\sigma_a + \Delta\sigma_r\right) - 2\Delta\varepsilon_r\Delta\sigma_r} \tag{1}$$

where $\Delta\sigma_a$ and $\Delta\sigma_r$ are the axial and lateral stress increment; $\Delta\varepsilon_a$ and $\Delta\varepsilon_r$ are the axial and lateral strain increment; E is elastic modulus.

When the axial stress increment $\Delta\sigma_a = 0$, the lateral stress increment $\Delta\sigma_r \neq 0$, relationship between stress and strain can be written as:

$$E = \frac{-2\Delta\sigma_r}{\Delta\varepsilon_a - 2\Delta\varepsilon_r} = \frac{\partial\left[2\left(\sigma_a - \sigma_r\right)\right]}{\partial\left(\varepsilon_a - 2\varepsilon_r\right)} \tag{2}$$

In case of hyperbola fitting for the relationship of $2(\sigma_{rc}-\sigma_r)$ and $\varepsilon_a-2\varepsilon_r$, where σ_{rc} is lateral consolidation pressure. At the same time, assuming that the initial tangent modulus changes with the axial consolidation pressure σ_{ac} changes, that is:

$$E_i = kp_a\left(\frac{\sigma_{ac}}{p_a}\right)^n \tag{3}$$

The Moore strength criterion for the destruction deviator stress is:

$$(\sigma_a-\sigma_r)_f = \frac{2c\cos\varphi+2\sigma_{ac}\sin\varphi}{1+\sin\varphi} \tag{4}$$

Because of $\sigma_a=\sigma_{ac}=\text{const}$, equation (2) can be turned into:

$$E_t = kp_a\left(\frac{\sigma_{ac}}{p_a}\right)^n \left\{1-R_f\frac{(\sigma_{rc}-\sigma_r)(1+\sin\phi)}{2c\cos\phi+2\sigma_{ac}\sin\phi-(\sigma_{ac}-\sigma_{rc})(1+\sin\phi)}\right\}^2 \tag{5}$$

For the isotropic consolidation, $\sigma_{rc}/\sigma_{ac}=k_0=1-\sin\varphi=1$, equation (5) can be turned into:

$$E_t = kp_a\left(\frac{\sigma_{ac}}{p_a}\right)^n \left\{1-R_f\frac{(\sigma_{rc}-\sigma_r)(1+\sin\varphi)}{2c\cos\varphi+2\sigma_{ac}\sin\varphi}\right\}^2 \tag{6}$$

$\sigma_{rc}=\sigma_{ac}=\sigma_1$, $\sigma_r=\frac{\sigma_2+\sigma_3}{2}$, the equation above can be turned into:

$$E_t = kp_a\left(\frac{\sigma_{ac}}{p_a}\right)^n \left\{1-R_f\frac{\left(\sigma_1-\frac{\sigma_2+\sigma_3}{2}\right)(1+\sin\varphi)}{2c\cos\varphi+2\sigma_1\sin\varphi}\right\}^2 \tag{7}$$

In addition, the expression of tangent bulk modulus:

$$B_t = k_b p_a\left(\frac{\sigma_3}{p_a}\right)^m \tag{8}$$

By the equations (7) and (8) can be seen, the improved Duncan-Chang model has seven parameters: c, φ, R_f, k, n, k_b m.

2.2 *Goodman surface unit*

In the pit excavation, the relative displacement occurred between soil and support structure, and, the soil and support structure is noncontinuous, so we need to set up continuous contact element. The Goodman unit (Goodman 1976) is a four node element without thickness, and two pieces of contact surface are imaging linked by the countless normal and tangential tiny springs, which can be used to simulate the contact surface dislocation and division, and widely used.

2.3 *Analysis of support*

In practical engineering, there are steel support, reinforced concrete support and various other forms of support. For simplicity, reflect the actual project situation in a certain extent, the elastic support form is used in simulation calculation. When the excavation to a certain depth, pile shift in pit, supporting the resulting displacement ΔL, and generates a reaction force F of piles. The equation $\varepsilon=\frac{\Delta L}{L}=\frac{F}{AE}$ can be deduced in this reaction F, the reaction in the pile body, iteration, and inverse displacement of pile body.

2.4 *Analysis of the excavation process*

Due to geotechnical engineering problems belong to the elastic-plastic problem, the strain and the displacement depends on not only the stress state, but also the stress history. So the final results by the finite element method have great relevance with the simulation of pit excavation process. Simulation of excavation in the finite element method, the key point is to make the excavation surface become stress free surface, and completely remove the stress from the excavation surface. Therefore, each excavation level needs to be determined, and the force which is from the upper soil to the lower soil has to be according to the pre-excavation stress. After excavation, the force is counterproductive to the excavation surface, and at the same time, the upper soil of the structure has to be removed and dug up, then the next step of finite element is the calculation.

3 PROGRAM CHART

The finite element program consists of a main program and several subroutines, as the program Chart shown in Figure 1.

4 EXAMPLE OF CALCULATION

Some pit engineering, calculation plane is 18 m*125 m, ground overload is 16 kpa, the excavation depth is 9 m, underground continuous wall supporting structure with 17.5 m depth

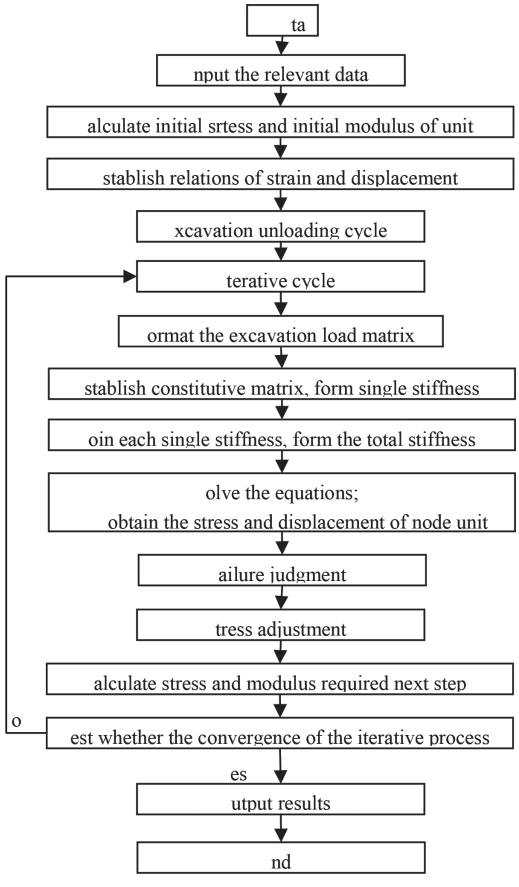

Figure 1. Program chart.

and 0.8 m thickness. Elastic modulus is 2.3×10^4 MPa, Poisson's ratio is 0.18. A total of two layers, first layer 2.0 m under the ground, second layer under the ground 5.5 m, and the support stiffness is 16800 kN/m. The soil is clay, its parameters (Zhao & Zhang 2009) are shown in Table 1.

The lateral displacement of retaining wall is calculated respectively for the Duncan-Chang model and the improved Duncan-Chang model by the finite element program, the calculation results of the two models and the measured values are drawing in Figure 2.

As can be seen from Figure 2, the maximum lateral displacement of the retaining wall according to the result of Duncan-Chang model is 34 mm, according to the improved Duncan-Chang model calculation result is 26 mm, the measured value is the 22 mm. Therefore, calculation result of the displacement of the retaining wall by using the improved Duncan-Chang model is more reasonable.

Table 1. Soil parameters.

Model type	c	φ	R_f	k	n	v	k_{ur}
Duncan-Chang Model	44	12	0.85	400	0.35	0.44	400
Improved Duncan-Chang Model	44	12	0.85	400	0.35	0.44	–

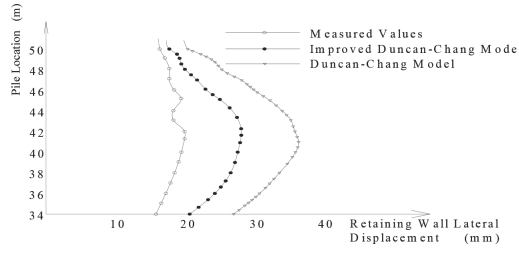

Figure 2. Lateral displacements of retaining wall on Duncan-Chang and improved Duncan-Chang and measured values.

5 CONCLUSION

According to the stress and displacement caused by pit excavation, the paper established a finite element model to analyze and calculate, and use the finite element program to calculate the retaining wall lateral displacement by Duncan-Chang model and improved Duncan-Chang model. Calculation results obtained by using the improved Duncan-Chang model are fairly approached the measured values, which verify the improved Duncan-Chang model is more reasonable, and provides a reference for the design of pit support.

ACKNOWLEDGMENTS

This work was financially supported by the principal fund project of East China Institute of Technology (DHXK1127) and research on teaching reform of colleges and universities in Jiangxi Province (JXJG-14-6-7).

REFERENCES

Abdulaziz, I.M., & Clough, G.W. 1981. Prediction of movements for braced cuts in clay. *Journal of the Geotechnical Division* 107(6): 759–775.

Donald, J.M., Clough, G.W. & Robert, S.W. 1975. Temporary excavation in varved clay. *Journal of the Geotechnical Engineering Division* 101(3): 279–295.

Goodman, R.E. 1976. *Methods of Geological Engineering in Discontinuous Rocks*. USA: West Publishing Company.

Li, G.X. 2004. *Advanced Soil Mechanics.* Beijing: Tsinghua University Press.

Li, X.Y. 2004. Fully coupling analysis of seepage and stress for deep foundation pit based on displacement back analysis. *Chinese Journal of Rock Mechanics and Engineering* 23(8): 1269–1274.

Lou, Y.H., Yu, S.F. & Wang, B.Y. 2003. Analysis on internal force and deformation of support structure for foundation pit. *Chinese Journal of Rock Mechanics and Engineering* 22(3): 462–466.

Yin, D.S., Wang, B.T. & Wang, Y.T. 2007. Tangent elastic modulus of Duncan-Chang model for different stress paths. *Chinese Journal of Geotechnical Engineering* 29(9): 1380–1385.

Yu, J.L. & Gong, X.N. 2002. Research on deformation of foundation-pit engineering. *China Civil Engineering Journal* 35(4): 86–90.

Zhao, Q.S. & Zhang, C.H. 2009. Improved Duncan-Chang model and its application in pit excavation simulation. *Journal of Hebei University of Science and Technology* 30(2): 149–150.

Civil Engineering and Urban Planning IV – Liu et al. (Eds)
© 2016 Taylor & Francis Group, London, ISBN 978-1-138-02903-3

Earthquake response of cable-stayed bridge with local cable vibration under long-period ground motion

Bai-Ben Chen, Zhong-Ren Feng & Bei-Bei He
School of Civil Engineering and Architecture, Wuhan University of Technology, Wuhan, Hubei, China

Xue-Feng Wang
China Highway Engineering Consulting Corporation, Beijing, China

ABSTRACT: Three typical long-period seismic waves were selected to compare the ordinary seismic waves for time domain and frequency domain analysis. Based on the results, the finite element software ANSYS was used to establish the finite element model of a half floating cable-stayed bridge which has long central span of 926 m and hybrid girder. Two finite element models of cable for large-span cable-stayed bridge, single-element cable system, and multiple-element cable system, can be used to complete the structural dynamic characteristics analysis. The nonlinear time-history analysis of earthquake response of structure under the long-period seismic waves were compared with that of ordinary seismic waves, and the earthquake response of the long-span cable-stayed bridge with local cable vibration was discussed, also the reference for seismic design of long-span bridges was provided.

1 INTRODUCTION

With long-period natural vibrations and obvious effects to structure by higher modes of vibration, the earthquake response to the long-span cable-stayed bridge is complex. Especially, the earthquake response analysis and seismic design will become more complicated when the nonlinear impact is taken into account. At present, ordinary seismic waves are usually used for excitation in the seismic design of long-span bridge ignore the long-period characteristics of structure. It makes that the earthquake response analysis doesn't reflect the most adverse effects to structure comprehensively under the action of earthquake ground motion (Li & Zhang 2006). The characteristics of long-period ground motion are complex and depend upon several parameters (Chen et al. 2014). The damage to the structure by long-period ground motion has happened in the history (Zang & You 2012). For the long-span cable-stayed bridge, the impact of long-period ground motion should be studied further, and it's necessary to analyze the earthquake response for the long-span cable-stayed bridge with local cable vibration under the long-period seismic waves.

Three typical long-period seismic waves were selected to compare with the ordinary seismic waves for time domain and frequency domain analysis. Based on the results, the finite element software ANSYS was used to establish the finite element model of a half floating cable-stayed bridge which has long central span of 926 m and hybrid girder. Two finite element models of cable for large-span cable-stayed bridge, Single-Element Cable System (SECS), and Multiple-Element Cable System (MECS), can be used to complete the structural dynamic characteristics analysis. The time history analysis of earthquake response of structure under the long-period seismic waves were compared with that of ordinary seismic waves, and the earthquake response of the long-span cable-stayed bridge with local cable vibration was discussed, also the reference for seismic design of long-span bridges was provided.

2 CHARACTERISTICS OF GROUND MOTION

2.1 *Characteristics of time domain analysis*

The long-period seismic waves have low frequency components in abundance (Boore 2004; Koketsu & Miyake 2008). The three selected long-period seismic waves are: TCU026 (NS) wave and TCU136 (EW) wave which recorded Chi-Chi earthquake (in 1999) in Taiwan, and CBGS (N89 W) wave was recorded in Christchurch Botanical Gardens in Darfield earthquake which happened in New Zealand in 2010. The ordinary seismic waves including El Centro (NS) wave, Taft (N21E) wave and San Fernando wave (in 1971) were chosen for

Table 1. Characteristics of selected seismic waves.

Seismic waves*	Year	Magnitude	Peak acceleration (gal)	Recording time (s)
TCU026 (NS)	1999	7.6	73.4	90
TCU136 (EW)	1999	7.6	117.9	90
CBGS (N89 W)	2010	7.0	139.8	150
El Centro (NS)	1940	6.4	341.7	53.76
Taft (N21E)	1952	7.7	152.7	54.38
San Fernando	1971	6.5	207.9	28

*Waves are from PEER ground motion database of pacific earthquake engineering research center.

comparison and analysis. The time domain characteristics of seismic waves were shown in Table 1, and two typical acceleration time history chart of seismic waves was shown in Figure 1. Some properties can be concluded by time domain analysis, which is that the long-period compositions of the long-period seismic waves are very rich as compared to ordinary seismic waves, the length of period is longer, and the peak acceleration is smaller. The moment which peak acceleration happened is later than the one of ordinary seismic waves.

2.2 *Characteristics of frequency domain analysis*

As compared to the ordinary seismic wave, long-period seismic wave has its unique properties in the frequency domain analysis. The frequency domain characteristics of seismic wave can be shown by Fourier amplitude spectrum (Xie et al. 1990). Mathematical software MATLAB was used to make Fast Fourier Transformation (FFT), and the Fourier amplitude spectrums of the six seismic waves were compared with each other. As Figure 2 shown and from the results, the frequency of El Centro (NS) wave mainly are 1–4 Hz; Taft (N21E) wave mainly are 1–5 Hz; and 0.5–6 Hz are belonged to the San Fernando wave; all of that have very rich high frequency components. Conversely, the frequency of TCU026 (NS) wave mainly are 0.1–1.7 Hz, TCU136 (EW) wave are 0.1–1 Hz, CBGS (N89 W) wave are 0.2–2 Hz, which frequency are concentrated in low frequency zone.

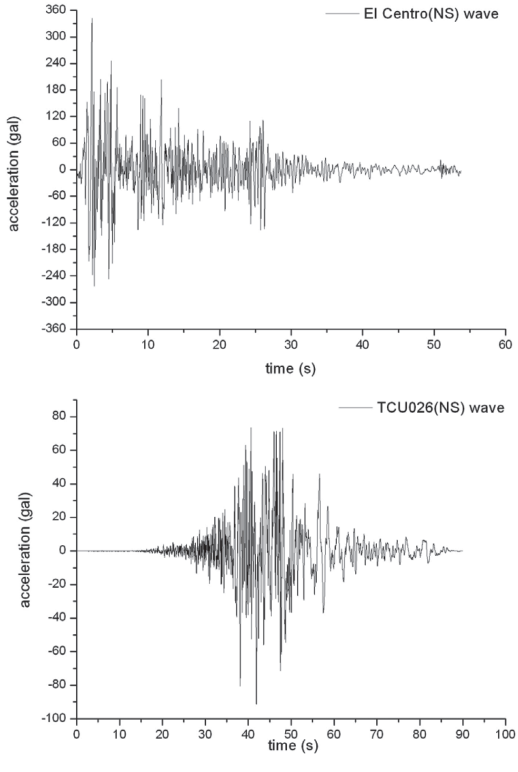

Figure 1. Acceleration time history chart of seismic waves.

2.3 *Standard acceleration response spectrum*

The acceleration response spectrum can reflect the impact on the structure by the seismic wave in the time range. In order to show the difference between the long-period seismic waves and ordinary seismic waves, two standard acceleration response spectrums with 5% damping ratio were drawn, which were long-period seismic waves and ordinary seismic waves, as shown in Figure 3. From this figure, the amplification coefficient β of long-period seismic waves are much greater than that of ordinary seismic waves in the long period parts, and the amplification effect on structure by ordinary seismic waves are mainly concentrated within the range of 0–2.5 s, the effect to the structure by the response spectrum of long-period seismic wave has a wide range of cycle domain, which is from 0 to 9 s. Thus, it can be seen that, the long period components of long-period seismic wave has great effect to the

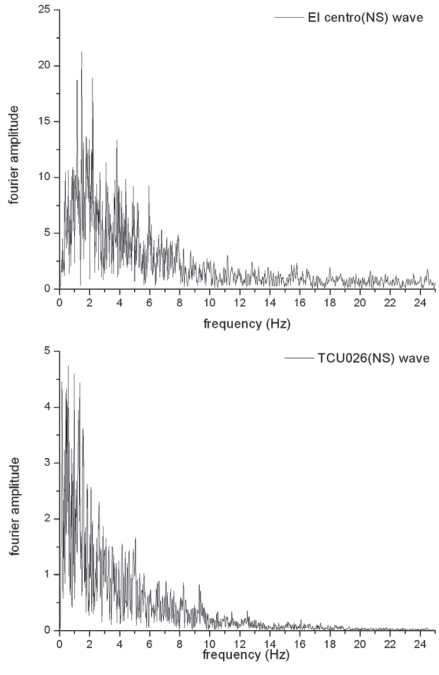

Figure 2. Fourier amplitude spectrum of seismic waves.

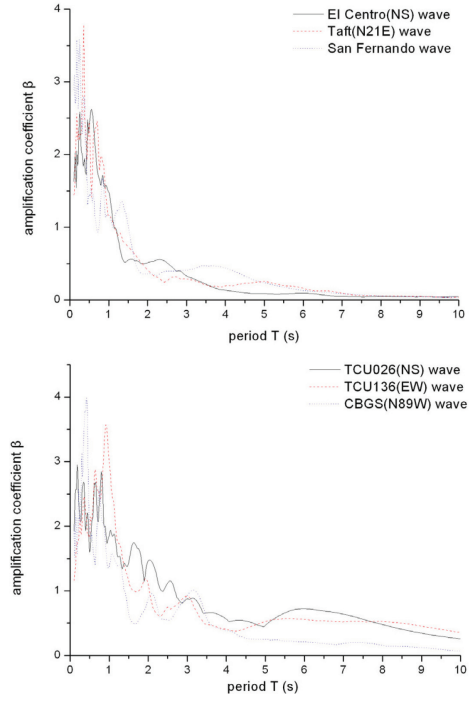

Figure 3. Standard acceleration response spectrums of seismic waves.

earthquake response of the structure in the long period parts, which also will have a significant effect to the structure with long natural vibration period.

3 FINITE ELEMENT MODEL AND DYNAMIC CHARACTERISTICS OF LOCAL VIBRATION

3.1 *Engineering background and finite element model*

The long-span cable-stayed bridge has two towers and hybrid girder with half floating system. Total length of the bridge is 1,476 meters, and the span arrangement is $3 \times 67.5 + 72.5 + 926 + 72.5 + 3 \times 67.5$ m, three auxiliary piers are set in both sides, and the main bridge is connected with approach bridges by auxiliary piers. The main girder of side span is pre-stressed concrete structure with box section, strength grading of concrete is C55. Separated pair of box section is used in the steel box girder, and the joint surface of steel and concrete is 12.5 m from the center line of the cable tower. The strength of cables is 1670 MPa, the whole bridge has 30 cables in each sector, and total has 240 cables.

Finite element software ANSYS was used to establish the model of the bridge, single-element cable system and multiple-element cable system were analyzed. "Fish bone beam model" is used to simulate the main girder. The main girder, main tower and pier were simulated by unit beam 188, cable simulated by unit link 10 and "fish bone beam" simulated by unit beam 4. The bottom of cable and the end of "fish bone beam" are linked together, and the top of cable and the main tower were coupled. The input of cable force is the final hanger force. The model took into account geometric stiffness of dead load. Finite element model of the bridge was shown in Figure 4.

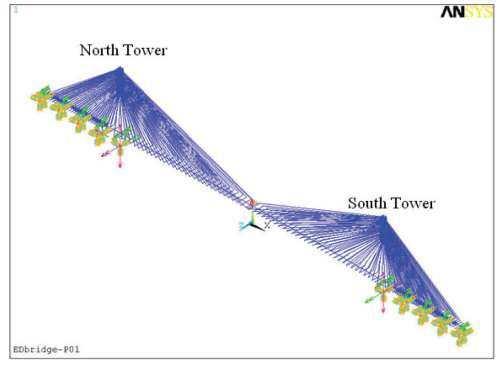

Figure 4. Finite element model of the bridge.

Table 2. Natural vibration period of the bridge (s).

Order	Model 1 (SECS)	Model 2 (cable dividing Num is 5)	Model 3 (cable dividing Num is 10)
1	11.107	11.044	11.036
2	6.507	6.354	6.334
3	4.499	4.398	4.386
4	3.894	3.844	3.837
5	3.664	3.600	3.593
6	3.039	3.026	3.024
7	2.583	2.541	2.536
8	2.486	2.466	2.466
9	2.467	2.422	2.414
10	2.217	2.174	2.169

Table 3. Dynamic properties of the bridge.

Order	Dynamic properties
1	Longitudinal floating of girder
2	First symmetrical side bending of girder
3	First symmetrical vertical bending of girder
4	First anti-symmetrical vertical bending of girder
5	Second symmetrical vertical bending of girder
6	Second anti-symmetrical vertical bending of girder
7	First anti-symmetrical side bending of girder
8	Second symmetrical vertical bending of girder
9	First side bending of left tower
10	Third anti-symmetrical vertical bending of girder

3.2 *Dynamic characteristics analysis of local vibration*

Block Lanczos method was used for structural vibration characteristics analysis, one set of SECS model and two sets of MECS model (segment of the cable is 5 or 10) were compared with each other's (Abdel-Ghaffar & Khalifa 1991), which shows that the vibration dynamic properties of the whole bridge, as shown in Tables 2 and 3. The first order fundamental period is long, and the period is around 11.1 s, which belongs to the long period structure. After considering local cable vibration, the impact on the natural periods of the structure is small, and the natural periods reduce slightly. More cable vibration modes and the cable and beam coupling vibration modes show up, which make the natural vibration modes of the whole bridge appear later.

4 ANALYSIS OF EARTHQUAKE RESPONSE

To analyze the earthquake response of bridge structure with local cable vibration under long-period seismic waves and normal seismic waves, the peak acceleration of selected seismic waves were adjusted to 50 gal (cm/s^2). The ground motion was placed along the x direction ignoring the horizontal and vertical ground motions. The spatial correlation of seismic wave weren't considered, using the consistent excitation input.

4.1 *Deformation analysis*

Taking the longitudinal displacement of node 1067 which is at the top of the north tower for analysis object, the displacement time history curves under two groups of seismic wave were shown in Figures 5–8. The longitudinal displacements at the top of tower and in the middle of main span under different seismic waves are shown in Tables 4 and 5.

From the figures and tables above, it can be concluded that the response of the same structure under the two groups of different seismic waves

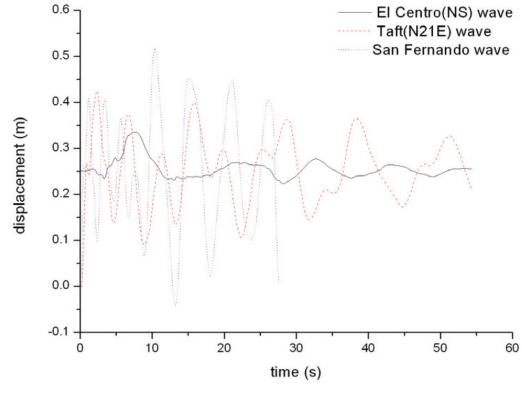

Figure 5. Displacement at the top of north tower under ordinary seismic waves (SECS model).

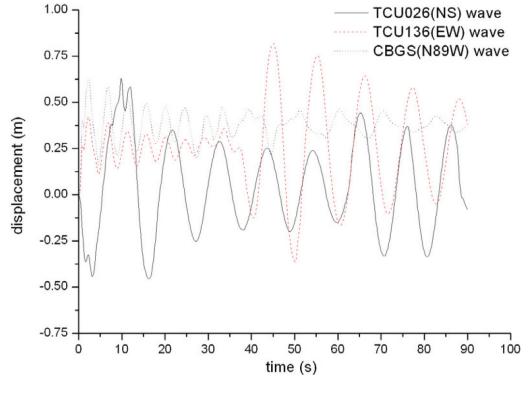

Figure 6. Displacement at the top of north tower under long-period seismic waves (SECS model).

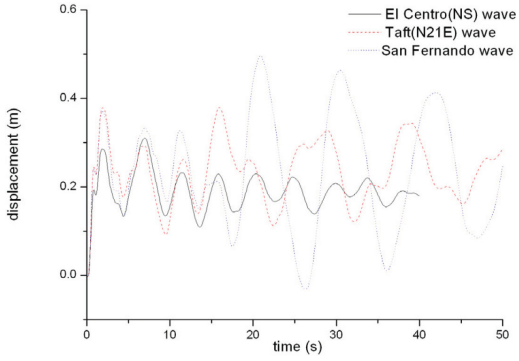

Figure 7. Displacement at the top of north tower under ordinary seismic waves (MECS model).

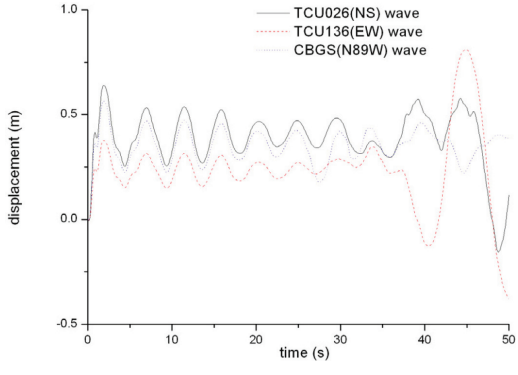

Figure 8. Displacement at the top of north tower under long-period seismic waves (MECS model).

Table 4. SECS model maximum displacements of the structure under different waves (m).

Seismic wave	Longitudinal displacement at the top of tower	Longitudinal displacement in the middle of span
TCU026 (NS)	0.629	0.389
TCU136 (EW)	0.819	0.536
CBGS (N89 W)	0.627	0.358
EI Centro (NS)	0.335	0.078
Taft (N21E)	0.424	0.091
San Fernando	0.517	0.111

were different from each other. The longitudinal displacements at the top of tower and in the middle of main span under long-period seismic waves were significantly higher than those under ordinary seismic waves. As in this bridge, the maximum longitudinal displacement under long-period seismic wave was 6.8 times more than the one of ordinary

Table 5. MECS model maximum displacements of the structure under different waves (m).

Seismic wave	Longitudinal displacement at the top of tower	Longitudinal displacement in the middle of span
TCU026 (NS)	0.619	0.390
TCU136 (EW)	0.809	0.537
CBGS (N89 W)	0.564	0.358
EI Centro (NS)	0.310	0.078
Taft (N21E)	0.380	0.091
San Fernando	0.497	0.112

Table 6. Maximum shear force at the bottom of tower under different waves (10^6 N).

Seismic wave	SECS model	MECS model
TCU026 (NS)	13.65	13.56
TCU136 (EW)	13.65	13.57
CBGS (N89 W)	13.64	13.56
EI Centro (NS)	12.91	12.86
Taft (N21E)	13.60	12.58
San Fernando	13.20	13.05

Table 7. Maximum bending moment at the bottom of tower under different waves (10^6 N·m).

Seismic wave	SECS model	MECS model
TCU026 (NS)	66.08	75.5
TCU136 (EW)	52.89	53.71
CBGS (N89 W)	41.38	51.96
EI Centro (NS)	10.37	11.93
Taft (N21E)	13.07	14.72
San Fernando	15.70	17.50

seismic wave, which showed the increasing effect of excitation by the long-period seismic wave. Comparing the analysis results of SCES model with MCES model, the longitudinal displacement at the top of tower had slight decreasing trend, and there was of no effect to the longitudinal displacement in the middle of main girder considering the local cable vibration. It meant that the local cable vibration has an impact on tower only, with less constrained and long-period seismic waves causing low frequency vibration of the structure.

4.2 *Internal force analysis*

The internal force of the structure was analyzed under different seismic waves. The maximum longitudinal shear force of structure is shown in Table 6,

and the maximum longitudinal bending moment of structure is shown in Table 7.

From Tables 6 and 7, the longitudinal shear force at the bottom of tower under long-period seismic wave was similar to the one under ordinary seismic wave, and the maximum shear force was slightly decreased considering the local cable vibration, which indicated that the local cable vibration has little impact to the structure. From the maximum bending moment of tower, the moment at the bottom of tower was increasing distinctly, at a rate much higher than that under ordinary seismic wave. The local cable vibration had increasing impact on the value of moment, and the amplitude trend was larger than the one of shear force.

5 CONCLUSION

Based on the characteristics of local cable vibration, finite element software ANSYS was used to analyze the nonlinear earthquake response of one long-span cable-stayed bridge under action of long-period seismic waves and ordinary seismic waves. The major conclusions drawn are as follows:

a. Compared with ordinary seismic wave, the long-period seismic wave has the characteristics including rich long period ingredient, longer duration and smaller peak acceleration, the main frequency are concentrated in the low frequency zone, and the amplification coefficient β is greater than that of an ordinary seismic wave.
b. The first order period of the long-span cable-stayed bridge is 11.1 s, which belongs to the long period structure. Local cable vibration has a certain impact on structural dynamic characteristics, which has performance of that the main mode of bridge is lagged, more cable self modes and coupled modes with cable and beam appear. It has less influence on the period of the whole structure.
c. The longitudinal displacements at the top of tower and in the middle of main span under long-period seismic waves were significantly higher than those under ordinary seismic wave action. The increasing effect induced by the excitation was enormous under long period seismic waves. After taking into account the local vibration of the cables, the longitudinal displacement on the top of tower was slightly reduced and there was no effect on the longitudinal displacement in the middle of main span.
d. The effect to the shear force at the bottom of tower was small by long-period seismic wave, but the maximum bending moment increased significantly under long-period seismic wave. Local cable vibration also had increasing effect for the longitudinal bending moment, and the increasing amplitude was greater than the value of shear force. Therefore, the safety problem of long-span bridge structure under the action of long-period seismic waves should be paid more attention.

REFERENCES

Abdel-Ghaffar, A.M. & Khalifa, M.A. 1991. Importance of cable vibration in dynamics of cable-stayed bridges. *Journal of Engineering Mechanics* 117(11): 2571–2589.

Boore, D.M. 2004. Effect of baseline correction on displacements and response spectra for several recordings of the 1999 Chi-Chi, Taiwan, Earthquake. *Bulletin of the Seismological Society of America* 91(5): 1199–1211.

Chen, Q.J., Zhang, T. & Chen, Z.H., et al. 2014. Traveling wave effect analysis of super-long-span cable-stayed bridge under long-period stochastic seismic excitation. *Journal of Hunan University* 41(4): 1–9.

Koketsu, K. & Miyake, H. 2008. A seismological overview of long-period ground motion. *Journal of Seismology* 12(2): 133–143.

Li, C.F. & Zhang, Y. 2006. Urgency of the study of long-period ground motion. *Seismological and Geomagnetic Observation and Research* 27(3): 1–8.

Xie, L.L., Zhou, Y.N. & Hu, C.X. 1990. Characteristics of response spectra of long-period earthquake ground motion. *Earthquake Engineering and Engineering Vibration* 10(1): 1–19.

Zang, M.M. & You, P.H. 2012. Analysis on long-period seismic responses for long-span bridge structure. *Journal of Henan University of Urban Construction* 21(2): 13–17.

Civil Engineering and Urban Planning IV – Liu et al. (Eds)
© 2016 Taylor & Francis Group, London, ISBN 978-1-138-02903-3

Physico-mechanical characteristics of dune sand concrete as an emerging building material for light constructions

Mohammed Chemrouk, Mohammed Boukerrou & Abdessamed Azzez Rahmani
University of Sciences and Technology Houari Boumediene (USTHB), Algiers, Algeria

ABSTRACT: For lightly loaded structural elements and load-bearing blocks for walls needed for light constructions such as housing and public shelters in general, dune sand concrete could be an emerging building material, particularly in areas where dune sand is in abundance and coarse aggregate is scarce such as in the Arabian Gulf and in the Southern part of the Maghreb. Dune sand concrete could really be a replacement material for affordable and suitable housing with all the modern facilities that the household needs today. An on-going research work showed that compressive strengths in the range of 25–30 MPa can be easily achieved with an addition of an optimum quantity of suitable fine fillers consisting of calcareous fillers or siliceous ones and that excellent architectonic effects with attractive surface finishes could be obtained with a relatively lower cost compared to ordinary concrete. This adds to the positive aspect related to the environment when using dune sand. Indeed, extracting coarse aggregates from quarries or from river beds is having serious environmental and ecological problems on our world.

This work presents a case study where a dune sand concrete is formulated. Its rheological as well as physico-mechanical properties are assessed so that this concrete material could be used as a building material for lightly loaded constructions such as mass housing and dwellings in regions where dune sand is abundant. This will certainly safeguard the ecological equilibrium of our nature, preserve it from any aggressive rock extractions and fulfil the requirements for a sustainable development since less energy would be consumed by the construction industry.

1 INTRODUCTION

The abundance of sand or other types of fine aggregates such as dune sand and the scarcity of coarse aggregate in some places of the world enabled sand concrete in general to emerge. In this sense, dune sand concrete is considered as a particular type of sand concrete. The difference between sand concrete and ordinary concrete is essentially the grading size of aggregate. Since the aggregate represents more than 70% of the total volume of concrete, such a difference in the skeleton of concrete greatly affects the construction properties of concrete, rheological as well as physico-mechanical. It also affects the overall cost of concrete constructions as both quarry and alluvial coarse aggregates require higher costs for their production and transportation to concrete plants. This is even more crucial in places lacking coarse aggregates and, as a result, huge mountains are completely devoured in some places of the world and disappear from Mother Nature ending up in seriously affecting the ecological equilibrium.

Sand concrete is a mixture of fine aggregate having less than 5 mm as the maximum size (sand), cement and other additives, essentially fillers. When sand consists of dune sand, this gives a dune sand concrete. There are no coarse aggregates in this type of concrete. The need for such concrete stems from the scarcity of coarse aggregates in some places and the cost related to their production and transportation to where they are needed. Furthermore, the quarry production of coarse aggregate is causing serious environmental problems to our world. In the same way, the extraction of round gravels from river beds is doing more ecological damage to our nature.

Faced with such problems, the construction industry is constantly searching for a substitute to ordinary concrete in many places of the world. In this sense, the abundance of sand in some places of the world, alluvial sand or dune sand, has instigated the study of this new material for its use in building construction, particularly in lightly loaded structures, not requiring higher compression strength, such as housing and dwellings and yet having comparable tensile strengths with that of ordinary concrete, if not more according to the present study. This presumed relatively improved tensile strength of dune sand concrete will allow for a relatively better behaviour towards cracking and hence an improved durability at the longer term.

Dune sand exists in large quantities in the Arabian Peninsula and in the southern part of the Maghreb, and hence could be an ideal ingredient for sand concrete to build lightly loaded framed structures for mass housing. Sand concrete in general and dune sand concrete in particular can also easily be used for producing load-bearing blocks locally for housing and dwellings with all the architectonic effects that result from this fine graded building material. The porous nature of the resulting dune sand concrete can be overcome by the addition of fine additive materials (less than 0.08 mm) such as calcareous fillers and siliceous fillers.

This paper studies the construction properties of dune sand concrete as a replacement to ordinary concrete in areas where coarse aggregates are costly to produce because of rarefaction and negative effects on the environment and where dune sand is in abundance.

2 DIFFERENCE BETWEEN ORDINARY CONCRETE AND SAND CONCRETE

The difference between ordinary concrete and sand concrete is essentially that of the grading of the material forming the skeleton. In the case of ordinary concrete, coarse aggregates create macro-voids which are filled with sand particles and the relatively small voids between sand particles are filled with fine cement particles. In the case of sand concrete, the cement and the fine additive particles fill-in the gaps between sand particles. However, in dune sand concrete, the gaps are numerous and hence a huge quantity of fines is needed to fill-in these gaps and reduce the porosity of the hardened building material. In effect, the porosity problem of sand concrete is even more complex with dune sand where practically all the sand particles have the same size. The fine gaps of dune sand concrete are filled with mixing water in excess and which evaporates with time, particularly under dry atmospheric conditions, inducing severe shrinkage to the dry concrete material and consequent fine cracking.

Fine additives, such as calcareous or siliceous fillers that fill-in these gaps are vital for dune sand concrete in order to make the material denser (Bali et al. 2002), hence to reduce its porosity. Masonry dust can also be used as possible fillers (Azzouz et al. 2002). Such fillers can be obtained from recycled masonry and hence relieve the environment from dumping non-degradable materials. This is because technically and economically it is not possible to fill-in all the sand concrete gaps, particularly the dune sand concrete gaps, with cement compounds, and hence the use of fine fillers becomes essential.

Technically, using more cementiteous material is not recommended since it causes a shrinkage problem and economically, the resulting concrete material is not viable. To tackle the porosity problem of sand concrete, particularly that of dune sand concrete and at the same time keeping the cement content to the level of that used in ordinary concrete, fillers should be used to fill-in the gaps between sand particles and then the mixture sand-fillers is stiffened with cement paste. The geological nature and the shape of fillers affect the quantity of water required for obtaining a workable mix. In this sense, spherical particles necessitate less water than angular ones and provide a better compactness for the hardened mix. The geological nature of fillers determines their possible activity with water in the same manner as cement and hence improves the properties of the hardened mix. These types of fillers are mainly calcareous fillers, siliceous fillers, blastfurnace slags and fly-ashes; the first two types of fillers are passive fillers. Both types of fillers may however react chemically with some cement hydrates to improve the bonding of sand particles. The proportion of added fillers varies from 20% to 75% by weight of cement, depending on the type of filler and the type of sand used in making sand concrete. One of the essential qualities of hard concrete is its compactness. The main parameters affecting compactness are:

- The grading of the mix
- The water content, since a part of such water will evaporate, creating voids.
- The means of placing and compacting the fresh concrete.

3 CASE STUDY: FORMULATION OF DUNE SAND CONCRETE

A dune sand of 0.6 mm maximum size was used, with an Equivalent Sand of 86. The mineral additives consisted of calcareous fillers and siliceous fillers having maximum size less than 0.08 mm and a specific surface around 3500 cm^2/g used in proportions of 100, 150, 200, 250 and 300 kg/m^3 respectively. The cement consisted of ordinary Portland cement, used in two proportions in the mix: 350 kg/m^3 and 400 kg/m^3. Three water/cement (W/C) ratios were used, namely 0.6, 0.7, and 0.8. Superplasticisers were used to lubricate the dune sand concrete mixes in proportions of 1.5% per weight of cement. Cylindrical (16×32) cm and prismatic ($4 \times 4 \times 16$) cm concrete specimens were made for characterizing the physico-mechanical properties of the hardened dune sand concrete produced. At the fresh state, the workability of concrete was assessed through the VB consistometer test as a function of the optimum addition of

fillers. The variation of the compactness of sand concrete with the addition of fillers was assessed through the density of the concrete material.

Examples of dune sand concrete mixes formulated are given below:

-For W/C = 0.6

Mix 1
Dune sand: **1390** kg/m³
Cement 350 kg/m³
Fillers: **150** kg/m³
Water 210 kg/m³
Plasticiser: 5.25 kg/m³

Mix 2
Dune sand: **1340** kg/m³
Cement: 350 kg/m³
Fillers: **200** kg/m³
Water: 210 kg/m³
Plasticiser: 5.25 kg/m³

Mix 3
Dune sand: **1310** kg/m³
Cement: 400 kg/m³
Fillers: **150** kg/m³
Water: 240 kg/m³
Plasticiser: 6.0 kg/m³

Mix 4
Dune sand: **1260** kg/m³
Cement: 400 kg/m³
Fillers: **200** kg/m³
Water: 240 kg/m³
Plasticiser: 6.0 kg/m³

-For W/C = 0.7

Mix 5
Dune sand: **1355** kg/m³
Cement: 350 kg/m³
Fillers: **150** kg/m³
Water: 245 kg/m³
Plasticiser: 5.25 kg/m³

Mix 6
Dune sand: **1305** kg/m³
Cement: 350 kg/m³
Fillers: **200** kg/m³
Water: 245 kg/m³
Plasticiser: 5.25 kg/m³

Mix 7
Dune sand: **1270** kg/m³
Cement: 400 kg/m³
Fillers: **150** kg/m³
Water: 280 kg/m³
Plasticiser: 6.0 kg/m³

Mix 8
Dune sand: **1210** kg/m³
Cement: 400 kg/m³
Fillers: **200** kg/m³
Water: 280 kg/m³
Plasticiser: 6.0 kg/m³

4 FRESH DUNE SAND CONCRETE— MIXING AND CONCRETING PROPERTIES

Fine additives of all types should be kept in silos in the same manner as cement. When mixing, it is advised that the "active" constituents be added last before the addition of water. The dispersion of fine elements can be achieved without difficulty in all classical mixers, and hence it is not advised to exaggerate the mixing time as is usually done for ordinary concrete. The fine grading of sand concrete in general, and that of dune sand concrete in particular, makes the segregation problem inexistent in this type of concrete and hence its transportation does not cause any problem. With its high fluidity and absence of segregation, sand concrete has a great pumping aptitude through longer distances, vertically and horizontally.

The reduced risk of segregation and the cohesion of the mixes help limit the bleeding despite the high water content. Although sand concrete can be placed by simply pouring the fresh mix in the mould or laying it on the surface (for roads), it is advised to vibrate it in order to obtain full compactness, particularly for heavily reinforced sections and slender shapes. Another advantage of sand concrete in general, is the good finish and architectonic effect after demoulding. This desired quality, however, is conditioned by well-prepared shafts and moulds in order to make them impervious to any grout loss, since this type of concrete is of a high fluidity. Architectural aesthetics are becoming more and more a criterion for selecting suitable building materials. In this sense, sand concrete is particularly favourable since it offers a magnificent surface finish and architectonic effects with less effort and cost. Factors such as the quality, the colour of the particles, the proportion of cement and fines, the geological nature of the sand and finally the quality of the mould are the key factors for obtaining architectonic effects.

Typical VB-time test results for workability are given in Figures 1 and 2 below for different

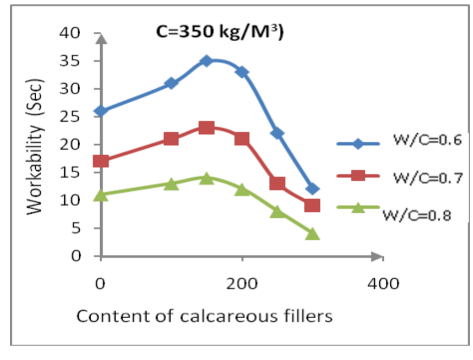

Figure 1. Workability of dune sand concrete mixes with calcareous fillers.

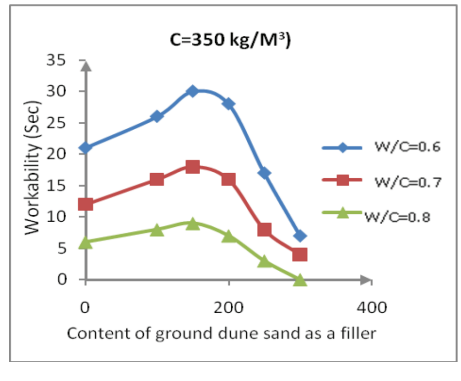

Figure 2. Workability of dune sand concrete mixes with siliceous fillers.

cement contents and with W/C ratios comparable to those used for ordinary concrete in a hot and dry climate. It can be seen that all the dune sand concrete mixes had VB times less than 40 seconds and could be considered as fairly workable mixes, particularly with the presence of siliceous fillers; the use of suplerplasticisers have helped improving such workability.

5 PHYSICO-MECHANICAL PERFORMANCES OF DUNE SAND CONCRETE

5.1 *Mechanical properties*

Generally, the compressive strength is lower than in ordinary concrete. This is due to the porosity and hence the lesser density of this type of concrete and even more so for dune sand concrete. The resisting skeleton, made with sand, fillers and cement particles, is not as strong as that of ordinary concrete made with coarse aggregate, sand and cement particles. The high percentage of fine particles in dune sand concrete requires more water, a part of which evaporates leaving voids. This porous internal structure of the material has a reduced compressive strength. In effect, an infinite number of micro-pores become full of water after mixing and placing of concrete. Under the effect of the climate conditions, such stored water evaporates with time leaving empty micro-pores in the hardened concrete structure. The only way to limit the existence of these micro-pores in the structure of concrete is to limit the quantity of mixing water using superplasticisers (Boukerrou 2012).

The results of the compressive and tensile strengths of the hardened dune sand concrete are illustrated by Figures 3 and 4 for different types of fillers.

For higher cement content (400 kg/m^3), the same evolution of the mechanical properties is observed with relatively higher peak values for both the compressive and the tensile strengths.

With the use of siliceous fillers, the compressive strength has reached a value of 35 MPa at 90 days of age and 32 MPa at 28 days, strengths sufficiently high for dune sand concrete to be used as a structural material, particularly when an optimum quantity of fillers is used in the mix to fill in the micro gaps. In the present study, such optimum quantity fluctuates between 150 kg/m^3 and 200 kg/m^3 depending on the cement content used. The tensile strength, appreciated through the modulus of rupture, is even higher than that of ordinary concrete having comparable W/C ratios and cement contents. Indeed, a value approaching 6 MPa is obtained for the modulus of rupture of this dune sand concrete when an optimum quantity of siliceous fillers is used, making the appearance of cracks to be relatively delayed in this type of concrete. The values of the tensile strengths obtained are more comparable to those of high performances concrete than to ordinary concrete. This could be explained by the absence of higher size aggregate particles which are more likely to have stress concentration around them and hence inducing early micro-cracks at the interface aggregate-cement paste. Higher size aggregate particles are also more prone to surface dust which affects the quality of the bond between the aggregate particles and the cement paste. Such bond quality is a key factor in the tensile strength of any concrete.

The trend of variation of the mechanical properties is the same for higher values of the W/C ratio, with relatively lower peak strength values as the quantity of water is increased; the higher values being obtained when siliceous fillers are used. The peak strengths were obtained for optimum filler content in the range of 150 kg/m^3 – 200 kg/m^3 as in the case of the previous W/C ratio and cement content.

The stress-strain curve follows approximately the same evolution as in ordinary concrete. However, the curve seems to reach a peak stress at strains in the range of 1500 μs to 2000 μs instead of 2000 μs to 2500 μs as in ordinary concrete. The shape of the stress-strain curve flattens when approaching the maximum stress, expressing clearly a better deformability of the material by comparison to ordinary Concrete. Dimensional variations of dune sand concrete are more important since they are not restrained by coarse aggregate. This results in a lesser Young's modulus than that of ordinary concrete having comparable strength. Indeed, a value of 21 000 MPa was recorded experimentally for a dune sand concrete as compared to the generally accepted value of 30 000 MPa for ordinary concrete. In this sense, sand concrete and especially dune sand concrete is more deformable as expressed by the stress-strain curve of the material and hence less sensitive to cracking, a particularly disruptive structural problem in a hot and dry climate such as that of the Arabic Gulf and the Arabic Maghreb. This delayed cracking behaviour is expressed by the higher values of the tensile strength as illustrated in the curves of Figures 3 and 4. Such a material is also expected to behave well in seismic regions since it tolerates more deformations and softens when failing, liberating smoothly the stored energy instead of failing catastrophically as in ordinary concrete.

5.2 *Physical properties*

Shrinkage is another source of disruptive cracking for concrete in the presence of internal obstacles such as aggregates and non-uniformly distributed reinforcement. Having more fines and hence

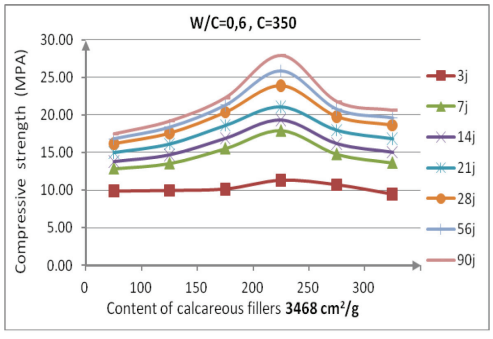

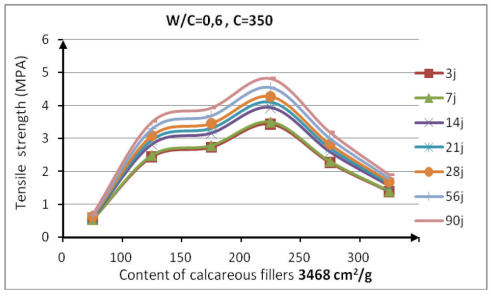

Figure 3. Evolution of the compressive strength and the tensile strength with age of a dune sand concrete with calcareous fillers.

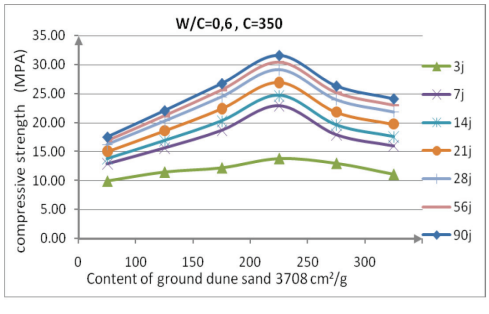

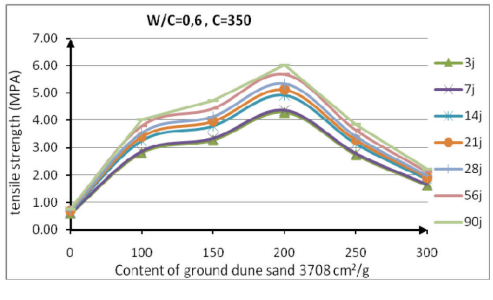

Figure 4. Evolution of the compressive strength and the tensile strength with age of a dune sand concrete with siliceous fillers.

containing more water and containing no coarse aggregates to restrain any deformation of the cement paste, dune sand concrete is expected to exhibit more shrinkage and creep than ordinary concrete. Indeed, the non-existence of coarse aggregate which constitutes the main obstacles for dimensional variations and the abundance of water required to wet all the fines, a large part of which evaporates afterwards, promote shrinkage in sand concrete and even more so in dune sand concrete. Shrinkage strain is essentially attributed to the cement paste which, in the case of ordinary concrete, is restrained by coarse aggregates not present in sand concrete. The absence of coarse aggregates makes dune sand concrete shrink relatively freely without major internal obstacles and hence without major cracking. It can be seen from Figures 5 and 6 that shrinkage increases with an increase in the W/C ratio and hence an increase in the quantity of water used. The W/C ratio is also an indication of the cement paste present in concrete. The two figures show that an increase in the cement paste leads to an increase in shrinkage;

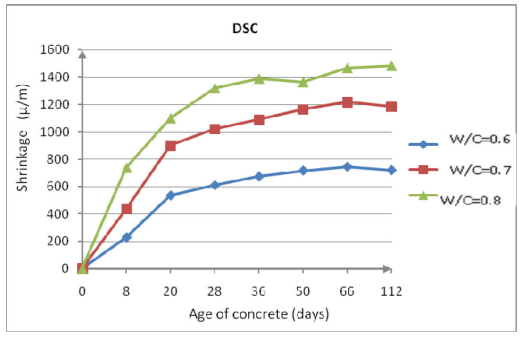

Figure 5. Shrinkage of dune sand concrete with an optimum quantity of calcareous fillers for different W/C ratios.

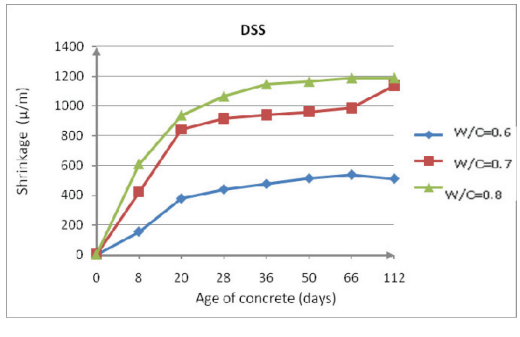

Figure 6. Shrinkage of dune sand concrete with an optimum quantity siliceous fillers for different W/C ratios.

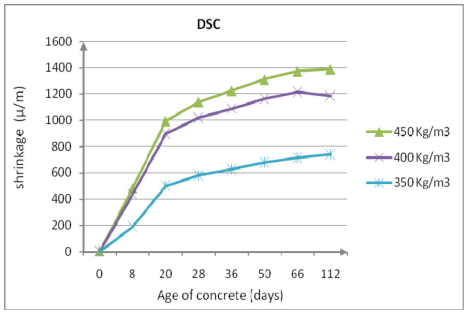

Figure 7. Shrinkage of dune sand concrete with calcareous fillers for various cement contents.

this is because any loss of water will reduce the paste volume and hence induce shrinkage.

Shrinkage of dune sand may be as high as three time that of ordinary concrete, particularly with higher quantities of mixing water. The use of siliceous fillers yields in a relatively lesser shrinkage by comparison to calcareous fillers. Indeed, with lesser water/cement ratio and the use of siliceous fillers, the shrinkage values are comparable to those of ordinary concrete in hot climate (Bendjilali et al. 2013). The results of the present study show that shrinkage of dune sand concrete with W/C = 0.6 is about twice that of ordinary concrete when calcareous fillers are used.

Figures 7 shows that an increase in the cement content increases the paste content and hence increases shrinkage. Such increase was found to be similar for both types of filler, since the paste generating shrinkage has the same content for both types of fillers and hence any loss of water will induce the same shrinkage.

Creep is a deformation induced by long-term loading and depends strongly on the internal structure of the material as in the case of shrinkage. The absence of coarse gravel representing the internal skeleton of concrete, which restrains the deformations of the cement paste, results in the development of more creep strains under the effect of loading, particularly in the presence of more water.

It can be deduced that the physical phenomenon of shrinkage and that of creep might limit the uses of dune sand concrete as a structural building material more than its compressive strength.

6 COMPACTNESS—LONG TERM DURABILITY OF DUNE SAND CONCRETE

In concrete in general, the aggregate fulfils the role of a skeleton in which the cement paste plays:

– First a rheological role (cohesion and fluidity) enabling concrete to be placed,
– Then a bonding role, gripping the aggregate particles so as to form a strong material which develops mechanical as well as durability properties.

Among the performances of a concrete material, an adequate compactness is vital to insure a better durability (Chemrouk & Attari 2003), a long-term performance which can be negatively affected by the ability of exchanging materials in a solid, liquid or gas state with the external environment. Compactness depends strongly on the grading of the mix and its water content and is thus weaker for sand concrete and even more so for dune sand concrete.

The lack of compactness in dune sand concrete is partly compensated by the use of an optimum content of fillers (Fig. 8) and in general the porosity of sand concrete, and that of dune sand concrete in particular, is more important than that of ordinary concrete. The porosity facilitates the permeability of the material to aggressive agents which could chemically attack concrete or cause the corrosion of steel (Chemrouk & Attari 2003). From this point of view, the durability of sand concrete and that of dune sand concrete is less than that of ordinary concrete. However, an optimum filler content in the range of 150 kg/m^3 to 200 kg/m^3 makes dune sand concrete denser (Fig. 8) and hence relatively more compact and durable at the longer term. Such optimum filler content was also found to yield the best mechanical strengths of the hardened material.

Nowadays, the development of the materials technology such as the use of fine fillers and superplasticisers and the advances in the concrete technology at all the stages (mixing, placing, curing) which, in effect, is an advantage for sand concrete, pledge for a compact dune sand concrete material and hence a durable material. However, a positive

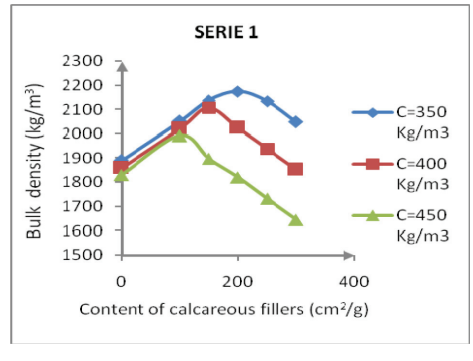

Figure 8. An optimum filler content makes dune sand concrete relatively denser.

aspect of the porosity is that the existence of the micro-pores and their uniform repartition within the material structure helps dune sand concrete to resist salt-weathering, frequent in desert regions, by offering sufficient pore space for the salt crystals after the evaporation of moisture and so avoiding the disruptive cracking which might be caused by higher volumes of salt crystals.

7 CONCLUSION

Dune sand concrete for desert places could be a substitute material to produce load-bearing blocks for affordable housing and dwellings. Compressive strengths in the range of 25 MPa are easy to achieve for dune sand concrete. For lightly loaded constructions, such a dune sand concrete with compressive strengths in the order of 25 MPa and above can be used as a structural material.

Dune sand concrete may have a higher tensile strength which delays the cracking of the material. The problem of porosity and hence shrinkage and long-term durability could be minimized by the use of selected additive fillers, suitable water reducers and a sufficient compaction. Shrinkage, although relatively more important than in ordinary concrete, may not however induce important cracking in the hardened sand concrete since its tensile strength is found to be relatively higher.

The abundance of local dune sand and the rarefaction of coarse aggregate together with the cost needed for the production and transportation of this latter mixing ingredient to the building site make dune sand concrete a material to rely on from an economic point of view in regions such as in the Maghreb and the Arabic Gulf, places where dune sand is in abundance. Sand concrete in general is a building material which yields better architectural aesthetics, a factor which has for long been a weakness point for concrete. Furthermore, from the environmental point of view, this material helps to relieve nature from dusty fillers, recycled or extracted from quarries, and by safeguarding the ecological equilibrium in places lacking coarse aggregate.

It is interesting to develop such concrete material to produce housing with a reduced cost, since more than 70% of the concrete ingredients are freely available in inexhaustible quantities. The negative aspects of shrinkage and creep behaviour can be overcome by a careful mix design, using suitable fine fillers and advanced water reducers.

REFERENCES

Azzouz, L., Bouhicha, M. & Kennai, S. 2002. Recycling of Waste Bricks in the Fabrication of Dune Sand Concrete. *International Congress on the Challenges of Concrete Construction—Sustainable Concrete Construction, Great Britain, 5–11 September, 665–673*. London: Thomas Telford.

Bali, A., Benmalek, M.C. & Queneudec, M. 2002. Proportion of a Low Cost Concrete with a Desert Dune Sand and Calcareous fillers. *International Congress on the Challenges of Concrete Construction—Sustainable Concrete Constructions, Great Britain, 5–11 September, 713–720.* London: Thomas Telford.

Bendjilali, K., Chemrouk, M., Goual, M.S. & Boulekbeche, B. 2013. Behaviour of Polypropylene Fibers' Mortars Conserved in Different Environments. *European Journal of Environmental and Civil Engineering (EJECE)* 17(8): 687–699.

Boukerrou, M. 2012. Etudes des propriétés Rhéologiques et Pyisico-Mécaniques du Béton de Sable avec Référence Particulière au Béton de Sable de Dune. MSc Research Thesis, Algiers: University of Sciences and Technology Houari Boumediene (USTHB).

Chemrouk, M. & Attari, N. 2003. Durability of Concrete with Particular Reference to High Performances Concrete; *Proceedings of the International Symposia: 'Celebrating Concrete—People and Practice', Dundee, Great-Britain, 3–4 September*. London: Thomas Telford.

This page intentionally left blank

Civil Engineering and Urban Planning IV – Liu et al. (Eds)
© 2016 Taylor & Francis Group, London, ISBN 978-1-138-02903-3

The elastic-plastic analysis of single buildings of prefabricated shear wall

Hu Qi, Ming Li & Kang Liu
China State Construction Engineering. Corporation Ltd., Technical Center, Shunyi District, Beijing, China

ABSTRACT: Structure analysis software YJF-EP is taken for the elastic-plastic analysis of a building of prefabricated shear wall, specifically, the whole anti-seismic performance under rare earthquake is analyzed. Three seismic waves, one artificial wave and two natural waves, are loaded according to code, and their reaction under an earthquake in the direction of X and Y is calculated. In order to study the anti-seismic performance of a structure with two floors set strengthened or three floors set strengthened, the dynamic responses under an earthquake are compared between the two structures, the result of which shows that the whole seismic responses of the structure are almost the same regardless of the number of floors strengthened as well as the anti-seismic performance.

1 INTRODUCTION

The selected prefabricated building, 22 floors in total, 2.9 m high for each floor, and 3.7 m high for basement, is entirely prefabricated above cast-in-place ground except for the basement. In order to study the whole anti-seismic performance of the structure and the anti-seismic performance impact of the height of the strengthened floor onto the 22 floors building under a rare earthquake, the elastic-plastic response of the structure is analyzed. According to the code, three waves, one artificial wave, and two natural waves are selected and studied for the seismic response in the main directions X and Y separately, the responses of the 22 floors building structure with two floors strengthened and three floors strengthened under the three waves of an earthquake are studied and compared.

2 THE STRUCTURE MODEL

The elastic-plastic analysis is taken for the 22 floors building, which is 63.8 m in height regarding the main body structure; YJK elastic-plastic calculation model (YJK-EP for short) is chosen as Figure 1. Two-floor and three-floor strengthened structures are chosen respectively in the elastic-plastic analysis of the model, as the confined boundary component height of the two models is different, the two models are different only in the component reinforcement area of the three floors, but are the same with regard to other parameters.

Considering the complex elastic-plastic analysis theory and practical reinforcement of the structure, the elastic-plastic model can be simplified properly in order to get steady and reliable results. Also, to make sure that YJK elastic-plastic analysis is unanimous with the designed model and YJK-EP model, the three models should be compared in terms of their overall computing. The result of the overall computing and the first three cycles comparison of the models are shown in Table 1, from which the overall index fits well. However, because of the difference among each unit and impact of reinforcement, the calculation result maybe not identical.

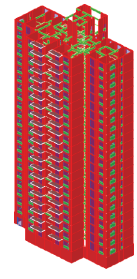

Figure 1. YJK model of 22 floors structure.

Table 1. Comparison of the calculation models.

	YJK	YJK-EP Two floors strengthened	YJK-EP Three floors strengthened
Mass (t)	12084	12702	12702
Period (s)			
T1	1.51	1.40	1.40
T2	1.50	1.42	1.42
T3	0.96	0.90	0.90

3 EARTHQUAKE WAVES

During the nonlinear time-history analysis, three earthquake waves are selected by YJK, one artificial wave, and two natural waves. The main direction oscillogram and response spectrum are seen in Figures 2 and 3.

From Table 2, the minimum base shear force of X direction by the earthquake waves time-history analysis is 11449 KN, which is larger than the 65% of the response spectrum base shear force of 15006 KN; the average of the base shear force from the three earthquake waves time-history analyses is 12122 KN, which is larger than the 80% of the response spectrum. The results of base shear force in Y direction also satisfy the above two conditions. The selected earthquake waves for the time-history analysis meet the requirement of the code for the seismic design of a building (GB50011-2010). Based on the features plane and façade of the structure, earthquake waves are put in the orthogonal direction plane and vertically, and the peek acceleration ratio in primary and secondary direction is 1:0.85:0.65, for which V direction and Y direction are calculated as primary direction; the peek acceleration in the primary direction is taken as 22 gal according to the code.

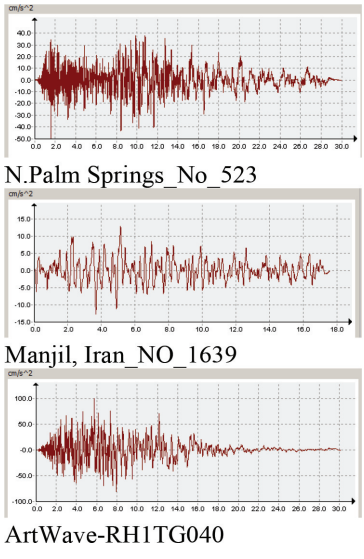

Figure 2. Earthquake wave.

Table 2. Comparison between earthquake wave base shear force and mode decomposition response spectrum base shear force.

	Shear force X direction (KN)	Shear force Y direction (KN)
Spectrum	15006	16358
ArtWave	11717	11693
N.Palm	11449	12352
Manjil	13200	16007
Average	12122	13351

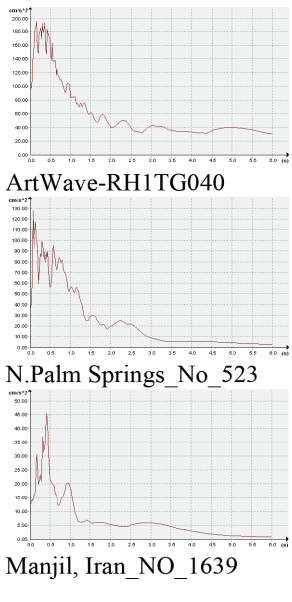

Figure 3. Spectrum of the earthquake wave.

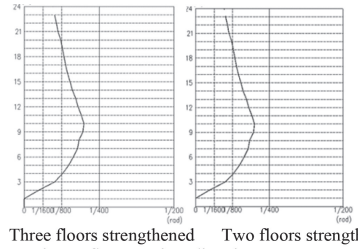

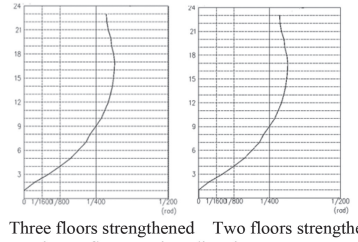

Manjil, Iran_NO_1639 (the displacement angle with 2 floors strengthened is the same with 3 floors strengthened, X, Y direction are: 1/501, 1/344)

Figure 4. (*Continued*)

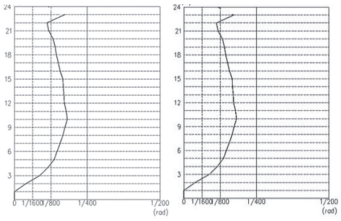

Three floors strengthened Two floors strengthened
Maximum floor rate in x direction

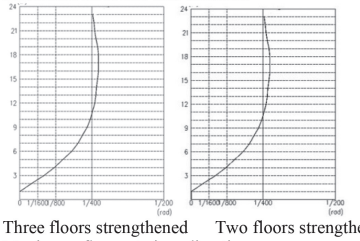

Three floors strengthened Two floors strengthened
Maximum floor rate in y direction
N.Palm Springs_No_523 (the displacement angle with 2 floors strengthened is the same with 3 floors strengthened, X, Y direction are: 1/551, 1/378)

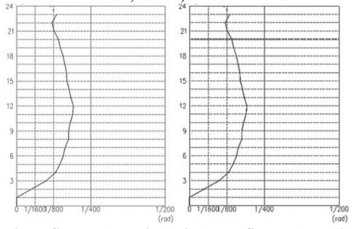

Three floors strengthened Two floors strengthened
Maximum floor rate in x direction

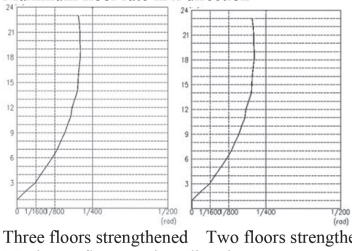

Three floors strengthened Two floors strengthened
Maximum floor rate in y direction
ArtWave-RH1TG040 (the displacement angle with two floors strengthened is the same with three floors strengthened, X, Y direction are: 1/522, 1/494)

Figure 4. The maximum story drift angle.

4 CALCULATION RESULTS

When two floors and three floors are set as strengthened floors, respectively, under the load of three waves, the maximum inter layer displacement angles of the structure by YJK-EP are compared in Figure 4.

The comparison between two floor strengthened structure and three floors strengthened structure is as follows.

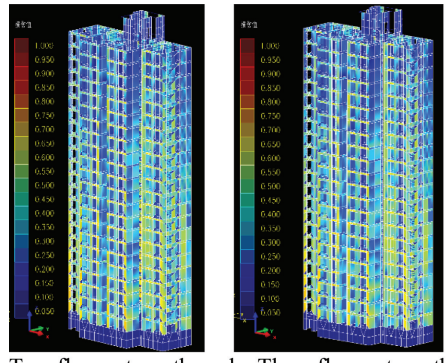

Two floors strengthened Three floors strengthened

Figure 5. Structure damage.

The maximum layer displacement angle by Manjil, Iran_NO_1639 wave is the largest; the structure damage picture under the wave is shown in Figure 5, from which the structure damage is focused on the structure coupling beam, the overall of the shear wall is little damaged, of which the damage is mainly focused on lower part, and decreasing as the floor rises.

5 CONCLUSION

When two floors and three floors are set as strengthened floors respectively, the inter layer displacement angle by elastic-plastic analysis is much smaller than the code limits (1/100) (JGJ3-2010), which indicates that three-floor and two-floor strengthened structures can both meet the requirement of the code in terms of overall anti-seismic performance. When two floors and three floors are set as strengthened floors, the structure displacement angle and structure damage are unanimous, which shows the structure of two floors strengthened or structure of three floors strengthened can rarely affect the structure performance during an earthquake. The structure damage picture shows that the structure damage is focused on the structure coupling beam; the overall of the shear wall is little damaged, with the damage mainly focused on the lower part, and decreasing as the floor rises.

REFERENCES

GB50011-2010. 2010. *Code for Seismic Design of Buildings.* Beijing: China Architecture & Building Press.

JGJ3-2010. 2010. Technical Specification for Concrete Structures of Tall Building. Beijing: China Architecture & Building Press.

This page intentionally left blank

Civil Engineering and Urban Planning IV – Liu et al. (Eds)
© 2016 Taylor & Francis Group, London, ISBN 978-1-138-02903-3

A new method for measuring hydraulic parameters of unsaturated soils

Pan-Pan Yi
Wuchang University of Technology, Wuhan, Hubei, China

Sheng-Kuan Niu
Changjiang Survey Planning Design and Research Co. Ltd., Wuhan, Hubei, China

ABSTRACT: In this paper, we present a new method to determine unsaturated soil hydraulic parameters. First, we carried out one-step outflow test to observe the curves of outflow with time. Then, the HYDRUS-1D water transport model was merged to obtain the curve parameters. Finally, the parameters were used to determine the soil–water characteristic curve and the hydraulic conductivity function. By comparing the measured data, it was shown that the difference between the estimated and measured values of soil–water characteristic curves was small. In addition, compared with traditional methods, the method can save a lot of time.

1 INTRODUCTION

Hydraulic properties of unsaturated soils include the soil–water characteristic curve and the conductivity function of the soils. The former represents a relationship between matric suction and degree of saturation, while the latter describes the dependence of conductivity on the degree of saturation or the matric suction. These properties play a crucial role in analyzing the processes related to unsaturated soils, such as the problem of deformation and strength of unsaturated soil, rainfall infiltration and slope stability, underground migration of pollutants (Fredlund & Xing 1996).

The most commonly used measurement of unsaturated soil hydraulic properties of the instrument has pressure plate apparatus, Tempe, and the combined testing system (Fredlund & Xing 1994). Tempe instrument can measure the equilibrium state of the soil–water characteristic. Based on the soil–water characteristic curve of the sample, the permeability function is calculated (Alexander 1986). In the pressure-plate test, the samples were removed when the weighing soil particles are easily peeled off, resulting in large experimental errors. The combined testing system can better measure the soil–water characteristic curve, but there is a long experiment measuring time, for the amount of experimental error of the larger issues of unsaturated hydraulic conductivity. These experimental tests were carried out under equilibrium conditions, it takes weeks or even months of testing based on different soil types. Therefore, it is very important to quickly and effectively measure unsaturated soil hydraulic parameters.

Recently, researchers have used methods to rapidly determine unsaturated soil hydraulic parameters of depth and extensive research. Gardner (1956) proposed the flow test method, which lasted for a short period of time, with no complex side boundary conditions, and was widely recognized. As a method for solving the nonlinear flow equation for unsaturated soil mechanics parameters, solution parameters are not the only problem; Doering (1965) obtained more satisfactory results using the method. Kool (1985) and Parker (1985) proposed one-step flow test and inverse methods and numerical methods for unsaturated soil hydraulic parameters, which have been used more widely.

In the flow test, the overflow water with the evolution of time, influenced not only by the size of suction applied, but also by the permeability of clay plate material constraints. Flow test previously mentioned did not take into account the effect of the sample overflow clay plate with time variation of the water. Recently, Ning (2006) pointed out that the entire testing process can be used as an initial/boundary value problem, and considered together with the ceramic plate and the sample flow process so that it is possible to simulate the effect of a good clay plate sample flow process, resulting in generating a more accurate water overflowing curve over time. On this basis, this paper carried out a step flow test. In this paper, a one-dimensional analysis of water flow software HYDRUS-1D was fitted with

overflow water flow rate versus time, and analyzed some of the anti-calculated hydraulic parameters that were measured accurately, and then obtained the unsaturated soil–water characteristic curve and the permeability function curve. In order to verify the reliability and practicality of the method, the results measured under the equilibrium soil–water characteristic curve and saturated hydraulic conductivity of the sample were compared.

2 MATHEMATICAL MODEL

2.1 *Basic equations of water movement*

Ignoring the soil level and lateral water movement, we consider only the one-dimensional vertical movement, changes in soil moisture by Richards' equation, namely

$$\frac{\partial \theta(h)}{\partial t} = \frac{\partial}{\partial z}\left(\mathrm{K}(h)\frac{\partial h}{\partial z} + \mathrm{K}(h) \right) \tag{1}$$

2.2 *Soil–water characteristic curve and the conductivity function*

Soil–water characteristic curve model uses the most commonly used van Genuchten model (van Genuchten 1980):

$$\theta(h) = \begin{cases} \theta_r + \dfrac{\theta_s - \theta_r}{[1+|\alpha h|^n]^m} & h < 0 \\ \theta_s & h \geq 0 \end{cases} \tag{2}$$

$$\mathrm{K}(h) = K_s S_e^l [1-(1-S_e^{1/m})^m]^2 \tag{3}$$

$$S_e = \frac{\theta - \theta_r}{\theta_s - \theta_r} \tag{4}$$

2.3 *Initial and boundary conditions*

2.3.1 *Initial conditions*

In the first step, before the sample is applied to the suction, it is applied with a smaller value (slightly larger than the sample intake values), and therefore, the sample changes from the saturated state to the unsaturated state:

$$h = h_0(z) + h' \quad t = 0, \quad 0 \leq z \leq H \tag{5}$$

2.3.2 *Boundary conditions*

The upper boundary flow constant is zero, whose mathematical expression is as follows:

$$Q = 0,\ t > 0,\ z = 0 \tag{6}$$

$$h = h(t),\ t > 0,\ z = H \tag{7}$$

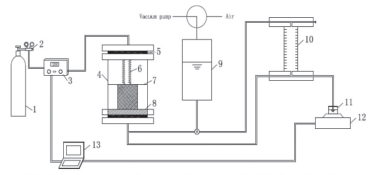

1- High-pressure nitrogen bottles 2- Valve 3- Pressure regulating pump 4- Pressure chamber 5- Seals 6- Spring 7- Barbed wire 8- High intake value clay plate 9- Water containers 10- Bubble Measurement System 11-Sheng cups 12-Electronic balance13-Data acquisition means

Figure 1. The sketch map of improved combined testing system.

3 IMPROVED COMBINED TESTING SYSTEM

The improved combined testing system is restructured on the basis of the original system. The diagram of the system is shown in Figure 1. The system consists of a pressure control systems, pressure chambers, water containers and bubble measurement systems, weighing systems, and data acquisition system structure.

Pressure control system consists of high-pressure nitrogen bottles, valves, pressure regulators, pumps and other parts. Pressure chamber has made greater improvement. The bottom of the pressure chamber increases the discharge path of bubbles, which can be discharged in the clay plate oozing bubbles, and then corrected for the sample of the overflow of water, which can make the measurements more accurate. Water containers and bubble measuring system are marked by a graduated glass tube and a plurality of line connection components. Before the experiment began to be put above the instrument storage container measurement system water flows into the bubble, thus, the sample is saturated. The weighing system consists of the balance and the cup, which has a small hole on the top. Small diameter holes can prevent water evaporation. The balance has a data cable connected to the backside of the computer, so data acquisition system capable of real-time acquisition to balance readings. Data acquisition systems with LabVIEW software to complete the data acquisition function, which have two data channels for recording the suction and the balance readings change with time. Collection interval can be set according to the experimental needs.

4 TEST PROGRAM AND MAIN EXPERIMENTAL PROCEDURE

4.1 *Test program*

Soil samples were taken from the Yellow River Delta, and their basic physical characteristics are presented in Table 1.

Table 1. Physical properties of the soil used in the test.

	Soil particles content/%			
Soil samples	Sand	Particles	Clay	Proportion
Silty sand	69.7	30.3	0	2.67

Soil samples were remodeled by using a 2 mm sieve, and then their proportion was measured. By designing dry density, initial water content was calculated to load the soil sample and the sample container quality, with the pressure of the soil sample method pushing a diameter of 5.4 cm, 3 cm-high cylindrical sample loading containers.

4.2 *The main experimental procedure*

The prepared samples and high intake value clay plate were placed in the vacuum apparatus by the pumping saturated (saturation) approach method. During the pumping (about 1 to 2 hours for sand; about 3 to 4 hours for clay), the inlet valve was opened and the water entered into the sample. In order to make the sample more saturated, the water level was controlled in three installments and the soil samples were submerged at intervals of about 1 hour, which would also effectively exclude part of the gas dissolved in the water.

The side storage container valve was opened, so that the amount of bubbles inside the water in the test tube was saturated. Then, each pipeline flush was turned on by adjusting the valve until all the air bubbles in the pipeline were saturated.

The saturated clay plate in the base was surrounded by a rubber band seal, then a sample of the saturated clay plate was placed, and the surrounding casing and bolts were covered to make the base seal. Next, a seal was put on the casing and the lid was covered with bolts to cover and seal the casing. The respective lines were connected by fast joints and the sample container was loaded.

Prior to testing, by adjusting the valve of the upper storage container of water into the bottom of the clay plate, on the bottom of the clay plate erosion, discharge sample loading process may enter the bottom of the clay bubble board. And the number shown in the bubble at this time measurement tube was recorded. LabVIEW data acquisition software was then applied to a small suction step (about 2 kPa for sand; about 8 kPa for powder and clay) of the sample, to make it unsaturated by the saturation. After the water was stable, the sample was applied to a large suction step until the overflow water was stable.

Because of the dehumidification of the sample period, some bubbles may overflow from the clay plate so that the water discharged from the bottom of the clay plate glass, so that the overflow of water measured is too large. So, after the end of the wet clay plate bottom, the segment should be flushed and the amount of bubbles should be recorded after measuring the scouring test tube readings to correct for the volume of air bubble overflow of the water sample.

5 TEST RESULTS

Based on the above steps for the prepared samples to be saturated, the sample was installed. First, the saturated sample was applied to a small suction at 1 kPa, a small amount of water overflow in the sample changed from the saturated state to the unsaturated state, and then the suction was increased to 80 kPa, to carry out the drying test. Once the water was constant, on the bottom of the clay plate erosion, the volume of the overflow bubble was recorded, and finally at zero suction, the wetting test was carried out. Suction step and the sample were applied to the overflow of water versus time curve, as shown in Figure 2.

5.1 *The soil–water characteristic curve and the conductivity function of drying*

Based on the corrected volume of the bubble overflow of the sample water, in terms of volume and water content, the water content that is obtained from the volume relationship changes over time. According to this curve, initial and boundary conditions, and the ceramic plate material parameters using HYDRUS-1D model of one-dimensional inverse water transport, fitting evolution overflowed water samples off the wet versus time. Measured data curve and fitting curve is shown in Figure 3, it can be seen from the figure, HYDRUS-1D model can fit inside the measured data well.

Based on these parameters, the use of VGM models, the sample can draw the soil–water

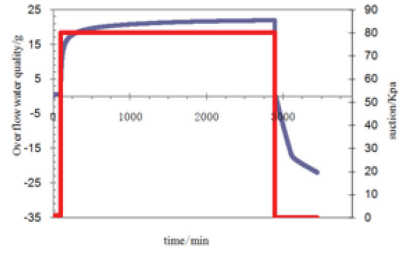

Figure 2. The curves of outflow and matric suction with time.

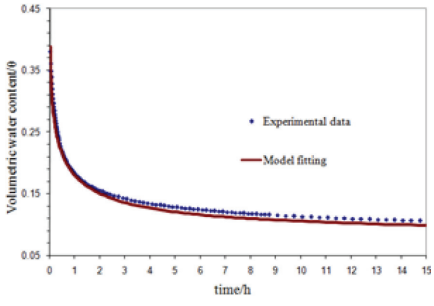

Figure 3. The comparison between the estimated and measured values of θ~t curve during drying.

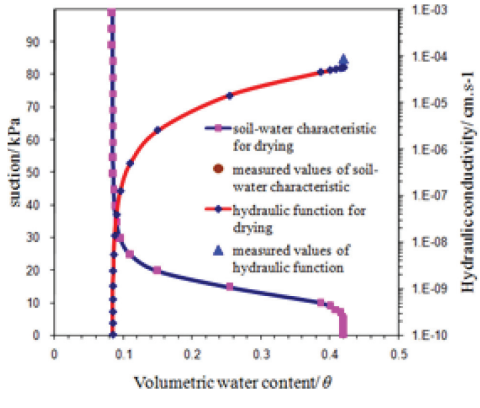

Figure 4. The curves of soil–water characteristic and hydraulic function during drying and some comparison with measured values.

characteristic curve and the conductivity function of the soils of drying, as shown in solid lines in Figure 4. Also, before you step flow test, the test system with a joint sample measured at equilibrium of soil–water characteristic curve and saturated hydraulic conductivity, is shown in Figure 4. Comparative analysis shows that the model of soil–water characteristic curves obtained with experimental results closer. In addition, it can be seen from the figure the value predicted by the model and the measured values are less saturated hydraulic system. Therefore, HYDRUS-1D one dimensional moisture transport model can be a good anti-unsaturated soil–water characteristic curve and permeability function curve count.

5.2 *The soil–water characteristic curve and the conductivity function of the soils of wetting*

The suction is reduced to zero; a water glass of water began to enter the sample. According to

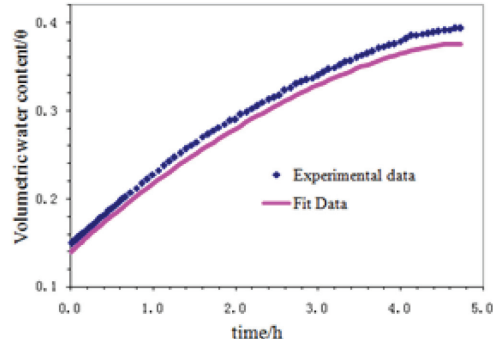

Figure 5. The comparison between the estimated and measured values of θ~t curve during wetting.

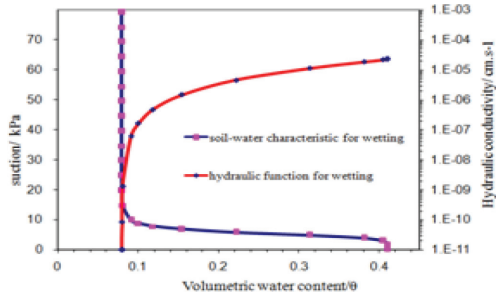

Figure 6. The curves of soil–water characteristic and hydraulic function during wetting.

volumetric water rates over time relational data, the initial and boundary conditions and material parameters of wet clay plate are off the stage, using HYDRUS-1D model of one-dimensional inverse water transport, fitting water overflowed the sample moisture the evolution curve over time. Curve fitting with the measured data of contrast curve is shown in Figure 5. As can be seen from the figure HYDRUS-1D model can fit inside the dehumidifying section of the sample volumetric water content variation with time.

VGM models of these input parameters can also draw the soil–water characteristic curve and the conductivity function of the soils of wetting, as shown in Figure 6.

6 CONCLUSIONS

Based on the analysis of this study, the following conclusion can be drawn:

– Improved combined testing system increases the efficiency of the bubble measurement system to accurately measure the volume of air

bubble overflow, correct overflow water, and then obtain the real value of the overflow water, thereby increasing erosion, and thus the bubble measurement system is necessary.

– HYDRUS-1D is a one-dimensional analysis of the impact of water flow through the sample software simulation clay plate percolation process that provides better results, thereby enabling more accurate fitting step flow test to measure the water overflow curve over time, soil–water characteristics of unsaturated soils derived by the inverse curve and permeability function, and the measured value was found to be close.
– Since this method is only applied to the specimen one suction step, by comparing the above-mentioned test, we can find that the suction step involving different hydraulic parameters obtained by the inverse calculation is also different from that of the test results obtained by applying suction step size constraints; this is the disadvantage of this method. So choosing a reasonable suction step is the key to the proposed method.

ACKNOWLEDGMENT

This research was financially supported by the project "The Test of Hydraulic Properties of Unsaturated Soils Based on Dynamic Method of the Construction Department of Hubei Province."

REFERENCES

Alexander, L. (ed.) 1986. Predicting unsaturated hydraulic conductivity from the soil water characteristic. *J. Transactions of the ASAE* 29(1): 176–184.

Doering, E.J. 1965. Soil-water diffusivity by the one-step method. *J. Soil Science* 99(5): 322–326.

Fredlund, D.G. &. Xing, A.Q. 1994. Predicting the permeability function for unsaturated soils using the soil-water characteristic curve. *J. Canadian Geotechnical Journal* 31(4): 533–546.

Fredlund, D.G. & Xing, A.Q. 1996. The relationship of the unsaturated soil shear strength to the soil-water characteristic curve. *J. Canadian Geotechnical Journal* 33(3): 440–448.

Gardner, W.R. 1956. Calculation of capillary conductivity from pressure plate outflow data. *J. Soil Science of America Proceeding* 20(2): 317–320.

Kool, J.B. (ed.) 1985. Determining soil hydraulic properties from one-step outflow experiments by parameter estimation: I, Theory and numerical studies. J. Soil Science Society of America Journal 49(3): 1348–1354.

Ning, L. 2006. Constant flow method for concurrently measuring soil-water characteristic curve and hydraulic conductivity function. *J. Geotechnical Testing Journal* 29(3): 1–12.

Parker, J.C. (ed.) 1985. Determining soil hydraulic properties from one-step outflow experiments by parameter estimation, II, Experimental studies. *J. Soil Science Society of America Journal* 49(2): 1354–1359.

van Genuchten, M.T. 1980. A closed-form equation for predicting the hydraulic conductivity of unsaturated soils. *J. Soil Science Society of America Journal* 44: 892–898.

This page intentionally left blank

Civil Engineering and Urban Planning IV – Liu et al. (Eds)
© 2016 Taylor & Francis Group, London, ISBN 978-1-138-02903-3

Cost risk analysis for the power transmission project-based network

Hong-Yu Shen, Peng Wang & Yi Liu
Jiangsu Electric Power Company Economic Research Institute, Nanjing, Jiangsu, China

ABSTRACT: The power transmission projects consist of large-scale investment, long construction period, wide line across a vast area, high technical level of equipment and devices, and significant social influence, which bring numerous uncertainties to the expected results. Based on the expert questionnaire, a three-level index system is used to determine the cost of risk, and then the Delphi method, AHP, network analysis, and fuzzy comprehensive evaluation are used to build a power transmission project cost risk index evaluation model. The results can be applied to the real project empirical analysis to provide reference to the cost of risk management and risk control system. It benefits similar projects to ensure the accuracy of the cost in the future.

1 INTRODUCTION

Fuzzy network analysis is an effective method, which is used for uncertainty evaluation with quantified uncertainty factors. Due to the complicated construction of the essential power transmission project, it presents several characters including large initial investment, the construction process, the present scale of investment, the long construction period, the wide construction area, the high technical level of equipment and devices, and the significant social influences. Those characters bring cost management into complex circumstances and various uncertain factors. Therefore, risk assessment of the power transmission project is a complicated system work; the accuracy of the evaluation result mainly depends on the selection of the rational index system and the relevance score made by experts for weighing the index system. On the other hand, the result may be influenced by a selected method as well. Therefore, the evaluation result may both relate to the evaluation objects and evaluation methods. This article is based on the theory of fuzzy network analysis, and cost risk index system assessment of the power transmission project is added as well. According to the characters of cost risk from the power transmission project, this article uses the Delphi method, Analytic Hierarchy Process (AHP) (Chang & Jiang 2007), network analysis method (Wang & Cai 2001), and fuzzy comprehensive evaluation method (Xue et al. 2012) to obtain a targeted evaluation of the power transmission project based on the fuzzy network analysis.

2 COST RISK EVALUATION INDEX SYSTEM BUILDING OF POWER TRANSMISSION PROJECT COST

Construct cost risk evaluation index system of the power transmission project should follow the principle of comprehensiveness, operability, and representativeness. This article was based on the feature mapping theory (Guo 2007) to indicate the project cost risk of the power transmission project. Based on the risk characteristic theory (Han et al. 2010), the project cost risk index can be divided into five first-level indicators and 16 secondary indicators after the subdivision. Basically, these indicators can cover all the risk factors of the power transmission project, which means it is operable. The set-up of the secondary cost risk evaluation index system of the power transmission project is shown as follows:

- Technical Risk (C_1): Technical Level (e_{11}); Design Proposal (e_{12}); and Design change (e_{13}).
- Management Risk (C_2): Mastery of Standard (e_{21}); Organization and Coordination (e_{22}); Management Level (e_{23}); and Professional Quality of Employees (e_{24}).
- Political Risk (C_3): Price Policy (e_{31}); Tax Policy (e_{32}); and Technical Standard (e_{33}).
- Economy Risk (C_4): Inflation (e_{41}); Price Increment (e_{42}); and Interest Increment (e_{43}).

– Environment Risk (C_5): Geological Hydrology Conditions of Construction Site (e_{51}); Climatic Conditions (e_{52}); and Natural Hazard (e_{53}).

3 COST RISK OF POWER TRANSMISSION PROJECT BASED ON FUZZY NETWORK ANALYSIS

3.1 *Project overview*

This study selected the Taichang to Wen dong 220 kv line project as the research object. The project is 220 kv double circuit engineering, the circuit is from 220 kv Taichang change to 220 kv Wendong change, the total length is 12.9 km. Among other charges, contained the basic tower 2 of 500 kV Taidou and Xingdou line increased renovation project. Special process contains demolition of basic tower 2. This project chose one-third of the road that is nearest to the highroad as its research project, with a total of 13 basic towers (seven of them are straight line towers).

Average staff's carrying length of this project (including road bend coefficient) is 0.2 km, average vehicle haul distance is 7 km. Tower foundation use excavation and filling pile foundation, the terrain of this project is flat ground 60%, mire 20%, river network 20%, and 0% of the hills. Geology is 68.765% of the ordinary soil, 24.445% of the puddle, 6.789% water puddle, and 0% of the hard soil and loose sand. A total of the towers are 43 (straight line towers within are 24).

3.2 *Evaluation and analysis*

Based on the multi-dimensional characteristics of the risk, the study is based on the evaluation of the secondary indexes by a single factor from the risk probability, consequences of the risk and risk control, respectively. We need to select a project manager and 20 relevant experts to investigate the evaluation of the cost risk secondary indicators' effective factors from Taichang to Wendong 220 kv line project. Twenty copies of the questionnaires were issued, recycled 20, the recovery rate of 100%, through sorting, statistics, get the evaluation results table as shown in matrix *U*. The reviews set is *N* (Highest risk, Higher risk, Medium risk, Lower risk, Lowest risk).

Based on the cost risk factors assessment survey statistics of Taichang to Wendong 220 kv route engineering project, the fuzzy judgment matrix can be constructed:

$$R=\begin{bmatrix}0.00 & 0.50 & 0.50 & 0.00 & 0.00\\ 0.00 & 0.40 & 0.50 & 0.10 & 0.00\\ 0.00 & 0.25 & 0.25 & 0.25 & 0.25\\ 0.00 & 0.00 & 0.50 & 0.25 & 0.25\\ 0.00 & 0.50 & 0.25 & 0.25 & 0.00\\ 0.00 & 0.25 & 0.25 & 0.15 & 0.35\\ 0.00 & 0.25 & 0.20 & 0.20 & 0.35\\ 0.10 & 0.25 & 0.25 & 0.40 & 0.00\\ 0.00 & 0.00 & 0.50 & 0.50 & 0.00\\ 0.75 & 0.25 & 0.00 & 0.00 & 0.00\\ 0.00 & 0.25 & 0.40 & 0.20 & 0.15\\ 0.00 & 0.25 & 0.40 & 0.30 & 0.05\\ 0.75 & 0.20 & 0.05 & 0.00 & 0.00\\ 0.50 & 0.25 & 0.25 & 0.00 & 0.00\\ 0.50 & 0.20 & 0.20 & 0.10 & 0.00\\ 0.75 & 0.25 & 0.00 & 0.00 & 0.00\end{bmatrix}$$

3.3 *Determination of the weights of F-ANP*

Based on the above method, the weights of F-ANP can be determined in order to determine the factors.

The quantitative matrix of primary risk cost indicators can be obtained as the set C_1 (Technical risks), which is fuzzy judgment matrix W_{11}:

$$W_{11}=\begin{bmatrix}0.637 & 0.258 & 0.258\\ 0.258 & 0.637 & 0.105\\ 0.105 & 0.105 & 0.637\end{bmatrix}$$

The structure of the quantitative matrix of other influencing factors C_2 can be obtained (management risks), which is the fuzzy judgment matrix W_{22}:

$$W_{22}=\begin{bmatrix}0.654 & 0.100 & 0.077 & 0.100\\ 0.077 & 0.700 & 0.192 & 0.100\\ 0.077 & 0.100 & 0.654 & 0.100\\ 0.192 & 0.100 & 0.077 & 0.700\end{bmatrix}$$

Similarly, the structure of the quantitative matrix of other influencing factors C_3 political risks) can be obtained, which is the fuzzy judgment matrix W_{33}:

$$W_{33}=\begin{bmatrix}0.600 & 0.200 & 0.200\\ 0.200 & 0.600 & 0.200\\ 0.200 & 0.200 & 0.600\end{bmatrix}$$

Similarly, we can obtain W_{12}, W_{13}, W_{21}, W_{23}, W_{24}, W_{31}, W_{32}, W_{41}, W_{42}, W_{43}, W_{51}, W_{52}, and W_{53}.

The final secondary quantitative index structure, the fuzzy matrix:

$$W = \begin{bmatrix}
0.637 & 0.258 & 0.258 & 0.333 & 0.333 & 0.637 & 0.333 & 0.333 & 0.333 & 0.333 & 0.333 & 0.333 & 0.333 & 0.333 & 0.333 \\
0.258 & 0.637 & 0.105 & 0.333 & 0.333 & 0.105 & 0.333 & 0.333 & 0.333 & 0.333 & 0.333 & 0.333 & 0.333 & 0.333 & 0.333 \\
0.105 & 0.105 & 0.637 & 0.334 & 0.334 & 0.258 & 0.334 & 0.334 & 0.334 & 0.334 & 0.334 & 0.334 & 0.334 & 0.334 & 0.334 \\
0.167 & 0.167 & 0.096 & 0.654 & 0.100 & 0.077 & 0.100 & 0.250 & 0.250 & 0.167 & 0.250 & 0.250 & 0.250 & 0.250 & 0.250 \\
0.500 & 0.500 & 0.250 & 0.077 & 0.700 & 0.192 & 0.100 & 0.250 & 0.250 & 0.500 & 0.250 & 0.250 & 0.250 & 0.250 & 0.250 \\
0.167 & 0.167 & 0.558 & 0.077 & 0.100 & 0.654 & 0.100 & 0.250 & 0.250 & 0.167 & 0.250 & 0.250 & 0.250 & 0.250 & 0.250 \\
0.166 & 0.166 & 0.096 & 0.192 & 0.100 & 0.077 & 0.700 & 0.250 & 0.250 & 0.166 & 0.250 & 0.250 & 0.250 & 0.250 & 0.250 \\
0.333 & 0.333 & 0.142 & 0.637 & 0.200 & 0.333 & 0.600 & 0.600 & 0.200 & 0.200 & 0.105 & 0.105 & 0.429 & 0.429 & 0.429 & 0.429 \\
0.333 & 0.333 & 0.429 & 0.105 & 0.200 & 0.333 & 0.200 & 0.200 & 0.600 & 0.200 & 0.258 & 0.258 & 0.258 & 0.142 & 0.142 & 0.142 \\
0.334 & 0.334 & 0.429 & 0.258 & 0.600 & 0.334 & 0.200 & 0.200 & 0.200 & 0.600 & 0.637 & 0.637 & 0.637 & 0.429 & 0.429 & 0.429 \\
0.200 & 0.333 & 0.333 & 0.333 & 0.333 & 0.333 & 0.333 & 0.200 & 0.200 & 0.200 & 0.637 & 0.258 & 0.200 & 0.333 & 0.200 & 0.200 \\
0.600 & 0.333 & 0.333 & 0.333 & 0.333 & 0.333 & 0.333 & 0.200 & 0.200 & 0.200 & 0.258 & 0.637 & 0.200 & 0.333 & 0.200 & 0.200 \\
0.200 & 0.334 & 0.334 & 0.334 & 0.334 & 0.334 & 0.334 & 0.600 & 0.600 & 0.600 & 0.105 & 0.105 & 0.600 & 0.334 & 0.600 & 0.600 \\
0.333 & 0.333 & 0.333 & 0.200 & 0.333 & 0.333 & 0.258 & 0.200 & 0.200 & 0.200 & 0.200 & 0.637 & 0.200 & 0.600 & 0.258 & 0.258 \\
0.333 & 0.333 & 0.333 & 0.200 & 0.333 & 0.333 & 0.105 & 0.600 & 0.600 & 0.600 & 0.200 & 0.105 & 0.200 & 0.200 & 0.637 & 0.105 \\
0.334 & 0.334 & 0.334 & 0.600 & 0.334 & 0.334 & 0.637 & 0.200 & 0.200 & 0.200 & 0.600 & 0.258 & 0.600 & 0.200 & 0.105 & 0.637
\end{bmatrix}$$

Make the ordering vector a_{ij} a composite of fuzzy weight matrix A:

$$A = \begin{bmatrix}
0.375 & 0.069 & 0.125 & 0.125 & 0.125 \\
0.125 & 0.419 & 0.125 & 0.125 & 0.125 \\
0.125 & 0.069 & 0.375 & 0.125 & 0.125 \\
0.125 & 0.069 & 0.125 & 0.375 & 0.125 \\
0.125 & 0.187 & 0.125 & 0.125 & 0.375
\end{bmatrix}$$

The fuzzy weighted matrix calculating weight is as follows. By calculating the limit rank, we can determine the final weighing result of this model as follows:

$$C = \begin{matrix} 0.055, 0.051, 0.047, 0.039, 0.053, 0.043, \\ 0.043, 0.050, 0.037, 0.066, 0.044, 0.044, \\ 0.065, 0.057, 0.056, 0.056 \end{matrix}$$

We can comprehensively evaluate the synthetic operator selection $M(\bullet,\oplus)$, which is the weighted average operator.

According to the formula $B = C \bullet R$, obtain $B = 0.321, 0.236, 0.231, 0.138, 0.074$.

By the maximum subordination principle, the maximum value is 0.321, which means this project has a high cost risk.

4 CONCLUSION

Based on the theory of fuzzy network analysis, the cost risk analysis of the power transmission project cost risk has the following conclusions:

– Based on the feature mapping theory to identify the engineering cost risk of the power transmission project. According to the risk characteristic theory, the cost risk assessment of the power transmission project's secondary index system is established.
– With the combination of the Delphi method, Analytic Hierarchy Process (AHP), network analysis method, and fuzzy comprehensive evaluation method, the cost risk index evaluation model of the power transmission project can be constructed.
– Applying the result of the power transmission project's cost risk evaluation model to the actual project, using the empirical analysis, the project cost risk management is promoted effectively, and the cost is guaranteed accurately.

REFERENCES

Chang, J.E. & Jiang, T.L. 2007. Study of determine the weight of Analytic Hierarchy Process (AHP). Journal of Wuhan University of Science and Technology, Information and Management Engineering 29(1): 153–156.

Guo, J. 2007. Feature mapping model and risk analysis of project application. Journal of Shandong University of Architecture 22(2): 154–157.

Han, Y., Gao, Q.M. & Luo, Y. 2010. Large public buildings risk characteristics analysis. Journal of Engineering Management 24(1): 37–40.

Wang, L.F. & Cai, H.O. 2001. Network process (ANP) in the theory and algorithm. Journal of Systems Engineering Theory and Practice 5(3): 44–50.

Xue, Y., Li, F.Y. & Liu, G.G. 2012. Survey method for determining weight fuzzy comprehensive evaluation set research. Cryogenic Architectural Technology 34(2): 121–122.

This page intentionally left blank

Civil Engineering and Urban Planning IV – Liu et al. (Eds)
© 2016 Taylor & Francis Group, London, ISBN 978-1-138-02903-3

Numerical modeling: The evolution of tectonic stress field in the Longmenshan region

Sheng-Rui Su, Ying Zhang & Peng Li
Department of Geological Engineering, Chang'an University, Xi'an, Shaanxi, China

ABSTRACT: In the Longmenshan region located in southwestern China and the northeastern edge of Qinghai-Tibetan plateau, the Wenchuan earthquake with a magnitude of 8.0 occurred in 2008. To study the evolution of the tectonic stress field before, during and after the earthquake, a two-dimensional numerical modeling was carried out. It was found that from the time period before the earthquake to the time period after the earthquake, the regional stress field had changed. The change coincides well with the deformation caused by the earthquake and the distribution of the after-shocks. The results may be applied in the prediction of earthquakes and the design of the underground constructions in the region.

1 INTRODUCTION

Tectonic stress field refers to the distribution of the tectonic stress within a certain range of space; it comprehensively reflects various powers acting on the geologic body and related to the movement in the crust (An 1992). Research on the distribution and evolution of tectonic stress field is the important basis of earthquake prediction, regional crustal stability evaluation, and research on the geological hazard, etc.

Longmenshan region is located in the southwestern region of China and the northeastern margin of Qinghai-Tibetan plateau. Due to the squeezing action of the Indian Plate and Eurasian Plate, Wenchuan Earthquake with 8.0 magnitude occurred in the Longmenshan region on May 12, 2008. As the focal depth is 10–20 km, and it lasted a long time, the Wenchuan earthquake had a tremendous destructiveness. Almost 70,000 people died and induced a large number of secondary disasters.

The change in the tectonic stress field in the earthquake areas has caused a wide attention (Tu et al. 2008; Jiang et al. 2003). To study the evolution of tectonic stress field before, during, and after the earthquake, a two-dimensional numerical modeling was carried out. The research result may provide a theoretical basis for an in-depth discussion of the regional geodynamic process in the eastern edge of the Qinghai-Tibet plateau and the prediction of the geological hazards.

2 RESEARCH AREA CHARACTERISTICS

Longmenshan region is located in the southwestern China and it is generally called the Longmenshan fault (abbreviated as LMS) zone. The study region is located in the Songpan-Ganzi blocks in the eastern edge of Qinghai-Tibet plateau. Its southwest area is intercepted by Xianshuihe fault (abbreviated as XSH), its east area is adjacent to the Yangtze platform, and its north area is Qinling orogenic belt (Fig. 1).

The Longmenshan fault zone consists of three reverse faults, which are named frontal Longmenshan fault, central Longmenshan fault, and back Longmenshan fault (Chen, et al. 2007; Li et al. 2006; Deng, et al.1994) from east to west (F3, F4 and F5 in Fig. 2). The inclination of these faults are NW and the dip angle are 50°–80°.

The research of the regional tectonic stress field shows that the orientation of the maximum principal stress in the Longmenshan region is NNW-SSE, but has certain partition variability. According to the result of the *in situ* stress measurement in the northeast parts of the Longmenshan Fault,

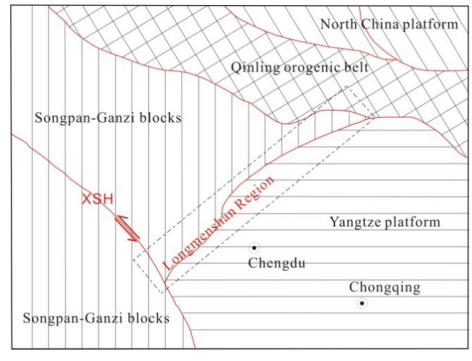

Figure 1. Geotectonic of the study region.

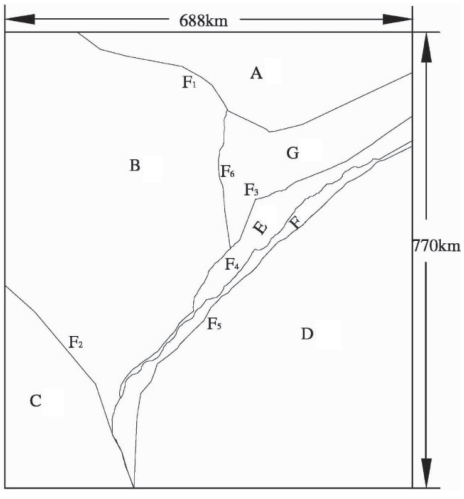

Figure 2. Geological model.

the orientation of the maximum principal stress is N28°E~N85°E, most of them are NEE-SWW (Chen et al. 2012), while in the rest of the region it is nearly east-west (Xie et al. 2003).

3 SET-UP OF THE MODEL

The paper has carried on a two-dimensional static analysis by using the ANSYS software. In the simulations, elastic isotropic properties are assumed for the intact rocks and Mohr-Coulomb model of the strength is assumed for the faults.

The scope of the model for simulation is determined after fully considering the tectonic stress field of Western China and the geological conditions of the Longmenshan region. Range of geographic coordinates is 101°–106°N, 29°–34°E. The model is about 688 km from the east to the west and 770 km from north to south, and the area is about 5.3×10^5 km^2.

Previous research indicates that the Longmenshan region includes the Xianshuihe fault (abbreviated as XSH, F_2), back Longmenshan fault (abbreviated as BL, F_3), central Longmenshan fault (abbreviated as CL, F_4), frontal Longmenshan fault (abbreviated as FL, F_5) (traditionally, the back, central, and frontal Longmenshan faults are collectively called Longmenshan fault zones in China), Minjiang fault (abbreviated as MJ, F_6), and Animaqing-Lueyang fault (abbreviated as AL, F_1). In the geomechanic model, the above mentioned six faults are included. The model is divided into seven regions taking the above mentioned six faults as boundaries (Table 1 and Fig. 2), and then we get the grid division model (Fig. 3).

Table 1. Zoning and major components.

Zoning code	Location	Major components
A	Qinling orogenic belt	Metamorphic rocks
B	Between XSH and LMS	Flysch clastic detritus
C	South of XSH	Proterozoic complex
D	Yangtze platform	Quaternary fluvial alluvial
E	Between BL and CL	Pre-Sinian complex
F	Between FL and CL	Paleozoic and Triassic strata
G	Between BL and AL	Similar to B

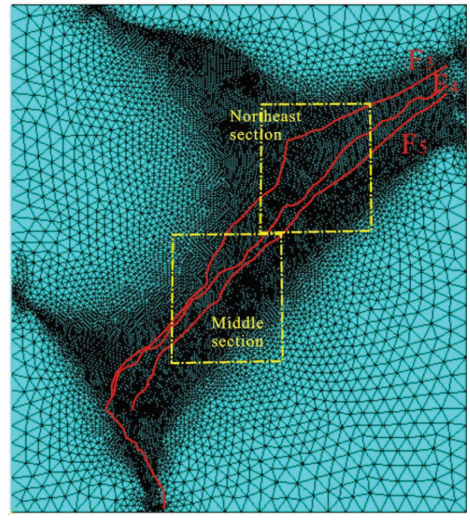

Figure 3. Grid division model.

4 MATERIAL PARAMETERS AND BOUNDARY CONDITIONS

4.1 *Material parameters*

By analyzing the formation lithology of the study area (Table 1) and referring to the previous empirical data (Committee of Engineering Geology Handbook 1992), the material parameters of rock mass can be determined (Table 2). For the mechanical parameters of the fault zones, the regional differences of their activity and the vibrational displacements in the Wenchuan earthquake are considered (Table 3).

It should be noted that the earthquake made a certain change in the original stress in rock mass and macroscopic continuity. In order to reflect these changes, the physical and mechanical parameters of the rock mass and fault zones are adjusted

Table 2. Physical and mechanical parameters of rocks*.

Zoning code	E (MPa)		Poison ratio		Unit weight	
	B	D&A	B	D&A	B	D&A
A	35×10^3	30×10^3	0.24	0.24	27	27
B	30×10^3	25×10^3	0.24	0.24	26	26
C	23×10^3	18×10^3	0.24	0.24	26	26
D	40×10^3	12×10^3	0.23	0.23	27	27
E	10×10^3	8×10^3	0.26	0.26	26	26
F	12×10^3	7×10^3	0.26	0.26	26	26
G	28×10^3	25×10^3	0.24	0.24	26	26

Zoning code	Cohesion (MPa)		Frictional angle (°)	
	B	D&A	B	D&A
A	1	0.9	40	37
B	1	0.9	40	40
C	9	0.8	45	45
D	5	1	35	41
E	0.9	0.7	35	35
F	0.8	0.8	34	34
G	1	0.7	38	35

*B-before the Wenchuan earthquake, D-during the earthquake, A-after the earthquake.

Table 3. Mechanical parameters of fault zones*.

Fault	Normal stiffness ($\times 10^2$ kN/m^2)			Shear stiffness ($\times 10^2$ kN/m^2)		
	B	D	A	B	D	A
F_1	4	4	4	4	4	4
F_2	4	4	4	1	1	1
F_3	30	30	30	2	0.2	0.2
F_4	30	3000	30	2	0.2	0.2
F_5	300	3000	3000	334	334	334
F_6	300	300	300	30	30	30
Fault	Cohesion (MPa)			Frictional angle (°)		
	B	D	A	B	D	A
F_1	0.1	0.008	0.008	15	15	15
F_2	1	0.008	0.008	23	23	23
F_3	0.5	0.05	0.05	30	20	20
F_4	0.2	0.05	0	10	10	5
F_5	0.5	0.2	0.1	25	25	25
F_6	0.8	0.7	0.6	25	20	18

*B-before the Wenchuan earthquake, D-during the earthquake, A-after the earthquake.

when they simulate the displacement and tectonic stress during the earthquake (Tables 2 and 3).

The material parameters of the rock mass after the earthquake is taken as the same with the one during the earthquake, but those of the fault zones are changed. As a diastrophism of the CL and a partial dislocation of the FL during the earthquake has reduced the strength of rock masses, the parameters of CL and FL are decreased but the parameters of other faults stay the same (Tables 2 and 3).

4.2 *Boundary conditions*

According to the regional tectonic stress field, an east-west tectonic stress is put on the west boundary, which lies to the north of XSH, a SE45° tectonic stress is put on the south of XSH, and east, south and north boundaries of model are constraint boundary.

5 ANALYSIS OF THE SIMULATION RESULTS

5.1 *Tectonic stress field before the earthquake*

5.1.1 *Maximum principal stress*

It is compressive and present stress concentration in the partial inflection point, fault endpoint, and intersection of faults. Especially in the intersection of AL fault and LMS, the intersection of LMS and XSH also exists. The stress magnitude along the LMS zone is obviously greater than that in the other regions (Fig. 4).

The maximum principal stress orientations have a partition characteristic. The predominant orientation of principal stress axes is east-west in north of XSH and LMS zones, which is consistent with the study of Xie et al. (2003). But in the area between MJ and BL, the predominant orientation of the principal compressive stress axes is NEE. In the area among FL, BL, and the west of XSH, the predominant orientation of the principal compressive stress axes is NW; the stress field is complex in the intersection of faults, the predominant orientation of the principal compressive stress axes start to change near Baiyang town, its southwest area gradually changed to an orientation nearly perpendicular to the strike, while the northeast area became gradually parallel to the strike.

Stress distribution is uniform along FL. The maximum principal stress changes greatly along BL and CL; the value is about 1.51 MPa near Wenchuan and Maoxian (BL) and the maximum value is about 1.72 MPa near Yingxiu (CL).

5.1.2 *Shear stress*

The gradient of shear stress contour in LMS is significantly greater than the other areas, and the maximum stress along the CL is the maximum (879 KPa), BL takes a second place (434 KPa) and FL is the minimum (184 KPa). The maximum shear stress along CL is near Yingxiu, and the maximum stress in BL is near Wenchuan and Maoxian.

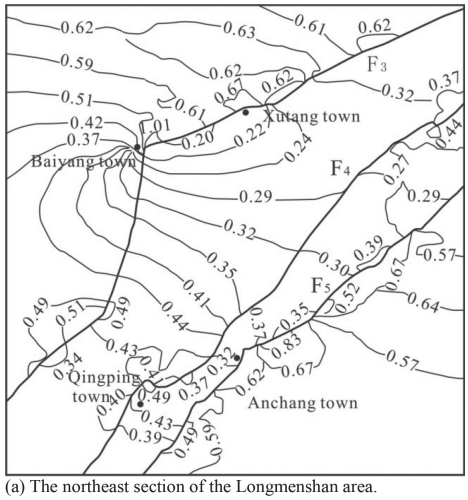

(a) The northeast section of the Longmenshan area.

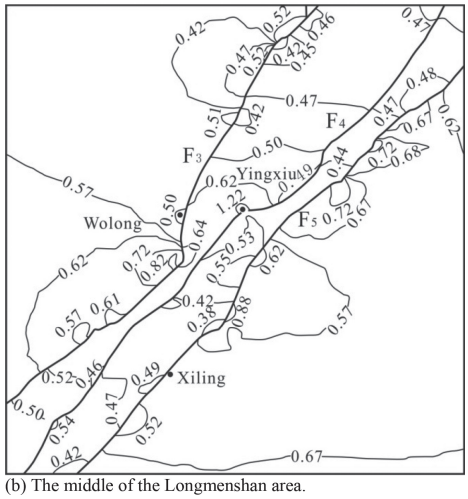

(b) The middle of the Longmenshan area.

Figure 4. The maximum principal stress isoline before the Wenchuan earthquake.

5.2 *Tectonic stress field during the earthquake*

5.2.1 *The maximum principal stress*

The whole study region is still in a compression state and it is complex along LMS. From the southwest to the northeast, the predominant orientation of stress axes show nearly east-west → SEE → nearly east-west along the central Longmenshan fault, which is basically consistent with the research results of Wang et al. (2009).

The concentration areas of the maximum principal stress mainly appears in the partial inflection point and intersection of faults, especially in the intersection of the LMS, XSH, and MJ, and the degree of stress concentration in the southwest of LMS is much greater than that in the northeast part.

The changes of the maximum principal stress in the southwest of LMS is greater than that in other areas during the earthquake: (a) in the intersection area of the southwest part of BL and zone B in Figure 2, principal compressive stress orientation centrally rotated nearly 30°, from before the earthquake SE60°–80° to NE83°–87°; (b) in the southwest zone E in Figure 2 (the intersection area of CL and BL), principal compressive stress orientation changes from nearly perpendicular to the strike before the earthquake to nearly east-west.

The magnitude of the maximum principal stress of southwest is bigger than that in the northeast of BL, but the variation is small along the strike. The largest maximum principal stress is 1.87 MPa, near Yingxiu (the epicenter of Wenchuan earthquake). It appears larger in its central part than the southwestern part, and the southeastern part is the smallest near BL. The maximum value appears in the north of Maoxian County, which is about 1.76 MPa.

5.2.2 *Shear stress*

The area where the shear stress concentration appears is basically the same as that before the earthquake, but the gradients of the shear stress contour line are different: (a) shear stress gradient changes significantly during the earthquake, the contour line between BL and CL is more intensive than those before the earthquake; (b) shear stress concentration is significant near Baiyang town (located on BL), and shear stress gradient increases more significantly than that before the earthquake; (c) shear stress contour line is more intensive than before the earthquake in the intersection of MJ and AL.

5.3 *Tectonic stress field after the earthquake*

5.3.1 *The maximum principal stress*

The stress orientation is NEE to SEE, but changes from NE83°–87° during the earthquake to SE83°–87° after the earthquake in the southwestern of BL. The stress in the central area is complex, part of the predominant orientation of principal stress axes is nearly perpendicular to the fault strike, part skew with the fault, and the others are parallel with the fault strike. The stress orientation in the northeast region is basically the same as during the earthquake stage. The stress in the southwest section of CL changes from nearly parallel, with the fault during the earthquake, to SEE after the earthquake. The stress orientation is NEE in the north of Xiaoyudong fault (central of FL), and the orientation is south-east in the south of Xiaoyudong.

According to the maximum principal stress's monitoring curves, the maximum principal stress's value changes only at the region near the intersections and the endpoint of the FL, in other regions

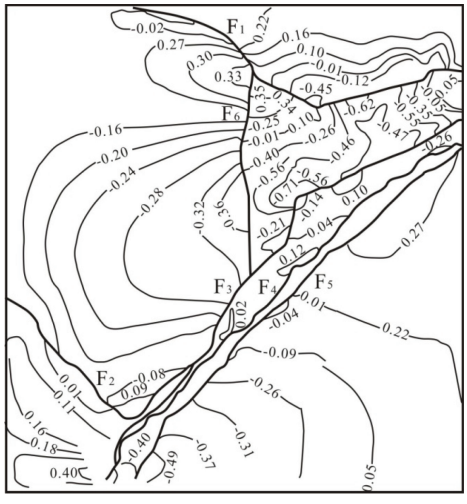

Figure 5. The maximum shear stress isoline after the earthquake.

along the strike the value becomes smaller gradually, and the curve is more gentle than during the earthquake. The stress curve of the CL goes up and down like waves, and the maximum value appears in the northeast of Yingxiu. The stress of the BL moves to the northeast along the fault, not in the region near Wenchuan and Maoxian.

5.3.2 *Shear stress*

After the earthquake, the shear stress contour line does not present an intensive area near Yingxiu (CL), but presents a stress concentration in the northeast of CL (Fig. 5). The change in the stress is significant and the concentration appears near Baiyang town (BL), the shear stress gradient is greater than that before the earthquake. The concentration also appears near Pingwu.

In the studied region, the maximum shear stress appears in the southernmost of FL, near Beichuan (CL), and near Baiyang town (BL).

6 EVOLUTION OF TECTONIC STRESS FIELD

From the numerical modeling results of the above three cases, it was found that the tectonic stress changed in magnitude and orientation. Some variations of the maximum principal stress are as follows:

1. In the whole study area, the maximum principal stress orientation was generally toward NEE to SEE except for the local region that is changing before, during, and after the earthquake.
2. In the southwestern region of BL, the maximum principal stress orientation was SE60°–80° before the earthquake, then changed to NE83°–87° during the earthquake, and finally became SE83°–87° after the earthquake (Fig. 6a).
3. The maximum principal stress orientation in the central area of BL was nearly perpendicular to the strike before the earthquake → nearly parallel to the strike during the earthquake → almost consistent with the changes during the earthquake (Fig. 6b).
4. In the Yingxiu area on CL, the maximum principal stress orientation was SE40°–50° before the earthquake, then changed to NE83°–87° during the earthquake and finally became SE83°–87° after the earthquake (Fig. 6c).
5. In the Xiaoyudong area (located between FL and CL), the maximum principal stress orientation was SE60°–70° before the earthquake, then changed to SE70°–80° during the earthquake and finally became SE40°–50° after the earthquake. Stress orientation near the Xiaoyudong

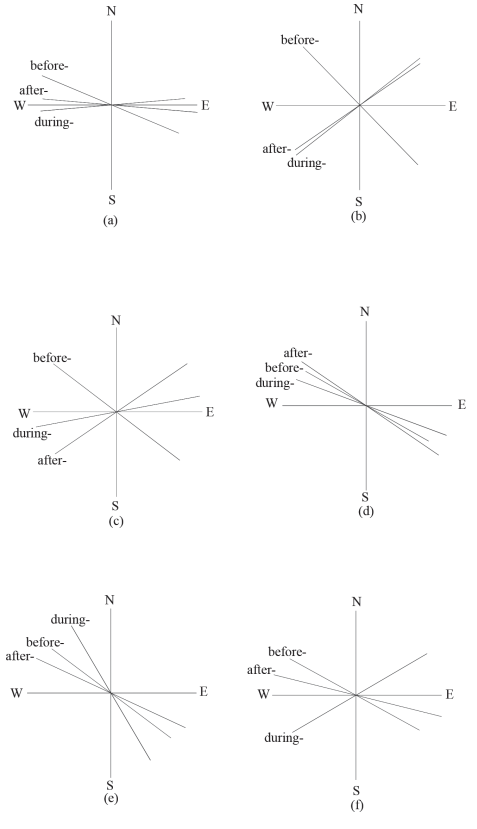

Figure 6. Changes in the maximum principal stress orientation before, during, and after the Wenchuan earthquake.

fault presents bifurcation, that is, the north of Xiaoyudong is NEE, while the south is east-south (Fig. 6d).
6. The maximum principal stress orientation was SE50°–60° before the earthquake, then changed to NW20°–30° during the earthquake to NW20°–30° after the earthquake in the area between Guangming town (BL) and Qingping town (CL) (Fig. 6e).
7. In the western area of Beichuan, the orientation of the maximum principal stress presented the following change: SE55°–60° → NE50°–60° → SE70°–80° (Fig. 6f).
8. The change in the vectors of the maximum principal stress was small through before, during, and after the earthquake in the area between the northeastern region of BL and AL, and the orientation of stress vectors was nearly parallel to the strike.

Variations of shear stress through before → during → after the Wenchuan earthquake are as follows:

1. The shear stress concentration region changed through before → during → after the earthquake, especially, in the area near Yingxiu, where the shear stress concentration was obviously significant before and during the earthquake. The shear stress value decreased obviously in CL and FL, but increased in BL after the earthquake.
2. The shear stress concentration region moved to the northeast along the CL after the Wenchuan earthquake, which was consistent with the distribution of the after-shocks of the Wenchuan earthquake that were concentrated in the northeast region of LMS.

7 CONCLUSION

Through the systematic numerical simulation, the tectonic stress field evolution of the Longmenshan region before and after the Wenchuan earthquake is revealed. The main conclusions are as follows:

1. The magnitude and orientation of maximum principal stress and shear stress all change through before, during, and after the earthquake in the Longmenshan region. The orientation of the maximum principal stress overall change from NEE to SEE, but the change is different in partial stress field. The change expression is different in different regions.
2. The change in shear stress through before, during, and after the earthquake in the Longmenshan region is as follows: the shear stress concentration appears in the partial region both before and during the earthquake, especially near Yingxiu; however, shear stress distribution is relatively homogeneous after the earthquake, and compared with that before the earthquake, the shear stress value decreased significantly in the frontal Longmenshan fault and the central Longmenshan fault but increased in the back Longmenshan fault. The shear stress concentration region moves to the northeast along the central Longmenshan fault, which is consistent with the distribution of the aftershocks of the Wenchuan earthquake.

ACKNOWLEDGMENTS

This work was financially supported by the major program of the National Natural Science Foundation of China (41030749), the National Natural Science Foundation of China (41072223), and the geological survey projects of Geological Survey Bureau of China (1212010914205).

REFERENCES

An, O. 1992. *Tectonic stress field.* Beijing: Seismological Press.

Chen, G.G., Ji, F.J. & Zhou, R.J. et al. 2007. Primary research of activity segmentation of Longmenshan fault zone since late-Quaternary. *Seismology and Geology* 29(3): 657–673.

Chen, Q.C., Feng, C.J., Meng, W. et al. 2012. Analusis of in situ stress measurements at the northeastern section of the Longmenshan fault zone after the 5.12 Wenchuan earthquake. *Chinese Journal of Geophysics* 55(12): 3923–3932.

Committee of Engineering Geology Handbook. 1992. *Engineering Geology Handbook (The third edition).* Beijing: China Architecture & Building Press.

Deng, Q.D., Chen, S.F. & Zhao, X.L. 1994. Tectonics, seismicity and dynamics of Longmenshan mountains and its adjacent regions. *Seismology and Geology* 26(2): 389–403.

Jiang, J.X., Yin, G.H. & Xu, F.Z. 2003. Relative stress field change of Kuerle region before 8.1 earthquake in western Kunlun Pass. *Earthquake* 23(3): 89–96.

Li, Y., Zhou, R.J. & Densmore, A.L. et al. 2006. *The eastern margin of continental dynamics process and geological response.* Beijing: Geological Press, 1–134.

Tu, H.W., Wan, X.H. & Gao, G. et al. 2008. Research of the reason for variations of the earthquake fault characters and the stress field in the Jiashi region of Xingjing from 1977 to 2006. *Progress in Geophysics* 23(4): 1038–1044.

Wang, Q.C., Chen, Z.L. & Zheng, S.H. 2009. Wenchuan earthquake aftershock sequence focal mechanism of space segmentation. *Chinese Science Bulletin* 53(16): 2348–2354.

Xie, F.R., Chen, Q.C. & Cui, X.F. et al. 2003. *Research of mainland China crustal stress environment.* Beijing: Geological Press.

Civil Engineering and Urban Planning IV – Liu et al. (Eds)
© 2016 Taylor & Francis Group, London, ISBN 978-1-138-02903-3

Field settlement observations made on four Concrete Face Rockfill Dams

Zhong-Zhi Fu & Ting-Bo Wang
Geotechnical Engineering Department, Nanjing Hydraulic Research Institute, Nanjing, Jiangsu, China

Sheng-Shui Chen
Key Laboratory of Failure Mechanism and Safety Control Techniques of Earth-Rock Dams, Nanjing, Jiangsu, China

ABSTRACT: Field settlement observations made on four Concrete Face Rockfill Dams (CFRDs) were studied with particular emphasis placed on the creep behavior of dams. It was found that the deformation mode of the CFRDs is primarily governed by the gravity of dam materials. However, creeps do occur during the construction, impounding and long term operation. Therefore, constitutive models capable of modeling the stress induced strain and creep strain in a unified manner was required to predict the deformation and stress behavior of CFRDs, particularly for those with a long duration of construction. Field observations also show that the settlement data of dams under constant loads could be well modeled by an exponential function, with one parameter controlling the final deformation and another one for the creep rate.

1 INTRODUCTION

Concrete Face Rockfill Dams (CFRDs) are increasingly built all over the world, during which the record of dam height has been continuously broken and more and more weak rocks have been used successfully with, however, a more rigorous compaction criteria (ICOLD 2010). Despite the great success achieved in the past in constructing higher and higher CFRDs, the design of such structures still largely depends on the empirical experiences gained in the previous practice. Nevertheless, large amounts of field observations have been collected and abundant laboratory experiments have been conducted with so many kinds of rockfill materials, providing a firm foundation for deepening the understanding of the behavior of both rockfill materials and concrete face rockfill dams. In this study, the field settlement observations made on the four CFRDs, including two hard rock CFRDs and two weak rock CFRDs, were studied. Particular attention was focused on the creep settlement that had taken place during the construction, impounding, and operation.

2 FIELD OBSERVATIONS MADE ON HARD ROCK CFRDS

2.1 *The Shuibuya CFRD*

The 233 m Shuibuya CFRD is the highest one of this type of dam ever built in the world up to date (Yang et al. 2010). This dam was constructed primarily with limestone of Maokou formation, limestone of Xixia formation and shale of Longtan formation. The limestones at both the formations are hard rocks, the average unconfined compressive strengths (UCS are 68.1 MPa and 46.4 MPa, respectively. The shale of Longtan formation is a kind of weak rock (UCS < 30 MPa) and they were only partially used in the secondary rockfill zone (3C). Therefore, most of the rockfill materials used in this dam are hard rocks.

The interior deformation monitoring instruments, including those for horizontal displacement and those for settlement, were installed in the three sections. In this paper, only the settlement data at the maximum cross section 0+212 is used. Figure 1 shows the locations of the five layers of settlement gauges installed in this section. Figure 2 plots the settlement histories of the five monitored points near the dam axis, i.e., SV01-1-7, SV01-1-18, SV01-1-27, SV01-1-33, and SV01-1-37. These monitoring gauges are selected herein because the vertical load and the settlement at these points are generally higher than the others at the same elevations. In addition, these points are far away from the surface of the dam and the influences of human activities and environmental events during the operation are negligible.

Three periods are involved in Figure 2, i.e., the construction period (before 2006/10), the impounding period (2006/10~2007/09), and the operation period (after 2007/09). It is clear that

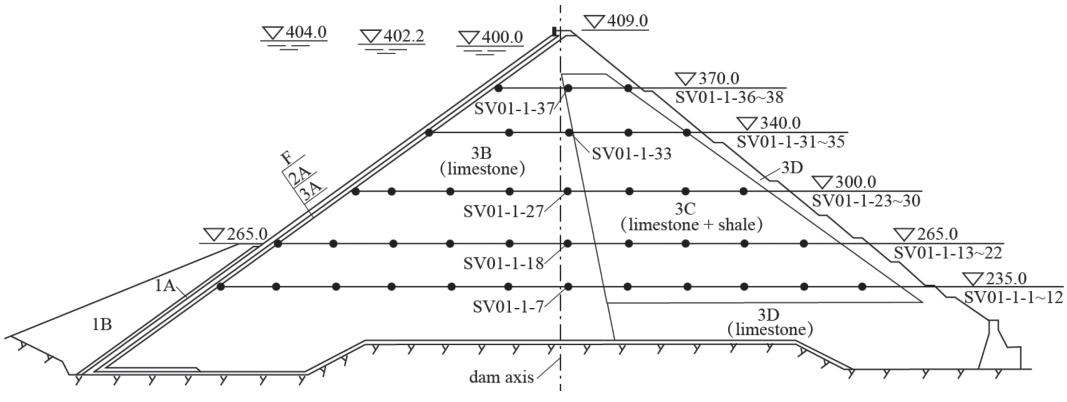

Figure 1. Location of settlement gauges installed in 0+212 section of Shuibuya CFRD.

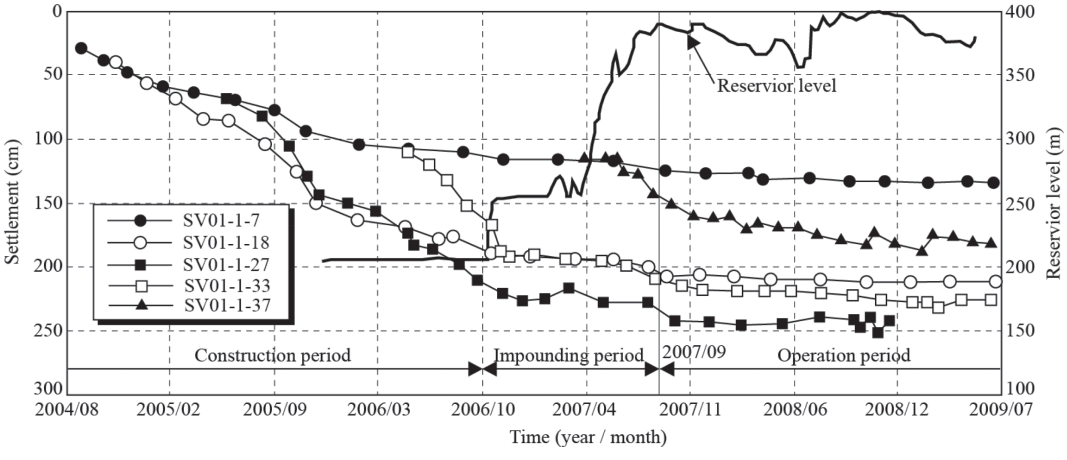

Figure 2. Settlement processes of five monitored points near the dam axis of Shuibuya CFRD.

the settlement induced by dam filling is much higher than that induced by reservoir impounding and that during the operation. That is to say, for CFRDs built with hard rocks, most of the settlement takes place during the construction period. Another important finding is the continuous increase of settlement at most of these monitoring points even when the reservoir level experienced a drop from Sep. 2007 to Jun. 2008. This means that the settlement induced by the creep of rockfill materials counterbalanced their elastic rebound, and indicated that the conventional way of considering the deformation caused by loading and by the creep of rockfill materials in a separated manner is irrational, particularly for high CFRDs with a long periods of construction and impounding.

In addition to the interior monitoring instruments, seven points were also established along the dam crest at the elevation of 405 m for the measurement of crest settlement (Zhou et al. 2011). Figure 3 shows the monitored settlement of these points except SL3 and SL7. The settlement data of SL3 are rather close to those of the SL4 and inclusion of them that makes the figure not very clear. Data of SL7 are not plotted herein because the monitored settlements are very small compared with others. The monitored points near the center of the canyon (SL4 and SL5) settled more evidently during the reservoir impounding than those points near the left and right abutments. This feature can be attributed to the thicker rockfill materials underlying the concrete slabs as well as the larger hydrostatic forces exerted upon the upstream slope near the center of the canyon. Taking the settlement from August 2007 to June 2008 as the post of construction deformation, we can find that all these post construction settlements could be well-modeled by the following function:

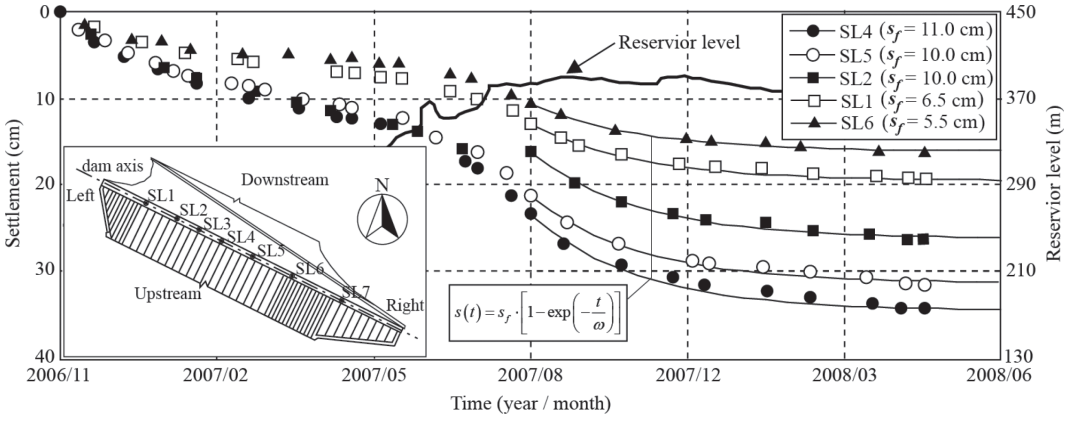

Figure 3. Crest settlement processes of Shuibuya CFRD.

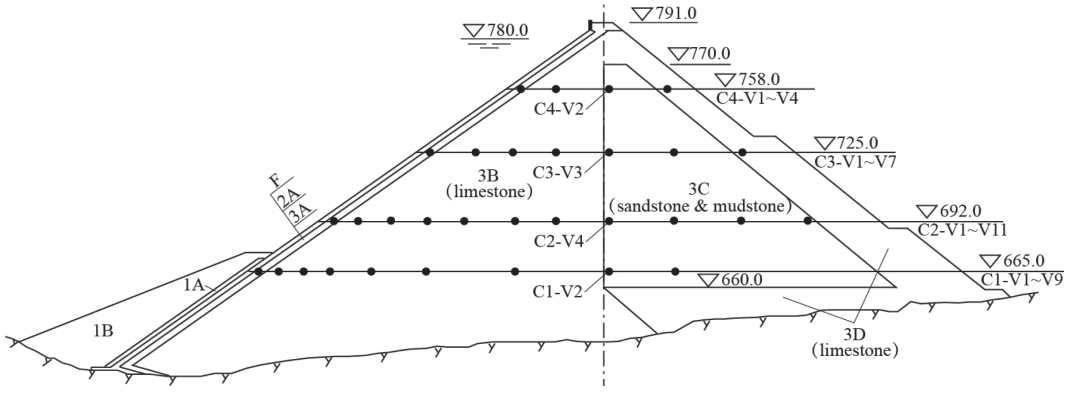

Figure 4. Locations of the settlement gauges installed in 0+630 section of Tianshengqiao CFRD.

$$s(t) = s_f \cdot \left[1 - \exp\left(-\frac{t}{\omega}\right)\right] \quad (1)$$

in which s_f denotes the final post construction settlement of the monitored point and ω is a parameter that controls the settlement rate. In the current case, ω is calibrated to be 5.5 months, and the values of s_f are given in Figure 3.

2.2 *The Tianshengqiao CFRD*

The 178 m Tianshengqiao CFRD is another high dam of this type built in China during the last decade of 20th century (Li 2011). The distinct feature of this dam is a vertical separation of the primary rockfill (3B) and the secondary rockfill (3C) as shown in Figure 4. This dam was constructed mainly with rockfill materials of the hard limestone except in the secondary rockfill zone (3C), which was filled mainly with the weak sandstone and mudstone excavated from the places of spillway, tunnel, and other structures. The vertical and horizontal displacement within the dam was monitored by the gauges installed in the three sections. Figure 4 shows the locations of the settled gauges installed in the maximum section (0+630) of the Tianshengqiao CFRD.

Filling of the dam started in February 1996 and ended in March 1999. Seven construction stages were designed considering the hydrological characteristics of the basin and the working intensity. The concrete slabs were cast in three stages (Zhang 2007). After casting the second-stage slabs to EL. 746 m in May 1998, the reservoir level was raised to EL. 740.36 m from that time to November 1998 for the power generation. The third-stage slabs were cast from April 1999 to May 1999 prior to the flood period of the river. Since then the reservoir level was raised to EL. 767.4 m until 24 August 1999. The first time that the reservoir was impounded to the normal level (780.0 m) was in 9 October 2000.

According to the above time schedule, we take the time before May 1999 as the construction period, and the time after October 2000 as the operational period. The duration in between is the impounding period.

Figure 5 shows the settlement histories of those monitored points at EL. 725.0 m. Some of the points were not included herein for the sake of clarity. Three general trends could be addressed in Figure 5. First, all the monitored points were settled much faster in the construction period than in the impounding period and the operation period, as was also observed in the Shuibuya CFRD. Second, although the points C3-V1, C3-V2, and C3-V3 are far away from the upstream surface of the dam and the influence of hydrostatic pressure upon them is less evident than the points C3-V5 and C3-V7, the former three points settled more than the latter two points during impounding. This observation can be explained by the larger creep deformation of the 3C zone than that of the 3B zone due to the difference in rockfill properties. Third, although the reservoir level changes periodically during the operation period, the settlement of all the monitored points, including the one near the upstream slope (C3-V7), almost show

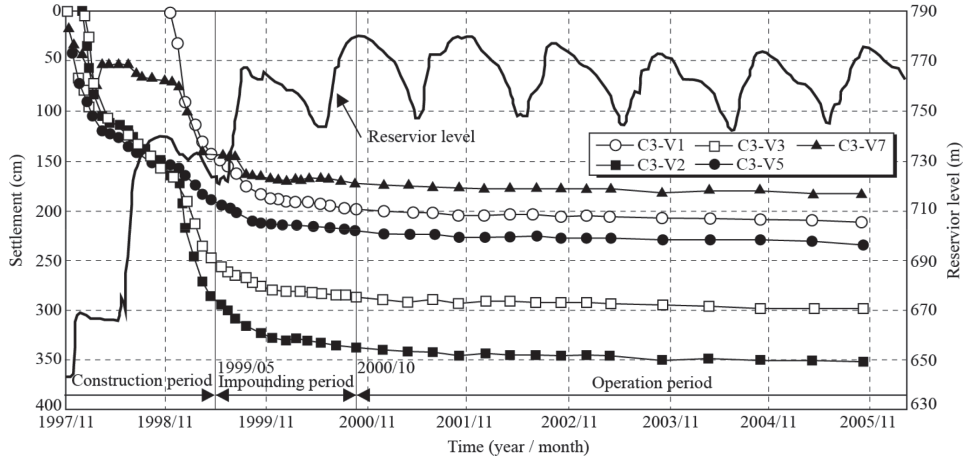

Figure 5. Settlement processes of the monitored points at EL. 725.0 m in Tianshengqiao CFRD.

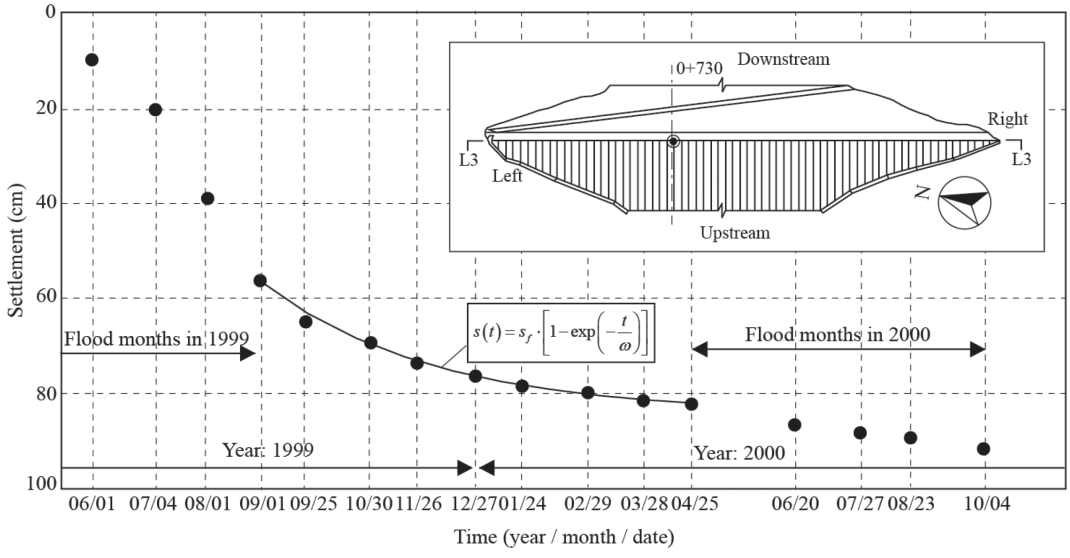

Figure 6. Settlement history of the point at 0+730 along the collimating line L3 in Tianshengqiao CFRD.

no dependence on the reservoir level. Nevertheless, slow settlement can still be observed at these points despite the marginal values.

Eight collimating lines parallel to the dam axis were also set to monitor the displacement of the points at the surface of the dam, among which collimating line L3 was used to monitor the movement of the cushion layer. Measurement was started at 18 Apr. 1999 when the dam was filled to EL. 787.3 m (elevation of the bottom of parapet wall). Figure 6 shows the settlement history of the monitored point set at section 0+730 m. Since this point is at the elevation of 787.3 m, which is quite close to the crest level, these data could be seen approximately as the crest settlement. It is found that the settlement rate before September 1999 is relatively higher than after that time. Two factors may account for this behavior. First, the reservoir level experienced a rapid increase from May 1999 to September 1999 as can be seen from the impounding curve in Figure 5. What's more, this period is the flood season of this basin and frequent rainfall resulted in accelerated creep of rockfill materials, particularly for the surface zones exposed to atmosphere. Accelerated settlement can also be seen from May 2000 for similar reasons. During the period from September 1999 to May 2000, the reservoir level underwent a drawdown and the settlement can be entirely attributed to the creep of the rockfill materials. The prediction made by Equation 1 with $s_f = 28$ cm and $\omega = 3.5$ months was also shown in Figure 6. The observed data could be modeled rather satisfactorily with the exponential function.

3 FIELD OBSERVATIONS MADE ON WEAK ROCK CFRDS

3.1 *The Da'ao CFRD*

The maximum height of the Da'ao CFRD is 90.2 m and the length of the dam crest is 244.5 m. At the very beginning of filling the primary rockfill zone (3B), it was found that the evident particle breakage occurs near the surface of the filled rockfill during compaction, and it resulted in a relatively impermeable layer (with a thickness of 3~8 cm) on the surface (Yang & Wang 2006). A large area of ponding occurred after the raining and it made the subsequent compaction quite difficult. This phenomenon was attributed to the evident particle breakage of the quarried rockfill materials (Zou 2001). Experiments also show that the UCS of the used sandstone was 25~40 MPa with an average value of 28.3 MPa, verifying a nature of weak rock. An inclined drainage zone was thus, added, between the transition layer (3A) and the primary rockfill zone (3B) to ensure that the 3B and 3C zones can keep dry even if a large quantity of leakage occurs (Fig. 7). Fresh hard rocks (with a UCS higher than 80 MPa) were used in the cushion layer (2A), the transition layer (3A) and the drainage zone. The weak rocks, however, were still used in 3B and 3C zones. According to the statistics, more than 70% of the dam was filled with weak rocks, resulting in a considerable saving of costs. To monitor the deformation behavior of the dam, eleven settlement gauges were installed in the maximum sections of the Da'ao CFRD in the three different elevations as shown in Figure 7.

Filling of the rockfill materials and the pouring of concrete slabs were finished on 5 April 1999, and the impounding of the reservoir was started on 28 June 1999. The first time that the reservoir level reached the normal operation elevation (217.0 m) was 23 April 2000. Figure 8 shows the settlement data of the typically monitored points. All the points underwent a rapid increase of the settlement during the impounding period from July 1999 to May 2000, including the points near the dam axis (V3, V7 and V10). The settlement continued to increase from May 2000, although, the reservoir level experienced a decrease of 16 m until

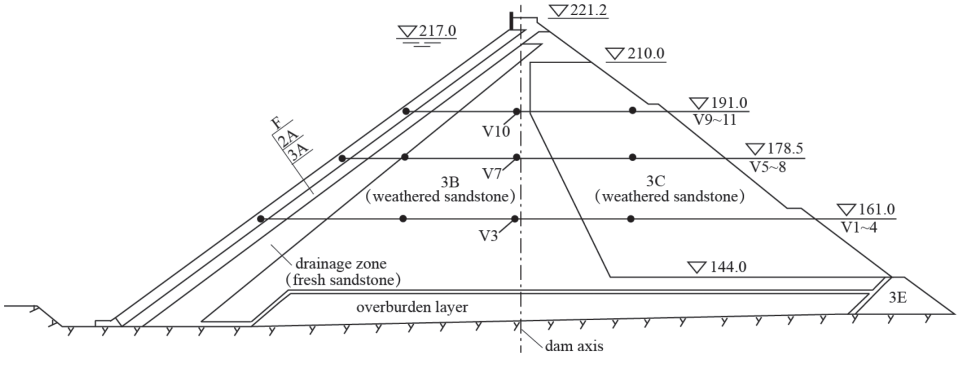

Figure 7. Locations of the settlement gauges installed in the maximum section of Da'ao CFRD.

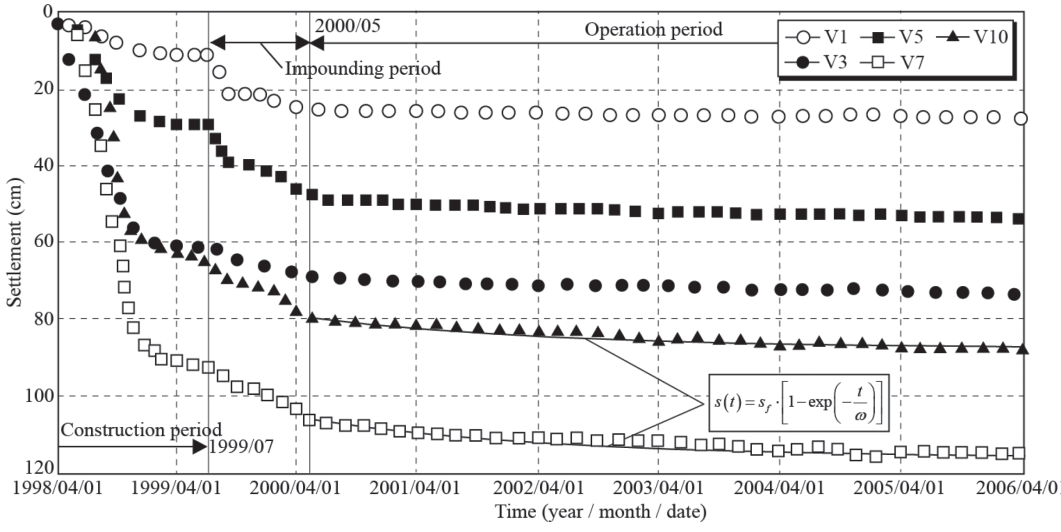

Figure 8. Settlement processes of the monitored points in Da'ao CFRD.

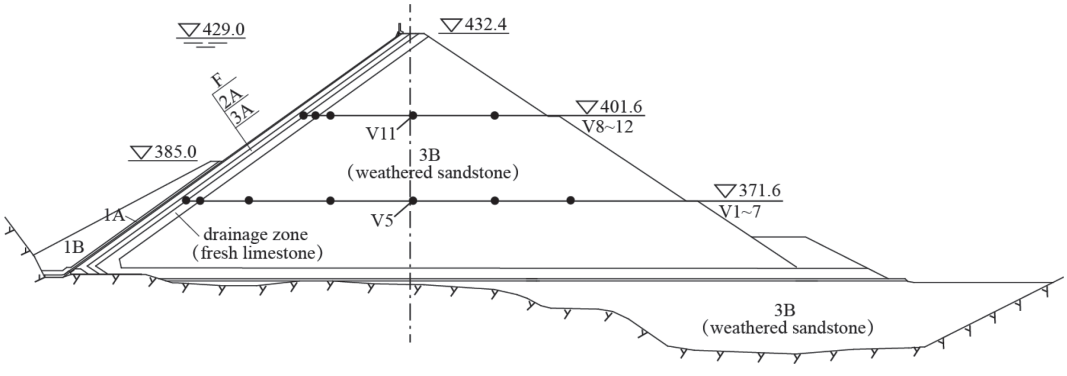

Figure 9. Locations of settlement gauges installed in the maximum section of Xiaojingou CFRD.

April 2001, indicating an evident contribution of the creep of rockfill materials. The general trends of the settlement data shown in Figure 8 also confirms that the post construction deformation of a dam constructed with weak rocks may last several years. Back analysis using the data of points V7 and V10 gives the values of the two creep parameters in Equation 1, i.e., $\omega = 2$ years; $s_f = 10$ cm for V7 and $s_f = 8$ cm for V10.

3.2 *Xiaojingou CFRD*

The Xiaojingou CFRD is one of the dams under construction in Sichuan province, China. The maximum height of the dam is 87.6 m. This dam was filled mainly with weathered sandstone with an average UCS of 40 MPa. According to the geological investigations and laboratory experiments, a high fraction of the rockfill materials excavated can be classified into weak rocks (UCS < 30 MPa). Similar problems like particle breakage during the compaction and ponding after raining were encountered during construction as in Da'ao CFRD. An "*L*" shaped drainage zone was also designed upstream of the 3B zone as shown in Figure 9. An evident feature of the dam is that no secondary rockfill zone (3C) was designed downstream of the dam axis. All the rockfill materials in the dam (3B), except the 2 A and 3 A zones, were filled with the same materials and compacted with the same criterion. Two layers of the settlement gauges were installed at two different elevations (371.6 m and 401.6 m) in the maximum cross section as shown in Figure 9.

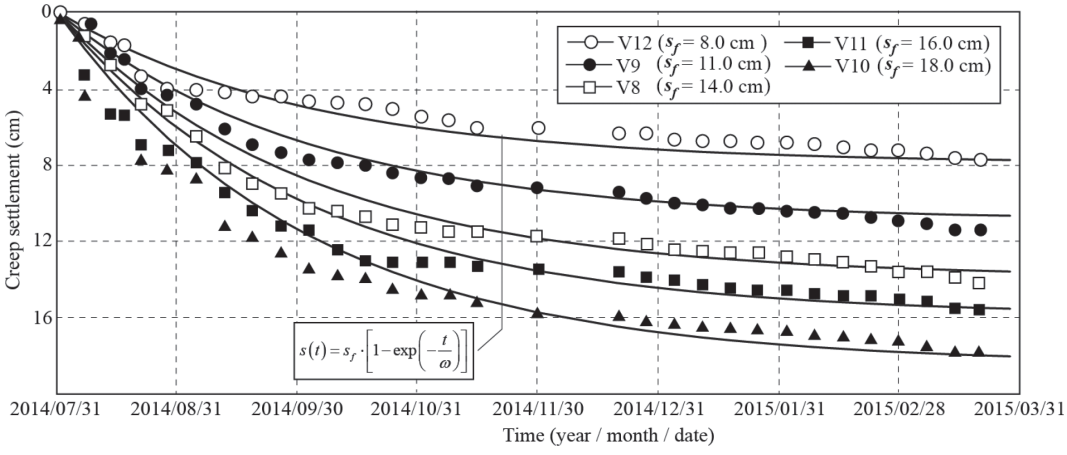

Figure 10. Settlement processes of monitored points in Xiaojingou CFRD.

Filling of rockfill materials started on 20 Jane 2013 and it was filled to EL. 430.2 m on 31 July 2014. As the immigration problems have not been thoroughly solved, the reservoir could not be impounded despite the completion of dam filling. Therefore, concrete slabs were not cast after 31 July 2014 and the dam continued to settle under gravity. Compared with the previous cases, the loading condition of this dam was relatively simple. Construction period of the dam was short and no impounding has been ever experienced. Until the end of March 2015, the dam has already settled 8 months. Figure 10 shows the settlement histories of the monitored points V8~12. Similar to the previous cases, the settlement rate of the monitored points decreases as the time elapses. In addition, the settlement data could be approximated by Equation 1 with the parameter ω = 62.5 days (≈2 months) and different values for s_f are shown in Figure 10.

4 CONCLUSION

Based on the observations made from the above four CFRDs, the following conclusions could be drawn:

1. CFRDs filled mainly with either hard rocks or weak rocks settle quickly during the construction. The settlement induced by the reservoir impounding and during operation is relatively smaller and slower than in construction. That is to say, the gravity of the materials is the governing factor that controls the deformation mode of a CFRD.
2. Regardless of the hard rock CFRDs or weak rock CFRDs, a recognizable creep deformation takes place after the completion of dam filling, resulting in a continuous increase of settlement during reservoir level variation and operation. Therefore, to predict the behavior of a CFRD reliably, a model that can describe the deformation induced by stress and creep in a unified manner is required, particularly for those high dams with a long duration of construction.
3. The creep deformation of CFRDs under constant loads can be modeled satisfactorily using an exponential function with two parameters. One governs the final deformation and the other one controls the rate of creep deformation.

REFERENCES

International Commission on Large Dams (ICOLD). 2010. *Concrete Face Rockfill Dams, Concepts for Design and Construction*. Beijing: China Water Power Press.

Li, N.H. 2011. Performance of high concrete face rockfill dams in China and its inspiration. *Chinese Journal of Geotechnical Engineering* 33(2): 165–173.

Yang, M. & Wang, N.B. 2006. Technologies of constructing the Da'ao concrete face rockfill dam with weak rocks. *China Science and Technology Information* 17(20): 48–51.

Yang, Q.G., Liu, N. & Sun, Y. 2010. *Construction Technologies in the Shuibuya Concrete Face Rockfill Dam*. Beijing: China Water Power Press.

Zhang, Z.L. 2007. Design and technical innovation of rockfill dam projects. *Chinese Journal of Geotechnical Engineering* 29(8): 1184–1193.

Zhou, W., Hua, J.J. & Chang, X.L. 2011. Settlement analysis of the Shuibuya concrete-face rockfill dam. *Computers and Geotechnics* 38(2): 269–280.

Zou, J.X. 2001. Design and technological characteristics of Da'ao concrete face rockfill dam. *Jiangxi Hydraulic Science and Technology* 27(2): 94–98.

This page intentionally left blank

Civil Engineering and Urban Planning IV – Liu et al. (Eds)
© 2016 Taylor & Francis Group, London, ISBN 978-1-138-02903-3

Analysis of the lifting law of the lakeshore deepwater berth

Hong-Wei Sun
School of Civil Engineering, Changchun Institute of Technology, Changchun, Jilin, China

ABSTRACT: According to the change form of lifting displacement curve established on the lakeshore deepwater berth's lifting displacement data observed and collected during the frosty period, this paper will analyze the influence of temperature on the lake ice frost-thawing situations and moisture contained in the foundation soil at the berth pile at different temperature periods, and reveal the berth lifting law when the conditions change in different temperature periods.

1 INTRODUCTION

The so-called lakeshore deepwater berth approaches the lakeshore and has the foundation pile with a long-time big soaking depth, as shown in Figure 1. Lakeshore first berth of Changchun Park under the experimental observation belongs to the deepwater berth, having a foundation pile with the soaking depth of 1.8 m. In the frosty period, there is still unfrozen water under the ice layer after the lake water under the berth is frozen to have certain thickness. Due to the function of thermal insulation, unfrozen water can make the foundation of the earth at the lake bottom to be always melted soil during the frosty period. For example, according to the ice-breaking test for the lakeshore first deepwater berth in Changchun Park: the thickness of the frozen layer on the lake surface intwo frosty periods is about 1–1.1 m, and the depth of the unfrozen water under the frozen layer is 0.7–0.8 m. The foundation earth at the lake bottom is melted soil with high moisture content. According to the stage analysis for lifting displacement curve (hereinafter referred to as berth lifting displacement curve) established for Changchun Park firstfirst

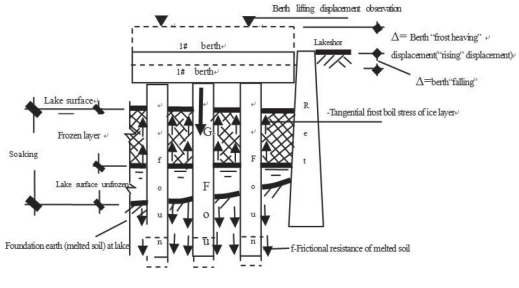

Figure 1. Diagram of lakeshore deepwater berth's frost boil mechanism and lifting displacement.

berth lifting displacement data observed in situ in two frosty periods: the berth happened periodic change in the frosty period, rising in earlier stage, falling in middle stage, and rising in later stage.

The research also showed that the berth lifting was closely related to the temperature influence on the freezing and thawing conditions of the lake water and water environment of the melted soil in different periods of the frosty period and appeared peculiar. This paper will research the lifting mechanism and law of the berth according to its lifting displacement curve state.

2 LAKESHORE DEEPWATER BERTH LIFTING DISPLACEMENT CURVE

According to the actual lifting displacement value of the first lakeshore deepwater berth of the Changchun Park, lifting displacement curves in two frosty periods and same-period temperature change curves have been established, as shown in Figures 2 and 3. For example: in Figure 2, each curve is the berth rising-falling-rising displacement curve established on the lifting displacement value measured on the different observation days in the whole frosty period at single lifting displacement observation points (see Fig. 1) on the berth. The displacement unit is mm. The same kind of displacement curves established on the frosty period lifting displacement value is collected at the four observation points (Sun 2007) on the first berth that are integrated into the graphical curve set. Dashed lines are the regression lines of the displacement at each observation point displacement, representing the average level of the lifting displacement; in the Figure 2, "frequency spectrum" curve is the same-period temperature change curve drawn according to the daily maximum and minimum temperatures in the frosty period. Dashed lines in the figure

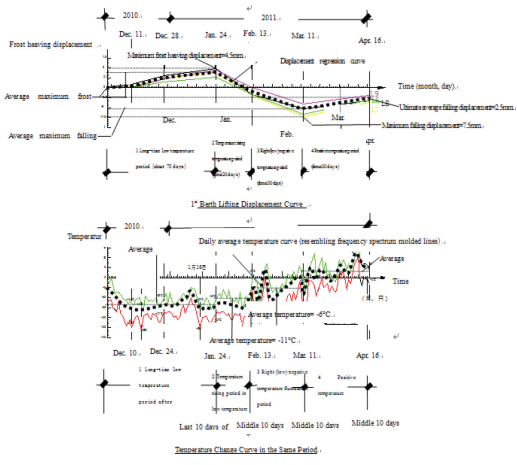

Figure 2. First frosty period Changchun park first lakeshore deepwater berth lifting displacement curve and same-period temperature change curve.

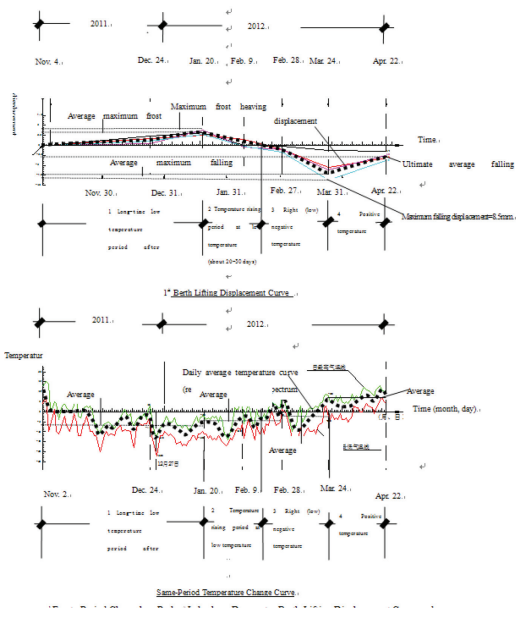

Figure 3. Second frosty period Changchun park first lakeshore deepwater berth lifting displacement curve and same-period temperature change curve.

stand for daily average temperature curves of regression. The frosty period is the experimental research period researched and decided according to the berth lifting law, which is selected for comprehensively and objectively reflecting the full view of the berth lifting displacement. The frosty period determined in this task is from mid-to-late November every year to mid-to-late April next year. The meaning of the Figure 3 is the same as the above.

3 ANALYSIS OF THE LAKESHORE DEEPWATER BERTH LIFTING LAW

Observe first lakeshore deepwater berth lifting displacement curve, as shown in Figures 2 and 3. Common features of the two frosty periods are: berth lifting displacement change form which is the same and displacement curves in the positive and negative areas appear "resembling sine curve shape."

4 ANALYSIS OF THE LAKESHORE DEEPWATER BERTH LIFTING LAW

Observe first lakeshore deepwater berth lifting displacement curve, as shown in Figures 2 and 3. Common features of two frosty periods are: berth lifting displacement change form is same, displacement curves in positive and negative areas appear "resembling sine curve shape" fluctuation trend by frosty period, and the corresponding lifting displacement in all rising and falling sections approximately appears linear change. The rising section on the displacement curve in the positive value area indicates that the berth has appeared constantly increasing rising displacement. According to the research findings: the rising displacement is the "frost heaving displacement" (Sun 2007) generated by the berth after the frost boil of the lake ice pushes the berth foundation pile (see the analysis for the following first period); after rising to the maximum frost heaving displacement, the berth will continuously fall to the lowest position; and then generate a limited rising to the height on the initial position lower than the frosty period at the end of the frosty period, leaving "surplus falling displacement." This surplus falling displacement is the net slippage of the berth in a frosty period, indicating that the lakeshore deepwater berth fell after the frosty period. For example: the maximum frost heaving displacement values (peak value displacement) in the positive value area in second frosty period is 3.5 mm and 4.5 mm, respectively, the average frost heaving displacement is 3.5 and 3 mm, that happened in the last 10 days of January next year; the minimum falling displacement in the negative value area is 7.5 mm and 8.5 mm, average falling displacement is 5.5 and 7.5 mm, which happened in the mid-to-late March next year. In the end of the frosty period, however, it generally happened in the mid-to-late April next year. The berth's surplus falling displacement is 2.5 and

3.5 mm, which will not develop as it enters the summer falling displacement. The frost heaving rising speed is about 0.044 mm/d, falling speed is about 0.163 mm/d, frost heaving rising speed only about 1/4 of the falling speed, which is the frost heaving rising speed that is relatively slow. It is, thus, clear that the maximum displacement (peak value displacement) of rising (frost heaving) and falling is not big and develops slowly, and the displacement curve form is "flat."

According to the scene investigation in the frosty period and the profound research for the displacement state: the above displacement state happened on the berth, which is closely related to the lack in ice freezing and thawing forms and the strength and moisture content of the foundation earth in different temperature periods in the frosty period, reflecting the changes in four temperature periods of "resembling sine curve shape" lifting the displacement curve. The displacement change causes the analysis and law analysis in each temperature period that is introduced below.

First period: Constant low temperature periods after temperature drop—from the beginning of November every year to the middle ten days of January next year, about 70–80 days. Average temperature in this period in two frosty periods is −14°C and −7°C. In this period, the approximate linearity of the berth lifting displacement curve increases, indicating that the berth happened continuous rising displacement. According to the analysis for the frost boil mechanism of the lake ice, this rising displacement is the "frost heaving" displacement caused because the berth foundation pile is pushed by the frost boil of the ice layer on the lake surface. As shown in Figures 2 and 3, the cause is continuous temperature drop with the atmosphere. The lake surface is frozen and coagulated to a certain thickness to form continuous frost zone. The frost zone is continuously coagulating and expanding its volume. The tangential frost boil stress τ' the expansive force of ice acts on the surface of the berth's foundation pile (as shown in Fig. 1) that will start pushing the foundation pile upward. When the tangential frost boil stress τ' increases until exceeding the sum of the pile and berth's dead load G and frictional force f of the melted soil layer at the lake bottom against the pile, that is, $\tau' \geq G + f$ (Sun 2008), the foundation pile and berth will entirely generate an upward frost heaving displacement (see Fig. 1). The thickened thick ice layer is extremely sensitive to low temperature change. With low temperature lasting for a long time in a later period, the freezing strength of the ice layer will increase gradually, the freezing strength (Chen & Wang 2006) on the surface of the ice and berth foundation pile will constantly increase accordingly, and the tangential frost boil stress acts on the foundation pile surface that will push the foundation pile to continuously generate a frost heaving displacement (that is, rising displacement). As the compaction and homogeneity of the ice is much higher than that of the frozen earth (Sun 2014a), and the approximate linearity of the generated tangential frost boil stress acts on the surface of berth foundation pile, showing that the frost heaving displacement of the berth in this period has appeared the feature of approximate linearity increase. Maximum frost heaving displacement happened in the end of this period. For example, the average value of the actual maximum frost heaving displacement of the berth in two frosty periods is 3.5 mm and 3 mm, and it happened around the middle ten days of February every year.

Second period: Temperature rising period at low temperature—from the last 10 days of January next year to first 10 days or the middle ten days of February (about 20–30 days). Average temperature of this period in the two frosty periods is −11°C and −5°C. Temperature in this period increases at a low (negative) temperature in the end of the section, but still below zero. The frost heaving displacement curve of the berth in this period appears in the trend of the approximate linearity reduction, as shown in Figures 2 and 3. One reason of the displacement reduction: very big temperature difference between day and night enables the ice layer on the lake surface to frequently suffer from "thermal expansion and cold contraction" and crack, and frequently happen in constant temperature rising period. Cracking of frost zone enables the ice's tangential frost boil stress that had acted on the berth foundation pile to be released partially, which means that the effective of tangential frost boil stress acting on the pile surface has decreased accordingly, and the berth and foundation pile will gradually and entirely drop under the dead load. Second reason: rheological characteristic (Sun 2014a) of the ice in this period has appeared, showing that the ice strength in the later period will reduce, the tangential frost boil stress acted on the surface of the foundation pile will reduce accordingly, and the berth and foundation pile will also entirely fall under a dead load. This is another factor resulting in the berth drop and frost heaving displacement. Third reason: frost boil of the ice layer on the lake surface has extruded the pile foundation, enabling the ice on the contact surface to melt and lubricate (Sun 2014a), destroying the freezing strength between ice and pile, relatively reducing the tangential frost boil stress, and assisting the berth falling. It goes without saying that the combined action of the above attenuation factors can reduce the tangential frost boil stress acted on the surface of the berth foundation pile, and weaken the function of the restraint. The berth

and the foundation pile are bound to fall as a whole due to the reduction of the constraint force. In the end, constant temperature gives rise to a negative temperature, the berth will drop to the initial position before the frosty period, and the frost heaving displacement will reduce to zero. At this time, the tangential frost boil stress that the frost zone acts on the berth foundation pile will become minimum and almost disappear. The berths will continuously sink under the dead load. In this period, drop of the approximate linearity of the berth's frost heaving displacement curve can indicate the comprehensive effect of all the factors.

Third period: Positive low (negative) temperature fluctuation period—from the middle ten days of February next year to the middle ten days of March, about 30 days. Average temperature of this period in two frosty periods is –6°C and –3°C. The displacement curve approximate linearity in this period decreases, indicating that the berth continuously generates falling displacement. The displacement curve shows "negative" displacement, appears negative growth trend, as shown in Figures 2 and 3. In this period, temperature is under frequent fluctuation between positive and negative temperatures, the surface of the lake surface ice layer absorbs the heat arising from the atmospheric temperature rise and starts melting, and the ice layer bottom also melts upward from the ice and water juncture. The tangential frost boil stress of the frost zone gradually disappears as the ice melts, the berth and foundation pile continuously fall as a whole under the dead load. The berth rising and falling can reflect the sedimentation displacement in this period appearing to of a linear "negative" growth, and drops to maximum displacement (about 6 mm) by the end of the period, as shown in the figures. Sedimentation will terminate. At this time, a new balance will form between the weight of the berth and foundation pile and frictional resistance of the melted soil layer at the lake bottom. Apparently, the drop displacement in this period is not caused by the frost boil of the ice, but by the loss of tangential frost boil stress of the lake ice, and the falling of berth and foundation pile under the dead load.

Fourth period: Positive temperature period—from the last 10 days of March next year to mid-to-late April, about 20–30 days. Average temperature of this period in the two frosty periods is 3°C and 7°C, as shown in Figures 2 and 3. In this period, the lake surface frost zone absorbs the atmospheric positive temperature to complete melting. Water absorption of the foundation earth surrounding the berth foundation pile is saturated, and the buoyancy of saturated soil increases gradually. The berth foundation pile floats upward under the combined action of the buoyancy (Zhou 2000) of the water and saturated foundation earth, and generates the rising displacement. The rising displacement gradually happened with water level on the lake surface lifted after thawing and foundation earth became saturated, this can be proved by approximate linearity increase of berth rising displacement curve in positive temperature period, as shown in Figures 2 and 3. Comparatively speaking, the buoyancy of the water and saturated foundation earth has limited action on the upward floating of the berth foundation pile and berth rising as well. For example: the berth in positive temperature period in two frosty periods will stop after rising (floating up) to a certain height, indicating that the buoyancy at this time becomes balanced with dead load of the berth structure and the rising will stop. Moreover, at the termination, the berth rising height is lower than the initial height of the berth before the frosty period. This height difference between them is the ultimate falling displacement generated by the berth after experiencing a frosty period of freezing-thawing cycle. For example: the average displacement of surplus drop of the berth in the end of two frosty periods is 2.5 and 3.5 mm. In addition, heat absorption and expansion of the berth plate at a positive temperature rise period will also result in berth rising.

It is, thus, clear that rising displacement of the berth in positive temperature period is caused by buoyancy of water and soil and thermal expansion of the berth. However, the fundamental reason is that the lake ice frost boil makes the berth's frost heaving cause foundation earth to loosen, and the loosened melted soil absorbs melted water and solidifies to enable buoyancy to increase.

5 CONCLUSION

The rising law of the lakeshore deepwater berth in the frosty period can be described as below.

The lifting displacement curve established according to the actual berth lifting displacement in the frosty period appears to be the lifting displacement development form of "resembling sine curve", and consists of the lifting displacement changes of four temperature periods, and the lifting displacements in each period is similar to the linearity change. The lifting displacement law in the period is introduced is as follows:

1. Constant low temperature period after temperature drop: under the drive of continuously increased tangential frost boil stress of the ice layer on lake surface, overall rising displacement of foundation pile and berth is frost heaving displacement, appearing approximate linearity growth law;

2. Temperature rising period at a low temperature: combined effect of lake surface ice's thermal expansion and cold contraction arising from temperature rise fluctuation at low temperature, rheology caused by long-term load-carrying of ice and freezing strength reduction arising from long-term extrusion of ice enables the tangential frost boil stress approximate linearity acted on the berth foundation pile to decrease, and the berth and foundation pile drop as a whole under dead load, showing that the approximate linearity of the berth's frost heaving displacement decreases. The berth lifting displacement curve in this period indicates the law of linear drop. In the end of this period, the berth will drop to the initial position before the frosty period;
3. Positive low (negative) temperature fluctuation period: positive and negative temperature fluctuation accelerates melting of lake ice. The tangential frost boil stress acted on the berth foundation pile continuously decreases and the berth continuously fall under the dead load. The berth lifting displacement curve in this period keeps representing the law of approximate linearity falling. In the end of this period, the berth drops to the minimum level and stops developing. The force blocking the berth from falling in this period is the continuously increasing frictional force generated by foundation earth when absorbing melted lake water and re-solidifying.
4. Positive temperature period: constant positive temperature enables the lake ice to be completely melted, and the foundation earth surrounding the berth foundation pile gradually transits to supersaturation state. The foundation earth in the supersaturation state and buoyancy of deepwater layer enables foundation pile and berth to float upward as a whole gradually, showing continuously rising displacement on the berth's lifting displacement curve. When the dead load and buoyancy of the berth and foundation pile is balanced with the frictional force of foundation earth, the berth rising will stop. The surplus descending displacement is the gross falling in a frosty period.

In summary, the rising and falling of lakeshore deepwater berth in the frosty period is influenced by the temperature of frosty period (Sun 2014b) revealing multi-change periods' change law.

REFERENCES

Chen, S.B. & Wang, Y.Q. 2006. *Frost Action of Soil and Foundation Engineering.* Beijing: Science Press. 254–496.

Sun, H.W. 2007. Observation of Artificial Lakeshore Pile Foundation "Frost Heaving" Phenomenon in Seasonal Frozen Earth Area. *Journal of Changchun Institute of Technology* 8(4): 1–4.

Sun, H.W. 2008. Presentation and Experiment of Control Measures for Artificial Lakeshore Berth Pile Foundation "Frost Heaving". *Journal of Changchun Institute of Technology* 9(1): 4–7.

Sun, H.W. 2014a. Study on Instability of Frozen Earth. *Journal of Changchun Institute of Technology* 15(1): 9–12.

Sun, H.W. 2014b. Research of Frozen Earth Theory of Miller and Beskow. *Journal of Changchun Institute of Technology* 15(2).

Zhou, Y.W. 2000. *Frozen Earth in China.* Beijing: Science Press. 10–216.

This page intentionally left blank

Civil Engineering and Urban Planning IV – Liu et al. (Eds)
© 2016 Taylor & Francis Group, London, ISBN 978-1-138-02903-3

Key technique in the movement of the Yellow River Museum

Zong-Min Zhang
North China University of Water Resources and Electric Power, Zhengzhou, Henan, China

Ling Cai
Jiang Xi Biotech Vocational College, Nanchang, Jiangxi, China

ABSTRACT: Integral Movement of Building has provided a new alternative to handle buildings to be demolished during urban planning. This paper begins with an analysis of the technical difficulties in the movement of the Yellow River Museum, such as the design of wall underpinning structure, the control of differential settlement, and the measures of vibration reduction, etc. Then, the authors simulate the force carrying mechanism of wall underpinning system with ANSYS, and propose relevant mechanical models and design methods on the basis of mechanics analysis. At last, the control of differential settlement, the measures of structural reinforcement and deformation supervision are analyzed in further detail. The research results from this paper can be reference for similar projects in the future.

1 PROJECT OVERVIEW

1.1 *Overview of the Yellow River Museum project*

Built in 1955, the Yellow River Museum is one of the earliest river museums in the world. This building is a textbook example of Russian architecture, with many cultural relics, hydro-geological data, river models and more than 600 historical pictures in it. The museum located in the center of Zhengzhou City, was a historic city landmark. In 2008, it was listed as a key cultural relic by the government of Henan province.

In 2012, to make space for the construction of the new metro, some engineers planed to demolish this building. In order to preserve it, the authorities decided to move it with technological measures after careful investigation.

The Yellow River Museum has a handsome two story brick-wood structure. With strip-shaped foundation and wooden frame, the building well typifies the rich extremes of Russian architecture. Before moving the building, technicians inspected the material intensity of the major components of the architecture. According to the results of the inspection, the strength of concrete was about C15, while the strength of masonry was about MU7.5, and the strength of mortar was about M1.8. The building seismic performance failed to meet the basic requirements of building codes, while the integrity is poor.

According to the requirements of design, only the main exhibition hall of the museum was to be moved (Du & Yang 2012). As shown in the Figure 1, the route of moving was designed as follows: (1) to move eastward for 33.2 meters, (2) southward for 15 meters, (3) eastward for 35.8 meters, (4) southward for 17.7 meters.

1.2 *Technical difficulties*

There are three difficulties in this project:

1. The route of moving was polyline, which brings forward higher requirements for the underpinning structure. The vertical loading needs to be transmitted to the track along the X axle, and the track along the Y axle. Besides, the exhibition hall has a special floor plan. So, the difference in the loads between different axes is huge. It is important to synchronize all axes by underpinning the structure with high rigidity and proportional distribution of the thrust (Wu & Chen 2011).

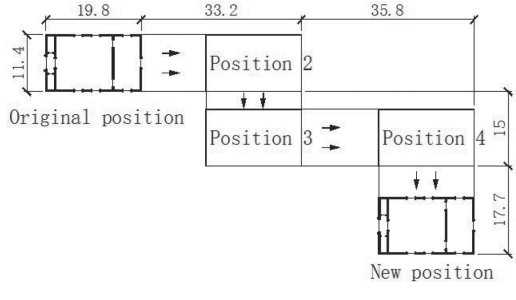

Figure 1. The moving route of the Yellow River Museum.

2. The new position is near to the original position. However, the bases of the two positions are of different compactness. In order to avoid the oversize sedimentation which might cause wreck, it is necessary to investigate the subsoil and to use an appropriate type of foundation (Wang & Wu 2011).
3. The long-span exhibition hall of the museum, which has poor space rigidity, had been in use for about 60 years. It is important to reduce the vibration of the building during the moving process.

2 DESIGN OF THE WALL UNDERPINNING STRUCTURE

2.1 *Underpinning structure and construction sequence*

The wall is the most significant bearing component for brick-wood structures. Currently, engineers in the field primarily rely on the use of two-beam-clamped structure and single-beam underpinning structure for underpinning the wall (Zhao & Wang 2013). Considering the practical features of the Yellow River Museum, the two-beam-clamped structure was used to underpin the bearing wall in side axis, while the single-beam underpinning structure was used to underpin the steel brace. The construction sequence of two-beam-clamped structure can be divided into four steps:

1. To strengthen and widen the original foundation. Construct the track beam, and pave steel plate above the track beam.
2. To place steel roller above the steel plate, and pave steel plate above the steel roller, as shown in Figure 2.
3. To band the reinforced bar of underpinning beam, erect the formwork, and cast the concrete of underpinning beam. After hardening, the underpinning beam is completed, as shown in Figure 3.
4. To sever the wall between the two steel plates. Then, the building becomes a removable house.

Figure 2. Construction of underpinning beam.

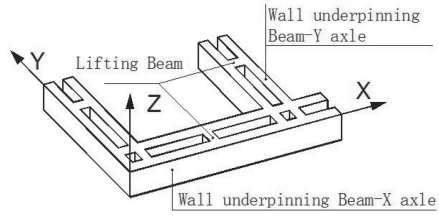

Figure 3. The completed underpinning beam.

As shown in Figure 1, when the building is moved from original position to position 2, the rollers are under the underpinning beam along the X-axis, while nothing is under the underpinning beam along the Y-axis. However, when the building is moved from position 2 to position 3, the operation is just the opposite. When the building is in position 2, we can jack the underpinning beam for about 5 mm to remove the roller under the underpinning beam along the X-axis and put the roller under the underpinning beam along the Y-axis. After all the rollers are replaced, the build can be moved along the Y-axis.

2.2 *Finite-element analysis*

At present, ANSYS software is widely used for finite element analysis. In order to study the load transfer and stress the distribution of underpinning beam in detail, we simulate the concrete with the element of **solid65**, and simulate the steel bar with the element of **link8**. Then, the 3-D finite element model is computed and analyzed. We apply the loading of the exhibition hall into the model and solve the problems related to the stress and strain. As shown in Figure 4, on top of the underpinning beam, the main stress is the tense in the direction of Y-axis. The axial tension on top of the beam is inhomogeneous and becomes maximum in the mid-span while minimum in the position of lifting beam. The changing trend of the axial tension on top of the whole beam is exactly the same as that of the reversed continuous beam. Based on the study concerning the stress distributed in the section of underpinning beam, it is clear that the friction force between wall and concrete can trigger torsion. So, we can design the beam as a reversed continuous beam under the load of flexure-shear-torsion.

2.3 *Mechanical analysis and reinforcement design*

All loads on the underpinning beam is shown in Figure 5 by mechanism analysis, and can be simplified as shown in Figure 6. Vertical load of wall (denoted by N) can easily be worked out by PKPM (PKPM was an excellent structure design software that has been widely used in engineering design).

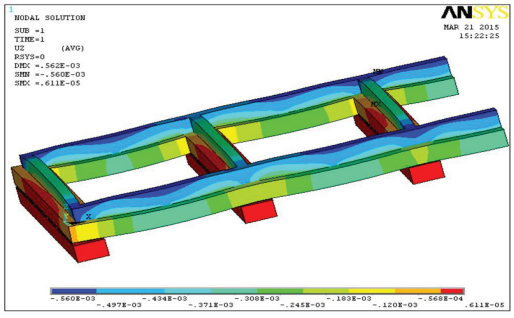

Figure 4. The result of finite element model.

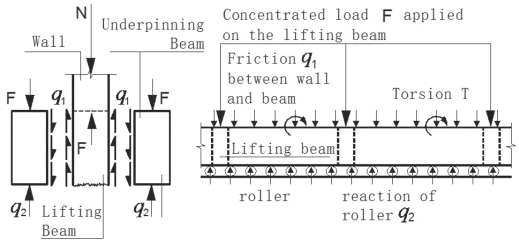

Figure 5. All the loads on the underpinning beam.

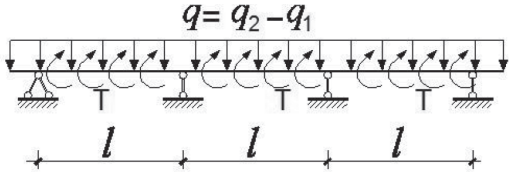

Figure 6. Simplified loads on the underpinning beam.

Sometimes, we must convert N (concentrated load) into q_2 (uniformly distributed load). The friction forces between the wall and the concrete vary dramatically according to the strength of material and construction technology. So we would better figure it out with field experiment. Considering the inhomogeneous of friction, we can use 60% of the experimental value as the value of q_1. Then, we can figure out F (the concentrated load on the lifting beam) and T (the torsion caused by friction). We can also calculate (q_2-q_1) as the uniformly distributed load, which can be applied to the reversed continuous beam. Based on the calculation, we can select the most unfavorable section and use the load to calculate the longitudinal steel bars and stirrups of the underpinning beam as a flexure-shear-torsion member. At last, we should check the crack width and load displacement according to the Chinese standards and criteria (MHURD 2010).

3 CONTROL OF DIFFERENTIAL SETTLEMENT

The foundation soil of the original position had been compacted for a long time, and the consolidation settlement has been stable. But the foundation soil of the new position had never been compacted. When one end of the building remains in the original position while the other end is moved to a new position, differential settlement might lead to leans in the building. If the differential settlement exceeds the allowable limit, cracks and damages may occur.

Referring to the new Geology Investigation Report, we calculated the settlement of the building with PKPM (an authoritative calculation program developed by China Academy of Build Research). The additional settlement value of building in original position was about 3~5 mm, but the additional settlement value of building in other position was about 17~21 mm. Therefore, the difference in the settlement value between the two positions was about 15 mm. The gradient of wall doesn't conform to the Chinese standards (MHURD 2011). Based on the

Figure 7. Outside reinforced structure.

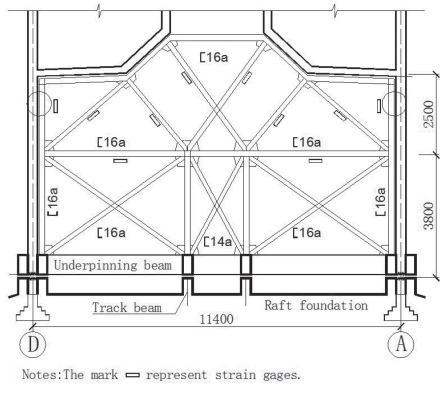

Figure 8. Sections of the interior reinforced structure.

Table 1. Partial strain monitoring data.

Original position	To position 2	To position 3	To position 4	To new position
Location of measuring points	Top of frame with wall	Bracing of mid-span	Bracing of side-span	Crossbeam
Number of measuring points	8	16	8	8
Observations (10×10^{-6})	−131~150	−86~92	−73~81	−56~78
Frequency of warning	2	0	0	0
Strain of warning (10×10^{-6})	150			

calculation and data analysis, the raft foundation was designed under the track beam. In such way, the differential settlement between the two type of foundation was controlled within 6 mm, and the gradient of the wall was safe according to the code for design.

4 MEASURES OF VIBRATION REDUCTION

4.1 *Strengthening measures*

In order to reduce structural vibrations, we built a steel frame with channel steel outside and inside the building. As shown in Figures 7 and 8, the steel frame was connected tightly to the underpinning beam in the bottom, and fastened tightly to the wall and the roof on the top. After the reinforcement, the structure vibration was reduced greatly. In addition, the strain gages were embedded in the joints. During the moving process, all the strains can be monitored and analysed directly. When any strain exceeds the default values, the system would beep to alert the engineers, and the movement would stop immediately (Gu 2013). The movement would be resumed only if the problem was found out and solved. With these measures, oversize relative displacement would be under control, and cracking would be greatly avoided.

4.2 *Precision monitor system*

With these strain gages, the strains will be monitored continuously as partly shown in Table 1. The movement can be divided into four stages. When the building is moved from position 2 to position 3, the deformation of the longest walls increase sharply because their orientation was perpendicular to the direction of movement, and the acceleration of movement increased correspondingly. This would usually lead to quick rise in the strain value of joints between walls and steel columns and may trigger the annunciator. Under such circumstance, the moving should stop. When the acceleration was adjusted, the strain value of those joints became normal. In the subsequent movement, the strain value of other joints ware controlled below the limit of the strain value, which ensured safe operation (Yu & Lu 2013).

5 CONCLUSIONS

The construction of foundation and moving process took 228 days in total. The accomplished effect is ideal. Most historic features of the old building are preserved during the movement. It has been about 2 years since the accomplishment of the movement, and everything has been normal with the building. This demonstrated that all measures during the process of moving are safe. The movement of the Yellow River Museum has great significance to the preservation of historic buildings. Finally, some researches concerning the design of moving construction are also presented in this paper, which can be good reference for the similar projects in the future.

REFERENCES

Du, Y.F. & Yang, Q.H. 2012. Imulation of unitary shifting of buildings with foundation and parameters of loading condition monitoring. *Journal of Lanzhou University of Technology* 38(6): 112–117.

Gu, Y.S. 2013. Discussion on design of underpin structure joint for shift engineering. *Building Structure* 43(s2): 711–713.

Ministry of Housing and Urban-Rural Development of the People's Republic of China. 2010. *Code for design of concrete structures* Beijing: China Architecture & Building Press.

Ministry of Housing and Urban-Rural Development of the People's Republic of China. 2011. *Code for design of building foundation* Beijing: China Architecture & Building Press.

Wang, J.Y. & Wu, E.J. 2011. Underpinning and Reinforcement in complex moving engineering of historic masonry-timber building. *Construction Technology* 40(337): 32–35.

Wu, E.J. & Chen, Z. 2011. Internal Force Analysis of Underpinning Structure at Adverse Construction Stage in Complex Moving Engineering. *Construction Technology* 2011(3): 33–38.

Yu, J. & Lu, P.Z. 2013. Analysis of vibration properties about two different types of buildings. China Civil Engineering Journal 46(s1): 81–86.

Zhao, S.Y. & Wang, T.C. 2013. Integral translation design and construction of ST.James' church. *Architecture Technology* 44(11): 966–968.

Civil Engineering and Urban Planning IV – Liu et al. (Eds)
© 2016 Taylor & Francis Group, London, ISBN 978-1-138-02903-3

Research on the hard brittle clay shale water content and the mechanical strength distribution rule

Guo-Ren Lu & Ming Liu
Shandong Jianzhu University, Jinan, Shangdong, China

Le-Wen Zhang
Shandong University, Jinan, Shangdong, China

Hao Zhou
Shandong Jianzhu University, Jinan, Shangdong, China

ABSTRACT: Wellbore stability problem in shale is a very complex and worldwide problem in drilling engineering. The Core tested in this paper is the seriously collapsed deep mud shale that is chosen from Shawodi area in Junggar basin. The strength parameters (cohesion, angle of internal friction, elastic modulus, Poisson ratio) of the shale with different water contents were measured based on the laboratory experiment, and the relation between shale water content and strength parameters is obtained through a regression analysis of the experimental data, and the distributing law of the water content in shale is deduced. This paper provides the experiment and theory for stress calculating of the wall rock of the shale after hydration and valuing wellbore stability.

1 INTRODUCTION

Borehole wall instability is a complex and worldwide difficult problem in drilling engineering. In shale rock mass we often consider the borehole instability problem. As more than 75% drilling formation is made up of shale, and about 90% of the borehole collapse problems refer to shale instability (Xu 1997; Zhao 1996). The engineering difficulties caused by the well instability is huge, for instance, hole shrinkage, hole collapse and pipe sticking, hole enlargement, pipe blocking, low cementing quality, etc. These accidents not only delay the drilling, but also bring technology difficulties to the conservation of oil. The sidewall instability problem causes a large number of economic losses, and it is still a very important problem to China and even all over the world.

The core tested in this study has seriously collapsed deep mud shale that has been chosen from the Shawodi area in the Junggar basin. The strength parameters (cohesion, angle of internal friction, elastic modulus, Poissons ratio) of shale with different water contents were measured; the relation between shale water content and the strength parameter is studied. The distributing law of the water content in shale is deduced by using seepage mechanics theory.

2 SHA-1 WELL FIELD SITUATION OVERVIEW

2.1 *Sha-1 well basic situation and formation situation*

Sha-1 well is an exploration Well in Shawodi NO.1 anticline in the newly developed western area, and belongs to the China Petroleum & Chemical. The preliminary drilling purpose is pre-prospects petroleum situation of the Jurassic, Triassic, cretaceous and Permian of ShaWo of NO. 1 anticline trap to establish the stratigraphic section of central sag in the Junggar basin area and get the relevant geophysical parameters. The designed well depth is 5500 m, actual depth is 5580 m, and the stop drilling layer is the Triassic Baikouquan formation. The oil and gas were found in the Sangong river, Badao bay, Baijian beach. There are 56 oil and gas layers, the total thickness of 151.5 m; and the well coring footage is 112.98 m, the cumulative core length is 105.89 m long, and the average harvest ratio is 93.72%.

2.2 *Sha-1 well drilling fluid usage and exception handling situation*

The mud system of Sha -1 well in different stage is polymer drilling fluid system, respectively,

non-dispersion polymer drilling fluid system, and polysulfide drilling fluid system. The detail situations are as follows: on September 8, 2002, drilling to 1056 m, mud performance: density is 1.15 g/cm3, viscosity is 39 s, plastic viscosity is 16 mPa.s, dynamic shear force is 3 pa, shear force is 1/3, and filtration is 6 ml, mud cake is 0.5 mm, silt content is 0.3% sand, PH is 8. 970 m to 920 m (tertiary, the palm red mudstone, light gray powder sandstone, argillaceous siltstone, interbred with different thicknesses is difficult to drill, and there is sticking when the drill moves upward or downward repeatedly even with the super pull force of 100 ~ 200 km. The reason is that the palm red mudstone is of poor lithology, large plastic, easy to absorb water, and easy to form a drill and drill-bit mud pack.

The pipe stuck during 709 ~ 3860 m period is still serious even after the equipment management and control is enhanced. Some additives for high temperature condition were added, and the viscosity of the drilling maintenance fluid were kept between 38 ~ 54 s under 3200 m. Since the formation mud is serious and the performance is difficult to control, the mud thickening phenomenon is serious. The reason is mainly due to the stratigraphic mud intrusive into the mud, the silty sand rock and small particles pollute the mud. The pipe stuck is serious in Donggou, Tugulu and Xishanyao, and the most serious situation has happened in Tugulu.

The mud is polluted and the mud cake quality is poor, for the collapse below 3860 m to 5580 m is serious and the high pressure layer is penetrated. Through the treatment by asphalt class anti-collapse agent, the mud cake quality has improved, the drilling difficulty is reduced or eliminated, and collapse phenomenon has also improved markedly. The highest bottom hole temperature is 113 °C by electrical measuring. The rheological properties of the drilling fluid has improved, the water loss and the formation of immersion has reduced, by adding a variety of additives for the high temperature condition.

The formation between 3840 ~ 4850 m is coal deposits, and there are a lot of intermittent cementation planes and collapses. Sometimes pumps get blocked suddenly, and cause drill sticking. In order to solve the wall collapse problem, the asphalt class collapse prevention agent was used; the wall collapse problem is solved effectively. At 5580 m depth, the high-pressure water overflow is opened, about 0.36 m^3 per hour, density up to 1.87 g/cm^3, the formation water still cannot be controlled.

2.3 *Main problem summaries*

The formation is drilled mostly is siltstone, sandstone, fine sandstone, and causes serious pollution to mud. Upper palm red mudstone has poor lithology, plastic is large, and water imbibition is strong and easy to form a drill mud pack.

Due to the discontinuity of the coal seam, the collapse of the 3860 ~ 5580 m layer of Sankai is serious; especially in the 3957 ~ 5265 m layer, small card often happens, server card twice, and red mudstone reducing, and drill blocking is serious.

The underground clay was intruded into mud, causing a serious mud thickening phenomenon, and silty sand rock and very small particles caused mud pollution. There is a serious short blockage tripping when drill in the Donggou, Tugulu and Xishanyao, the most serious one happens in the Tugulu group.

3 LABORATORY EXPERIMENT ON RELATION BETWEEN SHALE MOISTURE CONTENT AND STRENGTH

The experiment shows that under the multi field coupling situation, there is not only a pressure transmission, but also the mass transfer. The mass transfer changes with time and moisture content. The moisture content changes will lead to an obvious intensity change; this paper carries out laboratory experiment on the relationship between the shale water content and strength. Twelve cores were selected and divided into four groups, every three cores as a group, with the same water content. Each core has tested the peak intensity strength by a triaxial pressure experiment, then the core cohesion and internal friction angle will be identified. The results are shown in Table 1; the cohesion and internal friction angle under different moisture content are shown in Table 2.

The original water content of the shale is 0.74%, the cohesion and internal friction angle under this water content is:

$$C_0 = 38.92\ kPa,\ \varphi_0 = 22.78^{\circ}$$

In order to determine the relation between the water and the parameters including the Poisson ratio, elastic modulus, cohesion, and internal friction angle, the models have been established:

$$\begin{aligned} C &= C_0 e^{K_1 w + b_1} \\ \varphi &= \varphi_0 e^{K_2 w + b_2} \end{aligned} \tag{1}$$

The K_1, K_2, b_1, b_2 are regression coefficients, and the value of the four coefficients could be determined through experimental data analysis, and the results are:

$$K_1 = -0.27919 \qquad K_2 = -0.39 \qquad b_1 = 0.58$$
$$b_2 = 0.34$$

Relationships between the water content and the parameters include cohesion and internal friction and angle, which are shown in Figures 1 and 2.

Table 1. Strength experiment results.

Well name	Well section	Well depth	Water content/[%]	Confining pressure/[MPa]	Peak strength/ [MPa]
Sha-1	943/51	3970.79–3970.89	2.47	20	145.3
Sha-1	943/51	3970.79–3970.89	2.47	30	166.8
Sha-1	943/51	3970.79–3970.89	2.47	40	188.3
Sha-1	943/51	3970.79–3970.89	3.38	20	120.02
Sha-1	943/51	3970.79–3970.89	3.38	30	140.92
Sha-1	943/51	3970.79–3970.89	3.38	40	161.82
Sha-1	943/51	3970.79–3970.89	4.04	20	105.45
Sha-1	943/51	3970.79–3970.89	4.04	30	125.95
Sha-1	943/51	3970.79–3970.89	4.04	40	146.45
Sha-1	943/51	3970.79–3970.89	5.07	20	87.43
Sha-1	943/51	3970.79–3970.89	5.07	30	107.33
Sha-1	943/51	3970.79–3970.89	5.07	40	127.23

Table 2. Relation between water content and strength.

Water content/ [%]	Cohesion/ [kPa]	Internal friction angle/°	Elastic modulus/ [GPa]	Poisson ratio
2.47	34.87984	21.40347	14.303	0.232
3.38	27.0543	20.65718	6.867	0.243
4.04	22.50147	20.13225	4.695	0.252
5.07	16.87807	19.33956	2.888	0.266

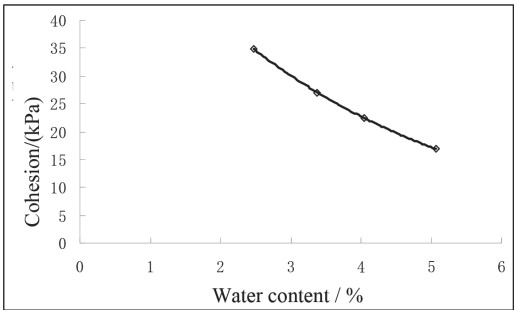

Figure 1. Relation between water content and cohesion.

The relation between water content and parameters including elastic modulus and Poisson ratios that were obtained as follows, and the relations were shown in Figures 3 and 4.

$$E = 105.33\, w^{-2.2238}$$

$$v = 0.0131\, w + 0.1992$$

E is the elastic modulus/(GPa); w is water content/%; v is Poisson ratio.

Figures 1 to 3 show that the water and the elastic modulus, cohesion, internal friction angle

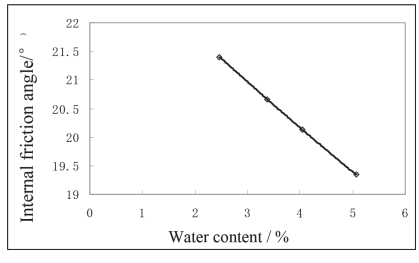

Figure 2. Relation between water content and internal friction angle.

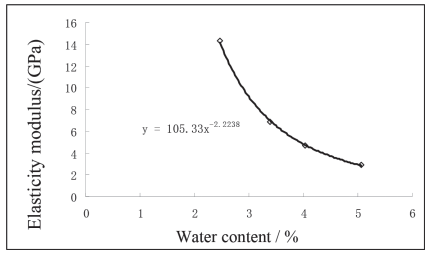

Figure 3. Relation between water content and elasticity modulus.

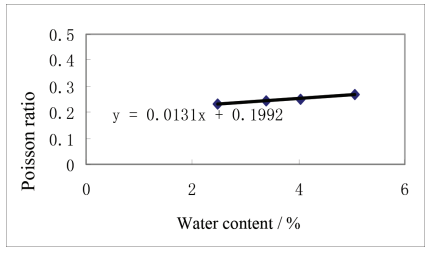

Figure 4. Relation between water content and Poisson ratio.

decreases with the increase of water content, the cohesion and elastic modulus reduced sharply. Figure 4 shows that the water content has little effect on the Poisson's ratio of shale.

4 WATER CONTENT DISTRIBUTION LAW RESEARCH

According to the seepage mechanics principle, the pore pressure could be changed under the hydraulic pressure difference and chemical potential difference. Seepage flow balance equation is shown in the Equation (2):

$$\frac{1}{r}\frac{\partial}{\partial r}(r\rho u_r)+\frac{\partial}{\partial t}(\phi\rho)=0 \tag{2}$$

The u_r, ρ, ϕ are volumes (cm^3/s), density (cm^3/s), and the porosity of the cell cube, respectively, and Equation (3) could be:

$$\frac{1}{r}\frac{\partial}{\partial r}(ru)+\frac{\partial}{\partial t}(\phi\rho)=0 \tag{3}$$

Relationship between the pore pressure and density could be got based on the definition of compression ratio, and hypothesis that the compression rate is constant. The physical relationship is shown as Equation (4).

$$\frac{\partial p}{\partial r}=\frac{1}{\rho C}\frac{\partial \rho}{\partial r} \tag{4}$$

The relationship between the pore pressure and the mass flow rate could be established as Equation (5):

$$\frac{1}{r}\frac{\partial(ru)}{\partial r}+\phi\rho C\frac{\partial P}{\partial r}=0 \tag{5}$$

The C, P is the fluid compression ratio and pore pressure (MPa).

The relationship between mass flow rate and water content could be obtained by mass balance equation,

$$\frac{1}{r}\frac{\partial(ru)}{\partial r}=\frac{\partial w}{\partial t} \tag{6}$$

And the equation (7) could be got by:

$$\frac{\partial w}{\partial t}+\phi\rho C\frac{\partial P}{\partial t}=0 \tag{7}$$

The w is the percentage of the adsorbed water (named water content for short in this paper) at some position and time.

The mathematical relationship between moisture content and pore pressure is established as Equation (6) and (7), and the water content distribution law can be got by combining the following distribution regularity of pore pressure (Lomba et al. 2000).

$$\begin{aligned}&\frac{\partial P}{\partial t}-\frac{K_1}{c}\frac{\partial^2 P}{\partial x^2}-\frac{nRTK_\Pi}{c}\frac{\partial^2 C_s}{\partial x^2}=0\\&\frac{\partial C_s}{\partial t}-\frac{\partial}{\partial x}\left(D_{eff}\frac{\partial C_s}{\partial x}\right)=0\end{aligned} \tag{8}$$

P—pore pressure
K_1, K_Π—coupling factor
c—fluid compressibility
C_s—solution concentration
C_{df}—drilling fluid solution concentration
D_{eff}—effective diffusion coefficient.

5 CONCLUSION

The following conclusions could be got through the analysis in this paper:

1. There are negative exponential functions between the water content and the parameters including elastic modulus, cohesion, and internal friction angle.
2. The elastic modulus, cohesion and internal friction angle decreased with the increase of water content, the cohesion and elastic modulus reduces sharply.
3. The water content has a small effect on the shale Poisson ratio.

The relation between the elastic modulus, cohesion, internal friction angle, and the water content, and the distribution law of the shale water content could be used in the wall rock pressure to calculate. The research in this paper can provide the basic method to evaluate the stability of the well.

REFERENCES

Lomba, R.F.T., Chenevert, M.E. & Sharma, M.M. 2000. The role of osmotic effects in fluid flow through shales. *Journal of Petroleum Science and Engineering* 25(1):25–35.

Xu T.T. 1997. Borehole wall stability technology research status and development direction. *Drilling Fluid and Completion Fluid* 14(4):36–43.

Zhao, Z.J. 1996. *Mechanical and chemical stability of borehole wall outside the mechanism and method of research*. Beijing: China Machine Press.

Civil Engineering and Urban Planning IV – Liu et al. (Eds)
© 2016 Taylor & Francis Group, London, ISBN 978-1-138-02903-3

Research development on seismic behavior of the short-pier shear wall

Long-Min Jiang & Jing-Fang He
Hunan University of Technology, Zhuzhou, Hunan, China

ABSTRACT: Characteristics and advantages of the short-pier shear wall are briefly introduced in this paper. It also made a comprehensive discussion on the seismic behavior of short-pier shear wall by means of theoretical analysis, pseudo-static test, and finite element analysis. Meanwhile, the paper brings forward the research direction of what is to be put emphasis on in the future.

1 INTRODUCTION

Academician Rong first introduced the short-pier shear wall structure in 1997. Compared with other structures, the short-pier shear wall has some advantages:

1. It well solves the problem of the members' protruding from the metope by putting vertical members and coupling beams in the partition wall, thus making this kind of structure better meet the demands of architecture function than that of frame structure.
2. As compared to the shear wall structure, it also has some unique identities. First of all, the number and length of walls are mainly in accordance with the need of lateral stiffness, and we can easily adjust the stiffness and the location of stiffness center by changing different section size. In addition, by means of substituting the shear wall for masonry filler wall, the short-pier shear wall becomes lighter and seismic response decreases.
3. In contrast with special-shaped column structure, the lateral load resistance of the short-pier shear wall can easily meet the requirements. The joint reinforcement is similar to that of the shear wall, therefore, it's easy to construct.

Being flexible and adjustable both in architecture and engineering, the short-pier shear wall structure fully meets the demands of people's expectation for the diversification of house. Giving all these advantages, it is widely used since it was first applied to an engineering project in the 1990s.

The short-pier shear wall structure, a new reinforced concrete structure between shear wall structure and frame structure, has distinct Chinese characteristics which results from Chinese real estate's rapid development as well as academic research. So far, research relevant to the short-pier shear wall is merely done at home, while there is no such research abroad. This paper is to summarize the research results in relation to the short-pier shear wall and preliminarily predict the trends of the research.

2 RELEVANT RESEARCH ON SEISMIC PERFORMANCE OF THE SHORT-PIER SHEAR WALL

2.1 *Theoretical analysis*

Cheng et al. (2001) puts forward a point of view that the short-pier shear wall should be designed as a combined wall. He also gives the discriminant of the symmetrical coupled shear wall with short piers and the limit value of the cross section height of pier.

Huang et al. (2002) comes to the conclusion that the lateral displacement curve of short-pier shear walls subjected to the horizontal forces belongs to the flexure shearing type deformation. Besides, the equations and diagrams used to define the inflection point in the lateral displacement curve are provided (Huang et al. 2003a). The effect of different pier strength coefficients, integrity coefficients and the reinforcement ratios in coupling beams on the elastic-plastic capability of the short-pier shear walls has been studied. With the increase of pier strength coefficient as well as the decrease of integrity coefficient and the reinforcement ratios in continuous beams, the bearing capacity of short pier shear wall decreases while its ductility increases (Huang et al. 2003b).

2.2 *Pseudo-static test*

Song et al. (2002a) had conducted the first experiment of the short-pier shear wall subjected to low cyclic loading. The results show that as for the wall

without flanges, longitudinal reinforcement at the bottom of the wall yields first when the limbs are short, while stirrups in the coupling beam yield first when the limbs are long. Compared with the specimens in the elastic state, those in the plastic state have an obvious phenomenon of stress redistribution. Strain at the bottom of the wall without flanges basically coincides with the plane section assumption, and the failure of specimen results from rapid development of the strain at each end of the coupling beams (Song et al. 2002b).

Cao et al. (2004) drew a multiple comparisons between normal short-pier shear walls and walls with concealed bracings. As indicated in the result, short-pier shear wall with concealed bracings gets an increase in cracking load, yield load and ultimate load, compared with those of the normal short-pier shear wall. Ductility factor rises, while stiffness degradation slows down. Hysteretic curves become plumber, and its energy dissipation capacity increases a lot. When specimen eventually fails, the number of cracks increases, meanwhile, the cracks become more concentrated (Cao et al. 2006).

Cai et al. (2005) summarized the influences of axial compression ratio and span-depth ratio of coupling beams on the mechanical characteristic parameters of the short-pier shear walls, basing on two groups of specimens undergoing low cyclic loading. The results indicate that compared with walls that are subject to low axial compression ratio, walls subject to high axial compression ratio have higher cracking load, yield load, and ultimate load, while ductility and energy dissipation capability decline as axial compression ratio increases; as the span-depth ratio of coupling beam decreases, the cracking load, yield load, and ultimate load of the walls gradually increase. However, when the span-depth ratio declines to a certain extent, the increase amplitude gradually decreases.

Huang et al. (2005) performed a pseudo-static experiment on two symmetric coupled short-pier shear walls. The results indicate that short-pier shear wall is a type of coupled wall with strong piers and weak beams. Beams yield earlier than piers, and the material capacity of the coupling beams could be sufficiently used due to the internal stress redistribution in the beams after they yield.

Li et al. (2006) introduced a new kind of structure named HPC short-pier shear wall with a pair of beams, and carried out a pseudo-static test on three four-story 1/3 scale HPC short-pier shear walls in order to analyze the bearing capacity, stiffness, ductility, energy dissipation, and failure characteristics of the models, which differed in types of coupling beams. It proves that walls with a pair of beams have better seismic performance than that of other kinds of walls.

Wei et al. (2010) performed several low cyclic loading tests on six short-pier shear walls belonging to three groups. Of each group, one specimen used uniform reinforcement, while the other one was placed with concealed columns under the same reinforcement ratio. The result shows that the capability, ductility, and energy dissipation of the walls with concealed columns are obviously better than those of the ordinary walls. As a consequence, it is suggested that the concealed columns be planted in the wall.

Zhang et al. (2010) researched on six short-pier shear walls with L-shape section by means of pseudo-static tests, and analyzed influences of axial compression ratio and depth to thickness ratio on the seismic behavior of specimens. Torsional deformations of the walls with L-shape are small when subjected to lateral forces. Bending and shear failure is the main failure mode. Besides, the smaller the shear span ratio and the bigger the axial compression ratio, the greater potential for shear damage. As depth to thickness ratio and axial compression ratio increase, the ultimate bearing capacity, energy dissipation capacity and ductility decrease. It is most appropriate when the depth to thickness ratio is 6.5:1.

Wu et al. (2009) conducted several low cyclic loading experiments to validate the seismic behavior of shape steel short-pier shear wall which has shape steel concealed columns at the end of web plate. The result shows that shape steel short-pier shear wall sees a remarkable improvement in bearing capability, ductility, energy dissipation, hysteretic behavior, and stiffness degradation compared with those of ordinary short-pier shear walls. In contrast to solid steel specimens, the lattice steel specimens have higher loading capacity and worse ductility (Wang et al. 2014).

Li et al. (2010) performed several pseudo-static tests on six L-shaped short-pier shear walls and six T-shaped short-pier shear walls to testify the seismic behavior of the walls. The result shows that there exists obvious asymmetric characteristics in the stiffness degradation curves of the T-shaped and L-shaped short-pier shear walls, as is shown in Figures 1 and 2. T-shaped short-pier shear wall is superior to L-shaped short-pier shear wall in seismic performance as its bearing capacity is higher and ductility is better. Short-pier shear wall is more ductile when the web is in tension and the flange in compression.

Li (2011) conducted several pseudo-static tests on six T-shaped short-pier shear walls and six L-shaped short-pier shear walls. The result shows that failure mode is mainly controlled by shear span ratio. Small shear span ratio results in shear compression failure while moderate shear span ratio leads to bending shear failure and high shear span

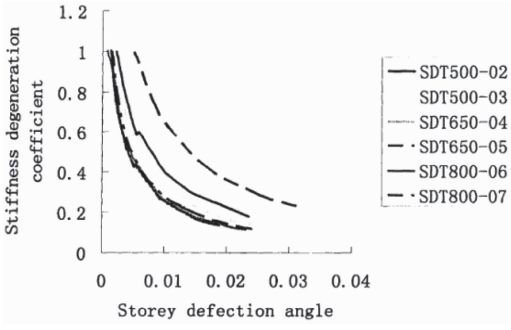

Figure 1. Stiffness degradation curves of T-section specimens.

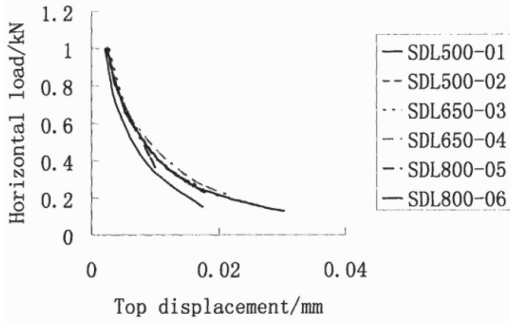

Figure 2. Stiffness degradation curves of L-section specimens.

ratio is more likely to experience bending failure. On account of the asymmetry of L-shaped short-pier shear wall in both principal axis directions, its centroid and stiffness center don't coincide with each other which makes it more likely to experience torsional failure than that of the T-shaped short-pier shear wall.

Zhang (2014) did several pseudo-static tests on four T-shaped short-pier shear walls and four L-shaped short-pier shear walls, which contain two walls with local joints respectively. The result indicates that hysteretic curves of the wall with local joints are more symmetric than those of the wall without local joints, and the area, obviously bigger than that of the wall without local joints, of its hysteretic curves are approximately equal in both directions. The ultimate displacement of specimens with local joints is bigger than that of the specimens without local joints. As a consequence, the former ones achieve significant improvement in ductility and energy dissipation. Though bearing capacity and elasticity of the specimens with local joints decrease in contrast with those of the specimens without local joints, they can meet the needs of engineering.

2.3 *Finite element analysis*

Gao (2003) did non-linear analyses on six short-pier shear walls subjected to monotonic loading, and obtained the variation of crack propagation, stress nephogram of failure, and skeleton curves. The result indicates that the result of finite element analysis is in accord with that of experiment, which confirms the rationality of finite program.

Zhang et al. (2006) simulated the whole procedure of multi-story short-pier shear wall from cracking to failure process using finite element analysis, and studied the effect of depth to thickness ratio, concrete strength grade, span-depth ratio of coupling beam, and axial compression ratio on bearing and deformation capability. The result shows that different factors have different influences on the mechanical behavior of short-pier shear wall, and appropriate selection of design factors can optimize the mechanical behavior of structure.

Yuan (2010) studied the short-pier shear walls under different depth to thickness ratios by means of elastic analysis when the specimens were subjected to frequently occurred earthquake actions and elasto-plastic time-history analysis when the specimens were subjected to rare earthquake actions, and acquired their seismic response. It suggests that the depth to thickness ratio be under 7.

3 DEVELOPMENT TRENDS OF SHORT-PIER SHEAR WALL IN THE FUTURE

Short-pier shear wall is still at the preliminary stage, though it's been 20 years since it was first introduced, there are still many theoretical and practical problems to be solved: 1) when it comes to daily use, short-pier shear wall frequently needs to be holed in the wall on account of laying pipelines and opening windows, thus having an impact on bearing capacity, ductility, lateral stiffness, etc. Therefore, it's of great necessity to study the seismic performance of short-pier shear wall with holes 2). It's requisite to do research on the reinforcement of short-pier shear wall and the holes in it as inappropriate design and construction, change in forces, natural disasters, and holes dug in the wall have already affected the architecture and its serviceability.

REFERENCES

Cai, Q.Z., Gao, Z., Li, H. & Peng, S.M. 2005. Experiment of SLW under monotonic and cyclic Reversed loading and its ansys analysis. *Journal of Wuhan University of Technology* 27(12): 49–52.

Cao, W.L., Dong, H.Y., Hu, G.Z., Zhang, J.W. & Huang, X.M. 2004. Experimental study on seismic behavior of RC coupled shear wall with concealed bracings. *Journal of Building Structures* 25(3): 22–28.

Cao, W.L., Zhang, J.W., Chang, W.H., Huang, X.M. & Zhao, C.J. 2006. Experiment study on seismic behavior of RC coupled short-pier shear wall with concealed bracings. *Earthquake Engineering and Earthquake Vibration* 26(1): 64–70.

Cheng, W.X., Jin, X.Q. & Wu, Z.B. 2001. Design and research of short-pier shear walls. *Building Structures* 31(7): 51–52.

Gao, Z. 2003. *ANSYS analysis and regularity distribution study of internal force on short-pier shear wall structure system*. Wuhan: Wuhan University of Technology.

Huang, D.S., Cheng, W.X. & Peng, F. 2003a. Study on elasto-plastic performances of shear walls with short piers. *Journal of Southeast University (Natural Science Edition)* 34(2): 164–167.

Huang, D.S., Cheng, W.X. & Peng, F. 2005. Low-cycle loading experiment study on symmetric double short-pier shearwalls. *Journal of Building Structures* 26(6): 51–56.

Huang, D.S., Cheng, W.X. & Peng, F. 2002. Design and research of short-pier shear walls(2). *Building Structures* 32(8): 10–11, 32.

Huang, D.S., Peng, F. & Cheng, W.X. 2003b. Design and research of short-pier shear walls(3). *Building Structures* 33(9): 24–25, 72.

Li, K.M., Sun, C.Y. & Li, J. 2006. Experimental study on HPC short-leg shear wall with a pair of beams. *Earthquake Engineering and Earthquake Vibration* 26(3): 121–123.

Li, Q.N., Li, X.L. & Lei, W.N. 2010. Study on destruction law and stiffness ductility of T-shaped and L-shaped short shear wall. *Journal of Building Structures* 40(2): 37–39, 44.

Li, X.L. 2011. *Mechanical model and test study of high-rise building on short-leg shear wall structure*. Xi'an: J.Xi'an Univ. of Arch. & Tech.

Rong, B.S. 1997. Short-pier shear wall system in elevator residence building. *Journal of Building Structures* 18(6): 14–19.

Song, J.X., Liu, L.X. & Peng, S.M. 2002b. A research on strain distribution evolution process of short-limbed wall structure under horizontal cyclic loading. *World Earthquake Engineering* 19(1): 77–80.

Song, J.X., Peng, S.M. & Liu, L.X. 2002a. Short-pier wall structure under horizontal cyclic loading test. *J. of Huazhong Univ. of Sci. & Tech. (Urban Science Edition)* 18(1): 91–94.

Wang, X.Y., Su, Y.S. & Yan, L.B. 2014. Experimental study on seismic behavior of steel reinforced high strength concrete short-pier shear walls with rectangular section. *Journal of Building Structures* 35(2): 46–54.

Wei, H., Gong, Z.W., Fang, X.D. & Chen, Z.C. 2010. Experimental research on seismic performance of short-pier shear wall structure with rectangular section. *Journal of Building Structures* 40(3): 71–74.

Wu, M.Z., Yang, Y.D. & Guo, D. 2009. An experiment study on the behavior of steel reinforced concrete short-limbed shear wall structure under different directional cyclic loading. *J. Xi'an Univ. of Arch. & Tech. (Natural Science Edition)* 41(4): 461–466.

Yuan, H. 2010. Study on seismic behavior of short-leg shear wall with different cross section. Hefei: Hefei University of Technology.

Zhang, M. 2014. Experimental research on seismic behavior of short-pier shear walls of T-shaped and L-shaped cross section with local joint. *World Earthquake Engineering* 30(3): 27–38.

Zhang, P.L., Li, Q.N. & Li, X.L. 2010. Experimental research on seismic performance of short-pier shear wall with L-shaped section. *Earthquake Engineering and Earthquake Vibration* 30(4): 51–56.

Zhang, S.J., Li, Q.N. & Xu, J.N. 2006. Simulative analysis on the static elasto-plastic property of shot-leg shear wall. *J. Xi'an Univ. of Arch. &Tech* 37(10): 199–203, 226.

Civil Engineering and Urban Planning IV – Liu et al. (Eds)
© 2016 Taylor & Francis Group, London, ISBN 978-1-138-02903-3

Influence factor of surrounding roads on compacting displacements of jacked piles

Zhan-You Luo, Bao-Ping Zhou & Yan-Li Tao
Zhejiang University of Science and Technology, Hangzhou, Zhejiang, China

ABSTRACT: Underground pipelines and their attachments were easily destroyed by the installed piles on the condition of the surrounding roads. Presently, the surrounding roads were neglected for the compacting displacements because of the installation complexity of jacked piles. An appropriate numerical simulation method adopting the Drucker–Prager failure criterion and the finite deformation theory was proposed according to the actual installation process of jacked pile. This model can simulate the interaction among the pile, the soil, and the continuous penetration. Compacting displacements of jacked piles were studied through the numerical simulation method. The results show that the width and the depth of the surrounding building foundations were the important influencing factors for the compacting displacements of jacked piles. The vertical displacements between the roads and the piles were larger than that without the consideration of the surrounding roads, but on the other hand horizontal displacements became less. The effective measures must be taken to prevent further damages for the underground pipes and the attachments near the surrounding roads during the installation of jacked piles.

1 INTRODUCTION

Compacting displacements of installed piles were affected by the surrounding roads in the urban engineering. The measured data showed that the compacting properties and the influence scopes were different (Hagerty & peck 1971; Sagaseta et al. 1997; Sagaseta et al. 2001; Luo et al. 2014). Therefore, it was necessary to obtain the compacting effect of installed piles with regard to the surrounding roads and protect the surrounding environment.

Extensive studies on compacting displacements had been conducted. Because of the installation complexity of jacked piles these studies were not involved in the influence of the surrounding roads. The calculating method of compacting displacements had the Cavity Expansion Method (CEM) (Cao et al. 2001; Yang et al. 2006), the Strain Path Method (SPM) (Randolph et al. 1979; Baligh 1985; Chow & The 1990) and the Numerical Simulation Method (NSM) (Mabsout et al. 1995 & Luo et al. 2008). The analytical solutions based on the Cavity Expansion Method (CEM) or the Strain Path Method (SPM) cannot obtain the horizontal and the vertical displacement fields of the whole pile-depth (Carter et al. 1986). Furthermore, the CEM or SPM solution cannot be taken into consideration the interface friction between the pile and the soil, therefore the analytical solutions may result in large errors. The Numerical simulation method obtained by the finite element method can effectively overcome these difficulties (Mabsout et al. 1995). In this paper, finite element model based on the interaction of pile–soil and continuous penetration was established. The compacting effects of jacked piles due to the depth and the width of the surrounding roads were analyzed.

2 FINITE ELEMENT MODEL

2.1 *Basic assumptions*

The installation model of jacked piles, especially for group piles or piles in row, involved the engineering properties of soil, finite deformation, contact problem and constitutive relation of the soil and the pile. In order to effectively simulate the installation procession of jacked piles, some assumptions were given as follows:

1. Stress analysis of the numerical simulation model was the total stress other than the effective stress.
2. The actual penetration process was simulated in two-dimensional plane strain space.
3. Constitutive relation of reinforced concrete pile was linear elastic and four-node element was used for numerical model pile.
4. Constitutive relation of engineering soil was elastic–plastic relation and the Drucker–Prager failure criterion was adopted. Moreover, the nonlinearly properties of material and geometry can be used.

5. Face–face friction contact elements were used for the interface of the pile and the soil. The friction type of the contact elements belonged to the coulomb friction theory.
6. Horizontal freedom of the surrounding roads was restricted, but the vertical movement was free.

2.2 *Equivalent transformation of piles in row*

In order to analyze the compacting effect of jacked piles, piles in row need to be converted to equivalent model (Fig. 1). According to the actual pile spacing, $k \cdot d$, the equivalent width of the piles in row was defined as:

$$w_{eq} = \frac{\pi}{4k} \cdot d \tag{1}$$

where w_{eq} was the equivalent width of the piles in row, d was the diameter of the single pile, and k was the coefficient of pile spacing.

2.3 *Finite element model*

Figure 2 shows the finite element model of pile–soil system. The equivalent width of the sheet pile was 0.4 m and its length was 20 m. The tip of the equivalent sheet pile was assumed parabolic shape. The width of the clay soil domain was taken as 50 times the one of the sheet pile and its depth was 100 times the width of the sheet pile. The soil surface was free. Lower and right surfaces were fixed boundary. Considering the continuum of soil, it was necessary to set a narrow opening before installation in order to make the pile penetration process become easy and avoid the large element mesh distortion. The effect for the simulation result of the compacting soil displacements can be neglected owing to the small size of the narrow opening. The distance between the pile center and the inner surrounding road was 2 m.

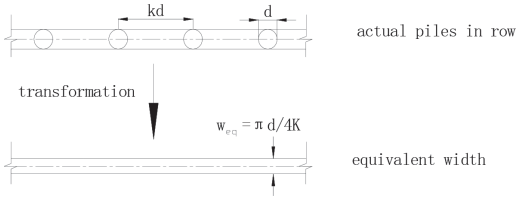

Figure 1. Equivalent transformation.

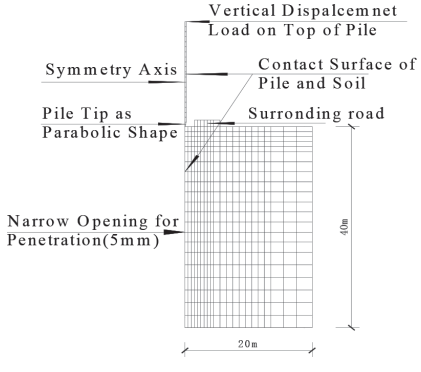

Figure 2. Finite element model.

3 COMPACTING DISPLACEMENTS OF JACKED PILES

3.1 *Simulation parameters*

In order to obtain the effective results, it was necessary to assume the soil was homogeneous. The parameters of the pile and the soil were shown in Table 1.

According to the existing urban roads, the width and the depth of the urban road was generally 3–8 m and 0–2 m, respectively. Figure 3 showed the sketch of the surrounding road. The parameters of the surrounding roads were shown in Table 2.

Table 1. Parameters of the pile and the soil.

Parameters	Soil	Pile
Modulus of elasticity, E (MPa)	2.0	2000
Poisson's ratio, ν	0.40	0.30
The density of concrete, ρ (kg·m^{-3})	1890	2500
Cohesion, C (kPa)	15.0	
Internal friction angle, Φ (°)	15.0	
Friction coefficient, μ	0.20	0.20
Maximum shear strength, τ (kPa)	20.0	20.0
Contact stiffness, kn (kN·m^{-1})	8000	

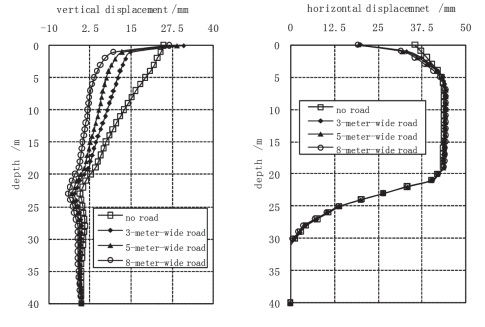

Figure 3. Variations of soil displacements with the depth (measured distance from the pile center is 1.2 m).

Table 2. Parameters of the surrounding roads.

Distance between pile and road (m)	Parameters of surrounding roads			
	Depth (m)		Width (m)	
2.0	0.0	1.0	2.0	3.0
2.0	0.0	1.0	2.0	5.0
2.0	0.0	1.0	2.0	8.0
No surrounding road	–	–	–	–
2.0※		1.0※		3.0※

※Basic calculating parameters for the finite element method.

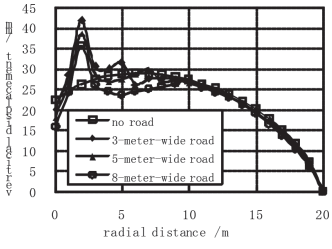

(a) Vertical displacements.

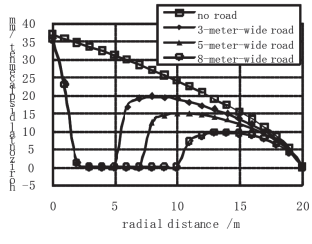

(b) Horizontal displacements.

Figure 4. Variations of soil displacements with the radial distance (z = 0 m).

3.2 *Compacting displacements affected by the width of the surrounding roads*

Figure 4 showed the horizontal and vertical displacements of the soil with depth and the position was 1.2 m from the pile center. For vertical displacements, the positive value indicated soil uplift, negative values indicated soil settlement. As could be seen from Figure 4, the vertical heave of the ground surface increased with the increasing road width, but the heave difference with the increasing soil depth became less. The horizontal displacements of the shallow-layer soils (–4 m) became larger than that compared with the absence of the surrounding roads. However, the displacements of the deep-layer soil (4–20 m) were almost as same as that with regard to the surrounding roads.

Figure 5 showed variation between the horizontal and the vertical displacements of soil with radial distance for ground surface. As could be seen from Figure 5, the vertical heave of the ground surface between pile and the road became larger than that without the surrounding roads; however the heave became less in the opposite direction of the surrounding roads. The heave of the ground surface increased with the increasing depth. Horizontal displacements of the ground surface had a considerable reduction in the constraint conditions of the surrounding roads. Moreover, the wider of the surrounding roads, the greater reduction of the horizontal displacements.

Figure 6 showed the variation between the horizontal and the vertical displacements of soil with a radial distance for 5 m depth soil. As could be seen

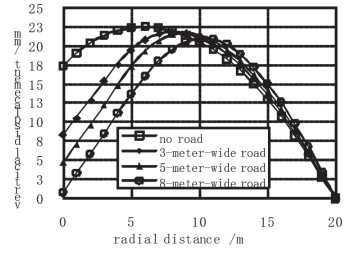

(a) Vertical displacements.

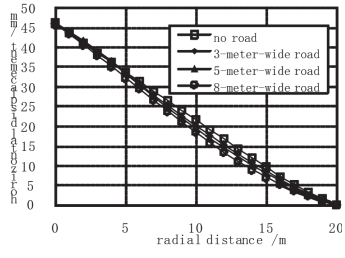

(b) Horizontal displacements.

Figure 5. Variations of soil displacements with the radial distance (z = 5 m).

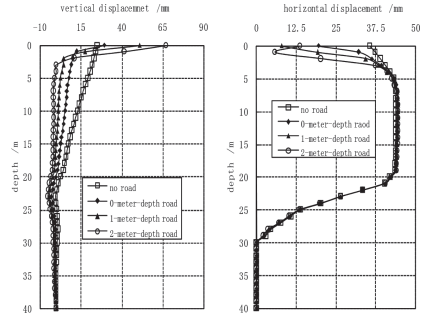

Figure 6. Variations of soil displacements with the depth.

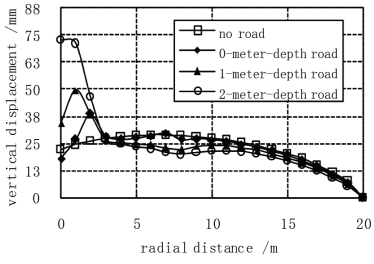

(a) Vertical displacements.

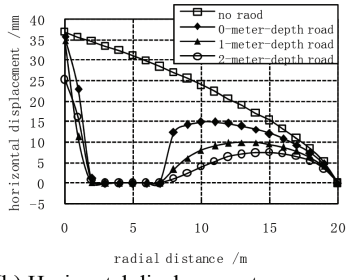

(b) Horizontal displacements.

Figure 7. Variations of soil displacements with the radial distance (z = 0 m).

from Figure 6, the vertical heave of the ground surface between the pile and the road became less than that without the surrounding road. The heave of the ground surface decreased with the increasing road depth. The horizontal displacements of 5 m depth were not obvious for the surrounding roads depth.

3.3 *Compacting displacements affected by the depth of the surrounding roads*

Figure 7 showed the horizontal and the vertical displacements between the road and the pile. The vertical displacements decreased with the increasing depth of road for the shallow-layer soils (0–3 m), but increased for the deep-layer soils (3–20 m). It could be seen from the Figure that the vertical displacements increased with the increasing depth of the road for the ground surface.

4 CONCLUSION

The relationship between the soil compacting displacements and the width or the depth of the road was analyzed according to the finite element model. Main conclusions were obtained as follows:

1. Surrounding roads can obviously affect the compacting displacements for the shallow-layer soils. However, the compacting effect became less for the deep-layer soils. The vertical displacements between the road and the pile would become larger than that without the consideration of the surrounding roads, but the horizontal displacements became less than that without the consideration of the surrounding roads.
2. It was more easily to be destroyed for underground pipelines and their attachments on the condition of the surrounding roads because of the larger vertical compacting displacements. Therefore it was very important to pay the attention to adverse effects from the surrounding roads during the installation of jacked pile.

ACKNOWLEDGMENTS

The research was supported by the National Natural Science Foundation of China (No. 41572299, No. 41172292, & No. 41427802), the New Century Excellent Talents in University (No. NCET-11-1080), and the 151 New Century Excellent of Zhejiang (No. 2012-1-076).

REFERENCES

Baligh, M.M. 1985. Strain path method. *Journal of geotechnical engineering* 111(9): 1108–1136.

Cao, L.F., The, C.I. & Chang, M.F. 2001. Undrainded cavity expansion in modified Cam clay I: Theoretical analysis. *Geotechnique* 51(4): 323–334.

Carter, J.P., Booker, J.R., & Yeung, S.K. 1986. Cavity expansion in cohesive frictional soils. *Geotechnique* 36(3): 345–358.

Chow, Y.K & The. C,I. 1990. A theoretical study of pile heave. *Geotechnique* 40(1): 1–14.

Hagerty, D.J. & Peck, R.B. 1971. Heave and lateral movements due to pile driving. *J. Soil Mech. And Found. Div., ASCE* 97(11): 1513–1532.

Luo, Z.Y., Xia, J.Z., Gong, X.N. & Zhu, X.R. 2008. Comparison study of dynamic simulation for compacting displacement of jacked pile and in-situ test. *Chinese Journal of Rock Mechanics and Engineering* 27(8): 1709–1714.

Luo, Z.Y., Xia J.Z., Gong, X.N. & Liu, W. 2014. Study on compacting soil displacements around jacked single pile based on excess pore pressure dissipation. *Chinese Journal of Rock Mechanics and Engineering*, 33(S1): 2765–2772.

Mabsout, M.E., Teese, L.C. & Tassoulas, J.L. 1995. Study of pile driving by finite-element method. *Journal of Geotechnical Engineering, ASCE* 121(7): 535–543.

Randolph, M.F, Carter, J.P. & Wroth, C.P. 1979. Driven piles in clay—the effects of installation and subsequent consolidation. *Geotechnique* 29(4): 361–393.

Sagaseta, C., Whittle, A.J. & Santagata M. 1997. Deformation analysis of shallow penetration in clays. *International Journal for Numerical and Analytical Methods in Geomechanics*, 21(10): 687–719.

Sagaseta, C. & Whittle, A.J. 2001. Prediction of ground movements due to pile driving in clay. *J.Geotech. Geoenviron. Eng* 127(1): 55–65.

Yang, J., Tham, L.G., Lee, P.K.K., Chan, S.T. & Yu, F. 2006. Behaviour of jacked and driven piles in sandy soil. *Geotechnique* 56(4): 245–259.

Civil Engineering and Urban Planning IV – Liu et al. (Eds)
© 2016 Taylor & Francis Group, London, ISBN 978-1-138-02903-3

Application and exploration of ground penetrating radar to pipe jacking construction

Kai Guo, Peng Chen & Lin Liu
College of Civil Engineering, Shenyang Jianzhu University, Shenyang, Liaoning, China

Yi Ma & Ren-Jie Sun
Shenyang Construction Quality Testing Center, Shenyang, Liaoning, China

ABSTRACT: Using ground penetrating radar to detect road geological condition, we solve the problem of subterranean cavity formed by pipe jacking construction over-excavation. By adjusting the center frequency of the radar antenna, the sampling rate, time Windows, measuring point distance and other factors get clear radar map. Via mean value method, the wavelet transforming method for radar map post-processing analysis. GPR test results are consistent with the results of the drilling sampling, which is recommended for road detection regularly and makes for road traffic safety and road life.

1 INTRODUCTION

Pipe jacking construction is a good laying pipelines technology, having many advantages including fast progress, low total cost, good construction quality and small impaction on environment and traffic, etc. At present in the construction of sewage pipes, industrial underground pipes and underground walkways use pipe jacking construction to avoid the destruction of underground structures and causing traffic congestion problems. Ahead of construction, investigating hydrology, geology, types and physical properties of foundation soil, soil density, water level, flow and surface water drainage investigations to control over-excavation in jacking to prevent the landslide. Ground penetrating radar is a new and gradually developed technology in recent years, with features such as continuous and non-destructive, economic and efficient (Luo 2006). Its Real-time image of Visual response test results, coupled with its high precision, high efficiency advantage and favored, make the methods developed very fast in the texting field.

2 PRINCIPLE OF GEOLOGICAL RADAR

Ground penetrating radar emits electromagnetic waves to detect the target through the transmitting antenna, by the receiving antenna receives the reflected wave from the target body interface. According to the theory of electromagnetic wave propagation, electromagnetic wave generates refraction and reflection. The receiving antenna receives the reflected echo information medium. The computer analysis information of the received signal is as shown in Figure 1. When electromagnetic wave propagates in the medium, its propagation velocity V is mainly decided by the dielectric constant ε_r of media. When electromagnetic wave comes to the surrounding dielectric constant different target boundary, it will produce the reflected wave received by the receiving antenna, so as to achieve Objective detection (Li 1994).

According to records of the time of GPR ground reflected wave and the subsurface reflected wave difference ΔT, you can calculate the depth of burial underground abnormal H according to equation (1)

$$H = V*\Delta T/2 \quad (1)$$

where, H is the target layer thickness; V is the velocity of propagation of electromagnetic waves

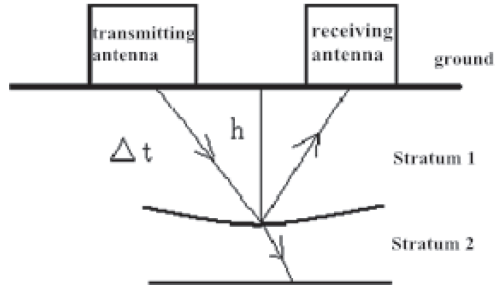

Figure 1. Geological radar working principle.

in the underground media, its size is determined by the formula (2):

$$V = C/\sqrt{\varepsilon} \quad (2)$$

where, C is the speed of electromagnetic wave in the atmosphere, approximately 3×10^8 m/s; ε is the relative dielectric constant, depending on the dielectric constant of the material layers constituting the underground.

Refraction and reflection characteristics of electromagnetic waves in the surface of the medium represented by the refraction coefficient R and reflection coefficient T. (Zhao & Lou 2004) For non-magnetic media, perpendicular to the incident electromagnetic wave, represented by the following formula:

$$T = \frac{2\sqrt{\varepsilon_1}}{\sqrt{\varepsilon_1} + \sqrt{\varepsilon_2}}$$

$$R = \frac{\sqrt{\varepsilon_1} - \sqrt{\varepsilon_2}}{\sqrt{\varepsilon_1} + \sqrt{\varepsilon_2}}$$

where: ε_1, ε_2 are the dielectric constant of the upper and lower medium.

The intensity of the reflected signal depends on the difference dielectric between ε_1 and ε_2, the greater the power difference, the stronger the reflected signal. Radar penetration depth depends on the center frequency of the wave and electrical resistance of underground media. The higher the conductivity, the smaller the penetration depth, vice versa the higher the center frequency, the smaller the penetration depth.

GPR electromagnetic frequencies emitted from several tens of megahertz to gigahertz. The theoretical maximum probing depth is twenty times than the wavelength of electromagnetic waves; theoretical minimum resolution detection of one tenth the wavelength of electromagnetic waves.

GPR propagating in lossy medium and the underground media can't be changed for the same area. So, the probing depth and resolution is only determined by the frequency of radar antenna. In practice, the detected media does not fully meet the dielectric extreme conditions, the depth of the environmental media showed an inverse relationship to conductivity σ and operating frequency f. For high-frequency radar antenna, its electromagnetic wave wavelength is smaller, and fast attenuation. So, its detected depth is shallow. But it has the higher resolution. The low-frequency antenna is on the contrary. When it requires probing deeper, due to the relatively large set, we should collect even more the number of samples to get deeper subsurface information. Then, electromagnetic round-trip time is also longer, making detection more slowly. When we choose the geological radar, we should consider these factors based on the actual situation to select the appropriate frequency antenna.

3 ENGINEERING EXAMPLE

3.1 *Project profile*

A city because of actual demand should lay a comprehensive pipeline. In the pipeline route planning, it involves passing through the normal running road. Taking economic factor of no undermining the existed roads, safety factor of solving traffic congestion and environmental factor of reducing environmental pollution into account, we decide to use pipe jacking technology to lay pipeline at the intersection of road and pipeline. According to the function, laying position and the different role, the diameter and depth of pipe also have different requirements. The maximum diameter of rainwater pipes is DN2600, the minimum diameter is DN500; maximum depth is 5.8 m, the minimum depth is 1.35 m; the maximum crossing length is 30 meters, the shortest crossing length is 23 m; diameter DN500 ~ DN600 pipes with PE pipes, diameter greater than DN600 pipe using concrete pipes and metal pipes. The maximum diameter of sewage pipes is DN1500, the minimum diameter is DN355; maximum depth is 7.03 meters, the minimum depth is 2.2 meters; the maximum crossing length is 30 meters, the shortest crossing length is 22 m; diameter less than DN600 pipe with PE pipe, diameter more than DN600 pipe using concrete pipe and metal pipe. Due to the pipe jacking construction overbreak may cause subterranean cavity disease around pipelines, it will seriously affect the integrity of road and pipeline and will bury a security risk to the use of road and pipeline.

3.2 *Detection scheme*

1. Survey line arranging
   The subterranean cavity disease most likely be located directly above the laying pipeline. Next, it is located on the top of the duct edge and pipe surrounding. Hence, it need to arrange a survey line directly above the the pipeline. In the meantime, it should arrange intensive survey lines on the both sides of pipeline axis. In order to obtain the desired radar detection maps, which can reflect the pipelines geological conditions accurately and comprehensively, setting the survey lines regulation as follows. ① For small diameter pipe with diameter DN800 or less, a survey line just above the pipeline was arranged. Meanwhile, survey lines were arranged intensively on the both sides of pipeline axis respectively, as shown in Figure 2. ② According to the diameter DN1000 to DN2000 pipe, a

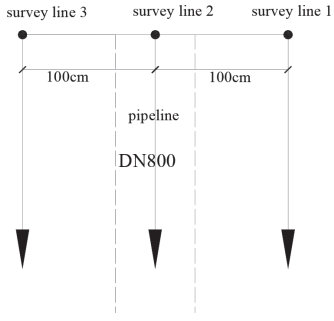

Figure 2. DN800 survey line.

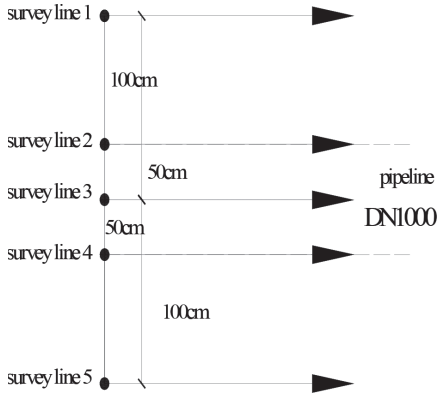

Figure 3. DN1000 survey line.

survey line was arranged just above the pipeline, then a survey line on the each side of the pipeline was arranged at the distance of 150 cm away from pipeline axis respectively, and at the left and right of the pipeline survey lines was arranged intensively at the distance of 50 cm away from pipeline axis respectively as shown in Figure 3. ③ For diameter more than DN2000 pipe, a survey line was arranged just above the pipeline, meanwhile on each side of the pipeline a survey line was arranged at the distance of 200 cm away from pipeline axis respectively, then intensive survey lines was arranged on the each side of the pipeline at the distance of 50 cm and 100 cm away from pipeline axis respectively, as shown in Figure 4. ④ When radar discover the suspected defects, it is needed to carry on intensive and repeated test in part area to confirm defects. When it comes to work, radar antennas are close to road surface, sliding along the survey line for fast acquisition. To ensure that the position of the measuring point on radar chart is corresponding to the actual detection mileage, setting a mileage mark every 5 meters as a detection section. This is for controlling the detection

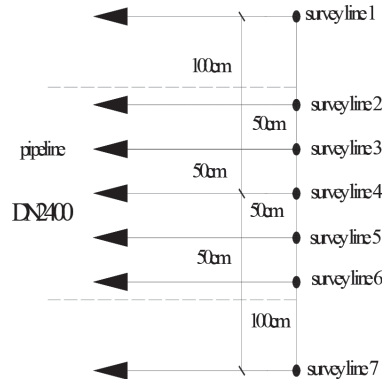

Figure 4. DN2400 survey line.

mileage and the relative position of diseases accurately in the testing process.

2. Measurement parameters selection

The radar detection effect is closely related to measurement parameters. The parameters contain: antenna center frequency, time Windows, sampling rate, measuring point distance etc.

Radar antenna center frequency selection must take target depth, target minimum size and antenna size into account. Generally, when the resolution and geological conditions is satisfied, we should try to use the antenna with the low center frequency (Li 1994). At the beginning, we use the low-frequency antenna with 200 MHz center frequency, getting a good result in terms of relatively deep pipeline. When we probed relatively shallow pipeline, the effect of low-frequency antenna is not ideal. So, we decide to change antenna frequency, using center frequency antenna with 600 MHz center frequency to replace of 200 MHz. Due to the wavelength of 600 MHz antenna is smaller, we should appropriately increase antenna window from 107ns to 213ns. This method contributes to adjust disease image to appear in the middle of the radar chart and observe image easily. Meantime, we appropriately increase the number of sampling points per sweep, transferring number from 384 to 512. In addition, we reduce the grating spacing to increase the amount of collected information. Using a single frequency scanning antenna would exit a problem that the frequency selection is too low or high. If the frequency is too low, we may be can't meet the accuracy requirement. Too high, deeper pipeline may be leaked detected. So, we take antenna array to compensate for this deficiency, lining up the same frequency or different frequencies antenna in a particular manner, and combining antennas with a specific combiner to work together. (Zhong 2010) Thus, the different

frequencies antenna has a sufficient resolution at different depths, different positions antenna can detect the same object at different angles. So you can get more than one radar map a time, complete deep and shallow probing at a much faster speed and higher resolution at the same time. That greatly improve the accuracy of detection and save time.

3.3 *Test results*

1. The total detection mileage is 20 km, including 78 pipelines and 39 intersections, with an average pipeline depth of about 3.3 meters, detection objects contain: pipe rack, heat pipes, telecommunication lines, water supply pipelines.
2. Subterranean cavity
   Soil and air have large electric property difference, when the electromagnetic wave propagates from soil to air and next from air to soil, it will produce a strong reflection interface. Then, up and down two interfaces have a reflection respectively. Abnormal light and dark radar cross-sectional view will be presented, which indicates the presence of voids or cracks, as shown in Figure 5.
3. Not dense phenomenon
   Between pipeline and road surface soil is not compacted, multiple interfaces will reflect electromagnetic waves many times. Therefore, not dense soils will be presented by clutter waveform radar on the radar cross-sectional view, as shown in Figure 6.

3.4 *Test results calibration*

To determine the accuracy of the radar images, drilling core samples correspond to underground cavity positions showed on radar chart. By contrasting to the result of drilling and radar images, we find that the results are basically the same, as shown in Figure 7–10.

According to Figures 7–10, there is a height difference between the bottom of the road and subsoil.

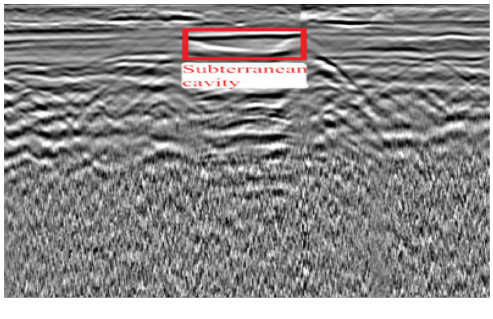

Figure 5. Subterranean cavity.

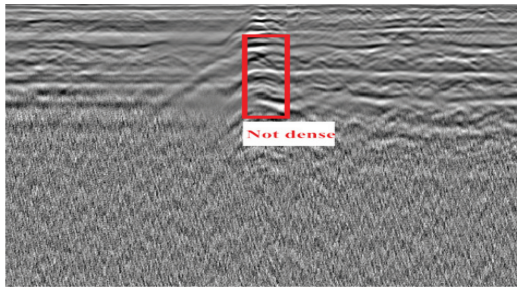

Figure 6. Not dense phenomenon.

Figure 7. Drilling pavement.

Figure 8. Cavity inside.

Then, it exists empty diseases in this position. This shows that using radar technology to measure the geological conditions of the project is feasible. Test results provide the disease location, shape, and size information for the remedial measures.

3.5 *Remedy program*

In order to prevent subterranean cavity further developing causing ground subsidence. So, it is

Figure 9. Depth of cavity bottom to pavement.

Figure 10. Depth of road bottom to pavement.

necessary to take measures to fill and repair underground voids. Here use shrinkage-compensating concrete material to fill and repair defection. According to the position showed by radar information, drilling through the road and underground hole, pouring shrinkage-compensating concrete into the cavity, as shown in Figure 11.

3.6 *Application development*

For the obtained radar map, there will be clutter wave signal having nothing to do with the scattering properties of the target, but it appears with target sub-waves in the same sampling time, windows and has similar spectral characteristics. The clutter wave has a serious impact on radar detection performance. So we should take measures to suppress radar clutter wave. Commonly simple technique is mean value method, which works for clutter wave produced by smooth surface effectively (Zhang 2005). For clutter wave produced by uneven surface, we often use wavelet transform method and Subspace method to suppress radar clutter wave caused by uneven surface.

Figure 11. Remedial scene.

4 CONCLUSION

1. According to the actual situation and detection purposes arranging reasonable testing route is the base of getting good results.
2. Choosing different frequency radar antenna and antenna array technology and adjusting radar parameters reasonably are the key to achieve the desired effect.
3. Using the average method and subspace method can suppress the influence of radar clutter wave to improve detection performance.
4. As an indirect means of detection, GPR also has many itself limitations, such as: radar antenna frequency selection, parameters adjustment, radar chart accurate judgment. Thus, it requires repeated comparison and careful analysis in the detection process.

ACKNOWLEDGEMENTS

We would like to express our gratitude for financial support from Shenyang Science and Technology Innovation Special Fund-Scientific and technological and social development projects (F14-117-9-00). Thanks for Shenyang Construction Quality Testing Center.

REFERENCES

Li, D.X. 1994. *Method and application of ground penetrating radar*. Beijing: Geological Publishing House.

Luo, Z.Q. 2006. Characteristics of radar detection *Quality of Highway Engineering* 23(4): 54–58.

Zhang, C.C. 2005. *Shallow ground penetrating radar signal processing technology research*. Chengdu: University of Electronic Science and Technology.

Zhao, Y.F & Lou, H. 2004. Highway road ground penetrating radar detection technology application. *Journal of Henan Normal Universit*y (Natural Science) 32(2): 98–100.

Zhong, L. 2010. Application of antenna array in the detection of municipal pipelines. *Fujian Building* 144(6): 122–124.

This page intentionally left blank

Civil Engineering and Urban Planning IV – Liu et al. (Eds)
© 2016 Taylor & Francis Group, London, ISBN 978-1-138-02903-3

Study on the drying shrinkage of the manufactured sand high-strength concrete

Da-Hong Wu
Guizhou Transportation Planning Survey and Design Academy Co. Ltd., Guiyang, Guizhou, China

ABSTRACT: In this paper, we conducted a comparative study on the drying shrinkage of the high-strength concrete of the manufactured sand and the natural sand. The results of the study show that the drying shrinkage of the high-strength concrete of the manufactured sand is greater than the natural sand, and the difference is bigger in the early days. As the time passes, there is a difference in the drying shrinkage. It tends to be stable, and the drying shrinkage is around $40–50 \times 10^{-6}$ after 7 days. Under the condition of same W/C and the dosage of cement, the compressive strength of the high-strength concrete of the manufactured sand is greater than the natural sand at the same age.

1 INTRODUCTION

When the tensile stress produced by the drying shrinkage of the concrete exceeds the tensile strength of the concrete itself or drying shrinkage strain exceeds the limit tensile strain of the concrete, the concrete can produce a dry crack that will accelerate the deterioration of the concrete and the steel bar corrosion, reducing the durability of the concrete structure (Almudaiheem & Hansen 1987, Almudaiheem 1992). Because of the prestressed steel corrosion rate is greater than the ordinary steel, drying shrinkage cracks of the prestressed reinforced concrete structure damage is greater.

Manufactured sand is processed by the broken rock, and it is made of the special machines (GB/T14684-2011, 2011). A large number of manufactured sand concrete is wildly used in the buildings nowadays, and it will be used more and more widely in the future. Manufactured sand high-strength concrete is used in the big bridges and buildings more and more. C50–C55 concrete strength grade is generally used in the highway bridges. The strength of the concrete is generally 60–70 MPa. The study is based on the engineering practice, which is the research of the drying shrinkage of the manufactured sand high-strength concrete in the highway bridges.

2 EXPERIMENTAL MATERIALS

1. Cement: 52.5 grade ordinary Portland cement, manufactured by the Conch cement plant of Yingde in the Guangzhou province, with 34.5 MPa and 56.4 MPa compressive strength at 3rd day and 28th day, respectively.
2. Manufactured sand: Manufactured sand production in Zhangyi of the Hunan province, parent rock for limestone, their physical characteristics are explained in Table 1 and Figure 1.
3. Natural sand: Natural sand production in Ruicheng of the Hunan province, their physical characteristics are explained in Table 2 and Figure 2.
4. Coarse aggregate: Coarse aggregate production in Zhangyi of the Hunan province, parent rock for limestone. Coarse aggregate is crushed stone with 5–25 mm continuous gradation, Gravel accounted for 15% of 4.75–9.5 mm, 35% of 9.5–16 mm, and 50% of 9.5–16 mm.
5. Admixture: Admixture is the polycarboxylate superplasticizer, from Hunan vanguard building materials co., Ltd, the dosage is 1.0% by the weight of the cement.
6. Water: Water is tap water.

Table 1. Physical properties of the sand.

Type	Name	Value
Manufactured sand	Fine content (%)	10.4
	MB (methylene blue value)	0.3
	Fineness module	3.2
	Crushed stone value (%)	16.3
Natural sand	Clay content (%)	0.7
	Clay lumps and friable particles content (%)	0.1
	Fineness module	2.7
	Soundness (%)	3.0

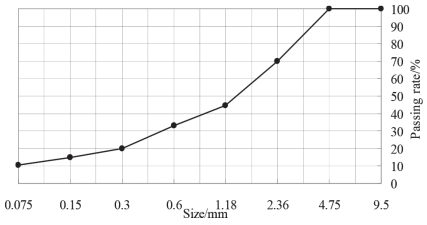

Figure 1. Grading of the manufactured sand.

Table 2. Composition of the concrete.

Concrete specimen	Mix proportions (kg/m^3) C	W	S	G	W/C	SP (%)
CS1: manufactured sand	481	154	708	1107	0.32	39
CS2: natural sand	481	154	635	1180	0.32	35

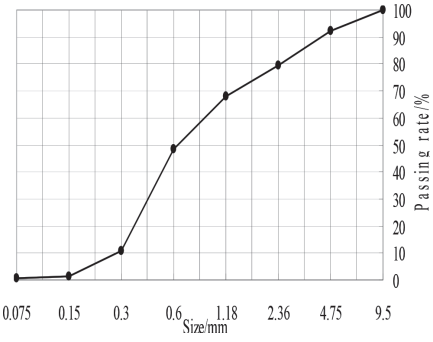

Figure 2. Grading of the manufactured sand.

3 EXPERIMENTAL METHODS

1. Properties of the fresh concrete are tested according to the Chinese national standard GB/T50080-2002.
2. Compressive strength is tested in response to GB/T50081-2002 of the Standard for Test Method of the Mechanical Properties of the Ordinary Concrete.
3. Drying shrinkage is tested according to the Chinese national standard GB/T50082-2009. Specimen size is 100 × 100 × 515 mm, the maintenance 3 d after ripping, and then placed in the constant temperature and humidity chamber (20 °C, 60% RH) test, shrinkage value using the dial gauge for testing (GB/T50082-2009, 2009). The test was done as shown in Figure 3.

Figure 3. Concrete drying shrinkage test.

4 RESULTS AND DISCUSSION

4.1 *Experimental results and the analyses about the workability and the strength*

According to the bridge engineering usage of the C50 concrete mix design, the principles for the design of the concrete must satisfy the following requirements:

- The workability of the fresh concrete is the same.
- The dosage of the concrete is the same.
- The W/C of the concrete is the same.
- The workability of the fresh concrete can be adjusted through adding the concrete admixture.

The compositions of the concrete are listed in Table 2. The test results of the workability and the strength of the concrete are listed in Table 3.

Experimental results show that the workability of the C50 concrete of the natural sand is better than the concrete of the manufactured sand under the condition of the same W/C and the dosage of the cement. The compressive strength of the C50 concrete of the manufactured sand is better than the concrete of the natural sand under the condition of the same W/C and the dosage of the cement, and the compressive strength is higher than the river sand concrete, about 8% in 28 days.

4.2 *Experimental results and the analyses about the drying shrinkage*

Drying shrinkage performance test results are shown in Figure 4. Experimental results show:

- The drying shrinkage of the high-strength concrete of the manufactured sand is greater than the natural sand at the same age.
- The difference of the drying shrinkage between the manufactured sand and the natural sand is big in the early days, but the difference tends to be stable, and the drying shrinkage is around 40–50 × 10^{-6} after 7 days at the later stage.

Table 3. Workability and strength of the concrete.

Concrete specimen	Mix proportions (kg/m^3) 3 d	7 d	28 d	Slump (mm)
CS1: manufactured sand	53.2	64.4	68.9	161
CS2: natural sand	52.3	60.6	64.1	205

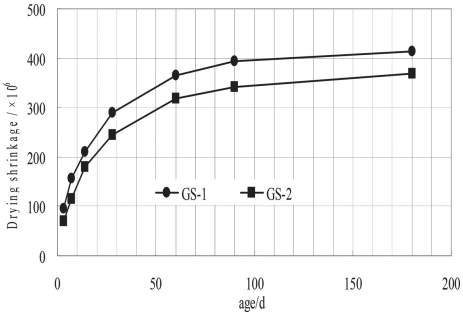

Figure 4. Drying shrinkage performance test results.

The results are obtained from the following reasons:

– The manufactured sand contain 10% fine, which led to the increase of the rate of the drying shrinkage.
– In order to ensure the workability of the manufactured sand concrete to meet the construction requirements, the general manufactured sand concrete sand rate is about 5% higher than the natural sand.

5 CONCLUSION

1. The drying shrinkage of the high-strength concrete of the manufactured sand is greater than the natural sand at the same age.
2. The difference of the drying shrinkage of the manufactured sand and the natural sand is bigger in the early days. As the growth of the time, the drying shrinkage difference tends to be stable.
3. Under the condition of same W/C and dosage of cement, the compressive strength of the high-strength concrete of the manufactured sand is greater than the natural sand at the same age.
4. Due to the existence of the fine in the manufactured sand and the high-sand ratio led to the mechanism of the high-strength concrete early drying shrinkage is larger, which should be taken seriously in the process of application. We can take the following measures to reduce the shrinkage of the concrete:
   – Adding fly ash in the manufactured sand concrete.
   – Adding expansive agent in the concrete.
   – Strengthening early wet curing to reduce the drying shrinkage value.

REFERENCES

Almudaiheem, J.A. 1992. An Improved Model to predict The ultimate Drying Shrinkage of Concrete. *Magazine of Concrete Research* 159(44):81–85.

Almudaiheem, J.A. and Hansen, W. 1987. Effect of Specimen Size and Shape on Drying Shrinkage of Concrete. *ACI Materials Journal* 84(2):130–135.

GB/T 50082-2009, 2009. *Standard for test methods of long-term performance and durability of ordinary concrete of People's Republic of China*. Beijing: China Standard Press. (in Chinese).

GB/T 14684-2011, 2011. *Standard of sand for construction of People's Republic of China*. Beijing: China Standard Press. (in Chinese).

This page intentionally left blank

Civil Engineering and Urban Planning IV – Liu et al. (Eds)
© 2016 Taylor & Francis Group, London, ISBN 978-1-138-02903-3

Finite element analysis of hollow cylinder test taking torque rate into consideration

Bin-Bin Xu
Tianjin Port Engineering Institute Ltd. of CCCC, Tianjin, China
Key Laboratory of Geotechnical Engineering of Tianjin, Tianjin, China
Key Laboratory of Geotechnical Engineering, Ministry of Communication, Tianjin, China

Toshihiro Noda
Nagoya University, Nagoya, Japan

ABSTRACT: In this paper, a soil-water coupled finite element analysis is carried out to investigate the behavior of monotonic hollow cylinder test in which the calculation model is regarded as a boundary value problem. The feasibility of finite element method is firstly reviewed and the effect of wall thickness is discussed in detail and the influence of loading patterns is also involved in this part. It is found that the uniformity of deformation becomes better as the wall thickness gets thinner. From the aspect of torque rate, it can be found that for the relatively low torque rate, the apparent behavior matches up very well mutually, which is also in accordance with the case with initial distributive velocity and acceleration indicating non-inertia effect. As the loading rate increases, the inertia term gradually plays a crucial role in excess pore water pressure and geometrical deformation.

1 INTRODUCTION

In order to clarify the soil properties and verify the validity of proposed constitutive model, various indoor experiments have been carried out to check the mechanical behavior of soil under different stress path, such as plane strain test, oedometer test and triaxial test, in which the triaxial compression test is the most popular test. However, the stress state in the triaxial test is not three dimensional and it cannot be called a true triaxial test. In practical geotechnical engineering, the soil in the ground is usually under a three dimensional stress state. Recently, the hollow cylinder test that is determined by four individual stresses is employed to simulate the practical stress state during the construction.

Specimen in laboratory testing including the above hollow cylindrical specimen is usually regarded as a single element possessing uniform deformation to verify the validity of constitutive model. However, as the progressing of loading, such uniformity will lose gradually, which may leads to inhomogeneous and localized deformation. Asaoka & Noda (1995) described the specimen as a boundary value problem with initial conditions under plain strain assumption and pointed out the importance of considering the effect of boundary value problem specially in the case of rapid loading and large deformation. (Jin et al. 2010) dealt with a three dimension triaxial test regarded as a boundary value problem and demonstrated the difference between soil specimen and the perfect element concerning cyclic frequency, confining pressure and so on using quasi-static FE analysis code.

This paper will also treat the monotonic undrained hollow cylinder torsional shear test as a three-dimensional boundary value problem with initial conditions taking into consideration of loading patterns, torque rate, and specimen thickness to investigate the influence of inhomogeneity. The analysis code is a soil-water coupled finite deformation analysis (Asaoka & Noda 2007, Noda et al. 2008) which can deal with static/dynamic behaviors incorporated into SYS Cam-clay model (Asaoka et al. 2000, 2002) that can clarify the loss of structure, overconsolidation and anisotropy during loading response in extensive natural deposited soils is employed to state the influence of several factors involved inertial effect.

2 ANALYSIS CONDITION

2.1 *Mesh and boundary condition*

The height, inter diameter and outer diameter of the specimen are 8 cm, 4 cm and 8 cm respectively. For the finite element partition, it is divided into 5, 32 and 20 elements in the radial, circumferential and vertical directions and there are totally 3200 elements and 4032 nodes in the calculation, which needs about four hours to finish one computation.

Table 1. Soil parameters and initial conditions.

Elasto-plastic parameters	
Compression index $\tilde{\lambda}$	0.108
Swelling index $\tilde{\kappa}$	0.025
Critical state constant M	1.55
Intercept of NCL* N	2.0
Poisson's ratio ν	0.3
Initial conditions	
Specific volume	1.747
Stress ratio	0.0
Degree of structure	1.0
Degree of overconsolidation ration	5.0
Soil particle density ρ (g/cm^3)	2.65
Permeability coefficient k (cm/s)	3.7×10^{-7}

* Specific volume on NCL of fully remolded soil when $p' = 98.1$ kPa, $q = 0$.

The mechanical boundary is exactly same as those in the practical test. Namely, the nodes at the bottom end are fixed in three directions and for the nodes at the top end a constant angular velocity of 0.005 rad/s, which is 0.1875%/sec, is applied on the nodes at the top end. Constant load is applied at the vertical direction and there is no displacement restriction. For the hydraulic boundary, the entire boundary is impermeable.

2.2 *Soil parameters*

The soil parameters are shown in Table 1. Here SYS Cam-clay model is employed as the constitutive model of the soil, in which the structure, overconsolidation ratio and anisotropy is evaluated with concept of plastic deformation based on the modified Cam-clay model. Details about the constitutive model and elasto-plastic parameters can be seen in Asaoka et al. (2000). As can be seen, the saturated clay is fully remolded and overconsolidated with a relative low permeability. It should also be noticed that the evolution parameters about loss of overconsolidation accompanying with plastic deformation is different from that used in Asaoka & Noda (1995). The gravity force is ignored in the analysis and the anisotropy is also neglected.

3 CALCULATION RESULTS

Various torque rates, 0.005 rad/s, 0.5 rad/s 5 rad/s and 1000 rad/s, namely 0.1875%/s, 18.75%/s, 187.5%/s and 37500%/s that is an extremely rapid loading rate only at the top end are adopted to investigate the influence of the torque rate namely the inertia term on the distribution of the deformation and the apparent behavior.

The apparent behavior for three torque velocities is given in Figure 1. The behavior matches up very well with each other when the loading rate is less than 18.75%/s. However, with the loading rate raising, the initial inertial effect is gradually playing a significant role in the loading process, indicated by the oscillation of deviator stress and pore water pressure, as shown in Figure 2. In the finite element calculation, the total torque T_θ is given by the dot product of the equivalent nodal force vector and the radial vector through Eq. (1),

$$T_\theta = \int_v \left([B]^T \{T'\} + \rho \{\dot{v}\} \right) dv \cdot \{r\} \tag{1}$$

where [B], T', ρ and r indicate the matrix transforming nodal velocity to strain vector, Cauchy's effective stress vector, the density of soil-water mixture and the vector in the radius. Also, the term of acceleration is included to take inertia effect into account.

Usually, the first term in the right becomes much more predominate than the second term including the acceleration for the quasi-static cases, however, as the loading rate increases, the weighted part of the inertia term raises to some extent to play an action on the total torque. As shown next in Figure 3 about the propagation of acceleration, the sudden rapid loading results in a significant acceleration wave inside the specimen which will spread

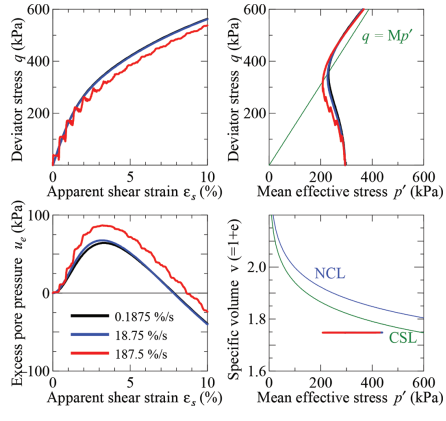

Figure 1. Influence of loading rate effect on apparent behavior at $\omega = 0.005$, 0.5 and 5 rad/s.

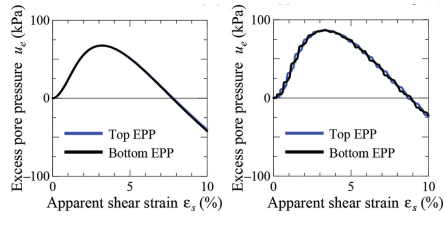

Figure 2. Difference of excess pore water pressure measured at top and bottom with $\omega = 0.5$ and 5 rad/s.

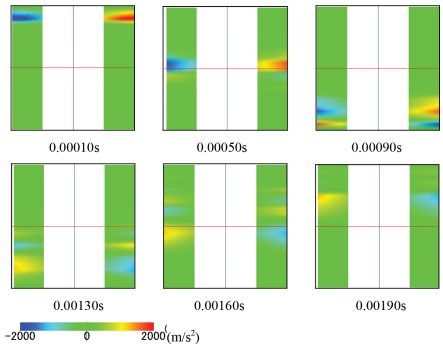

Figure 3. Propagation of acceleration in y-direction at $\omega = 5$ rad/s.

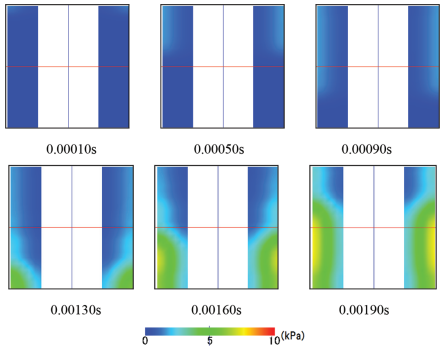

Figure 4. Propagation of excess pore water pressure at $\omega = 5$ rad/s.

towards the bottom surface and then reflect back. The resultant acceleration will enlarge the torque when two of them motion towards same direction while diminish it when opposite. For the first three torque rates, although remarkable difference appears in the apparent behavior, the distribution of shear strain seems to be no much difference.

Figure 4 denotes the propagation of the pore water pressure corresponding to the transmission of acceleration inside the specimen. Similarly, the pore pressure shows a remarkable inter-reflection up and down.

In order to make sure the influence of initial inertia term namely the acceleration on the apparent behavior of the specimen and the excess pore water pressure, a special loading scheme without initial inertia term is proposed. As analyzed in the above, when the torque rate is very high, the inertia term on the loading end becomes very large and the nodes at the loading end deform firstly and then propagate towards the end without the loading. Namely, initially the movement tendency of all the nodes in the specimen doesn't keep the same pace.

An initially distributed variables consisting of velocity and acceleration are artificially applied to each node according to its position in order to realize a perfectly static loading in certain direction, which contributes the inertia-free loading scheme. The angular velocity 250 rad/s with the opposite direction is applied at all the nodes at both ends and then the angular velocity of the nodes inside the nodes decreases linearly according to position. Finally at the middle of the specimen, there is no torque rate. In other words, there is a symmetrical plane at the middle height of the specimen, at the two side of which the linearly decreasing but opposite angular velocity and angular acceleration can be observed. The initial excess pore water pressure is also designated to each element in accordance with the local angular velocity and the radius. For the special loading scheme, because of the initial distributive variables, all the nodes inside the specimen would keep the same pace mutually and there is no propagation of disturbance no matter how great the initial loading rate is.

For the specimen with initially artificial velocity, acceleration and pore water pressure, it behaves like a specimen under quasi-static loading without considering the loading time and loading increment, even though the angular velocity is unimaginably large. When the distributive variables are applied, there is almost no migration of pore water, as shown in Figure 5. Figure 6 shows the distribution of the acceleration which indicates that the distribution of the acceleration is independent of the loading periods. Correspondingly, there is also no propagation of excess pore water pressure inside the specimen.

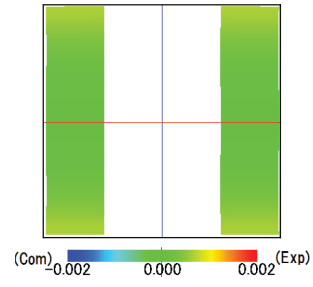

Figure 5. Distribution of specific volume change when $\gamma_s = 11.8\%$.

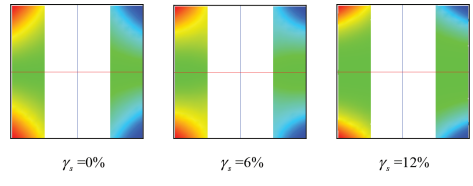

Figure 6. Distribution of y-acceleration at x-z cross section with distributive $\omega = 250$ rad/s.

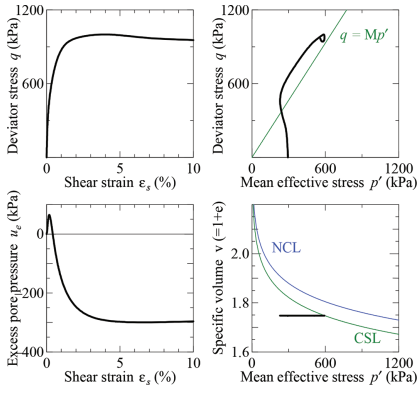

Figure 7. Apparent behavior at an extremely rapid torque rate of 1000 rad/s.

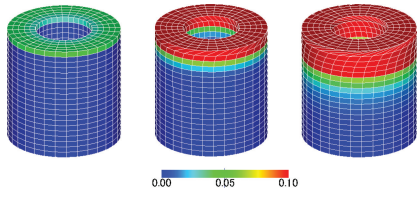

Figure 8. Effect of inertia term on geometrical deformation with torque rate of 1000 rad/s.

As an extreme case of the rapid torque rate, an angular velocity of 1000 rad/s (37500%/s) is carried out in order to check the influence of the inertial term on the geometry deformation. Figure 7 and Figure 8 present the apparent behavior where the pore water pressure is measured at the top end and the distribution of shear strain at different loading stages respectively. The specimen seems to reach a critical state fairly quickly in a relatively minor shear strain where the deviator stress and the excess pore water pressure reach stable. The shear strain distribution confirms the significant influence of the inertia term upon the geometry changes. The loading rate turns to be so huge that initially the shear strain only crowds at the top layer, following propagation downwards.

4 CONCLUSIONS

Monotonic undrained hollow cylinder torsional shear test has been treated as not a single element but a boundary value problem with initial conditions to carry out a series of simulation taking into consideration of loading rate effect about inertia term and wall thickness. The conclusions are as following:

1. Artificially imposed distributive velocity and acceleration on each nodes and distributed pore water pressure on each element at initial moment enables to eliminate the inertial effect during the loading, which can be regarded as a quasi-static problem irrespective of loading time and loading increment, although the torque rate seems to be beyond imagination.
2. The inertial term plays a crucial role as the loading rate increases with the absence of initially distributive quantities. As the torque is loaded within a very short time, tremendous disturbance would transmit towards the adjacent nodes in the form of acceleration wave, while at the same time, in order to maintain the validity of the former equilibrium equation, corresponded gradient of excess pore water pressure is induced inside the relevant element to counteract the unbalanced inertia force. Meanwhile, due to the uniform circular motion, the acceleration at the top varies from instant to instant with constant magnitude. To a certain extent, it is not a simple and temporary punch problem where the momentary acceleration wave is applied and then disappears in a short time, but a durative action with regular acceleration acting as the excitation origin even though it is called monotonic loading.

Therefore, the propagation of the acceleration and the pore water pressure would be induced and transmitted inside the specimen persistently with multiple-reflection, which may result in the oscillation of torque measured at the top end. If the loading rate gets even larger, the geometry deformation predominantly concentrates at the loading layer and propagates gradually downward.

REFERENCES

Asaoka, A. & Noda, T. 1995. Imperfection sensitive bifurcation of Cam-clay under plane strain compression with undrained boundaries. *Soils and Foundations* 35(1): 83–100.

Asaoka, A., Nakano, M. & Noda, T. 2000. Super-loading yield surface concept for highly structured soil behavior. *Soils and Foundations* 40(2): 99–110.

Asaoka, A., Noda, T., Yamada, E., Kaneda, K. & Nakano, M. 2002. An elasto-plastic description of two distinct volume change mechanisms of soils. *Soils and Foundations* 42(5): 47–57.

Asaoka, A. & Noda, T. 2007. All soils all states all round geo-analysis integration, *International Workshop on Constitutive Modelling-Development, Implementation, Evaluation, and Application*. Hongkong: ASCE: 11–27.

Jin, Y., Ye, B. & Zhang, F. 2010. Numerical simulation of sand subjected to cyclic load under undrained conventional triaxial test. *Soils and Foundations* 50(2): 177–194.

Noda, T., Asaoka, A. & Nakano, M. 2008. Soil-water coupled finite deformation analysis based on a rate-type equation of motion incorporating the SYS Cam-clay model. *Soils and Foundations* 48(6): 771–790.

Civil Engineering and Urban Planning IV – Liu et al. (Eds)
© 2016 Taylor & Francis Group, London, ISBN 978-1-138-02903-3

The research of the impact load of a vehicle applied to the bridge based on a model experiment

Xing-Fu Lin & Yong Ding
Department of Civil Engineering, Ningbo University, Ningbo, Zhejiang, China

Xiao-Dong Zhang & Guang-Wu Tang
Key Laboratory of Bridge Earthquake Resistance Technology, Ministry of Communications, Chongqing, China

ABSTRACT: The impact load of the vehicle tires is the main dynamic load applied on the bridges, and it is also one of the main factors leading to the damage of the bridge structures. To analyze this impact load, reduced scale models of bridge and vehicle are manufactured in this work. By measuring the supporting load of the bears of the bridge model, the local impact of the vehicle is evaluated. The global effect of the vehicle load is assessed by the middle-span deflection of the bridge model. The experimental results show that the local impact of the vehicle near the bridge expansion joint is obvious, and it is much higher than the global dynamic effect of the vehicle on the bridge. The width of the expansion joint and the velocity of the vehicle are the main factors affecting the impact load.

1 INTRODUCTION

Impact load of the vehicle tires is the main dynamic load applied on the bridges, and it is also one of the main factors leading to the damage of the bridge structures (Xia 2002; Lima & Brito 2009; Zhang et al. 2004). The impact can be divided into a local impact and a global impact according to the different influences of the scope. In the American bridge code and the British bridge code, the local impact factors of the tire load on the expansion joint are 0.75 and 0.33, respectively. In the Chinese bridge code, this impact factor for the tire load on the expansion joint has not been defined, and the local impact factor of the bridge structure is 0.3, which is adopted for simplification. According to the measurement on the practical bridge by Ding and the numerical simulation by Roeder, this impact factor maybe underestimate the practical tire load (Roeder 1998; Ding et al. 2013). There is a great difference for the local impact factors of the tire load of vehicle on the expansion joint in the bridge codes of different countries. So this impact load is worth paying more attention to.

In this paper, reduced scale models of vehicle and bridge are established. The supporting load of the bears of the bridge passing across the bridge expansion joint is measured to evaluate the local impact, and the middle-span deflection of the bridge is measured to evaluate the global impact. Meanwhile, the influences of the width of the expansion joint and the velocity of the vehicle on the impact load of vehicle are discussed.

2 REDUCED SCALE MODEL OF THE BRIDGE

The reduced scale bridge model is shown in Figure 1. Overall length and calculated span of the bridge are 380 cm and 377 cm, respectively. The width and the height of the cross section of the girder of bridge are 10.5 cm and 5 cm, respectively. The thickness of the bottom and the side wall is 0.2 cm and 0.16 cm, respectively.

Photos of the bridge model in the experiment are shown in Figure 2. There are three spans in this bridge model, and they are all simply supported on the ends. The expansion joint is placed between the adjacent spans, which are shown in Figure 2 (b). The middle span is adopted to test the impact

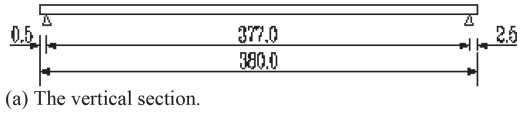

(a) The vertical section.

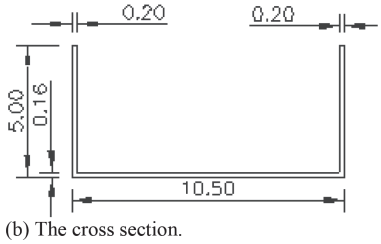

(b) The cross section.

Figure 1. The structure of the bridge model (unit: cm).

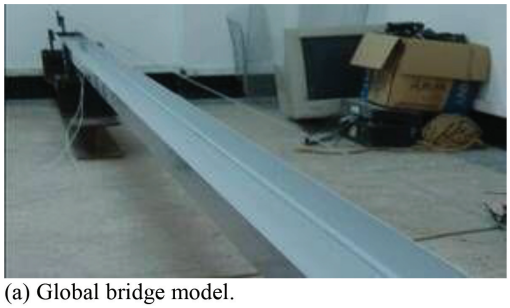

(a) Global bridge model.

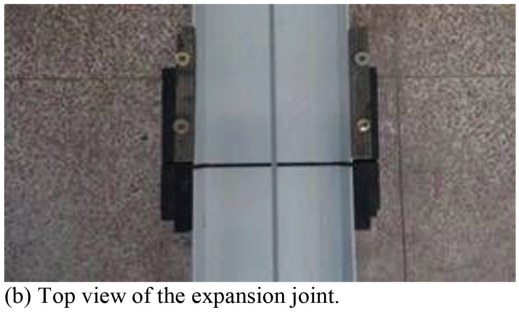

(b) Top view of the expansion joint.

(c) Rolling simply supported end.

Figure 2. Photos of the bridge model.

load of the vehicle. One end of the middle span is simply supported on a rolling bearing; the other is simply supported on two dynamic force sensors, which is shown in Figure 2 (c).

3 REDUCED SCALE MODEL OF THE VEHICLE

Photo of the vehicle model is shown in Figure 3. The length and the width of the vehicle model are 15 cm and 9 cm, respectively. It is fitted for the bridge model. This vehicle model is composed of elastic tires and rigid body. The iron slabs can be added on to adjust the mass of the vehicle.

On the practical bridge, contact patch exists between the tire and the bridge deck. The soft silicone is chosen as the material of the vehicle's tire to simulate the elasticity of the practical tire, so

Figure 3. Photo of the vehicle model.

that the contact patch also exists between the tire model and the bridge deck.

The vehicle model is pulled by the stepper motor. Velocity of the stepper motor can be controlled by inputting programs. The velocity of the vehicle can be adjusted from 0.1 m/s to 1 m/s. To give the vehicle model a stable speed on the middle span of the bridge model, a 1.3 m long acceleration section is designed on the first span. To stop the vehicle model, a 0.5 meter long deceleration section is designed on the third span.

4 DESIGN AND EXECUTION OF THE EXPERIMENT

4.1 *Local impact test*

When the local impact test is conducted, total weight of the vehicle is set as 4.6 kg. The steps of the experiment are as follows:

1. Setting the width of the expansion joint to 0 mm;
2. Dividing velocity of the vehicle into ten different grades, i.e., from 0.1 m/s to 1 m/s. Measuring the impact force by the dynamic force sensors placed at the begin of middle span of bridge, and collect the data at every velocity of the vehicle;
3. Setting the width of expansion joint as 0.5 mm, 1 mm, 1.5 mm, 2 mm, 2.5 mm, and 3 mm, respectively, and to repeat step (2).

The maximum dynamic force when the front tire of the vehicle model passing across the expansion joint is analyzed to evaluate the local impact.

4.2 *Global impact test*

The global impact test mainly studies the maximum mid-span deflection of the bridge. The steps of the experiment are as follows:

1. Setting the width of the expansion joint as 0 mm;

2. Dividing the velocity of the vehicle into ten different grades, i.e., from 0.1 m/s to 1 m/s. Measuring the mid-span deflection by LVDT sensor, and collect the data at every velocity of the vehicle;
3. Setting the width of the expansion joint as 0.5 mm, 1 mm, 1.5 mm, 2 mm, 2.5 mm, and 3 mm, respectively, and to repeat step (2).

5 RESULTS AND DISCUSSION

5.1 *Results and analysis of the local impact*

Figure 4 shows the maximum load of the front tire increases with the width of the expansion joint when the velocities of the vehicle model are kept as a constant. Figure 5 shows the maximum load of the front tire increases with the velocity of the vehicle model when the width of the expansion joint is 1.5 mm. Figure 6 shows that the position of the maximum load of the front tire load is in the range of 4 mm to 5.5 mm from the expansion joint. And the distance between the position of the maximum tire load and the expansion joint is less

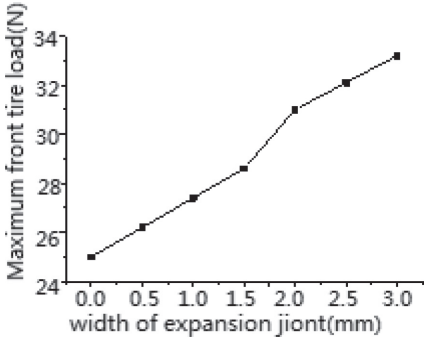

Figure 4. The relationship between the maximum front tire load and the width of the expansion.

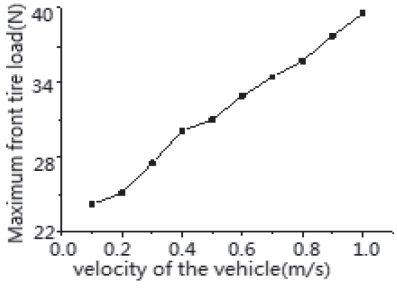

Figure 5. The relationship between the maximum front tire load and the velocity of the vehicle.

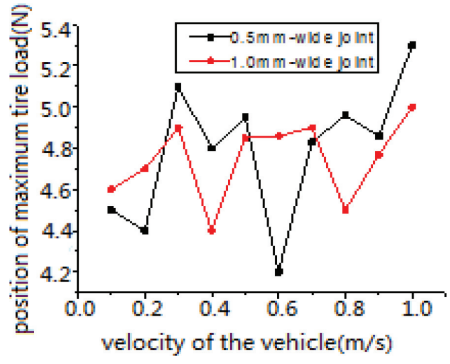

Figure 6. The relationship between the position of the maximum tire load and the velocity of the vehicle.

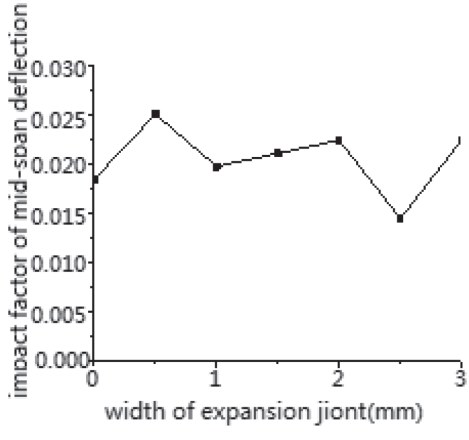

Figure 7. The relationship between the mid-span deflection and the width of the expansion joint.

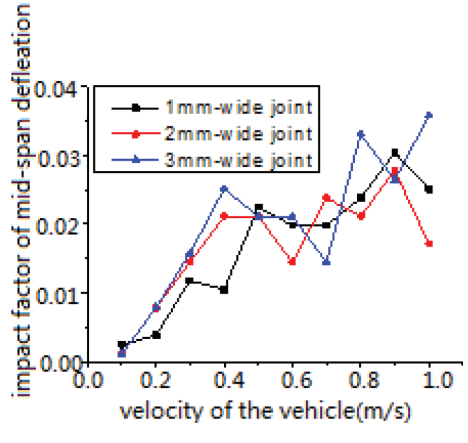

Figure 8. The relationship between the impact factor of the mid-span deflection and the velocity of the vehicle.

than 6.4 mm, which is the contact length of the tire indentation. So it is necessary to pay more attention to the effect of the local impact in the regions near the expansion joint when designing and maintaining the bridge.

5.2 *Results and analysis of the global impact*

Figure 7 shows the width of the expansion joint hardly affects the impact factor of the mid-span deflection when the velocities are kept as a constant. Figure 8 shows that the impact factor of the mid-span deflection increases with the increasing velocity of the vehicle model when the velocity is less than 0.4 m/s. When the velocity exceeds 0.4 m/s, the vehicle model is unsteady. The maximum impact factor of the mid-span deflection is only 0.036. It indicates that the global impact of the tire load of vehicle on the bridge is much smaller than the local impact of the tire load.

6 CONCLUSION

In this paper, the reduced scale models of the vehicle and the bridge are used to analyze the local and the global impact of the tire load of the vehicle on the bridge structure. Impact load of the tire and the mid-span deflection of the bridge are tested to evaluate the local impact and the global impact, respectively. The width of the expansion joint and the velocity of the vehicle are taken into consideration as factors affecting the impact load. Conclusions are as follows:

1. The impact factor of the tire load increases linearly with the width of the expansion joint.
2. Local impact factor increases with the velocity of vehicle when it is less than 1 m/s. The bumping on the expansion joint has little effect on the global impact factor of the mid-span deflection. Therefore, the analysis of the maximal mid-span moment and the dynamic deflection can ignore the effect of the bumping on the expansion joint.
3. The distance between the position of the peak of front tire load and the end of the expansion joint is less than the length of the tire indentation, so it is necessary to reinforce regions near the expansion joint when the bridge is designed.

ACKNOWLEDGMENT

This work was supported by the Fund of Key Laboratory of Bridge Earthquake Resistance Technology of the Ministry of Communications of PRC (201401), Zhejiang public welfare Technology Research Program (2015C33036), Demonstration Project of Science and Technology Services in Ningbo (2015F1008), and Science and Technology Program of Zhejiang Provincial Communication Department (2015-2-47).

REFERENCES

Ding, Y., Huang, Q. & Xie, X., et al. 2013. A computational method for the dynamic load in heavy-vehicle bumping at the bridge expansion joint and analysis of the influencing factors. *China Civil Engineering Journal* 46(7): 98–107.

González, A., Cantero, D. & O'Brien, E.J. 2011. Dynamic increment for shear force due to heavy vehicles crossing a highway bridge. *Computers & Structures* 89(23–24): 2261–2272.

Lima, J.M., Brito, J.D. 2009. Inspection survey of 150 expansion joints in road bridges. *Engineering Structures* 31(5): 1077–1084.

Roeder, C.W. 1998. Fatigue and dynamic load measurements on modular expansion joints. *Construction and Building Materials* 12(2–3): 143–150.

The Ministry of Communications of PRC. 2004. General Specification for Highway Bridge Design (JTJD60-2004), Beijing: China Communications Press

Xia, H. 2002. *Dynamic interaction of vehicle and bridge*. Beijing: Science Press.

Zhang, J.H., Yang, C.X., & Su, G.H. 2004. Bridge expansion joints damaged Cause and prevention of damage of expansion joints. *China Municipal Engineering* 108(2): 21–22, 26, 66.

Civil Engineering and Urban Planning IV – Liu et al. (Eds)
© 2016 Taylor & Francis Group, London, ISBN 978-1-138-02903-3

The state space method of free vibration analysis for frame-shear wall-thin-walled core skew structure

Hua Zhang & Li Huang
Institute of Civil Engineering, Hebei University of Science and Technology, Shijiazhuang, Hebei, China

ABSTRACT: To analyze the free horizontal vibration for the stepped tall buildings composed of a frame-shear wall and thin-walled core skew system in the vertical direction, the piecewise continuum technique was used for the structures. Simulating the space coordinate along with the height direction of the structure as the time coordinate, the state space equations are derived. The state vector equations can be calculated according to the state space theory and the initial state vector can be obtained from the boundary conditions of the structure. Then the natural frequency of the structure can be derived as well. Compared with other methods, the results demonstrate that the proposed method is simper to compute, more accurate, and more convenient for applications.

1 INTRODUCTION

With the increasing height of the buildings, the structures become more and more complicated. The skew structures composed by frames, shear walls, and thin-walled cores which are connected by the rigid floors become more and more popular. Because the forces along three dimensions are flexure–torsion coupled, the mechanics analysis of this kind of structures is comprehensive. With the increasing height, the vertical members are often designed to be with the varied sections in order to save the material and decrease the self-weight, and the mechanic analysis of this kind of structure becomes more comprehensive (Bao 1992).

The static analysis of the structure has been studied by using the initial parameter method (Hu & Zhang 2004) and the state space method (Hu & Zhang 2006), but there are relatively few researches for free vibration analysis for the structure. In this paper the state space method would be used to calculate the natural frequency of the skew combined building structure, in order to provide a numerical analysis method with a higher precision and simpler computation.

The basic assumptions as follows are adopted to build the calculation model (Bao 2001):

1. The floor stiffness is infinitely great in plane, but it is zero out of plane.
2. The members in the structure have stepped variable cross-sections.
3. The structural plane layout remains unchanged along with the height of the structure.

In this paper, by using the traditional continuum assumptions as above, the skew combined structure with the stepped parameters is simplified as a flexure–torsion beam with the stepped sections. In other words the shear wall and the thin-walled core are considered as combined cantilever members with the stepped sections, the total frame is considered as the elastic supports (Bao 1991). According to the conditions of physics and equilibrium, introducing deformations and initial forces as state vectors the state space equations are derived, the state space expressions of horizontal vibration for the tall building with stepped parameters have been derived. The solution of non-homogeneous equations is given by the iteration computing scheme. Combined with the boundary conditions of the structure, the frequency equation is obtained and the vibrational frequencies are obtained. The calculation process can be realized by programming in MATLAB language.

2 ESTABLISHMENT OF THE STATE SPACE EXPRESSION

The structure is divided into n segments and in every segment the structure has constant parameters. The global coordinate system and the local coordinate system are established in the structure. The equilibrium equation under the global coordinate system for the micro-segment is established, which is shown in Figure 1.

$$\{Q'\} = -[M_k]\frac{\partial}{\partial t^2}\{U\} = -[M_k]\{\ddot{U}\} \tag{1}$$

In the formula,

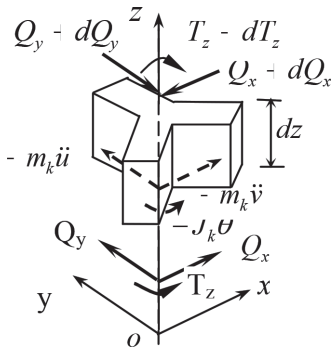

Figure 1. Micro section of segregation.

$$\{U\} = \{u \quad v \quad \theta\}^T, \{Q\} = \{Q_x \quad Q_y \quad T_z\}^T,$$
$$[M_k] = diag(m_k \quad m_k \quad J_k)$$

where u, v, and θ are the displacements of the mass center along x axis, y axis, and the torsion angle about z axis, respectively, Q_x, Q_y, T_z are the total shear along x axis, y axis, and the total torsion about z axis, respectively, m_k and J_k are the distributed mass and the moment of inertia of the segments, respectively.

For the i-th member in the segment, which is shown in Figure 2, including a shear wall and a thin-wall core), the relationships of every basic variable in the local coordinate system are as follows:

$$\begin{cases} \{\bar{U}_i'\} = \dfrac{\partial}{\partial z}\{\bar{U}_i\} \\ \{\bar{M}_i\} = -[D_{ik}]\{\bar{U}_i''\} = -[D_{ik}]\dfrac{\partial}{\partial z}\{\bar{U}'\} \\ \{\bar{Q}_i\} = -[D_{ik}]\{\bar{U}'''\} + [D_{tik}]\{\bar{U}'\} \\ \qquad = \dfrac{\partial}{\partial z}\{\bar{M}\} + [D_{tik}]\{\bar{U}'\} \end{cases} \tag{2}$$

where,

$$[D_{ik}] = E\begin{bmatrix} I_{yik} & & \\ & I_{yxk} & \\ & & I_{\omega ik} \end{bmatrix} [D_{tik}] = \begin{bmatrix} 0 & 0 & 0 \\ 0 & 0 & 0 \\ 0 & 0 & GJ_{dik} \end{bmatrix}$$

where I_{yi}, I_{xi} are the moment of inertias of members for their local coordinate system, $I_{\omega i}$ is the section moment of inertia, and J_{dik} is St. Venant constant of torque.

For the j-th frame in the segment, which is shown in Figure 3, the relationships of every basic variables in the local coordinate system are as follows:

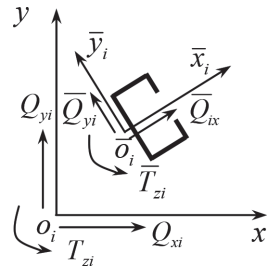

Figure 2. Whole and local co-ordinate systems (a).

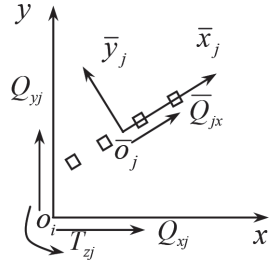

Figure 3. Whole and local co-ordinate systems (b).

$$\begin{cases} \{\bar{U}_j'\} = \dfrac{\partial}{\partial z}\{\bar{U}_j\} \\ \{\bar{Q}_i\} = [D_{Fjk}]\{\bar{U}'\} \end{cases} \tag{3}$$

In the formula,

$$\begin{cases} \{\bar{U}_j\} = \{\bar{u}_j \quad 0 \quad 0\}^T \\ \{\bar{Q}_j\} = \{\bar{Q}_{xj} \quad 0 \quad 0\}^T \end{cases}, \ [D_{Fjk}] = \begin{bmatrix} C_{Fjk} & 0 & 0 \\ 0 & 0 & 0 \\ 0 & 0 & 0 \end{bmatrix}$$

where C_{Fjk} is the anti-push rigidity of the j-th frame in the segment.

The conversion relations of the displacements between the global coordinate system and the local coordinate system are as follows:

$$\left.\begin{aligned} \{U\} &= [T_i]\{\bar{U}_i\} \\ \{U\} &= [T_j]\{\bar{U}_j\} \end{aligned}\right\} \tag{4}$$

In the formula,

$$[T_i] = \begin{bmatrix} \cos\alpha_i & -\sin\alpha_i & 0 \\ \sin\alpha_i & \cos\alpha_i & 0 \\ x_i^0\sin\alpha_i - y_i^0\cos\alpha_i & x_i^o\cos\alpha_i + y_i^o\sin\alpha_i & 1 \end{bmatrix}$$

The relationship of the basic unknown quantities under the global coordinate system and the local coordinate system are as follows:

$$\left.\begin{aligned}\left\{\bar{U}_i'\right\}&=\left[T_i\right]^T\left\{U_i'\right\}\\ \left\{\bar{U}_j'\right\}&=\left[T_j\right]^T\left\{U_j'\right\}\end{aligned}\right\} \tag{5}$$

$$\left\{\bar{M}_i\right\}=-\left[D_{ik}\right]\left[T_i\right]^T\frac{\partial}{\partial z}\left\{U'\right\} \tag{6}$$

$$\left.\begin{aligned}\left\{\bar{Q}_i\right\}&=\left[T_i\right]^T\frac{\partial}{\partial z}\left\{M_i\right\}+\left[D_{tik}\right]\left[T_i\right]^T\left\{U_i\right\}\\ \left\{\bar{Q}_j\right\}&=\left[D_{Fjk}\right]\left[T_j\right]^T\left\{U'\right\}\end{aligned}\right\} \tag{7}$$

Letting,

$$\begin{aligned}\left[A_k\right]&=\sum_i\left[T_i\right]\left[D_{ik}\right]\left[T_i\right]^T\\ \left[B_k\right]&=\sum_i\left[T_i\right]\left[D_{tik}\right]\left[T_i\right]^T+\sum_j\left[T_j\right]\left[D_{Fjk}\right]\left[T_j\right]^T\end{aligned} \tag{8}$$

The relationship of the basic unknown quantities of the k-th segment is as follows:

$$\begin{cases}\dfrac{\partial}{\partial z}\left\{U\right\}=\left\{U'\right\}\\ \dfrac{\partial}{\partial z}\left\{U'\right\}=-\left[A_k\right]^{-1}\left\{M\right\}\\ \dfrac{\partial}{\partial z}\left\{M\right\}=\left\{Q\right\}-\left[B_k\right]\left\{U'\right\}\\ \dfrac{\partial}{\partial z}\left\{Q\right\}=-\left[M_k\right]\left\{\ddot{U}\right\}\end{cases} \tag{9}$$

The displacements and the internal forces are related to time and coordinate when the structure is under the natural vibration, so their form can be written as follows:

$$\begin{cases}\left\{U\right\}=\left\{\hat{U}\right\}\sin\left(\varpi t+\varphi\right)\\ \left\{U'\right\}=\left\{\hat{U}\right\}\sin\left(\varpi t+\varphi\right)\\ \left\{M\right\}=\left\{\hat{M}\right\}\sin\left(\omega t+\varphi\right)\\ \left\{Q\right\}=\left\{\hat{Q}\right\}\sin\left(\omega t+\varphi\right)\end{cases} \tag{10}$$

Then the parameters in Equation (10) are transformed to the dimensionless form, the vibration equation can be written in matrix form as follows:

$$\begin{Bmatrix}\dfrac{d}{d\xi}\left\{X_1\right\}\\ \dfrac{d}{d\xi}\left\{X_2\right\}\\ \dfrac{d}{d\xi}\left\{X_3\right\}\\ \dfrac{d}{d\xi}\left\{X_4\right\}\end{Bmatrix}=\begin{bmatrix}0 & E & 0 & 0\\ 0 & 0 & -\left[\delta_k\right] & 0\\ 0 & -\left[\gamma_k\right] & 0 & E\\ \left[\beta_k\right] & 0 & 0 & 0\end{bmatrix}\begin{Bmatrix}\left\{X_1\right\}\\ \left\{X_2\right\}\\ \left\{X_3\right\}\\ \left\{X_4\right\}\end{Bmatrix} \tag{11}$$

In the equation, $\xi=z/H$

$$\left.\begin{aligned}\left\{X_1\right\}&=\left\{\frac{\hat{u}}{H}\quad\frac{\hat{v}}{H}\quad\hat{\theta}\right\}^T\\ \left\{X_2\right\}&=\left\{\hat{u}'\quad\hat{v}'\quad H\hat{\theta}'\right\}^T\\ \left\{X_3\right\}&=\left\{\frac{H}{D^*}\hat{M}_x\quad\frac{H}{D^*}\hat{M}_y\quad\frac{H^2}{D^*}\hat{M}_z\right\}^T\\ \left\{X_4\right\}&=\left\{\frac{H^2}{D^*}\hat{Q}_x\quad\frac{H^2}{D^*}\hat{Q}_y\quad\frac{H^3}{D^*}\hat{T}_z\right\}^T\end{aligned}\right\}$$

$$\left[\gamma_k\right]=\frac{H^2}{D^*}\left[B_k\right]\left[\beta_k\right]=-\frac{H^4\varpi^2}{D^*}\left[M_k\right]$$

$$\left[\delta_k\right]=D^*\left[A_k\right]^{-1}$$

where H is the total height of the structure, D^* is a specific value used as the structural characteristic stiffness, and E is a unit matrix with three-order.

Equation (11) can be simplified as follows:

$$\frac{d}{d\xi}\left\{X\right\}=\left[A_{2k}\right]\left\{X\right\} \tag{12}$$

where

$$\left\{X\right\}=\left\{\left\{X_1\right\}^T\quad\left\{X_2\right\}^T\quad\left\{X_3\right\}^T\quad\left\{X_4\right\}^T\right\}^T$$

$$\left[A_{2k}\right]=\begin{bmatrix}0 & E & 0 & 0\\ 0 & 0 & -\left[\delta_k\right] & 0\\ 0 & -\left[\gamma_k\right] & 0 & E\\ \left[\beta_k\right] & 0 & 0 & 0\end{bmatrix}$$

The formula is the state space expression for free vibration analysis of the k-th segment in the frame-shear wall-thin core skew combined structure with the stepped parameters. The solution is denoted as follows:

$$\left\{X\right\}=e^{A_{2k}\left(\xi-\xi_{k-1}\right)}\left\{X_{k-1}\right\} \tag{13}$$

where $\{X_{k-1}\}$ is the vector formed by no dimensional total displacement, rotation, moment of

shear wall, total frame, and thin walled core at the bottom of the k-th segment structure.

3 THE STATE TRANSFER MATRIX AND ITS CALCULATION

The matrix form of solution for the state space expression of free vibration can be expressed as follows:

$$\{X\} = \left[N_k\left(\xi - \xi_{k-1}\right)\right]\{X_{k-1}\} \tag{14}$$

where $\left[N_k\left(\xi - \xi_{k-1}\right)\right] = e^{A1_k(\xi-\xi_{k-1})}$.

This is the state transfer matrix of free vibration analysis for the frame-shear wall-thin walled core skew combined structures with the stepped parameters.

In this paper, the exponential matrix is calculated by means of the method of power series expansion as follows:

$$e^{[A_{1k}](\xi-\xi_{k-1})} = E + [A_{1k}](\xi - \xi_{k-1}) + \frac{[A_{1k}](\xi-\xi_{k-1})}{2!} + \frac{\left([A_{1k}](\xi-\xi_{k-1})\right)^3}{3!} + \frac{\left([A_{1k}](\xi-\xi_{k-1})\right)^4}{4!} + \cdots \tag{15}$$

In the calculation process of the state transfer matrix, the exponential matrix needs to be solved emphatically.

Quite a few experts have discussed about the calculation of these functions. In the paper, some techniques are adopted to simplify the calculation and make the results meet the precision requirement.

4 CALCULATION OF THE NATURAL FREQUENCY

Note that $[N_k] = \left[N_k\left(\xi_k - \xi_{k-1}\right)\right]$, which is called by the state transfer matrix of the k-th segment in the skew combined structure. Then it can be obtained by using recursive Equation (14) as follows:

$$\{X(1)\} = [N]\{X(0)\} \tag{16}$$

where $[N] = [N_n][N_{n-1}]\ldots[N_1] = [n_{ij}]_{12\times12}$, the square matrix is the whole state transfer matrix.

The boundary conditions of structure are as follows:

The bottom of structure is fixed, so

$$\begin{cases}\{X_3(1)\} = 0\\ \{X_4(1)\} = 0\end{cases} \tag{17}$$

The top of structure is free, so

$$\begin{cases}\{X_1(0)\} = 0\\ \{X_2(0)\} = 0\end{cases} \tag{18}$$

A binary linear equation group can be established by combining the Equation (17) and the boundary conditions of Equation (18).

$$\begin{bmatrix} n_{77} & n_{78} & \cdots & n_{7,12}\\ n_{87} & n_{88} & \cdots & n_{8,12}\\ \vdots & \vdots & \ddots & \vdots\\ n_{12,7} & n_{12,8} & \cdots & n_{12,12}\end{bmatrix}\begin{Bmatrix}\{X_3\}\\ \{X_4\}\end{Bmatrix} = \begin{Bmatrix}0\\0\\\vdots\\0\end{Bmatrix} \tag{19}$$

Only when the coefficient determinant including the natural frequency is zero, the Equation (19) has nonzero solution. According to this condition the natural frequency can be obtained.

5 EXAMPLE

There is a three-story structure with 3.0 m storey height. The parameters of the structure are as follows: $E = 2.5 \times 10^7$ kN/m^2, $\mu = 0.1$.

The wall thickness of the thin-walled core and the shear-wall are 0.15 m and 0.2 m, respectively. The section size of the column and the beam in frame are 0.5 m × 0.5 m and 0.6 m × 0.24 m, respectively.

The distributed mass are as follows: $m_1 = m_2 = 2$t/m, $m_3 = m_4 = 3$t/m. The moment of inertia is 398.7 t·m^2/m.

The plane layout of the third floor is same as other floors, but the stiffness and the mass are r times as other floors (which is shown in Fig. 4).

It can be seen from Table 1 that the results of the two calculation methods are very close to each other. It is shown that the free vibrations analysis

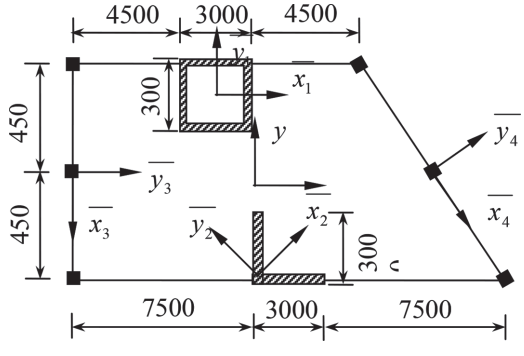

Figure 4. Plane layout of the structure.

Table 1. Natural frequency.

	r = 1		r = 0.5		r = 0.1	
	This paper	Refs 4	This paper	Refs 4	This paper	Refs 4
1	11.67	11.79	14.41	14.38	20.07	19.77
2	14.02	14.54	18.15	18.75	26.69	24.47
3	14.56	15.01	18.86	19.22	27.67	28.02
4	56.80	56.97	60.07	59.54	70.47	68.11
5	87.39	89.87	92.86	95.40	112.49	110.41
6	88.41	91.08	94.03	96.65	115.50	111.82
7	150.14	149.84	149.67	148.88	140.86	136.99
8	248.53	251.03	245.77	249.20	231.20	228.18

method for frame-shear wall-thin-walled core skew combined structure with the stepped parameters can be analyzed by the state space method, and the calculation results are quite accurate. The state space method has the advantages of clear and simple idea, convenient calculation, high precision, and a well applicability.

The studied achievements of this paper have good practicality and popularity, and they can provide a precise rule for the analysis and the calculation of the skew combined structures.

REFERENCES

Bao, S.H. 1991. Coupled vibrations for tall building cooperating systems by ODE solver. *Journal of Computational Structural Mechanics and Applications* 8(4): 379–386.

Bao, S.H. 1992. Flexure-torsion coupled vibrations for tall building flame-shear wal1-thin walled member cooperating systems. *China Civil Engineering Journal* 2(1): 12–20.

Bao, S.H. 2001. *Newly edited tall building structures*. Beijing: China Hydraulic and Water-Power Press.

Hu, Q.P. & Zhang, H. 2004. The internal parameter method for analysis of frame-shear wall-thin walled cores cooperating systems. *Journal of Hebei Institute of Architectural Science and Technology* 21(3): 37–41.

Hu, Q.P. & Zhang, H. 2006. State space method for the analysis of frame-shear wall-thin walled cores cooperating systems. *Engineering Mechanics* 23(4): 125–129.

This page intentionally left blank

Civil Engineering and Urban Planning IV – Liu et al. (Eds)
© 2016 Taylor & Francis Group, London, ISBN 978-1-138-02903-3

Finite element method analysis—the mechanism of anti-slide piles to reinforce the slope title

De-Bin Ren, Shi-Hai Yu & Jun-Yin Tu
Shenyang Jianzhu University, Shenyang, Liaoning, China

ABSTRACT: To find a kind of safer slope supporting measure, shear strength reduction finite element method is applied on the simulation to the back-slope of some hydropower house. The slope is reinforced using single-row and double-row anti-slide piles, which can be shown by the three-dimensional numerical analysis. It is feasible to apply shear strength reduction finite element method in analyzing this slop.

1 INTRODUCTION

Single-row anti-slide piles used in slope reinforcement cannot ensure the safe reliability of slope engineering when there is a big landslide thrust. To take a kind of safer slope supporting measure, in this research, there is a shear strength reduction finite element method applied in the simulation to the back-slope of some hydropower house. Compared with the safety factors above and those reached from the limit equilibrium analysis method, and after the three-dimensional numerical analysis to reinforced slope using single-row and double-row anti-slide piles, it is feasible to apply shear strength reduction finite element method in analyzing this slop. Moreover, adopting double-row anti-slide piles used in the slope reinforcement gets better performance than single-row anti-slide piles, because in kind of bending moment, displacement, and shear stress of piles, the figures measured from double-row anti-slide are less than those from single-row anti-slide piles in different degree. Under the premise of ensuring the safe reliability of anti-slide piles used in the slope reinforcement engineering, simulating slope reinforcement supporting measure can exert significant influence in guiding engineering and reducing the unnecessary waste.

1.1 *Introduction*

With the rapid development of the economic construction, more and more economic activities have been developed in mountainous areas, such as building roads, exploiting of mines, constructing of hydropower stations, and so on which lead to the difficult problems about the slope geological hazards (Lu et al. 2006) follow. So it is an important research project in geotechnical engineering world to find the way to manage the slopes as a protective measure. Recently single-row anti-slide piles as an important way in the slope supporting measure have been widely used in the engineering field (Ou & Wu 2008). But when the slope reinforcement cannot ensure the stability of slope, we would have to increase another row of anti-slide piles, which constitutes double-row anti-slide piles (Shen et al. 2008) Double-row anti-slide piles supporting structure is a new style supporting system which comes from single-row anti-slide piles and exploits "space effect". Generally, the type of double-row anti-slide piles can be divided into two classes where consists of double-row anti-slide piles with coupling beams or not. Because we do not know how to distribute landslide trust force and affect each other with pillar from front and back. Although, double-row anti-slide piles have started using in engineering, we have not a series of researches about it in academic circles at home and abroad. The traditional calculation method about anti-slide piles can bring and cause a lot of problems, which have neither considered interactions with piles-soil nor ensured the size and distribution shape of landslide trust force in soldier piles, leading to the designed calculation in deformation and internal force differ from reality in soldier pile. So it is necessary to analyze the fixed slope in this way named finite element method combined with the way of shear strength reduction. This article will make use of the finite element method to analyze the stability of slope (Ren et al. 2008; Zienkiewieo et al. 1975; Zheng et al. 2001) behind the powerhouse of hydroelectric station, later, based on strength reduction method (Zhao 2005; Cheng et al. 2007; Wu et al. 2006) using three-dimensioned numerical analysis to analyze the slope, which is underpinned by single-row anti-slide piles or double-row anti-slide piles,

at the same time, which can help us to analyze and find the difference of shapes and properties. After the operation of power, the slope behind the hydropower station repeatedly appears the crack of slope land and collapse. The phenomenon of slope deformation and distraction is obvious, which needs to take protecting measures at once, in order to prevent the slope developing from partial sliding to whole sliding. The gradient for the slope behind the hydropower station is about 1:1.5. Then the ground elevation building area is 230 m. The ground elevation of building area in the back hillside is 230 m–320 m, the edge of slope in back is 60.0 m, the edge of slope in the front is 40.0 m and the depth of foundation is 50.0 m.

2 FINITE ELEMENT ANALYSIS OF SLOPE BASED ON STRENGTH REDUCTION METHOD

2.1 *The basic assumptions for this model and basic structure of soil as well as basic parameters*

When analyzing through finite element method, in order to realize the convenience of calculation and correspond to engineering practice, the calculation model needs to be simplified as follows: (1) Ignore the impact which is brought by construction of supporting measure and ground-water lower and drainage for soil properties; (2) The angle of dilatation is equivalent to zero; and (3) Making use of symmetry we can adopt three-dimensional finite element model to conducting slope stability analysis. Geometrical shape and FEM mesh model. Surrounding soil may give the model some function of restraint, the bounding of model as shown: horizontal restraint on the X direction should be added to the left and right boundaries of model and horizontal on the Y direction should be added to the front and back boundaries of model. Basement in every direction should be restrained, but headpiece is free-surface. (4) Adopting Mohr–Coulomb model (Hu et al. 2008), we can imitate the basic structural system. (5) The calculation area of the finite element model is 160 m × 6.4 m × 90 m. Properties of the soil is listed in Table 1.

2.2 *The result of calculation and analysis*

It is essential to select failure criterion for the shear strength reduction method which concerns the accuracy of the finite element method. The displacement catastrophe at the top of slope regards the overall slope instability as a mark. From the destroying phenomenon shows, slope collapse and the slide body comes into moving state from stable static state simultaneously. Displacement will produce mutation at the top of slope and are accompanied by a dramatic increase in displacement of slide body. This phenomenon corresponds with the concept of slope failure (Lv et al. 2008).

Using postprocessor function of ABAQUS software which bears strong function, we can draw relationship curve between horizontal displacement of nodes at the top of slope and safety factor (as shown in Fig. 1). We can see from Figure 1 when there is a lack of support measure, there is an obvious inflection point between the horizontal displacement of nodes at the top of slope and safety factor for relationship curve, which can indicate the mutilation of displacement on nodes, and then a corresponding safety coefficient is 1.08. According to the project date (Morgenstern & Price 1965), we can the adopt moment balance method to calculating slope safety factor and get results which is 1.09, closing to the slope safety factor calculated by the strength reduction finite element method which illustrates that it is feasible to analyze the slope stability with the finite element method.

3 FINITE ELEMENT ANALYSIS OF SLOPE REINFORCEMENT BASED ON THE STRENGTH REDUCTION METHOD

When the slope is reinforced by single-row anti-slide piles and double-row anti-slide piles, its aim is to research the difference of lateral deformation and stress. We adopt two scenarios to reinforce the slope. Scenario 1: we use single-row anti-slide piles, and the length of piles is 45 m and piles spacing in the same row is 7.5 m. In order to imitate the pile of the real mechanism of action, we adopt a 1 m diameter circular column. Scenario 2: adopting the system of double-row anti-slide piles we choose it that length of the piles is 40 m and diameter of the

Table 1. Properties of the soil.

Property	Sever $\Gamma = kN/m^3$	*Cohesion C* (*kPa*)	Frictional angle Φ' (°)	Modulus of deformation *E* (*MPa*)	Poisson ration ν
Soil	19	12	18	200	0.25
Single-row piles	24			60 000	0.2
Double-row piles	24			60 000	0.2

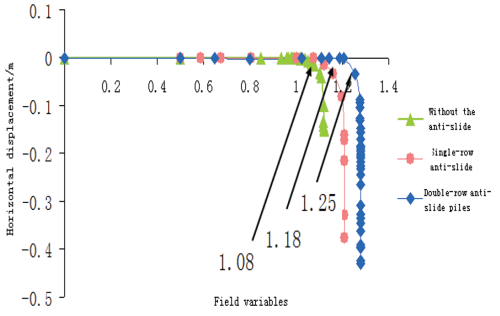

Figure 1. Relationship curve between the displacement of nodes and the change of the field variables.

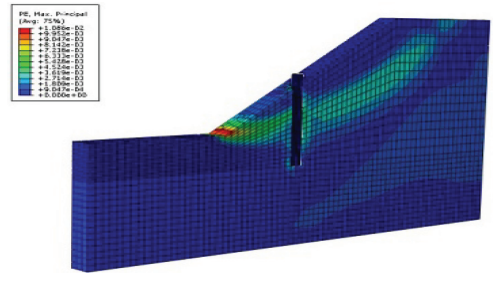

Figure 2. The plastic zone stress map of the single-row anti-slide piles.

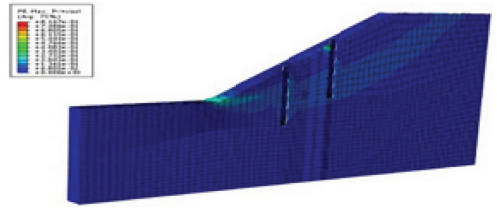

Figure 3. The plastic zone stress map of double-row anti-slide piles.

piles is 0.7 m and the length of front–back piles in row is equal and the stiffness of double-row anti-slide piles is half of the single-row anti-slide piles, meanwhile other parameters do not change. According to the literature (Wu et al. 2008), the distance is 3.5 m (5 d) for the front–back piles in row. We can get displacement distribution for piles, bending moment, and shear force. We should need to facilitate comparative analysis. Column parameters are listed in Table 1.

3.1 *Anti-slide piles to reinforce the slope before and after the comparison of safety factor*

Using postprocessor function of ABAQUS, we should firstly output the plastic zone stress maps at the displacement mutation point which are shown in Figures 2 and 3. Though the comparison and the analysis we can find that double-row anti-slide piles further prevent the slope soil at the upper from sliding down and causing sliding deformation, which hinders the connection of the plastic zone and do not appear the integral circular slip surface. Then we will draw the relationship curve between the displacement of nodes at the top of the slope which is followed by the change of field variables after the slope is reinforced by the single-row anti-slide piles (as shown in Fig. 1). It is known from Figure 1 that in the three cases no anti-slide piles, single-row anti-slides piles and double-row anti-slides piles have obvious infection point in relationship carve between displacement of nodes at the top of the slope and the change of the field variables. Meanwhile, mutational site corresponds to the change of field variables which is a safety factor. It is 1.18 for the safety factor of the single-row anti-slide piles which fits the slope safety level requirement but we can find that this safety factor has significantly smaller than the double-row anti-slide piles on equal conditions. It is 1.25 for the double-row anti-slide piles.

3.2 *The displacement distribution of the anti-slide piles*

Figure 4 is displacement of piles which is based on the analyzing result of the model. From Figure 4 we can know that the front piles and the back piles for double-row anti-slide piles have basically the same displacement variation tendencies. It is 0.6 for the maximum displacement of the front pile head, then it is 0.8 in the back piles. The back pile has greater displacement of pile than the front. Meanwhile, the maximum displacement of the pile head in single-row anti-slides piles is 1.2 m. Around 60% of it is the maximum displacement of the pile head in double-row anti-slides piles. Because the anti-slides piles is similar to the cantilever construction, the slope sliding resistance depends entirely on the elasticity of anti-slide piles embedded in enough depth to bear the earth pressure in the back of the pile and maintains its stability. The embedding depth of the single-row anti-slides is larger than the double-row anti-slides piles. In addition, from the displacement of pile form, the variation tendency of the double-row plies is more gentle than the single-row plies, which explains that the double-row plies is more difficult to lead to the phenomenon of slipping and snap.Thus, it can be seen that the double-row plies are more effective to control slope failure than the single-row piles.

3.3 *The bending moment distribution of anti-slide pile*

The contrast between the double-row anti-slides piles and the single-row anti-slides is shown in Figure 5. You can see in the figure that although the maximum moment for the front files in row and the back piles in row in the double-row files is at about 30 m below the pile top. The front piles and the back piles have great gap for bending moment, which always cannot reach the best working status at the same time. The maximum moment in the back piles in row has larger than the front piles in row, which tells me that it is equal to documentary records (Chen 2001; Bamiehon 2007). By contrasting the bending moment of the double-row anti-slides piles and the single-row anti-slides piles, we can find that the bending moment is zero at the top of piles and the bending moment of the double-row anti-slide piles is smaller than single-row anti-slide piles. It is not the same position for the maximum value of moment of two kinds of anti-slide piles, then we can know that the maximum value moment of the single-row anti-slide piles appears at about 27 m under the top of piles. The distribution of bending moment of anti-slide piles is similar to cantilever beam, then the maximum value of moment will appear at anchorage segment under the sliding surface.

3.4 *Distribution of the shearing force about the anti-slide piles*

It is distribution of shearing force about anti-slide piles in both approaches for Figure 6. From Figure 6 we can know that it is about zero for the shear stress of anti-slide piles at the top of piles in both approaches and that maximum for shear stress is distributed on the sliding surface and about at same position. Above the sliding surface, the shear distribution of loading segment is obviously larger in the single-row anti-slide piles than

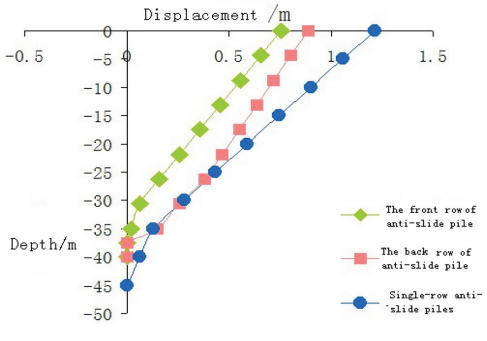

Figure 4. Displacements of piles.

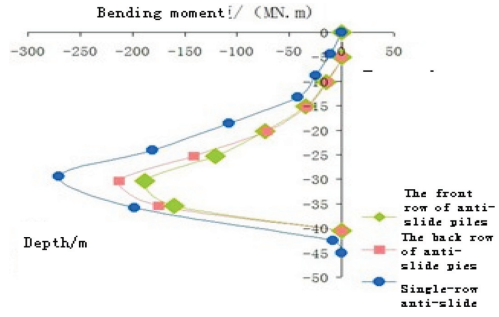

Figure 5. Bending moment of piles.

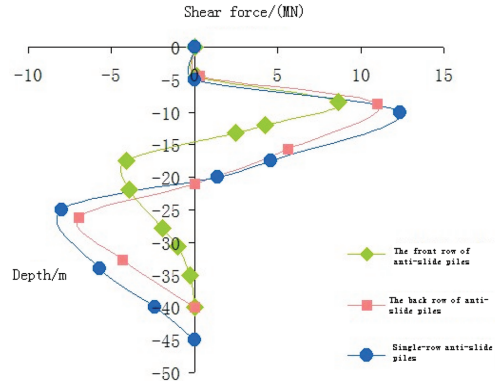

Figure 6. Shear stress of piles.

the double-row anti-slides piles below the sliding surface. The shear distribution of the loading segment in the single-row anti-slide piles is similar to the back anti-slide piles in the double-row piles. For the front piles and the back piles in double-row piles, the maximum of shear distribution can appear at the same position. Then the maximum of shear about the back piles is greater than the front piles. It follows that the distributed situation of displacement shear and bending moment as well as safety factor for the double-row anti-slides piles has a better effect than the single-row anti-slides piles. When landslide thrust force is larger, we should firstly adopt the double-row anti-slides piles in actual engineering.

4 CONCLUSION

Using the finite element method based on the shear strength reduction method and the traditional limit equilibrium method to analyze the stability of the slope. We can get a conclusion by comparing

with the results. It illustrates that the method which is used by this paper and the traditional limit equilibrium method have similar computed result, which indicates that it is feasible to analyze the stability of slope with the finite element shear strength reduction method and that the computed result is trustworthy. For using the single-row anti-slide piles and the double-row anti-slide piles to reinforce slopes, when the same rock and the earth produces landslide thrust with the shear strength reduction method, we should use postprocessor function of the finite element method to get accurately safety factor as well as distribution of displacement about pile, shear and bending moment. The effect of the double-row anti-slide piles is inordinately better than the single-row anti-slide piles.

Because the single-row anti-slide piles are the conventional form which has characters of the definite load conditions and simple construction, we should try to use the single-row anti-slide piles when conditions allow. But when the slope gets a bigger trust, the single-row anti-slide piles which is installed has failing slide-resistance action or cannot meet the requirement of security grade, we can adopt the system of the double-row anti-slide piles. Though computer simulation study we can know that it has an obvious gap for bending moment, shearing force, and displacement in the front-back pile in row, which exists in the support system of the double-row anti-slide piles. So the front–back piles in row have a different thrust to prevent the slippage. According to the different stress in the double-row piles the front piles, and the back piles should adopt a different section size and reinforcement method, as well as we should choose a reasonable spacing about pile in row and achieve the goal of economical and reasonableness in the design about the double-row piles.

REFERENCES

Bamiehon, J.D. 2007. Contribution of the bounding surface plasticity to the simulation of gallery excavation in plastic clays. *Engineering Geology* 64(23): 217–232.

Chen, C.Y. 2001. *Numerical analysis of slope stabilization concepts using piles.* Los Angeles: University of southern California.

Cheng, Y.M., Lansivaara, T. & Wei, W.B. 2007. Three-dimensional slope stability analysis by limit equilibrium and strength reduction methods. *Computers and Geotechnics* 34(3): 137–150.

Hu, X.Z., Gu, X.G., & Li, Y.C., 2008. Application of the modified mohr-coulomb failure criterion in oblique penetration simulation. *Journal of University of Science and Technology of China* 38(11): 1317–1320.

Lu, P.Y., Yang, J, & Han, L.J. 2006. Finite element analysis of double-row piles in consideration of dimensional effect. *Journal of Tianjin University* 39(8): 963–967.

Lv, Q., Sun, Y.H., & Shang, Y.Q. 2008. Slope failure criteria of shear strength reduction finite element method. *Journal of Zhejiang University (Engineering science)* 42(l): 83–87.

Morgenstern, N.R. & Price, V.E. 1965. The analysis of the stability of general slip surface. *Geotechnique* 15(1): 79–93.

Ou, Y.H. Wu, X.T. 2008. A case study on application of one optimal design method of anti-sliding pile. *Chinese Journal of Solid mechanics* 29(1): 115–117.

Ren, D.B., Wei, H., & Jia, H.T. 2008. Study on mechanical properties of glass fiber reinforced cementcomposite plate. *Journal of Shenyang Jianzhu Universit*y: Natural Science 24(6): 1005–1008.

Shen, Y.J. Lv, Q. & Shang, Y.Q. 2008. Effect of Pile row distance on internal stress of double-row anti-slide Piles. *Chinese Journal of Geology Engineering* 30(7): 1033–1037.

Wu, M., Fu, X.D., & Liu, H. 2006. By shear strength reduction method used in slope stability analysis. *Soil Eng. And Foundation* 20(1): 49–52.

Wu, G., Bai, B., & Nie, Q.K. 2008. Research on calculation method of double-row piles retaining structure for deep excavation. *Rock and Soil Mechanics* 29(10): 2753–2758.

Zienkiewieo, C., Humpheson, C., & Lewis, R.W. 1975. Associated and non-associated visco-plasticity and plasticity in soil mechanics. *Geotechnique* 25(4): 671–689.

Zheng, Y.R., Zhao, S.Y., & Shi, W.M. 2001. Some progress of slope stability analysis. *Under Ground Space* 21(4): 263–271. (in Chinese).

Zhao, S.Y., 2005. *Strength reduction finite element method and its application to soil and rock slopes*. Chongqing: Logistical Engineering University of PLA.

This page intentionally left blank

Civil Engineering and Urban Planning IV – Liu et al. (Eds)
© 2016 Taylor & Francis Group, London, ISBN 978-1-138-02903-3

Damage simulation of a concrete column in fire

Song-Hua Tang & Yu-Peng Cui
Key Laboratory of Concrete and Prestressed Concrete Structures of Ministry of Education, Southeast University, Nanjing, China
School of Civil Engineering, Central South University, Changsha, Hunan, China

Ying-She Luo & Shui-Ping Yin
College of Civil Engineering and Mechanics, Central South University of Forestry and Technology, Changsha, Hunan, China

ABSTRACT: Damage mechanics is an effective way to study the damage and failure of the structure. The damage process on fire can be studied by the damage mechanics method. The equations include the damage model, mechanical and heat conduction equations. In this way, the fire response simulation of a concrete column is simulated by ANSYS. The temperature and stress field are obtained, the damage and failure processes are observed from the killing or activating images, and the fire resistance of the column is obtained.

1 INTRODUCTION

Research on the calculation of fire resistance began in 1970s. The calculation is divided into two parts: temperature calculation and mechanics calculation. Some researchers compiled their own programs for the calculation (Ohash & Kodaira 1997; Zha 2003, Terro 1998; Capua & Mari 2007). Some researchers used the commercial FEM software to calculate the fire resistance (Xu 2005; Li 2008; Lin 2006).

Under the fire, the strength of concrete decreases with the temperature increasing, and when the temperature is above 550ºC, steel will lose a greater portion of its strength and stiffness. These changes have been observed by many researchers.

This deterioration of mechanical properties in material is mostly caused by the thermal damage at high temperatures, which should be included in the fire response calculation.

Some researchers have added the thermal damage effect to the fire response analysis. Huang et al. (Huang et al. 2001) put forward the deterioration layer units in the finite element analysis in fire. Cai et al. (Cai et al. 2003) proposed a beam-column unit that considers the material deterioration at high temperatures. Gawin et al. (Gawin et al. 2003) built a concrete constitutive model including the deterioration of materials under high temperatures for the calculation of fire response.

Damage mechanics is an effective way to study the damage and failure of the structure. In damage mechanics, the damage process can be analyzed by the damage model and mechanical equations, and many researchers have used this method to calculate the damage process of the structure (Li et al. 2001; Nechhnech et al. 2002; Tenchev & Purnel 2005; Li & Purkiss 2005).

Tang et al. (Tang et al. 2004) set the residual strength as the damage variable and built a thermal damage model at high temperatures, and this model can calculate up to 1000 ºC. By using this damage model with mechanical and heat conduction equations, a one-dimensional simulation of fire response for a concrete slab was obtained (Tang et al. 2013).

In this paper, a two-dimensional simulation of fire response for a concrete column was obtained by using the above method.

2 DAMAGE SIMULATION

A reinforced concrete column is shown in Figure 1. The size of the column is 305 × 305 × 3800 (mm). The strength of concrete specimens is 30 MPa, and the aggregate is siliceous (Su et al. 1992). The axial load is 343 kN, which is kept constant in the test. The column is exposed to the ASTME119 fire with four faces, as shown in Figure 2, and the temperature function is given by

$$T = 20 + 750\left[1 - \exp\left(-3.79553\sqrt{t}\right)\right] + 170.4\sqrt{t},$$

where the unit of t is hour.

Here, the finite element calculation of the fire response of the column with ANSIS is presented, and the damage process is analyzed. For symmetry, 1/4 of the column is studied and the cross-section is modeled, as shown in Figure 3. The finite element command flow file is programmed and the

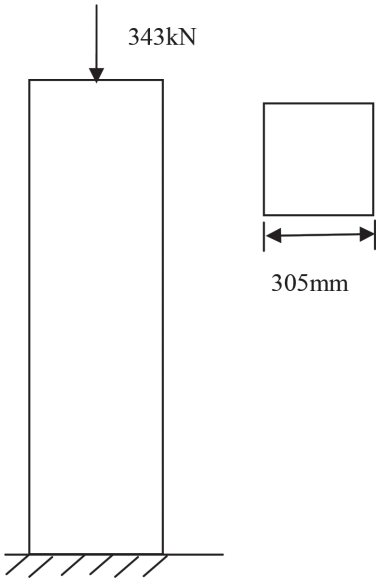

Figure 1. Reinforced concrete column.

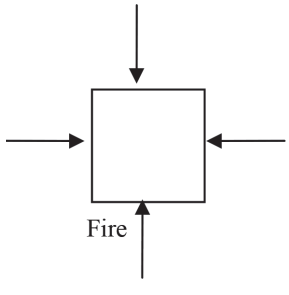

Figure 2. Four faces exposed to fire.

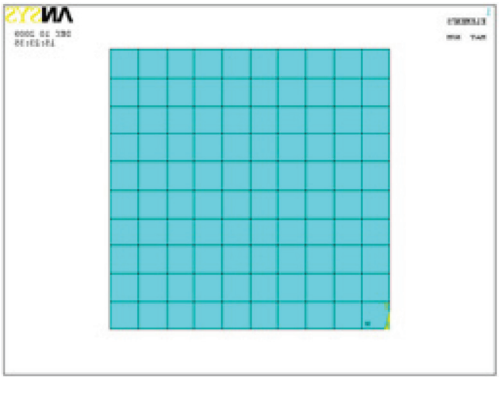

Figure 3. Finite element discretization of the cross-section.

temperature filed, and the stress field and the killing and activating process are calculated.

2.1 *Temperature field simulation*

The size in high direction is far greater than the sizes in the other two directions, so the heat conduction of the column can be analyzed as two-dimensional heat conduction that is unsteady. The following are its heat conduction equation, initial and boundary conditions:

$$\frac{\partial^2 T(x,y,t)}{\partial x^2}+\frac{\partial^2 T(x,y,t)}{\partial y^2} = \frac{1}{\alpha}\frac{\partial T(x,y,t)}{\partial t} \qquad (0\le x\le a, 0\le y\le b)$$

$$T=f(t) \quad x=0 \quad t>0$$

$$T=f(t) \quad x=a \quad t>0$$

$$T=f(t) \quad y=0 \quad t>0$$

$$T=f(t) \quad y=b \quad t>0$$

$$T=F(x,y) \quad 0\le x\le a,\ 0\le y\le b \quad t=0$$

where $\alpha = k/c\rho$ is the thermal diffusion coefficient; k is the thermal conductivity; c is the specific heat capacity and ρ is the density. And

$$f(t)=20+750\left[1-\exp(-3.79553\sqrt{t})\right]+170.4\sqrt{t},$$

which is the ASTME119 standard temperature curve.

For simplicity, the following assumptions are added in addition to the ones of the slab literature (Tang et al. 2013)

1. The temperature field is constant along the axis and irrelevant to the strain, stress and cracks.
2. The plane cross-section assumption.

The temperature field can be calculated with the ANSYS program by applying the above initial and boundary conditions and using the same thermal properties as the slab literature (Tang et al. 2013). Solid 5 unit is chosen to simulate the concrete. And two of the temperature results are shown in Figures 4 and 5.

2.2 *Stress field simulation*

Direct method of the thermal analysis in ANSYS is selected for calculation, i.e. the stress field is obtained with the temperature field at the same time. And two of the stress results are shown in Figures 6–7.

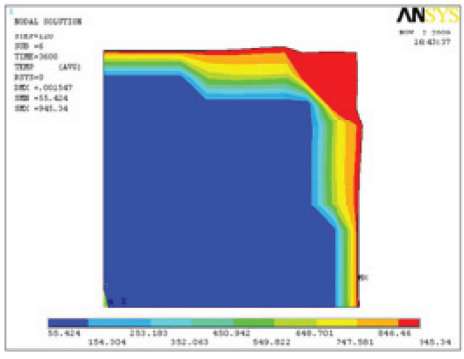

Figure 4. Temperature field (3600 s).

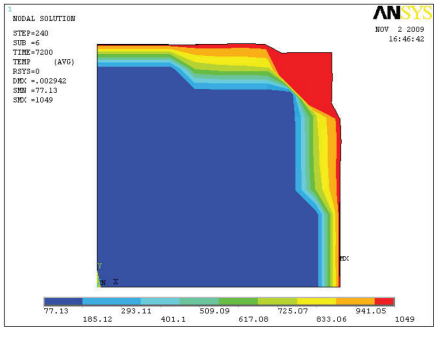

Figure 5. Temperature field (7200 s).

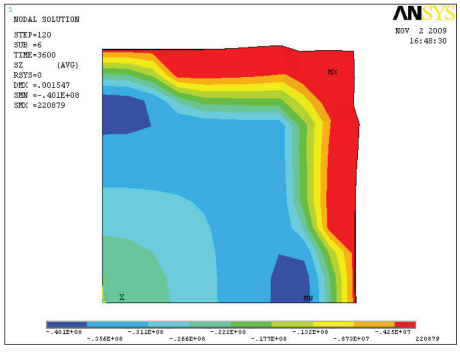

Figure 6. Stress field (3600 s).

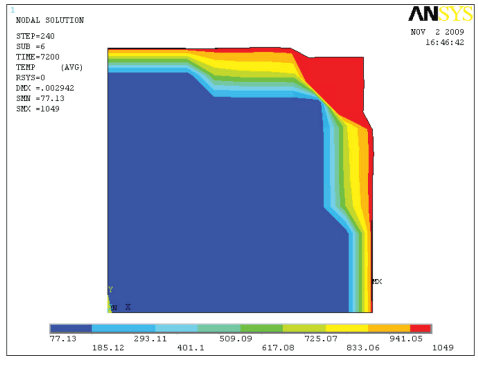

Figure 7. Stress field (7200 s).

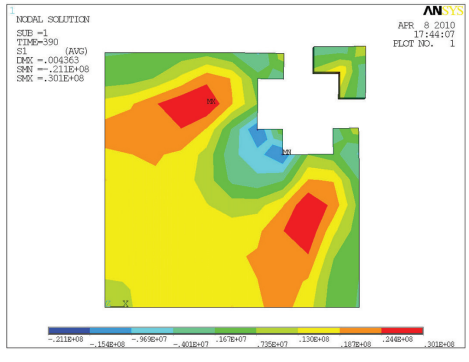

Figure 8. Image of killing or activating elements (390 s).

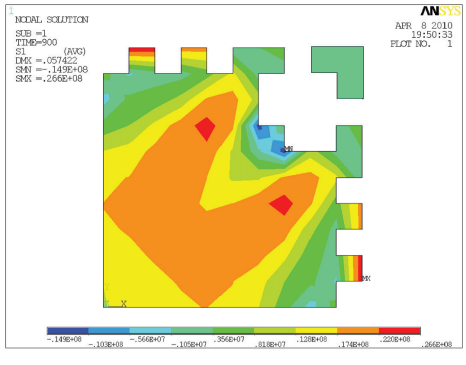

Figure 9. Image of killing or activating elements (900 s).

2.3 *Damage process simulation*

The damage process can be described by using the killing and activating skill in ANSYS. When one unit is damaged, i.e. the stress of this unit reaches the residual strength at this temperature, this unit will be killed. The process of damage and failure are shown in Figures 8–12.

2.4 *Analysis of the results*

1. The images shown in Figures 8–12 are selected from about 600 figures of killing and activating

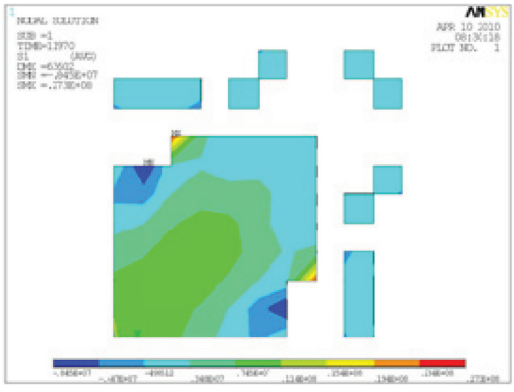

Figure 10. Image of killing or activating elements (11970 s).

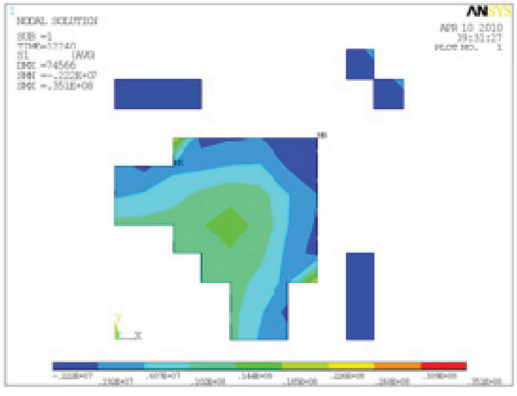

Figure 11. Image of killing or activating elements (12240 s).

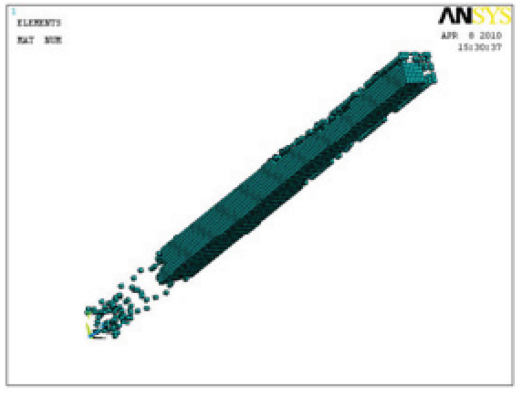

Figure 12. The column at failure.

elements. It can be seen that the residual area of the cross-section decreases gradually: at 12240 s, the residual area is 40% of the original area, i.e. 37.21 mm^2. And at 12270 s (3h24 min), the residual area is 5% of that, i.e. only 4.66 mm^2. At this time, the column cannot support the load and the procedure is ended, which indicates that the column fails and reaches the fire resistance, i.e. 3h24 min.

2. The calculation work of the simulation carried out using ANSYS is large. It takes 72 hours for the simulation of the column, and only 1/4 of the column is simulated. In the case of eccentric compression, when three or two faces exposed to fire, we cannot take 1/4 for analysis, so the calculation work will be larger. It is necessary to program special procedures for the simulation of the fire response.

3 CONCLUSIONS

The fire response of the structure on fire can be simulated by the damage mechanics method through the damage model, mechanical and heat conduction equations. A concrete column is simulated in this way by ANSIS. The temperature and stress field of the cross-section are obtained, and the damage and failure process of the column at high temperatures can be observed from the killing or activating images, and the fire resistance of the column is obtained.

For the asymmetric fire loads and complex structures, the calculation work determined using ANSIS will be larger, so it is necessary to program special procedures for the simulation.

REFERENCES

Capua, D.D. & Mari, A.R. 2007. Nonlinear analysis of reinforced concrete cross-sections exposed to fire. *Fire Safety* 42(2): 139–149.

Cai, J., Burgess, I. & Plank, R. 2003. A generalized teel/reinforced concrete beam column element model for fire conditions, *Engineering Structures* 25(6): 817–833.

Gawin, D., Pesavento, F. & Schrefle, B.A. 2003. Modeling of hydro-thermal behavior of concrete at high temperature with thermo chemical and mechanical material degradation, *Computer Methods in Applied Mechanics and Engineering*. (192): 1731–1771.

Huang, Z.H., Burgess, I.W. & Plank, R.J. 2001. Nonlinear structural modeling of a fire test subjected to high restraint, *Fire Safety* 36(8): 795–814.

Li, L.Y. & Purkiss, J. 2005. Stress-strain constitutive equations of concrete material at elevated temperatures. *Fire Safety* 40(7): 669–686.

Li, Y.C., Wang, H.W., Jiang, S.Q., Zhu, L.F. & Zhang, Z.Y. 2001. Research on the thermal viscoplastic constitutive relation of damaged materials and numerical simulation of circular tubes. *Fracture Explosion and Shock Waves* 21(2): 105–110.

Li, Y.H. 2008. Numerical simulation of reinforced concrete elements component under fire *Building Science* 24(3): 5–8.

Lin, X.Q. 2006. Calculation of the temperature field of reinforced concrete on fire. *Journal of Fujian University of Technology*. 4(3): 291–294.

Nechhnech, W., Meftah, F. & Reynouard J.M. 2002. An elasto-platic damage model for plain concrete subjected to high temperatures, *Engineering structures* (24): 597–611.

Ohash, H. & Kodaira, I.A. 1997. Calculation of load and deformation behavior of Structural elements taking into account 3-dimensional heat flow. *Melbourne: Fire safety science-proceedings of the fifth international symposium*: 1021–1032.

Su, N., Lin, T.D. & Lie T.T. 1992. Fire resistance of reinforced concrete columns. *China Civil Engineering* 25(6): 25–36.

Tang, S.H., Luo, Y.S., Zhou, Z.B. & Wang, Z.C. 2004 Thermal damage evolution of concrete. *Environment Effects on Fracture and Damage*, Zhejiang: Zhejiang University Press: 217–220.

Tang, S.H., Luo, Y.S., Yin, S.P., Li, Y.H., Chen, C. & Tian, F. 2013. Fire Response Calculation Based on Damage Mechanics. *Advanced Materials Research* (639–640): 1193–1199.

Tenchev, R. & Purnel, P. 2005. An application of a damage constitutive model to concrete at high temperature and prediction of spalling. *International Journal of Solids and Structures*. 42(26): 6550–6565.

Terro, M.J. 1998. Numerical modeling of the Behavior of Concrete Structures in Fire. *ACI Structural Engineering*, 95(2): 183–193.

Xu, Y.Y. 2005. Numerical simulation of reinforced concrete columns under elevated temperature, *Building Science*. 21(6): 41–44.

Zha, X.X. 2003. Three-dimensional non-linear analysis of reinforced concrete members in fire. *Building and Environment* 38(2): 297–307.

This page intentionally left blank

Civil Engineering and Urban Planning IV – Liu et al. (Eds)
© 2016 Taylor & Francis Group, London, ISBN 978-1-138-02903-3

Numerical analysis of foundation properties in a large artificial mountain

Wen-Dong Wang
Department of Geotechnical Engineering, Tongji University, Shanghai, China

Zhi-Rong Ye
Architectural Design and Research Institute, Tongji University, Shanghai, China

Kun Zeng
College of Civil Engineering, Tongji University, Shanghai, China

Cheng Zhao
Department of Geotechnical Engineering, Tongji University, Shanghai, China

He-Feng Chen & Hong-Wei Lu
Architectural Design and Research Institute, Tongji University, Shanghai, China

ABSTRACT: Based on the control of foundation strength, foundation deformation and stability of the Longhu piled mountain project in Zhengzhou, this paper aims at establishing a scientific and perfect design method and calculation system for the piled mountain project by theoretical and numerical analysis. The results indicate that the stability control consists of the mountain slope, the integral of slope and foundation, and foundation stability, which is influenced by the slope gradient, water level, soft soil layer and other factors. Large three-dimensional numerical analysis method can directly predict the final foundation deformation, analyze deformation law of foundation accurately, and provide a favorable reference for reducing the uneven settlement. By combining the strength growth theory with permission load method, the strength of foundation soil is controlled, which guarantees the effective utilization of the characteristics of soil consolidation and ensures the safety of the project.

1 INTRODUCTION

More and more cities have started to build artificial landscaping engineering to improve the urban living environment, which not only improves the city's image and solves the problem of solid waste disposal, but also provides a place for relaxation (Qi 2002; Wang et al. 2009; Meng & Wang 2012). However, during the piling construction, there exist some engineering geological problems such as uneven foundation settlement, shear destruction and slope failure instability (Gu et al. 2011; Liao 2014; Liu et al. 2004). So it is important to find the scientific design method and calculation system to choose the appropriate foundation treatment method and slope reinforcement method to ensure the safety of the artificial landscaping engineering.

The safety of the artificial landscaping engineering can be controlled by the following three aspects: strength of the foundation, deformation of the foundation and stability of the foundation. Many scholars (He 2007; Tang 2011; Zhao et al. 2011) have used finite element calculation software, such as ANSYS, FLAC and PLAXIS, to calculate the deformation of soil foundation and fill slopes. As a result, the design method of the artificial landscaping engineering can be achieved. Because of the complexity of the piling construction, today's study is usually based on a single problem but not on the system problem. In this paper, based on the piling construction of LongHu Park in Zhenzhou City, we use the software GEO-SLOPE to control the stability of the slope, foundation and the whole field, and use the numerical software ABAQUS to calculate the deformation of the foundation and the surrounding buildings. Besides, we also use the foundation intensity growth theory to control the strength of the foundation and the loading rate. This paper provides the whole design method of piling construction, which could provide useful information on similar engineering.

2 PROJECT OVERVIEW

2.1 *Background*

The project was conducted in the east-north area of LongHu Park in Zhenzhou City, including the Outer Ring Road, the Middle Ring Road and the Inner Ring Road around the LongHu Park in city planning. The Outer Ring Road was built, but the other roads have not yet been built. According to the design, parts of the roads will cross the mountain by using the buried tunnel design. The west of the mountain is close to the outer ring of Dragon Park, the north of the mountain is close to The First Street of Longyuan. In the mountain design, there are plans to utilize bulldozers to build the mountain and simulate the natural forest, which could make park space as a whole. The peak lies between the Middle Ring Road and Inner Ring Road, the distance from the mountain to the road is about 180 m, the height of the peak is about 49 m, and there are four secondary peaks, which form one-four basic skeletons. The mountain plan is as follows: the height of the peak is 49 m; the height of the secondary peaks is 15 m, 19 m, 15 m and 19 m; the bottom area of the mountain is about 351337 m^2; the length of the mountain from the east to the west is about 950 m, the length of the mountain from the south to the north is about 799 m; the degree of the mountain slope ranges from 10°to 20°. The sketch of the mountain is shown in Figure 1.

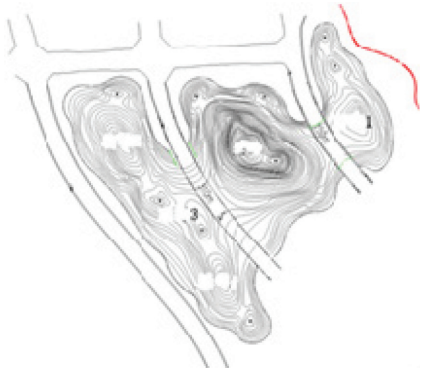

Figure 1. Sketch of Long-Hu Mountain.

2.2 *The engineering geological survey*

According to the result of geological drilling, *in situ* test and soil test, the newly sedimentary strata spread over from the surface to about 7 m; the quaternary Holocene alluvial strata spread over from 7 m to 30 m, and the ingredients of the soil are silt clay, silt and silt fine sand; the late Quaternary Pleistocene alluvial strata spread over from 30 m to 80 m, and the ingredients of the soil are silt and silt clay. According to the geological age and physical-mechanical properties, the soil within 80 m depth can be divided into nine types of engineering geological unit. The ground water mostly exists in the fourth and fifth sand layers, which is due to the strong water permeability of the sand. The stable groundwater depth is found to be about 6 m (the altitude is about 80 m) during the analysis. The physical-mechanical properties of different sands are as follows (Table 1): the permeability of the second and third sand layers is low, in order to speed up the consolidation of the foundation soil during loading and improve the strength of the foundation soil. We plan to insert the plastic draining board, whose length is about 9 m and pass through the third silt clay. At the same time, we pave the sand cushion in order to increase the way of the pore water discharge, shorten the distance of drainage, restrain the growth of excess pore water pressure and improve the mechanical properties of soil.

Table 1. The physical and mechanical indexes of foundation soil.

Layer	Soil type	Thickness (m)	Density (g/cm^3)	C (KPa)	φ (°)	Compression modulus (MPa)	Poisson's ratio	Bearing capacity value (KPa)	Permeability coefficient K (m/d)
(1)	Miscellaneous fill	1.5	19.55	12	18.5	9.0	0.3	–	–
(2)	Silt	3.7	19.55	12	18.5	9.0	0.3	140	0.5
(3)	Silt clay	1.3	19.33	20	15.5	3.5	0.3	90	0.1
(4)	Silt sand with silt	9	20.74	3.0	28.0	14.0	0.3	160	3.0
(5)	Sand	8.1	20.52	0.0	30.0	24.0	0.3	210	8.0
(6)	Silt with silt clay	5.7	20.52	24.0	16.5	15.5	0.3	220	0.1
(7)	Sand	7.2	20.52	0.0	30.0	30.5	0.3	300	9.0
(8)	Silt clay with clay	14.1	20.11	52.5	13.5	15	0.3	260	0.1
(9)	Silt clay with clay	9.4	20.19	50	13	15.5	0.3	270	0.1

The embankment of heaping mountain was excavated from the area of Dragon Park, in which the excavated soil mostly contained the second and third silt and silt clay, and the physical and mechanical indexes of the soil were determined. Adopting the indexes of the soil after remodeling and compacting, we obtained the Cohesion ($c = 12$ kPa) and internal friction angle ($\varphi = 18.5°$) from the laboratory test.

3 NUMERICAL ANALYSIS OF THE STABILITY OF HEAPING MOUNTAIN

During the analysis of the stability of heaping mountain, dimensional calculation method based on the limit equilibrium theory was used to calculate the most unfavorable factor of safety through analyzing the stability of different sections of the mountain. Some analysis methods such as Sweden Arc Method, Bishop Method, Janbu Method and Morgenstern-Price method were used to calculate the most unfavorable factor of safety. The stability of the mountain slope and the foundation are checked by the numerical analysis software Geo-Slope. In order to avoid the appearance of geological disasters such as landslide and foundation instability during the process of heaping mountain and after finishing the construction, we must control the favorable factor of safety. For example, we analyze the largest slope section by simulating the slope, analyzing the stability of the slope and discussing the factors that affect the stability of the slope. We import the data of the most disadvantaged sections into the Geo-Slope and create a model. The width of the foundation is two times the width of the mountain. The material parameters of every soil were built according to the physical and mechanical parameters of the foundation soil. The groundwater level is 6 m under the surface.

Through searching for the most unfavorable sliding surface of the slope, some results were found, as shown in Figure 2. The result of the calculation indicates that the most unfavorable sliding surface slope lies on the upper part of the slope and is close to the "projection" position, and the value of the sliding safety factor is 1.041. Through further analysis, we found that the value of the safety factor would increase when the height of the mountain water line is over the sliding surface. As a result, we should ensure the smoothness of the drainage channels during heaping mountain. Through searching for the most unfavorable sliding surface of the foundation and slope, some results were found, as shown in Figure 3. We could see that the toe lies on the most unfavorable sliding surface, and the failure type is the same as the cohesive slope failure mode that is existing. The most unfavorable

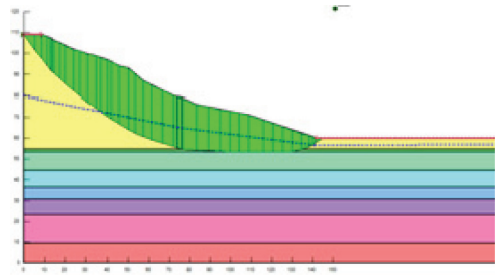

Figure 2. The most unfavorable sliding surface of the slope.

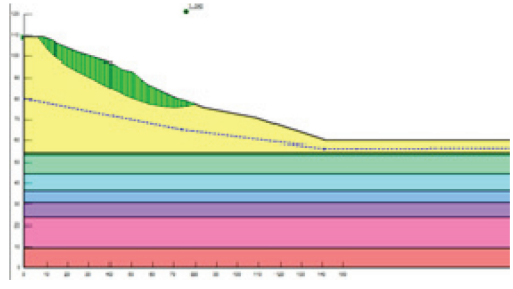

Figure 3. The most unfavorable sliding surface of the slope and the foundation.

sliding surface passes through the third weak layer and the groundwater line, and the existence of the weak layer will weaken the stability of the whole mountain. The value of the sliding safety factor is 1.044, which is close to the value of the slope sliding safety factor. We use the Circular Slide Method to analyze the stability of the foundation and avoid the instability failure of the foundation under loading on a large scale. Through searching for the most unfavorable sliding surface of the foundation, some results were found, as shown in Figure 4. We could see that the most unfavorable sliding surface affects on a large scale, which is bad to the surroundings, and when it appears, we must avoid it. The value of the sliding safety factor is 1.702, which is to some extent larger than the two values that have been referred.

From the above analysis, we could see that the sliding surface not only itself is prone to instability, but also affects the stability of the foundation and the slope. We could find that the value of the safety factor is lower than the value obtained from the engineering experience. The average of the section slope is about 20° and the angle of some parts reach to 24°. The value of the safety factor can be raised by improving the strength of the foundation, decreasing the average angle of the slope

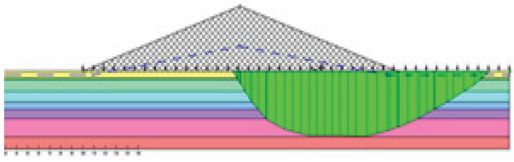

Figure 4. The most unfavorable sliding surface of the foundation.

and reinforcing the part that has a big angle of the slope. Taking the result and cost into consideration, we could choose the plan that decreases the average angle to 17° and increases the safety factor to 1.211.

4 GROUND DEFORMATION ANALYSIS

Due to the uniform loading during the piling construction, and because the post-load is larger, the foundation can produce not only large deformation, but also uneven settlement, which will have a great influence on the mountain surrounding the existing buildings. The traditional manual method of foundation settlement deformation evaluates only a specific location and cannot reflect the overall deformation and the trend of the reaction. So, it is necessary to determine mountain deformation based on the numerical simulation analysis. The calculation model is simplified and the ABAQUS6.11 software is used to obtain the deformation of the ground and the surrounding buildings. Because layered compaction is used in mountain design, according to the existing engineering practice, in the calculation of foundation deformation, the deformation of the mountain itself is not considered, and the deformation of the piled mountain is produced mainly by the foundation settlement.

Through the multiple choice of the appropriate size of the foundation model, it is ensured that the foundation of the boundary effect is small, close to the engineering practice. Finally, the geometric size of the foundation model is extended to a depth of one time, and the depth of the foundation is 2.4 times the height of the mountain. The foundation soil is used in the Mohr-Coulomb model, the material parameters are based on the survey report, and the elastic model is three times the compression modulus. The mountain and the foundation model are shown in Figure 5. *In situ* stress balance after gravity load on the mountain, in order to ensure the convergence, is consistent with the actual working condition and the applied gravity load step. By calculation, the deformation of the site is shown in Figure 6.

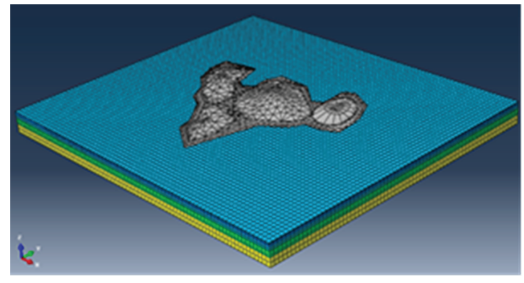

Figure 5. Numerical calculation model.

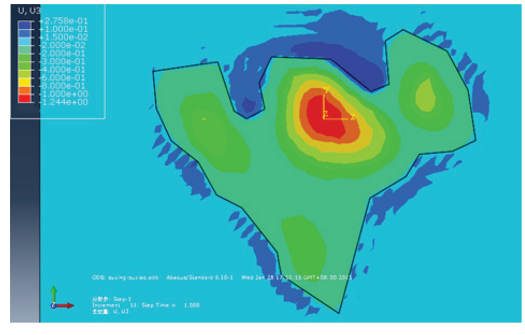

Figure 6. Site settlement cloud map.

As can be seen from the figure, the greater the absolute elevation of the mountain, the greater the foundation settlement; the settlement of the contour is a circular ring. The maximum ground settlement is calculated to be 1.244 m, located in the main peak projection area. It is worth noting that, at the peak of the foot of the slope, there is a different level of the ridged effect, and the location of the Himalayas is closer to the foot of the slope; the more bumps, the greater the amount. The largest foundation uplift is 275 mm, located in the northern area of the main peak. Therefore, the uneven settlement of the foundation and the slope of the mountain have a direct relationship.

The deformation characteristics of the surrounding roads in the mountain area are studied, and the deformation curves of the road are derived and analyzed. Figure 7 shows the vertical displacement curve of the road from the west to the east in the north.

From the figure, it can be seen that for the uneven uplift at 170 mm, and the maximum uplift occurs in the area near the main peak. Figure 8 shows the displacement curves of the outer ring of LongHu Park from the north to the south. From the figure, it can be seen that for the uneven uplift at 31 mm, the maximum uplift occurs one or tow times in the

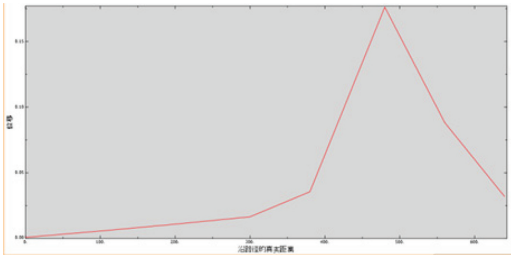

Figure 7. The displacement curve of the west-east direction in the north road.

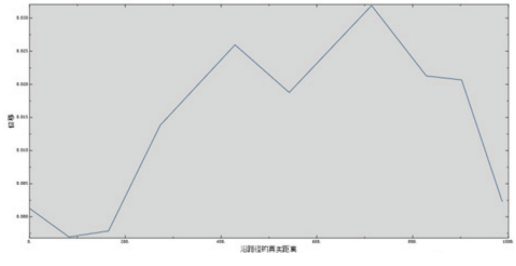

Figure 8. The displacement curves of the north-south direction in Long Lake.

western region Fufeng. Thus, we should strengthen the monitoring in the construction and adjust the construction plan dynamically. When the monitoring indexes exceed the alarm value, the measures should be taken immediately.

The deformation characteristics of the road around the mountain are analyzed by the numerical results, which shows the applicability of the numerical analysis method. Based on the results of the numerical analysis, we can develop effective treatment measures.

5 THE STRENGTH CONTROL OF THE FOUNDATION

The consolidation of the foundation occurs under load and with the drainage of pore water, and the strength of the foundation will increase. We can use this theory and the formula of Fellenius ($p1 = 5.52\ C_u/K$) to control the height of the load and the control of the strength. First, we use the shearing strength of the natural foundation to calculate the allowable load (p1) of the first level. The primary load safety factor K is 1.05. Based on the investigation report, we use the quick shear strength of 16.8 KPa as the natural foundation strength. P1 is 88 KPa, which is equivalent to 4.5 m-thick pile soil. When 1–3 layers of the degree of consolidation of soil reach 70%, we continue to apply the load at the next level. According to the formula $cu1 = cu + \Delta\sigma\ U \tan\varphi$, the foundation soil strength increases. According to the improved strength of the foundation, we estimate the next level load, until the piling construction is complete. In order to ensure engineering safety, the accurate load safety factor K dynamic increases as the height increases with the heap of soil.

Table 2. The improved strength of the foundation, allowable load and safety factor.

	The strength of the foundation (KPa)	Allowable load (KPa)	Safety factor
1	16.80	88.32	1.05
2	37.51	188.24	1.1
3	56.14	281.73	1.1
4	78.07	391.75	1.1
5	103.86	477.78	1.2
6	124.04	570.58	1.2
7	145.80	670.68	1.2
8	169.28	718.77	1.3

The improved strength of the foundation, allowable load and safety factor are given in Table 2. Because of the uneven load and its wide range, we cannot use the characteristic value bearing capacity to control the strength of the foundation according to the general design. So, using the strength growth theory and the method of allowable load, the strength of the foundation could be controlled, and thus could meet the project requirements better.

6 CONCLUSIONS AND SUGGESTIONS

Combined with engineering examples, the detailed design method of the piled mountain project is described.

In this paper, systematic analysis through the foundation strength calculation, foundation deformation control and stability control provide guidance for the engineering practice and reference for the design of the similar project.

1. The stability control consists of mountain slope, the integral of the slope and the foundation, and foundation stability. The height of water line, strength of soft soil layer, slope gradient and other factors have a great influence on stability, which must be carried out on the point of control.
2. The foundation settlement increases with the increase in the absolute elevation, and the uplift increases with the closer distance from the slope toe of the main peak position. Three-dimensional

numerical analysis methods could predict the final settlement based on observations, which can establish effective treatment measures.

3. The strength of foundation soil is controlled by combining the strength growth theory with permission load method, which guarantees the effective utilization of the characteristics of soil consolidation and also ensures the safety of the project.

REFERENCES

Gu, F.X., Yan, C.H. & Wang, B. 2011. Mechanism analysis of heap hill collapse in urban area of southern Jiangsu. *Journal of Engineering Geology* 19(5): 697–702.

He, D.W. 2007. Observation and Deformation Analysis on Construction Settlement of Piling mountain project in Olympic Forest Park. Xi'an: Xi'an University of Architecture and Technology.

Liao, H. 2014. Study on Failure Causes and Treatment of Soft Soil Foundation in Piling up Hill for Making Scenery Project. *Subgrade Engineering* (4): 222–226.

Liu, X.J., Li, H.Q. & Lei, H.Y. 2004. Application of large-scale software ANSYS to piling mountain project. *Rock and Soil Mechanics*. (supp 2): 357–360.

Meng, L. & Wang, G. 2012. Analysis on the landscape design of the new campus of a university in Tianjin. *XianDai Hortiaulure* (8): 129–129.

Qi, C.Q. 2002. Research on Piled Mountain landscape on construction waste landfill site in Tianjin. *Environmental Sanitation Engineering* 10(3): 113–115.

Tang, Z.G. 2011. Foundation deformation characteristics-Take heap hill project of ZhenJiangsports. Nanjing: NanJing University.

Wang, H.X., Han, Q. & Song, S.B. 2009 Architectural technology Heaping Mountain landscape bygarbage—Tsui Ping south park construction in Tianjin. *China Investigation & Design* (12): 82–84.

Zhao, B., Xu, B.T. & Yan, C.H. 2011. Numerical Analysis of Slope Stability for Artificial Landscape Hill. *Journal of Engineering Geology* 19(6): 859–864.

Civil Engineering and Urban Planning IV – Liu et al. (Eds)
© 2016 Taylor & Francis Group, London, ISBN 978-1-138-02903-3

Connection performance assessment of 2D steel frames under column-removal scenario

Cheng Chen, Hao-Ran Yu, Yan Xu & Wei-Bin Li
School of Civil Engineering, Southeast University, Nanjing, Jiangsu, P.R. China

ABSTRACT: Building performance test after earthquake is of great importance in Post-earthquake Examination. It showed that one of the weakest links in the steel frame systems is the beam–column joint. This paper proposed a method for finding the most vulnerable joint of steel frame structures under the scenario of sudden column loss. Three steel plane frames were designed according to different seismic conditions, analyzed and compared according to nonlinear dynamic method, and the distribution of moment normalized by yielding moment at the beam end in the direct influenced region was reached which suggested the structure designer should pay more attention to the joint with vulnerability.

1 INTRODUCTION

This paper proposed a method for finding the most vulnerable joint of steel frame structures under the scenario of sudden column loss which suggested the structure designer should pay more attention to the joint with vulnerability.

Uncertainties in the damage demand of the connections in the steel frame system were modelled through the dynamic response analysis in the FE software OpenSees. To consider the dynamic actions on the material properties, the yield strength of steel material was modified using the Cowper-Symonds model. The moment at the connection was selected as the assessment index of connection performance and the maximum normalized moment demand at beam end was under statistics.

2 FE SIMULATION

2.1 *Random parameters*

Due to large variations in material properties and loading conditions, the random parameters considered in this part included static yield strength of steel, gravity load.

For the material Q235, the static yield strength was modeled by the lognormal distribution with a mean value of 272 MPa (Wang et al. 2012) and a COV of 0.080 (Yu & He 2006). For gravity load, the dead load was modeled by the normal distribution with a mean value of 1.05 DL and a COV of 0.074; the live load was modeled by the extreme value type I distribution with a mean value of 0.305 LL and a COV of 0.212 (Cao & Cao 2006). Latin Hypercube Sampling (LHS) method was adopted to create 100 samples for the steel frame.

2.2 *Element and material*

In the software OpenSees, beams and columns were both modeled using dispBeamColumn elements with fiber sections to account for the interaction of moment and axial force (Mazzoni et al. 2006). Masses are calculated based on the gravity loads.

The constitutive model of steel Q235 was specified as multi-linear model with elastic stage, hardening stage and horizontal segment, shown in Figure 1. For steel Q235, Young's modulus was 206 GPa, and the tangent modulus in hardening stage was 1% of elastic modulus (Wang &

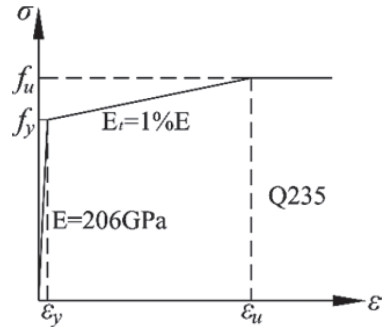

Figure 1. Constitutive model of steel Q235.

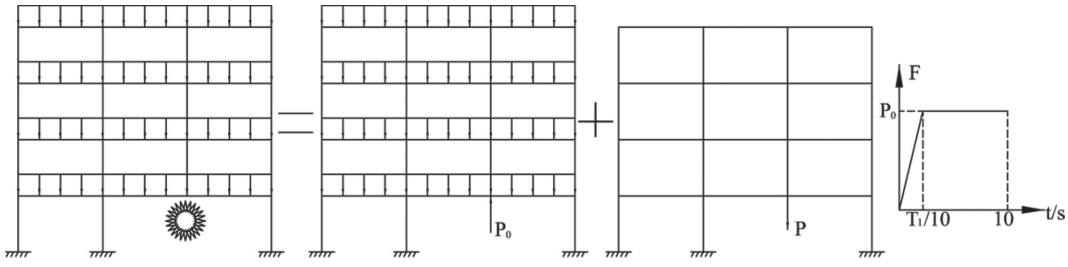

Figure 2. Loading procedure to simulate the nominal middle column removal.

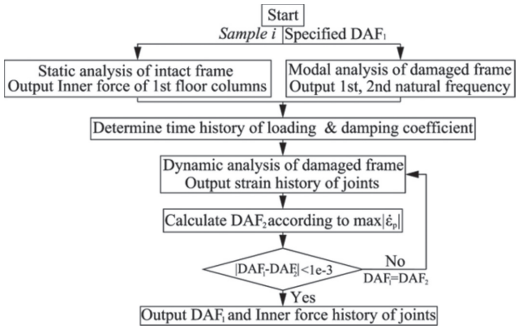

Figure 3. Dynamic analysis procedure of 2D steel frame.

Han 2009). The mean value of static yield strength was 272 MPa, and the mean value of static ultimate strength was 447 MPa (Wang et al. 2012).

High strain rate due to dynamic actions, would lead to the variation in mechanical properties of the material (DoD 2005). In this paper, only the dynamic effect on the material strength was considered. Dynamic Amplification Factor (DAF) of ultimate strength was assumed as 1.2 while DAF of yield strength was calculated according to Cowper-Symonds model,

$$\mathrm{DAF} = 1 + \left(\frac{\dot{\varepsilon}^{pl}}{\gamma} \right)^{m} \quad (1)$$

where $\dot{\varepsilon}^{pl}$ = equivalent plastic strain rate and the parameter γ, m was assumed as $40s^{-1}$, 0.2 (Izzuddin & Fang 1997).

2.3 *Load applying*

When structural system suffers extreme events like earthquake or blast, some members might induce a large response which is greater than bearing capacity and then fail to continue bearing. The local structure adjacent to initial failed member might experience mutation of loads and displacement boundary conditions, which contributes to further damage of the structural system.

Column removal method was selected to simulate the initial failure in the frame and the key elements specified as initial failure part were the middle and side columns in the first floor. The removal of a column did not affect the performance of corresponding joints. The loading procedure of middle column failure was illustrated in Figure 2.

The dynamic analysis procedure of steel frames following sudden column removal was shown in Figure 3.

3 EXAMPLE OF A PLANE FRAME

3.1 *Design information*

The study object was a four-storey three-span 2D steel frame with a floor height of 4 m shown in Figure 4. The span was 6 m and the width of beam loading was 6 m. The material selected was the carbon steel Q235. The dead load under the floor was 7.5 kN/m^2 and the live load was 4 kN/m^2. Three frames in zones with different fortification earthquake intensity were designed according to Chinese code and the geometrical information was listed in Table 1.

3.2 *Statistics of DAF of yield strength*

Dynamic Amplification Factor (DAF) of yield strength was obtained from the dynamic analysis and a lognormal distribution was fitted to the set of DAF. The statistic results in Table 2 showed that for a specified frame, the influence of sudden middle/side column removal on material properties was similar. But the influence was more obvious in Frame A, and mattered less in Frame C.

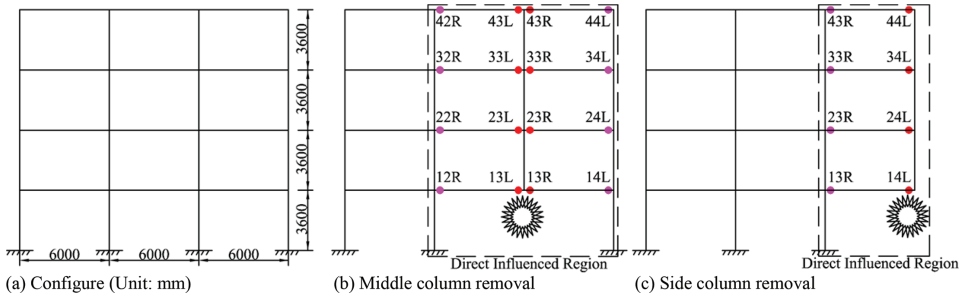

(a) Configure (Unit: mm) (b) Middle column removal (c) Side column removal

Figure 4. Configure of 2D steel frame.

Table 1. Geometrical information of three 2D frames (Unit: mm).

Name	Frame A (Intensity VI)	Frame B (Intensity VII)	Frame C (Intensity VIII)
Section of beam	H350 × 250 × 10 × 14	H350 × 250 × 10 × 16	H400 × 300 × 10 × 16
Section of column	H450 × 350 × 12 × 14	H450 × 350 × 14 × 16	H500 × 400 × 14 × 16

Table 2. Statistics of DAF of yield strength.

Name	Failed column	μ	σ	Mean	Standard variation
Frame A	Middle	0.24	0.0022	1.271	0.003
	Side	0.24	0.0024	1.272	0.003
Frame B	Middle	0.237	0.0029	1.267	0.004
	Side	0.237	0.0026	1.268	0.003
Frame C	Middle	0.224	0.0072	1.251	0.009
	Side	0.227	0.006	1.254	0.008

Table 3. Statistics of nM of joints in 1st floor among direct influenced region.

Failed column	Frame	Far from damaged column					Adjacent to damaged column				
		Joint	μ	σ	EX	Std	Joint	μ	σ	EX	Std
Middle	Frame A	12R	0.453	0.051	1.575	0.082	13L	0.198	0.031	1.220	0.038
		14L	0.446	0.046	1.563	0.072	13R	0.192	0.026	1.212	0.032
	Frame B	12R	0.41	0.04	1.508	0.061	13L	0.174	0.02	1.190	0.025
		14L	0.406	0.038	1.503	0.058	13R	0.171	0.018	1.187	0.022
	Frame C	12R	0.315	0.027	1.371	0.036	13L	0.119	0.032	1.127	0.034
		14L	0.312	0.028	1.366	0.038	13R	0.117	0.033	1.125	0.035
Side	Frame A	13R	0.451	0.055	1.573	0.088	14L	0.18	0.035	1.198	0.043
	Frame B	13R	0.408	0.04	1.505	0.061	14L	0.153	0.025	1.166	0.029
	Frame C	13R	0.318	0.026	1.375	0.036	14L	0.053	0.065	1.056	0.066

4 CONCLUSION

Maximum moment of joints among the direct influenced region following nominal column removal was under statistics, which was normalized by yield moment of the beam section, reaching maximum normalized moment (nM). Maximum normalized moment nM was modeled by a lognormal distribution and related parameters were listed in Table 3. It showed that for a specified frame, the mean value of nM for the joints far from damaged column in the direct influenced region was larger than that of

the joints adjacent to damaged column. The mean value of nM in Frame A was larger than that in Frame B and C.

REFERENCES

Baker, J.W., Schubert, M. & Faber, M.H. 2008. On the assessment of robustness. *Structural Safety* 30(3): 253–267.

Cao, Z.X. & Cao, P. 2006. *Structural Loads Theory in Architectural Engineering.* Beijing: China Water Power Press.

Izzuddin, B.A. & Fang, Q. 1997. Rate-sensitive analysis of framed structures Part I: Model formulation and verification. *Structural Engineering & Mechanics* 5(3): 221–237.

Lind, N.C. 1995. A measure of vulnerability and damage tolerance. *Reliability Engineering & System Safety* 48(1): 1–6.

Mazzoni, S., McKenna, F., Scott, M.H. & Fenves, G.L. 2006. *OpenSees Command Language Manual.* Berkeley: Pacific Earthquake Engineering Research Center.

Smith, J.W. 2006. Structural robustness analysis and the fast fracture analogy. *Structural Engineering International* 16(2): 118–123.

Starossek, U. & Haberland, M. 2008. Measures of Structural Robustness-requirements and Applications. *ASCE SEI Structures Congress, Apr. 2008.* Boston: Structure Engineering Institute of ASCE.

U.S. Department of Defense (DoD). 2005. Structures to resist the effects of accidental explosions. UFC 3-340-02. Washington, DC.

Wang, W.D. & Han, L.H. 2009. Hysteresis relationship in concrete filled steel tubular columns and steel beam planar frames. *Journal of Tsinghua University (Sci & Tech)* 49(12): 1934–1938.

Wang, Y.Q., Zhou, H., Shi, Y.J. & Chen, H. 2012. Seismic behavior analyses of welded beam-to-column connections based on fracture mechanics. *Engineering Mechanics* 29(4): 104–112.

Yu, Z.W. & He, S.S. 2006. Reliability analysis of ultimate bearing capacity of concrete-filled tubular steel stub columns. *Engineering Mechanics* 23(11): 139–144.

Civil Engineering and Urban Planning IV – Liu et al. (Eds)
© 2016 Taylor & Francis Group, London, ISBN 978-1-138-02903-3

Analysis of beam-column joint in steel frame structure based on connection failure probability

Hao-Ran Yu, Cheng Chen, Yan Xu & Wei-Bin Li
School of Civil Engineering, Southeast University, Nanjing, Jiangsu, China

ABSTRACT: Flange-welded web-bolted connection was analyzed in this paper, and the influential factors on weld fracture toughness demand at the connection are discussed, and through discussion, the length of the beam and the loading conditions in the finite element model of connection were determined. With respect to random parameters including material yield strength, critical value of weld fracture toughness (J Integral) and initial flaw at the interface of the beam bottom flange and column flange, the finite element analysis was conducted in ANSYS to find the relationship between section-normalized moment and J integral demand at the crack tip. Finally, the probabilistic model of connection failure was proposed including the relationship between nM and P_f.

1 INTRODUCTION

According to code for seismic design of buildings, under the action of earthquake, the joint in the beam can form the plastic hinge based on its ductility, dissipate the energy of earthquake input, and then avoid the destruction. However, in the Northridge earthquake and Japan Kobe earthquake, a lot of beam-column joints of steel frame did not form the plastic hinge but formed brittle fractures.

2 CONNECTION TYPE

The configuration of connections is illustrated in Figure 1, and the weld access hole was based on the recommendation in China's seismic design code (GB 50011-2010), as shown in Figure 2.

Assessment index of joint performance should have the feature of generality. Mf/Mp is regarded as the factor of joint performance (Matos & Dodds 2000), where Mf is the nominal moment at the beam end and Mp is the plastic ultimate moment. Since the plasticity coefficient of sectional resistance moment is influenced by the span, section height or loading features, and thus hard to assess, the nominal moment of the joints (Mf) in this paper is normalized by the yield moment of the section (My), denoted as nM.

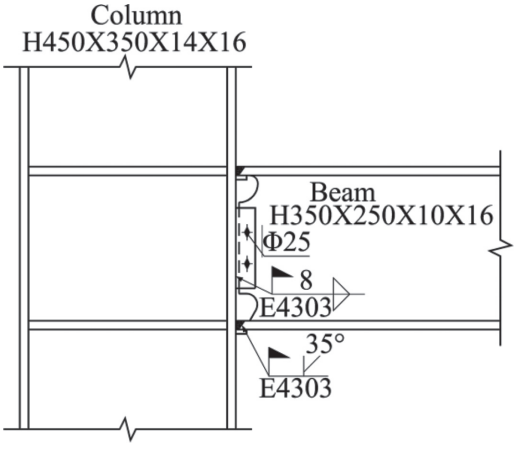

Figure 1. Configuration of connections (Frame B).

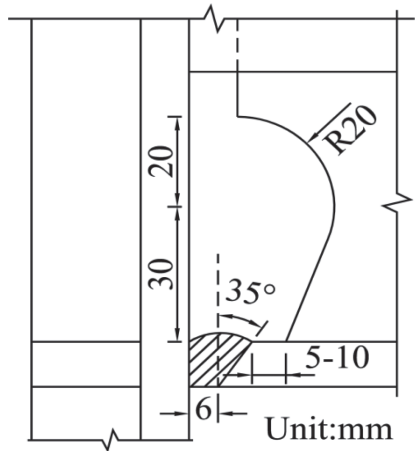

Figure 2. Configuration of weld access hole.

3 FE SIMULATION

3.1 *Random parameters*

Investigation reports of structural failure in the Northridge earthquake (Kaufmann et al. 1997) indicated a large scatter among several parameters such as initial crack size, yield strength of steel, and fracture toughness of the weld base. When investigating the performance of rigid connection, they should be regarded as significant parameters (Joh et al. 1999). The stochastic effect of these three parameters was considered in the pushdown analysis of connection.

3.2 *Elements and materials*

The constitutive model of steel Q235 and the Dynamic Amplification Factor (DAF) of yield strength was considered. The weld base E4303 was modeled as a multi-linear constitutive curve at the elastic stage, hardening stage and horizontal segment.

3.3 *Path of integration at the crack tip*

J integral theory is commonly used in elastic fracture mechanics. It is defined based on the contour integration of stress, strain and displacement in the surrounding areas of the crack tip. In the elastic-plastic state, the stress and strain field near the crack tip is uniquely determined by the J-integral. When the stress and strain field at the crack tip reaches the critical state of crack initiation, the J integral also reaches the critical value J_{IC} and then the crack body fractures. Therefore, the J integral can be used as a parameter to establish the basis of fracture judgment in the elastic-plastic state: $J \geq J_{IC}$ (Rice 1968).

Integral contour was conducted on the beam flange center (z = 0 mm) and edge (z = 124 mm) for calculation, the result of which showed a greater value.

4 MECHANICAL MODEL OF CONNECTIONS

SAC 96-01 (Venture 1996) investigated the failure mode of connections that were designed according to the Pre-Northridge earthquake code, and collected the deformation information of beam-column joints.

4.1 *Influence of loading mode and member length*

The models designed to validate the influence of the loading mode and member length on fracture toughness demand at the crack tip are shown in Figure 3. As shown in Figure 3a, the length of the beam was three times the beam height (3hb) and the whole length (Lb), respectively, and the beam was under the pure bending condition. As shown in Figure 3b, the length of the beam was three times the beam height (3hb) and the whole length (Lb), respectively, and the beam was under the combination of shearing force and bending.

The results shown in Figure 4 indicated that under the pure bending condition/combination of bending and shearing force, J integral demand at the crack tip was influenced little by the beam length at a specified inner force condition of connection.

4.2 *T-type joint and cruciform joint*

The models designed to validate the influence of the adjacent span are shown in Figure 5. The first joint model was T-type connection, while the second joint model was X-type connection. The result of J integral at the crack tip shown in Figure 6 indicated that the influence on J integral demand at the crack tip caused by neglecting the adjacent beam was small.

4.3 *Influence of shearing force at the beam end*

Information of the inner force (shearing force and moment) of joints adjacent to the failed columns obtained from the dynamic analysis of the frame model is provided in Table 1. The shearing force V was normalized by the web area A_{web}, while the moment M was normalized by the inertia moment W_x.

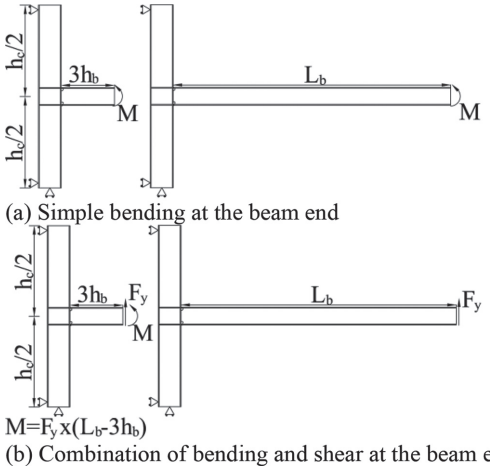

Figure 3. Joint models designed to validate the influence of the loading mode and member length.

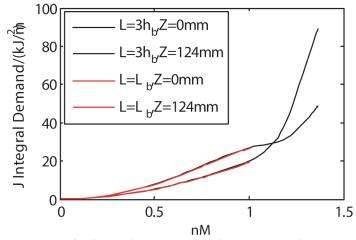

(a) Simple bending at the beam end

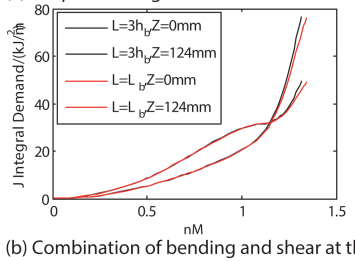

(b) Combination of bending and shear at the beam end

Figure 4. Relationship between normalized moment and J integral demand.

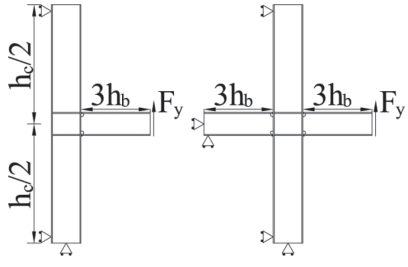

Figure 5. Models of T-type joint and cruciform joint.

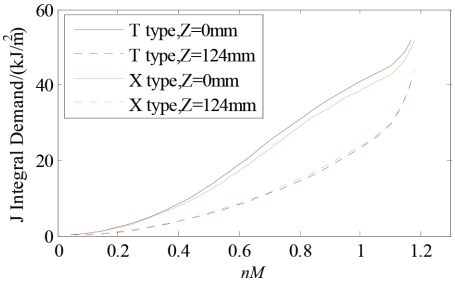

Figure 6. Relationship between normalized moment at the beam end and J integral demand.

Frames A, B and C mean frames in intensity categories 6, 7 and 8, respectively. Taking Frame B as an example, two models shown in Figure 7 were loaded with pure bending, bending and shearing, respectively, to consider the influence of shearing

Table 1. Statistics of shearing force/moment relationship for the joints adjacent to the failed columns.

Mean value of $\frac{V/A_{web}}{M_{max}/W_x}$	Frame A	Frame B	Frame C
Maximum	–0.01225	–0.02373	–0.06134
Minimum	–0.02466	–0.03195	–0.06904

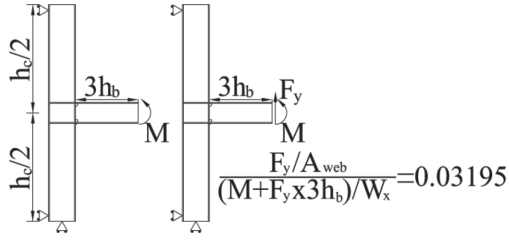

Figure 7. Model information with or without the consideration of shearing force.

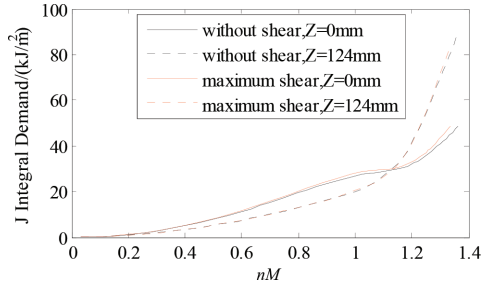

Figure 8. Relationship between normalized moment at the beam end and J integral demand.

force on J integral demand. The result shown in Figure 8 indicated that J integral demand at the crack tip at two loading conditions was similar. For the joints adjacent to the failed columns, the shearing force of joints had a little influence on J integral demand in the bottom beam flange.

4.4 *Influence of axial force at the beam end*

Information of the inner force (axial force and moment) of joints adjacent to the failed columns obtained from the dynamic analysis of the frame model is provided in Table 2. The axial force N was normalized by the section area A, while the moment M was normalized by the inertia moment W_x.

Taking Frame B as an example, two models shown in Figure 9 were loaded under pure bending, bending and axial force, respectively, to consider

Table 2. Statistics of axial force/moment relationship of joints adjacent to the failed columns.

Mean value of $\frac{N/A}{M_{max}/W_x}$	Frame A	Frame B	Frame C
Maximum	0.07469	0.05422	0.06529
Minimum	–0.06044	–0.06194	–0.07201

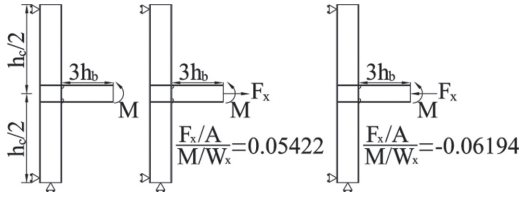

Figure 9. Model information with or without the consideration of axial force.

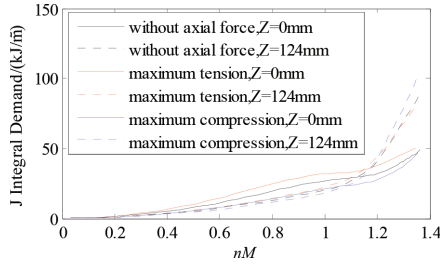

Figure 10. Relationship between normalized moment at the beam end and J integral demand.

the influence of axial force on J integral demand at the crack tip. The result shown in Figure 10 indicated that J integral demand at the crack tip at three loading conditions was obviously different. For the joints adjacent to the failed columns in this example, the axial force of joints had a large influence on J integral demand at the bottom beam flange and could not be neglected.

5 PROBABILISTIC MODEL OF CONNECTION FAILURE

5.1 *Calculation method of connection failure probability*

Since connection failure was considered as the situation in which the fracture toughness demand exceeded the critical value of fracture toughness of material E4303, the probability of the joint failure was calculated according to the following equation:

$$P_f = \iint_{p>m} f_p(p) f_M(m) dp dm$$
$$= \int_0^{\infty} f_p(p) \left(\int_0^p f_M(m) dm \right) dp = \int_0^p f_p(p) F_M(p) dp$$

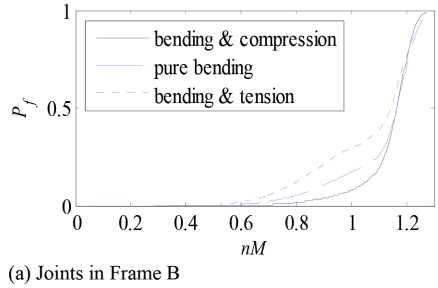

(a) Joints in Frame B

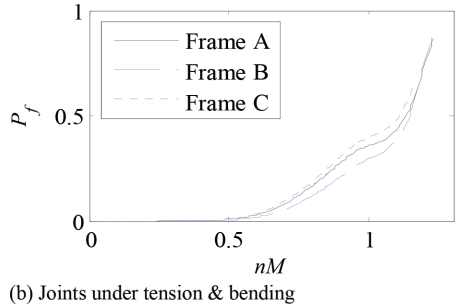

(b) Joints under tension & bending

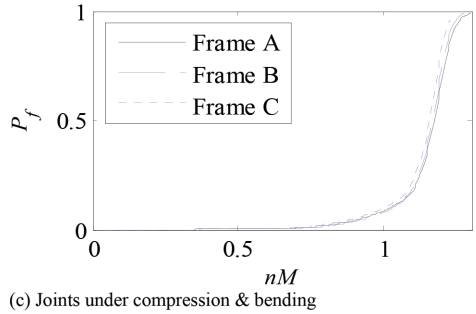

(c) Joints under compression & bending

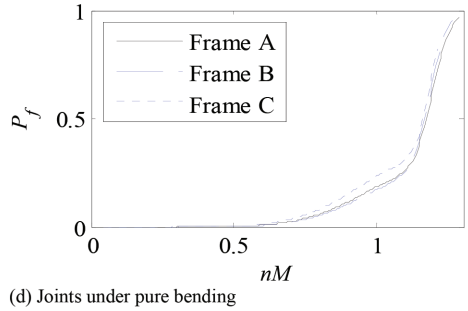

(d) Joints under pure bending

Figure 11. Probability model of connection failure at three representative inner force conditions.

where $f_P(p)$ is the probability density function of fracture toughness demand, and $f_M(m)$ is the probability density function of fracture toughness.

5.2 *Probability model for the discussed frame*

Figure 11 shows the relationship between connection failure probability and normalized moment. As shown in Figure 11a, at a representative moment, the failure probability of joints under the combination of bending and tension was the highest, while that under the combination of compression and bending was the lowest. As shown in Figure 11b, for joints under the combination of bending and tension, the unsmooth point in the Pf-nM curve was probably the turning point of the elastic/elasto-plastic stage. As shown in Figure 11c and d, Pf-nM curves for joints in frames A, B and C were similar.

6 CONCLUSIONS

From the results of the statistics, member length and the loading modes had a little significant influence on the J integral value of beam bottom flange, but the inner force at the end of the beam played a main role. And the shear at the end of the beam had a little effect on the J integral value, while the effect of the axial force cannot be ignored.

At the same node and an equivalent bending moment, the failure probability of joints was the highest when the beam was under the combination of bending and tension, intermediate under the pure bending, and lowest under the combination of compression and bending.

REFERENCES

Joh, C. & Chen, W. 1999. Fracture strength of welded flange-bolted web connections. *Journal of Structural Engineering* 125(5): 565–571.

Kaufmann, E.J., Fisher, J.W., Di, J.R.M. & Gross, J.L. 1997. *Failure Analysis of Welded Steel Moment Frames Damaged in the Northridge Earthquake*. Report NISTIR 5944. Gaithersburg: National Institute of Standards and Technology.

Matos, C.G. & Dodds, R.H. 2000. Modeling the effects of residual stresses on defects in welds of steel frame connections. *Engineering Structures* 22(9): 1103–1120.

Rice, J.R. 1968. A path independent integral and the approximate analysis of strain concentration by notches and cracks. *Journal of Applied Mechanics* 35(2): 379–386.

Venture, S.J. 1996. *Experimental Investigations of Beam-column Sub-assemblages*. Rep. No. SAC-96-01, Parts I & II. Sacramento.

Xu, G. & Ellingwood, B.R. 2011. Probabilistic robustness assessment of pre-Northridge steel moment resisting frames. *Journal of Structural Engineering* 137(9): 925–934.

This page intentionally left blank

Civil Engineering and Urban Planning IV – Liu et al. (Eds)
© 2016 Taylor & Francis Group, London, ISBN 978-1-138-02903-3

Linear optimal semi-active control of earthquake response of vibration-absorption megaframe structure

Min Zhang & Shu-Lan Hu
School of Civil Engineering and Architecture, Guangxi University of Science and Technology, Liuzhou, Guangxi, China

ABSTRACT: Earthquake response of vibration-absorption megaframe may be dominated according to the philosophy of linear optimal active control. The algorithm of an optimal active control has been developed to command the structure displacement, velocity and acceleration simultaneously, from which the Riccati equation has been revised. Based on the algorithm, the earthquake response of a 41 stories vibration-absorption megaframe has been controlled semi-actively by controllable dampers. The result indicates that the maximum vibration displacement and acceleration of the top of main frame may be reduced by 2/3, and the vibration accelerations of the floors of secondary frame may be decreased by 60%–75%.

1 INTRODUCTION

The vibration-absorption megaframe structure may be a new type of system. In this structure, the concrete tubes of the staircase and elevator lobby serve as the main-frame columns, and the huge beams spacing several floors work as the main-frame beams, whereas the secondary frames may be constructed on the main-frame beams. In order to evidently reduce the vibration response of the megaframe, and to greatly increase the effectiveness of vibration absorption, devices for the energy dissipation and vibration absorption may be designed between the main and the secondary frames, namely, the controllable damping isolation devices installed beneath the columns of the secondary frame and the controllable dampers designed at the top of secondary frame, which connect the secondary frames to the main frame.

Under the action of earthquake and pulsating wind, all secondary frames may be as the multistory frame beneath which the base isolation devices with controllable damp have been installed. Additionally, the secondary frames as huge mass blocks may constitute a large turned frequency mass damping system together with the main frame (TMD). Not only does the system possess the capacity of vibration absorption by means of TMD, but also may be characterized by base isolation and vibration absorption by way of damping energy dissipation.

The semiactive control with controllable damping devices may be a novel structure control method. The control combines the features of active and passive systems, which require a smaller power source to adjust actively the controllable damper parameters to produce the control forces which may be regulated according to the measured excitation and/or structure response. Owing to requiring a smaller power source to operate, the semiactive control has become one of the novel concepts of structure vibration control. In this paper, the dampers in the vibration-absorption megaframe structure may be designed to be variable so as to utilize the semiactive control of earthquake response of the structure (Calise & Sweriduk 1994).

2 SEMIACTIVE CONTROL ALGORITHMS

The geometrical configuration is shown in Figure 1, and the calculating diagram of this structure is show in Figure 2. The governing differential equation of motion for the main-frame with controllable dampers subjected to earthquake may be given.

$$[M]\{\ddot{X}\}+[C]\{\dot{X}\}+\left([K]-[\bar{K}_t]+[\bar{K}][H][E]\right)\{X\} -[\bar{K}][H]\{s\}=-[M]\{1\}\ddot{X}_0+[B]\{U\} \tag{1}$$

where $[M]$ is the mass matrix, $[C]$ is damping matrix, and $[K]$ is stiffness matrix. $\{X\}$ is the floor absolute displacement vector of the main-frame,

$\{s\}$ is the floor absolute displacement vector of secondary frames, and $\{U\}$ is the vector of adjustable damping force. $\bar{K}_1^{(i)}$ and $\bar{K}_t^{(i)}$ are respectively the stiffness of the base isolation device beneath the secondary-frame i and the controllable damper at top of the secondary-frame i. $u_1^{(i)}$ and $u_t^{(i)}$ are respectively adjustable damping force of the base isolation device and controllable damper in the secondary-frame i

$$[H]=\begin{bmatrix} \{e_1^{(1)}\}^T & \{0\}^T & \cdots & & & & \cdots & \{0\}^T \\ \{e_t^{(1)}\}^T & \{e_1^{(2)}\}^T & \{0\}^T & \cdots & & & \cdots & \{0\}^T \\ & & & \cdots & & & \cdots & \\ \{0\}^T & & & \cdots & \{0\}^T & \{e_t^{(i-1)}\}^T \quad \{e_1^{(i)}\}^T \quad \{0\}^T & \cdots & \{0\}^T \quad \{0\}^T \\ & & & \cdots & & & \cdots & \\ \{0\}^T & & & \cdots & & & \cdots & \{0\}^T \quad \{e_t^{(n)}\}^T \end{bmatrix}$$

$$\{e_t^{(i-1)}\}^T=[0 \ \cdots \ 0 \ 1],\ \{e_1^{(i)}\}^T=[1 \ 0 \ \cdots \ 0],$$

$$[E]=[[E_i]],\ \{U\}=\{\{u^{(i)}\}\}\ (i=1, 2, \ldots, n),$$

$$\{u^{(i)}\}=\begin{Bmatrix} u_1^{(i)} \\ u_t^{(i)} \end{Bmatrix}\quad [E_i]=\begin{bmatrix} 0 & \cdots & 0 & 1 & 0 & \cdots & 0 \\ 0 & \cdots & 0 & 1 & 0 & \cdots & 0 \\ & & & \cdots & & & \\ 0 & \cdots & 0 & 1 & 0 & \cdots & 0 \end{bmatrix}_{t_i\times(n+1)},$$

$$[\bar{K}_t]=\begin{bmatrix} 0 & & \cdots & & & & 0 \\ 0 & K_t^{(1)} & -K_t^{(1)} & 0 \cdots & & & 0 \\ & & \cdots & & & & \\ 0 & & \cdots & 0 & K_t^{(i)} & -K_t^{(i)} \quad 0 \cdots & 0 \\ & & \cdots & & & & \\ 0 & & \cdots & & & 0 \quad K_t^{(n)} & -K_t^{(n)} \end{bmatrix},$$

$$[\bar{K}]=\begin{bmatrix} 0 & \bar{K}_1^{(1)} & 0 & \cdots & & & 0 \\ 0 & \bar{K}_t^{(1)} & \bar{K}_1^{(2)} & 0 \cdots & & & 0 \\ & & & \cdots & & & \\ 0 & & & \cdots & 0 & \bar{K}_t^{(i-1)} \quad \bar{K}_1^{(i)} \quad 0 \cdots & 0 \\ & & & \cdots & & & \\ 0 & & & \cdots & & 0 \quad \bar{K}_t^{(n)} & 0 \end{bmatrix}.$$

The governing differential equation of motion for secondary-frame i may be given.

$$[m^{(i)}]\{\ddot{s}^{(i)}\}+[c^{(i)}]\{\dot{s}^{(i)}\}+\left([k^{(i)}]+[I^{(i)}][\bar{k}^{(i)}]\right)\{s^{(i)}\}$$
$$-[c^{(i)}][E_i]\{\dot{X}\}-[k_v^{(i)}]\{X\}=-[m^{(i)}]\{1\}\ddot{X}_0+[I^{(i)}]\{u^{(i)}\} \quad (2)$$

where [m(i)] is the floor mass matrix of secondary-frame i., [c(i)] and [k(i)] are respectively the damping and the stiffness matrix of secondary-frame i, [s(i)] is the floor absolute displacement vector of the secondary-frames i, and {u(i)} is the vector of adjustable damping force of the base isolation device and damper in the secondary-frame i.

$$[k_v^{(i)}]=[k^{(i)}][E_i]+[I^{(i)}][\bar{k}^{(i)}][E_i]+[I^{(i)}][\bar{k}^{(i)}][V_i]$$

$$[V_i]=\begin{bmatrix} 0 & & & & & & & & 0 \\ 1 & -1 & 0 & \cdots & & & & & 0 \\ & & & \cdots & & & & & \\ 0 & & & \cdots & 0 & 1 & -1 & 0 \cdots & 0 \\ & & & \cdots & & & & & \\ 0 & & & & & & \cdots & 0 \quad 1 & -1 \end{bmatrix}_{t_i\times(n+1)},$$

$$[I^{(i)}]=\begin{bmatrix} 1 & 0 \\ 0 & 0 \\ \cdots & \cdots \\ 0 & 0 \\ 0 & 1 \end{bmatrix}_{t_i\times 2},\quad [\bar{k}^{(i)}]=\begin{bmatrix} \bar{k}_1^{(i)} & 0 & \cdots & 0 & 0 \\ 0 & 0 & \cdots & 0 & \bar{k}_t^{(i)} \end{bmatrix}_{2\times t_i}$$
$$(i=1, 2, \ldots, n).$$

The governing differential equation of motion for the main and the secondary frame may be expanded as

$$[M_z]\{\ddot{w}\}+[C_z]\{\dot{w}\}+[K_z]\{w\}=\{L(t)\}+[T]\{U\} \quad (3)$$

where

$$[M_z]=\begin{bmatrix} [M] & [0] \\ [0] & diag\left([m^{(i)}]\right) \end{bmatrix},$$

$$[C_z]=\begin{bmatrix} [C] & [0] \\ \left\{-[c^{(i)}][E_i]\right\} & diag\left([c^{(i)}]\right) \end{bmatrix}\ (i=1, 2, \ldots, n),$$

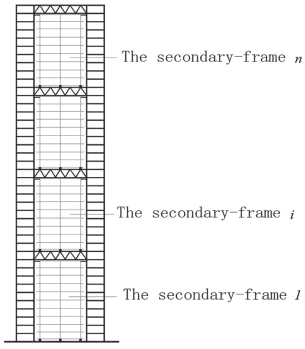

Figure 1. Geometrical configuration of megaframe.

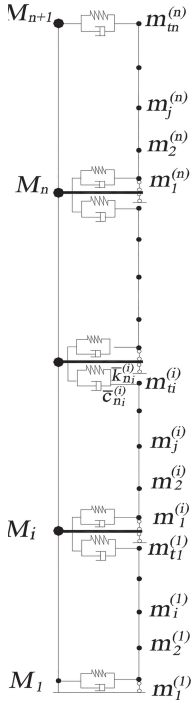

Figure 2. Calculating diagram of megaframe.

$$[K_z]=\begin{bmatrix}[K]-[\bar{K}_t]+[\bar{K}][H][E] & -[\bar{K}][H]\\ -\left\{\left[k_v^{(i)}\right]\right\} & diag\left(\left[k^{(i)}\right]+\left[I^{(i)}\right]\left[\bar{k}^{(i)}\right]\right)\end{bmatrix}$$

$(i=1, 2, \ldots, n)$,

$$\{L(t)\}=\begin{Bmatrix}-[M]\{1\}\ddot{X}_0\\ diag\left(-[m^{(i)}]\{1\}\right)\ddot{X}_0\end{Bmatrix},\ \{w\}=\begin{Bmatrix}\{X\}\\ \{s_i\}\end{Bmatrix},$$

$$[T]=\begin{bmatrix}[\bar{T}]\\ diag([I^{(i)}])\end{bmatrix}\quad (i=1, 2, \ldots, n)$$

$$[\bar{T}]=\begin{bmatrix}1 & 0 & & & & & & & & \\ 0 & 1 & 1 & 0 & & & & & & \\ & & & \cdots & & & & & & \\ 0 & & & \cdots & 0 & 1 & 1 & 0 & \cdots & 0 \\ & & & \cdots & & & & & & \\ 0 & & & \cdots & & & & & \cdots\ 0 & 1\end{bmatrix}_{n+1,2n}.$$

Using the state-space representation, equation (3) takes the form as follows.

$$\{\dot{z}\}=[A]\{z\}+[B]\{U\}+\{d\} \tag{4}$$

where

$$\{z\}=\begin{Bmatrix}\{w\}\\ \{\dot{w}\}\end{Bmatrix},\ [A]=\begin{bmatrix}[0] & [I]\\ -[M_z]^{-1}[K_z] & -[M_z]^{-1}[C_z]\end{bmatrix},$$

$$[B]=\begin{Bmatrix}[0]\\ [M_z]^{-1}[T]\end{Bmatrix},\ \{d\}=\begin{Bmatrix}[0]\\ [M_z]^{-1}\{L(t)\}\end{Bmatrix}.$$

3 LINEAR OPTIMAL SEMIACTIVE CONTROL ALGORITHM

In this algorithm, the control force $\{U(t)\}$ in equation (4) may be selected by minimizing. In order to simultaneously control the structure displacement, velocity and acceleration subjected to earthquake, the generalized cost function may be given as follows.

$$J=\frac{1}{2}\left\{z\left(t_f\right)\right\}^T[S]\left\{z\left(t_f\right)\right\}+\frac{1}{2}\int_0^{t_f}\left(\{z\}^T[Q_1]\{z\}+\{\dot{z}\}^T[Q_2]\{\dot{z}\}+\{U\}^T[R]\{U\}\right)dt \tag{5}$$

which t_f = duration of earthquake. $[Q_1]$, $[Q_2]$ and $[S]$ are all symmetric positive semidefinite weighting matrices, and $[R]$ is symmetric positive definite weighting matrix. If the elements of $[Q_1]$, $[Q_2]$ are large than those of $[R]$, reducing $[z(t)]$, $[\dot{z}(t)]$ has priority over reducing $\{U(t)\}$.

The vector $\{\dot{z}\}$ of equation (4) may be substituted in equation (5) and mathematically operated, and equation (5) has been given.

$$J=\frac{1}{2}\{z(t_f)\}^T[S]\{z(t_f)\}+\frac{1}{2}\int_0^{t_f}\left(\{z(t)\}^T[\bar{Q}]\{z(t)\}+\{\bar{U}(t)\}^T[\bar{R}]\{\bar{U}(t)\}\right)dt \tag{6}$$

where

$$[\bar{Q}] = [Q_1] + [A]^T [Q_2][A] - [\bar{S}][\bar{R}]^{-1}[\bar{S}]^T,$$
$$[\bar{S}] = [A]^T [Q_2][B],$$
$$[\bar{R}] = [R] + [B]^T [Q_2][B],$$
$$\{\bar{U}(t)\} = \{U(t)\} + [\bar{R}]^{-1}[\bar{S}]^T \{z(t)\}.$$

Minimizing (6) subject to the constraint of (4) results in the control force vector $\{U(t)\}$ regulated only by the state vector $\{z(t)\}$.

$$\{U(t)\} = -[\bar{R}]^{-1}\left([B]^T [\bar{P}(t)] + [\bar{S}]^T\right)\{z(t)\} \tag{7}$$

where the matrix $[\bar{P}(t)]$ is the solution of the revisal Riccati equation, which may be expressed as follows.

$$\begin{cases} -[\dot{\bar{P}}(t)] = [\bar{P}(t)][\bar{A}] + [\bar{A}]^T [\bar{P}(t)] + [\bar{Q}] \\ \qquad\qquad -[\bar{P}(t)][B][\bar{R}]^{-1}[B]^T [\bar{P}(t)] \\ [\bar{P}(t_f)] = [S], \end{cases} \tag{8}$$
$$[\bar{A}] = [A] - [B][\bar{R}]^{-1}[\bar{S}]^T;$$

Owing to the damping force of magnetic liquid damper regulated by varying magnetic field strength, the magnetic liquid damper may be used as controllable damper. The controllable damping isolation device may combine the magnetic liquid damper with isolation bearings. The optimal active control force given by equation (7) may be difficult for magnetic liquid damper to obtain totally, thus the damping force only approaches the optimal active control force by adjusting the parameter of magnetic liquid damper. Consequently, the algorithm of optimal semi-active control of adjusting the parameter of magneto liquid damper is given as follows.

$$\begin{cases} \bar{u}_{\max} \text{ when } \bar{u}_i \cdot u_i > 0 \text{ and } |\bar{u}_{\max}| < |u_i| \\ \bar{u}_i = u_i \text{ when } \bar{u}_i \cdot u_i > 0 \text{ and } |\bar{u}_{\max}| \geq |u_i| \geq |\bar{u}_{\min}| \\ \bar{u}_{\min} \text{ others,} \end{cases}$$

where $\bar{u}_{\max}$ and $\bar{u}_{\min}$ are the damping forces when magnetic field strength is respectively zero and maximum, u_i is the optimal damping force of the magnetic liquid damper, and $\bar{u}_i$ is the damping force of the magnetic liquid damper (Maria 1995).

4 CALCULATION AND ANALYSIS

A forty-one stories symmetric megaframe is showed in Figure 3. The frame columns of megaframe are concrete tubes designed in 4 corners of the structure. The 4 mega frame beams of the megaframe are reinforced concrete trusses designed in the megaframe. The megaframe contains 4 stories main frame, in which the concrete tube thicknesses of various stories are respectively 300 mm, 250 mm, 250 mm and 200 mm from the bottom up. The cross sectional dimensions of various members in the truss are respectively 700 mm × 700 mm for upper and lower chords, and 600 mm × 600 mm for web members.

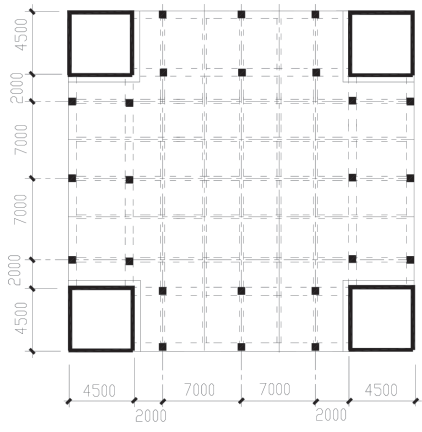

Figure 3. Plan diagram of vibration-absorption megaframe.

In the megaframe, the secondary frames are designed in various stories of the main frame, of which the numbers are respectively 1, 2, 3 and 4 from the bottom up, as is showed in Figure 1. The numbers of stories of secondary frames are respectively 10, 9, 9 and 9 from the bottom up. The cross sectional dimensions of the secondary frame are 600 mm × 600 mm for columns and 300 mm × 600 mm for beams of secondary frames. The story heights of all secondary frames are 3 m. The controllable damping isolation devices may be installed beneath columns of secondary frames, and the controllable damper may be designed at the top of secondary frames to connect with the main frame. The strength grade of concrete of the structures is C40. The structure may be subjected to EL centro earthquake of which the peak acceleration may be 110 cm/s^2.

Based on the linear optimal semiactive control algorithm, it is showed that the time history responses of displacement and acceleration at the top of the main frame in the semi-active control megaframe, which contrast with those of the corresponding aseismic megaframe in Figure 4.

In Figure 4, Δ and A are respectively defined as displacement and acceleration at the top of the main frame, and t is defined as time of earthquake. It may be indicated that the responses of

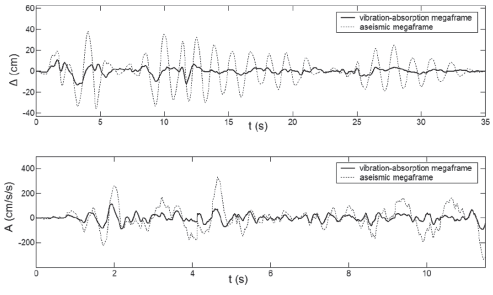

Figure 4. Time history responses of displacement and acceleration.

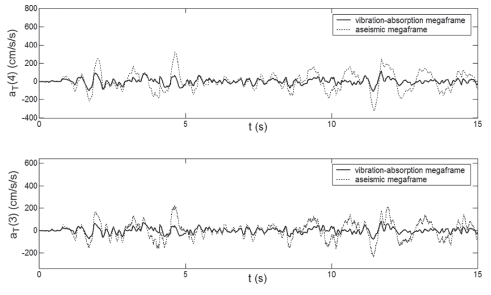

Figure 6. Time history responses of the absolute accelerations.

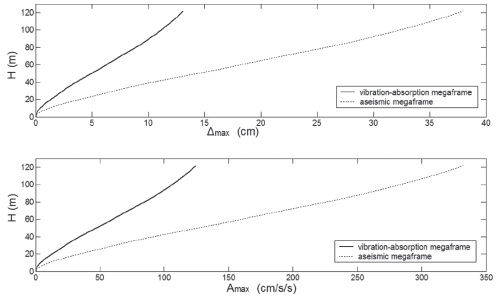

Figure 5. Maximum displacements and accelerations.

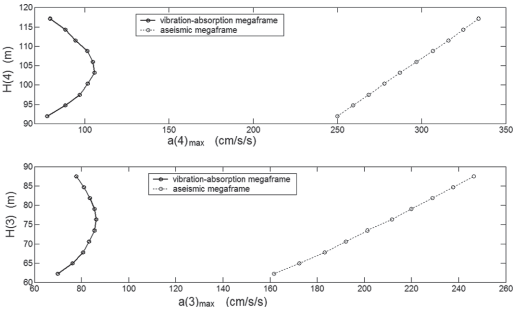

Figure 7. Maximum accelerations.

displacement and acceleration at the top of the main frame of vibration-absorption megaframe are much weaker than those of aseismic megaframe.

Figure 5 shows the maximum displacements and accelerations of various floors of main frame in the semi-active control structure and the corresponding aseismic structure, which indicate that the damping effect of the linear optimal semi-active control may be obvious, and the maximum displacement and acceleration at the top of the main frame may reduce by approximately 2/3 relatively to those of the corresponding aseismic structure.

In Figure 5, A_{max} and Δ_{max} are respectively defined as the maximum displacement and the maximum acceleration of various floors in the main frame, H is defined as the floor height of main frame.

Figure 6 shows the time history responses of the absolute accelerations at the top of the secondary-frame 3 and 4 in the semi-active control structure, which contrast with that of the corresponding aseismic structure.

In Figure 6, $a_T(4)$ and $a_T(3)$ are respectively defined as floor acceleration of secondary frame 4 and 3, and t is defined as time of earthquake.

Figure 7 shows the maximum accelerations of various floors of secondary frame 3 and 4 in the semi-active control structure and the corresponding aseismic structure, which indicate that the damping effect of the linear optimal semi-active control may be evident, and the maximum accelerations of various floors of the secondary frame 3 and 4 may decrease by 60%–75% relatively to that of the corresponding aseismic structure.

5 CONCLUSIONS

The overall objective of this study was to investigate the effectiveness of controllable dampers in reducing the earthquake response of vibration-absorption megaframe structure. Linear optimal semi-active control algorithm has been presented which can control simultaneously the structure displacement, velocity and acceleration subjected to earthquake, from which the Riccati equation has been revised. According to the algorithm, the earthquake responses of vibration-absorption megaframe structure have been analyzed. The results indicate that the semi-active control may be able to more effectively suppress the vibration displacement response of the main frame, and to more significantly reduce the vibration acceleration response of the main and the secondary frame.

REFERENCES

Calise, A.J. & Sweriduk, G.D. 1994. Active Damping of Building Structures Using Robust Control. *Proc. U.S. 5th Nat. Conf. Earthquake Engrg. Earthquake Engrg. Research Inst., El Cerrito, Calif.*.

Crai, J. 1993. et al. Active-passive Damping for Structural Response Attention in Building Using Cladding. *Proc. of ATC-17-1 Seminat on Seismic Isolation, Passive Dissipation, and Active Control, San Francisco.*

Dowdell, D.J., & Cherry, S. 1994b. Semi-active Friction Dampers for Seismic Response Control of Structures. *Proc. U.S. 5th Nat. Conf. Earthquake Engrg. Earthquake Engrg. Research Inst., El Cerrito, Calif.*.

Fahim, S. & Bijan, M. 1998. Semiactive control algorithms for structures with variable dampers. *Journal of Engineering Mechanics* 981(9): 534–541.

Hrovat, D., Barak, P., & Rabins, M. 1993. Semi-active versus passive or active tuned mass dampers for structural control. *J. Engrg. Mech. ASCE* 109(3): 231–238.

Kannan, S., Uras, H.M. & Aktan, H.M. 1995. Active control of building seismic response by energy Dissipation. *Earthquake Engrg. and Struct. Dyn.* 24(5): 76–82.

Loh, C.H. & Ma, M.J. 1994. Active-damping or Active-stiffness Control for Seismic Excited Buildings. *Proc. 1st World Conf. on Struct. Control. Int. Assoc. For Structural Control, Los Angeles, Calif.*.

Masata, A. 1996. Semi-active tuned mass dampers for seismic protection of civil structures. *Earthquake Engineering and Structural Dynamics* 25(6): 193–198.

Miller, R.K., Masri, S.F., Dehghanyer, T.J. & Caughey, T.K. 1988. Active vibration control of large civil structures. *Journal of Engineering Mechanics* 114(9): 123–128.

Feng, Q.M. and Akira, M. 1995. Vibration control of tall buildings using mega subconfiguration. *Journal of Engineering Mechanics* 10(3): 53–59.

Patten, W.N., Kuo, C.C., He, Q., Liu, L. & Sack, R.L. 1994a. Seismic Structural Control via Hydraulic Semi-active Vibration Dampers (SAVD). *Proc. 1st World Conf. on struct. Control. Int. Assoc. for structural Control, Los Angeles, Calif.*.

Tzan, S. & Pantelides, C.P. 1994. Hybrid structural control using viscoelastic dampers and active control system. *Earthquake Engrg. and Struc. Dyn.* 23(19): 112–118.

Civil Engineering and Urban Planning IV – Liu et al. (Eds)
© 2016 Taylor & Francis Group, London, ISBN 978-1-138-02903-3

Evaluation of Russia's innovation activity levels in construction

V.I. Telichenko & A.A. Benuzh
Moscow State University of Civil Engineering, Moscow, Russia

ABSTRACT: This article presents a comparative evaluation approach at the level of innovation activity in the construction industry in Russia. There are a total of 15 elements: Labor efficiency; Construction materials; Technologies and means of mechanization; Automation and intellect; Regulatory support; Legal and legislative frameworks; Pricing; Forecasting, planning, design; Information systems; Planning and management methods; Investment environment; Technetronic and ecological safety; Energy conservation; Education system and personnel training; Organization of scientific activities. These elements define the core spheres of the building sector that need to be identified. Based on the methods of expert evaluation, a quantitative index of the aforementioned elements is set in the range of /+3/ – / –3/. In terms of innovation levels and its dynamics, a simple analysis shows that Russia's construction industry succumbs to the same state of affairs as the innovation development of Russia's economy.

1 INTRODUCTION

In Russia, the term "innovation" became actively employed in construction and manufacturing industries about 8 to 10 years ago. At first, it was used with a sense of irony to it, i.e. there is no need to use foreign neologies since the Russian language has a variety of other words similar in meaning: development, novelty, improvement, and enhancement. "Innovation", however, spread in an avalanche-like manner into every part of modern life, propagating into a kind of worship and breaking through the stringiest of skeptics and conformists. Nowadays, from nanotechnology to business to traditional management and planning methods, few are bothered by "innovation". Furthermore, evaluation procedures exist to identify the level of innovation in a particular industry. Like a share of something new was discovered in what was thought to be a thoroughly examined trade. For example, a study (Fedoseyev 2012) demonstrated that companies focusing their activities on innovative procedures amount to around 5% in the construction industry and 9.3% in the manufacturing industry. Yet, prior to advancing into quantitative and qualitative analysis of innovation processes in construction, one must define the instances when the understanding of necessity and demand of development, novelties, improvements, and enhancements would occur.

The bases of any plant or production industries are "technologies". Numerous terms with systemic understanding attached to them such as "atomic technologies", "laser technologies", "medicinal technologies", "food technologies" and others are widely accepted.

Currently, the expression "construction technologies" carries a systemic meaning, which includes the following basic elements of industrial construction process: construction design, materials, resources, methods, medium, and parameters; these elements define the processes of production, management and control and ensure the creation of finished construction products in the broadest sense (Telichenko et al. 2012).

Obviously, the development of construction technology elements is uneven, since they are attributed to various segments of engineering. For example, rapid advancements in material sciences are supported rarely by the progress in construction machinery, which employ the newly discovered qualities of innovative materials. Similarly, this concept works on constructive building solutions when thermal protection issues are solved in terms of the thickness of the walls as opposed to effective thermo-isolation materials.

At different times, the discrepancy of some elements between other components of the integrated technological process becomes apparent. Thus, efficiency plunges, costs inflate and the quality of the end product drops. These periods, defined as "technological barriers", are possible to overcome the use of extensive novelties, i.e. innovations. Such a model of innovative advancement is indicative of construction technologies. Technological barriers are for the most part determined by the discrepancy in methods and forms of production organization, and production systems management, lagging behind in adopting new forms of management, control, pricing, rate setting, investment planning and other intangible production processes.

2 EVALUATION FRAMEWORK

Here, we consider 15 key components, in which the changes occur based on a continuous stream of novelties and could be defined as a process of innovation creation and implementation. We assume that these components hold an equally distributed weight in the overall evaluation of innovation levels in construction, allowing for a certain degree of discrepancy between them. Quantitative evaluation of each component's level is produced through expert methods when it is imperative to convert qualitative data into quantitative one. Comparative evaluation is composed of linguistic (verbal) criteria such as very high (+3), high (+2), medium (0 – +1), low (–2), and very low (–3). Each of the components is discussed in detail below.

2.1 *Labor efficiency*

This component is one of the main problems in the Russian construction industry, where numerous processes that are small and labor-intensive are difficult to execute with mechanical means. The level of labor efficiency in construction is very low and can only be compared with agriculture. This component is also one of the major reserves in advancing to a high-tech production industry. It is possible to properly apply this component through accurate and competent production management. Therefore, based on the method of expert evaluation mentioned above, labor efficiency is evaluated as (–3). For all the other components, the same method of expert evaluation will be used.

2.2 *Construction materials*

The level of innovation in material sciences in construction is fairly high. Moreover, many innovations find practical applications at a short span of time, becoming conventional and in demand, which further increases their innovation potential. We point out that material sciences for the most part define the knowledge content in construction utilizing advanced scientific instruments such as nanotechnology (+3).

2.3 *Technologies and means of mechanization*

In the face of widely spread applications of hand labor, many might think that technological processes in construction are poorly mechanized, but in fact that is not so. Modern construction technologies often represent huge technological complexes that are highly mechanized and even automated. Thy include "slurry wall", augur piles, cast-reinforced concrete, formwork systems and others. Modern construction machinery and mechanisms are up to par with requirements in terms of efficiency, product range, and handling convenience. The innovation cycle of mechanical equipment is unparalleled to that of construction materials and takes years, sometimes decades, which in part is often the cause of technological barriers (+2).

2.4 *Automation and intellect*

Construction industry is far behind when compared with high-tech industries such as automobile manufacturing. At the same time, the level of automation processes for developing materials in construction is fairly high. Currently, intelligent control systems are being developed, which can lead to construction shifting towards becoming a more high-tech industry. Overall, this component scores low (–1).

2.5 *Regulatory support*

The industry of construction has deteriorated significantly since the 1990s when a lean system of Soviet SNiP (construction rules and regulations) codes was abandoned. Stagnating now for over 20 years, a movement to recreate the rigid Soviet regulation system is seen. However, such an approach is difficult to identify as innovative. Furthermore, present conditions of this component are probably the main cause of technological barriers in the industry (–3).

2.6 *Legal and legislative frameworks*

This component corresponds to the overall situation of the industry. Legal and legislative frameworks are accepted, corrected, subjected to real-life practices and corrected again. The Town Planning Code illustrates this as it is still in the process of correction. This process can be characterized as innovative if not in principle then in form. Thus, the level of legal and legislative frameworks in construction could be evaluated as medium (+1).

2.7 *Pricing*

Pricing is in a worse shape than the previous component. For a long time, the industry has functioned by applying increasing coefficients, basing its judgments on the cost of materials, construction-assembly, project design work and other services. This in conjunction with the 94th code on project tenders destabilized the situation, causing the disruption of contracts, discreditable practices and, finally, a crisis in the construction market. Recently, pricing, the crucial part of the construction industry, has developed further, not only as an element of the market, but also as an instrument of control on various levels, corresponding to the current demands of energy efficiency, application of modern project

solutions, and safety. Overall, the level is evaluated as low (–1).

2.8 *Forecasting, planning, and design*

Forecasting, planning, and design always played a significant role in construction. Terms such as "structural design of airplanes" and "naval structural mechanics" exist for a reason. This terminology highlights the demands and practices for developing and accommodating project solutions. Nowadays, architects, project planners, and construction workers are able to form, calculate, design and build virtually any building or structure. However, the question of operating these structures efficiently and safely remains unanswered. This is where construction intersects other areas of human activities such as society, mentality, and personnel. The level is evaluated to be very high (+3).

2.9 *Information systems*

Construction specialists are removed from developing efficient information systems and professional software, but are their active users. It is difficult to imagine architectural and project offices, building companies and even construction platforms without modern information systems. Moreover terms such as virtual construction project exist, where a group of project participants cooperate, develop solutions, make corrections, and manage the projects remotely. CAD, CAM, and CALS technologies and other software are widely utilized and accepted as conventional (Telichenko & Morozenko 2012). The level is evaluated as very high (+2).

2.10 *Planning and management methods*

This component does not carry anything to be proud of. We often feel that the industry forgot about terms such as CMS, work performance project, process chart, and regulations. Planning and management methods are the reason for the high volumes of manual labor, overvaluation, and low quality. This can be interpreted as a side effect of low level of education and qualification, since almost everyone tries to get into construction. On the other hand, even professionals seem to have this management nihilism. For the most part, these negative processes are due to the significant decline in the number of knowledgeable workforce. This in part is a technological and staff barrier, leading the evaluation to stand at the low level (–1).

2.11 *Investment environment*

Construction industry can easily compete with any other in terms of this component's level and innovation dynamics. Construction workers are always interested in profitability, investment, absorption and circulation of money, employing governmental and private capital, and borrowing money from the public and from other construction agents. The development of the investment environment is often associated with high levels of competition and task division, where a prime contractor outsources parts of the project to various subcontractors, partners, and suppliers. Efficiency of investment ranks high on the list, which is predominantly determined by the long investment cycle. The level is evaluated as very high (+3).

2.12 *Technetronic and ecological safety*

Construction activities greatly influence the surrounding environment. Safety is one of the key principles of modern construction. During the last decade, the topic of technetronic and ecologically safe building has developed greatly. Terms such as "sustainable development", "construction system safety", "ecologically safe building", "complex construction safety", "green building", "biosphere compatibility", and others have become a commonplace in the industry.

These advancements could be considered as innovative development of this component. Innovations are introduced at a much slower pace in the actual construction, regulatory and legislative frameworks. This component has the potential to drag the industry to become a sci-tech priority. Today, the level of generating and studying innovations in terms of providing a plethora of security solutions in construction could be considered as medium (+1).

2.13 *Energy conservation*

Despite the relevance and innovativeness of this component in sci-tech and practical areas of construction, the industry has nothing to be proud of here. Vast room for improvement exists, yet all efforts are sidelined by outdated regulatory frameworks, investors focusing on quick short-term returns, rundown engineering communication lines, and fear of enormous capital expenditures to modernize housing and utilities infrastructure.

According to the specialists of "Korolev GmbH" from Germany, the euro investment amount to modernize only the heat supply systems in Russian cities would be around EUR 40 billion (Telichenko & Gogina 2012). Innovative solutions for this project are yet to find support from the industry, which is indicative of practical measures of fixing energy conservation issues in Russia. This is definitely a technological barrier that leads to have its level evaluated as very low (–3).

2.14 *Education system and personnel training*

In the Soviet Union and later in Russia, a lean training system existed for workers and specialists. The system covered every aspect that was essential to provide continuous education from high school to graduate to doctoral programs. Following the dissolution of the Soviet Union, the system suffered the same fate. Certain crucial elements such as basic vocational training were dropped, intermediate vocational training was significantly cut, and further vocational education became irrelevant, i.e. the system of talent management in construction. Practically, only higher construction education remained.

Universities were the ones that undertook the problem of education and scientific research within the industry (Telichenko 2011). Also, since the industry, with the dissolution of the Soviet Union, virtually disintegrated, practically all the responsibilities for innovation in construction education and science were piled up in the Ministry of Education, although this situation was indicative of not only the construction industry.

The efforts to consolidate industrial institutions and cooperation in terms of education and personnel training allow for the level of this component to be evaluated as high (+1).

2.15 *Organization of scientific activities*

Science has a special role in technological development, new knowledge creation, and generation of innovative ideas. Construction science has tremendous merits and traditions. Many science areas such as material science, mechanics, design, theory of machines and mechanisms, and organization and management of large systems were formed and developed by scientists in construction.

In the 1990s, various scientific-pedagogical schools closed their doors, causing the succession of generations to be cut off, resulting in great damage to science. Thus, today, the level of innovation potential of this component is evaluated as low (–1).

3 CONCLUSIONS

Hence, based on many decades' experience of the author Telichenko V.I.—Rector of the Moscow State University of Civil Engineering, following arithmetic of the indices awarded to each component, the sum equals to +3. Today, dividing that by 15 would give us the mean level of innovation in the construction industry. That number would amount to 0.2, which is the average of innovation potential in the construction industry in Russia. It is safe to say that the rumors of innovation underdevelopment in the construction industry in Russia are exaggerated. The potential for innovation is enormous, and it will be developed in a more dynamic fashion. We agree that this article is debatable in character. However, when it comes to development, new ideas and innovations, and debates are relevant.

REFERENCES

Fedoseyev, I. 2012. Will the construction of innovative activity area for the economy. *Innovation Journal 1*: 19–22.

Telichenko, V. 2011. Development of scientific and pedagogical schools MGSU as the basis of building science and education in Russia. *Building Equipment 8*: 2–4.

Telichenko, V. et al. 2012. Comprehensive approach to decision problems of the organization residential construction in the Russian Federation. *Industrial and Civil Construction 12*: 3–5.

Telichenko, V. & Gogina, H. 2012. Evaluation flexibility of investment and construction project on the basis of information technologies. *Urbanism 2*: 72–74.

Telichenko, V. & Morozenko, A. 2012. Complex approach to carrying energy efficient modernization of residential buildings and heating systems. *Industrial and Civil Construction 4*: 62–65.

Civil Engineering and Urban Planning IV – Liu et al. (Eds)
© 2016 Taylor & Francis Group, London, ISBN 978-1-138-02903-3

The influence of a bridge deck's relative height on the damping effect of a tower-girder elastic connecting device in cable-stayed bridges

Jian Huang, Wen-Xue Zhang, Lan-Lan Zhao & Jing-Jing Wang
Beijing University of Technology, Beijing, China

ABSTRACT: The seismic response of a cable-stayed bridge is greatly influenced by the structural system. Previous studies show that a proper elastic connection between the tower and girder can improve the seismic behavior of a cable-stayed bridge. However, the conclusions are limited by ignoring the influence of different heights of gravity centers on a tower-girder elastic connecting device's damping effect in a cable-stayed bridge. In the proposed study, the influence is considered systematically by taking a certain cable-stayed bridge as the model and changing the height of the gravity center of the lower tower. The result indicates that when the height of the gravity center is low, setting up an elastic connection between the tower and girder will improve the seismic behavior of the cable-stayed bridge effectively. When the height of gravity center reaches a certain extent, setting up an elastic connection will increase the seismic displacement response instead of reducing the seismic response of internal force.

1 INTRODUCTION

A cable-stayed bridge always consists of cable tower, auxiliary pier, staying cable, main beams, and junction device. Most of its mass is supported by the main beams and the bridge deck system which also bear most of the inertial force caused by earthquake. The inertial force is then transferred to the cable tower by the stay cable and the longitudinal junction device between the tower and girder. Generally, structure systems are classified by the constraint between the tower and girder. In different structural systems, the inertial force and the seismic response pass by different paths (Fan 1997; Zhang et al. 2010; Ye et al. 2002). As the structural system of a cable-stayed bridge is directly related to its seismic performance, selecting a reliable structure system is crucial to the bridge (Xu 2003; Zhang et al. 2012). Combined with specific cable-stayed bridge seismic designs, a reliable structure system with a resilient junction device to effectively improve the seismic performance between the tower and girder is found in the previous research (Li & Di 2011; Fang et al. 2010). However, most of the studies about elastic damping on cable-stayed bridges are limited to specific cable-stayed bridges without considering the impact of changes in the relative deck heights of cable-stayed bridges (Zhang et al. 2012; JTJ004 1999). Hence, it is necessary to study the effects of resilient junction device between the tower and girder on seismic performance of a cable-stayed bridge whose relative deck height varies.

2 PROJECT TO RELY ON AND MODELING

The main span of the cable-stayed bridge in the project is 386 m with the span portfolios of 60 m + 60 m + 160 m + 386 m. The type of cable tower is an inverted Y and constructed using C50 concrete. The main girder is the steel box presented as flat and streamlined. The height of the beam centerline is 3.5 m and the top width is 40.80 m. The ballast, 139 meters long, is distributed at the range of side spans. The total weight of the ballast on the bridge is 6388 t and the maximum ballast load is 63 t/m. The period of the response spectrum of the bridge site with exceeding probability of 2% in 50 years is 0.55 s and the peak acceleration is 149 cm/s^2. Based on the above statement, three artificial seismic waves are generated and the spectrum characteristics of that are shown in Figure 1.

Models with different connection stiffness between the tower and girder were built by SAP. In the models, cable towers, main girders, auxiliary piers, and the common piers were all discrete space beam elements. They were connected with double cable planes by means of the main and auxiliary constraints forming a fish-bone model. Fixed-end constraint simulation was adopted on the cable tower and bridge piers with transverse coupling constraint among main girder, auxiliary piers, and the common piers. As shown in Figure 2, no longitudinal constraint existed. The relative height of the deck of the cable-stayed bridge changed with the height of the lower pylon column. Take the

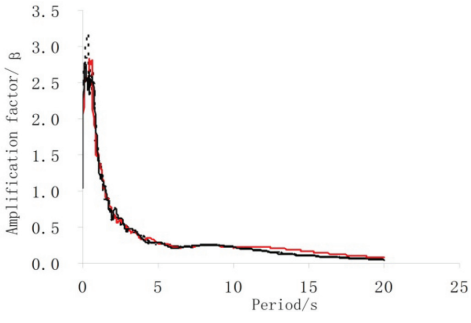

Figure 1. The spectrum characteristics of the three artificial seismic waves.

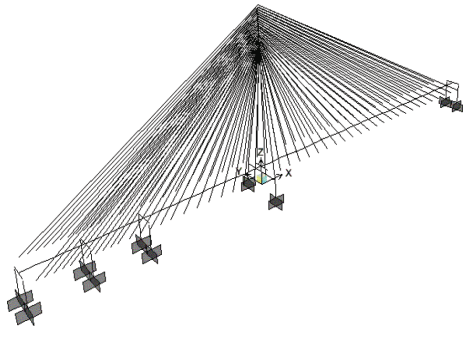

Figure 2. The finite element model for structure analysis.

ratio k = h_1/ h_0 as variable, where h_1 is the height of lower cable tower and h_0 is the total height of the cable tower, to analyze the influence of the relative height of the cable-stayed bridge deck on the damping effect of resilient junction device between the tower and the girder.

3 OPTIMIZING THE EFFECT OF RELATIVE HEIGHT OF DECK TO THE ELASTIC CONNECTION STIFFNESS

To analyze the effects of the relative height of the bridges on seismic response of the resilient junction system between the cable towers and the main girder, the models with different connection stiffness between cable towers and the main girder were built by varying k from 0.1 to 0.8, where k means the ratio of the height of lower cable tower h_1 to that of the whole tower h_0. The analyses of the results are shown below. The value in Figures 3–8 is the average value of the maximums of structural response under the three artificial waves shown in Figure 1.

3.1 *The internal force response optimization*

The results of internal force response of the cable-stayed bridge shown in the Figures 3–6 have different relative heights of bridge deck and resilient junction stiffness. The conclusions are:

– When the cable-stayed bridge has a relative low height (K = 0.1~0.4), namely a low-height gravity

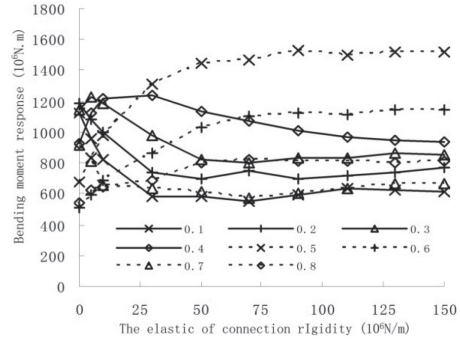

Figure 3. Bending moment response in tower bottom.

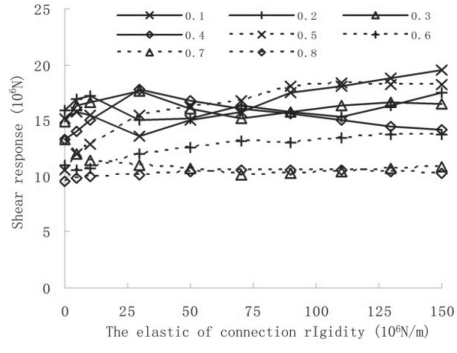

Figure 4. Shear response in tower bottom.

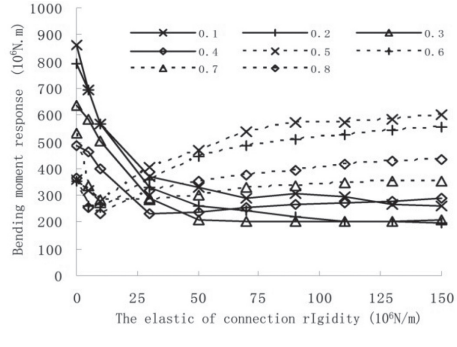

Figure 5. Bending moment response in upper tower bottom.

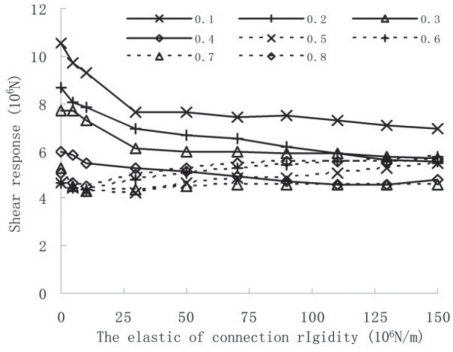

Figure 6. Shear response in upper tower bottom.

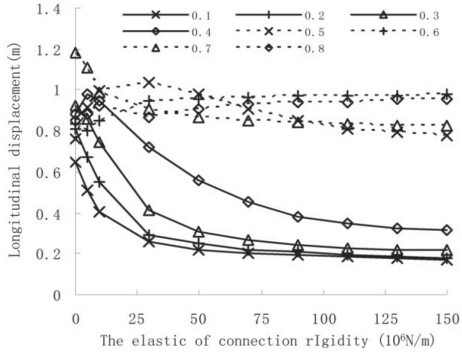

Figure 7. Longitudinal displacement response in beam end.

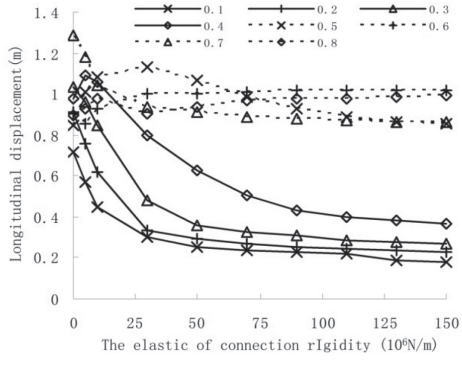

Figure 8. Longitudinal displacement response in tower top.

center cable-stayed bridge, the resilient junction device that is set between the tower and girder can reduce the structural seismic response effectively. When the resilient junction device has a small stiffness, it can effectively reduce the bending moment at the middle and bottom of cable-stayed bridge and cable tower and keep shear force stable. Meanwhile, for the main tower, the moment response of key sections decreases with the increase in stiffness. However, when the stiffness increases to a certain extent, the trend that the cable tower bottom bending moment response decreases with the increase of stiffness of the resilient junction device which brings down gradually and even has opposite trend. Meanwhile, a large fluctuation of the tower-bottom shear response appears.

- When the cable-stayed bridge has a relative high height, namely a medium-height gravity center cable-stayed bridge, the resilient junction device that is set between the tower and girder will not reduce the tower-bottom bending moment response. Instead, it increases the bending moment and shear force of the tower bottom. Therefore, in this case, the resilient junction device can't effectively improve the seismic internal force response for the medium-height gravity center cable-stayed bridge.
- When the cable-stayed bridge has a further relatively high height, namely a high-height gravity center cable-stayed bridge, the resilient junction could influence the moment and shear force of the tower-bottom in the cable-stayed bridge, and the influence can either be advantageous or not. However, the impact range is relatively slight.
- For the cable-stayed bridges whose relative height of deck is low, the resilient junction can reduce the damping effect of bending moment and shear force at the tower-bottom. And with the stiffness of elastic connection increasing, the bending moment and shear force of tower-bottom decrease more than 60% and 30%, respectively.
- For the cable-stayed bridges whose relative height of deck is high, the results of setting resilient junction device between the tower and girder depend on the stiffness of resilient junction device: when the stiffness of resilient junction device is less, the bending moment and shear responses of the tower bottom decrease with the stiffness increasing; however, when the stiffness increases to a certain extent, the responses increase with the stiffness increasing.

3.2 *Displacement response optimization*

When the relative heights of bridge deck are different, the stiffness influences of resilient junction device between the tower and girder on seismic displacement response of the cable-stayed bridge are shown in Figures 7 and 8, the conclusions are:

- The influences of setting the resilient junction device between the tower and girder on longitudinal displacement responses of beam end and

tower top are nearly the same for cable-stayed bridges with different heights of bridge deck.
- When the deck of the cable-stayed bridge is relatively low, such as the value of k is from 0.1 to 0.4, setting the resilient junction device between the tower and girder can effectively reduce the longitudinal displacement responses of the beam end and tower top, lowering by 40%~70%. When the stiffness of the resilient junction device is small, the longitudinal displacement responses of beam end and tower top reduce rapidly with the increase of stiffness of the resilient junction device; when the stiffness of the resilient junction device increases to a certain extent, the trend that the longitudinal displacement responses of beam end and tower top decrease with the increase of the stiffness of the resilient junction device begins to slow down obviously.
- When the deck of cable-stayed bridge is relatively high, such as the value of k is form 0.5 to 0.8, setting the resilient junction device between the tower and girder can't effectively reduce the longitudinal displacement response of the cable-stayed bridge. It may even lead to an increased response instead.

4 CONCLUSION

In this paper, the finite element analysis model was developed based on a project of a single-tower cable-stayed bridge. Then, the influence of relative height of the cable-stayed bridge deck on the damping effect of the resilient junction device between the tower and girder was studied systematically. The following conclusions can be drawn:

- The relative height of cable-stayed bridge deck has a great influence on the damping effect of the resilient junction device between the tower and beam. When the relative height of cable-stayed bridge deck is low, the bending moment response and displacement response of key sections of cable tower of cable-stayed bridge can be reduced significantly by optimizing the elastic connection stiffness with slight even no increase of the shear response at the bottom of the tower. In this way, a preferable shock-absorbing effect can be achieved.
- With the increase of relative height of the cable-stayed bridge deck, the damping effect of cable-stayed bridge achieved by setting the resilient junction device between the tower and girder decreases gradually. When the relative deck height increases to a certain extent, instead of reducing the seismic response of internal force, setting up an elastic connection will increase the seismic displacement response.
- When cable-stayed bridges are under seismic action, if the elastic connection between the girder and tower was set up properly, at the bottom of the bending moment, the shear force could be reduced and the vertical displacement of the tower and beam can have better inhibition. But the deck's relative height in cable-stayed bridges has a great effect on shock absorption effect of flexible connecting devices. The research results should be considered when cable-stayed bridges are designed. Then the elastic connection device can play a better role.

ACKNOWLEDGMENT

This work was supported by Projects of National Natural Science Foundation (51378034/E080505) and Beijing Natural Science Fund Project (8122007).

REFERENCES

Analysis of super-long-span cable-stayed bridge's structure system. *Journal of Tongji University* 31(4): 400–403.

Fan, L.C. 1997. *Bridge Seismic.* Shanghai: Tongji University Press.

Fang, Y., Li, J.Z., Peng, T.B. & Deng, Y.L. 2010. Influence of travelling-wave effect on seismic response of a long-span multi-tower cable stayed bridge. *Journal of Vibration and Shock* 29(10): 148–152.

Journal of Shijiazhuang Railway University 23(2): 88–93.

Li, Y.C. & Di, Q.S. 2011. Numerical simulation of dynamic characteristics of a cable-stayed aqueduct bridge. *Earthquake Engineering and Engineering Vibration* 10(4): 570–579.

Ministry of Transport of the People's Republic of China. 1999. *Seismic Design Specifications of Highway Construction (JTJ004-89).* Beijing: People's Communications Press.

Xu, L.P. 2003. Analysis of super-long-span cable-stayed bridge's structure system. *Journal of Tongji University* 31(4): 400–403.

Ye, A.J., Hu, S.D. & Fan, L.C. 2002. Research on aseismic structure system of cable-stayed bridge. *Bridge Construction* (4): 1–4.

Zhang, W.X., Bao, Y. & Wang, J.J. 2012. Influence of expansion joint clearance and longitudinal damper in cable-stayed bridge earthquake impact. *Highway Traffic Science and Technology* 29(8): 60–63.

Zhang, W.X., Wang, J.J. & Bao, Y. 2012. The study of Zhang, W.X., Wang, J.J. & Bao, Y. 2012. The study of cable-stayed bridge and approach bridge earthquake impact influence factors. *Vibration and Shock* 31(23): 115–117.

Civil Engineering and Urban Planning IV – Liu et al. (Eds)
© 2016 Taylor & Francis Group, London, ISBN 978-1-138-02903-3

Causes of explosion in section c of the diversion tunnel under construction at Zengwen reservoir

P.C. Lee & H.H. Pan
Department of Civil Engineering, Kaohsiung University of Applied Sciences, Kaohsiung, Taiwan

S.P. Ho
Department of Occupational Safety and Health, Chang Jung Christian University, Tainan, Taiwan

ABSTRACT: A diversion tunnel project at Zengwen Reservoir, Taiwan, was made to increase its water storage. During the cleanup operation after blasting this tunnel, flammable vapor clouds leaked from the rock drums and sunk down to where they contacted with a flammable source and exploded. This research conducted field investigations to assess the course of the accident and the scene after the explosion, while collecting oil and gas samples inside and from a nearby tunnel in order to undergo Gas Chromatography-Mass Spectrometer (GC-MS) analysis. By comparing the samples from different sections of the diversion tunnel, results showed that large amounts of flammable gases, light oil, and medium oil were inside the tunnel when it exploded. The application of GC-MS during investigation is crucial in the identification of material compositions. In addition, the top portions of the tunnel contained dead spaces where flammable gases could accumulate and reach explosion limits.

1 INTRODUCTION

Tunnels are a type of underpass which is mostly made for pedestrians, scooters, and general road and railway transportation. Nonetheless, some are made to transport water or have other specific purposes. Therefore, development of tunnels is beneficial for transportation convenience.

If flammable gases are released during construction of a tunnel, it could result in a fire or explosion. To avoid accumulation of hazardous gases inside tunnels, ventilation methods must be used to exhaust the gases. The Tunneling Association of Japan recommends that the wind speed inside tunnels be at least 0.5 m/s, while the ventilation design should allow the wind speed to be maintained at 1.0 m/s or higher in order to effectively prevent hazardous gases from accumulating at the arches of tunnels. If methane was to exist inside tunnels, the concentration should be lowered to 1.5% or lower (Ho 2004).

For measuring flammable gases, specified personnel should enter the tunnel every day before operation, after an earthquake, or any other scenario where there may be flammable gas leakage. Fixed automated detectors and portable detectors should both be used, and portable detectors should be used two to three times each day, while measurements should be repeated twice or thrice each time to ensure correct values. When choosing between detectors, the detection range and limitations of the instruments should be noted, while other factors in the environment which could affect detection should also be noted. Besides increasing the gas detection time and area, personnel advocacy and verification, equipment safety control, and personnel training, simple and convenient portable detection equipments should be provided to enhance efficiency of the people working on site, while also strengthening automated examinations (Wang 1998).

For the effect of explosions on pressure waves, Pang et al. (2014) used experiments and numerical simulations to propose the changes in shockwave overpressures against increasing distances for a methane pipe explosion. The trends are increasing overpressure values for increasing distance within 100 meters, and vice versa when the distance is more than 100 m. The flames and pressure waves caused by explosions produce temperature heat, which is one of the main hazards inside tunnels. Zhang & Ma (2015) reported that pressure waves caused by explosions can be divided into static pressure and dynamic pressure; the high-speed flow caused by gas burning is classified as dynamic pressure. At the tunnel entrance, the hazard of dynamic pressure far exceeds that of static pressure, while wind caused by air flow also results in serious damage. Experiment results by Zhang et al. (2013) showed that the more branches a tunnel contains, the

larger the overpressure values. This scenario can be observed during the construction of a tunnel, when a construction adit is created beside the main tunnel construction area, which accelerates the overall process. Tian et al. (2011) used numerical methods to show that for a tunnel with one end open and the other closed, the explosive field would be reflected by the closed side of the tunnel, which would result in a catch-up effect and overlapping with the other pressure waves, thus causing a larger explosion than if the tunnel was open on both ends. Tunnels which have one end open and the other closed are common among tunnel construction projects. A research conducted by Sasmito et al. (2013) indicated that adequate flow designs can enhance gas control whilst maintaining a low pressure drop. Furthermore, additional auxiliary ventilation also enhances gas control during tunnel constructions, which can be used as reference when designing the ventilation system for a tunnel.

The diversion tunnel construction at Zengwen reservoir is for the solving of water supply in southern Taiwan. Extra water, during the wet period of Laonong river and a tributary of Gaoping river (both rivers located in Kaohsiung and Pintung counties, Taiwan), is stored in the Zengwen reservoir, thus increasing the inflow of the reservoir and increasing the utilization of the dam and its water storage. However, the explosion which occurred during the construction was so powerful that it blew a truck parked at the tunnel entrance 10 meters out, subsequently killing two workers on November 4, 2007. This research collected oil samples and conducted assessments of the course of the accident and the scene after the explosion. A more complete inspection led to uncovering the cause of the explosion, which then could be the baseline to establish standards so as to lower chances of accidents while increasing the efficiency of the construction of the diversion tunnel (Lee et al. 2009).

2 RESEARCH METHODS

During the construction of the Zengwen reservoir diversion tunnel, an explosion occurred and initial assessment results indicated a gas explosion. To find the reason which caused the accident, this paper used the methods mentioned below.

2.1 *Field investigation*

This research conducted a field investigation of the tunnel site, while also asking the engineering staff about the on-site construction, ventilation system, gas detection, and project management, so as to assess the flammable gas accumulation situation and location of ignition, and further discover the reasons for the explosion.

2.2 *Use of GC-MS to analyze the gas and liquid leakage in the tunnel*

Gas Chromatography (GC) is conducted by injecting the sample directly into the column or by heating the sample after it has entered the column. The column is heated linearly or controlled by programs, while the carrier gas and stationary phase of the components would have differing distributions based on their thermodynamic properties (vapor pressure of compound under chromatograph temperature and selectivity of stationary phase). The carrier gas would carry the compound vapor through the column, and the components would be separated based on the varying vapor pressures and selectivity of stationary phases.

The GC detector used in this research was a Flame Ionization Detector (FID) and Thermal Conductivity Detector (TCD). The Flame Ionization Detector burns H_2 in O_2 to create flames, so when the sample ionizes within the flames (ionization), an ion current is formed under an electric field, and they are gathered at the electrode to create an electric current which is then detected. The basis of TCD is when an analysis is present, the thermal conductivity of the airflow changes and is detected.

The basis of MS (Mass Spectrometer) is the production of ions that are subsequently separated or filtered according to their mass-to-charge (m/z) ratio and detected. The resulting mass spectrum is a plot of the (relative) abundance of the produced ions as a function of the m/z ratio.

The Gas Chromatography-Mass Spectrometer (GC-MS) is an instrument which combines the separation capabilities of GC and differentiating abilities of MS; the component vapor separated by GC is sent into MS to obtain information on molecular structure.

During on-site investigation of the tunnel, unknown gases and liquids were found seeping through the ceiling, walls, and floor of the tunnel. After they were collected, composition analysis was accomplished by using GC-MS to confirm the existence of flammable materials inside the gases and liquids.

The gas chromatograph used was model HP-6890 N, while the mass spectrometer was model FIONS PLAYFORM II; chromatography column was 60 m long, film thickness was 0.25 um, inner diameter was 0.25 mm, analysis duration time was 110 min, temperature of injector was 310°C, mobile gas phase was helium, and linear flow rate was 1 mL/min.

3 RESULTS AND DISCUSSION

The situation inside the tunnel was given by on-site investigation, as shown in Figure 1 with two deaths found in the tunnel. Based on the burning of the equipment at the accident scene and the blown truck at the tunnel entrance, it was determined that the cause was a gas cloud explosion.

In order to uncover the cause of this accident, the location of the fire source had to be found first. A truck inside the tunnel (Fig. 1) had its shifter (gear lever) at the top position as shown in Figure 2, meaning that it was parked, thus proving it was turned off and therefore not the source. A BH120 excavator was found turned on with its lights on during the rescue of people from the accident; also, Figure 3 shows that the key in the excavator was in the "On" position, proving that it was the fire source of the explosion.

After determining the fire source, the accumulation of flammable gases was next. The tunnel possessed a ventilation system and some fixed gas detectors while personnel used handheld instruments to measure the gas concentration; nevertheless, an explosion still occurred, which is why this investigation focused on the ventilation and gas detection inside the tunnel.

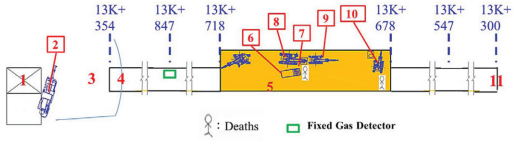

1. Control Room of Sewage treatment plant
2. Grouting Machine
3. Entrance
4. Tunnel Entrance
5. Near the Explosion Center
6. Truck
7. Middle of Excavator and Truck
8. Excavator-PC228
9. Excavator-BH120
10. Excavator-BH30
11. Excavation Position

Figure 1. Situation inside of the tunnel.

Figure 2. Truck inside tunnel with shifter at the top position.

Figure 3. BH120 excavator with the key in the "On" position.

3.1 *Situation of ventilation and gas detection inside tunnel*

After interviewing the workers on-site, it was recognized that hazardous gases would continuously be monitored during drilling and that flammable gas detectors (fixed automated detectors) shown in Figure 1 were installed at heights of 1.8 m inside the tunnel, with all of the measured values being lower than the permitted concentration. During the blasting operation of the construction, blowers at the entrance would provide ventilation after blasting. An on-site engineer (specified personnel) pairing with non-periodical measurements used a four-in-one gas detector (portable detectors) and detected hazardous gases from the tunnel entrance to the digging location at about 500 m away, with the height of detection at 1.3–1.6 m.

Due to influence of the air flow on the flammable gases, some of them lingered at the top of the tunnel which was 5.8 m high; the on-site personnel could not effectively measure the concentration of hazardous gases, resulting in detection values far lower than the lower explosive limits. When the gas cloud gradually spread from the top of the tunnel to the bottom, the flammable gases exploded as it came into contact with the fire source, which in this case was the starting induced by the BH120 excavator.

Investigation found that even under ventilation conditions, flammable gases could still accumulate at the arch of tunnels; even if the gases were heavier in density than air, they could still spread with the air flow, while uneven distribution would inhibit effective detection. This is why the measured gas

concentrations near the floor were all lower than the legal standard concentrations.

After the explosion, unknown gases and liquids were found seeping through the ceiling, walls, and floor of the tunnel; this research collected them and used GS-MS for composition analysis to determine the possibility of flammable gases leaking through the rocks in the tunnel.

3.2 *Gas and liquid composition analysis*

After the accident, locations 13 K and 300~400 m had cracks in the floor which were seeping unknown gases and oils. These were collected and analyzed, with the results arranged in Table 1.

The gases were analyzed using GCFID, with results showing in Table 2 that methane was the most at 844,535 ppm, and by using GCTCD, as listed in Table 3, methane occupied up to 94.86%, which means that large amounts of methane gas was leaking from the rocks. Methane is flammable and is lighter than air and floats upward easily which allowed it to accumulate at the arch of the tunnel 5.8 m above the floor. The gas detectors installed in the tunnel were at a lower position (1.8 m) while the handheld devices used by engineers were also used at lower heights (1.3~1.6 m), resulting in ineffective measurements. Methane would proceed to accumulate, and then exploded when a fire source was presented.

Table 1. Gas and oil samples in tunnel at locations 13 K and 300–400 m.

Location	Sample	Layer of exposure	Ignited or not
West tunnel 13 K + 300~400 m	Cracks in floor with bubbles	Limestone layer	ND

Table 2. GCFID analysis.

No	Substance	Concentration (ppm)
1	Methane	844,535.00
2	Ethane	31,669.70
3	Propane	3,544.18
4	iso-butane	501.32
5	n-butane	206.53
6	iso-pentane	52.65
7	n-pentane	9.79
8	n-hexane	1.61
9	n-C7	1.71
10	Benzene	34.77
11	n-C8	3.07
12	Toluene	28.19

Liquids were collected from two locations, one was a dark brown oil slick at 13 K + 300 m, which was analyzed by GC-MS and produced the total ion chromatogram labeled in Figure 4; the other was a dark brown suspended emulsion at 13 K + 340 m and its GC-MS results are shown in Figure 5.

The analysis of the oils from two locations at 13 K + 300 m and 13 K + 340 m were compared with a standard result from a mixture of gasoline and diesel fuel as shown in Figure 6.

Table 3. GCTCD analysis.

No	Substance	Percentage (%)
1	C5 = /C6+	0.0105
2	Carbon dioxide	0.2405
3	Propane	0.2177
4	i-Butane	0.0307
5	Ethane	3.4852
6	Propadiene	0.0005
7	n-Butane	0.0131
8	i-Pentane	0.0033
9	Oxygen	0.3227
10	Nitrogen	0.8144
11	Methane	94.8616

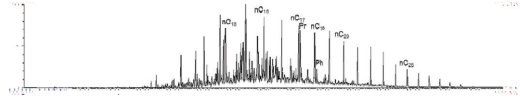

Figure 4. GC-MS results at 13 K + 300 m of tunnel.

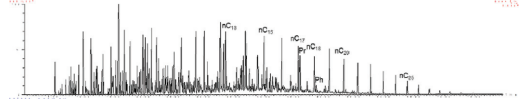

Figure 5. GC-MS results at 13 K + 340 m of tunnel.

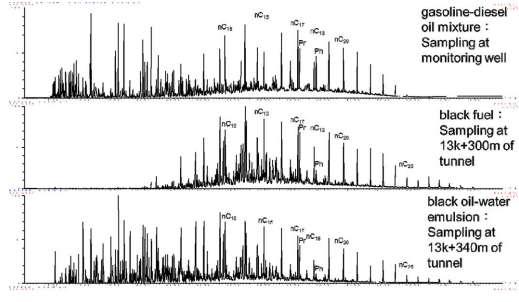

Figure 6. Composition comparison at 13 K + 300~400 m of tunnel.

Comparisons showed that the sample contains light oil and medium oil; also, oil collected inside the tunnel before the accident also contained light oil and medium oil, meaning the rocks in this tunnel contained flammable liquids besides flammable gases, which volatilized into flammable vapors that contributed to the explosion.

Based on the composition analysis from the scene, the rocks in the tunnel contained methane and ethane amongst other gases, and also light oil and medium oil amongst other liquids, which are all flammable substances, therefore being judged as the source of the explosion. From this case, the importance of using GC-MS and other equipment for composition analysis can be noted. In the future, chromatograms of oils and flammable gases should be established for the convenience of comparing the type of leaked substance if a tunnel explosion was to occur.

4 CONCLUSION

GC-MS analysis results of samples inside the tunnel showed that the tunnel contained large amounts of flammable gases along with light oil and medium oil. Methane posed as the majority, while the total of methane and ethane alone took up near the totality of all the gases combined. This shows that the rocks in the tunnel are filled with hazardous gases; when leaked into the tunnel and mixed with air, it produces a gas cloud explosion when upon contact with a flammable source. These results show that careful sampling and the use of GC-MS for comparisons can confirm the actual reasons for the accident.

This accident resulted from leaking flammable gases after excavation, which could have been a mixture of methane, toluene, xylene, and other flammable vapors. Surveying for flammable hydrocarbons before construction to ensure safety during excavation is required. Monitoring the concentration of hazardous gases during construction should also be considered, while fixed instruments should be used along with handheld instruments. Tunnels sections top, middle, and bottom and left, middle, and right should be measured, while the height should reach the tunnel arch; calculations should also be done for the detection delay time when the probe is touching the ceiling so as to ensure the validation of the measurements. Gas measurements have to be conduct periodically to avoid any negligence; if unknown leaking gases or liquids are detected, instrumental analysis should be conducted immediately to confirm the compositions of the gases or liquids, and corresponding protective measures and ventilation should be executed to ensure construction safety.

ACKNOWLEDGMENTS

This work was partially supported financially by the Taiwan Ministry of Science and Technology under MOST 103-2221-E-151-048.

REFERENCES

Ho, T.Y. 2004. Investigation and countermeasures during encounter of flammable gases in tunnel construction. *CECI Engineering Technology* (63).

Lee, B.C., Shu, F.Y. & Chen, M.C. 2009. Explosion disaster prevention for tunnel projects based on explosion case of diversion tunnel construction plan for Zengwen reservoir. *Industrial Safety and Health* 244: 48–57.

Pang, L., Wang, T., Zhang, Q., Ma, Q. & Cheng, L. 2014. Nonlinear distribution characteristics of flame regions from methane–air explosions in coal tunnels. *Process Safety and Environmental Protection* 92(3): 193–198.

Sasmito, A.P., Birgersson, E., Ly, H.C. & Mujumdar, A.S. 2013. Some approaches to improve ventilation system in underground coal mines environment–A computational fluid dynamic study. *Tunnelling and Underground Space Technology* 34: 82–95.

Tian, C.M., Wu, Y.B. & Lo, C.F. 2011. Characteristics of in-tunnel explosion-induced air shock wave and distribution law of reflected shock wave load. *Journal of Vibration and Shock* 30(1): 22–26.

Wang, S.L. 1998. Accident analysis–How to reach the goal. *Labor Safety and Health Newsletters* (27): 15–17.

Zhang, P., Du, Y., Zhou, Y., Qi, S., Wu, S.L. & Xu, J.F. 2013. Explosions of gasolineeair mixture in the tunnels containing branch configuration. *Journal of Loss Prevention in the Process Industries* 26(6): 1279–1284.

Zhang, Q. & Ma, Q.J. 2015. Dynamic pressure induced by a methane–air explosion in a coal mine. *Process Safety and Environmental Protection* 93(): 233–239.

This page intentionally left blank

Civil Engineering and Urban Planning IV – Liu et al. (Eds)
© 2016 Taylor & Francis Group, London, ISBN 978-1-138-02903-3

The effects of hole ratio on the failure probability of masonry structures

Ting Lv & Rong-Yue Zheng
Faculty of Architecture, Civil Engineering and Environment, Ningbo University, Ningbo, Zhejiang, China

ABSTRACT: In recent years, many masonry structure accidents happened and brought great dangers to the safety of people's life and property. A common cause of the collapse of masonry structures is people renovating their buildings unauthorized. In this paper, ANSYS software and Monte–Carlo method are combined to simulate the failure of masonry walls under different loads and with different hole ratios; probability design method is applied innovatively in the analysis of structural failure.

1 INTRODUCTION

Masonry structures are widely used and have a long history. According to statistics, masonry walls still account for more than 90% of all walls in urban and rural construction in China (Yan & Liu 2014). In addition, masonry structures play a significant role in the construction of socialist modernization. However, safety misadventures caused by the collapse of masonry structures are very common; these misadventures inflict great losses of life and property on people.

Due to the lack of experience in design and advanced construction technology, buildings constructed during the 1950s and 1980s are gradually outdated after long-term use. Besides people's living standards are improving with an expanding economy, higher demands for individuation, and complete function of buildings must surely follow. In an attempt to meet their demands, many people renovate their buildings unauthorized. It is rarely realized that these behaviors may lead to serious consequences (Paulo 2014).

On May 20, 2013, the collapse of an under renovation building in Fuzhou, Fujian province trapped more than a dozen people. The building was a hybrid structure built in the 1970s; illegal renovation was the major reason why the building collapsed. On December 16, 2012, a six-story civilian building collapsed in Ningbo, Zhejiang province. The accident killed one person and injured one more. There were two main reasons for this overall collapse: first, the load bearing walls were removed; second, the construction quality of the building was poor. Further research found that removing load bearing walls, illegal follow-up constructions, and changes in appearance were common in this building. The load-bearing walls of each floor had been transformed and the ground floor was the most serious part. Such tragedies happen repeatedly in the world. Therefore, it is important to do some modeling studies on anti-collapse capacity of masonry structures (José et al. 2013).

After consulting a large volume of academic literature, we found that a lot of scholars have carried out studies on the collapse of masonry structures, but few of them combined their studies with probability design and Monte–Carlo method (Ma & Lu 2001).

Given this, analog simulations about how illegal renovations affect the failure of masonry structures were performed. Our study not only has important innovation and practicability but also has some referenced values to correlational studies.

2 SIMULATION MODELS

2.1 *The object of study and physical models*

After summarizing the tragedies caused by the collapse of buildings, it was found that illegal alterations are very common. Among all alterations, the most typical behaviors involve opening holes in the walls and performing additional constructions during use. Using a masonry wall as a proxy, the above two situations were emulated, then their effects on the failure probability of the wall were studied.

Fired common brick walls 3000 mm long, 3000 mm tall, and 240 mm thick were selected as the subjects of our study; the physical model is shown in Figure 1.

Four different simulation models were designed without ring beams and constructional columns in all models. The specific parameters are as in Table 1.

2.2 *The type of finite element models*

Nowadays, there are two kinds of finite element models for masonry structure: the first model considers that masonry structures consist of two

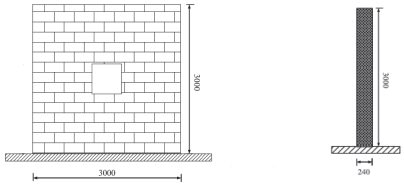

Figure 1. Front elevation (left) and left elevation (right) of the wall (units: mm).

Table 1. The specific parameters of four models.

Number of the model	Size of the hole (unit: mm)	Hole ratio (%)
1	0	0
2	600 × 600	4
3	1200 × 1200	16
4	1800 × 1800	36

kinds of materials and they should be modeled separately. The second model regards bricks and mortars as a single block (Fuschi et al. 1995). The first model requires multi-grid division and we can hardly simulate the cementation between bricks and mortars. As our goal is to study the overall reaction of the wall rather than the local details, the second method is more suitable.

2.3 *Material parameters of the model*

In our model, the strength class of mortar is M5, and the strength class of masonry is MU10. Elastic modulus of masonry structures in this case can be calculated by the following formula according to *People's Republic of China "Code for masonry structures" GB50003-2012*: E = 1600 f; f is the design value of the compressive strength of masonry structure. In this case, f = 1.5 MPa, so,

$$E = 1600 \times 1.5 = 2400 \text{ MPa}$$

According to the literature, the Poisson ratio of the masonry wall is 0.15, and the density is 1900 kg/m³ (Frankie et al. 2013).

The constitutive relation put forward by Tongji University is adopted to define the constitutive model of masonry walls. They obtain the stress–strain curve of masonry walls after regression analysis on the basis of experiments; the math expression is as follows:

$$\frac{\sigma}{f_m} = \frac{\varepsilon/\varepsilon_0}{0.2 + 0.8\,\varepsilon/\varepsilon_0} \quad (\varepsilon \le \varepsilon_0)$$

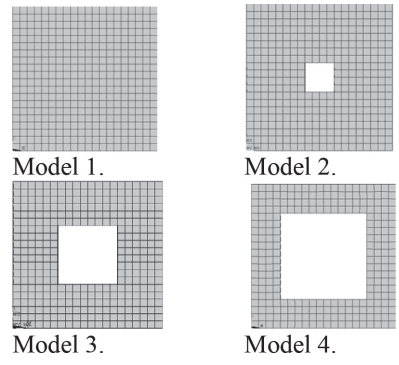

Figure 2. Four finite element models.

$$\frac{\sigma}{f_m} = 1.2 - 0.2\frac{\varepsilon}{\varepsilon_0} \quad (\varepsilon \ge \varepsilon_0)$$

ε_0 is the peak strain take for 0.02 and f_m is the average value of compressive strength of masonry.

2.4 *Loads and boundary conditions*

A vertical downward uniform surface load is applied on the top surface of the wall; the magnitude is *Fs*. In order to make the wall failure possible, *Fs* should be relatively large (Abrams et al. 2010). Considering that there is firm bounding between the wall and the ground, zero displacement constraint is applied at the bottom of the wall.

2.5 *Four finite element models*

According to the above conclusions, SOLID65 is selected to simulate the elements of monsory wall in the computational analysis. SOLID65 is in preparation for materials having similar properties as that of concrete (Mahmoud & Riveros 2013).

Finite element models are built and meshed in ANSYS, as in Figure 2.

3 PROBABILITY ANALYSIS AND MONTE–CARLO METHOD

According to the control variable method, in order to analyze how different hole ratios and loads affect the failure probability of the wall, the same load is applied on each model first and then the operation is repeated with different loads. The failure probability of each wall model is calculated with probability design method in the ANSYS software ultimately (Mahmoud & Riveros 2013).

The strength classes of the mortar and masonry are M5 and MU10, respectively. According to the state standard of the *People's Republic of China "Code for masonry structures" GB50003-012*, the design value of the compressive strength in this case is 1.5 MPa. Therefore, a statistical study should be conducted to calculate the probability of the compressive stress which is greater than the compressive strength after a large number of simulations; this is meant as the failure probability of a wall (Yang 2008).

Simulations are run using the Monte–Carlo sampling method. Monte–Carlo method, also known as stochastic simulation method or statistical experiment method, is very powerful (Ching & Hsieh 2007). Briefly, it creates a hypothesis, then provides a robust sample by simulation and reaches the conclusions by analyzing the similarities of all samples. It is based on statistical theory; according to the law of large numbers, complex problems, which can hardly be solved by the mathematical method, are approximately resolved (Ali & Page 1988). In any case, so long as the modeling is correct, we can come to a similar conclusion as that of the perfect mathematical method using the Monte–Carlo method.

By consulting massive literature, it is concluded that the density of the masonry wall ρ is uniformly distributed within the range of [1800, 2000], (units: kg/m³). The elastic modulus is subjected to Gaussian distribution with a mean value of 2400 MPa and the variance is 120. The applied force *Fs* is also subjected to Gaussian distribution with a mean of *Fs*; the confidence bounds are evaluated with a confidence level of 95%.

4 RESULTS

In order to improve the results and make them more reliable, three rounds of simulations are performed; each simulation contains three cycles and each cycle contains 1000 loops. Results are shown in Table 2 and a line chart is drawn in Figure 3.

Table 2. Simulation results.

Model no	Failure probability of the wall		
	First round of simulation (Fs = 400 kPa)	First round of simulation (Fs = 450 kPa)	First round of simulation (Fs = 500 kPa)
1	0	0	0
2	0	25.87%	68.89%
3	93.95%	99.38%	99.79%
4	1	1	1

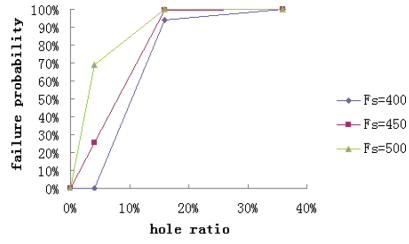

Figure 3. Line chart of simulation results.

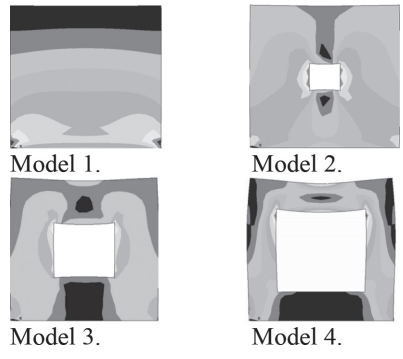

Figure 4. Four stress maps.

When *Fs* = 80 kPa, the stress maps of four models are as in Figure 4.

5 CONCLUSION

Conclusions obtained through the above-mentioned simulations results are as follows:

- Hole ratio has a significant effect on the anti-collapse capacity of masonry structures. Masonry structures perform well in collapse resistance. But once there is any hole in them, the anti-collapse capacity falls sharply.
- With the increase of hole ratio, the anti-collapse capacity of masonry structures becomes more vulnerable. Once the hole ratio reaches a certain extent, masonry structures will easily be destroyed even if the force applied is relatively small.
- For the same hole ratio, with the increase in applied force, the failure probability of masonry structures increases rapidly.

After the simulation, we learned that we absolutely could not change the housing structure unauthorized in order to avoid serious risks. If forced, the plan must be examined and verified by the designers at first. Only after doing a feasibility study can we carry on building reconstruction or perform additional constructions privately.

Collapse of masonry structures is a complex dynamic response process. This article performed simulations on failure probability of masonry structures, pioneered the use of probability theory and Monte–Carlo method in the research of building collapse, and developed a new thinking direction for many academics. However, there are still some deficiencies:

– As a numerical simulation, in order to deepen the study, more influencing factors, such as different configurations and different strengths of material, should be considered.
– As real experiments of structural collapse is destructive and expensive ande we need a lot of data with the Monte–Carlo method, we can hardly perform experiments to validate our simulation analysis.

Therefore, it calls for more intensive studies in order to overcome its shortcomings and get more precise results.

REFERENCES

Abrams, D., Fahnestock, L. & Eidini, M. 2010. Basic mechanism for Hybird masonry structures. Senapathi, S., Casey, K. & Hoit, M. eds. *Structures Congress* 2010: 987–997.

Ali, S. & Page, A. 1988. Finite element model for masonry subjected to concentrated loads. *Structural Engineering* 114(8):1761–1784.

Ching, J. & Hsieh, Y. 2007. Local estimation of failure probability function with direct Monte Carlo simulation. Kok-kwang, P. & Gordon, A.F. eds. *Probabilistic Applications in Geotechnical Engineering* 2007: 1–11.

Frankie, T., Gencturk, B. & Elnashai, A. 2013. Simulation-based fragility relationship for unreinforced masonry building. *Structural Engineering* 139(3): 400–410.

Fuschi, P., Giuseppe, G. & Rizzo, S. 1995. Nonlinear finite element analysis of no-tension masonry structures. In: *Meccanica.* Gambarotta, L. ed. Berlin:Springer.

José, del.coz., Díaz, J., Adam, J., Martínez-Luengas, A. & Alvarez Rabanal, F. 2013. Collapse of a masonry wall in an industrial building: diagnosis by numerical modeling. *Research J. Perform. Constr. Facil. Special Issue: Analysis of Structural Failures Using Numerical Modeling* 27: 65–76.

Ma, G., Hao, H. & Lu, Y. 2001. Homogenization of masonry using numerical simulations. *Engineering Mechanics* 127(5): 421–431.

Mahmoud, H. & Riveros, G. 2013. Fatigue reliability of stiffened panels using finite element Monte Carlo simulation. Leshko, B.J. & Mchugh, J. eds. *Structures Congress* 2013: 699–708.

Paulo, B.L. 2014. Masonry structure, overview. In: *Encyclopedia of Earthquake Engineering*. Beer, A. & Kougioumtzoglou A. eds. Berlin Heidelberg: Springer.

Spence, S., Gioffrè, M. & Grigoriu, M. 2008. Probabilistic model and simulation of irregular masonry walls. *Engineering Mechanics* 134(9): 750–762.

Yang, W.Z., 2008. Constitutive relation of masonry structure in the pressured stated. *Building Structure* 38(10): 80–82.

Yan, Q.W. & Liu. S.M. 2014. *Masonry Structure.* Hubei: Wuhan University Press.

Civil Engineering and Urban Planning IV – Liu et al. (Eds)
© 2016 Taylor & Francis Group, London, ISBN 978-1-138-02903-3

Dynamic behavior of a concrete building under mainshock-aftershock seismic sequence with a progressive damage and failure material model

J.M. Dulinska & I.J. Murzyn
Institute of Structural Mechanics, Krakow University of Technology, Krakow, Poland

ABSTRACT: In the paper the dynamic responses of a concrete structure subjected to mainshock-aftershock seismic sequences was investigated. Three components of the registered mainshock and aftershock were taken into account in the analysis. Peak ground acceleration equal 0.4 g was assumed for both shock. A one-storey shed was modeled with the ABAQUS software to represent a large concrete structure under the repeated earthquakes. For proper characterization of concrete structure behavior under the sequence of shocks a concrete damage plasticity model was assumed as a constitutive model of concrete. The obtained results indicate that aftershocks can have considerable effect on dynamic behavior of concrete structures in terms of enlarging zones affected by irreversible strains or additional damage evolution. The analysis revealed that aftershocks, which are usually not as strong as mainshocks, may result even in total loss of concrete material strength while performing in the mainshock-aftershock seismic sequence.

1 INTRODUCTION

Large seismic mainshocks are usually followed by numerous aftershocks within a short period of time. Aftershocks can have a significant effect on the dynamic behavior of a structure in terms of irreversible plastic strains and accumulated damage, as they affect a structure already weakened during a mainshock. The dynamic response of structures subjected to mainshock-aftershock seismic sequence has been extensively studied recently. Especially, concrete structures have the probability of severe damage while exposed to sequence of seismic events (Zhai et al. 2015; Massone et al. 2014). They may undergo plasticization or even collapse during aftershocks, since they are already degraded and cracked during the first shock. Only advanced constitutive models of the concrete material, which include progressive damage and failure phenomena, are advisable for examining dynamic behavior of concrete structures under mainshock-aftershock sequence.

In the paper the dynamic responses of a concrete building subjected to mainshock-aftershock seismic sequence are investigated. In order to compare damages under repeated earthquakes and assess the impact of both shocks on the structure, the concrete damage plasticity model, which describes multi-hardening plasticity and progressive damage (cracking), was implemented.

2 NUMERICAL MODEL OF THE ANALYZED CONCRETE STRUCTURE

The dynamic analysis of a concrete structure with a progressive damage and failure material model was carried out for a one-story engine shed located in an industrial area. The main dimensions of the structure are: the length of 19 m, the width of 14 m, the height of 15 m. The structural walls (20 cm thick) are built of a concrete material. The windows of the shed are strengthen by concrete heads. The structural roof system consists of steel trusses. The roof is covered by a steel sheeting. A 3D numerical

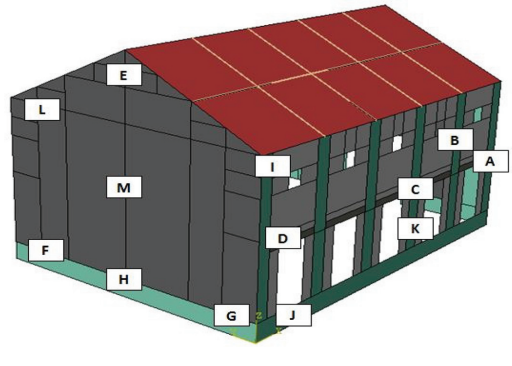

Figure 1. Numerical model of the concrete engine shed with monitoring points.

model, created with the ABAQUS package (Simulia 2013), is presented in Figure 1 along with points chosen for further dynamic analysis.

3 CONSTITUTIVE PARAMETERS FOR CONCRETE DAMAGED PLASTICITY MODEL

To represent the elastic-plastic behavior of the concrete engine shed under a sequence of seismic shocks the Concrete Damage Plasticity model (CDP) was assumed as a constitutive model of the concrete material (Lee & Fenves 1998; Lubliner et al. 1989; Simulia 2013). The model of the concrete material consists of the combination of non-associated multi-hardening plasticity and scalar damaged elasticity to describe the irreversible damage that occurs during the fracturing process. The yield surface is controlled by two variables representing equivalent plastic strains: $\tilde{\varepsilon}_t^{pl}$ and $\tilde{\varepsilon}_c^{pl}$, associated with failure mechanisms under tension and compression loading, respectively. The concrete damage is characterized by two different damage variables: d_t (for tension) and d_c (for compression). These variables are functions of equivalent plastic strains. They can take values from zero, which represents undamaged material, to one, which denotes total loss of strength. The CDP model assumes that the reduction of the elastic modulus E is given in terms of a scalar degradation variable $SDEG$ as:

$$E = (1 - SDEG)E_0 \tag{1}$$

where E_0 is the initial elasticity modulus of the undamaged material.

The essential constitutive parameters of the concrete material model are summarized in Table 1 (Schlangen 1993; Jankowiak & Lodygowski 2005). These properties were obtained through laboratory tests.

Other parameters of the concrete material were taken as follows: the elasticity modulus 34.0 GPa, the Poisson's ratio 0.19, the dilation angle 38°, the mass density 2400 kg/m^3.

The concrete damage plasticity model is specially recommended for calculations of concrete structures subjected to dynamic loadings, like earthquakes (Simulia 2013; Dulinska & Jasinska 2014).

Table 1. Constitutive parameters of concrete damage plasticity model (Schlangen 1993; Jankowiak & Lodygowski 2005).

Concrete tension stiffening		Concrete tension damage	
Stress [MPa]	Cracking strain [–]	d_t [–]	Cracking strain [–]
1.998930	0.0	0.0	0.0
2.842000	0.00003333	0.0	0.00003333
1.869810	0.000160427	0.406411	0.000160427
0.862723	0.000279763	0.69638	0.000279763
0.226254	0.000684593	0.920389	0.000684593
0.056576	0.00108673	0.980093	0.00108673
Concrete compression hardening		Concrete compression damage	
Stress [MPa]	Crushing strain [–]	d_c [–]	Crushing strain [–]
15.0	0.0	0.0	0.0
20.197804	0.0000747307	0.0	0.0000747307
30.000609	0.0000988479	0.0	0.0000988479
40.303781	0.000154123	0.0	0.000154123
50.007692	0.000761538	0.0	0.000761538
40.236090	0.002557559	0.195402	0.002557559
20.236090	0.005675431	0.596382	0.005675431
5.257557	0.011733119	0.894865	0.011733119

4 DATA OF THE SEISMIC MAINSHOCK AND THE AFTERSHOCK

In the dynamic analysis of the concrete structure earthquakes registered in Nocera Umbra (central Italy) were applied as kinematic excitations of the structure (ITACA 2015). The magnitude of the

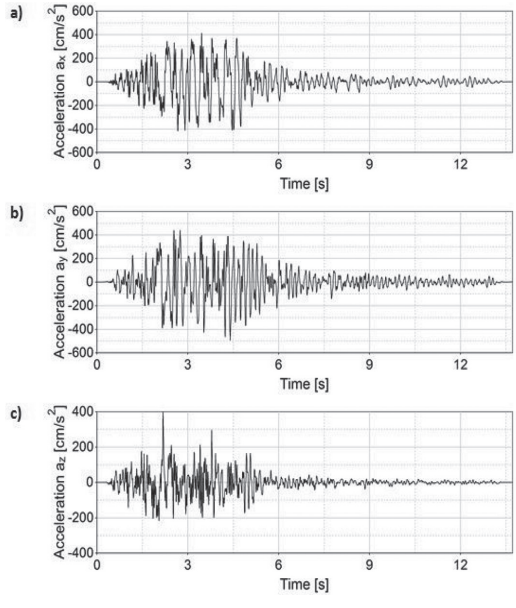

Figure 2. Time histories of the mainshock accelerations: (a) West-East direction: (b) North-South direction; (c) vertical direction.

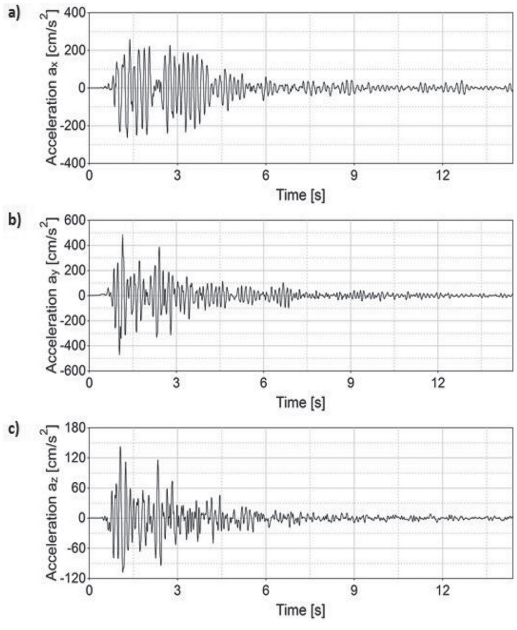

Figure 3. Time histories of the aftershock accelerations: (a) West-East direction: (b) North-South direction; (c) vertical direction.

Table 2. The Peak Ground Accelerations (PGA) of the mainshock and the aftershock.

	PGA [cm/s^2]		
	WE direction	NS direction	Vertical direction
Mainshock	414.96	492.16	398.23
Aftershock	263.29	485.88	142.79

mainshock was 6.1, whereas the magnitude of the aftershock equaled 5.7. The phase of the strong ground motion of both shocks approximately lasted 8s. Time histories of accelerations of the mainshock and the aftershock in three directions are presented in Figures 2 and 3, respectively. The Peak Ground Accelerations (PGA) of both shocks are summarized in Table 2.

5 DYNAMIC RESPONSES OF STRUCTURE TO THE MAINSHOCK AND AFTERSHOCK

The dynamic responses of the concrete structure to both shocks were calculated using full time history analysis. It was carried out with the Hilber-Hughes-Taylor time integration algorithm provided in the ABAQUS software for a direct step-by-step solution. As the progressive damage and failure model of concrete implements strong material nonlinearity a step of numerical integration was not fixed. The step varied from 10^{-5} to 10^{-2} s, according to convergence requirements. The geometric nonlinearity of the problem was also taken into account. A small value of artificial damping (0.05) was also introduced in the dynamic analysis to ensure numerical stability. The time shift between the mainshock and the aftershock equaled 10 s, that allowed the complete unloading of the structure.

For the dynamic analysis the Rayleigh model of mass and stiffness proportional damping was applied. The damping coefficients $\alpha = 0.466$ (referring to mass proportional damping) and $\beta = 0.005$ (referring to stiffness proportional damping) were determined for damping ratios of 3.5% referring to the first (4.3 Hz) and the second (5.1 Hz) natural frequencies, respectively.

The dynamic analyses were performed separately for the mainshock and the aftershock. The observed evolution plastic and damage measures, incorporated into the concrete damage plasticity model of the material, allowed to assess the impact of both shocks on the structure.

The distribution of plastic zones in the concrete wall resulted from the mainshock and the aftershock is presented in Figure 4a and b, whereas the evolution of the tensile damage is shown in Figure 5a and b, respectively.

It can be noticed that plasticization of the upper parts of pillars between windows was reported already after the mainshock (Fig. 4a). The aftershock resulted only in a slight growth of the area

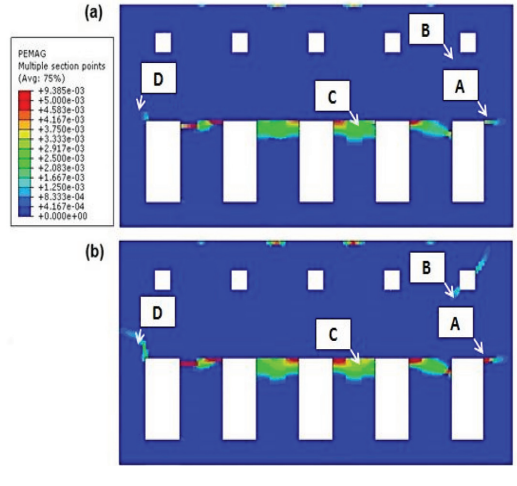

Figure 4. Distribution of plastic strains on the front wall resulted from: (a) the mainshock; (b) the aftershock.

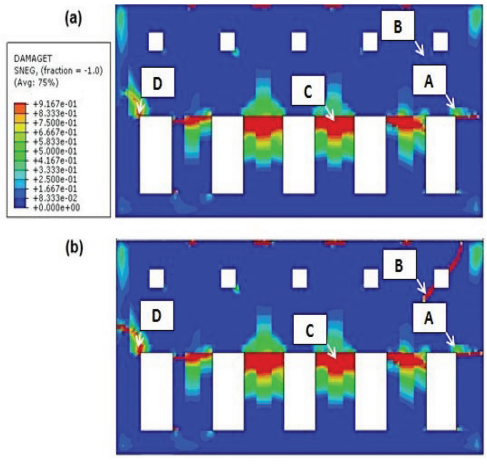

Figure 5. Tensile damage of the front wall: (a) due to the mainshock; (b) due to the aftershock.

affected by the plastic strains (see points B and D). The level of plastic strains at some points increased considerably (see point A) after the second seismic event. However, at the vast majority of analyzed points the level of plasticization did not undergo noticeable changes (see point C).

It also occurred that the tensile damage due to the mainshock affected mainly the upper parts of pillars between windows (Fig. 5a). The subsequent shock caused additional cracking in zones which did not undergo any damages during the first shock. The value of tensile damage variable reached 0.9 that indicates almost total loss of strength.

To present the plastic behavior and the progressive damage of the concrete material of the analyzed structure under the mainshock and the aftershock a detailed analysis of dynamic behavior of the concrete material at particular zones are presented in Figures 6–9. The following time histories of the plastic and progressive damage measures were examined: Logarithmic minimal Principal strains (LEP), equivalent plastic strains (PEEQ), tensile damage parameter of progressive Damage (DT). On the basis of the presented time histories some remarks concerning plastic behavior, progressive damage and failure in different zones of the structure can be formulated.

Four main scenarios of the dynamic behavior may be distinguished, depending on the locations of the analyzed points.

The first scenario of dynamic behavior could be observed on the time histories of plastic and damage measures obtained at point C (Fig. 6). This point was located in the area between two windows. It occurred that the concrete material at

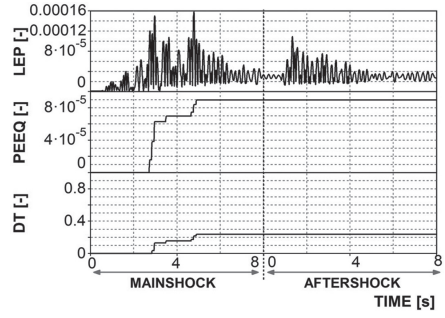

Figure 6. Time history of plastic (LEP, PEEQ) and Tensile Damage (DT) measures of the concrete material at point C due to the mainshock and the aftershock.

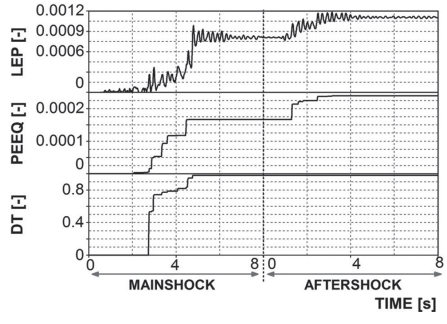

Figure 7. Time history of plastic (LEP, PEEQ) and Tensile Damage (DT) measures of the concrete material at point A due to the mainshock and the aftershock.

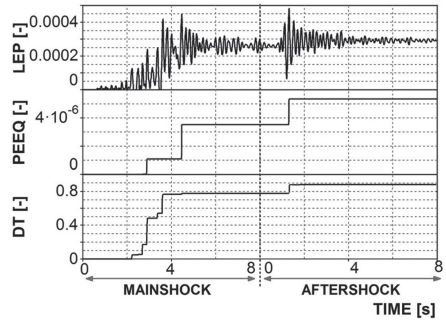

Figure 8. Time history of plastic (LEP, PEEQ) and Tensile Damage (DT) measures of the concrete material at point D due to the mainshock and the aftershock.

point C went plastic after approximately 3 seconds of the mainshock (see LEP and PEEQ charts). The process of plasticization at this point was accompanied by progressive tensile damage of the concrete material (see DT chart). The aftershock did not influence plastic and failure measures

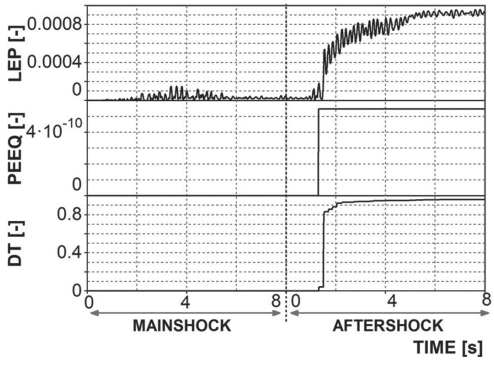

Figure 9. Time history of plastic (LEP, PEEQ) and Tensile Damage (DT) measures of the concrete material at point B due to the mainshock and the aftershock.

at point C. The level of PEEQ and DT variables was reported constant, whereas the LEP values oscillated around the value it had reached in the final phase of the mainshock.

The second scenario of dynamic behavior may be detected from the time histories of plastic and damage measures obtained at point A (see Fig. 7). Point A was placed just beneath the head of the window. It can easily be noticed that both the mainshock and the aftershock resulted in plastic behavior of that part of the wall. The increase of the plastic strains (see LEP and PEEQ charts) appeared at the beginning of the strong phase of both shocks. However, progressive damage (cracking) of the concrete material can be observed during the main event only (see DT chart).

The third possible situation can be observed on the time histories of plastic and damage measures obtained at point D (see Fig. 8). This point, like point A, was located just beneath the head of the window, but on the other side of the front wall. It turned out that the increase of the plastic strains (see LEP and PEEQ charts) appeared at the beginning of the strong phase of both shocks. Also the tensile damage time history indicated cracking at the same time (see DT chart).

The last analyzed scenario of dynamic behavior may be clearly recognized from the time histories of plastic and damage measures obtained at point B (see Fig. 9). This point was situated beneath the upper window (with no window head). It turned out that the mainshock resulted only in the elastic behavior of that part of the front wall. However, this zone underwent plasticization during the aftershock, which was applied to the structure already weakened by the mainshock (see LEP and PEEQ charts). In addition, new cracks appeared near point B (see DT chart), which was located on the trajectory of maximal principal stresses.

6 CONCLUSIONS

The following conclusions can be formulated on the basis of the dynamic analysis of the concrete engine shed subjected to mainshock-aftershock seismic sequence:

– The comparison of plastic and damage measures, increasing after subsequent seismic shocks, revealed that several scenarios can happen due to repeatability of seismic events. Both, the first stronger or the second lighter shock, can have crucial influence on plastic behavior and progressive damage of concrete structures.
– The obtained results indicate that aftershocks can have considerable effect on the dynamic behavior of concrete structure in terms of enlarging zones affected with plastic irreversible strains. The building may also exhibit additional progress in structural damage evolution such as shear wall cracking.
– Aftershocks are usually not so strong as mainshocks. Seismic shocks of similar size and magnitude would not cause any fracturing or failure if they strike an undamaged structure. But even being not large events, they may result in total loss of concrete material strength while performing in the mainshock-aftershock seismic sequence.

REFERENCES

Dulinska, J.M. & Jasinska, D. 2014. Performance of steel pipeline with concrete coating (modeled with concrete damage plasticity) under seismic wave passage. *Applied Mechanics and Materials* 459(2014): 608–613.

ITACA. The Italian Accelerometric Archive. 2015: *itaca.mi.ingv.it*.

Jankowiak, T. & Lodygowski, T. 2005. Identification of parameters of concrete damage plasticity constitutive model. *Foundations of Civil and Environmental Engineering* 6(2005): 53–69.

Lee, J. & Fenves, G.L. 1998. Plastic-damage model for cyclic loading of concrete structures. *Journal of Engineering Mechanics* 124(8): 892–900.

Lubliner, J., Oliver, J., Oller, S. & Oñate, E. 1989. A plastic-damage model for concrete. *International Journal of Solids and Structures* 25(3): 229–326.

Massone, L.M., Lemnitzer, A., Skolnik, D.A., Llera, J.C. & Wallace, J.W. 2014. Aftershock response of RC buildings in Santiago, Chile, succeeding the magnitude 8.8 maule earthquake. *Engineering Structures* 76(19): 324–338.

Schlangen, E. 1993. *Experimental and Numerical Analysis of Fracture Processes in Concrete*. Delft, Netherlands: Delft University of Technology.

Simulia ABAQUS Users' Manual v. 6.13. 2013. Dassault Systemes Simulia Corp., Providence, RI.

Zhai, C.H., Zheng, Z., Li, S. & Xie, L.L. 2015. Seismic analyses of a RCC building under mainshock-aftershock seismic sequences. *Soil Dynamics and Earthquake Engineering* 74(7): 46–55.

This page intentionally left blank

Civil Engineering and Urban Planning IV – Liu et al. (Eds)
© 2016 Taylor & Francis Group, London, ISBN 978-1-138-02903-3

Computational study on delamination detection in FRP beam with an ultrasonic-optic technique

Ying Xu, Yi Yu & Li Niu
Shenzhen Graduate School, Harbin Institute of Technology, Shenzhen, Guangdong, China

ABSTRACT: A novel technique for detecting delamination based on ultrasonic non-destructive technique is proposed. A PZT transmitter was employed to create the stress waves in the beam, and an optical fiber interferometric sensor was attached to the surface of the beam to detect the stress wave propagation in the beam. By analyzing the propagation characteristics of ultrasound and the wavelet time-frequency spectrum of the signal, the delamination location can be identified. Based on the theoretical analysis and simulation results, the feasibility of delamination detection with the proposed technique is demonstrated.

1 INTRODUCTION

Based on the physical structure, a composite is a multiphase material composed of matrix phase, reinforcing phase, and boundary phase. This special structure can be played to the advantages of various materials and expand their scope of application. A Fiber Reinforced Composite (FRP), as the most common and representative composite, shows advantages such as low mass, high intensity, convenient processing and molding, good elasticity, excellent chemical corrosion and weather resistance. Accordingly, it has been rapidly developed and widely applied in fields such as, aerospace, automobiles, marine, civil engineering and so on, and become a research hotspot at home and abroad (Patil et al. 2009; Teng et al. 2005; Wang et al. 2008).

Among numerous FRP materials, pultrusion-formed components are more widely studied and applied due to convenient batch production. As for architectural structures, Glass Fiber Reinforced Plastic (GFRP) has been used to replace steel or concrete so as to resolve the aging of steel beams and reinforced concrete bridge structures (Petrou et al. 2008; Salim et al. 1997) because its price/performance ratio, durability and intensity/quality ratio are higher than those of Carbon Fiber Reinforced Plastic (CFRP). For example, Beijing Miyun built a simply supported GFRP honeycomb box beam highway bridge with a span of 20.7 m and width of 9.2 m in 1982 (Ye et al. 2003), an expressway bridge on the M6 Motorway in England in 2006, the Friedberg Bridge with a span of 27 m in Germany in June 2008 (Jacob 2008), etc. Though GFRP pultrusion-formed components have been applied in many fields, such composites are highly non-homogeneous and anisotropic, which easily invalidates the boundary phase, causes the separation of two or more adjacent delamination surfaces or fibers and ultimately results in material failure and accidents (Heredia et al. 1996). For common I-shaped pultrusion-formed FRP beams during construction, if uneven loads are applied to the beam, side curvature at the top flange will distort the web plate, and may cause fatigue failure and then delamination between the flange and web plate due to long-term and continuous distortional deformation. Since such delamination is not located on the surface of the flange and is invisible to the naked eye, it can usually be detected only by nondestructive detection method.

The traditional ultrasonic detection technique imposes higher requirements for testers and equipment due to the multiple interface and high damping characteristic of FRP. In the literatures (Elvin et al. 1999; Xu et al. 2005; Leung et al. 2005), Xu Ying, Jiang Yi et al proposed that the delamination in a composite beam was detected by a 3×3 coupling optical fiber interferometer (Xu et al. 2005), from which a good experimental result was obtained. The detection principle is to compress the composite beam so as to distort it under external force. The optical fibers embedded in the composite will deform remarkably when the external force is applied at the delamination, and the optical fiber interferometer will show an output peak. A GFRP beam, however, is so hard that external force can barely distort it, and it is difficult to evenly control the force.

The authors have successfully detected delamination defects between the flange and web plate of an I-shaped beam based on References (Xu et al. 2007; Jiang et al. 2009) by using a piezoelectric acoustic transmitter (PZT) to generate ultrasonic pulses by means of numerical simulation,

replacing the normal transducer with a highly sensitive 3 × 3 coupling optical fiber interferometer to detect ultrasonic signals in the beam and then performing time-frequency analysis of the signals with wavelets.

2 DETECTION PRINCIPLE

2.1 *Finite element model*

Two sectional sizes are considered during the simulation, with detailed structures and sizes as shown in Figure 1 and Table 1 and material parameters in Table 2, GFRP fiber is directed towards the length of the beam. Delamination defects with height of 0.1 mm are constructed at the junction between the top flange and web plate through Boolean operations in ABAQUS software, and three common delamination distributions are considered during the simulation, including the same side and opposite side of the optical fiber, as well as penetration, as shown in Figure 2. The I-shaped beam is placed on two pedestals with a distance of 1000 mm while the optical fibers are affixed to the middle of the web plate. Integral strains between point C and D (see Fig. 1a) are calculated in ABAQUS to represent the integral strain of the optical fiber. The value and application time of PZT load are adjusted in order to keep the upper surface separated from the lower surface and reduce the influences of FRP on signal attenuation.

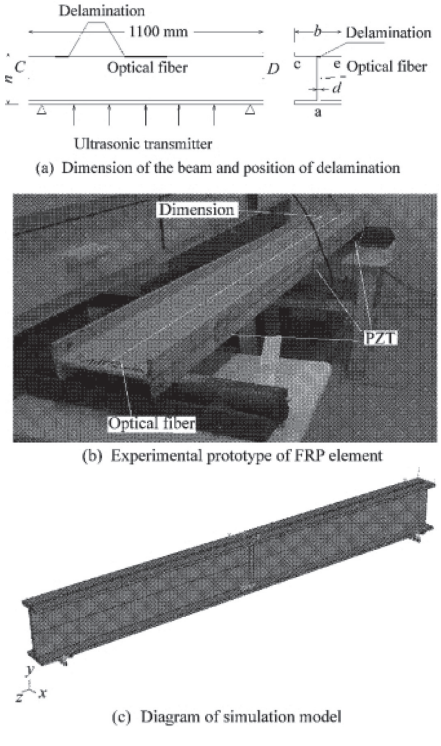

Figure 1. Illustration of the I-FRP beam.

Table 1. Size of I-beam.

I-beam models	Height *h* mm	Wide *b* mm	Thickness *d* mm
I100	100	68	4.5
I120	120	60	6.25

Table 2. Material properties of GFRP.

Elastic modulus Gpa	Shear modulus Gpa	Poisson's ratio
$E_{11} = 25.5$	$G_{12} = 5.07$	$v_{12} = 0.09$
$E_{22} = 8.5$	$G_{13} = 5.07$	$v_{13} = 0.09$
$E_{33} = 8.5$	$G_{23} = 3.07$	$v_{23} = 0.23$

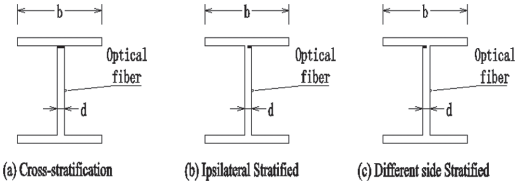

Figure 2. Schematic diagram of stratified distribution.

2.2 *Calculation of stress wave velocity (Zhang & Liu 2004)*

The diameter of a fiber is usually 5~20 μm, which is obviously smaller than the wavelength of the ultrasonic wave (the wavelength is greater than 100 μm at frequencies less than 20 MHz). As a result, the composite can be used as an even anisotropic material and the velocity of the stress wave is calculated by the propagation theory for the plane wave in the anisotropic material. During the calculation, Wang Xiaomin (Wang & Li 1998) quoted the direction vector representing the anisotropic characteristics of the media to deduce a strict analytical solution for the velocities of a quasi-longitudinal wave (qP wave) and 2 quasi-transverse waves (qSV wave and qSH wave). This calculation method is therefore adopted in this paper.

It is assumed that the direction of fibers in GFRP is identical with x1 (i.e., $\theta = 0$), and a coordinated system is established as shown in Figure 3. Therefore, the

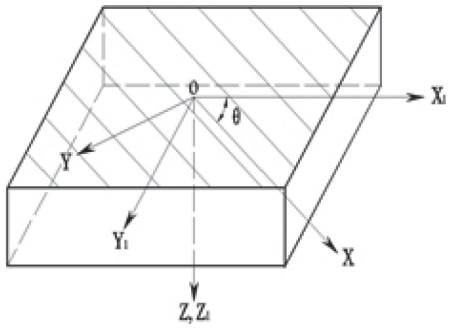

Figure 3. Geometry diagram of FRP materials.

stress-strain relationship in orthogonal anisotropic material is as follows (Kuo et al. 2008):

$$[\sigma]=\begin{bmatrix}\sigma_{11}\\ \sigma_{22}\\ \sigma_{33}\\ \sigma_{23}\\ \sigma_{31}\\ \sigma_{12}\end{bmatrix}=\begin{bmatrix}Q_{11} & Q_{12} & Q_{13} & & & \\ Q_{21} & Q_{22} & Q_{23} & & 0 & \\ Q_{31} & Q_{32} & Q_{33} & & & \\ & & & Q_{44} & 0 & 0 \\ & & & 0 & Q_{55} & 0 \\ & & & 0 & 0 & Q_{66}\end{bmatrix}\begin{bmatrix}\varepsilon_{11}\\ \varepsilon_{22}\\ \varepsilon_{33}\\ \gamma_{23}\\ \gamma_{31}\\ \gamma_{12}\end{bmatrix} \tag{1}$$

Since the local coordinate system for GFRP fiber matches the overall coordinate system, Equation (1) is still applicable to the overall stress-strain relationship (1). The wave propagation equation for stress waves in FRP composites is:

$$Q_{ijkl}\frac{\partial^2 u_k}{\partial x_j \partial x_l}=\rho\frac{\partial^2 u_i}{\partial t^2} \tag{2}$$

where, Q_{ijkl} shows elastic constant; u_i shows particle displacement; ρ shows density; t shows time.

$$u_j = A\exp\left(i\omega t\right) \tag{3}$$

where, A shows amplitude, ω shows circular frequency. When a harmonic plane wave (Equation (3)) is propagated in the media, Equation (3) is substituted into Equation (2) to deduce the Christoffel equation as follows:

$$\left(k^2\Gamma_{ik}-\rho\omega^2\delta_{ik}\right)u_k=0 \tag{4}$$

where, δ_{ik} shows the Kronecker symbol and the Christoffel stiffness is $\Gamma_{ik}=Q_{ijkl}n_j n_i (i,j,k,l=1,2,3)$. If a non-zero displacement solution is available in Equation (4), its coefficient matrix must be 0, and namely the characteristic equation shall be:

$$\left|k^2\Gamma_{ik}-\rho\omega^2\delta_{ik}\right|=0 \tag{5}$$

Pultrusion-formed GFRP section material, due to unicity of the fiber direction, is a transverse-isotropic media with Q22 = Q33, Q66 = Q55, Q12 = Q13, and Q44 = (Q33 – Q23)/2. The material parameters are substituted to deduce the velocities of three models of body waves in x2 x3 planes, with a qP wave of 2237.8 m/s, qSV wave of 1591.6 m/s and qSH wave of 1385.5 m/s.

2.3 *Wavelet analysis principle*

As the beam height (h) is much smaller than the beam length (l) (h/l = 6/55) and the load is vertical to x1, only the propagation conditions of the three stress waves in x2 x3 planes shall be considered during the analysis. The time needed for the first two propagations of the three stress waves in the complete beam and delamination beam to reach the optical fibers can be obtained by calculation, as shown in Table 3, in which there are few differences between the second arrival time for the qSV wave and qSH wave ($<2\times10^{-5}$ s). In view of the complexity of the I-shaped beam section and the diversity of stress waves in the beam (Liu et al. 2007), this study mainly extracts signals before 11×10^{-5} s for Morlet wavelet analysis to comprehensively investigate the time-frequency characteristics and changes of arrival time t when the qP wave reaches the optical fiber for the second time, and the distance of the reflection plane from the optical fiber is determined according to the following equation:

$$x=\frac{t\times22.378-h/2}{2}\ \ (mm) \tag{6}$$

Accordingly, the beam integrity can be determined and then the size of the delamination surface can be further analyzed.

3 ANALYTICAL EXAMPLES

3.1 *Detectable analysis of complete beam and mid-span penetrative delamination*

The C3D8R unit is used to simulate an intact beam and a 125 mm mid-span penetrative delamination beam, with material parameters as shown in Table 2, so as to calculate according to propagation of 10 grids within one period, with structured grid of 2.5 mm. Since the beam is symmetrical in its length direction, only the left half of the beam is analyzed.

The second-time arrival time t for qP wave can be obtained by extracting the time-interval curve of point C and D for integral strain under the different

Table 3. Ultrasonic dissemination time table for I-beams.

	I120 full beam	I120 layered beam	I100 full beam	I100 layered beam
Stress wave reach to FBG for the first time				
qP wave	2.68	2.68	2.23	2.23
qSV wave	3.77	3.77	3.14	3.14
qSH wave	4.33	4.33	3.61	3.61
Stress wave reach to FBG for the second time				
qP wave	8.04	7.48	6.70	6.29
qSV wave	11.31	10.51	9.42	8.85
qSH wave	13.00	12.08	10.83	10.16

excitation points and analyzing and verifying its Morlet wavelet time frequency. As for typical time-frequency analysis results, refer to Figure 4. The distance x from the reflection surface to the neutral layer of optical fibers under each excitation point can be determined according to Equation (6), with results as shown in Figure 5a and 5b. It can be seen from Figure 5 that the method proposed, in this paper can correctly detect the distribution of delamination in the beam's length direction, but there is a certain error of accurate positioning of delamination locations, with a maximum error of 2.02 mm in Figure 5b. An initial judgment shows that this error is mainly due to the greater beam grid partition which incurs an excessive simulation error in ultrasonic wave reflection. In order to, reduce this impact from the grid, the reflection simulation precision shall be verified again, and a grid of 1 mm shall be adopted for simulation calculations finally. Figure 5b shows that the left and right areas of delamination influence are up to 30 mm when the delamination is 125 mm. Then obviously, the area of coverage is related to both the size of delamination and the beam height h. The initial judgment of the detection results shows that the delamination sensitivity can be up to 10 mm if the single movable distance of the detection point is 5 during the detection process. The detectability of a delamination of 10 mm is studied below.

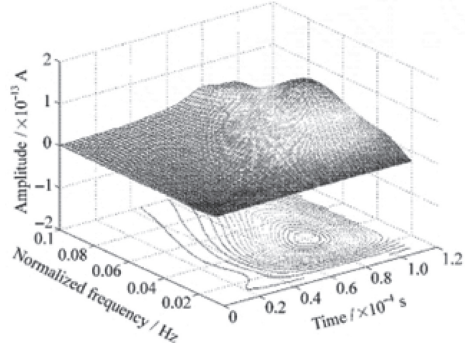

Figure 4. Typical wavelet time-frequency map.

3.2 *Detectability analysis of 10 mm mid-span delamination*

Via Boolean operation, simply supported I120 and I100 beams are constructed with delaminations (10 mm in length) in three distribution types at the junction between web plate and flange. The C3D8R unit is used to simulate the delaminated beams with no change of material parameters and a structured grid of 1 mm. The beams are symmetrical in the length direction, so it is only necessary to analyze the left sides of the beams. The simulated and analyzed results are referred to in Figure 6, from which it can be seen that this method can soundly determine the location on the beam in the length direction and also realize a higher precision of delamination positioning when the grid is 1 mm. From Figure 6a, 6b, 6c, and 6d, it can be seen that the reflection signals become weaker with the reduction of delamination areas, which results in an apparent changing trend in the precise delamination positioning error. However, the range and location of the delamination zones are still determined correctly. When comparing the detection results of two beams with different sectional sizes, it is found that the reduction in size can cause more complex reflection signals to some extent. However, a fiber optic interferometer rather than a traditional probe is used to detect the ultrasonic signals in the beams. This can provide a higher precision and sampling frequency through reasonable demodulation solutions, so the change of sectional size has less influence on the detection result. Through comparisons of the two delamination lines in Figure 6b and 6d, the relative locations of delamination and optical fibers show little influence on the detection results. The detection result curves under both conditions including the same side and opposite side are basically coincident. As for this method, therefore, there is a low requirement for embedment of optical fibers, which can

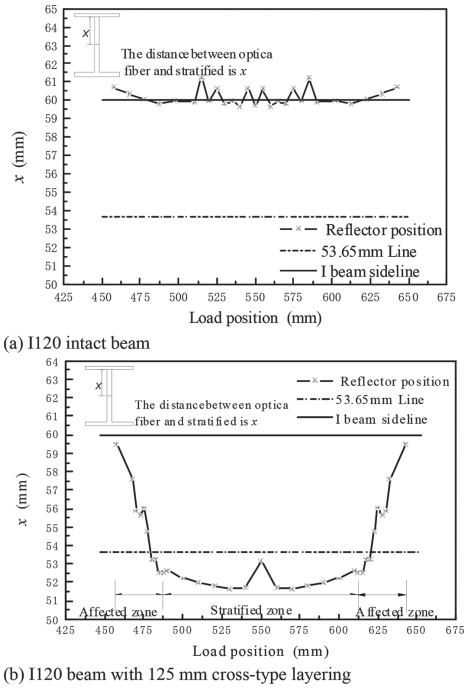

(a) I120 intact beam

(b) I120 beam with 125 mm cross-type layering

Figure 5. Reflector location of I120 intact beam and I120 layered beam.

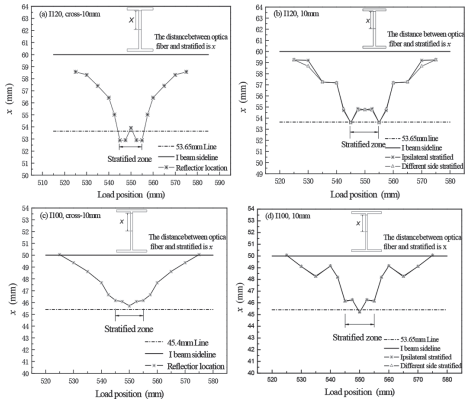

Figure 6. 10 mm reflector location of I120 and I100 cross-stratification beam.

be inserted externally or integrated into the components in advance.

3.3 *Detectability analysis of 10 mm quarter-span delamination*

In accordance with the method mentioned above, delaminated simply supported I120 and I100 beams of 10 mm at the quarter-span position are simulated with material parameters in Table 2 and a structured grid of 1 mm. In this case, the delamination is at the quarter-span position and it is not a symmetrical structure in the direction of beam length any longer. Therefore, the entire beam must be analyzed, with simulated analysis results as shown in Figure 7. The results demonstrate that this method can still correctly detect the delamination position when the delamination is at the quarter span, with a positioning error of no more than 2.5%. In comparison with the detection results of beams with two sectional sizes, it can be seen that the I120 beam is very sensitive to the boundary of the delamination area, the size of which can be well confirmed, but the delamination area boundary of the I100 beam is not obvious and can not be confirmed as precisely. Additionally, the positioning precision for the I100 beam delamination position is lower than that of the I120 beam. Based on a causal analysis, it is possible that the ultrasonic excitation point is closer to the beam end at the quarter-span position, and the reflection signals at the end of the beam couple with interference signals generated due to the reduction of sectional size, resulting in a deviation in the second signal peak, in which the detected t changes slowly. From two delamination lines in Figure 7b, the relative positions of delamination and optical fibers show little influence on the delamination detection result at the quarter-span position of the I120 beam. Comparison of the two delamination lines in Figure 7d shows that the relative positions of the delamination and optical fibers present less influence on individual points, with a maximum difference value of no more than 0.5 mm. The detection result curves basically coincide, so the relative positional influence of the optical fibers and

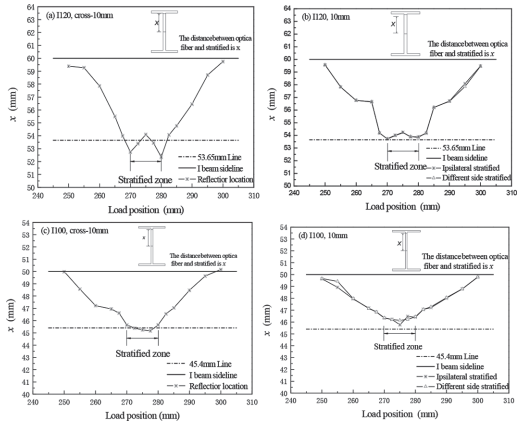

Figure 7. 10 mm reflector location of I120 and I100 a quarter of stratification beam.

delamination is still not considered when the optical fibers are arranged. Based on the figures above, the delamination asymmetry is considered during analysis, but the detection results are still approximately symmetric because the delaminated upper and lower surfaces have no contact with each other during the simulation. A symmetric relation is still approximately available when the beam body vibration actuated by PZT is neglected, so the detection result is still approximately symmetric.

4 CONCLUSION

The optical fiber ultrasonic detection technique is used in combination with wavelet signals to analyze and detect the delamination at the junction between the flange of the GFRP component and the web plate by means of numerical simulation.

Based on the simulation results, the method proposed in this paper can eliminate the influences of sectional forms and material properties on the detection results; additionally, it can more accurately detect the distribution of the delaminations in I-shaped beams with different sectional sizes in the beam length direction and accurately determine their positions.

Comparisons have demonstrated that the relative locations of optical fibers and delamination show little influence on the detection results. The arrangement of optical fibers can be accomplished through external attachment or integrated within the components to form intelligent components which allow comprehensive and repeated utilization of optical fibers. However, when detection is performed at a beam end, the influences of reflection signals from the beam end should be considered.

The consistency of the theoretical calculation with the simulation results sufficiently shows the feasibility of this method.

ACKNOWLEDGMENT

This paper has been supported by Funding of NSFC (51278156) and basic project of Shenzhen Science & Technology Program (JCYJ20140704172618811).

REFERENCES

Elvin, N., Leung, K.Y.C. & Sudarshanam, V.S. 1999. A novel fiber optic delamination detection scheme: Theoretical and experimental feasibility studies. *Journal of Intelligent Material, Systems and Structures* 10(4): 314–321.

Heredia, F.E., He, M.Y. & Evans, A.G. 1996. Mechanical performance of ceramic matrix composite I-beams. *Composites Part A: Applied Science and Manufacturing* 27(12): 1157–1167.

Jacob, A. 2008. Composite bridge decks cut life cycle costs. *Reinforced Plastics* 9(52): 30–32.

Jiang, Y., Leung, K.Y.C. & Ng, M. 2009. Delamination detection in an I-section glass fiber reinforced plastic beam with an optical fiber-based stress wave method. *Smart Materials and Structures* 18(6): 1–6.

Kuo, Y.M., Lin, H.J. & Wang C.N. 2008. Sound transmission across orthotropic laminates with a 3D model. *Applied Acoustics* 69(11): 951–959.

Leung, K.Y.C., Yang, Z. & Xu, Y. 2005. Delamination detection in laminate composites with an embedded fiber optical interferometric sensor. *Sensors and Actuators A: Physical* 119(2): 336–344.

Li, M., Wu, N. & Wu, L.Z. 2007. Scattering of anti-plane stress waves by a crack in a nonhomogeneous orthotropic medium. *Composite Structures* 79(2): 174–179.

Patil, S., Kostic, M. & Majumdar, P. 2009. Bridges with Glass Fibre Reinforced Polymers (GFRP) decks—The new road bridge in Friedberg (Hessen, Germany). *Stahlbau* 78(7): 462–470.

Petrou, M.F., Parler, D. & Harries, K.A. 2008. Strengthening of reinforced concrete bridge decks using carbon fiber-reinforced polymer composite materials. *Journal of Bridge Engineering* 13(5): 455–467.

Salim, H.A., Davalos, J.F. & Qiao, P.Z. 1997. Analysis and design of fiber reinforced plastic composite deck-and-stringer bridges. *Composite Structures* 38(1/4): 295–307.

Teng, J.G., Chen, J.F. & Smith, S.T. 2005. *FRP Reinforced Concrete Structures.* Beijing: China Architecture & Building Press.

Wang, L.M., Lu, J.J. & Liu, C.C. 2008. Mechanical properties of CFRP and its reinforced concrete beams. *Acta Materiae Compositae Sinica* 25(3): 167–169.

Wang, X.M. & Li, M.X. 1998. Propagation of elastic plane waves in homogeneous and transversely isotropic media. *Chinese Journal of Acoustics* 17(03): 280–288.

Xu, Y, Leung, K.Y.C. & Jiang, Y. 2007. Delamination detection at web/flange junction of I-section GFRP beam with fiber optical interferomenter sensor. *Acta Materiae Compositae Sinica* 24(2): 143–150.

Xu, Y., Jiang, Y. & Leung, K.Y.C. 2005. 3 × 3 coupler based mach-zehnder interferometer and its application in the delamination detection in composite. *Shenzhen Science and Technology* 12(2): 356–365.

Xu, Y., Leung, K.Y.C., Tong, P., et al. 2005. Interfacial delamination detection in bonded repair with fiber optical interferometric sensor. *Composites Science and Technology* 65(9): 1428–1435.

Ye, L.P., Feng, P. & Zhang, K. 2003. FRP in Civil Engineering in China: Research and Application. *6th International Symposium on Fibre-Reinforced Polymer-Reinforcement for Concrete Structures (FRPRCS-6), Singapore, Edited by Kiang Hwee Tan, World Scientific, July 2003*.

Zhang, H.Y. & Liu, Z.Q. 2004. Propagation of elastic plane waves in homogeneous anisotropic media. *Journal of Shanghai University: English Edition* 8(2): 164–168.

Civil Engineering and Urban Planning IV – Liu et al. (Eds)
© 2016 Taylor & Francis Group, London, ISBN 978-1-138-02903-3

Influence of Superabsorbent Polymer with different particle size and dosage on properties of cement mortar

Zhong-Lai Yi, Hua-Jian Li, Yan-Bin Tan & Yong-Jiang Xie
China Academy of Railway Sciences, Beijing, China

ABSTRACT: A Superabsorbent Polymer (SAP) was synthesized by aqueous solution polymerization, the influence of particle size on swelling behaviors of which was studied based on the diffusion-relaxation model. The fluidity of cement paste, the mechanical properties of hardened mortars and dimension shrinkage of hardening mortars during dry curing conditions were measured to investigate the impact of SAP with different particle size and dosage on the properties of mortars. The experimental results show that the particle size of SAP has further influence on swelling ability; the addition of SAP leads to a decrease of the fluidity of fresh mortars; the addition of SAP into mortars can remarkably reduce the dimension shrinkage of mortars under dry curing conditions, which can nevertheless severely reduce the mechanical properties of hardened mortars at early age under soaking curing conditions.

1 INTRODUCTION

Superabsorbent Polymer is a macromolecular polymer material with excellent water-absorbing and water-retention capabilities, which contains moderately crosslinking copolymerized hydrophilic groups as carboxyl and hydroxyl. SAP can imbibe and retain a large amount of aqueous solution (hundreds to thousands times of its weight), which have the abilities to either abstemiously and tardily release water or retain water under a certain pressure. Owing to these excellent properties, superabsorbent polymer have been contributing to applications in many fields such as industry, healthcare products, agriculture and horticulture, wastewater treatment, artificial intelligence water-gel system etc.

The main reason for drying shrinkage of cement-based materials as concrete and motar is the arefaction of cement hydration (caused by humidity run-off and autogenous drying). Consequently, the appropriate measures to compensate internal humidity run-off of cement hydration can availably alleviate the concrete shrinkage. Some researchers achieved an optimum cure of concrete without the need for applying external curing methods. The feasibility of curing concrete by adding water-soluble chemicals during mixing to reduce water evaporation in the set concrete, so called "self-curing", has been discussed (Dhir et al. 1994). Several different means to avoid crack formation due to self-desiccation are known. One example is based on addition of Lightweight Aggregate (LWA) particles to the concrete. LWA saturated with water can mitigate self-desiccation, however, this technique have some major defects, such as difficulties in controlling consistency and a significant reduction in strength and elastic modulus. R. Yoshida verified swelling mechanisms of SAP by microcosmic analysis, the results showed that when the thickness of gel was changed, the acceleration of swelling was delayed with increasing thickness, and the acceleration times agreed with theoretical values predicted from the model. The observed changes in diameter and thickness of the gel also supported the model (Ryo et al. 1994). Ole Mejlhede Jensen (Jensen & Hansen 2001) suggested that water entrainment with SAP might be beneficial to frost resistance of concrete. This is due to the gas-filled voids produced when the inclusions from entrained water are emptied due to chemical shrinkage. These voids are similar to voids created by air entrainment. The optimum size of the entrained water inclusions is around 100 μm. Reinhardt H.W. (Silvia et al. 1997) find that the SAP in concrete formed a large number of porosity. Compressive strength affected small, but flexural strength reduced significantly. Freezing resistance ability is greatly increased, and the chloride ion resistance is reduced. Lura et al. (2001) find that pore number and large hole number increased in the mortar with SAP by X ray analysis, and speculated that this is the main cause of concrete permeability resistance decreased.

This paper studied the swelling behavior of different particle size of SAP, the influence of SAP on the fluidity, mechanical properties and shrinkage performance of cement mortar with different particle size and dosage.

2 EXPERIMENTAL

2.1 *Materials*

The cement is chosen on the class of PO42.5 according with the Chinese standard. The fine aggregate is ISO standard sand. The polycarboxylate-based Superplasticizer (SP) with a solid content of approximately 20% is used. SAP is synthesized with analytical reagent grade reagents.

2.2 *Swelling measurements*

Swelling of the gel samples were measured gravimetrically at room temperature. A weighed amount of dry gel sample (usually 1 g) was taken in a pouch and immersed in distilled water in a beaker. The pouch was removed at specific time intervals and left to suspend for a while for drainage of excess water. The bag was dried by a soft paper and weighed. Net weight of the swollen gel was assigned by subtracting wet weight of the bag. Wet weight of the bag was determined separately by the same way.

$$Q = (W - W_0)/W_0 \quad (1)$$

where Q (g/g) was defined as swelling ratio of the gel, that is, water uptake per gram of dry polymer. W (g) and W_0 (g) are weights of the swollen and dry gels, respectively. The equilibrium swelling values were determined based on weights of the samples after contacting with water for 24 h.

2.3 *Mixtures*

Table 1 shows mix proportion of cement paste. The degree of fluidity of cement paste was measured according to "Test method for compatibility of cement and water-reducing agent" (JT/C 1083-2008). The dynamical viscosity degree of cement paste was measured by NDJ-1 model rotational viscometer.

2.4 *Specimen preparation and measurement*

Table 2 shows mix proportion of cement motar. The mixture is cast into molds and demoulded after 24 h. After demoulded, the specimens for mechanical properties were cured under water in a standard curing room where the temperature is 20 ± 1°C. The specimens for dimension shrinkage were cured in a laboratory condition (with temperature 20 ±1°C and RH 60 ± 3%) until testing ages. For each mixture, three 160 × 40 × 40 mm prism specimens were prepared for compressive and flexural strength test.

Table 1. Mix proportion of cement paste.

No.	SAP size (mesh)	m (SAP)/%	Cement/g	Water/g	w (SP)/%
1	>100	0.4	500	175	1
2	<200	0.4			
3	140~180	0.4			
4	140~180	0.2			
5	140~180	0.8			

Table 2. Mix proportion of cement mortar.

No.	SAP size (mesh)	m (SAP)/ %	Cement/ g	Sand/ g	Water/ g	w (SP)/ %
1	>100	0.4	450	1250	225	1
2	<200	0.4				
3	140~180	0.4				
4	140~180	0.2				
5	140~180	0.8				

3 RESULTS AND DISCUSSION

3.1 *Swelling kinetics*

Frisch's formula $\omega = kt^n$ is used to describe swelling kinetics of hydrophilic polymer, where ω is percentage of saturation; k is pervasion constant related to the water absorbency of SAP, n is exponential parameter as a criterion judging the modality of impregnant transmission in polymer. There is a functional simplification common to most of the treatments of intraparticle transport, i.e. the amount of solute adsorbed varies almost proportionally with half power of time, t1/2, rather than time itself, which is expressed as $\omega = kt^{0.5}$. The adsorption kinetic data was further processed to determine whether intraparticle diffusion was rate limiting.

Table 3 shows the swelling kinetics parameters of SAP with different particle size. The smaller the particle is, the smaller the ratio of swollen adsorption capacity (Wmax). Meanwhile, the more time is needed to reach the saturation point of swelling for the smaller particles. Figure 1 illustrates that the plot of adsorbate uptake vs. square root of time can be represented by a linear relationship but it does not pass through the origin. The curve of <200-mesh SAP is almost linear at the incipience of swelling, while that of 100-mesh SAP is an S-plot indicating that swelling rate is incipiently slow and becomes rapid after a certain interval.

The kinetics of adsorbate species transport from solution phase to the solid surface of adsorbent particle is often controlled by factors such as

Table 3. Kinetics parameters about SAP size.

SAP size (mesh)	Linear correlation square R2	Pervasion constant k	Swollen adsorption capacity Wmax (g/g)	Swelling time t (min)
>100	0.990	0.228	341.5	120
140–180	0.955	0.442	327.4	60
<200	0.967	0.780	295.3	10

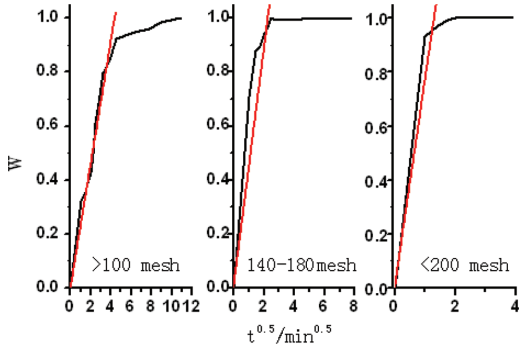

Figure 1. Effects of SAP particle size on the swelling kinetics.

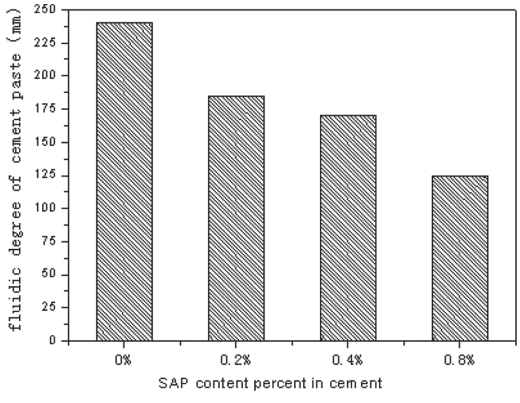

Figure 2. Effects of SAP dosage on the degree of fluidity.

film or boundary layer diffusion, diffusion of the adsorbate within the pores of the adsorbent (particle diffusion), pore surface diffusion and adsorption on the surface. The transport of adsorbate species into the pores of adsorbent (pore diffusion) is often the rate-controlling step, which is illustrated by the multilinearity of the plots because of the varying extent of adsorption in the initial and final stages. The initial curved portions of the plots are due to the liquid-film mass transfer while the linear portion is attributed to the intraparticle diffusion. The slope of the linear portion of these plots has been defined as a rate parameter k, a characteristic of the rate of adsorption in this region. Moreover, the particle diffusion would be the rate-controlling step if the line passes through the origin.

3.2 *Fluidity*

The proposition that a new additive should not influence the workability overmuch is chiefly considered in civil engineering. The primary effect of SAP addition on the workability of cement-based materials is the increase of fluidity and viscosity. Figures 2 and 3 display the degree of fluidity and dynamical viscosity vs. SAP dosage (percentage of cement). These figures show that the degree of fluidity declines while dynamical viscosity increases obviously, as the SAP content increases from 0.2% to 8%.

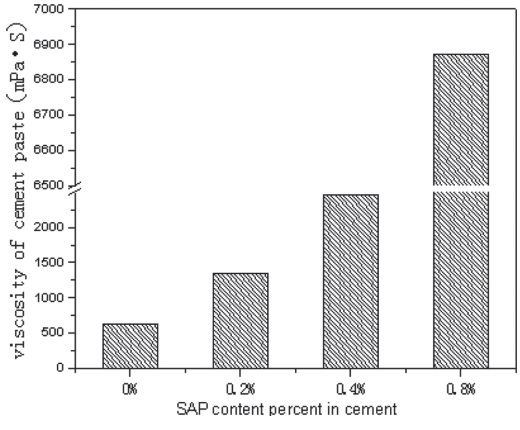

Figure 3. Effects of SAP particle dosage on the degree of viscosity.

For instance, compared to the pure paste, the degree of fluidity of paste with 0.8% SAP reduces almost by half, the degree of dynamical viscosity of which increase beyond 10 times. Because of the imbibition by SAP, accordingly, the reduction of water in cement leads to the decrease of fluidity; on the other hand, the formation of a spatial network of the SAP causes the increase of viscosity.

Figures 4 and 5 show the degree of fluidity and dynamical viscosity vs. SAP particle size (mesh). They show that the degree of fluidity declines while dynamical viscosity increases observably, as SAP particle size increases from >100 through 140–180 to <200 mesh. For example, compared to the pure cement paste, the degree of fluidity of paste with >100 SAP particles reduces beyond 30%, the degree of dynamical viscosity of which increase almost 15 times. These phenomena can be explained by swelling kinetics of SAP: the high specific surface and tiny granule diameter increase the area of interface with external solution; the augment of water absorbed by SAP heightens the viscosity cement paste. The larger particles have smaller velocity of water absorption, thus the water in cement paste increases.

3.3 *Mechanical strength*

Typical mechanical strength curves for motar specimens are shown in Figures 6 and 7, to facilitate comparison among test results for different dosage of SAP. As seen from Figure 6, average flexural strength of all specimens with SAP decreases from 6.5 MPa to 2.2 MPa at 1 day. SAP particles can reduce flexural strength of cement motar. Meanwhile, flexural strength only has a slight decrease as SAP content increase from 0.4% to 0.8% at 28 days. For example, compared to blank, flexural strength of motar with 0.4% and 0.8% SAP decrease 12% and 5% respectively, while that with 0.2% SAP increases appreciably. Figure 7 shows that the compressive strengths of motar are decreased gradually with the increase of SAP dosage. The influence of SAP at the early stage is more markedly than that at later stage. This is due to the high water absorbing capacity of SAP. At the early stage, the cement hydration water is reduced for SAP absorb many water. Only part of cement can be hydrated. The space between the aggregate

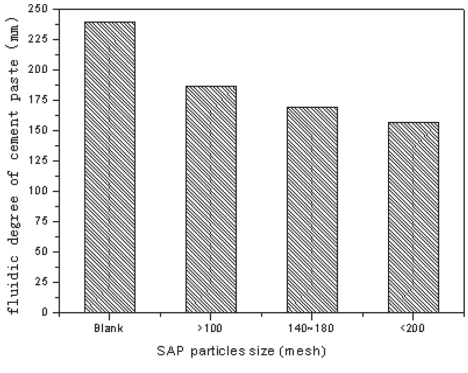

Figure 4. Effects of SAP particle size on the degree of fluidity.

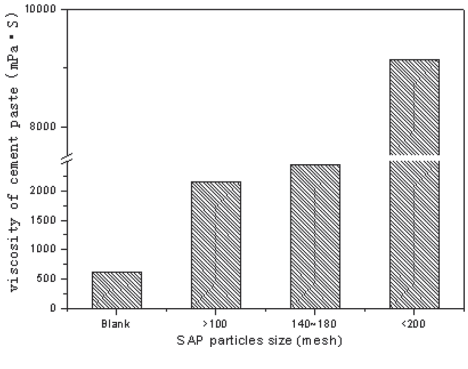

Figure 5. Effects of SAP particle size on the degree of viscosity.

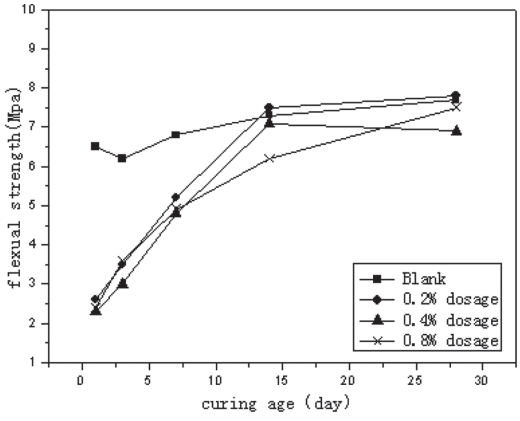

Figure 6. Effects of SAP dosage on flexural strength.

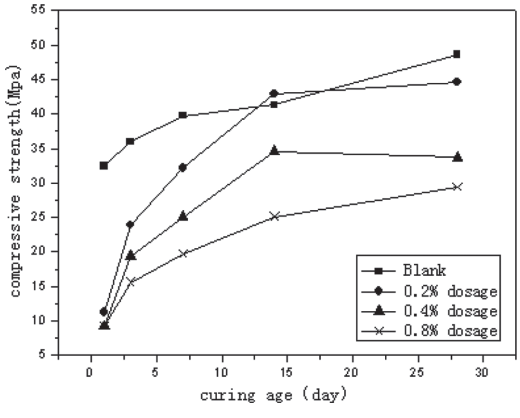

Figure 7. Effects of SAP dosage on compressive strength.

and mortar is porous for cement paste reduced. So the strength at early stage reduced greatly. With the growth of the curing age, the influence of SAP on the mechanical behavior of cement mortar reduced smaller and smaller. This is due to the SAP has high water absorption and water retention capacity for a long period of time, it can release the moisture to its surroundings in a long time. It can improve the degree of cement hydration. Hydration products structure is more compact, thus, increase the intensity of internal cement mortar. The strength of mortar can be increased.

Figures 8 and 9 show the effect of SAP particle size on the strength. From Figures 8 and 9, it can be seen that, with the decrease of the SAP particle size the decrease amplitude of flexural and compressive strength reduced, under the SAP content of 0.4%.

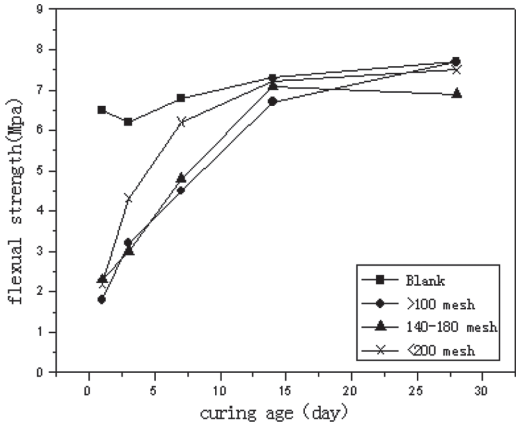

Figure 8. Effects of SAP particle size on flexural strength.

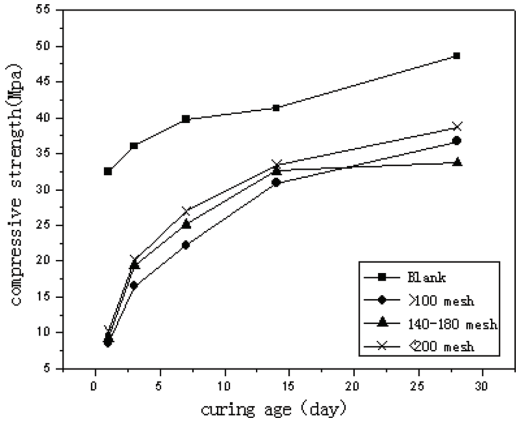

Figure 9. Effects of SAP particle size on compressive strength.

This may be due to the smaller the particle size of SAP, the smaller size of the hole in the cement mortar produced by SAP. And small particle size of SAP is more conducive to form polymerization network formation in the cement motar. Thus toughness of the mortar can be enhanced.

3.4 *Drying shrinkage*

Drying shrinkage in all motar to 28 days is shown in Figures 10 and 11. Each value represents an average value of three motar specimens. As displayed in Figure 10, the cement paste without SAP addition exhibits 350 microstrain of drying shrinkage at first day, whereas the cement motar with 0.4% SAP shrinks 150 microstrain. The size of the SAP particles affects their performance in motar, such as their mechanical stability during mixing and their influence on the rheology of the fresh motar. With respect to the ability of SAP to reduce autogenous shrinkage, the SAP particle size is also of

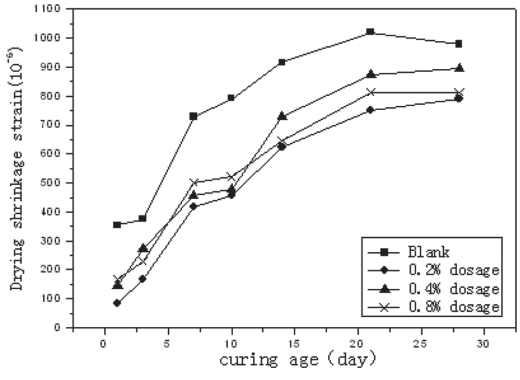

Figure 10. Effects of SAP dosage on drying shrinkage.

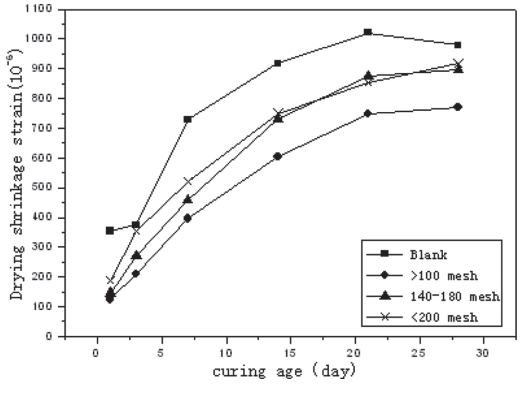

Figure 11. Effects of SAP particle size on drying shrinkage.

major importance. A series of preliminary drying deformation experiments indicate that an optimum SAP particle size exists, particles those are either smaller or larger than this optimum size are less effective in reducing autogenous shrinkage. Several phenomena may be involved in this. Figure 11 displays that the addition of >100 mesh SAP is more efficient to counteract build-up of restrained shrinkage which is counteracted partly at 0.4% SAP dosage compared with 140–180 and <200 mesh SAP, indicating that incorporation SAP particles can mitigate cracking in cement motar.

A possible mechanism contributing to the reduction of drying shrinkage in motar with SAP is water entrainment of SAP particles. The principles and theoretical background of water entrainment are described in a previous investigation. Introducing SAP particles into cement motar leads to a formation of controlled water-filled micropore inclusions, which prevent internal moisture evaporation to compensate water loss for curing motar specimens exposed in drying condition, promote hydration of unhydrated cement and reduce drying shrinkage of motar.

4 CONCLUSIONS

- The experiment result show that the smaller particles get the less ratio of swollen adsorption capacity (Wmax), meanwhile, the smaller particles need more time to reach the saturation point of swelling. The drawing curves of swelling kinetics vs. time $\omega = kt\ 0.5$ fitting line display that Fick's diffusion action plays a leading role in the primeval process of swelling, which sustains longer in larger particles of SAP.
- The primary effect of SAP addition on the cement paste is the increase of fluidity and viscosity. The degree of fluidity declines while dynamical viscosity increases observably as the increase of SAP content in the rage of 0.2%–0.8%, compared to that of the pure cement paste, the degree of fluidity of paste with 0.8% SAP reduces almost by half, the degree of dynamical viscosity of which increase beyond 10 times.
- SAP particles can reduce flexural and compressive strength of cement motar, while flexural strength only decreases slightly as SAP content increase from 0.4% to 0.8% at 28 days. SAP profoundly decease the compressive strength of motar, which almost reduces to 30% of that without SAP (blank). The specimens have nearly half of the compressive strength of blank ones at 28 days.
- The addition of SAP into mortars can remarkably reduce the dimension shrinkage of mortars under dry curing conditions. With respect to the ability of SAP to reduce autogenous shrinkage, the SAP particle size is also of major importance, >100 mesh SAP is more efficient in this paper.

ACKNOWLEDGEMENT

This work was financially supported by the National Natural Science Foundation of China (51308546).

REFERENCES

Dhir, R.K., Hewlett, P.C., Lota, J.S. et al. 1994. An investigation into the feasibility of formulating 'self-cure' concrete. *Materials and Structures* 27(10): 606–615.

Jensen, O.M. & Hansen, P.F. 2001. Water-entrained cement-based materials I. Principles and theoretical background. *Cement and Concrete Research* 31(4): 37–41.

Lura, P., van Breugel, K. & Maruyama, I. 2001. Effect of curing temprature and type of cement on early-age shrinkage of high-performance concrete. *Cement and Concrete Research* 31(12): 1867–1872.

Ryo, Y., Yukinari, O. & Kiyotaka, S. Sigmoidal swelling profiles for temperature-responsive poly (N-isopropylacrylamide-co-butyl methacrylate). *Journal of Membrane Science* 1994(89): 267–277.

Silvia, W. & Hans, W.R. 1997. A new generation of high performance concrete: Concrete with autogenous curing. *Advanced Cement Based Materials* 6(2): 59–68.

Civil Engineering and Urban Planning IV – Liu et al. (Eds)
© 2016 Taylor & Francis Group, London, ISBN 978-1-138-02903-3

Experiment study of retard-bonded pre-stressed concrete structure

Ting-Bin Liu
Lanzhou Jiaotong University, Lanzhou, Gansu, China

Jian-Chang Zhao
Gansu Construction Durability Research Center, Lanzhou, Gansu, China

ABSTRACT: Retard-bonded reinforcement is a kind of new prestressed reinforcement technology formed by wrapping a layer of retarded mortar on the surface of common prestressed reinforcement. In this paper, contrast analyses between retard-bonded prestressed members and conventional post-tensioned prestressed (with bonding and without bonding) members are made in crack moment, limit moment, formation of crack, load-deflection curve and other aspects through the test of retard-bonded prestressed members in bending (totally 16). We arrive at the conclusion of that there are the same working performances between prestressed members with bonding and retard-bonded prestressed members after retard-bonded prestressed members are tensioned for two months. According to the test results and engineering practice, we bring forward the design methods of retard-bonded prestressed members in bending and provide the base of promoting the use of this new prestressed system.

1 INTRODUCTION

According to the mode of design and construction, prestressed concrete systems can be divided into two categories, that is, pretensioned systems and post-tensioned systems. The post-tensioning (Tao 1996) systems can also be divided into ones with bonding and ones without bonding according to the bond between them. There are not only the advantages but also the insurmountable disadvantages in the two categories of post-tensioning systems (Benachour et al. 2008; Bonaldo et al. 2005; Climaco & Regan 2001). How to integrate them and make full use of their respective advantages is a problem that researchers of prestressed concrete have been searching for all along. Success on the development of super retarded mortar offers the possibility on the integration of post-tensioning system without bonding (Du et al. 2008; Harajli 2006) and one with bonding and form retard-bonded prestressed system (Cao et al. 2013; Fu et al. 2010; Li 2008; Zhao & Jin 2011; Feng & Zhou 2011). In the places holes need not to be performed, grouting is also not needed, and construction is as same as systems without bonding, but after the completion of construction, effects almost identical to prestressed with bonding reinforcement system will be achieved by means of the gradual condensation and hardening of retarded mortar wrapped on the prestressed reinforcement with the lapse of time. Contrast analysis between retard-bonded prestressed members and conventional post-tensioned prestressed (with bonding and without bonding (Kim & Lee 2012; Au & Du 2004) members are made in this paper in crack moment, limit moment, formation of crack (Feng & Zhou 2013; Zhao et al. 2009; Zhou & Feng 2011), load-deflection curve and other aspects through the test of 16 retard-bonded prestressed members in bending. We arrive at the conclusion of that there are the same working performances between prestressed members with bonding and retard-bonded prestressed members after retard-bonded prestressed members are tensioned for two months. According to the test result and engineering practice, we bring forward the design methods and construction programs of retard-bonded prestressed members in bending and provide the base of promoting the use of this new prestressed system.

2 A BRIEF INTRODUCTION TO SUPER-RETARD-SETTING MORTAR

Retard-bonded reinforcement is a kind of new prestressed reinforcement technology formed by wrapping a layer of retarded mortar on the surface of common prestressed reinforcement. It demands that there is no cementation between the wrapped mortar and prestressed reinforcement during retardation period, and tensile anchorage is just like reinforcement without bonding. After retardation period, retarded mortar will be hardened gradually and there will be cementation between

retarded mortar and tensioned prestressed reinforcement and finally they will attain certain strength and form reinforcement with bonding. It can be seen that retarded mortar plays a significant role in the whole retard-bonded prestressed system technology. Retarded mortar is mixed by water, cement, sand and compound retarder in a certain proportion. Before it is hardened, it can be seen as a kind of system made up of water and dispersed particle, having elasticity, stickiness, plasticity, corrosion resistance, microdilatancy and other characteristics. This kind of mortar, in a 5 to 40°C hermetic condition, should not be condensed within 20, 30 or 40 days according to the requirements of engineering and then be condensed gradually, and finally attains to a compression strength of more than 30 MPa. It takes several hours to more than ten hours for retarder commonly used for cement mortar to complete retardation. If we only increase mixture quantity to attain long-term retardation, this will result in the rapid reduction in the strength of mortar and even full loosening and no strength. In order to get super-retarded mortar which can meet all requirements of retard-bonded prestressed system, through repeated experiment, authors have developed special compound retarders, retardation periods of which are 20 days, 30 days and 40 days respectively, made up the corresponding super-retarded mortar with A type, B type and C type retardation periods, and carried out systematic experimental investigation for all kinds of engineering performances. The test results indicate:

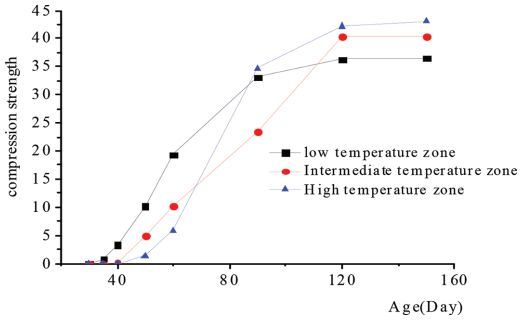

Figure 1. Influence of temperature on condensation and hardening of retarded mortar.

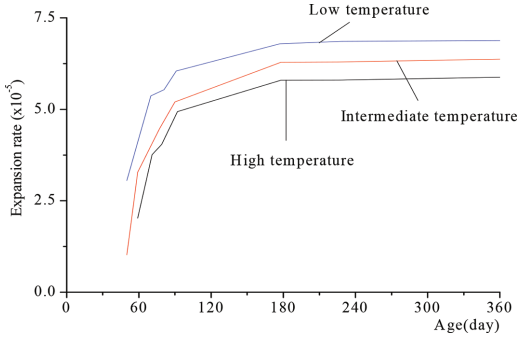

Figure 2. Change of expansion rate of retarded mortar under different temperatures.

- This retarded mortar has super retardation and its retardation period can be regulated flexibly according to different mixture ratio. It has good thixotropy and re-moldability during the retardation period.
- Temperature will influence retardation period and hardening strength of retarded mortar. Within 5 to 40°C, the higher temperature is, the longer retardation period is, the faster hardening speed and the higher later strength is, and vice verse. The influence of temperature on the condensation and hardening of retarded mortar is shown as Figure 1. Condensation and hardening of retarded mortar have nothing to do with the fact whether the ambient temperature is constant or not and the average temperature plays the key role.
- Retardation period of retarded mortar has something to do with the mixture quantity of compound retarder. The larger the mixture quantity is, the longer retardation period is. The final strength of the prepared retarded mortar may attain to 40 MPa.
- The super-retarded mortar has microdilatancy performance. As for the retarded mortar with same mixture ratio, the higher the maintenance temperature is, the smaller its expansion rate is, vice verse. The reason is that when the maintenance temperature is low, the condensation and hardening of retarded mortar are rapid, but the increase of strength is slow, so there is enough time for the production of more expansion components. At the same time because strength and expansion is a pair of contradictories, that is, the lower the strength is, the bigger expansion is. Under different temperatures, the change of expansion rate of retarded mortar is shown as Figure 2.
- The expansion rate of super-retarded mortar has something to do with retardation time. Under the condition of same temperature, the longer retardation time is, the smaller the expansion rate of retarded mortar is, and vice verse. The reason is that the longer retardation time is, the more expansion components are produced before retarded mortar has strength. However, at the moment the produced expansion components can not expand the volume of mortar, only can increase density of mortar. Under the

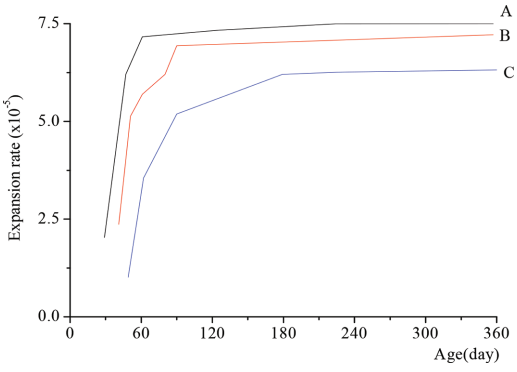

Figure 3. Changes of expansion rates of mortars with different retardation period under the condition of same temperature.

Table 1. Change of PH value of retarded mortar along with time.

Time	1	5	10	20	1	2	5	7
PH value	10	11	12	12.5	13	13	13	13

condition of same temperature, the changes of expansion rates of mortars with different retardation periods are shown in Figure 3.

– Retarded mortar will not result in the corrosion of reinforcement. The change of PH value of retarded mortar along with time is shown in Table 1. When PH value is not less than 12, there is no corrosion of reinforcement under the condition of normal temperature.

3 FABRICATION PROCESS AND TENSIONING FRICTIONAL RESISTANCE TEST OF RETARD-BONDED REINFORCEMENT

3.1 *Fabrication process of retard-bonded reinforcement*

The main process flow of wrapping and forming of retard-bonded reinforcement is shown as the following:

– The prepared retarded mortar should be painted on the plastic cloth of 5 cm width, with a thickness of 5 mm.
– One end of plastic cloth should be fastened with prestressed reinforcement and revolved with a constant force and then retarded mortar would be wrapped on the prestressed reinforcement.
– After completion of wrapping whole piece of prestressed reinforcement, worker should wrap a layer of plastic cloth counterclockwise on the surface again and the end should be fastened. The field of wrapping retard-bonded reinforcement is shown is Figure 4.
– The wrapped and formed retard-bonded reinforcements should be laid horizontally for future use and kept in shade to avoid solarization and drenching. It is necessary to cover straw mat on it and water to prevent dissipation of water. Yard field of retard-bonded prestressed reinforcement of horizontal partition of bridge tank type beam of Lanzhou Yintan Yellow River Bridge is shown in Figure 5.

3.2 *Tensioning frictional resistance test of retard-bonded prestressed reinforcement*

In order to fully observe the hardening process of preparing super retarded mortar, verify the reliability of forming by retard-bonded reinforcement technology, and provide frictional resistance parameters for design, we have simulated the tension technology of prestressed reinforcement. After pouring the concrete test pieces, according to age, we divide prestressed reinforcements into

Figure 4. Field of wrapping retard-bonded reinforcement.

Figure 5. Yard field of retard-bonded prestressed reinforcement.

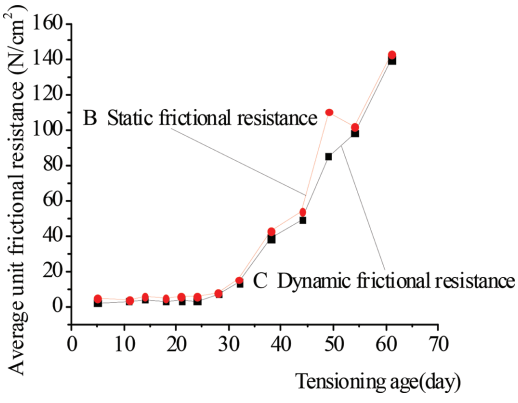

Figure 6. Relationship curve of tensioning age and tensioning frictional resistance.

14 groups, that is, 5, 11, 14, 18, 21, 24, 28, 32, 38, 44, 49, 54, 61, 66. There are 3 pieces of reinforcements in every group. We carry out tensioning test and get the relationship curve of tensioning age and tensioning frictional resistance (static frictional resistance and dynamic frictional resistance), shown in Figure 6. It can be seen that from Figure 6:

– Tensile frictional resistance of retard-bonded prestressed reinforcement basically keeps steady within the age of 30 days. The range of static frictional resistance per unit area is from 3.0 to 4.5 N/cm², and the counterpart of dynamic frictional resistance per unit area is from 1.77 to 3.5 N/cm². It can be seen that the prepared super retarded mortar will not be hardened for 30 days and has considerable plasticity.
– After the age is more than 30 days, there will be a rapid increase in the tensile frictional resistance, and after the age is more than 60 days, the tensile frictional resistance will attain 145 N/cm², which is mainly supplied by binding power in fact. It can be seen that super retarded mortar begins to harden after the age of 30 days, and once the commencement of hardening, there will be a rapid increase in its frictional resistance. The above two points show that the technology of wrapping super-retard-setting mortar is feasible.

4 TEST OF RETARD-BONDED PRESTRESSED MEMBERS IN BENDING

4.1 *Test program*

According to the test objective, we divide tension time into four periods, that is, 10 days, 15 days, 20 days and 25 days, considering the conditions which will take place on site when tensioning. There are two modes in distributing prestressed reinforcements, that is to say, linear reinforcement and curve reinforcement. In the mode of linear reinforcement, after the completion of tension of prestressed reinforcement, members may experience three circumstances: 1) They are transported immediately after tension. 2) Load is applied to them before retarded mortar attains the design strength. 3) Load is applied to them after retarded mortar attains the design strength. In order to have a contrast on the working performances between the retard-bonded prestressed members and prestressed members without bonding and prestressed members with bonding, two groups of prestressed member without bondings and prestressed members with bonding are arranged respectively. Prestressed without bonding reinforcement adopts the method of painting a layer of butter on the surface of prestressed reinforcement and then covering with bellows. Prestressed reinforcement with bonding adopts the traditional method. In the traditional method, we preform the holes firstly, and then tension the prestressed reinforcement after concrete attains the ultimate strength, lastly pour the mortar in the hole. In order to further study if retarded mortar, after hardening, and concrete and prestressed reinforcement attain the requirements of tight binding and combined deformation, after the completion of load test, we split the members, adopt the method of direct observation by eye, and sample to determine their strengths. The detailed programs of test are shown in Table 2. The number of members is 20.

4.2 *Facture and load-applying mode of members*

We adopt C40 concrete, and its proportioning rate of cement and sand and stone is 1:1.37:2.73. Cement adopts Portland cement and the range of grain diameters of broken gravels is from 0.5 to 2.0 cm. The member of linear reinforcement is shown as Figure 7. Steel mould is treated with natural maintenance and retarded mortar (B type) adopts the course of gradual hardening within the age of 30 days and getting the final hardening after three months and its compression strength attains 30 MPa. When fabricating members, we should set aside a $150 \times 150 \times 150$ cubic test block and three $100 \times 100 \times 300$ prismy test blocks for every member. We also should set aside a sample for every prestressed steel strand so as to determine its material properties. We should set aside test block for retarded mortar so as to determine the properties and final strength of retarded mortar. After tensioning and anchoring, we divide the member into three parts evenly in the lengthwise direction and applied the load, graded loading with one grade

Table 2. General test schedule of retard-bonded prestressed concrete member.

Type of prestress	Mode of steel distribution	Loading time	Tension time/day			
			10	15	20	25
Retard-bonded	Linear steel	1. Perturbation motion after tensioning (applied load after two months)			Number: 2 No.: 4-1, 4-2	Number: 2 No.: 2-1, 2-2
		2. Applied load when strength of retarded mortar is low. (one month)			Number: 2 No.: 5-1, 5-2	
		3. Applied load when retarded material is fully hardened. (two months)	Number: 2 No.: 1-1, 1-2	Number: 2 No.: 3-1, 3-2	Number: 2 No.: 6-1, 6-2	
	Curve steel	4. Applied load when retarded material is fully hardened. (two months)	Number: 2 No.: 9-1, 9-2		Number: 2 No.: 10-1, 10-2	
Without bonding	Linear steel				Number: 2 No.: 7-1, 7-2	
With bonding	Linear steel				Number: 2 No.: 8-1, 8-2	

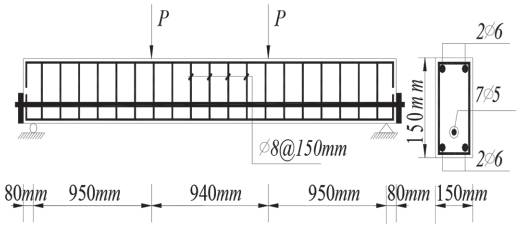

Figure 7. Member of linear reinforcement.

Figure 8. Arrangement of retard-bonded reinforcements before concrete pouring.

of 5 kN, on the middle two points according to the time specified by test program (see Figs. 7–9).

4.3 *Test results and analysis*

4.3.1 *Crack moment and limit moment*

From the commencement of applying load to the failure of structure, crack moments as well as limit moment of members are shown in Tables 3 and 4.

It can be seen from Table 3 that under same tension age the limiting moments of members (5-1, 5-2) loaded at one-month age are approximate to the ones of members without bonding (7-1, 7-2), which indicates that retarded mortar is not fully solidified when it is at the age of one month and the beam is just like the prestressed member without bonding at the moment. And the limiting moments of members (4-1, 4-2) and (6-1, 6-2) loaded at two-month age are approximate to the ones of prestressed members (8-1, 8-2) with bonding, which indicates that retarded mortar has been fully solidified and played the role of binding prestressed reinforcement with concrete and made

Figure 9. Abutments and loading devices.

prestressed reinforcement and concrete can experience operation and distortion together. Limiting moments of members (10-1, 10-2) with curve reinforcement are approximate to the members (4-1, 4-2) and (6-1, 6-2) with linear reinforcement. It can

Table 3. Measured value of crack moment and limit moment at the same tension age.

Mode of distributing steel	Surrounding of members	Member no.	Crack moment (kN·m)		Limit moment (kN·m)	
			Measured	Average	Measured	Average
Linear steel (retard-bonded steel)	1. Perturbation motion after tensioning (applied load after two months)	4-1/4-2	61.3/66.5	64.1	145.5/140.0	142.6
	2. Applied load when the strength of retarded mortar is low. (one month)	5-1/5-1	61.8/57.0	59.4	114.0/114.0	114.0
	3. Applied load when retarded material are fully hardened. (two months)	5-1/5-1	61.8/61.8	61.8	146.3/142.3	144.3
Linear steel	Reinforcement without bonding	7-1/7-2	61.8/57.0	59.3	109.3/114.0	111.6
	Reinforcement with bonding	8-1/8-2	66.5/61.8	64.1	133.0/137.8	135.4
Curve steel	Applied load when retarded material is fully hardened. (two months)	10-1/10-2	57.5/52.3	54.9	128.3/133.0	130.6

Table 4. Measured value of crack moment and limit moment at the different tension age.

Mode of distributing steel	Tension age/day	Member no.	Crack moment (kN·m)		Limit moment (kN·m)	
			Measured	Average	Measured	Average
Linear steel	10	1-1/1-2	66.3/68.2	67.7	123.5/128.3	125.9
	15	3-1/3-1	61.8/66.5	64.1	128.5/142.5	135.4
	20	6-1/6-2	61.8/61.8	61.8	146.3/142.3	144.3
	25	2-1/2-2	66.5/61.8	64.1	128.3/128.3	128.3
Curve steel	10	9-1/9-2	52.3/50.2	51.2	128.3/133.0	130.6
	20	10-1/10-2	57.5/52.3	54.9	128.3/133.0	130.6

be seen from Table 4 that tension age has a certain effect on the limiting moments and they will reach the maximum at the age of 20 days. It can be seen from Tables 3 and 4 that all crack moments are approximate no matter it is at the same tension age or not, which indicates that tension age and environment have few effects on the crack moments of members and the crack moments of members with curve reinforcement is smaller than the members with linear reinforcement. The reason for the above is that the tensile frictional resistance of curve reinforcement is bigger than linear reinforcement and effective prestress in midspan is smaller.

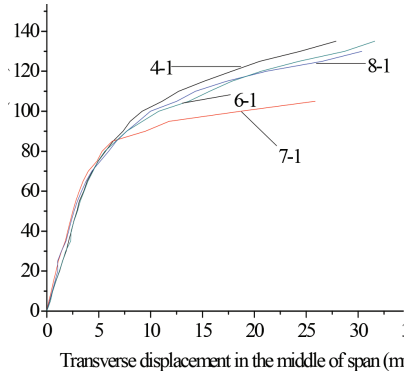

Figure 10. Load-deflection (p-f).

4.3.2 *Measured load-deflection (p-f) curve*

Figure 10 shows the load-deflection (p-f) curves of members (4-1, 6-1, 7-1, 8-1) when applied load two months after tensioning. It can be seen from Figure 10 that there are evident differences in the (p-f) curves between members (4-1, 6-1) when applied load two months after tensioning and member without bonding (7-1) but there is little difference between it and members with bonding, which indicate they have got the characteristics of prestressed member with binding.

In a word, it can be concluded that retard-bonded prestressed member can be fully deemed

as the prestressed member two months after tensioned.

5 DESIGN OF RETARD-BONDED PRESTRESSED REINFORCED CONCRETE STRUCTURE

The invention of retard-bonded prestressed concrete brings a revolution for prestressed concrete system. It is proved by tension frictional resistance test and load test of structural elements that not only retard-bonded prestressed concrete structural system is feasible on construction technologies, but also retarded mortar can fully play the role of binding prestressed reinforcement with concrete. Retard-bonded prestressed concrete structural system greatly simplifies construction technologies of prestressed concrete structural system with bonding of post-tension method, which doesn't cause many troubles in design. Except the little difference on the calculations of tensile frictional resistance, its calculation principles are fully identical to prestressed concrete structural system with bonding of post-tension method. The following factors should be taken into consideration when designing retard-bonded prestressed concrete structural system:

- When calculating the loss of tensile frictional resistance of retard-bonded prestress, the friction between prestressed reinforcement and retarded mortar should be taken into consideration. The design tensile force is calculated by 4.5 N/cm^2 for the loss of frictional resistance;
- When calculating section stress, the section should be considered as full section and the influence of pipe will not be considered again.
- Local stress and anti-crack checking computations under the anchor will not be controlled and the factor of reduction on the occupied duct area after the adoption of retard-bonded prestress technology will not be taken into consideration so as to enhance the safety stock.
- Due to the invention of special tension technology of retard-bonded reinforcement, control stress of steel strand under the anchor should be calculated by 0.78Ryb and the loss of frictional resistance at the mouth of anchor loop will not be considered.

6 CONCLUSIONS

Through super retarded material, the system without bonding and the system with bonding of post-tensioning method are combined by retard-bonded prestressed concrete system, learn from other's strong points to offset one's weaknesses each other, and make full use of respective advantages.

Contrast analysis between retard-bonded prestressed members and conventional post-tensioned prestressed (with bonding and without bonding) members are made in this paper in crack moment, limit moment, formation of crack, load-deflection curve and other aspects through the test of 16 retard-bonded prestressed members in bending. We arrive at the conclusion of that there are the same working performances between prestressed members with bonding and retard-bonded prestressed members after retard-bonded prestressed members are tensioned for two months.

With the successful invention of processing equipment of retard-bonded prestressed reinforcement, retard-bonded prestressed concrete structure, as a new prestress system, will be developed rapidly.

ACKNOWLEDGEMENTS

This work was financially supported by the Nation Natural Science Foundation (51368035), The Science and Technology Research Foundation of GURC (JK2012-13) and The Youth Science Foundation of LZJTU (2011032).

REFERENCES

ACI Committee 318. 2005. *Building Code Requirements for Structural Concrete and Commentary (ACI 318M-05)*. Farmington Hills: American Concrete Institute.

American Concrete Institute (ACI). 2011. *Building Code Requirements for Structural Concrete and Commentary*. Farmington Hills: ACI 318R-11, MI.

Au, F.T.K. & Du, J.S. 2004. Prediction of ultimate stress in unbonded tendons. *Mag Concr Res* 56(1): 1–11.

Benachour, A., Benyoucef, S. & Tounsi, A. 2008. Interfacial stress analysis of steel beams reinforced with bonded prestressed FRP plate. *Eng Struct* 30(11): 3305–3315.

Bonaldo, E., Barros, J.A.O. & Lourenco, P.B. 2005. Bond characterization between concrete substrate and repairing SFRC using pull-offtesting. *Int. J. Adhes. Adhes* 25(6): 463–474.

Cao, G.H., Hu, J.X., Zhang, K. & Wang, Z.P. 2013. Ultimate bearing capacity test of retard-bonded prestressed concrete beams. *Journal of Highway and Transportation Research and Development* 30(6): 49–55.

Climaco, J.C.T.S. & Regan, P.E. 2001. Evaluation of bond strength between old and new concrete in structural repairs. *Mag. Concr. Res* 53(6): 377–390.

Du, J.S., Au, F.T.K., Cheung, Y.K. & Kwan, A.K.H. 2008. Ductility analysis of prestressed concrete beams with unbonded tendons. *Eng Struct* 30(1): 13–21.

Feng, X. & Zhou, X.Y. 2011. Experiment and research on retard-bonded prestressed steel strands. *Highway* 21(3): 67–70.

Feng, X. & Zhou, X.Y. 2013. Experimental research on crack width of retard-bonded partially prestressed concrete beams. *Advanced Materials Research* 639–640(32): 211–215.

Fu, Q., Cao, X., Jin, L.Z., Zhu, W.X., Yang, H.X. & Shu, Z.B. 2010. Experimental study on the stress increment of prestressed tendons of retard-bonded prestressed concrete Continuous Beams. *Advanced Materials Research* 163–167(25): 1431–1435.

Harajli, M.H. 2006. On the stress in unbonded tendon at ultimate: Critical assessment and proposed change. *ACI Struct J* 103(6): 803–812.

Kim, K.S. & Lee, D.H. 2012. Flexural behavior of post-tensioned members with unbonded tendons. *Comput Concr* 10(5). (in press).

Li, P.X. 2008. Research on the retard-bonded prestressed technique and development prospects. *Industrial Construction* 38(11): 1–5.

Rosingnoli, M. 1999. Prestressed concrete box girder bridges with folded steel plane webs. *Proc Inst. Civ. Eng. Struct. Build* 134(1): 77–85.

Tao, X.K. 1996. *Post-tensioned Prestressed Concrete Design Handbook*. Beijing: China Architecture and Building Press.

Zhang, J.L., Song, Y.P. & Liu, Y. 2009. Cracking performance and crack closing of retard-bonded prestressed concrete beams. *Journal of Harbin Institute of Technology* 41(12): 128–132.

Zhao, X. & Jin, L.Z. 2011. Research of the calculation to prestress loss and the stretching friction of retard-bonded prestressed concrete continuous beams. *Journal of Jinggangshan University (Natural Science)* 32(6): 99–103.

Zhou, X.Y. & Feng, X. 2011. Experimental research on crack width of retard-bonded partially prestressed concrete T-beams. *Journal of Highway and Transportation Research and Development* 28(1): 56–61.

Civil Engineering and Urban Planning IV – Liu et al. (Eds)
© 2016 Taylor & Francis Group, London, ISBN 978-1-138-02903-3

Analysis of deformation characteristics of pre-stressed steel girder in high temperature (fire) environment

Qiang Sun, Yun Guan & Wei Tian
School of Civil Engineering, Anhui Jianzhu University, Hefei, Anhui, China

ABSTRACT: Mechanical properties of pre-stressed steel girder differs a lot in high temperature (fire) environment. Based on structural stability theory and fire hazard, formulas for calculating the deformation of prestressed steel girder are presented, and the influences of several factors (temperature, load, loss of prestress, cable arrangement height) in high temperature condition are analyzed. Researches show that these factors have a significant impact on deformation of girder. The method devised here is validated by precise experiments. The work in this paper provides some conclusions useful for pre-stressed steel girder fire-resistance design, and offers some proposals about how to reduce the deformation of pre-stressed steel girder in actual projects.

1 INTRODUCTION

Pre-stressed steel members offer such advantages as material saving, self-weight reduction, and lower cost. However, due to insufficient fire-resistance inherent in steel, building structures made of steel may undergo severe damage in the event of fire, so fire-resistance design of pre-stressed steel members is quite necessary. A lot of researches and explorations have been done into steel structure fire-resistance by both foreign and Chinese scholars since 1970s. Early-stage steel structure fire-resistance study was generally dominated by testing. Fire-resistance tests have been carried out using individual steel girders, columns, and built-up girders both in China and abroad by, among others, University of Sheffield (UK), CTICM (France), and Tongji University (China) (Lu et al. 2007; Li et al. 2006; Qing 2012; CSSAEC 2006).

In the middle and end of 1990s, certain scholars realized that the fire-resistance behavior of an entire structure is not identical to that of individual structural members; so some fire-resistance tests were performed on entire structures (Bai 2008; Liu 2001), including full-scale steel structure fire-resistance tests, among which the most famous was Cardington test in UK (BSI 1993; BSI 1994; Lenoi 1999; Noriaky 1993). In 2008, Jia Baorong, Dong Yuli, and Li Xiaodong, et al. completed testing researches into steel frame with different fire source locations and revealed the temperature field distribution and deformation pattern of individual members of the steel frame as well as the deformation and damage mechanism of the entire steel frame (Chung 1988; Saiidi 1995; Lenoi 1997; Zhou et al. 1995).

Considering the theories of fire science and the requirements of structural fire-resistance design and based on actual engineering situation and the potential accident condition of buildings, this paper analyzes the influence of fire factors and pre-stressing loss upon pre-stressed steel girder deformation. Illustrated by examples and for the purpose of improving the deformation capability of structures, this paper proposes some measures, which may have a value of reference to fire-resistance design of civil structures.

2 CALCULATION OF PRESTRESSED STEEL GIRDER DEFORMATION IN HIGH TEMPERATURE (FIRE) ENVIRONMENT

Pre-stressed steel girders are used typically in large-span structures and the member section area is usually less than that of their equivalent traditional steel girders so as to save steel. The rigidity is an important factor of controlling the normal work of the structure. As same as a pre-stressed concrete girder, prestress which is applied in the absence of external loads causes the girder to deform in a way opposite to the way which would otherwise be if only the external loads were applied (see Fig. 1a). When loads are applied to the girder, the camber generated by prestress is offset in the first place before the flexural deflection that deviates from the baseline occurs (see Fig. 1b). The deflection of the prestressed steel girder consists of two components: the deflection generated under the action of loads; the negative deflection generated under the prestress exerted on the lower flange (Luo 2011).

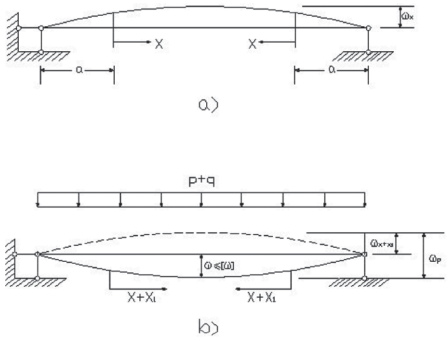

Figure 1. Flexural deflection of prestressed steel girder.

As such, the deflection of the girder may be estimated using:

$$\omega = \omega_P - \omega_{X+X_1} \tag{1}$$

where: ω_p is the deflection of the girder under the action of all the loads; ω_{X+X_1} is negative deflection (camber) of the girder caused by prestress and by the self-stress generated by loads.

The prestressing loss due to anchorage compression and cable relaxation becomes even more pronounced since external prestressing is used for most prestressed steel structure systems (Xiong et al. 2004) and the members in high temperature (fire) environment. The following formula may be used to estimate the deflection caused by prestressing loss (Wei & Dong 2007) due to anchorage compression and cable relaxation:

$$\omega = \omega_p - \omega_{X+X_1} + \omega_l \le [\omega] \tag{2}$$

where: ω_l is deflection caused by prestressing loss; $[\omega]$ is the allowable deflection given by steel structure code.

The following formula is suggested by Prof. Zhong Shantong of Harbin Institute of Technology (Zhong 1986) for computing the deflection of prestressed steel girders with straight-line cable arrangement and working at elastic stage:

$$\omega_X = \frac{Xel^2}{8EI}(1-4\varepsilon^2) \tag{3}$$

$$\varepsilon = \frac{a}{l} \tag{4}$$

where: X is amount of prestress exerted; e is distance between cable center and girder section gravity center; ε is ratio of support-cable end distance and span length; a is distance from prestressed member anchorage to support; l is span length.

The loss of prestress of steel girders at high temperature may be estimated using:

$$X_l = x_m + x_s = \frac{\Delta_a \times E_{1T} \times A_3}{l} + 0.125x_k \times \left(\frac{X_k}{f_{ptk}A_3\eta_T} - 0.5\right) \tag{5}$$

where: X_k is the controlling internal force for actual tensioning; X_l is loss of prestress with consideration given to high temperature; x_m is loss due to anchorage compression during tensioning with consideration given to the influence of high temperature; l is cable length; A_3 is cable section area; Δ_a is total compression amount of anchorage; E_{1T} is Elastic modulus of cable material with consideration given to temperature influence; x_s is loss due to continuing cable elongation after anchorage tensioning with consideration given to high temperature influence; f_{ptk} is standard value of tensile strength of cable material.

From equation (3), we get:

$$\omega_{X+X_1} = \frac{(X+X_1)el^2}{8EI}\left(1-4\varepsilon^2\right) \tag{6}$$

$$\omega_l = \frac{X_l el^2}{8EI}\left(1-4\varepsilon^2\right) \tag{7}$$

In combination with equations (3), (6) and (7), one may find the following formula for calculating the deformation of steel girders in high temperature (fire) condition:

$$\omega_T = \omega_{PT} - \frac{X_k + X_1 - X_l}{8E_T I}\left(1-4\varepsilon^2\right)el^2 \tag{8}$$

where: ω_T is deflection of prestressed steel girder in high temperature condition; ω_{pT} is deflection of steel girder under the action of all the loads in high temperature condition; X_1 is self-stressing tension caused by loads; E_T is elastic modulus of steel at high temperature (Li et al. 2006); I is moment of inertia of girder section.

With:

$$X_1 = \beta X - \gamma_T X = \frac{(M - fW_2)A}{W_2 + Ah_2} - \frac{fAW_2}{\gamma_T W_2 + \gamma_T Ah_2} \tag{9}$$

where: β is self-stress factor; γ_T is tensioning factor; M is sectional bending moment of girder used in calculation; f is design value of tensile strength of steel; A is section area of steel girder; W_2 is section modulus of the tensioned girder flange; h_2 is depth of sectional centroid to external edge of tensioned flange.

3 INFLUENCE OF DIFFERENT FACTORS UPON DEFORMATION CHARACTERISTICS OF PRESTRESSED STEEL GIRDER

3.1 *Influence of temperature upon steel girder deformation*

Working condition I: Given a cable-prestressed simply supported steel girder with $l = 18\,m$ and $A = 212.4\,cm^2$ (see Fig. 2), the girder is assumed to receive uniformly distributed loads, among which the permanent component is $q_d = 32\,kN/\text{m}$ and the live one $q_1 = 22\,kN/\text{m}$. The steel is Q235 and $90\phi5$ high strength steel wire ropes are used: $A_1 = 17.64\,cm^2$, $f_1 = 770\,Mpa, E_1 = E_2 = 2.06\times10^5 Mpa$, and the actual tensioning force $x_2 = 935\,kN$. The distance-load factor γ_T for the cable centroid to the sectional gravity center is taken at 1.0 and the allowable deflection $[\omega] = 1/250$.

Substituting the given conditions and relevant factors into equation (8), we find the deflection response of the cable-prestressed steel girder to temperature change, as shown in Figure 3.

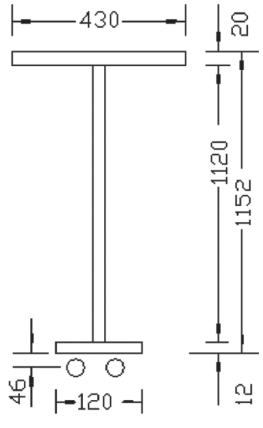

Figure 2. Cross section of prestressed steel girder.

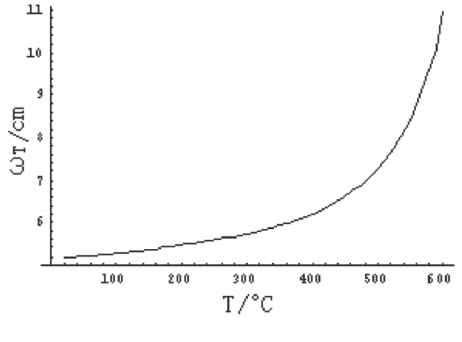

Figure 3. Member deflection—temperature curve.

The figure shows a direct proportion relation between the member deflection and the temperature at the initial temperature rising stage. At 20°C~250°C, the deflection does not change appreciably; however, when the temperature rises above 300°C the deflection becomes noticeable and no longer satisfies a linear relationship. When the temperature is around 500°C, the member so deforms that the allowable deflection is reached, i.e., the girder no longer meets the ultimate state for normal service. When the temperature exceeds 600°C, the member essentially loses its load-carrying capacity, which is evidenced by abruptly increasing mid-span deflection, and the member may be deemed as having failed. Considering the degrading factor given by EC3 for elastic modulus of steel at high temperature, one may find that the pattern of such degradation at high temperature looks largely similar in variation stages to the deflection of the member that increases with increasing temperature. It may be presumed naturally that the drop of elastic modulus of steel at high temperature is one of the key factors that lead to excessive member deflection in fire.

3.2 *Influence of different types of load upon steel girder deformation*

A comparison is made of the deformation occurred under the loads in three working conditions in order to analyze the deflection variation under different loads at high temperature. For the purpose of the rationality in comparison, the following three working conditions are so selected that the bending moment value at the controlling point (mid-span) is the same.

Working condition I: Identical to working condition I given in Section 2.1 “Influence of Temperature upon Steel Girder Deformation”;

Working condition II: The permanent load is uniformly distributed $q_d = 32\,kN/\text{m}$, the live load is a concentrated mid-span force $F = 198\,kN$, with the remaining condition identical to that of the above working condition I;

Working condition III: The permanent load is uniformly distributed $q_d = 32\,kN/\text{m}$, the live loads are two equidistantly spaced, concentrated, and equal forces $F_1 = F_2 = 148.5\,kN$ applied in the span, with the remaining condition identical to that of the above working condition I.

The code deduces the girder deflection calculation formula based on small deformation theory and requires that no local buckling shall occur when the girder is working in its normal elastic state. This deflection may be estimated using the beam deflection formula suggested in a textbook of mechanics of materials (Dai 2005).

The maximum deflection of the girder under uniformly distributed load is estimated using

$\omega_{\max} = \frac{5ql^4}{384EI}$; the maximum deflection of the girder under the action of one mid-span concentrated load is estimated using $\omega_{\max} = \frac{Fl^3}{48EI}$; the maximum deflection of the girder under the action of 2 identical and equidistantly spaced concentrated loads is estimated using $\omega_{\max} = \frac{6.81Fl^3}{384EI}$.

Figure 4 suggests that the member deflection increases with temperature for all the three working conditions. With the bending moment value of the controlling point kept the same for each working condition, the largest deflection is found in working condition I, i.e., the entire girder is subject to uniformly distributed load, and the second largest deflection occurs in working condition II, followed by condition III, which shows the least deflection.

3.3 *Influence of prestressing loss amount upon deformation characteristics of steel girder*

We take working condition I as the example to illustrate the influence upon the deflection of a steel girder at high temperature when consideration is given to the amount of prestressing loss. The amount of prestressing loss is 0~200 *kN*, and the member temperature is 20°C, 200°C, 400°C and 600°C respectively.

The calculation results are shown in Figure 5, which suggests that the member deflection increases progressively with the loss of prestress and an essentially direct proportion relation is apparent. One may find from the curve that the member deflection increases with temperature but does not differ very much at 20°C, 200°C, or 400°C. However, when the temperature is at 600°C the deflection is almost twice as large as would be at normal temperature. Before the temperature exceeds 400°C, the deflection varies by almost an identical amount for prestress losses not exceeding a certain limit and varies by an amount less than that when the temperature is 600°C for prestress losses not exceeding a certain limit.

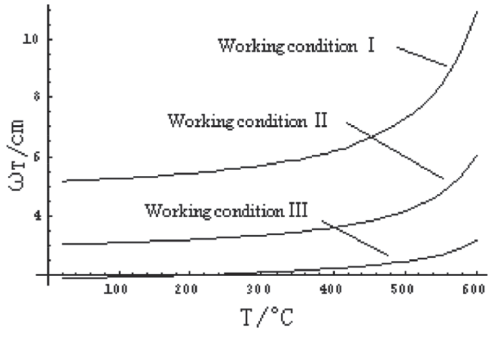

Figure 4. Member deflection—type of load curve.

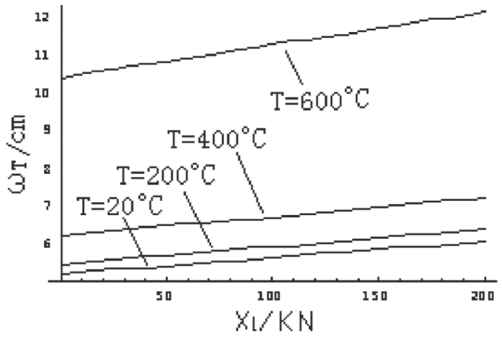

Figure 5. Member deflection—prestress loss curve.

Large deflection values increase progressively, i.e., with increasing temperature the member deflection varies more and more noticeably for a certain prestressing loss range.

3.4 *Influence of different support types upon deformation characteristics of steel girder*

The configuration of member supports influences both the internal force distribution of the entire girder and the member deflection, so intelligently devised support types are necessary to secure the strength and rigidity of a prestressed steel girder. The following paragraphs analyze the deflection variation with temperature at high temperature for a beam under uniformly distributed load with both ends simply supported, one end simply supported and the other fixed, or both ends fixed. From formulas of mechanics of materials (Dai 2005).

The deflection of a girder with both ends hinged and under uniformly distributed load may be estimated using $\omega_{\max} = \frac{5ql^4}{384EI}$; the deflection of a girder with one end hinged and the other fixed and under uniformly distributed load may be estimated using $\omega_{\max} = \frac{0.0054ql^4}{EI}$; the deflection of a beam with both ends fixed and under uniformly distributed load may be estimated using $\omega_{\max} = \frac{ql^4}{384EI}$.

The calculation is based on working condition I except for difference in support type.

The calculation results are illustrated in Figures 6–8, which suggest that the deflection for either support type increases temperature. At a given temperature, the deflection of the steel girder is the largest when its both ends are hinged (i.e., simply supported), followed by when one end is hinged and the other fixed, whereas the deflection is the smallest when the girder has its both ends fixed. Similarly, for a given temperature rise range, the prestressed steel girder deflection variation range depends upon the support type. The deflection increase magnitude is the largest when both

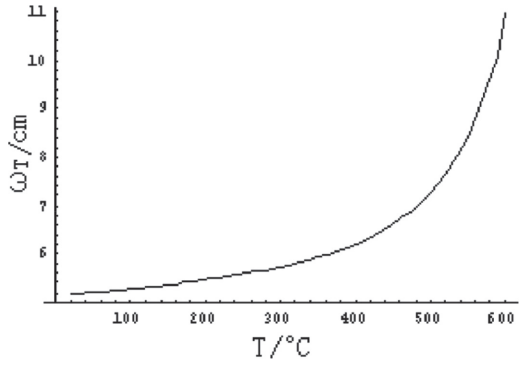

Figure 6. Deflection—prestressing loss curve for a member with both ends hinged.

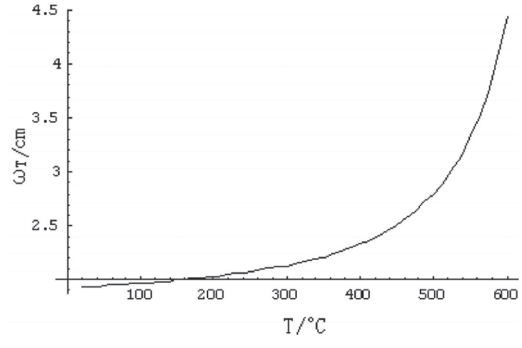

Figure 7. Deflection—prestressing loss curve for a member with both ends hinged.

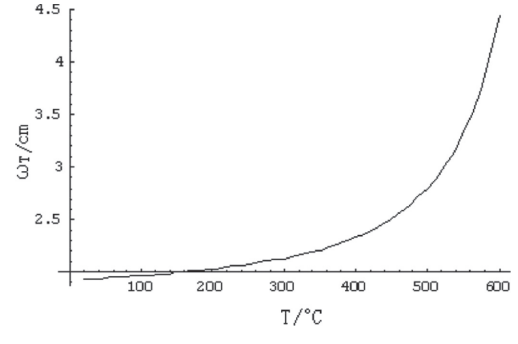

Figure 8. Deflection—prestressing loss curve for a member with both ends fixed.

ends are hinged, what comes next is when one end is hinged and the other fixed, and the deflection varies the least with the temperature when both ends are fixed. It is thus clear that the deflection of a steel girder at high temperature is closely related

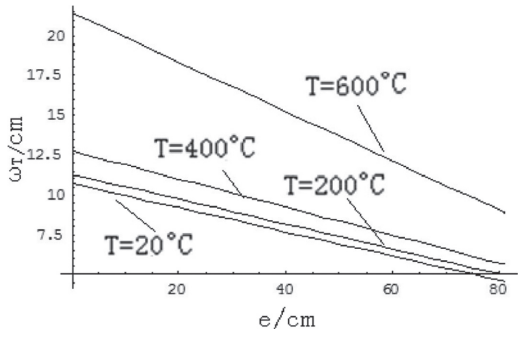

Figure 9. Member deflection—height of cable location curve at different temperatures.

to its restraint degree; hence, the choice of proper support type becomes mandatory if it is desirable to minimize deflection.

3.5 *Influence of height of cable location upon deformation characteristics of steel girder*

The analysis is again based on working condition I. The height of the cable location, or the distance e between the cable centroid and the sectional gravity center varies from 0~80 *cm* and the temperature is 20°C, 200°C, 400°C, and 600°C respectively.

The calculation results are given in Figure 9, which suggests that the deflection of the steel girder varies with the cable location height essentially in the same manner for 20°C and 200°C. For a given cable location height, the deflection increases with temperature. Similarly, for a given increase of cable location height, the largest decrease of deflection is observed when the temperature is 600°C, followed successively by 400°C, 200°C, and 20°C. Therefore, increasing the cable location height by a proper amount is effective in reducing member deflection.

4 CONCLUSION

This paper analyzes prestressed steel girder's deformation behavior in high temperature (fire) environment. The deflection of a cable-prestressed steel girder is broken down into three components: deflection caused by all the loads, negative deflection caused by applied prestress and by self-stress induced by loads, and deflection due to loss of prestress. Formulas are proposed for calculating prestressed steel girder deformation at high temperature with consideration given to prestressing loss. Analysis covers the influence of different factors upon member deflection at high temperature and such factors include temperature, load type,

amount of cable prestressing loss, support type, and height of cable location. Based on these analyses, some measures may be taken on actual jobs to minimize member deformation. For instance, intelligent selection of structural configuration and support type, selection of low-relaxation materials, employment of over-tensioning to compensate some prestressing loss, and proper location of cables.

ACKNOWLEDGEMENT

In this paper, the research was a project of: National Key Basic Research and Development Plan Project (2012CB719703), an Important Project of Provincial Level Natural Science Research of Higher Education Institutions in Anhui Province (KJ2014ZD06), and funded by Natural Science Fund of Anhui Province (1408085QE96).

REFERENCES

Bai, Y. 2008. *Research on Structural Performance and Fire-resistance of Large-space Steel Structures under Fire Conditions*. Beijing: Tsinghua University.

Chinese Steel Structure Association Expert Committee. 2006. *Technical Specification for Prestressed Steel Structures (CECS212:2006)*. Beijing: Chinese Overseas Press.

Chung, L. 1988. Experiments on active control of simic structures. *American Society of Civil Engineers Journal of Engineering Mechanics* 114(5): 241–256.

Dai, S. 2005. The calculation of stiffness of the beam considered the post-buckling strength. *Journal of Changzhou Institute of Technology* 18(s): 41–44.

European Committee for Standardization. 1993. *ENV 1993-1-2, Eurocode 3, Design of Steel Structures. Part 1.2: Structural Fire Design*, London: BSI.

European Committee for Standardization. 1994. *ENV 1994-1-2, Eurocode 4, Design of Composite and Concrete Structures. Part 1.2: Structural Fire Design*, London: BSI.

Hu, Y.Q. 2005. *Deformation and Plastic Research of Big Span Prestressed I-section Steel Girders*. Lanzhou: Lanzhou University of Technology.

Jia, Y.M., Gai, B.Z., Zhang, Y.G. & Ni, Y.Z. 2003. Theoretical analysis and experimental study of prestressed steel girders. *Engineering Mechanics* 20(3): 161–166.

Lenoi. G. 1997. Numerical analysis of thin walled beams with internal unbonded cables by the Ritz method. *International Journal of Solids and Structures* 35(6): 51–67.

Lenoi, G. 1999. Vibration of beams prestressed by internal frictionless cables. *Journal of Sound and Vibration* 222(1): 1–18.

Li, G.Q., Han, L.H., Lou, G.B. et al. 2006. *Fire Performance Design of Steel Structures and Steel-concrete Composite Structures*. Beijing: China Architecture & Building Press.

Liu, D.Z. 2001. Analysis and design of combined prestressed grids. *Journal of Harbin University of Civil Engineering and Architecture* 34(s): 40–42.

Lu, X.L., Yin, S.M. & Liu, X.L. 2007. *Modern Prestressed Steel Structures*. Beijing: China Communications Press.

Luo, C. 2011. Study on deflection calculation of prestressed reinforced concrete beam. *Journal of Waterway and Harbor* 32(1): 60–63.

Noriaky, H. 1993. Excitation of arch and suspension bridges by subwires. *Shock and Vibration* 1(3): 59–64.

Qing, B.T. 2012. The present and future of fire performance design of steel structures. *Technology Innovation and Application* 07(Z): 174.

Saiidi, M. 1995. Prestress force effect on vibration frequency of concrete bridges. *American Society of Civil Engineers Journal of Structural Engineering* 120(5): 2233–2241.

Wei, W. & Dong, D.M. 2007. Calculation for prestress losses due to deformation of anchorage device. *Journal of Architecture and Civil Engineering* 24(4): 86–90.

Xiong, X.Y., Gu, W. & Li, Y.M. 2004. The systems of external prestressing: State of the art review and prospects. *Industrial Construction* 34(7): 50–53.

Zhong, S.T. 1986. *Prestressed Steel Structures*. Harbin: Harbin Institude of Technology Press.

Zhou, D.Y., Zhang, H. & Lv, X.L. 1995. Design of a long span prestressed structures. *Structural Engineers* 35(4): 7–10.

Civil Engineering and Urban Planning IV – Liu et al. (Eds)
© 2016 Taylor & Francis Group, London, ISBN 978-1-138-02903-3

Experimental analysis on mechanical properties of different types of steel fiber-reinforced concrete

Jing-Gan Shao
Henan Vocational and Technical College of Communications, Zhengzhou, Henan, China

ABSTRACT: To study the work performance of different kinds of steel fiber-reinforced concrete, the design parameters of mix proportion were used according to the requirements of an expressway reconstruction project. And the indices of slump, slump flow, segregation resistance, bulk density, slump loss in 30 minutes, and mechanical strength of different kinds of steel fiber-reinforced concrete were tested and analyzed. The results indicated that the segregation resistance index is less than 15%, and the compressive strength of different kinds of steel fiber-reinforced concrete is about 68 Mpa. The splitting tensile strength-to-tensile compressive strength ratio of the milling-type steel fiber-reinforced concrete is much higher than the hook-type and indentation-type ones, which show that the toughness of milling-type steel fiber-reinforced concrete. The indices of the milling-type steel fibers reinforced concrete can satisfy the requirements of the technical standards better by using the milling-type steel fiber-reinforced concrete and the appropriate mix proportion in the construction of a late poured band of the bridge deck.

1 INTRODUCTION

Cao et al. (2012) and Chen et al. (2014) thought that steel fiber-reinforced concrete is a kind of heterogeneous composite material consisting of fine aggregate, coarse aggregate, cement and random distribution of steel fiber. Because of the resistance of steel fiber and the effect of reinforcement, the properties of steel fiber-reinforced concrete, such as tensile, shear and torsion, have been greatly improved. Domestic and foreign scholars have carried out some research on the mechanical properties of steel fiber-reinforced concrete, and obtained many results. Luo (2004) used the modified material testing machine to carry out the bending and splitting tensile test of steel fiber-reinforced concrete beams with 1% ~ 4% steel fiber volume fractions. The results indicate that the tensile strength of steel fiber-reinforced concrete is linear with the volume fraction of steel fiber-reinforced concrete. Wang et al. (2014) and Hao (2009) reported that different types of fiber in the fiber-reinforced concrete toughening mechanism exhibited different effects. The effect of a long diameter ratio on the toughness of steel fiber-reinforced concrete is more obvious. Domestic and foreign research have mainly focused on the mechanical properties and microstructure of steel fiber-reinforced concrete, while the performance of different types of steel fiber-reinforced concrete has been studied little.

There is a total length of 106 kilometers of highway project, the bridge uses steel fiber concrete pouring of post-cast strip, and the concrete strength level is required to reach above C50. Based on highway engineering, slump, bulk density and mechanical strength indices, an indoor experiment on different types of steel fiber-reinforced concrete is carried out, in order to provide guidance for the practical engineering and a certain reference for similar projects.

2 THE PERFORMANCE OF RAW MATERIALS

- Cement used in this study was rugged P.O 52.5 cement; its main performance index is presented in Table 1.
- Fly ash selected was mainly of Class I and Class II produced by the Luoyang thermal power plant; the main performance index is presented in Table 2.
- The main performance index of the coarse aggregate is 5~10 and 10~20 mm continuous graded limestone gravel, and its main performance index is presented in Table 3.
- Fine aggregate is made of natural river sand in Yiyang, and its main performance indices are presented in Table 4.
- The admixture is used in the HSP-GJS high performance water reducer, and its homogeneous properties are listed in Table 5.

Table 1. Cement performance index.

Specific surface area ($m^2 \cdot kg^{-1}$)	Standard consistency water (%)	Stability	Initial setting time	Final setting time	Compressive strength (MPa)		Flexural strength (MPa)	
					3d	28d	3d	28d
388	27.8	0.5	2:23	3:17	27.9	55.4	5.9	9.1

Table 2. Fly ash performance index of the Luoyang power plant.

Project	Fineness (0.045 mm sieve residue) (%)	Loss on ignition (%)	Water content (%)	Alkali content (%)	SO_3 (%)	Chlorine ion content (%)	Water demand ratio (%)	Activity index (%)	Grade
Results	9.8	2.1	0.3	1	0.64	0.007	93	84	I
	11	5.1	0.6	1	0.95	0.008	96	80	II

Table 3. Main performance indices of Yanshi stone.

Project	Apparent density (kg/m^3)	Packing density (kg/m^3)	Porosity (%)	Clay content (%)	Flakiness content (%)	Rock compressive strength (Mpa)	Chloride ion content (%)	Activity of Alkali (%)
Results	2658	1550	41.7	0.7	2.2	110	0.008	0.035

Table 4. Main performance indices of natural river sand in Yiyang.

Project	Fineness modulus	Apparent density (kg/m^3)	Packing density (kg/m^3)	Silt content (%)	Void fraction (%)	Chloride ion content (%)	Activity of Alkali (%)
Results	2.61	2662	1550	1.8	41.8	0.006	0.08

Table 5. Homogeneous index of polycarboxylate superplasticizer.

Project	Solid content (%)	Density (g/ml)	pH	Content of Cl^- (%)	Alkali content (%)
Results	20.4	1.08	6.4	0.041	1.69

3 DETERMINATION OF MIX RATIO OF STEEL FIBER-REINFORCED CONCRETE

3.1 *Steel fiber-reinforced concrete mix design principle*

In accordance with the "regulations of the mix proportion design of ordinary concrete" (JGJ 55-2011), Lv (2014) and Hu et al. (2001) reported that "the application technology of fiber reinforced concrete" (JGJ-T221-2010) and "regulations of structural design and construction of steel fiber reinforced concrete" (CECS2-92) and according to the actual demand, can be concluded as the steel fiber concrete mixture ratio design requirements:

- Water-to-cement ratio of steel fiber-reinforced concrete is 0.28–0.32; the sand ratio is 41% ~ 45%;
- If the steel fiber length diameter ratio lf/df is in the range of 50–70, then the fiber volume content should be 0.5%–2.0% and steel fiber surface needs to have anti-corrosion coating, which can be used in milling, end hook, indentation and other types of steel fiber, and steel fiber tensile strength should reach up to 600 MPa;
- If the steel fiber-reinforced concrete is prepared, the slump should be greater than 120 mm;
- The cement type used should be of high strength, good abrasion resistance, dry shrinkage and frost resistance of ordinary Portland cement or Portland cement, in order to ensure the mechanical properties of concrete;
- Fineness modulus of sand should ensure $2.6 < \mu < 3.0$, the desired particle hard wearing,

well-graded, angular surface roughness; limestone gravel stones should not be used, the maximum particle size should not be greater than 20 mm and 1/2 of steel fiber length.
– Polycarboxylic acid high-performance water reducer can be used as a suitable water reducer, and the amount of cement ranges from 0.5% to 1.5%;
– All kinds of raw materials should meet the requirements of the relevant standards, regulations and standards, in addition to meeting the above requirements.

According to the "Design specification for ordinary concrete mix proportion" (JGJ 55-2000) and the "Technical specification of fiber reinforced concrete" (JGJ-T221-2010), the steel fiber concrete mix proportion design requirements are as follows:

– Water-to-cement ratio of steel fiber-reinforced concrete is 0.30; the sand ratio is 43%; the dosage of the water reducing agent is 1.2% ~ 1.5%;
– The steel fiber in the concrete is as follows: the diameter is 0.75 mm, the length is 40 mm, and the volume fraction is 0.8%;
– If the steel fiber-reinforced concrete is prepared, the slump should be in the range of 100–120 mm;
– Fineness modulus of sand should be $2.6 < \mu < 2.8$; the gravel diameter should be 5–20 mm.

3.2 *Determination of the content of steel fiber*

Han et al. (2006) and Ji et al. (2015) indicated that the critical volume fraction of the fiber is the change in concrete failure mode: when the fiber content is less than the critical volume fraction of the fiber, the fiber cannot bear the load, which will destroy the structure of concrete. When the fiber content is larger than the critical volume fraction, the fiber can bear the load of the matrix transfer, even to improve the bearing capacities.

The critical mass ratio equation of the fiber is given in the paper of Sun et al. (2006), and the content of the fiber is determined by testing:

$$\rho_{fc} = \frac{f_{mu}}{f_{mu} + \eta_f (f_{fu} - \varepsilon_{mu} E_f)} \quad (1)$$

where
f_{mu}— the ultimate tensile strength (MPa) of fiber-reinforced concrete;
f_{fu}—the ultimate tensile strength (MPa) of fiber;
ε_{mu}—the ultimate tensile strain of the fiber-reinforced concrete matrix;
η_f—the effective coefficient of the fiber direction;
E_f—the elastic modulus of fiber (GPa).

For general C50 concrete, f_{mu} = 4.11 MPa, $\varepsilon_{mu} = 100 \times 10^{-6}$; for steel fiber, f_{fu} = 1450 MPa, E_f = 210 GPa, and η_f = 0.5, and by substituting Equation (1), the steel fiber critical volume rate is calculated to be 0.57%. On the basis of referring to a large amount of data and test data, taking into account the influence of the construction cost and the concrete design requirement, the volume fraction of steel fiber is 0.6%.

3.3 *Steel fiber concrete mix proportion scheme*

Three kinds of steel fiber shape can be used in the steel fiber concrete mix proportion scheme, such as milling type, end hook type, and indentation type, as shown in Figure 1. Based on a highway construction section, the strength grade of the bridge deck concrete is C50 and the 3d compressive strength of concrete should reach 50% of the design strength. Table 6 lists the design parameters according to the basic principle of steel fiber-reinforced concrete mix proportion design and the design requirements of steel fiber concrete mix proportion.

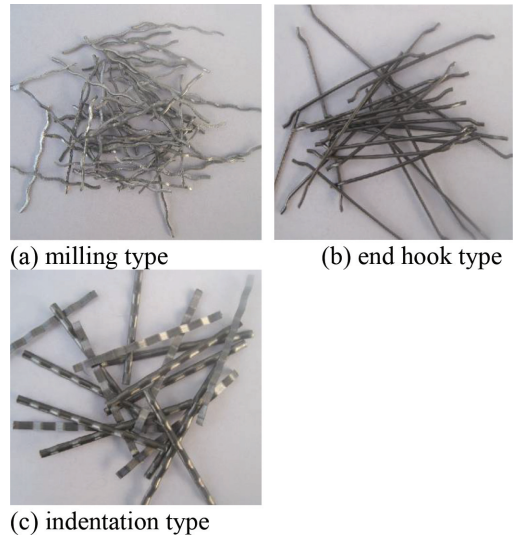
(a) milling type (b) end hook type (c) indentation type

Figure 1. Structure form of different types of steel fiber morphology.

Table 6. Mix ratio of steel fiber-reinforced concrete.

Cement (kg/m³)	Water (kg/m³)	Sand (kg/m³)	Stone (kg/m³)	Admixture (kg/m³)	Steel fiber (kg/m³)
475	140	750	1010	6.65	46.8

Table 7. Experimental results of steel fiber-reinforced concrete.

Number	Fiber type	Slump (mm)	Slump extension (mm)	Anti-segregation index (%)	Bulk density (kg/m^3)	30 min slump loss (%)
1	Milling	190	420 × 350	10.4	2406	/
2	End hook	175	330 × 330	9.8	2385	2.4
3	Indentation	175	390 × 330	11.7	2392	3.5

4 INDOOR EXPERIMENTAL RESULTS ANALYSIS

4.1 *Working performance of steel fiber-reinforced concrete*

The end hook type, milling type, and indentation type of steel fiber-reinforced concrete work performance (slump, slump extension, anti-segregation index, bulk density, and 30 min slump loss) were, respectively, studied by conducting indoor experiments. Table 7 summarizes the experimental results according to the "Standard test method for the performance of ordinary concrete" (GB/T 50080-2002) and the "European self-compacting concrete norms".

From Table 7, it can be concluded that the slump of milling type, end hook type, indentation type of steel fiber concrete, respectively, is 190 mm, 175 mm, and 175 mm, which is more than 175 mm, indicating that the liquidity has a certain loss, compared with the same strength grade concrete. The anti-segregation index of three forms of structure concrete is 10.4%, 9.8%, and 11.7%, respectively, which can meet the requirements of the European standard "specification and guidelines for Self-Compacting concrete", which is not more than 15%; 30 min slump loss of three structural forms of the steel fiber concrete is within 4%, which can fully meet the needs of the construction site.

4.2 *Mechanical strength of steel fiber-reinforced concrete*

The compressive strength and splitting tensile strength of steel fiber-reinforced concrete with three different shapes, namely the end hook type, the milling type and the indentation type, were tested for 3 days, 7 days, and 28 days, respectively. The experimental results are shown in Figure 2.

From Figure 2a, it can be seen that the compressive strength of three kinds of steel fiber reinforced concrete for 3 days is more than 50 MPa, reaching the limit value of the design strength; after 7 days, the compressive strength is more than 60 MPa, which can meet the design requirements; the average growth rate is 21% for 3–7 days and 8% for 7–28 days; for 28 days, the compressive strength of three kinds of steel fiber-reinforced concrete is of little difference. From Figure 2b, it can be seen that the splitting tensile strength is about 4.5 MPa for 3 days, an increase of 48% for 3–7 days, and 22% for 7–28 days, and the splitting tensile strength

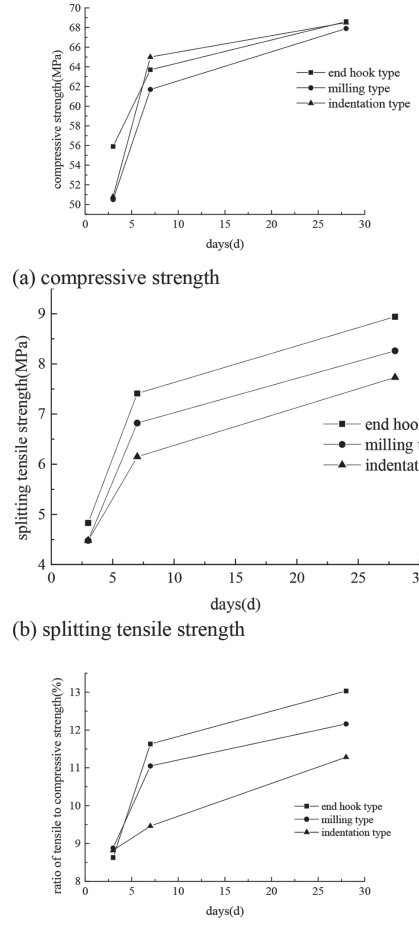

(a) compressive strength

(b) splitting tensile strength

(c) ratio of tensile to compressive strength

Figure 2. Mechanical strength of steel fiber-reinforced concrete.

of the milling type is greater than that of the end hook type and the indentation type at 28d.

The toughness of concrete is usually measured by the ratio of tensile strength to compressive strength. The larger ratio indicates that the toughness of concrete is better. The ratios of the three different shapes of steel fiber-reinforced concrete are shown in Figure 2c. With the age increasing, the ratio also increases gradually, and the tension and compression ratio of the milling type is the biggest at 7 days and 28 days, which shows that this steel fiber-reinforced concrete is the best. The tension and compression ratio of ordinary concrete is in the range of 5% to 8%, and for three kinds of steel fiber-reinforced concrete, it is 13.03%, 12.16%, and 11.28%, respectively. Compared with ordinary concrete, steel fiber can improve the toughness of concrete.

5 CONCLUSIONS

Based on the actual situation of a highway construction project, and according to the concrete conditions of the site and the design principle and the design requirements of the post-pouring strip of fiber-reinforced concrete, the concrete mix proportion parameters are determined. The main conclusions are as follows:

- The slump of steel fiber-reinforced concrete is more than 175 mm, indicating that the liquidity has a certain loss, compared with the same strength grade concrete; the anti-segregation index is within 15% and 30 min slump loss is within 4%, which satisfy the technical requirement of the relevant norms and the construction site.
- The compressive strength of three kinds of fiber reinforced concrete is about 68 MPa at 28 days, but the compressive strength, splitting tensile strength and the ratio of tensile strength to compressive strength of the milling steel fiber-reinforced concrete are better than those of the end hook type and the indentation type.
- With the age increasing, the upward trend of the tensile and compression ratio of milling steel fiber-reinforced concrete is the most obvious, which indicates that the steel fiber-reinforced concrete is the best and the toughness of concrete can be improved.

REFERENCES

Cao, Q.Y., Sun, W., Zhao, Y. et al. 2012. Performance of Cellulose Fiber Concrete and Application in Secondary Lining. *Journal of the China Railway Society (in Chinese)* 34(7): 103–107.

Chen, M., Bai, S. et al. 2014. Experimental research on comprehensive and tensile properties of hybrid fiber reinforced concrete. *Journal of Wuhan University of Technology (in Chinese)* 36(10): 113–117.

Han, H. 2001. *High Temperature Fatigue Properties of Steel Fiber Polymer Concrete*. Guangzhou: South China University of Technology.

Han, R., Zhao, S.B. & Qu. F.L. 2006. Experimental study on the tensile performance of steel fiber reinforced concrete. *China Civil Engineering Journal (in Chinese)* 30(11): 63–67.

Hao, W.F. 2009. *Experiential Study on the Mechanical Properties of Newly Steel Fiber Reinforced Concrete (in Chinese)*. Dalian: Dalian University of Technology.

Ji, X.X., Liang, Q. & Hou. G.Z. 2015. Mix design and test analysis of guardrail and bridge deck pavement concrete. *Road Machinery & Construction Mechanization* 32(1): 83–89.

Luo, Z. 2004. *Study on the Constitutive Relationship of Steel Fiber Reinforced Concrete under Intermediate Strain Rate (in Chinese)*. Changsha: Central South University.

Lv, Y.C. & Shao. J.G. 2014. Research on mixture ratio design and experiment of post-cast strip of bridge deck pavement with steel fiber concrete. *Highway Traffic Technology* 30(8): 162–164.

Sun, W., Jiang, J.Y., Dai, J., Jin, Z.Q. & Jing, W. 2006. Key performance and Experimental Study of the Super height Pumping Steel Fiber Reinforced Concrete. *Journal of Dalian University of Technology* 46(Suppl): 88–93.

Wang, R.L., Zhang, Q.M., Zhu, H.T. & Gao. D.Y. 2014. Analysis of the factors affecting the flexural strength of SFRC. *Journal of Hebei University of Technology (in Chinese)* 43(6): 39–42.

This page intentionally left blank

Civil Engineering and Urban Planning IV – Liu et al. (Eds)
© 2016 Taylor & Francis Group, London, ISBN 978-1-138-02903-3

Research on the stability of stiffened plates with trapezoidal closed ribs in orthotropic steel box girder

Xi Peng
School of Highway, Chang'an University, Xi'an, Shaanxi, China

Jin Di &Yang Zou
School of Civil Engineering, Chongqing University, Chongqing, China

ABSTRACT: Finite element (FEM) analysis is carried out in this paper for the strength of stiffened plates with trapezoidal closed ribs in the steel box girder of Hangzhou Bay Bridge, considering the influence of the aspect ratio β, and the thickness of parent plate. Through the comparison of the existent classical methods (Timoshenko and Ichiro Konishi methods) with the FEM, the results were close when the β is between 1.4 and 1.6. Due to ignoring the influence of torsional rigidity of stiffened ribs, the classic formulae of critical buckling stress will not be suitable for closed stiffened plates; and when β is 1.0, the thickness of the parent plate changes from 10 mm to 24 mm, the critical buckling load can be increased by 53%, indicating that increasing the thickness of parent plat can greatly improve the critical buckling load of the stiffened plates.

1 INTRODUCTION

Orthotropic steel box girder has been widely used in large-span cable-stayed bridges and suspension bridges, because it has a greater torsional rigidity and lateral bending stiffness, high strength, light weight, and good integrity (Cheng et al. 2010; Di et al. 2009; Li & Shao 2007). The longitudinal stiffened ribs in the steel box girder weld with decks, floors, and web which respectively become a whole, so as to constitute orthotropic stiffening plates. As important parts of the stiffening plates, the longitudinal stiffened ribs can increase the overall load carrying capacity of steel box girder, and improve local bending stiffness and the buckling stability capacity of stiffened plates.

The deck of the orthotropic steel box girder which needs to withstand local action of wheel loads and provides the necessary rigidity to the bridge pavement, generally uses closed trapezoidal stiffened ribs. Compared to open stiffened ribs, closed trapezoidal stiffened ribs not only have a large bending and torsional stiffness, but also they are easy to maintain (Wu 2006).

In order to study buckling performance of stiffened plates in the orthotropic steel box girder, international and local scholars carried out a large number of theories and experimental analysis (Ma et al. 2015; Zhao & Gao 2014). Timoshenko proposed the buckling analysis theory of a steel beam based on the elastic theory, which provided the theoretical basis for the early design specification in many European and American countries (Timoshenko 1965). The targeted research on the stability of compressed stiffened plates in our country remains insufficient; we don't even have relevant rules to follow till date. In this paper, the stability of stiffened plates with trapezoidal closed ribs was studied in details.

2 CHARACTERISTICS OF BUCKLING INSTABILITY

The compressed stiffened plates bearing the axial pressure generally have four failure forms as shown in Figure 1.

- *Overall buckling:* when the longitudinal stiffened ribs have lesser stiffness, the stiffened ribs will exhibit buckling failures outside the plane along with the parent plate.
- *Local buckling of parent plates:* when the longitudinal stiffened ribs have larger stiffness, the parent plate between the stiffened ribs will preferentially exhibit buckling failure, taking the longitudinal stiffened ribs as the wave nodes.
- *Local buckling of webs in stiffened ribs:* when the stiffened ribs have a larger width-to-thickness ratio, the web in stiffened ribs will buckle first.
- *Local buckling of stiffened ribs and parent plates:* The destructive forms (1) and (2) are the key points of the stiffened plate design, while we can use proper structural measures to avoid the latter two failure forms.

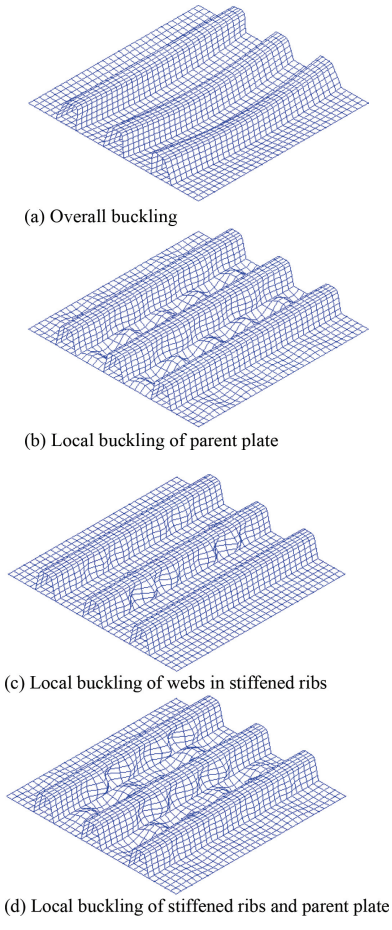

Figure 1. Buckling failure forms of stiffened plate.

3 INFLUENCE FACTORS OF BUCKLING

In this paper, a finite element (FEM) analysis was carried out for the stability of stiffened plates with closed ribs. This study was based on the stiffened plates with trapezoidal closed ribs in the steel box girder of Hangzhou Bay Bridge. The simple-supported stiffened rectangular plate with one couple edges under uniform compression was performed, which is arranged six trapezoidal stiffened ribs in the longitudinal (Fig. 2). In the calculation model, the element shell 63 is used to simulate stiffened plate, and the material is Q345 steel. The structure of the stiffened plates is shown in Figure 3, and its matching parameters are showed in Table 1.

3.1 *Aspect ratio of parent plates*

When the aspect ratio β was between 0.4~5.0, the ratio (σ_{cr}/σ_y) of the critical buckling stress and steel

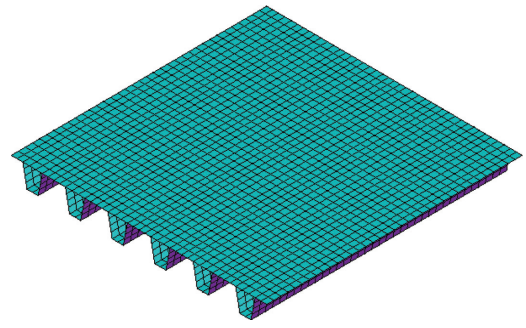

Figure 2. Finite element calculation model.

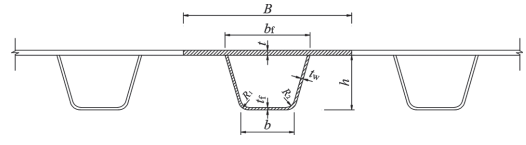

Figure 3. Basic structure of the stiffened plate.

Table 1. Parameters of stiffened plates (mm).

	Parameters							
Names	B	t	b_f	b	h	t_w	R_1	R_2
HZW1	600	20	300	170	280	8	40	32
HZW2	600	14	300	170	280	8	40	32
HZW3	850	14	400	250	260	6	30	24
HZW4	850	16	400	250	260	6	30	24

yield strength was performed, and compared with the results of Timoshenko and Ichiro Konishi methods. The difference of Timoshenko method and Ichiro Konishi method is that the former takes the lower edge of the parent plate as the reference axis to calculate the flexural stiffness of stiffened ribs, while the latter takes the middle of the parent plateas the reference axis (Ichiro 1983; Timoshenko 1965).

The results of stiffened plates HZW1~HZW4 are shown in Figures 4 to 7. When β is less than 1.4, the values (σ_{cr}/σ_y)of Timoshenko and Ichiro Konishi methods are far greater than the value of the finite element method; the difference decreased, while β increased. When β is equal to 0.4, the largest difference reached to 94%. When β is equal to 1.6, the values of Timoshenko and Ichiro Konishi methods were close to the value of the finite element method; Within the scope of $\beta \geq 1.8$, the values of Timoshenko method and Ichiro Konishi method were less than the value of the finite element method, and when $\beta = 5.0$, the difference measured was 82%.

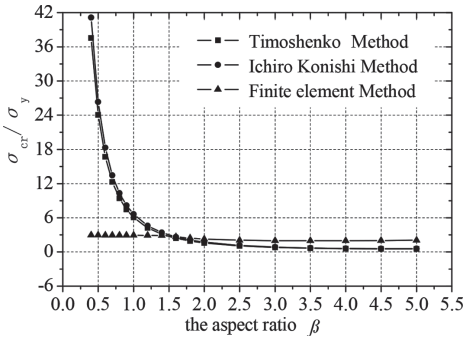

Figure 4. Critical buckling stress of HZW1.

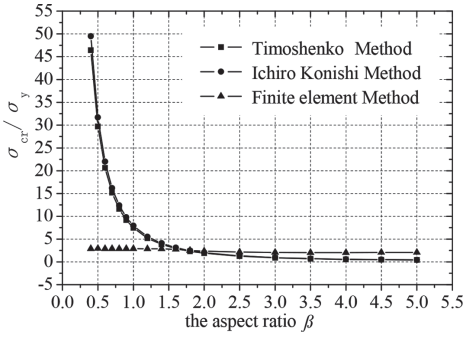

Figure 5. Critical buckling stress of HZW2.

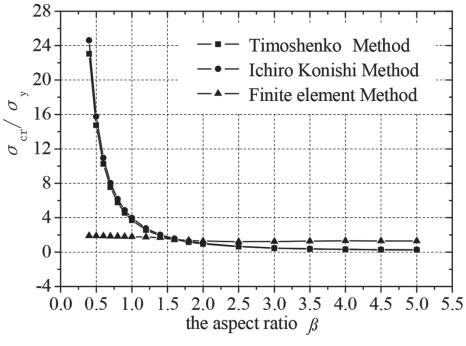

Figure 6. Critical buckling stress of HZW3.

As we can be clear from the above results, the critical stress calculated by the classic formula (Timoshenko or Ichiro Konish formulae) is quite different from the mathematical results of FEM. There are two concepts that are needed to explain the phenomenon.

– The buckling failure status in the finite element method is the partial buckling of the loading end of the parent plate or the trapezoid stiffened ribs while the classic formula of critical buckling stress assumes the lengthwise and transverse of the stiffened ribs as the overall buckling of half sine wave length, which is inconsistent with the actual buckling failure of the stiffened plates.
– The research object of the classic formula is the open stiffened ribs, and Timoshenko neglected the torsional strain energy as the torsional stiffness is relatively small. As for the closed stiffened ribs, they have relatively larger torsional stiffness. So, they will leave behind errors if the torsional stiffness of the closed ribs were still ignored during the process of formula derivation.

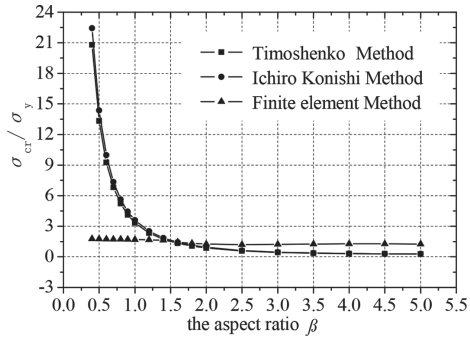

Figure 7. Critical buckling stress of HZW4.

Within the scope of $\beta \leq 1.4$, the first-order buckling mode of the stiffened plates is the partial buckling failures of the parent plate or stiffened ribs. The difference in calculation between critical buckling stress between classic formula and FEM is caused by reason (1) and (2). Within the scope of $\beta \geq 1.8$, the first-order mode of the stiffened plates is overall instabilities; the errors are mainly caused by the reason (2).

In 2009, Di Jin (Di 2009; Zhang et al. 2012), re-deduced the critical buckling stress calculation formula of the sides simple supported stiffened plates, considering the torsional strain energy of the stiffened ribs.

$$\sigma_{cr} = \frac{\pi^2 D}{b^2 t}\left[\frac{\left(1+\beta^2\right)^2+\gamma-1}{\beta^2\left[1+(n+1)\delta\right]}+\frac{(\alpha-1)(1-v)}{\left[1+(n+1)\delta\right]}\right] \quad (1)$$

In this formula, the former part inside the brackets is the effect of the bending strain energy of stiffened plates to the critical buckling stress, and the latter part is the effect of torsional strain energy of stiffened plates to the critical buckling stress. The effect of the torsional strain energy mainly depends on the size of the closed stiffened ribs, while the thickness change of the parent plate has very small influences on it. Given that the classic formula

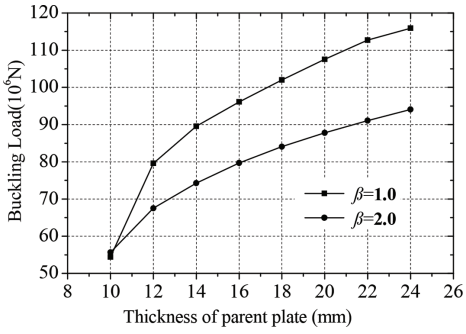

Figure 8. Buckling critical loads of the stiffened plate in different parent plate thickness.

cannot reflect the actual buckling conditions of the closed stiffened plates, the finite element method was only used in the subsequent analysis.

3.2 *Thickness of parent plates*

Taking example of HZW1, the ratio of critical buckling stress and steel yield strength was calculated, when the plate thickness is in the range of 12–24 mm and the aspect ratio β is equal to 1.0 or 2.0.

The results are presented in Figure 8. Assuming that β was equal to 1.0, when the plate thickness increased from 10 to 12 mm, the critical buckling load of stiffened plates changed from 54408 kN to 79610 kN. It increased 31.7%. When the plate thickness was in the range of 12–24 mm, it changed slowly from 79610 kN to 115924 kN, and increased by 31.3%. When β was 2.0 and the plate thickness changed from 10 to 12 mm, it increased from 55625 kN to 67523 kN, and increased by 17.6%. When the plate thickness is located in the range of 12 mm–24 mm, it changed from 67523 kN to 94097 kN, and increased by 28.2%.

The results show that within the common scope of the plate thickness in orthotropic steel box girders, the critical buckling load of the stiffened ribs rapidly increases with the increasing of the parent plate thickness, which means that the aspect ratio of the parent plate is reduced. It indicates that increasing the thickness of the parent plate plays an important part in improving the buckling critical loading of the stiffened plates.

4 CONCLUSION

Through the above research, we can draw the following conclusions:

– By using the finite element method, Timoshenko method and Ichiro Konishi method respectively, this paper calculated and contrasted the critical buckling stresses of the typical closed trapezoid stiffened ribs with different parent plate aspect ratio. The results show that the classical formula of the critical buckling stress neglects the torsional strain energy of the stiffened ribs, so it doesn't apply to the calculation of the closed stiffened plates. According to calculated results of FEM, it can be seen that the critical stress of closed stiffened ribs stays stable with the change in β, and is decreased slightly when the first-order buckling mode changes from local buckling to overall buckling.
– The buckling influence of parent plate thickness to stiffened plates with trapezoidal closed ribs was analyzed using FEM. When β was 1.0, as the parent plate thicknesses increased from 10 to 24 mm, the critical buckling load of the stiffened plates increased by 53%. When β is fixed as 2.0, it increased by 41%. The increase in the parent plate thickness, in turn, reduces the aspect ratio of the parent plate, and increases of the critical buckling load. Increasing the thickness of the parent plate can effectively improve the stability performance of the stiffened plate.

REFERENCES

Cheng, B., Xiao, R.C. & Zhao, J.C. 2010. Calculation of ultimate strength for slightly stiffened thick panels under biaxial compression. *China Civil Engineering Journal (in Chinese)* 43(6): 87–93.

Di, J. 2009. *Research on the Mechanical Behavior and Design Method of Trapezoidal Stiffened Plate in Steel Box Girder*. Shaanxi: Chang'an University.

Di, J., Zhou, X.H. & Lv, Z.D., et al. 2009. Experiment on ultimate bearing capacity of U-stiffened plate of orthotropic steel box girder. *China Journal of Highway and Transport (in Chinese)* 22(2): 59–64.

Ichiro, K. 1983. *Steel Bridges (Part Ninth)*. Beijing: China Railway Publishing House.

Li, L.F. & Shao, X.D. 2007. Theoretical study and model test on the capacity of orthotropic U-rib stiffened plates. *China Civil Engineering Journal (in Chinese)* 40(6): 42–48.

Ma, N.J., Wang, R.H. & Han, Q. 2015. Dynamical buckling of stiffened plates with initial geometrical imperfection. *Journal of Vibration and Shock (in Chinese)* 34(1): 123–127.

Timoshenko, S.P. & Gere J.M. 1965. *Elastic Stability Theory*. Beijing: Science Press.

Wu, C. 2006. *Modern Steel Bridges (Part I)*. Beijing: China Communications Press.

Zhang, Q., Jin, D. & Zhou X.H. 2012. Calculation method of critical buckling stress for stiffened plate with closed ribs. *Journal of Traffic and Transportation Engineering (in Chinese)* 12(5): 37–42.

Zhao, Q. & Gao, P. 2014. Comparison of calculation method of stiffened compression plate's stability bearing capability. *Journal of Fuzhou University (Natural Science Edition) (in Chinese)* 42(1):95–98.

Civil Engineering and Urban Planning IV – Liu et al. (Eds)
© 2016 Taylor & Francis Group, London, ISBN 978-1-138-02903-3

Experimental study on road performance parameters of micro bonded graded broken stone

Bao-Yang Yu
Institute of Transportation Engineering, Shenyang Jianzhu University, Shenyang, Liaoning, China

Yue Zhang
Highway Management Department, Fushun, Liaoning, China

Zi-Jing Wang
Institute of Transportation Engineering, Shenyang Jianzhu University, Shenyang, Liaoning, China

ABSTRACT: Due to the characteristics of micro bonded graded crushed stone material, it has its own advantages in the ordinary road construction. Through a series of indoor tests, the road performance index of different cement dosage skeleton dense type of micro bonded graded gravel is studied, and the characteristics of micro bonded graded gravel are studied, and provide guidance for design and construction.

1 INTRODUCTION

Semi-rigid base asphalt pavement is widely used in the construction of all levels of highway, has made a significant contribution for our country's highway construction. However, semi rigid base asphalt pavement has its own reflective cracking and other serious defects, resulting in serious pavement damage, which also increased the difficulty to the future maintenance work. Micro bonded graded crushed stone pavement is set up under the asphalt pavement, which has a high degree of structural strength, and it belongs to semi flexible material, which has a good dry shrinkage performance and can restrain the reflection cracks caused by temperature shrinkage. Therefore, this paper will study the cement dosage of 1%, 1.5%, 2%, 2.5%, 3% of the micro bonded graded crushed stone material of the road with the performance parameters of the research, for the future construction and design to provide a reference.

2 MICRO BONDED GRADED CRUSHED STONE MATERIAL

Micro bonded graded broken stone by the different size of the gravel material in a certain proportion, filling the gap gradually, with a small amount (less than 3%) of the cement as binder, according to the principle of combining with optimum gradation of compacted material, belonging to the dense structure.

Based on the project the construction of a micro bonded graded gravel base test road of Fushun City, Liaoning Province, the quarry to provide 4 file limestone, grain diameter of 0~10 mm, 5~20 mm, 10~5 mm, 20~40 mm. In order to guarantee the construction quality of micro bonded graded crushed stone, the physical and mechanical properties of the above 4 documents are tested, and the concrete data are shown in Table 1. Specific synthetic gradation and construction mix are shown in Tables 2 and 3.

Table 1. Physical and mechanical indexes.

Experiment project	Company	Aggregate test results								Specified value
		26.5 mm	19 mm	16 mm	13.2 mm	9.5 mm	4.75 mm	3~5 mm	0~3 mm	
Needle like content	%	0	3.9	0.8	3.9	2.3	7.5	–	–	<20%
Sand equivalent	%	–	–	–	–	–	–	133.7	132.5	>60%
Crushing value	%	–	–	–	–	23.6	–	–	–	<26%
Plasticity index	–	3.6								<9%

Table 2. Particle size distribution to achieve high density.

Material specifications	The following screen (mm) quality percentage/%												
	31.5	26.5	19	16	13.2	9.5	4.75	2.36	1.18	0.6	0.3	0.15	0.075
Compose graduation	99.8	89.0	66.6	50.7	42.8	40.9	31.0	19.3	12.6	9.9	7.5	6.4	5.5
Graduation range	100	85~95	66~80	44~56	37~48	38~41	28~38	18~28	12~20	8~14	5~11	3~9	0~6

Table 3. Particle size distribution in the construction mix.

Aggregate size	0~5 mm	5~10 mm	10~20 mm	20~40 mm
Dosage/%	33	8	45	14

Table 4. The optimum moisture content and maximum dry density of micro bonded graded crushed stone.

Cement dosage	1%	1.5%	2%	2.5%	3%
Optimum water content	4.27%	4.29%	4.75%	4.83%	4.89%
Maximum dry density	2.41	2.41	2.42	2.43	2.44

As the construction process need to be based on the optimum moisture content, and maximum dry density as the basis of micro bonded graded crushed stone base, so this paper will be in accordance with the design gradation cement dosage as 1%, 1.5%, 2%, 2.5%, 3% of the skeleton dense type of micro bonded graded crushed stone test, so as to determine the optimum moisture content and maximum dry density. The results are shown in Table 4.

3 TEST AND RESULTS OF ROAD PERFORMANCE OF MICRO BONDED GRADED CRUSHED STONE MATERIAL

In accordance with the *Test Procedure Of The Inorganic Material In The Highway Engineering*, the test method of the inorganic binder stabilized material (cylindrical) was made to produce micro bonded graded crushed stone. In accordance with the method of stable materials of inorganic binding materials for the health of micro bonded graded crushed stone, and unconfined compressive strength test of micro bonded graded crushed stone was performed on the 7 day unconfined compressive strength, splitting strength and indoor compressive resilient modulus test. Their specific results were shown in Tables 5–7.

Table 5. Unconfined compressive strength of different cement content of 7 days (1%~3%).

The quantity of cement/%	Unconfined compressive strength/MPa
1	0.86
1.5	1.32
2	2.04
2.5	3.10
3	4.00

Table 6. Splitting strength of different cement content (1%~3%).

The quantity of cement/%	Splitting strength/mpa
1	0.17
1.5	0.31
2	0.44
2.5	0.51
3	0.61

Table 7. Compressive resilient modulus of different cement content (1%~3%).

The quantity of cement/%	Compressive resilient modulus/mpa
1	202
1.5	299
2	357
2.5	546
3	853

Through Table 5, when the cement content is 2.5%, the 7 days of unconfined compressive strength can meet the requirements for the light traffic on pavement base. When the cement content is 3%, 7 days of the unconfined compressive strength can

meet the design specification of highway asphalt pavement in heavy traffic on the pavement base.

Tables 5–7 show that the 7 days of micro bonded graded broken stone, no side limit compression strength, splitting strength, compressive resilient modulus increases with the increase of cement content.

4 CONCLUSION

Through the 7 days of unconfined compressive strength, when the cement content is 2.5%, the 7 days of the 7 days of unconfined compressive strength can meet the requirements for the light traffic on pavement base. When the cement content is 3%, 7 days of the unconfined compressive strength can meet the design specification of highway asphalt pavement in heavy traffic on the pavement base.

7 days unconfined compressive strength, splitting strength and compressive resilience modulus of micro bonded graded crushed stone are increased with the increase of cement content.

ACKNOWLEDGEMENTS

This work was financially supported by Liaoning Provincial Department of education project (L2015454), Fushun Fu Yi Da Highway Engineering Technology Co. Ltd (14-08-71).

REFERENCES

JTG. 2006. *Highway Asphalt Pavement Design Specification D50-2006*. Beijing: People's Communications Press.

JTG. 2007. *Code for highway geotechnical testing E40-2007.* Beijing: People's Communication Press.

JTG. 2009. *Highway Engineering Inorganic Binding Material Test Code E51-2009*. Beijing: People's Communication Press.

This page intentionally left blank

Civil Engineering and Urban Planning IV – Liu et al. (Eds)
© 2016 Taylor & Francis Group, London, ISBN 978-1-138-02903-3

Performance observation and evaluation analysis of the graded broken stone base test road

Bao-Yang Yu
Institute of Transportation Engineering, Shenyang Jianzhu University, Shenyang, Liaoning, China

Yue Zhang
Highway Management Department, Fushun, Liaoning, China

Zi-Jing Wang
Institute of Transportation Engineering, Shenyang Jianzhu University, Shenyang, Liaoning, China

ABSTRACT: Paving two graded macadam base test road, the test road of Qiansanxian in Fushun and Henggaixian in Anshan was carried out in the field. The flip-type asphalt pavement structure and the fully flexible asphalt pavement structure were analyzed. The road surface deflection, crack investigation, and flatness of the test road were investigated, and the performance of the road was analyzed in three ways. The performance observation and analysis of the graded crushed stone base test road were observed and analyzed.

1 INTRODUCTION

In order to verify the effect of the asphalt pavement structure of the graded broken stone base course, in this paper, a total of two graded gravel road test roads were conducted, namely the Qiansanxian test road in Fushun and the Henggaixian test road in Anshan, respectively. The detection of the construction of both test roads was also carried out.

2 GRADED CRUSHED STONE BASE TEST ROAD IMPLEMENTATION SCHEME

2.1 *Qiansan line reconstruction project in Fushun*

The Qiansan line reconstruction project's general section of the pavement structure has been widely used in Liaoning Province for many years by using a 5 cm grain-type rubber powder modified asphalt concrete surface layer +30 cm cement stabilized gravel base (plant mixing method, cement dosage 5%) +25 cm natural gravel cushion. The pavement structure of the Qiansan line is divided into two kinds: the first one is that the graded crushed stone material is used as the base of asphalt pavement, and the bottom layer is the cement stabilized gravel; the other is the double layer graded crushed stone base structure, which is the original old road pavement. According to the gradation gravel layer thickness, the surface layer thickness, the gradation gravel structure type, a total of 5 pavement structure scheme, test road pavement, and the structure of the layout are shown in Figures 1 and 2.

Figure 1. Fushun test road.

2.2 *Anshan Huangai line test road*

Huangai line located in the eastern mountain area of Liaoning Province is a provincial highway connecting Benxi to Gaizhou. The starting point for the reconstruction of Dayingzi, terminus for the red flag, the design mileage is K274 + 675 – K291 + 000 and the full-length is 16.325 km. The test section is set at the pile number K276 + 000 – K277 + 000, and the total length is 1 km. The Anshan test road is used in the structure of the basic pavement structure on the skeleton dense graded aggregate. The old road pavement structure consists of 2.5 + 4 cm asphalt mix through the surface layer + 20 cm of the cement stabilized gravel base (mixed) + 20 cm natural gravel cushion. The two grade highways in the mountainous area, with the design speed of 40 km/h. The subgrade width is 9.5 m and the pavement width is 8.5 m. The full implementation of the GBM project and test road pavement structure layout are shown in Figure 3.

The general pavement structure is a surface layer of 3 cm modified asphalt concrete and 4 cm granular asphalt concrete. The basic part of the widening consists of 20 cm natural gravel and 35 cm cement

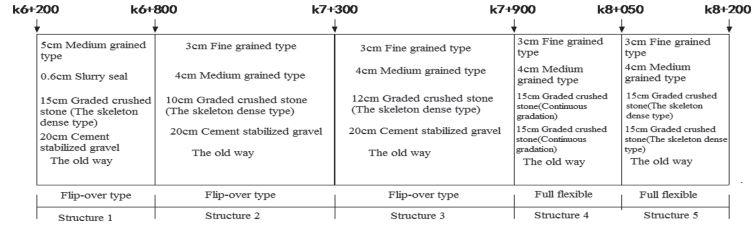

Figure 2. Pavement structures plan of the test road in Fushun.

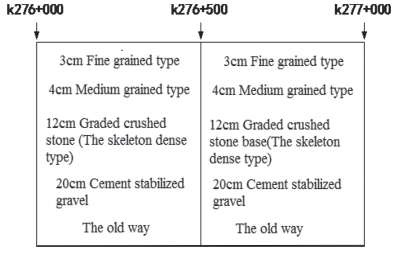

Figure 3. Pavement structure plan of the test road in Anshan.

stabilized gravel. The reinforcing period is 20 cm cement stabilized gravel.

3 TEST ROAD PAVEMENT PERFORMANCE OF THE LATE OBSERVATION

In order to accurately locate the graded crushed stone on the base asphalt pavement, it is necessary to carry out the investigation on traffic. In this paper, according to the Highway Asphalt Pavement Design Standard (JTGD50-2006), the number of different axle loads was converted, and the cumulative equivalent axle times were calculated.

Through the investigation of the traffic volume of the three tests, the cumulative equivalent axle times of the test road in the design period were calculated, and the traffic volume survey results are shown in Table 1.

3.1 *Observation results and analysis*

In this paper, the main content of the late stage of the test is: (1) the road surface deflection; (2) crack investigation; and (3) flatness.

3.1.1 *The Qiansan lines in Fushun*

1. Deflection detection

The members of the project group in July 2010 detected the bending of the Fushun Qiansan line test road sink in five kinds of pavement structure scheme of section 20 m per point. The Falling Weight Deflectometer (FWD) instrument was used to detect the surface of the test road. The detection results are shown in Table 2.

From the data given in the table, pavement structures 1, 2, and 3 were used for graded crushed stone base asphalt pavement structure, and pavement structures 4 and 5 were used for the double graded broken layer soft asphalt pavement structure. Thus, the graded gravel asphalt pavement will not be in actual use because of the low modulus and leads to the deflection of the phenomenon.

2. Crack detection

In order to grasp the time development and change of pavement crack, the first three line test road in Fushun was carried out three times, and the crack location, number, length, and width of the five pavement structures were detected, as well as the crack of the semi-rigid base asphalt pavement, which is adjacent to the test road, was detected (1 km). DR observation of pavement failure rate is shown in Table 3 and Figure 4.

Figure 5 shows the asphalt pavement (structures 1, 2, and 3) and the crack rate of the

Table 1. Summary results of test road traffic survey.

Test road	BZZ.100KN Cumulative standard axle (Ne)	Traffic grade
Fushun Qiansan line	317	Medium traffic
Anshan Huangai line	609	Medium traffic

Table 2. Test data aggregation results.

Pavement structure	Mean value (0.01 mm)	Standard deviation (0.01 mm)	Coefficient of variation (%)
1	22.19	8.56	38.57
2	24.45	5.53	22.57
3	21.65	3.55	16.38
4	24.63	2.58	10.46
5	31.17	5.9	18.94

Table 3. Calculation results of DR.

Time	Starting semi-rigid base	Pavement structure 1	Pavement structure 2	Pavement structure 3	Pavement structure 4	Pavement structure 5	Ending semi-rigid base
2010.4	0.898	0.313	0.505	0.447	0.000	0.000	0.907
2010.9	0.980	0.296	0.445	0.425	0.000	0.000	0.894
2011.4	1.180	0.325	0.615	0.596	0.067	0.000	1.825

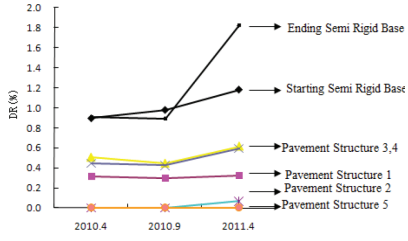

Figure 4. DR curve of the Fushun test road.

flexible base asphalt pavement with the graded broken stone (structures 4 and 5), which is based on the graded crushed stone pavement and is obviously lower than the pavement damage rate of the semi-rigid base asphalt pavement. In the first unfavorable season after no cracks, the particular use of the flexible base asphalt pavement with graded gravel to prevent and control the reflective crack is significant. In addition, the thickness of the gravel layer of pavement structures 2 and 3 is 10 cm and 12 cm, the thickness of pavement structure 1 is 15 cm, the thickness of pavement structures 4 and structure 5 is 30 cm. From the effect of preventing reflection cracks, the crack rate of the pavement is reduced.

3. Flatness detection

With 3 m ruler method for the detection of five kinds of pavement roughness condition, at the same time, it is compared with the flat degree of the semi-rigid base asphalt pavement, which is adjacent to the test road. The test results are shown in Figure 6.

From Figure 6, it can be seen that the pavement roughness of the five kinds of structure asphalt pavement is decreased, and it is generally lower than that of the semi-rigid base asphalt pavement. One final observation of the average value of structures 1, 2, and 3 for 3.53 mm, and the semi-rigid base asphalt pavement roughness for 2.75 mm, while the flexible base asphalt pavement (structures 4 and 5) is worst, which is obvious that the permanent deformation of the graded crushed stone of the thick base course is more obvious than that of the semi-rigid base asphalt pavement.

Through the investigation and calculation, the cumulative equivalent shaft of the Qiansan

Figure 5. Reflection cracks of Fushun test road.

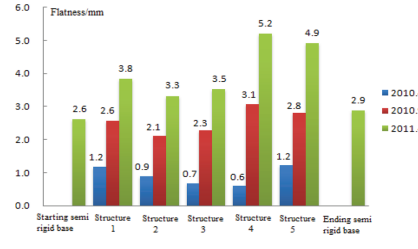

Figure 6. Smoothness of the Fushun test road.

line in Fushun is more than 3 000 000 times, after nearly two years of traffic load, from the above to the Fushun Qiansan line test road surface deflection, the crack rate and the whole test results, it was found that the graded crushed stone base can be competent for all kinds of indices under a medium traffic load.

3.1.2 *Anshan Huangai line*

The Anshan Huangai line was detected for deflection and cracks for one time.

1. Deflection detection

Anshan Huangai line deflection test results are shown in Figures 7 and 8.

As can be seen from the figure, Anshan Huangai line test road deflection was signifi-

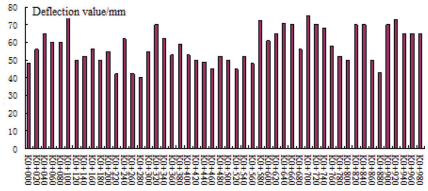

Figure 7. Deflection test result of the Anshan test road (left).

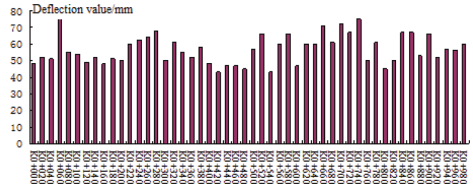

Figure 8. Deflection test result of the Anshan test road (right).

Table 4. Crack test result of the Anshan test road.

Number	Position	Crack width (mm)	Crack length	Remarks
1	K276 + 40	1	Full width	Gravel base thickness 12 cm
2	K276 + 160	3	Full width	Gravel base thickness 12 cm
3	K276 + 280	3	Full width	Gravel base thickness 12 cm
4	K276 + 310	1	5 m	Gravel base thickness 12 cm
5	K276 + 460	3	Full width	Gravel base thickness 12 cm
6	K276 + 500	1	6 m	Gravel base thickness 15 cm
7	K276 + 535	2	Full width	Gravel base thickness 15 cm
8	K276 + 565	1	6 m	Gravel base thickness 15 cm
9	K276 + 605	1	4 m	Gravel base thickness 15 cm
10	K276 + 635	1	5 m	Gravel base thickness 15 cm
11	K276 + 675	1	3 m	Gravel base thickness 15 cm
12	K276 + 735	1	4 m	Gravel base thickness 15 cm
13	K276 + 775	2	Full width	Gravel base thickness 15 cm
14	K276 + 875	1	4 m	Gravel base thickness 15 cm
15	K276 + 925	2	6 m	Gravel base thickness 15 cm
16	K276 + 985	1	4 m	Gravel base thickness 15 cm

cantly higher than that of the former Fushun Qiansan line. This is due to the construction of graded gravel on the basic level of compaction is not enough and the low modulus.

2. Crack detection
   The Anshan Huangai line test road crack detection results are shown in Table 4.
   From the above data, it can be seen that the 1 km test section of a total of 22 cracks, an average of 45 m, pavement damage rate, and the Qiansan line in the Fushun are similar, and thus the control of the reflective crack effect is obvious.

4 CONCLUSION

1. The actual investigation of the pavement cracks in the experimental road shows that the asphalt pavement structure with the graded crushed stone and the flexible base asphalt pavement structure with the graded broken stone both have great control of reflective cracks.
2. The actual investigation of the flat flatness test in the experimental road shows that in order to ensure the construction quality of graded gravel compaction, under the premise of meeting the design requirements, under a medium traffic load, two kinds of structures are not supposed to exhibit the phenomenon of excessive deflection, obviously permanent deformation, or the rutting phenomenon due to the graded broken stone layer.

ACKNOWLEDGMENTS

This work was financially supported by the Liaoning Provincial Department of Education Project (L2015454) and the Fushun Fu Yi Da Highway Engineering Technology Co. Ltd (14-08-71).

REFERENCES

He et al. 2009. Research on the mechanical characteristics of asphalt pavement with graded crushed stone base. Xi'an: Chang'an University Press.

Huang & Qian 2001. *Design theory and method grade asphalt pavement*. Beijing. Science Press.

Niekerk. 2002. *Mechanical Behavior and Performance of Granular Bases and Sub bases*. Pavement Press.

Sha 1998. *Semi rigid base asphalt pavement*. Beijing: People's Communications Press.

Civil Engineering and Urban Planning IV – Liu et al. (Eds)
© 2016 Taylor & Francis Group, London, ISBN 978-1-138-02903-3

Experiment study on the effect of freeze-thaw damage to chloride ion penetration performance of concrete

Xiao-Hang Hao
College of Urban and Rural Construction, Agricultural University of Hebei, Baoding, Hebei, China

Ya-Na Zhang
Zhongji Petrochemical Engineering Design Limited Company, Baoding, Hebei, China

Yan Liu & Ya-Di Hu
College of Urban and Rural Construction, Agricultural University of Hebei, Baoding, Hebei, China

ABSTRACT: In the paper, the fast freeze-thaw test method and Rapid Chloride Migration Test (RCM method) are applied to measure the chloride ion diffusion coefficient before and after freeze-thaw damage. At the same time, the relationships between the parameter of freeze-thaw damage (freeze-thaw cycles, mass loss and compressive strength) and the chloride ion diffusion coefficient are analysed. The analysis shows that the chloride ion migration coefficients of different strength grades concrete enhance along with the increasing of numbers of freeze-thaw cycles, the relationship is nonlinear.

1 INTRODUCTION

Concrete is the most widely used construction material, and its durability is getting more and more attention in the civil engineering field. In practical engineering, most of the concrete structure in the North China are subjected to freeze-thaw damage in varying degrees (Kang & Feng 1997; Pigeon & Pleau 1995) especially coastal concrete structure is so interfered with freeze-thaw cycles and chloride ion corrosion for a long term that it makes the reinforced concrete structures more susceptible to corrosion, which causes the salt-freezing damage of the concrete. Therefore, it is limited to establish the empirical formula when only one single factor (Yang 2007; Zhang 2010) is considered. Based on this, the chloride ion permeability after freeze-thaw damage is studied in the paper, further the influence of freeze-thaw damage parameters on chloride ion permeability are analysed. The salt-freezing theory of the concrete is supplemented and improved, which can provide a certain references for the practical engineering.

2 EXPERIMENTAL STUDY

The Ordinary Portland cement with a 42.5 strength grade was applied in this experiment. The dry river sand with a 2.4 fineness modulus was used for the fine aggregate, and its packing density and apparent density were 1550 kg/m^3 and 2590 kg/m^3 respectively. The crashed stone with a proper gradation was applied for the coarse aggregate, which packing density and apparent density were 1500 kg/m^3 and 2740 kg/m^3 respectively.

The concrete's mixture proportions are shown in Table 1.

2.1 *Experimental method*

Concrete splitting tensile strength and compressive strength were tested according to stand-

Table 1. Mixture proportions of concrete.

Concrete types	W/C	Sand ratio	Cement content (kg/m^3)	Fine aggregate (kg/m^3)	Coarse aggregate (kg/m^3)	Water content (kg/m^3)
C30	0.54	36%	389	659	1171	210
C40	0.42	36%	536	590	1049	225
C50	0.35	34%	514	588	1140	180
C55	0.32	34%	563	570	1106	180

ard test method. The freezing and thawing test was carried by the rapid frozen thaw method, through which the mass-loss rate and concrete cube strength value after freezing and thawing were obtained. The Cl^- permeability coefficient of concrete was obtained through the Cl^- penetration test which is conducted in the method of RCM.

2.2 *Experimental analysis*

2.2.1 *Effect of freeze-thaw cycles*

The Cl^- diffusion coefficient of every concrete strength grade under different freeze-thaw cycles are shown in Table 2. It can be found that Cl^- diffusion coefficient enhances with the increases of freeze-thaw cycles and different strength grades concrete present a similar increasing trend.

It can be found from Figure 1 that Cl^- diffusion coefficient of low strength grade concrete is higher than high strength grade concrete under the same number of freezing and thawing cycles. The Cl^- diffusion coefficient enhances with the increases of freeze-thaw cycles for the same strength grade concrete. The freeze-thaw cycles effect accelerates the diffusion of chloride ions in concrete and this promoting effect is very obvious (Zheng 2004), which can be interpreted that the process of freeze-thaw cycles damages the internal structure of concrete.

Table 2. The Cl^- diffusion coefficient under different freeze-thaw cycles.

Average	0	50	100	150
C30	11.8377	14.8363	18.122	32.1067
C40	8.4373	9.034	16.9072	27.5963
C50	3.6765	4.2238	15.457	17.7598
C55	2.5498	3.0515	10.7852	11.0832

2.2.2 *The relationship of mass-loss rate and Cl^- diffusion coefficient*

The mass loss rate of concrete under different freeze-thaw cycles and Cl^- permeability values are shown in Table 3. It can be found that the mass loss rate and Cl^- permeability coefficient enhance with the increase of freeze-thaw cycles on the whole. Meanwhile, the fitting relationship in the Figure 2 shows that at the 50 times freeze-thaw cycles state, the blocks' mass loss rate are negative, and the fitting curves appear anti-inflection points, which reflects that at the 50 times freeze-thaw condition, the concrete blocks' quality are not decreased, but increase slightly. When numbers of freeze-thaw cycles reach to 100, the increased tendency of mass loss and Cl^- permeability are accelerated. At this point, the freeze-thaw damage aggravates gradually, which provides a convenient condition for the Cl^- penetration.

2.2.3 *The relationship of compressive strength and Cl^- diffusion coefficient*

It can be found from the Figure 3 and Table 4 that with the increase of freeze-thaw cycles, different strength grades concrete present a decreased compressive strength and an increased Cl^- permeability coefficient. After 150 freeze-thaw cycles, the C30 specimens present a minimum compressive strength and the maximum Cl^- permeability coefficient (Point values are on the left). The compressive strength value of C40 is higher than C30 on the whole (The C40's value are all on the right side of the C30's under the same freeze-thaw cycles), and the Cl^- permeability coefficient value of C40 is lower than C30 under the same freeze-thaw cycles, which shows that the strength grade of concrete C40 is better than C30 at the same freeze-thaw cycles. Also, both compressive strength and resistance to Cl^- permeability of C50 are better than C30 and C40. It fully provided that at the same freeze-thaw cycles, the higher the concrete strength grade is, the higher the concrete

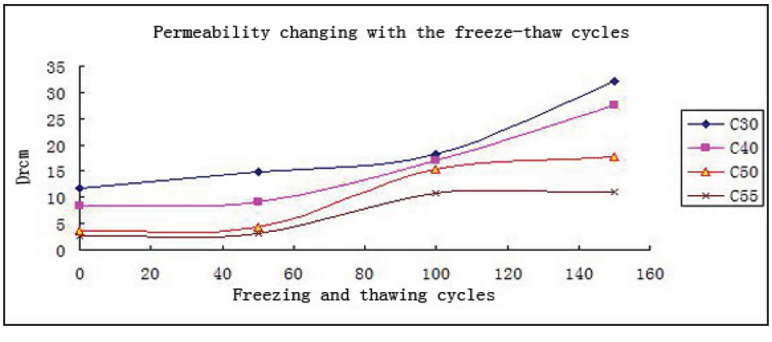

Figure 1. The relationship of freeze-thaw cycles and Cl^- diffusion coefficient.

Table 3. The relationship between Cl^- diffusion coefficient and mass loss rate.

Strength grade of concrete	The number of freeze-thaw cycles	Mass-loss rate	Cl^- diffusion coefficient
C30	0	0.00%	11.84
	50	–0.32%	14.84
	100	0.82%	18.12
	150	7.58%	32.11
C40	0	0.00%	8.44
	50	0.16%	9.03
	100	0.63%	16.91
	150	9.54%	27.60
C50	0	0.00%	3.68
	50	–0.78%	4.22
	100	0.56%	15.46
	150	6.91%	17.76
C55	0	0.00%	2.55
	50	–0.29%	3.05
	100	–0.64%	10.79
	150	1.34%	11.08

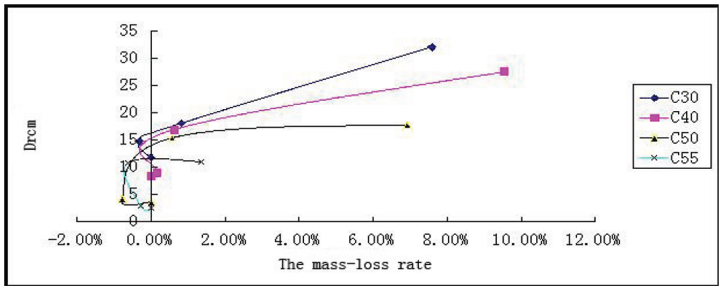

Figure 2. The relationship of mass loss rate and the chloride ion diffusion coefficient.

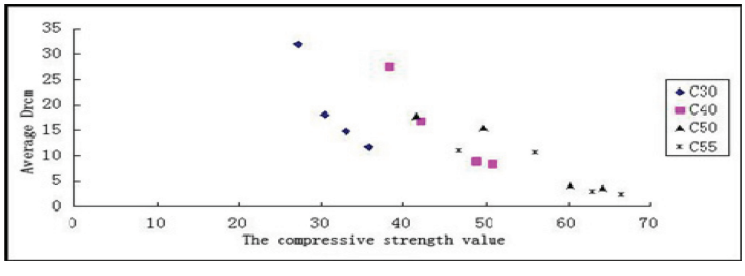

Figure 3. The relationship of average strength and Cl^- diffusion coefficient.

Table 4. The relationship of compressive strength and Cl^- diffusion coefficient.

	C30		C40		C50		C55	
	Average strength	Diffusion coefficient	Average strength	Diffusion coefficient	Average strength	Diffusion coefficient	Average strength	Diffusion coefficient
0	35.63	11.84	50.77	8.44	64.23	3.68	66.5	2.5498
50	32.93	14.84	48.77	9.03	60.23	4.22	62.83	3.0515
100	30.4	18.12	42.13	16.91	49.6	15.46	55.93	10.7852
150	27.2	32.11	38.3	27.60	41.6	17.76	46.57	11.0832

compressive strength is and the smaller the Cl^- permeability coefficient is.

3 CONCLUSIONS

1. The relationship between the freeze-thaw cycles and Cl^- permeability coefficient was studied through experiments. The Cl^- permeability coefficient of low strength grade concrete is higher than high strength grade concrete under the same number of freezing and thawing cycles.
2. The freeze-thaw cycle effect makes the concrete a mass-loss to some extent and a decreased compressive strength. The chloride ion permeability coefficient of different strength grades concrete present an increased tendency with the decrease of the compressive strength.
3. On the whole, the freeze-thaw cycle makes the concrete's mass decreased. However, under the small freeze-thaw cycles, the concrete presents a slight increase in the concrete mass. After 100 times of freeze-thaw cycles, the change of the mass loss rate of C30 and C40 is accelerated, and after 125 times of freeze-thaw cycles, the mass loss rate of C50 and C55 increases rapidly.

ACKNOWLEDGEMENTS

This research work was supported by Provincial Nature Science Foundation of Hebei Province (Grant No. E2015204111, Project Name: Study on concrete structure durability based on multi-factor coupling effect) and Science and Technology Foundation of Agricultural University of Hebei Province (Grant No. ZD201504, Project Name: Study on concrete structure durability based on the load damage).

REFERENCES

Kang, J.F. & Feng, N.Q. 1997. The durability problems of hydraulic concrete and high performance hydraulic concrete. *Concrete and Cement Products* 8(4): 4–10.

Pigeon, M. & Pleau, R. 1995. *Durability of concrete in cold climates.* Abingdon: Taylor & Francis.

Yang, Q.B. 2007. Effects of sodium chloride concrete action in saturation degree in concrete under freezing-thawing cycles. *Journal of the Chinese Ceramic Society* 35(1): 96–100.

Zhang, H. 2010. *Deicing salt resistance of cement concrete pavement.* Nanjing: Nanjing University of Aeronautics and Astronautics.

Zheng, J.J. 2004. *Long-term stability research of waste forms containing chromium residue based on cement*. Zhejiang: Zhejiang University of Technology.

Civil Engineering and Urban Planning IV – Liu et al. (Eds)
© 2016 Taylor & Francis Group, London, ISBN 978-1-138-02903-3

Numerical simulation study on the freeze-thaw process of concrete

Xiao-Hang Hao
College of Urban and Rural Construction, Agricultural University of Hebei, Baoding, Hebei, China

Wei Lan
Department of Finance, Shijiazhuang Vocational College of City Economy, Shijiazhuang, Hebei, China

Yan Liu & Ya-Di Hu
College of Urban and Rural Construction, Agricultural University of Hebei, Baoding, Hebei, China

ABSTRACT: Based on the testing, numerical simulation on concrete freeze-thaw test is analyzed through ABAQUS finite element method. The influence of different freeze-thaw cycles on various strength grade concrete are discussed, therefore the difference of concrete frost resistance in different strength grade is analyzed. It is feasible to simulate the freeze-thaw cycles of concrete because the analysis results are consistent with testing results. At the same time, numerical simulation analysis results can testify and explain testing results which is instructional for study of concrete freeze-thaw cycles.

1 INTRODUCTION

In the north temperate zone of our country, most of the concrete structures are suffering from freeze-thaw damage, which poses a serious threat to people property, so the study of freeze-thaw damage is necessary (Gong 2004). Due to the limitation of objective conditions in the experimental studies, the testing results can't represent the really material performance effectively in the actual loads and environment. Therefore, it is a new approach for numerical simulation method to study concrete freeze-thaw damage, including the law of the concrete freeze-thaw damage and comparison analysis with testing results.

In this paper, ABAQUS finite element method are applied for the numerical simulation of the concrete testing, and the thermos coupling model are applied to simulate the frost heaving force (Ji et al. 2010; Hale et al. 2009; Wu 2003). At the same time, the simulant results are compared with the test results and the law of the freeze-thaw damage is further analysed.

2 CONCRETE FREEZE-THAW TEST

2.1 *Experimental study*

The mixture proportions of C30, C40 and C50 are showed in Table 1. Cylinder blocks of Φ100 mm × 50 mm, cured for 28 days under the standard conditions, are used for the test specimens, and then the fast freeze-thaw test are carried out after soaking those blocks in the water for 4 days. Each of the three strength grades concrete is conducted the freeze-thaw test for 50, 100 and 150 times, and then the laws of concrete freeze-thaw damage are determined by analyzing the change in the appearance of concrete blocks, the mass loss rate and the strength loss rate.

2.2 *Testing result analysis*

The C30 concrete blocks are taken as examples in Figure 1. After 50 freeze-thaw cycles, C30 concrete blocks present less obvious damage and some microscopic cracks in the local, and the

Table 1. Mixture proportion of concrete.

Concrete types	W/C	Sand ratio	Cement content (kg/m^3)	Fine aggregate (kg/m^3)	Coarse aggregate (kg/m^3)	Water content (kg/m^3)
C30	0.54	38%	370	695	1134	200
C40	0.42	36%	452	633	1124	190
C50	0.35	34%	514	588	1140	180

Figure 1. The C30 concrete after suffering 50 (left), 100 (middle), 150 (right) cycles of freeze-thaw.

Table 2. The strength -loss rate and mass-loss rate of concrete.

Concrete types	Strength -loss rate			Mass-loss rate		
	50 cycles	100 cycles	150 cycles	50 cycles	100 cycles	150 cycles
C30	7.35%	16.04%	25.56%	0.30%	1.41%	8.12%
C40	6.23%	13.91%	23.14%	0.14%	1.02%	4.21%
C50	5.91%	12.84%	20.66%	0.11%	0.71%	1.54%

concrete surface remains smooth, but present a little rough (left); After 100 freeze-thaw cycles, the cracks on those blocks is more obvious, and the concrete surface is no longer smooth (middle); After 150 freeze-thaw cycles, the concrete blocks present obviously large cracks, leakage of the aggregate and serious spalling around the blocks; some even serious damage and losing its original shape (right). With the increase of freeze-thaw cycles, the degree of concrete appearance damage increases gradually.

The averages of strength loss rate and mass loss rate are showed in Table 2. It can be found that with the increases of freeze-thaw cycles, concrete strength loss rate and mass loss rate increase gradually, and with the decrease of the water cement ratio, concrete strength loss rate and mass loss rate are significantly reduced.

2.3 *The numerical simulation of concrete freeze-thaw process*

In this paper, the transient heat transfer analysis theory and sequence coupled thermal stress analysis method (Li 2013; Chen 2012) are applied for numerical simulation of the concrete freeze-thaw cycles. To be consistent with the test, the Φ100 mm × 50 mm cylinders are applied for the 3D models. The grid calculation area is shown in Figure 2, and the area is divided into 11121 tetrahedral elements and 2298 nodes. The Heat Transfer unit type is applied for this analysis.

In the analysis of thermal stress field, in order to simulate the frost heaving force, the unit type of the temperature field is converted to 3D stress, and the calculation results of temperature field are added to the model in the form of predefined field.

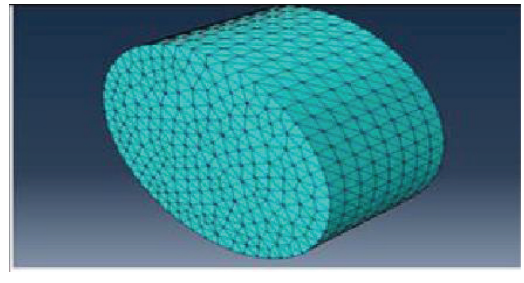

Figure 2. The diagram of grid partitioning.

2.4 *Analysis of the numerical simulation results*

The C30 concrete are taken as example to analysis the change rule of the concrete performance under different freeze-thaw cycles in Figures 3 and 4. It can be found that with the increase of freeze-thaw cycles, the proportion of the blue parts in the stress diagram decreases gradually, which indicates that the stress increases gradually. The change is more apparent in the strain diagram: the color changes from blue to orange. However, the change is not obvious when the freeze-thaw cycles are 100 and 150 times, which shows that the blocks may have reached the ultimate strain and presents a damaged state. It can be seen that with the increase of freeze-thaw cycles, the stress and strain both increase gradually, and the destruction of the concrete is more and more serious.

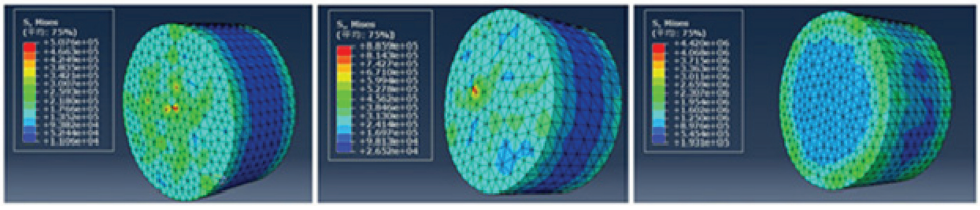

Figure 3. The stress diagram of C30 concrete suffering 50 (left), 100 (middle), 150 (right) cycles of freeze-thaw.

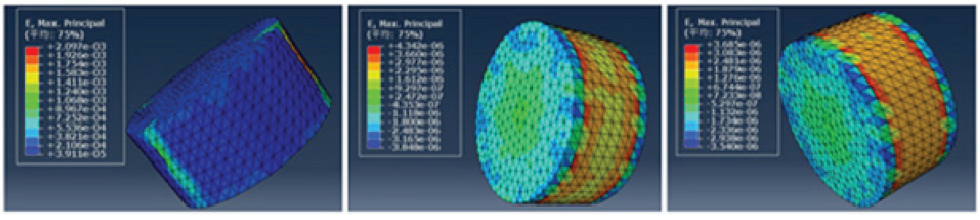

Figure 4. The strain diagram of C30 concrete suffering 50 (left), 100 (middle), 150 (right) cycles of freeze-thaw.

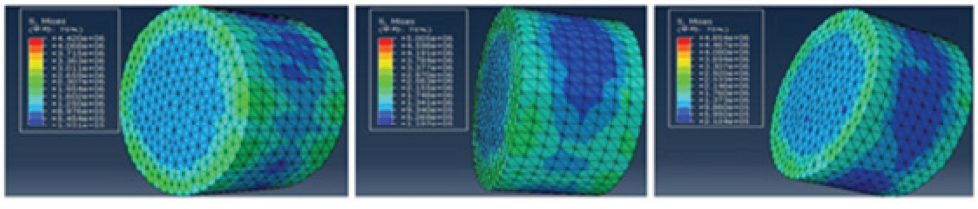

Figure 5. The cross-section stress diagram of C30 (left), C40 (middle) and C50 (right) concrete.

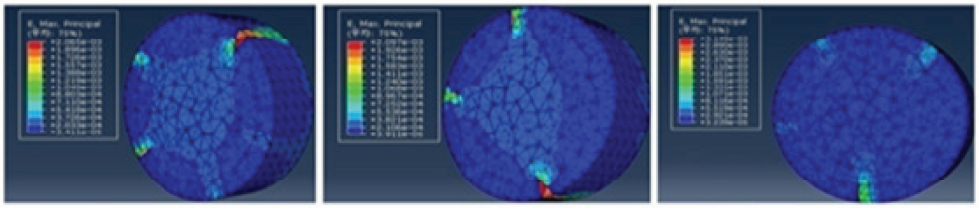

Figure 6. The cross-section strain diagram of C30 (left), C40 (middle), C50 (right) concrete.

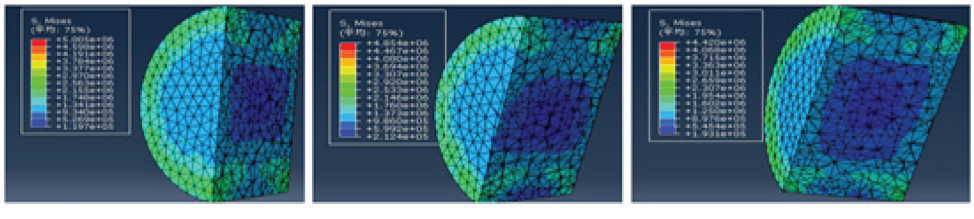

Figure 7. The longitudinal section stress diagram of C30 (left), C40 (middle) and C50 (right) concrete.

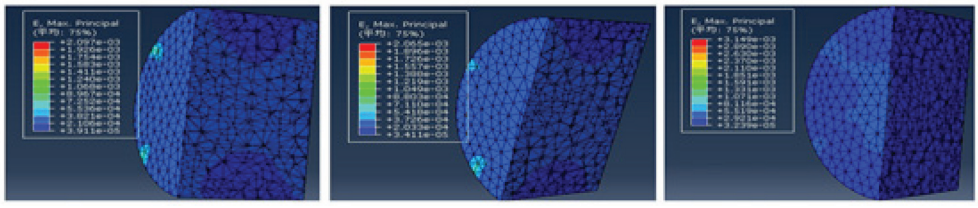

Figure 8. The longitudinal section strain diagram of C30 (left), C40 (middle) and C50 (right) concrete.

It can be found from Figures 5–8 that with the decrease of water cement ratio, the proportion of the dark blue parts in the stress diagram increases gradually, which indicates that the internal stress decreases gradually. In the strain diagram, when subjected to freeze-thaw damage, generally, the larger strains present firstly on the lateral surface, and then some cracks appear, and the strain along the crack spreads to the internal gradually. It can be found from the four figures that with the decrease of water cement ratio, the invasion scope and the extent of the freeze-thaw damage both decrease gradually.

3 CONCLUSIONS

In this paper, ABAQUS finite element method are applied for the numerical simulation of the freeze-thaw cycle test and compression test. In the simulation of freeze-thaw test, the changing law of the stress and strain is clearly observed and in the simulation of compression test, the maximum compressive strength is accurately determined. Therefore, numerical simulation analysis results can testify and explain testing results, which provides a new method for the study of concrete freeze-thaw cycles.

Through the study of numerical simulation on freeze-thaw test, it can be found that with the increase of freeze-thaw cycles, the stress and strain both increase gradually, and the damage degree of the concrete also increases gradually. However, with the decrease of water cement ratio, the frost resistance of the concrete increases gradually.

ACKNOWLEDGEMENTS

This research work was supported by Provincial Nature Science Foundation of Hebei Province (Grant No. E2015204111, Project Name: Study on concrete structure durability based on multi-factor coupling effect) and Science and Technology Foundation of Agricultural University of Hebei Province (Grant No. ZD201504, Project Name: Study on concrete structure durability based on the load damage).

REFERENCES

Chen, C.G. 2012. *Analysis on the Tensile Characteristic Test and Thermo-Hydro -Mechanics Coupling of Freeze-thaw Rock*. Xi'an: Xi'an University of Science and Technology.

Gong, L.S. 2004. *Design and contraction direction to concrete structure durability*. Beijing: China Building Industry Press.

Hale, W.M., Freyne, S.F. & Russell, B.W. 2009. Examining the frost resistance of high performance concrete. *Construction and Building Materials* 23(2): 878–888.

Ji, X.D., Song, Y.P. & Liu, J. 2010. Study on frost damage constitutive model of concrete. *Journal of Hydroelectric Engineering* 28(3): 461–467.

Li, S.M. 2013. *Numerical Simulation of the Concrete Damage Plastic Coupling under Temperature Effect and Application Research*. Shenyang: Shenyang University of Technology.

Wu, Y. 2003. *Study on deformation characteristic of concrete arch dam with MgO admixture*. Nanjing: Hohai University.

Civil Engineering and Urban Planning IV – Liu et al. (Eds)
© 2016 Taylor & Francis Group, London, ISBN 978-1-138-02903-3

Experimental study on the flexural behavior of concrete beams strengthened with near-surface mounted CFRP laminates

Li Huang, Xian Li & Hua Zhang
Institute of Civil Engineering, Hebei University of Science and Technology, Shijiazhuang, Hebei, China

ABSTRACT: In order to research the flexural behavior of the RC beams strengthened with Near-Surface Mounted (NSM) CFRP laminates, one reference beam, two strengthened undamaged beams, and two strengthened damaged beams were studied by experimentation. The influences of the grooves and strengthened conditions on the flexural behavior were investigated. The results indicate that the bearing-capacity of the strengthened RC beams with the two grooves is higher than that of beams with the three grooves. The strengthening effect is slightly significant for damaged beams rather than undamaged beams. Compared with the reference beam, the cracks in the strengthened beams are narrower, propagate more slowly and are well-distributed.

1 INTRODUCTION

In recent years, the method using near-surface mounted CFRP laminates to reinforce them is familiar. This method is to slot on the strengthened member, to embed the carbon fiber lath, to let the carbon fiber lath participate in the member's stress through the bonding of cementitious materials (Wu et al. 2010; Liang et al. 2009; He et al. 2008; Zeng et al. 2008). Compared with the outer pasting method, NSM CFRT laminates method has the advantages of less material consumption, high intensity, corrosion resistance, and so on. This paper conducts a loading test on the five concrete beams, compares and analyzes the bearing capacity, crack patterns, load-deflection curves at the mid span and load-strain curves of the test beams by different slot numbers and different reinforcement conditions (Cheng et al. 2008; Zhou et al. 2006).

2 EXPERIMENT GENERAL SITUATION

2.1 *Design of sample*

Making five beams with a rectangular section of the same size, No. L1~L5, the section size are $b \times h = 150\ mm \times 250\ mm$, the length of the beam is 2.1 m, and the clear span is 1.8 m. The design strength grade of the concrete is C30, the thickness of the concrete cover is 25 mm. The test beam has 2 tension reinforcing bars of 14HRB335, 2 compression reinforcing bars of 10HRB335, stirrups of the test beam are 8 at 100 of HPB300, length of the shear span and pure bending section is 600 mm. The test beam's size and reinforcements are as shown in Figure 1. The section of the strengthened beam L2 and L3 is as shown in Figure 2, and the section of strengthened beam L4 and L5 is as shown in Figure 3.

In order to analyze the influence of different groove numbers and the influence of the damaged beam or undamaged beam on the flexural behavior of the beams in the condition of the same amount of carbon fiber laminates, we design test beam L1 as an unstrengthened beam (i.e. comparison beam), L2, L3, L4, and L5 as beams with near-surface mounted CFRP laminates. Among them, L2 and L3 have 2 grooves, the width and thickness of the carbon fiber laminates is 13.46 mm and 1.4 mm, respectively. L4 and L5 have 3 slots, the width and thickness of carbon fiber laminates is 13.46 mm and 1.4 mm respectively. Size of the slots is 10 mm at width and 20 mm at depth. Using the epoxy resin as laminates and groove's bonding material, the bonding length is 1800 mm. Reinforcement conditions are: direct reinforcement without injury to L2 and L4, pre loading 65% of the ultimate load value to L3 and L5 (This value is obtained by comparison beam L1) and completely uninstalling, then reinforcing (i.e. damaged beam).

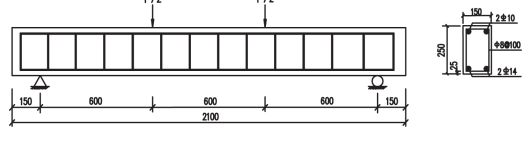

Figure 1. Dimensions and reinforcing steel configurations of the test beams.

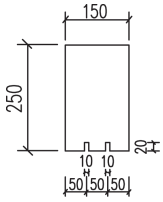

Figure 2. The cross-sections of L2 and L3.

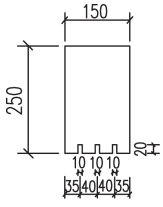

Figure 3. The cross-section of L4 and L5.

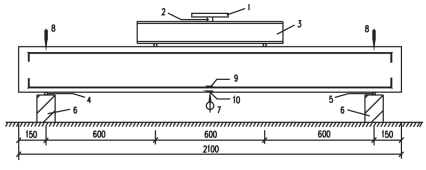

1-Hydraulic pressure testing machine 2-Pressure sensor
3-Distribution beam 4-The sliding hinge support
5-Fixed hinge bearing 6-Supporting pier 7-Dial indicator
8-Displacement meter 9-The strain foil of steel bars
10- The strain foil of carbon fiber
Figure 4. Loading device and measuring point arrangement of the test beams.

Figure 4. Loading device and measuring point arrangement of the test beams.

Table 1. Mechanical properties of the steel bars.

Diameter (mm)	Design value of tensile strength (MPa)	Steel bar's modulus of elasticity (MPa)	Steel bar's strength standard value (MPa)	The ultimate strength of steel bar (MPa)
8	270	2.1×10^5	324	458
10	300	2.0×10^5	338	492
14	300	2.0×10^5	346	589

Figure 4 shows the loading device and measuring point arrangement of the test beams.

2.2 *Material properties of experiment beams*

Table 1 gives the mechanical parameters of the steel bars. The design value of the axial compressive strength of the concrete is 14.3 MPa, the modulus of elasticity is 30 GPa. The main performance index of the carbon fiber plate is provided by the manufacturer, the tensile strength is 2450 MPa, the modulus of elasticity is 170 GPa, and the elongation is 1.72%.

3 ANALYSIS OF EXPERIMENT RESULTS

3.1 *Analysis of the beams' bearing capacity*

The bearing capacity of the beam is shown in Table 2.

As can be seen from Table 2, beams L2, L3, L4, and L5 are strengthened by carbon fiber laminates, and their yield load and ultimate load are all higher than that of L1 without reinforcement. Among them, their increase in the ultimate load is higher than that of the yield load. The strengthened beams whose extent of damage is 65% have a higher increase of the ultimate load than that of the undamaged beams. The strengthened beams with the two grooves have a higher increase of ultimate load than that of strengthened beams with three grooves.

It can be obtained from the test results: using the embedded reinforcement, the bearing capacity of aii the beams has been improved. For the undamaged beams L2 and L4, in the early stage of loading carbon fiber laminates, which are embedded at back surface of the concrete beams, restrain the development of concrete deformation and delay the cracking of concrete. After the concrete cracks, the original tensile force from the bottom of concrete beams is shared by the steel bars and carbon fiber laminates. Carbon fiber laminates play a big role after steels bars yield. For damaged reinforced beams L3 and L5, there have been cracks before strengthening. In the initial stage of loading, carbon fiber laminates participate in bearing the load together with the steel bars. When steel bars are out of work, all the loads transfer to the carbon fiber laminates until the beam destroys. The increase of the ultimate load is slightly higher than that of the undamaged beams.

Table 2. Bearing capacity of the test beams.

Test beams' no	The yield load (kN)	The ultimate load (kN)	The increase of yield load (%)	The increase of ultimate load (%)
L1	85	107.5	–	–
L2	92	145	8.2	34.9
L3	108	150	27.1	39.5
L4	96	124	12.9	15.3
L5	96	132	12.9	22.8

3.2 *Analysis of test beams' cracks*

The fracture shape of the test beams after destroying is as shown in Figure 5.

It can be observed from the process of loading to the beam L1, with the increase of load, when the steel bars yield, the concrete is crushed and presents the typical bending failure, the width of the main cracks are relatively large and cracks mainly distribute in pure bending section. It can be observed from the process of loading to L2, L3, L4, and L5, crack extension of strengthened beams is slower than beam L1, the distribution of cracks is more symmetrical than beam L1, the main crack branching of pure bending section is less, the crack width is smaller than beam L1. Among them, the number of cracks in the pure bending section of L3 is less than beam L1, other beams' crack numbers are no less than beam L1.

3.3 *Analysis of test beams' load-deflection curves*

The load-deflection curves is as shown in Figure 6.

It can be seen from Figure 6(a) that for beams with two grooves, in the initial stage of loading, deflection curves basically coincide, there is no significant effect to concrete beams with different reinforced conditions. But with the increase of load, for different reinforcement conditions of the beams, the deflection is different. Under the same load, the deflection of the unreinforced beam L1 is the maximum, the next is beam L2, the deflection of the beam L3 is the minimum. This is because

Figure 5. Cracks of the experimental beams.

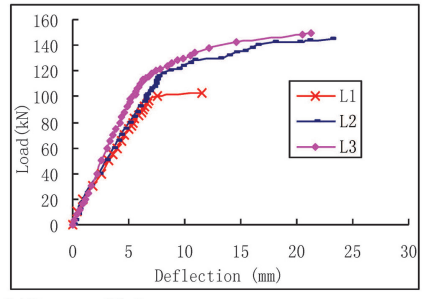

(a)Beams with 2 grooves

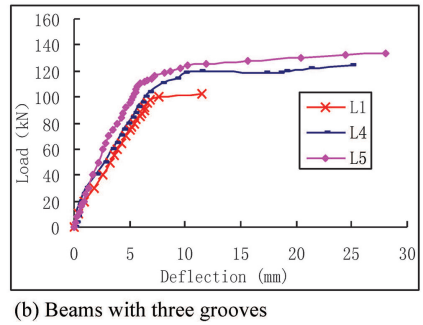

(b) Beams with three grooves

Figure 6. The load-deflection curves of the beams.

the carbon laminates of L2 and L3 have a control action on the original cracks' development when beams are beginning to stress. So their deflection is smaller than L1. When the load reaches the maximum value, the deflection of reinforced beam is obviously greater than the beam L1. This shows that the carbon fiber laminates of the strengthened beam has an inhibition effect for cracks and improves the flexural rigidity of the beam.

It can be seen from Figure 6(b) that for beams with three grooves, their deflection development trend and features are similar with beams which have two grooves.

3.4 *Load-strain analysis of the laminates*

Figure 7 is the load-strain curves of beams' laminates.

It can be seen from Figure 7(a) that in the early stage of loading for reinforced beams with two grooves, under the same load the strain of L3 is slightly larger than that of L2. This is because concrete of L2 hasn't cracked in the initial stage of loading, laminates can only participate in bearing load after concrete cracks. However, the concrete of L3 has cracked before strengthening; laminates participate in the bearing load in the early stage of loading. With the increase of load, the laminates'

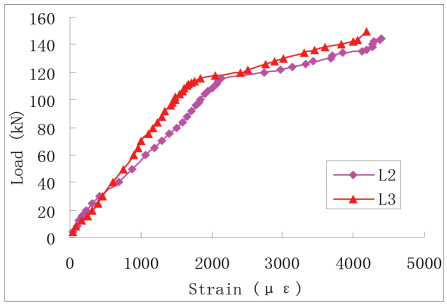

(a)Beams with two grooves

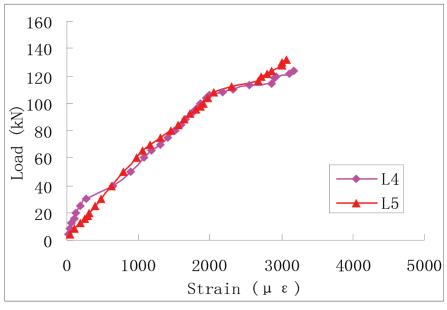

(b)Beams with three grooves

Figure 7. The load-strain curves of the beams.

strain of L3 is less than that of L2. After the yielding of the steel bars, the strain curve of the carbon fiber laminates shows a large turning. The strain increases rapidly and the curve tilts upward, the load is mainly born by a carbon fiber laminates.

It can be seen from Figure 7(b) that the beams with three grooves, the shape of carbon fiber laminates' load-strain curve is similar to beams with two grooves. But under the same load conditions, the difference between strain of L4 and L5 is small. This shows that the different conditions of the reinforcement have a certain influence on the strain of carbon fiber laminates for beams with two grooves. But there is little effect for beams with three grooves.

4 CONCLUSION

Beams that are reinforced by near-surface mounted CFRP laminates have higher yield load and ultimate load than unreinforced beams. And the increase of ultimate load is greater than the yield load. In this experiment, the increase of ultimate bearing capacity for beams with two grooves is 34.9% and 39.5%. The number for beams with three grooves is 15.3% and 22.8%. It shows at the same time, under the same amount of carbon fiber laminates, the increase of bearing capacity for beams with two grooves is higher than that of beams with three grooves.

For the beams with two grooves, beams with an extent of damage of 65% have a higher ultimate load than undamaged beams. For beams with three grooves, it is almost the same condition. This indicates that ultimate bearing capacity of damaged beams is slightly higher than that of undamaged beams.

The cracks' development of reinforced beams has some characteristics compared with the reference beam like the slow crack extension, small width and the more uniform distribution. Reinforced beams can effectively restrain the cracks development of concrete beams.

The strain gap of carbon fiber laminates is obvious for beams with two grooves in damaged or undamaged conditions. However, it is not too obvious for beams with three grooves.

REFERENCES

Cheng, X.L., Ren, Z.H., Xu, P. & Zeng, X.T. 2008. The loading-bearing capacity calculation of oblique section in concrete beams strengthened with near-surface mounted CFRP laminates. *Journal of Henan Polytechnic University (Natural Science)* 27(2): 228–233.

He, X.J., Zhou, C.Y. & Xu, L. 2008. Experimental study on the flexural behavior of reinforced concrete beams strengthened with near-surface mounted CFRP laminates. *China Civil Engineering Journal* 41(12): 14–20.

Liang, J.F, Yan, L.B. & Zhao, J.J. 2009. Experimental study on RC beams strengthened with near-surface mounted CFRP plate. *Concrete* (1): 46–49.

Wu, Y.L., Yao, J. & Zhu, X.X. 2010. Analysis on bonding performance test of mounted CFRP strengthened concrete beam. *Architecture Technology* 41(5): 454–456.

Zeng, X.T., Cheng, X.L. & Gao, B.L. 2008. Experimental study on flexural characteristics of RC beams strengthened with near-surface mountde CFRP laminates. *Engineering Mechanics* 25(12): 106–113.

Zhou, Z.Y, Xiang, C.J. & He, X.J. 2006. Prediction of Flexural Capacities for RC Beams Strengthened with NSM FRP Reinforcement. *Building Structures* 36(12): 19–21.

Civil Engineering and Urban Planning IV – Liu et al. (Eds)
© 2016 Taylor & Francis Group, London, ISBN 978-1-138-02903-3

Simulation analysis of the excavation with the support pile of the Shandong bookstore project

Yu Wang
Jinan Institute of Surveying and Mapping, Jinan, Shandong, China

Fen-Ting Lu
School of Civil Engineering, Shandong University, Jinan, Shandong, China

Wen-Kui Hu & Guang-Lei Hu
Jinan Institute of Surveying and Mapping, Jinan, Shandong, China

Yin-Jie Zheng
School of Civil Engineering, Shandong University, Jinan, Shandong, China

ABSTRACT: According to the materials of the foundation pit engineering of the Shandong Bookstore Project, this paper mainly studied the pile-anchor support form. With the numerical simulation of the whole construction process of the pile-anchor support, this paper analyzed the horizontal deformation of the pile, the horizontal deformation of the soil on the top of the pile and the change rule of the internal force of the anchor, and compared to the calculated result with the measured result, providing experiences for similar researches.

1 INTRODUCTION

Pile-anchor supporting structure is a novel anti-slide structure since the 1980s, forming by the supporting pile together with one or several layers of anchor. It is a statistically indeterminate structure with a good stability and high safety performance, which is commonly used in deep the foundation pit as an integrated slope protection technology (Zhang & Huo 2002, Huang et al. 1997).

Depending on the current specifications and the design level (Ministry of Construction of the People's Republic of China 2002; China Academy of Building Research 2012), the support scheme of the foundation pit of the Shandong Bookstore was defined by controlling the value of horizontal displacement and surrounding settlement with business software. This paper has built a three-dimensional model of the pile-anchor support by a finite element software to analyze the horizontal deformation of pile, the horizontal deformation of soil on the top of pile and the change rule of the internal force of anchor under excavation conditions, and compared with the measured values, providing experiences for design optimization and construction of the similar projects.

2 LOCATION AND GEOLOGICAL CONDITION OF THE PROJECT

Shandong Bookstore project, which has been proposed by the Shandong Publishing Group Co., Ltd., is located between the north of Jingshi Road and the south of Jingjiu Road, and is also located between Shengli Street and Minsheng Street in Jinan City, as shown in Figure 1.

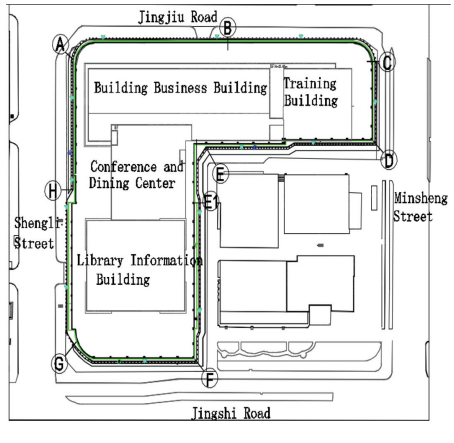

Figure 1. Plan view of excavation.

The total land area is 16328 m^2, the total construction area is 1,24,000 m^2, including 90,000 m^2 of the ground floor area and 34,000 m^2 of the underground floor area. The project contains library information building, conference and dining center, bookstore business building and the training center. Those four buildings are connected to a whole from south to north and west to east, surrounded by the underground garage in\an L-shaped. Respectively, the east and west lengths of the foundation pit are 161.9 meters and 70.6 meters, and the north and south length are 144.8 meters and 46.7 meters.

3 SUPPORTING SCHEME OF THE FOUNDATION PIT

The supporting scheme with a pile-anchor form studied here is for the GH section shown in Figure 1, and supported parameters are showed in Tables 1 and 2, support section is showed in Figure 2. The concrete scheme is as shown below:

1. For the support pile, the embedded depth is 50 meters, the diameter is 800 mm, the length is 20.05 meters, the horizontal spacing is 1.80 meters, the main reinforcement is HRB400, the stirrup is HPB300, the reinforcing rib is HRB335, the concrete grade is C30, the thickness of main reinforcement is 50 mm, crown beam anchors 50 mm into the pile top, main reinforcement anchors 700 mm into the crown beam.
2. For anchor, there are four layers of the anchor cables, the horizontal spacing is also 1.8 m, which means the anchor cables are located on pile bodies, the anchor hole diameter is 150 mm, the grouting material is of pure cement paste, water cement ratio is 0.5, grouting strength is not less than M20 by the twice pressure grouting method, that the first pressure is about 0.5 MPa and the second grouting pressure is about 2.5 MPa, two 25 A channel steels are used as waist beam.
3. For concrete crown beam on the pile top the plan view is 900 × 800 mm, the concrete grade is C30, the main reinforcement is HRB335, the stirrup is HPB300, and the thickness of main reinforcement is 25 mm.

The space between the two boundaries of the foundation pit is 68.850 m, so the boundary of the model is the symmetric spacing, 34.425 m, the depth is 60 m, and the unit width is 1.8 m.

Table 1. Physical and mechanical parameters of soils and rocks.

Soil	c (kPa)	Φ(°)	γ(N/m^3)	μ
Filling	15	15	19000	0.4
Loess	24.6	19.9	19000	0.4
Gravel	10	35	20000	0.4
Residual soil	19.6	20.5	17200	0.4
Seriously weathered rock	20	25	18000	0.38
Strong weathered rock	20	35	20000	0.36

4 CONSTRUCTION OF THE FINITE ELEMENT MODEL

Fixed hinge bearing is used for the bottom of the model by the assumption that the bottom is fixed. The displacement of the bottom is limited in all three directions, the top is free and there are 20 Kpa distributed additional load in 15 m from the edge of foundation pit. The displacement of the excavation faces are limited in its corresponding horizontal direction, which means limiting the displacement of Y axis if the face is parallel to Y axis, limiting the displacement of X axis if the face is parallel to X axis. The weight stress of the soil is calculated automatically during the analysis process. Considering the role of the pre-stressed anchor and the additional load, girdding of the soil element around the anchor is finer. The meshing is shown in Figure 3.

Table 2. Physical and mechanical parameters of anchor.

Layer	Serial number	Pore diameter (mm)	Length (m)	Design bearing capacity (kN)	Lock value
1	MG1	150	3 s15.2 stranded wire L = 17500@1800	328.0	60% of design value
2	MG2	150	3 s15.2 stranded wire L = 20000@1800	351.4	60% of design value
3	MG3	150	3 s15.2 stranded wire L = 19000@1800	444.5	60% of design value
4	MG4	150	3 s15.2 stranded wire L = 15000@1800	432.9	60% of design value

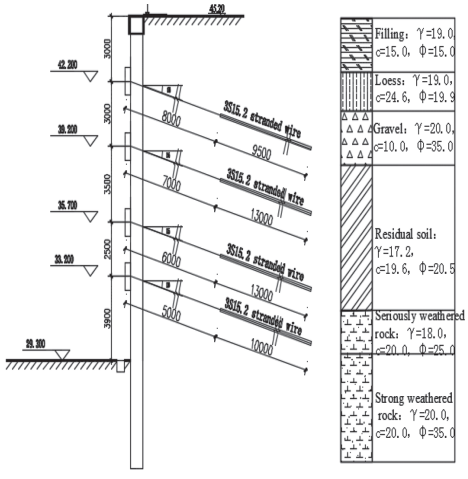

Figure 2. Typical section of support.

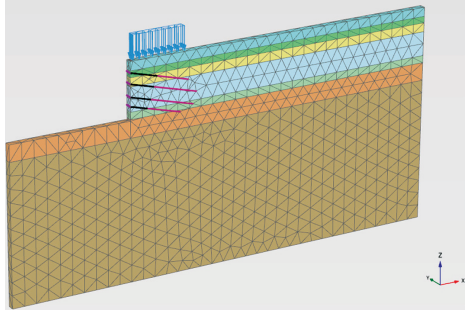

Figure 3. FEM model of typical section.

5 SIMULATION PROCESS

In this paper, the bottom of the pile is tied to soil by the use of Tie contact, the anchor section of the cable is embedded into the soil by way of an Embedded, the external anchoring end, which is tied to the retaining pile. The pre-stress of the anchor is applied by the equivalent cooling method (Wu & Gao 2008), and with the anisotropic temperature and strain coefficients, the strain will be obtained by the given temperature for the definition of the effect of applying pre-stress.

The numerical simulation of the construction process is divided into 10 steps:

Step-1. Balance the initial stress field and application of super load;
Step-2. Excavation of the first layer of soil;
Step-3. Installation of the first layer of anchor and its pre-stress;
Step-4. Excavation of the second layer of soil;
Step-5. Installation of the second layer of anchor and its pre-stress;
Step-6. Excavation of the third layer of soil;
Step-7. Installation of the third layer of anchor and its pre-stress;
Step-8. Excavation of the fourth layer of soil;
Step-9. Installation of the fourth layer of anchor and its pre-stress;
Step-10. Excavation of the last layer of soil.

6 ANALYSIS OF THE SIMULATION RESULTS

The stress clouds of soil after each excavation step are shown in Figures 4–8, and Figure 9 is the horizontal displacement of pile along the depth after each excavation step. It can be seen from Figure 9 that the horizontal displacement of pile is

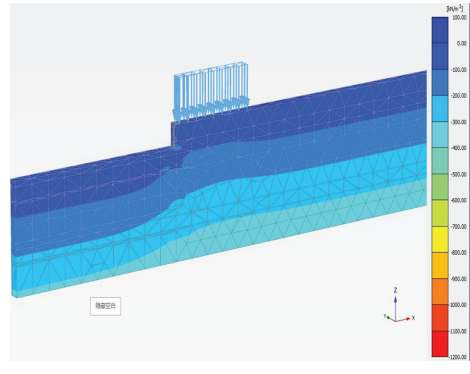

Figure 4. Contour of the principal stress σ_1 after Step-2.

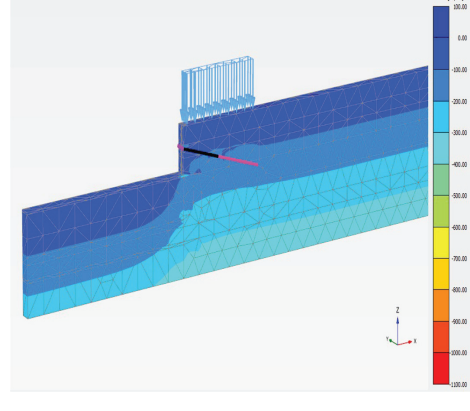

Figure 5. Contour of the principal stress σ_1 after Step-4.

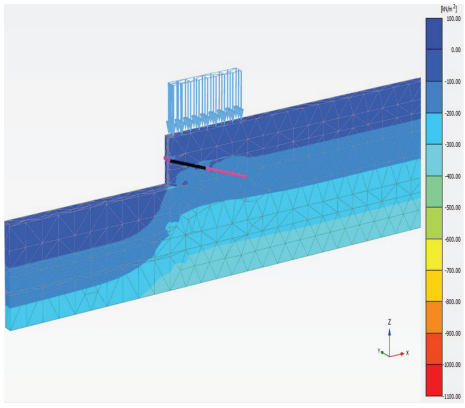

Figure 6. Contour of the principal stress σ1 after Step-6.

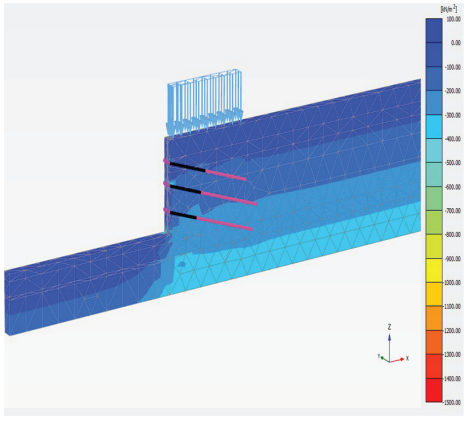

Figure 7. Contour of the principal stress σ1 after Step-8.

continuously increasing along with excavation steps, and reaches to the maximum value, 10.43 mm, in the range of 6.8~8.1 m under ground surface.

Figure 10 shows the horizontal displacement of the soil along the distance from the edge of the foundation pit. It can be seen that the magnitude of the displacement value decreases with the distance from the edge of the foundation pit, and the horizontal displacement is only 8.78 mm at the edge of the foundation pit after all excavation steps.

Table 3 shows the internal value of each layer of the anchor during the excavation. It can be seen from the table that the internal force of anchor increases gradually during the excavation, and the internal force of the lower anchor is larger than that of the upper anchor.

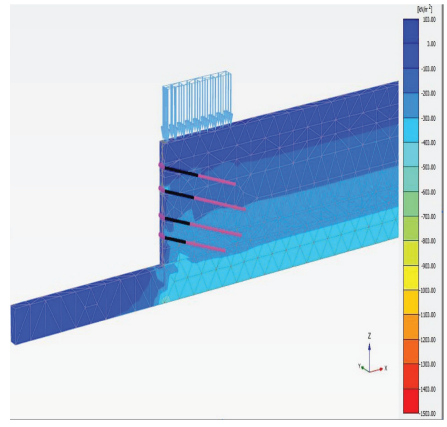

Figure 8. Contour of the principal stress σ_1 after Step-10.

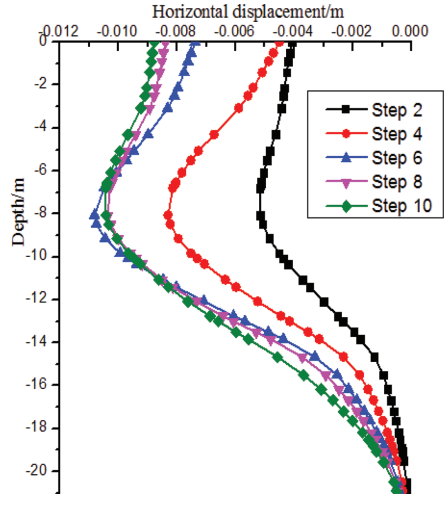

Figure 9. Horizontal displacement of the pile along the excavation depth.

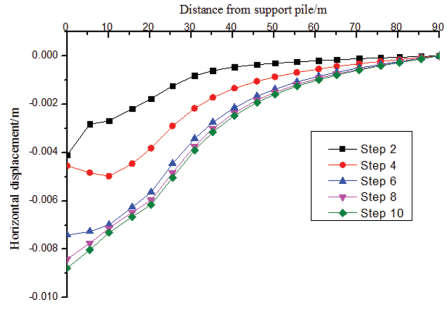

Figure 10. Horizontal displacement of the soil along the distance from the edge of the foundation pit.

Table 3. Axial force of the anchor in each construction step (kN).

Layer	Step-3	Step-4	Step-5	Step-6	Step-7	Step-8	Step-9	Step-10
1	196.80	228.39	198.08	208.28	217.42	215.98	220.24	217.98
2		–	210.80	267.93	215.25	232.61	225.44	228.32
3	–	–	–	–	266.70	307.38	263.84	283.72
4	–	–	–	–	–	–	259.70	310.69

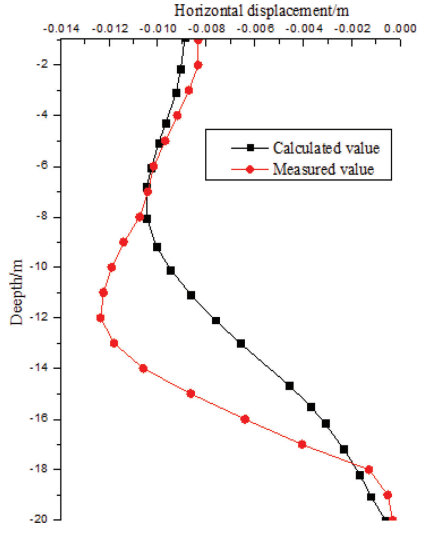

Figure 11. Comparison of the horizontal displacement of pile along the excavation depth.

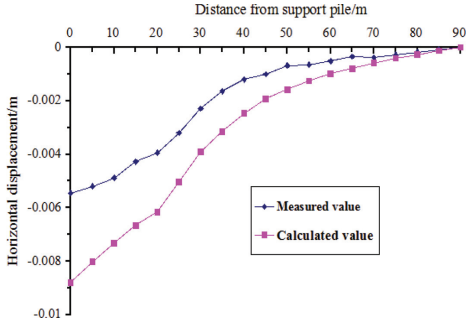

Figure 12. Comparison of the horizontal displacement of the soil along the distance from the edge of the foundation pit.

7 COMPARISON WITH MEASURED RESULTS

Figures 11 and 12, respectively, indicates the calculation data curve and the measured data curve of the horizontal displacement of the pile along the depth after each excavation step and the horizontal displacement of soil along the distance from the edge of the foundation pit. It can be seen that both of those two calculated deformation trends are consistent with the measured deformation trends. The measured values of deformation are smaller than the calculated values, which are in accordance with the practical situation.

8 CONCLUSION

Finite element software can simulate the whole process of the pile-anchor supporting the construction, obtain the horizontal deformation of pile body, horizontal deformation of the soil on the pile top and the variation of the internal force of anchor, and the results correspond to the measured results, providing guidance to the actual engineering design.

ACKNOWLEDGMENT

This research was financially supported by Promotive Research Fund for Excellent Young and Middle-aged Scientists of Shandong Province (Grant No. BS2013SF024).

REFERENCES

China Academy of Building Research. 2012. *Technical Specification for Retaining and Protection of Building Foundation Excavations*. Beijing: China Architecture & Building Press.

Huang, S.Y., Zhang, X.H. & Cao, H. 1997. *Foundation treatment and foundation pit bracing*. Wuhan: China University of Geo-sciences Press.

Ministry of Construction of the People's Republic of China. 2002 *Code for design of building foundation*. Beijing: China Architecture & Building Press.

Wu, Z.X. & Gao, Z.J. 2008. Application of the equivalent lowering temperature method in simulating pre-stress tension procedure to solve the form-search of BSS. *Journal of Zhejiang University of Technology* 36(5): 587–590.

Zhang, Q.X. & Huo, D. 2002. The Failure Models Of Anchor-pile Retaining Structures And Case Analysis. *Industrial Construction* 32(6): 77–79.

This page intentionally left blank

Civil Engineering and Urban Planning IV – Liu et al. (Eds)
© 2016 Taylor & Francis Group, London, ISBN 978-1-138-02903-3

Mechanical analysis of a new type of self-centering frame

Yue Liu, Meng-Xin Pan, Zhen Zhou, Ya-Kun Dong & Tian-Shuo Zhou
Key Laboratory of Concrete and Prestressed Concrete Structures of the Ministry of Education, Southeast University, Nanjing, Jiangsu, China
State Key Laboratory of Building Safety and Built Environment, Beijing, China

ABSTRACT: This paper illustrates the mechanical property of the new self-centering frame. First, based on the introduction of the structure mechanism, researchers analyze the internal distribution of the frame structure subjected to lateral loads. Then researchers build a numerical analysis model of this structure using OpenSEES, with Pushover analysis of single-story structure and seismic-resisting performance analysis of a three-story structure. The analysis demonstrates that the new self-centering frame subjected the seismic loads has a small residual deformation and good self-centering property, and it is a recoverable seismic-resisting structure.

1 INTRODUCTION

Recently, with the constant development of the seismic engineering, the design conception of seismic-resisting structure transformed from anti-collapse design to recoverable design. Conception of recoverable design is to control the peak deformation of the structure and the residual deformation. Not only it requires structure not to collapse, but also need to reduce structure repairing time and cost. Even some structure can be used normally without repairing after the earthquake (Seo & Sause 2005; Lv et al. 2011; Pan et al. 2011). The residual deformation has two effects on the property of structure after subjecting the seismic loads (Erochko 2013): one is reducing the ability to resist the following earthquake. The other one is increasing the structure repairing cost. In order to decrease the residual deformation of the structure, researchers have designed a self-centering structure with post-tension pre-stress technology. This structure aims to be self-centering by using the gaps between different components, while it remains elastic. As a consequence, it can effectively decrease the residual deformation of the structure subjected the seismic loads. Peak deformation of the structure is controlled by friction or yield energy dissipators.

Based on the design conception above, Hajjar and other researchers design the rocking wall whose foundation can free to rotate (Eatherton et al. 2008). Christopoulos and other scholars first proposed a structure that consists of inter tube, outer tube and post-tensioning strands (Christopoulos et al. 2008). During the earthquake, inter tube and outer tube will have different movement and a gap will appear and the post-tensioning strands will extend. After the earthquake, force from the strands will make the gap disappear and make the structure be recovered.

The traditional connection between column and beam will increase the distance between neighboring columns. As a consequence, the pull will appear between neighboring floors and it may destroy the floors. The new self-centering frame avoids this problem by the design of inter tube and outer tube. Kurama, Wada and other researchers did more further research of this frame (Kurama et al. 1999; Wada et al. 2008). The research demonstrates the special property of this frame subjected the seismic loads compared to traditional ones.

2 MECHANISM OF SC FRAME

Figure 1 shows the schematic of the structure and working mechanism of this new Self-Centering frame.

As shown in Figure 1, the bottom chord of the beam consists of two tubes. The inner tube is connected to the column by bolts at the height of the bottom chord, and the outer tube is connected to the top chord by T-beam. Top chord is connected

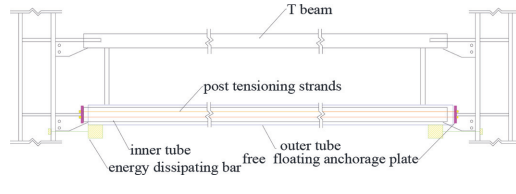

Figure 1. Configuration of the SC frame.

to the column by bolts and there is no connection between the inner tube and the outer tube. Free floating anchorage plates slide over the connectors at the end of the inner tube, but are held in place by the post-tensioning, whose strands pre-compress the concentric tubes. The post-tensioning acts to keep the inner and outer tube of the bottom chord in alignment and make them static relatively when there is no force on the frame.

When subjected to seismic action, the overall structure is equivalent to the one with horizontal force acting on it. Then the column rotates, which causes a relative horizontal displacement between the column at the height of the bottom chord and the column at the height of the top chord. Because the bottom chord outer tube displaces with the top chord, the inner tube and outer tube of the bottom chord move laterally relative to one another as the column rotates relative to the truss. Result from the relative displacement of the two bottom chord tubes, the post-tensioning strands elongate and provide the increasing restoring force that restraining the lateral displacement so that can get the minimum of the largest horizontal displacement.

The restoring force remains the same in the moment when seismic action ceases. The post-tensioning provides the restoring force that creates self-centering by bringing the two tubes back into alignment. The column gets back from tilt to a vertical position, so as to reduce the residual deformation of the structure after the earthquake.

Structural friction elements, setting between the inner and outer tubes, are utilized to dissipate seismic energy through inelastic deformations. During a strong ground motion in earthquake, there is rapid relative displacement in the inner and outer tubes. The friction element dissipates the seismic energy, thereby reducing the seismic response of the structure.

3 MECHANICAL ANALYSIS

Figure 2 shows the model of a single-story and single-bay SC Frame. Both the connections between columns and beams and between columns and basis are hinges. The post-tensioning strands inside the tubes underneath the bottom flange of beam pre-compress the concentric tubes and acts to keep the inner and outer tube in alignment. In this way, the post-tensioning creates the restoring force that drives self-centering, which makes the mechanism a complicated statically indeterminate structure.

Assume that a horizontal rightward point force F in Figure 2 is acted on the top of the frame, which consequently makes the whole frame lean rightward and a horizontal displacement gap is generated between the top flange and bottom flange. The gap separates the outer tube and the inner tube, as a result, the strands inside the tubes are elongated and the pulling stress of the strands increases proportionally to the extension. As the lean is big enough, the tension of the strands reaches a threshold which could balance the system and no more lean is added under the action of F.

Figure 3 shows the mechanical details of the isolated columns in Figure 2. Let F be the assuming rightward force and F2, F4 the force on the columns acted by the bottom flanges, which are caused by the pulling force of the strands. F1, F3 the force on the columns acted by the top flanges, which are the reaction to F, and F_5, F_6 the forced acted by foundation on which the columns are constructed.

Given the statically balanced condition:

$$\begin{cases} F_1 + F_3 = F_A \\ F_2 + F_4 = F_A \\ F_5 + F_6 = F \end{cases} \tag{1}$$

Assume that F5 = αF6, then:

$$\begin{cases} 3.96(F_1 - F) - 3.35F_2 = 0 \\ 3.96F_3 - 3.35F_4 = 0 \\ F + F_2 - F_1 - \dfrac{\alpha}{1+\alpha}F = 0 \\ F_4 - F_3 - \dfrac{1}{1+\alpha}F = 0 \end{cases} \tag{2}$$

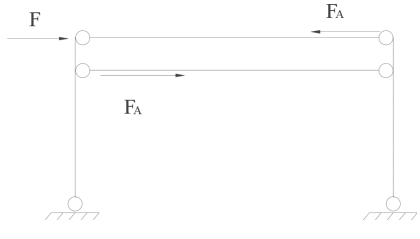

Figure 2. Mechanical model of single-story and single-bay SC frame.

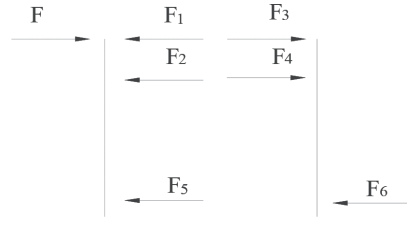

Figure 3. Mechanical details of the isolated columns of SC frame.

The following can be calculated:

$$F_1 = \frac{1+6.6\alpha}{1+\alpha}F,\ F_2 = \frac{6.6\alpha}{1+\alpha}F,\ F_3 = \frac{5.6}{1+\alpha}F$$
$$F_4 = \frac{6.6}{1+\alpha}F,\ F_A = 6.6F \tag{3}$$

Elongation of tensioned strands:

$$\Delta = \frac{(F_A - F_a)L}{EA} = \frac{(6.6F - 356)\times 10^3 \times 9100}{1.95\times 10^5 \times 1020} \tag{4}$$
$$= 0.04575\,(6.6F - 356)$$

Obliquity angle of columns:

$$\theta = \frac{\Delta_c}{h} = 7.5\times 10^{-5}(6.6F - 356) \tag{5}$$

Drift story:

$$\theta = \frac{\Delta_c}{h} = 7.5\times 10^{-5}(6.6F - 356) \tag{6}$$

When the gap between the top and bottom of the beam is over H/100, the structure is regarded as destroyed.

In this case, $\Delta_c = 39.6$ mm:

$$F = 71\ \text{kN} \tag{7}$$

So the maximum force the structure could bear is 71 KN.

Of all the above equations:

h: height of the beam; 600 mm;
H: height of the story; 3960 mm;
L: span of the beam; 10600 mm;
E: elasticity modulus of the strands; 1.95×10^5 MPa;
A: cross sectional area of the strands. 1020 mm^2;
Δ: elongation of tensioned strands;
Δ_c: gap between the top and bottom of the beam;
θ: obliquity angle of columns;
F_A: the pre-tensioned force of strands;
α: proportionality coefficient of the F_5 and F_6.

It is obvious that the value of α must be confirmed in order to know exactly the distribution of the internal force of the SC Frame.

4 OPENSEES MODEL FOR SC FRAME

Element analysis software OpenSEES is used to analyze the seismic performance of this structure. A single-story model is shown in Figure 4: Constant height of other stories is 3.96 m; the span is 9.1 m and

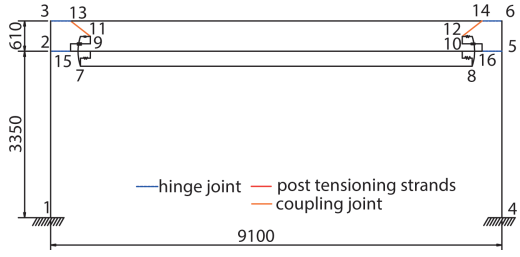

Figure 4. Single-story model.

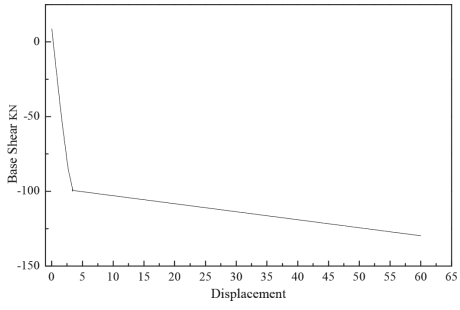

Figure 5. Relationship of Base Shear and top displacement.

the distance between top chord and bottom chord is 610 mm; the columns are pinned at the ground foundation. Nonlinear beam-column element is used to present beam and column with constitutive relation model Steel 01 Material. Free floating plate, the inner and outer tube are simulated by ENT element. ENT element is used to construct a uniaxial elastic-no tension material object. Inner and outer tube are endued with linear elastic material. Truss element with constitutive relation model Steel 02 Material is used for friction dissipating bars outside the outer tube.

As lateral load putting on the vertex of the frame, post tensioning strands are stretched causing the inner tube and outer tube separated. Meantime, friction element begins to dissipating earthquake energy. Figure 5 shows the relationship between base shear and displacement of vertex point under one amplitude load. By calculating the moment between point 13 and 15 along the loading period and the average of these proportion, we can get the coefficient of the internal force, $\alpha = 3.01$.

5 ANALYSIS OF THE SEISMIC-RESISTING PERFORMANCE

This paper takes the ASCE Benchmark Level III model structure with steel frame as the research

object (Ohtori et al. 2004), as shown in Figure 6: the bottom of the structure is base-rooms, height of the each story is 3.69 m. Material of each part in three model is similar as it in single-story model. Particularly, the column element is simulated with Steel 02 material instead of Steel 01 in order to demonstrate the P-Delta effect. Initial strain is set on the strands to present the post tensioning effect. Once the earthquake force is big enough, self-centering structure begins to work. And the initial stress is ensured to be larger than the friction to achieve the self-centering effect is feasible.

Los Angeles wave is selected as the earthquake excitations and analyses. Table 1 shows the probabilities of exceedence of 10%, 20% and 50% in 50 years respectively. Each POE group has three waves. And the average data would be taken as the result.

Figures 7 to 9 show the drift story, residual story and max drift acceleration respectively. Table 2 gives the comparison of the result. From the result we can see that max drift story at 50% POE appears at 1.43%. POE 10% corresponds to 2.36% and POE 2% correspond to 3.5%. As seen in the 3 series of waves, the deformation between stories appears to be well-distributed. It can be judged that the main structure don't suffer mass damage.

Average residual drift under each waves are 0.014%, 0.009% and 0.0149%, respectively (POE in descending order). It can be seen that residual drift is very low indicating an excellent performance of self-centering. The new SC frame exhibits the property of earthquake resistance. Figure 9 shows that

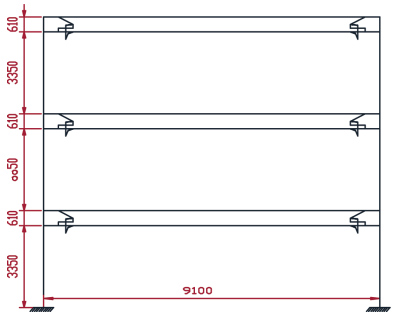

Figure 6. Three stories model.

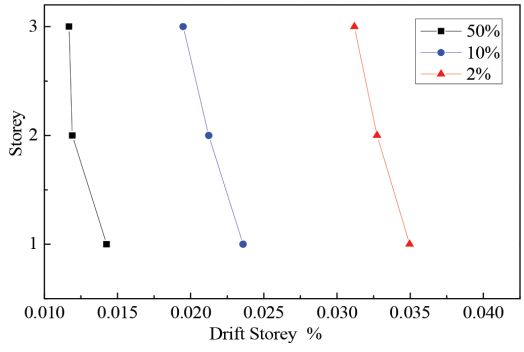

Figure 7. Drift Story under 3 series of waves.

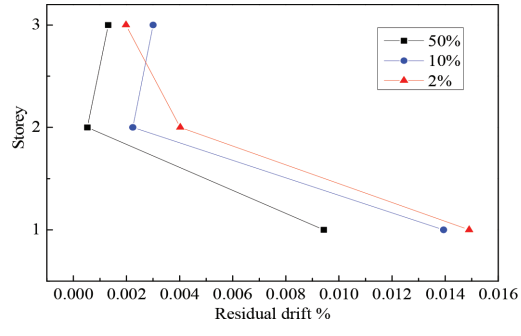

Figure 8. Residual story under 3 series of waves.

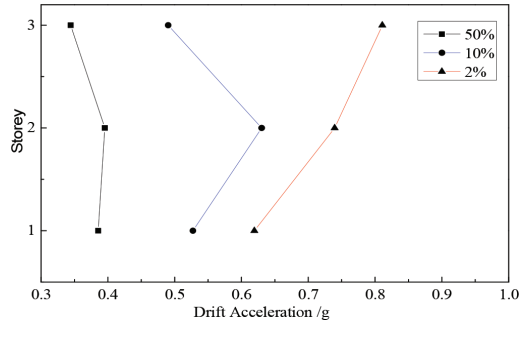

Figure 9. Max drift acceleration under 3 series of waves.

Table 1. Earthquake data.

	POE 10%			POE 50%			POE 2%		
Identifier	1	2	3	41	42	43	29	39	40
PGA (cm/sec^2)	452	662	386	578	326	141	793	490	613

Table 2. Maximum record under different earthquake.

	POE 50%	POE 10%	POE 2%
θ(%)	1.43	2.36	3.5
θ_r(%)	0.0094	0.0139	0.0149
α_g	0.395	0.63	0.811

acceleration under three type of waves doesn't reach one acceleration of gravity manifest a proponent property of control.

6 CONCLUSIONS

Compared to traditional ones the new SC frame can not only recover from the earthquake but also realize displacement coordination without any extra internal force. It also reflects compatibility of deformation between beam and frame comparing to the traditional SC beam. A reckoning procedure is compiled for the new SC frame. By calculating the moment proportion in single-story analysis in one amplitude, proportionality coefficient is obtained. Under different earthquake waves, the three story SC beam appears affine deformation of drift story and a tiny residual drift indicating palpable property of self-centering. A minor acceleration also embodies a definite control in the earthquake response.

ACKNOWLEDGEMENTS

The research described in this paper was financially supported by "National Natural Science Foundation of China" (grant no. 51208095), and "Opening Funds of State Key Laboratory of Building Safety and Built Environment" (grant no. BSBE2014-05) "Qing Lan Project of Jiangsu Province". The supports are gratefully acknowledged.

REFERENCES

Christopoulos, C., Tremblay, R., Kim, H.J. & Lacerte, M. 2008. Self-centering energy dissipative bracing system for the seismic resistance of structures: development and validation. *Journal of structural engineering* 134(1): 96–107.

Eatherton, M.R., Hajjar, J.F., Deierlein, G.G., et al. 2008. Controlle Drocking of Steel Framed Buildings with Replaceable Energy Dissipating Fuses. *The 14th World Conference on Earthquake Engineering, Beijing*.

Erochko, J.A. 2013. *Improvements to the Design and Use of Post-tensioned Self-Centering Energy-Dissipative (SCED) Braces*. Toronto: University of Toronto.

Kurama, Y., Sause, R., Pessiki, S. & Lu, L.W. 1999. Lateral load behavior and seismic design of unbonded post-tensioned precast concrete walls. *ACI Structural Journal* 96(4): 622–632.

Lv, X. et al. 2011. New concept of seismic design of structures-restorable structure. *Journal of Tongji University (Natural Science Edition)* 39(7): 941–948.

Ohtori, Y., Christenson, R.E., Spencer Jr, B.F., & Dyke, S.J. 2004. Benchmark control problems for seismically excited nonlinear buildings. *Journal of Engineering Mechanics* 130(4): 366–385.

Pan, Z. et al. 2011. Study on the self-centering steel structure. China Civil Engineering Journal of Building Structures (in Chinese) 32(9): 1–10.

Seo, C.Y., & Sause, R. 2005. Ductility demands on self-centering systems under earthquake loading. *ACI Structural Journal* 102(2): 275–285.

Wada, A., Qu, Z., Ito, H., et al. 2009. Seismic Retrofit Using Rocking Walls and Steel Dampers. *Proceedings of ATC/SEI Conference on Improving the Seismic Performance of Existing Buildings and Other Structures, San Francisco, CA, Dec. 2009*. USA: Applied Technology Council.

This page intentionally left blank

Civil Engineering and Urban Planning IV – Liu et al. (Eds)
© 2016 Taylor & Francis Group, London, ISBN 978-1-138-02903-3

Analysis of the displacement of soil around the shaft and cross channel based on MIDAS/GTS

Jian-Wen Zhong & Zhong-Yuan Duan
Institute of Urban Construction, University of South China, Hengyang, China

Yan-Jian Xu
Jiangxi Province Survey and Design Institute, Nanchang, China

ABSTRACT: The vertical shaft and the cross channel are the important part of the tunnel project, which belongs to the complex underground space structure. The change of stress and strain state of soil around. The vertical shaft and cross channel has space effect. According to the theory of the Mohr-Coulomb constitutive theory, the 3D numerical simulation of the vertical shaft and the cross channel is carried out by using the finite element analysis software MIDAS/GTS. Calculation results are basically consistent with the field monitoring data, proved the basic law of the displacement of soil around the complex underground space structures. The influence factors of the deviation between the calculated results and the field monitoring data are analyzed and the finite element analysis method of similar projects is summarized.

1 INTRODUCTION

In recent years, underground engineering accidents have brought many negative effects to the country and society. How to reduce the occurrence of those accidents, ensuring the safety of life and property during the construction stage, protecting the ecological environment around the site, reducing economic losses of state and society is a problem worthy of serious consideration. The key to ensure the safety of underground space structure is to control the displacement of soil around it (Zhu 1998). This paper takes a shaft and cross channel of Xiamen City Metro Line 1 as an example from the two aspects of field monitoring measurement and finite element numerical simulation to make a research on the displacement law of soil around the shaft and cross channel, exploring the monitoring and prediction method of soil displacement around the underground structures.

2 OVERVIEW

2.1 *Overview of the project*

One section of Xiamen Metro Line 1 turn to the Northwest along a arc radius of 450 meters, and a construction shaft was set up in the middle of this section. The shaft is located in an open field of a garden, no important buildings lie in the area of 3 times the depth of the shaft. There is a city trunk road on the east side of the site, the distance from the road center line to the shaft is about 40 m. The shaft is 6 meters long, 8 meters wide and 18 meters deep. Stratified excavation and support timely, the shaft was supported by: reinforced concrete wall (100 mm thick) in the 0~–3.0 m part; Steel grille waist beam + double layer reinforced net + Sprayed concrete in the part between –3.0 m~–7.0 m (the front 4 waist beam installed soil nailing which length 3.0 m, plum blossom type arrangement); double layer reinforced net + Sprayed concrete in the part between –7.0 m~–18.0 m. The shaft and the main tunnel was connected by a cross channel, which is 7.05 meters high and 5.5 meters wide, and the relative elevation of the vault is –9.40 m. The cross channel is built with mortar bolt (ring distance 1.0 m, longitudinal distance 1.5 m) + double layer reinforced net + sprayed concrete. In order to monitor the displacement of the surrounding soil in real time, the vertical surface displacement monitoring points and soil horizontal displacement monitoring tube around the shaft was installed before the shaft construction. The layout of the main monitoring points is shown in Figure 1.

2.2 *Overview of engineering geology*

The location of the project is a low mountain and hilly landform unit, and no bad geological phenomena such as fault zone were found. The filling soil has basically completed self weight consolidation; the main ingredient of the silty clay is powder and clay, the sand content of this layer is small; the bedrock is Granular granite and the weathering of bedrock is strong.

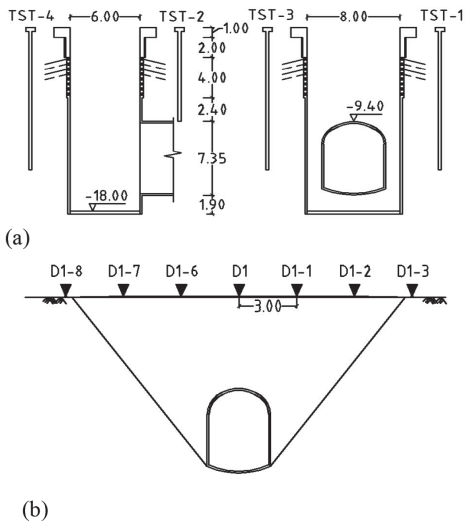

Figure 1. Main monitoring point layout.

Table 1. Mechanical parameters of rock and soil.

Name	h (m)	γ(kN/m³)	c	φ(°)	E (MPa)	ν
Plain fill	–1.6	17.5	10	13	–	–
Silty clay	–4.7	18.8	27	14	35	0.33
Residual soil	–7.1	19	32	19	50	0.30
Granite	–	21	35	28	150	0.27

The main rock and soil parameters of the site are shown in Table 1.

3 THEORETICAL DESCRIPTION

Displacement analysis is based on the analysis of stress state. The stress state of any point in the soil can be expressed by the 9 stress components:

$$\begin{bmatrix} \sigma_1 & \tau_{12} & \tau_{13} \\ \tau_{21} & \sigma_2 & \tau_{23} \\ \tau_{31} & \tau_{32} & \sigma_3 \end{bmatrix}$$

where $\tau_{12} = \tau_{21}$,$\tau_{13} = \tau_{31}$, $\tau_{23} = \tau_{32}$, to get the three dimensional stress state of a point is to solve the 6 independent stress components. (Shen 2000). Soil stress is consists of self weight stress and additional stress.

3.1 *Solution of self weight stress*

There are two kinds of calculation methods for the self weight stress of the soil in GTS. 1) The 6 stress components are calculated by using analytic solutions of ideal elastic solid by volume force in z direction; 2) The stress component of the z direction is calculated by using analytic solutions of ideal elastic solid by volume force in z direction, while the stress component of the horizontal direction is calculated by using the Coulomb earth pressure theory. For saturated soil, the pore water pressure should be considered, only the effective stress is used for displacement calculation (Li 2004).

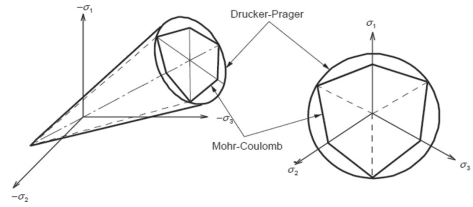

Figure 2. The Mohr—Coulomb yield surface.

3.2 *Additional stress*

The shaft surrounding additional load is mainly expressed as uniform load on the ground. Take any differential area of load surface to analyze, replace the uniform load equivalently with concentrated force, then using the Boussinesq solution to solve the independent stress components of the point in the soil mass. (Murthy 2002). Due to the hierarchical characteristics of soil, the displacement Can not calculated directly by the Boussinesq solution, the corresponding stress-strain constitutive relation is still needed.

3.3 *Constitutive model of soil*

Deformation of soil has complex characteristics, such as nonlinear, elastic-plastic, shear dilation, Compression hardens and time effect. (Mitchell 1993). In order to simplify the calculation, calculate the displacement of soil by using the elastic ideal plastic constitutive model. Assuming that soil mass is linear elastic before the yield stress, as long as the yield stress is reached, it turns to be ideal plasticity. This calculation uses the Mohr-Coulomb yield criterion.

Mohr-Coulomb yield surface in the principal stress space is shown in Figure 2.

4 FINITE ELEMENT NUMERICAL MODEL

4.1 *Basic assumption*

The site was flated before the shaft construction, which directly exposed the silty clay layer.

The following assumptions are made for the realization of the calculation:

1. The soil is considered as an ideal elastic-plastic material with uniform and isotropic material;
2. The anchor is equivalent to one dimensional element and it can only bear the tension.
3. The inner wall of the vertical shaft and the cross channel lining are equivalent to ideal plane strain elements. (Li et al. 2011).
4. The friction between the structure and the soil is considered.

4.2 *Numerical modeling*

The key part of this model is the connection between the shaft and the cross passage. In order to accurately simulate the displacement of surrounding rock and soil, take the soil to be excavated as the core of the model, divide the modeling into three steps to expand the size of the solid to the desired size.

Step 1. Establish the geometry solid of the soil to be excavated, and cut the section according to the actual construction progress, the mesh size is set to 1.0 m.

Step 2. Extended the solid to the part within 10 meters of the unloading surface set the mesh size consistent with soil mass to be excavated.

Step 3. Establish the solid 10 meters away from the unloading surface, the mesh size is set to expand along the direction away from the center to expand by equal proportion, and the maximum grid size is set to 3.0 m.

After the soil properties were assigned to the elements, normal displacement constraint was added to nodes on the boundary surface of the model. The temporary mobile board room and construction vehicles are considered as uniform load acting on the surface of the solid. The soil material is simulated by using the theory of Mohr-Coulomb while the elastic constitutive model is used to simulate the supporting structure.

The finite element model is shown in Figure 3.

5 RESULT

Simulation results shows that the displacement of the soil around the shaft and the cross channel is mainly occurred in range of the excavation depth of 1 times. The displacement cloud images are mushroom shaped, the displacement values are decreasing from the center to the periphery. The maximum displacement occurs at the junction of the shaft and the cross channel.

The displacement value and the distribution of soil are shown in Figure 4.

5.1 *Horizontal displacement of soil*

The horizontal displacement values of the nodes that located at the monitoring tube can be extracted in the GTS postprocessing module. The calculated values and the field monitoring values are plotted in the unified coordinate system, as shown in Figure 5. The positive displacement value indicates that the displacement is to the inside of the shaft. On the whole, the finite element analysis results are consistent with the field monitoring data, this calculation has basically realized the accurate simulation of the displacement of the surrounding soil. However, there are still deviations between the two values, the curve is not completely coincide.

As can be seen in Figure 5-(a), the deviation between the calculated curve and the measured curve is relatively large, and the maximum deviation (5.64 mm) occur at the position 4.0 meters below the ground, but the two curve are basically consistent at the depth of 5~11.0 m. The calculated curve and the measured curve of TST-2, as shown in Figure 5-(b), is consistent, the maximum deviation (2.18 mm) between them appears at the position of 9.5 meters deep from the ground. In Figure 5-(c), the calculated curve and the measured curve is intersect at the location of −10.5 m. Similar to TST-1, the calculated value of TST-2 is smaller than its measured value in the upper section of the monitoring tube and larger at the lower

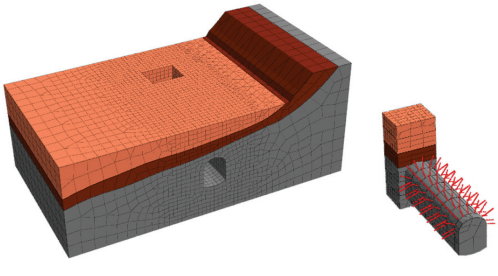

Figure 3. Finite element model.

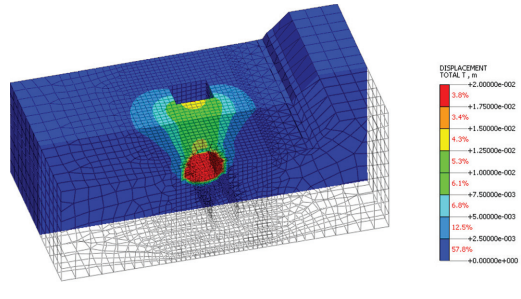

Figure 4. Cloud chart of soil mass total displacement.

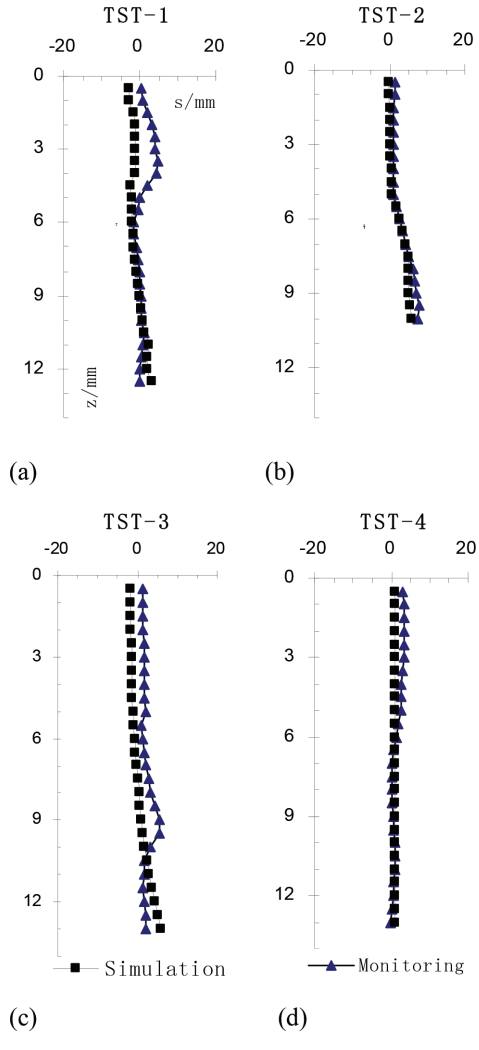

Figure 5. Chart of soil horizontal displacement.

end of the monitoring tube. In Figure 5-(d), the maximum difference of the tow curves of TST-4 is 2.50 mm and they are basically consistent at the lower end of the monitoring tube.

Generally, the curves of the measured displacement and the calculated displacement curves all showed the shape of letter "S". And the deviation between the two curves in each Figure mainly as follows: 1) In the upper soil, the measured displacement values are slightly larger than the calculated values, while at the bottom, the calculated values are slightly larger than the measured values.

Those differences reflect that: 1) the calculated value of displacement caused by the shaft excavation is smaller than the measured value during the shaft excavation; 2) the measured value of displacement happen at the construction stage of the cross channel is smaller than the calculated value at this stage. The main reason for this deviation should be as follows: 1) The time and space effect is not fully considered in the shaft construction, for example, overexcavation, leading to the construction of the supporting structure lags behind the excavation of the soil for a period of time. As a result, the measured value of soil displacement is greater than the calculated value. 2) Soil is not isotropic, as assumed, but similar to a kind of orthotropic material, so that deformation occurs in the upper soil mass caused by the excavation of the bottom soil is smaller than the calculated value at this stage. 3) The bottom of the monitoring tube is located in strong weathered granite. The rock material parameters used in the modeling are derived from the engineering investigation documents. The parameters in the engineering investigation file are reduced by the safety factor, which is usually smaller than the actual value. This is also a factor cause the deviation that can not be ignored.

To sum up, in spite of the existence of deviation, the simulation of the horizontal displacement of soil around the shaft and the cross channel by MIDSA/GTS is basically consistent with the actual horizontal displacement of soil. The value, distribution and development of soil displacement could be predicted before construction by using similar modeling and analysis method.

5.2 *Surface vertical displacement*

Surface vertical displacement is an important manifestation of soil displacement around the underground space structure. Accurate monitoring and measurement of surface subsidence by using optical measuring instruments is the key content of field monitoring. A set of monitoring points near the junction of the shaft and the cross channel was selected as the analysis objects here. These monitoring points belong to the same monitoring section, and the site monitoring data and numerical simulation results are shown in the following diagram.

As shown in Figure 6, the vertical displacement values of the ground surface appeared as spoon-shaped distribution: 1) the settlement value of the nodes close to the horizontal axis of the channel is relatively large, and decline along the direction away from the center. 2) As shown in the Figure 6 the displacement values on the left side are greater than the right side reflect that the vertical displacement value is inversely proportional to the burial depth of bedrock. The maximum value of field monitoring data of the surface settlement was –10.65 mm (D1), the minimum value is –4.30 mm (D1–3).

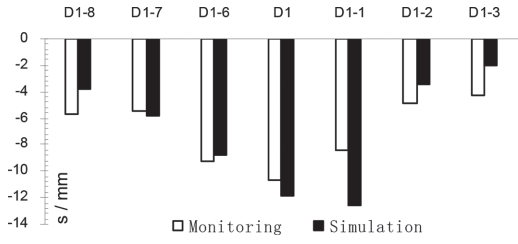

Figure 6. Chart of surface vertical displacement.

The maximum calculated value was –11.91 mm (D1–1); the minimum value was –2.07 mm (D1–1). Both the maximum and the minimum value, the calculated values are close to the measured values. The numerical simulation of vertical surface displacement results accurately reflect the actual situation.

6 CONCLUSION

Through comparative analysis of the results of field monitoring data and finite element simulation, the features of displacement of the soil around the shaft and the cross channel during construction can be summarized as the following points:

1. Deep horizontal displacement of the soil around the shaft and the cross channel showed the shape like letter "S". The increment of displacement occurs mainly in the construction stage of the cross channel. The construction method of reserving the soil in the bottom of the shaft is beneficial to the stability of the surrounding soil.
2. The vertical displacement of the ground surface shaped like a "spoon" type distribution, and shows an obvious trend of decline from the center to the edges.

Under the established design scheme, the 3D finite element calculation can simulate the stress and strain state of the surrounding soil of the underground space structure, and get the referencable displacement results. It has very important significance for the engineering safety assessment.

REFERENCES

Li, G.X. 2004. *Advanced soil mechanics*. Beijing: Tsinghua University press.

Li, H., Yang, L.S., Li Z., Zhu J.W. & Chui, P.F. 2011. Research on the space effect of ultra deep foundation pit based on MIDAS/GTS. *Railway Engineering* (4): 83–85.

Mitchell, J.K. 1993. *Fundamentals of Soil Behavior. 2nd ed.* New York: John Wiley & Sons, Inc.

Murthy, V.N.S. 2002. *Geotechnical Engeneering: Principles and practices of soil mechanics and foundation engineering*. New York: Taylor & Francis.

Shen, Z.J. 2000. *Theoretical soil mechanics*. Beijing: China Water & Power Press.

Zhu, B.F. 1998. *Principle and application of finite element method*. (2nd.ed). Beijing: China Water & Power Press.

This page intentionally left blank

Civil Engineering and Urban Planning IV – Liu et al. (Eds)
© 2016 Taylor & Francis Group, London, ISBN 978-1-138-02903-3

Numerical simulation of bearing characteristics of single pile in the Zhanjiang area

Yuan-Ming Liu
Shanghai Jianke Engineering Consulting Co. Ltd., Shanghai, China

Dong Fu
China First Metallurgical Group Co. Ltd., Wuhan, Hubei, China

Zhen-Xin Tong & Zhi-Qing Bao
Shanghai Jianke Engineering Consulting Co. Ltd., Shanghai, China

Bin Tang
College of Urban Construction, Wuhan University of Science and Technology, Wuhan, Hubei, China

ABSTRACT: Based on the nonlinear finite element software ABAQUS, we obtained the curves for the relationship between the pile tip resistance and pile top load with different pile lengths and pile diameters, and also the changes in pile side friction along the depth, by using the Duncan-Chang model to simulate the structured clay of the Zhanjiang group. This analysis indicates that within a certain range, the lateral friction resistance and tip resistance of short thin piles, under the same vertical load, plays a greater role than that of long thick piles.

1 INTRODUCTION

The Zhanjiang group's structured clay that is distributed in the Zhanjiang area, Guangdong Province, known for its special engineering properties, has gained widespread attention. Although it has a successful application in the academic and engineering field of pile foundation in Zhanjiang, the theoretical research lags behind the engineering practice. Therefore, carrying out the research on the bearing characteristics of pile foundation in the structured clay of the Zhanjiang group will be an urgent need and of great significance in the engineering field.

The main methods used for analyzing the single pile stress include the load transfer method, elastic theory method, shear displacement method, and numerical analysis method. It has been found that the single pile side friction changes with the depth and there is a relationship between the tip resistance and the pile top load, which are simulated by using the finite element analysis method; thus, it reveals the bearing character of single pile in the structural clay of the Zhanjiang group (Zhang 2006).

2 FINITE ELEMENT MODEL AND CALCULATION PARAMETERS

The single homogeneous Zhanjiang structural clay is used as the foundation soil, and the constitutive model belongs to the Duncan-Chang model. The material of the pile body adopts the linear elastic model. The grid division using the two-dimensional symmetric models is shown in Figure 1 (Fei & Zhang 2009). In order to reflect the deformation and stress of the pile more accurately, the soil around the pile and the pile end becomes more dense, and the pile end in the analysis area doubles its length downward, and it is also taken as a double pile length in the horizontal direction, which aims to minimize the influence on the analysis area that results from the boundary (Jiang 2012).

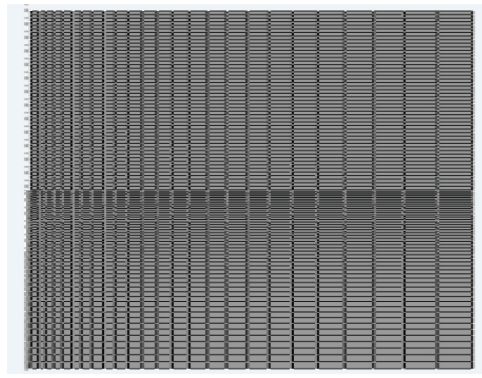

Figure 1. Finite element mesh.

Table 1. Duncan Chang model parameters of soil.

Parameter	v/KN*m^{-3}	C/kPa	φ/(^{0})	K	n
Soil	18.62	20	27.6	680	0.4
Parameter	R_f	G	F	D	
Soil	0.72	0.462	0.16	2.63	

Table 2. Parameters of pile body material.

Parameter	Modulus of elasticity E	Poisson's ratio V
Pile	20 GPa	0.2

A total of 6 single piles with different lengths are set up for the numerical simulation. The lengths of these piles are 10 m, 20 m, 30 m, 40 m, 50 m, 60 m, and the diameter of all the piles is 0.6 m; 4 single piles with different diameters are calculated, The lengths of the piles are 30 m each, and the diameter of the piles are 0.4 m, 0.6 m, 0.9 m and 1.3 m, respectively. The detailed calculation parameters of the piles with different lengths and diameters are listed in Tables 1 and 2.

3 NUMERICAL ANALYSIS OF BEARING CHARACTERISTICS OF SINGLE PILE IN THE ZHANJIANG GROUP'S STRUCTURED CLAY

3.1 *The exertion of side friction resistance*

From Figure 4 and Figure 2, it can be seen that the shorter or thinner the pile length is, the greater the effect of side friction resistance is. And the pile sides' friction resistance increases linearly along with the rise of the pile depth; but for single piles that are longer or thicker, the lateral friction resistance is not brought into full play; its distribution is that it first reaches a maximum and then reduces to a small value as the pile length increases. However, a slight increase can be seen near the pile end, which manifests a single hump-shape curve.

The following rules are shown in Figure 5 and Figure 3, for different lengths and diameters of single piles. When there is a small pile top load, the pile side friction resistance is almost uniformly distributed, with the increase in the load, the curve of side friction resistance begins to tilt, resulting in a single hump shape and a maximum. When the load is close to an ultimate load, the lateral friction curve is close to a straight line, which means that the side friction resistance of the pile is brought into full play.

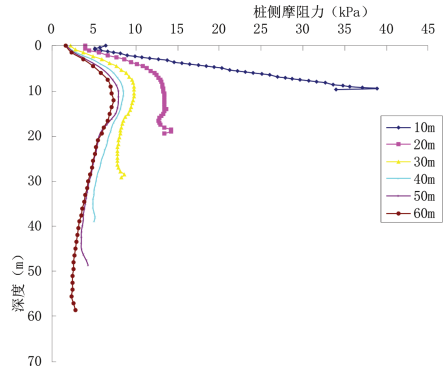

Figure 2. The depth curve of single piles' side friction resistance with different pile lengths under the load of 500 KN.

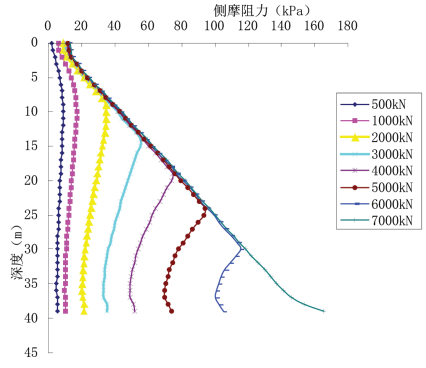

Figure 3. The depth curve of side piles' friction resistance for 40 m piles under different loading conditions.

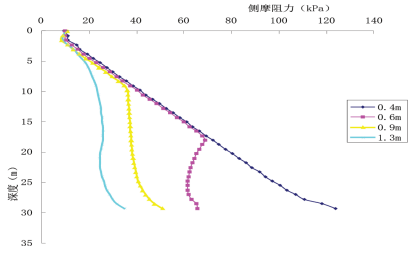

Figure 4. The depth curve of piles' side friction resistance with different diameters under the load of 3000 kN.

3.2 *The exertion of pile tip resistance*

From Figures 8 and 6, we can know the exertion of tip resistance for single piles with various lengths and diameters. Within certain realms, there is a linear relationship between the tip resistance of

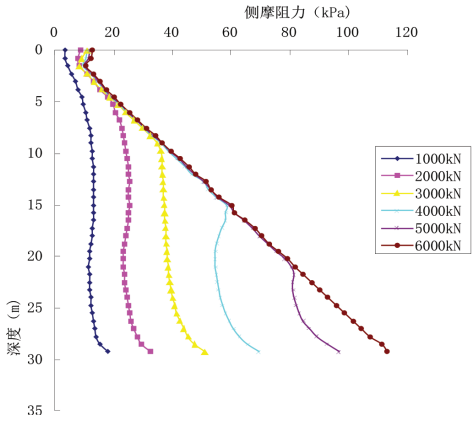

Figure 5. The depth curve of pile sides' friction resistance with 0.9 m diameter under different loading conditions.

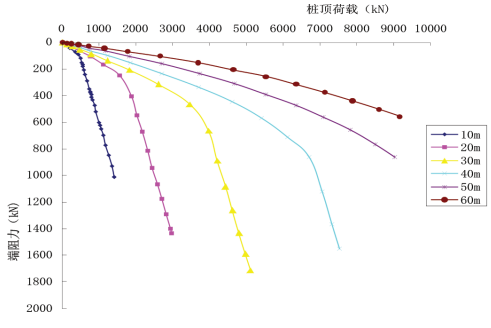

Figure 6. The relationship curve between the pile end resistance and pile loads with different pile lengths under the same load.

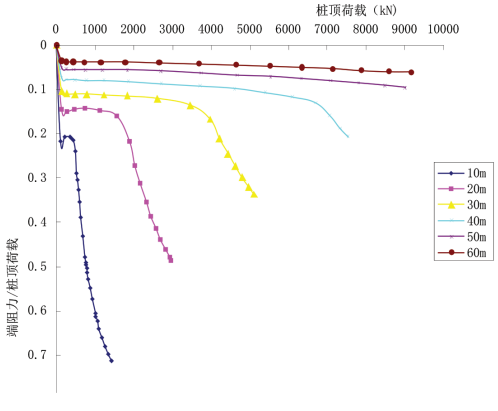

Figure 7. The relationship curve between the pile tip resistance/pile load and pile loads with different pile lengths under the same load.

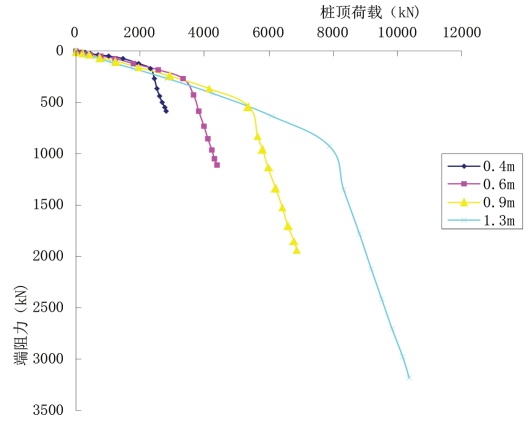

Figure 8. The relationship curve between the pile tip resistance and pile loads with different diameters under the same load.

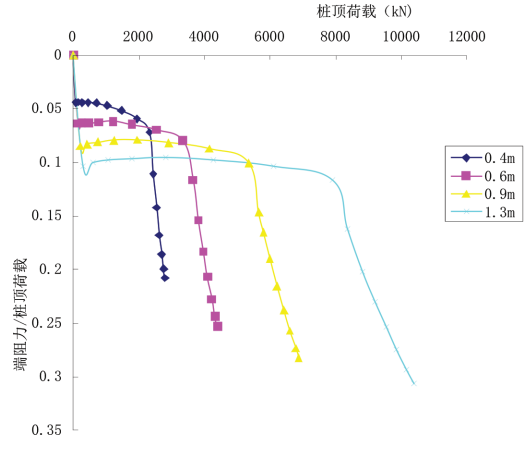

Figure 9. The relationship curve between the pile tip resistance/pile load and pile loads with different diameters under the same load.

single pile and the pile tip load, and the relation curve begins to bend following the augment of load; furthermore, the corresponding load of the relative bending point is not the same due to the different lengths and diameters, corresponding to the bending point, the longer the pile length or diameter becomes, the larger the load is. Beyond the bending point, the slope of the curve begins to elevate.

As shown in Figures 7 and 9, the curve that corresponds to different pile lengths and pile diameters, within a certain range, is nearly a horizontal line. The smaller line intercept can illustrate that the tip resistance accounts for a smaller proportion

of the load at the pile top, and when the pile top load is increasing, there is no evident change for its value; meanwhile, if the pile length is longer or the pile diameter is smaller, the intercept will also be smaller. Besides, when the pile top load exceeds a certain limit, the relationship curve begins to get steeper, and the tip resistance makes up a growing portion of the pile top load. It means that the tip resistance becomes gradually weak to a large extent when the load is increasing. The length and diameter of single piles are different; accordingly, the critical value of tip resistance that becomes gradually weak is also different; the longer the length of the pile is or the larger the diameter is, the greater the critical value will be. However, for the long and thick piles, the curve is still approximate to a horizontal line resulting from the small load, and the pile tip resistance and its function have not been fully realized. The bearing capacity of the single pile is mainly provided by the pile side friction resistance.

4 CONCLUSIONS

Through the finite element numerical analysis method, the exertion of side friction resistance and tip resistance, which is under the vertical load of single pile, is analyzed for different pile lengths and pile diameters in the Zhanjiang group, thus the following conclusions can be obtained.

First, with the increase in the pile top load, the depth curve of the lateral friction resistance is developed from a relatively flat curve to a single hump-shaped curve, and finally stretches into a straight line. In a specific range and under the same pile top's vertical load, the side friction resistance of the shorter and thinner piles will be larger than that of the longer and thicker piles; Second, when the load of the pile top is relatively small, the tip resistance of the pile is linear with the load of the pile top. And in a certain range, the tip resistance of the shorter and thinner piles, under the same pile top's vertical load, will be greater than that of the longer and thicker piles.

REFERENCES

Fei, K., Zhang, J.W. 2009. *The Application of the ABAQUS in Geotechnical Engineering.* Beijing: China Water & Power Press.

Jiang, C.Z. 2012. *The Numerical Analysis of Pipe Pile Vertical Bearing Characters Anhui Architecture Press* (2): 98–101.

Zhang, G.L. 2006. *The Numerical Simulation Research of the Single Bored Pile Vertical Capacity* Nanjing: Hohai University Press.

Civil Engineering and Urban Planning IV – Liu et al. (Eds)
© 2016 Taylor & Francis Group, London, ISBN 978-1-138-02903-3

The elastic mechanics equations of bi-curvature beam based on tensor theory

Jie-Min Liu
School of Science, Shenyang Jianzhu University, Shenyang, Liaoning, China

Zhi-Ying Zhang
School of Civil Engineering, Shenyang Jianzhu University, Shenyang, Liaoning, China

Qiu-Yu Wei
School of Science, Shenyang Jianzhu University, Shenyang, Liaoning, China

An-Guang Leng
Library, Shenyang Jianzhu University, Shenyang, Liaoning, China

ABSTRACT: Nonlinear elastic mechanics equations of bi-curvature beams, including curvatures-rotational angle equation, rotational angle-displacement equation, strain-displacement equation, and equilibrium equations are derived using tensor theory. These equations, established based on principle axes coordinate system of centroid, are clear in mechanical concept, concise in expression form, and provide a foundation for finite element analysis of large curvature and nonlinear special beams.

1 INTRODUCTION

A bi-curvature beam means a beam that has both curvature and twist ratio under initial configuration. The deformation theories of bi-curvature beams are more complex than those of straight beams. Special curved beams; such as circular, plane curved ones subjected to in-surface or out-surface forces were researched (Idström 2014; Kapania & Li 2003; Liu et al. 2013; Wu & Chiang 2011; Zeng 2010). In their works, some use natural coordinate system while the others use the coordinate system based on neutral axes. Thus, the equation forms of the same curved beam were different duo to difference of coordinate systems. Therefore, they are difficult to be application and widespread. Centroid principle axes coordinate system is clear in geometric concept and is defined easily even though for bi-curvature beams. In this paper, geometric equations, including curvatures-rotational angle equation, rotational angle-displacement equation, and strain-displacement equation, and equilibrium equations are set up based on principle axes coordinate system of centroid, using the tensor theory under plane normal assumption. These equations can be reduced to applying to various special curved beams.

2 THE ASSUMPTION OF DEFORMATION AND GEOMETRIC EXPRESSION OF BI-CURVATURE BEAMS

Tests show that the warping of cross-section of bi-curvature beam is not significant, even though under the condition of larger deformation. The normal of cross-section is approximately parallel to the centroid axis. In order to obtain geometric equation of bi-curvatures beams, an assumption of the bi-curvature beams deformation behavior is made as following: the cross-section, which is plane before deformation, maintains plane, and is still perpendicular to the axes after deformation. This assumption is called as plane perpendicular normal assumption.

The geometry description of a bi-curvature beam of curvature κ and twist ratio ν is shown in Figure 1. It is supposed that centroid principle axes coordinate system e_i and natural coordinate system $\boldsymbol{\tau nb}$ is consistent before deformation. Centroid principle axes basic vector $\boldsymbol{\tau}$, $\boldsymbol{n}$, and $\boldsymbol{b}$ is corresponding to $\boldsymbol{\tau}$, $\boldsymbol{n}$, and $\boldsymbol{b}$ of natural axes basic vector, respectively. Before deformation, the position vector of arbitrary centroid P on cross-section is $\boldsymbol{r}_0 = \boldsymbol{r}_0(x^1)$. Arbitrary point A on this cross-section is determined by position vector $\boldsymbol{r}$.

$$\boldsymbol{r} = \boldsymbol{r}_0(x^1) + x^2\boldsymbol{e}_2 + x^3\boldsymbol{e}_3 \tag{1}$$

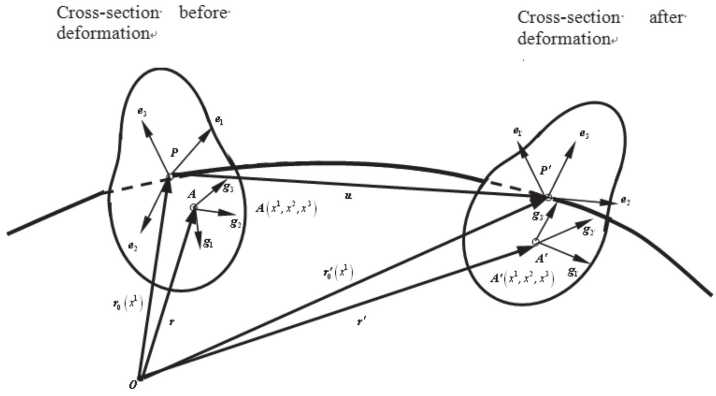

Figure 1. The geometry description of bi-curvature beam.

After deformation, point P moves to point p' and the displacement of point P is $u = u(x^1)$. The position vector of point p' is $\boldsymbol{r}_0' = \boldsymbol{r}_0 + \boldsymbol{u}$. The point A moves to point A', and the position vector point A' is expressed as

$$\begin{aligned}\boldsymbol{r}' &= \boldsymbol{r}_0' + x^2\boldsymbol{e}_{2'} + x^3\boldsymbol{e}_{3'} \\ &= \boldsymbol{r}_0(x^1) + u + x^2\boldsymbol{e}_{2'} + x^3\boldsymbol{e}_{3'} \\ &= \boldsymbol{r}_0(x^1) + u^i\boldsymbol{e}_i + x^2\boldsymbol{e}_{2'} + x^3\boldsymbol{e}_{3'}\end{aligned} \tag{2}$$

where, $\boldsymbol{e}_i'$ = centroid principle axes basic vector after deformation.

Due to deformation, the cross-section rotates around the principle axes of centroid the rotation angle of cross-section around x^i axis is θ^i (not shown in Fig. 1). Thus, $\boldsymbol{e}_{i'}$ is not consistent with natural axes basic vector after deflection.

According to the tensor theory

$$\boldsymbol{e}_1 = \boldsymbol{r}_{0,1}(x^1), \qquad \boldsymbol{e}_{1'} = \boldsymbol{r}_{0,1}' \tag{3}$$

According to the Frenet–Serret formula

$$\boldsymbol{e}_{i,1} = K_i^j\boldsymbol{e}_j, \qquad \boldsymbol{e}_{i',1} = K_{i'}^{j'}\boldsymbol{e}_{j'} \tag{4}$$

where

$$\begin{aligned}K_1^2 &= -K_2^1 = \kappa_1, \qquad K_1^3 = -K_3^1 = -\kappa_2 \\ K_2^3 &= -K_3^2 = \kappa_3, \qquad K_1^1 = K_1^1 = K_1^1 = 0\end{aligned} \tag{5}$$

$$\begin{aligned}K_{1'}^{2'} &= -K_{2'}^{1'} = \kappa_{1'}, \qquad K_{1'}^{3'} = -K_{3'}^{1'} = -\kappa_{2'} \\ K_{2'}^{3'} &= -K_{3'}^{2'} = \kappa_{3'}, \qquad K_{1'}^{1'} = -K_{2'}^{2'} = K_{3'}^{3'} = 0\end{aligned} \tag{6}$$

The principle curvatures of bi-curvature beams are defined as κ_i before deformation (i = 1, 2, 3) and as $\kappa_{i'}$ after deformation, respectively. κ_i and $\kappa_{i'}$ can be expressed as

$$\begin{aligned}&\kappa_1 = \upsilon, \ \kappa_2 = 0, \kappa_3 = \kappa \\ &\kappa_{1'} = \kappa_1 + \theta_{,1}^1, \kappa_{2'} = \kappa_2 + \theta_{,1}^2, \kappa_{3'} = \kappa_3 + \theta_{,1}^3\end{aligned} \tag{7}$$

The transformation relation of base vector $\boldsymbol{e}^i$ and $\boldsymbol{e}^{i'}$ are expressed as

$$\boldsymbol{e}^{i'} = T_{i'}^j\boldsymbol{e}_j \tag{8}$$

where, $T_{i'}^j$ is called as conversion tensor, and its components are shown as follows

$$T_{1'}^1 = \cos\theta^2\cos\theta^3 = 1$$

$$T_{2'}^2 = \sin\theta^1\sin\theta^2\sin\theta^3 + \cos\theta^1\cos\theta^3 = 1$$

$$T_{3'}^3 = \cos\theta^1\cos\theta^2 = 1$$

$$T_{1'}^2 = -T_{2'}^1 = -\left(\sin\theta^1\sin\theta^2\cos\theta^3 - \cos\theta^1\sin\theta^3\right) = \theta^3$$

$$\begin{aligned}T_{1'}^3 &= -T_{3'}^1 = -\left(\sin\theta^1\cos\theta^1\sin\theta^2\cos\theta^3 + \sin\theta^1\sin\theta^3\right) \\ &= -\theta^2\end{aligned}$$

$$T_{2'}^3 = -T_{3'}^2 = -\left(\cos\theta^1\sin\theta^2\sin\theta^3 - \sin\theta^1\cos\theta^3\right) = \theta^1$$

3 THE GEOMETRIC EQUATIONS (ROTATIONAL ANGLE-DISPLACEMENT, CURVATURE-ROTATIONAL ANGLE, AND STRAIN-DISPLACEMENT EQUATION) OF BI-CURVATURE BEAMS

According to the plane perpendicular normal assumption, we know

$$\boldsymbol{e}_{1'} \cdot \boldsymbol{e}_{2'} = 0, \qquad \boldsymbol{e}_{1'} \cdot \boldsymbol{e}_{3'} = 0 \tag{9}$$

Derivation of position vector $\boldsymbol{r}_0'$ to x^1 can be expressed as

$$\boldsymbol{e}_{1'} = \boldsymbol{r}'_{,1} = \boldsymbol{r}_{0,1} + \left(u^i_{,1} + K^i_{j'} u^j\right)\boldsymbol{e}_i \tag{10}$$

Substituting equations (8) and (10) into (9), we obtain

$$B^i T^i_2 = 0, \quad B^i T^i_3 = 0 \tag{11}$$

In which

$$B^1 = 1 + u^1_{,1} - \kappa_3 u^2 + \kappa_2 u^3 = 1 + u^1_{,1} - \kappa u^2$$

$$B^2 = u^2_{,1} + \kappa_3 u^1 - \kappa_1 u^3 = u^2_{,1} + \kappa u^1 - \upsilon u^3$$

$$B^3 = u^3_{,1} - \kappa_2 u^1 - \kappa_1 u^2 = u^3_{,1} - \upsilon u^2$$

Equations (11) are called as the equations of rotational angle-displacement of bi-curvature beam under large rotational angle and large displacement.

According to tensor theory, the covariant base $\boldsymbol{g}^i$ at point A and $\boldsymbol{g}^{i'}$ at point A' (see Fig. 1) can be expressed as

$$\boldsymbol{g}_i = \boldsymbol{r}_{,i}(x^j), \quad \boldsymbol{g}_{i'} = \boldsymbol{r}_{,i'}(x^{j'}) \tag{12}$$

Substituting Equations (1) and (2) into (17), we yield

$$\boldsymbol{g}_1 = \boldsymbol{e}_1 + (x^2 K^j_2 + x^3 K^j_3)\boldsymbol{e}_j, \quad \boldsymbol{g}_2 = \boldsymbol{e}_2, \quad \boldsymbol{g}_3 = \boldsymbol{e}_3 \tag{13}$$

$$\boldsymbol{g}_{1'} = \boldsymbol{u} = \boldsymbol{e}_1 + \alpha^i \boldsymbol{e}_i, \quad \boldsymbol{g}_{2'} = T^i_2 \boldsymbol{e}_i, \quad \boldsymbol{g}_{3'} = T^i_2 \boldsymbol{e}_i \tag{14}$$

$$\alpha^1 = B^1 + \beta^1_{,1} + \beta^j K^1_j - 1 \tag{15a}$$

$$\alpha^j = B^i + \beta^i_{,1} + \beta^j K^i_j \ (i = 2,3) \tag{15b}$$

$$\beta = x^2 T^i_2 + x^3 T^i_3 \tag{15c}$$

The metric tensor $\boldsymbol{g}_{ij}$ and $\boldsymbol{g}_{i'j'}$ are defined as respectively

$$g_{ij} = \boldsymbol{g}_i \cdot \boldsymbol{g}_j \tag{16a}$$

$$g_{i'j'} = \boldsymbol{g}_{i'} \cdot \boldsymbol{g}_{j'} \tag{16b}$$

The metric tensor matrix $\boldsymbol{G}$ and $\boldsymbol{G}'$ can be expressed as

$$\boldsymbol{G} = \begin{bmatrix} g_{11} & g_{12} & g_{13} \\ & g_{22} & g_{23} \\ \text{symm.} & & g_{33} \end{bmatrix} = \begin{bmatrix} g + (x^3\kappa_1)(x^3\kappa_1) + (x^2\kappa_1)(x^2\kappa_1) & -x^3\kappa_1 & x^2\kappa_1 \\ & 1 & 0 \\ \text{symm.} & & 1 \end{bmatrix} \tag{17}$$

$$\boldsymbol{G}' = \begin{bmatrix} g_{1'1'} & g_{1'2'} & g_{1'3'} \\ & g_{2'2'} & g_{2'3'} \\ \textit{symm.} & & g_{3'3'} \end{bmatrix} = \begin{bmatrix} 1 + 2\alpha^1 + \alpha^i\alpha^i & T^1_2 + \alpha^i T^i_2 & T^1_3 + \alpha^i T^i_3 \\ & 1 & 0 \\ & \textit{symm.} & 1 \end{bmatrix} \tag{18}$$

In which, $g = (1 - x^2\kappa_3 + x^3\kappa_2)^2 = (1 - x^2\kappa)^2$

Green-strain tensor can be definite as

$$\boldsymbol{E} = E_{ij}\boldsymbol{g}^i\boldsymbol{g}^j = \tfrac{1}{2}\left(g_{i'j'} - g_{ij}\right)\boldsymbol{g}^i\boldsymbol{g}^j = \varepsilon^{ij}\boldsymbol{e}_i\boldsymbol{e}_j \tag{19}$$

ε^{ij} is the strain tensor based on centroid principle axes. Due to $\boldsymbol{e}^i$ being orthogonal unit base vector, the covariant base vector $\boldsymbol{e}_i$ and contra-variant base vector $\boldsymbol{e}^i$ are equal, namely, $\boldsymbol{e}_i = \boldsymbol{e}^i$. Thus, $\varepsilon^{ij} = \varepsilon_{ij}$.

E_{ij} can be expressed as

$$E_{11} = \frac{1}{2}B^i B^i - \beta^i B^i_{,1} + \frac{1}{2}\beta^i_{,1}\beta^i_{,1} + \frac{1}{2}\beta^j\kappa^j_j\beta^k\kappa^j_k + \beta^j\kappa^j_j\beta^i_{,1} - \frac{1}{2}g - \frac{1}{2}(x^3\kappa_1)^2 - \frac{1}{2}(x^2\kappa_1)(x^3\kappa_1) \tag{20a}$$

$$2E_{12} = -x^2\theta^1_{,1} + x^3\theta^3_{,1}\theta^2 - x^3 T^i_1\kappa_i + x^3\kappa_1 \tag{20b}$$

$$2E_{13} = x^2\theta^1_{,1} - x^3\theta^3_{,1}\theta^2 + x^3 T^i_1\kappa_i - x^3\kappa_1 \tag{20c}$$

Since

$$\boldsymbol{e}_i\boldsymbol{e}_j = Q_{ik}Q_{jl}\boldsymbol{g}^k\boldsymbol{g}^l \tag{21}$$

$$Q_{ik} = \boldsymbol{e}_i \cdot \boldsymbol{g}_k \tag{22}$$

Substitution of Equations (13) to (22) leads to

$$Q_{11} = 1 - x^2\kappa_3 + x^3\kappa_2 = 0, Q_{22} = Q_{33} = 1 \tag{23a}$$

$$Q_{21} = -x^3\kappa_1, Q_{31} = x^2\kappa_1 \tag{23b}$$

$$Q_{12} = Q_{13} = Q_{23} = Q_{32} = 0 \tag{23c}$$

Thus,

$$\varepsilon^{ij}Q_{ik}Q_{jl} = E_{kl} \tag{24}$$

From Equation (24), the relation between ε_{ij} and E_{ij} can be got as

$$\begin{aligned} g\varepsilon_{11} &= E_{11} + 2x^3\kappa_1 E_{12} - 2x^2\kappa_1 E_{13} \\ \sqrt{g}\varepsilon_{12} &= \sqrt{g}\varepsilon_{21} = E_{12} \\ \sqrt{g}\varepsilon_{13} &= \sqrt{g}\varepsilon_{31} = E_{13} \end{aligned} \tag{25a}$$

$$\varepsilon_{22} = \varepsilon_{33} = \varepsilon_{23} = \varepsilon_{32} = 0 \tag{25b}$$

4 REDUCTION OF THE GEOMETRIC EQUATIONS

In the case of small rotational range, $\cos\theta^i = 1$, $\sin\theta^i = \theta^i$. $T_{i'}^{j}$ in Equation (8) is reduced as

$$\begin{aligned} &T_{1'}^{1} = T_{2'}^{2} = T_{3'}^{3} = 1, \quad T_{1'}^{2} = -T_{2'}^{1} = \theta^3 \\ &T_{1'}^{3} = -T_{3'}^{1} = -\theta^2, \quad T_{2'}^{3} = -T_{3'}^{2} = \theta^1 \end{aligned} \tag{26}$$

Equation (8) is reduced as

$$-B^1\theta^3 - B^3\theta^1 + B^2 = 0,\ B^1\theta^2 - B^2\theta^1 + B^3 = 0 \tag{27}$$

Equation (31) is always valid for arbitrary θ^1, therefore,

$$\theta^3 = B^2/B^1,\ \theta^2 = -B^3/B_1 \tag{28}$$

Equation (32) is called as the equations of rotational angle-displacement of bi-curvature beam under small rotational angle and large displacement.

For a plane curved beam, $\kappa_1 = 0, \kappa_3 = \kappa$, Equation (25a) is reduced as under small curvature and small deformation

$$\varepsilon_{11} = u_{,1}^1 - \frac{x^2\kappa_{,1}}{1-\kappa x^2}u^1 - \frac{\kappa}{1-\kappa x^2}u^2 - \frac{x^2}{1-\kappa x^2}u_{,11}^2 \tag{29}$$

For a circular curved beam, $\kappa_{,1} = 0$, Equation (28) is reduced as

$$\varepsilon_{11} = u_{,1}^1 - \frac{\kappa u^2}{1-\kappa x^2} - \frac{x^2}{1-\kappa x^2}u_{,11}^2 \tag{30}$$

For a plane straight beam, $\kappa = 0$, Equation (29) is reduced as

$$\varepsilon_{11} = u_{,1}^1 - x^2 u_{,11}^2 \tag{31}$$

5 EQUILIBRIUM EQUATIONS OF BI-CURVATURE BEAMS

The relation between internal intensity $\boldsymbol{p}$ and internal principal vector F, internal principal moment $\boldsymbol{M}$ are

$$\boldsymbol{F} = \boldsymbol{F}(x^1) = \int_A \boldsymbol{p}\cdot d\boldsymbol{A} = \int_A \boldsymbol{p}\cdot\boldsymbol{e}_1 dx^2dx^3 \tag{32}$$

$$\begin{aligned} \boldsymbol{M} &= \boldsymbol{M}(x^1) = \int_A \boldsymbol{r}\times\boldsymbol{p}dA \\ &= \int_A \left(x^2\boldsymbol{e}_2 + x^3\boldsymbol{e}_3\right)\times\boldsymbol{p}dA \end{aligned} \tag{33}$$

From Chuchy theory

$$\boldsymbol{p} = \boldsymbol{\sigma}\cdot\boldsymbol{e}_1 = \sigma_{ij}\boldsymbol{e}^i\boldsymbol{e}^j\cdot\boldsymbol{e}_1 = \sigma_{ij}\boldsymbol{e}^i\delta_1^j = \sigma_{i1}\boldsymbol{e}^i \tag{34}$$

Substituting Equations (3) into (1) and (2), we have

$$\boldsymbol{F}_i = \int_A \sigma_{i1}dx^2dx^3 \ (\boldsymbol{i} = 1, 2, 3) \tag{35}$$

$$M_1 = \int_A x^2\sigma_{31}dx^2dx^3 - \int_A x^3\sigma_{21}dx^2dx^3 \tag{36}$$

$$M_2 = \int_A x^3\sigma_{11}dx^2dx^3 \tag{37}$$

$$M_3 = -\int_A x^2\sigma_{11}dx^2dx^3 \tag{38}$$

Figure 2 shows bi-curvature beam infinitesimal portion subjected to external force and internal forces, and forces and force boundary condition of bi-curvature beam portion. $q = q(x^1)$ external force intensity and $\boldsymbol{m} = (x^1)$ is external moment intensity.

From equilibrium condition of the infinitesimal portion of bi-curvature beam, yield

$$\boldsymbol{F}_{,1} + \boldsymbol{q} = 0 \tag{39}$$

$$\boldsymbol{M}_{,1} + \boldsymbol{m} + \boldsymbol{F}\times\boldsymbol{e}_1 = 0 \tag{40}$$

Since

$$\begin{aligned} \boldsymbol{F}_{,1} &= (F_i\boldsymbol{e}^i)_{,1} = F_{i,1}\boldsymbol{e}^i + F_j\boldsymbol{e}^j{}_{,1} \\ &= F_{i,1}\boldsymbol{e}^i + F_jK_j^i\boldsymbol{e}_i = (F_{i,1} + F_jK_j^i)\boldsymbol{e}^i \end{aligned} \tag{41}$$

$$\begin{aligned} \boldsymbol{M}_{,1} &= (M_i\boldsymbol{e}^i)_{,1} = M_{i,1}\boldsymbol{e}^i + M_j\boldsymbol{e}^j{}_{,1} \\ &= M_{i,1}\boldsymbol{e}^i + M_jK_j^i\boldsymbol{e}_i = (M_{i,1} + M_jK_j^i)\boldsymbol{e}^i \end{aligned} \tag{42}$$

$$\boldsymbol{F}\times\boldsymbol{e}_1 = F^k\boldsymbol{e}_k\times\boldsymbol{e}_1 = F^k\boldsymbol{\varepsilon}_{k1i}\boldsymbol{e}^i \tag{43}$$

Therefore, substituting Equations (41)–(43) into (39) and (40), we obtain

$$F_{1,1} - F_2\kappa_3 + F_3\kappa_2 + q_1 = 0 \tag{44a}$$

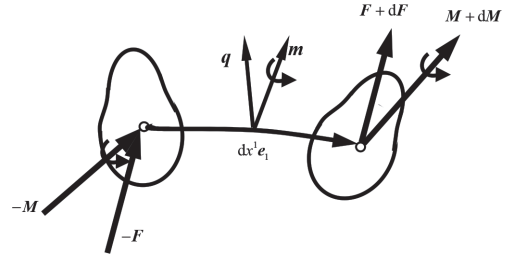

Figure 2. Infinitesimal portion subjected to external and internal forces.

$$M_{1,1} - M_2\kappa_3 + M_3\kappa_2 + m_1 = 0 \quad (44b)$$

$$F_{2,1} - F_1\kappa_3 + F_3\kappa_1 + q_2 = 0 \quad (44c)$$

$$M_{2,1} - M_1\kappa_3 + M_3\kappa_1 + F_3 + m_2 = 0 \quad (44d)$$

$$F_{3,1} - F_1\kappa_2 + F_2\kappa_1 + q_3 = 0 \quad (44e)$$

$$M_{3,1} - M_1\kappa_2 + M_2\kappa_1 - F_2 + m_3 = 0 \quad (44f)$$

6 CONCLUSION

Nonlinear elastic mechanics equations of bi-curvature beams are derived using tensor theory. These equations, including curvatures-rotational angle equation, rotational angle-displacement equation strain-displacement equation, and equilibrium equation are set up based on principle axes coordinate system of centroid. All of these explicit equations are strict in mathematics, clear in concept, and concise in form. Therefore, they can be used to conduct analysis of large curvature, and geometric nonlinear of bi-curvature beams.

REFERENCES

Idström, P. 2014. On the equations of motion for curved slender beams using tubular coordinates. *Mathematics Mathematics and Mechanics of Solids* 19(7): 758–804.

Kapania, R.K. & Li, J. 2003. On a geometrically exact curved/twisted beam theory under cross-section assumption. *Computational Mechanics* 30(8): 428–443.

Liu, T.L., Zhao, Y. & Wu, J.G. 2013. Explicit element stiffness matrix for curved beam with in-plane deformation. *Journal of Shenyang Jianzhu University* 29(6): 983–988.

Wu, J.S. & Chiang, L.K. 2011. Out-of-plane free vibration analysis of a horizontally circular curved beam carrying arbitrary sets of concentrated elements. *Journal of Structural Engineering* 137(2): 220–241.

Zeng, S., Chen, S.F., Qu, T. & Wang, H.D. 2010. Elasticity equations for spatial curved beams with large displacement and small rotation. *Engineering Mechanics* 27(12): 14–20.

This page intentionally left blank

Civil Engineering and Urban Planning IV – Liu et al. (Eds)
© 2016 Taylor & Francis Group, London, ISBN 978-1-138-02903-3

Analysis on the influence of buckling performance of the U-stiffened plate on deck surfacing and wheel load

Rui-Peng Zhao
China Railway First Survey and Design Institute Group Co. Ltd., Xi'an City, Shaanxi, China

ABSTRACT: In order to investigate the buckling performance of the U-rib stiffened plate under compression, the impact of the elastic modulus and thickness of deck surfacing and wheel load on the buckling performance of U-rib stiffened plates was studied by the finite element method. The results indicate that the changes in the elastic modulus of epoxy asphalt mixture were within the range of 500 MPa to 4500 MPa, the changes in the critical buckling stress of the stiffening plate were reduced by 2.77%, the changes in the thickness of the surfacing layer were within the range of 4 cm to 8 cm, and the changes in the critical buckling stress of the stiffening plate were reduced by 1.05%. Considering the out-of-plane wheel load, the critical buckling stress of the stiffening plate was reduced by 0.3%.

1 INTRODUCTION

Steel box girder is widely applied in large-span cable-stayed bridges and suspension bridges due to its advantages such as torsional and lateral bending stiffness (Hughes & Ma 1996), good integrity, homogeneity of the material, high strength, lightweight and highly developed in production in the factory (Thompson & Lewis 1972). As a major component of the top and bottom plates in the steel box girder structure, the application of the U-stiffened plate not only improves the bearing capacity of the whole girder, but also enhances the local bending stiffness and the stability under compression of the top and bottom plates (Graves Smith & Sridharan 1978).

Scholars from around the world have done research on the stability of the U-stiffened plate under elasticity and inelasticity conditions (Osama 1997; Osama 1998). The stability of the bridge deck structure under the service condition is also affected by the pavement and wheel load of the traffic (Wu et al. 2006). In order to provide a theoretical guidance and reference, this article demonstrated the FEM model by considering the stiffened plate and the pavement to analyze the effect of the pavement and wheel load on U-stiffened plates (Di et al. 2009; Li & Shao 2008).

2 EFFECT OF THE PAVEMENT ON THE ELASTIC STABILITY OF THE STIFFENED PLATE

2.1 *Introduction of the pavement on the steel box girder*

Several kinds of pavement commonly used on the steel box girder are placement asphalt concrete, SMA of modified asphalt and epoxy asphalt. Until now, in our country, epoxy asphalt pavement is used in most of the large-span bridges such as Sutong bridge, Runyang bridge, 3rd Nanjing Changjiang river bridge and Hangzhou Bay bridge. A large number of engineering applications and experiments have proved that epoxy asphalt is with high strength and ductility, high temperature stability and low temperature anti-cracking performance, anti-fatigue performance, water stability and chemical corrosion resistance.

In engineering practices, two important factors are considered to design the gradation of aggregates, namely skid resistance and anti-fatigue performance. The former factor needs relatively coarse grading to increase the roughness of the road surface. And the latter factor needs more fine grading to prolong the service lifespan of the pavement. Due to this uncertainty of gradation, the elasticity module of the epoxy asphalt pavement is dispersed.

2.2 *Effect of elasticity module of epoxy asphalt mixture on bridge deck buckling*

Taking north shipping channel bridge of Hangzhou Bay Bridge as an example, the effect of the elasticity module of epoxy asphalt mixture on the critical buckling stress of the closed-section stiffened plate h is analyzed. The FEM model is built under assumptions, which are as follows: 1. the elastic material of the pavement is homogeneous, continuous and isotropic, 2. the pavement is totally adhesive to the deck plate to bear the load, and the deck plate and pavement are considered as a whole entity, 3. the self-weight of the pavement and the

stiffened plate are ignored. The elasticity module of the pavement is set at 500 MPa, 1500 MPa, 2500 MPa, 3500 MPa and 4500 MPa, respectively. The pavement design of the north shipping channel bridge is shown in Figure 1.

U-stiffened plate FEM model was built by ANSYS 12.0 based on the structure parameter of the typical girder segment of the north shipping channel bridge. Every model contains six U-shape stiffeners, with a bridge deck plate, which are simulated by the Shell63 element. The pavement part is simulated by the Solid45 element. The pavement and the deck plate are connected by sharing nodes. The boundary condition is simply supported at four edges. The model is shown in Figure 2.

Critical buckling stress of the pavement with different elasticity modules is listed in Table 1 and Figure 3.

As shown in Table 1 and Figure 3, when the elasticity module of the pavement material is 500 MPa, the critical buckling stress of the U-stiffened plate increases by 1.27%, and the when the elasticity module increases from 500 MPa to 4500 MPa, the critical buckling stress of the U-stiffened plate increases by 2.77%. Therefore, considering the effect of the pavement makes no remarkable improvement to the critical buckling stress of the structure. And when the elasticity module of the pavement is increased, the critical buckling stress is hardly increased.

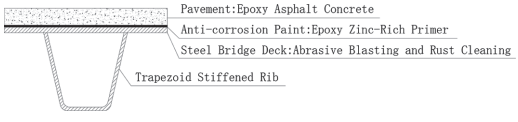

Figure 1. Pavement of the north shipping channel bridge.

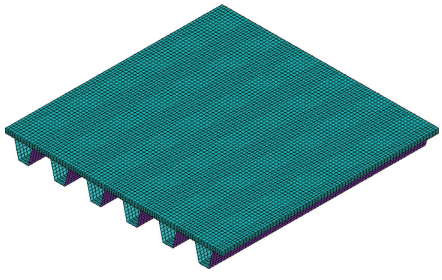

Figure 2. FEM model of the pavement.

Table 1. Critical buckling stress of the pavement with different elasticity modules (MPa).

Elasticity module	0	500	1500	2500	3500	4500
Critical buckling stress	280.7	284.3	287.9	289.6	290.9	292.1

*When the elasticity module is 0, it is equal to no pavement.

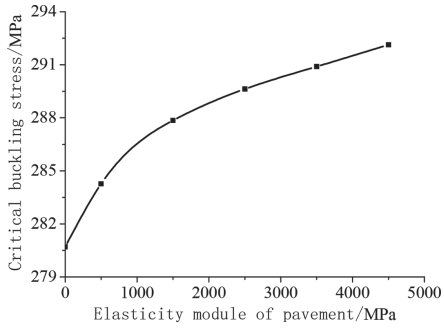

Figure 3. Curve of relation between the elasticity module and the critical buckling stress.

2.3 *The effect of the thickness of the pavement on the buckling of the deck plate*

Factors such as local temperature, precipitation, humidity of air and traffic condition have to be taken into consideration to design the pavement of the steel bridge deck. It needs to choose proper material and thickness based on the local condition. Nowadays, different countries often prefer different pavement thicknesses by their own experience. For example, the total thickness of the pavement in Britain is 4 cm, and in the United States and France, it is 5 cm. In our country, the form of the steel bridge deck pavement has a wide range, which is mainly single layer of double layer structure. In this section, thicknesses of epoxy asphalt ranging from 4 cm to 8 cm are calculated. The elasticity module is considered as 2500 MPa. The Poisson ratio is considered as 0.25. The critical buckling stress result is summarized in Table 2 and Figure 4.

As shown in Table 2 and Figure 4, when the elasticity module of the pavement is considered as 2500 MPa, the critical buckling stress of the stiffened plate increases by 1.05% as the thickness of the pavement increases from 4 cm to 8 cm. Therefore, the variation in the thickness of the pavement improves the critical buckling stress to a small extent when the material property is determined.

2.4 *Effect of wheel load on the elastic stability of the stiffened plate*

In this section, the effect of the pavement is ignored because it has a little effect on the critical buckling stress of the stiffened plate. In order to simulate the deformation of the deck plate under wheel

Table 2. Critical buckling stress of the pavement with different elasticity modules (MPa).

Thickness of pavement (cm)	0	4	5	6	7	8
Critical buckling stress (MPa)	280.7	287.5	288.8	289.6	290.1	290.5

*When the elasticity module is 0, it is equal to no pavement.

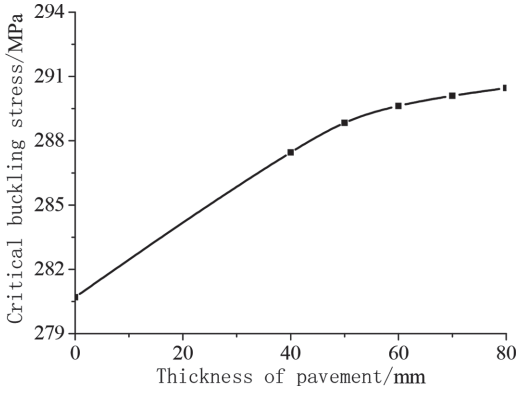

Figure 4. Curve of relation between the thickness of the pavement and the critical buckling stress.

load precisely, a FEM model is used with four diaphragms and six U-shape stiffeners. The model is built with shell element under the continuous boundary condition, as shown in Figure 5.

The tires of the vehicle become deformed when it is loaded on the deck plate, the contact area between the tire and the deck plate is the loading area. In this article, the wheel load is simplified as the typical back shaft load in the General Code for Design of Highway Bridges and Culverts (JTG D60-2004), which is 2×140 kN, ignoring the impact factor and the wheel load factor. The contact area of the wheels and deck plate is according to Table 4.3.1–2 in Chapter 4.3 of the design code, which is 0.6 m in width and 0.2 m in length. The wheel load is added to the mid-span of the model with a uniform distribution.

To analyze the effect of the lateral loading position of wheels on the local stress distribution of the stiffened plate, loading position 3 is chosen based on the location of the U-shape stiffener, as shown in Figure 6. Loading position 1 is among the two adjacent U-shape stiffeners, loading position 2 is at one edge of the U-shape stiffener, and loading position 3 is at the center line of the stiffener.

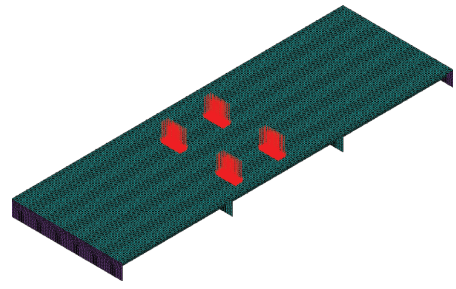

Figure 5. 3 span continuous U-stiffened plate FEM model.

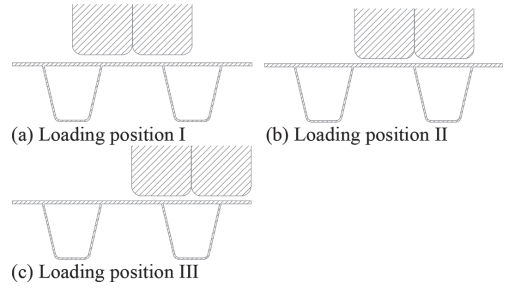

Figure 6. Loading position of wheels.

Table 3. Critical buckling stress of the U-stiffened plate under different wheel loads (MPa).

Loading position	No wheel load	Under wheel load		
		I	II	III
Stress	608.7	606.8	606.6	606.4

The critical stress of the U-stiffened plate under axial compression and different wheel loads are listed in Table 3.

As shown in Table 3, when considering the wheel load, the critical buckling stress of the stiffened plate decreases only by 0.3% and the change in the lateral loading position has no effect on the critical buckling stress.

3 CONCLUSION

Characteristics of the pavement on the steel box girder were introduced in this article. Taking north shipping channel bridge of Hangzhou Bay Bridge as an example, the effects of the elasticity module and thickness of the epoxy asphalt pavement on the critical buckling stress of the U-stiffened plate are analyzed. The result indicated that the increase

in the elasticity module and thickness of the epoxy asphalt pavement improves the critical buckling stress by less than 3%.

Considering the wheel load, the buckling performance of the U-stiffened plate under the axial compression and out-of-plane bending load is studied. The result from the analysis indicated that the wheel load only decreased the critical buckling stress of the U-stiffened plate by 0.3%, and the lateral loading position had a little effect on the buckling performance of the U-stiffened plate.

REFERENCES

Di, J., Zhou, X.H. & Lu, Z.D. 2009. Experiment on ultimate bearing capacity of U-stiffened plate of orthotropic steel box girder. *China Journal of Highway and Transport* 22(2): 59–64.

Graves Smith, T.R. & Sridharan, S. 1978. A finite strip method for the post-locally-buckled analysis of plate structures. *International Journal of Mechanical Sciences* 2011: 833–842.

Hughes, O.F. & Ma, M. 1996. Inelastic analysis of panel collapse by stiffener buckling. *Computer & Structures* 61(1): 107–117.

Li, L.F. & Shao, X.D. 2008. Theoretical analysis on stability property of U-rib stiffened plate of flat steel box girder. *Journal of Highway and Transportation Research and Development* 25(3): 88–92.

Osama, K.B. 1997. Analysis of stiffened plates under lateral loading using Sequential Quadratic Programming (SQP). *Computers & Structures* 62(1): 63–80.

Osama, K.B. 1998. A contribution to the stability of stiffened plates under uniform compression. *Computers and Structures* 66(5): 535–570.

Thompson, J.M.T. & Lewis, G.M. 1972. On the optimun design of thin-walled compression members. *J. Mech. Phys. Solids* 20(1): 101–109.

Wu, C., Zeng, M.G. & Feng, L.Y. 2006. Local part model test for ultimate bearing capacity of orthotropic panel of Sutong Bridge. *Bridge Construction* (2): 21–24.

Transportation engineering

This page intentionally left blank

Civil Engineering and Urban Planning IV – Liu et al. (Eds)
© 2016 Taylor & Francis Group, London, ISBN 978-1-138-02903-3

A new method for positioning Variable Message Signs

Yi-Rong Guo, Xiao-Ming Wang, Min Wang & Hong Zhang
College of Electrical and Information Engineering, Lanzhou University of Technology, Lanzhou, China

ABSTRACT: In order to distribute Variable Message Signs (VMS) in urban areas properly, based on actual guidance effect maximization, a new method for positioning the VMS is proposed. This method makes improvements in the original layout optimization model. Through the analysis of the complex components of VMS guidance effects, this method introduces repeated VMS traffic flow guidance effect and wasted VMS traffic flow guidance effect. This method also defines guidance coverage rate and guidance effect loss rate. At last, the greedy algorithm was used to solve the VMS layout optimization function. Through a road network example of 15 nodes, the model is proved to be simple and efficient. When seven VMS are collocated in the net, the guidance coverage rate is 0.75, and the guidance effect loss rate reaches 0.04; in Mei model 1, the guidance coverage rate is 0.56, and the guidance effect loss rate reaches 0.22; so it is an optimal configuration. Hence, it is more suitable for the needs of actual traffic flow guidance.

1 INTRODUCTION

1.1 *VMS positioning*

VMS is one of the effective ways of solving the problem of dynamic distribution of traffic flow. VMS, which is located in key road sections, can provide accurate information to travelers in real-time, so the travelers can adjust to the optimal travel path. Then the city traffic congestion is effectively alleviated and work efficiency is improved.

But compared with the continuous development of the traffic guidance system theory, the VMS positioning research is relatively backward, and the perfect VMS positioning theory system has not yet been created. The method of the specific working of VMS positioning is mostly experience dependent at home and abroad. Therefore, comprehensively using the relevant theories and methods according to the actual network situation for reasonable VMS positioning to accomplish maximum guidance effect, reduce unnecessary investment, and improve city traffic jam situations is of far-reaching significance (Mei et al. 2007).

1.2 *Research situation*

At present, at home and abroad, VMS research is mainly focused on the VMS positioning models, VMS characteristic analyses (Hou et al. 2012; Wen 2013), VMS design (Wang et al. 2014), and the available literature (Fan et al. 2014). The main VMS positioning models are as follows: cost minimization model (Wang & Wu 2013), VMS guidance effect maximization model (Niu et al. 2010), completely marginal model, grey decision model, fuzzy decision model (Lee et al. 2011), double level programming model (Song & Level 2013; Wei et al. 2013), cell transmission model (Doan et al. 2012; Sumalee et al. 2011).

Based on the existing VMS guidance effect maximization model, Niu's work puts forth a fuzzy-constraint based VMS programming model. The model makes improvements on the original attenuation factor, increases the constraints of benefit-cost, and introduces the fuzzy operator in the constraints; through the discussion of the random error term, providing road information, the study of Xu et al. (2013) determines traffic flow distribution. But none gave a specific calculation model.

For rational city traffic flow guidance based on the dual restriction of increase in the guidance coverage rate and decrease in the guidance effect loss rate, Mei's study proposes an optimization information board positioning method. On the premise of pursuit of maximum guided traffic flow, the author establishes and optimizes an information board layout function. (This paper is denoted as model 1)

$$\max Z = \sum_{j \in J} \sum_{i \in I} q_{ij} \delta_{ij} \tag{1}$$

In the above function, Z is the total traffic flow guided by VMS; q_{ij} is the traffic flow through the path i to the traffic destination j; δ_{ij} are the variables from 0 to 1.

But in the literature above, the analysis of regional VMS traffic guidance system is too

simple. For the same traffic flow, releasing the same information repeatedly cannot increase the understanding of guidance information; instead, repeated guidance will produce interference to the traveler. For the traffic flow to reach the destination in one or two intersections, it will have a waste effect to release guidance information. Therefore, based on the above issues, this paper analyses complex information demands of the traffic flow in a known regional network and traffic demand distribution area, puts forward a new VMS positioning method, and designs a greedy algorithm to optimize and solve the positioning function.

2 VMS POSITIONING METHOD

2.1 *Problem analysis*

Using Figure 1 to explain the guidance rules, from intersection 1 to intersection 8, the traffic demands are denoted by D_1~D_6 and VMS by S_1~S_6.

Because the information that the board can display is limited, let us suppose that each VMS can only display the traffic flow information in the distance of two intersections ahead. For example, the VMS S_1 can only display the information of the demand nodes D_1, D_2; the road section 2–3, 3–4; and the intersection 2, 3. It cannot display the nodes D_3 and intersection 4. The intersection of 4 can only be displayed by VMS S_2 and S_3.

If the same information is released repeatedly to the same traffic flow, the guidance effect is 0. On the way to the destination, if the same driver sees the same guidance information twice or more, he/she will ignore the interference caused by that redundant information. Hence, the same guidance information is invalid.

For traffic flow that will arrive at the destination in one or two intersections, there exists wasted guidance effect. For example, for the traffic flow to the destination D_1, the information of D_1 on VMS S_2 is invalid because the driver is near the destination. It is too near to select another route.

For the same traffic flow, different traffic information on a different VMS is valid. For the traffic flow to D_6, if VMS S_2 and S_4 all exist at the same time, the guidance effects they produce are all valid due to their display of different guidance information.

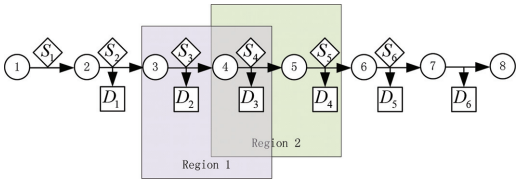

Figure 1. An example of VMS positioning.

Then, the optimization problem of VMS positioning, in the case of limited resources, is to select the appropriate combination of VMS setting and road section in the area to enable the VMS system to release as much guidance information as possible to the traffic drivers.

2.2 *The optimization model*

According to the analysis above, we improved the original information efficiency maximization model (model 1).

2.2.1 *The VMS guidance effect in theory*

The number of traffic OD paths in a regional is l; the number of all road section is m; the path is expressed as w_1, w_2, … w_i, … w_l, in which $w_i = (e_i^1, e_i^2, \ldots e_i^j, \ldots, e_i^m)$.

$$e_i^j = \begin{cases} 0 & j \text{ road section is not on } i \text{ path} \\ 1 & j \text{ road section is on } i \text{ path} \end{cases}$$

Set $q(w_i)$ as the traffic flow on the path w_i, then we can have the traffic flow matrix.

$$Q = \begin{pmatrix} q(w_1^1) & \ldots & q(w_1^j) & \ldots & q(w_1^m) \\ & & \ldots & & \\ q(w_i^1) & \ldots & q(w_i^j) & \ldots & q(w_i^m) \\ & & \ldots & & \\ q(w_l^1) & \ldots & q(w_l^j) & \ldots & q(w_l^m) \end{pmatrix}$$

The traffic flow of the road section j is the sum of the column j in traffic flow matrix, and the formula is

$$q(w^j) = \sum_{k=1}^{l} q(w_k^j) \tag{2}$$

In the region, there are m road sections that can set VMS. When the VMS number is n, the setting has to be $n \le m$ because setting to 2 and above VMS in the same road section is meaningless. Therefore, according to the analysis of the guidance rule in section 2.1, the total guidance effect in theory is

$$Z_{theory} = 2 \times \sum_{j=1}^{m} q(w^j)\delta_j, \ \sum_{j=1}^{m} \delta_j = n.$$

$$\delta_j = \begin{cases} 0 & VMS \text{ is not set on road section j} \\ 1 & VMS \text{ is set on road section j} \end{cases} \tag{3}$$

2.2.2 *The effect of repetitive VMS traffic flow guidance*

In actual traffic operation, the same information is released to a portion of the vehicles on the way to the destination in different road sections. This kind of guidance information is repeated, which will produce the repeated VMS traffic flow guidance effect.

As shown in Figure 1, concerning the released information on the S_2, S_3, the information on S_2 is region 1, and the information on S_3 is region 2. They all release the information of intersection 4 and traffic demand D_3. The traffic flow which will go through the road sections 2–3 and 3–4 are both guided by S_2 and S_3, named as $q(w(2\text{-}3\text{-}4))$. For this part of the traffic flow, the information of intersection 4 and traffic demand D_3 is released repeatedly, which in quantity is half of the guidance effect of the second VMS. The repetetive VMS traffic flow guidance effect is $Z_{\text{repeated}} = q(w(2\text{-}3\text{-}4))$.

Therefore, when the number of VMS is n, lets assume the selected road sections to set are w_{k1}, w_{k2}, … w_{kn}. For the two arbitrary road sections, assume the start and end intersections as (P_s^{start}, P_s^{end}), (P_t^{start}, P_t^{end}), respectively. If $(P_t^{start} = P_s^{end})$, or $(P_s^{start} = P_t^{end})$, then the traffic flow $q(w(P_t^{start} - P_s^{endt} - P_t^{end}))$ or $q(w(P_t^{start} - P_t^{endt} - P_s^{end}))$ is the repeated guided. Then, the repeated VMS traffic flow guidance effect is $Z_{repreated} = q(w(P_t^{start} - P_s^{endt} - P_t^{end}))$, or $Z_{repreated} = q(w(P_t^{start} - P_t^{endt} - P_s^{end}))$.

2.2.3 *Wasted VMS traffic flow guidance effect*

In the actual traffic system, when a part of the vehicle will arrive at the destination in one or two intersections, it will produce a wasted VMS traffic flow guidance effect.

As in Figure 1, if the guidance information is released on VMS S_4, then the S_4 will not produce any effect on the traffic flow to D_3, so the wasted guidance effect is $2 \times q(w(4\text{-}D_3))$. This kind of wasted effect is called first degree waste guidance effect.

If the guidance information is released on VMS S_3, then S_3 will produce a wasted guidance effect of $q(w(3\text{-}4\text{-}D_3))$ on the traffic flow D_3 because only one road section's information is necessary ahead. This kind of the wasted effect is called second degree waste guidance effect.

Therefore, when the number of VMS is n, lets assume the selected road sections to set are w_{k1}, w_{k2},... w_{kn}. For the arbitrary road section w_{ks}, assume that the start and end intersections are (P_s^{start}, P_s^{end}), respectively. If P_s^{end} is just the absorption node, then VMS will produce first degree waste effect. If P_s^{end} is adjacent to an absorption node P_t, and the traffic flow that through the nodes (P_s^{start}, P_s^{end}), P_t is $q(w(P_s^{start} - P_s^{end} - P_t))$, then the VMS will produce second degree waste guidance effect of $Z_{waste} = q(w(P_s^{start} - P_s^{end} - P_t))$.

2.2.4 *VMS guidance effect in reality*

Through the analysis above, the VMS guidance effect in reality is $Z_{reallity} = Z_{theory} - Z_{repeated} - Z_{waste}$.

The model is to find suitable road section combinations to get max $Z_{reality}$.

2.3 *The optimization step of the greedy algorithm*

The simple combination optimization problem can be solved by enumeration method. But with the expansion of the problem, the search space increases rapidly, and the solving efficiency is very low. For m road sections and n VMS problems, there are A_m^n kinds of combinations. While the city's road network is complex, the number of road sections is very large, so it is complex to solve the problem of VMS positioning. Then it is necessary to find an optimization algorithm to reduce the complexity.

Using the greedy algorithm, the steps to find the optimal combination of n VMS are as follows:

Step 1. To calculate the path flow and road section flow: we use the regional OD to distribute the traffic flow in paths, obtain the traffic flow matrix, and then obtain the traffic flow of the road sections.

Step 2. To sort the road section traffic flow in big to small order $w_{c1}^0, w_{c2}^0, \ldots, w_{cm}^0$.

Step 3. The method of the first VMS set: $Z_{theory}(w_{c1})$, $Z_{theory}(w_{c2})$, … $Z_{theory}(w_{cm})$, is the decreasing sequence. Calculate $Z_{reality}(w_{c1})$ first. If there is a waste guidance effect, then continue to calculate $Z_{reality}(w_{c2})$, $Z_{reality}(w_{c3})$, … until there is no waste guidance effect. Then in the sequence of $Z_{reality}(w_{c1})$, $Z_{reality}(w_{c2})$, …$Z_{reality}(w_{ck})$, the max one is the road section that sets the first VMS. In fact, 1 VMS positioning problem solving generally only requires 1step or 2 steps.

Step 4. The method of the second VMS set: Based on the first VMS road section $w_{cz(1)}$ selected, another road section is selected in this step. First, to delete the first road section $w_{cz(1)}$ from the original ordered sequence, a new ordered sequence $w_{c1}^1, w_{c2}^1, \ldots, w_{cm-1}^1$, is selected. Second, we select a new road section from the new sequence to form a two-element combination. Then we calculate the actual guidance effect of the combinations $Z_{reality}(w_{cz(1)}, w_{c1}^1)$, $Z_{reality}(w_{cz(1)}, w_{c2}^1)$, $Z_{reality}(w_{cz1}, w_{c3}^1)$, … respectively, until there is no loss guidance effect, or a combination's theory guidance effect is smaller than the actual guidance effect of a combination calculated before. Then in the sequence of $Z_{reality}(w_{cz(1)}, w_{c1}^1)$, $Z_{reality}(w_{cz(1)}, w_{c2}^1)$, $Z_{reality}(w_{cz(1)}, w_{c(3)}^1)$, …, the max one is the two road sections combination.

Step 5. The method of the n VMS set: based on the n-1 VMS road sections ($w_{cz(1)}$, $w_{cz(2)}$, … $w_{cz(n-1)}$)

selected, another road section is selected in this step. The selecting method is the same as described in step 4.

2.4 *The evaluation indexes*

In theory, with the increase in the number of VMS, the VMS guidance effect will also increase and that will inevitably produce repeated guidance effect and waste guidance effect. So it is not necessary to set VMS in each road sections. So now we discuss VMS positioning evaluation indexes. Two evaluation indexes are introduced to evaluate the efficiency of VMS system.

The Guidance Coverage Rate: In an n VMS system, the guidance coverage rate is the ratio of n VMS guidance effect in reality to the necessary guidance effect of the whole region. It indicates the VMS coverage in the road network and service level from the aspect of the traffic guidance effect, and we mark it K. The necessary guidance effect of the whole region is Z_{region}.

$$Z_{region} = \sum_{i=1}^{l}\left(\left(\sum_{j=1}^{m} e_i^j - 1\right) \times q\left(w^j\right)\right) \tag{4}$$

$$K = \frac{Z_{reality}}{Z_{region}},\ (K \le 1) \tag{5}$$

The Guidance Effect Loss Rate: The repeated VMS traffic flow guidance effect adds, and the wasted VMS traffic flow guidance effect loses the guidance effect; the guidance effect loss rate η is the guidance effect loss divided by the guidance effect in theory, which indicates the VMS use efficiency from the aspect of the economic benefits.

$$\eta = \frac{Z_{repeated} + Z_{waste}}{Z_{theory}},\ \eta < 1 \tag{6}$$

3 THE EXAMPLE ANALYSIS

3.1 *The example data*

The network example is shown in Figure 2. It has 15 nodes, 36 road sections, and the numbers marked in road sections indicate the section number and the impedance respectively.

Let us assume the origin nodes and destination nodes are nodes 1, 6, 11, 5, 10, 15, and we named them A, B, C, D, E, F. According to the OD matrix of the region, we assign the traffic flow to the various paths using the shortest path method in Table 1.

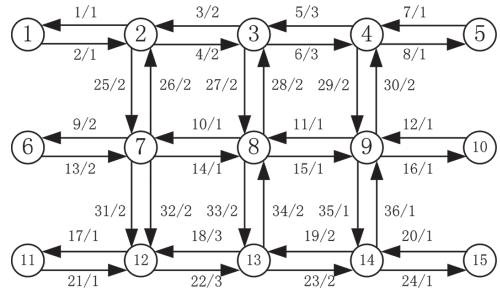

Figure 2. The example network.

Table 1. The traffic distribution path.

Path	Origin-destination nodes	The traffic flow	The road sections	The number of the road sections
r_1	A-B	100	2, 25, 9	3
r_2	A-C	60	2, 25, 31, 17	4
r_3	A-D	80	2, 4, 6, 8	4
r_4	A-E	30	2, 25, 12, 14, 16	5
r_5	A-F	70	2, 25, 12, 14, 35, 24	6
r_6	B-A	60	10, 26, 1	3
r_7	B-C	40	10, 31, 17	3
r_8	B-D	90	10, 12, 14, 30, 8	5
r_9	B-E	60	10, 12, 14, 16	4
r_{10}	B-F	90	10, 12, 14, 35, 24	5
r_{11}	C-A	100	18, 32, 26, 1	4
r_{12}	C-B	90	18, 32, 9	3
r_{13}	C-D	120	18, 32, 12, 14, 30, 8	6
r_{14}	C-E	50	18, 32, 12, 14, 16	5
r_{15}	C-F	80	18, 20, 22, 24	4
r_{16}	D-A	90	7, 5, 3, 1	4
r_{17}	D-B	100	7, 29, 13, 11, 9	5
r_{18}	D-C	100	7, 29, 13, 11, 31, 17	6
r_{19}	D-E	80	7, 29, 16	3
r_{20}	D-F	40	7, 29, 35, 24	4
r_{21}	E-A	70	15, 13, 11, 26, 1	5
r_{22}	E-B	50	15, 13, 11, 9	4
r_{23}	E-C	130	15, 13, 11, 31, 17	5
r_{24}	E-D	30	15, 30, 8	3
r_{25}	E-F	50	15, 35, 24	3
r_{26}	F-A	80	23, 36, 13, 11, 26, 1	5
r_{27}	F-B	60	23, 36, 13, 11, 9	5
r_{28}	F-C	80	23, 21, 19, 17	4
r_{29}	F-D	50	23, 36, 30, 8	3
r_{30}	F-E	100	23, 36, 16	3

Table 2. The sorted road sections.

Road section	w_{11}	w_{13}	w_{12}	w_{14}	w_{18}	w_{24}
Traffic flow	590	590	510	510	440	430
Road section	w_7	w_{17}	w_9	w_1	w_8	w_{26}
Traffic flow	410	410	400	400	370	370
Road section	w_{32}	w_2	w_{10}	w_{15}	w_{31}	w_{16}
Traffic flow	360	340	340	330	330	320
Road section	w_{29}	w_{30}	w_{23}	w_{25}	w_{35}	w_{36}
Traffic flow	320	290	270	260	250	230
Road section	w_3	w_5	w_4	w_6	w_{19}	w_{20}
Traffic flow	90	90	80	80	80	80
Road section	w_{21}	w_{22}	w_{27}	w_{28}	w_{33}	w_{34}
Traffic flow	80	80	0	0	0	0

The necessary guidance effect in the total region is $Z_{region} = 7370$.

3.2 *The greedy algorithm optimization process and evaluation index*

Using the greedy algorithm designed in this paper to calculate the maximum value of the positioning function, the process is as follows:

The road sections sorted from large to small are in Table 2.

Because the road sections 1, 8, 9, 16, 17, 24 are directly connected to the traffic destination notes, the traffic flow that went through this road section will all reach to the destinations, so it will produce the first degree waste guidance effect. So these road sections are not considered to set the VMS, and their VMS guidance effect is 0.

The VMS optimization positioning process is given in Table 3.

Table 3. The VMS optimization.

VMS no.	The VMS set road sections	The guidance effect in reality	The guidance coverage rate	The loss guidance effect rate	Choose or not
1	11	970			No
		The guidance effect in reality: q(w11) × 2-q(r17)-q(r22)-q(r27) = 590 × 2–100–50–60 = 970			
		The added loss guidance effect: Second Degree Waste Effect			
	13	1180	0.16	0	Yes
		The guidance effect in reality: q(w13) × 2 = 590 × 2 = 1180			
2	13, 11	1560			No
		The added loss guidance effect: Second Degree Waste guidance Effect, road section 13 and 11 have repeated guidance effect			
		The guidance effect in reality: (q(w13) + q(w11)) × 2-q(r17)-q(r18)-q(r21)-q(r22)-q(r23)-q(r25)-q(r27)-q(r17)-q(r22)-q(r27) = 1560			
	13, 12	2200	0.3	0	Yes
		The guidance effect in reality: (q(w13)+q(w12)) × 2 = (510+590) × 2 = 2200			
3	13, 12, 11	2580			No
		The added loss guidance effect: Second Degree Waste Effect, road section 13 and 11 have repeated guidance effect			
	13, 12, 14	2880			No
		The added loss guidance effect: road section 14 and 12 have repeated guidance effect			
	13, 12, 18	3080	0.42	0	Yes
		The guidance effect in reality: ((w13) + q(w12) + (w18)) × 2 = (510 + 590 + 440) × 2 = 3080			
4	13, 12, 18, 11	3460			No
		The added loss guidance effect: Second Degree Waste Effect, road section 13 and 11 have repeated guidance effect			
	13, 12, 18, 14	3510			No
		The added loss guidance effect: Second Degree Waste Effect			
	13, 12, 18, 7	3900	0.53	0	Yes
5	13, 12, 18, 7, 2	4580	0.62	0	Yes
6	13, 12, 18, 7, 2, 23	5120	0.69	0	Yes
7	13, 12, 18, 7, 2, 23, 10	5560	0.75	0.04	Yes
		The added loss guidance effect: road section 10 and 12 have repeated guidance effect			

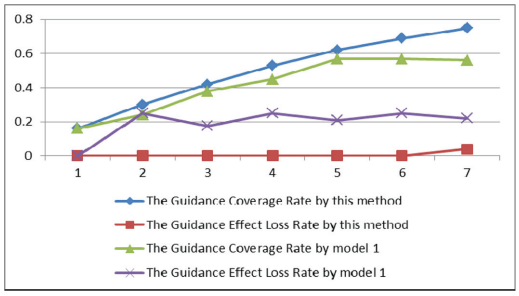

Figure 3. The VMS number and the evaluation indexes.

3.3 *The comparison and data analysis*

The comparison of the guidance coverage rate and the guidance effect loss rate with model 1 can be seen in Figure 3.

It is pointed out that when seven VMS are collocated in the net, the guidance coverage rate is 0.75, and the guidance effect loss rate reaches 0.04; in compared model 1, the guidance coverage rate is 0.56, and the guidance effect loss rate reaches 0.22; so it is optimal configuration. Comparing this configuration of VMS with model 1, we can see that the proposed method is better in guidance coverage rate with less guidance effect loss.

It can be seen from Figure 3 and Table 3 that, when the VMS number is small, VMS are basically set in the road sections of large traffic flow; when the VMS number is increased, the relationship between the VMS in combination should be considered.

Further analysis: when the VMS number is small, the VMS guidance coverage rate increased faster without guidance effect loss; with the increase of VMS number, the VMS guidance coverage rate gradually decreased, and finally guidance effect loss is produced. Because this network example and OD is relatively simple, the guidance effect loss rate is not obvious. In the actual network, with the increase of network complexity and OD, the distribution of traffic flow will also become more complex, so the relationship between the VMS number and the guidance coverage rate/the loss guidance effect rate will be more obvious.

4 CONCLUSION

This paper studied VMS positioning and its optimization. In a known network and traffic demand distribution, for maximum traffic flow guidance effect, complex VMS guidance situation is analyzed, and the corresponding mathematical model is established, and at last, the greedy algorithm is designed to solve the optimization function. Compared with the Mei model 1, this model is simpler, more effective, and more reasonable, which considers the complex situation better. In future practical applications, optimization of the VMS positioning model should also consider some other factors such as drivers' perceptions and reactions, road condition, cost, delay, etc.

REFERENCES

Doan, K., Ukkusuri & Satish, V. 2012. On the holding-back problem in the cell transmission based dynamic traffic assignment models. *Transportation Research: Part B* 46(9): 1218–1238.

Fan, L.L., Guan, W. & Gui, T.D. 2014. Spatial association rules of traffic guidance information release strategy. *Systems Engineering-Theory & Practice* 34(10): 2688–2694.

Hou, X.Y., Liu, W.F. & Yang, Y. 2012. Research on status of graphical information based on VMS. *Journal of Highway and Transportation Research and Development* 29(7): 118–123.

Lee, C.W., Kim, S.W. & Lee, S.B. 2011. Optimal check up and replacement periods of variable message signs: a case of the Seoul metropolitan transportation center. *Journal of Advanced Transportation* 45(3): 173–185.

Mei, Z.Y., Xiang, Y.Q., Chen, J. & Wang, W., 2007. Optimization method of configuration of traffic flow guidance information board in urban. *Journal of Traffic and Transportation Engineering* 7(5): 88–92.

Niu, S.Y., Liu, H. & Feng, J.G. 2010. The optimization of the planning and positioning of VMS based on fuzzy constrained conditions. *Systems Engineering* 28(3): 98–102.

Song, C. & Level, B. 2013. Programming models applied in urban transportation network design problems. *Advanced Materials Research* 791–793 (2013): 1172–1175.

Sumalee, A., Zhong, R.X., Pan, T.L. & Szeto, W.Y. 2011. Stochastic cell transmission model (SCTM): A stochastic dynamic traffic model for traffic state surveillance and assignment. *Transportation Research Part B: Methodological* 45(3): 507–533.

Wang, J.J. & Wu, Q. 2013. Study on multi-objective optimization model for VMS layout on expressways. *Applied Mechanics and Materials* 361–363(8): 2012–2015.

Wang, Y.S., Chen E.H. & Liu, J. 2014. Research on the key problems of city road VMS layout design standard. *Road Traffic & Safety* 14(2): 22–25.

Wei, M., Sun, B. & Jin, W.Z. 2013. A bi-level programming model for uncertain regional bus scheduling problems. *Journal of Transportation Systems Engineering and Information Technology* 13(4): 106–112.

Wen, M.F. 2013. *The Research on Cooperative Optimization and Traffic Guidance Technologies of Traffic Flow for Urban Intelligent Transportation System*. Changsha: Central South University.

Xu, Z., Hong, H.Z. & Yan, H. 2013. The configuration location designation of variable message signs. *Journal of Chongqing University* 36(10): 54–60.

Civil Engineering and Urban Planning IV – Liu et al. (Eds)
© 2016 Taylor & Francis Group, London, ISBN 978-1-138-02903-3

Traffic freight volume forecasting based on optimized GM (1,1) power model

Si-Jun Zhang & Shu-Yan Chen
School of Transportation, Southeast University, Nanjing, Jiangsu, China
Jiangsu Province Collaborative Innovation Center of Modern Urban Traffic Technologies, Nanjing, Jiangsu, China

ABSTRACT: Considering the theoretical defects in traditional GM (1,1) power model, both elements of background value and initial condition are taken into account to optimize the parameters in GM (1,1) power model. Firstly, error of background values in traditional GM (1,1) power model is analyzed and the background value formula is rebuilt according to the definition; Secondly, it is pointed out that the default initial condition is unreasonable, a method of selecting the initial conditions is established according to the minimum variance principle between original values and predicted values; Thirdly, the detailed steps are described in the field of prediction by the use of optimized model, meanwhile, an example of waterway freight volume in Shanghai from 1999 to 2008 is exploited to validate the effectivenesses, the results show that the optimized model possesses much higher precision in the simulation-prediction of waterway freight volume.

1 INTRODUCTION

Many methods have existed in the field of traffic freight volume forecasting, including Regression Analysis, Exponential Smoothing, Markov Analysis, Elasticity Coefficient method, etc. Freight volumes are multi-level, multi-factor complex variables, so it is difficult to modeling and determining the model parameters due to the lack of sufficient information. The using of prediction method such as Regression Analysis etc. is not only taking into account a variety of factors, but also collecting a lot of information, which will increase workload calculation and modeling difficulties. It will result in prediction failure in case that some information is difficult to be quantified and to determine the parameters of the model. Meanwhile, the using of moving averages, exponential smoothing such as time series methods are difficult to achieve high accuracy.

Since the birth of the gray system theory in the 1980s, it has been widely used in many areas with its 'small sample size, poor information' feature. The application has been particularly successful (Gross et al. 2011; Guo 2005; Liu & Lin 2011; Liu 2014), especially in the situation of uncertainty and lack of data. This theory gives new ideas for traffic freight volume forecasting. Currently, gray model are widely used in the prediction field (Poschmann et al. 2011; Xiong et al. 2010). In recent years, a number of experts and scholars have expanded and optimized GM (1,1) power model (Wang et al. 2012; Xiong et al. 2012; Dai et al. 2010; Zhao et al. 2014; Wang et al. 2009), the scope of application of the model has been greatly enriched. Through the researches on GM (1,1) power model, it can be found that most researchers focus on the parameters optimization of model from a single perspective, while the literature about considering parameters optimization from multi-perspective is uncommon. In view of this, the paper established optimization of gray GM (1,1) power model based on background value and initial condition, and the optimized model has been verified in the field of traffic freight volume forecasting with high simulation and prediction accuracy in the case of waterway freight volume in Shanghai.

2 DEFINITION OF GM (1,1) POWER MODEL

Definition (Liu 2014): Assume that $X^{(0)} = \{x^{(0)}(1), x^{(0)}(2),\ldots, x^{(0)}(n)\}$ is the original series, where $x^{(0)}$

$(i) \geq 0$, $i = 1, 2, \ldots, n$. Applying accumulated generating operation, it can be get $X^{(1)} = \{x^{(1)}(1), x^{(1)}(2), \ldots, x^{(1)}(n)\}$, where

$$x^{(1)}(k) = \sum_{i=1}^{k} x^{(0)}(i),\ k = 1, 2, \ldots, n.$$

The first order linear ordinary differential equation expressed as

$$\frac{dx^{(1)}}{dt} = ax^{(1)} = b(x^{(1)})^{a} \tag{1}$$

is called whitened differential equation of GM (1, 1) power model, of which the difference form is

$$x^{(0)}(k) = az^{(1)}(k) = b\left(z^{(1)}(k)\right)^{\alpha} \tag{2}$$

where a, b are parameters to be identified. a is called developing coefficient, b is called grey input, and α is called exponent of the model. The background value $z^{(1)}(k)$ in equation (2) is formulated as

$$z^{(1)}(k) = 0.5\left(x^{(1)}(k) + x^{(1)}(k-1)\right),\ k = 2, 3, \ldots, n. \tag{3}$$

solve it using least square method and obtain:

$$\hat{a} = (B^T B)^{-1} B^T Y \tag{4}$$

$$B = \begin{bmatrix} -z^{(1)}(2) & \left(z^{(1)}(2)\right)^{a} \\ -z^{(1)}(3) & \left(z^{(1)}(3)\right)^{a} \\ \vdots & \vdots \\ -z^{(1)}(n) & \left(z^{(1)}(n)\right)^{a} \end{bmatrix},\ Y = \begin{bmatrix} x^{(0)}(2) \\ x^{(0)}(3) \\ \vdots \\ x^{(0)}(n) \end{bmatrix} \tag{5}$$

in an initial condition of

$$\hat{x}^{(1)}(t)|_{t=1} = \hat{x}^{(1)}(1) = x^{(0)}(1)$$

the discrete solution of equation (1) is

$$\hat{x}^{(1)}(k+1) = \left\{\left[x^{(1)}(1)^{(1-\alpha)} - \frac{b}{a}\right]e^{-(1-\alpha)ak} + \frac{b}{a}\right\}^{\frac{1}{1-\alpha}} \tag{6}$$

When $\alpha = 0$, equation (6) is called traditional GM (1,1) model; when $\alpha = 2$, equation (6) is called traditional grey Verhulst model. The reduction value is:

$$\hat{x}^{(0)}(k+1) = \hat{x}^{(1)}(k+1) - \hat{x}^{(1)}(k) \tag{7}$$

When $k \leq n$, $\hat{x}^{(0)}(k)$ are simulated values; when $k \geq n$ $\hat{x}^{(0)}(k)$ are predicted values.

3 PARAMETER ESTIMATION BASED ON OPTIMIZED BACKGROUND VALUE

3.1 *Optimal estimation of a, b*

From the above equation (4), The accuracy of the model depends on the parameters a and b, while $z^{(1)}(k)$ is the most direct factor affecting a and b, it is one of the key factors that affect the accuracy of the model. Background value error analysis of traditional GM (1,1) power model is shown in Figure 1 (Xiong et al. 2012; Dai et al. 2010; Zhao et al. 2014).

Equation (1) is definite integrated over the interval $[k-1,k]$ and simplified:

$$x^{(0)}(k) + a\int_{k-1}^{k} x^{(1)}\mathrm{d}t = b\int_{k-1}^{k} (x^{(1)})^{\alpha}\mathrm{d}t \tag{8}$$

Comparing equations (2) and (8), it can be found:

$\int_{k-1}^{k} x^{(1)}(t)dt$ is replaced by $z^{(1)}(k) = 0.5\,[x^{(1)}(k) + x^{(1)}(k-1)]$; $\int_{k-1}^{k} (x^{(1)}(t))^{\alpha}dt$ is replaced by $\left(z^{(1)}(k)\right)^{\alpha}$.

It is necessary to optimize the structure of the background values to eliminate this systematic errors caused by approximate value, assume

$$\hat{z}^{(1)}(k) = \int_{k=1}^{k} x^{(1)}(t)dt,\ \hat{\mu}(k) = \int_{k=1}^{k} \left(x^{(1)}(t)\right)^{\alpha}\mathrm{d}t$$

where $k = 2, 3, \ldots, n$, because $x^{(1)}(t)$ satisfies the inhomogeneous exponential distribution, it can be assumed that $x^{(1)}(t) = Be^{A(t-1)} + C$, where A, B and C are undetermined coefficients, it is easy to get:

$$x^{(1)}(k) = Be^{A(k-1)} + C,\ (k = 1, 2, ..., n) \tag{9}$$

Applying regressived generating operation:

$$\begin{aligned} x^{(0)}(k) &= x^{(1)}(k) - x^{(1)}(k-1) \\ &= B(1 - e^{-A})e^{A(k-1)} = he^{A(k-1)} \end{aligned} \tag{10}$$

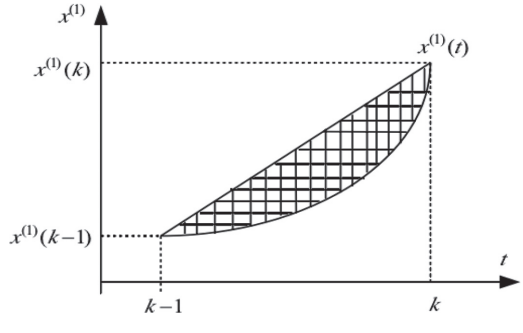

Figure 1. Schematic of background value error analysis.

where $h = B(1-\mathrm{e}^{-A})$. owing to:

$$x^{(1)}(k) = \sum_{i=1}^{k} x^{(0)}(k) = \frac{h\mathrm{e}^{A(k-1)}}{1-\mathrm{e}^{-A}} - \frac{h\mathrm{e}^{-A}}{1-\mathrm{e}^{-A}} \tag{11}$$

so

$$B = \frac{h}{1-e^{-A}},\ C = \frac{-he^{-A}}{1-e^{-A}} \tag{12}$$

owing to

$$\frac{x^{(0)}(k)}{x^{(0)}(k-1)} = \mathrm{e}^{A}$$

so

$$A = \ln x^{(0)}(k) - \ln x^{(0)}(k-1) \tag{13}$$

From equation (10), it can be known that

$$h = x^{(0)}(k)\left[\frac{x^{(0)}(k)}{x^{(0)}(k-1)}\right]^{(1-k)} \tag{14}$$

From equation (12), it can be known that

$$C = \frac{\left(x^{(0)}(k)\right)^{2-k} * \left(x^{(0)}(k-1)\right)^{k}}{x^{(0)}(k-1) - x^{(0)}(k)},$$

$$B = \frac{\left(x^{(0)}(k)\right)^{3-k}}{\left(x^{(0)}(k-1)\right)^{1-k} - \left(x^{(0)}(k) - x^{(0)}(k-1)\right)}$$

In this case

$$\begin{aligned}\hat{z}^{(1)}(k) &= \int_{k-1}^{k} x^{(1)}(t)dt = \int_{k-1}^{k} C + Be^{A(t-1)}dt \\ &= \frac{x^{(0)}(k)}{A} + C = \frac{x^{(0)}(k)}{\ln x^{(0)}(k) - \ln x^{(0)}(k-1)} \\ &\quad + \frac{\left(x^{(0)}(k)\right)^{2-k} * \left(x^{(0)}(k-1)\right)^{k}}{x^{(0)}(k-1) - x^{(0)}(k)} \\ &\quad \left(x^{(0)}(k-1) \neq x^{(0)}(k),\ k = 2, 3, \ldots, n\right)\end{aligned} \tag{15}$$

Owing to it is difficult to simplify $\hat{\mu}(k)$, this article will get its approximation by using computer processing tools. Matlab 8.0 is used here:

syms t;

$$\begin{aligned}&\hat{\mu}(k) \\ &= \mathrm{vpa}\left(\mathrm{int}\left(\left(B(k) * \exp\left(A(k) * (t-1)\right) + C(k)\right)^{\alpha}, \atop k-1,\ k\right)\right);\end{aligned}$$

Equation (2) is redefined based on optimized background value:

$$x^{(0)}(k) + a\hat{z}^{(1)}(k) = b\hat{\mu}(k),\ (k = 2, 3, \ldots, n) \tag{16}$$

Modify equation (5) as:

$$B = \begin{bmatrix} -\hat{z}^{(1)}(2) & \hat{\mu}(2) \\ -\hat{z}^{(1)}(3) & \hat{\mu}(2) \\ \vdots & \vdots \\ -\hat{z}^{(1)}(n) & \hat{\mu}(n) \end{bmatrix},\ Y = \begin{bmatrix} x^{(0)}(2) \\ x^{(0)}(3) \\ \vdots \\ x^{(0)}(n) \end{bmatrix} \tag{17}$$

3.2 *Estimation of* α

According to the references (Dai et al. 2010; Zhao et al. 2014; Wang et al. 2009), summarize estimation method of parameters α as:

$$\alpha = \frac{1}{n-2}\sum_{k=2}^{n-1} \alpha_k \tag{18}$$

where α_k is determined by equation (19) as:

$$\begin{aligned}&\alpha_k \\ &= \left\{\left[x^{(0)}(k+1) - x^{(0)}(k)\right]\hat{z}^{(1)}(k+1)\hat{z}^{(1)}(k)x^{(0)}(k)\right. \\ &\quad \left. - \left[x^{(0)}(k) - x^{(0)}(k-1)\right]\hat{z}^{(1)}(k+1)\hat{z}^{(1)}(k)x^{(0)}(k+1)\right\} \\ &\quad \Big/\left\{\left[x^{(0)}(k+1)\right]^2\hat{z}^{(1)}(k)x^{(0)}(k)\right. \\ &\quad \left. - \left[x^{(0)}(k)\right]^2\hat{z}^{(1)}(k+1)x^{(0)}(k+1)\right\}\end{aligned} \tag{19}$$

4 OPTIMIZED GM (1,1) POWER MODEL BASED ON INITIAL CONDITION

The selection of initial condition is another important factor affecting the model apart from the structure of background value.

$$\hat{x}^{(1)}(1) = x^{(0)}(1) \tag{20}$$

is often used as initial condition in the traditional GM (1,1) power model when solving whitened differential equation. According to the above-mentioned initial condition, the fitted curve must go through $(1, x^{(1)}(t))$ on the coordinate plane, while the fitting curve does not necessarily go through the first data point by the least squares principle, therefore, the above initial condition are not

accurate due to lack of theoretical basis (Zhang et al. 2002). In order to obtain more accurate predictions, in this paper,

$$\hat{x}^{(1)}(m) = x^{(0)}(m), (m = 1, 2, \ldots, n) \tag{21}$$

is considered as the initial condition. The discrete solution is rebuilt as:

$$\hat{x}^{(1)}(k) = \left\{\left[x^{(1)}(m)^{(1-\alpha)} - \frac{b}{a}\right]e^{-(1-\alpha)a(k-m)} + \frac{b}{a}\right\}^{\frac{1}{1-\alpha}}, \quad (k = 1, 2, ..., n) \quad (m = 1, 2, ..., n) \tag{22}$$

m can be determined by the following criteria:

$$\min_m S_0^2 = \sum_{k=1}^{n}\left[\left(x^{(0)}(k) - \hat{x}^{(0)}(k)\right)\right]^2 \tag{23}$$

where

$$\hat{x}^{(0)}(k) = \hat{x}^{(1)}(k) - \hat{x}^{(1)}(k-1) \tag{24}$$

5 MODELING STEPS OF OPTIMIZED GM (1,1) POWER MODEL

Specific modeling steps are as follows:
- Getting $X^{(1)}$ by applying accumulated generating operation;
- Obtaining parameters A,B,C and $\hat{Z}^{(1)}$ by optimized background value;
- Determining α_k and α;
- Getting $\hat{\mu}(n)$ by the use of optimized parameters A,B,C and α;
- Calculating parameters a,b based on the least squares principle;
- Establishing prediction equation and calculating prediction error when $m = 1, 2, \ldots, n$;
- Determining the best prediction equation according to the criteria;

6 APPLICATION AND ANALYSIS

An example of waterway freight volume in Shanghai from 1999 to 2008 is exploited to validate the effectiveness of the optimized model. The data comes from http://data.stats.gov.cn. For convenience, this article will record the optimized model as a Model 1. In modeling, the first 8 data of sequence $X^{(0)}$ are used as the original data of the prediction model 1, then the last two data are used to test the prediction accuracy of Model 1. The discrete solution of model 1 is:

$$\text{Model 1}: \hat{x}^{(1)}(k) = \left[-172.206 + 425.145e^{0.131(k-7)}\right]^{0.927} \quad (k = 1, 2, ..., 10)$$

Data analyses are shown in Table 1 and Figure 2.

6.1 *Model checking*

- Residual checking, shown in Table 1. calculated: model accuracy is 96%, higher than 90%.
- Relational degree checking, calculated:
- $r = 0.85$, higher than 0.60.
- Posterior-varian cechecking, calculated: $C = 0.09 < 0.35$, Error probability $P = 1 > 0.95$. According to criteria in Table 2, accuracy level of Model 1 is Level One, has better prediction accuracy.

In summary, the optimized model described in this article has advantages in simulation and prediction.

Table 1. Waterway freight volume simulated-predicted by Model 1 10^4 t.

Year	Practical value	Model 1'output	RE (%)
1999	16,335	17,096	4.66
2000	17,365	19,474	12.15
2001	20,931	21,221	1.39
2002	23,174	23,465	1.26
2003	26,621	26,119	1.89
2004	30,148	29,184	3.20
2005	34,674	32,689	5.72
2006	37,348	36,676	1.80
2007	41,543	41,202	0.82
2008	43,060	46,330	7.59

* http://data.stats.gov.cn

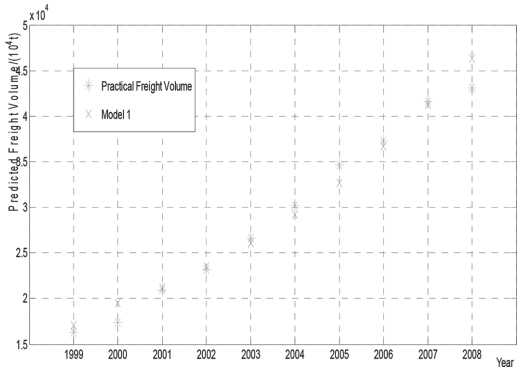

Figure 2. Comparison between simulated-predicted value and practical value.

Table 2. Model accuracy level.

Model accuracy level	Error probability P	Mean squared error C
Level one	$P > 0.95$	$C < 0.35$
Level two	$0.80 < P < 0.95$	$0.35 < C < 0.50$
Level three	$0.75 < P < 0.80$	$0.50 < C < 0.65$
Level four	$P < 0.70$	$C > 0.65$

7 CONCLUSION

Accurate prediction of waterway freight volume is not only conducive to grasp the development trend of the waterway market for the central and provincial transportation departments, but also conducive to the decision-making behaviors for the decision makers of waterway business. It brought a greater degree of difficulty to prediction accuracy of waterway freight volume due to the complexity and uncertainty in the future. This paper has built an optimized GM (1,1) power model from the definition by analyzing the theory error of traditional GM (1,1) power model, and it was introduced to the waterway traffic freight volume forecasting, the results show a higher prediction accuracy. The optimized model provides a basis for the relevant departments and personnel to grasp the waterway freight market and make decisions.

ACKNOWLEDGEMENT

This work was supported by National Natural Science Foundation of China under Grant No. 61374195.

REFERENCES

Dai, W.Z., Xiong, W. & Yang, A.P. 2010. Improved-grey Verhulst model and its application. *CIESC Journal* 61(8): 2097–2100.

Gross, T.J., Abrao, T. & Jeszensky, P.J.E. 2011. Distributed power control algorithm for multiple access systems based on Verhulst model. *AEU-International Journal of Electronics and Communications* 65(4): 361–372.

Guo, D.L. 2005. New methods and accuracy improvement of GM according to Laplace Transform. *The Journal of Grey System* 8(1): 13–24.

Liu, S.F. & Lin Y. 2011. *Grey Systems Theory and Application*. Berlin: Springer-verlag.

Liu, S.F. 2014. *Grey Systems Theory and Application.* 7th ed. Beijing: Science Press.

Poschmann, A., Moradi, A. & Khoo, K. 2011. Side-channel resistant crypto for less than 2300 GE. *Journal of Cryptology* 24(2): 322–345.

Wang, Z.X., Dang, Y.G. & Liu, S.F. 2009. Solution of GM (1,1) power model and its properties. *Systems Engineering and Electronics* 31(10): 2380–2383.

Wang, Z.X., Dang, Y.G. & Zhao, J.J. 2012. Optimized GM (1,1) power model and its application. *System Engineering-Theory & Practice* 32(9): 1973–1977.

Xiong, P.P., Dang, Y.G. & Qian, W.Y. 2010. The optimization of time response function in non-equidistant Verhulst model. *The Journal of Grey System* 22(3): 249–256.

Xiong, P.P., Dang, Y.G. & Yao, T.X., et al. 2012. The research on the modeling method of background value optimization in grey Verhulst model. *Chinese Journal of Management Science* 20(6): 154–158.

Zhao, H.H., Jian, L.R., Liu, Y., et al. 2014. Grey Verhulst Model and application based on background value and initial value optimization. *Systems Engineering* (32)3: 149–153.

This page intentionally left blank

Civil Engineering and Urban Planning IV – Liu et al. (Eds)
© 2016 Taylor & Francis Group, London, ISBN 978-1-138-02903-3

Modeling of tree-roots effects on pavement stresses and strains

M. Mostafa Hassan & J.A. Adedeji
Civil Engineering, Central University of Technology, Free State, South Africa

ABSTRACT: Using stress and strain in pavement design has become more prevalent through mechanistic-empirical design methods. Stresses and strains at any layer of the pavement determine the overall performance of such structure. Thus, the redistribution of these stresses and strains affects the stability of the pavement structure. Over the years, tree roots in pavement layers have contributed to its failure, although different recommendations to obviate the tree-roots effect have been suggested by arboriculturists and only a few contributions have been made by pavement engineers. Consequently, to date, pavement structure still experiences failure. However, with the help of the finite element model, the impact of tree roots in flexible pavement structure can be simulated and its effect on the stress and strain redistribution in pavement layers can be examined. The result of this study indicates that more stress is generated in overlay layers (asphalt and base layer) due to the presence of tree roots, which may later lead to cracks.

1 INTRODUCTION

Sustainability of pavement structure life has been a long-time global challenge to pavement engineers as a result of the continuously increasing cost of design, construction, maintenance and rehabilitation, with the design aspect being a major concern of all. Thus, the use of stress and strain in pavement design has become more prevalent through Mechanistic-Empirical Design Methods (ME-DM). The use of these methods are influenced by errors experienced and uneconomical reasons in the use of traditional empirical methods (Rahman et al. 2011; Shafabakhsh et al. 2013), and the inability of traditional methods to represent the actual scenario of pavement onsite. In ME-DM, stresses or strains at any layer of a pavement determine the overall performance of such structure. Consequently, redistribution of such stresses and strains further affects the stability and performance of the pavement structure.

Over the years, flexible pavement experience failures have been resulted from soil instability/expansion (Kordi et al. 2010), inappropriate use of materials, inadequacy in designs (Kordi et al. 2010; Shafabakhsh et al. 2013) and the presence of tree roots (D'Amato et al. 2002) in its layers. Focusing on the latter, tree is of great environmental importance in any urban design (Beecham 2012; Reavens 2001), yet its adverse effect (as a result of its roots) on the poor performance or sometimes failure experienced in pavement structure cannot be ignored.

1.1 *Tree roots and flexible pavement performances*

Tree is of great importance to any society. Some of its importance ranges from community and social values to ecological and environmental values (Beecham 2012; Reavens 2001; Roodt 2012). Ecologically, it sequestrates carbon dioxide and provides oxygen; improves air quality, climate amelioration and conserves water (Appleton et al. 2003; Rosenfeld et al. 1998), all of which contribute positively to the reduction of the global warming effect and carbon emissions. Also, trees are a positive component of urban infrastructure (Hauer et al. 1994), as they create a peaceful and aesthetically pleasing environment. Additionally, tree's shade has been found to be partially responsible for reduced pavement fatigue, cracking, shoving and other surface distress (McPherson & Muchnick 2005).

Contrary to the tree's importance, there have always been conflicts between it and the nearby infrastructures (Coder 1998; Randrup et al. 2003). Most of these conflicts result from the interaction of tree roots with the infrastructures. These roots serve as an anchor to the ground and gather water and nutrients that are transferable to all parts of the tree for reproduction, survival, energy storage and many other purposes (Russell & Culter 2003). Furthermore, roots are systems that differ from one species of the tree to the other (Day et al. 2010; Morgenroth 2011). Although, erroneously, it has been believed that roots mainly grow vertically downwards and have a limited lateral spread, but this is not true for all trees (Jim 2003). Roots

are typically shallow and widely spread (Morgenroth 2011); they are found in the upper 1 m of the soil and spread up to three times the diameter of the tree crown (Jim 2003). The root grows and expands radially and deforms the soil above them by the pressure it exerts. It further modifies its environment and develops stress and strain on various types of structures, resulting in conflicts (Nicoll & Coutts 1997). Consequently, growth of tree roots is considered an expensive nuisance and liability risk in many societies (Coder 1998; Roodt 2012). Various infrastructural conflicts exist with tree roots, some of which are sewer, storm water drains, water supply lines, foundations, sidewalks, walls, swimming pools and pavement structure (Coder 1998; Morell 1992; Nicoll & Coutts 1997; Randrup et al. 2003; Roodt 2012). Of all these conflicts, tree-root versus pavement is one of the most pervasive and costly problems (Appleton et al. 2003).

On the pavement structure, especially in category B and C road (the South African National Road Agency Ltd 2013), the shallow root growth conflicts with the overlaying pavement layers. Generally, tree roots do not just grow in pavement layers, but the presence of essential and valuable resources or thermal changes between materials that provide pore spaces further enhance their growth (Kopinga 1994). In addition, the presence of roots in this structure places a tensile stress on the upper surface of the overlay (i.e. base layer or surface layer). This stress that later results in damage is typically progressive, with the degree of distortion that increases gradually over time (Barrell 2011). On a comparative note, flexible pavement has less tensile strength across the surface than the rigid pavement, so it is prone to show damage more easily when compared with the rigid one (Coder 1998). Yet, the use of flexible pavement is widely acceptable because of various factors that include less tire-pavement noise generation, smoothness of surface, environmental sustainability and its economic value (Asphalt Pavement Alliance 2010; Jain et al. 2013). Therefore, it is considered in this study.

Previously, various studies on the effect of tree roots on different infrastructures have been considered with numerous recommendations, which include appropriate selection of tree species, application of root barriers, root pruning and herbicide impregnated geotextile fabrics (Appleton et al. 2003; Coder 1998; Hauer et al. 1994; Smiley 2003). Most of these recommendations are from an arboriculturist's point of view (Appleton et al. 2003; Coder 1998; Hauer et al. 1994), with few research contributions from pavement engineers. As a result, to date, pavement structure still experiences failures such as cracking, surface deformation, disintegration and surface defect (Adlinge & Gupta 2013). The majority of these failures have been associated with overloading of the structure, use of poor materials in the layers and base drainage, and inadequate pavement thickness and compaction (Pavement Failure Identification 2010; Rani 2007) without considering the presence of tree roots in pavement layers.

Among all these failures in the pavement structure, cracking is a major indicative of failure in pavement (Ahmed 2006) and one of the most common ones as it occurs in various forms: fatigue, longitudinal, transverse, block, edge, reflective and slippage (Adlinge & Gupta 2013; Kordi et al. 2010). Also, this failure further results in other failures such as potholes. Several reports have indicated its causes; however, only a few have considered tree-roots growth in the pavement layer as a possible cause. From Colombier's (1997) point of view, one of the causes of crakes in the pavement structure is the movements in the subgrade that results from shrinkage of clayey soil by excessive loss of moisture during a very dry period, which is aggravated by the presence of trees along the road. Likewise, D'Amato, et al. (2002) found that significantly root growth contributes to or worsens the cracks in the pavement, as its growth is located beneath the existing cracks that result from the increased soil aeration beneath the crack. The movement in the subgrade layer or of any layer in the structure (Fig. 1) affects the whole pavement that eventually results in the redistribution of stresses and strains in the structure. Therefore, these stresses and strains generated by tree roots need to be studied by the mechanistic-empirical design method for pavement analysis.

Figure 1. Tree roots in the subgrade of flexible pavement (retrieved and modified from line drawing 2013).

1.2 *Stresses and strains in pavement design*

Recently, there has been a shift in the design of pavement structure from the empirical design methods to ME-DM. This is as a result of limitations associated with the empirical design methods such as one climate condition, limited traffic, material type and new construction only (Huang 2004; Wang 2001). As with the empirical design methods, ME-DM exploits mathematical capability to calculate the stresses, strains and/or deflections in a multi-layered systems, such as pavement, when subjected to external loads (Hafeez 2010).

The stresses, strains and deflections generated in flexible pavements result from material properties, thickness of each layer, loading condition (Alkhateeb et al. 2011) and in the presence of another substance therein. With the use of finite element-based methods, one can calculate the theoretical stresses, strains and deformations that occur anywhere in the structure. However, there are a few critical locations that are of interest and are often used in pavement analysis (Darwish 2012; NCHRP 2004, Pavement Interactive 2008) such as

- Surface deflection;
- Tensile horizontal strain at the bottom of the surface course (for surface course fatigue cracking);
- Compressive vertical stresses/strains within the base/sub-base layers (for rutting of unbound layers), and
- Compressive vertical stresses/strains at the top of the subgrade (for subgrade rutting).

Looking closely at these critical positions, the presence of tree roots in or underneath any layer of the pavement structure can contribute massively to the failures experienced. Nonetheless, trees are inevitable to our urban environment.

Although the use of ME-DM in pavement design is widely acceptable, the use of the 3D Finite Element Method (FEM)-based software appears to be the best approach (Rahman et al. 2011, Shafabakhsh et al. 2013). Abaqus® 3D FEM software has applications in pavement analysis. Various researchers have used Abaqus® 3D FEM for the design of flexible pavement that yields positive results: Shafabakhsh et al. (2013) who investigated on the pavement thickness impact, Al-Azzawi (2012) on geogrid material positing in pavement and Yin (2013) on pavement and interactions with its instruments. With 3D capabilities, real-life monitoring of the behavior of pavement structure and the presence of tree roots can be studied. As a result, proper understanding of the causes of cracks and other failures in pavement can be achieved.

Considering the fact that 3D FEM calculates stresses and strains in the pavement structure, the redistribution of stresses and strains in flexible pavement induced by tree roots can be simulated and studied; thereafter, design and construction intervention can be taken into consideration. Therefore, this study aims at investigating cracking failures in flexible pavement via the impact of tree roots on its stress/strain redistribution.

2 SIMULATION DESIGN

In this study, four scenarios are developed. The first serves as a control model with the absence of tree roots in the pavement layers, while the second contains tree roots under the surface layer. Moreover, models with tree roots underneath the sub-base and in the subgrade serve as the third and fourth models, respectively. In scenarios 2, 3 and 4, the tree-root thicknesses vary in a range (25 mm–100 mm) to check for the continuous effect, as the root grows. These models are analyzed using the Abaqus® (6.13) 3D FEM software. However, for any successful FEM simulation, factors such as model geometry, material characterization, element type and meshing size, boundary condition and loading type need to be taken into consideration (Embraco 2006). Details of these factors for this present study are given below.

2.1 *Model geometry and material characterization*

The geometry and material characterization of the models are adopted from a previous research conducted by Rahman et al. (2011) (Table 1). Dimension and material characterization are the same for all scenarios, with the exception of the tree-roots system for the control model. Overall, this model

Table 1. Material property of pavement layers and tree roots.

Data	Asphalt surface	Granular base	Subgrade	Tree roots
Thickness (mm)	100	250	2000	25–100
Modulus of elasticity (MPa)	2175	415	52	12500
Poisson's ratio	0.35	0.4	0.45	0.33

geometry was considered to avoid edge errors. Material characterization and dimensions of an average pine species tree root with 12% moisture content are used based on a study by Green et al. (1999). Additionally, the dimension of tree roots is assumed to range from 25 mm to 100 mm and the pressure exert by its movement is taken as 0.4 MPa (Hartley 2012); this is actually to simulate the movement of tree roots. All layers of the pavement are assumed to be linearly elastic in behavior for simplicity.

2.2 *Finite element types and mesh size*

All scenarios are modeled using the 8-node continuum three-dimensional brick element (C3D8R) with reduced order numerical integration available in Abaqus® (6.13). C3D8R element has the capability of representing large deformation, geometric and material nonlinearity (Ibrahim et al. 2014; Rahman et al. 2011). Instead of the commonly used random mesh, structured mesh is defined for all layers of the pavement structure, so that the tire contact area can be controlled while sweep mesh is used for the tree root.

2.3 *Boundary condition, loading and contact modeling*

Under boundary and loading conditions, the models are all subjected to the static load in a linear perturbation analysis and the models are restrained in horizontal directions (i.e. degree of freedoms 1 and 3) with the subgrade base in all directions. Furthermore, the loading contact area is assumed to be rectangular (61575 mm^2), with a wheel pressure of 0.67 MPa (Rahman et al. 2011). Tie constraints are assumed as the interaction between the interfaces of the layers (i.e. layers are fully bounded with no friction) for the control model, while embedded constraints are used for interactions between tree-root and pavement layers.

3 RESULTS AND DISCUSSION

3.1 *Control model*

The results for the control model are presented in Figures 2 and 3, and these results are found to be of close match with those obtained by Rahman et al. (2011). From these figures, the strains and displacements in pavement layers are presented. Figure 3 shows that the compressive displacements generated in pavement layers by wheel loads decrease down the depth, and Figure 2 shows the increase in compressive strain through the layers. This is as a result of the arrangement of the layer with the highest load bearing capacity material (Asphalt) on the top and the lowest load bearing capacity material at the bottom.

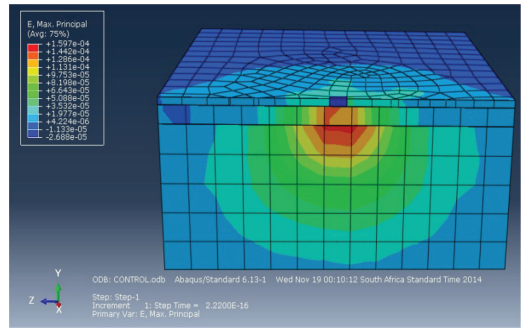

Figure 2. Strain distribution for the control model.

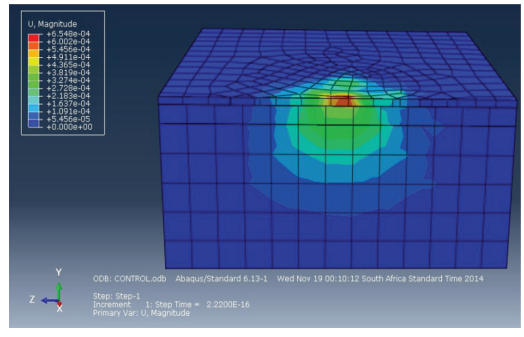

Figure 3. Deflection distribution for the control model.

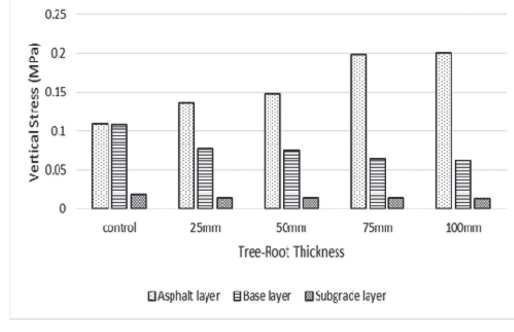

Figure 4. Stress redistribution for tree roots under the asphalt layer.

3.2 *Models with tree roots between the layers*

The results of these models, compared with the control model, are shown in Figures 4–9. Figures 4–6 show comparative graphs of the presence of tree roots underneath the asphalt (scenario 1), which show a decrease in vertical

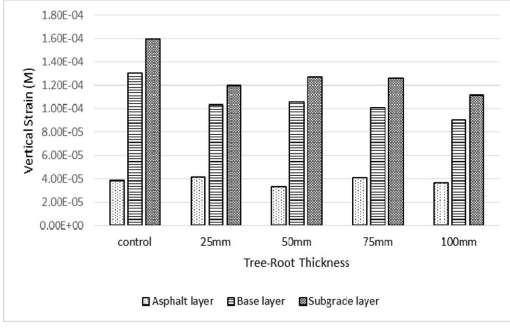

Figure 5. Strain redistribution for tree roots under the asphalt layer.

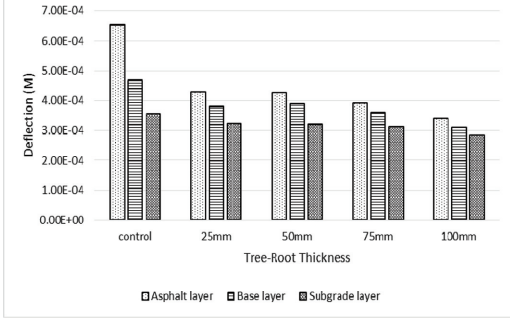

Figure 6. Deflection redistribution for tree roots under the asphalt layer.

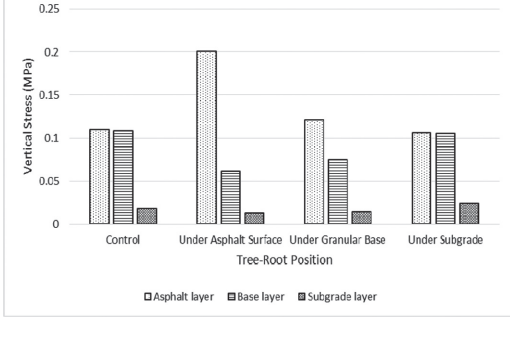

Figure 7. Stress redistribution for 100 mm tree roots.

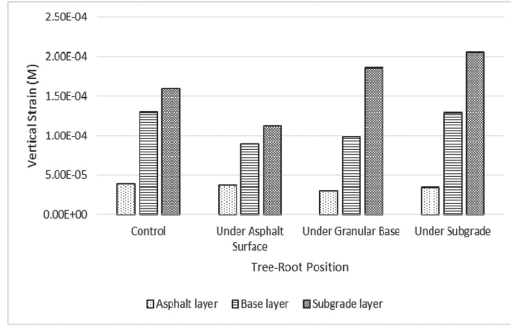

Figure 8. Strain redistribution for 100 mm tree roots.

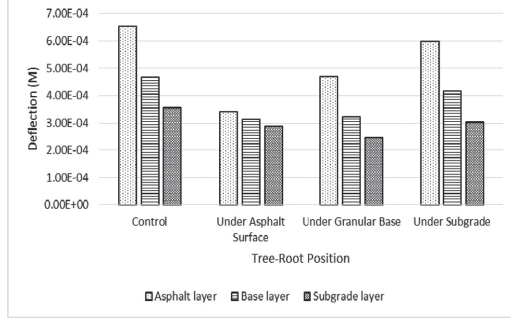

Figure 9. Deflection redistribution for 100 mm tree roots.

deflection (rutting) and strain in pavement layers; however, it was further observed to have increased the vertical stress in the asphalt layer that results in crack generation, while those of base and subgrade decrease. This implies that the stress that needs to be distributed downward the layers of the pavement is obstructed. Furthermore, Figures 7–9 show comparative graphs for stresses, strains and deflections by 100 mm-thick tree roots. The presence of tree roots underneath the base layer (scenario 2) shows a redistribution of stress and strain, as the vertical stress in the asphalt layer increases with the thickness of the tree root and the vertical strain increases in the subgrade layer, while the deflection decreases as in scenario 1. In scenario 3, the vertical stress and strain in the subgrade increases with little or no change in the other layers and the deflection still decreases. These results show that the presence of tree roots in the subgrade results in crack formation in the asphalt layer as the stress and strain are redistributed. Overall, in all scenarios, it was observed that the presence of tree roots in any pavement layer

have a significant effect on the stress generated in the asphalt layer and towards the edge (where the tree roots entered). Additionally, the movement of tree roots, which is the actual onsite scenario, was observed to cause an increase in the redistribution rate of stresses and strains.

4 CONCLUSION

In this study, the redistribution of stress, strain and deflection in flexible pavement through the tree-root impact is presented. A 3D FEM Abaqus® Software was used to analyze and understand the interaction between pavement layers and tree roots, and the results in terms of failures in pavement design.

The results indicated that tree roots essentially cause the redistribution of stress, strain and deflection. In the presence of tree roots, when the load is applied to the surface of the pavement, tree roots act like a reinforcement material, which is the cause of its elasticity nature that reduces deflection and strain in the layers. Nonetheless, it has a negative effect, as the stress that needs to be distributed downward the layers of the pavement is obstructed. This results in the generation of more stresses in overlay layers (asphalt and base layer), which later results in cracks. If these cracks are not maintained on time, it can lead to other failures such as surface lifting, potholes and raveling in the pavement structure.

REFERENCES

Adlinge, S.S. & Gupta, A.K. 2013. Pavement deterioration and its causes. *IOSR Journal of Mechanical & Civil Engineering* (IOSR-JMCE): 9–15.

Ahmed, H.Y. 2006. Effect of surface cracking on responses of flexible pavements structure. *Journal of Engineering Sciences*, *Assiut University* 34(3): 699–717.

Al-Azzawi, A.A. 2012. Finite element analysis of flexible pavements strengthen with geogrid. *ARPN Journal of Engineering and Applied Sciences* 7(10): 1295–1299.

Al-khateeb, L.A., Saoud, A. & Al-Msouti, M.F. 2011. Rutting prediction of flexible pavements using finite element modelling. *Jordan journal of Civil Engineering* 5(2): 173–189.

Appleton, B., Horsley, J. & Harris, V. 2002. *Trees for Parking Lots and Paved Areas.* Blacksburg: Virginia Cooperative Extension Publication.

Asphalt Pavement Alliance. 2010. *Perpetual Asphalt Pavements: A Synthesis*. Lanham, Maryland.

Barrell, J. 2011. Trees and Structural Damage. *www.barrelltreecare.co.uk*.

Beecham, S. 2012. Trees as Essential Infrastructure: Engineering and Design Considerations. *The 13th National Street Tree Symposium*, *the University of Adelaide, September 2012*.

Coder, K.D. 1998. Root Growth Control: Managing Perceptions and Realities. *The Landscape below Ground II. Second International Workshop on Tree Root Development in Urban Soils. Neely, D. & Watson, G. eds. Savoy, Ill, USA: International Society of Arboriculture, Champaign, IL*.

Colombier, G. 1997. *Cracking in Pavements: Nature and Origin of Cracks. Prevention of Reflective Cracking in Pavements*. RILEM Report.

D'Amato, N.E., Sydnor, T.D., Knee, M., Hunt, R. & Bishop, B. 2002. Which comes first, the root or the crack? *Journal of Arboriculture* 28(6): 277–289.

Darwish, S.G. 2012. Stress and Strain in Flexible Pavement. *http://www.unimasr.net/ums/upload/files/2012/Dec/UniMasr.com_892f9fb48f1aa1918a5cfbb7ad4d6f08.pdf*.

Day, S.D., Wiseman, P.E., Dickinson, S.B. & Harris, J.R. 2010. Contemporary concepts of root system architecture of urban trees. *Arboriculture & Urban Forestry* 36(4): 149–159.

Embraco, S.A. 2006. Some Aspects for the Simulation of a Non-Linear Problem with Plasticity and Contact. *http://www.ansys.com/staticassets/ANSYS/staticassets/resourcelibrary/confpaper/2006-Int-ANSYS-Conf-134.pdf*.

Green, D.W., Winandy, J.E. & Kretschmann, D.E. 1999. Mechanical properties of wood. *Wood handbook-Wood as An Engineering Material*. Madison, WI: U.S. Department of Agriculture, Forest Service, Forest Products Laboratory.

Hafeez, I. 2010. Empirical and Mechanistic Flexible Pavement Designed. *http://pec.org.pk/sCourse-files/Lec1.ppt*.

Hartley, M. 2012. *Tree Root Damage to Pipes*. The Arborist Network, Shanes Park NSW 2747.

Hauer, R.J., Miller, R.W. & Ouimet, D.M. 1994. Street tree decline and construction damage. *Journal of Arboriculture* 20(2): 94–97.

Huang, Y.H. 2004. *Pavement Analysis and Design*. 2nd ed. NJ: Pearson Education Inc.

Jain, S., Joshi, Y.P. & Golia, S.S. 2013. Design of rigid and flexible pavements by various methods and their cost analysis of each method. *International Journal of Engineering Research and Applications* 3(5): 119–123.

Jim, C.Y. 2003. Protection of urban trees from trenching damage in compact city environments. *Cities* 2(20): 87–94.

Kopinga, J. 1994. Aspects of the Damage to Asphalt Road Pavings Caused by Roots. *The Landscape below Ground. Proceedings of an International Workshop on Tree Root Development in Urban Soils. Watson, G. & Neely, D. eds. Champaign, IL: International Society of Arboriculture.*

Kordi, N.E., Endut, I.R. & Baharom, B. 2010. Types of Damages on Flexible Pavement for Malaysian Federal Road. *Proceeding of Malaysian Universities Transportation Research Forum and Conferences*, *2010*, Putrajaya, Kuala Lumpur: 421–432.

Line Drawing. 2013. Line Drawing Tree Roots#18409. *www.dawnc.eu/line-drawing-tree-roots/*.

McPherson, E.G. & Muchnick, J. 2005. Effects of street tree shade on asphalt concrete pavement performance. *Journal of Arboriculture* 31(6): 303–310.

Morell, J.D. 1992. Competition for space in the urban infrastructure. *Arboricultural Journal* 18(2): 73–75.

Morgenroth, J. 2011. Root growth response of platanus orientalis to porous pavements. *Arboriculture & Urban Forestry* 37(2): 45–50.

NCHRP. 2004. *Guide for Mechanistic-Empirical Design of New and Rehabilitated Pavement Structures: Appendix RR-Finite Element Procedures for Flexible Pavement Analysis.* Washington D.C.: Transportation Research Board, National Research Council.

Nicoll, B.C. & Coutts, M.P. 1997. Direct damage by urban tree roots: Paving the way for less damaging street trees. *Arboricultural Practice, Present and Future.* Claridge J. ed. Norwich, UK: Department of the Environment, Transport and the Regions.

Pavement Interactive. 2008. Flexible Pavement Mechanistic Models. *www.pavement-interactive.org/article/flexible-pavement-mechanistic-models/.*

PFI. 2010. Pavement Failure Identification. http://www.apai.net/cmdocs/apai/designguide/Appendix_A-B.pdf.

Rahman, M.T., Mahmud, K. & Ahsan, S. 2011. Stress-strain characteristics of flexible pavement using finite element analysis. *International Journal of Civil and Structural Engineering* 2(1): 233–240.

Randrup, T.B., McPherson, E.G. & Costello, L.R. 2003. A review of tree root conflicts with sidewalks, curbs, and roads. *Urban Ecosystems* 5(3): 209–225.

Rani, O.A. 2007. *The Effectiveness of Pavement Rehabilitation at Kuala Lumpur Karak Highway.* Johor: Universiti Teknologi Malaysia.

Roodt, L.D. 2012. Managing Trees in Road Reserves for Road Safety. *Abstracts of the 31st Southern African Transport Conference (SATC 2012), 9–12 July 2012.* Pretoria, South Africa: CSIR International Convention Centre,

Rosenfeld, A.H., Akbari, H., Romm, J.J. & Pomerantz, M. 1998. Cool communities: Strategies for heat island mitigation and smog reduction. *Energy and Buildings* 28(1): 51–62.

Russell, T. & Catherine, C. 2003. *The World Encyclopedia of Trees, Armadillo.*

Shafabakhsh, G.A., Motamedi, M. & Family, A. 2013. Influence of asphalt concrete thickness on settlement of flexible pavements. *Electronic Journal of Geotechnical Engineering* 18(Bund. C): 473–483.

Smiley, E.T. 2003. *Sidewalk Repair near Trees.* Bartlett Tree Research Laboratories Technical Report.

South African National Road Agency Ltd. 2013. *Pavement Design: South African Pavement Engineering Manual*. South Africa: An Initiative of the South African National Roads Agency Ltd.

Wang, J. 2001. *Three-Dimensional Finite Element Analysis of Flexible Pavements.* United States: Department of Civil Engineering, University of Maine.

Yin, H. 2013. The impact of strain gage instrumentation on localized strain responses in asphalt concrete pavements. *International Journal of Pavement Research and Technology* 6(3): 225–234.

This page intentionally left blank

Civil Engineering and Urban Planning IV – Liu et al. (Eds)
© 2016 Taylor & Francis Group, London, ISBN 978-1-138-02903-3

Navigation risk evaluation for channels based on the Belief Rule Base

Wei-Dong Gan & Zi-Yu Zhang
Tianjin Research Institute of Water Transport Engineering, Ministry of Communications, Tianjin, China

Yan-Wei Li
Strategic Development Department of CIMC Logistic (Shenzhen), Shenzhen, Guangdong, China

ABSTRACT: This paper analyzes the complex nonlinear relationship between the navigation risk in channels and each influence factor, to overcome fuzzy and subjective artificial evaluation. A Belief Rule Base (BRB) methodology is used to evaluate the risk of navigation in channels, which overcomes the shortcomings of traditional evaluation techniques that can only use expert knowledge or training data. Influence factors of navigation risk are identified by consulting the experts in the maritime transportation area. Data processing is formed on the belief rule base of navigation risk. The effective combination of qualitative knowledge and quantitative data is studied. The results of calculation examples indicate that the method is feasible and effective. The results provide an important reference to channel traffic management.

1 INTRODUCTION

With China's reform and opening-up policy waterway transportation developing considerably, the cargo throughput in ports has increased nearly 20 times in the recent 30 years. Followed by the sharp rise in the number of ships, traffic density has increased correspondingly, and the large-scale and high speed ships have also been developing rapidly, which makes the hardware conditions, such as channel resources, to be unsupported. Navigation risk in most waterways has increased. Due to the fact that part of the navigation conditions is limited and navigation risk is complex, the limited navigation resources cannot be fully utilized. As a result, accidents such as collisions and groundings occur frequently and the waterways are sometimes congested.

Ensuring ship traffic safety and improving the operation efficiency of ships are the focus of attention in the water transport field, and are also the basic requirements of the whole community of transport. The development prospect is to realize the efficient and unobstructed operation of the system on the safety basis. At present, qualitative ship navigation risk definition and quantitative calculation has a series of theories and methods. But research has mainly concentrated on two vessels or simple encounter risk situations, which makes it difficult to meet the development of water transportation. Few scholars have focused on the macro-perspective of risk prediction problems concerning navigable waters. This paper proposes a scientific prediction theory to study the main risk factor of navigable waters and scientific prediction of ship navigation risk of such waters, providing reference for the maritime departments in charge of supervision and effective organization of traffic schedule.

The present research lacks scientific and systematic approaches in a number of decision problems because they are often based on subjective knowledge. Decision problems usually carry uncertainties because of which the inner influence is relatively complicated, and the existing data are insufficient. Therefore, it is very difficult to solve the decision problem by means of traditional decision theory and modeling methods. Zhang et al. (2010) and Li et al. (2009) used expert scoring to aid analysis and decision-making. The problem of expert decision-making is that judgment given by experts is very subjective and thus difficult to unify standard because sometimes the data are incomplete and fuzzy. Yang (2001) and Yang et al. (2006) proposed a new decision method called the belief rule reasoning, which is based on the belief rule base. The method judges the system input by the activation weight of all the rules. Information fusion is then processed by using evidence fusion. This method can express the nonlinear relationship of the inner system and the process fuzzy problem better. The method has been successfully applied in areas of prediction, diagnosis and controlling (Yang et al. 2013; Zhang et al. 2013; Zhang et al. 2011).

2 BELIEF RULE BASE

The core method of the theory is evidential reasoning. The information expression of the belief rule and fusion needs to be achieved under the framework of evidence theory. Among them, the belief rule reasoning method is represented by four tuples $R = <X, A, D, F>$, which can be divided into two parts: antecedent and consequent variables. $X = \{X_i; i = 1 \ldots T\}$ is referred to the antecedent variables of rules. $A = \{A_1, A_2 \ldots A_T\}$ refers to the evaluation grade of the reference set. The whole value of X is in A. Moreover, X_i is distributed by A_i. The evaluation grade manifests the distributed nature, and can express the value by using the numerical or fuzzy version. $\{X_1 \rightarrow A_1, X_2 \rightarrow A_2 \ldots X_T \rightarrow A_T\}$ refers to the basic status of problem representation. Each of them can be expressed as the logical relationship "OR" and "AND", "or" expressed as OR and $\vee$, and "and" expressed as AND and $\wedge$. D is the distributed evaluation grade of the consequent variables. F is the logical relationship function between the antecedent and consequent rules.

The basic way of expression of the rules is in the IF-THEN form. For example, IF $A_1^K \wedge A_2^K \wedge A_3^K \wedge \ldots \wedge A_T^K$, THEN$\{(D_1, \beta_{1,K}), (D_2, \beta_{2,K}), \ldots, (D_N, \beta_{N,K})\}, \{0 \le \sum_{n=1}^{N} \beta_{n,K} \le 1\}$. In this method, belief rules need to take advantage of the weight of information fusion. The algorithm of the application is recursive basic evidential reasoning.

In short, the belief rule base is actually originated from the traditional expert system. But for simplification, the IF-THEN rule is optimized and joined with the belief level in the result by considering the weights of the attributes of the premise and the weights of the rules, and the formation of the belief rules. The belief rules of conditions and results fusion process are combined with related knowledge of evidence analysis theory.

3 RISK FACTOR IDENTIFICATION

The selected key risk factors in this paper are for predicting risk in real time. Three-angle assumption with human-ship surroundings is considered to identify the most characteristic or the influence of the most obvious effect of the factors in each type of factor. At last, the macro-risk of the channel is evaluated and predicted.

First, this paper pays attention to the channel risk, which has the following characteristics:

- The real-time state of channel running can be received. This paper focuses on the navigable waters of the macro-risk perspective. So, attention is paid to the real-time channel running state, rather than directly to the potential channel ability or extremal properties.
- The risk of real-time state of channel can be received. Different from previous studies, this paper focuses on the channel state parameter to reflect channel risk level, rather than on congestion and efficiency at the same time. Risk description in this paper is not from the angles of probability or the consequences of incident, while the concept is emphasized on risk or safety, which is the relative level of reaction under different conditions.
- Concerns about the ability of ship navigation can be received. Based on the height of the traffic organization, scheduling optimization should have the foresight. The main object is the ship that is about to enter a leg, the potential service object of the leg, transposition thinking from the ship's point of view, and more attention is paid to whether it can enter the leg under a low risk, i.e. the need to clear channel can receive ship capacity and the ship driver will form an acceptable risk impression in the subjective consciousness.

The concept of channel stock ratio and heading order is introduced. It is a key risk factor in this study. In addition to considering the correlation degree of visibility and ship accident rate, visibility is selected as the key risk factor.

The concept of channel stock ratio contents is as follows: at a certain period of time, there is a variation between the possible capacity of the channel section and ships' numbers in the channel section (according to the specified standard ship-type conversion), which is called as the channel section stock of the time. The ratio between the channel stock and the possible capacity is the channel stock ratio. Its expression is as follows:

$$P_R = \frac{C_r - Q}{C_r} \tag{1}$$

Here, P_R is the channel stock ratio and C_r is the channel navigation ability or possible traffic capacity. This can be calculated based on the overall ship domain model based on Fujii: take a long axis of 7 L in the general condition of channel, take a long axis of 6 L for the narrow leg, while considering the short axis data of the inland river ship domain model, take a short axis of 1 L. Q is the actual ship channel flow at the specified time.

For different channels, state division of their channel stock ratio is not the same, which is used to evaluate navigation risk. So, it adopts experts' scoring method, which consults the experienced ship's officers, pilot and VTS operators, and then determines the corresponding relationship between the channel stock and the risk from the related personnel in the subconscious based on the analysis

and processing of the statistical data. Therefore, the factor is actually a reaction result of human factors on the psychological quality and skill level.

Under certain navigation conditions of a channel in width, depth, navigation aids and channel stock ratio, interferences between the ships will be relatively small, the ship's courses are relatively concentrated, the ship navigational order is relatively orderly, and the whole channel of ship collision risk will also be relatively small, if the ships are in the same general navigation direction, and vice versa. Therefore, the number of ship's courses in the channel is taken into account in this paper; this factor can also play a complement role of channel stock ratio on the ship receiving ability of channel.

According to the "International Regulations for Preventing Collisions at Sea", ship course can be divided by considering the mutual position relationship on the basis of the statistics. It is worth mentioning that according to the relevant provisions of COLREGs (China MSA 2000), ship course is concerned with the ship's heading instead of the ship's track.

Considering that the ship's encounter situations in the channel are mainly overtaking and encountering, this paper assumed a two-way navigation in the uplink and downlink ship separately, without considering crossing the channel and large-angle crossing encounter situation in order to simplify the research. Overtaking on the ship position relationship requirement is before the vessel abaft the beam 22.5 degrees, encountering requirement of the ship in the opposite or nearly opposite course meet, in which the heading angle in 6 degrees is generally deemed as nearly opposite.

When distinguishing the ship course, assuming that a ship's heading and the uplink or downlink channel is completely consistent, the ship is considered as a reference standard for a specific note C_0 and a ship course C needs itself from the C_0 direction to starboard rotation that is positive, otherwise it is recorded as negative, and then the expression of a certain ship-course can be written as follows:

$$C = C_0 \pm \Delta C \tag{2}$$

Here, ΔC is the rotation angle for any ship course compared with the reference direction C_0.

In order to simplify the calculation, each of the uplink and downlink ship course is, respectively, divided into 3 categories. Course interval, denoted as $C_{interval}$, is the uplink and downlink course interval with a total of 6 course intervals, as shown in Figure 1. The uplink and downlink vessels of various interval expressions are as follows:

$$C^1{}_{\text{up}} = \{C|\ C = C_0 \pm 30\},\ C^1{}_{\text{down}} = \{C|\ C = C_0 \pm 30\};$$
$$C^2{}_{\text{up}} = \{C|\ C_0 + 30 < C < C_0 + 67.5\},$$

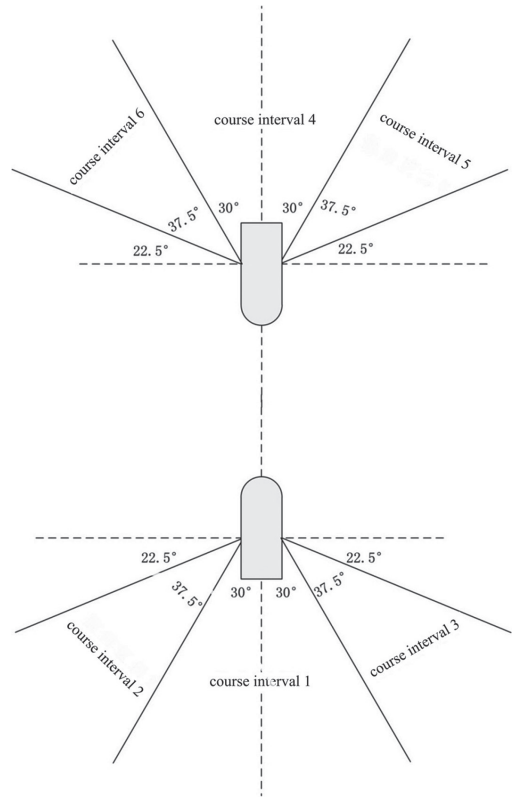

Figure 1. Schematic diagram of course interval division.

$$C^2{}_{\text{down}} = \{C|\ C_0 + 30 < C < C_0 + 67.5\};$$
$$C^3{}_{\text{up}} = \{C|\ C_0 - 67.5 < C < C_0 - 30\},$$
$$C^3{}_{\text{down}} = \{C|\ C_0 - 67.5 < C < C_0 - 30\}.$$

The domestic scholar (Guan 1997) analyzed the number of marine accidents occurred within 1000 hours, and obtained the function relationship between the visibility distance and marine accidents with the regression analysis. The expression of the equation can be written as follows:

$$N = 90 \times D^{-0.8} \tag{3}$$

Here, N is the marine accidents and D is the visibility distance (in km).

By analyzing the diagram of the visibility distance and the number of ship accidents in Figure 2, when the visibility distance is more than 4 km, the number of marine accidents is less and relatively stable. When the visibility distance is less than 4 km, the number of marine accidents increases rapidly with the visibility distance decreasing,

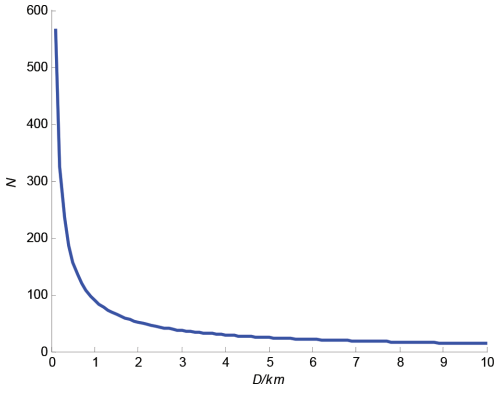

Figure 2. Visibility distance and accident number diagram.

which shows that the visibility distance starts to impact on the safety of navigation. When the visibility distance decreases to below 1 km, the number of marine accidents increases sharply; at this time, the visibility level is referred to as a danger factor for navigation safety.

4 MODEL CONSTRUCTION

According to the identification of risk factors, selected channel stock ratio, course order, visibility are considered as antecedent variables, and navigation risk as consequent variables.

4.1 *Determination of the reference value*

In this paper, the antecedent variables are divided into 3 grades, namely channel stock ratio {good, medium, poor}, course order {good, medium, poor}, visibility {good, medium, poor}, consequent variables selected channel risk {very low, low, general, high, very high}.

The above reference values are semantic value and should be quantified. Through consulting the ship's officers in the coastal waters, VTS operators and the pilot, the channel stock ratio equal to 0.7 can be defined as good, 0.5 as medium and 0.3 as poor, when the channel stock ratio is between the two numbers, which can be given expression belief distributed based on "good, medium, poor". Through the study of the statistical classification of ship course in the channel, we can get the number of actual course belonging to the course interval and then define the course order status on the basis of the course interval number. It simplifies the process of risk evaluation and prediction, and according to the result of expert scoring, the following processing can be made: when the number of ship course belonging to the interval is 1, the course order is defined as good. When the number is 3, it is defined as medium. When the number is 6, it is defined as poor. When the number is 2, 4 or 5, which can be given expression belief distributed based on 'good, medium, poor'. Figure 2 shows the function relation for state definition of degree of visibility, and then the real-time visibility distance classification, and the real-time visibility distance status will be as one of the inputs of the risk model for evaluation and prediction. On the basis of navigation habits, we can convert the unit of visibility distance with the km to the nautical mile (n mile), and can thus approximate the process. Visibility level is divided into "excellent, medium, poor". It is defined as excellent when the visibility distance is 2 n miles. It is defined as medium when the visibility distance is 1 n mile. It is defined as poor when the visibility distance is 0.5 n mile. When the visibility distance is between the two, which can be given expression belief distributed on the basis of "excellent, medium, poor". The quantitative results are summarized in Tables 1 to 4.

4.2 *Belief rule base establishment*

Through analyzing the experts' questionnaire data, the index weights of factors of ship collision risk in the channel are the channel stock ratio of 0.4, the course interval of 0.3 and the visibility of 0.3. Each index includes 3 states, making a total of 27 belief rules that are all in the form of belief and

Table 1. Channel stock ratio evaluation set P.

Semantic value	Good	Medium	Poor
Quantitative value	0.7	0.5	0.3

Table 2. Course order evaluation set C.

Semantic value	Good	Medium	Poor
Quantitative value	1	3	6

Table 3. Visibility evaluation set D.

Semantic value	Good	Medium	Poor
Quantitative value	2	1	0.5

Table 4. Navigation risk evaluation set W.

Semantic value	Very low	Low	General	High	Very high
Quantitative value	1	2	3	4	5

Table 5. Initial belief rule bases.

Number	Channel stock ratio P	Course order C	Visibility D	Navigation risk distributed evaluation results				
				Very low	Low	General	High	Very high
1	Good	Good	Excellent	0.75	0.24	0.01	0	0
2	Good	Good	Medium	0.6	0.29	0.11	0	0
3	Good	Good	Poor	0.31	0.28	0.21	0.16	0.04
4	Good	Medium	Excellent	0.43	0.32	0.17	0.06	0.02
5	Good	Medium	Medium	0.3	0.26	0.28	0.12	0.04
6	Good	Medium	Poor	0.18	0.18	0.32	0.22	0.1
7	Good	Poor	Excellent	0.19	0.22	0.3	0.23	0.06
8	Good	Poor	Medium	0.17	0.18	0.23	0.28	0.14
9	Good	Poor	Poor	0.09	0.12	0.25	0.32	0.22
10	Medium	Good	Excellent	0.53	0.26	0.15	0.03	0.03
11	Medium	Good	Medium	0.39	0.29	0.23	0.06	0.03
12	Medium	Good	Poor	0.19	0.23	0.28	0.22	0.08
13	Medium	Medium	Excellent	0.31	0.25	0.25	0.14	0.05
14	Medium	Medium	Medium	0.16	0.27	0.36	0.16	0.05
15	Medium	Medium	Poor	0.08	0.21	0.27	0.26	0.18
16	Medium	Poor	Excellent	0.06	0.25	0.34	0.26	0.09
17	Medium	Poor	Medium	0.03	0.22	0.35	0.28	0.12
18	Medium	Poor	Poor	0.01	0.07	0.26	0.33	0.33
19	Poor	Good	Excellent	0.26	0.19	0.29	0.2	0.06
20	Poor	Good	Medium	0.19	0.23	0.29	0.21	0.08
21	Poor	Good	Poor	0.11	0.18	0.27	0.26	0.18
22	Poor	Medium	Excellent	0.11	0.26	0.3	0.2	0.13
23	Poor	Medium	Medium	0.05	0.21	0.33	0.28	0.13
24	Poor	Medium	Poor	0.02	0.09	0.3	0.36	0.23
25	Poor	Poor	Excellent	0.03	0.11	0.26	0.38	0.22
26	Poor	Poor	Medium	0.01	0.05	0.22	0.38	0.34
27	Poor	Poor	Poor	0.00	0.02	0.11	0.32	0.55

form a belief rule base of navigation risk prediction. The efficient experts' questionnaire information is weighted mean and normalized, to get the initial belief rules as given in Table 5.

4.3 *Risk evaluation*

Inputting the value of each risk factor into the belief rule base, rule activation calculation and rule weight fusion, we can obtain the prediction results of navigation risk $B = (b_1, b_2, b_3, b_4, b_5)$.

4.4 *Result processing*

In order to make the results more clear, the final results are processed a second time and $R = BW^T$ is calculated, in which R values are found to be approximately 1~5; thus, the risk degree number corresponds to the waters' ultimate risk degree.

5 MODEL APPLICATION

This section takes the precautionary area in the Tianjin Port compound channel as a model verification example.

5.1 *Risk factor assignment*

– Channel stock ratio

At present, the channel section between No. 39 and No. 46 buoy light of the compound channel in the Tianjin port is a precautionary area. To exceed the limits of the Beaufort scale, the ship's breadth and provision goods, it implements one-way traffic. Taking into account the objective situation of the compound channel, and comprehensively referring to other domestic scholars, relevant research is conducted on the Tianjin Port compound channel and relevant rules and regulations, in which 146 m length and 10000 gross tonnage ship are selected as the standard type and ship domain is considered as the long axis of 6 L and the short axis of 1 L in accordance with the analysis of risk factors, for calculating the actual channel stock ratio. The "Ship navigation rules for Tianjin Port compound channel (Trial)" requirements are that the speed of a small ship should not be beyond 13 knots, and should not be less than 5 knots without permission. In fact, the section from No. 39 to No. 46 buoy light exists crossing flow,

and the speed should be reduced appropriately by 10 knots. In this paper, taking the macro-organization time for the next 1 hour, the channel stock ratio is 0.6.

– Course order
  This paper analyzes the statistics data of the ships' course between No. 39 and No. 46 buoy light within 1 hour. However, the time interval has not a large prediction range, i.e. 1 hour. According to the destination, the navigation condition, leeway and drift angle appropriately corrects the number of courses belonging to the interval at the observation time. Here, taking the course interval number as 3.
– Visibility
  In this paper, the visibility level is divided into "excellent, medium, poor". It is defined as excellent when the visibility distance is 2 n miles. It is defined as medium when the visibility distance is 1 n mile. It is defined as poor when the visibility distance is 0.5n mile. According to the meteorological data in the observation period, the visibility distance is about 2.5n miles; thus, the state is "excellent".

5.2 *Risk value calculation*

By inputting the risk factor status value into the belief rule base, rule activation calculation and rule weight fusion, we can draw the risk prediction results for the "very low 0.6815, low 0.2285, general 0.0656, high 0.0122, very high 0.0122".

5.3 *Result processing*

$R = BW^T = (0.6815,0.2285,0.0656,0.0122,0.0122) \times (1,2,3,4,5)^T = 1.4451$, and according to the navigation risk evaluation set W, R is between "very low" and "low", and is closer to "very low". So the navigation risk of the Tianjin port compound channel precautionary area is "very low". In recent years, statistical yearbook and the maritime accident results have been generally consistent with this result. That is to say, scientific and reasonable traffic organization and management of the Tianjin Port maritime safety authority works well in controlling navigational risk.

6 CONCLUSION

In this paper, the belief rule base is applied to the risk assessment of the approach channel of the Tianjin port. The belief rule base can not only fully utilize expert knowledge, but also systematically learn the historical data. The method can fit the development trend of the risk assessment method, which is the combination of qualitative knowledge and quantitative data. The results indicate that the method is feasible. Since the initial rule base established is simple and expert knowledge is limited, the setting parameter does not fully reflect the characteristics of the system. If we can make full use of expert experience and more different types of data, the evaluation results will be more accurate.

REFERENCES

China, MSA. 2000. *International Regulations for Preventing Collisions at Sea, 1972*. Beijing: CHINA, MSA. ed.

Guan, Z.J. 1997. Elementary analysis of marine traffic accidents. *Journal of Dalian Maritime University* 2(1): 46–51.

Li, H. & Wang, G.B. 2009. Operational effectiveness evaluation of foreign army's aircraft carrier formation based on fuzzy AHP comprehensive evaluation. *Ordnance Industry Automation* 28(3): 26–28.

Yang, J.B. 2001. Rule and utility based evidential reasoning approach for multi-attribute decision analysis under uncertainties. *European Journal of Operational Research* 131(1): 31–61.

Yang, J.B., Liu, J. & Wang, J. 2006. Belief rule-base inference methodology using the evidential reasoning approach RIMER. *IEEE Transactions on Systems, Man, and Cybernetics, Part A: Systems and Humans* 36(2): 266–285.

Yang, L.H., Cai, Z.L., Huang, Z.X., et al. 2013. Belief rule-base inference methodology for predicting probability of taking taxi. *Journal of Frontiers of Computer Science and Technology* 9(8): 985–994.

Zhang, B.C., Yin, X.J., Wang, Z.L., et al. 2013. Fault diagnosis for servo system of CNC based on RIMER. *Journal of Vibration, Measurement & Diagnosis* 33(4): 694–700.

Zhang, W., Shi, C.P. & Hu, C.H., et al. 2011. Fault diagnosis of engine based on RIMER expert system. *System Simulation Technology* 7(1): 11–15.

Zhang, Y.D., Guo, J. & Shan, N. 2010. Comprehensive evaluation of risk severity level of railway signal system. *Journal of Southwest Jiaotong University* 45(5): 758–762.

Civil Engineering and Urban Planning IV – Liu et al. (Eds)
© 2016 Taylor & Francis Group, London, ISBN 978-1-138-02903-3

Studying the effect of the difference in vehicles' mass on fatal accidents

S.M. Sadat Hoseini, F. Zera'at Peyma & S.S. Kashfi
Amin Police University, Tehran, Iran

ABSTRACT: Traffic accidents are a human tragedy that kills many people worldwide annually. In this research, causes of fatal accidents in the highway network of Isfahan city in Iran are studied. The survey just includes the killed persons in the scene of accident. The results indicate that vehicle mass is a crucial factor behind how injuries are distributed among the involved vehicles in a two-vehicle crash. A larger vehicle mass will protect the occupants in the vehicle, while at the same time inflict a higher injury or fatality risk on the occupants in the collision partner. This research was done on all fatal accidents that were recorded by police in the highway network of Isfahan city. This survey shows that most of fatal accidents occur when the difference in mass between the involved vehicles is high.

1 INTRODUCTION

Many studies have established that drivers of larger, heavier cars have lower risks in crashes than drivers of smaller, lighter cars (Severy et al. 1971) (Campbel et al. 1973) (O'Neill et al. 1974). The size and weight of cars are decreased to consume less fuel. This will lead to higher risk in a collision (Joksh et al. 1976) (Grime et al. 1979). However, the question of how the addition of mass to an existing car affects safety remains to be unanswered (Evans et al. 2001).

Hultkrantz et al. (2011) showed in Swedish data that 1 kg of curb weight of a vehicle will increase the accident cost in the collision partner given that the collision partner is lighter than the vehicle in question. At the same time, 1 kg of curb weight will decrease the own-vehicle accident cost, given a collision with a heavier vehicle. For the heavier vehicle in a collision, neither own weight nor the weight of the other vehicle has any significant influence on accident costs.

In each accident, the two involved vehicles are divided into the lighter vehicle and the heavier vehicle, and the effect of weight is examined separately for the two groups. The accident costs that fall on the lighter vehicle increase with the mass of the heavier vehicle and decrease with the own mass. Given that a vehicle is the heavier one in the crash, neither the own mass nor the mass of the lighter vehicle significantly affects the accident cost.

The expected external accident cost is calculated and it is shown to increase rapidly with vehicle mass. The paper discusses different solutions to internalize this external accident cost and calculates a mass-dependent multiplicative tax on the insurance premium in a no-fault insurance system (Jonsson et al. 2009).

For the injuries in two-vehicle crashes, it is important to take into account the concept of both crashworthiness and aggressiveness. Crashworthiness reflects the injury or fatality risk to the car occupants in a specific collision situation, while aggressiveness is a concept that instead reflects the injuries and the fatality risk to the occupants in the collision partner. A third concept that complicates the analysis is that of compatibility. This reflects the fact that a given vehicle can pose a different injury or fatality risk to different vehicles with the same crashworthiness due to a mismatch between vehicle parts (Joksh et al. 1998).

The strongest effect on the relative fatality risks in a collision is the weight ratio of the two vehicles. A weight ratio of 2:1, not rare in actual collisions, results in a fatality risk ratio of about 10:1, even in a collision between two cars (Joksh et al. 1998).

Table 1. Characteristics of Isfahan highways network.

Highway	Length (m)	Width (m)
Kharazi	4540	35
SayadShirazi	3144	35
Sofeh	2739	30
Agharebparast	4975	27
Keshvari	4500	25
Chamran	5450	37
Radani poor	2668	37
Agha Babaee	5263	28
Habibolahi	1644	27
Maysami	1427	35
West Highway	1045	25
ZoobAhan	2719	32

2 ISFAHAN HIGHWAYS NETWORK

Isfahan is a great city with a 42 km-long highway network with grade-separated junctions. Table 1 presents the characteristics of Isfahan highways.

This survey is a descriptive-periodic research on all fatal accidents in Isfahan highways that were recorded by police in 2008.

3 THEORETICAL BASIS OF ACCELERATION OF VEHICLES IN ACCIDENTS

This section investigated the acceleration of two vehicles with different masses in a crashing event by movement laws. Let us assume that two vehicles with different masses and speeds are moving, as shown in Figure 1.

In Figure 1, m and M are the mass of the small and big cars and V_m and V_M are the speed of the small and big cars, respectively. Let us assume that these two cars crashed and both of them changed to be a single mass and they are moving at the same speed. According to the conservation value of momentum, the following equation must be applied:

$$M \cdot V_M + m \cdot V_m = (M + m)V'$$

Here, the V′ is the final speed of two cars. According to the above relation, the final speed of two cars can be calculated by the following relation:

$$V' = \frac{M \cdot V_M + m \cdot V_t}{m + M}$$

The cause of injury to the driver in an accident is the acceleration of the vehicle. The acceleration of the bigger car can be calculated by the following equation:

$$a_M = \frac{V_M - V'}{dt} = \frac{m \cdot (V_M - V_m)}{dt \cdot (m + M)}$$

The acceleration of the small car can be calculated by the following equation:

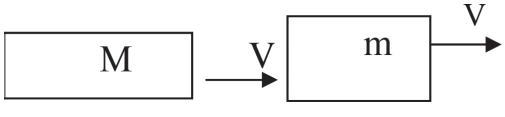

Figure 1. Two vehicles are moving.

$$a_m = \frac{V_m - V'}{dt} = \frac{M \cdot (V_M - V_m)}{dt \cdot (m + M)}$$

As can be seen, the acceleration of the smaller vehicle is greater than the bigger vehicle, which causes the high injury severity to the occupants of the smaller vehicle compared with the bigger vehicle. The higher the difference in mass, the higher the injury severity to the occupants of the smaller vehicle.

4 DESCRIPTION OF FATAL ACCIDENTS IN TERMS OF THE TYPE OF CRASH

The share of involved vehicles in fatal accidents of Isfahan highways is shown in Figure 2. Private cars have the biggest percent among the other vehicles, and pickup trucks and motorcycles are in the second and third positions.

Categorizing accidents according to the involved vehicles shows that pedestrian-vehicle crash (30%)

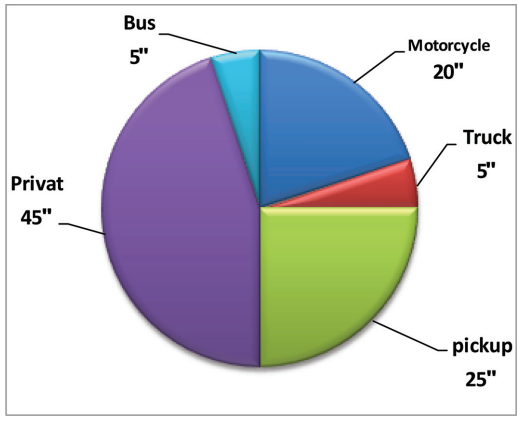

Figure 2. Share of fatal accidents between vehicles.

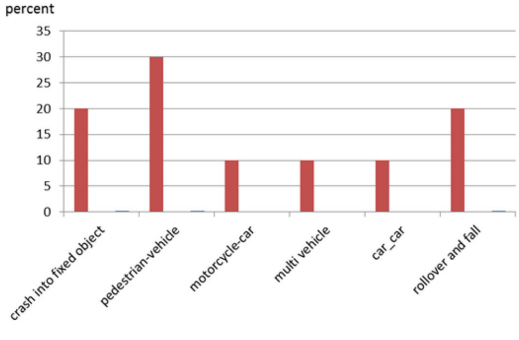

Figure 3. Share of fatal accidents between involved vehicles.

Table 2. Binomial test for the effect of difference in mass.

Difference in mass	Category	N	Observed prop.	Test prop.	Exact sig. (2-tailed)
Existence of difference of mass	1.00	12	0.60	0.50	0.012
Inexistence of deference of mass	0.00	8	0.40	–	–
Total	–	20	1.00	–	–

has the highest rate. In addition, it can be seen that 60% of fatal accidents relate to three major types of accidents in which there is a high difference in mass between the involved vehicles, which include pedestrian-vehicle crash, crash into fixed roadside objects and car-motorcycle crash. This is shown in Figure 3.

5 THE EFFECT OF THE DIFFERENCE IN VEHICLES' MASS ON FATAL ACCIDENTS

In this section, the effect of the difference in vehicles' mass on fatal accidents is tested. Here, the hypothesis that the high difference in mass between involved vehicles does not have the effects on fatal accidents is tested. It is assumed that there is a high difference in mass in the pedestrian-vehicle crash, crash into fixed roadside objects and car-motorcycle crash. In accidents of vehicle with a fixed object such as the bridge, the difference in mass is very high. According to these assumptions, the number of accidents in which the difference in mass between two vehicles is high, i.e. 12 out of 20 accidents, and the following hypothesis test is made:

H_0 = The high difference in mass between involved vehicles does not have the effects on fatal accidents.

H_1 = The high difference in mass between involved vehicles has the effects on fatal accidents.

For this assumption, binomial test was conducted, findings of which are summarized in Table 2.

The exact significance (2-tailed) is 0.012. Thus, the assumption of H_1 is accepted. In other words, on the basis of the high difference in mass between involved vehicles in accidents, the probability of fatality is also high.

6 CONCLUSION AND SUGGESTION FOR NEW RESEARCH

In this research, it was shown that the difference in mass between two vehicles has a significant effect on fatal accidents. It is advised that the traffic of heavy vehicles be limited in Isfahan highways and the enforcement of police be increased in these highways.

In future studies, highways of other cities and intercity highways should be investigated. Other types of roads, especially rural roads, should be studied for checking the effect of the difference in vehicles mass on the risk of fatality of the involved vehicles.

REFERENCES

Campbell, B.J. & Reinfurt, D.W. 1973. *The Relationship between Driver Crash Injury and Passenger Car Weight.* Chapel Hill, NC: Highway Safety Research Center, University of North Carolina.

Evans, L. 2001. Causal influence of car mass and size on driver fatality risk. *Am J Pub Health* (vol: 91): 1076–1081.

Grime, G. & Hutchinson, T.P. 1979. Mass of vehicles and driver injury. *Ergonomics* (vol: 22): 93–104.

Hultkrantz, L. & Lindberg, G. 2011. Accident Cost Speed and Mass of Vehicles Externalities and Insurance. *https://ideas.repec.org/p/oec/itfaab/2011-26-en.html.*

Joksch, H.C. 1976. *Analysis of the Future Effects of the Fuel Shortage and Increased Small Car usage upon Traffic Deaths and Injuries*. Report DOT-TSC-OST-75–21.

Joksch, H., Massie, D. & Pischler, R. 1998. *Vehicle Aggressivity: Fleet Characterization Using Traffic Collision Data*, DOT-HS-808-679. Washington, DC: National Highway Traffic Safety Administration, U.S. Dep't of Transportation.

Jonsson, L. & Lindberg, G. 2009. *Accident Externality and Vehicle Size—Evidence from Swedish Collision Accidents*. Sweden: Swedish National Road and Transport Research Institute (VTI).

O'Neill, B., Joksch, H. & Haddon, Jr., W. 1974. Empirical Relationships between Car Size, Car Weight and Crash Injuries in Car-to-car Crashes. *Proceedings of the Fifth International Technical Conference on Experimental Safety Vehicles, London, UK.* Washington, DC: National Highway Traffic Safety Administration.

Severy, D.M., Harrison, M.B. & Blaisdell, D.M. 1971. Smaller vehicle versus larger vehicle collisions. *SAE Transactions* (vol: 80): 2929–2958.

This page intentionally left blank

Civil Engineering and Urban Planning IV – Liu et al. (Eds)
© 2016 Taylor & Francis Group, London, ISBN 978-1-138-02903-3

Analysis and evaluation on depth perception of commercial vehicle drivers

Ling-Chao Zhang, Lang Wei, Jin-Cao Zhou, Shun Tian & Sheng-Chang Wang
Automobile College, Chang'an University, Xi'an, Shaanxi, China

ABSTRACT: Drivers' deep perception has a certain relation with distance estimation and judgment on the driving. It has an important significance to research its influence on traffic safety. First, the paper used a depth perception tester developed by the research group to detect the driver's depth perception of commercial vehicles, and collected 5,008 effective samples. Then, using the method of mathematical statistics, the paper obtained the result that the deep perception mean value had a positive correlation with accidents. Furthermore, according to the testing results of the instruments, the paper formulated a detection threshold with four levels for helping transportation companies to assess the commercial vehicle drivers. Finally, it was found that drivers' age and driving experience had an absolute relation with accidents, but there were no significant effects on the depth perception average value and stability, but young and low-driving experience drivers had bad detection ability.

1 INTRODUCTION

Currently, road traffic accidents are still in a high level state in the world, and major accidents often bring misfortune and disaster to the drivers and other people. In the driver-vehicle-road environment of traffic, with the progress of science and technology, the safety of road and car reliability increases continuously, but the safety reliability of drivers is difficult to improve (Liu & Zhang 2006). In 2009, the U.S. Department of Transportation claimed that more than 5.5 million motor vehicle accidents occurred in the United States. Among those accidents, the most common was collision with another motor vehicle (NHTSA 2009). On the road, drivers must constantly observe, analyze and judge the distance between their own cars and other cars and relative stationary objects to take the proper driving operations. Affected by different driving experiences, emotions, external environments and driving habit factors, some drivers are prone to produce driving illusion that leads to driving error and causes traffic accidents (Victoir et al. 2005). Research has shown that actual following distance is often smaller than the safety following distance (Yang & Guan 2008; Broughton et al. 2007). The error will increase with the improvement of speed, which is the main cause of rear-end accidents on the highway (Sun et al. 1997). According to the statistics, driving illusion can account for about 35% of the reasons for traffic accidents (Qi 1994). Penumaka et al. (2014) found that car drivers made perception and comprehension failures in a large proportion of cases.

Drivers are prone to accidents that are mainly related to their mental and physical qualities, so improving the drivers' psychological and physical quality is the key to accident prevention (Aili et al. 2010). Depth perception is an important physiological function that is different between the individuals. Zhang et al. (1994) studied drivers' visual depth perception, and found that there are significant differences between the safe driving groups and accident groups. Yan et al. (2011) investigated the influence of the expressway tunnel group on drivers' perceptual features, and found that the driver's age has no significant effect on the accuracy of depth vision, while driving experience and continuous driving time have a significant effect on the driver's depth vision. Said et al. (2012) briefly discussed the depth estimation method for a mobile platform using monocular vision.

As a test indicator of driving suitability, depth perception is an important measure to prevent traffic accidents.

2 RESEARCH INSTRUMENT AND METHOD

2.1 *Research instrument*

Froner et al. (2008) reported that user preference for a 3D display is not always a reliable guide to the ability to perform the human binocular depth perception. Care must be taken in selecting 3D display systems for tasks that critically rely on human depth judgment. Sun et al. (2010) integrated the monocular vision system with a laser system to

obtain an accurate depth estimation. The project group developed an instrument used to detect the driver's object space perception ability, as shown in Figure 1, which is a more cheap, convenient and popular application to assess drivers for passenger transportation enterprises.

Parts of the technical parameters are as follows: moving rod color, black; moving rod diameter, 3.5 mm; distance between the rods, 50 mm; rod movement range, 160 mm or more to the zero position; rod movement speed, 20 mm/s; light intensity of illumination in the instrument (lx), 1500~2500 lx; precision, 0.1 mm.

2.2 *Research method*

In order to ensure quality and reliability of the sample, test samples should be sufficient. The method of collective detection includes all the drivers in a corporation for making the test sample random and representative. To make the data more effective, the group uses two ways to collect the drivers' driving safety and traffic accidents data: one way is to directly obtain from the tested corporation recordings, and another way is to distribute a survey form to the driver to fill in at the scene. Drivers' age, driving experience, cultural level and other relevant information are collected before the test to analyze the correlation between depth perception and these factors later.

A total of 5,167 drivers working more than 3 years were detected from four large motor transportation companies in Fujian, Jiangsu and Anhui provinces. Then, we investigated their safe driving and accident records in the past three years. Finally, we collected an effective testing sample of 5008 for the depth perception analysis.

We mainly used statistical methods to analyze the collected data. The test measured the depth perception judgment error and then used the mean error of 3 times detection results as an evaluation index. A preliminary assumption is that the larger the mean error, the poorer the perception ability to the distance and location. This kind of drivers will be more prone to have accidents.

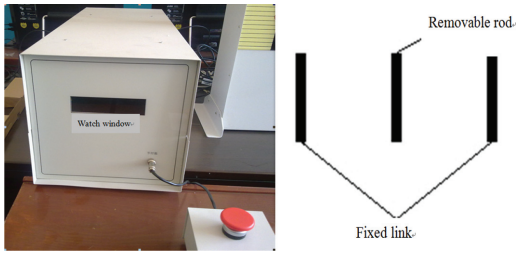

Figure 1. Depth perception instrument.

3 SAMPLE DATA STATISTICS AND ANALYSIS RESULTS

After cleaning up the initial data, the relation between depth perception detection data and accidents was investigated, and according to the detection data, the degree level of the drivers' deep perception detection threshold was formulated.

3.1 *The correlation analysis between the depth perception index and accidents*

From the statistical analysis of the effective testing samples, we calculated the mean value and standard variance of the drivers between the accident and non-accident groups. The results are summarized in Table 1.

Using SPSS software to test the normal distribution of the samples (Lisa et al. 2012; Sajad et al. 2013), Sig = 0.126 > 0.05, and the sample obeys the normal distribution. Making a T test for the accident and non-accident group samples, in the variance of the T test, Sig. (bilateral) = 0.000 < 0.05 while the variance is equal. As can be seen from Table 1, the drivers' depth perception mean value of the accident group is larger than that of the non-accident group, indicating that there is a significant difference between the two groups and a certain correlation between depth perception and accidents. Pearson's correlation coefficient is 0.358, proving that it is a positive correlation. With the increase in depth perception test mean value, accident probability related to the drivers will increase.

In addition, the standard variance value of the accident group is greater than that of the non-accident group, showing that there are gaps for the stability between the two groups, and the stability of the drivers' depth perception also affects the driving safety. Because there is incomplete possibility for the non-accident group's accident record, the correlation between depth perception and accidents will be more obvious.

3.2 *Formulating evaluation index detection threshold*

There was a significant difference between the accident and non-accident groups, so setting out

Table 1. Effective sample statistics between the accident and non-accident groups.

	Driver number	Mean value	Standard variance
Accident group	1132	13.57	9.31
Non-accident group	3876	12.21	8.66

Table 2. Deep perception evaluation index threshold.

Level	Good	Ordinary	Attention	Bad
Deep perception testing mean value threshold (mm)				
Maximum	2	9.5	17.5	
Minimum		2.1	9.6	17.6

the evaluation indicators to the following four categories: good, ordinary, attention and bad. Ordinary category takes the maximum proportion, and bad category is to be eliminated, taking the minimum proportion generally controlled within 5% (Li 2004). Through the cluster analysis, the results for class accidents' number and percentage and formulating evaluation index detection threshold of depth perception were obtained, as summarized in Table 2.

4 INFLUENCE OF AGE AND DRIVING EXPERIENCE ON DEPTH PERCEPTION

Finally, we investigated the drivers' age and driving experience of the accident group, and studied their relations with depth perception.

4.1 *Age factor analysis*

From the statistical analysis, the drivers' age of the accident group was mainly found to be in the range of 33–47 years, as shown in Figure 2. Age and accidents obeyed the normal distribution, and the correlation coefficient was 0.8067.

From Figure 3, we can see that the trend of 32- to 59-year-old drivers in the accident group is smooth and stable, but the depth perception mean value and standard deviation for 23- to 31-year-old drivers in the accident group are too large. In order to find the reason for this difference, next step characteristics and driving experience will be considered.

4.2 *Driving experience factor analysis*

From the statistical analysis, the drivers' driving experience in the accident group was found to be in the range of 7–26 years, as shown in Figure 4. Driving experience and accidents obeyed the normal distribution, and the correlation coefficient was 0.4223.

As seen from Figure 5, the mean value and standard deviation of depth perception from low driving year drivers are significantly higher than that high driving years drivers, which means low driving years drivers are weaker on the distance judgment and stability than high driving years drivers. The trend of the depth perception average value and stability fell slightly.

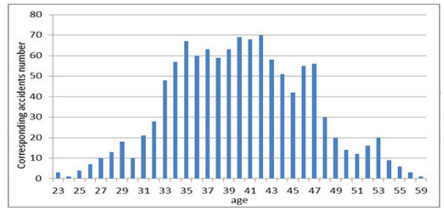

Figure 2. Age and corresponding driver number.

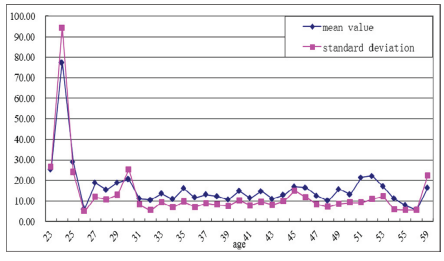

Figure 3. Age and depth perception diagram.

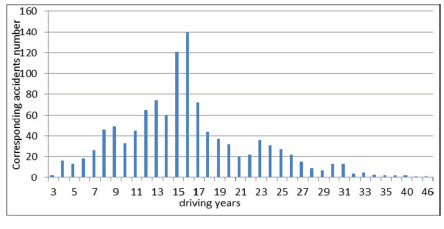

Figure 4. Driving years and corresponding driver number.

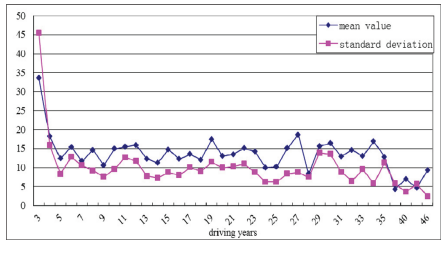

Figure 5. Driving years and depth perception diagram.

5 CONCLUSIONS

Firstly, we get the result that deep perception detection mean value has a positive correlation with accidents, which can be used to test the driver's suitability to drive as an evaluation index.

Then according to the testing instrument and data, formulating evaluation index detection threshold of depth perception, which can be used as a standard value for transportation companies to assess the drivers for preventing accidents. Finally, specific analysis was carried out on the influence of drivers' age and driving experience in the accident group on the depth perception. Drivers' age and driving experience have significant relations with accidents, but only young drivers and low-driving experience drivers in the accident group have a high detection mean value of depth perception and bad stability.

ACKNOWLEDGMENTS

This research was supported by the financial aid of the National Sci-Tech Support Plan Projects "Commercial Vehicle Safety Assurance Technology Development and Large-scale Applications" (No. 2009BAG13A04).

REFERENCES

Aili, S., Li, X. & Wei, J.D. 2010. Research on psychological and physiological characteristics of desert highway drivers. *Qinghai Transortation Technology* (3): 65–71.

Avinash, P.P., Savino, G. & Baldanzini, N. 2014. In-depth investigations of PTW-car accidents caused by human errors. *Safety Science* (68): 212–221.

Broughton, K.L., Switze, R.F. & Scott, D. 2007. Car following decisions under three visibility conditions and two speeds tested with a driving simulator. *Accident Analysis & Prevention* 39(1): 106–116.

Li, L.S. 2004. *Human Computer Interface Design.* Beijing: Science Press.

Lisa, R.M., Gireesh, V.G. & Joe, R.A. 2012. An evaluation of the psychometric properties of the purdue pharmacist directive guidance scale using SPSS and R software packages. *Research in Social and Administrative Pharmacy* 8(2): 166–171.

Liu, Y.Z. & Zhang, D.Y. 2006. Reliability analysis of vehicle driver. *Journal of Transportation Engineering and Information* 4(1): 1–4.

National Highway Traffic Safety Administration. 2009. *Traffic Safety Facts.* Washington, D.C.

Qi, J.W. 2003. The driver factor in the traffic accident—driving illusion and driving safety. *Road Traffic & Safety* (5): 29–33.

Said, Z., Sundaraj, K. & Wahab, M.N.A. 2012. Depth estimation for a mobile platform using monocular vision. *Procedia Engineering* (41): 945–950.

Sajad, S., Payam, J., Hekmat, R., et al. 2013. Mass modeling of Bam orange with ANFIS and SPSS methods for using in machine vision. *Measurement* 46(9): 3333–3341.

Sun, F.C., Zhou, Y. & Li, C. 2010. Research on Active SLAM with Fusion of Monocular Vision and Laser Range Data. *8th World Congress on Intelligent Control and Automation (WCICA 2010), Jinan, 7–9 July 2010.* Jinan: IEEE.

Sun, J.H., Yang, L.B. & Li, B.C. 1997. Research on eligibility detection system of professional motor drivers. *Automotive Researching* 16(3): 87–94.

Victoir, A. & Eertmans, A. 2005. Learning to drive safely: Social-cognitive responses are predictive of performance rated by novice drivers and their instructors. *Transportation Research Part F: Traffic Psychology and Behavior* 8(1): 59–74.

Yan, B., Chen, H. & Wei, J.Q. 2011. Influence of drivers' perceptual features on traffic safety in tunnel group. *China Safety Science Journal* 21(11): 16–21.

Yang, C.P. & Guan, H.F. 2008. Research on safe distance between vehicles for freeway anti-collision system. *Process Automation Instrumentation* 29(9): 19–21.

Zhang, J.D., Huang, Y., Liu, Z.H., et al. 1994. Research and discussion on forces the drivers' visual depth perception. *Auto Application* (48): 17–19.

Civil Engineering and Urban Planning IV – Liu et al. (Eds)
© 2016 Taylor & Francis Group, London, ISBN 978-1-138-02903-3

Research on the competitive character of urban rail transit and conventional bus—taking the Suzhou rail transit passenger corridor as an example

Li-Jing Wang, Wei-Zhou Xiao, Wei-Wei Shen & Jing Liu
School of Urban Rail Transportation, Soochow University, Suzhou, Jiangsu, China

ABSTRACT: With the rapid growth of motorization in big cities, traffic congestion becomes increasingly serious. Many cities began to develop an urban rail transit system with high capacity. As a latecomer to public transport market, rail transit will inevitably impact the conventional bus for its high speed, on time, and comfort. There are competitive relations between the two travel modes. This paper takes the Suzhou rail transit passenger corridor as an example to study the problem. Based on the utility function, a competitive selection model is established to analyze the choice behavior characteristics of passengers taking public transport. Thus, the paper compiles the competitive features of the two modes to provide references for the adjustment of the conventional bus lines within the corridor.

1 INTRODUCTION

With the rapid development of urban economy and constant improvement of urbanization, cities have expanded in scale and presented the problem of population aggregation and shortage of land. The rapid growth of motorization triggers the increasingly serious traffic congestion problem. Conventional buses, the principal part of the public transport system, have decreased in the average travel speed. Route buses become unpunctual and unreliable and can't meet the needs of residents' daily travel. The development experience of foreign cities indicates that the fundamental way to solve the problem of urban traffic is the development of urban rail transit with a high capacity (Lu et al. 2008). Many Chinese metropolises are in the process of developing rail transits. On the one hand, rail transit, which is rapid, punctual, and comfortable, will inevitably impact the number of passengers taking conventional bus lines within the rail corridor. On the other hand, the construction cost of rail transit is high and the formation of systematic transit operation networks is a long-term process. Also, rail transit has the disadvantage of a long walking distance because of longer station spacing and more transfers. Therefore, it is important to position the function of the two different travel modes in the public transport system properly. Also, it is necessary to take relevant measures to prevent unhealthy competition between the two modes and at the same time, realize orderly and effective competition.

Rail transit and conventional buses are the two main modes of public transportation in modern cities. There are many researches about the competitive relationship between the two modes. Foreign scholars began to research on traffic demand analysis based on the discrete choice model in 1970s; its representative men include McFadden, Ben-Akiva, Lerman, and so on. Their achievements put DCM into practical use in travel research. Domestically, C.Q. Ma calculated the passengers' contest region of rail transit and conventional bus by travel time and travel distance. He also established a Logit model, which was based on generalized cost, to get the share ratio curve of the two modes (Ma et al. 2007). K.M. Chen applied the Logit model and game theory to study the dynamic competition process between urban rapid rail transit and conventional bus (Chen & Luo. 2005). J.L. Chen made use of the data of the third residents' travel survey of Beijing to build a nested Logit model based on travel time. In this way, he analyzed how travelers' relevant attributes impact the travel mode choice behavior quantitatively. The study provided the reference for corresponding public transportation demand management policies (Chen et al. 2011). L.J. Liang took Shanghai rail transit line 6 as an example and revealed a preference survey on residents' transport travel. Based on this, she analyzed the change in travel time and cost after rail transit started operating and built a competitive model between bus and rail which was based on effect function and mode choice (Liang et al. 2009). This paper took the two rail transit lines in Suzhou as an example and created a survey on public transportation passengers within the rail transit corridor. Using these data, a competition model based on utility function is established

to study how travelers' features and the features of travel mode will influence travelers' choice behavior. Therefore, the two travel modes will be positioned reasonably to provide the reference for adjusting conventional bus lines.

2 ANALYSIS ON THE TRAVEL CHARACTERISTICS OF PUBLIC TRANSPORT PASSENGERS WITHIN THE SUZHOU RAIL TRANSIT CORRIDOR

To clear out the travel characteristics of public transport passengers within the Suzhou rail transit corridor, a questionnaire survey was made. The survey object is the passengers of the rail transit and the parallel conventional bus lines within the corridor. Travelers' personal basic information and their travel characteristics are investigated. The former includes the traveler's gender, age, profession, monthly income, educational level, and whether car owner. The latter includes whether workday, travel purpose, travel time, travel cost, transfer number, and so on.

This survey was carried out not only on workdays, but also on weekends. The survey sites included the vehicles and stations of the two travel modes. In Total1506 samples were obtained, which included 1127 conventional bus interviews and 379 rail transit passengers. The selection of interviews is random and the travel attributes of the two modes are all interviewed. Thus, the differences between the samples of each mode will not influence the analysis.

2.1 *P value test for relevant property*

Passengers' gender, age, profession, monthly income, educational level, whether car owner, whether workday, and travel purpose can be discretized. Then, the P value test is applied to identify whether these properties are significantly different between the two modes. Travel time, travel cost, and transfer number are considered separately.

In a hypothesis test problem, the smallest significance level that can be used to reject the original assumption H_0 is called the P value (see Mao et al. 2004). P value can be between 0 and 1 (see Liu. 2013). The process for P value test is: (1) Make the null hypothesis and alternative hypothesis. The null hypothesis H_0 here for the property means that there is no significant difference between the two modes. Alternative hypothesis H_1 is opposite. (2) Calculate the P value of each property. (3) Compare P values with the given significance level α to determine whether to refuse H_0. Table 1 shows the statistic results and P values of relevant properties.

Generally, we can strongly reject the null hypothesis if P value is smaller than 0.01. From Table 1, we know that there are four properties which are significantly different between the two modes. They are respectively profession, monthly income, whether car owner, and travel purpose. Then special attention should be paid to these properties in order to further study the differences between the two modes.

2.2 *Passengers' travel characters*

– Travel time

The travel time here refers to the whole time from the origin to the destination. It is obvious that rail transit can save passengers' riding time because of high speed and less delay. But its network has lower coverage which means longer access time and egress time. Passengers may also need to transfer to reach the destination, resulting in more cost and longer time. So the whole travel time of rail transit will not always be shorter. Table 2 shows passengers' choice distribution when rail transit can save different lengths of time.

The negative values in Table 2 mean that rail transit doesn't save total travel time. Here we regard the travel time of the two modes as the same if the time saved is between –5 and 5 min because of some random errors (Liang et al. 2009). The case that rail transit doesn't save travel time makes up 51.4%. Meanwhile, rail transit always brings about more travel cost, resulting in fewer passengers. As the time saved by rail transit becomes shorter, the choice proportion of conventional bus becomes larger. When the time saved is between 5 and 20 min, the choice proportion of conventional bus begins to surpass that of rail transit.

Rail transit can save travel time; nonetheless, it leads to more fares and transfers. Passengers will weigh between these elements before choosing the travel mode.

– Travel cost

Rail transit is rapid, on time, comfortable, and of high reliability, the fare is relatively high. The travel cost of the conventional bus which refers to total travel cost, is generally lower than rail transit. Table 3 shows passengers' choice distribution when conventional bus can save a different amount of cost.

Approximately 93.2% passengers pay less when choosing conventional bus. The majority travel cost saved is within 0 and 3. When the travel cost of rail transit is lower than that of conventional bus (this case is rare), all the passengers choose rail transit. When the costs for the two modes are the same, more passengers choose conventional bus. This is because senior citizens who don't need to pay for public tools prefer to take conventional bus. Broadly speaking, as the cost saved by using the conventional

Table 1. P value of passengers' personal attributes, whether workday and trip purpose.

Property	Travel mode	Proportion (%)		P value
Whether workday		*Workday*	*Weekend*	0.523
	Rail transit	65.1	34.9	
	Conventional bus	63.2	36.8	
Gender		*Male*	*Female*	0.860
	Rail transit	54.1	45.9	
	Conventional bus	53.6	46.4	
Whether car owner		*Yes*	*No*	0.001
	Rail transit	28.8	71.2	
	Conventional bus	20.2	79.8	

Age		*Under 20 years old*	*20–40 years old*	*40–60 years old*	*60 years old and above*	0.191
	Rail transit	6.7	72.8	14.7	5.9	
	Conventional bus	5.7	71.8	13.1	9.4	
Educational level		*Under high school*	*High school*	*Junior or regular college student*	*Postgraduate and above*	0.067
	Rail transit	8.3	20.5	67.2	4	
	Conventional bus	13.6	18.5	64.1	3.9	

Monthly income		*Under 2000¥*	*2001~3000¥*	*3001~5000¥*	*5001~8000¥*	*8000¥ and above*	0.001
	Rail transit	31.5	9.9	34.9	18.4	5.3	
	Conventional bus	22.9	17	39	15.6	5.5	

Position		*Employee*	*Civil servant*	*Business manager*	*Middle school student*	*College student*	*Retired*	*Self-employed laborer*	*Worker*	*Other*	0.002
	Rail transit	32.8	7.7	6.4	4.5	21.6	7.2	7.5	2.9	9.3	
	Conventional bus	41.8	7.4	5.6	1.9	15.1	9.7	5.5	4.7	8.3	
Travel purpose		*Work*	*School*	*Official business*	*Shopping*	*Fit and fun*	*Visit friends or relatives*	*See a doctor*	*Tourism*	*Other*	0.000
	Rail transit	17.9	1.9	7.7	16	14.9	8.3	3.7	10.4	19.2	
	Conventional bus	13.8	2.9	7.4	18.2	8.7	15.2	6.3	6	21.6	

Table 2. Distribution of travel time saved when choosing rail transit and mode choice proportion.

Time saved by rail transit (min)	Sample number	Choice proportion of rail transit (%)	Choice proportion of conventional bus (%)
40~70	18	94.4	5.6
20~40	136	64.0	36.0
5~20	455	44.2	55.8
−5~5	410	14.4	85.6
−15~−5	192	4.2	95.8
Under −15	41	4.9	95.1

Table 3. Distribution of travel cost saved when choosing conventional bus and mode choice proportion.

Cost saved by conventional bus (¥)	Sample number	Choice proportion of rail transit (%)	Choice proportion of conventional bus (%)
4 and above	155	3.2	96.8
3~4	152	13.8	86.2
2~3	261	21.8	78.2
1~2	286	44.8	55.2
0~1	331	40.8	59.2
0	50	24.0	76.0
Under 0	17	100	0

bus becomes higher, the choice proportion of conventional bus becomes larger.

– Transfer number

Generally, the transfer number of rail transit is larger because of smaller coverage areas. Table 4 shows passengers' choice distribution when rail transit causes more numbers of transfer.

The case that rail transit increases transfer numbers makes up 47.1%. As the transfer

numbers increased by rail transit become larger, the corresponding choice proportion becomes smaller.

2.3 *Comprehensive analysis*

Divide travel time into three categories according to the time change when a passenger chooses rail transit instead of conventional bus. When the travel time increases, it can be recorded by "Time +." When the travel time decreases, it can be recorded by "Time –." When the travel time remains the same, it can be recorded by "Time = ." The division method for travel cost and transfer number is the same. According to the change in the three factors, we get a variety of situations in Table 5.

We can find the follow conclusions:

- Situations 3, 4, 12, and 13 are common and make up 72.8% of the total sample. Their common feature is that rail transit doesn't save time, but causes more cost or transfer. Only situation 4 has a larger rail transit sharing proportion, which has less time, more cost, and equal transfer number when choosing rail transit.
- In situations 1, 11, and 14, all passengers choose rail transit. The common characteristic is that rail transit doesn't increase time, but has less cost or transfer. But these situations are rare and only make up 1.6% of the total sample. It is obvious that rail transit will always bring about more cost and transfer.
- In situations 3, 5, 7, 8, 9, 10, 12, 13, and 15, the share proportion of conventional bus is larger than that of rail transit. The sample proportion of these situations is as high as 68.7%. They have one trait in common: travel time can change, but at least one element in cost and transfer increases when choosing rail transit.
- In situation 16, the two modes have equal time, cost, and transfer; their choice proportions are the same. This indicates that public passengers have no significant preference between the two modes.

Table 4. Distribution of increase in transfer number when choosing rail transit and mode choice proportion.

Transfer number increased by rail transit	Sample number	Choice proportion of rail transit (%)	Choice proportion of conventional bus (%)
2	127	0.0	100.0
1	463	6.9	93.1
0	584	45.9	54.1
–1	72	95.8	4.2
–2	6	100	0

3 THE LOGIT MODEL BASED ON UTILITY FUNCTION AND ITS SOLUTION

3.1 *Model building*

As two main travel modes in public transport systems, rail transit competes with the conventional bus lines within its corridor because of the influence of different factors. These factors affect passengers' travel mode choice behavior and finally show up as

Table 5. Distribution of travel time, cost, and transfer change when choosing rail transit instead of bus and mode choice proportion.

Situation	Time	Cost	Transfer	Sample number	Choice proportion of rail transit (%)	Choice proportion of conventional bus (%)
1	–	–	–	14	100.0	0.0
2	–	+	–	58	94.8	5.2
3	–	+	+	216	9.7	90.3
4	–	+	=	292	67.8	32.2
5	–	=	+	3	0.0	100.0
6	–	=	=	15	60.0	40.0
7	+	+	+	133	0.8	99.2
8	+	+	=	80	11.2	88.8
9	+	=	+	9	0.0	100.0
10	+	=	=	10	0.0	100.0
11	=	–	–	3	100.0	0.0
12	=	+	+	223	4.5	95.
13	=	+	=	180	27.2	72.8
14	=	+	–	3	100.0	0.0
15	=	=	+	6	0.0	100.0
16	=	=	=	7	42.9	57.1

the allocation proportion of passenger volumes. To study how these factors impact passengers' mode choice behavior, it is necessary to analyze the utility of the two public trip modes. Among all models, Logit model is easy to understand in physical meaning and the selection probability of each mode is within 0 and 1. The sum of the selection probability for each mode is 1. Therefore, it is widely used in the study of utility function and sharing proportion of traffic modes (Zhang & Chen 2010).

A binary Logit model of rail transit and conventional bus is built in the following form:

$$\mathrm{Pr}_i = \frac{\exp(U_i)}{\exp(U_r) + \exp(U_b)}, \quad i = (r, b) \tag{1}$$

where Pr_i is the sharing proportion of mode i, i can be r (rail transit) and b (conventional bus). U_i is the utility function of mode i. It can be written as:

$$U_i = \alpha_i + \sum_J \beta_j X_{ij} \tag{2}$$

where α_i is constant term, X_{ij} is the jth travel element of mode i, β_j is the parameter to be calculated.

The key part in Logit model solution lies in the determination of the utility function. Repeated parameter selection and data correction are done to make the model conform to the traffic traveler behavior characteristics. This paper applies the software Biogeme to solve the model.

3.2 *Travel elements selection and model solving*

The property which is significantly different between the two modes can be ensured by the P value test. While repeated attempt needs to be done to select specific elements according to the results of model estimation. Table 6 shows the final model result.

The t value is used to measure whether the parameter's corresponding element is significant in interpreting the observed value. We can determine whether the element should be retained in the model by t value. Under the confidence level of 1%, the parameter with a t value greater than 2.58 shall be maintained. Under the confidence level of 5%, the parameter with a t value larger than 1.96 should be maintained. And the parameter with a t value greater than 1.65 shall be maintained under the confidence level of 10%. In the process of model solving, it is notable that passengers with a monthly income under 2000¥ prefer to choose rail transit. This is not consistent with common sense. After deep analysis, it is found that many of them are college students who have no source of income. The headquarters and north campuses of Soochow University are along the rail transit lines, so there are many college student passengers. To test if these groups are more inclined to take rail transit, a new element is formed by multiplying the variable whether college student with the variable whether monthly income under 2000¥. This is B_P5I1 in Table 6 which means they are college students with monthly incomes under 2000¥. Its corresponding parameter estimated is –1.71 with 10% confidence level.

3.3 *Analysis of model result*

After elements selection and parameter estimation, estimation results are obtained as shown in Table 6.

Table 6. Result of the choice model between rail transit and conventional bus.

Name of parameter	Meaning	Option the element in	Value of parameter	t value
ASC_R	The constant term of rail transit	Rail transit	–0.568	–1.35
B_PURPOSE1	Whether travel purpose is for work	Conventional bus	–0.659	–2.51
B_PURPOSE58	Whether travel purpose is for fit and fun or tourism	Conventional bus	–0.552	–2.53
B_CAROWNER	Whether car owner	Conventional bus	–0.553	–2.49
B_INCOME2	Whether monthly income is within 2001 and 3000¥	Conventional bus	0.724	2.45
B_P5I1	Whether college student with monthly income under 2000¥	Conventional bus	–0.437	–1.71
B_PROFESSION1	Whether employee	Conventional bus	0.547	2.64
B_BTIME	Travel time of conventional bus	Conventional bus	–0.124	–10.86
B_BCOST	Travel cost of conventional bus	Conventional bus	–0.852	–2.72
B_BTRANSFER	Transfer number of conventional bus	Conventional bus	–0.947	–1.76
B_RTIME	Travel time of rail transit	Rail transit	–0.129	–8.60
B_RCOST	Travel cost of rail transit	Rail transit	–0.344	–2.00
B_RTRANSFER	Transfer number of rail transit	Rail transit	–2.52	–8.20

It is reasonable that the corresponding parameters for time, cost, and transfer are negative. Thirteen parameters in the table meet the confidence level of 10% and ten parameters meet the confidence level of 5%. Parameters have high significance and the model has good precision.

From Table 6 we can find that personal properties will influence passengers' mode choice behavior in many ways. The model estimation process confirms that whether workday, gender, age, and educational level have no significant influence on travel mode choice. At present, tertiary industries in Suzhou have developed well and people of different professions have different workdays and days off. For the property "profession," the parameter for employees is 0.547, which indicates a preference for conventional bus. Now there are only two transit lines in Suzhou. Rail transit has lower coverage and poorer accessibility than bus. For the property "monthly income," it is found that college students with monthly incomes under 2000¥ prefer to choose rail transit and groups with monthly incomes between 2001 and 3000¥ prefer to choose bus. Other groups have no obvious difference. For the property "whether car owner," people who have cars were inclined to choose rail transit. These car owners have higher demand for punctuality and comfort and are more willing to choose rail transit. For the property "travel purpose," groups whose purposes are for work, fitness and fun, and tourism prefer to choose rail transit. Groups with other purposes have no significant selection bias. To understand passengers' concerns about travel time, cost, and transfer, this paper calculates the degree of characteristic elements' contribution to the utility function. The contribution degree reflects the element's influence on utility function. Calculating the average value of each element and putting these values into the utility function, the ratio between each element's utility and the total utility was calculated. The utility here should be the absolute value. Then we can get each element's contribution degree (Liang et al. 2009). The formula is:

$$C_{ij} = \frac{\left|\beta_j X_{ij}\right|}{\left|\alpha_i\right| + \sum_J \left|\beta_j X_{ij}\right|} \tag{3}$$

Table 7 shows the contribution degree of travel time, cost, and transfer.

From the table, we can see that travel time is the most concerned factor for all passengers. Compared with rail transit passengers, bus passengers are more concerned about travel time and cost, but pay less attention to transfer numbers.

It is observed that the Suzhou rail transit's disadvantage of short lines, low coverage range, and poor accessibility are the main factors that restrict its sharing proportion.

Table 7. The contribution proportion of each characteristic variable to the utility function.

Travel mode	Time	Cost	Transfer
Conventional bus	77.3%	20.8%	1.9%
Rail transit	61.6%	16.7%	21.7%

4 CONCLUSION

After opening a rail transit line, some passengers within the corridor will shift from the bus lines to rail transit. This will bring changes to the whole traffic structure. The model results show that currently there is a competitive relationship between two modes. Whether workday, gender, age, and educational level have no significant influence on travel mode choice. While whether car owner, profession, monthly income, and trip purpose have significant difference between the two modes. More importantly, bus passengers are more concerned about travel time and cost than rail transit passengers, but less about transfer numbers. At present, the Suzhou rail transit is still in the initial stage. Its disadvantages of short lines, low coverage range, and poor accessibility are the main factors that restrict its sharing proportion.

REFERENCES

Chen, J.L., Ma, Y.L. & Zhu, N. 2011. A study on bus travel mode choice behavior based on a nested Logit model. *Journal of Transportation Systems Engineering and Information Technology (in Chinese)* 11(S1): 120–125.

Chen, K.M. & Luo, X.Q. 2005. Game-theory of reasonable ticket price for urban railway transport. *Journal of Chang'an University (Natural Science Edition) (in Chinese)* 25(4): 52–55.

Liang, L.J., Wu, J.R. & Wang, H. 2009. Competition model between urban rail and bus transit. *Urban Mass Transit (in Chinese)* 12(9): 30–34.

Liu, Y. 2013. Application of various parameters in hypothesis testing. *Journal of Guizhou Normal College (in Chinese)* 29(3): 24–26.

Lu, F., Han, B.M., & Li, D.W. 2008. The backbone role of urban rail transit in urban passenger transport network. *Comprehensive Transportation (in Chinese)* (2): 67–69.

Ma, C.Q., Wang, Y.P. & Chen, K.M. 2007. Competition model between urban rail and bus transit. *Journal of Transportation Systems Engineering and Information Technology (in Chinese)* 7(3): 140–143.

Mao, S.S., Cheng, Y.M. & Pu, X.L. 2004. *Probability and Mathematical Statistics Course.* Beijing: Higher Education Press.

Zhang, Q.P. & Chen, Y.H. 2010. Study on traffic mode choice based on disaggregate model. *Railway Transport and Economy (in Chinese)* 32(1): 75–78.

Civil Engineering and Urban Planning IV – Liu et al. (Eds)
© 2016 Taylor & Francis Group, London, ISBN 978-1-138-02903-3

Modeling of fly ash stabilized base layers

J.A. Adedeji & M. Mostafa Hassan
Civil Engineering, Central University of Technology, Free State, South Africa

ABSTRACT: In South Africa and developing countries, the base or sub-base layer serves as the main structural element or bearing capacity of the pavement. As a result, more focus is placed on the base or sub-base layer for the accurate designing of the pavement structure. However, flexible pavement still experiences failures; these failures are generally caused by various factors such as soil expansion, inadequate soil stabilization, inappropriate use of materials in base courses and inadequacy in design. Consequently, the roads need regular maintenance and rehabilitation, which increases the operational cost of the roads. However, with an appropriate method of soil stabilization and the use of finite element-based software, the design and construction of flexible pavement can be enhanced. This paper attempts to validate the optimization of Cement-enhanced Class-F Fly ash usage, as the base layer stabilizer in the South African flexible pavement, using the ABAQUS model. The validation results are discussed in this paper.

1 INTRODUCTION

South Africa has the 10th longest total road network in the world, after the likes of the first three countries, namely the USA, China and India (Kannemeyer 2013). The road network in South Africa is approximately 746,978 km, of which only 153,791 km is paved (The South Africa National Roads Agency Ltd. (SANRAL) 2010). About 90 percent of the paved roads in South Africa are flexible pavement (De Beer et al. 1999); this can be attributed to the fact that flexible pavements are: cost-effective, generate less tire-pavement noise and are environmentally sustainable (Asphalt Pavement Alliance 2010; Jain et al. 2013). However, despite the fact that only 21 per cent of the road network is paved; approximately 62 per cent is in good conditions, 26 per cent is in fair conditions and the remaining 12 per cent is in poor or very poor conditions (Kannemeyer 2013).

Some of the poor conditions experienced in flexible pavement are as follows: permanent deformation, cracking of surface course and creation of potholes (Jassal 1998; Adlinge & Gupta 2013); these are generally caused by various factors such as soil expansion (Kordi et al. 2010), inappropriate use of materials in base courses, inappropriate soil stabilization (Paige-green 2008) and inadequate design (Kordi et al. 2010; Shafabakhsh et al. 2013, Pavement Failure Identification 2014). As a result, the roads need regular maintenance and rehabilitation, which increases the operational cost of the roads and consequently influences the national annual budget that skyrockets every year (Ndebele 2012).

The aforementioned conditions are the major factors that contribute to inappropriate soil stabilization and inadequate design because soil and pavement materials are part of the design process; therefore, these factors that lead to failure in the pavement structure can be averted if careful consideration is taken. However, with an appropriate method of soil stabilization and the use of Finite Element (FE) model, the possibility of designing and constructing quality and cost-effective flexible pavement can be enhanced. Thus, this paper attempts to close the gap through validation, between the state of practice (stabilization) and the state-of-the-art (FE design) in flexible pavement design.

1.1 *Stabilization of flexible pavement*

Flexible pavements with asphalt on the surface are used worldwide. This structure consists of various layers, with different strength and deformation characteristics, which make the layered system difficult to analyze in pavement engineering (Kim 2007). In flexible pavement, the material quality gradually and smoothly increases from the *in situ* subgrade up to the structural layers and surfacing (SANRAL 2013). Basically, the layers above the subgrade are selected to ensure that the transmitted stresses due to the loading are sufficiently reduced, so that the stress will not exceed the subgrade bearing capacity (Adu-Osei 2001).

Nevertheless, in South Africa and other developing countries, the main structural element or bearing capacity of the pavement is obtained from the deep and well-balanced unbounded granular base

or sub-base layer (Araya 2011; SANRAL 2013); using only thin asphalt (≤50 mm) on the surface to mainly provide protection against water ingress (De Beer et al. 1999; Araya 2011; SANRAL 2013). However, due to various factors such as inter-particle friction, particle distribution, particle hardness, cohesion, elasticity, durability and porosity (SANRAL 2013), which influence the behavior of the unbounded granular and other materials, the material characteristics of the entire pavement change continuously over time with environmental changes and later result in pavement failure.

The effects of these aforementioned factors are mostly significant for materials in its natural state. In order to stabilize the material behavior to a bearable or improved state, the concept of soil stabilization is introduced. However, stabilization concept is not new but the materials and the methods of stabilization are set to be evolving year after year. Stabilization primarily aims at improving the strength of soil or pavement materials and increasing the resistance to softening by water through bonding the soil particles together, water proofing the particles or combination of the two (Sherwood 1993; Takhelmayum 2013). This can be done by inducing vibration or compaction, and introducing a coarse or fine material and geosynthetic material (Hejazi et al. 2012); this process is known as mechanical stabilization. Also, chemical stabilization involves the addition of cementitious materials or soil minerals that produce the chemical reaction, thereby increasing the host material strength. Results have indicated that chemical stabilization is more advantageous (Makusa 2012; Heynes & Hassan 2013; Yadu & Tripathi 2013) but with few limitations such as the presence of organic matters, sulfate, sulfide and carbon dioxide in the stabilized soils, which may inhibit the stabilization process (Makusa 2012).

However, with the global increase in the production of by-products and waste materials such as blast furnace and steel slag, spent oil shale, china clay waste, slate waste, rice husk ash, millet husk ash, corn cob ash, coconut shell ash, waste foundry sand, cement kiln dust, fly ash, bottom ash, mining wastes, and demolition and construction waste (Hassan & Khalid 2010; Amin 2012; Bindu & Vysakh 2012; Heynes & Hassan 2013; Yadu & Tripathi 2013), also coupled with the challenge of disposal and environmental pollution, these factors have stimulated greater interest in their use in road construction (Nunes et al. 1996; Brennan & O'Flaherty 2002). Furthermore, in South Africa, mining wastes and fly ash tend to be common, which result from the fact that mining activities and coal play an important role in its economy, and also coal is a primary energy source for electricity generation (Furter 2011). Given the fly ash production of 30 mega ton per year in South Africa with only 6% utilized, the government is at the stage where it is strategically finding ways to reduce it through treatment, reuse and beneficiation (Furter 2011, Heyne & Hassan 2013).

Overall, fly ash has been found to be useful in pavement application purposes such as sub-grade, granular base or sub-base, asphalt surface and structural fill (United State Environmental Protection Agency 2009). However, unlike Class C, which is self-cementitious, Class F fly ash is often used alongside with other stabilizers (e.g. cement, lime or other industrial wastes) as a component of base or sub-base mixtures (Fhwa.dot.gov 2012), since pavements with a stabilized base or sub-base layer have proven to deliver better performance during their service life (Brennan & O'Flaherty 2002). According to Aydilek and Arora (2004), using fly ash as a stabilizer with cement increases the California Bearing Ratio (CBR), Unconfined Compressive Strength (UCS) and resilient modulus of the base layer, similarly Lav et al. (2006), using Class F fly ash with 2, 4, 8, and 10% of cement by total weight, discovered that the maximum dry density increases and optimum moisture content decreases upon addition of cement to fly ash to form an aggregate-free stabilized mixture for the pavement base. Recently, Heyns and Hassan (2013) in South Africa, utilizing three different types of fly ash (Kendal Dump Ash, Durapozz and Pozzfill) enhanced with cement on the G5 sub-base material classified according to the Committee of Land Transport Officials (COLTO) (1998), discovered that when the G5 sub-base material is stabilized, it can meet the C3 stabilized standard for the base layer as classified by the COLTO. Despite all the successes recorded in the empirical procedure of fly ash as a stabilizer, it has not yet been fully incorporated in the new pavement design method, which consequently may result in the failure of pavements (Paige-green 2008).

1.2 *Design innovations*

Pavement design has been transitioning from empirical methods to mechanistic approaches (Kim 2007). Empirical methods rely on more experience or observation of past pavement performance for the development of models, while mechanical approaches (layered elastic and FE method) involve the use of fundamental engineering mechanics to evaluate the state of stress in a pavement and thereby predict the response, behavior and performance of pavement (Seeds 2000). However, empirical methods tend to be simple and easy to use, yet these methods are limited and mostly confine to the location of development, and are probably not valid outside the location; as

a result, mechanistic methods are preferred (Wang 2001; Huang 2012).

The South African Mechanistic-Empirical Design Method (SAMDM) (Van Vuuren et al. 1974), developed in South Africa, works on the principle of layered elastic to determine pavement responses to the load; however, in recent years, the SAMDM has been scrutinized and criticized based on over sensitiveness to the change in the input variables and outdated damage models, a result that is presently under review (Jooste 2004; Theyse et al. 2011). However, mechanistic methods based on the FE model provide better material characterization options (Tiliouine & Sandjak 2014) and can be used to obtain stresses and strains at the bottom of the surface layer, compressive stress/strain within the base layer and at the top of the subgrade (Darwish 2014). Considering the increasing application of 3D models as the best compared with 2D models in the FE model (Rahman et al. 2011; Shafabakhsh et al. 2013), a 3D FE model was used in this study. Furthermore, Abaqus® 3D FE base software has been used extensively in pavement design (Kim 2007; Rahman, et al. 2011; Shafabakhsh et al. 2013). In addition, Abaqus® has a wide library of different element types and material models, and it also has the capability of analyzing a variety of problems (Rahman et al. 2011; Britto 2014). As a result of the extent of Abaqus® usage with its advantages and capability, it is considered in this study. Overall, the success of any FE model depends greatly on accurate material characterization.

2 NUMERICAL DESIGN

The Abaqus® (6.13) 3D FE model was used to represent the conventional three-layered flexible pavement structure in South Africa with both unbounded granular material (G5) and Cement-enhanced Class-F Fly ash as the base layer stabilizer. The following two scenarios were developed in this present study: in the first scenario, G5 material was used as the base layer; in the second scenario, G5 stabilized with cement (1%) and fly ash (20%) was used as the base layer (which is classified as C3) (Heynes and Hassan 2013). The description of the flexible pavement model used in this study is presented below.

2.1 *Description of pavement geometry and material characterization*

The model geometry is basically 3000 mm length by 3000 mm breath and the total depth varies based on the thickness of the base layer that changes over a range of 100 mm–300 mm (Fig. 1). This geometry is similar to that used by Ahmed (2006), with the aim of avoiding edge error when loaded. However, with respect to material characterization, there exist three levels of material characterization inputs in the mechanistic empirical design, but level 2 that relies on basic laboratory testing (CBR, UCS etc.) and correlations is commonly used based on the fact that level 1 depends on difficult laboratory testing such as triaxial test (Mallela 2004). Using the correlation proposed by Barenberg (1977), Equation (1) that was validated by Little et al. (2002) and Al-Jhayyish (2014), the material properties of the Cement-enhanced Class-F Fly ash as the base (C3) (Heynes & Hassan 2013) are obtained and other material properties are obtained from SANRAL (2013). All material characterizations used in this study are linear elastic for simplicity as nonlinear characterization requires a lot of input parameters and computational time (Al-Jhayyish 2014). Details of each layer of the pavement in terms of elastic modulus and Poisson's ratio with their thickness are presented in Table 1.

$$R_{(psi)} = 1200\ \mathrm{UCS}_{psi}. \quad (1)$$

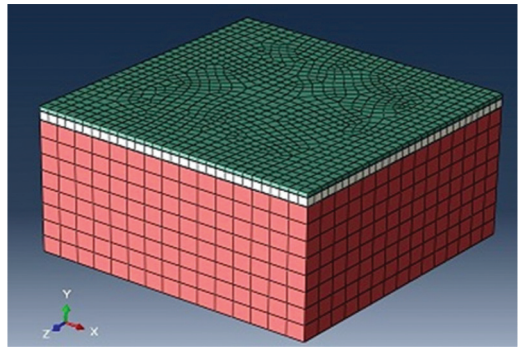

Figure 1. General geometry of pavement layers.

Table 1. Material properties of pavement layers.

Layer	Material code*	Thickness (mm)	Modulus of elasticity (Mpa)	Poisson's ratio
Surface	AG	50	3000	0.44
Granular base	G5	100–300	200	0.35
Stabilized base	C3	100–300	4596	0.35
Subgrade	G20	1500	45	0.35

*Classification according to the COLTO.

where M_R is the elastic modulus in psi; UCS is the unconfined compressive strength results in psi.

2.2 *Description of element type and meshing*

In this study, 8-node solid continuum elements (C3D8R) with reduction integration were used, as they had the capability of representing large deformation and material nonlinearity (Rahman et al. 2011; Ahmed 2006). Meshing of the geometry was done independently so that the thinnest layer (Surface) was finer (Fig. 1) (Tiliouine & Sandjak 2014).

2.3 *Description of boundary conditions and loadings*

The pavement layers were assumed to perfectly bond together and the model was fixed at the bottom of the element (subgrade) and roller constraints on the vertical boundaries. On loading, a standard equivalent single axel load with dual tires was used in this model. The load was applied and uniformly distributed over an equivalent circular area of dual tires (72557 mm^2) (Al-Jhayyish 2014) with a pressure of 0.65 Mpa (Theyse et al. 2011). Overall, all analyses were run as a static linear perturbation analysis procedure type.

3 ANALYSIS OF RESULTS AND DISCUSSION

In this study, the structural importance of the base layer was evaluated by considering Cement-enhanced Class-F Fly ash as the base layer stabilizer (C3); as a result, a critical area such as surface deflection, compressive vertical strain/stress within the base layer and at the top of the subgrade is used for the pavement verification analysis.

First, the increase in the thickness of the base layer (stabilized and unstabilized) decreases the deflection in the surface layer, thus it implies that the base layer is of structural importance in the pavement. However, the stabilized base layers show better results because the layer tends to act like a rigid surface (Table 2).

Table 2. The results of deflection in the surface layer.

Unstabilized base thickness (mm)	Deflection ($\times 10^{-5}$ m)	Stabilized base thickness (mm)	Deflection ($\times 10^{-5}$ m)
100	168.9	100	72.7
200	129.1	200	34.1
300	110.5	300	22.7

Second, the strain in the base and subgrade layers of the pavement is high in the y-direction (vertical); however, with the increase in the thickness of the stabilized base layer, it decreases. However, the stress in the base layer tends to be high in the x-direction (horizontal) (Table 3) and the stress in the stabilized layer against the unstabilized layer increases. This is due to the fact that the stabilized layer acts as a rigid surface and tends to absorb more stress as in the rigid pavement. The stress in the subgrade layer is high in the xy-direction (Table 4) and tends to decrease more in the stabilized layer because of the stress already absorbed by the stabilized base layer.

Finally, the stabilized base layer in the flexible pavement structure acts as a rigid layer, which uniformly distributes the stress generated by the traffic load, and it thus reduces the stress transferred

Table 3. The results of stress in the base layer.

Unstabilized base thickness (mm)	Stress (Mpa)	Stabilized base thickness (mm)	Stress (Mpa)
100	0.203	100	0.582
200	0.145	200	0.493
300	0.097	300	0.295

Table 4. The results of stress in the subgrade layer.

Unstabilized base thickness (mm)	Stress (Mpa)	Stabilized base thickness (mm)	Stress (Mpa)
100	0.028	100	0.001
200	0.017	200	0.003
300	0.011	300	0.002

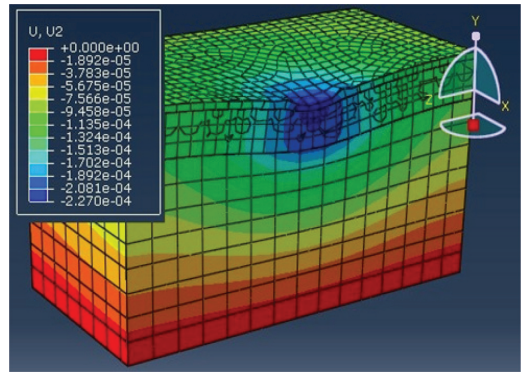

Figure 2. Stabilized base layer displacement distribution.

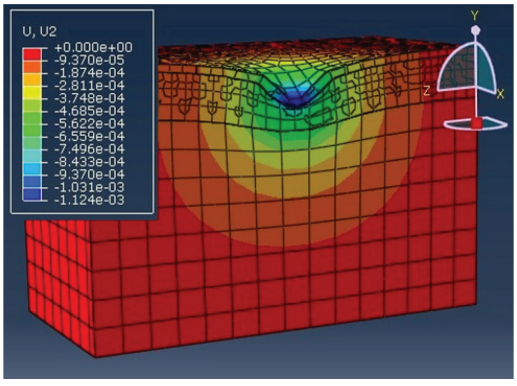

Figure 3. Unstabilized base layer displacement distribution.

to the subgrade when compared with the unstabilized base layer (Figs. 2 and 3).

4 CONCLUSION

Through the present study, the following conclusion can be drawn:

- The base layer in flexible pavement is the main structural element or bearing capacity of the pavement, and when stabilized, it can reduce the stress transferred to the subgrade; as a result, more attention should be paid to the design mix and laboratory testing of the base and other layers.
- The results of this study validate the use of Cement-enhanced Class-F Fly ash as an alternative stabilizer for the base layer in flexible pavement in place of the conventional use of cement only.
- Compared with the laboratory results, G5 stabilized with Cement-enhanced Class-F Fly ash at 20% can be used as the C3 material for base work.
- This work confirms that the use of Abaqus software has a great potential in the design and analysis of flexible and rigid pavements.

REFERENCES

Adlinge, S.S. & Gupta, A.K. 2013. Pavement deterioration and its causes. *International Journal of Innovative Research and Development* 2(4): 437–450.

Adu-Osei, A. 2001. *Characterization of Unbound Granular Layers in Flexible Pavements*. Technical Reported. Texas: Texas A&M University Texas Transportation Institute College Station.

Ahmed, H.Y. 2006. Effect of surface cracking on responses of flexible pavements structure. *Journal of Engineering Sciences* 34(3): 699–717.

Al-Jhayyish, A.K. 2014. *Incorporating Chemical Stabilization of the Subgrade in Pavement Design and Construction Practices*. Athens OH: Ohio University.

Amin, E.R. 2012. A review on the soil stabilization using low-cost methods. *Journal of Applied Sciences Research* 8(4): 2193–2196.

Araya, A.A. 2011. *Characterization of Unbound Granular Materials for Pavements*. Faculty of Civil Engineering and Geosciences. Delft, Netherlands: Delft University of Technology.

Asphalt Pavement Alliance. 2010. *Perpetual Asphalt Pavements: A Synthesis.* Maryland: APA 101, Lanham.

Aydilek, A.H. & Arora, S. 2004. Fly ash amended soils as highway base materials. *Journal of Materials in Civil Engineering* 17(6): 640–649.

Barenberg, E.J. 1977. *Evaluating Stabilized Materials.* National Cooperative Highway Research Program, Contract No. HR 63-4-1, Unpublished Report.

Bindu, J. & Vysakh, P. 2012. *Stabilisation of Lateritic Soil Using Coconut Shell, Leaf and Husk Ash.* Institution of Electrical and Electronics Engineers.

Brennan, M.J. & O'Flaherty, C.A. 2002. Materials used in road pavements. *Highways: The Location, Design, Construction & Maintenance of Road Pavement.* O'Flaherty, C.A. Oxford: Butterworth-Heinemann.

Britto, A. 2014. Running ABAQUS 6.9. *http://www-h.eng.cam.ac.uk/help/programs/fe/abaqus/doc/aba69f-double.pdf*.

Committee of Land Transport Officials (COLTO), 1998.

Darwish, S.G. 2012. Stress and Strain in Flexible Pavement. http://www.unimasr.net/ums/upload/files/2012/Dec/UniMasr.com_892f9fb48f1aa1918a5cfbb7ad4d6f08.pdf.

De Beer, M., Kannemeyer, L. & Fisher, C. 1999. Towards improved mechanistic design of thin asphalt layer surfacing based on actual tyre/pavement contact Stress-In-Motion (SIM) data in South Africa. *Proceedings of 7th Conf. Asphalt Pavements Southern Africa*, *Sun City, South Africa, 12–16 September 2004.*

Fhwa.dot.gov. 2012. Coal Fly Ash—User Guideline—Stabilized Base—User Guidelines for Waste and Byproduct Materials in Pavement Construction—FHWA-RD-97-148. *http://www.fhwa.dot.gov/publications/research/infrastructure/structures/97148/cfa55.cfm.*

Furter, E. 2011. Coal Fly Ash holds African Opportunities. *www.sheqafrica.com/fly-ash-conference/.*

Hassan, M.M. & Khalid, H. 2010. Mechanical and environmental characteristics of bituminous mixtures with incinerator bottom ash aggregates. *International Journal of Pavement Engineering* 11(2): 83–94.

Hejazi, S.M., Sheikhzadeh, M., Abtahi, S.M. & Zadhoush. A. 2012. A simple review of soil reinforcement by using natural and synthetic fibers. *Construction and Building Materials* 30(1): 100–116.

Heyns, M.W. & Hassan, M.M. 2013. South Africa class F fly ash for roads: Physical and chemical analysis, *Interim: Interdisciplinary Journal* 12(3): 28–41.

Huang, Y.H. 2012. *Pavement Analysis and Design*. 2nd edi. NJ: Pearson Education Inc.

Ibrahim, S.F., Gandhi, G.S. & Zaman, T.T. 2014. An approach in evaluating of flexible pavement in permanent deformation of paved and unpaved roads over sand dunes subgrade under repeated loads. *Journal of Environment and Earth Science* 4(14): 78–89.

Jain, S., Joshi, Y.P. & Golia, S.S. 2013. Design of rigid and flexible pavements by various methods and their cost analysis of each method. *International Journal of Engineering Research and Applications* 3(5): 119–123.

Jassal, K.S. 1998. *Development of Potholes from Cracks in Flexible Pavements*. Canada: Concordia University.

Jooste, F. 2004. Re-Evaluation of Some Aspects of the Mechanistic-Empirical Design Approach. *Proceedings of the 8th Conference on Asphalt Pavements for Southern Africa, Sun City, South Africa, 12–16 September 2004*.

Kannemeyer, L. 2013. Asset Management: General Status Overview. 25th Road Pavements Forum Meeting, Western Cape, 7–8 May, 2013.

Kim, M. 2007. *Three-Dimensional Finite Element Analysis of Flexible Pavements Considering Nonlinear Pavement Foundation Behavior*. Urbana-Champaign: Department of Civil Engineering, Graduate College of the University of Illinois at Urbana-Champaign.

Kordi, N.E., Endut, I.R. & Baharom, B. 2010. Types of Damages on Flexible Pavement for Malaysian Federal Road. *Proceeding of Malaysian Universities Transportation Research Forum and Conferences, Universiti Tenaga Nasional, 21 December 2010*.

Lav, A., Hilmi, M., Lav, A. & Goktepe, A.B. 2006. Analysis and design of a stabilized fly ash as pavement base material. *Fuel*. 85(16): 2359–2370.

Little, D., Snead, B., Godiwalla, A., Oshiro, P. & Tang. P. 2002. Characterization of Design Properties (Compressive Strength and Resilient Modulus) of Lime, Cement, Fly Ash Stabilized Structural Recycled Concrete Base As A Function of Curing Time. *Presentada en The 2002 Federal Aviation Administration Airport Technology Transfer Conference, Atlantic City, NJ, May 2002*.

Makusa, G.P. 2012. *Soil Stabilization Methods and Materials.* Luleå, Sweden: Department of Civil, Environmental and Natural resources, Luleå University of Technology.

Mallela, J., Harold Von Quintus, P.E., Smith, K.L. & Consultants, E.R.E.S. 2004. *Consideration of Lime-stabilized Layers in Mechanistic-empirical Pavement Design*. Arlington, Virginia: The National Lime Association.

Ndebele, S.J. 2012. *Keynote Address by the Minister of Transport*. Presented at the occasion of department's budget vote.

Nunes, N.C., Bridges, M.G. & Dawson, A.R. 1996. Assessment of secondary materials for pavement construction: Technical and environment aspects. *Waste Management* 16(1–3): 87–96.

Paige-green, P. 2008. A reassessment of some road material stabilization problems. *Proceedings of the 27th Southern African Transport Conference, Pretoria South Africa, July 7–11, 2008*.

PFI. 2010. Pavement Failure Identification. *http://www.apai.net/cmdocs/apai/designguide/Appendix_A-B.pdf*.

Rahman, M.T., Mahmud, K. & Ahsan, S. 2011 Stress-strain characteristics of flexible pavement using finite element analysis. *International Journal of Civil and Structural Engineering* 2(1): 233–240.

Seeds, S.B. 2000. *Flexible Pavement Design: Summary of the State of the Art*. Transportation in the New Millennium.

Shafabakhsh, G.A., Motamedi, M. & Family, A. 2013. Influence of asphalt concrete thickness on settlement of flexible pavements. *Electronic Journal of Geotechnical Engineering* 18(Bund. C): 473–483.

Sherwood, P. 1993. *Soil Stabilization with Cement and Lime. State of the Art Review*. London: Transport Research Laboratory, HMSO.

Takhelmayum, G. 2013. Laboratory study on soil stabilization using fly ash mixtures. *International Journal of Engineering Science and Innovative Technology* 2(1): 477–482.

The South Africa Natinal Roads Agency Ltd. 2010. Annal report 2010. *http://www.nra.co.za/content/Sanral_ARep_10_Web.pdf.*

The South African National Road Agency Ltd. 2013. *Materials Testing: South African Pavement Engineering Manual.* South Africa: An Initiative of the South African National Roads Agency Ltd.

Theyse, H.L., de Beer, M., Maina, J.M. & Kannemeyer. L. 2011. Interim Revision of the South African Mechanistic-Empirical Pavement Design Method for Flexible Pavements. *Presented at 10th Conference on Asphalt Pavements for Southern Africa, Champagne Sports Resorts, KwaZulu-Natal, South Africa, 11–14 September 2011.*

Tiliouine, B. & Sandjak, K. 2014. Numerical simulation of granular materials behavior for unbound base layers used in Algerian pavement structures. *International Journal of Civil and Structural Engineering* 4(3): 419–429.

United State Environmental Protection Agency. 2009. Using Recycled Industrial Materials in Roadways. *http://www.epa.gov/epawaste/conserve/imr/pdfs/roadways.pdf.*

Van Vuuren, D.J., Otte, E. & Paterson. W.D. 1974. The Structural Design of Flexible Pavements in South Africa. *Proceedings of the 2nd Conference on Asphalt Pavements in South Africa, Durban, South Africa, 1974.*

Wang, J. 2001. *Three-Dimensional Finite Element Analysis of Flexible Pavements*. United States: Department of Civil Engineering, University of Maine.

Yadu, L.K. & Tripathi. R.K. 2013. Stabilization of soft soil with granulated blast furnace slag and fly ash. *International Journal of Research in Engineering and Technology* 2(2): 115–119.

Civil Engineering and Urban Planning IV – Liu et al. (Eds)
© 2016 Taylor & Francis Group, London, ISBN 978-1-138-02903-3

Automatic extraction of vector road based on bus GPS data

Shi-Hao Xu & Fang-Zhen Li
School of Computer Science and Technology, Shandong University of Finance and Economics, Jinan, Shandong, China

Ling-Guo Meng
School of Physics, Shandong University, Jinan, Shandong, China

Qing-Tao Zhao
School of Information Science and Engineering, Shandong University, Jinan, Shandong, China

ABSTRACT: Acquiring the accurate geospatial information of road, the basic component of the RN (Road Network) is the precondition for the construction of high-precision vector RN. This paper presents a method for automatically extracting the vector representation of the routine pre-allocated for the bus from massive GPS (Global Positioning System) trajectories data. First, error and redundant data are eliminated and seed points that can roughly describe the road morphological structure are selected out. Then, those seed points are corrected by using the gravity method, and the core points, points on the road, are clustered from the corrected seed points. Finally, vector road is extracted and smoothed. The experimental result indicate that the method presented is effective and able to provide support for the subsequent construction of the vector RN map.

1 INTRODUCTION

Vector RN map is one of the main components of the ITS (Intelligent Transportation System) and plays a key role in many applications (Zhang et al. 2011). Traditional technologies for RN construction can be classified into two categories: field survey and RS (Remote Sensing) image digitalization (Gerke et al. 2004; Shahid & Zaman 2012). However, RN map generated by using traditional technologies is usually inconsistent with the current reality because the data they used are often out of date.

With the development of GPS technology and the popularity of embedded GPS devices, it is now possible to collect a large amount of accurate GPS data. GPS data contain abundant geospatial information, such as road structure and traffic signal, which enables automated methods for RN map generation or updating in real time. Seth et al. (2000) and Bruntrup et al. (2005) dedicated themselves to study how to update the existing RN map by using GPS data. Guo et al. (2007) developed a system named "Data Recycle" to collect vehicle GPS data during position mapping and realized road edge detection with the least square method based on those collected data. Chen & Cheng (2008) and Shi et al. (2009) designed methods to extract the RN from massive GPS data with operations in the binary mathematical morphology, respectively. Xie et al. (2014) presented a method to infer the RN from GPS traces by using the DTW (Dynamic Time Warping) algorithm. However, to generate or update the RN map needs huge amounts of GPS data. The data acquisition procedure by probing the car with special equipment is still costly and time-consuming. OSM (Open Street Map), founded in July 2004 by Steve squadron, tries to give a solution for free GPS data. Volunteers around the world are provided with a set of tools to contribute and edit their GPS traces. However, the process still relies on human intervention; furthermore, data from different sources are difficult to be integrated together (Haklay & Weber 2008).

Nowadays, in most cities, buses are installed with GPS terminals. A bus installed with the GPS terminal can send its location and speed to the database at regular intervals. As an important infrastructure of the city, the main roads are almost covered by routines of buses. Moreover, GPS data of buses are of high sampling rate, which can reflect the structure of roads in real time.

Indeed, complicated topology of the RN can be broken down into multiple consecutive roads. In this paper, we present an efficient method to extract vector road by using GPS data collected from buses, which supports further construction of the RN map. In our research, vector road is defined as a series of temporal-spatial ordered data

points, with which we can describe the continuous road from the start to the end covered by the routine of the bus. Utilization of GPS data of the bus for road extraction has the property of high verification because we can compare the extracted road with the routine of the bus displayed in the existing digital map, such as Baidu map. To our best knowledge, the present study is the first time to apply the bus GPS data for road extraction.

The remainder of this paper is organized as follows. In Section 3, we discuss our method step by step in detail. Afterwards, experiments are performed to assess our methods in Section 3. The last section makes some conclusions.

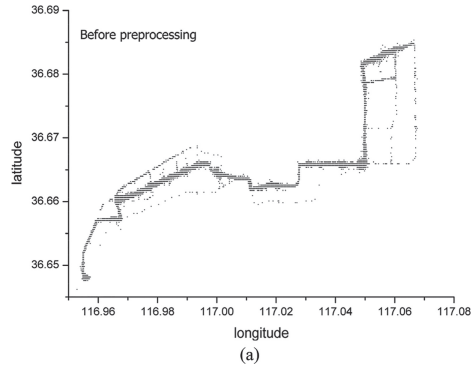

Figure 1(a). Distribution of all points.

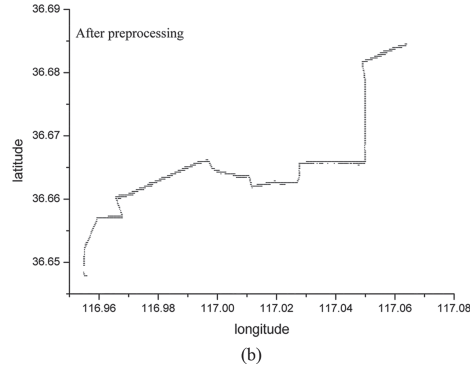

Figure 1(b). Distribution of seed points.

2 METHOD

2.1 *Data preprocessing*

A GPS trajectory, composed of a series of GPS data points, refers to the traveling trace of the bus. Each data point contains information such as longitude, latitude, speed and SQN (Station Sequence Number). Given a set of GPS trajectory data related to a certain routine pre-assigned for the bus, they are first preprocessed to get seed points that represent the morphological structure of the road covered by this routine. The data reprocessing procedure contains two steps: data partitioning and seed point selection.

2.1.1 *Data partitioning*

Each GPS trajectory is divided into two independent datasets: uplink and downlink. We denote SQN_{max} as the maximum of SQN in a trajectory. GPS points satisfying Equation (1) are classified to the uplink dataset and other points are classified to the downlink dataset. In practice, the uplink routine of a bus may not exactly coincide with the downlink routine. Thus, in our work, only uplink data are used to extract vector roads:

$$SQN < \left\lceil \frac{SQN_{max}}{2} \right\rceil \tag{1}$$

2.1.2 *Seed point selection*

The location of a spatial point can be described by its longitude and latitude. A spatial point may be hit by multiple data points. We find that the spatial points appear in the dataset and count the frequency of occurrence of the corresponding data points. Figure 1a shows the distribution of the spatial points that we found.

It is clearly observed from Figure 1a that most points are distributed on both sides of the road symmetrically, but some abnormal points fall on other areas rather than on the road covered by the routine of the bus. The reason for this is mainly due to the driver's behavior. Under some circumstances, drivers occasionally choose some other road segments but not the predefined routine. From the perspective of statistics, compared with the locations on the road, these noisy points should have a lower occurrence frequency, based on which the seed points can be selected. We sort all points in descending order by their occurrence frequency and select the top k (suggested 40) percent of high frequency points. Each of the selected points represents a seed point. The distribution of the seed points is shown in Figure 1b. It can be seen from Figure 1b that the morphological structure of the road is clearly represented by these seed points.

2.2 *Seed point correction*

Seed points need further processing, as they may still be inconsistent or redundant. From Figure 2, we can find that some seed points do not really fall on the road. In order to improve the accuracy of the seed points, we adopt the "neighborhood gravity" method, which is based on the moment balance theory, to correct the locations of the seed points.

Figure 2. Example of seed point distribution.

After data preprocessing, each seed point can be represented by longitude, latitude and frequency. Frequency can be seen as a weight. The larger the frequency, the higher the possibility that a seed point lays on the road. In this step, for each seed point, a circular neighborhood of the radius R is defined. The value of R is set equal to the error of the GPS terminal. We find all the seed points located in this circular neighborhood and calculate the weighted average of their coordinates as the new location of the investigated seed point. Figure 3 shows the schematic of the so-called neighborhood gravity method.

In Figure 3, the filled circle represents the original location before correction and the triangle indicates the corrected place of the seed point. Squares refer to the seed points within the circular neighborhood. The corrected location of the investigated seed point can be obtained by the following Equations (2) and (3):

$$x_0 = \frac{\sum_{i=0}^{n} x_i w_i}{\sum_{i=0}^{n} w_i} \tag{2}$$

$$y_0 = \frac{\sum_{i=0}^{n} y_i w_i}{\sum_{i=0}^{n} w_i} \tag{3}$$

2.3 *Core point calculation*

After correction, the seed points out of the road are closer to the road. Meanwhile, the distribution of the seed points is more clustered, which is unnecessary for extracting the road. A clustering algorithm is used to group these corrected seed points, and then a core point is calculated for each group. Core points give more compact and more accurate representation of the morphology of the road. There are many clustering algorithms, of which we choose the DBSACN (Density-Based Spatial Clustering of Applications with Noise)

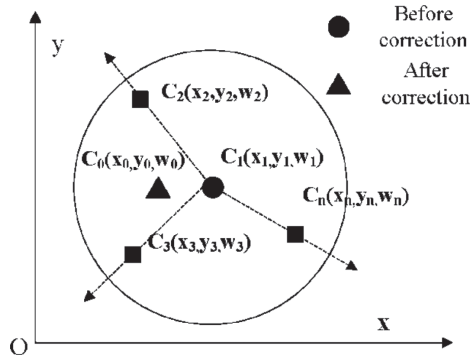

Figure 3. Seed point correction.

algorithm. DBSACN is a spatial clustering algorithm based on density (Borah & Bhattacharyya 2008). It is robust to noise, and the number of clusters need not to be supplied in advance. After clustering, we use Equations (2) and (3) to calculate the core point for each group. Figure 4 shows the distribution of the core points.

2.4 *Vector road extraction*

We obtained core points through the above processes, but they are unordered. In order to get the vector representation of the road, core points should be sorted according to the direction of bus driving. The direction of the road is consistent with the driving direction of the bus. Therefore, we choose the start of the bus as the start of the road, and then find the next core point with the nearest Euclidean distance. We repeat this step until all the core points are traversed. Finally, we get the ordered core points that are the vector representation of the road.

2.5 *Abnormal point removal*

Sudden structure changes may appear in some areas of the extracted road for the existence of abnormal points (see in Fig. 5). To identify these abnormal points, a method based on the bearing change rule is presented.

Three successive points are required for the abnormal point identification. We denote P_{i-1}, P_i, P_{i+1}, as the three successive points. First, bearing change (β_i), the angle between $\overrightarrow{P_{i-1}P_i}$ and $\overrightarrow{P_iP_{i+1}}$ that lies in the interval of 0–180 degrees, is calculated by Equation (4). We calculate the bearing change β_i for each core point (except for the first and the last) P_i. Point P_i is considered to be an abnormal point if β_i is greater than the predefined threshold E (suggested 105). After eliminating the abnormal points, a sudden change phenomenon disappears (see Fig. 5):

Figure 4. Example of core point distribution.

Figure 5. Example of abnormal removal.

$$\beta_i = \arccos\left(\frac{\overrightarrow{P_{i-1}P_i}\cdot\overrightarrow{P_iP_{i+1}}}{\left|\overrightarrow{P_{i-1}P_i}\right|\left|\overrightarrow{P_iP_{i+1}}\right|}\right) \quad (4)$$

2.6 *Corner detection and interpolation*

We regard a site where the bus changes its driving direction largely as a corner. Due to the lack of effective points around the corner, the curve is too stiff to show the real structure of the corner of the road (see Fig. 6).

To detect a corner, four successive points are required. We denote P_{i-1}, P_i, P_{i+1}, P_{i+2} as the four successive points. And β_{i-1}, β_i are the bearing change of points P_{i-1}, P_i, respectively (see Fig. 7). Because the driving direction of the bus often changes in a large amount at a corner, apparent bearing changes may occur consecutively upon the points around the corner. We judge that there exists a corner between P_{i-1} and P_i if the following two criteria are satisfied simultaneously: (1) $\beta_{i-1} + \beta_i$ is greater than the predefined threshold C (suggested 70); (2) β_{i-1} and β_i are in the same direction, i.e. both are clockwise or are counter clockwise. Criterion (2) can be expressed mathematically as follows:

$$\left(\overrightarrow{P_{i-2}P_{i-1}}\times\overrightarrow{P_{i-1}P_i}\right)\cdot\left(\overrightarrow{P_{i-1}P_i}\times\overrightarrow{P_iP_{i+1}}\right)>0 \quad (5)$$

Figure 6. Example of simulation point interpolation.

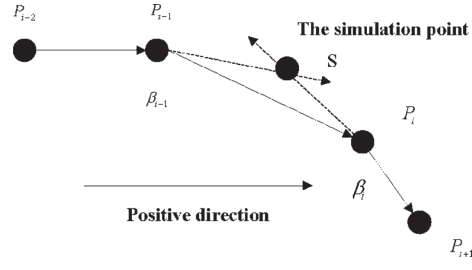

Figure 7. Simulation point interpolation algorithm.

We denote x_i, y_i as the coordinates of the point P_i and $\Delta x_i = x_i - x_{i-1}$, $\Delta y_i = y_i - y_{i-1}$. The above equation is equivalent to Equation (6):

$$(\Delta x_{i-1}\Delta y_i - \Delta x_i\Delta y_{i-1})(\Delta x_i\Delta y_{i+1} - \Delta x_{i+1}\Delta y_i) > 0 \quad (6)$$

After the corner is detected, a simulation point will be inserted between P_{i-1} and P_i. The simulation point, denoted S, is defined as the intersection of the two straight lines m and n, as shown in Figure 7. We select line m, such that the angle between m and $\overrightarrow{P_{i-2}P_{i-1}}$ is $(\beta_{i-1} + \beta_i)/3$. The angle between n and $\overrightarrow{P_iP_{i+1}}$ is also $(\beta_{i-1} + \beta_i)/3$. It can be easily proved that the angle between m and n is also $(\beta_{i-1} + \beta_i)/3$. So, the coordinates of S can be calculated through solving the equations of m and n.

The addition of the effective simulation point to the corner makes the structure of the corner smoother. Figure 6 shows the comparison before and after interpolating the simulation point around the corner.

3 EXPERIMENTS AND RESULTS

GPS trajectory data used in our experiment are collected from the first bus in Jinan city. The objective of our method is to extract a certain number of ordered points to represent the morphological

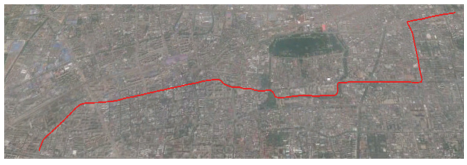

Figure 8. Comparison with road on Google Map.

Figure 9. Routine of the first bus in Jinan city.

structure of the road. We used one hundred thousand GPS points as the input for data preprocessing and then obtained 2321 seed points. Through clustering those corrected seed points, we obtained 362 core points. Finally, the road is represented by 323 points after removing the abnormal points and inserting the simulation point.

In order to assess the accuracy of the experimental results, the extracted road is compared with the Google Map and Baidu Map. By drawing the extracted road on Google Map, we find that it almost completely coincides with the road in Google Map, as shown in Figure 8.

The test result indicate that the coverage rate is up to 99.2%. In Figure 9, the blue line is the routine of the first bus. Obviously, it is consistent with the extracted road shown in Google map. Thus, the accuracy and reliability of our methods is established.

4 CONCLUSIONS

A method for automatic extraction of vector road based on the bus GPS data is presented in this paper. This method involves five steps: data preprocessing, seed point selection, core point computing, vector road construction and road smoothing. Our method opens the possibility to extract vector road in a very economical way with less human interference. Besides, it has no strict requirements on high speed and memory capacity for computing platform, even for long distance route extraction. Experimental results demonstrate the feasibility of our method, which can provide support for subsequent construction of the vector city RN map.

In the future, we aim to construct the city vector RN map based on roads extracted by using the method discussed in this paper. The emphasis is on how to detect and remove the overlapping road segments and identify the intersections of roads.

REFERENCES

Borah, B. & Bhattacharyya, D.K. 2008. A density differentiatedspatial clustering technique. *Journal of Computers* 3(2):72–79.

Bruntrup, R., Edelkamp, S., Jabbar, S. & Scholz, B.2005. Incremental map generation with GPS traces. *Proceedings of the 8th International IEEE Conference on Intelligent Transportation Systems, Vienna, Austria, September 13–16, 2005*. Florida: The Chemical Rubber Company Press.

Chen, C. & Cheng. Y.H. 2008. Roads Digital Map Generation with Multi-track GPS Data. *2008 International Workshop on Education Technology and Training & 2008 International Workshop on Geoscience and Remote Sensing, Shanghai, China, December2 1–22, 2008*. Piscataway, N.J.: IEEE Press.

Guo, T., Kazuaki, I. & Masashi, K. 2007. Towards High Accuracy Road Maps Generation from Massive GPS Traces Data. *Geoscience and Remote Sensing Symposium, 2007. IGARSS 2007, IEEE Internationa, Barcelona, Brazil, July 23–28, 2007*. Piscataway, N.J.: IEEE Press.

Gerke, M., Butenuth, M., Heipke, C. &Willrich, F. 2004. Graph-supported verification of road databases. *ISPRS Journal of Photogrammetry and Remote Sensing* 58(3–4):152–165.

Haklay, M. & Weber, P. 2008. OpenStreetMap: Usergenerated street maps. *IEEE Pervasive Computing* 7(4): 12–18.

Shahid, M.D. & Zaman, U.Z. 2012. Development of GIS-based Road Database Using High-resolution Satellite Image.*2012 2nd International Conference on Information Communication and Management (ICICM 2012). Hong Kong October 26–28, 2012*. Piscataway, N.J.: IEEE Press.

Seth, R. & Stefan S. 2000. Creating and Evaluating Highly Accurate Maps with Probe Vehicles. *IEEE 2000, IEEE Intellgent Transportation Systems Conference Proceedings, Dearborn (MI), USA, October l-3, 2000.* Piscataway, N.J.: IEEE Press.

Shi. W.H., Shen. S. &, Liu. Y.C. 2009. Automatic Generation of Road Network Map from Massive GPS Vehicle Trajectories. *Proceedings of the 12th International IEEE Conference on Intelligent Transportation Systems, St. Louis, MO, USA, October 3–7, 2009*. Piscataway, N.J.: IEEE Press.

Xie, X.Z., Wilfried, P. & Peter, V. 2014. Road Network Inference from GPS Traces using DTW Algorithm. *2014 IEEE 17th International Conference on Intelligent Transportation Systems (ITSC), Qingdao, China, October 8-11, 2014.* Piscataway, N.J.: IEEE Press.

Zhang, J.P., Wang, F.Y., Wang, K.F., Lin, W.H., Xu, X.& Chen, C. 2011. Data-driven intelligent transportation systems. *IEEE Transportations on Intelligent Transportation Systems*12(4): 1624–1639.

This page intentionally left blank

Civil Engineering and Urban Planning IV – Liu et al. (Eds)
© 2016 Taylor & Francis Group, London, ISBN 978-1-138-02903-3

Research on the crack resistance of the high-viscosity emulsified asphalt sand seal

Ya-Zhen Sun, Jia-Wei Pan & Xue-Ying Tang
Institute of Transportation Engineering, Shenyang Jianzhu University, Shenyang, Liaoning, China

Jin-Chang Wang
Institute of Transportation Engineering, Zhejiang University, Hangzhou, Zhejiang, China

ABSTRACT: In order to study the crack resistance of the high-viscosity emulsified asphalt sand seal, ABAQUS finite element software was carried out to build a pavement model to compare the stress at the crack tip and stress intensity factor with and without sand seal construction. The results indicate that the stress at the crack tip and stress intensity factor has a significant reduction after laying the sand seal directly or filling the crack before laying the sand seal. When there is more than one crack in the pavement, the reduction is also obvious. It can be concluded that the high-viscosity emulsified asphalt sand seal has a good performance on crack resistance.

1 INTRODUCTION

In recent years, with the rapid development of economy, semi-rigid base asphalt pavements are wildly used in the highway because of its high strength, stiffness and stability. Besides, it has a good performance on antifreeze. Therefore, the structural bearing capacity of the road can be improved significantly. But over time, the phenomenon has been found gradually that the semi-rigid base asphalt pavement is easy to crack. Through the investigation, it has been found that there are a large number of cracks in the semi-rigid base pavement after opening transport 1–2 years in our country, and there are many causes for crack such as nature, weather conditions, traffic load and construction of asphalt mixture and the base material (Yang 2011). So, in order to maintain its performance and to extend its service life, it is very necessary to repair these cracks.

Pavement maintenance is the key link along the whole road maintenance process. As a kind of brand new concept and technology, preventive maintenance has gained acceptance and application in our country. It is significant to change the situation of passive maintenance, which has a long history, and it is also meaningful to keep good pavement performance. Sand seal is a coating type used on surface layers and a new technique of preventive maintenance for pavements. The sand seal consists of sands that are laid on the roadway surface; after that, the surface is sprayed with emulsified asphalt and then embedment of the sand is accomplished by natural rolling. One of main functions of sand seal is to repair surface crack and prevent the propagation of crack. In order to study the crack resistance of the high-viscosity emulsified asphalt sand seal, ABAQUS finite element software was used to build a pavement model to compare the stress at the crack tip and stress intensity factor with and without sand seal construction. In addition, this paper took surface cracks as the main research object and carried out a series of numerical simulation analysis by using the finite element method.

2 FINITE ELEMENT MODEL

2.1 *Pavement structure*

A finite element with six structural layers was built to study the performance of the high-viscosity

Table 1. Parameters of the structural layer.

Layer	Thickness/ cm	Elastic modulus/ MPa	Poisson's ratio
Surface	4	1400	0.35
Middle surface course	6	1200	0.3
Bottom surface course	24	1000	0.3
Macadam	15	500	0.35
Cement stabilized macadam	20	1500	0.25
Base	–	40	0.4

emulsified asphalt sand seal based on the real pavement data. The parameters of each structural layer (Liao 2008) are listed in Table 1 and the finite element model is shown in Figure 1. The model of the pavement with sand seal is shown in Figure 2.

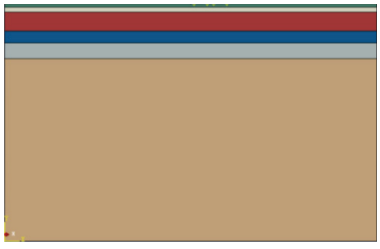

Figure 1. Finite element model of the original road.

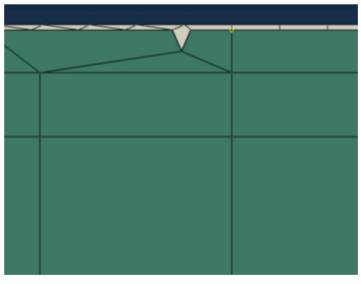

Figure 2. Finite element model after laying the sand seal.

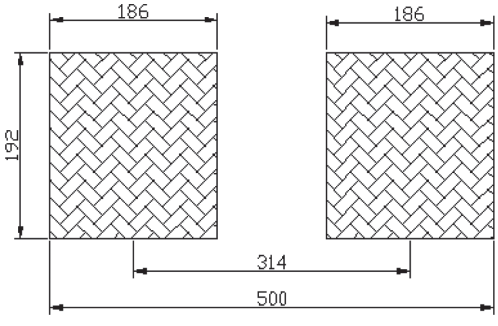

Figure 3. Traffic load.

2.2 *Traffic load*

The standard traffic load is 100 kN and the pressure is 0.7 MPa. According to the load stress equivalence principle, under the double rounds uniform load conversion into two rectangular loads, the size of each rectangle is 186 m × 192 mm (Saad et al. 2006) and the distance between two rectangular loads is 314 mm. The specific form is shown in Figure 3.

2.3 *Temperature load*

As we all know, asphalt concrete is a temperature-sensitive material (Lin 2015 a, b; He 2009).

When the temperature decreases, asphalt concrete suffers internal force that is due to thermal shrinkage. Surface crack will appear when the internal force is larger than the tensile strength of asphalt concrete. The internal force, in this paper, is caused by temperature changes from 0°C to –20°C. The expansion coefficient is presented in Table 2.

3 RESULTS

3.1 *The stress at the crack tip*

The result of stress under traffic loading is shown in Figure 4, and the stress at the crack tip under temperature loading is shown in Figure 5.

According to Figure 4, the values of stress at the crack tip in the original road, the road on which the sand seal is laid directly and the road on which the crack is filled before laying the sand seal are 0.334 MPa, 0.263 MPa, 0.175 MPa under traffic loading, respectively.

According to Figure 5, the values of stress at the crack tip in the original road and the road on which the crack is filled before laying the sand seal are 0.287 MPa and 0.146 MPa under temperature loading, respectively.

3.2 *Multi-crack effect*

In fact, there is more than one crack in the pavement. Therefore, the interaction between cracks has a significant impact on stress at the crack tip. So, the finite model built by ABAQUS is shown in Figure 6, which shows two cracks on the surface course. Figure 7 shows the result of the multi-crack effect with and without the sand seal.

Table 2. Expansion coefficient (m/°C).

Surface	Middle	Bottom	Macadam	Cement-stabilized macadam	Base
2.5×10^{-5}	2.5×10^{-5}	1.5×10^{-5}	1×10^{-5}	1×10^{-5}	5×10^{-5}

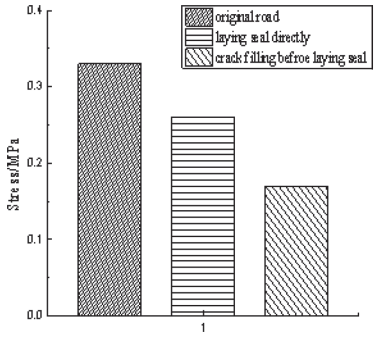

Figure 4. Stress at the crack tip under traffic loading.

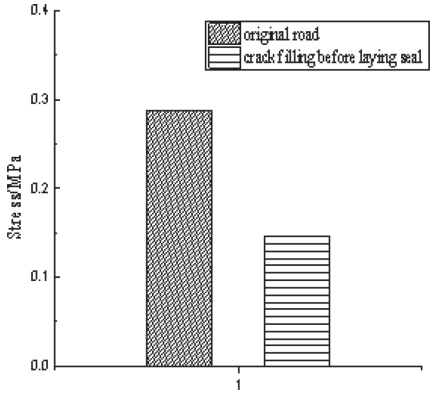

Figure 5. Stress at the crack tip under temperature loading.

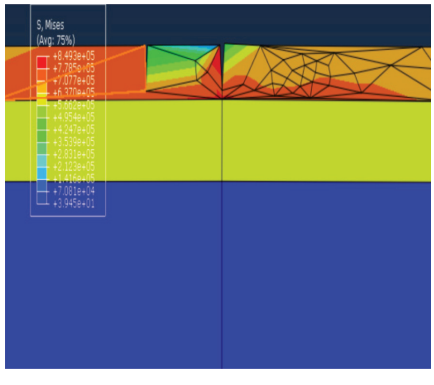

Figure 6. The finite model.

According to Figure 6, we found that when the distance between two cracks is close to 0.05 m, the effect of multiple cracks approaches a maximum value. The impact between two cracks would be negligible, and can be calculated as a single crack.

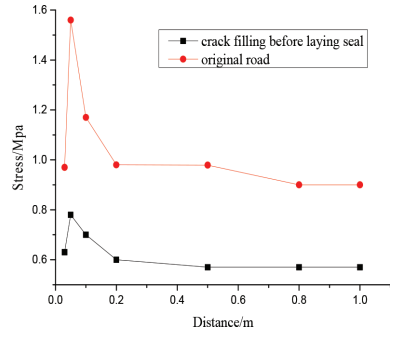

Figure 7. Distance effect.

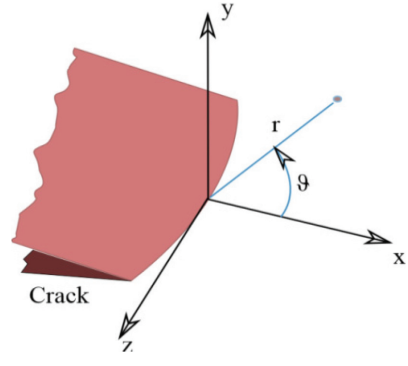

Figure 8. Polar coordinates at the crack tip.

3.3 *The stress intensity factor*

The Stress Intensity Factor (SIF) is used in fracture mechanics to predict the stress state (stress intensity) near the tip of a crack caused by a remote load or residual stresses (Zhang 2009). It is a theoretical construct usually applied to a homogeneous, linear elastic material and is useful for providing a failure criterion for brittle materials, and is a critical technique in the discipline of damage tolerance. The concept can also be applied to materials that exhibit small-scale yielding at a crack tip.

Linear elastic theory predicts the stress distribution (σ_{ij}) near the crack tip at polar coordinates (r, θ), as shown in Figure 8, with the origin at the crack tip, given in Equation (1):

$$\sigma_{ij}(r,\theta) = \frac{K}{\sqrt{2\pi r}} f_{ij}(\theta) \tag{1}$$

where K is the SIF and f_{ij} is a dimensionless quantity that varies with the load and geometry. This relation breaks down very close to the tip (small r) because as r approaches to 0, the stress σ_{ij} reaches

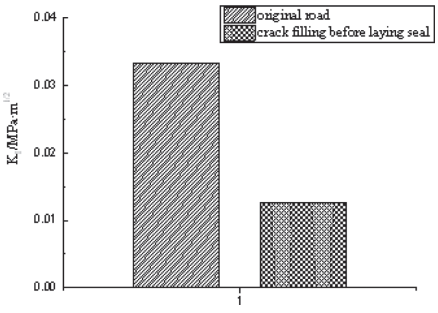

Figure 9. The stress intensity factor.

to ∞. Plastic distortion typically occurs at high stresses and the linear elastic solution is no longer applicable close to the crack tip. However, if the crack-tip plastic zone is small, it can be assumed that the stress distribution near the crack is still given by Equation (1).

Different subscripts are used to designate the stress intensity factor for the three different modes. The stress intensity factor for mode I is designated and applied to the crack opening mode. Mode II stress intensity factor applies to the crack sliding mode and mode III stress intensity factor applies to the tearing mode. These factors are formally defined in Equation (2) (Rooke et al. 1976):

$$K_I = \lim_{r \to 0} \sqrt{2\pi r}\,\sigma_y(r,0) \tag{2}$$

This study focused on determining the effect of temperature loading on the SIF of mode I (K_1). And the result is shown in Figure 9.

According to Figure 6, the values of the SIF in the original road and the road on which the crack is filled before laying the sand seal are 0.0334 MPa · $m^{1/2}$ and 0.0127 MPa · $m^{1/2}$, respectively.

4 CONCLUSIONS

– After laying the sand seal directly, the stress at the crack tip reduced by about 18 percent under traffic loading compared with the original road. If the crack is filled on the original road before laying the sand seal, the reduction would be 45 percent.
– The reduction in stress at the crack tip was 51 percent after filling the crack before laying the sand seal under temperature loading.
– When there is more than one crack in the pavement, the fissured effect must be considered. It can be concluded that when the distance between two cracks was close to 0.05 m, the effect was supreme. But when the distance was beyond 0.2 m, the effect can be overlooked.
– By comparing the SIF before and after laying the sand seal under temperature loading, the reduction of the SIF was found to be 51 percent.

ACKNOWLEDGMENTS

This work was financially supported by the National Natural Science Fund (51478276), the Natural Science Foundation of Liaoning Province (2014020070), the Liaoning Provincial Department of Education Project (L2014234), the Shenyang City Highway Project Management Office (14-08-130) and the Ministry of Housing and Urban Rural Construction Projects (2014-K5-024).

REFERENCES

He, C.Y. 2009. *Research on Preventive Maintenance Decision Making of Asphalt Pavement*. Hunan: Changsha University of Science & Technology.

Liao, G.Y. 2008. *The Application of ABAQUS in Road Engineering*. Nanjing: Publishing House of Southeast University.

Lin, C. 2015. *Numerical Simulation Analysis of Semi-rigid Pavement with Elaborate Loads*. Zhejiang: Zhejiang University.

Rooke, D.P. & Cartwright, D.J. 1976. *Compendium of Stress Intensity Factors*. HMSO Ministry of Defence. Procurement Executive.

Saad, B. & Mitri, H. 2006. 3D FE analysis of flexible pavement with geosynthetic reinforcement. *Journal of Transportation Engineering* 5(5): 402.

Yang, Q. 2011. *Application of XFEM in the Multiple Crack Propagation Analysis of Asphalt Pavement*. Hubei: Huazhong University of Science & Technology.

Zhang, X. 2009. *Damage and Fracture Mechanics*. Beijing: Beihang University Press.

Civil Engineering and Urban Planning IV – Liu et al. (Eds)
© 2016 Taylor & Francis Group, London, ISBN 978-1-138-02903-3

Reliability assessment of port area road based on Bayesian analysis

Xiang-Qun Song, Yong Zhou, Wen-Yuan Wang & Qi Zhang
Faculty of Infrastructure Engineering, Dalian University of Technology, Dalian, Liaoning, China

ABSTRACT: This paper proposes a reliability assessment model of the road in a Chinese container port from the perspective of uncertainty. First, we give a comparison on the attributes of road system and traffic between the port area and the urban area. Causal inference is then introduced to get the Bayesian network topology of connectivity reliability of the road segment in the port area. Based on the analysis and measurement of influence factors, connectivity reliability of both the road segment and different types of intersections can be evaluated, and then the assessment model of the connectivity reliability of the port area road is presented. An application of the reliability assessment model to the real road in a Chinese container port demonstrates the validity of the model. The results obtained from the reliability assessment model are used to help both port planners and operators make reasonable decisions.

1 INTRODUCTION

As a vital component of the collecting and dispatching system in container ports, port area roads transport nearly 62% of the total port freight in China. Some ports have been confronted with heavy road traffic congestion due to the expansion of container terminals, which has in turn brought more container truck traffic. This congestion not only worsens the level of service to container trucks, but also lowers the ports' efficiency and competitiveness. Therefore, how to plan and design the roads in the port area reasonably has raised increasing concerns in both academic and engineering communities. Real-time assessment of the reliability of the port area road considering various traffic conditions and emergencies, a key issue in port area road planning, is of great importance to make scientific decisions of road security management to eliminate the risk of time and prevent traffic accidents.

Reliability analysis has received very little attention in urban road network planning considering day-to-day operations and disaster scenarios, compared with other systems, e.g. electric power systems, water distribution systems, communication networks (Ang & Tang 2006). Road network connectivity reliability was first put forward by Mine & Kawai (1982), to reflect the probability that the network nodes remain connected. Another measurement of road network reliability is the travel time reliability or the coefficient of fluctuation of travel time (Asakura & Kashiwasani 1991). Chen et al. (2002) proposed the concept of road network capacity reliability in 1999 and systematically elaborated it in 2002. Our work is closest in spirit to Chen et al. (2011), who also aimed to present models based on Bayesian analysis to calculate the reliability of the road system for the need of a real-time decision-making in the safety management of the road network operation. However, road network in the urban area instead of the port area was considered in their study, and to the authors' knowledge, no relevant research has been conducted on port area road reliability in the literature.

This paper aims to make some revisions on research achievements related to urban road reliability in view of a comparison between the attributes of the road system in the port and urban areas, and proposes an efficient reliability assessment model of the road in a Chinese port. Especially, connectivity reliability of both the road segment and different types of intersections in the port area road system is evaluated using the Bayesian network based on the analysis and measurement of influence factors. The proposed assessment model of connectivity reliability of the port area road can provide a reference for truck traffic management and road system planning and layout.

2 PORT AREA ROAD ATTRIBUTES

Due to the features of container port traffic, the attributes of the road system and traffic in the port area differ from those in the urban area (Yang et al. 2010), as listed in Table 1. Based on the above comparison, we establish the reliability assessment model of the port area road via some revisions on the existing research achievements of urban road reliability.

Table 1. Comparison of attributes of the port area road and the urban area road.

	Urban area road	Port area road
Demand	Generated from the travel need of citizens	Generated from container transportation
	Fluctuation mainly depends on working-time	Fluctuation mainly depends on ship operations
	Travelers choose the optimal mode and path on account of travel time and cost	Drivers are usually aged above 40 years with higher driving skills but poorer physical health
	Many types of vehicles, but cars are the main ones with few trucks	Few optional paths
		Truck is the main mode with a higher failure rate and smaller safe speed and deviation
Supply	The road network is complex due to the large number of roads	The road network is quite simple with fewer intersections
	The road network covers the whole city, and has many connecting corridors with outsides	The railway affects road traffic strongly
	Several kinds of roadway, e.g. sidewalks and bikeways	Very few road types
Traffic flow	The pattern of traffic flow is fixed in time and direction, and can be predicted	Peak hours depend on handling operations, and are not fixed

3 METHODOLOGY

In this paper, port area road is simplified into a structure composed of road segments and various types of intersections connected in series. A sketch of the simplified port area road is shown in Figure 1.

As can be seen from the figure, several types of representative intersections are selected as part of the reliability model of the port area road system. In order to assess the connectivity reliability of the port area road, the reliability of both road segments and intersections needs to be calculated, which will be described below in detail.

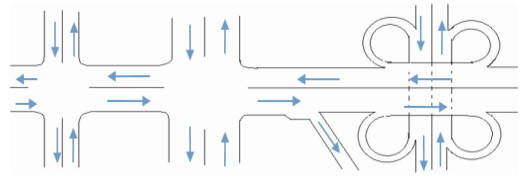

Figure 1. A sketch of a simplified port area road.

3.1 *Road segment reliability assessment*

Road segment traffic system consisting of driver, vehicle and road is considered in this paper. The whole system runs normally only when all the three factors work well. Based on the features of the series system, the connectivity reliability of the road segment equals the product of the reliability of these three factors, as given in Equation (1):

$$R_{rs} = R_d R_v R_r \tag{1}$$

where R_{rs} is the connectivity reliability of the road segment; R_d, R_v and R_r are the reliabilities of the driver, vehicle and road, respectively.

A Bayesian network structure of factors influencing the connectivity reliability of the road segment is constructed, as shown in Figure 2. Referring to the theory of the divisibility in the system and using Bayesian causal inference, the reliability of the road segment in the port area can be calculated.

Driver reliability is determined by driving skill and drivers' physical and mental health. It is not stable and hard to be calculated accurately. Some models widely used in ergonomics can be selected for calculating driver reliability.

Vehicle reliability is affected by vehicle conditions, travel speed, speed deviation, traffic density and traffic composition. These factors can be determined by either the statistical investigation or the expert evaluation method. For further details, the readers are referred to the paper by Chen et al. (2011).

Road reliability is influenced by adverse weather, road maintenance, road grade, road width and turning radius. With the design materials of the port area road and the existing evaluation functions, road reliability is not hard to be measured.

3.2 *Intersection reliability assessment*

Figure 1 shows the process of reliability assessment of different kinds of intersection. For the cross intersection, the connectivity reliability of eight road segments (four geographical orientations and two traffic directions) constituting this intersection, R_{rsi}, is calculated according to the assessment model proposed in the above section. In addition, the traffic flow on each road segment at a time period (generally in peak hours), q_i, is collected, and then the connectivity reliability of the cross intersection, R_I, can be calculated as follows:

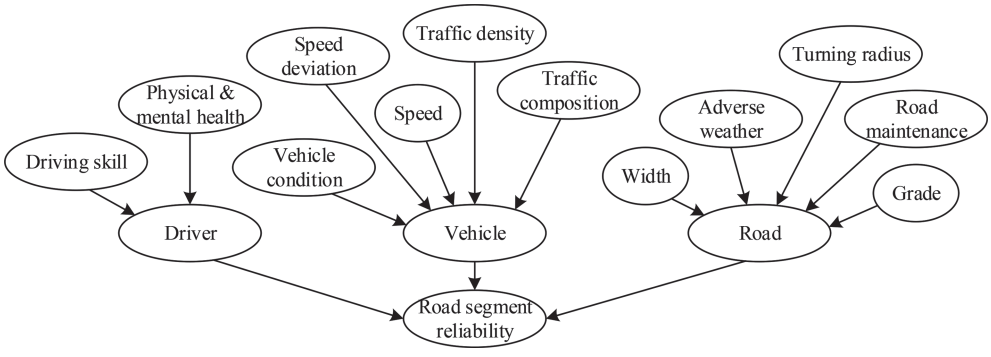

Figure 2. Bayesian network structure of the reliability model for the port area road segment.

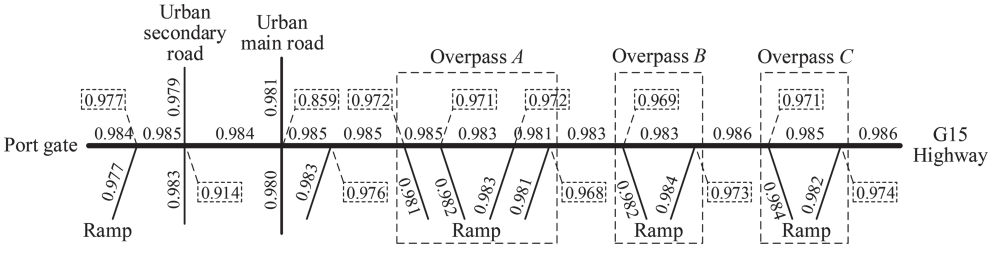

Figure 3. Connectivity reliability of road segments and intersections in the Dayaowan port area road system.

$$R_{\mathrm{I}} = \sum_{i=1}^{8} q_i R_{\mathrm{rs}i} / \sum_{i=1}^{8} q_i \tag{2}$$

The intersection of the port area road and ramp is composed of three segments, and the connectivity reliability calculation method of this kind of intersection is similar to that of the cross intersection. As for the overpass, it can be decomposed into two or four intersections of the port area and ramp for assessment.

3.3 *Port area road reliability assessment*

Port area road is composed of two road systems with an opposite direction of traffic flow connected in parallel, and each road system is made up of several road segments and intersections connected in series. With the assessment models of the road segment and various types of intersection, the connectivity reliability of the port area road can be calculated as follows:

$$R_{\mathrm{par}} = \frac{1}{2}\prod_{i=1}^{\mathrm{m}} R_{\mathrm{rs}i} \prod_{j=1}^{\mathrm{p}} R_{\mathrm{I}j} + \frac{1}{2}\prod_{i=1}^{\mathrm{n}} R'_{\mathrm{rs}i} \prod_{j=1}^{\mathrm{q}} R'_{\mathrm{I}j} \tag{3}$$

where R_{par} is the connectivity reliability of the port area road; m and n are the number of road segments in each direction; p and q are the number of intersections in each direction; $R_{\mathrm{rs}i}$ and $R_{\mathrm{rs}i}'$ are the connectivity reliability of the road segment i in each direction; $R_{\mathrm{I}j}$ and $R_{\mathrm{I}j}'$ are the connectivity reliability of the intersection j in each direction.

4 CASE STUDY

In this section, we assess the connectivity reliability of the Dayaowan port area road that connects the port gate with G15 highway using the Bayesian network structure. For simplicity, this port area road can be abstracted to the structure, as shown in Figure 3, and three kinds of intersections are involved in the road system. It can be noted that there are two entrance and exit ramps in overpass *A*, while one entrance and exit ramp both in overpasses *B* and *C*. According to field observations, peak hours occur between 16 and 18 o'clock. Related information such as traffic flow and composition of each road segment in this time period is collected to calculate its connectivity reliability, as shown in Figure 3. The results show that connectivity reliability of all road segments is high, which indicates that the probability of traffic jams occurring on the road segment is low. Figure 3 also

shows the values of connectivity reliability of all intersections in the port area road. As can be seen, most of the intersection reliability is above 0.9 except for the intersection of the urban main road and the port area road. Finally, based on the proposed assessment model, the connectivity reliability of the Dayaowan port area road is calculated to be 0.482.

5 CONCLUSIONS

With strong causal inference ability, the Bayesian network structure is a great tool for studying road reliability, involving a great number of uncertain variables. This paper builds a Bayesian network of the reliability model for the port area road segment, which intuitively describes the logical relationships among influential factors. Considering the features of the port area road and referring to the urban road reliability theory, a Bayesian network-based connectivity reliability assessment model of the port area road is presented. Compared with the conventional calculation model of road reliability, the model proposed in this paper is more simple and effective, and it is valuable for both port operation and port area road planning.

ACKNOWLEDGMENT

This research was financially supported by the National Natural Science Foundation of China under grant no. 51309049.

REFERENCES

Ang, A.H.S. & Tang, W.H. 2006. *Probability Concepts in Engineering: Emphasis on Applications to Civil and Environmental Engineering (2nd Edition)*. New York: Wiley.

Asakura, Y. & Kashiwasani, M. 1991. Road Network Reliability Caused by Daily Fluctuation of Traffic Flow. *Proceedings of the 19th PTRC Summer Annual Meeting, Brighton.*

Chen, A., Yang, H., Lo, H.K. & Tang, W.H. 2002. Capacity reliability of a road network: an assessment methodology and numerical results. *Transportation Research Part B: Methodological* 36(3): 225–252.

Chen, F., Liu, B., Guo, Z. & Chen, F. 2011. Reliability models of road traffic systems based on Bayesian analysis. *Journal of Tongji University (Natural Science)* 39(2): 220–225.

Mine, H. & Kawai, H. 1982. *Mathematics for Reliability Analysis*. Tokyo: Asakura-Shoten.

Yang, Z., Chen, G. & Moodie, D.R. 2010. Modeling road traffic demand of container consolidation in a Chinese port terminal. *Journal of Transportation Engineering* 136(10): 881–886.

Civil Engineering and Urban Planning IV – Liu et al. (Eds)
© 2016 Taylor & Francis Group, London, ISBN 978-1-138-02903-3

Study on the anti-cracking performance of fibrous high-viscoelastic asphalt sand

Ya-Zhen Sun, Xue-Ying Tang & Zheng Guo
Traffic Engineering Institute, Shenyang Jianzhu University, Shenyang, Liaoning, China

Jin-Chang Wang
Institute of Transportation Engineering, Zhejiang University, Hangzhou, Zhejiang, China

ABSTRACT: This paper presents an experimental investigation to understand the influence of different fibers on the tensile strength and fracture energy of fibrous high-viscoelastic asphalt sand. Three kinds of specimen, namely lignin fiber, basalt fiber and non-fiber, are selected for the direct tensile test. The maximum failure load is used to analyze the tensile strength, and the area surrounded by the load and displacement curve is used to analyze the fracture energy. The experimental results indicate that when the temperature is constant, the maximum load and fracture energy of the specimen are increased with the loading rate increased. The fracture energy at the loading rate of 20 mm/min for lignin fiber is 2.883 times, and at the loading rate of 2 mm/min for basalt fiber is 2.01 times and for non-fiber is 1.785 times, respectively, and we find that the lignin fiber is optimal for the growth of fracture energy.

1 INTRODUCTION

As the traffic volume and traffic axial load increasing, the demand of asphalt road is higher and higher. When the road is open to traffic, rutting, cracking and other diseases are produced. Reflection crack is a common disease of asphalt pavement. There are many measures of prevention for reflection crack; for example, stress-absorbing layer is a kind of effective measure. The stress-absorbing interlayer is set in the pavement to postpone reflective cracking to propagate. It has a lot of preferable merits in keeping the reflective cracking in the old cement concrete pavement rebuild project. It is becoming one of the important technological schemes in adding asphalt overlay on the old cement concrete road surface (Wang 2014). This paper mainly studies the trend of the maximum load and the fracture energy of specimens under different loadings, thus further evaluates the anti-cracking ability of fibrous high-viscoelastic asphalt sand.

2 EXPERIMENT

2.1 *Experimental material*

The asphalt in the test is a new kind of high-viscoelastic asphalt. It is composed of matrix asphalt, TCA additives, and active powder with a proportion of 84.35%, 9.13% and 6.52%, respectively. Aggregate is composed of gravel and stone chips. The gravel size is 5~10 mm and 3~5 mm, respectively, each for 50%. Stone chip size is 0~3 mm. Gradation composition for gravel 5~10 mm: gravel 3~5 mm: stone chips 0~3 mm is 25:25:50.

Lignin fiber and the basalt fiber are chosen as the test fibers. The mass proportion of the fiber is 0.4%. The lignin fibers are used in Shanghai factory production, whose model is FB-3002, as is shown in Figure 1. Its performance is tasteless, non-toxic, non-polluting and non-radioactive, and also has stable chemical properties (JTG E20-2011). Basalt fiber has good high temperature stability and good resistance to chemical corrosion. The basalt fiber is a kind of green environmental protection mineral fiber, which will not cause

Figure 1. Lignin fiber.

pollution to the environment (Liu 2010), as shown in Figure 2.

2.2 *Theory of fracture energy*

When the specimen is destroyed completely, fracture energy consumption must be considered. Fracture energy is the important parameter of anti-cracking and impact resistance of the material (Wang et al. 2013). Through the test, the curve of the force and displacement can be obtained, and the fracture energy is the area surrounded by the load and displacement of the curve, as shown in Figure 3 (Li et al. 2006).

2.3 *Specimen shape and dimension*

The specimen (300 mm × 300 mm × 50 mm) is prepared by the wheel rolling method according to the standard experiment methods of bitumen and bituminous, mixtures for highway engineering (JTG E20-2011), and then it is cut into a prism specimen with a cutting machine, which is 120 mm ± 1.0 mm long, 50 mm ± 1.0 mm wide and 50 mm ±1.0 mm high. The 1.5 mm-deep precutting fissure is cut to guarantee that the failure section is controlled in the middle of a tensile specimen. Specimen shape and dimension are shown in Figure 4.

Figure 2. Basalt fiber.

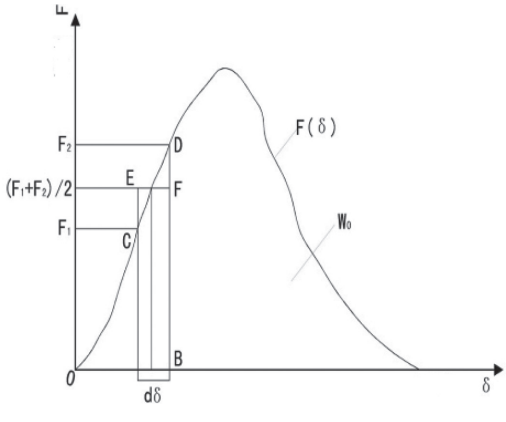

Figure 3. Fracture energy calculation curve.

2.4 *Experimental process*

In this experiment, the direct tensile test method is used to determine the tensile strength of the three kinds of specimen, namely non-fiber, lignin fiber and basalt fiber. The specimen is loaded by the automatic acquisition system. Fibrous high-viscoelastic asphalt is tested at three loading rates (2, 10 and 20 mm/min) at the temperature condition of 25ºC. The test involves specific steps, which are as follows:

– Putting the specimen in the oven for 4 h, then immediately put it in tensile test fixture, as shown in Figure 5, in order to avoid the friction between tensile fixtures and tensile specimen section, coated with vaseline on tensile fixtures to reduce the friction between them.
– The X-Y recorder is connected to the load sensors and displacement meter, the X axis is the

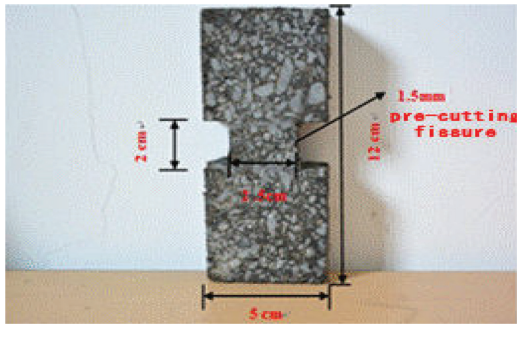

Figure 4. Specimen shape and dimension.

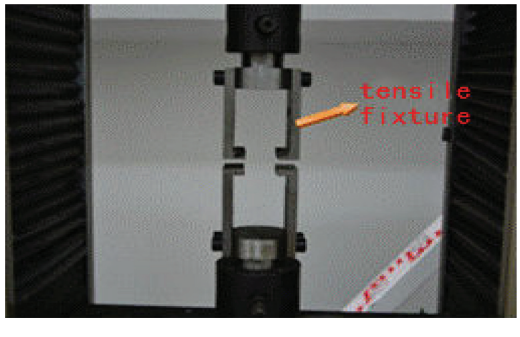

Figure 5. Tensile instrument.

Figure 6. X-Y recorder.

displacement, and the Y axis is the load. The instrument will automatically choose the appropriate range according to the load condition. The X-Y recorder is shown in Figure 6.

– The temperature of the test is 25°C and the loading rates selected are 2 mm/min, 10 mm/min, and 20 mm/min; at the same time, the X-Y recorder can record the corresponding load-deformation curve.

3 EXPERIMENTAL RESULTS

3.1 *The tensile strength analysis*

From Figure 7, it can be seen that the stress increased with the increased loading rate; when the specimen is destroyed completely, the stress reached the maximum. Before the maximum failure load, the stress increased with increased displacement, after the maximum failure load, the stress decreased with the increased displacement.

From Figure 8, it can be seen that when the loading rate is 2 mm/min, the basalt fiber tensile strength is maximum. When the loading rate is 10 mm/min, the maximum failure stress of basalt fiber and non-fiber is close and the maximum failure stress of lignin fiber is the minimum. When the loading rate is 20 mm/min, the lignin fiber and the basalt fiber tensile strength is close but greater than that of non-fiber. Above all, at the same loading rate, the tensile strength with fiber is much better than that of the specimens without fiber.

3.2 *Fracture energy analysis*

By comparing the anti-cracking of the three kinds of specimen, the magnitude of the fracture energy of per unit area is analyzed, as shown in Figures 9 and 10.

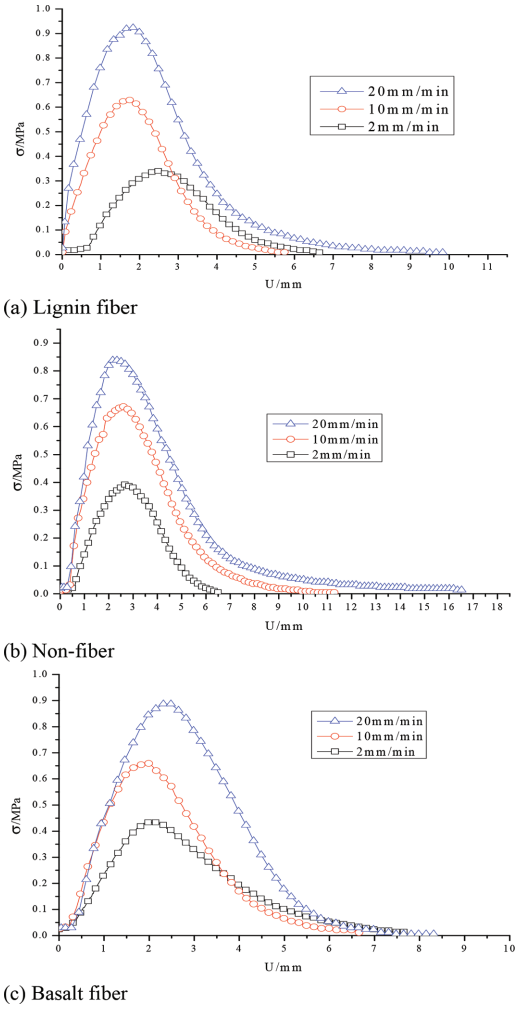

Figure 7. The stress-displacement curve for the specimen.

From Figure 9, it can be seen that when the temperature is constant, the fracture energy of the specimen increases with the increased loading rate. From Figure 10, it can be seen that when the loading rate is 2 mm/min and 10 mm/min, the basalt fiber fracture energy per unit area is maximum; when the loading rate is 20 mm/min, the fracture energy of the basalt fiber and lignin fiber per unit area are significantly greater than that of the non-fiber specimen. In summary, at the same temperature and same loading rate conditions, the addition of basalt fiber can obviously increase the fracture energy of the asphalt sand, which shows that the basalt fibers can increase the anti-cracking of high-viscoelastic asphalt sand.

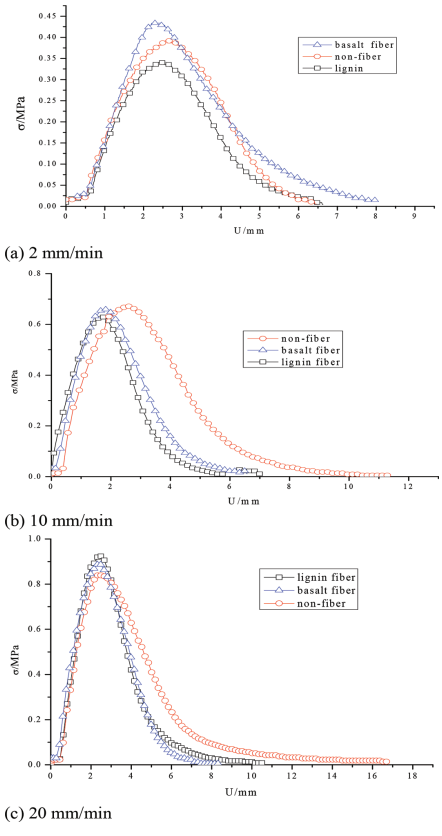

Figure 8. The stress-displacement curve for the different specimens at the same loading rate.

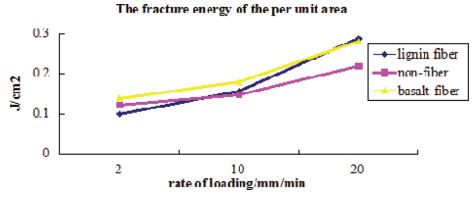

Figure 9. The same specimen at different loading rates.

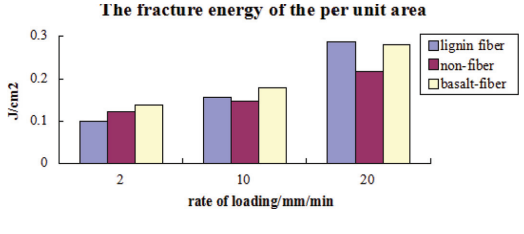

Figure 10. The different specimen at the same loading rate.

4 CONCLUSIONS

- When the temperature is constant, the tensile strength and fracture energy of the specimen are increased with the increased loading rate.
- The fracture energy at the loading rate 20 mm/min for lignin fiber is 2.883 times, and at the loading rate of 2 mm/min for basalt fiber is 2.01 times and for non-fiber is 1.785 times, respectively, and we find that the lignin fiber is optimal for the growth of fracture energy.
- When the loading rate and temperature are constant, the fracture energy of basalt fiber is larger than that of non-fiber.
- The addition of basalt fiber improves the tensile strength of high-viscoelastic asphalt sand while improving the anti-cracking of the material.

ACKNOWLEDGMENTS

This work was financially supported by the National Natural Science Fund (51478276), the Natural Science Foundation of Liaoning Province (2014020070), the Liaoning Provincial Department of Education Project (L2014234), the Shenyang City Highway Project Management Office (14-08-130) and the Ministry of Housing and Urban Rural Construction Projects (2014-K5-024).

REFERENCES

Liu, F.J. 2010. *The Study of the Asphalt Mixture Pavement Performance*. Harbin: Harbin Institute of Technology.

Qing, F.L., Peng, Z. & Chen, H.L. 2006. *Polypropylen Fibre Semi-rigid Base Crack Resistance Research*. Zhengzhou: The Yellow River Water Conservancy Press.

The Ministry of Transport Highway Research Institute. 2011. *Standard Test Methods of Bitumen and Bituminous Mixtures for Highway Engineering*. Beijing: China Communications Press.

Wang, J.C. 2014. *The Research and Application of the High Viscoelastic Asphalt Sand in Municipal Road*. Hangzhou: Zhejiang University.

Wang, Q., Zhu, L.L., Li, Z. & Liu, L. 2013. Study on the constitutive model of concrete and steel for explicit dynamic beam elements of ABAQUS. *Journal of Shenyang Jianzhu University (Natural Science)* 29(1): 56–64.

Civil Engineering and Urban Planning IV – Liu et al. (Eds)
© 2016 Taylor & Francis Group, London, ISBN 978-1-138-02903-3

Experimental study on the direct tensile experiment of high-viscoelastic asphalt sand

Ya-Zhen Sun
Traffic Engineering Institute, Shenyang Jianzhu University, Shenyang, Liaoning, China

Zhang-Yi Gu & Chang Liu
School of Science, Shenyang Jianzhu University, Shenyang, Liaoning, China

Zheng Guo
Traffic Engineering Institute, Shenyang Jianzhu University, Shenyang, Liaoning, China

ABSTRACT: In order to study the mechanical properties of high viscoelastic asphalt sand, the indoor direct tensile experiment is designed with different loading rates and temperatures. Technical index of raw materials was measured to perform experimental analysis according to the gradation requirements. The tensile experiment was carried out by the self-made tensile instrument and the data of stress and strain are recorded and then analyzed later. The experimental results showed that (1) the tensile stress of high viscoelastic asphalt sand increased and then decreased later with the increasing displacement, indicating that the ability to resist deformation of the specimen ranged from increasing to decreasing. In addition, the tensile stress reached the maximum value at the displacement of 5 mm. (2) Raising temperature was favorable to the ductility of asphalt sand. (3) Effect of the temperature on the tensile strength was more significant than the loading rate. (4) When the temperature was 25°C, and the loading rate was 10 mm/min, and the tensile stress approached a minimum value of 0.35 MPa, which can be used as the tensile strength under the control of the temperature and the loading rate.

1 INTRODUCTION

Reflective crack is the major distress observed in Asphalt Concrete (AC) pavements. Typically, these reflective cracks may be induced and quickly reflected upwards and throughout the asphalt pavement surface layer (Aben & Maeharah 1998; Yu & Zhang 2005; Wu & Ling 1998; Dumas & Vecoven 1993) under the effect of the traffic load and the temperature, which shortens the service life of the pavement. Such cracks not only affect the comfortable degree of the pavement, but also allow for the infiltration of water, which results in a rapid shortening of the life. Normally, one of the possible ways is to lay the stress absorbing layer. The stress absorbing layer located between the surface layer and the base layer has become the subject of intense research (Arabani et al. 2012; Long 2012; Xu 2013; Liu 2013). During the past decades, it has been noted that it may have a significant impact on preventing or retarding the propagation of the crack. However, there are only a few published reports on the testing of the high viscoelastic characteristic. The stress-absorbing layer would bear tensile stress from the original pavement. Once the tensile stress exceeds the tensile strength, it will lead to failure. The specific process is shown in Figure 1. Therefore, the tensile performance of high viscoelastic asphalt sand and the tensile strength could be obtained through the direct tensile test and thus the basic parameters and strength for the ABAQUS pavement model are determined.

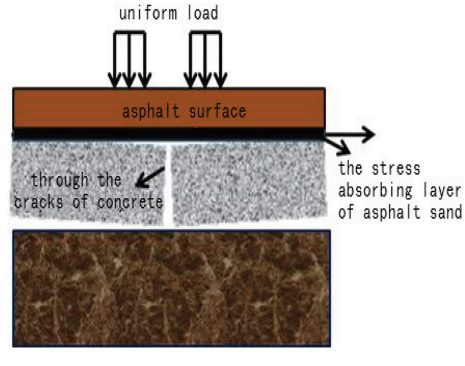

Figure 1. The tensile process of the stress absorbing layer.

2 MATERIALS AND METHODS

2.1 *Direct tension experiment design*

The same kind of load rather than the same loading rate is applied on the asphalt mixed material that changes the mechanical properties greatly, so the loading rate plays an important role in the mechanical properties of asphalt mixture. With the increasing temperature, the mechanical properties of asphalt mixture will be affected directly, so the temperature is another influence factor on the mechanical properties of asphalt mixture. In summary, the temperature and the loading rate can be considered as the controlling factors in the indoor experiment. Consequently, specimens were subsequently tested at loading rates of 10, 20 and 50 mm/min. Additionally, the testing temperatures were 5°C, 15°C and 25°C.

2.2 *Materials*

In this experiment, the road petroleum asphalt A-70#, SBS modified asphalt content of 7%, was used whose performance was consistent with the Technical Specifications for Construction of Highway Asphalt Pavements (JTG F40-2004). In addition, the asphalt-aggregate ratio was 8.8%.

Generally, sand and fine sand are recommended to be used in the stress absorbing layer of asphalt mixture. The amount of natural sand in the stress absorbing layer of asphalt mixture was less than 30%.

The gradation of asphalt sand was (0~3), (3~5) and (5~10) mm and the corresponding proportion was 50%, 33% and 17%. The gradation of asphalt sand mixture was designed on the basis of the Technical Specifications for Construction of Highway Asphalt Pavements (JTG F40-2004).

2.3 *Specimen preparation*

Rutting specimen (300 mm × 300 mm × 50 mm) was prepared by the wheel rolling method according to the Standard Experiment Methods of Bitumen and Bituminous Mixtures for Highway Engineering (JTG E20-2011), and then it was cut into the prism specimen with a cutting machine, which had the length of 120 mm ± 1.0 mm, the width of 50 mm ± 1.0 mm, and the height of 50 mm ± 1.0 mm. The 1.5 mm-deep pre-cutting fissure was cut to guarantee that the failure section was controlled in the middle of a tensile specimen, as shown in Figure 2.

2.4 *Experiment equipment*

The asphalt sand stress absorbing layer was paved between the asphalt surface layer and a concrete base in the transformation of the old road, as shown in Figure 1, which was mainly subjected to tension. Under the act of conventional universal testing machines, the result was no longer valid due to the induced additional local failure. To overcome this problem, a novel tensile test machine was designed, which was fabricated and employed for tensile testing to control the location of the failure surface.

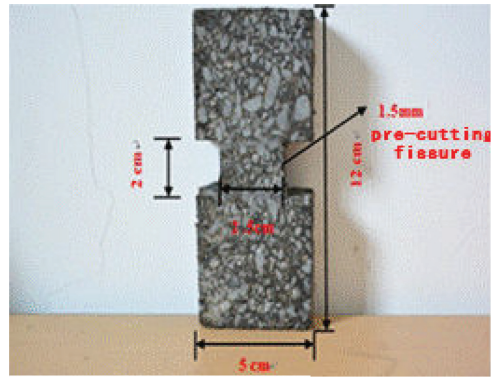

Figure 2. Dimension of the specimen.

As shown in Figure 3, the self-made tensile instrument mainly composed of mechanical sensors and tensile fixture installed on an electronic universal testing machine. The electronic universal material testing machine was used in this experiment, which had the maximum range of 100 kN. The load was measured with a sensor, the maximum of which should be at 20%~80% of its range. The electric signal was produced from the automatic acquisition sensor and the displacement meter and was stored in the data acquisition system, from which the force and displacement curve is drawn by the X-Y recorder.

2.5 *Experimental process*

In this case, the tensile instrument of high viscoelastic asphalt sand was used to measure the load-displacement curves that could determine the stress-displacement curves at different temperatures and loading rates. The experiment steps are as follows:

- Specimens were removed from the incubator and placed in a tensile experiment fixture immediately. Petrolatum was coated between the tensile fixture and the specimen in order to reduce the interface friction.
- The load sensor and the displacement sensor were connected to the X-Y recorder. The X, Y axis represents, respectively, the displacement and the load, and the appropriate range will be determined based on the loading conditions.

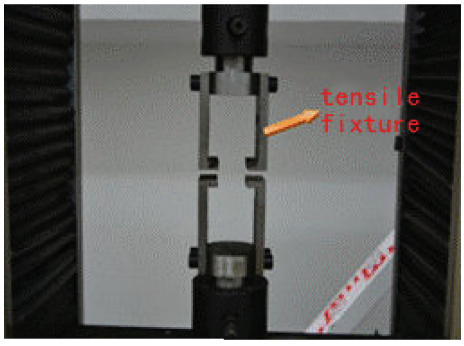

Figure 3. Tensile instrument.

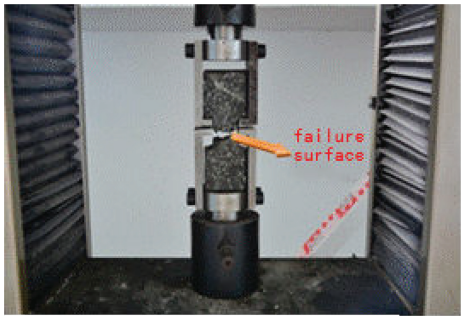

Figure 4. The failure surface of the tensile specimen.

– At the specified temperature and the loading rate, the load increased linearly was applied to the specimen until failure, and the failure surface is (the form of tensile specimen failure) shown in Figure 4. At the same time, the corresponding load-deformation curves were recorded by the X-Y recorder.

3 EXPERIMENTAL RESULTS

The failure surface of tension specimens generally occurred in the pre-cut section of specimens in the direct tension experiment. The failure surface occurred on the inclined shearing section rather than on the pre-cut section. Therefore, the data from the inclined shearing failure of the specimen should be eliminated, and the corresponding data from the tensile failure surface should be selected as the experimental results for the direct tensile experiment.

The maximum tensile stress varied with temperature and loading rate, as given in Table 1.

The plots of load displacement are typically almost nonlinear up to the point of discontinuity,

Table 1. The maximum tensile stress varies with temperature and loading rate.

Temperature/(°C)	5	15	25
Loading rate/(mm/min)			
5	0.6	0.35	0.35
20	1.1	0.60	0.50
50	1.6	0.75	0.65

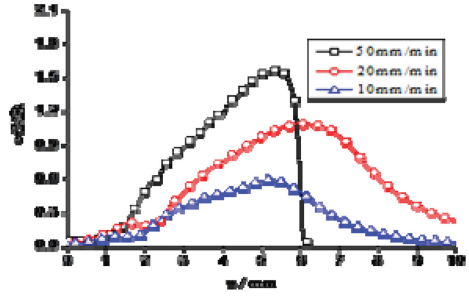

Figure 5. The curve of the tensile stress and displacement at 5°C.

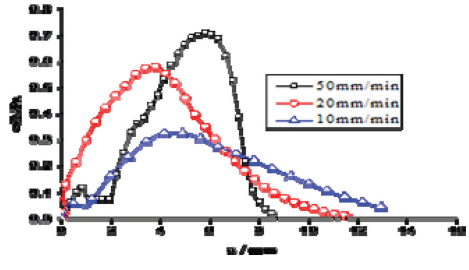

Figure 6. The curve of the tensile stress and displacement at 5°C.

which can be marked as the first stage. However, after the peak point, it can be observed that the load tends to be zero with the displacement increasing under different temperature conditions, which illustrates that the ability to resist deformation of the specimen ranges from increasing to decreasing, as is shown in Figures 5–7. This is called the second stage. The tensile stress decreased, respectively, by 41.6%, 54.5% and 59.3%, with the temperature increasing from 5°C to 25°C. In addition, the tensile stress decreased, respectively, by 46.1%, 53.3% and 62.5%, with the loading rate decreasing from 50 mm/min to 5 mm/min. The tensile strength of the specimen decreased with the temperature increasing, while it increased with the increasing loading rate. The results were similar but the loading rate increased by 10 times while the temperature increased by only 5 times. Therefore, the

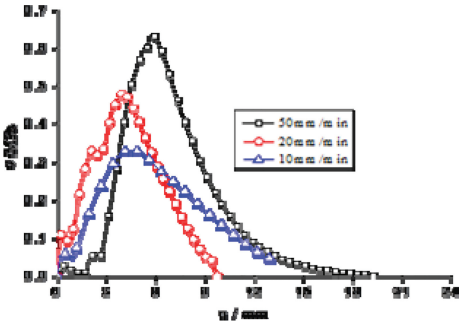

Figure 7. The curve of the tensile stress and displacement at 25°C.

behavior of the stress layer showed greater sensitivity at increasing temperature than at increasing loading rate.

All the peak values of the tensile stress could be reached when the displacement was 5 mm at different loading rates. The peak of tensile stress reached the maximum (1.6 MPa, 0.75 MPa, 0.65 MPa) at the 50 mm/min loading rate under different temperature conditions (5, 15, 25°C), and then presented the almost linear decreasing tendency, which indicates that the high viscoelastic asphalt sand would be subjected to failure more easily at the high loading rate.

As shown in Figures 5–7, the maximum displacement was increased from 10 mm to 19 mm and the peak displacement was increased from 5.5 mm to 7 mm, with the temperature increasing from 5°C to 25°C, which indicates that ductility could be increased effectively with the increasing temperature.

4 CONCLUSIONS

– From the two stages, the ability to resist deformation of the specimen ranges from increasing to decreasing. In addition, the tensile stress reaches the top at the displacement of 5 mm. Therefore, the displacement of 5 mm could be regarded as the recommended critical deformation index of high viscoelastic asphalt sand.
– The tensile stress decreased rapidly after the peak at the loading rate of 50 mm/min, which indicates that the high viscoelastic asphalt sand deterioration becomes serious at the high loading rate.
– The behavior of the stress layer shows greater sensitivity in increasing temperature than increasing loading rate.
– The maximum displacement of high viscoelastic asphalt sand is increased with the increased temperature, which indicates that ductility could be increased effectively with the temperature increasing.
– The tensile strength of 0.35 MPa at 25°C and the 10 mm/min loading rate is the minimum under all the conditions, so the parameter of the finite element model is obtained.

ACKNOWLEDGMENTS

This work was financially supported by the National Natural Science Fund (51478276), the Natural Science Foundation of Liaoning Province (2014020070), the Liaoning Provincial Department of Education Project (L2014234), the Shenyang City Highway Project Management Office (14-08-130), and the Ministry of housing and urban rural construction projects (2014-K5–024).

REFERENCES

Aben & Maeharah. 1998. Study of reflective cracking prevention effects using stress absorbing membrane interlayer. *Journal of JSCE* 1998(3): 245–249.

Arabani, M. et al. 2012. Estimating moisture sensitivity of warm mix asphalt modified with zycosoil as an antistrip agent using surface free energy method. *Journal of Materials in Civil Engineering* 24(7): 889–897.

Dumas, P. & Vecoven, J. 1993. Processes Reducing Reflective Cracking: Synthesis of Laboratory Tests. *Proceedings of the 2nd RILEM -Conference on Reflective Cracking Pavements* 1993(18): 220.

JTG F.40-2004. 2004. *Technical Specifications for Construction of Highway Asphalt Pavements.* Beijing: China Communication Press.

Liu, Q.T. 2013. Induction healing of porous asphalt concrete beams on an elastic foundation. *Mater. Civ. Eng.* 25(7): 880–885.

Long, G.C. 2012. Self-compacting concrete reinforced by waste tyre rubber particle and emulsified asphalt. *Sustainable Construction Materials* 2012: 92–104.

Wu, G.C & Ling, T.Q. 1998. The analysis of developing mechanism of thermal crack of the semi-rigid roadbase. *China Journal of Highway and Transport* 11(1): 21.

Xu, Y.L. 2013. Effect of a sand mix inter layer on thermal cracking in overlays. *Materials in Civil Engineering* 26(9): 309–313.

Yu, J.M. & Zhang, X.N. 2005. Evaluation of environmental factors to fatigue performance of asphalt mixes. *Journal of Southeast University* 2005(04): 486–489.

Civil Engineering and Urban Planning IV – Liu et al. (Eds)
© 2016 Taylor & Francis Group, London, ISBN 978-1-138-02903-3

An RFID based carbon footprint tracing method for product logistics

Shao-Li Chen, Jian-Jun Yi, Xiao-Min Zhu & Hui Jiang
Department of Mechanical Engineering, East China University of Science and Technology, Shanghai, China

ABSTRACT: The RFID (Radio-frequency identification) technology facilitates the rate of information flow and the efficiency of decision-making in the supply chain management. In this paper, a new RFID based method is proposed for the carbon footprint tracing throughout product logistics. During the four key stages in product logistics (i.e. delivering, loading, unloading and receiving), the logistics geographic location, time and other product properties can be stored in the RFID tags, which are attached on the packages of products and the vehicles. By scanning these RFID tags, the logistics-related information can be obtained, with which the carbon footprint of the product logistics process can be calculated. In addition, a case study for the logistics process of fifty servers is demonstrated in this paper to explain the procedure of this method. Finally, this paper provides reference value for the researches of RFID information systems and carbon footprint tracing systems.

1 INTRODUCTION

The whole lifecycle of industrial product mainly contains the processes of material purchasing, manufacturing, delivering, normal using and recycling/disposal (British Standards Institution 2008). Firstly, the suppliers provide the manufacturers with materials or parts for processing and assembling. After the manufacturing process, products will be transported to the dealers. Finally, these products will be sold out through a distribution network established by the dealers. It can be seen that transportation links different phases in the supply chain. Figure 1 shows the whole procedure of how products flow from one phase to another and finally to the buyers through a logistics system.

Primary ways of modern logistics, such as railway transportation, road transportation, waterway transportation and air transportation, consume large amounts of fossil fuels, leading to a particularly large carbon footprint that greatly affecting the environment (Sundarakani et al. 2010). One research shows that, in 2020, the carbon footprint caused by transportation will increase by 80% compared to that in 2015 (Piecyk & Mckinnon 2010). Although the PAS 2050 and ISO 14000 standards have provided the calculation methods for carbon footprint, the actual tracing of carbon footprint is extremely complex. Under this circumstance, in order to decrease the carbon footprint, it has become a research hotspot to find out how to efficiently trace the carbon footprint during the product logistics process and optimize the supply chain.

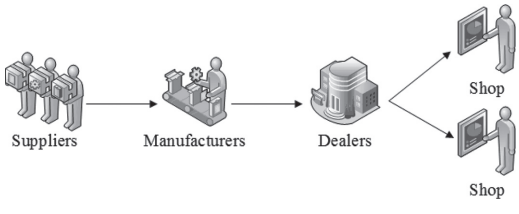

Figure 1. Diagram of the supply chain.

RFID (Radio Frequency Identification) is a kind of wireless identification technology. Recent years, the development of RFID brings some new potential solutions for the efficient and automatic tracing of the carbon footprint during the product logistics process. After collecting and analyzing current carbon footprint measuring standards, Ali Dada et al. (2009, 2010) put forward a method to trace the carbon footprint with RFID technology, and established a demonstration system; RFID tags were embedded in PCBs by ITRI (Industrial Technology Research Institute 2011) to trace the carbon footprint conveniently. Meanwhile, ITRI put forward a carbon footprint tracing framework using the EPC Global system.

RFID consists of RFID tags, RFID readers and related programs. Currently, the price of RFID tag is continuing to decline. In this paper, RFID tags are used as the carrier for the logistics-related information, and the reason lies in:

– Because RFID has been widely used in the logistics management and product tracing, it is easy to extend its function to realize the carbon footprint tracing during the product logistics process.

– RFID is reliability and has low implementation costs. RFID tags have strong adaptability to meet a diversity of demands (i.e. they are easy to be attached on various products and vehicles), and are able to work in a variety of harsh environment.
– RFID has long read-write distance and high read-write speed. Meanwhile, multiple RFID tags can be read simultaneously and automatically. Therefore, RFID can improve the efficiency of data collection and finally realize the automatic calculation for the carbon footprint during the product logistics.
– Data in RFID tags can be updated dynamically. Data generated by sensors such as vehicle GPS devices can also be saved in RFID tags. In addition, RFID data can be encrypted.
– RFID can access to the Internet of Things seamlessly.

This paper mainly focuses on how to apply RFID to the carbon footprint tracing during the logistics processes among the suppliers, manufacturers, dealers and the shops. The study provides reference value for the researches of RFID information systems and carbon footprint tracing systems. In the second section of this paper, a carbon footprint tracing method based on RFID is proposed. Then, a case study of the proposed method is introduced in the third section. Finally, a conclusion is given in the last section.

2 RFID BASED CARBON FOOTPRINT TRACING METHOD FOR PRODUCT LOGISTICS

The main advantage of applying RFID technology to logistics carbon footprint tracing is its efficient information-gathering ability. It is important to collect necessary information for the calculation of the carbon footprint. This section presents an RFID based carbon footprint tracing method for the transportation process of product logistics.

One of the key information of carbon footprint tracing is vehicle type. As shown in Figure 2, when goods are transported from location A to location B, different types of vehicles take different percentages of the total goods and have different impacts on the environment. Therefore, the calculation for the carbon footprints of them shall be classified. The other key information is transportation path which determines the carbon footprints for same vehicles. It can be extracted directly from the vehicle GPS devices, for example, recording the longitude and latitude of a vehicle regularly. Since traditional passive RFID tags cannot meet the needs of storing a mass of transportation information due to limited capacity, the key information is to be saved in the high memory active RFID tags attached on vehicles, named as tag-I in this paper.

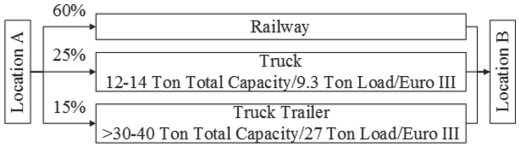

Figure 2. Transportation model.

Besides the information saved in tag-I, some other products-related information shall be saved in the passive RFID tags attached on the packages of goods, named as tag-II. In addition, a product logistics information center shall be established to store all the related information in the logistics transportation process. The structure of the proposed system is shown in Figure 3. In this diagram, the mobile/fixed RFID device is used to read/write data from/to RFID tags and upload/download collected data to/from the information center. The mobile device and the information center are both capable for calculating the carbon footprint according to the logistics information.

During the preparing period before the transportation process, the product ID (i.e. EPC: Electronic Product Code), together with some other information (shown in Table 1), is written into the tag-II and the database in the product logistics information center.

The information of the four stages during the transportation process are collected by RFID tags to calculate carbon footprint. As shown in

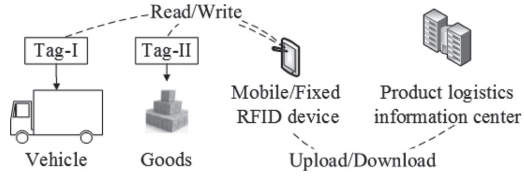

Figure 3. System structure of the RFID based carbon footprint tracing method.

Table 1. Data sheet of the product information in the preparing period.

Field name	Product name	Manufacturer	Amount	Weight (kg)
Sample data	EPC of product A	Manufacturer A	5	10

Figure 4, the four stages are: delivering (collecting the starting location and time), loading (updating the location and time, collecting the type of vehicle), unloading (updating the location and time) and receiving (updating the location and time, checking all the goods). With both information of the four stages and those in the information center, the carbon footprint of the transportation process can be calculated.

In the delivering stage, the data in the RFID tag-I is read out by an RFID device. Then, a data sheet shown in Table 2 will be created and stored into the database. In the meantime, these data shall be updated to the tag-II. The data can be used for indicating the starting location and starting time of the transportation.

In the loading stage, after reading the data from tag-I and tag-II, the database will create and store a data sheet shown in Table 3 according to the collected data. Besides, the data in tag-II will also be updated. In this data sheet, the Vehicle ID is used to identify the type of the vehicle and then the emission factor of the vehicle can be queried out; the Vehicle kilometrage is calculated by the combination of the location/date time in the delivering stage, the location/date time in current loading stage, and the transportation path recorded in the tag-I.

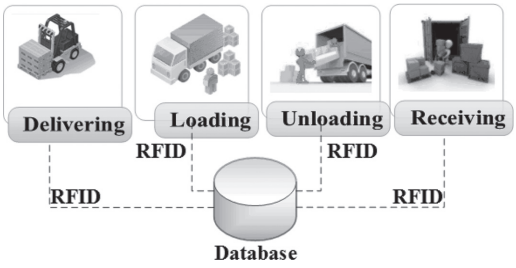

Figure 4. Four stages in the transportation process.

The operation process in the unloading stage is similar to the loading stage. Tag-I and tag-II are scanned by a mobile RFID device. Then, the data sheet shown in Table 4 will be created and stored into the database. Besides, the data in the tag-II will be updated. Since only a single vehicle is used during a pair of loading and unloading stages, the Vehicle ID in the unloading stage should be the same as that in the loading stage. Also, the transportation distance of this stage can be calculated.

In the receiving stage, when the product reaches the destination, the final data in the tag-I and tag-II can be read out through a fixed/mobile RFID reader. Then the data sheet shown in Table 5 will be created and stored into the database.

Figure 5 shows the data flow of the logistics process. In this process, the data in tag-I is updated automatically, and the data in tag-II is updated by RFID devices.

After experiencing the four stages and the preparing period above, with the collected RFID data which stored in the database, the carbon footprint for the transportation process of product logistics

Table 2. Data sheet of the delivering stage.

Field name	Stage	Reading device	Location	Date time
Sample data	Delivering	Fixed reader sr1	Longitude XX.XXXXXX, latitude XX.XXXXXXX	20150802140327

Table 3. Data sheet of the loading stage.

Field name	Stage	Reading device	Location	Date time	Vehicle ID	Vehicle kilometrage
Sample data	Loading	Mobile reader mr1	Longitude XX.XXXXXXX, latitude XX.XXXXXXX	20150802142210	V001	5

Table 4. Data sheet of the unloading stage.

Field name	Stage	Reading device	Location	Date time	Vehicle ID	Vehicle kilometrage
Sample data	Unloading	Mobile reader mr2	Longitude XX.XXXXXXX, latitude XX.XXXXXXX	20150802164127	V001	70

Table 5. Data sheet of the receiving stage.

Field name	Stage	Reading device	Location	Date time
Sample data	Receiving	Fixed reader sr2	Longitude XX.XXXXXXX, latitude XX.XXXXXXX	20150802171419

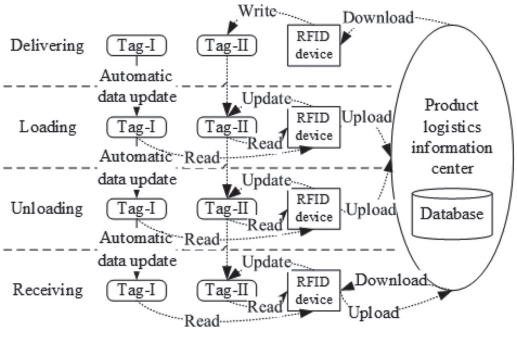

Figure 5. Data flow of the logistics process.

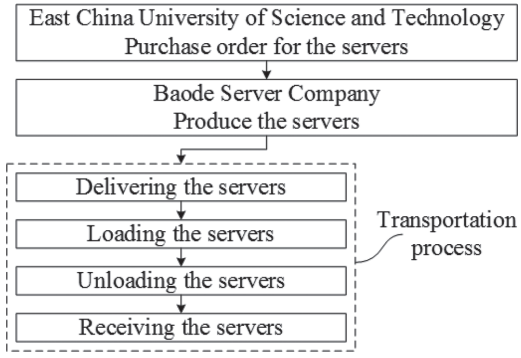

Figure 6. Process model of the transportation for fifty servers.

can be calculated. Assume all the necessary RFID data has been saved successfully, and then the following information can be extracted or deduced: the starting location, the receiving location, the type of vehicle, the transportation path, the transportation distance, the amount of products, the weight of products, etc. Finally the following equation can be used to calculate the carbon footprint generated during the product logistics process:

$$\textit{Carbon footprint} = \textit{Emission factor} \times \textit{Total weight} \times \textit{Transportation distance} \quad (1)$$

where the '*Total weight*' and '*Transportation distance*' are obtained directly from the database; the '*Emission factor*' of the vehicle is obtained by retrieving the LCA (Life Cycle Assessment) application program, and this retrieving process is implemented in accordance with the index of vehicle type.

The whole carbon footprint of logistics is the sum of each phase's carbon footprint. These phases include the 'supplier to manufacturer' phase, the 'manufacturer to dealer' phase and the 'dealer to shop' phase. In addition, the whole carbon footprint is to be divided by the 'amount' of the products to get the carbon footprint of every single product.

3 CASE STUDY

In this section, assume the following application scenario: East China University of Science and Technology (ECUST, Xuhui district, Shanghai) ordered fifty PT6280 N tower servers from Baode Server Company (Baoan district, Shenzhen). After Baode Server Company received the order and produced the servers, the servers were transported to ECUST by a truck. The process model is shown in Figure 6.

The size of the PT6280 N tower sever is 0.426 meter in height, 0.192 meter in width and 0.482 meter in depth. The total weight of 50 servers is 0.6 ton, and 12 kg per server (packing included). All the servers were transported by a light truck which met Euro II emission standard. In addition, an RFID tag-I was fixed in the truck.

During the preparing period before delivering, fifty RFID tag-IIs which saved the products information were attached on the packages of the servers, and the information was also written into the database as shown in Table 6.

In the delivering stage, the data in the tag-I was read by an RFID device. Then a corresponding data sheet (as shown in Table 7) was created and stored into the database. The key information in this stage is the location and the date time. Meanwhile, the tag-IIs' data was updated according to the data sheet.

In the loading stage, scanning all the RFID tags by a mobile RFID device, then the total number of servers could be checked. The data sheet shown in Table 8 was created and written into the database for the further calculation of the carbon footprint during the logistics process. In addition, the data in the tag-IIs should also be updated.

Similar to the last stage, in the unloading stage, the RFID data could be collected and updated by

Table 6. Data sheet of the preparing period for fifty servers.

Field name	Product name	Manufacturer	Amount	Weight (kg)
Data	67724B65516E6D54EE980C98	Baode Server Company	1	12
	67724B65516E6D54EE980C99	Baode Server Company	1	12
	…	…	…	…

Table 7. Data sheet of the delivering stage for fifty servers.

Field name	Stage	Reading device	Location	Date time
Data	Delivering	Fixed reader r1	Longitude 114.0697 E, latitude 22.69258 N	20150731100014

Table 8. Data sheet of the loading stage for fifty servers.

Field name	Stage	Reading device	Location	Date time	Vehicle ID	Vehicle kilometrage
Data	Loading	Mobile reader mr-a	Longitude 113.342613 E, latitude 23.149252 N	20150731124227	V3-66	124

Table 9. Data sheet of the unloading stage for fifty servers.

Field name	Stage	Reading device	Location	Date time	Vehicle ID	Vehicle kilometrage
Data	Unloading	Mobile reader mr-b	Longitude 121.431448 E, latitude 31.149165 N	20150801140310	V3-66	1443

Table 10. Data sheet of the receiving stage for fifty servers.

Field name	Stage	Reading device	Location	Date time
Data	Receiving	Fixed reader r2	Longitude 121.431448 E, latitude 31.149165 N	20150801142545

a mobile RFID device, and the data sheet shown in Table 9 could be created and written into the database.

When the servers reached ECUST, in the inspection process (i.e. the receiving stage), all the tags' data was read again by an RFID device and the data sheet shown in Table 10 could be created and written into the database. In this stage, the total number of products should be checked again.

The total distance of the logistics process could be obtained by the sum of the vehicle kilometrages recorded in the loading and unloading stages, and it turned out to be 1567 km. The total weight of the servers could also be obtained from the information in the database (or from the tag-IIs). Then, query the vehicle information database which is based on the CMP LCA database, and the emission factor of the light track with vehicle ID V3–66 could be found out as 168. Finally, the carbon footprint of this logistics process could be calculated according to the following equation:

$$168 \times 0.6 \times 1567 = 157953.6 \text{ g} = 157.9536 \text{ kg} \quad (2)$$

Furthermore, since the total carbon footprint value had been obtained, the carbon footprint

generated by a single server during this logistics process could also be calculated, which gives about 3 kg per server.

4 CONCLUSIONS

This paper proposed an RFID based carbon footprint tracing method for product logistics. In this method, all the logistics-related information (e.g. the location, time, product weight, vehicle type, etc.) is recorded in the RFID tags attached on the vehicle and the packages of products. The RFID data will be updated during the four key stages of logistics process: delivering, loading, unloading and receiving. In addition, a product logistics information center which has a database is established to store all the collected RFID data. After the whole logistics process, with all the collected information, the total transportation distance and the emission factor of the vehicle can be obtained. Finally, the carbon footprint of the logistics process can be calculated.

The innovation of this paper is the combination of the RFID technology and the carbon footprint tracing. With the help of RFID, all logistics information and product information can be recorded automatically and accessed conveniently. Meanwhile, RFID guarantees the accuracy of information. Moreover, the data security can also be ensured.

In this paper, a case study for the logistics process of fifty servers is used to demonstrate the detail of applying RFID to the logistics carbon footprint tracing. It shows that RFID simplifies the tracing operations and increases the tracing efficiency. In the future, the proposed method could be modified and expanded to realize the carbon footprint tracing during the manufacturing process.

ACKNOWLEDGEMENTS

This paper was supported by the Research Foundation of Science and Technology Commission of Shanghai under Grant No. 10DZ1500200; the National Nature Science Fundation of China (NSFC) under Grant Nos.: 50975088, 51275173, 51210105018; the Fundamental Research Funds for the Central Universities under Grant No. WH0913009; Shanghai Pujiang Program under Grant No. PJ201000353; and Shanghai Software and IC industry Development Special Fund under Grant No. 120493.

REFERENCES

British Standards Institution. 2008. *Guide to PAS 2050*. London: British Standards Institution.

Dada, A., Rau, A., Konkel, M., Staake, T. & Fleisch, E. 2010. The Potential of the EPC Network to Monitor and Manage the Carbon footprint of Products Part 2: Dynamic Carbon Footprint Demonstrators. *Auto-ID Labs White Paper*.

Dada, A., Staake, T. & Fleisch, E. 2009. The Potential of the EPC Network to Monitor and Manage the Carbon Footprint of Products Part 1: Carbon Accounting. *Auto-ID Labs White Paper*.

Industrial Technology Research Institute. 2011. RFID Embedded in PCBs for Carbon Footprint Tracking. *ITRI TODAY* 64, 1st Quarter 2011.

Swedish Life Cycle Center. 2008. CPM LCA Database. *http://cpmdatabase.cpm.chalmers.se*.

Piecyk, M.I. & Mckinnon, A.C. 2010. Forecasting the carbon footprint of road freight transport in 2020. *International Journal of Production Economics* 128(1): 31–42.

Sundarakani, B., Souza, R.D., Goh, M., Wagner, S.M., & Manikandan, S. 2010. Modeling carbon footprints across the supply chain. *International Journal of Production Economics* 128(1): 43–50.

Civil Engineering and Urban Planning IV – Liu et al. (Eds)
© 2016 Taylor & Francis Group, London, ISBN 978-1-138-02903-3

Left-turn track function of bicycle flow in intersection

Shui-Chao Zhang
School of Transportation, Ningbo University of Technology, Ningbo, Zhejiang, China
Jiangsu Key Laboratory of Urban ITS, Southeast University, Nanjing, Jiangsu, China

Kang-Kang He & Ren-Fa Yang
School of Transportation, Ningbo University of Technology, Ningbo, Zhejiang, China

ABSTRACT: The study of bicycle flow left-turn track is the basis of studying the traffic conflict between left-turn bicycles and motor vehicles. This paper built the two-dimensional coordinate system of intersection using its geometrical features, acquired the coordinate data of the left-turn bicycle traveling track through the video coordinate method, and applied the coordinate data to the two-dimensional coordinate system. Finally, the track function expression of the left-turn bicycle flow was founded using the method of regression analysis. This function is a quadratic function, and relevant parameters are only related to the geometric parameters of intersections. The construction of the intersection left-turn bicycle flow track function is significant to the optimization of intersection traffic management.

1 INTRODUCTION

The large quantity of traffic accidents in Chinese cities have shown that the traffic conflict between bicycles and motor vehicles is an important cause of intersection accidents, and the traffic conflict between left-turn bicycles and motor vehicles constitutes a large proportion of it. To understand the left-turn track of bicycles flow in the intersection is an important basis of studying the traffic characteristics of left-turn bicycle flow and the traffic conflict between left-turn bicycles and motor vehicles. Through systematic study, this paper proposed the left-turn bicycle flow track function based on intersection geometric conditions and grasped the travelling characteristics of the left-turn bicycles in the intersection, which would play an important role in optimizing the management and control method of intersections and improving safety in them.

2 LITERATURE REVIEW

So far, the research on bicycle travelling track is very limited at home and abroad. Yu et al. (2011), using the method of cluster analysis, worked out the division method of travelling stage when the bicycle group traveled through intersections and provided the travelling track at corresponding stages. Besides, Tilahun (2007) studied the basic methods of choosing bicycle transportation facilities in three aspects namely track, lane, and traffic volume. As for the data collection methods of bicycle travelling characteristics in the intersection, there are a limited number of researches at home and abroad, and existing research findings mainly concentrated on studying related data of traffic accidents through video analysis. For instance, Lu et al. (2005) adopted the digital photogrammetry to build the camera verifying model by means of aberration analysis of digital camera photos, and extrapolated the vehicle travelling data in accidents. Wang et al. (2008) built the photogrammetric two-dimensional analysis model of traffic accidents in the intersection, used road markings as calibrated reference materials, and calibrated the distances between accident vehicles. Tang et al. (2007) brought forth the two-step extended camera calibration method of accident scene photogrammetry and proposed the relatively accurate coordinate measuring method of vehicles in the intersection through image correction. Shen et al. (2010), according to the basic mapping information of intersections, put forward the method to calculate the travelling coordinate information of bicycles in the intersection based on the principle of photogrammetry. The mentioned data acquisition methods of intersection traffic travelling characteristics, although with relatively high accuracy, were proved to be complex, difficult to implement, and unsuitable for acquisition of large amounts of basic data in practical operation.

As a result, based on the research on left-turn bicycle track at home and abroad, this paper proposed the video coordinate method suitable for

data acquisition of left-turn bicycle flow track and the track function in the intersection, which provided the theoretic foundations for the optimization measures of intersection bicycle management and control.

3 METHODOLOGIES

3.1 *Intersection coordinate system*

To accurately study the track of bicycles in the intersection, the basic precondition is to acquire the time-varied coordinate positions when bicycles are travelling through intersections. Based on the coordinate positions we can analyze relevant characteristics of bicycles in the intersection such as their travelling track, and travelling speed, etc. Therefore, it is essential to build the coordinate system of intersections. For ordinary intersections, if we extend the rear lines of two intersecting crosswalk lines which will intersect at one point, and make this point as the origin of coordinates and fix the rear lines of the two crosswalk lines as the X-axis and Y-axis, thus we can build the two-dimensional coordinate system of the intersection as shown in Figure 1.

The crosswalk lines in the intersection are painted with one-meter intervals between one another, therefore, every crosswalk line can be regarded as a coordinate scale on the X-axis or Y-axis. If we connect the opposite crosswalk lines in the intersection with straight lines, an orthogonal grid system with one meter as the unit will be formed, thus we can conveniently specify the coordinates of every point in the intersection as shown in Figure 1.

As for irregular intersections, we can build corresponding coordinate systems through the transformation of coordinates.

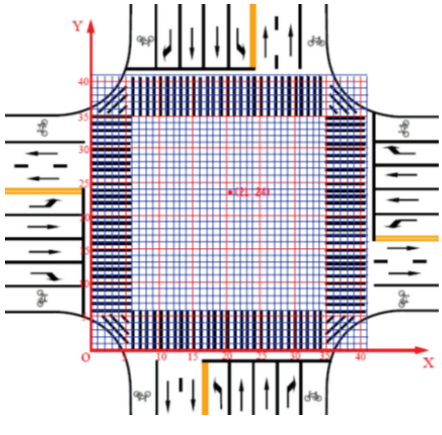

Figure 1. Intersection orthogonal grid system.

3.2 *Intersection bicycle track data investigation method*

As for the studied intersection, firstly we shot a video about the traffic in this intersection with a camera at high altitude. Then according to the geometrical characteristics of the intersection, we selected two intersected crosswalk rear lines as the X-axis and Y-axis of the intersection, and loaded the prepared grid system into the intersection video through the video software, thus building the coordinate system of the whole intersection as shown in Figure 2. Based on that, we can obtain the coordinates of every bicycle at every moment (to be more specific, their front wheel touchdown points) through manual observation. Thus we can find out the travelling characteristics of any single bicycle and then the whole bicycle group. This is the so-called video coordinate method.

3.3 *Track equation acquisition method*

In order to obtain more available track data of bicycle flow, this paper selected the intersections which have large bicycle flow to study, and carried out corresponding data acquisition. For instance, next we will analyze the intersection of West Huancheng Road and Lianfeng Road of Ningbo.

The intersection of West Huancheng Road (south-north direction) and Lianfeng Road (east-west direction), two primary roads of Ningbo, is located in the western part of the city center and has a relatively large motor vehicle and bicycle flow volume. In this intersection, the width of the broadening segment of east-west road is 54 meters and that of the south-north road is 48 meters. We built the coordinate system with the south-entrance crosswalk rear line as the X-axis and the west-entrance one as the Y-axis as shown in Figure 3.

We set the camera in the building near the intersection and took the video of the intersection at the evening traffic peak time. Then we loaded the

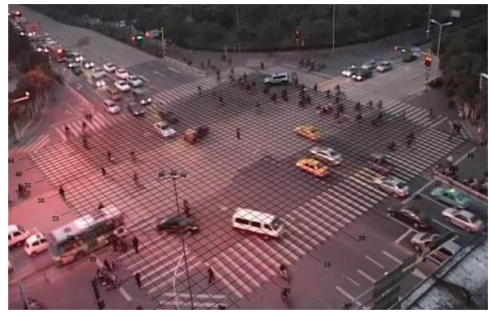

Figure 2. Video coordinate method schematic diagram.

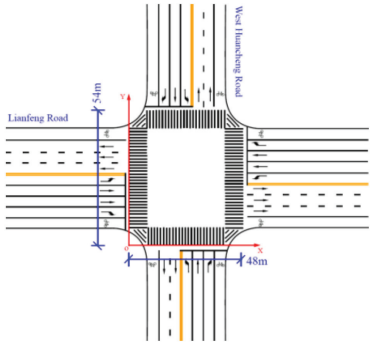

Figure 3. Lianfeng Road-West Huancheng Road intersection coordinate system.

Figure 4. The video screenshot after the left-turn bicycle flow became stabilized.

Table 1. Bicycle track coordinates list.

Number	X-axis coordinate	Y-axis coordinate	Number	X-axis coordinate	Y-axis coordinate
1	3	13	14	21	28
2	4	15	15	25	29
3	5	13	16	26	28
4	7	16	17	26	31
5	11	17	18	26	33
6	12	22	19	28	29
7	14	21	20	28	31
8	16	17	21	29	37
9	16	19	22	30	36
10	16	22	23	33	38
11	19	23	24	36	39
12	20	22	25	38	49
13	21	19	26	40	55

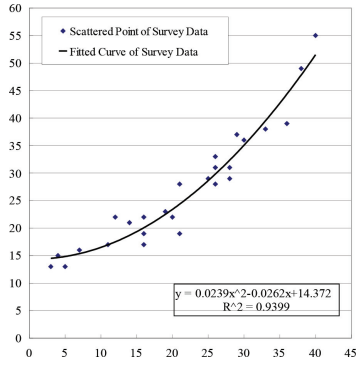

Figure 5. Track scatter diagram and regression analysis for left-turn bicycle.

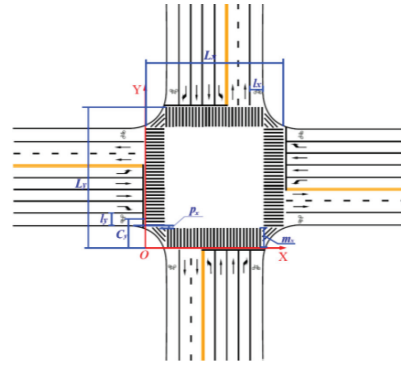

Figure 6. Intersection parameters schematic diagram.

grid coordinate system in the video and selected the left-turn bicycle flow at the west-entrance to study. After the left-turn bicycle flow at the west-entrance became stabilized, we paused the video as shown in Figure 4. Next, based on this video screenshot and built coordinate system, we recorded the coordinate data (with the front wheel touchdown point as the reference point of the bicycle) of every left-turn bicycle in the intersection at this point and acquired the data array in Table 1.

Based on the track coordinates of the left-turn bicycle flow shown in Table 1, we put them in the coordinate system of this intersection and then got the scatter diagram in Figure 5.

To acquire the track function and track characteristics of the left-turn bicycle flow, we made the regression analysis of the scattered point data and received the binomial regression analysis chart, which is also showed in Figure 6.

From Figure 6 we can see, the track curve of left-turn bicycle flow in the intersection can be adequately described by the quadratic function, and we can obtain corresponding function expression through regression analysis.

4 RELEVANT PARAMETERS IN THE LEFT-TURN TRACK FUNCTION

To promote and utilize the left-turn bicycle flow track function studied in this paper and apply it to ordinary intersections, we needed to acquire the relevant parameters in the left-turn track function and the correlations with the intersection geometric parameters. Meanwhile, it needs the normalizing processing of the ordinary intersections.

In the intersection coordinate system built in this paper, the X-axis and Y-axis were arranged along the rear parts of the crosswalk lines. In this coordinate system, the turning points of the left-turn bicycle flow usually drift some distance away from the X-axis, namely their Y-axis coordinates is not zero. Combined with real observation, especially for the four phase controlling intersection, after letting the straightly travelling bicycles go, the left-turn bicycles basically have occupied the whole bicycle stop line, so we can take the midpoint of the stop line as the starting point of the whole bicycle flow. Hence, the distance drifted away from the X-axis of the bicycle flow starting point can be expressed as follow:

$$C_y = (m_x + p_x) + l_y/2$$

In this expression,

C_y—the distance drifted away from the X-axis of the bicycle flow starting point (m), namely the vertical coordinate of this point;

l_y—the bicycle lane width in the Y-axis direction;

m_x—the crosswalk width in the X-axis direction;

p_x—the width of the crosswalk back curb in the X-axis direction, usually 1 meter wide.

These parameters are showed in Figure 6.

Meanwhile, combined with actual observation, when the left-turn bicycle flow turned into the bicycle lane of the intersecting road, its distribution mainly concentrated near the bicycle lane midline, that is we can hold that the end point of the bicycle flow left-turn track was located at the midpoint of the intersecting bicycle lane. Based on the coordinate system we have built, the horizontal coordinate of the turning-in point can be expressed as:

$$F_x = L_x - (m_y + p_y) - l_x / 2$$

In this expression,

F_x—the horizontal coordinate of the end point of the bicycle flow track;

L_x—the width of the entrance broadening segment in the X-axis direction;

l_x—the bicycle lane width in the X-axis direction;

m_y—the crosswalk width in the Y-axis direction;

p_y— the width of the crosswalk back curb in the Y-axis direction, usually 1 meter wide.

The specification of the intersection is represented mainly by the broadening segment length in the direction of X-axis and Y-axis that is L_x and L_y. Next is the basic expression of the left-turn bicycle flow track function:

$$y = ax^2 + bx + c$$

In this expression, the equation $c = C_y$ can be determined roughly by the geometrical parameters of the intersection specification, therefore, the parameters we should study with emphasis are a and b. With such a train of thoughts, we selected the relatively standard intersections with large bicycle flow volumes in Nanjing and Ningbo to acquire the video information of left-turn bicycle flow. The acquired data of the intersection basic parameters L_x and L_y and the parameters a and b in the bicycle flow left-turn track function was shown in Table 2 (Note: to improve the video utilization rate, we acquired the left-turn bicycle flow data both in the east-west and south-north direction).

If we made a simple transformation of Expression 3, we can get:

$$y = a\,(x + b/2a)^2 + c - b^2/4a$$

Combined with the left-turn bicycle flow track in Figure 5, in the expression above, a value is the important parameter reflecting the track opening shape and $b/2a$ value mainly reflects the drifted distance of track lowest point from the Y-axis, therefore, a value is more important to our study of left-turn bicycle flow track. Meanwhile, we can see from Table 2 that, in the measured intersection samples, $b/2a$ values are basically lower than 0.5, which indicates that in real intersection the drifted distance of the track lowest point from the Y-axis is relatively small in terms of the geometrical size of the intersections. To simplify the problem

Table 2. Statistical table of relevant parameters of the left-turn bicycle flow function in the intersection with different specifications.

Number	L_x/m	L_y/m	a	b	$R2$
1	48	54	0.0239	0.0262	0.9399
2	54	48	0.0202	0.0143	0.9246
3	40	42	0.0412	0.0233	0.9355
4	42	40	0.0325	0.0265	0.9348
5	44	52	0.0434	0.0328	0.9324
6	52	44	0.0237	0.0254	0.9168
7	36	38	0.0521	0.0436	0.9328
8	38	36	0.0428	0.0384	0.9557
9	40	44	0.0458	0.0288	0.9256
10	44	40	0.0326	0.0226	0.9523

without influencing its research nature, this paper regarded $b/2a$ value as a smaller number, namely we can ignore the value when reflecting the left-turn track function. Hence, we can get the simplified general expression of the left-turn track function:

$$y = ax^2 + c$$

In the above expression, $c = C_y$, when $x = F_x$, we found that $y = aF_x^2 + C_y = L_y$, namely $a = (L_y - C_y)/F_x^2$.

To sum up, when the relevant parameters of the intersection geometrical size (namely L_x, L_y, l_x, l_y, m_x, m_y) were determined the intersection left-turn bicycle flow track function can be represented as follows:

$$y = ax^2 + c$$

$$\text{Among them } \begin{cases} c = C_y \\ a = (L_y - C_y)/F_x^2 \end{cases}$$

5 DISCUSSION

Based on the geometrical characteristics of the intersections and using the built coordinate system, we can acquire the circular curve function between the west-entrance bicycle lane midline and the north-entrance bicycle lane midline (in this intersection, it is an elliptic curve), and draw this curve in Figure 7, as shown by the red point.

If we make a comparative analysis of the left-turn bicycle flow track curve between corresponding circular curves, we can find that the travelling track of the left-turn bicycle flow in the intersections is not on the circular curve but inside it, namely there are certain deviations between the two. The causes include, on one hand, after the green lights lighten, the travelling direction of bicycles was not tangent

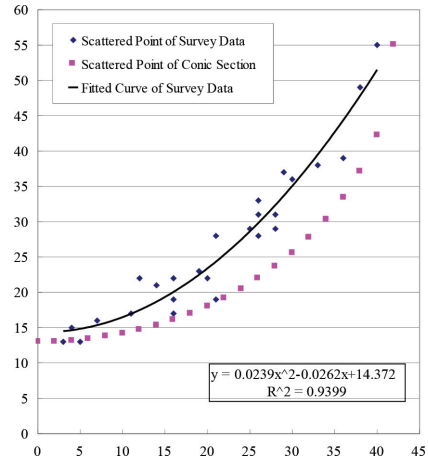

Figure 7. Comparing with the left-turn bicycle flow track and circular curve.

to the original bicycle lane; one the other hand, bicycles kept pursuing the shortest path when travelling in the intersections and, due to their flexibility, they kept changing their directions in this process and did not strictly abide by relevant equations of motion in physics. These two factors have led to the deviations between the travelling track of the left-turn bicycle flow in the intersection and the equations of motion in physics (they can be described by circular curve equations), but the former can be described by quadratic function equations.

6 CONCLUSION

This paper provided the track function of left-turn bicycle flow in the intersection. This function is the quadratic function and the relevant parameters are only related to the geometric parameters of the intersection. That is to say, if the geometric parameters of one intersection are given, the track function of left-turn bicycle flow also can be obtained. And the traveling track of the left-turn bicycle flow in the intersections is not on the circular curve but inside it, namely there are certain deviations between the two. The research results can be well used to optimize the management and control of bicycles in the intersection.

ACKNOWLEDGEMENTS

This research was supported by the National Natural Science Foundation of China (No. 51308311), Natural Science Foundation of Zhejiang Province, China (LQ13E080004) and Open Research Fund

of Jiangsu Key Laboratory of Urban ITS, Southeast University. We hereby express our gratitude for these.

REFERENCES

Fan, L.Q. 2013. Coordinated control of multi-intersectional traffic signals in road network. *International Journal of Applied Mathematics and Statistics* 51(22): 116–124.

Lu, Y.K., Jin, X.L. & Hou, X.Y. 2005. Application of digital photogrammetry in accident reconstruction. *Journal of Computer-Aided Design & Computer Graphics* 17(10): 116–120.

Pucher, J., Dill, J. & Handy, S. 2010. Infrastructure, programs, and policies to increase bicycling: An international review. *Preventive Medicine* 50(2): 106–125.

Rubins, D. & Hardy, S. 2005. Times of bicycle crossings: Case study of Davis, California. *Transportation Research Record: Journal of the Transportation Research Board* 50(12): 22–27.

Shen, J.J. & Wang, W. 2010. Study on the motor and non-motor mixed traffic conflict zone of urban intersections based on photogrammetry. *Journal of Yangzhou University (Natural Science Edition)* 13(1): 75–78.

Tang, Y.S., Li, J., Bai, Y. & Shi, J. 2007. Extended-two-step camera calibrated method of traffic accident scene measurement. *Journal of Traffic and Transportation Engineering* 7(1): 81–84.

Tilahun, N.Y., Levinson, D.M. & Krizek, K.J. 2007. Trails, lanes, or traffic: Valuing bicycle facilities with an adaptive stated preference survey. *Transportation Research Part A* 12(41): 287–301.

Wang, F.Y., Yang, C.H., Zou, X.D. & Zhou, Q.H. 2008. Application of photogrammetry in traffic accident scene measurement based on road mark. *Journal of Transportation Engineering and Information* 6(1): 1–5.

Wang, L.F., Chen, H. & Li, Y. 2013, Track-oriented urban traffic analysis based on network accessibility. *International Journal of Applied Mathematics and Statistics* 64(12): 61–68.

Yu, Q., Shi, L. & Li, N. 2011. Passing stage division of bicycle groups at signalized intersection. *Journal of Transportation Systems Engineering and Information Technology* 11(4): 135–139.

Civil Engineering and Urban Planning IV – Liu et al. (Eds)
© 2016 Taylor & Francis Group, London, ISBN 978-1-138-02903-3

Study on the test of the CRTSII slab reinforced with Basalt Fiber Steel Tendon

Zhao-Ping Feng, Hao Wang, Yong Wang, Shu-Xun Zhang, Peng Wang & Xiu-An Yan
National Space Frame and Steel Structures Quality Supervision and Inspection Center, Xuzhou, Jangsu, China

ABSTRACT: Basalt Fiber Steel Tendon (hereinafter referred to as BFST) provides an effective way to solve the issues on the poor insulation of the HRB500 bar (which is a new hot-rolled ribbed bar with a yield strength of 500 MPa) mesh and low bond force between HRB500 and concrete resulting from insulation treatment adopted currently to improve the transmission performance of the resonant track circuit at the Beijing-Shanghai high-speed rail. In this paper, research on the CRTSII slab reinforced with BFST is conducted by using the numerical simulation and static test. The results for the numerical simulation and test tend to be similar and the model of numerical simulation is reliable, CRTSII slab with BFST has good ductility to meet the carrying capacity requirements, and the BFST, as a kind of new material, is feasible to be used for track board. The calculation results can provide a reliable reference for non-ballasted track technology systems.

1 INTRODUCTION

CRTSII slab is a biaxial bending structure that is subjected to the vertical and horizontal bending moments (Academy of Railway Sciences 2005). The HRB500 bar is subjected to the vertical and horizontal bending moments that overlap with each other to form a closed loop of fixed steel mesh, which will generate electromagnetic induction at the moment of the passing train and could lead to the train control signal transmission circuit error. Currently, two methods can be used to resolve this issue: HRB500 bar surface coating insulating paint and arrangement of the insulating clamp or thermoplastic tubes at the overlapped node of HRB500 mesh; sometimes a combination of two methods can also be adopted. However, these methods not only make the construction process complicated and increase the costs but also reduce the bond force between the HRB500 bar and the concrete, which will affect the comprehensive force performance of the structure. In order to solve this problem, BFST, as a new kind of exterior insulation material, is used to replace the existing HRB500 bar, and then a contrast test is performed on the track slab with two kinds of steel bars. BFST can be used to make up for the lack of the HRB500 bar as well as to solve the corrosion problem after slab cracking, and improve the durability of the rail system due to better corrosion resistance of the BFST. Meanwhile, BFST has superior insulating properties that can fundamentally solve the safety problem and increase the safety of the rail system.

2 BFST

BFST can be made by the extrusion forming process through twisting steel wires outside of continuous filaments infiltrated with resin. The process is shown in Figure 1. This section mainly investigates the mechanical properties of the BFST for the application to the CRTSII slab.

BFST possesses excellent features such as high tensile strength, good corrosion resistance, lightweight, excellent fatigue resistance, superior insulation and excellent electromagnetic characteristics, and is widely used in civil engineering and water conservancy projects, especially in coastal areas, port projects, and large-span bridge engineering. There are also several drawbacks, including complex production processes, strict technical requirements, discreteness of material, higher cost than ordinary steel, low elastic modulus, low shear strength and large creep effect. In order to comprehend fully the characteristics of BFST, its relative performance in the pull-out test is investigated (General Administration of Quality Supervision, Inspection and Quarantine of People's Republic of China & China National Standardization Management Committee. 2009). The test is shown in Figure 2a, and the pull-out results are summarized in Table 1. Bond test on the BFST and the concrete is carried out for an in-depth understanding of the characteristics of the bond force between the BFST and concrete. The test process is shown in Figure 2b and 2c, and the test results are shown in Figure 3.

According to the slip-stress curve, the slip-stress curve residual segment of the BFST specimen is approximately sinusoidal and the HRB500 bar shows a slowly decreasing trend. The whole curve can be roughly divided into three stages: micro-slip stage, slip stage and fall stage (pull-out stage). The elastic modulus of BFST is lower than that of the HRB500 bar and the bonding performance of the spiral rib is superior than that of the crescent rib of the HRB500 bar, in response to stretching loads. The slope of the HRB500 bar is higher than that of the BFST at the tensile load. The results for three specimens at tensile load are summarized in Table 2.

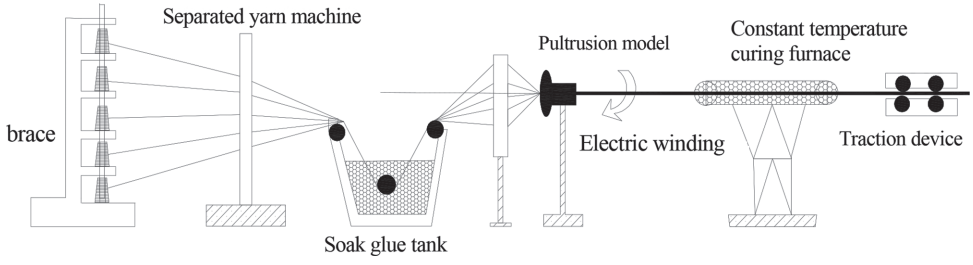

Figure 1. Process flow diagram of BFST.

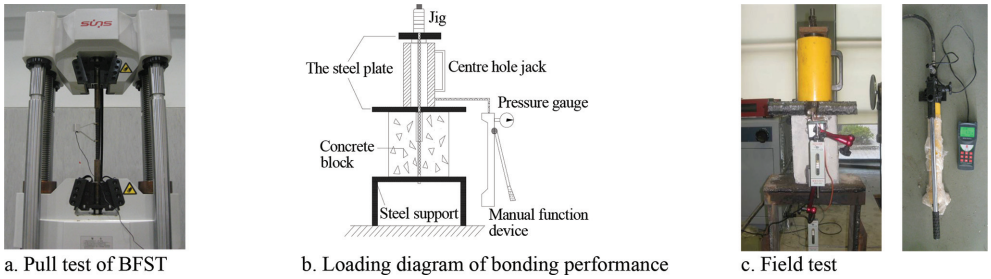

a. Pull test of BFST b. Loading diagram of bonding performance c. Field test

Figure 2. BFST test.

Table 1. BFST tensile results.

Name of the steel material	Diameter	Section area	Yield strength	Ultimate strength	Modulus of elasticity	Elongation
BFST	8 mm	50.3 mm^2	460 MPa	550 MPa	70 GPa	2.05%
	20 mm	314.2 mm^2	460 MPa	540 MPa	86 GPa	2.0%

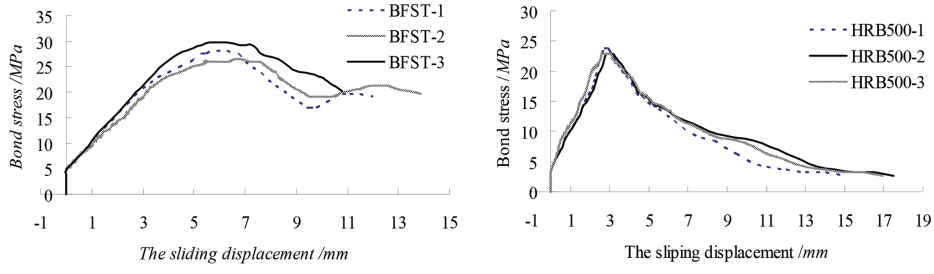

a. The bond-slip curve of BFST b. The bond-slip curve of HRB500 bar

Figure 3. Bond-slip contrast curves.

Table 2. Bonding test results.

Specimen number	Effective diameter (mm)	Ultimate load (kN)	Largest bond stress (MPa)	Slip value of the bond stress peak value (mm)	Free end outsourcing fiber damage
BFST-1	8	53.3	28.1	6.3	Intact
BFST-2	8	50.7	26.5	6.7	Cracked
BFST-3	8	56.1	29.7	5.6	Intact
HRB500 bar -1	8	45.2	23.9	2.9	–
HRB500 bar -2	8	43.1	22.8	3.0	–
HRB500 bar -3	8	43.9	23.0	3.1	–

From the test results, it can be found that the ultimate load and the maximum bond force of the BFST are greater than those of the HRB500 bar. This phenomenon can be explained by the surface shape of the BFST and the HRB500 bar. The height projection of spiral ribs adopted for the BFST and the contact region with concrete are superior than that for the HRB500 bar, so that the mechanical snap-in force of BFST is larger than that of the HRB500 bar.

3 CRTSII SLAB TENDONS

In this paper, the CRTSII slab application in the Beijing-Shanghai high-speed rail is lateral prestressing. Slab cracking is prevented at the use stage according to the design requirements. Each piece of the CRTSII slab includes 20 small slabs (Guo 2006). In this paper, each small slab was researched. The tendons of the slabs are shown in Figure 4, which are equipped with six prestressed tendons at the central slab and four longitudinal non-prestressed tendons at each of the up and down slabs and transverse tendons are structural bars of 8 mm in diameter. The research is carried out under the condition that the transverse tendons and prestressed tendons are kept constant and four longitudinal non-prestressed tendons are set at each of the up and down slabs to be the BFST.

4 MODELING ANALYSIS

Nonlinear finite element static analysis of the slab is conducted using the software ANSYS based on the constitutive relation of the material involved, failure criterion and boundary conditions considered in this paper (Shang et al. 2006). Furthermore, computerized analysis of model stress, strain and deflection is carried out by establishing the finite element model for the CRTSII slab. The feasibility verification of the finite element analysis is made

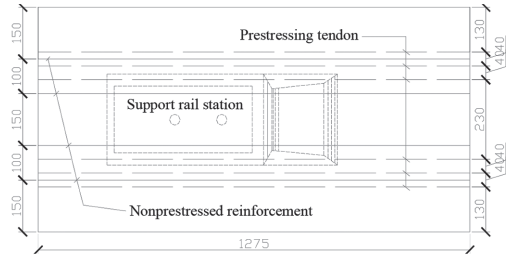

a. The longitudinal reinforcement

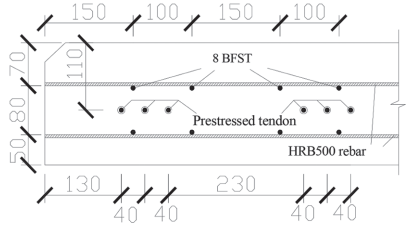

b. The section of reinforcement figure

Figure 4. Reinforcement figure.

through further research on the bending mechanism and damage characteristics of the slab under rail lines with static load.

Solid65 unit is adopted to simulate the model of the cross-sectional slab concrete and the link8 unit is adopted to simulate the model of tendons.

Material parameters involved in the model are taken from the above material mechanics test data and related literature specification. The unit of the corresponding value is taken as specific parameters in Tables 3 and 4.

In order to be closer to the actual situation, the sleeper of the rail slab is built during modeling. The existing bond-slip model based on the test data curve, shown in Figure 3, is revised. The revised constitutive relation model is shown in Figure 5, and, finally, the constitutive relation between concrete and all kinds of tendons is introduced to generate a complete model. Crushing closed and

Table 3. Concrete material parameter.

Content of the reinforced material	Shear transfer coefficient Closed	Shear transfer coefficient Open	Compressive strength *fcu* (MPa)	Axial compressive strength *Fc* (MPa)	Axis tensile strength *Ft* (MPa)	Modulus of elasticity (MPa)	Poisson's ratio
BFST	0.8	0.3	35.5	25.3	1.96	35500	0.2
HRB500	1.0	0.4					

Table 4. Reinforcement material parameter.

Name of the material	Diameter (mm)	Section area (mm^2)	Tensile strength (MPa)	Modulus of elasticity (GPa)	Elongation (%)	Poisson's ratio
BFST	8.0	50.3	550.0	70.0	2.05	0.23
HRB500	8.0	50.3	640.0	200.0	2.05	0.25
Spiral rib steel wire	10.0	78.5	1860.0	205.0	1.89	0.3

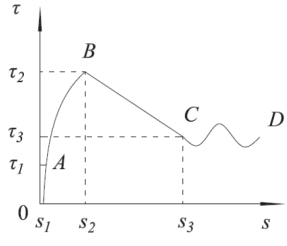

Figure 5. The revised constitutive relation model. *The parameters in the graph based on the test data curve are shown in Figure 3.

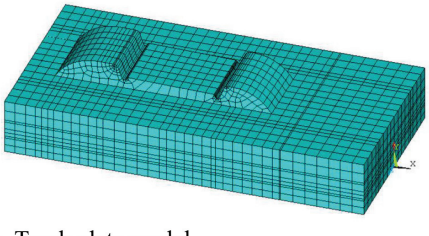

a. Track plate model

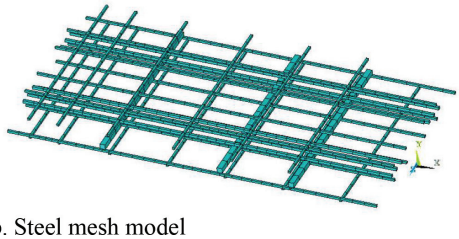

b. Steel mesh model

Figure 6. Model figure.

cracking switch arranged in the concrete near the site of constraints and loading avoided the stress concentration, which would further induce partial concrete damage, leading to non-convergence of calculation and affecting the calculation results. The model is shown in Figure 6.

5 STATIC TEST ON THE CRTSII SLAB

Two pieces of the slab of BFST and one piece of the slab of the HRB500 bar are selected for the static test according to the test requirements and the "Railway Passenger Dedicated Line of CRTSII slab ballast less track concrete slab temporary technical conditions" (People's Republic of China Ministry of Railways 2008). The test load is shown in Figure 7. The conditions for the deflection, stress and strain, ultimate bearing strength and cracking of rail slabs at graded load are recorded.

Slab cracking moment, non-prestressed tendon yield moment, ultimate damage moment, the corresponding vertical displacement and its ultimate failure mode are given in Table 5.

Cracking development is shown in Figure 8. Cracking development of the slab of BFST is more compact than that of the HRB500 bar. The difference is caused by the smaller modulus of elasticity of BFST than that of the HR500 bar; besides, the bond performance between the spiral ribs and the concrete is superior than that of the HRB500 bar, and the overall performance of BFST combined with concrete together is better.

Due to limited space, the data regarding two kinds of tendon of slabs are selected respectively to compare stress and strain, deflection and deformation, ultimate bearing load with test value data at the designed load condition. The simulation and test values on strain, cracking bend moment of compressed-area concrete are in fair good agreement. The values on deflection of simulation and test matched well before loading ratio reached 0.9. But when loading ratio reached 1, the deflection values became larger than before abruptly, at the very time it is inconvenient to control deflection measurement so that there is no match between the test values and the simulation values. The test and simulation data summarized in tabular form are as shown in Tables 6–8.

a. Load carrying test

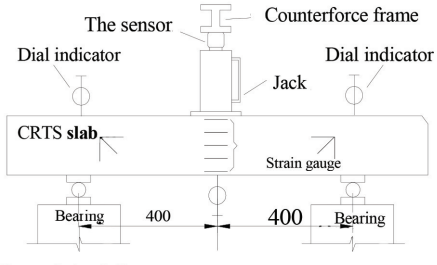

b. The static load diagram

Figure 7. Static test figure.

As can be seen from the three slabs, BFST can be used as the main tensile tendon. All the load-deflection curves of the slab have an obvious inflection point whose corresponding load is the cracking load. After concrete cracking, the increased rate for the mid-span deflection of the specimens with BFST slab is obviously more than that before the concrete cracking. Comparing the specimen of the BFST slab with the specimen of the steel concrete slab, though the specimen of the steel concrete slab has a inflection point, the second phase slope of the load-deflection curves is relatively large, indicating that the second phase of its deflection variation range is less than that of the test specimen of the BFST slab. This decrease is due to concrete cracking that prevents the working of the concrete slab at the bottom so that the bending deformation of the slab specimen of BFST is more obvious and the curve slope is relatively small, which lead to a rapid increase in deflection owing to the smaller elastic modulus of BFST compared with that of the HRB500 bar.

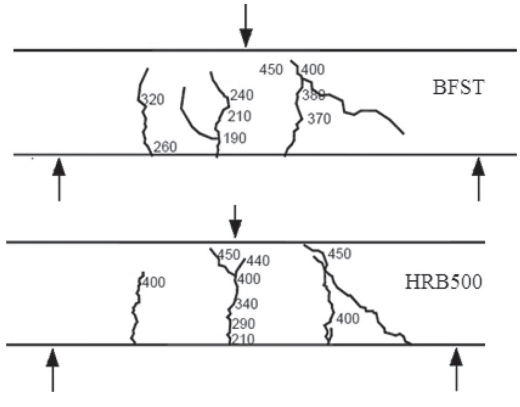

Figure 8. Crack propagation pattern.
* Load the value (unit kN) applied the figure represented, crack development to mark the position of the figure.

Table 5. Rail panel bending displacement and failure mode.

Serial number	Cracking moment Mcr	Yield moment My	Ultimate bending moment Mu	Yield displacement Δy	The fracture displacement Δu	Failure mode
BFST-1	36.16	57.81	79.02	2.91	7.02	Concrete crushed, BFST broken
BFST-2	37.50	54.72	75.0	2.70	6.83	Slab broken, BFST broken
HRB500	38.84	58.02	77.01	2.61	6.95	Concrete crushed, rebar broken

Table 6. Slab top concrete strain simulation value and experiment comparison (με).

Loading ratio	10%	20%	40%	60%	70%	80%	90%	100%
BFST								
Simulation value	–80	–161	–260	–540	–829	–1005	–1273	–1379
Test results	–92	–172	–314	–650	–887	–1132	–1399	–1498
HRB500								
Simulation value	–35	–74	–181	–427	–553	–650	–869	–967
Test results	–42	–85	–204	–480	–621	–756	–967	–1109

Table 7. Track slab midspan deflection simulation value and experiment comparison table (mm).

Loading ratio	10%	20%	40%	60%	70%	80%	90%	100%
BFST								
Simulation value	0.10	0.19	0.37	0.76	1.61	2.43	3.54	4.55
Test results	0.06	0.11	0.26	0.73	1.36	1.99	3.41	7.02
HRB500								
Simulation value	0.04	0.09	0.18	0.85	1.19	1.56	1.99	2.25
Test results	0.01	0.05	0.19	0.73	1.03	1.68	2.18	6.95

Table 8. Bearing capacity contrast test value and analog value (kN · m).

Project/Name	BFST-1	BFST-2	HRB500
Cracking moment/kN · m			
Test results	36.16	37.50	38.84
Simulation value	32.46		35.27
Ultimate bending moment/kN · m			
Test results	79.02	75.00	77.02
Simulation value	67.52		70.21

6 CONCLUSION

From the above discussion and test data comparison, it can be shown that the BFST has good mechanical properties and good working coordination with concrete. The simulation values of the BFST that theoretically enhanced rail slabs of CRTSII type match well with the test values, and the results from the analysis of the established model have a reference value. Although the slabs of the BFST have a bigger deflection and a smaller bearing load than the slabs of the HRB500 steel, the technical specification requirements could be met, so that BFST applied on the rail slabs of CRTSII type can not only solve the resonant track circuit interference problem caused by the ordinary steel closed loop, but also meet the structure force requirements of cross-sectional slabs under rail lines. The experimental results show that the BFST, as a kind of new material, is feasible to be used for track board. The calculation results provide a reliable reference for the ballastless track technology system.

REFERENCES

Academy of Railway Sciences. 2005. *Ballastless Track Design Guide.* Beijing: China Railway Publishing House.

General Administration of Quality Supervision, Inspection and Quarantine of People's Republic of China & China National Standardization Management Committee. 2009. *GB/T 13096-2008 Mechanical Tests on Plastic Rods Pultruded Glass Fiber Reinforced.* Beijing: China Standard Press.

Guo, T.Z. 2006. *High Speed Railway Ballastless Track Structure.* Beijing: China Railway Publishing House.

People's Republic of China Ministry of Railways. 2008. *Passenger Dedicated Railway CRTSII Type Slab Track Concrete Track Slab Temporary Technical Conditions.* Beijing: China Railway Press.

Shang, X.J., Qiu, F., Zhao, H.F. & Li, W.Y. 2006. *ANSYS Senior Structure Finite Element Analysis Method and Example Applications.* Beijing: China Water Conservancy and Hydropower Press.

The Ministry of Railways of the People's Republic of China. 2005. *TB10082-2005 Railway Track Design Specification.* Beijing: China Railway Publishing House.

Wang, X.M. 2007. *Numerical Analysis of ANSYS Engineering Structure.* Beijing: China Communications Press.

Yu, L., Zhang, J.W. & Zhao, G.T. 2009. The design and analysis of prestressed holes asymmetric non-ballast Track. *Railway Science and Engineering Newspaper* 4(6): 23–27.

Civil Engineering and Urban Planning IV – Liu et al. (Eds)
© 2016 Taylor & Francis Group, London, ISBN 978-1-138-02903-3

Optimal bus station locations using a Voronoi diagram model

Guang-Yu Zhu
MOE Key Laboratory for Transportation Complex Systems Theory and Technology, Beijing Jiaotong University, Beijing, China
Center of Cooperative Innovation for Beijing Metropolitan Transportation, Beijing, China
Key Laboratory of System Control and Information Processing, Ministry of Education, Shanghai, China

Wen-Xi Zhang
MOE Key Laboratory for Transportation Complex Systems Theory and Technology, Beijing Jiaotong University, Beijing, China
Center of Cooperative Innovation for Beijing Metropolitan Transportation, Beijing, China

Jing Wei
Hainan Communications Investment Holdings Co. Ltd., Hainan, China

Peng Zhang
Beijing Municipality Key Laboratory of Urban Traffic Operation Simulation and Decision Support, Beijing Transportation Research Center, Beijing, China

ABSTRACT: The layout of bus stations affects the travel efficiency of passengers and the traffic capacity of the road. A layout model for a bus station based on a Voronoi diagram is proposed in this paper aiming at minimizing the total travel cost of public transportation system as well as the number of passengers. First, the relationship between the layouts of bus stations and the total travel cost is analyzed, then the influencing factors are quantified. Second, a measuring function of travel cost of passengers is established. Then, all alternative stations are grouped based on Voronoi diagram. The layout model is set up to determine the final bus station locations. An example is given to show the validity and effectiveness of the proposed model.

1 INTRODUCTION

The planning and layout of bus stations has a direct impact on bus passengers' traveling efficiency. Thus, the optimization of the location and number of stations in bus lines play an important role in improving the service of public transportation and optimizing the resources of urban transportation infrastructure. Wang et al. (2004) put forward a method in programming and layout of the transit hub based on predicted data about the distribution of bus passengersiang (2006) put forward some basic principles of the layout of bus station locations.

In recent years, in order to make up for insufficient pure mathematical models on intuition and visibility, some scholars began to blend GIS in the planning of bus stations. Zhang (2011) analyzed the factors influencing the layout of bus stations using spatial analysis method. Novaes (2000) applied the Voronoi diagram in urban area planning. Gahegn & Leeput (2000) put forward some application examples to show the usage of different Voronoi models. Abellanas et al. (2003) gave a simple algorithm for computing the Time Voronoi Diagram. Oliveira et al. (2011) presented a model to optimize the bus station spacing of a bus line.

Wang et al. (2004) put forward a method in programming and layout of the transit hub based on predicted data about the distribution of bus passengers. Jiang (2006) put forward some basic principles on the layout of bus station locations.

2 THE INFLUENCING FACTORS CONCERNING THE LAYOUT OF THE BUS STATIONS

There are some factors affecting the procedure of the layout of bus stations to minimize the total travel cost of public transportation system as well as the number of passengers. Main factors are:

– The layout of land within the service range of the bus station.

– The walking distance from domicile to the bus station.
– The layout of bus stations within an area.
– The number of roads linked with one identical bus station.
– Traffic volume of the roads which are linked to one bus station.
– Traffic direction of the roads which are linked to one bus station.

3 THE LAYOUT MODEL OF BUS STATIONS

Assume n points $X_i(i = 1, 2, ..., n,)$ were set as control points distributed in a plane. A Voronoi diagram of these n points is composed of continuous polygons, which are constituted by lines connecting the perpendicular bisector with two adjacent points according to the Nearest Neighbor Rule. The area is divided into n blocks $V(i)(i = 1, 2, ..., n)$, which is called Voronoi region. An arbitrary point(x, y) in block $V(i)$, $X_i(i = 1, 2, ..., n)$ is the nearest point from (x, y). As shown in Figure 1, the Voronoi diagram is constituted by six points; the star points are Voronoi points and the pentagon is a Voronoi polygon.

4 SETTING UP THE LAYOUT MODEL OF BUS STATIONS

The weight of travel distribution density could be determined by investigating the travel generation source of each traffic zone. Generally, for the convenience of calculating, we set each centroid as the demand point of bus transit. Thus, the essence of the layout of bus station is to assign a certain number of bus stations to the demand points, with the minimized total travel cost of the whole public transport system, as well as the passengers.

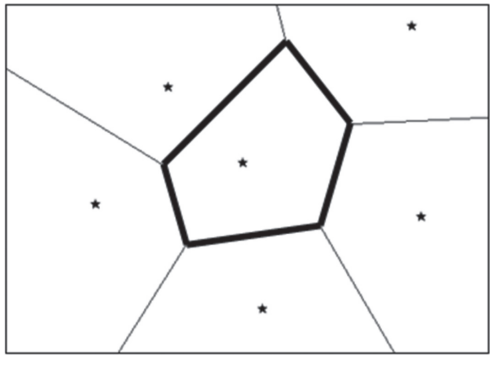

Figure 1. Voronoi diagram with six control points.

Set δ as a two-dimensional Euclidean coordinate. Then the public transport demand points and alternative bus stations were marked within the coordinate system according to their relative positions in the geographical space. The relative coordinates of the bus demand points $X_i(i = 1, 2, ..., n)$ is (x_i, y_i) in the coordinates δ; the relative coordinates of the alternative bus station $X_j(j = 1, 2, ..., n)$ is (x_j, y_j) in the coordinates δ. C_{ij} means the set of paths from demand points i to alternative points j in the coordinates δ.

Then, the layout model of bus station could be set up as equation (1).

$$\min(z) = \sum_i \sum_j k_i f_{ij}^c(x,y) Y_{ij} \quad (1)$$

$$s.t. \sum_{j=1} X_j = N$$

$$c \in C_{ij}, \forall i, j$$

$$X_{j(j=1,...,m)} = \begin{cases} 1 \\ 0 \end{cases}$$

$$Y_{ij} \in \{0,1\}, \forall i, j$$

k_i is the weight coefficient, meaning the influencing weight of the factors related to the layout of bus stations that affects the total costs of bus systems; N is the total number of bus stations needed to be deployed; $X_j = 1$ represents the alternative bus station finally selected as the public transport station, $X_j = 0$ means it isn't selected; $Y_{ij} = 1$ means assigning the public transport demand point i to the station j, $Y_{ij} = 0$ means it isn't assigned; c represents one path of the set C_{ij}, which includes all paths from the demand points i to alternative points j. $f_{ij}^c(x, y)$ is the metric function of public transport travel costs, meaning the generated travel costs of passengers choosing path c from i to j, in the premise of public transport demand point i having been selected as the alternat ive point j. The metric function can be the space distance function, cost function, travel time function, as well as the user-defined function.

The metric function selected in this paper is based on the shortest passenger travel distance (namely, the total weighted Euclidean distance between each public transport demand point and the alternative point). Assuming that the displacement distance between any two points is continuous, set $X_i(x_i, y_i)$ as the public transport demand point, $X_j(x_j, y_j)$ as the public transport alternative point, then the metric function $f_{ij}^c(x, y)$ is as follows:

$$f_{ij}^c(x,y) = \varepsilon\alpha\beta \left\| X_i - X_j \right\| = \varepsilon\alpha\beta \sqrt{\left(x_i - x_j\right)^2 + \left(y_i - y_j\right)^2} \quad (2)$$

ε is the distance correction coefficient, which is used to transform the residents' actual travel distances

from the zone centroid to the bus station into the approximate straight line of Euclidean distance; α, β, $\gamma(\alpha, \beta, \gamma \geq 1)$ represent the time correction coefficient, cost correction coefficient, and other correction coefficient, which are respectively, used for adjusting the influencing factors of traveling time, traveling cost, and traveling safety, which are connected with the residents' paths from the zone centroid to the bus station. According to the calibration of modification coefficients, the concept between these three factors and the distance can be unified.

5 PARAMETERS OF MODEL

The main parameter of the model is the weight coefficient k_i, representing the cost weight of the public transport system itself, namely, the influencing weight of the factors influencing the layout of bus stations that affect the total cost of bus systems. We can then make quantitative values of it based on the principle of bus station layouts and the condition of alternative bus stations.

Thus, in order to determine the weight coefficient k_i, first, we need to quantitatively process the influencing factors of the layout of bus stations. The quantitative values are shown as follows, from Tables 1 to 6:

Table 1. Quantitative table of land layouts in service radiation range of bus stations.

Land usage	Resident	Industry	Public facilities	Road and square	Urban green land
Quantitative value	1	1	2	3	4

Table 2. Quantitative table of the walking distance when passengers arrive at bus stations.

Passenger walking distance	<500 m	500–600 m	600–8000 m	800–1000 m	>1000 m
Quantitative value	1	2	3	4	5

Table 3. Quantitative table of the layout of bus station.

Road conditions	Road crossing		Road segment
	Road exit	Road entrance	
Quantitative value	1	2	3

Table 4. Quantitative table of multi-line sharing at identical bus stations.

Level of station service LOS	A	B	C	D	E	F
Effective time s/h	1200	1800	2400	2700	3000	3600
Line probability of buses α, %	1	2.5	10	20	35	50
Quantitative value	1	2	3	4	5	6

Table 5. Quantitative table of traffic volume for the attached road of the bus stations.

Traffic flow/person	<2000	2000–4000	4000–6000	6000–8000	8000–10,000	>10,000
Quantitative value	1	2	3	4	5	6

Table 6. Quantitative table of traffic directions at the attached road of the bus stations.

Traffic direction	Multi-direction	Bi-direction	Single direction
Quantitative value	1	2	3

6 SOLVING STEPS OF THE MODEL

The solving steps for layout model of bus station locations based on Voronoi diagram are given as follows:

- Making a traffic survey of service scope of radiation on regional bus lines. According to the concentration distribution of residents in the survey results, we can divide the service scope into several traffic zones. Then we further investigate the number of generating sources in each traffic zone. Determining the travel distribution center of the zone, they are bus demand points, $X_i(i = 1, 2, ..., n)$.
- Creating a Voronoi diagram in taking bus demand points $X_i(i = 1, 2, ..., n)$ as control points. $V(X_i)$ is the Voronoi polygon composed of the demand points of bus transit $X_i(i = 1, 2, ..., n)$. $V(Xi)$ divided the Attract Range of the bus route into n parts, where $X_j(j = 1, 2, ..., m)$ are the alternative bus stations and the alternative bus stations distributed in the $V(X_i)$ region.
- Taking the area of Voronoi polygon as the boundary, we place the alternative bus stations into a group located in the same polygons, using $Xs(i)(s < m)$ to represent the group. The distance

between a group of alternative bus stations $Xs(i)$ ($s < m$) and the corresponding control points of Voronoi polygon is the shortest.
– Selecting randomly a group of alternative bus stations $Xs(i)(s < m)$ in Voronoi polygon $V(X_i)$. Calculating each alternative bus station in the group in using the model (1), choosing the bus station accord with the goal of minimizing the total travel cost of the bus system and number of bus passengers as the optimal bus station.
– Repeating the previous step and determine all bus station in bus lines, and then the layouts of bus stations are completed.

7 APPLICATION CASE

The layout analysis of bus stations in a suburb of a city is set as the case to be studied.

Seven villages are contained in an area of 40.3 square kilometers (shown as Fig. 2). The optimization layout of bus station should be made using the Voronoi diagram.

Step 1. Making a survey to determine the service region of every bus line, shown in Table 7.

Step 2. Dividing the traffic generation source as per the traffic zone according to the concentration distribution of residents. Determining statistically the number of traffic generating sources in each traffic zone to determine the demand point of bus transit in every traffic zone. As shown in Figure 2, the six square points $X_i(i = 1, 2, ..., n)$ are six bus demand points of bus transits in each traffic zone, and they are distributed in the village F, village C, and village B.

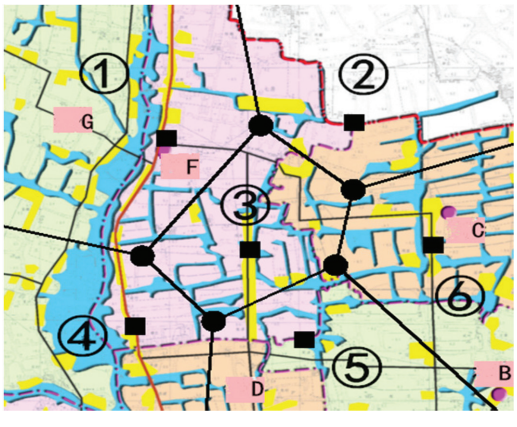

Figure 2. The Voronoi diagram of the layout for bus station.

Table 7. Distribution of the villages.

Village	A	B	C	D	E	F	G	Others
Number	91	97	89	127	159	118	266	46

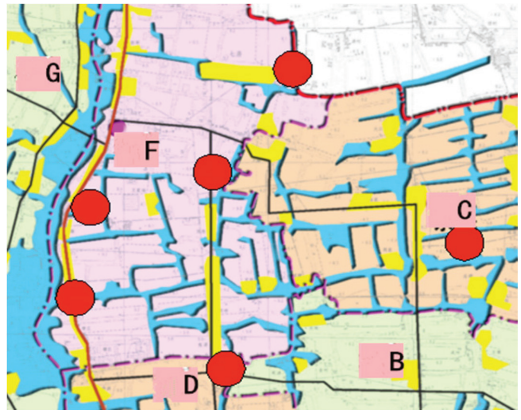

Figure 3. The layout of bus stations.

Step 3. A Voronoi diagram is set up based on six control points $X_i(i = 1, 2, ..., n)$, as shown in Figure 3. $V(X_i)$ is a Voronoi polygon composed of these six demand points. The Voronoi polygon divided the attract range of the bus line into six parts, as shown in Figure 2. Alternative bus stations of every regional $V(X_i)$ are $X_j(j = 1, 2, ..., m)$ and divide alternative bus stations of the same polygon into a group $Xs(i)(s < m)$.

Step 4. Selecting randomly a group of alternative bus stations $Xs(i)(s < m)$ in Voronoi polygon $V(X_i)$. Calculating each alternative bus station in the group based on the goal of minimizing the total travel cost of the bus system and bus passengers by using the model (1). In this way, we can determine the optimal bus station.

Step 5. Repeat the previous step, so we can determine all the bus stations in bus lines, then the layouts of bus stations are completed, as shown in Figure 3.

8 CONCLUSION

A layout model for bus stations based on a Voronoi diagram is proposed in this paper aiming to minimize the total travel cost of public transportation system as well as the passengers. A case was studied to show the validity and effectiveness of the proposed model. The layout model based on the Voronoi diagram is a method that synthesizes

the graph theory and the mathematical analyzing, which can be utilized for the planning and layout of bus stations.

At present, the Voronoi diagram is mainly used in geographic and economic areas, but it also has a great potential in spatial planning. It is necessary do further studies for the applications of weighed Voronoi diagrams in this model.

ACKNOWLEDGMENT

This work is supported by the National Science Foundation of China (Nos. 61572069 and 61503022), the Fundamental Research Funds for the Central Universities (No. 2014JBM211), the Open Project Program of Key Laboratory of System Control and Information Processing, Ministry of Education, Shanghai Jiaotong University (No. Scip201507), Beijing Municipality Key Laboratory of Urban Traffic Operation Simulation and Decision Support, and Beijing Transportation Research Center.

REFERENCES

Abellanas, M., Hurtado, F., Sacristan, V., Icking, C., Ma, L., Klein, R. et al. 2003. Voronoi diagram for services neighboring a highway. *Information Processing Letters* 86(5): 283–288.

Gahegan, M., & Lee, I. 2000. Data structures and algorithms to support interactive spatial analysis using dynamic voronoi diagrams. *Computers Environment & Urban Systems* 24(6): 509–537.

Jiang, W.T. 2006. Discuss about where to place bus station and how to lay it. *Traffic & Transportation* 7(1): 81–84.

Novaes, A.G. 2000. Logistics Districting With Multiplicatively Weighted Voronoi Diagrams. *XI Congreso Panamericanode Ingenieriade Transitoy Transport, Gramado, RS, 19*.

Oliveira, H.F., Gonçalves, M.B., Cursi, E.S. & Novaes, A.G. 2011. Development of a computational system to determine the optimal bus-stop spacing in order to minimize the travel time of all passengers. *Dynamics in Logistics*, 15–25.

Wang, Q., Wang, W. & Tie-Zhu, L.I. 2004. Transport planning for urban public traffic transfer hubs. *Journal of Transportation Systems Engineering and Information Technology* 4(3): 82–85.

Zhang, F. 2011. Application of gis spatial analysis to bus station locations choosing using. *Geospatial Information* 9(1): 118–120.

This page intentionally left blank

Civil Engineering and Urban Planning IV – Liu et al. (Eds)
© 2016 Taylor & Francis Group, London, ISBN 978-1-138-02903-3

Optimization of sustainable biofuel network based on hybrid genetic algorithm

Na-Na Geng & Yong Zhang
School of Transportation, Southeast University, Nanjing, Jiangsu, China

Yi-Xiang Sun
School of Civil Aviation, Nanjing University of Aeronautics and Astronautics, Nanjing, Jiangsu, China

Yun-Jian Jiang
School of Transportation, Southeast University, Nanjing, Jiangsu, China

ABSTRACT: At present, biofuel is developed as alternative fuels by the government in order to reduce air pollution. However, it is unable to realize the low pollution characteristics because in the transportation and delivery process, a lot of carbon emissions would be generated due to scattered supply nodes and obvious periodical fluctuation. Therefore, effective locating of the distribution center is very critical to biofuel. The main purpose of this article is to research the biofuel location problem from the perspective of carbon emissions, in which process a hybrid genetic algorithm is used to get the optimal location with applications in a cassava biofuel enterprise, for instance. First, a mathematic model is constructed in this paper based on the factors of location selection and requirements of the building process within the distribution center. Second, the mathematical methods, combined with genetic algorithm and mountain climbing algorithm are employed so as to analyze an enterprise example and acquire the locating result. Finally, this paper discusses the location result of the instance location, which thus proves the practicability of this paper. Moreover, the results obtained in this paper will help achieve sustainability of biofuel transport and distribution, thereby promoting the development of biofuel industry in China.

1 INTRODUCTION

Biofuel is increasingly considered as extremely important materials in addressing energy security problems, poverty reduction, decreased dependency on fossil fuels, and reduced Greenhouse Gas (GHG) emissions. Angela & Salvatore (2012) proposed that more and more vehicles have begun to use biofuel as an alternative fuel, while many governments have promoted the biofuel production. For these reasons, the volume of biofuel has been greatly increased. Therefore, biofuel network optimization is particularly important. According to the literature, the present study of the location allocation problem is mature and expanded into a wide field. Based on the most basic classification principles, Beamon (1998) indicated that the number of distribution centers can be divided into two groups, namely the single distribution center and multiple distribution centers. Yue et al. (2014) introduced the key challenges and opportunities in modeling and optimization of biomass-to-bioenergy supply chains. However, future biofuel supply chains should integrate with petroleum refinery supply chains to deal with carbon capture, modeling of sustainability and the treatment of uncertainties. Duarte et al. (2012) analyzed facility location and logistics networks in 7 biodiesels and 6 bio-ethanol production plants in Colombia, and provided a decision-making model to make a comparison between facility locations, taking account production costs and the logistics network into consideration Martinkusa et al. (2014) provided a framework for a quantitative approach for biorefinery siting and decision-making, and validated the social asset measures used for facility siting at the county level through retrospective prediction analysis. Miyazakia et al. (2014) employed a country-level spatially explicit hybrid integer linear programming model to identify the optimal Fischer-Tropsch biodiesel production plant locations in Finland. The model results indicated that five biodiesel production plants of 390 MW feedstock were needed to be built to meet the 2020 renewable energy target in transport (25.2 PJ). Azadeh et al. (2014) proposed a stochastic linear programming model, within a multi-period planning framework so as to maximize the expected profit. AtifOsmani & Jun Zhang (2013) presented a model not only to deal with a time-staged and

multi-commodity production/distribution system, facility locations and capacities, technologies and material flows, but also to propose a two-stage stochastic MILP model to maximize the expected profit by optimizing the strategic and tactical decisions and to find the location of biorefineries insensitive to the stochastic environment.

Nowadays, various models have been developed to design biofuel supply chains by optimizing the economic performance. More and more articles have focused on carbon emissions: Delivand et al. (2015) indicated that most of the mature biofuel markets used grain as feedstock, i.e. corn and wheat, and the performance is usually assessed by life-cycle tools, such as life-cycle energy and CO_2 analysis. Zhang et al. (2012) described the development of a simulation model with an easy-to-use graphical user interface for the biofuel supply chain. The model uses the delivered feedstock cost, energy consumption and GHG emissions as the system performance criteria. Akgul et al. (2014) used a Hybrid Integer Nonlinear Programming (MINLP) model of carbon-negative energy generation in the UK so as to examine the potential for existing power generation assets, thus acting as a carbon sink as opposed to a carbon source. Furthermore, they used the model to examine the technical and economic compromises implicit in transition from a dedicated fossil fuel only to a carbon-negative electricity generation network. Giarola et al. (2012) conducted an empirical hybrid integer programming model that considers market demand uncertainty, and studied the biofuel production system technology choice under the dual goals of the economic and GHG emissions, and the biological ethanol technology selection decision problem with a case study of Italy.

Articles considering the biofuel carbon have been mostly focusing on the perspective of supply chain optimization and studying the first generation of biofuel industry, thereby providing a solution path to the ultimate capacity of planning and transportation decision-making. While for cassava as the raw material of the second generation of biofuel, there is no further discussion on the relationship between carbon emissions and the objective function. Ren et al. (2015) indicated that a biofuel can be regarded as a promising alternative to fossil fuels for its significant advantages of renewability and sustainability performances; however, these papers just mainly take the cost of transportation, transformation technology and inventory cost into consideration, but there are rare papers considering the sustainable factors in the supply chain design decision research. Therefore, the main purpose of this article is to research the biofuel location problem from the perspective of carbon emissions and use a hybrid genetic algorithm to obtain the optimal location.

2 MODEL CONSTRUCTION

2.1 *Problem description*

As an important part of logistics activities, location allocation plays an essential role in the whole logistics system. Meloa et al. (2009) indicated that the reasonable location allocation result can promote the transport of goods in the direction of organization, integration and modernization.

The purpose of this article is to research a single distribution center location allocation problem.

The characteristics of the problem are as follows:

- The object of the study is the LAP problem with no function of warehousing;
- The goods transportation is a single variety of biomass fuel;
- Each user has only one distribution center and will be served by it;
- The unit freight cost is fixed;
- The carbon emission of unit freight is fixed.

2.2 *Model parameter*

d_{ij}: distance from the supplier i to the distribution center j;
d_{jk}: distance from the distribution center j to the demander k;
q_{ij}: transporting quantities from the supplier i to the distribution center j;
q_{jk}: transporting quantities from the distribution center j to the demander k;
F_j: fixed cost of constructing distribution center j;
c_1: transporting cost of unit freight from the supplier i to the distribution center j;
c_2: transporting cost of unit freight from the distribution center j to the demander k;
c_g: carbon trading price;
f_g: carbon emission of unit freight transporting;
M_j: the maximum capacity of the distribution center.

Based on the above definition of variables, the goal programming model is set up as follows:

$$\min Z_1 = F_j + \sum_i c_1 q_{ij} d_{ij} + \sum_j \sum_i c_2 q_{jk} d_{jk} \tag{1}$$

$$\min Z_2 = c_g f_g \left(\sum_i q_{ij} d_{ij} + \sum_j \sum_i q_{jk} d_{jk} \right) \tag{2}$$

Subject to:

$$\sum_{i=1}^{n} q_{ij} \le M_j \quad j = 1, 2, \ldots m \tag{3}$$

$$\sum_{i=1}^{n} q_{ij} = \sum_{k=1}^{l} q_{jk} \quad j = 1, 2, \ldots m \tag{4}$$

$$d_i = \left[\left(x_0 - x_i \right)^2 + \left(y_0 - y_i \right)^2 \right]^{1/2} \quad (5)$$

$$d_j = \left[\left(x_0 - x_j \right)^2 + \left(y_0 - y_j \right)^2 \right]^{1/2} \quad (6)$$

$$q_{ij} \geq 0,\ q_{jk} \geq 0, \quad j = 1, 2, ..., m \quad (7)$$

3 METHODS

In the previous literature, distribution center location mainly includes common heuristic algorithm: genetic algorithm (Diogo et al. 2014) simulated annealing algorithm (Chao 2015), ant colony algorithm (Martin 2014) and tabu search algorithm (Zhang et al. 2009). As a global random search method, Genetic Algorithm (GA) is widely used in many fields due to its simple operation and effectiveness in solving the problem. Marvin et al. (2006) proved that genetic algorithm can theoretically seek the optimal solution to the problem from the perspective of probability at random. However, on the one hand, in the practical application (Earl 2005), it is found that the genetic algorithm has its limits, such as premature phenomenon and poor local optimization ability. On the other hand, some optimization algorithm global optimization has a strong local search ability despite poor abilities of methods such as gradient method, climbing method and simulated annealing method. Therefore, this article uses a hybrid algorithm of genetic algorithm and mountain climbing algorithm to realize simple operation and improve the efficiency effectively in solving the locating problem.

The principle of the algorithm is to embed an additional local optimization module in the restructuring cycle of the genetic algorithm. In the process, local optimization techniques are used for each new offspring before entering into groups, and then they are moved to the nearest local optimal point. In terms of using the heuristic method for local optimization to chromosome, the advantages of genetic algorithm are taken for the global exploration. Specific operation process is as follows: search the global optimal solution process from a set of randomly generated initial solutions. It first generates a new set of individuals by genetic operations such as selection, crossover and mutation, and then operates the climbing process for generated independent individuals, using result as individuals in the next generation group. This process is repeated iteratively until a termination condition is satisfied.

4 CASE STUDY

4.1 *Case description*

In this paper, first, designing of the supply chain including eight 2 suppliers and customers is conducted. Then, a distribution center within the designated area is established according to the spread of customers and suppliers of the biofuel company. Lastly, the transportation task is completed with each surrounding customer within the minimum cost. Specific coordinates and other indicators are presented in Tables 1–3.

4.2 *Results and analysis*

The software of Matlab 7.0 is used to solve the modeling problem. Parameter settings are as follows: maximum iterations G = 100, population size N = 10, parameters in the crossing process = 0.4, crossover probability = 0.6 and mutation probability = 0.003. Then, the hybrid genetic algorithm is used to solve, iterate and reach the highest fitness value. At the same time, the result becomes stable and the convergent effect is better, as shown in Figure 1.

The hybrid genetic algorithm is used to solve the problems of the petitions. In the end, the simulation result is the optimal biofuel distribution center coordinates (50.74, 41.00). At the same time, by

Table 1. Biofuel supplier information.

No	Abscissa	Ordinate	Maximum supply quantity
1	80	30	8 t
2	50	10	14 t

Table 2. Biofuel demanding information.

No	Abscissa	Ordinate	Quantity demanded
1	50	62	0.6 t
2	45	36	0.7 t
3	42	54	0.9 t
4	47	51	1 t
5	84	60	0.5 t
6	65	75	0.3 t
7	53	49	0.9 t

Table 3. Other parameter values.

No	Parameter	Quantitative value
1	c_1	1 yuan/kg
2	c_2	0.8
3	N	8
4	cg	30 yuan/t
5	f	0.08 t
6	F	50000 yuan

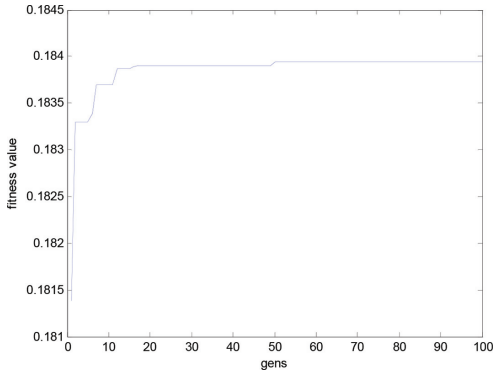

Figure 1. Changing curve of the fitness value in the genetic process.

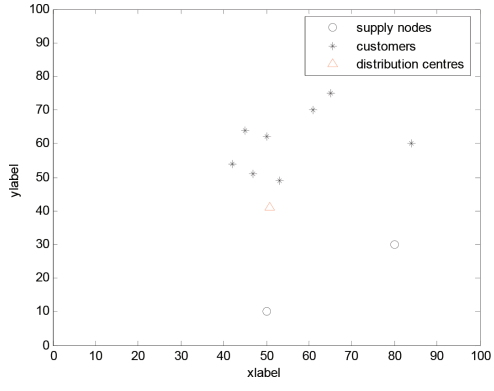

Figure 2. The specific location of the distribution center.

finding the distribution center location, the least cost of transportation and carbon emission can be obtained by calculation (543.640918), with a minimum total cost of 50543.640918. The specific location of the sustainable biofuel distribution center is shown in Figure 2.

5 CONCLUSION

Against the background of the widespread biofuel, the location problem of the enterprise distribution center, which has been regarded as a part of the whole logistics system, is becoming particularly important.

– In terms of the previous articles on the distribution center location, they are mostly based on the least transportation costs and the shortest transporting mileage, but at present, with the concept of sustainable logistics, air pollution has become even more important than cost reduction. Therefore, the important innovation of this article is the consideration of the carbon emissions, which are then added to the DC location model so as to optimize the whole network.
– Multi-objective model is adopted to solve more complex problems. This paper adopts the combination of genetic algorithm and mountain climbing algorithm as the solution. Through biofuel business cases, this algorithm can effectively solve this kind of problem with a stronger practicability and good practical value.

Of course, this article also has many limitations, which are as follows:

– In order to reduce the complexity of the model, in this paper, the average price trading by only recent days in the market is chosen for the carbon emissions assumptions. However, in the actual carbon trading process, the carbon price may change significantly.
– The hybrid genetic algorithm used in this paper could not test the selection of the crossover rate and the mutation rate, as they were adopted from previous papers.

ACKNOWLEDGMENTS

This work was supported by the National Natural Science Foundation of China (Project No. 71372198). We are grateful to these colleges for their valuable suggestions for improvement.

REFERENCES

Ae Duarte, Wasarache, Ca Cardoa-Dyna, 2012. Cost analysis of the location of colombian biofuels plants. *Dyna. Rev. Fac. Nac. Minas.* 79(176): 71–80.

Akgul, O., N. Mac Dowell, L.G. Papageorgiou, N. Shah. 2014. A Mixed Integer Nonlinear Programming (MINLP) supply chain optimization framework for carbon negative electricity generation using Biomass to Energy with CCS (BECCS) in the UK. *International Journal of Greenhouse Gas Control* 28(9): 189–202.

Ali Azadeh, Hamed Vafa Arani, Hossein Dashti. 2014. A stochastic programming approach towards optimization of biofuel supply chain. *Energy* 76(11): 513–525.

Angela D. & Salvatore Di F. 2012. Biofuels in developing countries: Are comparative advantages enough? *Energy Policy* 44(5): 101–117.

Atif, Osmani & Zhang, J. 2013. Stochastic optimization of a multi-feedstock lignocellulosic-based bioethanol supply chain under multiple uncertainties. *Energy* 59(9): 157–172.

Beamon, B.M. 1998. Supply chain design and analysis: Models and methods. *International Journal of Production Economics* 55(8): 281–294.

Diogo, R.M. Fernandes, Caroline Rocha, Daniel Aloise, Glaydston M. Ribeiro, Enilson M. Santos, Allyson Silva. 2014. A simple and effective genetic algorithm for the two-stage capacitated facility location problem. *Computers & Industrial Engineering* 75(9): 200–208.

Earl, C. 2005. *Fundamental Concepts of Genetic. Algorithms Fuzzy Modeling and Genetic Algorithms for Data Mining and Exploration*. Morgan Kaufmann.

Martin, Reed, Aliki, Yiannakou & Roxanne, Evering. 2014. An ant colony algorithm for the multi-compartment vehicle routing problem. *Applied Soft Computing* 15(2): 169–176.

Marvin, A. Arostegui, Jr., Sukran, N., Kadipasaoglu, Basheer M. Khumawala. 2006. An empirical comparison of Tabu Search, simulated annealing, and genetic algorithms for facilities location problems. *International Journal of Production Economics* 103(9): 742–754.

Meloa, M.T., S. Nickelb, F. Saldanha-da-Gamad. 2009. Facility location and supply chain management-A review. *European Journal of Operational Research* 196 (7): 401–412.

Mitra Kami Delivand, Anna Rita B. Cammerino, Pasquale Garofalo, Massimo Monteleone. 2015. Optimal locations of bioenergy facilities, biomass spatial availability, logistics costs and GHG (Greenhouse Gas) emissions: a case study on electricity productions in South Italy. *Journal of Cleaner Production* 14(3): 129–139.

Natalie Martinkusa, Wenping Shib, Nicholas Lovrichc, John Pierced, Paul Smithe, Michael Wolcotta. 2014. Integrating biogeophysical and social assets into biomass-to-biofuel supply chain siting decisions. *Biomass and Bioenergy* 66(7): 410–418.

Ren, J.Z., Dong, L., Sun, L., Goodsite, M.E., Tan, S.Y. & Dong, L.C. 2015. Life cycle cost optimization of biofuel supply chains under uncertainties based on interval linear programming. *Bioresource Technology* 187(7): 6–13.

Sara Giarola, Andrea Zamboni, Fabrizio Bezzo. 2012. Environmentally conscious capacity planning and technology selection for bioethanol supply chains. *Renewable Energy* 43(7): 61–72.

Takahiro, Miyazakia, Jyunpei, Sugiurab, Teppei, Nagatomic & Rafael Batresd. 2014. Integration of process synthesis and location-transportation for the design of biomass conversion systems. *Renewable Energy* 62(2): 319–330.

Wang, C., Mu, D., Zhao, F. & Sutherland, J.W. 2015. A parallel simulated annealing method for the vehicle routing problem with simultaneous pickup-delivery and time windows. *Computers & Industrial Engineering* 83(5): 111–122.

Yue, D.J., You, F.Q., Seth W. Snyder. 2014. Biomass-to-bioenergy and biofuel supply chain optimization. *Computers & Chemical Engineering* 66(7): 36–56.

Zhang, F.L., Johnson D.M. & Sutherland, J.W. 2012. Development of a simulation model of biomass supply chain for biofuel production. *Renewable Energy* 44(8): 380–391.

Zhang, R.Y., Yun, W.Y. & Ilkyeong, Moon. 2009. A reactive tabu search algorithm for the multi-depot container truck transportation problem. *Article Transportation Research Part E: Logistics and Transportation Review* 45(12): 904–914.

This page intentionally left blank

Civil Engineering and Urban Planning IV – Liu et al. (Eds)
© 2016 Taylor & Francis Group, London, ISBN 978-1-138-02903-3

Mode choice behavior for access to the airport under a new mode: A case study of Nanjing Lukou Airport

Dan-Wen Bao, Song-Yi Hua & Jun-Hua Jia
College of Civil Aviation, Nanjing University of Aeronautics and Astronautics, Nanjing, Jiangsu, China

ABSTRACT: Using Revealed Preference (RP) and Stated Preference (SP) data obtained in the survey of travel behaviors of passengers in Nanjing Lukou Airport, this paper analyzed the passengers' choice of airport access mode. Nested Logit (NL) and Mixed Logit (MXL) models were respectively established to identify the preferences of airport passengers after the construction of the airport railway. The comparison results indicated that the MXL model allowed a better estimate result for SP/RP combined data. Travel time and travel cost were the major factors affecting choice of airport access mode. Travel purpose and luggage quantity significantly affected the passengers' intention of selecting airport rail. Elasticity analysis results show that if the out-of-vehicle time of airport rail is shortened, more passengers will use the public transport mode to airport. Passengers who use taxis or airport buses to airport are significantly affected by travel cost, and they show the strongest intention to use airport railway to reach the airport.

1 INTRODUCTION

In recent years, aviation in China experienced rapid development: the average annual growth of passenger traffic from 2004 to 2014 reached 14% and passengers in 24 airports were over 10 million. In Nanjing Lukou Airport, the gateway airport in the second largest city in eastern China, the number of passengers in 2014 will reach 15 million which will rank 15th busiest airport in China. The access transportation system to Lukou Airport currently primarily relies on roads. The traffic pressure is high and the saturation degree at the traffic peak period exceeds 0.8. Therefore, in order to relieve the traffic pressure of the airport expressway, the Nanjing Municipal Government has built an airport rail line, which can connect the urban areas of Nanjing and Jiangning District to Lukou Airport to provide passengers a new more efficient and fast access mode.

In this paper, based on combined data of revealed preference (SP)/stated preference (RP) on passengers' travel behaviors in Lukou Airport, it analyzed the influence of the introduction of airport rail on choice of airport access mode and respectively compared the estimation results obtained using Nested Logit (NL) and Mixed Logit (MXL) models. Moreover, this paper determined the main influencing factors in access mode choice by airport passengers and quantified the diversion role of rail traffic on other travel modes. The results above can be used to guide the planning of airport rail traffic.

2 LITERATURE REVIEW

Harvey (1986) indicated that travel time and cost were the main influencing factors of travel mode. Lythgoe & Wardman (2002) studied the market shares of railway and airport and provided relevant prediction models. Soushi et al. (2014) studied the relationship between airport and travel modes. Travel time was the primary factor in the selection of travel modes. Mei (2010) explored the major influencing factors in the process when passengers selected travel model to airports. Sun (2006) proposed that among travel time, travel cost, travel accessibility, convenience, etc., traffic accessibility and traffic cost were the primary influencing factors in the selection of traffic modes. Becky (2008) indicated that airport flight fare, flight time, flight frequency, and the number of flight routes played a more important role in the selection of airport. Psaraki & Abacoumkin (2002) believed that travel time and cost were the primary factors to be considered by passengers. Hess & Polak (2005) studied passengers in northern London with ML Model and found that travel time, travel cost, flight frequency, and departure time were the influencing factors in travel mode selection.

In previous studies, the influence of rail traffic on airport access mode choice was seldom reported. Survey methods or estimation models for the introduction of a new traffic mode were not available. In the paper, we designed the questionnaire for airport access mode behavior characteristics of airport passengers and established a comprehensive

model based on existing travel modes and choice intention with SP/RP survey data.

3 CHOICE MODELING FRAMEWORK

3.1 *Nested logit model*

NL model proposed by David (2012) was widely used in the estimation of the RP/SP combined data. Zhang (2008) believed that the classification according to traffic mode allowed the better estimation results of NL Model than according to the properties of RP/SP data. In the paper, the data was classified first according to traffic mode, and then according to properties of RP/SP data. A two-layer NL mode was established as shown in Figure 1.

According to NL model, the probability that the passenger n selects the ith travel mode is expressed as:

$$P_{A_i n}=P_{(i/A)n}P_{An} \tag{1}$$

where: $P_{A_i n}$ is the probability that the passenger n selects the ith travel mode; A_i is the ith selection branch under the travel program A; $P_{(i/A)n}$ is the probability that the passenger n selects the ith travel mode based on the travel mode A; P_{An} is the probability that the passenger n selects the travel mode A.
wherein:

$$P_{An}=\frac{e^{\lambda_2 V_{An}}}{\sum_{A=1}^{2} e^{\lambda_2 V_{An}}} \tag{2}$$

$$P_{(i/A)n}=\frac{e^{\lambda_1 V_{(i/A)n}}}{\sum_{i=1}^{N} e^{\lambda_1 V_{(i/A)n}}} \tag{3}$$

where: V_{An} is the utility that the passenger n selects the ith travel mode; $V_{(i/A)n}$ is the fixed term in the variation of the utility with the combination of A_i; and A when the passenger n selects the ith travel mode.

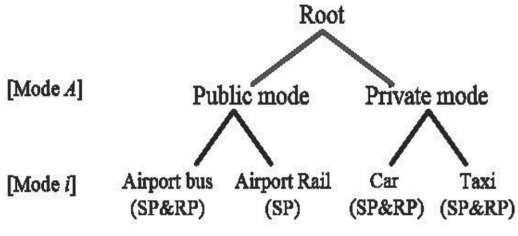

Figure 1. NL model structure.

3.2 *Mixed logit model*

Train (2010) proposed MXL model known as the random parameter logit model. In the model, it is assumed the utility that individual i selects the branch j is:

$$V_{ij}=\beta_j+X_{ij}+\varepsilon_{ij}=\mu_{\beta_j}X_{ij}+\eta_{\beta_j}X_{ij}+\varepsilon_{ij} \tag{4}$$

where: β_j and X_{ij} are, respectively, the row vector and column vector of the influencing factor k; $\beta_j=\mu_{\beta j}+\eta_{\beta j}$: $\mu_{\beta j}$ is the average of β_j, and $\eta_{\beta j}$ is the random error term of β_j and reflects the heterogeneity of the individual i; $\eta_{\beta j}X_{ij}+\varepsilon_{ij}$ is the error term of utility function. The first two terms on the right side of the equation, $\mu_{\beta j}X_{ij}+\eta_{\beta j}X_{ij}$, which indicate the random utility terms including the error term (ε_{ij}) of logit model and the random utility terms are dependent on each other.

4 SURVEY DESIGN AND DATA ANALYSIS

4.1 *Survey design*

The purpose of this survey is to grasp the variation in airport access mode choice of passengers after airport rail is put into operation. Therefore, travel modes are considered in RP survey include cars, taxis, and airport buses. Travel modes considered in SP survey include cars, taxis, airport buses, and rails.

The survey was performed from June 8 to June 14, 2014. The survey period consisted of working days and weekends. The survey data were acquired from passengers who obtained their boarding passes or waiting for flights in Terminal 1 of Lukou Airport. We received 621 questionnaires, including 592 valid questionnaires. RP survey was performed in the form of the paper questionnaire. Survey participants' travel features were directly recorded. SP survey was performed in the form of electronic questionnaire. Survey participants selected their travel modes among the simulation results. The survey participants could select the existing travel mode or the future new travel mode. In the survey, the main mode and transfer mode as well as the simulated travel characteristics data were recorded.

4.2 *Data analysis*

The level of passengers' socioeconomic attributes is showed in Table 1.

Table 2 shows the change of passengers' travel behaviors after introducing a new travel mode.

About 30% of passengers will change their travel modes. About 30.6% of passengers who select airport bus and 21.9% of passengers who select car will switch to use airport rail, indicating that airport rail has the significant impact on the selection of travel mode. Especially passengers with private cars are more willing to select the efficient and cheap rail mode. However, the passengers who select taxis will not change their travel mode because they are mostly tourists and require a higher travel comfort.

Table 1. Analysis on passengers' socioeconomic attributes.

Socioeconomic attributes	Sample size (%)
Gender	
Male	58.2
Female	41.8
Age	
≤20	4.0
21–30	18.6
31–40	26.3
41–50	24.6
51–60	17.2
≥61	9.3
Occupation	
Staff	18.6
Servants	19.1
Business	34.9
Student	11.2
Labor	8.5
Other	7.7
Education	
Under junior	2.5
Senior	21.1
Undergraduate	52.6
Graduate	23.8
Household income/year (RMB)	
Under 5	3.5
5–8	15.2
8–12	32.6
12–20	21.3
20–25	17.2
25 and above	10.2
Number of cars	
0	33.7
1	62.2
2 and above	4.1

5 ESTIMATION RESULTS AND ELASTICITY ANALYSIS

5.1 *Choice of airport access mode*

Table 3 shows the regression results obtained by NL and MXL models (choosing car access mode as the baseline mode).

Results obtained by the two models are different. The likelihood function value and McFadden (2006) determination coefficient of MXL model are larger than those of the NL model, indicating that MXL model allows a better overall fitting effect.

The results of NL model show that β coefficient of car ownership and household income of airport bus and airport rail are negative. However, in the results of MXL model, the two factors of airport rail are not significant, indicating that the choice of airport rail is not directly related to car ownership or household income. Passengers with official business purposes prefer to use airport rail because the timing of airport rail is more precise. Passengers with frequent aviation experiences prefer to use taxis. However, results of MXL model show that the travel frequency of passengers has no significant influence on choice of airport rail. Moreover, if more luggage is consigned, passengers prefer to use cars or taxis. But in the results of MXL model, more accompanied luggage show no significant influence on the passengers' choice of airport rail. Results indicate that setting up the large luggage well is the key factor to improve travel proportion of airport rail.

5.2 *Elasticity analysis*

Tables 4 and 5, respectively, show the elasticity analysis results of travel time and travel cost. The negative (diagonal) mean elasticity estimates are

Table 2. Comparison between the current and the past choices of airport access mode.

	Current access mode choice under a new mode (sample size (%))				
Contents	Car	Taxi	Airport bus	Airport rail	Total
Past access mode choice					
Car	70.7	1.2	6.2	21.9	100
Taxi	0.5	89.3	3.8	6.4	100
Airport bus	1.1	5.9	62.4	30.6	100
Total	39.3	21.3	18.8	20.6	100

Table 3. Comparison of RP/SP combined data estimation by NL and MXL model.

	NL model		*MXL model*	
Explanatory variables	*β*	*T-value*	*β*	*T-value*
Non-random parameters				
Taxi	1.533	2.197	2.132	1.638
Airport bus	–0.334	–3.534	–0.212	–4.766
Airport rail	–0.692	–2.441	–0.115	–3.205
Socioeconomic attributes (access mode)				
Number of cars (airport bus)	–1.354	–2.117	–0.846	–1.947
Number of cars (airport rail)	–0.732	–1.980	–1.733	–0.972
Household income (airport bus)	–0.538	–1.910	–1.384	–1.856
Household income (airport rail)	–0.246	–2.126	–0.433	–0.542
Trip characteristics (access mode)				
Business purpose (taxi)	0.315	3.012	1.094	3.177
Business purpose (airport rail)	2.187	2.803	2.051	6.189
Frequency of travel (taxi)	0.653	3.544	1.088	2.144
Frequency of travel (airport rail)	–1.536	–3.635	0.154	1.168
Check-in luggage (taxi)	2.565	5.353	2.127	7.083
Check-in luggage (airport bus)	–0.947	–4.864	–1.620	–5.942
Check-in luggage (airport rail)	–2.453	–7.955	–1.982	–6.602
Carry-on luggage (taxi)	1.537	3.059	0.863	2.597
Carry-on luggage (Airport rail)	–1.148	–2.063	–1.835	–1.113
Random parameters				
In-vehicle time	–0.442	–6.643	–0.764	–8.954
Out-of-vehicle time	–0.286	–7.253	–0.527	–7.678
Travel cost	–2.047	–5.547	–2.462	–9.335
Test parameters				
Likelihood function value	–1508.2		–1473.2	
McFadden coefficient	0.6382		0.6946	

*Only significant variables were listed in the table.

Table 4. Direct and cross elasticity of airport access mode (travel time).

	Car		Taxi		Airport bus		Airport rail	
Mode	Out-of-vehicle time	In-vehicle time	Out-of-vehicle time	In-vehicle time	Out-of-vehicle time	In-vehicle time	Out-of-vehicle time	In-vehicle time
Car	–0.06	–0.14	0.04	0.12	0.04	0.12	0.05	0.12
Taxi	0.031	0.06	–0.04	–0.08	0.03	0.06	0.03	0.06
Airport bus	0.15	0.32	0.14	0.31	–0.26	–0.58	0.16	0.39
Airport rail	0.30	0.84	0.29	0.84	0.31	0.85	–0.40	–0.85

the direct elasticity, and the off-diagonal (positive) estimates are the cross elasticity between modes.

As shown in Table 4, the absolute value of the elasticity of in-vehicle time is significantly greater than that of out-of-vehicle time, indicating that in-vehicle time has the more significant influence on travel mode than out-of-vehicle time. The average cross elasticity of airport rail is significantly higher than that of other travel modes. If the

Table 5. Direct and cross elasticity of airport access mode (travel cost).

Mode	Car	Taxi	Airport bus	Airport rail
Car	–1.084	0.375	0.377	0.373
Taxi	0.821	–1.026	0.829	0.832
Airport bus	0.654	0.655	–0.473	0.660
Airport rail	0.276	0.273	0.277	–0.683

out-of-vehicle time of airport rail increased by 1%, the proportions of cars, taxis, and airport buses to be selected will respectively increase by 0.302%, 0.294%, and 0.315%. If travel time of airport rail can be significantly shortened in the future, passengers will not use cars or taxis, thus relieving airport expressway congestion.

Similar conclusions about travel cost are shown in Table 5. The absolute values of direct elasticity of cars and taxis are the largest (−1.084 and −1.026), indicating that when fuel fare, roll toll, parking fee, taxi fare, and other travel costs are increased, the proportion of passengers who select cars or taxis will significantly decrease. The results indicate that passengers who select taxis or airport buses are easily affected by travel cost. They are the most potential passengers of airport rail.

6 CONCLUSION

In this paper, we examined the travel behaviors of passengers in Nanjing Lukou Airport after the introduction of airport rail and analyzed the survey data respectively with NL and MXL models. Estimation results with SP/RP combined data showed that MXL model requires the more significant influencing factors and allows more precise estimating results for the two travel modes: airport rail and airport bus. MXL model results indicate that travel time and cost are the most important factors affecting passengers' selection of airport access modes. According to direct elasticity and cross elasticity analysis results with MXL model, on the basis of the consideration of existing traffic services, if we can shorten external time of airport rail traffic, passengers will not use cars or taxis and switch to high-capacity public traffic modes. The passengers who select taxis or airport buses are easily affected by travel cost. They are the most potential passengers of airport rail.

ACKNOWLEDGMENT

This study is financially supported by Project supported by the National Natural Science Foundation of China (Grant No. 51508274) and the Natural Science Foundation of Jiangsu Province of China (Grant No. BK20140821). The authors also would like to thank the Department of Transportation at Nanjing University of Aeronautics and Astronautics for their contribution to the survey.

REFERENCES

Becky, P.Y. 2008. Passenger's airport choice within Multi-Airport Regions (MARs): some insight from a stated preference survey at HongKong International Airport. *Journal of Transport Geography* 16(2): 117–125.

David, A. 2012. Accounting for scale heterogeneity within and between pooled data sources. *Transportation Research Part A* 46(3): 480–486.

Harvey, G. 1986. Study of airport access mode choice. *Journal of Transportation Engineering* 112(5): 525–545.

Hess, S. & Polak, J.W. 2005. Mixed logit modeling of airport choice in multi-airport regions. *Journal of Air Transport Management* 11(2): 59–68.

Lythgoe, W.F. & Wardman, M.R. 2002. Demand for rail travel to and from airports transportation. *Transportation* 29(2): 125–143.

McFadden, D. & Train, K. 2006. Measurement of Simulation Variance in Parameter Stimation [EB/OL]. *http://citeseer.ist.psu.edu/mcfadden95measurement.html.*

Mei, L. & William, H.K. 2010. Incorporating passenger perceived service quality in airport ground access mode choice model. *Transport Metrical* 6(1): 3–17.

Psaraki, V. & Abacoumkin, C. 2002. Access mode choice for relocated airports: the Athens International airport. *Journal of Air Transport Management* 8(2): 89–98.

Soushi, S., Peter, N., Eric, P. & Piet, R. 2014. Comparative performance analysis of European airports by means of extended data envelopment analysis. *Journal of Advanced Transportation* 48(3): 185–202.

Sun, Y.J. 2006. Access mode and departure airport choice in San Francisco Bay area. *Regional Science* 85(4): 543–567.

Train, K.A. 2010. Control function approach to endogeneity in consumer choice models. *Journal of Marketing Research* 47(1): 3–13.

Zhang, T.R., Yang, D.Y. & Zhao, Y.L. 2008. Comparative study of RP/SP combined data estimation between mixed logit and nested logit model. *Journal of Tongji University* 36(8): 1073–1078.

This page intentionally left blank

Civil Engineering and Urban Planning IV – Liu et al. (Eds)
© 2016 Taylor & Francis Group, London, ISBN 978-1-138-02903-3

Effect of rail transit box-girder with web opening on the structure noise radiation

Lin-Ya Liu & Dai-Yan Xu
Engineering Research Center of Railway Environment Vibration and Noise Ministry of Education, East China Jiaotong University, Nanchang, Jiangxi, China

ABSTRACT: Box-girder structures vibrate and make low frequency noises under the dynamic force of trains causing great harm to human health. A 32-m single-span box-girder for mass transit was introduced as the object and two three-dimensional finite element models were built on the two conditions of vent web and vent-free web. Based on the calculation of the vibrations of the box beam owing to the train load, acoustic finite element-boundary element coupling method was used to calculate and analyze features of the noise radiation of the structure generated by opening the box-girder of the web plate. The following conclusion was drawn: the structure noise of the box-girder is mainly distributed in 0–50 Hz and the peak frequency of noise radiation is 20 Hz; the web opening of the box-girder has a good noise reduction effect. These results can be used for box-girders in urban rail transit construction and provide a theoretical reference to reduce vibration and noise.

1 INTRODUCTION

Box-girders of rail transit vibrate and emit noises in the surroundings under loading of trains. Among these noises, the noise at the frequency range of 0~100 Hz was referred to as low-frequency noise (Liu et al. 2002; Zhu et al. 2005). Long wavelength characteristics of low frequency noise makes it hard to attenuate the process and can be harmful to the human body (Gao et al. 2010; Jiang et al. 2004). Therefore, it is necessary to research on the structure noise of box-girders for rail transit and to take effective controlling measures.

Many factors can impact low frequency vibration and noise radiations from rail box-girders, such as vehicle speed, the shape and structure of bridge as well as the different designs of viaduct (Ngai et al. 2002). The sections of box-girders and other factors can also affect the transmissibility of structure vibrations on viaduct. Train loading can cause vibrations in the tracks and lower part of the bridge thereof producing secondary radiation noise which mainly depends on the impedance of the bridge (Janssens et al. 1996). Greater impedance of the bridge will lead to less radiation noise (Li et al. 2013). The scheme opening on the cylindrical shell scheme can reduce low frequency noise, and this provides a way to reduce the bridge's structure noise (Xie et al. 2008). Opening holes on the wheels can help reduce sound radiation efficiency of the wheels by creating an "acoustic short circuit" from the outside and inside (Daneryd et al. 1998; Yang et al. 2014).

A 32-m simply supported box beam of the Wuhan-Guangzhou high-speed railway is taken as the research object in this paper. In engineering, the design of ventilation holes is commonly used in order to adjust the temperature difference of the inside and outside box-girder structure cavity and reduce non-loading cracks due to temperature change. This kind of design can also cause the "acoustic short circuit" to reduce the noise of box-girder radiation because of the reduction of radiating surface. Based on the above reasons, two kinds of three-dimensional finite element models were built on the conditions of vent web and vent-free web. Based on the calculation of vibration of the box beam with the train load, an acoustic finite element-boundary element coupling method was used to calculate and analyze features of structure noise radiation generated by opening the box-girder of the web plate.

2 ACOUSTIC FINITE ELEMENT-BOUNDARY ELEMENT COUPLING MODEL FOR BOX-GIRDER

2.1 *Finite element analysis theory for box-girders and model building*

In finite element analysis, based on the transient dynamics analysis of structure dynamic response, node displacement, stress, speed, acceleration, and other responses of structures changing with time were obtained under loading. Transient dynamic analysis is also known as time history analysis. Its basic motion equation is:

$$[M]\{\ddot{u}(t)\}+[C]\{\dot{u}(t)\}+[K]\{u(t)\}=\{F(t)\} \quad (1)$$

where [*M*], [*C*], and [*K*] stands for the mass matrix for the system, damping matrix, and stiffness matrix, respectively; $\{\ddot{u}(t)\},\{\dot{u}(t)\},\{u(t)\}$ stands for acceleration, velocity, and displacement vectors, respectively; $\{F(t)\}$ is the nodal loading vector of system.

To compare and forecast the noise radiation of the rail box-girder and structure vibration under train loads precisely, finite element software was used to develop the three-dimensional finite element model of box-girder: the span of girder is 32 m; modulus is 36.2 Gpa, density is 2500 kg/M^3, Poisson's ratio is 0.2, damping ratio is 0.03, and bearing stiffness is 3.38×10^9 N/m; vertical stiffness of the fastener is 6×10^9 N/m with a damping ratio of 10^4 Ns/m and fastener spacing is 0.625 m.

The study ignored the influence of the bridge pier and ground reflection. The box beam simulation was taken as the solid45 element, simply supported and fixed on both ends of the bridge, and the elastic support simulation was taken as the combin14 element.

After mesh, finite element model is shown (Fig. 1a). This paper aimed to analyze the noise radiation characteristics of web box beams with openings. The web hole radius was 0.1 m with a distance of 2 m in between. The abdominal perforation of the box beam finite element model is shown (Fig. 1b).

2.2 *Radiating noise calculation theory and boundary element model of box-girders*

According to the principle of the conservation of fluid medium and some basic assumptions about the sound wave, the Helmholtz equation of acoustic radiation expression of box-girder is deduced as follow:

$$(\nabla^2+k^2)p=0 \quad (2)$$

where ∇^2 is the Laplace operator; $k = w/c$ is the acoustic wave number; c is the sound velocity in air medium; w is the circular frequency; p is sound pressure.

On the ground where the overlapping points on the sound field and solid structure coupling boundary share the same boundary conditions, sound pressure on the boundary of sound field can be calculated after knowing the results of displacement response on the solid boundary; then it is possible to obtain the sound pressure of any point in the whole acoustic field.

Compared with using the data from experiments to solve vibration noise level in large-scale complicated structures, the results based on the finite element-coupled acoustic boundary element method has relatively high accuracy (Jiao et al. 2012).

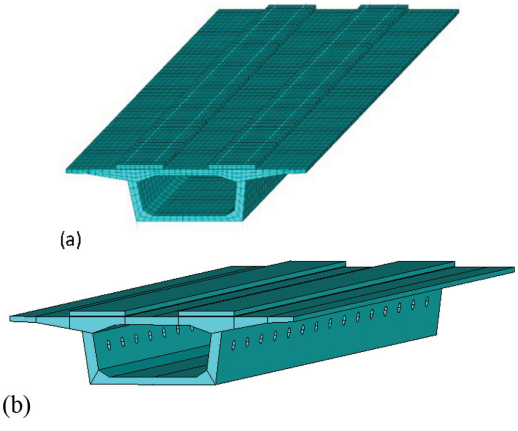

Figure 1. Finite element model for box-girder (a) and finite element model of box-girder with web opening (b).

3 SOUND PRESSURE AT THE FIELD POINT

In order to solve the vibration response of the box-girder under the train load, two CRH2 trains at 180 km/h speed, through the right line of single direction to simulate the real situation, are used to track irregularity taking the German low interference spectrum and using the method of Newmark–β to solve the bridge structure's dynamic response.

Taking the box-girder structure vibration acceleration as the initial condition of the acoustic boundary element, the sound pressure response of the sites was solved based on the acoustic boundary element software virtual.lab.

In order to study the sound field distribution at different distances from the bridge's centerline level, five locations were chosen along the horizontal. D1~D5 were listed at positions 1 m above the ground and perpendicular to the centerline of the line of distribution. The horizontal distances from the bridge centerline were 0 m, 5 m, 10 m, 20 m, and 25 m. Sound field outputs of box-girders are shown (Fig. 2a).

The noise emission at the sound pressure level of D1 and D5 are shown (Fig. 2b). D1 is located 1 m below the surface of box-girder. Figure 2b shows that the structure noise of the box-girder is mainly distributed in 0–50 Hz and the peak frequency of noise radiation is 20 Hz; the equivalent sound pressure level in web plate with openings in the box-girder has reduced at 20 Hz; but compared with the web plate without openings in

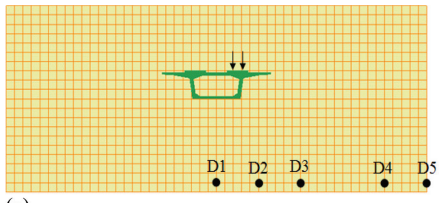

(a)

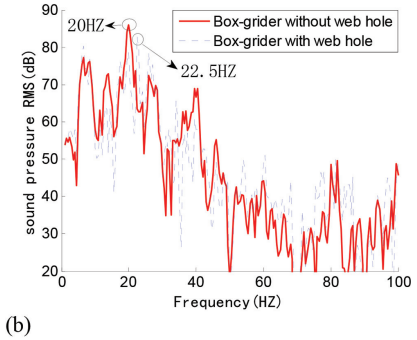

(b)

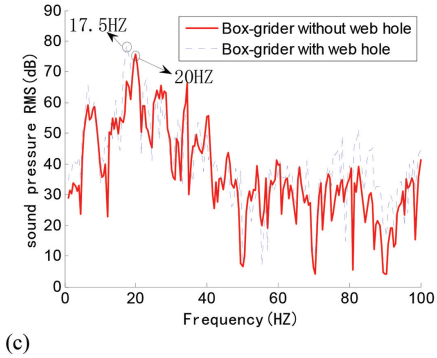

(c)

Figure 2. The site map of acoustic output of box-girders (a); noise emission sound pressure level of field point D1 (b) and noise emission sound pressure level of field point D5 (c).

the box-girder, the peak frequency of box-girder with web plate openings has increased to 22.5 Hz. Meanwhile, at the peak frequency, noise emission at the box-girder with web plate openings is lower than that of box-girder without web plate openings by about 3 db.

D5 is located 25 m away from the centerline of the box-girder horizontally. Peak frequency of noise radiation of the web plate with openings reached 17.5 Hz and decreases a little compared with the peak frequency of noise radiation of the web plate without openings (Fig. 2c); noise emission at the peak frequency increased and this can be attributed to the perforation aggregating transverse vibration and vertical vibration in center plates and flange end plates.

4 STRUCTURE NOISE REDUCTION EFFECT OF WEB PLATE WITH OPENINGS

In this paper, by using a 32-m single-span box-girder for mass transit as a study objective, we calculated and analyzed noise characteristics of box-girders having web plates with and without openings. The analysis showed that the peak frequency of noise radiation in web plate with openings increases at the near field points as shown (Fig. 3a); peak frequency of sound pressure level increases to 22.5 Hz at the D1 location blow bridge span and

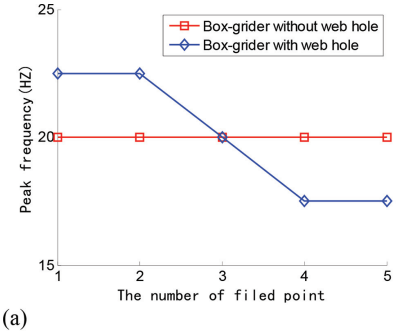

(a)

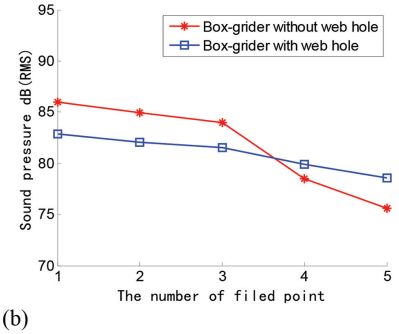

(b)

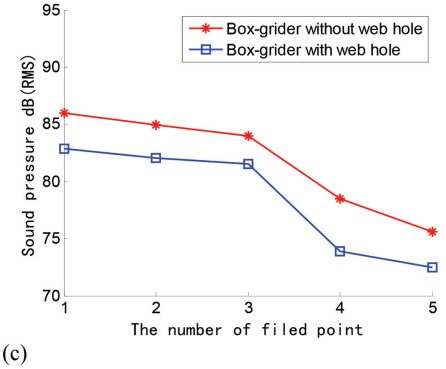

(c)

Figure 3. Field noise peak frequencies (a); peak noise level at the field (b) and the maximum sound pressure in range of 20–100 Hz (c).

Table 1. The maximum sound pressure in the range of 20–100 Hz.

Filed point	The maximum sound pressure (db)		
	Box-grider without web hole	Box-grider with web hole	Attenuation values
D1	86.0 (20 Hz)	82.8 (22.5 Hz)	3.16
D2	84.9 (20 Hz)	82.0 (22.5 Hz)	2.87
D3	84.0 (20 Hz)	81.5 (20 Hz)	2.45
D4	78.4 (20 Hz)	73.9 (20 Hz)	4.58
D5	75.5 (20 Hz)	72.4 (20 Hz)	3.1

at D2 5 m away from the centerline. Meanwhile peak frequency of sound pressure level decreases to 17.5 Hz at the D4 and D5 locations respectively by 20 m and 25 m away from the centerline.

Comparing the peak noise of every location, from D1 below the box-girder to D3 10 m away from the centerline, the sound pressure level of web plate with openings decreased by 3 db (Fig. 3b). Results show that by perforating the box-girder web, structure noise radiation in the near-field has better noise reduction results and far-field noise peak frequencies can also be reduced below the lowest frequency 20 Hz that the human ear can hear.

As the human ear's hearing threshold range is 20–2000 Hz, we discussed the sound pressure below 20 Hz frequency which is not very significant, considering the low frequency noise in the range of 20–100 Hz, get the maximum sound pressure level of sites D1–D5 are shown (Table 1), in diagram as shown (Fig. 3c).

Results show that considering the threshold range of the human ear, the maximum sound pressure of the box beam in midspan sites D1–D5 have a significant reduction effect (Fig. 3c). The best noise reduction effect is that the maximum sound pressure of the site D4 reduces to 4.58 db.

5 CONCLUSION

– The structure noise of the box-girder is mainly distributed in 0–50 Hz, which shows that the structure noise of the box beam is mainly about low frequency noise. This conclusion has very good consistency with (Gao et al. 2010).
– Measured opening holes on the web plate of box beam can effectively reduce the structure noise. This provides a new possible method of rail transit box-girder design to reduce the structure noise radiation.

ACKNOWLEDGMENTS

The research reported herein was supported by the National Natural Science Foundation of China (Grant No. 51268014).

REFERENCES

Daneryd, A. 1998. On Vibro-Acoustic and Mechanical Properties of Perforated Railway Wheel. *Proceedings of the 6th International Workshop on Railway and Tracked Transit System Noise.* Ile des Embiez: [s. n.]

Gao, F. 2010. Analysis and experimental study on the radiation noise of the elevated structures of Beijing metro line 5. *China Rail Way Science* 5(3): 134–139.

Janssens, M.H.A. 1996. A calculation model for the noise Irom steel railway bridges. *Journal of Sound and Vibration* 193(1): 295–305.

Jiang, B. 2004. Analysis of track structure noise of urban rail transit and related reduction measures. *Railway Engineering* 13(2): 62–65.

Jiao, Y.H. 2012. Vibration noise calculation and testing analysis of large vertical planetary transmission gearbox based on FEM and BEM. *Journal of Vibration and Shock* 4(3): 123–127.

Li, W.H. 2013. Analysis on vibration impedance and its transfer characteristics for rail transit viaducts. *Urban Rapid Rail Transit* 34(4): 29–32.

Liu, J.L. 2002. Vibration and noise of the urban rail transit. *Journal of Traffic and Transportation Engineering* 1(2): 29–33.

Ngai, K.W. 2002. Structure-noise and vibration of concrete box structure and rail viaduct. *Journal of Sound and Vibration* 255(2): 281–297.

Xie, W.P. 2008. Analysis of acoustic radiation from reinforced concrete cylindrical shell in air. *Noise and Vibration Control* 3(5): 109–112.

Yang, X.W. 2014. Effect of web hole on vibration noise radiation characteristics of railway wheel. *China Rail Way Science* 2(3): 58–64.

Civil Engineering and Urban Planning IV – Liu et al. (Eds)
© 2016 Taylor & Francis Group, London, ISBN 978-1-138-02903-3

A comprehensive model for facility location in disaster relief

Quan-Sheng Lei, Zhuo-Da Mo & Xiao-Guang Zhou
School of Automation, Beijing University of Posts and Telecommunications, Beijing, China

ABSTRACT: We consider a problem faced by international aid organizations after the occurrence of a natural disaster. Based on the domestic situations, a supply system with intermediate warehouses has to be established to provide affected people with relief commodities. Firstly we review the different location models in the literature that are related to regular emergency services. Secondly, based on Warehouse Location–Routing Problem (WLRP), we present a comprehensive model that describes the integrated supply chain operations in response to natural disasters. Compared to P-median problem, our proposed model can deliver the relief commodities faster to the disaster victims. Such a model provides the opportunity for a centralized operation plan that can eliminate delays and assign the limited resources in a way that is optimal for the entire system. Finally an illustrative example was discussed to show how the proposed models can be used to determine the facilities locations in disaster relief.

1 INTRODUCTION

In recent years, frequent natural disasters and man-made catastrophic have brought great loss to human beings. Every year, more than 500 disasters are estimated to strike our planet, killing 200 million others. After a natural disaster, the victims need to be provided with food, medicine and other relief goods, which should be dispatched to distribution centers in affected areas as soon as possible so that relief operations are accelerated. Emergency logistics is the bridge between preparedness and response, procurement and distribution-the critical role being coordination of all activities required to minimize the response time and to maximize the relief in a disaster zone.

However, due to the disaster, on one hand, massive demands often outstrip resources; on the other hand, the infrastructure in the affected region can be destroyed to a large extent. Therefore, a new supply (transportation) system including intermediate depots has to be established in order to be able to transport the relief goods from suppliers to the disaster victims. Referring to the logistics structure presented by Federal Emergency Management Agency (FEMA) in Abbas Afshar (2012), the transportation system that we consider is as follows. Relief goods are transported from suppliers to intermediate depots, then we deliver the relief goods to all victims in the affected areas from the intermediate depots. Suppliers are international airports, harbors, international aid organizations like the Red Cross, local emergency supplies warehouses, or local suppliers, where the latter are preferred in order to support the local economy.

Our model formulation will be based on the Warehouse Location–Routing Problem (WLRP) introduced by Perl & Daskin (1989). The standard WLRP formulation can be described as follows. Goods are to be shipped from a set of plants to one or more warehouses and from there to the customers. The number, size and location of the warehouses, the allocation of customers to warehouses and the delivery routes have to be determined with the objective of minimizing total cost. Total cost consists of warehousing cost and transportation cost. Warehousing cost is composed of the opening cost of a warehouse, which is a fixed cost, and throughput cost, which depends on the amount of goods shipped through a particular warehouse.

In order to make our model close to real-world, that is to say, we have to extend the formulation of the standard WLRP and to introduce problem specific constraints. Also in our case, customers or disaster victims, each of them having a given demand which can be adequately supplied by the supply sources, requires deliveries. However, contrary to the standard WLRP, there is no throughput cost of a warehouse. The objective of our model is a non-monetary benefit function and what we truly care is to minimize the total cost of time through suppliers to disaster victims.

The goal of this paper is to develop a comprehensive model that describes the integrated supply chain operations in response to natural disasters. This paper will offer a model that not only considers details such as resources allocation in the transportation system; but also considers finding the optimal location for temporary facilities as well as considering the allocation of customers to warehouses. Such a model provides the opportunity

for a centralized operation plan that can eliminate delays and assign the limited resources in a way that is optimal for the entire system.

Facility location problems have been extensively investigated by different researchers and practitioners in the field of emergency logistics. In the rest section, we review the prior work that is related to different emergencies settings.

On one hand, based on the objectives, these location models can be classified into covering models, P-median models, and P-center models.

Covering models are the most widespread location models for formulating the emergency facility location problem. Figure 1 presents an illustration of a feasible covering problem, where the coverage area of a facility is indicated by circles around the selected locations.

Another important way to measure the effectiveness of facility location is by evaluating the average (total) distance between the demand points and the facilities. This is P-median problem. This relationship applies to both private and public facilities such as supermarkets, post offices, as well as emergency service centers, for which proximity is desirable. We illustrate a P-median model in Figure 2.

In contrast to the P-median models, which concentrate on optimizing the overall performance of the system, the P-center model attempts to minimize the worst performance of the system and thus is also known as minimax model. In the last several decades, the P-center model and its extensions have been investigated and applied in the context of locating facilities such as Emergency Medical Service (EMS) centers, hospitals, fire station, and other public facilities. The objective function for the P-center model of the location solution in Figure 2 quantifies only the longest distance between a demand point and a selected location.

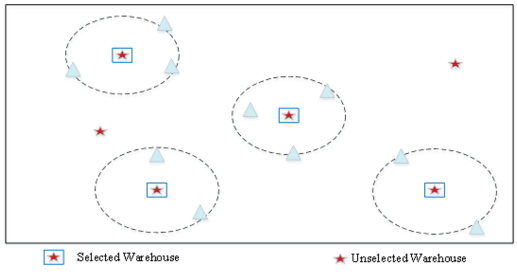

Figure 1. Covering problem example.

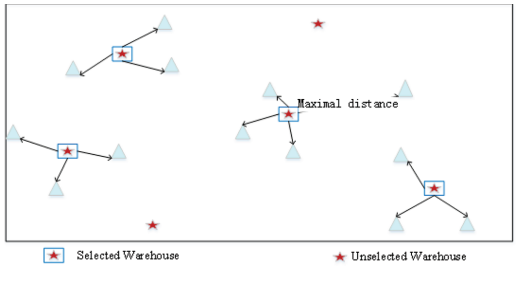

Figure 2. P-median/P-center problem example.

On the other hand, see Aakil M. Caunhye (2012), most facility location optimization models in emergency logistics combine the process of location with stock pre-positioning, evacuation, or relief distribution. The only location-alone models surveyed are published by Jia et al. (2005; 2007) and Dessouky et al. (2006). They are formulated as maximal covering location models with multiple quantity-of-coverage and quality-of-coverage requirements. Dessouky et al. (2006) additionally include a stochastic vehicle routing model to perform relief distribution.

Belardo et al. (1984) and Balcik & Beamon (2008) present such models, which deal with the assignment of stock to facilities such that demands can be satisfied and do not consider the routing of stock through a network, with the latter adding budgetary constraints and response time requirements. Iakovou et al. (1989) extend the framework to prescribe relief distribution by defining coverage in terms of a critical time to meet demands. This enables the investigation of arc-associated decision variables, such as the quantity of equipment to transport and time taken for such movement. Models that consider both relief distribution and stock pre-positioning aim to combine strategic and operational planning.

2 MATHEMATICAL MODEL FORMULATION AND NUMERICAL EXPERIMENT

In this section initially the notations and required parameters for the formulation are introduced. After that, the decision variables of the mathematical model are defined. Then the objective function formulation is presented followed by formulation and introduction of the constraints of the problem. Finally a set of numerical experiments are conducted to evaluate the features of the proposed formulation. The problem size is kept small so it can be solvable by commercial solver and the result can be analyzed easier. However the small-size problem still fully represents all elements of the proposed model.

2.1 *Notations*

$P = set\ of\ plants,\ i \in P\ are\ indices$

$W = set\ of\ potential\ depots,\ j \in W\ are\ indices$

$C = set\ of\ customers,\ k \in C\ are\ indices$

2.2 *Parameters*

$c_{ij} = time\ required\ to\ drive\ from\ node\ i\ to\ node\ j$

c_{jk} = *time required to drive from node j to node k*

f_j = *the fixed opening cost of a warehouse*

D_k = *demand of customer k*, $k \in C$

WN = *the maximum number of potential depots*

2.3 *Decision variables*

x_{ij} = *the amount of relief commodities delivered from node i to node j*

y_j = *the binary variable.*1 *if the potential depot is located at node j*; *equal to* 0 *otherwise*

z_{jk} = *the binary variable.* 1 *if a depot j services customer k*, *equal to* 0 *otherwise*

2.4 *Objective function*

$$Minimize \sum_{i\in P}\sum_{j\in W} c_{ij}x_{ij} + \sum_{k\in C}\sum_{j\in W} D_k c_{jk} z_{jk} + \sum_{j\in W} f_j y_j \quad (1)$$

$$s.t.: \sum_{j\in W} y_j \le WN \quad (2)$$

$$z_{jk} \le y_j \quad \forall\ j \in W,\ k \in C \quad (3)$$

$$\sum_{j\in W} z_{jk} \ge 1 \quad \forall\ k \in C \quad (4)$$

$$\sum_{i\in P} x_{ij} = \sum_{k\in C} D_k z_{jk} \quad \forall\ j \in W \quad (5)$$

$$x_{ij} \ge 0,\ \ y_j, z_{jk} \in \{0,1\} \quad \forall i \in P,\ j \in W,\ k \in C \quad (6)$$

The objective (1) is to minimize the total cost of time between the demand points and the supply points, including warehousing cost and total transportation cost. The transportation cost is composed of demand-weighted cost between the demand points and facilities and the cost between the supply points and the facilities. Constraint (2) states that there are WN warehouses to be located in a set W of possible locations. Constraint (3) allows assignment only to the sites at which facilities have been located. Constraint (4) ensures that there are at least one facilities servicing for one specific demand point. Constraint (5) is the flow equilibrium for each facility. Finally constraint (6) enforces the integrality of decision variables.

2.5 *Numerical experiment*

The experimental study complies with the logistic transportation system proposed above after disaster, and the scale of the problem is comparable to the real-world-size problems.

The following example is an imaginary scenario where a natural disaster strikes someplace. It is assumed that there are three supply points and five potential facilities as well as eight affected demand points. After the disaster, the number and the location of the warehouses should be determined by deciders. Then the relief commodities are to be shipped from supply points (such as airport, local suppliers) to one or more determined warehouses and from there to the customers. The input data required in mathematical model is presented in Tables 1 and 2.

CPLEX commercial solver is used to solve the MIP model formulations. Therefore, the facility location problem was solved to optimality using CPLEX12.5.1. Based on the input parameters defined above, we solve the classical P-median models of facility location problem for the emergency relief firstly. The solution is depicted in Figure 3. As the result shows, the serial number of selected warehouses are 1, 4, 5. The warehouse

Table 1. Time required from warehouse to customer and demand of customer.

	Customers—Time required from warehouse to customer								
Warehouses	C1	C2	C3	C4	C5	C6	C7	C8	Open cost
W1	5	10	7	20	30	40	45	50	1000
W2	40	20	30	30	40	55	50	70	1000
W3	20	20	15	10	10	15	25	25	1000
W4	30	20	15	3	5	5	15	15	1000
W5	50	45	40	20	15	5	5	5	1000
Demand	100	80	80	90	70	120	110	90	

Table 2. Time required from plant to warehouse.

Warehouses—Time required from plant to warehouse					
Plants	W1	W2	W3	W4	W5
P1	30	60	30	40	50
P2	40	70	25	35	45
P3	50	80	35	45	35

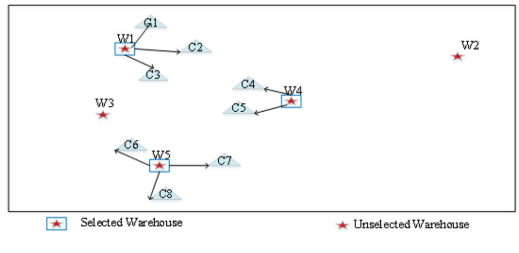

Figure 3. Solution of the P-median model.

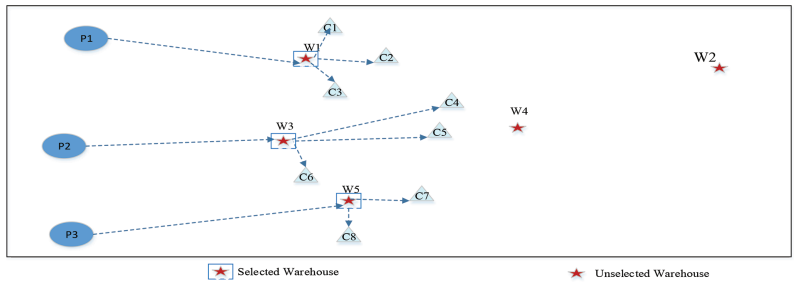

Figure 4. Solution of our proposed model.

1 serves a set of customers (1, 2, 3). The warehouse 4 serves a set of customers in (4, 5). The warehouse 5 serves a set of customers (6, 7, 8). The result is obvious, because the P-median problem minimize the average (total) distance between the demands and the selected facilities. But our proposed model minimize the total cost in the supply chain, i.e., including supply points, facilities and demand points. The solution is depicted in Figure 4. Contrary to the P-median model, the serial number of selected warehouses are 1, 3, 5. The warehouse 3 serves a set of customers (4, 5, 6), while the warehouse 5 serves a set of customers (7, 8). There is no doubt that our model minimizes the total cost of time in the transportation system.

3 CONCLUSIONS AND FUTURE DIRECTIONS

Facility location is so important issue in designing the emergency supply distribution system that it has been extensively investigated by different researchers and practitioners in the field of emergency logistics.

In this paper, we get the following conclusions. Firstly we should take into account the whole supply chain rather than optimizing the local commodities distribution between the demands and the selected facilities in disaster relief. Secondly, compared to the P-median problem, our proposed model, which objective is to minimize the total cost of time through the whole supply chain, can deliver the relief commodities faster to the disaster victims. Finally an illustrative example was discussed to show how the proposed models can be used to determine the facilities locations for rapid commodities supply distribution during the emergency with showing the efficiency increased by 5%.

An open research question is how to develop an overall response plan that takes into consideration all the different possible scenarios. Is it more efficient and cost effective to develop a single strategy that is robust to the different possibilities or is it better to develop a separate plan for each possible emergency? Another research direction is to develop efficient algorithms to solve the facility location problems.

ACKNOWLEDGMENT

We sincerely thank the editor. This work was supported by the Grain Welfare Industry Research Projects of China Grant No. 201313009–08 and the National Science Foundation of China Grant No. 71171022 and Industrial Project Foundation of Guizhou Province, China Grant GY [2013]3012.

REFERENCES

Afshar, A. & Haghani, A. 2012. Modeling integrated supply chain logistics in real-time large-scale disaster relief operations. *Socio-Economic Planning Sciences* 46(4): 327–338.

Balcik, B. & Beamon, B.M. 2008. Facility location in humanitarian relief. *International Journal of Logistics: Research and Applications* 11(2): 101e21.K. (unpublished).

Belardo, S., Harrald, J., Wallace, W.A. & Ward, J.A. 1984. Partial covering approach to siting response resources for major maritime oil spills. *Management Science* 30(10): 1184e96.

Caunhye, A.M., Nie, X.F. & Pokharel, S. 2012. Optimization models in emergency logistics: A literature review. *Socio-Economic Planning Sciences* 46(1): 4–13.

Dessouky, M., Ordóñez, F., Jia, H. & Shen, Z. 1984. Rapid distribution of medical supplies. In: *Delay Management in Health Care Systems.* New York: Springer.

Jia, H., Ordóñez, F. & Dessouky, M.A. 2005. Modeling framework for facility location of medical services for large-scale emergencies. *IIE Transactions* 39(1): 41e55.

Jia, H., Ordóñez, F. & Dessouky, M.M. 2007. Solution approaches for facility location of medical supplies for large-scale emergencies. *Computers & Industrial Engineering* 52(2): 257e76.

Perl, J. & Daskin, M.S. 1985. Warehouse location–routing problem. *Transportation Research* 19(5): 381–96.

Young, M. 1989. *The Technical Writer's Handbook.* Mill Valley, CA: University Science.

Civil Engineering and Urban Planning IV – Liu et al. (Eds)
© 2016 Taylor & Francis Group, London, ISBN 978-1-138-02903-3

A trans-shipment model for emergency relief distribution in unexpected disasters

Quan-Sheng Lei, Yan-Yan Wang & Xiao-Guang Zhou
School of Automation, Beijing University of Posts and Telecommunications, Beijing, China

ABSTRACT: We consider a two-stage supply system consisting of supply warehouses and demand points. According to the uncertainty of the actual demand, we use the fuzzy math method and assume the demand is a triangular fuzzy number for the model. And we only consider the transport cost and inventory cost; therefore, our objective function is to minimize their total. Then we solve the model by MATLAB; with specific parameters, we find that the objective function increases with increase in the confidence level and that the proportion of demand should be satisfied from supply warehouses to demand points. We also discovered that when a supply warehouse's stock is relatively large, the increase in its inventory holding cost will make selection a priority from the warehouse in the deployment. Therefore, the total transport quantity of the warehouse increases and at the same time the material allocation strategy changes.

1 INTRODUCTION

Over the past century, the cycle of all kinds of disasters has obviously shortened, and the frequency of their occurrences increased significantly. Last month, the 8.1-earthquake that occurred in Nepal caused heavy casualties. Not only did it damage the life of people in Nepal, but also it affected parts of the Chinese. In 2008 alone, 240,500 people lost their lives due to natural or man-made disasters. And the Great East Japan Earthquake in March of 2011 brought 15,883 confirmed deaths (Christine 2013). When an earthquake happens, immediate distribution of emergency supplies is pivotal in minimizing the damage and fatality. Therefore, it's the main focus of post-earthquake relief operations. Since time and resources are limited, emergency logistics decision-makers have to make optimal decisions in limited time, funds, and other resources.

The obvious feature of unexpected disasters is the uncertainty of demand. Beamon (2006) raised the concern that emergency supplies always showed that there were many types and numbers of supplies, demand had no law, and constraints were special. Through research, Arminas (2005) and Beamon (2004) came to the conclusion that time, variety, quantity, etc., were not accurately predicted but could only be forecast in probability. In recent years, because of incomplete information after a major natural disaster, Sheu (2010) created a dynamic demand management model for emergency logistics operations. He also verified the effectiveness of the model by an example and showed that the prediction error of the whole model was less than 10%. However, we will use fuzzy math, assume emergency supplies demand is a triangular fuzzy number, and then establish the model of the distribution of emergency supplies.

As regards distribution of emergency supplies, Yi and Kumar (2007) divided the original emergency logistics problem into two decision stages, namely: the building of vehicle routes and large scale distribution of emergency supplies, and then proposed a heuristic ant colony optimization method to solve it. By bringing stock of supplies and distribution model together, Lee (2007) raised different modes of the total costs. Through the study of the distribution of emergency supplies, Sowinski (2003) presented that different supplies should be identified by different labels, which can solve the problem of distribution; then on the basis of this, he discussed the inventory problem of emergency supplies. For the study of emergency supplies, Song (2005) studied the transport problem with the goal of minimizing transport costs under different constraints. In his research on inventory costs, Whybark (2007) presented that inventory costs under emergencies were different from the normal circumstances; the former needed to consider more questions. In the study, Santoso (2005) took into account the shortage of rescue and added it to the total costs; at the same time, he put forward the idea of integrating the emergency supply chain. In response to the distribution of supplies for a single disaster with limited time, quantity, and quality of resources, Fiedrich et al. (2000) gave a model that it transported supplies to disaster areas

by improving the quality of aid through effective use of resources in order to reduce death to the least. Likewise, in order to minimize the number of deaths, Fiedrich and Gehbauer (2000) applied the optimization model of distribution to multiple locations with limited time, quantity, and quality of resources after earthquake disasters. In 2004, in the article "Emergency Logistics Planning in Natural Disasters" published on operations, Linet and Turkish scholars, expanded the field of the study, abstracted the problem of emergency supplies distribution as the network flow question with multi-commodity and multi-mode, set the minimization of unsatisfied demand as the goal, then established a mixed integer programming model, and solved the model using the greed algorithm. Finally the model was tested and verified by the Turkey earthquake emergency deployment as an example. With respect to transport modes, Gulay et al. (2000) proposed a multi-tiered standard method to solve helicopter scheduling problems in relief, so that the number of helicopters and pilots dispatched to meet demand were at the lowest cost.

From the above study, we discover that although researches of emergency management are rich, the studies on stock of emergency supplies with quantitative research are lacking. According to the Federal Emergency Planning operational procedures, Nezih & Walter (2006), from the view of operation research and management science, reviewed emergency management issues related to the operation of the system and pointed out the importance of quantitative research was to improve emergency operation. Benita et al. (2006) established and analyzed three different inventory management strategies and applied these to the emergency work in Southern Sudan. This study also showed the importance of quantitative research for emergency management. In 2009, they also emphasized that the supplies chain should be coordinated. Therefore, in this paper we will study the distribution of stock in quantitative, which can provide valuable references for decision-makers.

Overall, the transport problem of emergency supplies is processed into the shortest transport path problem; then, we use various algorithms to get the optimal solution, or it is abstracted as a network flow problem of multi-materials and multi-modes, but there is little research on distribution. So the study of transfer of relief items is significant, and this not only helps to determine the quantity of overall supplies and delivery capabilities scientifically and reasonably, but also helps to reduce the cost of relief stored.

This paper mainly focuses on developing a transshipment model that describes the relief distribution in unexpected disasters. And the goal of our study is to minimize the sum of transport cost and inventory cost with a certain allocation plan. We study the distribution system of emergency supplies under emergency events. The system has two levels including warehouses and supply demand points. There is variation in the transport cost, and the total transport cost becomes bigger as transport quantity increases. At the same time, inventory holding cost is also in presence and the whole inventory cost increase with the goods in store. Therefore, the final result will be a compromise between transport cost and inventory cost in order to get the optimal objective function.

During the study, we select an earthquake as the example. Considering the uncertainty of demand, therefore, we use the fuzzy math method; then demand is assumed as a triangular fuzzy number. For the demand constraint, we assume the cargo from the warehouse to a demand point at a certain confidence level in order to simplify the model. After building the model, we use MATLAB software to solve the problem and reflect the scheduling decisions specifically. Then the results show that the optimal value of the objective function increases as the confidence level increases. When the stock of warehouse is relatively small, their inventory holding cost has no impact on transport quantity; however, when the stock is abundant, the total transport quantity in the warehouse increases as its inventory holding cost grows.

2 MODEL

This paper studies the distribution system of emergency supplies under the emergency event; reliefs are transported from the supply warehouses to demand points. When the inventory of warehouses remains after the deployment, there will be inventory costs. And when the inventory holding cost of warehouses is relatively large, in the distribution of supplies, it will give priority to allocate materials from the warehouses with a higher inventory holding cost for the deployment, but it will also be affected by the transport cost. Therefore, the final result will be a compromise between transport cost and inventory cost in order to get the objective function optimal. According to the characteristics of emergency logistics demand, we study the demand as a triangular fuzzy number.

2.1 *Parameters*

- c_{ik} the variable transport cost between warehouse i and demand point k per unit
- S_i the stock of warehouse i
- $\tilde{D}_k$ the fuzzy demand of demand point k
- h_i the inventory holding cost of warehouse i per unit

– Q_{ik} the transport quantity between warehouse i and demand point k
– y_i binary variable indicating if the warehouse i is needed to provide demand (value 1) or not (value 0)
– α the confidence level under the given constraints
– M a big number
– $Pos\{\cdot\}$ the fuzzy possibility of events in $\{\cdot\}$.

2.2 *Assumptions*

Assumption 1: Fuzzy demand D is a triangular fuzzy number, and $\tilde{D} = (d_L, d_M, d_R)$, its membership function is $u_{\widetilde{D(x)}}$, which is defined as follows:

$$u_{\widetilde{D(x)}} = \begin{cases} L(x) = \dfrac{x - d_L}{d_M - d_L} & d_L \le x \le d_M \\ R(x) = \dfrac{d_R - x}{d_R - d_M} & d_M \le x \le d_R \\ 0 & \text{otherwise} \end{cases} \quad (1)$$

Assumption 2: The total inventory of each warehouse is greater than the sum of all demands; unsatisfied demands will not exist, namely $\sum_{i=1}^{n} S_i \ge \sum_{k=1}^{n} \widetilde{D_k}$.

Assumption 3: Given θ is a non-empty set, $P(\theta)$ represents the power set of θ, and Pos is defined as a set function on $P(\theta)$, if Pos meets the following three conditions:

– $Pos(\theta) = 1$, namely the possibility of total set is 1;
– $Pos(\Phi) = 0$, namely the possibility of empty set is 0;
– For any set of set $\{A_k\}$ in the power set of $P(\theta)$, there is $Pos\{U_k A_k\} = \sup_k Pos\{A_k\}$;

Pos is called for the possibility measure. And there are the following definitions:

$$Pos\{\tilde{a} \le b\} = \sup\{\mu_{\tilde{a}}(x) \mid x \in R, x \le b\} \quad (2)$$

$$Pos\{\tilde{a} \ge b\} = \sup\{\mu_{\tilde{a}}(x) \mid x \in R, x \ge b\} \quad (3)$$

$$Pos\{\tilde{a} = b\} = \mu_{\tilde{a}}(b) \quad (4)$$

The objective function of the model is

$$\min\left[\sum_{i=1}^{n}\sum_{k=1}^{n} c_{ik} \cdot Q_{ik} + h_i \cdot \left(S_i - \sum_{k=1}^{n} Q_{ik}\right)\right] \quad (5)$$

As it can be seen from the above equation, we study the minimization of the total of transport cost and inventory cost, where $\sum_{i=1}^{n}\sum_{k=1}^{n} c_{ik} \bullet Q_{ik}$ shows the transport cost and $h_i \cdot (S_i - \sum_{k=1}^{n} Q_{ik})$ represents the cost of inventory when there are remaining goods after the deployment.

And the constraints of the model are the following:

$$\sum_{i=1}^{n} Q_{ik} = \widetilde{D_k} \quad k = 1, 2, ..., n \quad (6)$$

$$\sum_{k=1}^{n} Q_{ik} \le S_i \quad i = 1, 2, ..., n \quad (7)$$

$$\sum_{k=1}^{n} Q_{ik} \le M \cdot y_i \quad i = 1, 2, ..., n \quad (8)$$

$$Q_{ik} \ge 0 \quad i = 1, 2, ..., n \quad (9)$$

$$y_i \in \{0,1\} \quad i = 1, 2, ..., n \quad (10)$$

The existence of the fuzzy parameter $\widetilde{D_k}$ leads to no clear significance of constraints in the model. In order to solve this problem, we transform constraint (6) into the meaningful fuzzy chance constrain as follows:

$$Pos\left(\sum_{i=1}^{n} Q_{ik} = \widetilde{D_k}\right) \ge \alpha \quad k = 1, 2, ..., n \quad (11)$$

Constraint (11) states that the transport supplies from supply warehouses to demand points should meet the confidence level α at least to satisfy the demand; Constraint (7) ensures the transport quantity of goods from each warehouse is less than its inventory; Constraint (8) represents only used warehouses will be assigned with demand points; Constraint (9) is a non-negative constraint and Constraint (10) is an integer constraint.

In order to solve fuzzy chance constrained model, we use the theory of possibility degree and convert the chance constrained to the corresponding definition of equivalence classes.

Lemma 1 Given the triangular fuzzy number $\tilde{r} = (r_L, r_M, r_R)$, its membership function is $\mu_{\tilde{r}}(x)$, then for any given confidence level $a(0 \le \alpha \le 1)$, if and only if $Pos\{\tilde{r} = b\} \ge \alpha$ is:

$$\begin{cases} b \ge (1-\alpha) \cdot r_L + \alpha \cdot r_M \\ b \le (1-\alpha) \cdot r_R + \alpha \cdot r_M \end{cases} \quad (12)$$

So the fuzzy chance constraint $Pos\,(\sum_{i=1}^{n} Q_{ik} = \widetilde{D_k}) \ge \alpha$ can be transformed to the clear equivalence classes as follows:

$$\begin{cases} \sum_{i=1}^{n} Q_{ik} \ge (1-\alpha) \cdot D_{kL} + \alpha \cdot D_{kM} & k = 1, 2, \ldots, n \\ \sum_{i=1}^{n} Q_{ik} \le (1-\alpha) \cdot D_{kR} + \alpha \cdot D_{kM} & k = 1, 2, ..., n \end{cases} \quad (13)$$

Then the fuzzy chance constrained programming model can be transformed into a deterministic model.

3 NUMERICAL ANALYSIS

In this section, we will set some specific parameters to analyze the model in order to better compare the objective function changes under different circumstances. And we will analyze confidence level and inventory holding cost.

We assume that there are three supply warehouses and four demands points, namely $i = 1, 2, 3$ and $k = 1, 2, 3, 4$, respectively.

The parameters of the variable transport cost between warehouse i and demand point k per unit c_{ik} in Table 1, the stock of warehouse i S_i in Table 2, the fuzzy demand of demand point k $\tilde{D}_k$ in Table 3, and the inventory holding cost of warehouse i per unit h_i in Table 4 are as follows:

3.1 *The analysis of confidence level*

In the process of effect of confidence level for the objective function, because emergency supplies has an important influence on logistics, we take four confidence level values: 0.80, 0.85, 0.90, and 0.95 for research. Meanwhile, we set the inventory holding costs of the three warehouses as follows: $h_1 = 20, h_2 = 10, h_3 = 15$, and then use MATLAB to get the results as in Table 5.

Table 1. Values of variable transport cost.

c_{ik}	Demand point 1	Demand point 2	Demand point 3	Demand point 4
Warehouse 1	100	50	150	80
Warehouse 2	180	120	70	50
Warehouse 3	60	70	120	100

Table 2. Values of the stock of warehouse.

Warehouse i	1	2	3
S_i	500	4000	700

Table 3. Values of demand.

Demand point k	1	2	3	4
$\tilde{D}_k$	(400, 500, 550)	(600, 800, 900)	(650, 700, 800)	(850, 1000, 1200)

Table 4. Values of inventory holding cost.

Warehouse i	1	2	3
h_i	20	10	15

From Table 5, we can see that the optimal value of the objective function grows as the confidence level increases. This is because the higher the confidence level is, the more demands need to be satisfied, then the increase of transport cost is higher than the reduction of inventory cost, which leads to the conclusion that the objective function value becomes bigger. However, because the difference of fuzzy demand is relatively not large, the transport quantity changes little under different confidence levels. From the table, we see the value of a column is relatively small; therefore, our model needs to be improved in the further.

3.2 *The analysis of inventory holding cost*

Due to inventory holding cost, transport quantity from supply warehouse to demand point is small, which results the inventory cost becoming bigger. However, our objective function is the minimization of the total of transport cost and inventory cost; therefore, the change in inventory holding cost will change the transport quantity. In the study of the effect of inventory holding cost on transport quantity, we assume the confidence level is 0.90, then set two the warehouses' inventory holding costs from the three as 15, then change the value of the third warehouse, and observe the changes. The results are as follows:

From the data in Figures 1–3, we can see that when the stock of warehouse 1 and 3 is relatively small, their inventory holding cost has no impact on transport quantity. This is because when their inventory holding cost is zero, the inventory stock is all shipped out; even if their inventory holding cost continues to increase, no excess inventory can be deployed. But the stock of warehouse 2 is relatively abundant; when its inventory holding cost increases, demand will be shipped on priority from warehouse 2 in order to get the optimal objective function. So the inventory holding cost of warehouse 2 has an influence on the deployment of the transport system, namely the total transport quantity of warehouse increases when its inventory holding cost increases. Meanwhile, the transport quantity of warehouse 1 and 3 will change. We can get that when the stock of warehouse is relatively small, their inventory holding cost has no impact on transport quantity; however, when the stock is abundant, the total transport quantity of

Table 5. Values of objective function with different α.

α	Value of objective function	Q_{11}	Q_{12}	Q_{13}	Q_{14}	Q_{21}	Q_{22}	Q_{23}	Q_{24}	Q_{31}	Q_{32}	Q_{33}	Q_{34}
0.80	225850	174	0	0	326	296	760	0	644	10	0	690	0
0.85	227510	174	0	0	328	305	770	0	650	8	0	692	0
0.90	229180	172	0	0	328	313	780	0	657	5	0	695	0
0.95	230840	172	0	0	328	321	790	0	664	3	0	697	0

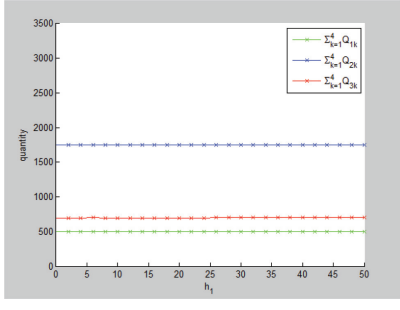

Figure 1. The total transport quantity of each warehouse in h_1.

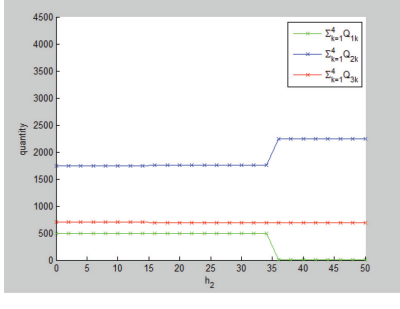

Figure 2. The total transport quantity of each warehouse in h_2.

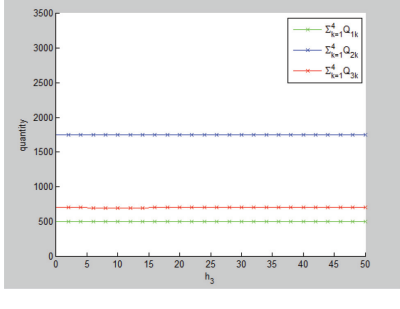

Figure 3. The total transport quantity of each warehouse in h_3.

the warehouse grows when its inventory holding cost increases.

4 CONCLUSION

In this paper, we focused on the deployment of emergency supplies in unexpected disaster situations. And we established an earthquake model as an example, set specific parameters to solve the model, and analyzed the same. Our model only consists of two stages, namely, demand supply warehouses and demand points; in the case of only considering transport cost and inventory cost, we get the minimization of total cost. And we assume the total supply quantity is more than the total demand. Based on the uncertainty of unexpected disasters, we use the fuzzy math method and assume the demand is a triangular number and adopt a certain confidence level to simplify the model in order to get the result. In numerical analysis, we assume that there are three supply warehouses before the earthquake and after there are four demand points, and then we allocate the relief items from warehouses to demand points reasonably. In this process there are variable transport costs and inventory holding costs. Thus, if inventory holding cost of some warehouses is relatively large, it will preferentially allocate goods from these warehouses. Our objective function is the minimization of the total of transport cost and inventory cost; therefore, we use an algorithm to get the balance between them in order to get the optimization. After using MATLAB to solve the model, we analyze the effect of confidence level and inventory holding cost for the entire system and get the conclusion that the value of objective function increases as the confidence level increases. However, the effect of inventory holding cost for the deployment is related to the stock of warehouses. When the stock is relatively small, at first the total transport quantity of the warehouse equals its maximum stock, inventory holding cost has no impact on the deployment at this time. But when the stock of warehouse is relatively large, the increase of inventory holding cost will lead to ship reliefs from the warehouse on priority in order

to get the optimization of the objective function, namely, the total transport quantity of the warehouse increases when its inventory holding cost increases. Then at the same time the material allocation strategy changes.

Although this study has some practical significance, due to the limit of technical and capabilities, there are still extensions on the subject. For example, when analyzing the effects of different confidence levels on the objective function, we find the transport quantity from a warehouse to a demand point is relatively small, although, now the model gets the optimization, but in reality this is unreasonable. That's why our model needs further optimization. Besides, we only study the single-period and single-material; in further study, it can be extended for multi-periods and multi-materials.

ACKNOWLEDGMENT

We sincerely thank the editor. This work was supported by the Grain Welfare Industry Research Projects of China (Grant No. 201313009-08) and the National Science Foundation of China Grant No. 71171022 and Industrial Project Foundation of Guizhou Province, China Grant GY [2013] 3012.

REFERENCES

Arminas, D. 2005. Supply lessons of tsunami aid. *Supply Management* 10(2): 14.

Beamon, B.M. 2004. Humanitarian Relief Chains: Issues and Challenges. *Proceedings of the 34th International Conference on Computers and Industrial Engineering, San Francisco, CA, USA, 2004*. Seattle, WA: University of Washington.

Beamon, B.M. & Kotleba, S.A. 2006. Inventory modeling for complex emergencies in humanitarian relief operations. *International Journal of Logistics: Research and Applications* 9(1): 1–18.

Beamon, B.M. & Kotleba, H.A. 2006. Inventory management support systems for emergency humanitarian relief operations in South Sudan. *The International Journal of Logistics Management* 17(2): 187–212.

Balcik, B, Beamon, B.M., Krejci, C.C., et al. 2010. Coordination in humanitarian relief chains: Practices, challenges and opportunities. *International Journal of Production Economics* 126(1): 22–34.

Christine, T., 2013. Mayor Briefs Indonesian Leader on Reconvery. *http://www.japantimes.co.jp/news/2013/11/22/national/mayor-briefs-indonesian-leader-on-recovery-2/*.

Fiedrich, F., Gehbauer, F. & Rickers, U. 2000. Optimized resource allocation for emergency response after earthquake disasters. *Safety Science* 35(1): 41–57.

Gulay, B., Linet, O. & Ahmet, C. 2002. An interactive approach for hierarchical analysis of helicopter logistics in disaster relief operations. *European Journal of Operational Research* 140(1): 118–133.

Lee, Y.H., Jung, J.W. & Jeon, Y.S. 2007. An effective lateral transshipment policy to improve service level in the supply chain. *International Journal of Production Economics* 106(1): 115–126.

Linet, O. & Ediz, E. 2004. Emergency logistics planning in natural disasters. *Annals of Operations Research* 129(1–4): 217–245.

Nezih, A. & Walter III, G.G. 2006. OR/MS research in disaster operations magement. *European Journal of Operational Research* 175(1): 475–493.

Santoso, T., Ahmed, S., Goetschalckx, M. & Shapiro, A. 2005. Astochastic programming approach for supply chain network design under uncertainty. *European Journal of Operational Research* 167(1): 96–115.

Sheu, J.B. 2010. Dynamic relief-demand management for emergency logistics operations under large–scale disasters. *Transportation Research Part E* 46(1): 1–17.

Song, M.A. 2005. *Constructing Modes of Urgent Rescue Logistics Distribution System (in Chinese)*. Taiwan, China: Institute of transportation, National Communication University.

Sowinski, L.L. 2003. The lean, mean supply chain and its Human counterpart. *World* 16(6): 18.

Wei, Y. & Kumar, A. 2007. Ant colony optimization for disaster relief operations. *Transportation Research Part E* 43(6): 660–672.

Whybark, D.C. 2007. Issues in managing disaster relief inventories. *International Journal of Production Economics* 108(1): 228–235.

Civil Engineering and Urban Planning IV – Liu et al. (Eds)
© 2016 Taylor & Francis Group, London, ISBN 978-1-138-02903-3

A cellular automata model for indoor evacuation based on artificial potential field and ant colony algorithm

Zhi-Wei Ye, Yu-Jie Yin, Xin-Lu Zong, Ming-Wei Wang & Ying-Li Jiang
Hubei University of Technology, Wuhan, Hubei, China

ABSTRACT: For handling the problem of evacuation routing inside buildings, a cellular automata model for indoor evacuation based on artificial potential field and ant colony algorithm is proposed in this paper. In this model, the actual region is modeled using cellular automata. In order to make full use of the cognition to known environment and guide the ant search, the integrated heuristic information is constructed using the potential field direction of node and the distance between node and the goal according to the potential field distribution of node locations. Finally, the model has been employed to simulate the whole evacuation process in a layer of teaching building. The experimental results show that the proposed model could get the optimal evacuation path effectively, which is better than the basic ant colony algorithm. It has better convergence and optimization precision and is able to produce a feasible evacuation planning route for crowds in buildings.

1 INTRODUCTION

During emergency accidents in public places (e.g. buildings, stadiums, subway stations and airports), if people fail to judge emergency exits, avoid obstacles, and escape from the place, they may be injured and even die. Therefore, in recent years, more and more attention is being paid to personnel safety evacuation problems in public places. In addition to large-scale military exercises and survey statistics, experimental simulation is one of the most important evacuation research methods. Evacuation simulation can be used to analyze the evacuation process of people and reduce the evacuation time required in danger. Some crowd evacuation models on evacuation work are put forward (Zheng et al. 2009). Among them, by defining simple rules and parallel computing updates, the cellular automata model can simulate pedestrian behavior. It is widely used in pedestrian evacuation dynamics (Song et al. 2013). In fact, building evacuation is a complex issue. Many problems are considered in the process of evacuation, including walking path for each evacuees, the time taken for entire evacuation, congestion of people. The diversity in evacuation requirements cannot be satisfied by traditional shortest path methods. But intelligent algorithms have good inspiration mechanisms, can optimize different evacuation targets to meet the needs of evacuation, and can better conform to practical evacuation applications.

Ant Colony Optimization (ACO) is a intelligent optimization algorithm for simulating ants' foraging behavior (Dorigo 1996). It was used to solve the traveling salesman problem initially. ACO has also been applied to the study of emergency evacuation in recent years. Ant colony algorithm is a good method of simulation; it is suitable for solving path planning in emergency evacuations (Zong et al. 2014). At the same time, due to its positive feedback characteristics and local search ability, it has good robustness and strong ability of global optimization. And it combines with other algorithms easily. However, it also has the shortcomings of slow convergence rate and premature convergence. Artificial Potential Field (APF) is a planning method for simulating electric potential field distribution (Khatib 1986). This method is simple in structure and is widely used for real-time obstacle avoidance and smooth path planning. People move in the direction of the potential field force under the combination of attraction and repulsion. The direction of movement can make people avoid known obstacles and reach the exit (Tan & Chen 2009).

An important way to improve algorithm performance is by combining different methods and carrying complementary advantages (Duan et al. 2013; Georgoudas et al. 2010; Selem et al. 2011). For handling the evacuation path planning problems in buildings, this paper establishes the environment model of cellular automata and combines the ant colony optimization algorithm and artificial potential field. The advantage of artificial potential field for rapid obstacle avoidance improves the transition rules of ants, and capabilities of ant

path search in turn speed up the optimization of ant colony algorithm. Meanwhile, the potential field force of artificial potential field, as a part of the ant heuristic information, guides ant searching, is easy to fall into local minimum points, and can solve problems of unreachable destinations. Finally the effectiveness of the proposed method is validated by simulation experiments.

The rest of the paper is organized as follows: In section 2, our improved model is proposed. The movement rules and algorithm steps are described. In section 3 simulation data and results analysis are shown. Finally, experimental conclusions are given.

2 CELLULAR AUTOMATA MODEL BASED ON ANT COLONY OPTIMIZATION AND ARTIFICIAL POTENTIAL FIELD

2.1 *Cellular automata model*

The cellular automata model has simulated the process of pedestrians' evacuation in buildings as follows. The building is described by a two-dimensional cellular space. The size of a cell corresponds to 0.5 × 0.5 m. Cellular automata have three states: occupied by obstacles, occupied by pedestrians, and free. Each cell has a different status and attributes. The neighborhood considered in the model is Moore's Neighborhood that includes eight cells surrounding the central cell. The central cell arrives to an adjacent empty cell in one time step.

2.2 *Ant colony optimization based on artificial potential field*

We propose Ant Colony Optimization based on Artificial Potential Field (ACO-APF) to optimize the pedestrian path on cellular automaton model for evacuation.

Initially, people are randomly placed in the cells. At t moment, person k's attraction potential energy and repulsion potential energy on cell i are given by equations (1) and (2).

$$U_{att}(i) = \frac{1}{2}\xi\rho^2{}_g(i) \tag{1}$$

$$U_{rep}(i) = \begin{cases} \frac{1}{2}\gamma\left(\frac{1}{\rho(i)} - \frac{1}{\rho_0}\right)^2, & \rho(i) \le \rho_0 \\ 0, & \rho(i) > \rho_0 \end{cases} \tag{2}$$

$\rho_g(i)$ is the Euclidean distance of cell i and goal point q_g. ξ,γ are direct proportion gain coefficients accordingly. $\rho(i)$ is the shortest distance of person k and obstacles, ρ_0 is the maximum distance of obstacles' influence on people. The attraction and repulsion of person k on cell i corresponding with potential negative gradients, are given by equations (3) and (4).

$$\overrightarrow{F_{att}}(i) = -\mathrm{grad}[U_{att}(i)] = \xi(i - q_g) \tag{3}$$

$$\begin{aligned}\overrightarrow{F_{rep}}(i) &= -\mathrm{grad}[U_{rep}(i)] \\ &= \begin{cases} \frac{\gamma}{\rho^2(i)}\left(\frac{1}{\rho(i)} - \frac{1}{\rho_0}\right)\nabla\rho(i), & \rho(i) \le \rho_0 \\ 0, & \rho(i) > \rho_0 \end{cases}\end{aligned} \tag{4}$$

$\nabla\rho(i)$ is the vector of obstacle to cell i; the total potential energy of the comprehensive factors for pedestrians on cell i is expressed by equation (5).

$$U_i = \sum U_{att}(i) + \sum U_{rep}(i) \tag{5}$$

By this time, the path selection probability of person k on cell i is given by equation (6).

$$p_{ij}^k(t) = \begin{cases} \frac{[\tau_{ij}(t)]^\alpha \times [\eta_{ij}(t)]^\beta}{\sum_{s \in J_i} [\tau_{is}(t)]^\alpha \times [\eta_{is}(t)]^\beta}, & \text{if } j \in \boldsymbol{J}_i \\ 0, & \text{otherwise} \end{cases} \tag{6}$$

α and β are the important parameters of pheromone and heuristic, J_i is a neighbor set of cell i. The heuristic function of ACO $\eta_{ij}(t)$ is updated by making use of the artificial potential field's percepted exits and obstacles, as given in equation (7).

$$\eta_{IJ}(t) = \frac{1}{\min\left\{d_{j,exits} \mid j \in J_i\right\} \times U_j} \tag{7}$$

U_j is the total potential energy of cell j, $d_{j,exits}$ is the shortest distance of cell j to exits. All pedestrians update the pheromone by equations (8) and (9) after one complete cycle.

$$\tau_{IJ}(t + \Delta t) = (1 - \rho) \times \tau_{IJ}(t) + \sum_{k=1}^{m} \tau_{IJ}^k(t + \Delta t) \tag{8}$$

$$\tau_{ij}^k(t + \Delta t) = \begin{cases} \frac{1}{L_k}, & edge(i,j) \in path_k \\ 0, & \text{otherwise} \end{cases} \tag{9}$$

L_k is the path length of person k in the loop. The pheromone will evaporate over time; ρ is the evaporation parameter of $\tau_{ij}, \rho \in [0,1]$. The more the pheromone of the path, the shorter the distance of the path, and the probability of choosing this path by person k will be greater. Because of this positive

feedback mechanism, all people will be attracted to the shortest path.

In the evacuation process of the ant colony, we set up the following rules:

A cell can only accommodate one pedestrian.

Pedestrians can walk in free cells, not stay in cells occupied by obstacles.

Pedestrians indoors can move to the cells of corridors and exits; pedestrians in corridors can only move toward exits and cannot move back indoors.

If more than one person competes with the same free cell at the same time, it chooses a person's entry randomly; others choose cells again, until all persons find themselves only the goal cells in the next moment on the grid.

When pedestrians can't choose the current optimal cell, they choose a sub-optimal cell without considering the exit directions.

Pedestrians can't choose the cell which is the step on the cell, unless the other cells can't be accessed.

3 EXPERIMENTS AND RESULTS

The potential energy field gain coefficient. The classrooms modeled in this paper are located on the first floor of an actual teaching building. Four classrooms are described on the grid. The classroom has two exits. The sides of the corridor are the evacuation destinations, as shown in Figure 1. Figure 2 is the plane potential energy distribution. The experimental processes were implemented by MATLAB R2011b and run on a PC with 3.20 GHz, 3.47 GB RAM. In the cellular automata model based on ACO-APF and ACO, the parameters used were set as follows:

$$\alpha = 2,\ \beta = 10,\ \rho = 0.1,\ NC_{\max=100},\ \xi = 20,\ \gamma = 1.$$

Pedestrians are scattered into the plane. We tested the independent experiment 10 times with ACO-APF and ACO algorithms. Pedestrians are evacuated with the corresponding algorithms. Their running at one time, 500 people's evacuation path length with iteration, and evacuation time step with iteration under different algorithms is shown on Figure 3.

From Figure 3, the evacuation path length and time step of two algorithms decreased with the increase in iterations below 50, and after 50 iterations the results of the two tended to be stable. From final iteration results, the evacuation performance of ACO-APF was better than the evacuation performance of ACO, the best path length is 1.522*104 m, and the best evacuation time step is 68 steps.

In Table 1, we listed the average path lengths and optimal path lengths of different people 10 times using two algorithms. With the increase in the number of people, the evacuation path length became longer. For a different number of people, the ant colony optimization based on the artificial potential field had a better solution for average

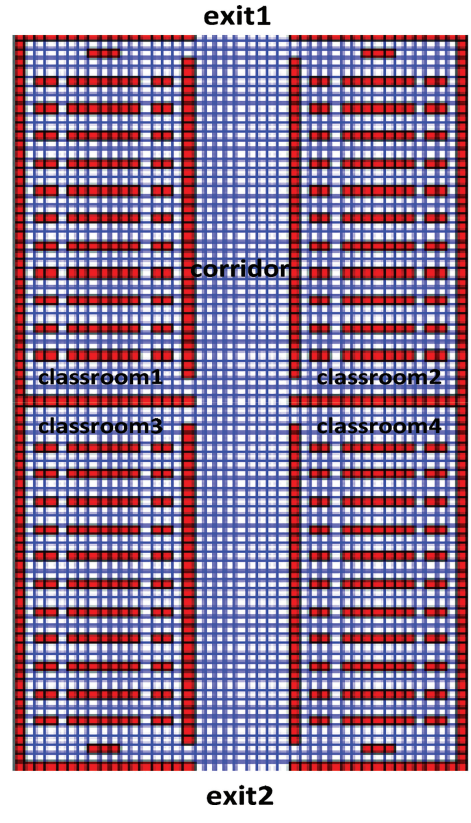

Figure 1. The layout of classrooms.

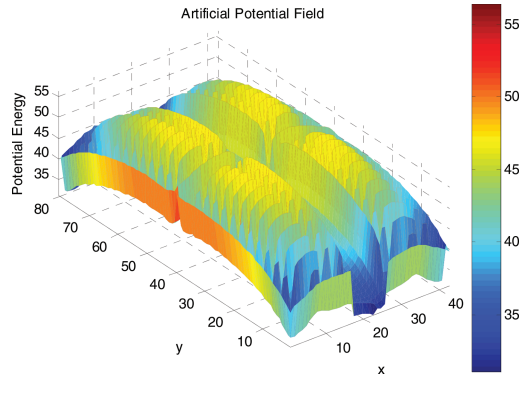

Figure 2. The classroom's potential energy distribution.

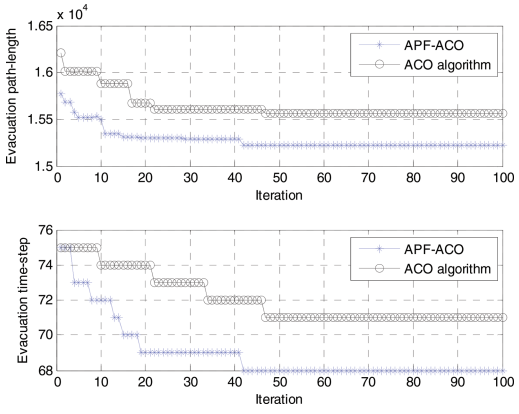

Figure 3. Five hundred people's evacuation path length and time step with iteration.

Table 1. Evacuation path lengths of different people with two algorithms.

Members	Evaluation criterion	ACO/m	ACO-APF/m
200	Average path	5509	5365
	Optimal path	5258	5075
500	Average path	15667	15326
	Optimal path	15564	15222
800	Average path	32351	31751
	Optimal path	31772	31098
1000	Average path	48873	47332
	Optimal path	47710	46423

Table 2. The evacuation time step of different algorithms.

Algorithm	Members	Average time steps of classrooms empty/time-step
ACO	200	55
	500	69
	800	98
	1000	118
ACO-APF	200	54
	500	68
	800	96
	1000	120

path and optimal path, and the path is relatively stable.

In Table 2, the average time-step of different people obtained using two algorithms 10 times were listed. From the table, we can see that the evacuation time step was longer with the increase in the number of people. The evacuation time-step of ant colony optimization based on artificial potential field was slightly better than basic ant colony optimization algorithm on the whole. The efficiency evacuation in emergency also improved.

Combining Tables 1 and 2, the proposed ant colony optimization based on artificial potential field in cellular automata evacuation model has a better effect than basic ant colony optimization on total evacuation path and evacuation time. Evacuation path length had decreased to save evacuation time. This model provides an effective solution for indoor evacuation.

4 CONCLUSION

Emergency evacuation model and evacuation path planning are the important key issues of an emergency system. This paper combines the ant colony algorithm and artificial potential field in a cellular automata model for indoor evacuation. It can be used to optimize the dynamic evacuation path. This method improves the heuristic function and makes full use of the cognition of the known environment to guide ant searching. It improves the speed of algorithm convergence and simulates the personnel congestion problems effectively. Experiment results show that this model has a better performance than the basic ant colony optimization algorithm in terms of evacuation path and evacuation time for solving evacuation problems. In addition, it also needs to further analyze the unsafe factors in different environments. There are many factors of pedestrians' routing selections. It remains to be further researched in the future.

ACKNOWLEDGMENT

This work was supported by Natural Science Foundation of China (Grant Nos. 61202287 and 41301371), the General Program for Natural Science Foundation of Hubei Province in China (No. 2015CFB594), and the scientific research foundation Natural Science Foundation of Hubei University of Technology (Grant #BSQD12034).

REFERENCES

Dorigo, M., Maniezzo, V. & Colorni, A. 1996. Ant system: Optimization by a colony of cooperating agents. *IEEE Transactions on Systems, Man, and Cybernetics, Part B: Cybernetics* 26(1): 29–41.

Duan, P., Xiong, S. & Li, H. 2013. Improved multiple ant colony algorithm for emergency evacuation in large building. *Jisuanji Yingyong Yanjiu* 30(2): 357–363.

Georgoudas, I.G., Kyriakos, P., Sirakoulis, G.C. & Andreadis, I.T. 2010. An FPGA implemented cellular automaton crowd evacuation model inspired by the electrostatic-induced potential fields. *Microprocessors and Microsystems* 34(7): 285–300.

Khatib, O. 1986. Real-time obstacle avoidance for manipulators and mobile robots. *The International Journal of Robotics Research* 5(1): 90–98.

Selem, B., Neji, Z., Jelassi, S. & Bouziri, H. 2011. Artificial Neural Networks for microscopic evacuation system. *2011 International Conference on Communications, Computing and Control Applications (CCCA), Hammamet, 3–5 March 2011*.

Song, Y., Gong, J., Li, Y., Cui, T., Fang, L. & Cao, W. 2013. Crowd evacuation simulation for bioterrorism in micro-spatial environments based on virtual geographic environments. *Safety Science* 53(2): 105–113.

Tan, X. & Chen, D. 2009. A Hybrid Approach of Path Planning for Mobile Robots Based on the Combination of ACO and APF Algorithms. *International Workshop on Intelligent Systems and Applications, ISA, Wuhan, 2009*.

Zheng, X., Zhong, T. & Liu, M. 2009. Modeling crowd evacuation of a building based on seven methodological approaches. *Building and Environment* 44(3): 437–445.

Zong, X., Xiong, S. & Fang, Z. 2014. A conflict–congestion model for pedestrian–vehicle mixed evacuation based on discrete particle swarm optimization algorithm. *Computers & Operations Research* 44(2): 1–12.

This page intentionally left blank

Civil Engineering and Urban Planning IV – Liu et al. (Eds)
© 2016 Taylor & Francis Group, London, ISBN 978-1-138-02903-3

Intercity rail transit pricing based on the Ramsey model

Qing-Yu Luo, Lie Mang, Hong-Fei Jia & Shu-Tao Gao
College of Traffic, Jilin University, Changchun, Jilin, China

ABSTRACT: There has been a long-existing problem, which will balance the social benefits with the normal profits of an enterprise by a reasonable pricing. This article tries to develop a scientific pricing system based on the Ramsey model for a new transit system. Although, many kinds of pricing methods are provided to the transport system, the intercity rail transit is more complicated. In this article, a set of Ramsey pricing method is put forward. It includes the establishment of the Ramsey pricing model and the calibration of parameters. Finally, a case study for pricing Qingdao–Rongcheng intercity rail transit is carried out to realize the application. The Ramsey pricing model is helpful in meeting the requirements of the rail transit enterprises and the intercity transit passengers.

1 INTRODUCTION

In recent years, the intercity rail transit has become a new traffic mode that deals the trips between urban agglomerations. Along with the popularity of the new mode, the pricing problem has been focused. For a long time, the pricing of the rail transit has been controlled by the government in China and was deemed to be lack of the theoretical basis. This caused a low fare level and restricted the development of the rail transit. It is a complicated problem to make a reasonable fare to balance the social benefits with the normal profits of the enterprises. The purpose of this article was to develop a scientific and reasonable pricing system that combines with the mathematical model. In this article, we use the Ramsey model for the intercity rail transit pricing, in order to form a reasonable pricing system and improve the competitiveness of the intercity rail transit.

2 LITERATURE

Initially, the researches on the rail transit pricing are often related with some literatures about the transit mode split. Nuzzolo et al. (2000) presents a choice model that can be used to simulate the impacts on users' choices by the variations of some railway service characteristics (e.g., timetable, travel time, and prices) in a medium-long distance. Kraus and Yoshida (2002) present the commuter's time-of-use decision into a model of optimal pricing and service in urban mass transit.

Gradually, researchers develop many kinds of pricing methods. Vuuren (2002) tried to establish the link between the well-developed economic theory of optimal pricing, the empirical analysis of the demand price elasticity, and the marginal cost estimates for the Netherlands Railways, and set up a pricing model according to the relationship between transport supply and demand. Si and Gao (2001) proposed a bi-level programming model for the rail transit pricing system and a three-tier programming model by considering the passenger flow distribution. Game theory was applied to the rail transit pricing by Levinson (2005). At the same time, he developed the two-side game to the tripartite game. Qi (2006) applied the system dynamics to transportation pricing and set up a pricing model.

Furthermore, Wardman (2006) estimated an enhanced model for forecasting railway demand and to explaining higher levels of growth in the 1990s in Great Britain. It points out that different pricing strategies have a direct influence on the total demand. Cantos-Sanchez et al. (2009) developed an interurban passenger transport pricing model based on the differences of characteristics. They attempted to adjust the fare rate to achieve the maximization of social welfare. Wang and Li (2011) applied the logit pricing model into the Wuhan–Guangzhou rail transit, and provided a basis for the reasonable pricing to intercity rail transit.

Although there are all kinds of pricing methods, some weaknesses hinder their application. Some methods are difficult in finding out the quantification functions and the calibration methods of parameters. And some methods require a large amount of samples and basic information. So, scholars began to search a pricing method to overcome those weaknesses. As a result, Zhou (2001) introduced the Ramsey theory into the subway pricing, and used the Ramsey peak pricing

to adjust the passenger flow in the Mass Transit Railway Corporation. Zhao (2005) applied the Ramsey model to make a price for the light rail of Chongqing, China. The Ramsey model has proved its way in finding the balance point between the maximum public welfare and the sustainable production of manufacturers. Chang and Li (2007) used the Ramsey model to set a price for the subway of Tianjin, and it was successful to bring the diversion of passenger flow and the maximum of social welfare. But all those researchers have not given a complete methodology to the pricing problem.

Moreover, the Ramsey pricing can be applied in the rail system of many cities, but the rail transit system between cities is different from that in a city. The Ramsey pricing method for the intercity rail transit system need to solve more complicated problems, such as pricing system, parameter determination, and so on. This paper attempts to give a complete methodology to the intercity rail transit pricing.

3 METHODOLOGY

3.1 *The Ramsey pricing theory*

The Ramsey pricing model is a neo-classical model of economic growth, which is based primarily on the work of Frank P. Ramsey (1928). It is not only considering the balance between income and expenditure, but also realizing the optimization of resource allocation. The price of this model is around the marginal costs. If the fixed investment in an industry is not big, and its marginal cost is incremental from a social perspective, the optimal price is equal to the marginal cost. If the fixed investment in the industry is great, such as telecommunications, subway, and light rail, the marginal cost is decreasing. In that case, the pricing according to the marginal cost will no way make the operators or producers recover their costs. Thus, a company can only accept the price greater than the marginal cost to balance the profit and loss. So, the Ramsey pricing is a kind of subprime pricing method which pursuits the suboptimal of social welfare.

The huge fixed costs of the intercity rail transit system lead to that the average cost is much greater than the marginal cost. If the marginal cost pricing is applied, the enterprise will suffer huge losses, the rail transit system will be too crowded, and some accidents might occur. On the contrary, if all the fixed costs are borne by passengers at the beginning of pricing, the fare will be too high and out of the reach of people. It is not conducive to the development of the intercity rail transit system. Therefore, we must make a reasonable price, not only to cover the normal costs of the rail transit enterprises, but also to maximize the social benefits. The Ramsey model is a good way to solve this problem.

3.2 *The Ramsey pricing model*

Now for a new intercity rail transit system, suppose the average fare of Ramsey is M, the passenger volume of rail transit is Q, the average income is MQ, and the operating cost is $C(Q)$. The condition of the balance of income and expenditure is that of $MQ - C(Q) = 0$. According to the knowledge of economics, the social welfare function is that $W = \int M(Q)dQ - C(Q)$. Therefore, in order to maximize the benefits with the balance of payment, the benefits can be calculated by the Lagrange multiplier method as follow:

$$F = \int M(Q)dQ - C(Q) + \lambda[MQ - C(Q)] \tag{1}$$

where λ is a parameter. Take the derivative of Equation (1), and let it be 0, then

$$\frac{\partial W}{\partial Q} = M - C'(Q) + \lambda\left[M + Q\frac{\partial M}{\partial Q} - C'(Q)\right] = 0 \tag{2}$$

The operating cost C and the passenger volume Q should satisfy the equation as follow:

$$C(Q) = bQ^e \tag{3}$$

where b and e are constants. With the fixedness of the constant cost, the marginal cost mc is the derivative of the operating cost for passenger volume:

$$mc = C'(Q) = \frac{\partial C(Q)}{\partial Q} = \frac{\partial (bQ^e)}{\partial Q} = beQ^{e-1} \tag{4}$$

The price elasticity of demand is calculated as;

$$\varepsilon = -\frac{M}{Q}\cdot\frac{\partial Q}{\partial M} \tag{5}$$

So the Equation (2) can be simplified as follow:

$$\frac{M - mc}{M} = \frac{\lambda}{1+\lambda}\cdot\frac{1}{\varepsilon} \tag{6}$$

Define the Ramsay coefficient $\eta = \frac{\lambda}{1+\lambda}$, then

$$\frac{M - mc}{M} = -\frac{\eta}{\varepsilon} \tag{7}$$

The average Ramsey fare can be calculated as:

$$M = mc \cdot \frac{1}{1+\frac{\eta}{\varepsilon}} = mc \cdot R \tag{8}$$

where $R = 1+\frac{\eta}{\varepsilon}$.

As in the Equation (8), according to the Ramsay pricing, the fare is the product of the marginal cost and a coefficient factor. Combining Equation (4) with Equation (7), we get the final Ramsay model as follow:

$$M = mc \cdot \frac{1}{1+\frac{\eta}{\varepsilon}} = beQ^{e-1}\frac{1}{1+\frac{\eta}{\varepsilon}}. \tag{9}$$

3.3 *Parameter calibration*

3.3.1 *Forecasting the future passenger volume*

– *Forecasting the sharing rate*

Passengers face with the choice of traffic modes when they travel between cities. The process of choosing mode is a multi-objective decision-making problem. Passengers will choose a certain traffic mode among the intercity rail, the common railway, and the highway bus in China. Combining with the personal characteristics and travel purposes, all relevant attributes, such as punctuality, economy, rapidity, convenience, and comfort, are considered. Passengers would like to select the mode of the maximized integrated utility.

There are many methods to forecast the sharing rate. Overcoming the massive questions of aggregate disaggregating models, disaggregate models have been used in various fields. The representative of disaggregate model, the Logit model, has a strong persuasion in the individual behavior research. And it has a simple structure and is easy to operate. Therefore, the Multinomial Logit (MNL) model as in the Equation (10) is chosen to forecast the sharing rate.

$$P_i = \frac{e^{U_i}}{\sum e^{U_i}} = \frac{e^{\Sigma\omega_{ij}\cdot r_{ij}}}{\sum e^{\Sigma\omega_{ij}\cdot r_{ij}}} \quad i \in I \tag{10}$$

where P_i is the probability of the i-th traffic mode chosen by travelers;

I is the traffic modes between cities can be chosen, including the intercity rail, the common rail, and the highway bus;

U_i is the utility function;

ω_{ij} is the weight of the service attribute (punctuality, rapidity, convenience and comfort);

r_{ij} is the normalized value that the j-th service attribute of the i-th traffic mode.

The characteristics of various traffic modes and their service attributes as shown in Table 1.

To calculate and normatively process each service attribute values in Table 1, the normalized attribute will be acquired.

The attribute value of rapidity
= Distance/Average speed + Connection time
(In this paper, the distance is 300 km).

The attribute value of comfort
= Per capita space + 1/Vibrational acceleration

The attribute value of convenience
= 1/Transfer times + 1/Transfer time + 1/Ticketing time

The normalized method is changing the attribute values of each service into scale [0, 1]. The attribute value of the maximum benefit is set as 1, the other attribute values are converted by the ratio of the maximum benefit, then r_{ij} can be set as in Table 2.

In summary, combining r_{ij} with ω_{ij}, the sharing rate of the intercity rail transit will be forecasted by the MNL model.

Table 1. Traffic modes and their service attributes.

Mode	Intercity rail	Common rail	Highway bus
Rapidity			
Average speed (km/h)	200	70	90
Connection time (h)	0.8	0.6	0.5
Comfort			
Per capita space (m^2)	3.0	1.4	1.6
Vibrational acceleration (m/s^2)	3.1	4.5	2.1
Punctuality			
On-schedule rate (%)	97	70	80
Convenience			
Transfer times	2	1	1
Transfer time (h)	0.8	0.5	0.5
Ticketing time (h)	0.2	0.2	0.1

Table 2. Normalized attribute values.

Mode	Intercity rail	Common rail	Highway bus
Rapidity	1.000	0.470	0.601
Comfort	1.000	0.486	0.514
Punctuality	1.000	0.722	0.825
Convenience	0.519	0.615	1.000

– *Forecasting the passenger volumes*
By collecting the past passenger volume, determine the OD volumes of each nodal cities located in new intercity rail transit, then, selecting the appropriate model to forecast OD volume between each nodal cities, combine the sharing rate, intercity rail transit volume of the nodal cities will be forecasted.

3.3.2 *Determining the marginal cost*
When the fixed cost remains unchanged, the marginal cost is the derivative of the operating cost to the passenger flow, take the logarithm of both sides of Equation (3),

$$\ln C(Q) = \ln b + e \ln Q \tag{11}$$

Select an intercity rail lines which have been built and put into operation to get the similar marginal cost. The selected line must meet the following requirements: (1) be similar to the topographic features of new urban rail transit area; (2) be similar to the urban nature; and (3) be similar in trip modes. With the regression analysis of the existing passenger volume and operating costs, the constants b and e can be determined, then the marginal cost of the intercity rail transit can be obtained.

3.3.3 *Determining the price elasticity of demand*
In the theory of price, the concept of elasticity is the sensitivity of demand or supply on price or other factors. In the quantification of the demand elasticity, the price variables used to include many factors, such as speed, comfort, punctuality, and convenience, etc. Those factors are interconnected and affect each other. We derive the price elasticity of demand by the MNL model.

According the Equation (10) and the derivation of r_{ij}, the price elasticity of demand can be getting it from from Equation (12).

$$\varepsilon = \sum\nolimits_j \left(-\frac{r_{ij}}{P_i} \cdot \frac{dP_i}{dr_{ij}} \right) = \sum \omega_{ij} r_{ij} (1 - P_i) \tag{12}$$

3.4 *The fare rate of the intercity rail transit*

3.4.1 *Determining the average travel distance*
Choose the important nodal cities on the rail traffic route (A, B, and C), and the OD passenger volume of A, B, and C can be respectively obtained through investigation. Taking an example of A, get the passenger product volume from A to B and the passenger attract volume from B to A, make the average value as the passenger volume between A and B (q_{AB}). Similarly, q_{AC} and q_{BC} can be obtained. Set the distances between AB, AC, and BC as d_{AB}, d_{AC}, and d_{BC}, the average travel distance is:

$$\bar{d} = \frac{q_{AB} \cdot d_{AB} + q_{AC} \cdot d_{AC} + q_{BC} \cdot d_{BC}}{q_{AB} + q_{AC} + q_{BC}} \tag{13}$$

3.4.2 *Determining the fare rate*
The equation of fare rate (q) is:

$$q = \frac{M}{\bar{d}}. \tag{14}$$

4 CASE STUDY

Qingdao–Rongcheng intercity rail transit in China is provided as an example. And we choose Qingdao, Weihai, and Yantai, those three cities as nodes of the network. Weihai–Qingdao and Weihai–Yantai are taken as the OD parts. The Ramsey model is used to make the price of Qingdao–Rongcheng intercity rail transit.

First of all, an investigation of passenger travel is conducted in Weihai. The passenger volume of Weihai was 17,760 in 2013. By determining the number of samples within the sample to ensure 90% confidence interval, the sample size is 285, the actual feedback is 283, and there are 276 effective questionnaires among the all questionnaires. The effective rate is 97.5%. The contents of the questionnaires include the transport service attributes (rapidity, comfort, punctuality, and convenience) ranked by passengers. The normalized result of survey is showed in Table 3. Since there is no common railway from Weihai to Qingdao and Yantai, the intercity rail transit and the highway bus are considered as two options. The service attribute values of different traffic modes and the weights from Weihai to Qingdao and Yantai are shown in Table 3.

Take the parameters above into the MNL model, the sharing rate of Qingdao–Rongcheng intercity rail transit is 54.1%.

A trend extrapolation can be forecasted by the SPSS software. Until 2015, the result of passenger volume from Weihai to Qingdao and Yantai is 18,323,000 people. Then, use the sharing rate to forecast the intercity rail transit passenger volume

Table 3. Service attribute values of two modes from Weihai to Qingdao and Yantai.

Attribute	Rapidity	Comfort	Punctuality	Convenience
Intercity rail	1.000	1.000	1.000	0.519
Highway bus	0.601	0.514	0.825	1.000
Weight value	0.310	0.230	0.230	0.230

from Weihai to Qingdao and Yantai. There are 9,913,000 people.

Weihai, Qingdao, and Yantai have many hills, and those three cities are all big or great cities. The rail transit from Guangzhou to Zhuhai is similar to the one from Weihai to Qingdao and Yantai, in terms of the terrain, the characteristics of the city and the travel ways of citizens. So the marginal cost of the intercity rail transit from Guangzhou to Zhuhai can be compared with that of Qingdao–Rongcheng.

The historical passenger volume and operate costs of Guangzhou–Zhuhai intercity rail transit are analyzed and shown in Figure 1.

From above, we can get that $b = 70{,}369$, $e = 0.54$, and bring these to the Equation (4), the marginal cost can be get as $mc = 22.99$ yuan.

From the Equation (12), combine with the statistic in Table 1, the price elasticity of demand can be getting as $\varepsilon = -0.41$. It satisfies the relevant literature for the price elasticity of demand in –0.5 to –0.2 (Litman 2004).

The relationship between the Ramsey fare and the Ramsey coefficient is pointed out in Figure 2.

Figure 2 shows that the value of the Ramsey coefficient should below 0.35, according to our research, the value is identified as $\eta = 0.179$. From the Equation (9), the final average Ramsey fare $M = 40.69$ yuan per people.

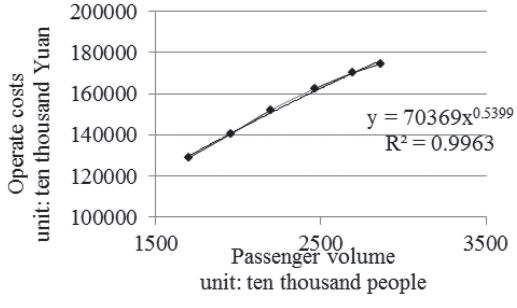

Figure 1. The relationship between passenger cost and the passenger volume.

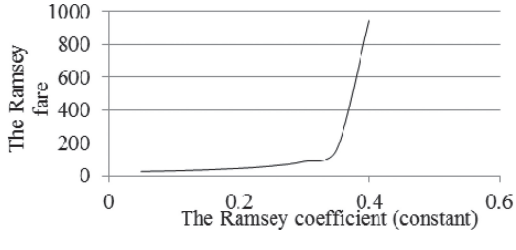

Figure 2. The relationship between the Ramsey fare and the Ramsey coefficient.

Based on the statistic of OD from Weihai, Qingdao and Yantai, from the Equations (13) and (14), the average distance of Qingdao–Rongcheng intercity rail transit can be calculated as 105 km, and the fare rate of Qingdao–Rongcheng intercity rail transit is 0.387 yuan per people per km.

5 CONCLUSION

This article builds up a pricing methodology based on the Ramsey model for the intercity rail transit system. In our methodology, the average fare can be evaluated using passenger volume, marginal cost, price elasticity of demand, and travel distance. The methods of measuring those variables are defined in detail and the relevant parameters are calibrated. The priority of our methodology lies in the following aspects.

First, the Ramsey model is superior to other pricing methods because it is helpful to find the balance between the sustainable benefits of manufacturers and the maximum public welfare. With the quantitative data collected by our questionnaire and interview surveys, the pricing method has been applied and verified by Qingdao–Rongcheng intercity rail transit. It turns out that applying Ramsay model to the monopoly welfare, such as intercity rail transit, can add an extra fare on the basis of marginal cost. For the enterprise operation of the intercity rail transit, the extra fares not only make up for the loss, but also reflect the social welfare.

Second, in our methodology, the new Ramsey pricing method contains the prediction of future passenger volume and the determination of the marginal cost, the price elasticity of demand and average travel distance. That is to say, most of the influential factors of fare have been considered and given definite calculation methods. The Ramsey pricing can reflect the reality accurately and make the conclusions more convincing. It provides a targeted and operational pricing method for the intercity rail transit system.

Furthermore, we can also adjust the fare rate combining with the characteristics of distance and passenger volume in different seasons and cities. The fare rate forecasted in this article is for the early operation stage of a new intercity rail transit. The Ramsey coefficient could be properly adjusted to forecast the medium and long-term fares. It can satisfy different pricing targets.

ACKNOWLEDGMENT

We would like to thank the fund project: National Natural Science Foundation of China (70901032)

and China Postdoctoral Science Foundation (2012M510884) for their help and support.

REFERENCES

Cantos-sánchez, P., Moner-colonques, R., Sem-peremonerris, J.J. & álvarez-sanjaime, Ó. 2009. Alternative pricing regimes in interurban passenger transport with externalities and modal competition. *Regional Science and Urban Economics* 39(2): 128–137.

Changli & Lilihong. 2007. Study of Tianjin metro ticket pricing based on Ramsey pricing model. *Railway Engineering cost Management* 22(6): 12–17.

Kraus, M. & Yoshida, Y. 2002. The commuter's time-of-use decision and optimal pricing and service in urban mass transit. *Journal of Urban Economics* 51(1): 170–195.

Levinson, D. 2005. Micro-foundations of congestion and pricing: A game theory perspective. *Transportation Research Part A: Policy and Practice* 39(7): 691–704.

Litman, T. 2004. Transit price elasticities and cross-elasticities. *Journal of Public Transportation* 7(2): 3.

Lixaimiao & Wang, H.J. 2011. Calculation and study of passenger flow transfer to Wuguang DPL based on logit mode. *Hunan Vocational College of Railway Technology* (2): 23–28.

Luo, C.Z. 2014. *Research on the Effects of Guangzhou-Zhuhai Intercity Rail on Highway Passenger Transport and Its Countermeasures*. Xi'an: Chang'an University.

Nuzzolo, A., Crisalli, U. & Gangemi, F. 2000. A behavioural choice model for the evaluation of railway supply and pricing policies. *Transportation Research Part A* 34(5): 395–404.

Qi. Y.J. 2006. *Research on the Development of Urban Rail Transit Fare in China*. Xi'an: Chang'an University.

Ramsey, F.P. 1928. A contribution to the theory of taxation. *The Economic Journal* 37(145): 47–61.

Si, B.F. & Gao, Z.Y. 2001. Sensitivity analysis for the relationship between passenger-ticket price and passenger volume of different sorting trains. *Journal of Northern Jiaotong University* 49–53+69.

Vuuren, D. 2002. Optimal pricing in railway passenger transport: theory and practice in the Netherlands. *Transport Policy* 9(2): 95–106.

Wardman, M. 2006. Demand for rail travel and the effects of external factors. *Transportation Research Part E: Logistics and Transportation Review* 42(3): 129–148.

Zhao, L.J., Chen, Y.H. & Che, T.Y. 2005. Study on the pricing plan of Chongqing light rail. *Railway Transport and Economy* 27(11): 40–42.

Zhou, L. 2001. Application of Ramsey pricing pattern for subway pricing. *Technology & Economy in Areas of Communications* 3(4): 47–49.

Civil Engineering and Urban Planning IV – Liu et al. (Eds)
© 2016 Taylor & Francis Group, London, ISBN 978-1-138-02903-3

A model of avoiding traffic accidents between drivers and pedestrians in signalized intersections in VANETs

Jun Sun
School of Information Engineering, Yangzhou University, Yangzhou, Jiangsu, China

ABSTRACT: With the development of society, more and more families have their own private vehicles. Thus, the total number of vehicles has been greatly increased in recent years, which has a bad effect on the process of achieving each family's convenient life aims due to traffic jams and traffic accidents. Especially, the traffic accidents that occurred around the intersections between drivers and pedestrians have already become serious society issues recently. Therefore, it is necessary to give useful measures to avoid these kinds of accidents. Therefore, according to the authors' knowledge, there have been no related measures until now, and currently it is just based on the personal judgments of the drivers and pedestrians. Hence, this paper gives a feasible scheme for how to avoid the traffic accidents between drivers and pedestrians in signalized intersections. A Markov chain-based scheme was proposed for the calculation of the traffic accident probability in the signalized intersections. Simulations were conducted to verify the performances of the proposed scheme, and its superiority could be observed by comparing with the situation of without accident avoiding schemes in typical urban road network scenarios.

1 INTRODUCTION

Along with the development of our community, more and more vehicles are being possessed by many families. However, the road capacity cannot match the number of vehicles, which has resulted in many traffic jams and traffic accidents.

Public roads consist of road conditions, vehicles, and pedestrians. Drivers' behaviors have dominant statuses in the traffic accidents. So recently, more and more researches concerning drivers' behaviors are conducted in the academic community. However, drivers' behavior is complicated, which consists of a multitude of factors, such as driver's driving habits and personal moods.

Good habits and good moods can help the driver make the right choice while facing emergency situations, which contributes to reducing traffic accidents. The relationships between risky driving habits and motor vehicle driver injury are analyzed, and the results confirm the need for interventions targeting risky driving and also suggested that different strategies may be required for different high-risk groups (Blows et al. 2005). It is necessary to provide effective strategies to reduce the traffic accident rate (Blows et al. 2005). Therefore, the causes of traffic accidents and secondary rear-end accidents in the emergency rescue of highway traffic accidents are found, and suggestions were proposed to reduce secondary accidents, and loss to life and property (Yu 2013). Several kinds of behaviors modes such as GHP model (Hamdar 2012), Gipps model, and safe-distance model were proposed previously (Wageningen-Kessels et al. 2014). A driver model was introduced and then extended to the proposed driver model to the distance behavior (Ludmann et al. 1997).

The heterogeneous traffic accident data are analyzed, which has revealed the hidden relationships finally. However, the authors could not propose the corresponding measures to solve the traffic accident (Depaire et al. 2008).

A feedback program was employed to help the drivers improving their safety behaviors based on the idea that particular types of driver errors result from contingency traps as defined by Fuller (Hutton et al. 2001). But the limitation was that it was designed to improve the behaviors of the drivers who expressed a desire to improve their own safety.

In this paper, we propose a Markov chain-based traffic flow model for calculating the probability of driving in the signalized intersections safely. Besides, we propose a bidirectional scheme to monitor the behaviors of drivers and pedestrians to avoid the traffic accident in the signalized intersections.

The rest of this paper is organized as follows: Section II describes the Markov chain-based traffic flow model in the signalized intersection and also provides a safe-distance model. The bidirectional scheme to monitor the behaviors of drivers and pedestrians is proposed in Section III. The performance evaluation of the proposed model is presented in Section IV. Finally, Section V concludes this paper and gives the future work.

2 PROPOSED MARKOV CHAIN-BASED TRAFFIC FLOW MODEL AND ADJACENT SAFE-DISTANCE MODEL

In this section, a Markov chain-based traffic flow model has been proposed for the calculation of the traffic accident probability in the signalized intersections. In order to ensure the safety of Vehicle to Vehicle (V2V), it is necessary to propose a safe-distance model between adjacent vehicles. Let us suppose that all the vehicles have installed the GPS and OBU devices, which are responsible for collecting the vehicles' related information and then sending the collected information to traffic light control center, respectively.

2.1 *Markov chain-based traffic flow model*

Suppose that vehicles can approach the next signalized intersection only after leaving from the previous signalized intersection in one traffic light cycle (green light, red light, yellow light). Setting the traffic light cycle as C_{cycle}, the maximum road capacity is g_m vehicles. The proposed Markov chain-based traffic flow model is shown in Figure 1.

In Figure 1, let u,h,w be the random variables, which represent the number of traffic light cycles for vehicles waiting around the signalized intersections, the remaining number of vehicles in the same direction of the road during the period of driving through the signalized intersections safely, and the state of drivers' behaviors on the road, respectively. The states of drivers' behavior are of two types: normal driving and abnormal driving. If drivers drive normally, then $w=-1$, others $w=0$. Let p_0 be the probability that drivers drive normally, and p_2 be probability that the drivers drive normally after driving abnormally, respectively.

As u represents the number of traffic light cycles for vehicles waiting around the signalized intersections, then u subtracts 1 at each traffic light cycle. The remaining numbers of vehicles in the same direction of the road may be changed or unchanged, which depends on the drivers' behavior state w. Here, we choose a subject vehicle queue 1^i ($0 \le i \le k$, k is the maximum periodicity of traffic light in one signalized intersection) at a certain time. Let p_1 denote the probability that the last vehicle in the subject vehicle queue cannot pass through the signalized intersection safely, and then a three-dimensional process u,h,w can be obtained.

The one-step transition probabilities can be presented as following:

$$P\{(i,h,-1)\,|\,(i,h-1,-1)\} = p_0;\ 0 \le i \le k,\ 1 \le h \le g_m \tag{1}$$

$$P\{(i,h,0)\,|\,(i,h,0)\} = 1-p_2;\ 0 \le i \le k,\ 1 \le h \le g_m \tag{2}$$

$$P\{(i,h-1,-1)\,|\,(i,h,0)\} = p_2;\ 0 \le i \le k,\ 1 \le h \le g_m \tag{3}$$

$$P\{(i,h,-1)\,|\,(i-1,1,-1)\} = \frac{p_1}{g_m};\ 0 \le i \le k,\ 1 \le h \le g_m \tag{4}$$

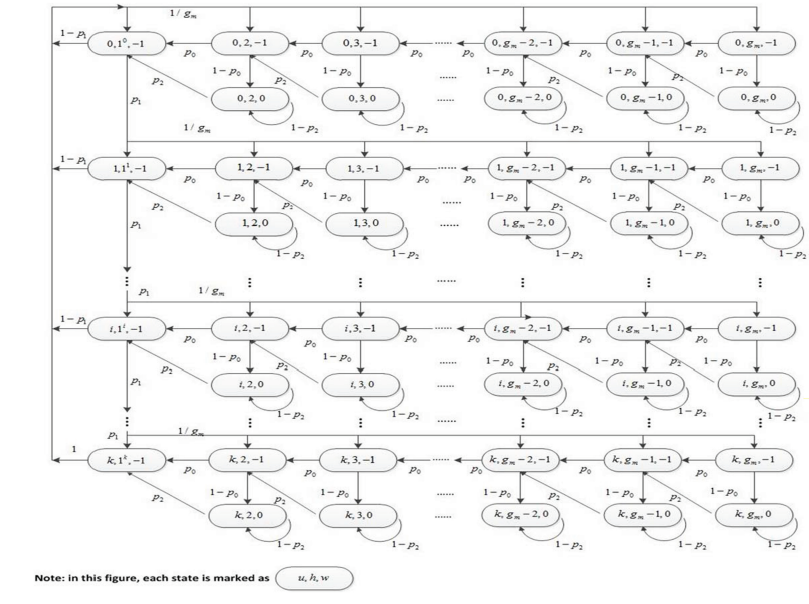

Figure 1. The Markov chain-based vehicles traffic flow model.

$$P\{(0,h,-1)\,|\,(k,1,-1)\} = \frac{1}{g_m};\ 1 \le h \le g_m \tag{5}$$

Equation 1 shows that the driver driving normally. Equations 2 and 3 show that the driver drives abnormally and normally after driving abnormally in the previous time, respectively. Equation 4 denotes that the marked vehicle should wait for the next traffic light cycle and a majority of the vehicles will drive into this road during the same cycle time. Here, only the first g_m vehicle will be considered in the waiting queue in the current traffic signal cycle, and the other vehicles located behind the first g_m vehicle will be considered in the next traffic signal cycle. Equation 5 is suitable for some special situations such as light traffic flow.

Let $P_{abnormal}$ be the probability that the driving behaviors are abnormal, $G_{(u,h,w)}$ be the steady state probability of vehicles staying at the state of (u, h, w). We can get $\sum_{u=0}^{k}\sum_{h=1}^{g_m} G_{(u,h,-1)} + \sum_{u=0}^{k}\sum_{h=2}^{g_m} G_{(u,h,0)} = 1$. Here, we obtain the steady-state probability p_3 of vehicles arriving at the signalized intersection, which corresponds to the state of $(i,1^i,-1)$ $(0 \le i \le k)$. Let $p_{safecross}$ represent the probability that vehicles can drive through the signalized intersection safely, and N be the total numbers of vehicles in road A and road B (shown in Fig. 4) in every hour, if j is the number of lane, the p_3 and $p_{safecross}$ can be written as:

$$p_3 = \frac{\sum_{u=0}^{k} G_{(u,1,-1)}}{1 - p_{abnormal}} = \frac{1 - p_1^{k+1}}{\sum_{u=0}^{k} \frac{g_m}{2} p_1^u (1-p_1) + (1 - p_1^{k+1})} \tag{6}$$

$$p_{safecross} = \frac{1}{2} N p_3^j \,(1-p_3)^{N-j} \tag{7}$$

2.2 *Adjacent safe-distance model*

The earliest car-following models include the cars following rules based on adjacently following vehicles in the nearby distance. Newell proposed a simple safe-distance model with a time delay as (Lint et al. 2014):

$$v_n = v_n\,(x_{n-1}\,(t-\tau) - x_n\,(t-\tau)) \tag{8}$$

where v_n is the current speed of the vehicle n; x_n is the driving distance of the vehicle n; $\tau$is the reaction time of driver; and τ_n is the reaction time of the driver n (suppose that the maximum and minimum values of the reaction time are τ_{max} and τ_{min}, respectively).

Later on, he simplified the model as:

$$x_n\,(t+\tau_n) = x_{n-1}(t) - s_{jam,n} \tag{9}$$

where $S_{jam,n}$ is the front to front distance between the two adjacent vehicles (e.g., vehicle n and vehicle n–1) at the standstill state and the average length of vehicles is L. In this paper, we employ this safe-distance model for the simulation in Section IV.

3 THE PROPOSED ACCIDENTS AVOIDING SCHEME OF MONITOR BEHAVIORS OF DRIVERS AND PEDESTRIANS

As shown in Figures 2 and 3, when pedestrians run when the light is red (the case 1 in the Figs. 2 and 3), the monitor gives an instant feedback to the traffic light control center, then messages will be informed by the traffic light control center to the first vehicle, which will arrive at the signalized intersection when pedestrians walk across the road at the red light ahead. Then the first vehicle sends the emergency message to the following subsequent vehicles by a multi-hop transmission.

When vehicles run at the red light (case 2 in Figs. 2 and 3), the monitor gives an instant feedback to the traffic light control center, then the traffic light control center informs the pedestrians

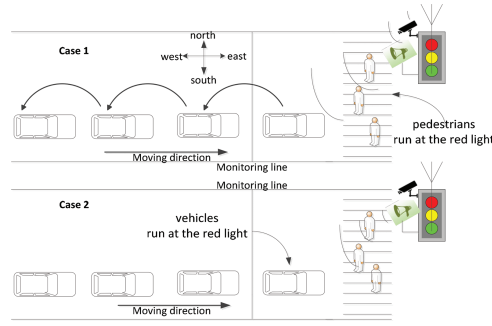

Figure 2. The proposed model for avoiding traffic accidents between drivers and pedestrians.

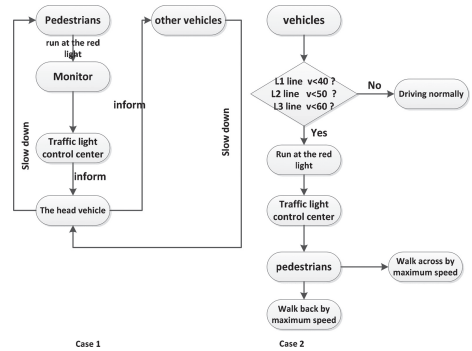

Figure 3. The process of the scheme.

via the loudspeaker that some vehicles may run at the red light in this intersection. As shown in Figure 3, when the speed of the vehicle at the speed of l_1 exceeds 40 km/h, it is suspected of running at the red light, so do other two conditions.

3.1 *Case 1: pedestrians run at the red light*

Suppose when the traffic light in the west-east direction is green, vehicles in this direction are driving at a normal speed. If some pedestrians are running at the red light in the north-south direction, the monitor will send this abnormal picture to the traffic light control center, which will communicate with the head vehicle that is driving toward the sidewalk in west-east direction and then relays this message to the other vehicles in the radio coverage area by the head vehicle. The judgment whether the picture is abnormal or not is up to the traffic light control center, which uses image-processing related techniques to make that decision. This paper does not discuss on this in detail. The off-the-peg abnormal cases are applied to the later simulation in Section IV.

Then, these vehicles send this emergency message to other vehicles that are not in the radio coverage area and RSUs by a multi-hop transmission, so that the head and subsequent vehicles will keep a safe distance with each other to avoid accidents among vehicles.

3.2 *Case 2: vehicles run at the red light*

When the traffic light is green in the north-south direction, pedestrians walk through the sidewalk in this direction. Once vehicles in the west-east direction intend to run at the red light, the OBUs in the vehicles will send the related information such as the current speed, direction, and the position to the traffic light control center. The traffic light control center will calculate this information; after their behavior is judged as abnormal, the control center will inform the pedestrians via a loudspeaker.

Here, a monitoring line is set as the detecting line when the vehicle arrives at the detecting line, as shown in Figure 2, and the OBU sends the related information to the traffic light control center immediately.

4 PERFORMANCE AND EVALUATION

According to the authors' knowledge, there have been no related traffic accident avoiding measures until now, and currently it is just based on the personal judgments of drivers and pedestrians. To evaluate the proposed model, we compare the proposed scheme with the situation of the without accident avoiding scheme (WOAA scheme).

A simple simulation is done based on the scenario (shown in Fig. 4 and the process is shown in Fig. 3) by using Matlab. The relevant parameters are shown in Table 1. Suppose that at every traffic light cycle, there are 10 pedestrians running at the red light and walking across the sidewalk normally when vehicles run at the red light, and the phenomenon of running at the red light on a single direction is considered in the simulation. Suppose that the allowed maximum speed of the vehicles is S_{max}, and the maximum deceleration speed is α_{max} and the maximum speed of the pedestrians is v_{max}.

As shown in Figure 4, the road near the sidewalk is divided into three parts, and each part has

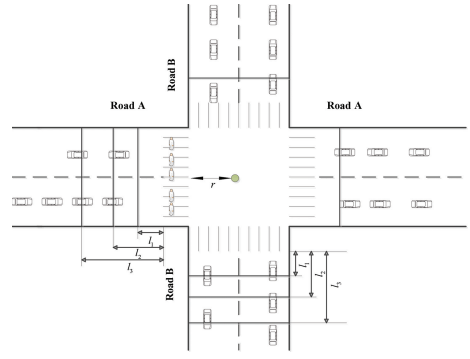

Figure 4. Simulation scenario.

Table 1. Simulation parameters.

Parameter	Meaning	Value
Road type	The road type	2-way 2-lane
S_{max}	Allowed maximum speed of vehicle	60 (km/h)
α_{max}	Maximum deceleration speed of vehicle	4 (m/s^2)
r	Half width of the road	7.5 (m)
N	Traffic flow in a hour	1000 (veh/h)
k	Maximum periodicity of traffic light	120
τ_{min}	Minimum reaction time of driver	0.4 (s)
τ_{max}	Maximum reaction time of driver	2.9 (s)
v_{max}	Maximum speed of pedestrians	2 (m/s)
L	Average length of vehicles	5 (m)
l_1	Distance between monitoring line and sidewalk	16 (m)
l_2	Distance between monitoring line and sidewalk	25 (m)
l_3	Distance between monitoring line and sidewalk	35 (m)

a monitoring line denoted by l_1, l_2 and l_3, which is responsible for collecting information of the related vehicles and sending the collected information to the traffic light control center.

The goal of the proposed scheme is to avoid accident between drivers and pedestrians. The performances of the proposed schemes are shown in Figures 5–9 by comparing with and without accident avoiding scheme (WOAA scheme). Only the unilateral condition is considered, that is just one side of the pedestrians or one direction of vehicles running at the red light. In other words, the behavior of bilateral vehicles running at the red light in one traffic light cycle is not considered.

There are two cases provided to evaluate the performances of the proposed strategy: pedestrians running at the red light and vehicles running at the red light.

1. Case 1: pedestrians running at the red light. Figure 5 shows the case that pedestrians run at the red light when vehicles run on the road normally. There are 10 pedestrians running at the red light, and the time spent by the pedestrian who is the first to arrive at the middle line (as shown in the Figure 4, the width of the road r is 7.5 m) of the road is 5 s; however, the last pedestrian spends 8 s as shown in the Figure 5. It is easy to understand that once the pedestrians arrive at the middle line, they can walk through the sidewalk safely under the unilateral condition.

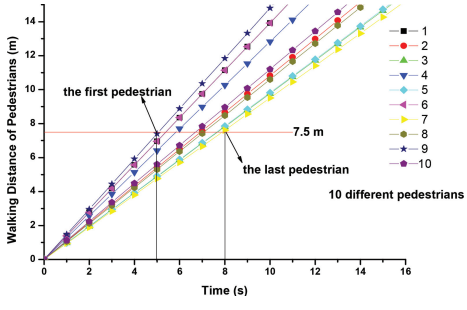

Figure 5. Walking distance of 10 pedestrians when they run at the red light.

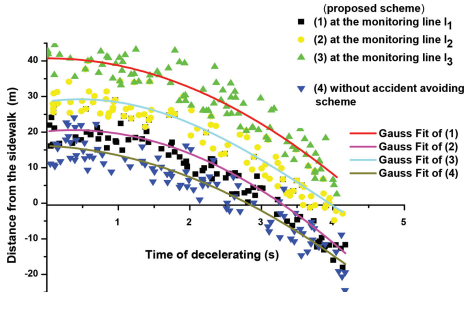

Figure 6. Distance from the sidewalk of head vehicle vs. time needed to slow down to stop when pedestrians run at the red light within 100 traffic light cycles.

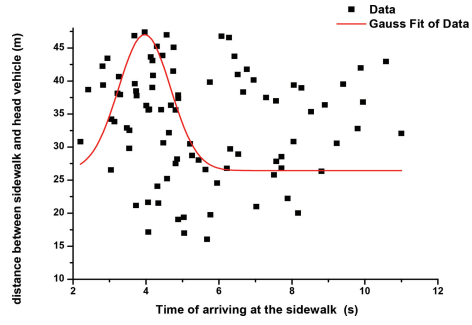

Figure 7. Distance from the sidewalk and time of arriving at the sidewalk of vehicles when they run at the red light within 100 traffic light cycles.

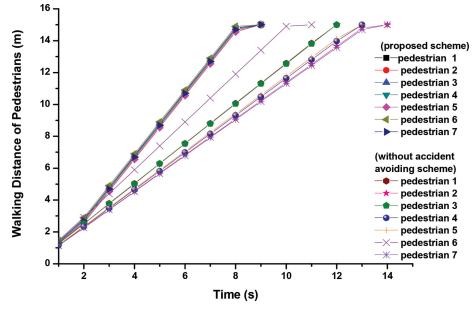

Figure 8. The first seven pedestrians' walking when vehicles run at the red light.

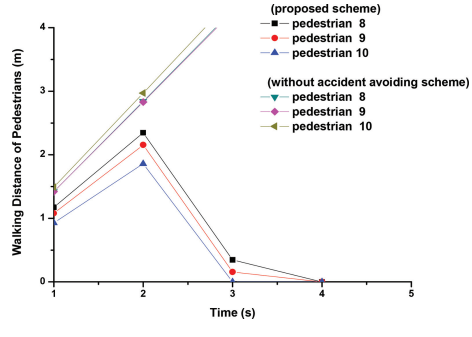

Figure 9. The latter three pedestrians' walking when vehicles run at the red light.

Figure 6 shows the distance from the sidewalk of the head vehicle when the traffic light

control center starts to inform and the needed time to slow down to stop under the proposed scheme and the WOAA scheme, respectively.

As shown in Figure 6, there are 20 points (indicated by a black square) and 8 points (indicated by a yellow dot) under the zero on the Y-axis when the vehicle is informed at the monitoring lines l_1 and l_2, respectively, which means there are 28 times of vehicle running across the sidewalk within 4.5 s. Further, when informed at the line l_3, all the points are above the zero point on the Y-axis. That means all vehicles can be slowed down to a standstill state before arriving at the sidewalk within 100 traffic light cycles. When it is informed at the line l1, most of the distances are under the 20 m; however, almost half and even more the distances are above 20 m when it is informed at the line l_3.

It is the driver who has to be aware of the illegal behavior of the pedestrian; however, the traffic accident is usually inevitable in this case due to the very short distance from the pedestrian.

As shown in Figure 5, the pedestrians need about 5 s to 8 s to walk across the middle line. However, there are 28 times of vehicle running across the sidewalk within 4.5 s by the proposed scheme. So the vehicles will arrive at the sidewalk 0.5 s earlier than the pedestrians run away toward the sidewalk. Therefore, accidents will now occur on the sidewalk.

Compared with the proposed scheme, there are 34 instances (indicated by a blue triangle) of vehicles running across the sidewalk within 4.5 s without accident avoiding scheme (as shown in Fig. 6). The accident rate is 34/100 under the without accident avoiding scheme. However, the accident rates are only 20/100, 8/100, and 0 under the proposed scheme at the lines l1, l2, and l3, respectively.

2. Case 2: vehicles running at the red light
When the green time is 2 s, the traffic light control center detects whether there is a vehicle running at the red light, then informs the pedestrians the information via the loudspeaker. If the pedestrians have walked r/3, they will walk across the sidewalk by maximum speed of v_{max}, others will walk back by the same speed. From Figures 8 and 9, it can be observed that there are three pedestrians returning (spend 3 s to 4 s) and others are picking up the pace to walk across the road (spend 4.2 s to 4.5 s approximately) in the proposed scheme. However, pedestrians always walk on the sidewalk, and they spend 4.9 s to 6.7 s to arrive at the middle line without the accident avoiding scheme.

There are 36 times that the vehicles arrive at the sidewalk within 4.5 s, and 75 times that the vehicles arriving at the sidewalk within 6.7 s (shown in Fig. 7). That is, the accident rate by our proposed scheme is 36%; however, the rate without accident avoiding scheme is 75%.

5 CONCLUSION

In this paper, we propose a Markov chain-based vehicles traffic flow control model for driving through the signalized intersections safely, which aims to calculate the traffic accident rate. Besides, we propose a new monitor model for directing drivers' and pedestrians' behaviors. Under the proposed scheme, the traffic light control center will give the warning to pedestrians in advance when there are vehicles running at the red light. Compared with the situation of the WOAA scheme, the traffic accident rate can be reduced by a large scale under the proposed scheme. Pedestrians' traffic habits and individual emotions will be taken into consideration in the next step. The delay of the reception and transmission of the signal will also be considered.

ACKNOWLEDGMENT

This work was supported by the National Natural Science Foundation of China (Grant No. 61401387, 61301111, 61472343), the Universities Natural Science Research Project of Jiangsu Province (No. 14 KJB510035), and the Natural Science Foundation of Yangzhou City (Grant No. YZ2014054).

REFERENCES

Blows, S., Ameratunga, S. & Ivers, R.Q. 2005. Risky driving habits and motor vehicle driver injury. *Accident Analysis & Prevention* 37(4): 619–624.

Depaire, B., Wets, G. & Vanhoof, K. 2008. Traffic accident segmentation by means of latent class clustering. *Accident Analysis & Prevention* 40(4): 1257–1266.

Hamdar, S. 2012. *Driver Behavior Modeling, Handbook of Intelligent Vehicles*. London: Springer: 537–558. http://link.springer.com/referenceworkentry/10.1007%2F978-0-85729-085-4_20

Hutton, K.A., Sibley, C.G. & Harper, D.N. 2001. Modifying driver behaviour with passenger feedback. *Transportation Researcher* 4(4): 257–269.

Ludmann, J., Neunzig, D. & Weilkes, M. 1997. Traffic Simulation with Consideration of Driver Models, Theory and Examples. *Vehicle System Dynamics: International Journal of Vehicle Mechanics and Mobility* 27(5): 491–516.

Wageningen-Kessels, F. V. & Lint, H.V. 2014. Genealogy of traffic flow models. *EURO Journal on Transportation and Logistics* 4(4): 45–73.

Yu, Q.Y. 2013. Causes and Prevention Measures of Secondary Rear-end Accidents in the Rescue of Highway Traffic Accidents. *Procedia Engineering* 52: 571–577.

Civil Engineering and Urban Planning IV – Liu et al. (Eds)
© 2016 Taylor & Francis Group, London, ISBN 978-1-138-02903-3

Hybrid life cycle and interval linear programming for the copying paper supply-chain management considering the Greenhouse Gas mitigation

Wen-Cong Yue
State Key Laboratory of Water Environment Simulation, School of Environment, Beijing Normal University, Beijing, China

Yan-Peng Cai
State Key Laboratory of Water Environment Simulation, School of Environment, Beijing Normal University, Beijing, China
Institute for Energy, Environment and Sustainable Communities, University of Regina, Regina Saskatchewan, Canada

Lin-Yu Xu, Chun-Hui Li, Xuan Wang & Qiang-Qiang Rong
State Key Laboratory of Water Environment Simulation, School of Environment, Beijing Normal University, Beijing, China

ABSTRACT: Concerns over the conflicts between Greenhouse Gas (GHG) reduction and industrial development are increasing for multiple stages of pulp and paper industry. Also, the conflict of such an industry is becoming serious in many regions of China. Greenhouse effects of the region's industrial activities are significantly linked with the transportation for supplying raw materials and paper products. In this research, to comprehensively support the decision-making in the supply-chain management and GHG reduction for the industry, a hybrid life-cycle and inexact programming approach was proposed. The approach can reflect the uncertainty of the supply and demand in real industrial activities. The interval linear programming model could help the solutions for the supply chains in mitigating the greenhouse effect. The developed method was then applied to a pulp and paper mill in the Shandong Province of China for demonstrating its application. The results indicated that the amount of copying paper production in each month would be in the range of 200–800 t. Road transportation would carry 5010 t of copying paper to four retailers in a year, accounting for more than 75% of the total amount.

1 INTRODUCTION

Governments around the world are setting targets and taking action to reduce carbon dioxide (CO_2) emissions in general. In China, for example, the executive meeting of the state council sets a target for 2020 that reduces 40–45% per Gross Domestic Product (GDP) compared to the emission amount of 2005. Anthropogenic Greenhouse Gas (GHG) emissions to the atmosphere are regarded as the chief contributor to the global warming (Dormer et al. 2013). Industry accounts for 40% of the global energy-related CO_2 emissions (Roddy 2013). In China, GHG emission and regional industrial activities are closely related. The greenhouse effect of the region's industrial activities is often linked with the transportation for the supplying raw materials and products. A sound supply-chain plan in the industries should, therefore, take the GHG reduction into account.

Along with the increasing concerns over global warming, Greenhouse Gas (GHG) emissions arising from products (goods and services) were assessed by the help of Life-Cycle Assessment (LCA). Similarly, to reflect a growing concern for the fight against the threat of global warming, the term "Carbon Footprint" (CF), came into wide use across media, governments, and the business world (Kimura et al. 2010). Dormer et al. (2013) calculated the CF of recycled PET trays. Muthu et al. (2011) studied the CF of different types of shopping bags. However, the uncertainty features of the life-cycle inventory were always not brought into the GHG emission accounting in the industrial system.

Comparatively, many inexact optimization tools can be used to remedy such disadvantages. There were numerous attempts on optimization models for decision-making in industrial system. For example, Ubando et al. (2013) developed a fuzzy fractional programming model for designing

a trigeneration system and for simultaneously optimizing the allocation of the CF per energy stream. Osmani and Zhang (2014) proposed a two-stage Linear Programming (LP) to maximize the annualized profit of an integrated dual-feedstock lignocellulosic-based bioethanol supply chain. Pekala et al. (2010) proposed a LP model to handle the minimization of the use of highest-quality energy sources. Thus, to improve the applicability of LCA for the decision-making support in the supply-chain management, interval LP approach needs to be incorporated into a general LCA framework.

Therefore, the objective of this research was to develop a hybrid life-cycle and interval linear optimization method for the design and operation of supply chains. In brief, the method can minimize the greenhouse effect in supply-chain transportation as well as satisfy customer demands. Meanwhile, the approach can reflect the uncertainty of the supply and demand in the real industrial activities. The developed method was then demonstrated in a pulp and paper mill in Shandong Province of China.

2 METHODOLOGY

2.1 *Life-cycle analysis*

2.1.1 *System boundary and functional unit*

Considering the features of the pulp and paper production, the functional unit of copying paper is the weight of copying paper (1000 kg). In brief, life-cycle analysis of copying paper is related to the following stages (Fig. 1).

2.1.2 *Life-cycle inventory*

Each greenhouse gas, i.e., CO_2, methane (CH_4), and nitrous oxide (N_2O) has a potential influence on greenhouse warming to a certain extent. The warming influence is estimated as the extent of relative to that of a greenhouse gas. According to IPCC (1996), the emissions of GHGs are measured in terms of a reference gas, CO_2. The GWPs of CO_2, CH_4, and N_2O (with a time span of 100 years) are 1, 21, and 310. The total emissions of greenhouse gases are determined as follows (Yousefi et al. 2014):

$$\text{Greenhouse effect} = \sum_i \text{GWP} \times M_i \tag{1}$$

where M_i is the mass (in kg) of the emission gas. The score is expressed in terms of CO_2 equivalents.

Several related decisions must be made to produce paper in the minimum amount of CF of products life cycle. An outline of the stock preparation problem is shown in Figure 1. Key decisions to be made are as follows:

1. The raw material composition, i.e., what mixture of chemical softwood and hardwood pulps and mechanical pulps to choose (Claassen 2014).
2. The transportation of pulp to the paper mill, i.e., the cellulose suppliers and the distance and mode of transportation do not consider the question of backhauling (Carlsson & Rönnqvist 2007).

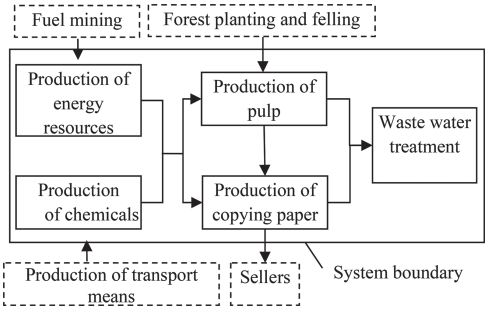

Figure 1. System boundary of copying paper.

2.2 *Uncertain analysis of the life-cycle inventory*

A number of factors contribute to the uncertainty in the life-cycle inventory, including uncertainties in source data, imputation and balancing, allocation, assuming proportionality and homogeneity, concordance, regional aggregation, temporal discrepancies, representativeness of model data, monetary exchange rates (for multiregion models), and price conversion (Wiedmann et al. 2011).

Data Quality Indicator (DQI) method has been extensively employed in qualitative dealing with LCA uncertainty issue (Wang et al. 2012). It uses a group of selected indicators (Table 4 shows an example of DQI matrix) to assess the quality of life-cycle inventory:

$$q = \frac{1}{n}\sum_{i=1}^{n} q_i \tag{2}$$

where q is the expectation value q_i.

$$R = \frac{q - \min q_i}{\max q_i - \min q_i} \tag{3}$$

where R is the percent of q in the matrix of data quality; min q_i is the minimum value of q_i; and max q_i is the maximum value of q_i. Then, values of DQIs and uncertain range of life-cycle inventory can be calculated from the DQI assignment matrix.

2.3 *Interval parameter programming models*

Interval LP (ILP) is used to deal with uncertainties in optimization problems, with all or part of the model parameters being expressed as interval numbers (Xu et al. 2010). The ILP allows the interval information to be directly communicated into the optimization process and resulting solution (Cai et al. 2007, Huang et al. 1995). An ILP model can be written as follows:

$$\text{Minimize } f^{\pm} = C^{\pm}X^{\pm} \tag{4}$$

such that

$$A^{\pm}X^{\pm} \geq B^{\pm} \tag{4a}$$

$$X^{\pm} \geq 0 \tag{4b}$$

$$C^{\pm},\ A^{\pm} \neq 0 \tag{4c}$$

$$\begin{aligned}\text{Min } G = {} & \sum GWP \times \theta_t \varpi_t \sum_{j=1}^{12}\sum_{i=1}^{n} ceil\left(x_{ijt}^{\pm}/8.4\right) \\ & + \sum GWP \times \theta_r \varpi_r \sum_{j=1}^{12}\sum_{i=1}^{n} ceil\left(x_{ijr}^{\pm}/17.5\right) \\ & + l_t \times 20 \sum_{j=1}^{12}\sum_{i=1}^{n} ceil\left(x_{ijr}^{\pm}/17.5\right)\end{aligned} \tag{5}$$

such that

$$\sum_{i=1}^{4}\left(x_{ijt}^{\pm} + x_{ijr}^{\pm}\right) \leq C_j^{\pm}, \forall j \tag{5a}$$

$$\sum_{j=1}^{12}\left(x_{tjt}^{\pm} + x_{ijr}^{\pm}\right) \geq D_i^{\pm},\ \forall i \tag{5b}$$

$$x_{tjt}^{\pm},\ x_{ijr}^{\pm},\ C_j^{\pm},\ D_i^{\pm} \geq 0,\ \forall i \tag{5c}$$

where G is the greenhouse effect in transportation for copying paper; θ is the emission factor of GHGs; and ϖ is the fuel consumption factor. $x_{ijt}^{\pm}$ is the amount of the product in road transported to the ith retailer in the jth month; l_r is the price of railway transportation; p_r is the distance of railway transportation; $x_{ijr}^{\pm}$ is the amount of the product in railway transportation to the ith retailer in the jth month; $C_j^{\pm}$ is the amount of production for the four retailers in the jth month; and $D_i^{\pm}$ is the amount of copying paper demand in a year for the ith retailer.

3 CASE STUDY

3.1 *Problem definition*

A pulp and paper mill located in the Shandong Province is chosen as a case in this paper. The main products of the mill exhibit multiple types of copying paper. The main aim of this section is to account for the amount of GHG emission in the supply chains of the mill.

3.2 *Life-cycle inventory*

1. Electricity production
   Relevant research results in the GHG emissions are in accordance with IPCC (2006) and Cui et al. (2012).
2. Pulp and paper mill
   According to the study of life-cycle analysis of copying paper from Yue et al. (2014) and Wang et al. (2011), the inventory of GHG emission in the process of 1000 kg of copying paper production is described in Table 1.
3. Transportation
   Average emission factors of the transportation machinery (Equation 6) are referred to the related study from IPCC (2006).

$$E = \sum_{j}\left(F_j \times EF_j\right) \tag{6}$$

where E is the emissions of the greenhouse gases (kg); F_j is the fuel consumed (as represented by the fuel sold) (TJ); EF_j is the emission factor (kg/TJ) of the jth fuel, with j being the fuel type. The average index of EF_j is referred to the default emission factors for road mobile machinery, railways, and ships from IPCC (2006). Thus, the emission factors of trucks in CO_2, CH_4, and N_2O are [72600, 74800], [1.6, 9.5], and [1.3, 12] kg/TJ; the emission factors of railways in CO_2, CH_4, and N_2O are [72600, 74800], [1.67, 10.4], and [14.3, 85.8] kg/TJ. Fuel consumption factors for cargo transportation by truck (capacity: 8 t) and train (capacity: 4000 t) are 0.13 kg/km, and 4.15 kg/km, respectively. The net calorific value of diesel oil is [4.14E-05, 4.33E-05] TJ/kg. In the base year, the output of copying paper was 5010 t. The distance of transportation for raw materials and products is listed in Table 2.

Table 1. GHG emission inventories of producing 1000 kg copying paper in the base year.

	Production process		
	1*	2	3
Energy consumption (KWh)	16.11	458	9.6
CO_2 emission (kg)	1517.63	–	–

Note: 1, pulp making; 2, paper making; and 3, wastewater treatment.

Table 2. Transportation for raw materials and copying paper in the base year.

Means	Amount (t)	Distance S*	R1	R2	R3	R4
s	4000	–	–	–	–	–
r	650	800	–	–	–	–
r	990	15	–	–	–	–
r	300	3500	–	–	–	–
r	3750	–	1600	1900	–	–
r	1260	–	–	–	2500	2800

*Note: S, supplier; R, retailer; s, ships; r, railways; t, trucks; 1, pulp; 2, chemicals; 3, packing materials; and 4, copying paper.

Table 3. Uncertainty analysis of life-cycle inventory.

Item*	DQI	R (%)	DQI	Range endpoints (%)
1	(3, 2, 1, 2, 2, 3)	58.33	3	±30
2	(5, 4, 3, 3, 5, 4)	50	2.5	±35
3	(3, 3, 3, 1, 1, 4)	75.00	4	±20

*Note: 1, electricity production; 2, pulp and paper mill; 3, transportation.

3.3 *Uncertainty analysis*

The uncertainty analysis is based on the methodology of DQI. The uncertainty of the life-cycle inventory of the UWMS in Dalian is listed in Table 3.

4 RESULTS AND DISCUSSION

Solutions of the model in Section 2.3 are presented in Table 4.

The final solutions contain the following two aspects.

1. The solutions of copying the paper production
   The maximum productive capacity of a month is 800 t of copying paper in the mill. Thus, the amount of copying paper production in each month would be in the range of 200–800 t. The amount for copying the paper production in December, i.e., [650, 745] t, would be the biggest in a year. The amount for copying the paper production in April, i.e., [163, 333] t, would be the smallest in a year. In the following five months, i.e., from May to July, and from September to November, the amounts for copying paper production would be [500, 593] t.

Table 4. Solution strategy for product supply in a year.

	Retailer 1		Retailer 2		Retailer 3		Retailer 4	
	T*	R	T	R	T	R	T	R
1	217	[0, 16]	179	[0, 42]	0	[0, 10]	104	[0, 27]
2	200	[0, 22]	0	[0, 80]	0	[0, 9]	0	[0, 52]
3	0	[0, 22]	96	[0, 80]	0	[0, 9]	104	[0, 52]
4	59	[0, 23]	0	[0, 85]	0	[0, 10]	104	[0, 52]
5	59	[0, 16]	337	[0, 42]	0	[0, 8]	104	[0, 27]
6	59	[0, 16]	203	[0, 42]	40	[0, 8]	199	[0, 27]
7	76	[0, 16]	151	[0, 42]	151	[0, 8]	122	[0, 27]
8	59	0	0	0	441	0	0	[0, 300]
9	76	[0, 16]	151	[0, 42]	151	[0, 8]	122	[0, 27]
10	76	[0, 16]	151	[0, 42]	151	[0, 8]	122	[0, 27]
11	59	[0, 19]	0	[0, 67]	133	[0, 8]	104	[0, 44]
12	59	[0, 20]	133	[0, 34]	133	[0, 13]	324	[0, 27]
T	[1000, 1201]		[1400, 1999]		[1200, 1300]		[1410, 2101]	

*Note: T, trucks; and R, railways.

2. The solutions of copying paper transportation
   Road transportation would carry 5010 t of copying paper to the four retailers in a year, accounting for more than 75% of the total amount. For Retailer 1, the amount for copying paper transportation in February, i.e., [200, 222] t, would be the biggest in a year. For Retailer 2, the amount for copying paper transportation in May, i.e., [337, 379] t, would be the biggest in a year. For Retailer 3, the amount for copying paper transportation in August, i.e., 441 t, would be the biggest in a year. For Retailer 4, the amount for copying paper transportation in December, i.e., [324, 351] t, would be the biggest in a year.

5 CONCLUSION

In this research, a hybrid life-cycle and inexact programming approach was developed for the design and operation of supply chains. Briefly, the method would minimize the greenhouse effect in the supply-chain transportation as well as satisfy customer demands. Meanwhile, the approach would characterize the supply chain systems that can reflect the uncertainty of supply and demand in real industrial activities. A case study illustrated the applicability of the hybrid approach for supply-chain management in industries. The results indicated that the amount of copying paper production in each month would be in the range of 200–800 t. Road transportation would carry 5010 t of copying paper to the four retailers in a year, accounting for more than 75% of the total amount. Further work will be required in terms of considering other environmental impacts on supply-chain management

and incorporating other life-cycle stages into the system boundary.

ACKNOWLEDGMENTS

This work was supported by the Fundamental Research Funds for the Central Universities (2014KJJCB10), the National Science & Technology Pillar Program, China (No. 2012BAC05B02), and the National Science Foundation for Innovative Research Group (No. 51121003).

REFERENCES

Cai, Y., Huang, G.H., Nie, X.H., Li, Y.P. & Tan, Q. 2007. Municipal solid waste management under uncertainty: A mixed interval parameter fuzzy-stochastic robust programming approach. *Environ Eng Sci* 24(3): 338–352.

Carlsson, D. & Rönnqvist, M. 2007. Backhauling in forest transportation: models, methods, and practical usage. *Can J Forest Res* 37: 2612–2623.

Claassen, G.H. 2014. Mixed integer (0–1) fractional programming for decision support in paper production industry. *Omega* 43: 21–29.

Cui, X., Hong, J. & Gao, M. 2012. Environmental impact assessment of three coal-based electricity generation scenarios in China. *Energy* 45(1): 952–959.

Dormer, A., Finn, D.P., Ward, P. & Cullen, J. 2013. Carbon footprint analysis in plastics manufacturing. *J. Clean Prod.* 51(15): 133–141.

Huang, G.H., Baetz, B.W. & Patry, G.G. 1995. Grey integer programming: an application to waste management planning under uncertainty. *European J Oper Res* 83: 594–620.

IPCC. 1996. *Climate change 1995: The science of climate change.* Cambridge, U.K.: Cambridge University Press.

IPCC. 2006. *IPCC Guidelines for national greenhouse gas inventories*. Hayama, Japan: Institute for Global Environmental Strategies.

Kimura, A., Wada, Y., Kamada, A., Masuda, T., Okamoto, M., Goto, S.-I., Tsuzuki, D., Cai, D., Oka, T. & Dan, I. 2010. Interactive effects of carbon footprint information and its accessibility on value and subjective qualities of food products. *Appetite* 55(2): 271–278.

Muthu, S.S., Li, Y., Hu, J.Y. & Mok, P.Y. 2011. Carbon footprint of shopping (grocery) bags in China, Hong Kong and India. *Atmos Environ* 45: 469–475.

Osmani, A. & Zhang, J. 2014. Economic and environmental optimization of a large scale sustainable dual feedstock lignocellulosic-based bioethanol supply chain in a stochastic environment. *Appl Energ* 114: 572–587.

Pekala, L.M., Tan, R.R., Foo, D.C.Y. & Jezowski, J.M. 2010. Optimal energy planning models with carbon footprint constraints. *Appl Energ* 87(6): 1903–1910.

Roddy, D.J. 2013. A syngas network for reducing industrial carbon footprint and energy use. *Appl Therm Eng* 53(2): 299–304.

Ubando, A.T., Culaba, A.B., Aviso, K.B. & Tan, R.R. 2013. Simultaneous carbon footprint allocation and design of trigeneration plants using fuzzy fractional programming. *Clean Technologies and Environmental Policy* 15: 823–832.

Wang, E., Shen, Z., Neal, J., Shi, J., Berryman, C. & Schwer, A. 2012. An AHP-weighted aggregated data quality indicator (AWADQI) approach for estimating embodied energy of building materials. *Int J Life Cycle Assess* 17(6): 764–773.

Wang, Y., Liu, J., Hansson, L., Zhang, K. & Wang, R. 2011. Implementing stricter environmental regulation to enhance eco-efficiency and sustainability: a case study of Shandong Province's pulp and paper industry, China. *J. Clean Prod* 19(4): 303–310.

Wiedmann, T.O., Suh, S., Feng, K., Lenzen, M., Acquaye, A., Scott, K. & Barrett, J.R. 2011. Application of hybrid life cycle approaches to emerging energy technologies—The case of wind power in the UK. *Environ Sci Tech* 45(13): 5900–5907.

Xu, Y., Huang, G.H., Qin, X.S., Cao, M.F. & Sun, Y. 2010. An interval-parameter stochastic robust optimization model for supporting municipal solid waste management under uncertainty. *Waste Manag* 30(2): 316–327.

Yousefi, M., Khoramivafa, M. & Mondani, F. 2014. Integrated evaluation of energy use, greenhouse gas emissions and global warming potential for sugar beet (Beta vulgaris) agroecosystems in Iran. *Atmos Environ* 92: 501–505.

Yue, W., Cai, Y., Rong, Q., Cao, L. & Wang, X. 2014. A hybrid MCDA-LCA approach for assessing carbon foot-prints and environmental impacts of China's paper producing industry and printing services. *Environmental Systems Research* 3: 1–9.

This page intentionally left blank

Civil Engineering and Urban Planning IV – Liu et al. (Eds)
© 2016 Taylor & Francis Group, London, ISBN 978-1-138-02903-3

Comparisons of resident trip characteristics in large and medium cities between the central and western regions in China

Tao Liu & Bao-Feng Li
College of Architecture and Urban Planning, Huazhong University of Science and Technology, Wuhan Hubei, China

ABSTRACT: In this article, six typical large and medium-sized cities from the central and western regions in China were selected. The common characteristics and individual difference between two regions, such as the trip frequency of urban residents, the trip mode structure, the purpose of the trip and the trip time were analyzed. Furthermore, causes of differences were explored, and verification was conducted by model building. Based on intrinsic relation of the traffic and economic characteristics, the related suggestions were presented.

Keywords: large and medium-sized cities; resident trip; trip characteristics

1 INTRODUCTION

Despite of different economic development layers, urbanization progress and different life levels, both central and western regions are confronted with huge traffic pressure and traffic problems are increasingly highlighted when faced with the rapid development of motorization in China (Yao et al. 2012, Xiong et al. 2012). By attempting to analyze and compare resident trip survey materials in some large and medium-sized cities of both regions, this article explores the common features of resident trip and individual traffic characteristics related to the levels of regional economic development in order to reveal the intrinsic relationships between urban traffic and economic development (Wang 2008). Based on this, appropriate suggestions are proposed so that the foundation can be made for the traffic problems among large and medium-sized cities with different economic development levels.

2 BASIC CONDITIONS OF COMPARATIVE CITIES

The large and medium-sized cities in this study are referred to those whose non-agricultural population is less than 500,000 in downtown and suburb areas (including designated towns). According to the years of transportation planning experience in large and medium cities, by considering the characteristics of social and economic development and urban internal spatial structure layout, the relatively underdevloped cities in the western region, such as Zunyi, Guigang, Datong, and the relatively developed cities in central China, such as Jingmen, Chenzhou, Yichang were selected. Although all the selected cities are large and medium-sized, there are large differences in economic development. The economic levels in the central region are higher than those in the western region as a whole. Basic conditions are shown in Table 1.

Table 1. Basic conditions of comparative cities (Zou 2012).

Category	City	Population (10e4)	Area (square kilometers)
Central region	Jingmen	46.8	51.82
	Chenzhou	62	56
	Yichang	106	112
Western region	Zunyi	110	515
	Guigang	46.9	51.1
	Datong	178	346.96
Category	Remark	Per capita GDP (Yuan)	Urban residents per capita disposable income (Yuan)
Central region	2011	22425	15526
	2011	24203	17606
	2010	23855	14282
Western region	2012	21970	19748
	2010	12932	19314
	2012	23259	18915

3 TRIP TIMES PER PERSON

3.1 *General characteristics of trip times*

Trip times mainly reflect residents trip ability and the needs, while trip gross is the basic measure

index of capacity limit for urban traffic system (Deng et al. 2000, Florian & Patrick 2014). Urban residents per capita trip times basically lie between 2.0 and 3.5 times/day. Due to the relatively low trip cost and relatively low trip time, trip times per person in the relatively small-sized city will be relatively high.

3.2 *Comparative analysis of resident trip times in large and medium-sized cities of two zones*

1. Trend comparison
   Trip times per person in a relatively developed and undeveloped area of six large and medium-sized cities are shown in Table 2.

   There are a variety of factors affecting trip times deeply, such as urban layout, urban scale, economic situation, lifestyle, transportation, communications facilities, etc. Well-developed economy and well-serviced traffic facilities definitely stimulate the increase of trip times, while convenient communication and falling environment quality will bring down the trip times. When there is no significant difference between city scale, and city layout, the economic difference takes up the dominant factor of trip times' variation. In the relatively developed large and medium-sized cities of central China, the investment of traffic infrastructure is larger than that of western region, thus the economic life is relatively more frequent, whose resident trip times per day per capita lie between 2.48 and 2.53, and the average trip times per capita is 2.51; On the other hand, in western region of large and medium-sized cities the resident trip times lie between 2.23 and 2.79, and the average trip time per capita is 2.46, which was lower than those in central China.
2. Model verification
   The following multiple linear regression model is established with the variables, trip times per capita per day N (times/day), population P (ten thousand people), the area A (square kilometers), urban disposable income (Yuan), and the Gross Domestic Product (GDP) per capita.

Table 2. Trip times per person's comparison of large and medium-sized cities in central and western region.

City	Trip times per person	Year
Jingmen	2.51	2011
Chenzhou	2.53	2011
Yichang	2.48	2012
Zunyi	2.23	2012
Guigang	2.79	2010
Datong	2.34	2010

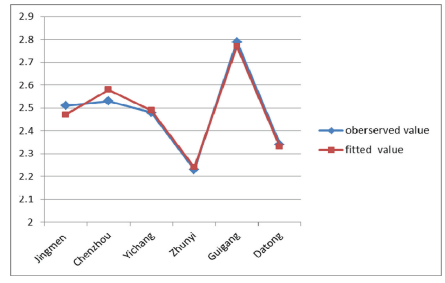

Figure 1. Fitting of observed value and model value.

Table 3. The correlation coefficient related to the dependent variables and trip times per capita.

Index	Population (10e4)	Area (square kilometers)	Per capita GDP (10 thousand Yuan)
Correlation coefficient	–0.000767	–0.0003888	0.0000617
Urban residents per capita disposable income (10 thousand Yuan)		Per capita GDP (10 thousand Yuan)	Per capita GDP (10 thousand Yuan)
0.00000414		0.0000617	0.0000617

$$N = 1.0829 - 0.000767 \times P - 0.000388 \times A + 4.14 \times 10^{-6} \times G + 6.17 \times 10^{-5} \times I$$

$$R^2 = 0.975$$

As shown in Figure 1, the model calculation results can better fitting status values.

Under the condition of linear correlation, the correlation coefficient between the independent variables and the dependent variables is calculated, and the close degree between the dependent variable and trip times is described, as shown in Table 3.

The results show that the trip times per capita is positively correlated to economy index, while it has negative correlation with the city scale. In the absence of significant difference with city layout and city scale, trip times per person will be increased when economy grows, but will not rise unlimitedly with the economic development. On the contrary, when the city scale expands, the trip times per capita will be reduced.

4 TRIP MODE CHARACTERISTICS

Trip mode structure, referred to the proportion of different trip modes for urban residents daily, is

an important index that reflects the development level of urban transportation. Generally speaking, the trip modes include walking, bicycle, motorcycle, public transit, private car, unit car, and so on. Different trip mode structures may display significant difference for the requirements of the urban traffic system. Usually the factors influencing the structure of trip modes include trip factor, social economic factor, the city layout factor, public transport factors, private traffic factor, and so on. Since there exist huge different between large and medium-sized cities and small cities in city scale and layout structure, the selection of trip modes forms into competitive situation among public transit, private cars and walking. Table 4 shows the data of trip mode structure of large and medium-sized cities in central and western regions.

4.1 *Total characteristic*

The total proportion of bus, car and walk is above 55%. This is because the larger the cities, the relatively larger proportion of long-distance trip, or higher degree of mobility.

4.2 *Disparity analysis*

The trip ridership in different cities have their own uniqueness, e.g. in the mountain city Zunyi, walking holds a small proportion, while the bus ridership is high. In Chenzhou City, the proportion of private car tripping is large, but the percentage of motorcycle tripping is very low.

There lies in difference of three main trip modes bus, private car and walking according to ranking order. In the relatively developed central region of the large and medium-sized cities, the three main modes rank as walking, bus and private car in terms of trip proportion While in the western region, within the three main modes the proportion of walking and private cars is relatively stable, in which walking accounts for 30%, and private cars are about 10%, but the bus tripping varies a lot.

Even for the same trip mode, the difference is significant. As a whole, the proportion of walking in the central region is larger than that in the western region. Among the three cities of the developed areas, the trip proportion of walking in Chenzhou City is the lowest as 35.49%, and is still higher than the highest proportion in western region of Guigang City as 34.08%. The proportion of bicycle in the central region is higher than that in the western region. Among the three cities in the central region, the trip proportion of bicycle in Jingmen City is the lowest as 15.39%, and is still higher than the highest proportion in western region of Guigang as 6.32%.

The main reason causing the diversity is the disparity of regional economy, the level of urbanization, urban layout and transportation management policy. In the central region the development of slow traffic is paid more attention to, and the infrastructure is much more complete compared to the western region, thus more people are willing to adopt slow trip mode; While the construction of the transport infrastructure in the western region is still in its infancy, and the development of transport still tend to attach more importance to vehicles, not people, thus the concept of slow traffic needs more attention.

After the "Smooth Traffic Project" is implemented in the central region, the use of motorcycles are limited in large and medium-sized cities, while in the western region of small cities, urban transport policy pays no attention to specific trip mode, so the management of the motorcycle is relatively loose, as a result, the developing trend of motorcycle is accelerated.

Table 4. The trip mode structure of large and medium-sized cities in central and western regions (%).

City	Walk	Bicycle	Bus	Taxi	Motorcycle	Car	Unit car	Other	Year
Jingmen	35.80	14.59	15.39	3.29	17.77	6.39	3.54	3.23	2011
Chenzhou	35.49	6.91	19.45	9.48	1.44	13.49	6.09	7.65	2011
Yichang	33.79	8.91	17.45	6.48	12.44	12.49	6.09	8.35	2011
Zunyi	20.57	1.72	46.62	4.24	8.25	10.72	6.79	1.09	2012
Guigang	34.08	6.32	6.83	0.53	28.49	10.02	1.57	12.18	2010
Datong	21.49	4.91	26.42	3.51	19.58	9.49	5.09	9.56	2011

5 TRIP PURPOSE

Trip purpose is trip motivation. It can be roughly divided into working, going to school, shopping, entertainment, and business, visiting friends and relatives and so on. Among these purposes, working, going to school and business trip is rigid categories, shopping, entertainment and other leisure trip belong to elastic trip. Social and economic development level, occupation, work (learning) systems all have significant effect on residents' trip purpose, in which the levels of social development mainly influence on trip purpose of life, culture, entertainment, etc. Table 5 gives statistical

Table 5. Resident trip purpose structure of large and medium-sized cities in central region and western region respectively (%).

City	Job	Study	Official business
Jingmen	23.30	10.8	2.34
Chenzhou	20.67	5.66	2.87
Yichang	22.25	8.32	2.46
Zunyi	26.62	7.66	0.84
Guigang	19.73	18.14	3.78
Datong	21.27	5.52	2.23
Shopping	Visit	Home	Entertainment
17.77	1.89	1.28	1.96
1.44	2.82	1.45	3.84
12.44	2.45	2.36	3.64
8.25	3.06	1.40	2.13
28.49	2.08	0.88	1.20
19.58	3.32	1.52	3.95
City	Office	Other	Year
Jingmen	51.48	2.34	2011
Chenzhou	53.90	5.62	2011
Yichang	46.12	4.42	2011
Zunyi	46.29	7.36	2012
Guigang	47.86	2.47	2010
Datong	50.24	5.06	2011

data structure of resident tripling in the large and medium-sized cities of the Midwest, whose overall characteristic conclude return trip, working and going to school account for over 75%, and going to work is the largest proportion generally above 19%, besides going home.

In relatively developed large and medium-sized cities of central region with economy, the leisure trip is generally higher than that of the western region for the purpose of leisure entertainment and shopping. Similarly, in relatively developed region with industry, the employment rate is higher, and the rigid trip rate for going to work is higher than that in a relatively undeveloped region, and the trip rate for going to school in a relatively undeveloped developed area is higher than that in a relatively developed area.

6 TRIP TIME

Trip time is referred to the time required for residents from the origin to the destination with one-way tripping, which can be determined by trip mode, trip distance and so on. It is an important indicator of performance to measure the rationality of overall layout, accessibility, urban road network and public transportation.

Table 6 and Table 7 show average trip time statistics data and trip distance distribution statistics in six large and medium-sized cities of both regions average trip consumption statistics data and trip distance distribution statistics.

6.1 *General characteristic*

Considering the trip time of different trip modes is an important indicator to measure whether the urban traffic structure is reasonable or not. Trip survey data indicate that the overall feature of the time is that the larger the city scale is, the longer the trip time, and the total trip time is generally similar for the residents with the same sized city (Zhou et al. 2007).

The average trip time in the six selected cities is about 18 minutes (In Zunyi it is a little bit higher while in Guigang it is a little bit lower), which is within the reasonable range; the average trip time cost in Zunyi and Guigang is larger than other cities because the city scale is larger.

Seen from the trip time of different modes, non-motorized modes show less average trip time, and walking is the minimal one; among motorized modes, other trip times are higher than the average trip time except the taxi, and the bus trip time is the largest in addition to the authorized cars. The results above show that bus network layout needs to be further improved and bus service level needs further promotion in two regions.

6.2 *Comparison characteristics*

Due to the differences in social & economic levels, resident income, transport management policy and trip mode structure, there are some differences of trip time in two regions.

Table 6. Average trip times of different trip mode (min).

City	Walk	Bicycle	Bus	Average	Year
Jingmen	17.18	17.36	23.95	17.39	2011
Chenzhou	16.79	18.02	24.95	19.79	2011
Yichang	15.46	18.14	22.45	18.49	2011
Zunyi	20.02	18.26	20.95	20.24	2012
Guigang	17.23	17.40	23.15	17.42	2010
Datong	18.39	18.44	22.68	19.46	2011
Motorcycle	Car	Unit car	Taxi	Other	Year
19.94	22.6	37.1	8.43	17.57	2011
18.94	24.6	38.2	7.44	18.98	2011
18.36	23.2	37.92	7.27	18.38	2011
19.23	26.6	39.4	9.32	19.57	2012
17.94	23.6	36.8	7.86	17.49	2010
18.64	23.4	38.1	8.34	18.62	2011

Table 7. Different time distance distribution of comparative cities (%).

Time distance (min)	Jingmen	Chenzhou	Yichang	Zunyi	Guigang	Datong
0–10	7.63	22	20.9	8.18	30.57	22.4
10–20	27.41	25.2	24.6	21.34	34.03	24.4
20–30	25.40	25.5	23.8	29.77	21.91	26.8
30–40	22.86	11.7	13.2	13.90	6.10	11.4
40–50	6.78	5.4	5.8	8.29	2.50	6.1
50–60	3.32	5.5	5.7	9.69	2.69	5.7
60–70	3.51	1.6	3.2	2.90	1.22	1.8
>70	3.09	3.0	2.8	5.93	0.98	3.4

1. Difference of average trip time
   In the relatively developed zones, such as Jingmen and Chenzhou, the proportion of motorized vehicle modes (especially the motorcycle) is large, and part of walking and cycling trips are replaced by motorcycles, leading to non-motorized trip time in large and medium-sized cities less than that in the relatively underdeveloped western region of; at the same time, because in the central region the economy is well developed, part of bus trips turn to private cars, causing more trip time and larger trip range than that in the large and medium-sized cities of western region; In Jingmen, Chenzhou and other cities, taxi serves more between cities and surrounding towns, thus the trip time turns to be longer. However, in Zunyi, Guizhou and other cities of western region taxi mainly serves in urban areas, hence the trip time is shorter than that in the relatively developed cities of central China significantly.
2. Difference of trip tolerance time
   There exists significant different of trip tolerance time. It is assumed that the trip time T of 90% residents (when 90% residents' trip time is less than T) are defined as the maximal acceptable trip time. On the basis of definition, the trip tolerance time in six cities for one trip is shown in Figure 2. The influencing mechanism of trip time is very complicated, generally speaking, the longer the trip distance, the longer the trip time is, while the higher the motorization degree is, the shorter the trip time is (Zou et al. 2008, Lu & Wang 2004). However, through comparison and analysis, it can be found that in the typical city scale without much difference, the trip tolerance time with high motorized degree of large and medium-sized cities in central region, is higher rather than that in the western region (about 5 minutes), which implies that tolerance degree of trip time for residents of large and medium-sized cities in central region is larger, whereas satisfactory degree threshold is lower than that in the central city.

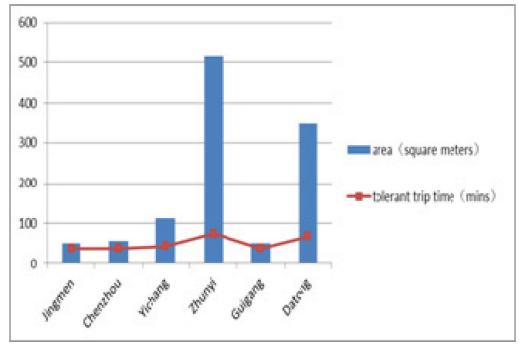

Figure 2. Tolerance trip time comparisons.

More reasonable explanation is that the economy in the large and medium-sized cities of western region is fallen behind and the urban and rural difference is significant, so the residents trip range focus on administrative area of the city, while the difference of urban and rural economy in relatively developed area is smaller, because of their more frequent communication, leading to wider trip range and larger trip tolerance time.

7 CONCLUSIONS AND RECOMMENDATION

7.1 *Conclusions*

In the absence of significant difference with city size and layout, for large and medium-sized cities, economy is the main factor for the variability of resident trip in the relatively developed city and the relatively undeveloped city.

In the relatively developed area average trip times per capita per day of urban residents is relatively higher than that in the western region, and the motorized trip mode structure proportion is also much higher than that in the western region, but

its non-motor mode is shrinking more and more; Moreover, the elastic trip proportion with leisure and entertainment in the central region is higher than that in the western area, and the motorized average trip time is longer than that in western region, but the non-motorized average trip time is lower than that in the western region of large and medium-sized cities; There exist certain difference between the trip time of two regions, and the most significant is that is the trip tolerance time in central region is 5 minutes longer than that in the western region of small cities.

7.2 *Recommendation*

Based on the internal relationship between traffic characteristics and the economy, the following suggestions are presented:

1. As the rapid development of economy and the speeding up of urbanization, space integration process of urban and rural is accelerated in large and medium-sized cities of central China and the trip distance for a quite number of urban residents will break through the traditional city range, therefore, it is recommended that to the trip tolerance the time be controlled within 40 minutes when planning. The economy in relatively developed central area should be integrated into the process of regional economic integration quickly, while the trip distance will be longer. It is necessary to strengthen the infrastructure integration in urban and rural area, and construct long-distance Bus Rapid Transit (BRT) system under the condition of keeping trip relatively stable.
2. In large and medium-sized cities of the western region walking and bicycle transportation system planning and humanized design should be strengthened to maintain the leading position of non-motorized vehicle split ratio. The motorcycle in relatively developed areas should be controlled with the excessive development in large and medium-sized cities of central area, and the trip mode of walking and bicycle should be advocated for the short distance trip.
3. Multi-level and diversified passenger transportation should be formed in order to satisfy the increasing and elastic leisure and entertainment trip demand with the economic development. To speed up the integration of urban and rural public transportation planning and construction, the level of bus service should be improved, and the integration of urban and rural space transportation support system should be established.
4. In the central China central-rising opportunity is confronted with. There is much space for their economy development and future planning for bearing capacity of urban transportation system should keep certain margin; the traffic infrastructure construction in large and medium-sized cities of central region has already been in shape, and. Traffic demand is relatively prosperous, so traffic demand management should be implemented firstly rather than in the western cities.

REFERENCES

Deng, M.Y. & Xie, L. 2000. The characteristics of the trips of the local residents and the transport policy in Guangzhou. *City Planning Review* 24(11): 45–49.

Florian, H. & Patrick, B. 2014. Falko D. Advanced leader election for virtual traffic lights. *ZTE Communications* 12(1): 11–16.

Lu, J. & Wang, W. 2004. Study of resident trip time consumption characteristic. *Journal of Highway and Transportation Research and Development* 21(10): 102–104.

Wang, L. 2008. Study on promotion of city public security and improvement of city planning. *China City Planning Review* 17(3): 30–37.

Xiong, Z., Sheng, H. & Rong, W.G. 2012. Intelligent transportation systems for smart cities: a progress review. *Science China (Information Sciences)* (12): 2908–2914.

Yao, X.H., Zhan, F.B. & Lu, Y.M. 2012. Effects of real-time traffic information systems on traffic performance under different network structures. *Journal of Central South University* (19): 586–592.

Zhou, Q., Lu, H.P. & Xu, W. 2007. Comparison and analysis of urban resident trip characteristics. *Journal of Central South Highway Engineering* 32(2): 145–149.

Zou, Z.Y. 2012. *Report of Transport Planning about Jingmen, Chenzhou, Zunyi, Guigang etc.* Wuhan: College of Traffic Science and Engineering of Huazhong University of Science and Technology.

Zou, Z.Y., Jiang, Z.H. & Hu, C. 2008. Analysis on resident trip characteristics in part of Chinese cities. *Journal of Wuhan University of Technology (Transportation Science & Engineering)* 32(3): 554–557.

Civil Engineering and Urban Planning IV – Liu et al. (Eds)
© 2016 Taylor & Francis Group, London, ISBN 978-1-138-02903-3

A multistage method on regional multimodal logistic network design from a logistic enterprise perspective: A case in China

Hua-Qiang Li
School of Automobile, Chang'an University, Xi'an, Shanxi, China

ABSTRACT: Regional multimodal transport and logistics network designing can promote the development of multimodal transport in China and provide support for transport enterprises to build the multimodal transport business. The aim of this paper is to develop a multi-stage method of regional multimodal transport and logistics network designing under a fuzzy environment using a fuzzy Technique for Order Performance Similar to the Ideal Solution (TOPSIS) and fuzzy 0–1 integer programming. Fuzzy TOPSIS approach was used to evaluate the ranking of candidate cities located in the Yangtze River Delta. Furthermore, the fuzzy 0–1 integer programming was erected to determine the optimized logistics network. Finally, the approach was demonstrated using the case of Jiangsu Jinling transportation group CO., LTD, China, which involved 16 candidate cities in the Yangtze River Delta. In the end, Jiangsu Jinling transportation group CO., LTD built a logistics network consisting of five logistics network hubs and 11 general nodes using the approached method. The application of a practical case indicates that this approach can provide effective decision support for Transport Corporation to establish a regional multimodal transport and logistics network.

1 INTRODUCTION

As an advantage of multimodal transport, Drop and Pull Transport refers to a transport mode in which the devices pulled by a power-driven vehicle, including semi-trailer, full-trailer, and even the container on the truck chassis, are dropped when reaching a certain destination and then will be replaced by other fully loaded devices for driving back to the point of origin or another destination. A series of policies and regulations have been introduced in recent years by relevant departments in the country to stimulate the development of Drop and Pull Transport. The Road Transport Department of Transport Ministry posited in July 2010 that the development of Drop and Pull Transport should be regarded as the target and key task of the 12th Five-Year Plan. All these show Drop and Pull Transport as an energy-saving and emission-reducing transport mode that will change the transport and production ways of road freight industry, and is attracting more and more attention from the government.

The high development requirement of Drop and Pull Transport in China, however, is in conflict with its short development time, leading to a gap between expectation and reality. There exist a lot of inevitable deficiencies including low Drop-Pull operation efficiency, poor infrastructure resources, lack of information platforms as well as the restrictions by government policies and regulations. As China lacks logistics enterprises of a certain scale, logistics companies usually focus their business on a certain region. In this case, we focus our effort on how to solve the logistics problems of a certain region.

A multistage method of a regional multimodal transport and logistics network design is presented in this paper in order to promote the development of multimodal transport in China and provide support for transport enterprises to build multimodal transport business. We also considered that a real situation is uncertain, so fuzzy numbers are introduced. And the steps and superiority of this method are illustrated via an actual project case—the construction of a multimodal transport and logistics network in the Yangtze River Delta by Jiangsu Jinling Transportation Group.

2 METHODS

TOPSIS (Technique for Order Preference by Similarity to Ideal Solution), was developed by Hwang and Yoon (1981) for the first time. It is a classical approach to Multi-Attribute or Multi-Criteria Decision-Making (MADM/MCDM) problems (Tan 2011). According to this technique, the best alternative would be one that is closest to the positive-ideal solution and farthest from the negative-ideal solution (Ertugrul & Karakasoglu 2009).

But traditional TOPSIS methods can only deal with a certain number. Ambiguity is a big challenge for Decision Makers (DMs). Because of this fact, researchers tried to apply TOPSIS in a fuzzy environment. An impressive variety of fuzzy TOPSIS algorithms and applications have developed in recent years. Thus, Fuzzy TOPSIS has become a useful approach to solve practical problems.

The 0–1 integer programming is a kind of special integer programming, which has broad application prospects. Considering the imprecise nature of human judgments, we combine 0–1 inter programming with fuzzy sets so as to solve practical problems.

Considering both tangible and intangible criteria, this study proposes integrated fuzzy techniques for order preference similar to Fuzzy TOPSIS and Fuzzy 0–1 integer programming approach evolved to solve the logistics network designing problem of multimodal transport.

As shown in Figure 1, our approach can be divided into two stages:

1. Determining the ranking of candidate cities by Fuzzy TOPSIS;
2. Building the fuzzy 0–1 integer programming and determine the regional multimodal logistics network.

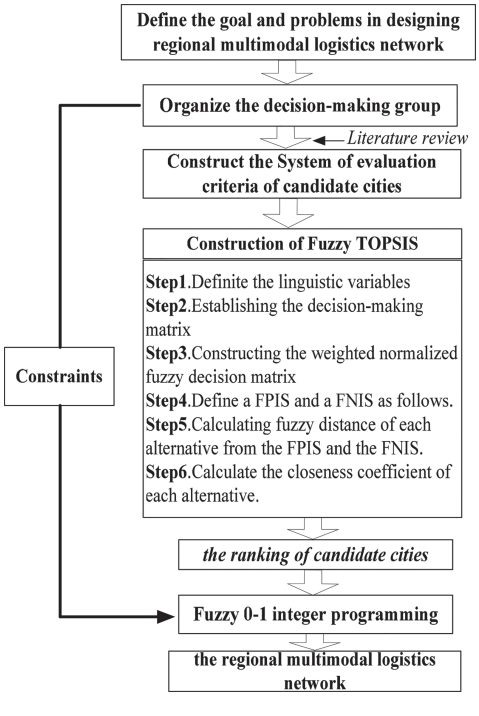

Figure 1. Method framework for logistics network design.

By this method, we can determine the logistics network based on the location of the hub of logistics networks and general logistics network node.

2.1 *Stage I. Determining the ranking of candidate cities*

2.1.1 *Step 1. Define the goal and problems in regional multimodal logistics networks and organize the decision-making groups.*

The design goal of a logistics network of multimodal transportation is to develop a single methodology to help transportation companies determine the optimal logistics network. According to the designing problem, we assume that a decision-making group to do the designing has K persons and that there are m candidate cities that could be selected to construct logistics hubs. The candidate cities are located in the Yangtze River Delta.

2.1.2 *Step 2. Construct the system of evaluation criteria of candidate cities.*

For evaluating the candidate nodes reasonably and synthetically, we must establish a scientific and effective evaluation system. We set the goal of choosing the site and making the evaluation system more scientific and user-friendly, and taking the correlation and pertinency into account, we sought out 12 indexes as follows:

1. F1, Gross Domestic Product (GDP)
   The Gross Domestic Product in the region will affect the amount of container packaging and goods needed to be transported to the area for production and consumption. In addition, Qi (2008) believed that GDP also affects the attract amount of transshipment containers. Therefore, an intermodal container node usually is selected in economically developed areas in order to ensure adequate supply.
2. F2, Trade volume of import and export
   In China, container multimodal transport is mainly composed of foreign trade transportation, and domestic trade transportation is complementary. Import and export trade provides an adequate supply for container transportation. Ge (2007) treated the throughput as technical conditions of the port and basis of port transit city layout in container multimodal transport. So the trade volume of import and export of nodal city will have important influences on multimodal transport network.
3. F3, Total freight volume of region
   The total freight volume of the region means the total amount of goods circulation in the region; it is an important index of developing and checking the transportation production plan, the research of development scale, and speed of transportation.

4. F4, Comprehensive conditions of carriage
   Comprehensive conditions of carriage refer to the environmental conditions of a series of operations, including container transportation infrastructure, organization levels, etc. It also affects the degree of container packaging and the attract amount of transshipment container. According to the research by Yang (2011), carriage factors can be divided into four factors: convenience of water transport, rail transport, highway transportation and air transport, and he has made a detailed quantitative analysis.
5. F5, Degree of container packaging suitability
   Container multimodal transport needs to package the goods by container, so the degree of container packaging suitability must be considered. International trade goods can be divided into 56 items, of which only 32 species are suitable for container transport. According to statistics, the container freight volume is only 10.7% of the total freight; the rest are not suitable for container transport or marginalized goods. Thus, it's the amount of goods that decides the suitable amount for container packaging (especially in the foreign trade) rather than the amount of total goods in the generation amount of container.
6. F6, Price of logistics land
   Construction of multimodal transport node needs to occupy a large area of land; what's more is that enough space for development is needed. So the price of logistics land will affect the node's dimensions directly. Kang & Wang (2009) think the index can be measured reasonably via unit land exploitation cost.
7. F7, Degree of the logistics market saturation
   Degree of logistics market saturation refers to the ratio of the amount of market share and market potential in the area of logistics industry. Market potential means the limit of the logistics market's demand (Li & Huang 2006). The analysis of the degree of market saturation relates to many market development aspects. A market with a higher saturation degree requires a higher development cost, thus a relatively lower profit. A market with a low saturation degree, although requiring a low cost, does not have stable customers in the market.
8. F8, Location conditions
   Location conditions include natural conditions and geographical position and largely determine the rationality and difficulty level in the construction of multimodal transport nodes. Feng (2008) found that natural conditions affect the cost of freight hub construction and the operations management fee when the node is put into use. Li (2003) thinks it's best that nodes distribute in an important transport hub city, logistically important nodes on the network, or an important economic center city on a regional or national comprehensive transportation network.
9. F9, Conditions of logistics policy
   Regional economic and transport construction must obey the country's macroeconomic development and transportation planning requirements. National policy guidance and support on regional economic and transport development will profoundly affect the regional economic development and the degree of perfection of the transportation network, as well as intermodal container related links. Therefore, multimodal transport nodes should be constructed in areas with national policy guidance to create better external conditions for the development of container services.
10. F10, Complementary conditions such as energy and labor supply
    Complementary conditions, such as energy and labor supply, affect the economic costs and efficiency of transport. It is better for constructing multimodal transport nodes that have a better energy supply, adequate labor, and logistics talents.
11. F11, Degree of fit enterprise strategy
    For container multimodal transport layout, a fitting corporate strategy would require that the layout should construct the right node layout according to the changes in the environment, resources, strength, and future development needs. The investment in node construction is big and the construction period is long. It should not only suit to current needs, but also advance moderately to leave room for future development.

2.1.3 *Step 3. Definite the linguistic variables.*

In this paper, the importance weights of various criteria and the ratings of qualitative criteria are considered as linguistic variables. They are named as follows: Very Low (VL), Low (L), Medium (M), high (H), and Very High (VH). These linguistic variables can be expressed in triangular fuzzy numbers as (0, 0, 0.25), (0, 0.25, 0.5), (0.25, 0.5 0.75), (0.5, 0.75, 1), and (0.75, 1, 1).

2.1.4 *Step 4. Constructing the decision-making matrix.*

Let $\tilde{e}_{ij}^{k}$ denote the value of the criteria F_j for candidate city C_i decided by the decision-maker D_k, and let $\tilde{w}_j^k$ denote the weight of the criteria F_j decided by decision-maker D_k.Then the weight of the criteria and the rating of alternatives with respect to each criterion can be calculated as equation (1) and (2):

$$\tilde{e}_{ij} = \frac{1}{K} \otimes \left(\tilde{e}_{ij}^{1} \oplus \tilde{e}_{ij}^{2} \oplus \cdots \oplus \tilde{e}_{ij}^{K} \right) \tag{1}$$

$$\tilde{e}_{ij} = \frac{1}{K} \otimes \left(\tilde{e}_{ij}^{1} \oplus \tilde{e}_{ij}^{2} \oplus \cdots \oplus \tilde{e}_{ij}^{K} \right) \tag{2}$$

As stated above, then the decision-making problem can be concisely expressed in matrix format as:

$$\tilde{E} = \begin{bmatrix} \tilde{e}_{11} & \tilde{e}_{12} & \cdots & \tilde{e}_{1n} \\ \tilde{e}_{21} & \tilde{e}_{22} & \cdots & \tilde{e}_{2n} \\ \vdots & \vdots & \ddots & \vdots \\ \tilde{e}_{m1} & \tilde{e}_{m2} & \cdots & \tilde{e}_{mn} \end{bmatrix} \tag{3}$$

$$\tilde{W} = [\tilde{w}_1, \tilde{w}_2, \ldots, \tilde{w}_n] \tag{4}$$

where $\tilde{e}_{ij}, \forall i, j$ and $\tilde{w}_j, \forall j$ are linguistic variables, can be described by triangular fuzzy numbers, and

$$\tilde{e}_{ij} = (a_{ij}, b_{ij}, c_{ij}), \ \tilde{w}_j = \left(\tilde{w}_{j1}, \tilde{w}_{j2}, \tilde{w}_{j3} \right).$$

2.1.5 *Step 5. Constructing the weighted normalized fuzzy decision matrix*

We can obtain the normalized fuzzy decision matrix denoted by $\tilde{F}$.

$$\tilde{F} = \left[\tilde{f}_{ij} \right]_{m \times n}, \tag{5}$$

where $\tilde{e}_{xy}, \forall x, y$ can be calculated by:

$$\tilde{f}_{ij} = \left(\frac{a_{ij}}{c_j^+}, \frac{b_{ij}}{c_j^+}, \frac{c_{ij}}{c_j^+} \right), \ c_j^+ = \max_i c_{ij}, \ if \ \ j \in J_1, \tag{6}$$

$$\tilde{f}_{ij} = \left(\frac{a_j^-}{c_{ij}}, \frac{a_j^-}{b_{ij}}, \frac{a_j^-}{a_{ij}} \right), \ a_j^- = \min_i c_{ij}, \ if \ \ j \in J_2, \tag{7}$$

where J_1 and J_2 represent the criteria of benefit and cost, respectively.

Considering the different importance of each criterion, we can obtain the weighted normalized fuzzy decision matrix denoted by $\tilde{G}$

$$\tilde{G} = [\tilde{g}_{ij}]_{m \times n}, i = 1, 2, \ldots, m, \ j = 1, 2, \ldots, n \tag{8}$$

2.1.6 *Step 6. Determining the positive ideal solution and negative ideal solution.*

The fuzzy positive ideal solution and the fuzzy negative ideal solution are shown in the following equations.

$$\begin{aligned} \tilde{P}^+ &= \left(\tilde{g}_1^+, \tilde{g}_2^+, \cdots \tilde{g}_n^+ \right) \\ &= (\max_i \tilde{g}_{ij}, \ j \in J_1; \ \min_i \tilde{g}_{ij}, \ j \in J_2) \end{aligned} \tag{9}$$

$$\begin{aligned} \tilde{P}^- &= (\tilde{g}_1^-, \tilde{g}_2^-, \cdots \tilde{g}_n^-) \\ &= (\min_i \tilde{g}_{ij}, \ j \in J_1; \ \max_i \tilde{g}_{ij}, \ j \in J_2) \end{aligned} \tag{10}$$

2.1.7 *Step 7. Calculating fuzzy distance of each fleet from $\tilde{P}^+$ and $\tilde{P}^-$.*

The distance of each candidate city from $\tilde{P}^+$ and $\tilde{P}^-$ can be currently calculated as

$$D_i^+ = \sum_{j=1}^{n} d(\tilde{g}_{ij}, \tilde{g}_j^+), i = 1, 2, \cdots, m \tag{11}$$

$$D_i^- = \sum_{j=1}^{n} d(\tilde{g}_{ij}, \tilde{g}_j^-), i = 1, 2, \cdots, m \tag{12}$$

where $d(\tilde{g}_{ij}, \tilde{g}_j^-)$ and $d(\tilde{g}_{ij}, \tilde{g}_j^+)$ are the distance measurements between two fuzzy numbers.

2.1.8 *Step 8: Calculate the closeness coefficient of each candidate city.*

The closeness coefficient of each candidate city is calculated as follows:

$$CC_i = \frac{D_i^-}{D_i^+ + D_i^-}, i = 1, 2, \ldots, m \tag{13}$$

The CC_i represents the suitability of building a logistics network hub of the i-th candidate city. A higher score corresponds to a better suitability.

2.2 *Build the fuzzy 0–1 integer programming and determine the optimized logistics network*

2.2.1 *Step 1: Modeling the fuzzy 0–1 integer programming*

If there are some constraints, such as investment and business volume of logistics enterprise, the capacity constraints of each candidate city use the sum of candidate cities as an objective function in fuzzy 0–1 integer programming to determine the optimized combination of candidate cities. The objective function and constraints of this fuzzy 0–1 integer programming is as follows:

$$\min \sum_{i=1}^{M} x_i \tag{14}$$

Subject to:

$$\sum_{i=1}^{M} \tilde{c}_i x_i \le TC \tag{15}$$

$$\sum_{i=1}^{M} \beta_i x_i \ge \tilde{\beta}_{\min} \tag{16}$$

$$\sum_{i=1}^{M} CC_i x_i - CC_{ave}\left(\sum_{i=1}^{M} x_i\right) \geq 0 \tag{17}$$

$$x_i \in \{0,1\}, \forall i \tag{18}$$

$$CC_{ave} = \frac{1}{M}\sum_{i=1}^{M} \varepsilon_i \tag{19}$$

where,

x_i: $x_i = 1$, the i-th city is selected; $x_i = 0$, the i-th city is not selected;
$\tilde{c}_i$: The fuzzy construction costs of the i-th candidate city;
TC: Maximum investment of logistics enterprises to build logistics nodes;
β: Maximum by capacity can be built of the i-th candidate city;
$\tilde{\beta}_{\min}$: Fuzzy estimates of logistics enterprises' business volume;
CC_i: Closeness coefficient of the i-th candidate city;
CC_{ave}: The average closeness coefficient can be calculated cities.

2.2.2 *Step 2: Defuzzification*

Considering the weights average method and α-cut method of Tanaka et al, constraints (15) and (16) can be converted to the exact coefficient constraints as follows:

$$\sum_{i=1}^{M} \left[(1-w)(c_i)_\alpha^L + w(c_i)_\alpha^U\right] x_i \leq TC \tag{20}$$

$$\sum_{i=1}^{M} \beta_i x_i \geq (1-w)(\beta_{\min})_\alpha^L + w(\beta_{\min})_\alpha^U \tag{21}$$

where, $w \in [0,1]$ denote the decision-making group's preference for upper and lower limits.

3 CASE STUDY

3.1 *Case background*

Jiangsu Jinling Transportation Group, founded in 1949, bore the national key task and dredging port cargo transport, as well as rescue and disaster relief emergency security task, as the national key transportation enterprise, the province's largest state-owned road transportation enterprise, in planning economy age. In 2004 under the Nanjing government unified deployment, Jiangsu Jinling Transportation Group completed the restructuring of the whole enterprise. In recent years, the enterprise development has expanded to include cargo logistics, passenger travel, business property, and transportation industry as an integrated transportation enterprise group, 27 in total either wholly-owned, holding subsidiaries, and participation.

With freight logistics as the main business of integrated transportation companies, container multimodal transport will play an important role. Node, as the basis to realize transport platform of intensification, specialization, and informationization, is an important basic guarantee of promoting rapid development of the multimodal transport, container transport, and modern logistics and plays an important role in the formation of norms and orderly, fair competition in the transportation market. Through a reasonable layout of multimodal transport nodes, it can enhance the capacity of enterprise transportation network of effective supply build a rapid transport system based on transportation networks, which plays a major role in improving the enterprise's overall efficiency and service level and accelerates the development of the modern transportation industry.

In order to suit the development goals of the Jiangsu Jinling Transportation Group, this article will establish a reasonable competitive multimodal transport network for the enterprise in the Yangtze

Figure 2. The distribution map of candidate cities.

Table 1. Linguistics variables evaluation and the weight matrix of the criteria.

	Decision-makers			
Criteria	D1	D2	D3	Weight
F1	H	VH	H	(0.58,0.83,1.00)
F2	H	H	H	(0.50,0.75,1.00)
F3	M	M	H	(0.33,0.58,0.83)
F4	VH	VH	VH	(0.75,1.00,1.00)
F5	M	L	L	(0.08,0.33,0.58)
F6	H	M	H	(0.42,0.67,0.92)
F7	M	L	M	(0.17,0.42,0.67)
F8	H	H	VH	(0.58,0.83,1.00)
F9	M	M	M	(0.25,0.50,0.75)
F10	L	VL	L	(0.00,0.17,0.42)
F11	M	L	VL	(0.08,0.25,0.50)

Table 2. Ratings of the 16 candidates by decision-makers under all criteria.

Cities		F1 (100 million yuan)	F2 (100 million dollar)	F3 (10000 tons)	F4	F5	F6	F7	F8	F9	F10	F11
C1	Shanghai	20101.3	4367.6	94376.3	VH	VH	(1000,1500,2000)	VH	VH	L	L	VH
C2	Nanjing	7201.6	552.4	41998.5	VH	H	(620,650,680)	H	VH	H	H	VH
C3	Suzhou	12011.7	3056.9	17700	H	H	(630,663,696)	VH	H	M	M	H
C4	Wuxi	7568.2	707.8	18267.7	H	M	(380,426,472)	H	H	M	M	H
C5	Chang zhou	6524.7	965.7	32600	H	H	(720,760,800)	M	M	H	H	H
C6	Zhenjiang	2630.1	114.1	13000	M	M	(300,338,376)	M	M	H	H	M
C7	Nantong	4558.7	263	26700	M	M	(270,300,330)	L	M	H	H	M
C8	Yangzhou	2933.2	102.0	12200	L	M	(280,310,340)	L	M	M	M	M
C9	Taizhou	2701.7	103.7	32375	M	H	(380,400,420)	M	M	M	M	M
C10	Hangzhou	7804.0	616.8	30200	VH	H	(800,1082,1364)	VH	VH	M	M	H
C11	Ningbo	3969.8	290.3	17794	H	M	(300,336,372)	H	H	M	M	H
C12	Huzhou	1662.0	87.4	19467	M	M	(600,625,650)	M	H	H	H	M
C13	Jiaxing	2884.9	287.4	6738	M	M	(800,1000,1200)	M	H	M	M	M
C14	Shaoxing	3620.1	321.0	9274	M	H	(320,350,380)	M	M	M	M	M
C15	Zhoushan	852.0	153.6	19939	L	H	(340,360,380)	H	M	M	M	L
C16	Taizhou	349.0	206.2	5358.22	L	H	(700,740,780)	M	M	M	M	L

River Delta region based on the actual situation of the enterprise. There are 16 cities of the Yangtze River Delta candidate cities and the geographical position distribution is shown in Figure 2.

3.2 *Calculation and result*

The proposed method is currently applied to solve this problem and the computational procedure is as follows:

First of all, a decision-making group who had extensive knowledge and experience in the field of logistics network designing was organized by the corporation of two professors and one engineer. Then the decision-making group used the linguistic variables (shown in Table 1) to assess the importance of the criteria and the rating of the candidate city (shown in Table 2). Then according to equation (1), the weight matrix was calculated, as shown in Table 1. Finally, according to equations (2–14), the closeness coefficient CC of each candidate city was calculated, as shown in Table 3.

According to a real case of the company, the decision-makers determined the fuzzy construction costs and maximum capacity of candidate cities could be built (shown in the Table 4). The maximum investment of the enterprises to build logistics network is ten thousand yuan and the fuzzy estimates of logistics enterprises' business volume can be expressed by the triangular fuzzy number as (450,500,550). Then, according to equations (15–21), the fuzzy 0–1 integer programming results based on different α and w was calculated as shown in Table 4.

Table 3. CC, C_i and β_i of candidate cities.

Candidate city		CC	C_i (ten thousand yuan)	β_i
C1	Shanghai	0.912847	(460,480,500)	90
C2	Nanjing	0.609956	(420,450,480)	100
C3	Suzhou	0.61157	(440,460,480)	105
C4	Wuxi	0.416067	(350,370,390)	110
C5	Changzhou	0.47979	(340,360,380)	120
C6	Zhenjiang	0.227617	(300,320,340)	95
C7	Nantong	0.229824	(290,300,310)	100
C8	Yangzhou	0.0997	(260,270,280)	115
C9	Taizhou	0.256272	(280,300,320)	100
C10	Hangzhou	0.583014	(440,470,500)	85
C11	Ningbo	0.341288	(340,360,380)	90
C12	Huzhou	0.331948	(330,350,370)	105
C13	Jiaxing	0.309799	(340,360,380)	120
C14	Shaoxing	0.222556	(260,270,280)	115
C15	Zhoushan	0.169267	(280,300,320)	100
C16	Taizhou	0.181295	(350,370,390)	130

Finally, decision-makers chose Shanghai, Nanjing, Zhenjiang, Nantong, and Ningbo to build the logistics network hub of multimodal transport based on the results of Fuzzy TOPSIS and Fuzzy 0–1 integer programming. As shown in the Figure 2, there are five logistics network hubs of multimodal transport and 11 general logistics network nodes, and the hubs have more developed traffic conditions of waterway, railway, and highway. Jiangsu Jinling transportation group CO., LTD built the logistics network consisting of the five logistics network

Table 4. Fuzzy 0–1 integer programming result.

w/α	w = 0	w = 0.2	w = 0.4	w = 0.6	w = 0.8	w = 1
α = 0	C2, C9, C13, C16	C1, C3, C6, C7, C11	C1, C7, C9, C13, C11	C1, C3, C6, C9, C11	C1, C10, C12, C13, C16	C2, C3, C9, C13, C16
α = 0.5	C1, C4, C6, C7, C11	C1, C6, C7, C9, C11	C1, C4, C6, C9, C11	C1, C6, C9, C13, C11	C1, C3, C9, C13, C11	C1, C2 , C6, C7, C11,
α = 1	C1, C2, C6, C7, C11	C1, C2, C6, C7, C11	C1, C2, C6, C7, C11	C1, C2, C6, C7, C11	C1, C2, C6, C7, C11	C1, C2, C6, C7, C11

hubs and 11 general nodes will promote the development of the company's multimodal transport greatly by satisfying the company's freight demand of each logistics network node and fully using the multimodal transport of each city.

4 CONCLUSION

This paper studies primarily the two-stage approach for logistics enterprises to design the regional multimodal logistics network based on 16 candidate cities in the Yangtze River delta under a fuzzy environment. One methodology to be used by logistics corporation in designing the regional multimodal logistics network has been established based on the fuzzy TOPSIS and fuzzy 0–1 integer programming, and the application of the method studied in this paper has been described for Jiangsu Jinling transportation group CO., LTD's designing of a regional multimodal logistics network.

The case of Jiangsu Jinling transportation group CO., LTD shows that the proposed method is of great realistic significance and effectiveness of designing regional multimodal logistics network. But how to operate an actual case of multimodal transport on the built logistics network needs to be continued.

REFERENCES

Ertugrul, I. & N. Karakasoglu, 2009. Performance evaluation of Turkish cement firms with fuzzy analytic hierarchy process and TOPSIS methods. *Expert Systems with Applications* 36(1): 702–715.

Feng, Y.X. 2008. *The Synthetic Evaluation Method of Logistics Park Location and Related Issues Research*. Changsha: Central South University (in Chinese).

Ge, R. 2007. Study on Rational Layout of Container Transferring Cities and Route Selection in Multimodal Container Transportation. Beijing: Beijing Jiaotong University (in Chinese).

Hwang, C.L. & Yoon, K. 1981. *Multiple attributes decision making methods and applications*. Berlin, Heidelberg: Springer.

Kang, X.Y. & W. Wang, 2009. Layout of Port Multimodal Transport Nodes Based on Fuzzy c-cluster Analysis. *Transportation* 28: 64–68 (in Chinese).

Li, Q. 2003. *The Study of Wuhan's Developing Towards Logistic Pivotal City.* Wuhan: Wuhan University of Technology (in Chinese).

Li, Y. & Huang, Y.F. 2006. *Marketing.* Tianjin: Science Press (in Chinese).

Qi, H. 2008. The Planning of Container Multimodal Transport Freight Station Based on Fuzzy Cluster Analysis. *Journal of Fuqing Branch of Fujian Normal University* (5): 13–16 (in Chinese).

Tan, C.Q. 2011. A multi-criteria interval-valued intuitionistic fuzzy group decision making with Choquet integral-based TOPSIS. *Expert Systems with Applications* 38(4): 3023–3033.

Yang, Y.H. 2011. *Analysis of Location of the fright cargo hubs based on Multimodal Transport*. Xian: Chang'an University (in Chinese).

This page intentionally left blank

Civil Engineering and Urban Planning IV – Liu et al. (Eds)
© 2016 Taylor & Francis Group, London, ISBN 978-1-138-02903-3

Research on mechanical properties of steel slag asphalt mixture

Wei Li, He-Di Wang, He-Bin Wang & Cheng-Yuan Wang
School of Civil Engineering, Shenyang Jianzhu University, Shenyang, Liaoning, China

ABSTRACT: The rapid growth of industrial waste and its slow degradation rate is the main contradiction of garbage disposal. Steel slag is one of the main by-products of the iron and steel industry. If it is utilized effectively, we can not only solve the problem of expropriation of land and environmental pollution, but also get a great economic benefit. In this paper, author does a Marshall test, split test, and water seepage test, to understand the mechanical properties of steel slag, to provide theory of using steel slag in subgrade and pavement.

1 INTRODUCTION

On the one hand Chinese make great quantities of steel every year. Chinese steel output reached 1.126 billion tons (NBSC 2015) and steel slag more than 100 million tons in 2014. This accumulated steel slag not only expropriated a lot of land, but also pollute the environment seriously. On the other hand, highway construction needs a large number of stone. Production of crushed stone will cause serious ecological and environmental problems such as the destruction of vegetation and bare hillside.

In recent years, domestic and foreign scholars have done a lot of research on the mechanical properties of steel slag (Poh et al. 2006; Shan 2000; Shi 2004). Steel slag swells seriously in water and strength properties of different types of steel slag are different. Therefore, the way that steel slag replace crushed stone as the main material for the integration in road construction has not been widely used. The authors continue to do research on steel slag, to provide theory basis for its application in road construction, in order to achieve its utilization scientifically and effectively in geotechnical engineering.

2 TEST SURVEY

2.1 *Properties of steel slag*

Due to the ore composition and production process, the chemical composition of steel slag change. According to the Japanese Association for the study of steel slag, the chemical composition is shown in Table 1 and physical properties in Table 2 (Cui 2008). Experimental results are in accordance with "Steel Slag for Road" (GB/T 25824-2010).

From Table 1, we can see the main chemical composition of steel slag consists of CaO, SiO_2, Fe_2O_3, Al_2O_3, and FeO, and the chemical composition is generally more than 80%. The other contains a small amount of MgO, MnO, P_2O_5, and f-CaO, where f-CaO content is no more than 3%, the volume of steel slag is relatively stable.

From Table 2, apparent relative density of coarse aggregate standard is required to be no less than 2.60 and test result is 3.24. Apparent relative density of fine aggregate standard is required to be no less than 2.50 and test result is 3.36. Test results generally indicate that the physical and mechanical properties of steel slag meet the provisions relating to road surface material in "Technical Specification for Construction of Highway Asphalt Pavements" (JTGF40-2004) in China. In addition, water absorption of expressway and arterial road is required to be no more than 2.0%, and other grade ordinary road is no

Table 1. Chemical constituents of steel slag.

Chemical constituents Species	Blast furnace slag	Converter slag	Electric furnace slag	
			Acid slag	Reducing slag
CaO	41.7%	45.8%	22.8%	55.1%
SiO_2	33.8%	11.0%	12.1%	18.8%
Fe_2O_3	4.4%	17.4%	29.5%	3.2%
MgO	7.4%	6.5%	4.8%	7.3%
Al_2O_3	13.4%	1.9%	6.8%	16.5%
FeO	6.2%	7.2%	4.5%	3.4%
P_2O_5	<0.1%	1.7%	0.3%	0.1%
MnO	0.3%	5.3%	7.9%	1.0%
f-CaO*	2.5%	2.8%	1.2%	1.5%

*f-CaO is free calcium oxide.

Table 2. Physical properties of steel slag.

Physical properties	Aggregate requirement	Test result
Crushing value	≤26%	17.5%
Apparent relative density (D10–15)*	≥2.60	3.24
Apparent relative density (D5–10)*	≥2.50	3.36
Water absorption (for expressway and arterial road)	≤2%	2.2%
Water absorption (for other grade ordinary road)	≤3%	2.2%
Adhesiveness of asphalt	≥Lv.4	Lv.4
Acicular content	≤15%	4.6%
Losangeles abrasion value	≤28%	18.5%
Polishing value	≥42	45
f-CaO	≤3%	0.04%
Efflorescence rate upper limit	≤5%	0.47%
Soaking expansion rate	≤2%	0.46%
Impact value	25%	14%

*D10–15 means aggregate diameter range from 10 mm to 15 mm, and D5–10 means 5 mm to 10 mm.

Table 3. Aggregate gradation.

AC-13*		AC-16*		AC-20*	
Sieve size (mm)	Percent passing %	Sieve size (mm)	Percent passing %	Sieve size (mm)	Percent passing %
0.075	5.4	0.075	5	0.075	5.8
0.15	6.6	0.15	7	0.15	7.8
0.3	7.9	0.3	9	0.3	11.2
0.6	12.1	0.6	11	0.6	14.3
1.18	19.5	1.18	17	1.18	18.9
2.36	29.7	2.36	26	2.36	26.6
4.75	40.3	4.75	48	4.75	39.3
9.5	72	9.5	74	9.5	52.7
13.2	92.4	13.2	90	13.2	67.8
16.0	100	16.0	96	16.0	87.3
		19.0	100	19.0	95.7
				26.5	100

*AC-13 asphalt aggregate ratio is 5.2%; AC-16 asphalt aggregate ratio is 4.8%; AC-20 asphalt aggregate ratio is 4.6%.

more than 3.0% in "Technical Specification for Construction of Highway Asphalt Pavements" (JTGF40-2004) in China. The test result of water absorption is 2.2%, and it is more than 2.0%. So we should pay attention to this situation in road construction.

2.2 *Mix proportion of steel slag asphalt mixture*

We use AH-90 of heavy traffic road asphalt and dense gradation asphalt mixture. Coarse aggregate and fine aggregate are all replaced by steel slag in asphalt mixture. They are used in asphalt highway surface and semi-rigid base. Steel slag asphalt mixture gradation is shown in Table 3 (Cheng et al. 2006; Ying & Zheng 2005; Zhang & Zhao 2006).

3 EXPERIMENTAL PROCEDURE

3.1 *Marshall stability test of steel slag asphalt mixture at high temperature*

Test specimen is shaped in the standard Marshall compaction method. The height meets 63.5 ± 1.3 mm and diameter meets 101.6 ± 0.2 mm. Automatic Marshall tester is used and the loading speed is 50 ± 5 mm/min. The pressure and deformation relationship are record by computer automatically. Figures 1–6 show the recorded pressure and deformation curves. The abscissa is a deformation and the ordinate is maximum load.

Marshall stability is generally required to be not less than 5 kN and the flow value is 2–5 mm in "highway engineering specifications" in China. Table 4 shows the results of Marshall stabilities and flow value. It seems that with the increase of coarse slag aggregate, the Marshall stabilities will become larger with the increase of coarse slag aggregate. The Marshall stabilities are all more than 8 kN; they satisfy the requirement of "highway engineering specifications" in China. And the flow value tends to become larger with the increase of coarse slag aggregate too.

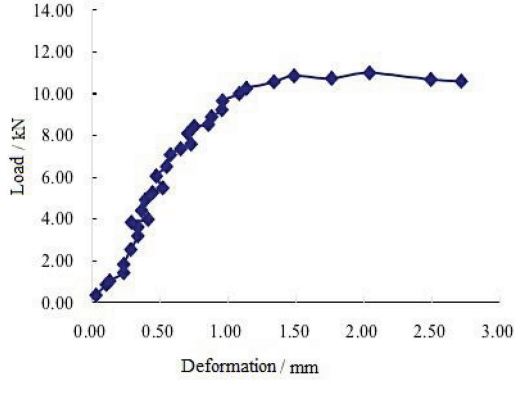

Figure 1. Load and deformation relationship for AC-13(1).

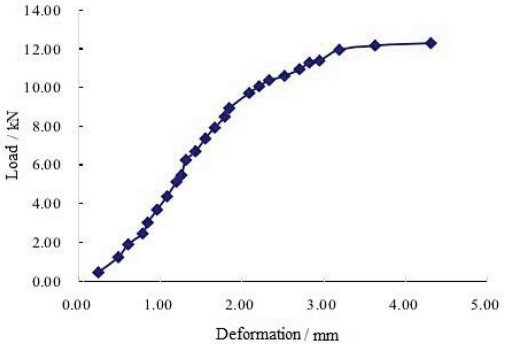

Figure 2. Load and deformation relationship for AC-13(2).

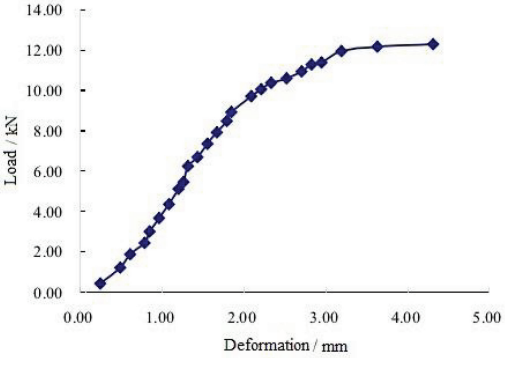

Figure 3. Load and deformation relationship for AC-16(1).

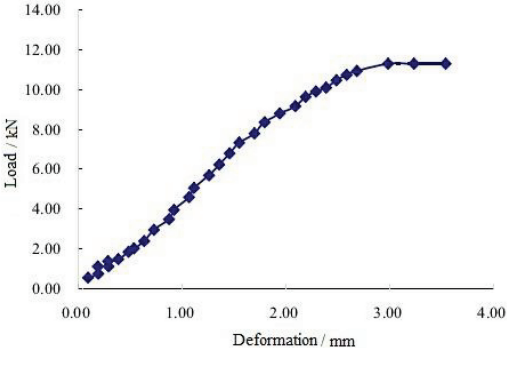

Figure 4. Load and deformation relationship for AC-16(2).

3.2 *Steel slag asphalt mixture crack resistance at low temperature*

Test specimen is made as the same as Marshall stability test of steel slag asphalt mixture at high temperature. Material testing machine is used

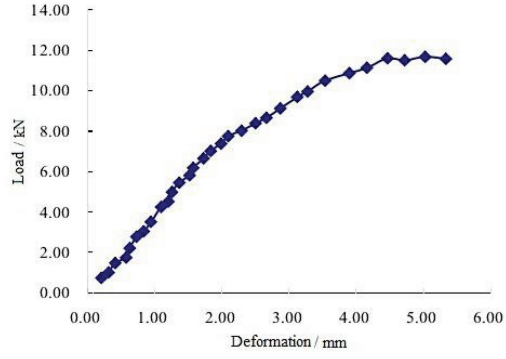

Figure 5. Load and deformation relationship for AC-20(1).

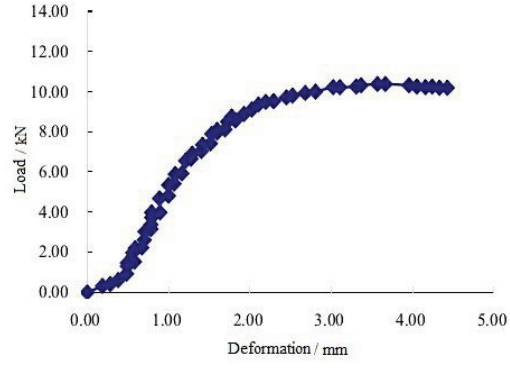

Figure 6. Load and deformation relationship for AC-20(2).

Table 4. Physical properties of steel slag.

Mix proportion	Marshall stability (N)	Flow value (mm)
AC-13(1)	10.80	2.62
AC-13(2)	10.21	3.96
AC-16(1)	11.59	4.60
AC-16(2)	11.74	3.77
AC-20(1)	12.80	4.92
AC-20(2)	12.21	4.86

and the loading speed is 50 mm/min. The load and horizontal deformation are recorded by computer automatically until test specimens splitting failure.

The average splitting tensile strengths of AC-13, AC-16 and AC-20 are calculated from experimental data are 1.21 MPa, 1.15 MPa and 1.08 MPa, respectively. In "highway engineering specifications" in

China, the splitting tensile strength is required to range from 1.2 MPa to 1.6 MPa for AC-13, and range from 0.8 MPa to 1.2 MPa for AC-16 and AC-20. The maximum load and height are shown in Table 5, and Figure 7 shows the comparison of splitting tensile strength between specification and different mixture ratio. The results show splitting tensile strength can meet the requirements of specification. In addition, the splitting tensile strength tends to become smaller with the increase of coarse slag aggregate.

Calculation formula is shown below:

$$R_T = 0.006287 P_T / h \quad (1)$$

where R_T = splitting tensile strength, MPa; P_T = the maximum load, N; h = height, mm.

3.3 *Seepage test of steel slag asphalt mixture*

Permeability performance is one key index of the asphalt pavement water stability. Test specimen of steel slag asphalt mixture is shaped by the wheel rolling method. The length is 300 mm, the width is 300 mm, and the height is 50 mm. Pavement seepage instrument is used to determine the permeability coefficient.

Table 5. Maximum load and height.

Mix proportion	The maximum load (N)	Height (mm)
AC-13(1)	11876	62.22
AC-13(2)	12078	62.24
AC-16(1)	12070	62.56
AC-16(2)	10800	63.14
AC-20(1)	10820	64.30
AC-20(2)	11310	64.40

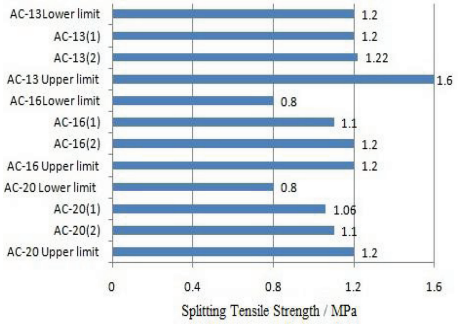

Figure 7. The comparison of splitting tensile strength between specification and different mixture ratio.

Table 6. Permeability coefficient.

	AC-13	AC-16	AC-20
Permeability coefficient	70 mL/min	88 mL/min	105 mL/min

Turn on the switch of pavement seepage instrument, and the water start to drop. We record the time that water drops to 100 ml. Read the instrument tube once per 60 seconds until the water drops to 500 ml. If the water drops slowly, we record the water permeability for 3 minutes. If the water drops fast, we record the time of water drop to 500 ml.

Calculation formula of permeability coefficient is shown below:

$$C_w = \frac{V_2 - V_1}{t_2 - t_1} \times 60 \quad (2)$$

where C_w = permeability coefficient of pavement; V_1 = the first reading volume 100 mL; V_2 = the second reading volume 500 mL; t_1 = the first reading time, s; t_2 = The second reading time, s.

Table 6 shows permeability coefficient from test results. The test results show permeability coefficient of AC-13, AC-16 and AC-20 are 70 mL/min, 88 mL/min and 105 mL/min, respectively. Same as Marshall stability test results, the permeability coefficient tends to become larger with the increase of coarse slag aggregate too.

4 CONCLUSION

In this paper, the author uses steel slag to replace the crushed stones, do many tests of mechanical properties about steel slag asphalt mixture, to verify the suitability of steel slag instead of crushed stones. The test results show as follow:

- In Marshall stability test of steel slag asphalt mixture, the results show stability and flow value can meet the requirements of specification. Marshall stability and flow value tends to become larger with the increase of coarse slag aggregate. In addition, it is also found that asphalt factors had no significant effect on stability, the stability changes is caused by change of gradation.
- In steel slag asphalt mixture splitting test, the results show splitting tensile strength can meet the requirements of specification. Splitting tensile strength tends to become smaller with the increase of coarse slag aggregate.

– In steel slag asphalt mixture seepage test, permeability coefficient is suitable. Permeability coefficient tends to become larger with the increase of coarse slag aggregate.

ACKNOWLEDGMENT

This research is supported by the talent engineering sustentation fund of Liaoning Province and Shenyang municipal science and technology plan (F13-066-2-00).

REFERENCES

Cheng, Y.W., He, X.H. & Zhang, W. 2006. Engineering design grading envelope of AC-16 bituminous mixture. *Journal of Wuhan Polytechnic University* 25(1): 78–81.

Cui, L. 2008. Research on proportion and properties of asphalt mixture with macroporous slag. *Municipal Engineering Technology* 26(2): 140–142.

Nation Bureau of Statistics of China. 2015. Industrial Production Operation in December 2014. *http://www.stats.gov.cn/english/PressRelease/201501/t20150120_671528.html*.

Poh, H.Y., Ghataora, G.S. & Ghazireh N. 2006. Soil stabilization using basic oxygen steel slag fines. *Journal of Materials in Civil Engineering* 18(2): 230–240.

Shan, Z.F. 2000. The state of treatment technique and comprehensive utilization to steel slag in China and abroad. *Safety & Environmental Protection Research Institute* 12(2): 27–32.

Shi, C. 2004. Steel slag-its production, processing, characteristics, and cementitious properties. *Journal of Materials in Civil Engineering* 16(3): 230–236.

Ying, R.H. & Zheng, J.L. 2005. The combination ratio designing of AC-20I bituminous mixture in the middle layer. *Journal of China & Foreign Highway* 25(3): 34–36.

Zhang, Y.P. & Zhao, Y.A. 2006. The combination ratio designing and construction quality control measures in the upper layer of AC 13. *Journal of Liaoning Provincial College of Communication* 8(2): 18–20.

This page intentionally left blank

Civil Engineering and Urban Planning IV – Liu et al. (Eds)
© 2016 Taylor & Francis Group, London, ISBN 978-1-138-02903-3

Multi-objective evaluation of different traffic organizations for twelve-lane freeways

Jing Han, Cheng-Cheng Xu & Wei Wang
Jiangsu Key Laboratory of Urban ITS and Jiangsu Province Collaborative Innovation Center of Modern Urban Traffic Technologies, Southeast University, Nanjing, Jiangsu, China

Xiao-Yan Tian & Xiao-Dong Li
Liaoning Provincial Transportation Planning and Design Institute, Liaoning, China

ABSTRACT: In recent few decades, numerous four or six-lane freeways have been expanded to meet the increasing traffic demand. However, there are relatively few studies about how to decide the priority of different traffic organizational modes of multi-lane freeways with more than eight lanes. Based on the data from Shen-Shan Segment of Jing-Ha Freeway, this paper aimed to establish a multi-objective evaluation index system for three different traffic organizational modes, including, the integral mode, the 'Long-distance artery & collecting and distributing rode' mode and the passenger-freight separated mode. VISSIM simulation studies were conducted to obtain various traffic flow parameters, and the Analytic Hierarchy Process was used to determine the priority of the three traffic organizational modes. The research results can help the decision makers to select a relatively better organizational mode in reconstruction and expansion projects of multilane freeways.

1 INTRODUCTION

With the rapid development of Chinese economy in recent years, transportation demand is increased day by day. To meet the increasing traffic demand, numerous freeways are reconstructed or expanded into 8 or more than 8-lane freeways. It is the future trend to construct multilane freeways in pivotal transport corridors. For safe and well-ordered traffic, lane management is common to be operated on freeways with more than 8 lanes overseas to restrain disorder driving between lanes. Previous studies in China have not developed adequately and are deficient in discriminant method for the traffic organization for 8 or more than 8-lane freeways.

Jack (1983) discussed the geometric design problems in the reconstruction of freeways systematically, especially made an accurate summary for problems in the design of the interchanges. Fan et al. (1983) made an analysis of the relationship between the traffic flow of freeways before and after expansion. Daganzo (2002) proposed a model of multilane freeway traffic flow based on the theory of driver behavior characteristics, and studied the freeway basic section and confluence area respectively. Lee (2010) studied the elements of four-lane, six-lane and eight-lane freeways respectively, established the poisson regression model and finally concluded that the main factors influencing the safety of the eight-lane freeway are lane types and lane width.

Previous studies about evaluations of traffic organizational modes for multi-lane freeways mainly used the traffic efficiency as the only criterion. Traffic safety, economic factors and environment factors were not considered in these studies for making a more comprehensive decision-making and optimization. Thus, considering analysis above, this paper selected a 12-lane freeway from Shen-Shan Freeway as the analysis object and does analysis of the comprehensive decision-making and optimization for different traffic organizational modes.

2 TRAFFIC ORGANIZATIONAL MODES OF MULTILANE FREEWAYS

In order to ensure the traffic efficiency, driving safety and the convenience of access, three traffic organizational modes of cross sections are generally considered in multilane freeways: integral mode, 'Long-distance artery & collecting and distributing rode' mode and passenger-freight separated mode.

– Integral mode
  Integral mode is usually used when the lane number of freeway is no more than 8. In some cases of 10-lane and 12-lane freeways where roadside land are limited, integral mode can also be used. Figure 1a and 2a illustrate the integral mode of Shen-Shan Segment of Jing-Ha

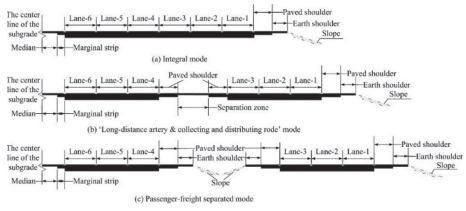

Figure 1. Section sketch of each mode.

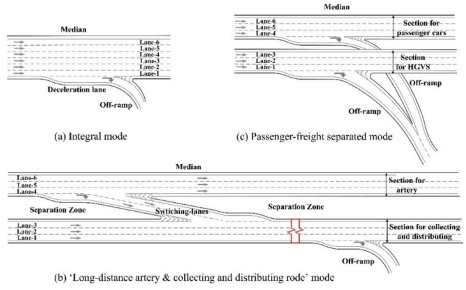

Figure 2. Aerial view of each mode.

Freeway, which was expanded to 6 lanes in each direction. All lanes serve both passenger and freight vehicles.

– 'Long-distance artery & collecting and distributing rode' mode
When there are more lanes in cross sections, separated modes are usually used in each direction. There are two types of separated modes. One type is that inner and outer parts are linked by switching lane every regular interval, which is called 'Long-distance artery & collecting and distributing rode' mode. Vehicles can transfer freely between the two parts and ramps of interchanges only connect with outer parts. Vehicles in the inner part have higher speed and less interference, which are mainly long-distance traffic. Vehicles in the outer part drive relatively slower and can transfer into or out of the inner part through switching lane. Figure 1b and 2b illustrate the 'Long-distance artery & collecting and distributing rode' mode of Shen-Shan Segment of Jing-Ha Freeway, which was broadened to 6 lanes in each direction.
– Passenger-freight separated mode
In the passenger-freight separated mode, the inner and outer parts are separated. Freight vehicles are only allowed to travel on the lane of outer parts, while the passenger cars are only allowed to travel on the lanes of inner parts. In this case, ramps of interchanges need to connect relatively with both inner and outer part. A 12-lane freeway in passenger-freight separated mode can actually be regarded as a combination of a 6-lane passenger freeway and a 6-lane freight freeway. Figure 1c and 2c illustrate the passenger-freight separated mode of Shen-Shan Segment of Jing-Ha Freeway, which was broadened to 6 lanes in each direction.

3 THEORETICAL FRAMEWORK

3.1 *Calibration of VISSIM simulation models*

Traffic simulation model VISSIM is used to generated the traffic flow data that are difficult obtained from field collections. One of the major benefits of VISSIM is that not only detailed geometric configurations such as medians, driveways, and turning bays, but also drivers' behavioral characteristics encountered in the transportation system can be modeled in simulation. Based on the results from the field research in Shen-Shan Segment of Jing-Ha Freeway, flow-speed curve was plotted and illustrated as Figure 3. With curves in Figure 3 as calibrated target of simulation platform, adjustments of distributions of desired speed under free flow condition of cars and heavy vehicles which take high ratios in traffic composition were made in this study. To verify simulation models, the method of testing capacities was used in this study. Through inputting traffic flows over capacities, capacity was ascertained as 2196 veh/h, critical speed as 75.1 km/h and calibration error as 0.2% when cars are only served while in another case when heavy vehicles are only served, capacity was ascertained as 1064 veh/h, critical speed as 44.1 km/h and calibration error as 3%. Simulation was verified at a 95% confidence level.

Adjusted plans of driving behavior parameters for different heavy-vehicle mixing rates are listed in 0.

3.2 *Multi-objective evaluation method*

– Multi-objective evaluation index system
A system of index is necessary in evaluating the superiority of a plan. Both qualitative and quantitative standards are needed in the index system. Appraisal indicators are determined by the designer or the panel considering the scope,

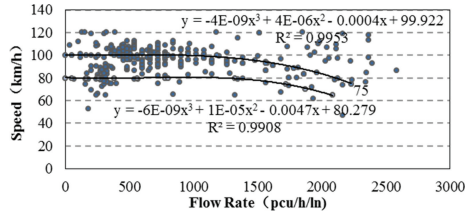

Figure 3. Actual flow-speed curve in Shen-Shan Segments of Jing-Ha Freeway.

Table 1. Parameter adjustment of car following model in driving behaviors.

Plan	a	b	c	d	e	f	g	h
	Percentage of HGV (%)							
Adjusted parameters	0	5	10	20	30	40	60	100
CC0 (standstill distance)	1.50	1.58	1.65	1.80	1.95	2.10	2.40	3.00
CC1 (headway time)	1.50	1.53	1.55	1.60	1.65	1.70	1.80	2.00
CC8 (standstill acceleration)	3.50	3.43	3.35	3.20	3.05	2.90	2.60	2.00
CC9 (acceleration at 80 km/h)	1.50	1.45	1.40	1.30	1.20	1.10	0.90	0.50

nature and complexity of the project. By setting up comprehensive and systematic evaluation index system, the deciders can measure the traits of various factors from both qualitative and quantitative angles and reveal the connection between all the factors from both horizontal and vertical aspects, so as to correctly select the appropriate traffic organizational mode. In this study, traffic safety, traffic efficiency, economic factor and environmental factor are the four main criterions of evaluating traffic organizational modes.

* Traffic safety
  Traffic safety is the premise and guarantee of normal operation of high efficiency. In this study, crash occurrence probability is used as a measure of traffic safety.
* Traffic efficiency
  Traffic efficiency is the fundamental aim of freeway's reasonable design. Traffic flow and running speed are considered in this paper as the main indicators of measuring traffic efficiency.
* Economic factor
  In the actual project implementation process, the economic factor is an important problem to be reckoned with, to which the authorities pay much attention. Two of the most important points in economic factors are project cost and construction difficulty.
* Environmental factor
  In this study, freeway occupation of land resource and pollutant discharge are selected as the indicators of consideration.

– Multi-objective evaluation theory

The Analytic Hierarchy Process (AHP) is a decision analysis method proposed by a famous American mathematician T.L. Saaty in the 1970s, which analyzes the decision-making problem displayed in different levels of the hierarchy. AHP uses hierarchical structure of a problem to consider qualitative and quantitative criteria.

The basic steps of the AHP method are as follows.

Firstly, creating a hierarchical structure of different levels, from the objective, through a variety of criteria, and with alternatives at the lowest level.

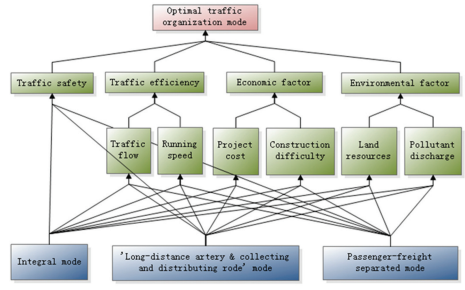

Figure 4. Hierarchical structure diagram.

Secondly, creating the comparison matrix. The comparison matrix of elements in one level in relation to elements at a higher level is constructed using individual comparison translated into scale values. The preferences of decision makers are quantified using Saaty's nine-point scale, and the meaning are as following: 1 = equally important, 3 = slightly important, 5 = very important, 7 = much more important, 9 = extremely more important. The 2, 4, 6, and 8 represent the values in between.

Thirdly, calculating the relative rankings for each level of the hierarchy by pairwise comparing each criteria or alternative. After creating all matrices, the vector of relative weight and maximum eigenvalue (λ_{max}) for each matrix is calculated.

Fourthly, calculating the consistency index and ratio. It is necessary to calculate a Consistency Index (CI) of an n*n matrix, which is defined as $CI = \frac{\lambda_{max} - n}{n-1}$. The Consistency Ratio (CR) is calculated as CR = CI/RI, where RI means the random consistency index.

The hierarchical structure established in this study is shown in Figure 4.

4 RESULTS AND DISCUSSION

4.1 *Traffic safety effects of different traffic organizational modes*

Xu et al. (2013) developed a model to link the probability of crash occurrences to various traffic flow

variables derived from detector data. The expression of logit model is shown as follows:

$$\ln\frac{P(x)}{1-P(x)} = -7.376 + 0.074\,DetOcc_u + 0.060\,SpdDev_u + 0.050\,SpdDev_d + 0.119\,OccDif_d + 0.092\,AvgCnt_{u-d} + 0.026\,AvgOcc_{u-d} + 0.886\,Weather + 1.057\,DetDist_{u-d} - 0.049\,Width_s - 0.856\,Width_o + 0.508\,Curve \quad (1)$$

where: $P(x)$ = the probability of the occurrence of a crash; $DetOccu$ = Average 30-s detector occupancy at the upstream station (%); $SpdDev_u$ = Std. dev. of 30-s mean speeds at the upstream station (mile/h); $SpdDev_d$ = Std. dev. of 30-s mean speeds at the downstream station (mile/h); $OccDif_d$ = Average absolute difference in 30-s detector occupancies between adjacent lanes at the downstream station; $AvgCnt_{u-d}$ = Average absolute difference in vehicle counts between upstream and downstream stations (veh/30 s); $AvgOcc_{u-d}$ = Average absolute difference in detector occupancies between upstream and downstream stations (%); $Weather$ = 1, adverse weather conditions (rain or fog); = 0, otherwise; $DetDist_{u-d}$ = Distance between upstream and downstream stations (mile); $Widths$ = Road surface width (ft); $Width_o$ = 1, if outer shoulder width > 10 ft; = 0, otherwise; and $Curve$ = 1, curve section; = 0, otherwise.

In view of the three kinds of traffic organizational modes, the operational organization and the probability of the occurrence of a crash are different from each other. In this study, entrances of the ramps to interchanges and interweave sections of the switching lanes, where are the freeway accident prone sections, are selected as the objects of study. The peak time of the accidents lies between 7 pm to 8 pm. In this study, 7 pm to 7:30 pm was chosen as the simulation time. Based on the traffic flow variables from the VISSIM simulation, and the probability of the occurrence of a crash can be calculated using equation (1). The probability of the occurrence of a crash under different traffic organizational mode in different periods of time are shown in Figure 5.

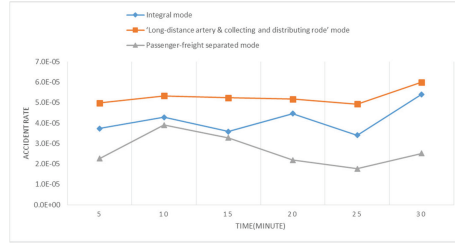

Figure 5. The probability of the occurrence of a crash under different traffic organizational modes.

4.2 *Traffic efficiency effects of different traffic organizational modes*

A series of formulas for calculating the traffic capacity of different traffic organizational modes were developed as follow.

The actual capacity of integral mode can be expressed as:

$$CAP = C_d * N * f_P * f_{HV} * f_{OL} * f_{IL} \quad (2)$$

where: N = number of lanes (in one direction) of the freeway; f_p = adjustment factor for driver population; f_{HV} = adjustment factor for presence of heavy vehicles; f_{OL} = adjustment factor for outer lane; f_{IL} = adjustment factor for inner and median lanes.

The actual capacity of 'Long-distance artery & collecting and distributing rode' mode can be expressed as:

$$CAP = C_D * N * f_P * f_{HV} * f_{OL} * f_{IL} * f_{LC} \quad (3)$$

where: f_{LC} = adjustment factor for switching lane. Concrete meaning of other parameters are the same with above.

The actual capacity of passenger-freight separated mode can be expressed as:

$$CAP = C_D^p * N^p * f_P^p * f_{OL}^p * f_{IL}^p + C_D^f * N^f * f_P^f * f_{OL}^f * f_{IL}^f \quad (4)$$

where: factors with superscript 'p' denote parameters of the passenger freeway while factors with superscript 'f' denote parameters of the freight freeway. Concrete meanings of related parameters are the same with above.

Detailed comparison of capacities among three modes are illustrated in 0.

Detailed comparison of traffic speeds among three modes are illustrated in 0.

4.3 *Economic effects of different traffic organizational modes*

In the stage of freeway route selection, economic factor should be an important evaluation index of the selected scheme. This research mainly takes the project cost and construction difficulty of different traffic organizational modes into consideration.

The project cost depends on the technical conditions and standard along with the nature, which has a great influence on the choosing of schemes.

For example, a certain highway in Tianjin with similar nature conditions on 2005, whose width of

Table 2. Comparison of capacities in three traffic organizational modes.

Modes	Calculating equation	Values of factors	Capacity (pcu/h)
Integral	Equation (2)	$C_D = 2200, N = 6, f_p = 0.981,$ $f_{HV} = 0.63, f_{OL} = 0.82, f_{IL} = 0.90$	6021
'Long-distance artery & collecting and distributing rode'	Equation (3)	$C_D = 2200, N = 6, f_p = 0.981, f_{HV} = 0.63,$ $f_{OL} = 0.94, f_{IL} = 0.96, f_{LC} = 0.95$	6994
Passenger-freight separated	Equation (4)	$C_D^p = 2200, C_D^f = 1100, N^p = 3,$ $N^f = 3, f_P^p = 0.981, f_P^f = 0.981,$ $f_{OL}^p = 0.94, f_{OL}^f = 0.92, f_{IL}^p = 0.96, f_{IL}^f = 0.97$	8732

Table 3. Comparison of traffic speeds in three traffic organizational modes.

		'Long-distance artery & collecting and distributing rode'		Passenger-freight separated	
	Integral	Long-distance artery	Collecting and distributing rode	Passenger	Freight
Average speed (km/h)	79.99636	92.78333	86.615	96.15224	87.40448
Standard deviation (km/h)	27.66	4.510446	7.20009	11.55294	6.757183

subgrade is 33 m, costing 5,115,840 thousand for Chienan fees, 792,450 thousand for building and maintaining the subgrade, 255,020 thousand for building and maintaining the pavement, 969,950 thousand for building bridge and culvert, 1,666,300 thousand for building the tunnel, 856,450 thousand for alternate construction, and 171,460 thousand for other projects along the line.

Comparing with the integral mode, the 'long-distance artery & collecting and distributing rode' mode needs to take the cost of adding up switching lane into consideration, while the passenger-freight separated mode should set the interchange ramp individually for both passenger lane and freight lane, and design for highway engineering, which costs more and gets more difficult for construction.

4.4 *Environmental effects of different ways of traffic organizational modes*

Environment should also be an important issue, along with safety, efficiency and economy. In this research, effect of different cross-section form of the land resources and discharge of pollutants under different traffic organizational modes is of great concern.

Comparing with the Integral mode in the aspect of land using, the 'long-distance artery & collecting and distributing rode' mode which contains 12 lanes, needs an extra switching lane directionally with the width of 3.75 m each. While the passenger-freight separated mode should set the interchange connections individually for both passenger lane and freight lane, and reserve some space between passenger lane and freight lane in the same direction.

In the aspect of pollutants, the results for discharge of pollutants per 30 s of the three modes collected by simulation are shown in Figure 6.

4.5 *Multi-objective decision-making results*

According to the engineering practice, weights of traffic safety, traffic efficiency, economic factor and environmental factor in the hierarchical structure are shown in Figure 7.

According to the designed evaluation index system, the results of the priority of the three traffic organizational modes are shown in Figure 8.

Therefore, after synthetically considering the traffic safety, traffic efficiency, economic factor and environmental factor, the reconstruction of Shen-Shan Segment of Jing-Ha Freeway is suggested to select the passenger-freight separated mode.

Influences of the weight value of the four criteria to the result of the priority of the three modes respectively are given in Figure 9.

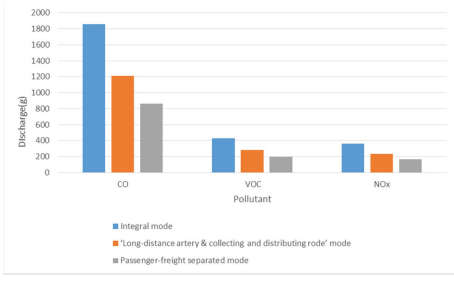

Figure 6. Discharge of pollutants under different traffic organizational modes.

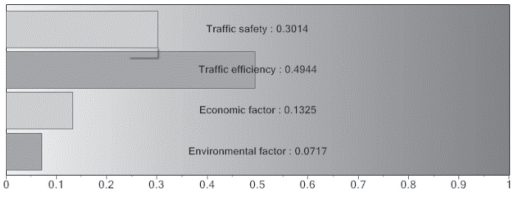

Figure 7. Weights of criteria in the hierarchical structure.

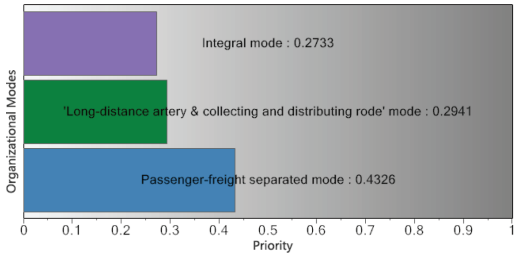

Figure 8. Result of the priority of the three traffic organizational modes.

As shown in Figure 9a, the priority scores for the 'long-distance artery & collecting and distributing rode' mode decreases with an increase in the assigned weights to the influence of traffic safety. While the priorities score for the integral mode and passenger-freight separated mode increase with an increase the assigned safety weights. Thus, the safety performance of integral mode and passenger-freight separated mode is better than that of the 'long-distance artery & collecting and distributing rode' mode. Figure 9b indicates that with an increase in the assigned weights to the influence of traffic efficiency, the priorities score for 'long-distance artery & collecting and distributing rode' mode and passenger-freight separated mode increase respectively while that scores for integral mode decreases, which means 'long-distance

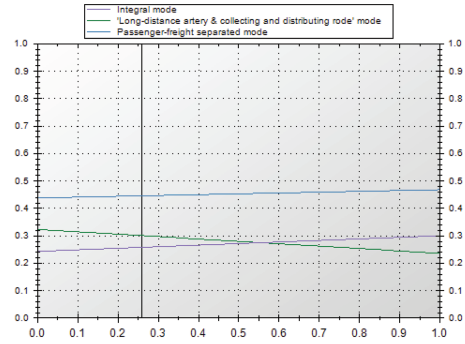

(a) Influence of traffic safety

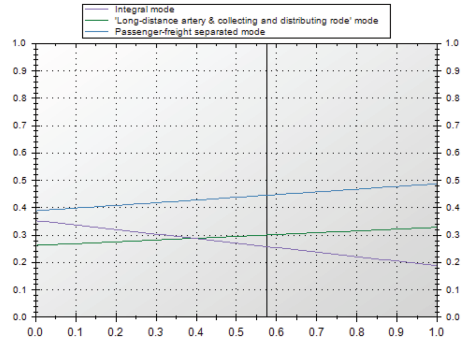

(b) Influence of traffic efficiency

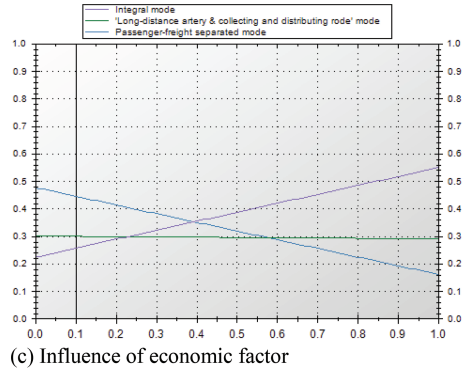

(c) Influence of economic factor

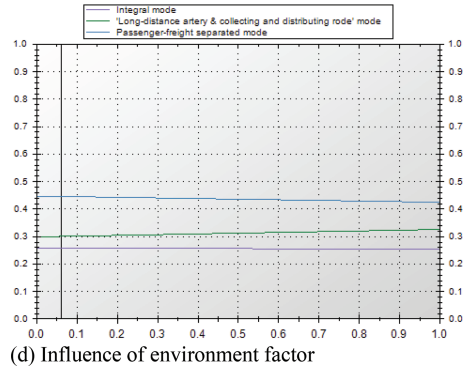

(d) Influence of environment factor

Figure 9. Influence of the four criteria to the priority of the three modes.

artery & collecting and distributing rode' mode and passenger-freight separated mode perform better than integral mode in the aspect of efficiency. Figure 9c shows that integral mode behaves better than the other two considering economy. As shown in Figure 9d, passenger-freight separated mode performs the best in the aspect of environment.

5 CONCLUSION

This research established a multi-objective evaluation index system for 12-lane freeway based on different layouts of section and traffic organizational modes. With the help of simulation software VISSIM, the traffic flow parameters were gathered to determine the value for each index and the priority for the three traffic organizational modes. As the research is mainly based on the data collected in the Shen-Shan Segment of Jing-Ha Freeway, which may also be applied to multi-objective decision-making for other multi-lane highway. During the process of determining the weights of safety efficiency economy and environment, it is subjective due to the limit of experience and knowledge, which may cause influence to the final results. A detailed research of impact of different weights on the final solution will be made in further study.

ACKNOWLEDGEMENT

This research was sponsored by the fund provided by the Liaoning Provincial Department of Communications. The authors would like to thank the reviews for the valuable comments of this manuscript.

REFERENCES

Daganzo, C.F. 2002. A behavioral theory of multi-lane traffic flow. Part I: Long homogeneous freeway sections. *Transportation Research Part B: Methodological* 36(2): 131–158.

Fan, S.S., Chang, T.C. & Liu, K.W. 1983. Feasibility Study on Widening of a High Volume Freeway Section. *Road Engineering Association of Asia and Australasia, Conference, 4th, Jakarta, Indonesia, 1983.*

Ilangkumaran, M. & Kumanan, S. 2009. Selection of maintenance policy for textile industry using hybrid multi-criteria decision making approach. *J Manuf Technol Manage* 20: 1009–1022.

Leisch, J.E. 1983. Planning/design features and case studies in freeway reconstruction. *ITE Journal* (10): 14–23.

Lee, S.B. 2010. Analysis of Design Elements for Urban Highway Safety. *4th IRTAD Conference, Seoul, Korea.*

Liu, P., Qu, X. et al. Development of a VISSIM simulation model for U-turns at unsignalized intersections. *Journal of Transportation Engineering* 138(11): 1333–1339.

Traffic Planning and Design Institute of Liaoning Province. 2014. *Capacity and Safety Studies of Multilane Freeway.* Shenyang.

Xu, C., Tarko, A.P., Wang, W. et al. 2013. Predicting crash likelihood and severity on freeways with real-time loop detector data. *Accident Analysis & Prevention* 57: 30–39.

This page intentionally left blank

Civil Engineering and Urban Planning IV – Liu et al. (Eds)
© 2016 Taylor & Francis Group, London, ISBN 978-1-138-02903-3

Urban public transportation system in China

Hao Huang & Lin Cheng
Southeast University, Nanjing, Jiangsu, China

ABSTRACT: In this paper, China's urban public transportation is paid on attention. First, the situation of China's urban public transportation is introduced to show an overall view on China's urban public transportation. Based on the current situation, two development strategies are proposed. Then five suggestions are promoted to solve problems in urban public transportation system.

1 INTRODUCTION

The urban traffic functions could be realized based on urban traffic and transportation system whose main component is passenger transport system. It is acknowledged that passenger transport system is an essential part in urban development.

Generally, passenger transport system contains two components: public transportation system and road traffic system that serves for private cars. As the rapid development of urbanization, serious congestion has become a great problem for many cities, especially for the megalopolises. Countries around the world have tried various methods to solve this problem, including road extension, facilities extension, etc. However, these methods have not reached expected results. According to these experiences, people start to realize the advantages of public transportation system. China, as a developing country with the largest population, is also facing the road congestion problem. In recent years, large cities in China have taken measures to promote public transportation system.

2 CHINA'S URBAN PUBLIC TRANSPORTATION

2.1 *The present situation and the analysis of China's urban public transportation text and indenting*

The development of urban public traffic in China comes from low levels of city motor vehicle ownership and narrow road space. Because of the rapid development of economy and the increased quantity of the accelerated urbanization process of residents travel distance growth, and the residents' concept of time strengthening, the quality of public transport service is put forward higher requirements. But in the mid 80 s, public transportation in big cities had been shrinking, from operating efficiency to the operation and management and from the level of service to the economic benefit of the recession. Around seventeen years (from 1978 to 1995), the national public transport vehicles' route length was increased by 2.5 and 2.8 times, public transit vehicle ownership was 0.62/one thousand (Liu 2013), but the public transportation vehicles operating by 12–14 km per hour speed were decreased to 5–10 km, thus, the new capacity was offset by the decline of transport efficiency. From 1992 to 1995, the urban population had been increased by 20%–30% in a number of cities, but the urban public transport passengers had fallen by 13.7%, hence the public transport industry had been shrinking. That, in turn, spawned a massive private traffic, especially the increase in private cars, further intensified the traffic congestion of the city. The deterioration of traffic for the sustainable development of urban economy has brought great obstacles.

For bus companies, road congestion and traffic congestion reduce the speed and the efficiency of the public transport vehicles. Because the bus companies rely on government subsidies for a long time, ticket prices problem is not solved; operational efficiency and with the operation and management, service quality is good or bad has nothing to do with the enterprise survival; thus losing money. City bus companies make the city's transport efficiency and the quality of residents travel to drop affects the development of urban economy.

In the second half of the 90 s, in order to relieve the contradictions of urban traffic, from national to local, successively adopted a series of measures to implement the policy of "bus priority," vigorously developed public transportation, and through a positive policy guidance, control individual transport, realized the most effective use of transport facilities, improved the transport efficiency.

From 1997 to 1998, 87.5% of the public transportation enterprises' operating income was increased,

12.5% of public transport enterprise income was reduced, but the overall operation increased the income, income growth averaging 14.49%. In 1997 cities survey, 86.96% of the public transportation enterprise was lost, the average transit enterprises loss was 49.55 million Yuan. In 1998, 82.61% of the public transportation enterprises had the loss of 48.30 million Yuan per bus enterprise. These circumstances, with the development of public transportation, though the bus operating income was increased, but it's hard to make up the losses of the policy of the bus companies, mainly to sideline work, because of the amount of income disparity is great, and can not fundamentally reverse bus company losses.

After years of reform, urban public transport by the state-owned enterprises "one world" the situation has been broken, the joint venture and foreign investment, cooperation, private as well as some limited liability companies, and joint stock co., Ltd. However, the dominance of state-owned enterprises has not fundamentally changed, in the vast majority of cities, the state-owned share of passenger bus companies throw major share, some important social obligation is mainly borne by the public transportation enterprises.

At present, the government gradually promotes enterprise to the market by the full implementation of enterprise autonomy, establishes modern enterprise system, it is undoubtedly for the urban public transport out of the woods, a rare opportunity to seek development. In a word, on the basis of learning and absorbing advanced experience both at home and abroad, based on the systematic study of urban public transport sustainable development system of our country, set up, and improve the urban public transport management system suitable for China's national conditions, to promote the development of the urban public traffic in China is of great significance.

2.2 *The main problems of the urban public traffic*

2.2.1 *Vehicle contradiction in urban traffic system: Growing too fast and a lack of road capacity*

Motor vehicles, which lead to traffic congestion, reduce travel time utilization, the root cause of environmental pollution, have increased in recent years. The city motor vehicle has already amounted to 5 million cars in 1994. According to our country car growth analysis, when car ownership growth rate is more than 20%, it will cause deterioration of the urban traffic.

And road conditions in our country are not optimistic. Urban per capita road area in China has long been at a low level, it was only in the 90 s began to have a rapid development, per capita road area 2.8 m^2 by up to 6.6 m^2. Although growth rate fast, it couldn't catch up with the city traffic growth of nearly 20% a year. Now more than 32 millions of people in the big cities across the country, there are 27 urban per capita road area is lower than the national average. Central Shanghai road area per capita is only 3.5 m^2, about 50% of the driveway saturation of 95%, the peak hours throughout the saturation is more than 70% on average, these sections is busy all day long, very crowded, some roads blocked more than 6.5 h continuously, central district average traffic speed setting down to about 10 km/h (Chang 1999).

Why heavily in construction of roads, traffic congestion is so serious? The most direct reason is lack of road area is serious. First of all, our country big city resident per capita road area is less than a third of the developed countries. Secondly, our country is in the process of urban suburbanization, new roads in recent years, mainly in new urban area and suburbs, contrast, road area of the central rate and no obvious improvement. Again, the urban real estate and commercial development mainly concentrated in the central district, generated a lot of traffic, the city road carrying serious overload. In addition, our country illegally occupy roads and sidewalks in the city problem for a long time can not be solved effectively, which makes the serious shortage of road area is more nervous.

Road area is less than originally lies in the lag of the construction of the road, not only makes the city after the summary of the existing road function become vague, road use efficiency is low, and cause waste of time and the cost of driving are huge. But so for the mass under the condition of road construction in alleviating traffic congestion original, raises the more traffic, more conflicts.

To solve the traffic problems, just rely on large road traffic engineering can only take temporary solution not effect a permanent cure, in the face of limited road traffic capacity, strengthen traffic management is the effective solution. So how to build a more perfect and more developed traffic network, provide more rapid and more direct transport services, how to guide people preferred their bus way, strengthen the consciousness of bus is a very long term emphasis in the future.

2.2.2 *Public transport management system has not been smooth*

Public transportation in our country by transportation, urban construction two departments to divide and rule, licensing, and certification, compete for administrative authority, think urban public traffic management confusion. State management of the public transportation is basically the management of the state-owned bus company, and no special functional organization management coordination of public transportation and the overall development of urban traffic planning and development

of bus urban traffic rules and coordinated development policy, land use planning.

Shenzhen high traffic of workers and peasants, for example, the business is mainly composed of transport and the public security traffic two departments coordinated management, ticket prices by the price bureau management, bus terminal to land use planning and management by the land planning bureau, multiple management department of power and influence on conflicts of interest to the state of the bus company. Have introduced several urban passenger transportation market competition at present, state-owned special properties of the bus company decided it can not be like other companies involved in comprehensive competition, and the present situation of the multiple management will not be able to maintain the reasonable interests of the state-owned enterprises, state-owned bus enterprises competitiveness is very weak but also in the fierce competition to keep a higher level of service to maintain the status quo of market share. Listing and numbering when listing facts use either the style tag List signs or the style tag List numbers.

2.3 *From the state to the stable where there is no public transportation construction capital source*

On infrastructure investment, the government's investment is still basically urban rapid road system and flyovers, most of the city bus transport investment is only about 5% of the urban road construction funds.

Overseas development of urban public traffic can largely be divided into two forms: one kind is the bus company fully in accordance with the instructions to complete the government regulation of public transport services, the government in a strong financial guarantee; The other is a transit business according to the principle of market economy, the government integrated use of economic, legal and administrative means to regulate operation of bus companies. Operation of urban public transportation mode in our country is with the developed countries, basically arranged by the state, namely the type of blood transfusion. But the western developed countries are "high-pressure & high-concentration & low-viscosity" (high input, high subsidies), low fare, but our country is take the "three low" (low input, low subsidies, and low fares) way (Zhou & Li 2007). Western countries choose the above model is based on solid economic strength, under the government's huge investment and subsidies, city bus get rapid development. And our country economic power co., Ltd., as a result, the way more walk more narrow, lead to some bus companies even simple reproduction and difficult to maintain.

2.3.1 *Public transport development policy has no stability*

And urban public transport as the development of industry of which has influence on the overall situation, the origin of the national economy status does not adapt, state of urban public transport has not been clear, stable economic support policies and practices subsidy system, around the survival and development of the bus around depends entirely on the government's attention degree, frequently change.

For example, the Shenzhen government's policy of the bus company loss subsidy has been adjusted, before 1998 is the real loss of real, subsidizing quota from 1998 to 2000, 2001 subsidies will be depending on the actual situation of the public transportation development.

2.3.2 *Excessive open public transportation enterprise competition*

The special properties of the bus company decided to not allow vicious competition in this industry, but the national policy in industry management did not fully consider the particularity, in order to enliven the market, hasty decision to allow competition in this industry in full swing. Competition between different bus companies can improve the bus service and reduce the cost, but will be potentially dangerous, now most of the potential problems, adopt contracting mode of operation of public transport vehicles in order to pursue the economic interests of the largest, random destruction of competition rules, serious short-term behavior, reduce the service quality, increase the urban pollution, and endanger the safety of passengers. At the same time make the bus companies to further get into trouble.

2.3.3 *The low level of traffic management technology*

At present, the urban traffic too much depends on the person's administrative management, static management of vehicles more than dynamic management, and for the modernization of traffic control and traffic safety management facilities are rare.

Due to lack of facilities obviously could not keep up with the needs of the development of traffic management technology, the traffic police prolonged spell of manpower, spelling a physical state, in the traffic management can not do nip in the bud.

3 DEVELOPMENT STRATEGY

3.1 *Development strategy for urban public transportation system*

3.1.1 *Factors of influence*

When planning the structure of public transportation system, it is necessary to consider population, city layout, use of land, economic level, economic structure, space factors, development strategy,

environmental factors, political factors, level of urbanization, and the structure of urban public transportation.

3.1.2 *Principles*

– Equity
  Urban public transportation system should ensure the right of using public transportation system for all citizens. It means that everyone have the ability to use public transportation system in terms of finance.
– Feasibility
  The construction of urban public transportation system must have feasibility, which contains the consideration of society, economy, and environment.
– Sustainability
  It is widely acknowledged that the construction of urban public transportation system should be sustainable.
– Marketization
  The construction of urban public transport investment projects can be completely market-oriented, adhering to the principle of market economy through the cost effectiveness, in order to save precious national investment. The costs and benefits are not just monetary costs and campus, but the costs and benefits of the whole society.

3.2 *Methods for construction of public transportation system*

Aiming at the opportunity and threat of public transportation system, with its advantages and disadvantages, people make feasible strategy of public transportation system and further evaluation, then select the most appropriate strategy.

The steps of making development strategy of urban public transportation system are as follows:

– Analysis of factors
  In this process, people list the factors which have direct and major impact on system development first, then present the factors which have indirect and minor impact.
– Making plans based on the action measures
  External factors of urban public transportation are unchangeable while internal factors can change in the direction of advancing public transportation system by people's subjective initiative. Under the guidance of this idea, people can draw a series of options for construction of urban transportation by match each factor.

  Analysis of urban transportation system includes the previous two aspects: environmental analysis and comprehensive analysis. The former is the basis for getting the advantages, disadvantages, threat, and threat of urban transportation. Then evaluate the pros and cons of the system on this basis. After comprehensive and systematic comparison, determine the final key strategy.

4 SUGGESTIONS

4.1 *Make overall target and consolidate its strategic positioning*

First, people should get aware of the public property of urban transportation system and confirm the responsibility and goals of government. By increasing transportation capacity, improving service level and enhancing the competitiveness and attractiveness of urban public transportation, people can build a motorized travel system whose main part is public transportation. Meanwhile, the travel condition for cycling and walking can be improved. People should develop various forms of large-capacity public transport to increase the capacity of public transportation. Meanwhile, it is important to optimize the transport hub and improve site coverage. It is necessary to build a public transportation system in which urban rail transit is backbone, regular bus is network, taxi is supplement and bicycle is extension. Then the public transportation is ensured its dominant role.

4.2 *Change management concept*

"Transit city" has become the development direction of the global metropolises, its core is that urban public transport urban development leads the city's development (Jiang et al. 2006). First, consider the transit corridor as city's development axis, which will gather residents and employment. Then the best travel portfolio "live + transit + work" is built. Secondly, set subway stations and bus stations as the city's development center. Develop around these areas to implement intensive urban growth. China's urbanization process developed rapidly in the previous stage, the development of public transport in a relatively passive and lagging behind, it is difficult to achieve the goal that urban public transport development leads city's development. Therefore, from now on, it is necessary to focus on the implementation of traffic projects assessment system and highlight the role of public transport planning in guiding urban space layout. New land development plan should be conducted a public transport security assessment and establish the "one-vote" effect of urban public transport in city's plan, based on the degree of land development. Meanwhile, implement various public transport modes to promote convergence and conveniently integrated development of urban and rural public transport.

4.3 *Implement tax for public transport development*

It seems necessary to implement tax for public transport development as soon as possible, which can establish a stable funding source for public transportation infrastructure and transit development. Meanwhile, some government could conduct congestion charging policy which is more sustainable than simply limiting license. We also can learn from Hong Kong where levy tax of initial use of private car. In addition, it is proposed exempt tax for relevant companies.

During "twelve five" period, the nation has exempted tax of newly acquired steam tram vehicle, tax of land use of urban public transport, tax of public transport travel. This policy can be given a clear definition in the future relevant law.

4.4 *Increase service level*

While limit private car trips, it is necessary to support equivalent public transportation service to ensure people's right to pursuit comfortable transport. In China, there is a problem that the public transportation is crowded, low speed, and not convenient to transfer. This problem decreases the attractiveness of public transportation.

In order to establish the dominant position of public transport, we must enhance the competitiveness of public transport as soon as possible. First, we need to expand the scope of public transportation service. We can adjust line network structure and improve line density and site coverage to meet the public demand for a variety of travel. We can support multi-level characteristics of public transport services such as peak line, commuter bus, community shuttle bus to facilitate passenger's travel. Secondly, we can improve the convenience level of transfer. Aiming at this, we can support car or bicycle parking facilities around bus terminal, stations of rail. Thirdly, we need to improve the quickness of travel. We can actively promote the construction of urban public transport priority lanes and priority signal system. Fourthly, we need to improve vehicle safety technology and the level of comfort. It is import to advance the process of eliminating the old vehicles with low safety level and low emission level. Fifthly, try to establish a pattern of urban and rural transport integration. We should build network in which the city is the leader, the country is the center, the town is the node and the road is the link. With this network, we can realize the goal that everyone can enjoy public transportation system.

5 CONTROL THE NUMBER OF CARS

To solve current traffic problems, we must take emphasis on both the development of urban public transportation and constraint of cars. In terms of control private cars, car quota system is implemented in Singapore to ensure the annual growth of cars. China should first control the number of official cars and enhance credibility of the government. At present, China has more than 2 million official cars. The phenomenon of overuse, high stand, high cost is outstanding. It is suggested to the State Council to implement relevant management policy as soon as possible. We can learn some advanced experience: in USA, the purchase of vehicles must be checked by the parliament and the government publishes the report of fuel-use; in France, it is illegal to use official cars for private goal, every resident can call the police whenever they see such phenomenon; in England, the use GPS to position and monitor the official cars.

6 CONCLUSION

Nowadays, China is still facing with road congestion, and the problem is getting worse. In this case, it seems necessary to promote public transportation because of its effectiveness and environmental protection. With the suggestions mentioned above, China may make great improvement in promoting the use of public transportation, and the problem of road congestion may be relieved.

REFERENCES

Chang, D.T. 1999. A new era for public transport development in China. *China Environment Series* 1999(3): 2000.

Liu, W., Lund, H. & Mathiesen, B.V. 2013. Modelling the transport system in China and evaluating the current strategies towards the sustainable transport development. *Energy Policy* 2013(58): 347–357.

Pucher, J., Peng, Z., Mittal, N. et al. 2007. Urban transport trends and policies in China and India: impacts of rapid economic growth. *Transport Reviews* 27(4): 379–410.

Yulin, J., Liguang, F., Hongyang, W. & Runlong, X. 2006. Challenges and Policy Options for Sustainable Urban Transportation Development in China. *Proceeding of EU-China Workshop on Sustainable Urban Transport, Beijing, China, 2006.*

Zhou, W. & Li, Y. 2007. Developing theory and method of urban public traffic in China. *Journal of Chang'an University (Natural Science Edition)* 2007(4): 014.

This page intentionally left blank

Civil Engineering and Urban Planning IV – Liu et al. (Eds)
© 2016 Taylor & Francis Group, London, ISBN 978-1-138-02903-3

Crowd management in emergency situations: What can be learned from the existing video data?

Bei-Bei Liu & Xiu-Cheng Guo
Southeast University, Nanjing, Jiangsu, China

ABSTRACT: The investigation of crowd management while evacuating under emergent situations is an important issue. Several articles have called attention to the importance of crowd evacuation in emergency. This article talks about the characteristics and influential factors of crowd evacuation. When estimating the effectiveness of crowd evacuation, time is an important index that should be considered. Group behavior can influence occupant behavior to some extent. By analyzing two existing videos (one is for emergency and, the other is under common condition), relative conclusions can be made about evacuation in emergency situations which help the crowd management. Relative personnel injuries and property damage can be decreased to the minimal level.

1 INTRODUCTION

The theoretical research of crowd evacuation has begun in the early 1970s. It is still one of the most important contexts in the area of crowd evacuation until now. The theoretical research of crowd evacuation mainly includes relative study on various parameters and the rule of pedestrian evacuation behaviors. Various influence factors during emergencies led to the development of a variety of evacuation models. Until now, two evacuation models building EXODUS (Gwynne et al. 2005) and SIMULEX (Thompson et al. 1996) have been developed to study the evacuation patterns under emergency and normal conditions. The characteristics of crowd evacuation vary a lot under emergency situations and normal conditions which should be put of special importance. This essay introduces the characteristics of crowd evacuation in the second part. In the third part, the influence factors of crowd evacuation are described. The fourth part is the case study, and the final section is conclusion.

2 THE CHARACTERISTICS OF CROWD EVACUATION

2.1 *Non-adaptive behaviors*

When facing emergent situation, people are easily stimulated by the dangerous environment, especially by those panic motions, so the normal psychological behavior patterns can be lost with ease which will leading to the wrong judgment of the current emergency and eventually the irrational evacuation behaviors, such as: jostling each other, knocking down others when running, and trampling each other. All of those irrational evacuation behaviors are called non-adaptive behaviors. A large amount of casualties under emergent situations are caused by the characteristics of non-adaptive behaviors. Sometimes this behavior is triggered in life-threatening situations such as fires in crowded buildings, at other time, stampedes can arise during the rush for seats or seemingly without cause. Although engineers all finding ways to alleviate the scale of such disasters, their frequency seems to be increasing with the number and size of mass events.

2.2 *Evacuation differences for various groups*

2.2.1 *For personal information*

For common people, only a small portion has received professional training under emergent situation. Most of them can react and evacuate timely when there is a real emergency compared with those never being trained before. For various aging groups, the older the group is, the less evacuating knowledge they control about evacuation. For male and female, there is a big difference when talking about the evacuation route in the building. More than half of the female have no idea of the clear evacuation route in the building (Guomin & Chen 2012).

2.2.2 *For psychological condition when evacuating*

Based on the gender difference, male and female have various sensitive degrees on emergent situation. Generally speaking, male are more cautious

and sensitive about emergency than female which means female can easily be neglectful and careless. For psychological conditions when evacuating, male are more calm compared with female. This concludes that the psychological endurance for female is weaker than male. When there is an emergency, female are easily to be panic and nervous. The psychological hint can be impacted by the educational degree. Generally speaking, the higher the education background is, the more proportion of the people having negative emotion will be.

2.2.3 *For evacuation behavior*

Evacuation behavior means a set of basic behaviors under emergent situations, such as the first behavioral responses. The first behavioral responses vary a lot during different aging groups. The proportion of people who choose to evacuate quickly is 63.93% in the aging group under 15. Adults during 30–60 account for 52.64% to evacuate at the first time. The proportion of youth during the age of 15–30 is 40%. Only 35% of the old choose to escape as their evacuation behavior. There is half of the old man who choose to inform others about the emergent situation which means the old are more likely to take care of others. The second one is the youth whose proportion is about 42%, only 31.25% of minors choose to inform others. The proportion to try to put out the fire is relatively small in all aging groups. By comparison, the youth during 15–30 have the higher proportion: 8.75%. The proportion of people waiting for rescue increases with the age increasing as the older the people are, the weaker they will be. Up to 15% of people choose to wait for rescue on the age of over 60.

3 CASE STUDY

To study the principles of crowd evacuation during emergency situation, normal situation, and the differences between them, this essay adopts video analysis to achieve correlated data and explores the characteristics of pedestrian flow. In this part, the video under emergency situation is the surveillance video which is about Wenchuan earthquake in a supermarket. The time data are collected at the exit of the supermarket. And the video under normal situation is recorded in Suzhou railway station.

3.1 *Emergency situation*

According to above description, human behavior under emergency situation turns out to be different compared with normal condition, which contributes to different characters of pedestrian evacuation. Here by taking down the specific moment when pedestrian pass through specified locations, deep research on time consumption and evacuation population can be conducted.

3.1.1 *Data collection*

In this case, two lines on the floor are selected as the base lines. Rather than the distance between the straight lines, the time when each individual arrive at the base lines is noted respectively. As the walking speed of all the people encountering emergency events is far faster than those under normal circumstances, the image in this video is really difficult to discriminate when several persons reach designated location. Then the video is replayed in slow motion in ULEAD video studio and the replaying speed is 25% of real one. After requiring time data is got, it is necessary to convert the recorded value to actual value. About 35 s in this video is observed.

3.1.2 *Data processing*

Assuming that there is a kind of relationship between time and amount of evacuating people, the raw data in Table 1 is converted into accumulated value preparing for subsequent analysis. The amount of total evacuation pedestrians is 174 in 35 s. The average evacuation speed is not up to 5 people.

3.1.3 *Data analyses*

Based on the raw data, scatter diagram reflecting evacuation change in seconds can be obtained as the following Figure 1.

The blue trend line shows the evacuating number in each second is increasing gradually during observation session. While subsequent data in

Table 1. Model aggregation results.

R	R square	Adjusted R square	Sig
0.999	0.998	0.998	0.000

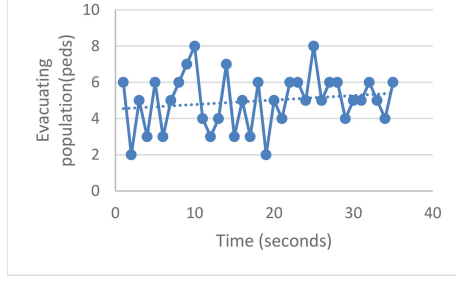

Figure 1. The evacuating population in each second.

emergency video is not available so that the trend should be extended to whole process of the earthquake. It just indicates that general evacuating speed is accelerating at the beginning.

Similarly, the scatter diagram can be achieved in excel (see Fig. 2).

The above figure clearly demonstrates the growing tendency of evacuating number with time in spite of some slightly statistical fluctuation and the variance of growth rate. As is mentioned before, the characteristics of crowd evacuation is affected by various complex factors. Owing to the diversity and complexity, the fluctuation and variance are logical and can be neglected if the values are within tolerance limits.

3.1.4 *Model construction*

Importing the data to SPSS software, linear regression is conducted in this part. In Section 1.2, the relationship is not given out directly. Here in the light of intuitive observation of Figure 2, it is assumed to be linear relation between time and accumulated evacuation. In this model, x is independent variable symbolizing time, and y is dependent variable denoting the accumulated value.

In SPSS, through a process: analyze–regression–linear regression, the model aggregation results are accessible in Table 1.

The value of R square is close to 1, which proves the linear relationship is reasonable, and the fitting formula will be in accordance with the practice. In addition, the value of significance is 0, which further justifies the reliability of the model results.

And the following Table 2 is about the coefficient values in the eventual model formula. The constant term is –3.027 and the coefficient of independent variable is 4.998. Then the equation of linear regression is:

$$y = 0\ 4.998x - 3.027$$

The T value shown in Table 2 illustrates the confidence level of fitted coefficient. T value

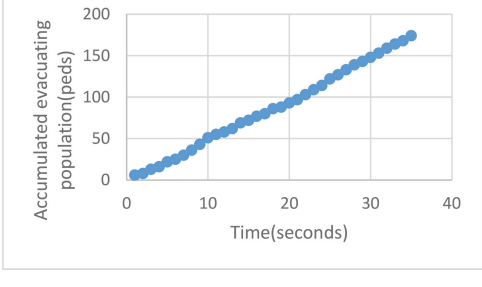

Figure 2. Accumulated evacuating population.

Table 2. Coefficient values in the fitting model.

Model	B	T value	Sig
Constant	–3.027	–3.796	0.001
x	4.998	129.364	0.000

of x 129.364 is high enough to support the reliability of the model results. The significance value of constant term is 0.001, close to 0, and that of coefficient of x is exactly 0. The small values provide evidence for the acceptability of the model. This equation can perfectly describe the principle of escaping population in the earthquake.

3.2 *Normal situation*

In normal conditions, the influence factors are similar to those in emergency situations but the importance levels will be different across factors. Thus the evacuating number and time consumption will be different legitimately. The research methodology for normal situation is the same as that for emergency situation. As in emergency system, the speed and time or other parameters appears random. Especially in normal situations, many pedestrians walk in a relative slow speed without nervous sense from panic.

3.2.1 *Data collection*

Railway passengers get off the train in the negative layer and this video is just recorded at one exit in this floor. Still two virtual lines are appointed on the floor as the base lines. And the timing when a commuter passing through the front and back base lines are recorded in the excel file. In this way all the data required is arranged by pedestrians' arriving order. The observation period is about 2 min during which 77 pedestrians walk out in total.

3.2.2 *Data processing*

It is meaningless to go into the time or speed logistic of each people. What is needed is to achieve universal law of crowd evacuation by considering the human factors comprehensively. Drawing lessons from the analyzing theory in emergency, the accumulated evacuation population during each consecutive 5 s can be calculated from original data.

According to this table, the number of evacuation also increases with time. And the amount of total evacuation pedestrians is 77 in 120 s. The average evacuation speed is about 0.64 people per second.

3.2.3 *Data analyses*

Utilizing the required original data list, scatter diagram is shown in Figure 3.

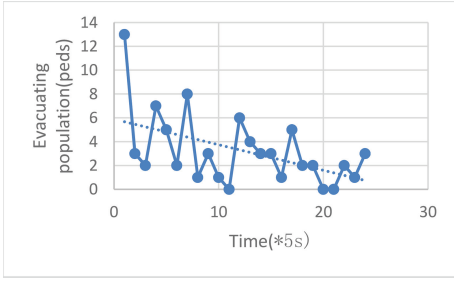

Figure 3. Evacuating volumes in each 5 s.

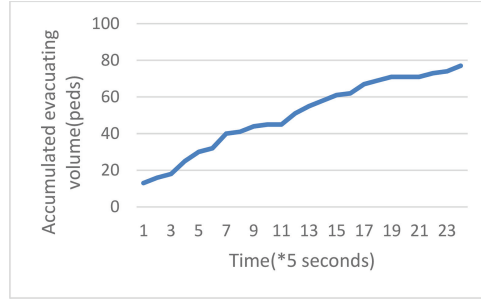

Figure 4. Accumulated evacuating volume.

The blue trend line shows the evacuating volume in each 5 s drops in general level. However, this tendency represents only the escaping volume fluctuation during the observing time period. Unlike emergency situation, the pedestrian crowd forms casually and continuously. The short-term data cannot depict the overall pattern of normal evacuation.

The broken line graph is also obtained (Fig. 4). Figure 4 describes the increasing tendency of evacuating pedestrian volume by every 5 s. Compared with Figure 3, the linear relationship is not obvious by sight. The level of fluctuation in normal situation is more severe than in emergency. The possible reason is that the pedestrians are urgent to escape for life during emergency. While in normal condition, not so many people care about the escaping efficiency.

3.2.4 *Model construction*

The linear relationship is explored in SPSS software. Like the model in emergency situation, x is independent variable symbolizing time and y is dependent variable denoting the accumulated value. The value of R square which demonstrating the uniformity of the model results with the physical truth is shown in Table 3.

The magnitude of R square is less than that of emergency situation, but it is still high enough to prove the linear relation with small significance. So the linear regression equation can be modeled as well. The coefficient values are given out in Table 4.

$$y = 2.800x + 15.370$$

The T values of constant term and coefficient of independent variable are reasonable for model results. And the significance values of them are both 0 which indicate that the fitting result is satisfying.

Table 3. Model aggregation results.

R	R square	Adjusted R square	Sig
0.984	0.967	0.966	0.000

Table 4. Coefficient values in the fitting model.

Model	B	T value	Sig
Constant	15.370	9.800	0.000
x	2.800	25.513	0.000

3.3 *Comparison between the normal situation and the emergency situation*

3.3.1 *Qualitative analysis*

As for physiological aspect, the consequences from differences in gender and age are easy to distinguish. Apparently, the male and young people have the ability to evacuate in relative high speed. Referring to psychological aspect, the reaction to emergent stimulus varies with each individual. Some people need less reaction time but some people response slowly in panic. In emergency situation, growing tension forces people to move quickly. While in normal conditions pedestrians expose less attention on speed or time so they prefer to move at a leisurely pace. And speaking of environmental factors, the geometric feature and surrounding obstacles should be focused on. Based on visual observation, the size of exit in supermarket is smaller than that in railway station and the passing ability in supermarket is lower. But the passing ability does not represent evacuation volume.

3.3.2 *Quantitative analysis*

As mentioned before, fundamental parameters are listed in the following Table 5. The evacuating volume and time are different between emergency and normal situations. The evacuation speed in emergency is 4.97 pedestrians per second which is higher than that of normal situation.

Besides the linear regression equations suggest that both situations share similar changing laws. The linear dependence between accumulated

Table 5. Fundamental parameters.

	Volume (peds)	Time (s)	Speed
Emergency	174	35	4.97
Normal	77	120	0.64

evacuating volume and time spent is a little stronger in emergency situation in the light of T value and significance.

4 CONCLUSION

On the basis of fundamental theory, research on the crowd evacuation has been conducted. Deep analysis about characteristics of crowd evacuation gives out details on non-adaptive behaviors and evacuation differences among various groups. And the influence factors of crowd evacuation have been explored with respect to physical aspect and psychology aspects. The individual decision-making has great effects on evacuation. Also route choice, occupant and group behavior, obstacle and many other factors play important roles in the effectiveness and efficiency of crowd evacuation. To study the features and some factors, both emergency and normal situations are taken into account. The video resource for emergency situation is downloaded from internet and the normal video is recorded. After collecting data from both videos and processing these data, parameters related to evacuating flow are calculated out. From the fitting models, the changing trend in both conditions is in agreement with linear relationship in spite of some tiny variation.

However, some shortages exist in this research procedure. The normal situation video has less representativeness because the evacuation varies with conditions significantly. And the accessibility to record appropriate videos which fully reflect the overall information about normal evacuation is limited. In addition, the sharpness and duration of emergency video is severely difficult to seek out. Sometimes, the time data in emergency video cannot be gotten accurately, which decreases the reliability of the model. The models can just indicate the tendency of related parameters helping to describe the evacuation process while they do not apply to widespread use in quantity.

REFERENCES

Bierlaire, M. & Robin, T. 2009. Pedestrians choices. In: *Pedestrian Behavior: Models, Data Collection and Applications*. Timmermans, H. ed. Emerald Group Publishing Limited.

Bovy, P.H.L & Stern, E. 1990. *Route Choice: Wayfinding in Transport Networks*. Dortrecht: Kluwer Academic Publishers.

Guomin, Z. & Chen, H. 2012. Investigation of individual characteristics and evacuation behavior patterns in complex construction. *Journal of Tianjin Institute of Urban Construction* 18(4): 296–299.

Gwynne, S., Galea, E.R., Owen, M., Lawrence, L. & Filippidis, L. 2005. A systematic comparison of building EXODUS predictions with experimental data from the Stapelfeldt trials and the milburn house evacuation. *Applied Mathematical Modelling* 29(2): 818–851.

Haurie, A. & Marcotte, P. 1985. On the relationship between Nash—Cournot and Wardrop Equilibria. *Networks* 15(3): 295–308.

Hoogendoorn, S.P. & Bovy, P.H.L. 2004. Pedestrian route-choice and activity scheduling theory and models. *Transp. Res. B-Meth* 38(2): 169–190.

Nilsson, D. 2009. *Exit Choice in Fire Emergencies—Influencing Choice of Exit with Flashing Lights*. Sweden: Lund University.

Nilsson, D. & Johansson, A. 2009. Social influence during the initial phase of a fire evacuation-analysis of evacuation experiments in a cinema theatre. *Fire Safety Journal* 44(1): 71–79.

Sime, J.D. 1985. Movement towards the familiar—person and place affiliation in a fire entrapment setting. *Environment and Behaviour* 17(6): 697–724.

Santos, G. & Aguirre, B.E. 2004. *A Critical Review of Emergency Evacuation Simulation Models, NIST Workshop on Building Occupant Movement during Fire Emergencies June 9–10, National Institute of Standards and Technology*. Washington, DC, USA: U.S. Department of Commerce.

Thompson, P.A., Wu, J. & Marchant, E.W. 1996. Modelling evacuation in multi-storey buildings with SIMULEX. *Fire Engineers Journal* 56(185): 6–11.

This page intentionally left blank

Civil Engineering and Urban Planning IV – Liu et al. (Eds)
© 2016 Taylor & Francis Group, London, ISBN 978-1-138-02903-3

Fuzzy-theory-based determination model for researching airport passenger flow radiative zone

Wei-Hua Zhang, Lin Zhou, Hai-Jian Bai & Qiang-Qiang Li
School of Transportation Engineering, Hefei University of Technology, Hefei, Anhui, China

ABSTRACT: With the rapid development of the economy, airports are becoming an important node and hub for transportation systems. Airport passenger flow radiative zone deeply influences the airport site selection, scale of construction, and daily operation, so it is essential to determine a reasonable boundary of airport passenger flow radiative zone. The paper studied the determination of airport passenger flow radiative zone based on fuzzy theory. A model was developed with the shortest landside traffic distance and some influencing factors were taken into consideration to optimize the model. And at the end of the paper, the case of Hefei city airport was taken to identify the scope of airport passenger flow radiative zone based on the model.

1 INTRODUCTION

In recent years, air transportation rapidly developed with its safe, accurate, and efficient characteristics. Airports, as the button of air transport, are converging and delivering a large number of stream of people, logistics, information flow, and cash flow. The scope of airport passenger flow radiative zone varies for city size, regional economy, airport size, airport property, and landside traffic to airport, so the scientific definition of the scope of airport passenger flow radiative zone has important significance to guide the airport site selection and promote development of economy.

2 ANALYSIS OF AIRPORT PASSENGER FLOW RADIATIVE ZONE

2.1 *Airport passenger flow radiative zone*

Airport passenger flow radiative zone refers to the area surrounding the city that the airport can affect, cover, and serve. Let us assume that the airport passenger radiative zone is a circle, and without external influencing factors it is an unlimited circular area spreading outward with the airport as the center (Hsu et al. 1997). The arrows represent the direction of the weakened impact of the airport passenger flow radiative zone. Figure 1 shows an ideal airport radiative zone. With the gradual increase in distance, influence of airport radiative zone will get weaker and weaker until it fades away. It is to say that the airport radiative zone is a limited area where the boundary is its largest scope.

When there is obvious difference in the scale of two airports, the scope of the two airports' radiative zones also has a great difference, Figure 2 shows this visibly. And when the two airports are almost the same, the two ideal airport passenger flow radiative zones are divided by obvious lines, which is shown in Figure 3. According to the breaking point theory, the cut-off point of the two radiative zones must be the point where the two airports have the same radiative ability. Apparently the ideal dividing line of the two airports passenger

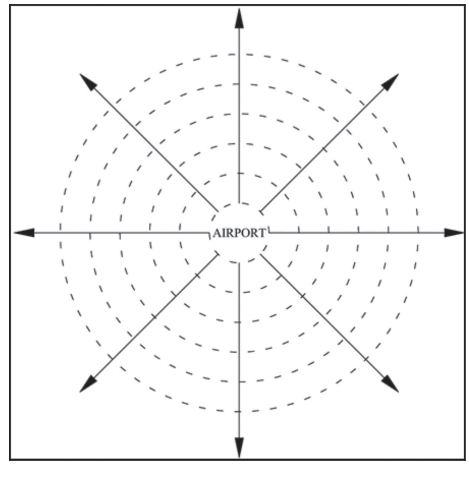

Figure 1. The radiative zone of independent ideal airport passenger flow.

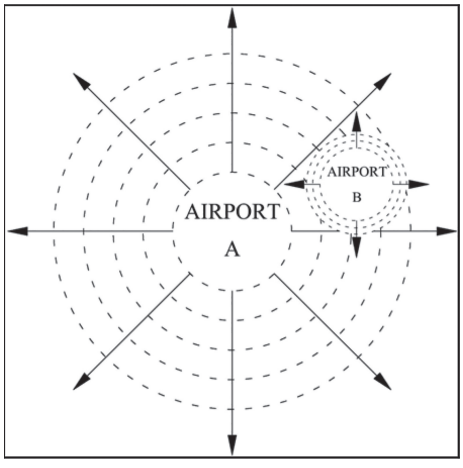

Figure 2. The radiative zone of the two different airport passenger flow.

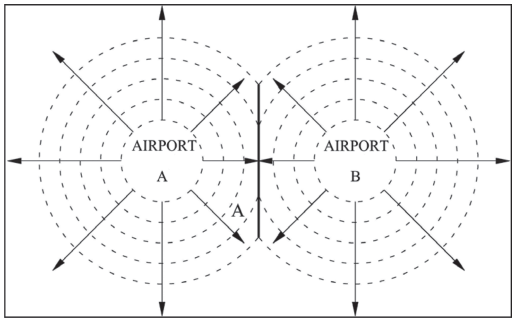

Figure 3. The radiative zone of the two same airport passenger flow.

radiative zones is midperpendicular to the two airports (Hess & Polak 2005).

2.2 *Influencing factor analysis of airport passenger flow radiative zone*

There are four main factors affecting the airport passenger flow radiative zone. We will introduce the factors in detail below.

2.2.1 *City scale and regional economy level*

Airports mainly serve the local city, so a city's scale directly affects the basic area of airport passenger radiative zone (Brooke et al. 1994). Regional economic development has been promoting the development of civil aviation, and the higher the regional economy level, the larger is the demand of civil aviation and the wider the scope of airport radiative zone will be.

2.2.2 *The airport size and airport property*

With a wider airport size, it is indicated that passengers of a wider region will use the airport, and the airport radiative zone will obviously get larger. Airport property refers to the type of airport strategic position; it also can affect the scope of the airport radiative zone.

2.2.3 *Airport operational efficiency*

Airport operational efficiency depends on air throughput, passenger flow characteristics, and capacity of facilities. Compared to the same type airport, it is often characterized by more efficient aviation services, more excellent level of management, and higher airline revenue (Chu 2009). With higher airport operational efficiency, the scope of airport radiative zone will be larger and larger.

2.2.4 *The landside traffic connected to the airport*

Efficient, punctual, and convenient landside traffic can effectively shorten the total travel time. With better landside traffic, airports can attract a wider range of passengers, and the scope of airport radiative zone will expand.

3 DETERMINATION MODEL OF AIRPORT PASSENGER FLOW RADIATIVE ZONE

3.1 *Model building*

Based on fuzzy theory, when there are multiple airports around an administrative unit, passengers of the administrative unit can accept aviation services in many airports (De Neufville 1995). Fuzzy rules are if there are a certain ratio of passengers in the administrative unit choosing certain airport for air travel, we can say the ratio of passengers of the administrative unit is the airport passenger flow radiative zone. We can get the scope of airport radiative zone by summing the ratios of each administrative unit for the same airport (Liu 2008). We assume that air passengers in the administrative unit feel comfortable with the landside traffic distance of d_1, feel common with d_2, and feel barely acceptable with d_3. Due to farther distance and inconvenience, people choose another airport or another means of transportation (Hess & Polak 2006). With the critical value of d_1, d_2, and d_3, we assume that the membership degree is f_0 when landside traffic distance is d_2. Without considering the difference in each airport and its surrounding environment, we establish membership functions that the administrative unit belongs to in the multi-airports radiative zone (Windle & Dresner 1995).

$$f\left(d_{ij}\right)=\begin{cases}1, & d_{ij}\le d_1\\ \dfrac{f_0-1}{d_2-d_1}d_{ij}+\dfrac{d_2-f_0d_1}{d_2-d_1}, & d_1<d_{ij}\le d_2\\ \dfrac{-f_0}{d_3-d_2}d_{ij}+\dfrac{f_0d_3}{d_3-d_2}, & d_2<d_{ij}\le d_3\\ 0, & d_3<d_{ij}\end{cases} \tag{1}$$

where $f(d_{ij})$ = membership of administrative unit i belonging to the scope of airport j radiative zone.

Combining Equation (1) and Figure 4 we can see that membership is the biggest when the landside traffic distance is less than d_1; when the distance is in (d_1,d_2) or (d_2,d_3), membership degree gradually reduced with the increase of landside traffic distance between administrative unit and the airport. When the distance is more than d_3, administrative unit passengers completely do not accept the airport for air services. It is to say that the administrative unit completely does not belong to the airport passenger flow radiative zone.

Adding all the membership degrees we can build the ratio model of the administrative unit belonging to a certain airport passenger radiative zone (Liu 2008).

$$r_{ij}=\frac{f\left(d_{ij}\right)}{\sum_{j=1}^{n}f\left(d_{ij}\right)},\qquad \sum_{j=1}^{n}r_{ij}=1 \tag{2}$$

where r_{ij} = the ratio of administrative unit i belonging to the airport j passenger radiative zone.

In combination with each administrative unit's air passenger volume, we can build the model of airport passenger flow radiative zone.

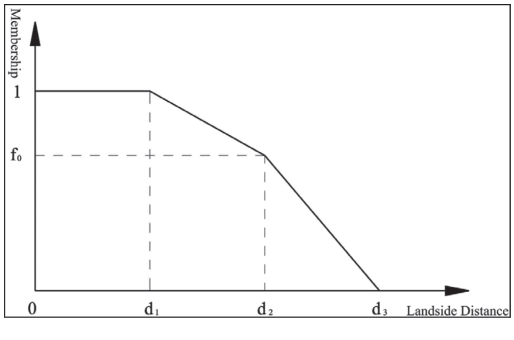

Figure 4. Membership function diagram of passenger flow radiative zone for multiple airports with a single administrative unit.

$$C_j=\sum_{i=1}^{m}C_ir_{ij} \tag{3}$$

where C_j = airport's total passenger volume j = radiative zone, and C_i = air passenger volume of administrative unit i.

Airport total passenger volume means the scope of airport passenger flow radiative zone. Its radiative ability to each administrative unit is reflected through air passenger volume, and each administrative unit does not only belong to the scope of a certain airport passenger radiative zone.

3.2 *Optimal model under multiple influencing factors*

Main factors that influence the scope of airport passenger flow radiative zone have been analyzed through the above analysis, the assumptions in Equation (1) do not consider the difference in each airport and its surrounding environment. It cannot reflect the airport passenger flow radiative zone well. So here we develop an optimal model to improve the existing model by adding some parameters.

$$f\left(d_{ij}\right)=\delta_i\varphi_i\eta_i\begin{cases}1, & d_{ij}\le d_1\\ \dfrac{f_0-1}{d_2-d_1}d_{ij}+\dfrac{d_2-f_0d_1}{d_2-d_1}, & d_1<d_{ij}\le d_2\\ \dfrac{-f_0}{d_3-d_2}d_{ij}+\dfrac{f_0d_3}{d_3-d_2}, & d_2<d_{ij}\le d_3\\ 0, & d_3<d_{ij}\end{cases} \tag{4}$$

where δ_i = the correction factor of membership degree that administrative unit i belongs to the scope of airport j radiative zone by airport size and regional economy level, φ_i = the correction factor of membership degree that administrative unit i belongs to the scope of airport j radiative zone by airport operational efficiency; η_i = the correction factor of membership degree that administrative unit i belonging to the scope of airport j radiative zone by the landside traffic connected to the airport.

4 PARAMETER CALIBRATION OF THE MODEL

4.1 *The correction factor of membership degree by airport scale and regional economy level*

We divide the airports into three types. Airport throughput of more than 10 million people is the first class airport; airport throughput between

1 and 10 million is second class airport; and airport throughput less than 1 million is third class airport. Table 1 shows the impact of regional economy (GDP), number of local tourism, per capita income to airport throughput (Zheng 2014), and this can reflect the influence of membership degree from the side.

4.2 *The correction factor of membership degree by operational efficiency of the airport*

Through operational efficiency DEA evaluation of China's main airports, we can see airport's average ranking of operation efficiency, as shown in Table 2 (Fu et al. 2013). Other airports can take the same type of indicators according to the DEA data.

4.3 *The correction factor of membership degree by the landside traffic connected to the airport*

Through quantitative processing of comfort level, degree of easy interchange, travel time, ticket price, transport capacity, and delay of landside traffic connected to the airport, we study the effect of the landside traffic in membership degree, and build the calculation model of airport air transportation competitiveness using the landside traffic with the data from London airport (Feng et al. 2014), and use the data of other airports in London to check. The model can reflect the influence of membership degree in some way.

$$y = -0.444 + 6.059x_1 - 0.386x_2 - 2.351x_3 + 13.338x_4 - 1.82x_5 \quad (5)$$

where y = the airport passenger transport competitiveness index, x_1–x_5 is airport landside walking distance, the landside travel time, ticket price, comfort level, and delay.

Table 1. The influence of regional economy, local tourism population, per capita income on the airport throughput.

Airport	First class airport (%)	Second class airport (%)	Third class airport (%)
1% change of GDP	1.9254	1.5154	2.2122
1% change of local tourism	0.2751	0.2192	0.3512
1% change of per capita income	0.1025	0.1920	0.0975

Table 2. Operational efficiency of some main Chinese airports.

Airport	Operational efficiency
Shanghai Hongqiao airport	1
Beijing Capital airport	0.997
Chongqing airport	0.976
Wuhan Tianhe airport	0.973
Tianjin Binghai airport	0.866
Hangzhou Xiaoshan airport	0.861

5 CASE ANALYSIS

We considered Hefei city airport, Huangshan city airport, Fuyang city airport, Anqing city airport, and Chizhou city airport in Anhui province. By data investigation and comparative analysis, we obtained the ratio of airport throughput in Hefei city airport in provincial total airport throughput as shown in Figure 5.

We used the optimal model to analyze Hefei city airport passenger flow radiative zone. Make the following assumptions first. Assuming that we ignore the influence of the airport outside the province, we did not consider the influence of airport operational efficiency on membership function, neglecting the effects of airways on airport passenger flow radiative zone. And when passengers choose airport, they feel comfortable by the landside traffic distance of less than 50 km, feel common when less than 100 km (Wang et al. 2006), and refuse to accept more than 200 km without the airport terminal in their local city and give the membership degree $f_0 = 0.3$. The distance of each city in Anhui Province is shown in Table 3.

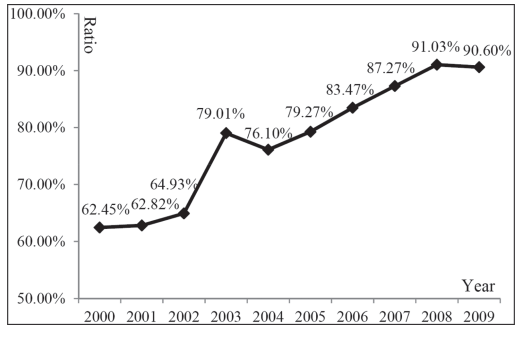

Figure 5. The ratio of Hefei city airport throughput in the provincial total throughput from 2000 to 2009.

Table 3. Statistics of landside distance between two cities of Anhui province.

Cities	Distance to Hefei	Distance to Huangshan	Distance to Fuyang	Distance to Chizhou	Distance to Anqing
	City airport (km)	City airport (km)	City airport (km)	City airport (km)	City airport (km)
Hefei	0	260	180	135	150
Wuhu	120	180	295	110	150
Bengbu	120	370	145	250	270
Ma'anshan	120	220	285	150	190
Suzhou	200	460	135	335	345
Anqing	150	160	185	45	0
Huainan	95	350	115	225	235
Tongling	110	150	285	45	85
Huangshan	260	0	430	130	160
Xuancheng	170	140	355	125	170
Chizhou	135	130	290	0	290
Chuzhou	110	290	245	200	230
Huaibei	240	495	150	370	380
Fuyang	180	430	0	290	185
Lu'an	75	290	140	155	145
Bozhou	260	520	105	390	390

Table 4. The correction factor of membership degree by airport size and regional economic level.

	Hefei city airport	Huangshan city airport	Fuyang city airport	Chizhou city airport	Anqing city airport
δ_i	13.95	2.67	1	1.86	1.96

Table 5. Reduced statistics of landside distances between two cities of Anhui province.

Cities	Distance to Hefei city airport (km)	Distance to Huangshan city airport (km)	Distance to Fuyang city airport (km)	Distance to Chizhou city airport (km)	Distance to Anqing city airport (km)
Hefei	0	–	180	135	150
Wuhu	85	180	–	110	150
Bengbu	85	–	145	–	–
Ma'anshan	85	–	–	150	190
Suzhou	140	–	135	–	–
Anqing	105	160	185	45	0
Huainan	65	–	115	–	–
Tongling	75	150	–	45	85
Huangshan	–	0	–	130	160
Xuancheng	120	140	–	125	170
Chizhou	95	130	–	0	–
Chuzhou	75	–	–	200	–
Huaibei	170	–	150	–	–
Fuyang	125	–	0	–	185
Lu'an	55	–	140	155	145
Bozhou	180	–	105	–	–

Table 6. Membership degree of the city belonging to each airport.

City	Membership of Hefei city airport	Membership of Huangshan city airport	Membership of Fuyang city airport	Membership of Chizhou city airport	Membership of Anqing city airport
Hefei	13.95	0	0	0	0
Wuhu	7.11	0.16	0	0.5	0.29
Bengbu	7.11	0	0.17	0	0
Ma'anshan	7.11	0	0	0.28	0.06
Suzhou	2.51	0	0.2	0	0
Anqing	3.98	0.32	0.05	1.86	1.96
Huainan	11.02	0	0.26	0	0
Tongling	9.07	0.4	0	1.86	1
Huangshan	0	2.67	0	0.39	0.23
Xuancheng	3.35	0.48	0	0.42	0.18
Chizhou	5.16	0.56	0	1.86	0
Chuzhou	9.07	0	0	0	0
Huaibei	1.26	0	0.15	0	0
Fuyang	3.14	0	1	0	0.09
Lu'an	12.97	0	0.18	0.25	0.32
Bozhou	0.84	0	0.29	0	0

Table 7. The scope of Hefei city airport passenger flow radiative zone.

City	Scope of Hefei city airport radiative zone (%)
Hefei	100.00
Wuhu	88.15
Bengbu	97.73
Ma'anshan	95.47
Suzhou	92.79
Anqing	48.73
Huainan	97.74
Tongling	73.56
Huangshan	0.00
Xuancheng	75.69
Chizhou	68.07
Chuzhou	100.00
Huaibei	89.33
Fuyang	74.26
Lu'an	94.51
Bozhou	74.60

Hefei city airport has airport terminals in 13 prefecture-level cities. The basic functions include all the functions at the airport terminals except boarding the plane, and passengers can go to the airport directly in other cities. It is time-saving and convenient. We set conditions of local cities without an airport terminal in and a distance of more than 200 km to the airport. We can then exclude the cities out of the airport radiative zone. And according to the information, GDP per capita of Hefei city is 2.38 times than Anqing city, 4.65 times than Fuyang city, 1.74 times than Huangshan city, and 2.50 times than Chizhou city.

Table 4 shows the correction factor δ_i of membership degree by airport size and regional economy level. As we considered the reduction of landside traffic distance about the impact of Hefei city airport, and the other four are almost the same state, we can choose $\eta_i = 1$. Above all, we can find the landside traffic distance after the reduction, which is shown in Table 5.

Considering that passengers living in Hefei city always choose Hefei city airport, we can use the fuzzy theory-based determination optimal model with the shortest landside traffic distance to calculate the membership of the city which belongs to the airport, which is shown in Table 6. And the scope of Hefei city airport passenger flow radiative zone is shown in Table 7.

6 CONCLUSION

- The paper studied the determination model of airport passenger flow radiative zone. By detailed analysis and careful consideration, a mathematic model was developed with the shortest landside traffic distance.
- Influencing factors of airport radiative zone were taken into consideration, and correction factors were introduced in the model to reflect the influencing factors. Then a new optimal model was developed with the correction factors to identify airport passenger flow radiative zone.

– By using the data of Hefei city airport, the optimal model proved to be effective to search the airport passenger flow radiative zone. Through parameter calibration, the model could be used by any airport to determine the airport passenger flow radiative zone.

ACKNOWLEDGMENT

The research was supported by the National Natural Science Foundation of China under Grant No. 51178158 and the National Natural Science Foundation of China under Grant No. 51308176.

REFERENCES

Brooke, A.S. et al. 1994. Methodology for predicting European shorthaul air transport demand from regional airports: An application to East Midlands international airport. *Journal of Air Transport Management* 1(1):37–46.

Chu, Y.C. 2009. *Research on Airport Operation Efficiency Evaluation and Improvement*. Tianjing: Tianjin University.

De Neufville, R. 1995. Management of multi-airport systems. *Journal of Air Transport Management* 2(2): 99–110.

Feng, J.P. et al. 2014. A study on land-side traffic's influence to the airports' passenger competitiveness. *Road Traffic & Safety* 14(2): 60–64.

Fu, S.N. et al. 2013. Operational efficiency of major airports in China based on dual-oriented DEA model. *Journal of Transportation Systems Engineering and Information Technology* 13(4): 193–199.

Hess, S. & Polak, J.W. 2005. Mixed logit modelling of airport choice in multi-airport regions. *Journal of Air Transport Management* 11(2): 59–68.

Hess, S. & Polak, J.W. 2006. Exploring the potential for cross-nesting structures in airport-choice analysis: a case-study of the Greater London Area. *Transportation Research Part E* 42(2): 63–81.

Hsu, C. & Wu, Y.H. 1997. The market size of a city-pair route at an airport. *The Annals of Regional Science* 31(4): 391–409.

Liu, X.M. 2008. *Intelligence Computational Based Air Passenger Flow Distribution in Uncertain Environment*. Nanjing: Nanjing University of Aeronautics and Astronautics.

Wang, J.E. et al. 2006. Research on spatial distribution and service level of Chinese airport system. *Geographic Research* 61(8): 829–838.

Windle, R. & Dresner, M. 1995. Airport choice in multiple-airport regions. *Journal of Transportation Engineering* 121(4): 332–337.

Zheng, Y.Q. 2014. *Study of the Correlation between Regional Economy and Development Scale of Airport*. Nanjing: Nanjing University of Aeronautics and Astronautics.

This page intentionally left blank

Civil Engineering and Urban Planning IV – Liu et al. (Eds)
© 2016 Taylor & Francis Group, London, ISBN 978-1-138-02903-3

Performance evaluation of recycled cement stabilized crushed stone

Jing Wang
Beijing University of Architecture and Civil Engineering, BJTICR Centre, Beijing, China

Shi-Fa Xu
Beijing University of Architecture and Civil Engineering, TRC, Beijing, China

Jie Qiao
Beijing Urban Road and Bridge Maintenance Centre, Beijing, China

Li-Ting Xu
Shell (China) Co. Ltd., Beijing, China

Yu-Jie Guo
Henan Province Highway Engineering Bureau Group Co. Ltd., Zhengzhou, Hunan, China

ABSTRACT: This paper first validated the feasibility of recycling cement stabilized crushed stone, research shows that under blending ratio 30% of reclaimed cement stabilized crushed stone, cement dosage 3.5%, the strength of recycled cement stabilized crushed stone can meet the specification requirements of new material. Second, the 7 d unconfined compressive strength, cleavage strength and drying shrinkage performance under different blending ratio were evaluated and compared. By comparing the performances we concluded that the recycled aggregate exert adverse effects on cement stabilized recycled crushed stone.

1 RESEARCH BACKGROUND

With the ongoing highway construction, more and more express ways come into overhaul stage, milling of pavement structures produces large amounts of waste of asphalt concrete, cement concrete and semi-rigid materials. Current recycling technology of asphalt concrete and cement concrete is relatively mature. The recycling technology of asphalt concrete include hot recycling technology, warm recycling technology and cold recycling technology, hot and warm recycling technology apply to surface layer and cold recycling technology is mainly used in base layer. Cement concrete is generally regenerated into cement concrete pavement or semi-rigid base course. Semi-rigid base course is usually thicker than asphalt surface layer and cement concrete slab, the pavement will produce more waste after milled and take up a lot of land resources. On the other hand, highway construction faces mineral aggregate lack problems, mining of mineral aggregate consumes a lot of energy, resulting in environmental pollution. Recycling of semi-rigid base course materials not only has huge economic benefits, but also has great environmental benefits. Widely used in high-grade Highway base, cement stabilized crushed stone is a common kind of semi-rigid base course materials and has the characteristics of high strength, high rigidity (JTJ034-2000).

At present, the main utilization pattern of milled semi-rigid base course materials is blending with lime or concrete, controlling quality by 7 d unconfined compressive strength. In the process of utilization it occurs the problems of performance weakness, quality variability and so on. Under overall blending mode of empirical method, this paper conducted feasibility study of milled materials of cement stabilized macadam. Contrast with new cement stabilized crushed stone under same aggregate grade, we analyzed the impact of milled materials to cement stabilized crushed stone. Because there is a limit blending ratio for overall blending mode, this article also studied the impact of blending ratio to cement stabilized stone performances under equal blending ratio, aiming to determine the best blending ratio of milled materials and ensuring the balance of performances and economy (JTG/T F20-2015).

2 FEASIBILITY STUDY OF CEMENT STABILIZED CRUSHED STONE RECYCLING TECHNOLOGY

2.1 *Grade design*

The experimental milled materials come from Zhumadian-Xinyang section of Beijing-Hong Kong-Macao express way. First we made a preliminary break and sieving. The new aggregate is limestone produced by some stone factory of Xinyang. The cement is P.C.42.5 composite Portland cement. Sieving results are shown in Table 1 (Hu 2004).

According to the Technical specifications of highway road base construction (JTJ034-2000), the maximum size of a single particle should not exceed 31.5 mm. The content of 4.75 mm-19 mm Size particles is up to 35.3% and limit the blending ratio of milled materials to 30%. The final design grade is shown in Figure 1: Aggregate 0–5 20%, Aggregate 10–30 50%, milled materials 30%, which meet Technical specifications' requirements (Zhang 2006).

2.2 *Determine the optimum water content and dry density*

The experiment method to determine optimum water content and dry density is Heavy compaction experiment. We carry out the experiment under 3.5%, 4.5% and 5.5% content of cement, 4% and 5% content of cement is determined according to interpolations. The optimum water content and dry density when blending ratio of milled materials is 30% is shown in Table 2. The optimum water content and dry density when blending ratio of milled materials is 0% is shown in Tables 2 and 3, both under the design grade.

Table 1. Sieving results.

Sieve size (%)	Aggregate 0–5	Aggregate 5–10	Aggregate 10–30	Milled materials
31.5	100	100	100	100
26.5	100	100	100	99.42
19	100	100	83.19	91.22
9.5	100	99.10	27.09	71.51
4.75	99.30	24.31	1.80	55.92
2.36	68.20	4.07	0.63	39.18
0.6	35.51	2.63	0.59	15.72
0.075	7.57	1.76	0.51	2.40
<0.075	0.00	0.00	0.00	0.00

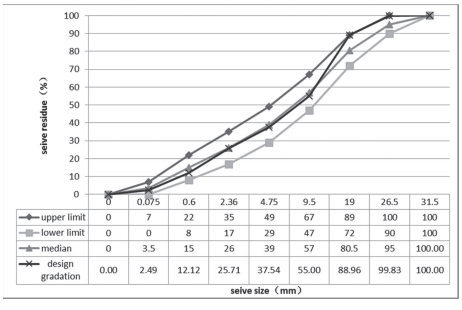

Figure 1. Design grade.

2.3 *Performance verification*

First we molded cylindrical specimens size of diameter × high = Φ150 mm × 150 mm according to JTG E51-2009 and beam specimens size of 100 mm × 100 mm × 450 mm according to T0843-2009. Second the specimens are cured under standard conditions (temperature 20°C±2°C, relative humidity above 95%) 6 day and soaked in water of 20°C±2°C 1 day. After cured, we tested the 7 d unconfined compressive strength, the 7 d cleavage strength, the shrinkage coefficient, 28 d TSR, 28 d compression rebound modulus. Experiment results are shown in Figures 2 to 7 (JTG E51-2009).

Table 2. Compaction results when blending ratio 30%.

Cement content	3.5%	4%	4.5%	5%	5.5%
Optimum water content (%)	7.0	7.1	7.1	7.2	7.2
Dry density (g/cm³)	2.30	2.30	2.30	2.29	2.28

Table 3. Compaction results when blending ratio 0%.

Cement content	3.5%	4%	4.5%	5%	5.5%
Optimum water content (%)	4.6	4.7	4.8	4.8	4.8
Dry density (g/cm³)	2.32	2.33	2.34	2.35	2.35

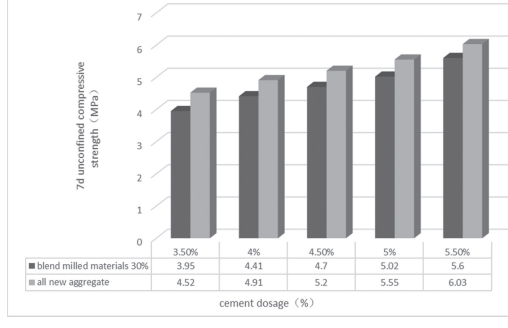

Figure 2. 7 d Unconfined compressive strength.

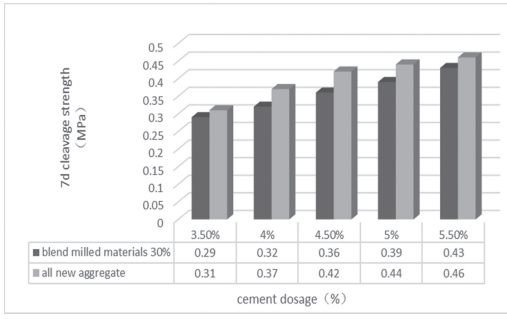

Figure 3. 7 d cleavage strength.

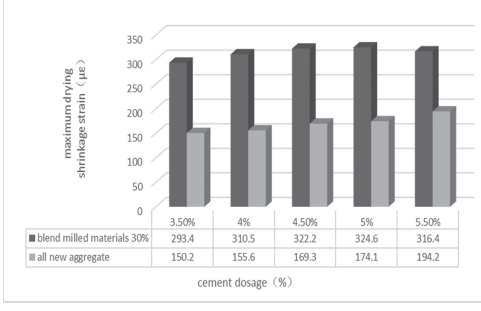

Figure 4. Maximum drying shrinkage strain.

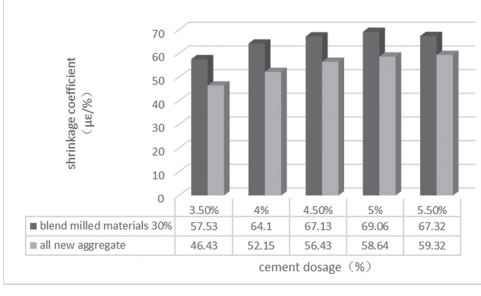

Figure 5. Shrinkage coefficient.

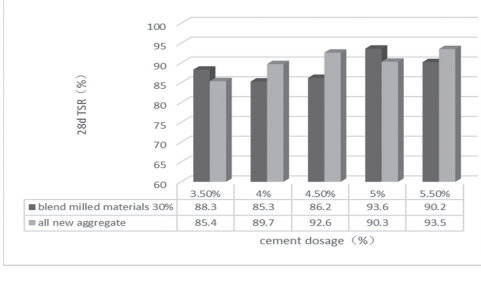

Figure 6. 28 d TSR.

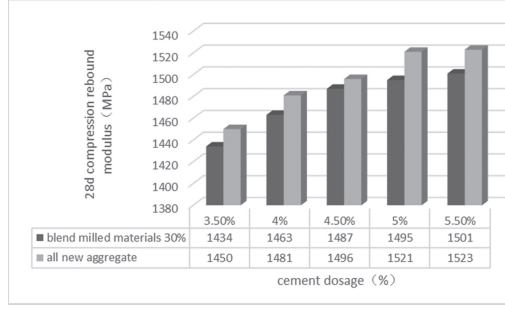

Figure 7. 28 d compression rebound modulus.

Experiment results show that the 7 d unconfined compressive strength, the 7 d cleavage strength of cement stabilized crushed stone blending with 30% milled materials increase along with the increase of cement dosage. When cement dosage is 3.5%, the 7 d unconfined compressive strength can meet regulatory requirements 3–5 MPa. Contrast with cement stabilized crushed stone absolutely utilizing new aggregates, road performance of cement stabilized crushed stone blending with 30% milled materials declined. There is a certain drop degree of 7 d unconfined compressive strength, 7 d cleavage strength, 28 d TSR and 28 d compression rebound modulus, but the maximum drying shrinkage strain and shrinkage coefficient raised. Milled materials have bad influences on cement stabilized crushed stone, and the influence on maximum drying shrinkage strain is most serious. For example: when cement dosage is 4.5%, The maximum drying shrinkage strain of cement stabilized crushed stone absolutely utilizing new aggregates is 169.3 με, but the maximum drying shrinkage strain of cement stabilized crushed stone blending with 30% milled materials is up to 322.2 με, which indicates more probabilities of reflective crack to asphalt pavement.

Causes of this phenomenon are as follows:

– The density of milled materials is relatively lower than new aggregates. Although under same quality, the milled materials take up more space than new aggregates.
– After a certain degree of grinding, the angularity of milled materials is much stronger, the specific surface area is larger, which exerts some influence on skeletal structure and compactness.
– The cement mortar wrapped around milled materials has a weak bearing capacity and many tiny cracks, which makes a finer grade.
– The cement mortar wrapped around milled materials is a kind of porous materials and has a high water absorbing capacity, but the cement of it is completely hydrated. The water of physical

absorption is easy to evaporate, which makes the contraction more serious.

3 CONCLUSIONS

- When cement dosage is 3.5%, the 7 d unconfined compressive strength can meet regulatory requirements 3–5 MPa.
- Compared to cement stabilized crushed stone absolutely utilizing new aggregates, road performance of cement stabilized crushed stone blending with 30% milled materials declined.
- Milled materials exert an adverse influence on cement stabilized crushed stone, and has the greatest impact on crack resistance.

REFERENCES

Application Handbook of Test Methods of Materials Stabilized Inorganic Binders for Highway Engineering (JTG E51-2009). Beijing: China Communications Press.

Hu, L.Q. 2004. *Research on Structural Characteristic and Component Design Methods for Semi-rigid Base Course Material*. Xi'an: Chang'an University.

Technical Guidelines for Construction of Highway Road Bases (JTG/T F20-2015). Beijing: China Communications Press.

Technical Specifications of Highway Road Base Construction (JTJ034-2000). Beijing: Research Institute of Highway Ministry of Transport.

Zhang, G.Z. 2006. *Mix Design and Road Performance of Cement and Flyash Stabilized Crushed-stones Roadbases.* Xi'an: Chang'an University.

Civil Engineering and Urban Planning IV – Liu et al. (Eds)
© 2016 Taylor & Francis Group, London, ISBN 978-1-138-02903-3

Performance evaluation of the recycling asphalt binder regenerated with vegetable oil

Qi Man & Jing Wang
School of Civil and Transportation Engineering, Beijing University of Civil Engineering and Architecture, Beijing, China

Shi-Fa Xu & Zhi Suo
School of Civil and Transportation Engineering, Beijing University of Civil Engineering and Architecture, Beijing, China
Beijing Urban Transportation Infrastructure Engineering Technology Research Center, Beijing, China

ABSTRACT: The traditional asphalt binder rejuvenators usually contain a great deal of fuel heavy oils to supply the light oil components of bitumen which decreased during a long-term aging procedure. However, there are many problems to use the fuel heavy oil as an asphalt rejuvenator. In this research, a cooking vegetable oil was used instead of the traditional rejuvenator. It can not only reduce the viscosity of the asphalt effectively but also improve the low-temperature performance of the asphalt. Meanwhile, it can help to solve the problem of waste oil pollution and reduce the costs of the asphalt regeneration. The performances of the aged asphalt before and after regeneration were evaluated, and the optimum adding amount of vegetable oil asphalt rejuvenator was calculated. This approach provides a developed design procedure for the recycling asphalt pavement material design.

1 INTRODUCTION

In recent years, modification and maintenance of the asphalt pavement are being implemented widely in China. It leads to a problem that a large number of Recycled Asphalt Pavement (RAP) materials are produced every year. As a kind of a waste material, the RAP would cause many serious environmental problems if it is not properly handled. Hot recycling of the asphalt pavement can save a lot of raw materials and reduce the energy consumption, because it takes a good advantage of RAP. It has been proved as an effective method to solve the problem of RAP accumulation (West et al. 2014; Xu et al. 2013).

The traditional rejuvenators usually contain a great deal of fuel heavy oils to supply the light oil component of bitumen, which decreased during a long-term aging procedure. However, the fuel heavy oils easily emit at a high recycling temperature (above 180 °C). The vegetable oils are rich in unsaturated fatty acids, which were similar to the light oil components and have a better temperature resistance. Based on the bitumen aging and rejuvenation theory, it can be used for the bitumen regeneration (Li et al. 2014; Shashwat et al. 2006).

Since 1970s, with the gradual development of the asphalt regeneration technology research, western countries began to develop a recycling agent. At the beginning of SHRP, Researchers have analyzed the change of composition in the asphalt ageing process. They try to recover the performance of the aging asphalt according to adding the missing components to it (Kallas 2014). However, the chemical structure of the asphalt is so complex, even though it has similar chemical composition (Shen et al. 2007; Mohanty 2002). Gordon Davies chose to use the soybean wax and the waste vegetable oil as the regeneration agent in 2010. His research indicated the direction for the development of the recycling agent (Gordon 2013).

In this research, the physical indexes of the recycled asphalt were tested, and the optimal addition amount of the vegetable oil rejuvenator was determined.

2 MATERIALS

The vegetable oil rejuvenator is a kind of mixture which takes the waste vegetable oil (soybean oil) used in cooking as the raw material, in which a stable component is present (Hameed 2009; Garciaa 2010). The properties of the vegetable oil rejuvenator are illustrated in Table 1.

Table 1. The physical properties of the vegetable oil rejuvenator.

Test items	Test results	Test items	Test results
Appearance	Black	Viscosity (60 °C)	0.160 Pa·s
PH-value	7 ± 0.5	Dielectric constant	2.8
Density	0.923 g/mL	Flash point	234 °C

Table 2. The physical properties of the virgin asphalt and the aged asphalt.

Test items	Standard	70# virgin asphalt	Aged asphalt
Penetration (0.1 mm) at 25 °C	ASTM D5	72	20.8
Softening point (°C)	ASTM D36	47	61
Ductility (cm) at 15 °C	ASTM D113	102	8.9
Viscosity (mPa·s) at 13 °C	ASTM D4402	485	713

The asphalt in this article is 70# virgin asphalt. As illustrated in Table 2, we simulated the aged process of the asphalt by PAV and tested the performance indexes of the virgin asphalt and the aged asphalt.

3 RESULTS AND DISCUSSION

3.1 *Physical properties*

Figures 1–3 show the results from the fundamental physical properties tests such as penetration, softening point and ductility for the 70# virgin asphalt, aged asphalt (extracted from the RAP materials) and recovered asphalt with different contents of the rejuvenators.

Penetration is used to divide the model of asphalt. The smaller the penetration, the higher the hardness, conversely the lower the hardness. From the results in Figure 2, it was observed that the penetration values increased linearly as the increasing content of the rejuvenator in the aged asphalt. The shifting trend of the penetrations roughly in line with "y = 862.86x + 20.19" and the correlation coefficient R^2 is 0.997. Similarly, we can also find that the penetration values of the recovered asphalt containing approximately 4–6% vegetable oil rejuvenator have similar grades as the 70# virgin asphalt.

In general, the higher the softening point, the higher the hardness, and the better the temperature stability. The relationship between the softening point values and the different content of the asphalt are shown in Figure 2. As illustrated in the graph, the softening point value decreases with the increasing content of the rejuvenator into

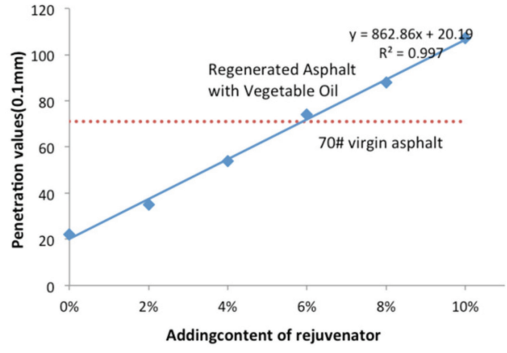

Figure 1. The influence of the rejuvenator content on penetration.

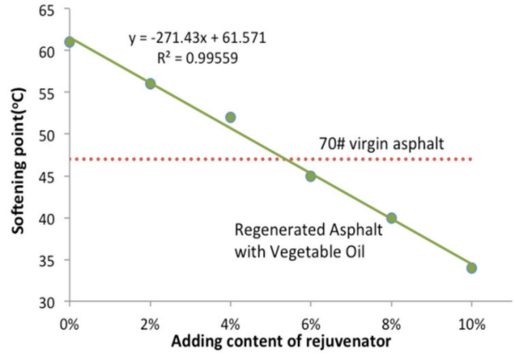

Figure 2. The influence of the rejuvenator content on softening point.

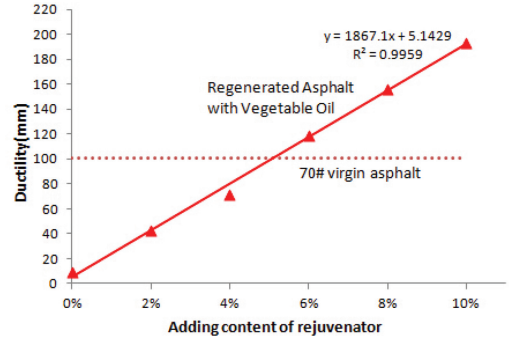

Figure 3. The influence of the rejuvenator content on ductility.

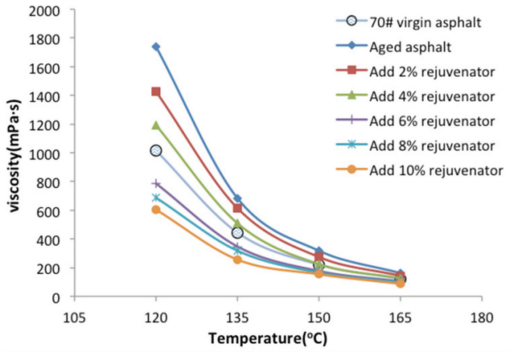

Figure 4. The influence of the rejuvenator content on viscosity.

the aged asphalt. The shifting trend of softening points roughly in line with "y = –271.43x + 61.57" and the correlation coefficient R^2 is 0.996. The softening point values of the recovered asphalt content approximately 4–6% vegetable oil rejuvenator have similar grade as the 70# virgin asphalt.

Ductility reflects the flexibility of the asphalt; the higher the ductility, the better the flexibility. As shown in Figure 4, the ductility values of the recovered asphalt increase with the increasing content of the rejuvenator. The shifting trend of the ductilities roughly in line with "y = 1867.1x + 5.14" and the correlation coefficient R^2 is 0.996. The ductility values of the recovered asphalt content approximately 4–6% vegetable oil rejuvenator have similar grades as the 70# virgin asphalt.

3.2 *High temperature viscosity*

The influence of the rejuvenator content on the viscosity of the recovered asphalt is shown in Figure 4. It is clear that the viscosity of the recovered asphalt decreases with the increasing rejuvenator content. From Figure 4 we can find that the viscosity values of the recovered asphalt containing 4–6% vegetable oil rejuvenator have similar grade comparing with the 70# virgin asphalt. It means that the addition of the vegetable oil rejuvenator can more effectively decrease the aged asphalt viscosity, which is the vital in decreasing the proportion of the asphaltenes in the recovered asphalt.

4 CONCLUSION

In this paper, some preliminary conclusions are as follows:

- The fundamental physical properties test shows that the fundamental physical properties of the asphalt can be recovered when approximately 4–6% vegetable oil rejuvenator is added. Vegetable oil rejuvenator can effectively reduce the hardness and improve the plasticity of the aged asphalt.
- The viscosity values of the recovered asphalt containing 4–6% vegetable oil rejuvenator content have similar grades of the control virgin asphalt. The viscosity of recovered asphalt more effectively decreases with the increasing rejuvenator contents.

REFERENCES

Garciaa, A., Schlangen, E., Ven, M. & Beltrana, G.S. 2010. Preparation of capsules containing rejuvenators for their use in asphalt concrete. *J. Hazard. Mater*. 184(21):603–611.

Gordon, D. 2013. *Release Agent Formulas and Methods*. US20 11/025878 A1.2013.

Hameed, B.H., Gol, C.S. & Chin, L.H. 2009. Process optimization for methyl ester production from waste cooking oil using activated carbon supported potassium fluoride. *Fuel Processing Technology* 90(12): 102–107.

Kallas, B.F. 2014. *Flexible Pavement Mixture Design Using Reclaimed Asphalt Concrete*. Report No. FHWA/RD-84/088, Final Report.

Li, B., Qiu, L.Q. & Song, S.F. 2014. Analysis of fatty acids in vegetable oils in gas chromatography. *Chinese Journal of Analysis Laboratory* 33(5):144–149.

Mohanty, A.K., Misra, M. & Drzal, L.T. 2002. Sustainable bio-composites from renewable resources: Opportunities and challenges in the green materials world. *Journal of Polymers and the Environment* 10(6):19–26.

Shashwat, S.B., Milind, V.J. & Radha, V.J. 2006. Treatment of oil spill by sorption technique using fatty acid grafted sawdust. *Chemosphere* 64(2006): 1026–1031.

Shen, J., Amirkhanian, S. & Jennifer, A.M. 2007. Effects of rejuvenating agents on superpave mixtures containing reclaimed asphalt pavement. *Journal of Materials in Civil Engineering* 14(5):376–384.

West, R. & Willis, J.R. 2013. *Improved Mix Design, Evaluation and Materials Management Practices for Hot Mix Asphalt with High Reclaimed Asphalt Pavement Content*. Washington D.C.: NCHRP Report 752.

Xu, S.F., Xu, L.T., Zheng, W. & Wang, X.X. 2013. Developmentand outlook of technology of hot recycling of reclaimed asphalt pavement. *Road Machinery and Construction Mechanization* 32(6):39–43.

This page intentionally left blank

Civil Engineering and Urban Planning IV – Liu et al. (Eds)
© 2016 Taylor & Francis Group, London, ISBN 978-1-138-02903-3

Review on three road surface roughness simulation methods

Fan Yang & Jiang-Tao Zhao
School of Mechanical Engineering, Qinghai University, Xining, Qinghai, China

ABSTRACT: Road surface roughness is an important factor on studying the comfortable degree of moving vehicles, the degree of road surface wear, and the vehicle-bridge vibration. There are three methods on simulating road surface roughness in the paper, MATLAB software was used to simulate B level road surface roughness with three different theories, respectively. The example showed that the trigonometric series method was the best method conforming to the actual road surface roughness, but the power spectrum had a great difference with the standard spectrum. The power spectrum, which was generated by inverse discrete Fourier transform, was roughly the same as the standard spectrum, however, the change of road surface roughness, which was generated by inverse discrete Fourier transform, was slow and the change trend had a great difference with the actual road surface roughness. The three-dimensional road surface roughness can generate the simulated road truly, the power spectrum was roughly the same as the standard spectrum, and hence three-dimensional road surface roughness had a great advantage on the vehicle-bridge vibration.

1 INTRODUCTION

The road surface roughness is an important factor on studying the comfortable degree of the moving vehicles, the degree of road surface wear, and the vehicle-bridge vibration. The vibration of vehicle is mainly caused by the road surface roughness during the vehicle going. The road surface roughness affects the comfortableness of the vehicle, work life of the vehicle, vehicle's gas mileage, vehicle smoothness and so on. When the vibration of vehicle-bridge studied, displacement of the bridge is passed on to the vehicle due to the road surface roughness. The road surface roughness decides the exactness and veracity of the whole research process. The accurate simulation of road surface roughness has an important significance to the researchers of the automotive engineering and the road and bridge project.

The early method of research to the pavement is the trial; plainness of the road surface is obtained by straight forward test used by the pavement thickness (Xie 2005). With the development of the technology of numerical simulation, scholars run the model and simulation of the road based on the theoretical test, and put forward various methods of the simulation of road surface roughness. The simulation of road surface roughness experienced the process from two-dimensional to three-dimensional. Over the research and simulation of road surface roughness in the past, model of two-dimensional road surface roughness mainly divides into four general categories (Duan 2009), the model of the analysis with power spectrum, time series, and fractal interpolation. Power spectrum model contains the trigonometric series method and white noise excitation method. Time series model contains AR (Auto Regression) and ARMA (Auto Regressive Moving Average) method. In the initial research of the vehicle-road system, the model of a quarter and a half of vehicle is used. The excitation which is an input in the above model ensures the roughness, which is perpendicular to the road with the model along the length of the road can satisfy the operation. With the constant research deep going innovations, the degree of freedom in the model is becoming more and more, full vehicle is needed to study the influence of the vehicles roll over, heel and sideslip caused by snow, ice, rain and wind, so more and more simulation methods of three-dimensional road surface roughness appear (Hong et al. 2011; Lu et al. 2014; Liang et al. 2011).

2 THEORY OF ROAD SURFACE ROUGHNESS

The actual measurement shows that the road surface roughness is a normal distribution with zero mean characteristic. And density of the power spectrum about road surface is shown in Equation (1) (Han & Chen 2008).

$$G_q(n) = G_q(n_0)\left(\frac{n}{n_0}\right)^{-W} \tag{1}$$

where $G_q(n)$ = road roughness power spectral density; n = space frequency, m^{-1}; n_0 = reference space

frequency, $n_0 = 0.1$, m^{-1}; $G_q(n_0)$ = road roughness coefficient, m^{-2}/ m^{-1}; w = frequency index, $w = 2$.

2.1 *Inverse discrete Fourier transform*

If the x_m ($m = 0, 1, \ldots, N-1$) is the sampled data of the road roughness, then its discrete Fourier transform is shown in Equation (2) (Liu & Qian 2008):

$$Z_k = \sum_{m=0}^{N-1} x_m e^{\frac{-j2\pi km}{N}} \quad (k = 0, 1, 2, \ldots, N-1) \tag{2}$$

$$|Z_k| = \sqrt{\frac{N}{2l} G_q(n_k)} \left(k = 0, 1, 2, \ldots, \frac{N}{2} \right) \tag{3}$$

$$Z_k = |Z_k| e^{j\varphi_k} \left(k = 0, 1, 2, \ldots, \frac{N}{2} \right) \tag{4}$$

The formula $n_k = k \cdot n$, φ_k is the random phase and it can be randomly chosen from [0, 2π]. The road roughness is obtained by inverse discrete Fourier transform in Equation (5).

$$Z_m = \frac{1}{N} \sum_{k=0}^{N-1} x_m e^{\frac{2\pi km}{N}} \quad (m = 0, 1, 2, \ldots, N-1) \tag{5}$$

2.2 *Trigonometric series method*

Dividing (f_1, f_2) into N portions, the center frequency of the portions in i is $f_{mid\text{-}i}$. When N is big enough, $f_{mid\text{-}i}$ can be used to take the place of numerical value of the density of the power spectrum. Multiply it with the frequency space f_i can obtain the density of the power spectrum in each portion, and it is shown in Equation (6) (Zhang & Yang 2010).

$$G_i = G_q(f_{mid\text{-}i}) \cdot f_i (i = 1, 2, 3 \ldots N) \tag{6}$$

The relation between the power spectrum and the amplitude spectrum is $A^2 = G$, so the roughness of the frequency in each section can be acquired in Equation (7).

$$A_i = \sqrt{G_i} = \sqrt{G_q(f_{mid\text{-}i}) g V f_i} \tag{7}$$

where A_i = the roughness amplitude of the frequency in each section. The super position of N cosine waves, which the standard deviation is A_i can get in Equation (8).

$$Z_m = \sum_{i}^{m} \sqrt{2} A_i \cos(2\pi f_i t + \varphi_k) \tag{8}$$

where Z_m is the displacement which is perpendicular to road, m. Bring $t = y/u$, $f_i = u \cdot n_i$ into Equation (8), then Equation (9) can be acquired.

$$Z_m = \sum_{i}^{m} \sqrt{2} A_i \cos(2\pi n_i y + \varphi_k) \tag{9}$$

where y = the displacement along the road length.

2.3 *The three-dimensional road surface roughness*

Liang et al. (2011) & Liu et al. (2014) made the spatial expansion on the basis of the two-dimensional road surface roughness and get the three-dimensional road surface roughness in Equation (10).

$$Z_k = \sum_{i=1}^{N} \sqrt{2} A_i \sin[2\pi n_i (x + y) + \varphi_k] \tag{10}$$

where x = the displacement along the road width, y = the displacement along the road length.

3 THE NUMERICAL SIMULATION OF THE ROAD SURFACE ROUGHNESS

The space frequency of the general road distributes in 0.011 m^{-1} < n < 2.830 m^{-1}, range of vehicle speed is 10 m/s < u < 40 m/s, and the range of temporal frequency is 0.44 Hz < f < 28.30 Hz. The natural frequency range of the suspended mass is 1.0 Hz < f < 2.0 Hz and the natural frequency range of unsuspended mass is 10.0 Hz < f < 15.0 Hz.

Range of time frequency was divided into 200 parts, $N = 200$, the sampling frequency was 0.01 s. equation (10) was used to simulate the three-dimensional B level road surface roughness with MATLAB software in ISO criterion as shown in Figure 1.

B level road surface roughness was simulated in Figure 1 with 40 m in length and 40 m in width. It can be seen that the variation range of the B

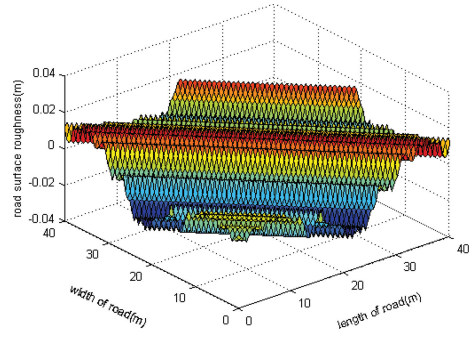

Figure 1. Three-dimensional B level road surface roughness.

level road surface roughness was mainly focused on –0.02 m ~ 0.02 m, and it fluctuated nearby the zero. It kept pace with the hypothesis that process of the road surface roughness is a normal distribution with a zero average value. Correctness of simulation was proved. The power spectrum generated in the direction of x and y moved around the standard spectrum up and down in Figure 2, but they did not deviate too much, and that tested the correctness of the simulated result.

The Figure 3 was the B level road surface roughness generated by inverse discrete Fourier transform, which the length was 40 m, and its transformation range was –0.01 m ~ 0.02 m, the entirety fluctuated around 0.005 m. The varied range of the numerical value of adjacent length was not very large, as it increased and decreased slowly. This trend was not the same as the actual road. The spatial frequency of the power spectrum and the standard spectrum, which were generated

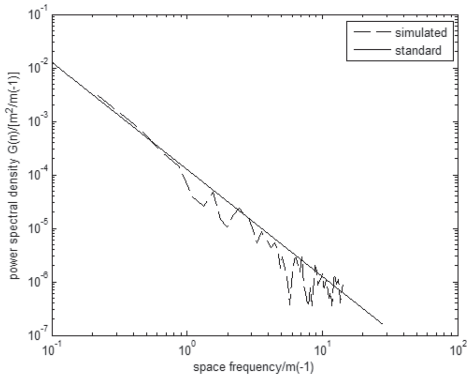

Figure 2. Comparison of the three-dimensional B level road surface roughness power spectrum and standard spectrum.

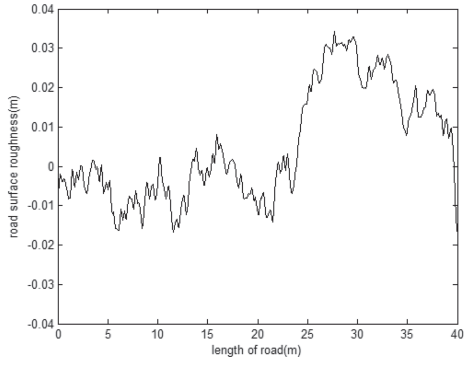

Figure 3. B level road surface roughness generated by inverse discrete Fourier transform.

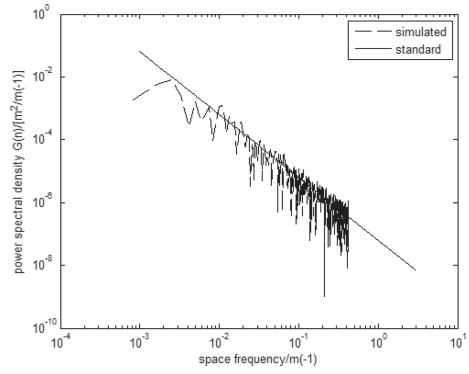

Figure 4. Comparison of power spectrum generated by inverse discrete Fourier transform and standard spectrum.

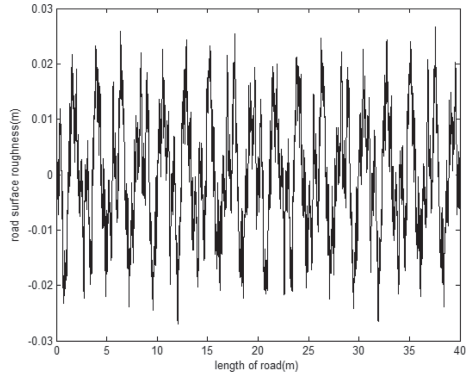

Figure 5. B level road surface roughness generated by trigonometric series method.

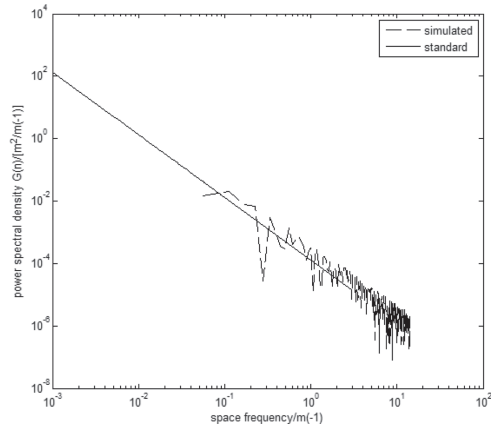

Figure 6. Comparison of power spectrum generated by trigonometric series method and standard spectrum.

by inverse discrete Fourier transform shown in Figure 4 agreed well.

The Figure 5 was B level road surface roughness generated by trigonometric series method, and its variation range was concentrated upon –0.02 m ~ 0.02 m. The result simulated fluctuated nearby the zero, and its range ability was faster than the other methods. Figure 6 showed that the power spectrum and the standard spectrum generated had the best simulating effect in the three methods.

4 CONCLUSION

The variation trend of trigonometric series method is the best method conforming to the actual road surface roughness, but the power spectrum which is generated has a great difference with the standard spectrum. The power spectrum generated by inverse discrete Fourier transform is roughly the same as the standard spectrum, but the road roughness generated by inverse discrete Fourier changes slowly, which has a great difference with the actual. The three-dimensional road surface roughness can generate the simulated road more truly and directly, and the power spectrum generated is roughly the same as the standard spectrum. When the full vehicle model to study the influence of the vehicle's roll over, heel and sideslip caused by snow, ice, rain, and wind is to be built, the three-dimensional road surface roughness has greater advantages in the vehicle-bridge vibration.

REFERENCES

Duan, H., Shi, F., & Xie, F. 2009. The review about the road roughness. *Vibration and Shock* 28(9): 95–102.

Grigoriu, M. 2006. Evaluation of Karhunen-Loeve, spectral and sampling representations for stochastic processes. *Journal of Engineering Mechanics* 132(2): 179–189.

Han, W.S. & Chen, A.R. 2008. Three-dimensional coupling vibration of wind-vehicle-bridge systems under random traffic flow. *China Civil Engineering Journal* 41(9): 97–103.

Hong, Y.T., Wang, G.L., Liu, J. et al. 2011. The design of the reconstructed system of 3-dimensional road for vehicle and realize. *Journal of the Mechanical Engineering* 27(8): 126–133.

Jiang, R.C., Chen, H.M., Liu, D.W. et al. 2012. The reconfiguration of vehicle 3-dimensiona road speed bump and realize. *Journal of Qingdao University (the Edition of Engineering)* 29(1): 32–36.

Liang, X.C., Zhang, J. & Xu, R. 2011. The simulation of the road reconfiguration of Trigonometric series method. *Journal of Automotive Engineering* 43(6): 442–447.

Liu, B., Wang, Y.Z. & An, J.J. 2014. The spatial model of vehicle -pavement coupling vibration and its dynamic responses analysis. *Journal of Shandong University: Engineering Science* 43(3): 83–90.

Liu, Y. & Qian, Z.D. 2008. Review of road roughness and vehicle vibration mode. *Journal of Highway and Transportation Research and Development* 25(1): 51–57.

Lu, Z.X., Xu, H., Liu, Y.G., et al. 2014. The reconfiguration of 3-dimensional road based on fractal interpolation and analyze. *Journal of Agriculture Engineering* 22(3): 188–194.

Ma, L., Han, W.S. & Ji, B.H. 2012. Study of vehicle-bridge coupling vibration under actual traffic flow. *China Journal of Highway and Transport* 25(6): 80–87.

Xie, W.D. 2005. The application of the stochastic signal in the simulation of road roughness. *Vibration Test and Diagnosis* 25(2): 126–131.

Zhang, H.L. & Yang, W.Q. 2010. Evaluation method of pavement roughness based on 5-DOF human-vehicle-road vibration model. *Journal of Traffic and Transportation Engneering* 10(4): 16–22.

Civil Engineering and Urban Planning IV includes the papers presented at the 4th International Conference on Civil Engineering and Urban Planning (CEUP 2015, Beijing, China, 25-27 July 2015). The contributions from experts and world-renowned scientists cover a wide variety of topics:

- Civil engineering;
- Architecture and urban planning;
- Transportation engineering;
- Geomatics;
- Natural hazards and risk, and
- Rock mechanics and rock engineering.

Civil Engineering and Urban Planning IV will appeal to professionals and academics involved in the above mentioned areas.

ISBN 978-1-138-02903-3

CRC Press
Taylor & Francis Group
an **informa** business
www.crcpress.com

6000 Broken Sound Parkway, NW
Suite 300, Boca Raton, FL 33487
Schipholweg 107C
2316 XC Leiden, NL
2 Park Square, Milton Park
Abingdon, Oxon OX14 4RN, UK

an **informa** business